K.H. Bennemann
J.B. Ketterson (Eds.)

The Physics of Superconductors

Vol. II Superconductivity in Nanostructures, High-T_c and Novel Superconductors, Organic Superconductors

Volume I

Springer

The Physics of Superconductors

Springer-Verlag Berlin Heidelberg GmbH

K.H. Bennemann J.B. Ketterson (Eds.)

The Physics of Superconductors

Vol. II. Superconductivity in Nanostructures, High-T_c and Novel Superconductors, Organic Superconductors

With 492 Figures, 14 in Colour, and 26 Tables

Springer

Prof. K.H. Bennemann
Freie Universität Berlin
Fachbereich für Physik – WE 2
Arnimallee 14
14195 Berlin, Germany
e-mail: khb@physik.fu-berlin.de

Prof. J.B. Ketterson
Dept. of Physics and Astronomy
Northwestern University
Evanston
Illinois 60208, USA
e-mail: j-ketterson@nwu.edu

Library of Congress Cataloging-in-Publication Data applied for

Die Deutsche Bibliothek - CIP-Einheitsaufnahme
Bibliographic information published by Die Deutsche Bibliothek.
Die Deutsche Bibliothek lists this publication in the Deutsche
Nationalbibliografie; detailed bibliographic data is available in the
Internet at <http://dnb.ddb.de>.

ISBN 978-3-642-62352-3 ISBN 978-3-642-18914-2 (eBook)

DOI 10.1007/978-3-642-18914-2

This work is subject to copyright. All rights are reserved, whether the whole or part of the material is concerned, specifically the rights of translation, reprinting, reuse of illustrations, recitation, broadcasting, reproduction on microfilm or in any other way, and storage in data banks. Duplication of this publication or parts thereof is permitted only under the provisions of the German Copyright Law of September 9, 1965, in its current version, and permission for use must always be obtained from Springer-Verlag. Violations are liable for prosecution under the German Copyright Law.

springeronline.com

© Springer-Verlag Berlin Heidelberg 2004
Originally published by Springer-Verlag Berlin Heidelberg New York in 2004

The use of general descriptive names, registered names, trademarks, etc. in this publication does not imply, even in the absence of a specific statement, that such names are exempt from the relevant protective laws and regulations and therefore free for general use.

Typesetting: Data prepared by the author using a Springer TEX macro package
Cover design: *design & production* GmbH, Heidelberg

Printed on acid-free paper SPIN 10889430 56/3141/XT 5 4 3 2 1 0

Preface

Superconductivity continues to be intensively studied and remains one of the most interesting research areas in physics. In particular, studies of superconductivity in nanostructures, novel superconducting materials like cuprates, ruthenates, heavy–fermion metals, novel metallic alloys and organics are presented. New and unexpected behaviors have been observed. As examples we note the two–gap–like superconductivity in MgB_2, non–conventional superconductors with $d_{x^2-y^2}$ symmetry, triplet–superconductivity and new organic superconductors. In parallel there have been impressive advances in the study of nano/mesoscopic superconducting structures and tunnel/proximity junctions.

Complimentary theoretical and experimental studies have advanced our understanding of systems with strong electronic correlations and the associated superconducting phase transitions. New experimental techniques and field–theoretical methods have emerged. The symmetry of the superconducting order–parameter in certain material classes seems different from the usual singlet, s–wave form found in conventional superconductors. There is strong evidence of a Cooper–pairing mechanism differing from the conventional one arising from the electron–phonon interaction. In view of the simultaneous occurrence of an enhanced magnetic response in many novel superconductors (cuprates, ruthenates and heavy-fermion metals), pairing due to exchange of spin–excitations has been proposed and studied. With this mechanism, triplet Cooper–pairing can also occur, in addition to singlet Cooper–pairing. This may be the case in Sr_2RuO_4 and heavy–fermion metals like UPt_3.

Many basic questions still await definite answers. Yet the fact that so many interesting results are already at hand justifies the production of two new books on the "Physics of the Superconductors", of which this is the second volume. Hopefully, they together serve the same purpose as did the previous and well–known "Bibles of Superconductivity" published in 1968 by our former colleague *R. D. Parks*. It is our intention that the present books should be of use to students, teachers and researchers; hopefully it will help the latter to further advance the field and stimulate new discoveries. We fully expect new surprises and discoveries in this century, continuing the trend of last century, which started with the discovery of superconductivity itself by Kamerling–Omnes in 1911.

The various chapters of this Volume treat in a comprehensive way important new classes of superconductors. The state of the art of research on mesoscopic structures, superconductivity in cuprates, ruthenates, heavy–fermion metals and organic metals is presented. The introduction gives a brief summary of important results and of recent developments. The first chapters treat

superconductivity in granular metals and nanostructures. Note, the interplay of lattice structure and superconductivity is one of the classic questions in the field of superconductivity. Mesoscopic structures involving superconductors may play a major role concerning further applications and technology. The book continues with a review of phase–transitions. Important general behavior of the superconducting phase–transition is discussed. One learns how to embed this phase–transition into the general theory of phase–transitions using statistical–mechanics. The next chapter illustrates the importance of photoemission, in particular of angular–resolved photoemission spectroscopy (ARPES), for studying the electronic structure of superconductors, in particular the elementary excitations in cuprates. The chapter "Concepts in High–Temperature Superconductivity" is a critical introduction to the present state of the theory of superconductivity. The following two chapters describe in a fairly complete way experiments on novel superconductors, organic superconductors and heavy–fermion metals. This is followed by a comparison of the experimental facts with the theory based on Cooper–pairing due to the exchange of spin–excitations. This tries to explain important experimental facts and complements the other theory chapter in this treatise. It may pave the way towards a general BCS–like theory for superconductivity in cuprates, heavy–fermions and other novel superconductors. The theory is applied to hole – and electron doped cuprates and to Sr_2RuO_4. Note, Sr_2RuO_4 exhibits interesting anisotropic magnetic activity and likely triplet Cooper–pairing. In a following chapter interesting superconductivity in Heavy–Fermion metals is reviewed. In a final chapter superconductivity and superfluidity are compared; this stimulates one to view superconductivity, superfluidity and Bose–Einstein condensation from a more general perspective. As an example, triplet superconductivity and superfluidity in ^{3}He are clearly intimately connected.

As in the previous volume, the authors have been encouraged to present the material in such a way that it will remain useful and interesting for some time to come, as was the case with the earlier Parks books. Simultaneously we wish the book to be stimulating and enlightening for both students and researchers including those at the forefront of the field.

We wish to thank all the authors for their careful work and their patience through the editing phase. Especially we are grateful for the contribution of Dr. V. Emery despite his difficult personal circumstances. Special thanks go to Christof Bennemann for his essential help in styling and preparing the book for publication. As with the first volume, he strove for accuracy and uniformity. We also thank Drs. D. Manske, I. Eremin, and F. Nogueira for their assistance. Finally we thank Drs. Ascheron and Lahee from Springer Verlag for their patience and help.

Berlin, November 2003 *K.H. Bennemann and J.B. Ketterson*

Contents

List of Contributors XIII

1 Recent Developments
K.H. Bennemann, J.B. Ketterson 1

1.1 Introduction: General Remarks 1
1.2 Novel Superconductors and Basic Facts 2
1.3 Granular Superconductors, Josephson–Junctions 14
1.4 Outlook 21

2 Nanostructured Superconductors
G. Deutscher 25

2.1 Introduction 25
2.2 Nanostructured Compounds 26
2.3 The Granular Structure 27
2.4 Normal State Transport 30
2.5 Single Grain Behavior 33
2.6 Weakly Coupled Grains:
Granular Insulators and Super–Insulators 39
2.7 Well Coupled Grains 44
2.8 Critical Temperature of Granular Superconductors 49

3 Proximity–Coupled Systems:
Quasiclassical Theory of Superconductivity
V. Chandrasekhar 55

3.1 Introduction 55
3.2 Transport Equations in the Diffusive Approximation 56
3.3 The Keldysh Green's Functions 61
3.4 The Quasiclassical Approximation 70
3.5 Non–Equilibrium Green's Functions for Superconducting Systems 76
3.6 Quasiclassical Superconducting Green's Functions 80
3.7 The Dirty Limit: The Usadel Equation 85
3.8 Parametrization of the Quasiclassical Green's Function 94
3.9 Applications of the Quasiclassical Equations
to Proximity–Coupled Systems 97

3.10 Summary 108

4 Universal Properties of Cuprate Superconductors: Evidence and Implications
Toni Schneider 111

4.1 Introduction 111
4.2 Critical Behavior at Finite Temperature 120
4.3 Quantum Critical Behavior and Crossover Phenomena 130
4.4 Thin Films 157
4.5 Concluding Remarks and Comparison with Other Layered Superconductors 158

5 Photoemission in the High–T_c Superconductors
J.C. Campuzano, M.R. Norman, M. Randeria 167

5.1 Introduction 168
5.2 Basics of Angle–Resolved Photoemission 169
5.3 The Valence Band 182
5.4 Normal State Dispersion and the Fermi Surface 184
5.5 Superconducting Energy Gap 202
5.6 Pseudogap 214
5.7 Photoemission Lineshapes and the Electron Self–Energy 228
5.8 Summary 265

6 Concepts in High Temperature Superconductivity
E.W. Carlson, V.J. Emery, S.A. Kivelson, D. Orgad 275

6.1 Introduction 276
6.2 High Temperature Superconductivity is Hard to Attain 279
6.3 Superconductivity in the Cuprates: General Considerations 285
6.4 Preview: Our View of the Phase Diagram 301
6.5 Quasi–1D Superconductors 303
6.6 Quasi–1D Physics in a Dynamical Stripe Array 321
6.7 Electron Fractionalization in $D > 1$ as a Mechanism of High Temperature Superconductivity 325
6.8 Superconductors with Small Superfluid Density 329
6.9 Lessons from Weak Coupling 344
6.10 Lessons from Strong Coupling 351
6.11 Lessons from Numerical Studies of Hubbard and Related Models 364
6.12 Doped Antiferromagnets 386
6.13 Stripes and High Temperature Superconductivity 401

7 Organic Superconductors
M. Lang, J. Müller 453

7.1 Introduction 453
7.2 Characteristics of Organic Charge–Transfer Conductors 456

7.3 Normal–State Properties 463
7.4 Superconducting–State Properties 494
7.5 Epilogue 538

8 Unconventional Superconductivity in Novel Materials
M.B. Maple, E.D. Bauer, V.S. Zapf, J. Wosnitza 555

8.1 Introduction 556
8.2 Conventional Superconductors Containing Localized Magnetic Moments 557
8.3 f–Electron Heavy Fermion Superconductors 587
8.4 Organic Superconductors 636
8.5 Layered Cuprate and Ruthenate Superconductors 668
8.6 Comparison of the Properties of Different Classes of Novel Superconductors 703

9 Electronic Theory for Superconductivity in High–T_c Cuprates and Sr_2RuO_4
D. Manske, I. Eremin, K.H. Bennemann 731

9.1 Introduction 732
9.2 Electronic Theory for Hole– and Electron–Doped Cuprates 750
9.3 Electronic Theory for Ruthenates (Sr_2RuO_4) 785
9.4 Results for Hole– and Electron–Doped Cuprates 799
9.5 Results for Sr_2RuO_4 839
9.6 Summary and Outlook 855

10 Heavy Fermion Superconductivity
P. S. Riseborough, G. M. Schmiedeshoff, J. L. Smith 889

10.1 Overview 890
10.2 Introduction 892
10.3 Properties of the Normal State 951
10.4 Properties of the Superconducting State 1007
10.5 Heavy Fermion Superconducting Compounds 1054
10.6 The Conclusion 1066

11 Superfluid ^{3}He and the Cuprate Superconductors
A.J. Leggett 1087

11.1 Introduction: Bose Condensation and Cooper Pairing 1087
11.2 The Normal State: Is the Fermi–Liquid Picture Valid? 1094
11.3 Response Functions: The MIR Peak in the Cuprates 1098
11.4 The Cooper–Paired States of Superfluid ^{3}He and the Cuprates: General Considerations 1100
11.5 Symmetry of the Order Parameter 1107
11.6 Conclusion 1111
11.7 Summary 1111

Author Index 1115

Subject Index 1121

Contents of Volume I

1 History of Superconductivity
K. H. Bennemann, J. B. Ketterson 1

1.1 Introduction 1
1.2 High Transition–Temperature Superconductivity and Novel Superconductors 9
1.3 Summary 20

2 Theoretical Foundation: Phenomenology and Microscopic Theory
L. Pitaevskii 23

2.1 Non–Diagonal Long Range Order and Superfluidity 23
2.2 Non–Diagonal Long Range Order in Superconductors 30
2.3 London Equation 33
2.4 Thermodynamics of Superconductors in a Magnetic Field 37
2.5 The Intermediate State of Superconductors 39
2.6 The Ginzburg–Landau Theory 41
2.7 Surface Energy at the Boundary Between Normal and Superconducting Phases 47
2.8 Superconductors of the Second Kind 52
2.9 Quantized Vortex Lines 53
2.10 Vortex–Vortex Interactions 59
2.11 Cooper–Pairing 63
2.12 Energy Spectrum of a Superconductor 67
2.13 Thermodynamic Properties of Superconductors 72
2.14 Elements of the Theory of Green's Functions 79
2.15 Green's Function of a Superconductor 85
2.16 Temperature Green's Functions 89
2.17 Temperature Green's Functions of a Superconductor 92

3 Fluctuation Phenomena in Superconductors
A. I. Larkin, A. A. Varlamov 95

3.1 Introduction 96
3.2 Ginzburg–Landau Formalism: Thermodynamics 101
3.3 Fluctuations Below the Critical Temperature 127

3.4 Ginzburg-Landau Theory of Fluctuations in Transport Phenomena 136
3.5 Fluctuations Near S-I Transition 151
3.6 Microscopic Derivation of the TDGL Equation 159
3.7 Fluctuation Conductivity 170
3.8 Manifestation of Fluctuations in Various Properties 188
3.9 Conclusions 222

4 Electron–Phonon Superconductivity
F. Marsiglio, J. P. Carbotte 233

4.1 Introduction 234
4.2 The Electron–Phonon Interaction: Overview 235
4.3 The Phonons 261
4.4 The Critical Temperature and the Energy Gap 276
4.5 Thermodynamics and Critical Magnetic Fields 293
4.6 Response Functions 298
4.7 Summary 322
4.8 Appendix: Microscopic Developments 326

5 Theory of Superconducting Alloys
L. P. Gor'kov 347

5.1 Introduction 347
5.2 Averages of Green Functions Over Impurities 349
5.3 Superconducting Alloys with a Small Gap 358
5.4 Paramagnetic Alloys and Gapless Superconductivity 370
5.5 Eilenberger Equations 374
5.6 Final Remark 382

6 High–T_c Superconductivity
H. R. Ott 385

6.1 Introduction 385
6.2 Typical Structural Characteristics 388
6.3 Occurrence of Superconductivity 399
6.4 Physical Properties of Copper Oxides 406
6.5 Physical Properties of Non–Cuprate High–T_c Superconductors 466
6.6 Final Remarks 481

7 Spin Fluctuation Model for d–wave Superconductivity
A. V. Chubukov, D. Pines, and J. Schmalian 495

7.1 Introduction and Overview 495
7.2 Spin–Fermion Model 509
7.3 Summary of Strong–Coupling Theory for Electron-Phonon Pairing 517

7.4 Strong–Coupling Approach to Spin-Fermion Interaction 521
7.5 Fingerprints of Spin Fermion Pairing 539
7.6 Comparison with the Experiments on Cuprates 557
7.7 Conclusions 579

8 Tunneling Spectroscopy of Conventional and Unconventional Superconductors
J. Zasadzinski 591

8.1 Introduction 591
8.2 Basic Tunneling Phenomenology 594
8.3 Tunneling and Strong–Coupling Effects: Microscopic Picture ... 603
8.4 Tunneling Spectroscopy of Conventional Superconductors 608
8.5 Tunneling in High–Temperature Superconductors 614
8.6 Heavy Fermion Superconductors 637
8.7 Organic Superconductors 639
8.8 Other Materials 640
8.9 Conclusions 641

9 Pairing Symmetry in Cuprate Superconductors: Phase–Sensitive Tests
C. C. Tsuei, J. R. Kirtley 647

9.1 Introduction 648
9.2 Phase–Sensitive Tests: Theoretical Background 654
9.3 Phase–Sensitive Tests: Experiments 664
9.4 Universality of the *d*–Wave Pair State 697
9.5 Implications of *d*–Wave Pairing Symmetry 704
9.6 Conclusions 711

10 Vortex Matter
G. Blatter, V. B. Geshkenbein 725

10.1 Introduction 726
10.2 Ginzburg–Landau– and London Theories 735
10.3 Vortex Lines 739
10.4 Vortex Lattice 750
10.5 Layered Materials 760
10.6 Anisotropic Scaling Theory 781
10.7 Statistical Mechanics 789
10.8 Quenched Disorder: Pinning and Creep 831
10.9 Uncorrelated Disorder: Collective Pinning and Creep 844
10.10 Correlated Disorder 890
10.11 Surface– and Geometrical Barriers 897
10.12 Vortex Glasses 903
10.13 Concluding Remarks 913

List of Contributors

Bauer, E. D.
Department of Physics and
Institute for
Pure and Applied Physical Sciences,
Univ. of California, San Diego
La Jolla, California, USA
ericb@physics.uscd.edu

Bennemann, K. H.
Institut für Theoretische Physik,
Freie Universität Berlin, Berlin,
Germany
khb@physik.fu-berlin.de

Campuzano, J. C.
Dept. of Physics, University of
Illinois at Chicago, USA and
Materials Science Division, Argonne
National Lab., Argonne, USA
jcc@uic.edu

Carlson, E. W.
Dept. of Physics, Boston University,
Massachusetts, USA
ericac@physics.bu.edu

Chandrasekhar, V.
Dept. of Physics, Northwestern
University, Evanston, Illinois, USA
v-chandrasekhar@nwu.edu

Deutscher, G.
School of Physics and Astronomy,
Department of Condensed Matter
Physics, Tel Aviv University,
Tel Aviv, Israel
guyde@post.tau.ac.il

Emery, V. J.
Brookhaven National Laboratory,
Department
of Physics, New York, USA
emery@cmth.phy.dnl.gov

Eremin, I.
Inst. für Theoretische Physik, Freie
Universität Berlin, Berlin, Germany
ieremin@physik.fu-berlin.de

Ketterson, J.
Dept. of Physics, Northwestern
University, Evanston, Illinois, USA
j-ketterson@nwu.edu

Kivelson, S. A.
Univ. of California at Los Angeles
Dept. of Physics, California, USA
stevek@physics.ucla.edu

Lang, M.
Physik-Institut der
Johann Wolfgang Goethe Univer-
sität, Frankfurt/Main, Germany
michael.lang@physik.uni-frankfurt.de

Leggett, A. J.
Dept. of Physics, University of
Illinois, Illinois, USA
tony@amaterasu.physics.uiuc.edu

Manske, D.
Inst. für Theoretische Physik, Freie Universität Berlin, Berlin, Germany
dmanske@physik.fu-berlin.de

Maple, M. B.
Dept. of Physics and Inst. for Pure and
Applied Physical Sciences, Univ. of California, San Diego La
Jolla, California, USA
mbmaple@ucsd.edu

Müller, J.
Max-Planck Institute for Chemical
Physics of Solids,
Dresden, Germany
mueller@cpfs.mpg.de

Norman, M. R.
Materials Science Division, Argonne National Laboratory, Argonne, USA
norman@thio.msd.anl.gov

Orgad, D.
Univ. of California at Los Angeles, Department of Physics, California, USA
dron@physics.ucla.edu

Randeria, M.
Tata Institute of Fundamental Research,
Mumbai, India
randeria@theory.tifr.res.in

Riseborough, P. S.
Department of Physics, Polytech University, NewYork, USA
prise@poly.edu

Schmiedeshoff, G. M.
Occidental College, Department of Physics,
California, USA gms@oxy.edu

Schneider, T.
Physik–Institut der Universität Zürich, Switzerland
tschnei@physik.unizh.ch

Smith, J. L.
National Laboratory Los Alamos, Nevada, USA jlsmith@lanl.gov

Wosnitza, J.
Institut für Angewandte Physik, TU Dresden, Dresden, Germany
wosnitza@physik.tu-dresden.de

Zapf, V. S.
Dept. of Physics and Inst. for Pure and
Applied Physical Sciences, Univ. of California, San Diego La
Jolla, California, USA
vzapf@physics.ucsd.edu

1 Recent Developments

K.H. Bennemann Dept. of Physics, Freie Universität Berlin, Germany
J.B. Ketterson Dept. of Physic and Astronomy Northwestern University, Evanston, USA

1.1 **Introduction: General Remarks** 1
1.2 **Novel Superconductors and Basic Facts** 2
1.3 **Granular Superconductors, Josephson–Junctions** 14
1.4 **Outlook** 21
Acknowledgements 21
References 22

1.1 Introduction: General Remarks

In 1911 Kamerling–Onnes discovered superconductivity in mercury at 4.2K, in 1933 the fundamental Meissner–Ochsenfeld effect ($\mathbf{j}_s \propto \mathbf{A}$) has been discovered and in 1957 Bardeen, Cooper, Schrieffer explained superconductivity using an electronic theory as resulting from the electron–phonon coupling (B.C.S.–theory). In many metals this interaction caused singlet Cooper–pairing ($\mathbf{k}\uparrow, -\mathbf{k}\downarrow$) of electrons within an energy–shell of the order of $2\omega_D$ around the Fermi–energy $\epsilon_F(\omega_D$ = Debye energy). The resultant superconductivity was described by an order–parameter $\Delta_{\mathbf{k}}$ having s–symmetry ($\Delta_{\mathbf{k}} = \Delta$). Most metals exhibited superconductivity below a relatively low transition–temperature T_c and $T_c \leq$ 20K [1]. In Fig. 1.1 we illustrate the occurence of superconductivity in the periodic table.

Thus, with the discovery of high T_c–superconductors, cuprates, by Bednorz and Müller in 1986 with T_c far above 20K a new era started [2]. Many novel superconductors among them cuprates, ruthenates, heavy–fermion metals and organic materials were discovered. For the cuprates one observed T_c–values ranging up to 150K, see Fig. 1.2 for illustration. Heavy–fermion metals (such as UPt_3, $CeIn_3$, $ZrZn_2$, $CePd_2Si_2$, etc.) and the other new superconductors had relatively low transition–temperatures T_c below a few K. Yet most of these novel superconductors exhibited behaviour rather different from B.C.S.–behaviour of the conventional superconductors. In particular one observed non s–symmetry of the order–parameter, strong electronic correlations including non Fermi–liquid behavior (electrical resistivity $\rho \propto T$, scattering rates $\propto \omega$,...) and unusual phase–diagrams. Possibly Sr_2RuO_4 and heavy–fermion metals (UPt_3, etc.) exhibit also triplet Cooper–pairing ($\mathbf{k}\uparrow, -\mathbf{k}\uparrow$) [3]. A recent surprise was also superconductivity in layered structured MgB_2 with $T_c \simeq$ 40K and two gaps [4].

Presently further observations are necessary and a B.C.S–like theory is needed to obtain a definite universal picture about the phenomenon superconductivity with all its facts and possibilities, in particular about all the

K. H. Bennemann et al. (eds.), *The Physics of Superconductors*
© Springer-Verlag Berlin Heidelberg 2004

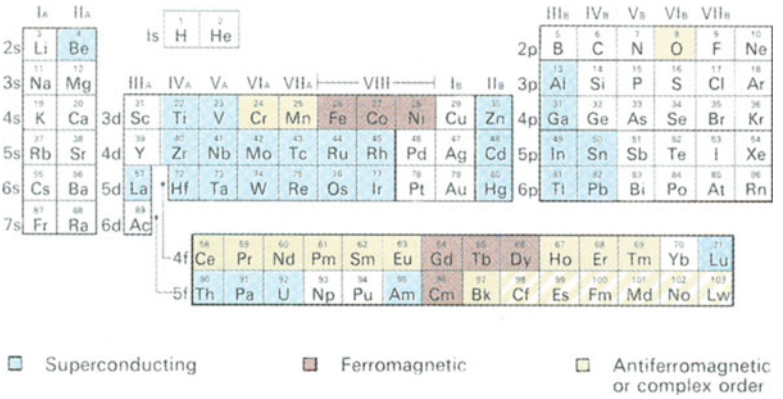

Fig. 1.1. The occurrence of superconductivity in the periodic table is illustrated. Clearly as the history of superconductivity shows alloys and compounds of the elements play a most important role

fields (phonons, spin–excitations, ...) which cause Cooper–pairing and thus superconductivity. A goal is also a unifying field–theory of superconductivity and superfluidity.

Metals with parallel magnetic– and superconducting activity are of central interest. Triplet Cooper–pairing relates such superconductors intimately to superfluid ^{3}He [3]. Superconductors with quantum–critical points are of special interest with respect to basic questions of quantum–mechanics [5]. Mesoscopic superconductivity, superconducting quantum–dot systems and nanostructures (arrays of Josephson–junctions, etc.) are of essential interest, also with respect to applications and technology [6].

By continuity one may assume safely that further surprises and discoveries lie ahead of us. Yet these will relate to what is known already and will need for an understanding many basic facts which are presented in the various chapters of this book. In the following we summarize some of the new observations.

1.2 Novel Superconductors and Basic Facts

We concentrate on the new superconductors having a non s–symmetry order–parameter like the cuprates, ruthenates and heavy–fermion metals. To contrast their behaviour from the conventional superconductor ones, we repeat first basic behaviour of B.C.S. superconductivity.

a) Conventional Superconductors

Most metals and alloys thereof exhibit electron–phonon coupling driven superconductivity with transition–temperatures ranging up to about 20K. The

A-15 compounds (Nb_3Ge,...) have the largest transition–temperatures T_c [1, 7]. The superconducting order–parameter $\Delta_{\mathbf{k}}$ has s–symmetry ($\Delta_{\mathbf{k}}$=const.).

Depending on the ratio of the coherence length ξ(T) and the penetration depth λ(T) magnetic flux may penetrate (vortex formation). Superconductors of type I ($\kappa \equiv \frac{\lambda}{\xi} < \frac{1}{\sqrt{2}}$) and type II ($\kappa > \frac{1}{\sqrt{2}}$) with vortices exist [1,2].

In conventional superconductors typically non–magnetic impurities reduce T_c relatively weak, while paramagnetic impurities have a strong destructive effect and may destroy superconductivity. External magnetic fields and electrical currents destroy the superconducting state, break up Cooper–pairs, and even may cause gapless superconductivity.

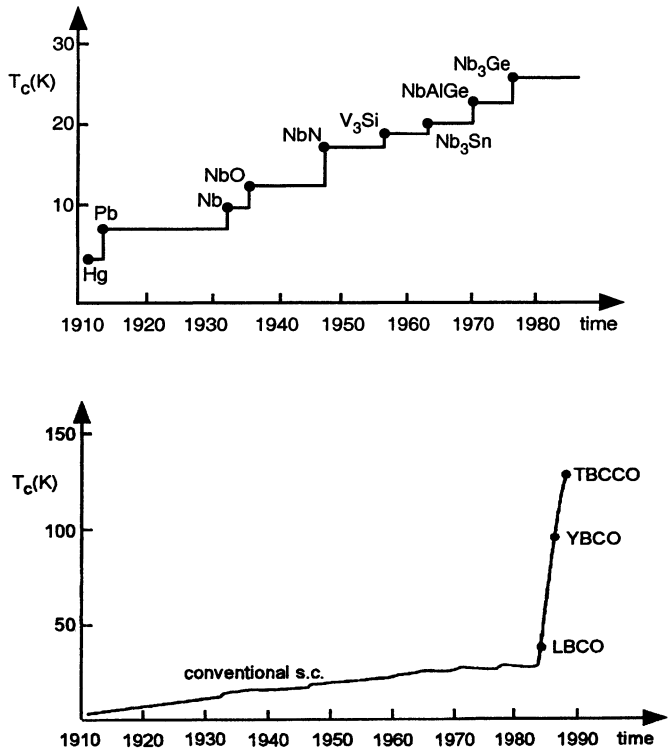

Fig. 1.2. History of the transition temperature T_c for the first 70 years following the discovery of superconductivity in 1911. The A–15 compounds were of particular interest in the search for higher T_c–superconductors. High–T_c cuprate superconductors were discovered by Bednorz and Müller in 1986. For $La_{2-x}Ba_xCuO_4$ a $T_c \simeq$ 35 K, for $YBa_2Cu_3O_{7-\delta}$ a T_c = 92 K, and for $HgBa_2Ca_2Cu_3O_{8+\delta}$ a transition–temperature T_c = 133 K was observed, for example

Tunnel–junctions of superconductors exhibit the Josephson–effect. The tunnelling current is given by

$$j \propto \sin(\Delta\Phi + \omega t) \quad .$$

$\Delta\Phi$ is the difference of the global phase of the two superconductors. The current results from the tunnelling of Cooper–pairs [8].

In all conventional superconductors phase–coherent Cooper–pairing occurs at the transition–temperature T_c. The structure of the order–parameter $\Delta_{\mathbf{k}}(\omega)$, seen in the spectral–density for example, reflects for conventional superconductors characteristic phonon frequencies involved in Cooper–pairing. The Meissner–effect occurs at T_c for phase–coherent Cooper–pairs. Part of the history of superconductivity is shown in Figs. 1.2.

It is expected that similar behaviour regarding basic facts can be expected also for the novel superconductors, in particular if electron–phonon interaction causes Cooper–pairing. This seems the case for the recently discovered (type II) superconductor MgB_2 with $T_c \simeq 40$ K and quasi two gaps, $\Delta_1 \simeq 4$ meV and $\Delta_2 \simeq 7.5$ meV due to π–and σ–type electrons [9]. Both gaps have s–symmetry and result from the highly anisotropic layer–structure of the MgB_2–lattice. Note, Boron–planes consisting of hexagon–B–rings characterize the structure. The dominating bonds of π– and σ–type cause superconductivity. As a consequence of this anisotropy one gets a critical magnetic field $H_{c2}^{||}$ and $H_{c2}^{\perp}$. One estimates $H_{c2}^{\perp} \sim (\xi^{||})^{-2} \sim 0.2\ H_{c2}^{||}$. Here the $H_{c2}^{||}$ and $H_{c2}^{\perp}$ refer to in–plane and perpendicular to B–plane upper critical field, respectively. Note, $H_{c2} \simeq \Phi_0/\pi\xi^2$, $\xi \sim \Delta^{-1}$, Φ_0 refers to the elementary flux quantum.

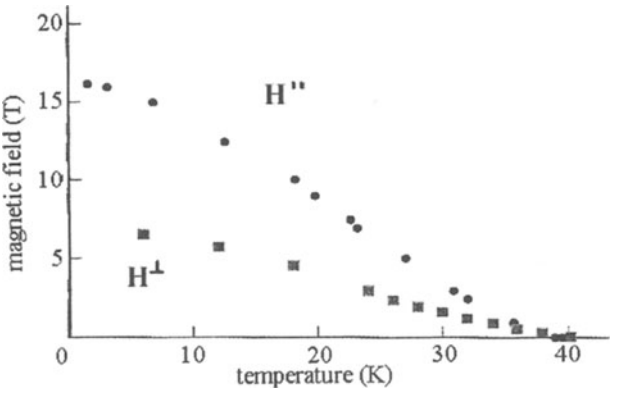

Fig. 1.3. Critical upper magnetic fields $H_{c2}''(T)$ and $H_{c2}^{\perp}(T)$ referring to the B–planes and direction perpendicular to it, respectively, in the layered structure of MgB_2. The anisotropic behavior of $H_{c2}(T)$ is indicative of the approximate two gap behavior

In Fig. 1.3 we illustrate the anisotropic behaviour of $H_{c2}(T)$ indicative of 2 gaps. It is interesting that MgB_2 can carry relatively strong superconducting currents in magnetic fields up to 3 T, which compares with that observed for high–T_c cuprates. Note, the isotope–effect as well as tunnel spectroscopy support phonon driven superconductivity. One gets that $Mg^{11} \longrightarrow Mg^{10}$ increases T_c by about 1 K in accordance with $T_c \propto (Mg)^{-1/2}$. Interestingly AlB_2 is not superconducting. Note, MgB_2 in another example for the interesting role played by the lattice structure regarding superconductivity.

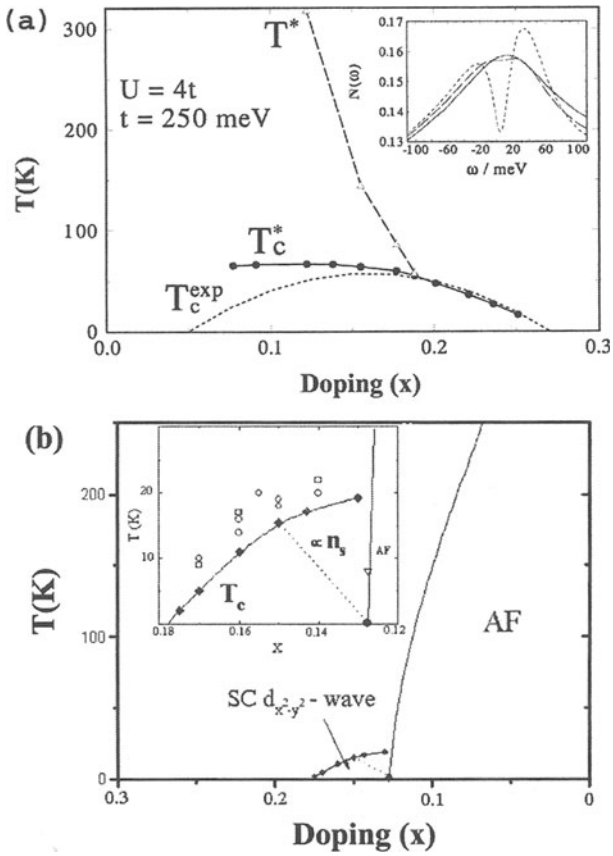

Fig. 1.4. Doping dependence of the superconducting transition temperature $T_c(x)$ of (a) hole ($La_{2-x}Sr_xCuO_4$, ...) and (b) electron ($Nd_{2-x}Ce_xCuO_4$, ...) doped cuprates. (T_c^* neglects C.P. phase fluctuations, T^* refers to the onset of pseudo–gap.) A.F. refers to the anti–ferromagnetic phase and n_s to superfluid density. The inset Fig. in (a) is a calculated spectral–density. The inset Fig. (b) refers to calculations. Here, $T_c \propto n_s$ for electron doping is an open question presently

b) Cuprates

The high T_c–superconductors LSCO($La_{2-x}Sr_xCuO_4$) and BSCCO($Bi_2Sr_2CaCu_2O_8$) etc. with T_c–values ranging up to 150K consist all of layered structures with CuO_2–layers (one or more per unit lattice–cell) which seem largely responsible for Cooper–pairing and superconductivity. Type II superconductivity and non–s–symmetry of the order–parameter, likely $d_{x^2-y^2}$–symmetry, is observed. Tunnel–spectroscopy, ARPES, and many other experiments support this. Parallel magnetic activity (anti–feromagnetic one) and superconducting one occurs. Typically an interdependence of these activities is observed. Singlet Cooper–pairing is present. Due to strong correlations unusual properties are exhibited, see for example the temperature–dependence of the electrical resistivity and other transport properties, a pseudo gap of $d_{x^2-y^2}$–symmetry in the quasi–particle dispersions, non–Fermi–liquid behavior (self–energy $\Sigma(\omega) \propto \omega$, etc.), and so on. As a consequence the elementary excitations in the cuprates seem to behave anomalously. The doping dependence of T_c indicates that phase–fluctuations of Cooper–pairs play a role, in particular in underdoped cuprates with stronger correlations among the quasi–particles. This seems reflected by

$$T_c \propto n_s \quad ,$$

where n_s denotes the doping dependent superfluid density ($n_s = n_s(x,T)$). Whether $T_c \propto n_s$ occurs also for electron doping needs to be verified. It is expected for low Cooper–pair density.

Fig. 1.4 illustrates the doping–dependent phase diagram of hole doped ($La_{2-x}Sr_xCuO_4$)–and electron ($Nd_{2-x}Ce_xCuO_4$)–doped cuprates [10]. In hole doped cuprates for increasing doping x one gets that T_c increases first due to increase of hole concentration and itinerancy and then T_c decreases again due to the disappearance of the antiferromagnetic spin–excitations. Note, electron doping consists largely of occupying the hybridized d–orbitals (upper Hubbard–band) of Cu, of quenching the Cu–spins, while hole doping of the oxygen p–states, destroying long–range anti–ferro–magnetism due to frustration, consists mainly of emptying the oxygen p–band. Thus with increasing hole doping anti–ferromagnetic excitations are weakened and itinerancy of the correlating hole–carriers is improved. One might expect somewhat different behaviour of hole– and electron doped cuprates.

c) Ruthenates

Due to advances in crystal growth the ruthenates have become a very interesting material class in condensed matter physics [3]. There are structural similarities with the cuprates [11]. In Sr_2RuO_4 layers of RuO_2 are separated by Sr and O atoms, in $SrRuO_3$ one has RuO_2–layers with Sr in between, and in $Sr_3Ru_2O_7$ a similar, but more 3d–type structure is present. Sr_2RuO_4 is a novel superconductor with T_c=1.5 K. Several measurements indicate triplet Cooper–pairing and p–symmetry of the superconducting order pa-

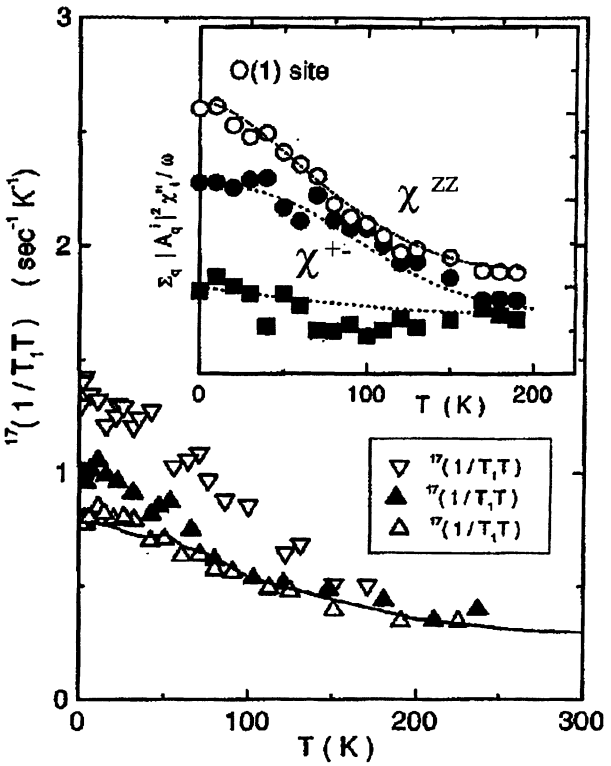

Fig. 1.5. Magnetic anisotropy $\chi^{+-}(T)$ and $\chi^{zz}(T)$ referring to in plane and perpendicular to RuO_2–plane response, respectively, in Sr_2RuO_4. The experimental results refer to spin–relaxation (T_1, Knight–shift)

rameter [3, 12], possibly:

$$\Delta_{\mathbf{k}} \propto \mathbf{z}(k_x + ik_y) \quad .$$

The anisotropy of H_{c2} is even larger than in the cuprates. $SrRuO_3$ is a ferromagnetic metal. Upon applying a magnetic field one observes a magnetic quantum critical point in $Sr_3Ru_2O_7$.

These facts suggest already that the ruthenates are a most important class of new materials in condensed matter physics. In particular triplet Cooper–pairs $(\mathbf{k}\uparrow, -\mathbf{k}\uparrow)$ in Sr_2RuO_4 may stimulate further studies of triplet pairing in superconducting heavy–fermion metals, in organic–systems and ferromagnetic metals like Fe under pressure and an unifying view on superconductivity and ^{3}He–superfluidity.

Concentrating on Sr_2RuO_4 note that superconductivity seems related to both antiferromagnetic– and ferromagnetic–activity. Most important is the

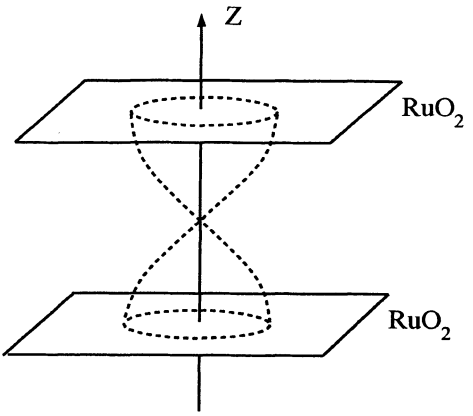

Fig. 1.6. Illustration of a possible form of the p–type superconducting order–parameter in Sr_2RuO_4. In principle incommensurability along z–axis may occur

recently observed anisotropic response to an external magnetic field h. This is illustrated in Fig. 1.5 [13]. Note, $\chi^{\pm} \ll \chi^{zz}$, where the susceptibilities refer to the response to a magnetic field parallel to the RuO_2–planes and perpendicular to these planes, respectively. It seems then possible that the Fermi–surface topology and the structure of the total spin–susceptibility $\chi(\mathbf{q}, \omega)$ cause triplet Cooper–pairing, since ferromagnetic spin–excitations dominate over antiferromagnetic ones.

The superconducting order–parameter seems of p–symmetry [3,11]:

$$\Delta_{\mathbf{k}} = \Delta_0 z \cos\frac{k_z c}{2}\{\sin\frac{k_x a}{2}\cos\frac{k_y a}{2} + i\sin\frac{k_y a}{2}\cos\frac{k_x a}{2}\} \quad , \tag{1.1}$$

with no nodes in the RuO_2–planes, but with nodes along the the z–direction perpendicular to the planes. The possible form of $\Delta_{\mathbf{k}}$ is illustrated in Fig. 1.6. Note, the spin of the Cooper–pairs, ($\mathbf{k}\uparrow$, $\mathbf{k}\downarrow$), is parallel to the RuO_2–planes, but with no preferable direction in these planes. The orbital angular momentum $\boldsymbol{l}$ of the Cooper–pairs points in z–direction perpendicular to the planes [3,12].

Of course, triplet Cooper–pairing (breaking time reversal symmetry) is reflected by corresponding thermodynamical and optical behavior. Due to the usual coupling between the orbital angular momentum $\boldsymbol{l}$ and the external magnetic field $\boldsymbol{h}$ one expects a rich response and different critical magnetic fields ($h_{c2}(T)$) dependent on whether $\boldsymbol{h}$ is parallel to the RnO_2–planes or $\boldsymbol{h}||z$, perpendicular to the RnO_2–planes. Furthermore, the breaking of time reversal symmetry will be seen by corresponding optical response, for example, its dependence on light polarization. The magnetic anisotropy is expected to lift the degeneracy of the three triplet states.

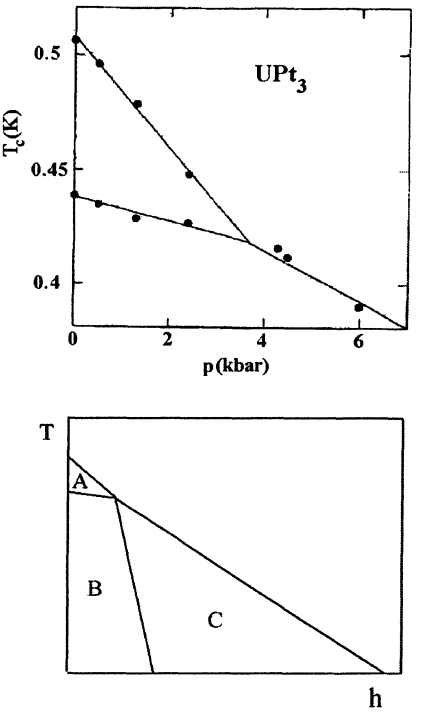

Fig. 1.7. The phase diagram $T_c(P)$ and $T_c(h)$ of the heavy–fermion metal UPt_3 is shown (h denotes the external magnetic field, p the pressure). A, B, C refers to different superconducting states

Note, it is of utmost significance to identify definitely triplet pairing and the pairing field (spin–excitations).

d) Heavy–Fermion Metals

The heavy–fermion metals are characterized by an unusually large electronic density of states (DOS) near the Fermi–energy, N(0). Thus, the effective mass m of the carriers is much larger then the bare electronic mass m_0. Note, m may range up to 100 m_0 or more. Typical heavy–fermion metals are listed in table 1.1 [14].

Due to the large electronic density of states (DOS) the heavy–fermion metals exhibit simultaneously interesting magnetic– and superconducting behaviour. Multiple magnetic and superconducting phases and generally complex thermodynamical behaviour exist [5, 15]. For example, this is demonstrated by the phase diagrams of T_c(h) and T_c(P) of UPt_3 shown in Fig. 1.7.

Note, while in conventional type II superconductors there are 2 superconducting phases in the h-T plane (low field Meissner phase and a high

Table 1.1. List of heavy–fermion metals. m and m_0 are the effective and bare electron mass and T_c the superconducting transition temperature. Note, the interesting dependence of T_c on pressure.

	UPt_3	UBe_{13}	UPd_2Al_3	UGe_2
m/m_0	360	1100	210	100
T_c(K)	0.55	0.85	2	0.7

field vortex phase above h_{c1}(T)) in UPt_3 there are five phases: vortex phase C, and phases A and B each exhibiting a Meissner– and vortex–phase. The phase–diagram T_c(P) exhibits also the superconducting phase A, appearing for pressure P=0 at $T_c \geq$ 5K, and phase B appearing for P=0 at $T_c \simeq$ 0.44K. The symmetry of the order parameter is certainly not simply s–wave like, but different for T_c(P,h). This is still analyzed as well as the mechanism for Cooper–pairing. However probably spin–excitations seem involved.

Several studies where performed for analyzing the supercondcuting phases by using a Ginzburg–Landau theory and allowing a more complex order–parameter including triplet Cooper–pairing. Note, the free–energy change may be described by

$$\Delta F = \alpha_1(T-T_{c1})|\Delta_1|^2 + \alpha_2(T-T_{c2})|\Delta_2|^2 + \beta_1|\Delta_1|^4 + \beta_2|\Delta_2|^4 + \beta_{12}|\Delta_1|^2|\Delta_2|^2 + \ldots . \quad (1.2)$$

Here, Δ_1, Δ_2 refer to the order–parameter of the different phase transitions. The coefficients are pressure dependent.

Of course, one may attempt an analysis using an electronic theory for $\chi(\mathbf{q},\omega)$ and $\Delta_\mathbf{k}$ for the cuprates and ruthenates (Sr_2RnO_4) [11] and for the heavy–Fermion metals. Then, the order–parameter is approximately given by (after linearization and for $T \to 0$)

$$\Delta_{\mathbf{k},\sigma} = -\Sigma_{\mathbf{k}',\sigma'} V_{\mathbf{k}\sigma,\mathbf{k}'\sigma'} \frac{\Delta_{\mathbf{k}'\sigma'}}{2E_\mathbf{k}} \quad . \quad (1.3)$$

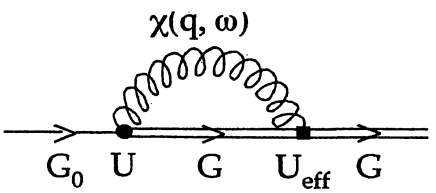

Fig. 1.8. Cooper–pairing due to the field represented by the dynamic susceptibility $\chi(\mathbf{q},\omega)$ to which the quasi–particles described by the matrix Green's function G couple by U. Here U_{eff} includes vertex corrections

Whether a B.C.S.– like universal theory can be derived as suggested by field–theory from the Feyman–diagram shown in Fig. 1.8 is still an open question. Strong correlations could prevent such simplifying Eliashberg–type theory. However, if the dynamics of the vertex corrections is not changing the general behaviour (obtained already for $U_{eff} \rightarrow U$) one may obtain already good qualitative results from such an effective Eliashberg–type theory.

In Fig. 1.9 we show more data on heavy–fermion metals indicating the role played by magnetic excitations. The superconducting transition–temperature T_c(P) of $CeIn_3$ may be of particular interest due to quantum criticality at P$\simeq$28 kbar where the Néel temperature $T_N \rightarrow 0$ and superconductivity appears [5]. This needs, however, further studies.

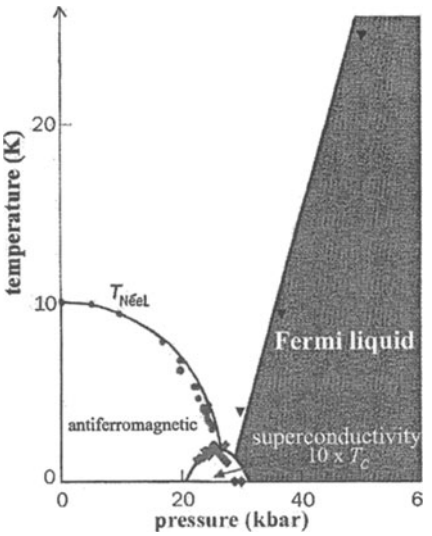

Fig. 1.9. Phase diagram of the heavy–fermion $CeIn_3$. Note the appearance of superconductivity at larger pressure

This is also the case regarding the phase diagram of UGe_2 where for P$\rightarrow$ 18 kbar, $T_c \rightarrow 0$ and $T_{curie} \rightarrow 0$. Not much is known about pairing mechanism and symmetry of the superconducting state appearing for pressure above P$\simeq$ 8 kbar. Typical phase diagrams indicative of the interplay of antiferromagnetism or ferromagnetism and Cooper–pairing are shown in Fig. 1.10. Note, further experiments may somewhat modify these interesting phase–diagrams.

It is of utmost interest to determine for UPt_3 and the other heavy–fermion for Fe and UGe_2 and related metals the interplay of magnetism and superconductivity, the symmetry of the superconducting order parameter, the thermodynamical properties and the role played by quantum critical points (Q.C.P.).

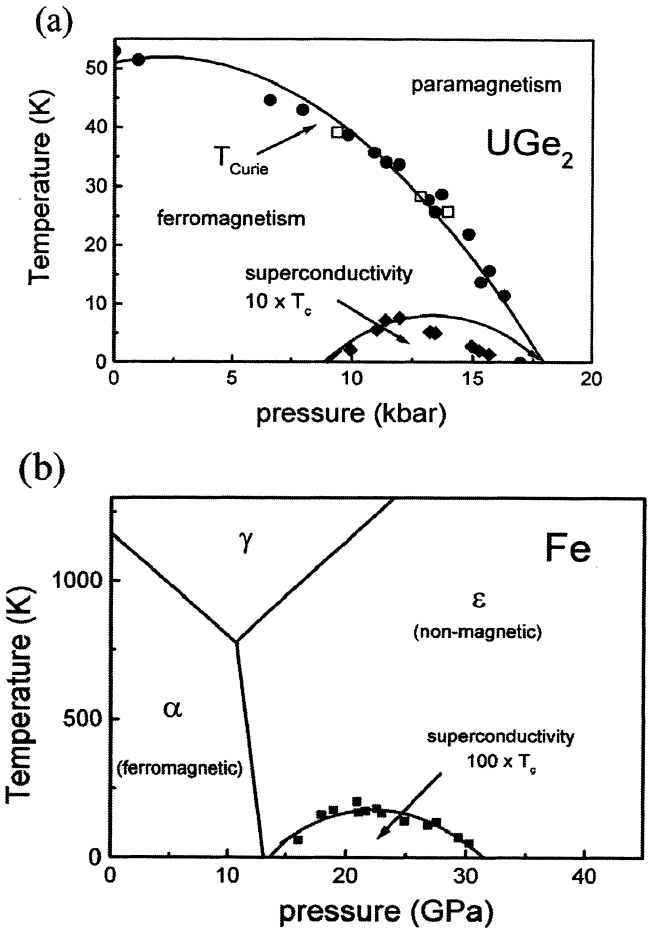

Fig. 1.10. (a) Phase diagram of UGe_2. (b) Superconducting hexagonal ϵ–phase Fe under strong pressure. α, β, ϵ refers to the various Fe phases

Besides Ginzburg–Landau type analysis electronic theories are needed to understand superconductivity in these systems.

Summarizing, the interdependence of magnetism and superconductivity has been a classical problem and seems nowadays due to technical advances regain interest. Note, the Larkin–Ovchinnikov state of a superconductor in the presence of an exchange field [16]

$$\Delta_k \sim \cos\,(\mathbf{k}\cdot\mathbf{r})$$

indicates already too that magnetism and superconductivity may seek a compromising arrangement. This is also known from Ginzburg–Landau theory

with two order–parameters which may coexist or exclude each other, depending on the parameters controlling the energetics.

e) Organic Superconductors

Recently, many studies have shown that organic metals are most interesting. A large class of crystalline organic systems are quasi–two–dimensional charge–transfer salts. Many become superconducting [17]. Various properties of these organic metals are shared with the cuprates like layered structures, strong correlations causing also antiferromagnetism and non–s–symmetry Cooper–pairing. The organic metals are very clean nearly impurity free systems. Also astonishingly superconductivity may be induced by strong magnetic fields. In Fig. 1.11 the interesting phase–diagram of κ-(BEDT-TTF)$_2$-Cu[N(CN)$_2$]Br a typical composition of a charge–transfer salt is shown. Such molecules are stacked into layers. Planes of Cu[N(CN)$_2$]Br aniones separate these layers. Within these layers the molecules form dimers and electrons or holes can hop then easily from one molecule to the next one, but not perpendicular to the layers (hence: quasi 2d–behavior). Thus, salts consist of conducting layers separated by a non–conducting environment (anions).

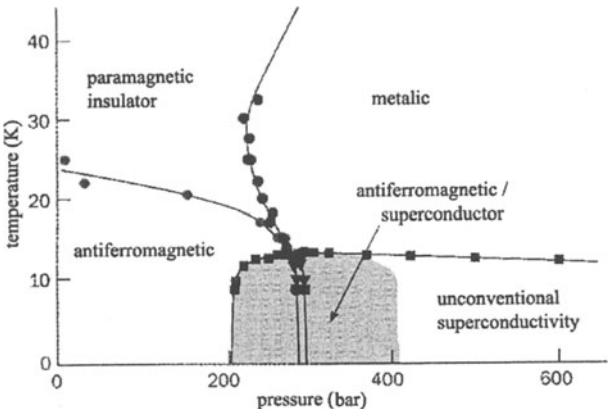

Fig. 1.11. Phase diagram of the organic metal κ-(BEDT-TTF)$_2$-Cu[N(CN)$_2$]Br (Bisethylenedithio–terathiofulene–X type salt)

Clearly bond–length changes, also due to pressure, will sensitively change the electrical properties. Also applying a magnetic field perpendicular to the layers (along the c–axis) affects the system due to the formation of Landau–levels which will pass the Fermi–energy as the external magnetic field varies (see de Haas – van Alphen oscillations). In stronger magnetic fields also quantum mechanical interband tunnelling occurs [17].

Superconductivity occurs at relatively low temperatures usually upon applying pressure, see Fig. 1.11. Various experiments indicate unconventional

Cooper–pairing ($2\Delta_0 \sim 7k_B T_c$, non–s–symmetry of $\Delta_{\mathbf{k}}$). Note, superconductivity occurs close to the antiferromagnetic–state like in the cuprates and heavy–fermion metals. Experiments indicate that the long range magnetic order is due to localized spins on the dimer and not due to the hopping carrier (holes or electrons). Antiferromagnetic spin–fluctuations occur as a precursor of superconductivity. How much these and phonons are involved in Cooper–pairing must be clearified by further analysis.

In an external magnetic field interesting behaviour may result due to the layered structure, Landau–level formation and spin–split bands. Possibly Cooper–pairs ($\mathbf{k}\uparrow, -\mathbf{k}+\mathbf{q}\downarrow$) may form. A Larkin–Ovchinnikov state [16,17] with $\Delta_{\mathbf{k}} \sim \cos(\mathbf{kr})$ may occur. In general the response to an external magnetic field is highly anisotropic. Furthermore, it is interesting that superconductivity may be induced in λ–$(BETS)_2FeCl_4$ by a magnetic field h which destroys long range magnetic order of the Fe^{3+}. Field induced superconductivity may also occur in α–$(BEDT\text{-}TTF)_2KHg(SCN)_4$ by affecting with the external magnetic field h the charge–density–wave (CDW) present in this system.

Clearly further experiments are needed to clarify the situation. However, rich behaviour may be expected in general, since CDW–, SDW– excitations, Landau–levels and 2d–properties are present.

1.3 Granular Superconductors, Josephson–Junctions

As early studies by Buckel and Hielsch and others have shown strongly disordered lattices and amorphous metals may effect sufficiently superconductivity due to changes in the electron–phonon coupling, phonon–spectrum, electronic parameters (DOS:N(0)) and surface effects. As a result superconductivity changes and might get strengthened, increase of T_c, and generally thermodynamical properties might change favorably, see Garland, Bennemann [18], and Deutscher and references therein. In the amorphous state some non–metallic systems become metallic and then also superconducting. In table 1.2 we illustrate the situation.

Table 1.2. Superconductivity in disordered and amorphous metals. Estimates of the superconducting transition–temperature T_c.

material	$(T_c/T_{c0})_{expt}$	$(T_c/T_{c0})_{calc.}$
Al	~ 5	4.9
Pb	~ 0	0
Ga	~ 8	8
Sn	~ 1.3	2
In	~ 1.3	1.2

Remarkable is also the occurrence of superconductivity PdH–systems where dependent on H–doping and disorder dramatic changes in T_c are ob-

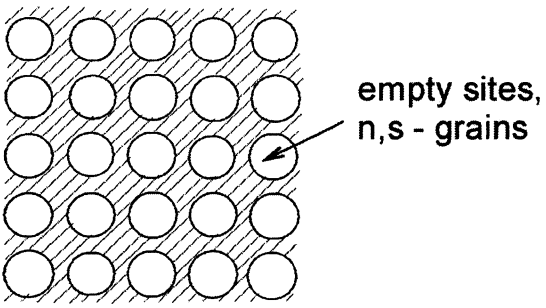

Fig. 1.12. Illustration of an ensemble of small particles, grains which are in the normal (n) or superconducting (s) state. For small particle size (radius R) and volume V the electronic energy spectrum gets discrete with level spacing $\delta(\delta = (N(0)V)^{-1} \approx \epsilon_F/n = (\hbar V_F/R)(Rh_F)^{-2}$; $N(0) = DOS$ at ϵ_F, $n = no$ of electrons). The grains may be in the normal (n)–or superconducting (s)–state. In such a grain structure some sites may be empty (0). Note, such a lattice like structure may resemble an alloy of sd– and n–state grains and also a nanostructure if small particles are removed irregularly from the lattice

served, see experiments by Buckel *et al.* [23] This is a good example of the potential of material science regarding superconductivity studies. Similarly this is the case for superconductivity in fullerides.

Extending these studies of granular materials one investigated small particles, nanostructures and metals consisting of an ensemble of small metallic grains, clusters [6], see Fig. 1.12. Thus, quantum size effects occur (discretization of electronic energy spectrum: $\epsilon_{\mathbf{k}} \rightarrow \epsilon_n$, granular size $l \sim \xi, \lambda$; ξ in the coherence length, λ in the penetration depth). In such granular superconductors surface effects and proximity effects become important. As a function of grain size metal insulator transitions and strong quantum–mechanical behaviour occurs. Note, on general grounds one expects, for example, that in reduced dimensions fluctuations play a more important role.

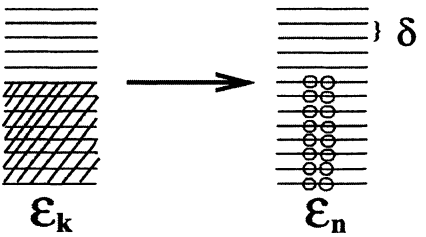

Fig. 1.13. Illustration of size effects in small particles having diameter of the order of R and n–electrons. The level spacing is $\delta \approx \epsilon_F/n \approx (\hbar V_F/R)(k_F R)^{-2}$ and the coherence length $\xi \sim (R\delta/kT_c)(Rk_F)^2 = \delta_0 N^{2/3} R$. Here, we introduced the dimensionless size parameter $\delta_0 = \delta/kT_c$

The discretization of the electronic energy spectrum, $\epsilon_{\mathbf{k}} \rightarrow \epsilon_n$, is illustrated in Fig. 1.13. Of course, the level spacing $\delta(\mathrm{T})$ affects various properties such as the coherence–length $\xi(\mathrm{n})$ and penetration depth $\lambda(\mathrm{n})$ and thus the thermodynamical and optical properties. Note, $\xi/\mathrm{R} \sim \mathrm{N}^{2/3}$ and hence $\xi \gg \mathrm{R}$ due to $\mathrm{N}^{2/3} \gg 1$. One expects that superconductivity disappears below a critical particle size ($\mathrm{R} < \xi$). The behaviour of small particles due to changes in the number n of electrons, for example $n \rightarrow n \pm 1$, and Cooper pairs by one, for example, is very interesting and may play a role for achieving a two level superconducting state (two charged states). This could be used for information technology (information storage, optical imprinting technology).

The charging of small particles is controlled by electrostatic energy. The change of the charge $Q = en \rightarrow Q \pm 1$ causes an energy change $\mathrm{e}^2/2\mathrm{C}$, C is the capacitance of the small particle and this may lead to a Coulomb blockade (in tunnelling, for example). Approximately at temperatures $T \simeq 0$ due to the electrostatic energy ($\mathrm{Q} = \mathrm{e}\Delta\mathrm{n}$) it is

$$E_n = \frac{Q^2}{2C} - \frac{Q}{C} C'V \tag{1.4}$$

(C, C′ capacitances, V=external potential) the blockade is periodically lifted as a function of n and V ($E_{n+1} = E_n$). In the superconducting state one has for $T \simeq 0$ that $\Delta > e^2/2C$. The situation is illustrated in Fig. 1.14. From $E_{n+1} + \Delta = E_n$ and $E_{n+2} = E_n$, n–even and large Cooper–pair sea, one gets a period–doubling with respect to the normal state. Note, $E_{n+2} = E_n$ might not hold for smaller density of Cooper–pairs.

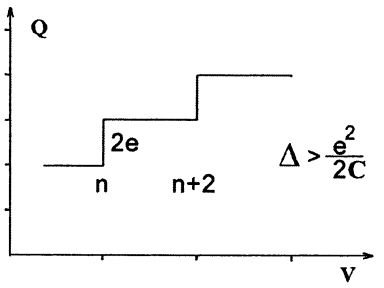

Fig. 1.14. Charging up behavior of a small superconductor with capacitance C and charge $Q = en$, n-even, in a potential ($\Delta > e^2/2C$). This behavior follows from $E_n = E_{n+2}$ and n-even and reflects Cooper–pair formation. One has also $E_n = E_{n+1} + \Delta$, where E_{n+1} has one unpaired electron. Then Q changes by e at $\Delta V \propto (2n + 1)$. V is the external voltage

In view of the strong quantum–mechanical behavior of small particles structures consisting of a larger number of small particles seem very interesting (mesoscopic systems).

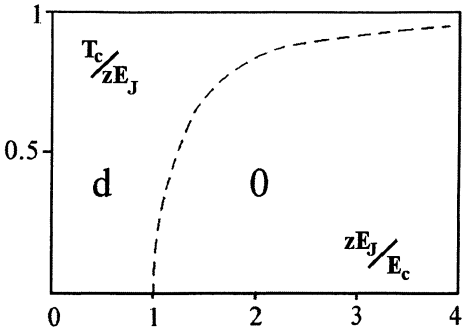

Fig. 1.15. Transitions in an ensemble of superconducting quantum dots controlled by the Josephson–energy E_J and the Coulomb–energy $E_c = e^2/2C$. T_c refers to the global superconducting transition–temperature of the ensemble. Phase O below T_c refers to a globally ordered superconducting state of the ensemble and phase d above T_c to superconducting grains with no global Cooper–pair phase coherence. z is the coordination number

An ensemble of grains for illustration may exhibit transitions to superconductivity at T_{c1}, where the single grains get superconducting, and at T_{c2} where globally and phase coherently the whole ensemble becomes superconducting ($T_{c2} \leq T_{c1}$), see Fig. 1.15. Generally an ensemble of grains may resemble an alloy like array of S/S and S/N junctions. (S=superconducting, N=normal state grains).

The behavior of an ensemble of grains depends of course on the coupling, on electron hopping between the grains. Also the structural order of the grains plays a role. A regular lattice like arrangement of the grains (1–dimensional, 2d–topology) is of particular interest. For small distances between the cluster particles electron tunnelling, inelastic Cooper pair tunnelling (Josephson–coupling) occurs. Hence, charge fluctuations are present in such granular superconductors. The resultant interesting Josephson effect can be described by [19]

$$H = H_T - \Sigma_{i,j}\, E_g(i,j) \cos \Phi_{ij} + \frac{2e^2}{C} \Sigma_{i,j}\, (N_i - N_j)^2 + \ldots \quad . \tag{1.5}$$

In equation (1.4) the first term refers to normal electron hopping between the grains, the second term to Cooper–pairs tunnelling between neighboring superconducting grains (Josephson–effect) and the last term is electrostatic energy due to different charges of neighboring grains i, j. For simplicity the same capacitance C and E_J–Josephson energy is taken. The phase difference $\Phi_{ij} = \Phi_i - \Phi_j$ refers to the phases Φ_i of the superconducting order parameter $\Delta_i = |\Delta_i| e^{i\Phi_i}$ of grain i. It is important to note that

$$[\Phi, N] = i \quad , \tag{1.6}$$

where N is the Cooper–pair number operator [6, 20]. Hence, Φ and N are canonically conjugate variables. Treating these as classical variables one finds immediately from the Hamilton–Jacobi equations the Josephson equations

$$j_J = (E_J/e) \sin \Delta\Phi$$

and

$$\dot{\Phi} = 2eV \quad .$$

Note, the commutator Eq. (1.6) implies the uncertainty relation

$$\Delta\Phi\Delta N \sim 1 \quad . \tag{1.7}$$

Consequently, large phase fluctuations, phase incoherence of the small particles make ΔN small and thus N a good quantum number. Hence, in view of Eq. (1.7) one may expect in an ensemble of superconducting grains an ensemble transition to a Mott–insulator if the capacitance C gets smaller and thus the Josephson–energy ($\sim E_J$) becomes smaller than the electrostatic energy $\sim 2e^2/\mathrm{C}$) [6,19]. The charge transport between the grains is suppressed while each grain is still superconducting. This behaviour is illustrated in Fig. 1.15 [19].

Note,if the capacitance C gets larger, ΔN increases and then all grains become phase–coherent ($\Delta\Phi \to 0$) [6,20].

For small particles (size <10nm, for example) proximity effect and Andreev–reflection [6,22] play an increasingly important role and may cause anomalous behaviour of the diamagnetic susceptibility and of the maximal Josephson–currents as a function of particle size, temperature etc.. For example, the Josephson–currents ($j_J = j_0 \sin \Delta\Phi$, $j_0 = \pi\Delta/2eR_T$, R_T resistance of tunnel barrier) may reverse ($j_J \to -j_J$, π–junctions) and maximal current j_0 reflects quantum size effects. In a Josephson–lattice of quantum dots: $j_0 = z\frac{e\Delta}{\hbar}$, where z is the lattice coordination number [6]. The ensemble topology of the small particles and their separation plays a role, since mean free path effects and phase coherency matter. A ring like arrangement of Josephson coupled quantum–dots is expected to be an interesting physics–toy regarding behaviour of 2–state superconductors and flux–pinning [20].

It is obvious that tunnel–junctions have become an interesting new area of solid state physics [21,22]. The tunnel medium (metals, insulators, molecules) can be manipulated, in particular optically, and new non–equilibrium physics could result. In Fig. 1.16 we illustrate a tunnel–junction describing in particular S/N/S, N/S/N junctions. Here, S may refer to singlet or triplet superconductors and N to normal state systems, metals and ferromagnets [22]. In the case of a $S_1/N_2/S_3$ sandwich, where S_1 and S_3 are singlet B.C.S.–type superconductors, the spin tunnel current is zero. If S_1 is a singlet– and S_3 a triplet superconductor, one expects for Josephson–tunnelling [22]

$$j_j = \sum_n (j_{1n} \sin n\Delta\phi + j_{2n} \cos n\Delta\phi) \quad . \tag{1.8}$$

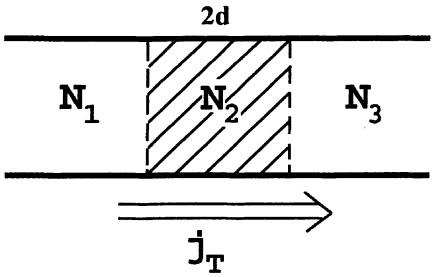

Fig. 1.16. Illustration of a tunnel junction $N_1/N_2/N_3$, where N_i may refer to singlet and triplet superconductors and to normal state metals, including ferromagnets, respectively. The tunnel current j_T may refer to single–electrons or Cooper–pairs and transport of charge and spin. Depending on the thickness $2d$ of the tunnel medium proximity effect and Andreev–reflection at S/N interfaces plays a role

Here, n=1,2,... and $\Delta\phi$ refers to the phase difference of the order parameter of S_1 and S_3. We assume that the thickness 2d of N_2 does not destroy phase coherence of the tunnelling electrons. Eq. (1.8) corresponds to a general Fourier–expansion of j_J. If time reversal symmetry is present (both S_1 and S_3 are singlet B.C.S. superconductors) one gets that the second term in Eq. (1.8) disappears, since $\Delta\phi \rightarrow -\Delta\phi$ implies $j_J \rightarrow -j_J$. Then approximately $j_J \sim \sin\Delta\phi$. If S_3, for example, refers to a triplet superconductor, then characteristically

$$j_J(n=1) = 0 \quad , \tag{1.9}$$

since the superconducting wave function $\psi_i = \eta_i^{spin}\,\varphi_i^{orbital}$ of i=1 and i=3 are orthogonal [22]. Thus to lowest order for a (singlet/N_2/ triplet) sandwich

$$j_J \sim \sin(2\Delta\phi) + \ldots \quad . \tag{1.10}$$

Clearly spin–active interfaces of the sandwich resulting from spin–orbit coupling or spin-excitations in N_2 may change the symmetry arguments and then j_J(n). Note, in case of spin–flip scattering selection rules change and spin– and orbital angular momentum need not to be conserved separately, but only the total angular momentum. As a consequence one might get contributions from j_{11} and j_{21} and from higher j_{in}.

In summary, one expects characteristic properties and differences for the (singlet/N_2/singlet), (singlet/N_2/triplet), and (triplet/N_2/triplet) junctions. Similarly, if N_2 is a ferromagnetic metal or insulator it will affect differently and characteristically junctions involving only singlet superconductors and those involving a triplet superconductor. Clearly, Josephson–tunnelling of singlet Cooper–pairs is more characteristically affected by a ferromagnet N_2 tunnelling medium than j_J for triplet superconductors.

Sandwiches ($F_1/S/F_3$) involving a superconductor S between two ferromagnets F_1 and F_3 with parallel or antiparallel orientation of the magnetization with also exhibit interesting behaviour. (We assume for simplicity that the thickness $2d$ of S is smaller than the spin–mean free path in S). Then charge (j_c)– and spin (j_{sp})– tunnel currents are expected. Due to spin–polarized tunnel currents provided by the exchange splitting of majority and minority bands in the ferromagnets one gets in general the functional behaviour

$$j_T = j_T\{\Delta, ...\} \quad , \Delta = \Delta\{j_T, ...\} \quad . \tag{1.11}$$

The spin polarized tunnel current j_T may cause presence of unpaired single electrons at the Fermi–energy ϵ_F besides Cooper–pairs and thus superconductivity is weakened. The effect should be different for singlet– and triplet–Cooper–pairs. A rich thermodynamical behaviour is expected. Due to proximity effect and Andreev–reflection [6, 22] the F/S interface coupling could cause the induction of a Larkin–Ovchinikov state [16] into the singlet superconductor ($\Delta_k \rightarrow \Delta_0 \cos kx + ...$), for example if $\lambda \sim 2d$. Then the electrons in the superconductor may feel the exchange field present in the ferromagnets. Also the exchange field accompanying the spin–polarized tunnel current might cause a similar change of the Cooper–pairing.

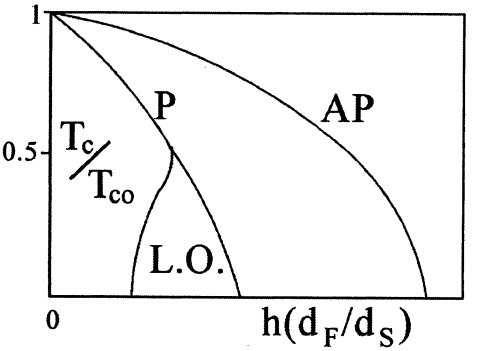

Fig. 1.17. Phase–diagram of a (F_1/S/F_3) sandwich. S refers to a singlet superconductor and F_1,F_3 to ferromagnets with T_c at P for parallel (P) orientation of their magnetization and T_c at AP for antiparallel (AP) one. L.O. is the Larkin–Ovchinnikov phase, h the exchange field and T_c and T_{co} the superconducting transition–temperature in the presence and absence, respectively, of the exchange field. d_F and d_S refer to the thickness of the ferromagnetic and superconducting film, respectively

Applying Usadel– and Eilenberger–type equations [22] for Cooper–pairing in external fields $\mathbf{h}$ one has

$$\{\omega_n^{'} + ih(\mathbf{r}) + \frac{1}{2}\mathbf{v}_F \cdot \nabla\} F = \Delta^{'}(\mathbf{r})G \,,$$

$$\omega_n^{'} = \omega_n + \frac{1}{2\tau}\int \frac{d\Omega}{4\pi} G(\mathbf{r}) \quad ,$$

and

$$\Delta^{'}(\mathbf{r}) = \Delta(\mathbf{r}) + \frac{1}{2\tau}\int \frac{d\Omega}{4\pi} F(\mathbf{r}) \quad . \tag{1.12}$$

Here, G and F are the usual Green's functions and τ is the elastic scattering term. Thus, one obtains the interesting phase–diagram for $(F_1/S/F_3)$ sandwiches shown in Fig. 1.17.

Recently, Nogueira and Bennemann discussed a Josephson like spin–current j_J^{spin} for $(F_1/N_2/F_3)$– sandwiches [20]. If the thickness $2d$ is smaller than the spin–mean free path the results could also be applied if N_2 is a superconductor.

1.4 Outlook

We have attempted to summarize developments in the area of superconductivity. Superconductivity in MgB_2, cuprates, ruthenates, heavy–fermion metals and organic systems shows that new metals continue to keep the field alive. This view is further supported by the results on small particles, nano–structures and sandwich–structures. The interdependence of structure and superconductivity and further of magnetism and superconductivity remains a key physical issue. Extreme quantum–mechanical behaviour due to $T \rightarrow 0$, reduced dimensionality, correlations, quantum–fluctuations and in particular at quantum critical points (Q.C.P.) might present new surprises in the future. Of course, still interesting remains the search for new superconductors. As an example, may serve superconductivity in intercalated $Na_xCoO_2(H_2O)$, $x \simeq 0.35$ and $y \simeq 1.3$,and with $T_c \leq 5K$ [24]. An unifying field theoretical analysis of Non–Fermi liquid behaviour and of superconductivity and superfluidity and of Bose–Einstein condensation remains a challenging goal. Systems consisting of superconducting quantum dots may become very useful for quantum information technology. Eqs. (1.4) and (1.5), where the charge changes are due to Cooper–pairs, describe the posto get 2–level superconducting states.

Acknowledgements
We thank D. Manske, I. Eremin, F. Nogueira and last not least E.v. Sulzbach for helpful discussions. We are also in particular grateful to W. Buckel, R.D. Parks, M. Peter and B. Mühlschlegel for many discussions over the years.

References

1. R.D.Parks: *Superconductivity*, Vol 1,2 (**Marcel Dekker Inc.**, New York, 1969); J.R. Schrieffer: *Theory of Superconductivity* (Benjamin, New York, 1964).
2. J.G. Bednorz and K.A Müller, Z. Phys. B **64** 189 (1986); K.H Bennemann and J.B. Ketterson: *The Physics of Superconductors*, Vol. 1 (Springer, 2002).
3. Y. Maeno *et al*, Nature **372**, 532 (1994); T.M. Rice, Nature **396**, 627 (1998); Y. Maeno, T.M. Rice, M. Sigrist, Physics Today **54**, 42, Physica C **341–348** 695 (2000).
4. J. Nagamatsu, N. Nakagawa, T. Muranaka, Y. Zenitani, and J. Akimitsu, Nature **410** 63 (2001); D.K. Finnemore, J.E. Ostenson, S.L. Bud'ko, G. Lapertot, and P.C. Canfield, Phys. Rev. Lett. **86** 2420 (2001).
5. M. Vojta, Phys. Bl. **55**, March 2002; S. Sachdev: *Quantum Phase Transitions* (Cambridge Univ. Press, 1999); J. Flouquet and A. Buzdin, Phys. World **15** 41(2002).
6. W. Belzig and C. Bruder, Phys. Bl. **56** (No.5) 35 (2000); C.W.J. Beenakker, in *Mesocopic Quantum Physics* (North Holland, Amsterdam 1995); B. Mühschlegel, Surface Rev. and Lett. **3** (No.1) 115 (1996), W.P. Halperin, Rev. Mod. Phys. **58**, 533 (1986); B. Janko, L. Smith, V. Ambegaokar, Phys. Rev. B **50**, 1152; M.T. Tuominen, J.M. Hergenrother, T.S. Tighe, and M. Tinkham, Phys Rev. Lett. **69** (1992) 1997; Mesoscopic Superconductivity Physica B **203**, 201 (1994); Y. Imry: *Introduction to Mesoscopic Physics* (Oxford Univ. Press, 1997); B.L. Altshuler *et al.*: *Mesoscopic Phenomena in Solids* (North Holland, Amsterdam 1991).
7. J.P. Carbotte and F. Marsiglio, in *The Physics of Superconductors* (Edts. K. Bennemann, J. Ketterson, Springer 2002).
8. B.D. Josephson, Phys. Lett **1** 251 (1962); P.W. Anderson in *Lectures on Many Body Problem* (Edt. E.R. Caionello, Academic Press, New York 1964).
9. H.J. Choi, D. Roundy, H. Sun, M.L. Cohen, and S.G. Louie, Nature **418**, 758 (2002).
10. D. Manske, I. Eremin, and K.H. Bennemann, Phys. Rev. B **62**, 13922 (2000).
11. D. Manske, I. Eremin, and K.H. Bennemann, in *The Physics of Superconductors*, Vol 2 (Springer 2003).
12. A. Mackenzie, Y. Maeno and S. Julian, Phys. World **15** (No4) 33 (2002).
13. I. Eremin, D. Manske and K.H. Bennemann, Phys. Rev. B **65**, 220502(R).
14. H.R. Ott in *The Physics of Superconductors Vol.1* (Edts. K.H. Bennemann, J.B. Ketterson, Springer 2002).
15. L. Degiorgi, Rev. Mod. Phys. **71** 687 (1999); F. Steglich *et al.* J. Phys. Chem. Sol. **59**, 2190 (1998); M.B. Maple, Physica C **341-348**, 47 (2000); C.R. Stewart, Rev. of Mod. Physics **73**, 797 (2001); R. Joynt and L. Taillefer, Rev. Mod. Phys. **74**, 235 (2002).
16. A.I. Larkin, Yu.N. Ovchinnikov, JETP **20**, 762 (1965).
17. J. Singleton and C. Mielke, Phys. World **15** (No1) 35 (2002), T. Ishiguo *et al.*: Organic Superconductors (Springer 1998), M. Lang in *The Physics of Superconductors Vol.2* (Edt. K.H. Bennemann, J.B. Ketterson, Springer 2003).
18. J.W. Garland, K.H. Bennemann, F.M. Mueller, Phys. Rev. Lett. **21**, 1315 (1968); W. Buckel, and R. Hilsch, Z. Phys. **138**, 109 (1954).
19. J.B. Ketterson and S.N. Long: *Superconductivity* (Cambridge Univ. Press 1999).
20. F.S. Nogueira and K.H. Bennemann, to be published cond-mat/0302528

21. L.B. Ioffe and M.V. Feigel'man, cond-mat /0203011; B. Doucot, M.V. Feigel'man and L.B. Ioffe, Phys. Rev. Lett. **90**, 107003 (2003).
22. I. Baladić, A. Buzdin, N. Ryzhanova and A.Vedyayev, Phys. Rev. B **63**, 54518 (2001); Y. Asano, Y. Tanaka, M. Sigrist, and S. Kashiwaya, cond-mat /0212353v1.
23. K.H. Bennemann, Z. Physik **260**, 367 (1973).
24. T. Takada, H. Sakurai, E. Takayama-Muromachi, F. Izumi, R.A. Dilanian, and T. Sasaki, Nature **422**, 53 (2003).

2 Nanostructured Superconductors

Guy Deutscher
School of Physics and Astronomy, Tel Aviv University, Israel

2.1 **Introduction** 25
2.2 **Nanostructured Compounds** 26
2.3 **The Granular Structure** 27
2.3.1 Grain Size 27
2.3.2 Granular to Amorphous Transformation and the Metal to Insulator Transition 29
2.3.3 The Percolative Random Structure 29
2.4 **Normal State Transport** 30
2.4.1 Transport in Random Percolating Structures 30
2.4.2 Transport in Granular Structures 31
2.4.3 Progressive Coulomb Blockade 31
2.5 **Single Grain Behavior** 33
2.5.1 Estimates of the Limiting Size of Superconductivity 34
2.5.2 Numerical Studies 35
2.5.3 Experiments on Nano–Size Grains 37
2.6 **Weakly Coupled Grains: Granular Insulators and Super–Insulators** 39
2.6.1 Small Grain Case: Percolative Behavior 40
2.6.2 Large Grain Case: Superconducting Insulators 40
2.6.3 Pseudogap Regime in the Superconducting Insulator 43
2.6.4 The Superinsulator Case 44
2.7 **Well Coupled Grains** 44
2.7.1 Granular Case 45
2.7.2 Random Case 47
2.8 **Critical Temperature of Granular Superconductors** 49
2.8.1 Grain Size Dependence of the Critical Temperature 49
2.8.2 Weak Screening Model 50
Acknowledgements 52
References 52

2.1 Introduction

We review the structure, transport and superconducting properties of compounds composed of small metallic grains connected in different ways. After a short description of the two main kinds of structures, normally granular, random and metal/insulator mixtures, an account is given of their normal state behavior near the metal to insulator transition. Superconductivity in single grains, weakly connected grains and well connected grains is then reviewed. Finally, some remarks are made on the T_c enhancement in granular superconductors.

K. H. Bennemann et al. (eds.), *The Physics of Superconductors*
© Springer-Verlag Berlin Heidelberg 2004

2.2 Nanostructured Compounds

It has been known for a long time by metallurgists that eutectic systems composed of two immiscible phases (elements or compounds) can assume different structures depending on the procedure followed in their preparation such as cooling and annealing schedules. Granular matter falls into that category. For instance, when Al is evaporated in a poor vacuum system it condenses in the form of a film composed of small Al grains, weakly coupled together through thin amorphous Al_2O_3 barriers. This was discovered accidentally by Abeles *et al.* [1] in the early sixties. Al-Al_2O_3 is a good eutectic system, because oxygen is essentially immiscible in Al, and Al_2O_3 is the only oxide of Al. This ensures a very sharp boundary between the metal and the oxide. In this way, Al grains as small as a couple of nanometers can be obtained. Another well studied eutectic system is Al-Ge, which can also assume a granular structure when the two elements are co–deposited onto a substrate held at room temperature, see Fig. 2.1. In that case also Al is crystalline and Ge amorphous [2]. But when such a film is annealed, or when it is deposited to start with at an elevated temperature, Ge is in crystalline form. The structure is then no longer granular. Rather, it is composed of Al and Ge small crystallites, randomly distributed in space. The structure is then of

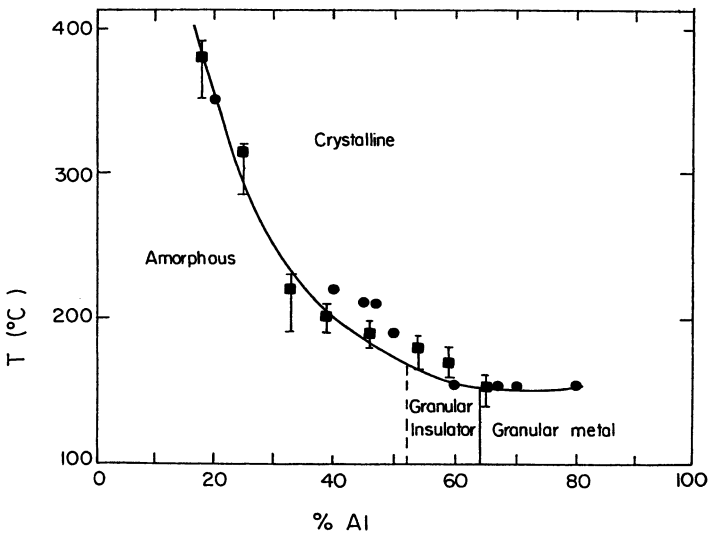

Fig. 2.1. Phase diagram of the Al–Ge system as a function of the growth temperature T, and %Al (volume fraction). The crystalline phase has the random percolating structure. The amorphous phase is insulating. The granular phase can be either metallic or insulating

the percolative type [3]. Other eutectic systems having similar properties are Sn-SnO_x, Sn-Ar, and Ni-SiO_2.

Abeles *et al.* discovered that granular Al films had many interesting properties. Their normal state resistivity was typically a few orders of magnitude higher than that of bulk Al. Their critical temperature could reach more than 3K compared to 1.2K for pure Al and the upper critical field several Tesla. These properties are structure sensitive. The same composite in its percolative form does not have an enhanced critical temperature. Its normal state properties are different, particularly in the vicinity of the metal to insulator transition at high insulator concentration.

These observations raise some interesting questions. Why does the metal form in the granular structure? How should the "poor metal properties" be understood? Why is the critical temperature higher than that of the bulk metal in the granular structure and not in the percolative one? Is the enhanced critical temperature a property of the small grain itself or is it a property of the coupled grains? Is it accidental that the maximum T_c enhancement occurs near the metal–to–insulator transition? This last property is the most intriguing one, because it resembles so much that of the cuprates whose highest T_c is also reached at an "optimum doping" very close to the metal–to–insulator transition. Is this similarity accidental? Is it a clue that may help understand the high T_c of the cuprates? Our answers to these questions are to–day still imperfect, but we certainly understand that granular matter is an even more interesting object of study than was realized at the time of its discovery.

2.3 The Granular Structure

Granular films can be obtained either by the reactive evaporation of the metal in the presence of a sufficient pressure of oxygen in the vacuum system as was first done un–intentionally by the RCA group or by the co–deposition of the metal and the insulator (for a review see for instance Ref. [3]). The metal and the insulator must be insoluble and must not form definite compounds. As already mentioned not all metal–insulator systems form granular structures and the type of structure that is obtained depends on the temperature of the substrate at the time of deposition. Granular structures may also transform into other structures upon annealing [5].

2.3.1 Grain Size

An important observation is that in granular films the metal is crystallized and the insulator (or semiconductor) amorphous. This has been shown explicitly for Al-Al_2O_3 and for Al-Ge. Furthermore, in these two systems the thickness of the dielectric is of atomic size [2]. The size of the metal grains is

a decreasing function of the dielectric concentration. At high dielectric concentration it is in the nanometer range. For dielectric concentrations roughly higher than 50 vol.%, the mixture turns amorphous, or at least the grain size becomes smaller than the electron microscope resolution.

Detailed studies of the grain size distribution have been performed by dark field electron microscopy. They have shown that this distribution is rather narrow, particularly at high dielectric concentration [6], see Fig 2.2 for illustration

These observations have suggested the following model for the growth mechanism of granular films [2]. During deposition metal grains nucleate and grow through diffusion of metal atoms in the amorphous as–deposited mixture. The dielectric atoms or molecules play a purely passive role in this process. They are expelled at the periphery of the growing metal grains. When a continuous dielectric layer is formed at the periphery, it acts as a barrier that slows down further grain growth. This continuous dielectric layer is formed at a grain size value that depends on the dielectric concentration in the composite. The higher it is the smaller is this grain size.

This model explains the observed relationship between the dielectric volume fraction and the grain size as well as the uniformity of the latter. The prediction that the dielectric thickness is of molecular size, is also in good agreement with experiment [2].

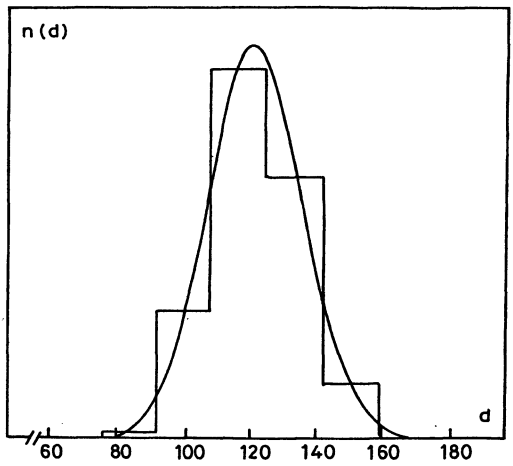

Fig. 2.2. A typical histogram of grain size distribution n(d) of Al grains in the Al–Ge granular phase. The size d is the grain diameter in Ångstrom

2.3.2 Granular to Amorphous Transformation and the Metal to Insulator Transition

The above correlations are is only valid at moderate insulator concentrations. Beyond a certain concentration the grain size becomes actually concentration independent. This limiting value depends on the temperature of deposition. It becomes smaller at lower temperatures suggesting that it is set by a diffusion mechanism. In this regime, as the dielectric concentration keeps increasing, the dielectric barriers between the metallic grains become thicker. Shortly thereafter the structure shifts to an amorphous mixture.

The geometrical growth model assumes a priori that the granular structure is energetically more favorable than the amorphous one. A clue as to what drives the structural transformation may be the fact that the metal–to–insulator transition (discussed later in detail) appears first, but quite close to it. When electrons become localized in the grains, since the dielectric barriers become thicker, their kinetic energy increases. This increase is on the order of the energy level splitting, which is inversely proportional to the grain's volume. For a grain of nanometer size, containing roughly a thousand electrons, this energy is of the order of a few tenths of an electron volt. Per grain this is a few times the thermal energy at room temperature. Depending on other factors such as the interface energy between the metal and the dielectric this may be sufficient to tip the balance in favor of the amorphous structure. Thus, the granular–to–amorphous transition may in fact be electronically driven.

2.3.3 The Percolative Random Structure

If at the time of deposition both the metal and the dielectric crystallites can nucleate, one obtains a structure in which they are randomly dispersed. By this we mean that the probability to find , say, a dielectric crystal next to a metallic one, is solely dictated by the respective volume fractions, at least if they are of similar sizes. This structure is obtained if the mixture is deposited at a temperature that is high enough to allow the nucleation of dielectric crystals. It is well known that metals will crystallize even when deposited at cryogenic temperatures, but that dielectrics can easily form in an amorphous structure unless the deposition temperature is several hundred degrees Celsius above room temperature. For instance, a random Al–Ge mixture will be formed if deposited at a temperature higher than about 300^0C.

Even though metallic and dielectric crystallites are not located at well defined sites on a lattice, the obtained structure is essentially similar to a random percolative one. Metallic and insulating clusters are formed, whose structure is fractal on scales intermediate between the crystallites size and the percolation correlation length for each respective type of cluster [3]. The percolation correlation length diverges at a certain critical volume fraction, whose value depends on the dimensionality. Below that volume fraction, only finite clusters are formed. Beyond it finite clusters are still present, but an

infinite cluster is formed as well. In three dimensions there are distinct thresholds for the two constituents. The phase diagram comprises three regions: at low metal volume fraction only the insulator forms an infinite cluster; beyond the critical metal volume fraction, both the metal and the insulator form infinite clusters; at still higher metal volume fraction, only the metal forms an infinite cluster. In two dimensions there is only one threshold: either the metal or the insulator will form an infinite cluster.

2.4 Normal State Transport

In this section, we review the behavior of the electrical resistivity and of the Hall effect for both kinds of structure, the granular and the random one. We start with the latter which is better understood.

2.4.1 Transport in Random Percolating Structures

What is well understood in the framework of percolation theory is the case of random mixtures where the metal M and the insulator I are randomly distributed in space, as we have described above.The resistivity is given by

$$\rho \propto (p - p_c)^{-t} \quad , \tag{2.1}$$

where p is the metal volume fraction and p_c the metal critical volume fraction at which an infinite metallic cluster is formed. The value of the exponent t depends on dimensionality, $t_{3D} = 2.0$ and $t_{2D} = 1,3.$.

In 2 dimensions ($2D$) theory predicts and experiment verifies that the Hall constant R_H does not diverge at the percolation threshold. In $3D$, however, one gets

$$R_H \propto (p - p_c)^{-g} \quad . \tag{2.2}$$

The $3D$ experimental value of g = 0.38±0.05 [7] is in good agreement with the theoretical result g = 0.29±0.05 from numerical simulations [8]. Hence percolation theory predicts and experiment verifies that in $3D$ one has

$$R_H \propto \rho^{0.15} \tag{2.3}$$

As long as there exists an infinite metallic cluster ($p > p_c$) the temperature dependence of the resistivity of the composite has metallic character. It decreases as the temperature is lowered. The Hall constant is temperature independent. These properties are also well observed experimentally. They are non–trivial. For instance, close enough to the percolation threshold the room temperature resistivity will be very high typical of a semiconductor rather than of a metal. Yet, upon measuring its temperature dependence, it will appear that it has the metallic character [9]. This statement is correct except for some subtle weak localization effects that will appear at low temperatures on the weakest parts of the infinite cluster, if the crystallites are small enough.

2.4.2 Transport in Granular Structures

The behavior experimentally observed in *granular* systems, where each metallic grain is surrounded by an insulating coating, is quite different from that of random systems. Contrary to the prediction of percolation theory verified in random systems the temperature dependence of the resistivity is activated beyond a certain value of the resistivity. Bandyopahyay *et al.* have found that in granular Al one finds $R_H \propto \rho^{0.5}$ [10] near the metal to insulator transition, while from percolation theory one would expect $R_H \propto \rho^{0.2}$. In comparing their results with other theories, Bandyopahyay *et al.* noted that the scaling theory of localization predicts that R_H should be temperature independent. Hence, in their samples where the conductivity is activated (R_H/ρ) should be temperature dependent contrary to their experiments. Theories based on interaction effects predict $R_H \propto \rho^2$, also in disagreement with experiment. Hence, the transport properties of granular films are not well explained by either percolation localization (or interaction) theories.

One essential difference between granular materials and random M/I mixtures consists in the existence in the former of a finite charging energy E_c necessary for the transfer of an electron from grain to grain. This is due to the insulating coating surrounding each metal grain. The question is then whether the M–I transition is still driven by disorder effects, characterized in this case by a distribution of intergrain resistances R and for which a percolation description might apply as in the case of random mixtures, or whether the charging energy plays a dominant role. One would expect the first mechanism to apply for large grain sizes (small charging energy) and the second one for small grains. In the case of the granular films studied by Bandyopahyay *et al.* the grain size is only of a few nanometers $E_c \approx (e^2/r)$. For the isolated grain it is of the order of 0.1 eV. One expects that electrostatic charging should play a dominant role near the M/I transition. We examine below the possible role of Coulomb blockade in transport phenomena in granular nano–structures.

2.4.3 Progressive Coulomb Blockade

A number of experiments support the idea of the Coulomb blockade [11] for electron tunnelling between small grains, even if this electrostatic effect can be washed out by quantum fluctuations in single tunnel junctions [12]. Thus, it is certainly not surprising that pure percolation models do not describe correctly the experimental situation of nano–strucured granular films. On the other hand, since the samples of Bandyopay *et al.* have a finite conductivity in the normal state above the superconducting transition, one might be tempted to say that electrostatic effects are negligible. Why should'nt percolation effects then dominate?

It has been proposed [13] that the behavior of R_H near the M/I transition can in fact be successfully described in a semi–classical manner [14]

by considering the effect of the charging energy in the form of a progressive Coulomb blockade in which more and more "free electrons" are frozen out from the conduction process.

Following Abeles [15] we discuss the conduction process in granular compounds in terms of the intergrain resistance R and capacity C. We assume that electrostatic effects dominate over disorder, or in other words that R and C are uniform. As Abeles first pointed out, when the classical relaxation time $\tau = RC$ becomes shorter than $\left(\frac{\hbar}{e^2}\right) C$, the link between two neighboring grains can in fact be considered as metallic. This occurs when $R < \left(\frac{\hbar}{e^2}\right)$independently of the capacitance value. Extending this two–grain criterion to the entire granular system, one obtains that it becomes macroscopically insulating beyond a critical resistivity $\rho_c = (\frac{\hbar}{e^2})d$, where d is the grain diameter. While this criterion is rather well verified empirically, it is of course not correct, since the existence of a Coulomb blockade depends on the connecting circuit itself, here the rest of the sample. However, we can modify Abeles argument so as to make it basically identical to that of Mott [16].

Consider a granular system and assume that it is *metallic.* We "isolate" one grain from the rest of the granular system to which it is coupled through R and C. If we charge this grain by the addition of one electron and if RC is larger than $(\frac{\hbar}{e^2})C$, this grain is effectively isolated from the system and transfer of the electron requires a finite electrostatic energy. However, this grain is just like any other grain. Hence, all of them are isolated and the medium must be *insulating,* contrary to our initial assumption. Hence, if $R > (\frac{\hbar}{e^2})$, the system cannot be metallic and it must be insulating.

In fact $\rho_c = (\frac{\hbar}{e^2})d$ is identical, apart from a numerical factor to Mott's minimum metallic conductivity criterion, with a carrier density d^{-3}. We can indeed recover it by using the conventional expression for the conductivity and assuming that each grain contributes *only one free carrier.* The effective carrier density is then $n = (n_0/N)$, where n_o is the carrier density in the bulk metal and N is the number of free electrons in a grain and the conductivity is given by

$$\sigma = \frac{n_o}{N}\frac{e^2\tau}{m^*} \quad . \tag{2.4}$$

Here, m* is the effective mass corresponding to the motion of the carriers in the lattice of grains. Denoting by l^*, v_F^*, the mean free path and Fermi velocity corresponding to inter–grain motion, one has

$$\sigma = \frac{e^2 l^*}{m^* v_f^* d^3} \quad . \tag{2.5}$$

Ioffe and Regel were the first to point out that the minimum value of l^* is the inter–atomic distance (the inter–grain distance) [17]. Thus, the minimum

metallic conductivity is given with $dk_f^* \sim 1$and $l^* \sim d$. We recover the result

$$\rho_c = \left(\frac{\hbar}{e^2}\right) d \quad . \tag{2.6}$$

Just as the intergrain resistance value $\frac{\hbar}{e^2}$ allows the metallic transfer of *one* electron from a grain to a neighboring one, and the system behaves as if it had *one* free electron per grain, we now remark that the value $R_p = \frac{\hbar}{p^2e^2}$ allows the simultaneous transfer of p electrons. In other words, a granular system with an inter–grain resistance R_p will behave as if it had p free electrons per grain. Its resistivity will be

$$\rho = \frac{\hbar d}{p^2 e^2} \quad , \tag{2.7}$$

and using the same approximation the Hall constant will be

$$R_H = \frac{d^3}{pe} \quad . \tag{2.8}$$

Hence, one has

$$R_H = d^{5/2} \left(\frac{\rho e^2}{\hbar}\right)^{1/2} \quad . \tag{2.9}$$

Thus, the progressive Coulomb blockade model predicts that the Hall constant varies as the square root of the normal state resistivity at constant grain size. This is in agreement with the experiments of Bandyopay *et al.*. Keep in mind that near the M/I transition the grain size remains constant [6].

We conclude that the available data are consistent with a Mott description of the M/I transition in granular systems having a small grain size. This transition takes place by a progressive freezing out of the bulk conduction carriers, until just before the transition each grain contributes effectively only one conduction electron. Simultaneous transfer of more than one electron per grain requires a finite activation energy. This can be at the origin of the negative coefficient of temperature in such films, while there is some evidence that their conductivity is finite at zero temperature.. We note that in this borderline situation electronic screening is strong within each grain, but weak between the grains. From that standpoint such grains become effectively zero–dimensional, which has some interesting consequences for superconductivity as will be discussed in more detail in a later section.

2.5 Single Grain Behavior

A fundamental question concerning superconductivity (as well as any other cooperative phenomenon) is to know the size below which superconductivity

cannot persist. This question is all the more relevant for superconductivity in view of the fact that the surface boundary condition for the order parameter is a mild one due to the fact that the coherence length is much larger than interatomic distances. To a good approximation it is the gradient of the order parameter in the direction perpendicular to the surface that is zero, rather than the order parameter itself (on the scale of the coherence length). The boundary condition does not prevent the occurrence of superconductivity in grains smaller than the coherence length. An exception to this rule are high temperature and short coherence length superconductors. This we shall discuss briefly at the end of this chapter.

What is then the limiting size of a superconducting grain? There are several ways in which we can try to answer this question. One of them is to calculate the thermodynamic fluctuations of the order parameter that result from the finie size and to determine at what size these fluctuations are of the same order of magnitude as the order parameter itself. The second one is to calculate at what size there will be only one Cooper pair per grain. A third one is to determine at what size the average separation between the single particle electronic levels is of the order of the gap. We shall briefly perform these estimates. A remarkable result is that they all give the same answer.

2.5.1 Estimates of the Limiting Size for Superconductivity

Assuming that the grain's size is smaller than ξ the boundary condition for the order parameter, $\mid \nabla\Psi \mid_{\perp} = 0$, together with the requirement that the order parameter cannot vary substantially on a length scale smaller than ξ,imposes that the order parameter is constant within the grain. We can then use a simplified Landau–Ginzburg expression for the free energy density:

$$F_s = F_n + a \mid \Psi \mid^2 + \frac{b}{2} \mid \Psi \mid^4 \quad . \tag{2.10}$$

Here, a is a linear function of the temperature that changes sign at the critical temperature T_c, and b is a constant. Fluctuations of the order parameter consist of a deviation from its equilibrium value:

$$\Psi = \Psi_0 + \delta\Psi \quad . \tag{2.11}$$

Above T_c, $\Psi_0 = 0$, and the excess free energy resulting from fluctuations is simply:

$$\delta F_s = a\langle \mid \delta\Psi \mid^2 \rangle \Omega \quad , \tag{2.12}$$

where Ω is the grain's volume. At a finite temperature T one has

$$\delta F_s \simeq k_B T \quad . \tag{2.13}$$

We are now in a position to calculate the quantity of interest:

$$\frac{\langle \mid \delta\Psi \mid^2 \rangle}{\mid \Psi_0 \mid^2} \simeq \frac{k_B T}{\left(\frac{a^2}{b}\right) \Omega} \quad . \tag{2.14}$$

This result is easily understood: fluctuations of the order parameter are of the order of the order parameter itself when the thermal energy $k_B T$ is of the order of the condensation energy in the grain. If we move somewhat away from T_c(let us say, around $T_c/2$), T is still of the order of T_c , and the condensation energy is already of the order of its value at $T = 0$. Using the BCS expression for the condensation energy in the limit $T = 0$, and noting that the gap is of the order of $k_B T_c$,the same criterion gives

$$\frac{1}{2} N(0) \Delta^2 \Omega \simeq \Delta \quad . \tag{2.15}$$

In other terms words one has

$$N(0) \Delta \Omega \simeq 1 \quad . \tag{2.16}$$

Since $N(0)\Delta$ is essentially the number of Cooper pairs per unit volume, this condition means that the number of Cooper pairs in the grain is of order unity.

Finally, let us consider the last criterion. The average separation of the quasi–particles energy levels near the Fermi level is the Fermi energy E_F, divided by the number of electrons n per unit volume times the volume of the grain. The last criterion then reads

$$\frac{E_F}{n\Omega} \simeq \Delta \quad . \tag{2.17}$$

In the free electron approximation it is $N(0) = \frac{3}{2} \frac{n}{E_F}$. This is the same condition as before. For a typical superconductor such as Al the limiting diameter for superconductivity comes out to be of the order of 100 Å.

2.5.2 Numerical Studies

The above estimates are only rough. Another factor to be taken into account to predict the properties of small grains is the odd or even number of electrons per grain. We can expect that when the number is odd and the size sufficiently small that the separation between the electronic levels is a substantial fraction of the gap. The unpaired electron will play the role of a pair breaker further weakening the superconducting ground state.

In small grains with $\delta \gtrsim \Delta$, ab–initio calculations of the effect of mesoscopic fluctuations on the heat capacity and the spin susceptibility have been recently performed [18]. These calculations take into account the odd or even number of electrons, and have been performed for an ensemble of monodispersed grains, where the single particle spectrum is statistically distributed

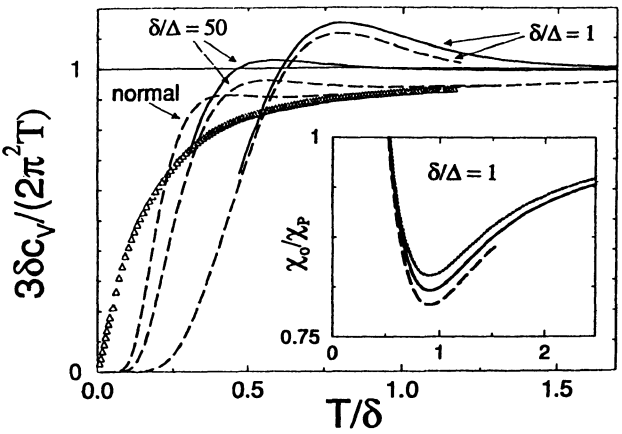

Fig. 2.3. Temperature dependence of the heat capacity and of the susceptibility of superconducting grains. Δ is the superconducting gap, and δ the separation between the electronic levels in the normal state. When both energies are of the same order, a smeared peak in the heat capacity can still be observed at the transition temperature. At the same temperature, a dip in the susceptibility is predicted

and characterized by level repulsion. Such calculations are relevant for comparison with experiments where measurements are carried out on a very large number of grains. Results differ from those of calculations for equally spaced, non–interacting levels. This can give some spurious results.

Results for the heat capacity predict for an ensemble of grains with even number of electrons an exponential decrease at low temperatures $T \ll \delta$, and at temperatures $T \sim \Delta$, an enhancement reminiscent of the heat capacity jump in bulk samples, see Fig. 2.3. For an ensemble of grains with odd number of electrons the low temperature behavior is the same as that of normal grains with a T^2 behavior and no enhancement is predicted at $T \sim \Delta$. In an experimental realisation, even and odd number of electrons will be mixed, so that the only effect related to superconducting pairing will be an enhancement at $T \sim \Delta$.This enhancement is substantial (about 20%) for $\delta \sim \Delta$, but vanishingly small for $\delta \sim 50\Delta$.

The spin susceptibility shows pairing effects for ensembles of grains with odd number of electrons. For even number of electrons the exponential decrease of the susceptibility at low temperatures is basically a normal state effect. For odd numbers the decrease below T_c (due to pairing) is followed by an upturn at lower temperatures due to the unpaired electron. This re–entrant behavior is a signature of pairing effects. It has been checked that in normal grains the susceptibility is continuously increasing as the temperature is lowered.

2.5.3 Experiments on Nano–Size Grains

Experiments have not been performed so far on physically isolated nano–grains, but on grains effectively uncoupled to neighboring ones. This is realized for instance in the case of granular composites consisting of metal grains separated by dielectric barriers sufficiently thick to prevent inter–grain Josephson coupling. For instance, Al–Ge mixtures are like this. Another case consists of a metal grain embedded in a dielectric barrier. The first case is appropriate for heat capacity measurements and the second one for tunneling spectroscopy.

Heat capacity measurements

The heat capacity transition of Al–Ge thin film composites has been measured for various compositions, near the metal/insulator transition [19]. In this region, the Al grain size (diameter) is of about 10nm. Measurements were performed for films ranging from metallic to insulating. A transition, characterized by a broaden peak in the heat capacity, was observed even for samples that were macroscopically insulating. This is explicitly shown Fig. 2.4. For that grain size, the separation between the electronic levels is of the order of the gap of bulk Al, as we have calculated above. This result is in agreement with the calculations of Falci *et al.* [18] in the sense that it clearly shows that superconductivity is not quenched down to sizes at which $\delta \sim \Delta$. If anything, the experimentally observed peak in the heat capacity is rather larger than predicted. However, one has to be careful in view of the uncertainties on the exact grain size and gap values in the grain. These are probably larger than in the bulk in view of the enhanced critical temperature.

Smaller grain sizes, down to a couple of nanometers, are achieved in the composite Al-Al_2O_3. In that case, $\delta \gg \Delta$. Heat capacity measurements on such films have shown that the transition disappears while the samples are still metallic, as shown Fig. 2.5. One thus reaches the conclusion that any sign of superconductivity in the heat capacity is quenched at a size between 10nm and 2nm, again in agreement with theory.

Tunneling into single grains

The spectroscopic properties of single grains have been studied by measuring the conductance of junctions where the current from one electrode to the other passes through a grain, which is weakly connected to them [20]. This device is sensitive to both the single level splitting and the superconductng gap. The conductance shows a series of peaks marking the bias values at which the transfer of an electron from one electrode (lead) to the other. Each peak corresponds to tunnelling via an electronic level on the particle. The even (odd) number of electrons on the grain (in the zero bias state) can be identified by the presence (absence) of field splitting of these peaks.

For the even case the bias where the first peak is observed decreases as a function of the applied field until a field is reached where it stays roughly constant. This decrease is associated with the decrease of the superconducting gap in the grain under the applied field. In this way, the value of the gap is

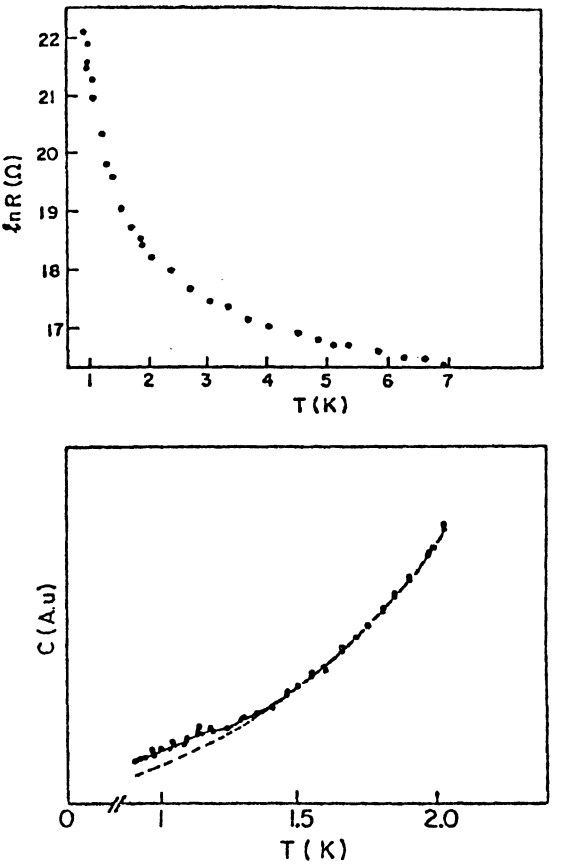

Fig. 2.4. Electrical resistance in *ln* scale (upper Fig.) and the heat capacity (lower Fig.) as a function of temperature for an Al–Ge sample in the granular insulating phase. The grain size distribution is similar to that shown in Fig. 2.2. Although the sample is macroscopically insulating, the heat capacity transition of the individual Al grains can be observed. The behavior of the heat capacity is similar to that predicted in Ref. [18], shown in Fig. 2.3

determined. In the odd case the first peak corresponds to a state where an additional electron pairs with the single one, while in the second one there must be two unpaired electrons. The difference in energy must therefore be twice the gap and it must go down as the field is increased. This is observed.

Gap values can in this way be clearly identified as long as they are larger than δ. For the studied Al grains, this corresponds to sizes larger than about 10 nm. Gap values obtained are larger than the bulk Al value by about 50%, in agreement with the increase in T_c observed in granular Al films. These measurements confirm the conclusion drawn from the heat capacity data,

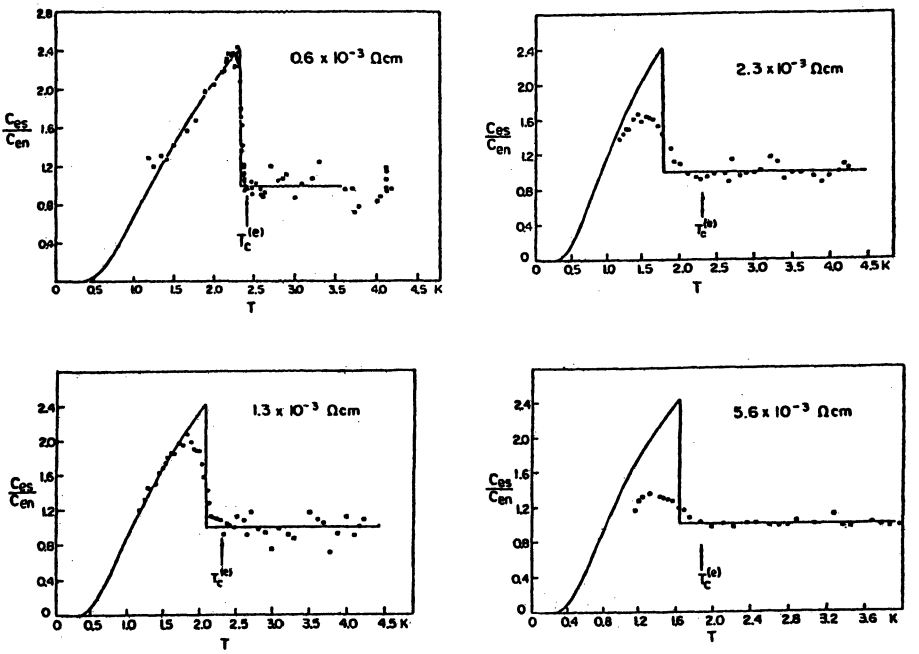

Fig. 2.5. Heat capacity transition temperatures $T_c^{(e)}$ of Al–Al_2O_3 films at various levels of the normal state resistivity. As the resistivity is increased from about $0.5x10^{-3}\Omega$cm to $5x10^{-3}\Omega$ cm, by increasing the oxide concentration, the transition goes from BCS like to very smeared. The grain diameter in these samples is about 40 $\AA$, below the size at which an isolated grain can show a transition, according to Ref. [18] (δ/Δ is substantially larger than one). Notice the increased transition temperature compared to that of bulk Al (1.2K), even in samples having a smeared transition. In this case, this increase cannot be attributed to the isolated grain, since for that size they are basically not superconducting

that superconductivity persists certainly down to a size where $\delta \sim \Delta$. They also confirm that the increase in T_c quoted before is a property of single grains. It is not due to intergrain coupling.

2.6 Weakly Coupled Grains: Granular Insulators and Super–Insulators

We now consider the case of superconducting grains having some degree of coupling between them. By this we mean that the granular compound is macroscopically very close to being an insulator in the normal state. This is different from the case considered in a later section where we discuss critical currents and critical fields. There it is implicitly assumed that the compound

is a metal in its normal state. Here we wish to review what is known for the more delicate situation where the coupling is not so weak that it can be ignored, but sufficiently weak that the compound is not really a metal. Some remarks concerning the normal state properties of such compounds have already been made in Section 2.3.

For the case of isolated grains, two energy scales had to be considered: the level spacing δ and the superconducting gap Δ. Here additional scales come into play: the normal state tunnelling coupling energy Vt, the charging energy E_c and the intergrain Josephson coupling E_J. The degree of disorder in the compound has also some importance This includes the widths of the grain size and of the Josephson coupling distributions.

We can distinguish between two cases, depending on whether $E_J \geq k_B T$, or $E_J \ll k_B T$. It is clear that only in the first case can macroscopic coherence be achieved.

2.6.1 Small Grain Case: Percolative Behavior

An interesting case where disorder effects dominate is when the individual grains are smaller than the critical size defined above. Grains can then become superconducting *only* if they couple together. Assuming that the grains are all of the same size, but that the coupling between them (defined by the normal state intergrain resistance R_N) has a substantial distribution width, one can then show that a percolating structure appears below some critical temperature [21]. As the temperature is lowered the condition $E_J > k_B T$ is met by an increasing fraction of junctions. When this fraction is sufficient an infinite cluster is formed. Under the simplifying assumption that only this infinite cluster contributes to the heat capacity the heat capacity transition can then be calculated. The only free parameter is the width of the R_N's distribution. As shown Fig. 2.6, the result of the calculation is in good agreement with experiments [22].

2.6.2 Large Grain Case: Superconducting Insulators

When the grains are larger than the critical size a relevant question to ask is whether the compound can be insulating in its normal state and still undergo a macroscopic transition to a coherent superconducting state. The tunnelling coupling energy V_t represents an effective band width for the granular compound. It is sufficient to make it a metal if it is larger than the electrostatic charging energy E_c and vice versa. Calling t the intergrain tunneling matrix element, the coupling energy is given by

$$V_t = \frac{t^2}{\delta} \quad , \tag{2.18}$$

where we have ignored numerical factors of order unity (such as the number of nearest neighbors) in view of the crudeness of our model for the

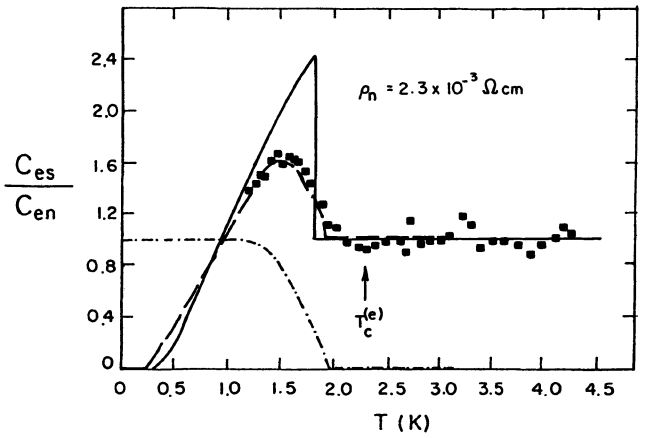

Fig. 2.6. Fit to a percolation model of the heat capacity transition for one of the samples shown in Fig. 2.5

metal/insulator transition. The compound is an insulator if

$$E_c > \frac{t^2}{\delta} \quad . \tag{2.19}$$

Hence, the question we are asking is whether the situation described by the conditions

$$E_J > E_c > \frac{t^2}{\delta} \tag{2.20}$$

can be realized. Note, this must be fulfilled if we want to have a superconducting insulator.

The intergrain conductance can be calculated from the Thouless expression

$$g = g_c \frac{V_t}{\delta} \quad , \tag{2.21}$$

where g_c is the universal conductance $\left(\frac{e^2}{\hbar}\right)$. Using this relation we can rewrite the Josephson expression

$$E_J = \frac{\hbar}{e} \frac{\Delta}{eR_N} \tag{2.22}$$

as

$$E_J = \Delta \frac{t^2}{\delta^2} \quad . \tag{2.23}$$

So we can have a superconducting insulator only if the gap is larger than the level spacing. This is our old large grain condition and not a very surprising

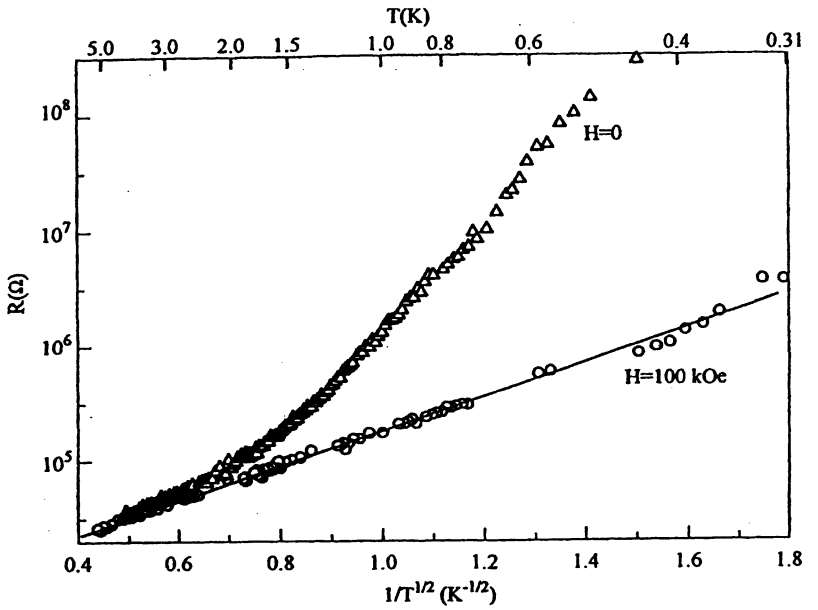

Fig. 2.7. Supra–insulator transition in an Al–Ge sample in the granular–insulating phase. At low temperatures, the resistance is higher when the grains are superconducting than when they are returned to the normal state by the application of a strong magnetic field [33]

result. The other condition that the Josephson coupling energy should be larger than the Coulomb energy is more interesting. For an isolated grain the Coulomb energy is $(\frac{e^2}{\epsilon a})$ where a is the grain's radius. For a 10 nm grain this energy is of the order of 0.1 eV. This is several orders of magnitude larger than the Josephson coupling energy. Hence, the existence of a superconducting insulator at grain sizes typical of granular materials seems to be ruled out.

Yet, early experiments by Shapira and Deutscher [23] had identified a narrow region near the M/I transition in Al–Ge films, where the superconducting insulating regime appeared to exist. The grain size was indeed of the order of 10 nm. The authors concluded that the Coulomb energy must in fact have been strongly reduced by a large effective dielectric constant ϵ_{eff} near the Metal/Insulator transition. These early experiments have been recently extended down to lower temperatures [24]. The claim for the existence of a superconductor–insulator regime has been fully confirmed (Fig. 2.7). It is therefore established that the effective dielectric constant in the granular compound can be increased by several orders of magnitude larger (at least three) near the M/I transition.

It is well known that the M/I transition is one of the most difficult problems in solid state physics. Localization (a la Anderson), Coulomb interac-

tions and disorder (percolation) may all play a role. A lingering question is whether this can be a (presumably second order) phase transition, and if such, what is the order parameter? So far the theory has not been able to give a full answer to this question. It could be that the true importance of the existence of the superconducting insulator near the M/I transition is that it implies a divergence of the dielectric constant. This would mean a second order phase transition. So far the experiments on Al/Ge granular compounds are the only ones that have clearly demonstrated this divergence. It could be that this is so, since the dielectric thickness in this compound is particularly uniform as discussed in Section 2.2. More work needs to be done to establish firmly under what conditions the M/I transition can indeed be a phase transition.

2.6.3 Pseudogap Regime in the Superconducting Insulator

Nozières and Pistolesi [25] have considered a model where a material has a gap E_g in the DOS in the normal state and at the same time can develop a superconducting order parameter below a temperature T_c. This model does not refer to the granular case in particular, although this could be one of its realizations. The parameters of the model are E_g and the critical temperature T_{c0} that the material would have in the absence of the normal state gap. It assumes that the interaction parameter V of the BCS theory is not modified by E_g. The critical temperature, the quasi–particle energy gap and the order parameter are calculated as a function of $\left(\frac{E_g}{\Delta_{00}}\right)$, where Δ_{00} is the BCS gap of the pristine material. The position of the Fermi energy is also taken into account.

The main results are that as $\left(\frac{E_g}{\Delta_{00}}\right)$ is increased the critical temperature goes down, the single particle excitation energy goes up and the order parameter goes down up to a value where superconductivity collapses all together. One of the signatures of the pseudogap regime is that the strong coupling ratio (energy gap/critical temperature) becomes very large near the point of collapse of superconductivity. As is well known, this behavior has been one of the main recent findings in the high T_c cuprates [26]. One of the interpretations proposed for the large gap is that it represents the energy required to break up preformed pairs above T_c. However, it was shown that in the pseudogap regime the coherence energy scale follows the same doping dependence as T_c, rather than that of the pseudogap. The pseudogap in the cuprates may thus just be a manifestation of the fact that in the underdoped regime the cuprates are basically superconducting insulators. Transport measurements have indeed shown that their normal state conductivity increases at low temperatures [27].

Tunneling experiments on Al/Ge films in the superconducting insulator regime have given some evidence for a large strong coupling ratio [28].

2.6.4 The Superinsulator Case

Out of the narrow concentration range where the superconducting insulator regime is observed one expects to enter into a regime where the grains are still superconducting (provided they are large enough), but the Josephson coupling is too weak to allow a macroscopically coherent state:

$$E_c > E_J > \frac{t^2}{\delta} \quad . \tag{2.24}$$

Here, we have assumed that the decrease of the dielectric constant away from the M/I transition is the main reason for the inversion of the order of E_c and E_J. The main point is that E_c becomes quickly larger by orders of magnitude upon lowering the temperature. Hence, an increase of E_J will not help to recover the superconducting state. There is, however, still another interesting regime, where E_c is not much larger than the value of the superconducting gap in the grains:

$$U \geq \Delta > E_J > \frac{t^2}{\delta} \quad . \tag{2.25}$$

In this regime, the intergrain resistance will be substantially increased by the known phenomenon of Giaever tunnelling between two superconductors which itself requires an energy of 2Δ. As the temperature is lowered below the critical temperature of the grains, the behavior will go from insulating (normal state exponential localization) to superinsulating.

Indeed, a change of slope in the lnR versus $T^{-\frac{1}{2}}$ representation has been clearly observed just outside the range of the superconducting insulator regime [23] at temperatures of the order of the critical temperature of the grains in Al/Ge films as shown Fig. 2.8. This experiment is another proof that superconductivity persists in Josephson–uncoupled grains having a size of about 10 nm.

2.7 Well Coupled Grains

In this section we consider the case where electrostatic charging can be completely neglected. In other words the granular compound is a metal in its normal state. The key parameters are then the grain size and the inter–grain coupling [28]. In an homogeneous superconductor the critical current density j_c and the upper critical field H_{c2} are determined by the coherence length $\xi(T)$. The Ginzburg Landau (GL) theory predicts that:

$$j_c = \frac{4en_s}{3\sqrt{3}} \frac{\hbar}{m\xi(T)} \tag{2.26}$$

and

$$H_{c2} = \frac{\Phi_0}{2\pi\xi^2(T)} \quad . \tag{2.27}$$

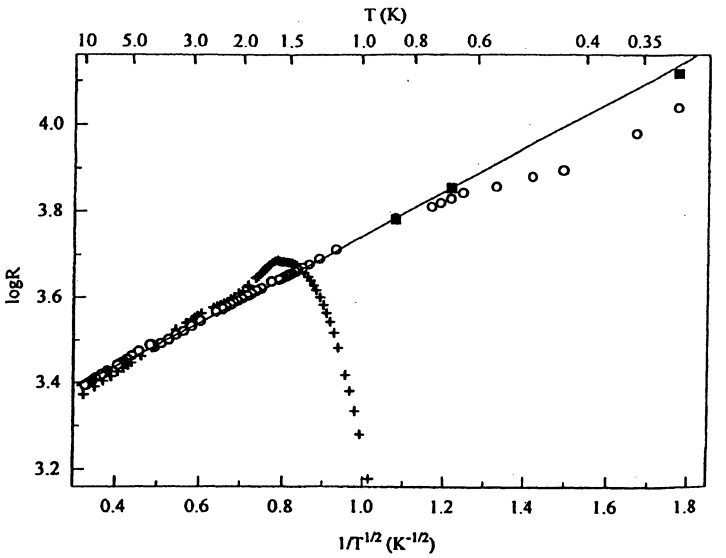

Fig. 2.8. An Al–Ge sample still in the granular insulating phase having a lower resistance than that shown in Fig. 2.7 has a transition to a superconducting state near 1K

In what follows we consider whether these relations are valid in a granular metal, taking care of course that the value of the coherence length correctly reflects the structure of the compound – granular or random.

2.7.1 Granular Case

The above relations remain valid for a granular superconductor as long as the grain size d is smaller than the coherence length. An expression for the coherence length valid for a granular superconductor has been given by Deutscher, Imry and Gunther (DIG) [29] on the basis of the free energy expression:

$$F_s = F_n + A\sum_i \mid \Delta_i \mid^2 + \frac{B}{2}\sum_i \mid \Delta_i \mid^4 + \frac{1}{2}C\sum_{i,j} \mid \Delta_i - \Delta_j \mid^2 \quad , \quad (2.28)$$

where the sum in the last term of the rhs runs over neighboring grains. This expression assumes that the grain size is smaller than the value of the coherence length of the parent material so that inside each grain the order parameter Δ is constant. If there are spatial variations of the order parameter due to thermodynamical fluctuations, it will then vary discontinuously from grain to grain. This is expressed in the last term of the rhs. This term replaces the usual gradient term of the GL theory. The value of the coefficient C is determined by the intergrain dielectric barrier. It is simply related to the

strength E_c of the Josephson intergrain coupling:

$$E_c = C \mid \Delta \mid^2 \quad . \tag{2.29}$$

The coherence length is given by

$$\xi(T) = \sqrt{\frac{C}{d \mid A \mid}} \quad . \tag{2.30}$$

This expression is valid as long as $\xi(T) > d$. When this condition is fulfilled the granular superconductor is effectively three dimensional. The coefficients A and B are equal to the GL coefficients of the parent material. The explicit value of C can be calculated from the Josephson expression for the coupling energy near T_c:

$$E_J = \frac{\pi\hbar \mid \Delta \mid^2}{8e^2 R k_B T_c} \quad , \tag{2.31}$$

where R is the intergrain normal state resistance.

The expression for $\xi(T)$ allows to check whether it is indeed larger than d, which is the condition for its validity. Apart from coefficients of order unity we can write

$$\frac{\xi(T)^2}{d^2} = \left(\frac{\hbar}{Re^2}\right)\left(\frac{\delta}{k_B T_c}\right)\frac{T_c}{T_c - T} > 1 \quad , \tag{2.32}$$

where

$$\delta = \frac{E_F}{N} \tag{2.33}$$

is the distance between the electronic levels in the grain and N is the number of electrons per grain.

The condition $\xi(T) > d$ is always valid near T_c. Far below T_c this is the case if the intergrain resistance is smaller than the quantum resistance $\left(\frac{\hbar}{e^2}\right)$, as long as the level splitting is of the order of $k_B T_c$ (or the gap). We have discussed in earlier sections the full importance of this condition..

In the three dimensional regime, when the critical current density is reached, the phase changes by π over many grains. In the presence of vortices their core extends over many grains. The granularity of the material has the effect to turn the superconductor into a strong type II one.The grain size itself is not directly reflected in the superconducting properties. This was the case treated by the group of Abeles [4].

In the regime $\xi(T) < d$ the coherence length evidently looses its meaning, since inside each grain the order parameter is constant. The granular superconductor then becomes *zero dimensional [6]*. If the individual grains remain superconducting in the 0D regime, which will happen under conditions that

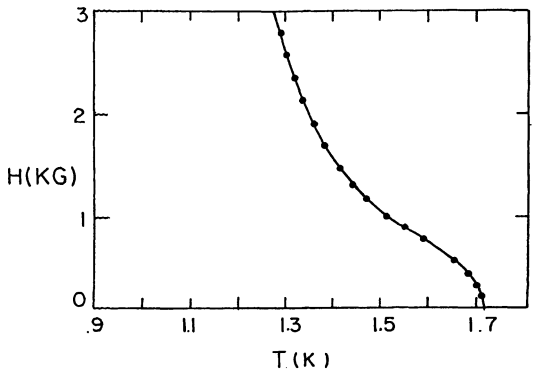

Fig. 2.9. Upturn to the critical field of an Al–Ge sample in the granular metallic regime

we have discussed above, the critical current will be determined by the critical current of the individual junctions:

$$j_c = I_c d^{-2} \quad , \tag{2.34}$$

where

$$I_c = \frac{2e}{\hbar} E_c \quad . \tag{2.35}$$

The critical field becomes equal to the critical field of the individual grains:

$$H_c(grain) = \frac{\Phi_0}{d^2}(1 - \frac{T}{T_c})^{\frac{1}{2}} \quad . \tag{2.36}$$

The transition to zero–dimensionality that occurs when $\xi(T) \leq d$ is directly reflected in the temperature dependence of the critical field. While it is linear in the 3 dimensional high temperature regime where $\xi(T) > d$, it becomes parabolic in the zero dimensional regime. The transition is thus marked by an upturn of the critical field [30], as seen Fig. 2.9.

2.7.2 Random Case

Here again the conventional expressions for the critical current density and of the upper critical field are valid as long as the coherence length is larger than the length scale that characterizes the inhomogeneity of the system. However now the inhomogeneity scale is not the grain size, but rather the *percolation correlation length* ξ_p:

$$\xi_p = \alpha d(p - p_c)^{-\nu} \quad , \tag{2.37}$$

where α is a numerical coefficient of order unity and ν is the critical index that governs the divergence of ξ_p near the threshold p_c. We are interested here

in the case where $p > p_c$. There is then an infinite cluster, which can be visualized as composed of "fat" blobs connected by thin weak links. The blobs consist of many interconnected threads, while the weak links are basically single chains of grains. More exactly, it has been shown that the number of parallel channels in a weak link does not diverge near p_c. The physical meaning of ξ_p is that it is the distance that separates nearest weak links. At scales larger than ξ_p the infinite cluster can be considered as being homogeneous. At scales smaller than ξ_p, the actual structure of the blobs which is fractal will determine the properties of the system.

The superconducting state probes the properties of the infinite cluster on the scale of the coherence length. Again, we have to consider two cases.

i) homogeneous limit $\xi(T) >> \xi_p$:

In this limit the percolating superconductor behaves as a homogeneous one. The critical current density is determined by the number of independent superconducting channels per unit cross section:

$$j_c \propto \xi_p^{-2} \propto (p - p_c)^{2\nu} \quad . \tag{2.38}$$

This dependence was observed experimentally for a series of Pb–Ge mixtures and offers directly a determination of the critical index of the correlation length. The coherence length and upper critical field are determined by the macroscopic coefficient of diffusion D which can be calculated from the Einstein relation for the macroscopic conductivity:

$$\sigma = 2e^2 N(0) D \quad . \tag{2.39}$$

Here the density of states $N(0)$ is given by the density of the infinite cluster which goes to zero at p_c with exponent β. Hence,

$$D \propto (p - p_c)^{t-\beta} \quad . \tag{2.40}$$

We can use the dirty limit expression to calculate the coherence length:

$$\xi^2(T) = \frac{\pi}{8} \frac{\hbar D}{k_B T} \frac{T_c}{T_c - T} \quad . \tag{2.41}$$

Due to the divergence of $\xi(T)$ at T_c the homogeneous limit will always apply close to the transition temperature. The upper critical field will then vary linearly with temperature and is roughly proportional to the normal state resistivity (exponent t is substantially larger than the exponent β (in 3D, $t = 2$ and $\beta = 0.4$)).

ii) inhomogeneous limit $\xi(T) < \xi_p$:

When $\xi(T)$ is smaller than the percolation correlation length, we are not allowed anymore to use the above expressions. This will happen when p is close to p_c (D then goes to zero) and if we are not too close to T_c. The new and interesting property that then arises is that the coefficient of diffusion is

now scale dependent. It is sensitive to the internal structure of the blobs as is the value of the upper critical field.

At short length scales diffusion is not governed by the usual diffusion law

$$x^2 = Dt \quad , \tag{2.42}$$

but rather by an anomalous diffusion law, which can be represented by an analogous equation, but where the diffusion coefficient is itself time dependent:

$$x^2 = D(t)t \quad . \tag{2.43}$$

At long time scales D goes back to its macroscopic, time independent value. At short length scales, namely at scales shorter than the percolation correlation length, it varies as a power law of t, in a way that is independent of the concentration. The idea here is that at these short length scales the diffusion process (or the conductance) is insensitive to the macroscopic structure of the cluster (whether it is finite or infinite).Now, if we apply a magnetic field we effectively probe the cluster on a scale

$$\xi(H) = \left(\frac{\Phi_0}{2\pi H}\right)^{\frac{1}{2}} \quad . \tag{2.44}$$

If $\xi(H) > \xi_p$, we are back to the usual case and the critical field is concentration dependent. It varies with the macroscopic conductivity in a way that is similar to that of a regular type II superconductor (there are some minor differences, due to the concentration dependence of the density of the infinite cluster). But if $\xi(H) < \xi_p$, the cluster is probed on a scale that is concentration independent. Then the upper critical field, which is here the field that will destroy the "blobs", is independent from the concentration, hence from the macroscopic conductivity.This saturation of the upper critical field in the vicinity of the percolation threshold, where the macroscopic resistivity diverges, has indeed been observed [31].

2.8 Critical Temperature of Granular Superconductors

It is a remarkable property of granular superconductors such as Al-Al_2O_3 and Al–Ge that their critical temperature increases as the grain size is decreased, reaching its maximum value near the metal to insulator transition. In this section we review the available data and make some remarks concerning the possible role of weak screening in the critical temperature enhancement.

2.8.1 Grain Size Dependence of the Critical Temperature

Enhancement of the critical temperature is observed in granular structures only. Random percolating mixtures of the same constituents, for instance Al

and Ge, do not show any critical temperature enhancement. Critical temperatures increase as the dielectric volume fraction is increased up to near the metal to insulator transition. Critical temperatures are higher when the films are deposited unto substrates held at low temperatures. For instance, the maximum critical temperature observed in Al-Al_2O_3 is about 2K when deposited at room temperature, and more than 3K when deposited at liquid nitrogen temperature (1,30).

As we have seen above the average grain size decreases when the dielectric volume fraction increases. The grain size is also decreased the deposition temperature is decreased. It has been shown that for a given eutectic system, T_c is in fact only a function of the grain size, itself determined by the dielectric volume fraction and the deposition temperature. More precisely, when plotted as a function of the surface to volume ratio σ, the critical temperature values of Al-Al_2O_3 films fall on a single curve for samples deposited at room temperature or liquid nitrogen temperature. The results are consistent with a simple dependence of the BCS interaction parameter NV on σ :

$$NV = (NV)_0(1 + 0.3\sigma) \quad . \tag{2.45}$$

Here we assume that the Debye temperature remains unchanged and that the interaction is enhanced over a surface layer having a thickness of about 3Å [27].

2.8.2 Weak Screening Model

Many models, well reviewed by Abeles [4], have been proposed to explain the T_c enhancement. Amongst them, the idea that T_c increase is induced by phonon softening at the surface received considerable attention. Yet, detailed tunnelling measurements performed on granular Al failed to give quantitative evidence for this model [32]. In addition, it is not clear how it could explain why there there is no enhancement at all in the case of the percolating structure. Here, we consider a different approach, based on our description of the metal to insulator transition in the granular structure.

When the Coulomb blockade becomes effective, reducing the number of electrons that can freely flow simultaneously from grain to grain, electrons at the grains surface become weakly screened while the screening in the interior of the grain remains strong. It is interesting to consider the effect of this weak surface screening on the interaction parameter.

Weak screening evidently enhances all Coulomb interactions. For specificity let us consider the Jellium model of these interactions in a metal:

$$V = \varepsilon \frac{4\pi e^2}{k_s^2 + q^2} + \frac{4\pi e^2}{k_s^2 + q^2} \frac{\omega_q^2}{\omega^2 - \omega_q^2} \quad , \tag{2.46}$$

where k_s is the inverse screening length, q the momentum transfer and ω_q the frequency of a phonon of momentum q. The first term of the r.h.s. is the

Coulomb repulsion, reduced by a factor $\varepsilon < 1$, which takes into account its renormalisation due to retardation effects. In the limit of zero frequency the net interaction is:

$$V = -\frac{4\pi e^2}{k_s^2 + q^2}(1 - \epsilon) \quad . \tag{2.47}$$

This evidently gets enhanced by a reduced screening parameter. But this enhanced interaction does not lead to an enhanced T_c, on the contrary. Multiplying the interaction potential by the normal state density of states, $N = \frac{k_s^2}{4\pi e^2}$,we obtain for a typical phonon wave vector q_0 in the zero frequency limit

$$NV = \frac{k_s^2}{k_s^2 + q_0^2}(1 - \epsilon) \quad . \tag{2.48}$$

Thus, the BCS parameter is in fact an *increasing* function of the screening parameter, as is well known. Although obtained here in the framework of a very crude model, we believe the conclusion to be quite general. Namely, that as a function of the screening parameter, the net interaction potential and the BCS parameter vary in opposite directions. This indicates a possible general way to obtain higher critical temperatures: one reduces screening *under the condition that at the same time the density of states is kept unchanged.* We can in principle do this, if reduced screening is obtained primarily through a reduced dimensionality, rather than through a reduced carrier density. In fact, in the 2D and 1D case, it may even be possible to have an *enhanced* density of states, if the Fermi level is properly located (A15, van Hove).

It would of course be risky to apply this very simple argument in a quantitative way to such complex materials as the cuprates or the organic superconductors. But it may not be unreasonable to apply this to the granular superconductors.

We consider a grain of a weak coupling superconductor (in the BCS sense) that is large enough so that we can neglect special cluster size effects on its electronic structure. We assume that the grain is located in an insulating matrix. Then reduced screening takes place at the atomic surface layer of the grain, while the density of states remains unchanged to a first approximation. We write

$$k_s^{-1} = k_{so}^{-1}(1 + \alpha\sigma) \quad , \tag{2.49}$$

where k_{so} is the screening parameter of the bulk material and α is a numerical coefficient of order unity whose value depends on the dielectric properties of the insulating matrix.The surface to volume ratio σ is the surface of the grain divided by its volume, multiplied by a length of the order of the screening length, say roughly 1Å. Assuming $\sigma \ll 1$,we can calculate the new value of the BCS parameter:

$$NV = NV_0(1 + \frac{2k_{so}^2}{k_{so}^2 + q_o^2}\sigma) \quad , \tag{2.50}$$

where $V_o$is the net interaction potential in the bulk material.

Let us take as example Al. From the BCS expression for T_c we get $NV_0 = 0.18$. The renormalized Coulomb repulsion is $\mu^* = 0.1$ From this we obtain $\left(\frac{k_{s0}^2}{k_{s0}^2+q_0^2}\right) = 0.3$,. Thus,

$$NV = NV_0(1 + 0.6\sigma) \quad . \tag{2.51}$$

In spite of the crudeness of our calculation, this result is in remarkable agreement with the data (7,30). No particular importance should of course be given to the value of the coefficient of σ in view of the approximations made. The weak screening model can also explain why no critical temperature enhancement is seen in percolating random structures. Even very near the percolation threshold the majority of metal grains that constitute the infinite cluster are not at the surface of this cluster, but are well connected within "blobs". Hence, the effective surface to volume ratio is too weak to have any effect on T_c.

Note, this naive model is unlikely to be the last word on the intriguing T_c enhancement in granular materials. Electronic effects and other may play an interesting role.

Acknowledgements

This chapter summarizes many collaborations, some of them over long periods of time. Ben Abeles and Richard Cohen, then at RCA Laboratories, were the ones who attracted my attention to the challenges posed by the understanding of granular superconductivity. A long collaboration followed with the neighboring Rutgers group, particularly with Peter Lindenfeld and the late William McLean, and their students and post docs, amongst them Tom Worthington and Tom Filler. At Tel Aviv University, Moshe Dayan, David Bergman, Henri Fenichel, Alexander Gerber, Meir Gershenson, Ilan Grave, Enrique Grunbaum, Y. Imry, Zvi Ovadyahu, Michael Rappaport, Yoash Shapira, O.Entin Wohlman all made important contributions. Inspiring discussions with the late Shlomo Alexander took place on a permanent basis. I take the opportunity to express my sincere gratitude to all of them. It is known that our work on granular Aluminium was one of the triggers that prompted Alex Muller to look for high temperature superconductivity in oxides. This may well have been the most important outcome of this work.

This work was supported by the Oren Family Chair for Experimental Solid State Physics.

References

1. B. Abeles, R.W. Cohen and G.W. Cullen, Phys. Rev. Lett. **17** ,632 (1966).
2. Y. Shapira and G. Deutscher, Thin Solid Films **87**, 29(1982).
3. G. Deutscher, A. Kapitulnik and M. Rappaport, in *Percolation, Structures and Processes*, Eds. G. Deutscher, R. Zallen and J. Adler, Annals of the Israel Physical Society **5**, 207 (1983).

4. B. Abeles, Adv. Phys. **24**, 407 (1975); Applied Solid State Science **6**,1 (1976).
5. A. Kapitulnik, M. Rappaport and G. Deutscher, J. Phys. Lett. **42**, L-541 (1981).
6. G. Deutscher, H. Fenichel, M. Gershenson, E. Grunbaum and Z. Ovadyahu, J. of Low Temp. Phys. **10**, 231 (1973).
7. U. Dai *et al.*, Phys. Rev. B **36**, 790 (1987).
8. D.J. Bergman *et al.*, Phys. Rev. Lett. **50**, 1512 (1983).
9. G. Deutscher, M. Rappaport and Z. Ovadyahu, Solid State Commun. **28**, 247 (1978).
10. B. Bandyopadhyay *et al.*, Phys. Rev. B **26**, 3476 (1982).
11. A. Fulton and G.J. Dolan, Phys.Rev.Lett. **59**, 109 (1987).
12. H. Devoret *et al.*, Phys. Rev. Lett. **61**, 1824 (1990).
13. G. Deutscher and M. Cyrot, unpublished.
14. N.F. Mott and Davis, in *Electronic processes in non cristalline materials*, Clarendon Press, Oxford (1971).
15. B. Abeles, Phys. Rev. B **15**, 2828 (1977).
16. N.F. Mott, Phil. Mag. **26**, 1015 (1972).
17. J. Ioffe and A. Regel, Prog. in Semiconductors **4**, 237 (1960).
18. G. Falci, A. Fubini and A. Mastellone, to be published
19. Y. Shapira, PhD. Thesis, Tel Aviv University (1986).
20. D.C. Ralph, C.T. Black and M. Tinkham, Phys. Rev. Lett. **74**, 3241 (1995).
21. G. Deutscher, O. Entin-Wohlman, S. Fishman and Y. Shapira, Phys. Rev. B **21**, 5041 (1980).
22. R.L. Filler *et al.*, Phys. Rev. B **21**, 5031 (1980).
23. Y. Shapira and G. Deutscher, Phys. Rev. B **27**, 4463 (1983).
24. P. Nozieres and F. Pistolesi, European Journal of Physics B **10**, 649 (1999).
25. G. Deutscher, Nature **397**, 410 (1999).
26. L. Nechustan, MSc. Thesis, Tel Aviv University (2002).
27. G. Deutscher, M. Gershenson, E. Grunbaum and Y. Imry, J. Vac. Sci. Technol. **10**, 674 (1973).
28. G. Deutscher, Phys. Lett. **35A**, 28 (1971).
29. G. Deutscher, Y. Imry and L. Gunther, Phys. Rev. B **10**, 4042 (1974).
30. G. Deutscher, O. Entin–Wohlman and Y. Shapira, Phys. Rev. B **22**, 4264 (1980).
31. A. Gerber and G. Deutscher, Physica B **126**, 477 (1984).
32. M. Dayan and G. Deutscher, Proceedings of Low Temperature Physics LT14, Vol. 2, 241 (1975), North Holland Publishers.
33. A. Gerber *et al.*, Phys. Rev. Lett. **78**, 4277 (1997).

3 Proximity–Coupled Systems: Quasiclassical Theory of Superconductivity

Venkat Chandrasekhar
Dept. of Physics and Astronomy, Northwestern University, Evanston, USA

3.1 **Introduction** 55
3.2 **Transport Equations in the Diffusive Approximation** 56
3.3 **The Keldysh Green's Functions** 61
3.4 **The Quasiclassical Approximation** 70
3.5 **Non–Equilibrium Green's Functions for Superconducting Systems** 76
3.6 **Quasiclassical Superconducting Green's Functions** 80
3.7 **The Dirty Limit: The Usadel Equation** 85
3.8 **Parametrization of the Quasiclassical Green's Function** 94
3.9 **Applications of the Quasiclassical Equations to Proximity–Coupled Systems** 97
3.9.1 Proximity–Coupled Wire 97
3.9.2 Superconductor–Metal Bilayer 104
3.9.3 The SNS Junction and Andreev Interferometers 106
3.10 **Summary** 108
References 108

3.1 Introduction

Although the physics of normal metals (N) in close proximity to superconductors (S) has been studied extensively for more than thirty years, it is only in the past decade that experiments have been able to probe directly the region close to the NS interface at temperatures far below the transition temperature T_c of the superconductor. These experiments have been made possible by the availability of microlithography techniques that enable the fabrication of heterostructure devices with submicron scale features. This size scale is comparable to the relevant physical length scales of the problem, and consequently, a number of new effects have been observed. A variety of systems have been studied, the variation primarily being in the type of normal metal coupled to the superconductor. Canonical normal metals such as copper and gold, semiconductors, insulators, and ferromagnets have been employed. Although a variety of theoretical techniques have been used to describe proximity–coupled systems, the quasiclassical theory of superconductivity [1–12] has proved to be a remarkably powerful tool in understanding the microscopic basis for the remarkable effects observed in these systems.

K. H. Bennemann et al. (eds.), *The Physics of Superconductors*
© Springer-Verlag Berlin Heidelberg 2004

A number of excellent recent articles [13–19] have explored the application of the quasiclassical theory of superconductivity to proximity coupled systems. In this review, a self–contained development of the quasiclassical theory is presented, starting from non–equilibrium Keldysh Green's functions for normal metal systems. If the normal metal is clean, quasiparticles in the normal metal travel ballistically over long length scales. In the samples studied in the majority of recent experiments, however, the quasiparticles are scattered elastically within a short distance, so that the quasiparticle motion is diffusive. Here, we shall concentrate on this diffusive case, where the elastic scattering length ℓ is the shortest relevant length scale in the problem. We shall also restrict ourselves to the case where the superconductor is of the canonical s–wave type, avoiding complications with non–spatially symmetric order parameters within the superconductor.

3.2 Transport Equations in the Diffusive Approximation

As an illustration of some of the issues that arise in dealing with non–equilibrium transport in mesoscopic diffusive systems, we consider first the classical Boltzmann equation in the diffusion approximation. Consider a one–dimensional diffusive normal metal wire of length L. We assume that all dimensions of the wire are larger than ℓ, the elastic mean free path of the conduction electrons. $f(E,x)$, the distribution function of electrons at energy E and at a point x along the wire, obeys the diffusion equation

$$D\frac{d^2f(E,x)}{dx^2} + C(f) = 0. \tag{3.1}$$

Here, $D = (1/3)v_F\ell$ is the three–dimensional electron diffusion constant, with v_F being the Fermi velocity of the electrons. $C(f)$ is the collision integral, which takes into account inelastic scattering of the electrons, and itself depends on the distribution function f. If we consider a mesoscopic wire whose length L is much shorter than any inelastic scattering length L_{in}, this term can be set to zero.

This diffusion equation has a simple solution in some specific geometries. Consider the case of a wire of length L sandwiched between two normal 'reservoirs,' which we shall call the left (at $x = 0$) and right (at $x = L$) reservoirs. The reservoirs are defined as having an equilibrium distribution function $f_L(E)$ and $f_R(E)$ respectively. Then the solution of the diffusion equation, Eq. (3.1), under the condition $L \ll L_{in}$ (so that $C(f) = 0$), and subject to the boundary conditions that $f(E,x) = f_L(E)$ at the left reservoir, and $f(E,x) = f_R(E)$ at the right reservoir, is given by [20]

$$f(E,x) = [f_R(E) - f_L(E)]\,\frac{x}{L} + f_L(E) \quad . \tag{3.2}$$

The electrical current I through the wire in the diffusion approximation is given by

$$I = -eAD \int N(E) \frac{\partial f}{\partial x} dE \quad , \tag{3.3}$$

where A is the cross–sectional area of the wire. With $f(E,x)$ given by Eq. (3.2), this can be written

$$I = -\frac{eAD}{L} \int N(E)[f_R(E) - f_L(E)]dE \quad . \tag{3.4}$$

In order to obtain a finite current, we must apply a voltage across the wire. Let us apply a voltage V to the left reservoir, keeping the right reservoir at ground ($V = 0$). This has the effect of shifting the energies of the electrons in the left reservoir by $-eV$, so that the electron distribution function there is given by $f_L(E) = f_0(E - eV)$, where $f_0(E)$ is the usual equilibrium Fermi distribution function

$$f_0(E) = \frac{1}{e^{E/k_BT} + 1} \tag{3.5}$$

and the energy E is measured from the Fermi energy E_F. Figure 3.1 shows the distribution function $f(E,x)$ in the wire. It has a step–function form, which varies linearly along the length of the wire. Evidence for such a non–equilibrium distribution has recently been seen experimentally in a series of beautiful experiments by the Saclay group. [21]

In the limit of small voltages V, the difference of distribution functions in Eq. (3.4) can be expanded as

$$\begin{aligned} f_R(E) - f_L(E) = f_0(E) - f_0(E - eV) &\approx f_0(E) - \left[f_0(E) + eV \left(-\frac{\partial f_0}{\partial E} \right) \right] \\ &= -eV \left(-\frac{\partial f_0}{\partial E} \right) \end{aligned} \tag{3.6}$$

so that

$$I = \frac{e^2AD}{L} V \int N(E) \left(-\frac{\partial f_0}{\partial E} \right) dE \approx \frac{N(0)e^2AD}{L} V \quad , \tag{3.7}$$

where $N(0)$ is the density of states at the Fermi energy. In performing the integral, we have assumed that we are at low enough temperatures so that the derivative of the Fermi function $(-\partial f_0/\partial E)$ can be approximated by $\delta(E)$. The electrical conductance is then given in the Nernst–Einstein form $G = N(0)e^2D(A/L) = \sigma_0(A/L)$.

The thermal current through the wire is given by an expression similar to Eq. (3.4):

$$I^T = \frac{AD}{L} \int EN(E)[f_R(E) - f_L(E)]dE \quad . \tag{3.8}$$

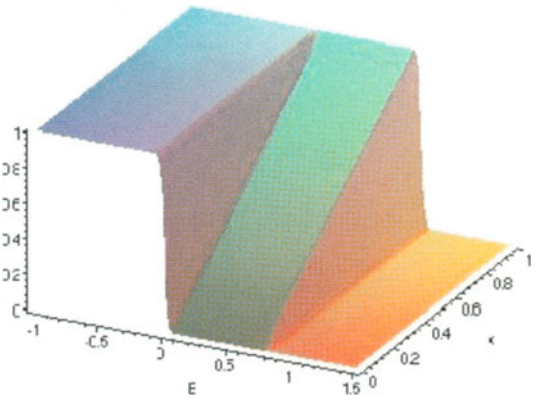

Fig. 3.1. Nonequilibrium electron distribution function f in a normal wire with a potential V applied across it as a function of energy E and position x. The position x is normalized to the length L of the wire

The critical difference between the expression for the thermal current and the expression for the electrical current is the presence of an additional factor of E in the integrand in Eq. (3.8), which has important consequences in the calculation of the thermal properties.

To obtain expressions for the thermal coefficients, let the temperature of the left reservoir be T and its voltage V, and let the temperature of the right reservoir $T+\Delta T$ and its corresponding voltage $V=0$. The distribution function in the left electrode is then $f_L(E) = f_0(E-eV,T)$, and the distribution function in the right electrode is $f_R(E) = f_0(E,T+\Delta T)$. In the limit of small $\Delta T, V$, the difference in the distribution functions in Eq. (3.4) can be expanded as

$$\begin{aligned} f_R(E) - f_L(E) &= \left[f_0(E,T) + \frac{E}{T}\Delta T\left(-\frac{\partial f_0}{\partial E}\right)\right] - \left[f_0(E,T) + eV\left(-\frac{\partial f_0}{\partial E}\right)\right] \\ &= \left[\frac{E}{T}\Delta T - eV\right]\left(-\frac{\partial f_0}{\partial E}\right) \quad . \end{aligned} \tag{3.9}$$

Putting this expression into the equations for the electrical and thermal currents, Eq. (3.4) and Eq. (3.8), one obtains the two transport equations

$$I = \frac{e^2AD}{L}\left[\int N(E)\left(-\frac{\partial f_0}{\partial E}\right)dE\right]V - \frac{eAD}{TL}\left[\int EN(E)\left(-\frac{\partial f_0}{\partial E}\right)dE\right]\Delta T, \tag{3.10a}$$

$$I^T = -\frac{eAD}{L}\left[\int EN(E)\left(-\frac{\partial f_0}{\partial E}\right)dE\right]V + \frac{AD}{TL}\left[\int E^2N(E)\left(-\frac{\partial f_0}{\partial E}\right)dE\right]\Delta T\,. \tag{3.10b}$$

These equations are equivalent to the usual form for the transport equations for a metal:

$$I = GV + \eta\Delta T \quad , \tag{3.11a}$$

$$I^T = \zeta V + \kappa\Delta T \quad , \tag{3.11b}$$

with the linear–response thermoelectric coefficients defined by

$$G = \frac{e^2AD}{L}\left[\int N(E)\left(-\frac{\partial f_0}{\partial E}\right)dE\right], \tag{3.12a}$$

$$\eta = -\frac{eAD}{TL}\left[\int EN(E)\left(-\frac{\partial f_0}{\partial E}\right)dE\right], \tag{3.12b}$$

$$\zeta = -\frac{eAD}{L}\left[\int EN(E)\left(-\frac{\partial f_0}{\partial E}\right)dE\right], \tag{3.12c}$$

$$\kappa = \frac{AD}{TL}\left[\int E^2N(E)\left(-\frac{\partial f_0}{\partial E}\right)dE\right]. \tag{3.12d}$$

If we approximate the derivative of the Fermi function by a δ function at low temperatures, as we did for the electrical conductance G, we see that all other coefficients vanish. In order to obtain a finite value, we use the Sommerfeld expansion for the integrals [22]

$$\int \Phi(E)\left(-\frac{\partial f_0}{\partial E}\right)dE = \Phi(0) + \frac{\pi^2(k_BT)^2}{6}\left[\frac{\partial^2\Phi(E)}{\partial E^2}\right]_{E=0} + \ldots \quad . \tag{3.13}$$

Using the fact that $N'(0) = N(0)/2E_F$, we obtain the following expressions for the last three coefficients

$$\eta = -\frac{\pi^2k_B^2T}{6}\frac{eAD}{L}\frac{N(0)}{E_F}, \tag{3.14a}$$

$$\zeta = -\frac{\pi^2(k_BT)^2}{6}\frac{eAD}{L}\frac{N(0)}{E_F}, \tag{3.14b}$$

$$\kappa = \frac{\pi^2k_B^2T}{3}\frac{AD}{L}N(0). \tag{3.14c}$$

Experimentally, the quantities often measured are the thermopower S and the thermal conductance G^T. The thermopower is defined as the thermal voltage generated by a temperature differential ΔT, under the condition that no

electrical current flow through the wire ($I = 0$). Putting this condition into the first transport equation, Eq. (3.10), we obtain

$$S = \frac{V}{\Delta T} = -\frac{\eta}{G} = \frac{\pi^2}{6}\frac{k_B}{e}\frac{k_B T}{E_F} \quad . \tag{3.15}$$

Note that since the expression for S contains a factor $k_B T/E_F$, the thermopower of a typical normal metal is very small.

The thermal conductance G^T is defined as the ratio of the thermal current I^T to the temperature differential ΔT, under the same condition of no electrical current flow ($I = 0$). From the equations above

$$G^T = \frac{I^T}{\Delta T} = \kappa + \zeta S \quad . \tag{3.16}$$

For typical metals, the second term is much smaller than the first, and is usually ignored, so that $G^T \approx \kappa$. If we take the ratio of the electrical to the thermal conductance, we obtain

$$\frac{G^T}{G} = \frac{\pi^2}{3}\frac{k_B^2}{e^2}T. \tag{3.17}$$

Consequently, one finds that the Wiedemann–Franz law holds, even though the scattering lengths for momentum relaxation (ℓ) and energy relaxation (L_{in}) are quite different. This is because the reservoirs are assumed to be perfect, so that any electron entering a reservoir immediately equilibrates with the other electrons in the reservoir.

Before we go on to discuss normal metals in contact with superconductors, it is worthwhile to review some important assumptions in the calculations above. First, in our calculations, we have assumed that the diffusion coefficient D is a constant independent of the energy E and position x. When coherence effects are important, as in the case of the proximity effect, the diffusion coefficient becomes a function of both these parameters, $D(E, x)$. The differential equation for the distribution function, Eq. (3.1) is then modified. $D(E, x)$ itself in general is determined by the distribution function $f(E, x)$, so one must solve a set of coupled differential equations to obtain a solution. This is difficult to do analytically in all but the simplest of cases, and more often must be done numerically. The remainder of this chapter will be devoted in great part to deriving the appropriate differential equations for the distribution functions and diffusion coefficient in the case of normal metals in contact with superconductors, using the quasiclassical equations for superconductivity.

Second, apart from the electrical conductance G, the thermal coefficients derived above would all vanish if the density of states at the Fermi energy $N(E)$, were assumed to be constant, so that it could be taken out of the integrals. The small variation in the density of states at the Fermi energy is

responsible for finite (but small) values of the off-diagonal transport coefficients η and ζ. For example, the thermopower S, which is non–zero only if there is an asymmetry between the properties of particles and holes near the Fermi energy, vanishes if $N(E)$ is assumed constant. The small difference in $N(E)$ above and below E_F gives rise to the small but finite thermopowers of typical normal metals. The conventional quasiclassical theory of superconductivity assumes particle–hole symmetry *a priori* in the definition of the quasiclassical Green's functions, in that $N(E)$ is assumed constant at E_F. Consequently, thermoelectric effects cannot be calculated in the conventional quasiclassical approximation; an extension of the theory is required.

Finally, we have been discussing here *currents* and *conductances*, rather than *current densities* and *conductivities*. These are the more relevant quantitites, since we will be discussing mesoscopic samples in which the measured properties are properties of the sample as a whole. This will be particularly important for the proximity effect, where long range phase coherence means that non–local effects are important.

3.3 The Keldysh Green's Functions

The starting point for developing the quantum analog to the classical Boltzmann transport equation is the Keldysh diagrammatic technique. We shall begin our discussion of the Keldysh technique in the notation of Lifshitz and Pitaevskii. [23] As in the equilibrium case, we define a non–equilibrium Green's function

$$G_{\sigma_1\sigma_2}(X_1, X_2) = -i \left\langle n \left| T\hat{\psi}_{\sigma_1}(X_1)\hat{\psi}^+_{\sigma_2}(X_2) \right| n \right\rangle \quad . \tag{3.18}$$

Here X_1 and X_2 take into account the three spatial coordinates (denoted by $\boldsymbol{r}_1$ and $\boldsymbol{r}_2$ respectively), and the time coordinate (t_1 and t_2). The difference between the non–equilibrium Keldysh Green's function above and the usual equilibrium Green's function is that the average is taken over any quantum state $|n>$ of the system, rather than just the ground state $|0>$. The time ordering operator T has the effect

$$G_{\sigma_1\sigma_2}(X_1, X_2) = \begin{cases} -i \left\langle n \left| \hat{\psi}_{\sigma_1}(X_1)\hat{\psi}^+_{\sigma_2}(X_2) \right| n \right\rangle & , \text{if } t_1 > t_2 \ , \\ +i \left\langle n \left| \hat{\psi}^+_{\sigma_2}(X_2)\hat{\psi}_{\sigma_1}(X_1) \right| n \right\rangle & , \text{if } t_2 > t_1 \ , \end{cases} \tag{3.19}$$

for fermion operators (the case of interest here). For simplicity, we label the spin indices and the coordinate indices by numbers. We shall define a set of

Green's functions that will be useful later:

$$G_{12}^{\alpha\alpha} = -i\left\langle T\hat{\psi}_1\hat{\psi}_2^+\right\rangle, \tag{3.20a}$$

$$G_{12}^{\beta\beta} = i\left\langle \tilde{T}\hat{\psi}_1^+\hat{\psi}_2\right\rangle, \tag{3.20b}$$

$$G_{12}^{\alpha\beta} = -i\left\langle \hat{\psi}_1\hat{\psi}_2^+\right\rangle, \tag{3.20c}$$

$$G_{12}^{\beta\alpha} = i\left\langle \hat{\psi}_2^+\hat{\psi}_1\right\rangle. \tag{3.20d}$$

The first Green's function is just the one defined above, in this new notation. The second Green's function is similar in definition to $G_{12}^{\alpha\alpha}$, except that it is defined with operator $\tilde{T}$ instead of T, which orders the operators in reverse chronological order. The last two Green's functions are defined without any time–ordering operators. The four Green's functions so defined are not linearly independent, but are related by linear equations of the form

$$G^{\alpha\alpha} + G^{\beta\beta} = G^{\alpha\beta} + G^{\beta\alpha}. \tag{3.21}$$

The retarded and advanced Green's functions G^R and G^A can be defined as in the equilibrium case

$$G_{12}^R = \begin{cases} -i\left\langle \hat{\psi}_1\hat{\psi}_2^+ + \hat{\psi}_2^+\hat{\psi}_1\right\rangle & \text{, if } t_1 > t_2\,, \\ 0 & \text{, if } t_2 > t_1 \end{cases} \tag{3.22}$$

and

$$G_{12}^A = \begin{cases} 0 & \text{, if } t_1 > t_2\,, \\ i\left\langle \hat{\psi}_1\hat{\psi}_2^+ + \hat{\psi}_2^+\hat{\psi}_1\right\rangle & \text{, if } t_2 > t_1\,. \end{cases} \tag{3.23}$$

and are related by

$$G_{12}^A = \left(G_{21}^R\right)^*. \tag{3.24}$$

G^R and G^A can be written in terms of the Keldysh Green's functions defined earlier as (we set $\hbar = 1$)

$$G^R = G^{\alpha\alpha} - G^{\alpha\beta} = G^{\beta\alpha} - G^{\beta\beta}\,, \tag{3.25a}$$

$$G^A = G^{\alpha\alpha} - G^{\beta\alpha} = G^{\alpha\beta} - G^{\beta\beta}\,. \tag{3.25b}$$

$G^{\alpha\alpha}$ satisfies the equation of motion

$$G_{01}^{-1}G_{12}^{(0)\alpha\alpha} = \delta(X_1 - X_2)\,, \tag{3.26}$$

where G_0^{-1} is the differential operator (in the free electron approximation)

$$G_0^{-1} = i\frac{\partial}{\partial t} + \frac{\nabla^2}{2m} + \mu \tag{3.27}$$

and the second subscript to G_0^{-1} denotes that the differentials in Eq. (3.27) are with respect to coordinates corresponding to this subscript. The argument of the delta function Eq. (3.26) includes space, time and spin coordinates, and the notation $G_{12}^{(0)\alpha\alpha}$ (with a superscript 0) signifies a Green's function for an ideal gas.

The δ function in Eq. (3.26) arises from the discontinuities in $G^{\alpha\alpha}$ at $t_1 = t_2$. G^R and G^A have similar discontinuities, and obey a similar equation. $G^{(0)\beta\beta}$ has a discontinuity of the opposite sign, and hence obeys the equation

$$G_{01}^{-1} G_{12}^{(0)\beta\beta} = -\delta(X_1 - X_2) \,. \tag{3.28}$$

$G^{\alpha\beta}$ and $G^{\beta\alpha}$ have no discontinuities at $t_1 = t_2$, and hence obey the equations

$$G_{01}^{-1} G_{12}^{(0)\beta\alpha} = 0 \,, \tag{3.29a}$$

$$G_{01}^{-1} G_{12}^{(0)\alpha\beta} = 0 \,. \tag{3.29b}$$

The diagram technique for Keldysh Green's functions is similar to that for equilibrium Green's functions, except that one needs to sum over the internal indices α and β, with a corresponding increase in the number of diagrams. For example, Fig. 3.2 shows two diagrams corresponding to the first order corrections to $G_{12}^{\alpha\alpha}$ in the presence of an external potential, which is represented by a dashed line.

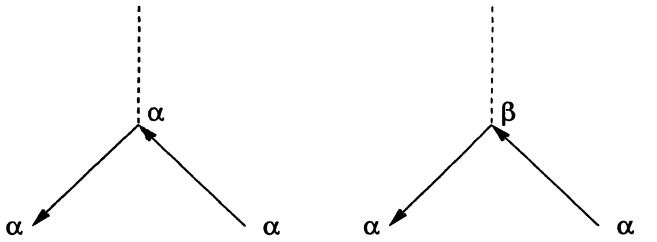

Fig. 3.2. Diagrams corresponding to the first order corrections to the Keldysh Green's function $G_{12}^{\alpha\alpha}$ in the presence of an external potential U, which is represented by a dashed line

In the same manner, Dyson's equation for the Green's function can be represented as shown in Fig. 3.2, where the ellipse represents the self–energy function $\Sigma^{\alpha\beta}$. In order to make the notation more compact and tractable, it is useful to introduce a matrix Green's function and corresponding self–energy matrix:

$$\check{G} = \begin{pmatrix} G^{\beta\beta} & G^{\alpha\beta} \\ G^{\beta\alpha} & G^{\alpha\alpha} \end{pmatrix} , \qquad \check{\Sigma} = \begin{pmatrix} \Sigma^{\beta\beta} & \Sigma^{\alpha\beta} \\ \Sigma^{\beta\alpha} & \Sigma^{\alpha\alpha} \end{pmatrix} . \tag{3.30}$$

Dyson's equation can then be written in matrix form as

$$\check{G}_{12} = \check{G}^0_{12} + \int \check{G}^0_{14}\check{\Sigma}_{43}\check{G}_{32}\, d^4X_3\, d^4X_4\,, \tag{3.31}$$

where the usual rules of matrix multiplication are used.

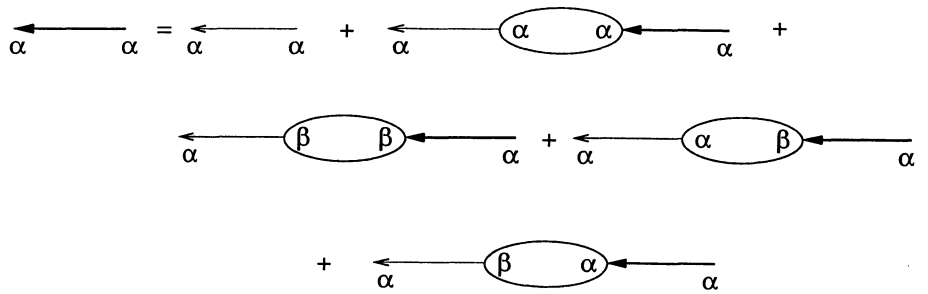

Fig. 3.3. Dyson's equation in diagrammatic form for the Keldysh Green's function $G^{\alpha\alpha}_{12}$. The thick line represents the exact Green's function $G^{\alpha\alpha}_{12}$, the thin line represents the Green's function for an ideal gas $G^{(0)\alpha\alpha}_{12}$, and the ellipse represents the self-energy Σ

As we saw earlier, the components of the Green's function matrix are not independent, but are linearly related. One can therefore perform a transformation to set one of the matrix components to zero. There are many ways to do this; the one we shall use here is the one employed in most recent literature on the quasiclassical theory of superconductivity. [11] The matrices above are first rotated in Keldysh space using the transformation $\check{G} \rightarrow \tau_3\check{G}$, where the τ matrices are identical in form to the Pauli spin matrices

$$\tau^0 = \begin{pmatrix} 1 & 0 \\ 0 & 1 \end{pmatrix}, \quad \tau^1 = \begin{pmatrix} 0 & 1 \\ 1 & 0 \end{pmatrix}, \quad \tau^2 = \begin{pmatrix} 0 & -i \\ i & 0 \end{pmatrix}, \quad \tau^3 = \begin{pmatrix} 1 & 0 \\ 0 & -1 \end{pmatrix}, \tag{3.32}$$

and then transformed $\check{G} \rightarrow Q\check{G}Q^\dagger$, where the matrix Q is given by

$$Q = \frac{1}{\sqrt{2}}(\tau^0 - i\tau^2). \tag{3.33}$$

The resulting matrices have the form

$$\check{G} = \begin{pmatrix} G^R & G^K \\ 0 & G^A \end{pmatrix}, \qquad \check{\Sigma} = \begin{pmatrix} \Sigma^R & \Sigma^K \\ 0 & \Sigma^A \end{pmatrix}, \tag{3.34}$$

where the retarded and advanced Green's functions G^R and G^A have been defined above, and the new Keldysh Green's function G^K is given by

$$G^K = G^{\alpha\alpha} + G^{\beta\beta} = G^{\alpha\beta} + G^{\beta\alpha}. \tag{3.35}$$

Σ^R, Σ^A and Σ^K are defined in a similar manner. In what follows, we shall use the 'check' to denote the Keldysh matrices. In order to avoid writing integrals over the space and time coordinates, we introduce the binary operator $\otimes$, which has the effect of integrating over the free space and time coordinates and performing matrix multiplication when applied between two Keldysh matrices. Thus, the Dyson equation for the Keldysh Green's function written above can be represented as

$$\check{G} = \check{G}^0 + \check{G}^0 \otimes \check{\Sigma} \otimes \check{G} \,. \tag{3.36}$$

$\check{G}^0$ obeys the equation of motion

$$G_{01}^{-1}\check{G}_{12}^0 = \delta(X_1 - X_2). \tag{3.37}$$

Operating G_{01}^{-1} on the Dyson equation Eq. (3.36) from the left, we obtain

$$G_{01}^{-1}\check{G} = \delta(X_1 - X_2) + \check{\Sigma} \otimes \check{G}. \tag{3.38}$$

The conjugate equation is[1]

$$\check{G}G_{02}^{-1} = \delta(X_1 - X_2) + \check{G} \otimes \check{\Sigma}. \tag{3.39}$$

Subtracting the two equations, we obtain

$$(G_0^{-1} \otimes \check{G} - \check{G} \otimes G_0^{-1}) - (\check{\Sigma} \otimes \check{G} - \check{G} \otimes \check{\Sigma}) = 0, \tag{3.40}$$

where we have suppressed the subscript '1' of G_{01}^{-1}. This can be written as a commutator

$$[G_0^{-1} \ominus \check{G}] - [\check{\Sigma} \ominus \check{G}] = 0$$

or

$$[G_0^{-1} \ominus \check{G}] = [\check{\Sigma} \ominus \check{G}] \tag{3.41}$$

where the $\ominus$ operator defines the commutator of two operators $[A \ominus B] = A \otimes B - B \otimes A$.

The mixed or Wigner representation

The Green's function $\check{G}_{12}$ oscillates rapidly with the difference $\boldsymbol{r}_2$ - $\boldsymbol{r}_1$, on the scale of the inverse Fermi wave vector k_F^{-1}. In the physical systems to be discussed, we are interested in variations on much longer length scales. We therefore perform a transformation to center–of–mass coordinates, $\boldsymbol{R}$, T, and difference coordinates, $\boldsymbol{r}$, $\boldsymbol{t}$, defined by the equations [24]

$$\boldsymbol{r}_1 = \boldsymbol{R} - \boldsymbol{r}/2, \qquad \boldsymbol{r}_2 = \boldsymbol{R} + \boldsymbol{r}/2 \tag{3.42a}$$

$$t_1 = T - t/2, \qquad t_2 = T + t/2 \tag{3.42b}$$

[1] From the right, we operate on the coordinate 2, hence we use the operator G_{02}^{-1}. G_{02}^{-1} operated on the right is equivalent to G_{02}^{-1*} operated on the left.

and then define a Fourier transform of $\check{G}_{12}$ with respect to the variables $\boldsymbol{r}$ and t:

$$\check{G}(\boldsymbol{R},T;\boldsymbol{r},t) = \int e^{-iEt} e^{i\boldsymbol{p}\cdot\boldsymbol{r}}\, \check{G}(\boldsymbol{R},T;\boldsymbol{p},E)\, d\boldsymbol{p}\, dE. \tag{3.43}$$

In Eq. (3.41) the part of the commutator involving G_0^{-1} can be written as

$$G_{01}^{-1} \otimes \check{G} - \check{G} \otimes G_{02}^{-1} = \left[i\left(\frac{\partial}{\partial t_1} + \frac{\partial}{\partial t_2} \right) - \frac{1}{2m}(\nabla_1^2 - \nabla_2^2) \right] \check{G}\,, \tag{3.44}$$

using Eq. (3.27) in the free electron approximation. Transforming to the coordinates, $\boldsymbol{R}, T, \boldsymbol{r}, t$, this can be written

$$\left(i\frac{\partial}{\partial T} + \frac{1}{m}\nabla_{\boldsymbol{r}} \cdot \nabla_{\boldsymbol{R}} \right) \check{G}\,. \tag{3.45}$$

From Eq. (3.35), the Keldysh component G^K of the Green's function can be written as the sum of the Green's functions $G^{\alpha\beta}$ and $G^{\beta\alpha}$. Keeping in mind the definitions of these functions given in Eq. (3.20), we can define a non-equilibrium distribution function $f(\boldsymbol{R},T,\boldsymbol{r})$, which is related to the function $G^{\beta\alpha}$ by

$$\begin{aligned} f(\boldsymbol{R},T,\boldsymbol{r}) &= \left\langle \hat{\psi}^+(\boldsymbol{R}+\boldsymbol{r}/2, T+t/2)\hat{\psi}(\boldsymbol{R}-\boldsymbol{r}/2, T-t/2) \right\rangle_{t=0} \\ &= -iG^{\beta\alpha}(\boldsymbol{R},T,\boldsymbol{r},t)_{t=0} \quad . \end{aligned} \tag{3.46}$$

Similarly, we have

$$\begin{aligned} \left\langle \hat{\psi}(\boldsymbol{R}+\boldsymbol{r}/2, T+t/2)\hat{\psi}^+(\boldsymbol{R}-\boldsymbol{r}/2, T-t/2) \right\rangle_{t=0} &= 1 - f(\boldsymbol{R},T,\boldsymbol{r}) \\ &= iG^{\alpha\beta}(\boldsymbol{R},T,\boldsymbol{r},t)_{t=0}\,. \end{aligned} \tag{3.47}$$

Subtracting the first equation from the second, we obtain

$$\begin{aligned} 1 - 2f(\boldsymbol{R},T,\boldsymbol{r}) = h(\boldsymbol{R},T,\boldsymbol{r}) &= i(G^{\alpha\beta}(\boldsymbol{R},T,\boldsymbol{r},t)_{t=0} + G^{\beta\alpha}(\boldsymbol{R},T,\boldsymbol{r},t)_{t=0}) \\ &= iG^K(\boldsymbol{R},T,\boldsymbol{r},t)_{t=0}\,, \end{aligned} \tag{3.48}$$

where we have defined a new distribution function $h(\boldsymbol{R},T,\boldsymbol{r})$. In terms of the mixed Fourier transform, Eq. (3.43), this can be written as

$$h(\boldsymbol{R},T,\boldsymbol{r}) = iG^K(\boldsymbol{R},T,\boldsymbol{r},t)_{t=0} = \frac{i}{2\pi}\int e^{i\boldsymbol{p}\cdot\boldsymbol{r}}\, G^K(\boldsymbol{R},T;\boldsymbol{p},E)\, d\boldsymbol{p}\, dE. \tag{3.49}$$

Taking the Keldysh component of Eq. (3.44) at $t = 0$, we obtain

$$\left(i\frac{\partial}{\partial T} + \frac{1}{m}\nabla_{\boldsymbol{r}} \cdot \nabla_{\boldsymbol{R}} \right) \int d\boldsymbol{p}\, \frac{dE}{2\pi}\, e^{i\boldsymbol{p}\cdot\boldsymbol{r}}\, G^K(\boldsymbol{R},T;\boldsymbol{p},E), \tag{3.50}$$

or, in terms of the Fourier components with respect to $\boldsymbol{r}$, corresponding to momentum $\boldsymbol{p}$,

$$\frac{\partial h(\boldsymbol{R},T,\boldsymbol{p})}{\partial T} + \frac{\boldsymbol{p}}{m} \cdot \nabla_{\boldsymbol{R}} h(\boldsymbol{R},T,\boldsymbol{p}) \,, \tag{3.51}$$

where the Fourier transform of the Wigner distribution function $h(\boldsymbol{R},T,\boldsymbol{p})$ is given by

$$h(\boldsymbol{R},T,\boldsymbol{p}) = \frac{i}{2\pi} \int G^K(\boldsymbol{R},T;\boldsymbol{p},E)\, dE \,. \tag{3.52}$$

In equilibrium, h is given by

$$h_0(\epsilon_{\boldsymbol{p}}) = 1 - 2f_0(\epsilon_{\boldsymbol{p}}) = \tanh(\epsilon_{\boldsymbol{p}}/2k_BT) \,. \tag{3.53}$$

Eq. (3.51), which is the Keldysh component of the left hand side of Eq. (3.41), has the form of the one side of the classical Boltzmann equation for the distribution function. (Using the definition of the function $h(\boldsymbol{R},T,\boldsymbol{p})$, this can also be written in a more conventional form in terms of $f(\boldsymbol{R},T,\boldsymbol{p})$.) The right hand side of the Keldysh component of Eq. (3.41) must therefore correspond to the collision terms. The right hand side of the Keldysh component can be written as $2(\Sigma^{\beta\alpha}G^{\alpha\beta} - \Sigma^{\alpha\beta}G^{\beta\alpha})$. Taking the limit at $t = 0$, and writing in terms of the distribution function $f(\boldsymbol{R},T,\boldsymbol{p})$ using Eq. (3.45) and Eq. (3.46), this Keldysh component of the right hand side of Eq. (3.41) can be written as [23]

$$-2i[\Sigma^{\beta\alpha}(R,T,p)(1 - f(\boldsymbol{R},T,\boldsymbol{p})) + \Sigma^{\alpha\beta}(R,T,p)f(\boldsymbol{R},T,\boldsymbol{p})] \,. \tag{3.54}$$

The first term in Eq. (3.54) with the factor $(1 - f(\boldsymbol{R},T,\boldsymbol{p}))$ has the usual form of a scattering–in term, corresponding to the gain of particles, while the second term has the form for a scattering–out term, corresponding to a loss of particles. Consequently, we see that the Keldysh component of the right–left subtracted Dyson equation gives the transport equation for the distribution function. From the diagonal components components of the same equation, one can obtain solutions for the other components of $\check{G}$ and $\check{\Sigma}$. More typically, the scattering terms on the right hand side of the Boltzmann equation make it difficult to solve, and some approximations must be employed. If the variation of the system with the center–of–mass coordinates T and $\boldsymbol{R}$ is small, then one can expand the Green's functions and self–energies, which are functions of $\boldsymbol{R},\boldsymbol{r},T,t$ about $\boldsymbol{R}$ and T in a Taylor's series to first order in $\boldsymbol{r}$ and t. This is the gradient expansion discussed by Kadanoff and Baym [24] and Larkin and Ovchinnikov [4], and we shall return to it at the end of this section.

Instead of taking the difference of Eq. (3.38) and its conjugate equation, Eq. (3.39). Thus, we take the sum, we obtain the equation

$$[G_0^{-1} \oplus \check{G}] = 2\delta(X_1 - X_2) + [\check{\Sigma} \oplus \check{G}] \,, \tag{3.55}$$

where the operator $\oplus$ defines the Keldysh anti–commutator, in the same way as the operator $\ominus$ defines the Keldysh commutator. The left hand side of Eq. (3.55) can be written as

$$G_{01}^{-1} \otimes \check{G} + \check{G} \otimes G_{02}^{-1} = \left[i \left(\frac{\partial}{\partial t_1} - \frac{\partial}{\partial t_2} \right) - \frac{1}{2m} (\nabla_1^2 + \nabla_2^2) \right] \check{G} \,. \tag{3.56}$$

Transforming to the mixed representation, we obtain

$$\left[2i \frac{\partial}{\partial t} + \frac{1}{m} \left(\frac{1}{4} \nabla_{\boldsymbol{R}}^2 + \nabla_{\boldsymbol{r}}^2 \right) \right] \check{G}(\boldsymbol{R}, T, \boldsymbol{r}, t) \tag{3.57}$$

Now, the assumption we are making is that the variations of G on the scale of $\boldsymbol{R}$ are much slower than the variations on the scale of $\boldsymbol{r}$. Hence, the terms in equation above involving derivatives with $\boldsymbol{R}$ contribute much less than the those with $\boldsymbol{r}$, and can be neglected in this approximation. If we consider the equation for G_0, for which the terms involving Σ on the right hand side of Eq. (3.55) are 0, then we obtain after transforming to Fourier components [25]

$$(E - \epsilon_{\boldsymbol{p}}) G_0(\boldsymbol{R}, T, \boldsymbol{p}, E) = 1 \tag{3.58}$$

or

$$G_0(\boldsymbol{R}, T, \boldsymbol{p}, E) = \frac{1}{(E - \epsilon_{\boldsymbol{p}})} \,, \tag{3.59}$$

where

$$\epsilon_{\boldsymbol{p}} = \frac{p^2}{2m} - \mu \sim v_F (p - p_F). \tag{3.60}$$

So far, we have assumed a free–electron model. If there is a slowly varying potential $U(\boldsymbol{R}, T)$, the equation above can be modified to

$$G_0(\boldsymbol{R}, T, \boldsymbol{p}, E) = \frac{1}{(E - \epsilon_{\boldsymbol{p}} - U(\boldsymbol{R}, T))} \,. \tag{3.61}$$

This equation has form of a Green's function for a free particle, but in a slowly varying potential $U(\boldsymbol{R}, T)$. The operator G_0^{-1} in the mixed representation can therefore be written as

$$G_0^{-1} = (E - \epsilon_{\boldsymbol{p}} - U(\boldsymbol{R}, T)) \,. \tag{3.62}$$

More accurately, one transforms Eq. (3.27) using the following equations

$$\frac{\partial}{\partial t_{1,2}} = \frac{1}{2} \frac{\partial}{\partial T} \pm \frac{\partial}{\partial t}, \tag{3.63a}$$

$$\nabla_{1,2} = \frac{1}{2} \nabla_{\boldsymbol{R}} \pm \nabla_{\boldsymbol{r}} \tag{3.63b}$$

$$\nabla_{1,2}^2 = \frac{1}{4} \nabla_{\boldsymbol{R}}^2 \pm \nabla_{\boldsymbol{r}} \cdot \nabla_{\boldsymbol{R}} + \nabla_{\boldsymbol{r}}^2. \tag{3.63c}$$

Again, assuming the functions in the mixed representation are slowly varying functions of $\boldsymbol{R}$, we can ignore the second derivatives with respect to $\boldsymbol{R}$, to obtain

$$G_0^{-1} = \frac{1}{2}\frac{\partial}{\partial T} + \frac{\partial}{\partial t} + \frac{\nabla_{\boldsymbol{r}}^2}{2m} + \frac{\nabla_{\boldsymbol{r}} \cdot \nabla_{\boldsymbol{R}}}{2m} + \mu \,. \tag{3.64}$$

In most applications of interest here, we also ignore the slow T dependence. Adding the potential $U(\boldsymbol{R}, T)$, and writing in terms of the partial Fourier transform with respect to $\boldsymbol{p}$ and E, we obtain

$$G_0^{-1} = E - \epsilon_{\boldsymbol{p}} + \frac{i}{2}\boldsymbol{v}_F \cdot \nabla_{\boldsymbol{R}} + \mu - U(\boldsymbol{R}, T), \tag{3.65}$$

where we have replaced $\boldsymbol{p}/m$ by $\boldsymbol{v}_F$, since the important region of interest is at the Fermi surface. Note that we still keep account of the *direction* of the momentum.

To conclude this section, we derive some expressions for the convolution of two operators in the mixed representation, the gradient expansion discussed above. Consider the convolution of two operators defined as an integral over the internal space and time coordinates

$$A \otimes B = \int d\boldsymbol{r}_3 \int dt_3 A(\boldsymbol{r}_1, \boldsymbol{r}_3, t_1, t_3) B(\boldsymbol{r}_3, \boldsymbol{r}_2, t_3, t_2) \,. \tag{3.66}$$

If we do a partial transform to $\boldsymbol{p}, \boldsymbol{R}$ (but do not transform the time coordinates), $A \otimes B$ can be represented as

$$A \otimes B = \int dt_3 e^{\frac{i}{2}(\nabla_{\boldsymbol{R}}^A \cdot \nabla_{\boldsymbol{p}}^B - \nabla_{\boldsymbol{p}}^A \cdot \nabla_{\boldsymbol{R}}^B)} A(\boldsymbol{R}, \boldsymbol{p}, t_1, t_3) B(\boldsymbol{R}, \boldsymbol{p}, t_3, t_2) \,, \tag{3.67}$$

where the superscripts to the derivatives denote that they operate only those functions. If the derivatives are small, we need to take only the first order expansion of this expression

$$\begin{aligned}(A \otimes B)(\boldsymbol{p}, \boldsymbol{R}) = & \int dt_3 \left[1 + \frac{i}{2}\left(\nabla_{\boldsymbol{R}}^A \cdot \nabla_{\boldsymbol{p}}^B - \nabla_{\boldsymbol{p}}^A \cdot \nabla_{\boldsymbol{R}}^B\right)\right] \\ & \times A(\boldsymbol{R}, \boldsymbol{p}, t_1, t_3) B(\boldsymbol{R}, \boldsymbol{p}, t_3, t_2) \,.\end{aligned} \tag{3.68}$$

Similarly we get

$$\begin{aligned}(B \otimes A)(\boldsymbol{p}, \boldsymbol{R}) = & \int dt_3 \left[1 + \frac{i}{2}\left(\nabla_{\boldsymbol{R}}^B \cdot \nabla_{\boldsymbol{p}}^A - \nabla_{\boldsymbol{p}}^B \cdot \nabla_{\boldsymbol{R}}^A\right)\right] \\ & \times B(\boldsymbol{R}, \boldsymbol{p}, t_1, t_3) A(\boldsymbol{R}, \boldsymbol{p}, t_3, t_2) \,.\end{aligned} \tag{3.69}$$

If we were dealing with functions alone, then the multiplication of the two function A and B is commutative. When A and B are matrices, however,

they do not in general commute, so we obtain

$$(A \ominus B)(\boldsymbol{p}, \boldsymbol{R}) = A \otimes B - B \otimes A$$
$$= \int dt_3 \, [A, B] + \frac{i}{2} \int dt_3 \, [\{\nabla_{\boldsymbol{R}} A, \nabla_{\boldsymbol{p}} B\} - \{\nabla_{\boldsymbol{p}} A, \nabla_{\boldsymbol{R}} B\}], \tag{3.70}$$

where $[A, B]$ notation stands for the commutator of the two functions, and $\{A, B\}$ stands for the anticommutator. A similar equation can be obtained if we transform the times to the mixed representation T, E

$$(A \ominus B)(T, E) = A \otimes B - B \otimes A$$
$$= \int d\boldsymbol{r}_3 \, [A, B] + \frac{i}{2} \int d\boldsymbol{r}_3 \, [\{\partial_T A, \partial_E B\} - \{\partial_E A, \partial_T B\}], \tag{3.71}$$

When we transform both sets of variables, we obtain

$$(A \ominus B)(\boldsymbol{p}, \boldsymbol{R}, T, E) = A \otimes B - B \otimes A =$$
$$[A, B] + \frac{i}{2} [(\{\partial_T A, \partial_E B\} - \{\partial_E A, \partial_T B\}) + (\{\nabla_{\boldsymbol{R}} A, \nabla_{\boldsymbol{p}} B\} - \{\nabla_{\boldsymbol{p}} A, \nabla_{\boldsymbol{R}} B\})]. \tag{3.72}$$

In most cases, we are interested in stationary situations, where there is no T dependence. In this case, the equation above reduces to

$$(A \ominus B)(\boldsymbol{p}, \boldsymbol{R}, T, E) = A \otimes B - B \otimes A$$
$$= [A, B] + \frac{i}{2} [\{\nabla_{\boldsymbol{R}} A, \nabla_{\boldsymbol{p}} B\} - \{\nabla_{\boldsymbol{p}} A, \nabla_{\boldsymbol{R}} B\}]. \tag{3.73}$$

These expressions will be useful in the calculations to follow.

3.4 The Quasiclassical Approximation

The non–equilibrium spectral function A is defined in the same way as in the equilibrium case [11, 26]

$$A = \frac{i}{2\pi}(G^R - G^A) = -\frac{1}{\pi}\mathrm{Im}(G^R), \tag{3.74}$$

where Im (G^R) denotes the imaginary part of the retarded Green's function. In the equilibrium case, A defines the spectrum of energy levels, for stationary quantum states, it has the form of a sum of δ–functions at each state energy. In the quasiparticle approximation, these δ–functions are broadened, but the width Γ of each state, defining its lifetime, is still small compared to its energy. If Γ is large, the quasiparticle approximation breaks down,

and one cannot obtain a kinetic equation for a distribution function by integrating over the energy E. However, for most perturbations of interest, the self–energies typically have a weak dependence on the magnitude of the momentum, this dependence being appreciable only near the Fermi energy. On the other hand, while the Dyson equation has a strong dependence on E and $\epsilon_{\boldsymbol{p}}$, the subtracted Dyson equation, Eq. (3.41), from which we will obtain the equations of motion, has a very weak dependence on both E and $\epsilon_{\boldsymbol{p}}$. In this case, it is possible to average over the particle energy to eliminate the dependence on the magnitude of the momentum, but keep the dependence on the direction of the momentum. Hence, one can think of replacing the Green's functions and self–energies by their values on the Fermi surface, multiplied by a δ–function in the form

$$G(\boldsymbol{R},\boldsymbol{p},t_1,t_2) \rightarrow \delta(\epsilon_{\boldsymbol{p}})g(\boldsymbol{R},\hat{p},t_1,t_2)\ . \tag{3.75}$$

To this end, we define the so–called quasiclassical Green's function

$$g(\boldsymbol{R},\hat{p},t_1,t_2) = \frac{i}{\pi}\int d\epsilon_{\boldsymbol{p}}\ G(\boldsymbol{R},\boldsymbol{p},t_1,t_2)\ . \tag{3.76}$$

Care must be taken in performing this integral, since the integrand falls off only as $1/\epsilon_{\boldsymbol{p}}$ for large $\epsilon_{\boldsymbol{p}}$. To avoid this, one can introduce a cut–off in the integral, as done by Serene and Rainer, [7] or following Eilenberger, [1] use a special contour for integration.

We would like to obtain an equation of motion for the quasiclassical Green's functions. If we obtain an equation of motion by operating G_0^{-1} in the form of Eq. (3.64) on Dyson's equation, and then integrating over $\epsilon_{\boldsymbol{p}}$, there are terms in the equation that will have large contributions. In order to eliminate these large terms, we start from the left–right subtracted equation of motion, Eq. (3.41), in which the troublesome terms are cancelled, and then integrate over $\epsilon_{\boldsymbol{p}}$. The terms on the right hand side of Eq. (3.41) are of the form

$$\check{\Sigma}\otimes\check{G} = \int dt_3\ dx_3^3\ \check{\Sigma}(x_1,t_1,x_3,t_3)\check{G}(x_3,t_3,x_2,t_2)\ . \tag{3.77}$$

We first Fourier transform this term with respect to $\boldsymbol{p}$, which takes care of the integral over x_3. We then average the resulting equation with respect to $\epsilon_{\boldsymbol{p}}$. The assumption here is that only $\check{G}$ has a strong dependence on the momentum $\boldsymbol{p}$, so the result of this averaging is a term of the form

$$\int dt_3\ \check{\Sigma}(\boldsymbol{R},\boldsymbol{p},t_1,t_3)\check{g}(\boldsymbol{R},\hat{p},t_3,t_2)\ . \tag{3.78}$$

Now, to complete the transformation, the self–energy $\check{\Sigma}$, which is a functional of the Green's functions $\check{G}$, must become a functional only of the quasiclassical

Green's functions $\check{g}$, $\check{\Sigma}[\check{G}] \rightarrow \check{\sigma}[\check{g}]$. With this final change, Eq. (3.41) for the quasiclassical Green's functions becomes

$$[(g_0^{-1} - \check{\sigma}) \circ \check{g}] = 0 \,. \tag{3.79}$$

The $\circ$ operator in the commutator $[A \circ B]$ involves an integral over the internal time coordinates in addition to the usual matrix multiplication for Keldysh matrices. If we transform the time coordinates as well, this integral can be removed, as shown at the end of the last section (Eq. 3.72). In this case, the commutator becomes a simple commutator (but involving matrix multiplication of the Keldysh matrices).

It remains to express the physical quantities of interest in terms of the Green's functions. The particle density is given by

$$\rho(1) = -2iG_{11}^{\beta\alpha} \tag{3.80}$$

and the current density in the absence of external fields is given by

$$\boldsymbol{j}(1) = -\frac{e}{m}\left(\nabla_1 - \nabla_2\right) G_{12}^{\beta\alpha}|_{2=1} \,. \tag{3.81}$$

From the definitions of G^R, G^A and G^K in terms of $G^{\alpha\beta}$, $G^{\beta\alpha}$ and $G^{\beta\beta}$, we can write the function $G^{\beta\alpha}$ as

$$G^{\beta\alpha} = \frac{1}{2}\left[G^K + (G^R - G^A)\right] \,. \tag{3.82}$$

G^R and G^A depend on the equilibrium properties of the system, and so do not contribute to the current on nonequilibrium density. Consequently, these terms can be dropped in the expression for the particle density and current. Writing in terms of the quasiclassical Green's functions, we can obtain expressions for the density and the current in the mixed representation. Consider the expression for charge density

$$\delta\rho(\boldsymbol{R}, T) = -ieG^K(\boldsymbol{R}, T, \boldsymbol{r} = 0, t = 0) \,, \tag{3.83}$$

where we use $\delta\rho$ instead of ρ to emphasize that this does not include the equilibrium contributions. Expanding G^K in terms of Fourier components in momentum space $\boldsymbol{p}$

$$\begin{aligned}\delta\rho(\boldsymbol{R}, T) &= -ie\left[\int \frac{d^3p}{(2\pi)^3}\, e^{i\boldsymbol{p}\cdot\boldsymbol{r}} G^K(\boldsymbol{R}, T, \boldsymbol{p}, t)\right]_{\boldsymbol{r}=0, t=0} \\ &= -ie\int \frac{dE}{2\pi} \int \frac{d^3p}{(2\pi)^3}\, G^K(\boldsymbol{R}, T, \boldsymbol{p}, E) \,,\end{aligned} \tag{3.84}$$

where we have used the fact that setting $t = 0$ in $G^K(t)$ is equivalent to integrating $G^K(E)$ over $dE/2\pi$.

The equivalent expression for the current density can also be written in terms of the quasiclassical Green's function. From Eq. (3.81) and Eq. (3.82) we have in the mixed representation

$$\boldsymbol{j}(\boldsymbol{R},T) = -\frac{e}{2m}\left[(\nabla_1 - \nabla_2)\, G^K(\boldsymbol{R},T,\boldsymbol{r},\boldsymbol{p})\right]_{\boldsymbol{r}=0,t=0} . \tag{3.85}$$

The integral over the momentum $\boldsymbol{p}$ can be rewritten as

$$\int \frac{d^3p}{(2\pi)^3} \to N_0 \int d\epsilon_{\boldsymbol{p}} \int \frac{d\Omega_p}{4\pi} , \tag{3.86}$$

where N_0 is the density of states at the Fermi energy, and $d\Omega_p$ is an element of solid angle in momemtum space p. Writing $\nabla_1 - \nabla_2 = 2\nabla_{\boldsymbol{r}}$ from Eq. (3.63b), we obtain

$$\boldsymbol{j}(\boldsymbol{R},T) = -\frac{e}{m}\left[\nabla_{\boldsymbol{r}} \int \frac{d^3p}{(2\pi)^3}\, e^{i\boldsymbol{p}\cdot\boldsymbol{r}} G^K(\boldsymbol{R},T,\boldsymbol{p},t)\right]_{\boldsymbol{r}=0,t=0} . \tag{3.87}$$

Operating $\nabla_{\boldsymbol{r}}$ on the exponential within the integral gives $i\boldsymbol{p}$. In the quasiclassical approximation, we assume that the major contribution comes from near the Fermi surface, so that $\boldsymbol{p}/m = \boldsymbol{v}_F$, the Fermi velocity. With this approximation, we obtain

$$\boldsymbol{j}(\boldsymbol{R},T) = -ie \int \frac{dE}{2\pi} \int \frac{d^3p}{(2\pi)^3}\, \boldsymbol{v}_F G^K(\boldsymbol{R},T,\boldsymbol{p},E) . \tag{3.88}$$

If we use the definition of the distribution function h given by Eq. (3.48), we obtain

$$\boldsymbol{j}(\boldsymbol{R},T) = -e \int \frac{d^3p}{(2\pi)^3}\, \boldsymbol{v}_F h(\boldsymbol{R},T,\boldsymbol{p}) \tag{3.89}$$

which is the expected classical form for the current. Recalling the definition of the quasiclassical Green's function, Eq. (3.76), we obtain

$$\boldsymbol{j}(\boldsymbol{R},T) = -\frac{1}{2} e N_0 \int dE \int \frac{d\Omega_p}{4\pi} \boldsymbol{v}_F g^K(E,\hat{p},\boldsymbol{R},T) , \tag{3.90}$$

where we have used Eq. (3.76) and Eq. (3.86). Note that writing these expressions in terms of the quasiclassical Green's functions necessitates reversing the order of integration over E and $\epsilon_{\boldsymbol{p}}$.

The transformation, Eq. (3.86), assumes that the density of states is constant at the Fermi energy, and hence assumes that particle–hole symmetry holds. Hence, within this approximation, we will not be able to obtain any results on physical phenomenon that depend on particle–hole asymmetry, in particular, thermoelectric effects. This should be contrasted with the derivation of the current in the diffusive limit that we performed in the introduction,

where the energy dependence of the density of states was taken into account explicitly.

So far, we have ignored the effects of external fields and potentials. In particular, the effect of a magnetic field is of interest. The magnetic field is introduced in the form of a vector potential $\boldsymbol{A}(\boldsymbol{R},T)$. Here, we shall consider only time independent fields. $\boldsymbol{A}(\boldsymbol{R})$ is introduced by making the change

$$\nabla_{\boldsymbol{R}} \rightarrow \nabla_{\boldsymbol{R}} - ie\boldsymbol{A}(\boldsymbol{R}) \equiv \partial_{\boldsymbol{R}} \tag{3.91}$$

in all equations involving the spatial derivative. For example, the operator $\tilde{G}_{01}^{-1}$ is now written

$$\tilde{G}_{01}^{-1} = i\frac{\partial}{\partial t_1} + \frac{\partial_{\boldsymbol{r}}^2}{2m} + \mu - e\phi \,. \tag{3.92}$$

In the equation above, we have also added a term $e\phi$, corresponding to the presence of a scalar potential.

In our formulation, we would like all observable quantities to be invariant under a gauge transformation of the vector potential

$$\boldsymbol{A} \rightarrow \boldsymbol{A} + \nabla\chi(\boldsymbol{r}) \,, \tag{3.93}$$

which also transforms the potential

$$\phi \rightarrow \phi - \frac{\partial\chi}{\partial t} \,. \tag{3.94}$$

Eq. (3.87) for the electrical current is then modified to

$$\boldsymbol{j}(\boldsymbol{R},T) = -\frac{2e}{m}\left[[\nabla_{\boldsymbol{r}} - ie\boldsymbol{A}(\boldsymbol{R})]\int \frac{d^3p}{(2\pi)^3}\, e^{i\boldsymbol{p}\cdot\boldsymbol{r}} G^{\beta\alpha}(\boldsymbol{R},T,\boldsymbol{p},t)\right]_{\boldsymbol{r}=0,t=0} \,, \tag{3.95}$$

where we have written the current in terms of $G^{\beta\alpha}$ rather than G^K. It follows that Eq. (3.88) can be written as

$$\begin{aligned}\boldsymbol{j}(\boldsymbol{R},T) = -i2e &\int \frac{dE}{2\pi}\int \frac{d^3p}{(2\pi)^3}\, \boldsymbol{v}_F G^{\beta\alpha}(\boldsymbol{R},T,\boldsymbol{p},E) + \frac{2ie^2}{m}\boldsymbol{A}(\boldsymbol{R}) \\ &\times \int \frac{dE}{2\pi}\int \frac{d^3p}{(2\pi)^3}\, G^{\beta\alpha}(\boldsymbol{R},T,\boldsymbol{p},E) \,.\end{aligned} \tag{3.96}$$

The second term in the equation above is called the diamagnetic term. It is cancelled by a contribution from the first term arising from energies far from the Fermi energy, which are not taken into account in the quasiclassical Green's function as defined by Eq. (3.76). [11] Note that such a cancellation does not occur in the case of a superconductor, and the second term gives rise to the supercurrent, which is proportional to the vector potential and the

phase gradient according to Eq. (3.94). With this high energy contribution cancelled by the diamagnetic term, the equation above transforms into the expression Eq. (3.90) for the electrical current, written now in terms of the Keldysh component of the quasiclassical Green's function.

Such a cancellation does not occur in transforming $\delta\rho$ in terms of the quasiclassical Green's functions, and the contribution of the integrals in Eq. (3.84) must be explicitly calculated. [11] The result that was obtained by Eliashberg [3] can be written as

$$\delta\rho(\boldsymbol{R},T) = -\frac{eN_0}{2}\int dE \int \frac{d\Omega_p}{4\pi} g^K(E,\hat{p},\boldsymbol{R},T) - 2e^2 N_0 \phi(\boldsymbol{R},T), \quad (3.97)$$

where $\phi(\boldsymbol{R},T)$ is now the scalar electrochemical potential. This expression can also be obtained by invoking gauge invariance arguments. Since we must preserve charge neutrality in the system, $\delta\rho = 0$, so that $\phi(\boldsymbol{R},T)$ is given by

$$\phi(\boldsymbol{R},T) = -\frac{1}{4e}\int dE \int \frac{d\Omega_p}{4\pi} g^K(E,\hat{p},\boldsymbol{R},T) \quad (3.98)$$

For completeness, we also write expressions for the thermal current and the density of states. The expression for the thermal current in terms of the Keldysh Green's function is given by

$$\boldsymbol{j}_{th}(\boldsymbol{R},T) = i\int \frac{dE}{2\pi}\int \frac{d^3p}{(2\pi)^3}\, E\boldsymbol{v}_F G^K(\boldsymbol{R},T,\boldsymbol{p},E), \quad (3.99)$$

and the corresponding form in terms of the quasiclassical Green's functions

$$\boldsymbol{j}_{th}(\boldsymbol{R},T) = \frac{1}{2}N_0\int dE \int \frac{d\Omega_p}{4\pi} E\boldsymbol{v}_F g^K(E,\hat{p},\boldsymbol{R},T). \quad (3.100)$$

As in the equilibrium case, the density of states is given directly by the spectral function A defined in Eq. (3.74), now expressed in the mixed representation

$$\begin{aligned} N(E,\boldsymbol{R},T) = A(E,\boldsymbol{R},T) &= -\frac{1}{\pi}\mathrm{Im}G^R(E,\boldsymbol{R},T) \\ &= -\frac{1}{\pi}\mathrm{Im}\int \frac{d^3p}{(2\pi)^3} G^R(E,\boldsymbol{p},\boldsymbol{R},T). \end{aligned} \quad (3.101)$$

Written in terms of the quasiclassical Green's function, this becomes

$$N(E,\boldsymbol{R},T) = N_0 \mathrm{Re}\int \frac{d\Omega_p}{4\pi} g^R(\boldsymbol{R},E,T), \quad (3.102)$$

where the notations Re and Im stand for the real and imaginary components respectively.

3.5 Non–Equilibrium Green's Functions for Superconducting Systems

The formalism that we have developed for non–equilibrium Green's functions for normal systems carries over into the superconducting case, except that the Green's functions for the superconducting case are more complicated. In order to show how the Green's functions are defined, we start by expressing the Green's functions in the superconducting case in terms of field operators in the Nambu–Gor'kov formalism. In this formalism, the field operators can be written as two–component column matrices

$$\hat{\Psi}_1 = \begin{pmatrix} \hat{\psi}_{1\uparrow} \\ \hat{\psi}^+_{1\downarrow} \end{pmatrix} , \tag{3.103}$$

where the up and down arrows refer to the spin indices, and the numbers now refer only to the time and space coordinates. The Hermitian adjoint of this operator can be written as a two–component row matrix

$$\hat{\Psi}^+_1 = \left(\hat{\psi}^+_{1\uparrow} \; \hat{\psi}_{1\downarrow} \right) . \tag{3.104}$$

The multiplication of two such operators is defined as the tensorial product of the two matrices. For example

$$\hat{\Psi}_1 \hat{\Psi}^+_2 = \begin{pmatrix} \hat{\psi}_{1\uparrow}\hat{\psi}^+_{2\uparrow} & \hat{\psi}_{1\uparrow}\hat{\psi}_{2\downarrow} \\ \hat{\psi}^+_{1\downarrow}\hat{\psi}^+_{2\uparrow} & \hat{\psi}^+_{1\downarrow}\hat{\psi}_{2\downarrow} \end{pmatrix} . \tag{3.105}$$

It is natural then to define the Green's functions in terms of these products. For example, the natural definition of the Green's function corresponding to $G^{\alpha\alpha}$, Eq. (3.20a), would be

$$G^{\alpha\alpha}_{12} = -i \left\langle T\hat{\Psi}_1 \hat{\Psi}^+_2 \right\rangle = -i \begin{pmatrix} \left\langle T\hat{\psi}_{1\uparrow}\hat{\psi}^+_{2\uparrow} \right\rangle & \left\langle T\hat{\psi}_{1\uparrow}\hat{\psi}_{2\downarrow} \right\rangle \\ \left\langle T\hat{\psi}^+_{1\downarrow}\hat{\psi}^+_{2\uparrow} \right\rangle & \left\langle T\hat{\psi}^+_{1\downarrow}\hat{\psi}_{2\downarrow} \right\rangle \end{pmatrix} . \tag{3.106}$$

However, we would like to keep the same form for the equations of motion and Dyson's equation as for the normal case, except, of course, the quantities will be matrices in Nambu–Gor'kov space. To see if the definition above fits this requirement, let us operate $i\partial/\partial t_1$ on the Green's function for an ideal gas, as defined above. With the definition

$$h_{01} = -\frac{\nabla^2_1}{2m} - \mu , \tag{3.107}$$

we have the matrix Equation

$$\begin{aligned} i\frac{\partial}{\partial t_1} G^{(0)\alpha\alpha}_{12} = h_{01} & \begin{pmatrix} \left\langle T\hat{\psi}_{1\uparrow}\hat{\psi}^+_{2\uparrow} \right\rangle & \left\langle T\hat{\psi}_{1\uparrow}\hat{\psi}_{2\downarrow} \right\rangle \\ -\left\langle T\hat{\psi}^+_{1\downarrow}\hat{\psi}^+_{2\uparrow} \right\rangle & -\left\langle T\hat{\psi}^+_{1\downarrow}\hat{\psi}_{2\downarrow} \right\rangle \end{pmatrix} \\ & + \begin{pmatrix} \delta(X_1 - X_2) & 0 \\ 0 & \delta(X_1 - X_2) \end{pmatrix} . \end{aligned} \tag{3.108}$$

This does not have the required form of the analogous equation for the normal case, Eq. (3.26). To remedy this, we define our Green's functions with an extra factor of τ^3. The definitions corresponding to Eq. (3.20) are then

$$\tilde{G}_{12}^{\alpha\alpha} = -i\tau^3 \left\langle T\hat{\Psi}_1\hat{\Psi}_2^+ \right\rangle = -i\tau^3 \begin{pmatrix} \left\langle T\hat{\psi}_{1\uparrow}\hat{\psi}_{2\uparrow}^+ \right\rangle & \left\langle T\hat{\psi}_{1\uparrow}\hat{\psi}_{2\downarrow} \right\rangle \\ \left\langle T\hat{\psi}_{1\downarrow}^+\hat{\psi}_{2\uparrow}^+ \right\rangle & \left\langle T\hat{\psi}_{1\downarrow}^+\hat{\psi}_{2\downarrow} \right\rangle \end{pmatrix}, \tag{3.109a}$$

$$\tilde{G}_{12}^{\beta\beta} = -i\tau^3 \left\langle \tilde{T}\hat{\Psi}_1\hat{\Psi}_2^+ \right\rangle = -i\tau^3 \begin{pmatrix} \left\langle \tilde{T}\hat{\psi}_{1\uparrow}\hat{\psi}_{2\uparrow}^+ \right\rangle & \left\langle \tilde{T}\hat{\psi}_{1\uparrow}\hat{\psi}_{2\downarrow} \right\rangle \\ \left\langle \tilde{T}\hat{\psi}_{1\downarrow}^+\hat{\psi}_{2\uparrow}^+ \right\rangle & \left\langle \tilde{T}\hat{\psi}_{1\downarrow}^+\hat{\psi}_{2\downarrow} \right\rangle \end{pmatrix}, \tag{3.109b}$$

$$\tilde{G}_{12}^{\alpha\beta} = -i\tau^3 \left\langle \hat{\Psi}_1\hat{\Psi}_2^+ \right\rangle = -i\tau^3 \begin{pmatrix} \left\langle \hat{\psi}_{1\uparrow}\hat{\psi}_{2\uparrow}^+ \right\rangle & \left\langle \hat{\psi}_{1\uparrow}\hat{\psi}_{2\downarrow} \right\rangle \\ \left\langle \hat{\psi}_{1\downarrow}^+\hat{\psi}_{2\uparrow}^+ \right\rangle & \left\langle \hat{\psi}_{1\downarrow}^+\hat{\psi}_{2\downarrow} \right\rangle \end{pmatrix}, \tag{3.109c}$$

and

$$\tilde{G}_{12}^{\beta\alpha} = i\tau^3 \left\langle \hat{\Psi}_2^+\hat{\Psi}_1 \right\rangle = i\tau^3 \begin{pmatrix} \left\langle \hat{\psi}_{2\uparrow}^+\hat{\psi}_{1\uparrow} \right\rangle & \left\langle \hat{\psi}_{2\downarrow}\hat{\psi}_{1\uparrow} \right\rangle \\ \left\langle \hat{\psi}_{2\uparrow}^+\hat{\psi}_{1\downarrow}^+ \right\rangle & \left\langle \hat{\psi}_{2\downarrow}\hat{\psi}_{1\downarrow}^+ \right\rangle \end{pmatrix}. \tag{3.109d}$$

Here, the 'tilde' over the Green's functions denotes that they are matrices in Nambu–Gor'kov space. The operator corresponding to Eq. (3.26) is then defined as

$$\tilde{G}_{01}^{-1} = i\tau^3 \frac{\partial}{\partial t_1} + \frac{\partial_1^2}{2m} + \mu. \tag{3.110}$$

Here it is understood that any 'scalar' quantities in the equation above and in what follows are mulitiplied by the identity matrix τ^0. With these modifications, all the equations derived for the Keldysh Green's functions for the normal case can be carried over directly to the superconducting case. In particular, the advanced and retarded Green's functions $\tilde{G}^R$ and $\tilde{G}^A$ are defined in terms of the Green's functions in Eq. (3.109) in the same manner as before. The Keldysh matrices corresponding to Eq. (3.34) are then

$$\hat{G} = \begin{pmatrix} \tilde{G}^R & \tilde{G}^K \\ 0 & \tilde{G}^A \end{pmatrix}, \qquad \hat{\Sigma} = \begin{pmatrix} \tilde{\Sigma}^R & \tilde{\Sigma}^K \\ 0 & \tilde{\Sigma}^A \end{pmatrix}, \tag{3.111}$$

Since each element of these matrices are themselves 2x2 matrices, the resulting Keldysh matrices for superconductors are 4x4 'supermatrices,' and we shall denote them by a 'hat' symbol ($\hat{}$). The equation of motion equivalent to Eq. (3.41) is

$$[\hat{G}_0^{-1} \ominus \hat{G}] = [\hat{\Sigma} \ominus \hat{G}]. \tag{3.112}$$

Before we go any further, we need to specify the self-energy $\tilde{\Sigma}$. At the temperatures of interest in the experiments on proximity systems, the important

self–energy terms are due to electron–phonon scattering ($\tilde{\Sigma}_{e-p}$), and electron impurity scattering ($\tilde{\Sigma}_{imp}$). For conventional superconductors, the elastic component ($\tilde{\Sigma}^R_{e-p} + \tilde{\Sigma}^A_{e-p}$) of the electron–phonon contribution is the one that leads to the coupling between superconducting electrons [8] (the other contributions of electron–phonon scattering will be ignored, under the assumption that we are at low enough temperatures so that inelastic electron–phonon scattering can be ignored). Perhaps a simpler way of dealing with this component of the electron–phonon interaction is to start directly with the Gor'kov equations of motion [26] for the Green's function Eq. (3.109a), which we write in the form (ignoring impurity scattering for the moment)

$$\begin{pmatrix} i\frac{\partial}{\partial t_1} + \frac{\nabla_1^2}{2m} + \mu & \Delta \\ -\Delta^* & -i\frac{\partial}{\partial t_1} + \frac{\nabla_1^2}{2m} + \mu \end{pmatrix} \tilde{G}^{\alpha\alpha}_{12} = \delta(X_1 - X_2)\,, \tag{3.113}$$

with the pair potential Δ defined as [2]

$$\Delta = \lambda \lim_{2\to 1+} < T\hat{\psi}_{1\uparrow}\hat{\psi}_{2\downarrow} >= i\lambda \lim_{2\to 1+} [\tilde{G}^{\alpha\alpha}_{12}]_{12} \tag{3.114}$$

in terms of the upper left component of the Green's function $\tilde{G}^{\alpha\alpha}_{12}$, which is frequently called the anomalous Green's function (or pair amplitude), and denoted by F. Here λ is the coupling constant. For a uniform bulk superconductor Δ is real. For a normal metal, λ vanishes, and hence, although the pair amplitude in a normal metal may be finite, the pair potential vanishes. Eq. (3.114) defines a self–consistent equation for the pair potential Δ; it is defined in terms of the anomalous Green's function F, which in turn is determined by an equation that depends on Δ. Note that unlike $[\tilde{G}^{\alpha\alpha}_{12}]_{11}$, $[\tilde{G}^{\alpha\alpha}_{12}]_{12}$ is continuous at $t_2 = t_1$, so that Δ can also be written in terms of $[\tilde{G}^{\alpha\beta}_{12}]_{12}$ or $[\tilde{G}^{\beta\alpha}_{12}]_{12}$ at $t_2 = t_1$.

Still ignoring impurity scattering, the equation of motion Eq. (3.112) can then be written in compact form as

$$\left[\left(i\hat{\tau}^3\frac{\partial}{\partial t_1} + \frac{\nabla_1^2}{2m} + \mu + \hat{\Delta}\right) \ominus \hat{G}\right] = 0\,. \tag{3.115}$$

Here $\hat{\Delta}$ represents a 4x4 matrix

$$\hat{\Delta} = \begin{pmatrix} \tilde{\Delta} & 0 \\ 0 & \tilde{\Delta} \end{pmatrix}\,, \tag{3.116}$$

where

$$\tilde{\Delta} = \begin{pmatrix} 0 & \Delta \\ -\Delta^* & 0 \end{pmatrix}\,, \tag{3.117}$$

[2] Δ defined this way differs from the conventional definition by a factor of i. Note that the signs associated with Δ in the matrix above are different from the conventional definition of Gor'kov's equation, because of the τ^3 factor in the definition of the Green's functions.

with Δ defined by Eq. (3.114), and

$$\hat{\tau}^3 = \begin{pmatrix} \tau^3 & 0 \\ 0 & \tau^3 \end{pmatrix} . \tag{3.118}$$

Before we move on to making the quasiclassical approximation, it is useful to obtain expressions for measurable quantities in terms of the Green's functions defined in this section. Following Eq. (3.49), one can define a distribution function by averaging the Keldysh component of the Green's function defined in Eq. (3.111)

$$\tilde{h}(\boldsymbol{R}, T, \boldsymbol{p}) = \frac{i}{2\pi} \int dE \, \tilde{G}^K(\boldsymbol{R}, T; \boldsymbol{p}, E) . \tag{3.119}$$

However, since $\tilde{G}^K$ is a 2x2 matrix, $\tilde{h}$ is also a 2x2 matrix, so that its interpretation as a simple distribution function (in the flavor of Eq. (3.49) for the equilibrium case, for example) is not immediately clear. A more physical interpretation can be obtained by diagonalizing the Gor'kov equations given in Eq. (3.113) [12]. The matrix on the left hand side of this equation can be diagonalized by a unitary transformation; this transformation, of course, is just the Bogoliubov–Valatin transformation, which results in a diagonal 'energy' matrix with eigenvalues

$$E_{\boldsymbol{p}}^2 = \epsilon_{\boldsymbol{p}}^2 + \Delta^2. \tag{3.120}$$

The same transformation also diagonalizes the *equilibrium* distribution matrix $\tilde{h}_0$, which now has the form

$$\tilde{h}_0 \simeq \begin{pmatrix} 1 - 2f_{0\uparrow}(E_{\boldsymbol{p}}) & 0 \\ 0 & 2f_{0\downarrow}(E_{\boldsymbol{p}}) - 1 \end{pmatrix} . \tag{3.121}$$

The top–left component is for electron–like excitations, and the bottom–right component for hole–like excitations. This suggests that for our combined Nambu–Gor'kov–Keldysh Green's functions, the equations for the electric current and thermal current should be modified to

$$\boldsymbol{j}(\boldsymbol{R}, T) = -\frac{ie}{2} \int \frac{dE}{2\pi} \int \frac{d^3p}{(2\pi)^3} \boldsymbol{v}_F \mathrm{Tr} \left[\tau^3 \tilde{G}^K(\boldsymbol{R}, T, \boldsymbol{p}, E) \right] , \tag{3.122}$$

and

$$\boldsymbol{j}_{th}(\boldsymbol{R}, T) = -\frac{i}{2} \int \frac{dE}{2\pi} \int \frac{d^3p}{(2\pi)^3} E \boldsymbol{v}_F \mathrm{Tr} \left[\tilde{G}^K(\boldsymbol{R}, T, \boldsymbol{p}, E) \right] . \tag{3.123}$$

Taking the trace of the matrix takes the contributions of both electrons and holes. Note that the expression for electrical current includes a factor of τ^3 in the argument of the trace, while the thermal current does not.

3.6 Quasiclassical Superconducting Green's Functions

In principle, the properties of the superconducting system may be calculated starting from Gor'kov's equations. In practice, however, such calculations are difficult in all but the simplest cases. The problem is that Gor'kov's equations contain information at length scales much finer than those of interest. The way around this is to make the quasiclassical approximation as we did for the case of the normal Green's functions, which we proceed to do below.

Taking into account impurity scattering, the equation of motion for the superconducting Green's function can now be written as

$$\left[\left(i\hat{\tau}^3\frac{\partial}{\partial t_1}+\frac{\partial_1^2}{2m}+\mu+\hat{\Delta}-\hat{\Sigma}_{imp}\right)\ominus\hat{G}\right]=0\,, \tag{3.124}$$

where the impurity self-energy $\hat{\Sigma}_{imp}$ includes contributions from both spin-flip and spin-independent elastic scattering.

The elastic contribution to the self-energy can be written as

$$\hat{\Sigma}_0(\boldsymbol{p})=N_i\int\frac{d^3p'}{(2\pi)^3}\left|v(\boldsymbol{p}-\boldsymbol{p}')\right|^2\hat{G}(\boldsymbol{p}')\,. \tag{3.125}$$

Here v is the impurity potential, and N_i the number of impurities per unit volume. We assume that $v(\boldsymbol{p})$ is independent of the magnitude of $\boldsymbol{p}$, so that

$$\hat{\Sigma}_0(p)=N_iN_0\int d\epsilon_{\boldsymbol{p}'}\,\frac{d\Omega_{p'}}{4\pi}\left|v(\hat{p}\cdot\hat{p}')\right|^2\hat{G}(\boldsymbol{p}')\,. \tag{3.126}$$

Defining the elastic scattering rate $1/\tau$ in the Born approximation by

$$\frac{1}{\tau}=2\pi N_iN_0\int\frac{d\Omega_{p'}}{4\pi}\left|v(\hat{p}\cdot\hat{p}')\right|^2\,, \tag{3.127}$$

we can write

$$\hat{\Sigma}_0=\frac{1}{2\pi\tau}\int d\epsilon_{\boldsymbol{p}}\,\hat{G}(p)\,. \tag{3.128}$$

Here $\hat{G}(p)$ is a function of the magnitude of $\boldsymbol{p}$ alone. Similarly, for the contribution from spin-flip scattering, one obtains

$$\hat{\Sigma}_{sf}=\frac{1}{2\pi\tau_{sf}}\int d\epsilon_{\boldsymbol{p}}\,\hat{\tau}^3\hat{G}(p)\hat{\tau}^3\,. \tag{3.129}$$

From Eq. (3.111), one has

$$\left[\left(i\hat{\tau}^3\frac{\partial}{\partial t_1}+\frac{\partial_1^2}{2m}+\mu+\hat{\Delta}-\hat{\Sigma}_0-\hat{\Sigma}_{sf}\right)\ominus\hat{G}\right]=0\,. \tag{3.130}$$

Converting the left hand side of this equation to relative coordinates using Eq. (3.63) (neglecting any derivatives with respect to the center–of–mass time T), and using only the first term of Eq. (3.73) to lowest order, we obtain

$$[\hat{\tau}^3 E + \hat{\Delta}, \hat{G}] + i\boldsymbol{v}_F \cdot \partial_{\boldsymbol{R}} \hat{G} - [\hat{\Sigma}_0 + \hat{\Sigma}_{sf}, \hat{G}] = 0 \,. \tag{3.131}$$

Note that there are no integrations over space or time coordinates in the equation above, but only matrix multiplications. Written in terms of the quasiclassical Green's functions, this becomes

$$[\hat{\tau}^3 E + \hat{\Delta}, \hat{g}] + i\boldsymbol{v}_F \cdot \partial_{\boldsymbol{R}} \hat{g} - [\hat{\sigma}_0 + \hat{\sigma}_{sf}, \hat{g}] = 0 \,, \tag{3.132}$$

where

$$\hat{\sigma}_0 = -i\frac{1}{2\tau}\hat{g}_s \,, \tag{3.133}$$

and

$$\hat{\sigma}_{sf} = -i\frac{1}{2\tau_{sf}}\hat{\tau}^3 \hat{g}_s \hat{\tau}^3 \,. \tag{3.134}$$

The subscript to the quasiclassical Green's functions denotes that they are averaged over all angles of $\boldsymbol{p}$. Eq. (3.132) is Eilenberger's equation [1] and is the starting point for many calculations on superconducting systems.

To complete the transformation to quasiclassical Green's functions, we express the equations for physically observable quantities in terms of the quasiclassical Green's functions. From Eq. (3.114), the gap parameter Δ can be expressed as

$$\Delta = i\lambda[\tilde{G}^{\alpha\beta}_{11+}]_{12} = \frac{i}{2}\lambda[\tilde{G}^{K}_{11+}]_{12} \tag{3.135}$$

using the definition Eq. (3.35) of the Keldysh Green's function. In the mixed representation, this can be written as

$$\begin{aligned}\Delta &= \frac{i\lambda}{2}\int\frac{dE}{2\pi}\int\frac{d^3p}{(2\pi)^3}[G^K(\boldsymbol{R},T,\boldsymbol{p},E)]_{12} \\ &= N_0\frac{\lambda}{4}\int dE\int\frac{d\Omega_p}{4\pi}[g^K(\boldsymbol{R},t,\hat{p},E)]_{12} \\ &= N_0\frac{\lambda}{8}\int dE\int\frac{d\Omega_p}{4\pi}\mathrm{Tr}\{(\tau^1 - i\tau^2)g^K(\boldsymbol{R},t,\hat{p},E)\} \,.\end{aligned} \tag{3.136}$$

From Eq. (3.122) and (3.123), the electrical current and thermal currents are given by

$$\boldsymbol{j}(\boldsymbol{R},T) = -\frac{eN_0}{4}\int dE\int\frac{d\Omega_p}{4\pi}\boldsymbol{v}_F \mathrm{Tr}\left[\tau^3\tilde{g}^K(\boldsymbol{R},T,\boldsymbol{p},E)\right] \tag{3.137}$$

and

$$\boldsymbol{j}_{th}(\boldsymbol{R},T) = -\frac{N_0}{4}\int dE \int \frac{d\Omega_p}{4\pi} E\boldsymbol{v}_F \mathrm{Tr}\left[\tilde{g}^K(\boldsymbol{R},T,\boldsymbol{p},E)\right] . \tag{3.138}$$

One can also define an equation that gives the amount of charge associated with quasiparticle excitations. In a superconductor in equilibrium, the number of particles and holes are equal, so the quasiparticle charge should vanish. If there is an imbalance in the population of electrons and holes, one can obtain a *charge imbalance*, [2,27] usually denoted by Q^*, which is given by

$$\begin{aligned} Q^* &= -\frac{ie}{2}\int \frac{dE}{2\pi}\int \frac{d^3p}{(2\pi)^3}\mathrm{Tr}\left[\tilde{G}^K(\boldsymbol{R},T,\boldsymbol{p},E)\right] \\ &= -\frac{eN_0}{4}\int dE \int \frac{d\Omega_p}{4\pi}\mathrm{Tr}\left[\tilde{g}^K(\boldsymbol{R},T,\boldsymbol{p},E)\right] \end{aligned} \tag{3.139}$$

Q^* is essentially the first term on the right hand side of Eq. (3.97). Invoking charge neutrality, this then would result in a electrochemical potential given Eq. (3.98)

$$\phi(\boldsymbol{R},T) = -\frac{1}{N_0 e}Q^* \tag{3.140}$$

The normalization condition and the distribution function

In obtaining the equation of motion of the Green's functions by subtracting the Dyson equation from its conjugate, some information was lost regarding the norm of the quasiclassical Green's function $\hat{g}$. The norm of $\hat{g}$ can be obtained by the normalization condition for the quasiclassical Green's function obtained by Eilenberger, [1] and Larkin and Ovchinnikov [4]

$$\hat{g}\hat{g} = \hat{\tau}^0, \tag{3.141}$$

where (4x4) matrix multiplication is implied. This normalization condition can be obtained by explicit calculation for a bulk system in equilibrium. Furthermore, it can be shown that the normalization condition is consistent with Eilenberger's equation Eq. (3.132).

Eq. (3.141) is equivalent to the three (2x2) matrix equations

$$\tilde{g}^R\tilde{g}^R = \tau^0 , \tag{3.142a}$$

$$\tilde{g}^A\tilde{g}^A = \tau^0 , \tag{3.142b}$$

and

$$\tilde{g}^R\tilde{g}^K + \tilde{g}^K\tilde{g}^A = 0 . \tag{3.142c}$$

As in the case of the E–integrated Green's functions, we would like to obtain an equation of motion for a distribution function, equivalent to the

quantum Boltzmann equation derived earlier. We introduce such a distribution function $\tilde{h}$ by the ansatz [11]

$$\tilde{g}^K = \tilde{g}^R\tilde{h} - \tilde{h}\tilde{g}^A \,. \tag{3.143}$$

This form of the quasiclassical Keldysh Green's function satisfies the normalization condition Eq. (3.142c), as can be verified by direct substitution

$$\tilde{g}^R(\tilde{g}^R\tilde{h} - \tilde{h}\tilde{g}^A) + (\tilde{g}^R\tilde{h} - \tilde{h}\tilde{g}^A)\tilde{g}^A = 0 \tag{3.144}$$

using Eq. (3.142a) and(3.142b). Note that the function $\tilde{h}$ is not uniquely defined; if $\tilde{h}$ is replaced by $\tilde{h} + \tilde{h}'$, where

$$\tilde{h}' = \tilde{g}^R\tilde{x} + \tilde{x}\tilde{g}^A \tag{3.145}$$

and $\tilde{x}$ is an arbitrary matrix function, the right hand side of Eq. (3.143) is unchanged. [7] This arbitrariness allows us some flexibility in choosing the distribution function $\tilde{h}$. At low frequencies, for example, following Schmid and Schön, [2] and Larkin and Ovchinnikov, [5] we may choose $\tilde{h}$ to be diagonal in particle–hole space

$$\tilde{h} = h_L\tau^0 + h_T\tau^3 \,. \tag{3.146}$$

The subscripts refer to the longitudinal (h_L) and transverse (h_T), a terminology introduced by Schmid and Schön to refer to changes that are associated with the magnitude (h_L) or phase (h_T) of the complex order parameter. In equilibrium, $h_L(E) = 1 - 2f_0(E)$ and $h_T(E) = 0$.

Another possible choice is one introduced by Shelankov [28]

$$\tilde{h} = h_1\tau^0 + \tilde{g}^R h_2 \,. \tag{3.147}$$

This representation has the advantage that the equation for the distribution function reduces to a form very similar to the Boltzmann equation when the quasiparticle approximation is valid. In what follows, we shall use the representation of Schmid and Schön.

The representation of the Keldysh Green's function in terms of a distribution function allows us to obtain an equation of motion for the distribution function from the equation of motion for the Green's function. From Eilenberger's equation (3.132), we obtain three equations of motion for the three components of the quasiclassical Green's function

$$[E\tau^3 + \tilde{\Delta}, \tilde{g}^R] + i\boldsymbol{v}_F \cdot \partial_{\boldsymbol{R}}\tilde{g}^R - [\tilde{\sigma}^R, \tilde{g}^R] = 0 \,, \tag{3.148a}$$

$$[E\tau^3 + \tilde{\Delta}, \tilde{g}^A] + i\boldsymbol{v}_F \cdot \partial_{\boldsymbol{A}}\tilde{g}^A - [\tilde{\sigma}^A, \tilde{g}^A] = 0 \,, \tag{3.148b}$$

$$[E\tau^3 + \tilde{\Delta}, \tilde{g}^K] + i\boldsymbol{v}_F \cdot \partial_{\boldsymbol{R}}\tilde{g}^K - \tilde{\sigma}^R\tilde{g}^K - \tilde{\sigma}^K\tilde{g}^A + \tilde{g}^R\tilde{\sigma}^K + \tilde{g}^K\tilde{\sigma}^A = 0 \,, \tag{3.148c}$$

where $\tilde{\sigma} = \tilde{\sigma}_0 + \tilde{\sigma}_{sf}$. Substituting $\tilde{g}^K$ from Eq. (3.143) into Eq. (3.148c), we obtain

$$[E\tau^3 + \tilde{\Delta}, \tilde{g}^R\tilde{h} - \tilde{h}\tilde{g}^A] + i\boldsymbol{v}_F \cdot \partial_{\boldsymbol{R}}(\tilde{g}^R\tilde{h} - \tilde{h}\tilde{g}^A) - \tilde{\sigma}^R(\tilde{g}^R\tilde{h} - \tilde{h}\tilde{g}^A)$$
$$-\tilde{\sigma}^K\tilde{g}^A + \tilde{g}^R\tilde{\sigma}^K + (\tilde{g}^R\tilde{h} - \tilde{h}\tilde{g}^A)\tilde{\sigma}^A = 0\,. \tag{3.149}$$

Subtracting from the equation above Eq. (3.148a) multiplied by $\tilde{h}$ on the right, and adding Eq. (3.148b) multiplied by $\tilde{h}$ on the left, we obtain

$$\tilde{g}^R B[\tilde{h}] - B[\tilde{h}]\tilde{g}^A = 0\,, \tag{3.150}$$

where

$$B[\tilde{h}] = [E\tau^3 + \tilde{\Delta}, \tilde{h}] + \tilde{\sigma}^K - (\tilde{\sigma}^R\tilde{h} - \tilde{h}\tilde{\sigma}^A) + i\boldsymbol{v}_F \cdot \partial_{\boldsymbol{R}}\tilde{h}\,. \tag{3.151}$$

Equation(3.150) is the required equation of motion for the distribution function $\tilde{h}$.

As an example, we shall calculate the Green's functions for the equilibrium case for a bulk superconductor, in the limit where $\sigma = 0$. Equation(3.148a) in this limit has the form

$$[E\tau^3 + \tilde{\Delta}, \tilde{g}^R] = 0\,. \tag{3.152}$$

First, if we represent the retarded Green's function by

$$\tilde{g}^R = \begin{pmatrix} g_{11} & g_{12} \\ g_{21} & g_{22} \end{pmatrix}\,. \tag{3.153}$$

The normalization condition Eq. (3.142a) and Eq. (3.152) together imply that

$$g_{11} = -g_{22}, \tag{3.154a}$$
$$g_{11}^2 + g_{21}g_{12} = 1\,, \tag{3.154b}$$
$$g_{21} = -g_{12}\frac{\Delta^*}{\Delta} \tag{3.154c}$$

and

$$g_{11} = g_{12}\frac{E}{\Delta}\,. \tag{3.154d}$$

Solving these equations, we obtain

$$\tilde{g}^R = \begin{pmatrix} \frac{E}{\sqrt{E^2-|\Delta|^2}} & \frac{\Delta}{\sqrt{E^2-|\Delta|^2}} \\ -\frac{\Delta^*}{\sqrt{E^2-|\Delta|^2}} & -\frac{E}{\sqrt{E^2-|\Delta|^2}} \end{pmatrix}\,. \tag{3.155}$$

In taking the square roots in the equation above, a factor of i will appear if $E^2 < |\Delta|^2$. This is the expected solution from Gor'kov's equations. Note that

g_{11} is just the normalized BCS density of states for $E^2 > |\Delta|^2$, so that g_{11} represents a generalized density of states.

From the equations above, it is clear that $g_{21} = -g_{12}^*$. To obtain $\tilde{g}^A$, we can use the relation Eq. (3.24), which in terms of Nambu–Gor'kov matrices reads

$$\tilde{G}^A = -\tau^3 \tilde{G}^{R+} \tau^3 \qquad \text{or} \qquad \tilde{g}^A = -\tau^3 \tilde{g}^{R+} \tau^3 \tag{3.156}$$

where the G^+ etc. denotes the Hermitian conjugate.

3.7 The Dirty Limit: The Usadel Equation

In systems where elastic impurity scattering is strong, the motion of quasiparticles is not ballistic, but diffusive. In this case, the effect of the strong impurity scattering is to randomize the momentum of the quasiparticles, so that it makes sense to average the properties of system over the directions of the momentum, keeping in mind that the magnitude of the momentum is still its value at the Fermi surface, p_F.

With this in mind, let us consider a system with strong impurity scattering, which we define as a system in which the impurity scattering rate $1/\tau$, as defined by Eq. (3.127), is much larger than any energy in the problem (E, Δ). In this case, we expand the quasiclassical Green's function to first order in momentum (essentially an expansion in spherical harmonics)

$$\hat{g} = \hat{g}_s + \hat{p}\hat{g}_p \,, \tag{3.157}$$

where $\hat{p}$ denotes a vector of unit magnitude in the direction of $\boldsymbol{p}$, and $\hat{g}_s$ and $\hat{g}_p$ are independent of the direction of $\boldsymbol{p}$, and the subscripts stand for s–wave and p–wave components of $\hat{g}$. The assumption is that $\hat{g}_p \ll \hat{g}_s$. The self–energy is expanded in a similar fashion

$$\hat{\sigma} = \hat{\sigma}_0 + \hat{\sigma}_{sf} = \hat{\sigma}_s + \hat{p}\hat{\sigma}_p \,. \tag{3.158}$$

We would like to calculate the components of $\hat{\sigma}$ in terms of the components of $\hat{g}$, for which we shall need the definition of $\hat{\sigma}$ in terms of $\hat{g}$. Ignoring spin–flip scattering for the moment, this relation is given by Eq. (3.126), which can be rewritten in terms of the quasiclassical Green's functions in the form

$$\begin{aligned} \hat{\sigma}_0(p) &= -i\pi N_i N_0 \int \frac{d\Omega_{p'}}{4\pi} |v(\hat{p}\cdot\hat{p}')|^2 \hat{g}(\boldsymbol{p}') \\ &= -i\pi N_i N_0 \int \frac{d\Omega_{p'}}{4\pi} |v(\hat{p}\cdot\hat{p}')|^2 (\hat{g}_s + \hat{p}'\hat{g}_{p'}) \,, \end{aligned} \tag{3.159}$$

using the expansion Eq. (3.157) for the Green's function above. In order to do this, we take the dot product of $\hat{p}$ with both sides of the equation above

$$\hat{p}\cdot\hat{\sigma} = \hat{p}\hat{\sigma}_s + (\hat{p}\cdot\hat{p})\hat{\sigma}_p = \hat{p}\hat{\sigma}_s + \hat{\sigma}_p \,. \tag{3.160}$$

We perform a similar operation on Eq. (3.159)

$$\hat{p}\cdot\hat{\sigma}_0(p) = -i\pi N_i N_0 \int \frac{d\Omega_{p'}}{4\pi}|v(\hat{p}\cdot\hat{p}')|^2(\hat{p}\hat{g}_s + (\hat{p}\cdot\hat{p}')\hat{g}_{p'}) \,. \tag{3.161}$$

Since both $\hat{p}$ and $\hat{g}_s$ are independent of the integration over $d\Omega_{p'}$, the first term under the integral in the equation above can be written as

$$-i\pi\hat{p}\hat{g}_s N_i N_0 \int \frac{d\Omega_{p'}}{4\pi}|v(\hat{p}\cdot\hat{p}')|^2 = -\frac{i}{2\tau}\hat{p}\hat{g}_s \tag{3.162}$$

using the definition Eq. (3.127) of $1/\tau$. If we consider non–spin–flip scattering alone, then $\hat{\sigma}$ can be obtained by equating like terms in Eq. (3.160) and (3.161). If we include spin–flip scattering, one can write

$$\hat{\sigma}_s = -\frac{i}{2\tau}\hat{g}_s - -\frac{i}{2\tau_{sf}}\hat{\tau}^3\hat{g}_s\hat{\tau}^3 \,, \tag{3.163}$$

as expected from Eq. (3.133) and (3.134). For the p–wave component, we consider only the contribution from non spin–flip impurity scattering, under the assumption that it is much stronger than the spin–flip scattering. The second term under the integral in Eq. (3.161) can be written as

$$\begin{aligned} &- i\pi N_i N_0 \int \frac{d\Omega_{p'}}{4\pi}|v(\hat{p}\cdot\hat{p}')|^2(\hat{p}\cdot\hat{p}')\hat{g}_{p'} = \\ &- i\pi N_i N_0 \hat{g}_p \int \frac{d\Omega_{p'}}{4\pi}|v(\hat{p}\cdot\hat{p}')|^2[1-(1-\hat{p}\cdot\hat{p}')] \,, \end{aligned} \tag{3.164}$$

where $\hat{g}_p$ can be taken out of the integral since it is independent of the direction of $\boldsymbol{p}$. The first term in the square bracket can be seen to be related to the elastic scattering rate $1/\tau$. The remaining terms can be written in terms of the transport time, defined by

$$\frac{1}{\tau_{tr}} = 2\pi N_i N_0 \int \frac{d\Omega_{p'}}{4\pi}|v(\hat{p}\cdot\hat{p}')|^2(1-\hat{p}\cdot\hat{p}') \,, \tag{3.165}$$

that is well known in the transport theory of metals. With this definition, $\hat{\sigma}_p$ can be written as

$$\hat{\sigma}_p = -\frac{i}{2}(\frac{1}{\tau} - \frac{1}{\tau_{tr}})\hat{g}_p \,. \tag{3.166}$$

By putting Eq. (3.157) into the normalization condition for the quasiclassical Green's function, and neglecting terms quadratic in $\hat{g}_p$, we also obtain the two equations

$$\hat{g}_s\hat{g}_s = 1 \tag{3.167a}$$

and

$$\hat{g}_s\hat{g}_p + \hat{g}_p\hat{g}_s = 0 \,. \tag{3.167b}$$

We now proceed to expand the Eilenberger equation, Eq. (3.132), in terms of the s and p–wave expansions of $\hat{g}$ and $\hat{\sigma}$. Replacing $\boldsymbol{v}_F$ by $v_F\hat{p}$, we obtain

$$[\hat{\tau}^3 E - \hat{\Delta}, \hat{g}_s] + \hat{p}[\hat{\tau}^3 E - \hat{\Delta}, \hat{g}_p] + iv_F\hat{p}\cdot\partial_{\boldsymbol{R}}(\hat{g}_s + \hat{p}\hat{g}_p) - [\hat{\sigma}_s, \hat{g}_s] - \hat{p}[\hat{\sigma}_s, \hat{g}_p] + [\hat{\sigma}_p, \hat{g}_s] + \hat{p}\cdot\hat{p}[\hat{\sigma}_p, \hat{g}_p] = 0\,. \tag{3.168}$$

The last term is second order in the small quantity $\hat{g}_p$, and can be neglected. Collecting the terms that are even in $\hat{p}$, we obtain

$$[\hat{\tau}^3 E + \hat{\Delta}, \hat{g}_s] + iv_F(\hat{p}\cdot\hat{p})\partial_{\boldsymbol{R}}\hat{g}_p = 0\,. \tag{3.169}$$

Averaging this equation over all directions of $\hat{p}$ gives

$$[\hat{\tau}^3 E + \hat{\Delta}, \hat{g}_s] + i\frac{v_F}{3}\partial_{\boldsymbol{R}}\hat{g}_p = 0\,. \tag{3.170}$$

Ignoring spin–dependent scattering for the moment, the terms that are odd in $\hat{p}$ can be written

$$[\hat{\tau}^3 E + \hat{\Delta}, \hat{g}_p] + iv_F\partial_{\boldsymbol{R}}\hat{g}_s - \frac{i}{2\tau_{tr}}[\hat{g}_p, \hat{g}_s] = 0\,, \tag{3.171}$$

where we have used Eq. (3.163) and (3.166) to write $\hat{\sigma}_s$ and $\hat{\sigma}_p$ in terms of $\hat{g}_s$ and $\hat{g}_p$. If elastic scattering is strong, the first term in the equation above can be neglected compared to the third, so we obtain

$$iv_F\partial_{\boldsymbol{R}}\hat{g}_s + \frac{i}{\tau_{tr}}\hat{g}_s\hat{g}_p = 0\,, \tag{3.172}$$

where we have used Eq. (3.167b) to simplify the second term. Multiplying this equation by $\hat{g}_s$ on the left and using Eq. (3.167a) we obtain

$$v_F\hat{g}_s\partial_{\boldsymbol{R}}\hat{g}_s = -\frac{1}{\tau_{tr}}\hat{g}_p\,, \tag{3.173}$$

or writing $\hat{g}_p$ in terms of $\hat{g}_s$ we get

$$\hat{g}_p = v_F\tau_{tr}\hat{g}_s\partial_{\boldsymbol{R}}\hat{g}_s = -\ell\hat{g}_s\partial_{\boldsymbol{R}}\hat{g}_s\,. \tag{3.174}$$

Here, we have introduced the elastic scattering length $\ell = v_F\tau_{tr}$. Putting this into Eq. (3.171) we obtain

$$[\hat{\tau}^3 E + \hat{\Delta}, \hat{g}_s] - i\frac{v_F\ell}{3}\partial_{\boldsymbol{R}}\hat{g}_s\partial_{\boldsymbol{R}}\hat{g}_s = 0\,. \tag{3.175}$$

Writing this in terms of the diffusion coefficient $D = (1/3)v_F\ell$, and reintroducing the spin–flip scattering term, we get

$$[\hat{\tau}^3 E + \hat{\Delta} - \hat{\sigma}_{sf}, \hat{g}_s] - iD\partial_{\boldsymbol{R}}\hat{g}_s\partial_{\boldsymbol{R}}\hat{g}_s = 0\,. \tag{3.176}$$

This is the equation first derived by Usadel [29] and forms the starting point for most discussions of dirty superconducting systems.

In the remainder of our development we shall neglect the spin–flip scattering term. Writing $\hat{g}_s$ as a matrix

$$\hat{g}_s = \begin{pmatrix} \tilde{g}_s^R & \tilde{g}_s^K \\ 0 & \tilde{g}_s^A \end{pmatrix} , \tag{3.177}$$

we can write the matrix equation, Eq. (3.176), as three separate equations

$$[\tau^3 E + \tilde{\Delta}, \tilde{g}_s^R] = iD\partial_{\boldsymbol{R}}(\tilde{g}_s^R \partial_{\boldsymbol{R}} \tilde{g}_s^R), \tag{3.178a}$$

$$[\tau^3 E + \tilde{\Delta}, \tilde{g}_s^A] = iD\partial_{\boldsymbol{R}}(\tilde{g}_s^A \partial_{\boldsymbol{R}} \tilde{g}_s^A) , \tag{3.178b}$$

and

$$[\tau^3 E + \tilde{\Delta}, \tilde{g}_s^K] = iD\partial_{\boldsymbol{R}} \left[(\tilde{g}_s^R \partial_{\boldsymbol{R}} \tilde{g}_s^K) + (\tilde{g}_s^K \partial_{\boldsymbol{R}} \tilde{g}_s^A)\right] . \tag{3.178c}$$

As before, the first two equations come from the diagonal components of the Usadel equation, and describe the equilibrium properties of the system, while the third equation comes from the off–diagonal or Keldysh component, and represents the kinetic equation for the distribution function. These equations are supplemented by the equations for measurable quantities corresponding to Eq. (3.137), (3.138) and (3.137). Expanding $\tilde{g}^K$ in Eq. (3.137 using Eq. (3.157) and Eq. (3.137), we have

$$\begin{aligned} \boldsymbol{j}(\boldsymbol{R}, T) &= -\frac{eN_0}{4} \int dE \int \frac{d\Omega_p}{4\pi} v_F \hat{p} \mathrm{Tr} \left[\tau^3 \left(\tilde{g}_s^K + \hat{p}\tilde{g}_p^K\right)\right] \\ &= \frac{eN_0 D}{4} \int dE \mathrm{Tr} \left[\tau^3 (\tilde{g}_s \partial_{\boldsymbol{R}} \tilde{g}_s)^K\right] , \end{aligned} \tag{3.179}$$

where the angular average over the p–wave component give a factor of (1/3), and we have replaced $(1/3)v_F\ell$ by the diffusion coefficient D. Now

$$(\tilde{g}_s \partial_{\boldsymbol{R}} \tilde{g}_s)^K = (\tilde{g}_s^R \partial_{\boldsymbol{R}} \tilde{g}_s^K) + (\tilde{g}_s^K \partial_{\boldsymbol{R}} \tilde{g}_s^A) \tag{3.180}$$

so that Eq. (3.180) above can be rewritten as

$$\boldsymbol{j}(\boldsymbol{R}, T) = \frac{eN_0 D}{4} \int dE \mathrm{Tr} \left[\tau^3 \left(\tilde{g}_s^R \partial_{\boldsymbol{R}} \tilde{g}_s^K + \tilde{g}_s^K \partial_{\boldsymbol{R}} \tilde{g}_s^A\right)\right] . \tag{3.181}$$

The equation for j_{th} is obtained in a similar way

$$\boldsymbol{j}_{th}(\boldsymbol{R}, T) = \frac{N_0 D}{4} \int dE \; E \; \mathrm{Tr} \left[\tilde{g}_s^R \partial_{\boldsymbol{R}} \tilde{g}_s^K + \tilde{g}_s^K \partial_{\boldsymbol{R}} \tilde{g}_s^A\right] . \tag{3.182}$$

The kinetic equation, Eq. (3.178c), can be recast in terms of a differential equation for a distribution function $\tilde{h}$, in the hopes of separating the equilibrium properties of the system, represented by $\tilde{g}_s^R$ and $\tilde{g}_s^A$, from the

non–equilibrium properties of the system, represented by $\tilde{h}$. To this end, as before, we substitute Eq. (3.143) for $\tilde{g}_s^K$ in Eq. (3.178c), which then becomes

$$\begin{aligned}&[\tau^3 E + \tilde{\Delta}, \tilde{g}_s^R \tilde{h}] - [\tau^3 E + \tilde{\Delta}, \tilde{h}\tilde{g}_s^A] \\ &= iD\partial_{\boldsymbol{R}} \left[\left(\tilde{g}_s^R (\partial_{\boldsymbol{R}} \tilde{g}_s^R) \tilde{h} - \tilde{h} \tilde{g}_s^A (\partial_{\boldsymbol{R}} \tilde{g}_s^A) \right) + \partial_{\boldsymbol{R}} \tilde{h} - \left(\tilde{g}_s^R \partial_{\boldsymbol{R}} \tilde{h} \tilde{g}_s^A \right) \right] . \end{aligned} \tag{3.183}$$

Taking the trace of both sides of the equation above gives

$$0 = iD\partial_{\boldsymbol{R}} \mathrm{Tr} \left\{ \partial_{\boldsymbol{R}} \tilde{h} + \tilde{g}_s^R (\partial_{\boldsymbol{R}} \tilde{g}_s^R) \tilde{h} - \tilde{h} \tilde{g}_s^A (\partial_{\boldsymbol{R}} \tilde{g}_s^A) - \tilde{g}_s^R (\partial_{\boldsymbol{R}} \tilde{h}) \tilde{g}_s^A \right\} , \tag{3.184}$$

using Eq. (3.178a) and (3.178b). In the linear regime, we can use the diagonal representation of $\tilde{h}$ given by Eq. (3.146) to obtain

$$\begin{aligned}&D\, \partial_{\boldsymbol{R}} \left[(\partial_{\boldsymbol{R}} h_L) \mathrm{Tr} \left\{ 1 - \tilde{g}_s^R \tilde{g}_s^A \right\} + h_T \mathrm{Tr} \left\{ \tau^3 \left(\tilde{g}_s^R (\partial_{\boldsymbol{R}} \tilde{g}_s^R) - \tilde{g}_s^A (\partial_{\boldsymbol{R}} \tilde{g}_s^A) \right) \right\} \right. \\ &\left. - (\partial_{\boldsymbol{R}} h_T) \mathrm{Tr} \left\{ \tilde{g}_s^R \tau^3 \tilde{g}_s^A \right\} \right] = 0 . \end{aligned} \tag{3.185}$$

Here, we have used the fact that

$$\begin{aligned}\mathrm{Tr}\{\partial_{\boldsymbol{R}} (\tilde{g}_s^R \tilde{g}_s^R)\} &= \mathrm{Tr}\{(\partial_{\boldsymbol{R}} (\tilde{g}_s^R)) \tilde{g}_s^R + \tilde{g}_s^R (\partial_{\boldsymbol{R}} (\tilde{g}_s^R))\} \\ &= 2\mathrm{Tr}\{\tilde{g}_s^R (\partial_{\boldsymbol{R}} (\tilde{g}_s^R))\} = 0 . \end{aligned} \tag{3.186}$$

Taking the trace after multiplying both sides of Eq. (3.183) by τ^3 gives

$$\begin{aligned}&D\partial_{\boldsymbol{R}} \left[\partial_{\boldsymbol{R}} h_T \mathrm{Tr}\{1 - \tilde{g}_s^R \tau^3 \tilde{g}_s^A \tau^3\} + h_L \mathrm{Tr}\{\tau^3 \left(\tilde{g}_s^R (\partial_{\boldsymbol{R}} \tilde{g}_s^R) - \tilde{g}_s^A (\partial_{\boldsymbol{R}} \tilde{g}_s^A) \right) \} \right. \\ &\left. - \partial_{\boldsymbol{R}} h_L \mathrm{Tr}\{\tilde{g}_s^R \tilde{g}_s^A \tau^3\} \right] \\ &= i \left[h_L \mathrm{Tr}\{\tau^3 [\tilde{g}_s^R - \tilde{g}_s^A, \tilde{\Delta}]\} - 2h_T \mathrm{Tr}\{\tilde{\Delta} (\tilde{g}_s^R + \tilde{g}_s^A)\} \right] . \end{aligned} \tag{3.187}$$

Equations (3.185) and (3.187) form a set of coupled differential equations for the distribution functions h_L and h_T. Let us define the quantities

$$Q = \frac{1}{4} \mathrm{Tr}\{\tau^3 \left(\tilde{g}_s^R (\partial_{\boldsymbol{R}} \tilde{g}_s^R) - \tilde{g}_s^A (\partial_{\boldsymbol{R}} \tilde{g}_s^A) \right) \} \tag{3.188}$$

and

$$M_{ij} = \frac{1}{4} \mathrm{Tr}\{\delta_{ij} \tau^0 - \tilde{g}_s^R \tau^i \tilde{g}_s^A \tau^j\} . \tag{3.189}$$

Then Eq. (3.185) and (3.187) can be written in the form

$$\partial_{\boldsymbol{R}} [M_{00} (\partial_{\boldsymbol{R}} h_L) + Q h_T + M_{30} \partial_{\boldsymbol{R}} h_T)] = 0, \tag{3.190a}$$

$$\begin{aligned}\partial_{\boldsymbol{R}} [M_{33} (\partial_{\boldsymbol{R}} h_T) + Q h_L + M_{03} \partial_{\boldsymbol{R}} h_L)] &= \frac{i}{4D} \left[h_L \mathrm{Tr}\{\tau^3 [\tilde{g}_s^R - \tilde{g}_s^A, \tilde{\Delta}]\} \right. \\ &\left. - 2h_T \mathrm{Tr}\{\tilde{\Delta} (\tilde{g}_s^R + \tilde{g}_s^A)\} \right] . \end{aligned} \tag{3.190b}$$

These equations are in the form of diffusion equations for the distribution function, more general forms of the diffusion equation discussed for the normal case in the introduction. As we shall see, the quantity Q is related to the *spectral* supercurrent in the system, D/M_{ij} are now the energy and position dependent diffusion coefficients, and Eq. (3.190) are essentially continuity equations for the spectral thermal and electric current. In the normal limit, $g^R = \tau^3$, $g^A = -\tau^3$, and $\tilde{\Delta} = 0$, so that $M_{00} = M_{33} = 1$, and $Q = M_{03} = M_{30} = 0$. Equations (3.190) then reduce to Eq. (3.1), as expected. Noting that the term in square brackets in Eq. (3.178c) is the same as the term in parenthesis in Eq. (3.181) and the term in square brackets in Eq. (3.182), the electric current can be written as

$$\boldsymbol{j}(\boldsymbol{R},T) = eN_0 D \int dE\ (M_{33}(\partial_{\boldsymbol{R}} h_T) + Q h_L + M_{03}\partial_{\boldsymbol{R}} h_L)\ . \tag{3.191}$$

The first term corresponds to quasiparticle (or dissipative) current, and the second term to the supercurrent. The third term, which is proportional to the derivative of h_L, is associated with an imbalance between particles and holes. The thermal current can be written in a similar way

$$\boldsymbol{j}_{th}(\boldsymbol{R},T) = N_0 D \int dE\ E[M_{00}(\partial_{\boldsymbol{R}} h_L) + Q h_T + M_{30}\partial_{\boldsymbol{R}} h_T]\ . \tag{3.192}$$

For the charge–imbalance Q^*, we note that only the s–wave part of the Keldysh Green's function in the square brackets in Eq. (3.139) survives after angular averaging. Writing g_s^K in the form given by Eq. (3.143), with $\tilde{h}$ given by Eq. (3.146), we have

$$\begin{aligned} Q^* &= -\frac{eN_0}{4}\int dE\ h_L \mathrm{Tr}\{g_s^R - g_s^A\} - \frac{eN_0}{4}\int dE\ h_T \mathrm{Tr}\{\tau^3(g_s^R - g_s^A)\} \\ &= -eN_0 \int dE\ h_T N(E)\ , \end{aligned} \tag{3.193}$$

since g_s^R and g_s^A are traceless. Here we have defined the normalized superconducting density of states by

$$N(E) = \frac{1}{4}\mathrm{Tr}\{\tau^3(g_s^R - g_s^A)\}\ , \tag{3.194}$$

which reduces to the conventional BCS density of states in the equilibrium case.

We can also recast the kinetic equations Eq. (3.190) in a slightly different form sometimes used in the literature. To do this, we subtract Eq. (3.178b) from Eq. (3.178a), multiply by τ^3, and take the trace. The result is

$$\mathrm{Tr}\{\tau^3[g_s^R - g_s^A, \tilde{\Delta}]\} = -iD\partial_{\boldsymbol{R}}(\mathrm{Tr}\{\tau^3[\tilde{g}_s^R \partial_{\boldsymbol{R}}\tilde{g}_s^R - \tilde{g}_s^A \partial_{\boldsymbol{R}}\tilde{g}_s^A]\})\ . \tag{3.195}$$

Using the definition of Q, we have

$$\partial_{\boldsymbol{R}} Q = \frac{i}{4D}\mathrm{Tr}\{\tau^3[g_s^R - g_s^A, \tilde{\Delta}]\}\ . \tag{3.196}$$

If we choose a gauge in which Δ is real, the right hand side of the equation vanishes, so that $\partial_{\boldsymbol{R}} Q = 0$. Clearly, $\partial_{\boldsymbol{R}} Q = 0$ also for a normal metal (even a proximity–coupled normal metal), where Δ vanishes. In either case, the spectral supercurrent Q is conserved. The right hand side of the equation above multiplied by h_L is the same as the second term of Eq. (3.190b). Subtracting Eq. (3.195) multiplied by h_L from Eq. (3.190b), we obtain

$$\partial_{\boldsymbol{R}} \left[M_{33}(\partial_{\boldsymbol{R}} h_T) + M_{03}(\partial_{\boldsymbol{R}} h_L)\right] + Q(\partial_{\boldsymbol{R}} h_L) = -\frac{i}{4D}\left[2h_T \mathrm{Tr}\{\tilde{\Delta}(\tilde{g}_s^R + \tilde{g}_s^A)\}\right] . \tag{3.197}$$

For real Δ, when $\partial_{\boldsymbol{R}} Q = 0$, Eq. (3.190a) can be written in a similar manner

$$\partial_{\boldsymbol{R}} \left[M_{00}(\partial_{\boldsymbol{R}} h_L) + M_{30}(\partial_{\boldsymbol{R}} h_T)\right] + Q(\partial_{\boldsymbol{R}} h_T) = 0 . \tag{3.198}$$

Finally, we can also write the kinetic equations in a form similar to Eq. (3.150)

$$\tilde{g}_s^R B[\tilde{h}] - B[\tilde{h}]\tilde{g}_s^A = 0 , \tag{3.199}$$

by performing similar manipulations on Eq. (3.178) as were performed on Eq. (3.148). For the diffusive case, $B[\tilde{h}]$ is a functional of $\tilde{h}$ now given by

$$\begin{aligned} B[\tilde{h}] &= [\tau^3 E + \tilde{\Delta}, \tilde{h}] \\ &\quad - iD\left[(\partial_{\boldsymbol{R}} \tilde{g}_s^R)(\partial_{\boldsymbol{R}} \tilde{h}) + \frac{1}{2}\left(\tilde{g}_s^R(\partial_{\boldsymbol{R}}^2 \tilde{h}) - (\partial_{\boldsymbol{R}}^2 \tilde{h})\tilde{g}_s^A\right) - (\partial_{\boldsymbol{R}} \tilde{h})(\partial_{\boldsymbol{R}} \tilde{g}_s^A)\right] . \end{aligned} \tag{3.200}$$

Boundary conditions for the quasiclassical equations of motion

Eq. (3.178) or their derivatives form a set of coupled differential equations for the quasiclassical Green's functions and the distribution function. In order to obtain a solution, however, we need to specify the boundary conditions for the Green's functions and the distribution function. To this end, we define the concept of a *reservoir*, where the Green's functions and distribution function have well–defined values.

For a normal reservoir, the retarded and advanced quasiclassical Green's functions are given by

$$g_{N0}^R = \tau^3; \qquad g_{N0}^A = -\tau^3, \tag{3.201}$$

and for the superconducting case, by Eq. (3.155), which we reproduce here

$$\tilde{g}^R = \begin{pmatrix} \frac{E}{\sqrt{E^2 - |\Delta|^2}} & \frac{\Delta}{\sqrt{E^2 - |\Delta|^2}} \\ -\frac{\Delta^*}{\sqrt{E^2 - |\Delta|^2}} & -\frac{E}{\sqrt{E^2 - |\Delta|^2}} \end{pmatrix} . \tag{3.202}$$

Here, g_{S0}^A is given by Eq. (3.156).

The equilibrium distribution function $\tilde{h}$ is given by Eq. (3.121) in both normal and superconducting reservoirs (since we are dealing only with excitations), where, as we noted earlier the $(1,1)$ component of the matrix applies to particle–like excitations, and the $(2,2)$ component of the matrix applies to hole–like excitations. From this point of view, the Fermi functions in Eq. (3.121) are given in terms of the usual equilibrium Fermi function Eq. (3.5) by $f_{0\uparrow}(E) = f_0(E)$ and $f_{0\downarrow}(E) = f_0(-E)$. (Since we are dealing with the static limit in all that follows, we again use the symbol T to refer to the temperature.) Looking ahead to where we might have a finite voltage V on a reservoir, the equilibrium form of $\tilde{h}$ can then be written as

$$\tilde{h}_0 = \begin{pmatrix} \tanh\left(\frac{E+eV}{2k_BT}\right) & 0 \\ 0 & \tanh\left(\frac{E-eV}{2k_BT}\right) \end{pmatrix} . \tag{3.203}$$

If we write $\tilde{h}_0$ in the form of Eq. (3.146) the equilibrium values of h_L and h_T can then be expressed as

$$h_{L,T} = \frac{1}{2}\left[\tanh\left(\frac{E+eV}{2k_BT}\right) \pm \tanh\left(\frac{E-eV}{2k_BT}\right)\right] . \tag{3.204}$$

If a finite voltage is put on the superconductor, we will obtain a time evolution of the phase in accordance with the Josephson relations. Since we have restricted ourselves here to the static case, we must assume that the voltage on the superconducting reservoir $V = 0$. In this case, $h_T = 0$ for the superconducting reservoir.

For a system with perfect interfaces between the superconducting and normal parts, the boundary conditions defined by the equations above are sufficient to solve the differential equations, the implicit assumption being that the Green's functions and the distribution functions are continuous across any interface. When the transparency of the interface is less than unity, this is no longer true. Zaitsev [30] derived the boundary conditions for the Green's functions at an interface of arbitrary transparency. Kupriyanov and Lukichev [31] simplified these equations for the diffusive case in the limit of small barrier transparency. Consider then an interface at $x = 0$ between two metals, say one a normal metal in the half–plane $x < 0$ (labeled by the index '1') and one a superconductor in the half–plane $x > 0$, (labeled by the index '2'), although it also could be an interface between two different normal metals or superconductors. The boundary conditions of Kupriyanov and Lukichev are then

$$v_{F1}D_1\hat{g}_{s1}(\partial_x\hat{g}_{s1}) = v_{F2}D_2\hat{g}_{s2}(\partial_x\hat{g}_{s2}) , \tag{3.205a}$$

$$\hat{g}_{s1}\partial_x\hat{g}_{s1} = \frac{1}{2r}[\hat{g}_{s1}, \hat{g}_{s2}] . \tag{3.205b}$$

Here ∂_x denotes a derivative in the positive x direction, and $r = R_b/R_N$ is a parameter that is nominally the ratio of the barrier resistance R_b to the

normal wire resistance per unit length R_N/L, but is inversely proportional to the transmission t of the interface. The first of the equations is clearly related to the conservation of current across the interface. The right hand side of the second equation has been shown to be the first term in an expansion of terms of the transmission coefficient t, [14] and hence, it is only valid for low t.

The diagonal part of Eq. (3.205b) gives the boundary condition for the Green's functions

$$\tilde{g}_{s1}^R \partial_x \tilde{g}_{s1}^R = \frac{1}{2r} \left[\tilde{g}_{s1}^R \tilde{g}_{s2}^R - \tilde{g}_{s2}^R \tilde{g}_{s1}^R \right] . \tag{3.206}$$

The off-diagonal part of Eq. (3.205b) gives the boundary condition for the distribution function

$$\tilde{g}_{s1}^R \partial_x \tilde{g}_{s1}^K + \tilde{g}_{s1}^K \partial_x \tilde{g}_{s1}^A = \frac{1}{2r} \left[\tilde{g}_{s1}^R \tilde{g}_{s2}^K + \tilde{g}_{s1}^K \tilde{g}_{s2}^A - \tilde{g}_{s2}^R \tilde{g}_{s1}^K - \tilde{g}_{s2}^K \tilde{g}_{s1}^A \right] . \tag{3.207}$$

If we put in Eq. (3.143) for $\tilde{g}_s^K$, with Eq. (3.146) for $\tilde{h}$, and then take as before the trace of the resulting equation, and the trace of the equation multiplied by τ^3, we will obtain boundary conditions for h_T and h_L. Noting that the left hand side of Eq. (3.207) is simply the term in square brackets on the right hand side of Eq. (3.178c), we obtain the two equations

$$2r \left[M_{00} (\partial_{\boldsymbol{R}} h_L) + Q h_T + M_{30} \partial_{\boldsymbol{R}} h_T) \right] = \alpha_1 , \tag{3.208a}$$

and

$$2r \left[M_{33} (\partial_{\boldsymbol{R}} h_T) + Q h_L + M_{03} \partial_{\boldsymbol{R}} h_L) \right] = \alpha_2 , \tag{3.208b}$$

where

$$\begin{aligned} \alpha_1 = \mathrm{Tr} \{ & \tilde{g}_1^R (\tilde{g}_2^R \tilde{h}_2 - \tilde{h}_2 \tilde{g}_2^A) + (\tilde{g}_1^R \tilde{h}_1 - \tilde{h}_1 \tilde{g}_1^A) \tilde{g}_2^A \\ & - \tilde{g}_2^R (\tilde{g}_1^R \tilde{h}_1 - \tilde{h}_1 \tilde{g}_1^A) - (\tilde{g}_2^R \tilde{h}_2 - \tilde{h}_2 \tilde{g}_2^A) \tilde{g}_1^A \} , \end{aligned} \tag{3.208c}$$

and

$$\begin{aligned} \alpha_2 = \mathrm{Tr} \{ & (\tau^3 \tilde{g}_1^R (\tilde{g}_2^R \tilde{h}_2 - \tilde{h}_2 \tilde{g}_2^A) + (\tilde{g}_1^R \tilde{h}_1 - \tilde{h}_1 \tilde{g}_1^A) \tilde{g}_2^A \\ & - \tilde{g}_2^R (\tilde{g}_1^R \tilde{h}_1 - \tilde{h}_1 \tilde{g}_1^A) - (\tilde{g}_2^R \tilde{h}_2 - \tilde{h}_2 \tilde{g}_2^A) \tilde{g}_1^A) \} . \end{aligned} \tag{3.208d}$$

We note that although the boundary conditions of Kupriyanov and Lukichev are valid for large r, they also give the correct boundary conditions (that of continuity of the Green's functions and distribution functions) in the limit of $r \to 0$. For arbitrary transmission of a barrier with n channels, the boundary condition can be represented as [19]

$$\hat{g}_{s1} \partial_x \hat{g}_{s1} = \gamma \frac{e^2}{\pi} \sum_n 2T_n \frac{[\hat{g}_{s1}, \hat{g}_{s2}]}{4 + T_n (\hat{g}_{s1} \hat{g}_{s2} + \hat{g}_{s2} \hat{g}_{s1} - 2)} , \tag{3.209}$$

where γ is a constant factor, and T_n is the transmission of the nth channel. It can be seen that for a single channel with small transmission T, this equation reduces to the boundary condition of Kupriyanov and Lukichev.

3.8 Parametrization of the Quasiclassical Green's Function

The normalization Eq. (3.167a) permits a parametrization of the quasiclassical Green's functions that is very convenient for calculations. Eq. (3.167a) is a matrix equation that is equivalent to the three equations (3.142) for the s–wave component of the Green's function. To take into account the macroscopic phase of the superconductor, we note that a gauge transformation that transforms the vector and scalar potentials according to Eq. (3.93) and (3.94) transforms the field operators according to the equations

$$\hat{\psi} \rightarrow \hat{\psi} e^{i\chi} , \tag{3.210a}$$

$$\hat{\psi}^{+} \rightarrow \hat{\psi}^{+} e^{-i\chi} . \tag{3.210b}$$

The Nambu–Gor'kov Green's functions defined in Eq. (3.109) are transformed accordingly. For example, two components of $\tilde{G}_{12}^{\beta\alpha}$ would transform according to

$$[\tilde{G}_{12}^{\beta\alpha}]_{11} \rightarrow [\tilde{G}_{12}^{\beta\alpha}]_{11} e^{-i(\chi(\boldsymbol{r}_1)-\chi(\boldsymbol{r}_2))} , \tag{3.211a}$$

$$[\tilde{G}_{12}^{\beta\alpha}]_{12} \rightarrow [\tilde{G}_{12}^{\beta\alpha}]_{12} e^{i(\chi(\boldsymbol{r}_1)+\chi(\boldsymbol{r}_2))} . \tag{3.211b}$$

Making the transformation (3.42a) to mixed coordinates, and taking the limit as $\boldsymbol{r} \rightarrow 0$, we see that the off–diagonal components of the Nambu–Gor'kov Green's functions are multiplied by a phase factor $e^{i\chi(\boldsymbol{R})}$ or $e^{-i\chi(\boldsymbol{R})}$, while the diagonal components remain unchanged. Consequently, Δ also transforms as

$$\Delta \rightarrow \Delta e^{i\chi(\boldsymbol{R})} . \tag{3.212}$$

Keeping this in mind, we can express $\tilde{g}_s^R$ as

$$\tilde{g}_s^R = \begin{pmatrix} \cosh\theta & \sinh\theta e^{i\chi} \\ -\sinh\theta e^{-i\chi} & -\cosh\theta \end{pmatrix} , \tag{3.213}$$

where θ and χ are complex functions of the energy E and position $\boldsymbol{R}$. This form satisfies the normalization condition $\hat{g}_s^R \hat{g}_s^R = \tau^0$. Note, one can also express $\hat{g}_s^R$ equivalently in terms of sin and cos. For completeness, we also give the expression for $\tilde{g}_s^A$:

$$\tilde{g}_s^A = \begin{pmatrix} -\cosh\theta^* & -\sinh\theta^* e^{i\chi^*} \\ \sinh\theta^* e^{-i\chi^*} & \cosh\theta^* \end{pmatrix} . \tag{3.214}$$

We now put this into the Usadel equation for $\tilde{g}^R$, Eq. (3.178a). Keeping in mind that the matrix for $\tilde{\Delta}$ involves additional factors of $e^{i\chi}$ and $e^{-i\chi}$ due to the gauge transformation, the diagonal (1,1) component of this matrix equation is

$$D\sinh^2\theta\, \partial_{\boldsymbol{R}}^2\chi + D\sinh 2\theta\, \partial_{\boldsymbol{R}}\chi\, \partial_{\boldsymbol{R}}\theta - 2i\mathrm{Im}(\Delta)\sinh\theta = 0, \tag{3.215a}$$

and the off–diagonal component (1,2) is

$$D\partial_{\boldsymbol{R}}^2\theta - \frac{D}{2}\sinh 2\theta\,(\partial_{\boldsymbol{R}}\chi)^2 + 2Ei\sinh\theta - 2i\mathrm{Re}(\Delta)\cosh\theta = 0, \qquad (3.215b)$$

where we have used Eq. (3.215a) to simplify Eq. (3.215b). Defining a current $j_s(E,\boldsymbol{R})$ by the equation

$$j_s(E,\boldsymbol{R}) = \sinh^2\theta(E,\boldsymbol{R})\partial_{\boldsymbol{R}}\chi(E,\boldsymbol{R}), \qquad (3.216)$$

we can rewrite Eq. (3.215a) as

$$D\partial_{\boldsymbol{R}} j_s(E,\boldsymbol{R}) - 2i\mathrm{Im}(\Delta)\sinh\theta = 0. \qquad (3.217)$$

$j_s(E,\boldsymbol{R})$ is proportional to $\sinh^2\theta$, which is proportional to the square of the pair amplitude, and it is also proportional to the gauge–invariant gradient of the phase. Consequently, it is similar in form to the conventional definition of the supercurrent, and is called the spectral supercurrent. Indeed, Eq. (3.217) is simply another way of writing Eq. (3.196), and Q and j_s are related by

$$Q(E,\boldsymbol{R}) = -\mathrm{Im}(j_s(E,\boldsymbol{R})). \qquad (3.218)$$

As we noted before, $\partial_{\boldsymbol{R}}Q = 0$ if Δ is purely real, and from Eq. (3.217), it can be seen that $\partial_{\boldsymbol{R}} j_s(E,\boldsymbol{R}) = 0$ also if Δ is real.

Equations(3.215) form a set of coupled equations that can be solved in principle for $\theta(E,\boldsymbol{R})$ and $\chi(E,\boldsymbol{R})$. In the case of a negligible spectral supercurrent, the equations decouple, and one needs to solve only Eq. (3.215b). In the limit of a bulk superconductor with a uniform real order parameter and no phase gradient, we recover the bulk value of the Green's function, Eq. (3.155). The differential equations must be supplemented by boundary conditions. From Eq. (3.155), in a superconducting reservoir, we have

$$\cosh\theta_{S0} = \frac{E}{\sqrt{E^2 - |\Delta|^2}}\,, \qquad (3.219)$$

so that the value of θ in the superconducting reservoir is given by

$$\theta_{S0} = \begin{cases} -i\frac{\pi}{2} + \frac{1}{2}\ln\frac{|\Delta|+E}{|\Delta|-E} & \text{if } E < |\Delta|\,, \\ \frac{1}{2}\ln\frac{E+|\Delta|}{E-|\Delta|} & \text{if } E > |\Delta|\,. \end{cases} \qquad (3.220)$$

The value of χ in a superconducting reservoir is just the macroscopic phase of the superconductor. In a normal reservoir, $\theta = 0$. The value of χ in a normal reservoir is meaningless, of course, and any choice that results in no phase gradient is valid.

In terms of the θ parametrization, the boundary conditions of Kupriyanov and Lukichev can be expressed as

$$r\sinh\theta_1(\partial_{\boldsymbol{R}}\chi_1) = \sinh\theta_2\sin(\chi_2 - \chi_1), \qquad (3.221a)$$

and

$$r\left[\partial_{\boldsymbol{R}}\theta_1 + i\sinh\theta_1\cosh\theta_1(\partial_{\boldsymbol{R}}\chi_1)\right] = \cosh\theta_1\sinh\theta_2 e^{i(\chi_2-\chi_1)} - \sinh\theta_1\cosh\theta_2 \ . \tag{3.221b}$$

Note, that for $r = 0$, the boundary conditions reduce to $\chi_1 = \chi_2$ and $\theta_1 = \theta_2$. In the absence of a supercurrent, $(\partial_{\boldsymbol{R}}\chi_1) = 0$, so that the equations above simplify to

$$\chi_1 = \chi_2, \tag{3.222a}$$

and

$$r(\partial_{\boldsymbol{R}}\theta_1) = \sinh(\theta_2 - \theta_1). \tag{3.222b}$$

Finally, we can write expressions for physical quantities in terms of θ and χ. These quantities can be written in terms of the M_{ij}

$$M_{00} = \frac{1}{2}\left[1 + \left(\cosh\theta\cosh\theta^* - \sinh\theta\sinh\theta^* e^{i(\chi-\chi^*)}\right)\right], \tag{3.223a}$$

$$M_{33} = \frac{1}{2}\left[1 + \left(\cosh\theta\cosh\theta^* + \sinh\theta\sinh\theta^* e^{i(\chi-\chi^*)}\right)\right], \tag{3.223b}$$

$$M_{03} = -\frac{i}{2}\left[\sinh\theta\sinh\theta^*\sin(\chi-\chi^*)\right], \tag{3.223c}$$

and

$$M_{30} = \frac{i}{2}\left[\sinh\theta\sinh\theta^*\sin(\chi-\chi^*)\right] \ . \tag{3.223d}$$

If χ is real, then the $M_{03} = M_{30} = 0$, and M_{00} and M_{33} simplify to

$$M_{00} = \cos^2(\mathrm{Im}(\theta)) \tag{3.224a}$$

and

$$M_{33} = \cosh^2(\mathrm{Re}(\theta)) \ . \tag{3.224b}$$

These relations will be used in the next section when we discuss applying the Usadel equation to derive the transport properties of some simple device geometries.

To conclude this section, we shall write an expression for the gap in terms θ. Replacing Eq. (3.143) for $\tilde{g}^K$ into Eq. (3.136) for the gap, we have

$$\Delta = N_0\frac{\lambda}{4}\int dE\ [\tilde{g}_s^R\tilde{h} - \tilde{h}\tilde{g}_s^A]_{12} \ , \tag{3.225}$$

where performing the angular average in Eq. (3.136) gives the s–components of the Green's functions. Putting in $\tilde{h}$ in the form of Eq. (3.146), we obtain

$$\Delta = N_0 \frac{\lambda}{4} \int dE \, [h_L(\tilde{g}_s^R - \tilde{g}_s^A) + h_T(\tilde{g}_s^R \tau^3 - \tau^3 \tilde{g}_s^A)]_{12} \, . \tag{3.226}$$

With $\tilde{g}_s^R$ and $\tilde{g}_s^A$ given by Eq. (3.213) and (3.214), we obtain

$$\begin{aligned} \Delta = N_0 \frac{\lambda}{4} \int dE \quad & [h_L(\sinh\theta e^{i\chi} + \sinh\theta^* e^{i\chi^*}) \\ & -h_T(\sinh\theta e^{i\chi} - \sinh\theta^* e^{i\chi^*})] . \end{aligned} \tag{3.227}$$

As an example, consider the case of a bulk superconductor, where $\chi = 0$ and $h_T = 0$. We then have

$$\begin{aligned} \Delta &= N_0 \frac{\lambda}{2} \int dE \; h_L \mathrm{Re}(\sinh\theta) \\ &= N_0 \frac{\lambda}{2} \int dE \; \tanh(E/2k_BT) \mathrm{Re}\left(\frac{\Delta}{\sqrt{E^2 - \Delta^2}}\right) , \end{aligned} \tag{3.228}$$

which is the usual self–consistent equation for the gap.

3.9 Applications of the Quasiclassical Equations to Proximity–Coupled Systems

We shall conclude our discussion of the quasiclassical theory by applying the equations that we have derived to some simple devices incorporating normal metals in close proximity with superconductors. Since the equations of motion in the diffusive limit are in general nonlinear, solving them usually requires numerical techniques, except in the limit of large resistances between the superconductor and the normal metal, where the Usadel equation can be linearized. We shall restrict ourselves to one–dimensional examples; these are the ones discussed most in the literature.

3.9.1 Proximity–Coupled Wire

We start with the simplest possible device, a one–dimensional normal–metal wire of length L connected on one end to a superconducting reservoir and at the other end to a normal metal reservoir. For definitiveness, let us take the superconducting reservoir to be at $x = 0$ and the normal–metal reservoir at $x = L$, and let us consider first the case of a perfect SN interface, so that the interface barrier resistance parameter $r = 0$. In this geometry, there can be no supercurrent, so that Q (or alternatively, j_s) is zero. Furthermore, we can take the phase χ to be zero in the superconducting reservoir without loss of

generality, and we note again that $\Delta = 0$ in the normal metal. Under these conditions, only M_{00} and M_{33} are non–zero in Eq. (3.190), which now read

$$M_{00}(\partial_R h_L) = K_1, \tag{3.229a}$$

and

$$M_{33}(\partial_R h_T) = K_2\ , \tag{3.229b}$$

where K_1 and K_2 are constants of integration. On integrating these equations from $x = 0$ to $x = L$, we obtain

$$h_L(x = L) - h_L(x = 0) = K_1 \int_0^L \frac{1}{M_{00}} dx, \tag{3.230a}$$

$$h_T(x = L) - h_T(x = 0) = K_2 \int_0^L \frac{1}{M_{33}} dx\ . \tag{3.230b}$$

To calculate the conductance of the normal–metal wire in the linear approximation, we apply a small voltage V on the normal–metal reservoir, keeping the superconducting reservoir at $V = 0$. If we consider the second equation, $h_T(x = 0) = 0$, and expanding $h_T(x = L)$ in a Taylor's expansion to first order, we obtain from Eq. (3.230b)

$$K_2 = \frac{eV}{2k_BT \cosh^2\left(\frac{E}{2k_BT}\right)} \int_0^L \frac{1}{M_{33}(E,x)} dx\ . \tag{3.231}$$

The electric current in the linear response regime can then be obtained from Eq. (3.191)

$$j = \frac{N_0 e^2 VD}{2k_BT} \int dE \frac{1}{\cosh^2(E/2k_BT)} \int_0^L \frac{1}{M_{33}(E,x)} dx\ . \tag{3.232}$$

There are two differences between this equation and the equivalent equation for a normal metal in the classical regime (Eq. (3.10) that we derived earlier. First, the equation above involves an integral over energy and position. One can define a energy and position dependent electrical diffusion coefficient

$$D_3(E,x) = \frac{D}{M_{33}(E,x)} \tag{3.233}$$

instead of the constant diffusion coefficient D in Eq. (3.10). Second, the current in Eq. (3.232) does not involve temperature differentials. Indeed, if one assumes that the superconducting reservoir is at a temperature T, and the normal reservoir at a temperature $T + \Delta T$, and expand $h_T(x = L)$ to first order in ΔT, the terms involving ΔT cancel, so that there is no term proportional to ΔT. As a consequence, thermoelectric phenomena cannot be

described using the quasiclassical equations, and an extension to the theory is required to take them into account.[3]

From Eq. (3.232), one can define a spectral or energy dependent conductance of the wire

$$G(E) = G_N \int_0^L \frac{1}{M_{33}(E,x)} dx \,, \tag{3.234}$$

where G_N is the normal state conductance of the wire. The total conductance is then

$$G = \int dE \frac{G(E)}{2k_B T \cosh^2(E/2k_B T)} \,. \tag{3.235}$$

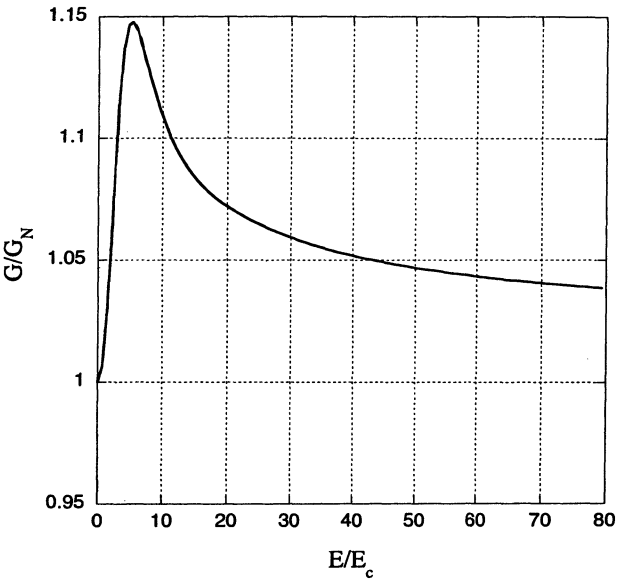

Fig. 3.4. Spectral conductance $G(E)$ of a one–dimensional wire of length L as a function of energy E, normalized to the correlation energy E_c. The barrier interface parameter r=0, and the gap is set to be $\Delta = 1000E_c$

Figure 3.4 shows the results of a numerical calculation of $G(E)/G_N$ as a function of the normalized energy E/E_c. The normalization factor $E_c = D/L^2$ is called the correlation energy or Thouless energy (from the theory of disordered metals, where it also occurs), [32] and is dependent on the length L of the wire. At high energies, $G(E)$ approaches its normal state value, as expected. As the energy is lowered, the conductance increases, as might be

[3] See, for example, F. Wilhelm, PhD Thesis, Universität Karlsruhe, 2000

expected in a proximity–coupled normal metal. However, instead of continually increasing as the energy is reduced, it reaches a maximum of around 1.15 G_N at an energy of $E \simeq 5E_c$, and then decreases, reaching its normal state value at $E = 0$. This non–monotonic behavior of the conductance is called reentrance, and has been observed in experiments by a number of groups. [33] It should be emphasized that the relevant energy scale where the maximum in conductance is observed is set not by the gap Δ of the superconductor, but by E_c, which itself depends inversely on the square of the length of the sample L. Hence in very long or macroscopic samples, the energy (and correspondingly, the temperature) at which the minimum would occur is far below the experimentally accessible range, and one regains the monotonic behavior expected from the simple Ginzburg–Landau theory of de Gennes. [34]

The temperature dependent conductance $G(T)$ can be obtained from $G(E)$ using Eq. (3.235); the result of this calculation, plotted in terms of the normalized resistance $R(T)/R_n$, is shown in Fig. 3.5. In obtaining this plot, we have used a value of $\Delta = 32E_c$, corresponding to a weak–coupling transition temperature of $T_c = 1.764\Delta/k_B$, typical parameters for Al films. We have also assumed that the gap is temperature dependent. Like $G(E)$, $R(T)$ is also non–monotonic, with a minimum at some intermediate temperature. We would expect the minimum in $R(T)$ to be around $T \simeq 5E_c/k_B$, based on the behavior of $G(E)$. However, the temperature dependence of the superconducting gap modifies this behavior, so that the minimum in resistance occurs at a somewhat higher temperature when the interface between the normal metal and the superconductor is perfect. Figure 3.5 shows additional curves corresponding to progressively increasing values of the interface barrier parameter r. Increasing the resistance of the NS interface decreases the leakage of superconducting correlations from the superconductor into the normal metal, and consequently results in a smaller increase in the conductance of the proximity–coupled normal metal. In addition, the temperature T_{min} at which the minimum in resistance occurs is also shifted down.

From Eq. (3.194), the normalized density of states $N(E)$ can be expressed in terms of θ as

$$N(E) = \cosh\left(\mathrm{Re}(\theta)\right)\cos\left(\mathrm{Im}(\theta)\right) \ . \tag{3.236}$$

Figure 3.6 shows the density of states as a function of energy and position along the wire of length L. There is a proximity–induced decrease of $N(E)$ near the superconducting reservoir. In fact, at the NS interface, there is a divergence in $N(E)$ at the gap energy, and it goes to zero at $E = 0$, just as one would expect for a superconductor. However, unlike a superconductor, it is not strictly zero for $E < \Delta$, but still has a finite amplitude. As one moves away from the NS interface into the proximity–coupled normal wire, both the amplitude of this effective gap and the divergence are smoothly reduced, so that at the normal reservoir, one recovers the normal density of states.

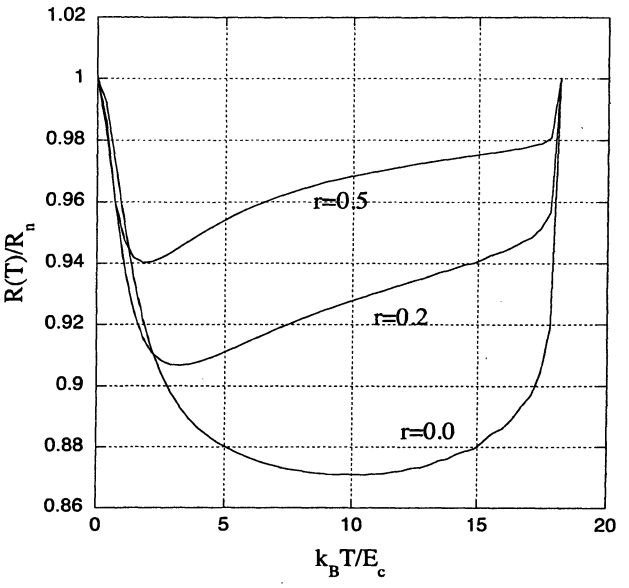

Fig. 3.5. Temperature dependent resistance $R(T)$ normalized to the normal state resistance R_N, as a function of the temperature T normalized to E_c, for different values of the interface resistance parameter r. The gap is set to be $\Delta = 32E_c$

This position dependent variation of the density of states has been observed in experiments. [35]

In our analysis above of the proximity effect in a normal metal coupled to a superconductor, we have ignored the effects of electron decoherence on the proximity correction. Phase coherence is essential to observing the proximity effect; if the phase coherence length L_ϕ is less than the length of the sample L, a finite spatial cutoff of the proximity effect is introduced. Phenomenologically, this can be taken into account by saying that the length of the wire is now L_ϕ instead of L. Since L_ϕ is typically of the order of a few microns even at low temperatures, this sets the dimensions of the samples that are required to observe this mesoscopic proximity effect.

While L_ϕ sets the upper cutoff for observing the proximity effect, a second relevant length scale for the problem can be obtained by considering the length at which E_c is equal to k_BT. This length is

$$L_T = \sqrt{\frac{\hbar D}{k_B T}}\,, \tag{3.237}$$

where L_T is called variously the thermal diffusion length or the Thouless length, again from the theory of disordered metals, where it also occurs. [32] (We put in here explicitly the factor of $\hbar$.) In fact, here it is simply the diffusive form of the superconducting coherence length in the normal metal, familiar

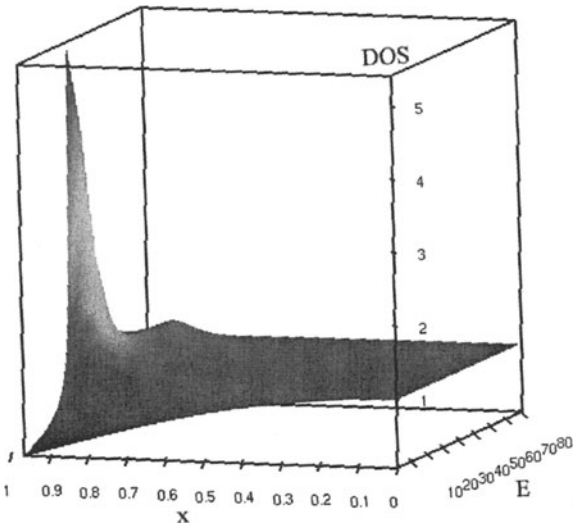

Fig. 3.6. Density of states $N(E, X)$ normalized to the normal state density of states N_0 for a one dimensional wire of length L, as a function of E/E_c and position x along the wire. The superconducting reservoir is at $x = 1.0$, and the normal reservoir is at $x = 0$. The density of states is suppressed at low energies near the superconducting reservoir

from the de Gennes/Ginzburg–Landau theory of the proximity effect, [34] which in the clean limit is given by

$$\xi_N = \frac{\hbar v_F}{k_B T} \,. \tag{3.238}$$

At low temperatures, when L_T is longer than L, the superconducting correlations induced in the normal metal extend throughout its length. At higher temperatures, they are restricted to a region of length L_T near the superconductor. L_T is also on the order of a few microns in typical metallic samples in accessible temperature regimes, so it also sets a limit on the dimensions of the samples in which one can see a proximity effect.

To calculate the thermal conductance of the wire, we proceed from Eq. (3.230a). We now consider a small temperature differential ΔT applied across the wire. Expanding h_L in a first–order Taylor's expansion, as we did for h_T, we obtain

$$K_1 = -\frac{E\Delta T}{2k_B T^2 \cosh^2\left(\frac{E}{2k_B T}\right)} \int_0^L \frac{1}{M_{00}(E,x)} dx \,. \tag{3.239}$$

We then obtain from Eq. (3.192)

$$j_{th} = -\frac{N_0 D \Delta T}{2k_B T^2} \int dE \frac{E^2}{\cosh^2(E/2k_B T)} \int_0^L \frac{1}{M_{00}(E,x)} dx \,. \tag{3.240}$$

As with the electrical conductance, we can define a thermal diffusion coefficient

$$D_0(E,x) = \frac{D}{M_{00}(E,x)} \,, \tag{3.241}$$

and a spectral thermal conductance

$$G_{th}(E) = G_{thN} \int_0^L \frac{1}{M_{00}(E,x)} dx, \tag{3.242}$$

where G_{thN} is related to the normal state electrical conductance by Eq. (3.17)

$$G_{thN} = G_N \frac{\pi^2}{3} \frac{k_B^2}{e^2} T \,. \tag{3.243}$$

Finally, the thermal conductance itself is given by an integral over energy

$$G_{th} = \frac{3}{\pi^2} \frac{1}{2(k_B T)^3} \int dE \frac{E^2 G_{th}(E)}{\cosh^2(E/2k_B T)} \,. \tag{3.244}$$

Of course, as noted by Andreev [36], the thermal conductance of a normal metal wire sandwiched between a normal–metal reservoir on one end and a superconducting reservoir on the other end must vanish, since the superconductor acts as a thermal insulator, so that no thermal current can flow through the device as a whole. However, one may consider a normal–metal wire with the superconducting reservoir connected off to one side, so that it does not block the flow of thermal current through the proximity–coupled wire. One may then consider the thermal conductance of the normal metal wire itself. Figure 3.7 shows the thermal conductance of this geometry, as a function of temperature, for different transmissivities of the interface barrier. The thermal conductance shows a monotonic decrease as T is lowered below T_c, although there are no distinct features at any particular temperature, unlike for the electrical conductance. In a superconductor, the exponential decrease in the thermal conductivity is associated with the opening of the gap in the quasiparticle density of states, since it is the quasiparticles that carry the thermal current. Noting the decrease in the density of states in the proximity–coupled normal metal wire, shown in Fig. 3.6, it is not surprising that this system will also show a decrease in the thermal conductance. The thermal conductance of the wire is strongly dependent on the transmission of the NS interface, characterized by the parameter r, and approaches the normal state thermal conductance as r increases.

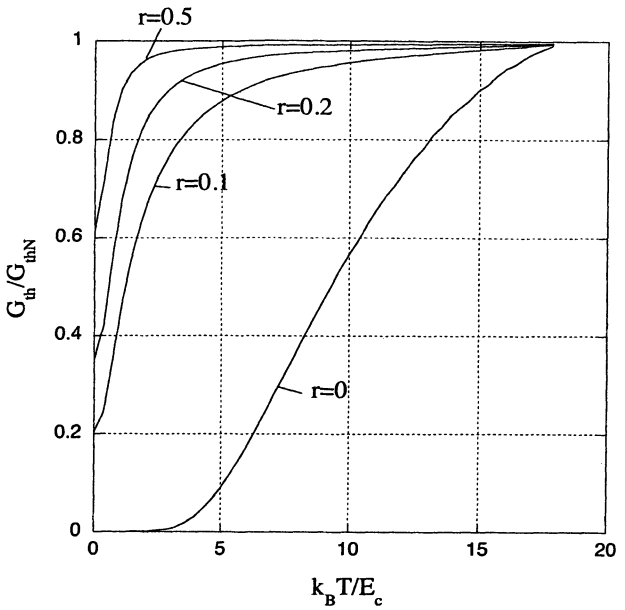

Fig. 3.7. Thermal conductance G_{th} of a normal wire connected to a superconducting reservoir on one end, and a normal metal reservoir on the other, as a function of the normalized temperature T, for a number of different values of the interface barrier parameter r. The gap is set to be $\Delta = 32E_c$, corresponding to a transition temperature of $T = 18.14E_c$

We note here again that, in our current approximation, a small voltage drop across the S/n–wire/N device will not result in a contribute to a thermal current through the system, since any terms proportional to voltage in the expansion of h_L will cancel. This is the converse of the case for the electrical current, where a small temperature drop did not contribute to the electrical current, emphasizing again that the conventional quasiclassical approximation cannot take into account thermoelectric effects.

3.9.2 Superconductor–Metal Bilayer

Instead of a normal reservoir on one side of the wire, if we consider a wire of length L connected only on one end to a superconducting reservoir (with the other end open), then a true gap in the density of states opens up in the proximity–coupled normal metal. The magnitude of the gap is related to E_c; hence, one can consider the proximity–coupled normal–metal in this case as a superconductor with a gap of E_c.

If the superconductor is not a reservoir, but a thin layer itself, then one will suppress superconductivity in the superconducting layer due to the proximity of the normal metal, an inverse proximity effect. The suppression of super-

conductivity is expected to reduce the gap in the superconductor. It is an interesting exercise to calculate the transition temperature of the bilayer in the quasiclassical approximation. We shall loosely follow here the treatment given by Martinis *et al.* [37] and Guéron [38].

Let the thickness of the superconductor be t_S, and the thickness of the normal metal t_N. We take the origin, $x = 0$, at the NS interface, and the superconductor extends from $x = -t_S$ to $x = 0$, and the normal metal from $x = 0$ to $x = t_N$. Near the transition, the order parameter in the superconductor is small, so we may the small θ limit of Eq. (3.215b). Since the phase is not important in this problem, we take $\chi = 0$. The resulting equation is

$$D\partial_x^2\theta + 2Ei\theta - 2i\Delta = 0\,, \tag{3.245}$$

where we have assumed that the gauge is chosen so that Δ is real. Let us assume that θ at $x = 0$ in the superconductor is θ_{0S}, and that variations of θ about this mean value are small. Under these conditions, we can also assume that the gap Δ in the superconductor is uniform. We can then expand θ_S to second order in x

$$\theta_S = \theta_{0S} + ax + bx^2\,. \tag{3.246}$$

Now, at $x = -t_S$, (and also at $x = t_N$), we have a vacuum interface, where $\partial_x\theta = 0$. Hence $a = 2bt_S$, and from the differential equation (3.245) taken at $x = 0$, $b = (i/D)(\Delta - E\theta_{0S})$, so that

$$\theta_S = \theta_{0S} + \frac{i}{D}(\Delta - E\theta_{0S})(2t_S x + x^2)\,. \tag{3.247}$$

Similarly

$$\theta_N = \theta_{0N} + \frac{i}{D}E\theta_{0N}(2t_N x - x^2)\,. \tag{3.248}$$

From the boundary condition Eq. (3.222b), we have the two equations

$$\frac{2irt_S}{D}(\Delta - E\theta_{0S}) = \theta_{0N} - \theta_{0S}\,, \tag{3.249a}$$

$$\frac{2irt_N}{D}E\theta_{0N} = \theta_{0N} - \theta_{0S}\,. \tag{3.249b}$$

Solving this pair of equations for θ_{0S}, we have

$$\theta_{0S} = \frac{\Delta}{E}\frac{D^2t_S(t_S + t_N) + 4r^2t_N^2t_S^2 - 2irDt_n^2}{D^2(t_s + t_N)^2 + 4r^2t_S^2t_N^2}\,. \tag{3.250}$$

Putting this into Eq. (3.228) for the gap, with $T = T_c$, and with the approximation that $\sinh(\theta) \simeq \theta$, we obtain

$$1 = N_0\frac{\lambda}{2}\int\frac{dE}{E}\tanh(E/2k_BT_c)\left[1 - \frac{t_N(t_S + t_N)}{(t_S + t_N)^2 + (4r^2/D^2)t_S^2t_N^2}\right]\,. \tag{3.251}$$

The first term in the square brackets gives the bare transition temperature T_{c0} of the superconducting film, and the second term corresponds to the corrections associated with the inverse proximity effect. For a perfect interface, with $r = 0$, the suppression of T_c is directly proportional to the normal fraction of the bilayer, and $T_c \to 0$ as t_N increases. For a highly resisitive barrier ($r \to \infty$), the second term in the square brackets goes to zero, so that there is little effect of the normal metal film on T_c of the superconducting film, as expected.

3.9.3 The SNS Junction and Andreev Interferometers

As our final example of the application of the quasiclassical equations of superconductivity, we consider the case of a dirty SNS junction. The model we consider is a normal metal wire of length L sandwiched between two superconducting reservoirs. As is well known, the application of a phase difference between the two superconducting reservoirs will result in the flow of a supercurrent through the normal wire. The phase difference can be applied, for example, by connecting one of the superconducting reservoirs to the other, thereby forming a loop with two different arms, one superconducting and one normal. This configuration is commonly called an Andreev interferometer. The phase between the two superconducting reservoirs can be varied by applying an Aharonov–Bohm type magnetic flux through the area of the loop; in this respect, we put together all contributions in the gauge–invariant phase χ. Due to the single–valued nature of the wave functions, a phase factor of $2\pi\Phi/\Phi_0$ is picked up in going aroung the loop, where Φ is the magnetic flux threading the Andreev interferometer, and $\Phi_0 = h/2e$ is the superconducting flux quantum. In a superconductor, the supercurrent I_S that is generated is directly proportional to the phase gradient; if I_S is small compared to the critical current I_c, the phase dropped across the superconductor will be small. Since I_c of the superconducting part of the Andreev interferometer is so much greater than the critical current of the proximity coupled normal–metal wire, most of the phase change will occur across the length L of the normal metal wire.

This fact allows us to map the Andreev interferometer that is coupled with an Aharonov–Bohm flux Φ to a SNS system with a phase difference $\phi = 2\pi\Phi/\Phi_0$ across it. In terms of our model, we consider the superconductors to be reservoir; this means applying a boundary condition for the gauge–invariant phase χ at the superconducting reservoirs. For our purposes, we apply this boundary condition anti–symmetrically, with a phase $\chi_L = -\pi\Phi/\Phi_0$ at the superconducting reservoir at $x = 0$, and $\chi_R = \pi\Phi/\Phi_0$ at the superconducting reservoir at $x = L$. We then must solve Eq. (3.215) in the normal–metal wire for θ and χ, with $\Delta = 0$, subject to the boundary condition for χ noted above, and the boundary condition $\theta = \theta_{S0}$ (where θ_{S0} is given by Eq. (3.220)) at both $x = 0$ and $x = L$. In general, both θ and χ are complex functions of x and E, and the solution of Eq. (3.215) must be

done numerically. Following Yip [39], we consider first the supercurrent Q,

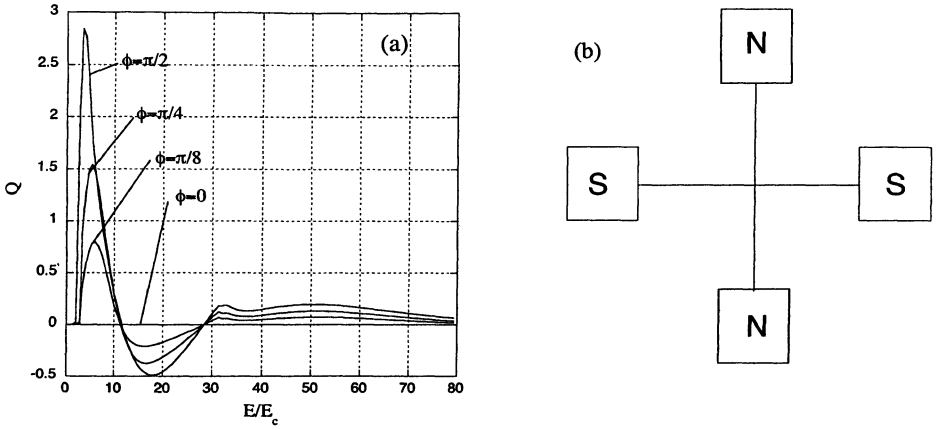

Fig. 3.8. (a) Spectral supercurrent Q in a normal wire between two superconducting reservoirs, as a function of the normalized energy E/E_c, for different values of the phase difference ϕ between the superconducting reservoirs. (b) Geometry of an Andreev interferometer, essentially a cross with one arm connected to superconducting reservoirs, and the other arm connected to normal reservoirs

given by Eq. (3.218). Some insight into the contributions to j_s can be gained by looking again at the case of a bulk superconductor. From Eq. (3.202), the major contribution to j_s comes from energies near the gap. For a long proximity wire with $E_c < \Delta$, however, the major contribution comes from energies of order E_c. Figure 3.8(a) shows a plot of Q as a function of energy for various values of the phase difference ϕ between the two superconducting reservoirs, for the case of a perfectly transparent interface, and $\Delta = 32E_c$. Of course, for zero phase difference, the supercurrent vanishes. As ϕ is increased from zero, there is a peak in $Q(E)$ at $E \simeq 6E_c$. This peak moves down in energy as ϕ increases. At larger values of E, Q becomes negative. For shorter wires, this region of negative Q is less prominent. The total supercurrent is given by the second term in Eq. (3.191)

$$J_s = eN_0 D \int dE\, Q(E) h_L(E), \tag{3.252}$$

and therefore depends also on the distribution of quasiparticles. Any change in this distribution will affect the supercurrent. For example, the distribution can be changed by increasing the temperature, which has the result of decreasing the supercurrent. As we demonstrated in the introduction, a non–equilibrium quasiparticle distribution can also be generated by injecting a normal current into the proximity wire in the SNS geometry by attaching two additional leads to the center of the normal wire, forming a normal

cross, with two of the wires attached to superconducting reservoirs, and the two other wires attached to normal reservoirs, as shown in Fig. 3.8(b). The current in the SNS junction is then a function of the current injected between the normal reservoirs, and the supercurrent can even change sign depending on magnitude of the injected normal current. [39, 40] This effect has been observed in recent experiments. [41]

Due to long–range phase coherence, the Green's function in the arms of the cross attached to the normal reservoirs will also depend on the phase difference between the two superconducting reservoirs in the structure shown in Fig. 3.8(b). Consequently, the electrical conductance measured between the two normal reservoirs will also be a periodic function of the phase difference between the two superconducting reservoirs. Experimentally, the conductance of such Andreev interferometers have been found to oscillate periodically with an applied external flux, with a fundamental period of $\phi_0 = h/2e$. [42–44] Similar oscillations are also expected in the thermal conductance as well. Periodic oscillations are also observed in the thermopower of Andreev interferometers [45], although these thermopower oscillations cannot be described within the framework of the current quasiclassical theory.

3.10 Summary

The quasiclassical theory of superconductivity has proved to be a powerful tool for the quantitative description of long–range phase coherent phenomena in diffusive proximity coupled systems. As we have shown, the linear electrical and thermal conductance of complicated devices incorporating normal and superconducting elements can be calculated in principle, although the solutions frequently involve numerical techniques. Extension to the nonlinear regime, with finite voltages across the normal reservoirs, is also conceptually straightforward, although numerically challenging.

Application of finite voltages to the superconducting elements is trickier, as it involves time dependent evolution of the phase, and is only beginning to be examined theoretically. Finally, the quasiclassical theory for diffusive systems, in its present form, does not deal at all with thermoelectric phenomena. Extensions to incorporate thermoelectric effects in the theoretical framework have been attempted [46], but still require further work to be complete.

References

1. G. Eilenberger, Z. Phys **214**, 195 (1968).
2. A. Schmid and G. Schön, J. Low. Temp. Phys. **20**, 207 (1972).
3. G.M. Eliashberg, Zh. Eksp. Teor. Fiz. **61**, 1254 (1971), Sov. Phys. JETP **34**, 668 (1972).
4. A.I. Larkin and Yu. N. Ovchinnikov, Zh. Eksp. Teor. Fiz. **68**, 1915 (1976), Sov. Phys. JETP **41**, 960 (1976).

5. A.I. Larkin and Yu. N. Ovchinnikov, Zh. Eksp. Teor. Fiz. **73**, 299 (1977), Sov. Phys. JETP **46**, 155 (1978).
6. C.-R. Hu, Phys. Rev. B **21**, 2775 (1980).
7. J.W. Serene and D. Rainer, Physics Reports **101**, 221 (1983).
8. G. Schön, in *Nonequilibrium Superconductivity*, edited by D.N. Langenberg and A.I. Larkin, Elsevier, 1986.
9. A.G. Aronov, Yu.M. Gal'perin, V.L. Gurevich and V.I. Kozub, *Nonequilibrium Properties of Superconductors (Transport Equation Approach)*, in *Nonequilibrium Superconductivity*, edited by D.N. Langenberg and A.I. Larkin, Elsevier, 1986; Advances in Physics **30**, 539 (1981).
10. J. Beyer, C.J. Pethick and J. Rammer, *Pair Breaking in Nonequilibrium Superconductors*, in *Nonequilibrium Superconductivity*, edited by D.N. Langenberg and A.I. Larkin, Elsevier, 1986.
11. J. Rammer and H. Smith, Rev. Mod. Phys. **58**, 323 (1986).
12. H. Smith and H.H. Jensen, *Transport Phenomena*, Clarendon, Oxford, 1989.
13. A.F. Volkov, A.V. Zaitsev and T.M Klapwijk, Physica C **210**, 21 (1993).
14. C.J. Lambert and R. Raimondi, J. Phys.: Condens. Matter **10**, 901 (1998).
15. A.F. Volkov and V.V. Pavlovskii, in *Proceedings of the AIP conference: lectures on superconductivity in networks and mesoscopic systems*, New York, 1998.
16. A.A. Golubov, F.K. Wilhelm, and A.D. Zaikin, Phys. Rev. B **55**, 1123 (1997).
17. F.K. Wilhelm, A.D. Zaikin and G. Schön, J. Low Temp. Phys. **106**, 305 (1997).
18. W. Belzig, F.K. Wilhelm, C. Bruder, G. Schön and A.D. Zaikin, Superlattices and Microstructures **25**, 1251 (1999).
19. Yu. V. Nazarov, Superlattices and Microstructures **25**, 1221 (1999).
20. K.E. Nagaev, Phys. Lett. A **169**, 103 (1992); Phys. Rev. B **52**, 4740 (1995).
21. See, for example, F. Pierre, H. Pothier, D. Esteve, M.H. Devoret, A.B. Gougam, and N.O. Birge, in *Kondo effect and dephasing in low-dimensional metallic systems*, edited by V. Chandrasekhar, C. Van Haesendonck and A. Zawadowski, NATO Science Series, vol. II/50, Kluwer Academic Publishers, Dordrecht, 2001.
22. J.M. Ziman, *Principles of the theory of solids*, 2nd edition, Cambridge University Press, Cambridge, 1972.
23. E.M. Lifshitz and L.P. Pitaevskii, *Physical Kinetics*, vol. 10 of the Landau and Lifshitz *Course of Theoretical Physics*, Pergamon Press, Oxford, 1981.
24. L.P. Kadanoff and G. Baym, *Quantum Statistical Mechanics*, Addison–Wesley, Redwood City, 1962.
25. J.B. Ketterson and S.N. Song, *Superconductivity*, Cambridge University Press, Cambridge 1999.
26. A.A. Abrikosov, L.P. Gor'kov and I.E. Dzyaloshinski, *Methods of Quantum Field Theory in Statistical Physics*, Dover, New York, 1975.
27. M. Tinkham, Phys. Rev. B **6**, 1747 (1972).
28. A.L. Shelankov, J. Low Temp. Phys. **60**, 29 (1985).
29. K.D. Usadel, Phys. Rev. Lett. **25**, 507 (1970).
30. A.V. Zaitsev, Zh. Eksp. Teor. Fiz. **86**, 1742 (1984), Sov. Phys. JETP **59**, 1015 (1985).
31. M.Yu. Kuprianov and V.F. Lukichev, Zh. Eksp. Teor. Fiz. **94**, 139 (1988), Sov. Phys. JETP **67**, 1163 (1988).
32. B.L. Altshuler, P.A. Lee and R.A. Webb, *Mesoscopic Phenomena in Solids*, North–Holland, Amsterdam, 1991.
33. See, for example, P. Charlat, H. Courtois, Ph. Gandit, D. Mailly, A.F. Volkov and B. Pannetier, Phys. Rev. Lett. **77**, 4950 (1996).

34. P.G. de Gennes, *Superconductivity of Metals and Alloys*, Addison–Wesley, Redwood City, 1966.
35. S. Guéron, H. Pothier, N.O. Birge, D. Esteve, and M.H. Devoret, Phys. Rev. Lett. **77**, 3025 (1996).
36. A.F. Andreev, Zh. Eksp. Teor. Fiz. **46**, 1823 (1964), Sov. Phys. JETP **19**, 1228 (1964).
37. J.M. Martinis, G.C. Hilton, K.D. Irwin and D.A. Wollman, Nuclear Instruments and Methods in Physics Research A **444**, 23 (2000).
38. S. Guéron, PhD thesis, Université Paris 6, (1997).
39. S.-K. Yip, Phys. Rev. B **58**, 5803 (1998).
40. F.K. Wilhelm, G. Schön and A.D. Zaikin, Phys. Rev. Lett. **81**, 1682 (1998).
41. J.J.A. Baselmans, A.F. Morpugo, B.J. van Wees and T.M Klapwijk, Nature **397**, 43 (1999).
42. H. Pothier, S. Guéron, D. Esteve, and M.H. Devoret, Phys. Rev. Lett. **73**, 2488 (1994).
43. V.T. Petrashov, V.N. Antonov, P. Delsing, and T. Claeson, Phys. Rev. Lett. **74**, 5268 (1995).
44. S.G. den Hartog, B.J. van Wees, T.M. Klapwijk, Yu.V. Nazarov and G. Borghs, Phys. Rev. B **56**, 13738 (1997).
45. J. Eom, C-J Chien and V. Chandrasekhar, Phys. Rev. Lett. **81**, 437 (1998).
46. F. Wilhelm, PhD thesis, Universität Karlsruhe, 2000.

4 Universal Properties of Cuprate Superconductors: Evidence and Implications

Toni Schneider
Physik–Institut der Universität Zürich, Switzerland

4.1 **Introduction** 111
4.2 **Critical Behavior at Finite Temperature** 120
4.2.1 Sketch of the Scaling Predictions 120
4.2.2 Evidence for Finite Temperature Critical Behavior 124
4.3 **Quantum Critical Behavior and Crossover Phenomena** 130
4.3.1 Sketch of the Scaling Predictions 130
4.3.2 Evidence for Doping Tuned Quantum Phase Transitions 135
4.3.3 Evidence for Substitution Tuned Quantum Phase Transitions 149
4.3.4 Evidence for Magnetic Field Tuned Quantum Phase Transitions 152
4.4 **Thin Films** 157
4.5 **Concluding Remarks and Comparison with other Layered Superconductors** 158
Acknowledgements 161
References 161

4.1 Introduction

Establishing and understanding the phase diagram of cuprate superconductors in the temperature – dopant concentration plane is one of the major challenges in condensed matter physics. Superconductivity is derived from the insulating and antiferromagnetic parent compounds by partial substitution of ions or by adding or removing oxygen. For instance La_2CuO_4 can be doped either by alkaline earth ions or oxygen to exhibit superconductivity. The empirical phase diagram of $La_{2-x}Sr_xCuO_4$ [1–9] depicted in Fig. 4.1 shows that after passing the so called underdoped limit ($x_u \approx 0.047$), T_c reaches its maximum value T_c^m at $x_m \approx 0.16$. With further increase of x, T_c decreases and finally vanishes in the overdoped limit $x_o \approx 0.273$. This phase transition line is thought to be a generic property of cuprate superconductors [10] and is well described by the empirical relation

$$T_c(x) = T_c(x_m)\left(1 - 2\left(\frac{x}{x_m} - 1\right)^2\right) = \frac{2T_c(x_m)}{x_m^2}(x - x_u)(x_o - x)\ , \tag{4.1}$$

K. H. Bennemann et al. (eds.), *The Physics of Superconductors*
© Springer-Verlag Berlin Heidelberg 2004

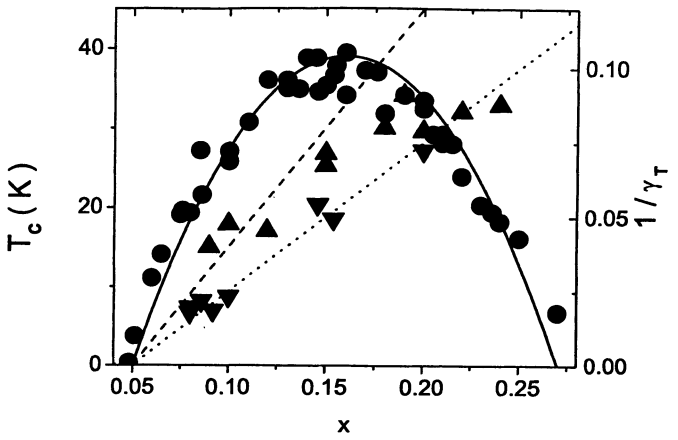

Fig. 4.1. Variation of T_c (open circles) [1–9] and γ_T with x for $La_{2-x}Sr_xCuO_4$. Filled circles correspond to $1/\gamma_{T_c}$ [1,2,4,6,7] and filled triangles to $1/\gamma_{T=0}$ [8,9]. The solid curve is Eq. (4.1) with $T_c^m = 39K$. The dashed and dotted lines follow from Eq. (4.2) with $\gamma_{T_c,0} = 2$ and $\gamma_{T=0,0} = 1.63$

proposed by Presland *et al.* [11], with $x_m = 0.16$. Approaching the endpoints along the axis x, $La_{2-x}Sr_xCuO_4$ undergoes at zero temperature doping tuned quantum phase transitions. As their nature is concerned, resistivity measurements reveal a quantum superconductor to insulator (QSI) transition in the underdoped limit [3,12–15] and in the overdoped limit a quantum superconductor to normal state (QSN) transition [15].

Another essential experimental fact is the doping dependence of the anisotropy. In tetragonal cuprates it is defined as the ratio $\gamma = \xi_{ab}/\xi_c$ of the correlation lengths parallel (ξ_{ab}) and perpendicular (ξ_c) to CuO_2 layers (ab–planes). In the superconducting state it can also be expressed as the ratio $\gamma = \lambda_c/\lambda_{ab}$ of the London penetration depths due to supercurrents flowing perpendicular (λ_c) and parallel (λ_{ab}) to the ab–planes. Approaching a nonsuperconductor to superconductor transition ξ diverges, while in a superconductor to nonsuperconductor transition λ tends to infinity. In both cases, however, γ remains finite as long as the system exhibits anisotropic but genuine 3D behavior. There are two limiting cases: $\gamma = 1$ characterizes isotropic 3D– and $\gamma = \infty$ 2D–critical behavior. An instructive model where γ can be varied continuously is the anisotropic 2D Ising model [16]. When the coupling in the y direction goes to zero, $\gamma = \xi_x/\xi_y$ becomes infinite, the model reduces to the 1D case and T_c vanishes. In the Ginzburg–Landau description of layered superconductors the anisotropy is related to the interlayer coupling. The weaker this coupling is, the larger γ is. The limit $\gamma = \infty$ is attained when the bulk superconductor corresponds to a stack of independent slabs of thickness d_s. With respect to experimental work, a

considerable amount of data is available on the chemical composition dependence of γ . At T_c it can be inferred from resistivity ($\gamma = \xi_{ab}/\xi_c = \sqrt{\rho_{ab}/\rho_c}$) and magnetic torque measurements, while in the superconducting state it follows from magnetic torque and penetration depth ($\gamma = \lambda_c/\lambda_{ab}$) data. In Fig. 4.1 we included the doping dependence of $1/\gamma_T$ evaluated at T_c (γ_{T_c}) and $T = 0$ ($\gamma_{T=0}$). As the dopant concentration is reduced, γ_{T_c} and $\gamma_{T=0}$ increase systematically, and tend to diverge in the underdoped limit. Thus the temperature range where superconductivity occurs shrinks in the underdoped regime with increasing anisotropy. This competition between anisotropy and superconductivity raises serious doubts whether 2D mechanisms and models, corresponding to the limit $\gamma_T = \infty$, can explain the essential observations of superconductivity in the cuprates. From Fig. 4.1 it is also seen that $\gamma_T(x)$ is well described by

$$\gamma_T(x) = \frac{\gamma_{T,0}}{x - x_u}. \tag{4.2}$$

Having also other cuprate families in mind, it is convenient to express the dopant concentration in terms of T_c. From Eqs. (4.1) and(4.2) we obtain the correlation between T_c and γ_T:

$$\frac{T_c}{T_c(x_m)} = 1 - \left(\frac{\gamma_T(x_m)}{\gamma_T} - 1\right)^2, \quad \gamma_T(x_m) = \frac{\gamma_{T,0}}{x_m - x_u}. \tag{4.3}$$

Provided that this empirical correlation is not merely an artefact of $La_{2-x}Sr_x$ CuO_4, it gives a universal perspective on the interplay of anisotropy and superconductivity, among the families of cuprates, characterized by $T_c(x_m)$ and $\gamma_T(x_m)$. For this reason it is essential to explore its generic validity. In practice, however, there are only a few additional compounds, including $HgBa_2CuO_{4+\delta}$ [17] and $Bi_2Sr_2CuO_{6+\delta}$, for which the dopant concentration can be varied continuously throughout the entire doping range. It is well established, however, that the substitution of magnetic and nonmagnetic impurities, depress T_c of cuprate superconductors very effectively [18, 19]. To compare the doping and substitution driven variations of the anisotropy, we depicted in Fig. 4.2 the plot $T_c/T_c(x_m)$ versus $\gamma_T(x_m)$ / γ_T for a variety of cuprate families. The collapse of the data on the parabola, which is the empirical relation (4.3), reveals that this scaling form appears to be universal. Thus, given a family of cuprate superconductors, characterized by $T_c(x_m)$ and $\gamma_T(x_m)$, it gives a universal perspective on the interplay between anisotropy and superconductivity.

The effect of a substitution for Cu by other magnetic or nonmagnetic metals was also investigated extensively [15, 18, 19]. A result common to all of these studies is that T_c is suppressed in the same manner, independent of wether the substituent is magnetic or nonmagnetic. For this reason, the phase diagram of $La_{2-x}Sr_xCu_{1-y}Zn_yO_4$, depicted in Fig. 4.3, applies quite generally. Apparently, the substituent axis (y) extends the complexity and

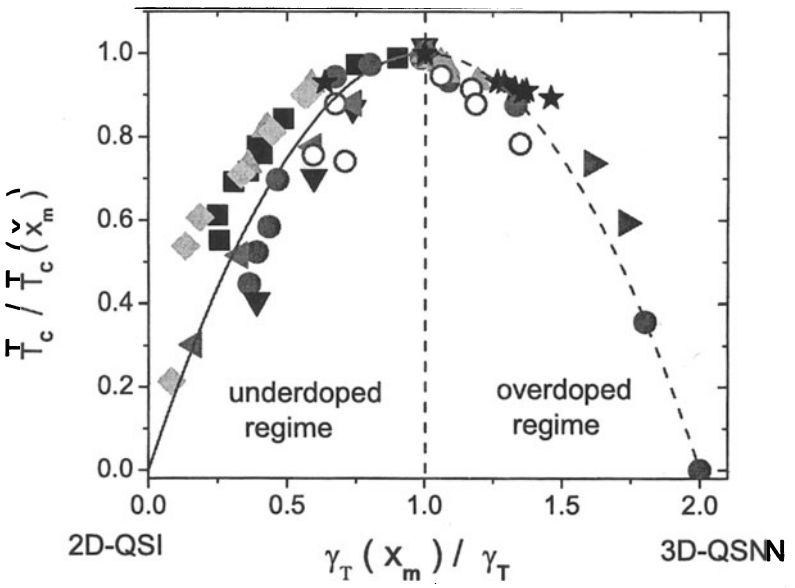

Fig. 4.2. $T_c/T_c(x_m)$ versus $\gamma_T(x_m)/\gamma_T$ for $La_{2-x}Sr_xCuO_4$ (•, $T_c(x_m) = 37$K, $\gamma_{T_c}(x_m) = 20$) [1, 2, 4, 6, 7] , (○, $T_c(x_m) = 37$K, $\gamma_{T=0}(x_m) = 14.9$) [8, 9], $HgBa_2CuO_{4+\delta}$ (▲, $T_c(x_m) = 95.6$K, $\gamma_{T_c}(x_m) = 27$) [17], $Bi_2Sr_2CaCu_2O_{8+\delta}$ (★, $T_c(x_m) = 84.2$K, $\gamma_{T_c}(x_m) = 133$) [20], $YBa_2Cu_3O_{7-\delta}$ (♦, $T_c(x_m) = 92.9$K, $\gamma_{T_c}(x_m) = 8$) [21], $YBa_2(Cu_{1-y}Fe_y)_3O_{7-\delta}$ (■, $T_c(x_m) = 92.5$K, $\gamma_{T_c}(x_m) = 9$) [22], $Y_{1-y}Pr_yBa_2Cu_3O_{7-\delta}$ (▼, $T_c(x_m) = 91$K, $\gamma_{T_c}(x_m) = 9.3$) [23], $BiSr_2Ca_{1-y}Pr_yCu_2O_8$ (◄, $T_c(x_m) = 85.4$K, $\gamma_{T=0}(x_m) = 94.3$) [24] and $YBa_2(Cu_{1-y}\ Zn_y)_3O_{7-\delta}$ (►, $T_c(x_m) = 92.5$K, $\gamma_{T=0}(x_m) = 9$) [25]. The solid and dashed curves are Eq. (4.18), marking the flow from the maximum T_c to QSI and QSN criticality, respectively

richness of the phase diagram considerably. The blue curve corresponds to a line of quantum phase transitions, given by $y_c(x)$. The pink arrow marks the doping tuned insulator to metal crossover and the green arrow corresponds to a path along which a QSI and QSN transition occurs. From Fig. 4.4 it can be inferred that isotope substitution, though much less effective, has essentially the same effect. T_c is lowered and the underdoped limit x_u shifts to some $y_c(x)$. This suggests that substitution induced local distortions, rather than magnetism, is the important factor. For $y > y_c(x)$ superconductivity is suppressed due to the destruction of phase coherence.

The point of reference for magnetic field tuned transitions is embodied in the schematic phase diagram shown in Fig. 4.5. It is strongly affected by the combined effect of pinning, thermal and quantum fluctuations, anisotropy and dimensionality [27]. In clean cuprates and close to $T_c(x, H = 0)$ thermal fluctuations are thought to be responsible for the existence of a first–order

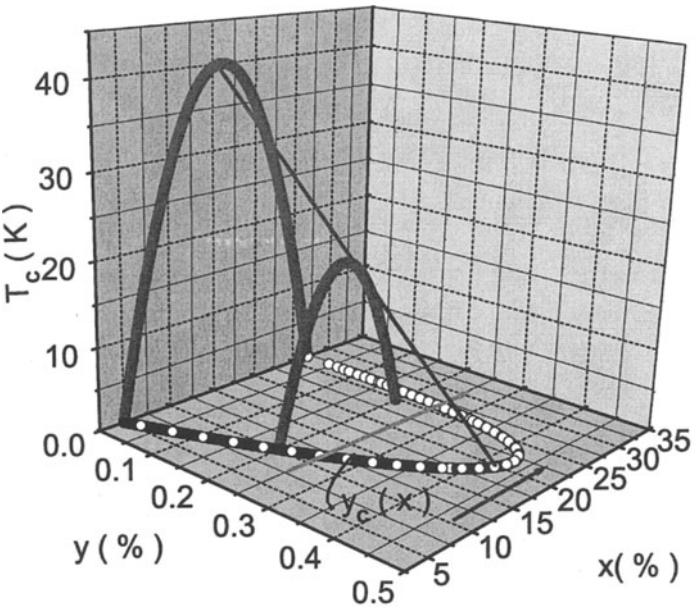

Fig. 4.3. Phase diagram of $La_{2-x}Sr_xCu_{1-y}Zn_yO_4$. The blue solid curve corresponds to $y_c(x)$, a line of quantum phase transitions. The pink arrow marks the doping tuned insulator to metal crossover and the green arrow marks a path where a QSI and QSN transition occurs. Experimental data taken from Momono *et al.* [15]

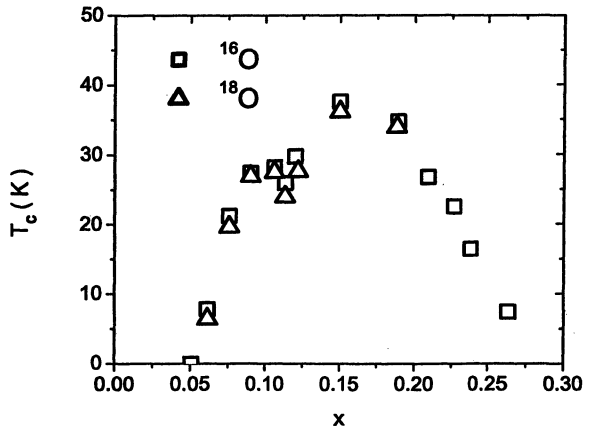

Fig. 4.4. T_c (^{16}O) and T_c (^{18}O) versus x for $La_{2-x}Sr_xCuO_4$. From Guo–Meng Zhao *et al.* [26]

vortex melting transition. In the presence of disorder, however, the long–range order of the vortex lattice is destroyed and the vortex solid becomes a glass [28]. Since a sufficiently large magnetic field suppresses superconductivity, due to the destruction of phase coherence, there is a line $H_m\,(x)$ of quantum phase transitions, connecting the zero field QSI and QSN transitions. Indeed, recent experiments revealed that sufficiently–intense magnetic fields suppress superconductivity and mediate a metal to insulator (MI) crossover [29–32].

The QSI transition can also be traversed in films by changing their thickness [13]. An instructive example are the measurements on $YBa_2Cu_3O_{7-\delta}$ slabs of thickness d separated by 16 unit cells ($\approx$ 187 A) of $PrBa_2Cu_3O_7$. Due to their large separation the $YBa_2Cu_3O_{7-\delta}$ slabs are essentially uncoupled. As shown in Fig. 4.6, T_c was found to vary with the thickness d of the $YBa_2Cu_3O_{7-\delta}$ slabs as

$$\frac{T_c\,(d)}{T_c^{bulk}} = \frac{d_s}{d}\left(\frac{d}{d_s} - 1\right), \tag{4.4}$$

with T_c^{bulk} = 91K and d_s = 10.1A [33]. d_s is the critical film thickness below which superconductivity is lost. Although the decrease of T_c is partially due to the 3D–2D crossover, the occurrence of the QSI transition points to the dominant role of disorder and quantum fluctuations. Nevertheless, it is

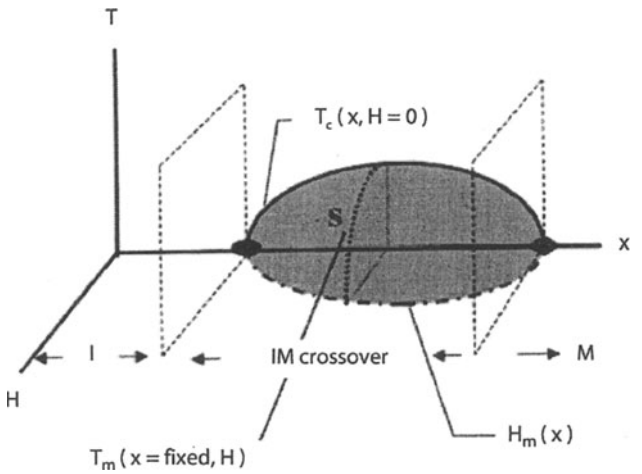

Fig. 4.5. Schematic (x, H, T)–phase diagram. There is the superconducting phase (S), bounded by the zero–field transition line, $T_c\,(x, H = 0)$, the critical lines of the vortex melting or vortex glass to vortex fluid transitions, $T_m\,(x = \text{fixed}, H)$ and the line of quantum critical points, $H_m\,(x, T = 0)$. Along this line superconductivity is suppressed and the critical endpoints coincide with the 2D–QSI– and 3D–QSN–critical points at x_u and x_o, respectively

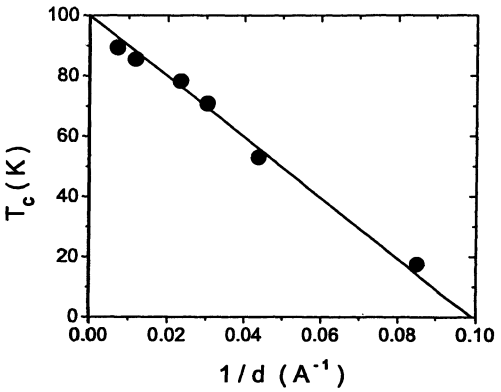

Fig. 4.6. Zero resistance T_c versus $1/d$ of $YBa_2Cu_3O_{7-\delta}$ layers of thickness d separated by 16 $PrBa_2Cu_3O_7$ unit cells. Taken from Goodrich *et al.* [33]. The straight line is a linear fit to Eq. (4.4)

conceivable that in sufficiently clean films superconductivity may also occur at and slightly below d_s.

This review aims to analyze the empirical correlations and phase diagrams from the point of view of thermal and quantum critical phenomena, to identify the universal properties, the effective dimensionality and the associated crossover phenomena. In view of the mounting evidence for 3D–XY–universality close to optimum doping [7,13,34–40], we concentrate here on the thermodynamic and ground state properties emerging from the QSI– and QSN– transitions, including the associated crossover phenomena. For this purpose we invoke the scaling theory of quantum critical phenomena [13,41].

Zero temperature phase transitions in quantum systems differ fundamentally from their finite temperature counterparts in that their thermodynamics and dynamics are inextricably mixed. Nevertheless, by means of the path integral formulation of quantum mechanics, one can view the statistical mechanics of D–dimensional $T = 0$ quantum system as the statistical mechanics of a $D+z$ dimensional classical system with a fake temperature which is some measure of the dynamics, characterized by the dynamic critical exponent z. This allows one to apply the scaling theory developed for classical critical phenomena to quantum criticality. In particular this leads to an understanding of the low T and crossover behavior close to quantum phase transitions and to universal relations between various properties. Evidence for power law behavior should properly consist of data that cover several decades in the parameters to provide reliable estimates for the critical exponents. In cuprate superconductors, the various power laws span at best one decade. Accordingly, more extended experimental data are needed to determine the

critical exponents of the quantum phase transitions. Nevertheless, irrespective of their precise value, the evidence for scaling and with that for data collapse exists. It uncovers the relationship between various properties and the significance of the empirical correlations and offers an understanding of the doping, substitution and magnetic field tuned quantum phase transition points and lines (see Figs. 4.1, 4.3 and 4.5). Evidently, the anisotropy, the associated dimensional crossover and the scaling relations between various properties close to the OSI and QSN criticality provide essential constraints for the understanding of the phase diagrams and the microscopic theory of superconductivity in these materials.

Note that this scenario is not incompatible with the zoo of microscopic models, relying on competing order parameters [42–52]. Here it is assumed that in the doping regime where superconductivity occurs, competing fluctuations, including antiferromagnetic and charge fluctuations, can be integrated out. The free–energy density is then a functional of a complex scalar, the order parameter of the superconducting phase, only. Given the generic phase diagrams (Figs. 4.1, 4.3 and 4.5) the scaling theory of finite temperature and quantum critical phenomena leads to predictions, including the universal properties, which can be confronted with experiment. As it stands, the available experimental data appears to be fully consistent with a single complex scalar order parameter, a doping tuned dimensional crossover and a doping, substitution or magnetic field driven suppression of superconductivity, due to the loss of phase coherence. When the evidence for this scenario persists, antiferromagnetic and charge fluctuations turn out to be irrelevant close to criticality. Moreover, it implies that a finite transition temperature and superfluid aerial superfluid density in the ground state, require in chemically doped systems a finite anisotropy. The important conclusion there is that a finite superfluid density in the ground state of bulk cuprates oxides is unalterably linked to an anisotropic but 3D condensation mechanism. Thus despite the strongly two–dimensional layered structure of cuprate superconductors, a finite anisotropy associated with the third dimension, perpendicular to the CuO_2 planes, is an essential factor in mediating superfluidity.

The paper is organized as follows. Sec. 4.2 is devoted to the finite temperature critical behavior. Since a substantial review on this topic is available [13], we concentrate on the specific heat. In Sec. 4.1 we sketch the scaling theory of finite temperature critical phenomena in anisotropic superconductors falling into the 3D–XY universality class. This leads naturally to universal critical amplitude combinations, involving the transition temperature and the critical amplitudes of specific heat, correlation lengths and penetration depths. The universality class to which the cuprates belong is thus not only characterized by its critical exponents but also by various critical–point amplitude combinations which are equally important. Indeed, though these amplitudes depend on the dopant concentration, substitution etc., their universal combinations do not. Evidence for 3D–XY universality and their implication for

the vortex melting transition is presented in Sec. 4.2. Here we also discuss the limitations arising from the inhomogeneities and the anisotropy, which render it difficult to observe 3D–XY critical behavior along the entire phase transition line $T_c(x)$ (Fig. 4.1) or on the entire surface $T_c(x, y)$ (Fig. 4.3).

In Sec. 4.3 we examine the quantum phase transitions and the associated crossover phenomena. The scaling theory of quantum phase transitions [41], extended to anisotropic superconductors [13], is reviewed in Sec. 4.1. Essential predictions include a universal amplitude relation in D=2 involving the transition temperature and the zero temperature in–plane penetration depth, as well as a fixed value of the in–plane sheet conductivity. Moreover we explore the scaling properties of transition temperature, penetration depths, correlation lengths, anisotropy and specific heat coefficient at 2D–QSI and 3D–QSN criticality. In Sec. 4.2 we confront these predictions with the empirical correlations (4.1), (4.2) and (4.3) and pertinent experiments. Although the experimental data are rather sparse, in particular close to the 3D–QSN transition, we observe a flow pattern pointing consistently to a 2D–QSI transition with $z = 1$ and $\overline{\nu} \approx 1$, and 3D–QSN criticality with $z = 2$ and $\overline{\nu} \approx 1/2$. z is the dynamic critical exponent and $\overline{\nu}$ the correlation length exponent. The estimates for the 2D–QSI transition coincide with the theoretical prediction for a 2D disordered bosonic system with long–range Coulomb interactions [53,54]. This reveals that in cuprate superconductors the loss of phase coherence, due to the localization of Cooper pairs, is responsible for the 2D–QSI transition. On the other hand, $z = 2$ and $\overline{\nu} \approx 1/2$ point to a 3D–QSN critical point, compatible with a disordered metal to d–wave superconductor transition at weak coupling [55]. Here the disorder destroys superconductivity, while at the 2D–QSI transition it destroys superfluidity. A characteristic feature of the 2D–QSI transition is its rather wide and experimentally accessible critical region. For this reason we observe consistent evidence that it falls into the same universality class as the onset of superfluidity in ^{4}He films in disordered media, corrected for the long–rangeness of the Coulomb interaction. As also discussed in this section, the existence of 2D–QSI and 3D–QSN critical points implies a doping and substitution tuned dimensional crossover. A glance to Fig. 4.2 shows that it is due to the dependence of the anisotropy on doping and substitution. An important implication is, that despite the small fraction, which the third dimension contributes to the superfluid energy density in the ground state, a finite transition temperature and superfluid density in bulk cuprates is unalterably linked to a finite anisotropy. Thus, despite their strongly two–dimensional layered structure, a finite anisotropy associated with the third dimension, perpendicular to the CuO_2 planes, is an essential factor in mediating pair condensation. This points unambiguously to the conclusion that theories formulated for a single CuO_2 plane cannot be the whole story. Moreover, the evidence for the flow to 2D–QSI criticality also implies that the standard Hamiltonian for layered superconductors [56] is incomplete. Although its critical properties fall into the 3D–XY universal-

ity class, disorder and quantum fluctuations must be included to account for the flow to 2D–QSI and 3D–QSN criticality.

Sec. 4.4 is devoted to the magnetic field tuned quantum phase transitions. Contrary to finite temperature, disorder is an essential ingredient at $T = 0$. It destroys superconductivity at 3D–QSN criticality and superfluidity at 2D–QSI critical points. On the other hand, superconductivity is also destroyed by a sufficiently large magnetic field. Accordingly, one expects a line $H_m(x)$ of quantum phase transitions, connecting the zero field 2D–QSI and 3D–QSN transitions (see Fig. 4.5). The relevance of disorder at this critical endpoints suggests a line of quantum vortex glass to vortex fluid transitions. Although the available experimental data is rather sparse, it points to the existence of a quantum critical line $H_m(x)$ and 2D localization, consistent with 2D–QSI criticality.

In Sec. 4.5 we treat cuprates with reduced dimensionality. Empirically it is well established that a quantum superconductor to insulator transition in thin films can also be traversed by reducing the film thickness. There is a critical film thickness (d_s) where T_c vanishes and below which disorder destroys superconductivity [13]. In chemically doped cuprates the critical thickness is comparable to the c–axis lattice constant. Moreover, the empirical correlation (4.3), displayed in Fig. 4.2, implies that in the bulk superconductivity disappears in the 2D limit. Thus, the combined effect of disorder and quantum fluctuations appears to prevent the occurrence of strictly 2D superconductivity. For this reason it is conceivable that in sufficiently clean films superconductivity may also occur at and below this value of d_s. Since chemically doped materials with different carrier densities also have varying amounts of disorder, the third dimension appears to be needed to delocalize the carriers and to mediate superfluidity. The comparison with other layered superconductors, including organics and dichalcogenides is made in Sec. 4.6.

4.2 Critical Behavior at Finite Temperature

4.2.1 Sketch of the Scaling Predictions

In superconductors the order parameter is a complex scaler, but it can also be viewed as a two component vector (XY). Supposing that sufficiently close to the phase transition line, separating the superconducting and non superconducting phase, 3D–XY–fluctuations dominate, the scaling form of the singular part of the bulk free energy density adopts then the form [13,57]

$$f_s = -k_B T Q_3^{\pm} \left(\xi_x^{\pm} \xi_y^{\pm} \xi_z^{\pm}\right)^{-1} \tag{4.5}$$

where $\xi_i^{\pm}$ is the correlation length diverging as

$$\xi_i^{\pm} = \xi_{i,0}^{\pm} |t|^{-\nu}, \; i = x, y, z, \; \pm = sign(t), \; t = \frac{T - T_c}{T_c} \tag{4.6}$$

and $Q_3^{\pm}$ are universal constants. In this context it should be kept in mind, that in superconductors the pairs carry a non zero charge in addition to their mass and the charge ($\Phi_0 = hc/2e$) couples the order parameter to the electromagnetic field via the gradient term in the Ginzburg–Landau Hamiltonian. In extreme type II superconductors, however, the coupling to vector potential fluctuations appears to be weak [58], but nonetheless, in principle, these fluctuations drive the system very close to criticality, to a charged critical point [60]. In any case, inhomogeneities in cuprate superconductors appear to prevent from entering this regime, due to the associated finite size effect [13]. For these reasons, the neglect of vector potential fluctuations appears to be justified and the critical properties at finite temperature are then those of the 3D–XY – model, reminiscent to the lambda transition in superfluid helium, extended to take the anisotropy into account [13,34].

In the superconducting phase the order parameter Ψ can be decomposed into a longitudinal ($\Psi_0 + \Psi_{lo}$) and transverse (Ψ_{tr}) part:

$$\Psi = \Psi_0 + \Psi_{lo} + i\Psi_{tr}, \tag{4.7}$$

where $\Psi_0 = \langle \Psi \rangle$ is chosen to be real. At long wavelength and in the superconducting phase the transverse fluctuations dominate and the correlations do not decay exponentially, but according to a power law [13,57]. This results in an inapplicability of the usual definitions of a correlation length below T_c. However, in terms of the helicity modulus, which is a measure of the response of the system to a phase–twisting field, a phase coherence length can be defined [59]. This length diverges at critical points and plays the role of the standard correlation length below T_c. In the presence of a phase twist of wavenumber k_i, the singular part of the free energy density adopts the scaling form

$$f_s = -\frac{k_B T Q_3^-}{\xi_x^{tr}\xi_y^{tr}\xi_z^{tr}} \Phi\left(k_x\sqrt{\xi_y^{tr}\xi_z^{tr}}, k_y\sqrt{\xi_x^{tr}\xi_z^{tr}}, k_z\sqrt{\xi_x^{tr}\xi_y^{tr}}\right), \tag{4.8}$$

yielding for the helicity modulus the expression

$$\Upsilon_i = - = \left.\frac{\partial^2 f_s}{\partial k_i^2}\right|_{\mathbf{k}=\mathbf{0}} = \frac{k_B T Q_3^-}{\xi_i^{tr}} \left.\frac{\partial^2 \Phi}{\partial k_i^2}\right|_{\mathbf{k}=\mathbf{0}} \tag{4.9}$$

where the normalization, $Q_3^- \left(\partial^2\Phi/\partial k_i^2\right)_{\mathbf{k}=\mathbf{0}} = 1$, has been chosen. At T_c this leads to the universal relation

$$(k_B T_c)^3 = \xi_{x0}^{tr}\xi_{y0}^{tr}\xi_{z0}^{tr}\Upsilon_{x0}\Upsilon_{y0}\Upsilon_{z0} = \left(\frac{\Phi_0^2}{16\pi^3}\right)^3 \frac{\xi_{x0}^{tr}\xi_{y0}^{tr}\xi_{z0}^{tr}}{\lambda_{x0}^2\lambda_{y0}^2\lambda_{z0}^2} \tag{4.10}$$

and the definition of the phase coherence lengths, also referred to as the transverse correlation lengths. The critical amplitudes of the transverse correlation length, ξ_{i0}^{tr}, helicity modulus, Υ_{i0} and penetration depth, λ_{x0}, are the defined as

$$\xi_i^{tr} = \xi_{i0}^{tr}\,|t|^{-\nu}\,, \quad \Upsilon_i = \Upsilon_{i0}\,|t|^{\nu}\,, \quad \lambda_i = \lambda_{i0}\,|t|^{-\nu/2}\,. \tag{4.11}$$

The relationship between helicity modulus and penetration depth, used in Eq. (4.10), is obtained as follows. From the definition of the supercurrent

$$j_i = c\frac{\delta f_s}{\delta A_i}, \tag{4.12}$$

where $\mathbf{A}$ is the vector potential and c the speed of light, we obtain for the magnetic penetration depth the expression

$$\frac{1}{\lambda_i^2} = -\left(\frac{4\pi j_i}{cA_i}\right)_{\mathbf{A}=\mathbf{0}} = -\frac{16\pi^3}{\Phi_0^2}\left.\frac{\partial^2 f_s}{\partial k^2}\right|_{k=0} = \frac{16\pi^3}{\Phi_0^2}\Upsilon_i, \tag{4.13}$$

by imposing the twist, $k_i = 2\pi A_i/\Phi_0$.

Noting then that the transverse correlation function decays algebraically,

$$S_{tr}(R_i) = \langle \Psi_{tr}(R_i)\,\Psi_{tr}(0)\rangle \propto \langle \Psi_0\rangle^2 \frac{\sqrt{\xi_j^{tr}\xi_{j'}^{tr}}}{R_i},\ j \neq j' \neq i, \tag{4.14}$$

it is readily seen that the length scales ξ^- correspond to the real space counterparts of the transverse correlation length defined in terms of the helicity modulus. These length scales are related by

$$\xi_i^- = \sqrt{\xi_j^{tr}\xi_{j'}^{tr}},\ j \neq j' \neq i \tag{4.15}$$

so that,

$$\xi_{x0}^-\xi_{y0}^-\xi_{z0}^- = \xi_{x0}^{tr}\xi_{y0}^{tr}\xi_{z0}^{tr}. \tag{4.16}$$

From the singular behavior of the specific heat

$$\frac{C}{Vk_B} = -\frac{T}{k_B}\frac{\partial^2 f_s}{\partial t^2} \approx \frac{A^\pm}{\alpha}|t|^{-\alpha}, \tag{4.17}$$

it the follows that the combination of critical amplitudes

$$\left(R^\pm\right)^3 = A^\pm\xi_x^\pm\xi_y^\pm\xi_z^\pm = A^\pm\xi_{x0}^{tr}\xi_{y0}^{tr}\xi_{z0}^{tr} = -Q_3^\pm\alpha(1-\alpha)(2-\alpha), \tag{4.18}$$

is universal, provided that

$$3\nu = 2 - \alpha, \tag{4.19}$$

holds. Moreover, additional universal relations include

$$\frac{A^-}{A^+} = R_A,\ \frac{\xi_{x0}^-\xi_{y0}^-\xi_{z0}^-}{\xi_{x0}^+\xi_{y0}^+\xi_{z0}^+} = \frac{\xi_{x0}^{tr}\xi_{y0}^{tr}\xi_{z0}^{tr}}{\xi_{x0}^+\xi_{y0}^+\xi_{z0}^+} = R_\xi. \tag{4.20}$$

Thus, the critical amplitudes are expected to differ from system to system and to depend on the dopant concentration, the universal combinations (4.10),

(4.18) and (4.20) should hold for all cuprates and irrespective of the doping level, except at the critical endpoints of the 3D–XY critical line.

A characteristic property of cuprate superconductors is their anisotropy. In tetragonal systems, where $\xi_a = \xi_b = \xi_{ab}$, it is defined as the ratio $\gamma = \xi_{ab}/\xi_c$, of the correlation length parallel and perpendicular to the ab–planes. Noting that according to Eqs. (4.9) and (4.13)

$$\frac{\Upsilon_x}{\Upsilon_z} = \frac{\xi_z^{tr}}{\xi_x^{tr}} = \frac{\xi_z^{tr}\xi_y^{tr}}{\xi_x^{tr}\xi_y^{tr}} = \frac{\lambda_z^2}{\lambda_x^2} = \left(\frac{\xi_x^-}{\xi_z^-}\right)^2, \tag{4.21}$$

holds, we obtain for γ the relation

$$\gamma_{T_c} = \frac{\xi_{ab0}^-}{\xi_{c0}^-} = \frac{\lambda_{c0}}{\lambda_{ab0}}. \tag{4.22}$$

the universal relation (4.10) can then be rewritten in the form

$$k_B T_c = \frac{\Phi_0^2}{16\pi^3} \frac{\xi_{ab,0}^-}{\lambda_{ab,0}^2 \gamma_{T_c}}. \tag{4.23}$$

Clearly, T_c, $\xi_{ab,0}^-$, $\lambda_{ab,0}$ and γ depend on the dopant concentration, but universality implies that this relation applies at any finite temperature, irrespective of the doping level. An other remarkable consequence follows from the universal relation

$$k_B T_c^3 = \left(\frac{\Phi_0^2}{16\pi^3 k_B}\right)^3 \frac{(R^-)^3}{A^- \lambda_{x0}^2 \lambda_{y0}^2 \lambda_{z0}^2} \tag{4.24}$$

which follows from Eqs. (4.10) and (4.18). Indeed, considering the effect of doping, substitution and pressure, denoted by the variable y, we obtain

$$\frac{3}{T_c}\frac{dT_c}{dy} = -\frac{1}{A^-}\frac{dA^-}{dy} + \sum_i \lambda_{i0}^2 \frac{d\left(1/\lambda_{i0}^2\right)}{dy}. \tag{4.25}$$

Thus, the effect of doping, substitution and pressure on transition temperature, specific heat and penetration depths are not independent, but related by this law.

In an applied magnetic field the singular part of the free energy density adopts the scaling form [13, 39]

$$f_s = -\frac{k_B T Q_3^{\pm}}{\xi_x^{\pm}\xi_y^{\pm}\xi_z^{\pm}} G_3^{\pm}(\widetilde{z}) \quad , \quad G_3^{\pm}(0) = 1, \tag{4.26}$$

where

$$\widetilde{z} = \frac{1}{\Phi_0}\sqrt{H_x^2\xi_y^2\xi_z^2 + H_y^2\xi_x^2\xi_z^2 + H_z^2\xi_x^2\xi_y^2}, \tag{4.27}$$

and $G_3^{\pm}(\widetilde{z})$ is a universal scaling function of its argument. Note that in the isotropic case, where $\xi = \xi_x = \xi_y = \xi_z$, this scaling form is identical to that of uniformly rotating ^{4}He near the superfluid transition. Magnetic field and rotation frequency are related by $H \rightarrow m_4 c\Omega/e$ [61]. In the presence of a magnetic field and $T < T_c$ the correlations do no longer decay algebraically. The Fourier transform of $S_{tr}(R)$ behaves for small wavenumbers q as

$$S_{tr}(q) \propto \frac{1}{q^2 + 1/\xi^2}. \tag{4.28}$$

Supposing then that there is a phase transition in the (H,T)–plane for $T < T_c$ the scaling function must have a singularity at some value $\widetilde{z}_c$. Examples are the vortex melting and vortex glass transition. Since the vortex melting transition is first order, ξ does not diverge but is bounded by

$$\frac{1}{\Phi_0}\sqrt{H_x^2\xi_y^2\xi_z^2 + H_y^2\xi_x^2\xi_z^2 + H_z^2\xi_x^2\xi_y^2} = \widetilde{z}_m. \tag{4.29}$$

Invoking Eqs. (4.6) we obtain for the first order transition line with H $\|$c$\|z$ the expression,

$$H_{cm} = \frac{\Phi_0\widetilde{z}_m}{\xi_{a,0}\xi_{b,0}}\left(\frac{T_c - T}{T_c}\right)^{2\nu}, \quad \frac{T_c - T_{cm}}{T_c} = \left(\frac{\xi_{a,0}\xi_{b,0}}{\widetilde{z}_m\Phi_0}\right)^{1/2\nu} H_c^{1/2\nu}. \tag{4.30}$$

In the interval $T_{cm} < T < T_c$ one expects a remnant of the zero field specific heat singularity. Because the correlation length is bounded, there is a magnetic field induced finite size effect. At the melting transition the limiting length is $L^2 = (\widetilde{z}_m\Phi_0)/H_c$ (Eq. (4.29)). Close to T_c on expects on dimensional grounds, $L^2 \approx (\Phi_0)/H_c$ to hold. Since the correlation length cannot exceed L, the zero field singularity, i.e. in the specific heat, is removed. As a remnant of this singularity, the specific heat will also exhibit a maximum at T_p which is located below T_c according to

$$\frac{T_c - T_p}{T_c} \approx \left(\frac{\xi_{a,0}\xi_{b,0}}{\Phi_0}\right)^{1/2\nu} H_c^{1/2\nu}. \tag{4.31}$$

4.2.2 Evidence for Finite Temperature Critical Behavior

Provided that the thermal critical behavior is fluctuation–dominated (i.e. non–mean–field) and the fluctuations of the vector potential can be neglected, cuprate superconductors fall into the 3D–XY universality class. We have seen that the universality class to which a given system belongs is not only characterized by its critical exponents but also by various critical–point amplitude combinations. The implications include: (i) The universal relations hold irrespective of the dopant concentration and material; (ii) Given the nonuniversal critical amplitudes of the correlation lengths, $\xi_{i,0}^{\pm}$, and the universal

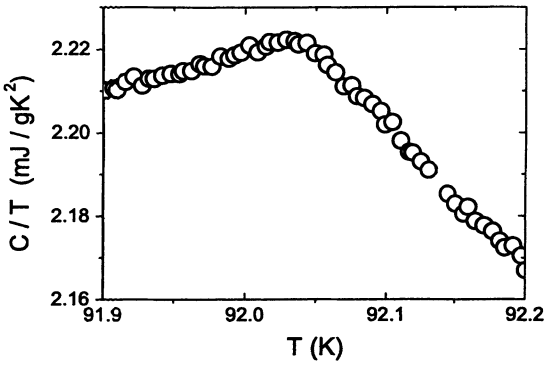

Fig. 4.7. Specific heat coefficient C/T (mJ/gK^2) versus T (K) of $YBa_2Cu_3O_{7-\delta}$ (sample YBCO3 [62])

scaling function $G_3^{\pm}(\widetilde{z})$, universal properties can be derived from the singular part of the free energy close to the zero field transition. These properties include the specific heat, magnetic torque, diamagnetic susceptibility, melting line, etc. Although there is mounting evidence for 3D–XY–universality in cuprates [7, 13, 34–40], it should be kept in mind, that evidence for power laws and scaling should properly consist of experimental data that covers several decades of the parameters. In practice, there are inhomogeneities and cuprates are homogeneous over a finite length L only. In this case, the actual correlation length $\xi(t) \propto |t|^{-\nu}$ cannot grow beyond L as $t \to 0$, and the transition appears rounded. Due to this finite size effect, the specific heat peak occurs at a temperature T_P shifted from the homogeneous system by an amount $L^{-1/\nu}$, and the magnitude of the peak located at temperature T_P scales as $L^{\alpha/\nu}$. To quantify this point we show in Fig. 4.7 the measured specific heat coefficient of $YBa_2Cu_3O_{7-\delta}$ [62]. The rounding and the shape of the specific heat coefficient clearly exhibits the characteristic behavior of a system in confined dimensions, i.e. rod or cube shaped inhomogeneities [63].

A finite–size scaling analysis [13] reveals inhomogeneities with a characteristic length scale ranging from 300 to 400 A, in the $YBa_2Cu_3O_{7-\delta}$ samples YBCO3, UBC2 and UBC [62]. Note that recent measurements by a variety of techniques suggest that superconductivity is not homogeneous in cuprates [64–66].For this reason, deviations from $3D$–XY critical behavior around T_p do not signal the failure of $3D$–XY universality, as previously claimed [62], but reflect a finite–size effect at work. Indeed from Fig. 4.8 it is seen that the finite–size effect makes it impossible to enter the asymptotic critical regime. To set the scale we note that in the λ–transition of ^{4}He the critical properties can be probed down to $|t| = 10^{-9}$ [67, 68]. In Fig. 4.7 we marked the intermediate regime where consistency with the 3D–XY–critical behavior, $C/T = \widetilde{A}^{\pm} 10^{-\alpha \log_{10}|t|} + \widetilde{B}^{\pm}$ for $\alpha = -0.013$ and $\widetilde{A}^{+}/\widetilde{A}^{-} = 1.07$,

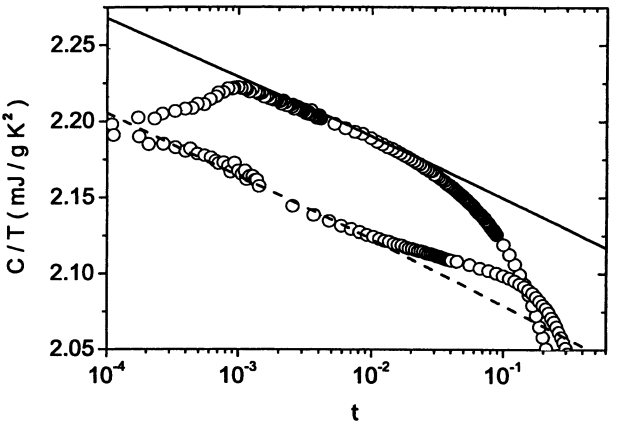

Fig. 4.8. Specific heat coefficient C/T (mJ/(gK^2)) versus $\log_{10}|t|$ for $YBa_2Cu_3O_{7-\delta}$ with $T_c = 92.12$K (sample YBCO3 [62])

can be observed in terms of full circles. The upper branch corresponds to $T < T_c$ and the lower one to $T > T_c$. The open circles closer to T_c correspond to the finite–size affected region, while further away the temperature dependence of the background, usually attributed to phonons, becomes significant. Hence, due to the finite size effect and the temperature dependence of the background the intermediate regime is bounded by the temperature region where the data depicted in Fig. 4.8 fall nearly on straight lines. In this context it should be kept in mind that the effect of disorder and inhomogeneities is quite different. Since the critical exponent α of the specific heat is negative at the 3D–XY transition, Harris criterion implies that disorder is irrelevant so that the critical behavior will be that of the pure system [69]. To provide quantitative evidence for 3D–XY universality in this regime, we invoke the universal relations (4.10) and (4.18) to calculate T_c from the critical amplitudes of specific heat and penetration depth. Using $A^+ = 8.4\ 10^{20}$ cm^3, derived from the data shown in Fig. 4.8 for sample YBCO3 with $T_c = 92.12$K, $\lambda_{a,0} = 1153$A, $\lambda_{b,0} = 968$A and $\lambda_{c,0} = 8705$A, derived from magnetic torque measurements on a sample with $T_c = 91.7K$ [39], together with the universal numbers $A^+/A^- = 1.07$ and $R^- \approx 0.59$ [13], we obtain $T_c = 88.2$K . Hence, the universal 3D–XY–relations (4.10) and (4.18) are remarkably well satisfied.

Another difficulty in observing 3D–XY critical properties stems from the fact that most cuprates are highly anisotropic. A convenient measure of the anisotropy is γ_{T_c} (Eq. (4.22)), which depends on the dopant concentration (see Figs. 4.1 and 4.2). Although the strength of thermal fluctuations grows with increasing γ, they become essential 2D slightly away from T_c. Accordingly, the 3D–XY – critical regime shrinks and the corrections to scaling

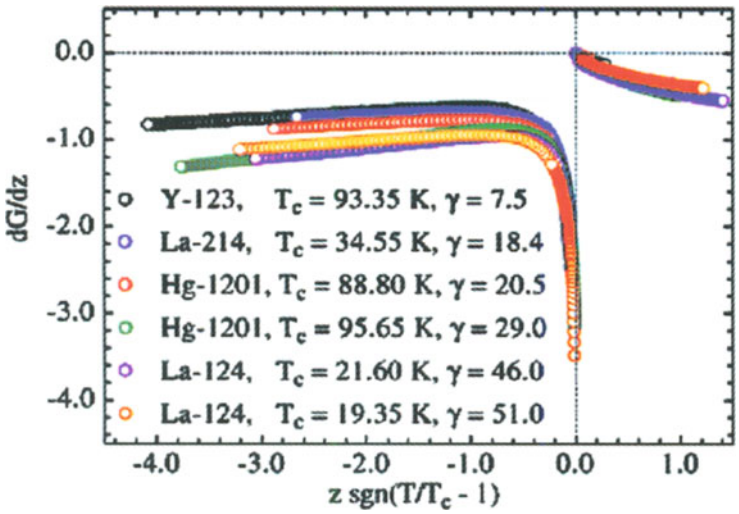

Fig. 4.9. Scaling function $dG_3^{\pm}(\widetilde{z})/d\widetilde{z}$ derived from the angular dependence of the magnetic torque for $YBa_2Cu_3O_{6.93}$, $La_{1.854}Sr_{0.146}CuO_4$, $HgBa_2CuO_{4.108}$, $HgBa_2CuO_{4.096}$, $La_{1.914}Sr_{0.086}CuO_4$ and $La_{1.920}Sr_{0.080}CuO_4$ (taken from [7])

become significant. To document this point we depicted in Fig. 4.9 estimates for the derivative of the universal scaling function $G_3^{\pm}(\widetilde{z})$ derived from magnetic torque measurements [7]. Even though the qualitative behavior is the same for all samples, the deviations increase with rising γ_{T_c}. This systematics cannot be attributed to the experimental uncertainties of about 40%. It is more likely that it reflects the reduction of the temperature regime where 3D–fluctuation dominates so that corrections to scaling become important [13]. In this view it is clear that due its moderate anisotropy [13,39], optimally doped $YBa_2Cu_3O_{7-\delta}$ is particularly suited to observe and check the consistency with 3D–XY critical behavior. In contrast to this, in highly anisotropic cuprates like $Bi_2Sr_2CaCu_2O_{8-\delta}$, it will be difficult to enter the regime where 3D fluctuations dominate [70]. Nevertheless, since the critical behavior of the charged fixed point is the only alternative left, it becomes clear that even the intermediate critical behavior of highly anisotropic cuprates like $Bi_2Sr_2CaCu_2O_{8-\delta}$ falls into the 3D–XY universality class. fluctuations grows with increasing γ, they become essential 2D slightly away from T_c. Accordingly, the 3D–XY – critical regime shrinks and the corrections to scaling become significant. To document this point we depicted in Fig. 4.9 estimates for the derivative of the universal scaling function $G_3^{\pm}(\widetilde{z})$ derived from magnetic torque measurements [7]. Even though the qualitative behavior is the same for all samples, the deviations increase with rising γ_{T_c}. This systematics cannot be attributed to the experimental uncertainties of about 40%. It is

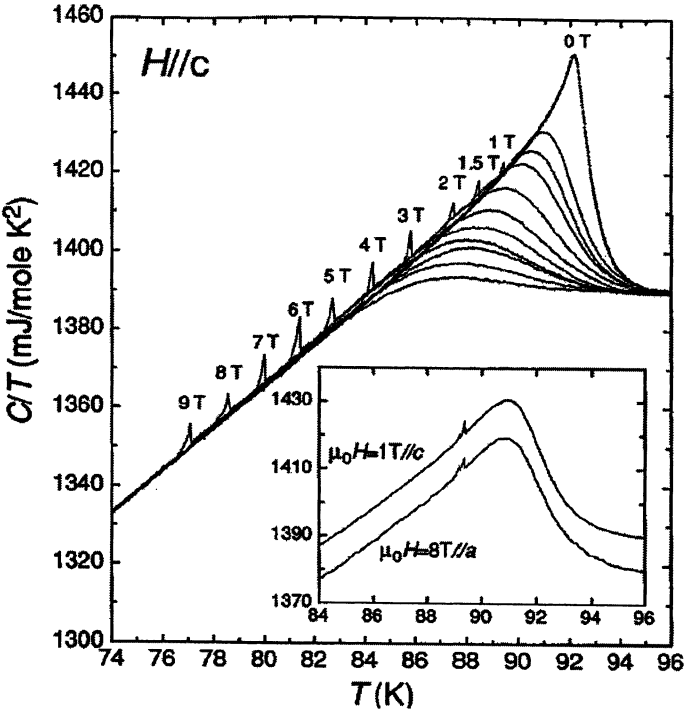

Fig. 4.10. Temperature dependence of the specific heat coefficient for various applied magnetic fields ($H \| c$) of an untwined $YBa_2Cu_3O_{7-\delta}$ single crystal. The numbers on the top of the peak like features denote the applied field strength. The inset shows representative data for $H = 1\text{T}$ ($H \| c$) and $H = 8\text{T}$ ($H \| (a, b)$), data shifted vertically by 10 mJ/molK^2 (taken from [72])

more likely that it reflects the reduction of the temperature regime where 3D–fluctuation dominates so that corrections to scaling become important [13]. In this view it is clear that due its moderate anisotropy [13, 39], optimally doped $YBa_2Cu_3O_{7-\delta}$ is particularly suited to observe and check the consistency with 3D–XY critical behavior. In contrast to this, in highly anisotropic cuprates like $Bi_2Sr_2CaCu_2O_{8-\delta}$, it will be difficult to enter the regime where 3D fluctuations dominate [70]. Nevertheless, since the critical behavior of the charged fixed point is the only alternative left, it becomes clear that even the intermediate critical behavior of highly anisotropic cuprates like $Bi_2Sr_2CaCu_2O_{8-\delta}$ falls into the 3D–XY universality class.

The melting transition of the vortex lattice was discovered in 1993 in $Bi_{2.15}Sr_{1.85}CaCu_2O_{8-\delta}$ using the μSR technique [71]. An anomaly attributed to this transition was observed in specific heat measurements of $YBa_2Cu_3O_{7-\delta}$ [72]. In Fig. 4.10 we depicted the temperature dependence of the specific heat coefficient of an untwined $YBa_2Cu_3O_{7-\delta}$ single crystal for various applied

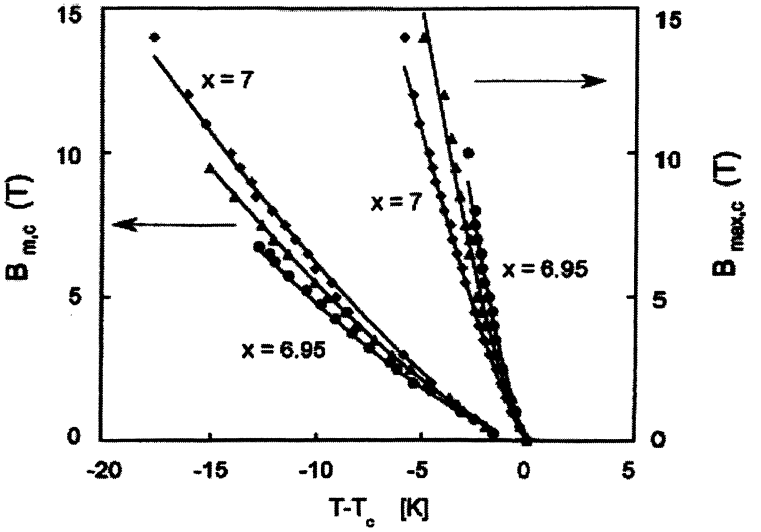

Fig. 4.11. Melting line $H_{c,m}$ and $H_{c,\max}$ versus $T - T_c$ for a $YBa_2CuO_{7-\delta}$ single crystal with $\delta = 0$ (♦), $\delta = 0.03$ (▲) and $\delta = 0.053$ (•) for H||c. Taken from [74]. The curves correspond to $H_{cm} = A_{cm}\left(\frac{T_c - T}{T_c}\right)^{2\nu}$ and $H_{cp} = A_{cp}\left(\frac{T_c - T}{T_c}\right)^{2\nu}$ with $\nu = 2/3$

fields H||c. Of particular interest in this context is the small anomaly below the main peak, marked by the strength of the applied field. It is attributed to the vortex melting transition. Evidence for the first order nature of the transition stems from magnetization measurements, revealing a jump at H_m [73], which signals the singularity in the scaling function $G_3^{\pm}(\tilde{z})$ at $\tilde{z} = \tilde{z}_m$ (Eq. (4.26)).

Due to the first order nature of the transition, the correlation lengths remain bounded, so that the melting line H_{cm} and the temperature T_P, where the broad peak in the specific heat coefficient adopts its maximum value, should scale according to Eqs. (4.30) and (4.31). A glance at Fig. 4.11 shows that this behavior is experimentally well confirmed. Note that the variation of the amplitudes A_{cm} and A_{cp} is due to the doping dependence of $\xi_{a,0}\xi_{b,0}$ (see Eqs. (4.30) and (4.31)). From Eq. (4.29) it is seen that the melting line also yields useful information on the anisotropy. As an example we consider the angular dependence in the (c,a) plane. Eq. (4.29) yields

$$H_m(\delta) = H_m(\delta = 0)\,\gamma_{ca}\left(\sin^2(\delta) + \gamma_{ca}^2\cos^2(\delta)\right)^{-1/2}, \tag{4.32}$$

where

$$\gamma_{ca} = \frac{\xi_a}{\xi_c}, \quad H_m(\delta = 0) \propto (1 - T/T_c)^{2\nu}.$$

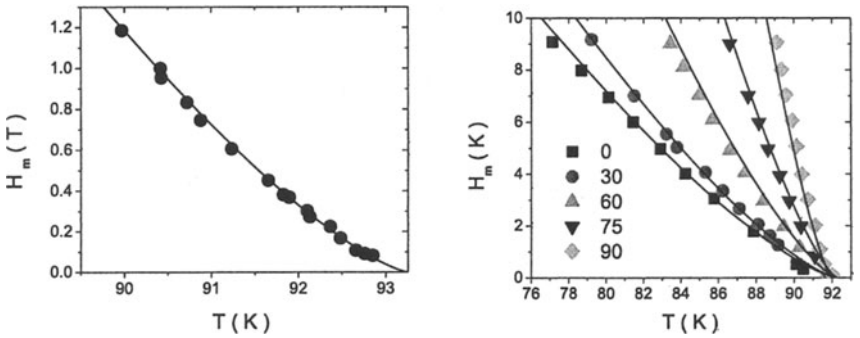

Fig. 4.12. Left panel: Melting line for $YBa_2Cu_3O_{7-\delta}$ with $T_c = 93.25K$ derived from field (◯)– and angular–dependent (□) torque curves. The solid line corresponds to $H_m \propto (1 - T/T_c)^{2\nu}$ with $\nu = 2/3$. Data taken from [75]. Right panel: Melting lines $H_m(\delta, T)$ for $YBa_2Cu_3O_{7-\delta}$ with $T_c = 92K$, detected by a direct measurement of the entropy change. The symbols denote experimental data taken at different magnetic field orientations in the (c,a) plane, measured by the angle δ [76]. The solid lines are Eq. (4.32) with $\gamma_{ca} = 7.6$ and $\nu = 2/3$

From Fig. 4.12 it is seen that this behavior is well confirmed. In this context the question arises, whether or not phase coherence and with that superfluidity persists above the melting line. Recently, numerical simulations revealed that the vortex liquid is incoherent, i.e. phase coherence is destroyed in all directions, including the direction of the applied magnetic field, as soon as the vortex lattice melts [77,78].

To summarize, there is considerable evidence that the intermediate finite temperature critical behavior of cuprate superconductors, when attained, is equivalent to that of superfluid helium. Moreover, we saw that finite size scaling is a powerful tool to identify and characterize inhomogeneities.

4.3 Quantum Critical Behavior and Crossover Phenomena

4.3.1 Sketch of the Scaling Predictions

Given the empirical phase transition line $T_c(x)$ or surface $T_c(x, y)$ with critical endpoints or lines (see Figs. 4.1 and 4.3) doping and substitution tuned quantum phase transitions can be expected. To invoke and sketch the scaling theory of quantum critical phenomena we define δ, measuring the relative distance from quantum critical points, in terms of

$$\delta = \begin{cases} y = 0 & : \delta = (x - x_u)/x_u \\ y = 0 & : \delta = (x_o - x)/x_o \\ y \neq 0, \quad x_u \leq x \leq x_o & : \delta = (y_c(x) - y)/y_c(x) \end{cases} . \tag{4.33}$$

At $T = 0$ and close to quantum criticality one has two kind of correlation lengths [13,41]. The usual spatial correlation length in direction i

$$\overline{\xi_i^-} = \overline{\xi}_{i,0}^- \delta^{-\overline{\nu}} \tag{4.34}$$

and the temporal one

$$\overline{\xi_\tau^-} = \overline{\xi}_{\tau,0}^- \delta^{-\overline{\nu}_\tau},$$

where the dynamic critical exponent is defined as the ratio

$$z = \frac{\overline{\nu}_\tau}{\overline{\nu}}. \tag{4.35}$$

The singular part of the free energy density adopts then the scaling form [13,14,41]

$$f_s(\delta, T) = \overline{Q}_D \left(\overline{\xi}_{\tau,0}^- \prod_{i=1}^{D} \overline{\xi}_{i,0}^- \right)^{-1} \delta^{\overline{\nu}(D+z)} F_D(\overline{y}), \quad \overline{y} = k_B T \overline{\xi}_\tau = k_B T \overline{\xi}_{\tau,0} \delta^{-z\overline{\nu}}, \tag{4.36}$$

where $F_D(\overline{y})$ with $F_D(\overline{y} = 0) = 1$ is a universal scaling function and Q_D a universal constant. Another quantity of interest is the helicity modulus which adopts the scaling form [13,14]

$$\Upsilon_i^D(\delta, T) = \overline{Q}_D \left(\overline{\xi}_{i,0}^- \right)^2 \left(\overline{\xi}_{\tau,0}^- \prod_{i=1}^{D} \overline{\xi}_{i,0}^- \right)^{-1} \delta^{\overline{\nu}(D-2+z)} Y_D(\overline{y}), \tag{4.37}$$

where $Y_D(\overline{y})$ with $Y_D(y = 0) = 1$ is a universal scaling function of its argument. As a first application we consider a line of finite temperature transitions $T_c(\delta)$ ending at a quantum critical point at $T = 0$ and $\delta = 0$. The scaling forms then require that

$$k_B T_c = \frac{\overline{y}_c}{\overline{\xi}_{\tau,0}^-} \delta^{z\overline{\nu}}, \tag{4.38}$$

where y_c is the universal value of the scaling function argument at which the scaling functions exhibit a singularity at finite temperature. Combining Eqs. (4.37) and (4.38) we obtain in $D = 2$

$$\frac{k_B T_c}{\Upsilon_{ab}^{D=2}(\delta, 0)} = \overline{R}_2, \quad \overline{R}_2 = \frac{\overline{y}_c}{Y_2(\overline{y}_c)\overline{Q}_2}, \tag{4.39}$$

yielding the universal relation

$$T_c \lambda_{ab}^2(0) = \frac{\Phi_0^2 \overline{R}_2}{16\pi^3 k_B} d_s, \tag{4.40}$$

between transition temperature and zero temperature in–plane penetration depth. d_s denotes the thickness of the superconducting slab and $\overline{R}_2$ is a universal dimensionless constant. Analogously, in $D = 3$ Eqs. (4.37) and (4.38) yield

$$\frac{k_B T_c}{\Upsilon_{ab}^{D=3}(\delta,0)} = \overline{R}_3 \overline{\xi}_c^-, \quad \overline{R}_3 = \frac{\overline{y}_c}{Y_3(\overline{y}_c)\,\overline{Q}_3}, \tag{4.41}$$

so that T_c, $\lambda_{ab}^2(0)$, $\overline{\xi}_c^-$ and $\overline{\xi}_{ab}^-$ are related by

$$T_c \lambda_{ab}^2(0) = \frac{\Phi_0^2\,\overline{R}_3}{16\pi^3 k_B}\overline{\xi}_c^- = \frac{\Phi_0^2\,\overline{R}_3}{16\pi^3 k_B}\frac{\overline{\xi}_{ab}^-}{\gamma_{T=0}}. \tag{4.42}$$

This is just the quantum analogy of the universal finite temperature relation (4.23). When there is an anisotropy tuned 3D–2D crossover, where $\gamma_{T=0} \to \infty$, matching of Eqs. (4.40) and (4.42) requires that

$$\overline{R}_3 \overline{\xi}_c^- = \overline{R}_3 \frac{\overline{\xi}_{ab}^-}{\gamma_{T=0}} = \overline{R}_2 d_s. \tag{4.43}$$

Noting then that the universal relation (4.42) applies close to both, the 2D–QSI and 3D–QSN transition it is expected to provide useful information on the correlation lengths ($\overline{\xi}_c^-$, $\overline{\xi}_{ab}^-$), given experimental data for $T_c\lambda_{ab}^2(0)$ and $\gamma_{T=0}$.

Moreover, useful scaling relations for the specific heat coefficient γ_c are readily derived from the singular part of the free energy density (4.36), namely:

$$\gamma_c|_{T=0} = \frac{c}{T}\Big|_{T=0} = \frac{\partial^2 f_s}{\partial T^2}\Big|_{T=0} \propto \delta^{\overline{\nu}(D-z)} \propto T_c^{(D-z)/z} \propto H_c^{(D-z)/2}, \tag{4.44}$$

since H_c scales as $H_c \propto \left(\overline{\xi}_{ab}^-\right)^{-2}$ [13], when applied parallel to the c–axis, and

$$\frac{d\gamma_c}{dT}\Big|_{T=0} = \frac{d}{dT}\left(\frac{c}{T}\right)\Big|_{T=0} = \frac{\partial^3 f_s}{\partial T^3}\Big|_{T=0} \propto \delta^{\overline{\nu}(D-2z)} \propto T_c^{(D-2z)/z}. \tag{4.45}$$

Finally, considering a 2D quantum critical points resulting from a 3D–2D crossover in the ground state, Eq. (4.43) implies that close to 2D quantum criticality the anisotropy diverges as

$$\gamma_{T=0} = \frac{\overline{\xi}_{ab}^-}{\overline{\xi}_c^-} = \frac{\overline{R}_3 \overline{\xi}_{ab,0}^-}{\overline{R}_2 d_s}\delta^{-\overline{\nu}} \propto T_c^{-1/z}. \tag{4.46}$$

Combining the scaling relations (4.38), (4.40), (4.43) and (4.46) a 2D quantum critical point resulting from a 3D–2D crossover is then characterized by

$$T_c \propto \lambda_{ab}^{-2}(0) \propto n_s^{\square}(0) \propto \gamma_{T=0}^{-z} \propto \delta^{z\overline{\nu}}, \quad \gamma_c|_{T=0} \propto T_c^{(2-z)/z} \propto H_c^{(2-z)/2}. \tag{4.47}$$

$n_s^{\square}(0) = \left(d_s/\lambda_{ab}^2(0)\right)$ denotes aerial superfluid density. In particular it relates the superconducting properties to the anisotropy parameter, fixing the dimensionality of the system. It reveals that an anisotropy driven 3D–2D crossover destroys superconductivity even in the ground state.

From Eq. (4.42), rewritten in the form

$$\overline{\xi}_c^- = \frac{16\pi^3 k_B}{\Phi_0^2\,\overline{R}_3} T_c \lambda_{ab}^2(0)\,, \quad \overline{\xi}_{ab}^- = \frac{16\pi^3 k_B}{\Phi_0^2\,\overline{R}_3} T_c \lambda_{ab}^2(0)\,\gamma_{T=0}, \tag{4.48}$$

it is seen that $T_c\lambda_{ab}^2(0)$ and $T_c\lambda_{ab}^2(0)\,\gamma_{T=0}$ are appropriate indicators for the occurrence of quantum phase transitions. Close to 3D–QSN criticality $\overline{\xi}_c^-$ and $\overline{\xi}_{ab}^-$ diverge according Eq. (4.34) as

$$\text{3D-QSN}: \overline{\xi}_c^- \propto \overline{\xi}_{ab}^- \propto \delta^{-\overline{\nu}} \propto T_c^{-1/z}, \tag{4.49}$$

because $\gamma_{T=0}$ remains finite. This differs from the 2D–QSI transition, where according to relation (4.46)

$$\text{2D-QSI}: \overline{\xi}_c^- = \frac{\overline{R}_2}{\overline{R}_3} d_s, \quad \overline{\xi}_{ab}^- = \frac{\overline{R}_2}{\overline{R}_3} d_s \gamma_{T=0} \propto \delta^{-\overline{\nu}} \propto T_c^{-1/z}, \tag{4.50}$$

applies. Here $\overline{\xi}_c^-$ tends to a finite value, proportional to the thickness d_s of the sheets.

Another quantity of interest is the zero temperature condensation energy. Close to 2D–QSI and 3D–QSN criticality it scales according to Eqs. (4.36) and (4.38) as

$$-E(T=0) \propto \delta^{\overline{\nu}(D+z)} \propto T_c^{(D+z)/z}. \tag{4.51}$$

As expected, when superconductivity disappears, the condensation energy vanishes.

Next we turn to the critical behavior of the conductivity. In the normal state and close to a 3D–XY critical point, the DC conductivities, parallel (σ_{ab}^{DC}) and perpendicular (σ_c^{DC}) to the layers, scale as [13]

$$\sigma_{ab}^{DC} \propto \frac{\xi_\tau}{\xi_c}, \; \sigma_c^{DC} \propto \frac{\xi_c \xi_\tau}{\xi_{ab}^2}, \tag{4.52}$$

where ξ_τ is the correlation length associated with the finite temperature critical dynamics. At T_c the ratio is then simply given by the anisotropy

$$\frac{\sigma_c^{DC}}{\sigma_{ab}^{DC}} = \left(\frac{\xi_c}{\xi_{ab}}\right)^2 = \left(\frac{1}{\gamma_{T_c}}\right)^2. \tag{4.53}$$

Approaching 2D–QSI criticality, the scaling relation (4.47) implies

$$\gamma_{T_c} = \gamma_{T_c,0}\delta^{-\overline{\nu}} \tag{4.54}$$

Another essential property of this critical point is that for any finite T_c the in–plane areal conductivity is always larger than [13,41]

$$\sigma_{ab}^{DC} d_s = \sigma_0 \frac{4e^2}{h}. \tag{4.55}$$

This follows from the fact that close to 2D–QSI the in–plane resistivity adopts the scaling form [13,41]

$$\rho_{ab} = \frac{h}{4e^2\sigma_0} F(\overline{y}), \quad \overline{y} = k_B T \overline{\xi}_\tau. \tag{4.56}$$

Thus, close to a 2D–QSI transition the normal state resistivity $\rho_c^{DC}(T_c^+) = 1/\sigma_c^{DC}(T_c^+)$, evaluated close but slightly above T_c, is predicted to diverge as

$$\rho_c^{DC}(T_c^+) = \gamma_{T_c}^2 \frac{h}{4e^2\sigma_0} = \gamma_{T_c,0}^2 \delta^{-2\overline{\nu}} \frac{h}{4e^2\sigma_0}. \tag{4.57}$$

$F(y)$ is a scaling function of its argument and $F(0) = 1$. This behavior uncovers the 3D–2D crossover associated with the flow to 2D–QSI criticality in the normal state. To establish a relation between normal and superconducting properties, we express δ in terms of $\lambda_c(0)$. Using Eq. (4.47) we obtain

$$\lambda_c(0) = \Omega_s \left(\sigma_c^{DC}(T_c^+)\right)^{-(2+z)/4}, \quad \Omega_s = \gamma_{0,0}\lambda_{ab,0}(0) \left(\frac{4e^2\sigma_0}{h\gamma_{T_c,0}^2}\right)^{(2+z)/4}, \tag{4.58}$$

where

$$\gamma_T = \gamma_{T,0}\delta^{-\overline{\nu}}, \quad \lambda_{ab,0}(0) = \lambda_{ab,0}(0)\,\delta^{-z\overline{\nu}/2}, \tag{4.59}$$

are the zero temperature critical amplitudes. The scaling relation (4.58) differs from the mean–field prediction for bulk superconductors in the dirty limit [79] and layered BCS superconductors, treated as weakly coupled Josephson junction [80–82]:

$$\lambda_c(0) = \Omega_s \left(\sigma_c^{DC}(T_c^+)\right)^{-1/2}, \tag{4.60}$$

where

$$\Omega_s = \left(\frac{\hbar c^2}{4\pi^2 \Delta(0)}\right)^{1/2}, \quad \Delta(0) = 1.76 k_B T_c \tag{4.61}$$

and $\Delta(0)$ denotes the zero temperature energy gap.

Approaching 3D–QSN criticality, the finite temperature relations (4.52) and (4.53) still apply, but both, ρ_c^{DC} and ρ_{ab}^{DC} diverge at T_c, while the

anisotropy γ_{T_c} remains finite. For this reason ξ_τ, the correlation length associated with the finite temperature critical dynamics, cannot be eliminated. Nevertheless, since ξ_τ scales as, $\xi_\tau \propto \xi_{ab}^{z_{cl}}$, where z_{cl} is the critical exponent of the finite temperature dynamics, we obtain from Eq. (4.52) the relation

$$\sigma_c^{DC} \propto \frac{\xi_c \xi_\tau}{\xi_{ab}^2} \propto \frac{\xi_\tau}{\gamma_{T_c} \xi_{ab}} \propto \xi_{ab}^{z_{cl}\ -1} \propto \xi_{ab,0}^{z_{cl}\ -1} \left|t\right|^{-\nu(z_{cl}\ -1)}, \tag{4.62}$$

valid close to 3D–XY critical points. Since close to a 3D–QSN criticality, the doping dependence of the finite temperature critical amplitude $\xi_{ab,0}$ is given by $\overline{\xi}_{ab}$ (see Eqs. (4.23) and (4.42)), we finally obtain with $\lambda_c(0) \propto \delta^{-\frac{\overline{\nu}}{2}(1+z)}$ (Eq. (4.37)) the relationship between $\lambda_c(0)$ and $\sigma_c(T_c^+)$ the relationship

$$\lambda_c(0) \propto \left(\sigma_c\left(T_c^+\right)\right)^{\frac{1+z}{2(z_{cl}-1)}}, \tag{4.63}$$

characterizing the flow to a 3D–QSN critical point in the $(\lambda_c(0), \sigma_c(T_c^+))$ plane.

Noting that the in–plane resistivity tends close to 2D–QSI criticality to a fixed value (Eq. (4.56)), ρ_{ab} can also be used as a parameter measuring the distance from the critical point. This is achieved by setting $y = k_B T \overline{\xi}_\tau \propto T\delta^{-z\overline{\nu}} \propto T\left(\left(\rho_{ab}^0 - \rho_{ab}\right)/\rho_{ab}^0\right)^{-z\overline{\nu}}$. Given then a transition line $T_c(\delta)$ ending at the 2D–QSN critical point the scaling form (4.56) requires that

$$T_c \propto \left(\frac{\rho_{ab}^0 - \rho_{ab}}{\rho_{ab}^0}\right)^{z\ \overline{\nu}}, \quad \rho_{ab}^0 = \frac{h}{4e^2\sigma_0} \tag{4.64}$$

because the scaling function $F(y)$ exhibits a singularity at y_c, signaling the finite temperature transition line.

4.3.2 Evidence for Doping Tuned Quantum Phase Transitions

The empirical correlations between T_c, dopant concentration x and anisotropy γ_T (Eqs. (4.1)-(4.3)) clearly point to the existence of quantum critical endpoints. A glance to Fig. 4.2 shows, when T_c vanishes in the underdoped limit, the anisotropy γ_T tends to infinity. Accordingly a 2D–QSI transition is expected to occur. In the overdoped limit, T_c vanishes again but the finite anisotropy implies a 3D–QSN transition. Since the aforementioned empirical correlations turned out to be remarkably generic (see Fig. 4.2) they appear to reflect universal properties characterizing these quantum phase transitions. Indeed, the empirical correlation (4.1) points with the scaling law (4.38) to $z\overline{\nu} = 1$ in both transitions. Moreover, the empirical relation between T_c and γ_T (4.3) implies according to the scaling law (4.46) a 2D–QSI transition with $\overline{\nu} = 1$. Thus, the universality classes emerging from the empirical relations are characterized by the critical exponents:

$$\text{2D-QSI}: z = 1,\ \overline{\nu} = 1, \tag{4.65}$$

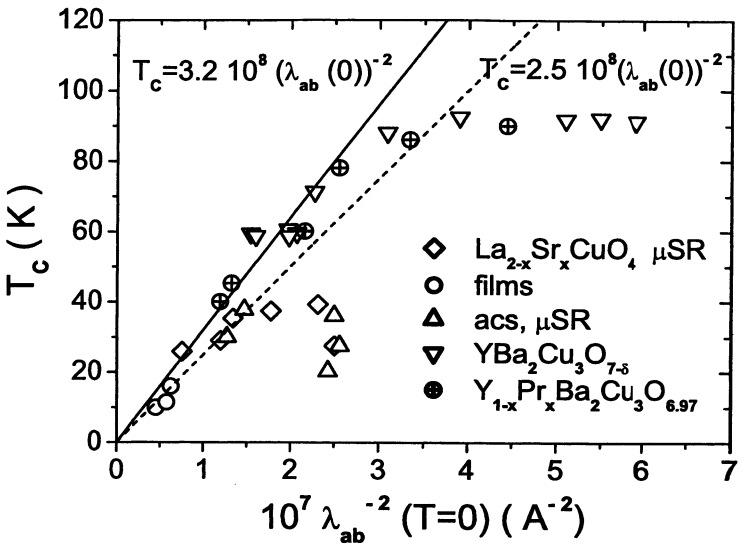

Fig. 4.13. T_c versus $\lambda_{ab}(T=0)^{-2}$ for $La_{2-x}Sr_xCuO_4$ (○: [85], ▲: [9], □: [84]) $YBa_2Cu_3O_{7-\delta}$ (▽: [86]) and $Y_{1-x}Pr_xBa_2Cu_3O_{6.97}$ (⊗: [87]). The dashed and solid lines correspond to Eq. (4.68)

$$\text{3D-QSN}: z\overline{\nu} = 1. \tag{4.66}$$

These 2D–QSI exponents are consistent with the theoretical prediction for a 2D disordered bosonic system with long–range Coulomb interaction. Here the loss of superfluidity is due to the localization of the pairs, which is ultimately responsible for the transition [53, 54]. A potential candidate for the 3D–QSN transition is the Ginzburg–Landau theory proposed by Herbut [55]. It describes a disordered d–wave superconductor to metal transition at weak coupling and is characterized by the critical exponents $z = 2$ and $\overline{\nu} = 1/2$, except in an exponentially narrow region. Since the resulting $z\overline{\nu}$ coincides with the value implied by the empirical correlation (4.1), one expects with the estimate (4.66),

$$\text{3D-QSN}: z = 2,\ \overline{\nu} = 1/2. \tag{4.67}$$

A characteristic property of a 2D–QSI transition, irrespective of the value of $z\overline{\nu}$, is the universal relation (4.40) between transition temperature and zero temperature penetration depth. An instructive example is the onset of superfluidity in ^{4}He films adsorbed on disordered substrates, where the linear relationship between T_c and aerial superfluid density $n_s^{\square}(0) \propto d_s/\lambda_{ab}^2(0)$ is well confirmed [83]. In cuprates, a nearly linear relationship between T_c and $\lambda_{ab}(T=0)^{-2}$ has been established some time ago by Uemura *et al.* [84]. In the present context, it is not strictly universal, because d_s, the thickness of

the independent slabs, is known to adopt family dependent values [13, 88]. This fact can be anticipated from Fig. 4.13, showing experimental data for T_c versus $1/\lambda_{ab}^2\,(T=0)$ of $La_{2-x}Sr_xCuO_4$ [9,84,85], $YBa_2Cu_3O_{7-\delta}$ [86] and $Y_{1-x}Pr_xBa_2Cu_3O_{6.97}$ [87]. With T_c in K and $\lambda_{ab}(T=0)$ in A, the dashed and solid straight lines correspond to

$$T_c \approx \frac{3.2\ 10^8}{\lambda_{ab}^2\,(T=0)},\ \frac{2.5\ 10^8}{\lambda_{ab}^2\,(T=0)}. \tag{4.68}$$

Invoking then the universal relation (4.40) we obtain the estimate,

$$\frac{d_s\,(YBa_2Cu_3O_{7-\delta})}{d_s\,(La_{2-x}Sr_xCuO_4)} \approx \frac{3.2}{2.5} \approx 1.3, \tag{4.69}$$

which is consistent with , $d_s\,(YBa_2Cu_3O_{7-\delta})\ /\ d_s\,(La_{2-x}Sr_xCuO_4) \approx 10.1\ A\ /7.6\ A \approx 1.33$, derived from the thickness tuned QSI transition and the crossing point phenomenon, respectively [13, 88]. Consequently, $dT_c/d(1/\lambda_{||}^2(T=0))$ is not strictly universal. Nevertheless, due to the small variations of d_s within a family of cuprates it adopts there a nearly unique value. For this reason the empirical proportionality of T_c and $\lambda_{ab}\,(T=0)^{-2}$ for underdoped members of a given family confirms the flow to 2D–QSI criticality.

Next we turn to the behavior of the resistivity close to 2D–QSI criticality. In Fig. 4.14 we displayed the data of Semba and Matsuda [89] for the temperature dependence of the in-plane resistivity ρ_{ab} of $YBa_2Cu_3O_y$ at various dopant concentrations y. Below $y \approx 6.3$ the resistivity increases with decreasing temperature, signaling the onset of insulating behavior in the zero temperature limit. Above $y \approx 6.3$ and as the temperature is reduced, the resistivity drops rapidly and vanishes at and below T_c. Thus, for $y \gtrsim 6.3$ there is a superconducting phase and the 2D–QSI–transition occurs at $y \approx 6.3$. Moreover, the temperature dependence of ρ_c/ρ_{ab}, depicted in Fig. 4.14, is in accord with the scaling relations (4.38) and (4.53), yielding $\rho_c/\rho_{ab} = \gamma_{T_c}^2 \propto \delta^{-2\overline{\nu}} \propto T_c^{2/z}$. Indeed, the anisotropy increases by approaching the 2D–QSI transition. In contrast, near the 2D–QSI transition ($y \approx 6.3$), there is a finite threshold in–plane resistivity $\rho_{ab}^{th} \approx 0.8 m\Omega cm$ (see Fig. 4.14). According to the scaling relation (4.55) this is a characteristic feature of a 2D–QSI transitions. For $d_s \approx 11.8A$ and $\sigma_0 \approx 1$ this leads to the sheet resistance $\rho_{ab}^{th}/d_s \approx h/\left(4e^2\right) \approx 6.5\ \ k\Omega$. Since $\rho_c \propto \gamma^2\rho_{ab}$ and $\rho_{ab}^{th} \to d_s h/\left(4e^2\right)$ it also becomes evident that the rise of ρ_c for $T > T_c$ simply reflects the increasing anisotropy and with that the flow to 2D–QSI criticality. Together with the doping dependence of γ_{Tc} (see Figs. 4.1 and 4.2), these features clearly confirm the occurrence of a 2D–QSI transition.

According to Eqs. (4.40) and (4.64)a 2D–QSI–transition is also characterized by the scaling relation

$$k_B T_c = c\left(\frac{\rho_{0c}-\rho_0}{\rho_{0c}}\right)^{z\,\overline{\nu}} = \frac{\Phi_0^2}{16\pi^3\overline{Q}_2}\frac{d_s}{\lambda_{ab}^2(T=0)}, \tag{4.70}$$

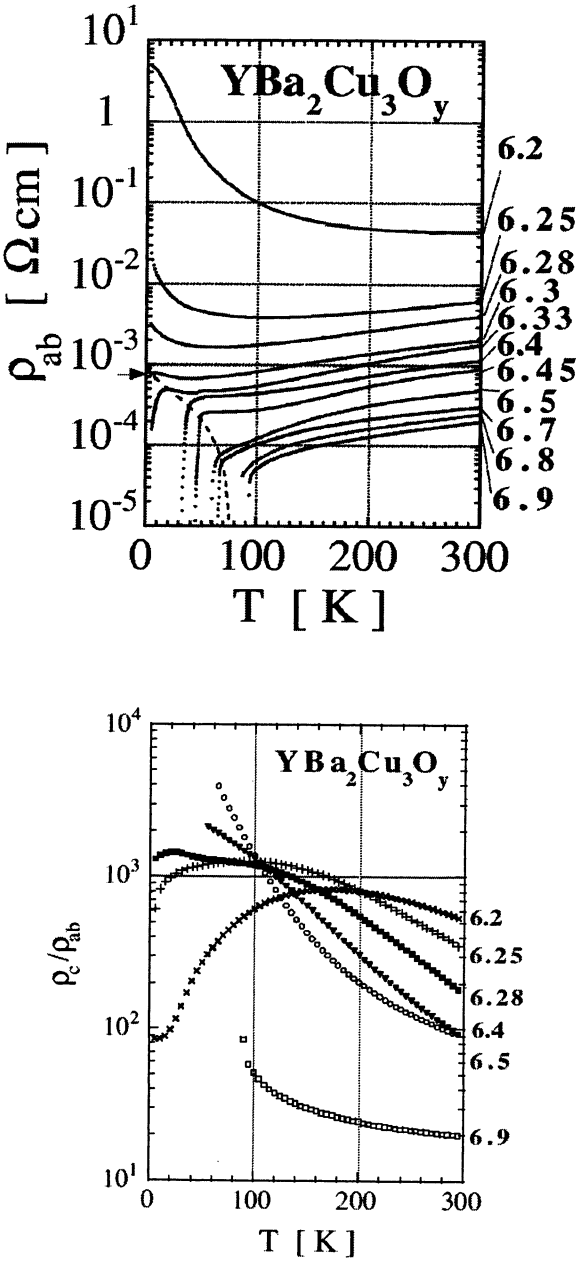

Fig. 4.14. Upper panel: Temperature dependence of the in–plane resistivity ρ_{ab} of $YBa_2Cu_3O_y$ at various dopant concentrations y. Taken from Semba and Matsuda [89]. The threshold resistivity is indicated by an arrow. Above panel: ρ_c/ρ_{ab} versus T of underdoped $YBa_2Cu_3O_y$ (taken from Semba and Matsuda [89])

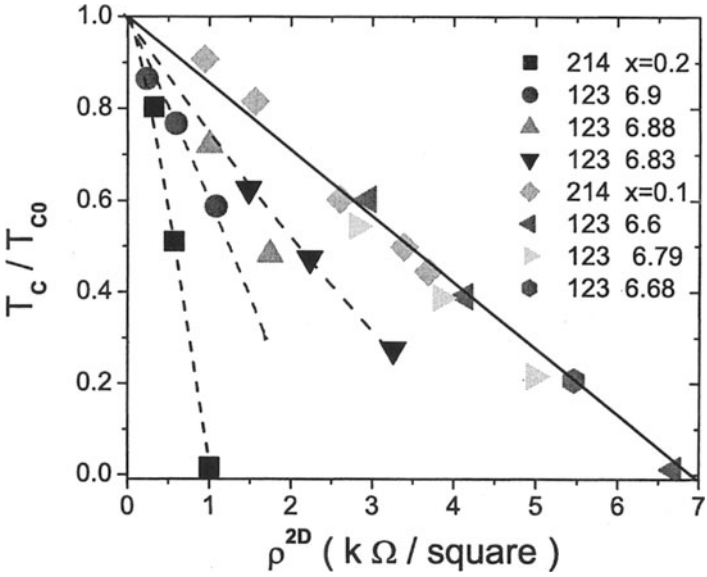

Fig. 4.15. Residual in–plane resistance versus normalized critical temperature for Zn–substituted $La_{2-x}Sr_xCuO_4$ and $YBa_2Cu_3O_{7-\delta}$. T_{c0} is the transition temperature of the Zn free compound (taken from Fukuzumi *et al.* [3]

where ρ_0 and ρ_{0c} denote the residual and critical residual sheet resistivity, respectively. This prediction is well confirmed by the data of Fukuzumi *et al.* for Zn–substituted $La_{2-x}Sr_xCuO_4$ and $YBa_2Cu_3O_{7-\delta}$ [3] displayed in Fig. 4.15. Approaching the underdoped limit the data merge on a straight line. With the scaling relation (4.70) this points to $z\overline{\nu} = 1$ consistent with the value emerging from the empirical correlations (Eq. (4.65)).

Next we turn to the isotope effect. Since universal relations like (4.18), (4.23) and (4.40) should apply irrespective of the doping and substitution level, the isotope effects on the quantities involved, are not independent. As an example we consider the universal relation (4.40), predicting that close to the 2D–QSI transition the isotope effect on transition temperature and zero temperature in–plane penetration depth are related by

$$\beta_{T_c} = \beta_{d_s} + \beta_{1/\lambda^2_{ab}(0)}, \tag{4.71}$$

where

$$\beta_B = -\frac{m}{B}\frac{\Delta B}{\Delta m} \tag{4.72}$$

ΔB denotes the shift of B upon isotope substitution. Although the available experimental data on identical samples are rather sparse, the results shown in Fig. 4.16 for the oxygen isotope effect in $La_{2-x}Sr_xCu_{1-x}O_4$ [90, 91] and

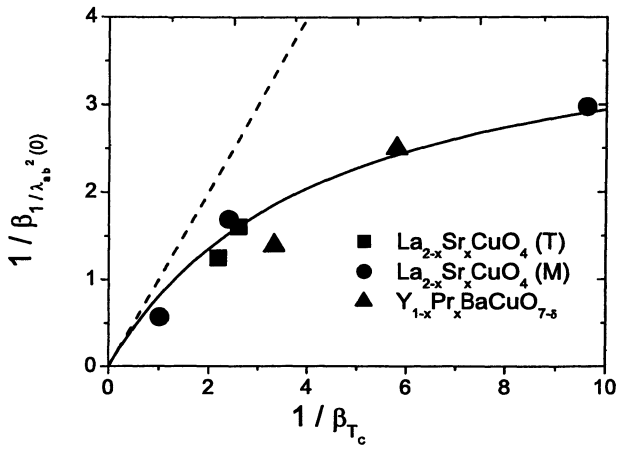

Fig. 4.16. Oxygen isotope effect for underdoped $La_{2-x}Sr_xCuO_4$ in terms of $1/\beta_{1/\lambda_{ab}^2(0)}$ versus $1/\beta_{T_c}$. The dashed line marks the critical behavior at the 2D–QSI transition ($\beta_{1/\lambda_{ab}^2(0)} \to \beta_{T_c} \to \infty$), while the solid curve is Eq. (4.71) with $\beta_{d_s} = -0.2$. Experimental data taken from Refs.: • [90], ■ [91] and ▲ [92]

$Y_{1-x}Pr_xBa_2Cu_3O_7$ clearly reveal the crossover to the asymptotic 2D–QSI behavior marked by the dashed straight line. The solid curve is a fit to Eq. (4.71), yielding the estimate

$$\beta_{d_s} \approx -0.2, \tag{4.73}$$

for the isotope coefficient of d_s. An essential result is that the flow to 2D–QSI criticality implies that the isotope coefficients β_{T_c} and $\beta_{1/\lambda_{ab}^2(0)}$ diverge. Some insight is obtained by noting that in the doping regime of interest, isotope substitution does not affect the dopant and substitution concentrations. [90]. In contrast it lowers the transition temperature and shifts the underdoped limit x_u [35,93]. From the relation $T_c = a\,\delta^{z\nu}$ (Eq. (4.38)), yielding

$$\frac{\Delta T_c}{T_c} = -\frac{z\nu}{x/x_u - 1}\frac{\Delta x_u}{x_u}, \tag{4.74}$$

we obtain for the isotope coefficient the expression

$$\beta_{T_c} = \frac{1}{\bar{r}}\left(\frac{T_c(x_m)}{T_c}\right)^{1/z\nu}, \quad \frac{1}{\bar{r}} = z\nu\frac{m}{\Delta m}\frac{\Delta x_u}{x_u}\left(\frac{a}{T_c(x_m)}\right)^{1/z\nu}, \tag{4.75}$$

applicable close to the 2D–QSI transition. Here we rescaled T_c by $T_c(x_m)$, the transition temperature at optimum doping, to reduce variations of T_c between different materials [35].

In Fig. 4.17 we show the experimental data for $Y_{1-x}Pr_xBa_2Cu_3O_7$ [93], $La_{1.85}Sr_{0.15}Cu_{1-x}Ni_xO_4$ [94] and $YBa_{2-x}La_xCu_3O_7$ [95] in terms of $1/\beta_{T_c}$

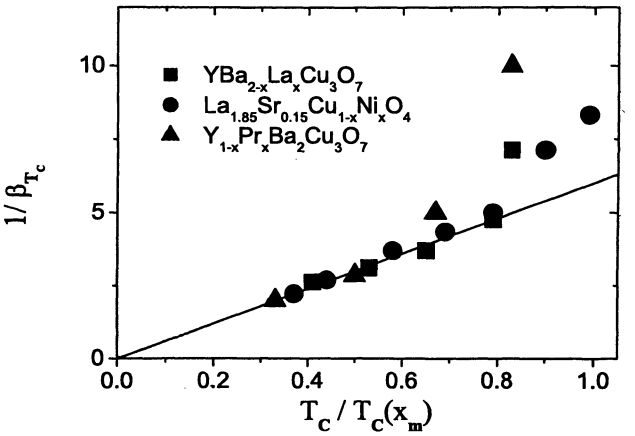

Fig. 4.17. Inverse isotope coefficient $1/\beta_{T_c}$ versus T_c/T_c^m for $Y_{1-x}Pr_xBa_2Cu_3O_7$ [93], $La_{1.85}Sr_{0.15}Cu_{1-x}Ni_xO_4$ [94] and $YBa_{2-x}La_xCu_3O_7$ [95]. The straight line corresponds to $1/\beta_{T_c} = \overline{r}\, T_c/T_c^m$ (Eq. (4.75)) with $z\overline{\nu} = 1$ and $\overline{r} = 6$

versus $T_c/T\,(x_m)$. As predicted by Eq. (4.75), approaching the 2D–QSI transition $T_c/T_c\,(x_m) = 0$, the data collapse on a straight line, pointing again to $z\overline{\nu} \approx 1$(Eq. (4.65)). Accordingly, the strong doping dependence of the isotope coefficients of transition temperature and zero temperature in–plane penetration depth in underdoped cuprates follows naturally from the doping tuned 3D–2D crossover and the associated 2D–QSI transition in the underdoped limit. One might hope that this novel point of view about the isotope effects in cuprate superconductors [96] will stimulate further experimental work to obtain new data to confirm or refute these predictions.

A property suited to shed light on the critical behavior of both, the 2D–QSI and 3D–QSN transition is the magnetic field dependence of the specific heat coefficient in the limit of zero temperature. From the scaling relation $\gamma_c|_{T=0} \propto H_c^{(D-z)/2}$ (Eq. (4.44)) it is seen that for both transition $\gamma_c|_{T=0} \propto H_c^{1/2}$ holds, provided that $z = 1$ and $z = 2$ at 2D–QSI and 3D–QSN criticality, respectively. The experimental data displayed in Fig. 4.18 shows that in $La_{2-x}Sr_xCuO_4$ $(D-z)/2 = 1/2$ holds irrespective of the doping level. Thus these data provide rather unambiguous evidenced for a 2D–QSI transition with $z = 1$ and a 3D–QSN criticality with $z = 2$. This implies that $\gamma_c|_{T=0} \propto H_c^{1/2}$ is not a characteristic feature of d–wave pairing, as proposed by Volovik [98], Won and Maki [99].

The above comparison with experiment provides rather clear evidence for the occurrence of a 2D–QSI transition with $z = 1$ and $\overline{\nu} = 1$ in the underdoped and a 3D–QSI critical point $z = 2$ and $\overline{\nu} = 1/2$ in the overdoped limit. Next, to substantiate this scenario further, we consider the crossover between these quantum critical points. Noting that $1/\lambda_{ab}^2\,(0)$ scales close to

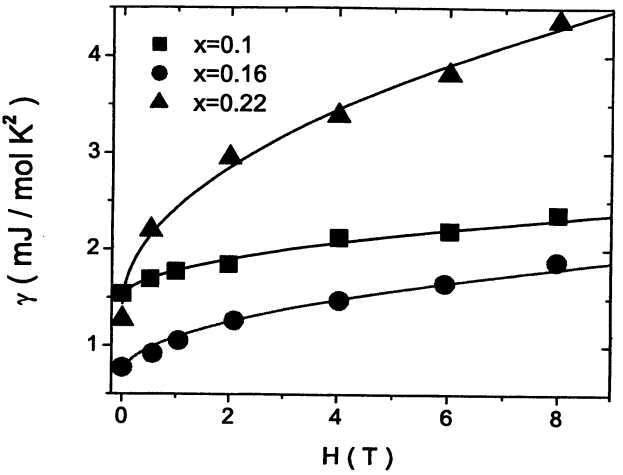

Fig. 4.18. Magnetic field dependence of the specific heat coefficient at zero temperature $\gamma_c|_{T=0}$ for $La_{2-x}Sr_xCuO_4$ at x=0.1, 0.16 and 0.22 (taken from Chen *et al.* [97])

these critical points as (Eq. (4.37))

$$\frac{1}{\lambda_{ab}^2(0)} \propto \Upsilon_{ab}^D(0) \propto \delta^{\overline{\nu}((D-2+z))}, \tag{4.76}$$

we invoke

$$\lambda_{ab}^2(0) = \frac{a_\lambda}{x - x_u} + \frac{b_\lambda}{(x_o - x)^{3/2}}, \tag{4.77}$$

to interpolate between the 2D–QSI and 3D–QSN transition. A fit to the experimental data of $La_{2-x}Sr_xCuO_4$, yielding the parameters

$$a_\lambda = 5.42\ 10^5\ A^2, \quad b_\lambda = 6.9\ 10^3\ A^2, \tag{4.78}$$

is shown Fig. 4.19.

It is remarkable that this simple interpolation scheme, reducing in the under– and overdoped limit to the expected asymptotic behavior, describes the data so well. Due to this agreement, this interpolation function provides in conjunction with the empirical law for $T_c(x)$ (Eq. (4.1)), a realistic description of the doping dependence of the zero temperature out–of–plane correlation length $\overline{\xi}_c$, given by Eq. (4.48), yielding $\overline{\xi}_c \propto T_c\lambda_{ab}^2(0)$, close to 2D–QSI and 3D–QSN criticality. The doping dependence of $T_c\lambda_{ab}^2(0)$ is displayed in Fig. 4.20 for $La_{2-x}Sr_xCuO_4$. Since $T_c \propto d_s/\lambda_{ab}^2(0)$ holds in the underdoped limit (see Eq. (4.40) and Fig. 4.13), it is clear that $T_c\lambda_{ab}^2(0)$ tends to a constant value, proportional to d_s, the thickness of the independent sheets. Since initially $d/dx\left(T_c\lambda_{ab}^2(0)\right) \approx -T_c(x_m)\, a_\lambda x_o$, the linear decrease simply reflects the parabolic form of the empirical law (4.1). Finally,

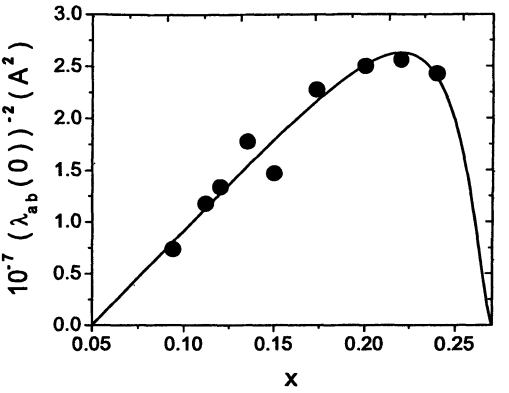

Fig. 4.19. $1/\lambda_{ab}^2(0)$ versus x for $La_{2-x}Sr_xCuO_4$. •: experimental data taken from [9,84]. The solid curve is a fit to Eq. (4.77) with the parameters listed in Eq. (4.78). It indicates the crossover from a 2D–QSI transition with $z = 1$ and $\overline{\nu} = 1$ to a 3D–QSN criticality with $z = 2$ and $\overline{\nu} = 1/2$

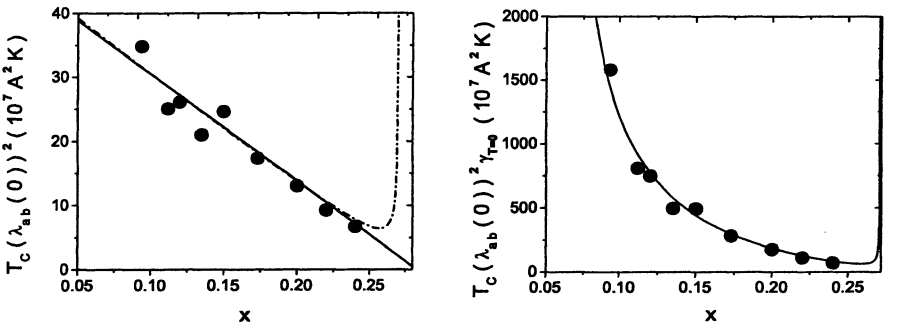

Fig. 4.20. (a) $T_c\lambda_{ab}^2(0)$ versus x for $La_{2-x}Sr_xCuO_4$. •: taken from [9] and [84]. The solid line is Eqs. (4.1) and (4.77) with $T_c(x_m) = 39.8$K and the parameters listed in Eq. (4.78). Note that close to the 2D–QSI and 3D–QSN transition $T_c\lambda_{ab}^2(0) \propto \overline{\xi}_c$. (b) $T_c\lambda_{ab}^{-2}(0)\gamma_{T=0}$ versus x for $La_{2-x}Sr_xCuO_4$. • : T_c and $\lambda_{ab}^{-2}(0)$ taken from [9,84] and $\gamma_{T=0}$ from Eq. (4.2) with $\gamma_{T=0,0} = 2$. Note that $T_c\lambda_{ab}^{-2}(0)\gamma_{T=0} \propto \overline{\xi}_{ab}$(4.48). The solid curve indicates the crossover from 2D–QSI ($z = 1$, $\overline{\nu} = 1$) to 3D–QSN ($z = 2$, $\overline{\nu} = 1/2$) criticality according to Eqs. (4.1), (4.2), (4.76) and (4.77)

the upturn close to the overdoped limit, a regime which experimentally has not yet been attained, signals the 3D–QSN transition, where $\overline{\xi}_c \propto T_c\lambda_{ab}^2(0)$ diverges. In this context it is also instructive to consider the zero temperature in–plane correlation length. By definition it diverges at a 2D and 3D quantum phase transition. According to the scaling relation (4.48) it can be measured in terms of $\overline{\xi}_{ab} \propto T_c\lambda_{ab}^2(0)\gamma_{T=0}$. In Fig. 4.20 we displayed the experimental data for $\overline{\xi}_{ab} \propto T_c\lambda_{ab}^2(0)\gamma_{T=0}$ versus x. For comparison we in-

cluded the behavior resulting from Eqs. (4.1), (4.2),(4.76) and (4.77) in terms of the solid curve. While the rise of $\bar{\xi}_{ab}$ in the underdoped regime, signaling the occurrence of a 2D–QSI transition, is well confirmed, it does not extend sufficiently close to the overdoped limit to detect 3D–QSN criticality. From Fig. 4.21, showing the doping dependence of the T–linear term of the specific heat coefficient of $La_{2-x}Sr_xCuO_4$, it is seen that this quantity tends to a finite value in the underdoped limit and increases in the overdoped regime. This behavior is fully consistent with the scaling relation $d\gamma_c/dT|_{T=0} \propto \delta^{\overline{\nu}(D-2z)}$ (Eq. (4.45)). Indeed at 2D–QSI criticality with $z = 1$, $d\gamma_c/dT|_{T=0}$ tends to a constant value and diverges close to the 3D–QSN critical point for $z > 3/2$. Unfortunately, the data does not extend sufficiently close to the overdoped limit to provide reliable estimates of the exponent combination $\overline{\nu}(3-2z)$.

Provided that the linear T–term of $1/\lambda_{ab}^2(T)$ in the zero temperature limit exists, the scaling relations (4.37) and (4.38) yield close to quantum criticality the universal relation

$$T_c \frac{d}{dT}\left(\frac{\lambda_i(0)}{\lambda_i(T)}\right)^2\Bigg|_{T=0} = \overline{y}_c \left.\frac{dY_D}{d\overline{y}}\right|_{\overline{y}=0}, \tag{4.79}$$

where D=2 and D=3 for the 2D–QSI and 3D–QSN transition, respectively. In Table 4.1 we collected additional estimates for various cuprates and doping levels. The rise of the magnitude of $T_c\, d/dT\,(\lambda_{ab}(\delta,0)/\lambda_i(\delta,T))^2\big|_{T=0}$ with increasing doping level reflects the 2D–3D–crossover in the scaling function Y_D. Noting that most compounds are close to optimum doping it is not surprising that the listed values scatter around -0.61, the value of nearly optimally doped $La_{2-x}Sr_xCuO_4$.

Before turning to the substitution tuned quantum transitions it is useful to express the doping dependence in the interpolation formula (4.77) in terms of

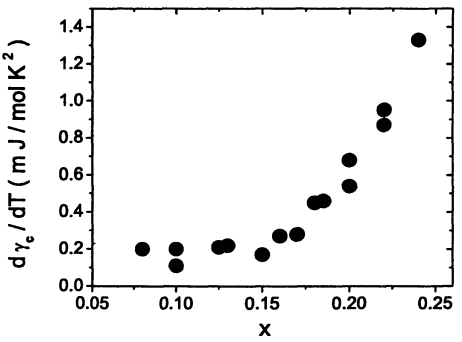

Fig. 4.21. $T_c d\gamma_c/dT|_{T=0}$ versus x for $La_{2-x}Sr_xCuO_4$. Data taken from Ref. [15] and [100]

Table 4.1. Estimates for $T_c\, d/dT\,(\lambda_{ab}(0)/\lambda_{ab}(T))^2|_{T=0}$ derived from the experimental data of: slightly underdoped $HgBa_2Ca_2Cu_3O_{8+\delta}$, slightly overdoped $HgBa_2CuO_{4+\delta}$ [101], under–, optimally– and over–doped $La_{2-x}Sr_xCuO_4$ [9], $Bi_2Sr_2CaCu_2O_{8+\delta}$ [102], $Y_{0.94}Ca_{0.6}Ba_2Cu_4O_8$, $YBa_2Cu_4O_8$, $Y_{1.925}La_{0.075}Cu_4O_8$ and $Y_{1.9}La_{0.1}Cu_4O_8$ [103].

	$\lambda_{ab}(0)$ (A)	T_c (K)	$T_c \frac{d}{dT}\left(\frac{\lambda_i(\delta,0)}{\lambda_i(\delta,T)}\right)^2\Big\vert_{T=0}$
$HgBa_2Ca_2Cu_3O_{8+\delta}$	1770	135	-0.59
$HgBa_2CuO_{4+\delta}$	1710	93	-0.65
$La_{1.9}Sr_{0.1}CuO_4$	2800	30	-0.49
$La_{1.85}Sr_{0.15}CuO_4$	2600	39	-0.61
$La_{1.8}Sr_{0.2}CuO_4$	1970	35	-0.72
$La_{1.78}Sr_{0.22}CuO_4$	1930	27.5	-0.72
$La_{1.76}Sr_{0.24}CuO_4$	1940	19	-0.94
$Bi_2Sr_2CaCu_2O_{8+\delta}$	2600	91	-0.61
$Y_{0.94}Ca_{0.06}Ba_2Cu_4O_8$	1361	88	-0.51
$YBa_2Cu_4O_8$	1383	81	-0.58
$YBa_{1.925}La_{0.075}Cu_4O_8$	1521	74	-0.61
$YBa_{1.9}La_{0.1}Cu_4O_8$	1593	72	-0.63

the transition temperature. This is achieved by invoking the empirical correlation 4.1 between T_c and doping concentration x . In Fig. 4.22 we displayed the resulting Uemura plot, T_c versus $1/\lambda_{ab}^2(0)$ for $La_{2-x}Sr_xCuO_4$ in terms of the solid and dashed curves, resembling the outline of a fly's wing. The solid curve marks the flow from $T_c(x_m)$ to the 2D–QSI critical point and the dashed one the flow to 3D–QSN criticality. The dotted line indicates the universal 2D–behavior (Eqs. (4.40)) and (4.68)). For comparison we included the experimental data of Panagopoulos *et al.* [9] and Uemura *et al.* [84]. Although the data does not attain the respective critical regimes, together with the theoretical curves, they provide a generic perspective of the flow to 2D–QSI and 3D–QSN criticality. Indeed convincing evidence for these flows emerges from the μSR data displayed in Fig. 4.23 for $Y_{0.8}Ca_{0.2}Ba_2(Cu_{1-y}Zn_y)O_{7-\delta}$ ($Y_{0.8}Ca_{0.2}$-123), $Tl_{0.5-y}Pb_{0.5+y}Sr_2Ca_{1-x}Y_xCu_2O_7$ (Tl-1212) [104] and $TlBa_2CuO_{6+\delta}$ (Tl-2201) [105]. In analogy to Fig. 4.22, the solid curves mark the flow from $T_c(x_m)$ to the 2D–QSI critical point and the dashed ones the approach to 3D–QSN criticality.

Additional confirmation of this flow emerges from Fig. 4.24, showing the condensation energy versus hole concentration p for $Y_{0.2}Ca_{0.2}Ba_{0.2}Cu_3O_{7-\delta}$ taken from Tallon and Loram [106]. The solid and dashed curves are Eqs. (4.51), in terms of

$$-E(T=0) \propto \delta^{(z+D)/z} \propto (p-p_u)^3 \propto T_c^3,$$
$$-E(T=0) \propto (p_o-p)^{5/2} \propto T_c^{5/2}, \qquad (4.80)$$

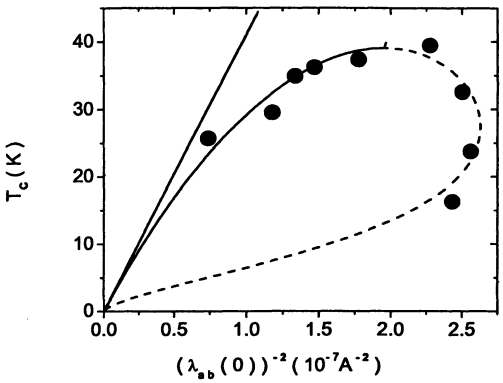

Fig. 4.22. T_c versus $1/\lambda_{ab}^2(0)$ for $La_{2-x}Sr_xCuO_4$. •: experimental data taken from [9, 84]. The solid and dashed curves result from the empirical law (4.1) and the interpolation function (4.77) with $T_c(x_m)$=39.8 K and the parameters listed in Eq. (4.78). The solid line indicates the flow from optimum doping to 2D–QSI criticality and the dashed one to the 3D–QSN critical point

with $(z+D)/z = 3$ and $(z+D)/z = 5/2$, the values appropriate for the 2D–QSI (Eq. (4.65)) and 3D–QSN (Eq. (4.67)), respectively.

A generic flow to the 2D–QSI critical point also emerges from the plot $\lambda_c(0)$ versus $\sigma_c(T_c^+)$ displayed in Fig. 4.25 for $YBa_2Cu_3O_{7-\delta}$, $La_{2-x}Sr_xCuO_4$ and $Bi_2Sr_2CaCu_2O_y$ at various doping levels. An empirical, nearly linear, correlation between these quantities has been proposed by Basov *et al* [107]. From the scaling relation (4.58) it is seen that the systematic rise of $\lambda_c(0)$ with decreasing $\sigma_c(T_c^+)$, tuned by decreasing dopant concentration and the associated rise of the anisotropy γ_T, reflects again the flow to 3D–QSI criticality. The straight line marks the asymptotic behavior $La_{2-x}Sr_xCuO_4$ for $z = 1$ and $\Omega_s \approx 24\mu m(\Omega cm)^{3/4}$. Since Ω_s depends on the critical amplitudes $\gamma_{0,0}$, $\lambda_{ab,0}(0)$, $\gamma_{T_c,0}$ and the thickness d_s (Eqs. (4.58) and (4.59)), its value is unique within a family of cuprates. $\Omega_s \approx 24\mu m(\Omega cm)^{3/4}$ follows from $\gamma_{0,0} \approx 1.63$, $\gamma_{T_c,0} \approx 2$ (see Fig. 4.1), $d_s \approx 6.6$ A, $\sigma_0 \approx 1$ and $\lambda_{ab,0}(0) \approx 736$ A (Eq. (4.78). Although the experimental data is still quite far from the underdoped limit, the flow to 2D–QSI criticality with family dependent values of Ω_s can be anticipated. This differs from the mean–field prediction for bulk superconductors in the dirty limit and layered BCS superconductors, treated as weakly coupled Josephson junctions (see Eqs. (4.60) and (4.61)) where $\Omega_s \propto T_c^{-1/2}$. Moreover, as the optimally doped and underdoped regimes are approached, systematic deviations from the straight line behavior appear, indicating the flow to 3D–QSN–criticality (Eq. (4.63)).

According to the empirical correlation between T_c and anisotropy γ_T (see Eq. (4.3) and Fig. 4.2), the initial value of the dopant concentration determines whether the flow leads to 2D–QSI or 3D–QSN criticality. For initially

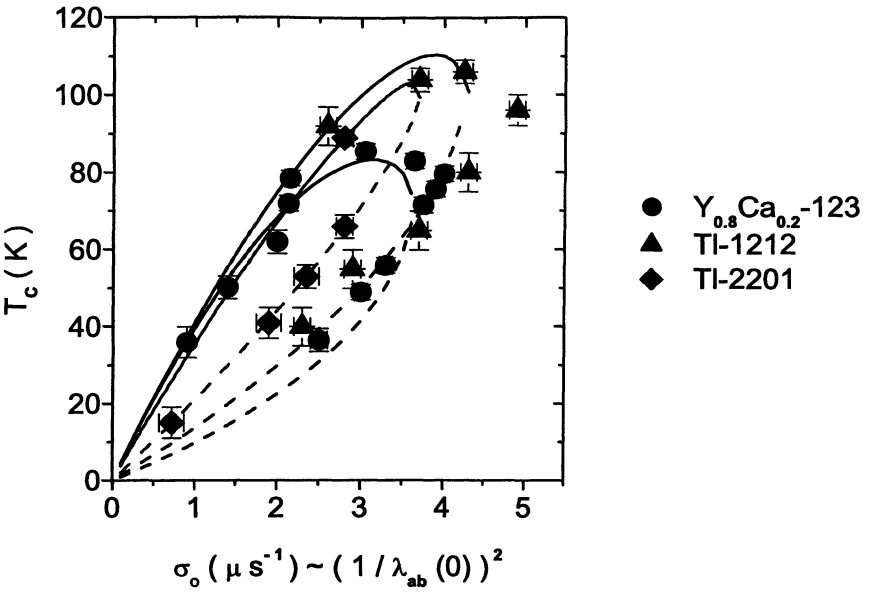

Fig. 4.23. T_c versus $\sigma_0 \propto \lambda_{ab}^{-2}(0)$ for $Y_{0.8}Ca_{0.2}Ba_2(Cu_{1-y}Zn_y)O_{7-\delta}$ ($Y_{0.8}Ca_{0.2}$-123), $Tl_{0.5-y}Pb_{0.5+y}Sr_2Ca_{1-x}Y_xCu_2O_7$ (Tl-1212) [104] and $TlBa_2CuO_{6+\delta}$ (Tl-2201) [105]. The solid and dashed curves result from the empirical law (4.1) and the interpolation function (4.77). The solid curves indicate the flow from optimum doping to 2D–QSI criticality and the dashed ones to the 3D–QSN critical point

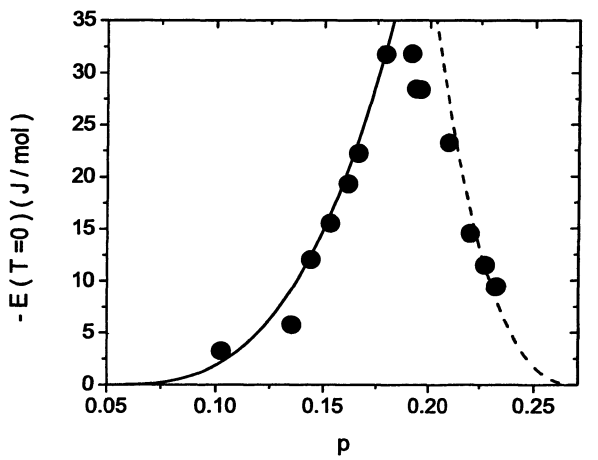

Fig. 4.24. Condensation energy $-E(T=0)$ versus hole concentration p for $Y_{0.2}Ca_{0.2}Ba_{0.2}Cu_3O_{7-\delta}$. The experimental data is taken from Tallon and Loram [106]. The solid and dashed lines are Eqs. (4.80), indicating the approach to 2D–QSI and 3D–QSN criticality

underdoped cuprates, the rise of γ_T , tuned by the doping induced reduction of T_c, directs the flow to 2D–QSI criticality. Conversely, in initially overdoped cuprates, the fall of γ_T to a finite value drives the flow to the 3D–QSN critical point. As the nature of the quantum phase transitions is concerned we have seen that the 2D–QSI transition has a rather wide and experimentally accessible critical region. For this reason we observed considerable and consistent evidence that it falls into the same universality class as the onset of superfluidity in ^{4}He films in disordered media, corrected for the long–rangeness of the Coulomb interaction. The resulting critical exponents, $z = 1$ and $\overline{\nu} \approx 1$, are also consistent with the empirical relations (Eqs. (4.1), (4.2) and (4.3)) and the observed temperature and magnetic field dependence of the specific heat coefficient in the limit of zero temperature. These properties also point to a 3D–QSN transition with $z = 2$ and $\overline{\nu} \approx 1/2$, describing a d–wave superconductor to disordered metal transition at weak coupling. Here the disorder destroys superconductivity, while at the 2D–QSI transition it localizes the pairs and with that destroys superfluidity. Due to the existence of the 2D–QSI and 3D–QSN critical points, the detection of finite temperature 3D–XY critical behavior will be hampered by the associated crossovers which reduce the temperature regime where thermal 3D–XY fluctuations dominate. In any case, our analysis clearly revealed that the universality of the empirical correlations reflect the flow to 2D–QSI and 3D–QSN criticality. Moreover, the doping tuned superconductivity in bulk cuprate superconductors turned out to be a genuine 3D phenomenon, where the interplay of anisotropy and superconductivity destroys the latter in the 2D limit.

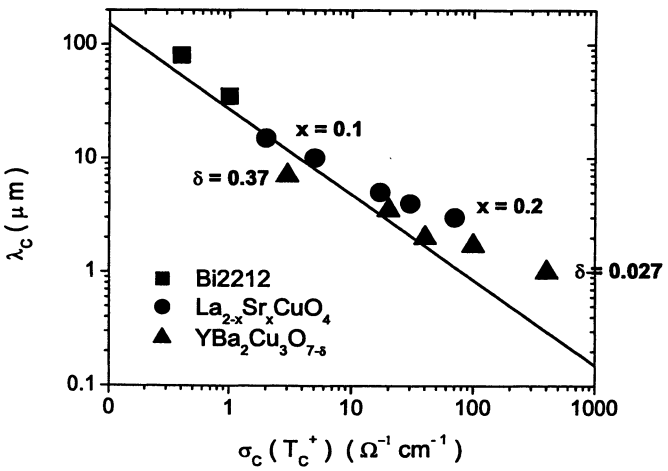

Fig. 4.25. $\lambda_c(0)$ versus $\sigma_c\left(T_c^+\right)$ for $YBa_2Cu_3O_{7-\delta}$ (▲), $La_{2-x}Sr_xCuO_4$ (•) [108] and $Bi_2Sr_2CaCu_2O_y$ (■) [109]. The straight line is Eq. (4.58) with $z = 1$ and $\Omega_s \approx 24\mu m\,(\Omega cm)^{3/4}$, the estimate for $La_{2-x}Sr_xCuO_4$

4.3.3 Evidence for Substitution Tuned Quantum Phase Transitions

It is well established, both experimentally and theoretically, that in conventional superconductors (e.g., A15 compounds or the Chevrel phases) the presence of magnetic impurities depresses the superconducting transition temperature more efficiently than does the introduction of nonmagnetic ions [110], and this has been ascribed to the breaking of pairs by the magnetic impurities. To determine wether the cuprates behave similarly with respect to magnetic impurities, extensive studies involving the substitution for Cu by other 3d metals have been performed [18, 19]. A result common to all these studies is that T_c is depressed in the same manner, independent of wether the substituent is magnetic or nonmagnetic, and in contrast to that observed in conventional superconductors.

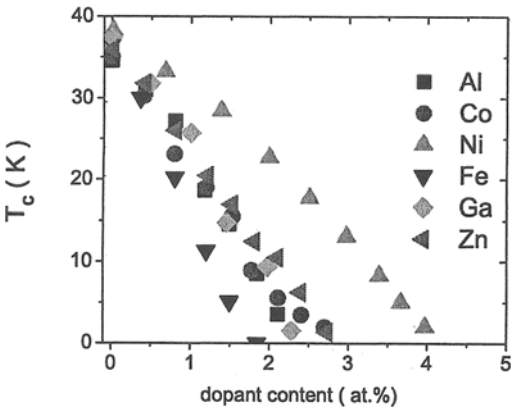

Fig. 4.26. Variation of T_c with substitution for $La_{1.95}Sr_{0.15}Cu_{1-y}A_yO_4$ (A=Fe, Cu, Ni, Zn, Ga and Al) (taken from Xiao *et al.* [18])

To illustrate this point we depicted in Fig. 4.26, the variation of T_c with substitution for $La_{1.95}Sr_{0.15}Cu_{1-y}A_yO_4$ (A=Fe, Cu, Ni, Zn, Ga and Al) [18]. T_c is seen to vanish at a critical substitution concentration y_c, where a quantum phase transition occurs. The experimental data for $La_{2-x}Sr_xCu_{1-y}Zn_yO_4$, $Y_{0.8}Ca_{0.2}Ba_2Cu_{3-3y}Zn_{3y}O_{7-\delta}$ [111] and $Bi_2Sr_2CaCu_{2-2y}Co_{2y}O_{8+\delta}$ [112] shows that this behavior is not restricted to optimum doping. Thus T_c dependence on both, the dopant (x) and substitution concentration (y). Fig. 4.3 shows the resulting (T_c, x, y) diagram for $La_{2-x}Sr_xCu_{1-y}Zn_yO_4$. The blue curve, $y_c(x)$, is a line of quantum phase transitions. At the corresponding critical endpoints the system undergoes a 2D–QSI and 3D–QSN transition. Along the path marked by the green arrow, a QSI and QSN transition is

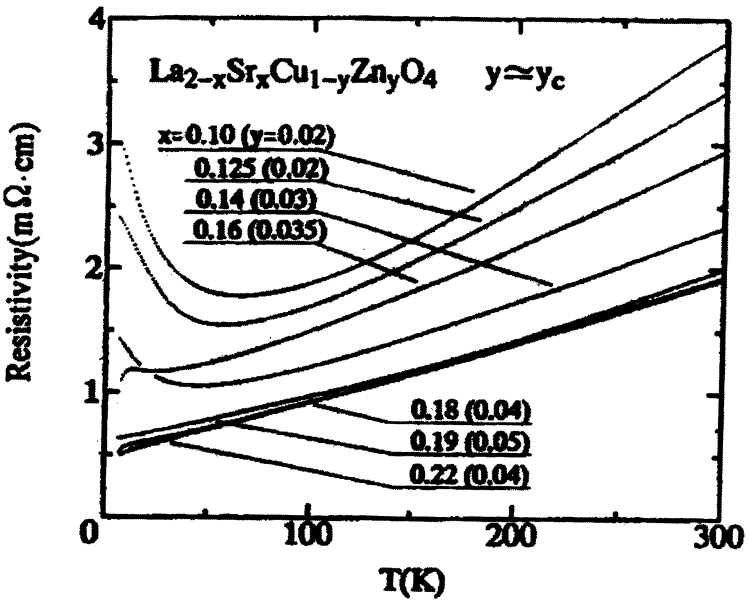

Fig. 4.27. Temperature dependence of the resistivity for $La_{2-x}Sr_xCu_{1-y}Zn_yO_4$ at $y_c(x)$ (taken from Momono *et al.* [15])

expected to occur. The pink arrow indicates the crossover from insulating to metallic behavior.

This scenario, emerging from the temperature dependence of the resistivity of $La_{2-x}Sr_xCu_{1-y}Zn_yO_4$ [15], is shown in Fig. 4.27. Along the phase transition line $y_c(x)$ superconductivity is disappears and for $x \gtrsim 0.16$ metallic behavior sets in, while for $x \lesssim 0.16$ the resistivity exhibits insulating behavior at low temperatures. For fixed x and close to $y_c(x)$, T_c scales according to Eqs. (4.33) and (4.38) as

$$T_c(y) \propto \left(1 - \frac{y}{y_c(x)}\right)^{z\overline{\nu}}. \tag{4.81}$$

Since $z\overline{\nu} = 1$ is expected to hold in both, the doping tuned 2D–QSI and 3D–QSN transition (Eqs. (4.65) and (4.67)), this combination should hold along the entire line $y_c(x)$. Although the data shown in Fig. 4.26 is remarkably consistent with $z\overline{\nu} = 1$ it remains to be understood, why the linear relationship applies almost over the entire substitution regime. Close to the 2D–QSI and 3D–QSN transitions, the singular part of the free energy density scales in analogy to Eq. (4.36) as

$$f_s \propto \delta^{\overline{\nu}(D+z)} \mathcal{F}\left(y\delta^{-\overline{\nu}}\right), \ \delta = x/x_u - 1, \ 1 - x/x_o. \tag{4.82}$$

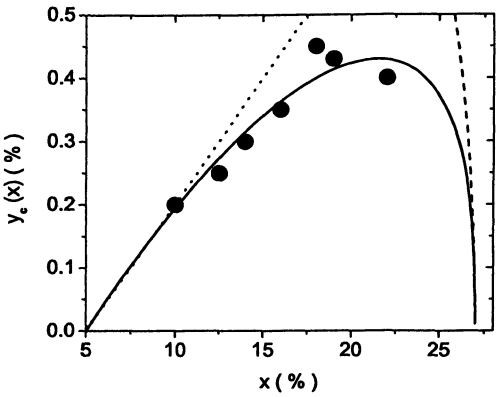

Fig. 4.28. y_c versus x for $La_{2-x}Sr_xCu_{1-y}Zn_yO_4$. • : Taken from Momono *et al.* [15]. The solid curve interpolates between the critical behavior of a 2D–QSI transition with $\overline{\nu} = 1$ (dotted line: $y_c(x) = 0.03(x-5)$) and a 3D–QSN transition with $\overline{\nu} = 1/2$ (dashed line: $y_c(x) = 0.46(27-x)^{1/2}$)

$\mathcal{F}$ is a scaling function of its argument. A phase transition is signaled by a singularity of the scaling function at some value of its argument. Thus,

$$y_c(x) \propto \delta^{\overline{\nu}}, \tag{4.83}$$

with $\overline{\nu} = 1$ close to the 2D–QSI (Eqs. (4.65)) and $\overline{\nu} = 1/2$ near the 3D–QSN transition (Eq. (4.67)). The resulting phase transition line is shown in Fig. 4.28 for $La_{2-x}Sr_xCu_{1-y}$
Zn_yO_4, where we included the experimental data for comparison. As expected from the doping dependence of the correlation lengths (see Fig. 4.20) $y_c(x)$ exhibits close to the 3D–QSN transition a very narrow critical regime. For this reason the data considered here is insufficient to provide an estimate for $\overline{\nu}$. Nevertheless, $\overline{\nu} = 1/2$ yields a reasonable qualitative description of the quantum critical line $y_c(x)$.

The picture we no have is summarized in the phase diagram shown in Fig. 4.3. The blue curve corresponds to the line of quantum phase transitions $y_c(x)$ shown in Fig. 4.28. Along this line, $z\overline{\nu} = 1$ is expected to hold (Eqs. (4.65) and (4.67)), while $\overline{\nu} \approx 1$(Eqs. (4.65)) at the 2D–QSI ($y = 0$ and $x = x_u$) and $\overline{\nu} = 1/2$ at the 3D–QSN (($y = 0$ and $x = x_o$) transition. According to the empirical correlation between T_c and anisotropy γ_T (see Eq. (4.3) and Fig. 4.2), the initial value of the dopant concentration determines whether the flow upon substitution leads to 2D–QSI or 3D–QSN criticality. For initially underdoped cuprates, the rise of γ_T , tuned by the substitution induced reduction of T_c, drives the flow to 2D–QSI criticality. Conversely, in initially overdoped cuprates, the fall of γ_T to a finite value directs the flow to 3D–QSN criticality. The mechanism whereby the substitution of Cu

leads to a reduction of T_c and finally to the quantum critical line $y_c(x)$ appears to be not well understood. When the aforementioned universality classes of the 2D–QSI and 3D–QSN transitions hold true (Eqs. (4.65) and (4.67)), disorder plays an essential role. At 2D–QSI criticality it localizes the pairs and destroys superfluidity [53, 54] and at the 3D–QSN transition it destroys superfluidity and the pairs [55]. In this context we also note that the phase diagram of $La_{2-x}Sr_xCuO_{4+\delta}$ shown in 4.4, reveals that isotope substitution leads to identical behavior, although less pronounced [26]. Since isotope substitution is accompanied by local lattice distortions, we conclude that in addition to disorder, lattice degrees of freedom tune superconductivity in an essential manner. Another essential facet emerges from the fact that the doping and substitution tuned flow to the 2D–QSI critical point is associated with an enhancement of γ_T. Thus, despite the fact that the fraction $\eta = \left(1/\lambda_c^2(0)\right) / \left(1/\lambda_a^2(0) + 1/\lambda_b^2(0) + 1/\lambda_c^2(0)\right) = 1/\left(1 + 2\gamma_{T=0}^2\right)$ [13], which the third dimension contributes to the superfluid energy density in the ground state, is very small, this implies that a finite T_c is inevitably associated with an anisotropic but 3D condensation mechanism, because γ_T is finite whenever superconductivity occurs (see Fig. 4.2). This points unambiguously to the conclusion that theories formulated for a single CuO_2 plane cannot be the whole story. It does not imply, however, a 3D pairing mechanism because in the presence of fluctuations pairing and superfluidity occur separately.

4.3.4 Evidence for Magnetic Field Tuned Quantum Phase Transitions

We have seen (Sec. 3.2) that a strong magnetic field destroys superconductivity at finite temperature. In sufficiently clean systems this destruction occurs at the first order vortex melting transition. However, in the presence of disorder, the long–range order of the vortex lattice is destroyed and the vortex solid becomes a glass [28]. The vortex fluid to glass transition appears to be a second–order transition, signaled by the vanishing of the zero–frequency resistance in the vortex glass phase. Since disorder plays an essential role at 2D–QSI and 3D–QSN criticality, one expects a line $H_m(x)$ of vortex–glass to fluid quantum phase transitions, leading to the schematic phase diagram depicted in Fig. 4.5.There is the superconducting phase (S), bounded by the zero–field transition line, $T_c(x, H = 0)$, the critical lines of the vortex melting or vortex glass to vortex fluid transitions, $T_m(x = fixed, H)$ and the line of quantum critical points, $H_m(x, T = 0)$. Along this line superconductivity is suppressed and the critical endpoints coincide with the 2D–QSI and 3D–QSN critical points at x_u and x_o, respectively. To fix the critical line $H_m(x, T = 0)$ close to the 2D–QSI and 3D–QSN transitions, we note that the singular part of the ground state energy density scales in analogy to Eq. (4.36) as

$$f_s(\delta, T) = \overline{Q}_D \left(\overline{\xi}_{\tau,0}^{-} \prod_{i=1}^{D} \overline{\xi}_{i,0}^{-} \right)^{-1} \delta^{\overline{\nu}(D+z)} \overline{G}_D(\overline{z}), \quad \overline{z} = \frac{H \overline{\xi}_a \overline{\xi}_b}{\Phi_0} \tag{4.84}$$

where H corresponds to a field applied parallel to the c–axis. Supposing that in the (H, δ)–plane there is a continuous transition first order melting transition. Then the scaling function $\overline{G}_D(\overline{z})$ will exhibit a singularity at some universal value $\overline{z} = \overline{z}_m$. Thus close the 2D–QSI and 3D–QSN critical endpoints the quantum critical line (see Fig. 4.5) is given by,

$$H_m(\delta) = \frac{\overline{z}_m \Phi_0}{\xi_{a,0}\xi_{b,0}}\, \delta^{2\overline{\nu}}, \tag{4.85}$$

with $\overline{\nu} \approx 1$ (Eq. (4.65)) and $\overline{\nu} \approx 1/2$ (Eq. (4.67)) close to 2D–QSI and 3D–QSN criticality, respectively. Moreover, the singular behavior of the scaling function $\overline{G}_D(\overline{z})$ must be such as enable the correlation length when $H \neq 0$ to correspond to the vortex glass transition, so that

$$\overline{\xi}_H = \overline{\xi}_{H,0} \left| \frac{H - H_m(\delta)}{H_m(\delta)} \right|^{-\overline{\nu}_m}. \tag{4.86}$$

$\overline{\nu}_m$ is the correlation length exponent of the vortex glass to fluid transition. Noting that $T_c \propto \delta^{\overline{\nu} z} \propto \xi^{-z}$ (see Eqs. (4.34) and (4.38), we obtain with Eq. (4.86) for the magnetic field induced reduction of T_c the relation

$$T_c(H) \propto (H_m(\delta) - H)^{\overline{\nu}_m z_m}. \tag{4.87}$$

z_m is the dynamic critical exponent of the vortex glass to fluid transition.

The existence of a quantum phase transition line $H_m(\delta)$ can be anticipated from the in–plane resistivity data for $YBa_2Cu_{3-z}Zn_zO_y$ of Segawa *et al.* [31] shown in the left panel of Fig. 4.29. With increasing magnetic field strength T_c is depressed. In the sample with $y = 6.7$ and $z = 2.7\%$ the temperature dependence of ρ_{ab} clearly points to a magnetic field tuned QSI transition around $16 < H_m(y = 6.7, z = 2.7\%) \lesssim 18T$. Since $H_m(\delta)$ scales as $\delta^{2\overline{\nu}} \propto (z_c - z)^{2\overline{\nu}}$(Eq. (4.85)), $H_m(y = 6.7, z)$ should increase with reduced Zn concentration z. This behavior is consistent with the data for $z = 2.3\%$, where $H_m(y = 6.7, z = 2.3\%) > 18T$. The emerging (H, T) phase diagram, consisting of finite temperature transition lines (vortex glass to fluid transitions) with 2D–QSI critical endpoints is displayed in the right panel of Fig. 4.29. In the schematic (x, H, T)–phase diagram shown in Fig. 4.5, these lines result from cuts near the zero field 2D–QSI–transition with x replaced by z.

Related behavior was also observed in $La_{2-x}Sr_xCuO_4$ [30] and $Bi_2Sr_{2-x}La_xCuO_{6+\delta}$ [32]. In the hole doped $La_{2-x}Sr_xCuO_4$ [30] and the electron doped $Pr_{2-x}Ce_xCu_{4+\delta}$ a magnetic field tuned metal to insulator crossover was observed close to optimum doping, while in $Bi_2Sr_{2-x}La_xCuO_{6+\delta}$ [32] the crossover sets in well inside the underdoped regime. The phase diagram of $Bi_2Sr_{2-x}La_xCuO_{6+\delta}$ is displayed in the left panel of Fig. 4.30. In the underdoped limit ($x \approx 0.84$) the transition temperature vanishes and a 2D–QSI transition is expected to occur. Evidence for this transition emerges from the temperature dependence of ρ_{ab} shown in the right panel of Fig. 4.30 [32],

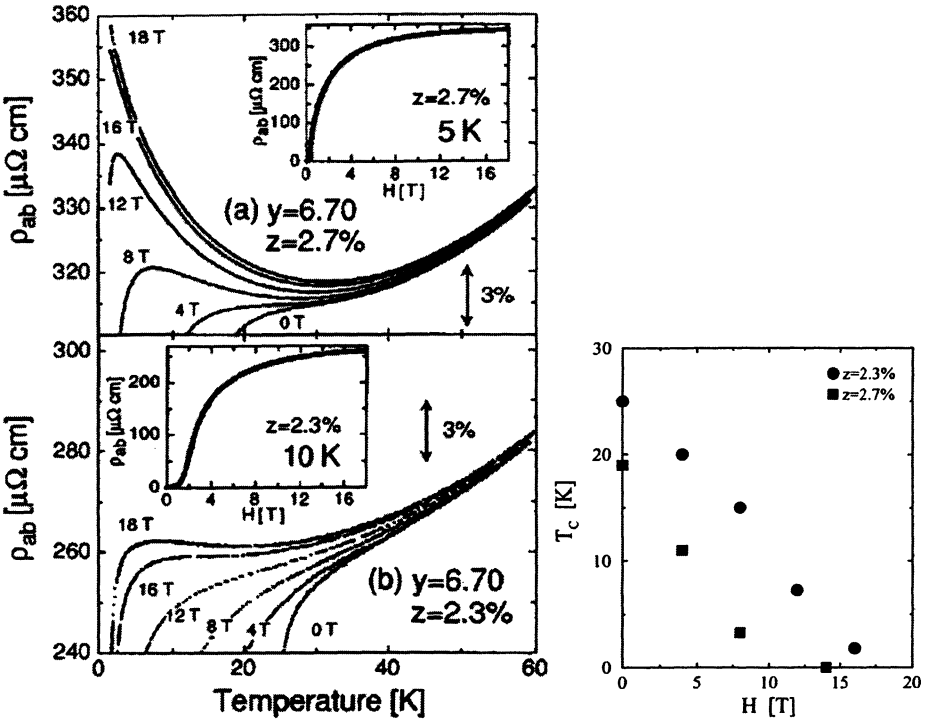

Fig. 4.29. Left panel: In–plane resistivity ρ_{ab} versus T at $H = 0$, 4, 8, 16 and $18T$ for $YBa_2Cu_{3-z}Zn_zO_y$. a: $y = 6.7, z = 2.7\%$ and b: $y = 6.7, z = 2.3\%$. Taken from Segawa *et al.* [31]. Right panel: Schematic (H,T)–phase diagram of $YBa_2Cu_{3-z}Zn_zO_y$ derived from the data shown in the left panel

taken at $H = 0$ and $60T$ for six doping levels x. To strengthen this point we plotted in Fig. 4.31 the resulting T_c versus $\rho_{0,c} - \rho_0$ for $x = 0.76, 0.73$ and 0.66 and $\rho_{0,c} \approx 0.5\ m\Omega cm$ at $H = 0$. Apparently there is suggestive consistency with the 2D–QSI scaling relation (4.42) with $z\overline{\nu} \approx 1$, as well as with the corresponding data for $La_{2-x}Sr_xCuO_4$ and $YBa_2Cu_3O_{7-\delta}$ shown in Fig. 4.15. As the 60T data (symbols) are concerned, the samples closest to the QSI transition ($x = 0.76$ and 0.84) exhibit in ρ_{ab} a pronounced upturn at low temperatures. This points to an insulating normal state. Indeed, the weak upturn below 6 K at $x = 0.73$, visible in the inset to Fig. 4.30, signals the proximity to the onset of insulating behavior, while the low T behavior of the $x = 0.66$ sample with $T_c\,(H = 0) = 23$K exhibits metallic behavior. Thus, there is a metal to insulator (MI) crossover. The emerging (x, T, H)–phase diagram is displayed in Fig. 4.32. The arrows mark the flows emerging from the experimental data displayed in Fig. 4.30 for $x = 0.84$ (1) and $x = 0.66$ (2).

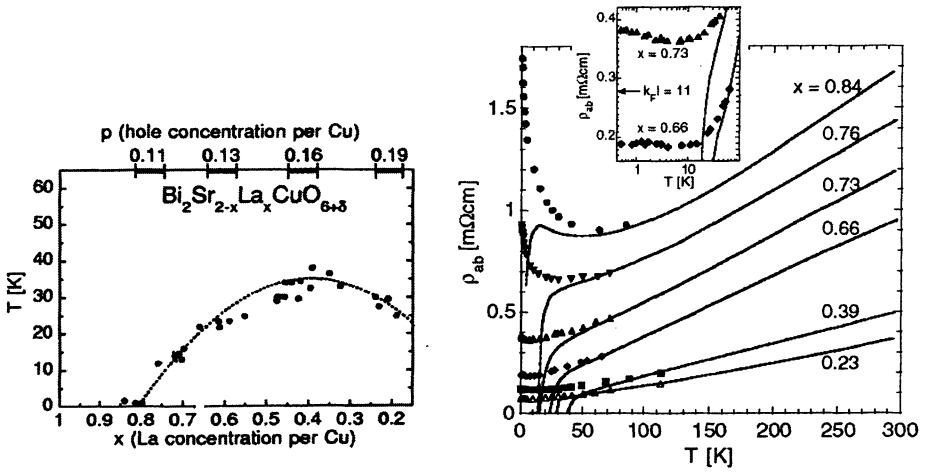

Fig. 4.30. Left panel: Phase diagram of $Bi_2Sr_{2-x}La_xCuO_{6+\delta}$ in the doping concentration (x or p)–temperature plane. Taken from Ono *et al.* [32]. Right panel: Temperature dependence of ρ_{ab} for a $Bi_2Sr_{2-x}La_xCuO_{6+\delta}$ crystal in $H = 0$ and 60T for various dopant concentrations x. The insets shows a clearer view of the low temperature behavior for $x = 0.66$ and 0.73 (taken from Ono *et al.* [32])

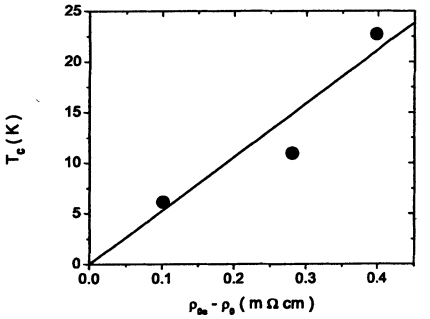

Fig. 4.31. T_c versus $\rho_{0,c} - \rho_0$ for $Bi_2Sr_{2-x}La_xCuO_{6+\delta}$. Deduced from the data shown in Fig. 4.30 for x=0.76, 0.73 and 0.66 and $\rho_{0,c} = 0.5$ mΩcm. The straight line is the scaling relation (4.70) with $z\overline{\nu} \approx 1$

This differs from the behavior observed in $La_{2-x}Sr_xCuO_4$ where the detectable MI– crossover appears to set in close to optimum doping. In Fig. 4.33 we depicted the logarithmic plot of $\rho_{ab}(T)$ for $Bi_2Sr_{2-x}La_xCuO_{6+\delta}$ and $La_{2-x}Sr_xCuO_4$ crystals for $H = 0$ and 60T and various doping concentrations [32]. Concentrating on the presence or absence of an upturn, it is clearly seen that in $La_{2-x}Sr_xCuO_4$ the MI–crossover occurs around $x \approx 0.15$, corresponding to optimum doping. However, it should be kept in mind that this

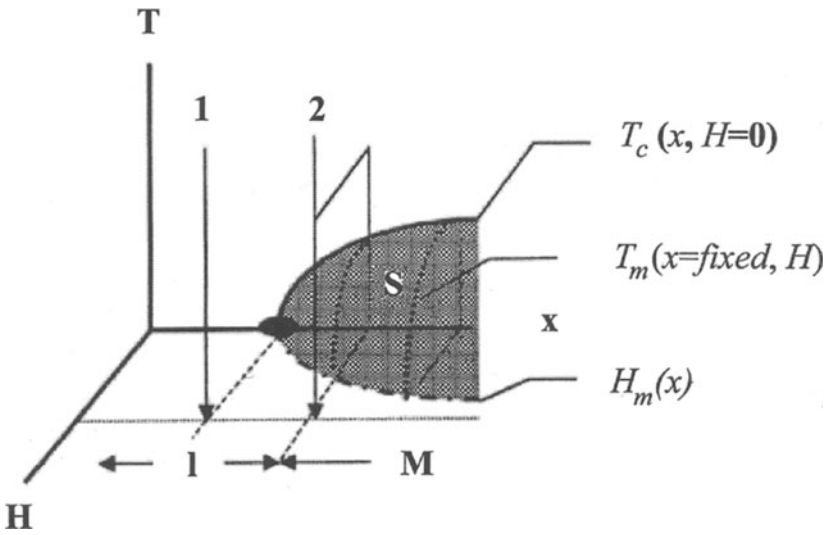

Fig. 4.32. Schematic (x,T,H)–phase diagram close to the 2D–QSI transition. There is the superconducting phase (S), bounded by the zero–field transition line, $T_c\,(x, H = 0)$, the lines of the vortex melting or vortex glass to vortex fluid transitions $T_m\,(x = fixed, H)$ and the quantum critical line $H_m\,(x)$. The critical lines $T_c\,(x, H = 0)$ and $H_m\,(x)$ merge in the underdoped limit ($x = x_u$) where a doping driven quantum superconductor to insulator (QSI) transition (•) occurs. The arrows mark the flows emerging from the experimental data shown in Fig. 4.31 at $x = 0.84$ (1), $x = 0.66$ (2)

crossover is nonuniversal. For this reason, the dopant concentration where insulating behavior is detectable is expected to be material dependent.

The magneto resistance $\rho_{ab}\,(H, T)$ of underdoped $La_{2-x}\,Sr_xCuO_4$ films with $x \approx 0.048$ ($T_c = 0.45$K) and 0.051 ($T_c = 4$K) was also studied in magnetic fields up to 0.5T and at temperatures down to $30mK$ [113]. The temperature dependence of $\rho_{ab}\,(H, T)$ of the film closest to the 2D–QSI transition ($x \approx 0.048$, $T_c = 0.45$K) was found to be consistent with $\rho_{ab} \propto exp\left((T/T_0)^{1/3}\right)$ below 1K and for fields from 4 to 6T. Thus this study points to 2D–localization. On the other hand, the data of Ando *et al.* [29] (Fig. 4.33) appears to be consistent with a logarithmic divergence of the normal–state resistivity down to $0.7K$ for $x = 0.08$ and $H = 60$T, suggesting 2D weak localization. In any case, the evidence for 2D localization confirms an essential property of 2D–QSI criticality: disorder localizes the pairs and destroys superfluidity [53, 54].

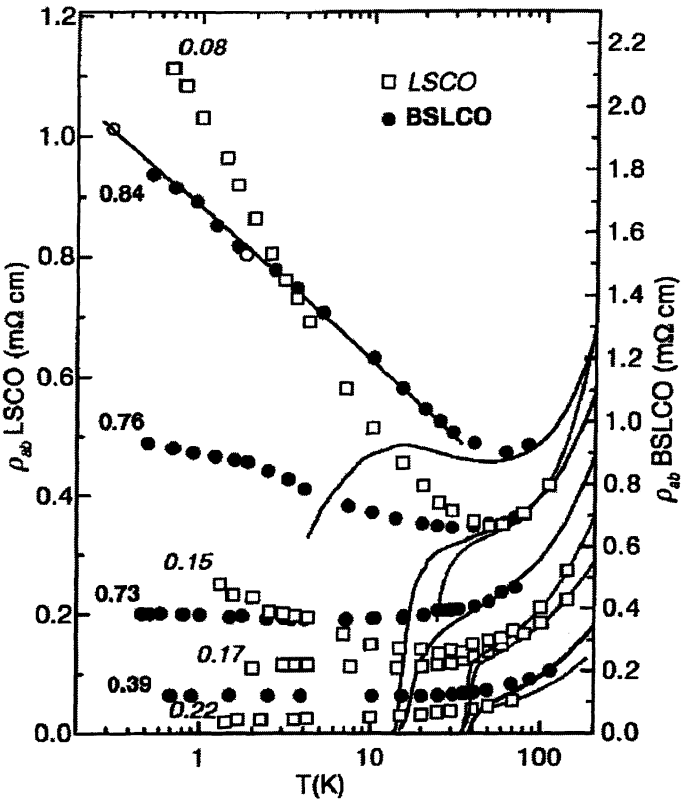

Fig. 4.33. Logarithmic plot of ρ_{ab} (T) for $Bi_2Sr_{2-x}La_xCuO_{6+\delta}$ and $La_{2-x}Sr_xCuO_4$ crystals in H=0T (solid lines) and 60 T (filled circles), labelled by La concentration, x. The straight line indicates consistency with the $log(1/T)$ behavior at $x = 0.84$. and open circles are $H = 30$T data. La_{2-x} Sr_xCuO_4 data in $H = 0$T (dashed lines) and in 60T (open squares), labelled by the Sr concentration x (taken from Ono *et al.* [32])

4.4 Thin Films

There is considerable evidence that the quantum superconductor to insulator transition in thin films can also be traversed by changing a parameter such as film thickness, disorder etc. [13]. As cuprates are concerned, an instructive example are the measurements of $YBa_2Cu_3O_{7-\delta}$ slabs of thickness d separated by 16 unit cells (≈ 187 A) of $PrBa_2Cu_3O_7$. Due to the large separation the $YBa_2Cu_3O_{7-\delta}$ slabs can be considered to be essentially to be uncoupled. As shown in Fig. 4.6 in $YBa_2Cu_3O_{7-\delta}$ slabs of thickness d the transition temperature was found to vary according to Eq. (4.4). Together with the scaling relation (4.38) this points to a 2D–QSI transition with $z\overline{\nu} = 1$, in agreement with our previous estimate (Eq. (4.65)). Since quantum fluctuations

alone are not incompatible with superconductivity, this 2D–QSI transition must be attributed to the combined effect of disorder and quantum fluctuations. Nevertheless, it is conceivable that in cleaner films superconductivity may also occur at and below this value of d_s, which is close to the estimate derived from the bulk (Eq. (4.69)). What's seen is then superconductivity in 2D and due to the reduced dimensionality fluctuations will be enhanced over the full range of dopant concentrations. As it stands, in the bulk (see e.g. Fig. 4.2) and chemically doped films superconductivity disappears in the 2D–limit. Since chemically doped materials with different carrier densities also have varying amounts of disorder, the third dimension is apparently needed to delocalize the carriers and to mediate superfluidity.

4.5 Concluding Remarks and Comparison with Other Layered Superconductors

Evidence for power laws and scaling should properly consist of data that cover several decades in the parameters. The various power laws which we have exhibited span at best one decade and the evidence for data collapse exists only over a small range of the variables. Consequently, though the overall picture of the different types of data is highly suggestive, it cannot really be said that it does more than indicate consistency with the scaling expected near a quantum critical point or a quantum critical line. Nevertheless, the doping, substitution and magnetic field induced suppression of T_c clearly reveal the existence and the flow to 2D–QSI and 3D–QSN quantum phase transition points and lines (see Figs. 4.1, 4.2, 4.3 and 4.5). In principle, their universal critical properties represent essential constraints for the microscopic theory and phenomenological models. As it stands, the experimental data is fully consistent with a single complex scalar order parameter, a doping induced dimensional crossover, a doping, substitution or magnetic field driven suppression of superconductivity, due to the loss of phase coherence. When the evidence for this scenario persists, antiferromagnetic and charge fluctuations are irrelevant close to criticality. Moreover, given the evidence for the flow to 2D–QSI criticality, the associated 3D–2D crossover, tuned by increasing anisotropy, implies that a finite T_c and superfluid density in the ground state of bulk cuprates is unalterably linked to a finite anisotropy. This raises serious doubts that 2D models are potential candidates to explain superconductivity in bulk cuprates. Thus, there is convincing evidence that the combined effect of disorder and quantum fluctuations plays an essential role and even destroys superconductivity in the 2D limit of chemically doped cuprates. Thus, as the nature of the quantum phase transitions in chemically doped cuprates is concerned, disorder is an essential ingredient. We have seen that the 2D–QSI transition has a rather wide and experimentally accessible critical region. For this reason we observed considerable and consistent evidence that it falls into the same universality class as the onset of superfluidity in ^{4}He films in

disordered media, corrected for the long–rangeness of the Coulomb interaction. The resulting critical exponents, $z = 1$ and $\overline{\nu} \approx 1$ are also consistent with the empirical relations (Eqs. (4.1), (4.2) and (4.3)) and the observed temperature and magnetic field dependence of the specific heat coefficient in the limit of zero temperature. These properties also point to a 3D–QSN transition with $z = 2$ and $\overline{\nu} \approx 1/2$, describing a d–wave superconductor to disordered metal transition at weak coupling. Here the disorder destroys superconductivity, while at the 2D–QSI transition it localizes the pairs and with that destroys superfluidity. Due to the existence of the 2D–QSI and 3D–QSN critical points, the detection of finite temperature 3D–XY critical behavior will be hampered by the associated crossovers which reduce the temperature regime where thermal 3D–XY fluctuations dominate. In any case, our analysis clearly revealed that superconductivity in chemically doped cuprate superconductors is a genuine 3D phenomenon and that the interplay of disorder (anisotropy) and superconductivity destroys the latter in the 2D limit. As a consequence, the universality of the empirical correlations reflects the flow to 2D–QSI and 3D–QSN criticality, tuned by chemical doping, substitution and an applied magnetic field. A detailed account of the flow from 2D–QSI to 3D–QSN criticality is a challenge for microscopic theories attempting to solve the puzzle of superconductivity in these materials. Although the mechanism for superconductivity in cuprates is not yet clear, essential constraints emerge from the existence of the quantum critical endpoints and lines. However, much experimental work remains to be done to fix the universality class of the 2D–QSI and particularly of the 3D–QSN critical points unambiguously.

In conclusion we note that universal properties emerging from thermal and quantum fluctuations are not restricted to cuprate superconductors. Potential candidates are the highly anisotropic organic superconductors which are close to a metal–insulator boundary. A glance to Fig. 4.34 shows that the correlation between $\lambda_c(0)$ and $\sigma_c^{DC}(T_c^+)$ is particularly rewarding. In various classes of layered superconductors, including organics, transition metal dichalcogenides and cuprates, $\lambda_c(0)$ is systematically suppressed with increase of normal state conductivity $\sigma_c^{DC}(T_c^+)$. Without thermal and quantum fluctuations the DC conductivity is given by

$$\sigma_c^{DC} = \frac{ne^2}{m_c}\tau_{tr} = \frac{c^2\tau_{tr}}{4\pi\lambda_c^2(0)}. \tag{4.88}$$

τ_{tr} is the mean scattering time of the normal electrons in transport properties with number density per unit volume n and effective mass m_c. Provided that the variations of τ_{tr} are small, superconductors where fluctuations can be neglected (mean–field superconductors) are then characterized by the dotted line in Fig. 4.34, which is

$$\lambda_c(0) \propto \left(\sigma_c^{DC}\right)^{-1/2}. \tag{4.89}$$

It agrees with the data of mean–field superconductors rather well. Inter-

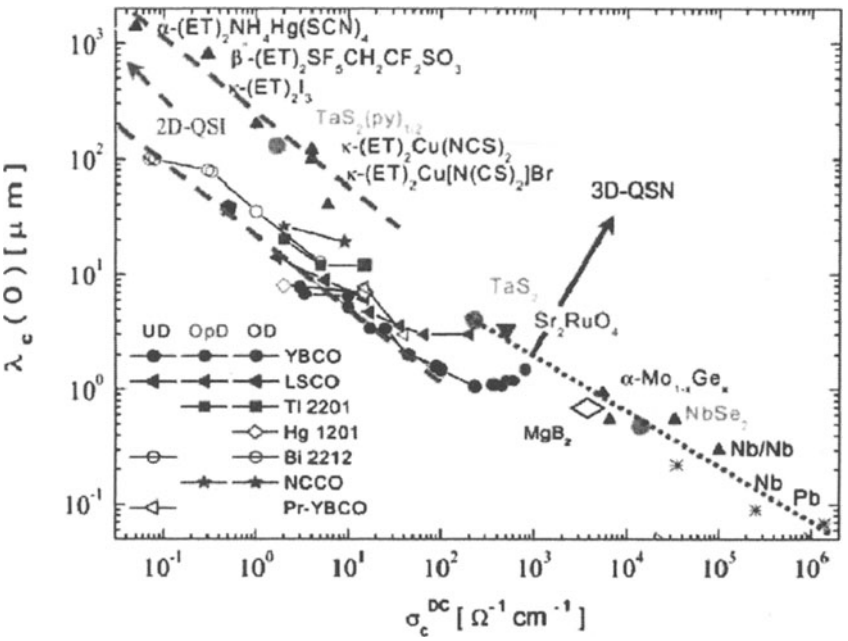

Fig. 4.34. $\lambda_c(0)$ versus σ_c^{DC} for a variety of superconductors. $YBa_2Cu_3O_{7-\delta}$ (YBCO) [115–119], $La_{2-x}Sr_xCuO_{4+\delta}$ (LSCO) [117, 120, 121], $HgBa_2CuO_{4+\delta}$ (Hg1201) [122], $Tl_2Ba_2CuO_{6+\delta}$ (Tl2201) [123–125], $Bi_2Sr_2CaCu_2O_{8+\delta}$ (Bi2212) [126, 127], $Nd_{2-x}Ce_xCuO_{4+\delta}$ (NCCO) [128]. Blue points –underdoped (UD), green –optimally doped (OpD) and red –overdoped (OD). Transition metal dichalcogenides [145, 146]; $(ET)_2X$ compounds [136–144]; $(TMTSF)_2$ ClO_4 [129–135]; Sr_2RuO_4 [147, 148]; MgB_2 [149–151]; Nb [152, 153]; Pb [153]; Nb Josephson junctions [154]; αMo_{1-x} Ge_x [155]. The dotted line is Eq. (4.88) and the dashed ones Eq. (4.58). The red arrows indicate the flow to 2D–QSI and for overdoped $YBa_2Cu_3O_{7-\delta}$ to 3D–QSN criticality, respectively

estingly enough, MgB_2 and Sr_2RuO_4 appear to fall into this class, as well. Prominent and systematic deviations from this behavior occur for the highly anisotropic organics and underdoped cuprates. As $\lambda_c(0)$ increases with the reduction of the normal state conductivity σ_c^{DC}, we observe that the data tends to scatter around two branches, consistent with $\lambda_c(0) = \Omega_s \left(\sigma_c^{DC}\right)^{-3/4}$, which is the scaling relation (4.58) with $z = 1$, describing the critical behavior close to 2D–QSI critical points. The most prominent deviations from these trends occur for overdoped cuprates (see also Fig. 4.23). In particular the data for overdoped $YBa_2Cu_3O_{7-\delta}$ (YBCO) exhibit an upturn, signaling the crossover to 3D–QSN criticality (Eq. (4.63)). Since organics undergo superconductor to insulator transitions [156], are highly anisotropic and γ can be varied over a rather extended interval, i.e. $\gamma_{T_c} = 180$ for κ-$(ET)_2$ $Cu[N(CS)_2$

]Br, $\gamma_{T_c} = 350$ for κ-(ET)$_2$ Cu(NCS)$_2$ [157] and. $\gamma_{T_c} = 2\ 10^3$ for α– (BEDT–TTF)$_2$NH$_4$Hg(SCN)$_4$, it becomes clear that the organics line in Fig. 4.34 indicates the flow of this class of superconductors to 2D–QSI criticality, where the scaling relation (4.58) applies.

Thus unlike the organics the cuprates undergo a doping tuned crossover from 2D–QSI to 3D–QSN criticality, where $\sigma_c^{DC}(T_c^+)$ and $\lambda_c(0)$ tend to infinity, while T_c vanishes. These critical points are attained in the underdoped and overdoped limit, respectively, where T_c vanishes. In this crossover the cuprates either pass the organics or the dotted mean–field line, spanned by conventional superconductors (see Fig. 4.34). $YBa_2Cu_3O_{7-\delta}$(YBCO) and $La_{2-x}Sr_xCuO_{4+\delta}$(LSCO) cross the dotted mean–field line in the neighborhood of TaS_2, Sr_2RuO_4 and MgB_2 . In this region of the $\lambda_c(0)$-$\sigma_c^{DC}(T_c^+)$ plane fluctuations do not play a dominant role. Indeed, Sr_2RuO_4 exhibits Fermi liquid normal state properties [158]. However, overdoped cuprates flow to 3D–QSN criticality, where disorder destroys the phase coherence and the pairs. On the contrary, the organics evolve rather smoothly from the mean–field regime, to which Pb, Nb, Nb–junctions, α-$Mo_{1-x}Ge_x$ and the dichalcogenides belong. Thus, these flows provide a perspective of the regimes where fluctuations and disorder are essential.

Acknowledgements
It is a pleasure to thank H. Keller and K.A. Müller for numerous helpful discussions.

References

1. M. Suzuki and M.Hikita, Phys. Rev. B **44**, 249 (1991).
2. Y. Nakamura and S. Uchida, Phys. Rev. **B** 47, 8369 (1993)).
3. Y. Fukuzumi, K. Mizuhashi, K. Takenaka, and S. Uchida, Phys. Rev. Lett. **76**, 684 (1996).
4. M. Willemin, C. Rossel, J. Hofer, H. Keller, and A. Revcolevschi, Phys. Rev. B **59**, 717 (1999).
5. T.Kimura, K. Kishio, T. Kobayashi, Y. Nakayama, N. Motohira, K. Kitazawa, and K. Yamafuji, Physica C **192**, 247 (1992).
6. T. Sasagawa, Y. Togawa, J. Shimoyama, A. Kapitulnik, K. Kitazawa, and K. Kishio, Phys. Rev. B **61**, 1610 (2000).
7. J. Hofer, T. Schneider, J.M. Singer, M. Willemin, H. Keller, T. Sasagawa, K. Kishio, K. Conder, and J. Karpinski, Phys. Rev. B **62**, 631 (2000).
8. T. Shibauchi, H. Kitano, K. Uchinokura, A. Maeda, T. Kimura, and K. Kishio, Phys. Rev. Lett. **72**, 2263 (1994).
9. C. Panagopoulos, J.R. Cooper, T. Xiang, Y.S. Wang, and C.W. Chu, Phys. Rev. B **61**, 3808 (2000).
10. J. L. Tallon, C. Bernhard, H. Shaked,R.L. Hitterman, and J.D. Jorgensen, Phys. Rev. B **51**, 12911 (1995).
11. M.R. Presland, J.L. Tallon, R.G. Buckley, R.S. Liu, and N.E. Flower, Physica C **176**, 95 (1991).
12. T. Schneider, Acta Physica Polonica A **91**, 203 (1997).

13. T. Schneider and J. M. Singer, *Phase Transition Approach To High Temperature Superconductivity*, Imperial College Press, London, (2000).
14. T.Schneider and J.M.Singer, J. Supercond. **13**, 789(2000).
15. N. Momono, M. Ido, T. Nakano, M. Oda, Y. Okajima, and K. Yamaya, Physica C **233**, 395 (1994).
16. L. Onsager, Phys. Rev. **65**, 117 (1944).
17. J. Hofer, J. Karpinski, M. Willemin, G.I. Meijer, E.M. Kopnin, R. Molinski, H. Schwer, C. Rossel, and H. Keller, Physica C **297**, 103 (1998).
18. G. Xiao, M.Z. Cieplak, J.Q. Xiao, and C.L. Chien, Phys. Rev. B **42**, 8752 (1990).
19. J.M. Tarascon, E. Wang, S. Kivelson, B.G. Bagley, G.W. Hull, and R. Ramesh, Phys. Rev. B **42**, 218 (1990).
20. S. Watauchi, H. Ikuta, H. Kobayashi, J. Shimoyama, and K. Kishio, Phys. Rev. B **64**, 64520 (2001).
21. T.R. Chien, W.R. Datars, B.W. Veal, A.P. Paulikas, P. Kostic, C. Gu, and Y. Jiang, Physica C **229**, 273 (1994).
22. T.R. Chien, W.R. Datars, M.D. Lan, J.Z. Liu, and R.N. Shelton, Phys. Rev. B **49**, 1342 (1994).
23. T.R. Chien, W.R. Datars, J.Z. Liu, M.D. Lan, and R.N. Shelton, Physica C **221**, 428 (1994).
24. X.F. Sun, X. Zhao, X.-G. Li, and H.C. Ku, Phys. Rev. B **59**, 8978 (1999).
25. C. Panagopoulos, J.R. Cooper, N. Athanassopoulou, and J. Chrosch, Phys. Rev. B **54**, 12721 (1996).
26. Guo-Meng Zhao *et al.*, unpublished.
27. G. Blatter, M.V. Feigel'man, V.B. Geshkenbein, A.I. Larkin, and V.M. Vinokur, Rev. Mod. Phys. **66**, 1125 (1994).
28. See, e.g., T. Schneider, G.I. Meijer, J. Perret, J.-P. Locquet, and P. Martinoli, Phys. Rev. B **63**, 144527 (2001).
29. Y. Ando, G.S. Boebinger, A. Passner, T. Kimura, and K. Kishio, Phys. Rev. Lett. **75**, 4662 (1995).
30. G.S. Boebinger, Y. Ando, A. Passner, T. Kimura, M. Okuya, J. Shimoyama, K. Kishio, K. Tamasaku, N. Ichikawa, and S. Uchida, Phys. Rev. Lett. **77**, 5417 (1996).
31. K. Segawa and Y. Ando, Phys. Rev. B **59**, 3948 (1999).
32. S. Ono, Y. Ando, T. Murayama, F.F. Balakirev, J.B. Betts, and G.S. Boebinger, Phys. Rev. Lett. **85**, 638 (2000).
33. R. G. Goodrich, P. W. Adams, H. Lowndes and D. P. Norton, Phys. Rev. B **56**, 14299 (1997).
34. T. Schneider and D. Ariosa, Z. Phys. B Cond. Mat. **89**, 267 (1992).
35. T. Schneider and H. Keller, Int. J. Mod. Phys. B **8**, 487 (1993).
36. M. A. Hubbard *et al.*, Physica C **259**, 309 (1996).
37. S. Kamal, D.A. Bonn, N. Goldenfeld, P.J. Hirschfeld, R. Liang, and W.N. Hardy, Phys. Rev. Lett. **73**, 1845 (1994); S. Kamal, R. Liang, A. Hosseini, D.A. Bonn, and W.N. Hardy, Phys. Rev. B **58**, 8933 (1998).
38. V. Pasler, P. Schweiss, Ch. Meingast, B. Obst, H. Wuehl, A.I. Rykov, and S. Tajima, Phys. Rev. Lett. **81**, 1094 (1998).
39. T. Schneider *et al.*, Eur. Phys. J. B **3**, 413 (1998).
40. T. Schneider and J. M. Singer, Physica C **341-348**, 87 (2000).
41. K.Kim and P.B.Weichman, Phys. Rev. B **43**, 13583 (1991).

42. S. Sachdev and J. Ye, Phys. Rev. Lett. **69**, 2411 (1992).
43. P. Monthoux and D. Pines, Phys. Rev. B **50**, 16015 (1994).
44. C. Castellani, C. Di Castro, and M. Grilli, Phys. Rev. Lett. **75**, 4650 (1995).
45. C. M. Varma, Acta Physica Polonica A **91**, 191 (1997).
46. S.C. Zhang, Science **275**, 1089 (1997).
47. S. Kivelson, E. Fradkin and V.J. Emery, Nature **393**, 550 (1998).
48. M. Randeria, in *Proceedings of the tenth International School of Physics "Enrico Fermi " Varenna*, edited by G.Iadonisi and J.R. Schrieffer (IOS Press Amsterdam, 1998).
49. S. Caprara, M. Sulpizi, A. Bianconi, C. Di Castro, and M. Grilli, Phys. Rev. B **59**, 14980 (1999).
50. S. Chakravarty, R.B. Laughlin, D.K. Morr, and Ch. Nayak, Phys. Rev. B **63**, 094503 (2001).
51. M. Voijta, Y. Zhang and S. Sachdev, Phys. Rev. Lett. **85**, 4940 (2000).
52. P.W. Anderson, Science **288**, 480 (2000).
53. M.P.A. Fisher, G. Grinstein, and S.M. Girvin, Phys. Rev. Lett. **64**, 587 (1990).
54. I.F. Herbut, Phys. Rev. B **61**, 14723 (2000).
55. I.F. Herbut, Phys. Rev. Lett. **85**, 1532 (2000).
56. L.I. Glazman and A.E. Koshelev, Phys. Rev. B **43**, 2835 (1991).
57. P.C. Hohenberg, A. Aharony, B.I. Halperin, and E.D. Siggia, Phys. Rev. B **13**, 2986 (1976).
58. D.S. Fisher, M.P.A. Fisher, and D.A. Huse, Phys. Rev. B **43**, 130 (1991).
59. M.E. Fisher, M.N. Barberm and D. Jasnow, Phys. Rev. A **8**, 1111 (1973).
60. I.F. Herbut and Z. Tesanovic, Phys. Rev. Lett. **76**, 4588 (1996).
61. W. F. Vinen, in *Superconductivity II*, edited by R. D. Parks (Marcel Dekker, INC., New York, 1969).
62. M. Charalambous, O. Riou, P. Gandit, B. Billon, P. Lejay, J. Chaussy, W.N. Hardy, D.A. Bonn, and R. Liang, Phys. Rev. Lett. **83**, 2042 (1999).
63. E. Schultka and E. Manusakis, Phys. Rev. Lett. **75**, 2710 (1995).
64. E. S. Bozin, G. H. Kwei, H. Takagi and S. J. L. Billinge, Phys. Rev. Lett. **84**, 5856 (2000).
65. K. M. Lang, V. Madhavan, J.E. Hoffman, E.W. Hudson, H. Eisaki, S. Uchida, J.C. Davis, cond-mat/0112232.
66. A.W. Hunt, P.M. Singer, A.F. Cederstrom, and T. Imai, cond-mat/0011380.
67. A. Singsaas and G. Ahlers, Phys. Rev. B **30**, 5103 (1994).
68. S. Mehta *et al.*, J. Low Temp. Phys. **114**, 467 (1999).
69. see, e.g. M. Ma, *Modern Theory of Critical Phenomena*, (Benjamin, Reading, 1976).
70. A. Junod, M. Roulin, B. Revaz, and A. Erb, Physica B **280**, 214 (2000).
71. S.L. Lee, P. Zimmermann, H. Keller, M. Warden, I.M. Savic, R. Schauwecker, D. Zech, R. Cubitt, E.M. Forgan, P.H. Kes, T.W. Li, A.A. Menovsky, and Z. Tarnawski, Rev. Lett. **71**, 3862 (1993).
72. A. Schilling, R.A. Fisher, N.E. Phillips, U. Welp, W.K. Kwok, and G.W. Crabtree, Phys. Rev. Lett. **78**, 4833 (1997).
73. R. Liang, D.A. Bonn, and W.N. Hardy, Phys. Rev. Lett. **76**, 835 (1996).
74. M. Roulin, A. Junod, and E. Walker, Physica C **296**, 137 (1998).
75. M. Willemin, A. Schilling, H. Keller, C. Rossel, J. Hofer, U. Welp, W.K. Kwok, R.J. Olsson, and G.W. Crabtree, Phys. Rev. Lett. **81**, 4236 (1998).

76. A. Schilling, R.A. Fisher, N.E. Phillips, U. Welp, W.K. Kwok, and G.W. Crabtree, Phys. Rev. B **58**, 11157 (1998).
77. X. Hu, S. Miyashita, and M. Tachiki, Phys. Rev. Lett. **79**, 3498 (1997).
78. A. K. Nguyen and A. Sudbo, Phys. Rev. B **58**, 2802 (1998).
79. M. Tinkham, Introduction to Superconductivity (Mc Graw Hill, New York, 1975).
80. L. N. Bulaevskii, Sov. Phys. JETP **37**, 1133 (1973).
81. V. Ambegaokar and A. Baratoff, Phys. Rev. Lett. **10**, 486 (1963).
82. G. Deutscher and O. Entin-Wohlman, J. Phys. C **10**, L433 (1977).
83. P.A. Crowell, F.W van Keuls, and J. R. Reppy, Phys. Rev. B **55**, 12620 (1997).
84. Y.J. Uemura, V.J. Emery, A.R. Moodenbaugh, M. Suenaga, D.C. Johnston, A.J. Jacobson, J.T. Lewandowski, J.H. Brewer, R.F. Kiefl, S.R. Kreitzman, G.M. Luke, T. Riseman, C.E. Stronach, W.J. Kossler, J.R. Kempton, X.H. Yu, D. Opie, and H.E. Schone, Phys. Rev. B **38**, 909 (1988), Y.J. Uemura, G.M. Luke, B.J. Sternlieb, J.H. Brewer, J.F. Carolan, W.N. Hardy, R. Kadono, J.R. Kempton, R.F. Kiefl, S.R. Kreitzman, P. Mulhern, T.M. Riseman, D. Ll. Williams, B.X. Yang, S. Uchida, H. Takagi, J. Gopalakrishnan, A.W. Sleight, M.A. Subramanian, C.L. Chien, M.Z. Cieplak, G. Xiao, V.Y. Lee, B.W. Statt, C.E. Stronach, W.J. Kossler, and X.H. Yu, Rev. Lett. **62**, 2317 (1989).
85. J. Perret, Thesis, University of Neuchatel (1999).
86. P. Zimmermann, H. Keller, S.L. Lee, I.M. Savic, M. Warden, D. Zech, R. Cubitt, E. M. Forgan, E. Kaldis, J. Karpinski, and C. Krueger, Phys.Rev. B **52**, 541 (1995).
87. C.L. Seaman, J.J. Neumeier, M.B. Maple, L.P. Le, G.M. Luke, B.J. Sternlieb, Y.J. Uemura, J.H. Brewer, R. Kadono, R.F. Kiefl, S.R. Krietzman, and T.M. Riseman, Phys.Rev. B **42**, 6801 (1990).
88. T. Schneider and J. M. Singer, Physica C **313**, 188 (1999).
89. K. Semba and A. Matsuda, Phys. Rev. Lett. **86**, 496 (2000).
90. G.M. Zhao *et al.*, J. Phys. Condens. Matter **10**, 9055 (1998).
91. J. Hofer, K. Conder, T. Sasagawa, G. Zhao, M. Willemin, H. Keller, and K. Kishio, Phys. Rev. Lett. **84**, 4192 (2000).
92. R.Khasanov, A.Shengelaya, K.Conder, E.Morenzoni, I.M.Savic, and H.Keller, cond-mat/0201165.
93. P. Franck *et al.*, Physica C **162-164**, 733 ((1989), ibid. **185-189** (1991), Phys. Rev. B **44**, 5318 (1991).
94. N. Babushkina, A. Inyushkin, V. Ozhogin, A. Taldenkov, I. Kobrin, T. Vorob'eva, L. Molchanova, L. Damyanets, T. Uvarova, and A. Kuzakov, Physica C **185-189**, 901 (1991).
95. H.J. Bornemann and D.E. Morris, Phys. Rev. B **44**, 5322 (1991).
96. T. Schneider and H. Keller, Phys. Rev. Lett. **86**, 4899 (2001).
97. S. J. Chen, C.F. Chang, H.L. Tsay, H.D. Yang, and J.-Y. Lin, Phys. Rev. B **58**, 14753 (1998).
98. G. E. Volovik, JETP Lett. **58**, 469 (1993).
99. H. Won and K. Maki, Europhys. Lett. **73**, 2744 (1995).
100. J.W. Loram *et al.*, 10^{th} Ann. HTS Workshop (World Scientifique 1996) p.341.
101. C. Panagopoulos, B.D. Rainford, J.R. Cooper, W. Lo, J.L. Tallon, J. W. Loram, J. Betouras, Y.S. Wang, and C.W. Chu, Phys. Rev. B **60**, 14617 (1999).
102. T. Jacobs, S. Sridhar, Q. Li, G.D. Gu, and N. Koshizuka, Phys. Rev. Lett. **75**, 4516 (1995).

103. A. Shengelaya, C.M. Aegerter, S. Romer, H. Keller, P.W. Klamut, R. Dybzinski, B. Dabrowski, I.M. Savic, and J. Klamut, Phys. Rev. B **58**, 3457 (1998).
104. C. Bernhard, J. L. Tallon, Th. Blasius, A. Golnik, and Ch. Niedermayer, Phys. Rev. Lett. **86**, 1614 (2001).
105. C. Niedermayer, C. Bernhard, U. Binninger, and H. Glueckler, J.L. Tallon, E.J. Ansaldo, J.I. Budnick, Phys. Rev. Lett. **71**, 1764 (1993).
106. J. L. Tallon and J. W. Loram, Physica C **349**, 53 (2001).
107. D.N. Basov, T. Timusk, B. Dabrowski, J.D. Jorgensen, Phys. Rev. B **50**, 3511 (1994).
108. S. Uchida and K. Tamasaku, Physica C **293**,1 (1997).
109. H. Shibata and A. Matsuda, Phys. Rev. B **59**, 11672 (1999).
110. A. A. Abrikosov and L.P. Gor'kov, Zh. Eksp. Teor. Fiz. **39**, 1781 (1969) [Sov.Phys.-JETP **12**, 1243 (1961)].
111. J. L. Tallon, C. Bernhard, G.V.M. Williams, and J.W. Loram, Phys. Rev. Lett., **79**, 5294 (1997).
112. J. L. Tallon, Phys. Rev. B **58**, 5956 (1998).
113. K. Karpinska, A. Malinowski, M.Z. Cieplak, S. Guha, S. Gershman, G. Kotliar, T. Skoskiewicz, W. Plesiewicz, M. Berkowski, and P. Lindenfeld, Phys. Rev. Lett. **77**, 3033 (1996).
114. S.V.Dordevic, E.J.Singley, D.N.Basov, S. Komiya, Y. Ando, E.Bucher, C.C.Homes, and M.Strongin, Phys. Rev. B **65**, 134511 (2002).
115. D.N. Basov, T. Timusk, B. Dabrowski, and J.D. Jorgensen, Phys. Rev. B **50**, 3511 (1994).
116. C.C. Homes *et al.*, Physica C **254**, 1 1995.
117. S. Uchida and K. Tamasaku, Physica C **293**, 1 1997.
118. J. Schutzmann, S. Tajima, S. Miyamoto, and S. Tanaka, Phys. Rev. Lett. **73**, 174 (1994).
119. C. Bernhard,D. Munzar, A. Wittlin, W. Koenig, A. Golnik, C.T. Lin, M. Klaeser, Th. Wolf, G. Mueller-Vogt, and M. Cardona, Phys. Rev. B **59**, 6631 (1999).
120. D.N. Basov, H.A. Mook, B. Dabrowski, and T. Timusk, Phys. Rev. B **52**, 13141 (1995).
121. S. Uchida, K. Tamasaku, and S. Tajima, Phys. Rev. B **53**, 14558 (1996).
122. J.R. Kirtley, K. A. Moler, G. Villard, and A. Maignan, Phys. Rev. Lett. **81**, 2140 (1998).
123. D. N. Basov *et al.*, Science **288**, 468 (2000).
124. K. A. Moler *et al.*, Science **279**, 1193 (1998).
125. A.S. Katz, S.I. Woods, E.J. Singley, T.W. Li, M. Xu, D.G. Hinks, R.C. Dynes, and D.N. Basov, Phys. Rev. B **61**,5930 (2000).
126. J. R. Cooper *et al.*, Nature **343**, 444 (1990).
127. T. Motohashi, J. Shimoyama, K. Kitazawa, K. Kishio, K.M. Kojima, S. Uchida, and S. Tajima, Phys. Rev. B **61**, 9269 (2000).
128. A. Pimenov, A.V. Pronin, A. Loidl, U. Michelucci, A.P. Kampf, S.I. Krasnosvobodtsev, V.S. Nozdrin, and D. Rainer, Phys. Rev. B **62**, 9822 (2000).
129. P. Garoche *et al.*, Sol. Stat. Comm. **19**, 455 (1976).
130. L.P. Le, G.M. Luke, B.J. Sternlieb, W.D. Wu, Y.J. Uemura, J.W. Brill, and H. Drulis, Physica C **185-189**, 2715 (1991).
131. J.J. Finley and B.S. Deaver, Solid Stat. Commun. **36**, 493 (1980).
132. P. de Trey *et al.*, J. Low Temp. Phys. **11**, 421 (1973).

133. K. Onabe *et al.*, J. Phys .Soc. Jap. **45**, 50 (1978).
134. R. J. Kennedy *et al.*, Can. J. Phys. **62**, 776 (1984).
135. A.H. Thompson, F.R. Gamble, and R.F. Koehler, Phys. Rev. B **5**, 2811 (1972).
136. X. Su, F. Zuo, J.A. Schlueter, A.M. Kini, and J.M. Williams, Phys. Rev. B **58**, 2944 (1998).
137. A. Carrington, I.J. Bonalde, R. Prozorov, R.W. Giannetta, A.M. Kini, J. Schlueter, H.H. Wang, U. Geiser, and J.M. Williams, Phys. Rev. Lett. **83**, 4172 (1999).
138. T. Shibauchi *et al.*, Phys. Rev. B **55**, 11979 (1997).
139. M. Dressel, O. Klein, G. Gruener, K.D. Carlson, H.H. Wang, and J.M. Williams, Phys. Rev. B **50**, 13603 (1994).
140. H. Taniguchi, H. Sato, Y. Nakazawa, and K. Kanoda, Phys. Rev. B **53**, 8879 (1996).
141. S. Wanka, D. Beckmann, J. Wosnitza, E. Balthes, D. Schweitzer, W. Strunz, and H.J. Keller, Phys. Rev. B **53**, 9301 (1996).
142. K. Kajita, Y. Nishio, S. Moriyama, W. Sasaki, R. Kato, H. Kobayashi, and A. Kobayashi, Sol. Stat. Comm. **64**, 1279 (1987).
143. X. Su, F. Zuo, J.A. Schlueter, J.M. Williams, P.G. Nixon, R.W. Winter, and G.L. Gard, Phys. Rev. B **59**, 4376 (1999).
144. R. Prozorov, R.W. Giannetta, J. Schlueter, A.M. Kini, J. Mohtasham, R.W. Winter, and G.L. Gard, Phys. Rev. B **63**, 052506 (2001).
145. H. Schwenk, K. Andres, F. Wudl, and E. Aharon-Shalom, Solid State Commun. **45**, 767 (1983).
146. K. Murata *et al.*, J. Phys. Soc. Jpn. **50**, 3529 (1981).
147. Y. Maeno *et al.*, Nature **372**, 532 (1994).
148. K. Yoshida, Y. Maeno, T. Fujita, and S. Nishizaki, Physica C **263**, 519 (1996).
149. C. Panagopoulos, B.D. Rainford, T. Xiang, C.A. Scott, M. Kambara, and I.H. Inoue, Phys. Rev. B **64**, 094514 (2001).
150. M. Angst, R. Puzniak, A. Wisniewski, J. Jun, S.M. Kazakov, J. Karpinski, J. Roos, and H. Keller, Phys. Rev. Lett. **88**, 167004 (2002).
151. D.K. Finnemore, J.E. Ostenson, S.L. Bud'ko, G. Lapertot, and P.C. Canfield, Phys. Rev. Lett. **86**, 2420 (2001).
152. A.V. Pronin, M. Dressel, A. Pimenov, A. Loidl, I.V. Roshchin, and L.H. Greene, Phys. Rev. B **57**, 14416 (1998).
153. O. Klein, E.J. Nicol, K. Holczer, and G. Gruener, Phys. Rev. B **50**, 6307 (1994).
154. E. Goldobin, M.Yu. Kupriyanov, I.P. Nevirkovets, A.V. Ustinov, M.G. Blamire, and J.E. Evetts, Phys. Rev. B **58**, 15078 (1998).
155. S.J. Turneaure, Th.R. Lemberger, J.M. Graybeal, Phys. Rev. Lett. **84**, 987 (2000).
156. Y. Nakazawa, H. Taniguchi, A. Kawamoto, and K. Kanoda, Phys. Rev. B **61**, 16295 (2000).
157. S. Kawamata *et al.*, J. Low. Temp. Phys. **105**, 1721 (1996).
158. C. Bergemann, S.R. Julian, A.P. Mackenzie, S. NishiZaki, and Y. Maeno, Phys. Rev. Lett. **84**, 2662 (2000), and references therein.

5 Photoemission in the High–T_c Superconductors

J.C. Campuzano Dept. of Physics University of Illinois at Chicago, USA and Materials Science Division, Argonne Nat. Lab., USA
M.R. Norman Materials Science Division, Argonne Nat. Lab., USA
M. Randeria Tata Institute of Fundamental Research, Mumbai, India

5.1 **Introduction** 168
5.2 **Basics of Angle–Resolved Photoemission** 169
5.2.1 Matrix Elements and Selection Rules 171
5.2.2 The One–Step Model 172
5.2.3 Single–Particle Spectral Function 174
5.2.4 Spectral Functions and Sum Rules 176
5.2.5 Analysis of ARPES Spectra: EDCs and MDCs 179
5.3 **The Valence Band** 182
5.4 **Normal State Dispersion and the Fermi Surface** 184
5.4.1 Normal State Dispersion in Bi2212: A First Look 185
5.4.2 Improved Methods for Fermi Surface Determination 188
5.4.3 Summary of Results on the Optimally Doped Fermi Surface: .. 199
5.4.4 Extended Saddle Point Singularity 199
5.4.5 Bilayer Splitting? 200
5.5 **Superconducting Energy Gap** 202
5.5.1 Particle–Hole Mixing 203
5.5.2 Quantitative Gap Estimates 206
5.5.3 Doping Dependence of the SC Gap 210
5.6 **Pseudogap** 214
5.6.1 Pseudogap near $(\pi,0)$ 214
5.6.2 Anisotropy of the Pseudogap 217
5.6.3 Fermi Arcs 217
5.6.4 Evolution of the Fermi Surface with Doping 222
5.6.5 Low Energy vs High Energy Pseudogaps 225
5.6.2 Origin of the Pseudogap? 226
5.7 **Photoemission Lineshapes and the Electron Self–Energy** 228
5.7.1 Self–Energy Extraction 230
5.7.2 Temperature Dependence of Self–Energy 233
5.7.3 Modeling the Self–Energy 235
5.7.4 Peak/Dip/Hump – Experiment 240
5.7.5 Mode Model 244
5.7.6 Doping Dependence 248
5.7.7 Dispersion Kink of Nodal Quasiparticles 253
5.7.8 Condensation Energy 263
5.8 **Summary** 265
Acknowledgments 265
References 265

K. H. Bennemann et al. (eds.), *The Physics of Superconductors*
© Springer-Verlag Berlin Heidelberg 2004

5.1 Introduction

Angle resolved photoemission spectroscopy (ARPES) has played a major role in the elucidation of the electronic excitations in the high temperature cuprate superconductors. Several reasons have contributed to this development. First, the great improvement in experimental resolution, both in energy and momentum, aided by the large energy scales present in the cuprates, allows one to see features on the scale of the superconducting gap. More recently the resolution has improved to such an extent, that now features in traditional superconductors like Nb and Pb, with energy scales of a meV, can be observed by ARPES [1].

Second, most studies have focused on $Bi_2Sr_2CaCu_2O_8$ (Bi2212) and its single layer counterpart, $Bi_2Sr_2CuO_6$ (Bi2201). These materials are characterized by weakly coupled BiO layers, with the longest interplanar separation in the cuprates. This results in a natural cleavage plane, with minimal charge transfer. This is crucial for ARPES, since it is a surface sensitive technique; for the photon energies typically used, the escape depth of the outgoing electrons is only of the order of $\sim 10\mathring{A}$. For this reason, we elect to concentrate on these materials in the current article, since the data are known to be reproducible among the various groups.

The third reason is the quasi–two dimensionality of the electronic structure of the cuprates, which permits one to unambiguously determine the momentum of the initial state from the measured final state momentum, since the component parallel to the surface is conserved in photoemission. Moreover, in two dimensions, ARPES directly probes the the single particle spectral function, and therefore offers a complete picture of the many body interactions inherent in these strongly correlated systems.

There are other reasons to point out as well. For example, the very incoherent nature of the excitations near the Fermi energy in the normal state does not allow the application of traditional techniques, such as the de Haas van Alphen effect. The electrons simply do not live long enough to complete a cyclotron orbit. Another important reason why ARPES has played a major role is the highly anisotropic nature of the electronic excitations in the cuprates, which means that momentum resolved probes are desirable when attempting to understand these materials.

It is satisfying to compare the earlier ARPES papers to more recent ones, and observe the remarkable progress the field has undergone. But this satisfaction must be tempered by the knowledge that the current literature is still full of unresolved issues. Undoubtedly, some of what is described here will be viewed in a new light in the future, and we will try to point out the contentious points, but the reader must keep in mind that the writers, by necessity, approach this task with their own set of biases. For a complementary view, the reader is refered to the recent review by Damascelli, Shen and Hussain [2]. An earlier review of ARPES studies of high T_c superconductors can be found in the book by Lynch and Olson [3].

5.2 Basics of Angle–Resolved Photoemission

The basics of angle–resolved photoemission have been described in detail in the literature [4]. We will limit ourselves to a brief review of some salient points, emphasizing those aspects of the technique which will be useful in understanding ARPES studies of high T_c superconductors. We start by looking at a simple independent particle picture, and subsequently include the effects of strong interactions.

The simplest model of ARPES is the three step model [5], which separates the process into photon absorption, electron transport through the sample, and emission through the surface. In the first step, the incident photon with energy $h\nu$ is absorbed by an electron in an occupied initial state, causing it to be promoted to an unoccupied final state, as shown in Fig. 5.1a. There is conservation of energy, such that

$$h\nu = BE + \Phi + E_{\text{kin}} \,, \tag{5.1}$$

where Φ is the work function, and BE and E_{kin} are the binding and kinetic energies of the electron, respectively. We will not discuss the subsequent two steps of the three step model, photoelectron transport to the surface and transmission through the surface into the vacuum, as they only affect the number of emitted electrons, and thus the absolute intensity [4].

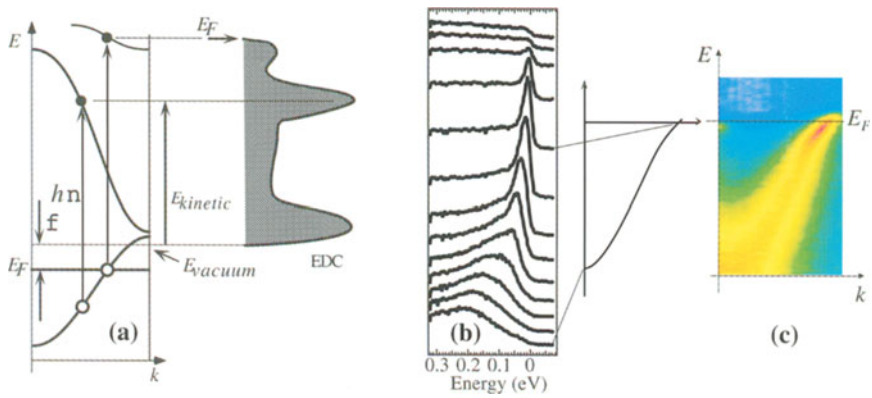

Fig. 5.1. a: Independent particle approximation view of ARPES; To the right is the resulting energy distribution curve (EDC); b: Experimental EDCs along a path in momentum space in Bi2212; c: Intensity map from these data

The kinetic energy of the electrons is measured by an electron energy analyzer. If the number of emitted electrons is then plotted as a function of their kinetic energy, as shown in Fig. 5.1, peaks are found whenever an

allowed transition takes place. Eq. (5.1) then yields the kinetic energy of the electron if the work function is known. Measuring Φ accurately is not a trivial task, but fortunately, in the case of a metallic sample one does not need to know Φ. By placing the sample in electrical contact with a good metal (e.g., polycrystalline gold) one can measure the binding energy in the sample with respect to the chemical potential (Fermi level E_f) of Au. The photoemission signal from Au will simply be a Fermi function convolved with the experimental energy resolution, and from the mid point of its leading edge one estimates E_f.

The existence of the sample surface breaks (discrete) translational invariance in the direction normal to the surface. However, two–dimensional translational invariance in the the directions parallel to the surface is still preserved, and thus $\mathbf{k}_{\|}$, the component of the electron momentum parallel to the surface, is conserved in the emission process. This allows us to obtain the in–plane momentum of the initial state by identifying it with the parallel momentum of the emitted electron

$$k_{\|} = \sqrt{\frac{2mE_{\rm kin}}{\hbar}} \sin\theta \cos\phi \tag{5.2}$$

of the outgoing electron emitted along the (θ, ϕ) direction with a kinetic energy $E_{\rm kin}$, as shown in Fig. 5.2a.

The momentum perpendicular to the sample surface k_z is not conserved, and thus knowledge of the final state k_z^f does not permit one to say anything useful about the initial state k_z^i, except in the case where $\mathbf{k}_{\|} = 0$, in which case $k_z^i = k_z^f$. We should emphasize that a given outgoing electron corresponds to a fixed, but apriori unknown, k_z^i. In materials with three–dimensional electronic dispersion it is, of course, essential to fully characterize the initial state, and many techniques have been developed to estimate k_z^i; see Ref. [4]. Aside from making $\mathbf{k}_{\|} = 0$ as described above, one can vary the incident photon energy $h\nu$ thereby changing the kinetic energy of the outgoing electron. For fixed $\mathbf{k}_{\|}$ this amounts to changing the initial state k_z. (One also has to take into account the changes in intensity brought about by the photon energy dependence of the matrix elements).

We will not be much concerned about methods of k_z determination here, since the high T_c cuprates are quasi–two–dimensional (2D) materials with, in many cases (e.g., Bi2212), no observable k_z–dispersion. In fact, this makes ARPES data from 2D materials much easier to interpret, and is one of the reasons for the great success of the ARPES technique for the cuprates. In the remainder of this article, we will use the symbol $\mathbf{k}$ to simply denote the two–dimensional momentum parallel to the sample surface, unless explicitly stated otherwise.

In the independent particle approximation, the ARPES intensity as a function of momentum $\mathbf{k}$ (in the 2D Brillouin zone) and energy ω (measured

with respect to the chemical potential) is given by Fermi's Golden rule as

$$I(k,\omega) \propto |\langle\psi_f|\,\mathbf{A}\cdot\mathbf{p}\,|\psi_i\rangle|^2\, f(\omega)\delta(\omega-\varepsilon_k)\,, \tag{5.3}$$

where ψ_i and ψ_f are the initial and final states, $\mathbf{p}$ is the momentum operator, and $\mathbf{A}$ the vector potential of the incident photon [6]. Here $f(\omega) = 1/[\exp(\omega/T)+1]$ is the Fermi function at a temperature T in units where $\hbar = k_B = 1$. It ensures the physically obvious constraint that photoemission only probes *occupied* electronic states.

For noninteracting electrons, the emission at a given $\mathbf{k}$ is at a sharp energy $\epsilon_{\mathbf{k}}$ corresponding to the initial state dispersion. As we will discuss below, the effect of interactions (either electron–electron or electron–phonon) is to replace the delta function by the one–particle spectral function, which is a non–trivial function of both energy and momentum. Although now the peaks will in general shift in energy and acquire a width, the overall intensity is still governed by the same matrix element as in the non–interacting case. Thus the lessons learned from studying general properties of the matrix elements are equally applicable in the fully interacting case.

5.2.1 Matrix Elements and Selection Rules

The dipole matrix element $M_{fi} = \langle\psi_f|\,\mathbf{A}\cdot\mathbf{p}\,|\psi_i\rangle$ is in general a function of the the momentum $\mathbf{k}$, of the incident photon energy $h\nu$, and of the polarization $\mathbf{A}$ of the incident light. Here we discuss dipole selection rules which arise from very general symmetry constraints imposed on M_{fi}, and which are very useful in interpreting ARPES data. Our approach is a simplified version of Hermanson's analysis [7].

Let the photon beam be incident along a plane of mirror symmetry of the sample ($\mathcal{M}$), with detector placed in the same mirror plane; see Fig. 5.2(a). The final state ψ_f must then be even with respect to reflection in $\mathcal{M}$, because if it were odd the wave function would vanish at the detector. (For this discussion it is simpler to imagine changing the photon polarization, keeping the detector fixed. In the actual experiment, however, it is the polarization which is fixed and the detector is moved when checking dipole selection rules.)

The dipole transition is allowed if the entire matrix element has an overall even symmetry. Thus two possibilities arise. (1) For an initial state ψ_i which is even with respect to $\mathcal{M}$, the light polarization $\mathbf{A}$ must also be even, i.e. parallel to $\mathcal{M}$. (2) For an initial state odd with respect to $\mathcal{M}$, $\mathbf{A}$ must also be odd, i.e. perpendicular to $\mathcal{M}$. This can be summarized as:

$$\langle\psi_f\,|\mathbf{A}\cdot\hat{\mathbf{p}}|\,\psi_i\rangle \begin{cases} \psi_i \textit{ even } \langle+|+|+\rangle \Rightarrow \mathbf{A} \textit{ even}\,, \\ \psi_i \textit{ odd } \langle+|-|-\rangle \Rightarrow \mathbf{A} \textit{ odd}\,. \end{cases} \tag{5.4}$$

Consider hybridized Cu3d-O2p initial states, as shown in Fig. 5.2(b), which have a $d_{x^2-y^2}$ symmetry about a Cu site. These states are even under reflection in $(0,0)-(\pi,0)$ (i.e. the plane defined by this symmetry axis and

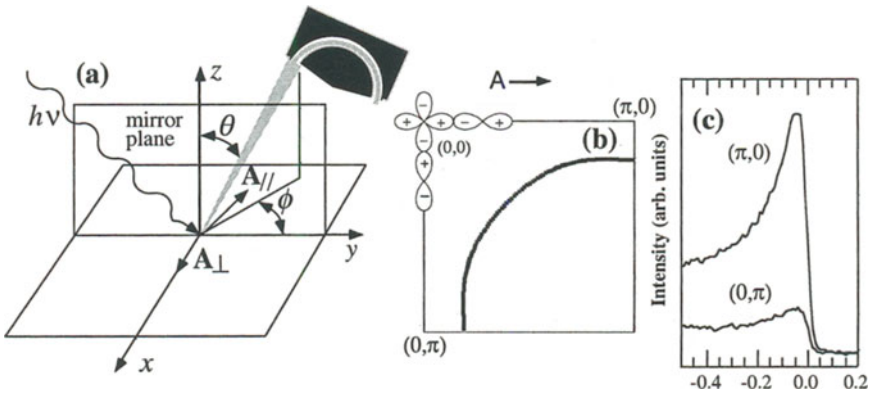

Fig. 5.2. (a) Arrangement of the photon beam and detector in order to make use of the photoemission selection rules. (b) Symmetry of the Cu3$d_{x^2-y^2}$ orbitals hybridized with the O2p orbitals. (c) EDCs showing the symmetry of the orbitals in (b) obtained at $\hbar\nu$ =22 eV

the z–axis) and odd with respect to $(0,0)-(\pi,\pi)$. Therefore, measurement along the $(0,0)-(\pi,0)$ direction will be dipole–allowed (forbidden) if the polarization vector **A** is parallel (perpendicular) to this axis. Fig. 5.2(c) shows that, consistent with an initial state which is even about $(0,0)-(\pi,0)$, the signal is maximized when **A** lies in the mirror plane and minimized when **A** is perpendicular to this plane. (The reasons for small non–zero intensity in the dipole forbidden geometry are the small, but finite, **k**–window of the experiment and the possibility of a small misalignment of the sample). Similarly, we have checked experimentally (for Bi2212 in the Y–quadrant where there are no superlattice complications) that the initial state is consistent with odd symmetry about $(0,0)-(\pi,\pi)$ (see also Ref. [8]).

While the dipole matrix elements are strongly photon energy dependent, the selection rules are, of course, independent of photon energy. This has been checked by measurements at 22 eV and 34 eV. [9] All of these results are consistent with the fact that we are probing Cu3d-O2p initial one–electron states with $d_{x^2-y^2}$ symmetry. We will see below that these selection rules are extremely useful in disentangling the main CuO_2 "band" from its umklapp images due to the superlattice in Bi2212.

5.2.2 The One–Step Model

The three–step model of photoemission gives a very useful zeroth order description of the photoemission process, but it needs to be put on a firmer footing, both as regards the calculation of photoemission intensities from ab–initio electronic structure calculations, and also for developing a deeper understanding of how many–body effects influence ARPES spectra. We now

briefly review the so called "one–step" model of photoemission with these goals in mind.

Ever since Hertz and Hallwachs discovered photoemission [10], it is known that the photo–electron current at the detector is proportional to the incident photon flux, i.e., to the *square* of the vector potential. Thus photoemission measures a *nonlinear* response function, and the relevant correlation function is a three current correlator, as first emphasized by Schaich and Ashcroft [11]. It is instructive to briefly review their argument. As in standard response function calculations, let's look at an expansion of the current at the detector (the response) in powers of the vector potential of incident photons (the perturbation). Let $\mathbf{R}$ be the location of the detector in vacuum and $\mathbf{r}$ denote points inside the sample. The zeroth order contribution $\langle 0|j_\alpha(\mathbf{R},t)|0\rangle$ vanishes as there are no currents flowing in the ground state $|0\rangle$ of the unperturbed system. The linear response also vanishes, with $\langle 0|j_\alpha(\mathbf{R},t)j_\beta(\mathbf{r},t')|0\rangle = 0$ and $\langle 0|j_\alpha(\mathbf{r},t')j_\beta(\mathbf{R},t)|0\rangle = 0$, since there are no particles at the detector, in absence of the electromagnetic field, and $j_\beta(\mathbf{R},t)|0\rangle = 0$. Thus the leading term which survives is

$$\langle j_\gamma(\mathbf{R},t)\rangle \propto \int d\mathbf{r}'dt'd\mathbf{r}''dt''A_\alpha(\mathbf{r}',t')A_\beta(\mathbf{r}'',t'') \times\langle 0|j_\alpha(\mathbf{r}',t')j_\gamma(\mathbf{R},t)j_\beta(\mathbf{r}'',t'')|0\rangle \,, \tag{5.5}$$

where only current operators *inside* the sample act on the unperturbed ground state on either side and the current at the detector is sandwiched in between.

The three current correlation function can be represented by the triangle diagram shown in Fig. 5.3(A) [12], where the line between the two external photon vertices is the Greens function of the "initial state" or "photo–hole" and the two lines connecting the photon vertex to the current at the detector represent the "photo–electron" which is emitted from the solid. There is a large literature on the evaluation of the (bare) triangle diagram incorporating the results of ab–initio electronic structure calculations of a semi–infinite solid, including the effects of realistic surface termination and multiple scattering effects in the photo–electron final states. Detailed calculations using this formalism were first carried out by Pendry [13] for a system with one atom per unit cell, and later generalized to more complex crystals [14–16].

This approach is very reliable for calculating photoemission intensities, and gives important information about "matrix element effects", i.e., the dependence of the ARPES intensity on $\mathbf{k}$, and on the incident photon energy and polarization. (It does not, however, shed light on the many–body aspects of the lineshape). Such ab–initio methods have been extensively used by Bansil, Lindroos and coworkers [17] for the high T_c cuprates.

As an example of the usefulness of ab–initio methods, we show the comparison between the observed and calculated ARPES intensities for YBCO in Fig. 5.4. Since the calculated intensity is a sensitive function of the termination plane, such a comparison suggests that the crystal breaks at the

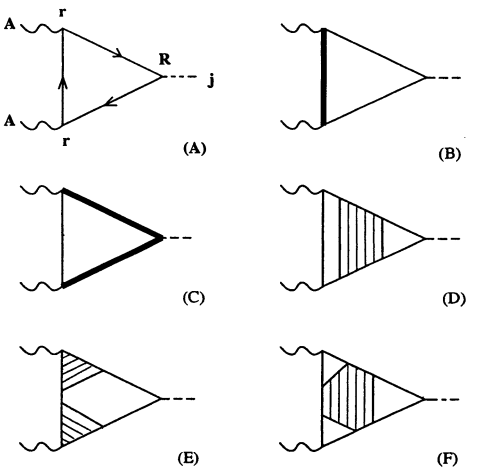

Fig. 5.3. Diagrams contributing to the three–current correlator of ARPES. The physical processes that each diagram represents is discussed in the text

chains, a conclusion later confirmed by STM measurements [18]. In fact, it was the complexity of the termination in YBCO, plus the fact that none of the possible cleavage planes of YBCO are charge neutral, and thus involve significant charge transfer, that convinced us to focus primarily on the Bi–based cuprates (Bi2212 and Bi2201). These materials have two adjacent BiO planes which are van der Waals bonded, and thus cleavage leads to neutral surfaces which are not plagued by uncontrolled surface effects. The highly two–dimensional Bi–based cuprates are thus ideal from the point of view of ARPES studies.

5.2.3 Single–Particle Spectral Function

Although the one step model gives a reasonable interpretation of the overall *intensity* in the photoemission process, much of what we really want to learn from the experiment relates to the spectral *lineshape*, which, as we will show, is strongly influenced by correlations. We must then ask ourselves the important question of how the initial state lineshape enters the ARPES intensity and to what extent this is revealed in the observed lineshape. Although a fully rigorous justification of a simple interpretation of ARPES spectra is not available at the present time, a reasonable case can be made for analyzing the data in terms of the single particle spectral function of the initial state.

We begin by considering the various many–body renormalizations of the bare triangle diagram which are shown in Fig. 5.3. These renormalizations can arise, in principle, from either electron–phonon or electron–electron interactions. These self energy effects and vertex corrections are easy to draw,

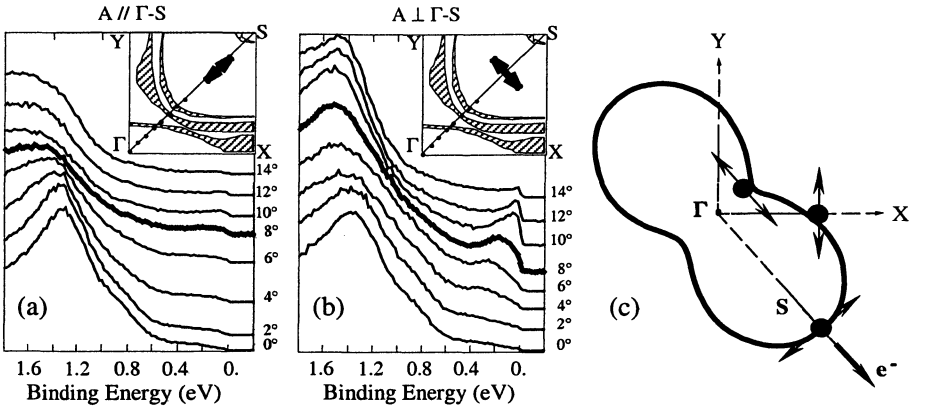

Fig. 5.4. Comparison of the photoemission intensity of states along the zone diagonal in YBCO with (a) even polarization and (b) odd polarization, showing that this state is odd with respect to reflection about the diagonal to the Cu–O bond direction. (c) Comparison of the photoemission intensity to the observed one as a function of polarization. The detailed polarization comparison gives confidence to the interpretation of the observed peak as arising from the Cu–O plane states

but impossible to evaluate in any controlled calculation. Nevertheless, they are useful in obtaining a qualitative understanding of the the various processes and estimating their relative importance. Diagram (B) represents the self–energy corrections to the occupied initial state that we are actually interested in studying; (C) and (D) represent final state line–width broadening and inelastic scattering; (E) is a vertex correction that describes the interaction of the escaping photo–electron with the photo–hole in the solid; (F) is a vertex correction which combines features of (D) and (E). (An additional issue in a quantitative theory of photoemission is related to the modification of the external vector potential inside the medium, i.e., renormalizations of the photon line. These are considered in detail in Ref. [17]).

If the sudden approximation is valid, we can neglect the vertex corrections: the outgoing photo–electron is moving so fast that it has no time to interact with the photo–hole. Let us make simple time scale estimates for the cuprates with 15 - 30 eV (ultraviolet) incident photons. The time t spent by the escaping photo–electron in the vicinity of the photo–hole is the time available for their interaction. A photoelectron with a kinetic energy of (say) 20 eV has a velocity $v = 3 \times 10^8$ cm/s. The relevant length scale, which is the smaller of the screening radius (of the photo–hole) and the escape depth, is $\sim 10\mathring{A}$. Thus $t = 3 \times 10^{-16}$ s, which should be compared with the time scale for electron–electron interactions (which are the dominant source of interactions at the high energies of interest): $t_{ee} = (2\pi)/\omega_p = 4 \times 10^{-15}$ s, using a plasma frequency $\omega_p = 1$ eV for the cuprates (this would be even slower if c–axis plasmons are involved). *If* $t \ll t_{ee}$, then we can safely ignore vertex

corrections. From our very crude estimate $t/t_{ee} = 0.1$, so that the situation with regard to the validity of the impulse approximation is not hopeless, but clearly, experimental checks are needed, and we present these in the next subsection.

Very similar estimates can be made for renormalizations of the outgoing photo–electron due to its interaction with the medium; again electron–electron interactions dominate at the energies of interest. The relevant length scale here is the escape depth, which leads to a process of self–selection: those electrons that actually make it to the detector with an appreciable kinetic energy have suffered no collisions in the medium. Such estimates indicate that the "inelastic background" must be small and we will show how to experimentally obtain its precise dependence on $\mathbf{k}$ and ω later.

Finally, one expects that final state linewidth corrections are small for quasi–2D materials based on the estimates made by Smith *et al.* [19] In fact, this is yet another reason for the ease of interpreting ARPES data in quasi–2D materials. A clear experimental proof that these effects are negligible for Bi2212 will be presented later, where it will be seen that deep in the superconducting state, a resolution limited leading edge is obtained for the quasiparticle peak.

5.2.4 Spectral Functions and Sum Rules

Based on the arguments presented in the preceding subsection, we assume the validity of the sudden approximation and ignore both the final–state linewidth broadening and the additive extrinsic background. Then (B) is the only term that survives from all the terms described in Fig. 5.3 and the ARPES intensity is given by [20,21]

$$I(\mathbf{k},\omega) = I_0(\mathbf{k}) f(\omega) A(\mathbf{k},\omega) \,, \tag{5.6}$$

where $\mathbf{k}$ is the initial state momentum in the 2D Brillouin zone and ω the energy relative to the chemical potential. The prefactor $I_0(\mathbf{k})$ includes all the kinematical factors and the square of the dipole matrix element (shown in Eq. (5.3)), $f(\omega)$ is the Fermi function, and $A(\mathbf{k},\omega)$ is the one–particle spectral function which will be described in detail below.

We first describe some general consequences of Eq. (5.6) based on sum rules and their experimental checks. The success of this strategy employed by Randeria *et al.* [21] greatly strengthens the case for a simple $A(\mathbf{k},\omega)$ interpretation of ARPES data.

The one–particle spectral function represents the probability of adding or removing a particle from the interacting many–body system, and is defined as $A(\mathbf{k},\omega) = -(1/\pi)\mathrm{Im}G(\mathbf{k},\omega + i0^+)$ in terms of the Green's function. It can be written as the sum of two pieces $A(\mathbf{k},\omega) = A_-(\mathbf{k},\omega) + A_+(\mathbf{k},\omega)$, where the spectral weight to add an electron to the system is given by $A_+(\mathbf{k},\omega) = Z^{-1}\sum_{m,n} e^{-\beta\mathcal{E}_m} |\langle n|c^\dagger_{\mathbf{k}}|m\rangle|^2 \delta(\omega + \mathcal{E}_m - \mathcal{E}_n)$, and that to extract an electron

is $A_-(\mathbf{k},\omega) = Z^{-1}\sum_{m,n} e^{-\beta\mathcal{E}_m}|\langle n|c_\mathbf{k}|m\rangle|^2\delta(\omega+\mathcal{E}_n-\mathcal{E}_m)$. Here $|m\rangle$ is an exact eigenstate of the many-body system with energy $\mathcal{E}_m$, Z is the partition function and $\beta = 1/T$. It follows from these definitions that $A_-(\mathbf{k},\omega) = f(\omega)A(\mathbf{k},\omega)$ and $A_+(\mathbf{k},\omega) = [1-f(\omega)]\,A(\mathbf{k},\omega)$, where $f(\omega) = 1/[\exp(\beta\omega)+1]$ is the Fermi function. Since an ARPES experiment involves removing an electron from the system, the simple golden rule Eq. (5.3) can be generalized to yield an intensity proportional to $A_-(\mathbf{k},\omega)$

We now discuss various sum rules for $A(\mathbf{k},\omega)$ and their possible relevance to ARPES intensity $I(\mathbf{k},\omega)$. While the prefactor I_0 depends on $\mathbf{k}$ and also on the incident photon energy and polarization, it does *not* have any significant ω or T dependence. Thus the energy dependence of the ARPES lineshape and its T dependence are completely characterized by the spectral function and the Fermi factor. The simplest sum rule $\int_{-\infty}^{+\infty} d\omega A(\mathbf{k},\omega) = 1$ is not useful for ARPES since it involves both occupied (through A_-) *and unoccupied* states (A_+). Next, the density of states (DOS) sum rule $\sum_\mathbf{k} A(\mathbf{k},\omega) = N(\omega)$ is also not directly useful since the prefactor I_0 has very strong $\mathbf{k}$-dependence. However it may be useful to $\mathbf{k}$-sum ARPES data $N_p(\omega) = \sum_\mathbf{k} I_0(\mathbf{k})A(\mathbf{k},\omega)$ in an attempt to simulate the angle-integrated photoemission intensity.

The important sum rule for ARPES is

$$\int_{-\infty}^{+\infty} d\omega f(\omega)A(\mathbf{k},\omega) = n(\mathbf{k}), \tag{5.7}$$

which directly relates the energy-integrated ARPES intensity to the momentum distribution $n(\mathbf{k}) = \langle c_\mathbf{k}^\dagger c_\mathbf{k}\rangle$. (The sum over spins is omitted for simplicity). Somewhat surprisingly, the usefulness of this sum rule has been overlooked in the ARPES literature prior to Ref. [21].

We first focus on the Fermi surface $\mathbf{k} = \mathbf{k}_F$. One of the major issues, that we will return to several times in the remainder of this article, will be the question of how to define "$\mathbf{k}_F$" at finite temperatures in a strongly correlated system which may not even have well-defined quasiparticle excitations, and how to determine it experimentally. For now, we simply define the Fermi surface to be the locus of gapless excitations in $\mathbf{k}$-space in the normal state, so that $A(\mathbf{k}_F,\omega)$ has a peak at $\omega = 0$.

To make further progress with Eq. (5.7), we need to make a weak particle-hole symmetry assumption: $A(\mathbf{k}_F,-\omega) = A(\mathbf{k}_F,\omega)$ for "small" ω, where "small" means those frequencies for which there is significant T-dependence in the spectral function. It then follows that [21] $\partial n(\mathbf{k}_F)/\partial T = 0$, i.e., *the integrated area under the EDC at* $\mathbf{k}_F$ *is independent of temperature.* To see this, rewrite Eq. (5.7) as $n(\mathbf{k}_F) = \frac{1}{2} - \frac{1}{2}\int_0^\infty d\omega \tanh(\omega/2T)\,[A(\mathbf{k}_F,\omega) - A(\mathbf{k}_F,-\omega)]$ and take its T-derivative. It should be emphasized that we cannot say anything about the *value* of $n(\mathbf{k}_F)$, only that it is T-independent. (A much stronger assumption, $A(\mathbf{k}_F,-\omega) = A(\mathbf{k}_F,\omega)$ for *all* ω, is sufficient to give $n(\mathbf{k}_F) = 1/2$ independent of T). We emphasize the approximate nature of the $\mathbf{k}_F$-sum-rule since there is no exact symmetry that enforces it.

We note that we did not make use of any properties of the spectral function other than the weak particle–hole symmetry assumption, and to the extent that this is also valid in the superconducting state, our conclusion $\partial n(\mathbf{k}_F)/\partial T = 0$ holds equally well below T_c. There is the subtle issue of the meaning of "$\mathbf{k}_F$" in the superconducting state. In analogy with the Fermi surface as the "locus of gapless excitations" above T_c, we can define the "minimum gap locus" below T_c. We will describe this in great detail in Section 5.1 below; it suffices to note here that "$\mathbf{k}_F$" is independent of temperature, within experimental errors, in both the normal and superconducting states of the systems studied thus far [22].

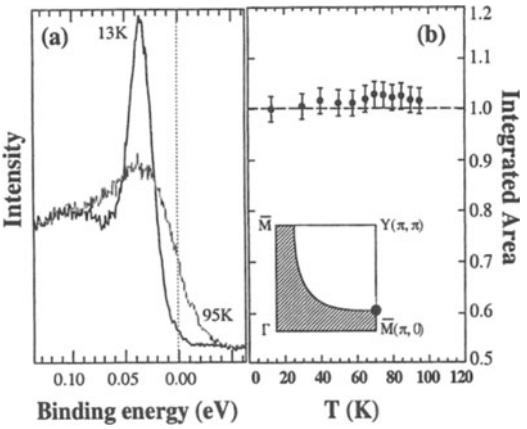

Fig. 5.5. (a) ARPES spectra for Bi2212 at the $\mathbf{k}_F$ point shown in the zone inset in the normal and superconducting states. (b) Integrated intensity as a function of temperature at the same k point

In Fig. 5.5(a) we show ARPES spectra for near–optimal Bi2212 ($T_c = 87$ K) at $\mathbf{k}_F$ along $(\pi, 0)$ to (π, π) at two temperatures: $T = 13$ K, which is well below T_c, and $T = 95$ K, which is in the normal state. The two data sets were normalized in the positive energy region, which after normalization was chosen to be the common zero baseline. (The essentially ω–independent emission at positive energies, which is not cut–off by the Fermi function, is due to higher harmonics of the incident photon beam, called "second order light"). For details, see Ref. [21].

In Fig. 5.5(b) we plot the integrated intensity as a function of T and find that, in spite of the remarkable changes in the lineshape from 95K to 13K, the integrated intensity at $\mathbf{k}_F$ is very weakly T–dependent, verifying the sum rule $\partial n(\mathbf{k}_F)/\partial T = 0$. The error bars come from the normalization due to the low count rate in the $\omega > 0$ background.

Let us discuss several other potential complications in testing the T–independence of the integrated intensity at $\mathbf{k}_F$. Note that matrix elements have no effect on this result, since they are T–independent. The same is true for a T–independent additive extrinsic background. In an actual experiment the observed intensity will involve convolution of Eq. (5.6) with the energy resolution and a sum over the $\mathbf{k}$–values within the momentum window. While energy resolution is irrelevant to an integrated quantity, sharp $\mathbf{k}$–resolution is of the essence.

The T–independence of the integrated intensity is insensitive to the choice of the integration cutoff at negative ω, provided it is chosen beyond the dip feature. It has been observed experimentally that the normalized EDCs at $\mathbf{k}_F$ have identical intensities for all $\omega < -100$meV. This is quite reasonable, since we expect the spectral functions to be the same for energies much larger than the scale associated with superconductivity. The fact that one has to go to 100meV (much larger than $T_c \sim 10meV$) in order to satisfy the sum rule suggests that electron–electron interactions are involved in superconductivity.

5.2.5 Analysis of ARPES Spectra: EDCs and MDCs

In the preceding subsections we have presented evidence in favor of a simple spectral function interpretation of ARPES data on the quasi 2D high T_c cuprates. In the process, we saw that the ARPES intensity in Fig. 5.5 has a nontrivial lineshape which has a significant temperature dependence. We now introduce some of the basic ideas which will be used throughout the rest of the article to analyze and understand the ARPES lineshape.

The one–electron Green's function can be generally written as $G^{-1}(\mathbf{k},\omega) = G_0^{-1}(\mathbf{k},\omega) - \Sigma(\mathbf{k},\omega)$ where $G_0(\mathbf{k},\omega) = 1/[\omega - \varepsilon_{\mathbf{k}}]$ is the Green's function of the noninteracting system, $\varepsilon_{\mathbf{k}}$ is the "bare" dispersion, and the (complex) self–energy $\Sigma(\mathbf{k},\omega) = \Sigma'(\mathbf{k},\omega) + i\Sigma''(\mathbf{k},\omega)$ encapsulates the effects of all the many–body interactions. Then using its definition in terms of ImG, we obtain the general result

$$A(\mathrm{k},\omega) = \frac{1}{\pi} \frac{\Sigma''(\mathbf{k},\omega)}{\left[\omega - \varepsilon_{\mathbf{k}} - \Sigma'(\mathbf{k},\omega)\right]^2 + \left[\Sigma''(\mathbf{k},\omega)\right]^2} \,. \tag{5.8}$$

We emphasize that this expression is entirely general, and does not make any assumptions about the validity of perturbation theory or of Fermi liquid theory.

New electron energy analyzers, which measure the photoemitted intensity as a function of energy and momentum simultaneously, allow the direct visualization of the spectral function, as shown in Fig. 5.6, and have also suggested new ways of plotting and analyzing ARPES data.

(a) In the traditional energy distribution curves (EDCs), the measured intensity $I(\mathbf{k},\omega)$ is plotted as a function of ω (binding energy) for a fixed value of $\mathbf{k}$; and

(b) In the new [23] momentum distribution curves (MDCs), $I(\mathbf{k}, \omega)$ is plotted at fixed ω as a function of $\mathbf{k}$.

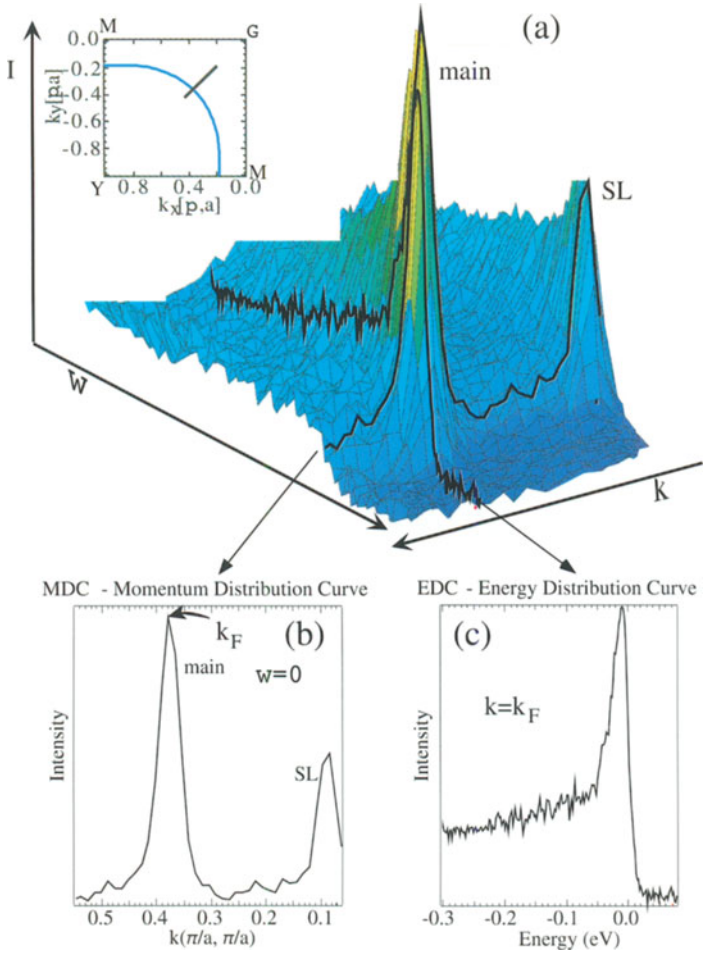

Fig. 5.6. (a) The ARPES intensity as a function of $\mathbf{k}$ and ω at $h\nu$=22eV and T=40K. main is the main band, and SL a superlattice image. (b) A constant ω cut (MDC) from (a). (c) A constant $\mathbf{k}$ cut (EDC) from (a). The diagonal line in the zone inset shows the location of the $\mathbf{k}$ cut; the curved line is the Fermi surface.

Until a few years ago, the only data available were in the form of EDCs, and even today this is the most useful way to analyze data corresponding to gapped states (superconducting and pseudogap phases). These analyses will be discussed in great detail in subsequent sections. We note here some of the issues in analyzing EDCs and then contrast them with the MDCs. First, note

that the EDC lineshape is non–Lorentzian as a function of ω for two reasons. The trivial reason is the asymmetry introduced by the Fermi function $f(\omega)$ which chops off the positive ω part of the spectral function. (We will discuss later on ways of eliminating the effect of the Fermi function). The more significant reason is that the self energy has non–trivial ω dependence and this makes even the full $A(\mathbf{k},\omega)$ non–Lorentzian in ω as seen from Eq. (5.8). Thus one is usually forced to model the self energy and make fits to the EDCs. At this point one is further hampered by the lack of detailed knowledge of the additive extrinsic background which itself has ω–dependence. (Although, as we shall see, the MDC analysis give a new way of determining this background).

The MDCs obtained from the new analyzers have certain advantages in studying gapless excitations near the Fermi surface [23–25]. In an MDC the intensity is plotted as a function of k varying normal to the Fermi surface in the vicinity of a fixed $\mathbf{k}_F(\theta)$, where θ is the angle parametrizing the Fermi surface. For k near k_F we may linearize the bare dispersion $\varepsilon_{\mathbf{k}} \simeq v_F^0(k-k_F)$, where $v_F^0(\theta)$ is the bare Fermi velocity. We will not explicitly show the θ dependences of k_F, v_F^0, or other quantities considered below, in order to simplify the notation.

Next we make certain simplifying assumptions about the remaining $\mathbf{k}$–dependences in the intensity $I(\mathbf{k},\omega)$. We assume that: (i) the self–energy Σ is essentially independent of k normal to the Fermi surface, but can have arbitrary dependence on θ along the Fermi surface; and (ii) the prefactor $I_0(\mathbf{k})$ does not have significant k dependence over the range of interest. It is then easy to see from Eqs. 5.6 and 5.8 that $I(\mathbf{k},\omega)$ plotted as function k (with fixed ω and θ) has the following lineshape. The MDC is a Lorentzian:
(a) centered at $k = k_F + [\omega - \Sigma'(\omega)]/v_F^0$; with
(b) width (HWHM) $W_M = |\Sigma''(\omega)|/v_F^0$.

Thus the MDC has a very simple lineshape, and its peak position gives the renormalized dispersion, while its width is proportional to the imaginary self energy. The consistency of the assumptions made in reaching this conclusion may be tested by simply checking whether the MDC lineshape is fit by a Lorentzian or not. Experimentally, excellent Lorentzian fits are invariably obtained (except when one is very near the bottom of the "band" or in a gapped state [26]).

Finally, note that the external background in the case of MDCs is also very simple. One can fit the MDC (at each ω) to a Lorentzian plus a constant (at worst Lorentzian plus linear in k) background. From this one obtains the value of the external background including its ω dependence. Now this ω–dependent background can be subtracted off from the EDC also, if one wishes to. Note that estimating this background was not possible from an analysis of the EDCs alone.

5.3 The Valence Band

The basic unit common to all cuprates is the copper–oxide plane, CuO_2. Some compounds have a tetragonal cell, $a = b$, such as the Tl compounds, but most have an orthorhombic cell, with a and b differing by as much as 3% in YBCO. There are two notations used in the literature for the reciprocal cell. The one used here, appropriate for Bi2212 and Bi2201, has $\Gamma - M$ along the $Cu - O$ bond direction, with $M \equiv (\pi, 0)$, and $\Gamma - X(Y)$ along the diagonal, with $Y \equiv (\pi, \pi)$. The other notation, appropriate to YBCO, has $\Gamma - X(Y)$ along the $Cu - O$ bond direction and $\Gamma - S$ along the diagonal. This difference occurs because the orthorhombic distortion in one compound is rotated 45° with respect to the other. The main effect of the orthorhombicity in Bi2212 and Bi2201 is the superlattice modulation along the b axis, with Q_{SL} parallel to $\Gamma - Y$. Except when refering to this modulation, we will assume tetragonal symmetry in our discussions. For a complete review of the electronic structure of the cuprates, see Ref. [27].

The Cu ions are four fold coordinated to planar oxygens. Apical (out of plane oxygens) exist in some structures (LSCO), but not in others. Either way, the apical bond distance is considerably longer than the planar one, so in all cases, the cubic point group symmetry of the Cu ions is lowered, leading to the highest energy Cu state having $d_{x^2-y^2}$ symmetry. As the atomic $3d$ and $2p$ states are nearly degenerate, a characteristic which distinguishes cuprates from other 3d transition metal oxides, the net result is a strong bonding–antibonding splitting of the Cu $3d_{x^2-y^2}$ and O $2p$ σ states, with all other states lying in between. In the stochiometric (undoped) material, Cu is in a d^9 configuration, leading to the upper (antibonding) state being half filled. According to band theory, the system should be a metal. But in the undoped case, integer occupation of atomic orbitals is possible, and correlations due to the strong on–site Coulomb repulsion on the Cu sites leads to an insulating state. That is, the antibonding band "Mott–Hubbardizes" and splits into two, one completely filled (lower Hubbard band), the other completely empty (upper Hubbard band) [28].

On the other hand, for dopings characteristic of the superconducting state, a large Fermi surface is observed by ARPES (as discussed in the next section). Thus, to a first approximation, the basic electronic structure in this doping range can be understood from simple band theory considerations. The simplest approximation is to consider the single Cu $3d_{x^2-y^2}$ and two O $2p$ (x,y) orbitals. The resulting secular equation is [29]

$$\begin{pmatrix} \epsilon_d & 2t\sin(k_x a) & -2t\sin(k_y a) \\ 2t\sin(k_x a) & \epsilon_p & 0 \\ -2t\sin(k_y a) & 0 & \epsilon_p \end{pmatrix}, \tag{5.9}$$

where ϵ_d is the atomic $3d$ orbital energy, ϵ_p is the atomic $2p$ orbital energy, and t is the Cu–O hopping integral. Diagonalization of this equation leads to

a non–bonding eigenvalue $E_{nb} = \epsilon_p$, and

$$E_{\pm} = \frac{\epsilon_p + \epsilon_d}{2} \pm \sqrt{(\frac{\epsilon_p - \epsilon_d}{2})^2 + 4t^2(\sin^2(k_x a) + \sin^2(k_y a))}\,, \tag{5.10}$$

where + refers to antibonding, – to bonding. This dispersion is shown in Fig. 5.7(a)

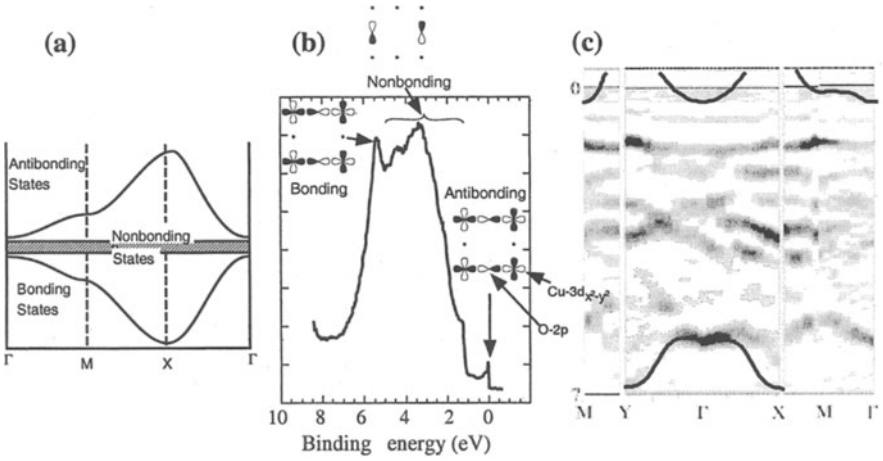

Fig. 5.7. (a) Simple three band estimate of the electronic structure of the Cu-O plane states; (b) EDC showing the whole valence band at the $(\pi, 0)$ point; c) Intensity map of the whole valence band obtained by taking the second derivative of spectra such as the one in (b). The orbitals in (b) are based on the three band model, where black and white lobes corresponding to positive and negative wavefunctions

In Fig. 5.7(b), we show an ARPES spectrum obtained at the $(\pi, 0)$ point of the Brillouin zone for Bi2212. Three distinct features can be observed: the bonding state at roughly -6eV, the antibonding state near the Fermi energy, and the rest of the states in between. This rest consists of the non–bonding state mentioned above, as well as the remainder of the Cu $3d$ and O $2p$ orbitals, plus states originating from the other (non Cu–O) planes. It is difficult to identify all of these "non–bonding" states, as their close proximity and broadness causes them to overlap in energy. Perhaps surprisingly, the overall picture of the electronic structure of the valence band has the structure that one would predict by the simple chemical arguments given above, as shown in Fig. 5.7(c). The most important conclusion that one can derive from Fig 5.7 is the early prediction by Anderson [30], namely that there is a single state relevant to transport and superconducting properties. This state, the antibonding state in Fig 5.7, is well separated from the rest of the states,

and therefore any reasonable theoretical description of the physical properties of these novel materials should arise from this single state.

Despite these simple considerations, correlation effects do play a major role, even in the doped state. The observed antibonding band width is about a factor of 2-3 narrower than that predicted by band theory [31]. In fact, the correlation effects are the ones we are most interested in, as they give rise to the many unusual properties of the cuprates, including the superconducting state.

As mentioned above, in the magnetic insulating regime, the picture is quite different. The antibonding band splits into two, with the chemical potential lying in the gap [32]. Upon doping with electrons or holes, the chemical potential would move up or down. One would then expect to observe small Fermi surfaces, hole pockets centered at $(\pi/2, \pi/2)$ with a volume equal to the hole doping, x. These can be generated at the mean field level by folding Fig. 5.7(a) back into the magnetic zone with Q=(π, π), and turning on an interaction, U_{eff}, between the two folded bands. This can be contrasted with the large Fermi surface of the unfolded case, typically centered at (π, π) with a volume $1 + x$. It is still an open question whether there is a continuous evolution between these two limits, or whether there is a discontinuous change at a metal–insulator transition point. In any case, a proper description of the electronic structure must take the strong electron–electron correlations into account, even in the superconducting regime.

5.4 Normal State Dispersion and the Fermi Surface

The Fermi surface is one of the central concepts in the theory of metals, with electronic excitations near the Fermi surface dominating all the low energy properties of the system. In this Section we describe the use of ARPES to elucidate the electronic structure and the Fermi surface of the high T_c superconductors.

It is important to discuss these results in detail because ARPES is the only experimental probe which has yielded useful information about the electronic structure and the Fermi surface of the planar Cu–O states which are important for high T_c superconductivity. Traditional tools for studying the Fermi surface such as the deHaas–van Alphen effect have not yielded useful information about the cuprates, because of the need for very high magnetic fields, and possibly because of the lack of well defined quasiparticles. Other Fermi surface probes like positron annihilation are hampered by the fact that the positrons appear to preferentially probe spatial regions other than the Cu–O planes.

The first issue facing us is: what do we mean by a Fermi surface in a system at high temperatures where there are no well–defined quasiparticles? (Recall that quasiparticles, if they exist, manifest themselves as sharp peaks in the one–electron spectral function whose width is less than their energy,

and lead to a jump discontinuity in the momentum distribution at $T = 0$.) Clearly, the traditional $T = 0$ definition of a Fermi surface defined by the jump discontinuity in $n(\mathbf{k})$ is not useful for the cuprates. First, the systems of interest are superconducting at low temperatures. But even samples which have low T_c's have normal state peak widths at E_f which are an order of magnitude broader than the temperature [25,33]. If, as indicated both by ARPES and transport, sharp quasiparticle excitations do not exist above T_c, there is no possibility of observing a thermally–smeared, resolution–broadened, discontinuity in $n(\mathbf{k})$.

It is an experimental fact that in the cuprates ARPES sees broad peaks which disperse as a function of momentum and go through the chemical potential at a reasonably well–defined momentum. We can thus adopt a practical definition of the "Fermi surface" in these materials as "the locus of gapless excitations".

Historically, the first attempts to determine the Fermi surface in cuprates were made on YBCO [34], however, surface effects as well as the presence of chains appear to complicate the picture, so we will focus principally on Bi2212 and Bi2201, which have been studied the most intensively. Other cuprates which have also been studied by ARPES, include the electron–doped material NCCO [35] and, more recently, LSCO as a function of hole doping [36].

We discuss below various methods used for the determination of the spectral function peaks in the vicinity of E_f. In addition, we supplement these methods with momentum distribution studies, taking due care of matrix element complications. We will then discuss three topics: the extended saddle–point in the dispersion, the search for bilayer splitting in Bi2212, and (in Section 5.6.4) the doping dependence of the Fermi surface.

5.4.1 Normal State Dispersion in Bi2212: A First Look

We begin with the results obtained by using the traditional method of deducing the dispersion and Fermi surface by studying the EDC peaks as a function of momentum. This method was used for the cuprates by Campuzano *et al.* [34], Olson *et al.* [31], and Shen and Dessau [8], culminating in the very detailed study of Ding *et al.* [37]. The use of EDC peak dispersion has some limitations which we discuss below. Nevertheless, it has led to very considerable understanding of the overall electronic structure, Fermi surface, and of superlattice effects in Bi2212, and therefore it is worthwhile to review its results first, before turning to more refined methods.

The main results of Ding *et al.* [37] on the electronic dispersion and the Fermi surface in the normal state ($T = 95$K) of near–optimal OD Bi2212 ($T_c = 87$K) using incident photon energies of 19 and 22 eV are summarized in Fig. 5.8. The peak positions of the EDC's as a function of $\mathbf{k}$ are marked with various symbols in Fig. 5.8(b). The filled circles are for odd initial states (relative to the corresponding mirror plane), open circles for even initial states, and triangles for data taken in a mixed geometry (i.e. the photon

polarization was at 45° to the mirror plane). The Fermi surface crossings corresponding to these dispersing states are estimated from the k–point at which the EDC peak positions go through the chemical potential when extrapolated from the occupied side. The k_F estimates are plotted as open symbols in Fig. 5.8(a).

We use the following square lattice notation for the 2D Brillouin zone of Bi2212: $\Gamma\bar{M}$ is along the CuO bond direction, with $\Gamma = (0,0)$, $\bar{M} = (\pi,0)$, $X = (\pi,-\pi)$ and $Y = (\pi,\pi)$ in units of $1/a^*$, where $a^* = 3.83\mathring{A}$ is the separation between near–neighbor planar Cu ions. (The orthorhombic a axis is along X and b axis along Y).

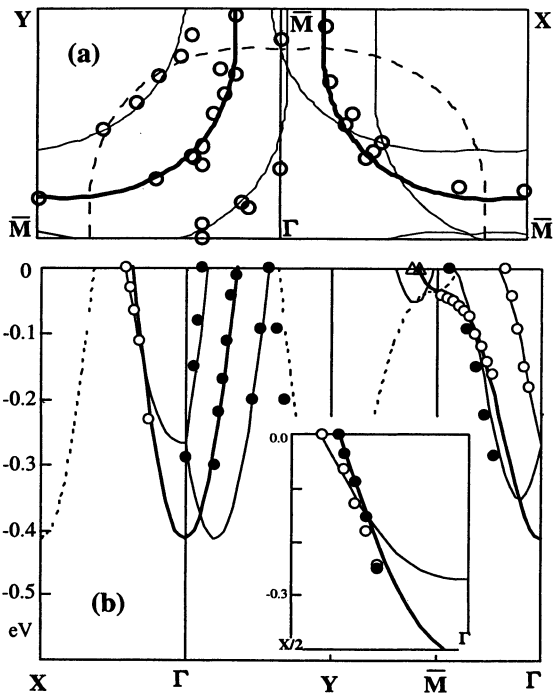

Fig. 5.8. Fermi surface (a) and dispersion (b) obtained from normal state measurements. The thick lines are obtained by a tight binding fit to the dispersion data of the main band with the thin lines $(0.21\pi, 0.21\pi)$ umklapps and the dashed lines (π,π) umklapps of the main band. Open circles in (a) are the data. In (b), filled circles are for odd initial states (relative to the corresponding mirror plane), open circles for even initial states, and triangles for data taken in a mixed geometry. The inset of (b) is a blowup of ΓX

In addition to the symbols obtained from data in Fig. 5.8, there are also several curves which clarify the significance of all of the observed features. The thick curve in Fig. 5.8(b) is $\epsilon(\mathbf{k})$, a six–parameter tight–binding fit [38] to the dispersion data in the Y–quadrant; this represents the main CuO_2 "band". It cannot be overemphasized that, although this dispersion looks very much like band theory (except for an overall renormalization of the bandwidth by a factor of 2 to 3), the actual normal state lineshape is highly anomalous. As discussed in Section 5.7 below, there are no well defined quasiparticles in the normal state.

The thin curves in Fig. 5.8(b) are $\epsilon(\mathbf{k}\pm\mathbf{Q})$, obtained by shifting the main band fit by $\pm\mathbf{Q}$ respectively, where $\mathbf{Q} = (0.21\pi, 0.21\pi)$ is the superlattice (SL) vector known from structural studies [39]. We also have a few data points lying on a dashed curve $\epsilon(\mathbf{k} + \mathbf{K}_\pi)$ with $\mathbf{K}_\pi = (\pi, \pi)$; this is the "shadow band" discussed below.

The thick curve in Fig. 5.8(a) is the Fermi surface contour obtained from the main band fit, while the Fermi surfaces corresponding to the SL bands are the thin lines and that for the shadow band is dashed. It is very important to note that the shifted dispersion curves and Fermi surfaces provide an excellent description of the data points that do not lie on main band. We note that the main Fermi surface is a large hole–like barrel centered about the (π, π) point whose enclosed area corresponds to approximately 0.17 holes per planar Cu. One of the key questions is why *only one* CuO main band is found in Bi2212 which is a bilayer material with two CuO planes per unit cell. We postpone discussion of this important issue to end of this Section.

The "shadow bands" seen above, were first observed by Aebi et al. [40] in ARPES experiments done in a mode similar to the MDCs by measuring as a function of $\mathbf{k}$ the intensity $\int_{\delta\omega} d\omega f(\omega)A(\mathbf{k}, \omega)$ integrated over a small range $\delta\omega$ near $\omega = 0$. The physical origin of these "shadow bands" is not certain at the present time. They were predicted early on to arise from short ranged antiferromagnetic correlations [41]. In this case the effect should become stronger with underdoping toward the AFM insulator, for which there is little experimental evidence [42]. An alternative explanation is that the shadow bands are of structural origin: Bi2212 has a face–centered orthorhombic cell with two inequivalent Cu sites per plane, which by itself could generate a (π, π) foldback. Interestingly, it has been recently observed that the shadow band intensity is maximal at optimal doping [43].

We now turn to the effect of the superlattice (SL) on the ARPES spectra. This is very important, since a lack of understanding of these effects has led to much confusion regarding such basic issues as the Fermi surface topology (see below), and the anisotropy of the SC gap (see Section 5.5). The data strongly suggest [44] that these "SL bands" arise due to diffraction of the outgoing photoelectron off the structural superlattice distortion (which lives primarily) on the Bi–O layer, thus leading to "ghost" images of the electronic structure at $\epsilon_{\mathbf{k}\pm\mathbf{Q}}$.

We emphasize the use of polarization selection rules (discussed in Section 5.2.1) for ascertaining various important points. First, we use them to carefully check the absence of a Fermi crossing for the main band along $(0,0) - (\pi,0)$, i.e. $\Gamma\bar{M}$. Note that the Fermi crossing that we do see near $(\pi,0)$ along $\Gamma\bar{M}$ in Fig. 5.8(a) is clearly associated with a superlattice umklapp band, as seen both from the dispersion data in Fig. 5.8(b) and its polarization analysis. This Fermi crossing is only seen in the $\Gamma\bar{M}$ $\perp$ (odd) geometry both in our data and in earlier work [45]. Emission from the main $d_{x^2-y^2}$ band, which is even about $\Gamma\bar{M}$, is dipole forbidden, and one only observes a weak superlattice signal crossing E_f. (We will return below to newer data at different incident photon energies where the possibility of a Fermi crossing along $\Gamma\bar{M}$ is raised again).

Second, we use polarization selection rules to disentangle the main and SL bands in the X–quadrant where the main and umklapp Fermi surfaces are very close together; see Fig. 5.8(a). The point is that ΓX (together with the z–axis) and, similarly ΓY, are mirror planes, and an initial state arising from an orbital which has $d_{x^2-y^2}$ symmetry about a planar Cu–site is odd under reflection in these mirror planes. With the detector placed in the mirror plane the final state is even, and one expects a dipole–allowed transition when the photon polarization **A** is perpendicular to (odd about) the mirror plane, but no emission when the polarization is parallel to (even about) the mirror plane. While this selection rule is obeyed along ΓY it is violated along ΓX. In fact this apparent violation of selection rules in the X quadrant was a puzzling feature of all previous studies [8] of Bi2212. It was first pointed out in Ref. [46], and then experimentally verified in Ref. [37], that this "forbidden" $\Gamma X||$ emission originates from the SL umklapps. We will come back to the $\Gamma X||$ emission in the superconducting state below.

5.4.2 Improved Methods for Fermi Surface Determination

We now discuss more recently developed methodologies for Fermi surface determination. The need for these improvements arises in part from the practical difficulty of determining precisely where in **k**–space a state goes through E_f. This problem is particularly severe in the vicinity of the $(\pi,0)$ point of the zone where one is beset by the following complications in both Bi2201 and 2212:

(1) The normal state ARPES peaks are very broad. This has important implications about the (non–Fermi–liquid) nature of the the normal state, as discussed later (Section 5.7).

(2) The electronic dispersion near $(\pi,0)$ is anomalously flat ("extended saddle–point").

(3) In Bi2212 the superlattice structure complicates the interpretation of the data as described above. Fortunately this complication is greatly reduced in Pb–doped Bi2201 and 2212.

(4) The final complication comes from the strong variation of the **k**–dependent

ARPES matrix elements with incident photon energy. This makes the use of changes in absolute intensity as a function of $\mathbf{k}$ to estimate Fermi surface crossings highly questionable.

Note that the first two points are intrinsic problems intimately related to the physics of high T_c superconductivity, the third is a material–specific problem, while the last is specific to the technique of ARPES. Nevertheless, all of these issues must be dealt with adequately before ARPES data on Bi2212 can be used to yield definitive results on the Fermi surface.

Eliminating the Fermi function

Recall that the peak of the EDC as a function of ω corresponds to that of $f(\omega)A(\mathbf{k},\omega)$, which in general does *not* coincide with the peak of the spectral function $A(\mathbf{k},\omega)$. If one has a broad spectral function, which at k_F is centered about $\omega = 0$, then the peak of the EDC will be at $\omega < 0$ (positive binding energy), produced by the Fermi function $f(\omega)$ chopping off the peak of A, in addition to resolution effects.

Since the goal is to study the dispersive peaks in $A(\mathbf{k},\omega)$, rather than in the EDC, one must effectively eliminate the Fermi function from the observed intensity. We present two ways of achieving this goal, and illustrate it with data on Bi2201 where it permits us to study the broad and weakly dispersive spectral peaks (points (1) and (2) above) near $(\pi, 0)$ without the additional complication of the superlattice.

One approach is simply to divide the data by the Fermi function; more accurately one divides the measured intensity $I(\mathbf{k}_F,\omega)$ by $f(\omega) * R(\omega)$, the convolution of the Fermi function with the energy resolution. Although this does not rigorously give the spectral function (because of the convolution), this is a good approximation in situations where the energy resolution is very sharp. An excellent example of such an approach can be seen in the work of Sato *et al.* [47] on Pb–doped Bi2201 ($Bi_{1.80}Pb_{0.38}Sr_{2.01}CuO_{6-\delta}$) which is overdoped with a $T_c < 4K$. In Fig. 5.9 we show the raw data in the vicinity of M at various temperatures in the left panel and the corresponding data "divided by the Fermi function" in the right panel. The "divided" data permits one to clearly observe the dispersion well above E_f particularly at high temperatures, and thereby identify the Fermi crossings with a great degree of confidence.

An alternative approach [9] to eliminating the Fermi function is to symmetrize the data. For each $\mathbf{k}$ define the symmetrized intensity by $I_{\rm sym}(\mathbf{k}_F,\omega) = I(\mathbf{k}_F,\omega) + I(\mathbf{k}_F,-\omega) = I_0\, A_{sym}(\mathbf{k}_F,\omega)$. It is easy to show that $I_{\rm sym}(\omega)$ will exhibit a local minimum, or dip, at $\omega = 0$ for an occupied $\mathbf{k}$ state, while it will show a local maximum at $\omega = 0$ for an unoccupied $\mathbf{k}$ state. In practice, then, the Fermi crossing $\mathbf{k}_F$ is determined as follows: All EDCs along a cut are symmetrized and $\mathbf{k}_F$ is identified as the boundary in $\mathbf{k}$–space between points where $I_{\rm sym}$ has a local maximum versus a local minimum at $\omega = 0$. As shown in Ref. [9], these arguments work even in the presence of finite resolution effects. We note that this method, and the one presented above,

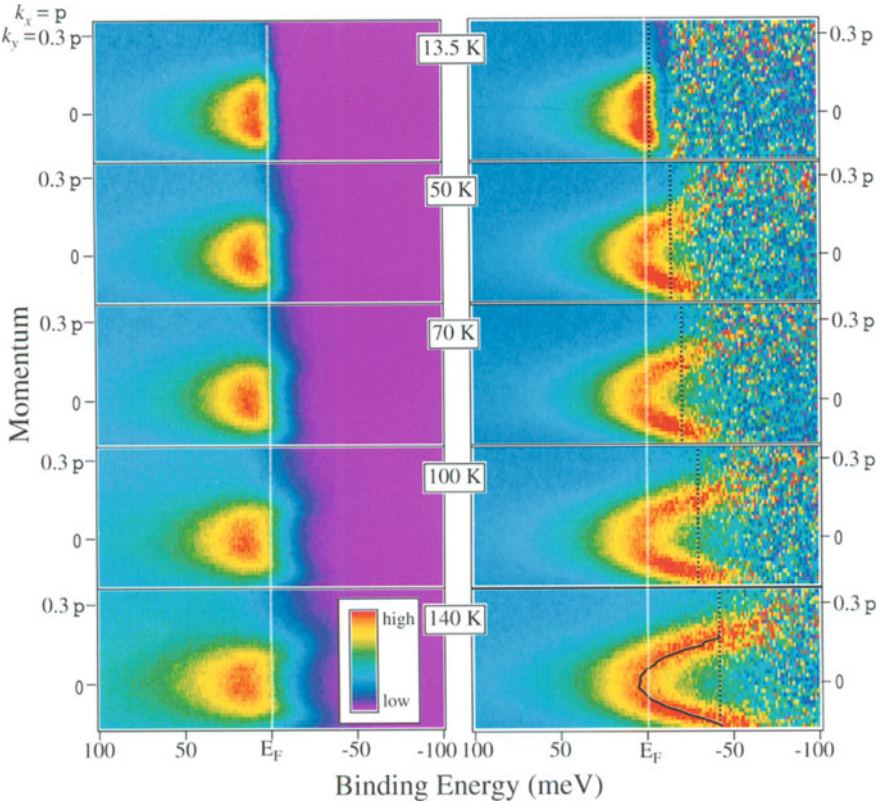

Fig. 5.9. Left panel: temperature dependence of ARPES intensity of OD Bi2201 ($T_c < 4K$) along the $(\pi, 0) - (\pi, \pi)$ cut. Right panel: same divided by the Fermi function at each temperature convoluted with a Gaussian of width 11 meV (energy resolution). Dotted lines show the energy above E_f at which the Fermi function takes a value of 0.03. The solid line in the 140 K data indicates the peak positions obtained by fitting with a Lorentzian

for eliminating the Fermi function require a very accurate determination of the chemical potential (zero of binding energy).

In Fig. 5.10 we show the results [9] of a symmetrization analysis for an OD 23K Bi2201 ($Bi_{1.6}Pb_{0.4}Sr_2CuO_{6-\delta}$) sample. From the raw data along cuts parallel to $(\pi, 0)$ to (π, π) (see Fig. 7 of Ref. [9]) and along $(0, 0) \rightarrow (2\pi, 0)$ (shown in Fig. 5.10(d)) one sees broad peaks whose dispersion is very flat near $(\pi, 0)$, thus making it hard to determine $\mathbf{k}_F$ from EDC dispersion alone. Nevertheless, the symmetrized data provide completely unambiguous results: in the top panels (a,b, and c) of Fig. 5.10 we illustrate the use of symmetrized data to determine $\mathbf{k}_F$ using the criterion described above. Two

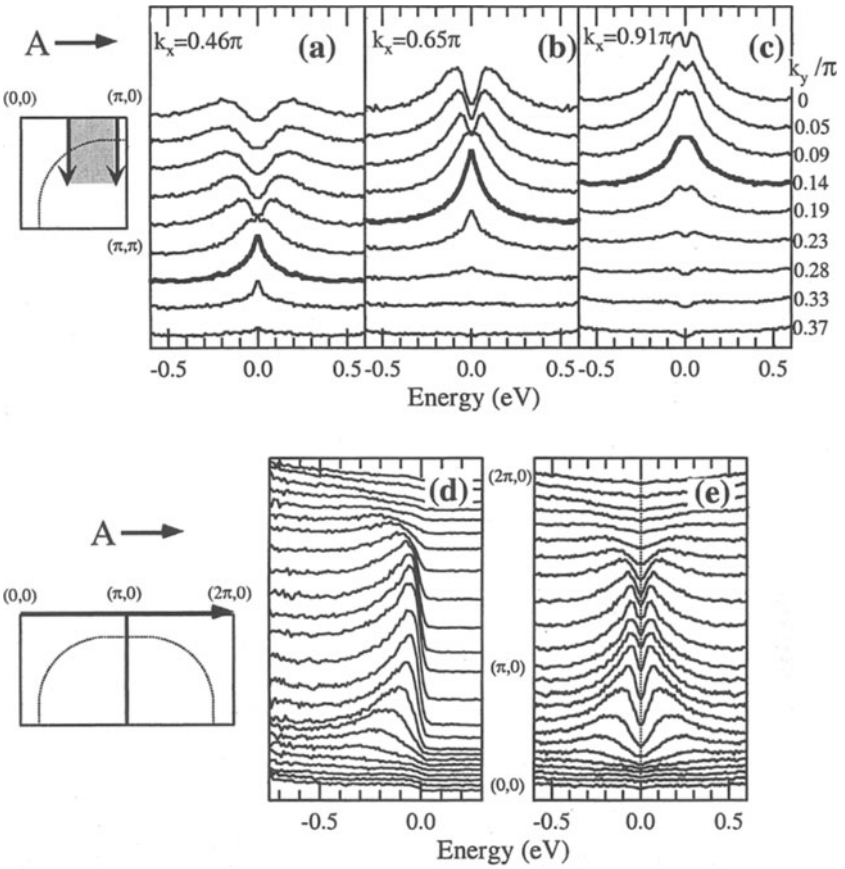

Fig. 5.10. (a,b,c) Symmetrized EDCs along cuts parallel to $(\pi, 0)$ to (π, π) for OD 23K Bi2201 at $T = 25K$ using $h\nu = 22eV$ photons. The curve corresponding to $\mathbf{k}_F$ along each cut is determined as explained in the text and is shown by a thick line. The lower panel (d) shows EDCs along the $(0, 0) \rightarrow (2\pi, 0)$ direction; panel (e) shows symmetrized curves corresponding to the data in (d) and shows the absence of a Fermi surface crossing along $(0, 0)$ to $(\pi, 0)$

other features about this analysis are worth noting. First, on approaching $\mathbf{k}_F$ from the occupied side, resolution effects are expected to lead to a flat topped symmetrized spectrum. Second, one expects an intensity drop in the symmetrized spectrum upon crossing $\mathbf{k}_F$, assuming that matrix elements are not strongly $\mathbf{k}$–dependent. Both of these effects are indeed seen in the data and further help in deducing $\mathbf{k}_F$.

It is equally important to be able to ascertain the *absence* of a Fermi crossing along a cut. In this respect, the raw data along $(0, 0) - (\pi, 0) - (2\pi, 0)$ in Fig. 5.10(d)is difficult to interpret: the "flat band" remains extremely close

to E_f but does it cross E_f? It is simple to see from the symmetrized data in Fig. 5.10(e) the answer is "no". The symmetrized data do not show a peak centered at $\omega = 0$ for any $\mathbf{k}$, thus establishing the absence of a Fermi crossing along this cut.

Intensity Plots

A different method for determining the Fermi surface is to make a 2D plot as a function of $\mathbf{k}$ of $\int_{\delta\omega} d\omega I(\mathbf{k}, \omega)$, the observed intensity integrated over a suitably chosen narrow energy interval $\delta\omega$ about the Fermi energy. At first sight this seems to be a very direct way to find out the $\mathbf{k}$–space locus on which the low energy excitations live. However, as we discuss below, one has to be very careful in interpreting such plots since one is now focusing on the *absolute* intensity of the ARPES signal, which can be strongly affected by the $\mathbf{k}$–dependence of the photoemission matrix elements.

This approach was pioneered in the cuprates by Aebi and coworkers [40], and in recent times with the availability of Scienta detectors with dense $\mathbf{k}$–sampling it has been used by several groups [48–52]. We show as an example in Fig. 5.11 results from our group [51] on an optimally doped $T_c = 90$K Bi2212 sample [53] using 33eV incident photons.

Before commenting on the controversies about the Fermi surface crossing near the $(\pi, 0)$ point, we first examine EDCs along the ΓY direction (middle panel of Fig. 5.11, where the left panel shows a two dimensional plot of the energy and momentum dependent intensity of photoelectrons along the ΓY cut). All of the features — main band (MB), superlattice umklapp bands (UB) and the shadow band (SB) — seen before [37] and discussed above are confirmed. We also see weaker, second order umklapps from the superlattice (corresponding to $\pm(0.42, 0.42)$, twice the superlattice wavevector), which confirms the diffraction origin of the superlattice bands.

We now turn to panels (c,d) of Fig. 5.11 where we plot the integrated intensity within a ± 100 meV window about the chemical potential. We note the very rapid suppression of intensity beyond $\sim 0.8\Gamma$M [48], which does not occur in data taken with 22eV incident photons. This has led some authors [50, 54] to suggest the existence of an electron–like Fermi surface with a crossing at this point. However, Fretwell *et al.* [51] and independently Borisenko *et al.* [52] have argued that this Fermi crossing along $(0, 0)$ to $(\pi, 0)$ is actually due to one of the umklapp bands, and the near optimally doped Fermi surface is indeed hole like as earlier shown by Ding *et al.* [37].

This can be seen most clearly in Pb–doped samples, where the umklapp bands are not visible. In Fig. 5.12, we show the Fermi energy intensity map of Borisenko *et al.* [52], where the hole surface centered around (π, π) and its shadow band partner are quite apparent.

One of the main reasons for the controversy surrounding the topology of the optimal doped Fermi surface is the fact that data taken at different incident photon energies $h\nu$ lead to different intensity patterns. Our assertion, based on Refs. [9, 51], is that the superlattice umklapp band is more

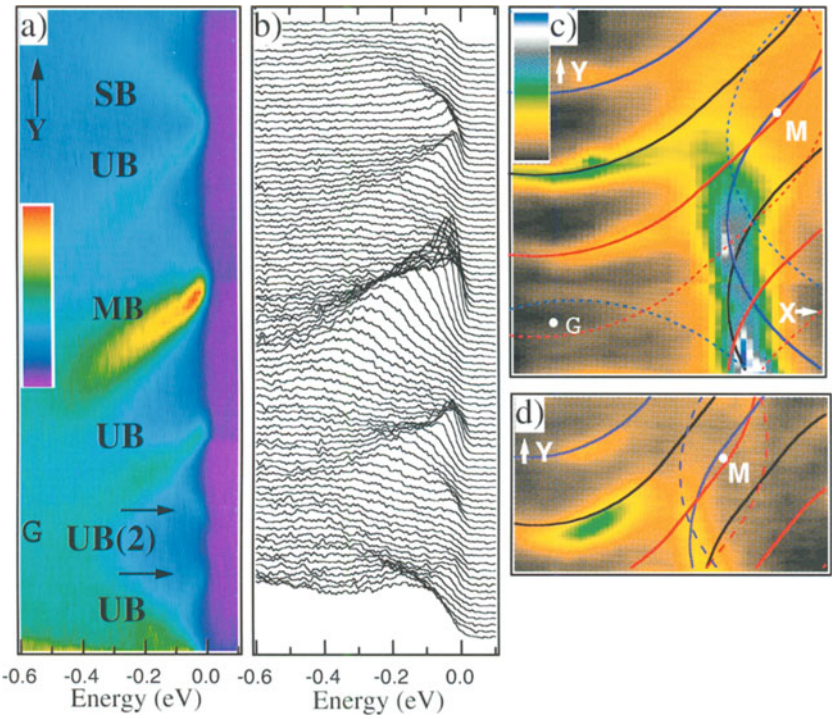

Fig. 5.11. (a) Intensity $I(\mathbf{k}, \omega)$ and (b) EDCs along ΓY measured on an optimally doped sample (T_c=90K) at T=40K with 33 eV photons polarized along ΓX. (c) Integrated intensity (-100 to +100 meV) covering the X and Y quadrants of the Brillouin zone. Data were collected on a regular lattice of $\mathbf{k}$ points (spacing 1° along ΓX and 0.26° along ΓY). (d) Integrated intensity (± 40 meV) as in (c), but in the normal state (T = 150K). Overlaid on (c) is the main band (black), ± umklapps (blue/red), and ± 2nd order umklapps (dashed blue/red lines) Fermi surfaces from a tight binding fit [38]

noticeable at $h\nu$ = 33eV compared with 22 eV since matrix element effects suppress the main band intensity at 33 eV. For a detailed discussion about how to discriminate between a main band and superlattice Fermi crossing, we refer the reader to the cited papers, and also to Refs. [9,37] for the use of polarization selection rules for this purpose.

Matrix Element Effects

There is an important general lesson to be learned from the above discussion which is equally relevant for the $n(\mathbf{k})$ methods to be discussed below. Changes in the ARPES intensities (either integrated over a small energy window or over a large energy range) as a function of $\mathbf{k}$ can be strongly affected by matrix element effects. This is, of course, obvious from the expression for the

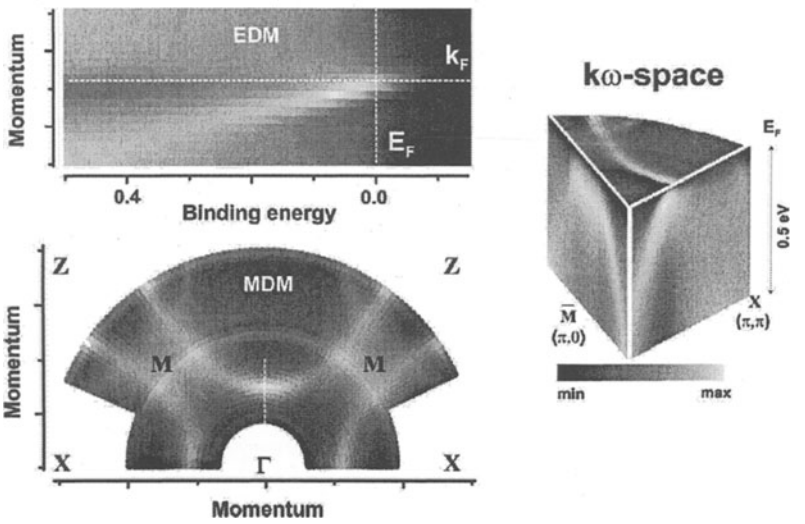

Fig. 5.12. Upper panel: Energy distribution map from the $\Gamma - (\pi, \pi)$ direction in the Brillouin zone of Pb–doped BSCCO recorded at room temperature. Lower panel: momentum distribution map of Pb–doped BSCCO, recorded at room temperature (raw data). White horizontal dashed line represents a $\mathbf{k}_F$–EDC, vertical ones correspond to an E_F–MDC. In both cases the gray scale represents the photoemission intensity as indicated. The inset shows the three dimensional (k_x, k_y, ω) space, which is probed in ARPES of quasi–2D systems (from Ref. [52])

the ARPES intensity: $I(\mathbf{k}, \omega) = I_0(\mathbf{k}; \nu; \hat{\mathbf{A}}) f(\omega) A(\mathbf{k}, \omega)$. The key question is: after integration over the appropriate range in ω, how do we differentiate between the $\mathbf{k}$ dependence coming from the matrix elements I_0 (which we are not interested in per–se) from the $\mathbf{k}$ dependence coming from the spectral function?

One possibility is to have *a priori* information about the matrix elements from electronic structure calculations [17]. But as we now show, even in the absence of such information, one can experimentally separate the effects of a strong $\mathbf{k}$–variation of the matrix element from a true Fermi surface crossing. The basic idea is to exploit the fact that changing the incident photon energy one only changes the ARPES matrix elements and not the spectral function (or the resulting momentum distribution) of the initial states.

We will use Bi2201 to illustrate our point since it has all the complications (points (1),(2) and (4)) listed above without the superlattice (point (3)). Fig. 5.13 (a), from Ref. [9], shows the intensity (integrated over a large energy range) as a function of $\mathbf{k}$ for OD 23K Bi2201, and highlights the differences between data obtained at 22 eV and 34 eV incident photon energies. At 22 eV the maximum intensity occurs close to $(\pi, 0)$ and decreases both toward $(0, 0)$ and (π, π), while at 34 eV there is a strong depression of intensity on

approaching $(\pi, 0)$, resulting in a shift of the intensity maximum away from $(\pi, 0)$.

From the discussion of Section 5.2.4, we can write the integrated intensity as: $I(\mathbf{k}) = \int_{-\infty}^{+\infty} d\omega I(\mathbf{k}, \omega) = I_0(\mathbf{k}; \nu; \mathbf{A}) n(\mathbf{k})$. We attribute this loss in intensity around $(\pi, 0)$ at 34 eV seen in Fig. 5.13(a) to strong $\mathbf{k}$–dependence of I_0 rather than $n(\mathbf{k})$. Experimentally we prove this by showing that the EDCs at the same point in the Brillouin zone obtained at the two different photon energies show exactly the same lineshape, i.e. one can be rescaled onto the other as shown in Fig. 5.13(b). As an independent check of this, we have also shown that the symmetrization analysis leads to the same conclusion that there is no Fermi crossing along $(0, 0) \rightarrow (\pi, 0)$; see Fig. 9 of Ref. [9].

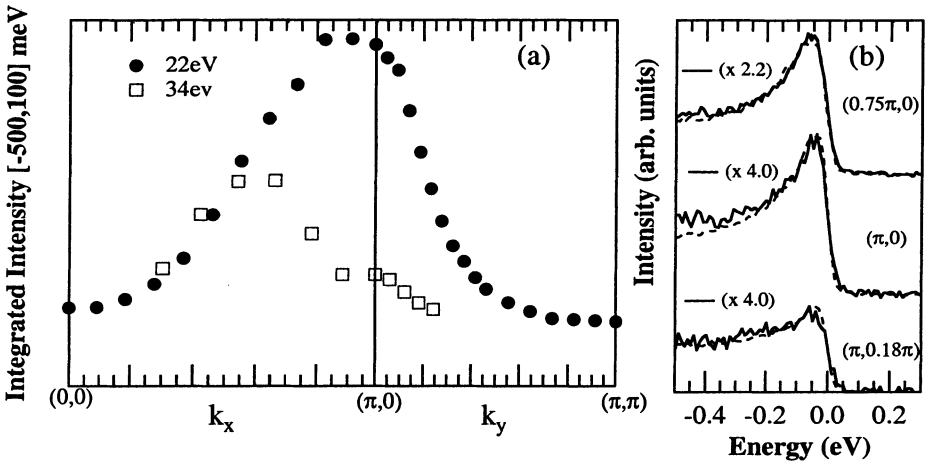

Fig. 5.13. Bi2201–OD23K, (a) Integrated intensity (over the range is −500 to 100 meV) along the $(0, 0) \rightarrow (\pi, 0) \rightarrow (\pi, \pi)$ directions for two incident photon energies $h\nu$ =22 and 34 eV. (b) Comparison of the ARPES lineshape measured at 22 (dashed lines) and 34 eV (solid lines) at three different $\mathbf{k}$ points. One curve has been scaled by the multiplicative constant indicated to make it lie on top of the other

For completeness, we note that another possible source of incident $h\nu$–dependence in ARPES is k_z–dispersion. If there was c–axis dispersion, different photon energies would probe initial states with different k_z values consistent with energy conservation. However the scaling shown in Fig. 5.13(b) proves that it is the *same* two–dimensional (k_z–independent) initial state which is being probed in the data shown here, and the $h\nu$–dependence arises entirely from the different final states that the matrix element couples to.

Methods based on the Momentum Distribution

Finally we turn to the use of the momentum distribution sum rule [21] (discussed in Section 5.2.4) in determining the Fermi surface. In principle,

locating the rapid variation of $n(\mathbf{k})$ offers a very direct probe of the Fermi surface which we emphasize is not restricted to Fermi liquids. (The $T = 0$ momentum distribution for known non–Fermi liquid systems, such as Luttinger liquids in one dimension, do show a inflection point singularity at $\mathbf{k}_F$.) However in practice, one needs to be very careful about the $\mathbf{k}$–dependence of the matrix elements, as clearly recognized in the original proposal [21].

Here we discuss two approaches using the $n(\mathbf{k})$ method to obtain information about the Fermi surface. The first method is to study the $\mathbf{k}$–space gradient of the logarithm of the integrated intensity. The second method is to study the temperature–dependence of the integrated intensity and use the approximate sum rule [21] $\partial n(\mathbf{k}_F)/\partial T = 0$ discussed in Section 5.2.4.

The gradient method was used in our early work [37, 55] where $\mathbf{k}_F$ was estimated from the location of $\max |\nabla_{\mathbf{k}} n(\mathbf{k})|$. The same method has also been successfully used later by other authors [56, 57]. In the presence of strong matrix element effects, it is even more useful to plot the magnitude of the logarithmic gradient: $|\nabla_{\mathbf{k}} I(\mathbf{k})|/I(\mathbf{k})$ which emphasizes the rapid changes in the integrated intensity. The logarithmic gradient filters out the less abrupt changes in the matrix elements and helps to focus on the intrinsic variations in $n(\mathbf{k})$.

As an example we show in Fig. 5.14 the results [9] of such an analysis for an OD 0K Bi2201 sample. In the top panels (a) and (c) we show the integrated intensity $I(\mathbf{k})$ around the $(\pi, 0)$ point obtained at two different photon energies: 22 eV and 28 eV respectively. In the lower panels 11(b) and (d), we plot $|\nabla_{\mathbf{k}} I(\mathbf{k})|/I(\mathbf{k})$. Note that there are large differences between the two top panels, due to different matrix elements at 22 eV and 28 eV. However, as explained above, the logarithmic gradients in the bottom panels, which are more influenced by the intrinsic $n(\mathbf{k})$, are much more similar. The Fermi surface can be clearly seen as two high intensity arcs curving away from the $(\pi, 0)$ point. Once matrix element effects are taken care of, the Fermi surface results obtained at the two different photon energies are quite similar, and in good agreement with the results obtained from independent methods like symmetrization on the same data set [9].

Our final method for the determination of a Fermi crossing goes back to the sum rule [21] that we had introduced earlier, $\partial n(\mathbf{k}_F)/\partial T = 0$. Assuming that the matrix elements are T–independent on the temperature scales of interest, this immediately implies the integrated intensity at (and only at) $\mathbf{k}_F$ is T–independent. In Section 5.2.4, we had used this sum rule to get confidence in the validity of the single–particle spectral function interpretation of ARPES by verifying at $\mathbf{k}_F$ assuming that $\mathbf{k}_F$ was known (by some other means). Now we can invert the logic: we can look at the T dependence of the integrated intensity, and identify $\mathbf{k}_F$ as that point in $\mathbf{k}$–space where the integrated intensity is T–independent. This is illustrated in Fig. 5.15 from the work of Sato et al. [47], who determine $\mathbf{k}_F$ along the $(\pi, 0) - (\pi, \pi)$ cut for a highly OD Bi2201 sample. The result is completely consistent with that

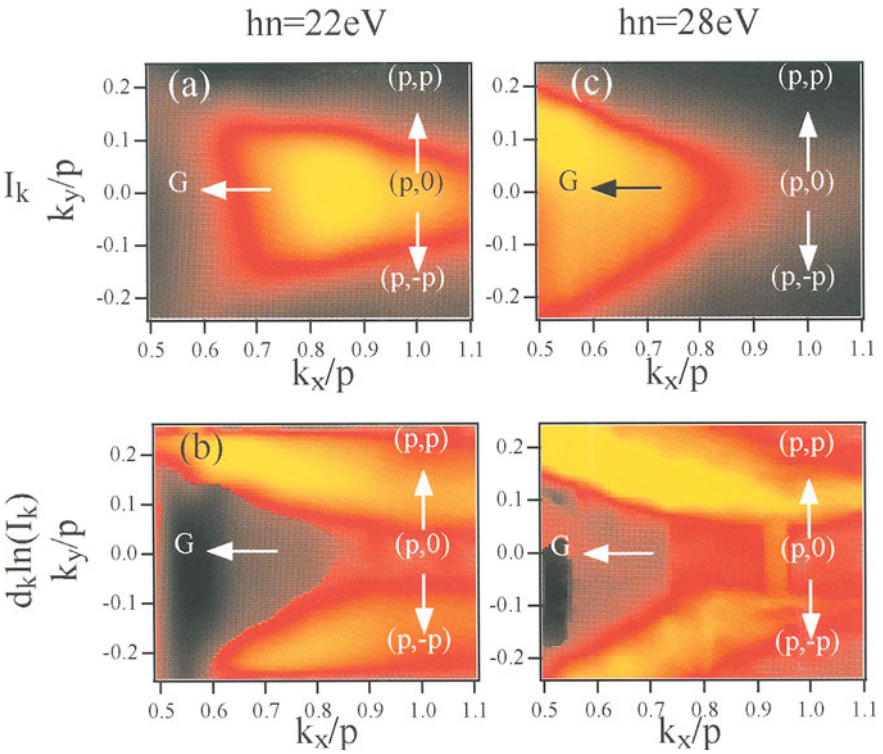

Fig. 5.14. Bi2201–OD0K: (a and c) Integrated intensity (over -350 to +50 meV) $I(\mathbf{k})$ measured at $\hbar\nu$ =22 and 28 eV around the $(\pi, 0)$ point. Notice that the intensity maximum depends strongly upon the photon energy $\hbar\nu$.(b and d) Corresponding gradient of the logarithm, $|\nabla_{\mathbf{k}} I(\mathbf{k})|/I(\mathbf{k})$, the maxima which correspond to Fermi crossings and clearly show that, *independent of the photon energy*, the Fermi surface consists of a hole barrel centered around (π, π)

obtained by other methods, such as "division by the Fermi function" on the same sample (see Fig. 5.9).

EDCs vs MDCs

To conclude this discussion, let us note a very recent development for determining k_F and the near–E_f dispersion based on the MDCs, which are plots of the ARPES intensity as a function of k (in this case normal to the expected Fermi surface), at various fixed values of ω. As shown in Section 5.2.5, the MDC peak position in the vicinity of the Fermi surface, i.e, near $(\mathbf{k} = \mathbf{k}_F, \omega = 0)$ is given by: $k = k_F + [\omega - \Sigma'(\omega)]/v_F^0$.

Thus k_F is determined by the peak location of the MDC at $\omega = 0$. The fully renormalized Fermi velocity $v_F = v_F^0/[1 - \partial\Sigma'/\partial\omega]$ is given by the slope of the MDC peak dispersion. We note that the factor arising from the k–dependence of the self–energy is already included in v_f^0, so that $v_f^0 =$

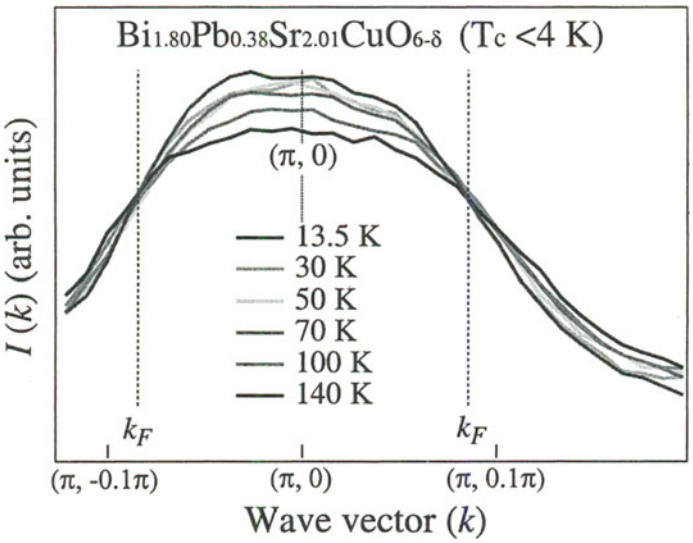

Fig. 5.15. Temperature dependence of the integrated ARPES intensity $I(\mathbf{k})$ along the $(\pi, 0) - (\pi, \pi)$ cut, obtained by integrating the ARPES intensity from -100 to 100 meV. (An angle–integrated temperature–independent background is subtracted before integration)

$v_f^{\text{bare}}[1 + \partial\Sigma'/\partial\varepsilon_{\mathbf{k}}]$. (To see this, note that the analysis of Section 5.2.5 can be easily generalized to retain the first order term $\partial\Sigma'/\partial\varepsilon_{\mathbf{k}}$ without spoiling the Lorentzian lineshape of the MDC provided this k–dependence does not enter Σ'').

As discussed earlier, the above results derive from the Lorentzian lineshape of the MDC which arises when three conditions are satisfied: the matrix elements do not depend on k, the self energy does not depend on k (except for the $(k - k_F)$ variation of Σ' noted above) and dispersion can be linearized near the Fermi surface. The validity of these assumptions can be checked self–consistently by the Lorentzian MDC lineshape and the dispersion deduced from the data.

The significance of this approach is that, as emphasized by Kaminski *et al.* [25], the dispersions of the EDC and MDC peak positions are actually different in the cuprates; see Fig. 5.54(a) in Section 5.7.7. This difference arises due to the non–Fermi liquid nature of the normal state, so that the EDC peak dispersion is *not* given by the condition $\omega - v_F^0(k - k_F) - \Sigma' = 0$ but also involves in general Σ''. In contrast the MDC peak dispersion is rigorously described by the expression described above, and is much simpler to interpret.

We expect that the MDC method for determining the dispersion and k_F which has thus far been used mainly along the zone diagonal, will eventually

be the method of choice, except when one is very close to the bottom of the band where linearization fails.

5.4.3 Summary of Results on the Optimally Doped Fermi Surface

We have discussed a large number of methods for determination of the Fermi surface in Bi2201 and Bi2212 in the previous subsection. These include: (a) dispersion of EDC peaks through E_f, (b) dispersion of peaks after division by the Fermi function, (c) symmetrization, (d) maps of intensities at E_f, (e) gradient of $n(\mathbf{k})$, (f) T–dependence of $n(\mathbf{k})$, and (g) MDC dispersion. In addition we also discussed using the $h\nu$–dependence of the data and polarization selection rules to eliminate matrix element effects and to identify superlattice Fermi crossings.

The reader might well ask: why so many different methods? The reason is that the development of all of these methods has taken place to deal with the complications of accurately identifying the Fermi surface in the presence of the four problems listed at the beginning of the preceding subsection. Each method has its pros and cons, so that some, like (b) and (c) require very accurate E_f determination, which is not the case in (e) and (f) which use energy–integrated intensities. Most methods require dense sampling in $\mathbf{k}$ space, while method (f) requires in addition data at several temperatures.

Given the complications of the problem at hand it is important to look for crosschecks and consistency between various ways of determining the Fermi surface. We believe that for optimally doped Bi2201 and 2212 there is unambiguous evidence for a single hole barrel centered about the (π, π) point enclosing a Luttinger volume of $(1 + x)$ holes where x is the hole doping. We discuss further below the issues of the doping–dependence of the Fermi surface and of bilayer splitting in Bi2212.

5.4.4 Extended Saddle Point Singularity

The very flat dispersion near the $(\pi, 0)$ point observed in all of the data is striking. Specifically, along $(0, 0)$ to $(\pi, 0)$ there is an intense spectral peak corresponding to the main band, which disperses toward E_F but stays just below it. This is often called the "flat band" or "extended saddle point", and appears to exist in all cuprates, though at different binding energies in different materials [8, 45, 58].

In our opinion this flat band is not a consequence of the bare electronic structure, but rather a many–body effect, because a tight–binding description of such a dispersion requires fine–tuning (of the ratio of the next–near neighbour hopping to the near–neighbour hopping) which would be unnatural even in one material, let alone many.

An important related issue is whether this flat band leads to a singular density of states. It is very important to recognize that, while Fig. 5.8(b) *looks*

like a conventional band structure, the dispersing states whose "peak positions" are plotted are extremely broad, with a width comparable to binding energy, and these simply cannot be thought of as quasiparticles. This general point is true at all $\mathbf{k}$'s, but specifically for the flat band region it has the effect of spreading out the spectral weight over such a broad energy range that any singularity in the DOS would be washed out. This is entirely consistent with the fact that other probes (tunneling, optics, etc.) do not find any evidence for a singular density of states either.

5.4.5 Bilayer Splitting?

On very general grounds, one expects that the two CuO_2 layers in a unit cell of Bi2212 should hybridize to produce two electronic states which are even and odd under reflection in a mirror plane mid–way between the layers. Where are these two states? Why then did we find only one main "band" and only one Fermi surface in Bi2212?

Let us first recall the predictions of electronic structure calculations [59]. In systems like Bi2212, the intra–bilayer hopping as a function of the in–plane momentum $\mathbf{k}$ is of the form [29,60] $t_\perp(\mathbf{k}) = -t_z(\cos k_x - \cos k_y)^2$. Thus the two bilayer states are necessarily degenerate along the zone diagonal. However they should have a maximum splitting at $\bar{M} = (\pi, 0)$ of order 0.25 eV, which may be somewhat reduced by many–body interactions.

Depending on the exact doping levels and on the presence of Bi–O Fermi surface pockets, which are neither treated accurately in the theory nor observed in the ARPES data, we must obtain one of the two following situations: (1) the bilayer antibonding (A) state is unoccupied while the bonding (B) state is occupied at $(\pi, 0)$. This would lead to an A Fermi crossing along $(0,0) - (\pi,0)$ and a B Fermi crossing along $(\pi,0) - (\pi,\pi)$. As described at great length above we did not find evidence for a main band Fermi crossing along $(0,0) - (\pi,0)$ at least for the near optimal doped sample, therefore this possibility is ruled out.

(2) The second possibility is that both the A and B bilayer states are occupied at the $(\pi, 0)$. In this case, there should be two (in principle, distinct) Fermi crossings along $(\pi,0) - (\pi,\pi)$, although they might be difficult to resolve in practice. Nevertheless, one would definitely expect to see two distinct occupied states at the $(\pi, 0)$ point. Unfortunately, the normal state spectrum at $(\pi, 0)$ is so broad in the optimally doped and underdoped materials that it is hard to make a clear case for bilayer splitting. Thus an effort was made to search for this effect in the superconducting state at $T \ll T_c$, when a sharp feature (quasiparticle peak) is seen (see Fig. 5.16) and one might hope that the bilayer splitting should be readily observable.

The issue then is how to interpret the peak–dip–hump structure seen in the ARPES lineshape at $(\pi, 0)$ in Fig. 5.16. The peak–dip–hump structure will be discussed at length in Section 5.7 below. Nevertheless, here we will briefly address the question of whether: (I) the peak and the hump are the

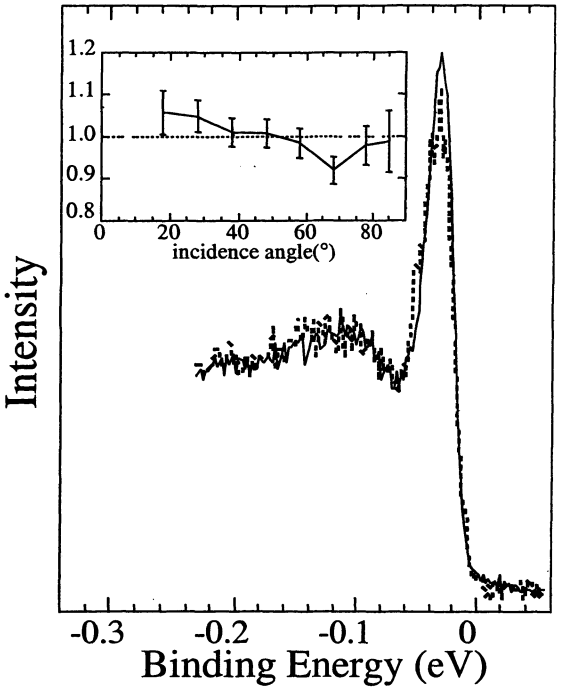

Fig. 5.16. Low temperature (T=13K) EDC's of near optimal $T_c = 87$K Bi2212 at $(\pi, 0)$ for various incident photon angles. The solid (dashed) line is 18° (85°) from the normal. The inset shows the height of the sharp peak for data normalized to the broad bump, at different incident angles

two bilayer split states, which are resolved below T_c once the peak becomes sharp? Or (II) is the non–trivial line shape due to many–body effects in a single spectral function $A(\mathbf{k}, \omega)$?

Three pieces of evidence will be offered in favor of hypothesis (II) as opposed to (I), so that no bilayer spliting is observable even in the superconducting state of near optimal doped Bi2212. The first evidence comes from studying the polarization dependence of the ARPES matrix elements. For case (I) there are two independent matrix elements which, in general, should vary differently with photon polarization $\mathbf{A}$, and thus the intensities of the two features should vary independently as $\mathbf{A}$ is varied. On the other hand, for case (II), the intensities of the two features are governed by a single matrix element. As shown in Fig. 5.16 it was found in Ref. [37] that by varying the z–component of $\mathbf{A}$, the peak and hump intensities scale together, and thus the peak–dip–hump are all part of a single spectral function for Bi2212.

A second piece of evidence comes from a comparison [61] of the normal and superconducting state dispersions near the $(\pi, 0)$ point, which will be

discussed in detail in connection with Figs. 5.43 and 5.44 of Section 5.7.4. From these data, we argue that there is no evidence for a feature above T_c, which would correspond to the dispersionless quasiparticle peak below T_c. Thus the dispersionless peak must be of many–body origin.

The third and final piece of evidence comes from both ARPES and SIS tunneling. In the ARPES data [62] shown in Fig. 5.50 of Section 5.7.6 one sees the striking fact that while the energy scales of both the quasiparticle peak and the $(\pi, 0)$ hump increase with underdoping, their ratio is essentialy doping independent. Since the location of the peak is the (maximum) superconducting gap — as discussed in detail in Section 5.5 — the $(\pi, 0)$ hump energy scales with the gap. SIS tunneling data also finds the same correlation on a very wide range of materials (including some which have a single CuO plane) whose gap energies vary by a factor of 30 [63]. This provides very strong evidence that both the peak and hump are related to many–body effects and not manifestations of bilayer spliting.

We note that Anderson [64] had predicted that many–body effects within a single layer could destroy both the quasiparticles and the coherent bilayer splitting *in the normal state.* But why the splitting should not be visible in the superconducting state, where sharp quasiparticles do exist, is not clear from a theoretical point of view.

Recently, the above picture has been challenged by a number of authors [65–67]. What has become clear is that bilayer splitting is indeed present for heavily overdoped Bi2212 samples, and has been seen now by several groups, including our own. In Fig. 5.17, we show (a) the bilayer split Fermi surfaces and (b) the bilayer split EDCs observed by the Stanford group for a heavily overdoped (T_c=65K) Bi2212 sample. Note that the bilayer splitting can even be seen in the umklapp bands. The resulting dispersion is reproduced in Fig. 5.18, where one sees that the momentum dependence of the splitting follows that expected from electronic structure considerations [29, 60].

How this effect evolves as a function of doping, though, is still controversial. In particular, if it is present for optimal doping, it is difficult to resolve. Moreover, some authors who advocate bilayer splitting still argue that the peak/dip/hump structure in the superconducting state is largely a many–body effect [65] as we adovcate here. This is supported by the fact that the same lineshape is seen in trilayer Bi2223 [68], where one would expect three features if layer splitting were causing these effects. And similar lineshapes have been seen by tunneling in single layer systems, in support of a many–body interpretation. The reader is refered to Ref. [2], where the issue of bilayer splitting is discussed in greater detail than here.

5.5 Superconducting Energy Gap

In this Section, we will first establish how the superconducting (SC) gap manifests itself in ARPES spectra, and then directly map out its variation with $\mathbf{k}$

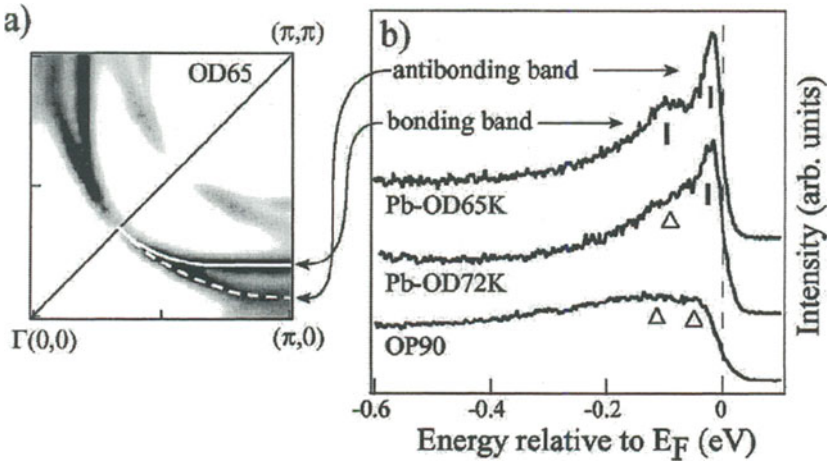

Fig. 5.17. (a) Bilayer–split Fermi surfaces of heavily overdoped OD65; the two weaker features are their superstructure counter parts. Solid and dashed lines represent the bonding and antibonding Fermi surfaces, respectively. (b) Normal state photoemission spectra of Bi2212 taken at $(\pi, 0)$ for three different doping levels. Data were taken with $h\nu = 22.7$ eV photon. Bars indicate identified feature positions, and triangles indicate possible feature positions. (from Ref. [65])

along the Fermi surface. This is the only available technique for measuring the momentum dependence of the energy gap, and complements phase–sensitive tests of the order parameter symmetry [69]. Thus ARPES has played an important role [70], [71] in establishing the d–wave order parameter in the high T_c superconductors [69]. At the end of the Section, we will discuss the doping dependence of the SC gap and its anisotropy, and the implications of this study for various low temperature experiments like thermal conductivity and penetration depth.

5.5.1 Particle–Hole Mixing

To set the stage for the experimental results it may be useful to recall particle–hole (p–h) mixing in the BCS framework (even though, as we shall see in Section 5.7, there are aspects of the data which are dominated by many body effects beyond weak coupling BCS theory). The BCS spectral function is given by

$$A(\mathbf{k},\omega) = u_{\mathbf{k}}^2 \Gamma/\pi((\omega - E_{\mathbf{k}})^2 + \Gamma^2) + v_{\mathbf{k}}^2 \Gamma/\pi((\omega + E_{\mathbf{k}})^2 + \Gamma^2) \qquad (5.11)$$

where the coherence factors are $v_{\mathbf{k}}^2 = 1 - u_{\mathbf{k}}^2 = \frac{1}{2}(1 - \epsilon_{\mathbf{k}}/E_{\mathbf{k}})$ and Γ is a phenomenological linewidth. The normal state energy $\epsilon_{\mathbf{k}}$ is measured from E_f and the Bogoliubov quasiparticle energy is $E_{\mathbf{k}} = \sqrt{\epsilon_{\mathbf{k}}^2 + |\Delta(\mathbf{k})|^2}$, where

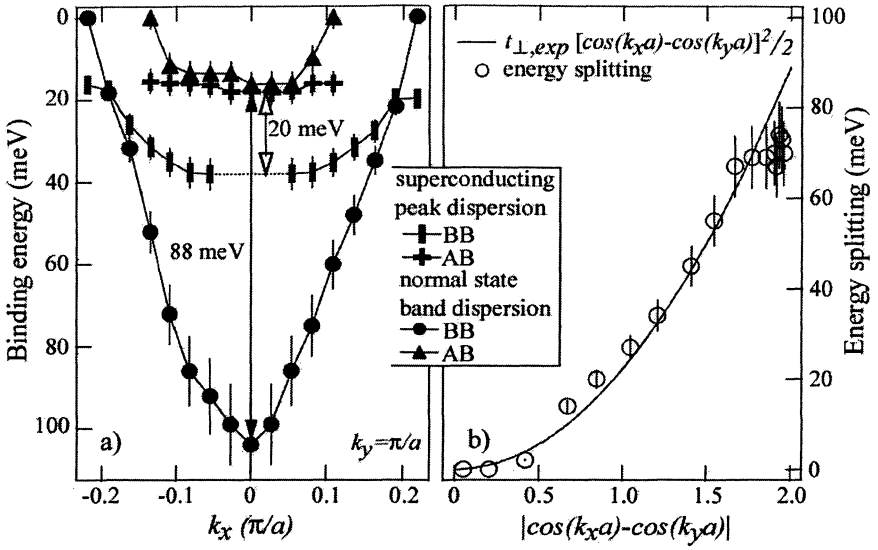

Fig. 5.18. (a) Dispersion extracted from heavily overdoped OD65. (b) Energy splitting along the antibonding Fermi surface, which is obtained from data shown in Fig. 5.17. It is simply the binding energy of the bonding band, since the binding energy of the antibonding band is zero at its Fermi surface. The curve is $\frac{1}{2}t_{\perp,\mathrm{exp}}[\cos(k_x a)-\cos(k_y a)]^2$, where $t_{\perp,\mathrm{exp}} = 44 \pm 5$ meV. Error bars are due to the uncertainties in determining the energy position (from Ref. [65])

$\Delta(\mathbf{k})$ is the gap function. Note that only the second term in Eq. (5.11), with the $v_{\mathbf{k}}$–coefficient, would be expected to make a significant contribution to the EDCs at low temperatures.

In the normal state above T_c, the peak of $A(\mathbf{k},\omega)$ is at $\omega = \epsilon_{\mathbf{k}}$ as can be seen by setting $\Delta = 0$ in Eq. (5.11). We would thus expect to see in ARPES a spectral peak which disperses through zero binding energy as $\mathbf{k}$ goes through $\mathbf{k}_F$ (the Fermi surface). In the superconducting state, the spectrum changes from $\epsilon_{\mathbf{k}}$ to $E_{\mathbf{k}}$; see Fig. 5.19. As $\mathbf{k}$ approaches the Fermi surface the spectral peak shifts towards lower binding energy, but no longer crosses E_f. Precisely at $\mathbf{k}_F$ the peak is at $\omega = |\Delta(\mathbf{k}_F)|$, which is the closest it gets to E_f. This is the manifestation of the gap in ARPES. Further, as $\mathbf{k}$ goes beyond $\mathbf{k}_F$, in the region of states which were unoccupied above T_c, the spectral peak *disperses back*, receding away from E_f, although with a decreasing intensity (see Eq. (5.11)). This is the signature of p–h mixing.

Experimental evidence for particle–hole mixing in the SC state was first given in Ref. [55]. In Fig. 5.20 we show normal and SC state spectra for Bi2212 for $\mathbf{k}$'s along the cut shown in the inset. In the normal state data in panel (b) we see the electronic state dispersing through E_f: the $\mathbf{k}$'s go from occupied (top of panel) to unoccupied states (bottom of panel). The normal

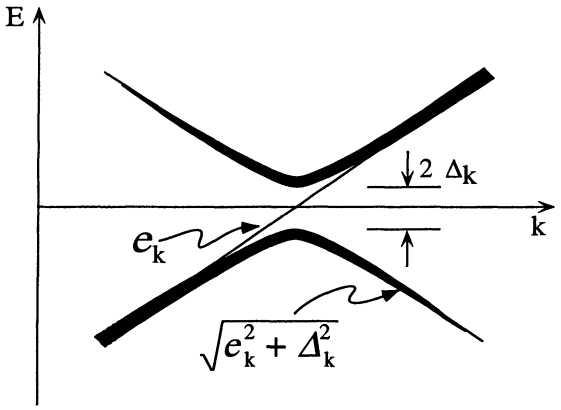

Fig. 5.19. Schematic dispersion in the normal (thin line) and superconducting (thick lines) states following BCS theory. The thickness of the superconducting state lines indicate the spectral weight given by the BCS coherence factors u and v

state dispersion is plotted as black dots in Fig. 5.21 (b). The $\mathbf{k}_F$ obtained from this dispersion is in agreement with that estimated from the $|\nabla_{\mathbf{k}} n(\mathbf{k})|$ analysis of the normal state data shown in Fig. 5.21 (a).

We see from Fig. 5.20 (a) that the SC state spectral peaks do not disperse through the chemical potential, rather they first approach $\omega = 0$ and then recede away from it. The difference between the normal and SC state dispersions is clearly shown in Fig. 5.21 (b).

There are three important conclusions to be drawn from Fig. 5.21 (b). First, the bending back of the SC state spectrum for $\mathbf{k}$ beyond $\mathbf{k}_F$ is direct evidence for p–h mixing in the SC state. Second, the energy of closest approach to $\omega = 0$ is related to the SC gap that has opened up at the FS, and a quantitative estimate of this gap will be described below. Third, the location of closest approach to $\omega = 0$ ("minimum gap") coincides, within experimental uncertainties, with the $\mathbf{k}_F$ obtained from analysis of normal state data.

In fact by taking cuts in $\mathbf{k}$–space which which are perpendicular to the normal state Fermi surface one can map out the "minimum gap locus" in the SC state, or for that matter in any gapped state (e.g., the pseudogap regime to be discussed in the following Section). We emphasize that particle–hole mixing leads to the appearance of the "minimum gap locus" and this locus in the gapped state gives information about the underlying Fermi surface. (By this we mean the Fermi surface on which the SC state gap appears below T_c). In fact, the observation of p–h mixing in the ARPES spectra is a clear way of asserting that the gap seen by ARPES is due to superconductivity rather than of some other origin, e.g., charge– or spin–density wave formation.

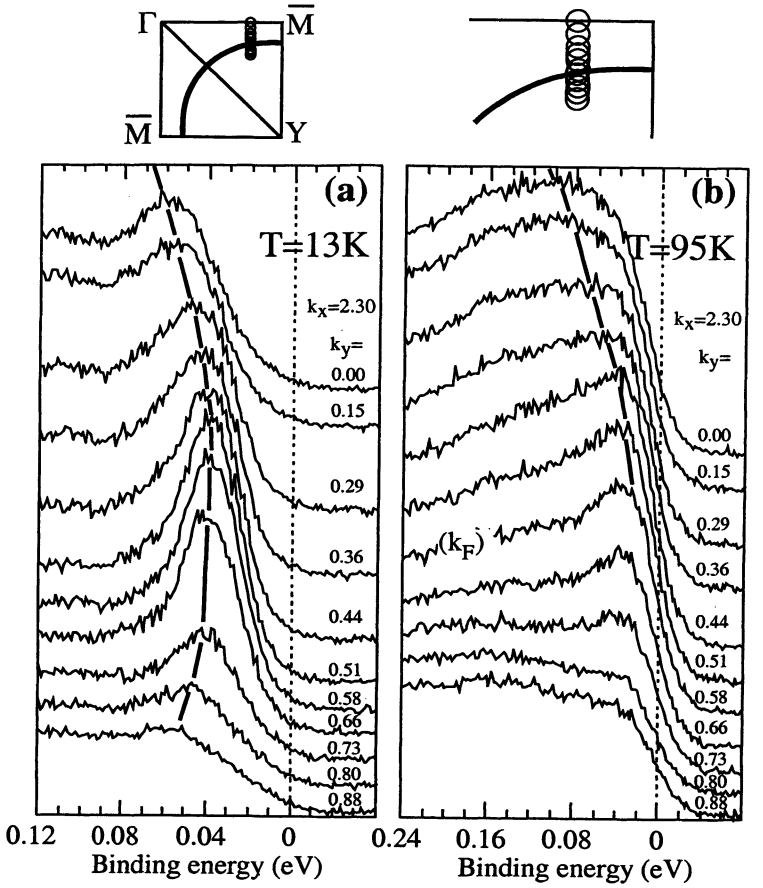

Fig. 5.20. (a) Superconducting state and (b) normal state EDC's for a near optimal $T_c = 87$K Bi2212 sample for a set of **k** values (in units of $1/a$) shown in the Brillouin zone at the top. Note the different binding energy scales in panels (a) and (b)

5.5.2 Quantitative Gap Estimates

The first photoemission measurements of the SC gap in the cuprates was by Imer *et al.* [72] using angle–integrated photoemission, and by Olson and coworkers [73] using angle–resolved photoemission. The first identification of a large gap anisotropy consistent with d–wave pairing was made by Shen and coworkers [70]. Ding *et al.* [22,71] subsequently made quantitative fits to the SC state spectral function to study the gap anisotropy in detail.

We now discuss the quantitative extraction of the gap at low temperatures ($T \ll T_c$) following Ding *et al.* [71]. In Fig. 5.23, we show the $T = 13$K EDCs for an 87K T_c sample for various points on the main band FS in the Y–quadrant. Each spectrum shown corresponds to the minimum observable

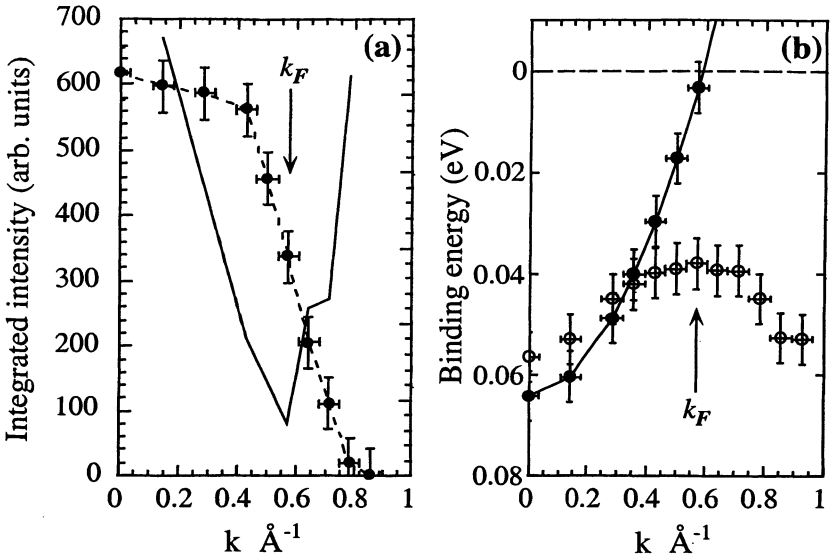

Fig. 5.21. (a) Integrated intensity versus **k** from the normal state data of Fig. 5.20 (b) shown by black dots gives information about the momentum distribution $n(\mathbf{k})$. The derivative of the integrated intensity is shown by the black curve (arbitrary scale). The Fermi surface crossing $\mathbf{k} = \mathbf{k}_F$ is identified by the minimum in the derivative. (b) Normal state dispersion (closed circles) and SC state dispersion (open circles) obtained from EDC's of Fig. 5.20. Note the back–bending of the SC state dispersion for **k** beyond $\mathbf{k}_F$ which is a clear indication of particle–hole mixing. The SC state EDC peak position at $\mathbf{k}_F$ is an estimate of the SC gap at that point on the Fermi surface

gap along a set of **k** points normal to the FS, obtained from a dense sampling of **k**–space [74]. We used 22 eV photons in a ΓY $\perp$ polarization, with a 17 meV (FWHM) energy resolution, and a **k**–window of radius $0.045\pi/a^*$.

The simplest gap estimate is obtained from the mid–point shift of the leading edge of Bi2212 relative to a good metal (here Pt) in electrical contact with the sample. This has no obvious quantitative validity, since the Bi2212 EDC is a spectral function while the polycrystalline Pt spectrum (dashed curve in Fig. 5.22) is a weighted density of states whose leading edge is an energy–resolution limited Fermi function. We see that the shifts (open circles in Fig. 5.23) indicate a highly anisotropic gap which vanishes in the nodal directions, confirming earlier results by Shen *et al.* [70]. These results are qualitatively similar to one obtained from the fits described below.

Next we turn to modeling [22,71] the SC state data in terms of spectral functions. It is important to ask how can we model the non–trivial line shape (with the dip–hump structure at high ω) in the absence of a detailed theory, and, second, how do we deal with the extrinsic background? We argue as

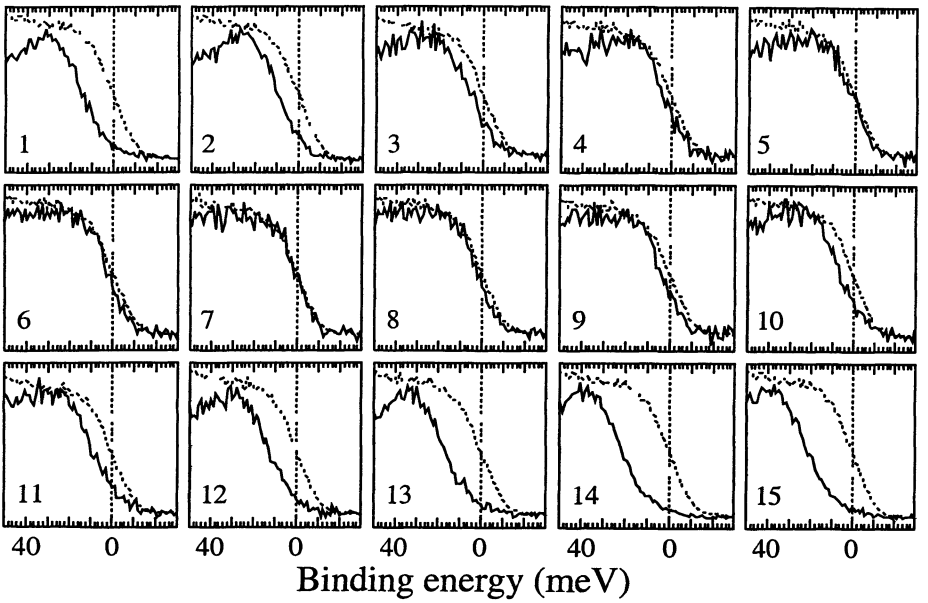

Fig. 5.22. Bi2212 spectra (solid lines) for an 87K T_c sample at 13K and Pt spectra (dashed lines) versus binding energy (meV) along the Fermi surface in the Y quadrant. The photon polarization and BZ locations of the data points are shown in inset to Fig. 5.23

follows: in the large gap region near $(\pi, 0)$, we see a linewidth collapse for frequencies smaller than $\sim 3\Delta$ upon cooling well below T_c. Thus for estimating the SC gap at the low temperature, it is sufficient to look at small frequencies, and to focus on the coherent piece of the spectral function with a resolution–limited leading edge. (Note this argument fails at higher temperatures, e.g., just below T_c). This coherent piece is modeled by the BCS spectral function, Eq. (5.11).

The effects of experimental resolution are taken into account via

$$\tilde{I}(\mathbf{k},\omega) = I_0 \int_{\delta\mathbf{k}} d\mathbf{k}' \int_{-\infty}^{+\infty} d\omega' R(\omega-\omega') f(\omega') A(\mathbf{k}',\omega') \,, \tag{5.12}$$

where $R(\omega)$, the energy resolution, is a normalized Gaussian and $\delta\mathbf{k}$ is the $\mathbf{k}$–window of the analyzer. In so far as the fitting procedure is concerned, all of the incoherent part of the spectral function is lumped together with the experimental background into one function which is added to the $\tilde{I}$ above. Since the gap is determined by fitting the resolution–limited leading edge of the EDC, its value is insensitive to this drastic simplification. To check this, we have made an independent set of fits to the small gap data where we do not

use any background fitting function, and only try to match the leading edges, not the full spectrum. The two gap estimates are consistent within a meV. Once the insensitivity of the gap to the assumed background is established, there are only two free parameters in the fit at each $\mathbf{k}$: the overall intensity I_0 and the gap $|\Delta|$; the dispersion $\epsilon_{\mathbf{k}}$ is known from the normal state study, the small linewidth Γ is dominated by the resolution.

The other important question is the justification for using a coherent spectral function to model the rather broad EDC along and near the zone diagonal. As far as the early data being discussed here is concerned, such a description is self–consistent [22, 71], though perhaps not unique, with the entire width of the EDC accounted for by the large dispersion (of about 60 meV within our $\mathbf{k}$–window) along the zone diagonal. More recent data taken along $(0,0)$ to (π,π) with a momentum resolution of $\delta\mathbf{k} \simeq 0.01\pi/a^*$ fully justifies this assumption by resolving coherent nodal quasiparticles in the SC state; see Section 5.7.7.

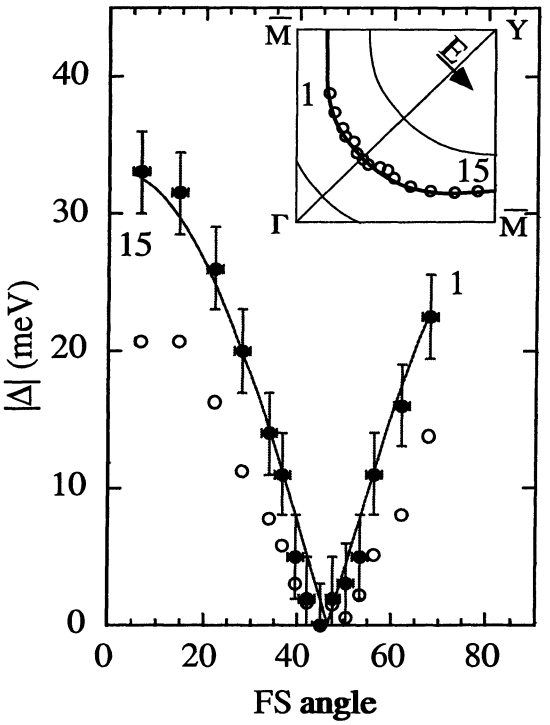

Fig. 5.23. Y quadrant gap in meV versus angle on the Fermi surface (filled circles) from fits to the data of Fig. 5.22. Open symbols show leading edge shift with respect to Pt reference. The solid curve is a d–wave fit to the filled symbols

The gaps extracted from fits to the spectra of Fig. 5.22 are shown as filled symbols in Fig. 5.23. For a detailed discussion of the the error bars (both on the the gap value and on the Fermi surface angle), and also of sample–to–sample variations in the gap estimates, we refer the reader to Ref. [71]. The angular variation of the gap obtained from the fits is in excellent agreement with $|\cos(k_x) - \cos(k_y)|$ form. The ARPES experiment cannot of course measure the phase of the order parameter, but this result is in strong support of $d_{x^2-y^2}$ pairing [69]. Such an order parameter arises naturally in theories with strong correlations and/or antiferromagnetic spin fluctuations [75]. Moreover, the functional form of the anisotropy we find is consistent with electrons in the Cooper pair residing on neighboring Cu sites. That is, ARPES gives information on the spatial range of the pair interaction which is difficult to obtain from other techniques.

Finally we comment on the temperature dependence of the gap. Unfortunately with increasing temperature the linewidth grows and a simple BCS–type modeling (valid for $T \ll T_c$) of just the coherent part of the spectral function is not possible. While T–dependence of the leading edge can certainly be used as a rough guide, this estimate is affected by both the gap and the linewidth (the diagonal self–energy). We will discuss methods for modeling the SC state data in Section 5.7.

For completeness, we add a remark clarifying the earlier observation of two nodes in the X–quadrant [22], and the related non–zero gap along ΓX in the $\Gamma X||$ geometry [22, 76]. It was realized soon afterwards that these observations were related to gaps on the superlattice bands [46], and not on the main band. To prove this experimentally, the X–quadrant gap has been studied in the $\Gamma X \perp$ geometry [71] and found to be consistent with Y–quadrant $d_{x^2-y^2}$ result described above.

5.5.3 Doping Dependence of the SC Gap

There are two important issues to be addressed about the doping dependence: How does the maximum gap change with doping? and how does the gap anisotropy evolve with doping?

ARPES results on underdoped samples show that the maximum gap *increases* [77, 78] with decreasing hole concentration. For a recent compilation of gap versus doping results [62] in Bi2212, see Fig. 5.50 of Section 5.7.6. Identical results have also been obtained by tunneling spectroscopy [79]. This was at first quite unexpected since T_c decreases as one underdopes from optimality. The fact that $2\Delta/k_BT_c$ is not constant with doping and can become an order of magnitude larger than its BCS weak–coupling value is very clear evidence that the SC phase transition on the underdoping side is qualitatively different from the BCS transition, a point that we will return to in the next Section on pseudogaps.

We next turn to the question of the SC gap anisotropy as a function of doping. In this case it is the behavior of the gap in the vicinity of the

node which is the most important since all low temperature $T \ll T_c$ thermodynamic and transport properties are controlled by thermal excitation of quasiparticles in the vicinity of the nodes (where the SC gap vanishes on the Fermi surface). These low energy excitations have a Dirac–like spectrum $E(\mathbf{k}) = \sqrt{v_F^2 k_\perp^2 + v_2^2 k_\parallel^2}$ where $k_\perp$ ($k_\parallel$) are the components of the $\mathbf{k}$ perpendicular (tangential) to the Fermi surface, and measured from the nodal point. Here v_F is the nodal Fermi velocity controlling the dispersion perpendicular to the Fermi surface, while $v_2 = \partial \Delta_\mathbf{k}/\partial k_\parallel$ is the the gap slope at the nodal point.

The density of states for low energy excitations is then given by $N(\omega) = 2\omega/(\pi v_F v_2)$ for $\omega \ll \Delta$ (in units where $\hbar = 1$). This leads to characteristic temperature dependences for various low temperature properties with coefficients essentially determined by v_F and v_2. Specifically for $T \ll T_c$, the specific heat goes like $C(T) = c_1 T/(v_F v_2)$; the thermal conductivity goes like $\kappa(T)/T = c_2\,(v_F/v_2 + v_2/v_F)$ and the superfluid density goes like $\rho_s(T) = \rho_s(0) - c_3(v_F/v_2)T$. Here c_1 and c_2 are known constants while c_3 contains (apriori unknown) multiplicative Fermi liquid parameters [80, 81].

Clearly ARPES has a unique ability to independently measure both v_F, using the dispersion of the nodal quasiparticle, and v_2, using the slope of the SC gap at the node. One can then make detailed comparison with various bulk measurements, and thereby test the validity of the description of the low temperature properties of the SC state in terms of weakly interacting quasiparticles [80–82]. This is particularly important given the lack of sharply defined quasiparticles in the normal state of the cuprates.

With these motivations in mind, a detailed measurement of the shape of the superconducting gap in Bi2212 as a function of doping was carried out by Mesot *et al.* [83]. Although these measurements were carried out at a time when the energy and momentum resolutions were lower than those currently available, they still give useful information because the gap over the full range of angles over the irreducible zone was measured. Using the simple BCS spectral function fits (described above) and taking into account the measured dispersion and the known energy and momentum resolutions, Mesot *et al.*found the results shown in Fig. 5.24. The simple d–wave gap $\Delta = \Delta_0 \cos(2\phi)$ (Fig. 5.23) is modified by the addition of the first harmonic $\Delta_\mathbf{k} = \Delta_\mathbf{max}[B\cos(2\phi) + (1-B)\cos(6\phi)]$, with $0 \le B \le 1$. Note that the $\cos(6\phi)$ term in the Fermi surface harmonics can be shown to be closely related to the tight binding function $\cos(2k_x) - \cos(2k_y)$, which represents next nearest neighbours interaction, just as $\cos(2\phi)$ is closely related to the near neighbor pairing function $\cos(k_x) - \cos(k_y)$. From Fig. 5.24 we find that while the overdoped data are consistent with $B \simeq 1$, the parameter B decreases as a function of underdoping.

Before discussing the doping dependence of the results in detail, let us first look at the comparisons between ARPES and other probes near optimality. Low temperature specific heat data on Bi2212 is not available, but the

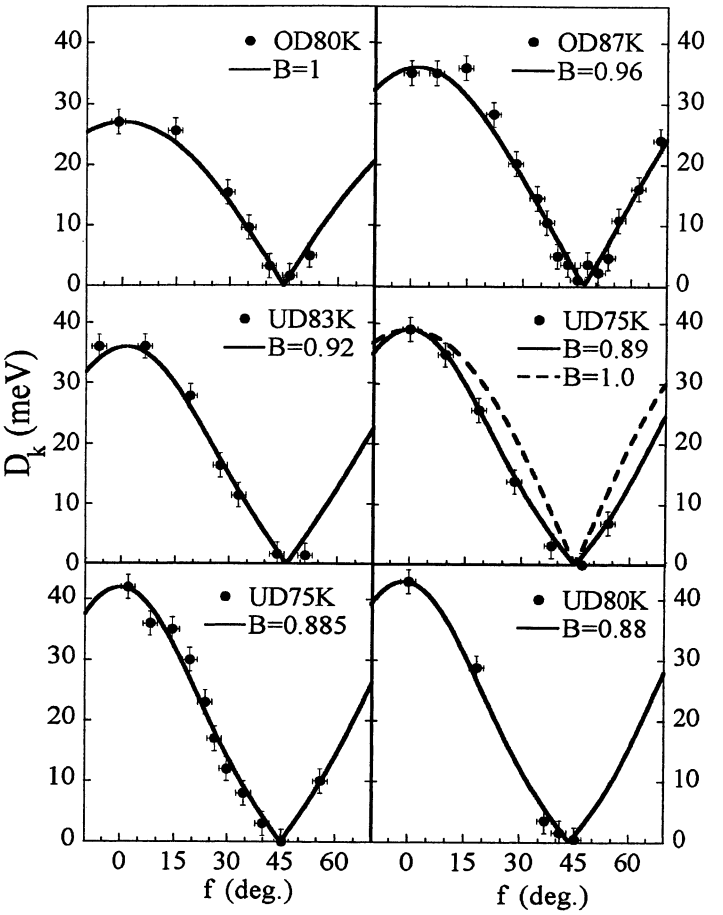

Fig. 5.24. Values of the superconducting gap as a function of the Fermi surface angle ϕ obtained for a series of Bi2212 samples with varying doping. Note two different UD75K samples were measured, and the UD83K sample has a larger doping due to sample aging [42]. The solid lines represent the best fit using the gap function: $\Delta_k = \Delta_{\max}[B\cos(2\phi) + (1-B)\cos(6\phi)]$ as explained in the text. The dashed line in the panel of an UD75K sample represents the gap function with B=1

thermal conductivity has been measured by Taillefer and coworkers [82] on an optimal $T_c = 89$K sample. Now one can use the κ/T formula given above with the coefficient $c_2 = k_B^2 n/3\hbar d$, where n/d is the stacking density of CuO_2 planes. It is important to note that c_2 is *not* renormalized by either vertex corrections or Fermi liquid parameters [81]. Thus one infers $v_F/v_2 = 19$ from the thermal transport data [82], which is in remarkable agreement with the ARPES estimate [83] of $v_F/v_2 \simeq 20$ coming from the measured values of $v_F = 2.5 \times 10^7$ cm/s and $v_2 = 1.2 \times 10^6$ cm/s for the near optimal $T_c = 87$K

sample of Fig. 5.24. (We note that in Ref. [83] we used the notation v_Δ for one-half the gap slope at the node, which is related to v_2 defined above by $v_2 = 2v_\Delta/\hbar k_F$.)

The comparison of ARPES results with the slope of the superfluid density $\rho_s \sim 1/\lambda^2$ obtained from penetration depth measurements is more complicated, as discussed in more detail in Ref. [83], for two reasons. Experimentally, there seem to be discrepancies between the $d\lambda^{-2}/dT$ results of various groups, and theoretically the slope of ρ_s is renormalized by doping-dependent Fermi liquid parameters [80,81] which are not known apriori. These parameters characterize the residual interactions between the nodal quasiparticles in the superconducting state. Thus, e.g., even at optimality the slope $d\lambda^{-2}/dT$ obtained using the ARPES estimate of v_F/v_2 and ignoring Fermi liquid renormalization is almost three times as large as the experimentally measured value of $d\lambda^{-2}/dT$ in near optimal Bi2212 [84]. This indicates the importance of Fermi liquid renormalizations in order to make a quantitative comparison. For more details on the doping dependence of these renormalizations, see Ref. [80,83,85].

Finally, let us return to the doping dependence of the results of Fig. 5.24. In contrast to the maximum gap (at the $(\pi,0)-(\pi,\pi)$ Fermi surface crossing) increasing as a function of underdoping, noted earlier, we see the gap slope at the node, which determines v_2, decreasing with underdoping. This is a result of the doping dependence of the B parameter introduced above.

This surprising observation raises several questions. First, could the flattening at the node be, in fact, evidence for a "Fermi arc", a line of gapless excitations, in the underdoped materials, especially since such arcs are seen above T_c (See Sect. 4.6.3 for further discussion of Fermi arcs in underdoped materials). Given the error bars on gap estimates in Fig. 5.24, it is impossible to rule out arcs in all the samples. Nevertheless, it is clear that there are samples (especially OD87K, UD80K and UD75K) where there is clear evidence in favor of a point node rather than an arc at low temperatures. Furthermore, it is very important to note that a linear T dependence of $\rho_s(T)$ at low temperature, for all doping levels, in clean samples gives independent evidence for point nodes, at least in YBCO [86].

Second, is the change in gap anisotropy intrinsic, or related to impurity scattering [87]? We can eliminate the latter explanation on two grounds. The maximum gap *increases* as the doping is reduced, opposite to what would be expected from pair breaking due to impurities. Also, impurity scattering is expected to lead to a characteristic "tail" to the leading edge [88], for which there is no evidence in the observed spectra.

Thus the flattening near the nodes with underdoping does appear to be an intrinsic feature which may be related to the increased importance of longer range pairing interactions as one approaches the insulator. It would be of great interest to study the details of the doping dependence of the

gap anisotropy with the new Scienta detectors which have greatly improved energy and momentum resolution.

5.6 Pseudogap

In this Section we describe one of the most fascinating developments in the study of high T_c superconductors: the appearance of a pseudogap above T_c which is seen most prominently on the underdoped side of the cuprate phase diagram. Briefly the "pseudogap" phenomenon is the loss of low energy spectral weight in a window of temperatures $T_c < T < T^*$; see Fig. 5.25. The pseudogap regime has been probed by many techniques like NMR, optics, transport, tunneling, μSR and specific heat; for reviews and references, see Refs. [89,90]. ARPES, with its unique momentum–resolved capabilities, has played a central role in elucidating the pseudogap phenomenon [42,91–94].

We will discuss in this Section ARPES results on the anisotropy of the pseudogap, its T–dependence, its doping dependence, and its effect on the normal state Fermi surface. We emphasize that for the most part we will focus on the "low energy" or leading edge pseudogap, and only mention ARPES evidence for the "high energy pseudogap" toward the end. We will conclude the Section with a summary of the constraints put by the ARPES data on various theoretical descriptions of the pseudogap.

5.6.1 Pseudogap near $(\pi, 0)$

In the underdoped materials, T_c is suppressed by lowering the carrier (hole) concentration as shown in Fig. 5.25. In the samples used by our group [42,93,94] underdoping was achieved by adjusting the oxygen partial pressure during annealing the float–zone grown crystals. These crystals also have structural coherence lengths of at least 1,250$\mathring{A}$ as seen from x–ray diffraction, and optically flat surfaces upon cleaving, similar to the slightly overdoped T_c samples discussed above. We denote the underdoped (UD) samples by their onset T_c: the 83K sample has a transition width of 2K and the highly underdoped 15K and 10K have transition widths > 5K. Other groups have also studied samples where underdoping was achieved by cation substitution [91,92].

We now contrast the remarkable properties of the underdoped samples with the near–optimal Bi2212 samples which we have been mainly focusing on thus far. We will first focus on the behavior near the $(\pi, 0)$ point where the most dramatic effects occur, and come back to the very interesting $\mathbf{k}$–dependence later. In Fig. 5.26 [78] we show the T–evolution of the ARPES spectrum at the $(\pi, 0) \rightarrow (\pi, \pi)$ Fermi crossing for an UD 83K sample. At sufficiently high temperature, the leading edge of the UD spectrum at $\mathbf{k}_F$ and the reference Pt spectrum coincide, but below a crossover temperature $T^* \simeq$ 180K the leading edge midpoint of the spectrum shifts below the chemical potential. In Fig. 5.26 one can clearly see a loss of low energy spectral weight

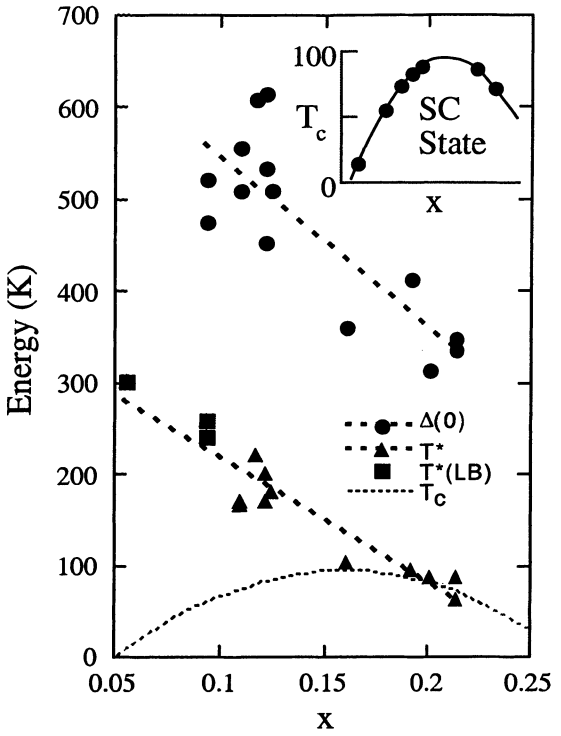

Fig. 5.25. T^* (triangles for determined values and squares for lower bounds) and T_c (dashed line) as a function of hole doping x. The x values for a measured T_c were obtained by using the empirical relation $T_c/T_c^{max} = 1 - 82.6(x - 0.16)^2$ [95] with T_c^{max} =95 K. Also shown is the low temperature (maximum) superconducting gap $\Delta(0)$ (circles). Note the similar doping trends of $\Delta(0)$ and T^*

at 120K and 90K. It must be emphasized that this gap–like feature is seen in the normal (i.e., non–superconducting) state for $T_c = 83K < T < T^* = 180K$.

The doping dependence of the temperature T^*, below which a leading–edge pseudogap appears near $(\pi, 0)$, is shown in Fig. 5.25. Remarkably T^* increases with underdoping, in sharp contrast with T_c, but very similar to the low temperature SC gap, a point we will return to at the end of the Section. The region of the phase diagram between T_c and T^* is called the pseudogap region.

It is important to emphasize that our understanding of the lightly UD samples (e.g., the UD 83K sample) is the best among the UD materials. In such samples all three regimes — the SC state below T_c, the pseudogap regime between T_c and T^* and the gapless "normal" regime above T^* — can be studied in detail. In contrast, in the heavily UD samples (e.g. the UD 10K and UD 15K samples), not only is the SC transition broad, one also has such

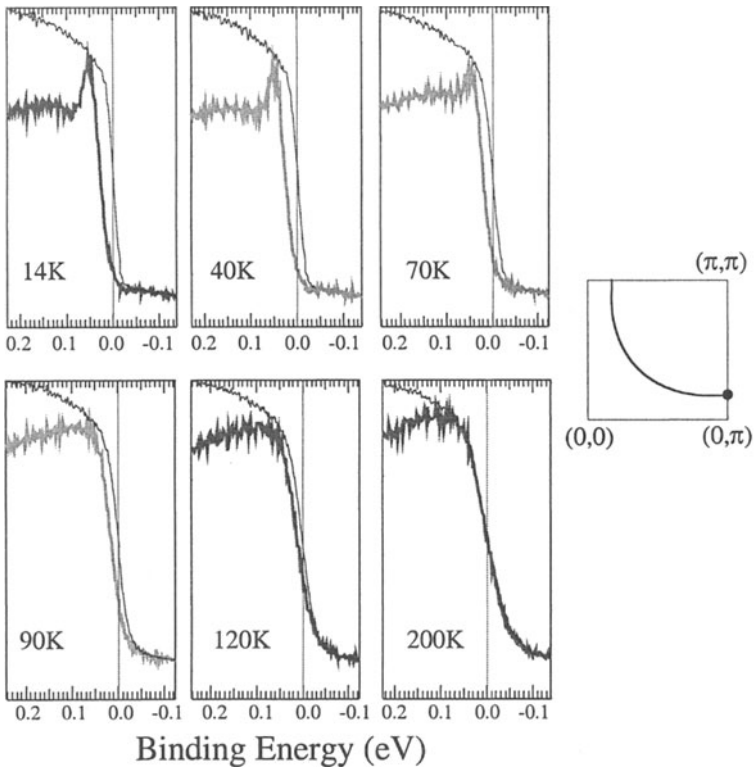

Fig. 5.26. ARPES spectra along the $(\pi, 0) \rightarrow (\pi, \pi)$ direction for an 83 K underdoped sample at various temperatures (solid curves). The thin curves in each panel are reference spectra from polycrystalline Pt used to accurately determine the zero of binding energy at each temperature

low T_c's and such high T^*'s that only the pseudogap regime is experimentally accessible. Nevertheless, the results on the heavily underdoped samples appear to be a natural continuation of the weakly underdoped materials and the results (the trends of gap and T^*) on the low T_c samples are in qualitative agreement with those obtained from other probes (see Ref. [89,90]).

The T–dependence of the leading–edge midpoint shift appears to be completely smooth through the SC transition T_c. In other words, the normal state pseudogap evolves smoothly into the SC gap below T_c. Nevertheless, there *is* a characteristic change in the lineshape in passing through T_c associated with the appearance of of a sharp feature below T_c in Fig. 5.26. This can be identified as the coherent quasiparticle peak for $T \ll T_c$. The existence of a SC state quasiparticle peak is quite remarkable given that the normal state spectra of UD materials are even broader than at optimality, and in fact become progressively broader with underdoping. In fact, the low temperature

SC state spectra near $(\pi, 0)$ in the UD systems (see Fig. 5.50 of Section 5.7.6) are in many ways quite similar to those at optimal doping, with the one crucial difference that the spectral weight in the coherent quasiparticle peak diminishes rapidly with underdoping [96, 97].

5.6.2 Anisotropy of the Pseudogap

We have already indicated that the pseudogap above T_c near the $(\pi, 0)$ point of the zone evolves smoothly through T_c into the large SC gap below T_c, and thus the two also have the same magnitude. Since the SC gap has the d–wave anisotropy (discussed in detail in the preceding Section), it is natural to ask: what is the **k**–dependence of the pseudogap above T_c?

The first ARPES studies [91–93] showed that the pseudogap is also highly anisotropic and has a **k**–dependence which is very similar to that of the SC gap below T_c. Later work [94] further clarified the situation by showing that the anisotropy has a very interesting temperature dependence. We now describe these developments in turn.

In Fig. 5.27 [93] we plot the leading edge shifts for three samples at 14K: the slightly overdoped 87K and UD 83K samples are in their SC states while the UD 10K sample is in the pseudogap regime. The gap estimate for each sample was made on the "minimum gap locus" (explained earlier in the context of the SC gap; see further below). The large error bars on the UD 10K sample come from the difficulty of accurately locating the midpoint of a broad spectrum. Also there is a flattening of the gap near the node, a feature that we discussed earlier for the SC gap in UD samples.

The remarkable conclusion is that the normal state pseudogap has a very similar **k**–dependence and magnitude as the SC gap below T_c.

5.6.3 Fermi Arcs

The T–dependence and anisotropy of the pseudogap was investigated in more detail in Ref. [94] motivated by the following question. Normal metallic systems are characterized by a Fermi surface, and optimally doped cuprates are no different despite the absence of sharp quasiparticles (see Section 5.4). On the underdoped side of the phase diagram, however, how does the opening of pseudogap affect the locus of low lying excitations in **k**–space?

In Fig. 5.28 we show ARPES spectra for an UD 83K sample at three **k** points on the Fermi surface for various temperatures. The superconducting gap, as estimated by the position of the sample leading edge midpoint at low T, is seen to decrease as one moves from point a near $(\pi, 0)$ to b to c, closer to the diagonal $(0, 0) \rightarrow (\pi, \pi)$ direction, consistent with a $d_{x^2-y^2}$ order parameter. At each **k** point the quasiparticle peak disappears above T_c as T increases, with the pseudogap persisting well above T_c, as noted earlier.

The striking feature which is apparent from Fig. 5.28 is that the pseudogap at different **k** points closes at different temperatures, with larger gaps

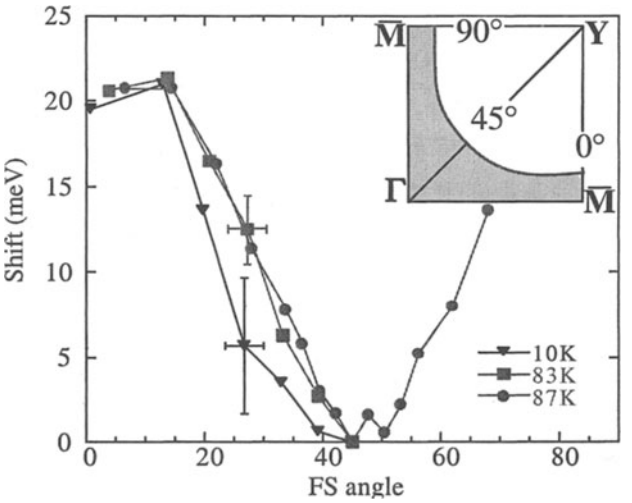

Fig. 5.27. Momentum dependence of the gap estimated from the leading-edge shift in samples with T_c's of 87K (slightly overdoped), 83K (UD) and 10K (UD), measured at 14K. For the sake of comparison between samples we made vertical offsets so that the shift at 45° is zero; the offsets are −3meV for the 83K and +2meV for the 10K sample. The inset shows the Brillouin zone with the large Fermi surface

persisting to higher T's. At point a, near $(\pi, 0)$, there is a pseudogap at all T's below 180K, at which the Bi2212 leading edge matches that of Pt. As discussed above, this defines T^* above which the the largest pseudogap has vanished within the resolution of our experiment, and a closed contour of gapless excitations — a Fermi surface — is obtained. The surprise is that if we move along this Fermi surface to point b the sample leading edge matches Pt at 120K, which is smaller than T^*. Continuing to point c, about halfway to the diagonal direction, we find that the Bi2212 and Pt leading edges match at an even lower temperature of 95K. In addition, spectra measured on the same sample along the Fermi contour near the $(0,0) \rightarrow (\pi, \pi)$ line shows no gap at any T (even below T_c) consistent with $d_{x^2-y^2}$ anisotropy.

One simple way to quantify the behavior of the gap is to plot the midpoint of the leading edge of the spectrum; see Fig. 5.28(e). We note that a leading edge midpoint at a negative binding energy, particularly for **k** point c, indicates the formation of a peak in the spectral function at $\omega = 0$ at high T. Further, we will say that the pseudogap has closed at a **k** point when the midpoint equals zero energy, in accordance with the discussion above. A clearer way of determining this will be presented below when we discuss the symmetrization method, but the results will be the same. From Fig. 5.28, we find that the pseudogap closes at point a at a T above 180K, at point b at 120 K, and at point c just below 95 K. If we now view these data as a function of decreasing T, the picture of Fig. 5.28(f) clearly emerges.

With decreasing T, the pseudogap first opens up near $(\pi, 0)$ and progressively gaps out larger portions of the Fermi contour. Thus one obtains gapless arcs which shrink as T is lowered, eventually leading to the four point nodes of the d–wave SC gap. The existence of such arcs is apparent from the first

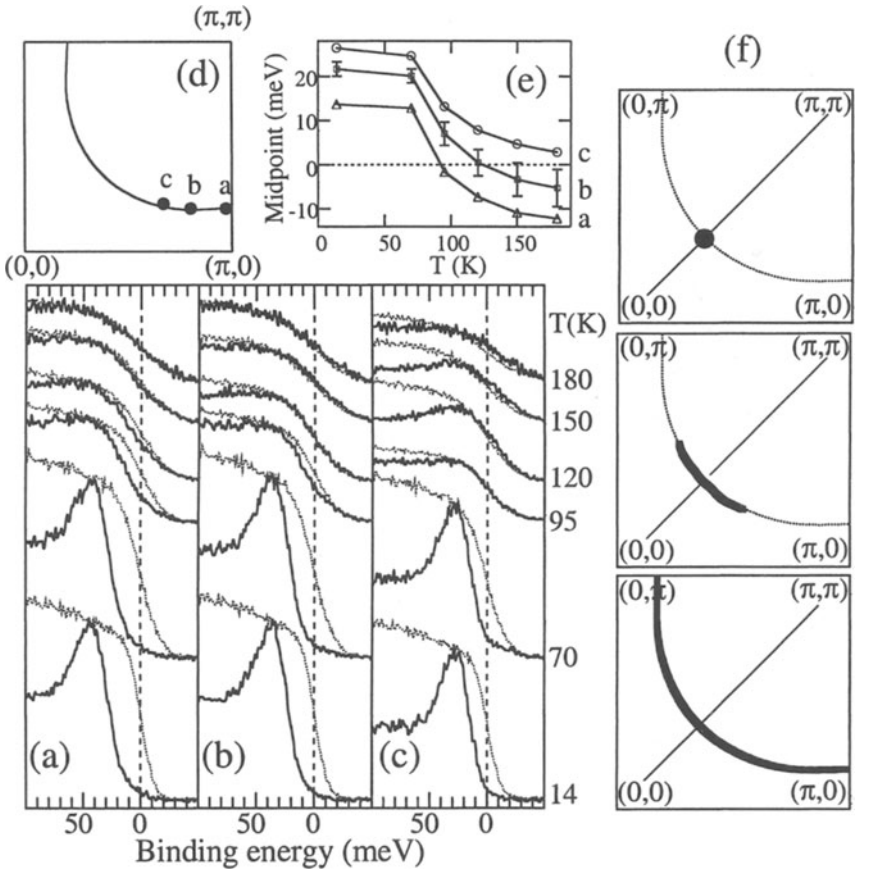

Fig. 5.28. (a,b,c): Spectra taken at three **k** points in the Y quadrant of the zone (shown in (d)) for an 83K underdoped Bi2212 sample at various temperatures (solid curves). The dotted curves are reference spectra from polycrystalline Pt (in electrical contact with the sample) used to determine the chemical potential (zero binding energy). Note the closing of the spectral gap at different T for different **k**'s, which is also apparent in the plot (e) of the midpoint of the leading edge of the spectra as a function of T. Panels (f) show a schematic illustration of the temperature evolution of the Fermi surface in underdoped cuprates. The d–wave node below T_c (top panel) becomes a gapless arc above T_c (middle panel) which expands with increasing T to form the full Fermi surface at T^* (bottom panel)

ARPES work on the pseudogap [91], where it was noted that the Fermi contours in the pseudogap phase did not extend all the way to the zone boundary (see Fig. 5.29). Whether the arcs shrink to a point precisely at T_c or below

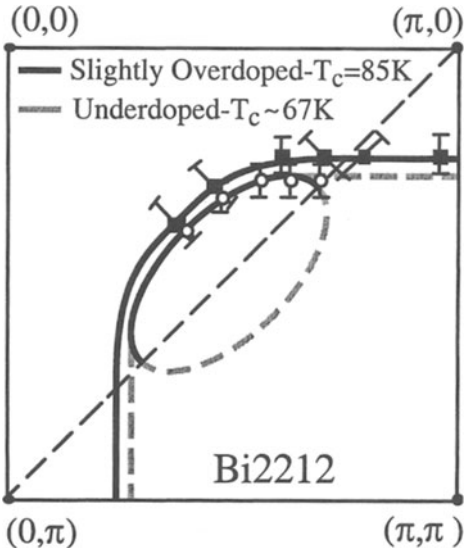

Fig. 5.29. Fermi level crossings from two Bi2212 samples of differing oxygen content. The entire zone can be reconstructed by fourfold rotation about (0,0) (from Ref. [91])

T_c is not clear from the existing data. As discussed in the preceding Section, we do believe that arcs do not survive deep into the SC state where there is point node at $T \ll T_c$ in clean samples, as also evidenced by the linear T drop in the superfluid density at low T.

We next turn to a powerful visualization aid that makes these results very transparent. This is the symmetrization method introduced in Ref. [94], which effectively eliminates the Fermi function f from ARPES data and permits us to focus directly on the spectral function A. Given ARPES data described by [21] $I(\omega) = \sum_{\mathbf{k}} I_0 f(\omega) A(\mathbf{k}, \omega)$ with the sum over a small momentum window about the Fermi momentum $\mathbf{k}_F$, we can generate the symmetrized spectrum $I(\omega) + I(-\omega)$. Making the reasonable assumption of particle–hole (p-h) symmetry for a small range of ω and $\epsilon_{\mathbf{k}}$, we have $A(\epsilon_{\mathbf{k}}, \omega) = A(-\epsilon_{\mathbf{k}}, -\omega)$ for $|\omega|, |\epsilon|$ less than few tens of meV. It then follows, using the identity $f(-\omega) = 1 - f(\omega)$, that $I(\omega) + I(-\omega) = \sum_{\mathbf{k}} I_0 A(\mathbf{k}, \omega)$ which is true even after convolution with a (symmetric) energy resolution function; for details see the appendix of Ref. [9]. The symmetrized spectrum coincides with the raw data for $\omega \leq -2.2 T_{eff}$, where $4.4 T_{eff}$ is the 10%-90% width

of the Pt leading edge, which includes the effects of both temperature and resolution. Non–trivial information is obtained for the range $|\omega| \leq 2.2T_{eff}$, which is then the scale on which p–h symmetry has to be valid. We have extensively checked this method, and studied in detail the errors introduced by incorrect determination of the chemical potential or of $\mathbf{k}_F$ (which lead to spurious narrow features in the symmetrized spectra), and the effect of the small (1° radius) $\mathbf{k}$–window of the experiment (which was found to be small).

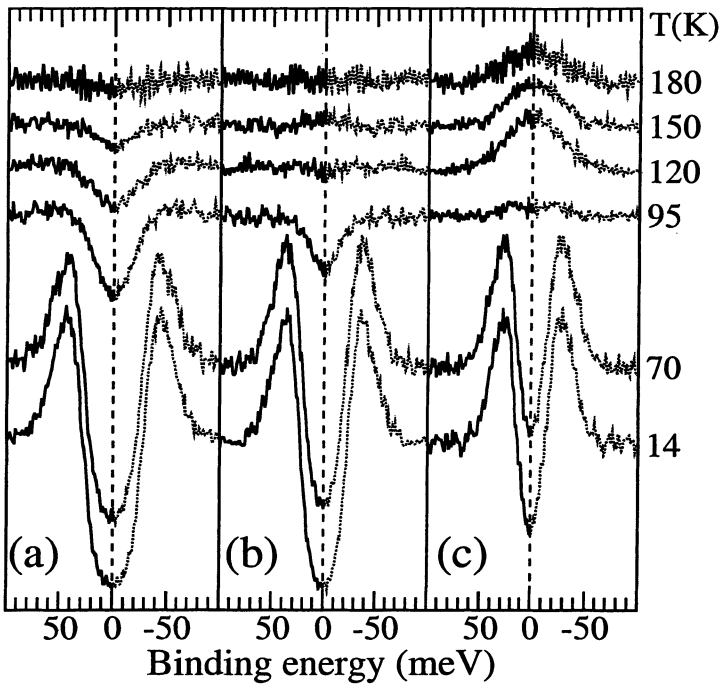

Fig. 5.30. Symmetrized spectra corresponding to the raw spectra (a,b,c) of Fig. 5.28. The gap closing in the raw spectrum of Fig. 5.28 corresponds to when the pseudogap depression disappears in the symmetrized spectrum. Note the appearance of a spectral peak at higher temperatures in c

In Fig. 5.30 we show symmetrized data for the UD 83K underdoped sample corresponding to the raw data of Fig. 5.28. To emphasize that the symmetry is put in by hand, we show the $\omega > 0$ curve as a dotted line. At $\mathbf{k}$ point a near $(\pi, 0)$ the sharp quasiparticle peak disappears above T_c but a strong pseudogap suppression, on the same scale as the superconducting gap, persists all the way up to 180K (T^*). Moving to panels b and c in Fig. 5.30 we again see pseudogap depressions on the scale of the superconducting gaps at those points, however the pseudogap fills up at lower temperatures: 120K at b and 95K at c. In panel c, moreover, a spectral peak at zero energy

emerges as T is raised. All of the conclusions drawn from the raw data in Fig. 5.28 are immediately obvious from the simple symmetrization analysis of Fig. 5.30.

There are many important issues related to these results that will be taken up in Section 5.7.3 where we describe modeling the electron self–energy in the pseudogap state. We will discuss there the remarkable T–dependent lineshape changes and the T–dependence of the gap itself. Here we simply note that, without any detailed modeling, the data [94] clearly show qualitative differences in the T–dependence at different $\mathbf{k}$–points. Near the $(\pi, 0)$ point the gap goes away with increasing temperature with the spectral weight filling–in, but no perceptible change in the gap scale with T. On the other hand, at $\mathbf{k}_F$ points halfway to the node, one sees a suppression of the gap scale with increasing temperature.

We conclude this discussion with a brief mention of the implications of our results. We believe that the unusual T–dependence of the pseudogap anisotropy will be a very important input in reconciling the different crossovers seen in the pseudogap regime by different probes. The point here is that each experiment is measuring a $\mathbf{k}$–sum weighted with a different set of $\mathbf{k}$–dependent matrix elements or kinematical factors (e.g., Fermi velocity). For instance, quantities which involve the Fermi velocity, like dc resistivity above T_c and the penetration depth below T_c (superfluid density), should be sensitive to the region near the zone diagonal, and would thus be affected by the behavior we see at $\mathbf{k}$ point c. Other types of measurements (e.g. specific heat and tunneling) are more "zone–averaged" and will have significant contributions from $\mathbf{k}$ points a and b as well, thus they should see a more pronounced pseudogap effect. Interestingly, other data we have indicate that the region in the Brillouin zone where behavior like $\mathbf{k}$ point c is seen shrinks as the doping is reduced, and thus appears to be correlated with the loss of superfluid density [98]. Further, we speculate that the disconnected Fermi arcs should have a profound influence on magnetotransport given the lack of a continuous Fermi contour in momentum space.

5.6.4 Evolution of the Fermi Surface with Doping

We now discuss the doping dependence of the normal state Fermi surface on the underdoped side of the phase diagram. The first issue to face up to is: can the Fermi arcs described above be a manifestation of a Fermi surface with small closed contours centered about $(\pi/2, \pi/2)$? Such hole–pockets enclosing x holes (per planar Cu) are suggested by some theories of lightly doped Mott insulators [99] as alternatives to the large Fermi surfaces containing $(1 + x)$ holes which would be consistent with the Luttinger counting.

The T–dependence of the arcs is by itself evidence against their being part of a pocket Fermi surface. Nevertheless, if there were such small hole pockets then one should observe two features in the ARPES data: a closure of the Fermi arc on the other side of $(\pi/2, \pi/2)$, which would be clear evidence for a

"shadow band"-like dispersion ((π, π)-foldback of the main band) in the UD samples. In a variety of UD samples we have carefully searched for both these features and found no evidence for either [42]. However this is a tricky issue, given the very broad spectra and possible materials problems in the highly UD samples. Nevertheless, given the available evidence, the gapless arcs that we observe [94] are simply an intermediate state in the smooth evolution of d-wave nodes into a full Fermi surface. This smooth evolution was carefully checked on an UD 83K sample where a dense mapping was done in $\mathbf{k}$ space at $T = 90$K, revealing only a small Fermi arc just above T_c.

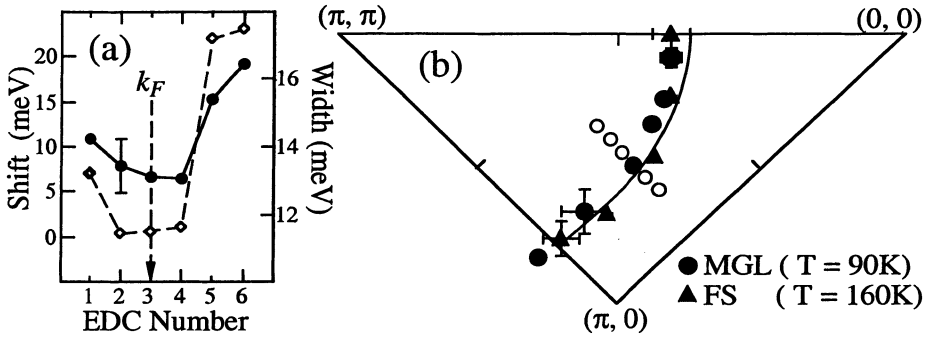

Fig. 5.31. (a) Midpoint shifts (dots) and widths (diamonds) for an UD 83K sample at a photon energy of 22 eV at 90K for a cut shown by the open dots in (b). (b) Fermi surface at 160K (solid triangles) and minimum gap locus at 90K (solid dots). Notice that the two surfaces coincide within error bars. The error bars represent uncertainties of Fermi crossings as well as possible sample misalignment. The solid curve is a rigid band estimate of the Fermi surface

The other issue related to the Fermi surface is: what is its doping dependence above T^* where the pseudogap effects are absent. While one can easily compare the near optimal and lightly UD Fermi surfaces, the rapid rise of T^* with underdoping does not permit us to address this question. However, one can study the "minimum gap locus" in any gapped state, in close analogy with the manner in which this was defined in the SC state; see Section 5.5.

There is also a more fundamental reason to study the "minimum gap locus" in the pseudogap regime. One wants to know whether the pseudogap is "tied" to the Fermi surface, or if it has some other characteristic momentum $\mathbf{Q}$ (unrelated to $\mathbf{k}_f$). In Fig. 5.31(a) [42] we follow the dispersion of an UD 83K sample in the pseudogap regime. Moving perpendicular to the (expected) Fermi surface from occupied to unoccupied states, one finds that that the dispersion first approaches the chemical potential and then recedes away from it. This locates a $\mathbf{k}$-point on the minimum gap locus. For a lightly UD sample we find in Fig. 5.31(b) that this locus in the pseudogap regime coincides,

within experimental error bars, with the Fermi surface determined above T^* where there is no pseudogap. The pseudogap is thus tied to the Fermi surface in the same way the SC gap is, and is in contrast with, say, charge or spin density waves, which are tied to other characteristic **Q** vectors.

In the more heavily underdoped samples, it is not possible to compare the minimum gap locus in the pseudogap state with the Fermi surface above T^*, or the minimum gap locus below T_c, since the latter two are not measurable with T^* too high and T_c too low. Nevertheless, if one *assumes*, by continuity, that the minimum gap locus in the pseudogap state gives information about the Fermi surface that got gapped out, then even for an highly UD sample one finds a large underlying Fermi surface, satisfying the Luttinger count of $(1 + x)$ holes per planar Cu [42] as shown in Fig. 5.32.

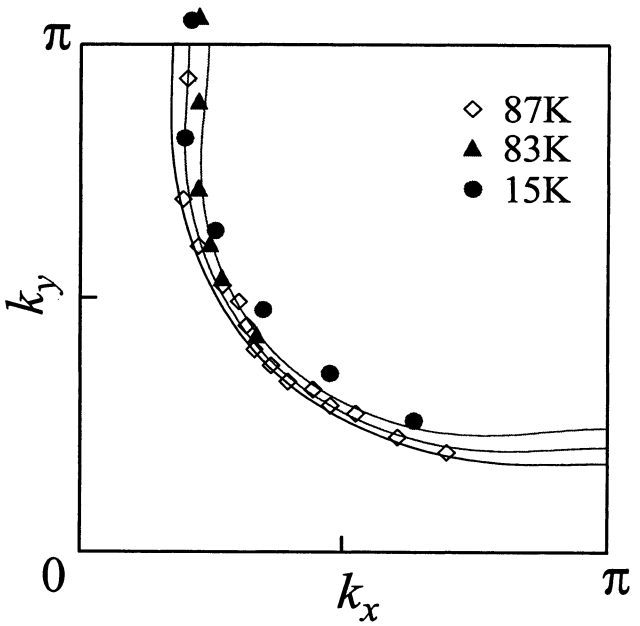

Fig. 5.32. Fermi surfaces of the 87K, 83K, and 15K samples. All surfaces enclose a large area consistent with the Luttinger count (see text). The solid lines are tight binding estimates of the Fermi surface at 18%, 13%, and 6% doping assuming rigid band behavior

The same conclusion has been recently reached by the Dresden group [43]. Fig. 5.33 reproduces their Fermi energy intensity maps as a function of doping, where a large Fermi surface (plus its shadow band image) is always visible. They argue, though, that the volume is not quite 1+x, and they attribute this difference to the presence of bilayer splitting.

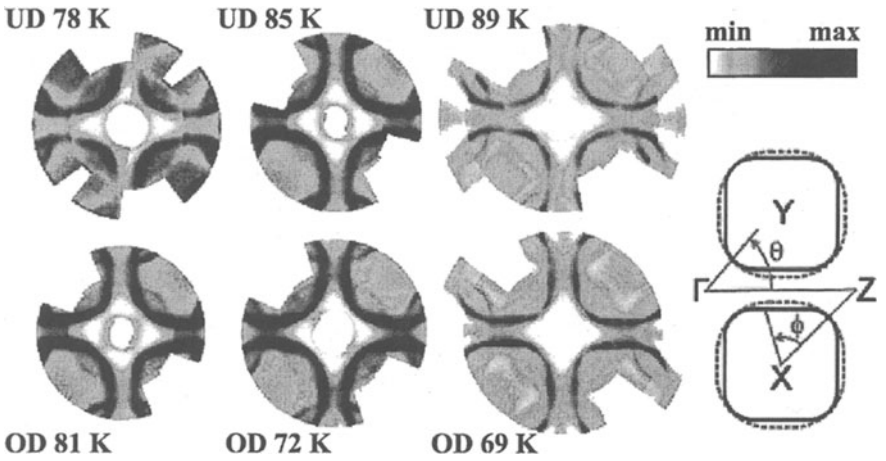

Fig. 5.33. Basal plane projection of the normal–state (300 K) Fermi surface of Bi(Pb)–2212 from high–resolution ARPES. The E_F intensity (normalized to the signal at $\omega = 0.3$ eV) is shown in grayscale. The T_c of each sample is indicated. The raw data cover half of the grey–black area of each map and have been rotated by 180 around the Γ point to give a better k–space overview. The line dividing raw and rotated data runs almost vertically for the UD76K map and from top left to bottom right in all other maps. The sketch shows the Fermi surface for the OD69K data set as black barrel–like shapes defined by joining the maxima of fits to the normalized E_F MDCs (from Ref. [43])

5.6.5 Low Energy vs High Energy Pseudogaps

In all of the preceding discussion we have focussed on the "low energy" or leading–edge pseudogap. It is important to point out that the phrase pseudogap is (somewhat confusingly) also used to describe a higher energy feature, which we call the "high energy pseudogap".

The presence of a high energy pseudogap was evident in the first ARPES work on the pseudogap, reproduced in Fig. 5.34 [91]. As the doping is reduced from optimal doped, a gap opens up in a region around the $(\pi, 0)$ points of the zone. The energy of this gap is significantly higher than the leading edge gap emphasized in later work [92, 93]. The resulting dispersion of this high energy feature looks reminiscent of what is expected for a spin density wave gap. As the doping is further reduced, an energy gap then opens up along the (π, π) direction, and the material becomes truly insulating.

In Fig. 5.35 [62] we show the temperature dependence of the $(\pi, 0)$ spectrum for an UD 89K sample. Note that there is no coherent quasiparticle peak until the system is cooled below T_c, with only a broad incoherent spectrum observed for all $T > T_c$. The leading edge pseudogap which develops below T^* is difficult to see on the energy scale of this figure; the midpoint shift at 135 K is 3 meV. However, a higher energy feature can easily be iden-

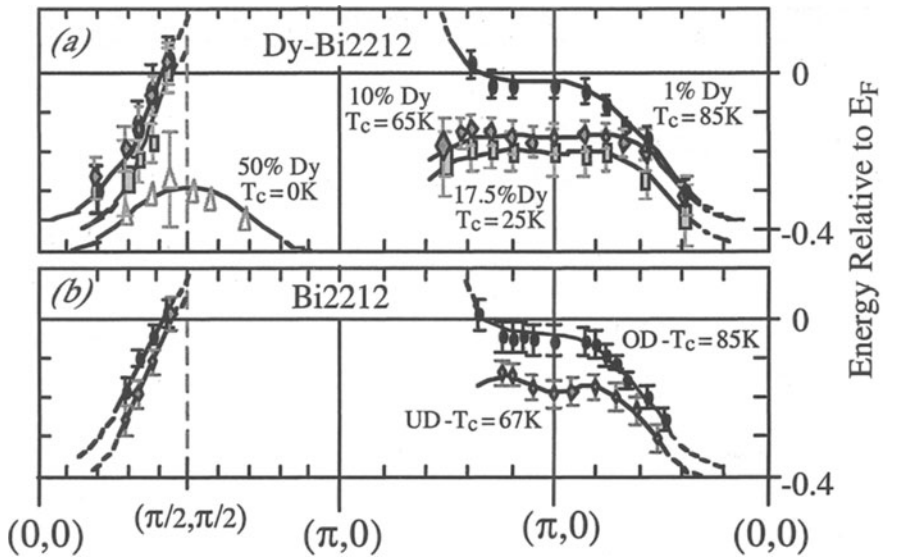

Fig. 5.34. (a),(b) Map peak centroids vs k for $Bi_2Sr_2Ca_{1-x}Dy_xCu_2O_{8+\delta}$ thin films and deoxygenated $Bi_2Sr_2CaCu_2O_{8+\delta}$ bulk samples, respectively, with various hole doping levels. (a) Filled oval, 1% Dy near optimal doping with T_c = 85 K; gray diamond, 10% Dy underdoped with T_c = 65 K; gray rectangular, 17.5% Dy underdoped with T_c = 25 K; triangle, 50% Dy insulator. (b) Filled oval, 600 air annealed slightly overdoped with T_c = 85 K; gray diamond, 550 argon annealed underdoped with T_c = 67 K (from Ref. [91])

tified by a change in slope of the spectra as function of binding energy; this is also very clear in the data of Fig. 5.48 of Section 5.7.6. At the highest temperature $T = 247$K this feature is just due to the Fermi function cutoff, but in the pseudogap regime, this feature actually represents the onset of loss of spectral weight on a high energy scale, and hence may be called the "high energy pseudogap". It can also be seen from Fig. 5.35 that the energy scale of this feature is very similar to that of the well–known $(\pi, 0)$–hump of the peak–dip–hump structure seen in the SC state. This connection will be discussed in detail in Section 5.7.6 where we also argue that the high energy pseudogap and the hump have similar dispersions [62].

5.6.6 Origin of the Pseudogap?

We conclude with a summary of ARPES results on the pseudogap and a brief discussion of its theoretical understanding.

As described above, the low–energy (leading edge) pseudogap has the following characteristics.

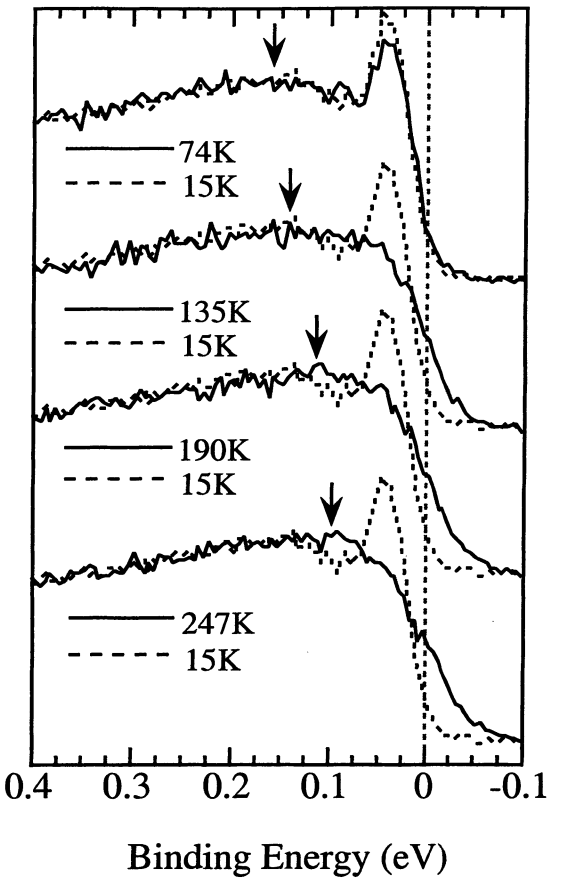

Fig. 5.35. Spectra at the $(\pi, 0)$ point for an UD 89K sample at various temperatures compared with the low temperature (15K) spectrum. The position of the high energy feature is marked by an arrow

- The magnitude of the pseudogap near $(\pi, 0)$, i.e., the scale of which there is suppression of low energy spectral weight above T_c, is the same as the maximum SC gap at low temperatures. Further both have the same doping dependence.
- There is a crossover temperature scale T^* above which the full Fermi surface of gapless excitations is recovered. The pseudogap near $(\pi, 0)$ appears below T^*.
- The normal state pseudogap evolves smoothly through T_c into the SC gap as a function of decreasing temperature.
- The pseudogap is strongly anisotropic with **k**–dependence which resembles that of the d–wave SC gap. The anisotropy of the pseudogap seems

to be T–dependent leading to the formation of disconnected Fermi arcs below T^*.

- The pseudogap is "tied" to the Fermi surface, i.e., the minimum gap locus in the pseudogap regime coincides with the Fermi surface above T^* and the minimum gap locus deep in the SC state, at least in those samples where all three loci can be measured.

The simplest theoretical explanation of the pseudogap, qualitatively consistent with the ARPES observations, is that it arises to due pairing fluctuations above T_c [90, 100]. The SC gap increases with underdoping while T_c decreases. Thus in the underdoped regime T_c is not controlled by the destruction of the pairing amplitude, as in conventional BCS theory, but rather by fluctuations of the phase [101] of the order parameter leading to the Uemura scaling $T_c \sim \rho_s$ [98]. Even though SC order is destroyed at T_c, the local pairing amplitude survives above T_c giving rise to the pseudogap features. A natural mechanism for such a pseudogap coming from spin pairing in a doped Mott insulator exists within the RVB framework [102], with possibility of additional chiral current fluctuations [103].

More recently the pairing origin of the pseudogap has been challenged. Some experiments [104] have been argued to suggest a non–pairing explanation with a competition between the pseudogap and the SC gap. A specific realization of this scenario is the staggered flux or d–density wave mechanism [105] in which T^* is actually a phase transition below which both time–reversal and translational invariance are broken. A more subtle phase transition with only broken time–reversal has also been proposed [106] as the origin of the pseudogap.

Although a qualitative understanding of some of the characteristics of the pseudogap within the non–pairing scenarios is not clear at this time, these theories make sharp predictions about broken symmetries below T^* which can be tested. A very recent ARPES study [107] of circular dichroism finds evidence in favor of broken time reversal, thus casting some doubt on the pairing fluctuation ideas. The last word has clearly not been said on this subject, either theoretically or experimentally, and the origin of the pseudogap remains one of the most important open questions in the field of high T_c superconductors.

5.7 Photoemission Lineshapes and the Electron Self–Energy

Under certain conditions, which were discussed in Section 5.2, ARPES measures the occupied part of the single particle spectral function, $A(\mathbf{k},\omega)f(\omega)$, with $A = ImG/\pi$ where G is the Greens function. The latter can be expressed as $G^{-1} = \omega - \epsilon_{\mathbf{k}} - \Sigma(\mathbf{k},\omega)$ where $\epsilon_{\mathbf{k}}$ is the single–particle energy (defined by the kinetic energy and single–particle potential energy terms of

the Hamiltonian) and Σ is the Dyson self–energy (i.e., everything else). Often, this form is associated with a perturbative expansion used to estimate Σ, but of course the expression is itself tautological. The purpose of writing G in this form is that it isolates all many–body effects in the function Σ. An advantage of ARPES is that one has the possibility of extracting Σ directly from the data, allowing comparison to various microscopic predictions for Σ.

One of the more trivial examples of this is when one fits ARPES data to determine the superconducting gap, Δ. For instance, the work described in Section 5.5 [22] used a broadened form of BCS theory to fit the leading edge of the spectra. This is equivalent to $\Sigma = -i\Gamma + \Delta_{\mathbf{k}}^2/(\omega + \epsilon_{\mathbf{k}} + i\Gamma)$, $\Gamma = 0$ describing standard BCS theory. The advantage of this procedure is the actual gap function, Δ, is extracted from the data, rather than ill defined quantities, such as the often utilized leading edge shift (midpoint of the leading edge) which is not the same as Δ because of lifetime and resolution effects. When this is done, a Δ_k is obtained which has rather spectacular agreement with that expected for a d–wave order parameter. Although ARPES contains no phase information of the order parameter, the linear behavior of Δ_k along the Fermi surface near the gap zero (node) implies a sign change. Moreover, ARPES has the additional advantage of determining the shape of Δ_k in the Brillouin zone, which gives important information on the spatial range of the pairing interaction [83], as also discussed in Section 5.5.

Even when fitting data at low temperatures including energy and momentum resolution, a non–zero Γ is always needed. The origin of this residual Γ is still debated. It is larger than what is expected based on impurity scattering, and certainly larger than that implied by various conductivity probes (thermal, microwave, and infrared). Although the transport scattering rate is different from $\mathrm{Im}\Sigma$ (and in particular, only Umklapp processes contribute to electrical conductivity), the discrepancy is still large enough to be noticeable, even when taking into account the fact that in the simple approximation being employed here, Γ represents some average of $\mathrm{Im}\Sigma$ over a frequency range of order Δ.

Although it has been suggested that the residual Γ is due to surface inhomogeneity effects (in particular, a distribution of Δ due to local oxygen inhomogeneities [108]), a more likely possibility is that it is the same effect which is seen in normal metals like $TiTe_2$. In the latter case, it was convincingly argued that this was the expected final state lifetime contamination effect when attempting to extract Σ from ARPES spectra [109]. Although the latter is expected to vanish in the pure 2D limit, even small 3D effects can lead to a noticeable effect, since final state lifetimes are large. For instance, in simple models, its contribution to Γ is of order $(v_c^i/v_c^f)\Gamma_f$, where v_c^i is the c–axis velocity of the initial state, v_c^f that of the final state, and Γ_f is the final state lifetime [19]. Since Γ_f is typically of order 1 eV, then a velocity ratio of only 0.01 is sufficient to cause a residual Γ of 10 meV.

With this as an introduction, in this section, we desire to take a more serious look at the issue of extracting Σ from the data. The most commonly employed strategy is to come up with some model for Σ, and then see how well it fits the data, as illustrated by the simple example above. We will discuss this approach in more detail later. We start, though, with discussing an alternate approach which we have recently advocated.

5.7.1 Self–Energy Extraction

Let us first assume we know A. Given that, we can easily obtain Σ. A Kramers–Kronig transform of A will give us the real part of G

$$\mathrm{Re}G(\omega) = P\int_{-\infty}^{+\infty} d\omega' \frac{A(\omega')}{\omega' - \omega}\,, \tag{5.13}$$

where P denotes the principal part of the integral. Knowing now both ImG and ReG, then Σ can be directly read off from the definition of G.

$$\begin{aligned}
\mathrm{Im}\Sigma &= \frac{\mathrm{Im}G}{(\mathrm{Re}G)^2 + (\mathrm{Im}G)^2} \\
\mathrm{Re}\Sigma &= \omega - \epsilon - \frac{\mathrm{Re}G}{(\mathrm{Re}G)^2 + (\mathrm{Im}G)^2}\,.
\end{aligned} \tag{5.14}$$

To obtain ReG using Eq. (5.13), we need to know A for *all* energies. From ARPES, though, we only know the product of A and f. (While unoccupied states can be studied by inverse photoemission, its resolution at present is too poor to be useful for our purposes). This is not a limitation if an occupied $\mathbf{k}$–state is being analyzed and one can either ignore the unoccupied weight or use a simple extrapolation for it (except that only $Re\Sigma + \epsilon$ is determined). On the other hand, one is usually interested in k vectors near the Fermi surface. Therefore a key assumption will have to be made. We can implement our procedure if we make the assumption of particle–hole symmetry, $A(\epsilon_{\mathbf{k}}, \omega) = A(-\epsilon_{\mathbf{k}}, -\omega)$, within the small $\mathbf{k}$–window centered at $\mathbf{k}_F$. Then, A is obtained by exploiting the identity $A(\epsilon_{\mathbf{k}}, \omega)f(\omega) + A(-\epsilon_{\mathbf{k}}, -\omega)f(-\omega) = A(\epsilon_{\mathbf{k}}, \omega)$, which holds even in the presence of the energy resolution convolution. Note, this can only be invoked at $\mathbf{k}_F$, and was used previously to remove the Fermi function from ARPES data [94], where it was denoted as the symmetrization procedure (note that the "symmetrized" data will correspond to the raw data for $\omega <\sim -2.2kT$). Although the particle–hole symmetry assumption is reasonable for small $|\omega|$ where it can be tested in the normal state by seeing whether the "symmetrized" spectrum has a maximum at the Fermi energy (E_F), it will almost certainly fail for sufficiently large $\omega > 0$. Nevertheless, since we only expect to derive Σ for $\omega < 0$, then the unoccupied spectral weight will affect the result only in two ways. The first is through the sum rule $\int d\omega A(\omega) = 1$ which must be used to eliminate the intensity prefactor of the ARPES photocurrent. From Eq. (5.14), we see that violation of the

sum rule will simply rescale ImΣ, but not ReΣ due to the $\omega - \epsilon$ factor. Our normalization, though, is equivalent to assuming n_{k_F}=0.5, and thus does not involve "symmetrized" data. The second influence comes from the Kramers–Kronig transformation in Eq. (5.13), which is a bigger problem. Fortunately, the contribution from large $\omega' > 0$, for which our assumption is least valid, is suppressed by $1/(\omega' - \omega)$. Further, for $\mathbf{k}_F$, $\epsilon_{\mathbf{k}}$=0 and thus ReΣ is not plagued by an unknown constant.

When using real data, it is sometimes desirable to filter the noise out of the data, as well as to deconvolve the energy resolution, before employing the above procedure. These details can be found in Ref. [110]. Moreover, it is assumed that any "background" contribution (see Section 5.2) has been subtracted from the data as well.

In Fig. 5.36a, we show T=14K symmetrized data for a T_c=87K Bi2212 overdoped sample at the $(\pi, 0)$ point [110]. We note the important differences in this superconducting state spectrum, compared with the normal state one (which can be fit by a simple Lorentzian), due to the opening of the superconducting gap, with the appearance of a sharp quasiparticle peak displaced from E_F by the superconducting gap, followed by a spectral dip, then by a "hump" at higher binding energies. The resulting Σ is shown in Fig. 5.36b and c. At high binding energies, one obtains a constant ImΣ with a very large value ($\sim$ 300 meV). Near the spectral dip, ImΣ has a small peak followed by a sharp drop.

Despite this sharp drop below 70 meV, ImΣ remains quite large at low frequencies. Then, below 20 meV, there is a narrow spike in ImΣ. This is the imaginary part of the BCS self-energy, $\Delta^2/(\omega + i0^+)$, which kills the normal state pole at ω=0. The resulting $1/\omega$ divergence of the real part ReΣ, which creates new poles at $\pm\Delta$=32meV, is easily seen in Fig. 5.36c. This is followed by a strong peak in ReΣ near the spectral dip energy, which follows from the Kramers–Kronig transformation of the sharp drop in ImΣ. The strong peak in $Re\Sigma$ explains why the low energy peak in A is so narrow despite the large value of ImΣ. The halfwidth of the spectral peak is given by $\Gamma = z$ImΣ where $z^{-1} = 1 - \partial$Re$\Sigma/\partial\omega$ (z is the quasiparticle residue). In the vicinity of the spectral peak, z^{-1} is large ($\sim$9), giving a Γ of $\sim$14 meV. We note, though, that Γ is still quite sizeable, and thus the peak is not resolution limited, as discussed above.

We can contrast this result with that obtained in the pseudogap phase. In Fig. 5.37a, we show T=95K symmetrized data from a T_c=85K underdoped Bi2212 sample at the $(\pi, 0) - (\pi, \pi)$ Fermi crossing. One again sees (Fig. 5.37b) a peak in ImΣ at ω=0, but it is broadened relative to that of the superconducting state, and the corresponding divergence of ReΣ (Fig. 5.37c) is smeared out. Such behavior would be consistent with replacing the BCS self-energy $\Delta^2/(\omega + i0^+)$ by $\Delta^2/(\omega + i\Gamma_0)$, and can be motivated by considering the presence of pair fluctuations above T_c, as will be discussed further below. Note from Fig. 5.37 that although the equation ω–Re$\Sigma(\omega) = 0$ is

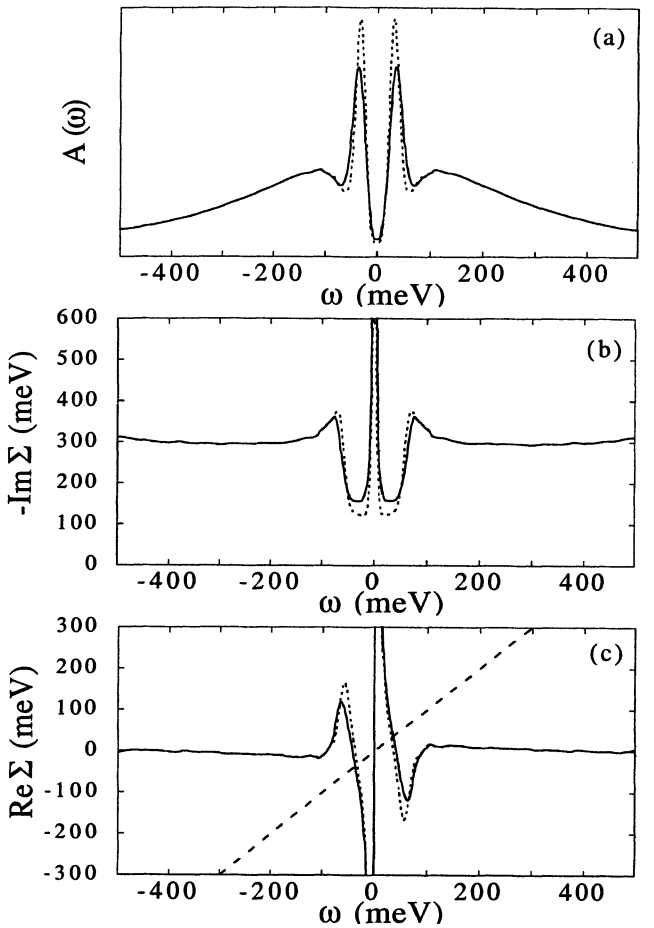

Fig. 5.36. (a) Symmetrized spectrum for overdoped Bi2212 (T_c=87K) at T=14K at $(\pi, 0)$ with (dotted line) and without (solid line) energy resolution deconvolution. The resulting ImΣ and ReΣ are shown in (b) and (c). The dashed line in (c) determines the condition Re$\Sigma = \omega$

still satisfied at $|\omega| \sim \Delta$, zImΣ is so large that the spectral peak is strongly broadened in contrast to the sharp peak seen below T_c. Actually, to a good approximation, the spectral function is essentially the inverse of ImΣ in the range $|\omega| <\sim 2\Delta$. We can also contrast this case with data taken above T^*, the temperature at which the pseudogap "disappears". In that case, the spectrum is featureless, and the peak in ImΣ is strongly broadened. As the doping increases, this peak in ImΣ disappears. Further doping causes a depression in ImΣ to develop around $\omega = 0$, indicating a crossover to more Fermi liquid like behavior.

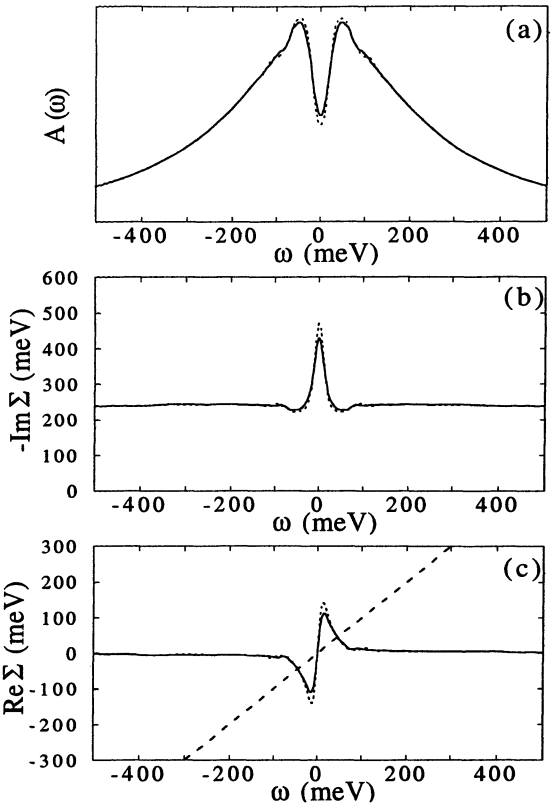

Fig. 5.37. (a) Symmetrized spectrum for underdoped Bi2212 (T_c=85K) at T=95K (pseudogap phase) at the $(\pi, 0) - (\pi, \pi)$ Fermi crossing with (dotted line) and without (solid line) energy resolution deconvolution. The resulting ImΣ and ReΣ are shown in (b) and (c). The dashed line in (c) determines the condition $Re\Sigma = \omega$

5.7.2 Temperature Dependence of Self-Energy

We now turn to the rather controversial issue of how the spectrum at $(\pi, 0)$ varies as a function of temperature, that is, how one interpolates between Figs. 5.36 and 5.37.

In Fig. 5.38, we show data taken for an optimal doped (T_c=90K) Bi2212 sample [111]. The leading edge of the spectral peak is determined by the superconducting gap, whose energy stays fairly fixed in temperature, and persists above T_c (the pseudogap). On the trailing edge, one sees a spectral dip, whose energy also remains fixed in temperature, and becomes filled in above T_c due to broadening of the trailing edge of the peak.

In Fig. 5.39a, ImΣ is plotted for various temperatures. At low temperatures and energies, it is again characterized by a peak centered at zero

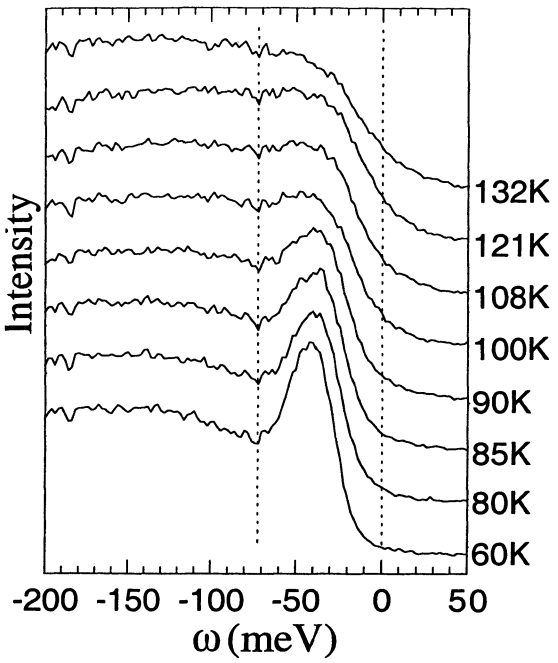

Fig. 5.38. Temperature dependence of ARPES data at $(\pi, 0)$ for a T_c=90K Bi2212 sample. The vertical dotted lines mark the spectral dip energy and the chemical potential

energy due to the superconducting energy gap, and a "normal" part which can be treated as a constant plus an ω^2 term. A maximum in ImΣ occurs near the energy of the spectral dip. Beyond this, ImΣ has a large, nearly frequency independent, value. As the temperature is raised, the zero energy peak broadens, the constant term increases, and the ω^2 term goes away.

In Fig. 5.39b, the quantity ω−ReΣ is plotted. At low temperatures and energies, there is a $1/\omega$ term due to the energy gap, and a "normal" part which is linear in ω. As expected, the zero crossing is near the location of the spectral peak. Beyond this, there is a minimum near the specral dip energy, then the data are approximately linear again, but with a smaller slope than near the zero crossing. As the temperature is raised, the gap $(1/\omega)$ term broadens out and the low energy linear in ω term decreases, paralleling the behavior discussed above for ImΣ.

From Figs. 5.38 and 5.39, we see that rather than the spectral peak decreasing in weight with increasing temperature, it disappears by broadening strongly in energy. This can be seen directly by inspecting Fig. 5.39, in that as the temperature increases, ImΣ (Fig. 5.39a) in the vicinity of the peak increases in magnitude with T, and z^{-1} (roughly the slope in Fig. 5.39b near the zero crossing) decreases with T. In fact, it is the strong T variation of

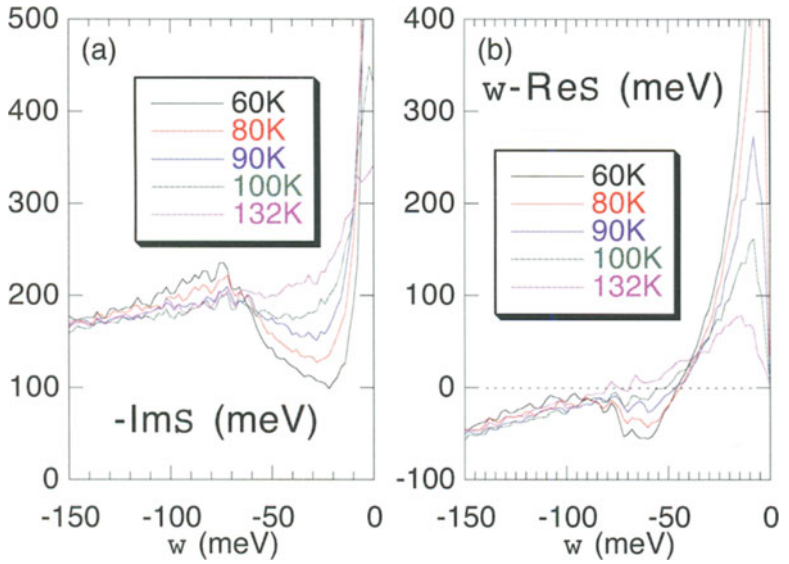

Fig. 5.39. Temperature dependence of (a) ImΣ and (b) ReΣ derived from the data of Fig. 5.38

ImΣ and z^{-1}, and the fact that they operate in concert, which is responsible for the rapid variation in the effective width of the spectral peak with T.

The above analysis is important in that it shows how coherence is lost in the system. It is apparent from Figs. 5.38 and 5.39 that once a temperature is reached where the spectral peak is no longer discernable in the data, the difference in behavior of the self–energy between low energies and high energies is lost. That is, once the spectral dip is filled in, the low and high energy behaviors have merged, and the sharp peak and broad hump at low temperature is simply replaced by a single broad peak (with a leading edge gap due to the pseudogap). This is consistent with the spectral peak simply losing its integrity as the temperature is raised. The analysis does not support a picture of a well defined quasiparticle peak whose weight simply disappears upon heating, as has been suggested by other authors [96].

5.7.3 Modeling the Self–Energy

This behavior can be further quantified by fitting the self–energy for binding energies smaller than the dip energy to that expected for a superfluid Fermi liquid, and exploring the temperature dependence of the resulting parameters. The reader can find this analysis in Ref. [111]. Rather, we will discuss here a simpler analysis we performed where we contrasted the temperature dependence of overdoped and underdoped samples [112]. In this case, we chose to look at data at the $(\pi, 0) - (\pi, \pi)$ Fermi crossing (antinode). The dip/hump

structure is considerably weaker here than at the $(\pi, 0)$ point, allowing us to concentrate on more general aspects of the spectra.

We begin with the overdoped sample, where there is no strong pseudogap effect. The simplest self–energy which can describe the low energy data at all T is

$$\Sigma(\mathbf{k}, \omega) = -i\Gamma_1 + \Delta^2/[(\omega + i0^+) + \epsilon(\mathbf{k})]. \tag{5.15}$$

Here Γ_1 is a single–particle scattering rate taken, for simplicity, to be an ω–independent constant. It is effectively an average of the (actual ω–dependent) Σ'' over the frequency range of the fit. (In Ref. [111], we generalized this to a constant plus an ω^2 term, and included the resulting linear ω contribution to Σ'). The second term is the BCS self–energy discussed previously.

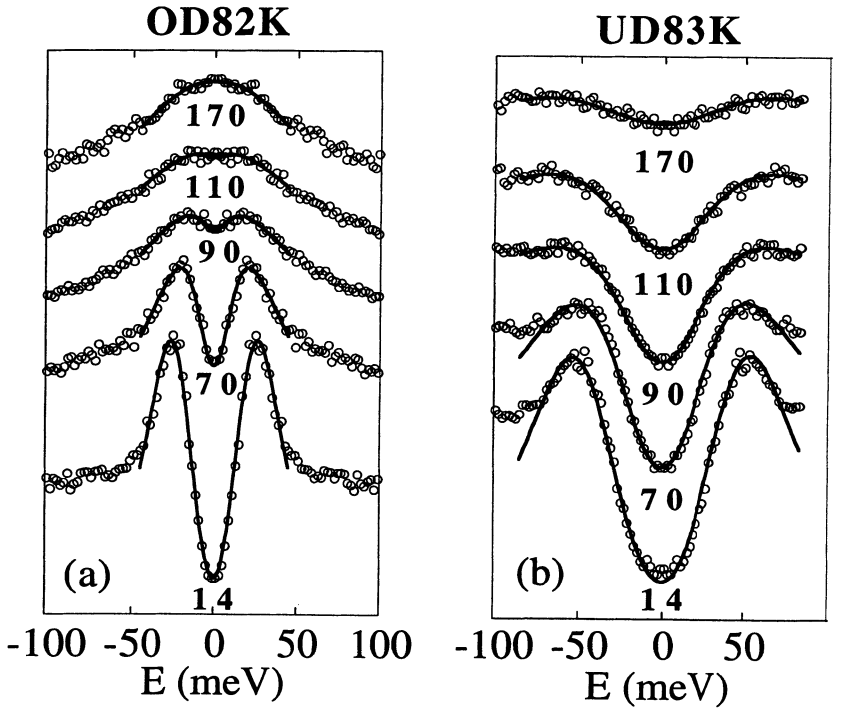

Fig. 5.40. Symmetrized data for (a) a T_c=82K overdoped sample and (b) a T_c=83K underdoped sample at the $(\pi, 0) - (\pi, \pi)$ Fermi crossing at five temperatures, compared to the model fits described in the text

In Fig. 5.40a, we show symmetrized data for an overdoped T_c=82K sample at the antinode together with the fits obtained as follows [112]. Using Eq.

(5.15), we calculate the spectral function

$$\pi A(\mathbf{k},\omega) = \Sigma''(\mathbf{k},\omega)/\left[(\omega - \epsilon_{\mathbf{k}} - \Sigma'(\mathbf{k},\omega))^2 + \Sigma''(\mathbf{k},\omega)^2\right], \tag{5.16}$$

convolve it with the experimental resolution, and fit to symmetrized data. The fit is restricted to a range of ±45 meV given the small gap in the overdoped case and the sharpness of the quasiparticle peaks below T_c. We find that Eq. (5.15) describes the low energy data quite well.

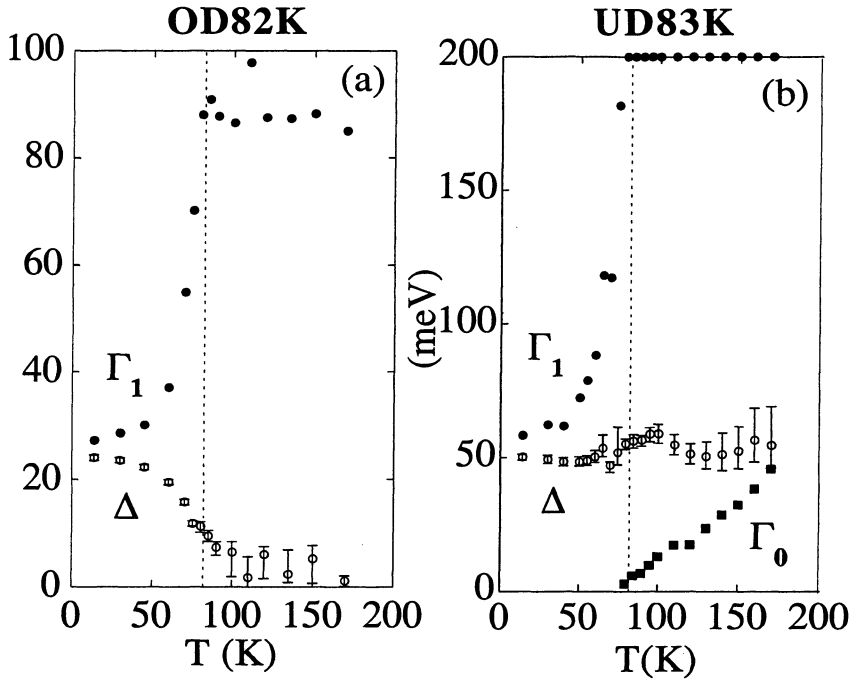

Fig. 5.41. Δ (open circles), Γ_1 (solid circles), and Γ_0 (solid squares) versus T at the $(\pi,0) - (\pi,\pi)$ Fermi crossing for (a) a T_c=82K overdoped sample and (b) a T_c=83K underdoped sample. The dashed line marks T_c. The error bars for Δ are based on a 10% increase in the RMS error of the fits

The T-variation of the fit parameters Δ and Γ_1 are shown in Fig. 5.41a. $\Delta(T)$ decreases with T, and although small at T_c, it only vanishes above T_c, indicating the possibility of a weak pseudogap. This effect is sample dependent, in that several overdoped samples we have looked at, the gap vanishes closer to T_c. We caution that the error bars shown in Fig. 5.41a are based on the RMS error of the fits, but do not take into account experimental errors in μ and $\mathbf{k}_F$.

$\Gamma_1(T)$ is found to be relatively T–independent in the normal state. Below T_c, we see that Γ_1 decreases very rapidly, and can be perfectly fit to the form $a + bT^6$. This rapid drop in linewidth leading to sharp quasiparticle peaks at low T, which can be seen directly in the ARPES data, is consistent with microwave and thermal conductivity measurements, and implies that electron–electron interactions are responsible for Γ_1. Note the clear break in Γ_1 at T_c, despite the fact Δ has not quite vanished. We have seen similar behavior to that described above for a variety of overdoped samples at several $\mathbf{k}$ points.

We next turn to the more interesting underdoped case. We find that near $(\pi, 0)$ the self–energy (5.15) cannot give an adequate description of the data, in that it does not properly describe the pseudogap and its unusual "filling in" above T_c. Theoretically, we cannot have a divergence in $\Sigma(\mathbf{k}_F, \omega = 0)$ in a state without broken symmetry. A simple modification of the BCS self–energy rectifies both these problems:

$$\Sigma(\mathbf{k}, \omega) = -i\Gamma_1 + \Delta^2/[\omega + \epsilon(\mathbf{k}) + i\Gamma_0]. \tag{5.17}$$

The new term $\Gamma_0(T)$ should be viewed as the inverse pair lifetime. The theoretical motivation for Eq. (5.17) is given in Ref. [112]. We stress that this three parameter form is again a minimal representation of the pseudogap self–energy. Since it is not obviously a unique representation, it is very important to see what one learns from the fits.

In Fig. 5.40b, we show symmetrized data at the antinode for a T_c=83K underdoped sample. Below T_c we see quasiparticle peaks. Above T_c these peaks disappear but there is still a large suppression of spectral weight around ω=0. As T is raised further, the pseudogap fills in (rather than closing) leading to a flat spectrum at a temperature of T^* (200K). The self–energy, Eq. (5.17), gives a good fit to the data. These fits were done below T_c over a larger energy range (±75 meV) than in the overdoped case because of the larger gap. The range above T_c was increased to ±85 meV so as to properly describe the pseudogap depression.

In Fig. 5.41b, we show the T–dependence of the fit parameters. We find a number of surprises. First, Δ is independent of T within error bars. Similar behavior has been inferred from specific heat and tunneling data. This T–independence is in contrast to the behavior of the overdoped 82K sample with almost identical T_c at the same $\mathbf{k}$ point. In addition, for the underdoped sample, the gap evolves smoothly through T_c.

The single–particle scattering rate $\Gamma_1(T)$ for the underdoped sample is found to be qualitatively similar to the overdoped case. It is consistent with being T–independent above T_c, but with a value over twice as large as the overdoped case (allowing Γ_1 to vary above T_c does not improve the RMS error of the fits). Second, we see the same rapid decrease in Γ_1 below T_c as in the overdoped case. Note again the clear break at T_c.

The most interesting result is $\Gamma_0(T)$. We find $\Gamma_0 = 0$ below T_c and proportional to $T - T_c$ above. This behavior is robust, and is seen in all the fits

that we have tried. Moreover, a non–zero Γ_0 is needed above T_c to obtain a proper fit to the data (its effect cannot be reproduced by varying the other parameters). The fact that this T–dependence is exactly what one expects of an inverse pair lifetime is a non–trivial check on the validity of the physics underlying Eq. (5.17). Further, we observe from Fig. 5.41 that T^* corresponds to where $\Delta(T) \sim \Gamma_0(T)$. This condition can be understood from the small ω expansion of Eq. (5.17).

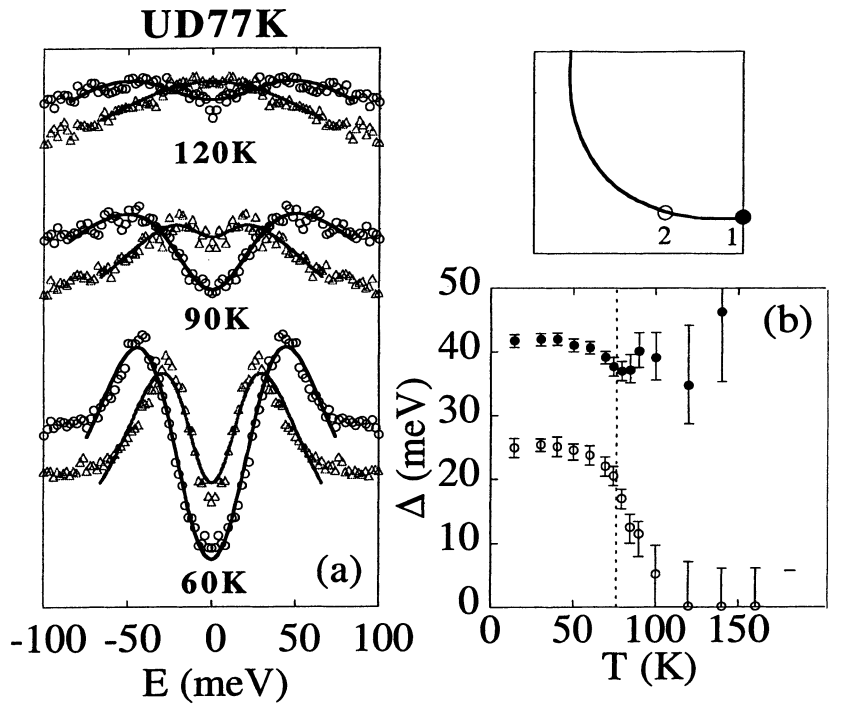

Fig. 5.42. (a) Symmetrized data for a T_c=77K underdoped sample for three temperatures at (open circles) $\mathbf{k}_F$ point 1 in the zone inset, and at (open triangles) $\mathbf{k}_F$ point 2, compared to the model fits. (b) $\Delta(T)$ for these two k points (filled and open circles), with T_c marked by the dashed line

The next important question is whether the T–dependence at the antinode described above exists at other $\mathbf{k}_F$–points. To answer this, we have looked at T–dependent data for a number of underdoped samples at two different $\mathbf{k}$ vectors. All data at the antinode give results similar to those for the 83K sample. However at the second $\mathbf{k}$–point, about halfway between the antinode and the node along the $(0,0) - (\pi,\pi)$ direction, we see quite different behavior. We demonstrate this in Fig. 5.42a where symmetrized data for a

77K underdoped sample are shown. For the antinode, one clearly sees the gap fill in above T_c, with little evidence for any T–dependence of the position of the spectral feature defining the gap edge, just as for the 83K sample. In contrast, at the second $\mathbf{k}$ point, the gap is clearly closing, indicating a strong T–dependence of Δ. Similar behavior is seen in other underdoped samples with T_c between 75 and 85K.

In Fig. 5.42b, we show the T–dependence of Δ obtained from fits (over a range of ± 66 meV) at the second $\mathbf{k}$ point for the 77K sample. Δ is found to be strongly T–dependent, being roughly constant below T_c, then dropping smoothly to zero above. The strong T–dependence of Δ makes it difficult to unambiguously determine Γ_0 from the fits at this $\mathbf{k}$–point. On theoretical grounds, we expect that, here too, there is a non–zero Γ_0, and the closing of the pseudogap is again determined by $\Delta(T) \sim \Gamma_0(T)$, however this condition is satified by the rapid drop in $\Delta(T)$, rather than the rise in $\Gamma_0(T)$. For completeness, we also show $\Delta(T)$ for this sample at the antinode, which has a similar behavior to that of the 83K sample.

We see that these results give further evidence for the unusual $\mathbf{k}$–dependences first noted in Ref. [94]. Strong pairing correlations are seen over a very wide T–range near $(\pi, 0)$, but these effects are less pronounced and persist over a smaller T–range as one moves closer to the zone diagonal. This is clearly tied to the strong $\mathbf{k}$–dependence of the effective interaction and the unusual (anomalously broad and non–dispersive) nature of electronic states near $(\pi, 0)$.

5.7.4 Peak/Dip/Hump – Experiment

We now turn to a detailed discussion of the peak/dip/hump lineshape. As mentioned above, a very broad normal state spectrum near the $(\pi, 0)$ point of the zone evolves quite rapidly for $T < T_c$ into a narrow quasiparticle peak, followed at higher binding energies by a dip then a hump, the latter corresponding to where the spectrum recovers to its normal state value [113]. Similar effects are observed in tunneling spectra [114].

In Fig. 5.43, we show spectra for a T_c =87K Bi2212 sample along $\Gamma - \bar{M} - Z$, i.e., $(0,0) - (\pi, 0) - (2\pi, 0)$, in (a) the normal state (105 K) and (b) the superconducting state (13 K), from which we note two striking features [61]. First, we see that the low energy peak in the superconducting state persists over a large range in $\mathbf{k}$–space, even when the normal state spectra have dispersed away from the Fermi energy. Second, when the hump in the superconducting state disperses, it essentially follows that of the normal state spectrum. This is accompanied by a transfer of weight to the hump from the low frequency peak, which is fairly fixed in energy. The same phenomena are also seen along $\bar{M}$ to Y (Fig. 5.43c). We will argue that the unusual dispersion seen in the superconducting state of Fig. 5.43 is closely tied to the lineshape change discussed earlier (Fig. 5.38).

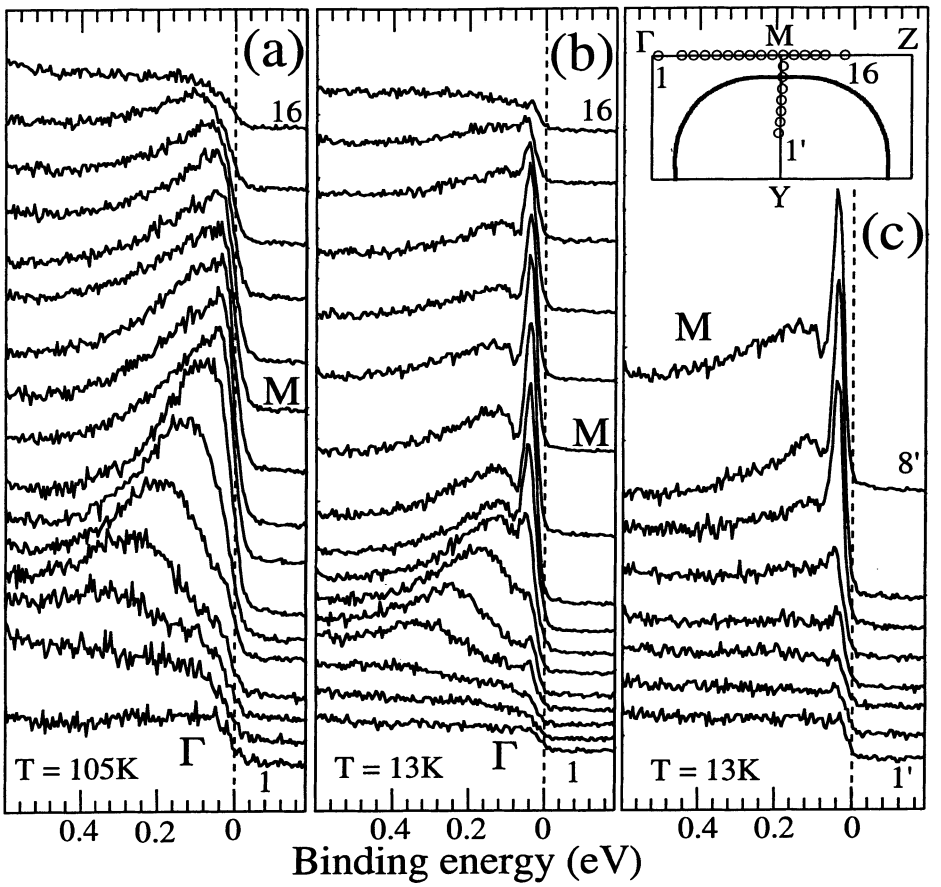

Fig. 5.43. Spectra in (a) the normal state (105 K) and (b) the superconducting state (13 K) along the line $\Gamma - \bar{M} - Z$, and (c) the superconducting state (13 K) along the line $\bar{M} - Y$ for an overdoped (T_c=87K) Bi2212 sample. The zone is shown as an inset in (c) with the curved line representing the observed Fermi surface

The simplest explanation of the superconducting state spectra would be the presence of two bands (e.g., due to bilayer splitting), one responsible for the peak and the other for the hump. However, this explanation is untenable [115]. First, if the sharp peak were associated with a second band, then this band should also appear above T_c. But there is no evidence for it in the normal state data. Second, if the peak and hump were from two different bands, then their intensities must be governed by different matrix elements. However, we found [37] that the intensities of both features scaled together as the photon polarization was varied from in to out of plane, as if they were governed by a common matrix element (Section 5.4.5). These arguments

suggest that the unusual lineshape and dispersion represent a single electronic state governed by non–trivial many–body effects, as assumed in the previous discussion (Figs. 5.36-5.39). For more overdoped materials, though, bilayer splitting should be taken into account, as discussed in Section 5.4.5.

Under this assumption, the data are consistent with a strong reduction of the imaginary part of the self–energy ($\mathrm{Im}\Sigma$) at low energies in the superconducting state (Fig. 5.36). If the scattering is electron–electron like in nature, then $\mathrm{Im}\Sigma$ at frequencies smaller than $\sim 3\Delta$ will be suppressed due to the opening of the superconducting gap [116]. On closer inspection, though, a more interesting story emerges. First, from Figs. 5.36 and 5.43, we see that the superconducting and normal state data match beyond 90 meV. From 90 meV, the dip is quickly reached at 70 meV, then one rises to the sharp peak. Notice that since the width of the peak is around 20 meV, then the change in behavior of the spectra (from hump, to dip, to the trailing edge of the peak) is occuring on the scale of the energy resolution. That means that the intrinsic dip must be quite sharp. This implies that the large $\mathrm{Im}\Sigma$ at high energies must drop to a small value over a narrow energy interval to be consistent with the data, i.e., there is essentially a step in $\mathrm{Im}\Sigma$. In fact, the data are not only consistent with a step in $\mathrm{Im}\Sigma$, but the depth of the dip is such that it is best fit by a peak in $\mathrm{Im}\Sigma$ at the dip energy, followed by a rapid drop to a small value. This behavior can again be seen from the independent analysis shown in Figs. 5.36 and 5.39.

What are the consequences of this behavior in $\mathrm{Im}\Sigma$? If $\mathrm{Im}\Sigma$ has a sharp drop at $\tilde{\omega}$, then by Kramers–Kronig transformation, $\mathrm{Re}\Sigma$ will have a sharp peak at $\tilde{\omega}$ (Fig. 5.36). This peak can very simply explain the unusual dispersion shown in Fig. 5.43, as it will cause a low energy quasiparticle pole to appear even if the normal state binding energy is large. The most transparent way to appreciate this result is to note that a sharp step in $\mathrm{Im}\Sigma$ is equivalent to the problem of an electron interacting with a sharp (dispersionless) mode, since in that case, the mode makes no contribution to $\mathrm{Im}\Sigma$ for energies below the mode energy, and then makes a constant contribution for energies above. This problem has been treated by Engelsberg and Schrieffer [117], and extended to the superconducting state by Scalapino and coworkers [118]. The difference in our case is that since the effect only occurs *below* T_c, it is a consequence of the opening of the superconducting gap in the electronic energy spectrum, and thus of a collective origin, rather than a phonon.

To facilitate comparison to this classic work, in Fig. 5.44 we plot the position of the low energy peak and higher binding energy hump as a function of the energy of the single broad peak in the normal state. This plot has a striking resemblance to that predicted for electrons interacting with a sharp mode in the superconducting state, and one clearly sees the low energy pole which we associate with the peak in $\mathrm{Re}\Sigma$. On general grounds, the flat dispersion of the low energy peak seen in Fig. 5.44 is a combination of two effects: (1) the peak in $\mathrm{Re}\Sigma$, which provides an additional mass renormalization of the

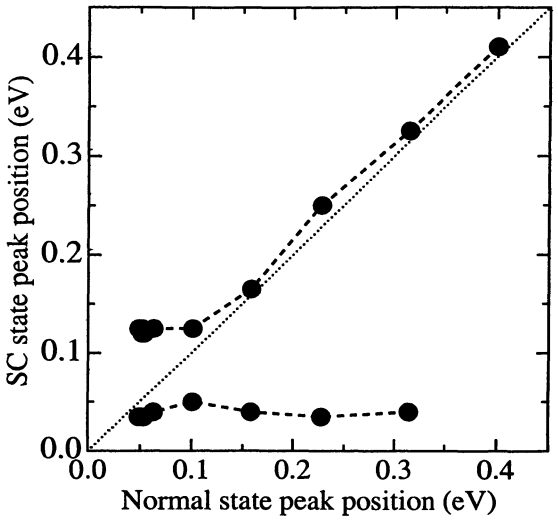

Fig. 5.44. Positions of the sharp peak and the broad hump in the superconducting state versus normal state peak position obtained from Fig. 5.43a and 5.43b. Solid points connected by a dashed line are the data, the dotted line represents the normal state dispersion

superconducting state relative to the normal state, and thus pushes spectral weight towards the Fermi energy, and (2) the superconducting gap, which pushes spectral weight away. This also explains the strong drop in intensity of the low energy peak as the higher binding energy hump disperses.

An important feature of the data is the dispersionless nature of the sharp peak. The mode picture discussed above would imply a dispersion of the peak from Δ_k to $\tilde{\omega} = \omega_0 + \Delta_k$ as the normal state binding energy increases (where ω_0 is the mode energy). However, this dispersion turns out to be weak. From the data of Fig. 5.36, we infer an $\omega_0 = 1.3\Delta_{max}$, ω_0 being essentially the energy separation of the peak and dip. Since Δ_k is known to be of the $d_{x^2-y^2}$ form, then Δ_k should go to zero as we disperse towards the Γ point. Therefore, the predicted dispersion is only from Δ_{max} to $1.3\Delta_{max}$ (32 to 42 meV).

Since the dip/hump structure is most apparent at the $(\pi, 0)$ points, it is natural to assume that it has something to do with $Q = (\pi, \pi)$ scattering, as discussed by Shen and Schrieffer [119]. But here, we find a new effect. If one compares the data of Figs. 5.43b and 5.43c, one sees that a low energy peak also exists along $(\pi, 0) - (\pi, \pi)$ for approximately the same momentum range as the one from $(\pi, 0) - (0, 0)$. That is, if there is a peak for momentum p, one also exists for momentum $p + Q$. This can be understood, since the self-energy equations for p and $p + Q$ will be strongly coupled if Q scattering is dominant.

5.7.5 Mode Model

For now, we ignore the complication of momentum dependence. The lowest order contribution to electron–electron scattering is represented by the Feynman diagram shown in the inset of Fig. 5.45. In the superconducting state, each internal line will be gapped by Δ. This implies that the scattering will be suppressed for $|\omega| < 3\Delta$. This explains the presence of a sharp quasiparticle peak at low temperatures. What is not so obvious is whether this in addition explains the strong spectral dip. Explicit calculations show only a weak dip–like feature [120]. To understand this in detail, we equate the bubble plus interaction lines (Fig. 5.45 inset) to an "α^2F" as in standard strong–coupling literature. In a marginal Fermi liquid (MFL) at T=0, $\alpha^2F(\Omega)$ is simply a constant in Ω. The effect of the gap is to force α^2F to zero for $\Omega < 2\Delta$. The question then arises where the gapped weight goes. It could be distributed to higher energies, but in light of the above discussion, we might expect it to appear as a collective mode inside of the 2Δ gap. For instance, if the bubble represents spin fluctuations, a sharp mode will appear if the condition $1 - U\chi_0(\mathbf{q}, \Omega) = 0$ is satisfied for $\Omega < 2\Delta$. These three cases (MFL, gapped MFL, gapped MFL plus mode) are illustrated in Fig. 5.45.

Σ is easy to obtain analytically if we ignore the complication of the superconducting density of states from the $\mathbf{k} - \mathbf{q}$ line of Fig. 5.45 and just replace this by a step function at Δ. The resulting ImΣ for the gapped MFL and gapped MFL plus mode models are shown in Fig. 5.46a [121] in comparison to the normal state MFL. Note that structure in α^2F at Ω appears in Σ at $|\omega| = \Omega + \Delta$ due to the gap in the $\mathbf{k} - \mathbf{q}$ line. Moreover, the MFL plus mode is simply the normal state MFL cut–off at 3Δ (this is obtained under

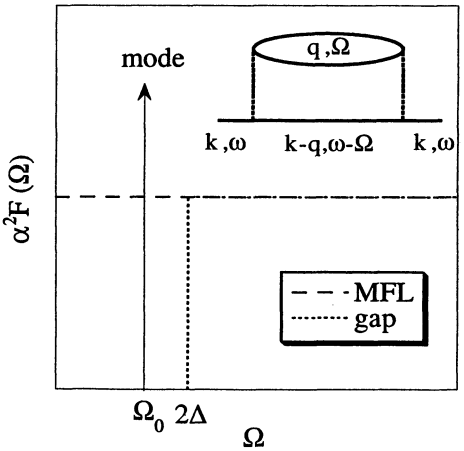

Fig. 5.45. α^2F for three models, MFL (dashed line), gapped MFL (dotted line), and gapped MFL plus mode (dotted line plus δ function). Inset: Feynman diagram for the lowest order contribution to Σ from electron–electron scattering

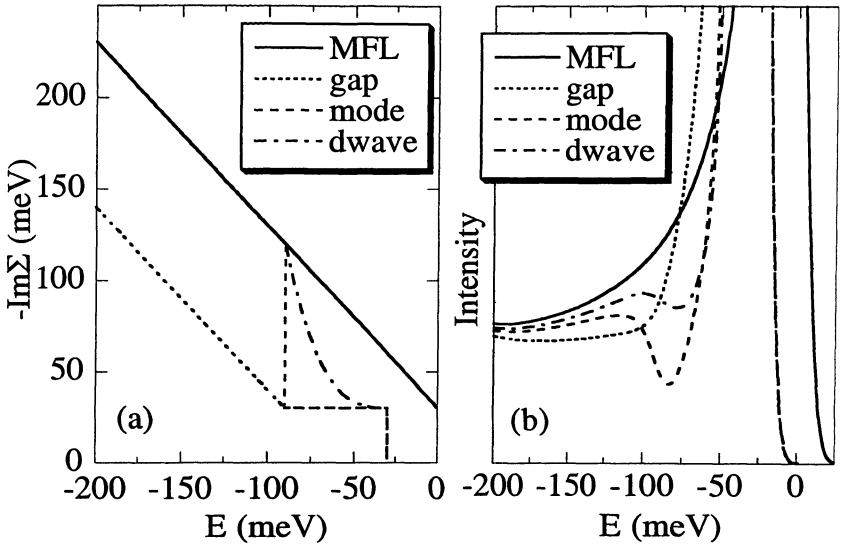

Fig. 5.46. (a) ImΣ for MFL (solid line), gapped MFL (dotted line), gapped MFL plus mode (dashed line), and simple d-wave model (dashed-dotted line). Parameters are α=1, ω_c=200meV, Δ=30meV (0 for MFL), Ω_0=2Δ, and Γ_0=30meV. (b) Spectral functions (times a Fermi function with T=14K) convolved with a resolution gaussian of σ=7.5 meV for these four cases (ϵ=-34meV)

the assumption that all the gapped weight in α^2F shows up in the mode). In contrast, the gapped MFL decays linearly to zero at 3Δ.

The Nambu spectral function is given by

$$A(\omega) = \frac{1}{\pi} Im \frac{Z\omega + \epsilon}{Z^2(\omega^2 - \Delta^2) - \epsilon^2}\,, \tag{5.18}$$

with (a complex) $Z(\omega) = 1 - \Sigma(\omega)/\omega$. These are shown in Fig. 5.46b and were convolved with a gaussian of σ=7.5 meV, typical of high resolution ARPES, with a constant ImΣ (Γ_0) added for $|\omega| > \Delta$ to reduce the size of the quasiparticle peak. We note that there is no dip as such for the gapped MFL model, whereas the addition of the mode causes a significant dip. The latter behavior is consistent with experiment. Moreover, the mode model has the additional advantage that ImΣ recovers back to the normal state value by 3Δ, which is also in agreement with experiment in that the normal and superconducting state spectra agree beyond 90 meV (Figs. 5.36 and 5.43).

We contrast this behavior with that expected for a simple d-wave model. To a first approximation, this can be obtained by replacing the step drop in ImΣ in the MFL plus mode model with $(|\omega| - \Delta)^3$ for $|\omega| < 3\Delta$ [122]. This is shown in Fig. 5.46a as well, with the resulting spectrum in Fig. 5.46b. Only a weak dip appears. Moreover, we have analyzed models with

the exponent 3 replaced by some n and have found that n must be large to obtain a dip as strong as seen in experiment. Therefore, the upshot is that at the least, something similar to a step is required in $\mathrm{Im}\Sigma$ to be consistent with experiment.

In principle, we could take the above MFL plus mode model and fit experiment with it. We consider a simpler model. There are several reasons for this. First, the MFL model has a number of adjustable parameters associated with it. There is the coupling constant (α), the cut–off frequency (ω_c), and the mode energy (which is not in general 2Δ). Moreover, the spectrum for $\mathbf{k}$ points near the $(\pi, 0)$ point does not appear to be MFL–like in nature. We have found that the normal state Bi2212 spectrum is fit very well by a Lorentzian plus a constant background in an energy range less than 0.5eV. This is also true for Bi2201 spectrum where the normal state can be accessed to much lower temperatures.

In the resulting Lorentzian model, the normal state Σ is purely an imaginary constant, and $\alpha^2 F$ is a mode at zero energy. In the superconducting state, this mode gets pushed back to some energy within 2Δ. This model is artificial in the sense that all the self–energy is being generated by the mode. That is why we went through the above discussion motivating the mode more properly as a rearrangement of $\alpha^2 F$ due to the superconducting gap. In practice, though, the results are very similar to the MFL plus mode model, and has the further advantage of having the several parameters of that model collapse to just the mode strength (Γ_1) and mode position (Ω_0) of the Lorentzian model. Moreover, analytic results can still be obtained for Σ when the superconducting density of states for the $\mathbf{k} - \mathbf{q}$ line of Fig. 5.45 is taken into account. The result is [121]

$$\begin{aligned} -Im\Sigma(\omega) &= \Gamma_0 N(|\omega|) + \Gamma_1 N(|\omega| - \Omega_0),\ |\omega| > \Omega_0 + \Delta \\ &= \Gamma_0 N(|\omega|),\ \Delta < |\omega| < \Omega_0 + \Delta \\ &= 0,\ |\omega| < \Delta \end{aligned} \tag{5.19}$$

where $N(\omega) = \omega/\sqrt{\omega^2 - \Delta^2}$ is the BCS density of states, and

$$\begin{aligned} \pi \mathrm{Re}\Sigma(\omega) &= \Gamma_0 N(-\omega) \ln\left[|-\omega + \sqrt{\omega^2 - \Delta^2}|/\Delta\right] \\ &+ \Gamma_1 N(\Omega_0 - \omega) \ln\left[|\Omega_0 - \omega + \sqrt{(\omega - \Omega_0)^2 - \Delta^2}|/\Delta\right] \\ &- \{\omega \to -\omega\}\,. \end{aligned} \tag{5.20}$$

Here, it has again been assumed that Δ is a real constant in frequency. An s–wave density of states has been used to obtain an analytic result. A d–wave density of states will not be that different. The advantage of an analytic result is that it is useful when having to take spectra and convolve with resolution to compare to experiment. Our results are not very sensitive to Γ_0, included again to damp the quasiparticle peak.

The resulting real (Eq. (5.20)) and imaginary (Eq. (5.19)) parts of Σ at $(\pi, 0)$ are shown in Fig. 5.47a. Note the singular behaviors at Δ (peak

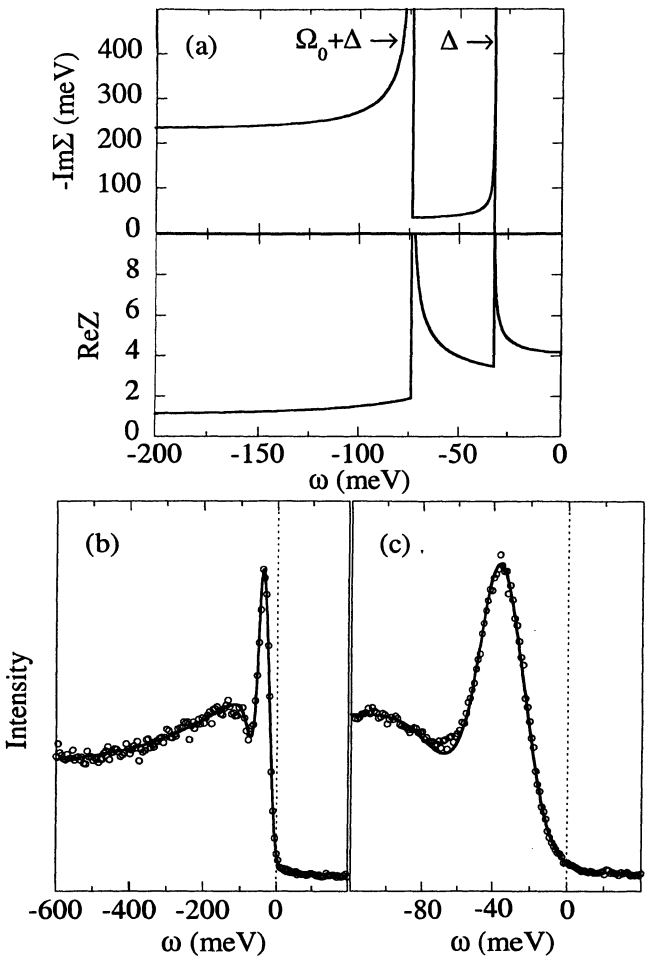

Fig. 5.47. (a) ImΣ and ReZ at $(\pi, 0)$ from Eqs. 5.19 and 5.20 (Γ_1=200meV, Γ_0=30meV, Δ=32meV, Ω_0=1.3Δ). Comparison of the data at $(\pi, 0)$ for (b) wide and (c) narrow energy scans with calculations based on Eqs. 5.18-5.20, with an added step edge background contribution

energy) due to the Γ_0 term and at $\Omega_0 + \Delta$ (dip energy) due to the Γ_1 term. In both cases, step drops in ImΣ would also give singularities in $Re\Sigma$. The advantage of peaks in ImΣ (due to the SC density of states) is that it makes the dip deeper in better agreement with experiment. In Fig. 5.47b and 5.47c, we show a comparison of the resulting spectral function (convolved with the experimental energy and momentum resolution) to experimental data at $(\pi, 0)$ for both wide and narrow energy scans, where a step edge background

with a gap of Δ is added to the calculated spectrum. The resulting agreement is excellent.

It is interesting to note that the mode energy we infer from the data is 41 meV, equivalent to a magnetic resonant mode energy observed in YBCO [123] and Bi2212 [124] by neutron scattering data at $\mathbf{Q} = (\pi, \pi)$. The Q dependence of this mode correlates well with the observations of Fig. 5.43. To explore this in greater detail, we now consider the doping dependence of the peak/dip/hump structure.

5.7.6 Doping Dependence

We show data along $(\pi, 0) \rightarrow (\pi, \pi)$ for an underdoped 75K sample in the superconducting state (Fig. 5.48a) and in the pseudogap state (Fig. 5.48b) [62]. Below T_c, the sharp peak at low energy is essentially dispersionless, while the higher energy hump rapidly disperses from the $(\pi, 0)$ point towards the $(\pi, 0) \rightarrow (\pi, \pi)$ Fermi crossing seen above T^*. Beyond this, the intensity drops dramatically, but there is clear evidence that the hump disperses back to higher energy. In the pseudogap state, the high energy feature also shows strong dispersion, much like the hump below T_c, even though the leading edge is non–dispersive like the sharp peak in the superconducting state.

In Fig. 5.49 we show the dispersion of the sharp peak and hump (below T_c), for a variety of doping levels, in the vicinity of the $(\pi, 0)$ point along the two principal axes. The sharp peak at low energies is seen to be essentially non–dispersive along both directions for all doping levels, while the hump shows very interesting dispersion. Along $(\pi, 0) \rightarrow (0, 0)$ (Fig. 5.49a), the hump exhibits a maximum, with an eventual dispersion away from the Fermi energy, becoming rapidly equivalent to the binding energy of the broad peak in the normal state as one moves away from the region near $(\pi, 0)$. In the orthogonal direction (Fig. 5.49b), since the hump initially disperses towards the $(\pi, 0) \rightarrow (\pi, \pi)$ Fermi crossing, which is known to be a weak function of doping, one obtains the rather dramatic effect that the dispersion becomes stronger with underdoping. We also note that there is an energy separation between the peak and the hump due to the spectral dip. In essence, the hump disperses towards the spectral dip, but cannot cross it, with its weight dropping strongly as the dip energy is approached. Beyond this point, one sees evidence of the dispersion bending back to higher binding energy for more underdoped samples.

Fig. 5.50a shows the evolution of the low temperature spectra at the $(\pi, 0)$ point as a function of doping. The sharp quasiparticle peak moves to higher energy, indicating that the gap increases with underdoping (although this is difficult to see on the scale of Fig. 5.50a). We see that the hump moves rapidly to higher energy with underdoping. These trends can be seen very clearly in Fig. 5.50b, where the energy of the peak and hump are shown as a function of doping for a large number of samples. Finally, we observe that the quasiparticle peak loses spectral weight with increasing underdoping, as

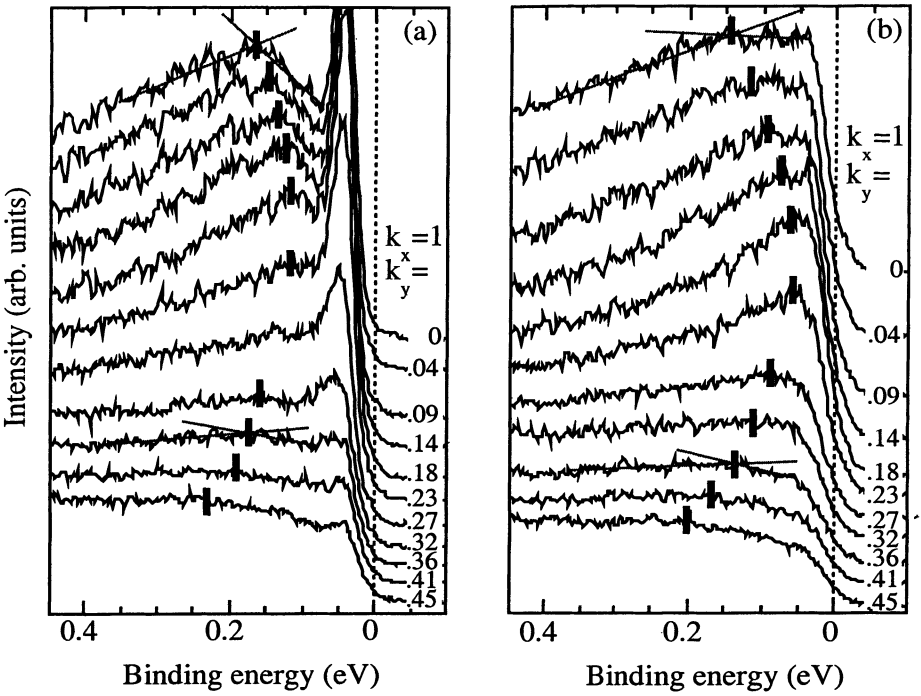

Fig. 5.48. Spectra along $(\pi, 0) \rightarrow (\pi, \pi)$ in (a) the superconducting state (T=60K), and (b) the pseudogap state (T=100K) for an underdoped 75K sample (curves are labeled in units of π/a). The thick vertical bar indicates the position of the higher energy feature, at which the spectrum changes slope as highlighted by the intersecting straight lines

expected for a doped Mott insulator; in addition the hump also loses spectral weight though less rapidly.

This effect has recently been quantified in greater detail, where it was found that the spectral weight of the peak varies linearly with doping, as reproduced in Fig. 5.51. [96,97]. We remark that Ding *et al.* [97] also found the unusual relation that the product of the peak weight times the peak energy is constant with doping.

The hump below T_c is clearly related to the superconducting gap, given the weak doping dependence of the ratio between the hump and quasiparticle peak positions at $(\pi, 0)$, shown in Fig. 5.50c. Tunneling data find this same correlation on a wide variety of high-T_c materials whose energy gaps vary by a factor of 30 [63].

To motivate the analysis below that firmly establishes the mode interpretation of of the peak/dip/hump spectra and its connection with neutron data, we note that the spectral dip represents a pairing induced gap in the in-

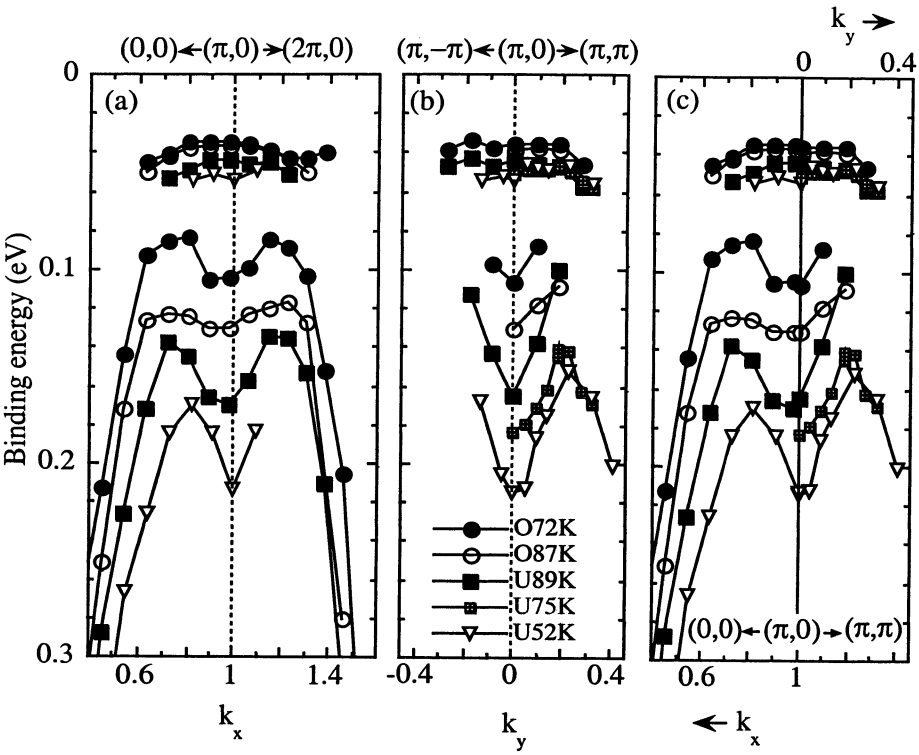

Fig. 5.49. Doping dependence of the dispersion from (a) $(\pi, 0) \rightarrow (\pi \pm \pi, 0)$, (b) $(\pi, 0) \rightarrow (\pi, \pm\pi)$, and (c) both directions, for the peak and hump in the superconducting state. U is underdoped and O is overdoped. Points were obtained by polynomial fits to the data, and are consistent with the simpler criterion used in Fig. 5.48

coherent part of the spectral function at $(\pi, 0)$ occurring at an energy $\Delta + \Omega_0$, where Δ is the superconducting gap and Ω_0 is the mode energy. We can estimate the mode energy from ARPES data from the energy difference between the dip $(\Delta + \Omega_0)$ and the quasiparticle peak (Δ).

In Fig. 5.52b we plot the mode energy as estimated from ARPES for various doping levels as a function of T_c and compare it with neutron measurements. We find striking agreement both in terms of the energy scale and its doping dependence [125]. The same agreement, in greater detail, has been recently found using tunneling data [126], as shown in Fig. 5.53. We note that the mode energy inferred from ARPES decreases with underdoping, just like the neutron data, unlike the gap energy (Fig. 5.50b), which increases. This can be seen directly in the raw data, shown in Fig. 5.52a. This is also seen from the tunneling data, where they have found that the mode energy scales with doping as $5T_c$, just like the neutron resonance. An interesting

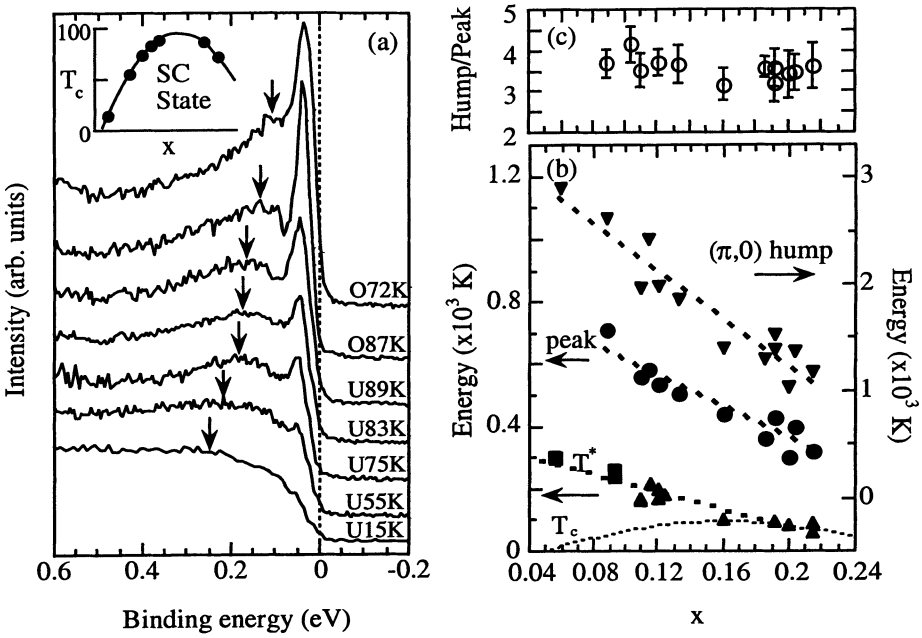

Fig. 5.50. Dependence of energy scale on carrier density: (a) Doping dependence of the spectra (T=15K) at the $(\pi, 0)$ point. The inset shows T_c vs. doping. (b) Doping dependence of T^*, and the peak and hump binding energies in the superconducting state along with their ratio (c), as a function of doping, x. The empirical relation between T_c and x is given by $T_c/T_c^{max} = 1 - 82.6(x - 0.16)^2$ with T_c^{max}=95K. For T^*, solid squares represent lower bounds

point from the tunneling is that the ratio of the mode energy to the gap energy saturates to 2 in the overdoped limit, as would be expected for a collective mode sitting below a continuum with a gap of 2Δ. Moreover, there is strong correlation between the temperature dependences in the ARPES and neutron data. While neutrons see a sharp mode only below T_c, a smeared out remnant persists up to T^* [127]. As the sharpness of the mode is responsible for the sharp spectral dip, one then sees the correlation with ARPES where the dip disappears above T_c, but with a remnant of the hump persisting to T^*.

An important feature of the neutron data is that the mode only exists in a narrow momentum range about (π, π), and is magnetic in origin. To see a further connection with ARPES, we return to the results of Fig. 5.49. Note the dispersion along the two orthogonal directions are similar (Fig. 5.49c), unlike the dispersion inferred in the normal state. As these two directions are related by a (π, π) translation $((x, 0) \equiv (0, -x); (0, -x) + (\pi, \pi) = (\pi, \pi - x))$, we see that the hump dispersion is clearly reflecting the (π, π) nature of the

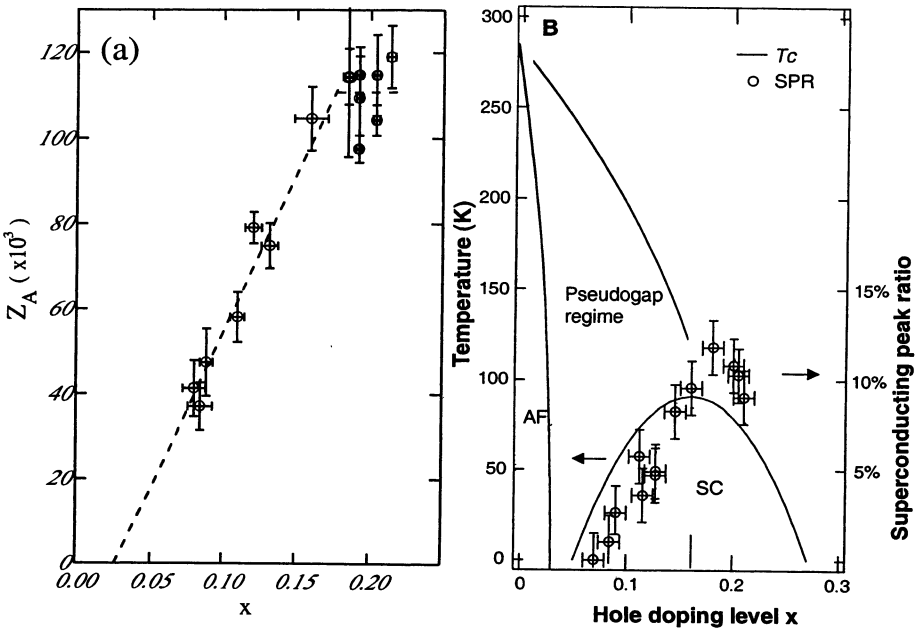

Fig. 5.51. (a) Doping dependence of the low–T (14 K) coherent weight (z_A). The dashed line is a guideline showing that z_A increases linearly on the underdoped side, and tapers off on the overdoped side. (from Ref. [97]) (b) The doping dependence of the superconducting peak ratio (SPR) is plotted over a typical Bi2212 phase diagram. The solid line is a guide to the eye. Horizontal error bars denote uncertainty in determining the doping level (±0.01); vertical error bars denote uncertainty in determining the SPR (±1.5%). AF, antiferromagnetic regime; SC, superconducting regime (from Ref. [96])

collective mode. This dispersion is also consistent with a number of models in the literature which identify the high energy feature in the pseudogap regime as a remnant of the insulating magnet [128]. We note, though, that the mode is due to quasiparticle pair creation and thus not just a continuation of the spin wave mode from the antiferromagnet [129].

This brings up a question that is at the heart of the high T_c problem: how can a feature which can be understood as a strong coupling effect of superconductivity, as discussed above, turn out to have a dispersion that resembles that of a magnetic insulator? The reason is that the collective mode has the same wavevector, (π, π), which characterizes the magnetic order of the insulator. It is easy to demonstrate that in the limit that the mode energy goes to zero (long range order), one actually reproduces a symmetric dispersion similar to that in Fig. 5.49c, with the spectral gap determined by the strength of the mode [41]. This is in accord with the increase in the hump energy with underdoping (Fig. 5.50b) tracking the rise in the neutron mode intensity.

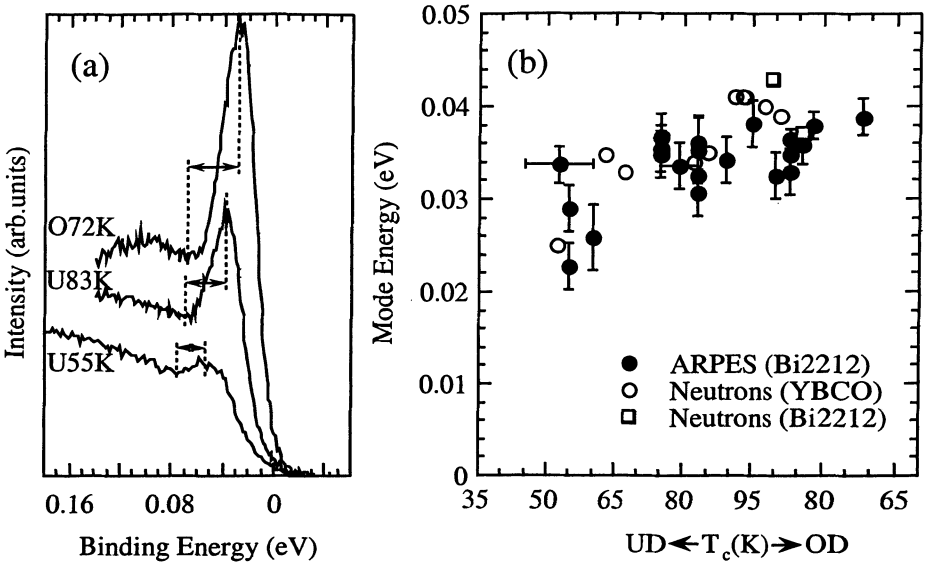

Fig. 5.52. Doping dependence of the mode energy: (a) Spectra at $(\pi, 0)$ showing the decrease in the energy separation of the peak and dip with underdoping. Peak and dip locations were obtained by independent polynomial fits and carefully checked for the effects of energy resolution. (b) Doping dependence of the collective mode energy inferred from ARPES together with that inferred from neutron data [125]

Since the hump scales with the superconducting gap, the obvious implication is that the mode is intimately connected with pairing, a conclusion which can also be made by relating the mode to the superconducting condensation energy [130]. That is, high T_c superconductivity is likely due to the same magnetic correlations which characterize the insulator and give rise to the mode.

5.7.7 Dispersion Kink of Nodal Quasiparticles

So far, our discussion has largely been centered on behavior near the $(\pi, 0)$ point of the zone. We now turn to consideration of other $\mathbf{k}$ vectors.

Remarkably, we find that the effects discussed above are manifest even on the zone diagonal where the gap vanishes, with significant changes in both the spectral lineshape and dispersion below T_c, relative to the normal state where the nodal points exhibit quantum critical scaling [23]. Specifically, below T_c a kink in the dispersion develops along the diagonal at a finite energy ($\sim$70 meV) [24,25]. This is accompanied, as required by Kramers–Kronig relations, by a reduction in the linewidth leading to well-defined quasiparticles [33]. As one moves away from the node, the renormalization increases, and the kink

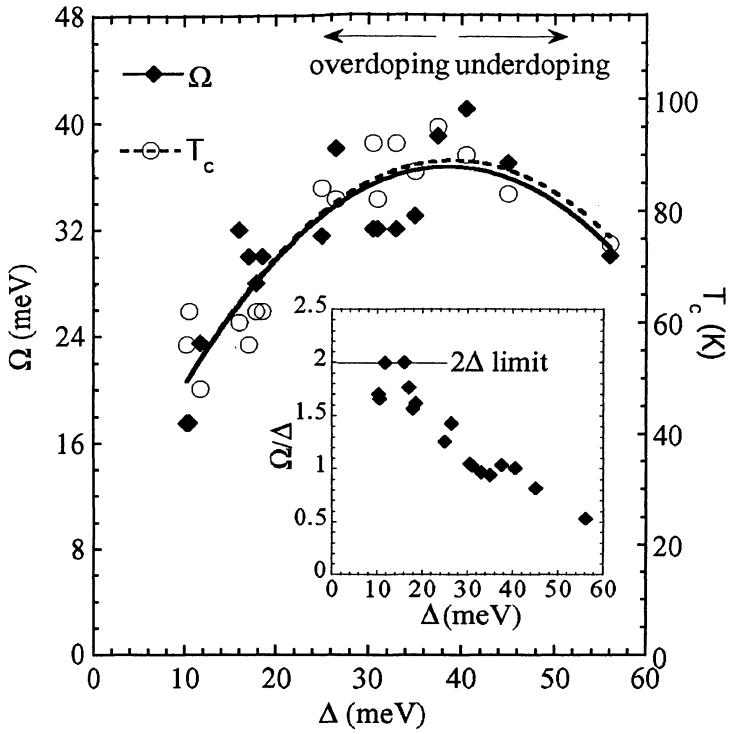

Fig. 5.53. Measured mode energy Ω and bulk T_c value vs. measured gap value Δ for 17 junctions over a wide doping range from UD74K to OD48K. Solid and dashed lines are quadratic fits of Ω and T_c vs. Δ. Inset shows Ω/Δ vs. Δ (from Ref. [126])

in dispersion along the diagonal smoothly evolves into the spectral dip, with the same characteristic energy scale throughout the zone.

In Fig. 5.54a, we plot the dispersion of the spectral peak above T_c obtained from constant $\mathbf{k}$ scans (energy distribution curves or EDCs), and the peak in momentum obtained from constant ω scans (momentum distribution curves or MDCs) [23] from data for a T_c=90K sample along the (π, π) direction [25]. We find that the EDC and MDC peak dispersions are very different, a consequence of the ω dependence of Σ.

To understand this, we start by noting that since $\epsilon_{\mathbf{k}} \simeq v_F^0(k - k_F)$, then from Eq. (5.8) the MDC at fixed ω is a Lorentzian centered at $k = k_F + [\omega - \Sigma'(\omega)]/v_F^0$, with a width (HWHM) $W_M = |\Sigma''(\omega)|/v_F^0$, *provided* (i) Σ is essentially independent of k normal to the Fermi surface, *and* (ii) the dipole matrix elements do not vary significantly with k over the range of interest. That these two conditions are fulfilled can be seen by the nearly Lorentzian MDC lineshape observed in ARPES [23].

On the other hand, in general, the EDC at fixed $\mathbf{k}$ has a non–Lorentzian lineshape reflecting the non–trivial ω–dependence of Σ, in addition to the Fermi cutoff at low energies. Thus the EDC peak is *not* given by $\omega - v_F^0(k - k_F) - \Sigma'(\omega) = 0$ but also involves Σ'', unlike the MDC peak. Further, if the EDC peak is sharp enough, making a Taylor expansion we find that its width (HWHM) is given by $W_E \simeq |\Sigma''(E_k)|/[1 - \partial\Sigma'/\partial\omega|_{E_k}]$, where E_k is the peak position.

We see that it is much simpler to interpret the MDC peak positions, and thus focus on the change in the MDC dispersion going from the normal (N) to the superconducting (SC) state shown in Fig. 5.54b. The striking feature of Fig. 5.54b is the development of a kink in the dispersion below T_c. At fixed ω let the dispersion change from k_N to k_{SC}. Using $v_F^0(k_N - k_{SC}) = \Sigma'_{SC}(\omega) - \Sigma'_N(\omega)$, we directly obtain the change in real part of Σ plotted in Fig. 5.54c. The Kramers–Kronig transformation of $\Sigma'_{SC} - \Sigma'_N$ then yields $\Sigma''_N - \Sigma''_{SC}$, plotted in Fig. 5.54d, which shows that $|\Sigma''_{SC}|$ is smaller than $|\Sigma''_N|$ at low energies.

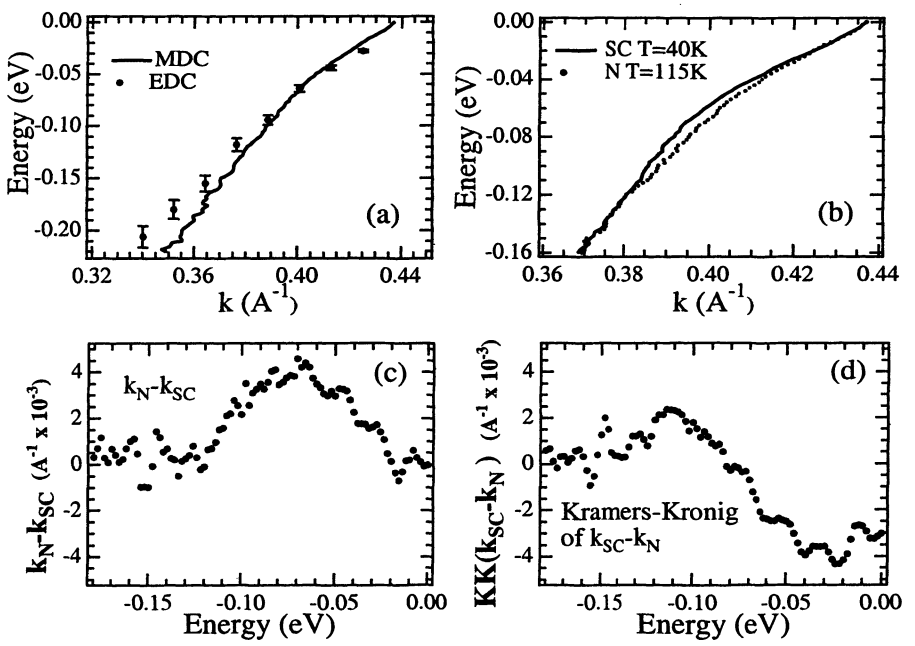

Fig. 5.54. ARPES data along the (π, π) direction at $h\nu$=28eV. (a) EDC dispersion in the normal state compared to the MDC dispersion. The EDCs are shown in Fig. 5.55d. (b) MDC dispersions in the superconducting state (T=40K) and normal state (T=115K). (c) change in MDC dispersion from (b). (d) Kramers–Kronig transform of (c)

We compare these results in Fig. 5.55a with the $W_M = |\Sigma''|/v_F^0$ estimated directly from the MDC Lorentzian linewidths. The normal state curve was obtained from a linear fit to the corresponding MDC width data points in Fig. 5.55a, and then the data from Fig. 5.54d was added to it to generate the low temperature curve. We are thus able to make a quantitative connection between the appearance of a kink in the (MDC) dispersion below T_c and a drop in the low energy scattering rate in the superconducting state relative to the normal state, which leads to the appearance of quasiparticles below T_c [33]. We emphasize that we have estimated these T–dependent changes in the complex self–energy without making fits to the EDC lineshape, thus avoiding the problem of modeling the ω dependence of Σ and the extrinsic background.

In Fig. 5.55b, we plot the EDC width obtained as explained in Ref. [33] from Fig. 5.55d. As an interesting exercise, we present in Fig. 5.55c the ratio of this EDC width to the MDC width of Fig. 5.55a (dotted lines), and compare it to the renormalized MDC velocities, $1/v \equiv dk/d\omega$, obtained directly by numerical differentiation of Fig. 5.54b (solid lines). We note that only for a sufficiently narrow EDC lineshape is the ratio $W_E/W_M \simeq v_F^0/[1-\partial\Sigma'/\partial\omega] = v_F$. Interestingly, only in the superconducting state below the kink energy do these two quantities agree, which implies that only in this case does one have a Fermi liquid.

Similar kinks in the dispersion have been seen by ARPES in normal metals due to the electron–phonon interaction [131]. Phonons cannot be the cause here, since the kink disappears above T_c. Rather, this effect is suggestive of coupling to an electronic collective excitation which only appears below T_c. Recently, this view has been challenged by Lanzara *et al.* [132], and we discuss this work at the end of this subsection.

We now study how the lineshape and dispersion evolve as we move along the Fermi surface. An analysis similar to the above is possible, but more complicated due to the presence of an energy gap [26]. We will thus confine ourselves here to a general description of the data. In Fig. 5.56, we plot raw intensities for a series of cuts parallel to the MY direction (normal state in left panels, superconducting state in middle panels). We start from the bottom row that corresponds to a cut close to the node and reveals the same kink described above. As we move towards $(\pi, 0)$, the dispersion kink (middle panels) becomes more pronounced and at around k_x=0.55 develops into a break separating the faster dispersing high energy part of the spectrum from the slower dispersing low energy part. This break leads to the appearance of two features in the EDCs, shown in the right panels of Fig. 5.56. Further towards $(\pi, 0)$, the low energy feature, the quasiparticle peak, becomes almost dispersionless. At the $(\pi, 0)$ point, this break effect becomes the most pronounced, giving rise to the peak/dip/hump in the EDC. We note that there is a continuous evolution in the zone from kink to break, and these features all occur at exactly the same energy.

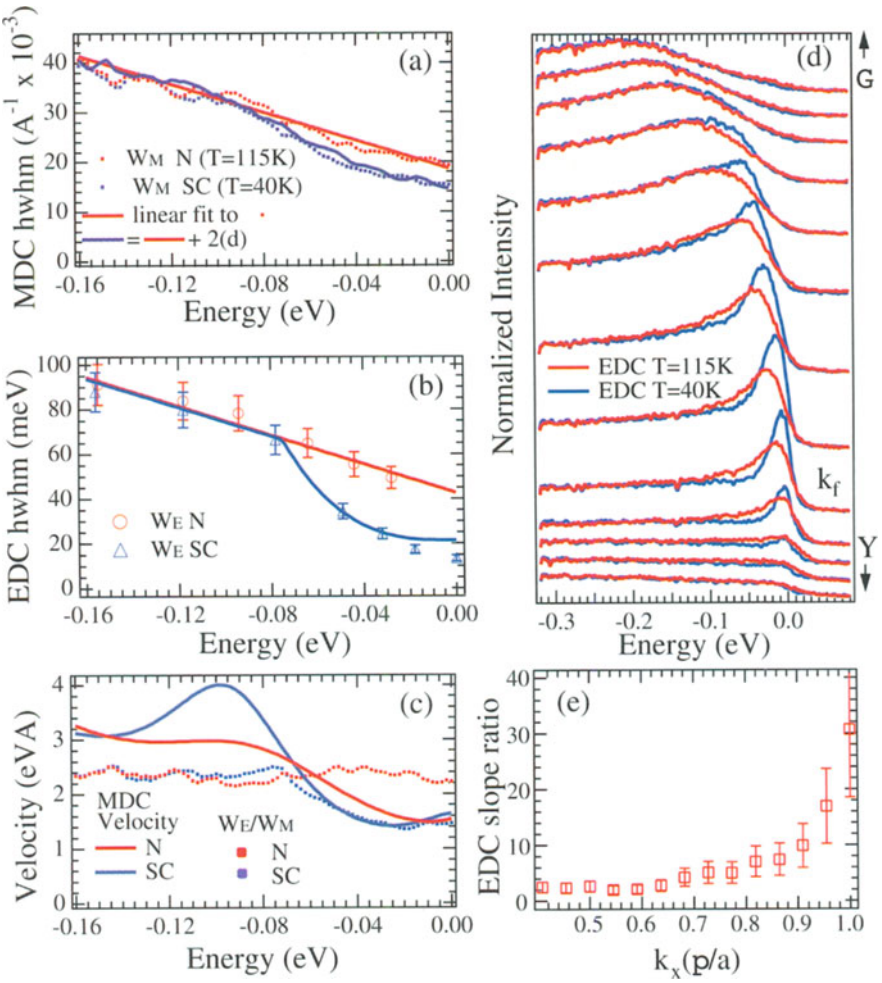

Fig. 5.55. (a) Comparison of change in Σ'' obtained directly from the MDC widths (HWHM) to the one obtained from the dispersion in Fig. 5.54d by using the Kramers–Kronig transform. (b) HWHM width obtained from EDCs shown in (d). Lines marked by fit are linear in normal state and linear/cubic in superconducting state. The data in (b) fall below the fits at low energies because of the Fermi cut–off of the EDCs. (c) Renormalized MDC velocity obtained from differentiating Fig. 5.54b (solid lines), compared to the ratio W_E/W_M from (a) and (b). (e) Ratio of EDC dispersion slopes above and below the kink energy at various points along the Fermi surface (from middle panels of Fig. 5.56)

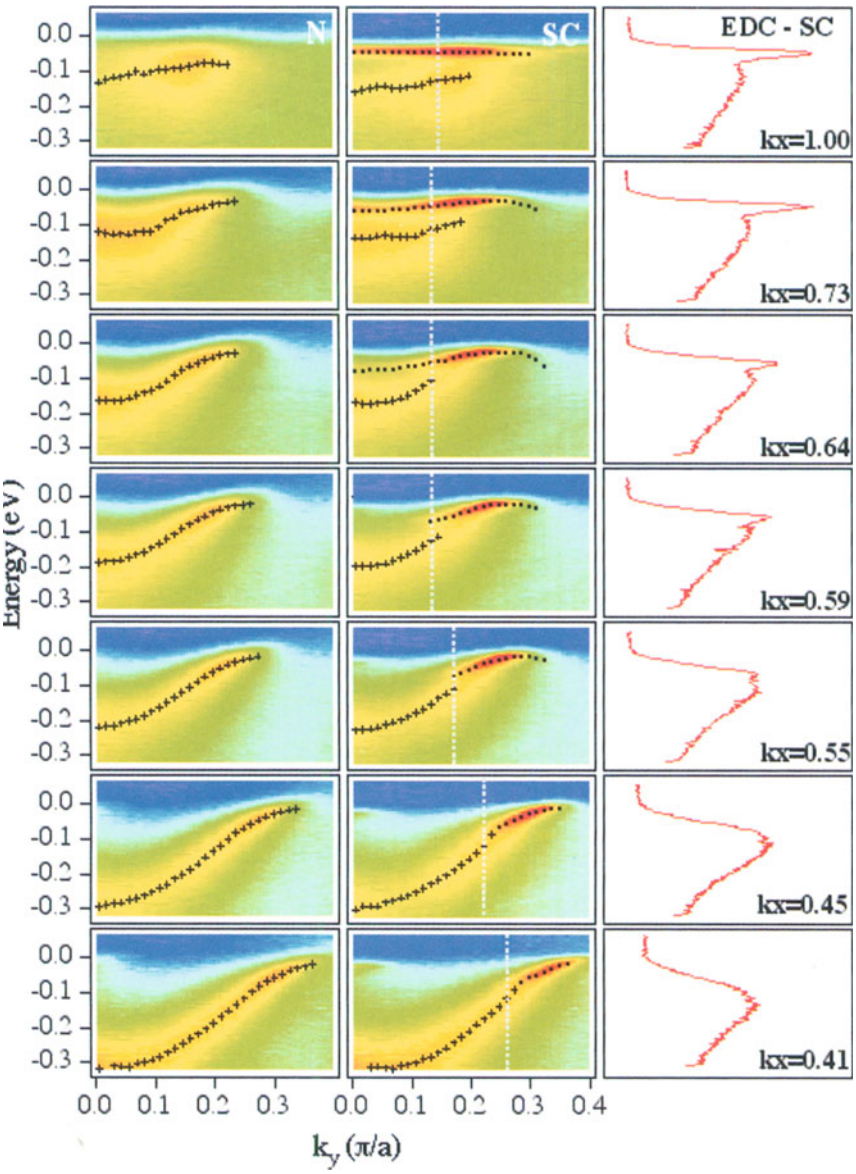

Fig. 5.56. Left panels: Log of normal state ($h\nu$=22eV, T=140K) ARPES intensity along selected cuts parallel to MY. EDC peak positions are indicated by crosses. Middle panels: Log of superconducting state (T=40K) intensity at the same cuts as for left panels. Crosses indicate positions of broad high energy peaks, dots sharp low energy peaks. Right panels: EDCs at locations marked by the vertical lines in the middle panels

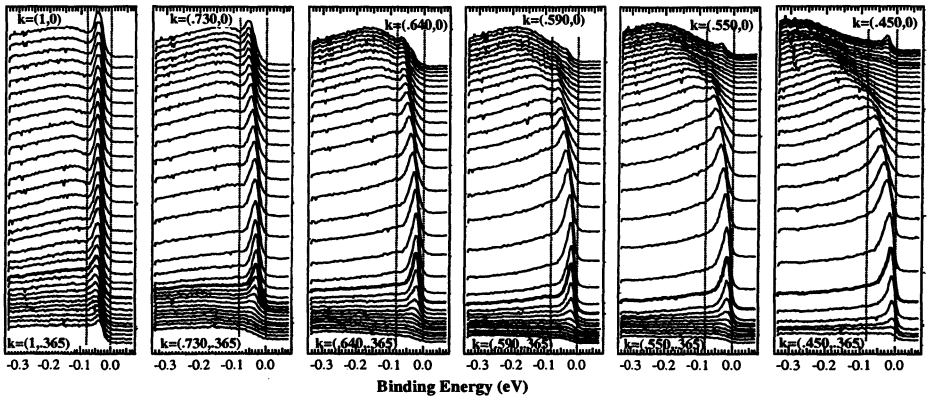

Fig. 5.57. ARPES intensity (T=40K) along selected cuts from Fig. 5.56. The thick lined curves correspond approximately to $\mathbf{k}_F$. Vertical lines are at 0 and -80 meV

The above evolution is suggestive of the self–energy becoming stronger as the $(\pi, 0)$ point is approached. This can be quantified from the observed change in the dispersion. In Fig. 5.55e we plot the ratio of the EDC dispersion slope above and below the kink energy at various points along the Fermi surface obtained from middle panels of Fig. 5.56. Near the node, this ratio is around 2, but becomes large near the $(\pi, 0)$ point because of the nearly dispersionless quasiparticle peak. A different behavior was inferred in Ref. [132], but in their case, the cuts near $(\pi, 0)$ were perpendicular to ours, and thus not normal to the Fermi surface.

The lineshape also indicates that the self–energy is larger near $(\pi, 0)$, as is evident in Fig. 5.57. Along the diagonal, there is a gentle reduction in Σ'' at low energies, as shown in Fig. 5.55a and b, with an onset at the dispersion kink energy scale. In contrast, near the $(\pi, 0)$ point there must be a very rapid change in Σ'' in order to produce a spectral dip, as discussed above. Despite these differences, it is important to note that these changes take place throughout the zone at the same characteristic energy scale (vertical line in Fig. 5.57).

As also discussed above, the $(\pi, 0)$ ARPES spectra can be naturally explained in terms of the interaction of the electron with a collective mode of electronic origin which only exists below T_c. It was further speculated that this mode was the neutron resonance. Here we have shown that dispersion and lineshape anomalies have a continuous evolution throughout the zone and are characterized by a single energy scale. This leads us to suggest that the same electron–mode interaction determines the superconducting lineshape and dispersion at all points in the zone, including the nodal direction. In essence, there is a suppression of the low energy scattering rate below the

finite energy of the mode. Of course, since the neutron mode is characterized by a (π, π) wavevector, one would expect its effect on the lineshape to be much stronger at points in the zone which are spanned by (π, π), as observed here.

A similar conclusion has been reached by Johnson *et al.* [133], where they find that the kink energy scales with doping like the neutron resonance (Fig. 5.58a), and that the temperature dependence of Σ' tracks that of the resonance intensity (Fig. 5.58b). Moreover, they find that Σ' increases with underdoping (Fig. 5.58a), much like that extracted from the peak/dip/hump lineshape at $(\pi, 0)$.

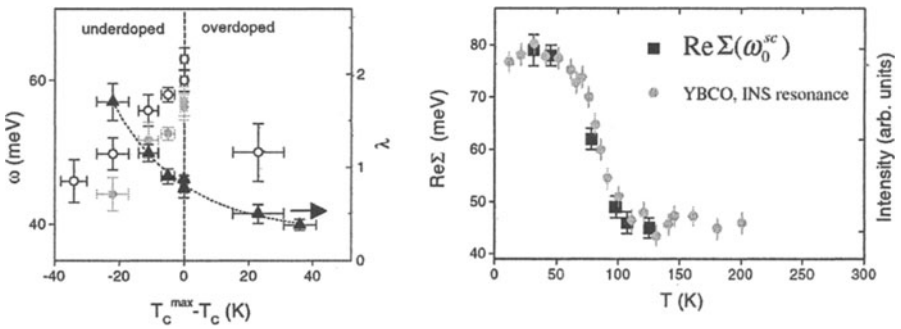

Fig. 5.58. Left panel: Plot of ω_0, the energy of the maximum value of ReΣ in the superconducting state (open circles), and ω_0^{SC} (gray circles), the energy of the maximum in difference between the superconducting and normal state values plotted as a function of T_c referenced to the maximum T_c^{max} ($\equiv$ 91 K). The coupling constant λ (black triangles) is referenced to the right–hand scale. Right panel: Temperature dependence of Re$\Sigma(\omega_0^{SC})$ from the nodal line for the UD69K sample (black squares) compared with the temperature dependence of the intensity of the resonance mode observed in inelastic neutron scattering studies of underdoped $YBa_2Cu_3O_{6+x}$, T_c = 74 K (gray circles) (adapted from Ref. [133])

Detailed calculations which take into account the momentum dependence of the neutron resonance give an extremely good description of the experimental data [134]. These results can be understood by studying the Feynman diagram of Fig. 5.45. The key point is that the neutron resonance has a finite width in momentum space, corresponding to a short correlation length of order 2 lattice constants. Because of this, there is now an internal sum over momentum in the diagram, which will be dominated by the flat regions of the fermionic dispersion around the $(\pi, 0)$ points. This means that structure in the electron self–energy will occur at an energy of $\Delta_{max} + \Omega_{res}$, independent of external momentum. This explains why the energy scale is invariant throughout the zone. On the other hand, as the external momentum is swept,

the momentum dependence of the neutron form factor is probed. Since the latter peaks at $Q = (\pi, \pi)$, then the magnitude of the self–energy will be maximal at $(\pi, 0)$, since these points are connected by Q, and minimum at the node. This explains why the peak/dip/hump effect first weakens into a "break" effect and then into a dispersion kink as the node is approached. These calculations have been recently extended to incorporate bilayer splitting effects [135], and are able to explain a number of unusual lineshape and dispersion features present in data on heavily overdoped Bi2212 [65–67, 136]

As mentioned above, this picture has been challenged by Lanzara *et al.* [132]. These authors claim that the kink is still present above T_c, except it is smeared in energy. Moreover, they find that a kink is present in a large variety of cuprates, including Bi2201 and LSCO, with an energy which is material and doping independent, as shown in Fig. 5.59. They argue that all of these observations are in support of a phonon interpretation of the kink.

Although initially attractive, there are some problems with this scenario. First, in regards to the kink above T_c, it has been claimed by Johnson *et al.* [133] that the "kink" above T_c is simply the curvature in the dispersion one expects based on marginal Fermi liquid theory. In support of this, they argue that the maximum in the real part of Σ is at a different energy in the normal state than in the superconducting state. Though this appears to be the case, there is indeed residual structure in the normal state self–energy at the kink energy in the optimal doped sample we have looked at. On the other hand, our normal state data actually corresponds to the pseudogap phase, and as a residual of the neutron resonance is present in the pseudogap phase, the residual "kink" above T_c (if really there) does not rule out a magnetic interpretation. Moreover, as Johnson *et al.*convincingly showed (Fig. 5.58b), there is definitely a large component to the self–energy which follows the same order parameter like temperature variation that the neutron resonance intensity does. This observation is supported by recent work of Gromko *et al.* [136] concerning a dispersion kink in the bonding band of heavily overdoped Bi2212 near $(\pi, 0)$.

Second, in regards to constancy of the energy scale, this is indeed an interesting observation, though we note this statement contradicts that of Johnson *et al.*concerning the doping dependence of the kink energy mentioned above (Fig. 5.58). Also, even in a phonon model, the kink energy should occur at the sum of the maximum gap energy plus the phonon energy. Why the sum of these two numbers should be doping and material independent is a real puzzle (as it would be for a magnetic interpretation as well). And, why only one phonon would be relevant, despite the large number of phonons present in the cuprates, is another puzzle. Still, a phonon model for the kink has certain attractions, as discussed by Lanzara *et al.* [132]. Certainly, more work is needed to definitively resolve the controversies surrounding the origin of the dispersion kink.

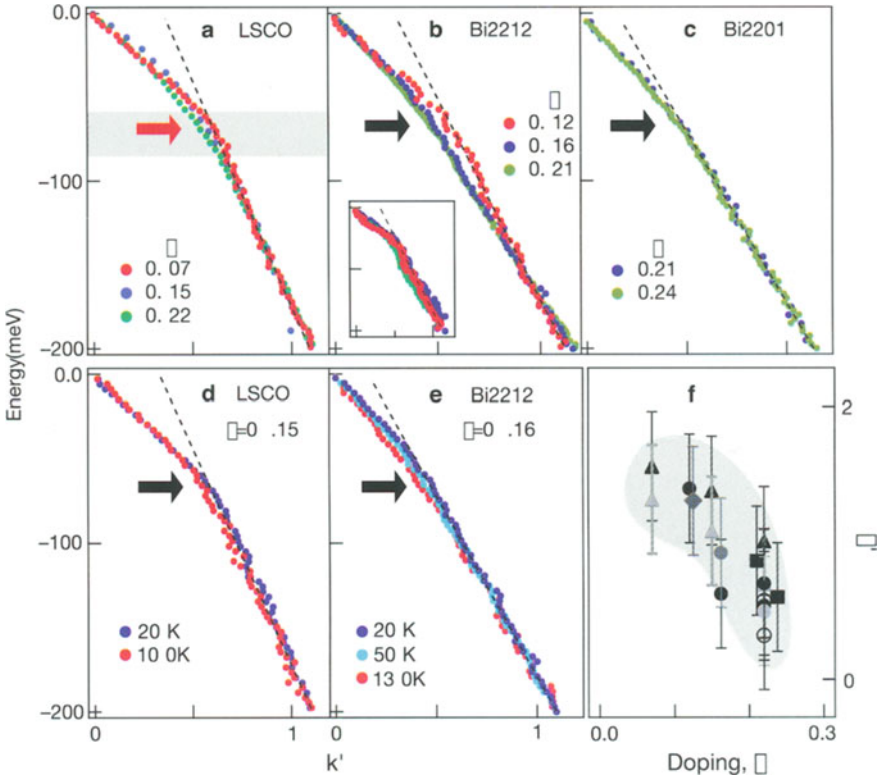

Fig. 5.59. Ubiquity of a sudden change ('kink') in the dispersion. Top panels are plots of the dispersion (derived from the momentum distribution curves) along $(0,0) - (\pi,\pi)$ (except panel **b** inset, which is off this line) versus the rescaled momentum k' for different samples and at different doping levels. a–c, Doping (δ) dependence of LSCO (at 20 K; a), Bi2212 (superconducting state, 20 K; b), and Bi2201 (normal state, 30 K; c). Dotted lines are guides to the eye. The kink position in **a** is compared with the phonon energy at $q = (\pi, 0)$ (thick red arrow) and the phonon width and dispersion (shaded area) from neutron data. The doping was determined from the T_c versus doping universal curve. Inset in b, dispersions off the (0, 0) – (π,π) direction, showing also a sharpening of the kink on moving away from the nodal direction. The black arrows indicate the position of the kink in the dispersions. **d,e**, Temperature dependence of the dispersions for LSCO (d, optimally doped) and Bi2212 (e, optimally doped). f, Doping dependence of λ along the (0, 0) – (π,π) direction as a function of doping. Data are shown for LSCO (filled triangles) and NdLSCO (1/8 doping; filled diamonds), Bi2201 (filled squares) and Bi2212 (filled circles in the first Brillouin zone, and unfilled circles in the second zone). The different shadings represent data obtained in different experimental runs. Blue area is a guide to the eye. (adapted from Ref. [132])

5.7.8 Condensation Energy

We conclude this section by discussing the relation of ARPES data to the superconducting condensation energy.

We begin with the assumption that the condensation energy does not have a component due to phonons. To proceed, we assume an effective single–band Hamiltonian which involves only two particle interactions. Then, simply exploiting standard formulas for the internal energy $U = \langle H - \mu N \rangle$ (μ is the chemical potential, and N the number of particles) in terms of the one–particle Green's function, we obtain [137]

$$U_N - U_S = \sum_{\mathbf{k}} \int_{-\infty}^{+\infty} d\omega (\omega + \epsilon_k) f(\omega) \left[A_N(\mathbf{k}, \omega) - A_S(\mathbf{k}, \omega) \right] , \qquad (5.21)$$

where the spin variable has been summed over. Here and below the subscript N stands for the normal state, S for the superconducting state. $A(\mathbf{k}, \omega)$ is the single–particle spectral function, $f(\omega)$ the Fermi function, and ϵ_k the bare energy dispersion which defines the kinetic energy part of the Hamiltonian. Note that the μN term has been absorbed into ω and ϵ_k, that is, these quantities are defined relative to the appropriate chemical potential, μ_N or μ_S. In general, μ_N and μ_S will be different. This difference has to be taken into account, since the condensation energy is small.

The condensation energy is defined by the zero temperature limit of $U_N - U_S$ in the above expression. Note that this involves defining (or somehow extrapolating to) the normal state spectral function at $T = 0$. Such an extrapolation, which we return to below, is not specific to our approach, but required in all estimates of the condensation energy. We remark that Eq. (5.21) yields the correct condensation energy, $N(0)\Delta^2/2$, for the BCS theory of superconductivity.

We also note that Eq. (5.21) can also be broken up into two pieces to individually yield the thermal expectation value of the kinetic energy (using $2\epsilon_k$ in the parentheses in front of $f(\omega)$), and that of the potential energy (using $\omega - \epsilon_k$ instead).

The great advantage of Eq. (5.21) is that it involves just the occupied part of the single particle spectral function, which is measured by ARPES. Therefore, in principle, one should be able to derive the condensation energy from such data, if an appropriate extrapolation of the normal state spectral function to T=0 can be made. On the other hand, a disadvantage is that the bare energies, ϵ_k, are *a priori* unknown. Note that these are not directly obtained from the measured ARPES dispersion, which already includes many–body renormalizations. Rather, they could be determined by projecting the kinetic energy operator onto the single–band subspace.

Some of the problems associated with an analysis based on experimental data can be appreciated. First, the condensation energy is obtained by subtracting two large numbers. Therefore, normalization of the data becomes a central concern. Problems in this regard when considering $n(\mathbf{k})$, which is the

zeroth moment of the ARPES data, were discussed previously [138]. For the first moment, these problems are further amplified due to the ω weighting in the integrand. When analyzing real data, we have found that the high energy tail contribution to the first moment is very sensitive to how the data are normalized. Different choices of normalization can even lead to changes in sign of the first moment.

Another concern concerns the $\mathbf{k}$ sum in Eq. (5.21). ARPES has $\mathbf{k}$–dependent matrix elements, which lead to weighting factors not present in Eq. (5.21). These effects can in principle be factored out by either theoretical estimates of the matrix elements [139], or by comparing data at different photon energies to obtain information on them [9].

Another issue in connection with experimental data is an appropriate extrapolation of the normal state to zero temperature. Information on this can be obtained by analyzing the temperature dependence of the normal state data, remembering that the Fermi function will cause a temperature dependence of the data which should be factored out before attempting the $T = 0$ extrapolation. We finally note that the temperature dependence issue is strongly coupled to the normalization problem mentioned above. In ARPES, the absolute intensity can change due to temperature dependent changes in absorbed gasses, surface doping level, and sample location. Changes of background emission with temperature is another potential problem.

Despite these concerns, we believe that with careful experimentation, many of these difficulties can be overcome, and even if an exact determination of Eq. (5.21) is not possible, insights into the origin of the condensation energy will certainly be forthcoming from the data. This is particularly true for ARPES, which has the advantage of being $\mathbf{k}$ resolved and thus giving one information on the relative contribution of different $\mathbf{k}$ vectors to the condensation energy.

Insights into what real data might indicate have been offered by us [137] in the context of the "mode" model illustrated in Fig. 5.47. What we found was that for parameters characteristic of optimal doped ARPES data, the superconducting condensation was driven by kinetic energy lowering, as opposed to the potential energy lowering found in BCS theory. This occurs because n_k becomes sharper in the superconducting state than in the normal state. In essence, the normal state is a non Fermi liquid and the superconducting state is a Fermi liquid, so what occurs is that the effect of quasiparticle formation on sharpening n_k is greater than the effect of particle–hole mixing on smearing it. The net result is a sharpening, leading to a lowering in kinetic energy. In BCS theory, the normal state is a Fermi liquid, and thus only the particle–hole mixing effect is present, leading to a net smearing of n_k and thus an increase in the kinetic energy. The same model can be used to evaluate the optical sum rule [140], and what is found is a violation of the sum rule with a sign and magnitude consistent with recent optics experiments [141]. It

will be of great interest to see whether these results can be confirmed directly from ARPES data, as speculated early on by Anderson [142].

5.8 Summary

We review angle resolved photoemission spectroscopy (ARPES) results on the high T_c superconductors, focusing primarily on results obtained on the quasi–two dimensional cuprate $Bi_2Sr_2CaCu_2O_8$ and its single layer counterpart $Bi_2Sr_2CuO_6$. The topics treated include the basics of photoemission and methodologies for analyzing spectra, normal state electronic structure including the Fermi surface, the superconducting energy gap, the normal state pseudogap, and the electron self–energy as determined from photoemission lineshapes.

Acknowledgments

Much of the experimental work described in this article was done in collaboration with Hong Ding, Adam Kaminski, Helen Fretwell, Kazimierz Gofron, Joel Mesot, Stephan Rosenkranz, Tsunehiro Takeuchi, and the group of Takashi Takahashi, including Takafumi Sato and Takayoshi Yokoya. We were very fortunate to have available to us the samples from Kazuo Kadowaki, T. Mochiku, David Hinks, Prasenjit Guptasarma, Boyd Veal, Z. Z. Li, and Helene Raffy. We have also benefited from many interactions over the years with Phil Anderson, Alex Abrikosov, Jim Allen, Cliff Olson, Ole Andersen, Al Arko, Bertram Batlogg, Arun Bansil, Matthias Eschrig, Atsushi Fujimori, Peter Johnson, Bob Laughlin, Bob Schrieffer, Z. X. Shen, and Chandra Varma.

This work was supported by the National Science Foundation, Grant No. DMR 9974401 (JCC) and the U.S. Department of Energy, Office of Science, under Contract No. W-31-109-ENG-38 (JCC and MRN). MR is grateful for partial support from the Indian DST through the Swarnajayanti scheme.

References

1. A. Chainani, T. Yokoya, T. Kiss, S. Shin, Phys. Rev. Lett. **85**, 1966 (2000).
2. A. Damascelli, Z.-X. Shen, Z. Hussain, Rev. Mod. Phys. (2002), cond-mat/0208504.
3. D.L. Lynch and C.G Olson, *Photoemission studies of high–temperature superconductors* (Cambridge University Press, Cambridge, UK, 1999).
4. S. Hüfner, *Photoelectron Spectroscopy* (Springer–Verlag, Berlin, 1996), and references therein.
5. C.N. Berglund and W.E. Spicer, Phys. Rev. **136**, A1030 and A1044 (1964).
6. In general, the matrix element also contains a $\mathbf{p} \cdot \mathbf{A}$ term. Above the bulk plasma frequency, the light penetrates deeply into the solid, making this term small. This "surface photoemission" has not been prominent in the many studies of the cuprates, and we will henceforth ignore it.
7. J. Hermanson, Solid State Comm. **22**, 9 (1977).

8. For a review of the first five years of work on the cuprates, see Sec. 4 and 5 of Z. X. Shen and D. S. Dessau, Phys. Repts. **253**, 1 (1995).
9. J. Mesot, M. Randeria, M. R. Norman, A. Kaminski, H.M. Fretwell, J. C. Campuzano, H. Ding, T. Takeuchi, T. Sato, T. Yokoya, T. Takahashi, I. Chong, T. Terashima, M. Takano, T. Mochiku, and K. Kadowaki, Phys. Rev. B **63**, 224516 (2001).
10. H. Hertz, Ann. Physik **31**, 983 (1887).
11. W. L. Schaich and N. W. Ashcroft, Phys. Rev. B **3**, 2452 (1971).
12. C. Caroli, D. Lederer–Rozenblatt, B. Roulet, and D. Saint-James, Phys. Rev. B **8**, 4552 (1973).
13. J. B. Pendry, Surf. Sci. **57**, 679 (1976). For a review of applications of these methods to the cuprates, see: A. Bansil and M. Lindroos, J. Phys. Chem. Solids **56**, 1855 (1995).
14. C.G. Larsson, Surface Science **152/153**, 213 (1985); *ibid* **162**, 19 (1985).
15. P.A.P. Lindberg, L.I. Johansson and A.N. Christensen, Surface Science **197**, 353 (1987).
16. F.L. Hopkinson, J.B. Pendry, and D.J. Titterington, Comput. Phys. Comm. **26**, 111 (1980).
17. A. Bansil, M. Lindroos, and J.C. Campuzano, Proc. Mater. Res. Soc. **253**, 519 (1992); M. Lindroos, A. Bansil, K. Gofron, H. Ding, J.C. Campuzano, R. Liu, and B.W. Veal, Physica C **212**, 347 (1993).
18. H.L. Edwards, J.T. Markert and A.L. de Lozanne, Phys. Rev. Lett. **69**, 2967 (1992).
19. N. V. Smith, P. Thiry, and Y. Petroff, Phys. Rev. B **47**, 15476 (1993).
20. See, e.g., L. Hedin and S. Lundquist, *Solid State Physics* **23**, 1 (Academic, New York, 1969).
21. M. Randeria, H. Ding, J-C. Campuzano, A. Bellman, G. Jennings, T. Yokoya, T. Takahashi, H. Katayama-Yoshida, T. Mochiku, and K. Kadowaki, Phys. Rev. Lett. **74**, 4951 (1995).
22. H. Ding, J. C. Campuzano, A. F. Bellman, T. Yokoya, M. R. Norman, M. Randeria, T. Takahashi, H. Katayama-Yoshida, T. Mochiku, K. Kadowaki, G. Jennings, Phys. Rev. Lett. **74**, 2784 (1995) and **75**, 1425 (E) (1995).
23. A. V. Federov, T. Valla, P. D. Johnson, Q. Li, G. D. Gu, N. Koshizuka, Phys. Rev. Lett. **82**, 2179 (1999); T. Valla, A.V. Fedorov, P.D. Johnson, B.O. Wells, S.L. Hulbert, Q. Li, G.D. Gu, and N. Koshizuka, Science **285**, 2110 (1999); T. Valla, A. V. Fedorov, P. D. Johnson, Q. Li, G. D. Gu, N. Koshizuka, Phys. Rev. Lett. **85**, 828 (2000).
24. P.V. Bogdanov, A. Lanzara, S.A. Kellar, X.J. Zhou, E.D. Lu, W.J. Zheng, G. Gu, J.-I. Shimoyama, K. Kishio, H. Ikeda, R. Yoshizaki, Z. Hussain, and Z. X. Shen, Phys. Rev. Lett. **85**, 2581 (2000).
25. A. Kaminski, M. Randeria, J. C. Campuzano, M. R. Norman, H. Fretwell, J. Mesot, T. Sato, T. Takahashi, and K. Kadowaki, Phys. Rev. Lett. **86**, 1070 (2001).
26. M. R. Norman, M. Eschrig, A. Kaminski, J. C. Campuzano, Phys. Rev. B **64**, 184508 (2001).
27. W. E. Pickett, Rev. Mod. Phys. **61**, 433 (1989).
28. P. W. Anderson, *The Theory of Superconductivity in the High-T_c Cuprates* (Princeton Univ. Pr., Princeton, 1997).
29. O. K. Andersen A. I. Liechtenstein, O. Jepsen, F. Paulsen, J. Phys. Chem. Solids **56**, 1573 (1995).

30. P. W. Anderson, Science **235**, 1196 (1987).
31. C. G. Olson, R. Liu, D. W. Lynch, R. S. List, A. J. Arko, B. W. Veal, Y. C. Chang, P. Z. Jiang, and A. P. Paulikas, Phys. Rev. B **42**, 381 (1990).
32. The electronic structure of the insulator has been extensively studied by the Stanford group, confirming beautifully the predicted valence band maximum at $(\pi/2, \pi/2)$, see B. O. Wells, Z.-X. Shen, A. Matsuura, D. M. King, M. A. Kastner, M. Greven, and R. J. Birgeneau, Phys. Rev. Lett. **74**, 964 (1995).
33. A. Kaminski, J. Mesot, H. Fretwell, J. C. Campuzano, M. R. Norman, M. Randeria, H. Ding, T. Sato, T. Takahashi, T. Mochiku, K. Kadowaki, and H. Hoechst, Phys. Rev. Lett. **84**, 1788 (2000).
34. J. C. Campuzano, G. Jennings, M. Faiz, L. Beaulaigue, B. W. Veal, J. Z. Liu, A. P. Paulikas, K. Vandervoort, H. Claus, Phys. Rev. Lett. **64**, 2308 (1990).
35. D. M. King, Z.-X. Shen, D. S. Dessau, B. O. Wells, W. E. Spicer, A. J. Arko, D. S. Marshall, J. DiCarlo, A. G. Loeser, C. H. Park, E. R. Ratner, J. L. Peng, Z. Y. Li, R. L. Greene, Phys. Rev. Lett. **70**, 3159 (1993); R. O. Anderson, R. Claessen, J. W. Allen, C. G. Olson, C. Janowitz, L. Z. Liu, J.-H. Park, M. B. Maple, Y. Dalichaouch, M. C. de Andrade, R. F. Jardim, E. A. Early, S.-J. Oh, W. P. Ellis, *ibid* **70**, 3163 (1993); N. P. Armitage, D. H. Lu, C. Kim, A. Damascelli, K. M. Shen, F. Ronning, D. L. Feng, P. Bogdanov, Z.-X. Shen, Y. Onose, Y. Taguchi, Y. Tokura, P. K. Mang, N. Kaneko, M. Greven, *ibid* **87**, 147003 (2001); N. P. Armitage, F. Ronning, D. H. Lu, C. Kim, A. Damascelli, K. M. Shen, D. L. Feng, H. Eisaki, Z.-X. Shen, P. K. Mang, N. Kaneko, M. Greven, Y. Onose, Y. Taguchi, Y. Tokura, *ibid* **88**, 257001 (2002).
36. A. Ino, C. Kim, T. Mizokawa, Z.-X. Shen, A. Fujimori, M. Takaba, K. Tamasaku, H. Eisaki, S. Uchida, J. Phys. Soc. Japan **68**, 1496 (1999); A. Ino, C. Kim, M. Nakamura, T. Mizokawa, Z.-X. Shen, A. Fujimori, T. Kakeshita, H. Eisaki, S. Uchida, Phys. Rev. B **62**, 4137 (2000); A. Ino, C. Kim, M. Nakamura, T. Yoshida, T. Mizokawa, Z.-X. Shen, A. Fujimori, T. Kakeshita, H. Eisaki, S. Uchida, *ibid* **65**, 094504 (2002); T. Yoshida, X. J. Zhou, M. Nakamura, S. A. Kellar, P. V. Bogdanov, E. D. Lu, A. Lanzara, Z. Hussain, A. Ino, T. Mizokawa, A. Fujimori, H. Eisaki, C. Kim, Z.-X. Shen, T. Kakeshita, S. Uchida, *ibid*, **63**, 220501 (2001).
37. H. Ding, A. F. Bellman, J. C. Campuzano, M. Randeria, M. R. Norman, T. Yokoya, T. Takahashi, H. Katayama-Yoshida, T. Mochiku, K. Kadowaki, G. Jennings, and G. P. Brivio, Phys. Rev. Lett. **76**, 1533 (1996).
38. M. R. Norman, M. Randeria, H. Ding, and J. C. Campuzano, Phys. Rev. B **52**, 615 (1995).
39. R. L. Withers, J. G. Thompson, L. R. Wallenberg, J. D. Fitzgerald, J. S. Anderson, B. G. Hyde, J. Phys. **C 21**, 6067 (1988).
40. P. Aebi, J. Osterwalder, P. Schwaller, L. Schlapbach, M. Shimoda, T. Mochiku and K. Kadowaki, Phys. Rev. Lett. **72**, 2757 (1994); J. Osterwalder, P. Aebi, P. Schwaller, L. Schlapbach, M. Shimoda, T. Mochiku and K. Kadowaki, Appl. Phys. A **60**, 247 (1995).
41. A. Kampf and J. R. Schrieffer, Phys. Rev. **B 42**, 7967 (1990).
42. H. Ding, M.R. Norman, T. Yokoya, T. Takuechi, M. Randeria, J.C. Campuzano, T. Takahashi, T. Mochiku, and K. Kadowaki, Phys. Rev. Lett. **78**, 2628 (1997).
43. A. A. Kordyuk, S. V. Borisenko, M. S. Golden, S. Legner, K. A. Nenkov, M. Knupfer, J. Fink, H. Berger, L. Forro, R. Follath, Phys. Rev. B **66**, 014502 (2002).

44. This would allow us to understand (1) why polarization selection rules are obeyed for the $\Gamma\bar{M}$ mirror plane, and (2) qualitatively, why the intensities for odd and even polarizations along ΓX are comparable.
45. D. S. Dessau, Z.X. Shen, D. M. King, D. S. Marshall, L. W. Lombardo, P. H. Dickinson, A. G. Loeser, J. DiCarlo, C.H Park, A. Kapitulnik, and W. E. Spicer, Phys. Rev. Lett. **71**, 2781 (1993).
46. M. R. Norman, M. Randeria, H. Ding, J. C. Campuzano, and A. F. Bellman, Phys. Rev. B **52**, 15107 (1995).
47. T. Sato, T. Kamiyama, T. Takahashi, J. Mesot, A. Kaminski, J. C. Campuzano, H. M. Fretwell, T. Takeuchi, H. Ding, I. Chong, T. Terashima, M. Takano, Phys. Rev. B **64**, 054502 (2001).
48. N. L. Saini, J. Avila, A. Bianconi and A. Lanzara, M. C. Asensio, S. Tajima, G. D. Gu, and N. Koshizuka, Phys. Rev. Lett. **79**, 3467 (1997).
49. J. Mesot, M. R. Norman, H. Ding, J. C. Campuzano, Phys. Rev. Lett. **82**, 2618 (1999); N. L. Saini, A. Bianconi, A. Lanzara, J. Avila, M. C. Asensio, S. Tajima, G. D. Gu, N. Koshizuka, *ibid* 2619 (1999).
50. Y.-D. Chuang, A. D. Gromko, D. S. Dessau, Y. Aiura, Y. Yamaguchi, K. Oka, A. J. Arko, J. Joyce, H. Eisaki, S. I. Uchida, K. Nakamura, and Yoichi Ando, Phys. Rev. Lett. **83**, 3717 (1999).
51. H.M. Fretwell, A. Kaminski, J. Mesot, J. C. Campuzano, M. R. Norman, M. Randeria, T. Sato, R. Gatt, T. Takahashi, and K. Kadowaki, Phys. Rev. Lett. **84**, 4449 (2000).
52. S. V. Borisenko, M. S. Golden, S. Legner, T. Pichler, C. Durr, M. Knupfer, J. Fink, G. Yang, S. Abell, H. Berger, Phys. Rev. Lett. **84**, 4453 (2000); S. V. Borisenko, A. A. Kordyuk, S. Legner, C. Durr, M. Knupfer, M. S. Golden, J. Fink, K. Nenkov, D. Eckert, G. Yang, S. Abell, H. Berger, L. Forro, B. Liang, A. Mailouck, C. T. Lin, B. Keimer, Phys. Rev. B **64**, 094514 (2001).
53. The data in Ref. [51] is taken in the superconducting state ($T = 40$K) of the $T_c = 90$K sample. We note that the integration range (± 100 meV) employed for the intensity patterns is much larger than the gap energy scale, and the minimum gap locus (to be discussed below in Section 5.6) in the superconducting state is essentially identical to the normal state Fermi surface.
54. D.L. Feng, W.J. Zheng, K.M. Shen, D.H. Lu, F. Ronning, J.-I. Shimoyama, K. Kishio, G. Gu, D. Van der Marel, Z.-X. Shen, cond-mat/9908056.
55. J. C. Campuzano, H. Ding, M. R. Norman, M. Randeria, A. F. Bellman, T. Yokoya, T. Takahashi, H. Katayama-Yoshida, T. Mochiku, and K. Kadowaki, Phys. Rev. B **53**, R14737 (1996).
56. Th. Straub, R. Claessen, P. Steiner, S. Hufner, V. Eyert, K. Friemelt and E. Bucher, Phys. Rev. B **55**, 13473 (1997).
57. M. C. Schabel, C.-H. Park, A. Matsuura, Z.-X. Shen, D. A. Bonn, Ruixing Liang, and W. N. Hardy, Phys. Rev. B **57**, 6107 (1998).
58. K. Gofron, J. C. Campuzano, H. Ding, C. Gu, R. Liu, B. Dabrowski, B. W. Veal, W. Cramer, G. Jennings, J. Phys. Chem. Sol. **54**, 1193 (1993); K. Gofron, J. C. Campuzano, A. A. Abrikosov, M. Lindroos, A. Bansil, H. Ding, D. Koelling, B. Dabrowski, Phys. Rev. Lett. **73**, 3302 (1994).
59. S. Massida, J. Yu, and A.J. Freeman, Physica **C 152**, 251 (1988); O. K. Andersen, O. Jepsen, A. I. Liechtenstein, I. I. Mazin, Phys. Rev. **B 49**, 4145 (1994).
60. S. Chakravarty, A. Sudbo, P. W. Anderson and S. Strong, Science **261**, 337 (1994).

61. M.R. Norman, H. Ding, J.C. Campuzano, T. Takeuchi, M. Randeria, T. Yokoya, T. Takahashi, T. Mochiku, and K. Kadowaki, Phys. Rev. Lett. **79**, 3506 (1997).
62. J. C. Campuzano, H. Ding, M. R. Norman, H. M. Fretwell, M. Randeria, A. Kaminski, J. Mesot, T. Takeuchi, T. Sato, T. Yokoya, T. Takahashi, K. Kadowaki, P. Guptasarma, D. G. Hinks, Z. Konstantinovic, Z. Z. Li, and H. Raffy, Phys. Rev. Lett. **83**, 3709 (1999).
63. J. Zasadzinski, L. Ozyuzer, Z. Yusof, J. Chen, K. E. Gray, R. Mogilevsky, D. G. Hinks, J. L. Cobb, J. T. Markert, SPIE **2696**, 338 (1996); See also J. Zasadzinski *et al.* (unpublished) in Fig. 1 of D. Coffey, J. Phys. Chem. Solids **54**, 1369 (1993).
64. P. W. Anderson, Science **256**, 1526 (1992).
65. D.L. Feng, N.P. Armitage, D.H. Lu, A. Damascelli, J.P Hu, P. Bogdanov, A. Lanzara, F. Ronning, K.M. Shen, H. Eisaki, C. Kim, and Z.-X. Shen, Phys. Rev. Lett. **86**, 5550 (2001); D.L. Feng, C. Kim, H. Eisaki, D.H. Lu, A. Damascelli, K.M. Shen, F. Ronning, N. P. Armitage, N. Kaneko, M. Greven, J.-I. Shimoyama, K. Kishio, R. Yoshizaki, G.D. Gu, Z.-X. Shen, Phys. Rev. B **65**, 220501 (2002).
66. Y. D. Chuang, A. D. Gromko, A. Fedorov, D. S. Dessau, Y. Aiura, K. Oka, Y. Ando, H. Eisaki, S. I. Uchida, Phys. Rev. Lett. **87**, 117002 (2001); Y. D. Chuang, A. D. Gromko, A. Fedorov, Y. Aiura, K. Oka, Y. Ando, D. S. Dessau, cond-mat/0107002.
67. A. A. Kordyuk, S. V. Borisenko, T. K. Kim, K. Nenkov, M. Knupfer, M. S. Golden, J. Fink, H. Berger, R. Follath, Phys. Rev. Lett. **89**, 077003 (2002).
68. D.L. Feng, A. Damascelli, K.M. Shen, N. Motoyama, D.H. Lu, H. Eisaki, K. Shimizu, J.-I. Shimoyama, K. Kishio, N. Kaneko, M. Greven, G.D. Gu, X.J. Zhou, C. Kim, F. Ronning, N. P. Armitage, and Z.-X. Shen, Phys. Rev. Lett. **88**, 107001 (2002); D.L. Feng, H. Eisaki, K.M. Shen, A. Damascelli, C. Kim, D.H. Lu, Z.-X. Shen, K. Shimizu, J.-I. Shimoyama, K. Kishio, N. Motoyama, N. Kaneko, M. Greven, G.D. Gu, Intl. J. of Mod. Phys. **16**, 1691 (2002); T. Sato, H. Matsui, S. Nishina, T. Takahashi, T. Fujii, T. Watanabe, and A. Matsuda, Phys. Rev. Lett. **89**, 067005 (2002).
69. D. J. Van Harlingen, Rev. Mod. Phys **67**, 515 (1995); C. C. Tsuei and J. R. Kirtley, *ibid* **72**, 969 (2000).
70. Z. X. Shen, D. S. Dessau, B. O. Wells, D. M. King, W. E. Spicer, A. J. Arko, D. Marshall, L. W. Lombardo, A. Kapitulnik, P. Dickinson, S. Doniach, J. DiCarlo, A. G. Loeser, C. H. Park, Phys. Rev. Lett. **70**, 1553 (1993).
71. H. Ding, M. R. Norman, J. C. Campuzano, M. Randeria, A. Bellman, T. Yokoya, T. Takahashi, T. Mochiku, and K. Kadowaki, Phys. Rev. B **54**, R9678 (1996).
72. J.-M. Imer, F. Patthey, B. Dardel, W.-D. Schneider, Y. Baer, Y. Petroff, A. Zettl, Phys. Rev. Lett. **62**, 336 (1989).
73. C. G. Olson, R. Liu, A.-B. Yang, D. W. Lynch, A. J. Arko, R. S. List, B. W. Veal, Y. C. Chang, P. Z. Jiang, A. P. Paulikus, Science **245**, 731 (1989).
74. The large dispersion along ΓY, of about 60 meV within our momentum window $\delta\mathbf{k} = 0.045\pi/a^*$, makes it hard to locate $\mathbf{k}_F$ accurately and to map out the nodal region. To this end the we use a step size of $\delta\mathbf{k}/2$ normal to the Fermi surface and $\delta\mathbf{k}$ along it.
75. See: D. Pines and P. Monthoux, J. Phys. Chem. Solids **56**, 1651 (1995) and D. J. Scalapino, Phys. Rep. **250**, 329 (1995).

76. R. J. Kelley, J. Ma, C. Quitmann, G. Margaritondo, M. Onellion, Phys. Rev. B **50**, 590 (1994).
77. J. M. Harris, Z.-X. Shen, P. J. White, D. S. Marshall, M. C. Schabel, J. N. Eckstein, I. Bozovic, Phys. Rev. B **54**, R15665 (1996).
78. H. Ding, J. C. Campuzano, M. R. Norman, M. Randeria, T. Yokoya, T. Takahashi, T. Takeuchi, T. Mochiku, K. Kadowaki, P. Guptasarma, and D. G. Hinks, J. Phys. Chem. of Solids **59**, 1888 (1998).
79. Ch. Renner, B. Revaz, J.-Y. Genoud, K. Kadowaki, O. Fischer, Phys. Rev. Lett. **80**, 149 (1998); N. Miyakawa, P. Guptasarma, J. F. Zasadzinski, D. G. Hinks, K. E. Gray, *ibid* **80**, 157 (1998).
80. A. J. Millis, S. M. Girvin, L. B. Ioffe, and A. I. Larkin, J. Phys. Chem. Solids **59**, 1742 (1998).
81. A. C. Durst and P. A. Lee, Phys. Rev. **62**, 1270 (2000).
82. M. Chiao, P. Lambert, R. W. Hill, C. Lupien, R. Gagnon, L. Taillefer, P. Fournier, Phys. Rev. **62**, 3554 (2000).
83. J. Mesot, M. R. Norman, H. Ding, M. Randeria, J. C. Campuzano, A. Paramekanti, H. M. Fretwell, A. Kaminski, T. Takeuchi, T. Yokoya, T. Sato, T. Takahashi, T. Mochiku, and K. Kadowaki, Phys. Rev. Lett. **83**, 840 (1999).
84. For penetration depth measurements on Bi2212, see: S.-F. Lee, D. C. Morgan, R. J. Ormeno, D. M. Broun, R. A. Doyle, J. R. Waldram, K. Kadowaki, Phys. Rev. Lett. **77**, 735 (1996); T. Jacobs, S. Sridhar, Q. Li, G. D. Gu, N. Koshizuka, *ibid* **75**, 4516 (1995); O. Waldmann, F. Steinmeyer, P. Muller, J. J. Neumeier, F. X. Regi, H. Savary, J. Schneck, Phys. Rev. B **53**, 11825 (1996).
85. A. Paramekanti and M. Randeria, Physica C **341 - 348**, 827 (2000).
86. W. N. Hardy, D. A. Bonn, D. C. Morgan, R. Liang, K. Zhang, Phys. Rev. Lett. **70**, 3999 (1993); D. A. Bonn, S. Kamal, A. Bonakdarpour, R. Liang, W. N. Hardy, C. C. Homes, D. N. Basov, T. Timusk, Czech. J. Phys. **46**, 3195 (1996).
87. S. Haas, A. V. Balatsky, M. Sigrist and T. M. Rice, Phys. Rev. B **56**, 5108 (1997).
88. R. Fehrenbacher and M. R. Norman, Phys. Rev. B **50**, 3495 (1994).
89. T. Timusk and B. W. Statt, Rept. Prog. Phys. **62**, 61 (1999).
90. M. Randeria, in *Proceedings of the International School of Physics "Enrico Fermi" Course CXXXVI on High Temperature Superconductors*, ed. G. Iadonisi, J. R. Schrieffer, and M. L. Chiafalo, (IOS Press, 1998), p. 53 - 75; [Varenna Lectures, 1997] cond-mat/9710223.
91. D.S. Marshall, D.S. Dessau, A.G. Loeser, C-H. Park, A.Y. Matsuura, J.N. Eckstein, I. Bozovic, P. Fournier, A. Kapitulnik, W.E. Spicer, and Z.-X. Shen, Phys. Rev. Lett. **76**, 4841 (1996).
92. A. G. Loeser, Z.-X. Shen, D. S. Dessau, D. S. Marshall, C. H. Park, P. Fournier, A. Kapitulnik, Science **273**, 325 (1996).
93. H. Ding, T. Yokoya, J.C. Campuzano, T. Takahashi, M. Randeria, M.R. Norman, T. Mochiku, K. Kadowaki, and J. Giapintzakis, Nature **382**, 51 (1996).
94. M. R. Norman, H. Ding, M. Randeria, J. C. Campuzano, T. Yokoya, T. Takeuchi, T. Takahashi, T. Mochiku, K. Kadowaki, P. Guptasarma, and D. G. Hinks, Nature **392**, 157 (1998).
95. M.R. Presland, J.L. Tallon, R.G. Buckley, R.S. Liu, and N.E. Flower, Physica C **176**, 95 (1991).

96. D.L. Feng, D.H. Lu, K.M. Shen, C. Kim, H. Eisaki, A. Damascelli, R. Yoshizaki, J.-I. Shimoyama, K. Kishio, G.D. Gu, S. Oh, A. Andrus, J. O'Donell, J.N. Eckstein, Z.-X. Shen, Science **289**, 277 (2000).
97. H. Ding, J.R. Engelbrecht, Z. Wang, J.C. Campuzano, S.-C. Wang, H.-B. Yang, R. Rogan, T. Takahashi, K. Kadowaki, and D. G. Hinks, Phys. Rev. Lett. **87**, 227001 (2001).
98. Y. J. Uemura, G. M. Luke, B. J. Sternlieb, J. H. Brewer, J. F. Carolan, W. N. Hardy, R. Kadono, J. R. Kempton, R. F. Kiefl, S. R. Kreitzman, P. Mulhern, T. M. Riseman, D. L. Williams, B. X. Yang, S. Uchida, H. Takagi, J. Gopalakrishnan, A. W. Sleight, M. A. Subramanian, C. L. Chien, M. Z. Cieplak, G. Xiao, V. Y. Lee, B. W. Statt, C. E. Stronach, W. J. Kossler, X. H. Yu, Phys. Rev. Lett. **62**, 2317 (1989).
99. For a review, see: P. A. Lee, Normal state properties of the oxide superconductors: a review, in *High Temperature Superconductivity*, ed. K. S. Bedell, D. Coffey, D. E. Meltzer, D. Pines, J. R. Schrieffer, p. 96-116 (Addison-Wesley, New York, 1990).
100. M. Randeria, N. Trivedi, A. Moreo, and R.T. Scalettar, Phys. Rev. Lett. **69**, 2001 (1992); N. Trivedi and M. Randeria, Phys. Rev. Lett. **75**, 312 (1995).
101. V. Emery and S. Kivelson, Nature **374**, 434 (1995).
102. G. Baskaran, Z. Zou and P. W. Anderson, Solid St. Comm. **63**, 973 (1987); G. Kotliar and J. Liu, Phys. Rev. B **38**, 5142 (1988); H. Fukuyama, Prog. Theor. Phys. Suppl. **108**, 287 (1992).
103. P. A. Lee and X. G. Wen, Phys. Rev. Lett. **76**, 503 (1996) and Phys. Rev. B **63**, 224517 (2001).
104. J. Tallon and J. Loram, Physica C **349**, 53 (2001).
105. S. Chakravarty, R. B. Laughlin, D. K. Morr and C. Nayak, Phys. Rev. B **63**, 094503 (2001).
106. C. M. Varma, Phys. Rev. Lett. **83**, 3538 (1999).
107. A. Kaminski, S. Rosenkranz, H. Fretwell, J. C. Campuzano, Z. Li, H. Raffy, W. G. Cullen, H. You, C. G. Olson, H. Hoechst, Nature **416**, 610 (2002).
108. S. H. Pan, J. P. O'Neal, R. L. Badzey, C. Chamon, H. Ding, J. R. Engelbrecht, Z. Wang, H. Eisaki, S. Uchida, A. K. Gupta, K.-W. Ng, E. W. Hudson, K. M. Lang, J. C. Davis, Nature **413**, 282 (2001).
109. L. Perfetti, C. Rojas, A. Reginelli, L. Gavioli, H. Berger, G. Margaritondo, M. Grioni, R. Gaal, L. Forro, F. Rullier Albenque, Phys. Rev. B **64**, 115102 (2001).
110. M. R. Norman, H. Ding, H. Fretwell, M. Randeria, and J. C. Campuzano, Phys. Rev. B **60**, 7585 (1999).
111. M. R. Norman, A. Kaminski, J. Mesot, J. C. Campuzano, Phys. Rev. B **63**, 140508 (2001).
112. M. R. Norman, M. Randeria, H. Ding, and J. C. Campuzano, Phys. Rev. B **57**, R11093 (1998).
113. D.S. Dessau, B.O. Wells, Z.-X. Shen, W.E. Spicer, A.J. Arko, R.S. List, D.B. Mitzi, and A. Kapitulnik, Phys. Rev. Lett. **66**, 2160 (1991); D.S. Dessau, Z.-X. Shen, B.O. Wells, D. M. King, W.E. Spicer, A.J. Arko, L. W. Lombardo, D.B. Mitzi, and A. Kapitulnik, Phys. Rev. B **45**, 5095 (1992).
114. Q. Huang, J.F. Zasadzinski, K.E. Gray, J.Z. Liu, and H. Claus, Phys. Rev. B **40**, 9366 (1989).
115. Bilayer splitting is discussed in Section 5.4.5.

116. Y. Kuroda and C. M. Varma, Phys. Rev. B **42**, 8619 (1990).
117. S. Engelsberg and J. R. Schrieffer, Phys. Rev. **131**, 993 (1963).
118. D. J. Scalapino, in *Superconductivity*, ed. R. D. Parks (Marcel Decker, New York, 1969), Vol 1, p. 449.
119. Z.-X. Shen and J. R. Schrieffer, Phys. Rev. Lett. **78**, 1771 (1997).
120. P. B. Littlewood and C. M. Varma, Phys. Rev. B **46**, 405 (1992).
121. M. R. Norman and H. Ding, Phys. Rev. B **57**, R11089 (1998).
122. S. M. Quinlan, P. J. Hirschfeld, and D. J. Scalapino, Phys. Rev. B. **53**, 8575 (1996).
123. J. Rossat-Mignot, L.P. Regnault, C. Vettier, P. Bourges, P. Burlet, J. Bossy, J.Y. Henry, and G. Lapertot, Physica C **185-189**, 86 (1991); H.A. Mook, M. Yethiraj, G. Aeppli, T. E. Mason, T. Armstrong, Phys. Rev. Lett. **70**, 3490 (1993); Hung Fai Fong, B. Keimer, P.W. Anderson, D. Reznik, F. Dogan and I.A. Aksay, Phys. Rev. Lett. **75**, 316 (1995).
124. H.F. Fong, P. Bourges, Y. Sidis, L.P. Regnault, A. Ivanov, G.D. Gu, N. Koshizuka, and B. Keimer, Nature **398**, 588 (1999).
125. Neutron results are reviewed by P. Bourges, in *The gap symmetry and fluctuations in high T_c superconductors*, ed. J. Bok, G. Deutscher, D. Pavuna, and S.A. Wolf (Plenum, New York, 1998), p. 349.
126. J.F. Zasadzinski, L. Ozyuzer, N. Miyakawa, K.E. Gray, D.G. Hinks, C. Kendziora, Phys. Rev. Lett. **87**, 067005 (2001).
127. P. Dai, M. Yethiraj, H. A. Mook, T. B. Lindemer, and F. Doğan, Phys. Rev. Lett. **77**, 5425 (1996).
128. R. Preuss, W. Hanke, C. Grober, and H. G. Evertz, Phys. Rev. Lett. **79**, 1122 (1997); J. Schmalian, D. Pines, and B. Stojkovic, *ibid.* **80**, 3839 (1998); X.-G. Wen and P. A. Lee, *ibid.* **76**, 503 (1996).
129. E. Demler and S.-C. Zhang, Phys. Rev. Lett. **75**, 4126 (1995).
130. P. Dai, H. A. Mook, S. M. Hayden, G. Aeppli, T. G. Perring, R. D. Hunt, and F. Doğan, Science **284**, 1344 (1999).
131. M. Hengsberger, D. Purdie, P. Segovia, M. Garnier, Y. Baer, Phys. Rev. Lett. **83**, 592 (1999); T. Valla, A. V. Fedorov, P. D. Johnson, S. L. Hulbert, *ibid.*, 2085 (1999).
132. A. Lanzara, P.V. Bogdanov, X.J. Zhou, S.A. Kellar, D.L. Feng, E.D. Lu, T. Yoshida, H. Eisaki, A. Fujimori, K. Kishio, J.-I. Shimoyama, T. Noda, S. Uchida, Z. Hussain, and Z.-X. Shen, Nature **412**, 510 (2001).
133. P.D. Johnson, T. Valla, A.V. Fedorov, Z. Yusof, B.O. Wells, Q. Li, A.R. Moodenbaugh, G.D. Gu, N. Koshizuka, C. Kendziora, Sha Jian, and D.G. Hinks, Phys. Rev. Lett. **87**, 177007 (2001).
134. M. Eschrig and M. R. Norman, Phys. Rev. Lett. **85**, 3261 (2000) and cond-mat/0202083.
135. M. Eschrig and M. R. Norman, cond-mat/0206544.
136. A. D. Gromko, A. V. Federov, Y.-D. Chuang, J. D. Koralek, Y. Aiura, Y. Yamaguchi, K. Oka, Y. Ando, D. S. Dessau, cond-mat/0202329; A. D. Gromko, Y.-D. Chuang, A. V. Federov, Y. Aiura, Y. Yamaguchi, K. Oka, Y. Ando, D. S. Dessau, cond-mat/0205385.
137. M. R. Norman, M. Randeria, B. Janko, J. C. Campuzano, Phys. Rev. B **61**, 14742 (2000).
138. J. C. Campuzano, H. Ding, H. Fretwell, J. Mesot, A. Kaminski, T. Sato, T. Takahashi, T. Mochiku, and K. Kadowaki, cond-mat/9811349.

139. A. Bansil and M. Lindroos, Phys. Rev. Lett. **83**, 5154 (1999).
140. M. R. Norman and C. Pepin, Phys. Rev. B **66**, 100506 (2002).
141. H. J. A. Molegraaf, C. Presura, D. van der Marel, P. H. Kes, M. Li, Science **295**, 2239 (2002); A. F. Santander-Syro, R. P. S. M. Lobo, N. Bontemps, Z. Konstantinovic, Z. Z. Li, H. Raffy, cond-mat/0111539.
142. P. W. Anderson, Phys. Rev. B **42**, 2624 (1990).

6 Concepts in High Temperature Superconductivity

E. W. Carlson, S. A. Kivelson, D. Orgad
Univ. of California at Los Angeles Dept. of Physics, USA
V. J. Emery
Brookhaven National Laboratory Dept. of Physics, USA

6.1 Introduction 276
6.2 High Temperature Superconductivity is Hard to Attain 279
6.2.1 Effects of the Coulomb Repulsion and Retardation on Pairing 280
6.2.2 Pairing *vs.* Phase Ordering 282
6.2.3 Competing Orders 283
6.3 Superconductivity in the Cuprates: General Considerations 285
6.3.1 A Fermi Surface Instability Requires a Fermi Surface 287
6.3.2 There is no Room for Retardation 287
6.3.3 Pairing is Collective! 288
6.3.4 What Determines the Symmetry of the Pair Wavefunction? 288
6.3.5 What does the Pseudogap mean? 291
6.4 Preview: Our View of the Phase Diagram 301
6.5 Quasi–1D Superconductors 303
6.5.1 Elementary Excitations of the 1DEG 303
6.5.2 Spectral Functions of the 1DEG–Signatures of Fractionalization 310
6.5.3 Dimensional Crossover in a Quasi–1D Superconductor 317
6.5.4 Alternative Routes to Dimensional Crossover 320
6.6 Quasi–1D Physics in a Dynamical Stripe Array 321
6.6.1 Ordering in the Presence of Quasi–Static Stripe Fluctuations 322
6.6.2 The General Smectic Fixed Point 325
6.7 Electron Fractionalization in $D > 1$ as a Mechanism of High Temperature Superconductivity 325
6.7.1 RVB and Spin–Charge Separation in two Dimensions 326
6.7.2 Is an Insulating Spin Liquid Ground State Possible in $D > 1$? 327
6.7.3 Topological Order and Electron Fractionalization 329
6.8 Superconductors with Small Superfluid Density 329
6.8.1 What Ground State Properties Predict T_c? 330
6.8.2 An illustrative Example: Granular Superconductors 331
6.8.3 Classical Phase Fluctuations 336
6.8.4 Quantum Considerations 340
6.8.5 Applicability to the Cuprates 342

K. H. Bennemann et al. (eds.), *The Physics of Superconductors*
© Springer-Verlag Berlin Heidelberg 2004

6.9 Lessons from Weak Coupling 344
6.9.1 Perturbative RG Approach in $D > 1$ 344
6.9.2 Perturbative RG Approach in $D = 1$ 348
6.10 Lessons from Strong Coupling 351
6.10.1 The Holstein Model of Interacting Electrons and Phonons . 352
6.10.2 Insulating Quantum Antiferromagnets 354
6.10.3 The Isolated Square 358
6.10.4 The Spin Gap Proximity Effect Mechanism 361
6.11 Lessons from Numerical Studies of Hubbard and Related Models 364
6.11.1 Properties of Doped Ladders 365
6.11.2 Properties of the two Dimensional t–J Model 377
6.12 Doped Antiferromagnets 386
6.12.1 Frustration of the Motion of Dilute Holes in an antiferromagnet 386
6.12.2 Coulomb Frustrated Phase Separation and Stripes 394
6.12.3 Avoided Critical Phenomena 396
6.12.4 The Cuprates as Doped Antiferromagnets 398
6.12.5 Additional Considerations and Alternative Perspectives 399
6.13 Stripes and High Temperature Superconductivity 401
6.13.1 Experimental Signatures of Stripes 403
6.13.2 Stripe Crystals, Fluids, and Electronic Liquid Crystals 407
6.13.3 Our view of the Phase Diagram—Reprise 410
6.13.4 Some open Questions 414
Acknowledgements 422
References 423

6.1 Introduction

It is the purpose of our study to explore the theory of high temperature superconductivity. Much of the motivation for this comes from the study of cuprate high temperature superconductors. However, we do not focus in great detail on the remarkable and exciting physics that has been discovered in these materials. Rather, we focus on the core theoretical issues associated with the mechanism of high temperature superconductivity. Although our discussions of theoretical issues in a strongly correlated superconductor are intended to be self contained and pedagogically complete, our discussions of experiments in the cuprates are, unfortunately, considerably more truncated and impressionistic.

Our primary focus is on physics at intermediate temperature scales of order T_c (as well as the somewhat larger "pseudogap" temperature) and energies of order the gap maximum, Δ_0. Consequently (and reluctantly) we have omitted any detailed discussion of a number of fascinating topics in cuprate superconductivity, including the low energy physics associated with nodal quasiparticles, the properties of the vortex matter which results from the application of a magnetic field, the effects of disorder, and a host of material specific issues.

Note, conventional superconductors are good metals in their normal states, and are well described by Fermi liquid theory and BCS theory. They also exhibit a hierarchy of energy scales, $E_F \gg \hbar\omega_D \gg k_B T_c$, where E_F and $\hbar\omega_D$ are the Fermi and Debye energies, respectively, and T_c is the superconducting transition temperature. Moreover, one typically does not have to think about the interplay between superconductivity and any other sort of collective ordering, since in most cases the only weak coupling instability of a Fermi liquid is to superconductivity. These reasons underlie the success of the BCS–Eliashberg–Migdal theory in describing metallic superconductors [1].

By contrast, the cuprate high temperature superconductors [2] (and various other newly discovered materials with high superconducting transition temperatures) are highly correlated "bad metals," [3, 4] with normal state properties that are not at all those of a Fermi liquid. Also the assumptions of BCS theory are violated by the high temperature superconductors. There is compelling evidence that the cuprates are better thought of as doped Mott insulators, rather than as strongly interacting versions of conventional metals [5–7]. The cuprates also exhibit numerous types of low temperature order which interact strongly with the superconductivity, the most prominent being antiferromagnetism and the unidirectional charge and spin density wave "stripe" order. These orders can compete or coexist with superconductivity. Furthermore, whereas phase fluctuations of the superconducting order parameter are negligibly small in conventional superconductors, fluctuation effects are of order one in the high temperature superconductors because of their much smaller superfluid stiffness.

Apparently, none of this complicates the fundamental character of the superconducting order parameter: it is still a charge 2e scalar field, although it transforms according to a nontrivial representation of the point group symmetry of the crystal—it is a "d–wave superconductor." At asymptotically low temperatures and energies, there is every reason to expect that the physics is dominated by nodal quasiparticles that are similar to those that one might find in a BCS superconductor of the same symmetry. Indeed, there is considerable direct experimental evidence that this expectation is realized [8–11]. However, the failure of Fermi liquid theory to describe the normal state and the presence of competing orders necessitates an entirely different approach to understanding much of the physics, especially at intermediate scales of or-

der $k_B T_c$, which is the relevant scale for the mechanism of high temperature superconductivity.

It is the purpose of this paper to address the physics of high temperature superconductivity at these intermediate scales. We pay particular attention to the problem of charge dynamics in doped Mott insulators. We also stress the physics of quasi–one dimensional superconductors, in part because that is the one *theoretically* well understood limit in which superconductivity emerges from a non–Fermi liquid normal state. To the extent that the physics evolves adiabatically from the quasi–one to the quasi–two dimensional limit, this case provides considerable insight into the actual problem of interest. The soundness of this approach can be argued from the observation that $YBa_2Cu_3O_{7-\delta}$ (YBCO) (which is strongly orthorhombic) exhibits very similar physics to that of the more tetragonal cuprates. Since the conductivity and the superfluid density in YBCO exhibit a factor of 2 or greater anisotropy within the plane, [12,13] this material is already part way toward the quasi–one dimensional limit without substantial changes in the physics! In the second place, because of the delicate interplay between stripe and superconducting orders observed in the cuprates, it is reasonable to speculate that the electronic structure may be literally quasi–one dimensional at the local level, even when little of this anisotropy is apparent at the macroscopic scale.

A prominent theme of this article is the role of *mesoscale structure* [14]. Because the kinetic energy is strongly dominant in good metals, their wavefunctions are very rigid and hence the electron density is highly homogeneous in real space, even in the presence of a spatially varying external potential (*e.g.* disorder). In a highly correlated system, the electronic structure is much more prone to inhomogeneity [15–17], and intermediate scale structures (stripes are an example) are likely an integral piece of the physics. Indeed, based on the systematics of local superconducting correlations in exact solutions of various limiting models and in numerical "experiments" on t–J and Hubbard models, we have come to the conclusion that mesoscale structure may be *essential* to a mechanism of high temperature superconducting pairing. (See Sections 6.10 and 6.11.) This is a potentially important guiding principle in the search for new high temperature superconductors.

This is related to a concept that we believe is central to the mechanism of high temperature superconductivity: the condensation is driven by a lowering of kinetic energy. A Fermi liquid normal state is essentially the ground state of the electron kinetic energy, so any superconducting state which emerges from it must have *higher* kinetic energy. The energy gain which powers the superconducting transition from a Fermi liquid must therefore be energy of interaction—this underlies any BCS–like approach to the problem. In the opposite limit of strong repulsive interactions between electrons, the normal state has high kinetic energy. It is thus possible to conceive of a *kinetic energy driven mechanism of superconductivity*, in which the strong frustration

of the kinetic energy is partially relieved upon entering the superconducting state [18–24]. Such a mechanism does not require subtle induced attractions, but derives directly from the strong repulsion between electrons. As will be discussed in Section 6.10, the proximity effect in the conventional theory of superconductivity is a prototypical example of such a kinetic energy driven mechanism: when a superconductor and a normal metal are placed in contact with each other, the electrons in the metal pair (even if the interactions between them are repulsive) in order to lower their zero point kinetic energy by delocalizing across the interface. A related phenomenon, which we have called the "spin gap proximity effect" [20,25] (see Section 6.10.4), produces strong superconducting correlations in t–J and Hubbard ladders [26], where the reduction of kinetic energy transverse to the ladder direction drives pairing. It is unclear to us whether experiments can unambiguously distinguish between a potential energy and a kinetic energy driven mechanism. (Recent papers by Molegraaf *et al* [27] and Santadner–Syro *et al* [28] present very plausible experimental evidence of a kinetic energy driven mechanism of superconductivity in at least certain high temperature superconductors.) But since the interaction between electrons is strongly repulsive for the systems in question, we feel that the *a priori* case for a kinetic energy driven mechanism is very strong.

Our approach in this article is first to analyze various aspects of high temperature superconductivity as abstract problems in theoretical physics, and then to discuss their specific application to the cuprate high temperature superconductors. (While examples of similar behavior can be found in other materials, for ease of exposition we have focused on this single example.) We have also attempted to make each section self contained. Although many readers no doubt will be drawn to read this compelling article in its entirety, we have also tried to make it useful for those readers who are interested in learning about one or another more specific issue. The first eleven sections focus on theoretical issues, except for Section 6.4, where we briefly sketch the mechanism in light of *our* view of the phase diagram of the cuprate superconductors. In the final section, we focus more directly on the physics of high temperature superconductivity in the cuprates, and summarize some of the experimental issues that remain, in our opinion, unsettled. Except where dimensional arguments are important, we will henceforth work with units in which $\hbar = k_B = 1$.

6.2 High Temperature Superconductivity is Hard to Attain

We explore the reasons why high temperature superconductivity is so difficult to achieve from the perspective of the BCS–Eliashberg approach. Because of retardation, increasing the frequency of the intermediate boson cannot

significantly raise T_c. Strong coupling tends to reduce the phase ordering temperature, and promote competing instabilities.

Superconductivity in metals is the result of two distinct quantum phenomena: pairing and long range phase coherence. In conventional homogeneous superconductors, the phase stiffness is so great that these two phenomena occur simultaneously. On the other hand, in granular superconductors and Josephson junction arrays, pairing occurs at the bulk transition temperature of the constituent metal, while long range phase coherence, if it occurs at all, obtains at a much lower temperature characteristic of the Josephson coupling between superconducting grains. To achieve high temperature superconductivity requires that both scales be elevated simultaneously. However, given that the bare interactions between electrons are strongly repulsive, it is somewhat miraculous that electron pairing occurs at all. Strong interactions, which might enable pairing at high scales, typically also have the effect of strongly suppressing the phase stiffness, and moreover typically induce other orders (magnetic, structural, *etc.*) in the system which compete with superconductivity.

It is important in any discussion of the theory of high temperature superconductivity to have clearly in mind why conventional metallic superconductors, which are so completely understood in the context of the Fermi liquid based BCS–Eliashberg theory, rarely have T_c's above 15K, and never above 30K. In this section, we briefly discuss the principal reasons why a straightforward extension of the BCS–Eliashberg theory *does not* provide a framework for understanding high temperature superconductivity, whether in the cuprate superconductors, or in C_{60}, or *possibly* even BaKBiO or MgB_2.

6.2.1 Effects of the Coulomb Repulsion and Retardation on Pairing

In conventional BCS superconductors, the instantaneous interactions between electrons are typically repulsive (or at best very weakly attractive)—it is only because the phonon induced attraction is retarded that it (barely) dominates at low frequencies. Even if new types of intermediate bosons are invoked to replace phonons in a straightforward variant of the BCS mechanism, the instantaneous interactions will still be repulsive, so any induced attraction is typically weak, and only operative at low frequencies.

Strangely enough, the deleterious effects of the Coulomb interaction on high temperature superconductivity has been largely ignored in the theoretical literature. The suggestion has been made that high pairing scales can be achieved by replacing the relatively low frequency phonons which mediate the pairing in conventional metals by higher frequency bosonic modes, such as the spin waves in the high temperature superconductors [29–32] or the shape modes [33,34] of C_{60} molecules. However, in most theoretical treatments of this idea, the Coulomb pseudopotential is either neglected or treated

in a cavalier manner. That is, models are considered in which the instantaneous interactions between electrons are strongly attractive. This is almost certainly [14,20,35–37] an unphysical assumption!

In Section 6.9, we use modern renormalization group (RG) methods [38, 39] to derive the conventional expression for the Coulomb pseudopotential, and how it enters the effective pairing interaction at frequencies lower than the Debye frequency, ω_D. This theory is well controlled so long as $\omega_D \ll E_F$ and the interaction strengths are not too large. It is worth reflecting on a well known, but remarkably profound result that emerges from this analysis: As electronic states are integrated out between the microscopic scale E_F and the intermediate scale, ω_D, the electron–phonon interaction is unrenormalized (and so can be well estimated from microscopic considerations), but the Coulomb repulsion is reduced from a bare value, μ, to a renormalized value,

$$\mu^* = \mu/[1 + \mu \log(E_F/\omega_D)]. \tag{6.1}$$

Here, as is traditional, μ and μ^* are the dimensionless measures of the interaction strength obtained by multiplying the interaction strength by the density of states. We define λ in an analogous manner for the electron–phonon interaction. Thus, even if the instantaneous interaction is repulsive (*i.e.* $\lambda - \mu < 0$), the effective interaction at the scale ω_D will nonetheless be attractive ($\lambda - \mu^* > 0$) for $\omega_D \ll E_F$. Below this scale, the standard RG analysis yields the familiar weak coupling estimate of the pairing scale T_p:

$$T_p \sim \omega_D \exp[-1/(\lambda - \mu^*)]. \tag{6.2}$$

The essential role of retardation (an essential feature of the BCS mechanism) is made clear if one considers the dependence of T_p on ω_D:

$$\frac{d\log[T_p]}{d\log[\omega_D]} = 1 - \left[\mu^* \log\left(\frac{T_p}{\omega_D}\right)\right]^2. \tag{6.3}$$

So long as $\omega_D \ll E_F \exp[-(1-\lambda)/\lambda\mu]$, we have $\frac{d\log[T_p]}{d\log[\omega_D]} \approx 1$, and T_p is a linearly rising function of ω_D, giving rise to the conventional isotope effect. (Recall, for phonons, $d\log[\omega_D]/d\log[M] = -1/2$.) However, when $\omega_D > T_p \exp[1/\mu^*]$, we have $\frac{d\log[T_p]}{d\log[\omega_D]} < 0$, and T_p becomes a decreasing function of ω_D! Clearly, unless ω_D is exponentially smaller than E_F, superconducting pairing is impossible by the conventional mechanism. (In the present discussion we have imagined varying ω_D while keeping fixed the electron–phonon coupling constant, $\lambda = \frac{C}{M\omega_D^2} = \frac{C}{K}$, where C is proportional to the (squared) gradient of the electron–ion potential and K is the "spring constant" between the ions. If we consider instead the effect of increasing ω_D at fixed C/M, it leads to a decrease in λ and hence a very rapid suppression of the pairing scale.)

This problem is particularly vexing in the cuprate high temperature superconductors and similar materials, which have low electron densities, and

incipient or apparent Mott insulating behavior. This means that screening of the Coulomb interaction is typically poor, and μ is thus expected to be large. Specifically, from the inverse Fourier transform of the $\boldsymbol{k}$ dependent gap function measured [40] in angle resolved photoemission spectroscopy(ARPES) on $Bi_2Sr_2CaCu_2O_{8+\delta}$, it is possible to conclude (at least at the level of the BCS gap equation) that the dominant pairing interactions have a range equal to the nearest neighbor copper distance. Since this distance is less than the distance between doped holes, it is difficult to believe that metallic screening is very effective at these distances. From cluster calculations and an analysis of various local spectroscopies, a crude estimate [20] of the Coulomb repulsion at this distance is of order 0.5eV or more. To obtain pairing from a conventional mechanism with relatively little retardation, it is necessary that the effective attraction be considerably larger than this!

We are therefore led to the conclusion that the only way a BCS mechanism can produce a high pairing scale is if the effective attraction, λ, is very large indeed. This, however, brings other problems with it.

6.2.2 Pairing vs. Phase Ordering

In most cases, it is unphysical to assume the existence of strong attractive interactions between electrons. However, even supposing we ignore this, strong attractive interactions bring about other problems for high temperature superconductivity: 1) There is a concomitant strong reduction of the phase ordering temperature and thus of T_c. 2) There is the possibility of competing orders. We discuss the first problem here, and the second in Section 6.2.3.

Strong attractive interactions typically result in a large increase in the effective mass, and a corresponding reduction of the phase ordering temperature. Consider, for example, the strong coupling limit of the negative U Hubbard model [41] or the Holstein model [42], discussed in Section 6.10. In both cases, pairs have a large binding energy, but they typically Bose condense at a very low temperature because of the large effective mass of a tightly bound pair—the effective mass is proportional to $|U|$ in the Hubbard model and is exponentially large in the Holstein model. (See Section 6.10.)

Whereas in conventional superconductors, the bare superfluid stiffness is so great that even a substantial renormalization of the effective mass would hardly matter, in the cuprate high temperature superconductors, the superfluid stiffness is small, and a substantial mass renormalization would be catastrophic. The point can be made most simply by considering the result of simple dimensional analysis. The density of doped holes per plane in an optimally doped high temperature superconductor is approximately $n_{2d} = 10^{14}\text{cm}^{-2}$. Assuming a density of hole pairs that is half this, and taking the rough estimate for the pair effective mass, $m^* = 2m_e$, we find a phase ordering scale,

$$T_\theta = \hbar^2 n_{2d}/2m^* \approx 10^{-2} eV \approx 100K \; . \tag{6.4}$$

Since this is in the neighborhood of the actual T_c, it clearly implies that any large mass renormalization would be incompatible with a high transition temperature. What about conventional superconductors? A similar estimate in a $W = 10\mathring{A}$ thick Pb film gives $T_\theta = \hbar^2 n_{3d} W/2m^* \approx 1eV \approx 10,000K$! Clearly, phase fluctuations are unimportant in Pb. This issue is addressed in detail in Section 6.8.

We have seen how T_p and T_θ have opposite dependence on coupling strength. (A general principle is proposed: "optimal" T_c occurs as a crossover.) If this is a general trend, then it is likely that any material in which T_c has been optimized has effectively been tuned to a crossover point between pairing and condensation. A modification of the material which produces stronger effective interactions will increase phase fluctuations and thereby reduce T_c, while weaker interactions will lower T_c because of pair breaking. In Section 6.8 it will be shown that optimal doping in the cuprate superconductors corresponds to precisely this sort of crossover from a regime in which T_c is determined by phase ordering to a pairing dominated regime.

6.2.3 Competing Orders

A Fermi liquid is a remarkably robust state of matter. In the absence of nesting, it is stable for a range of repulsive interactions; the Cooper instability is its only weak coupling instability. (As long as the interactions are not too strong.) The phase diagram of simple metals consists of a high temperature metallic phase and a low temperature superconducting state. When the superconductivity is suppressed by either a magnetic field or appropriate disorder (*e.g.* paramagnetic impurities), the system remains metallic down to the lowest temperatures.

The situation becomes considerably more complex for sufficiently strong interactions between electrons. In this case, the Fermi liquid description of the normal or high temperature phase breaks down (whether it breaks down for fundamental or practical reasons is unimportant) and many possible phases compete. In addition to metallic and superconducting phases, one would generally expect various sorts of electronic "crystalline" phases, including charge ordered phases (*i.e.* a charge density wave—CDW—of which the Wigner crystal is the simplest example) and spin ordered phases (*i.e.* a spin density wave—SDW—of which the Néel state is the simplest example).

Typically, one thinks of such phases as insulating, but it is certainly possible for charge and spin order to coexist with metallic or even superconducting electron transport. For example, this can occur in a conventional weak coupling theory if the density wave order opens a gap on only part of the Fermi surface, leaving other parts gapless [43]. It can also occur in a multicomponent system, in which the density wave order involves one set of electronic orbitals, and the conduction occurs through others—this is the traditional understanding of the coexisting superconducting and magnetic order in the Chevrel compounds [44].

Such coexistence is also possible for less conventional orders ("Stripe" order). One particular class of competing orders is known loosely as "stripe" order. Stripe order refers to unidirectional density wave order, *i.e.* order which spontaneously breaks translational symmetry in one direction but not in others. We will refer to charge stripe order, if the broken symmetry leads to charge density modulations and spin stripe order if the broken symmetry leads to spin density modulations, as well. Charge stripe order can occur without spin order, but spin order (in a sense that will be made precise, below) implies charge order [45]. Both are known on theoretical and experimental grounds to be a prominent feature of doped Mott insulators in general, and the high temperature superconductors in particular [6, 46–51]. Each of these orders can occur in an insulating, metallic, or superconducting state.

In recent years there has been considerable theoretical interest in other types of order that could be induced by strong interactions. From the perspective of stripe phases, it is natural to consider various partially melted "stripe liquid" phases, and to classify such phases, in analogy with the classification of phases of classical liquid crystals, according to their broken symmetries [52]. For instance, one can imagine a phase that breaks rotational symmetry (or, in a crystal, the point group symmetry) but not translational symmetry, *i.e.* quantum (ground state) analogues of nematic or hexatic liquid crystalline phases. Still more exotic phases, such as those with ground state orbital currents [53–58] or topological order [59], have also been suggested as the explanation for various observed features of the phenomenology of the high temperature superconductors.

Given the complex character of the phase diagram of highly correlated electrons, it is clear that the conventional approach to superconductivity, which focuses solely on the properties of the normal metal and the pure superconducting phase, is suspect. A more global approach, which takes into account some (or all) of the competing phases is called for. Moreover, even the term "competing" carries with it a prejudice that must not be accepted without thought. In a weakly correlated system, in which any low temperature ordered state occurs as a Fermi surface instability, different orders generally *do* compete: if one order produces a gap on part of the Fermi surface, there are fewer remaining low energy degrees of freedom to participate in the formation of another type of order. For highly correlated electrons, however, the sign of the interaction between different types of order is less clear. It can happen [60] that under one set of circumstances, a given order tends to enhance superconductivity and under others, to suppress it.

The issue of competing orders, of course, is not new. In a Fermi liquid, strong effective attractions typically lead to lattice instabilities, charge or spin density wave order, etc. Here the problem is that the system either becomes an insulator or, if it remains metallic, the residual attraction is typically weak. For instance, lattice instability has been seen to limit the superconducting transition temperature of the A15 compounds, the high temperature super-

conductors of a previous generation. Indeed, the previous generation of BCS based theories which addressed the issue always concluded that competing orders suppress superconductivity [44].

More recently it has been argued that near an instability to an ordered state there is a low lying collective mode (the incipient Goldstone mode of the ordered phase) which can play the role of the phonon in a BCS–like mechanism of superconductivity [29,61,62]. In an interesting variant of this idea, it has been argued that in the neighborhood of a zero temperature transition to an ordered phase, quantum critical fluctuations can mediate superconducting pairing in a more or less traditional way [63, 64, 66]. There are reasons to expect this type of fluctuation mediated pair binding to lead to a depression of T_c. If the collective modes are nearly Goldstone modes (as opposed to relaxational "critical modes"), general considerations governing the couplings of such modes in the ordered phase imply that the superconducting transition temperature is depressed substantially from any naive estimate by large vertex corrections [67]. Moreover, in a regime of large fluctuations to a nearby ordered phase, one generally expects a density of states reduction due to the development of a pseudogap; feeding this psuedogapped density of states back into the BCS–Eliashberg theory will again result in a significant reduction of T_c.

6.3 Superconductivity in the Cuprates: General Considerations

Some of the most important experimental facts concerning the cuprate high temperature superconductors are described with particular emphasis on those which indicate the need for a new approach to the mechanism of high temperature superconductivity. A perspective on the pseudogap phenomena and the origin of d–wave–like pairing is presented.

While the principal focus of the present article is theoretical, the choice of topics and models and the approaches are very much motivated by our interest in the experimentally observed properties of the cuprate high temperature superconductors. In this section, we discuss briefly some of the most dramatic (and least controversial) aspects of the phenomenology of these materials, and what sorts of constraints those observations imply for theory. As we are primarily interested in the origin of high temperature superconductivity, we will deal here almost exclusively with experiments in the temperature and energy ranges between about $T_c/2$ and a few times T_c.

Before starting, there are a number of descriptive terms that warrant definition. The parent state of each family of the high temperature superconductors is an antiferromagnetic "Mott" insulator with one hole (and spin 1/2) per planar copper [65]. These insulators are transformed into superconductors by introducing a concentration, x, of "doped holes" into the copper

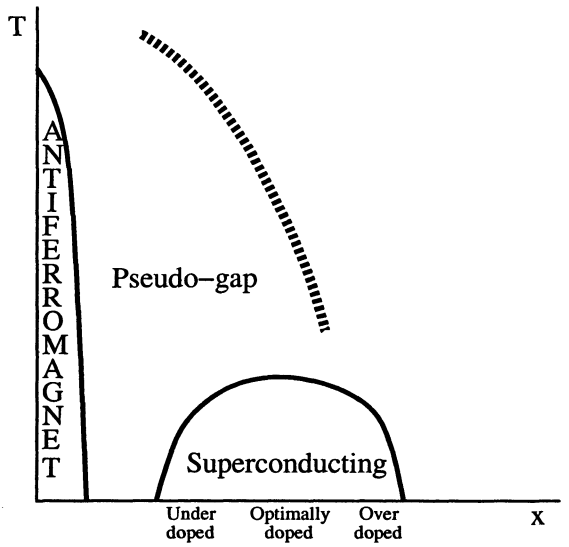

Fig. 6.1. Schematic phase diagram of a cuprate high temperature superconductor as a function of temperature and x—the density of doped holes per planar Cu. The solid lines represent phase transitions into the antiferromagnetic (AF) and superconducting (SC) states. The dashed line marks the opening of a pseudogap (PG). The latter crossover is not sharply defined and there is still debate on its position; see Refs. [82,83]

oxide planes. As a function of increasing x, the antiferromagnetic transition temperature is rapidly suppressed to zero, then the superconducting transition temperature rises from zero to a maximum and then drops down again. (See Fig. 6.1.) Where T_c is an increasing function of x, the materials are said to be "underdoped." They are "optimally doped" where T_c reaches its maximum at $x \approx 0.15$, and they are "overdoped" for larger x. In the underdoped regime there are a variety of crossover phenomena observed [82,83] at temperatures above T_c in which various forms of spectral weight at low energies are apparently suppressed—these phenomena are associated with the opening of a "psuedogap." There are various families of high temperature superconductors, all of which have the same nearly square copper oxide planes, but different structures in the regions between the planes. One characteristic that seems to have a fairly direct connection with T_c is the number of copper–oxide planes that are close enough to each other that interplane coupling may be significant; T_c seems generally to increase with number of planes within a homologous series, at least as one progresses from "single layer" to "bilayer," to "trilayer" materials [4,84].

6.3.1 A Fermi Surface Instability Requires a Fermi Surface

As has been stressed, for instance, by Schrieffer [1], BCS theory relies heavily on the accuracy with which the normal state is described by Fermi liquid theory. BCS superconductivity is a Fermi surface instability, which is only a reasonable concept if there is a well defined Fermi surface. BCS–Eliashberg theory relies on the dominance of a certain class of diagrams, summed to all orders in perturbation theory. This can be justified from phase space considerations for a Fermi liquid, but need not be valid more generally. To put it most physically, BCS theory pairs well defined quasiparticles, and therefore requires well defined quasiparticles in the normal state.

There is ample evidence that in optimally and underdoped cuprates, at least, there are no well defined quasiparticles in the normal state. This can be deduced directly from ARPES studies of the single particle spectral function [85–92], or indirectly from an analysis of various spin, current, and density response functions of the system [3, 4]. (Many, though not all, of these response functions have been successfully described [93–95] by the "marginal Fermi liquid" phenomenology.) Because we understand the nature of a Fermi liquid so well, it is relatively straightforward to establish that a system is a non–Fermi liquid, at least in extreme cases. It is much harder to establish the cause of this behavior—it could be due to the proximity of a fundamentally new non–Fermi liquid ground state phase of matter, or it could be because the characteristic coherence temperature, below which well defined quasiparticles dominate the physics, is lower than the temperatures of interest. Regardless of the reason for the breakdown of Fermi liquid theory, a description of the physics at scales of temperatures comparable to T_c can clearly *not* be based on a quasiparticle description, and thus cannot rely on BCS theory.

6.3.2 There is no Room for Retardation

As stressed in Section 6.2.1, retardation plays a pivotal role in the BCS mechanism. In the typical metallic superconductor, the Fermi energy is of order 10eV, while phonon frequencies are of order 10^{-2}eV, so $E_F/\omega_D \sim 10^3$! Since the renormalization of the Coulomb pseudopotential is logarithmic, this large value of the retardation is needed. In the cuprate superconductors, the bandwidth measured in ARPES is roughly $E_F \approx 0.3$eV—this is a renormalized bandwidth of sorts, but this is presumably what determines the quasiparticle dynamics. Independent of anything else, the induced interaction must clearly be fast compared to the gap scale, $\omega_D > 2\Delta_0$, where Δ_0 is the magnitude of the superconducting gap. From either ARPES [96, 97] or tunnelling [98] experiments, we can estimate $2\Delta_0 \approx 0.06$eV. Thus, a rough upper bound $E_F/\omega_D < E_F/2\Delta_0 \sim 5$ can be established on how retarded an interaction in the cuprates can possibly be. That is almost not retarded at all!

6.3.3 Pairing is Collective!

For the most part, the superconducting coherence length, ξ_0, cannot be directly measured in the high temperature superconductors because, for $T \ll T_c$, the upper critical field, H_{c2}, is too high to access readily. However, it can be inferred indirectly [99–103] in various ways, and for the most part people have concluded that ξ_0 is approximately 2 or 3 lattice constants in typical optimally doped materials. This has lead many people to conclude that these materials are nearly in a "real space pairing" limit [104–108], in which pairs of holes form actual two particle bound states, and then Bose condense at T_c. This notion is based on the observation that if x is the density of "doped holes" per site, then the number of pairs per coherence area, $N_p = (1/2)x\pi\xi_0^2/a^2$, is a number which is approximately equal to 1 for "optimal doping," $x \approx 0.15 - 0.20$.

However, there are strong *a priori* and empirical reasons to discard this viewpoint.

On theoretical grounds: In a system dominated by strong repulsive interactions between electrons, it is clear that pairing must be a collective phenomenon. The Coulomb interaction between an isolated pair of doped holes would seem to be prohibitively large, and it seems unlikely that a strong enough effective attraction can emerge to make such a strong binding possible. (Some numerical studies of this have been carried out, in the context of ladder systems, by Dagotto and collaborators [109].) Moreover, it is far from clear that the dimensional argument used above makes any sense: Why should we only count doped holes in making this estimate? What are the rest of the holes doing all this time? If we use the density of holes per site $(1 + x)$, which is consistent with the area enclosed by the Fermi surface seen in ARPES [110], the resulting N_p is an order of magnitude larger than the above estimate [111].

On experimental grounds: The essential defining feature of real space pairing is that the chemical potential moves below the bottom of the band. Incipient real space pairing must thus be associated with significant motion of the chemical potential toward the band bottom with pairing [104,105,113, 114]. However, experimentally, the chemical potential is found to lie in the middle of the band, where the enclosed area of the Brilloin zone satisfies Luttinger's theorem, and no significant motion at T_c (or at any pseudogap temperature in underdoped materials) has been observed [115–119]. This fact, alone, establishes that the physics is nowhere near the real space pairing limit.

6.3.4 What Determines the Symmetry of the Pair Wavefunction?

Independent of but contemporary with the discovery of high temperature superconductivity in the cuprates, Scalapino, Loh, and Hirsch [120], in a prescient work suggested the possibility of superconductivity in the two dimensional Hubbard model in the neighborhood of the antiferromagnetic state

at half filling. This work, which was in spirit a realization of the ideas of Kohn and Luttinger [121], concluded that the dominant superconducting instability should have $d_{(x^2-y^2)}$ symmetry, as opposed to s symmetry. Immediately after the discovery of high temperature superconductivity, a large number of other theorists [29, 122–127] came to the same conclusion, based on a variety of purely theoretical analyses, although at the time the experimental evidence of such pairing was ambiguous, at best. By now it seems very clear that this idea was correct, *at least* for a majority of the cuprate superconductors, based on a variety of phase sensitive measurements [128–130]. This represents one of the great triumphs of theory in this field. (There are still some experiments which appear to contradict this symmetry assignment [131], so the subject cannot be said to be completely closed, but it seems very unlikely that the basic conclusion will be overturned.)

While the names "s" and "d" relate to the rotational symmetries of free space, it is important to understand what is meant by s–wave and d–wave in a lattice system which, in place of continuous rotational symmetry, has the discrete point group symmetry of the crystal. Consequently, the possible pairing symmetries correspond to the irreducible representations of the point group: singlet orders are even under inversion and triplet orders are odd. In the case of a square crystal [1], the possible singlet orders (all corresponding to one dimensional representations) are colloquially called s, $d_{(x^2-y^2)}$, $d_{(xy)}$, and g, and transform like 1, (x^2-y^2), (xy), and $(x^2-y^2)(xy)$, respectively. As a function of angle, the gap parameter in an s–wave order always has a unique sign, the d–wave gap changes sign four times, and the g–wave changes sign 8 times. A fifth type of order is sometimes discussed, called extended–s, in which the gap function changes sign as a function of the magnitude of $\boldsymbol{k}$, rather than as a function of its direction—this is not a true symmetry classification, and in any generic model there is always finite mixing between s and extended s.

In crystals with lower symmetry, there are fewer truly distinct irreducible representations. For instance, if the square lattice is replaced with a rectangular one, the distinction between s and $d_{(x^2-y^2)}$ is lost (they mix), as is that between $d_{(xy)}$ and g. On the other hand, if the elementary squares are sheared to form rhombuses, then the s and $d_{(xy)}$ symmetries are mixed, as are $d_{(x^2-y^2)}$, and g. Both of these lower symmetries correspond to a form of orthorhombic distortion observed in the cuprates—the former is the correct symmetry group for $YBa_2Cu_3O_{7-\delta}$ and the latter for $La_{2-x}Sr_xCuO_4$. However, so long as the physics does not change fundamentally as the lattice symmetry is reduced, it is reasonable to classify order parameters as "d–wave–like" or "s–wave–like." We define an order parameter as being d–

[1] The pairing symmetries should really be classified according to the point group of a tetragonal crystal, but since the cuprates are quasi–two dimensional, it is conventional, and probably reasonable, to classify them according to the symmetries of a square lattice.

wave–like if it changes sign under 90^o rotation, although it is only a true d–wave if its magnitude is invariant under this transformation. Conversely, it is s–wave–like if its sign does not change under this rotation, or when reflected through any approximate symmetry plane. In almost all cases what is really being seen in phase sensitive measurements on the cuprates is that the order parameter is d–wave–like. (It is worth noting that in t–J and Hubbard ladders, d–wave–like pairing is the dominant form of pairing observed in both analytic and numerical studies, as discussed below.)

There is a widespread belief that d–wave symmetry follows directly from the presence of strong short range interactions between electrons, irrespective of details such as band structure. The essential idea here follows from the observation that the pair wavefunction, at the level of BCS mean field theory, is expressed in terms of the gap parameter, $\Delta_{\boldsymbol{k}}$, and the quasiparticle spectrum, $E_{\boldsymbol{k}}$, as

$$\phi_{pair}(\boldsymbol{r}) = \sum_{\boldsymbol{k}} \frac{1}{L^{d/2}} e^{i\boldsymbol{k}\cdot\boldsymbol{r}} \frac{\Delta_{\boldsymbol{k}}}{2E_{\boldsymbol{k}}} \ . \tag{6.5}$$

In the presence of strong short range repulsion (and weaker longer range attraction) between electrons, it is favorable for ϕ_{pair} to vanish at $\boldsymbol{r} = \boldsymbol{0}$, which it does automatically if the pairing is not s–wave. While this argument makes some physical sense, it is ultimately *wrong*. In the limit of dilute electrons, where the coherence length is much smaller than the inter–electron distance, the pairing problem reduces to a two particle problem. It is well known that in the continuum the lowest energy two particle spin singlet bound state is nodeless. Given certain mild conditions on the band structure one can also prove it on the lattice. (This is true under conditions that the hopping matrix, *i.e.* the band structure, satisfies a Peron–Frobenius condition). Therefore, in this limit, the order parameter is necessarily s–wave–like!

The above discrepancy teaches us that it is the presence of the kinematical constraints imposed by the Fermi sea that allows for non s–wave pairing. The ultimate pairing symmetry is a reflection of the distribution in momentum space of the low energy single particle spectral weight. The reason for this is clear within BCS theory where the energy gain, which drives the transition, comes from the interaction term

$$\text{Potential Energy} = \sum_{\boldsymbol{k},\boldsymbol{k}'} V_{\boldsymbol{k},\boldsymbol{k}'} \frac{\Delta_{\boldsymbol{k}}}{2E_{\boldsymbol{k}}} \frac{\Delta_{\boldsymbol{k}'}}{2E_{\boldsymbol{k}'}} \ , \tag{6.6}$$

which is maximized by a gap function that peaks in regions of high density of states unless the pairing potential that connects these regions is particularly small. (Although we do not know of an explicit justification of this argument for a non–BCS theory, for example one which is driven by gain in kinetic energy, we feel that the physical consideration behind it is robust.)

Finally, there is another issue which is related to order parameter symmetry in a manner that is more complex than is usually thought—this is the

issue of the existence of nodal quasiparticles. While nodal quasiparticles are natural in a d–wave superconductor, d–wave superconductors can be nodeless, and s–wave superconductors can be nodal. To see this, it is possible to work entirely in the weak coupling limit where BCS theory is reliable. The quasiparticle excitation spectrum can thus be expressed as

$$E_{\boldsymbol{k}} = \sqrt{\varepsilon_{\boldsymbol{k}}^2 + \Delta_{\boldsymbol{k}}^2}\,, \tag{6.7}$$

where $\varepsilon_{\boldsymbol{k}}$ is the quasiparticle dispersion in the normal state (measured from the Fermi energy). Nodal quasiparticles occur wherever the Fermi surface, that is the locus of points where $\varepsilon_{\boldsymbol{k}} = 0$, crosses a line of gap nodes, the locus of points where $\Delta_{\boldsymbol{k}} = 0$. If the Fermi surface is closed around the origin, $\boldsymbol{k} = 0$, or about the Brilloin zone center, $\boldsymbol{k} = (\pi, \pi)$ (as it is most likely in optimally doped $Bi_2Sr_2CaCu_2O_{8+\delta}$ [132]), then the d–wave symmetry of $\Delta_{\boldsymbol{k}} = 0$ implies the existence of nodes. However, if the Fermi surface were closed about $\boldsymbol{k} = (0, \pi)$ (and symmetry related points), there would be no nodal quasiparticles [133]. Indeed, it is relatively easy to characterize [134, 135] the quantum phase transition between a nodal and nodeless d–wave superconductor which occurs as a parameter that alters the underlying band structure is varied. Conversely, it is possible to have lines of gap nodes for an extended s–wave superconductor, and if these cross the Fermi surface, the superconductor will posses nodal quasiparticles.

6.3.5 What does the Pseudogap mean?

What experiments define the pseudogap?

One of the most prominent, and most discussed features of the cuprate superconductors is a set of crossover phenomena [54, 82, 83] which are widely observed in underdoped cuprates and, to various extents, in optimally and even slightly overdoped materials. Among the experimental probes which are used to locate the pseudogap temperature in different materials are:

1)**ARPES and c–axis tunnelling**

There is a suppression of the low energy single particle spectral weight, shown in Figs. 6.2 and 6.3 at temperatures above T_c as detected, primarily, in c–axis tunnelling [136] and ARPES [96, 97] experiments. The scale of energies and the momentum dependence of this suppression are very reminiscent of the d–wave superconducting gap observed in the same materials at temperatures well below T_c. This is highly suggestive of an identification between the pseudogap and some form of local superconducting pairing. Although a pseudogap energy scale is easily deduced from these experiments, it is not so clear to us that an unambiguous temperature scale can be cleanly obtained from them. (The c–axis here, and henceforth, refers to the direction perpendicular to the copper–oxide planes, which are also referred to, crystallographically, as the ab plane.)

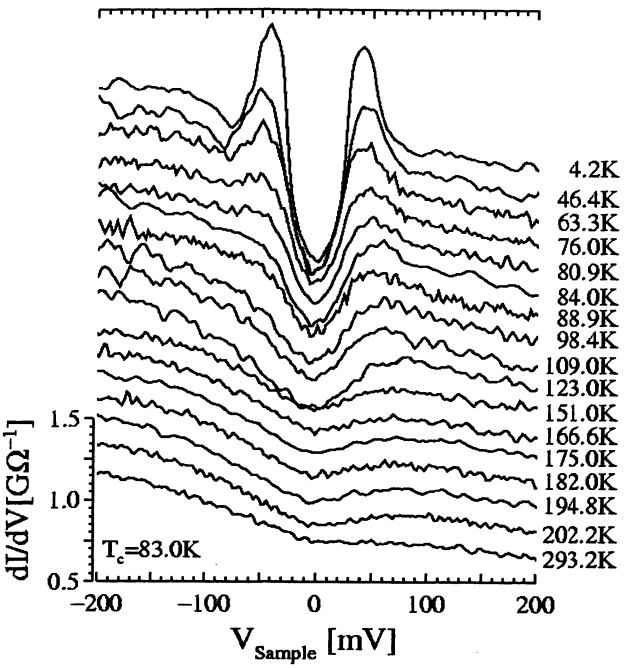

Fig. 6.2. Tunnelling density of states in a sample of underdoped $Bi_2Sr_2CaCu_2O_{8+\delta}$ (T_c=83K) as a function of temperature. Note that there is no tendency for the gap to close as T_c is approached from below, but that the sharp "coherence peaks" in the spectrum do vanish at T_c (from Ref. [98])

2)Cu NMR

There is a suppression of low energy spin fluctuations as detected [137] primarily in Cu NMR. In some cases, two rather different temperature scales are deduced from these experiments: an upper crossover temperature, at which a peak occurs in χ', the real part of the uniform spin susceptibility (*i.e.* the Knight shift), and a lower crossover temperature, below which $1/T_1T$ drops precipitously. (See Fig. 6.4.) Note that $1/T_1T \propto \lim_{\omega\to 0} \int d\boldsymbol{k} f(\boldsymbol{k})\chi''(\boldsymbol{k},\omega)/\omega$, the $\boldsymbol{k}$ averaged density of states for magnetic excitations, where $f(\boldsymbol{k})$ is an appropriate form factor which reflects the local hyperfine coupling. Although the temperature scale deduced from χ' is more or less in accordance with the pseudogap scale deduced from a number of other spectroscopies, it is actually a measure of the reactive response of the spin system. The notion of a gap can be more directly identified with a feature in χ''. (*A note of warning*: while the structure in $1/T_1T$ can be fairly sharp at times, the observed maxima in χ' are always very broad and do not yield a sharply defined temperature scale without further analysis.)

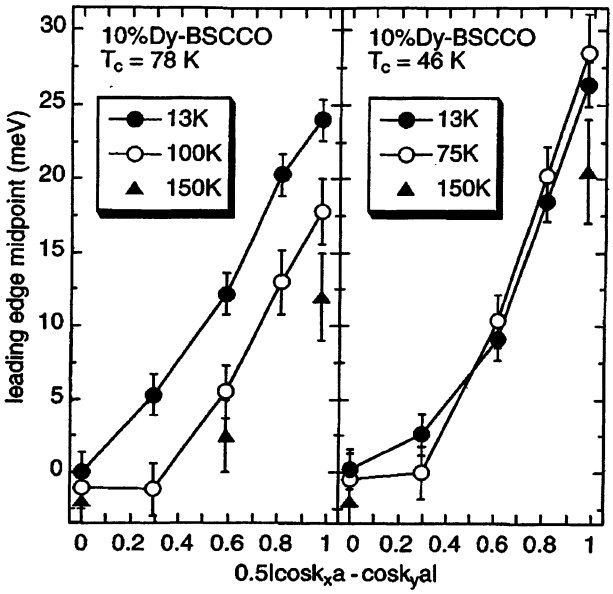

Fig. 6.3. The angular dependence of the gap in the normal and superconducting states of underdoped $Bi_2Sr_2Ca_{1-x}Dy_xCu_2O_{8+\delta}$ as deduced from the leading edge energy of the single hole spectral function $A^<(\boldsymbol{k},\omega)$ measured by ARPES. A straight line in this plot would correspond to the simplest $d_{x^2-y^2}$ gap, $|\Delta_{\boldsymbol{k}}| = \Delta_0|\cos(k_x) - \cos(k_y)|$ (from Ref. [96])

3)Resistivity

There is a significant deviation [138,139] of the resistivity in the ab plane from the T linear temperature dependence which is universally observed at high temperatures. A pseudogap temperature is then identified as the point below which $d\rho_{xx}/dT$ deviates (increases) significantly from its high temperature value. (See Fig. 6.5.) In some cases, a similar temperature scale can be inferred from a scaling analysis of the Hall resistance, as well.

The pseudogap also appears in the c–axis resitivity, although in a somewhat different manner [140,141]. In this direction, the pseudogap results in a strong increase in the resistivity, reminiscent of the behavior of a narrow gap semiconductor, as shown in Fig. 6.6. If we imagine that the c–axis transport is dominated by tunnelling events between neighboring planes, it is reasonable that a bulk measurement of ρ_c will reflect the pseudogap in much the same way as the c–axis tunelling does.

4)Specific heat

There is a suppression of the expected electronic specific heat [83]. Above the pseudogap scale, the specific heat is generally found to be linear in temperature, $C_V \approx \gamma T$, but below the pseudogap temperature, C_V/T begins to decrease with decreasing temperature. (See Fig. 6.7.) Interestingly, since the

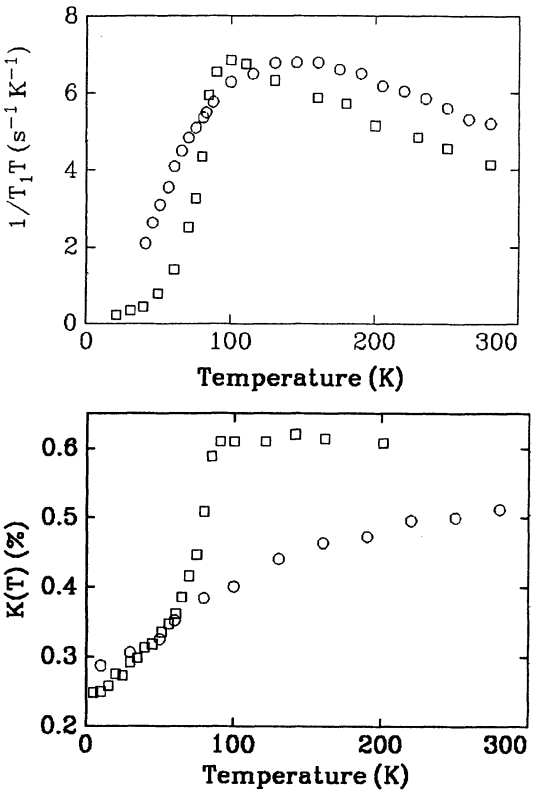

Fig. 6.4. Temperature dependence of the planar ^{63}Cu relaxation rate $1/T_1T$ and Knight shift K in optimally doped $YBa_2Cu_3O_{6.95}$ (squares) and underdoped $YBa_2Cu_3O_{6.64}$ (circles) (from Ref. [82])

value of γ above the pseudogap temperature appears to be roughly doping independent, the drop in the specific at lower temperatures can be interpreted as a doping dependent loss of entropy, $\Delta S(x) \equiv S(x,T) - S(x_{optimal},T)$, with a magnitude which is independent of temperature for any $T > T^*$. This is the origin of the famous (and still not understood) observation of Loram and collaborators [142] that there is a large entropy, $k_B/2$, which is somehow associated with each doped hole. *A word of warning*: except at the lowest temperatures, the electronic specific heat is always a small fraction of the total specific heat, and complicated empirical subtraction procedures, for which the theoretical justification is not always clear to us, are necessary to extract the electronic contribution.

5)**Infrared conductivity**

There is an anomalous motion of infrared spectral weight to low energies [143, 144]. The pseudogap is most clearly identified by plotting [144] the frequency

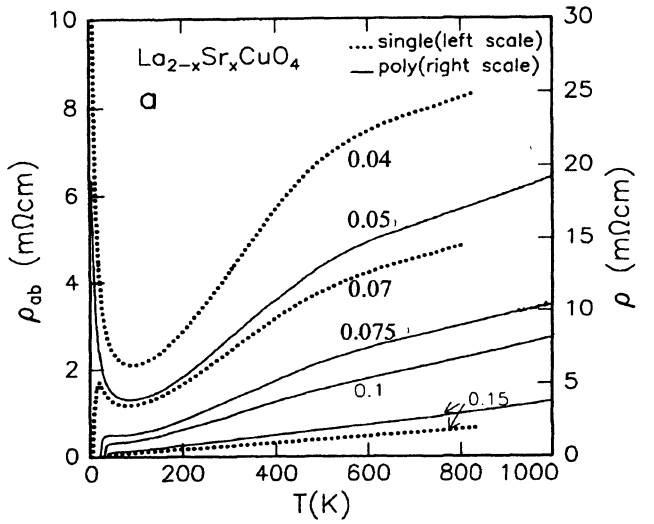

Fig. 6.5. The temperature dependence of the longitudinal resistivity in underdoped and optimally doped $La_{2-x}Sr_xCuO_4$. The dotted lines correspond to the in–plane resistivity (ρ_{ab}) of single crystal films while the solid lines depict the resistivity (ρ) of polycrystalline samples. The doping levels are indicated next to the curves (from Ref. [138])

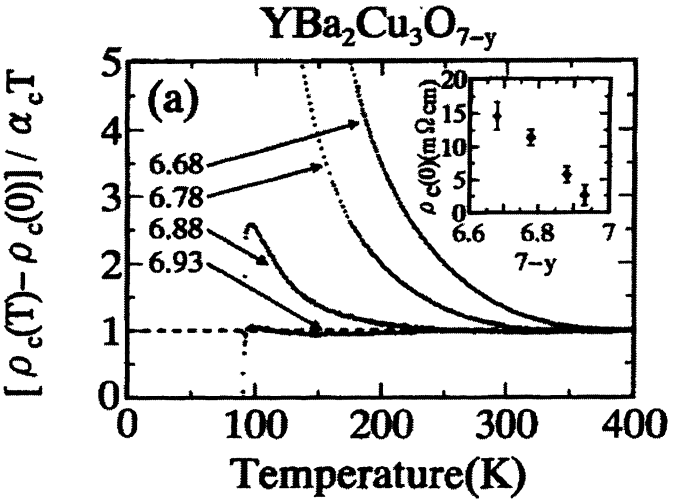

Fig. 6.6. The temperature dependence of the c–axis resistivity in underdoped and optimally doped $YBa_2Cu_3O_{7-\delta}$. Here α_c and $\rho_c(0)$ are the slope and the intercept, respectively, when the metallic part of ρ_c is approximated by a linear–T behavior. The inset shows how $\rho_c(0)$ varies with oxygen content (from Ref. [140])

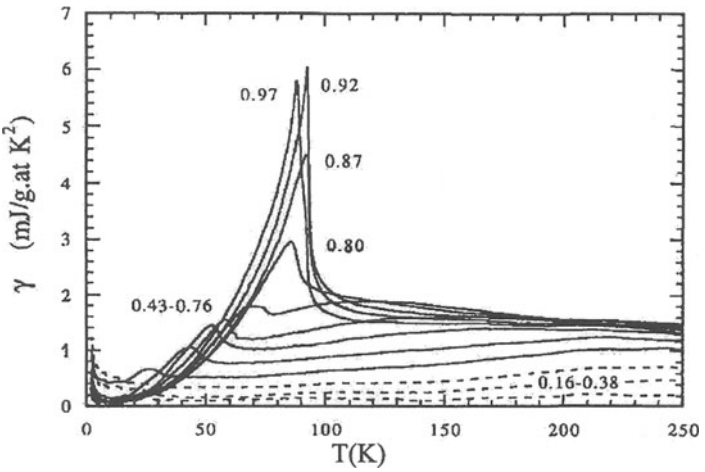

Fig. 6.7. Thermal density of "electronic" states, $\gamma \equiv C_V/T$ as a function of temperature for various oxygen concentrations in underdoped $YBa_2Cu_3O_{6+x}$ (from Ref. [142]). As discussed in [142], a complicated proceedure has been used to subtract the large nonelectronic component of the measured specific heat

dependent scattering rate, defined either as $1/\tau^*(\omega) \equiv \omega\sigma'_{ab}(\omega)/\sigma''_{ab}(\omega)$, or as $1/\tau(\omega) = [\omega_P^2/4\pi]\mathrm{Re}[1/\sigma(\omega)]$ where ω_P is the plasma frequency; the pseudogap is rather harder to pick out from the in–plane conductivity, σ'_{ab}, itself. At large ω, one generally sees $1/\tau(\omega) \approx A\omega$, and it then drops to much smaller values, $1/\tau \ll \omega$, below a characteristic pseudogap frequency, see Fig. 6.8. (A is generally a bit larger than 1 in underdoped materials and roughly equal to 1 in optimally doped ones.)

While in optimally doped materials, this manifestation of a pseudogap is only observed at temperatures less than T_c, in underdoped materials, it is seen to persist well above T_c, and indeed to be not strongly temperature dependent near T_c. A characteristic pseudogap energy is easily identified from this data, but, again, it is not clear to us to what extent it is possible to identify a clear pseudogap temperature from this data. A pseudogap can also be deduced directly [145, 146] from an analysis of $\sigma'_c(\omega)$, where it manifests itself as a suppressed response at low frequencies, as shown in Fig. 6.9.

6)Inelastic neutron scattering

There are temperature dependent changes in the dynamic spin structure factor as measured by inelastic neutron scattering. Here, both features associated with low energy incommensurate magnetic correlations (possibly associated with stripes) [147] and the so–called "resonant peak" are found to emerge below a temperature which is very close to T_c in optimally doped materials, but which rises considerably above T_c in underdoped materials [148]. (See Fig. 6.10.)

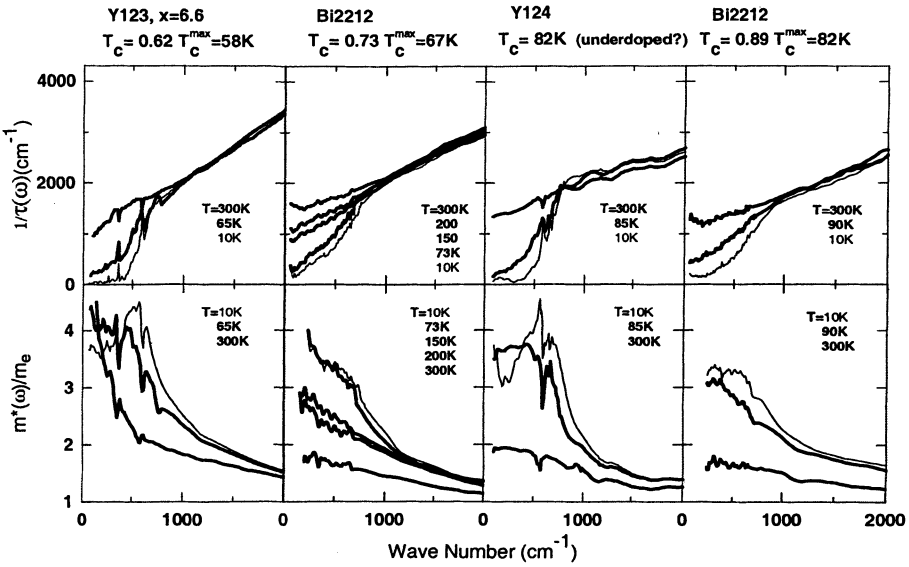

Fig. 6.8. Upper panels: Frequency dependent scattering rate for a series of underdoped cuprate superconductors above, near and below the superconducting transition temperature. Lower pannels: The effective mass enhancement $m^*/m_e = 1 + \lambda(\omega)$. Both are deduced from fitting infrared conductivity data to an extended Drude model $\sigma = (\omega_P^2/4\pi)/[1/\tau(\omega) - i\omega(1 + \lambda(\omega))]$ (from Ref. [144])

What does the pseudogap imply for theory?

It is generally accepted that the pseudogap, in one way or another, reflects the collective physics associated with the growth of electronic correlations. This, more than any other aspect of the data, has focused attention on theories of the collective variables representing the order parameters of various possible broken symmetry states [20, 51–54, 62, 78, 149–160]. Among these theories, there are two rather different classes of ways to interpret the pseudogap phenomena.

1) It is well known that fluctuation effects can produce local order which, under appropriate circumstances, can extend well into the disordered phase. Such fluctuations produce in the disordered phase some of the local characteristics of the ordered phase, and if there is a gap in the ordered phase, a pseduogap as a fluctuation effect is eminently reasonable—see Fig. 6.1. As is discussed in Section 6.8, the small superfluid density of the cuprates leads to the unavoidable conclusion that superconducting fluctuations are an order 1 effect in these materials, so it is quite reasonable to associate some pseudogap phenomena with these fluctuations. However, as the system is progressively underdoped, it gets closer and closer to the antiferromagnetic insulating state, and indeed there is fairly direct NMR evidence of increasingly strong local

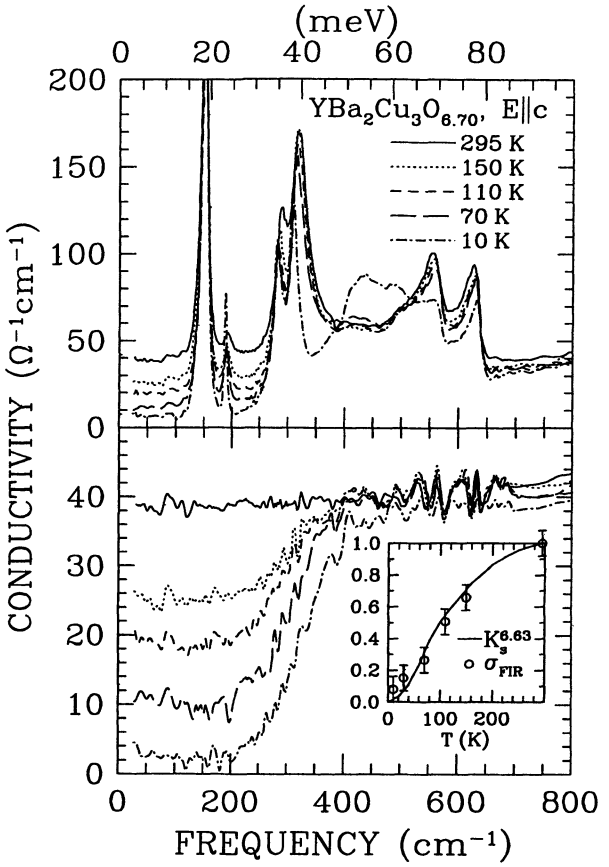

Fig. 6.9. The c–axis optical conductivity of underdoped $YBa_2Cu_3O_{7-\delta}$ ($T_c = 63$K) as a function of temperature (top panel). The optical conductivity after the substraction of the phonon features is presented in the lower panel. The inset compares the low frequency conductivity with the Knight shift (from Ref. [145])

antiferromagnetic correlations [161]. It is thus plausible that there are significant effects of antiferromagnetic fluctuations, and since the antiferromagnetic state also has a gap, one might expect these fluctuations to contribute to the pseudogap phenomena as well. There are significant incommensurate charge and spin density (stripe) fluctuations observed directly in scattering experiments on a variety of underdoped materials [47, 147, 162–164], as well as the occasional stripe ordered phase [165–169]. These fluctuations, too, certainly contribute to the observed pseudogap phenomena. Finally, fluctuations associated with more exotic phases, especially the "staggered flux phase" (which we will discuss momentarily) have been proposed [150, 170] as contributing to the pseudogap as well.

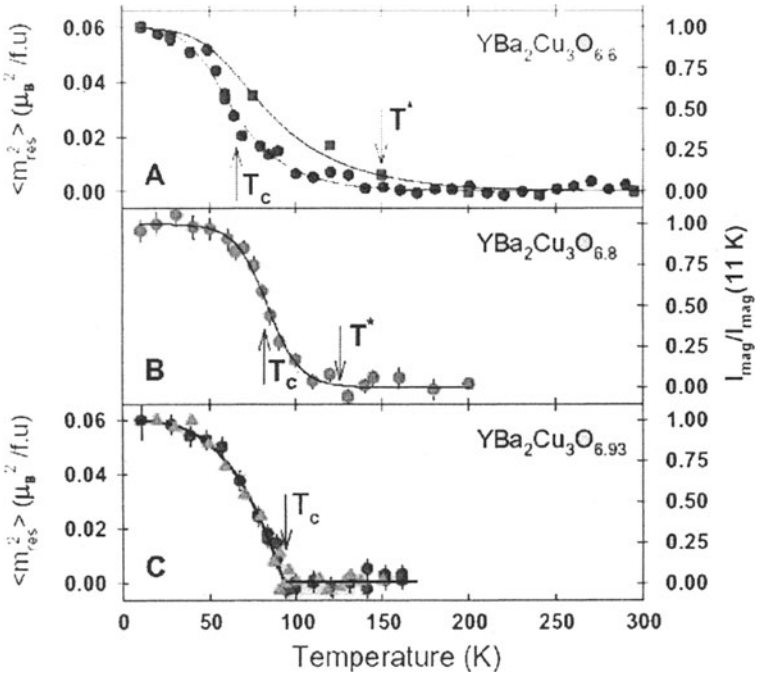

Fig. 6.10. The temperature dependence of the intensity of the so called resonant peak observed in neutron scattering in underdoped $YBa_2Cu_3O_{7-\delta}$ (from Ref. [148])

There has been a tremendous amount of controversy in the literature concerning which of these various fluctuation effects best account for the observed pseudogap phenomena. Critical phenomena, which are clearly associated with the phase fluctuations of the superconducting order parameter, have been observed [171–174] in regions that extend between 10% to 40% above and below the superconducting T_c in optimally and underdoped samples of $YBa_2Cu_3O_{7-\delta}$ and $Bi_2Sr_2CaCu_2O_{8+\delta}$; in our opinion, the dominance of superconducting fluctuations in this substantial range of temperatures is now beyond question. However, pseudogap phenomena are clearly observed in a much larger range of temperatures. Even if fluctuation effects are ultimately the correct explanation for all the pseudogap phenomena, there may not truly be one type of fluctuation which dominates the physics over the entire range of temperatures.

To illustrate this point explicitly, consider a one dimensional electron gas (at an incommensurate density) with weak attractive backscattering interactions see Section 6.5. If the backscattering interactions are attractive ($g_1 < 0$), they produce a spin gap Δ_s. This gap persists as a pseudogap in the spectrum up to temperatures of order $\Delta_s/2$. Now, because of the nature of fluctuations in one dimension, the system can never actually order at any finite tempera-

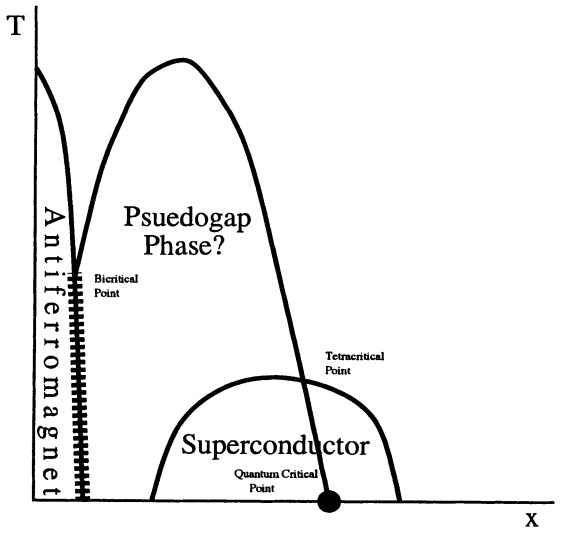

Fig. 6.11. There are many ideas concerning the meaning of the pseudogap. Defined purely phenomenologically, as shown in Fig. 6.1, it is a region in which there is a general reduction in the density of low energy excitations, and hence is bounded by an ill–defined crossover line. It is also possible that, to some extent, the pseudogap reflects the presence of a broken symmetry, in which case it must be bounded by a precise phase boundary, as shown in the present figure. There are many ways such a pseudogap phase could interact with the other well established phases. For purposes of illustration, we have shown a tetracritical and a bicritical point where the pseudogap meets, respectively, the superconducting and antiferromagnetic phases. One consequence of the assumption that the transition into the pseudogap phase is continuous is the exisence of a quantum critical point (indicated by the heavy circle) somewhere under the superconducting dome. See, for example, Refs. [20,52,54,62,175]

ture. However, there is a very real sense in which one can view the pseudogap as an effect of superconducting fluctuations, since at low temperatures, the superconducting susceptibility is proportional to Δ_s. The problem is that one can equally well view the pseudogap as an effect of CDW fluctuations. One could arbitrarily declare that where the CDW susceptibility is the most divergent, the pseudogap should be viewed as an effect of local CDW order, while when the superconducting susceptibility is more divergent, it is an effect of local pairing. However, this position is untenable; by varying the strength of the forward scattering (g_2), it is possible to pass smoothly from one regime to the other without changing Δ_s in any way !

2) There are several theoretical proposals [52–54] on the table which suggest that there is a heretofore undetected electronic phase transition in underdoped materials with a transition temperature well above the superconduct-

ing T_c. As a function of doping, this transition temperature is pictured as decreasing, and tending to zero at a quantum critical point somewhere in the neighborhood of optimal doping, as shown schematically in Fig. 6.11. If such a transition occurs, it would be natural to associate at least some of the observed pseudogap phenomena with it. Since these scenarios involve a new broken symmetry, they make predictions which are, in principle, sharply defined and falsifiable by experiment. However, there is an important piece of phenomenology which these theories must address: if there is a phase transition underlying pseudogap formation, why hasn't direct thermodynamic evidence (*i.e.* nonanalytic behavior of the specific heat, the susceptibility, or some other correlation function of the system) been seen in existing experiments? Possible answers to this question typically invoke disorder broadening of the proposed phase transition [54], rounding of the transition by a symmetry breaking field [52], or possibly the intrinsic weakness of the thermodynamic signatures of the transition under discussion [53, 176].

6.4 Preview: Our View of the Phase Diagram

The pseudogap phenomena is just the tip of the iceberg, and any understanding of the physics of the cuprate high temperature superconductors will necessarily be complicated. For this reason, we have arranged this article to focus primarily on high temperature superconducitivity as an abstract theoretical issue, and only really discuss how these ideas apply to the cuprates in Section 6.13. However, to orient the reader, we will take a moment here to briefly sketch *our* understanding of how these abstract issues determine the behavior, especially the high temperature superconductivity of the cuprates.

Fig. 6.12 is a schematic representation of the temperature *vs.* doping phase diagram of a representative cuprate. There are four energy scales relevant to the mechanism of superconductivity, marked as T^*_{stripe}, T^*_{pair}, T^*_{3D} and T_c. Away from the peak of the superconducting dome, these energy scales are often well separated. At least some of the pseudogap phenomena are, presumably, associated with the two crossover scales, T^*_{pair} and T^*_{stripe}.

Stripe Formation T^*_{stripe}

The kinetic energy of doped holes is frustrated in an antiferromagnet. As the temperature is lowered through T^*_{stripe}, the doped holes are effectively ejected from the antiferromagnet to form metallic regions, thus relieving some of this frustration. Being charged objects, the holes can only phase separate on short length scales, since the Coulomb repulsion enforces charge homogeneity at long length scales. As a result, at T^*_{stripe}, the material develops significant one dimensional charge modulations, which we refer to as charge stripes. This can be an actual phase transition (*e.g.* to a "nematic phase"), or a crossover scale at which significant local charge stripe correlations develop.

Pair Formation T^*_{pair}

While stripe formation permits hole delocalization in one direction, hole mo-

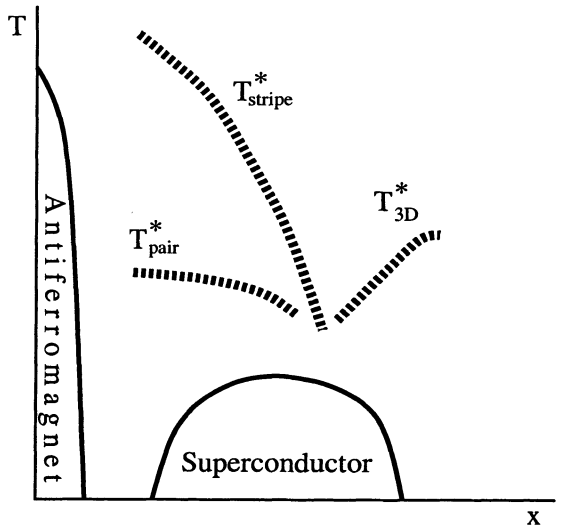

Fig. 6.12. Phase diagram as a function of temperature and doping within the stripes scenario

tion transverse to the stripe is still restricted. It is thus favorable, under appropriate circumstances, for the holes to pair so that the pairs can spread out somewhat into the antiferromagnetic neighborhood of the stripe. This "spin gap proximity effect" [20] (see Section 6.10.4), which is much like the proximity effect at the interface between a normal metal and a conventional superconductor, results in the opening of a spin gap and an enhancement of the superconducting susceptibility on a single stripe. In other words, T^*_{pair} marks a crossover below which the superconducting order parameter amplitude (and therefore a superconducting pseudo gap) has developed, but without global phase coherence.

Superconductivity T_c

Superconducting long ranged order onsets as the phase of the superconducting order parameter on each charge stripe becomes correlated across the sample. Since it is triggered by Josephson tunnelling between stripes, this is a kinetic energy driven phase ordering transition.

Dimensional Crossover T^*_{3D}

Superconducting long range order implies coherence in all three dimensions, and hence the existence of well defined electron–like quasiparticles [21, 151, 177]. Where the stripe order is sufficiently strong (in the underdoped regime), the dimensional crossover to 3D physics is directly associated with the onset of superconducting order. However, in overdoped materials, where the electron dynamics is less strongly influenced by stripe formation, we expect the dimensional crossover to occur well above T_c. (See Section 6.5.)

6.5 Quasi–1D Superconductors

The well developed theory of quasi–one dimensional superconductors is introduced as the best theoretical laboratory for the study of strongly correlated electron fluids. The normal state is a non–Fermi liquid, in which the electron is fractionalized. It can exhibit a broad pseudogap regime for temperatures above T_c but below the high temperature Tomonaga–Luttinger liquid regime. T_c marks a point of dimensional crossover, where familiar electron quasiparticles appear with the onset of long range superconducting phase coherence.

In this section we address the physics of the one dimensional electron gas and quasi–one dimensional systems consisting of higher dimensional arrays of weakly coupled chains. Our motivation is twofold. Firstly, these systems offer a concrete realization of various non–Fermi liquid phenomena and are amenable to *controlled* theoretical treatments. As such they constitute a unique theoretical laboratory for studying strong correlations. In particular, for whatever reason,much of the experimentally observed behavior of the cuprate superconductors is strongly reminiscent [85, 87, 151] of a quasi–1D superconductor. Secondly, we are motivated by a growing body of experimental evidence for the existence of electron smectic and nematic phases in the high temperature superconductors, manganites and quantum Hall systems [6, 178–182]. It is possible that these materials actually are quasi 1D on a local scale.

Our emphasis will be on quasi–one dimensional superconductors, the different unconventional signatures they exhibit as a function of temperature, and the conditions for their expression and stability. We will, however, include some discussion of other quasi–one dimensional phases which typically tend to suppress superconductivity. It is also worth noting that, for the most part, the discussion is simply generalized to quasi–1D systems with different types of order, including quasi–1D CDW insulators.

6.5.1 Elementary Excitations of the 1DEG

We begin by considering the continuum model of an interacting one dimensional electron gas (1DEG). It consists of approximating the 1DEG by a pair of linearly dispersing branches of left ($\eta = -1$) and right ($\eta = 1$) moving spin 1/2 ($\sigma = \pm 1$ denotes the z spin component) fermions constructed around the left and right Fermi points of the 1DEG. This approximation correctly describes the physics in the limit of low energy and long wavelength where the only important processes are those involving electrons in the vicinity of

the Fermi points. The Hamiltonian density of the model is

$$\begin{aligned}\mathcal{H} = & - iv_F \sum_{\eta,\sigma=\pm 1} \eta \psi^\dagger_{\eta,\sigma} \partial_x \psi_{\eta,\sigma} \\ & + \frac{g_4}{2} \sum_{\eta,\sigma=\pm 1} \psi^\dagger_{\eta,\sigma} \psi^\dagger_{\eta,-\sigma} \psi_{\eta,-\sigma} \psi_{\eta,\sigma} \\ & + g_2 \sum_{\sigma,\sigma'=\pm 1} \psi^\dagger_{1,\sigma} \psi^\dagger_{-1,\sigma'} \psi_{-1,\sigma'} \psi_{1,\sigma} \\ & + g_{1\parallel} \sum_{\sigma=\pm 1} \psi^\dagger_{1,\sigma} \psi^\dagger_{-1,\sigma} \psi_{1,\sigma} \psi_{-1,\sigma} \\ & + g_{1\perp} \sum_{\sigma=\pm 1} \psi^\dagger_{1,\sigma} \psi^\dagger_{-1,-\sigma} \psi_{1,-\sigma} \psi_{-1,\sigma} \ , \end{aligned} \tag{6.8}$$

where, *e.g.*, $\psi_{1,1}$ destroys a right moving electron of spin 1/2. The g_4 term describes forward scattering events of electrons in a single branch. The g_2 term corresponds to similar events but involving electrons on both branches. Finally, the $g_{1\parallel}$ and $g_{1\perp}$ terms allow for backscattering from one branch to the other. The system is invariant under $SU(2)$ spin rotations provided $g_{1\parallel} = g_{1\perp} = g_1$. In the following we consider mostly this case.

Umklapp processes of the form

$$g_3 \psi^\dagger_{-1,\uparrow} \psi^\dagger_{-1,\downarrow} \psi_{1,\downarrow} \psi_{1,\uparrow} e^{i(4k_F - G)x} + \text{H.c.} \ ,$$

are important only when $4k_F$ equals a reciprocal lattice vector G. When the 1DEG is incommensurate ($4k_F \neq G$), the rapid phase oscillations in this term render it irrelevant in the renormalization group sense. We will assume such incommensurability and correspondingly ignore this term. We will also neglect single particle scattering between branches (for example due to disorder) and terms that do not conserve the z component of the spin.

It is important to stress [183] that in considering this model we are focusing on the long distance physics that can be precisely derived from an effective field theory. However, all the coupling constants that appear in Eq. 6.8 are effective parameters which implicitly include much of the high energy physics. For instance, the bare velocity which enters the model, v_F, is not necessarily simply related to the dispersion of the band electrons in a zeroth order, noninteracting model, but instead includes all sorts of finite renormalizations due to the interactions. The weak coupling perturbative renormalization group treatment of this model is discussed in Section 6.9, below; the most important result from this analysis is that the Fermi liquid fixed point is always unstable, so that an entirely new, nonperturbative method must be employed to reveal the low energy physics.

Bosonization

Fortunately, such a solution is possible; the Hamiltonian in Eq. (6.8) is equivalent to a model of two independent bosonic fields, one representing the charge and the other the spin degrees of freedom in the system. (For reviews

and recent perspectives see Refs. [38, 183–189].) The two representations are related via the bosonization identity

$$\psi_{\eta,\sigma} = \frac{1}{\sqrt{2\pi a}} F_{\eta,\sigma} \exp[-i\Phi_{\eta,\sigma}(x)] \,, \tag{6.9}$$

which expresses the fermionic fields in terms of self dual fields $\Phi_{\eta,\sigma}(x)$ obeying $[\Phi_{\eta,\sigma}(x), \Phi_{\eta',\,\sigma'}(x')] = -i\pi\delta_{\eta,\eta'}\delta_{\sigma,\sigma'}\mathrm{sign}(x-x')$. They in turn are combinations of the bosonic fields ϕ_c and ϕ_s and their conjugate momenta $\partial_x\theta_c$ and $\partial_x\theta_s$

$$\Phi_{\eta,\sigma} = \sqrt{\pi/2}\,[(\theta_c - \eta\phi_c) + \sigma(\theta_s - \eta\phi_s)] \,. \tag{6.10}$$

Physically, ϕ_c and ϕ_s are, respectively, the phases of the $2k_F$ charge density wave (CDW) and spin density wave (SDW) fluctuations, and θ_c is the superconducting phase. In terms of them the long wavelength component of the charge and spin densities are given by

$$\rho(x) = \sum_{\eta,\sigma} \psi^\dagger_{\eta,\sigma}\psi_{\eta,\sigma} - \frac{2k_F}{\pi} = \sqrt{\frac{2}{\pi}}\partial_x\phi_c \,, \tag{6.11}$$

$$S_z(x) = \frac{1}{2}\sum_{\eta,\sigma} \sigma\psi^\dagger_{\eta,\sigma}\psi_{\eta,\sigma} = \sqrt{\frac{1}{2\pi}}\partial_x\phi_s \,. \tag{6.12}$$

The Klein factors $F_{\eta,\sigma}$ in Eq. (6.9) are responsible for reproducing the correct anticommutation relations between different fermionic species and a is a short distance cutoff that is taken to zero at the end of the calculation.

The widely discussed separation of charge and spin in this problem is formally a statement that the Hamiltonian density can be expressed as a sum of two pieces, each of the sine–Gordon variety, involving only charge or spin fields

$$\mathcal{H} = \sum_{\alpha=c,s} \left\{ \frac{v_\alpha}{2}\left[K_\alpha(\partial_x\theta_\alpha)^2 + \frac{(\partial_x\phi_\alpha)^2}{K_\alpha}\right] + V_\alpha\cos(\sqrt{8\pi}\phi_\alpha)\right\} \,. \tag{6.13}$$

Note, in 1D spin and charge separate when the Hamiltonian is separable, wavefunctions, and therefore correlation functions, factor. (See Eqs. (6.24) and (6.25).) In terms of the parameters of the fermionic formulation Eq. (6.8) the charge and spin velocities are given by

$$v_c = \frac{1}{2\pi}\sqrt{(2\pi v_F + g_4)^2 - (g_{1\parallel} - 2g_2)^2} \,, \tag{6.14}$$

$$v_s = \frac{1}{2\pi}\sqrt{(2\pi v_F - g_4)^2 - g_{1\parallel}^2} \,, \tag{6.15}$$

while the Luttinger parameters K_α, which determine the power law behavior of the correlation functions, are

$$K_c = \sqrt{\frac{2\pi v_F + g_4 - 2g_2 + g_{1\parallel}}{2\pi v_F + g_4 + 2g_2 - g_{1\parallel}}}\,, \tag{6.16}$$

$$K_s = \sqrt{\frac{2\pi v_F - g_4 + g_{1\parallel}}{2\pi v_F - g_4 - g_{1\parallel}}}\,. \tag{6.17}$$

The cosine term in the spin sector of the bosonized version of the Hamiltonian (Eq. (6.13)) originates from the back scattering term in Eq. (6.8) where the amplitudes are related according to

$$V_s = \frac{g_{1\perp}}{2(\pi a)^2}\,. \tag{6.18}$$

The corresponding term in the charge sector describes umklapp processes and in view of our assumption will be set to zero $V_c = 0$. Eqs. (6.14-6.18) complete the exact mapping between the fermionic and bosonic field theories.

In the absence of back scattering ($g_1 = 0$) this model is usually called the Tomonaga–Luttinger model. Since $\partial_x \theta_{c,s}$ and $\phi_{c,s}$ are canonically conjugate, it is clear from the form of the bosonized Hamiltonian (Eq. (6.13)) that it describes a collection of independent charge and spin density waves with linear dispersion $\omega_{c,s} = v_{c,s}k$. The quadratic nature of the theory and the coherent representation (Eq. (6.9)) of the electronic operators in terms of the bosonic fields allow for a straightforward evaluation of various electronic correlation functions.

For $g_1 \neq 0$ the spin sector of the theory turns into a sine–Gordon theory whose renormalization group flow is well known [190]. In particular, for repulsive interactions ($g_1 > 0$) the backscattering amplitude is renormalized to zero in the long wavelength low energy limit and consequently at the fixed point $K_s = 1$. On the other hand, in the presence of attractive interactions ($g_1 < 0$) the model flows to strong (negative) coupling where the cosine term in Eq. (6.13) is relevant. As a result ϕ_s is pinned in the sense that in the ground state, it executes only small amplitude fluctuations about its classical ground state value (*i.e.* one of the minima of the cosine). There is a spin gap to both extended phonon–like small amplitude oscillations about this minimum and large amplitude soliton excitations that are domain walls at which ϕ_s changes between two adjacent minima.

The susceptibility of the interacting one dimensional electron gas to various instabilities can be investigated by calculating the correlation functions of the operators that describe its possible orders. They include, among others, the $2k_F$ CDW and SDW operators

$$O_{CDW}(x) = e^{-i2k_F x} \sum_\tau \psi^\dagger_{1,\tau}(x)\psi_{-1,\tau}(x)\,, \tag{6.19}$$

$$O_{SDW_\alpha}(x) = e^{-i2k_F x} \sum_{\tau,\tau'} \psi^\dagger_{1,\tau}(x)\sigma^\alpha_{\tau,\tau'}\psi_{-1,\tau'}(x)\,, \tag{6.20}$$

where σ are the Pauli matrices, the $4k_F$ CDW (or Wigner crystal) order

$$O_{4k_F}(x) = e^{-i4k_F x} \sum_{\tau} \psi^{\dagger}_{1,\tau}(x)\psi^{\dagger}_{1,-\tau}(x)\psi_{-1,-\tau}(x)\psi_{-1,\tau}(x) \,, \tag{6.21}$$

and the singlet (SS) and triplet (TS) pair annihilation operators

$$O_{SS}(x) = \sum_{\tau} \tau\psi_{1,\tau}(x)\psi_{-1,-\tau}(x) \,, \tag{6.22}$$

$$O_{TS_\alpha}(x) = \sum_{\tau,\tau'} \tau\psi_{1,\tau}(x)\sigma^{\alpha}_{\tau,\tau'}\psi_{-1,-\tau'}(x) \,. \tag{6.23}$$

They can also be written in a suggestive bosonized form. For example the CDW and the singlet pairing operators are expressed as [2]

$$O_{CDW}(x) = \frac{e^{-2ik_F x}}{\pi a} \cos[\sqrt{2\pi}\phi_s(x)] e^{-i\sqrt{2\pi}\phi_c(x)} \,, \tag{6.24}$$

$$O_{SS}(x) = \frac{1}{\pi a} \cos[\sqrt{2\pi}\phi_s(x)] e^{-i\sqrt{2\pi}\theta_c(x)} \,. \tag{6.25}$$

The distinct roles of spin and charge are vividly apparent in these expressions: the amplitude of the order parameters is a function of the spin fields while their phase is determined by the charge degrees of freedom. Similar relations are found for the SDW and triplet pairing operators. However, the $4k_F$ CDW order is independent of the spin fields. Note, 1D order parameters have "spin" amplitudes and "charge" phases.

If in the bare Hamiltonian, $g_1 > 0$ and V_s is not too large, the system flows to the Gaussian fixed point with $K_s = 1$ and no spin gap. The gapless fluctuations of the amplitude (spin) and phase (charge) of the various orders lead then to an algebraic decay of their zero temperature space–time correlation functions (with logarithmic corrections which reflect the slow renormalization of marginally irrelevant operators near the fixed point [191]):

$$\begin{aligned}
\langle O^{\dagger}_{CDW}(x) O_{CDW}(0)\rangle &\propto e^{2ik_F x} x^{-(1+K_c)} \ln^{-3/2}(x) \,, \\
\langle O^{\dagger}_{SDW_\alpha}(x) O_{SDW_\alpha}(0)\rangle &\propto e^{2ik_F x} x^{-(1+K_c)} \ln^{1/2}(x) \,, \\
\langle O^{\dagger}_{4k_F}(x) O_{4k_F}(0)\rangle &\propto e^{4ik_F x} x^{-4K_c} \,, \\
\langle O^{\dagger}_{SS}(x) O_{SS}(0)\rangle &\propto x^{-(1+1/K_c)} \ln^{-3/2}(x) \,, \\
\langle O^{\dagger}_{TS_\alpha}(x) O_{TS_\alpha}(0)\rangle &\propto x^{-(1+1/K_c)} \ln^{1/2}(x) \,,
\end{aligned} \tag{6.26}$$

where the proportionality involves model dependent constants and where sub–leading terms have been omitted. In the presence of interactions that break spin rotation symmetry ($g_{1\parallel} \neq g_{1\perp}$) the model flows, for moderately repulsive bare $g_{1\parallel}$, to a point on a fixed line with $V_s = 0$ and $K_s > 1$. Correspondingly, the spin contribution to the decay exponent of the correlation

[2] For a discussion of some delicate points involving Klein factors in such expressions see Refs. [186] and [188].

functions (see Eq. (6.26)) changes from 1 to K_s for the CDW, SS, and the z component of the SDW order, and from 1 to $1/K_s$ for TS and the x and y components of the SDW order. (For $K_s \neq 1$, there are no logarithmic corrections and the leading behavior is that of a pure power law [191].)

The temporal dependence of the above correlation functions is easily obtained owing to the Lorentz invariance of the model (Eq. (6.13)). By Fourier transforming them one obtains the related susceptibilities whose low temperature behavior for the spin rotationally invariant case is given according to

$$\begin{aligned}
\chi_{CDW} &\propto T^{K_c-1}|\ln(T)|^{-3/2}\,, \\
\chi_{SDW} &\propto T^{K_c-1}|\ln(T)|^{1/2}\,, \\
\chi_{4k_F} &\propto T^{4K_c-2}\,, \\
\chi_{SS} &\propto T^{1/K_c-1}|\ln(T)|^{-3/2}\,, \\
\chi_{TS} &\propto T^{1/K_c-1}|\ln(T)|^{1/2}\,.
\end{aligned} \tag{6.27}$$

Therefore in the absence of a spin gap and for $1/3 < K_c < 1$, the $2k_F$ fluctuations are the most divergent, and the SDW is slightly more divergent than the CDW. In the presence of strong repulsive interactions when $K_c < 1/3$, the $4k_F$ correlations dominate. If $K_c > 1$, the pairing susceptibilities diverge at low temperatures and triplet pairing is the dominant channel. Note, without a spin gap, SDW and triplet pairing fluctuations are most relevant.

When $g_1 < 0$, a spin gap opens of magnitude

$$\Delta_s \sim \frac{v_s}{a}\left(\frac{|g_1|}{2\pi v_s}\right)^{1/(2-2K_s)}\,. \tag{6.28}$$

This can be explicitly demonstrated at the special Luther–Emery point [192] $K_s = 1/2$, where the spin sector is equivalent to a massive free Dirac theory. At this point, a new set of spinless fermions can be defined

$$\Psi_\eta \equiv \frac{1}{\sqrt{2\pi a}} F_\eta \exp[i\sqrt{\pi/2}(\theta_s - 2\eta\phi_s)]\,, \tag{6.29}$$

in terms of which the spin part of the Hamiltonian can be refermionized

$$\mathcal{H}_s = -iv_s \sum_\eta \eta \Psi_\eta^\dagger \partial_x \Psi_\eta + \Delta_s(\Psi_1^\dagger \Psi_{-1} + H.c.)\,, \tag{6.30}$$

and readily diagonalized to obtain the spin excitation spectrum

$$E_s = \sqrt{v_s^2 k^2 + \Delta_s^2}\,. \tag{6.31}$$

In the spin gapped phase (with a spin gap, CDW or singlet pairing fluctuations are the most relevant), correlations involving spin 1 order parameters,

such as SDW and triplet pairing, decay exponentially with correlation length $\xi_s = v_s/\Delta_s$. On the other hand the amplitude of the CDW and SS order parameters acquire a vacuum expectation value. Actual long range order, however, does not occur due to the phase fluctuations associated with the still gapless charge modes. Nevertheless, the CDW and SS susceptibilities are enhanced compared to the case with no spin gap and in a spin rotationally invariant system are given by

$$\chi_{CDW} \propto \Delta_s T^{K_c-2} ,$$
$$\chi_{SS} \propto \Delta_s T^{1/K_c-2} . \tag{6.32}$$

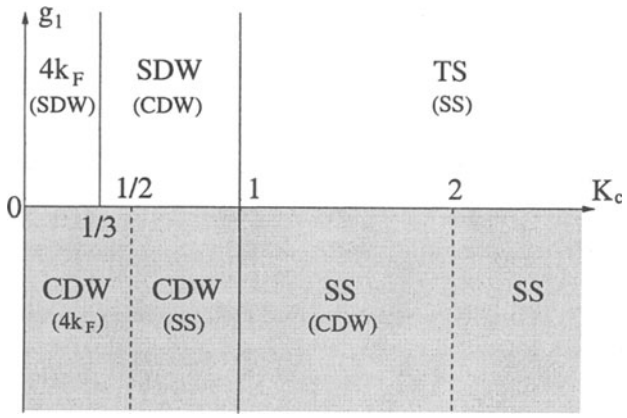

Fig. 6.13. Phase diagram for the one dimensional spin rotationally invariant electron gas showing where various zero temperature correlations diverge. Parentheses indicate subdivergent correlations and the shaded region contains the spin gapped phases. The order parameters that appear in the figure are: singlet superconductivity (SS); triplet superconductivity (TS); $2k_F$ spin density wave (SDW); $2k_F$ charge density wave (CDW); and $4k_F$ charge density wave ($4k_F$)

As long as $K_c > 1/2$ the singlet pairing susceptibility is divergent but it becomes more divergent than the CDW susceptibility only when $K_c > 1$. The latter diverges for $K_c < 2$ and is the predominant channel provided $K_c < 1$. Figure 6.13 summarizes the situation for low temperatures showing where in parameter space each type of correlation diverges.

We see that the low energy behavior of a system with a spin gap is basically determined by a single parameter K_c. For a Hubbard chain with repulsive interactions, it is well known [193] that $K_c < 1$, but this is not a general physical bound. For instance, numerical experiments on two leg Hubbard ladders (which are spin gapped systems as we discuss in Sections 6.10 and 6.11) have found a power law decay $r^{-\theta}$ of the singlet d–wave pairing

correlations along the ladder. Fig. 6.14 presents the minimal value of the decay exponent θ obtained for ladders with varying ratio of inter– to intra–leg hopping $t_\perp/t$ as a function of the relative interaction strength U/t [194]. By comparing it with the corresponding exponent $\theta = 1/K_c$ calculated for a spin gapped one dimensional system, one can see that $K_c > 1/2$ over the entire range of parameters and that for some ranges $K_c > 1$. Our point is that in a multicomponent 1DEG, it is possible to have $K_c > 1$ (and thus singlet superconductivity as the most divergent susceptibility) even for repulsive interactions.

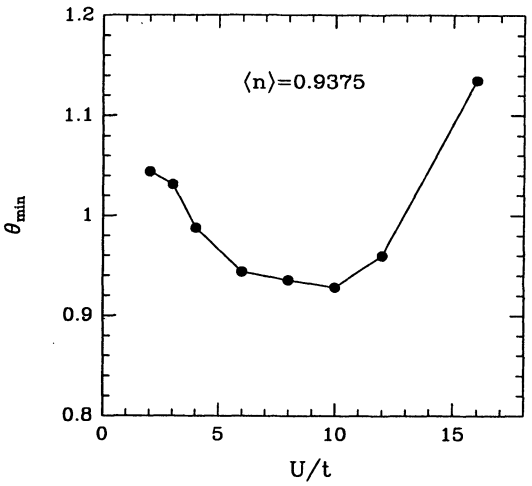

Fig. 6.14. Minimal value of the decay exponent, $\theta = 1/K_c$, of the d–wave singlet pairing correlations in a two leg ladder with varying hopping ratio $t_\perp/t$ as a function of U/t. The electron filling is $\langle n \rangle = 0.9375$. (From Noack et al. [194])

6.5.2 Spectral Functions of the 1DEG–Signatures of Fractionalization

The fact that one can obtain a strong (power law) divergence of the superconducting susceptibility from repulsive interactions between electrons is certainly reason enough to look to the 1DEG for clues concerning the origins of high temperature superconductivity—we will further pursue this in Sections 6.10 and 6.11, below. What we will do now is to continue to study the 1DEG as a solved model of a non–Fermi liquid.

In a Fermi liquid the elementary excitations have the quantum numbers of an electron and a nonvanishing overlap with the state created by the electronic creation operator acting on the ground state. As a result the single particle spectral function, $A(\boldsymbol{k}, \omega)$, is peaked at $\omega = \epsilon(\boldsymbol{k}) = \boldsymbol{v}_F(\boldsymbol{k}_F) \cdot (\boldsymbol{k} - \boldsymbol{k}_F)$,

where $\epsilon(\boldsymbol{k})$ is the quasiparticle dispersion relation. This peak can be and has been [195] directly observed using angle resolved photoemission spectroscopy (ARPES) which measures the single hole piece of the spectral function

$$A^{<}(\boldsymbol{k},\omega) = \int_{-\infty}^{\infty} d\boldsymbol{r}\, dt\, e^{i(\boldsymbol{k}\cdot\boldsymbol{r}+\omega t)} \langle \psi_\sigma^\dagger(\boldsymbol{r},t)\psi_\sigma(0,0)\rangle \ . \tag{6.33}$$

The lifetime of the quasiparticle, $\tau(\boldsymbol{k})$, can be determined from the width of the peak in the "energy distribution curve" (EDC) defined by considering $A^{<}(\boldsymbol{k},\omega)$ at fixed $\boldsymbol{k}$ as a function of ω:

$$1/\tau = \Delta\omega \ . \tag{6.34}$$

In a Fermi liquid, so long as the quasiparticle excitation is well defined (*i.e.* the decay rate is small compared to the binding energy) this width is related via the Fermi velocity to the peak width Δk in the "momentum distribution curve" (MDC). This curve is defined as a cross section of $A^{<}(\boldsymbol{k},\omega)$ taken at constant binding energy, ω. Explicitly

$$\Delta\omega = v_F \Delta k \ . \tag{6.35}$$

A very different situation occurs in the theory of the 1DEG where the elementary excitations, charge and spin density waves, do not have the quantum numbers of a hole. Despite the fact that the elementary excitations are bosons, they give rise to a linear in T specific heat that is not qualitatively different from that of a Fermi liquid. However, because of the separation of charge and spin, the creation of a hole (or an electron) necessarily implies the creation of two or more elementary excitations, of which one or more carries its spin and one or more carries its charge. Consequently, $A^{<}(k,\omega)$ does not have a pole contribution, but rather consists of a multiparticle continuum which is distributed over a wide region in the (k,ω) plane. The shape of this region is determined predominantly by the kinematics. The energy and momentum of an added electron are distributed between the constituent charge and spin pieces. In the case where both of them are gapless [see Figs. 6.15(a) and 6.15(b)] this means

$$\begin{aligned} E &= v_c|k_c| + v_s|k_s| \ , \\ k &= k_c + k_s \ , \end{aligned} \tag{6.36}$$

where energy and momentum are measured relative to E_F and k_F respectively. Consequently any point above the dispersion curve of the slower excitation (taken here to be the spin) may be reached by placing an appropriate amount of energy and momentum into the spin degrees of freedom, and the remaining energy and momentum into the charge degrees of freedom, as shown in Fig. 6.15(c). The addition of a hole is similarly constrained kinematically, and the corresponding zero temperature ARPES response has weight only within the shaded regions of Fig. 6.15(d).

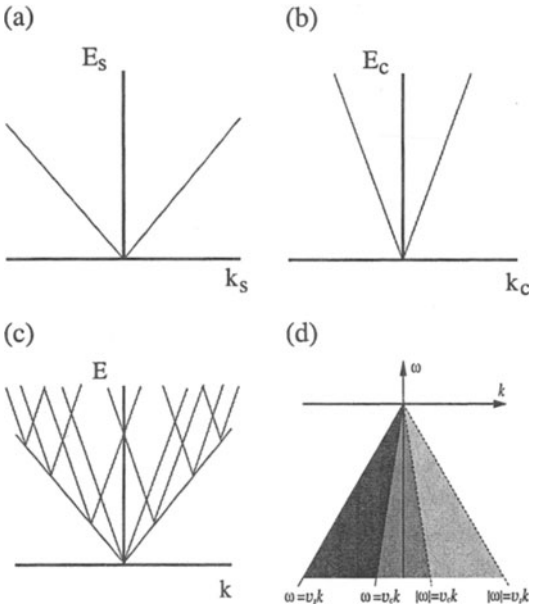

Fig. 6.15. Kinematics of the 1DEG: (a) Dispersion of the spin excitations. (b) Dispersion of the charge excitations. (c) The available electronic states. (d) Kinematic constraints on the spectral function: $A^<(k,\omega)$ for the 1DEG is nonzero at $T = 0$ only in the shaded region of the (k,ω) plane. In the spin rotationally invariant case, $K_s = 1$, $A^<(k,\omega) = 0$ in the lightly shaded region, as well. If in addition, $K_c = 1$, $A^<(k,\omega) = 0$ outside of the darkest region. We have assumed $v_c > v_s$, which is usually the case in realistic systems

Further constraints on the distribution of spectral weight may arise from symmetries. In the spin rotationally invariant case, at the fixed point $K_s = 1$, the spin correlators do not mix left and right moving pieces. As a consequence, $A^<(T = 0)$ for a right moving hole vanishes when ω is in the range $v_s k \leq |\omega| \leq v_c k$ (assuming $v_s < v_c$ and $k > 0$), even if the kinematic conditions are satisfied; See Fig. 6.15(d) (while the kinematic constraints are symmetric under $k \to -k$, the dynamical considerations are not, since although we have shifted the origin of k, we are in fact considering a right moving electron, *i.e.* one with momentum near $+k_F$). If in addition $K_c = 1$, so that the charge piece also does not mix left and right movers, $A^<(T = 0)$ vanishes unless $k < 0$ and $v_s|k| \leq |\omega| \leq v_c|k|$, (the darkest region in Fig. 6.15(d)). While $K_s = 1$ is fixed by symmetry, there is no reason why K_c should be precisely equal to 1. However, if the interactions are weak, (*i.e.* if K_c is near 1) most of the spectral weight is still concentrated in this region. It spreads throughout the rest of the triangle with increasing interaction strength.

Clearly, the total width of the MDC is bounded by kinematics and is at most $\Delta k_{max} = 2|\omega|/\min(v_c, v_s)$. Any peak in the MDC will have a width which equals a fraction of this, depending on the interactions and symmetries of the problem, but in any case will vanish as the Fermi energy is approached. By contrast, at $k = 0$, the shape of the EDC is not given by the kinematics at all, but is rather determined by the details of the matrix elements linking the one hole state to the various multi particle–hole states which form the continuum. In this case, the spectrum has a nonuniversal power law behavior with exponents determined by the interactions in the 1DEG. Whenever such a dichotomy between the MDC and EDC is present, it can be taken as evidence of electron fractionalization [87].

These general considerations can be substantiated by examining the explicit expression for the spectral function of the Tomonaga–Luttinger model [196–199]. The quantum criticality and the spin–charge separation of the model imply a scaling form for its correlation functions

$$A^{<}(k,\omega) \propto T^{2(\gamma_c+\gamma_s)+1} \int dq\, d\nu\, G_c(q,\nu)\, G_s(\tilde{k} - rq, \tilde{\omega} - \nu) \,, \tag{6.37}$$

where we introduce the velocity ratio $r = v_s/v_c$ and define the scaling variables

$$\tilde{k} = \frac{v_s k}{\pi T} \quad , \quad \tilde{\omega} = \frac{\omega}{\pi T} \,. \tag{6.38}$$

Since the spin and charge sectors are formally invariant under separate Lorentz transformations, the functions $G_\alpha, (\alpha = c, s)$ also split into right and left moving parts

$$G_\alpha(k,\omega) = \frac{1}{2} h_{\gamma_\alpha + \frac{1}{2}} \left(\frac{\omega + k}{2} \right) h_{\gamma_\alpha} \left(\frac{\omega - k}{2} \right) \,, \tag{6.39}$$

where h_γ is expressed via the beta function

$$h_\gamma(k) = \mathrm{Re} \left[(2i)^\gamma B \left(\frac{\gamma - ik}{2}, 1 - \gamma \right) \right] \,, \tag{6.40}$$

and the exponents

$$\gamma_\alpha = \frac{1}{8}(K_\alpha + K_\alpha^{-1} - 2) \,, \tag{6.41}$$

are defined so that $\gamma_\alpha = 0$ for noninteracting fermions.

Fig. 6.16 depicts MDC's at the Fermi energy ($\omega = 0$) and EDC's at the Fermi wavevector ($k = 0$) for a spin rotationally invariant ($\gamma_s = 0$) Tomonaga–Luttinger model for various values of the parameter γ_c. While the MDC's broaden somewhat with increasing interaction strength they remain relatively sharp with a well defined peak structure. On the other hand any

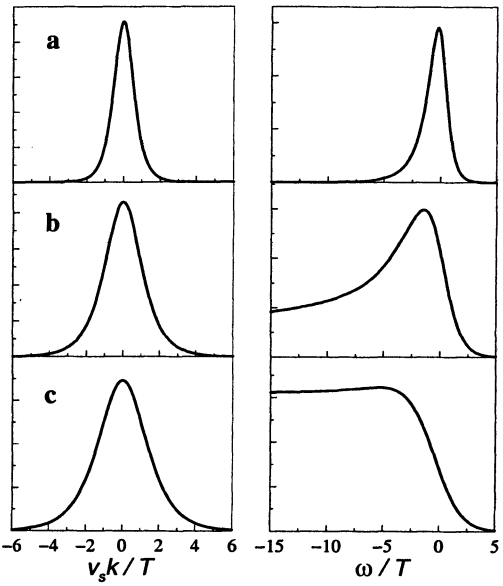

Fig. 6.16. MDC's at $\omega = 0$ (left) and EDC's at $k = 0$ (right), for a spin rotationally invariant Tomonaga–Luttinger liquid, with $v_c/v_s = 3$ and a) $\gamma_c = 0$, b) $\gamma_c = 0.25$, and c) $\gamma_c = 0.5$

corresponding structure in the EDC's is completely wiped out in the presence of strong interactions. Such behavior has been observed in ARPES studies of quasi–one dimensional compounds as depicted in Fig. 6.17 as well as in the cuprate high temperature superconductors [87].

Away from the Fermi energy and Fermi wavevector and for not too strong interactions the peaks in the MDC and EDC split into a double peak structure, one dispersing with v_s and the other with v_c. If observed this can be taken as further evidence for spin–charge separation.

We now turn to the interesting case in which the superconducting susceptibility is enhanced due to the opening of a spin gap, Δ_s. At temperatures large compared to Δ_s, the spin gap can be ignored, and the spectral function is well approximated by that of the Tomonaga–Luttinger liquid. However, even below the spin gap scale, many of the characteristics of the Tomonaga–Luttinger spectral function are retained. Spin–charge separation still holds in the spin gapped Luther–Emery liquids and there are no stable "electron–like" excitations. The charge excitations are still the gapless charge density waves of the Tomonaga–Luttinger liquid but the spin excitations now consist of massive spin solitons with dispersion $E_s(k) = \sqrt{v_s^2 k^2 + \Delta_s^2}$. As a result the spin piece of the spectral function is modified and from kinematics it follows that it consists of a coherent one spin soliton piece and an incoherent

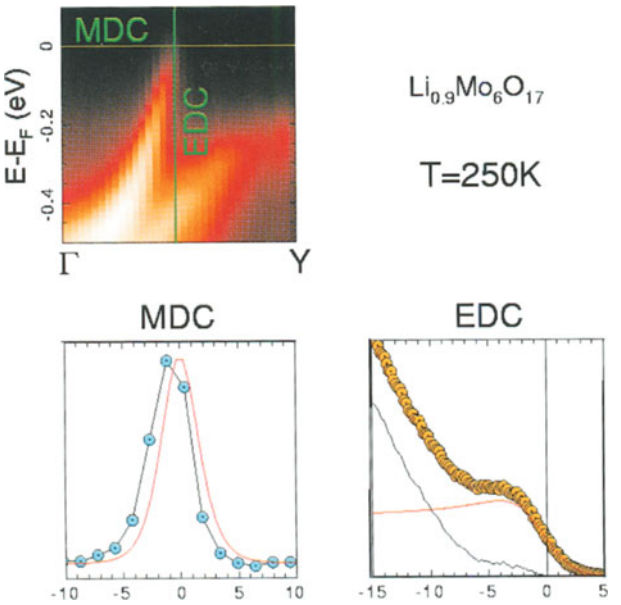

Fig. 6.17. ARPES intensity map for the purple bronze $Li_{0.9}Mo_9O_{17}$. The lower left panel depicts the MDC at the Fermi energy together with a Tomonaga–Luttinger theoretical curve. The lower right panel contains the EDC at the Fermi wavevector. The red line corresponds to the Tomonaga–Luttinger result and the black curve is its deviation from the experimental data (from Ref. [200])

multisoliton part

$$G_s(k,\omega) = Z_s(k)\delta[\omega + E_s(k)] + G_s^{(multi)}(k,\omega) \ , \tag{6.42}$$

where the multisoliton piece is proportional (at $T = 0$) to $\Theta[-\omega - 3E_s(k/3)]$. (For $K_s < 1/2$ formation of spin soliton–antisoliton bound states, "breathers", may shift the threshold energy for multisoliton excitations somewhat). The form of $Z_s(k)$ has been calculated explicitly [201], but a simple scaling argument gleans the essential physics [151]. It follows from the fact that the Luther-Emery liquid is asymptotically free that at high energies and short distances compared to the spin gap, the physics looks the same as in the gapless state. Therefore the dependence of the correlation functions on high energy physics, such as the short distance cutoff a, cannot change with the opening of the gap. Since in the gapless system G_s is proportional to $a^{2\gamma_s - 1/2}$, it is a matter of dimensional analysis to see that

$$Z_s(k) = (\xi_s/a)^{\frac{1}{2} - 2\gamma_s} f_s(k\xi_s) \ , \tag{6.43}$$

where f_s is a scaling function and $\xi_s = v_s/\Delta_s$ is the spin correlation length.

is a pseudogap state. Despite the appearance of a coherent piece in the spin sector, the spectral function (Eq. 6.37) still exhibits an overall incoherent response owing to the convolution with the incoherent charge part. The result is grossly similar to the gapless case, aside from the fact that the Fermi edge (the tip of the triangular support of $A^<$ in Fig. 6.15d) is pushed back from the Fermi energy by the magnitude of the spin gap (thus rounding the tip of the triangle). If, as suggested in Section 6.3, the Luther–Emery liquid is the paradigmatic example of a pseudogap state, clearly the above spectral function gives us an impression of what to expect the signature of the pseudogap to be in the one electron properties.

6.5.3 Dimensional Crossover in a Quasi–1D Superconductor

Continuous global symmetries cannot be spontaneously broken in one dimension, even at $T = 0$. Since the one dimensional Hamiltonian (Eq. (6.8)) is invariant under translations and spin $SU(2)$ and charge $U(1)$ transformations, no CDW, SDW, or superconducting long range order can exist in its ground state. Therefore, in a quasi–one dimensional system made out of an array of coupled 1DEG's, a transition into an ordered state necessarily signifies a dimensional crossover at which, owing to relevant interchain couplings, phases of individual chains lock together [23,151]. The ultimate low temperature fate of the system is fixed by the identity of the first phase to do so. This, in turn, is determined by the relative strength of the various couplings and the nature of the low energy correlations in the 1DEG.

In the spin gapped phase, which we consider in the rest of this section, both the CDW and the superconducting susceptibilities are enhanced. To begin with, we will analyze the simplest model of a quasi–one dimensional superconductor. We defer until the following section any serious discussion of the competition between CDW and superconducting order. We will also defer until then any discussion of the richer possibilities which arise when the quasi–one dimensional physics arises from a self–organized structure, *i.e.* stripes, with their own additional degrees of freedom.

Interchain coupling and the onset of order

The simplest and most widely studied model of a quasi–one dimensional spin gapped fluid is

$$\mathcal{H} = \sum_j \mathcal{H}_j + \mathcal{J} \sum_{\langle i,j \rangle} [O^\dagger_{SS}(i,x) O_{SS}(j,x) + \text{H.C.}] + \mathcal{V} \sum_{\langle i,j \rangle} [O^\dagger_{CDW}(i,x) O_{CDW}(j,x) + \text{H.C.}] \,, \tag{6.44}$$

where $\mathcal{H}_j$ describes the Luther–Emery liquid on chain, pairs of nearest neighbor chains are denoted $\langle i,j \rangle$, and $O_\alpha(j,x)$ is the appropriate order parameter field on chain j. The bosonized form of these operators is given in Eqs. (6.24) and (6.25), above. It is assumed that the interchain couplings, $\mathcal{J}$ and $\mathcal{V}$, are

small compared to all intrachain energies. There are two more or less complementary ways of approaching this problem:
1) The first is to perform a perturbative renormalization group (RG) analysis about the decoupled fixed point, *i.e.* compute the beta function perturbatively in powers of the interchain couplings. To lowest order, the beta function is simply determined by the scaling dimension, D_α, of each operator – if $D_\alpha < 2$, it means that O_α is perturbatively relevant, and otherwise it is irrelevant. It turns out that the CDW and SC orders are dual to each other, so that

$$D_{SS} = 1/K_c \quad , \quad D_{CDW} = K_c \, . \tag{6.45}$$

This has the implication that one, or the other, or both of the interchain couplings is always relevant. From this, we conclude with a high level of confidence that at low temperature, even if the interchain couplings are arbitrarily weak, the system eventually undergoes a phase transition to a higher dimensional ordered state. An estimate of T_c can be derived from these equations in the standard way, by identifying the transition temperature with the scale at which an initially weak interchain coupling grows to be of order 1. In this way, for $D_{SS} < 2$, one obtains an estimate of the superconducting transition temperature

$$T_c \sim E_F[\mathcal{J}/E_F]^{1/(2-D_{SS})} = \mathcal{J}[\mathcal{J}/E_F]^{(D_{SS}-1)/(2-D_{SS})}, \tag{6.46}$$

and similarly for the CDW ordering temperature. Note that as $D_{SS} \to 2^-$, $T_c \to 0$, and that $T_c \gg \mathcal{J}$ for $D_{SS} < 1$. Clearly, the power law dependence of T_c on coupling constant offers the promise of a high T_c when compared with the exponential dependence in BCS theory.
2) The other way is to use interchain mean field theory [202]. Here, one treats the one dimensional fluctuations exactly, but the interchain couplings in mean field theory. For instance, in the case of interchain SS ordering, one considers each chain in the presence of an external field

$$\mathcal{H}^{eff} = \mathcal{H}_j + [\Delta^*_{SS} O_{SS}(j,x) + \text{H.C.}] \, . \tag{6.47}$$

Here, Δ_{SS} is determined self–consistently by

$$\Delta_{SS} = z\mathcal{J}\langle O_{SS}(j,x)\rangle \, , \tag{6.48}$$

where z is the number of nearest neighbor chains and the expectation value is taken with respect to the effective Hamiltonian. This mean field theory is exact [151,203] in the limit of large z, and is expected to be reliable so long as the interchain coupling is weak. It can be shown to give exact results in the limit of extreme anisotropy for the Ising model, even in two dimensions (where $z = 2$) [202]. More generally, it is a well controlled approximation at least for temperatures $T \gg \mathcal{J}$ (which includes temperatures in the neighborhood

of T_c as long as $D_{SS} < 1$). This approach gives an estimate of T_c which is related to the susceptibility of the single chain,

$$1 = z\mathcal{J}\chi_{SS}(T_c)\,, \tag{6.49}$$

which, from the expression in Eq. (6.32), can be seen to produce qualitatively the same estimate for T_c as the perturbative RG treatment. The advantage of the mean field treatment is not only that it gives an explicit, and very physical expression for T_c, but that it permits us to compute explicitly the effect of ordering on various response functions, including the one particle spectral function. The case of CDW ordering is a straightforward extension.

Emergence of the quasiparticle in the ordered state

The excitation spectrum changes dramatically below T_c when the interchain "Josephson" coupling $\mathcal{J}$ triggers long range order [151]. The fractionalized excitations of the Tomonaga–Luttinger and the Luther–Emery liquids are replaced by new excitations with familiar "BCS" quantum numbers. Formally, superconducting order leads to a confinement phenomenon. While the spin gap in the Luther–Emery state already implies suppressed fluctuations of ϕ_s on each chain, and correspondingly a finite amplitude $\cos(\sqrt{2\pi}\phi_s)$ of the superconducting order parameter, it is the interchain Josephson coupling that tends to lock its phase θ_c from one chain to the next. (Note, Superconducting order binds fractionalized excitations into "ordinary" quasiparticles.)

Operating with the hole operator, Eq. (6.9), on the ground state at the position of the jth chain creates a pair of kinks (solitons) of magnitude $\sqrt{\pi/2}$ in both the charge and spin fields θ_c and ϕ_s of this chain. As a result the phase of the order parameter changes by π upon passing either the spin or the charge soliton. This introduces a negative Josephson coupling between the affected chain and its neighbors along the entire distance between the charge and spin solitons. The energy penalty due to this frustration grows linearly with the separation between the solitons and causes a bound pair to form. In fact, all solitonic excitations are confined into pairs, including charge–charge and spin–spin pairs. The bound state between the charge and the spin pieces restores the electron, or more precisely the Bogoliubov quasiparticle, as an elementary excitation, causing a coherent (delta function) peak to appear in the single particle spectral function.

An explicit expression for the spectral function in the superconducting state can be obtained in the context of the effective Hamiltonian in Eq. (6.47):

$$A^{<}(k,\omega) = Z(k)\delta[\omega - E(k)] + A^{(incoherent)}(k,\omega)\,, \tag{6.50}$$

where $E(k) = \sqrt{v_s^2 k^2 + \Delta_0^2}$. Here $\Delta_0 = \Delta_s + \Delta_c/2$ is the creation energy of the bound state where $\Delta_c \propto \Delta_{SS}$ is the mean field gap ($\Delta_c \ll \Delta_s$) that opens in the charge sector below T_c [151]. The multiparticle incoherent piece has a threshold slightly above the single hole threshold at $\omega = E(k) + 2\Delta_c$. The shape of $A^{<}(k,\omega)$ at $T = 0$ is presented schematically in Fig. 6.18.

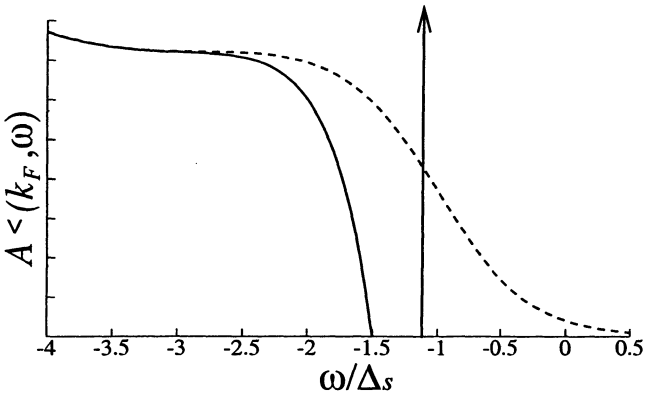

Fig. 6.18. The temperature evolution of the spectral function. The dashed line depicts $A^<$ at intermediate temperatures below the spin gap Δ_s but above T_c. The solid line represents the spectral function at zero temperature. A coherent delta function peak onsets near T_c at energy $\Delta_0 = \Delta_s + \Delta_c(0)/2$. The multiparticle piece starts at a threshold $2\Delta_c(0)$ away from the coherent peak

Once again, we may employ the asymptotic freedom of the system to construct a scaling argument. In this case, high energy physics dependent upon either the cutoff or the spin gap (which is by assumption much larger than T_c) cannot change upon entering the superconducting state. Comparing the form of the spectral response in the normal spin gapped state with that of the superconductor reveals the weight of the coherent peak

$$Z(k) = Z_s(0)(\xi_c/a)^{-\frac{1}{2}-2\gamma_c} f(k\xi_c) \,, \tag{6.51}$$

where f is a scaling function and $\xi_c = v_c/\Delta_c$ is the charge correlation length. Physically, the dependence of the weight on Δ_c, which also equals the (local) superfluid density [151], reflects the fact that the superfluid stiffness between chains controls the strength of the bound state forming the quasiparticle.

Since the superfluid density is a rapid function of temperature upon entering the superconducting state, the weight of the coherent peak will also rapidly increase as the temperature is lowered. Because the Josephson coupling is weak, the energy of the bound state is largely set by the spin gap, so that the energy of the coherent peak will not be a strong function of temperature in the neighborhood of T_c. Likewise, since the gap is not changing rapidly, the scattering rate and therefore the lifetime of the new quasiparticle will not have strong temperature dependence either. All of the above signatures have been observed in ARPES measurements of the coherent peak in $Bi_2Sr_2CaCu_2O_{8+\delta}$ [90,92,204,205] and $YBa_2Cu_3O_{7-\delta}$ [12].

The temperature evolution of the spectral function is in sharp contrast to that of a conventional superconductor, where the gap opens precisely at

T_c. Since in that case the gap is a rapid function of temperature, so is the energy of the conventional quasiparticle peak. Moreover, scattering processes are rapidly gapped out upon entering the BCS superconducting state, so that the quasiparticle often sharpens substantially as the temperature is lowered below T_c. Most importantly, in the conventional case, quasiparticles exist above the transition temperature, so the intensity (Z factor) of the peak does not change much upon entering the superconducting state. By contrast, in a quasi–one dimensional superconductor, there are no quasiparticle excitations in the normal state. The existence of the quasiparticle is due to the dimensional crossover to the three dimensional state, and is an entirely collective effect!

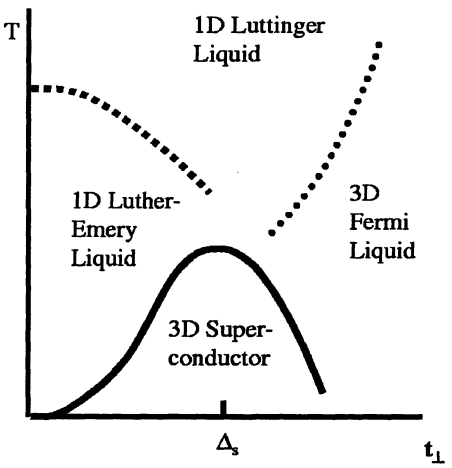

Fig. 6.19. *Two Routes to Dimensional Crossover.* In an array of multicomponent 1DEG's, for temperatures large compared to the transverse single particle tunnelling, $t_\perp$, the system behaves as a collection of independent (1D) Luttinger Liquids. For weak $t_\perp$, the dimensional crossover may proceed as described in Section 6.5.3, with a crossover first to a (1D) Luther–Emery Liquid, and a lower temperature dimensional crossover to a (3D) superconductor. For large $t_\perp$, there may be a dimensional crossover into a (3D) Fermi liquid, before the system becomes a (3D) superconductor

6.5.4 Alternative Routes to Dimensional Crossover

Until now, we have assumed that the spin gap is large compared to the interchain couplings, and this assumption leads inevitably to the existence of a quasi–1D pseudogap regime above T_c and a dimensional crossover associated with the phase ordering at T_c. Since under some circumstances, the spin

gap in 1D can be zero or exponentially small compared to E_F, it is possible for a system to be quasi–1D, in the sense that the interchain couplings are small compared to the intrachain interactions, and yet have the dimensional crossover occur above any putative spin gap scale. In this case, most likely the dimensional crossover is triggered by the relevance of the interchain, single particle hopping operator—since any spin gap is negligible, the previous argument for its irrelevance is invalidated. What this means is that there is a dimensional crossover, T_{3D}^*, at which the system transforms from a Luttinger liquid at high temperatures to a Fermi liquid at lower temperatures. (See Fig. 6.12.) If there are residual effective attractive interactions, the system will ultimately become a superconductor at still lower temperatures. However, in this case, the transition will be more or less of the BCS type—a Fermi surface instability (albeit on a highly anisotropic Fermi surface) with well defined quasiparticles existing both above and below T_c.

The crossover from a Luttinger liquid to a Fermi liquid is not as well characterized, theoretically, as the crossover to a superconductor. The reason is that no simple form of interchain mean field theory can be employed to study it. Various energy scales associated with the crossover can be readily obtained from a scaling analysis. A recent interesting advance [203, 206, 207] has been made on this problem using "dynamical mean field theory," again based on the idea of using $1/z$ (where z is the number of neighboring chains) as a small parameter, which gives some justification for a widely used RPA–like approximation for the spectral function [187]. However, there are still serious shortcomings with this approximation [203, 208]. Clearly more interesting work remains to be done to sort out the physics in this limit, which may be a caricature of the physics of the overdoped cuprates. More complicated routes to dimensional crossover can also be studied [134], relevant to systems with more than one flavor of chain. For instance, it has recently been found that it is possible for a two component quasi–1D system to produce a superconducting state which supports gapless "nodal quasiparticles," even in the limit of extreme anisotropy [134].

6.6 Quasi–1D Physics in a Dynamical Stripe Array

An interesting generalization of the quasi-1D system occurs when the background geometry on which the constituent 1DEG's reside is, itself, dynamically fluctuating. This situation arises in conducting stripe phases.

While in strictly 1D systems CDW and superconducting fluctuations happily coexist, interchain coupling typically leads to a low temperature state where one is ordered and the other is suppressed. As mentioned before, in the simplest microscopic realizations of the 1DEG with repulsive interactions, $0 < K_c < 1$ and hence the CDW susceptibility is the most divergent as $T \to 0$ (See Eq. (6.32).) This seemingly implies that the typical fate of a

quasi–one dimensional system with a spin gap is to wind up a CDW insulator in which CDW modulations on neighboring chains phase lock to each other. And, indeed, many quasi–one dimensional metals in nature suffer precisely this fate—the competition between CDW and SS order is a real feature of quasi–1D systems. Recall, however, that in more complicated realizations of the 1DEG, K_c can be greater than one even for repulsive interactions, as shown in Fig. 6.14 above. (Note, Competition between CDW and SS is key in quasi–1D systems.)

What we will examine in this section is another way in which the balance between CDW and SS ordering can be affected. [52, 209, 210] Specifically, we will show below that transverse fluctuations of the backbone on which the quasi–1D system lives significantly enhance the tendency to SS while suppressing CDW ordering. Such fluctuations are unimportant in conventional quasi–one dimensional solids, where the constituent molecules, upon which the electrons move, have a large mass and a rigid structure. But when the 1DEG's live along highly quantum electronic textures, or "stripes," transverse stripe fluctuations are probably always large.

6.6.1 Ordering in the Presence of Quasi–Static Stripe Fluctuations

Consider a two dimensional array of stripes that run along the x direction, and imagine that there is a 1DEG which lives on each stripe. To begin with, we will consider the case in which the stripe fluctuations are sufficiently slow that they can be treated as static—in other words, we consider an array of imperfectly ordered stripes, over whose meanderings we will eventually take an equilibrium (annealed) average. We will use a coordinate system in which points on the stripes are labeled by the coordinate x, the stripe number j, and in which transverse displacements of the stripe in the y direction are labeled by $h_j(x)$, as shown in Fig. 6.20. We therefore ignore the possibility of overhangs which is a safe assumption in the ordered state.

We now consider the effect that stripe geometry fluctuations have on the inter–stripe couplings. Because the CDW order (and any other $2k_F$ or $4k_F$ orders) occurs at a large wave vector, the geometric fluctuations profoundly affect its phase. As shown in the cartoon in Fig. 6.20, the transverse stripe fluctuations lead to a dephasing of the CDW order on neighboring stripes. To study this effect formally, we note that the local CDW order parameter (see Eqn. 24) has the form:

$$O_{CDW}(j,x) = \frac{e^{-2ik_F L_j(x)}}{\pi a} \cos[\sqrt{2\pi}\phi_s(j,x)] e^{-i\sqrt{2\pi}\phi_c(j,x)};, \tag{6.52}$$

where

$$L_j(x) = \int_0^x dx' \sqrt{1 + (\partial_{x'} h_j)^2} \tag{6.53}$$

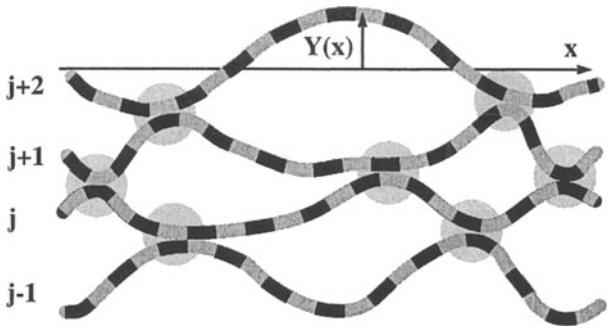

Fig. 6.20. Schematic representation of a smectic stripe phase. Stripe collisions are denoted by the light grey circles, the top left of which shows a favorable relative phase for a CDW along neighboring stripes. However, once this favorable phase is set, the top right collision is out of phase by half of a wavelength, and maximally unfavorable. As described in the text, any ordering with a finite wavevector along the stripe direction experiences this kind of destructive interference due to transverse stripe fluctuations. With the CDW ground state thus avoided, superconductivity (a $k = 0$ order) can flourish. Stripe collisions also enhance the Josephson coupling, further encouraging superconductivity

is the arc length, *i.e.* the distance measured along stripe j to point x. In contrast, the superconducting order parameter O_{SS} and any other $k = 0$ order are unaffected by the geometric fluctuations (see Eqn. 25). This results in a fundamental difference in the way CDW and Josephson inter–stripe couplings evolve with growing stripe fluctuations.

The CDW and Josephson couplings between neighboring stripes are of the form

$$H_{\mathcal{V}} = \frac{1}{(2\pi a)^2} \sum_j \int dx \mathcal{V}(\Delta_j h) \cos[\sqrt{2\pi}\phi_s(j,x)] \cos[\sqrt{2\pi}\phi_s(j+1,x)] \times \cos[\sqrt{2\pi}\Delta_j \phi_c + 2k_f \Delta_j L] \,, \tag{6.54}$$

$$H_{\mathcal{J}} = -\frac{1}{(2\pi a)^2} \sum_j \int dx \mathcal{J}(\Delta_j h) \cos[\sqrt{2\pi}\phi_s(j,x)] \cos[\sqrt{2\pi}\phi_s(j+1,x)] \times \cos[\sqrt{2\pi}\Delta_j \theta_c] \,, \tag{6.55}$$

where $\Delta_j h \equiv h(j+1,x) - h(j,x)$ etc. The coupling constants $\mathcal{V}(\Delta_j h)$ and $\mathcal{J}(\Delta_j h)$, depend on the local spacing between adjacent stripes, since they are more strongly coupled when they are close together than when they are far apart. This is particularly important for the Josephson coupling which depends on the pair tunnelling amplitude and therefore roughly exponentially on the local spacing between the stripes

$$\mathcal{J}(\Delta_j h) \approx \mathcal{J}_0 e^{-\alpha \Delta_j h} \,. \tag{6.56}$$

By integrating out the stripe fluctuations h one obtains the effective Hamiltonian of an equivalent rigid system of stripes. To first order in $\mathcal{V}$ the CDW coupling is similar to Eq. (6.54) but with $\Delta_j L$ set equal to 0 in the last term and $\mathcal{V}(\Delta_j h)$ replaced by

$$\langle \mathcal{V}(\Delta_j h) \rangle \exp[-2k_F^2 \langle (\Delta_j L)^2 \rangle] \,, \tag{6.57}$$

where $\langle\ \rangle$ signifies averaging over transverse stripe fluctuations. (Note, stripe fluctuations dephase CDW order.) Since $\Delta_j L = L_{j+1}(x) - L_j(x)$ is a sum of contributions with random signs, which are more or less independently distributed along the distance $|x|$, we expect it to grow roughly as in a random walk, *i.e.* $\langle (\Delta_j L)^2 \rangle \sim D|x|$, where D is a constant. Indeed one can show [52] that at finite temperature $\langle (\Delta_j L)^2 \rangle \sim T|x|$ while at $T = 0$ $\langle (\Delta_j L)^2 \rangle \sim \hbar\bar{\omega} \log |x|$, where $\hbar\bar{\omega}$ is a suitable measure of the transverse stripe zero point energy. As a result of this dephasing effect, coupling between CDW's vanishes rapidly except in a narrow region near the ends of the stripes and hence can be ignored in the thermodynamic limit. In short, transverse stripe fluctuations cause destructive interference of $k \neq 0$ order on neighboring chains, strongly suppressing those orders.

The effects of stripe fluctuations on the Josephson coupling can be analyzed in the same way. To first order in the inter–stripe coupling, $\mathcal{J}(\Delta_j h)$ is simply replaced by its average value, $\bar{\mathcal{J}} \equiv < \mathcal{J}(\Delta_j h) \rangle$. In other words, once quasi–static stripe fluctuations are integrated out, the result is once again the Hamiltonian we studied in Eq. (6.44), above, but with $\mathcal{V} = 0$ and $\mathcal{J} = \bar{\mathcal{J}}$. Moreover, due to the exponential dependence of $\mathcal{J}(\Delta_j h)$ on $(\Delta_j h)$, it is clear that $\bar{\mathcal{J}} > \mathcal{J}(0)$, *i.e.* transverse stripe fluctuations strongly enhance the Josephson coupling between stripes. (There is a similar enhancement of the CDW coupling but it is overwhelmed by the dephasing effect.) Physically, this enhancement reflects the fact that the mean value of $\mathcal{J}$ is dominated by regions where neighboring stripes come close together. In the case of small amplitude fluctuations, this enhancemnt can be viewed as an inverse Debye–Waller factor,

$$\langle \mathcal{J} \rangle \approx \mathcal{J}_0 e^{\frac{\alpha^2}{2} \langle (\Delta_j h)^2 \rangle} \,. \tag{6.58}$$

Here, the transverse stripe fluctuations are comparable in magnitude to the inter–stripe spacing, the mean Josephson coupling is geometrically determined by the mean density of points at which neighboring stripes actually "bump" (i.e. are separated by about one lattice constant a – see Fig. 6.20). In this limit, treating the stripe fluctuations as a random walk yields the estimate

$$\mathcal{J} \sim \left(\frac{a}{R}\right)^2 \mathcal{J}_0 \,, \tag{6.59}$$

where R is the mean distance between stripes.

6.6.2 The General Smectic Fixed Point

The quasi–static limit discussed above is presumably inadequate at low enough temperatures, where the quantum dynamics of stripe fluctuations must always be relevant. The complete problem, in which both the stripe dynamics and the dynamics of the 1DEG's are treated on an equal footing remains unsolved. However, since in a crystalline background, the stripe fluctuations are typically not gapless, we expect that at low enough temperatures, the stripe fluctuations can be treated as fast, and be integrated out to produce new effective interactions. So long as the stripes are reasonably smooth, these induced interactions will consist of long wavelength (around $k = 0$) density–density and current–current interactions between the neighboring Luttinger liquids—interactions that we have ignored until now. These interactions should undoubtedly be present in the bare model, as well, even in the absence of stripe fluctuations. They are marginal operators and should be included in the fixed point action.

The effect of these marginal interactions has been treated in several recent papers – the interested reader is referred to Refs. [209, 211]. The results bear some similarity to the quasi–static results described in the previous section. Specifically, repulsive interchain interactions suppress the tendency to CDW order, thereby enhancing the possibility of superconductivity from repulsive interactions. An exotic "smectic metal" phase with neither superconducting nor CDW order, but infinite anisotropy at low energies, has been found on the basis of this analysis as well.

Extensions of this model to a three dimensional array of chains [212] and the inclusion of a magnetic field [213] have been considered as well. In particular, it is found that the magnetic field supresses the region of superconducting order in the phase diagram, thus expanding the regime in which the smectic metal is stable. Similar considerations lead one naturally to consider other states obtained when the stripe fluctuations become still more violent. Assuming that the long range stripe order is destroyed by such fluctuations, while the short distance physics remains that of quasi–1DEG's living along the locally defined stripes, one is led to investigate the physics of electron nematic and stripe liquid phases. We shall return to this point in the final section.

6.7 Electron Fractionalization in $D > 1$ as a Mechanism of High Temperature Superconductivity

Spin–charge separation seems to offer an attractive route to high temperature superconductivity. It occurs robustly in 1D, but is now known to occur in higher dimensions as well, although seemingly only under very special circumstances.

We briefly discuss here a remarkable set of ideas for a novel mechanism of high temperature superconductivity based on higher dimensional generalizations of the 1D notion of spin–charge separation. Boasting a high pairing scale as well as crisp experimental predictions, these theories have many attractive features. They also bear a strong family resemblance to the "spin gap proximity effect mechanism," which we develop in some detail in Section 6.10.4. These appealing ideas, while valid, require the proximity of a spin liquid phase which in turn appears to be a fragile state of matter; for this reason, and others which will be made clear below, it is our opinion that these ideas are probably not applicable to the cuprate superconductors. The discussion in this section is therefore somewhat disconnected from the development in the rest of the paper. We merely sketch the central ideas, without providing any derivations. There are a number of recent papers dealing with this subject to which the interested reader can refer; see Refs. [78,81,185,214,215].

6.7.1 RVB and Spin–Charge Separation in Two Dimensions

Immediately following the discovery of high temperature superconductivity [2], Anderson proposed [5] that the key to the problem lay in the occurrence of a never before documented state of matter (in $D > 1$), a spin liquid or "resonating valence bond" (RVB) state, related to a state he originally proposed [216] for quantum antiferromagnets on a triangular (or similarly frustrating) lattice. In this context [81], a spin liquid is defined to be an insulating state with an odd number of electrons per unit cell (and a charge gap) which breaks neither spin rotational nor translational symmetry. Building on this proposal, Kivelson, Rokhsar, and Sethna [70] showed that a consequence of the existence of such a spin liquid state is that there exist quasiparticles with reversed charge spin relations, just like the solitons in the 1DEG discussed in Section 6.5, above. Specifically, there exist charge 0 spin 1/2 "spinons" and charge e spin 0 "holons." Indeed, these quasiparticles were recognized as having a topological character [70,217] analogous to that of the Laughlin quasiparticles in the quantum Hall effect.

There was a debate at the time concerning the proper exchange statistics, with proposals presented identifying the holon as a boson [69,70], a fermion [218], and a semion [219]. It is now clear that all sides of this debate were correct, in the sense that there is no universal answer to the question. The statistics of the fractionalized quasiparticles is dynamically determined, and is sensitive to a form of "topological order" [59,79,214,218,220] which differentiates various spin liquids. There are even transitions between states in which the holon has different statistics [220,221].

Two features of this proposal are particularly attractive:

1) It is possible to envisage a high pairing scale in the Mott insulating parent state, since the strong repulsive interactions between electrons, which result in the insulating behavior, are insensitive to any subtler correlations between electrons. Thus, the "μ^* issue" does not arise: the spin liquid can be viewed

as an insulating liquid of preformed Cooper pairs [5, 70, 71], or equivalently a superconductor with zero superfluid density (an oxymoron since in this case $T_\theta = T_c = 0$, but the intuitive notion is clear: we refer to a state which is derived from a superconductor by taking the limit of zero superfluid density while holding the pairing scale fixed). If this pairing scale is somehow preserved upon doping, then the transition temperature of the doped system is determined by superfluid stiffness and is not limited by a low pairing scale, as it would be in a BCS superconductor. Indeed, as in the case of the 1D Luther–Emery liquid discussed in Section 6.5, pairing becomes primarily a property of the spin degrees of freedom, and involves little or no pairing of actual charge.

2) When the holons are bosonic, their density directly determines the superfluid density. Thus the superconducting T_c can be crudely viewed as the bose condensation temperature of the holons. The result is that for small concentration of doped holes x [5], the transition temperature is proportional to a positive power of x (presumably [70] $T_c \sim x$ in 2D), in contrast to the exponential dependence on parameters in a BCS superconductor.

In short, many of the same features that would make a quasi–1D system attractive from the point of view of high temperature superconductivity (see Sections 6.5 and 6.10) would make a doped spin liquid even more attractive. However, there are both theoretical and phenomenological reasons for discounting this idea in the context of the cuprates.

6.7.2 Is an Insulating Spin Liquid Ground State Possible in $D > 1$?

The most basic theoretical issue concerning the applicability of the fractionalization idea is whether a spin liquid state occurs at all in $D > 1$. The typical consequence of the Mott physics is an antiferromagnetically ordered ("spin crystalline") state, especially the Néel state, which indeed occurs at $x = 0$ in the cuprates. Moreover, the most straightforward quantum disordering of an antiferromagnet will lead to a spin Peierls state, rather than a spin liquid, as was elegantly demonstrated by Haldane [222] and Read and Sachdev [72]. Indeed, despite many heroic efforts, the theoretical "proof of principle," *i.e.* a theoretically tractable microscopic model with plausible short range interactions which exhibits a spin liquid ground state phase, was difficult to achieve. A liquid is an intermediate phase, between solid and gas, and so cannot readily be understood in a strong or weak coupling limit [81].

Very recently, Moessner and Sondhi [80] have managed to demonstrate just this point of principle! They have considered a model [71] on a triangular lattice (thus returning very closely to the original proposal of Anderson) which is a bit of a caricature in the sense that the constituents are not single electrons, but rather valence bonds (hard core dimers), much in the spirit pioneered by Pauling.(Indeed, it is tempting to interpret the dimer model as the strong coupling, high density limit of a fluid of Cooper pairs [71].)

The model is sufficiently well motivated microscopically, and the spin liquid character robust enough, that it is reasonable to declare the spin liquid a theoretical possibility. The spin liquid state of Moessner and Sondhi does not break any obvious symmetry. This work was, to some extent, anticipated in studies of large N generalizations of the Heisenberg antiferromagnet. [72])

That said, the difficulty in finding such a spin liquid ground state in model calculations is still a telling point. (Spin liquids are fragile.) A time reversal invariant insulating state cannot be adiabatically connected to a problem of noninteracting quasiparticles with an effective band structure. (In a time reversal symmetry broken state, the band structure need not exhibit the Kramer's degeneracy, so that a weak coupling state with an odd number of electrons per unit cell is possible.) Band insulators always have an even number of electrons per unit cell. Thus, an insulating spin liquid is actually quite an exotic state of matter. Presumably, it only occurs when all more obvious types of ordered states are frustrated, *i.e.* those which break spin rotational symmetry, translational symmetry, or both. The best indications at present are that this occurs in an exceedingly small corner of model space, and that consequently spin liquids are likely to be rather delicate phenomena, if they occur at all in nature. This, in our opinion, is the basic theoretical reason for discarding this appealing idea in the cuprates, where high temperature superconductivity is an amazingly robust phenomenon.

One could still imagine that the insulating state is magnetically ordered, as indeed it is in the cuprates, but that upon doping, once the magnetic order is suppressed, the system looks more like a doped spin liquid than a doped antiferromagnet. (The cuprates appear to be doped spin crystals, not doped spin liquids.) In this context, there are a number of phenomenological points about the cuprates that strongly discourage this viewpoint. In the first place, the undoped system is not only an ordered antiferromagnet, it is a nearly classical one: its ground state and elementary excitation spectrum [223–226] are quantitatively understood using lowest order spin wave theory. This state is as far from a spin liquid as can be imagined! Moreover, even in the doped system, spin glass and other types of magnetic order are seen to persist up to (and even into) the superconducting state, often with frozen moments with magnitude comparable to the ordered moments in the undoped system [226–229]. These and other indications show that the doped system "remembers" that it is a doped antiferromagnet, rather a doped spin liquid.

Regardless of applicability to the cuprates, it would be worthwhile to search for materials that do exhibit spin liquid states, and even more so to look for superconductivity when they are doped. Numerical studies [230–233] indicate that good candidates for this are electrons on a triangular lattice with substantial longer range ring exchange interactions, such as may occur in a 2D Wigner crystal near to its quantum melting point [234], and the Kagomé lattice. It is also possible, as discussed in Section 6.11, to look for super-

conductivity in systems that exhibit some form of spin–charge separation at intermediate length scales. (See also Ref. [14].)

6.7.3 Topological Order and Electron Fractionalization

Finally, we address the problem of classifying phases in which true electron fractionalization occurs, *e.g.* in which spinons are deconfined. It is now clear from the work of Wen [79] and Senthil and Fisher [59] that the best macroscopic characterization of fractionalized phases in two or more dimensions is topological, since they frequently possess no local order parameter. Specifically, a fractionalized phase exhibits certain predictable ground state degeneracies on various closed surfaces—degeneracies which Senthil and Fisher have given a physical interpretation in terms of "vison expulsion." Unlike the degeneracies associated with conventional broken symmetries, these degeneracies are not lifted by small external fields which break either translational or spin rotational symmetry. It has even been shown [59, 220, 235] (as funny as this may sound) that topological order is amenable to experimental detection. Once topological classification is accepted, the one to one relation between spin liquids and electron fractionalization, implied in our previous discussion, is eliminated. Indeed, it is possible to imagine [59, 77] ordered (broken symmetry) states, proximate to a spin liquid phase, which will preserve the ground state degeneracies of the nearby spin liquid, and hence will exhibit spin–charge separation.

6.8 Superconductors with Small Superfluid Density

In contrast to the case of conventional superconductors, in superconductors with small superfluid density, fluctuations of the phase of the superconducting order parameter affect the properties of the system in profound ways.

A hallmark of BCS theory is that pairing precipitates order. But it is possible for the two phenomena to happen separately: pairing can occur at a higher temperature than superconductivity. In this case, there is an intermediate temperature range described by electron pairs which have not condensed. In the order parameter language, this corresponds to a well developed amplitude of the order parameter, but with a phase which varies throughout the sample. Superconductivity then occurs with the onset of long range phase coherence. (This is how ordering occurs in a quasi–1D superconductor, as discussed in Section 6.5, above.) Such superconductors, while they may have a large pairing scale, have a small stiffness to phase fluctuations, or equivalently a small superfluid density.

6.8.1 What Ground State Properties Predict T_c?

When the normal state is understood, it is reasonable to describe superconductivity as an instability of the normal state as temperature is lowered, which BCS theory does quite successfully in simple metals. Another approach, useful especially when the normal state is not well understood, is to consider which thermal fluctuations degrade the superconducting order as the temperature is raised. Put another way, we address the question, "What measurable ground state ($T = 0$) properties permit us to predict T_c?"

Two classes of thermal excitations are responsible for disordering the ground state of a superconductor: amplitude fluctuations of the complex order parameter (associated with pair breaking), and fluctuations of the phase (associated with pair currents).

The strength of the pairing (one energy scale) at $T = 0$ is quantifiable as a typical gap value, Δ_0, where

$$T_p \equiv \Delta_0/2 \,, \tag{6.60}$$

is the characteristic temperature at which the pairs fall apart. In a BCS superconductor, it is possible to estimate that $T_c \approx T_p$. (The factor $1/2$ in this definition approximates the weak coupling BCS expression, $T_c = \Delta_0/1.78$.) Certainly, more generally, T_p marks a loose upper bound to T_c, since if there is no pairing, there is probably no superconductivity.

We can construct another ground state energy scale as follows: Divide the sample into blocks of linear dimension, L, and ask how much energy it costs to flip the sign of the superconducting order parameter at the center of one such region. So long as L is larger than the coherence length, ξ_0, the cheapest way to do this is by winding the phase of the order parameter, so the energy is determined by the superfluid phase stiffness

$$T_\theta = \frac{1}{2} A \gamma L^{d-2} \,, \tag{6.61}$$

where d is the number of spatial dimensions, A is a geometry dependent dimensionless number of order 1 and the "helicity modulus", γ, is traditionally expressed in terms of the ratio of the superfluid density, n_s, to the pair effective mass, m^*:

$$\gamma \equiv \frac{\hbar^2 n_s}{m^*} \,. \tag{6.62}$$

(We will discuss the quantitative aspects of this relation in Subsection 6.8.3.) Note that for $d = 2$, this energy is independent of L, while for $d = 3$ it is minimized for the smallest allowable value of $L \sim \xi_0$. Clearly, when the temperature is comparable to T_θ, thermal agitation will produce random phase changes from block to block, and hence destroy any long range order. Again, a rough upper bound to T_c is obtained in this way.

In short, it is possible to conclude on very general grounds that

$$T_c \leq min[T_p, T_\theta] \; . \tag{6.63}$$

When $T_p \ll T_\theta$, phase fluctuations can be completely neglected except in the immediate neighborhood of T_c—this is the case in BCS superconductors.

If $T_p \gg T_\theta$, quasiparticle excitations, *i.e.* the broken Cooper pairs, play no significant thermodynamic role up to T_c. In this case a considerable amount of local pairing, and consequently a pseudogap, must persist to temperatures well above T_c. When both T_p and T_θ are comparable to T_c, as is the case in most optimally doped high temperature superconductors, neither class of thermal excitation can be safely neglected.

In Table 6.1, following Ref. [270], we tabulate T_θ, T_p, and T_c for various superconducting materials. Clearly, in bulk Pb, phase fluctuations are not terribly important, while in the cuprate superconductors (and the ET superconductors), phase fluctuations are an order 1 effect. Of this there is no possible doubt! Looking more closely at the table, one sees that the ratio of T_θ/T_c is generally smaller for the underdoped materials, and larger for overdoped, which implies that phase fluctuations are progressively less dominant with increasing doping. The ratio of T_p/T_c varies in the opposite manner with doping.

The obvious implication of the trends exhibited in Table 6.1 is that optimal doping marks a gradual crossover from an underdoped regime, where T_c is predominantly a phase ordering transition, to an overdoped regime in which it is predominantly a pairing transition. This also implies that both pairing and phase fluctuation physics play a nonnegligible role, except in the regimes of extreme underdoping or overdoping where $T_c \to 0$.

6.8.2 An Illustrative Example: Granular Superconductors

We now turn to a beautiful set of experiments carried out by Merchant *et al.* [271] on granular Pb films with a thin coating of Ag. This is a system in which the microscopic physics is well understood. The T_c of bulk Pb is 7.2K while Ag remains normal down to the lowest accessible temperatures, so that T_θ can be varied with respect to T_p by changing the thickness of Ag. In this way, the system can be tuned from an "underdoped" regime, where T_c is a phase ordering transition and pairing persists to much higher temperatures, to an "overdoped" regime, where the transition is very BCS–like.

Figure 6.21 shows the log of the resistance *vs.* temperature for a sequence of films (a–j) obtained by adding successive layers of Ag to a granular Pb substrate. Films a and b are seen to be globally insulating, despite being locally superconducting below $7.2K$. Films g–j are clearly superconductors. Films c–f are anomalous metals of some still not understood variety.

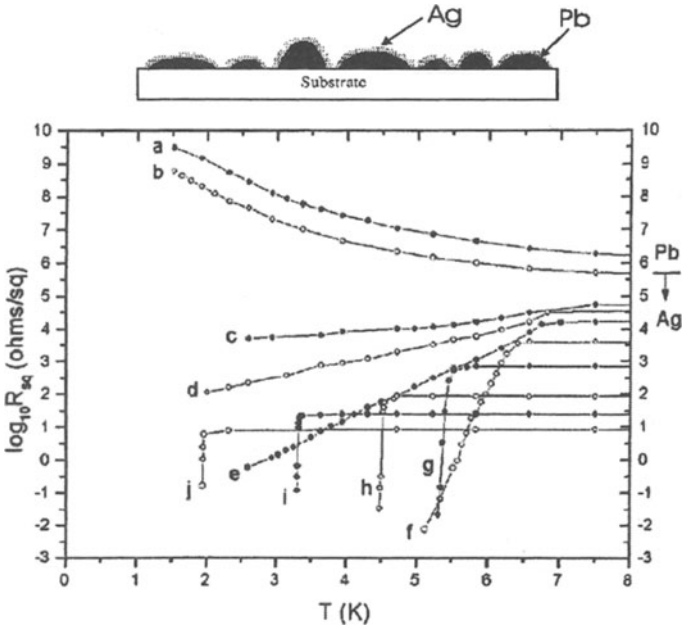

Fig. 6.21. The logarithm of the resistance *vs.* temperature for a sequence of films, starting with a granular Pb film (a) to which is added successively larger coverage of Ag. From Fig. 5 of Merchant *et al.* [271]

Table 6.1. Zero temperature properties of the superconducting state as predictors of T_c. Here, T_p is computed from Eq. (6.60) using values of Δ_0 obtained from either tunnelling or ARPES, except for overdoped Tl-2201, for which we have used Raman data. In computing T_θ from Eq. (6.61) for nearly isotropic materials (those above the double line), we have taken $d = 3$, $A = 2.2$, $L = \sqrt{\pi}\xi_0$, and $n_s/2m^* = (8\pi)^{-1}(c/e)^2\lambda_L^{-2}$ where λ_L and ξ_0 are the zero temperature London penetration depth and coherence length, respectively. For layered materials, we have taken $d = 2$, $A = 0.9$, and the areal superfluid density $n_s/2m^* = (8\pi)^{-1}(c/e)^2 L\lambda_L^{-2}$ where L is now the mean spacing between layers and λ_L is the in–plane London penetration depth. The precise numerical values of A and the factor of $\sqrt{\pi}$ should not be taken seriously—they depend on microscopic details, which can vary from material to material as discussed in Section 6.8.3. Penetration depth measurements on Y-123 refer to polycrystalline $Y_{0.8}Ca_{0.2}Ba_2Cu_3O_{7-\delta}$, and report λ_{ab}. The two entries for Hg-1223 assume that the superfluid density resides in all three planes (L=5.3Å), or the outer two planes only (L=7.9Å). In the case of the high temperature superconductors, the notations 'ud', 'op', and 'od' refer to under, optimally, and overdoped materials, respectively.

Table 6.1.

Material	L [Å]	λ_L[Å]	T_p[K]	T_c[K]	T_θ[K]	Ref.
Pb	830	390	7.9	7.2	6×10^5	[236,237]
Nb_3Sn	60	640	18.7	17.8	2×10^4	[238]
UBe_{13}	140	10,000	0.8	0.9	10^2	[239–241]
$Ba_{0.6}K_{0.4}BiO_3$	40	3000	17.4	26	5×10^2	[242,243]
K_3C_{60}	30	4800	26	20	10^2	[244–246]
MgB_2	50	1400	15	39	1.4×10^3	[247–249]
ET	15.2	8000	17.4	10.4	15	[250,251]
PCCO	6.2	2800	23	23	86	[252–254]
Tl-2201 (op)	11.6		122	91		[255]
Tl-2201 (od)	11.6	2000		80	160	[251,256]
Tl-2201 (od)	11.6	2200		48	130	[251,256]
Tl-2201 (od)	11.6		26	25		[257]
Tl-2201 (od)	11.6	4000		13	40	[251,256]
Bi-2212 (ud) x=.11	7.5		275	83		[98,258]
Bi-2212 (op)	7.5		220	95		[258]
Bi-2212 (op)	7.5	2700		90-93	60	[252,259]
Bi-2212 (op)	7.5	1800		84	130	[260,261]
Bi-2212 (od) x=.19	7.5		143	82		[258]
Bi-2212 (od) x=.225	7.5		104	62		[258]
Y-123 (ud) x=.075	5.9	2800		38	42	[262]
Y-123 (ud) x= .1	5.9	1900		64	90	[262]
Y-123 (op) x=.16	5.9	1500		85.5	140	[262,263]
Y-123 (op)	5.9		116	91-92		[100]
Y-123 (od) x=.19	5.9	1300		79	180	[262]
Y-123 (od) x=.23	5.9	1500		55	140	[262]
Y-248	6.8	1600		82	150	[264]
Hg-1201 (op)	9.5	1700	192	95-97	180	[263,265]
Hg-1212 (op)	6.4	1700	290	108	130	[265,266]
Hg-1223 (op)	5.3	1500	435	132-135	130	[263,265,266]
Hg-1223 (op)	7.9	1500		135	190	[263,266]
LSCO (ud) x=.1	6.6	2800	75	30	47	[267–269]
LSCO (op) x=.15	6.6	2600	58	38	54	[267,268]
LSCO (od) x=.20	6.6	1950		34	96	[268]
LSCO (od) x=.22	6.6	1900		27	100	[268]
LSCO (od) x=.24	6.6	1900		20	100	[268]

It is important to note that Fig. 6.21 is plotted on a log–linear scale, so that although it is unclear whether films c–f will ever become truly superconducting, films e and f, for example, have low temperature resistances which are 5 or 6 orders of magnitude lower than their normal state values, due to significant superconducting fluctuations; see Fig. 6.22.

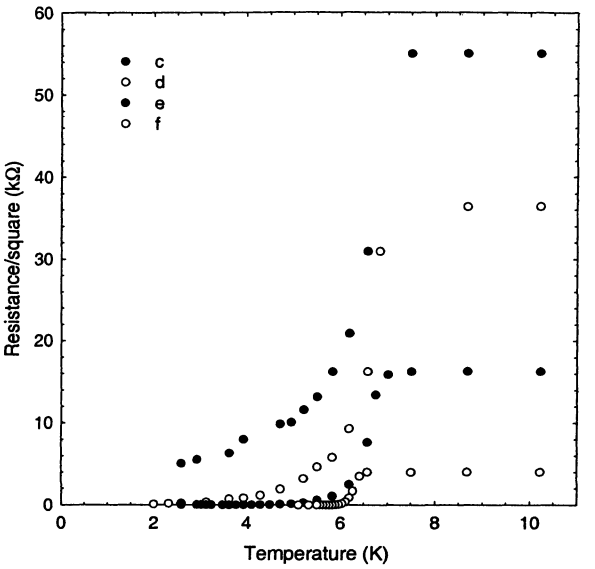

Fig. 6.22. The same data as in Fig. (6.21), but on a linear, as opposed to a logarithmic, scale of resistivity

Figure 6.23 shows I–V curves obtained from planar tunnelling in the direction perpendicular to the same set of films. As dI/dV is proportional to the single particle density of states at energy V, this can be interpreted as the analogue of an ARPES or tunnelling experiment in the high temperature superconductors. Among other things, the gap seen in films a–d is roughly independent of Ag coverage, and looks precisely like the gap that is seen upon tunnelling into thick Pb films. In these films, the gap seen in tunnelling is clearly a superconducting pseudogap.

The analogy between the behavior of these films as a function of Ag coverage, and the cuprate high temperature superconductors as a function of hole concentration is immediately apparent:

With little or no Ag, the typical Josephson coupling, J, between far separated grains of Pb is small; thermal phase fluctuations preclude any possibility of long range phase order for $T > J$. Clearly, increasing Ag coverage increases the coupling between grains, or more correctly, since the granular character of the films is gradually obscured with increasing Ag coverage, it increases

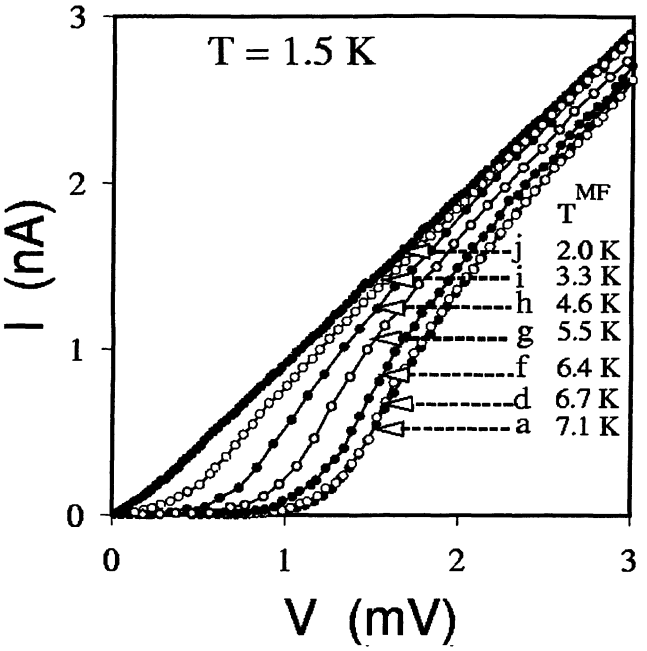

Fig. 6.23. I–V curves from planar tunnelling into the same sequence of films shown in Fig. (6.21) (from Fig. 6 of Merchant *et al.* [271])

the phase stiffness or superfluid density. This causes the phase ordering temperature to rise, much like the underdoped regime of the cuprates.

However, the pairing scale, or equivalently the mean field T_c, is a decreasing function of Ag coverage due to the proximity effect. Since the Pb grains are small compared to the bulk coherence length, ξ_0, the granularity of the films has little effect on the BCS gap equation. The pairing scale is equivalent to that of a homogeneous system with an effective pairing interaction,

$$\lambda^{eff} = \lambda_{Pb} \times f_{Pb} + 0 \times f_{Ag} \,, \tag{6.64}$$

where f_{Pb} and f_{Ag} are, respectively, the volume fraction of Pb and Ag. Consequently, the pairing gap,

$$\Delta_0 \sim \exp[-1/(\lambda^{eff} - \mu^*)] \tag{6.65}$$

is a decreasing function of Ag coverage. So long as $f_{Ag} \ll 1$ (films a–f) this effect is rather slight, as can be seen directly from the figures, but then the gap value can be seen to plummet with increasing Ag coverage. In films g–j, this leads to a decrease of T_c, reminiscent of overdoped cuprates.

Of course, it is clear that there is more going on in the experiment than this simple theoretical discussion implies:

1) *Disorder:* The effects of disorder are neglected in this discussion. A priori these should be strong, especially at low Ag coverage.
2) *Coulomb Blockade:* As best one can tell from the existing data, films a–f are not superconductors with a reduced T_c—in fact films a and b appear to be headed toward an insulating ground state, presumably due to quantum phase fluctuations induced by the charging energy of the grains. The energy to transfer a Cooper pair (charge 2e) between grains is

$$V_C = 4\alpha e^2/L\,, \tag{6.66}$$

where L is the grain size and α is a dimensionless constant which takes into account the grain shape and screening. When $V_C > J$, the number of pairs per grain becomes fixed at low temperature and the ground state is a type of paired Mott insulator. Since the number of pairs and the phase are quantum mechanically conjugate on each grain, when number fluctuations are suppressed by the charging energy, quantum phase fluctuations flourish, and prevent superconducting order. The screening of the Coulomb interaction can mitigate this effect. Screening clearly improves with increasing Ag coverage, so coverage dependent effects of quantum phase fluctuations contribute to the evolution observed in the experiments, as well.
3) *Dissipation:* There is even more to this story than the $\omega = 0$ charging energies. In contrast with classical statistical mechanics, the dynamics and the thermodynamics are inexorably linked in quantum statistical mechanics, and finite frequency physics becomes important. This issue has been addressed experimentally by Rimberg *et al.* [272] While there has been considerable progress in understanding the theory of quantum phase fluctuations (See, for example, Ref. [273] for a recent review), there are still many basic issues that are unresolved. For instance, films c–f show no sign of becoming truly superconducting or insulating as $T \to 0$! What is the nature of this intermediate state? This is a widely observed phenomenon in systems which are expected to be undergoing a superconductor to insulator transition [273,274]. The physics of this anomalous metallic state is not understood *at all*, even in systems, such as the present one, where the microscopic physics is believed to be understood. (See Section 6.8.4 for a taste of the theoretical subtleties involved.)

6.8.3 Classical Phase Fluctuations

We now undertake a critical analysis of thermal phase fluctuations. We will for now ignore the effects of thermal quasiparticle excitations, as well as the quantum dynamics which certainly dominate the phase mode physics at temperatures low compared to its effective Debye temperature. These important omissions will be addressed in Section 6.8.4.

Superconductors and classical XY models

When $T_\theta \ll T_p$, the superconducting transition temperature $T_c \approx T_\theta$, and the

transition can be well described by a phase only model. On general symmetry grounds, the free energy associated with time independent deformations of the phase must be of the form

$$V_{phase} = (\gamma/2) \int d\boldsymbol{r} (\nabla\theta)^2 \,, \tag{6.67}$$

where the helicity modulus, γ, is given by the superfluid density (the superfluid density sets the phase stiffness), n_s, and the effective pair mass, m^*, according to Eq. (6.62). Since $\boldsymbol{v}_s = \frac{\hbar}{m^*}\nabla\theta$ is the superfluid velocity, V_{phase} is easily seen to have an interpretation as the kinetic energy of the superfluid, $V_{phase} = \int d\boldsymbol{r} n_s m^* v_s^2/2$, so that classical phase fluctuations correspond to thermally induced pair currents. Eqs. (6.67) and (6.62) establish the sense in which the superfluid density controls the stiffness to phase fluctuations.

Eq. (6.67) is the continuum form of the classical XY model. Both in a superconductor and in the XY model, θ is a periodic variable (defined modulo 2π). Thus, we must handle the short distance physics with some care to permit the vortex excitations which are the expression of that periodicity. When this is done, typically by defining the model on a lattice, it captures the essential physics of the transition between a low temperature ordered and a high temperature disordered state.

To be concrete, let us consider an XY model on a d dimensional hypercubic lattice

$$H_{XY} = -\sum_{\langle i,j \rangle} \mathcal{V}(\theta_i - \theta_j) \,, \tag{6.68}$$

where $\langle i,j \rangle$ are nearest neighbor sites and $\mathcal{V}$ is an even, periodic function $\mathcal{V}(\theta) = \mathcal{V}(\theta + 2\pi) = \mathcal{V}(-\theta)$, with a maximum at $\theta = 0$ such that the Hamiltonian is minimized by the uniform state. The lattice constant, a, in this model has a physical interpretation—it defines the size of the vortex core. To generalize this model to the case of an anisotropic (*e.g.* layered) superconductor, we let both the lattice constant, a_μ, and the potential, $\mathcal{V}_\mu(\theta)$, depend on the direction, μ.

At zero temperature, the helicity modulus can be simply computed:

$$\gamma_\mu(T=0) = 2[a_\mu^2/\nu]\mathcal{V}_\mu''(0) \,, \tag{6.69}$$

where $\nu = (\prod_\nu a_\nu)$ is the unit cell volume. Thus, the relation between $\gamma(0)$ and T_θ, the ordering temperature of the model, depends both on the detailed form of $\mathcal{V}$ and on the lattice cutoff. In constructing Table 6.1 above, we have taken $\mathcal{V} = V\cos(\theta)$, and identified the area of the vortex core, $\pi\xi_0^2$, with the plaquette area, a^2 – this is the origin of the somewhat arbitrary $\sqrt{\pi}$ which appears in the three dimensional expression for T_θ. Fortuitously, for layered materials, $\gamma_x = \gamma_y \equiv \gamma_{xy}$ depends only on the spacing between planes, a_z, and not on the in–plane lattice constant.

One can, in principle, handle the short distance physics in a more systematic way by solving the microscopic problem (probably numerically) on large systems (large compared to ξ_0), and then matching the results with the short distance behavior of the XY model. In this way, one could, in principle, derive explicit expressions for $\mathcal{V}$ and a_μ in terms of the microscopic properties of a given material. However, no one (to the best of our knowledge) has carried through such an analysis for any relevant microscopic model. (How much does the detailed shape of $\mathcal{V}$ matter?)

What we [275] have done, instead, is to keep at most the first 2 terms in a Fourier cosine series of Eq. (6.68). With the cuprates in mind, we have studied planar systems:

$$H = -J_{\|} \sum_{\langle ij \rangle_{\|}} \{\cos(\theta_{ij}) + \delta \cos(2\theta_{ij})\} \\ -J_{\perp} \sum_{\langle ij \rangle_{\perp}} \{\cos(\theta_{ij})\} \ , \tag{6.70}$$

where $\langle ij \rangle_{\|}$ denotes nearest neighbors within a plane, and $\langle ij \rangle_{\perp}$ denotes nearest neighbors between planes. It is assumed that $J_{\|}$, $J_{\perp}$, and δ are positive, since there is no reason to expect any frustration in the problem, [276] and that $\delta \leq 0.25$, since for $\delta > 0.25$ there is a secondary minimum in the potential for $\theta_{ij} = \pi$, which is probably unphysical. Since dimensional analysis arguments of the sort made above are essentially independent of δ, varying δ permits us to obtain some feeling for how quantitatively robust the results are with regard to "microscopic details."

Properties of classical XY models

The XY model is one of the most studied models in physics [277]. We [275] have recently carried out a series of quantitative analytic and numerical studies of XY models (using Eq. (6.70)). In particular, we have focused on the thermal evolution of the superfluid density and the relation between the superfluid density and the ordering temperature.

As long as $J_{\perp}$ is nonzero, this model is in the universality class of the 3D XY model, and near enough to T_c, $\gamma(T) \sim |T_c - T|^{\nu}$, where ν is the correlation length exponent of the 3D XY model, $\nu \approx .67$. For sufficient anisotropy, there may be a crossover from 2D critical behavior close (but not too close) to T_c, to 3D critical behavior very near T_c. In practice, this crossover is very hard to see due to the special character of the critical phenomena of the 2D XY model; even a very weak $J_{\perp}$ significantly increases the transition temperature.

To see this, consider the case in which $J_{\|} \gg J_{\perp}$; in this limit, one can study the physics of the system using an asymptotically exact interplane mean field theory [202]. We define the order parameter, $m(T) \equiv \langle \cos[\theta_j] \rangle$, and consider the behavior of a single decoupled planar XY model in the presence of an external field, $h(T) = 2J_{\perp} m(T)$ due to the mean field of the neighboring two planes. The self–consistency condition thus reads

$$m(T) = m_{2D}(T, h) \ , \tag{6.71}$$

where $m_{2D}(T,h)$ is computed for the 2D model. A simple estimate for T_c can be obtained by linearizing this equation:

$$1 = 2J_\perp \chi_{2D}(T_c) \,. \tag{6.72}$$

Here the 2D susceptibility is

$$\chi_{2D} \sim T_{2D}^{-1} exp\left\{A_\chi \sqrt{T_{2D}/(T_c - T_{2D})}\right\} \,, \tag{6.73}$$

where T_{2D} is the Kosterlitz–Thouless transition temperature and A_χ is a nonuniversal number of order 1. A consequence of this is that even a very small interlayer coupling leads to a very large fractional increase in T_c

$$T_c - T_{2D} \sim T_{2D} A_\chi^2 / \log^2[J_\parallel / J_\perp] \,. \tag{6.74}$$

Only if $(T_c - T_{2D})/T_{2D} \ll 1$ will there be clear 2D critical behavior observed in the thermodynamics.

To make contact with a range of experiments it is necessary that we focus attention not only on universal critical properties, but also on other properties which are at least relatively robust to changes in microscopic details. One such property is the width of the critical region, but we are not aware of any systematic studies of the factors that influence this. For the simple ($\delta = 0$) isotropic 3D XY model, the critical region certainly does not extend further than 10% away from T_c.

Another such property is the low temperature slope of superfluid density curves as a function of temperature. (The superfluid density is linear at low T.) Using linear spin wave theory [278,279], one can obtain a low temperature expansion of the in–plane helicity modulus,

$$\frac{\gamma_\parallel(T)}{a_\perp} = J_\parallel(1+4\delta) - \frac{\alpha(1-16\delta)}{4(1+\delta)} T + \mathcal{O}(T^2) \,, \tag{6.75}$$

where we have used $a_x = a_y \equiv a_\perp$ and $\gamma_x = \gamma_y \equiv \gamma_\parallel$ for a planar system and α is a nonuniversal number which depends on $J_\perp/J_\parallel$. It is easy to show [275] that $\alpha = 1$ in the two dimensional limit ($J_\perp/J_\parallel = 0$), and that $\alpha = 2/3$ in the three dimensional limit ($J_\perp = J_\parallel(1+4\delta)$). The T-linear term is independent of $J_\parallel$, so that we expect the slope of scaled superfluid density curves, $\gamma_\parallel(T)/\gamma_\parallel(0)$ *vs.* T/T_c, to be much less sensitive to microscopic parameters (*i.e.* material dependent properties such as doping in the cuprates) than is $\gamma_\parallel(0)$. That this expectation is realized can be seen from our Monte Carlo simulation results presented in Fig. 6.24.

In addition, we find that there is a *characteristic shape* to the superfluid density vs. temperature curves in XY models. We have used Monte Carlo simulations to focus on two other dimensionless nonuniversal parameters: $A_1 = T_c/\gamma_\parallel(0)$ and $A_2 = T_c\gamma_\parallel'(0)/\gamma_\parallel(0)$, where $\gamma_\parallel'(0) = d\gamma_\parallel(0)/dT$. A_1 is a measure of how well the ground state property $\gamma_\parallel(0)$ (measurable through

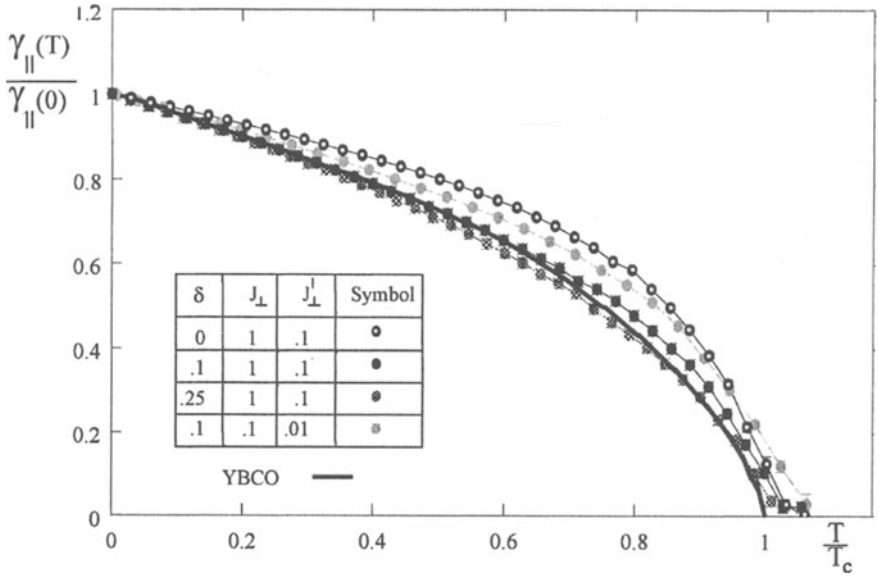

Fig. 6.24. Superfluid density *vs.* temperature, scaled by the zero temperature superfluid density and by T_c, respectively, from Ref. [275]. Experimental data on *YBCO* is depicted by the black line, and is taken from Kamal *et al.* [280] (The data are essentially the same for a range of doping concentration.) Our Monte Carlo results for system size $16 \times 16 \times 16$ are the filled symbols. Calculations are for two planes per unit cell, with coupling $J_\| = 1$ within each plane, and $J_\perp$ and $J'_\perp$ between alternate planes. Monte Carlo points above T_c are nonzero due to finite size effects. Except where explicitly shown, error bars are smaller than symbol size

the superfluid density) predicts T_c, which is equivalent to T_θ in this model. A_2 can be expressed in the more intuitive form $A_2 = T_c/T_{ex}$, where $T_{ex} \equiv \gamma_\|(0)/\gamma'_\|(0)$, is the estimate of T_c one would obtain by extrapolating from the low temperature slope of $\gamma_\|(T)$ to the point at which the superfluid stiffness would vanish. Over *orders of magnitude* of couplings ($0 \leq J_\perp/J_\| \leq .1$), and throughout the range $0 \leq \delta \leq .25$, A_1 and A_2 are remarkably robust: $A_1 \sim .6 - 1.7$, and $A_2 \sim .2 - -.5$. (The shape of $\gamma(T)$is robust!)

6.8.4 Quantum Considerations

In quantum systems, the dynamics affects the thermodynamics. However, the role of quantum effects on the phase dynamics is a large topic, and one in which many uncertainties remain. We will briefly discuss the simplest case here, mostly to illustrate the complexity of the problem.

Let us consider a simple two fluid model [3] in which a phase fluctuating superconductor is capacitively coupled to a normal fluid. The continuum limit

of the effective action obtained upon integrating out the normal fluid can be derived from simple hydrodynamic considerations. From the Josephson relation, it follows that the electric field

$$\boldsymbol{E} = -(\hbar/2e)\boldsymbol{\nabla}\dot{\theta} \, . \tag{6.76}$$

The Euclidean effective action is obtained by augmenting the classical action, Eq. (6.67), with the Maxwell term, and analytically continuing to imaginary time:

$$S[\theta] = \int_0^\beta d\tau \left\{ \int d\boldsymbol{r} \mathcal{L}_{quantum} + V_{phase} \right\}, \quad \mathcal{L}_{quantum} = \boldsymbol{E} \cdot \boldsymbol{D}/8\pi \, , \tag{6.77}$$

where $\beta = 1/T$, $\boldsymbol{D}(\boldsymbol{k},\omega) = \epsilon_0(\boldsymbol{k},\omega)\boldsymbol{E}(\boldsymbol{k},\omega)$, and ϵ_0 is the normal fluid dielectric function (analytically continued to imaginary time). Again, this effective action must be cutoff at short distances in such a way as to preserve the periodicity of θ by allowing vortex excitations.

An analysis of the Maxwell term, $S_{quantum}$, allows us to illustrate some of the complexity of this problem. (The order of limits matters.) At $\boldsymbol{k} = \boldsymbol{0}$ and small ω, $\epsilon_0 \approx 4\pi\sigma_0/i\omega$, where σ_0 is the D.C. conductivity of the normal fluid. Thus, if we first consider the spatial continuum limit before going to low frequencies, $S_{quantum} \sim \sum_{\omega_n} \int d\boldsymbol{r}\sigma_0|\omega_n||\boldsymbol{\nabla}\theta|^2$, where $\omega_n = 2\pi nT$ are the Matsubara frequencies. We recognize the resulting action as the continuum limit of an array of resistively shunted Josephson junctions [281,282] (RSJ). Here, the normal fluid plays the role of an "Ohmic heat bath."

On the other hand, if we first take $\omega = 0$, and then k small, $\epsilon \approx (k_{TF}/k)^2$ where k_{TF} is the Thomas–Fermi screening length. In this limit, the Maxwell term has the form of a phase kinetic energy, $\mathcal{L}_{quantum} \sim (M_\theta/2)|\dot{\theta}|^2$, with an effective mass, $M_\theta \propto [e^2/k_{TF}^2]^{-1}$ inversely proportional to an appropriately defined local charging energy. The resulting effective action is the continuum limit of the "lattice quantum rotor" (QR) model, also a widely studied problem [283]. The RSJ and QR models have quite different behavior at low temperatures. Without a rather complete understanding of the physics of the normal fluid, it is impossible in general to determine which, if either, of these limits captures the essential quantum physics.

There is nonetheless one important issue which can be addressed in a theoretically straightforward fashion: the temperature scale below which quantum effects dominate. The classical physics we studied in the previous section is readily obtained from the quantum model by suppressing all fluctuations with nonzero Matsubara frequency. We thus estimate a classical to quantum crossover temperature, T_{cl}, by comparing the classical ($\omega = 0$) and first finite frequency ($\omega = \omega_1 = 2\pi T$) contributions to $S[\theta]$. This leads to the implicit equation for T_{cl}:

$$T_{cl} = \sqrt{e^2 n_s/\epsilon_0 m^*} \, , \tag{6.78}$$

where ϵ_0 is evaluated at temperature $T = T_{cl}$, frequency $\omega \sim 2\pi T_{cl}$, and a typical momentum, $k \sim 1/a$. So long as $T \gg T_{cl}$, the imaginary time

independent (classical) field configurations dominate the thermodynamics. Clearly, depending on how good the screening is, T_{cl} can be much smaller or much larger than T_c. If we approximate ϵ_0 by its finite frequency, $k \to 0$ form, this estimate can be recast in an intuitively appealing form [275]:

$$T_{cl} \sim \left(\frac{\sigma_Q}{\sigma_0}\right) T_\theta \,, \tag{6.79}$$

where $\sigma_Q = e^2/(ha)$ is the quantum of conductance in which the vortex core radius enters as the quantum of length.

Recent theoretical developments have uncovered yet more subtleties. Although the low energy physics involves only phase fluctuations, phase slips (short imaginary time events where the phase spontaneously "slips" by 2π) involve amplitude fluctuations. In the presence of an ohmic heat bath, there are subtle, long time consequences of these amplitude fluctuations [284–286]. Another interesting possibility is electron fractionalization. Under some circumstances, it has been proposed [59] that hc/e vortices may be energetically preferred to the usual $hc/2e$ vortices, leading to a fractionalized state.

Combine this exciting but incomplete jumble of theoretical ideas with the remarkably simple but entirely unexplained behavior observed experimentally in granular superconducting films as they crossover from superconducting to insulating behavior, and one is forced to concede that the theory of quantum phase fluctuations is seriously incomplete. (This is an important unsolved problem!)

6.8.5 Applicability to the Cuprates

Both phase and pair breaking fluctuations are more prevalent at low T in the cuprate superconductors than in conventional BCS superconductors. The low superfluid density provides only a weak stiffness to thermal phase fluctuations of the order parameter. In addition, the nodes in the gap mean that there are low energy quasiparticle excitations down to arbitrarily low temperature. However, it is important to remember that nodal quasiparticles occupy only a small fraction of the Brillouin zone so long as $\Delta_o \gg T$.

T_c is unrelated to the gap in underdoped cuprates

As mentioned in Section 6.3, in underdoped cuprates, many probes detect a pseudogap in the normal state, such as NMR, STM, junction tunnelling, and ARPES. Whereas BCS theory would predict $T_c \sim \Delta_o/2$, where Δ_o is the superconducting gap maximum at zero temperature, the low temperature magnitude of the single particle gap as measured by ARPES or tunnelling experiments does not follow this relation, qualitatively or quantitatively. On the underdoped side, T_c increases with increasing doping, whereas Δ_o moves in the opposite direction in all cases studied to date. Even at optimal doping, T_c is always considerably smaller than the BCS value of $\Delta_o/2$. In optimally

doped BSCCO, for example, $T_c \sim \Delta_o/5$, where Δ_o is the peak energy observed in low temperature tunnelling experiments. [152, 287, 288] (See also Table 6.1.)

The ARPES experiments provide k–space information demonstrating that the gap, above and below T_c, has an anisotropy consistent with a d–wave order parameter. Furthermore, $\Delta_o(T)$ is largely undiminished in going from $T = 0$ to $T = T_c$ in underdoped samples, and the size and shape of the gap are basically unchanged through the transition. Add to this the contravariance of T_c with the low temperature magnitude of the gap as the doping is changed, and it appears the gap and T_c are simply independent energies [136,289]. The gap decreases with overdoping, which may be responsible for the depression of T_c in that region, so that the transition may be more conventional on the overdoped side. (There is no signature of the transition in the single particle gap.)

T_c is set by the superfluid density in underdoped cuprates

As emphasized above, the superfluid density in cuprates is orders of magnitude smaller than in conventional superconductors. [270] In addition, when the superfluid density is converted to an energy scale, it is comparable to T_c, whereas in conventional superconductors this phase stiffness energy scale is far above the transition temperature. In those conventional cases, BCS theory works quite well, but in the cuprates, the phase stiffness energy scale should also be considered.

This is further emphasized by the Uemura plot [108], which compares the transition temperature to the superfluid density. For underdoped systems, the relationship is linear within experimental errors. This is strong evidence that T_c is determined by the superfluid density, and therefore set by phase ordering.

Experimental signatures of phase fluctuations

In YBCO, $3DXY$ critical fluctuations have been observed in the superfluid density within 10% of T_c [174, 290], implying that the temperature dependence of the superfluid density below and near T_c is governed by phase fluctuations. It needs to be stressed that in conventional superconductors, such fluctuations that are seen are Gaussian in character—that is they involve fluctuations of both the amplitude and the phase of the order parameter [3]. The purely critical phase fluctuations observed in YBCO are entirely different. At low temperature (as low as $T = 1$K [292]), the superfluid density is a linearly decreasing function of temperature [9]. While this linear behavior is generally believed to be the result of amplitude fluctuations of an order parameter with nodes, it is difficult [150, 153, 293, 294] from this perspective to understand why the slope is nearly independent of x and of Δ_0/T_c. This feature of the data is naturally explained if it is assumed that the linear temperature dependence, too, arises from classical phase fluctuations, but then

[3] An interesting way to identify separate Gaussian and phase fluctuation regimes in YBCO is presented in Ref. [291], see also Ref. [80].

it is hard to understand [275, 295] why quantum effects would not quench these fluctuations at such low temperatures.

6.9 Lessons from Weak Coupling

The weak coupling renormalization group approach to the Fermi liquid and the 1DEG is presented. The role of retardation, the physics of the Coulomb pseudopotential, and the nonrenormalization of the electron phonon coupling in a BCS superconductor are systematically derived. The strong renormalization of the electron–phonon interaction in the 1DEG is contrasted with this—it is suggested that this may be a more general feature of non-Fermi liquids.

6.9.1 Perturbative RG Approach in $D > 1$

In recent years, Fermi liquid theory, and with it the characterization of the BCS instability, has been recast in the language of a perturbative renormalization group (RG) treatment. We will adopt this approach as we reconsider the conventional BCS–Eliashberg theory of the phonon mediated mechanism of superconductivity in simple metals. In particular, we are interested in exploring the interplay between a short ranged instantaneous electron–electron repulsion of strength μ and a retarded attraction (which we can think of as being mediated by the exchange of phonons) of strength λ, which operates only below a frequency scale ω_D. Although we will make use of a perturbative expression for the beta function which is valid only for μ and λ small compared to 1, the results are nonperturbative in the sense that we will recover the nonanalytic behavior of the pairing scale, T_p, expected from BCS mean field theory. The results are valid for any relative strength of μ/λ and, moreover, the corrections due to higher order terms in the beta function are generally smooth, and so are not expected to have large qualitative effects on the results so long as μ and λ are not large compared to 1.

All the results obtained in this section have been well understood by experts since the golden age of many–body theory, along with some of the most important higher order corrections which occur for λ of order 1 (which will be entirely neglected here). Our principal purpose in including this section is to provide a simple derivation of these results in a language that may be more accessible to the modern reader. A most insightful exposition of this approach is available in the articles by Polchinski, Ref. [39], and Shankar, Ref. [38], which can be consulted wherever the reader is curious about parts of the analysis we have skipped over. The one technical modification we adopt here is to employ an energy shell RG transformation, rather than the momentum shell approach adopted in Ref. [38]; this method allows us to handle the retarded and instantaneous interactions on an equal footing. It can also be

viewed as an extension of the analogous treatment of the 1D problem adopted in Ref. [296], as discussed in the next subsection.

We start by defining a scale invariant (fixed point) Euclidean action for a noninteracting Fermi gas

$$S_{fp}[\Psi_\uparrow, \Psi_\downarrow] = (2\pi)^{-(d+1)} k_F^{d-1} \sum_\sigma \int d\omega d\hat{k} dk \mathcal{L}_0[\Psi_\sigma] \,, \tag{6.80}$$

$$\mathcal{L}_0[\Psi_\sigma] = \bar{\Psi}_\sigma [i\omega + v_F(\hat{k})k] \Psi_\sigma \,,$$

where $d\boldsymbol{k} = k_F^{d-1} d\hat{k} dk$, the unit vector $\hat{k}$ is the direction of $\boldsymbol{k}$ and k is the displacement from the Fermi surface; we have assumed a simple spherical Fermi surface. The treatment that we present here breaks down when the Fermi surface is nested or contains Van Hove singularities. To regularize the theory, it is necessary to cut off the integrals; whereas Shankar confines k to a narrow shell about the Fermi surface, $|k| < \Lambda \ll k_F$, we allow k to vary from $-\infty$ to $+\infty$, but confine the ω integral to a narrow shell $|\omega| < \Omega \ll E_F$.

We now introduce electron–electron interactions. Naive power counting leads to the conclusion that the four fermion terms are marginal, and all higher order terms are irrelevant, so we take

$$\begin{aligned} S_{int} = \sum_{\sigma,\sigma'} \int \prod_{j=1}^{3} \frac{d\boldsymbol{k}_j d\omega_j}{(2\pi)^{d+1}} \bar{\Psi}_\sigma(\boldsymbol{k}_1, \omega_1) \bar{\Psi}_{\sigma'}(\boldsymbol{k}_2, \omega_2) \\ \times [g(\boldsymbol{k}_2 - \boldsymbol{k}_3) + \Theta(\omega_D - |\omega_2 - \omega_3|) \tilde{g}(\boldsymbol{k}_2 - \boldsymbol{k}_3)] \\ \times \Psi_{\sigma'}(\boldsymbol{k}_3, \omega_3) \Psi_\sigma(\boldsymbol{k}_1 + \boldsymbol{k}_2 - \boldsymbol{k}_3, \omega_1 + \omega_2 - \omega_3) \,, \end{aligned} \tag{6.81}$$

where Θ is the Heavyside function, and g and $\tilde{g}$ are, respectively, the instantaneous and retarded interactions. Signs are such that positive g corresponds to repulsive interactions. The distinction between retarded and instantaneous interactions is important so long as $\Omega \gg \omega_D$. We have invoked spin rotation invariance in order to ignore the dependence of g and $\tilde{g}$ on the spin indices.

It should be stressed, as already mentioned in Section 6.5, that this should already be interpreted as an effective field theory, in which the microscopic properties that depend on the band structure away from the Fermi surface such as mixing with other bands, more complicated three and four–body interactions, etc. have already fed into the parameters that appear in the model. What we do now is to address the question of what further changes in the effective interactions are produced when we integrate out electronic modes in a narrow shell between Ω and $\Omega e^{-\ell}$, ($\ell > 0$ and small), and then rescale all frequencies according to

$$\omega \to e^\ell \omega, \quad k \to e^\ell k \quad \text{and} \quad \Psi \to e^{-(3/2+\eta_F)\ell} \Psi \,, \tag{6.82}$$

to restore the cutoff to its original form and where, as usual, η_F is a critical exponent that is determined by the the properties of the interacting fixed point. We will carry this procedure out perturbatively in powers of g and $\tilde{g}$—to the one loop order we (and everyone else) analyzes, $\eta_F = 0$.

To first order in perturbation theory, simple power counting insures that the entire effective action is invariant under the RG transformation, other than the parameter ω_D which changes according to

$$d\omega_D/d\ell = \omega_D \ . \tag{6.83}$$

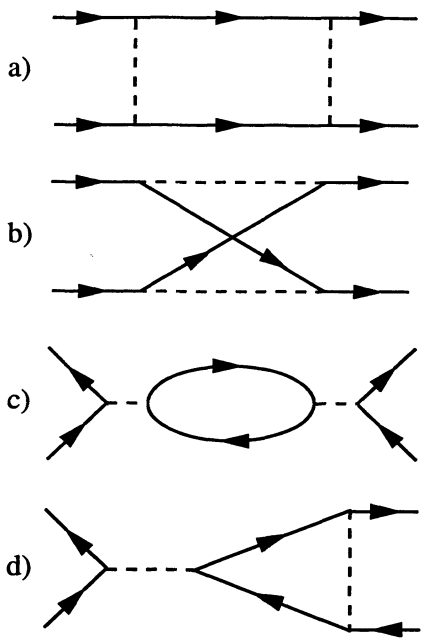

Fig. 6.25. The one loop diagrams that are invoked in the discussion of the renormalization of the effective interactions. a) and b) are referred to as the "Cooper channel" and c) and d) as "particle–hole channels". The loop is made out of electronic propagators with frequencies in the shell which is being integrated. The dashed lines represent interactions

To second (one loop) order, the forward scattering interactions are still unchanged; they produce the Fermi liquid parameters, and should actually be included as part of the fixed point action and treated non–peturbatively. This can be done straightforwardly, but for simplicity will be ignored here. The one loop diagrams which potentially produce contributions to the beta function are shown in Fig. 6.25. All internal legs of the diagrams refer to electron propagators at arbitrary momenta but with their frequencies constrained to lie in the shell which is being integrated out, $\Omega > |\omega| \geq \Omega e^{-\ell}$. The dashed lines represent interactions. All external legs are taken to lie on or near the

Fermi surface. Clearly, the energy transfer along the interaction lines in the Cooper channel, Figs. 6.25a and 6.25b, is of order Ω, and so for $\Omega \gg \omega_D$, $\tilde{g}$ does not contribute, while in Figs. 6.25c and 6.25d there is zero frequency transfer along the interaction lines, and so g and $\tilde{g}$ contribute equally.

Since $\Omega \ll E_F$, we can classify the magnitude of each diagram in powers of Ω; any term of order $|\Omega|^{-1}$ makes a logarithmically divergent contribution to the effective interaction upon integration over frequency, while any terms that are proportional to E_F^{-1} are much smaller and make only finite contributions which can be ignored for the present purposes. When the Cooper diagrams, shown in Figs. 6.25a and 6.25b, are evaluated for zero center of mass momentum, (*i.e.* if the momenta on the external legs are $\boldsymbol{k}_F$ and $-\boldsymbol{k}_F$), the bubble is easily seen to be proportional to Ω^{-1}. However, if the center of mass momentum is nonzero (*i.e.* if the external momenta are $\boldsymbol{k}_F + \boldsymbol{q}$ and $-\boldsymbol{k}_F$), the same bubble is proportional to $1/v_F|\boldsymbol{q}|$, and hence is negligible. The particle–hole diagrams in Figs. 6.25c and 6.25d are a bit more complicated. The bubble is zero for total momentum 0, and proportional to $1/v_F k_F$ for momentum transfer near $2k_F$. Thus, in more than one dimension, the particle hole bubbles can be neglected entirely. (We will treat the 1d case separately, below.) Putting all this together in the usual manner, we are left with the one–loop RG equations for the interactions between electrons on opposing sides of the Fermi surface,

$$\frac{dg_l}{d\ell} = -\frac{1}{\pi v_F} g_l^2 \,, \qquad \frac{d\tilde{g}_l}{d\ell} = 0 \,, \tag{6.84}$$

where l refers to the appropriate Fermi surface harmonic; for the case of a circular Fermi surface in two dimensions, l is simply angular momentum. (Implicit in this is the fact that odd l are associated with interactions in the triplet channel while even l are in the singlet channel.)

These equations describe the changes in the effective interactions upon an infinitesimal RG transformation. They can be easily integrated to obtain expressions for the scale dependent interactions. However, these equations are only valid so long as all the interactions are weak (to justify perturbation theory) and so long as $\Omega \gg \omega_D$. Assuming that it is the second condition that is violated first, we can obtain expression for the effective interactions at this scale by integrating to the point at which $\Omega = \omega_D$; the result is

$$\mu(\omega_D) = \frac{\mu_0}{1 + \mu_0 \log(\Omega_0/\omega_D)} \,, \quad \lambda(\omega_D) = \lambda_0 \,, \tag{6.85}$$

where $\mu = g/\pi v_F$, $\lambda = \tilde{g}/\pi v_F$, the symmetry labels on g and $\tilde{g}$ are left implicit, and the subscript "0" refers to the initial values of the couplings at a microscopic scale, $\Omega_0 \sim E_F$. (Note the nonrenormalization of λ for $\Omega > \omega_D$.)

The fact that the retarded interactions do not renormalize is certainly as noteworthy as the famous renormalization of μ. This means that it is

possible to estimate λ from microscopic calculations or from high temperature measurements, such as resistivity measurements in the quasi–classical regime where $\rho \propto \lambda T$.

Once the scale $\Omega = \omega_D$ is reached, a new RG procedure must be adopted. At this point, the retarded and instantaneous interactions are not distinguishable, so we must simply add them to obtain a new, effective interaction, $g^{eff}(\omega_D) = g(\omega_D) + \tilde{g}$, which upon further reduction of Ω renormalizes as a nonretarded interaction. If $g^{eff}(\omega_D)$ is repulsive, it will be further reduced with decreasing Ω. However, if it is attractive in any channel, the RG flows carry the system to stronger couplings, and eventually the breaks down at the pairing scale. perturbation theory breaks down. We can estimate the characteristic energy scale at which this breakdown occurs by integrating the one loop equations until the running coupling constant reaches a certain finite value $-1/\alpha$:

$$\Omega_1 = \omega_D e^{\alpha} \exp[-1/|g^{eff}(\omega_D)|] \,. \tag{6.86}$$

Of course, the RG approach does not tell us how to interpret this energy scale, other than that it is the scale at which Fermi liquid behavior breaks down. However, we know on other grounds that this scale is the pairing scale, and that the breakdown of Fermi liquid behavior is associated with the onset of superconducting behavior.

6.9.2 Perturbative RG approach in $D = 1$

The one loop beta function

In one dimension, the structure of the perturbative beta function is very different from in higher dimensions. In addition to the familiar logarithmic divergences in the particle–particle (or Cooper) channel, there appear similar logarithms in the particle–hole channel. That these lead to a serious breakdown of Fermi liquid theory can be deduced directly from the perturbation theory, although it is only through the magic of bosonization (discussed in Section 6.5) that it is possible to understand what these divergences lead to.

To highlight the differences with the higher dimensional case, we will treat the 1d case using the perturbative RG approach, but now taking into account the dimension specific interference between the Cooper and particle–hole channels. However, having belabored the derivation of the perturbative beta function for the higher dimensional case, we will simply write down the result for the 1d case; the reader interested in the details of the derivation is referred to Refs. [296] and [297].

In 1d, there are only two potentially important momentum transfers which scatter electrons at the Fermi surface, as contrasted with the continuum of possibilities in high dimension. It is conventional to indicate by g_1 the interaction with momentum transfer $2k_F$, and by g_2 that with zero momentum transfer. If we are interested in the case of a nearly half filled band, we also

need to keep track of the umklapp scattering, g_3, which involves a momentum transfer 2π to the lattice (see Section 6.5). Consequently, we must introduce a chemical potential, μ, defined such that $\mu = 0$ corresponds to the half filled band. Finally, we consider the retarded interactions, $\tilde{g}_1$, $\tilde{g}_2$, and $\tilde{g}_3$ which operate at frequencies less than ω_D. For simplicity, we consider only the case of spin rotationally invariant interactions.

The one loop RG equations (obtained by evaluating precisely the diagrams in Fig. 6.25), under conditions $\Omega \gg \omega_D, \mu$, are

$$\frac{dg_1}{d\ell} = -\frac{g_1^2}{\pi v_F} , \quad \frac{dg_c}{d\ell} = -\frac{g_3^2}{\pi v_F} , \quad \frac{dg_3}{d\ell} = -\frac{g_3 g_c}{\pi v_F} ,$$

$$\frac{d\tilde{g}_\pm}{d\ell} = -\frac{g_\pm}{\pi v_F}[\frac{3}{2}g_1 \pm g_3 + \frac{1}{2}g_c + \tilde{g}_\pm] , \quad \frac{d\tilde{g}_2}{d\ell} = 0 ,$$

$$\frac{d\mu}{d\ell} = \mu , \quad \frac{d\omega_D}{d\ell} = [1 + \frac{\tilde{g}_+}{\pi v_F}]\omega_D , \tag{6.87}$$

where $g_c \equiv g_1 - 2g_2$ and $\tilde{g}_\pm = \tilde{g}_1 \pm \tilde{g}_3$. For $\mu \gg \Omega \gg \omega_D$, the same equations apply, except now we must set $g_3 = \tilde{g}_3 = 0$. And, of course, if $\omega_D > \Omega$, we simply drop the notion of retarded interactions, altogether. (The electron–phonon interaction in a non–Fermi liquid can be strongly renormalized.)

There are many remarkable qualitative aspects to these equations, many of which differ markedly from the analogous equations in higher dimensions. The most obvious feature is that the retarded interactions are strongly renormalized, even when the states being eliminated have energies large compared to ω_D. What this means is that in one dimension, the effective electron–phonon interaction at low energies is *not* simply related to the microscopic interaction strength. Some of the effects of this strong coupling on the spectral properties of quasi–one dimensional systems can be found in Refs. [297–299].

Away from half filling

To see how this works out, let us consider the typical case in which the nonretarded interactions are repulsive (g_1, and $g_2 > 0$) and the retarded interactions are attractive ($\tilde{g}_\pm < 0$) and strongly retarded, $\omega_D/E_F \ll 1$. Far from half filling, we can also set $g_3 = \tilde{g}_3 = 0$. The presence or absence of a spin gap is determined by the sign of g_1. Thus, just as in the 3d case, in order to derive the effective theory with nonretarded interactions which is appropriate to study the low energy physics at scales small compared to ω_D, we integrate out the fermionic degrees of freedom at scales between E_F and ω_D, and then compute the effective backscattering interaction,

$$g_1^{eff} = g_1(\omega_D) + \tilde{g}_1(\omega_D) . \tag{6.88}$$

If $g_1^{eff} > 0$ (*i.e.* if $g_1(\omega_D) > |\tilde{g}_1(\omega_D)|$), then the Luttinger liquid is a stable fixed point, and in particular no spin gap develops. If $g_1^{eff} < 0$, however, the

Luttinger liquid fixed point is unstable; now, the system flows to a Luther–Emery fixed point with a spin gap which can be determined in the familiar way to be

$$\Delta_s \sim \omega_D \exp[-\pi v_F / g_1^{eff}] \,. \tag{6.89}$$

This looks very much like the BCS result from high dimensions. The parallel with BCS theory goes even a bit further, since under the RG transformation, a repulsive g_1 scales to weaker values in just the same way as the Coulomb pseudopotential in higher dimensions:

$$g_1(\omega_D) = \frac{g_1^0}{1 + (g_1^0/\pi v_F) \log (E_F/\omega_D)} \,, \tag{6.90}$$

where $g_1^0 \equiv g_1(E_F)$. However, in contrast to the higher dimensional case, $\tilde{g}_1$ is strongly renormalized; integrating the one–loop equations, it is easy to show that

$$\tilde{g}_1(\omega_D) = \left(\frac{\tilde{g}_1^0}{1 + \tilde{g}_1^0 L}\right) \left(\frac{g_1(\omega_D)}{g_1^0}\right)^{3/2} \left(\frac{E_F}{\omega_D}\right)^{-g_c/2\pi v_F} \,, \tag{6.91}$$

$$L = \int_0^{\log(E_F/\omega_D)} \frac{dx}{\pi v_F} \frac{\exp[-g_c x/2\pi v_F]}{[1 + (g_1^0/\pi v_F)x]^{3/2}} \,. \tag{6.92}$$

Various limits of this expression can easily be analyzed—we will not give an exhaustive analysis here. For $g_1 = g_c = 0$, Eq. (6.92) reduces to the same logarithmic expression, Eq. (6.90), as for g_1, although because $\tilde{g}_1$ has the opposite sign, the result is a logarithmic *increase* of the effective interaction; this is simply the familiar Peierls renormalization of the electron–phonon interaction. For $g_c < 0$, this renormalization is substantially amplified. Thus, in marked contrast to the higher dimensional case, strong repulsive interactions actually enhance the effects of weak retarded attractions!

Finally, there is bad news as well as good news. As discussed in Section 6.5, the behavior of the charge modes is largely determined by the "charge Luttinger exponent, K_c, which is in turn determined by the effective interaction

$$g_c^{eff} = g_c + \tilde{g}_1^{eff} - 2\tilde{g}_2 \,, \tag{6.93}$$

according to the relation (See Eq. (6.16).)

$$K_c = \sqrt{\frac{1 + (g_c^{eff}/\pi v_F)}{1 - (g_c^{eff}/\pi v_F)}} \,. \tag{6.94}$$

In particular, the relative strength of the superconducting and CDW fluctuations are determined by K_c; the smaller K_c, *i.e.* the more negative g_c^{eff},

the more dominant are the CDW fluctuations. It therefore follows from Eq. (6.93) that a large negative value of $\tilde{g}_1^{eff}$ due to the renormalization of the electron–phonon interaction only throws the balance more strongly in favor of the CDW order. For this reason, most quasi 1D systems with a spin gap are CDW insulators, rather than superconductors.

Half filling

Near half filling, the interference between the retarded and instantaneous interactions becomes even stronger. In the presence of Umklapp scattering, an initially negative g_c renormalizes to stronger coupling, as does g_3 itself. Without loss of generality, we can take $g_3 > 0$ since its sign can be reversed by a change of basis. Then we can see that both g_3 and g_c contribute to an inflationary growth of $\tilde{g}_-$. The RG equations have been integrated in Ref. [300], and we will not repeat the analysis here. The point is that all the effects discussed above apply still more strongly near half filling. In addition, we now encounter an entirely novel phenomenon—we find that the effective electron–phonon interaction strength at energy scale ω_D is strongly doping dependent, as well. It is possible [300], as indeed seems to be the case in the model conducting polymer polyacetylene, for the electron–phonon coupling to be sufficiently strong to open a Peierls gap of magnitude 2eV (roughly, 1/5 of the π–band width) at half filling, and yet be so weak at a microscopic scale that for doping concentrations greater than 5%, no sign of a Peierls gap is seen down to temperatures of order 1K!

How many of the features seen from this study of the 1DEG are specific to one dimensional systems is not presently clear. Conversely, these results prove by example that familiar properties of Fermi liquids cannot be taken as generic. In particular, strongly energy and doping dependent electron phonon interactions are certainly possibilities that should be taken seriously in systems that are not Fermi liquids.

6.10 Lessons from Strong Coupling

In certain special cases, well controlled analytic results can be obtained in the limit in which the bare electron–electron and/or electron–phonon interactions are strong. We discuss several such cases, and in particular we demonstrate a theoretically well established mechanism in one dimension, the "spin gap proximity effect," by which strong repulsive interactions between electrons can result in a large and robust spin gap and strongly enhanced local superconducting correlations. We propose this as the paradigmatic mechanism of high temperature superconductivity.

In certain special cases, well controlled analytic results can be obtained in the limit in which the bare electron–electron interactions are nonperturbative. We discuss several such models.

6.10.1 The Holstein Model of Interacting Electrons and Phonons

The simplest model of strong electron–phonon coupling is the Holstein model of an optic phonon, treated as an Einstein oscillator, coupled to a single tight binding electron band,

$$H_{Hol} = -t \sum_{\langle i,j\rangle,\sigma} [c^{\dagger}_{i,\sigma} c_{j,\sigma} + \text{H.C.}] + \alpha \sum_j x_j \hat{n}_j + \sum_j \left[\frac{P_j^2}{2M} + \frac{K x_j^2}{2} \right] , \quad (6.95)$$

where $\hat{n}_j = \sum_\sigma c^{\dagger}_{j,\sigma} c_{j,\sigma}$ is the electron density operator and P_j is the momentum conjugate to x_j.

In treating the interesting strong coupling physics of this problem, it is sometimes useful to transform this model so that the phonon displacements are defined relative to their instantaneous ground state configuration. This is done by means of the unitary transformation,

$$U = \prod_j \exp[i(\alpha/K) P_j \hat{n}_j] , \quad (6.96)$$

which shifts the origin of oscillation as $U^{\dagger} x_j U = x_j - (\alpha/K)\hat{n}_j$. Consequently, the transformed Hamiltonian has the form

$$U^{\dagger} H_{Hol} U = - t \sum_{\langle i,j\rangle,\sigma} [\hat{S}_{ij} c^{\dagger}_{i,\sigma} c_{j,\sigma} + \text{H.C.}] - \frac{U_{eff}}{2} \sum_j [\hat{n}_j]^2 + \sum_j \left[\frac{P_j^2}{2M} + \frac{K x_j^2}{2} \right] , \quad (6.97)$$

where $\hat{S}_{i,j} = \exp[-i(\alpha/K)(P_i - P_j)]$ and $U_{eff} = \alpha^2/K$.

There are several limits in which this model can be readily analyzed:

Adiabatic limit: $E_F \gg \omega_D$

In the limit $t \gg \omega_D$, where $\omega_D = \sqrt{K/M}$ is the phonon frequency and for α not too large, this is just the sort of model considered in the weak coupling section, or any other conventional treatment of the electron–phonon problem. Here, Migdal's theorem provides us with guidance, and at least for not too strong coupling, the BCS–Eliashberg treatment discussed in Section 6.9 can be applied. While U_{eff} is, indeed, the effective interaction which enters the BCS expression for the superconducting T_c, because the fluctuations of P_i are large if M is large, it is not useful to work with the transformed version of the Hamiltonian.

Inverse adiabatic limit; negative U Hubbard model

In the inverse adiabatic limit, $M \to 0$, fluctuations of P_j are negligible, so that $\hat{S}_{ij} \to 1$. Hence, in this limit, the Holstein model is precisely equivalent to the Hubbard model, but with an effective negative U. If $U_{eff} \ll t$, this is again a weak coupling model, and will yield a superconducting T_c given by

the usual BCS expression, although in this case with a prefactor proportional to t rather than ω_D.

In contrast, if $U_{eff} \gg t$, a strong coupling expansion is required. Here, we first find the (degenerate) ground states of the unperturbed model with $t = 0$, and then perform perturbation theory in small t/U_{eff}. In the zeroth order ground states, each site is either unoccupied, or is occupied by a singlet pair of electrons. The energy of this state is $-U_{eff}N^{el}$, where N^{el} is the number of electrons. These states can be thought of as the states of infinite mass, hard core charge 2e bosons on the lattice. There is a gap to the first excited state of magnitude U_{eff}. Second order perturbation theory in the ground state manifold straightforwardly yields an effective Hamiltonian which is equivalent to a model of hard core bosons ($[b_i^\dagger, b_j] = \delta_{i,j}$)

$$H_{boson} = -t_{eff} \sum_{\langle i,j \rangle} [b_i^\dagger b_j + \text{H.C.}] + V_{eff} \sum_{\langle i,j \rangle} b_i^\dagger b_i b_j^\dagger b_j + [\infty] \sum_j b_j^\dagger b_j [b_j^\dagger b_j - 1] \,, \tag{6.98}$$

with nearest neighbor hopping $t_{eff} = 2t^2/U_{eff}$ and nearest neighbor repulsion $V_{eff} = 2t_{eff}$. This effective model is applicable for energies and temperatures small compared to U_{eff}. (Clearly, $\tilde{b}_j \equiv c_{j\uparrow}c_{j\downarrow}$ does not satisfy the same–site piece of the bosonic commutation relation, but the hard core constraint on the b_j bosons corrects any errors introduced by neglecting this.)

The properties of this bosonic Hamiltonian, and closely related models where additional interactions between bosons are included, have been widely studied [301, 302]. It has a large number of possible phases, including superconducting, crystalline, and striped or liquid crystalline phases. The equivalence between hard core bosons and spin–1/2 operators can be used to relate this model to various spin models that have been studied in their own right. However, for the present purposes, there are two clear lessons we wish to draw from this exercise. The first is that there are ordered states, in particular insulating charge ordered states, which can compete very successfully with the superconducting state in strong coupling. The second is that, even if the system does manage to achieve a superconducting ground state, the characteristic superconducting T_c will be proportional to t_{eff}, and hence to the small parameter, t/U_{eff}. In summary, strong attractions impede coherent motion, and enhance charge ordering.

Large U_{eff}: bipolarons

More generally, in the strong coupling limit, $U_{eff} \gg t$, a perturbative approach in powers of t/U_{eff} can be undertaken, regardless of the value of M. Once again, the zeroth order ground states are those of charge $2e$ hard core bosons, as in Eq. (6.98). However, now the phonons make a contribution to the ground state—the ground state energy is $-U_{eff}N^{el} + (1/2)\omega_D N$ where N is the number of sites, and the gap to the first excited state is the smaller of U_{eff} and ω_D. Still, we can study the properties of the model at energies and temperatures small compared to the gap in terms of the hard core bosonic

model. Now, however,

$$t_{eff} = 2\frac{t^2}{U_{eff}} F_+(X) \ ,$$
$$V_{eff} = 4\frac{t^2}{U_{eff}} F_-(X) \ , \tag{6.99}$$

where $X \equiv \frac{U_{eff}}{\omega_D}$ and

$$F_\pm(X) = \int_0^\infty dt \exp\{-t - X[1 \pm \exp(-t/X)]\} \ . \tag{6.100}$$

This is often referred to as a model of bipolarons. In the inverse adiabatic limit, $F_\pm(X) \to 1$ as $X \to 0$, and hence these expressions reduce to those of the previous subsection. However, in the adiabatic limit, $X \gg 1$, $F_+(X) \sim e^{-2X}$, so t_{eff} is exponentially reduced by a Frank–Condon factor! However, $F_-(X) \to 1$ as $X \to \infty$, so V_{eff} remains substantial. Clearly, the lessons concerning the difficulty of obtaining high temperature superconductivity from strong coupling drawn from the negative U Hubbard model apply even more strongly to the case in which the phonon frequency is small. A bipolaron mechanism of superconductivity is simply impossible unless the phonon frequency is greater than or comparable to U_{eff}; in the opposite limit, the exponential suppression of t_{eff} relative to the effective interactions, V_{eff}, strongly suppresses the coherent Bose–condensed state, and favors various types of insulating, charge ordered states.

6.10.2 Insulating Quantum Antiferromagnets

We now turn to models with repulsive interactions. To begin with, we discuss the "Mott limit" of the antiferromagnetic insulating state. Here, we imagine that there is one electron per site, and such strong interactions between them that charge fluctuations can be treated petrubatively. In this limit, as is well known, the only low energy degrees of freedom involve the electron spins, and hence the problem reduces to that of an effective quantum Heisenberg antiferromagnet.

Quantum antiferromagnets in more than one dimension

In recent years, there has been considerable interest [77,80,81,214,231–233, 303,304] in the many remarkable quantum states that can occur in quantum spin models with sufficiently strong frustration—these studies are beyond the scope of the present review. On a hypercubic lattice (probably on any simple, bipartite lattice) and in dimension 2 or greater, there is by now no doubt that even the spin 1/2 model (in which quantum fluctuations are the most severe) has a Nèel ordered ground state [223]. Consequently, the properties of such systems at temperatures and energies low compared to the antiferromagnetic exchange energy, J, are determined by the properties of interacting

spin waves. This physics, in turn, is well described in terms of a simple field theory, known as the $O(3)$ nonlinear sigma model. While interesting work is still ongoing on this problem, it is in essence a solved problem, and excellent modern reviews exist [305].

In its ordered phase, the antiferromagnet has: i) gapless spin wave excitations, and ii) reduced tendency to phase ordering due to the frustration of charge motion. Since the superconducting state possesses a spin gap (or, for d–wave, a partial gap) and is characterized by the extreme coherence of charge motion, it is clear that both these features of the antiferromagnet are disadvantageous for superconductivity. (There is a very interesting line of reasoning [156] which takes the opposite viewpoint: it is argued that the important point to focus on is that both the superconductor and the antiferromagnet have gapless Goldstone modes, not whether those modes are spinless or spinful. In this line of thought there is a near symmetry, which turns out to be SO(5), between the d–wave superconducting and the Néel ordered antiferromagnetic states. This is an attractive notion, but it is not clear to us precisely how this line of reasoning relates to the more microscopic considerations discussed here.)

There is a body of thought [29–32] that holds that it is possible, at sufficiently strong doping of an antiferromagnet to reach a state in which the antiferromagnetic order and the consequent low energy spin fluctuations are eliminated and electron itineracy is restored, which yet has vestiges of the high energy spin wave excitations of the parent ordered state that can serve to induce a sufficiently strong effective attraction between electrons for high temperature superconductivity. Various strong critiques of this approach have also been articulated [18]. in a nearly antiferromagnetic electron fluid is critiqued. We feel that the theoretical viability of this "spin fluctuation exchange" idea has yet to be firmly established. As an example of how this could be done, one could imagine studying a two component system consisting of a planar, Heisenberg antiferromagnet coupled to a planar Fermi liquid. One would like to see that, as some well articulated measure of the strength of the antiferromagnetism is increased, the superconducting pairing scale likewise increases. If such a system could be shown to be a high temperature superconductor, it would establish the point of principal. However, it has been shown by Schrieffer [67] that Ward identities, which are ultimately related to Goldstone's theorem, imply that long wavelength spin waves cannot produce any pairing interaction at all. A model of this sort that has been analyzed in detail is the one dimensional Kondo–Heisenberg model, which is the 1D analogue of this system [306–308]. This system does not exhibit significant superconducting fluctuations of any conventional kind. While there certainly does not exist a "no–go" theorem, it does not seem likely to us that an exchange of spin waves in a nearly anitferromagnetic system can ever give rise to high temperature superconductivity. (Under circumstances in which antiferromagnetic correlations are very short ranged, it may still be possible

to think of an effective attraction between electrons mediated by the exchange of very local spin excitations [31]. This escapes most of the critiques discussed above—neither Ward identities nor the general incompatibility between antiferromagnetism and easy electron itineracy have any crisp meaning at short distances. By the same token, however, it is not easy to unambiguously show that such short range magnetic correlations are the origin of strong superconducting correlations in any system, despite some recent progress along these lines [309].)

Spin gap in even leg Heisenberg ladders

The physics of quantum antiferromagnets in one dimension is quite different from that in higher dimension, since the ground state is not magnetically ordered. However, its general features have been well understood for many years. In particular, for spin–1/2 Heisenberg ladders or cylinders with an even number of sites on a rung, quantum fluctuations result in a state with a spin gap. This is a special case of a general result [310], known as "Haldane's conjecture," that any 1D spin system with an even integer number of electrons per unit cell has a spin rotationally invariant ground state and a finite spin gap in the excitation spectrum. This conjecture has not been proven, but has been validated in many limits and there are no known exceptions. (One can hardly fail to notice that the Haldane conjecture is closely related to the conventional band structure view that insulators are systems with a gap to both charge and spin excitations due to the fact that there are an even number of electrons per unit cell and all bands are either full or empty.)

The physics of interacting electrons on ladders—*i.e.* "fat" 1D systems, will be discussed at length below. We believe this is an important, paradigmatic system for understanding the physics of high temperature superconductivity. The fact that even the undoped (insulating) ladder has a spin gap can be interpreted as a form of incipient superconducting pairing. Where that gap is large, *i.e.* a substantial fraction of the exchange energy, J, it is reasonable to hope that doping it will lead to a conducting state which inherits from the parent insulating state this large gap, now directly interpretable as a pairing gap.

Let us start by considering an N leg spin–1/2 Heisenberg model

$$H = \sum_{\langle i,j \rangle} J_{ij} \boldsymbol{S}_i \cdot \boldsymbol{S}_j \ , \tag{6.101}$$

where $\boldsymbol{S}_i$ is the spin operator on site i, so for $a, b, c = \{x, y, z\}$, $[S_i^a, S_j^b] = i\delta_{ij}\epsilon^{abc}S_i^c$ and $\boldsymbol{S}_i \cdot \boldsymbol{S}_i = 3/4$. Here, we still take the lattice to be infinite in one ("parallel") direction but of width N sites in the other. At times, we will distinguish between a ladder, with open boundary conditions in the "perpendicular" direction, and a cylinder, with periodic boundary conditions in this direction. We will typically consider isotropic antiferromagnetic couplings, $J_{ij} = J > 0$.

Ladders with many legs

In the limit of large N, it is clear that the model can be viewed as a two dimensional antiferromagnet up to a crossover scale, beyond which the asymptotic one dimensional behavior is manifest. This viewpoint was exploited by Chakravarty [311] to obtain a remarkably accurate analytic estimate of the crossover scale. His approach was to first employ the equivalence between the Heisenberg model and the quantum nonlinear sigma model. One feature of this mapping is that the thermodynamic properties of the d dimensional Heisenberg model are related to a $d+1$ dimensional sigma model, with an imaginary time direction which, by suitable rescaling, is *precisely* equivalent to any of the spatial directions. The properties of the Heisenberg model at finite temperatures are then related to the sigma model on a generalized cylinder, which is periodic in the imaginary time direction with circumference $\hbar v_s/T$ where v_s is the spin wave velocity. What Chakravarty pointed out is that, through this mapping, there is an equivalence between the Heisenberg cylinder with circumference $L = Na$ at zero temperature and the infinite planar Heisenberg magnet at temperature, $T = v_s/L$. From the well known exponential divergence of the correlation length with decreasing temperature in the 2d system, he obtained the asymptotic expression for the dimensional crossover length in the cylinder,

$$\xi_{dim} \sim a \exp[0.682N] \; . \tag{6.102}$$

As this estimate is obtained from the continuum theory, it is only well justified in the large N limit. However, comparison with numerical experiments described in Section 6.11 (some of which predated the analytic theory [312]) reveal that it is amazingly accurate, even for $N = 2$, and that the distinction between ladders and cylinders is not very significant, either.

This result is worth contemplating. It implies that the special physics of one dimensional magnets is only manifest at exponentially long distances in fat systems. Correspondingly, it means that these effects are confined to energies (or temperatures) smaller than the characteristic scale

$$\Delta_{dim} = v_s/\xi_{dim} \; . \tag{6.103}$$

As a practical matter, it means that only the very narrowest systems, with N no bigger than 3 or 4, will exhibit the peculiarities of one dimensional magnetism at any reasonable temperature.

To understand more physically what these crossover scales mean, one needs to know something about the behavior of one dimensional magnets. Since even leg ladders and cylinders have a spin gap, it is intuitively clear (and correct) that Δ_{dim} is nothing but the spin gap and ξ_{dim} the correlation length associated with the exponential fall of magnetic correlations at $T = 0$. For odd leg ladders, ξ_{dim} is analogous to a Josephson length, where correlations crossover from the two dimensional power law behavior associated with the

existence of Goldstone modes, to the peculiar quantum critical behavior of the one dimensional spin 1/2 Heisenberg chain.

The two leg ladder

It is often useful in developing intuition to consider limiting cases in which the mathematics becomes trivial, although one must always be sensitive to the danger of being overly influenced by the naive intuitions that result.

In the case of the two leg ladder, there exists such a limit, $J_\perp \gg J_\parallel$, where $J_\perp$ and $J_\parallel$ are, respectively, the exchange couplings across the rungs, and along the sides of the ladder. Here the zeroth order ground state is a direct product of singlet pairs (valence bonds) on the rungs of the ladder. Perturbative corrections to the ground state cause these valence bonds to resonant, locally, but do not fundamentally affect the character of the ground state. The ground state energy per site is

$$E_0 = -(3/8)J_\perp[1 + (J_\parallel/J_\perp)^2 + \ldots] \,. \tag{6.104}$$

Since each valence bond is nothing but a singlet pair of electrons, this makes it clear that there is a very direct sense in which the two leg ladder can be thought of as a paired insulator. The lowest lying spin–1 excited states are a superposition of bond triplets on different rungs, and have a dispersion relation which can easily be derived in perturbation theory:

$$E_{triplet} = J_\perp + J_\parallel \cos(k) + \mathcal{O}(J_\parallel^2/J_\parallel) \,. \tag{6.105}$$

This, too, reveals some features that are more general, such as a minimal spin gap of magnitude $\Delta_s = J_\perp[1 - (J_\parallel/J_\perp) + \mathcal{O}(J_\parallel^2/J_\parallel^2)]$ at what would be the antiferromagnetic ordering wavevector $k = \pi$.

6.10.3 The Isolated Square

While we are considering mathematically trivial problems, it is worth taking a minute to discuss the solution of the t–J model (defined in Eq. (6.119), below) on an isolated 4–site square. The pedagogic value of this problem, which is exactly diagonalizable, was first stressed by Trugman and Scalapino [313]. This idea was recently carried further by Auerbach and collaborators [314, 315], who have attempted to build a theory of the 2D t–J model by linking together fundamental squares. The main properties of the lowest energy states of this system are given in Table 5.2 for any number of doped holes.

The "undoped" state of this system (*i.e.* with 4 electrons) is a singlet with ground state energy $E_0 = -3J$. However, interestingly, it is not in the identity representation of the symmetry group of the problem—it is odd under 90° rotation. If we number the sites of the square sequentially from 1 to 4, then the ground state wavefunction is

$$|4 - electron\rangle = [\hat{P}^\dagger_{1,2}\hat{P}^\dagger_{3,4} - \hat{P}^\dagger_{1,4}\hat{P}^\dagger_{2,3}]|0\rangle \,, \tag{6.106}$$

Table 6.2. The low energy spectrum of the 4–site t–J square for 0 holes (4 electrons), 1 hole (3 electrons), and 2 holes (2 electrons).

0 holes

	Energy	Spin	Momentum
g.s.	$E=-3J$	$S=0$	$P=\pi$
1^{st} e.s.	$E=-2J$	$S=1$	$P=0$

1 hole

	Energy	Spin	Momentum
$0<J/t<0.263$			
g.s.	$E=-2t$	$S=3/2$	$P=0$
1^{st} e.s.	$E=-J-\sqrt{J^2/4+3t^2}$	$S=1/2$	$P=\pm\pi/2$
$0.263<J/t<2/3$			
g.s.	$E=-J-\sqrt{J^2/4+3t^2}$	$S=1/2$	$P=\pm\pi/2$
1^{st} e.s.	$E=-2t$	$S=3/2$	$P=0$
$2/3<J/t<2$			
g.s.	$E=-J-\sqrt{J^2/4+3t^2}$	$S=1/2$	$P=\pm\pi/2$
1^{st} e.s.	$E=-3J/2-t$	$S=1/2$	$P=\pi$
$2<J/t$			
g.s.	$E=-3J/2-t$	$S=1/2$	$P=\pi$
1^{st} e.s.	$E=-J-\sqrt{J^2/4+3t^2}$	$S=1/2$	$P=\pm\pi/2$

2 holes

	Energy	Spin	Momentum
$0<J/t<2$			
g.s.	$E=-J/2-\sqrt{J^2/4+8t^2}$	$S=0$	$P=0$
1^{st} e.s.	$E=-2t$	$S=1$	$P=\pm\pi/2$
$2<J/t$			
g.s.	$E=-J/2-\sqrt{J^2/4+8t^2}$	$S=0$	$P=0$
1^{st} e.s.	$E=-J$	$S=0$	$P=\pi,\pm\pi/2$

where $\hat{P}^\dagger_{i,j}=\hat{P}^\dagger_{j,i}=[c^\dagger_{i,\uparrow}c^\dagger_{j,\downarrow}+c^\dagger_{j,\uparrow}c^\dagger_{i,\downarrow}]/\sqrt{2}$ creates a singlet pair of electrons on the bond between sites i and j. Manifestly, $|4-electron\rangle$ has the form of an odd superposition of nearest neighbor valence bond states—in this sense, it is the quintessential resonating valence bond state. The lowest lying excitation is a spin–1 state with energy $-2J$, so the spin gap is J.

There are level crossings as a function of J/t in the "one hole" (3 electron) spectrum. For $0<J/t<(8-\sqrt{52})/3\approx 0.263$ the ground state is a spin 3/2 multiplet with energy $E_1=-2t$. It is orbitally nondegenerate with zero momentum (we consider the square as a 4–site chain with periodic boundary conditions and refer to the momentum along the chain.) For $(8-\sqrt{52})/3<J/t<2$ the ground state has spin 1/2, is two–fold degenerate with crystal

momentum $\pm\pi/2$, and has energy $E_1 = -[2J + \sqrt{J^2 + 12t^2}]/2$. For $2 < J/t$, the ground state has spin 1/2, zero momentum, and energy $E_1 = -3J/2 - t$.

The two hole (2 electron) ground state has energy $E_2 = -[J + \sqrt{J^2 + 32t^2}]/2$, and spin 0. It lies in the identity representation of the symmetry group. The lowest excitation is a spin 1 state. For $0 < J/t < 2$ it has crystal momentum $k = \pm\pi/2$ (*i.e.* it has a two–fold orbital and 3–fold spin degeneracy) and has energy $E_2(S = 1) = -2t$. For $2 < J/t$ it is orbitally nondegenerate with energy $E_2(S = 1) = -J$.

One important consequence of this, which follows directly from the Wigner–Eckhart theorem, is that the pair annihilation operator that connects the zero hole and the two hole ground states must transform as $d_{x^2-y^2}$. This is, perhaps, the most important result of this exercise. It shows the robustness of the d wave character of the pairing in a broad class of highly correlated systems. The dominant component of this operator is of the form

$$\phi_1 = \hat{P}_{12} - \hat{P}_{23} + \hat{P}_{34} - \hat{P}_{41}. \tag{6.107}$$

It also includes terms that create holes on next nearest neighbor diagonal sites [316, 317].

There are a few other interesting aspects of this solution. In the single hole sector, the ground state is maximally polarized, in agreement with Nagaoka's theorem, for sufficiently large t/J, but there is a level crossing to a state with smaller spin when t/J is still moderately large. Moreover, even when the single hole state is maximally polarized, the two hole state, like the zero hole state, is always a spin singlet. Both of these features have been observed in numerical studies on larger t–J clusters [318].

If we look still more closely at the $J/t \to 0$ limit, there is another interesting aspect of the physics: It is intuitively clear that in this limit, the holes should behave as spinless fermions. This statement requires no apology in the maximum spin state. Thus, the lowest energy spin–1 state with two holes has energy $E_2(S = 1) = -2t$ in this limit. It corresponds to a state in which one spinless fermion has crystal momentum $k = 0$ and energy $-2t$, and the other has crystal momentum $\pm\pi/2$ and energy 0. However, what is more interesting is that there is also a simple interpretation of the two hole ground state in the same representation. The antisymmetry of the spins in their singlet state means that they affect the hole dynamics through a Berry's phase as if half a magnetic flux quantum were threaded through the square. This Berry's phase implies that the spinless fermions satisfy antiperiodic boundary conditions. The ground state is thus formed by occupying the single particle states with $k = \pm\pi/4$ for a total ground state energy of $E_2 = -2\sqrt{2}t$, precisely the $J/t \to 0$ limit of the expression obtained above. The interesting thing is that, in this case, it is the hole kinetic energy, and *not* the exchange energy, which favors the singlet over the triplet state. This simple exercise provides an intuitive motivation for the existence of various forms of "flux phase" in strongly interacting systems [319].

Finally, it is worth noting that pair binding occurs, in the sense that $2E_1 - E_0 - E_2 > 0$, so long as $J/t > \sqrt{(39 - \sqrt{491})/\sqrt{3}} \approx 0.2068$. We will return to the issue of pair binding in Section 6.11 where we will show a similar behavior in Hubbard and t–J ladders.

6.10.4 The spin gap Proximity Effect Mechanism

The final strong coupling model we will consider consists of two inequivalent 1DEG's weakly coupled together—a generalization of a two leg ladder. Each 1DEG is represented by an appropriate bosonized field theory—either a Luttinger liquid or a Luther–Emery liquid. Most importantly, the two systems are assumed to have substantially different values of the Fermi momentum, k_F and $\tilde{k}_F$. We consider the case in which the interactions between the two systems are weak, but the interactions within each 1DEG may be arbitrarily large. The issue we address is what changes in the properties of the coupled system are induced by these interactions. (For all technical details, see Refs. [20] and [25].)

There is an important intuitive reason to expect this system to exhibit a novel form of kinetic energy driven superconducting pairing. Because $k_F \neq \tilde{k}_F$, single particle tunnelling between the two 1DEG's is not a low energy process—it is irrelevant in the renormalization group sense, and can be ignored as anything but a high energy virtual fluctuation. The same conclusion holds for any weak coupling between the $2k_F$ or $4k_F$ density wave fluctuations. There are only two types of coupling that are potentially important at low energies: pair tunnelling, since the relevant pairs have 0 momentum, and coupling between long wavelength spin fluctuations.

The magnetic interactions are marginal to leading order in a perturbative RG analysis—they turn out to be marginally relevant if the interactions are antiferromagnetic and marginally irrelevant if ferromagnetic [306, 308]. The effect of purely magnetic interactions has been widely studied in the context of Kondo–Heisenberg chains, but will not be discussed here. The effect of triplet pair tunnelling has only been superficially analyzed in the literature [25, 320, 321]—it would be worthwhile extending this analysis, as it may provide some insight into the origin of the triplet superconductivity that has been observed recently in certain highly correlated materials. However, in the interest of brevity, we will ignore these interactions.

Singlet pair tunnelling interactions between the two 1DEG's have a scaling dimension which depends on the nature of the correlations in the decoupled system. Under appropriate circumstances, they can be relevant. When this is the case, the coupled system scales to a new strong coupling fixed point which exhibits a total spin gap and strong global superconducting fluctuations. This is what we refer to as the spin gap proximity effect, because the underlying physics is analogous to the proximity effect in conventional superconductors. The point is that even if it is energetically costly to form pairs in one or

both of the 1DEGs, once the pairs are formed they can coherently tunnel between the two systems, thereby lowering their zero point kinetic energy. Under appropriate circumstances, the kinetic energy gain outweighs the cost of pairing. This mechanism is quite distinct from any relative of the BCS mechanism—it does not involve an induced attraction.

The explicit model which is analyzed here is expressed in terms of four bosonic fields: ϕ_c and ϕ_s represent the charge and spin degrees of freedom of the first 1DEG, and $\tilde{\phi}_c$ and $\tilde{\phi}_s$ of the other, as is discussed in Section 6.5, above. The Hamiltonian of the decoupled system is the general bosonized Hamiltonian described in that section, with appropriate velocities and charge Luttinger exponents, v_s, v_c, $\tilde{v}_s$, $\tilde{v}_c$, K_c, and $\tilde{K}_c$ if both are Luttinger liquids, and values of the spin gap, Δ_s and $\tilde{\Delta}_s$ in the case of Luther–Emery liquids (*i.e.* if the cosine potential in the sine–Gordon theory for the spin degrees of freedom is relevant). If we ignore the long wavelength magnetic couplings and triplet pair tunnelling between the two systems, the remaining possibly important interactions at low energy,

$$H_{inter} = \int dx[\mathcal{H}_{for} + \mathcal{H}_{pair}] \,, \tag{6.108}$$

are the forward scattering (density–density and current–current) interactions in the charge sector

$$\mathcal{H}_{for} = V_1 \partial_x \phi_c \partial_x \tilde{\phi}_c + V_2 \partial_x \theta_c \partial_x \tilde{\theta}_c \,, \tag{6.109}$$

where θ designates the field dual to ϕ (see Section 6.5), and the singlet pair tunnelling

$$\mathcal{H}_{pair} = \mathcal{J} \cos[\sqrt{2\pi}\phi_s] \cos[\sqrt{2\pi}\tilde{\phi}_s] \cos[\sqrt{2\pi}(\theta_c - \tilde{\theta}_c)] \,. \tag{6.110}$$

As discussed previously, the singlet pair creation operator involves both the spin and the charge fields.

The forward scattering interactions are precisely marginal, and should properly be incorporated in the definition of the fixed point Hamiltonian. $\mathcal{H}_{pair}$ is a nonlinear interaction; the coupled problem with nonzero $\mathcal{J}$ has not been exactly solved. However, it is relatively straightforward to asses the perturbative relevance of this interaction, and to deduce the properties of the most likely strong coupling fixed point (large $\mathcal{J}$) which governs the low energy physics when it is relevant.

The scaling dimension of the pair tunnelling interaction is introduced. The general expression for the scaling dimension of $\mathcal{H}_{pair}$ is a complicated analytic combination of the parameters of the decoupled problem

$$\delta_{pair} = \frac{1}{2}\left[\frac{A}{K_c} + \frac{B}{\tilde{K}_c} + K_s + \tilde{K}_s\right] \,, \tag{6.111}$$

where $A = 1$ and $B = 1$ in the absence of intersystem forward scattering interactions, but more generally A and B are complicated functions of the coupling

constants. For illustrative purposes, one can consider the explicit expression for these functions under the special circumstances $V_2 = -(\tilde{v}_c/v_c)(K_c\tilde{K}_c)V_1$; then $A = \sqrt{1 - (V_1^2 K_c\tilde{K}_c/v_c\tilde{v}_c)}$ and $B = (v_c - V_1 K_c)^2/\sqrt{v_c^4 - V_1^2 v_c\tilde{v}_c K_c\tilde{K}_c}$. Here, if both 1DEG's are Luttinger liquids, spin rotational invariance implies that $K_s = \tilde{K}_s = 1$. If one or the other 1DEG is a Luther–Emery liquid, one should substitute $K_s = 0$ or $\tilde{K}_s = 0$ in the above expression.

Pair tunnelling is perturbatively relevant if $\delta_{pair} < 2$, and irrelevant otherwise. Clearly, having a preexisting spin gap in either of the 1DEG's dramatically decreases δ_{pair}—if there is already pairing in one subsystem, then it stands to reason that pair tunnelling will more easily produce pairing in the other. However, even if neither system has a preexisting spin gap, there are a wide set of physical circumstances for which $\delta_{pair} < 2$. Notice, in particular, that repulsive intersystem interactions, $V_1 > 0$, produce a reduction of δ_{pair}. Again, the physics of this is intuitive—an induced anticorrelation between regions of higher than average electron density in the two 1DEG's means that where there is a pair in one system, there tends to be a low density region on the other which is just waiting for a pair to tunnel into it. (See, also, Section 6.6.)

In the limit that $\mathcal{J}$ is large, the spin fields in both 1DEG's are locked, which implies a total spin gap, and the out–of–phase fluctuations of the dual charge phases are gapped as well. This means that the only possible gapless modes of the system involve the total charge phase, $\phi \equiv [\phi_c + \tilde{\phi}_c]/\sqrt{2}$, and its dual, $\theta \equiv [\theta_c + \tilde{\theta}_c]/\sqrt{2}$. θ is simply the total superconducting phase of the coupled system, and ϕ the total CDW phase. At the end of the day, this strong coupling fixed point of the coupled system is a Luther–Emery liquid, and consequently has a strong tendency to superconductivity. In general, there will be substantial renormalization of the effective parameters as the system scales from the weak to the strong coupling fixed point. Thus, it is difficult to estimate the effective Luttinger parameters which govern the charge modes of the resulting Luther–Emery liquid. A naive estimate, which may well be unreliable, can be be made by simply setting $\mathcal{J} \to \infty$. In this case, all the induced gaps are infinite, and the velocity and Luttinger exponent that govern the dynamics of the remaining mode are

$$K_c^{total} = \sqrt{\frac{v_c K_c + \tilde{v}_c\tilde{K}_c + 2V_2}{v_c/K_c + \tilde{v}_c/\tilde{K}_c + 2V_1}}\,, \tag{6.112}$$

$$v_c^{total} = \frac{1}{4}\sqrt{[v_c K_c + \tilde{v}_c\tilde{K}_c + 2V_2][v_c/K_c + \tilde{v}_c/\tilde{K}_c + 2V_1]}\,.$$

6.11 Lessons from Numerical Studies of Hubbard and Related Models

The careful use of numerical studies to understand the physics on scales relevant to the mechanism of high temperature superconductivity is advocated.

High temperature superconductivity is a result of strong electronic correlations. Couple this prevailing thesis with the lack of controlled analytic methods for most relevant models, and the strong motivation for numerical approaches becomes evident. Such numerical studies are limited to relatively small systems, due to a rapid growth in complexity with system size. However, many of the interesting aspects of the high temperature superconductors, especially those which relate to the "mechanism" of pairing, are moderately local, involving physics on the length scale of the superconducting coherence length ξ. Since ξ is typically a few lattice spacings in the high T_c compounds, one expects that numerical solutions of model problems on clusters with as few as 50–100 sites should be able to reveal the salient features of high temperature superconductivity, if it exists in these models. Moreover, numerical studies can guide our mesoscale intuition, and serve as important tests of analytic predictions.

Notwithstanding these merits, a few words of caution are in order. Even the largest systems that have been studied so far[4] are still relatively small. Therefore, the results are manifestly sensitive to the shape and size of the cluster and other finite size effects. Some features, especially with regard to stripes, appear particularly sensitive to small changes in the model such as the presence of second neighbor hopping, [325, 326], the type of boundary conditions [327], *etc.* Less subtle modifications seem to have important consequences, too [330], most notably the inclusion of long range Coulomb forces (although this has been much less studied). This sensitivity has resulted in considerable controversy in the field concerning the true ground state phase diagrams of the stated models in the thermodynamic limit; see Refs. [327–329] and [331], among others.

The best numerical data, especially in terms of system size, exists for narrow Hubbard and t–J ladders. We therefore begin by considering them. Apart from their intrinsic appeal, these systems also offer several lessons which we believe are pertinent to the two dimensional models. The second part of this section provides a brief review of the conflicting results and views which have emerged from attempts to extrapolate from fat ladders and small periodic clusters to the entire plane.

What do we learn from numerical studies? We feel that numerical studies are *essential* in order to explore the important mesoscale physics of highly

[4] The largest are about 250 sites [322,323] using the density matrix renormalization group method (DMRG) and up to approximately 800 sites in Green function Monte Carlo simulations. [324]

correlated systems, but except in the few cases where a careful finite size scaling analysis has been possible over a wide range of system sizes, conclusions concerning the long distance physics should be viewed as speculative. Even where the extrapolation to the thermodynamic limit has been convincingly established for a given model, the established fact that there are so many closely competing phases in the strong correlation limit carries with it the corollary that small changes in the Hamiltonian can sometimes tip the balance one way or the other. Thus, there are significant limitations concerning the conclusions that can be drawn from numerical studies. In the present section we focus on the reproducible features of the local correlations that follow robustly from the physics of strong, short ranged repulsions between electrons, paying somewhat less attention to the various controversies concerning the actual phase diagram of this or that model.

We entirely omit any discussion of the technical details of the numerical calculations. Methods that have been used include exact diagonalization by Lanczos techniques, Monte Carlo simulations of various sorts, numerical renormalization group approaches, and variational ansatz. The reader who is interested in such aspects is invited to consult Refs. [332–337].

6.11.1 Properties of Doped Ladders

Ladder systems, that is, quasi–one dimensional systems obtained by assembling chains one next to the other, constitute a bridge between the essentially understood behavior of strictly one dimensional models and the incompletely understood behavior in two dimensions. Such systems are not merely a theoretical creation but are realized in nature [338, 339]. For example, two leg $S = 1/2$ ladders (two coupled spin-1/2 chains) are found in vanadyl pyrophosphate $(VO)_2P_2O_7$. Similarly, the cuprate compounds $SrCu_2O_3$ and $Sr_2Cu_3O_5$ consist of weakly coupled arrays of 2–leg and 3–leg ladders, respectively. It is likely that ladder physics is also relevant to the high temperature superconductors, at least in the underdoped regime, where ample experimental evidence exists for the formation of self–organized stripes.

In this section we review some of the most prominent features of Hubbard and especially t–J ladders. As we shall see the data offers extensive support in favor of the contention that a purely electronic mechanism of superconductivity requires mesoscale structure [14]. Specifically, we will find that spin gap formation and pairing correlations, with robust d–wave–like character, are intimately connected. Both of these signatures of local superconductivity appear as distinct and universal features in the physics of doped ladders. Nevertheless, they tend to diminish, in some cases very rapidly, with the lateral extent of the ladder, thus strongly suggesting that such structures are *essential* for the attainment of high temperature superconductivity. In addition we shall demonstrate the tendency of these systems to develop charge density wave correlations upon doping; it is natural to imagine that as the trans-

verse width of the ladder tends to infinity, these density wave correlations will evolve into true two dimensional stripe order.

Spin gap and pairing correlations: Hubbard chains

The purely one dimensional Hubbard model can be solved exactly using Bethe ansatz [340, 341] and thus may seem out of place in this section. However, like other models in this section, it is a lattice fermion model. In analyzing it, we will encounter many of the concepts that will figure prominently in our discussion of the other models treated here, most notably the importance of intermediate scales. Anyway, in many cases, the Bethe ansatz equations themselves must be solved numerically, so we can view this as simply a more efficient numerical algorithm which permits us to study larger systems (up to 1000 sites [14] or more).

The Hubbard Hamiltonian is

$$H_U = -t \sum_{\langle i,j \rangle, s} (c^\dagger_{i,s} c_{j,s} + h.c.) + U \sum_i n_{i,\uparrow} n_{i,\downarrow} \,, \tag{6.113}$$

where $\langle\ \rangle$ denotes nearest neighbors on a ring with an even number of sites N and $N+Q$ electrons. We define $E(Q,S)$ to be the lowest lying energy eigenvalue with total spin S and "charge" Q. Whenever the ground state is a spin singlet we can define the spin gap Δ_s as the energy gap to the lowest $S=1$ excitation

$$\Delta_s(Q) = E(Q,1) - E(Q,0) \,. \tag{6.114}$$

The pair binding energy is defined as

$$E_{pb}(Q) = 2E(Q+1) - E(Q+2) - E(Q) \,, \tag{6.115}$$

where $E(Q)$ has been minimized with respect to S. A positive pair binding energy means that given $2(N+Q+1)$ electrons and two clusters, it is energetically more favorable to place $N+Q+2$ electrons on one cluster and $N+Q$ on the other than it is to put $N+Q+1$ electrons on each cluster. In this sense, a positive E_{pb} signifies an effective *attraction* between electrons. The exact particle–hole symmetry of the Hubbard model on a bipartite lattice implies that electron doping $Q>0$ is equivalent to hole doping $Q<0$.

Fig. 6.26 displays the pair binding energy for electrons added to $Q=0$ rings. The role of intermediate scales (scales play an important role) is apparent: E_{pb} vanishes for large N and is maximal at an intermediate value of N. (The fact that pair binding occurs for $N=4n$ rings but not when $N=4n+2$ is readily understood from low order perturbation theory in U/t [14]). Moreover, the spin gap Δ_s reaches a maximum at intermediate interaction strength, and then decreases for large values of U, as expected from its proportionality to the exchange constant $J=4t^2/U$ in this limit. The pair binding energy E_{pb} follows suit with a similar dependence, as seen from Fig. 6.27.

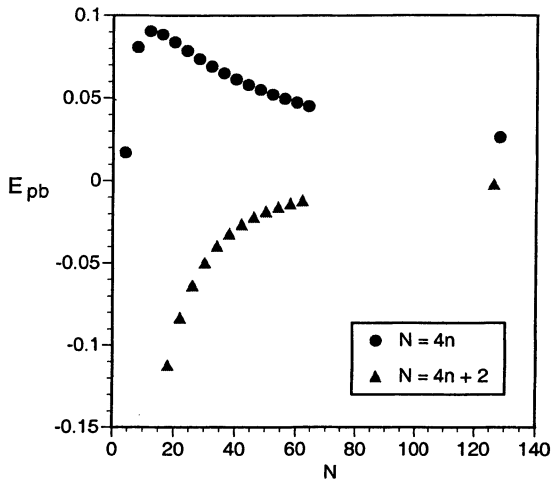

Fig. 6.26. Pair binding energy, E_{pb}, of $N = 4n$ and $N = 4n + 2$ site Hubbard rings with $t = 1$ and $U = 4$ (from Chakravarty and Kivelson [14])

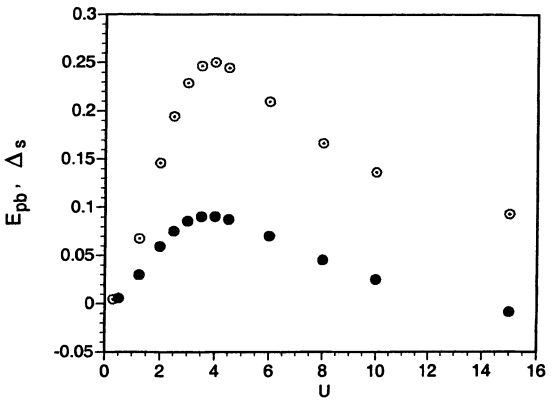

Fig. 6.27. Pair binding energy, E_{pb} (solid symbols), and spin gap, Δ_s (open symbols), of a 12 site $Q = 0$ Hubbard ring as a function of U in units of $t = 1$ (from Chakravarty and Kivelson [14])

We have already seen the intimate relation between the spin gap and the superconducting susceptibility in the context of quasi–one dimensional superconductors (see Section 6.5). Further understanding of the relation between pair binding and the spin gap can be gained by using bosonization to study the Hubbard model in the large N limit [14,341]. The result for $N = 4n \gg 1$

is

$$\Delta_s = \frac{v_s}{N}\left[B_1 \ln^{1/2}(N) + B_2\right] + \dots \,, \tag{6.116}$$

$$E_{pb} = \Delta_s + B_3\frac{v_s}{N} - \frac{B_4}{N^2}\left[\frac{{v_c}^2}{\Delta_c}\right] + \dots \,. \tag{6.117}$$

Here, v_s and v_c are the spin and charge velocities, respectively (in units in which the lattice constant is unity), and Δ_c is the charge gap in the $N \to \infty$ limit. The constants, B_j, are numbers of order unity. The important lesson of this analysis is that pair binding is closely related to the phenomenon of spin gap formation. Indeed, for large N, $E_{pb} \approx \Delta_s$. (The spin gap and pairing are related.)

Hubbard and t–J ladders

In the thermodynamic limit, where the number of sites $N \to \infty$, Hubbard chains, and their strong coupling descendants the t–J chains, have no spin gap and a small superconducting susceptibility, irrespective of the doping level. In contrast, ladder systems can exhibit both a spin gap and a strong tendency towards superconducting order even in the thermodynamic limit. While these systems are infinite in extent, the mesoscopic physics comes in through the finiteness of the transverse dimension.

In the large U limit and at half filling (one electron per site) the Hubbard ladder is equivalent to the spin–1/2 Heisenberg ladder

$$H_J = J\sum_{\langle i,j\rangle} \mathbf{S}_i \cdot \mathbf{S}_j \,, \tag{6.118}$$

where $\mathbf{S}_i$ is a spin 1/2 operator, $J = 4t^2/U \ll t$ is the antiferromagnetic exchange interaction, and $\langle i,j\rangle$ now signifies nearest neighbor sites of spacing a on the ladder. As discussed in Section 6.10, there is a marked difference between the behavior of ladders with even and odd numbers of chains or "legs". While even leg ladders are spin gapped with exponentially decaying spin–spin correlations, odd leg ladders are gapless and exhibit power law falloff of these correlations (up to logarithmic corrections). This difference is clearly demonstrated in Fig. 6.28. The spin gaps for the first few even leg ladders are known numerically [312, 342].

For the two, four, and six leg ladders, $\Delta_s = 0.51(1)J$, $\Delta_s = 0.17(1)J$, and $\Delta_s = 0.05(1)J$, respectively. This gap (widening the ladder closes the gap) appears to vanish exponentially with the width W of the system, in accordance with the theoretical estimate [311] $\Delta_s \sim 3.35J\exp[-0.682(W/a)]$, as discussed in Section 6.10. Although odd leg Heisenberg ladders are gapless, they are characterized by an energy scale which has the same functional dependence on W as Δ_s. Below this energy, the excitations are gapless spinons analogous to those in the Heisenberg chain [311], while above it they are weakly interacting spin waves. Based on our experience with the Hubbard rings we expect that spin gap formation is related to superconductivity. As

we shall see below this is indeed the case once the ladders are doped with holes. On the face of it, this implies that only rather narrow ladders are good candidates for the mesoscopic building blocks of a high temperature superconductors.

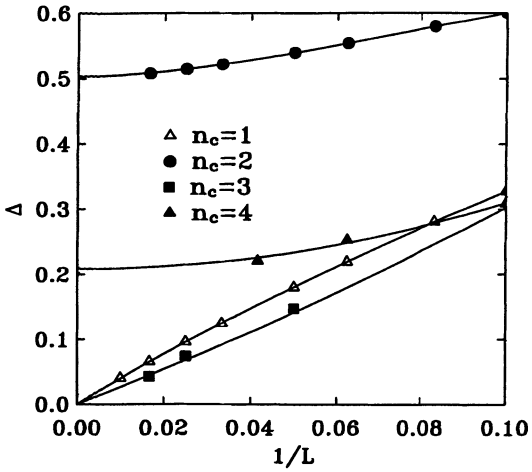

Fig. 6.28. Spin gaps as a function of system size L for open $L \times n_c$ Heisenberg ladders (from White *et al.* [312])

When the Hubbard ladder is doped with holes away from half filling, its strong coupling description is modified from the Heisenberg model (Eq. (6.118)) to the t–J model

$$H_{t-J} = -t \sum_{\langle i,j\rangle,s} (c^{\dagger}_{i,s} c_{j,s} + h.c.) + J \sum_{\langle i,j\rangle} \left[\mathbf{S}_i \cdot \mathbf{S}_j - \frac{1}{4} n_i n_j \right] , \qquad (6.119)$$

which is defined with the supplementary constraint of no doubly occupied sites. This is the version which has been most extensively studied numerically. Unless otherwise stated, we will quote results for representative values of J/t in the range $J/t = 0.35$ to 0.5.

Numerical studies of the two leg Hubbard model [343, 344] have demonstrated that doping tends to decrease the spin gap *continuously* from its value in the undoped system but it persists down to at least an average filling of $\langle n \rangle = 0.75$, as can be seen from the inset in Fig. 6.29. A similar behavior is observed in the t–J ladder although the precise evolution of the spin gap upon doping depends on details of the model [325].

Pairs of holes in two leg Hubbard or t–J ladders form bound pairs as can be seen both from the fact that the pair binding energy is positive, and from the fact that positional correlations between holes are indicative of a bound state. The pairs have a predominant $d_{x^2-y^2}$ symmetry as is revealed by the

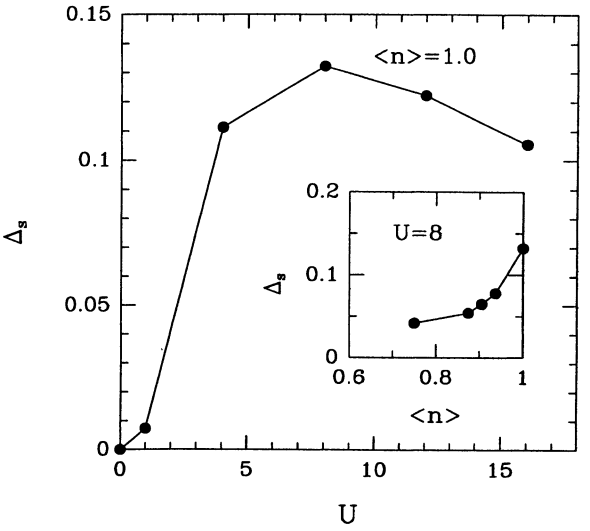

Fig. 6.29. The spin gap as a function of U for a half filled 2×32 Hubbard ladder. The inset shows Δ_s as a function of filling $\langle n \rangle$ for $U = 8$. Energies are measured in units of $t = 1$ (from Noack *et al.* [344])

relative minus sign between the ground state to ground state amplitudes for adding a singlet pair on neighboring sites along and across the legs [194,343]. It seems that the dominance of the $d_{x^2-y^2}$ channel is universally shared by all models over the entire range of doping that has been studied. (See Section 6.10.3 for a discussion of this phenomenon in the 2×2 plaquette.)

The doping dependence of the pair binding energy roughly follows the spin gap in various versions of the two leg ladder as shown in Fig. 6.30. The correlation function $D(l)$ of the pair field

$$\Delta_i^\dagger = (c_{i1\uparrow}^\dagger c_{i2\downarrow}^\dagger - c_{i1\downarrow}^\dagger c_{i2\uparrow}^\dagger) \,, \tag{6.120}$$

exhibits behavior consistent with a power law decay [194,343,345,346]

$$D(l) = \langle \Delta_{i+l} \Delta_i^\dagger \rangle \sim l^{-\theta} \,. \tag{6.121}$$

There exists less data concerning its doping dependence, but from the relevant studies [194,343] we can conclude that the pair correlations increase from the undoped system to a maximum at $x \sim 0.0625$ and then decrease when more holes are added to the system.

Both the spin gap and the pairing correlations in doped Hubbard and t–J ladders can be appreciably enhanced by slight generalizations of the models. For example, the exponent θ in Eq. (6.121), which depends on the coupling strengths U/t or J/t and the doping level x, is also sensitive to the ratio of the hopping amplitudes between neighboring sites on a rung and within a

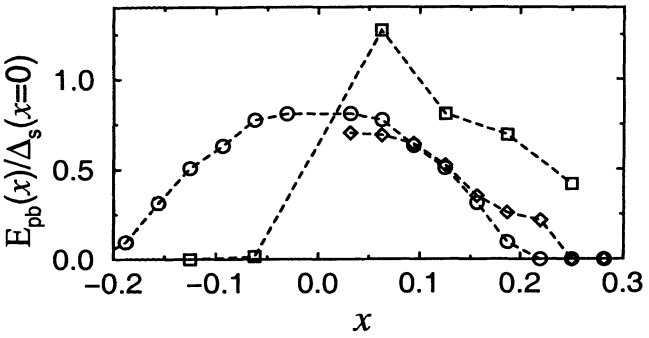

Fig. 6.30. The ratio of the pair binding energy to the undoped spin gap as a function of hole doping $x = 1 - \langle n \rangle$. The diamonds are for a 32×2 t–J ladder with $J/t = 0.3$. The circles are for a one band 32×2 Hubbard ladder with $U/t = 12$. The squares are for a three band Hubbard model of a two leg Cu-O ladder, i.e. a ladder made of Cu sites where nearest neighbor sites are connected by a link containing an O atom. Here $U_d/t_{pd} = 8$, where U_d is the on–site Cu Coulomb interaction and t_{pd} is the hopping matrix element between the O and Cu sites. The energy difference between the O and Cu sites is $(\epsilon_p - \epsilon_d)/t_{pd} = 2$, and the calculation is done on a 16×2 ladder (from Jeckelmann *et al.* [347])

chain $t_\perp/t$. By varying this parameter, the exponent θ can be tuned over the range $0.9 \leq \theta \leq 2.1$. In particular, for $x = 0.0625$ and intermediate values of the (repulsive) interaction $5 \leq U/t \leq 15$, it can be made smaller than 1 [194]; see Fig. 6.14. This is significant since, as we saw in Section 6.5.1, whenever $\theta < 1$ the superconducting susceptibility is the most divergent among the various susceptibilities of the ladder. Adding a nearest neighbor exchange coupling, J, to H_U also leads to stronger superconducting signatures owing to an increase in the pair mobility and binding energy [348]. The moral here is that details are important as far as they reveal the nonuniversal properties of the Hamiltonians that we study, and indicate relevant directions in model space. It should also imprint on us a sense of humility when attempting to fit real world data with such theoretical results.

We already noted that, in contrast to the two leg ladder, the three leg system does not possess a spin gap at half filling. This situation persists up to hole doping of about $x = 1 - \langle n \rangle = 0.05$, as can be seen in Fig. 6.31.[5] However, with moderate doping a spin gap is formed which reaches a maximum value at a doping level of $x = 0.125$. For the system shown here, with $J/t = 0.35$, the gap is only 20 percent smaller than that of the undoped two leg Heisenberg ladder. Upon further doping, the spin gap decreases and possibly vanishes as x gets to be 0.2 or larger.

[5] The nonvanishing spin gap in this region is presumably a finite size effect; see Fig. 6.28.

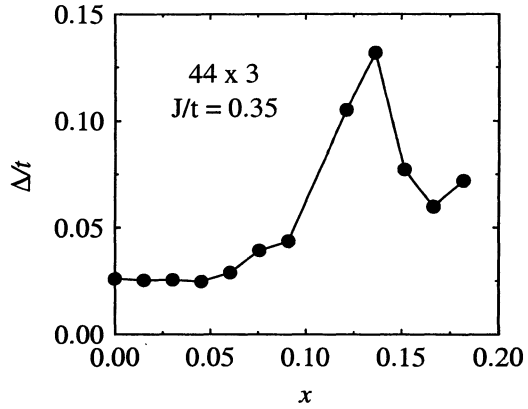

Fig. 6.31. Spin gap for a 44 × 3 ladder with open boundary conditions and $J/t = 0.35$ as a function of doping (from White and Scalapino [349])

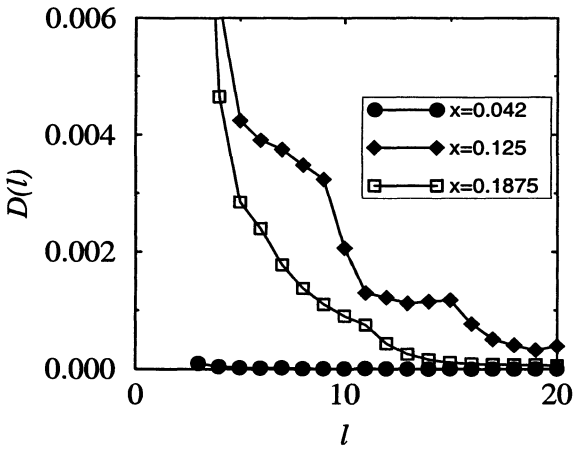

Fig. 6.32. The $d_{x^2-y^2}$ pair field correlations $D(l)$ for three different densities, calculated on 32 × 3 ($x = 0.1875$) and 48 × 3 ($x = 0.042$, $x = 0.125$) open t–J ladders with $J/t = 0.35$. (From White and Scalapino [349])

The establishment of a spin gap is concurrent with the onset of pairing correlations in the system. While two holes introduced into a long, half filled three chain ladder do not bind [316], indications of pairing emerge as soon as the spin gap builds up [349, 350]. As an example, Fig. 6.32 plots the pair field–pair field correlation function of Eq. (6.121) for various values of the hole doping, defined with

$$\Delta_i^\dagger = c_{i,2\uparrow}^\dagger (c_{i+1,2\downarrow}^\dagger + c_{i-1,2\downarrow}^\dagger - c_{i,1\downarrow}^\dagger - c_{i,3\downarrow}^\dagger) - (\uparrow \leftrightarrow \downarrow) \tag{6.122}$$

which creates a $d_{x^2-y^2}$ pair around the ith site of the middle leg (the leg index runs from 1 to 3). (There also exists a small s–wave component in the pair field due to the one dimensional nature of the cluster.) In the regime of low doping $x \leq 0.05$, the pair field correlations are negligible. However, clear pair field correlations are present at $x = 0.125$, where they are comparable to those in a two leg ladder under similar conditions. The pair field correlations are less strong at $x = 0.1875$; they follow an approximate power law decay as a function of the distance. [346,349] (The oscillations in $D(l)$ are produced by the open boundary conditions used in this calculation.) This behavior can be understood from strong coupling bosonization considerations [20] in which the two even modes (with respect to reflection about the center leg) form a spin gapped two leg ladder and for small doping the holes enter the odd mode giving rise to a gapless one dimensional electron gas. As the doping increases, pair hopping between the two subsystems may induce a gap in the gapless channel via the spin gap proximity effect [20].

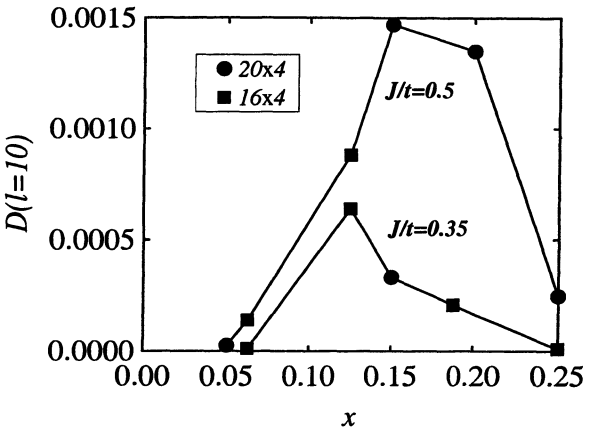

Fig. 6.33. The $d_{x^2-y^2}$ pair field correlation $D(l)$ at a separation of $l = 10$ rungs as a function of doping x, for 20×4 and 16×4 open ladders with $J/t = 0.35$ and 0.5. (From White and Scalapino [351])

Increasing the number of legs from three to four leads to behavior similar to that exhibited by the two leg ladder. The system is spin gapped and two holes in a half filled four leg ladder tend to bind. The pair exhibits features common to all pairs in an antiferromagnetic environment, including a d–wave–like symmetry [316]. Further similarity with the two leg ladder is seen in the d–wave pair field correlations $D(l)$. Fig. 6.33 shows $D(l = 10)$ for a t–J four leg ladder as a function of doping (extended s–wave correlations are much smaller in magnitude). The pairing correlations for $J/t = 0.5$ increase with doping, reaching a maximum between $x = 0.15$ and $x = 0.2$, and then

decrease. The magnitude of the correlations near the maximum is similar to that of a two leg Hubbard ladder with $U = 8t$ (corresponding to $J \sim 4t^2/U = 0.5$) with the same doping, but smaller than the maximum in the two leg ladder which occurs at smaller doping [194, 343]. For $J/t = 0.35$ the peak is reduced in magnitude and occurs at lower doping. The behavior of $D(l)$ near the maximum is consistent with power law decay for short to moderate distances but seems to fall more rapidly at long distances (perhaps even exponentially. [352])

Lastly, we present in Fig. 6.34 the response of a few ladder systems to a proximity pairing field

$$H_1 = d \sum_i (c^\dagger_{i,\uparrow} c^\dagger_{i+\hat{y},\downarrow} - c^\dagger_{i,\downarrow} c^\dagger_{i+\hat{y},\uparrow} + h.c.) \,, \tag{6.123}$$

which adds and destroys a singlet electron pair along the ladder. The response is given by the average $d_{x^2-y^2}$ pair field

$$\langle \Delta_d \rangle = \frac{1}{N} \sum_i \langle \Delta_i \rangle \,, \tag{6.124}$$

with Δ_i defined in Eq. (6.120). We see that the pair field response tends to decrease somewhat with the width of the system but is overall similar for the two, three and four leg ladders. We suspect it gets rapidly smaller for wider ladders.

Phase separation and stripe formation in ladders

We now address the issue of whether there is any apparent tendency to form charge density and/or spin density wave order in ladder systems, and whether there is a tendency of the doped holes to phase separate. Since incommensurate density wave long range order, like superconducting order, is destroyed by quantum fluctuations in one dimension, we will again be looking primarily at local correlations, rather than actual ordered states. Of course, we have in mind that local correlations and enhanced susceptibilities in a one dimensional context can be interpreted as indications that in two dimensions true superconductivity, stripe order, or phase separation may occur.

Phase Separation

Phase separation was first found in the one dimensional chain [353, 354] and subsequently in the two leg ladder [355–357]. As a rule, the phase separation line has been determined by calculating the coupling J at which the compressibility diverges. (See, however, Ref. [324].) This is in principle an incorrect criterion. The compressibility only diverges at the consolute point. Thermodynamically appropriate criteria for identifying regimes of phase separation from finite size studies include the Maxwell construction (discussed explicitly in Section 6.12, below), and measurements of the surface tension in the presence of boundary conditions that force phase coexistence. The divergent compressibility is most directly related to the spinodal line, which is not even strictly well defined beyond mean field theory. Thus, while in many

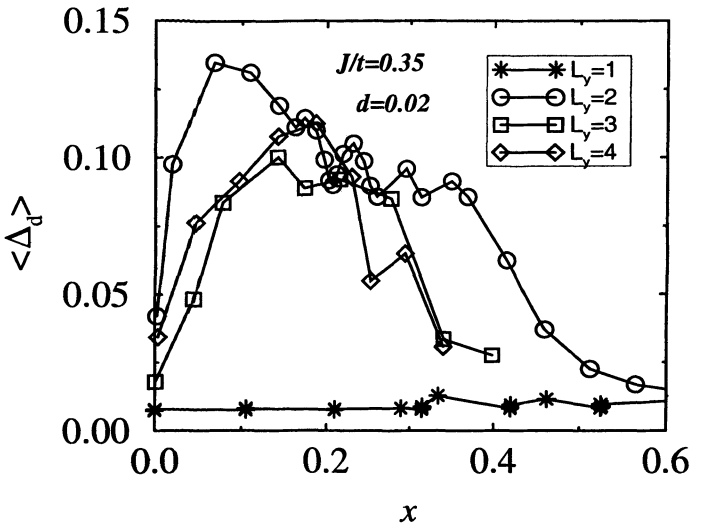

Fig. 6.34. The $d_{x^2-y^2}$ pairing response to a proximity pair field operator as a function of doping for a single chain and two, three, and four leg ladders. For the single chain, near neighbor pairing is measured. (From White and Scalapino [349])

cases the phase diagrams obtained in this way may be qualitatively correct, they are always subject to some uncertainty.

More recently Rommer, White, and Scalapino [358] have used DMRG methods to extend the study to ladders of up to six legs. Since these calculations are carried out with open boundary conditions, which break the translational symmetry of the system, they have used as their criterion the appearence of an inhomogeneous state with a hole rich region at one edge of the ladder and hole free regions near the other, which is a thermodynamically correct criterion for phase separation. However, where the hole rich phase has relatively low hole density, and in all cases for the six leg ladder, they were forced to use a different criterion which is not thermodynamic in character, but is at least intuitively appealing. From earlier studies (which we discuss below) it appears that the "uniform density" phase, which replaces the phase separated state for J/t less than the critical value for phase separation, is a "striped" state, in which the holes congregate into puddles (identified as stripes) with fixed number of holes, but with the density of stripes determined by the mean hole density on the ladder. With this in mind, Rommer *et al.* computed the interaction energy between two stripes, and estimated the phase separation boundary as the point at which this interaction turns from repulsive to attractive. The results, summarized in Fig. 6.35, agree with the thermodynamically determined phase boundary where they can be compared.

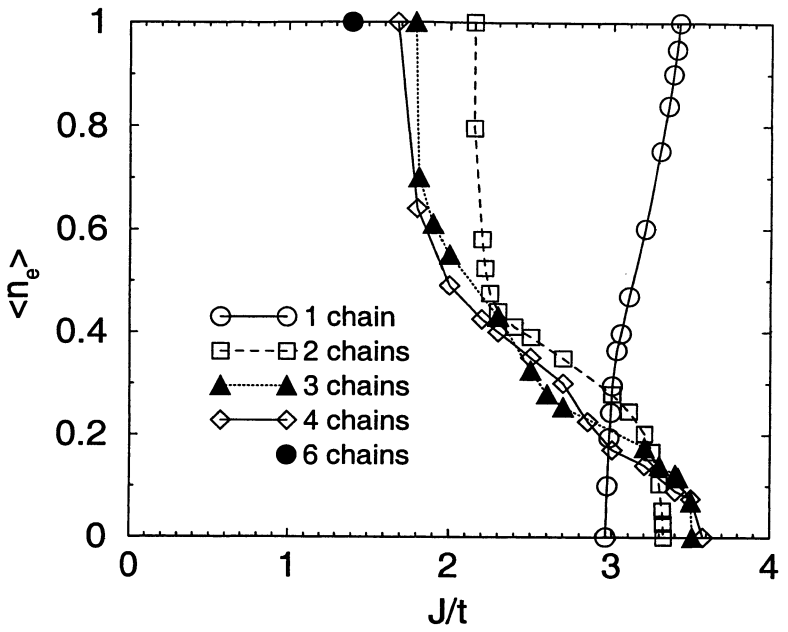

Fig. 6.35. Boundary to phase separated region in t–J ladders. Open boundary conditions were used in both the leg and rung directions except for the six leg ladder where periodic boundary conditions were imposed along the rung. Phase separation is realized to the right of the curves. $\langle n_e \rangle$ is the total electron density in the system (from Rommer *et al.* [358])

For large enough values of J/t, both the single chain and the ladders are fully phase separated into a Heisenberg phase ($\langle n_e \rangle = 1$) and an empty phase ($\langle n_e \rangle = 0$). However, the evolution of this state as J/t is reduced is apparently different for the two cases. For the chain, the Heisenberg phase is destroyed first by holes that diffuse into it; this presumably reflects the fact that hole motion is not significantly frustrated in the single chain system. In the ladders, on the other hand, the empty phase is the one that becomes unstable due to the sublimation of electron pairs from the Heisenberg region. This difference is evident in Fig. 6.35 where the phase separation boundary occurs first at high electron density in the chain and high hole density in the ladders. It is also clear from looking at this figure that the value of J/t at which phase separation first occurs for small electron densities is hardly sensitive to the width of the ladder. However, as more electrons are added to the system (removing holes), phase separation is realized for smaller values of J/t in wider ladders. Whether this is an indication that phase separation

takes place at arbitrarily small J/t for small enough hole densities in the two dimensional system is currently under debate, as we discuss in Section 6.11.2.

"Stripes" in ladders

At intermediate values of J/t, and not too close to half filling, the doped holes tend to segregate into puddles which straddle the ladders, as is apparent from the spatial modulation of the mean charge density along the ladder. (Stripes appear at smaller J/t.) Intuitively, we can think of this state as consisting of an array of stripes with a spacing which is determined by the doped hole density. From this perspective, the total number of doped holes associated with each puddle, $N_{puddle} = \varrho L$, is interpreted as arising from a stripe with a mean linear density of holes, ϱ, times the length of the stripe, L. (L is also the width of the ladder.) On a long, N site, 4 leg ladder with $4n$ holes, where $n \ll N$, one typically observes n or $2n$ distinct peaks in the rung–averaged charge density, which is then interpreted as indicating a stripe array with $\varrho = 1$ or $\varrho = 1/2$, respectively. In the thermodynamic limit, long wavelength quantum fluctuations of the stripe array would presumably result in a uniform charge density, but the ladder ends, even in the longest systems studied to date, are a sufficiently strong perturbation that they pin the stripe array [359]. In two and three leg ladders, the observed stripes apparently always have $\varrho = 1$. For the four leg ladder, typically $\varrho = 1$, but under appropriate circumstances (especially for $x = 1/8$), $\varrho = 1/2$ stripes are observed. In six and eight leg ladders, the charge density oscillations are particularly strong, and correspond to stripes with $\varrho = 2/3$ and $1/2$, respectively. Various arguments have been presented to identify certain of these stripe arrays as being "vertical" (*i.e.* preferentially oriented along the rungs of the ladder) or "diagonal" (*i.e.* preferentially oriented at 45^o to the rung), but these arguments, while intuitively appealing, do not have a rigorous basis.

We will return to the results on the wider ladders, below, where we discuss attempts to extrapolate these results to two dimensions.

6.11.2 Properties of the Two Dimensional t–J Model

It is a subtle affair to draw conclusions about the properties of the two dimensional Hubbard and t–J models from numerical studies of finite systems. The present numerical capabilities do not generally permit a systematic finite size scaling analysis. As a result, extrapolating results from small clusters with periodic boundary conditions, typically used when utilizing Monte Carlo or Lanczos techniques, or from strips with open boundary conditions as used in DMRG studies, is susceptible to criticism [327, 331]. It comes as no surprise then that several key issues concerning the ground state properties of the two dimensional models are under dispute. In the following we present a brief account of some of the conflicting results and views. However, at least two things do not seem to be in dispute: 1) there is a strong tendency for doped holes in an antiferromagnet to clump in order relieve the frustration of hole motion [360], and 2) where it occurs, hole pairing has a $d_{x^2-y^2}$ character.

Thus, in one way or another, the local correlations that lead to stripe formation and d–wave superconductivity are clearly present in t–J–like models!

Phase separation and stripe formation

There have been relatively few numerical studies of large two dimensional Hubbard model clusters. Monte Carlo simulations on square systems with sizes up to 12×12 and temperatures down to roughly $t/8$ have been carried out, typically with $U/t = 4$ [332]. A signature of phase separation in the form of a discontinuity in the chemical potential as a function of doping was looked for and not found. No evidence of stripe formation was found, either. Given the limited size and temperature range of these studies, and the absence of results that would permit a Maxwell construction to determine the boundary of phase separation, it is difficult to reach a firm conclusion on the basis of these studies. Certainly at relatively elevated temperatures, holes in the Hubbard model do not show a strong tendency to cluster, but it is difficult to draw conclusions concerning lower temperature, or more subtle tendencies. (Variational "fixed node" studies by Cosentini *et al* [361] are suggestive of phase separation at small x, but more recent studies by Becca *et al.* [362] reached the opposite conclusion.)

There are many more studies of phase separation in the t–J model. Most of them agree on the behavior in the regime of very low electron density $n_e = 1 - x \ll 1$. The critical J/t value for phase separation at vanishingly small n_e was calculated very accurately by Hellberg and Manousakis [363] and was found to be $J/t = 3.4367$. However, there are conflicting results for systems close to half filling ($n_e \sim 1$) and with small t–J. This is the most delicate region where high numerical accuracy is hard to obtain. Consequently, there is no agreement on whether the two dimensional t–J model phase separates for all values of J/t at sufficiently low hole doping x.

Emery *et al.* [364, 365] presented a variational argument (recently extended and substantially improved by Eisenberg *et al.* [366]) that for $J/t \ll 1$ and for x less than a critical concentration, $x_c \sim \sqrt{J/t}$, phase separation occurs between a hole free antiferromagnetic and a metallic ferromagnetic state. Since for large J/t there is clearly phase separation for all x, they proposed that for sufficiently small x, phase separation is likely to occur for all J/t. To test this, they computed the ground state energy by exact diagonalization of 4×4 doped t–J clusters. If taken at face value and interpreted via a Maxwell construction, these results imply that for any $x < 1/8$, phase separation occurs at least for all $J/t > 0.2$. Hellberg and Manousakis [324, 333] calculated the ground state energy on larger clusters of up to 28×28 sites using Green function Monte Carlo methods. By implementing a Maxwell construction, they reached the similar conclusion that the t–J model phase separates for all values of J/t in the low hole doping regime.

On the other hand, Putikka *et al.* [367] studied this problem using a high temperature series expansion extrapolated to $T = 0$ and concluded that phase separation only occurs above a line extending from $J/t = 3.8$ at zero filling

to $J/t = 1.2$ at half filling. In other words, they concluded that there is no phase separation for any x so long as $J/t < 1.2$. Exact diaganolization results for the compressibility and the binding energy of n–hole clusters in systems of up to 26 sites by Poilblanc [368] were interpreted as suggesting that the ground state is phase separated close to half filling only if $J/t > 1$. Quantum Monte Carlo simulations of up to 242 sites using stochastic reconfiguration by Calandra *et al.* [369] have found a phase separation instability for $J/t \sim 0.5$ at similar doping levels, but no phase separation for $J/t < 0.5$, while earlier variational Monte Carlo calculations [370] reported a critical value of $J/t = 1.5$. Using Lanczos techniques to calculate the ground state energy on lattices of up to 122 sites, Shih *et al.* [371, 372] estimate the lower critical value for phase separation as $J/t = 0.3 - 0.5$, a somewhat lower bound than previously found using similar numerical methods [373]. Finally, DMRG calculations on wide ladders with open boundary conditions in one direction by White and Scalapino [322, 323] found striped ground states for $J/t = 0.35$ and $0 < x < 0.3$, but no indication of phase separation.

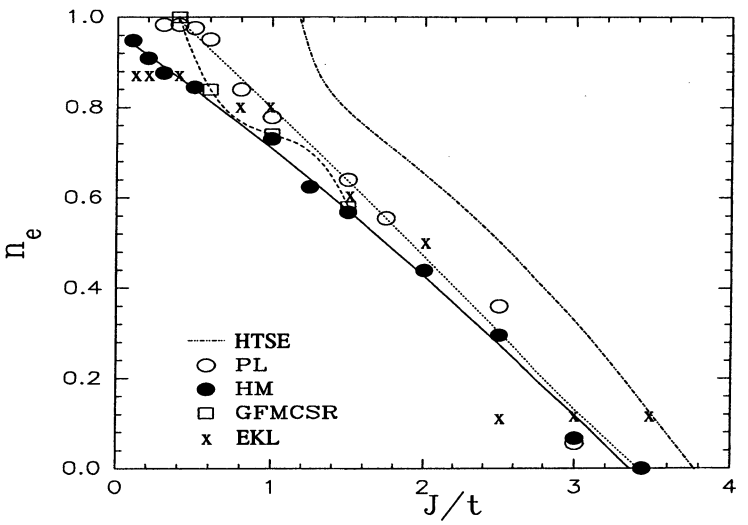

Fig. 6.36. Phase separation boundary of the two dimensional t–J model according to various numerical studies. The dashed–dotted line represents the high temperature series expansion results by Putikka *et al.* [367]. Also shown are results from calculations using the Power–Lanczos method by Shin *et al.* [372] (open circles), Greens function Monte Carlo simulations by Hellberg and Manousakis [333] (closed circles) and by Calandra *et al.* [369] (open squares), and exact diagonalization of 4×4 clusters by Emery *et al.* [364] (x's) (adapted from Shin *et al.* [372])

For comparison, we have gathered a few of the results mentioned above in Fig. 6.36. The scatter of the data at the upper left corner of the $n_e - J/t$

plane is a reflection of the near linearity of the the ground state energy as a function of doping in this region [331]. High numerical accuracy is needed in order to establish a true linear behavior which would be indicative of phase separation. While there is currently no definitive answer concerning phase separation at small doping, it seems clear that in this region the two dimensional t–J model is in delicate balance, either in or close to a phase separation instability.

The nature of the ground state for moderately small J/t beyond any phase separated regime is also in dispute. While DMRG calculations on fat ladders [322, 323] find striped ground states for $J/t = 0.35$ and $x = 1/8$, Monte Carlo simulations on a torus [327] exhibit stripes only as excited states. Whether this discrepancy is due to finite size effects or the type of boundary conditions used is still not settled. (The fixed node Monte Carlo studies of Becca *et al.* [374] likewise conclude that stripes do not occur in the ground state, although they can be induced by the addition of rather modest anisotropy into the t–J model, suggesting that they are at least energetically competitive.) While these conflicting conclusions may be difficult to resolve, it seems inescapable to us that stripes are important low energy configurations of the two dimensional t–J model for small doping and moderatly small J/t.

The most reliable results concerning the internal structure of the stripes themselves come from studies of fat t–J ladders, where stripes are certainly a prominent part of the electronic structure. Typically stripes are quarter–filled antiphase domain walls. In all studies of ladders, the doped holes aggregate into "stripes" which are oriented either perpendicular or parallel to the extended direction of the ladder, depending on boundary conditions. In many cases the spin correlations in the hole poor regions between stripes locally resemble those in the undoped antiferromagnet but suffer a π–phase shift across the hole rich stripe. This magnetic structure is vividly apparent in studies for which the low energy orientational fluctuations of the spins are suppressed by the application of staggered magnetic fields on certain boundary sites of the ladders—then, these magnetic correlations are directly seen in the expectation values of the spins [375]. However, such findings are not universal: in the case of the four leg ladder, with stripes along the ladder rungs, Arrigoni *et al.* [330] recently showed that in long systems (up to 4×27), these antiphase magnetic correlations are weak or nonexistent, despite strong evidence of charge stripe correlations. Ladder studies have also demonstrated that stripes tend to favor a linear charge density of $\varrho = 1/2$ along each stripe. (Note, at about the same time, Nayak and Wilczek [376] presented an interesting analytic argument which leads to the same bottom line.) Specifically, by applying boundary conditions which force a single stripe to lie along the long axis of the ladder, White *et al* [323] were able to study the energy of a stripe as a function of ϱ. They found an energy which is apparently a smooth function of ϱ (*i.e.* with no evidence of a nonanalyticity which would lock ϱ

to a specific value), but with a pronounced minimum at $\varrho = 1/2$. Moreover, with boundary conditions favoring stripes perpendicular to the ladder axis, they found that for $x \leq 1/8$ stripes tend to form with $\varrho = 1/2$ so that the spacing between neighboring stripes is approximately $1/2x$, while at larger x, a first order transition occurs to "empty domain walls" with $\varrho = 1$ and an inter–stripe spacing of $1/x$. In the region $0.125 < x < 0.17$ the two types of stripes can coexist.

It is worth noting that the original indications of stripe order came from Hartree–Fock treatments [377–380]. Hartree–Fock stripes are primarily spin textures. In comparison to the DMRG results on ladders, they correspond to "empty" ($\varrho = 1$) antiphase (π–phase shifted) domain walls, and so are insulating and overemphasize the spin component of the stripe order, but otherwise capture much of the physics of stripe formation remarkably accurately.

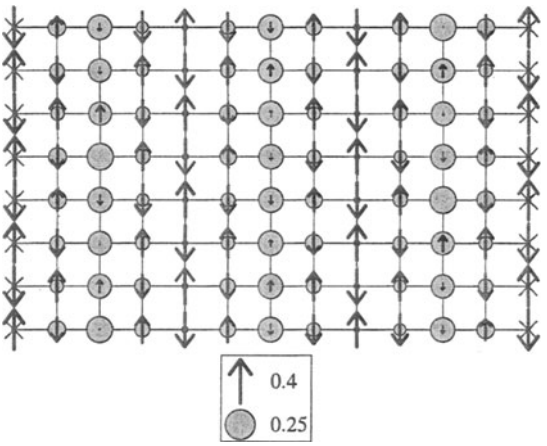

Fig. 6.37. Hole density and spin moments on a 13×8 cylinder with 12 holes, $J/t = 0.35$, periodic boundary conditions along the y direction and π–shifted staggered magnetic field of magnitude $0.1t$ on the open edges. The diameter of the circles is proportional to the hole density $1 - \langle n_i \rangle$ and the length of the arrows is proportional to $\langle S_i^z \rangle$ (from White and Scalapino [375])

Further insight into the physics that generates the domain walls can be gained by looking more closely at their hole density and spin structures. Both site–centered and bond–centered stripes are observed. They are close in energy and each type can be stabilized by adjusting the boundary conditions [322]. Fig. 6.37 depicts three site–centered stripes in a 13×8 system with 12 holes, periodic boundary conditions along the y direction and a π–shifted staggered magnetic field on the open ends of magnitude $0.1t$. These stripes

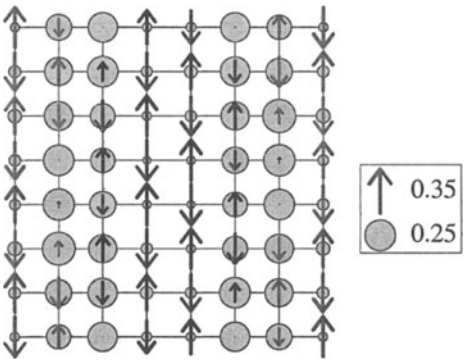

Fig. 6.38. Hole density and spin moments on a central section of a 16×8 cylinder with 16 holes, $J/t = 0.35$, with periodic boundary conditions along the y direction and staggered magnetic field of magnitude $0.1t$ on the open edges. The notation is similar to Fig. 6.37 (from White and Scalapino [375])

are quarter–filled antiphase domain walls. Fig. 6.38 shows a central section of a 16×8 cluster containing two bond–centered domain walls. This system is similar to the one considered above except that the magnetic field on the open ends is not π–shifted. Like their site–centered counterparts, the bond–centered stripes are antiphase domain walls, but with one hole per two domain wall unit cells.

The π–phase shift in the exchange field (the topological character of spin stripes can be inferred from local considerations) across the stripe can probably be traced, in both the bond– and site–centered cases, to a gain in the transverse kinetic energy of the holes. To demonstrate this point consider a pair of holes in a 2×2 t–J plaquette, as was done in Section 6.10.3. One can simulate the effect of the exchange field running on both sides of the plaquette through a mean field h which couples to the spins on the square [375]. For the in–phase domain wall such a coupling introduces a perturbation $h(S_1^z - S_2^z - S_3^z + S_4^z)$ which, to lowest order in h, lowers the ground state energy by $-h^2/\sqrt{J^2 + 32t^2}$. For the π–shifted stripe the perturbation is $h(S_1^z + S_2^z - S_3^z - S_4^z)$ with a gain of $-4h^2/\sqrt{J^2 + 32t^2}$ in energy, thereby being more advantageous for the pair. Indeed, this physics has been confirmed by several serious studies, which combine analytic and numerical work, by Zachar [381], Liu and Fradkin [382], and Chernyshev *et al.* [383] These studies indicate that there is a transition from a tendency for in–phase magnetic order across a stripe for small ϱ, when the direct magnetic interactions are dominant, to antiphase magnetic order for $\varrho > 0.3$, when the transverse hole kinetic energy is dominant.

Superconductivity and stripes

There is no unambiguous evidence for superconductivity in the Hubbard

model. The original finite temperature Monte Carlo simulations on small periodic clusters with $U/t = 4$ and $x = 0.15$ [332, 384] found only short range pair–pair correlations. The same conclusion was reached by a later zero temperature constrained path Monte Carlo calculation [385].

There are conflicting results concerning the question of superconductivity in the t–J model.

In the unphysical region of large J/t, solid conclusions can be reached: Emery *et al* [364] showed that proximate to the phase separation boundary at $J/t \leq 3.8$, the hole rich phase (which is actually a dilute electron phase with $x \sim 1$) has an s–wave superconducting ground state. This result was confirmed and extended by Hellberg and Manousakis [324], who further argued that in the dilute electron limit, $x \rightarrow 1^-$, there is a transition from an s–wave state for $2 < J/t < 3.5$ to a p–wave superconducting state for $J/t < 2$, possibly with a d–wave state at intermediate J/t. Early Lanczos calculations were carried out by Dagotto and Riera [332, 386, 387] in which various quantitites, such as the pair field correlation function and the superfluid density, were computed to search for signs of superconductivity in 4×4 t–J clusters. In agreement with the analytic results, these studies gave strong evidence of superconductivity for large J/t. Interestingly, the strongest signatures of superconductivity were found for $J/t = 3$ and $x = 0.5$ and decayed rapidly for larger J/t. This was interpreted as due to a transition into the phase separation region. (Note, however, that *all* the studies summarized in Fig. 6.36 suggest that $x = 0.5$ is already inside the region that, in the thermodynamic limit, would be unstable to phase separation.)

More recent Monte Carlo simulations by Sorella *et al.* [388, 389] showed evidence for long range superconducting order in $J/t = 0.4$ clusters of up to 242 sites with periodic boundary conditions and for a range of $x > 0.1$, as shown in Fig. 6.39. No signs of static stripes have been found in the parameter region that was investigated in these studies. A slight tendency towards incommensurability appears in the spin structure factor at (and sometimes above) optimal doping, suggesting perhaps very weak dynamical stripe correlations. Both the evidence for superconductivity and the absence of stripes are in conflict with the resuts of other studies. For example, Shih *et al.* [372] have shown that the pair binding energy on small clusters decreases with cluster size, and extrapolates to positive values in the thermodynamic limit for $J/t < 0.8$. (A similar conclusion was reached earlier by Boninsegni and Manousakis [390].) Stripe ground states were found for the same values of parameters in DMRG [322, 323] and other calculations. [391]

Notwithstanding this controversy, these results seem to add to the general consensus that *static* stripe order and superconductivity compete. This is not to say that stripes and superconductivity cannot coexist. Note, static stripes hamper superconductivity, but dynamic stripes may enhance it. As we saw, evidence for both stripes and pairing have been found in three and four leg t–J ladders [349, 351]. In fact pairing is enhanced in both of these systems when

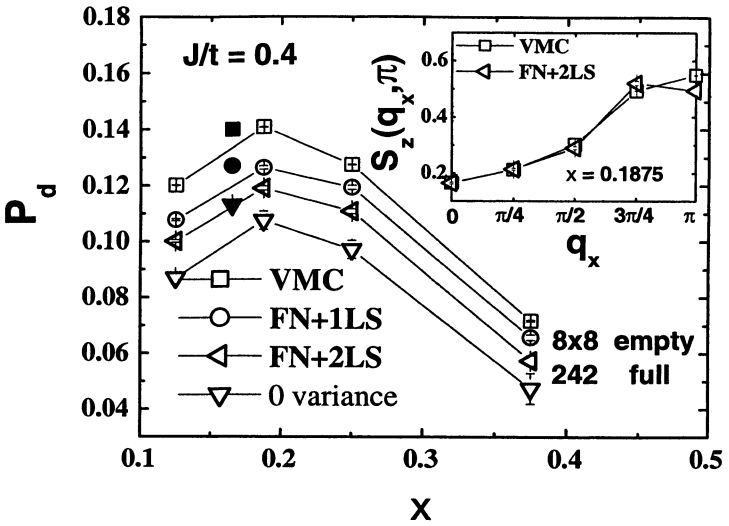

Fig. 6.39. The superconducting order parameter $P_d = 2 \lim_{l\to\infty} \sqrt{D(l)}$ calculated for the largest distance on a 8×8, $J/t = 0.4$ cluster as function of hole doping x. Results for $x = 0.17$ on a 242 site cluster are also shown. The different sets of data correspond to various Monte Carlo techniques. The inset shows the spin structure factor at $x = 0.1875$ (from Sorella *et al.* [389])

stripes are formed compared to the unstriped states found at small doping levels. Because of the open boundary conditions that were used in these studies the stripes were open ended and more dynamic. Imposing periodic boundary conditions in wider ladders (and also the four leg ladder) results in stripes that wrap around the periodic direction. These stripes appear to be more static, and pairing correlations are suppressed. A similar behavior is observed when the stripes are pinned by external potentials.

Further evidence for the delicate interplay between stripes and pairing comes from studies of the $t-t'-J$ model in which a diagonal, single particle, next nearest neighbor hopping t' is added to the basic t–J model [326,391]. Stripes destabilize for either sign of t'. This is probably due to the enhanced mobility of the holes that can now hop on the same sublattice without interfering with the antiferromagnetic background. Pairing is suppressed for $t' < 0$ and enhanced for $t' > 0$. (This is surprising since T_c is generally higher for hole doped cuprates (believed to have $t' < 0$) than it is for electron doped cuprates (which have $t' > 0$).) It is not clear whether the complete elimination of stripes or only a slight destabilization is more favorable to pairing correlations. Fig. 6.40 suggests that optimal pairing occurs in between the strongly modulated ladder and the homogeneous system.

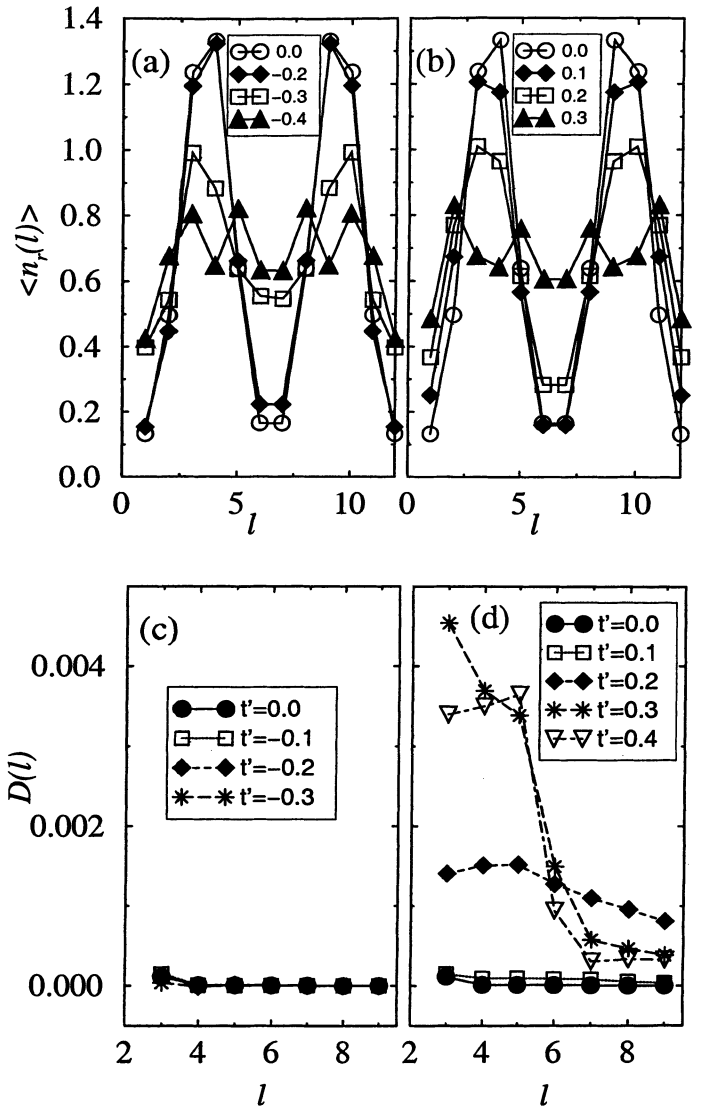

Fig. 6.40. Hole density per rung for a 12 × 6 ladder with periodic boundary conditions along the rungs, 8 holes, $J/t = 0.35$ and a) $t' \leq 0$ and b) $t' \geq 0$. c) and d) depict the d–wave pairing correlations for the same systems (from White and Scalapino [326])

Finally, allowing for extra hopping terms in the Hamiltonian is not the only way tip the balance between static charge order and superconductivity. So far we have not mentioned the effects of long range Coulomb interactions

on the properties of Hubbard related systems. This is not a coincidence since the treatment of such interactions in any standard numerical method is difficult. Nevertheless, a recent DMRG study of four leg ladders with open and periodic boundary conditions which takes into account the Coulomb potential in a self–consistent Hartree way [330], gives interesting results. It suggests that the inclusion of Coulomb interactions suppresses the charge modulations associated with stripes while enhancing the long range superconducting pairing correlations. At the same time the local superconducting pairing is not suppressed. Taken together, these facts support the notion that enhanced correlations come from long range phase ordering between stripes with well–established pairing. This enhanced phase stiffness is presumably due to pair tunnelling between stripes produced by increased stripe fluctuations.

6.12 Doped Antiferromagnets

There are many indications that the cuprate superconductors should be viewed as doped antiferromagnetic insulators. The motion of dilute holes in an aniterromagnet is highly frustrated, and attempts to understand the implications of this problem correspondingly frustrating. However, one generic solution is macroscopic or microscopic phase separation into hole poor antiferromagnetic and hole rich metallic regions (where the hole motion is unfrustrated).

The undoped state of the cuprate superconductors is a strongly insulating antiferromagnet. It is now widely believed that the existence of such a parent correlated insulator is an essential feature of high temperature superconductivity, as was emphasized in some of the earliest studies of this problem [5,122]. However, the doped antiferromagnet is a complicated theoretical problem–to even cursorily review what is known about it would more than double the size of this document. In this section we very briefly discuss the aspects of this problem which we consider most germane to the cuprates, and in particular to the physics of stripes. More extensive reviews of the subject can be found in [6,15,360,392].

6.12.1 Frustration of the Motion of Dilute holes in an Antiferromagnet

The most important local interactions in a doped antiferromagnet are well represented by the large U Hubbard model, the t–J model, and their various relatives. To be concrete, we will focus on the $t-J-V$ model [365] (a slight generalization of the t–J model, Eq. (6.119), to which it reduces for for $V=-J/4$.)

$$H=-t\sum_{\langle i,j\rangle,\sigma}\left\{c^{\dagger}_{i,\sigma}c_{j,\sigma}+\text{h.c.}\right\}+\sum_{\langle i,j\rangle}\left\{J\boldsymbol{S}_i\cdot\boldsymbol{S}_j+Vn_in_j\right\}\,, \tag{6.125}$$

where $\boldsymbol{S}_i = \sum_{\sigma,\sigma'} c^\dagger_{i,\sigma} \boldsymbol{\sigma}_{\sigma,\sigma'} c_{i,\sigma'}$ is the spin of an electron on site i. Here $\boldsymbol{\sigma}$ are the Pauli matrices and $\langle i,j \rangle$ signifies nearest neighbor sites on a hypercubic lattice in d dimensions. There is a constraint of no double occupancy on any site,

$$n_i = \Sigma_\sigma c^\dagger_{i,\sigma} c_{i,\sigma} = 0,1 \ . \tag{6.126}$$

The concentration of doped holes, x, is taken to be much smaller than 1, and is defined as

$$x = N^{-1} \sum_j n_j \ , \tag{6.127}$$

where N is the number of sites.

The essential feature of this model is that it embodies a strong, short range repulsion between electrons, manifest in the constraint of no double occupancy. The exchange integral J arises through virtual processes wherein the intermediate state has a doubly occupied site, producing an antiferromagnetic coupling. Doping is assumed to remove electrons thereby producing a "hole" or missing spin which is mobile because neighboring electrons can hop into its place with amplitude t.

Like a good game, the rules are simple: antialign adjacent spins, and let holes hop. And like any good game, the winning strategy is complex. The ground state of this model must simultaneously minimize the zero point kinetic energy of the doped holes and the exchange energy, but the two terms compete. The spatially confined wavefunction of a localized hole has a high kinetic energy; the t term accounts for the tendency of a doped hole to delocalize by hopping from site to site. However, as holes move through an antiferromagnet they scramble the spins: each time a hole hops from one site to its nearest neighbor, a spin is also moved one register in the lattice, *onto the wrong sublattice.* So it is impossible to minimize both energies simultaneously in $d > 1$. Moreover, in the physically relevant range of parameters, $t > J > tx$, neither energy is dominant. On the one hand, because $t > J$, one cannot simply perturb about the $t = 0$ state which minimizes the exchange energy. On the other hand, because $J > tx$ one cannot simply perturb about the ground state of the kinetic energy. (Note, for $t > J > xt$, the problem is highly frustrated.)

A number of strategies, usually involving further generalizations of the model, have been applied to the study of this problem, including: large n [393], large S [394, 395], large d [396], small t/J [364], large t/J [364, 397, 398], and various numerical studies of finite size clusters. (Some of the latter are reviewed in Section 6.11.) For pedagogic purposes, we will frame aspects of the ensuing discussion in terms of the large d behavior of the model since it is tractable, and involves no additional theoretical technology, but similar conclusions can be drawn from a study of any of the analytically tractable limits listed above (in some ways, the large S limit is the most physically

transparent of all these approaches–see Ref. [395] for further discussion). One common feature of these solutions is a tendency of the doped holes to phase separate at small x. The reason for this is intuitive: in a phase separated state, the holes are expelled from the pure antiferromagnetic fraction of the system, where the exchange energy is minimized and the hole kinetic energy is not an issue, while in the hole rich regions, the kinetic energy of the holes is minimized, and the exchange energy can be neglected to zeroth order since $J < tx_{rich}$, where x_{rich} is the concentration of doped holes in the hole rich regions. (It is still controversial whether or not phase separation is universal in $d = 2$ and 3 at small enough x– see Refs. [324,331,360,371,399–401].)

We employ the following large dimension strategy. We take as the unperturbed Hamiltonian the Ising piece of the interaction:

$$H_o = \sum_{\langle i,j \rangle} \left\{ J_z S_i^z S_j^z + V n_i n_j \right\} , \tag{6.128}$$

and treat as perturbations the XY piece of the interaction and the hopping:

$$H_1 = \frac{J_\perp}{2} \sum_{\langle i,j \rangle} \left\{ S_i^+ S_j^- + \text{h.c.} \right\} , \tag{6.129}$$

$$H_2 = -t \sum_{\langle i,j \rangle, \sigma} \left\{ c_{i,\sigma}^\dagger c_{j,\sigma} + \text{h.c.} \right\} . \tag{6.130}$$

Expansions derived in powers of $J_\perp/J_z$ and t/J_z can be reorganized in powers of $1/d$, [396] at which point we will again set $J_\perp = J_z \equiv J$ as in the original model (Eq. (6.125)), and allow the ratio t/J to assume physical values.

One hole in an antiferromagnet

It is universally recognized that a key principle governing the physics of doped antiferromagnets is that the motion of a single hole is highly frustrated. To illustrate this point, it is convenient to examine it from the perspective of a large dimension treatment in which the motion of one hole in an antiferromagnet is seen to be frustrated by a "string" left in its wake (see Fig. 6.41), which costs an energy of order $(d-1)J$ times the length of the string. The unperturbed ground state of one hole on, say, the "black" sublattice, is $N/2$-fold degenerate (equal to the number of black sublattice sites), once a direction for the Néel order is chosen (the other $N/2$ degenerate ground states describing a hole on the "red" sublattice form a disjoint Hilbert space under the operation of H_1 and H_2). These ground states are only connected in degenerate perturbation theory of third or higher order, via, *e.g.* two operations of H_2 and one of H_1. They are connected in perturbation theory of sixth or higher order by operations solely of the hopping term H_1 via the Trugman [402] terms, in which a hole traces any closed, nonintersecting path two steps less than two full circuits; see Fig. 6.42 for an example (such paths become important when $J \ll t$). In this manner a hole can "eat its own string". Owing to such processes a hole can propagate through an antiferromagnet. However, the high order in the perturbation series and the energetic

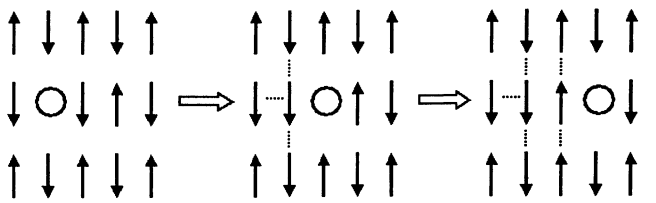

Fig. 6.41. Frustration of one hole's motion in an antiferromagnet. As the hole hops, it leaves behind a string of frustrated bonds designated here by dashed lines

barriers involved render the effective hopping matrix elements significantly smaller than their unperturbed values.

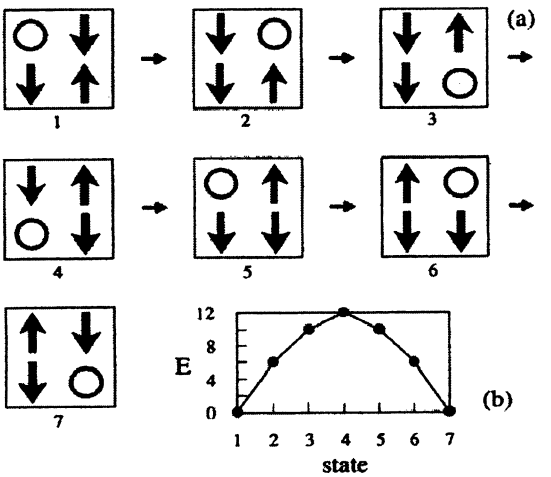

Fig. 6.42. Trugman terms. (a) A hole moving one and a half times around a plaquette translates a degenerate ground state without leaving a frustrated string of spins behind. (b) The energy of the intermediate states in units of J. The hole has to tunnel through this barrier as it moves (from Ref. [402])

Two holes in an antiferromagnet

In early work on high temperature superconductivity, it was often claimed that, whereas the motion of a single hole is inhibited by antiferromagnetic order, pair motion appears to be entirely unfrustrated. It was even suggested [19] that this might be the basis of a novel, kinetic energy driven mechanism of pairing–perhaps the first such suggestion. However, a flaw with this argument was revealed in the work of Trugman [402], who showed that this mode of propagation of the hole pair is frustrated by a quantum ef-

fect which originates from the fermionic character of the background spins. While Trugman's original argument was based on a careful analysis of numerical studies in $d = 2$, the same essential effect can be seen analytically in the context of a large d expansion. The effective Hamiltonian of two holes can be written as follows [396]:

$$H_2^{eff} = U^{eff} \sum_{\langle i,j \rangle} c_i^\dagger c_j^\dagger c_j c_i - T^{eff} \sum_{\langle i,j,k \rangle} c_j^\dagger c_i^\dagger c_j c_k + \mathcal{O}(1/d^2) \,, \tag{6.131}$$

where $\langle i, j, k \rangle$ signifies a set of sites such that i and k are both nearest neighbors of j, and the $c_i^\dagger$ creates a hole at site i. To lowest order in $(1/d)$, $U^{eff} = V - J/4$ and $T^{eff} = t^2/Jd$. For states with the two holes as nearest neighbors, H_2^{eff} can be block diagonalized by Fourier transform, yielding d bands of eigenstates labeled by a band index and a Bloch wavevector $\boldsymbol{k}$. The result is that $d - 1$ of these bands have energy U^{eff} and do not disperse. The remaining band has energy $U^{eff} + 4T^{eff} \sum_{a=1}^{d} sin^2(k_a/2)$, where k_a is the component of $\boldsymbol{k}$ along a. This final band, which feels the effects of pair propagation, has the largest energy. This counterintuitive result follows

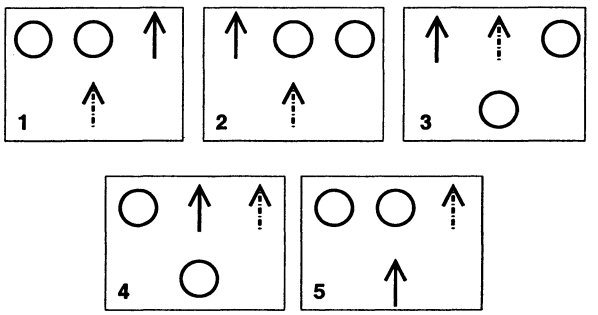

Fig. 6.43. Frustration of a hole pair's motion in an antiferromagnet. The figure shows a sequence of snapshots in a process that takes a pair of holes back to their original position, but with a pair of spins switched. The sequence is as follows: 1) Initial two hole state. 2) A spin has moved two sites to the left. 3) The other spin has moved one site up. 4) A hole has moved two sites to the left. 5) A hole has moved up. Due to the fermionic nature of the spins, the above process leads to an increase in the pair energy, so that pair propagation is not an effective mechanism of pair binding

from the fermionic nature of the background spins. A similar calculation for bosons would differ by a minus sign: in that case, the final band has energy $U^{eff} - 4T^{eff} \sum_{a=1}^{d} sin^2(k_a/2)$, which is much closer to what one might have

expected.[6] The interference effect for the fermionic problem is illustrated in Fig. 6.43. Different paths that carry the system from one hole pair configuration to another generally interfere with each other, and when two such paths differ by the exchange of two electrons, they interfere destructively in the fermionic case and constructively in the bosonic. It follows from this argument that pair motion, too, is frustrated–it actually results in an effective kinetic repulsion between holes, rather than in pair binding. (It is apparent that second neighbor hopping terms, t', produce less frustration of the single particle motion, and "pair hopping" terms, which arise naturally in the t/U expansion of the Hubbard model, lead to unfrustrated pair motion [158]. However, t' is generally substantially smaller than t, and if pair hopping is derived from the Hubbard model, it is of order J, and hence relatively small.)

Many holes: phase separation

In large d, the frustration of the kinetic energy of doped holes in an antiferromagnet leads to a miscibility gap [396]. Perhaps this should not be surprising, since phase separation is the generic fate of mixtures at low temperatures. At any finite temperature, two–phase coexistence occurs whenever the chemical potentials of the two phases are equal. In the present case, one of the phases, the undoped antiferromagnet, is incompressible, which means that at $T = 0$ its chemical potential lies at an indeterminate point within the Mott gap. Under these circumstances, phase coexistence is instead established by considering the total energy of the system:

$$\begin{aligned} E_{tot} &= N_{AF} e_{AF} + N_h e_h \\ &= N e_{AF} + N_h (e_h - e_{AF}) \,, \end{aligned} \tag{6.132}$$

where N_{AF} and N_h are the number of sites occupied by the undoped antiferromagnet and by the hole rich phase, respectively; $N = N_{AF} + N_h$; e_{AF} is the energy per site of the antiferromagnet and e_h is the energy per site of the hole rich phase, in which the concentration of doped holes is $x_{rich} = x(N/N_h) \geq x$. If E_{tot} has a minimum with respect to N_h at a value $N_h < N$, there is phase coexistence. This minimization leads to the equation

$$\mu = \frac{e_{AF} - e_h(\mu)}{1 - n(\mu)} \,, \tag{6.133}$$

where μ is the chemical potential of the hole rich phase, and $n = 1 - x_c$ is the electron density in the hole rich phase.

As we shall see, in the limit of large dimension, $n(\mu)$ (and hence e_h as well) is either 0 or exponentially small, so Eq. (6.133) reduces to

$$\mu \approx e_{AF} \,. \tag{6.134}$$

We can see already how phase separation can transpire. As the electron density is raised from zero (*i.e.* starting from $x = 1$ and lowering x), the chemical potential of the electron gas increases. Once μ reaches e_{AF}, the added

[6] This corrects similar expressions in Ref. [396].

electrons must go into the antiferromagnetic phase, and the density of the electron gas stops increasing. We can employ a small k expansion of the electronic dispersion, $\epsilon(\boldsymbol{k}) = -2td + tk^2 + \ldots$, to determine that $\mu \approx -2td + tk_F^2$. Thus if $e_{AF} < -2td$, the electron gas is completely unstable, and there is phase separation into the pure antiferromagnet, and an insulating hole rich phase with $n = 0$. In this case, $x_c = 1$. (Of course, phase separation occurs below a critical concentration of doped holes.) Otherwise, the density of the electron gas is

$$n = \frac{2A_d}{d}\left(\frac{k_F}{2\pi}\right)^d = \frac{2A_d}{d}\left(\frac{\sqrt{(\mu + 2td)/t}}{2\pi}\right)^d . \tag{6.135}$$

Here A_d is the hypersurface area of a d dimensional unit sphere. In large d, the energy per site of the pure antiferromagnet approaches that of the classical Néel state:

$$e_{AF} = -d\left(\frac{J}{4} - V\right)\left[1 + \mathcal{O}(1/d^2)\right] . \tag{6.136}$$

From this, it follows that the hole rich phase is insulating (*i.e.* it has no electrons) if $J - 4V > 8t$ and it is metallic ($x_c < 1$) if $J - 4V < 8t$. However, even when the hole rich phase is metallic, its electron density is exponentially small (as promised):

$$n = 1 - x_c = \frac{2}{\sqrt{\pi d}}\left[\frac{e}{\pi}\left(1 - \left[\frac{J - 4V}{8t}\right]\right)\right]^{d/2}\left[1 + \mathcal{O}(1/d)\right] , \tag{6.137}$$

where we have used the asymptotic large d expression [396] $A_d \approx \sqrt{\frac{d}{\pi}}(\frac{2\pi e}{d})^{d/2}$. As illustrated in Fig. 6.44 in large d, so long as $0 < x < x_c$, the ground state of the $t-J-V$ model is phase separated, with an undoped antiferromagnetic region and a hole rich region which, if $8t > J - 4V$, is a Fermi liquid of dilute electrons, or if $8t < J - 4V$, is an insulator. (Under these same circumstance, if $x_c < x < 1$, the ground state is a uniform, Fermi liquid metal[7].)

In the low dimensions of physical interest, such as $d = 2$ and $d = 3$, the quantitative accuracy of a large dimension expansion is certainly suspect. Nonetheless, we expect the qualitative physics of $d = 2$ and $d = 3$ to be captured in a large dimension treatment, since the lower critical dimension of most long range $T = 0$ ordered states is $d = 1$. For comparison, in Fig. 6.45 we reproduce the phase diagram of the 2D t–J model which was proposed by Hellberg and Manousakis [324] on the basis of Monte Carlo studies of systems with up to 60 electrons. There is clearly substantial similarity between this and the large D result in Fig. 6.44.

In one sense phase separation certainly can be thought of as a strong attractive interaction between holes, although in reality the mechanism is

[7] This statement neglects a possible subtlety due to the Kohn–Luttinger theorem.

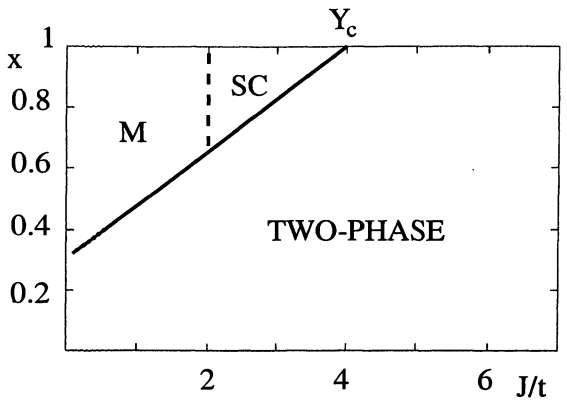

Fig. 6.44. Phase diagram of the t–J model deduced from large the d expansion. In the figure, we have set $d = 2$. "Two–phase" labels the region in which phase separation occurs between the pure antiferromagnet and a hole rich phase, "SC" labels a region of s–wave superconductivity, and "M" labels a region of metallic behavior. At parametrically small $J/t \propto 1/\sqrt{d}$, a ferromagnetic phase intervenes at small doping (from Ref. [396])

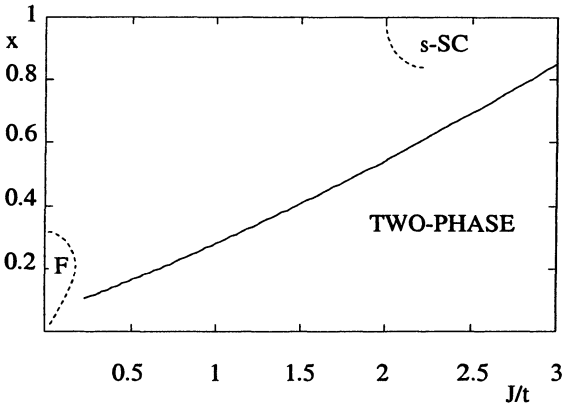

Fig. 6.45. Phase diagram of the t–J model in two dimensions at zero temperature, deduced from numerical studies with up to 60 electrons. "Two–phase" labels the region of phase separation, "s–SC" labels a region of s–wave superconductivity, and "F" labels a region of ferromagnetism. This figure is abstracted from Hellberg and Manousakis [324].

more properly regarded as the ejection of holes from the antiferromagnet. (Like salt crystallizing from a solution of salt water, the spin crystal is pure.) The characteristic energy scale of this interaction is set by magnetic energies,

so one expects to see phase separation only at temperatures that are small compared to the antiferromagnetic exchange energy J.

6.12.2 Coulomb Frustrated Phase Separation and Stripes

Were holes neutral, phase separation would be a physically reasonable solution to the problem of frustrated hole motion in an antiferromagnet. But there is another competition if the holes carry charge. In this case, full phase separation is impossible because of the infinite Coulomb energy density it would entail. Thus, there is a second competition between the short range tendency to phase separation embodied in the t–J model, and the long range piece of the Coulomb interaction. The compromise solution to this second level of frustration results in an emergent length scale [403]–a crossover between phase separation on short length scales, and the required homogeneity on long length scales. Depending upon microscopic details, many solutions are possible [404] which are inhomogeneous on intermediate length scales, such as checkerboard patterns, stripes, bubbles, or others. (Stripes are a unidirectional density wave.)

Of these, the stripe solution is remarkably stable in simple models [364, 396, 405], and moreover is widely observed in the cuprates [6]. A stripe state is a unidirectional density wave state–we think of such a state, at an intuitive level, as consisting of alternating strips of hole rich and hole poor phase. A fully ordered stripe phase has charge density wave and spin density wave order interleaved.

Certain aspects of stripe states can be made precise on the basis of long distance considerations. If we consider the Landau theory [45] of coupled order parameters for a spin density wave $\boldsymbol{S}$ with ordering vector $\boldsymbol{k}$ and a charge density wave ρ with ordering vector $\boldsymbol{q}$, then if $2\boldsymbol{k} \equiv \boldsymbol{q}$ (where $\equiv$, in this case, means equal modulo a reciprocal lattice vector), then there is a cubic term in the Landau free energy allowed by symmetry,

$$F_{coupling} = \gamma_{stripe} \left[\rho_{-\boldsymbol{q}} \boldsymbol{S}_{\boldsymbol{k}} \cdot \boldsymbol{S}_{\boldsymbol{k}} + \text{C.C.}\right]. \tag{6.138}$$

There are two important consequences of this term. Firstly, the system can lower its energy by locking the ordering vectors of the spin and charge density wave components of the order, such that the period of the spin order is twice that of the charge order. At order parameter level, is the origin of the antiphase character of the stripe order[8]. Secondly, because this term is linear in ρ, it means that if there is spin order, $\langle \boldsymbol{S}_{\boldsymbol{k}} \rangle \neq 0$, there must *necessarily*[9] be charge order, $\langle \rho_{2\boldsymbol{k}} \rangle \neq 0$, although the converse is not true.

[8] In the context of Landau–Ginzburg theory, the situation is somewhat more complex, and whether the spin and charge order have this relation, or have the same period turns out to depend on short distance physics, see footnote 10 and [406].

[9] Here, we exclude the possibility of perfectly circular spiral spin order, in which $\text{Re}\{\langle \boldsymbol{S} \rangle\} \cdot \text{Im}\{\langle \boldsymbol{S} \rangle\} = 0$ and $[\text{Re}\{\langle \boldsymbol{S} \rangle\}]^2 = [\text{Im}\{\langle \boldsymbol{S} \rangle\}]^2 \neq 0$.

The Landau theory also allows us to distinguish three macroscopically distinct scenarios for the onset of stripe order. If charge order onsets at a higher critical temperature, and spin order either does not occur, or onsets at a lower critical temperature, the stripe order can be called "charge driven." If spin and charge order onset at the same critical temperature, but the charge order is parasitic, in the sense that $\langle \rho_{2\boldsymbol{k}} \rangle \sim \langle \boldsymbol{S}_{\boldsymbol{k}} \rangle^2$, the stripe order is "spin driven." Finally, if charge and spin order onset simultaneously by a first order transition, the stripe order is driven by the symbiosis between charge and spin order. This is discussed in more detail in Ref. [45].

The antiphase nature of the stripes was first predicted by the Hartree–Fock theory and has been confirmed as being the most probable outcome in various later, more detailed studies of the problem [322,381,382,407]. In this case, the spin texture undergoes a π phase shift across every charge stripe, so that every other spin stripe has the opposite Néel vector, cancelling out any magnetic intensity at the commensurate wavevector, $\langle \pi, \pi \rangle$. This situation [408,409] has been called "topological doping." And, indeed, the predicted factor of two ratio between the spin and charge periodicities has been observed in all well established experimental realizations of stripe order in doped antiferromagnets. [47] Still, it is important to remember that nontopological stripes are also a logical possibility [381,382,399,406,410,411], and we should keep our eyes open for this form of order, as well.[10]

In the context of frustrated phase separation, the formation of inhomogeneous structures is predominantly a statement about the charge density, and its scale is set by the Coulomb interaction. This has several implications. Firstly, this means that charge stripes may begin to self–organize (at least locally) at relatively high temperatures, *i.e.* they are charge driven in the sense described above.[11] Secondly, charge density wave order always couples linearly to lattice distortions, so we should expect dramatic signatures of stripe formation to show up in the phonon spectrum. Indeed, phonons may significantly affect the energetics of stripe formation [412]. Thirdly, although we are used to thinking of density wave states as insulating, or at least as having a dramatically reduced density of states at the Fermi energy, this is not necessarily true. If the average hole concentration on each stripe is determined primarily by the competition between the Coulomb interaction and the local tendency to phase separation, the linear hole density per site along each stripe can vary as a function of x and consequently there is no reason to expect the Fermi energy to lie in a gap or pseudogap. In essence, stripes may be intrinsically metallic, or even superconducting. Moreover, such compressible stripes are highly prone to lattice commensurability effects which tend to pin the inter–stripe spacing at commensurate values. Conversely, if the stripes are a consequence of some sort of Fermi surface nesting, as is

[10] For example, an analogous Landau theory of stripes near the Néel state must include the order parameter $\boldsymbol{S}_{\pi}$, which favors in–phase domain walls [406].

[11] In Hartree–Fock theory, stripes are spin driven.

the case in the Hartree–Fock studies [377, 380, 413] of stripe formation, the stripe period always adjusts precisely so as to maintain a gap or pseudogap at the Fermi surface: there is always one doped hole per site along each charge stripe. This insulating behavior is likely a generic feature of all local models of stripe formation [408], although more sophisticated treatments can lead to other preferred linear hole densities along a stripe [322, 376].

In short, stripe order is theoretically expected to be a common form of self–organized charge ordering in doped antiferromagnets. ("Stripe glasses" and "stripe liquids" are also possible.) In a d–dimensional striped state, the doped holes are concentrated in an ordered array of parallel $(d-1)$ dimensional hypersurfaces: solitons in $d = 1$, "rivers of charge" in $d = 2$, and sheets of charge in $d = 3$. This "charge stripe order" can either coexist with antiferromagnetism with twice the period (topological doping) or with the same period as the charge order, or the magnetic order can be destroyed by quantum or thermal fluctuations of the spins. Moreover, the stripes can be insulating, conducting, or even superconducting. It is important to recall that for $d < 4$ quenched disorder is always a relevant perturbation for charge density waves, [414] so rather than stripe ordered states, real experiments may often require interpretation in terms of a "stripe glass" [415–418]. Finally, for many purposes, it is useful to think of systems that are not quite ordered, but have substantial short range stripe order as low frequency fluctuations, as a "fluctuating stripe liquid". We will present an example of such a state in the next subsection.

6.12.3 Avoided Critical Phenomena

Let us examine a simple model of Coulomb frustrated phase separation. We seek to embody a system with two coexisting phases, which are forced to interleave due to the charged nature of one of the phases. To account for the short range tendency to phase separation, we include a short range "ferromagnetic" interaction which encourages nearest neighbor regions to be of the same phase, and also a long range "antiferromagnetic" interaction which prevents any domain from growing too large:

$$H = -L \sum_{\langle i,j \rangle} \boldsymbol{S}_i \cdot \boldsymbol{S}_j + \frac{Q a^{d-2}}{2} \sum_{i \neq j} \frac{\boldsymbol{S}_i \cdot \boldsymbol{S}_j}{|\boldsymbol{R}_i - \boldsymbol{R}_j|^{d-2}} \,. \tag{6.139}$$

Here, $\boldsymbol{S}_j$ is an N component unit vector, $\boldsymbol{S}_i \cdot \boldsymbol{S}_i = 1$, L is a nearest neighbor ferromagnetic interaction, Q is an antiferromagnetic "Coulomb" term which represents the frustration (and is always assumed small, $Q \ll L$), d is the spatial dimension, $\langle i, j \rangle$ signifies nearest neighbor sites, a is the lattice constant, and $\boldsymbol{R}_j$ is the location of lattice site j. The Ising ($N = 1$) version of this model is the simplest coarse grained model [360, 419] of Coulomb frustrated phase separation, in which $S_j = 1$ represents a hole rich, and $S_j = -1$ a hole poor region. In this case, $L > 0$ is the surface tension of an interface

between the two phases, and Q is the strength of the Coulomb frustration. While the phase diagram of this model has been analyzed [419] at $T = 0$, it is fairly complicated, and its extension to finite temperature has only been attempted numerically [420]. However, all the thermodynamic properties of this model can be obtained [421,422] exactly in the large N limit.

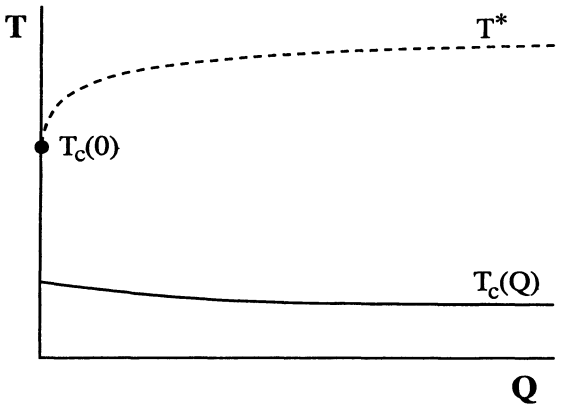

Fig. 6.46. Schematic phase diagram of the model in Eq. (6.139) of avoided critical phenomena. The thick black dot marks $T_c(Q = 0)$, the ordering temperature in the absence of frustration; this is "the avoided critical point". Notice that $T_c(Q \to 0) < T_c(Q = 0)$. From Ref. [422]

Fig. 6.46 shows the phase diagram for this model. Both for $Q = 0$ and $Q \neq 0$, there is a low temperature ordered state, but the ordered state is fundamentally different for the two cases. For the unfrustrated case, the ordered state is homogeneous, whereas with frustration, there is an emergent length scale in the ordered state which governs the modulation of the order parameter. To be specific, in dimensions $d > 2$ and for $N > 2$, there is a low temperature ordered unidirectional spiral phase, which one can think of as a sort of stripe ordered phase [422]. Clearly, as $Q \to 0$, the modulation length scale must diverge, so that the homogeneous ordered state is recovered. However, like an antiferromagnet doped with neutral holes, there is a discontinuous change in the physics from $Q = 0$ to any finite Q: for $d \leq 3$, $\lim_{Q \to 0} T_c(Q) \equiv T_c(0^+)$ is strictly less than $T_c(0)$. In other words, an infinitesimal amount of frustration depresses the ordering temperature discontinuously.

Although for any finite Q the system does not experience a phase transition as the temperature is lowered through $T_c(0)$, the avoided critical point heavily influences the short range physics. For temperatures in the range $T_c(0) > T > T_c(0^+)$, substantial local order develops. An explicit expression

for the spin–spin correlator can be obtained in this temperature range: At distances less than the correlation length $\xi_0(T)$ of the unfrustrated magnet, $R_{ij} < \xi_0(T)$, the correlator is critical,

$$\langle \boldsymbol{S}_i \cdot \boldsymbol{S}_j \rangle \sim (a/R_{ij})^{d-2-\eta} \ , \tag{6.140}$$

but for longer distances, $R_{ij} > \xi_0(T)$, it exhibits a damped version of the Goldstone behavior of a fluctuating stripe phase,

$$\langle \boldsymbol{S}_i \cdot \boldsymbol{S}_j \rangle \sim (a/R_{ij})^{\frac{d-1}{2}} \cos[KR_{ij}] \exp[-\kappa R_{ij}] \ . \tag{6.141}$$

At $T_c(Q)$, the wavevector K is equal to the stripe ordering wavevector of the low temperature ordered state, $K(T_c) = (Q/L)^{1/4}$. As the temperature is raised, K decreases until it vanishes at a disorder line marked T^* in the figure. The inverse domain size is given by

$$\kappa(T) = \sqrt{(Q/L)^{1/4} - K^2(T)} \ . \tag{6.142}$$

For a broad range of temperatures (which does not narrow as $Q \to 0$), this model is in a fluctuating stripe phase in a sense that can be made arbitrarily precise for small enough Q.

6.12.4 The Cuprates as doped Antiferromagnets

General considerations

There is no question that the undoped parents of the high temperature superconductors are Mott insulators, in which the strong short range repulsion between electrons is responsible for the insulating behavior, and the residual effects of the electron kinetic energy (superexchange) lead to the observed antiferromagnetism. Indeed, one of the great theoretical triumphs of the field is the complete description, based on interacting spin waves and the resulting nonlinear sigma model, of the magnetism in these materials. [224, 225, 305]

However, it is certainly less clear that one should inevitably view the superconducting materials as doped antiferromagnets, especially given that we have presented strong reasons to expect a first order phase transition between $x = 0$ and $x > 0$. Nonetheless, many experiments on the cuprates are suggestive of a doped antiferromagnetic character. In the first place, various measurements of the density of mobile charge, including the superfluid density [108,243], the "Drude weight" measured in optical conductivity [423], and the Hall number [424, 425], are all consistent with a density proportional to the *doped hole* density, x, rather than the total hole density, $1 + x$, expected from a band structure approach. Moreover, over a broad range of doping, the cuprates retain a clear memory of the antiferromagnetism of the parent correlated insulator. Local magnetism abounds. NMR, μSR, and neutron scattering find evidence (some of which is summarized in Section 6.13.1) of

static, or slowly fluctuating, spin patterns, including stripes, spin glasses, and perhaps staggered orbital currents. Static magnetic moments, or slowly fluctuating ones, are hard to reconcile with a Fermi liquid picture. There is also some evidence from STM of local electronic inhomogeneity [101,102,426] in BSCCO, indicative of the short range tendency to phase separate. The Fermi liquid state in a simple metal is highly structured in k–space, and so is highly homogeneous (rigid) in real space. This is certainly in contrast with experiments on the cuprates which indicate significant real space structure. (Note, the cuprates should be viewed as doped antiferromagnets.)

Stripes

There is increasingly strong evidence that stripe correlations, as a specific feature of doped antiferromagnets, occur in *at least some* high temperature superconducting materials. The occurrence of stripe phases in the high temperature superconductors in particular, and in doped antiferromagnets more generally, was successfully predicted by theory [377, 380, 413]. The theoretical predictions predated any clear body of well accepted experimental facts, although in all fairness it must be admitted that there was some empirical evidence of stripe–like structures which predated all of the theoretical inquiry: Even at the time of the first Hartree–Fock studies, there was already dramatic experimental evidence [427,428] of incommensurate magnetic structure in $La_{2-x}Sr_xCuO_4$. Indeed, it is clear that a fair fraction of the theoretical inferences discussed in Section 6.12.2 are, at least in broad outline, applicable to a large number of materials, including at least some high temperature superconductors [6]. In particular, the seminal discovery [429] that in $La_{1.6-x}Nd_{0.4}Sr_xCuO_4$, first charge stripe order, then spin stripe order, and then superconductivity onset at successively lower critical temperatures is consistent with Coulomb frustrated phase separation. (See Fig. 6.47 in Section 6.13.1.) Somewhat earlier work on the closely related nickelates [430] established that the charge stripes are, indeed, antiphase domain walls in the spin order.

Controversy remains as to how universal stripe phases are in the cuprate superconducting materials, and even how the observed phases should be precisely characterized. This is also an exciting topic, on which there is considerable ongoing theoretical and experimental study. We will defer further discussion of this topic to Section 6.13.

6.12.5 Additional Considerations and Alternative Perspectives

There are a number of additional aspects of this problem which we have not discussed here, but which we feel warrant a mention. In each case, clear discussions exist in the literature to which the interested reader is directed for a fuller exposition.

Phonons

There is no doubt that strong electron–phonon coupling can drive a system

to phase separate. Strong correlation effects necessarily enhance such tendencies, since they reduce the rigidity of the electron wavefunction to spatial modulation. (See, *e.g.*, the 1D example in Section 6.9.2.) In particular, when there is already a tendency to some form of charge ordering, on very general grounds we expect it to be strongly enhanced by electron–phonon interactions.

This observation makes us very leery of any attempt at a *quantitative* comparison between results on phase separation or stripe formation in the t–J or Hubbard models with experiments in the cuprates, where the electron–phonon interaction is manifestly strong [431]. Conversely, there should generally be substantial signatures of various stripe–related phenomena in the phonon dynamics, and this can be used to obtain an experimental handle on these behaviors [162]. Indeed, there exists a parallel development of stripe–related theories of high temperature superconductivity based on Coulomb frustration of a phase separation instability which is driven by strong electron–phonon interactions [16,61,432]. The similarity between many of the notions that have emerged from these studies, and those that have grown out of studies of doped antiferromagnets illustrates both how robust the consequences of frustrated phase separation are in highly correlated systems, and how difficult it is to unambiguously identify a "mechanism" for it. For a recent discussion of many of the same phenomena discussed here from this alternative viewpoint, see Ref. [62].

Spin–Peierls order

Another approach to this problem, which emerges naturally from an analysis of the large N limit [72], is to view the doped system as a "spin–Peierls" insulator, by which we mean a quantum disordered magnet in which the unit cell size is doubled but spin rotational invariance is preserved.[12] While the undoped system is certainly antiferromagnetically ordered, it is argued that when the doping exceeds the critical value at which spin rotational symmetry is restored, the doped Mott insulating features of the resulting state are better viewed as if they arose from a doped spin–Peierls state. Moreover, since the spin–Peierls state has a spin gap, it can profitably be treated as a crystal of Cooper pairs, which makes the connection to superconductivity very natural. Finally, as mentioned in Section 6.7, this approach has a natural connection with various spin liquid ideas.

Interestingly, it turns out that the doped spin–Peierls state also generically phase separates [393,435–437]. When the effect of long range Coulomb interactions are included, the result is a staircase of commensurate stripe phases [437]. Again, the convergence of the pictures emerging from diverse starting points convinces us of the generality of stripey physics in correlated systems. For a recent discussion of the physics of stripe phases, and their con-

[12] Alternatively, this state can be viewed as a bond–centered charge density wave [433,434].

nection to the cuprate high temperature superconductors approached from the large N/spin–Peierls perspective, see Ref. [438].

Stripes in other systems

It is not only the robustness of stripes in various theories that warrants mention, but also the fact that they are observed, in one way or another, in diverse physical realizations of correlated electrons. Stripes, and even a tendency to electronic phase separation, are by now well documented in the manganites—the colossal magnetoresistance materials. (For recent discussions, which review some of the literature, see Refs. [17,439] and [109].) This system, like the nickelates and cuprates, is a doped antiferromagnet, so the analogy is quite precise.

Although the microscopic physics of quantum Hall systems is quite different from that of doped antiferromagnets, it has been realized for some time [440,441] that in higher Landau levels, a similar drama occurs due to the interplay between a short ranged attraction and a long range repulsion between electrons which gives rise to stripe and bubble phases. Evidence of these, as well as quantum Hall nematic phases, [180,442] has become increasingly compelling in recent years. (For a recent review, see [181].) On a more speculative note, it has been noticed that such behavior may be expected in the neighborhood of many first order transitions in electronic systems, and it has been suggested that various charge inhomogeneous states may play a role in the apparent metal–insulator transition observed in the two dimensional electron gas [443].

6.13 Stripes and High Temperature Superconductivity

We present a coherent view–our view–of high temperature superconductivity in the cuprate superconductors. This section is more broadly phenomenological than is the rest of this paper.

In this article, we have analyzed the problem of high temperature superconductivity in a highly correlated electron liquid, with particular emphasis on doped antiferromagnets. We have identified theoretical issues, and even some solutions. We have also discussed aspects of the physics that elude a BCS description. This is progress.

However, we have not presented a single, unified solution to the problem. Contrast this with BCS, a theory so elegant it may captured in haiku:

Instability
Of a tranquil Fermi sea
Broken symmetry.

Of course, to obtain a more quantitative understanding of particular materials would require a few more verses—we might need to study the Eliashberg

equations to treat the phonon dynamics in a more realistic fashion, and we may need to include Fermi liquid corrections, and we may also have to wave our hands a bit about μ^*, *etc.* But basically, in the context of a single approximate solution of a very simple model problem, we obtain a remarkably detailed and satisfactory understanding of the physics. And while we may not be able to compute T_c very accurately—it does, after all, depend exponentially on parameters—we can understand what sort of metals will tend to be good superconductors: metals with strong electron-phonon coupling, and consequently high room temperature resistances, are good candidates, as are metals with large density of states at the Fermi energy. We can also compute various dimensionless ratios of physical quantities, predict dramatic coherence effects (which *do* depend on microscopic details), and understand the qualitative effects of disorder.

The theory of high temperature superconductivity presented here reads more like a Russian novel, with exciting chapters and fascinating characters, but there are many intricate subplots, and the pages are awash in familiars, diminutives, and patronymics. To some extent, this is probably unavoidable. Fluctuation effects matter in the superconducting state: the phase ordering temperature, T_θ, is approximately equal to T_c, and the zero temperature coherence length, ξ_0, is a couple of lattice constants. In addition, the existence of one or more physical pseudogap scales (the T^*'s) in addition to T_c means that there are multiple distinct qualitative changes in the physics in going from high temperature to $T = 0$. Moreover, various other types of ordered states are seen in close proximity to or in coexistence with the superconducting state. Thus, it is more plausible that we will weave together a qualitative understanding of the basic physics in terms of a number of effective field theories, each capturing the important physics in some range of energy and length scales. Ideally, these different theories will be nested, with each effective Hamiltonian derived as the low energy limit of the preceding one.

While not as satisfying as the unified description of BCS–Eliashberg–Migdal theory, there is certainly ample precedent for the validity of this kind of multiscale approach. The number of quantitative predictions may be limited, but we should expect the approach to provide a simple understanding of a large number of qualitative observations. In fact, we may never be able to predict T_c reliably, or even whether a particular material, if made, will be a good superconductor, but a successful theory should certainly give us some guidance concerning what *types* of new materials are good candidate high temperature superconductors [444, 445].

Before we continue, we wish to state a major change of emphasis. Up until this point, we have presented only results that we consider to be on secure theoretical footing. That is, we have presented a valid theory. (High temperature superconductivity being a contentious field, it will not surprise the reader to learn that there is controversy over how important each of the issues discussed above is to the physics of the cuprates. As the field

progresses, and especially as new data are brought to light, it may be that in a future version of this article we, too, might change matters of *emphasis*, but we are confident that no new understanding will challenge the *validity* of the theoretical constructs discussed until now.) We now allow ourselves free rein to discuss the *applicability* of these ideas to the real world. In particular, we discuss the cuprate high temperature superconductors, and whether the salient physics therein finds a natural explanation in terms of stripes in doped antiferromagnets. Various open issues are laid out, as well as some general strategies for addressing them.

6.13.1 Experimental Signatures of Stripes

At the simplest level, stripes refer to a broken symmetry state in which the discrete translational symmetry of the crystal is broken in one direction: stripes is a term for a *unidirectional density wave*. "Charge stripes" refer to a unidirectional charge density wave (CDW). "Spin stripes" are unidirectional colinear spin density waves (SDW). (Note, spiral SDW order has somewhat different character, even when unidirectional, and is not generally included in the class of striped states.) More subtle local forms of stripes, such as stripe liquids, nematics and glasses are addressed in Section 6.13.2.

Where do stripes occur in the phase diagram?

As discussed in Sections 6.11 and 6.12, holes doped into an antiferromagnet have a tendency to self–organize into rivers of charge, and these charge stripes tend to associate with antiphase domain walls in the spin texture. As shown in Section 6.12.2, stripe order is typically either "charge driven," in which case spin order onsets (if at all) at a temperature less than the charge ordering temperature, or "spin driven," if the charge order onsets as a weak parasitic order at the same temperature as the spin order. To the extent that stripes are indeed a consequence of Coulomb frustrated phase separation, we expect them to be charge driven, in this sense.

Neutron scattering has proven the most useful probe for unambiguously detecting stripe order. Neutrons can scatter directly from the electron spins. However, neutrons (and, for practical reasons, X–rays as well) can only detect charge stripes indirectly by imaging the induced lattice distortions. Alternatively, (as discussed in Section 6.12.2) since spin stripe order implies charge order, the magnetic neutron scattering itself can be viewed as an indirect measure of charge order. Since stripe order is unidirectional, it should ideally show up in a diffraction experiment as pairs of new Bragg peaks at positions $\boldsymbol{k}_{\pm} = \boldsymbol{Q} \pm 2\pi\hat{e}/\lambda$ where $\hat{e}$ is the unit vector perpendicular to the stripe direction, λ is the stripe period, and $\boldsymbol{Q}$ is an appropriate fiduciary point. For charge stripes, $\boldsymbol{Q}$ is any reciprocal lattice vector of the underlying crystal, while for spin stripes, $\boldsymbol{Q}$ is offset from this by the Néel ordering vector, $\langle \pi, \pi \rangle$. Where both spin and charge order are present, the fact that the charge stripes are associated with magnetic antiphase domain walls is reflected in the fact that $\lambda_{spin} = 2\lambda_{charge}$, or equivalently $\boldsymbol{k}_{charge} = 2\boldsymbol{k}_{spin}$.

$La_{1.6-x}Nd_{0.4}Sr_xCuO_4$ (LNSCO) is stripe ordered, and the onset of stripe ordering with temperature is clear. Fig. 6.47 shows data from neutron scattering, NQR, and susceptibility measurements [416]. In this material, charge stripes form at a higher temperature than spin stripes. Note also that static charge and spin stripes coexist with superconductivity throughout the superconducting dome. In fact experiments reveal quartets of new Bragg peaks, at $\boldsymbol{Q} \pm 2\pi\hat{x}/\lambda$ and $\boldsymbol{Q} \pm 2\pi\hat{y}/\lambda$. In this material, the reason for this is understood to be a bilayer effect—there is a crystallographically imposed tendency for the stripes on neighboring planes to be oriented at right angles to each other, giving rise to two equivalent pairs of peaks. Charge and spin peaks have also been detected [446] in neutron scattering studies of $La_{1.875}Ba_{0.125-x}Sr_xCuO_4$ (LBCO).

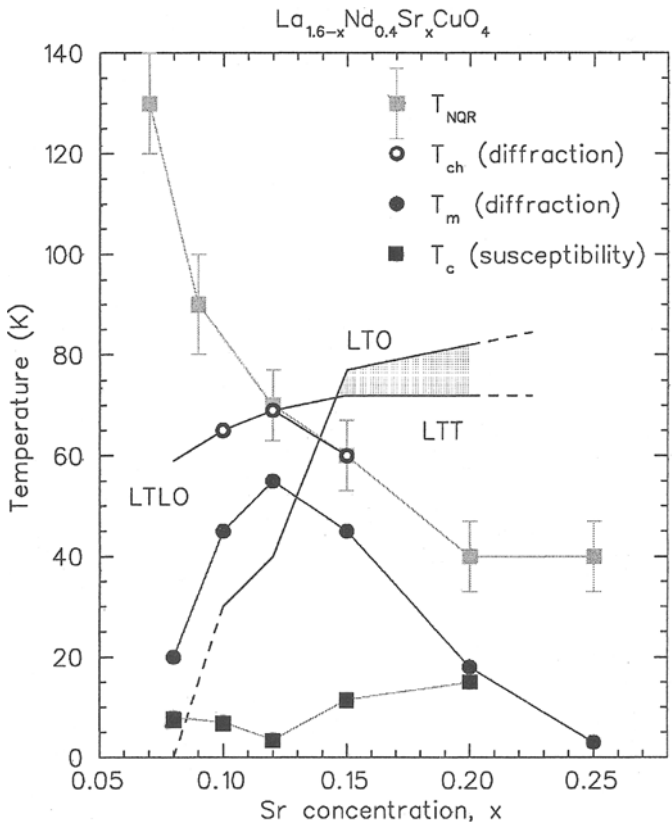

Fig. 6.47. Data points refer to the onset of charge inhomogeneity (NQR), to the onset of incommensurate magnetic peaks (T_m) and to the superconducting T_c, from Ichikawa *et al.* [416]

Spin stripe order has also been observed from elastic neutron scattering in $La_{2-x}Sr_xCuO_4$ (LSCO) for dopings between $x = .02$ and $x = .05$ where the material is not superconducting at any T; these stripes are called diagonal, because they lie along a direction rotated 45^o to the Cu-O bond direction [166]. Above $x = .05$ [447], the stripes are vertical, *i.e.* along the Cu-O bond direction, and the samples are superconducting at low temperature. We should say *mostly* vertical. Careful neutron scattering work [167,448] on LSCO and LCO has shown that the incommensurate peaks are slightly rotated from the $Cu-O$ bond direction, corresponding to the orthorhombicity of the crystal.. For dopings between $x = .05$ and $x = .13$, the stripes have an ordered (static) component. In the region $x = .13$ to $x = .25$, incommensurate magnetic peaks have been detected with inelastic neutron scattering. Because of the close resemblance between these peaks and the static order observed at lower doping, this can be unambiguously interpreted as being due to slowly fluctuating stripes.

Neutron scattering has also detected spin stripes in $La_2CuO_{4+\delta}$ (LCO) with $\delta = .12$ [448]. In this material, static stripes coexist with superconductivity even at optimal doping. In the $T_c = 42K$ samples (the highest T_c for this family thus far), superconductivity and spin stripe order onset simultaneously [168,448]. Application of a magnetic field suppresses the superconducting transition temperature, but has little effect on the ordering temperature of the spins [449].

In very underdoped nonsuperconducting LSCO, because the stripes lie along one of the orthorhombic axes, it has been possible to confirm [450, 451] that stripe order leads, as expected, to pairs of equivalent Bragg spots, indicating unidirectional density wave order. In both superconducting LSCO and LCO, quartets of equivalent Bragg peaks are observed whenever stripe order occurs. This could be due to a bilayer effect, as in LNSCO, or due to a large distance domain structure of the stripes within a given plane, such that different domains contribute weight to one or the other of the two pairs of peaks. However, because the stripe character in these materials so closely resembles that in LNSCO, there is no real doubt that the observed ordering peaks are associated with stripe order, as opposed to some form of checkerboard order.

In $YBaCu_2O_{6+y}$ (YBCO), incommensurate spin fluctuations have been identified throughout the superconducting doping range. [147,162,165,452] By themselves, these peaks (which are only observed at frequencies above a rather substantial spin gap) are subject to more than one possible interpretation [453], although their similarity [454] to the stripe signals seen in LSCO is strong circumstantial evidence that they are associated with stripe fluctuations. Recently, this interpretation has been strongly reinforced by several additional observations. Neutron scattering evidence [165] has been found of static charge stripe order in underdoped YBCO with $y = .35$ and $T_c = 39$K. The charge peaks persist to at least $300K$. The presence of a static stripe

phase in YBCO means that inelastic peaks seen at higher doping are very likely fluctuations of this ordered phase. In addition, phonon anomalies have been linked to the static charge stripes at $y = .35$, and used to detect charge fluctuations at $y = .6$ [162]. By studying a partially detwinned sample with $y = .6$, with a 2 : 1 ratio of domains of crystallographic orientation, Mook and collaborators were able to show that the quartet of incommensurate magnetic peaks consists of two inequivalent pairs, also with a 2:1 ratio of intensities in the two directions [455]. This confirms that in YBCO, as well, the signal arises from unidirectional spin and charge modulations (stripes), and not from a checkerboard–like pattern.

Empirically, charge stripe formation precedes spin stripe formation as the temperature is lowered, and charge stripes also form at higher temperatures than T_c. Both types of stripe formation may be a phase transition, or may simply be a crossover of local stripe ordering, depending upon the material and doping. Where it can be detected, charge stripe formation occurs at a higher temperature than the formation of the pairing gap,[13] consistent with the spin gap proximity effect (see Section 6.10.4).

Although some neutron scattering has been done on $Bi_2Sr_2CaCu_2O_{8+\delta}$ (BSCCO), the probe has only produced weak evidence of significant incommensurate structure [456]. The weak coupling of planes in BSCCO makes neutron scattering difficult, as it is difficult to grow the requisite large crystals. However, BSCCO is very well suited to surface probes such as ARPES and STM. Recent STM data, both with [457] and without [458] an external magnetic field have revealed a *static* modulation in the local density of states that is very reminiscent of the incommensurate peaks observed with neutron scattering. Indeed, in both cases, the Fourier transform of the STM image exhibits a clear quartet of incommensurate peaks, just like those seen in neutron scattering in LSCO and YBCO. Here, however, unlike in the neutron scattering data, phase information is available in that Fourier transform. Using standard image enhancement methods, this phase information can be exploited [458] to directly confirm that the quartet of intensity peaks is a consequence of a domain structure, in which the observed density of states modulation is locally one dimensional, but with an orientation that switches from domain to domain. The use of STM as a probe of charge order is new, and there is much about the method that needs to be better understood [459] before definitive conclusions can be reached, but the results to date certainly look very promising.

Finally, striking evidence of electronic anisotropy has been seen in untwinned crystals of $La_{2-x}Sr_xCuO_4$ ($x = 0.02 - 0.04$) and YBa_2CuO_{6+y} ($y = 0.35 - 1.0$) by Ando and collaborators [99]. The resistivity differs in the two in-plane directions in a way that cannot be readily accounted for by crystalline anisotropy alone. It is notable that in YBCO, the anisotropy increases as y is decreased. That is, the electrical anisotropy *increases* as the

[13] See our discussion of the pseudogap(s) in Section 6.3.5.

orthorhombicity is *reduced.* In some cases, substantial anisotropy persists up to temperatures as high as 300K. Furthermore, for $y < 0.6$, the anisotropy increases with decreasing temperature, much as would be expected [460] for an electron nematic. These observations from transport correlate well with the evidence from neutron scattering [455], discussed above, of substantial orientational order of the stripe correlations in YBCO, and with the substantial, and largely temperature independent anisotropy of the superfluid density observed in the same material. [13] Together, these observations constitute important, but still preliminary evidence of a nematic stripe phase in the cuprates.

6.13.2 Stripe Crystals, Fluids, and Electronic Liquid Crystals

Stripe ordered phases are precisely defined in terms of broken symmetry. A charge stripe phase spontaneously breaks the discrete translational symmetry and typically also the point group symmetry (e.g. four–fold rotational symmetry) of the host crystal. A spin stripe phase breaks spin rotational symmetry as well. While experiments to detect these orders in one or another specific material may be difficult to implement for practical reasons and because of the complicating effects of quenched disorder, the issues are unambiguous. Where these broken symmetries occur, it is certainly reasonable to conclude that the existence of stripe order is an established fact. That this can be said to be the case in a number of superconducting cuprates is responsible for the upsurge of interest in stripe physics.

It is much more complicated to define precisely the intuitive notion of a "stripe fluid". (For the present purposes, the term "fluctuating stripes" is taken to be synonymous with a stripe fluid. See, for example, Refs. [408] and [461].) Operationally, it means there is sufficient short ranged stripe order that, for the purposes of understanding the mesoscale physics, it is possible to treat the system *as if* it were stripe ordered, even though translational symmetry is not actually broken. It is possible to imagine intermediate stripe liquid phases which are translationally invariant, but which still break some symmetries which directly reflect the existence of local stripe order. The simplest example of this is an "electron nematic" phase. In classical liquid crystals, the nematic phase occurs when the constituent molecules are more or less cigar shaped. It can be thought of as a phase in which the cigars are preferentially aligned in one direction, so that the rotational symmetry of free space is broken (leaving only rotation by π intact) but translational symmetry is unbroken. In a very direct sense, this pattern of macroscopic symmetry breaking is thus encoding information about the microscopic constituents of the liquid. In a similar fashion, we can envisage an electron nematic as consisting of a melted stripe ordered phase in which the stripes meander, and even break into finite segments, but maintain some degree of orientational order—for instance, the stripes are more likely to lie in the x rather than the

y direction; see Fig. 6.48. In summary, some stripe liquids break rotational symmetry.

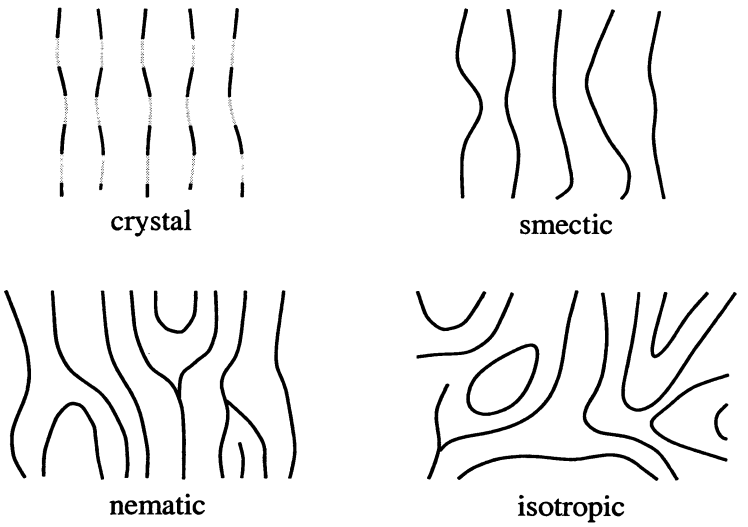

Fig. 6.48. Schematic representation of various stripe phases in two dimensions. The broken lines represent density modulations along the stripes. In the electronic crystal, density waves on neighboring stripes are locked in phase and pinned. The resulting state is insulating and breaks translation symmetry in all directions. Solid lines represent metallic stripes along which electrons can flow. They execute increasingly violent transverse fluctuations as the system is driven towards the transition into the nematic phase. The transition itself is associated with unbinding of dislocations that are seen in the snapshot of the nematic state. The isotropic stripe fluid breaks no spatial symmetries of the host crystal, but retains a local vestige of stripe order

One way to think about different types of stripe order is to imagine starting with an initial "classical" ordered state, with coexisting unidirectional SDW and CDW order. As quantum fluctuations are increased (metaphorically, by increasing $\hbar$), one can envisage that the soft orientational fluctuations of the spins will first cause the spin order to quantum melt, while the charge order remains (Melting stripes). If the charge order, too, is to quantum melt in a continuous phase transition, the resulting state will still have the stripes generally oriented in the same direction as in the ordered state, but with unbound dislocations which restore translational symmetry.

It is also possible to view the electron nematic from a weak coupling perspective, where it occurs as a Fermi surface instability [462], sometimes referred to as a Pomeranchuk instability. [463, 464] This instability is "nat-

ural" when the Fermi surface lies near a Van Hove singularity. The relation between the weak coupling and the stripe fluid pictures is currently a subject of ongoing investigation [465]. If the underlying crystal is tetragonal [466], this state still spontaneously breaks the crystal point group symmetry. In analogy with the corresponding classical state, it has been called an electron nematic, but it could also be viewed as an electronically driven orthorhombicity. This is still a state with broken symmetry, so in principle its existence should be unambiguously identifiable from experiment.

It is probable that when nematic order is lost, the resulting stripe liquid phase is not thermodynamically distinct from a conventional metallic phase, although the local order is sufficiently different that one might expect them to be separated by a first order transition. However, it is also possible that some more subtle form of order could distinguish a stripe liquid from other electron liquid phases—for instance, it has been proposed by Zaanen and collaborators [467] that a stripe liquid might posses an interesting, discrete topological order which is a vestige of the antiphase character of the magnetic correlations across a stripe. The order parameter can be identified with the matrix elements of any traceless symmetric tensor quantity, for instance the traceless piece of the dielectric or conductivity tensors.

With this physics in mind, we have sketched a qualitative phase diagram, shown in Fig. 6.49, which provides a physical picture of the consequences of melting a stripe ordered phase. As a function of increasing quantum and thermal transverse stripe fluctuations one expects the insulating electronic crystal, which exists at low temperatures and small $\hbar$, to evolve eventually into an isotropic disordered phase. At zero temperature this melting occurs in a sequence of quantum transitions [52]. The first is a first order transition into a smectic phase, then by dislocation unbinding a continuous transition leads to a nematic phase that eventually evolves (by a transition that can be continuous in $D = 2$, but is first order in a cubic system) into the isotropic phase. Similar transitions exist at finite temperature as indicated in Fig. 6.49.

We have also sketched a superconducting phase boundary in the same figure. Provided that there is a spin gap on each stripe, and that the charge Luttinger exponent $K_c > 1/2$, then (as discussed in Section 6.5) there is a divergent superconducting susceptibility on an isolated stripe. In this case, the superconducting T_c is determined by the Josephson coupling between stripes. Since, as discussed in Section 6.6, the mean Josephson coupling increases with increasing stripe fluctuations, T_c also rises with increasing $\hbar$ throughout the smectic phase. While there is currently no well developed theory of the superconducting properties of the nematic phase,[14] to the extent that we can think of the nematic as being locally smectic, it is reasonable to expect a continued increase in T_c across much, or all of the nematic phase, as shown in the figure. However, as the stripes lose their local integrity toward the transition

[14] Some very promising recent progress toward developing a microscopic theory of the electron nematic phase has been reported in Refs. [462] and [468].

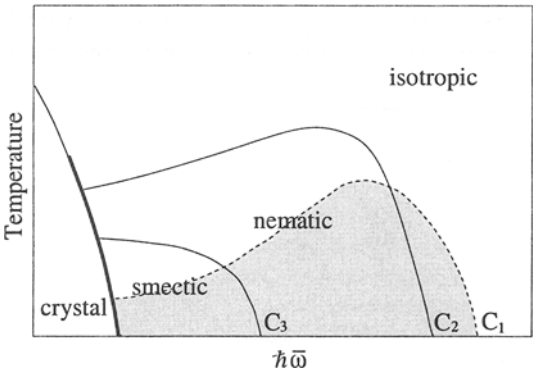

Fig. 6.49. Schematic phase diagram of a fluctuating stripe array in a (tetragonal) system with four–fold rotational symmetry in $D = 2$. Here $\hbar\bar{\omega}$ is a measure of the magnitude of the transverse zero point stripe fluctuations. Thin lines represent continuous transitions and the thick line a first order transition. We have assumed that the superconducting susceptibility on an isolated stripe diverges as $T \to 0$, so that at finite stripe density, there will be a transition to a globally superconducting state below a finite transition temperature. On the basis of qualitative arguments, discussed in the text, we have sketched a boundary of the superconducting phase, indicated by the shaded region. Depending on microscopic details the positions of the quantum critical points C_1 and C_2 could be interchanged. Distinctions between various possible commensurate and incommensurate stripe crystalline and smectic phases are not indicated in the figure. Similarly, all forms of spin order are neglected in the interest of simplicity

to the isotropic phase we expect, assuming that stripes are essential to the mechanism of pairing, that T_c will decrease, as shown.

The study of electronic liquid crystalline phases is in its infancy. Increasingly unambiguous experimental evidence of the existence of nematic phases has been recently reported in quantum Hall systems [180, 182, 442, 460, 469] in addition to the preliminary evidence of such phases in highly underdoped cuprates discussed above. Other more exotic electronic liquid crystalline phases are being studied theoretically. This is a very promising area for obtaining precise answers to well posed questions that may yield critical information concerning the important mesoscale physics of the high temperature superconductors.

6.13.3 Our View of the Phase Diagram – Reprise

Since the motion of dilute holes in a doped antiferromagnet is frustrated, the minimization of their kinetic energy is a complicated, multistage process. We have argued that this is accomplished in three stages: (a) the formation of static or dynamical charge inhomogeneity (stripes) at T^*_{stripe}, (b) the creation of local spin pairs at T^*_{pair}, which creates a spin gap, and (c) the establishment

of a phase–coherent superconducting state at T_c. The zero point kinetic energy is lowered along a stripe in the first stage, and perpendicular to the stripe in the second and third stages. Steps (a), (b), and (c) above are clearcut only if the energy scales are well separated, that is, if $T^*_{stripe} >> T^*_{pair} >> T_c$. On the underdoped side at least, if we identify T^*_{stripe} and T^*_{pair} with the appropriate observed pseudogap phenomena (see Section 6.3.5) there is a substantial (if not enormous) separation of these temperature scales.

Pseudogap scales

At high temperatures, the system must be disordered. As temperature is lowered, the antiferromagnet ejects holes, and charge stripe correlations develop. This may be either a phase transition or a crossover. We have called this temperature T^*_{stripe} in Fig. 6.12. Even if it is a phase transition, for instance a transition to a stripe nematic state, local order may develop above the ordering temperature, and probes on various time scales may yield different answers for T^*_{stripe}. As the antiferromagnet ejects holes, local antiferromagnet correlations are allowed to develop. Probes bearing on this temperature include the Knight shift, NQR, and diffraction. At a lower temperature, through communication with the locally antiferromagnetic environment, a spin gap develops on stripes. We identify this spin gap with the pairing gap, and have labeled this temperature (which is always a crossover) T^*_{pair}. Probes bearing on this temperature measure the single particle gap, and include ARPES, tunnelling, and NMR.

Dimensional crossovers

Looking at this evolution from a broader perspective, there are many consequences that can be understood based entirely on the notion that the effective dimensionality of the coherent electronic motion is temperature dependent. At high temperatures, before local stripe order occurs, the electronic motion is largely incoherent—*i.e* the physics is entirely local. Below T^*_{stripe}, the motion crosses over from quasi 0D to quasi 1D behavior. (It is intuitively clear that kinetic energy driven stripe formation should lead to increased hole mobility, as is observed, but how the famous T–linear resistivity can emerges from local quasi–0D physics is not yet clear. See, however, Refs. [360, 470–472].) Here, significant $\boldsymbol{k}$ space structure of various response functions is expected, and there may well emerge a degree of coherence and possibly pseudogaps, but the electron is not an elementary excitation, so broad spectral functions and non–Fermi liquid behavior should be the rule. Then, at a still lower temperature, a 1D to 3D crossover occurs as coherent electronic motion between stripes becomes possible. At this point coherent quasiparticles come to dominate the single particle spectrum, and more familiar metallic and/or superconducting physics will emerge. If the spin gap is larger than this crossover temperature (as it presumably is in underdoped materials), then this crossover occurs in the neighborhood of T_c. However, if the spin gap is small, then the dimensional crossover will likely occur at temperatures well above T_c, and T_c itself will have a more nearly BCS character, as discussed in Section 6.5.3—this

seems to be crudely what happens in the overdoped materials [473]. Since once there are well developed quasiparticles, there is every reason to expect them to be able to move coherently between planes, there is actually no substantial region of quasi 2D behavior expected. Although it may be hard, without a macroscopically oriented stripe array, to study the dimensional crossover by measuring in–plane response functions, the dimensional crossover can be studied by comparing in–plane to out–of plane behavior. (Much of the successful phenomenology of dimensional crossover developed in conjunction with the interlayer pairing mechanism of superconductivity [21] is explained in this way in the context of a stripe theory.)

The cuprates as quasi–1D superconductors

When $T^*_{stripe} >> T^*_{pair} >> T_c$, the model of a quasi–one dimensional superconductor introduced in Section 6.5.3 is applicable in the entire temperature range below T^*_{stripe}. The application of these results to the overdoped side is suspect, since that is where all of these energy scales appear to crash into each other.

ARPES and stripes

The temperature dependence of the spectral response of a quasi–one dimensional superconductor may be described as follows: At temperatures high compared to both the Josephson coupling and the spin gap, the system behaves as a collection of independent (gapless) Luttinger liquids. Spin–charge separation holds, so that an added hole dissolves into a spin part and a charge part. Consequently the spectral response exhibits broad EDC's and sharp MDC's.[15] In the intermediate temperature regime (below the spin gap), spin–charge separation still holds, and the ARPES response still exhibits fractionalized spectra, but with a pseudogap. In the low temperature phase, Josephson coupling between stripes confines spin and charge excitations, restoring the electron as an elementary excitation, and a sharp coherent peak emerges from the incoherent background, with weight proportional to the coupling between stripes.

There is a wealth of ARPES data on BSCCO, a material which lends itself more to surface probes than to diffraction. However, as mentioned previously, the presently available evidence of stripes in this material is compelling, but not definitive, so it requires a leap of faith to interpret the ARPES data in terms of stripes. The best evidence of stripes comes from STM data which is suggestive of local stripe correlations [457,458]. Since STM observes a static modulation, any stripes observed in STM can certainly be considered static as far as ARPES is concerned. (Unfortunately,there is currently little direct experimental information concerning the temperature dependence of the stripe order in BSCCO, although what neutron scattering evidence does exist [456], suggests that substantial stripe correlations survive to temperatures well above the superconducting T_c.) As long as the stripes have integrity over

[15] See Section 6.5 for a description of EDC's and MDC's.

a length scale at least as large as $\xi_s = v_s/\Delta_s$, it is possible for the stripes to support superconducting pairing through the spin gap proximity effect.

ARPES spectra from the antinodal region resemble a quasi–1D superconductor. At any rate, many features of the ARPES spectra, especially those for $\boldsymbol{k}$ in the antinodal region of the Brillouin zone (near $(\pi, 0)$) in BSCCO are unlike anything seen in a conventional metal, and highly reminiscent of a quasi–1D superconductor. Above T_c, ARPES spectra reveal sharp MDC's and broad EDC's. We take this [87] as evidence of electron fractionalization. Below T_c, a well defined quasiparticle peak emerges [90], whose features are strikingly similar to those derived in this model. The quasiparticle peak is nearly dispersionless along the $(0, 0)$ to $(\pi, 0)$ direction, and within experimental bounds its energy and lifetime are temperature independent. The only strongly temperature dependent part of the spectrum is the intensity associated with the superconducting peak. The temperature dependence of the intensity is consistent with its being proportional to a fractional power of the local condensate fraction or the superfluid density. Similar behavior has been measured now in an untwinned single crystal of YBCO [12] as well.

The most dramatic signatures of superconducting phenomena in ARPES experiments, both the development of the gap *and* the striking onset of the superconducting peak with phase coherence, occur in the *same* regions of k–space most associated with stripes: Specifically, an array of "horizontal" charge stripes embedded in a locally antiferromagnetic environment [474–477] has most of its low energy spectral weight concentrated near the $(\pi, 0)$ regions of k–space. Similarly, the strongest gap develops in the $(\pi, 0)$ regions, and in both BSCCO and YBCO, the only dramatic change in the ARPES response upon entering the superconducting state is the coherent peak seen in these same regions.

The ARPES spectrum from the nodal region ($\boldsymbol{k}$ near $(\pi/2, \pi/2)$) is less obviously one dimensional in character, although the nodal spectrum is certainly *consistent* with the existence of stripes, as has been demonstrated in several model calculations [135, 474–476, 478]. However, to a large extent, the spectrum in the nodal region is insensitive to stripe correlations. [135] Nodal quasiparticles are certainly important for the low temperature properties of the superconducting state. Moreover, there is indirect evidence that they dominate the in–plane transport above T_c. But the fact that the ARPES spectrum in the nodal direction does not change [479] in any dramatic fashion from above to below T_c, as one would have deduced even from the simplest BCS considerations, suggests that they do not play a direct role in the mechanism of superconductivity. This observation, however, must not be accepted unconditionally. There is an apparent contradiction between the smooth evolution of the spectral function observed in ARPES and the evolution inferred from macroscopic transport experiments [480, 481]; the latter suggest that a catastrophic change in the nodal quasiparticle lifetime occurs in the immediate neighborhood of T_c.

Inherent competition

Finally, it should be made clear that a stripes based mechanism of high temperature superconductivity *predicts* competition between stripes and superconductivity: static stripes may be good for pairing, but are certainly bad for the Josephson coupling (superfluid stiffness) between stripes. On the other hand, fluctuating stripes produce better Josephson coupling, but weaker pairing. The dependence of the gap on stripe fluctuations finds its origin in the spin gap proximity effect, where the development of the spin gap hinges on the one dimensionality of the electronic degrees of freedom [20], whereas stripe fluctuations cause the system to be more two dimensional. In addition, as described in Section 6.6, stripe fluctuations work against $2k_F$ CDW order along a stripe, but strengthen the Josephson coupling (stripes compete with superconductivity).

This is consistent with the empirical phase diagram: on the underdoped side there is a large gap, small superfluid stiffness, small transition temperature, and static stripes have been observed. With increasing doping, stripes fluctuate more, reducing the pairing gap, but increasing the Josephson coupling between stripes. This is a specific example of the doping dependent crossover scenario proposed in Refs. [112,270], in which underdoped cuprates have a strong pairing scale but weak phase stiffness and T_c is determined more or less by T_θ, whereas the overdoped cuprates have a strong phase stiffness but weak pairing scale and T_c is more closely associated with T^*_{pair}. Optimal doping is a crossover between a dominantly phase ordering transition and a dominantly pairing transition. Recently, direct evidence that optimal doping is a crossover of two energy scales was reported in an ARPES study of homologous compounds. [482]

6.13.4 Some Open Questions

As has been stressed by many authors, the cuprate superconductors are exceedingly complex systems. Crisp theoretical statements can be made concerning the behavior of simplified models of these systems, but it is probably ultimately impossible to make clean predictions about whether the results will actually be found in any given material. We are therefore reliant on experiment to establish certain basic empirical *facts*. In this subsection, we will discuss some of the fundamental issues of fact that are pertinent to the stripe scenario presented above, and make a few comments about the present state of knowledge concerning them. A word of caution is in order before we begin: positive results have clearer implications than negative results. Especially in these complicated materials, there can be many reasons to fail to see an effect.

Are stripes universal in the cuprate superconductors?

If stripes are not, in some sense, universal in the high temperature superconductors, then they cannot be, in any sense, essential to the mechanism of high temperature superconductivity. So an important experimental issue is whether stripes are universal in the cuprate superconductors.

The evidence from neutron scattering is discussed in Section 6.13.1: Incommensurate (IC) spin peaks (whether elastic or inelastic) have been detected throughout the doping range of superconductivity in the lanthanum compounds. In YBCO, IC spin peaks are seen with inelastic scattering, but it is presently unclear how much of that scattering intensity should be associated with stripe fluctuations, and how much should be associated with the "resonance peak". Neutron scattering has produced some evidence [456] of IC spin peaks in BSCCO, but this result is controversial [483]. No such peaks have been reported in TlBaCaCuO or HgBaCaCuO, although little or no neutron scattering has yet been done on crystals of these materials.

CDW order turns out to be much harder to observe, even when we know it is there. Charge stripe order has only been observed directly in $La_{1.6-x}Nd_{0.4}Sr_xCuO_4$ [416] and very underdoped $YBa_2Cu_3O_{7-\delta}$ [165], although the general argument presented in Section 6.12.2 implies that it must occur wherever spin stripe order exists. Given the difficulty in observing the charge order where we know it exists, we consider an important open question to be: Where does charge stripe order exist in the general phase diagram of the cuprate superconductors?

As mentioned before, STM experiments point to local charge stripes in BSCCO, both with [457] and without [458] a magnetic field. But there is nowhere near enough systematic data to know whether charge stripes are ubiquitous as a function of doping and in all the superconducting cuprates, how pronounced it is, and over what range of temperatures significant stripe correlations exist, even where we know they exist at low temperatures. Perhaps, in the future, this issue can be addressed further with STM, or even with ARPES or new and improved X–ray scattering experiments.

Are stripes an unimportant low temperature complication?

There is a general tendency for increasingly subtle forms of order to appear as systems are cooled—involving residual low energy degrees of freedom that remain after the correlations that are the central features of the physics have developed. (A classic example of this is transitions involving ordering of the nuclear moments at ultra–low temperatures in a metal.) While such forms of order are fascinating in their own right, one would not, typically, view them as important aspects of the basic materials physics of the studied system. There is a body of thought that holds that the various forms of stripe order that have been observed are in this class of phenomena—interesting side shows, but not the main event. It is also true that actual, static stripe order has only been observed under rather restrictive conditions—mostly in highly underdoped materials or materials with significantly depressed superconducting T_c's, and at temperatures less than or of order the optimal superconducting T_c.

To be central to the physics of high temperature superconductivity, charge stripes must occur at high enough energies and temperatures that they are relevant to zeroth order. Specifically, we want to look for evidence that local stripes persist up to temperatures which are greater than or equal to T_c.

If stripes are universal, then there must be a characteristic crossover scale below which significant stripe correlations emerge—clearly, at high enough temperature, no significant self-organization is possible. Undoubtedly, there is a high energy scale associated with one or more pseudogap crossovers in many underdoped materials—can we associate some of this crossover with the scale at which local stripe correlations become significant? If so, then manifestly stripes are a central player in the drama. If not, and if no still higher energy scale can be identified at which stripe physics begins, it would become increasingly difficult to envisage a starring role for stripes in the physics of the cuprates.

This issue has not been unambiguously resolved. There is substantial (yet not definitive) evidence that local stripe order persists to rather high temperatures. Evidence of local stripe order from observed [484] infrared active phonon modes has been seen to persist to at least 300K in highly underdoped $La_{2-x}Sr_xCuO_4$. Phonon anomalies, which have been tentatively associated with stripes, have been observed in neutron scattering experiments in slightly underdoped $YBa_2Cu_3O_{7-\delta}$ up to comparable temperatures [162]. Still more indirect evidence also abounds. This is a key question, and much more work is necessary to resolve it.

Are the length and time scales reasonable?

As emphasized above, to understand the mechanism of high temperature superconductivity, we are primarily concerned with mesoscopic physics, on length scales a few times the superconducting coherence length and time scales a few times $\hbar/\Delta_0$. So the real question we want to address is: Does stripe order exist on these length and time scales? Given that it is so difficult to determine where long range charge stripe order occurs, it is clearly still more complicated to determine where substantial stripey short range order occurs, or even precisely how much short range order is sufficient.

Are stripes conducting or insulating?

The earliest theoretical studies which predicted stripes as a general feature of doped antiferromagnets envisaged insulating stripes [377,379,380]. These stripes are conceptually close relatives of conventional CDW's in that they are obtained as a Fermi surface instability due to near perfect nesting of the Fermi surface. Such stripes have no low lying fermionic excitations. This perspective has led to an interesting theory of superconductivity which relies on stripe defects for charge transport [485].

The strongest evidence that charge stripes are incompressible, and therefore insulating, comes from plotting the magnetic incommensurability against the doping concentration. If this relationship is strictly linear, it implies that the concentration of holes on a stripe does not change, but rather the only effect of further doping is to change the concentration of stripes in a plane, bringing the stripes closer together. The data for LSCO are close to linear in the range $.024 \leq x \leq .12$, despite the change in orientation from diagonal to vertical at $x = .05$, [169,486] but the small deviation from linearity below

$x = .06$ does exceed the error bars. At present, the data leave open the possibility that the relationship is not strictly linear, and is also consistent with compressible (metallic) stripes throughout the doping range where they are observed. (See, *e.g.*, Fig. 5.7 of Ref. [447].)

Most of the other experiments we have mentioned support the notion that the stripes are intrinsically metallic. Of course, the observed coexistence of static stripe order and superconductivity is a strong indicator of this, as presumably it would be hard to attribute long distance charge transport to stripe motion. (One could envisage stripe defect motion which transports charge perpendicular to the stripes, [485] but certainly the effective number of carriers due to this effect must be small.) The situation is most dramatic in nonsuperconducting LSCO with $0.02 < x < 0.05$, where the stripes are ordered [169,486], and far enough separated that the intrinsic properties of an individual stripe must surely determine the electronic structure—the mean stripe spacing [486] grows to be as large as $350\mathring{A}$ or so for $x = 0.02$. (This is equivalent to 64 (orthorhombic) lattice constants, $b^*_{ortho} = 5.41\mathring{A}$. [166].) These materials exhibit [99,487] a metallic (linear in T) temperature dependence of the resistivity down to moderate temperatures. More remarkably, as shown [487] by Ando *et al.*, although the magnitude of the resistance is large compared to the quantum of resistance at all temperatures, when interpreted in terms of a model in which the conduction occurs along dilute, metallic stripes, the inferred electron mobility within a stripe is nearly the same as that observed in optimally doped LSCO!

Are stripes good or bad for superconductivity?

Striking empirical evidence which suggests that stripes and superconductivity are related comes from the Yamada plot [447], which reports T_c *vs.* the incommensurability seen in neutron scattering, *i.e.* the inverse spacing between stripes. First noted in LSCO, the relationship is remarkably linear for the underdoped region of the lanthanum compounds [447]. For far separated stripes, the transition temperature is depressed. As the stripes move closer together, and the Josephson coupling between them increases, T_c increases. In addition, the similarities between the Yamada plot and the Uemura plot [108], which shows a linear relationship between T_c and the superfluid density, indirectly imply that the Josephson coupling between stripes plays an important role in determining the macroscopic superfluid density.

It has been argued that since stripes compete with superconductivity, they cannot be involved in the mechanism of superconductivity [51]. (We would point out that, at the very least, such competition must imply that stripes and superconductivity are strongly connected.) The empirics are presently unclear on the issue. There is some evidence that static stripes compete with superconductivity, whereas fluctuating stripes enhance it. In instances where stripes are pinned, T_c is generally suppressed, such as with Nd doping, Zn doping, or at the 1/8 anomaly. An exception to this trend occurs in the LCO family, which exhibits its highest T_c for a static stripe ordered material.

Recently, Ichikawa *et al.* [416] have argued that it is spin stripe order, rather than charge stripe order, which competes with superconductivity. Whatever the details, the gross trend in materials other than LCO seems to be that the highest transition temperatures are achieved for dopings that presumably do not support actual (static) stripe order. It is also worth noting that in LSCO [488] and YBCO [148], neutron scattering shows a gap developing in the incommensurate magnetic fluctuations at T_c, perhaps indicating that superconductivity favors fluctuating stripes.

On the other hand, T_c is a nonmonotonic function of x, and pretty clearly determined by the lesser of two distinct energy scales. But the superconducting gap, as deduced from low temperature tunnelling or ARPES experiments deep in the superconducting state, is a monotonically decreasing function of x. It is generally believed that stripe correlations are similarly strongest when x is small and vanish with sufficient overdoping, although in truth the direct experimental evidence for this intuitively obvious statement is not strong. Thus, there is at least a generally positive correlation between the degree of local stripe order and the most obvious scale characterizing pairing. This leads us to our next question:

Do stripes produce pairing?

It is well known that the physics of an antiferromagnet is kinetic energy driven, and phase coherence must be kinetic energy driven when $T_{pair} >> T_c$, since spatial fluctuations of the phase drive pair currents. But can pair formation be kinetic energy driven? In particular, do stripes produce pairing? As reviewed in Section 6.11, numerical studies do find pairing in "fat" 1D systems.

However, there is no experiment we can point to that proves the pairing is either kinetic energy driven or due to stripes.

The brilliantly conceived high precision measurements of the optical conductivity of van der Marel and collaborators [27], and more recently by Bontemps and collaborators [28], are highly suggestive in this regard. In optimally doped BSCCO, they observe a strongly temperature dependent change in the optical spectral weight integrated up to frequencies two orders of magnitude greater than T_c—if interpreted in terms of the single band sum rule, this observation implies a decrease in the kinetic energy upon entering the superconducting state of a magnitude comparable to reasonable estimates of the condensation energy. This is very striking, since in a BCS superconductor, the kinetic energy would *increase* by precisely this amount. However, neither the single band sum rule, nor the notion of a condensation energy are unambiguously applicable in the present problem. This is *the best* existing evidence that the mechanism of superconductivity is kinetic energy driven, but it is not yet evidence that would stand up in court.

Nor is it clear what such an experiment would be. There are ways to falsify the conjecture that stripes produce pairing, such as a demonstration that stripes are not in some sense ubiquitous in the cuprates, or a demonstration

that pairing generally precedes local charge stripe formation as the temperature is lowered. We have discussed many predictions which find some support in experiments, such as the fact that static stripes are good for pairing but bad for phase coherence, and vice versa, and the systematics of the superconducting coherence peak. But these interpretations are not necessarily unique. Much of the phenomenology is *consistent* with a spin gap proximity effect mechanism of pairing, but we see no smoking gun.

Do stripes really make the electronic structure quasi–1D?

Does the existence of stripes provide a sufficient excuse to treat the cuprates as self–organized quasi–1D conductors? If so, then we can apply many of the insights we have obtained directly, and without apology to the interpretation of experiment. As has been discussed in previous sections, and in considerably more detail in other places [6,20,87,151,474,475,477], there are many striking experiments in the cuprates that can be simply and naturally understood in this way. But do they actually affect the electronic structure so profoundly as to render it quasi–1D?

The most direct evidence comes from the ARPES results of Shen and collaborators [88] on the stripe ordered material, $La_{1.6-x}Nd_{0.4}Sr_xCuO_4$. These experiments reveal a remarkable confinement of the majority of the electronic spectral weight inside a dramatically 1D Fermi surface. This experiment probes fairly high energy excitations, and so demonstrates a profound effect of an ordered stripe array on all aspects of the electronic structure. More generally, studies have shown [87,151,474,477] that many of the most striking features of the ARPES spectra of the cuprates are readily rationalized on the basis of an assumed, locally quasi–1D electronic structure.

Transport measurements are macroscopic, so even if locally the electronic structure is strongly quasi–1D, the effects of stripe meandering, domain formation, and disorder will always produce a substantially reduced effective anisotropy at long distances. From this perspective, the order 1, strongly temperature dependent transport anisotropies observed by Ando and collaborators [99] in LSCO and YBCO provide tangible evidence of a strong susceptibility of the electron liquid in the copper oxide planes to develop anisotropies in tensor response functions. Less direct, but even more dramatic evidence that stripes make the electron dynamics quasi–1D has been adduced from Hall effect measurements on the stripe ordered material, $La_{1.6-x}Nd_{0.4}Sr_xCuO_4$, by Noda *et al.* [489] They have observed that the Hall coefficient, R_H, which is relatively weakly temperature dependent above the stripe ordering transition temperature, T_{co}, drops dramatically for $T < T_{co}$, such that $R_H \to 0$ as $T \to 0$ for doped hole concentration, $x \leq 1/8$, and R_H tends to a reduced but finite value for $x > 1/8$. This observation was initially interpreted [489] as evidence that ordered stripes prevent coherent transverse motion of electrons within the copper oxide plane; this interpretation was later shown to be not entirely correct [209], although the basic conclusion that the stripes render the electron dynamics quasi–one dimensional is

probably sound. Further evidence that stripe formation inhibits transverse electronic motion is strongly suggested by the observed suppression of c–axis coherent charge motion in the stripe ordered state of the same materials [490].

However, it would be very desirable to develop new strategies to directly address this issue. For instance, a defect, such as a twin bounary, could purposely be introduced to locally aline the stripe orientation, and the induced electronic anisotropy then be detected with STM.

What about overdoping?

On the underdoped side of the phase diagram of the cuprates, the energy scales of T^*_{stripe}, T^*_{pair}, and T_c are generally sufficiently separated to make the application of many of these ideas plausible. Yet on the overdoped side, the energy scales seem to come crashing into each other, depressing T_c. Furthermore, on the overdoped side, we have $T_\theta > T_{pair}$, in violation of a common assumption we have made throughout this article. The very existence of stripes on the overdoped side is questionable. The Uemura and Yamada plot are not satisfied there. If there are no stripes, and yet there is superconductivity, this does not bode well for a stripes based mechanism. Indeed, it is easier to believe that a mean field like solution is crudely applicable on the overdoped side, where T_c is closer to T_{pair} than it is to T_θ.

One possibility is that the superconducting state far on the overdoped side (especially, where T_c is low and the normal state ARPES spectrum begins to look more Fermi liquid–like) is best approached in terms of a Fermi surface instability and a BCS–Eliashberg mechanism, while on the underdoped side it is best viewed from a stripes perspective. In keeping with the multiscale approach advocated above, it may be no simple matter to unify these approaches in a smooth way.

However, there is an attractive possibility that is worth mentioning here. As we have mentioned, in a stripe liquid, so long as the characteristic stripe fluctuations frequency, $\hbar\bar{\omega}$, is small compared to the superconducting gap scale, the stripes can be treated as quasi–static for the purposes of understanding the mechanism of pairing. Conversely, when $\hbar\bar{\omega} \gg \Delta_0$, the stripe fluctuations can be integrated out to yield an effectively homogeneous system with an induced interaction between electrons. Indeed, it has previously been proposed [127] that stripe fluctuations themselves are a candidate for the "glue" that mediates an effective attraction between electrons. It is easy to imagine that $\hbar\bar{\omega}/\Delta_0$ is a strongly increasing function of x. A sort of unification of the two limits could be achieved if stripe fluctuations play the role of the intermediate boson which mediates the pairing in highly overdoped materials, while in underdoped and optimally doped materials the system can be broken up into quasi–1D ladders, which exhibit the spin gap proximity effect.

How large is the regime of substantial fluctuation superconductivity?

This important question is fundamentally ill–defined. It is important, because

its answer determines the point of view we take with regard to a number of key experiments. But it is ill–defined in the following sense: in the neighborhood of any phase transition, there is a region above T_c where substantial local order exists, but how broad the fluctuation region is said to be depends on exactly how "substantial" is defined, or measured. There has been an enormous amount written on this subject already, so we will just make a few brief observations.

Because in one dimension, phase fluctuations always reduce the superconducting T_c to zero, in a quasi–one dimensional superconductor (*i.e.* in the limit of large anisotropy), there is necessarily a parametrically large fluctuation regime between the mean field transition temperature and the actual ordering temperature.

The finite frequency superfluid density measured in BSCCO [172] with $T_c = 74K$ shows a local superfluid density persists up to at least $90K$, indicative of fluctuation superconductivity in that regime. Both microwave absorption [173] and thermal expansivity measurements [171] on optimally doped YBCO detect significant critical superconducting fluctuations within $\pm 10\%$ of T_c. All of these experiments are well accounted for in terms of the critical properties of a phase–only (XY) model, and are not well described as Gaussian fluctuations of a Landau–Ginzburg theory. Thus, there is no question that there is a well defined magnitude of the order parameter, and substantial local superconducting order for at least 10K to 20K above T_c, and a correspondingly broad range of substantial phase fluctuations below T_c.

There are, however, some experiments that suggest that substantial local pairing persists in a much broader range of temperatures. [491] Nernst measurements [492,493] have detected vortex–like signals up to $100K$ above T_c in LSCO and YBCO, *i.e.* to temperatures up to 5 times T_c! In both cases, however, the final word has yet to be spoken concerning the proper interpretation of these intriguing experiments. [494] ARPES [97,495] and tunnelling [98] studies find that the gap in BSCCO persists up to $100K$ above T_c, *i.e.* to temperatures of order two or more times T_c.

Finally, there are preliminary indications that there may be substantial local superconducting order in severely underdoped materials in which no macroscopic indications of superconductivity appear at any temperature. Presumably, if this is the case, long range phase coherence has been suppressed in these materials by quantum phase fluctuations [288] which proliferate due to the small bare superfluid stiffness and the poor screening of the Coulomb potential. In particular, experiments on films of severely underdoped nonsuperconducting YBCO have revealed that a metastable superconducting state can be induced by photodoping. This has permitted the patterning of small scale superconducting structures, in which it has been shown [496] that substantial Josephson coupling between two superconducting regions can persist even when they are separated by as much as $1000\mathring{A}$.

This "anomalous proximity effect" implies that there is a substantial pair field susceptibility in this nonsuperconducting material.

What about phonons?

Phonons are clearly strongly coupled to the electron gas in the cuprates. Certainly, when there is charge order of any sort, it is unavoidable that it induces (or is induced by) lattice distortions. Manifestly, phonons will enhance any electronic tendency to phase separation or stripe formation [126]. They will also tend to make any stripes "heavy," and so suppress quantum fluctuations—likely, this leads to a depression of superconductivity. There is a dramatic isotope effect anomaly seen [497] in some materials when the doped hole density, $x = 1/8$; presumably, this is related to just such a phonon–induced pinning of the stripe order [429]. Recently, there has been considerable controversy generated by the suggestion [431] that certain features of the ARPES spectrum of a wide class of cuprates reflect the effects of strong electron–phonon coupling. This is clearly an area in which much work remains to be done. In our opinion, other than in 1D, the effects of electron–phonon coupling in a strongly correlated electron gas is an entirely unsolved problem.

What are the effects of quenched disorder?

We have said essentially nothing about the effects of quenched disorder on the materials of interest, although the materials are complicated, and disorder is always present. There are even some theories which consider the disorder to be essential to the mechanism of high temperature superconductivity [498]. A strong case against this proposition is made by the observation that as increasingly well ordered materials are produced, including some which are stoichiometric and so do not have any of the intrinsic disorder associated with a random alloy, the superconducting properties are not fundamentally altered, and that if anything T_c and the superfluid density both seem to rise very slightly as disorder is decreased.

However, other properties of the system are manifestly sensitive to disorder. Since disorder couples to spatial symmetry breaking order parameters in the same way that a random field couples to a magnetic order parameter, it is generally a relevant perturbation. Among other things, this means that none of the stripe orders discussed above will ever occur as true long range order, and the putative transitions are rounded and rendered glassy [417,499–501]. So even the supposedly sharp statements discussed above are only sharp, in practice, if we can study such highly perfect crystals that they approximate the disorder→0 limit. This is a general problem. Progress has been made in recent years in growing more and more perfect single crystals of particular stoichiometric superconductors. Clearly, advances in this area are an essential component of the ongoing effort to unravel the physics of these materials.

Acknowledgements

We would especially like to acknowledge the profound influence on our understanding of every aspect of the physics discussed in this paper of discussions with our colleagues and collaborators, John Tranquada, Vadim Oganesyan,

and Eduardo Fradkin. We also want to explicitly aknowledge the extremely helpful suggestions and critiques we obtained from J. W. Allen, Y. Ando, N. P. Armitage, A. Auerbach, D. A. Bonn, R. J. Birgeneau, E. Dagotto, A. H. Castro Neto, E. Fradkin, S. Sachdev, D. J. Scalapino, S. L. Sondhi, J. M. Tranquada, and O. Zachar. Finally, we have benefited greatly from discussion of the ideas presented herein with more colleagues than we can hope to acknowledge, but we feel we must at least acknowledge our intellectual debts to G. Aeppli, J. W. Allen, P. B. Allen, Y. Ando, D. N. Basov, M. R. Beasley, A. H. Castro Neto, S. Chakravarty, E. Dagotto, P. C. Dai, J. C. S. Davis, C. Di Castro, R. C. Dynes, H. Eisaki, A. Finkelstein, M. P. A. Fisher, T. H. Geballe, M. Granath, P. D. Johnson, C. Kallin, A. Kapitulnik, H.-Y. Kee, Y.-B. Kim, R. B. Laughlin, D-H. Lee, Y. S. Lee, K. A. Moller, H. A. Mook, C. Nayak, Z. Nussinov, N. P. Ong, J. Orenstein, S. Sachdev, D. J. Scalapino, J. R. Schrieffer, Z-X. Shen, S. L. Sondhi, B. I. Spivak, T. Timusk, T. Valla, J. Zaanen, O. Zachar, S-C. Zhang, and X. J. Zhou. This work was supported, in part, by NSF grant DMR-0110329 at UCLA, DOE grant DE-FG03-00ER45798 at UCLA and BNL, and NSF grant DMR-97-12765 and the Office of the Provost at Boston University.

References

1. J.R. Schrieffer, Theory of Superconductivity, Frontiers in Physics (Addison-Wesley) (1988).
2. J.G. Bednorz and K.A. Muller, "Possible high T_c superconductivity in the Ba-La-Cu-O system," *Z. Phys. B*, **64**, 189–193 (1986).
3. V.J. Emery and S.A. Kivelson, "Superconductivity in bad metals," *Phys. Rev. Lett.*, **74**, 3253–3256 (1995).
4. P.W. Anderson, "Experimental constraints on the theory of high-Tc superconductivity," *Science*, **256**, 1526–1531 (1992).
5. P.W. Anderson, "The resonating valence bond state in La_2CuO_4 and superconductivity," *Science*, **235**, 1169–1198 (1987).
6. V.J. Emery, S.A. Kivelson, and J.M. Tranquada, "Stripe phases in high-temperature superconductors," *Proc. Natl. Acad. Sci.*, **96**, 8814–8817 (1999).
7. P.A. Lee, "Pseudogaps in underdoped cuprates," *Physica C*, **317-318**, 194–204 (1999).
8. L. Taillefer, B. Lussier, R. Gagnon, K. Behnia, and H. Aubin, "Universal heat conduction in $YBa_2Cu_3O_{6.9}$," *Phys. Rev. Lett.*, **79**, 483–486 (1997).
9. P.J. Turner, R. Harris, S. Kamal, M.E. Hayden, D.M. Broun, D.C. Morgan, A. Hosseini, P. Dosanjh, J.S. Preston, R. Liang, D.A. Bonn, and W.N. Hardy, "Broadband microwave spectroscopy of d-wave quasiparticles in oxygen-ordered $YBa_2Cu_3O_{6.50}$," *cond-mat/0111353, submitted to PRL* (2002).
10. K.A. Moller, D.J. Baar, J.S. Urbach, R. Liang, W.N. Hardy, and A. Kapitulnik, "Magnetic field dependence of the density of states of $YBa_2Cu_3O_{6.95}$ as determined from the specific heat," *Phys. Rev. Lett.*, **73**, 2744–2747 (1994).
11. B. Revaz, J.-Y. Genoud, J.K. Neumaier, A. Erb, and E. Walker, "*d*-wave scaling relations in the mixed-state specific heat of $YBa_2Cu_3O_7$," *Phys. Rev. Lett.*, **80**, 3364–3368 (1998).

12. D.H. Lu, D.L. Feng, N.P. Armitage, K. M. Shen, A. Damascelli, C. Kim, F. Ronning, Z.X. Shen, D.A. Bonn, R. Liang, W.N. Hardy, A.I. Rykov, and S. Tajima, "Superconducting gap and strong in-plane anisotropy in untwinned $YBa_2Cu_3O_{7-\delta}$," *Phys. Rev. Lett.*, **86**, 4370–4373 (2001).
13. D. Basov, R. Liang, D.A. Bonn, W.N. Hardy, B. Dabrowski, D.B.T.M. Quijada, J.P. Rice, D.M. Ginsberg, and T. Timusk, "In-plane anisotropy of the penetration depth in $YBa_2Cu_3O_{7-x}$ and $YBa_2Cu_4O_8$," *Phys. Rev. Lett.*, **74**, 598–601 (1995).
14. S. Chakravarty and S. Kivelson, "Electronic mechanism of superconductivity in the cuprates, C_{60}, and polyacenes," *Phys. Rev. B*, **64**, 064511–064519 (2001).
15. V.J. Emery and S.A. Kivelson, "Frustrated electronic phase separation and high-temperature superconductors," *Physica C*, **209**, 597–621 (1993).
16. S. Caprara, C. Castellani, C. Di Castro, and M. Grilli, "Phase separation and superconductivity in strongly interacting electron systems," *Physica C*, **235-240**, 2155–2156 (1994).
17. A. Moreo, S. Yunoki, and E. Dagotto, "Phase separation scenario for manganese oxides and related materials," *Science*, **283**, 2034–2040 (1999).
18. P.W. Anderson, "A re-examination of concepts in magnetic metals: the 'nearly antiferromagnetic Fermi liquid'," *Adv. Phys.*, **46**, 3–11 (1997).
19. J.E. Hirsch, "Antiferromagnetism, localization, and pairing in a two-dimensional model for CuO2," *Phys. Rev. Lett.*, **59**, 228–231 (1987).
20. V.J. Emery, S.A. Kivelson, and O. Zachar, "Spin-gap proximity effect mechanism of high-temperature superconductivity," *Phys. Rev. B*, **56**, 6120–6147 (1997).
21. S. Chakravarty, A. Sudbo, P.W. Anderson, and S. Strong, "Interlayer tunneling and gap anisotropy in high-temperature superconductors," *Science*, **261**, 337–340 (1993).
22. E. Demler and S.-C. Zhang, "Quantitative test of a microscopic mechanism of high-temperature superconductivity," *Nature*, **396**, 733–737 (1998).
23. A.H. Castro Neto and F. Guinea, "Superconductivity, Josephson coupling, and order parameter symmetry in striped cuprates," *Phys. Rev. Lett.*, **80**, 4040–4043 (1998).
24. J.E. Hirsch, "The true colors of cuprates," *Science*, **295**, 2226–2227 (2002).
25. V.J. Emery, S.A. Kivelson, and O. Zachar, "Classification and stability of phases of the multicomponent one-dimensional electron gas," *Phys. Rev. B*, **59**, 15641–15653 (1999).
26. D.J. Scalapino, "The 2-leg Hubbard ladder: Computational studies of new materials," *cond-mat/0109125* (2001).
27. H.J.A. Molegraaf, C. Presura, D. van der Marel, P.H. Kes, and M. Li, "Superconductivity-induced transfer of in-plane spectral weight in $Bi_2Sr_2CaCu_2O_{8+\delta}$," *Science*, **295**, 2239–2241 (2002).
28. A.F. Santander-Syro, R.P.S.M. Lobo, N. Bontemps, Z. Konstantinovic, Z.Z. Li, and H. Raffy, "Pairing in cuprates from high energy electronic states," *cond-mat/0111539* (2001).
29. P. Monthoux, A.V. Balatsky, and D. Pines, "Toward a theory of high-temperature superconductivity in the antiferromagnetically correlated cuprate oxides," *Phys. Rev. Lett.*, **67**, 3448–3451 (1991).
30. N. Bulut and D.J. Scalapino, "$d(x^2 - y^2)$ symmetry and the pairing mechanism," *Phys. Rev. B*, **54**, 14971–14973 (1996).

31. D.J. Scalapino, "Superconductivity and spin fluctuations," *J. Low Temp. Phys.*, **117**, 179–188 (1999), international Conference on Physics and Chemistry of Molecular and Oxide Superconductors. MOS'99, Stockholm, Sweden, 28 July-2 Aug. 1999. Kluwer Academic/Plenum Publishers.
32. R.J. Radtke, S. Ullah, K. Levin, and N.R. Norman, "Constraints on superconducting transition temperatures in the cuprates: antiferromagnetic spin fluctuations," *Phys. Rev. B*, **46**, 11975–11985 (1992).
33. C.M. Varma, J. Zaanen, and K. Raghavachari, "Superconductivity in the fullerenes," *Science*, **254**, 989–992 (1991).
34. M. Schluter, M. Lannoo, M. Needels, G.A. Baraff, and D. Tomanek, "Electron-phonon coupling and superconductivity in alkali-intercalated C_{60} solid," *Phys. Rev. Lett.*, **68**, 526–529 (1992).
35. P. Morel and P.W. Anderson, "Calculation of the superconducting state parameters with retarded electron-phonon interaction," *Physical Review*, **125**, 1263–1271 (1962).
36. J.R. Schrieffer, D.J. Scalapino, and J.W. Wilkins, "Effective tunneling density of states in superconductors," *Phys. Rev. Lett.*, **10** (1963).
37. S. Chakravarty, S. Khlebnikov, and S. Kivelson, "Comment on "Electron-phonon coupling and superconductivity in alkali-intercalated C_{60} solid"," *Phys. Rev. Lett.*, **69**, 212 (1992).
38. R. Shankar, "Renormalization-group approach to interacting fermions," *Rev. Mod. Phys.*, **66**, 129–192 (1994).
39. J. Polchinski, "Renormalization and effective lagrangians," *Nucl. Phys. B*, **231**, 269–295 (1984).
40. Z.-X. Shen, D.S. Dessau, B.O. Wells, D.M. King, W.E. Spicer, A.J. Arko, D. Marshal, L.W. Lombardo, A. Kapitulnik, P. Dickinson, S. Doniach, J. DiCarlo, A.G. Losser, and C.H. Park, "Anomalously large gap anisotropy in the $a-b$ plane of bi2212," *Phys. Rev. Lett.*, **70**, 1553–1556 (1993).
41. R. Micnas, J. Ranninger, and S. Robaszkiewicz, "Superconductivity in narrow-band systems with local nonretarded attractive interactions," *Rev. Mod. Phys.*, **62**, 113–234 (1990).
42. T. Holstein, "Studies of polaron motion: I," *Annals of Physics.*, **8**, 325–342 (1959).
43. G. Gruner, Density waves in solids (Perseus Books Group) (2000).
44. G. Bilbro and W.L. McMillan, "Theoretical model of superconductivity and the martensitic transformation in A15 compounds," *Phys. Rev. B*, **14**, 1887–1892 (1976).
45. O. Zachar, S.A. Kivelson, and V.J. Emery, "Landau theory of stripe phases in cuprates and nickelates," *Phys. Rev. B*, **57**, 1422–1426 (1998).
46. J.M. Tranquada, "Phase separation, charge segregation and superconductivity in layered cuprates," *Neutron Scattering in Layered Copper-Oxide Superconductors, A. Furrer, Editor*, **83**, 225–260 (1998), kluwer, Dordrecht, The Netherlands.
47. J.M. Tranquada, "Experimental evidence for topological doping in the cuprates," *AIP-Conference-Proceedings*, **483**, 336–340 (1999).
48. J. Zaanen, "High-temperature superconductivity: stripes defeat the Fermi liquid," *Nature*, **404**, 714 (2000).
49. S. Sachdev, "Quantum criticality: competing ground states in low dimensions," *Science*, **288**, 475–80 (2000).

50. J. Orenstein and A.J. Millis, "Advances in the physics of high-temperature superconductivity," *Science*, **288**, 468–474 (2000).
51. G. Baskaran, "Competition between superconductivity and charge stripe order in high-Tc cuprates," *Mod. Phys. Lett. B*, **14**, 377–384 (2000).
52. S.A. Kivelson, E. Fradkin, and V.J. Emery, "Electronic liquid-crystal phases of a doped Mott insulator," *Nature*, **393**, 550–553 (1998).
53. C.M. Varma, "Non Fermi-liquid states and pairing of a general model of copper-oxide metals," *Phys. Rev. B*, **55**, 14554–14580 (1997).
54. S. Chakravarty, R.B. Laughlin, D.K. Morr, and C. Nayak, "Hidden order in the cuprates," *Phys. Rev. B*, **63**, 094503–094510 (2001).
55. I. Affleck and J.B. Marston, "Large-n limit of the Heisenberg-Hubbard model: Implications for high-T_c superconductors," *Phys. Rev. B*, **37**, 3774–3777 (1988).
56. G. Kotliar, "Resonating valence bonds and d-wave superconductivity," *Phys. Rev. B*, **37**, 3664–3666 (1998).
57. D.A. Ivanov, P.A. Lee, and X.-G. Wen, "Staggered-vorticity correlations in a lightly doped t-J model: A variational approach," *Phys. Rev. Lett.*, **34**, 3958–3961 (2000).
58. Q.H. Wang, J.H. Han, and D.H. Lee, "Staggered currents in the mixed state," *Phys. Rev. Lett.*, **87**, 7004–7007 (2001).
59. T. Senthil and M.P.A. Fisher, "Fractionalization in the cuprates: Detecting the topological order," *Phys. Rev. Lett.*, **86**, 292–295 (2000).
60. S.A. Kivelson, G. Aeppli, and V.J. Emery, "Thermodynamics of the interplay between magnetism and high-temperature superconductivity," *Proc. Nat. Acad. Sci.*, **98**, 11903–11907 (2001).
61. C. Castellani, C. Di Castro, and M. Grilli, "Singular quasiparticle scattering in the proximity of charge instabilities," *Phys. Rev. Lett.*, **75**, 4650–4653 (1995).
62. S. Andergassen, S. Caprara, C. Di Castro, and M. Grilli, "Anomalous isotopic effect near the charge-ordering quantum criticality," *Phys. Rev. Lett.*, **87**, 56401–56403 (2001).
63. A.V. Chubukov, S. Sachdev, and J. Ye, "Theory of two-dimensional quantum Heisenberg antiferromagnets with a nearly critical ground state," *Phys. Rev. B*, **49**, 11919–11961 (1994).
64. N.D. Mathur, F.M. Grosche, S.R. Julian, I.R. Walker, D.M. Freye, R.K.W. Haselwimmer, and G.G. Lonzarich, "Magnetically mediated superconductivity in heavy fermion compounds," *Nature*, **394**, 39–43 (1998).
65. The term "Mott insulator" means many things to many people. One definition is that a Mott insulator is insulating because of interactions between electrons, rather than because a noninteracting band is filled. This is not a precise definition. For example, a Mott insulating state can arise due to a spontaneously broken symmetry which increases the size of the unit cell. However, this is adiabatically connected to the weak coupling limit, and can be qualitatively understood via generalized Hartree–Fock theory. There is still a *quantitative* distinction between a weak coupling "simple" insulator on the one hand, which has an insulating gap that is directly related to the order parameter which characterizes the broken symmetry, and the "Mott" insulator on the other hand, which has an insulating gap which is large due to the strong repulsion between electrons. In the latter case, the resistivity begins to grow very large compared to the quantum of resistance well above the temperature at

which the broken symmetry occurs. The undoped cuprate superconductors are clearly Mott insulators in the quantitative sense that the insulating gap is of order 2eV, while the antiferromagnetic ordering temperatures are around 30 meV.

However, for those who prefer [68] a sharp, *qualitative* distinction, the term "Mott insulator" is reserved for "spin liquid" states which are distinct zero temperature phases of matter, do not break symmetries, and cannot be understood in terms of any straightforward Hartree–Fock description. Many such exotic states have been theoretically envisaged, including the long [5,69] and short ranged [70–72] RVB liquids, the chiral spin liquid [73–75], the nodal spin liquid [76,77] and various other fractionalized states with topological order [78,79]. Very recently, in the first "proof of principle," a concrete model with a well defined short ranged RVB *phase* has been discovered [80,81].

66. S.A. Grigera, R.S. Perry, A.J. Schofield, M. Chiao, S.R. Julian, G.G. Lonzarich, S.I. Ikeda, Y. Maeno, A.J. Millis, and A.P. Mackenzie, "Magnetic field–tuned quantum criticality in the metallic ruthenate $Sr_3Ru_2O_7$," *Science*, **294**, 329–332 (2001).
67. J.R. Schrieffer, "Ward's identity and the suppression of spin fluctuation superconductivity," *J. Low Temp. Phys.*, **99**, 397–402 (1995).
68. R.B. Laughlin, "A critique of two metals," *Adv. Phys.*, **47**, 943–958 (1998).
69. G. Baskaran, Z. Zou, and R.B. Laughlin, "The resonating valence bond state and high–T_c superconductivity - a mean field theory," *Solid State Comm.*, **63**, 973–976 (1987).
70. S.A. Kivelson, D.S. Rokhsar, and J.P. Sethna, "Topology of the resonating valence-bond state: Solitons and high–T_c superconductivity," *Phys. Rev. B*, **35**, 8865–8868 (1987).
71. D.S. Rokhsar and S.A. Kivelson, "Superconductivity and the quantum hard-core dimer gas," *Phys. Rev. Lett.*, **61**, 2376–2379 (1988).
72. N. Read and S. Sachdev, "Large-N expansion for frustrated quantum antiferromagnets," *Phys. Rev. Lett.*, **66**, 1773–1776 (1991).
73. V. Kalmeyer and R.B. Laughlin, "Theory of the spin liquid state of the Heisenberg antiferromagnet," *Phys. Rev. B*, **39**, 11879–11899 (1989).
74. X.G. Wen, F. Wilcek, and A. Zee, "Chiral spin states and superconductivity," *Phys. Rev. B*, **39**, 11413–11423 (1989).
75. P.B. Wiegmann, "Superconductivity in strongly correlated electronic systems and confinement versus deconfinement phenomenon," *Phys. Rev. Lett.*, **60**, 821–824 (1988).
76. L. Balents, M.P.A. Fisher, and C. Nayak, "Nodal liquid theory of the pseudogap phase of high–T_c superconductors," *Int. J. Mod. Phys. B*, **12**, 1033–1068 (1998).
77. L. Balents, M.P.A. Fisher, and C. Nayak, "Dual order parameter for the nodal liquid," *Phys. Rev. B*, **60**, 1654–1667 (1999).
78. T. Senthil and M.P.A. Fisher, "Z2 gauge theory of electron fractionalization in strongly correlated systems," *Phys. Rev. B*, **62**, 7850–7881 (2000).
79. X.G. Wen, "Topological orders in rigid states," *Int. J. Mod. Phys. B*, **4**, 239–271 (1990).
80. R. Moesner and S.L. Sondhi, "Resonating valence bond phase in the triangular lattice quantum dimer model," *Phys. Rev. Lett.*, **86**, 1881–1884 (2001).

81. R. Moessner, S.L. Sondhi, and E. Fradkin, "Short-ranged resonating valance bond physics, quantum dimer models, and Ising gauge theories," *Phys. Rev. B*, **65**, 024504–024516 (2002).
82. T. Timusk and B. Statt, "The pseudogap in high-temperature superconductors: an experimental survey," *Rep. Prog. Phys.*, **62**, 61–122 (1999).
83. J.L. Tallon and J.W. Loram, "The doping dependence of T^* - what is the real high T_c phase diagram?" *Physica C*, **349**, 53–68 (2001).
84. A. Leggett, "Cuprate Superconductivity: Dependence of T_c on the c-Axis Layering Structure," *Phys. Rev. Lett.*, **83**, 392–395 (1999).
85. P.W. Anderson, The Theory of Superconductivity in the Cuprates (Princeton University Press, Princeton, NJ) (1997).
86. R.B. Laughlin, "Evidence for quasiparticle decay in photoemission from underdoped cuprates," *Phys. Rev. Lett.*, **79**, 1726–1729 (1997).
87. D. Orgad, S.A. Kivelson, E.W. Carlson, V.J. Emery, X.J. Zhou, and Z. X. Shen, "Evidence of electron fractionalization from photoemission spectra in the high temperature superconductors," *Phys. Rev. Lett.*, **86**, 4362–4365 (2001).
88. X.J. Zhou, P. Bogdanov, S.A. Kellar, T. Noda, H. Eisaki, S. Uchida, Z. Hussain, and Z.-X. Shen, "One-dimensional electronic structure and suppression of d-Wave node state in $La_{1.28}Nd_{0.6}Sr_{0.12}CuO_4$," *Science*, **286**, 268–272 (1999).
89. T. Valla, A.V. Fedorov, P.D. Johnson, Q. Li, G.D. Gu, and N. Koshizuka, "Temperature dependent scattering rates at the Fermi surface of optimally doped $Bi_2Sr_2CaCu_2O_{8+\delta}$," *Phys. Rev. Lett.*, **85**, 828–831 (2000).
90. A.V. Fedorov, T. Valla, P.D. Johnson, Q. Li, G.D. Gu, and N. Koshizuka, "Temperature dependent photoemission studies of optimally doped $Bi_2Sr_2CaCu_2O_8$," *Phys. Rev. Lett.*, **82**, 2179–2182 (1999).
91. D.L. Feng, D.H. Lu, K.M. Shen, S.Oh, A. Andrus, J.O'Donnell, J. N. Eckstein, J. Shimoyama, K. Kishio, and Z. X. Shen, "On the similarity of the spectral weight pattern of $Bi_2Sr_2CaCuO_{8+\delta}$ and $La_{1.48}Nd_{0.4}Sr_{0.12}CuO_4$," *Physica C*, **341**, 2097–2098 (2000).
92. A.G. Loeser, Z.-X. Shen, M.C. Schabel, C. Kim, M. Zhang, A. Kapitulnik, and P. Fournier, "Temperature and doping dependence of the Bi-Sr-Ca-Cu-O electronic structure and fluctuation effects," *Phys. Rev. B*, **56**, 14185–14189 (1997).
93. C.M. Varma, P.B. Littlewood, S. Schmittrink, E. Abrahams, and A.E. Ruckenstein, "Phenomenology of the normal state of the Cu-O high-temperature superconductors," *Phys. Rev. Lett.*, **63**, 1996–1999 (1989).
94. C.M. Varma, Z. Nussinov, and W. van Saarloos, "Singular Fermi liquids," *cond-mat/0103393* (2001).
95. E. Abrahams and C.M. Varma, "What angle-resolved photoemission experiments tell us about the microscopic theory for high-temperature superconductors," *Proc. Natl. Accad. Sci.* (2000).
96. J.M. Harris, Z.-X. Shen, P.J. White, D.S. Marshall, M.C. Schabel, J.N. Eckstein, and I. Bozovic, "Anomalous superconducting state gap size versus Tc behavior in underdoped $Bi_2Sr_2Ca_{1-x}Dy_xCu_2O_8$," *Phys. Rev. B*, **54**, R15665–R15668 (1996).
97. H. Ding, T. Yokoya, J.C. Campuzano, T. Takahashi, M. Randeria, M.R. Norman, and T.M. K.H.J. Giapintzakis, "Spectroscopic evidence for a pseudogap in the normal state of underdoped high-T_c superconductors," *Nature*, **382**, 51–54 (1996).

98. C. Renner, B. Revaz, J.-Y. Genoud, K. Kadowaki, and O. Fischer, "Pseudogap precursor of the superconducting gap in under- and overdoped $Bi_2Sr_2CaCu_2O_{8+\delta}$," *Phys. Rev. Lett.*, **80**, 149–152 (1998).
99. Y. Ando, K. Segawa, S. Komiya, and A.N. Lavrov, "Electrical resistivity anisotropy from self-organized one-dimensionality in high-temperature superconductors," *Phys. Rev. Lett.*, **88**, 137005–137008 (2002).
100. I. Maggio-Aprile, C. Renner, A. Erb, E. Walker, and O. Fischer, "Direct vortex lattice imaging and tunneling spectroscopy of flux lines on $YBa_2Cu_3O_{7-\delta}$," *Phys. Rev. Lett.*, **75**, 2754–2757 (1995).
101. C. Howald, P. Fournier, and A. Kapitulnik, "Inherent inhomogeneities in tunneling spectra of $Bi_2Sr_2CaCu_2O_{8-x}$ crystals in the superconducting state," *Phys. Rev. B*, **64**, 100504–100507 (2001).
102. S.H. Pan, J.P. O'Neal, R.L. Badzey, C. Chamon, H. Ding, J.R. Engelbrecht, Z. Wang, H. Eisaki, S. Uchida, A.K. Guptak, K.W. Ng, E.W. Hudson, K.M. Lang, and J.C. Davis, "Microscopic electronic inhomogeneity in the high T_c superconductor $Bi_2Sr_2CaCu_2O_{8+x}$," *Nature*, **413**, 282–285 (2001).
103. J.E. Sonier, J.H. Brewer, R.F. Kiefl, D.A. Bonn, S.R. Dunsiger, W.N. Hardy, R. Liang, W.A. MacFarlane, R.I. Miller, and T.M. Riseman, "Measurements of the fundamental length scales in the vortex state of $YBa_2Cu_3O_{6.60}$," *Phys. Rev. Lett.*, **79**, 2875–2878 (1997).
104. C.A.R.S. de Melo, M. Randeria, and J.R. Engelbrecht, "Crossover from BCS to Bose superconductivity: Transition temperature and time-dependent Ginzburg-Landau theory," *Phys. Rev. Lett.*, **71**, 3202–3205 (1993).
105. Q. Chen, I. Kosztin, B. Janko, and K. Levin, "Pairing fluctuation theory of superconducting properties in underdoped to overdoped cuprates," *Phys. Rev. Lett.*, **81**, 4708–4711 (1998).
106. A.S. Alexandrov and N.F. Mott, "Thermal transport in a charged Bose gas and in high-T_c oxides," *Phys. Rev. Lett.*, **71**, 1075–1078 (1993).
107. A.S. Alexandrov and N.F. Mott, "Bipolarons," *Rep. Prog. Phys.*, **57**, 1197–1288 (1994).
108. Y.J. Uemura, G.M. Luke, B.J. Sternlieb, J.H. Brewer, J.F. Carolan, W.N. Hardy, R. Kadono, J.R. Kempton, R.F. Kiefl, S.R. Kreitzman, P. Mulhern, T.M. Riseman, D.L. Williams, B.X. Yang, S. Uchida, H. Takagi, J. Gopalakrishnan, A.W. Sleight, M.A. Subramanian, C.L. Chien, M.Z. Cieplak, G. Xiao, V.Y. Lee, B.W. Statt, C.E. Stronach, W.J. Kossler, and X.H. Yu, "Universal correlations between Tc and ns / m* (carrier density over effective mass) in high-T_c cuprate superconductors," *Phys. Rev. Lett.*, **62**, 2317–2320 (1989).
109. E. Dagotto, T. Hotta, and A. Moreo, "Colossal magnetoresistant materials: the key role of phase separation," *Physics Reports*, **344**, 1–153 (2001).
110. J.M. Luttinger, "Fermi surface and some simple equilibrium properties of a system of interacting fermions," *Phys. Rev.*, **119**, 1153–1163 (1960).
111. A theory of real space pairs which includes all the electrons and the repulsive interactions between them can be caricatured as a hard core quantum dimer model [71]. Here the pairing is collective, due to the high density of pairs. Indeed, N_p involves all of the electrons (the doped holes are not paired at all), but the superfluid density is small, involving only the density of doped holes. This contrasts markedly with the case of clean metallic superconductors where the density of pairs (that is, the density of electrons whose state is significantly altered by pairing) is small, $\sim N(E_F)\Delta_0$, while the superfluid density is large

and involves all the electrons. There is some evidence that the former situation in fact pertains to the high temperature superconductors [112].

112. V.J. Emery and S.A. Kivelson, "Crossovers and phase coherence in cuprate superconductors," *J. Phys. Chem. Solids*, **59**, 1705–1710 (1998).
113. A.N. Kocharian, C. Yang, and Y.L. Chiang, "Self-consistent and exact studies of pairing correlations and crossover in the one-dimensional attractive Hubbard model," *Phys. Rev. B*, **59**, 7458–7472 (1999).
114. A.N. Kocharian, C. Yang, and Y.L. Chiang, "Phase diagram and BCS-Bose condensation crossover in 1D and 2D Hubbard models," *Physica C*, **364-365**, 131–133 (2001).
115. J.W. Allen, C.G. Olson, M.B. Maple, J.-S. Kang, L.Z. Liu, J.-H. Park, R.O. Anderson, W.P. Ellis, J.T. Market, Y. Dalichaouch, and R. Liu, "Resonant photoemission study of $Nd_{2-x}Ce_xCuO_{4-y}$: Nature of electronic states near the Fermi level," *Phys. Rev. Lett.*, **64**, 595–598 (1990).
116. R.O. Anderson, R. Cleassen, J.W. Allen, C.G. Olson, C. Janowitz, L.Z. Liu, J.-H. Park, M.B. Maple, Y. Dalichaouch, M.C. de Andrade, R.F. Jardim, E.A. Early, S.-J. Ho, and W.P. Ellis, "Luttinger Fermi surface of metallic gap spectral weight in $Nd_{1.85}Ce_{0.15}CuO_{4-y}$," *Phys. Rev. Lett.*, **70**, 3163–3166 (1993).
117. T. Watanabe, T. Takahashi, S. Suzuki, S. Sato, and H. Katayama-Yoshida, "Inverse-photoemission study of hole-concentration dependence of the electronic structure in $Bi_2Sr_2Ca_{1-x}Y_xCu_2O_8$ (x=0.0-0.05)," *Phys. Rev. B*, **44**, 5316–5317 (1991).
118. A. Ino, C. Kim, M. Nakamura, T. Yoshida, T. Mizokawa, Z.-X. Shen, A. Fujimori, T. Kakeshita, H. Eisaki, and S. Uchida, "Electronic structure of $La_{2-x}Sr_xCuO_4$ in the vicinity of the superconductor-insulator transition," *Phys. Rev. B*, **62**, 4137–4141 (2000).
119. G. Rietveld, N.Y. Chen, and D. van der Marel, "Anomalous temperature dependence of the work function in $YBa_2Cu_3O_{7-\delta}$," *Phys. Rev. B*, **69**, 2578–2581 (1992), a rather larger value of the chemical potential shift at T_c, but still very small compared to the bandwidth, was obtained from high precision measurements of the work function.
120. D.J. Scalapino, J.E. Loh, and J.E. Hirsch, "d-wave pairing near a spin density wave instability," *Phys. Rev. B*, **34**, 8190–8192 (1986).
121. W. Kohn and J.M. Luttinger, "New mechanism for superconductivity," *Phys. Rev. Lett.*, **15**, 524–526 (1965).
122. V.J. Emery, "Theory of high-T_c superconductivity in oxides," *Phys. Rev. Lett.*, **58**, 2794–2797 (1987).
123. G. Kotliar and J. Liu, "Superexchange mechanism and d-wave superconductivity," *Phys. Rev. B*, **38**, 5142–5145 (1988).
124. C. Gros, R. Joynt, and T.M. Rice, "Superconductivity instability in the large-U limit of the two-dimensional Hubbard model," *Z. Phys. B*, **68**, 425–432 (1987).
125. D.J. Scalapino, E. Loh, and J.E. Hirsch, "Fermi-surface instabilities and superconducting d-wave pairing," *Phys. Rev. B*, **35**, 6694–6698 (1987).
126. M. Grilli, R. Raimondi, C. Castellani, C. Di Castro, and G. Kotliar, "Superconductivity, phase separation, and charge-transfer instability in the U=∞ limit of the three-band model of the CuO_2 planes," *Phys. Rev. Lett.*, **67**, 259–262 (1991).

127. A. Perali, C. Castellani, C. Di Castro, and M. Grilli, "d-wave superconductivity near charge instabilities," *Phys. Rev. B*, **54**, 16216–16225 (1996).
128. D.A. Wollman, D.J.V. Harlingen, W.C. Lee, D.M. Ginsberg, and A.J. Leggett, "Experimental determination of the superconducting pairing state in YBCO from phase coherence in YBCO-Pb SQUIDs," *Phys. Rev. Lett.*, **71**, 2134–2147 (1993).
129. C.C. Tsuei, J.R. Kirtley, C.C. Chi, L.S. Yu-Jahnes, A. Gupta, T. Shaw, J.Z. Sun, and M.B. Ketchen, "Pairing symmetry and flux quantization in a tricrystal superconducting ring of $YBa_2Cu_3O_{7-\delta}$," *Phys. Rev. Lett.*, **73**, 593 (1994).
130. K.A. Kouznetsov, A.G. Sun, B. Chen, A.S. Katz, S.R. Bahcall, J. Clarke, R.C. Dynes, D.A. Gajewski, S.H. Han, M.B. Maple, J. Giapintzakis, J.-T. Kim, and D.M. Ginsberg, "C-axis Josephson tunneling between $YBa_2Cu_3O_{7-\delta}$ and Pb: direct evidence for mixed order parameter symmetry in a high-T_c superconductor," *Phys. Rev. Lett.*, **79**, 3050–3053 (1997).
131. R.A. Klemm, G. Arnold, A. Bille, and K. Scharnberg, "Theory of c-axis twist Bi2212 Josephson junctions: Strong evidence for incoherent tunneling and s-wave superconductivity," *Physica* **C**, **341**, 1663–1664 (2000).
132. A. Damascelli, D.H. Lu, and Z.-X. Shen, "From Mott insulator to overdoped superconductor: Evolution of the electronic structure of cuprates studied by ARPES," *J. Electron Spectr. Relat. Phenom.*, **165**, 117–118 (2001).
133. J.R. Schrieffer, S.C. Zhang, and X.G. Wen, "Spin-bag mechanism of high-temperature superconductivity," *Phys. Rev. Lett.*, **60**, 944–947 (1988).
134. M. Granath, V. Oganesyan, S.A. Kivelson, E. Fradkin, and V.J. Emery, "Nodal quasiparticles in stripe ordered superconductors," *Phys. Rev. Lett.*, **87**, 167011–167014 (2001).
135. M. Vojta, Y. Zhang, and S. Sachdev, "Quantum phase transitions in d-wave superconductors," *Phys. Rev. Lett.*, **85**, 4940–4943 (2000).
136. M. Kugler, O. Fischer, C. Renner, S. Ono, and Y. Ando, "Scanning tunneling spectroscopy of $Bi_2Sr_2CuO6 + \delta$: new evidence for the common origin of the pseudogap and superconductivity," *Phys. Rev. Lett.*, **86**, 4911 (2001).
137. N.J. Curro, P.C. Hammel, B.J. Suh, M. Hucker, B. Buchner, U. Ammerahl, and A. Revcolevschi, "Inhomogeneous low frequency spin dynamics in $La_{1.65}Eu_{0.2}Sr_{0.15}CuO_4$," *Phys. Rev. Lett.*, **85**, 642–645 (2000).
138. H. Takagi, B. Batlogg, H.L. Kao, J. Kwo, R.J. Cava, J.J. Krajewski, and W.F.P. Jr., "Systematic evolution of temperature-dependent resistivity in $La_{2-x}Sr_xCuO_4$," *Phys. Rev. Lett.*, **69**, 2975–2978 (1992).
139. B. Bucher, P. Steiner, J. Karpinski, E. Kaldis, and P. Wachter, "Influence of the spin gap on the normal state transport in $YBa_2Cu_4O_8$," *Phys. Rev. Lett.*, **70**, 2012–2015 (1993).
140. K. Takenaka, K. Mizuhashi, H. Takagi, and S. Uchida, "Interplane charge transport in $YBa_2Cu_3O_{7-y}$: Spin-gap effect on in-plane and out-of-plane resistivity," *Phys. Rev. B*, **50**, 6534–6537 (1994).
141. A.N. Lavrov, Y. Ando, and S. Ono, "Two mechanisms of pseudogap formation in Bi-2201: evidence from the c-axis magnetoresistance," *Euro. Phys. Lett*, **57**, 267–273 (2002).
142. J.W. Loram, K.A. Mirza, J.R. Cooper, and W.Y. Liang, "Electronic specific heat of $YBa_2Cu_3O_{6+x}$ from 1.8 to 300 K," *Phys. Rev. Lett.*, **71**, 1740–1743 (1993).

143. J. Orenstein, G.A. Thomas, A.J. Millis, S.L. Cooper, D.H. Rapkine, T. Timusk, L.F. Schneemeyer, and J.V. Waszczak, "Frequency- and temperature-dependent conductivity in $YBa_2Cu_3O_{6+x}$ crystals," *Phys. Rev. B*, **42**, 6342–6362 (1990).
144. A. Puchkov, D.N. Basov, and T. Timusk, "Pseudogap state in high–T_c superconductors: an infrared study," *J.Phys Cond. Matt.*, **8**, 10049 (1996).
145. C.C. Homes, T. Timusk, R. Liang, D.A. Bonn, and W.N. Hardy, "Optical conductivity of c axis oriented $YBa_2Cu_3O_{6.70}$: Evidence for a pseudogap," *Phys. Rev. Lett.*, **71**, 1645–1648 (1993).
146. D. Basov, H.A. Mook, B. Dabrowski, and T. Timusk, "c-axis response of single- and double-layered cuprates," *Phys. Rev. B*, **52**, R13141–R13144 (1995).
147. M. Arai, T. Nishijima, Y. Endoh, T. Egami, S. Tajima, K. Tomimoto, Y. Shiohara, M. Takahashi, A. Garrett, and S.M. Bennington, "Incommensurate spin dynamics of underdoped superconductor $YBa_2Cu_3O_{6.7}$," *Phys. Rev. Lett.*, **83**, 608–611 (1999).
148. P.C. Dai, H.A. Mook, S.M. Hayden, G. Aeppli, T.G. Perring, R.D. Hunt, and F. Doğan, "The magnetic excitation spectrum and thermodynamics of high T_c superconductors," *Science*, **284**, 1344–1347 (1999).
149. B. Batlogg and V.J. Emery, "Crossovers in cuprates," *Nature*, **382**, 20 (1996).
150. X.G. Wen and P.A. Lee, "Theory of underdoped cuprates," *Phys. Rev. Lett.*, **76**, 503–506 (1996).
151. E.W. Carlson, D. Orgad, S.A. Kivelson, and V.J. Emery, "Dimensional crossover in quasi-one-dimensional and high T_c superconductors," *Phys. Rev. B*, **62**, 3422–3437 (2000).
152. B.G. Levi, *Physics Today*, **49**, 17 (1996).
153. D.-H. Lee, "Superconductivity in a doped Mott insulator," *Phys. Rev. Lett.*, **84**, 2694–2697 (2000).
154. S. Sachdev, "Kagome-acute- and triangular-lattice Heisenberg antiferromagnets: Ordering from quantum fluctuations and quantum-disordered ground states with unconfined bosonic spinons," *Phys. Rev. B*, **45**, 12377–12396 (1992).
155. M.U. Ubbens and P.A. Lee, "Superconductivity phase diagram in the gauge-field description of the t-J model," *Phys. Rev. B*, **49**, 6853–6863 (1994).
156. S.-C. Zhang, "SO(5) quantum nonlinear sigma model theory of the high–T_c superconductivity," *Science*, **275**, 1089–1096 (1997).
157. S.-C. Zhang, J.-P. Hu, E. Arrigoni, W. Hanke, and A. Auerbach, "Projected SO(5) models," *Phys. Rev. B*, **60**, 13070–13084 (1999).
158. A. Auerbach and E. Altman, "Projected SO(5) Hamiltonian for cuprates and its applications," *Int. Jour. Mod. Phys. B*, **15**, 2509–2518 (2001).
159. J.Ye, "Thermally generated vortices, gauge invariance, and electron spectral function in the pseudogap regime," *Phys. Rev. Lett.*, **87**, 227003–227006 (2001).
160. A. Abanaov, A.V. Chubukov, and J. Schmalian, "Fingerprints of spin mediated pairing in cuprates," *Journal of Electron Spectroscopy and Related Phenomena*, **117-118**, 129–151 (2001).
161. M. Takigawa, A.P. Reyes, P.C. Hammel, J.D. Thompson, R.H. Heffner, Z. Fisk, and K.C. Ott, "Cu and O NMR studies of the magnetic properties of $YBa_2Cu_3O_{6.63}$ (T_c=62 K)," *Phys. Rev. B*, **43**, 247–257 (1991).

162. H.A. Mook and F. Dogan, "Charge fluctuations in YBa2Cu3O$_{7-x}$ high-temperature superconductors," *Nature*, **401**, 145–148 (1999).
163. P. Dai, H.A. Mook, and F. Dogan, "Incommensurate magnetic fluctuations in $YBa_2Cu3O_{6.6}$," *Phys. Rev. B*, **80**, 1738–1741 (1998).
164. J.M. Tranquada, P.M. Gehring, G. Shirane, S. Shamoto, and M. Sato, "Neutron-scattering study of the dynamical spin susceptibility in $YBa_2Cu_3O_{6.6}$," *Phys. Rev. B*, **46**, 5561–5575 (1992).
165. H.A. Mook, P. Dai, and F. Dogan, "Charge and spin structure in $YBa_2Cu_3O_{6.35}$," *Phys. Rev. Lett.*, **88**, 097004–097007 (2002).
166. S. Wakimoto, R.J. Birgeneau, M.A. Kastner, Y.S. Lee, R. Erwin, P.M. Gehring, S.H. Lee, M. Fujita, K. Yamada, Y. Endoh, K. Hirota, and G. Shirane, "Direct observation of a one-dimensional static spin modulation in insulating $La_{1.95}Sr_{0.05}CuO_4$," *Phys. Rev. B*, **61**, 3699–3706 (2000).
167. H. Kimura, H. Matsushita, K. Hirota, Y. Endoh, K. Yamada, G. Shirane, Y.S. Lee, M.A. Kastner, and R.J. Birgeneau, "Incommensurate geometry of the elastic magnetic peaks in superconducting $La_{1.88}Sr_{0.12}CuO_4$," *Phys. Rev. B*, **61**, 14366–14369 (2000).
168. B.O. Wells, Y.S. Lee, M.A. Kastner, R.J. Christianson, R.J. Birgeneau, K. Yamada, Y. Endoh, and G. Shirane, "Incommensurate spin fluctuations in high-transition temperature superconductors," *Science*, **277**, 1067–1071 (1997).
169. M. Matsuda, M. Fujita, K. Yamada, R.J. Birgeneau, Y. Endoh, and G. Shirane, "Electronic phase separation in lightly doped $La_{2-x}Sr_xCuO_4$," *Phys. Rev. B*, **65**, 134515 (2002).
170. P.A. Lee and N. Nagaosa, "Gauge theory of the normal state of high-T_c superconductors," *Phys. Rev. B*, **46**, 5621–39 (1992).
171. C. Meingast, V. Pasler, P. Nagel, A. Rykov, S. Tajima, and P. Olsson, "Phase fluctuations and the pseudogap in $YBa_2Cu_3O_{7-\delta}$," *Phys. Rev. Lett.*, **86**, 1606–1609 (2001).
172. J. Corson, R. Mallozzi, J. Orenstein, J.N. Eckstein, and I. Bozovic, "Vanishing of phase coherence in underdoped $Bi_2Sr_2CaCu_2O_{8+\delta}$," *Nature*, **398**, 221–223 (1999).
173. D.A. Bonn, S. Kamal, A. Bonakdarpour, L. Ruixing, W.N. Hardy, C.C. Homes, and D.N.B.T. Timusk, "Surface impedance studies of YBCO," *Czech. J. Phys.*, **46**, 3195–3202 (1996).
174. V. Pasler, P. Schweiss, C. Meingast, B. Obst, H. Wuhl, A.I. Rykov, and S. Tajima, "3D-XY critical fluctuations of the thermal expansivity in detwinned $YBa_2Cu_3O_{7-\delta}$ single crystals near optimal doping," *Phys. Rev. Lett.*, **81**, 1094–1097 (1998).
175. C. Varma, "Pseudogap phase and the quantum-critical point in copper-oxide metals," *Phys. Rev. Lett.*, **83**, 3538–3541 (1999).
176. S. Chakravarty, *unpublished*.
177. T. Valla, P.D. Johnson, Z. Yusof, B. Wells, Q. Li, S.M. Loureiro, R.J. Cava, M. Mikami, Y. Mori, M. Yoshimura, and T. Sasaki, "Coherence-incoherence and dimensional crossover in layered strongly correlated metals," *submitted to Science* (2002).
178. J. Zaanen, "Superconductivity: self-organized one dimensionality," *Science*, **286**, 251–252 (1999).
179. Preliminary evidence of the existence of nematic order in $La_{2-x}Sr_xCuO_4$ and $YBa_2Cu_3O_{7-\delta}$ can be found in [99].

180. J.P. Eisenstein, M.P. Lilly, K.B. Cooper, L.N. Pfeiffer, and K.W. West, "New collective states of 2D electrons in high Landau levels," *Physica E*, **9**, 1–8 (2001).
181. M.M. Fogler, "Stripe and bubble phases in quantum Hall systems," *cond-mat/0111001* (2001).
182. M.M. Fogler, "Quantum Hall liquid crystals," *cond-mat/0111049* (2001).
183. V.J. Emery, "Theory of the one-dimensional electron gas," in "Highly Conducting One-Dimensional Solids," edited by J.T. Devreese, R.P. Evrard, and V.E. van Doren, 327 (Plenum, New York) (1979).
184. J. Solyom, "The Fermi gas model of one-dimensional conductors," *Adv. Phys.*, **28**, 201–303 (1979).
185. E. Fradkin, Field Theories of Condensed Matter Systems (Addison-Wesley, Massachusetts) (1991).
186. J. von Delft and H. Schoeller, "Bosonization for beginners - Refermionization for experts," *Annalen Phys.*, **7**, 225–305 (1998).
187. A.O. Gogolin, A.A. Nersesyan, and A.M. Tsvelik, Bosonization and Strongly Correlated Systems (Cambridge University Press, Cambridge) (1998).
188. H.J. Schulz, G. Guniberti, and P. Pieri, "Fermi liquids and Luttinger liquids," *cond-mat/9807366* (1998).
189. J. Voit, "One-dimensional Fermi liquids," *Rep. Prog. Phys.*, **58**, 977–1116 (1995).
190. J.M. Kosterlitz and D.J. Thouless, "Ordering, metastability and phase transitions in two-dimensional systems," *J. Phys. C*, **6**, 1181–1203 (1973).
191. T. Giamarchi and H.J. Schulz, "Correlation functions of one-dimensional quantum systems," *Phys. Rev. B*, **39**, 4620–4629 (1989).
192. A. Luther and V.J. Emery, "Backward scattering in the one-dimensional electron gas," *Phys. Rev. Lett.*, **33**, 589–592 (1974).
193. N. Kawakami and S.K. Yang, "Luttinger anomaly exponent of momentum distribution in the Hubbard chain," *Phys. Lett. A*, **148**, 359–362 (1990).
194. R.M. Noack, N. Bulut, D.J. Scalapino, and M.G. Zacher, "Enhanced $d_{x^2-y^2}$ pairing correlations in the two-leg Hubbard ladder," *Phys. Rev. B*, **56**, 7162–7166 (1997).
195. T. Valla, A.V. Fedorov, P.D. Johnson, and S.L. Hulber, "Many-body effects in angle-resolved photoemission: Quasiparticle energy and lifetime of a Mo(110) surface state," *Phys. Rev. Lett.*, **83**, 2085–2088 (1999).
196. A. Luther and I. Peschel, "Single-particle states, Kohn anomaly and pairing fluctuations in one dimension," *Phys. Rev. B*, **9**, 2911–2919 (1974).
197. V. Meden and K. Schönhammer, "Spectral functions for the Tomonaga-Luttinger model," *Phys. Rev. B*, **46**, 15753–15760 (1992).
198. J. Voit, "Charge-spin separation and the spectral properties of Luttinger liquids," *Phys. Rev. B*, **47**, 6740–6743 (1993).
199. D. Orgad, "Spectral functions for the Tomonga-Luttinger and Luther-Emery liquids," *Phil. Mag. B*, **81**, 377–398 (2001).
200. G.-H. Gweon, J.W. Allen, and J.D. Denlinger, "Ubiquitous generalized spectral signatures of electron fractionalization in quasi-low dimensional metals,"
201. F.H.L. Essler and A.M. Tsvelik, "Weakly coupled one-dimensional Mott insulators," *Phys. Rev. B*, **65**, 115117–115129 (2002).
202. D.J. Scalapino, Y. Imry, and P. Pincus, "Generalized Ginzburg-Landau theory of pseudo-one-dimensional systems," *Phys. Rev. B*, **11**, 2042–2048 (1975).

203. E. Arrigoni, "Crossover to Fermi-liquid behavior for weakly coupled Luttinger liquids in the anisotropic large-dimension limit," *Phys. Rev. B*, **61**, 7909–7029 (2000).
204. D.L. Feng, D.H. Lu, K.M. Shen, C. Kim, H. Eisaki, A. Damascelli, R. Yoshizaki, J. Shimoyama, K. Kishio, G.D. Gu, S. Oh, A. Andrus, J.O'Donnell, J.N. Eckstein, and Z.X. Shen, "Signature of superfluid density in the single-particle excitation spectrum of $Bi_2Sr_2CaCu_2O_{8+\delta}$," *Science*, **289**, 277–281 (2000).
205. H. Ding, J.R. Engelbrecht, Z. Wang, J.C. Campuzano, S.-C. Wang, H.-B. Yang, R. Rogan, T. Takahashi, K. Kadowaki, and D.G. Hinks, "Coherent quasiparticle weight and its connection to high- Tc superconductivity from angle-resolved photoemission," *Phys. Rev. Lett.*, **87**, 227001–227004 (2000).
206. S. Biermann, A. Georges, A. Lichtenstein, and T. Giamarchi, "Deconfinement transition and Luttinger to Fermi liquid crossover in quasi-one-dimensional systems," *Phys. Rev. Lett.*, **87**, 276405–276408 (2001).
207. S. Biermann, A. Georges, T. Giamarchi, and A. Lichtenstein, "Quasi-one-dimensional organic conductors: dimensional crossover and some puzzles," *cond-mat/0201542* (2002).
208. L. Yin and S. Chakravarty, "Spectral anomaly and high temperature superconductors," *Int. J. Mod. Phys. B*, **7**, 805–45 (1996).
209. V.J. Emery, E. Fradkin, S.A. Kivelson, and T.C. Lubensky, "Quantum theory of the smectic metal state in stripe phases," *Phys. Rev. Lett.*, **85**, 2160–2163 (2000).
210. A.H. Castro Neto, "Stripes, vibrations, and superconductivity," *Phys. Rev. B*, **64**, 104509–104535 (2001).
211. A. Vishwanath and D. Carpentier, "Two-Dimensional anisotropic non-Fermi-liquid phase of coupled Luttinger liquids," *Phys. Rev. Lett.*, **86**, 676–679 (2001).
212. R. Mukhopadhyay, C.L. Kane, and T.C. Lubensky, "Sliding Luttinger liquid phases," *Phys. Rev. B*, **64**, 045120–045137 (2001).
213. S.L. Sondhi and K. Yang, "Sliding phases via magnetic fields," *Phys. Rev. B*, **63**, 054430–054436 (2001).
214. S.A. Kivelson, "Electron fractionalization," *Synth. Met.*, **125** (2001).
215. T. Senthil and O. Motrunich, "Microscopic models for fractionalized phases in strongly correlated systems," *cond-mat/0201320* (2002).
216. P. Fazekas and P.W. Anderson, "On the ground state properties of the anisotropic triangular antiferromagnet. (Application of anisotropic Heisenberg model)," *Phil. Mag.*, **30**, 423–440 (1974).
217. R.B. Laughlin, "The relationship between high-temperature superconductivity and the fractional quantum Hall effect," *Science*, **242**, 525–533 (1988).
218. N. Read and B. Chakraborty, "Statistics of the excitations of the resonating-valence-bond state," *Phys. Rev. B*, **40**, 7133–7140 (1989).
219. V. Kalmeyer and R.B. Laughlin, "Equivalence of the resonating-valence-bond and fractional quantum Hall states," *Phys. Rev. Lett.*, **59**, 2095–2098 (1987).
220. S.A. Kivelson, "Statistics of holons in the quantum hard-core dimer gas," *Phys. Rev. B*, **39**, 259–264 (1989).
221. E. Demler, C. Nayak, H.-Y. Kee, Y.B. Kim, and T. Senthil, "Fractionalization patterns in strongly correlated electron systems: Spin-charge separation and beyond," *cond-mat/0105446* (2001).

222. F.D.M. Haldane, "O(3) nonlinear sigma model and the topological distinction between integer- and half-integer-spin antiferromagnets in two dimensions," *Phys. Rev. Lett.*, **61**, 1029–32 (1988).
223. S. Chakravarty, B.I. Halperin, and D. Nelson, "Two-dimensional quantum Heisenberg antiferromagnet at low temperatures," *Phys. Rev. B*, **39**, 2344–2371 (1989).
224. S. Chakravarty, B.I. Halperin, and D. Nelson, "Low-temperature behavior of two-dimensional quantum antiferromagnets," *Phys. Rev. Lett.*, **60**, 1057–1060 (1988).
225. R. Coldea, S.M. Hayden, G. Aeppli, T.G. Perring, C.D. Frost, T.E. Mason, S.-W. Cheong, and Z. Fisk, "Spin waves and electronic interactions in La_2CuO_4," *Phys. Rev. Lett.*, **86** (2001).
226. R.J. Birgeneau, A. Aharony, N.R. Belk, F.C. Chou, Y. Endoh, M. Greven, S. Hosoya, M.A. Kastner, C.H. Lee, Y.S. Lee, G. Shirane, S. Wakimoto, B.O. Wells, and K. Yamada, "Magnetism and magnetic fluctuations in $La_{2-x}Sr_xCuO_4$ for x=0 (2D antiferromagnet), 0.04 (3D spin glass) and x=0.15 (superconductor)," *Jour. Phys. Chem. Solids*, **56**, 1912–1919 (1995).
227. A. Weidinger, C. Niedermayer, A. Golnik, R. Simon, E. Recknagel, J.I. Budnick, B. Chamberland, and C. Baines, "Observation of magnetic ordering in superconducting $La_{2-x}Sr_xCuO_4$ by muon spin rotation," *Phys. Rev. Lett.*, **62** (1989).
228. C. Niedermayer, C. Bernhard, T. Blasius, A. Golnik, A. Moodenbaugh, and J.I. Budnick, "Common phase diagram for antiferromagnetism in $La_{2-x}Sr_xCuO_4$ and $Y_{1-x}Ca_xBa_2Cu_3O_6$ as seen by muon spin rotation," *Phys. Rev. Lett.*, **80** (1999).
229. C. Panagopoulos, J.L. Tallon, B.D. Rainford, T. Xiang, J.R. Cooper, and C.A. Scott, "Evidence for a generic novel quantum transition in high-Tc cuprates," *cond-mat/0204106* (2002).
230. P. Azaria, C. Hooley, P. Lecheminant, C. Lhuillier, and A.M. Tsvelik, "Kagome lattice antiferromagnet stripped to its basics," *Phys. Rev. Lett.*, **81**, 1694–1697 (1998).
231. W. LiMing, G. Misguich, P. Sindzingre, and C. Lhuillier, "From Neel long-range order to spin liquids in the multiple-spin exchange model," *Phys. Rev. B*, **62**, 6372–6377 (2000).
232. G. Misguich, B. Bernu, C. Lhuillier, and C. Waldtmann, "Spin liquid in the multiple-spin exchange model on the triangular lattice: ^{3}He on graphite," *Phys. Rev. Lett.*, **81**, 1098–1101 (1998).
233. C. Lhuillier and G. Misguich, "Frustrated quantum magnets," *cond-mat/0109146* (2001).
234. S. Chakravarty, S.A. Kivelson, C. Nayak, , and K. Volker, "Wigner glass, spin liquids and the metal-insulator transition," *Phil. Mag. B*, **79** (1999).
235. A.V. Chubukov, S. Sachdev, and T. Senthil, "Quantum phase transitions in frustrated quantumantiferromagnets," *Nucl. Phys. B*, **426**, 601–643 (1994).
236. R. Meservey and B.B. Schwartz, "equilibrium properties: comparison of experimental results with predictions of the BCS theory," in "Superconductivity," edited by R.D. Parks, vol. 1 (Marcel Deckker, Inc., New York, NY) (1969).
237. E.A. Lynton, Superconductivity (Methuen, London) (1962).
238. T.P. Orlando, E.J. McNiff Jr., S. Foner, and M.R. Beasley, "Critical fields, Pauli paramagnetic limiting, and material parameters of Nb3Sn and V3Si," *Phys. Rev. B*, **19**, 4545–4561 (1979).

239. Y.G. Naidyuk and I.K. Yanson, "Point-contact spectroscopy of heavy-fermion systems," *J. Phys. Cond. Matt.*, **10**, 8905–8938 (1998).
240. M.B. Maple, J.W. Chen, S.E. Lambert, Z. Fisk, J.L. Smith, H.R. Ott, J.S. Brooks, and M.J. Naughton, "Upper critical magnetic field of the heavy-fermion superconductor UBel3," *Phys. Rev. Lett.*, **54**, 477–480 (1985).
241. F. Gross, K. Andres, and S. Chandrasekhar, "Experimental determination of the absolute value of the London penetration depth in the heavy fermion superconductors UBe_{13} and UPt_3," *Physica C*, **162-164**, 419–420 (1989).
242. F. Sharifi, A. Pargellis, R.C. Dynes, B. Miller, E.S. Hellman, J. Rosamilia, and E.H.H. Jr., "Electron tunneling in the high-Tc bismuthate superconductors," *Phys. Rev. B*, **44**, 12521–12524 (1991).
243. Y.J. Uemura, L.P. Le, G.M. Luke, B.J. Sternlieb, W.D. Wu, J.H. Brewer, T.M. Riseman, C.L. Seaman, M.B. Maple, M. Ishikawa, D.G. Hinks, J.D. Jorgensen, G. Saito, and H. Yamochi, "Basic similarities among cuprate, bismuthate, organic, chevrel-phase, and heavy-fermion superconductors shown by penetration-depth measurements," *Phys. Rev. Lett.*, **66**, 2665–2668 (1991).
244. O. Gunnarsson, "Superconductivity in fullerides," *Rev. Mod. Phys.*, **69**, 575–606 (1997).
245. Y.J. Uemura, A. Keren, L.P. Le, G.M. Luke, B.J. Sternlieb, W.D. Wu, J.H. Brewer, R.L. Whetten, S.M. Huang, S. Lin, R.B. Kaner, F. Diederich, S. Donovan, G. Gruner, and K. Holczer, "Magnetic-field penetration depth in K_3C_{60} measured by muon spin relaxation," *Nature*, **352**, 605–607 (1991).
246. A.P. Ramirez, *Superconductivity Rev.*, **1**, 1–101 (1994).
247. A.S. Alexandrov, "Nonadiabatic polaronic superconductivity in MgB_2 and cuprates," *Physica C*, **363**, 231–236 (2001).
248. H. Schmidt, J.F. Zasadzinski, K.E. Gray, and D.G. Hinks, "Evidence for two-band superconductivity from break junction tunneling on MgB_2," *Phys. Rev. Lett.*, **88**, 127002–127005 (2002).
249. A.V. Sologubenko, J. Jun, S.M. Kazakov, J. Karpinski, and H.R. Ott, "Temperature dependence and anisotropy of the bulk upper critical field H_{c2} of MgB_2," *Phys. Rev. B*, **65**, R180505–R180508 (2002).
250. T. Arai, K. Ichimura, K. Nomur, S. Takasaki, J. Yamada, S. Nakatsuji, and H. Anzai, "Superconducting and normal-state gaps in κ-(BEDT-TTF)$_2$Cu(NCS)$_2$ studied by STM spectroscopy," *Solid State Commun.*, **116**, 679–682 (2000).
251. Y.J. Uemura, A. Keren, L.P. Le, G.M. Luke, W.D. Wu, Y. Kubo, T. Manako, Y. Shimakawa, M. Subramanian, J.L. Cobb, and J.T. Markert, "Magnetic-field penetration depth in $Tl_2Ba_2CuO_{6+\delta}$ in the overdoped regime," *Nature*, **364**, 605–607 (1993).
252. R. Prozorov, R.W. Giannetta, A. Carrington, P. Fournier, R.L. Greene, P. Guptasarma, D.G. Hinks, and A.R. Banks, "Measurements of the absolute value of the penetration depth in high-T_c superconductors using a low-T_c superconductive coating," *Appl. Phys. Lett.*, **77**, 4202 (2000).
253. A. Biswas, P. Fournier, V.N. Smolyaninova, R.C. Budhani, J.S. Higgins, and R.L. Greene, "Gapped tunneling spectra in the normal state of $Pr_{2-x}Ce_xCuO_4$," *Phys. Rev. B*, **64**, 104519–104526 (2001).
254. Kajitani, K. Hiraga, S. Hosoya, and T.F.K.O.-I.Y. Syono, "Structural study of oxygen-saturated or quenched $Pr_{2-x}Ce_xCuO_4$ with x¡=0.15," *Physica C*, **178**, 397–404 (1991).

255. L. Ozyuzer, Z. Yusof, J.F. Zasadzinski, R. Mogilevsky, D.G. Hinks, and K.E. Gray, "Evidence of $d_{x^2-y^2}$ symmetry in the tunneling conductance density of states of $Tl_2Ba_2CuO_6$," *Phys. Rev. B*, **57**, R3245–R3248 (1998).
256. C. Niedermayer, C. Bernhard, U. Binninger, H. Glückler, J.L. Tallon, E.J. Ansaldo, and J.I. Budnick, "Muon spin rotation study of the correlation between Tc and ns/m* in overdoped $Tl_2Ba_2CuO_{6+\delta}$," *Phys. Rev. Lett.*, **71**, 1764 (1993).
257. M. Kang, G. Blumberg, M.V. Klein, and N.N. Kolesnikov, "Resonance Raman study of the superconducting gap and low energy excitations in $Tl_2Ba_2CuO_{6+\delta}$ superconductors," *Phys. Rev. Lett.*, **77**, 4434 (1996).
258. N. Miyakawa, P. Guptasarma, J.F. Zasadzinski, D.G. Hinks, and K.E. Gray, "Strong dependence of the superconducting gap on oxygen doping from tunneling measurements on $Bi_2Sr_2CaCu_2O_{8-\delta}$," *Phys. Rev. Lett.*, **80**, 157–160 (1998).
259. M. Niderost, R. Frassanito, M. Saalfrank, A.C. Mota, G. Blatter, V.N. Zavaritsky, T.W. Li, and P.H. Kes, "Lower critical field H_{c1} and barriers for vortex entry in $Bi_2Sr_2CaCu_2O_{8+\delta}$ crystals," *Phys. Rev. Lett.*, **81**, 3231 (1998).
260. S.L. Lee, P. Zimmermann, H. Keller, M. Warden, I.M. Savic, R. Schauwecker, D. Zech, R. Cubitt, E.M. Forgan, P.H. Kes, T.W. Li, A.A. Menovsky, and Z. Tarnawski, "Evidence for flux-lattice melting and a dimensional crossover in single-crystal $Bi_{2.15}Sr_{1.85}CaCu_2O_{8+\delta}$ from muon spin rotation studies," *Phys. Rev. Lett.*, **71**, 3862–3865 (1993).
261. M. Weber, P. Birrer, F.N. Gygax, B. Hitti, E. Lippelt, H. Maletta, and A. Schenck, "Measurements of the London penetration depth in Bi-based high-T_c compounds," *Hyp. Int.*, **63**, 93 (1993).
262. C. Bernhard, J.L. Tallon, T. Blasius, A. Golnik, and C. Neidermayer, "Anomalous peak in the superconducting condensate density of cuprate high-Tc superconductors at a unique doping state," *Phys. Rev. Lett.*, **86**, 1614–1617 (2001).
263. C. Panagopoulos, J.R. Cooper, and T. Xiang, "Systematic behavior of the in-plane penetration depth in d-wave cuprates," *Phys. Rev. B*, **57**, 13422–13425 (1998).
264. P. Zimmermann, H. Keller, S.I. Lee, I.M. Savic, M. Warden, D. Zech, R. Cubitt, E.M. Forgan, E. Kaldis, J. Karpinski, and C. Kruger, "Muon-spin-rotation studies of the temperature dependence of the magnetic penetration depth in the $YBa_2Cu_3O_x$ family and related compounds," *Phys. Rev. B*, **52**, 541–552 (1995).
265. J.Y.T. Wei, C.C. Tsuei, P.J.M. van Bentum, Z. Xiong, C.W. Chu, and M.K. Wu, "Quasiparticle tunneling spectra of the high-Tc mercury cuprates: Implications of the d-wave two-dimensional van Hove scenario," *Phys. Rev. B*, **57**, 3650–3662 (1998).
266. L. Fàbrega, A. Calleja, A. Sin, S.P. nol, X. Obradors, J. Fontcuberta, and P.J.C. King, "Muon spin relaxation in Re-substituted $HgA_2Ca_{n-1}Cu_nO_{2n+2+x}$ (A = Sr,Ba; n = 2,3) superconductors," *Phys. Rev. B*, **60**, 7579–7584 (1999).
267. A. Fujimori, A. Ino, T. Yoshida, T. Mizokawa, M. Nakamura, C. Kim, Z.X. Shen, T. Kakeshita, H. Eisaki, and S. Uchida, "Fermi surface, pseudogap and superconducting gap in $La_{2-x}Sr_xCuO_4$," *Physica C*, **341-348**, 2067 (2000).

268. C. Panagopoulos, B.D. Rainford, J.R. Cooper, W. Lo, J.L. Tallon, J.W. Loram, J. Betouras, Y.S. Wang, and C.W. Chu, "Effects of carrier concentration on the superfluid density of high-Tc cuprates," *Phys. Rev. B*, **60**, 14617–14620 (1999).
269. P.G. Radaelli, D.G. Hinks, A.W. Mitchell, B.A. Hunter, J.L. Wagner, B. Dabrowski, K.G. Vandervoort, H.K. Viswanathan, and J.D. Jorgensen, "Structural and superconducting properties of $La_{2-x}Sr_xCuO_4$ as a function of Sr content," *Phys. Rev. B*, **49**, 4163–4175 (1994).
270. V.J. Emery and S.A. Kivelson, "Importance of phase fluctuations in superconductors with small superfluid density," *Nature*, **374**, 434–437 (1995).
271. L.M. Merchant, J. Ostrick, R.P.B. Jr., and R.C. Dynes, "Crossover from phase fluctuation to amplitude-dominated superconductivity: A model system," *Phys. Rev. B*, **63**, 134508–134514 (2001).
272. A.J. Rimberg, T.R. Ho, C. Kurdak, J. Clarke, K.L. Campman, and A.C. Gossard, "Dissipation-driven superconductor-insulator transition in a two-dimensional Josephson-junction array," *Phys. Rev. Lett.*, **78**, 2632–2635 (1997).
273. A. Kapitulnik, N. Mason, S.A. Kivelson, and S. Chakravarty, "Effects of dissipation on quantum phase transitions," *Phys. Rev. B*, **63**, 125322–125333 (2001).
274. N. Mason and A. Kapitulnik, "True superconductivity in a two-dimensional superconducting-insulating system," *Phys. Rev. B*, **64**, 60504–60508 (2001).
275. E.W. Carlson, S.A. Kivelson, V.J. Emery, and E. Manousakis, "Classical phase fluctuations in high temperature superconductors," *Phys. Rev. Lett.*, **83**, 612–615 (2000).
276. B.I. Spivak and S.A. Kivelson, "Aharonov-Bohm oscillations with period hc/4e and negative magnetoresistance in dirty superconductors," *Phys. Rev. B*, **45**, 10490–10495 (1992), electron correlations could change this assumption.
277. P.M. Chaikin and T.C. Lubensky, Principles of condensed matter physics (Cambridge) (1995).
278. E. Roddick and D. Stroud, "Effect of phase fluctuations on the low-temperature penetration depth of high- Tc superconductors," *Phys. Rev. Lett.*, **74**, 1430–1433 (1995).
279. M.W. Coffey, "Effect of superconductor phase fluctuations upon penetration depth," *Phys. Lett. A*, **200**, 195–200 (1995).
280. S. Kamal, D.A. Bonn, N. Goldenfeld, P.J. Hirschfeld, R. Liang, and W.N. Hardy, "Penetration depth measurements of 3D XY critical behavior in $YBa_2Cu_3O_{6.95}$ crystals," *Phys. Rev. Lett.*, **73**, 1845–1848 (1994).
281. S. Chakravarty, G. Ingold, S.A. Kivelson, and A. Luther, "Onset of global phase coherence in Josephson-junction arrays: a dissipative phase transition," *Phys. Rev. Lett.*, **56** (1986).
282. K.-H. Wagenblast, A.V. Otterlo, G. Schon, and G.T. Zimanyi, "Superconductor-insulator transition in a tunable dissipative environment," *Phys. Rev. Lett.*, **79** (1997).
283. S. Sachdev, Quantum Phase Transitions (Cambridge University Press, Cambridge, UK) (1999).
284. M.V. Feigel'man, A.I. Larkin, and M.A. Skvortsov, "Quantum superconductor-metal transition in a proximity array," *Phys. Rev. Lett.*, **86**, 1869–1872 (2001).

285. B.I. Spivak, A. Zyuzin, and M. Hruska, "Quantum superconductor-metal transition," *Phys. Rev. B*, **64**, 132502–132505 (2001).
286. Y. Oreg and E. Demler, "Fermions and bosons in superconducting amorphous wires," *cond-mat/0106645* (2001).
287. L. Ozyuzer, J.F. Zasadzinski, and N. Miyakawa, "Tunneling spectra and superconducting gap in $Bi_2Sr_2CaCu_2O_{8+\delta}$ and $Tl_2Ba_2CuO_{6+\delta}$," *Int. J. Mod. Phys. B*, **13**, 3721–3724 (1999).
288. S. Doniach and M. Inui, "Long-range Coulomb interactions and the onset of superconductivity in the high-Tc materials," *Phys. Rev. B*, **41**, 6668–6678 (1990).
289. J.M. Harris, P.J. White, Z.-X. Shen, H. Ikeda, R. Yoshizaki, H. Eisaki, S. Uchida, W.D. Si, J.W. Xiong, Z.-X. Zhao, and D.S. Dessau, "Measurement of an anisotropic energy gap in single plane $Bi_2Sr_{2-x}La_xCuO_{6+\delta}$," *Phys. Rev. Lett.*, **79**, 143–146 (1997).
290. T. Schneider and H. Keller, "Extreme type II superconductors. Universal properties and trends," *Physica*, **207**, 366–380 (1993).
291. F. a recent analysis of the doping dependence of ξ_0 see Y. Ando and K. Segawa, "Magnetoresistance of untwinned $YBa_2Cu_3O_y$ single crystals in a wide range of doping: anomalous hole-doping dependence of the coherence length," *Phys. Rev. Lett.*, **88**, 167005 (2002).
292. C.P.B. W.N. Hardy, D. A. Bonn, and R. Liang, "Magnetic field dependence of lambda in $YBa_2Cu_3O_{6.95}$: results as a function of temperature and field orientation," *Phys. Rev. Lett.*, **83**, 3277–3280 (1999).
293. X.-G. Wen and P.A. Lee, "Theory of quasiparticles in the underdoped high-T_c superconducting state," *Phys. Rev. Lett.*, **80**, 2193–2196 (1998).
294. A.J. Millis, S.M. Girvin, L.B. Ioffe, and A.I. Larkin, "Anomalous charge dynamics in the superconducting state of underdoped cuprates," *Jour. Phys. Chem. Solids*, **59**, 1742–1744 (1998).
295. L. Benfatto, S. Caprara, C. Castellani, A. Paramekanti, and M. Randeria, "Phase fluctuations, dissipation, and superfluid stiffness in *d*-wave superconductors," *Phys. Rev. B*, **63**, 174513–21 (2001).
296. G.T. Zimanyi, S.A. Kivelson, and A. Luther, "Superconductivity from predominantly repulsive interactions in quasi one-dimensional systems," *Phys. Rev. Lett.*, **60**, 2089–2092 (1988).
297. S.A. Kivelson and G.T. Zimanyi, "High temperature superconductors, RVB, and conducting polymers," *Molec. Cryst. and Liq. Cryst*, **160**, 457–481 (1988).
298. A.M. Finkel'stein and S.A. Brazovsky, "Interchain coupling in linear conductors," *J. Phys. C*, **14**, 847–857 (1981).
299. S.A. Brazovsky and A.M. Finkel'stein, "The influence of phonons on the optical properties and conductivity of quasi-one-dimensional metals," *Solid State Comm.*, **38**, 745 (1981).
300. S.A. Kivelson and M.I. Salkola, "Metal-non-metal transition in polyacetylene," *Synth. Met.*, **44**, 281–291 (1991).
301. G.G. Batrouni, R.T. Scalettar, G.T. Zimanyi, and A.P. Kampf, "Supersolids in the Bose-Hubbard Hamiltonian," *Phys. Rev. Lett.*, **74**, 2527–2530 (1995), see also [502].
302. M.P.A. Fisher, P.B. Weichman, G. Grinstein, and D.S. Fisher, "Boson localization and the superfluid-insulator transition," *Phys. Rev. B*, **40**, 546–570 (1989).

303. C. Nayak and K. Shtengel, "Microscopic models of two-dimensional magnets with fractionalized excitations," *Phys. Rev. B*, **64**, 064422–064428 (2001).
304. R. Coldea, D.A. Tennant, A.M. Tsvelik, and Z. Tylczynski, "Experimental realization of a 2D fractional quantum spin liquid," *Phys. Rev. Lett.*, **86**, 1335–1338 (2001).
305. S. Chakravarty, "Magnetic properties of La_2CuO_4," (Addison-Wesley, Redwood City, CA, USA) (1990).
306. A.E. Sikkema, I. Affleck, and S.R. White, "Spin gap in a doped Kondo chain," *Phys. Rev. Lett.*, **79**, 929–932 (1997).
307. O. Zachar, V.J. Emery, and S.A. Kivelson, "Exact results for a 1D Kondo lattice from bosonization," *Phys. Rev. Lett.*, **77**, 1342–1345 (1996).
308. O. Zachar, "Staggered liquid phases of the one-dimensional Kondo-Heisenberg lattice model," *Phys. Rev. B*, **63**, 205104–205113 (2001).
309. D.J. Scalapino and S.R. White, "Numerical results for the Hubbard model: implications for the high-T_c pairing mechanism," *Foundations of Physics*, **31**, 27–39 (2001).
310. F.D.M. Haldane, "Continuum dynamics of the 1-D Heisenberg antiferromagnet: identification with the O(3) nonlinear sigma model," *Phys. Lett. A*, **93**, 464–468 (1983).
311. S. Chakravarty, "Dimensional crossover in quantum antiferromagnets," *Phys. Rev. Lett.*, **77**, 4446–4449 (1996).
312. S.R. White, R.M. Noack, and D.J. Scalapino, "Resonating valence bond theory of coupled Heisenberg chains," *Phys. Rev. Lett.*, **73**, 886–889 (1994).
313. D.J. Scalapino and S.A. Trugman, "Local antiferromagnetic correlations and $d_{x^2-y^2}$ pairing," *Philos. Mag. B*, **74**, 607–610 (1996).
314. M. Havilio and A. Auerbach, "Superconductivity and quantum spin disorder in cuprates," *Phys. Rev. Lett.*, **83**, 4848–4851 (1999).
315. M. Havilio and A. Auerbach, "Correlations in doped antiferromagnets," *Phys. Rev. B*, **62**, 324–336 (2000).
316. S.R. White and D.J. Scalapino, "Superconductivity in ladders and coupled planes," *Phys. Rev. B*, **45**, 5744–5747 (1992).
317. D. Poilblanc, "Internal structure of the singlet $d_{x^2-y^2}$ hole pair in an antiferromagnet," *Phys. Rev. B*, **495**, 1477–1479 (1993).
318. Y. Fang, A.E. Ruckenstein, E. Dagotto, and S. Schmitt-Rink, "Holes in the infinite-U Hubbard model: instability of the Nagaoka state," *Phys. Rev. B*, **40**, 7406–7409 (1989), see also [503].
319. D. Rokhsar, "Quadratic quantum antiferromagnets in the fermionic large-N limit," *Phys. Rev. B*, **42**, 2526–2531 (1990).
320. C.M. Varma and A. Zawadowskii, "Scaling in an interacting two-component (valence-fluctuation) electron gas," *Phys. Rev. B*, **32**, 7399–7407 (1985).
321. H.-H. Lin, L. Balents, and M.P.A. Fisher, "N-chain Hubbard model in weak coupling," *Phys. Rev. B*, **56**, 6569–6593 (1997).
322. S.R. White and D.J. Scalapino, "Density matrix renormalization group study of the striped phase in the 2D t-J model," *Phys. Rev. Lett.*, **80**, 1272–1275 (1998).
323. S.R. White and D.J. Scalapino, "Energetics of domain walls in the 2D t-J model," *Phys. Rev. Lett.*, **81**, 3227–3230 (1998).
324. S. Hellberg and E. Manousakis, "Phase separation at all interaction strengths in the t-J model," *Phys. Rev. Lett.*, **78**, 4609–4612 (1997).

325. D. Poilblanc, O. Chiappa, J. Riera, S.R. White, and D.J. Scalapino, "Evolution of the spin gap upon doping a 2-leg ladder," *Phys. Rev. B*, **62**, R14633–R14636 (2000).
326. S.R. White and D.J. Scalapino, "Competition between stripes and pairing in a t-t'-J model," *Phys. Rev. B*, **60**, R753–R756 (1999).
327. S.C. Hellberg and E. Manousakis, "Stripes and the t-J model," *Phys. Rev. Lett.*, **83**, 132 (1999), see also Refs. 328,329.
328. S.R. White and D.J. Scalapino, "Comment on "Stripes and the t-J Model"," *Phys. Rev. Lett.*, **84**, 3021 (2000).
329. S.C. Hellberg and E. Manousakis, "Reply: Hellberg and Manousakis," *Phys. Rev. Lett.*, **84**, 3022 (2000).
330. E. Arrigoni, A.P. Harju, W. Hanke, B. Brendel, and S.A. Kivelson, "Stripes and superconducting pairing in the t-J model with Coulomb interactions," *Phys. Rev. B*, **65**, 134503–134507 (2002).
331. S.R. White and D.J. Scalapino, "Phase separation and stripe formation in the two-dimensional t-J model: A comparison of numerical results," *Phys. Rev. B*, **61**, 6320–6326 (2000).
332. E. Daggoto, "Correlated electrons in high-temperature superconductors," *Rev. Mod. Phys.*, **66**, 763–840 (1994).
333. S.C. Hellberg and E. Manousakis, "Green's-function Monte Carlo for lattice fermions: Application to the t-J model," *Phys. Rev. B*, **61**, 11787–11806 (2000).
334. S. Sorella, "Green function Monte Carlo with stochastic reconfiguration," *Phys. Rev. Lett.*, **80**, 4558–4561 (1998).
335. Y.C. Chen and T.K. Lee, "t-J model studied by the power Lanczos method," *Phys. Rev. B*, **51**, 6723–6726 (1995).
336. S.R. White, "Density-matrix algorithms for quantum renormalization groups," *Phys. Rev. B*, **48**, 10345–10356 (1993).
337. S.R. White, "Spin gaps in a frustrated Heisenberg model for CaV_4O_9," *Phys. Rev. Lett.*, **77**, 3633–3636 (1996).
338. E. Dagotto and T.M. Rice, "Surprises on the way from one- to two-dimensional quantum magnets: the ladder materials," *Science*, **271**, 618–623 (1996).
339. E. Dagotto, "Experiments on ladders reveal a complex interplay between a spin-gapped normal state and superconductivity," *Rep. Prog. Phys.*, **62**, 1525–1571 (1999).
340. E. Lieb and F.Y. Wu, "Absence of Mott transition in an exact solution of the short-range, one-band model in one dimension," *Phys. Rev. Lett.*, **20**, 1445–1448 (1968).
341. H.J. Schulz, in "Proceedings of the 9th Jerusalem Winter School for Theoretical Physics," edited by V. J. Emery (World Scientific, New York) (1993).
342. B. Frischmuth, B. Ammon, and M. Troyer, "Susceptibility and low-temperature thermodynamics of spin-1/2 Heisenberg ladders," *Phys. Rev. B*, **54**, R3714–R3717 (1996).
343. R.M. Noack, S.R. White, and D.J. Scalapino, "Correlations in a two-chain Hubbard model," *Phys. Rev. Lett.*, **73**, 882–885 (1994).
344. R.M. Noack, D.J. Scalapino, and S.R. White, "The ground state of the two-leg Hubbard ladder. A density-matrix renormalization group study," *Physica C*, **270**, 281–296 (1996).
345. E. Dagotto, J. Riera, and D. Scalapino, "Superconductivity in ladders and coupled planes," *Phys. Rev. B*, **45**, 5744–5747 (1992).

346. T. Kimura, K. Kuroki, and H. Aoki, "Pairing correlation in the three-leg Hubbard ladder-renormalization group and quantum Monte Carlo studies," *J. Phys. Soc. Jpn.*, **67**, 1377–1390 (1998).
347. E. Jeckelmann, D.J. Scalapino, and S.R. White, "Comparison of different ladder models," *Phys. Rev. B*, **58**, 9492–9497 (1998).
348. S. Daul, D.J. Scalapino, and S.R.White, "Pairing correlations on t-U-J ladders," *Phys. Rev. Lett.*, **84**, 4188–4191 (2000).
349. S.R. White and D.J. Scalapino, "Ground-state properties of the doped three-leg t-J ladder," *Phys. Rev. B*, **57**, 3031–3037 (1998).
350. T.M. Rice, S. Haas, M. Sigrist, and F.-C. Zhang, "Lightly doped t-J three-leg ladders: An analog for the underdoped cuprates," *Phys. Rev. B*, **56**, 14655–14667 (1997).
351. W.R. White and D.J. Scalapino, "Ground states of the doped four-leg t-J ladder," *Phys. Rev. B*, **55**, R14701–R14704 (1997).
352. D.J. Scalapino, *private communication*.
353. M. Ogata, M.U. Luchini, S. Sorella, and F.F. Assaad, "Phase diagram of the one-dimensional t-J model," *Phys. Rev. Lett.*, **66**, 2388–2391 (1991).
354. C.S. Hellberg and E.J. Mele, "Luttinger-liquid instability in the one-dimensional t-J model," *Phys. Rev. B*, **48**, 646–649 (1993).
355. M. Troyer, H. Tsunetsugu, and T.M. Rice, "Properties of lightly doped t-J two-leg ladders," *Phys. Rev. B*, **53**, 251–267 (1996).
356. C.A. Hayward and D. Poilblanc, "Luttinger-liquid behavior and superconducting correlations in t-J ladders," *Phys. Rev. B*, **53**, 11721–11728 (1996).
357. G. Sierra, M.A. Martin-Delgado, J. Dukelsky, S.R. White, and D.J. Scalapino, "Dimer-hole-RVB state of the two-leg t-J ladder: A recurrent variational ansatz," *Phys. Rev. B*, **57**, 11666–11673 (1998).
358. S. Rommer, S.R. White, and D.J. Scalapino, "Phase separation in t-J ladders," *Phys. Rev. B*, **61**, 13424–13430 (2000).
359. S.R. White, I. Affleck, and D.J. Scalapino, "Friedel oscillations and charge density waves in chains and ladders," *Phys. Rev. B*, **65**, 165122–165134 (2002).
360. S.A. Kivelson and V.J. Emery, "Strongly Correlated Electronic Materials: The Los Alamos Symposium 1993," (Addison-Wesley, Redwood City, CA, USA) (1994).
361. A.C. Cosentini, M. Capone, L. Guidoni, and G.B. Bachelet, "Phase separation in the two-dimensional Hubbard model: A fixed-node quantum Monte Carlo study," *Phys. Rev. B*, **58**, R14685–R14688 (1998).
362. F. Becca, M. Capone, and S. Sorella, "Spatially homogeneous ground state of the two-dimensional Hubbard model," *Phys. Rev. B*, **62**, 12700–12706 (2001).
363. S. Hellberg and E. Manousakis, "2-Dimensional t-J Model at Low Electron Density," *Phys. Rev. B*, **52**, 4639–4642 (1995).
364. V.J. Emery, S.A. Kivelson, and H.Q. Lin, "Phase separation in the t-J model," *Phys. Rev. Lett.*, **64**, 475–478 (1990).
365. S.A. Kivelson, V.J. Emery, and H.Q. Lin, "Doped antiferromagnets in the weak-hopping limit," *Phys. Rev. B*, **42**, 6523–6530 (1990).
366. E. Eisenberg, R. Berkovits, D.A. Huse, and B.L. Altshuler, "The breakdown of the Nagaoka phase in the 2D t-J model," *Phys. Rev. B*, **65**, 134437–134443 (2002).
367. W. O. Putikka, M.U. Luchini, and T.M. Rice, "Aspects of the phase diagram of the two-dimensional t-J model," *Phys. Rev. Lett.*, **68**, 538–541 (1992).

368. D. Poilblanc, "Phase diagram of the two-dimensional t-J model at low doping," *Phys. Rev. B*, **52**, 9201–9204 (1995).
369. M. Calandra, F. Becca, and S. Sorella, "Charge fluctuations close to phase separation in the two-dimensional t-J model," *Phys. Rev. Lett.*, **81**, 5185–5188 (1998).
370. H. Yokoyama and M. Ogata, "Phase diagram and pairing symmetry of the two-dimensional t-J model by a variation theory," *J. Phys. Soc. Japan*, **65**, 3615–3629 (1996).
371. C.T. Shih, Y.C. Chen, and T.K. Lee, "Phase separation of the two-dimensional t-J model," *Phys. Rev. B*, **57**, 627–631 (1998).
372. C.S. Shin, Y.C. Chen, and T.K. Lee, "Revisit phase separation of the two-dimensional $t - J$ model by the Power-Lanczos method," *cond-mat/0104067* (2001).
373. M. Khono, "Ground-state properties of the two-dimensional t-J model," *Phys. Rev. B*, **55**, 1435–1441 (1997).
374. F. Becca, L. Capriotti, and S. Sorella, "Stripes and spin incommensurabilities are favored by lattice anisotropies," *Phys. Rev. Lett.*, **87**, 167005–167008 (2001).
375. S.R. White and D.J. Scalapino, "Why do stripes form in doped antiferromagnets and what is their relationship to superconductivity?" *cond-mat/0006071* (2000).
376. C. Nayak and F. Wilczek, "Possible electronic structure of domain walls in Mott insulators," *Int. J. Mod. Phys. B*, **10**, 2125–2136 (1996).
377. J. Zaanen and O. Gunnarsson, "Charged magnetic domain lines and the magnetism of high-T_c oxides," *Phys. Rev. B*, **40**, 7391–7394 (1989).
378. D. Poilblanc and T.M. Rice, "Charged solitons in the Hartree-Fock approximation to the large-U Hubbard model," *Phys. Rev. B*, **39**, 9749–9752 (1989).
379. H.J. Schulz, "Domain walls in a doped antiferromagnet," *J. de Physique*, **50**, 2833–2849 (1989).
380. K. Machida, "Magnetism in La_2CuO_4 based compounds," *Physica C*, **158**, 192–196 (1989).
381. O. Zachar, "Stripes: Why hole rich lines are antiphase domain walls?" *cond-mat/0001217* (2000).
382. W.V. Liu and E. Fradkin, "Antiferromagnetic spin ladders effectively coupled by one-dimensional electron liquids," *Phys. Rev. Lett.*, **86**, 1865–1868 (2001).
383. A.L. Chernyshev, S.R. White, and A.H. Castro Neto, "Charge stripe in an antiferromagnet: 1d band of composite excitations," *cond-mat/0111474* (2001), see also Ref. 411.
384. A. Moreo, "Pairing correlations in the two-dimensional Hubbard model," *Phys. Rev. B*, **45**, 5059–5061 (1992).
385. S.-C. Zhang, J. Carlson, and J.E. Gubernatis, "Constrained path Monte Carlo method for fermion ground states," *Phys. Rev. B*, **55**, 7464–7477 (1997).
386. E. Dagotto and J. Riera, "Indications of $d_{2^x-y^2}$ superconductivity in the two dimensional t-J model," *Phys. Rev. Lett.*, **70**, 682–685 (1993).
387. E. Dagotto, A. Moreo, F. Ortolani, D. Poilblanc, and J. Riera, "Static and dynamical properties of doped Hubbard clusters," *Phys. Rev. B*, **45**, 10741–10760 (1992).
388. M. Calandra and S. Sorella, "From antiferromagnetism to d-wave superconductivity in the two-dimensional t-J model," *Phys. Rev. B*, **61**, R11894–R11897 (2000).

389. S. Sorella, G.B. Martins, F. Becca, C. Gazza, L. Capriotti, A. Parola, and E. Dagotto, "Superconductivity in the two-dimensional t-J model," *cond-mat/0110460* (2001).
390. M. Boninsegni and E. Manousakis, "Two-hole d-wave binding in the physical region of the t-J model: A Green's-function Monte Carlo study," *Phys. Rev. B*, **47**, 11897–11904 (1993).
391. T. Tohyama, C.G. C.T. Shih, Y. C. Chen, T. K. Lee, S. Maekawa, and E. Dagotto, "Stripe stability in the extended t-J model on planes and four-leg ladders," *Phys. Rev. B*, **59**, R11649–R11652 (1999).
392. E. L. Nagaev, Physics of Magnetic Semiconductors (Mir, Moscow) (1983).
393. A. Auerbach and B.E. Larson, "Doped antiferromagnet: The instability of homogeneous magnetic phases," *Phys. Rev. B*, **43**, 7800–7809 (1991).
394. A. Auerbach and B.E. Larson, "Small-polaron theory of doped antiferromagnets," *Phys. Rev. Lett.*, **66**, 2262–2265 (1990).
395. A. Auerbach, "Spin tunneling, Berry phases, and doped antiferromagnets," *Phys. Rev. B*, **48**, 3287–3289 (1993).
396. E.W. Carlson, S.A. Kivelson, Z. Nussinov, and V.J. Emery, "Doped antiferromagnets in high dimension," *Phys. Rev. B*, **57**, 14704–14721 (1998).
397. P.B. Visscher, "Phase separation instability in the Hubbard model," *Phys. Rev. B*, **10**, 943–945 (1974).
398. L.B. Ioffe and A.I. Larkin, "Two-dimensional Hubbard model with strong electron repulsion," *Phys. Rev. B*, **37**, 5730–5737 (1988).
399. L. Pryadko, D. Hone, and S.A. Kivelson, "Instability of charge ordered states in doped antiferromagnets," *Phys. Rev. Lett.*, **80**, 5651–5654 (1998).
400. J.K. Freericks, E.H. Lieb, and D. Ueltschi, "Segregation in the Falicov-Kimball model," *math-ph/0107003* (2001).
401. E.L. Nagaev, "Lanthanum manganites and other giant-magnetoresistance magnetic conductors," *Usp. Fiz. Nauk.*, **166**, 833 (1996).
402. S. Trugman, "Interaction of holes in a Hubbard antiferromagnet and high-temperature superconductivity," *Phys. Rev. B*, **37**, 1597–1603 (1988).
403. A.H. Castro Neto, "Landau theory of phase separation in cuprates," *Phys. Rev. B*, **51**, 3254–3256 (1995).
404. M. Seul and D. Andelman, "Domain shapes and patterns - the phenomenology of modulated phases," *Science*, **267**, 476–483 (1995).
405. B.P. Stojkovic, Z.G. Yu, A.R. Bishop, A.H. Castro Neto, and N. Gronbech-Jensen, "Charge ordering and long-range interactions in layered transition metal oxides," *Phys. Rev. Lett.*, **82**, 4679–4682 (1999).
406. L.P. Pryadko, S. A. K. V.J. Emery, Y.B. Bazaliy, and E.A. Demler, "Topological doping and the stability of stripe phases," *Phys. Rev. B*, **60**, 7541–7557 (1999).
407. A.L. Chernyshev, A.H. Castro Neto, and A.R. Bishop, "Metallic stripe in two dimensions: stability and spin-charge separation," *Phys. Rev. Lett.*, **84**, 4922–4925 (2000).
408. S.A. Kivelson and V.J. Emery, "Topological doping of correlated insulators," *Synthetic Metals*, **80**, 151–158 (1996).
409. J. Zaanen and Z. Nussinov, "Stripes and nodal fermions as two sides of the same coin," *cond-mat/0006193* (2000).
410. J. Han, Q.H. Wang, and D.H. Lee, "Antiferromagnetism, stripes, and superconductivity in the t-J model with Coulomb interaction," *Int. J. Mod. Phys.* **B**, **15**, 1117–1126 (2001).

411. A.H. Castro Neto, "Luttinger stripes in antiferromagnets," *Z. Phys. B*, **103**, 185–192 (1997).
412. J. Zaanen and P.B. Littlewood, "Freezing Electronic Correlations by Polaronic Instabilities in Doped La_2NiO," *Phys. Rev. B*, **50**, 7222–7225 (1994).
413. H.J. Schulz, "Incommensurate antiferromagnetism in the two-dimensional Hubbard model," *Phys. Rev. Lett.*, **64**, 1445–1448 (1990).
414. A.I. Larkin, "Effect of inhomogeneities on the structure of the mixed state of superconductors," *Sov. Phys. JETP*, **31**, 784–786 (1970).
415. V.J. Emery and S.A. Kivelson, "Charge inhomogeneity and high temperature superconductivity," *J. Phys. Chem. Sol.*, **61**, 467–471 (2000).
416. N. Ichikawa, S. Uchida, J.M. Tranquada, T. Niemoller, P. M. Gehring, S. H. Lee, and J. R. Schneider, "Local magnetic order vs superconductivity in a layered cuprate," *Phys. Rev. Lett.*, **85**, 1738–1741 (2000).
417. J. Schmalian and P.G. Wolynes, "Stripe glasses: Self-generated randomness in a uniformly frustrated system," *Phys. Rev. Lett.*, **85**, 836–839 (2000).
418. J. Burgy, M. Mayr, V. Martin-Mayor, A. Moreo, and E. Dagotto, "Colossal effects in transition metal oxides caused by intrinsic inhomogeneities," *Phys. Rev. Lett.*, **87**, 277202–277205 (2001).
419. U. Löw, V.J. Emery, K. Fabricius, and S.A. Kivelson, "Study of an Ising model with competing long- and short-range interactions," *Phys. Rev. Lett.*, **72**, 1918–1921 (1994).
420. M. Grousson, G. Tarjus, and P. Viot, "Monte Carlo study of the three-dimensional Coulomb frustrated Ising ferromagnet," *Phys. Rev. E*, **64**, 036109–036117 (2001).
421. L. Chayes, V.J. Emery, S.A. Kivelson, Z. Nussinov, and G. Tarjus, "Avoided critical behavior in a uniformly frustrated system," *Physica A*, **225**, 129–153 (1996).
422. Z. Nussinov, J. Rudnick, S.A. Kivelson, and L.N. Chayes, "Avoided critical behavior in O(n) systems," *Phys. Rev. Lett.*, **83**, 472–475 (1999).
423. D. B. Tanner and T. Timusk, "Optical properties of high-temperature superconductors," in "Physical Properties of High Temperature Superconductors Vol. III," edited by D. M. Ginsberg (World Scientific, Singapore) (1992).
424. N.P. Ong, "Transport properties of high T_c cuprates," in "Physical Properties of High Temperature Superconductors Vol. II," edited by D. M. Ginsberg (World Scientific, Singapore) (1992).
425. K. Krishana, J.M. Harris, and N.P. Ong, "Quasiparticle mean free path in $YBa_2Cu_3O_7$ measured by the thermal Hall conductivity," *Phys. Rev. Lett.*, **75**, 3529–3532 (1995).
426. K.M. Lang, V. Madhavan, J.E. Hoffman, E.W. Hudson, H. Eisaki, S. Uchida, and J. C. Davis, "Imaging the granular structure of high-T_c superconductivity in underdoped $Bi_2Sr_2CaCu_2O_{8+delta}$," *Nature*, **415**, 412–416 (2002).
427. T.R. Thurston, R.J. Birgeneau, M.A. Kastner, N.W. Preyer, G. Shirane, Y. Fujii, K. Yamada, Y. Endoh, K. Kakurai, M. Matsuda, Y. Hidaka, and T. Murakami, "Neutron scattering study of the magnetic excitations in metallic and superconducting $La_{2-x}Sr_xCuO_{4-y}$," *Phys. Rev. B*, **40**, 4585–4595 (1989).
428. S.-W. Cheong, G. Aeppli, T.E. Mason, H. Mook, S.M. Hayden, P.C. Canfield, Z. Fisk, K.N. Clausen, and J.L. Martinez, "Incommensurate magnetic fluctuations in $La_{2-x}Sr_xCuO_4$," *Phys. Rev. Lett.*, **67**, 1791–1794 (1991).

429. J.M. Tranquada, B.J. Sternlieb, J. D. Axe, Y. Nakamura, and S. Uchida, "Evidence for stripe correlations of spins and holes in copper oxide superconductors," *Nature*, **375**, 561–563 (1995).
430. J. M. Tranquada, D.J. Buttrey, V. Sachan, and J.E. Lorenzo, "Simultaneous ordering of holes and spins in $La_2NiO_{4.125}$," *Phys. Rev. Lett.*, **73**, 1003–1006 (1994).
431. A. Lanzara, P.V. Bogdanov, X.J. Zhou, S.A. Kellar, D.L. Feng, E.D. Lu, T. Yoshida, H. Eisaki, A. Fujimori, K. Kishio, J.-I. Shimoyama, T. Noda, S. Uchida, Z. Hussain, and Z.-X. Shen, "Evidence for ubiquitous strong electron-phonon coupling in high-temperature superconductors," *Nature*, **412**, 510–514 (2001).
432. L.P. Gor'kov and A.V. Sokol, "On the problem of the phase diagram of new superconductors," *J. Physique*, **50**, 2823–32 (1989).
433. A.J. Heeger, S.A. Kivelson, J.R. Schrieffer, and W. Su, "Solitons in conducting polymers," *Rev. Mod. Phys.*, **60**, 781–850 (1988).
434. D.K. Campbell, A.R. Bishop, and K. Fesser, "Polarons in quasi-one-dimensional systems," *Phys. Rev. B*, **26**, 6862–6874 (1982).
435. L.B. Ioffe and A. Larkin, "Superconductivity in the liquid-dimer valence-bond state," *Phys. Rev. B*, **40**, 6941–6947 (1989).
436. M. Marder, N. Papanicolaou, and G.C. Psaltakis, "Phase separation in a t-J model," *Phys. Rev. B*, **41**, 6920–32 (1990).
437. M. Vojta and S. Sachdev, "Charge order, superconductivity and a global phase diagram of doped antiferromagnets," *Phys. Rev. Lett.*, **83**, 3916–3919 (1999).
438. S. Sachdev and S.-C. Zhang, "Tuning order in cuprate superconductors," *Science*, **295**, 452 (2002).
439. D.I. Khomskii and K.I. Kugel, "Why stripes? Spontaneous formation of inhomogeneous structures due to elastic interactions," *Europhys. Lett.*, **55**, 208–213 (2001).
440. A.A. Koulakov, M.M. Fogler, and B.I. Shklovskii, "Charge density wave in two-dimensional electron liquid in weak magnetic field," *Phys. Rev. Lett.*, **76**, 499–502 (1996).
441. R. Moessner and T.J. Chalker, "Exact results for interacting electrons in high Landau levels," *Phys. Rev. B*, **54**, 5006–5015 (1996).
442. M.P. Lilly, K.B. Cooper, J.P. Eisenstein, L.N. Pfeiffer, and K.W. West, "Evidence for an anisotropic state of two-dimensional electrons in high Landau levels," *Phys. Rev. Lett.*, **82**, 394–397 (1999).
443. B. Spivak, "Title: Phase separation in the two-dimensional electron liquid in MOSFETs," *cond-mat/0205127* (2002).
444. S.A. Kivelson, "Making high-T_c higher: a theoretical proposal," *Physica B*, **61-67**, 61–67 (2002).
445. T.H. Geballe and B.Y. Moyzhes, "Qualitative understanding of the highest T_c cuprates," *Physica C*, **342**, 1821–1824 (2000).
446. M. Fujita, H. Goka, K. Yamada, and M. Matsuda, "Competition between charge/spin-density-wave orders and superconductivity in $La_{1.875}Ba_{0.125-x}Sr_xCuO_4$," *Phys. Rev. Lett.*, **88**, 167008–167011 (2002).
447. K. Yamada, C.H. Lee, K. Kurahashi, J. Wada, S. Wakimoto, S. Ueki, H. Kimura, Y. Endoh, S. Hosoya, G. Shirane, R.J. Birgeneau, M. Greven, M.A. Kastner, and Y. J. Kim, "Doping dependence of the spatially modulated dynamical spin correlations and the superconducting-transition temperature in $La_{2-x}Sr_xCuO_4$," *Phys. Rev. B*, **57**, 6165–6172 (1998).

448. Y.S. Lee, R.J. Birgeneau, M.A. Kastner, Y. Endoh, S. Wakimoto, K. Yamada, R.W. Erwin, S.-H. Lee, and G. Shirane, "Neutron-scattering study of spin-density wave order in the superconducting state of excess-oxygen-doped La_2CuO_{4+y}," *Phys. Rev. B*, **60**, 3643–3654 (1999).
449. B. Khaykovich, Y.S. Lee, R. Erwin, S.-H. Lee, S. Wakimoto, K.J. Thomas, M.A. Kastner, and R.J. Birgeneau, "Enhancement of long-range magnetic order by magnetic field in superconducting La_2CuO_{4+y}," *cond-mat/0112505* (2001).
450. H. Kimura, K. Hirota, H. Matsushita, K. Yamada, Y. Endoh, S.-H. Lee, C.F. Majkrzak, R. Erwin, G. Shirane, M. Greven, Y.S. Lee, M.A. Kastner, and R. J. Birgeneau, "Neutron-scattering study of static antiferromagnetic correlations in $La_{2-x}Sr_xCu_{1-y}Zn_yO_4$," *Phys. Rev. B*, **59**, 6517–6523 (1999).
451. M. Fujita, K. Yamada, H. Hiraka, P.M. Gehring, S.H. Lee, S. Wakimoto, and G. Shirane, "Static magnetic correlations near the insulating-superconducting phase boundary in $La_{2-x}Sr_xCuO_4$," *Phys. Rev. B*, **65**, 064505–064511 (2002).
452. P. Dai, H.A. Mook, R.D. Hunt, and F. Dogan, "Evolution of the resonance and incommensurate spin fluctuations in superconducting $YBa_2Cu_3O_{6+x}$," *Phys. Rev. B*, **63**, 054525–054544 (2001).
453. P. Bourges, Y. Sidis, H.F. Fong, L.P. Regnault, J. Bossy, A. Ivanov, and B. Keimer, "The spin excitation spectrum in superconducting $YBa_2Cu_3O_{6.85}$," *Science*, **288**, 1234–1237 (2000).
454. G. Aeppli, S. M. Hayden, P. Dai, H.A. Mook, R.D. Hunt, T.G. Perring, and F. Dogan, "The weights of various features in the magnetic spectra of cuprates," *Phys. Stat. Sol.*, **215**, 519–522 (1999).
455. H.A. Mook, P.C. Dai, F. Dogan, and R.D. Hunt, "One-dimensional nature of the magnetic fluctuations in $YBa_2Cu_3O_6$," *Nature*, **404**, 729–731 (2000).
456. H.A. Mook and B.C. Chakoumakos, "Incommensurate fluctuations in $Bi_2Sr_2CaCu_2O_8$," *Jour. Superconductivity*, **10**, 389–392 (1997).
457. J.E. Hoffman, E.W. Hudson, K.M. Lang, V. Madhavan, H. Eisaki, S. Uchida, and J.C. Davis, "A four unit cell periodic pattern of quasi-particle states surrounding vortex cores in $Bi_2Sr_2CaCu_2O_{8+x}$," *Science*, **295**, 466–469 (2002).
458. C. Howald, H. Eisaki, N. Kaneko, and A. Kapitulnik, "Coexistence of charged stripes and superconductivity in $Bi_2Sr_2CaCu_2O_{8+\delta}$," *cond-mat/0201546*.
459. J.E. Hoffman, K. McElroy, D.-H. Lee, K.M. Lang, H. Eisaki, S. Uchida, and J.C. Davis, "Imaging quasiparticle quantum interference in BSCCO," *submitted to* Science (2002).
460. E. Fradkin, S.A. Kivelson, E. Manousakis, and K. Nho, "Nematic phase of the two-dimensional electron gas in a magnetic field," *Phys. Rev. Lett.*, **84**, 1982–1985 (2000).
461. J. Zaanen, M.L. Horbach, and W.V. Saarloos, "Charged domain-wall dynamics in doped antiferromagnets and spin fluctuations in cuprate superconductors," *Phys. Rev. B*, **53**, 8671–8680 (1996).
462. V. Oganesyan, S.A. Kivelson, and E. Fradkin, "Quantum theory of a nematic Fermi fluid," *Phys. Rev. B*, **64**, 195109–195114 (2001).
463. C. Halboth and W. Metzner, "d-wave superconductivity and Pomeranchuk instability in the two-dimensional Hubbard model," *Phys. Rev. Lett.*, **85**, 5162–5165 (2000).
464. V. Hankevych, I. Grote, and F. Wegner, "Pomeranchuk and other instabilities in the $t-t'$ Hubbard model at the Van Hove filling," *cond-mat/0205213* (2002).

465. V. Oganesyan, E. Fradkin, and S.A. Kivelson, *work in progress* (2002).
466. A. Abanov, V. Kalatsky, and V.L. Pokrovsky, "Phase diagram of ultrathin ferromagnetic films with perpendicular anisotropy," *Phys. Rev. B*, **51**, 1023–1038 (1995).
467. J. Zaanen, O.Y. Osman, H.V. Kruis, Z. Nussinov, and J. Tworzydlo, "The geometric order of stripes and Luttinger liquids," *Phil. Mag. B*, **81**, 1485–1531 (2002).
468. Y.-B. Kim and H.-Y. Kee, "Pairing instability in a nematic Fermi liquid," *cond-mat/0204037* (2002).
469. K.B. Cooper, M. Lilly, J.P. Eisenstein, L.N. Pfeiffer, and K.W. West, "The onset of anisotropic transport of two-dimensional electrons in high Landau levels: An isotropic-to-nematic liquid crystal phase transition?" *cond-mat/0203174* (2002).
470. V.J. Emery and S. Kivelson, "Mapping of the two-channel Kondo problem to a resonant-level model," *Phys. Rev. B*, **46**, 10812–10817 (1992).
471. V.J. Emery and S.A. Kivelson, "Solution of an orbital Kondo array," *Phys. Rev. Lett.*, **71**, 3701–3704 (1993).
472. D. Chang and D.H. Lee, "Transport in inhomogeneous strongly correlated systems," *cond-mat/0205057* (2002).
473. Z.M. Yusof, B.O. Wells, T. Valla, A.V. Fedorov, P.D. Johnson, Q. Li, C. Kendziora, S. Jian, and D.G. Hinks, "Quasiparticle liquid in the highly overdoped $Bi_2Sr_2CaCu_2O_{8+\delta}$," *Phys. Rev. Lett.*, **88**, 167006–167009 (2002).
474. M. Granath, V. Oganesyan, D. Orgad, and S.A. Kivelson, "Distribution of spectral weight in a system with disordered stripes," *Phys. Rev. B*, **65**, 184501–184510 (2002).
475. M.I. Salkola, V.J. Emery, and S.A. Kivelson, "Implications of charge ordering for single-particle properties of high T_c superconductors," *Phys. Rev. Lett.*, **77**, 155–158 (1996).
476. M.G. Zacher, R. Eder, E. Arrigoni, and W. Hanke, "Stripes in doped antiferromagnets: single-particle spectral weight," *Phys. Rev. Lett.*, **85**, 2585–2588 (2000).
477. M.G. Zacher, R. Eder, E. Arrigoni, and W. Hanke, "Evolution of the stripe phase as a function of doping from a theoretical analysis of angle-resolved photoemission data," *Phys. Rev. B*, **65**, 045109–045117 (2002).
478. M. Vojta, Y. Zhang, and S. Sachdev, "Renormalization group analysis of quantum critical points in d-wave superconductors," *Int. J. Mod. Phys.B*, **14**, 3719–3734 (2000).
479. T. Valla, A.V. Fedorov, P.D. Johnson, B.O. Wells, S.L. Hulbert, Q. Li, G.D. Gu, and N. Koshizuka, "Evidence for quantum critical behavior in the optimally doped cuprate $Bi_2Sr_2CaCu_2O_8$," *Science*, **285**, 2110–2113 (1999).
480. Y. Zhang, N.P. Ong, P.W. Anderson, D.A. Bonn, R. Liang, and W.N. Hardy, "Giant enhancement of the thermal Hall conductivity kappa(xy) in the superconductor $YBa_2Cu_3O_7$," *Phys. Rev. Lett.*, **86**, 890–893 (2001).
481. D.A. Bonn, P. Dosanjh, R. Liang, and W.N. Hardy, "Evidence for rapid suppression of quasi-particle scattering below T_c in $YBa_2Cu_3O_7$," *Phys. Rev. Lett.*, **68**, 2390–2393 (1992), see also Ref. 504.
482. D.L. Feng, A. Damascelli, K.M. Shen, N. Motoyama, D.H. Lu, H. Eisaki, K. Shimizu, J.i. Shimoyama, K. Kishio, N. Kaneko, M. Greven, G.D. Gu, X.J. Zhou, C. Kim, F. Ronning, N.P. Armitage, and Z.-X. Shen, "Electronic

structure of the trilayer cuprate superconductor $Bi_2Sr_2Ca_2Cu_3O_{10+\delta}$," *cond-mat/0108386* (2001).

483. H.F. Fong, P. Bourges, Y. Sidis, L.P. Regnault, A. Ivanov, G.D. Gul, N. Koshizuka, and B. Keimer, "Neutron scattering from magnetic excitation in $Bi_2Sr_2CaCu_2O_{8+\delta}$," *Nature*, **398**, 588–591 (1999).
484. M. Dumm, D.N. Basov, S. Komiya, and Y. Ando, "Anistropic electromagnetic response of $La_{1.97}Sr_{0.03}CuO_4$ in the regime of spin stripes," *unpublished* (2002).
485. H.V. Kruis, Z. Nussinov, and J. Zaanen, "Emergent Z_2 gauge symmetry and spin-charge separation in one dimensional physics," *cond-mat/0110055* (2001).
486. M. Matsuda, M. Fujita, K. Yamada, R.J. Birgeneau, M.A. Kastner, H. Hiraka, Y. Endoh, S. Wakimoto, and G. Shirane, "Static and dynamic spin correlations in the spin-glass phase of slightly doped $La_{2-x}Sr_xCuO_4$," *Phys. Rev. B*, **62**, 9148–9154 (2000).
487. A.N. Lavrov, Y. Ando, S. Komiya, and I. Tsukada, "Unusual magnetic susceptibility anisotropy in untwinned $La_{2-x}Sr_xCuO_4$ single crystals in the lightly doped region," *Phys. Rev. Lett.*, **87**, 017007–017010 (2001).
488. B. Lake, G. Aeppli, T.E. Mason, A. Schroder, D.F. McMorrow, K. Lefmann, M. Isshiki, M. Nohara, H. Takagi, and S.M. Hayden, "Spin gap and magnetic coherence in a clean high-temperature superconductor," *Nature*, **400**, 43–46 (1999).
489. T. Noda, H. Eisaki, and S.I. Uchida, "Evidence for one-dimensional charge transport in $La_{2-x-y}Nd_ySr_xCuO_4$," *Science*, **286**, 265–268 (1999).
490. S. Tajima, T. Noda, H. Eisaki, and S. Uchida, "C-axis optical response in the static stripe ordered phase of the cuprates," *Phys. Rev. Lett.*, **86**, 500–503 (2001).
491. I. Iguchi, T. Yamaguchi, and A. Sugimoto, "Diamagnetic activity above T_c as a precursor to superconductivity in $La_{2-x}Sr_xCuO_4$," *Nature*, **412**, 420–23 (2001).
492. Y. Wang, Z. A. Xu, T. Kakeshita, S. Uchida, S. Ono, Y. Ando, and N.P. Ong, "Onset of the vortexlike Nernst signal above T_c in $La_{2-x}Sr_xCuO_4$ and $Bi_2Sr_{2-y}LaCuO_6$," *Phys. Rev. B*, **64**, 224519–224528 (2001).
493. Z.A. Xu, N. Ong, Y. Wang, T. Kakeshita, and S. Uchida, "Vortex-like excitations and the onset of superconducting phase fluctuation in underdoped $La_{2-x}Sr_xCuO_4$," *Nature*, **406**, 486–488 (2000).
494. I. Ussishkin, S.L. Sondhi, and D.A. Huse, "Gaussian superconducting fluctuations, thermal transport, and the Nernst effect," *cond-mat/0204484*.
495. A.G. Loeser, Z.-X. Shen, D.S. Dessau, D.S. Marshall, C.H. Park, P. Fournier, and A. Kapitulnik, "Excitation Gap in the Normal State of Underdoped $Bi_2Sr_2CaCu_2O_{8+\delta}$," *Science*, **273**, 325–329 (1996).
496. R.S. Decca, H.D. Drew, E. Osquiguil, B. Maiorov, and J. Guimpel, "Anomalous proximity effect in underdoped $YBa_2Cu_3O_{6+x}$ josephson junctions," *Phys. Rev. Lett.*, **85**, 3708–3711 (2000).
497. M.K. Crawford, M.N. Kunchur, W.E. Farneth, and E.M. McCarron, "Anomalous oxygen isotope effect in $La_{2-x}Sr_xCuO_4$," *Phys. Rev. B*, **41**, 282–287 (1990).
498. J.C. Phillips and J. Jung, "Nanodomain structure and function of high temperature superconductors," *Phil. Mag. B*, **81**, 745–756 (2001).

499. S.A. Kivelson and V.J. Emery, "Stripes and Related Phenomena," 91 (Kluwer Academic/Plenum Publishing, New York) (2000).
500. O. Zachar, "Stripes disorder and correlation lengths in doped antiferromagnets," *Phys. Rev. B*, **62**, 13836–13839 (2000).
501. N. Hasselmann, A.H. Castro Neto, C. Morais Smith, and Y. Dimashko, "Striped phase in the presence of disorder and lattice potentials," *Phys. Rev. Lett.*, **82**, 2135 (1999).
502. R.T. Scalettar, G.G. Batrouni, A.P. Kampf, and G.T. Zimanyi, "Simultaneous diagonal and off-diagonal order in the Bose-Hubbard Hamiltonian," *Phys. Rev. B*, **51**, 8467–8480 (1995).
503. S.R. White and I. Affleck, "Density matrix renormalization group analysis of the Nagaoka polaron in the two-dimensional t-J model," *Phys. Rev. B*, **64**, 024411–024416 (2001).
504. D.A. Bonn, K. Zhang, S. Kamal, R. Liang, P. Dosanjh, W.N. Hardy, C. Kallin, and A.J. Berlinsky, "Evidence for rapid suppression of quasi-particle scattering below T_c in $YBa_2CuO_{7-\delta}$," *Phys. Rev. Lett.*, **72**, 1391–1391 (1994).

7 Organic Superconductors

Michael Lang Physik–Institut der J.W. Goethe Univ. Frankfurt, Germany
Jens Müller Max–Planck–Institut für Chemische Physik fester Stoffe, Dresden, Germany

7.1 **Introduction** 453
7.2 **Characteristics of Organic Charge–Transfer Conductors** 456
7.2.1 Molecular Building Blocks 456
7.2.2 Structural Aspects 458
7.3 **Normal–State Properties** 463
7.3.1 Electronic Structure 463
7.3.2 Transport and Optical Properties 469
7.3.3 Thermal and Magnetic Properties 476
7.3.4 Anion Ordering and Glassy Phenomena 483
7.3.5 Phase Diagrams 488
7.4 **Superconducting–State Properties** 494
7.4.1 The Superconducting Phase Transition 494
7.4.2 Superconducting Parameters 504
7.4.3 Mixed State 509
7.4.4 Magnetic–Field–Induced Superconductivity 515
7.4.5 The Superconducting State – Pairing Mechanism and Order–Parameter Symmetry 515
7.5 **Epilogue** 538
Acknowledgements 540
References 540

7.1 Introduction

Over the past twenty years the research on organic conductors has developed into a most active branch of modern condensed–matter physics. The main difference of molecular conductors compared to conventional metals is that the former are made up of building blocks constructed from carbon atoms and their combinations with other elements such as sulfur, selenium or oxygen. As a result, when forming a crystal, these molecular units preserve to a large extent their specific features such as the molecular orbitals, the ionization energy and the intramolecular vibrational modes. Molecular materials thus have the potential of providing a flexible building–block system where the physical properties can be tuned by small modifications in the arrangements and bridging of these functional units. In contrast to the molecular crystals formed by weakly van der Waals–bond neutral entities, organic conductors consist of open–shell molecular units which are the result of a partial oxidation and reduction of the donor and acceptor molecules in the crystal–growth

K. H. Bennemann et al. (eds.), *The Physics of Superconductors*
© Springer-Verlag Berlin Heidelberg 2004

process. It is the unpaired electron residing in the π–molecular orbital (π–hole) of the donor unit which is responsible for the electronic properties of these charge–transfer salts. Due to a π–orbital overlap between adjacent molecules, the π–holes can delocalize throughout the crystal giving rise to metallic conductivity.

The unique chemistry of carbon, which, on the one hand, provides a rich basis of potential organic donor molecules, and the manifold possibilities of combining them with charge–compensating acceptor units, on the other, have enabled the synthesis of an enormous number of conducting organic charge–transfer salts. The geometry of the building blocks and the way they are packed together in the crystal determine the effective dimensionality of the electronic structure of the compound. The planar shape of the TMTSF (tetramethyltetraselenafulvalene) molecule – a derivative of the prototype TTF (tetrathiafulvalene) – permits an infinite stacking of these units in the crystal structure. As a consequence, a significant intermolecular overlap of the π–orbitals occurs only along the stacking axis giving rise to a quasi–one–dimensional conduction band. In contrast, packing of the larger BEDT–TTF (bisethylenedithio–tetrathiafulvalene) molecules often results in a quasi–two–dimensional electronic structure.

These low–dimensional organic conductors constitute a peculiar class of materials which has gained strong interest among scientists due to the wealth of interesting phenomena that have been observed over the last two decades or so. Above all it was the discovery of superconductivity in pressurized $(TMTSF)_2PF_6$ by Jérome *et al.* in 1979 [1] which created much excitement among both solid–state chemists and physicists. Indeed, this finding was a result of interdisciplinary efforts in synthesizing and characterizing organic conductors – activities which started up in the early 1950's by the pioneering work of Akamatu *et al.* [2] and which received a fresh impetus in 1964 thanks to the work of Little [3]. He proposed that in a suitably designed one–dimensional conductor embedded in a polarizable medium, superconductivity at high temperatures should be possible. Although it soon became clear that the nature of the superconducting state in the $(TMTSF)_2PF_6$ salt is of a fundamentally different type from what had been discussed in Little's model, this finding set the stage for the discovery of a large number of conducting charge–transfer salts including up to the latest count, more than 80 superconductors. Many of these systems superconduct even at ambient pressure with the highest T_c value of about 12 K received in the quasi–two–dimensional BEDT–TTF–based systems. Besides superconductivity, the organic charge–transfer salts reveal a variety of other interesting collective phenomena including spin–Peierls and density–wave states as well as phases with localized charges and commensurate–type antiferromagnetic order. These states have been found to depend most sensitively on factors such as the acceptor ions, the magnetic field or external pressure.

One of the key features underlying the above phenomena is the low dimensionality of the materials. The confinement of the carrier motion to one or two spatial dimensions together with the low charge–carrier concentration enhance the effect of the interactions between the electrons. Another important feature specific to these molecular systems is a considerably strong coupling of the charge carriers to the lattice degrees of freedom. For molecular crystals, this coupling includes both the interactions with high–frequency intramolecular modes and the low–lying intermolecular vibrations. The present organic metals thus represent ideal model systems for exploring the interplay of strong electron–electron and electron–phonon interactions in reduced dimensions. In particular, the close proximity of superconductivity to a magnetically–ordered state encountered not only in the organic materials but also in other strongly–correlated electron systems such as the heavy–fermion metals and high–temperature superconductors continues to challenge our understanding of superconductivity. While for the latter systems evidence is growing that, indeed, the magnetism and superconductivity are intimately related to each other, the nature of the superconducting state for the present materials is far from being understood.

The discussion of the superconducting–state properties for the present organic materials is complicated by the existence of contradictory experimental evidences. In some cases, this controversy even encompasses results on the same quantity when the measurements have been carried out by different groups. While about one half of the data seem to support an anisotropic superconducting state, with a d–wave order parameter being the most favored one, the other half are consistent with an order parameter which is finite everywhere on the Fermi surface.

Closely related to the issue of superconductivity in the proximity to antiferromagnetic order is the nature of the state above T_c. For the quasi–two–dimensional organic conductors, for example, unusual metallic properties have been observed posing the question whether this phenomenon is related to the equally unusual behavior seen in the other class of quasi–two–dimensional superconductors, the high–T_c cuprates [4].

This article will give an overview on the normal– and superconducting–state properties of organic superconductors. There are a number of review articles on this subject [5–10] – most of them focus on either the quasi–one–dimensional or two–dimensional materials. The intention of the present review is therefore to provide a discussion which covers aspects common to both families on the same footing. Instead of reviewing the whole diversity of behaviors found among the various compounds with all their structural and chemical modifications, we will mainly focus on selected compounds of both families. These are the most extensively studied and best characterized $(TMTSF)_2X$ and $(BEDT–TTF)_2X$ slats whose properties are representative for a wide class of materials. Special attention is paid to the more recent developments including the controversial discussions of some aspects, in par-

ticular the discussion on the nature and symmetry of the superconducting state.

7.2 Characteristics of Organic Charge–Transfer Conductors

7.2.1 Molecular Building Blocks

The prerequisites of forming conducting molecular solids are essentially (i) the creation of unpaired electrons and (ii) their delocalization throughout the crystal. For the organic superconductors discussed in this article, condition (i) is satisfied by a partial transfer of charge between the two constituent parts of a charge–transfer complex: an organic electron–donor molecule D is combined with an – in most cases inorganic – electron–acceptor complex X according to the reaction $[D_m] + [X_n] \rightarrow [D_m]^{+\delta} + [X_n]^{-\delta}$, where m and n are integers. Since the π–electrons of the D molecule with orbits extending perpendicularly to the planes of the molecules have low binding energies – much lower than those of the σ–electrons – they can easily be excited which can be seen in the charge–transfer process. Accordingly, the so created charge carriers have a π–electron (hole) character. In most cases, the negatively charged anions $[X_n]^{-\delta}$ adopt a closed–shell configuration and thus do not contribute to the electrical conductivity. When the crystal is formed, a delocalization of the charge carriers (ii) may be obtained by a dense packing of the donor molecules. As a result, the π–orbitals of the partially filled outer molecular shells overlap and an electronic band structure is formed.

The conductivity of solids depends on both the number of free carriers and their mobility in the crystal. In organic charge–transfer salts, the carrier concentration is determined by the electronegativity of the donor, the electron affinity of the acceptor molecule and the chemical bonds. A high mobility is obtained by a relatively large bandwidth which is the result of a considerably strong overlap of the π–orbitals from adjacent molecules.

Organic superconductors have been derived from a variety of different organic electron–donor molecules, where most of them are derivatives of the archetype TTF molecule. Its combination with the electron acceptor TCNQ (tetracyanoquinodimethane) in 1973 led to the synthesis of the first quasi–one–dimensional (quasi–1D) organic conductor TTF–TCNQ [11, 12]. This material and its derivatives served for a long time as model systems for exploring the physical properties of quasi–1D conductors.

In the vast majority of D_mX_n salts, the donor–acceptor molecular ratio $m : n$ is fixed to 2 : 1, i.e., two donor molecules transfer one electron to the acceptor X. Organic and organometallic chemistry have provided an enormous number of donor molecules which may serve as building blocks for organic conductors and superconductors. The main examples are the

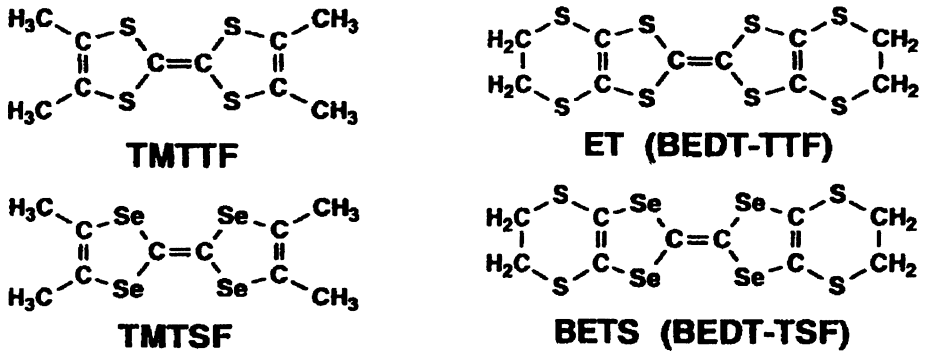

Fig. 7.1. Principal structures of donor molecules that furnish organic superconductors

TTF derivatives TMTSF, TMTTF[1], BEDT–TTF (commonly abbreviated as ET) and BEDT–TSF[2] (or simply BETS), see Fig. 7.1. The TMTSF differs from TMTTF in that the four sulfur atoms of the latter have been replaced by selenium. In the same way, BEDT–TSF is derived from BEDT–TTF. It is interesting to note that organic superconductors have been synthesized not only by using these symmetric molecules, but also on the basis of asymmetric complexes. These are the DMET (dimethylethylenedithio–diselenedithiafulvalene) [13,14], which is a hybride of TMTSF and BEDT–TTF, MDT–TTF (methylenedithio–TTF) [13,14] and BEDO–TTF (bisethylenedithioxy–TTF) [15], see [5] for an overview.

The TMTSF molecule provides the basis for the so–called Bechgaard salts $(TMTSF)_2X$ which form with a variety of inorganic monovalent acceptor molecules X. Indeed, it was $(TMTSF)_2PF_6$ where in 1979 superconductivity had been observed for the first time in an organic compound [1]. At ambient–pressure conditions, the material was found to undergo a metal–to–insulator transition around 12 K which had been identified as a spin–density–wave (SDW) ordering [6]. By the application of hydrostatic pressure of 12 kbar the SDW instability can be suppressed and superconductivity forms below $T_c = 0.9$ K [1,16]. A replacement of PF_6 by ClO_4 has resulted in the first and – till now – only member of the quasi–1D salts which becomes superconducting at ambient pressure [17].

Apparently, the strong tendency of the Bechgaards salts to undergo a metal–insulator transition, inherent to quasi–1D electron systems, counteracts with their ability to become superconducting. In order to achieve ambient–pressure superconductivity in these organic complexes with possibly even higher transition temperatures it is necessary to increase their dimensionality. According to this strategy, in 1982 the first metallic compound based on

[1] TMTTF stands for tetramethyltetrathiafulvalene

[2] BEDT–TSF stands for bisethylenedithio–tetraselenafulvalene

the new electron donor molecule BEDT–TTF [18], cf. Fig. 7.1, was synthesized by Saito *et al.* [19]. The underlying idea was to enhance the overlap between π–orbitals of adjacent molecules by enlarging the π–electron system on each molecule. This has been accomplished by adding rings of carbon and sulfur atoms at the outer ends of the TTF skeleton. In contrast to the Bechgaard salts where the donor molecules form infinite stacks, steric effects specific to the BEDT–TTF molecules prevent such an infinite face–to–face stacking in the $(BEDT–TTF)_2X$ salts. As a consequence, the side–by–side overlap between π–orbitals of adjacent molecules becomes stronger and, in some cases, comparable to the face–to–face interaction resulting in a quasi–2D electronic structure of the BEDT–TTF–based salts. The combination of BEDT–TTF with the monovalent anion $X = Cu(NCS)_2$ achieved in 1988 led to the discovery of the first ambient–pressure superconductor in this class of materials – the second generation of organic superconductors – with transition temperatures in the range of 10 K [20].

The quasi–1D and –2D systems tend to grow in needle– and plate–like shapes, with the latter usually showing well developed smooth and shiny metallic surfaces. The synthesis of organic molecular conductors can be divided into two steps: (1) the synthesis of the neutral donor and acceptor molecules and (2) the oxidation and reduction of the donors and acceptors to radical cations and radical anions. For step (1) several independent methods have been discussed and used even for selected donor and acceptor molecules, see e.g. [18]. Conversely, to perform step (2), the redox process, the electrocrystallization technique has proved to be the method of choice for synthesizing high–quality crystals. For details on the chemical synthesis and crystal growth techniques, the reader is referred to [5, 18, 21] and references cited therein.

7.2.2 Structural Aspects

Figure 7.2 shows exemplarily the crystal structure of $(TMTSF)_2PF_6$ viewed almost perpendicular to the stacking axis (a–axis) – the direction of highest conductivity. All members of the $(TM)_2X$ family, where TM stands for TMTSF and TMTTF, are isostructural with triclinic symmetry. The conducting stacks are separated by the anions which are located at inversion centers of the lattice. The donor molecules which are nearly planar and almost perpendicular to the chain axis are arranged in a zigzag–type manner along the chains with two slightly different intrachain distances corresponding to a weak dimerization. The fairly close Se $\cdots$ Se distance of 3.87 Å along the b–axis being smaller than the sum of the van der Waals radii of 4 Å results in a weak interchain overlap [6] and thus a weakly 2D electronic character. An important structural aspect of the $(TM)_2X$ compounds is related to the symmetry of the anion X. Where these anions are centrosymmetric such as the octahedral $X = PF_6$, AsF_6, SbF_6 or TaF_6 complexes, their orientation is fixed in the structure. In contrast, $(TM)_2X$ salts formed with

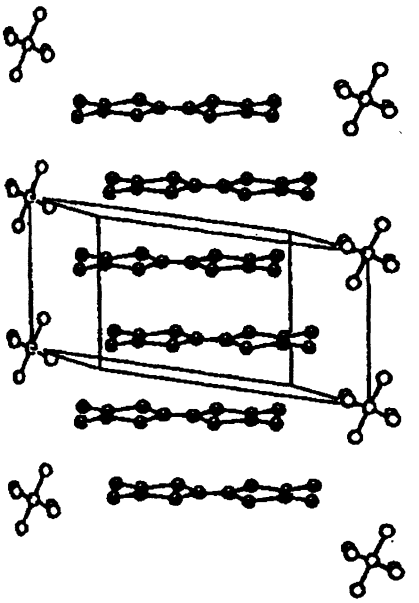

Fig. 7.2. Crystal structure of $(TMTSF)_2PF_6$ (side–viewed tilted). The axis with the highest conductivity is the vertical a'–axis, the one with the lowest conductivity the horizontal c–axis. a' is the projection of the a–axis onto the direction perpendicular to the bc–plane

non–centrosymmetric tetrahedral anions such as ClO_4 or FeO_4 undergo a structural transition from a disordered high–temperature state to an ordered low–temperature phase [22].

While all members of the $(TM)_2X$ family share the same crystal structure, the rather loose intra–stack coupling of the $(BEDT–TTF)_2X$ salts gives rise to a variety of polymorphic phases (packing motifs) which are distinguished by Greek characters; the most important amongst them are the α–, β–, and κ–phases, see e.g. [23] for a comprehensive review of the structural properties of these salts. In some cases, as for instance realized in the compound with the linear anion $X = I_3$, various structural modifications exist even for the same anion, cf. Fig. 7.3. The α–type structure consists of stacks arranged in a herring–bone pattern. The ET molecules are connected via $S \cdots S$ contacts being shorter than the sum of the van–der–Waals radii of 3.6 Å. The β–type packing is reminiscent of the stacking arrangement found in the Bechgaard salts. However, the smaller inter–stack distances in β–$(ET)_2I_3$ lead to a more two–dimensional electronic structure. The κ–phase is unique in that it does not consist of interacting stacks but rather of interacting dimers formed by two face–to–face aligned ET molecules. Adjacent dimers are arranged almost

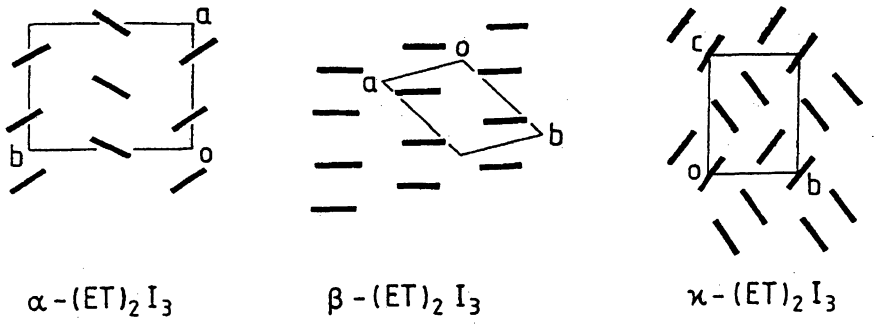

Fig. 7.3. Schematic packing motifs of the ET molecules in the α–, β– and κ–phases of $(ET)_2I_3$ viewed along the long axis of the ET molecules

orthogonal to each other so that the *intra*– and *inter*–dimer interactions are of the same size. This results in a quasi–2D electronic structure with a small in–plane anisotropy. The κ–type compounds with polymere–like anions are of particular interest with respect to their superconducting properties as they exhibit the highest transition temperatures.

In forming the crystal, apart from the ethylene $[(CH_2)_2]$ groups at the outer ends of the molecules, the charged ET molecules $C_6S_8[(CH_2)_2]_2$ untwist at their centre and become planar. As shown schematically in Fig. 7.4, the relative orientation of the outer C–C bonds can either be parallel (eclipsed) or canted (staggered). At high temperatures, the ethylene endgroups become disordered due to the strong thermal vibrations. Upon cooling to low temperatures, the endgroups adopt one of the two possible conformations, depending on the anion and the crystal structure. As will be discussed in section 7.3.4 for the κ–$(ET)_2X$ salts, disorder in the conformation of the $[(CH_2)_2]$ groups

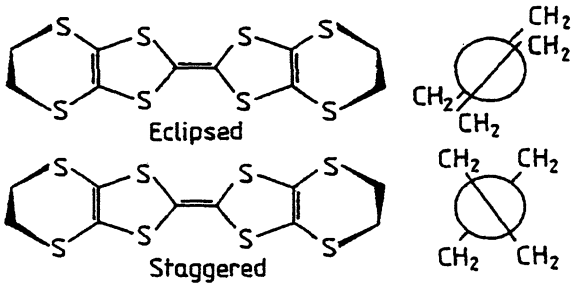

Fig. 7.4. Schematic view of the relative orientations of the ethylene endgroups $[(CH_2)_2]$ of the ET molecule. Right side shows the view along the long axis of the molecule

can have a severe influence on the electronic properties in these compounds, in particular the superconductivity.

The planar C_6S_8 skeleton of the ET molecules permits a rather dense packing with a variety of possible packing arrangements. As a result, the interdimer interaction becomes comparable to that within the dimers giving rise to a quasi–2D electronic structure. Besides the intermolecular S···S contacts, i.e. the donor–donor interaction, the donor–acceptor couplings also play an important role for the physical properties of these multilayer systems. The latter interaction is provided by electrostatic forces as a consequence of the charged molecules and the hydrogen bonds joining between the carbon atoms at the donor site and the sulfur, carbon or nitrogen atoms being located at the acceptor site. The relative strength of these different interactions, the conformational degrees of freedom of the ethylene groups along with the flexibility of the molecular framework give rise to a variety of different ET complexes [5, 23].

Despite their complex crystal structure with rather low symmetry (cf. Table 7.1) it is convenient to think of the $(ET)_2X$ compounds as layered systems consisting of conducting sheets formed by the ET molecules which are intersected by more or less thick insulating anion layers. Prime examples are the κ–phase $(ET)_2X$ salts with X=Cu(NCS)$_2$, Cu[N(CN)$_2$]Br and Cu[N(CN)$_2$]Cl which are the most intensively studied and best characterized members of this class of materials. These compounds are of particular interest not only because of their relatively high superconducting transition temperatures but also owing to certain similarities in their normal– and superconducting–state properties with those of the high–temperature cuprate

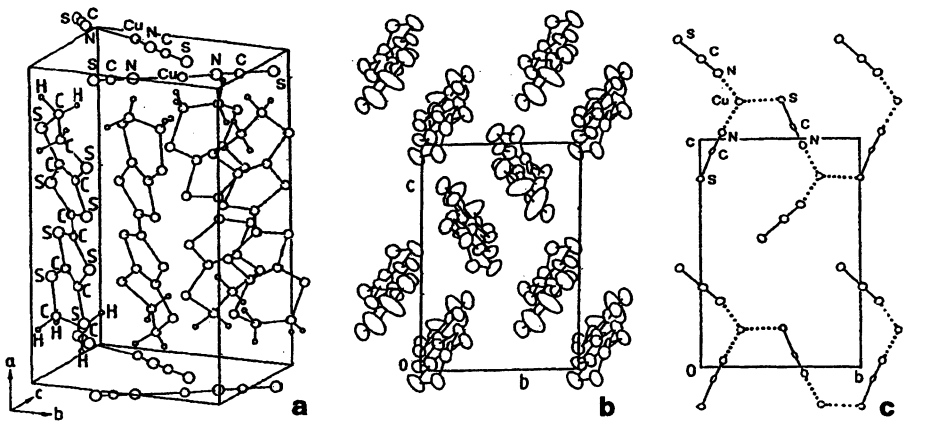

Fig. 7.5. (a) Crystal structure of κ-(BEDT-TTF)$_2$Cu(NCS)$_2$. The arrangement of the ET molecules (b) and the Cu(NCS)$_2$ anions (c) when viewed along the a^* direction, i.e. perpendicular to the conducting planes. The a–axis is slightly tilted from the a^*–axis which is normal to the conducting bc–plane

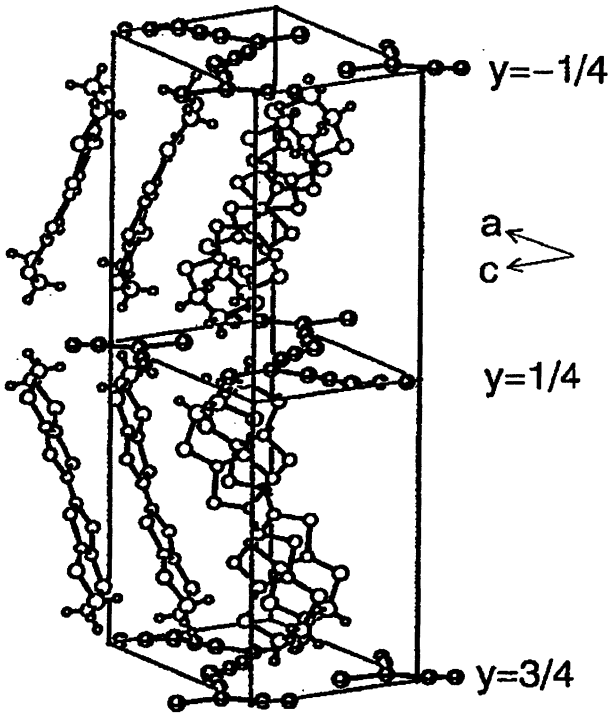

Fig. 7.6. Crystal structure of κ-(BEDT–TTF)$_2$Cu[N(CN)$_2$]Z, with Z = Br and Cl. Here the direction perpendicular to the conducting plane is the crystallographic b–axis. The anion layers are parallel to the ac–plane at y = −1/4, 1/4 and 3/4. The polymeric–like anion chains are running along the a direction

superconductors [4,9]. Figures 7.5 and 7.6 display the crystal structures of κ-(ET)$_2$Cu(NCS)$_2$ and κ–(ET)$_2$Cu[N(CN)$_2$]Z. In both cases the layered structure consists of conducting planes with the characteristic κ–type arrangement of the ET molecules separated by insulating anion layers. While the crystal structure of κ-(ET)$_2$Cu(NCS)$_2$ has monoclinic symmetry with two dimers, i.e. two formular units per unit cell, the κ–(ET)$_2$Cu[N(CN)$_2$]Z salts are orthorhombic with a unit cell containing four dimers, see Table 7.1. Due to the particular arrangement of their polymeric anions, these crystals lack a center of inversion symmetry.

Subtle changes in the intermolecular spacing or relative orientation of the ET molecules as e.g. induced by either external pressure or anion substitution may significantly alter the π–electron overlap between adjacent molecules. This can have a severe influence on the electronic properties as demonstrated for the κ–(ET)$_2$Cu[N(CN)$_2$]Z system for various Z: while the compound with Z=Br is a supercondutor with T_c = 11.2 K [24], replacement of Br by the

slightly smaller Cl results in an antiferromagnetic insulating ground state. On the other hand, the application of hydrostatic pressure of only about 300 bar drives the latter system to a superconductor with a T_c of 12.8 K [25–27], the highest transition temperature found among this class of materials so far.

A new class of materials which has recently gained considerable interest is based on the donor molecule BETS and its combination with the discrete anions MX_4 (M= Fe, Ga, In; X= Cl, Br). Two structural modifications have been found. These are the orthorhombic κ–type structure (Pnma) which results in plate–like crystals and the triclinic ($P\bar{1}$) λ–type variant which grow in a needle–like manner [28–30]. The λ-$(BETS)_2GaCl_4$ salt is a superconductor with $T_c = 6$ K [31]. Upon substituting Ga by Fe in λ-$(BETS)_2Fe_xGa_{1-x}Cl_4$ superconductivity becomes continuously suppressed with increasing x [32] and, for $x \geq 0.5$, replaced by an antiferromagnetic insulating ground state.

Some structural data for a selection of organic superconductors are summarized in Table 7.1.

7.3 Normal–State Properties

7.3.1 Electronic Structure

As for ordinary metals, the electronic properties of organic charge-transfer salts are determined by the quasiparticles at the Fermi surface (FS).[3] The

[3] This implies the applicability of the Fermi–liquid concept which is questionable for the most anisotropic $(TM)_2X$ salts, see e.g. [33].

Table 7.1. Room–temperature crystallographic data of some $(ET)_2X$ superconductors including the space group SG, lattice parameters a,b and c, unit–cell volume V, number of formular units per unit cell z as well as T_c values. In the case of quasi–2D $(ET)_2X$ salts the lattice parameter perpendicular to the conducting planes is underlined.

	SG	a(Å)	b(Å)	c(Å)	V(Å^3)	z	T_c(K)
$(TMTSF)_2PF_6$	$P\bar{1}$	7.297	7.711	13.522	713.14	1	1.1 (6.5 kbar)
κ-$(ET)_2Cu(NCS)_2$	$P2_1$	<u>16.248</u>	8.440	13.124	1688	2	10.4
κ-$(ET)_2Cu[N(CN)_2]Br$	$Pnma$	12.949	<u>30.016</u>	8.539	3317	4	11.2
κ-$(ET)_2Cu[N(CN)_2]Cl$	$Pnma$	12.977	<u>29.977</u>	8.480	3299	4	12.8 (300 bar)
β''-$(ET)_2SF_5CH_2CF_2SO_3$	$P\bar{1}$	9.260	11.635	<u>17.572</u>	1836	2	5.3
α-$(ET)_2NH_4Hg(SCN)_4$	$P\bar{1}$	10.091	<u>20.595</u>	9.963	2008	2	1.1
κ-$(ET)_2I_3$	$P2_1/c$	<u>16.387</u>	8.466	12.832	1688	2	3.5
λ-$(BETS)_2GaCl_4$	$P\bar{1}$	16.141	18.58	6.594	1774	2	6

energy–band structures for both the quasi–1D $(TM)_2X$ and the quasi–2D $(ET)_2X$ salts have been calculated employing a tight–binding scheme with a few simplifications [34]. The calculations are based on the assumption that the *intra*molecular interactions are much stronger than the interactions *between* adjacent molecules reducing the complexity of the problem enormously. In a first step, σ– and π–molecular orbitals are constructed using linear combinations of atomic s– and p–orbitals of the constituent atoms. In the molecular–orbital (MO) approximation, the electrons (holes) are considered to be spread over the whole molecule and only those electrons (holes) near the Fermi surface in the highest occupied (HOMO) and lowest unoccupied molecular orbitals (LUMO) are taken into account. Due to the overlap between molecular orbitals of adjacent molecules, the corresponding π–electrons (holes) are delocalized. Using available structural data, the overlap integrals and transfer energies can be obtained from quantum chemistry. These are input parameters for a standard tight–binding calculation based on molecular orbitals obtained by the extended Hückel approximation (EHA) from which the band structure and Fermi surfaces are derived [23, 35–37].

Based on the above approximations, Grant *et al.* have calculated a model band structure for the quasi–1D materials $(TM)_2X$ [38], see upper panel of Fig. 7.7. The FS consists of two open sheets which are slightly corrugated due to weak interactions perpendicular to the stacking axis. While the standard magnetic–quantum–oscillation studies cannot be used for these quasi–1D metals, some important information on the FS can still be derived from angular–dependent magnetoresistance measurements, see e.g. [39]. Of crucial importance are the topological aspects of the FS, i.e. the nesting properties, and the band filling. The conduction band can accommodate four electrons per $(TM)_2$ unit. Due to the weak structural dimerization which is more pronounced in the TMTTF compared to the TMTSF salts, a dimerization gap splits the conduction band into two parts. Therefore, removing one electron per unit cell in the charge–transfer process results in a half–filled conduction band.

The FS topology of the quasi–2D materials has been studied in great detail employing measurements of the de Haas–van Alphen (dHvA) and Shubnikov–de Haas (SdH) effect, the angular–dependent magnetorestistance (AMRO) and the cyclotron resonance, see [40, 41]. These results clearly demonstrate the presence of a well–defined Fermi surface and quasiparticle excitations in accordance with the Fermi–liquid theory.

The lower panel of Fig. 7.7 shows the results of EHA band–structure calculations for the superconductor κ-$(ET)_2Cu(NCS)_2$. Since any *inter*layer electron transfer has been neglected in these calculations, the resulting FS is strictly two dimensional. Despite the various simplifications employed, the main features of the so–derived FS are generally found to be in remarkable agreement with the experimental results [40], although a more elaborated analysis reveals certain details which are not adequately described [10, 44].

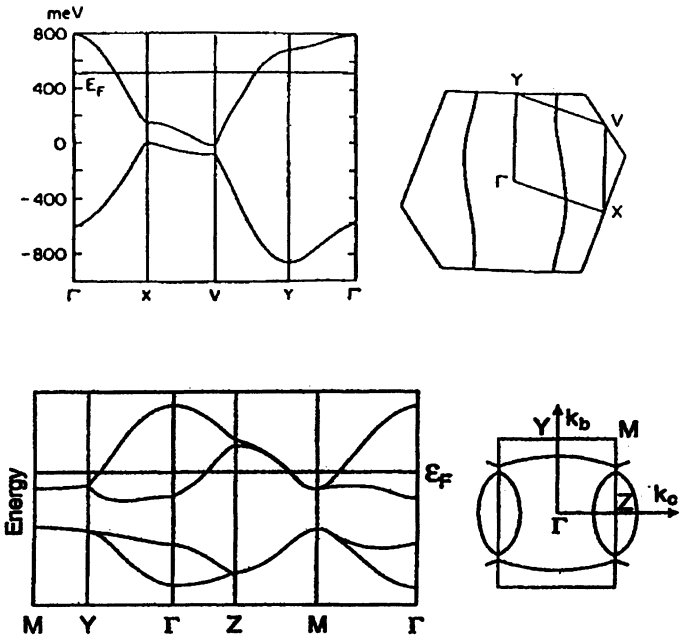

Fig. 7.7. Calculated energy dispersion and Fermi surface of $(TMTSF)_2X$ [38] (upper panel) and κ-$(ET)_2Cu(NCS)_2$ [42,43] (lower panel)

The four bands correspond to the four ET molecules in the unit cell, each represented by its HOMO. Due to the lack of a center–of–inversion symmetry, an energy gap opens at the Z–M zone boundary. As a consequence, the FS consists of closed hole–like quasi–2D orbits (α–pockets) and a pair of open quasi–1D corrugated sheets. According to a charge transfer of one electron per pair of ET molecules, the conduction band is three quarters filled. Due to the strong dimerization of the ET molecules in the κ–type structure, the conduction bands split up so that the upper band becomes half filled. Band–structure calculations based on high–temperature crystallographic data reveal FS topologies which are very similar among the various κ-$(ET)_2X$ systems [36,37], except for the degeneracy of the upper two bands along the Z–M zone boundary for the linear anion X = I_3. While the α– and κ–phase $(ET)_2X$ salts still combine quasi–1D and –2D bands, the FS of β–type salts is even more simple. It is of almost cylindrical shape and closed within the first Brillouin zone, reflecting the isotropic in–plane interactions between adjacent ET molecules.

Fermi–surface studies

In a magnetic field B, the transverse motion of electrons becomes quantized and their allowed states in $\boldsymbol{k}$–space are confined to so–called Landau levels. Periodic oscillations in magnetization and resistivity as a function of $1/B$

arise from the oscillatory behavior of the density of states at the Fermi level E_F as the Landau levels pass through the Fermi surface. From the oscillation period $\Delta(1/B)$ the extremal area of the FS cross section, S_F, perpendicular to the magnetic-field direction can be derived [45]:

$$S_F = \frac{2\pi e}{\hbar} \frac{1}{\Delta(1/B)}, \tag{7.1}$$

where $-e$ is the electron charge and $\hbar$ the Planck constant. A quantitative description of the oscillatory magnetization was given by Lifshitz and Kosevich [46]. According to their work, the amplitude of the oscillations is given by:

$$A \propto \frac{T}{\sqrt{B}} \frac{\exp(-\frac{\lambda m_c^* T_D}{m_e B})}{\sinh(\frac{\lambda m_c^* T}{m_e B})}, \tag{7.2}$$

where the effect on the electron spin has been neglected. m_e denotes the free electron mass and m_c^* the cyclotron effective mass, $\lambda = 2\pi^2 m_e k_B/(e\hbar)$ with k_B being the Boltzmann constant. $T_D = \hbar/(2\pi k_B \tau)$ is the Dingle temperature which accounts for the broadening of the Landau levels due to scattering of the electrons where τ is the relaxation time averaged over a cyclotron orbit. For state-of-the-art crystals of the $(ET)_2X$ salts, the Dingle temperatures are usually far below about 1 K, as e.g. $T_D \sim 0.5$ K as reported for κ-$(ET)_2Cu(NCS)_2$ [47], which reflect the high quality of these materials.

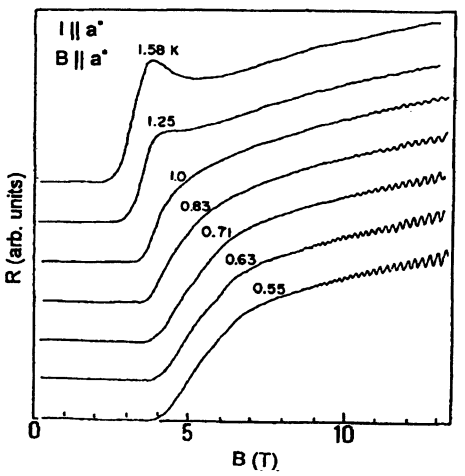

Fig. 7.8. Magnetorestistance of κ-$(ET)_2Cu(NCS)_2$ at different temperatures. Electrical current and magnetic field were applied along the a^*-axis, i.e. perpendicular to the conducting planes. Shubnikov-de Haas oscillations starts to become visible below 1 K, taken from [42]

Figure 7.8 shows early magnetoresistance data on κ-$(ET)_2Cu(NCS)_2$ [42]; see also [41] for more recent data. At the low–field side of the data sets, the transition from the superconducting to the normal state is visible. With increasing the field and at temperatures below 1 K, Subnikov–de Haas (SdH) oscillations caused by the closed α–orbits of the FS are superimposed. As expected from the simple FS topology (lower panel of Fig. 7.7), a single frequency according to only one extremal orbit (α–orbit) dominates the oscillatory behavior at lower fields. At higher magnetic fields, however, a second high–frequency component becomes superimposed [48, 49]. The latter corresponds to the so–called magnetic breakdown effect which is due to tunnelling of charge carriers across the energy gaps at the FS. It is common to refer to the magnetic–breakdown orbit which encompasses the whole FS as the β–orbit. For a detailed description of the FS studies on quasi–1D and quasi–2D charge–transfer salts, see [40, 41] and references therein.

Effective masses and renormalization effects

The experimentally derived effective cyclotron masses m_c^* for the various $(ET)_2X$ salts are significantly larger than the band masses m_b predicted by the above band–structure calculations, which are of the order of the free–electron mass m_e (see below). For the κ-$(ET)_2Cu(NCS)_2$ salt, for example, experiments reveal $m_c^* = (3.5 \pm 0.1)\, m_e$ for the α–orbit and (6.9 ± 0.8) for the magnetic–breakdown β–orbit [48]. A mass enhancement of comparable size is observed also for the thermodynamic effective mass m_{th}^* as determined by measurements of the specific heat $C(T)$. For a quasi–2D material consisting of stacks of metallic planes with interlayer spacing s, the Sommerfeld coefficient $\gamma^{2D} = C/T$ is given by:

$$\gamma^{2D} = \frac{\pi k_B^2}{3} \frac{m_{th}^*}{\hbar^2} \frac{1}{s}. \tag{7.3}$$

For κ-$(ET)_2Cu(NCS)_2$ one finds $\gamma = (23 \pm 1)\,\mathrm{mJ/mol\,K^2}$ [50, 51] which corresponds to $m_{th}^* = (4.7 \pm 0.2)\, m_e$. Both m_c^* and m_{th}^* are renormalized compared to the band mass m_b. The latter takes into account the fact that the electrons are moving in a periodic potential associated with the crystal lattice. The band masses estimated from tight–binding calculations and interband optical measurements are of the order of the free electron mass: Caulfield *et al.* applied the effective dimer model to κ-$(ET)_2Cu(NCS)_2$ and found $m_b^\alpha = 0.64\, m_e$ and $m_b^\beta = 1.27\, m_e$ [47] corresponding to a width of the conduction band of $W = 0.5 \sim 0.7\,\mathrm{eV}$. These values have to be compared with $m_b^\alpha = (1.72 \pm 0.05)\, m_e$ and $m_b^\beta = (3.05 \pm 0.1)\, m_e$ as derived from first–principles self–consistent local–density calculations [52]. For a discussion on the band masses derived from band–structure calculations and their relation to the cyclotron effective masses, see e.g. [53]. The substantial enhancement of the cyclotron masses compared to the band masses suggest an appreciable quasiparticle renormalization due to many–body effects, i.e. electron–electron and electron–phonon interactions. It has been proposed that a direct tool to

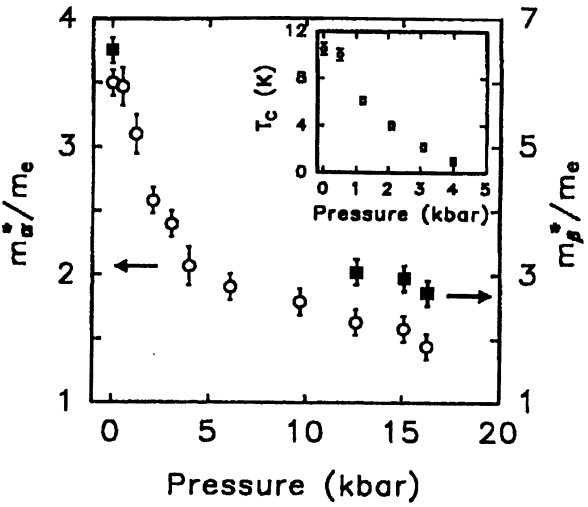

Fig. 7.9. Cyclotron effective masses of the α– (open circles, left scale) and β– (full squares and right scale) orbits as a function of hydrostatic pressure for κ-$(ET)_2Cu(NCS)_2$. The inset shows T_c against pressure, taken from [47]

determine the relative role of electron–electron correlations in the mass enhancement is provided by cyclotron resonance measurements [54]. According to the Kohn theorem the effective mass determined by cyclotron resonance experiments, m_{cr}^*, is independent of the electron–electron interactions. As a consequence, the experimental finding of $m_{cr}^* \approx m_b$ has been attributed to a dominant role of the Coulomb interaction for the mass renormalization [47]. However, recent studies on different $(ET)_2X$ systems along with theoretical calculations showed that the general applicability of the Kohn theorem for the quasi–2D organic superconductors is questionable, see [10,41].

On the other hand, various experiments such as optical studies [55–60], thermal conductivity [51, 61, 62] as well as inelastic neutron scattering experiments [63] indicate a substantial coupling of the charge carriers to the lattice vibrations. Taken together, it is likely that for the present molecular conductors both electron–electron as well as electron–phonon interactions are responsible for the mass–renormalization.

By means of pressure–dependent Shubnikov–de Haas experiments a striking interrelation between the suppression of superconductivity and changes in the effective masses have been found [47]. Figure 7.9 shows the hydrostatic–pressure dependence of the effective masses for κ-$(ET)_2Cu(NCS)_2$ [47]. As the pressure increases, m_c^* rapidly decreases, an effect which has been observed also for other $(ET)_2X$ compounds [64]. Above some critical pressure of about $4 \sim 5$ kbar the rate of suppression of m_c^* becomes much weaker. As this is about the same pressure value above which superconductivity becomes completely suppressed (see inset of Fig. 7.9), an intimate interrelation be-

tween mass enhancement and superconductivity has been suggested [47]. This is consistent with recent results of reflectivity measurements which showed that the pressure dependence of the 'optical masses', which are closely related to the bare band masses, do not show such a crossover behaviour [65]. Consequently, the pressure–induced reduction of the effective cyclotron masses has to be associated with a decrease in the strength of the electron–electron and/or electron–phonon interactions.

7.3.2 Transport and Optical Properties

Electrical resistivity

The organic superconductors discussed in this article are fairly good metals at room temperature with resistivities that vary over wide ranges depending on the particular compound and the current direction in respect to the crystal axes. The pronounced anisotropies found in the electrical properties are direct manifestations of the strongly directional–dependent overlap integrals.

For the $(TM)_2X$ series (cf. Fig. 7.2) one typically finds $\rho_a : \rho_b : \rho_c$ of the order of 1 : 200 : 30.000, where a is along the stacking axis. These numbers correspond to a ratio of the overlap integrals $t_a : t_b : t_c$ of about 10 : 1 : 0.1 with $t_a \approx 0.1 \sim 0.24\,\mathrm{eV}$ and $0.36\,\mathrm{eV}$ for the TMTTF and TMTSF compounds, respectively [6,33]. Figure 7.10 compiles temperature profiles of

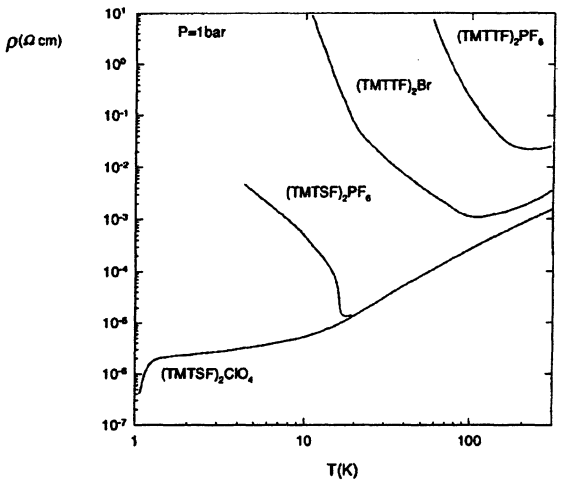

Fig. 7.10. Resistivity vs temperature for various $(TMTTF)_2X$ and $(TMTSF)_2X$ salts at ambient–pressure conditions in a double–logarithmic plot [66]

the resistivity for various $(TM)_2X$ compounds. Below a temperature T_ρ, depending on the anion, the resistivity of the sulfur–containing $(TMTTF)_2X$

compounds changes from a metallic–like high–temperature into a thermally–activated low–T behavior. Upon further cooling through $T_{SP} \simeq 20K < T_\rho$ (not shown), the $(TMTTF)_2PF_6$ salt undergoes a phase transition into a spin–Peierls (SP)–distorted nonmagnetic ground state, see e.g. [66] and references cited therein. With the application of moderate pressure both T_ρ and T_{SP} were found to decrease. By increasing the pressure to $p \geq 10$ kbar, the spin–Peierls ground state becomes replaced by an antiferromagnetic Néel state similar to the one found at normal conditions in $(TMTTF)_2Br$.

In the selenium–containing $(TMTSF)_2PF_6$ salt the metallic range extends down to lower temperatures until the sudden increase in the resistivity indicates the transition into an insulating SDW ground state. Above a critical pressure of about 6 kbar, the SDW state of $(TMTSF)_2PF_6$ becomes unstable giving way to superconductivity at lower temperatures, cf. the phase diagrams Figs. 7.21 and 7.22 in section 7.3.5.

Interestingly enough, when the spin–Peierls salt $(TMTTF)_2PF_6$ is exposed to sufficiently high pressure in excess of 43.5 kbar, a superconducting state can be stabilized [67, 68] which completes – for a single compound – the sequence of ground states indicated in the generic phase diagram in Fig. 7.21.

In their metallic regime the resistivity of the $(TM)_2X$ salts along the most conducting direction decreases monotonically with a power–law temperature dependence $\rho \propto T^\alpha$, where the exponent α, depending on the temperature interval, varies between 1 and 2, see e.g. [33, 69]. For $(TMTSF)_2PF_6$ for example, $\alpha \approx 1.8$ between 300 and 100 K and approaches approximately 2 at lower temperatures down to the metal–SDW transition [33]. A T^2 dependence in the resistivity has been frequently observed not only in the quasi–1D [69] but also for the various $(ET)_2X$ salts, see below.

A question of high current interest for the present quasi–1D conductors concerns the nature of their low–energy excitations. Is a Fermi–liquid approach still adequate or do we have to treat these materials within the framework of a Tomonaga–Luttinger liquid – a concept which has been proposed for dimensionality D = 1 [70–72]. Arguments in favor of a Luttinger–liquid behavior have been derived from various observations, not all of which have been generally accepted. Undisputed are, however, the non–Fermi–liquid features in the sulfur compounds $(TMTTF)_2X$: these materials undergo a charge localization at elevated temperatures $T_\rho = 250$ K for $X = PF_6$ and 100 K for $X = Br$ (cf. Fig. 7.10) which leaves the static magnetic susceptibility unaffected [6, 33]. This apparent separation of spin and charge degrees of freedom is one of the hallmarks of a Luttinger liquid, see e.g. [73]. Indications for a spin and charge separation have been reported also for other $(TM)_2X$ salts from optical– and thermal–conductivity experiments [74, 75]. The other signatures of a Luttinger liquid are (ii) a power–law decay at long distances of the spin or charge correlation functions which suppresses long–range order in 1D systems and (iii) the absence of any discontinuity in the distribution func-

tion for electron states at the Fermi energy. Indications for (ii) and (iii) have been reported from NMR [33], photoemission [76, 77] as well as transverse (c–axis) dc–resistivity [78] measurements.

The resistivity for the various $(ET)_2X$ and related compounds can be roughly classified into two distinct types of temperature dependences. While some of the materials show a more or less normal metallic–like T behavior, i.e. a monotonic decrease of $\rho(T)$ upon cooling, a pronounced $\rho(T)$ maximum above about 80 K has been found for a number of $(ET)_2X$ compounds. Among them are the κ-$(ET)_2X$ salts with polymere–like anions such as X = $Cu(NCS)_2$ or $Cu[N(CN)_2]Br$ [24, 79–81], the α-$(ET)_2NH_4Hg(SCN)_4$ [82] as well as the κ– and λ–type BETS salts [29]. The occurrence of the same kind of $\rho(T)$ anomaly in $(DMET)_2AuBr_2$ [83] demonstrates that (i) this feature is not a property specific to ET– or BETS–based salts and (ii) does not rely on the presence of Cu ions. Fig. 7.11 shows the in–plane resistivity of κ-$(ET)_2Cu(NCS)_2$ as a function of temperature at various pressures [79]. With decreasing temperatures, $\rho(T)$ first increases to a maximum at around 100 K before a metallic behavior sets in at lower temperatures. Under hydrostatic pressure, the maximum shifts to higher temperatures and becomes progressively suppressed. This is accompanied by a significant reduction of T_c (see also inset of Fig. 7.9). The origin of the anomalous $\rho(T)$ hump has been discussed by many authors and various explanations have been suggested including the formation of small polarons [84], a metal–metal phase transition [85], a valence instability of Cu [86], an order–disorder transition of the terminal ethylene groups of the ET molecules [87–89] as well as a crossover from localized small–polaron to coherent large–polaron behavior [90]. In this context it is interesting to note that for the κ-$(ET)_2Cu[N(CN)_2]Br$ system this maximum has been found to be sample dependent: using a different synthesis route, Thoma *et al.* [91] and Montgomery *et al.* [92] succeeded in preparing superconducting crystals which lack the anomalous resistance hump.

A closer look on the resistivity of κ-$(ET)_2Cu(NCS)_2$ below the maximum discloses an abrupt change in the slope at temperatures around $45 \sim 50$ K [93]. A similar behavior is found for κ-$(ET)_2Cu[N(CN)_2]Br$ [94] and has been interpreted as a crossover from a regime of antiferromagnetic fluctuations of localized spins at high temperatures to a low–T Fermi–liquid regime [95, 96]. More recent results, however, suggest that this temperature marks a density–wave–type *phase transition* [97–99], see section 7.3.3 for a detailed discussion.

At temperatures below the inflection point, the resistivity turns into an approximate $\rho(T) = \rho_0 + AT^2$ behavior until superconductivity sets in around 10 K. As mentioned above, a resistivity roughly following a T^2 law – even at elevated temperatures – is not an exception in the present molecular conductors, see e.g. [5]. In some high–quality crystals of β– and κ–type $(ET)_2I_3$, it has been observed over an extraordinarily wide temperature range up to temperatures as high as 100 K [100]. It has been argued that the T^2 depen-

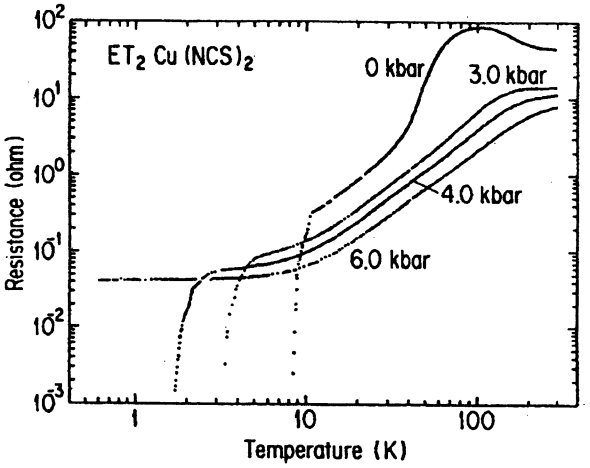

Fig. 7.11. Temperature dependence of the resistivity measured along the in–plane b–axis of κ-$(ET)_2Cu(NCS)_2$ at various pressures, taken from [79]

dence of the resistivity indicates a dominant role of electron–electron scattering in these materials [7]. On the other hand, for such a mechanism to predominate the resisitivity at temperatures as high as 45 K for the X = $Cu(NCS)_2$ and even 100 K for the X = I_3 salt implies that there is only a minor contribution from electron–phonon scattering. In light of the considerable electron–phonon coupling in these materials as proved by various experiments, such a scenario appears questionable. Alternatively, the T^2 law has been attributed to the scattering of electrons by phonons via electron–libron [101] or a novel electron–phonon scattering mechanism proposed for the high–T_c cuprates [100] which invokes electron–electron interactions [102,103]. For the discussion of the temperature dependence of the resisitivity, it is important to bear in mind, however, that due to the large pressure coefficients of the resisitivity of about $\partial \ln \rho / \partial p \simeq --20\,\%$/kbar at room temperature together with the extraordinary strong thermal contraction, it is difficult to make a comparison with theoretical predictions. Since the theory usually describes the temperature dependence at constant volume, a detailed comparison is meaningful only after transforming the constant–pressure into constant–volume profiles by taking into account the thermal expansion of the material.

Similar to the quasi–1D $(TM)_2X$ salts, the room–temperature resistivities of the quasi–2D (BEDT–TTF)$_2$X materials are generally rather high. For the κ-$(ET)_2Cu(NCS)_2$ salt for example, one finds $\rho_b \approx 6 \cdot 10^4\,\mu\Omega$cm and $\rho_c \approx 3 \cdot 10^4\,\mu\Omega$cm [104], which exceed the values for Cu by several orders of magnitude. This is partly due to the relatively low charge–carrier concentration of only about $10^{21}\,\mathrm{cm}^{-3}$.

In accordance with their quasi–2D electronic structure, a pronounced in–plane vs out–of–plane anisotropy has been observed which amounts to $10^{-3} \sim 10^{-5}$ [41]. In this respect it is interesting to ask whether under these conditions the interlayer transport is coherent or not, i.e. whether there is a coherent motion of band states associated with well–defined wave vectors or if the motion from layer to layer is diffusive and a Fermi velocity perpendicular to the layers cannot be defined [105]. This question has been addressed in recent magnetoresistance studies on the κ-$(ET)_2Cu(NCS)_2$ salt [106]. Here the interlayer–transfer integral has been estimated to be $t_\perp \approx 0.04\,\mathrm{meV}$ [106] as compared with $t_\parallel \sim 150\,\mathrm{meV}$ for the intralayer transfer [47]. According to this work, the Fermi surface is extended along the interlayer direction corresponding to a coherent transport.

Optical conductivity

Optical investigations by means of infrared and Raman measurements provide important information on the electronic parameters such as the plasma frequency, the optical masses and also the bandwidths and collision times for the carriers. In addition, they permit an investigation of vibrational properties and their coupling to the charge carriers. Using polarized light it is also possible to look for anisotropies in these quantities, as e.g. in the effective masses. The optical properties of quasi–1D and –2D organic conductors have been reviewed by several authors [6, 33, 107–110], see also [5, 10]. For a detailed discussion on the normal– and superconducting–state optical properties of the $(ET)_2X$ salts see [111]. A summary of Raman results on $(ET)_2X$ salts is given in [112, 113].

First extensive optical studies of the electronic properties of $(TM)_2X$ by Jacobsen *et al.* [114] provided information on the energy of charge–transfer processes and on the electron–phonon coupling: the large absorption features observed in the optical conductivity of the TMTTF salts have been assigned to intra– and intermolecular vibrations [115]. These studies have been supplemented by a series of more detailed investigations covering also the low frequency range, see [110] and references therein. In accordance with the expectations for a strongly anisotropic material with open Fermi surface, the optical response of the Bechgaards salts $(TMTSF)_2X$ was found to deviate strongly from that of a simple metal. The main features are a gap–like structure around 25 meV for $X = PF_6$ and a zero–frequency mode which grows upon decreasing the temperature. The latter contribution, having only a small spectral weight corresponding to 1 % of the carriers, is responsible for the metallic conductivity of the compound [110]. At high frequencies, i.e. at energies in excess of the interchain transfer integral t_b but below the intraband width $4t_a$, the data for the optical conductivity follow a $\sigma_1(\omega) \propto \omega^{-\gamma}$ dependence with $\gamma = 1.3$ [110]. Here $\gamma = 4n^2K_\rho - 5$, where K_ρ is the Luttinger–liquid–correlation parameter and n the degree of commensurability. From the experimentally derived γ value and assuming $n = 2$, i.e. a dominant quarter–filled band Umklapp scattering, $K_\rho \simeq 0.23$ has been de-

termined which agrees reasonably well with photoemission [76,116,117] and transport data [78]. These observations are consistent with a dimensional crossover in $(TMTSF)_2PF_6$ from a high–temperature Luttinger–liquid phase to a low–temperature (anisotropic) 3D Fermi liquid induced by interchain coupling.

For the various ET salts, the reflectance spectra are generally characterized by intensive sharp features due to molecular vibrations superimposed on a broad electronic background with the plasma edge at a frequency of about $4500 \sim 5000\,\mathrm{cm}^{-1}$. Fig. 7.12 shows optical conductivity data of superconducting deuterated κ-$(D_8\text{-}ET)_2Cu(NCS)_2$ (left panel) and insulating κ-$(ET)_2Cu[N(CN)_2]Cl$ (right panel) at various temperatures obtained from reflectivity measurements after a Kramers–Kronig analysis [118,119]. The far–infrared conductivities have been found to agree reasonably well with the dc–conductivities in showing a rapid increase below 50 K for κ-$(ET)_2Cu(NCS)_2$. The low–frequency feature has been interpreted as a Drude peak which increases with decreasing temperature or increasing pressure, i.e. when the metallic character of the material increases. The data are in good agreement with results of other studies, see [10, 90, 111] and references cited therein. However, the interpretation of the spectra may vary from author to author: Kornelsen *et al.* attributed the mid–infrared peak ($1000 \sim 4000\,\mathrm{cm}^{-1}$) to interband transitions superimposed on the free–carrier tail [118]. Wang *et al.* [90] argued that the sharp Drude peak in the conductivity that develops at low temperature, together with the large mid–infrared spectral weight indicate polaronic effects. According to this interpretation, the change from non–metallic to metallic behavior around $90 \sim 100\,\mathrm{K}$ as observed in the resistivity is due to a crossover from localized small–polaron to coherent

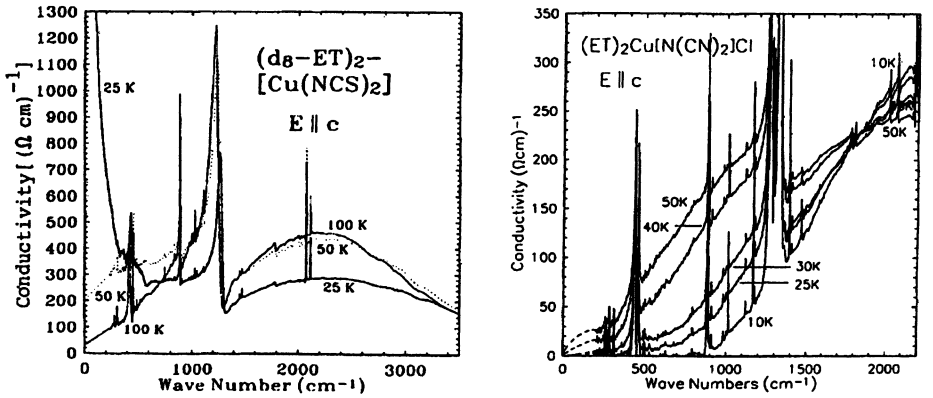

Fig. 7.12. Optical conductivity of κ-$(D_8\text{-}ET)_2Cu(NCS)_2$ (left panel) and κ-$(ET)_2Cu[N(CN)_2]Cl$ (right panel) at various temperatures for $E \parallel c$. Taken from [118] and [119], respectively

large–polaron behavior [90]. In contrast to the metallic/superconducting κ-$(ET)_2Cu(NCS)_2$ salt, the optical conductivity in the low–energy region for insulating κ-$(ET)_2Cu[N(CN)_2]Cl$ rapidly decreases below 50 K, indicating a large temperature–dependent semiconducting energy gap with a value of about 900 cm^{-1} at 10 K [119].

Electron–phonon coupling

Infrared reflectivity measurements can also be used to obtain information on the electron–phonon interaction. In molecular crystals, the coupling between the conduction electrons and the phonons is twofold. One kind of interaction, the so–called electron–molecular–vibration (EMV) coupling, involves the *intra*molecular vibrations which are characteristic of the molecular structure. This has to be distinguished from the electron–*inter*molecular–vibration coupling which refers to the interaction of the charge carriers with motions of almost rigid molecules around their equilibrium positions and orientations (translational and librational modes).

Electron–molecular–vibration coupling

It is well known [120] that electrons in the HOMO's of the TTF molecule and its derivatives couple strongly to the totally symmetric (A_g) molecular vibrations via the modulation of the HOMO energy, E_{HOMO}, by the atomic displacements. The linear EMV coupling constant g_i for mode i is defined as:

$$g_i = \frac{1}{h\nu_i} \frac{\partial E_{\mathrm{HOMO}}}{\partial Q_i}, \tag{7.4}$$

where Q_i is an intramolecular normal coordinate and ν_i the mode frequency. The effective electron–intramolecular–phonon coupling constant λ_i can then be calculated using $\lambda_i = 2g_i^2 h\nu_i N(E_F)$ where $N(E_F)$ is the density of states at the Fermi level.

The sharp features superimposed on the electronic background in Fig. 7.12 can be attributed to molecular vibrations. An assignment of these features to the various vibrational modes [121] is feasible by comparing spectra of different isotopically labelled salts with calculations based on a valence–force–field model by Kozlov *et al.* [124,125]. For the ET molecule, the modes with the strongest coupling constants are those involving the central carbon and sulfur atoms [124–126] at which the HOMO's have the largest amplitudes [35]. The frequencies of these C=C stretching and ring–breathing modes are $\nu_2 = 1465\,cm^{-1}(g_2 = 0.165), \nu_3 = 1427\,cm^{-1}(g_3 = 0.746)$ and $\nu_9 = 508\,cm^{-1}(g_9 = 0.476)$, where the calculated coupling constants are given in the brackets. Despite these sizable coupling constants, several studies – especially those of the mass isotope shifts on T_c for the ET salts [127] – indicate that the EMV coupling seems to play only a minor role in mediating the attractive electron–electron interaction, cf. section 7.4.5.

Electron–intermolecular–vibration coupling

While much experimental data are available on the EMV coupling, relatively little is known about the coupling of the charge carriers to the low–lying intermolecular phonons. This interaction is provided by the modulation of the

charge–transfer integrals t_{eff} between neighbouring molecules during their translational or librational motions. Within the Eliashberg theory, the dimensionless electron–intermolecular-phonon coupling constant λ is given by

$$\lambda = 2 \int \frac{\alpha^2(\omega)}{\omega} F(\omega) d\omega, \tag{7.5}$$

where $\alpha(\omega)$ is the electron–phonon–coupling constant, ω the phonon frequency and $F(\omega)$ the phonon density of states. The Eliashberg function $\alpha^2(\omega)F(\omega)$ can, in principle, be derived from tunneling characteristics of strong–coupling superconductors or via point–contact measurements. The latter experiments have been carried out by Nowack *et al.* on the β–type $(ET)_2X$ salts with X = I_3 and AuI_2 [128, 129] yielding $\lambda \simeq 1$. Some of the frequencies of the intermolecular modes have been determined by employing Raman and far–infrared measurements [60, 130–132]. More recent studies including inelastic–neutron [63] and Raman–scattering [57–60] have focused on investigation of the role of intermolecular phonons for superconductivity. These experiments yielded quite sizable superconductivity–induced phonon–renormalization effects which clearly indicate a significant coupling of the superconducting charge carriers to the intermolecular phonons and suggest an important role of these modes in the pairing interaction, cf. section 7.4.5.

7.3.3 Thermal and Magnetic Properties

Common to both the quasi–1D and –2D charge–transfer salts is the variety of ground states the systems can adopt depending on parameters such as the chemical composition or external pressure. Most remarkable is the fact that for both families the superconducting phase shares a common phase boundary with a long–range magnetically ordered state.

For the $(TMTSF)_2PF_6$ salt, cooling at ambient pressure leads to a metal–insulator transition at $T_{MI} \sim 12\,\text{K}$. The insulating ground state in the $(TMTSF)_2X$ series has been identified via NMR [133, 134] and susceptibility [135] measurements as a spin–density–wave ordering whose wave vector $\boldsymbol{q} = 2\,\boldsymbol{k_F}$ is determined by the optimum nesting condition of the quasi–1D Fermi surface [6]. The application of hydrostatic pressure to the X = PF_6 salt suppresses the magnetic state by destroying the nesting properties and instead stabilizes superconductivity below about $T_c = 1.1\,\text{K}$ at 6.5 kbar [136]. As has been shown again by NMR experiments, short–range spin–fluctuations with the same wave vector $\boldsymbol{q}$ remain active up to ~ 100 K, i.e. far above the SDW ordering in this salt. Moreover, these fluctuations are present also in the normal state of the ClO_4 compound despite its superconducting ground state [137].

For the quasi–2D κ–phase $(ET)_2X$ compounds, the nesting properties are expected to be less strongly pronounced, cf. the Fermi surface in Fig. 7.7. Nevertheless, as in the case of the quasi–1D salts, superconductivity lies

next to an antiferromagnetic insulating state in the pressure–temperature phase diagram, see section 7.3.5. While the compounds with the complex anions X=Cu(NCS)$_2$ and Cu[N(CN)$_2$]Br are superconductors with T_c values of 10.4 K and 11.2 K, respectively, κ-(ET)$_2$Cu[N(CN)$_2$]Cl is an antiferromagnetic insulator with $T_N = 27$ K which can be transformed into a superconductor with $T_c = 12.8$ K by the application of a small hydrostatic pressure of only 300 bar [25]. Likewise seen in the quasi–1D salts, the metallic state above T_c in these quasi–2D systems reveals indications for magnetic fluctuations. This has been demonstrated by NMR measurements on the various κ-(ET)$_2$X salts [138–142]. As shown in Fig. 7.13 the spin–lattice relaxation rate divided by temperature, $(T_1T)^{-1}$, for the superconductors κ-(ET)$_2$Cu(NCS)$_2$ and κ-(ET)$_2$Cu[N(CN)$_2$]Br behaves quite differently from what would be expected for a simple metal and realized to a good approximation in some other organic superconductors as, e.g. α-(ET)$_2$NH$_4$Hg(SCN)$_4$ [96, 140]. For both κ–phase compounds, the $(T_1T)^{-1}$ values at higher temperatures are enhanced by a factor $5 \sim 10$ compared to a conventional Korringa–type behavior. Upon cooling, $(T_1T)^{-1}$ gradually increases down to a temperature $T^* \simeq 50$ K, below which a steep decrease sets in. Both the overall enhancement of $(T_1T)^{-1}$ along with its anomalous peak around 50 K have been assigned to the effect of strong antiferromagnetic spin fluctuations with a finite wave vector [96,138,140,143]. The latter might be related to the ordering wave

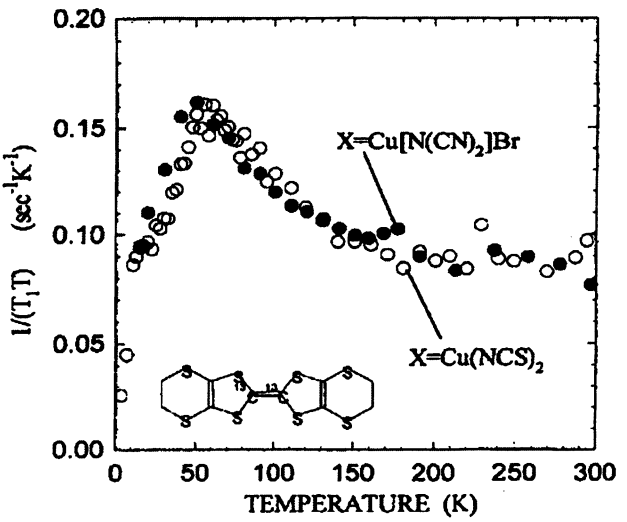

Fig. 7.13. Spin–lattice relaxation rate divided by temperature, $(T_1T)^{-1}$, for κ-(ET)$_2$Cu(NCS)$_2$ and κ-(ET)$_2$Cu[N(CN)$_2$]Br as a function of temperature, taken from [140]. For the ^{13}C–NMR measurements, the ^{12}C atoms of the central C = C double bond in the ET molecule have been replaced by ^{13}C

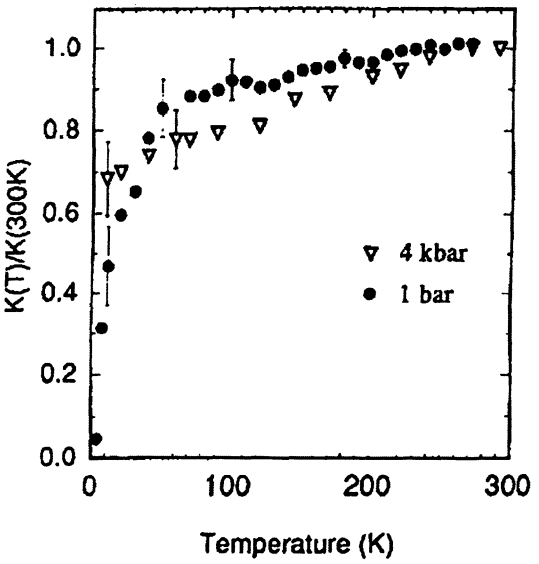

Fig. 7.14. Knight-shift, K_S, for κ-$(ET)_2Cu[N(CN)_2]Br$ as a function of temperature at ambient pressure and $p = 4\,\mathrm{kbar}$, taken from [138]

vector that characterizes the AF phase of κ-$(ET)_2Cu[N(CN)_2]Cl$ [96,138,143]. It has been emphasized by these authors that despite the rapid drop below $T^* \simeq 50\,\mathrm{K}$ the overall enhancement of $(T_1T)^{-1}$ persists until the onset of superconductivity indicative of the highly-correlated nature of the metallic state in these compounds [96,140]. NMR investigations performed at various pressures revealed that with increasing the pressure, the maximum at T^* shifts to higher temperatures while its size becomes progressively reduced. At pressures above 4 kbar the peak is replaced by a normal Korringa-type behavior, i.e. $(T_1T)^{-1} = \mathrm{const.}$ [138,139]. In [95,96] the abrupt reduction of $(T_1T)^{-1}$ below $T^* \simeq 50$ has been linked phenomenologically to a spin-gap behavior as discussed also in connection with the high-T_c cuprates. Indeed, the formation of a pseudogap was first proposed by Kataev *et al.* [144] on the basis of their ESR measurements. These authors observed a reduction of the spin susceptibility around 50 K, indicating a decrease of the electronic density of states at the Fermi level $N(E_F)$ near T^*. The same conclusion has been drawn from results of the static magnetic susceptibility [140] and Knight-shift (K_S) measurements [138]. Figure 7.14 shows K_S as a function of temperature for the κ-$(ET)_2Cu[N(CN)_2]Br$ salt. While the data at ambient pressure reveal a clear drop below about 50K, a rather smooth behavior with a gradual reduction upon cooling was found at 4 kbar [138]. The variation of the spin susceptibility in the high-temperature region has been attributed to the lattice contraction [143]. Although these experiments show clear evidence

for a reduction of the density of states at E_F below $T^* \simeq 50$, the nature of this phenomenon and its interrelation to superconductivity are still unclear.

Cooling through $T^* \simeq 50$ does not only cause anomalies in the above magnetic properties but also leads to clear signatures in transport, acoustic, optical and thermodynamic quantities. As mentioned above, for both superconducting compounds a distinct peak shows up in the temperature derivative of the electrical resistivity $\mathrm{d}\rho/\mathrm{d}T$ [93, 94] indicating a change in the density of states at E_F. A pronounced softening of ultrasound modes for κ-$(ET)_2Cu[N(CN)_2]Br$ and κ-$(ET)_2Cu(NCS)_2$ with distinct minima at $T^* \simeq 38\,K$ and 46 K, respectively, have been attributed to a coupling between acoustic phonons and antiferromagnetic fluctuations [145, 146]. An interaction between the phonon system and magnetism has also been suggested by Lin *et al.* based on their Raman scattering experiments [113,147]. Recent theoretical studies have attempted to explain both the acoustic and Raman experiments by a correlation–induced crossover from a coherent Fermi liquid at low temperatures to an incoherent bad metal at high temperatures [148,149]. According to this work, pronounced phonon anomalies as well as anomalous transport and thermodynamic properties are expected to occur at the crossover temperature T^*. Based on their NMR results, Kawamoto *et al.* [141] and Kanoda [95, 96] argued that T^* marks the crossover temperature from a region of antiferromagnetic fluctuations of localized spins at high T to a Fermi–liquid regime at low temperatures. This differs from the interpretation given by the Orsay group [138, 139, 143] who analyzed their NMR results in terms of strong antiferromagnetic fluctuations enhanced by Coulomb repulsion and the nesting properties of the Fermi surface.

More insight into the nature of the anomaly at T^* and its interrelation with superconductivity can be obtained by studying the coupling to the lattice degrees of freedom. This has been done by employing high–resolution thermal expansion measurements which also allow for studying directional–dependent effects [88, 97, 150]. Figure 7.15 compares the linear coefficient of thermal expansion, $\alpha(T) = \partial \ln l(T)/\partial T$, where $l(T)$ is the sample length, perpendicular to the planes for the superconducting κ-$(ET)_2Cu[N(CN)_2]Br$ (left panel) with that of the non–metallic κ-$(ET)_2Cu[N(CN)_2]Cl$ salt (right panel). For both compounds, various anomalies have been observed as indicated by the arrows [97,151]. These are (i) large step–like anomalies at $T_g = 70 \sim 80\,K$ which are due to a kinetic, glass–like transition associated with the ethylene endgroups, cf. section 7.3.4 and (ii) a distinct peak in $\alpha(T)$ at T^*. The latter feature, also observed for the superconductor κ-$(ET)_2Cu(NCS)_2$ (not shown) is absent in the non–metallic κ-$(ET)_2Cu[N(CN)_2]Cl$ salt, cf. right panel of Fig. 7.15 [97]. As demonstrated in the insets of Fig. 7.15, the transitions into the superconducting ($T_c = 11.8\,K$) and antiferromagnetic ($T_N = 27.8\,K$) ground states for the X=$Cu[N(CN)_2]Br$ and X=$Cu[N(CN)_2]Cl$ salts, respectively, are accompanied by distinct second–order phase transition anomalies in the coefficient of thermal expansion.

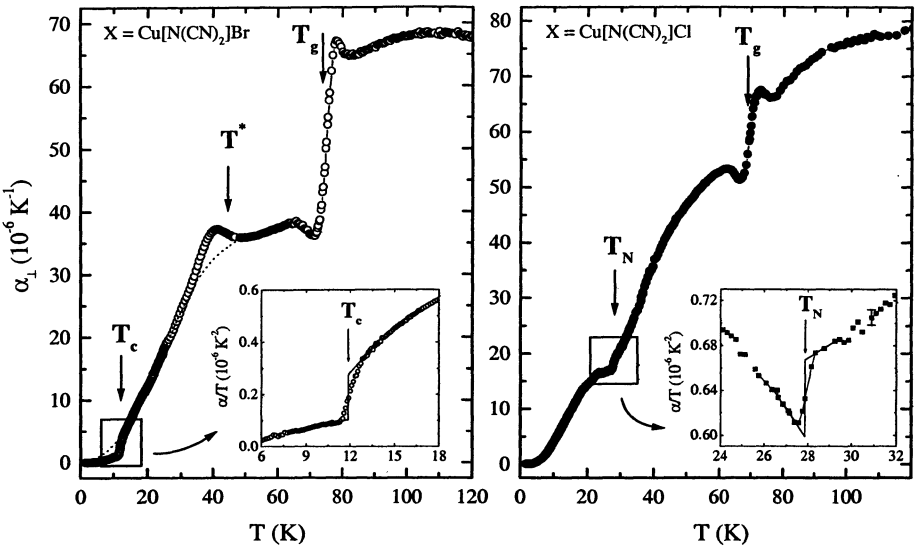

Fig. 7.15. Linear thermal expansion coefficient perpendicular to the planes of highest conductivity, $\alpha_\perp$, as a function of temperature for superconducting κ-$(ET)_2Cu[N(CN)_2]Br$ (left panel) and insulating κ-$(ET)_2Cu[N(CN)_2]Cl$ (right panel). The inset shows details of $\alpha_\perp$ for both salts as $\alpha_\perp/T$ vs T at the superconducting (X=Cu[N(CN)2]Br) and antiferromagnetic (X=Cu[N(CN)2]Cl) phase transition. Arrows indicate different kinds of anomalies as explained in the text, taken from [97]

Figure 7.16 shows the anomalous contribution, $\delta\alpha_i(T) = \alpha_i(T) - \alpha_{ib}(T)$, to the uniaxial thermal expansion coefficients along the principal axes, $\alpha_i(T)$, at T_c and T^* for the superconducting salts X=Cu[N(CN)2]Br (left panel) and X=$Cu(NCS)_2$ (right panel) obtained after subtracting a smooth background α_{ib} (dotted line in the left panel of Fig. 7.15) [98]. Judging from the shape of the anomalies at T^*, i.e. their sharpness and magnitude, it has been suggested that this feature be assigned to a second–order phase transition [98]. Figure 7.16 uncovers an intimate interrelation between the phase–transition anomalies at T_c and T^*: while both features are correlated in size, i.e. a large (small) anomaly at T_c complies with a large (small) one at T^*, they are anti-correlated in sign. A positive peak at T_c goes along with a negative anomaly at T^* and vice versa. According to the Ehrenfest relation

$$\left(\frac{\partial T^*}{\partial p_i}\right)_{p_i \to 0} = V_{\mathrm{mol}} \cdot T^* \cdot \frac{\Delta\alpha_i}{\Delta C}, \tag{7.6}$$

which relates the uniaxial–pressure dependence of a second–order phase–transition temperature T^* to the discontinuities in α_i, $\Delta\alpha_i$, and that of the specific heat, ΔC, the above findings imply that the uniaxial–pressure coefficients of T_c and T^* are strictly anticorrelated. In [97, 98] it has been argued that

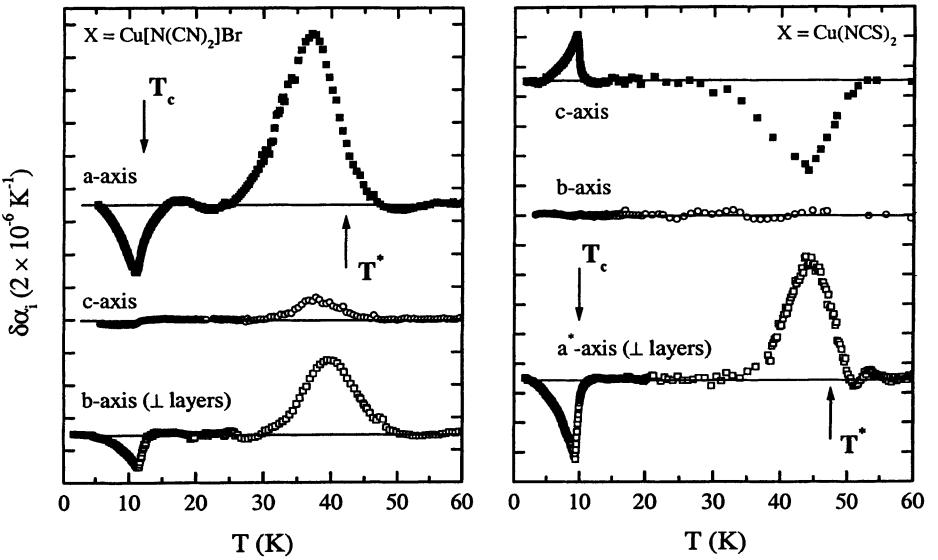

Fig. 7.16. Anomalous contributions, $\delta\alpha_i(T) = \alpha_i(T) - \alpha_{ib}(T)$, to the uniaxial thermal expansion coefficients, $\alpha_i(T)$, along the three principal axes for the superconducting salts κ-$(ET)_2Cu[N(CN)_2]Br$ (left panel) and κ-$(ET)_2Cu(NCS)_2$ (right panel), taken from [98]

the transition at T^* is not of structural but of electronic origin and related to the Fermi–surface topology. Based on the above uniaxial–pressure results, it has been proposed that T_c and T^* mark competing instabilities on disjunct parts of the Fermi surface [97, 98]: while the instability at T^* most likely involves only the minor quasi–1D fractions (see Fig. 7.7 and [138]), the major quasi–2D parts are subject to the superconducting instability at lower temperatures. As a result, these studies hint at the opening of a real gap associated with T^* on the small 1D–parts of the FS as opposed to a pseudogap on the major quasi–2D fractions. The condensation of parts of the FS into a density–wave below T^* would imply the onset of anisotropies in magnetic and transport properties. In fact, this has been found in recent orientational–dependent studies on both compounds [99]: cooling through T^* is accompanied by the onset of a small but distinct anisotropy in the magnetic susceptibility. As can be seen in Fig. 7.17, T^* affects also the charge degrees of freedom where below T^* the b–axis transport becomes more resistive compared to that along the c–axis [99]. These authors proposed that below T^* a static or fluctuating charge–density–wave (CDW) on minor parts of the FS coexists with the metallic phase on the remaining quasi–2D fractions.

The above discussion on the nature of the anomalies at T^* for the superconducting salts κ-$(ET)_2Cu[N(CN)_2]Br$ and κ-$(ET)_2Cu(NCS)_2$ poses the question whether this phenomenon is related to the magnetic signatures

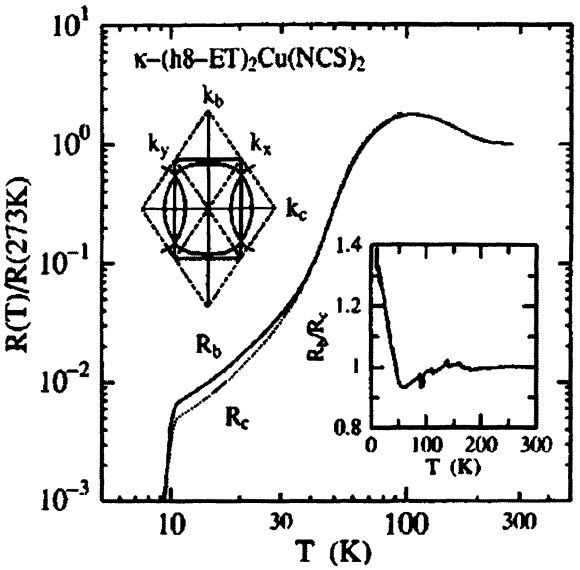

Fig. 7.17. Temperature dependence of the normalized resistance along the in–plane *b*– and *c*–axis of κ-$(ET)_2Cu(NCS)_2$. The top left inset shows the FS and the Brillouin zone, taken from [99]

found in the non–metallic κ-$(ET)_2Cu[N(CN)_2]Cl$. Earlier magnetization measurements on κ-$(ET)_2Cu[N(CN)_2]Cl$ revealed a shallow decrease below 45 K which was interpreted as the onset of an antiferromagnetic order [152]. In addition, indications were found for a weak ferromagnetic state at 22 K with a small saturation moment of $8 \cdot 10^{-4}\,\mu_B$/dimer. However, according to more recent NMR experiments, the spins order in a commensurate antiferromagnetic structure below $T_N \approx 27$ K with a sizable magnetic moment of $(0.4 - 1.0)\,\mu_B$/dimer [153]. From these measurements, along with magnetization studies, it has been inferred that the easy magnetic axis is aligned perpendicular to the planes and that a small canting of the spins causes a weak ferromagnetic moment parallel to the planes below about $22 \sim 23$ K, see also [154]. Recent ^{13}C–NMR experiments confirmed the commensurate character of the magnetic structure yielding a moment of $0.45\,\mu_B/(ET)_2$ [155].

Three different proposals have been put forward on the origin of the magnetic moments and the nature of the antiferromagnetic insulating state in κ-$(ET)_2Cu[N(CN)_2]Cl$: (i) electron localization due to lattice disorder accompanied by an incomplete compensation of their spins, i.e. an inhomogeneous frozen–in magnetic state [156], (ii) an itinerant SDW–type magnetism associated with the good nesting properties of the quasi–1D parts of the Fermi surface [119, 143, 157] and (iii) a correlation–induced Mott–Hubbard type

metal–insulator transition leading to a magnetic state characterized by localized spins [153].

Although proposal (i) has been ruled out by a recent thermal expansion study providing clear thermodynamic evidence for a phase transition at T_N [97] (see inset of the right panel of Fig. 7.15), the nature of the ordered state is still unclear. So far the results of optical, thermal and magnetic properties seem to indicate that certain elements of the models (ii) and (iii) would be applicable to κ-$(ET)_2Cu[N(CN)_2]Cl$.

7.3.4 Anion Ordering and Glassy Phenomena

In discussing molecular conductors and superconductors, an important issue which should not be overlooked is disorder and its possible implications on the electronic properties. In this respect we have to distinguish between different kinds of imperfections. The *extrinsic* disorder, i.e. impurity concentrations, contaminations or crystal defects can be vastly controlled in the preparation process although some aspects remain puzzling, see e.g. the discussion on the resistivity maximum in section 7.3.2. In a study of the alloy series β-$(ET)_2X$ with $X = (I_3)_{1-x}(IBr_2)_x$ $(0 \leq x \leq 1)$ – where the salts with the two limiting compositions with $x = 0$ and $x = 1$ are superconductors – a clear correlation between the residual–resistivity ratio (RRR) and T_c was found [158]. These experiments show that superconductivity is very sensitive to the induced random potentials which lead to electron localization. The effect of random potentials created by radiation damage effects – resulting in a suppression of superconducivity – has been studied for the Bechgaard salts as well as for β-$(ET)_2I_3$. For more details, the reader is referred to [5] and references therein.

$(TM)_2X$ salts

However, certain kinds of *intrinsic* disorder are unavoidable and can be of particular importance for experiments attempting to explore superconducting–state properties. The latter type of imperfections concerns materials where, by symmetry, certain structural elements can adopt one of two possible orientations which are almost degenerate in energy [159, 160].

This can be seen in the $(TM)_2X$ salts with non–centrosymmetric anions such as tetrahedral ClO_4. As a result, these anions are disordered at room temperature with an equal occupation for both orientations. Upon cooling, entropy is gained by a more or less perfect ordering of the anions, depending on how fast the system is cooled through the ordering temperature T_{AO}. A perfect long–range anion ordering, realized to a good approximation when cooled sufficiently slowly, then introduces a new periodicity of the lattice. Depending on the anion this can have quite different implications on the electronic properties: for the $(TMTSF)_2ClO_4$ salt, for example, the anion ordering below 24 K is accompanied by a doubling of the periodicity along the b–axis, i.e. perpendicular to the stacking axis which leaves the conducting properties almost unaffected. In contrast, the anion ordering for $(TMTSF)_2ReO_4$

opens up a large gap at the Fermi level leading to an insulating ground state. If the compound had been cooled quickly through T_{AO}, a disordered

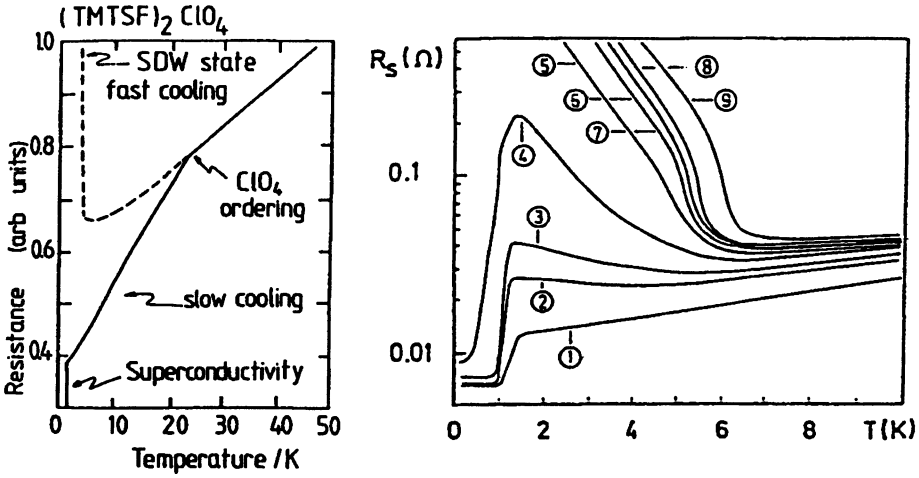

Fig. 7.18. Left panel: Effects of anion ordering in $(TMTSF)_2ClO_4$ at $T_{AO} = 24\,K$, on the resistivity, from [161]. Right panel: Semilogarithmic plot of the resistance vs temperature in states with various degrees of disorder characterized by T_Q numbered from 1 to 9 (see text), from [162]

"quenched" state is adopted at low temperatures whose properties are quite different from the "relaxed" state obtained after slow cooling.

The left panel of Fig. 7.18 shows the effect of anion ordering on $(TMTSF)_2ClO_4$. For a slowly cooled system, the anion–ordering phase transition occurs at $T_{AO} = 24\,K$. This is accompanied by a decrease of the resistivity due to the reduction of scattering by randomly distributed anion potentials. Upon further cooling, superconductivity sets in with $T_c = (1.2 \pm 0.2)\,K$. In contrast, for a crystal cooled rapidly, the high–temperature disordered state becomes quenched and the system undergoes a metal–to–insulator transition at $T_{MI} = 6.05\,K$. The insulating quenched state has been identified via NMR and ESR measurements [163, 164] as a SDW state with an energy gap $2\Delta_0/k_BT_{SDW} = 3.64$ close to the mean–field value of 3.52 [162]. The phase transition at T_{SDW} has been explored recently by specific heat measurements [165]. The right panel of Fig. 7.18 shows that the low–temperature resistivity may change over several orders of magnitude depending on the thermal history of the sample. Intermediate states with various degrees of frozen anion disorder have been produced by rapidly cooling the crystal from different temperatures $T_Q \geq T_{AO}$. Recent specific heat measurements showed that there is no difference between the specific heat anomalies at T_{AO} of slowly cooled and those of quenched–cooled samples, i.e. the structural transition is

independent of the kinetic conditions. From these results, the authors concluded that the reordering transition of the anions is of second order and occurs within the experimental timescales [165]. This is contrary to what would be expected for a glass–like transition. Such a glassy behavior, however, has been observed at the ordering temperatures of the compounds with $X = ReO_4$ ($T_{AO} = 180\,K$) and FSO_3 ($T_{AO} = 86\,K$). For more details see [5,33] and references therein.

κ-(BEDT–TTF)$_2$X salts

Indications for frozen–in disorder have been also reported for the quasi–2D salts of the κ–$(ET)_2X$ family. In an ac-calorimetry study, a glass–like transition has been found for κ-$(ET)_2Cu[N(CN)_2]Br$ and κ-$(ET)_2Cu[N(CN)_2]Cl$ [166–168]. The authors observed step–like anomalies in the heat capacity around 100 K, which have been attributed to a freezing out of the intramolecular motions of the ethylene endgroups at the ET molecules. Clear evidence for a glass–like transition have also been derived from thermal expansion measurements [97] which are extremely sensitive to structural rearrangements such as those involved in the glass–like freezing process. The outcome of this study confirmed, on the one hand, the above–mentioned specific heat results and clarified on the other, the nature of the thermal expansion anomalies previously reported by Kund *et al.* [88,150]. In addition, this study showed that a glass–like transition also exists for the κ-$(ET)_2Cu(NCS)_2$ salt. A glass transition is due to a relaxation process where, below a characteristic temperature T_g the relaxation time $\tau(T)$ of certain structural elements or molecules becomes so large that they can no longer reach thermodynamic equilibrium. As a result, a short range order, which is characteristic for this temperature T_g, becomes frozen in. Figure 7.19 shows exemplarily the linear coefficient of thermal expansion for κ-$(ET)_2Cu[N(CN)_2]Br$ measured parallel to the conducting planes at temperatures near T_g. As discussed in [97] the anomaly at $T_g \simeq 75\,K$ shows all the characteristics expected for a glassy transition [169], i.e. a step in the thermal expansion coefficient, a pronounced hysteresis between heating and cooling (left inset) and a cooling–rate dependent characteristic temperature T_g. The inset on the right side of Fig. 7.19 shows in an Arrhenius plot the inverse of the glass–transition temperatures, T_g^{-1}, vs the cooling rate $|q_c|$. The data nicely follow a linear behavior as expected for a thermally activated relaxation time [170,171]:

$$\tau(T) = \nu_0^{-1} \cdot \exp\left(\frac{E_a}{k_B T}\right), \tag{7.7}$$

where E_a denotes the activation energy barrier. The prefactor represents an attempt frequency ν_0. A linear fit to the data of Fig. 7.19 yields $E_a = (3200 \pm 300)\,K$.

The characteristic activation energy of the $[(CH_2)_2]$ conformational motion (cf. Fig. 7.4) was determined to $E_a = 2650\,K$ by ^1H–NMR measurements [143]. The similar size of the activation energy derived from Fig. 7.19

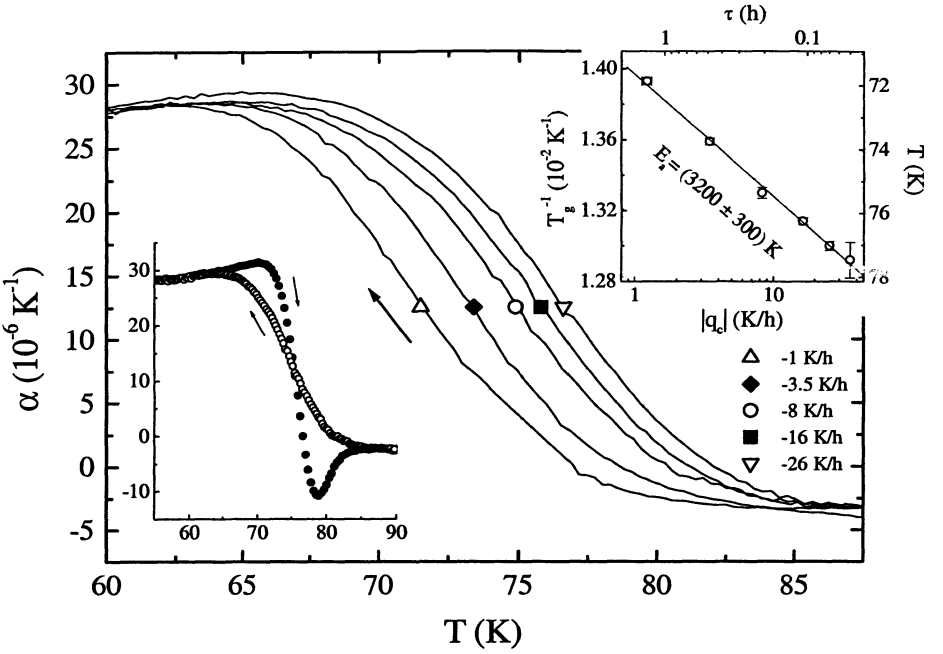

Fig. 7.19. Linear thermal expansion coefficient, α, vs T measured parallel to the conducting planes of κ-$(ET)_2Cu[N(CN)_2]Br$ in the vicinity of the glass transition defined as the midpoint of the step–like change in α for varying cooling rates q_c. Insets: hysteresis between heating and cooling curves around T_g (left side) and Arrhenius plot of T_g^{-1} vs $|q_c|$ and τ (right side), where $|q_c|$ is the cooling rate and τ the relaxation time (taken from [97])

along with the observation of a mass–isotope shift when replacing the hydrogen atoms in $[(CH_2)_2]$ by deuterium provide clear evidence that the ethylene endgroups are the relevant entities involved in the relaxation process [97].

An influence of the thermal history of the samples around 70 ∼ 80 K on the electronic properties had been realized by various authors and interpreted in different ways. Based on resistance measurements of structural relaxation kinetics on κ-$(ET)_2Cu[N(CN)_2]Br$, Tanatar *et al.* [89] claimed that the ethylene–endgroup ordering is associated with a sequence of first–order phase transitions around 75 K. A pronounced kink in the resistivity at 75 K accompanied by hysteresis between heating and cooling had been reported early on for κ-$(ET)_2Cu[N(CN)_2]Br$ [80, 174]. Similar behavior in the vicinity of T_g was observed also for κ-$(ET)_2Cu(NCS)_2$ [87]. Besides that, more recent measurements on κ-$(ET)_2Cu[N(CN)_2]Br$ yielded interesting time dependences affecting not only the electronic properties around 70 ∼ 80 K but also the properties at lower temperatures: Su *et al.* reported relaxation effects in $R(T)$ and a separation of the curves below about 80 K as a function of the cooling rate q_c. As shown in the inset of Fig. 7.20 (left panel) the residual re-

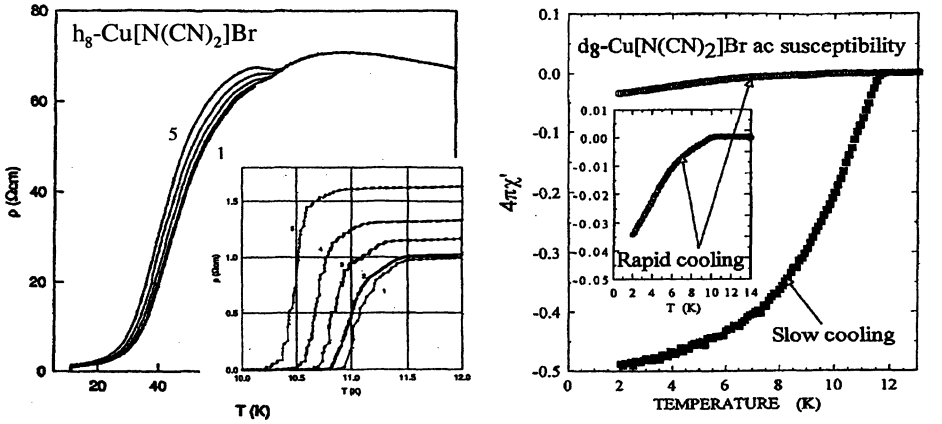

Fig. 7.20. Left panel: resistivity as a function of temperature for a sample of κ-$(H_8\text{-}ET)_2Cu[N(CN)_2]Br$ cooled at different rates ranging from about 0.5 K/min, lower curve (1), to 60 K/min upper curve (5). The inset shows an expansion of the data near the superconducting transition. Reproduced from [172]. Right panel: ac–susceptibility of κ-$(D_8\text{-}ET)_2Cu[N(CN)_2]Br$ after slow and rapid cooling (taken from [173])

sistivity increases with increasing $|q_c|$ [172,175]. The inset also shows that the way of cooling through $70 \sim 80$ K may influence the superconducting properties such that T_c decreases on increasing $|q_c|$. In addition, magnetization measurements revealed that with increasing $|q_c|$, a growing amount of disorder is induced causing an enlarged penetration depth [176]. In reference [177] an ac–susceptibility investigation of the magnetic penetration depths and their dependence on the cooling–rate–dependent intrinsic disorder have been performed. The authors found that the superconducting–state properties are critically determined by the time scale of the experiment around T_g.

For the deuterated κ-$(ET)_2Cu[N(CN)_2]Br$ salt, it has been reported that rapid cooling through 80 K drives the superconducting ground state into an insulating antiferromagnetic state [173,178]. [4] As shown in the right panel of Fig. 7.20 the ac–susceptibility data reveal a strong suppression of the superconducting volume fraction with increasing cooling rate [173]. It is tempting to assign the apparent deterioration of superconductivity to the frozen disorder at T_g: via the C-H$\cdots$ donor and C-H$\cdots$ anion contact interactions,

[4] The ground state of deuterated κ-$(D_8\text{-}ET)_2Cu[N(CN)_2]Br$ is strongly sample dependent; there are both superconducting as well as non–superconducting samples. In [173] it is claimed that the crystals always contain superconducting and non–superconducting components, whereas the latter have a magnetic character, possibly similar to that of κ-$(ET)_2Cu[N(CN)_2]Cl$. It is thus believed that the system is situated in the critical region of the phase diagram just between the superconducting and antiferromagnetic phases, see section 7.3.5.

disorder in the ethylene groups introduces a random potential that may alter the effective transfer integrals t_{eff} and, by this, may destroy superconductivity, see also [37].

7.3.5 Phase Diagrams

$(TM)_2X$ salts

Figure 7.21 comprises in a pressure–temperature plane results of various experiments on the quasi-1D charge-transfer salts $(TMTTF)_2X$ and their selenium analogues $(TMTSF)_2X$. The arrows indicate the position of the various salts at ambient pressure (cf. also Fig. 7.10). The generic character of the phase diagram – first proposed by Jérome *et al.* [137] – has been demonstrated recently by pressure studies on the $(TMTTF)_2PF_6$ salt [67,68,179] for which the ambient–pressure ground state is a dimerized spin–Peierls state. With increasing pressure, the system was found to pass through the whole sequence of ground states as shown in Fig. 7.22 and eventually becoming superconducting at high pressures above 43.5 kbar [68,179]. On the low–pressure (left)

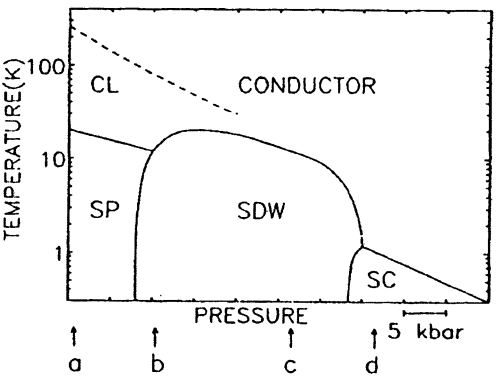

Fig. 7.21. Generalized phase diagram for the quasi–1D $(TM)_2X$ salts as proposed first by Jérome [137]. Arrows indicate the positions of the salts with different anions X at ambient pressure: (a) $(TMTTF)_2PF_6$, (b) $(TMTTF)_2Br$, (c) $(TMTSF)_2PF_6$, (d) $(TMTSF)_2ClO_4$. The following abbreviations are used: charge–localised insulator (CL), spin Peierls (SP), incommensurate spin–density–wave (SDW) and superconductivity (SC) (taken from [180])

side of the phase diagram in Figs. 7.21 and 7.22 the molecular stacks can be considered as only weakly–coupled chains, i.e. the system is close to be truly 1D. In fact upon cooling, the $(TMTTF)_2PF_6$ compound behaves very much like canonical 1D conductors where spin and charge degrees of freedom are decoupled: below $T_\rho = 250\,\text{K}$ the resistivity increases by several orders of magnitude due to charge localization while the spin susceptibility remains

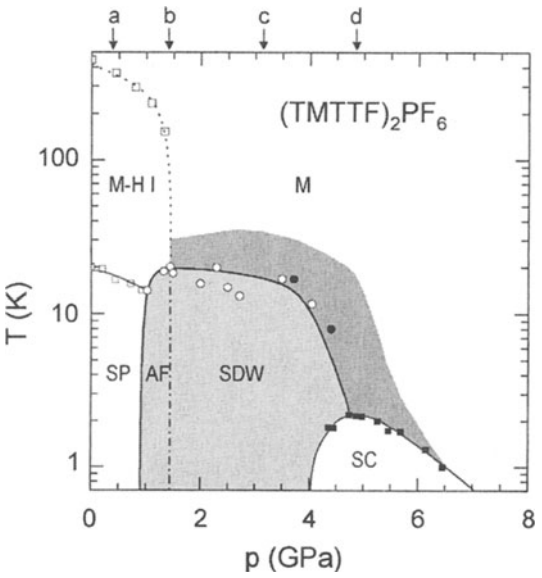

Fig. 7.22. Temperature–hydrostatic–pressure phase diagram for $(TMTTF)_2PF_6$. The abbreviations are: Mott–Hubbard insulating state (M-H I), metallic (M) and superconducting (SC) state, spin–Peierls (SP), commensurate (AF) and incommensurate (SDW) antiferromagnetic spin–density–wave state. Arrows: ambient–pressure ground–state location of other salts; (a) $(TMTTF)_2BF_4$, (b) $(TMTTF)_2Br$, (c) $(TMTSF)_2PF_6$, (d) $(TMTSF)_2ClO_4$ (taken from [68])

unaffected [6, 33, 78]. The phase below T_ρ has been interpreted as a Mott insulating state. Upon further cooling to $T_{SP} = 19\,\mathrm{K}$ a spin gap opens and the system enters a distorted spin–Peierls ground state. In $(TMTTF)_2Br$, position (b) Figs. 7.21 and 7.22, a long–range magnetic order is established below the spin–density–wave transition at $T_{SDW} \approx 13\,\mathrm{K}$. Toward the right side of the phase diagram, which can be carried out either by varying the anion or by the application of hydrostatic pressure, inter–stack interactions become more important. In this region of the phase diagram the electron–phonon interaction is less dominant and electron–electron interactions along with the good nesting properties of the Fermi surface (cf. Fig. 7.7) lead to a spin–density–wave ground state as observed, e.g. in the Bechgaard salt $(TMTSF)_2PF_6$ at ambient pressure. After suppression of the SP phase in $(TMTTF)_2PF_6$ with increasing pressure, a commensurate antiferromagnetic state is adopted before an incommensurate SDW phase is stabilized. With increasing pressure, T_{SDW} becomes progressively reduced until, above some critical pressure, the systems remain metallic and superconductivity replaces the SDW ground state. The effect of pressure is to increase the π–orbital overlap also in the transverse direction, i.e. perpendicular to the stacking axis. As a result the almost perfect nesting properties are destroyed and the systems

become more 3D in character.[5] According to NMR experiments [33,66] and recent transport measurements under hydrostatic pressure [68,179] strong SDW correlations are still active in the metallic state even when the SDW instability is replaced by superconductivity in $(TMTSF)_2ClO_4$. The range of strong SDW correlations for $(TMTTF)_2PF_6$ derived from these experiments is indicated in Fig. 7.22 by the shaded region above the SDW and SC phase boundaries.

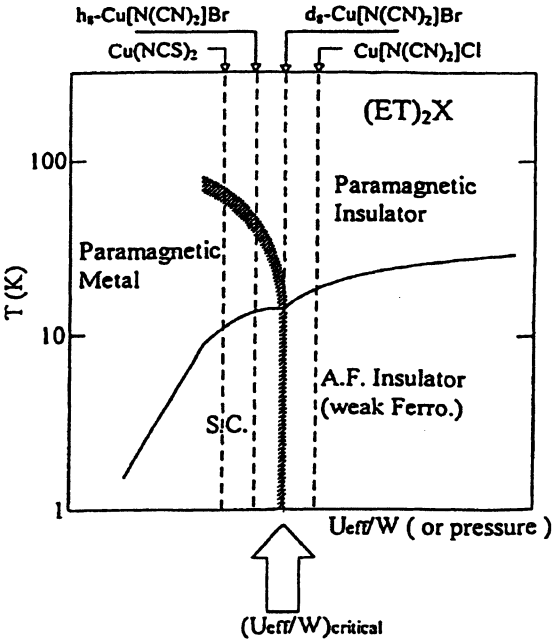

Fig. 7.23. Conceptual phase diagram for κ–phase $(ET)_2X$ as proposed by Kanoda [96]. Note that hydrostatic pressure decreases the ratio $U_{\rm eff}/W$, i.e. the low pressure side is on the right end of the phase diagram. The arrows indicate the ambient–pressure position of the various systems and AF and SC denote an antiferromagnetic insulator and superconductor, respectively

κ-(BEDT–TTF)$_2$X salts Figure 7.23 shows a conceptual phase diagram proposed by Kanoda for the dimerized κ–type BEDT–TTF salts. Here it

[5] Recent measurements under uniaxial strain revealed that the SDW transition is most strongly suppressed and superconductivity can be induced by the strain along the stacking a–axis [181,182]. Considerably smaller effects were observed for strain along the b'– and c'–axes – although the former direction is directly associated with the denesting of the quasi–1D Fermi surface [181]. This has been interpreted in terms of a pressure–induced decrease in the density of states at the FS [183].

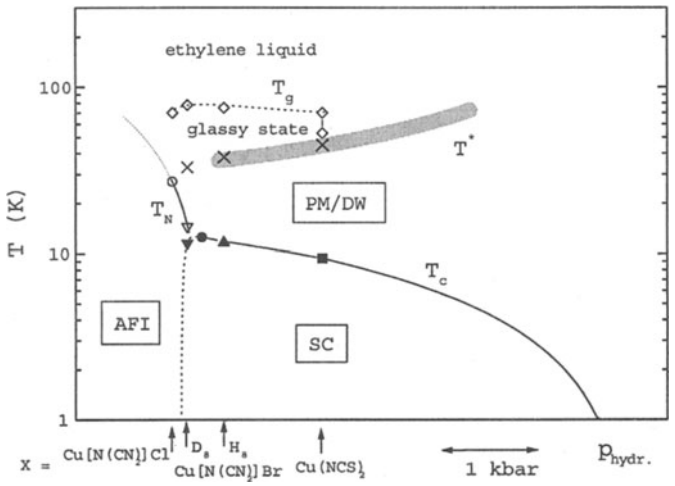

Fig. 7.24. Temperature–hydrostatic–pressure phase diagram for the κ-$(ET)_2X$ compounds. Arrows indicate the positions of the various compounds at ambient pressure. Circles correspond to results on κ-$(ET)_2Cu[N(CN)_2]Cl$ while down and up triangles indicate phase–transition temperatures on deuterated and hydrogenated κ-$(ET)_2Cu[N(CN)_2]Br$, respectively, and squares stand for results on κ-$(ET)_2Cu(NCS)_2$. The transitions into the superconducting and antiferromagnetic states are represented by closed and open symbols, respectively. Diamonds denote the glass–like freezing of ethylene disorder and crosses the density–wave (DW) transition on minor parts of the Fermi surface. These anomalies coincide with various features observed in magnetic, transport and acoustic properties (shaded area, see section 7.3.3) (taken from [97, 187])

has been assumed that it is the effective on–site (dimer) Coulomb interaction U_{eff} normalized to the bandwidth W which is the key factor associated with the various phases and phase transitions [95, 96]. The positions of the various salts are determined by their ambient–pressure ground–state properties. The deuterated κ-$(D_8\text{-ET})_2Cu[N(CN)_2]Br$ salt is situated right at the AFI/SC border. The system lies in between the antiferromagnetic insulating $X = Cu[N(CN)_2]Cl$ and the superconducting hydrogenated κ-$(H_8\text{-ET})_2Cu[N(CN)_2]Br$ salts. It has been proposed that a *partial* substitution of the 2×4 H–atoms by D–atoms allows for fine–tuning the κ-$(ET)_2Cu[N(CN)_2]Br$ system across the AFI/SC border [184–186]. The close proximity of an antiferromagnetic insulating to a superconducting phase has been considered – in analogy to the high–T_c cuprates – as a strong indication that both phenomena are closely connected to each other [4].

Figure 7.24 summarizes experimental data of a detailed thermodynamic study on the various κ-$(ET)_2X$ compounds in a pressure–temperature phase diagram [97, 187]. The positions of the various salts at ambient pressure are

indicated by the arrows.[6] The solid lines representing the phase boundaries between the paramagnetic (PM) and the superconducting (SC) or antiferromagnetic insulating (AFI) states refer to the results of hydrostatic–pressure studies of T_c and T_N [81,188,189].

At elevated temperatures, a glass–like transition at a temperature T_g (dotted line) has been identified. It marks the boundary between an ethylene–liquid at $T > T_g$ and a glassy state at $T < T_g$. While at temperatures above T_g, the motional degrees of freedom of the ethylene endgroups are excited with an equal occupancy for the two possible ethylene conformations, a certain disorder becomes frozen in at temperatures below T_g. The glass–like transition which is structural in nature has been shown to cause time dependences in electronic properties and may have severe implications on the ground–state properties of the κ-$(ET)_2Cu[N(CN)_2]Br$ salt depending on the cooling rate employed at T_g (see section 7.3.4).

At intermediate temperatures T^*, anomalies in the coefficient of thermal expansion have been found and assigned to a density–wave transition involving only the quasi–1D parts of the Fermi surface. These anomalies coincide with various features observed in magnetic, transport and acoustic properties (thick shaded line in Fig. 7.24, see also section 7.3.3). In [97,98] it has been proposed that instead of a pseudogap on the quasi–2D parts of the Fermi surface, a real gap associated with a density wave opens on the minor quasi–1D parts below T^*, see also [99]. This scenario implies that the density wave and superconductivity involve disjunct parts on the Fermi surface and compete for stability.

Details of the pressure–temperature phase diagram of the antiferromagnetic insulating salt κ-$(ET)_2Cu[N(CN)_2]Cl$ have been reported by Ito *et al.* [190] and Lefebvre *et al.* [191]. In the latter work, it has been shown that the superconducting and antiferromagnetic phases overlap through a first–order boundary that separates two regions of an inhomogeneous phase coexistence [191]. It has been argued that this boundary curve merges with a first–order line of the metal–insulator transition and that this line ends at a critical point at higher temperature, see Fig. 7.25. The figure also suggests the existence of a point–like region where the metallic, insulating, antiferromagnetic as well as superconducting phases all meet. This would imply the absence of a boundary between metallic and complete antiferromagnetic phases which would be incompatible with an itinerant type of magnetism [191].

$(BEDT–TSF)_2X$ salts

Figure 7.26 shows the phase diagram for the quasi–2D alloy system λ-$(BETS)_2$

[6] Note that hydrostatic pressure has been used as an abscissa for the purpose of compatibility with the conceptual phase diagram in Fig. 7.23. It has been found, however, that the uniaxial–pressure dependences for the various phase boundaries are strongly anisotropic [97,98,151] with a non–uniform behavior for the uniaxial–pressure coefficients of both the density–wave instability at T^* and those of T_c, cf. Figs. 7.16 and 7.31.

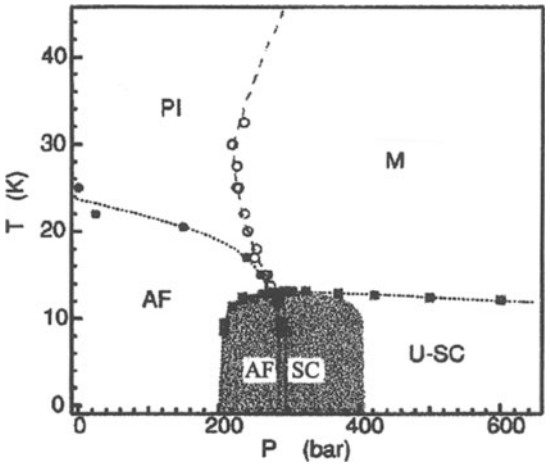

Fig. 7.25. Pressure–temperature phase diagram for κ-$(ET)_2Cu[N(CN)_2]Cl$. The antiferromagnetic (AF) transition temperature $T_N(p)$ (closed circles) were determined from the NMR relaxation rate while $T_c(p)$ (closed squares) and $T_{MI}(p)$ (open circles) were obtained from ac–susceptibility measurements. U–SC denotes uniform superconductivity; the AF–SC boundary line separates two regions of inhomogeneous phase coexistence (shaded area) (taken from [191])

$Fe_xGa_{1-x}Cl_4$ which has recently gained strong interest due to its interesting magnetic and superconducting properties [192]. The system is based on the donor molecule BEDT–TSF or simply BETS which represents the Se analogue to BEDT–TTF, see section 7.2. λ-$(BETS)_2$ $GaCl_4$ on the left side is a nonmagnetic salt which becomes superconducting at $T_c = 6\,K$ [31]. A magnetic field of 13 T aligned parallel to the highly conducting planes destroys superconductivity and stabilizes a paramagnetic metallic state. Conversely, λ-$(BETS)_2FeCl_4$ shows a metal–insulator (M-I) transition around 8 K which is accompanied by an antiferromagnetic order of the Fe^{3+} moments in the anion layers [28]. Applying a magnetic field in excess of about 10 T destabilizes the insulating phase and the paramagnetic phase recovers [193,194]. In the mixed series λ-$(BETS)_2Fe_xGa_{1-x}Cl_4$, the M-I transition becomes suppressed as the concentration x of magnetic Fe ions decreases and a superconducting ground state is formed for $x \leq 0.35$. A striking feature is the metal–superconductor–insulator transition for $0.35 \leq x \leq 0.5$, see Fig. 7.26. Apparently, the various phases contained in the above phase diagram originate from an intimate coupling between the magnetic moments of the Fe^{3+} $3d$ electrons and the π–conduction–electron spins of the BETS molecule, see e.g. [32,194,195].

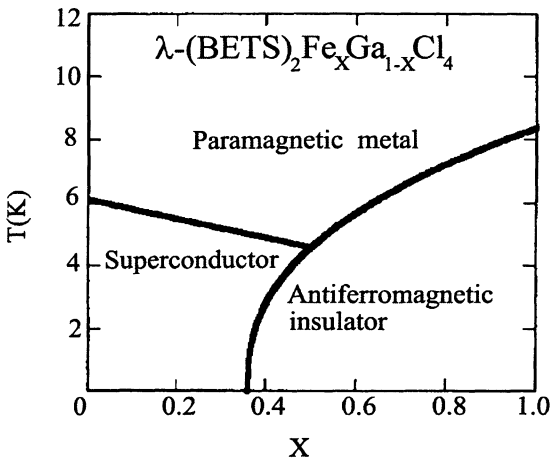

Fig. 7.26. Phase diagram for λ-$(BETS)_2Fe_xGa_{1-x}Cl_4$ taken from [32]

7.4 Superconducting–State Properties

Since the discovery of superconductivity in pressurized $(TMTSF)_2PF_6$ in 1979 [1], continuing efforts to design new potential donor and acceptor molecules have led to more than about 80 organic superconductors.[7] In the vast majority of cases, the donor molecules are derivatives of the prototype TMTSF molecule including BEDT–TTF as well as the selenium and oxygen substituted variants BEDT–TSF and BEDO–TTF, respectively. In addition, superconductors have been derived using asymmetric hybrides such as DMET and MDT–TTF. For a comprehensive list of organic superconductors the reader is referred to [5].

In the following discussion of superconducting properties we will confine ourselves to a few selected examples. These are the $(TMTSF)_2X$ and the quasi–2D $(BEDT\text{–}TTF)_2X$ and $(BEDT\text{–}TSF)_2X$ salts which are representative for a wide class of materials.

7.4.1 The Superconducting Phase Transition

Organic superconductors are characterized by a highly anisotropic electronic structure, a low charge carrier concentration and unusual lattice properties. As will be discussed below, the combination of these unique material parameters lead to a variety of remarkable phenomena of the superconducting state

[7] The materials discussed in this article have to be distinguished from another class of molecular superconductors – the alkali–metal–doped fullerenes discovered in 1991 [196] – which are usually not referred to as organic materials as they contain only carbon atoms.

such as pronounced thermal fluctuations, an extraordinarily high sensitivity to external pressure and anomalous mixed–state properties.

Superconducting anisotropy

The abrupt disappearance of the electrical resistance is one of the hallmarks that manifests the transition from the normal into the superconducting state for usual 3D superconductors. For the present low–dimensional organic superconductors – as in the layered high–T_c cuprates – however, strong fluctuations of both the amplitude and phase of the superconducting order parameter may cause a substantial broadening of the superconducting transition. This becomes particularly clear when a strong magnetic field is applied. As a consequence, for these materials zero–resistance is no longer a good measure of the superconducting transition temperature in a finite magnetic field. Therefore, for a precise determination of the upper critical fields, thermodynamic investigations such as magnetization, specific heat or thermal expansion measurements are necessary.

For materials with strongly directional–dependent electronic properties, a highly anisotropic superconducting state is expected as well. In an attempt to account for these anisotropies, the phenomenological Ginzburg–Landau and London models have been extended by employing an effective–mass tensor [197]. In the extreme case of a quasi–2D superconductor characterized by a superconducting coherence length perpendicular to the planes, $\xi_\perp$, being even smaller than the spacing between the conducting layers, s, these anisotropic 3D models are no longer valid. Instead, the superconductor has to be described by a model that takes the discreteness of the structure into account. Such a description is provided by the phenomenological Lawrence–Doniach model [198] which encloses the above anisotropic Ginzburg–Landau and London theories as limiting cases for $\xi_\perp > s$. This model considers a set of superconducting layers separated by thin insulating sheets implying that the 3D phase coherence is maintained by Josephson currents running across the insulating layers. In fact, the presence of an intrinsic Josephson effect has been demonstrated for several layered superconductors including some of the high–T_c cuprates and the present κ-$(ET)_2Cu(NCS)_2$ salt [199,200].

To quantify the degree of anisotropy, it is convenient to compare the results of orientational–dependent measurements with the above anisotropic models. For layered systems such as the present (BEDT–TTF)$_2X$ compounds, it is customary to use the effective–mass ratio $\Gamma = m_\perp^*/m_\parallel^*$, where $m_\perp^*$ and $m_\parallel^*$ denote the effective masses for the superconducting carriers moving perpendicular and parallel to the conducting planes, respectively. In the London and Ginzburg–Landau theories, Γ is directly related to the anisotropies in the magnetic penetration depths λ and coherence lengths ξ by

$$\sqrt{\Gamma} = \frac{\lambda_\perp}{\lambda_\parallel} = \frac{\xi_\parallel}{\xi_\perp}. \tag{7.8}$$

As an example for the highly anisotropic response of the superconducting transition to a magnetic field, we show in Fig. 7.27 results of the coefficient

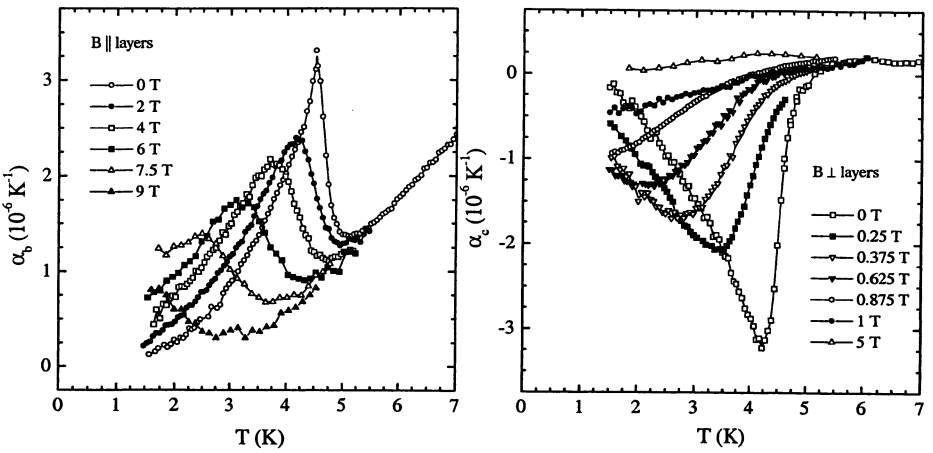

Fig. 7.27. Coefficient of thermal expansion of β''-$(ET)_2SF_5CH_2CF_2SO_3$ measured parallel (left panel) and perpendicular (right panel) to the conducting planes in varying fields applied along the measuring directions (taken from [151])

of thermal expansion $\alpha(T)$ near T_c for β''-$(ET)_2SF_5CH_2CF_2SO_3$.[8] While for fields parallel to the planes (left panel) the phase transition in $\alpha(T)$ is still visible even in $B = 9$ T, a field of 1 T applied perpendicular to the conducting planes is sufficient to suppress almost completely superconductivity (right panel of Fig. 7.27). In addition, for this field orientation, a pronounced rounding of the phase–transition anomaly even for very small fields can be observed. From these measurements the upper critical fields, B_{c_2}, can be determined permitting an estimate of the anisotropy parameter Γ:

$$B_{c_2}^{\perp\prime} = \left|\frac{\mathrm{d}B_{c_2}^{\perp}}{\mathrm{d}T}\right| = \frac{\phi_0}{2\pi\xi_{\parallel}^2 T_c} \quad \text{and} \quad \frac{B_{c_2}^{\perp\prime}}{B_{c_2}^{\parallel\prime}} = \frac{\xi_{\perp}}{\xi_{\parallel}} = \frac{1}{\sqrt{\Gamma}}, \tag{7.9}$$

where $B_{c_2}^{\perp\prime}$ and $B_{c_2}^{\parallel\prime}$ are the initial slopes of the upper critical fields for B perpendicular and parallel to the conducting planes, respectively [203, 204] and ϕ_0 is the flux quantum. For β''-$(ET)_2SF_5CH_2CF_2SO_3$ one finds $\xi_{\parallel} = (144\pm9)$ Å, $\xi_{\perp} = (7.9\pm1.5)$ Å and $\Gamma \approx 330$ [151] (cf. Table 7.1 in section 7.2.2 and Table 7.2 in section 7.4.2), which underlines the quasi–2D character of the superconducting state in this material. The large anisotropy parameter $\Gamma \approx 330$ exceeds the value of $\Gamma \approx 100$ found for the κ-$(ET)_2Cu(NCS)_2$ salt in dc–magnetization experiments [205].

The so–derived Γ values, however, may serve only as a rough estimate of the actual anisotropy parameters. The latter can be probed most sensitively by employing torque-magnetometry. For κ-$(ET)_2Cu(NCS)_2$ for example, Γ

[8] This salt of the β''–type structure contains large discrete anions and is unique in being the first superconductor free of any metal atoms [201, 202].

values ranging from 200 to 350 have been reported [206, 207] which place this material in the same class of quasi–2D superconductors as the most anisotropic high–T_c cuprates with $\Gamma = 150 \sim 420$ for $Bi_2Sr_2CaCu_2O_{8+x}$ [208, 209].

Fluctuation effects

The highly anisotropic response of the present quasi–2D superconductors to a magnetic field is also demonstrated in Fig. 7.28 where the temperature dependence of the magnetization around the superconducting transition is shown for κ-$(ET)_2Cu(NCS)_2$. While for fields aligned perpendicular to the planes (left panel) the transition considerably broadens with increasing field strength, there is only a little effect on the transition for fields parallel to the layers (right panel) [205], cf. also Fig. 7.27. This behavior is quite different from that which is found in a usual 3D superconductor and indicates the presence of strong superconducting fluctuations which are strongly enhanced in systems with reduced dimensionality [210].

A measure of the strength of thermal order–parameter fluctuations is provided by the so–called Ginzburg number

$$G = \frac{|T - T_c|}{T_c} = \frac{1}{2}\left(\frac{k_B T}{B_{c_{th}}^2(0)\xi_{\parallel}^2\xi_{\perp}}\right)^2, \tag{7.10}$$

where $B_{c_{th}}(0)$ is the thermodynamic critical field. G measures the ratio of thermal energy to the condensation energy per coherence volume. For classical 3D superconductors like niobium G amounts to about $G \sim 10^{-11}$. In contrast, for the present compounds and some of the high–T_c cuprates one finds $G \sim 10^{-2} - 10^{-3}$ [205, 211, 212]. Here, the relatively high transition temperatures together with a low charge–carrier concentration – the latter results in a small Fermi velocity, v_F, and thus a short coherence length $\xi \propto \hbar v_F/(k_B T_c)$ – enhance the effect of superconducting fluctuations. The strong rounding of the phase–transition anomaly with increasing magnetic fields aligned perpendicular to the conducting planes is then understood to be a result of a field–induced dimensional crossover: while the electronic state in small fields is quasi–2D, the confinement of the quasiparticles to their lower Landau levels in high fields leads to a quasi–zerodimensional situation [213, 214]. As a result, the relatively sharp phase–transition anomaly in zero field becomes progressively rounded and smeared out with increasing field. Instead of a well defined phase boundary between normal and superconducting states, the high–field range of the B–T phase diagram is characterized by a crossover behavior with extended critical fluctuations. Here, the assertion of a mean–field transition temperature, $T_c^{mf}(B)$, from the raw data is difficult and a fluctuation analysis has to be invoked.

The effect of fluctuations on transport and thermodynamic properties has been studied by several authors [215, 216]. Assuming the lowest–Landau–level approximation and taking into account only non–interacting Gaussian fluctuations, Ullah and Dorsey obtained an expression for a scaling function

of various thermodynamic quantities as the magnetization M or the specific heat C:

$$\Xi_i = F_i\left(A\frac{T - T_c^{\mathrm{mf}}(B)}{(TB)^n}\right), \tag{7.11}$$

with $\Xi_i = M/(TB)^n$ or C/T [211]. F_i is an unknown scaling function, A a temperature– and field–independent coefficient characterizing the transition width and $n = 2/3$ for anisotropic 3D materials and $n = 1/2$ for a 2D system. Thus from a scaling analysis both the actual dimensionality as well as the mean–field–transition temperature $T_c^{\mathrm{mf}}(B)$ can be determined.

Figure 7.29 shows the data of the dc–magnetization of κ-$(ET)_2Cu(NCS)_2$ (Fig. 7.28) and thermal expansion of β''-$(ET)_2SF_5CH_2CF_2SO_3$ (Fig. 7.27) taken in varying fields in the proper scaling forms $M/(TH)^{(n)}$ vs $(T - T_c^{\mathrm{mf}}(B))/(TB)^n$ and α_c^{sc}/T vs $(T - T_c^{\mathrm{mf}}(B))/(TB)^{1/2}$, respectively, where α_c^{sc} denotes the superconducting contribution to the coefficient of thermal expansion. [9] As shown in Fig. 7.29 the various field curves $\alpha_c^{sc}(T, B)$ show the 2D scaling over a rather wide temperature and field range, see also [211,217]. Ac-

[9] Since the volume coefficient of thermal expansion, $\beta(T)$, is related to the specific heat via the Grüneisen relation $\beta(T) = \gamma \cdot \frac{\kappa_T}{V_{mol}} \cdot C_V(T)$, where κ_T denotes the isothermal compressibility, V_{mol} the molar volume and γ a field– and temperature–independent Grüneisen parameter, the scaling form holds also for α/T.

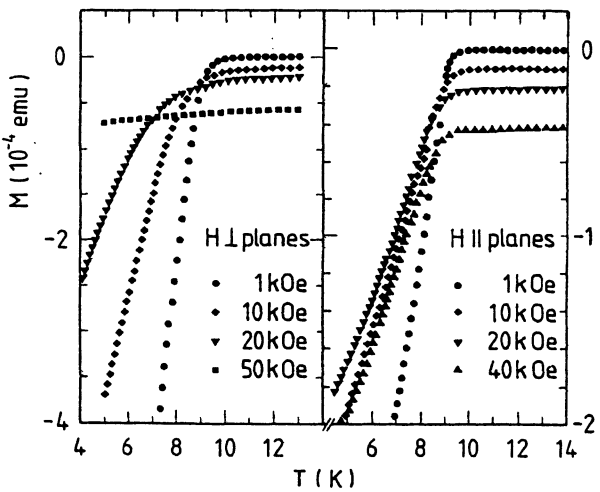

Fig. 7.28. Raw data of the dc–magnetization of single crystalline κ-$(ET)_2Cu(NCS)_2$ in various fields perpendicular (left panel) and parallel (right panel) to the conducting planes. The offset of each curve is due to contributions from the core electrons, the spin susceptibility as well as a small background signal (taken from [205])

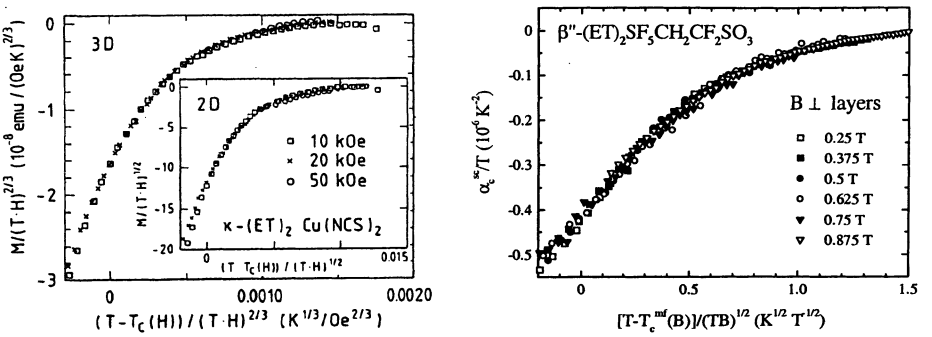

Fig. 7.29. Scaling behavior of the superconducting contribution to the magnetization of κ-$(ET)_2Cu(NCS)_2$ (left panel) [205] and the linear coefficient of thermal expansion of β''-$(ET)_2SF_5CH_2CF_2SO_3$ (right panel) [151] in magnetic fields applied perpendicular to the planes

cording to the scaling analysis of the high–field magnetization in Fig. 7.29 as well as the high–field conductivity in [218], κ-$(ET)_2Cu(NCS)_2$ is at the threshold from being a strongly anisotropic 3D to a 2D superconductor. On the other hand, a distinct 2D behavior has been claimed from a scaling analysis of low–field magnetization data by Ito *et al.* [219].

Pressure dependence of T_c

By applying pressure to a superconductor, one can study the volume dependence of the pairing interaction through changes of T_c. For the $(TMTSF)_2X$ and $(ET)_2X$ superconductors, one generally finds an extraordinarily high sensitivity to external pressure and, in the vast majority of cases, a rapid decrease of T_c with pressure. Figure 7.30 shows the variation of T_c for a selection of β– and κ–type $(ET)_2X$ salts under hydrostatic–pressure conditions. The initial slope of the pressure dependence of T_c, $(\partial T_c/\partial p)_{p\to 0}$, determined via resistivity measurements ranges from $-0.25\,\mathrm{K/kbar}$ for α-$(ET)_2NH_4Hg(SCN)_4$ ($T_c = 1\,\mathrm{K}$) [220] to $-3.2\,\mathrm{K/kbar}$ for κ-$(ET)_2Cu[N(CN)_2]Cl$ ($T_c = 12.8\,\mathrm{K}$ at $0.3\,\mathrm{kbar}$) [81]. For $(TMTSF)_2PF_6$, one finds $-(8\pm1)\cdot10^{-2}\,\mathrm{K/kbar}$ ($T_c = 1.1\,\mathrm{K}$ at $6.5\,\mathrm{kbar}$) [136]. At first glance a strong pressure dependence of T_c appears not surprising in view of the weak van der Waals bonds between the organic molecules, giving rise to a highly compressible crystal lattice. In fact, the isothermal compressibility $\kappa_T = -\partial \ln V/\partial p$ for κ-$(ET)_2Cu(NCS)_2$ of $\kappa_T = (122\,\mathrm{kbar})^{-1}$ [221, 222] exceeds the values found for ordinary metals by about a factor of five. To account for this "lattice effect" one should, therefore, consider the physically more meaningful volume dependence of T_c:

$$\frac{\partial \ln T_c}{\partial \ln V} = \frac{V}{T_c}\cdot\frac{\partial T_c}{\partial V} = -\frac{1}{\kappa_T \cdot T_c}\cdot\frac{\partial T_c}{\partial p}. \tag{7.12}$$

Using the above isothermal compressibility, one finds $\partial \ln T_c/\partial \ln V \approx 40$ for κ-$(ET)_2Cu(NCS)_2$ [151] which exceeds the values found for ordinary metallic

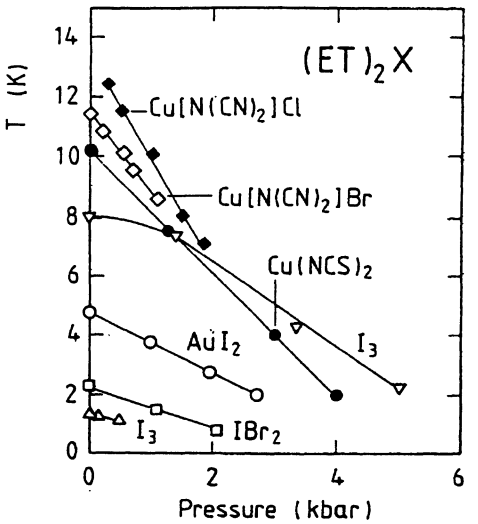

Fig. 7.30. Hydrostatic–pressure dependence of T_c for various β– and κ–type $(ET)_2X$ superconductors, reproduced from [5]

superconductors, as e.g. for Pb with $\partial \ln T_c / \partial \ln V = 2.4$ [223], or the layered copper–oxides with $-(0.36 \sim 0.6)$ reported for $YBa_2Cu_3O_7$ [224] by $1 \sim 2$ orders of magnitude.

For strongly anisotropic superconductors like those discussed here, even more information on the relevant microscopic couplings can be obtained by studying the effect of uniaxial pressure on T_c. Different techniques have been employed to determine the uniaxial–pressure coefficients of T_c for the $(TMTSF)_2X$ and $(ET)_2X$ salts including measurements under uniaxial strain or stress [225–228] or by using a thermodynamic analysis of ambient–pressure thermal expansion and specific heat data [97, 151, 229, 230]. The latter approach is based on the Ehrenfest relation which connects the pressure coefficients of T_c for uniaxial pressure along the i–axis (in the limit of vanishing pressure) to the phase–transition anomalies at T_c in the coefficient of thermal expansion, $\Delta\alpha_i$, and specific heat, ΔC:

$$\left(\frac{\partial T_c}{\partial p_i}\right)_{p_i \to 0} = V_{mol} \cdot T_c \cdot \frac{\Delta\alpha_i}{\Delta C}, \tag{7.13}$$

with V_{mol} being the molar volume. Figure 7.31 shows results of the linear thermal expansion coefficients along the three principal crystal axes of the superconductors β''-$(ET)_2SF_5CH_2CF_2SO_3$, κ-$(D_8$-$ET)_2Cu(NCS)_2$ and κ-$(ET)_2Cu[N(CN)_2]Br$. In all three cases, the uniaxial expansion coefficients are strongly anisotropic with striking similarities in the α_i's for the β'' and κ-$(ET)_2Cu(NCS)_2$ salts.

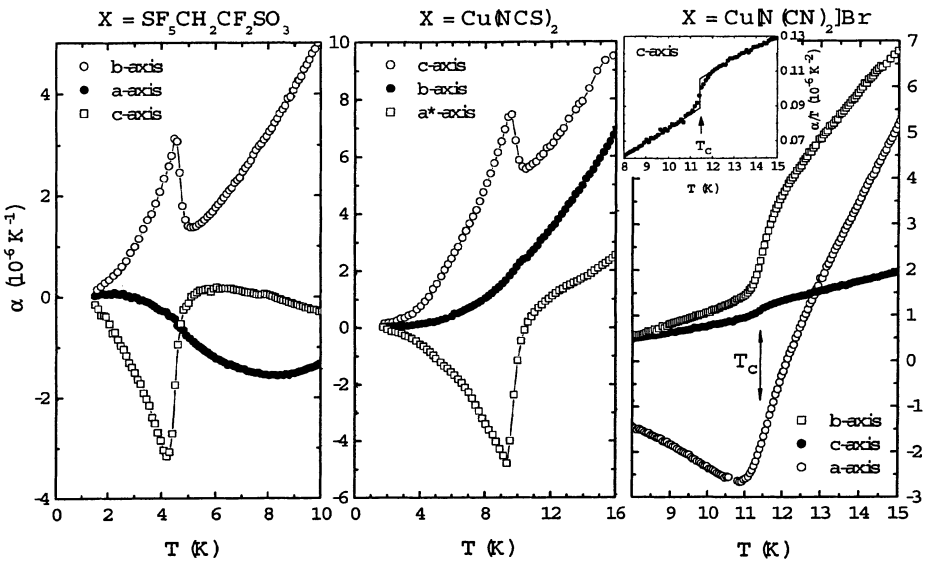

Fig. 7.31. Uniaxial coefficients of thermal expansion, α_i, vs temperature around the superconducting transition for $(ET)_2X$ with $X = SF_5CH_2CF_2SO_3$ (left), $Cu(NCS)_2$ (middle) and $Cu[N(CN)_2]Br$ (right panel), taken from [97, 151, 187]. Open squares indicate α data perpendicular to the planes; open and closed circles correspond to the in–plane expansion coefficients

Using equation (7.13), the uniaxial–pressure coefficients can be derived [97,151]. For κ-$(ET)_2Cu[N(CN)_2]Br$ one finds $\partial T_c/\partial p_b = -(1.26\pm0.25)$ K/kbar for the out–of–plane coefficient and $\partial T_c/\partial p_a = -(1.16 \pm 0.2)$ K/kbar and $\partial T_c/\partial p_c = -(0.12 \pm 0.05)$ K/kbar for the in–plane coefficients, employing a jump height in the specific heat ΔC as reported by [267]. In the same way, one obtains for β''-$(ET)_2SF_5CH_2CF_2SO_3$ $-(5.9\pm0.25)$ K/kbar along the out–of–plane c–axis and $+(3.9 \pm 0.15)$ K/kbar and $+(0.39 \pm 0.1)$ K/kbar for the in–plane coefficients along the b– and a–axis, respectively, using the ΔC value given in [231]. To check for consistency, the hydrostatic–pressure dependences can be calculated by summing over the uniaxial–pressure coefficients yielding $\partial T_c/\partial p_{hydr} = \sum_i (\partial T_c/\partial p_i) = -(2.54 \pm 0.5)$ K/kbar and $-(1.6 \pm 0.5)$ K/kbar for the κ and the β'' salt, respectively. These values are found to be in good agreement with the results obtained by hydrostatic–pressure experiments, i.e. $-(2.4 \sim 2.8)$ K/kbar for κ-$(ET)_2Cu[N(CN)_2]Br$ [94, 189] and -1.43 K/ kbar for β''-$(ET)_2SF_5CH_2CF_2SO_3$ [231]. [10]

[10] Figure 7.31 shows that there is a strikingly similar behavior for the uniaxial thermal expansion coefficients and thus the uniaxial–pressure coefficients of T_c of β''-$(ET)_2SF_5CH_2CF_2SO_3$ and κ-$(D_8\text{-}ET)_2Cu(NCS)_2$. The same observation was made also for the hydrogenated κ-$(H_8\text{-}ET)_2Cu(NCS)_2$ compound [187,230].

An obvious step towards a microscopic understanding of this class of superconductors is to trace out those uniaxial–pressure effects which are common to all systems and thus reflect a generic property. Such information would provide a most useful check of theoretical models attempting to explain superconductivity and its interrelation with the various other instabilities in the pressure–temperature plane. As Fig. 7.31 demonstrates, an extraordinarily large negative uniaxial–pressure coefficient of T_c for uniaxial pressure perpendicular to the conducting planes is common to all three superconductors shown there. Apparently, it is this huge component which predominates the large response of T_c under hydrostatic pressure. On the other hand, and in contrast to what has been frequently assumed, the systems behave quite non–uniformly concerning the in–plane pressure effects. While for κ-$(ET)_2Cu(NCS)_2$ the in–plane pressure coefficients of T_c are either vanishingly small or positive, they are both negative for the related κ-$(ET)_2Cu[N(CN)_2]Br$ system [97].

The above finding of a large negative uniaxial–pressure coefficient of T_c for pressure perpendicular to the planes as the only universal feature common to the κ-$(ET)_2X$ family is supported by results on the related κ-$(ET)_2I_3$ salt, see [233]. [11]

As has been discussed in [9], a large cross–plane pressure effect on T_c may arise from several factors: (i) Pressure–induced changes in the interlayer interaction. This effect includes changes of both the interlayer coupling, i.e. the degree of two–dimensionality, as well as changes in the electron–electron and electron–phonon coupling constants and (ii) changes in the phonon frequencies. Likewise, changes in the vibrational properties could be of relevance for the intraplane–pressure effects on T_c. In addition, in–plane stress effectively modifies the electronic degrees of freedom by changing the transfer integrals between the HOMO's of the nearest–neighbour ET molecules. Most remarkably, for some compounds like κ-$(ET)_2Cu(NCS)_2$ the in–plane–stress effect is either positive or zero. This makes a purely density–of–states effect account for the pressure–induced T_c shifts very unlikely: pressure–induced changes in the density–of–states should be strongest for in–plane stress owing to the quasi–2D electronic band structure. According to the simple BCS

Due to the lack of specific heat data for the deuterated salt, the uniaxial–pressure coefficients of κ-$(ET)_2Cu(NCS)_2$ can only be discussed qualitatively. According to a recent comparative study on the pressure dependences of the normal– and superconducting–state properties of hydrogenated and deuterated κ-$(ET)_2Cu(NCS)_2$, the latter compound reveals an even stronger pressure dependence of T_c [232].

[11] A different situation is encountered for the α-$(ET)_2MHg(SCN)_4$ salt, where uniaxial pressure perpendicular to the planes is found to either induce superconductivity by suppressing an ambient–pressure density–wave ground state for M = K, or enhance T_c for $M = NH_4$ [187, 226]. This behavior is most likely related to the exceptionally thick anion layers specific to this compound resulting in a strong decoupling of the conducting layers.

relation [234]

$$T_c = 1.13\,\Theta_D \exp(-\frac{1}{\lambda}) \quad \text{with} \quad \lambda = \frac{N(E_F)\langle I^2\rangle}{M\bar{\omega}^2}, \tag{7.14}$$

where Θ_D denotes the Debye temperature, $\langle I^2\rangle$ the electron–phonon matrix element averaged over the Fermi surface, M the ionic mass and $\bar{\omega}$ an average phonon energy, an in–plane–stress–induced increase in the π–orbital overlap, i.e. a reduced density–of–states at the Fermi level $N(E_F)$ is expected to cause a reduction of T_c. This is in contrast to the experimental observations.

An important piece of information contained in the above uniaxial–pressure results is that there is *no* uniform behavior in the intralayer–pressure effects on T_c for the various $(ET)_2X$ superconductors. It is especially the results on κ-$(ET)_2Cu(NCS)_2$ which show that in–plane pressure can even cause an increase of T_c [151,228]. This is in contrast to what has been assumed in the 2D electronic models discussed in [235,236]. In addition, the studies revealed a predominant effect of uniaxial pressure perpendicular to the planes clearly demonstrating that attempts to model the pressure–temperature phase diagrams by solely considering *in–plane* electronic degrees of freedom are inappropriate, see also [237].

Isotope substitution

Studying the effect of isotope substitutions on the superconducting transition temperature is one of the key experiments to illuminate the role of phonons in the pairing mechanism. For elementary superconductors, the observation of a $M^{-1/2}$ dependence of T_c where M is the isotopic mass, provided convincing evidence that the attractive interaction between the electrons of a Cooper pair is mediated by the exchange of lattice deformations, i.e. by phonons.

For the κ–phase $(ET)_2X$ compounds, the mass–isotope effect on T_c has been intensively studied, see [5], including isotope substitutions in both the ET donor molecule as well as the charge compensating anions. A most comprehensive study has been performed by the Argonne group on κ-$(ET)_2Cu(NCS)_2$ where overall seven isotopically labelled BEDT–TTF derivatives – with partial substitutions of ^{13}S, ^{34}C and ^{2}D – as well as isotopically labelled anions $[Cu(^{15}N^{13}CS)_2]^-$ have been used [127]. As will be discussed below in section 7.4.5, these studies revealed a genuine mass–isotope effect on T_c.

An "inverse" isotope effect on T_c has been observed for κ-$(ET)_2Cu(NCS)_2$ where T_c of deuterated samples κ-$(D_8$-$ET)_2Cu(NCS)_2$ was found to be higher than that of hydrogenated salts, see [5]. This effect has been confirmed and quantified by the above mentioned study where particular care has been taken to guarantee otherwise comparable quality of both the labelled and unlabelled crystals [127]. The physical reason for the inverse isotope effect is still unclear. A geometric H-D isotope effect has also been found for two other $(ET)_2X$ compounds κ_L-$(ET)_2Ag(CF_3)_4$(solvent) and β''-$(ET)_2SF_5CH_2CF_2SO_3$ having different packing motifs and anion structures. Although the T_c values vary considerably among these salts ranging from 2.9 K to 9.2 K the investigations reveal an almost identical "universal" shift of T_c of $\Delta T_c = +(0.26 \pm 0.06)$ K

[238, 239]. Taking into account the results of thermal expansion and X–ray studies of the lattice parameters [151, 240], it has been proposed that the inverse isotope effect is not directly related to the pairing mechanism. Instead it has been attributed to a geometrical isotope effect, i.e. changes in the internal chemical pressure: provided that the interlayer lattice parameter is identical for both compounds, the effectively shorter C–D bond of the deuterated salt [241] corresponds to a higher chemical pressure perpendicular to the planes for the hydrogenated salt. The negative values of $\partial T_c/\partial p_\perp$ then result in a higher T_c for the deuterated compound [238, 239], see also [187].

An alternative explanation has been proposed recently by Biggs *et al.* based on their measurements of the Shubnikov–de Haas effect focusing on pressure–induced changes of the Fermi–surface topology of deuterated and protonated κ-$(ET)_2Cu(NCS)_2$ [232]. It has been suggested that the superconducting mechanism is most sensitively influenced by the exact topology of the Fermi surface. Since the latter has been found to change more drastically with pressure in the deuterated salt, this effect might also be responsible for the inverse isotope effect [232]. In addition from recent millimeter–wave magnetoconductivity experiments it has been inferred that the quasi–one–dimensional FS sheets (see Fig. 7.7) are more corrugated in the deuterated salt (higher T_c) suggesting that the "nestability" of the FS may be important for T_c [242].

7.4.2 Superconducting Parameters

$(TMTSF)_2X$ salts

As a consequence of the highly anisotropic electronic structure, strong directional dependences are also expected for the superconducting–state properties such as the lower and upper critical fields. Among the $(TMTSF)_2X$ salts, the latter have been extensively studied for the ambient–pressure superconductor X = ClO_4, see [5, 33] and, more recently, also for pressurised $(TMTSF)_2PF_6$, see also section 7.4.5 below. For $(TMTSF)_2ClO_4$ the Meissner and diamagnetic shielding effects have been examined for magnetic fields aligned along the three principal axes [243]. From these experiments the lower critical field values B_{c_1} (at 50 mK) have been determined to 0.2, 1 and 10 (in units of 10^{-4} T) along the *a*–, *b*– and *c*–axis, respectively. The thermodynamic critical field, as estimated from the condensation energy, amounts to $B_{c_{th}} = (44 \pm 2) \cdot 10^{-4}$ T [244]. Figure 7.32 shows the temperature dependence of the upper critical fields, $B_{c_2}(T)$, for $(TMTSF)_2ClO_4$ as determined by early resistivity measurements [245]. The $B_{c_2}(0)$ values of 2.8 T, 2.1 T and 0.16 T for the *a*–, *b*– and *c*–axis, respectively, have been obtained from the data of Fig. 7.32 by an extrapolation to zero temperature. The so–derived value for fields aligned parallel to the *a*–axis, where B_{c_2} is the largest, is close to the Pauli limiting field B_P which is the critical value required to break spin–singlet (S = 0) Cooper pairs. For a non–interacting electron gas this is

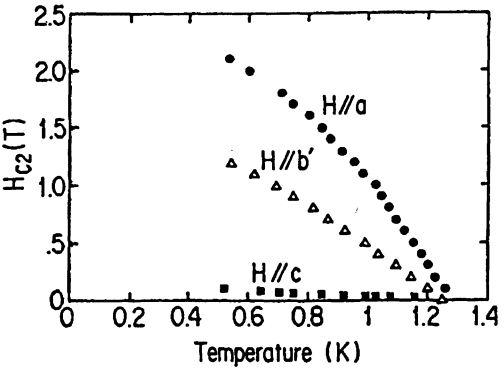

Fig. 7.32. Upper critical fields B_{c_2} determined from resistivity measurements as a function of temperature for $(TMTSF)_2ClO_4$ for the three principal crystal axes [245]

the case when the Zeeman energy just equals the condensation energy, i.e.

$$B_P = \Delta_0 \frac{1}{\sqrt{2}\mu_B}, \tag{7.15}$$

where μ_B denotes the Bohr magneton [246,247]. Assuming a BCS ratio for the energy gap $\Delta_0 = 1.76\, k_B T_c$ yields B_P (in Tesla) $= 1.84 \times T_c$ (in K) $= 2.3$ T for $(TMTSF)_2ClO_4$. The fairly good coincidence with the experimentally derived critical field has been taken as an indication for a spin–singlet pairing state [245,248,249]. As will be discussed in more detail in section 7.4.5, more recent resistivity measurements on the pressurized X = PF_6 salt down to lower temperatures revealed upper critical field curves which show an upward curvature for $T \rightarrow 0$ with no sign of saturation down to 0.1 K [250]. It has been argued in [250] that this unusual enhancement of B_{c_2} which exceeds the Pauli paramagnetic limit by a factor of 4 is strongly suggestive of a spin–triplet (S=1) pairing state.

Yet from the initial slopes of the upper critical field curves in Fig. 7.32, $B_{c_2}^{i'}$, the Ginzburg–Landau coherence lengths $\xi_i(0)$ can be derived using the following relation: $B_{c_2}^{i'} = \phi_0/(2\pi\xi_j\xi_k T_c)$, where i, j and k can be a, b and c [203,204]. The so–derived ξ_c value of about 20 Å being much smaller than the numbers for the a– and b–axis coherence lengths of 700 Å and 335 Å respectively, but comparable to the lattice parameter $c = 13.5$ Å indicates that superconductivity has, in fact, a more quasi–2D character. For the London penetration depth for B parallel to the a–axis, the axis of highest conductivity, a value of $\bar{\lambda} = 40\,\mu$m has been reported [251]. This number exceeds the GL coherence lengths by orders of magnitude indicating that the present system is an extreme type–II superconductor.

$(BEDT–TTF)_2X$ and $(BEDT–TSF)_2X$ salts

Due to the strong effects of fluctuations in these superconductors of reduced

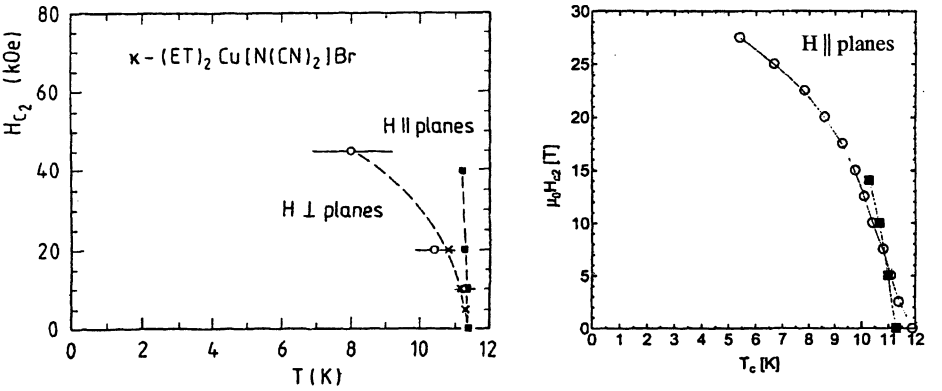

Fig. 7.33. Upper critical fields of κ-$(ET)_2Cu[N(CN)_2]Br$. Left panel: anisotropy of B_{c_2} as a function of temperature as determined from dc–magnetization measurements, taken from [205]. Right panel: $B_{c_2}(T)$ for fields aligned parallel to the conducting planes as determined from resistivity measurements using different criteria (closed and open symbols), reproduced from [252]

dimensionality, an accurate determination of the upper critical fields is difficult and in many cases not free of ambiguities. This holds true in particular for resistivity measurements in finite fields aligned perpendicular to the highly conducting planes as phase fluctuations of the order parameter give rise to a resistive state which tends to descend far below the mean–field transition temperature. A more reliable way to determine the upper critical fields is provided by measuring thermodynamic properties and employing a fluctuation analysis as described in section 7.4.1. The left panel of Fig. 7.33 shows B_{c_2} curves for κ-$(ET)_2Cu[N(CN)_2]Br$ as determined from dc–magnetization measurements [9, 205] using equation (7.11), cf. Figs. 7.28 and 7.29. The $B_{c_2}(T)$ curve for B aligned parallel to the highly conducting planes as determined from resistivity measurements are shown in the right panel of Fig. 7.33 over an extended field range. For the layered superconductors with negligible in–plane anisotropy, the expression (7.9) can be used to determine the GL coherence lengths perpendicular and parallel to the conducting planes.

Table 7.2 compiles the B_{c_2} values together with other superconducting parameters for the above BEDT–TTF compounds. For comparison, the table also contains data for the BETS–based system λ-$(BETS)GaCl_4$. As indicated in the table, the transition temperatures reported in the literature show a considerably large variation depending on the method and criterion used to determine T_c. This may partly be related to the fact that the superconducting transition is usually found to be relatively broad. Even for high quality single crystals with an in–plane mean free path of typically $\sim$ 2000 Å [106], the transition can be broadened due to internal strain fields as a consequence of the extraordinarily large pressure dependence of T_c. In addition, the quasi–

Table 7.2. Superconducting–state parameters of two representative κ–phase $(ET)_2X$ salts X = $Cu(NCS)_2$ and $Cu[N(CN)_2]Br$ as well as λ–(BETS)$GaCl_4$.

	κ-$(ET)_2Cu(NCS)_2$	κ-$(ET)_2Cu[N(CN)_2]Br$	λ-$(ET)_2GaCl_4$
T_c	$8.7 \sim 10.4$	$11.0 \sim 11.8$	$5 \sim 6$
$B_{c_2}^{\perp}(0)$ (T) [12]	6	$8 \sim 10$	3
$B_{c_2}^{\parallel}(0)$ (T) [13]	$30 \sim 35$	> 30	12
$B_{c_1}^{\perp}(0)$ (mT) [14]	6.5	3	
$B_{c_1}^{\parallel}(0)$ (mT) [15]	0.2		
$B_{c_{th}}(0)$ (mT) [16]	54	65	
$\xi_{\perp}(0)$ (Å) [17]	$5 \sim 9$	$5 \sim 12$	$9 \sim 14$
$\xi_{\parallel}(0)$ (Å) [18]	$53 \sim 74$	$28 \sim 64$	143
$\xi_{\parallel}(0)$ (Å) [19]	74	60	105
$\lambda_{\perp}(0)$ (μm) [20,21]	$40 \sim 200$	$38 \sim 133$	
$\lambda_{\parallel}(0)$ (Å) [22]	$5100 \sim 20000$	$6500 \sim 15000$	1500
$\kappa_{\parallel}$ [23]	$100 \sim 200$	$200 \sim 300$	107

2D nature of the electronic structure gives rise to pronounced fluctuations which cause a rounding of the transition [10].

According to recent magnetoresistivity studies, the in–plane Fermi surface of λ–(BETS)$GaCl_4$ strongly resembles that of κ-$(ET)_2Cu(NCS)_2$ with the effective masses being almost identical for both compounds [253]. However, the interplane transfer integral of $t_{\perp} \approx 0.21$ meV for the BETS salt is about a factor of 5 larger [253], indicating that λ-(BETS)$GaCl_4$ is more three–dimensional. Figure 7.34 compares the magnetic field–temperature phase di-

[12] [9,253–255]
[13] [252,255–258]
[14] [40,259]
[15] [40]
[16] $B_{c_{th}}(0) = T_c \cdot \sqrt{\frac{\mu_0 \gamma}{2 V_{mol}}}$
[17] [9,40,187,205,253,255,260]
[18] [9,40,205,255,260]
[19] $\xi_{\parallel}(0) = \sqrt{\frac{\phi_0}{2\pi B_{c_2}^{\perp}}}$
[20] $\lambda_{\perp}$ and $\lambda_{\parallel}$ denote the screening of supercurrents flowing perpendicular and parallel to the conducting planes, respectively, and *not* the direction of the magnetic field.
[21] [260–262]
[22] [253,260,262–266]
[23] [9,253]

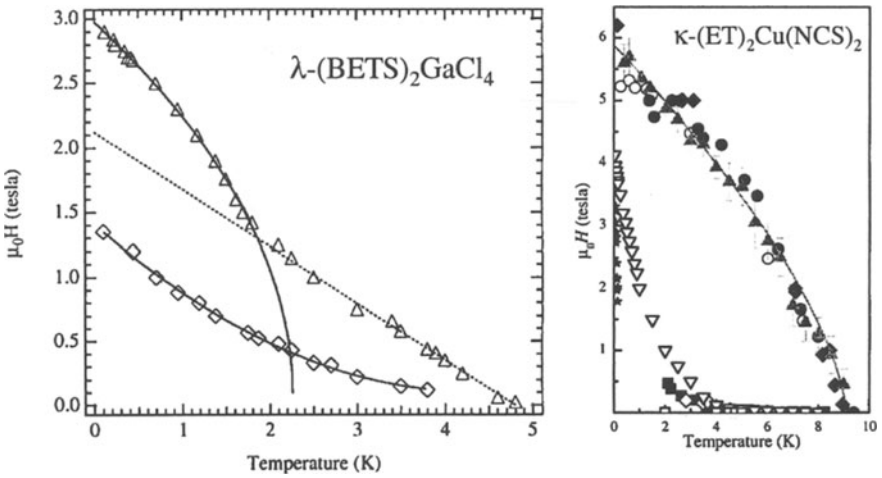

Fig. 7.34. Left panel: Upper critical field for $B \perp$ to the planes (triangles) of λ-(BETS)$GaCl_4$. Upper solid curve is $B_{c_2} \propto (T^* - T)^{1/2}$; the dashed curve $B_{c_2} \propto (T_c - T)$ (see text). Diamonds and the lower solid curve indicate the flux–lattice melting line (see also section 7.4.3). Right panel: $B_{c_2}(T)$ for B $\perp$ to the planes of κ-$(ET)_2Cu(NCS)_2$ as determined from different experimental techniques, see [253]. The solid curve is $B_{c_2} \propto (T_c - T)^{2/3}$ (see text). Also shown are transition and crossover lines in the mixed state, cf. Figs. 7.35 and 7.36 in section 7.4.3 below. Reproduced from [253]

agrams of the above compounds for fields aligned perpendicular to the planes. A dimensional crossover has been suggested to account for the unusual temperature dependence of $B_{c_2}^{\perp}$(T) observed for the BETS–based compound (left panel): B_{c_2}(T) shows a 3D–like linear behavior close to T_c which turns into a power–law dependence characteristic for a 2D superconductor with weakly coupled layers below some crossover temperature labelled as T^* [10,253]. In contrast, B_{c_2}(T) for the κ-$(ET)_2Cu(NCS)_2$ salt follows a $B_{c_2}(T) \propto (T-T_c)^{2/3}$ over the whole temperature range. The additional crossover and transition lines in the mixed state below the $B_{c_2}(T)$ curves indicated in Fig. 7.34 will be discussed in section 7.4.3.

Important information on the spin state of the Cooper pairs can be gained by comparing the experimentally determined $B_{c_2}(T)$ for $T \to 0$ with the Pauli–limiting field, B_P, as defined in equation (7.15). Using this formula, which neglects any orbital effects, and assuming a weak–coupling BCS ratio for the gap, i.e. $\Delta_0 = 1.76\, k_B T_c$, B_P amounts to $\sim$ 18 T and $\sim$ 21 T for κ-$(ET)_2Cu(NCS)_2$ and κ-$(ET)_2Cu[N(CN)_2]Br$, respectively. Apparently, these numbers are significantly smaller than the $B_{c_2}^{\parallel}(0)$ values found experimentally and listed in Table 7.2. On the other hand, clear evidence for a spin–singlet pairing state has been inferred from Knight shift measurements

on κ-$(ET)_2Cu[N(CN)_2]Br$ yielding a vanishingly small spin susceptibility at low temperatures [254]. These deviations might find a natural explanation by recalling that equation (7.15) is valid only in the weak–coupling limit. For a strong–coupling superconductor, on the other hand, the density of states is renormalized leading to a Pauli field which is enhanced by a factor of $(1+\lambda)^{1/2}$ [203,246], where λ denotes the interaction parameter, see equation (7.14). Clear evidence for a strong–coupling type of superconductivity has been found in specific heat experiments on the κ-$(ET)_2Cu[N(CN)_2]Br$ and κ-$(ET)_2Cu(NCS)_2$ salts [50,51,267,268], see section 7.4.5. As an alternative mechanism to account for a $B_{c_2}^{\parallel}(0)$ value in excess of the Pauli field, a transition into a Fulde–Ferrell–Larkin–Ovchinnikov (FFLO) state [269,270] has been proposed [257,271] and discussed controversially, see e.g. [10,272]. In such a scenario, a superconductor with suitable materials parameter adopts a new state at sufficiently high fields where the order parameter is spatially modulated. A more detailed discussion on this issue will be given in section 7.4.3 below.

Besides T_c and the upper critical fields, Table 7.2 contains further superconducting-state parameters such as the lower and the thermodynamic critical fields B_{c_1} and $B_{c_{th}}$, respectively, as well as the GL coherence lengths $\xi_{\parallel,\perp}$ and the London penetration depths $\lambda_{\parallel,\perp}$. B_{c_1} is usually determined by measuring the magnetization as a function of field under isothermal conditions where B_{c_1} corresponds to the field above which flux starts to penetrate the sample. Due to the smallness of B_{c_1}, the plate–like shapes of the crystals and the peculiar pinning properties of these layered superconductors, an accurate determination of B_{c_1} is difficult. A more reliable way to determine $B_{c_1}^{\perp}(0)$ has been proposed by Hagel *et al.* based on a model for thermally activated flux creep yielding $B_{c_1}^{\perp}(0) = (3 \pm 0.5)\,\mathrm{mT}$ for κ-$(ET)_2Cu[N(CN)_2]Br$ [259]. The values for the thermodynamic critical fields, $B_{c_{th}}$, in Table 7.2 are estimated from specific heat results using $B_{c_{th}}(0) = T_c \cdot \sqrt{\mu_0\,\gamma/(2\,V_{\mathrm{mol}})}$ where γ is the Sommerfeld coefficient. These values roughly agree with those calculated from $B_{c_{th}} = B_{c_2}/(\kappa\sqrt{2}) = B_{c_1}\sqrt{2}\kappa/\ln\kappa$, where $\kappa = \lambda/\xi$ is the GL parameter. The large numbers of κ reflect the extreme type–II character of these superconductors.

Also listed in Table 7.2 are values of the magnetic penetration depth λ, the characteristic length over which magnetic fields are attenuated in the superconductor. While the absolute values for λ derived from various experimental techniques are in fair agreement within a factor $4 \sim 5$, no consensus has yet been achieved concerning its temperature dependence, see section 7.4.5 below.

7.4.3 Mixed State

The peculiar material parameters of the present organic superconductors such as the pronounced anisotropy of the electronic states, the small coherence lengths and large magnetic penetration depths give rise to highly anomalous

mixed–state properties and a rich B-T phase diagram in the superconducting state. Exploring the unusual features of extreme type–II layered superconductors continues to be a subject of considerable interest owing to the variety of exciting phenomena that has been found in these materials, see e.g. [273]. Among them is a first–order melting transition of the Abrikosov vortex lattice into a vortex–liquid phase [274,275] not known for usual 3D superconductors. One of the striking early observations related to the anomalous mixed–state properties was the appearance of a so–called irreversibility line, $B_{\rm irr}$, which separates the B-T plane into an extended range $B_{\rm irr} < B < B_{c_2}$ where the magnetization is entirely reversible from a magnetically irreversible state at $B < B_{\rm irr}$. When a layered superconductor is exposed to a magnetic field $B > B_{c_1}$ aligned perpendicular to the planes, the confinement of the screening currents to the superconducting layers results in a segmentation of the flux lines into two–dimensional objects, the so–called vortex pancakes [276]. The coupling between vortex segments of adjacent layers is provided by their magnetic interaction and the Josephson coupling. The latter interaction drives tunnelling currents when two vortex segments are displaced relative to each other. As a result of both effects, the vortex pancakes tend to align thereby forming extended stacks.

A quite different situation arises for fields aligned parallel to the layers. In the limiting case of a quasi–2D superconductor characterized by a cross–plane coherence length $\xi_\perp$ being smaller than the interlayer distance s, the vortex cores slip into the insulating layers where the superconducting order parameter is small. Such a Josephson vortex has an elliptically deformed cross section and lacks a normal core. Since the Josephson screening currents across the insulating layers are very weak, the material is almost transparent for fields parallel to the planes corresponding to a large value for the upper critical field $B_{c_2}^{\parallel}$, cf. Table 7.2. Below we will discuss some of the anomalous mixed–state properties such as the vortex–lattice melting transition, the irreversibility line, the lock–in transition as well as the possible realization of an anomalous high–field state.

Muon spin rotation measurements on the κ-$(ET)_2Cu(NCS)_2$ salt have shown that a 3D flux–line lattice exists only at very low fields $B < 7\,\mathrm{mT}$ [277].[24] Using a decoration technique, Vinnikov *et al.* succeeded in imaging the vortex lattice in the low–field range [278]. Upon increasing the field to above some dimensional crossover field, B_{2D}, the vortex lattices of adjacent layers become effectively decoupled. Theory predicts that the crossover field is related to the anisotropy parameter Γ and the interlayer distance s by $B_{2D} = \phi_0/(\Gamma^2 s^2)$ [273], which for the κ-$(ET)_2Cu(NCS)_2$ salt results in $B_{2D} = 7.3 \sim 30\,\mathrm{mT}$ [277, 279]. An anomalous second peak in magnetization curves indicating a redistribution of pancake vortices at more suitable pinning centers, has been associated with B_{2D} [279, 280]. According to mea-

[24] Here the sample was arranged so that the superconducting planes enclose an angle of 45° in respect to the magnetic field.

surements of the interlayer Josephson–plasma resonance [281], a long–range quasi–2D order among vortices within the individual layers characterizes the state above B_{2D} and persists up to the irreversibility line. In this region of the B-T plane the pancake vortices of adjacent layers become effectively decoupled leading to a pinned quasi–2D vortex solid in each layer with no correlations between the locations of vortices among the layers [282]. A somewhat different point of view is taken in [280,283], where B_{2D} marks the crossover from a 3D flux line lattice below B_{2D} to a state with less strong interlayer coupling on a long range scale above, where a coupling between the layers is, to some extent, still present.

Another striking property common to the present quasi–2D superconductors is an extended vortex–liquid phase above $B_{\rm irr}$. Here the magnetization behaves entirely reversible upon increasing and decreasing the magnetic field, indicating that in this range flux pinning is ineffective. The abrupt onset of magnetic hysteresis at $B \leq B_{\rm irr}$ indicates a drastic increase in the pinning capability. The temperature dependence of the irreversibility field has been studied in detail for κ-$(ET)_2Cu(NCS)_2$ and κ-$(ET)_2Cu[N(CN)_2]Br$ using a variety of techniques including ac–susceptibility [259], dc–magnetization [205], magnetic torque [279,284] or Josephson–plasma–resonance experiments [281]. Figure 7.35 shows on a linear scale the irreversibility line in the B-T phase diagram of κ-$(ET)_2Cu(NCS)_2$ deduced from torque–magnetometry measurements in fields perpendicular to the planes [284]. As demonstrated in the left panel of Fig. 7.35, the irreversibility field at the lowest temperatures lies well below the upper critical field. Thus quantum fluctuations of the vor-

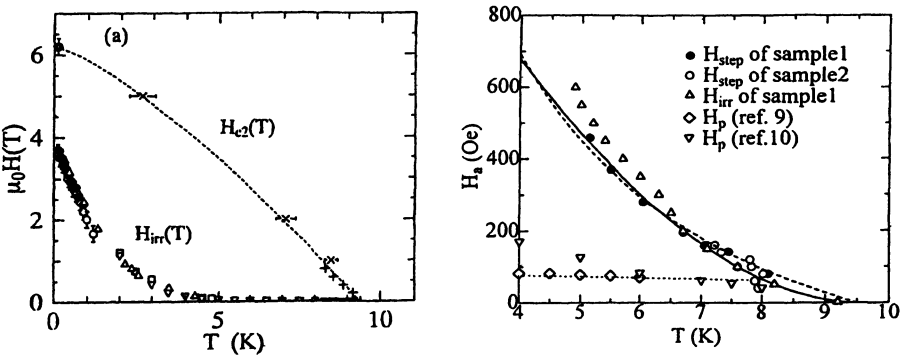

Fig. 7.35. Details of the B-T phase diagram for fields perpendicular to the conducting planes of κ-$(ET)_2Cu(NCS)_2$. Left panel: temperature dependence of the irreversibility field and the upper critical field taken from [284]. Right panel: first–order transition line (open and closed circles) determined by a step in the local induction. Solid and dashed curves represent theoretical predictions for the melting and decoupling transitions, respectively, see text. Open diamonds and down triangles indicate an anomalous second peak in magnetization associated with the dimensional–crossover field B_{2D} of the vortex system, taken from [280]

tices as opposed to thermally driven motions are responsible for the vortex liquid state in this region of the phase diagram [284]. The crossover from quantum to thermal fluctuations manifests itself in the temperature dependence of $B_{\rm irr}(T)$. Below ~ 1 K where quantum fluctuations are predominant, $B_{\rm irr}(T)$ varies linearly with temperature [284], whereas in the thermal fluctuation regime an exponential behavior $B_{\rm irr} = B_0 \exp(-AT/T_c)$ has been observed above the dimensional crossover field B_{2D} in contrast to a power–law behavior in the 3D vortex line lattice region below B_{2D} [205, 279]. A similar behavior has been observed also for κ-$(ET)_2Cu[N(CN)_2]Br$ where the crossover in the temperature dependence of the irreversibility line has been interpreted as a crossover from 2D to 3D pinning [259].

Indications for a first–order phase transition associated with a melting and/or a decoupling of the quasi–2D vortex lattice near the irreversibility line – similar to what has been found in some high–T_c cuprates [274, 275] – have been reported for κ-$(ET)_2Cu(NCS)_2$ [280, 285]. This refers to results from micro Hall–probe experiments where the local induction as a function of temperature at constant fields shows step–like changes. As shown in the right panel of Fig. 7.35 the first–order transition line can be fitted equally well by a melting or a decoupling transition. Steps in the equilibrium and local magnetization have been observed also in SQUID and micro–hall–probe measurements, respectively, for κ-$(ET)_2Cu[N(CN)_2]Br$ [283,286]. In addition, Josephson–plasma–resonance experiments revealed evidence that at the first–order transition, the interlayer coherence becomes lost indicating that the melting and the decoupling occur simultaneously [283].

Figure 7.36 shows in a semi–logarithmic plot the B-T phase diagram for κ-$(ET)_2Cu(NCS)_2$ as proposed by [282]. Note that here the crossover field B_{2D} separating the 3D flux–line lattice from the quasi–2D vortex solid is temperature dependent in contrast to the results shown in Fig. 7.35. A first–order melting transition driven by quantum fluctuations has been inferred from torque–magnetization measurements at very low temperatures [282].

An interesting situation arises when the magnetic field is aligned parallel to the planes enabling the vortices to slip in between the superconducting layers where the order parameter is small. For small tilt angles of the field in respect to the exact alignment, the vortex lattice can gain energy by remaining in this parallel "lock–in" configuration. This new state remains stable until the perpendicular field component, $B_\perp$, exceeds a threshold field at which the energy required to expel $B_\perp$ exceeds that associated with the creation of normal cores in the layers. Evidence for coreless Josephson vortices parallel to the superconducting layers and a lock–in state has been reported from ac–susceptibility measurements for κ-$(ET)_2Cu(NCS)_2$ [261] and from torque magnetometry on κ-$(ET)_2Cu(NCS)_2$ and κ-$(ET)_2Cu[N(CN)_2]Br$ [207, 287], see also [9].

Further interest in the behavior of the present quasi–2D organic superconductors in fields precisely aligned parallel to the planes arose from the

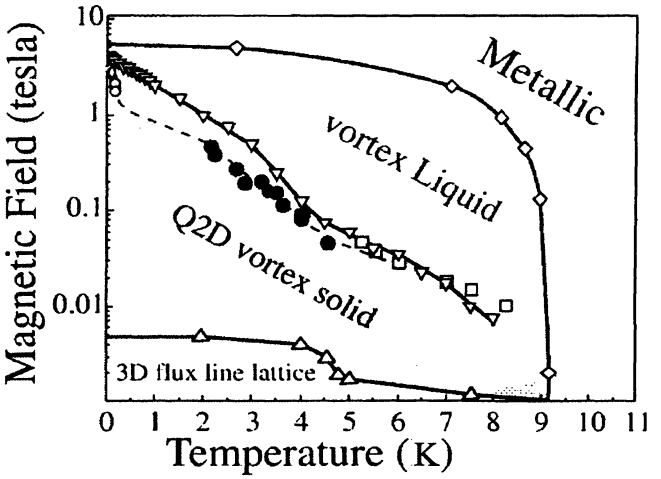

Fig. 7.36. Mixed–state B-T phase diagram for κ-$(ET)_2Cu(NCS)_2$ for B $\perp$ planes in a semi–logarithmic representation. B_{irr} is indicated by down triangles, the dimensional–crossover field by up triangles. Open squares denote a first order decoupling and/or melting transition. Closed and open circles refer to thermal melting or depinning and quantum melting transition from a quasi–2D vortex lattice to a liquid phase, respectively, taken from [282]

proposal that these systems are possible candidates for a Fulde–Ferrell–Larkin–Ovchinnikov (FFLO) state [288]. Under suitable conditions, a spin–singlet superconductor can reduce the pair–breaking effect of a magnetic field by adopting a spatially modulated order–parameter along the field direction [269, 270]. The wavelength of the modulation is of the order of the coherence length which results in a periodic array of nodal planes perpendicular to the vortices [269, 270]. In the case of an anisotropic superconductor, calculations show that the FFLO state might lead to an enhancement of the upper critical field to between 1.5 and 2.5 times the Pauli paramagnetic limit [288, 289].

By studying the magnetic behavior and the resistivity of κ-$(ET)_2Cu(NCS)_2$ in high magnetic fields employing a tuned circuit differential susceptometer, changes in the rigidity of the vortex arrangement at certain fields B_L *within* the superconducting state have been found for fields precisely aligned parallel to the planes [257, 271]. These effects have been interpreted as the manifestation of a phase transition from the superconducting mixed state into an FFLO state.

According to [269, 270], see also [291, 292], the stabilization of a FFLO state requires: (i) a large electronic mean free path $l > \xi_0$, i.e. clean limit, (ii) a Pauli limiting that predominates the orbital pair–breaking effect, (iii) a Zeeman energy that overcompensates the loss of superconducting conden-

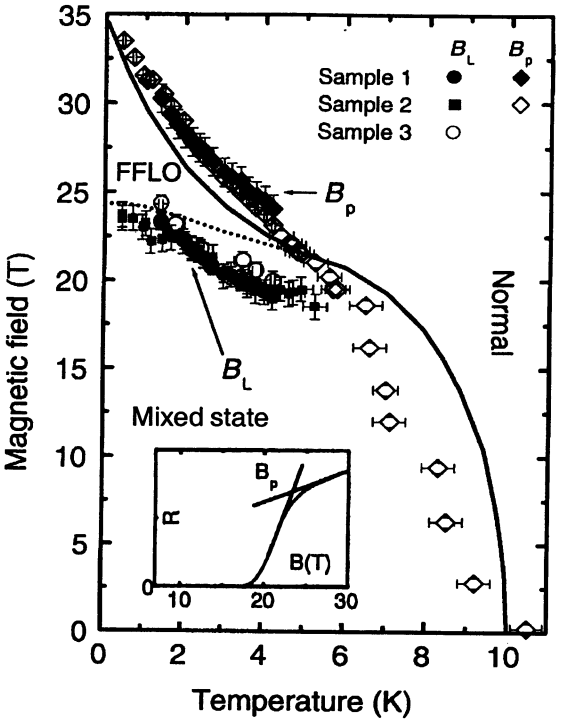

Fig. 7.37. Magnetic field–temperature phase diagram of κ-$(ET)_2Cu(NCS)_2$ for B aligned parallel to the planes compared with the theoretical FFLO phase diagram discussed in [290]. B_P as defined in the inset serves as a rough estimate for B_{c_2}. B_L indicates changes in the rigidity of the vortex arrangement within the superconducting state. Reproduced from [10,257]

sation energy and (iv) a short coherence length (or a large GL parameter $\kappa = \lambda/\xi$). As already discussed in section 7.4.2, the criteria (i) and (iv) are met for the present κ-$(ET)_2X$ salts. Condition (ii) is fulfilled since $H_P = \frac{1}{2}H_c(\pi\chi_{Spin})^{-1/2} \approx 17\,T$ is considerably smaller than the orbital critical field as derived from equation (7.9) taking the values from Table 7.2. To check for condition (iii) one has to compare the Zeemann energy with the condensation energy. Using $\chi_{Spin} = 4 \cdot 10^{-4}$ emu/mol for κ-$(ET)_2Cu(NCS)_2$ [86] and the upper critical field of 35 T yields a Zeeman–energy density of $E_Z = \frac{1}{2}\chi_{Spin}H_{c_2}^2 = 5\,mJ/cm^3$ $(= 5 \cdot 10^4\,erg/cm^3)$, which exceeds the condensation–energy density of $E_c = H_c^2/(8\pi) = \frac{1}{4}\cdot\gamma/V_{mol}\cdot T_c^2 = 1\,mJ/cm^3$ $(= 10^4\,erg/cm^3)$ calculated by employing the experimentally determined Sommerfeld coefficient $\gamma = (23 \pm 1)\,mJ/mol\,K^2$ for κ-$(ET)_2Cu(NCS)_2$ [50,51].

Figure 7.37 shows the temperature dependence of B_L and B_P, the latter serves as a rough estimate of B_{c_2} [257,271], see inset of Fig. 7.37. Comparing the results with theoretical calculations derived for a generic quasi–2D metal

[290] (solid and dotted lines in Fig. 7.37) using the parameter $B_{c_2}(0) = 35\,\mathrm{T}$ yielded a fairly good agreement with the predictions of the FFLO model. In particular, the temperature T^* below which the new state is stabilized was found to meet the theoretical predictions of $T^* = 0.56\,T_c$. However, recent magnetic torque measurements failed to detect any indication for such a transition [282].

7.4.4 Magnetic–Field–Induced Superconductivity

The λ-$(BETS)_2FeCl_4$ systems has attracted strong interest recently owing to the intriguing behavior found when the system is exposed to a magnetic field [293]. With increasing field aligned parallel to the planes, the low–temperature antiferromagnetic insulating state becomes suppressed and vanishes above about 10 T. At higher fields the paramagnetic metallic state which governs the $B = 0\,\mathrm{T}$ behavior above the Néel temperature of about 10 K is restored. For fields aligned exactly parallel to the highly conducting planes, a further increase to above 17 T has been found to induce a superconducting state at low temperatures, see Fig. 7.38. For this field configuration, the orbital effect is strongly suppressed so that superconductivity is limited only by the Zeeman effect, i.e. the Pauli limit, resulting in a high upper critical field. The field–induced superconducting state which is stable up to 41 T has been attributed to the Jaccarino–Peter effect, where the external magnetic field compensates the exchange field of the aligned Fe^{3+} moments [294]. The field–induced superconductivity is suppressed if the magnetic field is tilted from the conducting plane.

In the concentration range $0.35 \leq x \leq 0.5$ of the series λ-$(BETS)_2Fe_xGa_{1-x}Cl_4$ (cf. Fig. 7.26 in section 7.3.5), where superconductivity shares a common phase boundary with an antiferromagnetically ordered insulating state, a field–induced afm insulator–to–superconductor transition has been observed [295]. It has been suggested that the pairing interaction arises from the magnetic fluctuations through the paramagnetic Fe moments [293].

7.4.5 The Superconducting State – Pairing Mechanism and Order–Parameter Symmetry

Understanding the nature of superconductivity in all its variants continues to pose a challenging problem of enormous complexity. Elementary superconductors like Al or Zn are well described by the BCS model [296] which envisages pairing between quasiparticles in a relative zero angular momentum (L=0) and spin–singlet (S=0) state, with an attractive pairing interaction mediated by the exchange of virtual phonons. In the ground state, all electron pairs (Cooper pairs) are in the same quantum–mechanical state described by a single macroscopic wavefunction. Excitations, i.e. the creation of unpaired quasiparticles, require an energy in excess of $2\,\Delta$, where Δ is the energy gap, known as the order parameter. In the BCS model the gap amplitude $\Delta(\boldsymbol{k})$ is

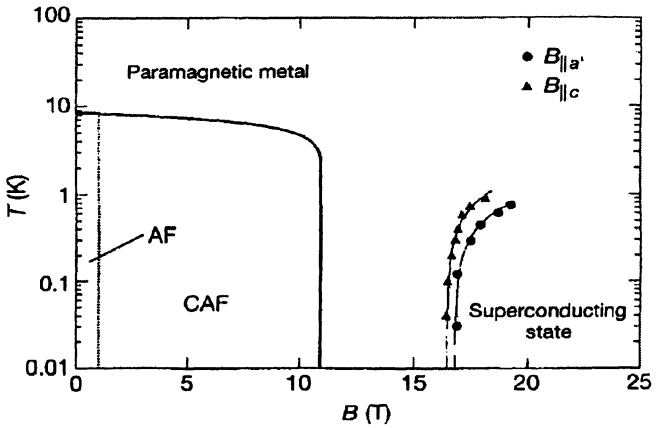

Fig. 7.38. Temperature vs magnetic field phase diagram for λ-$(BETS)_2FeCl_4$ with the magnetic field aligned parallel to the conducting planes. AF and CAF indicate the antiferromagnetic and canted antiferromagnetic phase, respectively (taken from [293])

uniform over the whole Fermi surface. In addition, the following quantitative relations are implied in the BCS model: a universal ratio $\Delta_0/k_BT_c = 1.76$, where Δ_0 is the energy gap at zero temperature, and $\Delta C/\gamma T_c = 1.43$ with ΔC being the jump height in the specific heat at T_c and γ the Sommerfeld coefficient.

In recent decades, novel classes of superconductors have been discovered in complex materials such as heavy–fermion metals [297], cuprates [298], ruthenates [299] and the present organic materials [1]. These systems have properties which are markedly different from those of the simple elements Al or Zn. The differences manifest themselves particularly clearly in the role of electron–electron interactions, which are strong in the new superconductors but of no relevance in the simple metals. The question at hand is whether superconductivity in the new materials is of a fundamentally different type to what is described in the BCS model and proved valid to a good approximation in so many superconductors. As for the present organic materials this question covers the following aspects

(i) Are the superconducting carriers "BCS–type" pairs of electrons that form below T_c (Cooper–pairs)? Or do tightly bound electron pairs preexist already at higher temperatures $T > T_c$ which undergo a Bose–Einstein condensation?

(ii) Is the relevant pairing mechanism different from a conventional phononic mechanism? The exchange of antiferromagnetic spin fluctuations as one of the models discussed for the high–T_c cuprates and also for the present organic materials is an example for an unconventional pairing interaction.

(iii) Is the symmetry of the order parameter lower than that of the Fermi surface? It is customary to refer to an unconventional superconducting state as one where the order parameter breaks at least one of the crystal symmetries.
(iv) Is the spin part of the superconducting pair wavefunction an antisymmetric singlet or a symmetric triplet state?

Although a local pairing scheme as distinguished from the BCS–type pairing has been discussed also for the present organic systems [300,301], the bulk of experimental observations do not support such a scenario. Rather the formation of Cooper–pairs below T_c implying an energy gap Δ with a maximum at $T = 0$ that vanishes for $T \geq T_c$ has been widely established, see e.g. [9].

The discussion of the above issues (ii)–(iv) in the context of the organic superconductors is complicated by the fact that even for the most fundamental properties contradictory experimental evidences exist. Since some of these discrepancies might simply reflect extrinsic effects as a consequence of an incomplete sample characterization, we shall therefore concentrate the discussion on those materials which are best characterized and where most data are available. These are the κ-phase $(ET)_2X$ and the $(TMTSF)_2X$ salts.

On the nature of the superconducting state

The central question for the present organic superconductors concerns the nature of the pairing interaction. The excitonic mechanism proposed by Little [3,302] for certain quasi–1D organic polymers was of great importance historically in giving the initial impetus to the development of the field. From today's perspective, however, it is fair to say that the search for materials with suitable chemical and physical properties for such a mechanism to work has been unsuccessful so far.

In the discussion of the transport and optical properties in section 7.3.2 it became clear that there is a substantial coupling of the charge carriers to both intra– as well as intermolecular phonons. Consequently, some researchers in the field believe in a conventional electron–phonon coupling mechanism. On the other hand, the fact that for the present materials – as for the cuprates and heavy–fermion systems – the superconducting region in the phase diagram lies next to a magnetically ordered state suggests that magnetic interactions are involved in the pairing mechanism.

Models considering the role of phonons in the pairing mechanism

One example for a conventional electron–phonon pairing scenario has been discussed by Yamaji [303]. In this model he considers an attractive interaction mediated by several high–frequency internal molecular vibrations in addition to one low–frequency intermolecular phonon.

A more general account for the complex role of phonons for superconductivity has been given by Girlando *et al.* [60,304,305]. By calculating the lattice phonons for the κ-$(ET)_2I_3$ and β-$(ET)_2I_3$ superconductors using the quasi–harmonic–lattice–dynamics method and evaluating the coupling to the electrons, λ, they succeeded in reproducing all available experimental data

related to the phonon dynamics, for example the lattice specific heat. They showed that a lattice mode that couples particularly strongly to the electrons is one in which the relative displacement of the ET molecule is along the long axis of the molecule, i.e. perpendicular to the conducting planes. As an interesting side result of their study on κ-$(ET)_2I_3$, it is mentioned, that the coupling of acoustic phonons is very anisotropic and likely to cause gap anisotropies, though of a conventional type. In addition, it has been shown that the lattice phonons alone cannot account for the T_c values in these compounds. High–frequency intramolecular phonons modulating the on–site electronic energies have to be taken into account to reproduce the critical temperatures [304].

Recently, a distinct kind of phonon–mediated pairing has been suggested for the $(ET)_2X$ salts [306]. It is based on the idea that in a system in which Coulomb correlations are screened to be short range, i.e. Hubbard type, the electron–phonon scattering is dominated by forward processes. This results in an effective small–q pairing potential. Subsequent self–consistent solutions of the BCS gap equation using a band structure based on the effective–dimer approximation, lead to a gap structure where d– and anisotropic s–wave states are nearly degenerate. Furthermore it has been argued that the conflicting experimental results about the gap symmetry may originate in the decorrelation of superconductivity on various parts of the Fermi surface – a consequence of small–q dominated pairing – and the near degeneracy of s– and d–wave superconducting gap states [306].

Models which consider a magnetic interaction

On the other hand, the rich phase diagram and the anomalous properties of the metallic state of these materials may suggest that the key elements dominating the physical behavior are the layered structure and the strong interactions between the electrons [4]. As a consequence, some researchers even resign from considering any coupling to the phonons and instead consider mechanisms which are solely based on two–dimensional electronic interactions. Most of these proposals deal with a spin–fluctuation–mediated pairing mechanism. The latter is motivated by the close proximity of the superconducting region in the phase diagram to an antiferromagnetic insulating state which – in analogy to the high–T_c cuprates – suggests that both phenomena are closely connected to each other [4, 235, 307].

An approach in this direction has been proposed by Kino and Fukuyama [235] who studied the effects of on–site Coulomb interaction and dimer structure in a strictly two–dimensional system within the Hartree–Fock approximation, see also [308]. In their picture, the antiferromagnetic insulating state of κ-$(ET)_2X$ is a Mott insulator. The Mott–Hubbard scenario for the present organic superconductors implies a half–filled conduction band, together with strong electron correlations. Because of the approximate square–lattice configuration of the dimers the authors expect a similar spin–fluctuation medi-

ated superconductivity with probably $d_{x^2-y^2}$ symmetry as in the cuprates [235].

Such a possibility has been studied in detail by Schmalian [307]. Using a two–band Hubbard model to describe the antibonding orbitals on the ET dimer he succeeded in creating a superconducting state with $T_c \simeq 10\,\mathrm{K}$ mediated by short–ranged antiferromagnetic spin fluctuations. It has been argued that despite the frustrating interactions and in–plane anisotropies which distinguish the organic materials from the high–T_c cuprates, the origin of superconductivity is very similar for both material classes [307].

A spin–fluctuation–based superconductivity similar to that of the cuprates has been claimed also by Kondo and Moriya [309–311]. They investigated the properties of a half–filled Hubbard model in a fluctuation exchange approximation (FLEX) with a right–angle isosceles triangular lattice with transfer matrices $-\tau'$ and $-\tau$. They revealed an energy gap of $d_{x^2-y^2}$ symmetry which upon cooling grows much faster compared to that expected in the BCS model. In addition they showed, that the appearance of d–wave superconductivity near an antiferromagnetic instability requires a suitable electronic structure, i.e. $\tau'/\tau > 0.3$ [236, 309, 310].

A spin–fluctuation mediated d–wave superconducting state has been found also by several other approaches including FLEX, perturbation theory or quantum Monte Carlo simulation applied to κ-$(\mathrm{ET})_2\mathrm{X}$ [312–315] or the quasi–one–dimensional $(\mathrm{TM})_2\mathrm{X}$ salts [314, 316]. In [317] and [316] an explanation for the pseudogap behavior at elevated temperatures T^* has been proposed in terms of strong antiferromagnetic spin–fluctuations.

While the starting point of the above models is in the limit of strong correlations, i.e. near the Mott–insulating state, a somewhat different viewpoint is taken in the work by Louati *et al.* [318]. These authors studied the effect of spin fluctuations in a two–dimensional model in the weak correlation regime by varying the bandwidth and the nesting properties of the Fermi surface. They argued that spin fluctuations are enhanced by the good nesting properties which may account for the anomalous NMR relaxation rate observed at temperatures T^* above T_c in the κ-$(\mathrm{ET})_2\mathrm{Cu}[\mathrm{N}(\mathrm{CN})_2]\mathrm{Br}$ salt. Furthermore they found that spin fluctuations can induce a superconducting coupling with d–wave symmetry that lies next to a spin–density–wave instability [318].

The above models address systems at half filling, which is realized in the dimerized κ–phase $(\mathrm{ET})_2\mathrm{X}$ and $(\mathrm{TMTSF})_2\mathrm{X}$ salts, suggesting spin–fluctuation–mediated superconductivity with a $d_{x^2-y^2}$ symmetry. A different scenario has been proposed for the θ and β'' structures [319]. Here the ET molecules are not dimerized which results in a quarter–filled hole band. In this case, a nearby insulating phase is believed to be due to a charge ordering, driven by strong inter–site Coulomb correlations. Applying slave–boson theory to an extended Hubbard model at quarter filling, superconductivity mediated by charge fluctuations has been found. This results in a d_{xy} symmetry of the

superconducting state [319] as opposed to the $d_{x^2-y^2}$ symmetry for the above spin–fluctuation mechanism.

Experiments probing the superconducting state

On the experimental side, the determination of the actual pairing mechanism is a most difficult task as there is no decisive probe to pin down the relevant pairing interaction. There are, however, some crucial experiments which may help to delineate the various possibilities. Investigating the mass–isotope effect on T_c is such a key experiment. Another one is to study the phonon system to probe the role of electron–phonon interactions. If phonons are involved in the pairing interaction this would result in renormalization effects in the temperature dependences of the phonon frequencies and linewidths upon cooling through T_c. Likewise, if a non–phononic mechanism is at work leading to an anisotropic gap with nodes along certain directions on the Fermi surface, a determination of the orientation of the gap zeroes by angular–dependent measurements can provide important information on the pairing mechanism.

For classical phonon–mediated superconductors the gap amplitude $\Delta(\boldsymbol{k})$ is assumed to be isotropic or at least to have an isotropic component combined with a $\boldsymbol{k}$–dependent part which obeys all symmetries of the crystal lattice. In contrast to such a conventional "finite–gap" state, the above mentioned electronic coupling schemes lead to a pairing state with higher angular momentum where $L = 2$ (d–wave) being the most favored one. In this case the amplitude of the Cooper–pair wave function vanishes at the origin of the relative coordinate which keeps the constituent quasiparticles of the Cooper pair apart. Therefore, $L \neq 0$ pairing states are good candidates for materials with strong on–site Coulomb repulsion. The gap–function of such an $L \neq 0$ state has a $\boldsymbol{k}$–dependence which is given by the spherical harmonics of the same angular momentum. For those states where the $\Delta(\boldsymbol{k})$ functions vanish at certain $\boldsymbol{k}$–vectors at the Fermi surface, the quasiparticle excitation spectrum at low energies is markedly different from that of an isotropic finite gap state. For the above d–wave order parameter $\Delta(\boldsymbol{k}) = \Delta_0 (\cos(k_x a) - \cos(k_y b))$ the zero crossings along the diagonals correspond to line nodes at the Fermi surface. This should be reflected in all quantities that depend on the number of thermally excited quasiparticles such as specific heat, NMR relaxation rate, magnetic penetration depth, etc. in the form of simple power–law dependences at sufficiently low temperatures. In contrast, an exponentially weak T–dependence in these quantities characterizes an isotropic non–vanishing order parameter. Thus, careful measurements of the above thermal properties should, in principle, provide a handle on the order–parameter symmetry, or at least permit to discriminate whether gap zeroes exist or not. In this context, it should be noted, however, that the observation of a non–exponential or power–law T–dependence in one of these quantities does not necessarily imply a gap structure with nodes. As an example, we mention gapless superconductivity via pair breaking which destroys an exponential behav-

ior [320,321]. Likewise, a power–law T–dependence could be of conventional origin, as e.g. a T^3 dependence in the specific heat for $0.2\,T_c < T < T_c$ which has been attributed to strong–coupling effects [322,323].

To our knowledge, the only example where a non–phononic mechanism has been clearly identified is the heavy–fermion superconductor UPd_2Al_3. Here, the combination of tunnel spectroscopy [324] and neutron scattering experiments [325] has provided sound evidence for a magnetic pairing interaction, i.e. the exchange of magnetic excitons.

Although numerous experiments have been devoted to the issue of the order parameter symmetry for the organic materials, no consensus has yet been achieved. It is fair to say that for the present systems direct evidence for a non–phononic mechanism such as the one mentioned above does not exist. Also phase–sensitive experiments as those applied successfully to the high–T_c cuprates [326,327] have not been performed so far for the organic materials.

In what follows we shall give a discussion of a selection of experimental results on the pairing mechanism and the symmetry of the order parameter. To begin with we shall focus on the $(ET)_2X$ salts.

Experiments on the pairing mechanism:
Isotope effect and electron–phonon coupling

The effect of isotope substitution has been studied for various members of the $(ET)_2X$ superconductors. Isotopes have been substituted in the ET molecule by replacing ^1H by ^2D in the ethylene endgroups, by a partial exchange of ^{12}C by ^{13}C or ^{32}S by ^{34}S atoms in the inner skeleton of the molecule. In addition, systems have been studied where the acceptor molecule has been isotopically labelled. First experiments focused on the role of the electron–molecular–vibration (EMV) coupling by substituting ^{13}C for ^{12}C in the central double bond of the ET molecule. The large decrease of T_c of $\Delta T_c/T_c = -2.5\,\%$ found for the high–temperature variant (β_H) of β-$(ET)_2I_3$ by the Orsay group [328] could not be reproduced by a subsequent study where no systematic decrease of T_c could be detected [329]. Most intensive studies on the isotope effect have been carried out on the κ-$(ET)_2Cu(NCS)_2$ salt by the Argonne group [127]. Their investigations include isotope substitutions on both the BEDT–TTF molecules (all together seven differently labelled BEDT–TTF derivatives) as well as the anions. In each case, a batch of unlabelled samples has been synthesized under strictly parallel experimental conditions. These crystals serve as a reference for comparison. By sampling a large number of crystals, typically eight or more of both labelled and unlabelled material, a genuine mass–isotope effect on T_c has been found: upon replacing all eight sulfur atoms by ^{34}S and the outer–ring–carbon atoms of the $[(CH_2)_2]$ endgroups by ^{13}C, which corresponds to a 5 % increase of the ET molecule's mass, a shift of $\Delta T_c = -(0.12 \pm 0.08)\,K$ has been observed. Assuming a BCS–like mass–isotope effect $T_c \propto M^{-\alpha}$ with the whole ET molecule as the relevant mass entity M, this shift corresponds to $\alpha = 0.26 \pm 0.11$. This experiment

provides clear evidence that the *inter*molecular (lattice) phonon modes are strongly involved in the pairing mechanism. On the other hand, the same group demonstrated the absence of a comparable isotope effect on T_c for κ-$(ET)_2Cu(NCS)_2$ and κ-$(ET)_2Cu[N(CN)_2]Br$ upon a partial substitution of the central C=C and also a simultaneous replacement of both the central and ring C=C atoms. The same holds true for a substitution of the eight sulfur atoms, see [127] and references therein. These results indicate that the *intra*molecular C=C and C–S bond–stretching vibrational modes of the ET molecule do not provide a substantial contribution to the Cooper pairing.

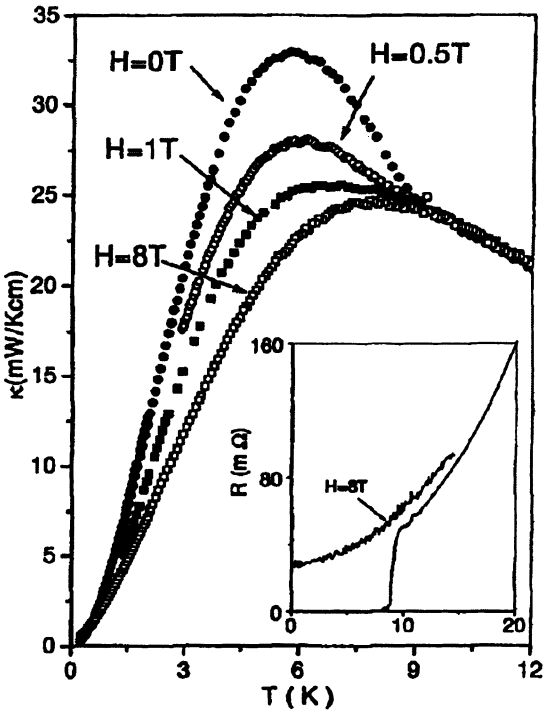

Fig. 7.39. Temperature dependence of the thermal conductivity of κ-$(ET)_2Cu(NCS)_2$ for B applied perpendicular to the planes. Inset: temperature dependence of the resistance, taken from [61]

Further indications for a strong electron–phonon coupling have been inferred from measurements of the thermal conductivity on κ-$(ET)_2Cu(NCS)_2$ and κ-$(ET)_2Cu[N(CN)_2]Br$ [51, 61, 62]. As shown in Fig. 7.39, the thermal conductivity $\kappa(T)$ of κ-$(ET)_2Cu(NCS)_2$ exhibits an upturn at the onset of superconductivity followed by a pronounced maximum just below T_c. It has been convincingly argued by the authors that the enhancement of $\kappa(T)$ in the

superconducting state is a consequence of the condensation of electrons into Cooper pairs which strengthens the heat transport by freezing out the scattering of the main heat carriers, the phonons. By employing the Wiedemann–Franz law it has been found that just above T_c the electronic contribution amounts to only 5 % of the total thermal conductivity [61]. Figure 7.39 also shows $\kappa(T)$ data taken at varying fields applied perpendicular to the conducting planes. In the normal state, a magnetic field of 8 T does not affect the thermal conductivity within the resolution of the experiment but induces a sizeable decrease in the charge conductivity (see inset) which is an additional indication of lattice–dominated thermal conductivity in the vicinity of T_c.

Temperature–dependent Raman scattering studies of the phonon dynamics of κ-$(ET)_2Cu(NCS)_2$ and κ-$(ET)_2Cu[N(CN)_2]Br$ substantiate the strong coupling of the superconducting charge carriers to intermolecular phonons [55–60]. The observed anomalous temperature dependence of the low–frequency phonons around and below T_c were found to be consistent with an isotropic gap $2\Delta_0$ close to 2.8 meV [59]. From the reported frequency shifts the electron–phonon coupling constants λ_i have been calculated yielding a total coupling constant of $\lambda_{tot} = 0.97 \pm 0.11$ [59].

Superconductivity–induced phonon renormalization

As a consequence of the interaction of charge carriers with the phonon system, the opening of a gap in the electronic density of states below T_c induces changes in the phonon frequencies and linewidths. These effects were first observed in the classical superconductors Nb_3Sn and Nb [330,331]. The results of these studies support the generally accepted picture that superconductivity in these materials is phonon–mediated. Inelastic neutron–scattering experiments have been performed on single crystals of κ-$(ET)_2Cu(NCS)_2$ on both hydrogenated and deuterated crystals [63,332]. Due to the extraordinarily large incoherent crosssection of the protons, the study of κ-$(H_8$-$ET)_2Cu(NCS)_2$ allows for a selective investigation of those vibrational modes that involve the hydrogen atoms at the terminal ethylene groups. The analysis of measurements above and below T_c suggest a substantial coupling of these modes to the superconducting charge carriers [332]. Figure 7.40 shows the results of inelastic neutron–scattering experiments on deuterated κ-$(ET)_2Cu(NCS)_2$ carried out by Pintschovius *et al.* [63]. The data reveal a sudden increase of the frequencies of transverse acoustic phonons upon cooling through T_c. This phonon hardening was found to be most pronounced for the wave vector $\boldsymbol{q} = (-0.225, 0, 0.45)$ and a phonon energy 2.4 meV. As discussed by Zeyher and Zwicknagl [333], significant changes are expected only for those phonons whose energy $\hbar\omega$ is close to the gap value 2Δ with a softening (hardening) for $\hbar\omega < 2\Delta$ ($\hbar\omega > 2\Delta$) [333]. The above results thus imply $2\Delta \simeq 2.4$ meV, i.e. $2\Delta/k_BT_c \simeq 3.1$, which is close to the BCS ratio of 3.52. The salient feature of this study is that intermolecular modes strongly couple to the superconducting charge carriers and may thus provide a substantial contribution to the pairing interaction [63].

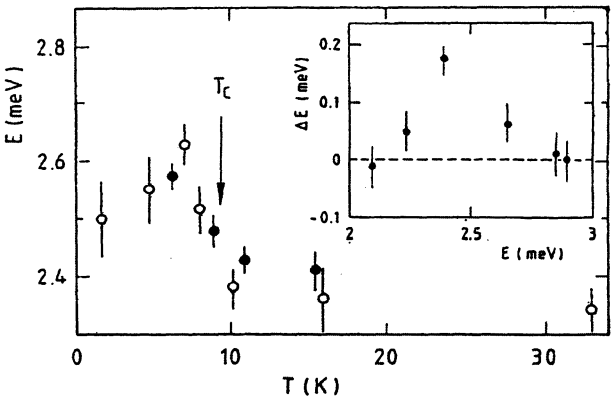

Fig. 7.40. Temperature dependence of the energy of the transverse acoustic phonon with wave vector $q = (-0.225, 0, 0.45)$ derived from inelastic neutron scattering on two different single crystals (open and closed circles) of deuterated κ-$(ET)_2Cu(NCS)_2$. Inset: observed frequency shifts $[\Delta E = E(T < T_c) - E(T > T_c)]$ of transverse acoustic phonons in the $[-\zeta, 0, 2\zeta]$ direction, reproduced from [63]

On the order–parameter symmetry in (BEDT-TTF)$_2$X: Measurements of the gap anisotropy

A new development in the investigation of the order–parameter symmetry is to probe the gap anisotropy directly by using orientational–dependent measurements. For the present organic superconductors, these techniques include mm–wave transmission [334], STM spectroscopy [335] and thermal conductivity [62] studies.

A *mm–wave magneto–optical technique* was used to determine the angle dependence of the high–frequency conductivity of κ-$(ET)_2Cu(NCS)_2$ [334, 336]. The results have been interpreted to support an anisotropic gap with "X shape", i.e. with nodes along the *b*– and *c*–direction [334], consistent with a $d_{x^2-y^2}$ symmetry of the order parameter as theoretically suggested by Schmalian [307]. However, these results have been critically commented upon by other groups [337, 338].

The superconducting gap structure of the same compound has been investigated using *STM spectroscopy* by Arai *et al.* [335]. The tunneling curves observed on the *bc*–plane (parallel to the conducting layers) in the low–energy region could be well fitted by a *d*–wave gap model. The corresponding $2\Delta_0/k_BT_c$ ratio was found to be 6.7 which is smaller than a previously reported value of 9 [339] but substantially larger than the BCS value of 3.52. In addition, the in–plane gap anisotropy was investigated, see Fig. 7.41. The dI/dV-V curves observed on the lateral surfaces were found to be also consistent with a *d*–wave gap. For this configuration a very large $2\Delta_0/k_BT_c$ ratio of 8.7 $\sim$ 12.9 has been obtained. The analysis of the angular dependence revealed that the direction of the line nodes of the gap is $\pi/4$ from the k_b–

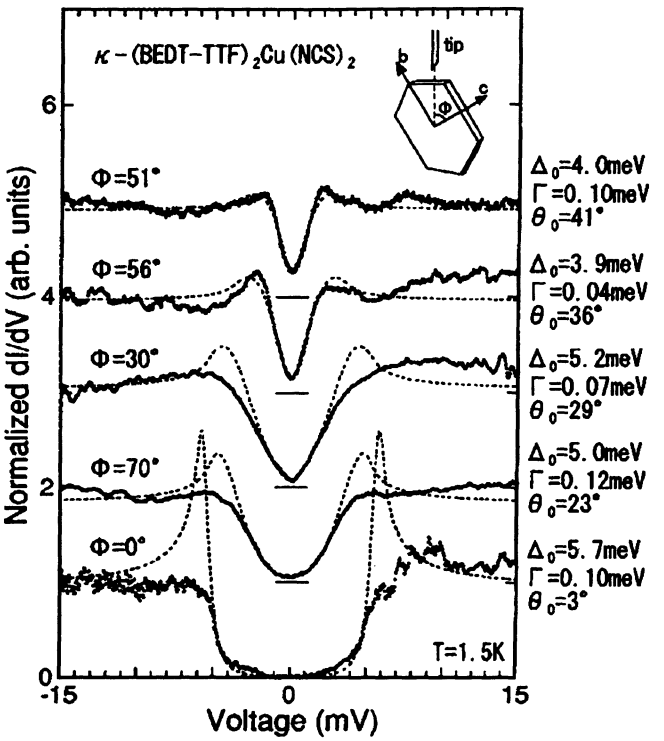

Fig. 7.41. dI/dV-V curves taken at 1.5 K on the lateral surfaces of κ-$(ET)_2Cu(NCS)_2$ single crystals. Data have been taken along various tunneling directions at different angles ϕ as defined in the inset. The dashed line represents the calculated curve based on the d–wave gap model with a $\boldsymbol{k}$ dependent tunneling, taken from [335]

and k_c–axes, i.e. the gap has $d_{x^2-y^2}$ symmetry [335]. It has been noted that these orientations of the gap nodes are at variance with those inferred from the above mm–wave–transmission experiments.

The *thermal conductivity* has been used as another directional–dependent probe. When compared to STM measurements, for example, this quantity has the advantage that it is free of surface effects. The implications of the symmetry of gap zeroes on the thermal conductivity in the vortex state have been theoretically investigated by various authors, see e.g. Won and Maki [340]. Measurements have been performed for the κ-$(ET)_2Cu(NCS)_2$ salt in a magnetic field rotating within the 2D superconducting plane. Figure 7.42 shows the angular variation of κ at a fixed field of $B = 2\,\mathrm{T}$. Θ denotes the angle between the heat current flowing along the crystallographic b direction and the magnetic field, i.e. $\Theta = 0°$ for $B \parallel b$. The salient result of this study is the occurrence of a $\kappa(\theta)$ contribution with a fourfold symmetry, $\kappa_{4\theta}$, at

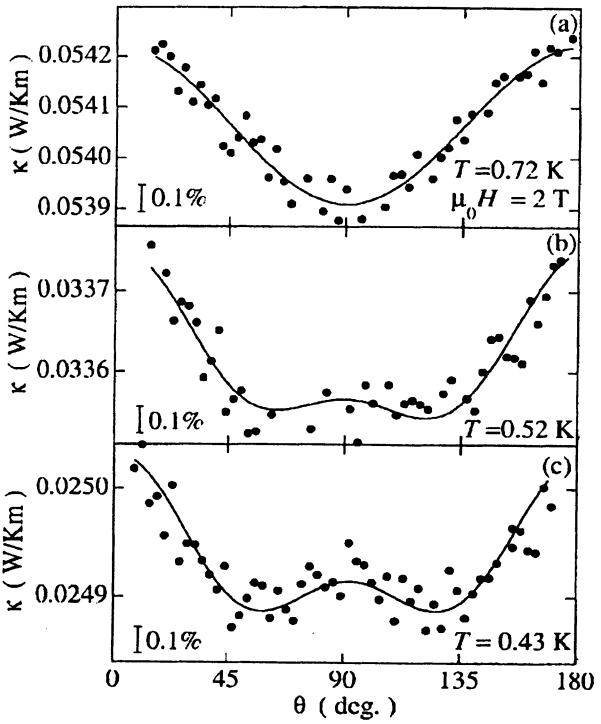

Fig. 7.42. Angular variation of $\kappa(B,\Theta)$ at 2 T for different temperatures where Θ denotes the angle between a rotating magnetic field in respect to the heat current flowing along the b–axis of the κ-$(ET)_2Cu(NCS)_2$ crystal. The solid lines represent the results of a fit using the function $\kappa(B,\Theta) = C_0 + C_{2\Theta}\cos 2\Theta + C_{4\Theta}\cos 4\Theta$, where C_0, $C_{2\Theta}$ and $C_{4\Theta}$ are constants, taken from [62]

low temperatures $T \leq 0.52\,K$ that adds to a predominant term with twofold symmetry. While the latter has been interpreted as being mainly phononic in origin, it is argued that the former is of a purely electronic nature and reflects the nodal gap structure [62]. Their analysis revealed that the gap zeroes are oriented along the directions rotated by 45° relative to the b– and c–axes. It has been pointed out in [62] that this nodal structure is inconsistent with the theories based on antiferromagnetic spin fluctuation where the nodes are expected to be along the b– and c–directions. Based on this observation Izawa *et al.* proposed a d_{xy} symmetry (referring to the magnetic Brillouin zone, see inset of Fig. 1 in [62]) which has been theoretically suggested for a charge–fluctuation scenario [319,341].

NMR measurements

A more indirect information on the symmetry of the superconducting order parameter is provided by temperature–dependent measurements of quantities

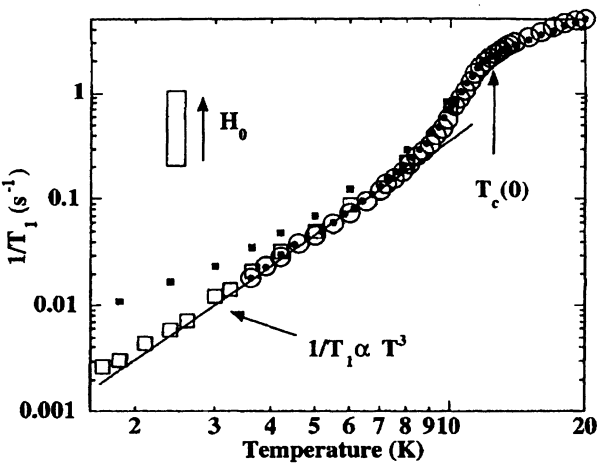

Fig. 7.43. Spin–lattice–relaxation rate $(T_1)^{-1}$ at fields of 5.6 T (open circles), 7.8 T (black circles) and 7 T (open squares) applied parallel to the conducting planes of κ-$(ET)_2Cu[N(CN)_2]Br$. Black squares correspond to a field of 7 T with a small misalignment, taken from [254]

which depend on the quasiparticle excitation spectrum. In this context NMR experiments, i.e. measurements of the Knight shift K_S and the spin–lattice relaxation rate $(T_1)^{-1}$ are of particular interest. The ^{13}C spin–lattice relaxation rate and Knight shift of κ-$(ET)_2Cu[N(CN)_2]Br$ have been investigated by various groups [142, 254, 342] with similar results. In these experiments single crystalline material was used where both ^{12}C atoms in the central carbon double bond of the ET molecule had been replaced by ^{13}C. For the investigation of electronic properties, these nuclei are superior since their coupling to the π–electron system is much stronger than that of the protons in the ethylene endgroups of the ET molecules. The salient results of these studies are: (i) Knight–shift measurements performed in fields aligned parallel to the conducting planes reveal a spin susceptibility that tends to zero at low temperatures. Since any contributions from the pancake vortices have been excluded for this field configuration, the above results have been taken as evidence for the spin–singlet character of the pairing state. (ii) The spin–lattice relaxation rate, $(T_1)^{-1}$, measured in the same parallel field configuration lacks a Hebel–Slichter peak and shows a power–law T^n behavior at low T, with n being close to 3, see Fig. 7.43. For the experimental conditions chosen, the authors ascribed the dominant source of relaxation to the quasiparticle excitations in the superconducting state. Consequently, the power–law temperature dependence in $(T_1)^{-1}$ has been interpreted as indicating an anisotropic pairing with nodes in the gap function [142, 254, 342].

Thermal conductivity

Investigations of the thermal conductivity on quasi–2D organic superconductors at low temperatures have been performed first on κ-$(ET)_2Cu(NCS)_2$ [61] and more recently also on κ-$(ET)_2Cu[N(CN)_2]Br$ [51]. These studies reveal that the onset of superconductivity is associated with a sudden increase of $\kappa(T)$ which can be suppressed by a moderate magnetic field. The enhancement of $\kappa(T)$ at the onset of superconductivity has been attributed to a strengthening of the phonon heat transport by reducing the scattering due to the gap formation. Their argument is based on a quantitative analysis of the data employing the Wiedemann–Franz law. It showed that just above T_c the electronic contribution amounts to only 5 % of the total thermal conductivity. A lattice–dominated thermal conductivity around T_c is also consistent with the absence of a magnetic field dependence of κ in this temperature range [61]. As for the question of the gap symmetry, the data at low temperature have been interpreted as indicating an excitation spectrum with gap zeroes: an extrapolation of the data for κ-$(ET)_2Cu(NCS)_2$ to $T \to 0$ revealed a finite in–T linear term which has been attributed to a residual electronic contribution [61]. The latter is expected for an unconventional superconductor due to impurity scattering of residual quasiparticles [343,344].

On the other hand, recent thermal conductivity measurements on the κ-$(ET)_2Cu[N(CN)_2]Br$ salt showed that down to the lowest temperatures the phonon scattering length is strongly influenced by quasiparticle scattering [51] which renders the analysis of the data on κ-$(ET)_2Cu(NCS)_2$ [61] as being questionable.

Magnetic penetration depth

The quantity which has been studied most intensively for the κ-$(ET)_2X$ superconductors in connection with the question on the order–parameter symmetry is the magnetic penetration depth.

According to the London theory, the penetration depth λ_L in the limit $T \to 0$ is directly related to the density of superconducting electrons n_s via

$$\lambda_L(0) = \sqrt{\frac{m^* c^2}{4\pi n_s e^2}}, \tag{7.16}$$

where m^* is the effective mass of the superconducting carriers [204]. Employing a two–fluid model with $n_e = n_s(T) + n_n(T)$ and n_e the density of conduction electrons, the temperature dependence of $\lambda_L(T)$ provides information on the normal–conducting component $n_n(T)$, i.e. the quasiparticle excitation spectrum. Since $n_s(T \to 0) = n_e$, the low–temperature value $\lambda(T \to 0)$ is a measure of the pair condensate, i.e. $\lambda_L^2(0) \propto m^*/n_s(0)$. For a conventional weak–coupling superconductor, the BCS theory predicts a mean–field temperature dependence of λ_L around T_c and an exponentially small variation

at low temperatures $T \ll T_c$ [345]:

$$\lambda_L(T) \simeq \lambda(0) \left[1 + \left(\frac{2\pi\Delta}{k_B T} \right)^{\frac{1}{2}} \exp\left(-\frac{\Delta}{k_B T} \right) \right] . \tag{7.17}$$

This holds true also for an anisotropic gap function without nodes, where for $k_B T \ll \Delta_{\min}$ the exponential low–temperature behavior is governed by the minimum value of the gap $\Delta_{\min}$. In contrast, an energy gap which vanishes along lines or at points at the Fermi surface will result in a power–law dependence of $\lambda_L(T)$ for $T \ll T_c$.

For the present materials the magnetic penetration depth has been determined by a variety of different techniques including ac–susceptibility [262, 346], muon–spin relaxation [263, 347], dc–magnetization [264, 265], surface impedance [260, 266] and a related high–frequency technique using a tunnel diode oscillator [348]. The results of these studies, however, are quite inconsistent regarding both the temperature dependence as well as the absolute values of $\lambda_L(T \to 0)$ (see Table 7.2 in section 7.4.2) and have led to quite different conclusions as to the symmetry of the superconducting order parameter.

Interestingly enough, these inconsistencies do not only involve results from different experimental techniques. Contradictory conclusions have been drawn also on the basis of seemingly identical experiments performed by different groups. This is the case for surface impedance studies where the penetration depth can be extracted from the complex conductivity. The latter is derived from the frequency shifts and variations of the quality factor of the resonator caused by the sample. While the surface impedance studies using a microwave perturbation technique on κ-$(ET)_2Cu(NCS)_2$ and κ-$(ET)_2Cu[N(CN)_2]Br$ by Klein *et al.* [349] and Dressel *et al.* [260] were found to be in good agreement with the BCS predictions, other studies by Achkir *et al.* [266] on κ-$(ET)_2Cu(NCS)_2$ revealed an in–T linear behavior at low temperatures indicative of an order parameter with zeroes on the Fermi surface. Deviations from an exponential temperature dependence of $\lambda_L(T)$ for the above two κ-$(ET)_2X$ compounds have been observed also in a more recent experiment using an rf tunnel–diode oscillator [348]. In contrast to the above measurements by Achkir *et al.*, however, their data of the in–plane penetration depth rather follow a $T^{\frac{3}{2}}$ power law (see Fig. 7.44). As has been argued by the authors, the data would still be consistent with a quasi–linear variation of the superfluid density as expected for a d–wave superconductor with impurities or a small residual gap [348]. Alternatively, the authors point out that the exponent 3/2 may arise naturally in a model proposed for short–coherence–length superconductors exhibiting a pseudogap [350].

An inconsistency exists also for μSR experiments performed by different groups. Here λ_L can be determined by measuring the field inhomogeneities in the mixed state, i.e. the spatial variation of the local induction of the vortex lattice. This technique was first applied to κ-$(ET)_2Cu(NCS)_2$ by Harshman

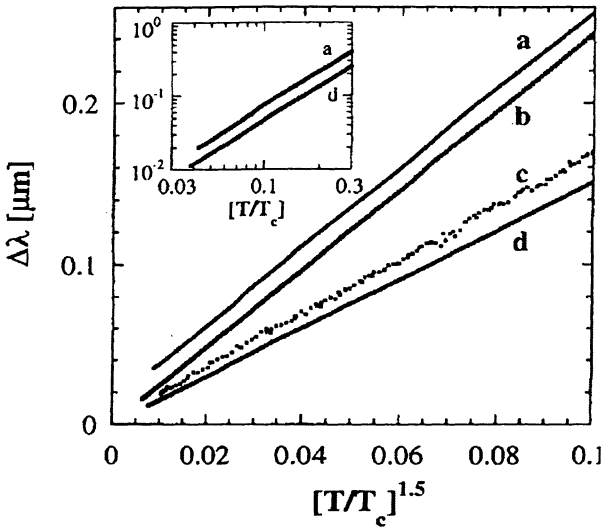

Fig. 7.44. Changes of the in–plane penetration depth $\Delta\lambda_{\parallel}(T)$ of κ-$(ET)_2Cu[N(CN)_2]Br$ [two samples (a),(b)] and κ-$(ET)_2Cu(NCS)_2$ [(c),(d)] plotted versus $(T/T_c)^{\frac{3}{2}}$. The data have been offset, taken from [348]

et al. [263] who could fit their data by a BCS temperature dependence. Subsequently, Le *et al.* [347] carried out similar experiments on the same system as well as on the κ-$(ET)_2Cu[N(CN)_2]Br$ salt and found an in–T linear variation for the in–plane penetration depth at low temperatures $\lambda_{\parallel}(T) \approx 1+\alpha\cdot(T/T_c)$.

A power law temperature dependence of $\lambda_{\parallel}(T)$ consistent with d–wave superconductivity has been observed also by ac–susceptibility measurements performed by different groups [177,262,346]. The latter experiments as well as the surface impedance studies are operating at very small external magnetic fields ($B < B_{c_1}$) attempting to probe the Meissner state. Possible difficulties in these experiments that may arise from flux–pinning–related phenomena near the surface of the superconductor, i.e. an inhomogeneous superconducting state, have been discussed in [9].

An alternative way to determine the penetration depth is to make use of the reversible mixed–state magnetization, a peculiarity of these strongly anisotropic superconductors with short coherence lengths.

According to the London model, the field dependence of the magnetization is given by

$$\frac{\mathrm{d}M}{\mathrm{d}(\ln H)} = \frac{\phi_0}{32\pi^2\lambda_{\mathrm{eff}}^2}, \tag{7.18}$$

where $\lambda_{\mathrm{eff}}^2 = \lambda_{\parallel}^2$ for $B \perp$ planes and $\lambda_{\mathrm{eff}}^2 = \lambda_{\parallel}\lambda_{\perp}$ for $B \parallel$ planes. In 3D superconductors, vortex pinning usually gives rise to an inhomogeneous distribution of the vortices in the mixed state and thus to an irreversible behavior of

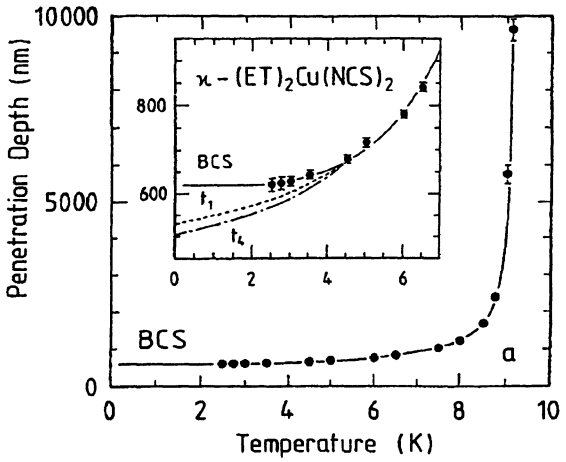

Fig. 7.45. In–plane penetration depth for single crystalline κ-$(ET)_2Cu(NCS)_2$. The solid line represents a BCS fit. The model calculations labelled t_1 and t_4 represent those anisotropic states proposed by Hasegawa *et al.* [351] and used by Le *et al.* to explain their μSR data [347] which have the weakest and strongest T dependences, respectively, taken from [264]

the magnetization upon increasing and decreasing the field. This may cause substantial uncertainties in determining the penetration depth from magnetization data. On the contrary, for quasi–2D superconductors with short coherence length the magnetization is entirely reversible over an extended field range, i.e. $B_{c_1} < B_{\rm irr} < B < B_{c_2}$ with $B_{\rm irr}$ being the temperature–dependent irreversibility line (see section 7.4.3). For κ-$(ET)_2Cu(NCS)_2$ and κ-$(ET)_2Cu[N(CN)_2]Br$ a reversible magnetization has been observed over an extended range in the B-T plane which thus allows for a precise determination of the in–plane penetration depth [264, 265]. The in–plane penetration depths $\lambda_{\|}(T)$ were determined, see Fig. 7.45, from the slopes $dM/d(\ln H)$ of the isotherms taken at different temperatures and using equation (7.18). The solid line represents a BCS fit [345] to the data. For both systems, the data reveal only a weak variation with temperature at low T consistent with an exponential temperature dependence as expected for a finite gap.

Specific heat

The above variety of contradictory results on the magnetic penetration depth indicate an extraordinarily high sensitivity of this quantity to extrinsic effects such as disorder or pinning–related phenomena. As a possible source, we mention the disorder associated with the glass transition of the ethylene endgroups, see section 7.3.4 and [177].

A quantity which is less sensitive to the above problems but can still provide fundamental information on the gap structure is the specific heat. In case this integral thermodynamic quantity were to find a low temperature elec-

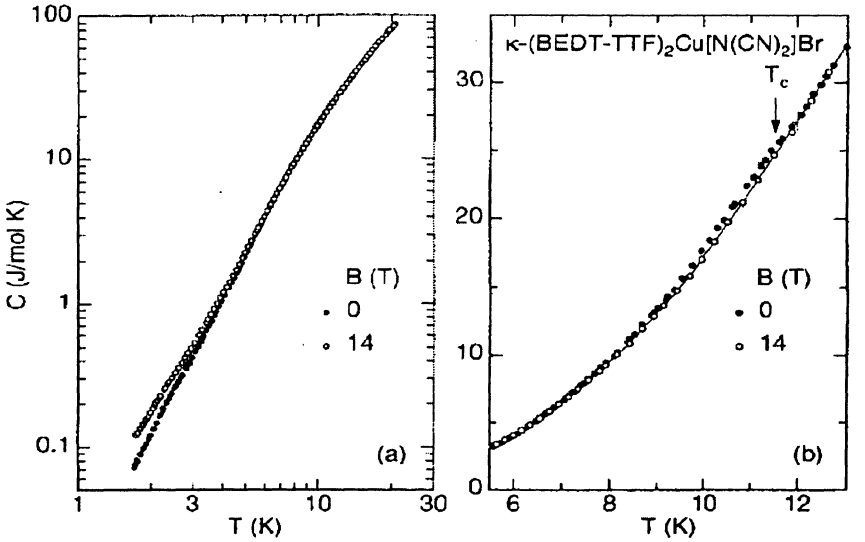

Fig. 7.46. Temperature dependence of the specific heat of κ-$(ET)_2Cu[N(CN)_2]Br$ in the superconducting ($B = 0$) and normal state ($B = 14\,T$) over an extended temperature range (left panel) and in the vicinity of $T_c = 11.5\,K$ (right panel). The solid line is a polynomial fit to the 14 T data, taken from [267]

tronic quasiparticle contribution, C_{es}, that varies exponentially weakly with the temperature, the existence of gap zeroes on the Fermi surface could be definitely ruled out. On the other hand, the observation of a non–exponential temperature dependence does not necessarily prove the existence of gap zeroes as this result might originate in extraneous contributions such as impurity phases, normal–conducting regions or pair–breaking effects. First specific heat measurements were focussing on the determination of the discontinuity at T_c which provides information on the coupling strength. From the results of Andraka *et al.* [352] and Graebner *et al.* [268] on κ-$(ET)_2Cu(NCS)_2$ yielding a ratio of $\Delta C/\gamma T_c > 2$ a strong–coupling behavior has been inferred for this salt. In a series of subsequent experiments, the temperature dependence of the electronic contribution, C_{es}, at lower temperatures was at the focus of the investigations. From experiments on κ-$(ET)_2Cu[N(CN)_2]Br$ Nakazawa *et al.* [353] reported a quadratic temperature dependence of C_{es} at low temperatures, which was taken as an indication for line nodes in the gap. However, recent high–resolution specific heat measurements on the same compound revealed an exponentially weak low–T electronic contribution to the specific heat implying a finite energy gap [267]. Moreover it has been shown in the latter study that the T^2 dependence in the C_{es} data by Nakazawa *et al.* [353] most likely originates in their incorrect determination of the phonon background [354]. Figures 7.46 and 7.47 show the results of specific heat measure-

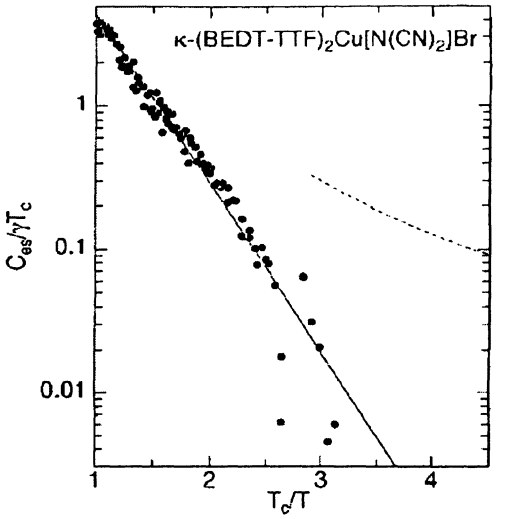

Fig. 7.47. A semi–logarithmic plot of $C_{es}/(\gamma T_c)$ vs T_c/T as determined from the data shown in Fig. 7.46. The solid line indicates the exponential variation of C_{es}. The dashed line corresponds to C_{es} as determined by Nakazawa *et al.* [353] (see text and [354]), taken from [267]

ments performed by Elsinger *et al.* [267]. The phonon contribution, which predominates the specific heat near T_c has been determined from measurements in an overcritical field. This standard procedure is valid as long as there are no magnetic contributions to the specific heat which might change with the field. From the absence of any measurable field dependence in the data above T_c this assumption appears justified. Figure 7.47 shows the exponential decrease of C_{es} with decreasing temperatures. The lack of a finite C_{es} for $T \to 0$ rules out the existence of zeroes in the energy gap.

A similar behavior has been observed also for κ-$(ET)_2Cu(NCS)_2$ [50,51]. Figure 7.48 shows the difference $\Delta C(T) = C(T, B = 0) - C(T, B = 8\,\mathrm{T} > B_{c_2})$ used to analyze the specific heat data. The advantage of using this quantity means that the unknown phonon contribution drops out. As Fig. 7.48 demonstrates, $\Delta C(T)$ deviates markedly from the weak–coupling BCS behavior in both the jump height at T_c as well as the overall temperature dependence. However, as was found also for κ-$(ET)_2Cu[N(CN)_2]Br$ [267], a much better description of the data is obtained by using the semi–empirical extension of the BCS formalism to strong–coupling superconductors – the so–called α–model [355]. It contains a single free parameter $\alpha \equiv \Delta_0/k_BT_c$ which scales the BCS energy gap $\Delta(T) = (\alpha/\alpha_{BCS}) \cdot \Delta_{BCS}(T)$ with $\alpha_{BCS} = 1.764$. As Fig. 7.48 clearly demonstrates, the strong–coupling BCS model with $\alpha = 2.8 \pm 0.1$ provides an excellent description of the data over the entire temperature range investigated [50]. Similar to what has been found for

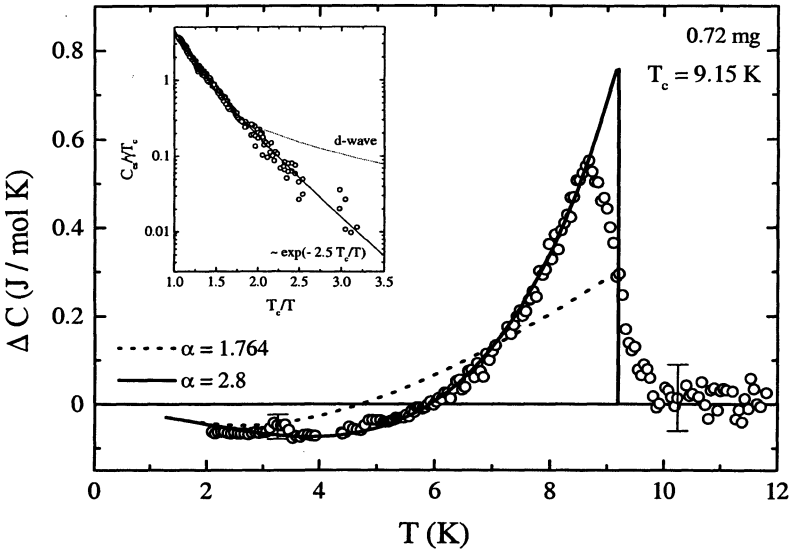

Fig. 7.48. Specific heat difference $\Delta C = C(0\,\mathrm{T}) - C(8\,\mathrm{T})$ of a κ-$(ET)_2Cu(NCS)_2$ single crystal of m = 0.72 mg (main panel). The dotted and solid thick lines represent the BCS curves for weak and strong coupling, respectively. The inset shows the quasiparticle contribution to the specific heat in the superconducting state as $C_{es}/\gamma T_c$ vs T_c/T in a semi-logarithmic representation. Here the solid line represents the strong-coupling BCS behavior while the dotted line indicates a T^2 behavior as expected for a d-wave order parameter [356], taken from [50,187]

κ-$(ET)_2Cu[N(CN)_2]Br$ (Fig. 7.47), the data for κ-$(ET)_2Cu(NCS)_2$ (inset of Fig. 7.48) are fully consistent with an exponentially small C_{es} at low temperatures, i.e. an energy gap without zeroes at the Fermi surface. The same behavior has been previously observed for other $(ET)_2X$ superconductors [51,357,358]. The above findings of an exponentially weak specific heat at low temperatures are clearly incompatible with the existence of gap zeroes as claimed by various of the above mentioned experiments. It has to be shown by future studies whether or not this controversy can be removed by taking properly into account the influence of magnetic fields even when applied parallel to the planes and other extraneous effects such as the cooling-rate-dependent disorder associated with the ethylene groups.

On the pairing state in $(TMTSF)_2X$

As for the BEDT-TTF systems, the nature of superconductivity in the Bechgaard salts $(TMTSF)_2X$ is still far from being understood and continues to be a controversial issue. Early suggestions of a spin-triplet (S=1) state were based on the proximity of superconductivity to a SDW state in the pressure-temperature phase diagram (cf. section 7.3.5). This situation resembles the theoretical expectation for an interacting 1D electron gas [359] where a SDW

phase lies next to triplet superconductivity. Further arguments for a spin-triplet p–wave superconductivity were derived from the observation that T_c is extremely sensitive to the introduction of nonmagnetic defects [360, 361] and substitutional impurities [362,363], see also [364,365]. As discussed in section 7.3.5, depending on external pressure and magnetic field, the Bechgaard salts can be tuned to either a superconducting or a SDW ground state which has led to the proposal that the order parameters of both phases are not independent of each other. The superconducting properties of the Bechgaard salts have been reviewed by several authors [5, 33, 366]. Since these articles are comprehensive up to 1998, we shall give only a brief overview on the early results and concentrate the discussion on the more recent developments including the possibility of spin–triplet superconductivity.

Among the $(TMTSF)_2X$ superconductors, the $X = PF_6$ and ClO_4 salts are the most extensively studied materials although the number of experimental investigations of the superconducting properties is much less compared to that of the BEDT-TTF salts and their derivatives. The reason for this is most likely related to the low T_c values of the former systems which require extensive low–temperature equipment and, in the case of $X = PF_6$, external pressure of $p \geq 5.8\,\text{kbar}$ [367] to stabilize the superconducting state. For the ambient–pressure superconductor $(TMTSF)ClO_4$ it is the anion ordering which renders the experimental situation difficult (see section 7.3.4). By slowly cooling through the anion–ordering temperature T_{AO} at around 24 K an ambient pressure superconducting state below $T_c = (1.2 \pm 0.2)\,\text{K}$ can be stabilized. In this case, the anions are believed to be well ordered. On the other hand, for samples that have been cooled rapidly across T_{AO}, an insulating state forms below $T_{MI} \simeq 6.1\,\text{K}$.

Early specific heat measurements on $(TMTSF)_2ClO_4$ focusing on the temperature range close to T_c revealed a discontinuity at T_c, $\Delta C/\gamma T_c = 1.67$ which is in fair agreement with the BCS value of 1.43 [244]. On the other hand, deviations from a BCS–type of superconductivity have been observed in NMR measurements by Takigawa *et al.* [368]. These authors reported the absence of a Hebel–Schlichter peak and a T^3 dependence in the spin–lattice relaxation rate. This has led to the proposal of a d–wave order parameter with a gap that vanishes along lines on the Fermi surface [368]. These results are at variance with more recent thermal conductivity data on the same salt, showing a rapid decrease of the electronic contribution to the heat transport below T_c which indicates the absence of low–lying excitations [369]. Their results provide strong evidence for a nodeless gap function. However, as pointed out by the authors, this result is not necessarily associated with an s–wave order parameter.

By enumerating possible gap functions for quasi–1D systems, Hasegawa and Fukuyama [351] showed that besides an anisotropic spin–singlet d–wave also a spin–triplet p–wave state – in both cases the order parameters vanish along lines on the FS – is possible. The authors suggested the possibility of

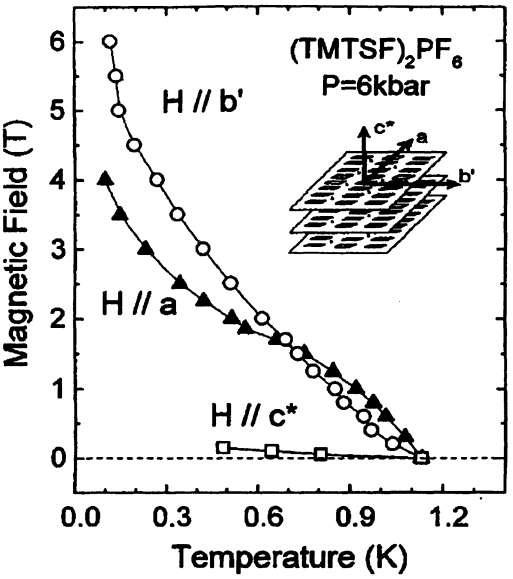

Fig. 7.49. *B-T* phase diagram of $(TMTSF)_2PF_6$ at a pressure of 6 kbar for magnetic fields aligned along three perpendicular axes as defined in the inset, taken from [250]

an antiferromagnetic spin–fluctuation pairing mechanism for the Bechgaard salts.

Arguments in favor of such a spin–fluctuation–mediated superconductivity with *d*–wave symmetry have been derived from a recent resistivity study under pressure [68, 179]. According to these results, a minimum in the resistivity $\rho_a(T)$ at $T_{\min}$ marks the onset of AF fluctuations before, at lower temperatures, an itinerant antiferromagnetic state (SDW) is stabilized. The width of the region of critical AF fluctuations in the T–p phase diagram (see Fig. 7.22 in section 7.3.5) is enhanced when the SDW ground state is approached from the high–pressure side, where the system is close to the SDW/SC border and largest where $T_c(p)$ reaches its optimum value. The correlation between the spin–fluctuation regime above the onset of superconductivity and the T_c value is taken as a strong argument for a pairing mechanism mediated by the exchange of these fluctuations [68, 179].

In a recent series of papers on the upper critical fields, the discussion of a possible realization of a triplet–pairing state in the Bechgaard salts has again been raised [250, 367, 370]. Lee *et al.* examined the upper critical field $B_{c_2}(T)$ and its directional dependence in $(TMTSF)_2PF_6$ under pressure via resistivity measurements. The resulting magnetic field–temperature phase diagram is depicted in Fig. 7.49 for fields aligned along the three crystal axes [250]. While the upper–critical–field curves near T_c were found to be consistent

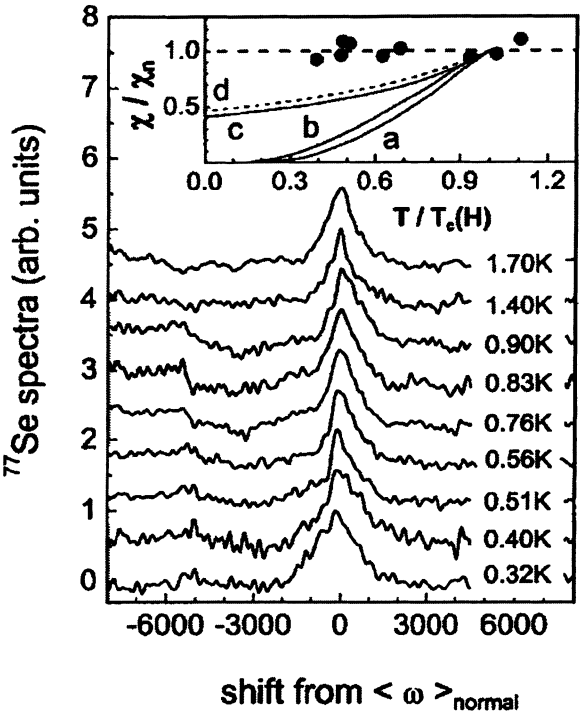

Fig. 7.50. ^{77}Se NMR spectra of $(TMTSF)_2PF_6$ under 7 kbar at various temperatures above and below T_c which is 0.81 K at the applied field of 1.43 T aligned along the most conductive a axis. The inset shows normalized χ_{Spin} data compared with theoretical calculations. Curves a and b are for a singlet state in applied fields B/B_{c_2} near zero and 0.63, respectively, as calculated by Fulde and Maki [371] while curves c and d represent a scenario where the vortex cores induce normal regions of a fraction equal to B/B_{c_2}, taken from [372]

with earlier results on the same and related compounds, which indicated a more conventional behavior (see also Fig. 7.32 in section 7.4.2) [245,248,249], the extension of the measurements to lower temperatures uncovered important new features: (i) the upper critical fields for B aligned along the a– and b–directions display strong positive curvatures *without* saturation. This behavior was found to be independent of the criterion used to extract B_{c_2} from the resistance profiles. (ii) $B^b_{c_2}$ becomes larger than $B^a_{c_2}$, i.e. the anisotropy inverts upon cooling, and (iii), the critical fields in both directions exceed the Pauli limiting field of $B_P = 1.84 \times T_c \simeq 2.2\,\mathrm{T}$ [246, 247]. In a subsequent resistivity study under fields along the b–axis and optimum pressure settings [367], the onset of superconductivity was found to persist even up to 9 T, which is more than four times B_P. The authors discussed various

proposals attempting to explain an upturn in the upper critical field. Among them are strong spin–orbit scattering [373,374], a magnetic–field–induced dimensional crossover from 3D to 2D [375,376] and the formation of a spatially inhomogeneous Fulde–Ferrell–Larkin–Ovchinnikov (FFLO) state [269,270]. It has been argued by Lee *et al.* that, even with a field–induced dimensional crossover which greatly enhances the orbital critical field, an additional effect is required to exceed the paramagnetic limit. This could be either the formation of the FFLO state or triplet superconductivity. The fact that no indications for a first–order phase transition into the FFLO state have been observed thus points to the possibility of a spin–triplet superconducting state.

This interpretation has gained further support from recent NMR measurements of the Knight shift K_S in the superconducting state of pressurized $(TMTSF)_2PF_6$ [372]. Since K_S is proportional to the spin–susceptibility χ_{Spin}, which is different for spin singlet ($\chi_{Spin} \rightarrow 0$ for $T \rightarrow 0$) and triplet (χ_{Spin} remains unchanged on cooling through T_c) superconductors, measurements of K_S provide a direct probe of the spin parity of the superconductor. Figure 7.50 shows that in contrast to the expectations for the various scenarios involving singlet superconductivity there is no significant change in K_S for $B \parallel a$ on cooling into the superconducting state. These observations together with similar results of a previous study for $B \parallel b$ [377] thus argue for a spin–triplet pairing. Besides K_S, the above studies included also measurements on the spin–lattice relaxation rate $1/T_1$ which exhibits a small peak near T_c. In light of the absence of such a peak in previous reports of zero field proton–NMR measurements [368] its identification with a Hebel–Schlichter peak is unclear.

7.5 Epilogue

Studies on superconductivity in organic charge–transfer salts have been carried out for more than twenty–years. The joint efforts of researchers from the fields of synthetic chemistry and solid–state physics have created this new class of molecular conductors which exhibits fascinating properties. Key features are a pronounced anisotropy of the electronic states spanning the whole range from quasi–1D to anisotropic 3D, a low charge carrier concentration and a strong coupling of the charge carriers to the lattice degrees of freedom. The combination of these extraordinary material parameters make the organic conductors ideal model systems for exploring the interplay of strong electron–electron and electron–phonon interactions in reduced dimensions. In fact, this material class has enriched the solid–state physics by a wealth of interesting collective phenomena such as spin–Peierls or density–wave instabilities, Mott–type metal–insulator transitions, and, above all, superconductivity. Most remarkably, these systems offer a unique opportunity to scan through the various ground states either in discrete steps by chemical means, or even in a continuous way through changes of the applied pressure.

Thanks to the intense interdisciplinary efforts from research groups in chemistry and physics, our level of understanding of these materials has progressed substantially. The basis for this development was accomplished by advances in organic and organometallic chemistry which have provided a rich and varied supply of molecules serving as building blocks for conductors and superconductors. By employing state–of–the–art preparation techniques, it is possible nowadays to synthesize crystals of unprecedented high quality which permit highly accurate measurements of their electronic parameters. In particular, these clean materials enable direct experimental access to the electronic band structure with a high level of accuracy. For the 2D materials, the various experiments agree in that the normal–state electronic properties are well described by quasiparticles within a Fermi–liquid approach. These quasiparticles reveal a considerable mass renormalization due to both electron–electron as well as electron–phonon interactions. This contrasts with the behavior found in the quasi–1D salts, where non–Fermi–liquid properties have been reported for transport and optical properties. Indeed, these results indicate the separation of spin and charge degrees of freedom – one of the hallmarks of a Luttinger liquid.

The phase diagrams of the quasi–1D and 2D materials have been mapped out in great detail utilizing a wide spectrum of experimental techniques – some of which have been applied under extreme conditions such as high magnetic fields and high pressure. These studies confirmed, on the one hand, the universal character of the phase diagrams for both families and revealed, on the other hand, intriguing new details of the interplay of the various phases. Despite such detailed information, in particular on the phase boundary between superconductivity and magnetism, there is still no generally accepted picture on the nature of the superconducting state. The fact that both phases share a common phase boundary have led some researchers to believe that both phenomena have the same origin. In such a scenario, the attractive pairing interaction would have to be provided by the exchange of antiferromagnetic spin fluctuations. In fact, some of the experimental data seem to indicate an anisotropic pairing state compatible with such a magnetic pairing interaction. While for the quasi–2D salts a spin–singlet state with d–wave symmetry is the most favored one among the anisotropic states proposed, a number of experiments on the quasi–1D materials even suggest triplet superconductivity. However, for the quasi–2D salts, the notion of an anisotropic superconducting state is in clear conflict with results of other experiments – in particular specific heat measurements – which demonstrate the existence of a finite superconducting energy gap on the whole Fermi surface.

It is remarkable that despite the continuous experimental efforts to unravel the fundamental features of the superconducting state, the above controversy still persists. These efforts include the application of standard experimental techniques, some of which have been driven to an extraordinarily

high resolution, as well as new, more sophisticated methods such as angular–dependent investigations of the gap functions.

An important lesson to be learnt from this controversy concerns the role of disorder, in particular the *intrinsic*–type of disorder which is inherent to many of the materials even when prepared under ideal conditions. As was recognized early on for the quasi–1D materials but has now proved to be true also for the quasi–2D systems, *intrinsic* disorder can be of crucial importance and should not be overlooked in exploring and discussing superconducting–state properties. This is of concern for all those materials where, by the symmetry, certain structural elements can adopt more than one orientation. Since these states are almost degenerate in energy, a cooling–rate dependent frozen *intrinsic* disorder will result at low temperatures which may have a severe influence on both the electronic and also the elastic properties of the sample. It is to be hoped that part of the above controversy can be removed by taking these disorder effects into account properly.

In viewing the field of organic conductors and superconductors as a whole, it is clear that these materials have provided a considerable contribution to our understanding of strongly interacting electrons in low dimensions, though important questions still remain open. This concerns, in particular, the nature of the metallic state above T_c and the role of electron–electron and electron–phonon interactions in the pairing mechanism. In light of the progress we have made in recent years, one can be optimistic that more systematic investigations on the relationship between molecular properties and crystal structure on the one hand, and the collective features of the bulk, on the other, will not only provide an answer to these questions but also will be a guidance for the synthesis of new materials with hopefully even more fascinating properties.

Acknowledgements

We are indebted to many colleagues and friends for collaborations, discussions and the support over the last years, especially M. Dressel, A.M. Kini, M. Köppen, F. Kromer, C. Langhammer, K. Maki, T. Sasaki, J.A. Schlueter, D. Schweitzer, F. Steglich, N. Toyota and J. Wosnitza. The technical assistance of C. Agnew is greatly acknowledged. Part of the work is supported by the Deutsche Forschungsgemeinschaft under the auspieces of the FOR 412.

References

1. D. Jérome, A. Mazaud, M. Ribault, K. Bechgaard, J. Physique Lett. **41**, L95 (1980).
2. H. Akamatu, H. Inokuchi, Y. Matsunaga, Nature **173**, 168 (1954).
3. W.A. Little, Phys. Rev. A **134**, 1416 (1964).
4. R.H. McKenzie, Science **278**, 820 (1997); Comments Cond. Mat. Phys. **18**, 309 (1998).
5. T. Ishiguro, K. Yamaji, G. Saito, *Organic superconductors*, 2nd edn. (Springer, Berlin 1998).

6. The review 'Organic conductors and superconductors' by D. Jérome and H.J. Schulz, Adv. Phys. **31**, 229 (1982) on the quasi–1D organic conductors has been republished in: Adv. Phys. **51**, 293 (2002).
7. L.N. Bulaevskii, Adv. Phys. **37**, 443 (1988).
8. J.-P. Farges (editor), *Organic Conductors – Fundamentals and Applications*, (M. Dekker, New York 1994).
9. M. Lang, *Quasi–Twodimensional Organic Superconductors*, Superconductivity Review **2**, 1 (1996).
10. J. Singleton, C. Mielke, *Quasi–two–dimensional organic superconductors: a review*, Contemp. Phys. **43**, 63 (2002).
11. L.B. Coleman, M.J. Cohen, D.J. Sandman, F.G. Yamagishi, A.F. Garito, A.J. Heeger, Solid State Commun. **12**, 1125 (1973).
12. J. Ferraris, D.O. Cowan, V. Walatka, Jr., J.H. Perlstein, J. Am. Chem. Soc. **95**, 948 (1973).
13. G.C. Papavassiliou, G.A. Mousdis, J.S. Zambounis, A. Terzis, A. Hountas, B. Hilti, C.W. Mayer, J. Pfeiffer, Synth. Met. **27**, B379 (1988).
14. A.M. Kini, M.A. Beno, D. Son, H.H. Wang, K.D. Carlson, L.C. Porter, U. Welp, B.A. Vogt, J.M. Williams, D. Jung, M. Evain, M.-H. Whangbo, D.L. Overmyer, J.E. Schirber, Solid State Commun. **69**, 503 (1989).
15. M.A. Beno, H.H. Wang, A.M. Kini, K.D. Carlson, U. Geiser, W.K. Kwok, J.E. Thompson, J.M. Williams, J. Ren, M.-H. Whangbo, Inorg. Chem. **29**, 1599 (1990).
16. K. Bechgaard, C.S. Jacobsen, K. Mortensen, H.J. Pedersen, N. Thorup, Solid State Commun. **33**, 1119 (1980).
17. K. Bechgaard, K. Carneiro, M. Olsen, F.B. Rasmussen, C.S. Jacobsen, Phys. Rev. Lett. **46**, 852 (1981).
18. L.K. Montgomery, 'Chemical Synthesis and Crystal Growth Techniques'. In: *Organic Conductors – Fundamentals and Applications.* ed. by J.-P. Farges (M. Dekker, New York 1994) pp. 115–145
19. G. Saito, T. Enoki, K. Toriumi, H. Inokuchi, Solid State Commun. **42**, 557 (1982).
20. K. Oshima, H. Urayama, H. Yamochi, G. Saito, Physica C **153–155**, 1148 (1988).
21. J.M. Williams, J.R. Ferraro, R.J. Thorn, K.D. Carlson, U. Geiser, H.H. Wang, A.M. Kini, M.-H. Whangbo, *Organic Superconductors (Including Fullerenes).* (Prentice Hall, Englewood Cliffs, N.J. 1992) chapter 2.
22. R. Moret, J.P. Pouget, In: *Crystal Chemistry and Properties of Materials with Quasi–One–Dimensional Structures.* ed. by J. Rouxel (D. Reidel, Dordrecht, The Netherlands, 1986) pp. 87–143.
23. T. Mori, Bull. Chem. Soc. Japan **71**, 2509 (1998); T. Mori, H. Mori, S. Tanaka, *ibid.* **72**, 179 (1999); T. Mori, *ibid.* **72**, 2011 (1999).
24. A.M. Kini, U. Geiser, H.H. Wang, K.D. Carlson, J.M. Williams, W.K. Kwok, K.D. Vandervoort, J.E. Thompson, D.L. Supka, D. Jung, M.-H. Whangbo, Inorg. Chem. **29**, 2555 (1990).
25. J.M. Williams, A.M. Kini, H.H. Wang, K.D. Carlson, U. Geiser, L.K. Montgomery, G.J. Pyrka, D.M. Watkins, J.M. Kommers, S.J. Boryschuk, A.V. Strieby Crouch, W.K. Kwok, J.E. Schirber, D.L. Overmyer, D. Jung, M.-H. Whangbo, Inorg. Chem. **29**, 3272 (1990).

26. H.H. Wang, K.D. Carlson, U. Geiser, A.M. Kini, A.J. Schultz, J.M. Williams, L.K. Montgomery, W.K. Kwok, U. Welp, K.G. Vandervoort, S.J. Boryshuk, A.V. Strieby Crouch, J.M. Kommers, D.M. Watkins, J.E. Schirber, D.L. Overmyer, D. Jung, J.J. Novoa, M.-H. Whangbo, Synth. Met. **41-43**, 1983 (1991).
27. Yu.V. Sushko, K. Andres, Phys. Rev. B **47**, 330 (1993).
28. A. Kobayashi, R. Kato, T. Naito, H. Kobayashi, Synth. Met. **56**, 2078 (1993).
29. A. Kobayashi, T. Udagawa, H. Tomita, T. Naito, H. Kobayashi, Chem. Lett. **1993**, 2179 (1993).
30. L.K. Montgomery, T. Burgin, C. Husting, L. Tilley, J.C. Huffmann, K.D. Carlson, J.D. Dudek, G.A. Yaconi, U. Geiser, J.M. Williams, Mol. Cryst. Liq. Cryst. **211**, 283 (1992).
31. H. Kobayashi, H. Akutsu, E. Arai, H. Tanaka, A. Kobayashi, Phys. Rev. B **56**, R8526 (1997).
32. S. Uji, C. Terakura, T. Terashima, T. Yakabe, Y. Terai, M. Tokumoto, A. Kobayashi, F. Sakai, H. Tanaka, H. Kobayashi, Phys. Rev. B **65**, 113101 (2002).
33. D. Jérome, 'Organic Superconductors: From $(TMTSF)_2PF_6$ to Fullerenes'. In: *Organic Conductors – Fundamentals and Applications.* ed. by J.-P. Farges (M. Dekker, New York 1994) pp. 405–494.
34. For a comprehensive overview on the band–structure calculations and Fermi–surface studies see [5] and references cited therein.
35. T. Mori, A. Kobayashi, Y. Sasaki, H. Kobayashi, G. Saito, H. Inokuchi, Bull. Chem. Soc. Jpn. **57**, 627 (1984).
36. M.-H. Whangbo, J.J. Novoa, D. Jung, J.M. Williams, A.M. Kini, H.H. Wang, U. Geiser, M.A. Beno, K.D. Carlson, 'Organic superconductivity'. ed. by V.Z. Kresin and W.A. Little (Plenum Press, New York 1990) p. 243.
37. U. Geiser, A.J. Schultz, H.H. Wang, D.M. Watkins, D.L. Stupka, J.M. Williams, J.E. Schirber, D.L. Overmyer, D. Jung, J.J. Novoa, M.-H. Whangbo, Physica C **174**, 475 (1991).
38. P.M. Grant, J. Phys. C3 **44**, 847 (1983).
39. G.M. Danner, W. Kang, P.M. Chaikin, Phys. Rev. Lett. **72**, 3714 (1994).
40. J. Wosnitza, *Fermi Surfaces of Low–Dimensional Organic Metals and Superconductors*, (Springer, Berlin 1996).
41. J. Singleton, *Studies of quasi–two–dimensional organic conductors based on BEDT–TTF using high magnetic fields*, Rep. Prog. Phys. **63**, 1111 (2000).
42. K. Oshima, T. Mori, H. Inokuchi, H. Urayama, H. Yamochi, G. Saito, Phys. Rev. B **38**, 938 (1988).
43. H. Mori, S. Tanaka, M. Oshima, G. Saito, T. Mori, Y. Maruyama, H. Inokuchi, Bull. Chem. Soc. Jpn. **63**, 2183 (1990).
44. N. Harrison, E. Rzepniewski, J. Singleton, J.P. Gee, M.M. Honold, P. Day, M. Kurmoo, J. Phys.: Cond. Mat. **11**, 7227 (1999).
45. L. Onsager, Phil. Mag. **43**, 1006 (1952).
46. L.F. Lifshitz, A.M. Kosevich, Zh. Eksp. Teor. Fiz. **29**, 730 (1955); Sov. Phys. JETP **2**, 636 (1956).
47. J. Caulfield, W. Lubczynski, F.L. Pratt, J. Singleton, D.Y.K. Ko, W. Hayes, M. Kurmoo, P. Day, J. Phys., Cond. Mat. **6**, 2911 (1994).
48. T. Sasaki, H. Sato, N. Toyota, Solid State Commun. **76**, 507 (1990).
49. T. Sasaki, H. Sato, N. Toyota, Physica C **185–189**, 2687 (1991).

50. J. Müller, M. Lang, R. Helfrich, F. Steglich, T. Sasaki, Phys. Rev. B **65**, R140509 (2002).
51. J. Wosnitza, S. Wanka, J. Hagel, M. Reibelt, D. Schweitzer, J.A. Schlueter, Synth. Met. (2002), in press.
52. Y.-N. Xu, W.Y. Ching, Y.C. Jean, Y. Lou, Phys. Rev. B **52**, 12946 (1995).
53. J. Merino, R.H. McKenzie, Phys. Rev. B **62**, 2416 (2000).
54. J. Singleton, F.L. Pratt, M. Doporto, T.J.B.M. Janssen, M. Kurmoo, J.A.A.J. Perenboom, W. Hayes, P. Day, Phys. Rev. Lett. **68**, 2500 (1992).
55. J.E. Eldridge, Y. Xie, H.H. Wang, J.M. Williams, A.M.Kini, J.A. Schlueter, Spectrochim. Acta A **52**, 45 (1996).
56. J.E. Eldridge, Y. Xie, Y. Lin, H.H. Wang, J.M. Williams, J.A. Schlueter, Synth. Met. **86**, 2067 (1997).
57. D. Pedron, G. Visentini, R. Bozio, J.M. Williams, J.A. Schlueter, Physica C **276**, 1 (1997).
58. D. Pedron, R. Bozio, J.A. Schlueter, M.E. Kelly, A.M. Kini, J.M. Williams, Synth. Met. **103**, 2220 (1999).
59. E. Faulques, V.G. Ivanov, C. Mézière, P. Batail, Phys. Rev. B **62**, R9291 (2000).
60. A. Girlando, M. Masino, G. Visentini, A. Brillante, R.G. Della Valle, E. Venuti, Synth. Met. **109**, 13 (2000).
61. S. Belin, K. Behnia, A. Deluzet, Phys. Rev. Lett. **81**, 4728 (1998).
62. K. Izawa, H. Yamaguchi, T. Sasaki, Y. Matsuda, Phys. Rev. Lett. **88**, 027002 (2002).
63. L. Pintschovius, H. Rietschel, T. Sasaki, H. Mori, S. Tanaka, N. Toyota, M. Lang, F. Steglich, Europhys. Lett. **37**, 627 (1997).
64. H. Weiss, M.V. Kartsovnik, W. Biberacher, E. Steep, E. Balthes, A.G.M. Janssen, K. Andres, N.D. Kushch, Phys. Rev. B **59**, 12370 (1999).
65. A.-K. Klehe, R.D. McDonald, A.F. Goncharov, V.V. Struzhkin, Ho-kwang Mao, R.J. Hemley, T. Sasaki, W. Hayes, J. Singleton, J. Phys.: Cond. Mat. **12**, L247 (2000).
66. P. Wzietek, F. Creuzet, C. Bourbonnais, D. Jérome, K. Bechgaard, P. Batail, J. Phys. I France **3**, 171 (1993).
67. T. Adachi, E. Ojima, K. Kato, H. Kobayashi, J. Am. Chem. Soc. **122**, 3238 (2000).
68. H. Wilhelm, D. Jaccard, R. Duprat, C. Bourbonnais, D. Jérome, J. Moser, C. Carcel, J.M. Fabre, Eur. Phys. J. B **21**, 175 (2001); H. Wilhelm, D. Jaccard, D. Jérome, J. Moser, R. Duprat, C. Bourbonnais, In: *Frontiers of High Pressure Research II: Application of High Pressure to Low-Dimensional Novel Electronic Materials.* ed. by H.D. Hochheimer *et al.*, 423 (2001).
69. J.R. Cooper, B. Korin–Hamzić, 'Organic Metals'. In: *Organic Conductors – Fundamentals and Applications.* ed. by J.-P. Farges (M. Dekker, New York 1994) pp. 359–403.
70. S. Tomonaga, Prog. Theor. Phys. **5**, 554 (1950).
71. J. Luttinger, J. Math. Phys. **4**, 1154 (1963).
72. H.J. Schulz, Int. J. Mod. Phys. B **5**, 57 (1991).
73. C. Bourbonnais, D. Jérome, Physics World (September 1998) p. 41.
74. V. Vescoli, L. Degiorgi, W. Henderson, G. Grüner, K.P. Starkey, L.K. Montgomery, Nature **281**, 1181 (1998).
75. T. Lorenz, M. Hofmann, M. Grüninger, A. Freimuth, G.S. Uhrig, M. Dumm, M. Dressel, Nature **418**, 614 (2002).

76. B. Dardel, D. Malterre, M. Grioni, P. Weibel, Y. Baer, J. Voit, D. Jérome, Europhys. Lett. **24**, 687 (1993).
77. V. Vescoli, F. Zwick, W. Henderson, L. Degiorgi, M. Grioni, G. Gruner, L.K. Montgomery, Eur. Phys. J. B **13**, 503 (2000).
78. J. Moser, M. Gabay, P. Auban-Senzier, D. Jérome, K. Bechgaard, J.M. Fabre, Eur. Phys. J. B **1**, 39 (1998).
79. K. Murata, M. Tokumoto, H. Anzai, Y. Honda, N. Kinoshita, T. Ishiguro, N. Toyota, T. Sasaki, Y. Muto, Synth. Met **27**, A263 (1988).
80. H. Sato, T. Sasaki, N. Toyota, Physica C **185-189**, 2679 (1991).
81. J.E. Schirber, D.L. Overmyer, K.D. Carlson, J.M. Williams, A.M. Kini, H.H. Wang, H.A. Charlier, B.J. Love, D.M. Watkins, G.A. Yaconi, Phys. Rev. B **44**, 4666 (1991).
82. M. Oshima, H. Mori, G. Saito, K. Oshima, 'The physics and chemistry of organic superconductors'. ed. by G. Saito, S. Kagoshima (Springer, Berlin, Heidelberg 1990) p. 257.
83. K. Kikuchi, Y. Honda, Y. Ishikawa, K. Saito, I. Ikemoto, K. Murata, H. Anzai, T. Ishiguro, Solid State Commun. **66**, 405 (1988).
84. K. Yamaji, Synth. Met. A **27**, 115 (1988).
85. S. Gärtner, E. Gogu, I. Heinen, H.J. Keller, T. Klutz, D. Schweitzer, Solid State Commun. **65**, 1531 (1998).
86. N. Toyota, T. Sasaki, H. Sato, Y. Watanabe, Physica C **178**, 339 (1991).
87. I.D. Parker, R.H. Friend, M. Kurmoo, P. Day, C. Lenoir, P. Batail, J. Phys. Cond. Mat. **1**, 4479 (1989).
88. M. Kund, H. Müller, W. Biberacher, K. Andres, Physica C **191**, 274 (1993).
89. M.A. Tanatar, T. Ishiguro, T. Kondo, G. Saito, Phys. Rev. B **59**, 3841 (1999).
90. N.L. Wang, B.P. Clayman, H. Mori, S. Tanaka, J. Phys.: Cond. Mat. **12**, 2867 (2000).
91. B. Thoma, Diploma Thesis, Stuttgart University (1996), unpublished.
92. L.K. Montgomery, R.M. Vestal, K.P. Starkey, B.W. Fravel, M.J. Samide, D.G. Peters, C.H. Mielke, J.D. Thompson, Synth. Met. **103**, 1878 (1999).
93. K. Murata, M. Ishibashi, Y. Honda, N.A. Fortune, M. Tokumoto, N. Kinoshita, H. Anzai, Solid State Commun. **76**, 377 (1990).
94. Y.V. Sushko, V.A. Bondarenko, R.A. Petrosov, N.D. Kushch, E.B. Yagubskii, J. Phys. I France **1**, 1375 (1991).
95. K. Kanoda, Hyperfine Int. **104**, 235 (1997).
96. K. Kanoda, Physica C **282–287**, 299 (1997).
97. J. Müller, M. Lang, F. Steglich, J.A. Schlueter, A.M. Kini, T. Sasaki, Phys. Rev. B **65**, 144521 (2002).
98. M. Lang, J. Müller, F. Steglich, J.A. Schlueter, A.M. Kini, T. Sasaki, Synth. Met. (2002), in press.
99. T. Sasaki, N. Yoneyama, A. Matsuyama, N. Kobayashi, Phys. Rev. B **65**, 060505 (2002).
100. M. Weger, M. Tittelbach, E. Balthes, D. Schweitzer, H.J. Keller, J. Phys.: Cond. Mat. **5**, 8569 (1993).
101. M. Weger, M. Kaveh, H. Gutfreund, Solid State Commun. **37**, 421 (1981).
102. M. Weger, D. Schweitzer, Synth. Met. **70**, 889 (1995).
103. M. Weger, Acta Physica Polonica A **87**, 723 (1995).
104. L.I. Buravov, A.V. Zvarykina, N.D. Kushch, V.N. Laukhin, V.A. Merzhanov, A.G. Khomenko, E.B. Yagubskii, Sov. Phys. JETP **68**, 182 (1989).

105. R.H. McKenzie, P. Moses, Phys. Rev. Lett. **81**, 4492 (1998).
106. J. Singleton, P.A. Goddard, A. Ardavan, N. Harrison, S.J. Blundell, J.A. Schlueter, A.M. Kini, Phys. Rev. Lett. **88**, 037001 (2002).
107. C.S. Jacobsen, In: *Low-Dimensional Conductors and Superconductors.* ed. by D. Jérome and L.G. Caron (Plenum Press, New York 1987) p. 253.
108. A. Graja, 'Optical Properties'. In: *Organic Conductors, Fundamentals and Applications.* ed. by J.-P. Farges (M. Dekker, New York 1994) pp. 229–267.
109. M. Dressel, Synth. Met. **85**, 1503 (1997).
110. L. Degiorgi, V. Vescoli, W. Henderson, G. Gruner, L.K. Montgomery, J. Phys. IV France **10**, Pr3-103 (2000).
111. M. Dressel, 'Optical properties of layered organic superconductors'. In: *Studies of High Temperature Superconductors*, Vol. **34**. (Nova Science, New York 2000).
112. J.E. Eldridge, Y. Lin, H.H. Wang, J.M. Williams, A.M. Kini, Phys. Rev. B **57**, 597 (1998).
113. Y. Lin, J.E. Eldridge, J.A. Schlueter, H.H. Wang, A.M. Kini, Phys. Rev. B **64**, 024506 (2001).
114. C.S. Jacobsen, D.B. Danner, K. Bechgaard, Phys. Rev. Lett. **46**, 1142 (1981); Phys. Rev B **28**, 7019 (1983); C.S. Jacobsen, K. Mortensen, M. Weger, K. Bechgaard, Solid State Commun. **38**, 423 (1981).
115. D. Pedron, R. Bozio, M. Meneghetti, C. Pecile, Phys. Rev B **49**, 10893 (1994).
116. F. Zwick, S. Brown, G. Margaritondo, C. Merlic, M. Onellion, J. Voit, M. Grioni, Phys. Rev. Lett. **79**, 3982 (1997).
117. F. Zwick, D. Jérome, G. Margaritondo, M. Onellion, J. Voit, M. Grioni, Phys. Rev. Lett. **81**, 2974 (1998).
118. K. Kornelsen, J.E. Eldridge, H.H. Wang, J.M. Williams, Phys. Rev. B **44**, 5235 (1991).
119. K. Kornelsen, J.E. Eldridge, H.H. Wang, H.A. Charlier, J.M. Williams, Solid State Commun. **81**, 343 (1992).
120. N.O. Lipari, M.J. Rice, C.B. Duke, R. Bozio, A. Girlando, C. Pecile, Int. Quantum Chem. Symp. **11**, 583 (1977).
121. Important references are [55, 118, 122, 123], see [9, 111] for both earlier and more recent citations.
122. J.E. Eldridge, C.C. Homes, J.M. Williams, A.M. Kini, H.H. Wang, Spectrochim. Acta A **51**, 947 (1995).
123. G. Visentini, M. Masino, C. Bellitto, A. Girlando, Phys. Rev. B **58**, 9460 (1998).
124. M.E. Kozlov, K.I. Pokhodnia, A.A. Yurchenko, Spectrochim. Acta A **43**, 323 (1987).
125. M.E. Kozlov, K.I. Pokhodnia, A.A. Yurchenko, Spectrochim. Acta A **45**, 437 (1989).
126. M. Meneghetti, R. Bozio, C. Pecile, J. Phys. **47**, 1377 (1986).
127. A.M.Kini, K.D. Carlson, H.H. Wang, J.A. Schlueter, J.D. Dudek, S.A. Sirchio, U. Geiser, K.R. Lykke, J.M. Williams, Physica C **264**, 81 (1996); A.M.Kini, K.D. Carlson, J.D. Dudek, U. Geiser, H.H. Wang, J.M. Williams, Synth. Met. **85**, 1617 (1997).
128. A. Nowack, M. Weger, D. Schweitzer, H. Keller, Solid State Commun. **60**, 199 (1986).
129. A. Nowack, U. Poppe, M. Weger, D. Schweitzer, H. Schenk, Z. Phys. B **68**, 41 (1987).

130. S. Sugai, H. Mori, H. Yamochi, G. Saito, Phys. Rev. B **47**, 14374 (1993).
131. K.I. Pokhodnia, A. Graja, M. Weger, D. Schweitzer, Z. Phys. B **90**, 127 (1993).
132. M. Dressel, J.E. Eldridge, J.M. Williams, H.H. Wang, Physica C **203**, 247 (1992).
133. A. Andrieux, D. Jérome, K. Bechgaard, J. Phys. (Paris) Lett. **42**, L87 (1981).
134. E. Barthel, G. Quirion, P. Wzietek, D. Jérome, J.B. Christensen, M. Jorgensen, K. Bechgaard, Europhys. Lett. **21**, 87 (1993).
135. K. Mortensen, Y. Tomkiewicz, K. Bechgaard, Phys. Rev. B **25**, 3319 (1982).
136. R.L. Greene, E.M. Engler, Phys. Rev. Lett. **45**, 1587 (1980).
137. D. Jérome, Science **252**, 1509 (1991).
138. H. Mayaffre, P. Wzietek, C. Lenoir, D. Jérome, P. Batail, Europhys. Lett. **28**, 205 (1994).
139. H. Mayaffre, P. Wzietek, S. Charfi–Kaddour, C. Lenoir, D. Jérome, P. Batail, Physica B **206 & 207**, 767 (1995).
140. A. Kawamoto, K. Miyagawa, Y. Nakazawa, K. Kanoda, Phys. Rev. Lett. **74**, 3455 (1995).
141. A. Kawamoto, K. Miyagawa, Y. Nakazawa, K. Kanoda, Phys. Rev. B **52**, 15522 (1995).
142. S.M. De Soto, C.P. Slichter, A.M. Kini, H.H. Wang, U. Geiser, J.M. Williams, Phys. Rev. B **52**, 10364 (1995).
143. P. Wzietek, H. Mayaffre, D. Jérome, S. Brazovskii, J. Phys. I France **6**, 2011 (1996).
144. V. Kataev, G. Winkel, D. Khomskii, D. Wohlleben, W. Crump, K.F. Tebbe, J. Hahn, Solid State Commun. **83**, 435 (1992).
145. K. Frikach, M. Poirier, M. Castonguay, K.D. Truong, Phys. Rev. B **61**, R6491 (2000).
146. T. Shimizu, N. Yoshimoto, M. Nakamura, M. Yoshizawa, Physica B **281 & 282**, 896 (2000).
147. Y. Lin, J.E. Eldridge, H.H. Wang, A.M. Kini, J.M. Williams, J.A. Schlueter, Phys. Rev. B **58**, R599 (1998).
148. J. Merino, R.H. McKenzie, Phys. Rev. B **62**, 16442 (2000).
149. J. Merino, R.H. McKenzie, Phys. Rev. B **61**, 7996 (2000).
150. M. Kund, K. Andres, H. Müller, G. Saito, Physica B **203**, 129 (1994).
151. J. Müller, M. Lang, F. Steglich, J.A. Schlueter, A.M. Kini, U. Geiser, J. Mohtasham, R.W. Winter, G.L. Gard, T. Sasaki, N. Toyota, Phys. Rev. B **61**, 11739 (2000).
152. U. Welp, S. Fleshler, W.K. Kwok, G.W. Crabtree, K.D. Carlson, H.H. Wang, U. Geiser, J.M. Williams, V.M. Hitsman, Phys. Rev. Lett. **69**, 840 (1992).
153. K. Miyagawa, A. Kawamoto, Y. Nakazawa, K. Kanoda, Phys. Rev. Lett. **75**, 1174 (1995).
154. M. Pinterić, M. Miljak, N. Biškup, O. Milat, I. Aviani, S. Tomić, D. Schweitzer, W. Strunz, I. Heinen, Eur. Phys. J B **11**, 217 (1999).
155. K. Miyagawa, A. Kawamoto, K. Uchida, K. Kanoda, Physica B **284–288**, 1589 (2000).
156. H. Posselt, H. Müller, K. Andres, G. Saito, Phys. Rev. B **49**, 15849 (1994).
157. M.A. Tanatar, T. Ishiguro, H. Ito, M. Kubota, G. Saito, Phys. Rev. B **55**, 12529 (1997).
158. M. Tokumoto, H. Anzai, K. Murata, K. Kajimura, T. Ishiguro, Japan J. Appl. Phys. **26** Suppl. 26–3, 1977 (1987).

159. J.P. Pouget, S. Ravy, J. Phys. I France **6**, 1501 (1996).
160. S. Ravy, R. Moret, J.P. Pouget, Phys. Rev. B **38**, 4469 (1988).
161. S. Tomic *et al.*, J. Phys. C3 **44**, 1083 (1983).
162. H. Schwenk, K. Andres, F. Wudl, Phys. Rev. B **29**, 500 (1984).
163. T. Takahashi, D. Jérome, K. Bechgaard, J. Physique Lett. **43**, L565 (1982).
164. K. Mortensen, C.S. Jacobsen, A. Lindegaard–Andersen, K. Bechgaard, J. Physique **44**, C3-963 (1983).
165. H. Yang, J.C. Lasjaunias, P. Monceau, J. Phys.: Cond. Mat. **12**, 7183 (2000).
166. K. Saito, H. Akutsu, M. Sorai, Solid State Commun. **111**, 471 (1999).
167. H. Akutsu, K. Saito, M. Sorai, Phys. Rev. B **61**, 4346 (2000).
168. A. Sato, H. Akutsu, K. Saito, M. Sorai, Synth. Met. **120**, 1035 (2001).
169. For a review, see e.g., R.W. Cahn (editor): 'Glasses and Amorphous Materials'. In: *Materials Science and Technology* Vol. **9** (Verlag Chemie, Weinheim 1991) p. 137; W. Kauzmann: *The nature of the glassy state and the behavior of liquids at low temperatures*, Chem. Rev. **43**, 219 (1948).
170. M.A. deBolt, A.J. Easteal, P.B. Macedo, and C.T. Moynihan, J. Am. Ceram. Soc. **59**, 16 (1976).
171. P. Nagel, V. Pasler, C. Meingast, A.I. Rykov, S. Tajima, Phys. Rev. Lett. **85**, 2376 (2000).
172. X. Su, F. Zuo, J.A. Schlueter, M.E. Kelly, J.M. Williams, Phys. Rev. B **57**, R14056 (1998).
173. A. Kawamoto, K. Miyagawa, K. Kanoda, Phys. Rev. B **55**, 14140 (1997).
174. Y. Watanabe, H. Sato, T. Sasaki, N. Toyota, J. Phys. Soc. Japan **60**, 3608 (1991).
175. X. Su, F. Zuo, J.A. Schlueter, M.E. Kelly, and J.M. Williams, Solid State Commun. **107**, 731 (1998).
176. A. Aburto, L. Fruchter, C. Pasquier, Physica C **303**, 185 (1998).
177. M. Pinterić, S. Tomić, M. Prester, D. Drobac, K. Maki, cond–mat/0206574 (2002).
178. H. Ito, T. Ishiguro, T. Kondo, G. Saito, Phys. Rev. B **61**, 3243 (2000).
179. D. Jaccard, H. Wilhelm, D. Jérome, J. Moser, C. Carcel, J.M. Fabre, J. Phys.: Cond. Mat. **13**, L1 (2001).
180. L. Balicas, K. Behnia, W. Kang, E. Canadell, P. Auban–Senzier, D. Jérome, M. Ribault, J.M. Fabre, J. Phys. I France **4**, 1539 (1994).
181. F. Guo, K. Murata, A. Oda, Y. Mizuno, H. Yoshino, J. Phy. Soc. Japan, **69**, 2164 (2000).
182. H. Hirai, R. Kondo, M. Maesato, T. Shibata, S. Kagoshima, Synth. Met. **120**, 963 (2001).
183. M. Miyazaki, K. Kishigi, Y. Hasegawa, J. Phy. Soc. Japan, **69**, 997 (2000).
184. A. Kawamoto, H. Taniguchi, K. Kanoda, J. Am. Chem. Soc. **120**, 10984 (1998).
185. H. Taniguchi, A. Kawamoto, K. Kanoda, Phys. Rev. B **59**, 8424 (1999); Physica B **284–288**, 519 (2000).
186. Y. Nakazawa, H. Taniguchi, A. Kawamoto, and K. Kanoda, Phys. Rev. B **61**, R16295 (2000).
187. J. Müller, Thermodynamische Untersuchungen an quasi–zweidimensionalen organischen Supraleitern. PhD Thesis, Dresden University, Dresden (2001), (Shaker Verlag, Aachen 2002).
188. J.E. Schirber, E.L. Venturini, A.M. Kini, H.H. Wang, J.R. Witworth, J.M. Williams, Physica C **152**, 157 (1988).

189. J.E. Schirber, D.L. Overmyer, J.M. Williams, A.M. Kini, H.H. Wang, Physica C **170**, 231 (1990).
190. H. Ito, T. Ishiguro, M. Kubota, G. Saito, J. Phys. Soc. Japan **65**, 2987 (1996).
191. S. Lefebvre, P. Wzietek, S. Brown, C. Bourbonnais, D. Jérome, C. Mézière, M. Fourmigué, P. Batail, Phys. Rev. Lett. **85**, 5420 (2000).
192. A. Sato, E. Ojima, H. Akutsu, H. Kobayashi, A. Kobayashi, P. Cassoux, Chem. Lett. **1998**, 673 (1998).
193. F. Goze, V.N. Laukhin, L. Brossard, A. Audouard, J.P. Ulmet, S. Azkenazy, T. Naito, H. Kobayashi, A. Kobayashi, M. Tokumoto, P. Cassoux, Physica B **211**, 290 (1995).
194. L. Brossard, R. Clerac, C. Coulon, M. Tokumoto, T. Ziman, D.K. Petrov, V.N. Laukhin, M.J. Naughton, A. Audouard, F. Goze, A. Kobayashi, H. Kobayashi, P. Cassoux, Eur. Phys. J. B **1**, 439 (1998).
195. C. Hotta, H. Fukuyama, J. Phys. Soc. Japan **69**, 2577 (2000).
196. A.F. Hebard, M.J. Rosseinsky, R.C. Haddon, D.W. Murphy, S.H. Glarum, T.T.M. Palstra, A.P. Ramirez, A.R. Kortan, Nature (London) **350**, 600 (1991).
197. V.G. Kogan, Phys. Rev. B **24**, 1572 (1981).
198. W.E. Lawrence, S. Doniach, In: *Proceedings to the Twelfth International Conference on Low–Temperature Physics*, Kyoto 1970. ed. E. Kanada (Keigaku, Tokyo 1971) p. 361.
199. R. Kleiner, F. Steinmeyer, G. Kunkel, P. Müller, Phys. Rev. Lett. **68**, 2394 (1992).
200. P. Müller, Advances in Solid State Physics **34** (Vieweg–Verlag, Braunschweig 1994).
201. U. Geiser, J.A. Schlueter, H.H. Wang, A.M. Kini, J.M. Williams, P.P. Sche, H.I. Zakowicz, M.L. VanZile, J.D. Dudek, P.G. Nixon, R.W. Winter, G.L. Gard, J. Ren, M.-H. Whangbo, J. Am. Chem. Soc. **118**, 9996 (1996).
202. J.A. Schlueter, U. Geiser, J.M. Williams, J.D. Dudek, M.E. Kelly, J.P. Flynn, R.R. Wilson, H.I. Zakowicz, P.P. Sche, D. Naumann, T. Roy, P.G. Nixon, R.W. Winter, G.L. Gard, Synth. Met. **85**, 1453 (1997).
203. T.P. Orlando, E.J. McNiff, Jr., S. Foner, M.R. Beasly, *Phys. Rev. B* **19**, 4545 (1979).
204. M. Tinkham, *Introduction to Superconductivity*, 2nd edn. (McGraw–Hill, New York 1996).
205. M. Lang, F. Steglich, N. Toyota, T. Sasaki, Phys. Rev. B **49**, 15227 (1994).
206. D.E. Farrell, C.J. Allen, R.C. Haddon, S.V. Chichester, Phys. Rev. B **42**, 8694 (1990).
207. S. Kawamata, K. Okuda, T. Sasaki, N. Toyota, Solid State Commun. **89**, 955 (1994).
208. J.C. Martinez, S.H. Brongersma, A. Koshelev, B. Ivlev, P.H. Kes, R.P. Griessen, D.G. de Groot, Z. Tarnavski, A.A. Menovsky, Phys. Rev. Lett. **69**, 2276 (1992).
209. Y. Matsuda, Marat B. Gaifullin, K. Kumagai, M. Kosugi, K. Hirata, Phys. Rev. Lett. **78**, 1972 (1997).
210. W.J. Skocpol, M. Tinkham, Rep. Prog. Phys. **38**, 1049 (1975).
211. U. Welp, S. Fleshler, W.K. Kwok, R.A. Klemm, V.M. Vinokur, J. Downey, B. Veal, G.W. Crabtree, Phys. Rev. Lett. **67**, 3180 (1991).
212. V. Pasler, PhD Thesis, Karlsruhe University, Karlsruhe (2000).

213. G. Bergmann, Z. Phys. **225**, 430 (1969).
214. P.A. Lee, S.R. Shenoy, Phys. Rev. Lett. **28**, 1025 (1972).
215. R. Ikeda, T. Ohmi, T. Tsuneto, J. Phys. Soc. Japan **59**, 1397 (1990).
216. S. Ullah, A.T. Dorsey, Phys. Rev. B **44**, 262 (1991).
217. Q. Li, In: *Physical Properties of High–Temperature Superconductors* Vol. **V**. ed. by D.M. Ginsberg (World Scientific, Singapore 1996).
218. S. Friemel, C. Pasquier, Y. Loirat, D. Jérome, Physica C **259**, 181 (1996).
219. H. Ito, M. Watanabe, Y. Nogami, T. Ishiguro, T. Komatsu, G. Saito, N. Hosoito, Jpn. J. Appl. Phys. Series **7**, 419 (1992).
220. J.S. Brooks, X. Chen, S.J. Klepper, S. Valfells, G.J. Athas, Y. Tanaka, T. Kinoshita, N. Kinoshita, M. Tokumoto, H. Anzai, C.C. Agosta, Phys. Rev. B **52**, 14457 (1995).
221. D. Chasseau, J. Gaultier, M. Rahal, L. Ducasse, M. Kurmoo, P. Day, Synth. Met. **41–43**, 2039 (1991).
222. M. Rahal, D. Chasseau, J. Gaultier, L. Ducasse, M. Kurmoo, P. Day, Acta Cryst. B **53**, 159 (1997).
223. G. Gladstone, M.A. Jensen, J.R. Schrieffer, In: *Superconductivity* Vol. **2**. ed. by R.D. Parks (M. Dekker, New York 1969) p. 655.
224. C. Meingast, B. Blank, H.Bürkle, B. Obst, T. Wolf, H. Wühl, V. Selvamanickam, K. Salama, Phys. Rev. B **41**, 11299 (1990).
225. H. Kusuhara, Y. Sakata, Y. Ueba, K. Tada, M. Kaji, T. Ishiguro, Solid State Commun. **74**, 251 (1990).
226. C.E. Campos, J.S. Brooks, P.J.M. van Bentum, J.A.A.J. Perenboom, S.J. Klepper, P.S. Sandhu, S. Valfells, Y. Tanaka, T. Kinoshita, N. Kinoshita, M. Tokumoto, H. Anzai, Phys. Rev. B **52**, R7014 (1995).
227. S. Kagoshima, M. Maesato, R. Kondo, T. Shibata, H. Hirai, Synth. Met. **120**, 683 (2001); M. Maesato, Y. Kaga, R. Kondo, H. Hirai, S. Kagoshima, Synth. Met. **120**, 941 (2001).
228. E.S. Choi, J.S. Brooks, S.Y. Han, L. Balicas. J.S. Qualls, Phil. Mag. B **81**, 399 (2001).
229. M. Kund, H. Veith, H. Müller, K. Andres, G. Saito, Physica C **221**, 119 (1994).
230. M. Kund, J. Lehrke, W. Biberacher, A. Lerf, K. Andres, Synth. Met. **70**, 949 (1995).
231. S. Sadewasser, C. Looney, J.S. Schilling, J.A. Schlueter, J.M. Williams, P.G. Nixon, R.W. Winter, G.L. Gard, Solid State Commun. **102**, 571 (1997).
232. T. Biggs, A.-K. Klehe, J. Singleton, D. Bakker, J. Symington, P. Goddard, A. Ardavan, W. Hayes, J.A. Schlueter, T. Sasaki, M. Kurmoo, J. Phys.: Cond. Mat. **14**, L495 (2002).
233. J. Müller, M. Lang, J.A. Schlueter, U. Geiser, D. Schweitzer, Synth. Met. **120**, 855 (2001).
234. P.B. Allen, R.C. Dynes, Phys. Rev. B **12**, 905 (1975).
235. H. Kino, H. Fukuyama, J. Phys. Soc. Japan **65**, 2158 (1996).
236. H. Kondo, T. Moriya, Physica B **281 & 282**, 940 (2000).
237. A. Painelli, A. Girlando, A. Fortunelli, Phys. Rev. B **64**, 054509 (2001).
238. A.M. Kini, J.A. Schlueter, B.H. Ward, U. Geiser, H.H. Wang, Synth. Met. **120**, 713 (2001).
239. J.A. Schlueter, A.M. Kini, B.H. Ward, U. Geiser, H.H. Wang, J. Mohtasham, R.W. Winter, G.L. Gard, Physica C **351**, 261 (2001).
240. Y. Watanabe, T. Shimazu, T. Sasaki, N. Toyota, Synth. Met. **86**, 1917 (1997).

241. J.M. Williams, A.J. Schultz, U. Geiser, K.D. Carlson, A.M. Kini, H.H. Wang, W.K. Kwok, M.-H. Whangbo, J.E. Schirber, Science **252**, 1501 (1991).
242. R.S. Edwards, A. Narduzzo, J. Singleton, A. Ardavan, J.A. Schlueter, cond-mat/0208086 (2002).
243. D. Mailly, M. Ribault, K. Bechgaard, J. Physique **44**, C3-1037 (1983).
244. P. Garoche, R. Brusetti, D. Jérome, K. Bechgaard, J. Physique Lett. **43**, L147 (1982).
245. K. Murata, M. Tokumoto, H. Anzai, K. Kajimura, T. Ishiguro, Jpn. J. Appl. Phys. **26**, Suppl. 26–3, 1367 (1987).
246. A.M. Clogston, Phys. Rev. Lett. **9**, 266 (1962).
247. B.S. Chandrasekhar, Appl. Phys. Lett. **1**, 7 (1962).
248. R.L. Greene, P. Haen, S.Z. Huang, E.M. Engler, M.Y. Choi, P.M Chaikin, Mol. Cryst. Liq. Cryst. **79**, 539 (1982).
249. P.M. Chaikin, M.Y. Choi, R.L. Greene, J. Magn. Magn. Mater. **31**, 1268 (1983).
250. I.J. Lee, M.J. Naughton, G.M. Danner, P.M. Chaikin, Phys. Rev. Lett. **78**, 3555 (1997).
251. H. Schwenk, K. Andres, F. Wudl, E. Aharon–Shalom, Solid State Commun. **45**, 767 (1983).
252. Y. Shimojo, A.E. Kovalev, S. Kamiya, E. Ohmichi, T. Ishiguro, H. Yamochi, G. Saito, A. Ayari, P. Monceau, Physica B **294–295**, 427 (2001).
253. C. Mielke, J. Singleton, M.-S. Nam, N. Harrison, C.C. Agosta, B. Fravel, L.K. Montgomery, J. Phys.: Cond. Mat. **13**, 8325 (2001).
254. H. Mayaffre, P. Wzietek, D. Jérome, C. Lenoir, P. Batail, Phys. Rev. Lett. **75**, 4122 (1995).
255. T. Kawasaki, M.A. Tanatar, T. Ishiguro, H. Tanaka, A. Kobayashi, H. Kobayashi, Synth. Met. **120**, 771 (2001).
256. F. Zuo, J.S. Brooks, R.H. McKenzie, J.A. Schlueter, J.M. Williams, Phys. Rev. B **61**, 750 (2000).
257. J. Singleton, J.A. Symington, M.S. Nam, A. Ardavan, M. Kurmoo, P. Day, J. Phys.: Cond. Mat. **12**, L641 (2001).
258. M.A. Tanatar, T. Ishiguro, H. Tanaka, A. Kobayashi, H. Kobayashi, J. Supercond. **12**, 511 (1999).
259. J. Hagel, S. Wanka, D. Beckmann, J. Wosnitza, D. Schweitzer, W. Strunz, M. Thumfart, Physica C **291**, 213 (1997).
260. M. Dressel, O. Klein, G. Grüner, K.D. Carlson, H.H. Wang, J.M. Williams, Phys. Rev. B **50**, 13603 (1994).
261. P.A. Mansky, P.M. Chaikin, R.C. Haddon, Phys. Rev. B **50**, 15929 (1994).
262. M. Pinterić, S. Tomić, M. Prester, D. Drobac, O. Milat, K. Maki, D. Schweitzer, I. Heinen, W. Strunz, Phys. Rev. B **61**, 7033 (2000).
263. D.R. Harshman, R.N. Kleiman, R.C. Haddon, S.V. Chichester–Hicks, M.L. Kaplan, L.W. Rupp Jr., T. Pfiz, D.L. Williams, D.B. Mitzi, Phys. Rev. Lett. **64**, 1293 (1990).
264. M. Lang, N. Toyota, T. Sasaki, H. Sato, Phys. Rev. Lett. **69**, 1443 (1992).
265. M. Lang, N. Toyota, T. Sasaki, H. Sato, Phys. Rev. B **46**, 5822 (1992).
266. D. Achkir, M. Poirier, C. Bourbonnais, G. Quirion, C. Lenoir, P. Batail, D. Jérome, Phys. Rev. B **47**, 11595 (1993).
267. H. Elsinger, J. Wosnitza, S. Wanka, J. Hagel, D. Schweitzer, W. Strunz, Phys. Rev. Lett. **84**, 6098 (2000).

268. J.E. Graebner, R.C. Haddon, S.V. Chichester, S.H. Glarum, Phys. Rev. B **41**, 4808 (1990).
269. P. Fulde, R.A. Ferrell, Phys. Rev. **135**, A550 (1964).
270. A.I. Larkin, Y.N. Ovchinnikov, Sov. Phys. JETP **20**, 762 (1965).
271. J.A. Symington, J. Singleton, M.-S. Nam, A. Ardavan, M. Kurmoo, P. Day, Physica B **294–295**, 418 (2001).
272. T. Ishiguro, J. Phys. IV France **10**, Pr3–139 (2000).
273. G. Blatter, M.V. Feigel'man, V.B. Geshkenbein, A.I. Larkin, V.M. Vinokur, Rev. Mod. Phys. **66**, 1125 (1994).
274. E. Zeldov, D. Majer, M. Konczykowski, V.B. Geshkenbein, V.M. Vinokur, H. Shtrikman, Nature **375**, 373 (1995).
275. S. Schilling, R.A. Fisher, N.E. Phillips, U. Welp, D. Dasgupta, W.K. Kwok, G.W. Crabtree, Nature **382**, 791 (1996).
276. J.R. Clem, Phys. Rev. B **43**, 7837 (1991).
277. S.L. Lee, F.L. Pratt, S.J. Blundell, C.M. Aegerter, P.A. Pattenden, K.H. Chow, E.M. Forgan, T. Sasaki, W. Hayes, H. Keller, Phys. Rev. Lett. **79**, 1563 (1997).
278. L.Ya. Vinnikov, T.L. Barkov, M.V. Kartsovnik, N.D. Kushch, Phys. Rev. B **61**, 14358 (2000).
279. T. Nishizaki, T. Sasaki, T. Fukase, N. Kobayashi, Phys. Rev. B **54**, R3760 (1996).
280. M. Inada, T. Sasaki, T. Nishizaki, N. Kobayashi, S. Yamada, T. Fukase, J. Low Temp. Phys. **117**, 1423 (1999).
281. M.M. Mola, J.T. King, C.P. McRaven, S. Hill, J.S. Qualls, J.S. Brooks, Phys. Rev. B **62**, 5965 (2000).
282. M.M. Mola, S. Hill, J.S. Brooks, J.S. Qualls, Phys. Rev. Lett. **86**, 2130 (2001).
283. T. Shibauchi, M. Sato, S. Ooi, T. Tamegai, Phys. Rev. B **57**, R5622 (1998).
284. T. Sasaki, W. Biberacher, K. Neumaier, W. Hehn, K. Andres, T. Fukase, Phys. Rev. B **56**, 10889 (1998).
285. N. Yoneyama, A. Higashihara, T. Sasaki, N. Kobayashi, S. Yamada, Synth. Met. (2002), in press.
286. L. Fruchter, A. Aburto, C. Pham–Phu, Phys. Rev. B **56**, R2936 (1997).
287. F. Steinmeyer, R. Kleiner, P. Müller, H. Müller, K. Winzer, Europhys. Lett. **25**, 459 (1994).
288. H. Shimahara, J. Phys. Soc. Japan **66**, 541 (1997).
289. H. Shimahara, J. Phys. Soc. Japan **67**, 1872 (1998).
290. H. Shimahara, Phys. Rev. B **50**, 12760 (1994).
291. M. Tachiki, S. Takahashi, P. Gegenwart, M. Weiden, M. Lang, C. Geibel, F. Steglich, R. Modler, C. Paulsen, Y. Ōnuki, Z. Phys. B **100**, 369 (1996).
292. P. Gegenwart, M. Deppe, M. Köppen, F. Kromer, M. Lang, R. Modler, M. Weiden, C. Geibel, F. Steglich, T. Fukase, N. Toyota, Ann. Physik **5**, 307 (1996).
293. S. Uji, H. Shinagawa, T. Terashima, T. Yakabe, Y. Terai, M. Tokumoto, A. Kobayashi, H. Tanaka, H. Kobayashi, Nature, **410**, 908 (2001).
294. L. Balicas, J.S. Brooks, K. Storr, S. Uji, M. Tokumoto, H. Tanaka, H. Kobayashi, A. Kobayashi, V. Barzykin, L.P. Gor'kov, Phys. Rev. Lett. **87**, 0670021 (2001).
295. S. Uji, C. Terakura, T. Terashima, T. Yakabe, Y. Imanaka, Y. Terai, S. Yasuzuka, M. Tokumoto, F. Sakai, A. Kobayashi, H. Tanaka, H. Kobayashi, L. Balicas, J.S. Brooks, Synth. Met. (2002), in press.

296. J. Bardeen, L.N. Cooper, J.R. Schrieffer, Phys. Rev. **108**, 1175 (1957).
297. F. Steglich, J. Aarts, C.D. Bredl, W. Lieke, D. Meschede, W. Franz, H. Schäfer, Phys. Rev. Lett. **43**, 1892 (1979).
298. J.G. Bednorz, K.A. Müller, Z. Phys. B **64**, 189 (1986).
299. Y. Maeno, H. Hashimoto, K. Yoshida, D. Nishizaki, T. Fujita, J.G. Bednorz, F. Lichtenberg, Nature **372**, 532 (1994).
300. S. Mazumdar, Solid State Commun. **66**, 427 (1988).
301. Y.J. Uemura, L.P. Le, G.M. Luke, B.J. Sternlieb, W.D. Wu, J.H. Brewer, T.M. Riseman, C.L. Seaman, M.B. Maple, M. Ishikawa, D.G. Hinks, J.D. Jorgensen, G. Saito, H. Yamochi, Phys. Rev. Lett. **66**, 2665 (1991).
302. W.A. Little, 'Organic Conductors: An Overview'. In: *Organic Conductors, Fundamentals and Applications.* ed. by J.-P. Farges (M. Dekker, New York 1994) pp. 1–24.
303. K. Yamaji, Solid State Commun. **61**, 413 (1987).
304. A. Girlando, M. Masino, A. Brillante, R.G. Della Valle, E. Venuti, Phys. Rev. B **66**, 100507(R) (2002).
305. A. Girlando, M. Masino, G. Visentini, R.G. Della Valle, A. Brillante, E. Venuti, Phys. Rev. B **62**, 14476 (2000).
306. G. Varelogiannis, Phys. Rev. Lett. **88**, 117005 (2002).
307. J. Schmalian, Phys. Rev. Lett. **81**, 4232 (1998).
308. E. Demiralp, W.A. Goddard III, Phys. Rev. B **56**, 11907 (1997).
309. H. Kondo, T. Moriya, J. Phys. Soc. Japan **67**, 3695 (1998).
310. H. Kondo, T. Moriya, J. Phys. Cond. Mat. **11**, L363 (1999).
311. H. Kondo, T. Moriya, J. Phys. Soc. Japan **68**, 3170 (1999).
312. H. Kino, H. Kontani, J. Phys. Soc. Japan **67**, 3691 (1998).
313. M. Vojta, E. Dagotto, Phys. Rev. B **59**, R713 (1999).
314. K. Kuroki, H. Aoki, Phys. Rev. B **60**, 3060 (1999).
315. T. Jujo, K. Yamada, J. Phys. Soc. Japan **68**, 1331 (1999).
316. H. Kino, H. Kontani, J. Phys. Soc. Japan **68**, 1481 (1999).
317. T. Jujo, K. Yamada, J. Phys. Soc. Japan **68**, 2198 (1999).
318. R. Louati, S. Charfi–Kaddour, A. Ben Ali, R. Bennaceur, M. Héritier, Phys. Rev. B **62**, 5957 (2000).
319. J. Marino, R.H. McKenzie, Phys. Rev. Lett. **87**, 237002 (2001).
320. K. Maki, In: *Superconductivity* Vol. **2**. ed. by R.D. Parks (M. Dekker, New York 1969) p. 1035.
321. A.A. Abrikosov, L.P. Gor'kov, Sov. Phys. JETP **12**, 1243 (1969).
322. H. Keiber, C. Geibel, B. Renker, H. Rietschel, H. Schmidt, H. Wühl, G.R. Stewart, Phys. Rev. B **30**, 2542 (1984).
323. B. Lüthi, M. Herrmann, W. Assmus, H. Schmidt, H. Rietschel, H. Wühl, U. Gottwick, G. Sparn, F. Steglich, Z. Phys. B. **60**, 387 (1985).
324. M. Jourdan, M. Huth, H. Adrian, Nature **398**, 47 (1999).
325. N.K. Sato, N. Aso, K. Miyake, S. Shiina, P. Thalmeier, G. Varelogiannis, C. Geibel, F. Steglich, P. Fulde, T. Komatsubara, Nature 410, 340 (2001).
326. C.C. Tsuei, J.R. Kirtley, C.C. Chi, Lock See Yu–Jahnes, A. Gupta, T. Shaw, J.Z. Sun, M.B. Ketchen, Phys. Rev. Lett. **73**, 593 (1994).
327. D.J. van Harlingen, 'Phase–sensitive tests of the symmetry of the pairing state in the high–temperature superconductors – Evidence for $d_{x^2-y^2}$ symmetry', Rev. Mod. Phys. **67**, 515 (1995).
328. P. Auban–Senzier, C. Bourbonnais, D. Jérome, C. Lenoir, P. Batail, E. Canadell, J.P. Buisson, S. Lefrant, J. Phys. I France **3**, 871 (1993).

329. K.D. Carlson, J.N. Williams, U. Geiser, A.M. Kini, H.H. Wang, R.A, Klemm, S.K. Kumar, J.A. Schlueter, J.R. Ferraro, K.R. Lykke, P. Wurz, D.H. Parker, J.D.M. Sutin, Inorg. Chem. **114**, 10069 (1992).
330. J.D. Axe, G. Shirane, Phys. Rev. B **8**, 1965 (1973).
331. S.M. Shapiro, G. Shirane, Phys. Rev. B **12**, 4899 (1975).
332. N. Toyota, M. Lang, S. Ikeda, T. Kajitani, T. Shimazu, T. Sasaki, K. Shibata, Synth. Met. **86**, 2009 (1997).
333. R. Zeyher, G. Zwicknagl, Z. Phys. B **78**, 175 (1990).
334. J.M. Schrama, E. Rzepniewski, R.S. Edwards, J. Singleton, A. Ardavan, M. Kurmoo, P. Day, Phys. Rev. Lett. **83**, 3041 (1999).
335. T. Arai, K. Ichimura, K. Nomura, S. Takasaki, J. Yamada, S. Nakatsuji, H. Anzai, Phys. Rev. B **63**, 104518 (2001); Solid State Commun. **116**, 679 (2000).
336. J.M. Schrama, J. Singleton, Phys. Rev. Lett. **86**, 3453 (2001).
337. S. Hill, N. Harrison, M. Mola, J. Wosnitza, Phys. Rev. Lett. **86**, 3451 (2001).
338. T. Shibauchi, Y. Matsuda, M.B. Gaifullin, T. Tamegai, Phys. Rev. Lett. **86**, 3452 (2001).
339. H. Bando, S. Kashiwaya, H. Tokumoto, H. Anzai, N. Kinoshita, K. Kajimura, J. Vac. Sci. Technol. A **8**, 479 (1990).
340. H. Won, K. Maki, Physica B **312–313**, 44 (2002).
341. D.J. Scalapino, E. Loh, Jr., J.E. Hirsch, Phys. Rev. B **35**, 6694 (1987).
342. K. Kanoda, K. Miyagawa, A. Kawamoto, Y. Nakazawa, Phys. Rev. B **54**, 76 (1996).
343. M.J. Graf, S.K. Yip, J.A. Sauls, D. Rainer , Phys. Rev. B **53**, 15147 (1996).
344. M.R. Norman, P.J. Hirschfeld, Phys. Rev. B **53**, 5706 (1996).
345. B. Mühlschlegel, Z. Phys. **155**, 313 (1959).
346. K. Kanoda, K. Akiba, K. Suzuki, T. Takahashi, G. Saito, Phys. Rev. Lett. **65**, 1271 (1990).
347. L.P. Le, G.M. Luke, B.J. Sternlieb, W.D. Wu, Y.J. Uemura, J.H. Brewer, T.M. Riseman, C.E. Stronach, G. Saito, H. Yamochi, H.H. Wang, A.M. Kini, K.D. Carlson, J.M. Williams, Phys. Rev. Lett. **68**, 1923 (1992).
348. A. Carrington, I.J. Bonalde, R. Prozorov, R.W. Giannetta, A.M. Kini, J.A. Schlueter, H.H. Wang, U. Geiser, J.M. Williams, Phys. Rev. Lett. **83**, 4172 (1999).
349. O. Klein, K. Holczer, G. Grüner, J.J. Chang, F. Wudl, Phys. Rev. Lett. **66**, 655 (1991).
350. I. Kosztin, Q.J. Chen, B. Janko, K. Levin, Phys. Rev. B **58**, R5936 (1998); Q.J. Chen, I. Kosztin, B. Janko, K. Levin, Phys. Rev. Lett. **81**, 4708 (1998); Q. Chen, I. Kosztin, K. Levin, Phys. Rev. Lett. **85**, 2801 (2000).
351. Y. Hasegawa, H. Fukuyama, J. Phys. Soc. Japan **56**, 877 (1987).
352. B. Andraka, J.S. Kim, G.R. Stewart, K.D. Carlson, H.H. Wang, J.M. Williams, Phys. Rev. B **40**, 11345 (1989).
353. Y. Nakazawa, K. Kanoda, Phys. Rev. B **55**, R8670 (1997).
354. In [353] the lattice specific heat of κ-$(ET)_2Cu[N(CN)_2]Br$ was estimated by measuring a second, deuterated sample after quench cooling to suppress superconductivity. The data analysis in [353] is based on the assumption that by this procedure the lattice specific heat remains unaffected and is identical to that of the hydrogenated superconducting compound. In [267] it has been shown, however, that the so-derived phonon background differs substantially from that determined in an overcritical field. The reason for this might be

related to the glass–like transition at T_g observed in this system [97], see section 7.3.4.
355. H. Padamsee, J.E. Neighbor, C.A. Shiffman, J. Low Temp. Phys. **12**, 387 (1973).
356. N. Momono, M. Ido, Physica C **264**, 311 (1996).
357. J. Wosnitza, X. Liu, D. Schweitzer, H.J. Keller, Phys. Rev. B **50**, 12747 (1994).
358. S. Wanka, J. Hagel, D. Beckmann, J. Wosnitza, J.A. Schlueter, J.M. Williams, P.G. Nixon, R.W. Winter, G.L. Gard, Phys. Rev. B **57**, 3084 (1998).
359. J. Solyom, Adv. Phys. **28**, 201 (1979).
360. M.Y. Choi, P.M. Chaikin, S.Z. Huang, P. Haen, E.M. Engler, R.L. Greene, Phys. Rev. B **25**, 6208 (1982).
361. S. Bouffard, M. Ribault, R. Brusetti, D. Jérome, K. Bechgaard, J. Phys. C **15**, 2951 (1982).
362. C. Coulon, P. Delhaes, J. Amiell, J.P. Manceau, J.M. Fabre, L. Giral, J. Phys. (Paris) **43**, 1721 (1982).
363. S. Tomić, D. Jérome, D. Mailly, M. Ribault, K. Bechgaard, J. Phys. (Paris) Colloq. **44**, C3–1075 (1983).
364. A.A. Abrikosov, J. Low Temp. Phys. **53**, 359 (1983).
365. L.P. Gor'kov, D. Jérome, J. Phys. (Paris) Lett. **46**, L643 (1985).
366. M. Dressel, Physica C **317–318**, 89 (1999).
367. I.J. Lee, P.M. Chaikin, M.J. Naughton, Phys. Rev. B **62**, R14669 (2000).
368. M. Takigawa, H. Yasuoka, G. Saito, J. Phys. Soc. Jpn. **56**, 873 (1987).
369. S. Belin, K. Behnia, Phys. Rev. Lett. **79**, 2125 (1997).
370. I.J. Lee, P.M. Chaikin, M.J. Naughton, Phys. Rev. B **65**, 180502 (2002).
371. P. Fulde, K. Maki, Phys. Rev. **139**, A788 (1965).
372. I.J. Lee, S.E. Brown, W.G. Clark, M.J. Strouse, M.J. Naughton, W. Kang, P.M. Chaikin, Phys. Rev. Lett. **88**, 017004 (2002).
373. R.A. Klemm, A. Luther, M.R. Beasley, Phys. Rev. B **12**, 877 (1975).
374. X. Huang, K. Maki, Phys. Rev. B **39**, 6459 (1989).
375. A.G. Lebed', JETP Lett. **44**, 114 (1986); L.I. Burlachkov, L.P. Gor'kov, A.G. Lebed', Europhys. Lett. **4**, 941 (1987).
376. N. Dupuis, G. Montambaux, C.A.R. Sá de Melo, Phys. Rev. Lett. **70**, 2613 (1993).
377. I.J. Lee, D.S. Chow, W.G. Clark, J. Strouse, M.J. Naughton, P.M. Chaikin, S.E. Brown, cond-mat/0001332, (2000).

8 Unconventional Superconductivity in Novel Materials

M. Brian Maple, Eric D. Bauer, Vivien S. Zapf
Department of Physics and Institute for Pure and Applied Physical Sciences
University of California, San Diego La Jolla, California, USA
Jochen Wosnitza
Institut für Festkörperphysik, TU Dresden, Dresden, Germany

8.1 **Introduction** 556
8.2 **Conventional Superconductors Containing Localized Magnetic Moments** 557
8.2.1 Introduction 557
8.2.2 Superconducting–Magnetic Interactions 558
8.2.3 Paramagnetic Impurities in Superconductors 559
8.2.4 Magnetic Field Induced Superconductivity 584
8.3 **f–Electron Heavy Fermion Superconductors** 587
8.3.1 Introduction 587
8.3.2 Normal–State Properties 588
8.3.3 Superconducting–State Properties 594
8.3.4 UPd_2Al_3 598
8.3.5 Quantum Critical Points 604
8.3.6 Non–Fermi Liquid Behavior 613
8.3.7 Magnetically Ordered Heavy–Fermion Superconductors 621
8.3.8 Multiple Superconducting Phases 625
8.3.9 Concluding Remarks 635
8.4 **Organic Superconductors** 636
8.4.1 Introduction 636
8.4.2 Normal–State Properties 638
8.4.3 Superconducting State Properties 649
8.4.4 Concluding Remarks 666
8.5 **Layered Cuprate and Ruthenate Superconductors** 668
8.5.1 Introduction 668
8.5.2 The Materials 668
8.5.3 Structure and Charge Carrier Doping 675
8.5.4 Superconducting Properties 677
8.5.5 Normal–State Properties 689
8.5.6 Concluding Remarks 702
8.6 **Comparison of the Properties of Different Classes of Novel Superconductors** 703
Acknowledgements 705
References 706

K. H. Bennemann et al. (eds.), *The Physics of Superconductors*
© Springer-Verlag Berlin Heidelberg 2004

8.1 Introduction

The past three decades have witnessed a series of spectacular developments in the field of superconductivity, driven by advances in the synthesis of new and complex materials. This has spawned several classes of novel superconducting materials, including magnetically ordered superconductors, heavy fermion superconductors, organic superconductors, high T_c cuprate superconductors, ruthenate superconductors, as well as several other interesting superconducting materials such as $Ba_{1-x}K_xBiO_3$, the fcc "buckeyball" compound Rb_3C_{60}, and MgB_2. The extraordinary physical properties of these materials are reviewed in this chapter.

The focus of this article is on the unconventional superconductivity displayed by heavy fermion f–electron materials, organic compounds, and copper and ruthenium oxides (Sections 8.3 – 8.6). In these novel materials, the superconducting phase often occurs in the vicinity of a magnetic phase in the hyperspace of temperature, chemical composition, pressure and magnetic field. This has been widely regarded as evidence that spin fluctuations play an important role in the pairing of superconducting electrons in these materials. In a few cases, this scenario has received additional support from experiments such as electron tunneling, although it has not been definitively established. The unconventional superconductivity observed in many of these materials is characterized by an anisotropic energy gap that appears to vanish at points or along lines on the Fermi surface. This suggests that the superconducting electrons are paired in states with angular momentum greater than zero (p– or d–wave superconductivity). Multiple superconducting phases have been discovered in the heavy fermion compounds UPt_3 and $U_{1-x}Th_xBe_{13}$ and attributed to a multicomponent superconducting order parameter coupled to a second order parameter. In the case of UPt_3, the second order parameter appears to be antiferromagnetic in nature. Recently, superconductivity has been observed under pressure in several antiferromagnetic Ce–based compounds (e.g., $CeIn_3$ [1], $CePd_2Si_2$ [2]) at low temperatures near the critical pressure where the Néel temperature extrapolates to 0 K (quantum critical point). An even more surprising development is the discovery of superconductivity under pressure in a ferromagnetic U–based compound (UGe_2 [3]) within the ferromagnetic phase in the vicinity of the critical pressure where the Curie temperature drops abruptly to 0 K. These striking results all point toward an intimate relationship between superconductivity and magnetism in these novel materials.

In order to provide a perspective for the role played by magnetism in the unconventional superconductivity of the heavy fermion f–electron, organic, and cuprate and ruthenate compounds described in Sections 8.3 – 8.6, the extraordinary phenomena produced by the interplay between superconductivity and magnetism in conventional superconducting systems are briefly described in Section 8.2. In conventional superconductors, the pairing of superconducting electrons is mediated by phonons, the superconducting elec-

trons are paired in singlet states with zero angular momentum (s–wave superconductivity), and the superconducting energy gap is constant, or nearly so, over the Fermi surface. Conventional s–wave spin–singlet superconductivity is adversely affected by the presence of localized magnetic moments in both paramagnetic and magnetically ordered states. Nevertheless, the interaction between superconductivity and magnetism generates new and unusual physical phenomena that include: (i) the destruction of superconductivity at a second critical temperature $T_{c2} < T_{c1}$, where T_{c1} is the superconducting critical temperature, (referred to as reentrant superconductivity) in a superconducting material containing paramagnetic impurities that exhibits the Kondo effect; (ii) the coexistence of superconductivity and antiferromagnetic order; (iii) the destruction of superconductivity by the onset of ferromagnetic order at a second critical temperature $T_{c2} \lesssim \theta_c < T_{c1}$, where θ_c is the Curie temperature and T_{c1} is the superconducting critical temperature; (iv) the development of a new sinusoidally modulated magnetic state with a wavelength $\lambda \sim 10^2$ Å that coexists with superconductivity in a narrow temperature range above T_{c2} due to superconducting–ferromagnetic interactions; and (v) magnetic field induced superconductivity (known as the Jaccarino–Peter effect [4]).

The emphasis of this review is on experiment. In view of the enormous scope of the subject, this article is not comprehensive and the choice of examples discussed is very selective. The chapter is divided into the following Sections:

1. Introduction
2. Conventional superconductors containing localized magnetic moments
3. f–electron heavy fermion superconductors
4. Organic superconductors
5. Layered cuprate and ruthenate superconductors
6. Comparison of the properties of different classes of novel superconductors

It should be noted that the magnetic field is denoted by the symbol **H** throughout the text, and by both **H** and **B** in the figures.

8.2 Conventional Superconductors Containing Localized Magnetic Moments

8.2.1 Introduction

The focus of this article is on the unconventional superconductivity displayed by several classes of novel superconductors, including heavy fermion f–electron compounds, organic compounds, and layered cuprates and ruthenates. As noted above, there is a preponderance of evidence for pairing of superconducting electrons with angular momentum $L > 0$ and a strong perception that magnetic interactions play a dominant role in mediating the electron

pairing in these materials. However, in order to put these developments in perspective, we first describe the extraordinary effects that occur when magnetic moments are embedded in s–wave superconductors. We consider two situations: one in which magnetic ions dissolved in a superconducting host have a small concentration and do not exhibit spin glass or long–range magnetic order (paramagnetic impurities), and another in which a large concentration of magnetic ions occupy a sublattice in a superconducting intermetallic compound and exhibit long range magnetic order (magnetically ordered superconductors). Our discussion is brief; the interested reader is referred to several more extensive articles on the subject for further reference [5–13].

The interrelation between superconductivity and magnetism has a long history that spans nearly a half century. The first theoretical inquiry into the coexistence of superconductivity and magnetism was made by Ginzburg in 1957 [14] and experimental investigations by Matthias, Suhl, and Corenzwit soon followed in 1958 [15]. The early experiments were carried out on binary and pseudobinary systems in which a rare earth (R) impurity with a partially–filled $4f$ electron shell and corresponding magnetic moment was dissolved in a superconducting element or binary compound; e.g., $La_{1-x}R_x$ and $Y_{1-x}R_xOs_2$. (Note that throughout this Chapter, rare earth R includes Y and the lanthanides La through Lu, upon successive filling of the f–electron shell.) These experiments were very provocative, but largely inconclusive with regard to questions concerning the coexistence of superconductivity and long–range magnetic order, primarily due to complications associated with chemical clustering and/or short–range or "glassy" types of magnetic order. However, the experiments stimulated some imaginative theoretical developments which, although largely inapplicable to the binary and pseudobinary systems then being investigated, anticipated several important phenomena that were later discovered in the 1970's. A significant "spin–off" of the early experimental and theoretical work on the coexistence problem was the achievement of a rather good understanding of superconductivity in the presence of paramagnetic impurities, including the effects of the crystalline electric field, Kondo scattering, localized spin fluctuations, etc. [5,6].

8.2.2 Superconducting–Magnetic Interactions

In a conventional superconductor, the superconductivity involves electron pairs (Cooper pairs) in which the two electrons have opposite momentum $\mathbf{k}$ and spin $\mathbf{s}$ - ($\mathbf{k}\uparrow, -\mathbf{k}\downarrow$). An applied magnetic field $\mathbf{H}$ or the magnetic moment $\boldsymbol{\mu}$ of an ion in a superconductor can interact with the superconducting electrons in two ways: via the Zeeman interaction of $\mathbf{H}$ or the exchange field generated by $\boldsymbol{\mu}$ with the spin $\mathbf{s}$ of a conduction electron ($\mathbf{s}\cdot\mathbf{H}$), and via the electromagnetic interaction of the vector potential associated with $\mathbf{H}$ or $\boldsymbol{\mu}$ with the momentum $\mathbf{k}$ of a conduction electron (the $\mathbf{k}\cdot\mathbf{A}$ term in the one electron Hamiltonian). Both of these interactions raise the energy of one member of a Cooper pair and lower the energy of the other. Such

"pair breaking" interactions are very destructive for superconductivity and generally lead to strong depressions of T_c. In a type II superconductor that does not contain ions carrying magnetic moments, superconducting electron pairs can be broken by both the Zeeman interaction of the applied magnetic field **H** with the spin of a superconducting electron, and the electromagnetic interaction of **H** with the momentum of a superconducting electron. The Zeeman interaction leads to the paramagnetic limiting field $H_p = [N(E_F)/(\chi_n - \chi_s)]^{1/2}$, where $N(E_F)$ is the density of states at the Fermi level E_F, and χ_n and χ_s are the normal and superconducting state Pauli susceptibilities, respectively [16,17], while the electromagnetic interaction yields the orbital critical field $H_{c2}^{\star} = \Phi_0/2\xi^2$, where Φ_0 is the flux quantum and ξ is the superconducting coherence length [18,19]. According to the BCS theory, $\chi_s(0) = 0$, and $H_p = H_{p0} = 1.84\ T_c$ [tesla]. However, spin orbit scattering can increase χ_s and, in turn, H_p.

How does a superconductor overcome these magnetic pair breaking interactions? One way that has been experimentally established is to set up a modulated spin structure with a period (lattice constant) $a < \xi$. This condition is satisfied in the known antiferromagnetic superconductors in which $\xi \gtrsim 10^2$ Å. In ferromagnetic superconductors, this condition can be satisfied by setting up a new sinusoidally modulated state that screens the exchange interaction at long wavelengths. Another way involves the presence of a negative (antiparallel) exchange field that compensates the applied magnetic field, allowing superconductivity to persist in magnetic fields much higher than the upper critical field. Yet another possibility is to utilize magnetic interactions to produce an unconventional superconducting state involving triplet spin pairing of electrons. These and other situations in which superconductivity and magnetism coexist are surveyed in this Chapter.

8.2.3 Paramagnetic Impurities in Superconductors

The effect of magnetic impurities on superconductivity has received a great deal of attention ever since the discovery that they produce a precipitous drop in the superconducting transition temperature T_c [15,20]. Herring [21] and Suhl and Matthias [22] noted that the conduction electron–impurity spin exchange interaction could account for this strong depression of T_c. Assuming that exchange scattering of conduction electrons by impurity spins may be adequately described within the first Born approximation (to second order in the exchange interaction parameter $\mathcal{J}$), Abrikosov and Gor'kov (hereafter AG) [23] developed in 1960 what is now a classic theory for superconductors containing paramagnetic impurities. Their theory successfully explained the basic features of these early experiments and further predicted the striking phenomenon of gapless superconductivity. However, studies of local moments in metals in the normal state have shown that the assumptions upon which the AG theory is founded are not applicable to many matrix–impurity systems that nonetheless exhibit a strong depression of T_c. In these systems,

the hybridization of the localized d– or f–electron states of the solute ion with conduction electron states results in a continuous demagnetization of the solute ion below a characteristic temperature T_0. The characteristic temperature T_0 can be associated with fluctuations of localized moments with a frequency τ_{sf}^{-1} or compensation of the localized moments by the conduction electron spins (Kondo effect). Large depressions of T_c are found even when the solute ions are weakly magnetic at superconducting temperatures (i.e., $T_0 \ll T_c$).

Exchange interaction

For transition metal impurity ions where the orbital angular momentum $\mathbf{L}$ is quenched, the exchange interaction Hamiltonian is given by

$$\mathcal{H}_{ex} = -2\mathcal{J}\mathbf{S} \cdot \mathbf{s}, \tag{8.1}$$

where $\mathcal{J}$ is the exchange interaction parameter, $\mathbf{S}$ is the paramagnetic impurity spin, and $\mathbf{s}$ is the conduction electron spin density at the impurity site. For R impurities, where $\mathbf{L}$ is not quenched, $\mathbf{S}$ is replaced by its projection on the total angular momentum vector $\mathbf{J} = \mathbf{L} + \mathbf{S}$ of the Hund's rule ground state. Then the exchange interaction Hamiltonian becomes

$$\mathcal{H}_{ex} = -2\mathcal{J}(g_J - 1)\mathbf{J} \cdot \mathbf{s}, \tag{8.2}$$

where g_J is the Landé g–factor for the Hund's rule ground state of the R ion.

Generally, $\mathcal{J}$ is approximated as

$$\mathcal{J} \sim \mathcal{J}_0 + \mathcal{J}_1, \tag{8.3}$$

where $\mathcal{J}_0$ (> 0) is the Heisenberg exchange term, while $\mathcal{J}_1$ (< 0) arises from covalent mixing between the localized d– or f–electron states and conduction electron states. In terms of the Schrieffer–Wolff transformation [24], $\mathcal{J}_1$ is given by

$$\mathcal{J}_1 \sim \frac{\langle V_{k\ell}^2 \rangle U}{\epsilon_\ell(\epsilon_\ell + U)} < 0, \tag{8.4}$$

when $|\epsilon_\ell| \gg \Delta$. Here, $V_{k\ell}$ is a matrix element mixing localized states with itinerant states, $\Delta = \pi \langle V_{k\ell}^2 \rangle N(E_F)$ is the Hartree–Fock (HF) half–width of the resonant state, $\epsilon_\ell = E_\ell - E_F$, E_ℓ is the energy of the centroid of the localized d– or f–state, E_F is the Fermi energy, and U is the intra–atomic Coulomb repulsion which splits spin–up and spin–down states in the Friedel–Anderson model [25,26]. In the limit that $U \gg |\epsilon_\ell|$, this expression takes the form

$$\mathcal{J} \sim \frac{\langle V_{k\ell}^2 \rangle}{\epsilon_\ell} < 0. \tag{8.5}$$

For partially–filled f–electron shells of rare earth ions with stable valence such as Pr, Nd, Gd, Tb, Dy, Ho, and Er, the hybridization between the

$4f$–electron and conduction electron states is weak and $\mathcal{J}$ is dominated by $\mathcal{J}_0$ ferromagnetic exchange). In contrast, for partially–filled d– or f–electron shells of transition metal ions, rare earth ions with unstable f–valence such as Ce, occasionally Pr, Sm, Eu, Tm, and Yb, and actinide ions, the hybridization is appreciable and $\mathcal{J}$ is dominated by $\mathcal{J}_1$ (antiferromagnetic exchange). The superconducting properties of matrix–paramagnetic impurity systems for the cases of ferromagnetic and antiferromagnetic exchange are dramatically different and are described below.

The exchange interaction also produces spin glass or long–range magnetic ordering in metals containing localized magnetic moments via the Ruderman–Kittel–Kasuya–Yosida (RKKY) mechanism. This is the primary source of long range magnetic ordering in ternary rare earth compounds, discussed later in this Section, although dipolar contributions may be important in certain cases. The polarized rare earth magnetic moments can then interact with the conduction electrons in two ways: by means of the Zeeman interaction of the exchange field and the conduction electron spins, and via the electromagnetic interaction of the magnetization and the persistent current.

Ferromagnetic exchange interaction

The effect of paramagnetic impurities on superconductivity for ferromagnetic exchange is best illustrated for Gd impurity ions in situations where the interactions between Gd impurities are sufficiently weak that they may be neglected over an appreciable temperature range below T_{c0}, the superconducting critical temperature of the superconducting matrix into which they have been dissolved. Since Gd is an S–state ion, this also avoids complications associated with the lifting of the degeneracy of the Hund's rule ground state by the crystalline electric field (CEF). Experimentally, it has been found that the curves of T_c/T_{c0} vs n/n_{cr} (T_c is the superconducting transition temperature of the alloy with paramagnetic impurity concentration n, and n_{cr} is the critical concentration above which superconductivity does not occur at any temperature) and $\Delta C/\Delta C_0$ vs T_c/T_{c0} (ΔC and ΔC_0 are the specific heat jumps at T_c and T_{c0}, respectively) behave in characteristic manners, both of which can be represented well by universal functions that have been calculated on the basis of the theory of AG [6]. Shown in Fig. 8.1 is a plot of T_c/T_{c0} vs n/n_{cr} for the $La_{1-x}Gd_xAl_2$ system; $T_{c0} = 3.3$ K is the T_c of the $LaAl_2$ host compound ($x = 0$) and $n_{cr} = 0.59$ at. % is the critical concentration where T_c vanishes [27]. The solid line, which has been fitted to the T_c/T_{c0} vs n/n_{cr} data, is the AG theoretical curve. Also shown in Fig. 8.1 are the Curie–Weiss temperatures θ_p, plotted as θ_p/T_{c0} vs n/n_{cr}, for the $La_{1-x}Gd_xAl_2$ system where the solid line is a guide to the eye [5,27]. Apparently, interactions between the Gd magnetic moments are sufficiently weak in this system to allow the AG theory to be tested to concentrations in the vicinity of n_{cr}. Shown in Fig. 8.2 is the behavior of $\Delta C/\Delta C_0$ vs T_c/T_{c0} for the $La_{1-x}Gd_xAl_2$ system [28] and the $Th_{1-x}Gd_x$ system [29], compared to calculations by Skalski *et al.* [30] based on the AG theory. As can be seen in Figs. 8.1 and 8.2, the

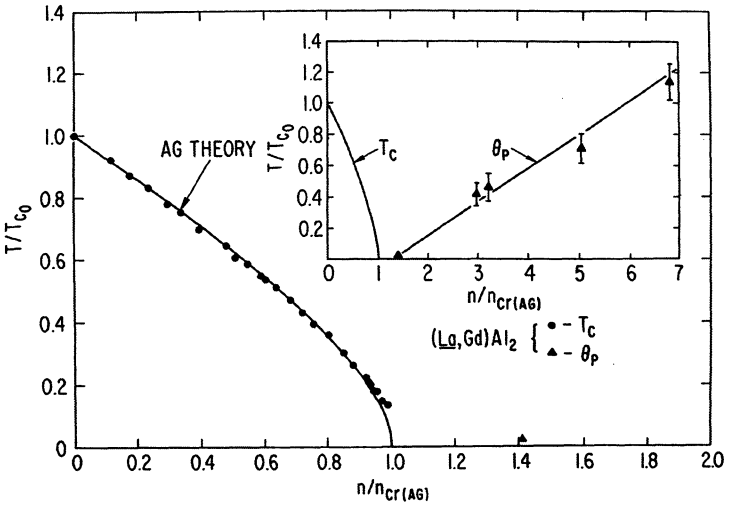

Fig. 8.1. Reduced superconducting critical temperature T_c/T_{c0} vs reduced Gd impurity concentration n/n_{cr} for the $La_{1-x}Gd_xAl_2$ system. The value of the superconducting critical temperature T_{c0} of the $LaAl_2$ host compound is 3.3 K, while the value of the critical concentration n_{cr} where $T_c = 0$ is 0.59 at. % Gd. The line denoted AG is the theoretical curve of Abrikosov and Gor'kov [23] that has been fitted to the data. Inset: Curie–Weiss temperatures θ_p determined from magnetic susceptibility measurements, plotted as θ_p/T_{c0} vs n/n_{cr}. The line through the data is a guide to the eye, after Refs. [5,27]

experimental T_c/T_{c0} vs n/n_{cr} and $\Delta C/\Delta C_0$ vs T_c/T_{c0} curves are well represented by the AG theory. The basic assumptions embodied in the AG theory are that (1) the superconducting order parameter does not vary with position, (2) the spins of the impurities are fixed and randomly oriented in space, and (3) scattering of conduction electrons by the paramagnetic impurities can be calculated within the first Born approximation. The first assumption requires that the impurities be randomly distributed throughout the superconducting matrix, while the second precludes any correlations between the spins of the impurities such as those that would arise from magnetic order.

If one regards the impurity spin direction as fixed, the exchange interaction is not time reversal invariant. As a result, the lifetime τ_s of the time–reversed single particle paired states of which the superconducting wave function is comprised is no longer infinite. In the AG theory, the superconducting properties in the presence of solute spins are characterized by a pair breaking parameter $\alpha = \tau_s^{-1}$. The theory predicts a second order transition to the superconducting state and a rapid decrease of the superconducting transition temperature with α given by the universal relation

$$\ln\left(\frac{T_c}{T_{c0}}\right) = \psi\left(\frac{1}{2}\right) - \psi\left(\frac{1}{2} + 0.14\frac{\alpha T_{c0}}{\alpha_{cr} T_c}\right), \tag{8.6}$$

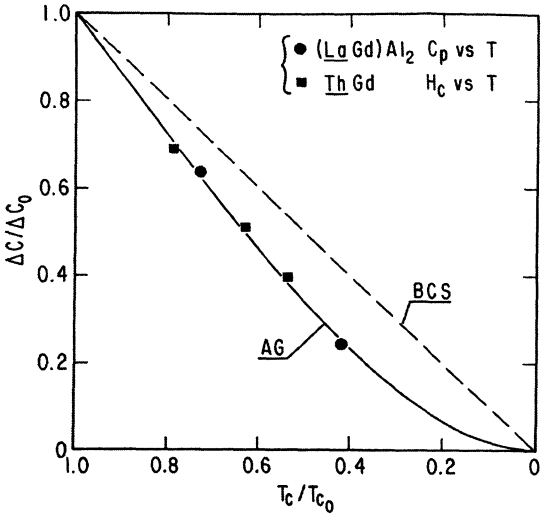

Fig. 8.2. Reduced specific heat jump $\Delta C/\Delta C_0$ vs reduced critical temperature T_c/T_{c0} for the matrix–impurity systems $La_{1-x}Gd_xAl_2$ and $Th_{1-x}Gd_x$. The $La_{1-x}Gd_xAl_2$ data were derived from $C(T)$ measurements by Luengo and Maple [28] and the $Th_{1-x}Gd_x$ data were derived from $H_{c2}(T)$ measurements by Decker and Finnemore [29]. The dashed line represents the BCS law of corresponding states, whereas the solid line is the result of the AG theory as calculated by Skalski *et al.* [30], after Ref. [6]

where T_{c0} corresponds to $\alpha = 0$, $\alpha_{cr} = k_B T_{c0}/4\hbar\gamma$ ($\ln\gamma$ is Euler's constant) corresponds to $T_c = 0$ (complete destruction of superconductivity) and ψ is the digamma function.

This expression has the linear asymptotic form

$$\frac{T_c}{T_{c0}} = 1 - 0.691\left(\frac{\alpha}{\alpha_{cr}}\right), \tag{8.7}$$

as $\alpha \to 0$.

It is apparently sufficient to calculate the pair breaking parameter α within the first Born approximation (to second order in $\mathcal{J}$), which for superconductors containing paramagnetic R ions gives the result

$$\alpha \equiv \frac{1}{\tau_s} = \frac{n}{\hbar}\left[\frac{N(E_F)}{2k_B}\right]\mathcal{J}^2(g_J - 1)J(J+1), \tag{8.8}$$

where n is the paramagnetic impurity concentration and $N(E_F)$ is the density of states at the Fermi level for the matrix.

It is important to note that α is proportional to n and independent of temperature. Hence, α/α_{cr} can be replaced by n/n_{cr} in Eqs. 8.6 and 8.7 where

n_{cr} is the critical concentration for the complete suppression of superconductivity. Thus, the theory predicts that the reduced critical temperature T_c/T_{c0} will be a universal function of reduced concentration n/n_{cr}

$$\ln\left(\frac{T_c}{T_{c0}}\right) = \psi\left(\frac{1}{2}\right) - \psi\left(\frac{1}{2} + 0.14\frac{nT_{c0}}{n_{cr}T_c}\right), \tag{8.9}$$

or

$$\frac{T_c}{T_{c0}} = \mathcal{U}\left(\frac{n}{n_{cr}}\right), \tag{8.10}$$

The specific heat jump ΔC at T_c as a function of T_c has also been calculated on the basis of the AG theory by Skalski *et al.* [30]. They find that the reduced specific heat jump $\Delta C/\Delta C_0$ is a universal function $\mathcal{V}$ of T_c/T_{c0},

$$\frac{\Delta C}{\Delta C_0} = \mathcal{V}\left(\frac{T_c}{T_{c0}}\right), \tag{8.11}$$

which deviates markedly from the linear BCS law of corresponding states

$$\frac{\Delta C}{\Delta C_0} = \frac{T_c}{T_{c0}}. \tag{8.12}$$

One of the most striking predictions of the AG theory is the phenomenon of gapless superconductivity. This results from the fact that the finite lifetime τ_s corresponds to an energy broadening $\Gamma \sim \hbar/\tau_s$ which introduces states into the gap and spreads out the BCS peak in the density of states. As a consequence, the energy gap $\Omega_G(\alpha)$ no longer corresponds to the order parameter $\Delta(\alpha)$ and with increasing α (or n), $\Omega_G(\alpha)$ goes to zero faster that $T_c(\alpha)$. For all concentrations, the superconductor is gapless at temperatures sufficiently near T_c; while for $n > 0.91\ n_{cr}$, the superconductor is gapless at all temperatures. For example, the theory predicts an attenuated specific heat jump at T_c (compared to the BCS law of corresponding states; see Fig. 8.2), and a linearly temperature–dependent term in the specific heat below T_c in the gapless region $n > 0.91\ n_{cr}$. Other predictions of the AG theory have been verified experimentally as described in other reviews [5, 6] (Note, the recent study by Overhauser *et al.* Phys. Rev. B **49**, 15799 (1994)). The AG theory yields an initial depression of T_c with n that is linear with a rate, for superconductors containing R impurities, given by

$$\left(\frac{dT_c}{dn}\right)_{n=0} = -\left[\frac{\pi^2 N(E_F)}{2k_B}\right]\mathcal{J}^2(g_J - 1)^2 J(J+1), \tag{8.13}$$

where the quantity $(g_J-1)^2J(J+1) = \mathcal{D}(R)$ is called the deGennes factor [33]. The variation of $(-dT_c/dn)_{n=0}$ with R for the $La_{1-x}R_x$ system scales with the function $\mathcal{D}(R)$ if $\mathcal{J}^2$ is assumed to decrease slightly with increasing R atomic number, except for Ce where $(-dT_c/dn)_{n=0}$ is anomalously large [15].

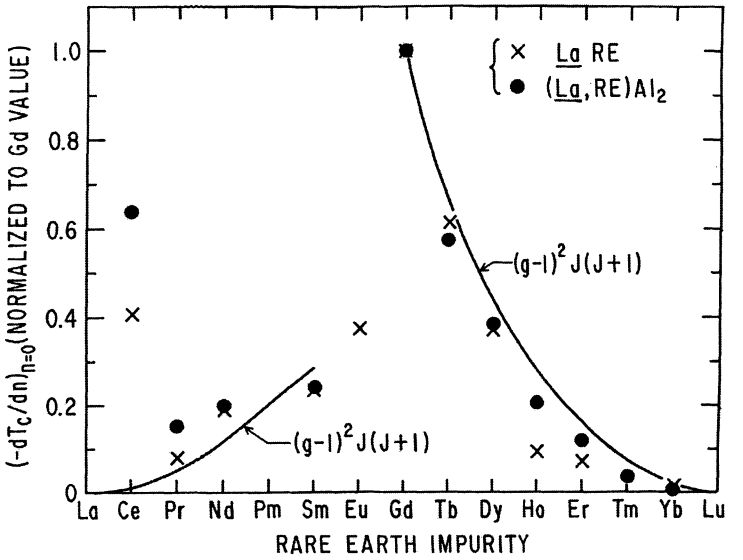

Fig. 8.3. Initial rate of depression of the superconducting critical temperature T_c with paramagnetic impurity concentration n, $(-dT_c/dn)_{n=0}$, vs rare earth R impurity for the $La_{1-x}R_x$ and $La_{1-x}R_xAl_2$ systems, after Refs. [5,32]

Investigations of the effect of substituted R ions on superconductivity of $LaAl_2$, which has a T_c of 3.3 K, revealed a variation of $(-dT_c/dn)_{n=0}$ with R similar to that of $La_{1-x}R_x$, with a corresponding anomalously large rate of depression of T_c with n for R = Ce [32]. The $(-dT_c/dn)_{n=0}$ vs R data for both $La_{1-x}R_x$ and $La_{1-x}R_xAl_2$, normalized to the value for Gd, are displayed in Fig. 8.3 [5,32].

It should be noted that, according to the AG theory, the depression of T_c depends on the magnitude of $\mathcal{J}$ but not on its sign. However, neglected in the AG theory are contributions to α of higher order than $\mathcal{J}^2$ which must be taken into account when $\mathcal{J}$ is negative. These contributions give rise to spectacular temperature dependent pair breaking effects which are considered below.

Antiferromagnetic exchange interaction

The anomalous depression of T_c with n for Ce substituents in La and $LaAl_2$ is associated with the hybridization of the localized $4f$–electron states of Ce and the conduction electron states [5]. The large depression of T_c with Ce concentration is due to the large negative contribution to the exchange interaction and the occurrence of the Kondo effect with $T_K \sim T_{c0}$, where T_K is the Kondo temperature and T_{c0} is the T_c of the La or $LaAl_2$ matrix (see below).

The Kondo temperature is a characteristic temperature that separates high temperature magnetic behavior, where $\chi(T)$ behaves as a Curie–Weiss law, from low temperature nonmagnetic behavior, where $\chi(T)$ approaches a constant value. A physical picture of the nonmagnetic ground state that has emerged from theories of the Kondo effect involves the gradual formation, as T decreases through T_K, of a many body singlet ground state in which the spin of each paramagnetic impurity ion is screened by the antiferromagnetically aligned spins of the conduction electrons. The Kondo temperature is given by

$$T_K \sim T_F \exp\left(\frac{-1}{N(E_F)|\mathcal{J}|}\right), \tag{8.14}$$

where T_F is the Fermi temperature.

The phenomenon of reentrant superconductivity due to the Kondo effect was discovered in the $La_{1-x}Ce_xAl_2$ system. Here, a sample within a certain range of Ce impurity concentrations becomes superconducting below a critical temperature T_{c1} and then loses its superconductivity below a second critical temperature T_{c2} [34,35]. The destruction of superconductivity at T_{c2} is associated with the competition between singlet spin pairing of electrons in the superconducting state, with characteristic energy $k_B T_c$, and the formation of the Kondo many body singlet state involving the conduction electrons and each Ce impurity ion, with characteristic energy $k_B T_K$. Shown in Figs. 8.4 (a) and (b), respectively, are ac magnetic susceptibility vs temperature data and the reentrant T_c vs n curve of the $La_{1-x}Ce_xAl_2$ system. The values of T_c in Fig. 8.4 (b) and the transition curves in Fig. 8.4 (a) from which they were inferred are identified with letters [34]. In addition to the remarkable behavior exhibited by the T_c/T_{c0} vs n curve, the $\Delta C/\Delta C_0$ vs T_c/T_{c0} curve also displays some interesting features which are shown in Fig. 8.5. Here, it can be seen that the curve of $\Delta C/\Delta C_0$ vs T_c/T_{c0} shows a pronounced downward deviation from both the BCS law of corresponding states and, as well, the AG theory. The two specific heat jumps for a specimen at 0.64 at.% Ce are indicated in Fig. 8.5 by the solid squares.

Electrical resistivity measurements on the $La_{1-x}Ce_xAl_2$ system in the normal state revealed the occurrence of a Kondo effect, as evidenced by a minimum in $\rho(T)$ at low temperatures [39]. The Ce impurity contribution to $\rho(T)$ was found to diverge as $-\ln T$ with decreasing T down to ~ 1 K, indicating a low Kondo temperature $T_K \lesssim 1$ K. Shown in Fig. 8.6 are specific heat C vs T data for a $La_{1-x}Ce_xAl_2$ alloy ($x = 0.64$ at.% Ce) in various magnetic fields up to 38 kOe [38]. Curves a – c, which have been drawn to fit more accurate data for a $La_{1-x}Ce_xAl_2$ alloy with $x = 0.906$ at.% Ce, correspond to an entropy of $R\ln 2$ per mol Ce, showing that the Ce^{3+} ground state is a doublet. Curve d is consistent with calculations of Bloomfield and Hamann [40] for $S = 1/2$ and $T_K = 0.42$ K. The two zero field superconducting critical temperatures T_{c1} and T_{c2} are indicated by arrows in the figure.The Kondo anomalies in the normal state properties of the $La_{1-x}Ce_xAl_2$ system

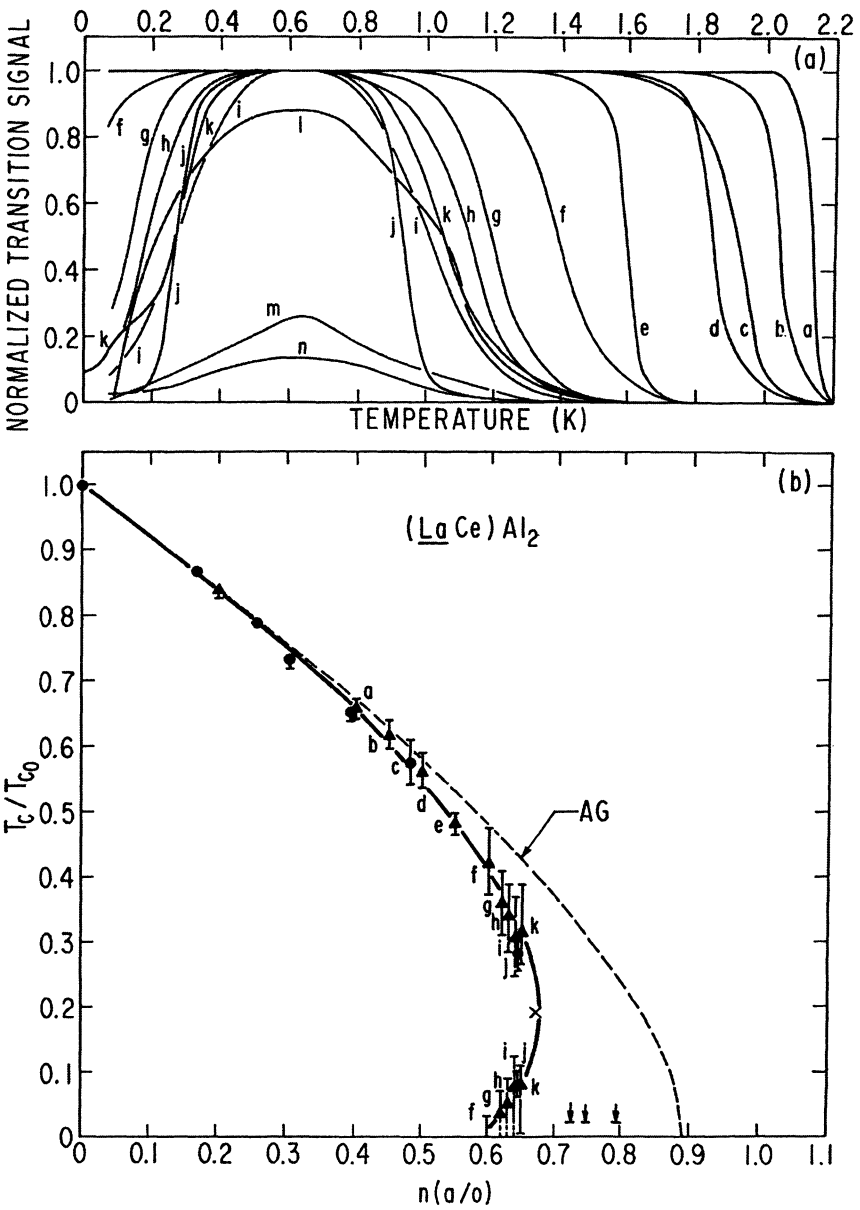

Fig. 8.4. (a) Normalized transition signal, based on ac magnetic susceptibility measurements, vs temperature for the $La_{1-x}Ce_xAl_2$ system. (b) Reduced superconducting critical temperature T_c/T_{c0} vs Ce impurity concentration n for the $La_{1-x}Ce_xAl_2$ system. The value of the superconducting critical temperature T_{c0} of the $LaAl_2$ host compound is 3.3 K. The data identified by letters are derived from the corresponding transition curves in (a), after Ref. [34]

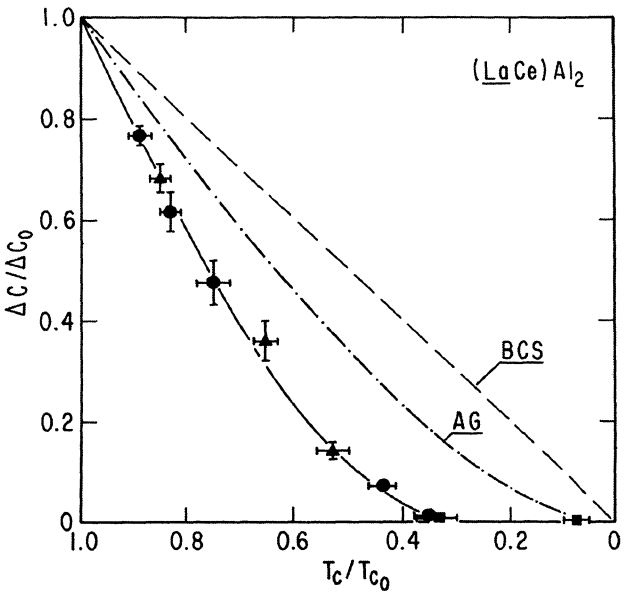

Fig. 8.5. Reduced specific heat jump $\Delta C/\Delta C_0$ vs reduced critical temperature T_c/T_{c0} for the $La_{1-x}Ce_xAl_2$ system. The solid triangles, circles and squares represent data from Luengo *et al.* [36], Armbrüster *et al.* [37], and Bader *et al.* [38], respectively. The dashed line represents the BCS law of corresponding states, the dot-dashed line indicates the AG result, and the solid line is a smooth curve drawn through the data, after Ref. [6]

have also been well characterized and used to test theoretical models of the Kondo effect. Subsequently, reentrant superconductivity was discovered in the $(La_{1-y}Th_y)_{1-x}Ce_x$ system in the low Th concentration range $0 < y \leq 0.25$ [41].

Superconductivity was studied in superconducting matrix–impurity systems in which the impurity ions were nonmagnetic at superconducting temperatures (i.e., $T_{c0} \ll T_0$, where T_0 is a characteristic temperature that separates low temperature nonmagnetic behavior from high temperature magnetic behavior, such as the Kondo temperature T_K). These studies revealed that the T_c vs n curves have positive curvature and can be described by a relation proposed by Kaiser [42], who considered the effect of nonmagnetic resonant d– and f–electron states of impurity ions on superconductivity. In this case T_c is a modified exponential relation of the form

$$T_c = T_{c0} \exp\left[-\frac{An}{(1-Dn)}\right], \tag{8.15}$$

where A and D are fitting parameters that can be related to parameters describing the conduction electrons ($N(E_F)$ and V, where V is the electron–

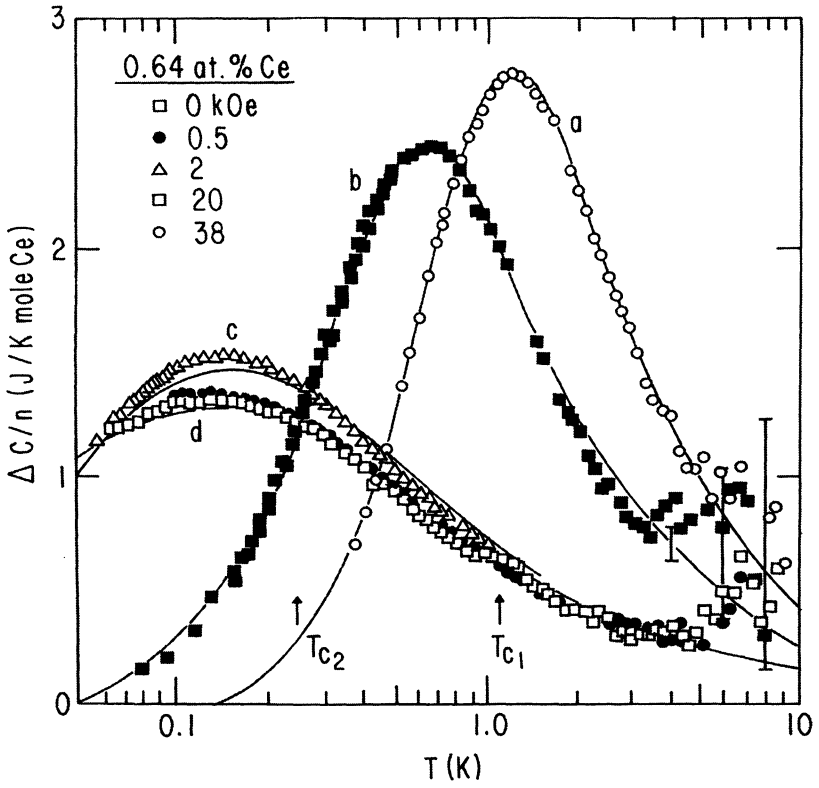

Fig. 8.6. Specific heat of a $La_{1-x}Ce_xAl_2$ alloy (0.64 at.% Ce) vs temperature in various magnetic fields up to 38 kOe. Curves a–c, which have been drawn to fit more accurate data for a $La_{1-x}Ce_xAl_2$ alloy with 0.906 at.% Ce, correspond to an entropy of $R\ln 2$ per mole Ce, showing that the Ce^{3+} ground state is a doublet. Curve d is consistent with calculations of Bloomfield and Hamann [40] for $S = 1/2$ and $T_K = 0.42$ K. The two zero field superconducting transitions are indicated, after Ref. [38]

phonon interaction parameter) and the localized d– or f–electrons ($N_\ell(E_F), U$, and L, where $N_\ell(E_F)$ is the density of states at E_F of the localized d– or f–electrons, U is the intra–atomic Coulomb interaction parameter, and L is the d– or f–electron orbital angular momentum). Shown in Fig. 8.7 are plots of T_c/T_{c0} vs n/n_0 for three systems [6] in which $T_0 \gg T_{c0}$, $Th_{1-x}U_x$ [43], $Th_{1-x}Ce_x$ [44], and $Al_{1-x}Mn_x$ [45]. Displayed in Fig. 8.8 are reduced specific heat jump $\Delta C/\Delta C_0$ vs reduced critical temperature T_c/T_{c0} data for the $Th_{1-x}U_x$ [46–48], $Al_{1-x}Mn_x$ [49, 50], and $Th_{1-x}Ce_x$ [51] systems. The nonmagnetic character of the f–electron states in these systems at superconducting temperatures where $T \ll T_0$ is reflected in the conformance of the $\Delta C/\Delta C_0$ vs T_c/T_{c0} data with the BCS law of corresponding states. The

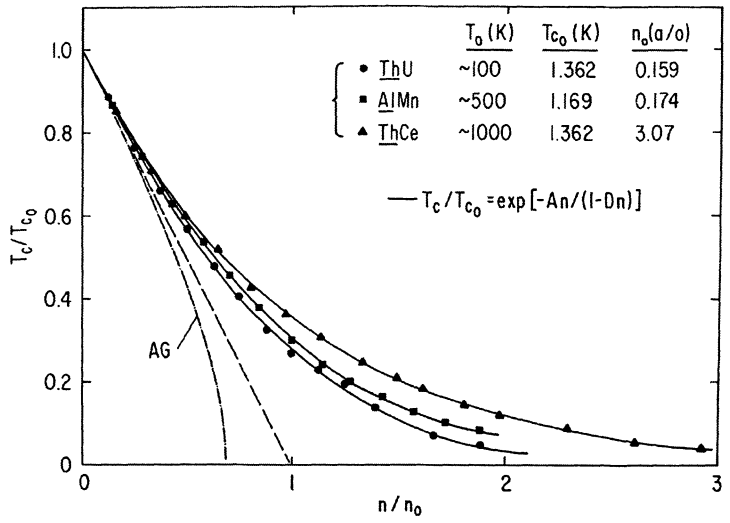

Fig. 8.7. Reduced superconducting critical temperature T_c/T_{c0} vs reduced impurity concentration n/n_0 for the $Th_{1-x}Ce_x$, $Th_{1-x}U_x$, and $Al_{1-x}Mn_x$ systems. The solid lines represent the modified exponential relation given in the figure that describes the weakening of superconducting electron pairs by nonmagnetic localized states [42]. The dot–dashed line is the AG curve, while the dashed line is a straight line to which the other curves have been scaled in the initial linear region at low concentrations. The values of the characteristic (or Kondo) temperature T_0, superconducting critical temperature of the host T_{c0}, and the scaling concentration n_0 are indicated in the figure, after Ref. [6]

$Th_{1-x}U_x$ system [43] provides an interesting example of the Kondo effect in the electrical resistivity. Shown in Fig. 8.9 (a) are ρ vs T data for $Th_{1-x}U_x$ samples with $x = 0, 0.01, 0.015$, and 0.02, in which the resistivity minimum phenomenon is evident. Displayed in Fig. 8.9 (b) are $\Delta\rho$ vs T^2 data, where $\Delta\rho(x,T) = \rho(x,T) - \rho(0,T)$ is the U contribution to the resistivity, that can be described by the relation $\rho(x,T) = \rho(x,0)[1 - (T/T_K)^2]$ with $T_K \sim 100$ K, consistent with the local Fermi–liquid behavior expected for the Kondo effect at low temperatures $T \ll T_K$ [43].

Reentrant superconductivity associated with the Kondo effect was predicted to occur in the limit $T_K \ll T_{c0}$, where T_{c0} is the critical temperature of the superconducting host metal, by Müller–Hartmann and Zittartz (MHZ) [52] and Ludwig and Zuckermann (LZ) [53]. MHZ and LZ obtained exponential–like curves of T_c vs n in the limit $T_K \gg T_{c0}$. Calculations of Zuckermann [54] and MHZ [55] for the initial depression of T_c with n, $(-dT_c/dn)_{n=0}$, yielded a maximum as a function of T_K/T_{c0} at $T_K/T_{c0} \approx 10$.

The magnetic state of an impurity in a superconducting matrix–impurity system can be continuously tuned by applying an external pressure P or al-

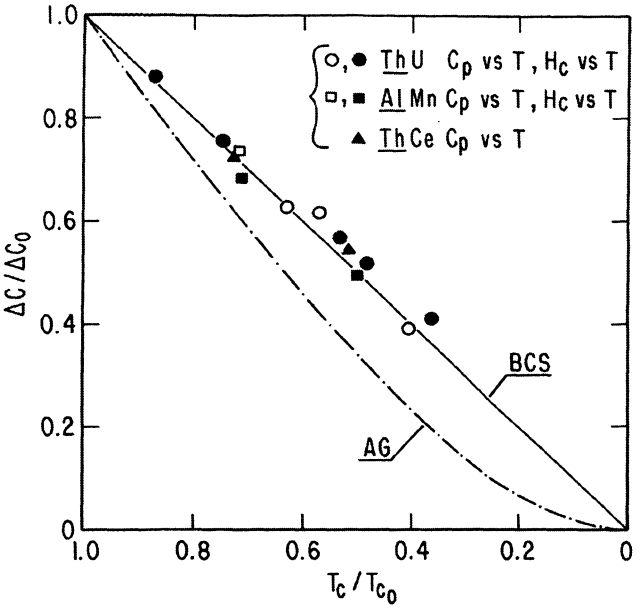

Fig. 8.8. Reduced specific heat jump $\Delta C/\Delta C_0$ vs reduced critical temperature T_c/T_{c0} for the $Th_{1-x}Ce_x$, $Th_{1-x}U_x$, and $Al_{1-x}Mn_x$ systems. The solid line represents the BCS law of corresponding states, whereas the dot–dashed line indicates the AG result. Open circles – data from Luengo *et al.* [46, 47]; solid circles – data from Watson *et al.* [48]; open square – data from Martin [49]; solid squares – data from Smith [50]; solid triangles – data from Dempesy [51], after Ref. [6]

loying the matrix with a suitable element. An example of the first case is illustrated in Fig. 8.10, which shows T_c vs pressure for the system $La_{1-x}Ce_x$ with several concentrations x of Ce [57]. With increasing Ce concentration, a minimum in T_c as a function of pressure P develops near 15 kbar which becomes more pronounced the higher the Ce concentration. The data for the $La_{1-x}Ce_x$ sample with $x = 0.02$ are particularly striking; the application of pressure drives T_c to zero at about 5 kbar, T_c remains zero up to $\sim$ 15 kbar, whereupon superconductivity reappears and T_c increases with pressure. The initial depression of T_c, $\Delta T_c/n$, increases markedly with pressure up to a maximum near 15 kbar and thereafter decreases to a value that, above $\sim$ 100 kbar, is more than an order of magnitude smaller than the maximum depression. Isobars of T_c vs n in the inset of Fig. 8.10 evolve with increasing pressure from nearly linear depressions with slight negative curvature to depressions with strong positive curvature. These results can be interpreted in terms of an increase of T_K, and, in turn, the ratio T_K/T_{c0}, with pressure. As T_K/T_{c0} increases under pressure, the initial depression of T_c with x is expected to increase, pass through a maximum, and then decrease, according to the the-

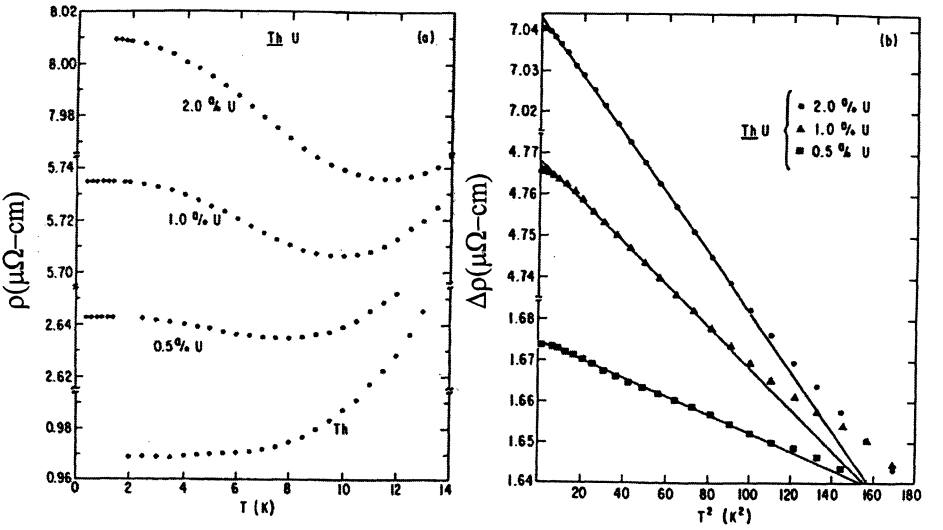

Fig. 8.9. (a) Electrical resistivity ρ vs temperature T of $Th_{1-x}U_x$ alloys with $x = 0.5, 1$, and 2 at. % U at low temperatures. (b) Incremental resisitivity $\Delta\rho(x,T) = \rho(x,T) - \rho(0,T)$ vs T^2 of $Th_{1-x}U_x$ alloys with $x = 0.5, 1$, and 2 at. % U, after Ref. [43]

ory of MHZ [55]. However, at the highest pressures, such large values of T_K are required ($\sim 10^6$ K!) that it was concluded that the Ce $4f$–state must demagnetize within the context of the Friedel–Anderson model.

An example of the second case is provided by the $La_{1-x}Ce_x$ system when Th is substituted for La. With increasing Th concentration y in the $(La_{1-y}Th_y)_{1-x}Ce_x$ system, the rate of the initial depression of T_c with Ce concentration passes through a pronounced maximum and T_c vs n changes continuously from curves with negative curvature and reentrant behavior to curves with positive curvature and exponential–like shapes [41]. Concomitantly, the normal state magnetic susceptibility [58] and electrical resistivity [59] evolve continuously from magnetic to nonmagnetic behavior. A self consistent analysis of the rates of the initial depression of T_c with n and the value of the specific heat jump at T_c demonstrated that the MHZ theory provides a good description of the data from $T_K/T_{c0} \approx 0.1$ to 100 [60,61].

Magnetically–ordered superconductors

The series of isostructural ternary rare earth compounds that have been investigated the most extensively in connection with the interaction between superconductivity and long–range magnetic order include the rhombohedral rare earth molybdenum chalcogenides RMo_6S_8 and RMo_6Se_8 (Chevrel phases), and the tetragonal rare earth rhodium borides RRh_4B_4 [7,8]. The long–range magnetic order that many of these compounds exhibit can be traced in part to the ordered R sublattice. The persistence of superconduc-

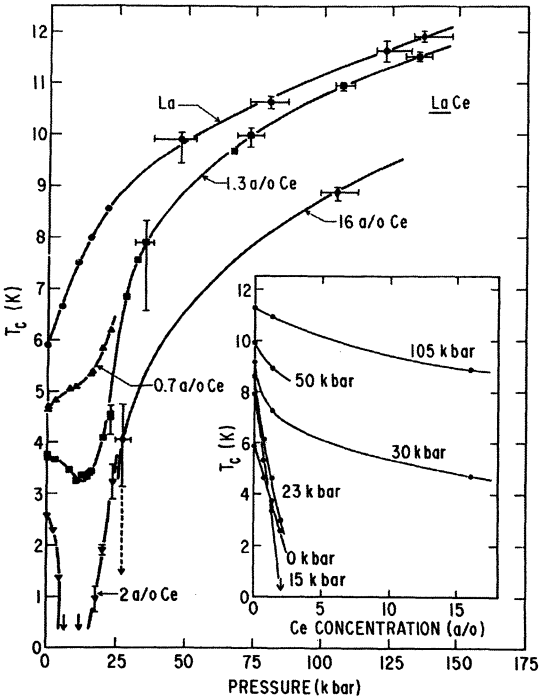

Fig. 8.10. Superconducting critical temperature T_c vs pressure for the $La_{1-x}Ce_x$ system. Isobars of T_c vs Ce concentration are shown in the inset, after Ref. [57]

tivity, even in the presence of relatively large concentrations of R ions, can be attributed to the relatively weak exchange interaction between the conduction electron spins and the R magnetic moments. This, in turn, appears to be associated with transition metal molecular units or "clusters" which, along with the R ions, are the basic building blocks of these ternary R phases. The superconductivity is believed to be primarily associated with the transition metal *d*–electrons that are relatively confined within the clusters and thereby interact only weakly with the R ions. Equation 8.13 has been used to estimate the magnitude of $\mathcal{J}$ for the RRh_4B_4 compounds from the depression of T_c of $LuRh_4B_4$ by R impurities with partially–filled $4f$ electron shells [62]. The initial depression of T_c of $LuRh_4B_4$ by Gd impurities, $(dT_c/dn)_{n=0} = -19$ K per atomic fraction of Gd in Lu, yields the value $|\mathcal{J}| = 2.3 \times 10^{-2}$ eV–atom, assuming $N(E_F) = 0.35$ states/eV–atom–spin direction [62]. Other ternary R systems have been investigated such as $RRh_{1.1}Sn_{3.5}$, $R_2Fe_3Si_5$, $RRuB_2$, etc. [7,8].

Antiferromagnetic superconductors

The coexistence of superconductivity and long–range antiferromagnetic order was discovered in the latter part of the 1970's in the R molybdenum selenides

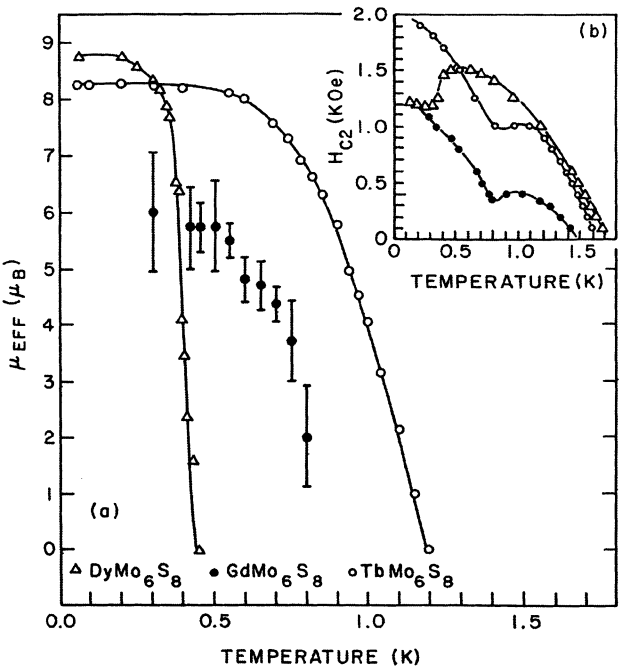

Fig. 8.11. Temperature dependence of the sublattice magnetization for RMo_6S_8 compounds with R = Gd, Tb, and Dy. The inset shows the measured upper critical field $H_{c2}(T)$ [63], after Ref. [64]

RMo_6Se_8 (R = Gd, Tb, and Er) [8,65] and R rhodium borides RRh_4B_4 (R = Nd, Sm and Tm) [8,66] at the University of California, San Diego, and in the R molybdenum sulfides RMo_6S_8 (R = Gd, Tb, Dy and Er) [8,63] at the University of Geneva. The occurrence of antiferromagnetic ordering of the R magnetic moments in the superconducting state was inferred from a λ-type anomaly in the heat capacity and a cusp in the magnetic susceptibility for the RMo_6Se_8 compounds [8,65], and from a feature in the upper critical field H_{c2} vs temperature T curve in the RMo_6S_8 compounds [8,63]. Neutron diffraction measurements on $GdMo_6Se_8$ [67] and RMo_6S_8 compounds with R = Gd, Tb, and Dy [68] confirmed the antiferromagnetic ordering of the sublattice of R ions in the Chevrel phase structure. The magnetic structure consists of alternating ferromagnetic [100] planes in the nearly cubic R sublattice in which the magnetic moments are parallel or antiparallel to the rhombohedral [111] axis. Plots of the sublattice magnetization vs temperature for RMo_6S_8 compounds with R = Gd, Tb, and Dy are shown in Fig. 8.11 where they are compared with data for H_{c2} vs temperature displayed in the inset of the figure [64]. There is a clear correlation between the onset of the sublattice magnetization and the depression of the H_{c2} curve below T_N.

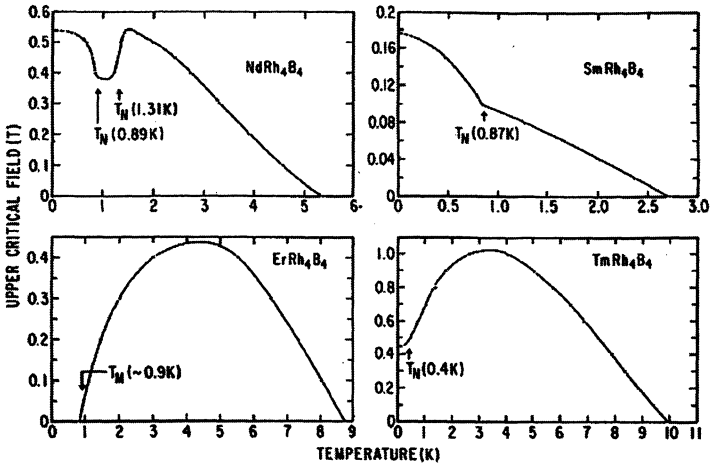

Fig. 8.12. Resistively determined upper critical field H_{c2} vs temperature T for polycrystalline samples of $NdRh_4B_4$, $SmRh_4B_4$, $ErRh_4B_4$, and $TmRh_4B_4$, after Ref. [9]

The anomalous depression of H_{c2} in the vicinity of T_N and other properties of antiferromagnetic superconductors have been addressed by numerous theories [69]. Several mechanisms by means of which superconductivity is modified by antiferromagnetic order have been considered. These include: (i) Reduction in pair breaking due to the decrease in the mean magnetization and, in turn, the conduction electron spin polarization below T_N. (ii) Increase in pair breaking due to magnetic moment fluctuations in the vicinity of T_N. (iii) Decrease of the attractive phonon mediated electron–electron pairing interaction by antiferromagnetic magnons. (iv) Reduction of the available phase space for virtual pair scattering by the change in lattice periodicity associated with antiferromagnetic order. (v) Pairing of electrons with finite momentum. Finite momentum pairing of electrons in states $(\mathbf{k}, \uparrow; \mathbf{k}+\mathbf{Q}, \downarrow)$, where $\mathbf{Q}$ corresponds to translation by a reciprocal lattice vector, was originally proposed by Baltensperger and Strassler [70] in 1963, and has been incorporated into several subsequent theories [69].

It should be emphasized that there are some antiferromagnetic superconductors where H_{c2} actually increases below T_N, or, in other words, superconductivity seems to be enhanced below T_N. A notable example is the compound $SmRh_4B_4$ whose resistively determined H_{c2} vs T curve, shown in Fig. 8.12, exhibits a sharp break in slope at $T_N = 0.87$ K [9]. In contrast, the H_{c2} vs T curves of the other two RRh_4B_4 antiferromagnetic superconductors shown in Fig. 8.12 display different behaviors with decreasing temperature; for $NdRh_4B_4$, which undergoes two antiferromagnetic transitions at $T_{N1} = 1.31$ K and $T_{N2} = 0.89$ K, H_{c2} decreases abruptly at T_{N1} and then increases

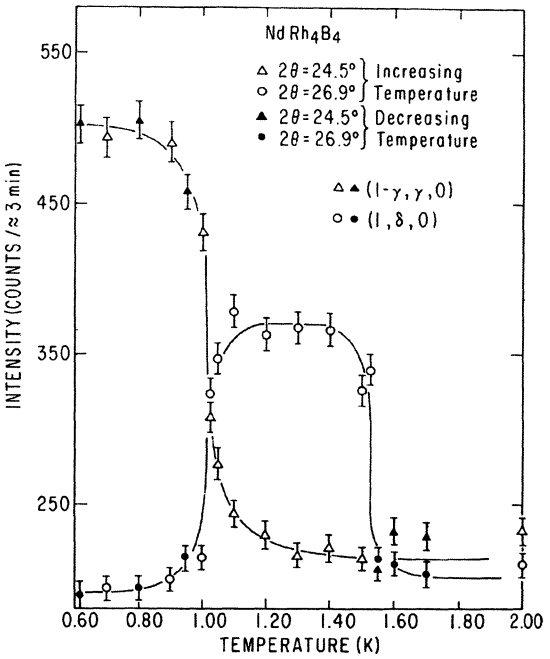

Fig. 8.13. Temperature dependence of the neutron scattering intensity of a representative satellite from each of the two magnetic phases of $NdRh_4B_4$, after Ref. [71]

sharply at T_{N2}, whereas for $TmRh_4B_4$, H_{c2} hardly changes at $T_N = 0.4$ K [9]. Neutron diffraction experiments indicate that the magnetic phases of $NdRh_4B_4$ in zero magnetic field are body–centered tetragonal antiferromagnetic structures in which the Nd^{3+} moments are alternately aligned parallel and antiparallel to the c–axis, with a sinusoidal modulation along the [100] direction with $\lambda = 46.5$ Å in the high temperature phase, and along the [110] direction with $\lambda = 45.2$ Å in the low temperature magnetic phase [71]. The temperature dependences of the neutron diffraction intensity of a representative satellite from each of the two magnetic phases of $NdRh_4B_4$ are shown in Fig. 8.13. The data in Fig. 8.12 indicate that there is no universal behavior of H_{c2} vs T for antiferromagnetic superconductors. Both enhancements and depressions of H_{c2} are found below T_N, which appear to be determined by a combination of the mechanisms enumerated above.

Recently, superconductivity was discovered in rare earth transition metal borocarbide quaternary systems [72–74]. For intermetallic compounds, these materials have high values of T_c; $T_c \approx 13.5$ K for $YNi_2B_3C_{0.2}$ [72], $T_c \approx 16.5$ K for RNi_2B_2C (R = Y, Tm, Er, Ho, La) [73], and $T_c \approx 23$ K for $YPd_5B_3C_{0.3}$ [74]. A value $T_c \approx 21.5$ K was reported for a Th based palladium borocarbide in the Th–Pd–B–C system which also has a relatively high extrapolated upper critical field $H_{c2}(0) > 17$ tesla [75]. Coexistence of su-

perconductivity and antiferromagnetism has been reported in RNi_2B_2C for R = Tm, Er, Ho, Dy [76]. Single crystals of RNi_2B_2C compounds have been prepared and investigated extensively by means of a variety of experimental techniques [77–80]. For example, Grigereit and coworkers [79] have performed neutron scattering measurements on the reentrant antiferromagnetic superconductor $HoNi_2B_2C$ which becomes superconducting at $\sim$ 7.5 K, re–enters the normal conducting state at 5 K, and quickly recovers superconductivity at lower temperature. The experiments reveal that the magnetic order that first forms upon cooling is oscillatory in nature and is directly coupled to the superconducting order parameter. However, in contrast to the ferromagnetic superconductors (discussed below), the oscillatory state in $HoNi_2B_2C$ is detrimental to superconductivity, and the superconducting state only survives at low temperatures because of a first order transition to a compensated antiferromagnet. A brief review of the phenomena that arise from the interplay between superconductivity and magnetism in the RNi_2B_2C compounds can be found in Ref. [80].

Ferromagnetic superconductors

Reentrant superconductivity due to the onset of long–range ferromagnetic ordering of the R magnetic moments was discovered in 1977 in $ErRh_4B_4$ [81] at the University of California, San Diego, and in $HoMo_6S_8$ [82] at the University of Geneva. These two materials, which become superconducting at an upper critical temperature T_{c1}, lose their superconductivity at a lower critical temperature $T_{c2} \approx T_M$, where T_M is the Curie temperature. Thermal hysteresis in various physical properties and a spike–shaped feature in the heat capacity near T_{c2} indicate that a first–order transition from the superconducting to the ferromagnetic normal state occurs at T_{c2} [9].

Typical ac magnetic susceptibility and electrical resistance vs temperature data for $ErRh_4B_4$ are displayed in Fig. 8.14 [83]. The thermal hysteresis at T_{c2} is evident in both properties. The resistively determined H_{c2} vs T curve for $ErRh_4B_4$ is shown in Fig. 8.12 [9].

Neutron diffraction measurements established that the ground states of the compounds $ErRh_4B_4$ [84, 85] and $HoMo_6S_8$ [86] are ferromagnetic. In addition, small angle scattering studies of $ErRh_4B_4$ [85,87] and $HoMo_6S_8$ [88] revealed the existence of a sinusoidally modulated magnetic state with a wavelength of the order of 10^2 Å that coexists with superconductivity in a narrow temperature interval above T_{c2}. Moreover, in $ErRh_4B_4$ the regions within which superconductivity and the sinusoidally modulated magnetic state coexist appear to be interspersed with normal ferromagnetic domains to form a spatially inhomogeneous state.

Shown in Fig. 8.15 is a plot of the heat capacity of $ErRh_4B_4$ and the isostructural nonmagnetic compound $LuRh_4B_4$ below 18 K [89]. The data reveal a jump in the heat capacity at $T_{c1} = 8.7$ K on a broad background with negative curvature that is a Schottky anomaly arising from the partial lifting by the CEF of the 16–fold degeneracy of the $Er^{3+} J = 15/2$ Hund's

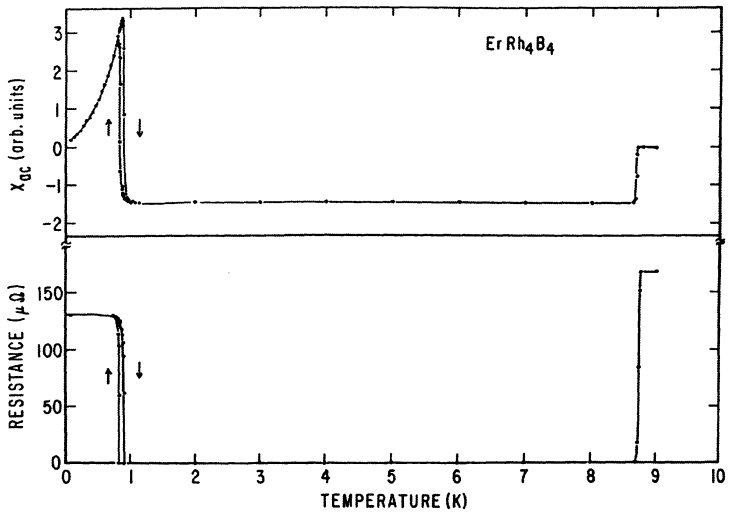

Fig. 8.14. Typical ac magnetic susceptibility χ_{ac} and electrical resistance vs temperature data for $ErRh_4B_4$, after Ref. [83]

rule multiplet. At lower temperatures (see inset), there is a spike–shaped feature at $T_{c2} = 0.93$ K (measured upon warming) superimposed on another anomaly that is apparently associated with the long–range ferromagnetic ordering of the Er^{3+} magnetic moments in the vicinity of T_{c2} [68]. There is also a shoulder in the heat capacity above T_{c2} whose origin may be attributable to the formation of a sinusoidally modulated magnetic state that coexists with superconductivity that is discussed below.

Measurements of the normalized neutron scattering intensity of the [101] reflection for $ErRh_4B_4$ [85] indicate that the ferromagnetic transition is broad, extending up to ~ 1.4 K, well above the temperature of the reentrant superconducting transition at $T_{c2} \sim 0.9$ K. Also, there is definite thermal hysteresis between ~ 0.8 K and ~ 1.4 K. The width of the ferromagnetic transition has been attributed to a distribution of effective Curie temperatures within the material, while the hysteresis may be caused by the nucleation of normal–ferromagnetic domains within the superconducting regions between T_{c2} and ~ 1.4 K. The heat capacity data also reveal thermal hysteresis, part of which appears to be associated with the formation of ferromagnetic domains (between ~ 0.9 K and ~ 1.3 K), and part of which is due to the reentrant transition at T_{c2}.

Neutron intensity vs scattering angle data at various temperatures on a polycrystalline $ErRh_4B_4$ sample, whose reentrant superconducting transition occurs at ~ 0.7 K, revealed the development of a peak near 1° which grows in intensity as the temperature is decreased and then disappears abruptly when the sample becomes normal below T_{c2} (see Fig. 8.16). The data were

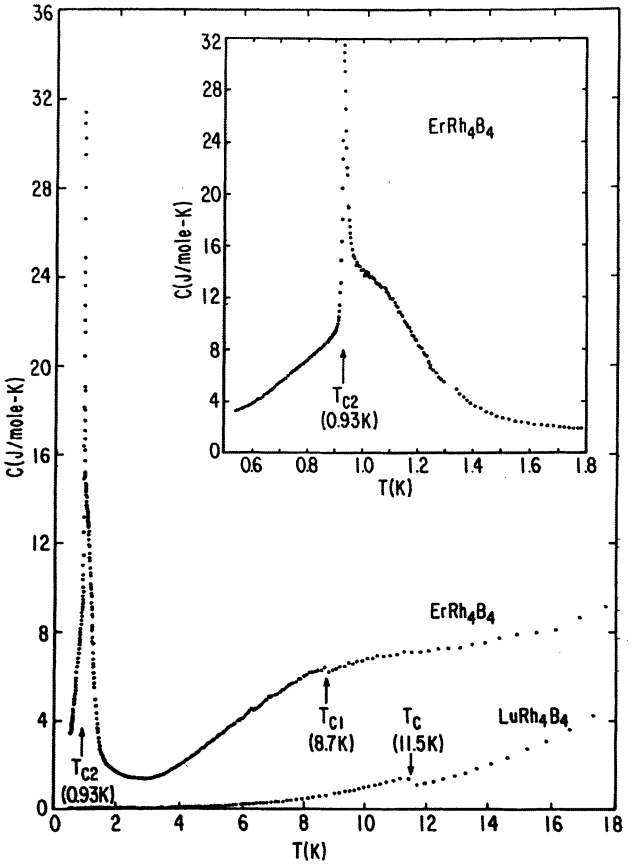

Fig. 8.15. Specific heat C vs temperature T for $ErRh_4B_4$ and $LuRh_4B_4$. The inset shows a detailed plot of C vs T for $ErRh_4B_4$ in the vicinity of the reentrant superconducting transition at T_{c2}, after Ref. [89]

interpreted in terms of fluctuations into a state in which the magnetization is sinusoidally modulated with a wavelength $\lambda \sim 100$ Å that was assumed to take the form of a spiral. Subsequently, neutron scattering experiments on an $ErRh_4B_4$ single crystal were performed by Sinha *et al.* [87]. Their findings are consistent with the neutron scattering experiments on polycrystalline $ErRh_4B_4$ by Moncton *et al.* [85], but revealed that the sinusoidally–modulated magnetic state is a transverse linearly polarized long–range magnetic state with a wavelength of ~ 100 Å. The linearly polarized sinusoidal modulation lies along the [010] axis and the propagation directions are at 45° to the [001] and the [100] axes. The neutron scattering measurements on a single crystal of $ErRh_4B_4$ are summarized in Fig. 8.17.

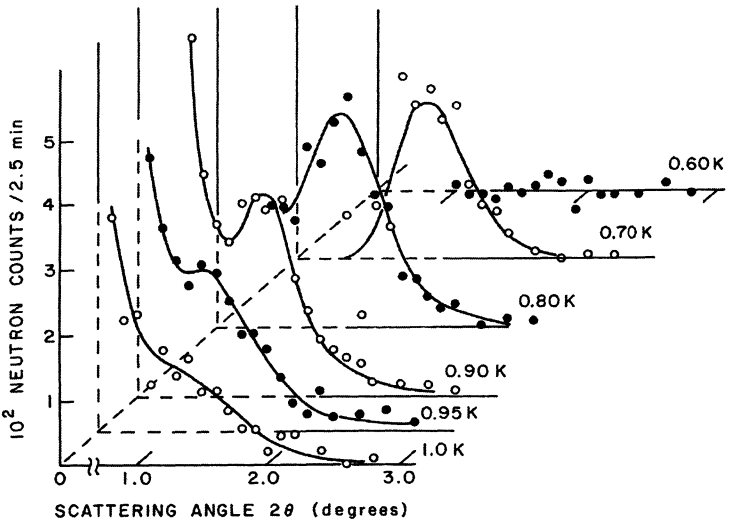

Fig. 8.16. Small angle neutron scattering results on $ErRh_4B_4$ obtained at various temperatures. The peak at $2\theta = 1.4°$ indicates an oscillatory magnetization with a wavelength of 100 Å, after Ref. [85]

Neutron diffraction experiments on a $HoMo_6S_8$ single crystal by Rossat–Mignod *et al.* [90] revealed that the wavelength of the sinusoidally modulated phase is twice as large as observed in powdered specimens and is transverse, with the moments oriented along the [111] direction while the wave vector is along the [110] direction. The large value of the wavelength ($\lambda \sim 570$ Å at 0.1 K) and the existence of a ferromagnetic phase in microdomains of the order of 1000 Å to 1500 Å was taken as evidence that the modulated phase is actually induced by the electromagnetic interaction between the persistent current and the magnetic moments.

The sinusoidally modulated magnetic state that coexists with superconductivity in $HoMo_6S_8$ and $ErRh_4B_4$ is reminiscent of the cryptoferromagnetic state proposed by Anderson and Suhl [91] in 1959 and has been the subject of much theoretical interest during the late 1970's and early 1980's. Whereas the original theory of Anderson and Suhl is based on the exchange interaction, more recent theories such as those of Blount and Varma [92], Ferrell *et al.* [93], and Matsumoto *et al.* [94] are based on the electromagnetic interaction. Although, as discussed earlier, the exchange interaction is operative in these materials, the electromagnetic interaction appears to be primarily responsible for the sinusoidally modulated magnetic state that coexists with superconductivity. Other possibilities for the periodic magnetic structure above T_{c2} that have been considered are (i) a spontaneous vortex lattice, (ii) a laminar structure, stabilized by the R magnetization in a

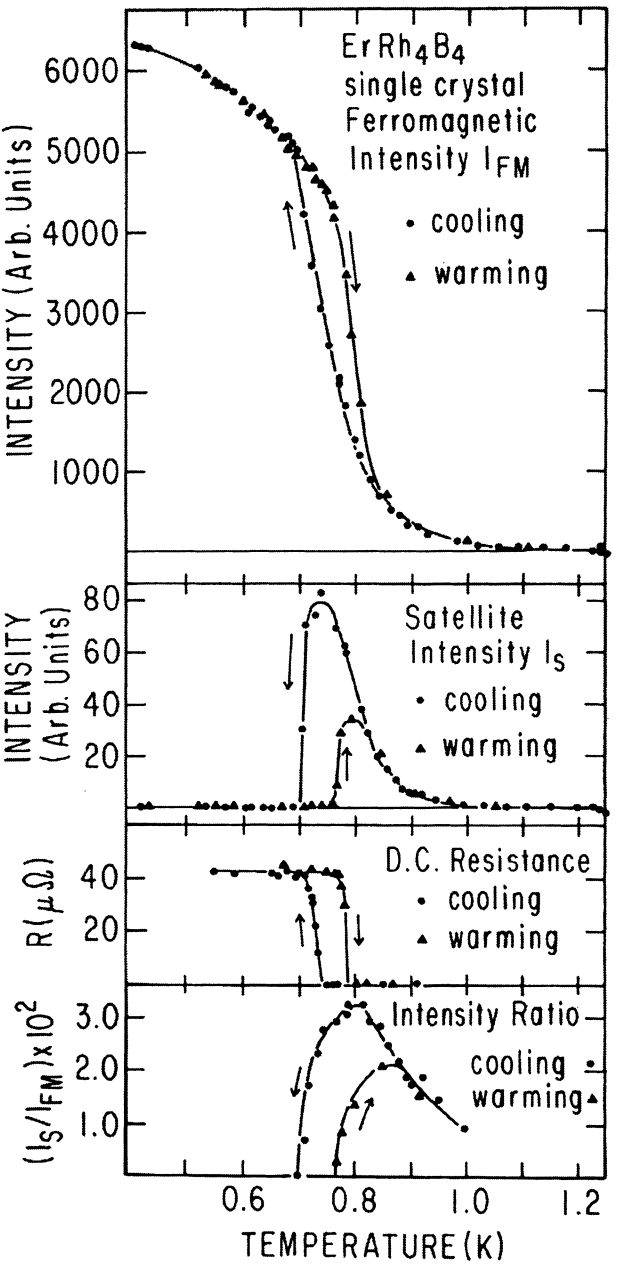

Fig. 8.17. Temperature dependence of the ferromagnetic intensity from the (101) Bragg peak, the satellite intensity, the dc resistance and the ratio of the satellite to the ferromagnetic intensity for the (101) reciprocal lattice point, after Ref. [87]

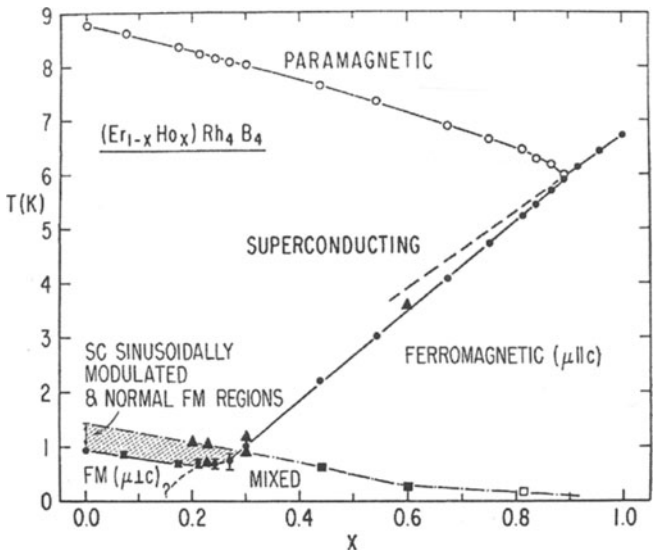

Fig. 8.18. Low temperature phase diagram for the $(Er_{1-x}Ho_x)Rh_4B_4$ pseudoternary system, after Refs. [95–97]

self–consistent manner, and (iii) combined spiral magnetic and spontaneous vortex states [69].

Many other techniques have been applied to investigate the physical properties of $HoMo_6S_8$ and $ErRh_4B_4$, and the reader is referred to several reviews on this subject that can be found in Ref. [8].

Superconductivity and competing magnetic interactions

Experiments on pseudoternary R compounds provide an alternative method for studying the interaction between superconductivity and long–range magnetic order, as well as for exploring the effects of competing types of magnetic moment anisotropy and/or magnetic order. Two types of RRh_4B_4 pseudoternaries have been formed, one in which a second R element is substituted at the R sites, and another in which a different transition element is substituted at the Rh sites.

An example of the first type of pseudoternary RRh_4B_4 system is $(Er_{1-x}Ho_x)Rh_4B_4$ whose low temperature phase diagram, delineating the paramagnetic, superconducting, and magnetically ordered phases, is shown in Fig. 8.18. The phase boundaries have been determined from ac magnetic susceptibility [95,96] and neutron diffraction measurements [97]. The phase diagram displays regions in which the Er^{3+} and Ho^{3+} magnetic moments independently order ferromagnetically within the basal plane and along the tetragonal c–axis, respectively, separated by a region of mixed magnetic phases. The temperature interval above T_{c2} within which the sinusoidally modulated magnetic phase in $ErRh_4B_4$ coexists with normal ferromagnetic domains is

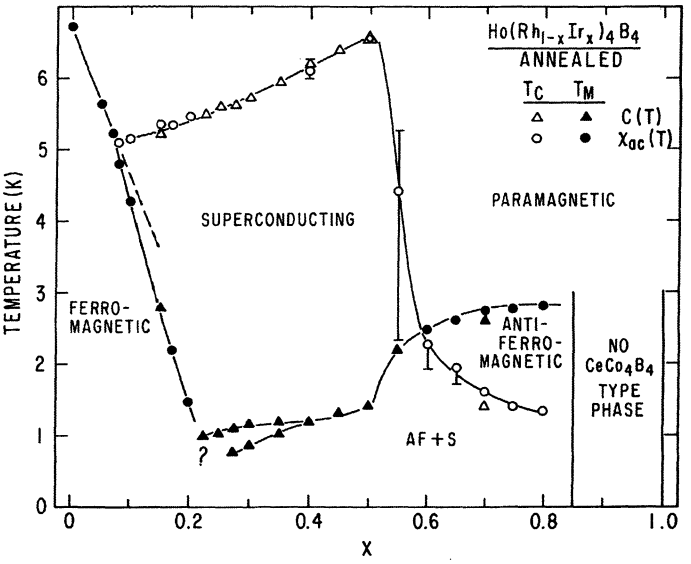

Fig. 8.19. Low temperature phase diagram for the $Ho(Rh_{1-x}Ir_x)_4B_4$ pseudoternary system, after Refs. [95, 99]

also indicated in Fig. 8.18. This inhomogeneous phase presumably persists within a certain region in the $T - x$ plane (shaded area in the figure). There is a tricritical point at the concentration $x_c = 0.89$ at which T_{c1}, T_{c2} and T_M become coincident. The T_{c2} vs x phase boundary for $x < x_c$ is depressed relative to a linear extrapolation of T_M vs x for $x > x_c$ (dashed curve in Fig. 8.18). Analysis of neutron diffraction data on an $(Er_{0.4}Ho_{0.6})Rh_4B_4$ sample [98] indicates that the actual T_M of 3.67 K is about 0.2 K less than it would have been in the absence of superconductivity, in accord with the dashed–line extrapolation as well as theoretical predictions.

A striking example of the second type of pseudoternary RRh_4B_4 system is $Ho(Rh_{1-x}Ir_x)_4B_4$. This system was first investigated by Ku *et al.* [100] and provided evidence for the coexistence of superconductivity and antiferromagnetic order with $T_N > T_c$ for $x > 0.6$. Subsequently, several detailed investigations of a $Ho(Rh_{0.3}Ir_{0.7})_4B_4$ compound were carried out; heat capacity measurements [89] confirmed the bulk character of the antiferromagnetic order in this material, while neutron diffraction experiments [101] revealed the magnetic structure. The low temperature phase diagram of the $Ho(Rh_{1-x}Ir_x)_4B_4$ system [95, 99], based on low temperature specific heat, ac magnetic susceptibility, and electrical resistance measurements, is shown in Fig. 8.19. The first study of this system yielded a similar phase diagram, but with no evidence for magnetic ordering at temperatures $T > 1.2$ K for $0.2 < x < 0.6$.

Several other pseudotenary RRh_4B_4 systems have been investigated, and the reader is referred to more comprehensive reviews for discussion and references [8, 13].

8.2.4 Magnetic Field Induced Superconductivity

One of the most dramatic manifestations of the interaction between superconductivity and magnetism is the induction of superconductivity through the application of a high magnetic field. The mechanism that is apparently responsible or this phenomenon, referred to as the exchange field compensation effect, was proposed by Jaccarino and Peter [4] more than twenty years before magnetic field induced superconductivity (MFIS) was firmly established experimentally [102].

The best example of MFIS is illustrated in Fig. 8.20 which shows H_{c2} vs T for the compound $Eu_{0.75}Sn_{0.25}Mo_6S_{7.2}Se_{0.8}$, taken from the work of Meul *et al.* [102]. The normalized electrical resistance (R/R_N) vs applied magnetic field H at several temperatures is displayed in the inset of Fig. 8.20. At the lowest temperature (0.37 K), the data reveal a sequence of transitions with increasing magnetic field from superconducting to normal, to superconducting again, and, finally, back to normal (S–N–S–N). From a series of measurements of R/R_N vs H at various temperatures, the phase diagram in the $H - T$ plane was constructed (Fig. 8.20); two separate domains of superconductivity are found, one at low fields and another at high fields, whereas only one domain of superconductivity at low fields is present for a conventional superconductor.

MFIS occurs in type II superconductors in which $H_{c2}(T)$ is determined by the paramagnetic limiting field H_p and which contain magnetic moments that are antiferromagnetically coupled to the spins of the conduction electrons. The magnetic moments in the $Eu_xSn_{1-x}Mo_6S_{8-y}Se_y$ compounds are carried by the divalent Eu ions and their coupling to the conduction electron spins generates an "effective" magnetic field, the exchange field H_J, that acts on the conduction electron spins in the same manner as an applied magnetic field. If the sign of the coupling between the Eu magnetic moments and the conduction electron spins is negative, the direction of H will be opposite to that of H_J; i.e., the effect of H_J will be "compensated" by H (see inset of Fig. 8.21). The net magnetic field H_T is then given by $H_T = H - |H_J|$. The sequence of S–N–S–N transitions shown in the inset of Fig. 8.20 can be explained in terms of the relationship between H_T and H_p as illustrated schematically in Fig. 8.21 [11]. The upper and lower curves show the applied field H and the exchange field H_J, respectively, the sum of which yields the net magnetic field H_T. The variation of H_T with respect to the value of H determines the superconducting behavior of the material.

In zero applied field, the compound is superconducting. As the applied magnetic field is increased, the Eu magnetic moments become aligned in the direction of the field at a relatively low H–value and $|H_J|$ attains its maximum

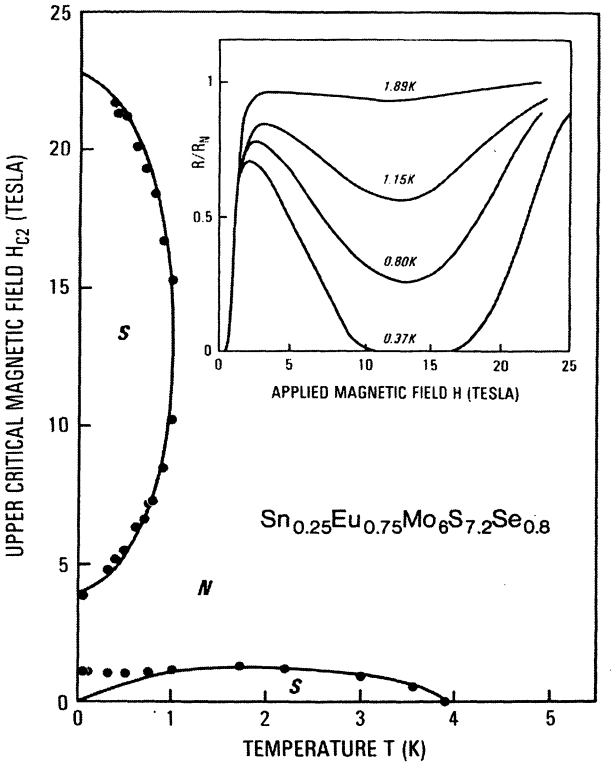

Fig. 8.20. Magnetic field H – temperature T phase diagram for the compound $Eu_{0.75}Sn_{0.25}Mo_6S_{7.2}Se_{0.8}$. The symbols S and N denote superconducting and normal regions, respectively. The solid circles represent the $H_{c2}(T)$ measurements of Meul *et al.* [102], and the solid lines are the boundaries predicted by theory. Normalized electrical resistance R/R_N, vs applied magnetic field data at several temperatures are shown in the inset, after Ref. [102]

value $|H_J^{max}|$ of 30–50 tesla. Consequently, provided $|H_J|$ is greater than H_p, the magnitude of H_T (which is now negative) can become larger than H_p and drive the material into the normal state. As the applied magnetic field is increased further, the net magnetic field starts to decrease in magnitude, until its magnitude falls below H_p when the compound once more becomes superconducting. Thereafter, H_T increases linearly with H, vanishing and then changing sign at $H = |H_J^{max}|$ where H_J is completely compensated, until H_T (now positive) exceeds H_p, when the system once again becomes normal. Because the value of the exchange field can be rather large, the compensation effect can take place at very high magnetic fields.

In actuality, the second transition from superconductivity to the normal state will also occur if H surpasses the orbital critical field H_{c2}^* of the compound. Thus, in order to observe MFIS, it is important that H_{c2}^*,

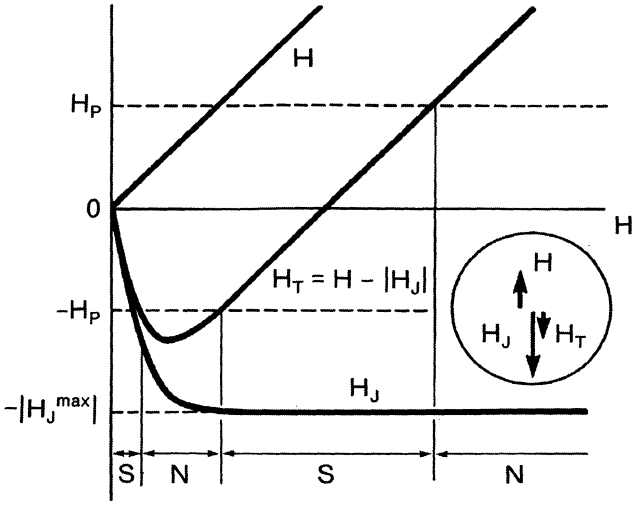

Fig. 8.21. Schematic diagram of the S–N–S–N transition sequence in an applied magnetic field H. H_T is the net magnetic field acting on the conduction electron spins, H_J is the exchange field produced by localized magnetic moments, and H_p is the paramagnetic limiting field. The material is superconducting (S) when $|H_J| < H_p$ and normal (N) when $|H_T| > H_p$, after Ref. [11]

which can also limit the value of the upper critical field H_{c2}, is large enough to allow superconductivity to occur in this magnetic field range (that is, $H_{c2}^* > |H_J^{max}| - H_p$), since the orbital effects are not compensated by the Jaccarino–Peter mechanism. The compensation of the exchange field by the applied magnetic field in several $Eu_xM_{1-x}Mo_6S_8$ systems (where M is a metal such as Sn, Pb, La [103] or Yb [104]) and in $EuMo_6S_8$ under pressure [105], had been inferred from an enhancement and anomalous temperature dependence of H_{c2} in these materials.

Following the initial suggestion by Jaccarino and Peter that MFIS could occur in a ferromagnet due to exchange field compensation, several theoretical investigations of MFIS in paramagnetic systems were carried out [106–108]. One model, based on the theory of type II superconductivity including the effect of the exchange field [107], was used by Meul *et al.* to analyse their $H_{c2}(T)$ measurements on the $Eu_xSn_{1-x}Mo_6S_8$ system. The calculated boundaries of the two superconducting domains observed for the compound $Eu_{0.75}Sn_{0.25}Mo_6S_{7.2}Se_{0.8}$ are indicated by the solid lines in Fig. 8.20 where the parameters of the theory have been adjusted to give the best fit to the data. The excellent description of the $H - T$ superconducting phase boundaries shown in Fig. 8.20 is striking confirmation of the Jaccarino–Peter compensation mechanism. Jaccarino and Peter originally suggested MFIS in a weakly ferromagnetic material, assuming that it would be superconducting

in the absence of ferromagnetic ordering. MFIS in a ferromagnet remains to be discovered.

8.3 f–Electron Heavy Fermion Superconductors

8.3.1 Introduction

In heavy–fermion compounds, strong electronic interactions between the conduction electrons and the localized f–electrons of rare earth or actinide ions results in large quasiparticle effective masses, up to several hundred times the free–electron mass. These compounds display a wide variety of striking correlated–electron phenomena including valence fluctuations, the Kondo effect, magnetic order, non–Fermi liquid behavior, and, of course, superconductivity.

As discussed in Section 8.2, magnetic moments in conventional superconductors suppress and eventually destroy superconductivity with increasing concentration of magnetic ions. In fact, for decades it was generally accepted that magnetism and superconductivity were inimical. Thus, the 1979 discovery of superconductivity in the heavy–fermion compound $CeCu_2Si_2$ [109], in which the sublattice of Ce ions possess well–defined local moments at high temperatures, posed a major puzzle to researchers. Since then, the list of superconducting heavy–fermion compounds has expanded to include about twenty Ce, U, Pu, and Pr–based compounds. The known heavy fermion f–electron superconductors and their crystal structure and lattice parameters are listed in Table 8.1. Many of these compounds display the coexistence of antiferromagnetism (AFM) and superconductivity, and, recently, ferromagnetic superconductors have been added to the list (UGe_2 [3], URhGe [110]).

The study of superconductivity in heavy–fermion compounds has lead to a range of unexpected phenomena and new theories. It is now widely suspected that heavy–fermion superconductivity (HFSC) is magnetically mediated, with an unconventional superconducting order parameter (p–, or d–wave symmetry) that vanishes at lines or points on the Fermi surface. In UPt_3 and $U_{1-x}Th_xBe_{13}$, multiple superconducting phases are observed which is evidence for a complex, multi–component superconducting order parameter. Very recently, superconductivity was discovered [120, 130] in $PrOs_4Sb_{12}$, in which the superconductivity may be mediated by electric quadrupolar interactions rather than magnetic interactions of the Pr ions, suggesting a new mechanism for superconductivity in heavy fermion systems. Two decades later, the question of how superconductivity and magnetism can coexist still remains a formidable challenge and further research into this subject will no doubt greatly expand our understanding of superconductivity.

In this Section, we briefly review the normal and superconducting properties of heavy–fermion superconductors, in general. We then focus on a few exemplary compounds such as the $CeMIn_5$ (M = Rh, Co, Ir), UGe_2, and $PrOs_4Sb_{12}$. The compound UPd_2Al_3 serves as an example to illustrate how

Table 8.1. Crystal structure and lattice parameters of heavy–fermion superconductors.

Compound	Structure Type	Lattice Parameters (Å)			Ref.
		a	b	c	
$CeCu_2Si_2$	$ThCr_2Si_2$ (Tetr. $I4/mmm$)	4.103		9.94	[111]
$CePd_2Si_2$	$ThCr_2Si_2$ (Tetr. $I4/mmm$)	4.24		9.88	[112]
$CeRh_2Si_2$	$ThCr_2Si_2$ (Tetr. $I4/mmm$)	4.09		10.18	[112]
$CeNi_2Ge_2$	$ThCr_2Si_2$ (Tetr. $I4/mmm$)	4.150		9.854	[113]
$CeCu_2Ge_2$	$ThCr_2Si_2$ (Tetr. $I4/mmm$)	4.18		10.18	[114]
$CeIn_3$	$AuCu_3$ (Cub. $Pm3m$)	4.689			[115]
$CeRhIn_5$	$HoCoGa_5$ (Tetr. $P4/mmm$)	4.652		7.542	[116]
$CeIrIn_5$	$HoCoGa_5$ (Tetr. $P4/mmm$)	4.668		7.515	[117]
$CeCoIn_5$	$HoCoGa_5$ (Tetr. $P4/mmm$)	4.62		7.56	[118]
Ce_2RhIn_8	Ho_2CoGa_8 (Tetr. $P4/mmm$)	4.665		12.244	[119]
$PrOs_4Sb_{12}$	$LaFe_4P_{12}$ (Cub. $Im\bar{3}$)	9.3017			[120]
UBe_{13}	$NaZn_{13}$ (Cub. $Fm\bar{3}c$)	10.268			[121]
UPt_3	$SnNi_3$ (Hex. $P6_3/mmc$)	5.764		4.899	[122]
URu_2Si_2	$ThCr_2Si_2$ (Tetr. $I4/mmm$)	4.121		9.681	[123]
UPd_2Al_3	$PrNi_2Al_3$ (Hex. $P6/mmm$)	5.365		4.186	[124]
UNi_2Al_3	$PrNi_2Al_3$ (Hex. $P6/mmm$)	5.207		4.018	[125]
UGe_2	$ZrGa_2$ (Orth. $Cmmm$)	4.036	14.928	4.116	[126]
URhGe	TiNiSi (Orth. $Pnma$)	6.855	4.327	7.501	[127]
U_6Fe	Mn_6Fe (Tetr. $I4/mcm$)	10.302		5.239	[128]
$PuCoGa_5$	$HoCoGa_5$ (Tetr. $P4/mmm$)	4.232		6.786	[129]

various spectroscopic techniques have been used to elucidate the nature of heavy–fermion superconductivity.

8.3.2 Normal–State Properties

Specific heat

For most metals, the normal–state specific heat C at low temperatures can be described by the sum of an electronic contribution that varies linearly with temperature T, and a phonon term that varies as T^3, i.e.,

$$C(T) = \gamma T + \beta T^3. \tag{8.16}$$

This equation is valid for temperatures well below the Fermi and Debye temperatures. Due to significant correlations between electrons at the Fermi–surface, the physics of heavy–fermion materials is most effectively described in terms of quasiparticle excitations. The effective mass of these quasiparticles can be much larger than that of free electrons, and is proportional to the electronic specific heat coefficient $\gamma = C/T$.

For an ordinary metal, γ is close to the value for a free–electron gas $\gamma_0 = (\pi^2/3k_B^2)N(E_F)$, where $N(E_F)$ is the density of states at the Fermi

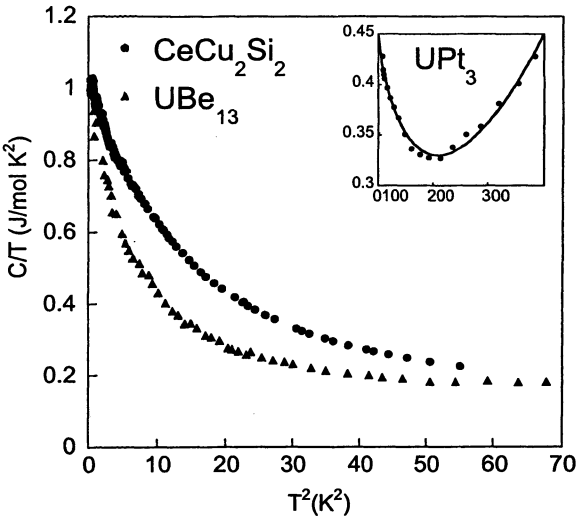

Fig. 8.22. Normal–state specific heat $C(T)$ plotted as C/T vs T^2 for $CeCu_2Si_2$ (circles) [109] and UBe_{13} (triangles) [131]. The inset shows C/T vs T^2 for the compound UPt_3 [132], where the solid line is a fit to Eq. 8.17

Energy; e.g., for sodium, $\gamma/\gamma_0 \approx 1.3$. In heavy–fermion compounds, γ/γ_0 can range from $10 - 1000$. In these materials, strong electronic or magnetic correlations between the electrons at the Fermi surface lead to high effective masses up to several hundred times the free–electron mass. The effective mass is proportional to the density of states at the Fermi energy, and therefore to the specific heat coefficient γ. Values of $\gamma(T = 0)$ for various heavy–fermion materials are shown in Table 8.2. For many heavy–fermion compounds, $C(T)$ deviates from Eq. 8.16 at low temperatures, such that $\gamma(T) = C(T)/T$ increases with decreasing temperature, sometimes reaching a maximum. The specific heat of the heavy–fermion compounds UBe_{13} and $CeCu_2Si_2$, plotted as C/T vs T^2 are shown in Fig. 8.22. The value of γ of both compounds diverges at temperatures below ~ 4 K, reaching a value of 1 J/mol K^2 as T approaches 0 K. This may be an indication of NFL behavior, to be discussed in section 8.3.6, or a low effective Fermi temperature, below which the density of states at the Fermi energy increases.

For the heavy–fermion systems UPt_3 and UAl_2, the specific heat at low temperatures can be described by

$$C(T) = \gamma T + \delta T^3 \ln T + \beta T^3 \tag{8.17}$$

for $T < 20$ K. The additional $\delta T^3 \ln T$ term was first observed in ^{3}He [159], and is predicted [160, 161] for long range spin fluctuations. The specific heat of UPt_3 is shown in the inset to Fig. 8.22, where the solid line is a fit to Eq. 8.17.

Table 8.2. Normal–state properties of heavy–fermion superconductors at ambient pressure, unless noted otherwise. γ is the electronic specific specific heatheat coefficient at low temperatures, taken at T_c. $\rho(300\ \mathrm{K})$ and ρ_0 are the room temperature and low temperature resistivities, respectively. T_M is the magnetic ordering temperature at ambient pressure. The order type refers to antiferromagnetism (AFM), ferromagnetism (FM) or spin density wave (SDW). T_{coh} is the temperature at which the screening of local moments by the Kondo effect reduces magnetic scattering, and is identified with a gradual shoulder in the electrical resistivity.

Compound	γ (mJ/mol K^2)	ρ_{300K} ($\mu\Omega$ cm)	ρ_0 ($\mu\Omega$ cm)	T_M (K)	Order type	T_{coh} (K)
$CeCu_2Si_2$	700 [109]	90 [133]	4.8 [134]	0.8 [135]	SDW	20 [133]
$CePd_2Si_2$		47	2 [136]	10 [137]	AFM	
$CeRh_2Si_2$	80	17	6[a]	35 [138]	AFM	
$CeNi_2Ge_2$	350 [113]	14/16	2.6/0.9 [139]			50 [140]
$CeCu_2Ge_2$		225[b]	120[b] [141]	4.15 [142, 143]	AFM	
$CeIn_3$			0.7 [144]	10.1	AFM	50 [145]
$CeRhIn_5$	200[c] [146]	33[c]	< 1	3.8	AFM	25[c] [116]
$CeIrIn_5$	720	40	1.25			50 [117]
$CeCoIn_5$	290	17	3			30 [118]
Ce_2RhIn_8	$\sim$ 400[a] [147]	70	65	2.8	AFM	10[a] [119]
$PrOs_4Sb_{12}$	350[d] [120, 148]	200	6			
UBe_{13}	900 [149]	140	200 [131]			10
UPt_3	420 [150]	225/100 [151]	0.5	6 [152]	AFM	10
URu_2Si_2	65 [123, 153]	330/170	30/30 [154]	17.5	AFM	50
UPd_2Al_3	150 [124]	140	10	14	AFM	75
UNi_2Al_3	120 [125]	1000	25	4.5	SDW	100
UGe_2	30[a] [155, 156]	200	0.2	53	FM	
URhGe	160 [157]		2 [110]	10	FM	
U_6Fe	280 [158]		50			
$PuCoGa_5$	80[d] [129]	250	30			

[a] 7.3 kbar
[b] 160 kbar
[c] 16 kbar
[d] determined from normal and superconducting–state properties.

Magnetization

The magnetic susceptibility χ in heavy–fermion systems tends to follow a Curie–Weiss law at high temperatures

$$\chi(T) = \frac{N_A \mu_{eff}^2}{3k_B(T - \theta_{CW})} \tag{8.18}$$

where N_A is Avogadro's number, k_B is Boltzmann's constant, μ_{eff} is the effective magnetic moment, and θ_{CW} is the Curie–Weiss temperature. The effective moment is often reduced somewhat with respect to the free ion value for Ce ($2.54\mu_B$) or U ($3.6\mu_B$), which can be attributed to valence fluctuations, the Kondo effect, or crystalline electric field (CEF) effects. The Curie–Weiss temperature is generally large and negative due to valence fluctuations or Kondo interactions if the temperature range of the Curie–Weiss fits is much

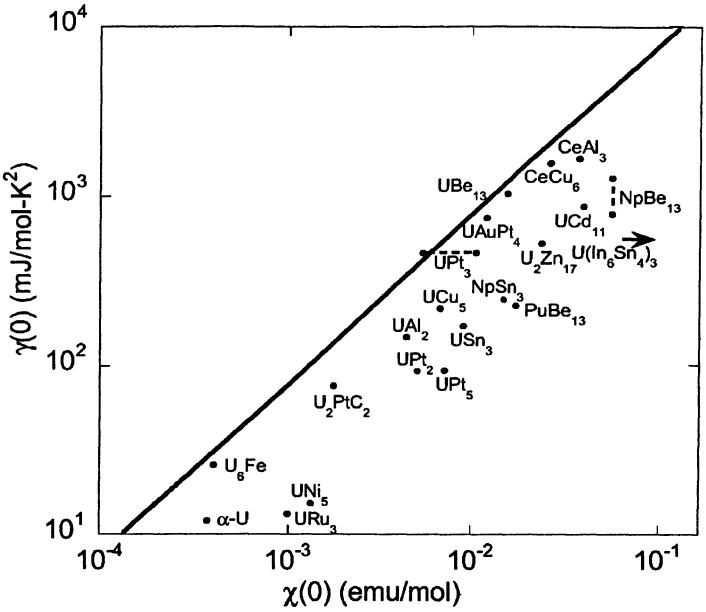

Fig. 8.23. Electronic specific heat coefficient γ plotted as a function of magnetic susceptibility χ at low temperatures on a log–log scale for various heavy–fermion materials. The solid line is the free–electron prediction for the Wilson ratio ($R = 1$), after Ref. [162]

larger than the CEF splitting of the lanthanide or uranium f–electron energy levels. $\theta_{\rm CW}$ is found to be a rough measure of the Kondo temperature, i.e., $T_{\rm K} \sim (3-4)\theta_{\rm CW}$.

At low temperatures (e.g. $\sim$ 50 K for $CeMIn_5$ (M = Rh, Ir, Co), 300 K for UPt_3) the magnetic susceptibility $\chi(T)$ typically deviates from a Curie–Weiss law. The direction of this deviation varies from compound to compound. For example, UPt_3 has a larger susceptibility at low temperatures than is predicted by the Curie–Weiss law, whereas UBe_{13} has a smaller susceptibility. There are various mechanisms which could be responsible for these deviations, including CEF effects, magnetic ordering, quenching of the local moments by the Kondo effect (which would only explain a suppression of the magnetization), and valence fluctuations of the f–electrons.

The Pauli susceptibility of heavy–fermion materials at the lowest temperatures, $\chi(0)$, is much larger than that of ordinary metals, typically by a factor of $10-100$. It is empirically found [162] to scale with the electronic specific heat coefficient $\gamma(0)$. In Fig. 8.23, $\gamma(0)$ is plotted as a function of $\chi(0)$ for various heavy–fermion materials. This scaling of the magnetic susceptibility and the electronic specific heat coefficient is predicted by Wilson for Kondo

systems [163] where the Wilson–Sommerfeld ratio

$$R = \frac{\pi^2 k_B^2}{\mu_{eff}^2} \frac{\chi(0)}{\gamma(0)} \tag{8.19}$$

is on the order unity for most heavy–fermion compounds. The predictions give $R = 1$ for the non–interacting electron model, and $R = 2$ for the Kondo model [163]. In a more general context the Wilson ratio is also known as the Sommerfeld ratio.

Many heavy–fermion superconductors order antiferromagnetically (e.g., UPd_2Al_3, $CeIn_3$) or exhibit spin glass freezing at low temperatures, and a very small number also order ferromagnetically (e.g., UGe_2). The magnetic ordering temperatures of all the heavy–fermion superconductors are listed in Table 8.3. The heavy–fermion compounds that order antiferromagnetically fall into two classes. Compounds in the first class (e.g., UPd_2Al_3, UNi_2Al_3, $CeIn_3$ and $CeRhIn_5$) have ordered magnetic moments in the range $(0.2 - 1)\mu_B$, and appear to have standard dipolar order parameters. Compounds in the second class (URu_2Si_2 and UPt_3) have very small ordered moments ($\sim 0.01\mu_B$), although the Néel temperatures of these compounds are comparable to those of the first class. One possible explanation for these small moments is quadrupolar ordering, although only the dipolar moment has been detected by means of neutron scattering experiments. In UPt_3 and $U_{1-x}Th_xBe_{13}$, an additional tiny (0.001 μ_B) magnetic moment is associated with the onset of a second superconducting phase.

Electrical resistivity

The electrical resistivity ρ of heavy–fermion materials is remarkably different than that of conventional metals. For a typical metal, (e.g., Pd), the resistivity decreases with decreasing temperature due to electron–phonon scattering for $T > \theta_D$, where θ_D is the Debye temperature. At low temperatures, Fermi liquid theory predicts that $\rho(T)$ saturates as $\rho(T) \propto AT^2 \propto (T/T_F)^2$, with a coefficient A of the order of 10^{-6} $\mu\Omega\,\mathrm{cm/K^2}$. This AT^2 term is so small in simple metals that it is obscured by other electron scattering processes. In heavy–fermion materials on the other hand, the AT^2 term can be up to five orders of magnitude larger than in ordinary metals, reflecting a low effective Fermi temperature $T_F^* \sim 10 - 100$ K, and is often observed at low temperatures. A universal relation between the large magnitude of A and the enhanced electronic specific heat coefficient γ in heavy–fermion materials was found by Kadowaki and Woods [173]. They observed that most HF compounds obeyed the relation $A/\gamma^2 = 1 \times 10^{-5}$ $\mu\Omega\,\mathrm{cm\,(mol\,K/mJ)^2}$, as illustrated in Fig. 8.24, provided the materials are not too close to a magnetic instability. Displayed in Fig. 8.25 are the $\rho(T)$ curves for two typical heavy–fermion compounds, UBe_{13} and $CeAl_3$. The resistivity of these and many other heavy–fermion materials is of the order of $100\mu\Omega\,\mathrm{cm}$ near room temperature, some $10 - 100$ times that of normal metals, and reflects the large exchange (Kondo) interaction between the local moments and the conduction electrons. A weak temperature dependence of $\rho(T)$ is most often

Table 8.3. Magnetic properties of some heavy–fermion superconductors. θ_{CW} and μ_{eff} are Curie–Weiss fit parameters to the susceptibility at high temperatures, and μ_{ord} is the ordered moment determined from neutron diffraction. (H parallel/perpendicular to c axis).

Compound	$\chi(0)$ (cm^3/mol)	θ_{CW} (K)	μ_{eff} (μ_B)	μ_{ord} (μ_B)
$CeCu_2Si_2$	0.082	140	2.68 [164]	
$CeNi_2Ge_2$	> 0.009	170	2.6 [140]	
$CeCu_2Ge_2$	0.3 [114]			
$CeRhIn_5$	0.022/0.005	16/−79	2.38 [116]	0.75 [165, 166]
$CeIrIn_5$	0.018/0.009	12.5/−67.4	2.28 [117]	
$CeCoIn_5$	0.014/0.008	−83/−54	2.59 [118]	
Ce_2RhIn_8	0.013/0.016	12/−40	2.38/2.32	0.55 [167]
$PrOs_4Sb_{12}$	0.06 [120]	−16	3.0	
UBe_{13}	0.015 [162]	−53	3.1	
UPt_3	0.19/0.10 [168]	−200	3.0	0.01 [169]
URu_2Si_2	0.01/0.06	−65	3.5	0.03 [123]
UPd_2Al_3	0.015 [124]	−47	3.2	0.85 [170]
UNi_2Al_3	0.06 [125]			0.2 [171]
UGe_2		55 [3]	2.7	1.5 [155]
URhGe		1.8 [110]	10	0.42 [127]
U_6Fe	0.003 [172]			
$PuCoGa_5$	0.031	−2	0.68 [129]	

observed in these materials at higher temperatures, follow by a maximum or shoulder at $T_{coh} \sim 50 - 100$ K. The resistivity drops rapidly just below T_{coh} due the formation of coherent Bloch states as the lattice of the local moments of the f–ion sublattice is screened by the conduction electrons. At the lowest temperatures, the resistivity exhibits Fermi liquid properties, i.e., $\rho(T) = \rho_0 + AT^2$, as shown in the inset of Fig. 8.25 for $CeAl_3$. A departure from the T^2 behavior of the electrical resistivity at low temperatures is observed in some heavy fermion materials, and is referred to as non–Fermi liquid behavior. This is discussed in detail in section 8.3.6.

Thermoelectric power

The thermoelectric power S is a sensitive function of the shape of the density of states near the Fermi level, therefore, large values of S are often observed in heavy–fermion compounds, compared to those of simple metals, due to the presence of a narrow f– or d–band at the Fermi level. A simple expression for the thermopower due to electron diffusion, that is valid for $T \gg \theta_D$, is given by

$$S = \frac{\pi^2 k_B^2 T}{3e} \left(\frac{\mathrm{d}(\ln \sigma(E))}{\mathrm{d}E} \right)_{E_F} \tag{8.20}$$

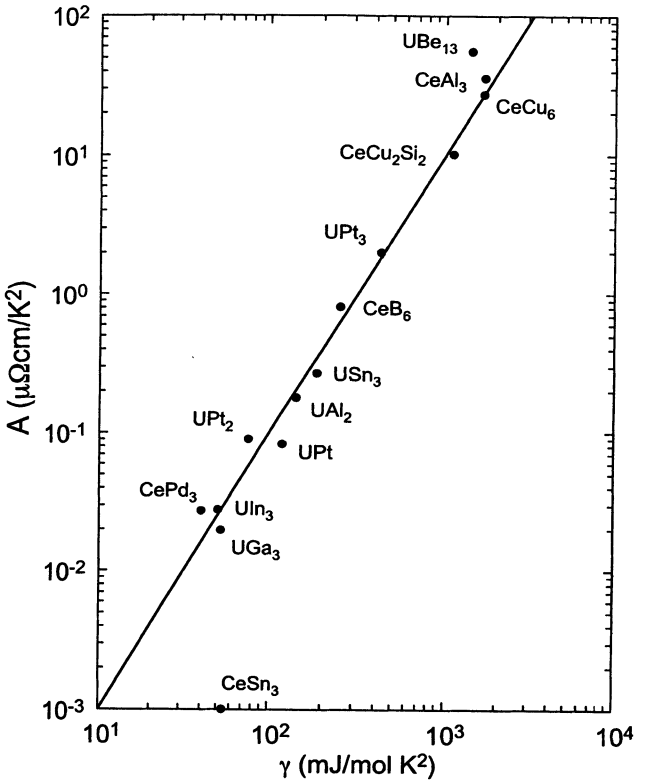

Fig. 8.24. Kadowaki–Woods plot: coefficient of the T^2 term in the electrical resistivity A vs electronic specific heat coefficient γ. The line has a slope $A/\gamma^2 = 1 \times 10^{-5} \mu\Omega\,\mathrm{cm\,(mol\,K/mJ)^2}$, after [173]

where $\sigma(E)$ is the value of the conductivity of the material at a energy E. A maximum in S is expected at a temperature of the order of the Kondo temperature. An anomalously large and positive value of S is often observed for Ce–based heavy–fermion compounds, with a maximum centered at T_K or at the CEF splitting if CEF effects are present. For Yb–based heavy–fermion materials, S is usually large and negative reflecting the fact that the electronic configuration of Yb is the one–hole counterpart to the one–electron configuration of Ce.

8.3.3 Superconducting–State Properties

Specific heat

The specific heat in the superconducting state of heavy–fermion materials differs markedly from that of conventional superconductors. Whereas $C(T)$ in a conventional superconductor varies as $C(T) \propto \exp(-\Delta/k_B T)$, in accordance with BCS theory, the specific heat of heavy–fermion materials can

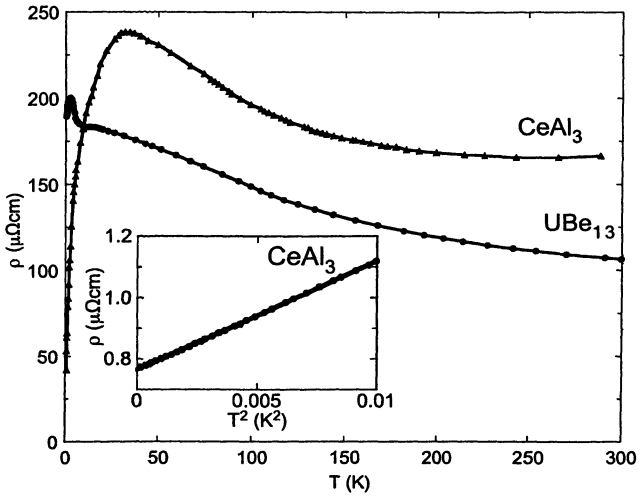

Fig. 8.25. Electrical resistivity ρ vs T of the heavy–fermion compounds UBe_{13} and $CeAl_3$. Inset: ρ vs T^2 for $CeAl_3$ at low temperatures , after [131,174,175]

often be described by a power law

$$C(T) = \gamma_s T + \delta T^n \tag{8.21}$$

where the power law exponent $n \sim 2-3$. Both the residual specific heat γ_s and the power law behavior suggest an unconventional superconducting gap that vanishes at lines ($n = 2$) or points ($n = 3$) on the Fermi surface.

In heavy–fermion materials, the magnitude of the specific heat jump ΔC at T_c is a large fraction of the value of $C(T_c)$. Values of $\Delta C/\gamma T_c$ are listed in Table 8.4. The quantity $\Delta C/\gamma T_c$ is predicted by BCS theory to be 1.43 (weak coupling) or 1.6 (strong coupling). The fact that $\Delta C/\gamma T_c$ for heavy–fermion materials is of the order of unity, where γ is the value derived from the normal–state specific heat, implies that the superconductivity in these materials is a bulk phenomenon, and that the same electrons responsible for the heavy–fermion behavior in the normal state are participating in the superconductivity. The specific heat jumps for the compounds UBe_{13} and $CeCoIn_5$ are shown in Fig. 8.26. For $CeCoIn_5$, the specific heat jump is unusually large such that $\Delta C/\gamma T_c = 4.5-5$ [117,176]. For this compound, $C(T)$ below T_c can be fit by Eq. 8.21 with $n = 2.3$ and $\gamma_0 = 110$ mJ/mol K^2.

Upper critical field

All of the known superconducting heavy–fermion compounds are type–II superconductors with upper critical fields H_{c2} of the order of a few tens of kOe and lower critical fields H_{c1} of the order of tens of Oe, corresponding to values of $\kappa \equiv \lambda/\xi_0 \sim 50-100$, where λ is the penetration depth and ξ_0 is the superconducting coherence length. These unusually large values of H_{c2} and small values of H_{c1} reflect the large effective masses of the superconducting

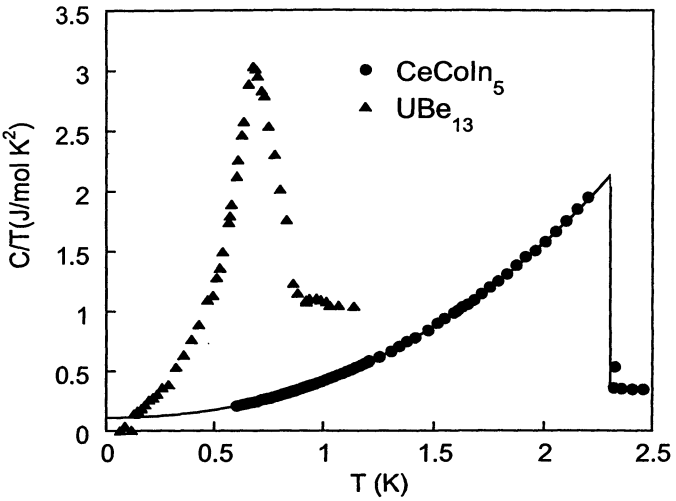

Fig. 8.26. Superconducting jump in the specific heat plotted as C/T vs T of UBe_{13} (triangles) [131] and $CeCoIn_5$ (circles) [176]. The line below T_c is a fit to the expression $C = \gamma T + \delta T^n$

quasiparticles which can be understood by noting that $H_{c1} \propto 1/\lambda^2 \propto 1/m^*$ and $H_{c2} \propto 1/\xi_0^2 \propto m^{*2}$. Most heavy–fermion superconductors have a large initial slope of the upper critical field near T_c, $-(dH_{c2}/dT)_{T_c}$, and sometimes exhibit a linear T–dependence at lower temperatures. For example, the initial slope of UBe_{13} is enormous, $-(dH_{c2}/dT)_{T_c} = 420$ kOe/K [131], as shown in the inset of Fig. 8.27. Below $T = 0.6$ K, the upper critical field of UBe_{13} is linear in temperature with a slope of -91 kOe/K (Fig. 8.27). The zero temperature value of the orbital critical field can be estimated from the initial slope of the upper critical field by the following formula [188]:

$$H_{c2}^*(0) = 0.693 T_c(-dH_{c2}/dT)_{T_c}, \tag{8.22}$$

from which the superconducting coherence length ξ_0 can be determined from the relation [189]

$$H_{c2}^*(0) = \Phi_0/2\pi\xi_0^2, \tag{8.23}$$

where $\Phi_0 = 2.07 \times 10^{-7}$ Oe cm^2 is the flux quantum. The value of ξ_0 can be used to estimate the Fermi velocity from the relation $\xi_0 \propto 0.18\hbar v_F/kT_c$; thus, the effective mass can be obtained via $m^* = \hbar k_f/v_F$ within a spherical–Fermi–surface approximation. The values of the coherence length and the effective mass estimated in this fashion for the heavy–fermion superconductors are collected in Table 8.4. Many heavy–fermion superconductors have anisotropic upper critical fields of the order of $H_{c2}^{||}/H_{c2}^{\perp} \approx 1.5$ near T_c (with respect to the c axis).

Table 8.4. Superconducting properties of heavy–fermion superconductors. T_c: superconducting transition temperature at P_c; H_{c2}: upper critical field at $T = 0$ K; $-(dH_{c2}/dT)_{T_c}$: slope of the upper critical field; m^*: effective mass determined from H_{c2} as discussed in section 8.3.3; $\Delta C/\gamma T_c$: superconducting specific heat jump $\Delta C/T_c$ divided by electronic specific heat coefficient γ; ξ_0: superconducting coherence length determined from Eq. 8.22. Values are listed as H parallel/perpendicular to the c–axis.

Compound	T_c (K)	P_c (kbar)	$H_{c2}(0)$ (kOe)	$-(dH_{c2}/dT)_{T_c}$ (kOe/K)	ξ_0 (Å)	$\Delta C/\gamma T_c$	m^* (m_e)
$CeCu_2Si_2$	0.49 [109]		20/25	230/230 [133]	65		351 [177]
$CePd_2Si_2$	0.43	28 [137]	13/7	16/12.7 [178]	230/300		97
$CeRh_2Si_2$	0.4	6	35	13	307		118 [179]
$CeNi_2Ge_2$	0.23	23	> 15	5 [139]	642		75
$CeCu_2Ge_2$	~ 2	165 [180]	35	11 [141]	147		37
$CeIn_3$	0.17	25 [2]	4.5 [181]	32	300		191
$CeRhIn_5$	2.17	16 [116]	160 [146]	140 [116]	40	0.36 [146]	104
$CeIrIn_5$	0.40		5/9	24/48	223/141	0.76 [117]	100
$CeCoIn_5$	2.3 [118]		50/120	7/15 [182]	50/32	4.5 [118]	121
Ce_2RhIn_8	2 [119]	23	−/54	−/92	51		94
$PrOs_4Sb_{12}$	1.85 [120]		22	19	116	~ 3 [148]	44
UBe_{13}	0.85		90 [183]	420 [183]	37	1.23 [131]	351
UPt_3	0.55 [184]		18	63	117	0.5 – 1.0 [150]	265
URu_2Si_2	1.5 [123, 153]		100	92	59	0.56	184
UPd_2Al_3	1.9		30	43	76 [185]	1.2 [124]	187
UNi_2Al_3	1.0		10	13	191 [185]	0.4 [125]	147
UGe_2	0.7 [3, 186]	10	20	58 [187]	108 [187]	0.25	235
URhGe	0.3 [110]		7	40	199	0.5	281
U_6Fe	3.7 [158]		~ 100	34	61	~ 2	109
$PuCoGa_5$	18.5 [129]		~ 750	59	21	~1	37

Nuclear magnetic resonance

Nuclear magnetic resonance (NMR) measurements yield a T^3 power law T–dependence of the $1/T_1$ relaxation rate for most heavy–fermion materials, instead of the exponential temperature dependence observed in conventional superconductors. Analogous to the specific heat, a T^3 (T^5) power law dependence of $1/T_1$ is indicative of a superconducting gap that vanishes at lines (points) on the Fermi surface. The T^5 power law has never been observed, but since NMR measurements are generally performed on powdered samples, the directionality of the point nodes would be lost. Also, if both point and line nodes are present, the T^3 dependence is expected to dominate.

In conventional BCS superconductors, a peak is observed in $1/T_1$ below T_c, known as the Hebel–Slichter peak. This peak does not occur in heavy–fermion superconductors, further confirming the exotic nature of the superconductivity.

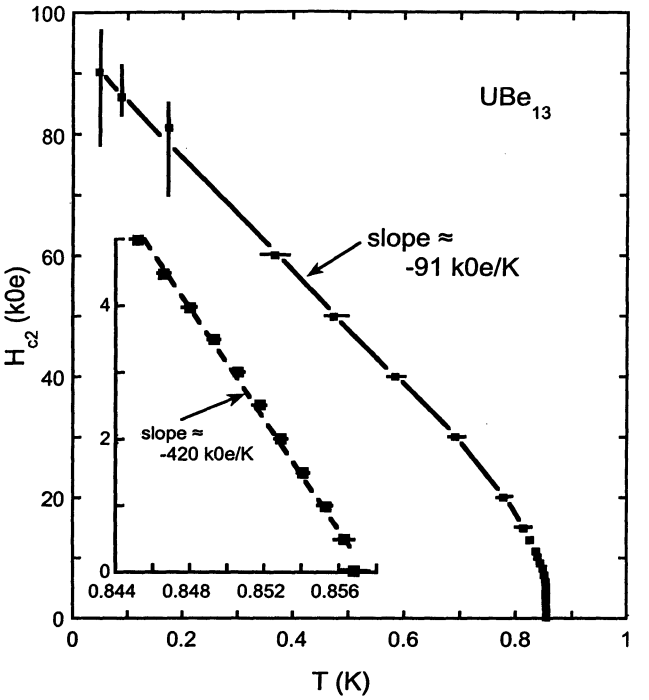

Fig. 8.27. Upper critical field H_{c2} vs T of UBe_{13}. Inset: Expanded view of $H_{c2}(T)$ of UBe_{13} near T_c. The line is a fit to the data yielding a slope $-(dH_{c2}/dT)_{T_c} = 420$ kOe/K, after Ref. [131]

8.3.4 UPd_2Al_3

Introduction

The heavy–fermion compound UPd_2Al_3 belongs to the ever–growing class of materials which display the coexistence of antiferromagnetic (AFM) order and superconductivity at low temperatures. This class, which includes such compounds as UPt_3 and $CeIn_3$, has attracted considerable attention during the last decade due to the unusual nature of the superconductivity. The detailed nature of the superconductivity in these compounds has been investigated using an assortment of optical and spectroscopic techniques including NMR, Josephson tunnelling, and inelastic neutron scattering, which suggests that the superconductivity is magnetically mediated and has d–wave order parameter symmetry. In this section, we use UPd_2Al_3 as an example to illustrate how spectroscopic techniques have been used to elucidate the nature of heavy–fermion superconductivity.

UPd_2Al_3 is a heavy–fermion compound with an electronic specific heat coefficient γ of ≈ 100 mJ/mol K^2, which corresponds to an effective electron mass of $m^* \approx 50\ m_e$. The specific heat of UPd_2Al_3 reveals antiferromagnetic

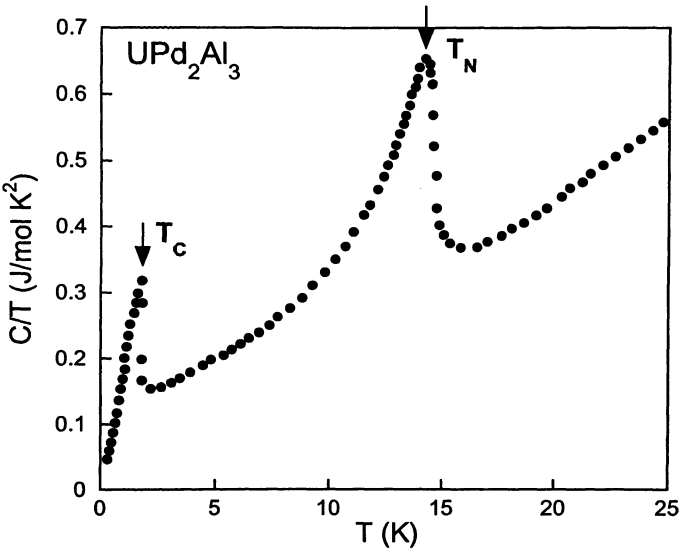

Fig. 8.28. Specific heat divided by temperature C/T plotted vs temperature T of polycrystalline UPd_2Al_3. The Néel temperature T_N and superconducting transition temperature T_c are indicated, after Ref. [124]

order at $T_N = 14$ K, and superconductivity at $T_c = 2$ K, as shown in Fig. 8.28.

Magnetic and Crystal Structure

Neutron diffraction measurements [190] show that UPd_2Al_3 crystalizes in the hexagonal $PrNi_2Al_3$ structure with lattice parameters $a = 5.37$ Å and $c = 4.19$ Å. The antiferromagnetic structure of UPd_2Al_3 consists of ferromagnetic sheets in the easy hexagonal plane with a relatively large ordered magnetic moment of 0.85 μ_B, which alternate in the c–direction. The magnetism arises from localized uranium moments with practically no spin transfer from the Pd ions, as confirmed by studies of neutron diffraction, NMR, and band–structure calculations [191–193].

The first neutron diffraction measurements [194, 195] on UPd_2Al_3 found that the AFM order remains almost unchanged in the superconducting state. However, recent high–resolution neutron diffraction data indicate [196] that as the temperature is lowered below the superconducting critical temperature T_c, a small 1 % reduction occurs in the intensity of the AFM Bragg peaks.

Inelastic Neutron Scattering

The inelastic neutron scattering profile measured at the AFM wave vector $Q = (0, 0, 0.5)$ is shown in Fig. 8.29. In addition to the zero energy divergence of the Bragg peak, two finite energy (inelastic) features are evident in the data: a peak at $\Delta E = 1.5$ meV due to the spin density wave, and a sharper peak at $\Delta E = 0.36$ K which results from an energy gap in the magnetic

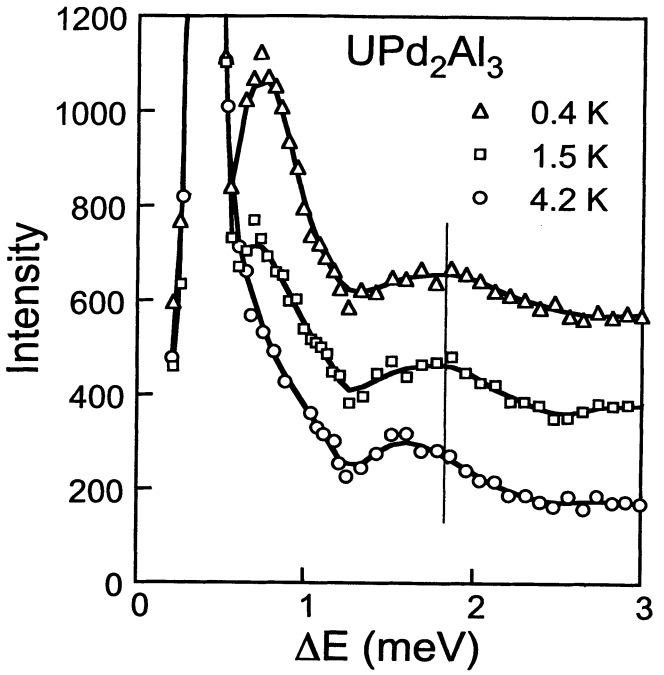

Fig. 8.29. Inelastic neutron diffraction data for UPd_2Al_3 at temperatures above and below $T_c = 2$ K. The lines are guides to the eye, after Ref. [196]

spectrum. The spin density wave is unusual in that it persists at temperatures well below T_N. It is localized about the AFM vector $Q = (0, 0, 0.5)$, since the peak intensity of the spin density wave peak drops off rapidly away from Q. The orientation of the spin density wave has been determined to be in the a-b crystallographic plane, transverse to the sublattice magnetization, from polarized inelastic neutron scattering measurements [197].

The energy gap in the magnetic spectrum observed in Fig. 8.29 occurs only in the superconducting state below $T_c = 2$ K and $H_c = 30$ kOe. The temperature dependence of the gap is surprisingly similar to the BCS theory prediction for a superconducting energy gap. At the lowest temperatures, the energy gap extrapolates to 0.36 meV, which corresponds to $2\Delta = 2.2k_BT_c$. This is comparable to the weak–coupling BCS theory result of $2\Delta = 3.5k_BT_c$. The appearance of this energy gap in the magnetic spectrum in the superconducting state suggests magnetically mediated superconductivity.

Superconducting energy gaps at slightly larger energies (up to $5.5k_BT_c$) have been observed in UPd_2Al_3 by NMR [191, 198, 199] and electron tunnelling [200] measurements. The discrepancy between the results of the different techniques is probably due to anisotropy of the energy gap; the power–law behavior of the specific heat and $1/T_1$ relaxation rate from NMR measure-

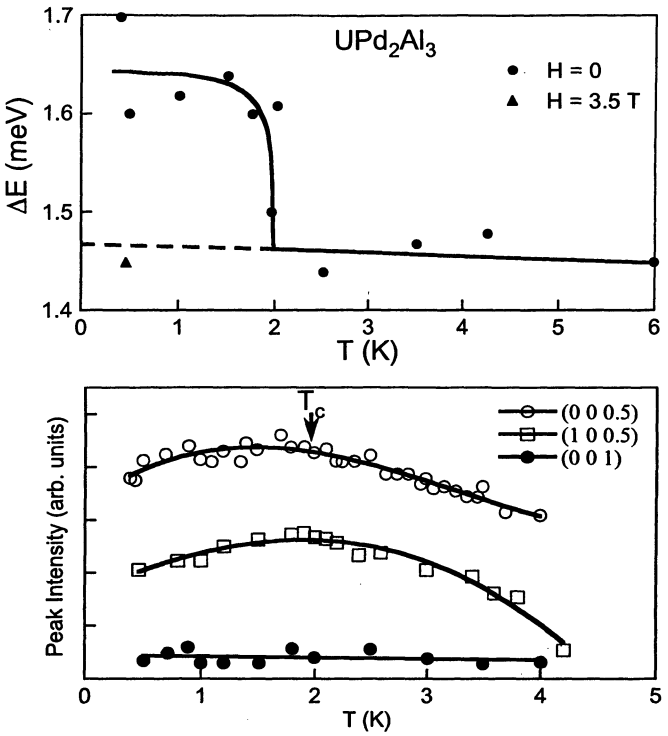

Fig. 8.30. UPd_2Al_3 inelastic neutron diffraction data [196]. Top panel: Activation energy ΔE of the spin density wave peak vs T. Bottom panel: Maximum of the spin density wave peak vs temperature T at various wave vectors

ments imply that the energy gap in UPd_2Al_3 must vanish at lines or points on the Fermi surface.

The onset of superconductivity has a marked effect on the spin density wave peak in the neutron diffraction data. As shown in Fig. 8.30, both the energy of the spin density wave peak and its line width increase abruptly at T_c. At the same time, the intensity of the peak reaches a maximum at T_c, and then decreases at lower temperatures. These effects are only apparent at fields below the critical field of UPd_2Al_3, and the normal–state spin density wave reappears in fields of $H = 35$ kOe. Thus, there appears to be a coupling between the superconducting and magnetic order parameters.

A temperature T_0, which characterizes the frequency spread (line width) of the spin wave, can be derived by fitting the energy spectrum to a Lorentzian function, yielding $T_0 \approx 28$ K for UPd_2Al_3. It has been suggested on the basis of theoretical work [201] that T_0 is proportional to T_c for spin–wave mediated superconductors. In fact, this relation is found to hold between

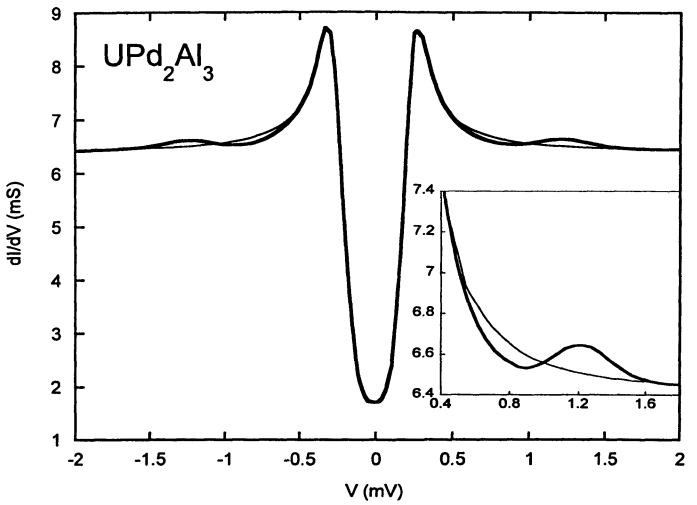

Fig. 8.31. Normalized differential conductivity of a UPd_2Al_3-AlO_x–Pb tunnel junction. The thinner line is a fit to the Dynes formula with $\Delta = 235$ μeV and $\gamma = 35$ μeV. The inset shows a feature associated with strong–coupling spin–fluctuations, after Ref. [203]

UPd_2Al_3 and the high–T_c superconductors, in which magnetically mediated superconductivity is also thought to occur [202].

These inelastic neutron scattering measurements show that the antiferromagnetism is almost unchanged by the onset of superconductivity and suggest that the superconductivity is mediated by transverse spin fluctuations in the *a-b* plane. An energy gap in the magnon spectrum of $\Delta(0) = 0.36$ meV was observed with a temperature dependence and magnitude close to the BCS prediction for a superconducting energy gap.

Electron Tunnelling

Further evidence for magnetically–mediated superconductivity in UPd_2Al_3, as well as details of the symmetry of the order parameter, have been elucidated by recent directional tunnelling measurements on thin films [203]. The UPd_2Al_3 thin films, which were grown by molecular beam epitaxy in the [001] orientation, are separated from a thin film of Pb by a 4 nm layer of aluminum oxide. Applying a magnetic field $H = 300$ Oe, which is above the H_{c2} of Pb, but well below the H_{c2} of UPd_2Al_3, results in a superconductor–insulator–normal tunnel junction. The resulting tunnelling spectrum is shown in Fig. 8.31, where the thin line is a fit to the Dynes formula. The most important feature of this tunnelling spectrum is a peak at $V = 1.22$ meV, which is above the gap energy, and below typical phonon frequencies ($\theta_D \approx 150$ K for UPd_2Al_3). The energy of this feature is very close to the energy gap $\Delta E = 1.5$ meV of a dispersive spin wave at the magnetic Bragg point $Q = (0, 0, 0.5)$, which was determined from inelastic neutron scattering measurements dis-

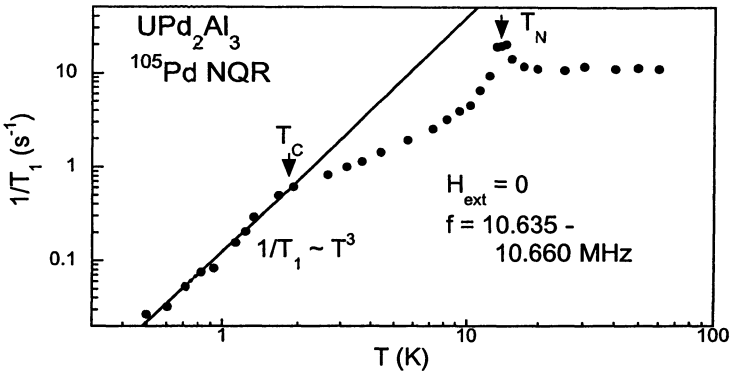

Fig. 8.32. Spin–lattice relaxation rate $1/T_1$ of UPd_2Al_3 as a function of temperature T determined from ^{105}Pd NQR measurements in the vicinity of the Néel temperature T_N and superconducting transition temperature T_c, after Ref. [191]

cussed in section 8.3.4. Thus, these measurements strongly suggest a coupling of the superconducting order parameter to a spin–fluctuation with an energy gap $\Delta E = 1.5$ meV. Furthermore, the directional nature of the tunnelling measurements provides information about the symmetry of the superconducting order parameter. Order parameters of odd parity can be ruled out due to the strong Pauli limiting that is observed in UPd_2Al_3, and there is only one even d–wave point group that does not show a gap node along the c axis. The authors conclude therefore that only the fully symmetric A_{1g} d–wave representation is consistent with the measurements.

Nuclear Magnetic Resonance

Two types of NMR and NQR measurements have been performed on UPd_2Al_3: ^{27}Al measurements by Kyogaku and coworkers in the early 1990s [204], and more recently ^{105}Pd NMR measurements by Matsuda et al. [191]. Both types of measurements agree as to the nature of the superconductivity in UPd_2Al_3. The spin–lattice relaxation rate T_1 derived from ^{105}Pd NQR results is plotted as $1/T_1$ vs temperature T in Fig. 8.32. Between T_c and T_N, $1/T_1$ varies as T in accordance with the Curie–Weiss law. Below T_c, $1/T_1$ follows a T^3 temperature dependence, and the Hebel–Slichter peak usually seen in BCS superconductors is absent. These data are consistent with the presence of unconventional superconductivity with an anisotropic energy gap that has line nodes on the Fermi surface. The best fit to the $1/T_1$ vs T data gives a superconducting energy gap of $2\Delta(0) = 5.5\ k_B T_c$. This energy gap is larger than that measured by neutron diffraction, perhaps due to anisotropy of the energy gap. In contrast to the NMR and NQR results, the T^3 temperature dependence of the specific heat implies point nodes on the Fermi surface. Additional NQR measurements at lower T are necessary to resolve this discrepancy. It is also possible that both point and line nodes are present and only one dominates in each measurement.

The magnetic properties of UPd_2Al_3 can only be discerned from ^{105}Pd NMR and not from ^{27}Al NMR measurements. This is because the Al atoms are located interstitially between Pd–U sheets, so transferred hyperfine fields from neighboring anti–aligned U moments are cancelled almost perfectly, and T_1 reflects only the susceptibility of the conduction electrons. On the other hand, the Pd atoms are surrounded ferromagnetically by U moments, which affect the Pd T_1 relaxation via the hyperfine interaction. The results of a recent ^{105}Pd NMR and NQR study are described below.

^{105}Pd NQR measurements show [191] a resonance line at ≈ 5 MHz which is split into two lines in the AFM state. The splitting can be explained by the presence of a 2.9 kOe internal field in the a–b plane. The temperature dependence of this internal field, which extrapolates to zero at T_N, closely matches that of the sublattice magnetization measured by neutron diffraction measurements [170,194]. The presence of a local field throughout the sample below T_c confirms the microscopic coexistence of antiferromagnetism and unconventional superconductivity.

The hyperfine coupling constant, deduced from the Knight shift, is very small (0.3 kOe/μ_B), indicating that there is no significant polarization density of Pd 4d electrons. Furthermore, the large value of T_1 above T_N confirms that the Pd ions are nonmagnetic and only very weakly coupled to the U ions.

The NMR and NQR measurements of UPd_2Al_3 confirm unconventional superconductivity with an energy gap that goes to zero at lines on the Fermi surface. The ^{105}Pd NMR and NQR measurements show that the antiferromagnetism is due to U local moments with a local field $H = 2.9$ kOe in the a–b plane. Furthermore, the results unambiguously demonstrate the coexistence of antiferromagnetism and superconductivity.

8.3.5 Quantum Critical Points

Introduction

Quantum phase transitions (QPT) are observed in many f–electron heavy–fermion systems, in which an antiferromagnetic (AFM) or ferromagnetic (FM) transition temperature, spin glass freezing temperature, or spin density wave (SDW) is suppressed to $T = 0$ K by pressure or chemical substitution. When the QPT is a second–order phase transition, it is referred to as a quantum critical point (QCP). A wide variety of f–electron materials display QPTs or QCPs including $CeIn_3$ and $CePd_2Si_2$ (AFM), UGe_2 (FM), and $CeCu_2Si_2$ (SDW). In the vicinity of the critical pressure or concentration δ_C at which the QCP occurs, so–called non–Fermi–liquid (NFL) behavior is often observed; it manifests as unusual power law temperature dependences of the physical properties at low temperatures. NFL behavior is discussed in more detail in Section 8.3.6. In some compounds, superconductivity also occurs in a narrow region around the critical pressure P_c at the QCP. The presence of superconductivity in the vicinity of the QCP suggests that the superconducting electron pairing mechanism may be mediated by magnetic

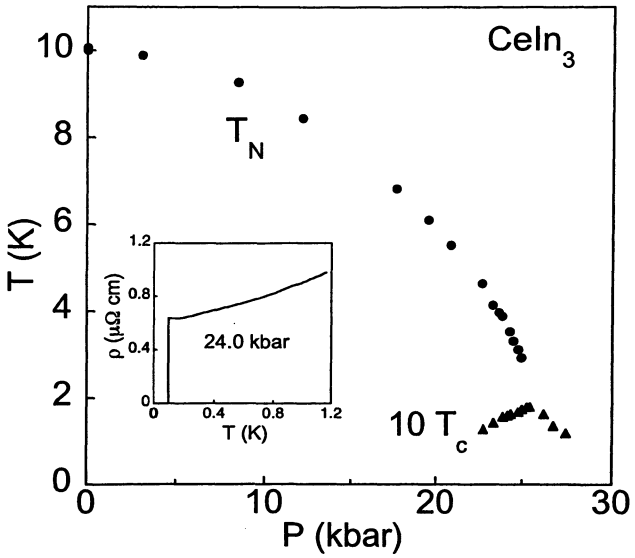

Fig. 8.33. Temperature–pressure $T - P$ phase diagram of $CeIn_3$ showing the Néel temperature T_N and superconducting transition temperature T_c (plotted as $10xT_c$). The inset shows the superconducting transition in the resistivity ρ vs temperature T at $P = 24$ kbar, after Ref. [1]

fluctuations. QCPs are also observed in the high-T_c cuprate superconductors as discussed in Section 8.5.

$CePd_2Si_2$ and $CeIn_3$

Recently, Lonzarich and coworkers [1,2] reported measurements of the temperature dependence of the electrical resistivity of single crystal specimens of the AFM compounds $CeIn_3$ and $CePd_2Si_2$ at various pressures up to ~ 30 kbar. The Néel temperature T_N, determined from a discontinuity in the slope $d\rho/dT$ at T_N, was found to decrease monotonically with increasing P for both compounds and to extrapolate to zero at a critical pressure P_c of ≈ 26 kbar for $CeIn_3$ and ≈ 28 kbar for $CePd_2Si_2$.

At temperatures below 1 K and pressures in a narrow region near P_c, $\rho(T)$ was found to drop abruptly, indicative of superconductivity for both compounds. The dependence of T_c on P has an inverted parabolic shape, reminiscent of the shape of the T_c vs charge carrier concentration curve found for the high T_c cuprate superconductors. The Néel temperature and superconducting transition temperature are plotted vs pressure in Fig. 8.33 for $CeIn_3$. The inset to this figure shows the superconducting transition in $\rho(T)$ at 24 kbar.

At $P = P'$, the pressure at which the maximum in T_c occurs, the superconductivity and AFM appear to coexist. However, at pressures above P', T_N can no longer be defined from the electrical resistivity measurements. The

transition from the AFM to the paramagnetic state appears to become first order or to be broadened in temperature due to pressure inhomogeneity such that it can no longer be detected in $\rho(T)$ measurements.

The observation of superconductivity near P_c, the pressure at which T_N extrapolates to zero, suggests that AFM spin fluctuations may be responsible for the pairing of superconducting electrons in these two compounds. Spin-fluctuation theories predict [205–208] that the resistivity in the vicinity of the QCP should vary as T^n with $n = 3/2$ for 3D AFM fluctuations and $n = 1$ for 2D AFM fluctuations (Table 8.5). In $CeIn_3$ and $CePd_2Si_2$, it was observed that near P_c and above T_c, $\rho(T)$ varies as T^n with $n = 1.6$ for $CeIn_3$ and $n = 1.2$ for $CePd_2Si_2$. These results suggest that the spin fluctuations have 3D character in cubic $CeIn_3$ and 2D character in tetragonal $CePd_2Si_2$. Spin-fluctuation theory also predicts that the magnetic ordering temperature near P_c should vary as $(P_c - P)^y$ where $y = 2/3$ for 3D and 1 for 2D fluctuations. While a linear dependence of T_N on P_c was observed in $CePd_2Si_2$, consistent with 2D fluctuations, a power law has not yet been distinguished for $CeIn_3$.

$CeMIn_5$ (M = Co, Ir, Rh)

The $CeMIn_5$ (M = Co, Rh, Ir) family of heavy-fermion compounds was discovered only a few years ago, yet has attracted an enormous amount of attention due to the variety of interesting phenomena that occur in these systems, including unconventional superconductivity, antiferromagnetism, quantum critical points, and non-Fermi liquid behavior [116–118, 147, 167, 209, 210]. $CeRhIn_5$ displays AFM order at $T_N = 3.8$ K, but becomes superconducting under pressure with a T_c of about 2.2 K at 21 kbar [116]. $CeIrIn_5$ is a superconductor at ambient pressure with a bulk $T_c = 0.4$ K, but a resistive superconducting transition at a higher temperature of $T_c = 1.2$ K [117]. Finally, $CeCoIn_5$ becomes superconducting at 2.3 K, which is the highest T_c of any Ce-based heavy-fermion superconductor yet discovered [118]. Measurements of power law T-dependences in the specific heat [117,118], NMR relaxation rate [211,212], and thermal conductivity [213] show that $CeCoIn_5$ and $CeIrIn_5$ are unconventional superconductors with nodal gaps. In particular, Izawa and coworkers measured [214] the directional thermal conductivity of $CeCoIn_5$ single crystals in an external magnetic field rotated in the a–b plane. Due to Andreev scattering, the thermal conductivity is enhanced when the magnetic field is along a nodal direction. The thermal conductivity data show a four-fold symmetry with peaks when the magnetic field is aligned in the [110] direction. These data are consistent with $d_{x^2-y^2}$ symmetry of the superconducting energy gap.

Before discussing quantum critical points in the $CeMIn_5$ (M = Rh, Co, Ir) systems, a description of the unusual nature of the superconductivity in $CeCoIn_5$ will be presented. Recent measurements [182, 214–217] of specific heat, magnetization, thermal conductivity, and thermal expansion show that the superconducting transition of $CeCoIn_5$ becomes first-order for applied magnetic fields above 47 kOe in the [001] direction, and 100 kOe in the

[100] direction. Evidence for the first order transition is also found in quasi–adiabatic magnetic field sweeps where the temperature of a thermally isolated sample is measured as a function of applied magnetic field [215]. For fields in the [001] direction, the temperature vs field data show a kink at temperatures above 0.72 K, corresponding to a second–order transition, and a step at temperatures below 0.72 K, corresponding to the latent heat released by a first–order transition.

First–order superconducting transitions were predicted in 1964 by Maki and Tsuneto [19,218] for superconductors in the clean limit where spin–orbit scattering can be neglected. However, $CeCoIn_5$ is the first superconductor to date to unambiguously demonstrate a first–order transition in specific heat measurements. The application of a magnetic field to a spin–singlet superconductor can destroy the superconductivity via two effects: orbital pair breaking, in which the field–induced kinetic energy of the Cooper pair exceeds the superconducting condensate energy, and Pauli paramagnetic limiting, in which it is energetically favorable for the electron spins to align with the magnetic field, thus breaking the Cooper pairs (See Section 8.2.x). The critical field determined by orbital pair breaking is given by Eq. 8.22, whereas the critical field from Pauli paramagnetic limiting is $H_p = \Delta_0/\sqrt{2}\mu_B$. The Maki parameter $\alpha = \sqrt{2}H_{c2}(0)/H_p$ is a measure of the relative strengths of these two effects. When Pauli paramagnetism is dominant and $\alpha \geq 1.8$, the superconducting transition is predicted to become first order at temperatures below a reduced temperature $t_0 = T_0/T_c$ [219]. Several groups have calculated the Maki parameter for $CeCoIn_5$ [215,220,221] with results ranging from 3.2 to 13. While there are varying techniques and experimental difficulties in determining the precise value of α, all the measurements agree that $\alpha > 1.8$ indicating that $CeCoIn_5$ is paramagnetically limited. Furthermore, thermal conductivity measurements indicate that $CeCoIn_5$ is in the clean limit with $l/\xi_0 = 14$ [213].

Very recent measurements on $CeCoIn_5$ have revealed that when T_c is suppressed below 0.3 K by magnetic fields, another transition occurs below T_c that is second–order. This transition has been observed in specific heat vs magnetic field [220], specific heat vs temperature [217], and in penetration–depth measurements using a self–resonant tank circuit [221]. This second transition is most prominent for H in the a–b plane; however, Bianchi *et al.* also observe a small effect for H along the crystallographic c–axis. The shape of the phase diagram is strongly suggestive of an "FFLO" state occurring between the second and the first–order transitions. In this state, which was independently predicted by Fulde and Ferrell [223] and Larkin and Ovchinnikov [224] in 1964, the superconductor lowers its energy in a magnetic field by forming periodic regions of superconductivity separated by domains of aligned spins. The order parameter is spatially modulated and changes sign, either sinusoidally or more abruptly. The FFLO state is predicted to occur at high fields, and at temperatures $T_{FFLO} < T < T_c$ in samples which are in the

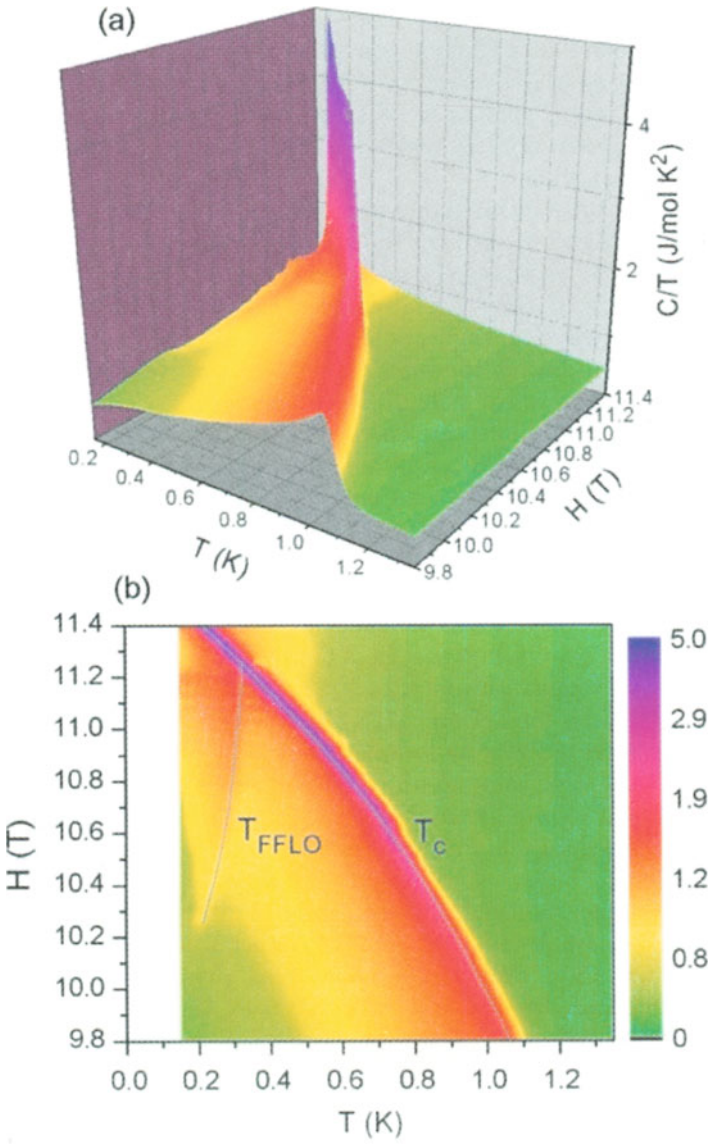

Fig. 8.34. (a) Electronic specific heat of $CeCoIn_5$ plotted as C/T vs temperature T and field H for H || [110]. (b) Contour plot of the data in (a) with the same color scale. Plots are from Bianchi *et al.* [217]

clean limit and for which spin–orbit scattering can be neglected. The FFLO state has been suggested to occur in $CeRu_2$ and UPd_2Al_3; however, in $CeRu_2$ the candidate FFLO transition was later found to be associated with vortex flux–line melting [225–227], and UPd_2Al_3 transition was not consistent with theory [228]. $CeCoIn_5$, however, is an excellent candidate for an FFLO state. It is in the clean limit with $l/\xi_0 \sim 14$ [213], has a nearly two–dimensional Fermi–surface [229,230] and a d–wave superconducting order parameter. Specific heat data as a function of temperature and magnetic field by Bianchi *et al.* [217] exhibiting a first–order superconducting transition and the possible FFLO region is shown in Fig. 8.34. Further work such as STM measurements or neutron–diffraction will be necessary to confirm the existence of the FFLO state in this system.

The unconventional superconducting state in $CeCoIn_5$ appears to evolve out of an equally unusual non–Fermi–liquid normal state. The resistivity above T_c varies linearly with temperature, and the specific heat diverges logarithmically with temperature when a magnetic field of 5 T (greater than H_{c2}) is applied along the [001] direction. However, at higher magnetic fields and low temperatures, Fermi–liquid behavior is recovered in the specific heat and electrical resistivity [118,217,222]. The high field phase diagram has been investigated by Paglione *et al.* [222] and by Bianchi *et al.* [217]. The phase diagram by Paglione *et al.* based on electrical resistivity and specific heat measurements is shown in Fig. 8.35. Furthermore, Bianchi *et al.* find scaling of the Sommerfeld coefficient $\gamma = C/T$ with $(H - H_c)/T$ over a broad range of temperatures and fields both in the FL and the NFL regime [217]. It is extremely unusual to find a QCP associated with a superconducting transition, and, in fact, the scaling behavior is indicative of a second–order QCP whereas the superconductivity is first–order. Both groups have therefore suggested that the QCP responsible for the NFL is in fact a second–order antiferromagnetic one, where the antiferromagnetic order is prevented or "hidden" by the superconductivity.

Another quantum critical point in $CeCoIn_5$ may occur at negative pressures [210]. Evidence for this comes from the fact that $CeRhIn_5$ is an antiferromagnet with a larger unit cell than $CeCoIn_5$. The Néel temperature of $CeRhIn_5$ can be suppressed with pressure leading to superconductivity above $P = 16$ kbar, with a $T_c = 2$ K, remarkably close to that of $CeCoIn_5$. At this pressure, the unit cell volume of $CeRhIn_5$ is also close to that of $CeCoIn_5$. In fact, there is a general correlation in the $CeMIn_5$ (M = Rh, Co, Ir) compounds between the superconducting transition temperature T_c and the lattice parameters [231]. It appears that, with the exception of the compounds displaying antiferromagnetism, T_c varies as a linear function of the lattice anisotropy c/a where c and a are the tetragonal lattice parameters. In Fig. 8.36, T_c is shown as a function of c/a for members of the $CeMIn_5$ family both under ambient pressure and hydrostatic pressures.

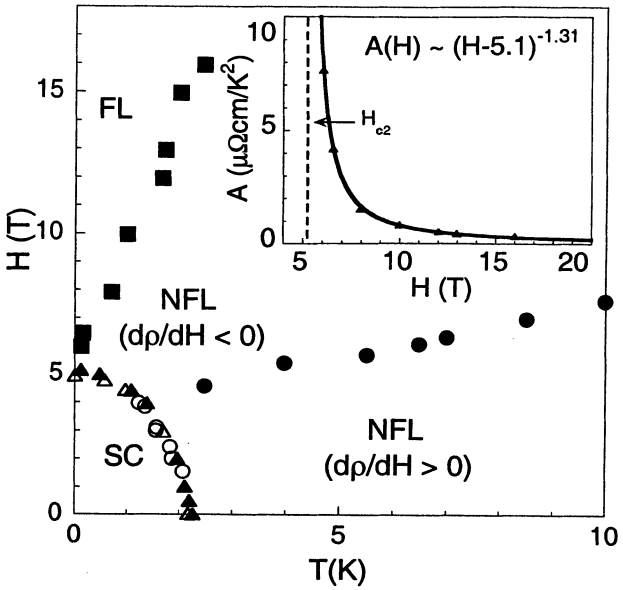

Fig. 8.35. Magnetic field H vs temperature T phase diagram of $CeCoIn_5$. Solid squares are the boundary between Fermi–liquid (FL) behavior with $\rho(T) = \rho_0 + AT^2$ and non–Fermi liquid (NFL) behavior. Solid circles indicate a maximum in magnetoresistivity, solid triangles are H_{c2} determined from resistivity, and open triangles and open circles are H_{c2} from resistivity and specific heat data in Ref. [118]. The inset shows the coefficient A in the FL regime as a function of field, which diverges near the upper critical field H_{c2} of $CeCoIn_5$, after Ref. [222]

Thus, $CeRhIn_5$ could be considered equivalent to $CeCoIn_5$ with an expanded lattice parameter, or "negative pressure". When pressure is applied to $CeCoIn_5$, T_c goes through a maximum at $P = 15$ kbar and is suppressed by $P \sim 37$ kbar. When the $CeRhIn_5$ and $CeCoIn_5$ phase diagrams are combined, considering $CeCoIn_5$ at ambient pressure equivalent to $CeRhIn_5$ at $P = 16$ kbar, the resulting phase diagram looks remarkably similar to those of the high–T_c cuprates (Section 8.5). In fact, several groups suggest the formation of a pseudogap near the QCP based on electrical resistivity and ^{115}In NQR measurements [210, 233]. The $T - P$ phase diagrams of $CeRhIn_5$ and $CeCoIn_5$ are shown in Fig. 8.37. Fermi–liquid behavior in the resistivity with a T^2 temperature–dependence is recovered at higher pressures, as shown.

An interesting question is therefore what happens when $CeRhIn_5$ and $CeCoIn_5$ are mixed to form $CeRh_{1-x}Co_xIn_5$, and whether tuning the lattice parameters via concentration is equivalent to tuning the lattice parameters with pressure. Substitution studies of both $CeRh_{1-x}Ir_xIn_5$ and $CeRh_{1-x}Co_xIn_5$ systems have been carried out and the phase diagrams are shown in Fig. 8.38 [176,234]. Both systems show a strikingly similar suppres-

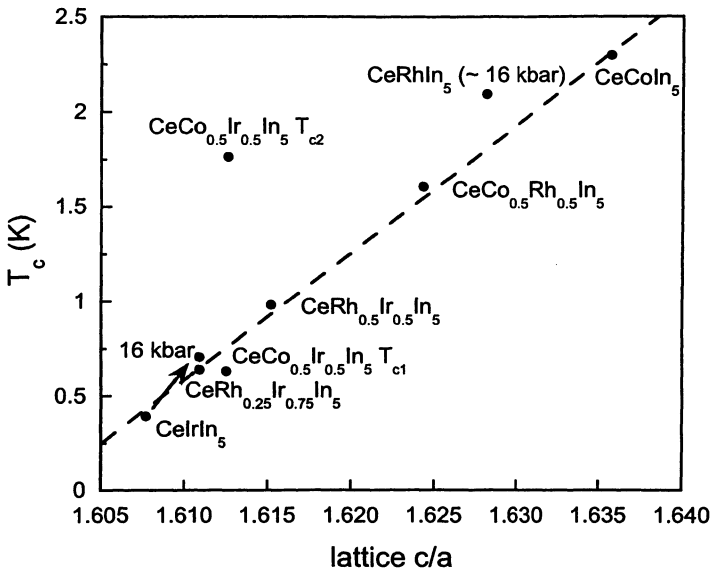

Fig. 8.36. Superconducting transition temperature T_c plotted vs the ratio of the hexagonal lattice constants c/a for various compounds in the $CeMIn_5$ family (M = Rh,Co,Ir), after Ref. [231]

sion of the Néel temperature T_N with increasing x, with T_N extrapolating to zero at a QCP at $x \sim 0.6 - 0.8$. The phase diagrams look similar to those of the $T - P$ phase diagram shown in Fig. 8.37, except that in the substituted systems, antiferromagnetism and superconductivity appear to coexist over a significant range of concentrations from $x = 0.4$ to $x = 0.7$. This is in contrast to $CeRhIn_5$ under pressure, in which specific heat measurements found no coexistence of antiferromagnetism and superconductivity [146], but $1/T_1$ measurements have found a coexistence over a narrow range of pressures [233, 235, 236]

For the $CeRh_{1-x}Co_xIn_5$ system, the specific heat plotted as C/T vs T for various Co concentrations x is shown in Fig. 8.39 [176]. (These data are very similar to those of the $CeRh_{1-x}Ir_xIn_5$ system in Ref. [234].) Each specific heat curve contains either one or two peaks. The peaks for $T < 2$ K are associated with the superconducting transition, whereas the peaks for $T > 3$ K are attributed to AFM transitions. The $C(T)/T$ data for samples with $0.4 \leq x \leq 0.6$ contain two peaks, indicating that these samples exhibit coexistence of superconductivity and antiferromagnetism. The magnitudes of the superconducting peaks are quite large, with $\Delta C/\gamma T_c \approx 1$ for most samples, and ~ 5 for $CeCoIn_5$, indicating that the superconductivity is a bulk phenomenon involving the heavy electrons. The magnitude of the superconducting peaks is suppressed with decreasing x, whereas the magnitude of the AFM peaks is enhanced with decreasing x. The entropy at 7 K, which

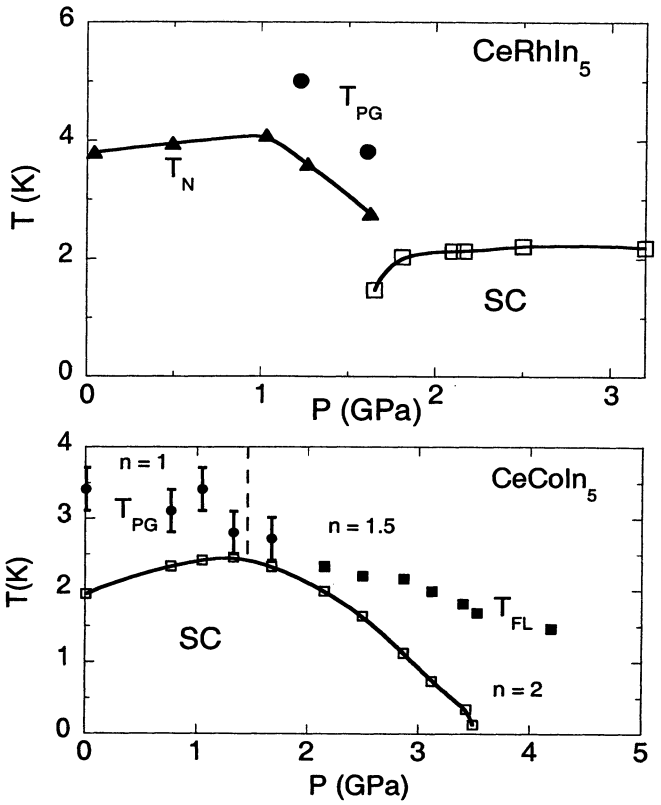

Fig. 8.37. Upper figure: temperature–pressure $T - P$ phase diagrams of $CeRhIn_5$ from electrical resistivity and ac susceptibility measurements (after Kitaoka *et al.* [232]). Lower figure: $T - P$ phase diagram of $CeCoIn_5$ based on electrical resistivity (after Sidorov *et al.* [210])

corresponds to the total area under the superconducting and AFM peaks, is constant for the samples with $x < 1$, implying that the same heavy electrons are participating in both the superconductivity and the antiferromagnetism. The question arises whether the superconductivity and magnetism coexist on a microscopic scale or if there are macroscopic concentration variations of Co and Rh within the sample. This question has been investigated for the $CeRh_{1-x}Ir_xIn_5$ system by Morris and coworkers [237]. μSR measurements in zero field of the $CeRh_{0.5}Ir_{0.5}In_5$ sample show that the antiferromagnetism exists over at least 85% of the sample, and ac magnetization measurements indicate at least 85% shielding of the sample. Thus, magnetism and superconductivity most likely coexist microscopically in this sample.

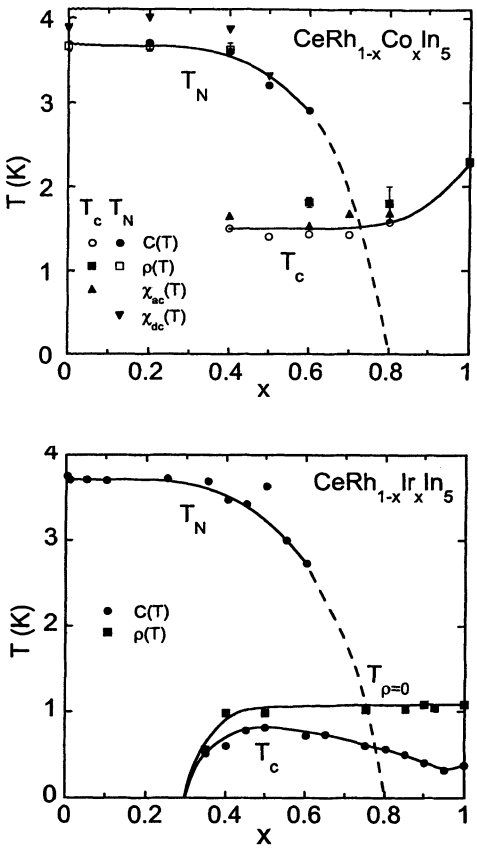

Fig. 8.38. Phase diagrams of $CeRh_{1-x}Ir_xIn_5$ and $CeRh_{1-x}Co_xIn_5$. The Néel temperature T_N, superconducting transition temperature T_c, and the temperatures at which the resistivity goes to zero $T_{\rho=0}$ are shown vs Ir or Co concentration x. The lines are guides to the eye (after [176, 234])

8.3.6 Non–Fermi Liquid Behavior

At the time of their discovery, nearly all of the heavy–fermion superconductors were found to have Fermi liquid properties, i.e., $\rho(T) \propto T^2$ and $C(T)/T \propto \chi(T) \propto$ constant. However, unusual temperature dependences of the physical properties, such as a linear T–dependence of the electrical resistivity [238], known as non–Fermi liquid behavior, have been observed in many heavy–Fermion compound since their first observation in UBe_{13}. In particular, the relatively weak magnetic field dependence of the electrical resistivity and specific heat, and the absence of a quasi–elastic peak in neutron scattering measurements in UBe_{13} do not follow the expected behavior of a conventional Kondo effect, which is thought to be the origin of the heavy–fermion characteristics. These experimental data led Cox to propose a two

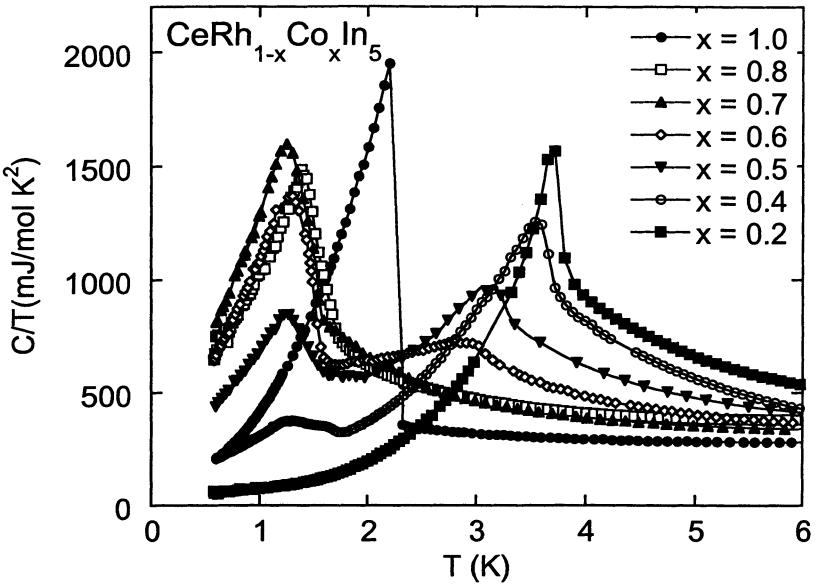

Fig. 8.39. Specific heat $C(T)$ shown as a plot of C/T vs temperature T for various $CeRh_{1-x}Co_xIn_5$ compounds. The peaks for $T < 2$ K are attributed to superconducting transitions, whereas the peaks for $T > 3$ K are ascribed to antiferromagnetic phase transitions, after Ref. [176]

channel quadrupolar Kondo model, in which the interaction between the electric quadrupole moments of a U^{4+} nonmagnetic doublet ground state in a cubic crystalline electric field and the charges of the conduction electrons give rise to NFL behavior at low temperatures [239, 240].

A few years later, NFL behavior was observed [241] in the $Y_{1-x}U_xPd_3$ system over a wide range of U concentrations x in the paramagnetic phase below the critical concentration $x_{cr} = 0.2$ where the magnetic transition temperature (later identified as the spin glass freezing temperature [242, 243]) vanished. This discovery started a period of intense research in f–electron materials in order to further investigate the occurrence and origin of non–Fermi liquid behavior [244, 246, 247, 504]. Non–Fermi liquid behavior in f–electron systems is characterized by weak power law or logarithmic temperature dependences of the physical properties at low temperatures $T \ll T_0$ for most f–electron systems and can be summarized as follows:

$$\rho \propto \left[1 - a\left(\frac{T}{T_0}\right)^n\right] \text{ where } |a| \approx 1 \text{ and } n \approx 1 - 1.5; \tag{8.24}$$

$$\frac{C}{T} \propto -\left[\frac{1}{T_0}\right] \ln\left(\frac{T}{T_0}\right) \text{ or } T^{-1+\lambda} \ (\lambda \approx 0.7 - 0.8); \tag{8.25}$$

$$\chi \propto \left[1 - \left(\frac{T}{T_0}\right)^n\right] \text{ with } n \approx 0.5, \; -\ln\left(\frac{T}{T_0}\right), \text{ or } T^{-1+\lambda} \; (\lambda \approx 0.7 - 0.8); \tag{8.26}$$

$$\chi''(\omega, T) \text{ scales as } \frac{\omega}{T}. \tag{8.27}$$

In several of these systems, the scaling temperature T_0 can be identified with the Kondo temperature T_K. The characteristic NFL temperature dependences were first established from studies of chemically substituted f–electron materials such as $Y_{1-x}U_xPd_3$ [241,248], $UCu_{5-x}Pd_x$ [249,250], and $CeCu_{6-x}Au_x$ [251,252], but more recently have been found in stoichiometric compounds at ambient pressure (e.g., $YbRh_2Si_2$ [253]) and under applied pressure (e.g., $CeIn_3$ [145], $CePd_2Si_2$ [254]). These experiments suggest that different mechanisms may be responsible for the NFL behavior observed in these f–electron materials. Several NFL models with distinct origins have been proposed and can be grouped into three main categories: (i) single–ion models based on a multichannel Kondo effect, (ii) disorder–driven NFL models, and (iii) models involving quantum fluctuations of an order parameter at a second–order $T = 0$ K phase transition (QCP). Various theoretical models have been proposed based on single–ion physics involving an unconventional Kondo effect, of either magnetic or electric (quadrupolar) origin [239,255–258]. In these multichannel Kondo models, the magnetic (quadrupolar) moments are over–compensated by a number of channels of conduction electrons due to additional orbital (spin) degrees of freedom, giving rise to power law or logarithmic temperature dependences of the physical properties at low temperatures. Theoretical models which incorporate the effects of disorder include the Kondo disorder model [259–261], in which a distribution of Kondo temperatures T_K due to chemical disorder with finite weight at $T_K = 0$ K leads to NFL properties, and an inhomogeneous Griffiths–McCoy phase [262], which consists of magnetic clusters in a paramagnetic phase formed as a result of the competition between the Kondo effect and the Ruderman–Kittel–Kasuya–Yosida (RKKY) interaction in the presence of magnetic anisotropy and disorder.

The critical behavior near a quantum critical point has been considered by a number of investigators [205–207,263–267]. Hertz [263] and later Millis [208,264] studied the fluctuations of an order parameter near a $T = 0$ K second order phase transition using renormalization techniques. They found that the critical behavior is determined by both spatial and temporal fluctuations in an effective dimension $d_{\text{eff}} = d + z$, where d is the spatial dimension and z is the dynamical exponent. The physical properties predicted by the Hertz/Millis theory including $\rho(T), \chi(T), C(T)/T$ and the dependence of the ordering temperature on the control parameter δ are listed in Table 8.5. Similar results were obtained by Moriya [205,206] with a self consistent renormalization group model of spin fluctuations in weak itinerant magnetic systems and also by a spin fluctuation theory by Lonzarich and coworkers [207]. A

Table 8.5. Spin–fluctuation theory predictions for the temperature dependences of the resistivity ρ and specific heat divided by temperature C/T, and the dependence of the magnetic ordering temperature T_M on the control parameter δ (pressure or carrier concentration) for 3– and 2– dimensional ferromagnetic (FM) and antiferromagnetic (AFM) spin fluctuations.

	3D FM	3D AFM	2D FM	2D AFM
ρ	$T^{5/3}$	$T^{3/2}$	$T^{4/3}$	T
C/T	$-\ln(T/T_0)$	$\gamma_0 - \beta T^{1/2}$	$T^{-1/3}$	$-\ln(T/T_0)$
T_M	$(\delta - \delta_c)^{3/4}$	$(\delta - \delta_c)^{2/3}$		$\delta - \delta_c$

recent paper by Si examines the effect of non–Gaussian fluctuations near a quantum critical point, and suggests a model in which the Kondo temperature is suppressed to zero at the same point as the second order phase transition, but from the opposite side of the phase diagram [268].

In recent years, non–Fermi liquid behavior has also been observed in three systems that are based on the heavy–fermion AFM superconductor UPd_2Al_3 (discussed in Sec. 8.3.4): $U_{1-x}M_xPd_2Al_3$ for M=Th, La, and Y. The magnetic phase diagrams of these three systems are shown in Fig. 8.40. It is remarkable that although these three systems have the same parent compound, the phase diagram of $U_{1-x}Th_xPd_2Al_3$ is quite different from those of $U_{1-x}La_xPd_2Al_3$ and $U_{1-x}Y_xPd_2Al_3$. Both the AFM order and superconductivity are only slightly suppressed with Th substitution (Fig. 8.40a) at $x = 0.2$, and the system crosses over to an NFL regime at $x \approx 0.6$. The NFL properties of $U_{1-x}Th_xPd_2Al_3$ at low temperatures scale with U concentration indicating the NFL behavior is associated with single–ion physics such as an unconventional Kondo effect.

In the $U_{1-x}Y_xPd_2Al_3$ system, the antiferromagnetism and superconductivity are rapidly suppressed with Y substitution (Fig. 8.40c). Similar behavior is found for $U_{1-x}La_xPd_2Al_3$ (Fig. 8.40b). The Néel temperature decreases from $T_N \approx 14$ K in UPd_2Al_3 to $T_N \approx 7$ K by $x = 0.2$, after which spin glass behavior is observed at $T_{SG} \approx 1$ K. The spin glass transition is no longer observed at a critical concentration $x_c \approx 0.7$ near the concentration where the NFL behavior occurs [270]. It appears that T_{SG} vanishes nearly linearly with x as $x \rightarrow x_c$. These results suggest that the NFL behavior in this system is associated with fluctuations of a magnetic order parameter above the spin glass freezing transition at $T = 0$ K. An example of the NFL behavior observed in these systems is shown in Fig. 8.41 for a $U_{1-x}Y_xPd_2Al_3$ sample with a composition ($x = 0.8$) close to that of the QCP at $x_c \approx 0.7$. The physical properties of $U_{0.2}Y_{0.8}Pd_2Al_3$ at low temperatures have the following T–dependences: $\rho \propto T$, $C/T \propto -\ln T$ (or T^n with $n = 0.2$), and $\chi \propto [1 - (T/T_0)]^{1/2}$.

Although the magnetic phase diagram of $U_{1-x}La_xPd_2Al_3$ is similar to that of $U_{1-x}Y_xPd_2Al_3$, the non–Fermi liquid behavior is close to that of

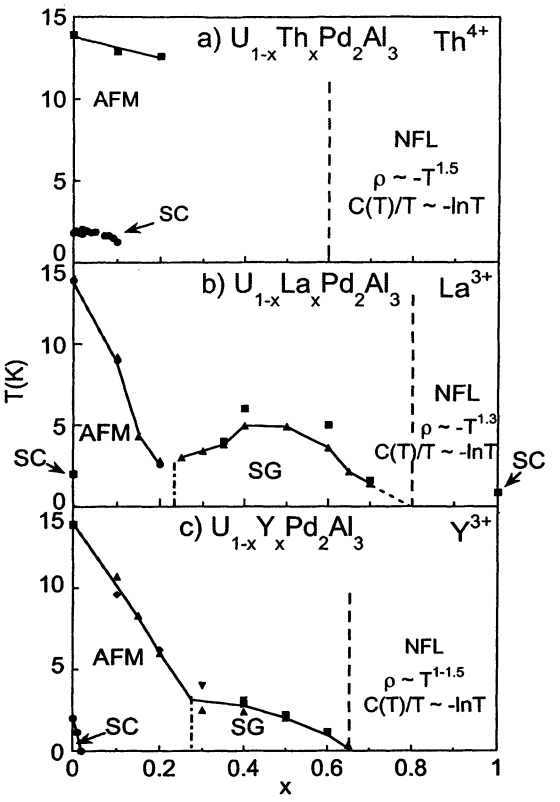

Fig. 8.40. Temperature – M concentration (T–x) phase diagrams of the $U_{1-x}M_xPd_2Al_3$ (M = Th, La, Y) systems. Regions of antiferromagnetic order (AFM), spin glass freezing (SG), superconductivity (SC) and non–Fermi liquid behavior (NFL) determined from measurements of the specific heat C, magnetic susceptibility χ, and electrical resistivity ρ as a function of temperature T are indicated in the T–x plane. The temperature dependences of ρ and C/T observed in the NFL regions are indicated in the figure, after Ref. [269]

$U_{1-x}Th_xPd_2Al_3$. This suggests that disorder from local expansion of the lattice by the larger Th and La ions could be driving the NFL behavior in these compounds. Substitution with Y leaves the lattice unchanged [269].

Non–Fermi liquid behavior has also been found in the vicinity of a ferromagnetic quantum critical point in systems such as $Th_{1-x}U_xCu_2Si_2$ [274] and $URu_{2-x}Re_xSi_2$ [273]. The substitution of Re or Tc for Ru in the heavy–fermion AFM superconductor URu_2Si_2 has been found to suppress both AFM order and superconductivity and induce ferromagnetism (FM) [271, 272]. The superconducting transition temperature T_c of $URu_{2-x}Re_xSi_2$ decreases rapidly from $T_c = 1.5$ K at $x = 0$ to below 200 mK at $x = 0.01$, while the Nèel

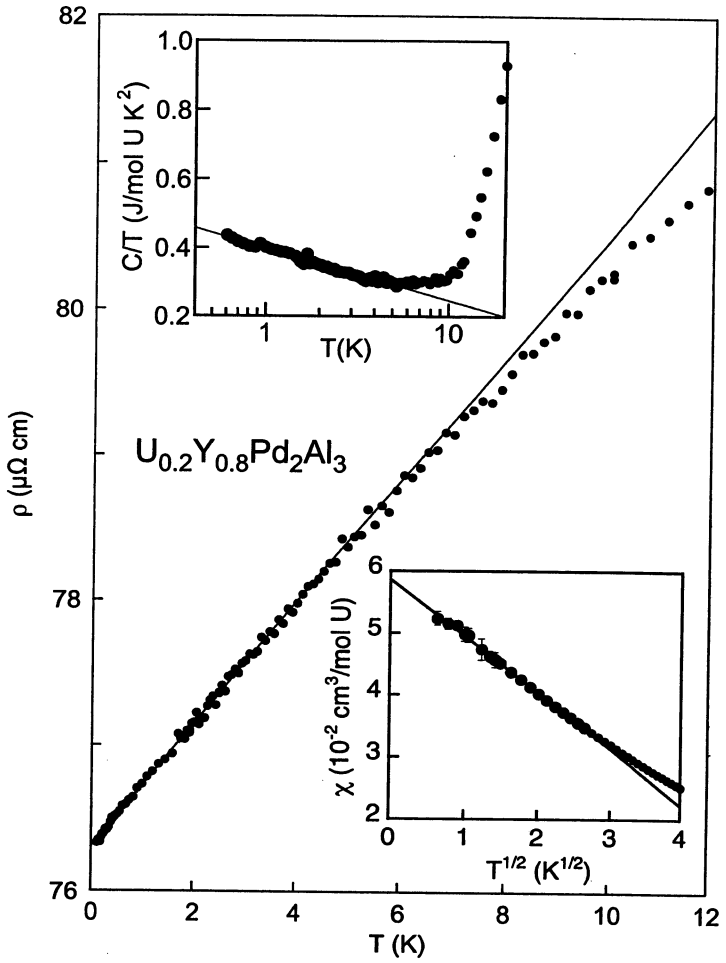

Fig. 8.41. Electrical resistivity ρ versus T, specific heat divided by temperature, C/T, versus log T (upper inset), and magnetic susceptibility χ versus $T^{1/2}$ (lower inset) for $U_{0.2}Y_{0.8}Pd_2Al_3$, after Ref. [270]

temperature T_N associated with the formation of the small moment antiferromagnetism ($\sim 0.03\ \mu_B$/U atom) or a spin density wave at 17.5 K decreases less rapidly with x and appears to vanish by $x = 0.15$ as shown in the $T - x$ phase diagram in Fig. 8.42. Ferromagnetic order occurs in the concentration range $0.3 \leq x \leq 1.4$ where the Curie temperature θ_C, saturation moment μ_{sat}, and electronic specific heat coefficient γ, exhibit maxima at $x = 0.8$ of 38 K, 0.44 μ_B/U atom, and 160 mJ/mol K^2 [271], respectively, as displayed in Fig. 8.43. Magnetic measurements indicate that the suppression of FM order occurs at $x_c^{FM} = 0.3$. For samples close to both the AFM ($x_c^{AFM} = 0.15$) and

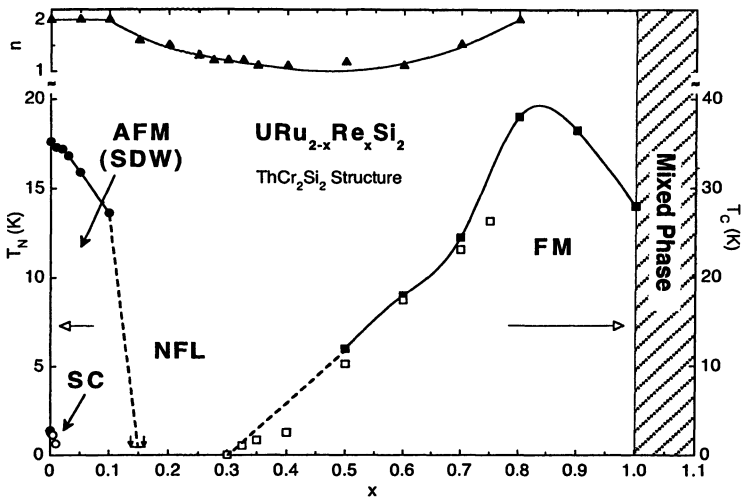

Fig. 8.42. Magnetic phase diagram of the $URu_{2-x}Re_xSi_2$ system showing the antiferromagnetic (AFM/SDW, filled circles), superconducting (SC, open circles), and ferromagnetic (FM, squares) regions. The power law exponent of the electrical resistivity, n, is shown in the top part of the diagram. Some data from Refs. [271,272], after Ref. [273]

FM ($x_c^{FM} = 0.3$) critical points with Re concentrations $0.15 < x \leq 0.6$, the non–Fermi liquid behavior is characterized by $C/T \propto -\ln T$ and $\rho(T) \propto T^n$ with $1 \leq n < 2$ at low temperatures [273]. Therefore, it appears that the NFL behavior persists well into the ferromagnetic state.

NFL behavior is observed in a wide range of $CeMIn_5$ (M = Rh, Co, Ir) compounds. In addition to the NFL behavior found in stoichiometric $CeCoIn_5$, studies of the chemically substituted systems $Ce_{1-x}(La,Y)_xRhIn_5$ and $Ce_{1-x}La_xCoIn_5$ have revealed logarithmic or power–law divergences of the specific heat and magnetic susceptibility once the superconductivity or antiferromagnetism in the parent compounds is suppressed [275–277]. In $Ce_{1-x}(La,Y)_xRhIn_5$ compounds, additional humps in the specific heat and peaks in the magnetic susceptibility are observed that coexist with NFL behavior and decrease with increasing x. These features can described by the Ce^{3+} $J = 5/2$ Hund's rule multiplet being split by a tetragonal CEF [275]. The humps in the specific heat have also been attributed to short–range 2D antiferromagnetic correlations. [276,278].

An interesting new theory for NFL behavior has arisen out of studies of the $CeMIn_5$ compounds. In this model, the specific heat and magnetization are decomposed into two components: a Kondo–gas part which obeys the single–ion Kondo model, and results from onsite coupling between Ce local moments and conduction electrons, and a Kondo–liquid portion resulting from intersite coupling between the Ce moments. This model was proposed for the

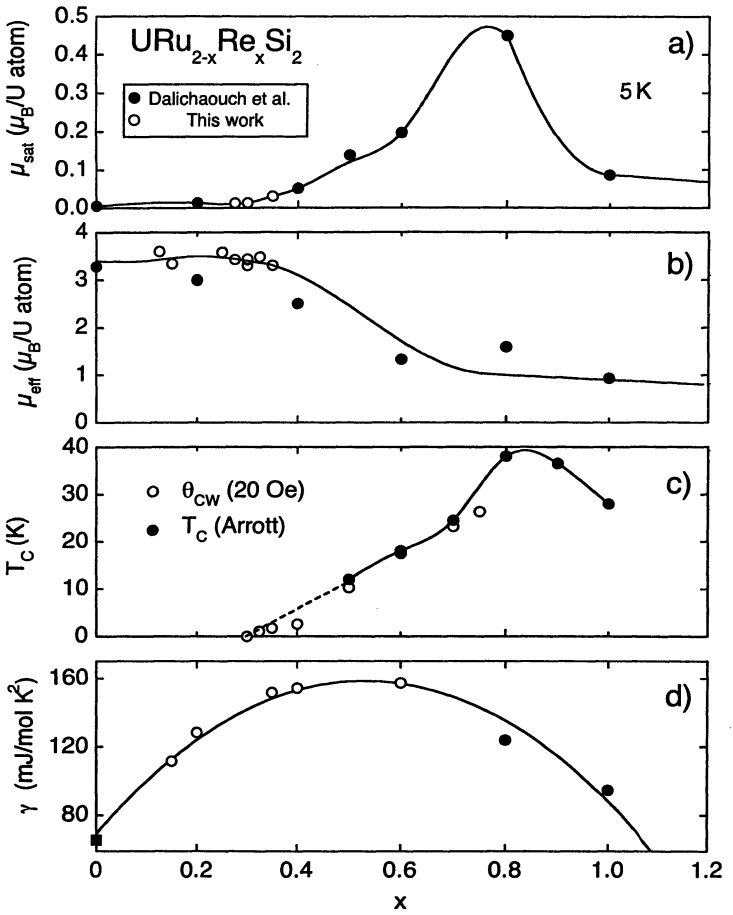

Fig. 8.43. Physical properties of $URu_{2-x}Re_xSi_2$ vs Re concentration x: a) saturation moment μ_{sat} (at 5 K), b) effective moment μ_{eff}, c) Curie temperature T_C and Curie–Weiss temperature θ_{CW}, and d) electronic specific heat coefficient γ (at 1 K). The filled circles are from Ref. [271]. Data for $x = 0$ from Ref. [153]. The lines are guides to the eye, after Ref. [273]

$Ce_{1-x}La_xCoIn_5$ system [279], and can also be applied to the $Ce_{1-x}Y_xRhIn_5$ system [280]. For these two systems, the fraction f_K of electrons participating in the single–ion Kondo effect increases roughly linearly as a function of x until it saturates at $x = 0.9$, at which point the Kondo–liquid portion goes to zero and the system entirely obeys the single–ion Kondo model. The fraction f_K also varies as a function of temperature. For pure $CeCoIn_5$, the Kondo gas condenses into a Kondo liquid below $T \sim 45$ K, resulting in a sudden downturn in the electrical resistivity or "coherence shoulder". This model provides an intriguing new possibility for the origin of NFL behavior, at least

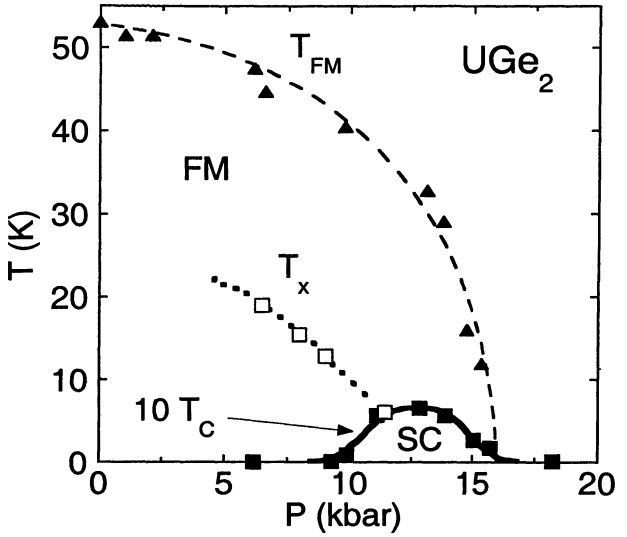

Fig. 8.44. Temperature–pressure $T - P$ phase diagram of UGe_2. T_{FM} denotes the Curie temperature; T_c denotes the superconducting transition (the T_c values are scaled by a factor of 10 for clarity; T_x denotes the feature in the $\rho(P,T)$ curves possibly due to a SDW/CDW transition. The solid and dashed lines are guides to the eye, after Refs. [3, 155]

in the $CeMIn_5$ compounds, and its applicability to other systems needs to be investigated.

8.3.7 Magnetically Ordered Heavy–Fermion Superconductors

UGe_2

Superconductivity under pressure was observed by Saxena *et al.* in single crystal specimens of the ferromagnetic (FM) compound UGe_2 within the ferromagnetic phase up to the critical pressure $P_c \approx 16$ kbar where the ferromagnetism vanishes [3]. Shown in Fig. 8.44 is the $T - P$ phase diagram for single crystals of UGe_2 [3]. The Curie temperature T_{FM} decreases from 53 K at ambient pressure to ≈ 12 K at $P = 15$ kbar, above which the FM transition can no longer be determined from the $\rho(T)$ curves, suggesting a first–order–like transition. A small feature in the resistivity curves is observed at applied pressures $P < 13$ kbar, perhaps related to a spin density wave (SDW) or charge density wave (CDW), and is denoted in Fig. 8.44 as T_x [155, 186]. Superconductivity is confined to a narrow pressure region 10 kbar $\leq P < 16$ kbar reaching a maximum value of $T_c = 0.7$ K at $P_x = 13$ kbar where features associated with the possible SDW/CDW can no longer be observed [3] (the phase diagram of polycrystalline UGe_2 samples, discussed below, is similar [186]). No superconductivity is observed at or above P_c, indicating that the

ferromagnetism and superconductivity are intimately related. Recent magnetization measurements under pressure confirm the first–order FM phase transition at P_c and reveal that the transition at T_x is also first–order [281].

It has been suggested that UGe_2 is a p–wave superconductor, in which the superconducting electrons do not suffer from the pair–breaking interaction caused by the large internal magnetic field, since the mean free path $l \sim 1500$ Å is much larger than the superconducting coherence length $\xi_0 \sim 130 - 200$ Å [3, 187]. Specific heat experiments under applied pressure reveal a finite value of C/T as $T \rightarrow 0$ K, which is consistent with the superconducting gap vanishing at lines or points on the Fermi surface [156, 187]. In addition, neutron diffraction measurements yield no evidence of a change in the magnetic moment upon entering the superconducting state, consistent with p–wave superconductivity [155]. Spin–triplet superconductivity mediated by coupled SDW/CDW spin fluctuations has been put forth in recent theoretical work by Watanabe and Miyake [282]. This theory can explain the anomalous reentrant behavior observed in upper critical field measurements along the a–axis of UGe_2 and the anisotropy of H_{c2} [155]; however, neutron diffraction measurements do not reveal any static order associated with a SDW/CDW. While these results can be explained within a spin–triplet scenario of superconductivity, an investigation on polycrystalline samples of UGe_2 with electron mean free paths of the order of the superconducting coherence length, discussed below, indicates that the superconductivity in UGe_2 may have s–wave character [186].

It is widely believed that p–wave superconductors are quite sensitive to nonmagnetic impurities, resulting in the suppression of superconductivity when $l \approx \xi_0$, where l is the electron mean free path and ξ_0 is the superconducting coherence length. Two of the leading candidates for p–wave superconductivity are Sr_2RuO_4 [283, 284] and UPt_3 [285, 286]. When the ratio $l/\xi_0 \sim 1$, T_c is completely suppressed for Sr_2RuO_4 [287] and decreases by 15 % for UPt_3 [286]. However, in UGe_2 superconductivity was observed in some polycrystalline samples with residual resistivities ρ_0 as high as 3 μΩcm, corresponding to a mean free path $l \sim 100$ Å, without any apparent diminution of T_c. Since the superconducting coherence length ξ_0 is $\sim 130 - 200$ Å [3, 187], this represents a ratio $l/\xi_0 \approx 1$, considerably reduced from the value $l/\xi_0 \approx 10$ observed for the single crystal specimens of UGe_2. This suggests that the superconductivity observed in UGe_2 under pressure may have s–wave character. It is noteworthy that several theories have recently been proposed in which s–wave, rather than p–wave, superconductivity is predicted to occur in the ferromagnetic state [288–292].

In the low temperature FL–like phase, the residual resistivity ρ_0 and the coefficient A of the T^2 contribution to the resistivity, $\rho(T) = \rho_0 + AT^2$, are both strongly dependent on pressure as shown in Fig. 8.45 for polycrystalline samples of UGe_2 and exhibit peaks at 15 kbar and 11 kbar, respectively (inset of Fig. 8.45). It is interesting that the maximum in ρ_0 correlates with

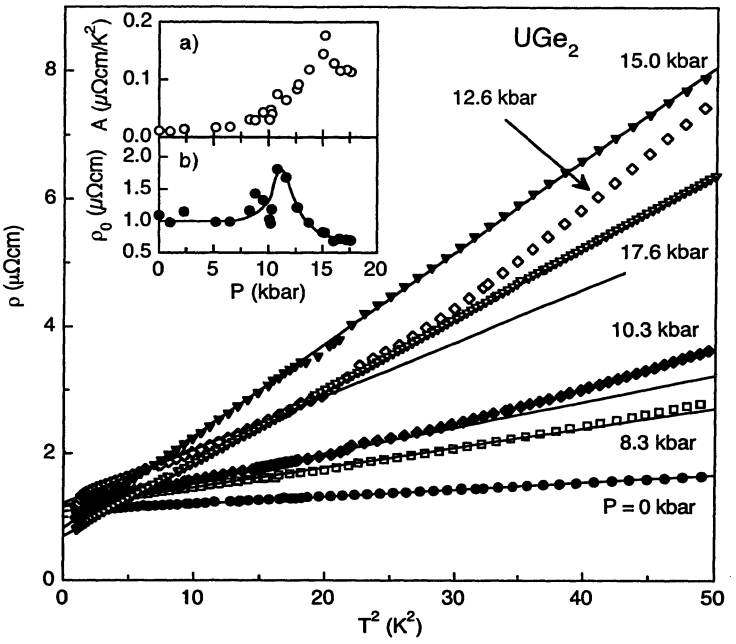

Fig. 8.45. Electrical resistivity ρ vs T^2 for UGe_2 at various applied pressures P. The lines are fits to the data of the form $\rho = \rho_0 + AT^2$. Inset a): Coefficient of the T^2 term of $\rho(T)$, A, vs P, Inset b): Residual resistivity ρ_0 vs P, after Ref. [186]

the broad maximum in $T_c(P)$ that is centered near the same pressure. Specific heat measurements on polycrystalline samples of UGe_2 reveal that γ increases with pressure up to 15 kbar [156]. The increase of γ is consistent with the behavior of $A(P)$ according to the Kadowaki–Woods relation $A = 1.0 \times 10^{-5} \gamma^2 \mu\Omega\,\mathrm{cm\,(mol\,K/mJ)^2}$ [173]. Since T_c of a conventional s–wave superconductor increases with $N(E_F)$, which is proportional to γ, and is not strongly affected by potential scattering, the correlation between T_c, γ, and ρ_0 is qualitatively consistent with s–wave superconductivity.

A precedent for the macroscopic coexistence of ferromagnetism and s–wave superconductivity is found in the compound $ErRh_4B_4$, discussed in Section 8.2.x, which exhibits localized moment ferromagnetism, in contrast to UGe_2, which is regarded as an itinerant ferromagnet. The compound $ErRh_4B_4$ becomes superconducting at a critical temperature $T_{c1} \approx 8.7$ K, FM at a Curie temperature $T_{FM} \approx 1.5$ K, and normal again at a second critical temperature $T_{c2} \approx 0.9$ K [81]. There is evidence, based on neutron scattering and specific heat measurements [85], for the macroscopic coexistence of FM and superconducting regions in the temperature interval between T_{c2} and θ_c. Within the superconducting regions between T_{c2} and θ_c, a sinusoidally modulated magnetic state with a wavelength of ~ 100 Å that coexists

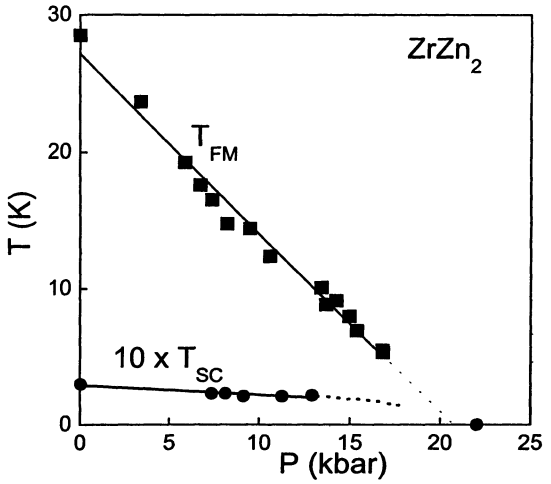

Fig. 8.46. Pressure–temperature phase diagram of $ZrZn_2$. T_{FM}: Curie temperature; T_c: Superconducting critical temperature. The values of T_c have been multiplied by a factor of 10 for clarity, after Ref. [295]

with superconductivity has been detected by means of small angle neutron scattering measurements [85]. The sinusoidally modulated magnetic state is believed to be produced by screening of the magnetic field associated with the ferromagnetically aligned Er magnetic moments by the supercurrents at long wavelengths [293]. Similar behavior has been found for the localized moment FM superconductor $HoMo_6S_8$ [294]. It seems reasonable that such an inhomogeneous FM s–wave superconducting state could also exist in UGe_2, in spite of the fact that it is an itinerant ferromagnet.

Irrespective of whether the superconductivity in UGe_2 is of s–wave (spin–singlet) or p–wave (spin–triplet) variety, it appears to be strongly connected to the ferromagnetism. For s–wave superconductivity, it seems possible that the onset of superconductivity occurs when the Curie temperature drops to a value such that the superconductivity is no longer suppressed by the internal field in the ferromagnet, while near P_c where the Curie temperature vanishes, the superconductivity is suppressed by the ferromagnetic spin fluctuations. Alternatively, the longitudinal spin fluctuations may actually produce pairing of electrons in spin–singlet s–wave states as proposed recently by Suhl [291] and developed further by Abrikosov [292]. The competition between these two effects could then lead to the maximum in T_c at a pressure below P_c. For triplet–spin superconductivity, the superconductivity would seem to require the presence of the ferromagnetism and be optimized at a pressure below P_c. Further experiments will be required to develop an understanding of the origin and nature of superconductivity in this remarkable material.

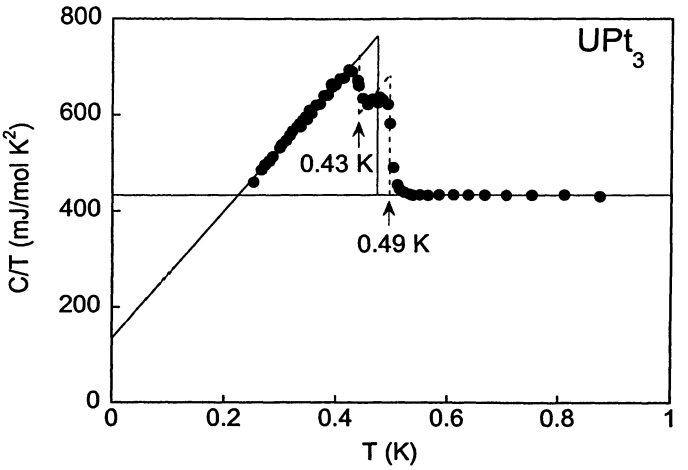

Fig. 8.47. Specific heat of UPt_3 in the vicinity of the superconducting transition plotted as C/T vs T. The dashed lines represent two idealized jumps, and the solid line represents a single jump with the same entropy, after Ref. [296]

The coexistence of superconductivity and ferromagnetism was recently reported in URhGe [110] and $ZrZn_2$ [295] below the Curie temperature at ambient pressure. For $ZrZn_2$, a superconducting transition at $T_c \approx 0.3$ K was observed to decrease with increasing pressure and vanish near the critical pressure P_c at which T_{FM} vanishes as shown in Fig. 8.46. The absence of a superconducting anomaly in specific heat, and the occurrence of superconductivity within the ferromagnetic state only in very pure samples suggest the possibility of a spin–triplet pairing mechanism, although trace amounts of a superconducting impurity phase cannot be ruled out at this point.

8.3.8 Multiple Superconducting Phases

UPt_3 and $U_{1-x}Th_xBe_{13}$

The first direct evidence for unconventional superconductivity was found for the compound UPt_3, which displays at least three distinct superconducting phases. Multiple superconducting phases were also found in the heavy–fermion compound $U_{1-x}Th_xBe_{13}$ when substituted with $2-4$ % Th, and more recently in $PrOs_4Sb_{12}$ (discussed in section 8.3.8). The appearance of multiple superconducting phases, which cannot be explained in terms of a conventional s–wave order parameter, has prompted a flurry of investigations into these exciting compounds.

UPt_3 exhibits antiferromagnetic (AFM) order below $T_N = 5$ K with a very small ordered moment of 0.02 μ_B/U atom aligned in the basal plane [169]. Early measurements on as–grown samples showed a single broad superconducting transition in the specific heat at 0.5 K; however, later measurements

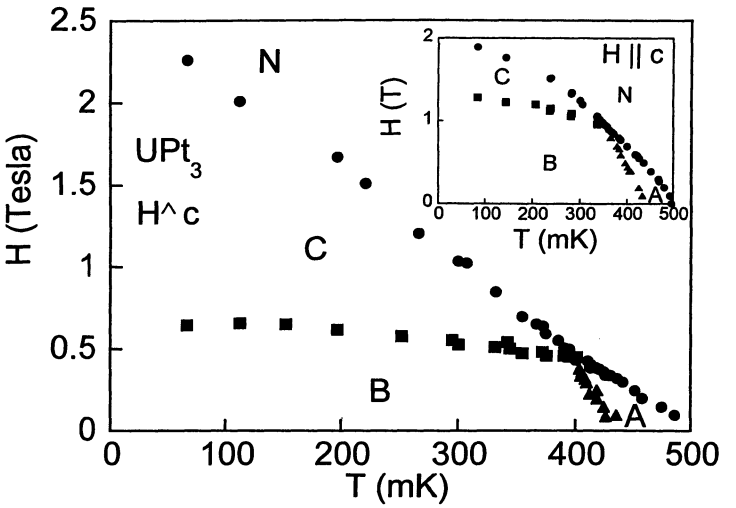

Fig. 8.48. Superconducting phase diagram of UPt_3 determined from ultrasonic velocity measurements. [298]. The data points delineate the second order phase transition lines between three superconducting phases "A", "B", and "C", and the normal state "N", after Ref. [298]

of annealed samples revealed two peaks in the specific heat near T_c at temperatures T_c^+ and T_c^- [296]. The specific heat vs temperature of a single crystal of UPt_3 is plotted in Fig. 8.47. The double kink feature has been verified in many different crystals, and while the values of the T_c's vary between samples, the kinks are always separated by about 50 mK. These data, along with anomalies in ultrasonic attenuation [297], and a kink in H_{c2} vs T point to multiple superconducting phases.

The superconducting phase diagram of UPt_3 determined from sound velocity measurements [298] is shown in Fig. 8.48, where "N" indicates the normal (antiferromagnetic) state, and the three superconducting phases are labelled "A", "B", and "C". The T_c^+ and T_c^- transitions observed in the specific heat at zero field correspond to the N–to–A and the A–to–B phase transition lines. Measurements of muon spin relaxation reveal that the transition to the B phase at T_c^- is accompanied by the onset of a small internal field at 475 mK. These data might lead to the conclusion that the phase transition at T_c^- just signifies the onset of magnetic order. However, the peak in the specific heat at the first transition is so large that it occupies most of the Fermi surface, and there is not enough entropy left for an equally large magnetic transition at T_c^-. The second transition can only be explained in terms of a transition to a different superconducting phase. Both transitions satisfy the relation $\Delta C/\gamma T_c \sim 1$ indicating that heavy electrons are responsible for the superconductivity, see rev. H. von Löhneysen, Physica **B197**, 551 (1994).

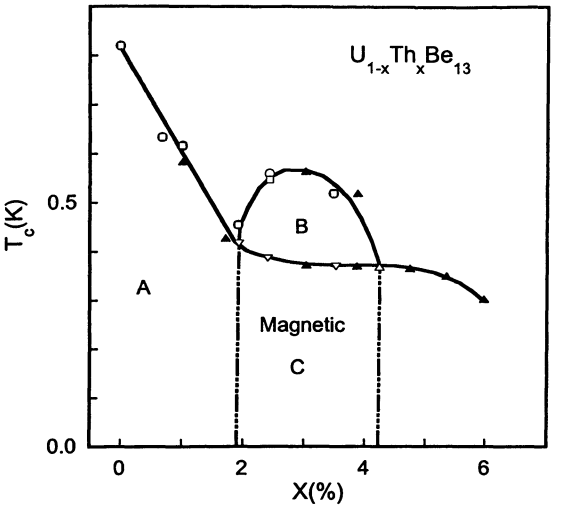

Fig. 8.49. Phase diagram of $U_{1-x}Th_xBe_{13}$, after Ref. [300]

The heavy–fermion compound $U_{1-x}Th_xBe_{13}$ also shows a rich phase diagram with multiple superconducting phases. The phase diagram determined from specific heat, upper critical field, and μSR studies is shown in Fig. 8.49 where "A" and "B" indicate the two superconducting phases [300]. As in UPt_3, the second superconducting transition is accompanied by a transition to very small moment magnetism (0.001 μ_B/U) [301]. Recent point contact spectroscopy measurements on UPt_3 [302] are consistent with line nodes in the *a-b* plane and point nodes along the *c* axis. NMR measurements of both compounds show T^3 temperature dependence below T_c, indicating lines of nodes; however, since the measurements were performed on powdered samples, the directionality of the point nodes would be lost.

Measurements of $T_c(P)$ on the $U_{1-x}Th_xBe_{13}$ system are displayed in Fig. 8.50 as isobars of T_c vs x for $0 \leq x \leq 12$ kbar [303]. Two different types of behavior are present for each pressure, separated by the minimum in $T_c(x)$ at x_{min}. For $x < x_{min}$, a monotonic decrease of $T_c(x)$ is observed as the pressure increases, and the magnitude of the slope dT_c/dP also becomes larger with increasing x. For $x > x_{min}$, an abrupt increase of T_c occurs with a maximum and subsequent decrease for higher x. The position of this maximum is pressure dependent, moving to higher concentration as P increases. It is tempting to infer from the $T_c(x)$ curves the existence of two distinct superconducting phases, one in the regions $0 \leq x \leq x_{min}$ (A phase) and the other at $x > x_{min}$ (B phase), where x_{min} is a function of pressure. The way the $T_c(x)$ curves evolve with pressure suggests that the $T_c(x)$ phase boundary for $x < x_{min}$ extends approximately linearly with the same slope to the region $x > x_{min}$.

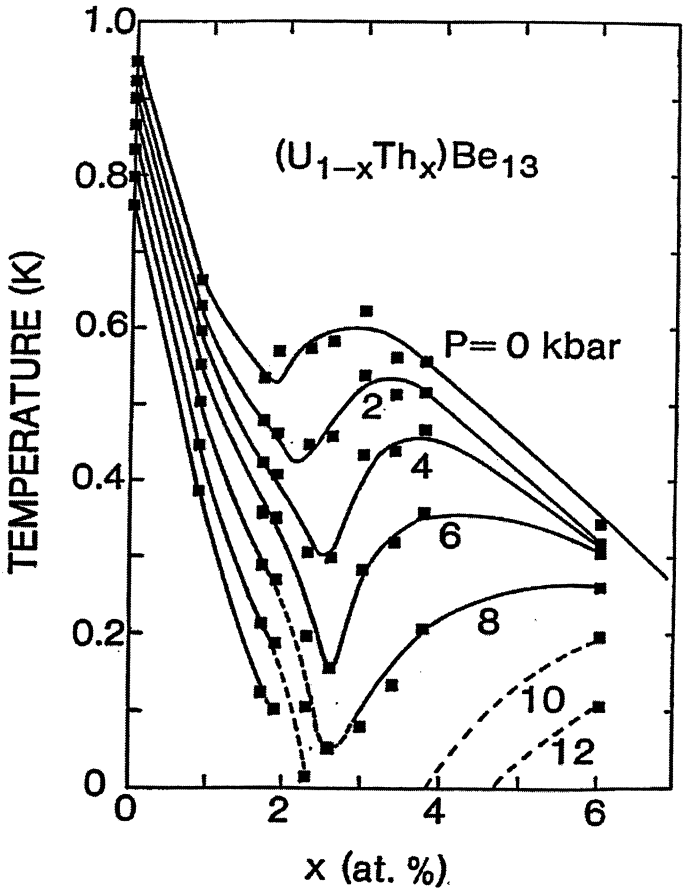

Fig. 8.50. Isobars of the superconducting critical temperature T_c vs x for $U_{1-x}Th_xBe_{13}$ between 0 and 12 kbar, after Ref. [303]

A variety of theories have been advanced to explain the unconventional superconductivity in UPt_3 and $U_{1-x}Th_xBe_{13}$. These theories have been extensively reviewed in Refs. [304–306]. For UPt_3, most of the data points to a spin singlet [307] or spin triplet [306, 308] complex (two component) superconducting order parameter [304]. Another possibility that is difficult to rule out is the presence of two different superconducting phases with different symmetries that happen to be nearly degenerate in temperature [309, 310]. The small moment magnetism in the "B" superconducting states could be explained by a superconducting order parameter that breaks time reversal symmetry. On the other hand, the magnetism could simply result from the onset of a spin density wave. The coupling between superconductivity and magnetism is a key issue that still needs to be resolved.

In the case of $U_{1-x}Th_xBe_{13}$, there are three second–order phase transitions that meet at a tri–critical point, which is theoretically not allowed [311]. This implies the existence of other phase transition lines. An additional phase transition has indeed been observed by assuming that Th substitution is equivalent to pressure, and measuring specific heat as a function of applied pressure for a sample with x = 0.019. One of the more popular models for $U_{1-x}Th_xBe_{13}$ [305,312] assumes multiple degenerate superconducting phases with different symmetries, as was mentioned for UPt_3. The pure UBe_{13} compound is assumed to have a *d*–wave symmetry and an *s*–wave phase with a lower T_c. The *d*–wave phase is suppressed with Th doping more rapidly than the *s*–wave phase, causing the two transition lines to cross. Thus for intermediate Th concentrations there is a pure *s*–wave phase at high temperatures and a mixed $s-d$ phase at lower temperatures.

$PrOs_4Sb_{12}$

Recently, superconductivity was observed in the filled skutterudite compound $PrOs_4Sb_{12}$ at $T_c = 1.85$ K [120, 130]. The superconductivity evidently involves heavy-fermion quasiparticles with an effective mass $m^* \approx 50\ m_e$, as inferred from the normal-state electronic specific heat coefficient γ, the jump in the specific heat at T_c, and the slope of the upper critical field near T_c. This compound appears to be the first example of a Pr-based heavy-fermion superconductor. A possible scenario for the heavy–fermion behavior could be the quadrupolar Kondo effect which involves screening of Pr^{3+} electric quadrupole moments of a nonmagnetic Γ_3 doublet ground state in the CEF by the charges of the conduction electrons [239,240], analogous to the screening of the magnetic dipole moments of paramagnetic ions by conduction electron spins that occurs in the magnetic Kondo effect. Another scenario could involve virtual excitations from either a Γ_1 singlet or a Γ_3 nonmagnetic doublet ground state to a low lying (~ 10 K) Γ_5 triplet state [314]. The issue of whether the CEF ground state of Pr^{3+} in $PrOs_4Sb_{12}$ is a Γ_1 singlet or a Γ_3 nonmagnetic doublet has not yet been resolved, as there is ample evidence for either possibility.

Evidence for the heavy–fermion behavior in $PrOs_4Sb_{12}$ was provided by the magnitude of the superconducting specific heat jump on a pressed pellet of single crystals as displayed in the inset of Fig. 8.51. (The $C(T)$ data have been corrected for excess Sb derived from the molten Sb flux in which the crystals were grown.) An equal entropy construction, in which the entropy is conserved just above and below T_c, yields $\Delta C/T_c = 632$ mJ/mol K^2. The value of the electronic specific heat coefficient from the weak–coupling BCS prediction ($\Delta C/\gamma T_c = 1.43$) is $\gamma \approx 440$ mJ/mol K^2. In the normal state, the specific heat can be described by $C(T) = \gamma T + \beta T^3 + C_{Sch}(T)$, where γT and βT^3 are electronic and phonon contributions, respectively, and $C_{Sch}(T)$ is a Schottky anomaly for a two level system consisting of a doublet ground state and a triplet excited state at an energy Δ above the ground state. The best fit of this expression to the data yields the values $\gamma = 607$ mJ/mol K^2,

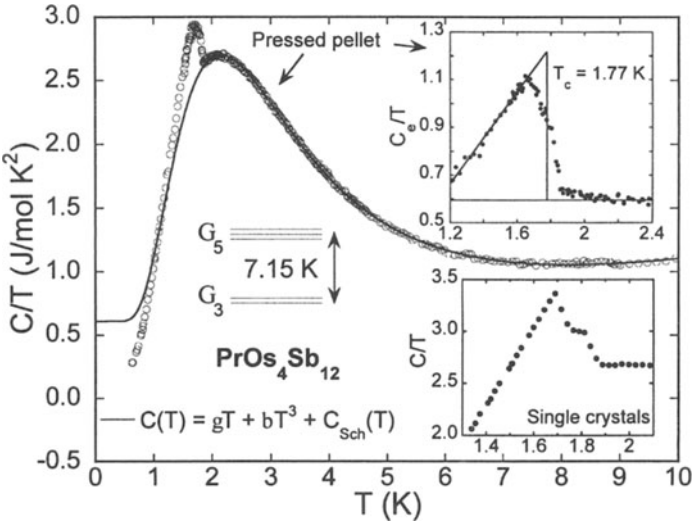

Fig. 8.51. Specific heat C divided by temperature T, C/T, vs T for a $PrOs_4Sb_{12}$ pressed pellet. The line represents a fit of the sum of electronic, lattice, and Schottky contributions to the data. Upper inset: C_e/T vs T near T_c for a $PrOs_4Sb_{12}$ pressed pellet (C_e is the electronic contribution to C). Lower inset: C/T vs T near T_c for $PrOs_4Sb_{12}$ single crystals, showing the structure in ΔC near T_c. Data from Refs. [120,130]

$\beta = 3.95$ mJ/mol K^4 (corresponding to a Debye temperature $\theta_D = 203$ K), and $\Delta = 7.15$ K.

Thermodynamic measurements on $PrOs_4Sb_{12}$ provide evidence for the formation of a nonmagnetic quadrupolar Γ_3 ground state due to splitting of the $J = 4$ multiplet of Pr in a cubic crystalline electric field. The Schottky–like anomaly in specific heat and the peak in magnetic susceptibility at $T \approx 3$ K just above the superconducting transition are consistent with a Γ_3 ground state and a low–lying Γ_5 first excited state separated by $\delta \approx 10$ K, followed by Γ_4 (111 K) and Γ_1 (313 K) excited states [120,148]. Low–temperature inelastic neutron scattering experiments reveal peaks in intensity in the excitation spectrum at 0.72 meV (8.2 K) and 11.4 meV (120 K), corresponding to ground state transitions that are in excellent agreement with this CEF energy level scheme [316]. Furthermore, ultrasonic measurements, a direct probe of CEF excitations, provide strong evidence for Γ_3 ground state in this material [317].

Other measurements suggest a nonmagnetic Γ_1 ground state in $PrOs_4Sb_{12}$ [318,319]. In this scenario, hybridization between the Γ_1 and excited f^2 states (i.e., Γ_4) gives rise to a heavy Fermi–liquid ground state [314,320]. Specific heat measurements by Aoki and co–workers [318] do not reveal a significant fraction of $R \ln 2$ of entropy released below 0.2 K in magnetic field expected from a splitting of the doublet Γ_3 ground state with H, thus indicating a

Γ_1 ground state. However, this hypothesis relies crucially on the assumption that there is no hybridization between the Γ_3 ground state and conduction electron states, which is unlikely given the large value of γ in this material. The magnetic susceptibility is also consistent with the CEF scheme: Γ_1(0 K), Γ_5(6 K), Γ_4(65 K) and Γ_3(111 K) [120]. Based on the near isotropy of the magnetization along the [100] and [110] directions and on the occurrence of a high–field ordered phase (discussed below), Tayama *et al.* suggested that such a Γ_1 ground state scenario better described the properties of $PrOs_4Sb_{12}$ than the Γ_3 ground state scenario. Neutron diffraction measurements reveal a small antiferromagnetic moment ($\mu_{AFM} = 0.025\mu_B$) parallel to the [010] direction in magnetic fields above $H \sim 5$ T at $T = 0.25$ K [321]. A crystalline electric field analysis based on a Γ_1 ground state suggests that antiferroquadrupolar order arises from a level crossing of the Γ_1 ground state with an excited state in magnetic fields, consistent with the diffraction results. Clearly, further measurements are necessary to determine the exact nature of the ground state in $PrOs_4Sb_{12}$.

A number of experimental results suggest unconventional superconductivity in $PrOs_4Sb_{12}$. Recent specific heat measurements [148,316] on single crystals of $PrOs_4Sb_{12}$ show a double superconducting jump reminiscent of UPt_3 (Fig. 8.47). The two superconducting transitions are estimated to occur at $T_{c1} = 1.75$ K and $T_{c2} = 1.85$ K using an entropy conserving construction. This double transition has been observed for several different combinations of single crystals as well as for individual single crystals [148,316]. In fact, the only specific heat measurement of $PrOs_4Sb_{12}$ that does not show the double jump feature is the original measurement of a pressed powder sample, in which a single broad transition is observed, probably due to strain effects [120]. These two transitions have also been observed in a variety of other measurements including: thermal expansion [322], magnetization [319, 324, 325], and penetration depth studies [327]. The thermal expansion measurements [322] reveal that, from the Ehrenfest relation, T_{c1} and T_{c2} have different pressure dependences suggesting that they are associated with two distinct superconducting phases.

The nature of the superconductivity of $PrOs_4Sb_{12}$ was investigated by means of thermal transport measurements in aligned magnetic fields by Izawa and coworkers [328]. The thermal transport shows an anisotropy as the magnetic field is rotated in the $a - b$ crystallographic plane as shown in Fig. 8.52, which is coupled to anisotropy in the superconducting order parameter. As the temperature is lowered below T_{c1}, the thermal transport changes symmetry from four–fold to two–fold in the $a-b$ plane. Group theoretical arguments given the cubic crystal structure of $PrOs_4Sb_{12}$ suggest that the high–temperature superconducting phase between T_{c1} and T_{c2} has six point nodes, whereas the low temperature phase below T_{c1} has two point nodes. The compound $PrOs_4Sb_{12}$ is the first heavy–fermion superconductor for which there is evidence of point nodes rather than line nodes in the superconducting order

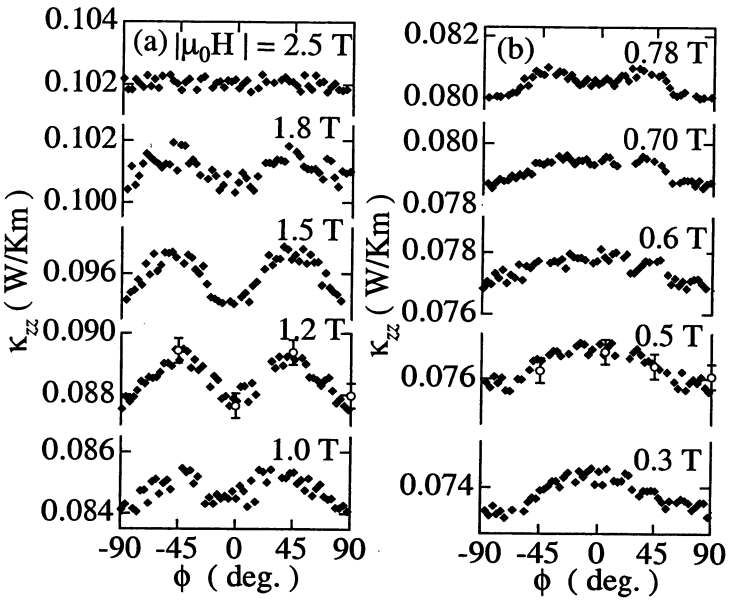

Fig. 8.52. (a),(b) Angular variation of κ_{zz} in a magnetic field rotating within the ab–plane at 0.52 K above and below $H_{c2}(\simeq 2.0$ T), from Ref. [328]

parameter. Izawa *et al.* also established the $H - T$ phase diagram of the two superconducting phases from thermal transport measurements as shown in Fig. 8.53, in which T_{c1} is suppressed by 25 kOe, and T_{c2} is suppressed by 7 kOe. On the other hand, recent transverse field μSR [329] and Sb–NQR measurements [330] on $PrOs_4Sb_{12}$ are consistent with an isotropic energy gap. Along with the specific heat, these measurements indicate strong coupling superconductivity. These findings suggest an s–wave, or, perhaps, a Balian–Werthamer p–wave order parameter. The Balian–Werthamer p–wave order parameter, originally suggested for the "B" phase of ^{3}He, involves Cooper pairs with aligned spins in the $L = 1$ angular moment state, and results in an isotropic energy gap [331]. It is also interesting to note that zero–field μSR measurements reveal the presence of internal magnetic fields below $T_{c2} = 1.85$ K indicating time–reversal symmetry breaking in the superconducting state [332] of $PrOs_4Sb_{12}$.

There is also evidence for a high field ordered phase (HFOP) in $PrOs_4Sb_{12}$. The $H - T$ phase diagram, depicting the superconducting region and the HFOP, is shown in Fig. 8.54 [325, 333]. The HFOP was first detected by means of features in $\rho(H,T)$ data [316,324,325]. The line that intersects the high field ordered state represents the inflection point of the "roll–off" in $\rho(T)$ at low temperatures and is a measure of the splitting between the Pr^{3+} ground state and the first excited state, which decreases with field. The HFOP

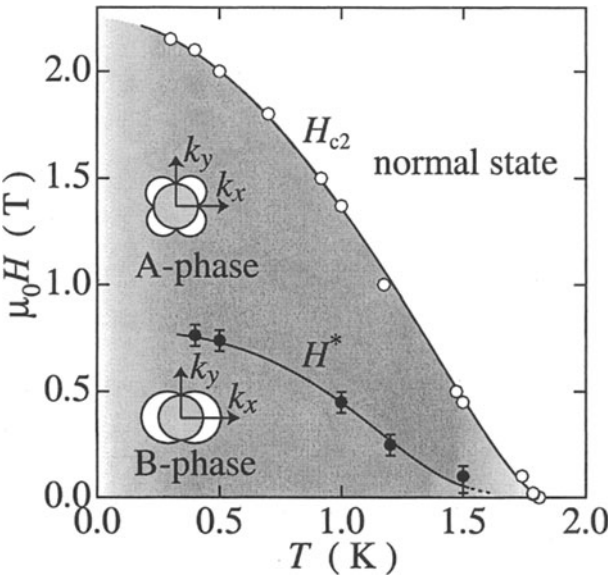

Fig. 8.53. Phase diagram of the superconducting gap symmetry of $PrOs_4Sb_{12}$ determined from thermal conductivity measurements. The filled circles represent the magnetic field H^* at which the transition from fourfold to twofold symmetry takes place. The open circles represent H_{c2}. The area of the gap function with fourfold symmetry is shown by pink (A–phase) and the area of the gap function with twofold symmetry is shown by blue (B–phase), from Ref. [328]

has also been observed by means of large peaks in the specific heat [148,318], thermal expansion [322, 323], and kinks in the magnetostriction [323] and $M(H)$ curves [315,316,325,334].

The heavy–fermion superconductor $PrOs_4Sb_{12}$ is an intriguing material because of the possibility that the heavy–fermion behavior and the superconductivity [335,336] arise from quadrupolar fluctuations, i.e., the screening of the quadrupole moments of the Pr^{3+} ions in a Γ_3 ground state by the charges of the conduction electrons. It is also only the second superconductor (after UPt_3) that exhibits two distinct superconducting phases with different order parameter symmetries. The heavy fermion state and unconventional superconductivity observed in this material represent a challenge for theoretical description [335–339].

$PuCoGa_5$

Superconductivity has been observed in the Pu–based material $PuCoGa_5$, which crystallizes in the same structure as the $CeMIn_5$ materials, with a critical temperature $T_c = 18.5$ K [129], an order of magnitude larger than that of other heavy–fermion superconductors. The specific heat of $PuCoGa_5$, shown in Fig. 8.55, reveals a large specific heat jump at T_c, $\Delta C/T_c = 110$ mJ/mol K^2, confirming bulk superconductivity in this material. If one as-

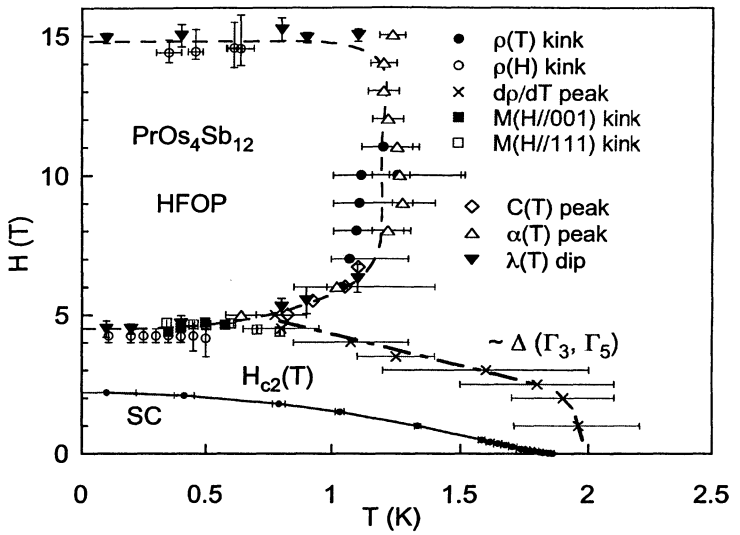

Fig. 8.54. Magnetic field – temperature ($H - T$) phase diagram of $PrOs_4Sb_{12}$ showing the regions exhibiting superconductivity (SC) and the high field ordered phase (HFOP). The dashed line is a measure of the splitting between the Pr^{3+} Γ_3 ground state and Γ_5 excited state (see text for further details), data from Refs. [148, 315, 316, 322, 324, 325]

sumes the BCS value $\Delta C/\gamma T_c = 1.43$, the electronic specific heat coefficient is $\gamma = 77$ mJ/mol K^2, indicating a moderate enhancement of the effective mass. Further evidence for bulk superconductivity is provided by electrical resistivity and magnetic susceptibility measurements (Fig. 8.55). In addition to the unusually large value of T_c for an intermetallic compound, the upper critical field is correspondingly large. An initial slope $dH_{c2}/dT = -59$ kOe/K yields an orbital critical field $H^*_{c2}(0) = 740$ kOe (Eq. 8.22). From this value of $H^*_{c2}(0)$, the superconducting coherence length is estimated to be $\xi_0 = 21$ Å, from which an effective mass $m^* = 37\ m_e$ is determined. This estimate of m^* yields $\gamma = 126$ mJ/mol K^2, providing further evidence for heavy–fermion behavior in $PuCoGa_5$. The critical current density is also quite large, $J_C > 10^4$ A/cm^2 for $T > 0.9T_c$, presumably due to pinning defects caused by the radioactive decay of Pu.

The nature of superconductivity in $PuCoGa_5$ has not been established; however, there are some indications that it is unconventional. Several measurements suggest that the f–electron localization lies in between that of $CeCoIn_5$, a local–moment heavy–fermion superconductor with $T_c = 2.3$ K, and $UCoGa_5$, which exhibits temperature–independent paramagnetism consistent with itinerant f–electron behavior. Both the characteristic temperature scale deduced from electrical resistivity measurements, which increases from $CeCoIn_5$ to $PuCoGa_5$ to $UCoGa_5$, and the electronic specific heat co-

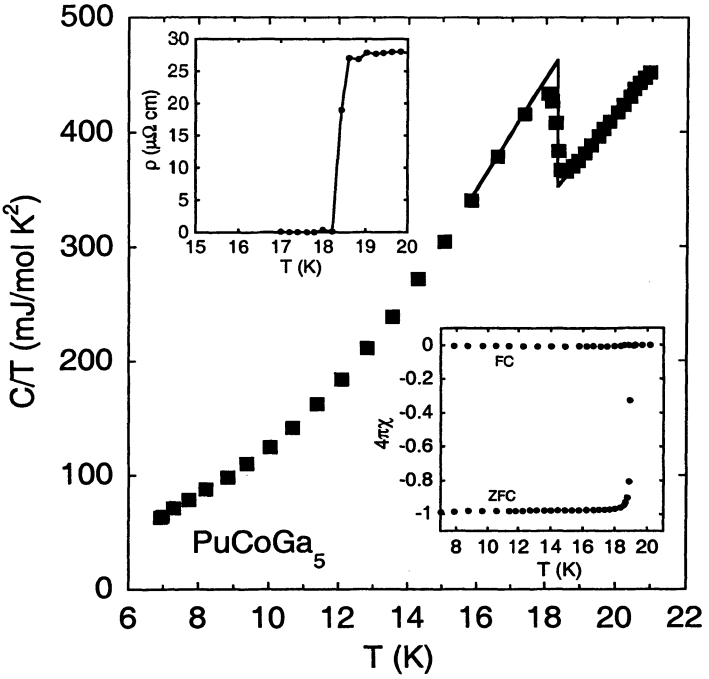

Fig. 8.55. Specific heat over temperature C/T, electrical resistivity ρ and magnetic susceptibility χ as a function of temperature T for $PuCoGa_5$ showing a superconducting transition at 18 K, after Ref. [129]

efficient, which increases from $\gamma \sim 10$ mJ/mol K^2 in $UCoGa_5$ to ~ 100 mJ/mol K^2 in $PuCoGa_5$ to ~ 1000 mJ/mol K^2 in $CeCoIn_5$, are consistent with this picture. In a scenario of unconventional superconductivity, the order–of–magnitude increase in T_c of $PuCoGa_5$ compared to that of $CeCoIn_5$ is expected from the increased bandwidth of the $5f$ electrons relative to the $4f$ electrons. The magnetic susceptibility exhibits Curie–Weiss behavior with an effective moment $\mu_{\text{eff}} = 0.68\ \mu_B$, close to the value expected for Pu^{3+}. Thus, it appears that superconductivity occurs in the presence of a sublattice of well defined magnetic moments, which is difficult to reconcile with a phonon–mediated pairing mechanism. Further investigations on $PuCoGa_5$ and other transuranic intermetallic compounds may provide new and exciting areas of research in superconductivity.

8.3.9 Concluding Remarks

The past two decades of research into heavy–fermion superconductors have consistently yielded a rich variety of new compounds, new phenomena, and new insights into the nature of superconductivity. When heavy–fermion su-

perconductivity was first discovered in $CeCu_2Si_2$ in 1979 by Steglich and coworkers, the coexistence of magnetism and superconductivity had only been established in ternary rare earth compounds such as the rare earth molybdenum chalcogenides RMo_6X_8 (X = S, Se) and the rare earth rhodium borides RRh_4B_4. Since then about 20 different Ce–, Pr–, U–, and Pu–based heavy–fermion superconductors have been discovered and the list will continue to grow. The past few years have seen renewed interest in heavy–fermion superconductors with the discovery of the coexistence of ferromagnetism and superconductivity in UGe_2, URhSi, and, possibly, $ZrZn_2$. The exciting discovery of superconductivity in $PrOs_4Sb_{12}$, which contains two superconducting phases which appear to have different order parameter symmetries, and may have a quadrupolar origin, suggests a new route to unconventional superconductivity. Heavy–fermion superconductors continue to be a fertile area of research and enhance our understanding of superconductivity.

8.4 Organic Superconductors

8.4.1 Introduction

The first organic superconductor, $(TMTSF)_2PF_6$, was discovered more than 20 years ago by Jérome *et al.* [340]. It belongs to a class of compounds known as Bechgaard salts, named after the first person to synthesize them, Klaus Bechgaard. $(TMTSF)_2PF_6$ undergoes a transition from a quasi–one–dimensional (1D) metal to a superconductor as the temperature is lowered below 1 K under an applied pressure of ~12 kbar. At ambient pressure, however, it experiences a Peierls metal–insulator transition to a spin–density–wave (SDW) state at low temperatures. With one exception, SDW phase transitions are observed in all Bechgaard salts based on TMTSF. The molecule TMTSF (tetramethyltetraselenafulvalene) is shown in Fig. 8.56.

Within a few years of this stimulating discovery, a large variety of other superconductors based on different molecular building blocks were found. Of the approximately 100 different organic superconductors known to date [341], the largest number are based on the molecule BEDT–TTF (bisethylenedithio–tetrathiafulvalene or ET for short), which is also shown in Fig. 8.56. The usual stoichiometry of these quasi–two–dimensional (2D) organic metals is $(ET)_2X$, where X represents a monovalent anion such as I_3^- or $Cu(NCS)_2^-$. [341,342]. Charge transfer from the neutral ET molecule to the anion leads to partially filled molecular bands, resulting in metallic conductivity. To date, the highest values of T_c are 11.5 K at ambient pressure for κ-$(ET)_2Cu[N(CN)_2]Br$ [343] and about 13 K for the isostructural material κ-$(ET)_2Cu[N(CN)_2]Cl$ under a moderate pressure of about 0.3 kbar [344].

Beyond the main building blocks, TMTSF and ET, of crystalline organic superconductors, a number of additional organic molecules are known to form superconducting species [341]. A very promising new class of 2D organic metals is based on the donor BETS (bisethylenedithio–tetraselenafulvalene),

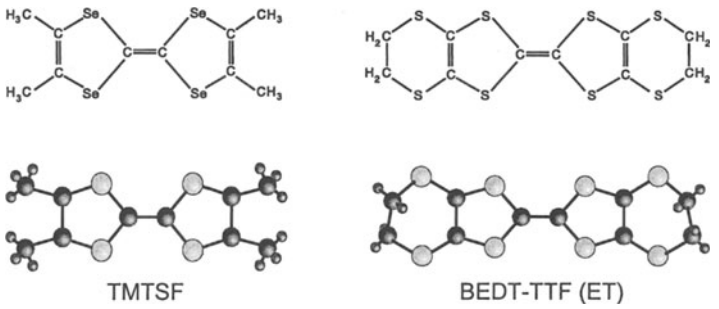

Fig. 8.56. The molecular structures of TMTSF (tetramethyltetraselenafulvalene) and BEDT–TTF (bisethylenedithio-tetrathiafulvalene, or ET for short), which are the main building blocks of crystalline molecular conductors. In contrast to TMTSF, the ET molecule is not completely planar

a selenium–substituted ET analogue. Molecular crystals of this donor with Fe^{3+}–containing anions are prone to magnetic interactions between the BETS π–electron system and the iron d electrons [345,346]. This makes these materials a fascinating playground for studying the competing magnetic and superconducting interactions. For example, reentrant superconductivity upon cooling (Section 8.2.3) and magnetic field induced superconductivity (Section 8.2.4) can be found in these systems.

Besides superconductivity, the organic metals show a wealth of different ground states such as antiferromagnetism, spin–Peierls, SDW, and charge–density–wave (CDW) states. These ground states are accessible by tuning the structure, counter anion, magnetic field, temperature, and pressure. The study of these fertile phase diagrams has led to new theoretical concepts; however, a solid understanding of some of these states still remains a challenge. Even the normal metallic state of these electronically low–dimensional metals reveals unusual properties sometimes not in line with conventional Fermi–liquid theory.

Many superconducting properties of the organic superconductors, especially of the 2D materials, resemble the behavior found in the cuprate superconductors [347–350]. The $H-T$ phase diagrams and the vortex dynamics are very similar in these layered strongly type–II superconductors. In contrast to the high–T_c cuprates, however, much less is known about the nature of the superconducting state in organic metals. Clear–cut experimental proof for unconventional non–BCS–like superconductivity is missing. However, for the 1D Bechgaard salts, recent sophisticated experiments support triplet pairing of the Cooper pairs. For the 2D organic superconductors, on the other hand, where singlet pairing has been established, an ongoing debate persists as to the exact symmetry of the order parameter (see [351–353] for recent reviews). Some experimental results hint at line nodes in the superconducting energy gap, i.e., d–wave symmetry, whereas other experiments, in particular, specific

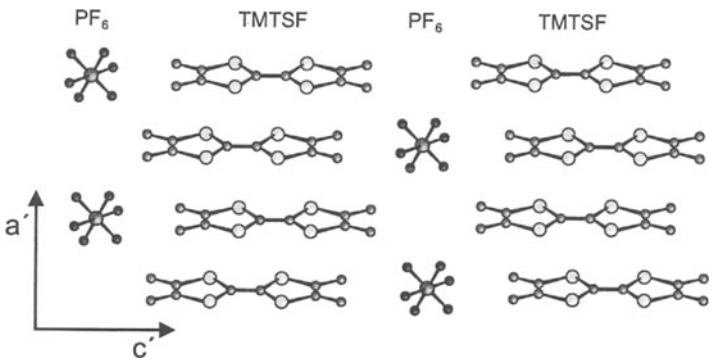

Fig. 8.57. Crystal structure of $(TMTSF)_2PF_6$ viewed somewhat tilted relative to the b direction. a' and c' are projections of a, the most–conducting direction, and c, the least–conducting direction

heat data, suggest the existence of a node–less energy gap, fully consistent with BCS–like s–wave symmetry.

A further unsolved issue is the mechanism responsible for Cooper–pair coupling. While there is some belief in the existence of a non–phonon–mediated coupling mechanism, as appears to be operative in unconventional superconductors such as the cuprates, Sr_2RuO_4, and heavy–fermion compounds, this issue remains unclear and heavily debated for the organic superconductors. The proximity of antiferromagnetic or SDW states to the superconducting state spurred the notion that antiferromagnetic fluctuations are responsible for the coupling. On the other hand, a number of experiments indicate that some interaction between phonons and superconductivity exists. In any case, it is clear that the excitonic mechanism originally proposed by Little [354] is not responsible for the pairing of superconducting electrons. Nevertheless, Little's prediction of very high transition temperatures in organic materials was an important stimulus for the search for organic superconductors.

8.4.2 Normal–State Properties

Ordinarily, the term "organic materials" implies plastics, i.e., polymeric carbon-based chains. However, the 1D and 2D organic metals discussed here are high–quality single crystals usually grown by electrocrystallization from appropriate solutions, the details of which are reviewed in depth in Ref. [342]. During this process the oxidation of the donor molecules occurs together with the crystal growth at the electrodes. The resulting charge–transfer salts weigh up to a few milligrams and are usually shaped like needles or plates.

Quasi–one–dimensional organic metals

All 1D organic superconductors based on the donor molecule TMTSF crystallize in the same triclinic crystal structure which is depicted in Fig. 8.57 for $(TMTSF)_2PF_6$ [355]. Some crystal parameters are given in Table 8.6. TMTSF

is a planar brick–like molecule that tends to stack in columns. These columns are formed along the a axis, which is the axis with the highest conductivity since in this direction the Se–Se distances are short, resulting in a strong π–orbital overlap. Along the b axis the Se–Se distances are similar; however, the overlap integrals are much smaller due to the side–by–side orientation of the Se atoms. Along the c axis, the PF_6^- anions (see Fig. 8.57) separate the columns. This results in only a weak electronic coupling along c with correspondingly small overlap integrals. The approximate ratio of the overlap integrals along the crystallographic directions is $t_a : t_b : t_c = 300 : 30 : 1$. These numbers reveal that the Bechgaard salts are by no means ideal one–dimensional metals. It is, however, exactly this tendency towards two dimensionality which shifts the insulating SDW state to low temperatures and allows superconductivity under moderate pressure (see below).

The calculation of the electronic band structure of the organic charge–transfer salts from first principles is a highly sophisticated task. Although steady progress has been made in dealing with the large unit cells in high–level first–principle studies [356], the usual method for obtaining the band structure is based on the extended Hückel tight–binding approximation. These calculations result in surprisingly reliable band structures for most 1D and 2D organic metals, at least for the dispersion relations in the neighborhood of the Fermi energy. The calculated band structure and the 2D Fermi surface (FS) for $(TMTSF)_2PF_6$ is shown in Fig. 8.58. For different anions, the dispersion relations and the FS are almost indistinguishable [357].

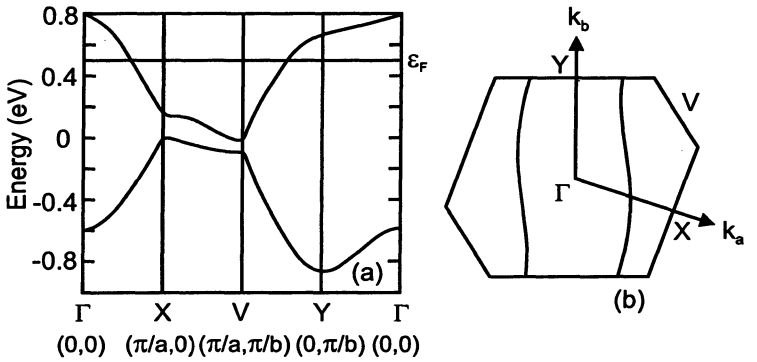

Fig. 8.58. (a) Calculated dispersion relation and (b) Fermi surface of $(TMTSF)_2PF_6$. These results are representative of all $(TMTSF)_2X$ salts [357]

For the Bechgaard salts, there is a strong mutual interaction between the 1D electronic system and the three–dimensional lattice. In general, metals with a pronounced 1D character have a tendency to develop an insulating ground state in a combined lattice and electronic phase transition. They are unstable against a Peierls transition, which is a perturbation with a wave (or

nesting) vector of $2k_F$, where k_F is the Fermi wave vector. This perturbation can either be a charge redistribution, i.e., a charge density wave (CDW), or a spin redistribution (SDW). This leads to a reconstruction of the crystallographic or magnetic unit cell resulting in a modified band structure and Fermi surface. Whether a Peierls transition occurs and at which temperature crucially depends on the dimensionality of the electronic system. For an ideal one–dimensional metal, a Peierls transition is inevitable.

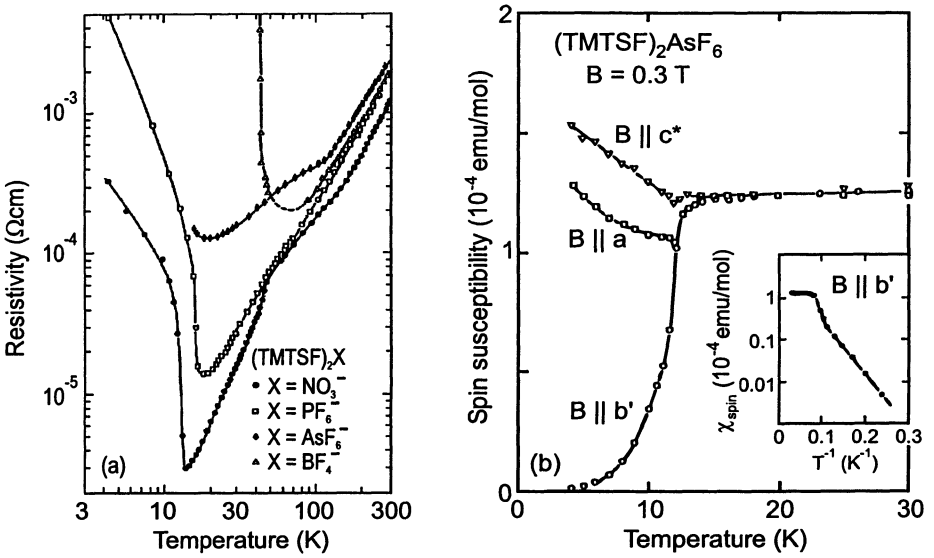

Fig. 8.59. (a) Temperature dependence of the resistivity for various $(TMTSF)_2X$ salts [358]. Below the Peierls transition, the resistivity shows insulating behavior. (b) Temperature dependence of the static spin susceptibility of $(TMTSF)_2AsF_6$. The inset shows the exponential decrease of the susceptibility in the b' direction (perpendicular to a and c^*) below the metal–insulator transition [359]

Most of the 1D Bechgaard salts show a Peierls transition at ambient pressure. However, this metal–insulator transition occurs at rather low temperatures, $T_{MI} \sim 10$ K (Fig. 8.59) since, as stated above, an appreciable overlap along the b direction leads to an increased dimensionality and reduces the electronic energy gained at the Peierls phase transition. The transition is clearly seen in the electrical–resistivity and magnetic–susceptibility data (Fig. 8.59) [358, 359]. These data prove the SDW nature of the distortion [360]; in contrast to an isotropic decrease of the magnetic susceptibility expected for a CDW, the susceptibility vanishes exponentially only along the b' direction (inset of Fig. 8.59(b)) [359]. Such behavior is characteristic of an antiferromagnetically ordered state with alternating spin orientation along the b' direction. This type of spin ordering has been confirmed by a number

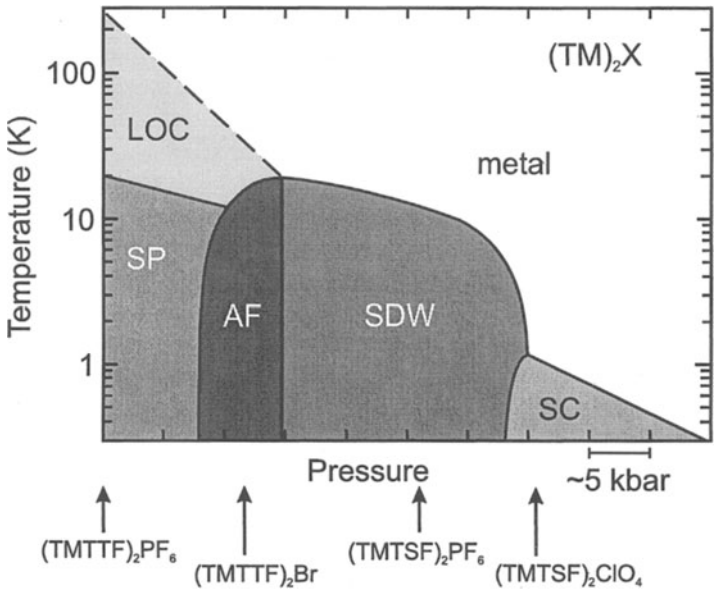

Fig. 8.60. Schematic pressure–temperature phase diagram of the $(TM)_2X$ salts based on TMTSF and TMTTF. The arrows indicate the ambient pressure of various molecular crystals. LOC = charge–localized insulator, SP = spin–Peierls, SDW = spin density wave, AF = antiferromagnetic insulator, and SC = superconductor

of additional experimental techniques, and by the fact that the measured SDW nesting vector is compatible with the calculated band structure shown in Fig. 8.58 [341,361].

As mentioned previously, moderate pressure of a few kbar suppresses the SDW state and superconductivity evolves. The generic pressure–temperature ($P - T$) phase diagram for the $(TM)_2X$ salts is shown in Fig. 8.60. TM stands for TMTSF or TMTTF (= tetramethyltetrathiofulvalene), the sulfur analogue of TMTSF. For the organic metals and superconductors, the crucial parameter is pressure, not charge–carrier concentration, as is the case for the cuprate superconductors. An increasing pressure is equivalent to a better overlap of the molecular wave functions which results in a reduced anisotropy and, consequently, in an increased dimensionality. The only Bechgaard salt which becomes superconducting at ambient pressure ($T_c = 1.2\,K$) is $(TMTSF)_2ClO_4$ [362]. In order for this to occur, the material has to be cooled slowly to allow the randomly oriented low–symmetry ClO_4 anions to order at about 24 K, where a superlattice is formed with a doubled lattice parameter along the b direction [341]. If, on the other hand, the sample is quenched rapidly with a cooling rate greater than 50 K/min, the high–temperature anion disorder persists down to low temperature and superconductivity does not appear.

TMTTF–based salts are electronically more one dimensional than the TMTSF analogues. For $(TMTTF)_2PF_6$, which is located at the far left side of the phase diagram in Fig. 8.60 at ambient pressure, an insulating state (LOC) occurs at high temperatures of about 230 K. The localization of the interacting electrons is believed to be due to a Mott–Hubbard transition. At lower temperatures, a spin–Peierls (SP) transition takes place resulting in a dimerization of the antiferromagnetically ordered spin chains. In recent sophisticated high–pressure studies [363–365], two groups were able to tune $(TMTTF)_2PF_6$ through all of the phases shown in Fig. 8.60. Indeed, at pressures of about 50 kbar superconductivity was induced. These data validate the $P-T$ phase diagram that was originally proposed by Jérome on the basis of experimental data obtained for different $(TM)_2X$ salts [366].

More information on the directional dependence of the strongly anisotropic molecular interactions can be gained by uniaxial–pressure studies. However, these are hampered by the high fragility of the organic superconductors. One of the few uniaxial–pressure investigations was recently reported for $(TMTSF)_2PF_6$ [367]. Surprisingly, the strongest suppression of the SDW transition temperature was found for pressure applied along the most–conducting a direction. The larger overlap along a results in an increased bandwidth and, concomitantly, in a decreased density of states and, therefore, a reduced energy gain in the electronic system at the SDW transition. Apparently, this effect is more important than the simultaneous increase in Fermi–surface nesting [368].

Magnetic fields can have a strong influence on the electronic properties of the organic superconductors. One fascinating phenomenon is the occurrence of field–induced spin density waves (FISDW) which become evident in Shubnikov–de Haas(SdH)–like oscillations in the longitudinal resistivity and in quantized steps of the Hall resistivity. Indeed, this was the first observation of a quantum Hall effect in a bulk crystal [369,370]. Stimulated by these intriguing results, a theory now commonly known as the "standard model" for FISDW was developed [371]. The principal effect of the applied magnetic field is an effective reduction of the electronic dimensionality. Therefore, the magnetic field can counterbalance the pressure–increased dimensionality leading to a transition into a SDW state at high enough field strengths. For more details, see Ref. [341].

In the 1D organic metals, a number of electrical–transport properties exist that cannot be explained by the conventional Fermi–liquid theory. In fact, for 1D metals a non–Fermi–liquid state, i.e., a spin–charge separated Luttinger liquid, is predicted. The observed field and temperature dependences of the resistivity [372,373] as well as recent thermal–conductivity data [374] have been interpreted along these lines. At zero field, $(TMTSF)_2PF_6$ is believed to be a marginal three–dimensional Fermi liquid which can be destabilized by the application of small fields in certain directions [375,376]. Above a threshold field (~ 0.2 T along the b direction), electronic transport shows

incoherent non–Fermi–liquid properties. Consequently, the "normal state" of the Bechgaard salts behaves nonmetallicly in the presence of small magnetic fields (see Refs. [377,378] for recent reviews).

Quasi–two–dimensional organic metals

In contrast to the isostructural 1D Bechgaard salts, a number of different crystal structures exist for the ET–based charge–transfer salts. They mainly differ in the packing motifs of the nonplanar ET molecules and are labeled by different greek letters (see Table 8.6) [341,342]. Figure 8.61 shows the crystal

Table 8.6. Crystallographic data and T_c for some organic metals based on the donor molecules TMTSF and ET. Z is the number of formula units per unit cell. For T_c the usually stated values are given independent from the experimental determination. The actual thermodynamic values may differ slightly. For the ET–based compounds the out–of–plane lattice parameter is underlined.

Compound	sp-gr.	a(Å)	b(Å)	c(Å)	α(°)	β(°)	γ(°)	Z	Ref.	T_c(K)
$(TMTSF)_2PF_6$	$P\bar{1}$	7.297	7.711	13.522	83.39	86.27	71.01	1	[355]	0.9[a]
$(TMTSF)_2ClO_4$	$P\bar{1}$	7.266	7.678	13.275	84.58	86.73	70.43	1	[379]	1.2
β-$(ET)_2I_3$	$P\bar{1}$	6.615	9.100	15.286	94.38	95.59	109.78	1	[380,381]	1.4
β-$(ET)_2IBr_2$	$P\bar{1}$	6.593	8.975	15.093	93.79	94.97	110.54	1	[382]	2.8
κ-$(ET)_2I_3$	$P2_1/c$	16.387	8.466	12.832	90	108.56	90	2	[383]	3.5
κ-$(ET)_2Cu(NCS)_2$	$P2_1$	16.256	8.456	13.143	90	110.28	90	2	[384]	10.4
κ-$(ET)_2Cu[N(CN)_2]Br$	$Pnma$	12.949	30.016	8.539	90	90	90	4	[343]	11.5
κ-$(ET)_2Cu[N(CN)_2]Cl$	$Pnma$	12.977	29.977	8.480	90	90	90	4	[344]	12.8[b]
α-$(ET)_2KHg(SCN)_4$	$P\bar{1}$	10.082	20.565	9.933	103.70	90.91	93.06	2	[385]	–[c]
α-$(ET)_2NH_4Hg(SCN)_4$	$P\bar{1}$	10.091	20.595	9.963	103.67	90.47	93.30	2	[386]	1.1
β''-$(ET)_2SF_5CH_2CF_2SO_3$	$P\bar{1}$	9.260	11.635	17.572	94.69	91.70	103.10	2	[387]	5.2

[a] this value was reported in Ref. [340] for a pressure of 12 kbar. A pressure of $\sim$ 6 kbar is however sufficient to suppress the SDW state and enable superconductivity with $T_c \approx 1.1$ K. See, for example, Ref. [388,389].

[b] at a pressure of $\sim$ 0.3 kbar.

[c] recently superconductivity with $T_c \approx 100$ mK was reported to occur at 2.5 kbar [390].

structure of β-$(ET)_2I_3$, a typical example of most $(ET)_2X$ salts. The common structural feature is the packing of the ET molecules into layers which are separated by poorly conducting anion planes (I_3^- planes in Fig. 8.61). The principal difference between the crystal structures of the ET families (α, β, β'', κ, etc.) is the arrangement of the ET donors within the layers. There are, however, always sufficiently close contacts between the π orbitals of the sulfur atoms of neighboring intralayer ET molecules. This results in the formation of molecular bands with only relatively small in–plane anisotropies (typically within a factor of two). The anions which are responsible for the

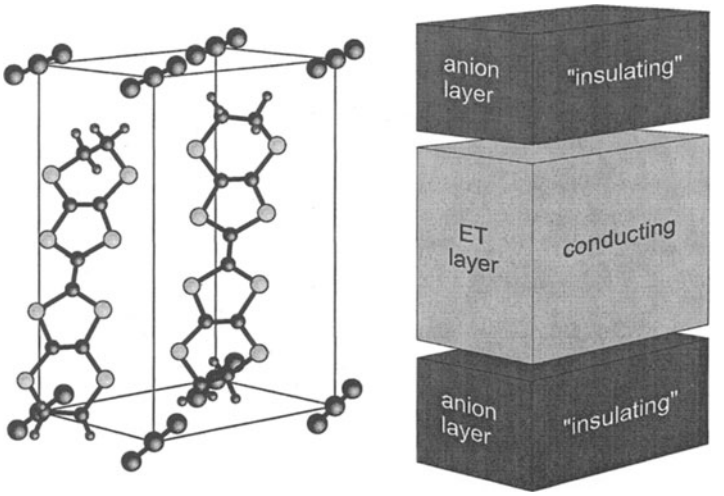

Fig. 8.61. Characteristic layered structure of the quasi–two–dimensional (2D) organic metals, exemplified by the crystal structure of β-$(ET)_2I_3$. The short distances between the sulfur atoms of different ET molecules result in a good conductivity within the ET layers. The ET layers are separated by the poorly conducting anion layers, schematically shown on the right side

charge transfer lead to partially filled molecular bands, enabling metallic conductivity. The anion layers are sandwiched between the highly conducting ET layers. This results in very strong anisotropies of the physical properties parallel and perpendicular to the layers. The electrical resistivity perpendicular to the layers is larger by about $3-6$ orders of magnitude than for electronic transport within the ET layers [341,351]. One should mention, however, that the exact value of this anisotropy is difficult to determine since any dislocation disturbing the in–plane transport will immediately lead to an enhanced in–plane resistance. This 2D structure, which is also reflected in the superconducting properties, is observed in all ET phases and resembles that of many layered cuprates, such as $Bi_2Sr_2CaCu_2O_{8-\delta}$ [348].

Although the layered structure occurs in all ET–based superconductors, the varying in–plane packing motifs of the organic molecules lead to different 2D electronic structures. The overlap integrals vary considerably depending on whether the ET molecules are aligned face–to–face or side–by–side. [391, 392]. The in–plane transfer energies can be obtained from these overlap integrals that, together with the known crystal structures, allow the electronic band structures to be calculated using the well–established extended Hückel tight–binding approximation. Two examples of the resulting energy dispersions and of the in–plane Fermi surfaces are shown in Fig. 8.62.

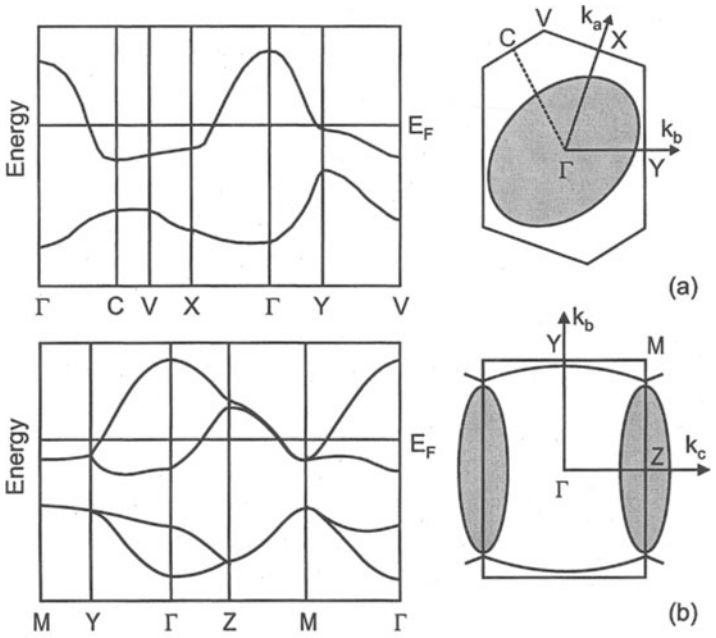

Fig. 8.62. Calculated energy dispersions and Fermi surfaces for (a) β–phase and (b) κ–phase ET salts (after [391,392] and [393])

For the β phase, one electron per unit cell is transferred to the anion leaving the highest occupied molecular orbital half filled. The nearly isotropic in–plane overlap integrals lead to an almost circular free–electron–like FS (Fig. 8.62(a)) [391,392]. The validity of this result has been verified by measurements of magnetic quantum oscillations and angular dependent magnetoresistance oscillations [361]. Indeed, only one closed orbit with the predicted area (shaded area in Fig. 8.62(a)) and only slightly more cornered shape [394] could be reconstructed from the data.

For the κ phase, the resulting FS is almost as simple as for the β phase. Here, the ET molecules form dimers where adjacent pairs in the plane are rotated by approximately 90° with respect to each other. This doubles the unit cell, resulting in two transferred electrons on two highest occupied molecular orbitals (see the dispersion relation in Fig. 8.62(b)). The resulting FS again resembles the free–electron picture where the FS cuts the first Brillouin zone with small gaps opening at the zone boundary due to Bragg reflections [393]. In fact, for κ-$(ET)_2Cu(NCS)_2$, larger gaps at the zone boundary are found due to the lack of a center of symmetry [395]. Again, de Haas–van Alphen (dHvA) and Shubnikov–de Haas (SdH) experiments confirm the predicted band structures for the κ–phase materials as well as for most other phases. However, the calculated effective masses are often much smaller than the experimental

values, sometimes close to the free–electron value. This is usually ascribed to the fact that many–body effects like electron–electron and electron–phonon interactions are typically not included in band–structure calculations. For more details on Fermi–surface studies, see the reviews in [361, 396].

Although the extended–Hückel treatment has been successful in describing the in–plane electronic band structure of organic metals and superconductors, it leaves the interlayer band structure unclear. The large separation of the conducting organic layers by relatively thick anion layers has led to the question of whether a real 3D Fermi surface exists at all. When the interlayer transport is incoherent, i.e., when an electron loses its phase information between successive tunnelling processes, no Bloch state can evolve and the band picture breaks down [397]. Although there is no experimental proof for this scenario, certain experimental features can be utilized to verify the coherent transport and the existence of a 3D Fermi surface [397, 398].

The most direct test of the 3D nature of the FS, which even gives a number for the interlayer transfer integral $t_\perp$, is the detection of nodes in magnetic quantum oscillations. Figure 8.63(a) shows the dHvA signal for β-$(ET)_2IBr_2$. The fast dHvA oscillations visible in the magnetization can be ascribed to the closed FS shown in Fig. 8.62(a). The existence of a corrugated FS, sketched in the inset of Fig. 8.63(a), results in two slightly different extremal orbits for the field H normal to the layer, leading to the beating nodes observed in the dHvA signal. At certain angles θ of the field relative to the normal to the ET planes, only one extremal orbit perpendicular to H remains and, consequently, no beating node appears in the dHvA signal. The careful determination of the angular dependence of these nodes allows a reliable extraction of $t_\perp$ [399].

Although solid proof exists for the coherent motion of electrons in band or Bloch states in β–phase ET salts, such evidence is missing for other organic metals. For example, the magnetization of β''-$(ET)_2SF_5CH_2CF_2SO_3$ shows sawtooth–like dHvA oscillations which follow the behavior expected for a 2D metal with fixed chemical potential almost perfectly (Fig. 8.63(b)) [400]. Furthermore, from the absence of any beating node in dHvA and SdH oscillations, which start at about 1.4 T deep in the superconducting state [401], any possible FS corrugation must be extremely small. Indeed, additional tests for the existence of a 3D FS failed for this material [402], making it a likely candidate for the 2D metal with incoherent interlayer transport envisioned by McKenzie and Moses [397]. Along these lines, deviations from the conventional Bloch–Boltzmann transport theory were observed in the interlayer magnetoresistance, i.e., a field–induced metal–insulator transition was found [403]. In spite of these highly unusual properties which contradict Fermi–liquid theory, the interlayer resistance at $H = 0$ is metallic over the whole investigated temperature range (see Fig. 8.64) and the measured quantum oscillations are consistent with an in–plane Fermi liquid. A possible realization of the FS of β''-$(ET)_2SF_5CH_2CF_2SO_3$ is depicted in the inset of Fig. 8.63(b).

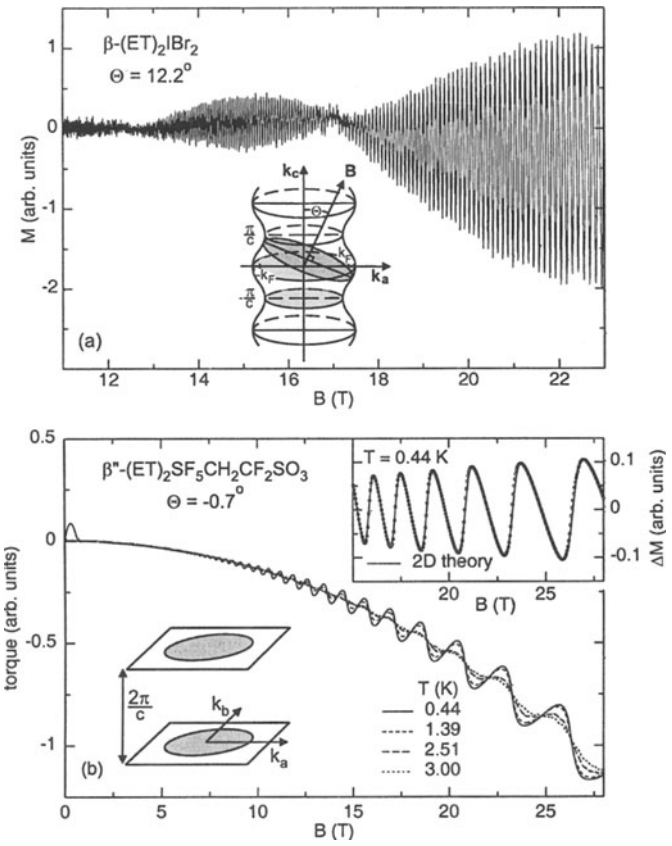

Fig. 8.63. (a) de Haas–van Alphen (dHvA) oscillations in the magnetization of β-$(ET)_2IBr_2$ at $T = 0.4\,K$. The nodes in the signal are caused by the slightly corrugated FS perpendicular to the conducting ET planes. The schematic sketch in the inset greatly exaggerates this corrugation. (b) Torque as a function of magnetic field of β''-$(ET)_2SF_5CH_2CF_2SO_3$. The dHvA signal (open circles in the upper inset) can be described almost perfectly by a 2D theory (solid line in the upper inset). The FS can be regarded as ideally 2D (lower inset)

For some organic superconductors, such as κ-$(ET)_2Cu[N(CN)_2]Br$, the interlayer resistivity increases upon cooling, reaching a maximum before metallic behavior sets in at lower temperature [341, 351]. There were speculations that this might be caused by antiferromagnetic fluctuations, especially since NMR measurements of the spin–lattice relaxation rate $1/T_1$ revealed a maximum in $1/(T_1T)$ close to the temperature where the maximum in R was observed (see also the dashed line in Fig. 8.70 below) [404, 405]. However, the sample dependence of the maximum in $R(T)$ shows that inhomogeneities and impurities have a substantial influence. As presented in Fig. 8.64, metallic

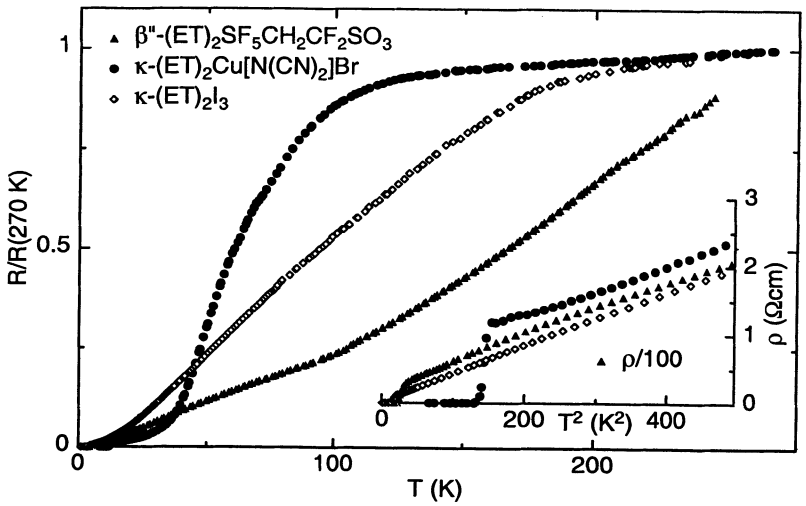

Fig. 8.64. Temperature dependence of the interlayer resistance R, normalized by R at 270 K, for three different organic superconductors. The inset shows the resistivity ρ as a function of T^2. Note that ρ for β''-$(ET)_2SF_5CH_2CF_2SO_3$ has been divided by 100

behavior is found for κ-$(ET)_2Cu[N(CN)_2]Br$ as well as for two other organic superconductors all the way from room temperature down to the lowest T. At high temperature, there is no generic T dependence for the different metals. Towards lower T, however, the interlayer resistivity can fairly well be described by $\rho = \rho_0 + AT^2$ (inset of Fig. 8.64). This T^2 behavior, which is also observed for many other organic metals [341], is usually taken as a sign of a well–behaved Fermi liquid where scattering is dominated by electron–electron interactions. However, although electronic correlations certainly are present in these low–dimensional metals, the wide temperature range over which the T^2 behavior can be found is not typical. Usually, this temperature dependence of ρ can only be observed at very low temperatures. The coefficient A depends on the strength of the electron–electron interaction and is roughly proportional to γ^2, where γ is the Sommerfeld coefficient of the specific heat [173]. As discussed in Section 8.3, for narrow–band systems like heavy–fermion metals, where electronic correlations are undoubtedly much more dominant than for organic metals, $A/\gamma^2 \approx 10^{-5}\ \Omega\,\mathrm{cm(mol\,K/J)^2}$. For transition metals, A/γ^2 is even a factor 100 smaller. Using a Sommerfeld coefficient $\gamma \approx 25\,\mathrm{mJ/mol\,K^2}$ derived from the specific heat of the organic metals (see below), $A \approx 6 \times 10^{-9}\ \Omega\,\mathrm{cm\,K^{-2}}$ would be expected for narrow–band metals. This is 6 to 8 orders of magnitude smaller than is actually observed for the organic metals ($A \approx 4\ \mathrm{m\Omega\,cm\,K^{-2}}$ for the κ–phase salts and about 100 times larger for the β'' salt). When using the in–plane resistivity data,

A is still at least two orders of magnitude larger than expected. Thus, it seems highly questionable to seek the origin of this T^2 behavior of the resistivity solely within the electronic system [406]. Scattering of 2D electrons at phonons might be the relevant mechanism. Interestingly, a number of other novel superconductors, including MgB_2 and the borocarbides, reveal a T^2 dependence as well, hinting at a possible common mechanism.

A further point which should be noted is the extraordinarily high interlayer resistivity ρ of the organic metals. For κ-$(ET)_2Cu[N(CN)_2]Br$, $\rho \approx 1\,\Omega$ cm just above T_c, which is about a factor of 10^6 larger than for lead at T_c. For β''-$(ET)_2SF_5CH_2CF_2SO_3$, ρ is another factor ~ 50 larger. The mean–free path derived from these values of ρ according to the usual transport theory is much smaller than the interatomic distances. This effect becomes even more pronounced towards higher temperatures. Again one has to ask, in analogy to the high–T_c cuprates, whether the interlayer transport can be understood in terms of the usual Fermi–liquid theory.

8.4.3 Superconducting State Properties

The organic superconductors, as well as all other novel superconductors discussed here, are strongly type–II superconductors. The lower critical fields, H_{c1}, of the organic superconductors are only a few mT and the upper critical fields, H_{c2}, are in the tesla range. These fields depend strongly on the direction of the applied field. For H applied within the planes, perpendicular to the least–conducting direction, H_{c2} often exceeds the Pauli paramagnetic limit [16, 246]. As will be discussed below in more detail, this is taken as an indication for triplet pairing in the 1D materials. For the 2D organic superconductors, on the other hand, many–body effects seem to explain the observed moderate H_{c2} enhancement.

Above a certain threshold field H_{irr} within the Shubnikov phase, the magnetic flux can move freely leading to dissipative phenomena and phase diagrams similar to those studied in great detail for the high–T_c materials. In spite of their moderate values of T_c, the layered structure and the high purity of the organic superconductors lead to a large reversible range in the mixed state. In contrast to the high–T_c superconductors, the upper critical fields of the organic superconductors are relatively low and more experimentally accessible. Thus, we can conveniently study the complete superconducting phase diagrams and the rich physics of the vortex phase. Recently, as previously observed in high–T_c cuprates, the first–order vortex–lattice melting transition close to H_{irr} was resolved in two κ–phase ET superconductors by means of sophisticated magnetization experiments [407, 408]. Another common feature observed for the highly anisotropic cuprates and the equally anisotropic ET superconductors is the occurrence of Josephson plasma resonances in magneto–optical experiments [410].

1D organic superconductors

All the known 1D Bechgaard superconductors, except for $(TMTSF)_2ClO_4$,

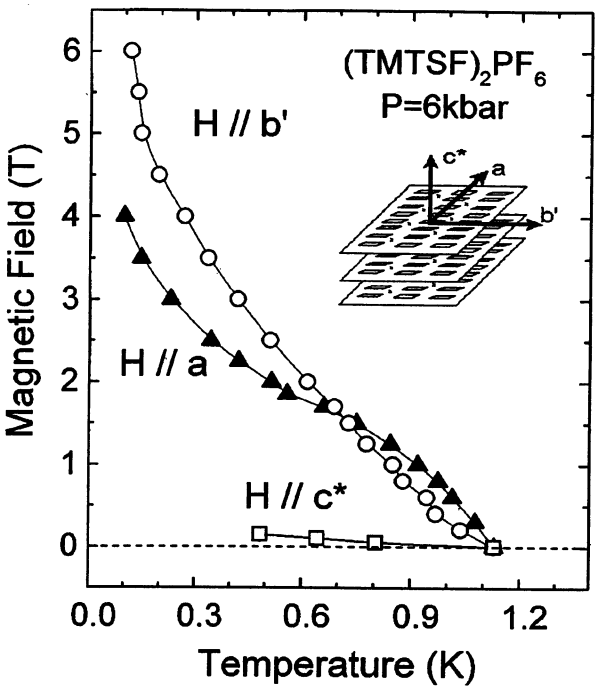

Fig. 8.65. $H-T$ phase diagram of $(TMTSF)_2PF_6$ at an applied pressure of 6 kbar for fields aligned along the a, b', and c^* directions (see inset). The data are extracted from electrical–resistance measurements [388, 389]

need pressure above at least 6 kbar to become superconducting at transition temperatures around 1 K. The amount of pressure needed to suppress the insulating ground state depends on the quality of nesting, i.e., on the electronic energy which can be gained at a Peierls transition. In other words, a certain degree of two–dimensionality is necessary to allow superconductivity to appear. In fact, an almost linear relationship has been observed between the lattice parameter b (see Fig. 8.57) and the critical pressure which suppresses the SDW state and induces superconductivity [411].

A further increase in pressure P results in a rapid decrease of T_c on the order of $dT_c/dP \approx 0.1\,K/kbar$. A decreasing T_c with pressure is a common feature in many conventional superconductors, however, with a much smaller dT_c/dP. This enhanced slope dT_c/dP can be explained by stiffening of the lattice under pressure that results in an increase of the average phonon frequency. This lattice stiffening is expected to be especially strong in soft organic crystals. Since T_c depends sensitively on the phonon frequency, T_c decreases.

For the highly anisotropic organic metals, a correspondingly strong directional dependence of the critical fields is observed. The lowest upper criti-

cal fields are found for H aligned along the c^* direction ($H_{c2} \approx 0.16\,\mathrm{T}$ for $(TMTSF)_2ClO_4$) [341]. For this field orientation, orbital effects, i.e., diamagnetic currents running in the ab' plane, limit H_{c2}. For magnetic fields along b' and a, this orbital limiting is largely suppressed due to the short c^*–axis coherence length. Consequently, in early experiments upper critical fields of ~ 2 and $\sim 2.8\,\mathrm{T}$, respectively, were reported [412]. This result was discussed in light of a possible Pauli–limited H_{c2}, suggesting that the Cooper pairs in the Bechgaard salts are in the singlet state. Neglecting spin–orbit coupling and many–body effects, the Pauli (or Clogston) limit is given by $H_p = (1.85\,\mathrm{T/K})T_c$ [16, 246], i.e., $H_p \approx 2.3\,\mathrm{T}$ for $(TMTSF)_2ClO_4$ with $T_c = 1.25\,\mathrm{K}$.

Since H_{c2} displays a strong anisotropy, an exact alignment of the field with respect to the principal axes, a, b', and c^* is required for its correct determination. Indeed, by carefully aligning H, Lee *et al.* proved impressively that for $(TMTSF)_2PF_6$ under pressure, H_{c2} definitely exceeds the Pauli paramagnetic limit (Fig. 8.65) [388, 389]. This occurs for H oriented along the a direction but even more pronounced for H aligned along the b' direction. For these field orientations, the orbital motion of the charge carriers is greatly suppressed due to the weak interplane transfer. The $H-T$ phase diagram was extracted from electrical–resistance data. The validity of this determination has recently been verified for $(TMTSF)_2ClO_4$ utilizing torque magnetization measurements [413]. The observed strong H_{c2} enhancement triggered the proposal by Lebed of triplet or p–wave pairing occurring in the 1D organic superconductors [414].

In order to provide further evidence for triplet pairing, a joint effort by several different groups tackled the challenging task of performing NMR measurements under pressure at dilution–refrigerator temperatures [415, 416]. The resulting ^{77}Se NMR data revealed no observable change in the Knight shift between the normal metallic and the superconducting state (Fig. 8.66). This provides strong support for triplet pairing since for singlet Cooper pairs with antiparallel spins, the Knight shift, which depends linearly on the electron–spin susceptibility, should drop rapidly below T_c. Indeed, the unchanged Knight shift observed previously for Sr_2RuO_4 [283] is one of the primary pieces of evidence for a triplet state in this superconductor. Stimulated by the experiments for $(TMTSF)_2PF_6$, Lebed suggested a triplet vector order parameter with the spins oriented along the b axis [417]. This proposal fits nicely with the observed features that a magnetic field applied along the b' direction cannot destroy superconductivity. It further predicts a finite energy gap over the whole FS, which is consistent with thermal–conductivity results for $(TMTSF)_2ClO_4$ [418]. In another work, spin–triplet f–wave–like pairing was suggested, which should be in competition with singlet d–wave pairing [419]. It should be noted that previous measurements already showed a strongly enhanced H_{c2} for $(TMTSF)_2AsF_6$ [420]. This and the suppression

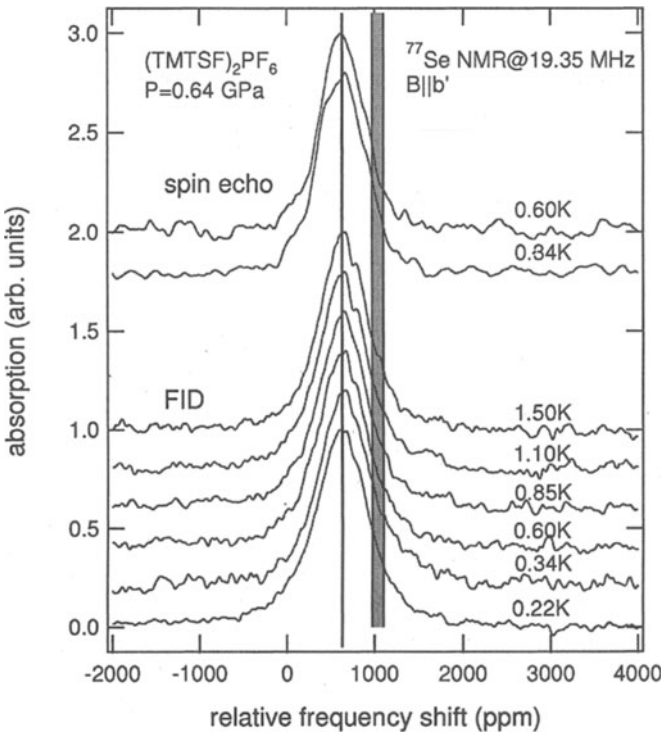

Fig. 8.66. ^{77}Se NMR spectra below and above T_c for $(TMTSF)_2PF_6$ with a magnetic field $H = 2.38\,T$ aligned along the b'–axis. The center of the NMR peak is virtually independent of temperature (solid line), whereas the hashed region marks the expected range where it should occur for a singlet ground state below T_c. [389,415]

of superconductivity by defects and by chemical substitution motivated early suggestions of a possible p–wave symmetry in the 1D organic metals [421,422].

Although the experimental data are consistent with the triplet scenario, other theoretical models have also been proposed. It was shown that even conventional s–wave pairing with an appropriate anisotropic orbital momentum may lead to the critical–field curve shown in Fig. 8.65 [423]. Another possibility is an unconventional d–wave state where the line nodes of the d–wave gap function are assumed to be eliminated by the anion ordering in $(TMTSF)_2ClO_4$ [424]. This would explain the thermal–conductivity data, but neglects the above mentioned Knight–shift results. Nevertheless, NMR Knight–shift data for $(TMTSF)_2ClO_4$ would be highly desirable since they could eliminate the possibility of s– or d–wave superconductivity in this material.

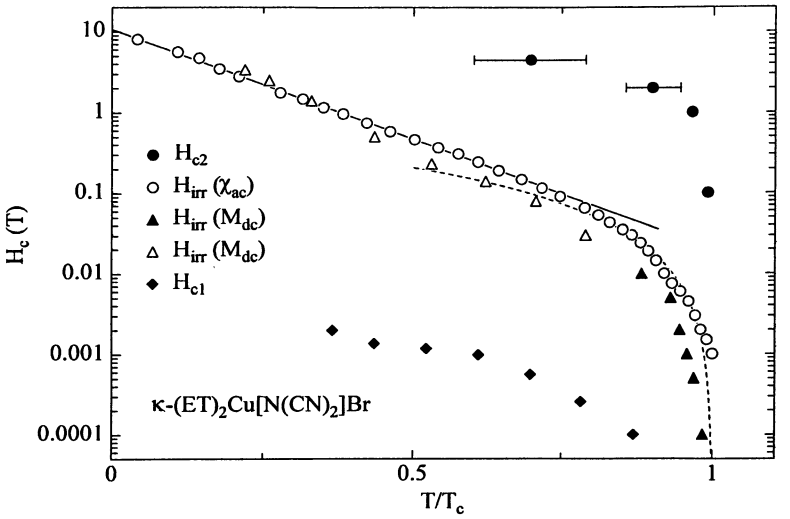

Fig. 8.67. Temperature dependences of H_{c1}, H_{c2}, and of the irreversibility field, H_{irr} of κ-(ET)$_2$Cu[N(CN)$_2$]Br. The data points (•, △) are from [425]. The solid line is an exponential fit, $H_{irr} \propto \exp(-AT/T_c)$, at low T. A $T^{3/2}$ dependence near T_c is denoted by the dashed line

2D organic superconductors

Equally intense and even more controversial is the discussion on the nature of the superconducting state in the 2D organic superconductors. However, before discussing this issue in more detail some principal superconducting properties as well as some high–field peculiarities will be presented.

Superconducting properties

A typical magnetic phase diagram of the 2D organic superconductors is exemplified for κ-(ET)$_2$Cu[N(CN)$_2$]Br in Fig. 8.67. The magnetic field is applied perpendicular to the ET planes. H_{c1} and H_{c2} are obtained from dc–magnetization measurements, M_{dc}, whereas H_{irr} is derived from measurements of ac susceptibility, χ_{ac} [425,426]. The magnetization is broadened considerably in fields due to superconducting fluctuations, and a scaling analysis was performed in order to obtain H_{c2} (Fig. 8.67) [425], in a manner similar to that done for the high–T_c cuprates.

The lower critical field is often extracted from the first deviation from perfect diamagnetism. For the strongly type–II superconductors, like the organic and high–T_c superconductors, however, this may overestimate H_{c1} since above H_{c1}, flux can only penetrate into the sample over a final energy barrier. This leads to magnetic relaxation effects which become increasingly slow close to H_{c1} [351,426]. Since no time–dependence of M is expected to occur in the Meissner state, H_{c1} is defined as the field at which the magnetic relaxation vanishes [426]. The H_{c1} data are depicted in Fig. 8.67.

For κ-$(ET)_2Cu[N(CN)_2]Br$, an upper critical field of $(12 \pm 2)\,T$ and a lower critical field of $(3 \pm 1)\,mT$ for $T = 0$ can be estimated. From these results the thermodynamic critical field $H_c \approx 100\,mT$, the in–plane coherence length $\xi_{\|} \approx 5\,nm$, and the Ginzburg–Landau parameter $\kappa \approx 100$ can be derived. With an average in–plane lattice parameter on the order $d \approx 1\,nm$, $\xi_{\|}/d$ is approximately 5, which is considerably smaller than the value of $\sim 10^3$ typical for pure metals, but comparable to what is found in high–T_c cuprates and other 'exotic' superconductors. The BCS coherence length is given by $\xi_0 = 0.18\hbar v_F/k_B T_c \approx 6.7\,nm$, using an estimate of the Fermi velocity $v_F \approx 5.6 \times 10^4\,m/s$ from dHvA data. With a mean–free path l of 200 to 400 Å, determined from magnetic quantum oscillations, this organic superconductor is just barely in the clean limit with $l/\xi_0 \approx 5$. In this case, one expects $\xi_{\|} = 0.74\xi_0 \approx 5\,nm$ which agrees quite well with the experimental value for $\xi_{\|}$. For fields parallel to the ET layers, H_{c1} is considerably smaller than the earth's field, making it nearly impossible to measure [427]. From the estimated value of H_{c2} at $T = 0$ for in–plane field orientations, an approximate interplane coherence length of $\xi_{\perp} \approx 0.5\,nm$ can be determined, which is much smaller than the layer distance of about 1.6 nm [348]. For other 2D organic superconductors, similar superconducting parameters have been found.

The physics of vortex dynamics in type–II superconductors, extensively studied for the high–T_c cuprates, has also been investigated in detail for the organic metals. Above the threshold field H_{irr} of type–II superconductors, vortices are free to move and, therefore, the magnetization is reversible. Below H_{irr}, the vortices are pinned, resulting in magnetic hysteresis, a diamagnetic ac–susceptibility signal, and a vanishing electrical resistivity. Since the depinning of the vortices is an activated process, slightly different values for H_{irr} are obtained depending on the method used and the criterion applied. Nonetheless, the gross temperature and angular dependences of H_{irr} are largely unaffected by these ambiguities [426, 428]. The H_{irr} data in Fig. 8.67 show a clear crossover at $T/T_c \approx 0.75$, independent of the method used to obtain the data. The same behavior has been observed for another κ–phase organic superconductor as well [428]. A crossover from 3D vortex fluctuations to 2D fluctuations is predicted at a magnetic field $H_{cr} \approx 4\Phi_0/\gamma^2 d^2 \approx 0.08\,T$, where $\Phi_0 = 2.07 \times 10^{-15}\,Tm^2$ is the magnetic–flux quantum, $d \approx 1.6\,nm$ is the interlayer distance, and $\gamma \approx 200$ is the anisotropy parameter estimated from magnetic–torque measurements for κ–phase superconductors [429, 430]. This prediction is in excellent agreement with the experimental value of $H_{cr} \approx 0.05\,T$.

Thermally activated 3D vortices are believed to be responsible for the power–law T dependence of $H_{irr} \propto T^{3/2}$ close to T_c (Fig. 8.67) [431], whereas the low–temperature exponential behavior can be understood by the breakdown of proximity–induced superconductivity (see [426] for details). This suggests that superconductivity is induced in the normal–conducting anion

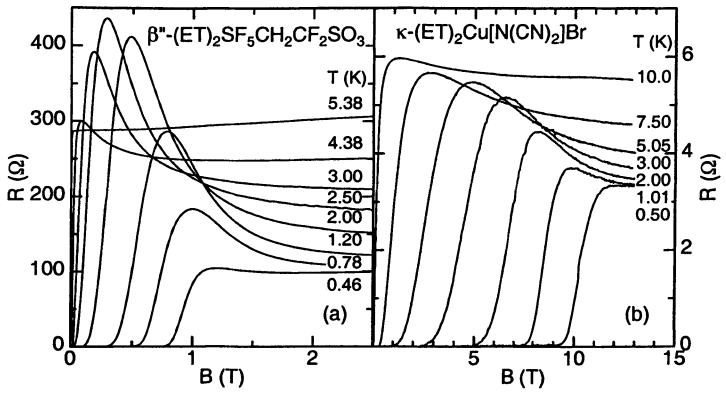

Fig. 8.68. The interlayer magnetoresistance of (a) β''-$(ET)_2SF_5CH_2CF_2SO_3$ and (b) κ-$(ET)_2Cu[N(CN)_2]Br$ for fields applied perpendicular to the ET planes with strong peaks before superconductivity occurs

layers by the superconducting ET layers. Above a certain threshold field H_{irr} for this proximity–induced superconductivity, the superconducting layers are effectively decoupled, and the vortices are weakly pinned 2D objects (pancake vortices). Measurements of the angular dependence of H_{irr} have verified that in the low–T 2D pinning regime, $H_{irr}(\theta)$ exhibits 2D behavior as predicted by Tinkham for $H_{c2}(\theta)$ of 2D films [189, 432]. Close to T_c, the Lawrence–Doniach model [433] for 3D anisotropic superconductors describes the data well [426, 428].

In contrast to most conventional superconductors, the short coherence lengths and large anisotropies in 2D organic superconductors lead to strong thermal fluctuations close to T_c, clearly visible in the electrical resistivity, the diamagnetic signal, and the specific heat. Estimates for the width of the temperature regime where thermal fluctuations are relevant can be made using the Ginzburg criterion, $G = |T - T_c|/T_c \propto (T_c H_c^{-2} \xi_{\|}^{-2} \xi_{\perp}^{-1})^2$. For the ET superconductors with $T_c \sim 10$ K, a value of $G \approx 10^{-2}$ results, which is comparable to values found for high–T_c cuprates where the larger T_c is compensated by the correspondingly larger thermodynamic critical field H_c [347, 348, 351]. For elemental superconductors, G is of the order 10^{-8} due to the much larger coherence lengths. The fluctuation width becomes much broader in applied magnetic fields, an effect visible in resistivity and magnetization data, and it has been studied extensively in both organic and high–T_c superconductors [341, 348].

One peculiar feature of the 2D organic superconductors is the occurrence of pronounced peaks in the interlayer resistance R close to the superconducting phase boundary (Fig. 8.68), which is believed to be caused by thermal fluctuations. With decreasing field, a peak in R is observed before superconductivity sets in. This peak is observed over a range of temperatures up

to T_c. Although a number of models have been suggested (see [347, 351] for an overview), a feasible explanation is based on the fluctuation–induced decrease of the normal density of states at the Fermi level. Combined with the other conductivity contributions caused by fluctuations (Aslamazov–Larkin and Maki–Thompson contributions), the observed behavior can be qualitatively reproduced taking into account the high anisotropy of the superconductors [347,434,435]. Nevertheless, the origin of this peak effect in the resistance measurements is still not well understood.

Measurements of the physical properties of 2D organic superconductors in high magnetic fields reveal a number of intriguing features. For the organic superconductor κ-$(ET)_2Cu(NCS)_2$, measurements using a tuned–circuit differential susceptometer revealed a change in the vortex rigidity at in–plane magnetic fields of about 22 T [436]. This has been suggested to indicate the onset of a Fulde–Ferrell–Larkin–Ovchinnikov (FFLO) state. This FFLO state is predicted to evolve at high magnetic fields when an attractive interaction between the Zeeman–split spin–up and spin–down quasiparticles leads to pairs with non–zero total momentum [224, 269]. 2D organic superconductors are good candidates for this scenario when the magnetic field is applied in plane, which prevents the appearance of orbital pair–breaking effects. However, besides the vortex–matter change reported in Ref. [436], no clear experimental evidence for the FFLO scenario exists.

A second fascinating aspect of the high–field work on organic superconductors is the observation of field–induced dissipation–less diamagnetic currents in the organic metal α-$(ET)_2KHg(SCN)_4$ [437,438]. This material is now believed to be in a CDW state at low temperatures (below 8 K) and fields below about 23 T [439, 440]; the material stays metallic with only a partial nesting of the 1D FS sheets. Early experimental data were interpreted in favor of a SDW state (see Ref. [361] for details). At higher fields above 23 T, when the Zeeman splitting deteriorates the nesting condition for the spin–up and spin–down bands, a spatially modulated incommensurate so–called CDW_x state is believed to evolve (analogous to the FFLO state for superconductors) [441]. It is within this high–field, low–temperature state that properties resembling a superconducting vortex state appear. More precisely, a field–induced diamagnetic signal [438] and hysteresis loops comparable to the irreversible region of the Shubnikov phase are observed [437, 439, 442]. Although Fröhlich superconductivity has been suggested [353], further justification of this proposal is absent. Recently, Harrison has suggested that the coexistence of the CDW with a strongly field–dependent orbital magnetization, caused by the Landau quantization of the 2D FS, may lead to nonequilibrium persistent currents [443]. This effect might explain the hysteresis loops observed in α-$(ET)_2KHg(SCN)_4$. In any case, the new and interesting physics of this field–induced phase deserves further research.

Finally, magnetic field induced superconductivity (MFIS) has been found between 18 and 41 T in λ-$(BETS)_2FeCl_4$ [444, 445]. At first glance, the evo-

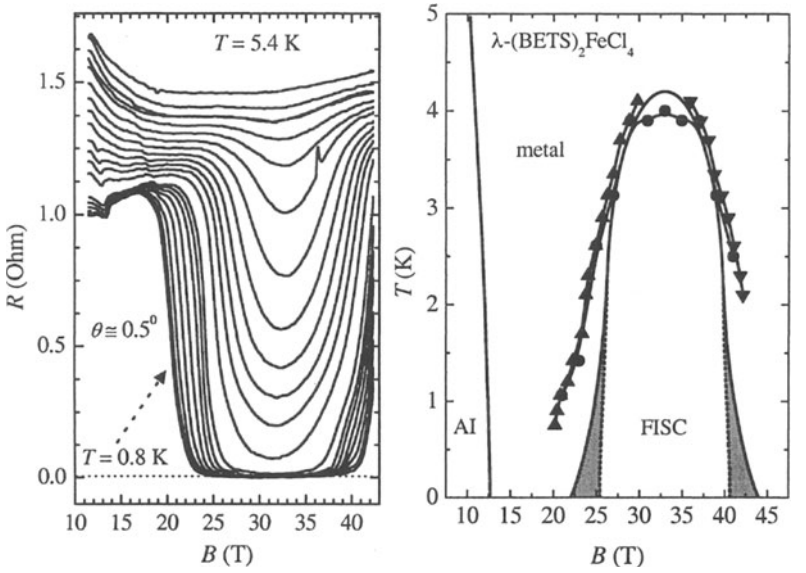

Fig. 8.69. Left panel: in–plane field dependence of the resistance R of λ-$(BETS)_2FeCl_4$ for different temperatures from 0.8 to 5.4 K. Right panel: the $H-T$ phase diagram indicates that after the suppression of an antiferromagnetic insulating (AI) low–field state with magnetic field, field–induced superconductivity (FISC), referred to in the text as magnetic field induced superconductivity (MFIS), is observed between about 18 to 41 T [445]

lution of a superconducting state in a magnetic field is surprising since the magnetic field usually destroys superconductivity. In the first experiment in magnetic fields up to 20 T [444], the increase of T_c with field led to speculations about unconventional pairing interactions caused by magnetic fluctuations via the Fe moments. In another experiment in fields up to 42 T, however, a more complete superconducting phase diagram evolved as shown in Fig. 8.69 [445]. At the lowest temperature (about 0.8 K), the resistance drops to zero at an in–plane field of about 18 T and becomes finite again at a field of about 41 T. The superconducting phase could be resolved up to about 4 K. It was also shown that only the in–plane field component is relevant for the occurrence of superconductivity.

One possible explanation for the MFIS observed in λ-$(BETS)_2FeCl_4$ is the Jaccarino–Peter field–compensation effect [4], as mentioned in [444]. In this scenario the applied magnetic field aligns the $S = 5/2$ Fe^{3+} moments, which impress an exchange field $\mathcal{J}\langle S\rangle$ on the spins s of the conduction electrons via the exchange interaction $\mathcal{J}\boldsymbol{S}\cdot\boldsymbol{s}$, as described in Section 8.2. For $\mathcal{J} < 0$, the applied magnetic field becomes compensated by the exchange field and may reach values less than the Pauli paramagnetic limit, thereby allowing the field–induced superconducting state to occur. One of the most striking

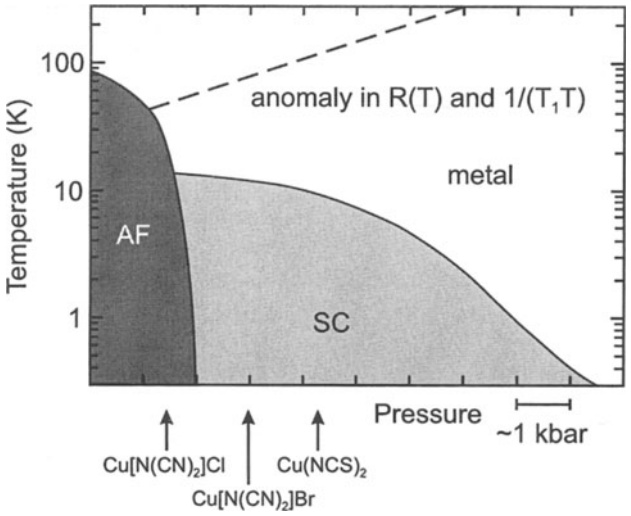

Fig. 8.70. Schematic $P-T$ phase diagram for the κ-$(ET)_2X$ salts depicting regions of antiferromagnetic insulator behavior (AFM) and superconductivity (SC). The arrows indicate starting points for the different materials at ambient pressure

examples of the Jaccarino–Peter effect, is provided by the Chevrel–phase superconductor $Eu_xSn_{1-x}Mo_6S_8$ containing small quantities of Br or Se [102]. In this case, superconductivity with $T_c \approx 3.9\,K$ is first destroyed at about 1 T and then restored above about 4 T but only below 1 K. In λ-$(BETS)_2FeCl_4$, the antiferromagnetic state has to be suppressed in high magnetic fields before the superconducting state can evolve out of a paramagnetic state.

The nature of the superconducting state

For the 2D organic superconductors, the controversial experimental situation still prevents a definite conclusion as to whether conventional BCS or unconventional superconductivity exists. It is generally believed that the Cooper pairs are in a singlet spin state. Evidence for a superconducting ground state with singlet spin pairing includes a vanishing spin susceptibility detected by NMR experiments [446–448] and the value of the paramagnetic–limited upper critical field [449]. For the latter analysis, however, the above mentioned weak–coupling estimate is not appropriate, since many–body effects have to be taken into account. An elegant determination of the Pauli limit has been performed by Zuo *et al.* using known thermodynamic quantities such as the superconducting condensation energy from specific heat data and the Pauli spin susceptibility and is taken as further evidence for a singlet ground state [450].

One motivation for suggesting an unconventional order parameter, i.e., of singlet d–wave symmetry, is the nature of the $P-T$ phase diagram of the κ–phase superconductors first proposed in Ref. [451] (Fig. 8.70). Next

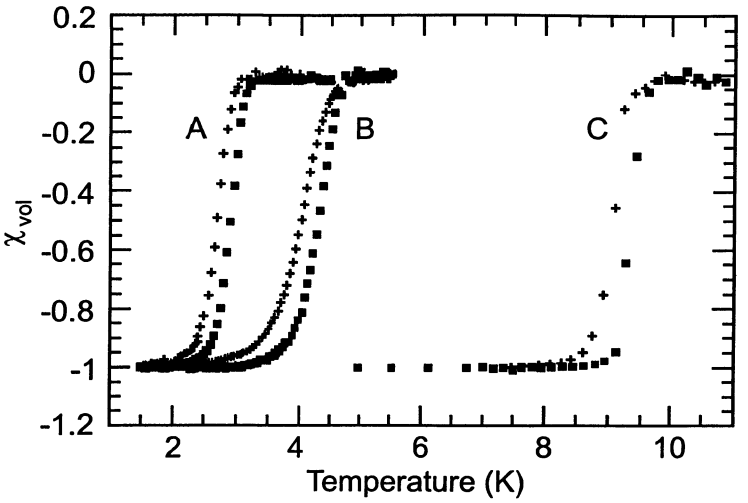

Fig. 8.71. Representative superconducting transition curves measured by ac susceptibility for (A) κ_L-$(ET)_2Ag(CF_3)_4$, (B) β''-$(ET)_2SF_5CH_2CF_2SO_3$, and (C) κ-$(ET)_2Cu(NCS)_2$. Plus symbols are for hydrogenated, filled squares for deuterated samples [458]

to the superconducting state an antiferromagnetic insulating state exists, similar to that observed for the 1D Bechgaard salts and reminiscent of the phase diagram of many high-T_c materials. However, there is only one κ–phase material known that displays an antiferromagnetic insulating state at ambient pressure that can be suppressed by pressure. For κ-$(ET)_2Cu[N(CN)_2]Cl$, a pressure of 300 bar is sufficient to induce superconductivity at a record T_c of about 12.8 K (Fig. 8.70) [344]. A further increase in the hydrostatic pressure rapidly suppresses the superconducting ground state. In fact, the compound κ-$(ET)_2Cu(NCS)_2$ displays the largest pressure dependence of T_c yet observed for any superconductor, $\Delta T_c/\Delta p \approx -3\,\mathrm{K/kbar}$ [452]. Thermal-expansion measurements revealed that T_c is most sensitive to uniaxial pressure perpendicular to the planes [453, 454] indicating that, at least for the κ phase, an enlargement of the anion–layer thickness might increase T_c even further. However, as evidenced by the $P-T$ phase diagram, the κ–phase materials containing large anions reside close to an insulating state, which is proposed to be a Mott–Hubbard insulating state driven by the small bandwidth and a large Coulomb interaction [349, 350, 455–457].

A key experiment that provided evidence for the electron–phonon interaction as the pairing interaction in the early superconductors was the detection of an isotope effect, i.e., the increase of T_c proportional to $m^{-1/2}$ as predicted by BCS theory. For the organics, m is some average molecular mass. At first sight, a somewhat confusing picture exists for the 2D organic superconductors. Substitution of all eight hydrogens in the ET ethylene end groups by

deuterium causes an enhancement of T_c by about 0.3 K for three different organic superconductors (Fig. 8.71) [458]. This effect is not only inverse to what is expected but, in addition, the size of the T_c shift is much larger than would be explicable by a simple molecular–mass change. Apparently, the interaction between the outer parts of the ET molecules and the anions plays a crucial role in the pairing strength. This interaction is expected to be rather sensitive to uniaxial pressure perpendicular to the planes. As mentioned, this was indeed confirmed by thermal–expansion measurements which extracted an initial reduction of T_c by 6 K/kbar for β''-$(ET)_2SF_5CH_2$-CF_2SO_3 and κ-$(ET)_2Cu(NCS)_2$ [454]. With this result in mind, the inverse isotope effect can be understood by the smaller zero–point displacement of the carbon–deuterium bonds compared to the lighter hydrogen–deuterium bonds. This results in a reduced internal lattice pressure and, consequently, in an increased T_c for the deuterated samples [458].

In order to avoid any changes of the anion–hydrogen interaction, experiments were carried out on samples in which only central atoms of the ET molecules were exchanged. Substitution of four ^{12}C atoms by ^{13}C and all eight ^{32}S atoms by ^{34}S resulted in a reduction of T_c of about 1% [459]. This agrees well with the BCS expectation and provides strong support for a Cooper–pair coupling which is at least partially mediated by phonons. Additional support for this scenario comes from Raman data which showed a clear hardening of the Raman modes below T_c for κ-$(ET)_2Cu[N(CN)_2]Br$ [460] and from inelastic neutron–scattering experiments [461]. In the latter measurement a significant shift of a phonon branch was observed below T_c, an effect hardly seen this clearly in any other superconductor. Consequently, there are a number of experiments indicating an electron–phonon mechanism for superconductivity in organic superconductors, whereas the argument for a pairing mechanism mediated by antiferromagnetic fluctuations is largely based on the $P - T$ phase diagram (Fig. 8.70).

Apart from the coupling mechanism in the organic superconductors, the symmetry of the order parameter is a highly controversial issue. The experimental situation appears to be rather inconclusive and only some aspects shall be presented. For further discussion of this topic see Refs. [347,348,351–353].

One quantity which should reflect the symmetry of the order parameter is the magnetic penetration depth, $\lambda(T)$. For a conventional BCS s–wave gap, λ should exhibit an exponential temperature dependence, whereas for a superconducting gap with nodes a power–law T dependence is expected. The serious experimental problems in determining λ reliably are illustrated in Fig. 8.72. In Fig. 8.72(a) the magnetic penetration depth is determined by dc–magnetization measurements [462]; whereas, in Fig. 8.72(b) the same quantity is extracted utilizing a tunnel–diode–oscillator technique [463]. In the former experiment by Lang *et al.*, the magnetization data can be very well described by the conventional weak–coupling BCS theory as shown by

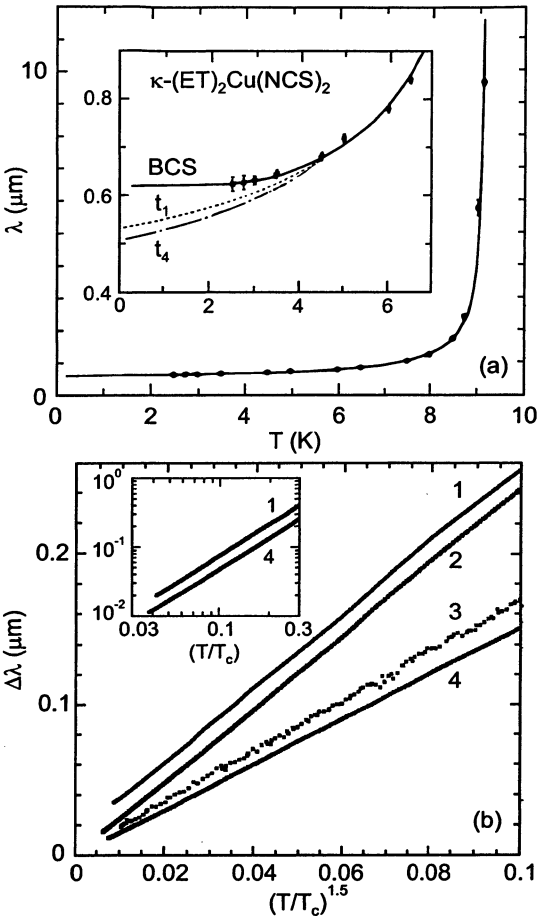

Fig. 8.72. Temperature dependences of the in–plane penetration depths extracted from (a) dc–magnetization measurements [462] and (b) by use of a high–frequency tunnel–diode–oscillator technique [463]. The inset in (a) shows the low–T data in an enlarged scale together with model curves for BCS (solid line) and for two triplet states, t_1 and t_4 (broken curves). The data in (b) are for two samples of κ-$(ET)_2Cu[N(CN)_2]Br$ (1,2) and two samples of κ-$(ET)_2Cu(NCS)_2$ (3,4)

the solid line in Fig. 8.72(a). The broken lines represent model curves for two earlier suggested triplet states. In the high–resolution data of Carrington *et al.* [463], a $T^{3/2}$ variation of λ is found, in contrast to the BCS results of Lang *et al.* as well as other groups, and, in addition, different from the T^2 behavior previously reported by others. This inconclusive picture prevails in a number of other experiments utilizing different techniques which report either BCS or unconventional behavior of λ (see [347,348,351–353] for more details).

The temperature dependence of the spin–lattice relaxation rate, $1/T_1$, from NMR measurements is often used to obtain information about nodes in the superconducting energy gap. Usually, an increase of $1/T_1$ just below T_c is expected, known as the Hebel–Slichter coherence peak (see Fig. 8.74). Although the occurrence of this peak is an important proof of BCS superconductivity, its absence cannot disprove conventional superconductivity as evidenced by the missing peak for the BCS superconductors Nb and V. At low temperatures, $1/T_1$ is predicted to vanish exponentially for a fully–gapped superconductor, and display a power–law T dependence when the superconducting energy gap goes to zero at points or lines on the Fermi surface (see Fig. 8.74).

Early proton–NMR experiments received particular attention when reporting an unexpected enhancement of $1/T_1$ by about a factor of 10 at $\sim T_c/2$ as seen in Fig. 8.73(a) [464,465]. Similar results were reported for many other organic superconductors and caused considerable confusion at the time. This feature was only understood a number of years later when an NMR measurement of the angular–dependence of $1/T_1$ [466] showed that the strong enhancement of $1/T_1$ below T_c vanishes when the magnetic field is aligned within the ET planes (Fig. 8.73(b)). Below T_c, $1/T_1$ exhibits a sharp dip in a narrow angular region about 4° wide around this field orientation ($\theta = 90°$). It is therefore clear that this effect is connected with the flux–line vortex dynamics in the Shubnikov state. In the reversible region, the flux lines are free to move which results in a rapidly changing magnetic field at the hydrogen sites and, consequently, causes the strongly enhanced relaxation rate. However, when the magnetic field lies within the ET planes the flux lines prefer to stay within the poorly conducting anion layers, which results from a well–known phenomenon called intrinsic pinning. For this field orientation, the magnetic field at the hydrogen sites remains approximately constant and $1/T_1$ approaches the expected intrinsic value. In the organic metals, the hydrogen nucleus has a relatively weak coupling to the conduction electrons residing in the spatially distant ET layers. Therefore, the relaxation due to the moving flux lines easily dominates. This is in contrast to the situation for the cuprate superconductors, where very large relaxation rates due to the conduction electrons occur that mask the flux–line effect.

After realizing this important additional relaxation channel, NMR experiments were performed with the magnetic field aligned within the ET layers and, in addition, the ^{13}C nuclei were chosen as a local probe since they are located in the center of the ET molecules, closer to the itinerant–electron system. Three groups almost simultaneously reported comparable results [446–448], two of which are shown schematically in Fig. 8.74. There are several marked differences between the experimental results and the behavior for a BCS superconductor (shown as a solid line) [467]. First, the coherence peak just below T_c is absent (although this is not conclusive evidence for unconventional superconductivity, as mentioned above). Second,

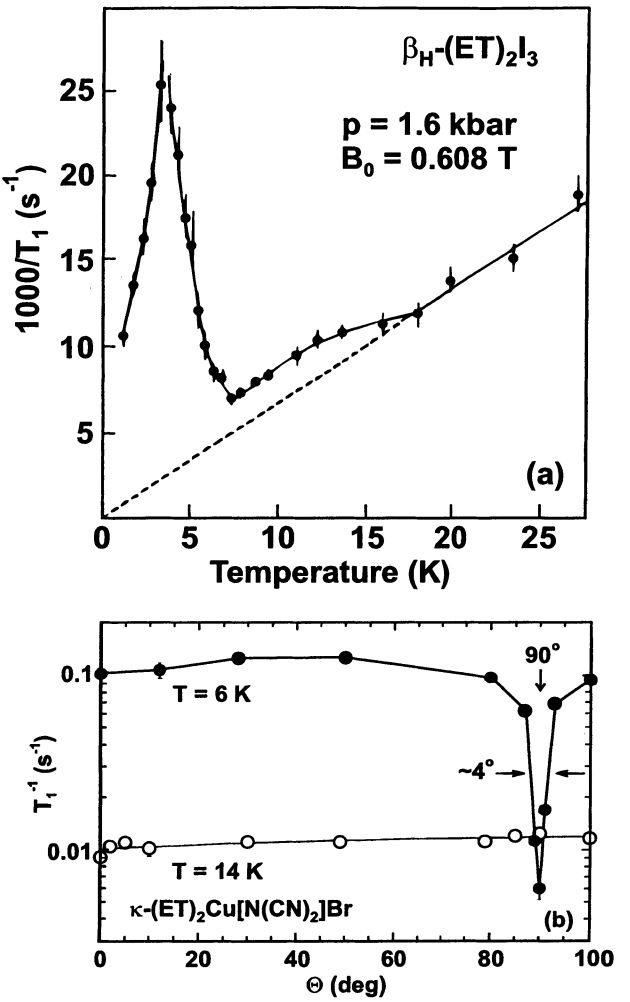

Fig. 8.73. Proton NMR spin–lattice relaxation rates T_1^{-1}: (a) Temperature dependence of $1000/T_1$ for β_H-$(ET)_2I_3$ ($T_c \approx 8\,K$) [464,465]. (b) Angular dependence of $1/T_1$ for κ-$(ET)_2Cu[N(CN)_2]Br$ ($T_c \approx 11.5\,K$) above and below T_c [466]

$1/T_1$ follows a T^3 dependence that provides strong evidence for a node–like structure of the energy gap. The rapid decrease of $1/T_1$ just below T_c suggests a very fast gap opening, i.e., much faster than is realized for a conventional superconductor. One should bear in mind, however, that all of the NMR experiments were performed in an applied magnetic field, which might influence the gap structure even if the vortex dynamics can be neglected.

In light of the controversial issue of the symmetry of the superconducting gap in the 2D organic superconductors, all of the above measurements as well

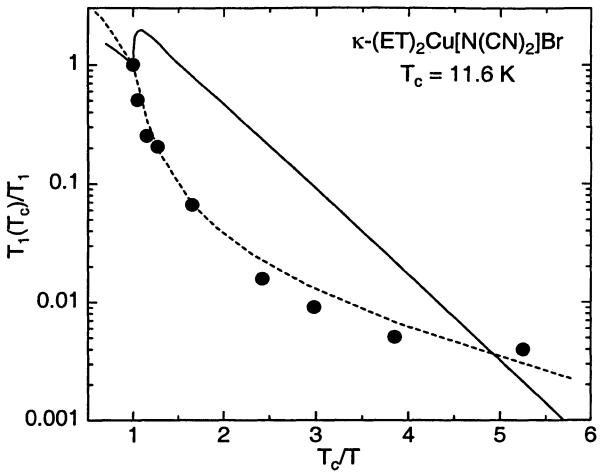

Fig. 8.74. Temperature dependence of the normalized spin–lattice relaxation rate. The solid line depicts the behavior for the weak–coupling BCS superconductor aluminum [467]. Data from ^{13}C NMR for κ-$(ET)_2Cu[N(CN)_2]Br$ in fields parallel to the conducting ET planes are shown as closed circles [446] and dashed line [447]. There is no Hebel–Slichter peak and the relaxation rate decreases as T^3 rather then exponentially

as the specific heat measurements discussed below provide no information about the detailed node topology. Therefore, the recent attempts to measure the possible anisotropy of the order parameter directly received particular attention. The first report of gap nodes in κ-$(ET)_2Cu(NCS)_2$ [468] was argued to be a misinterpretation of the millimeter–wave magneto–optical data [469]. In other work, scanning–tunnelling spectroscopy (STM) was utilized to measure the in–plane anisotropy of the superconducting gap [471]. The STM tip was placed on various as–grown or in–air prepared surfaces perpendicular to the interlayer direction. Strongly anisotropic current–voltage spectra were recorded, which were interpreted as being consistent with *d*–wave pairing. In line with this result, thermal–conductivity measurements in applied magnetic fields revealed a fourfold symmetry of the electronic contribution to the thermal conductivity [472]. Both of these experiments determined that the node directions are rotated by 45° with respect to the in–plane crystal axes of κ-$(ET)_2Cu(NCS)_2$. However, one should keep in mind that both experiments can only manifest an asymmetry of their signals but cannot verify real zero points of the energy gap. Furthermore, STM investigations are naturally extremely sensitive to surface states and should, therefore, be performed on well–characterized surfaces. Finally, the thermal conductivity due to quasiparticle excitation had to be measured in an applied magnetic field leading to similar difficulties as mentioned for the NMR experiments above.

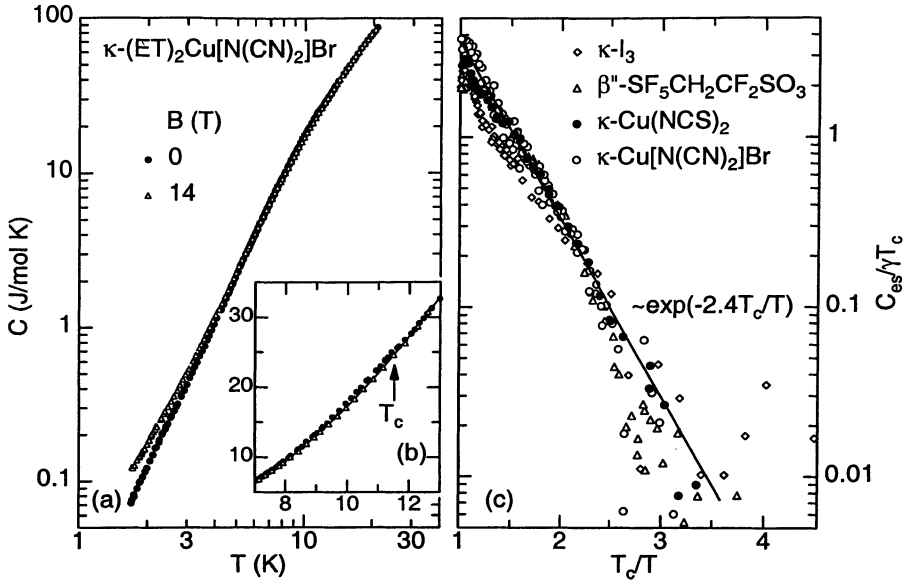

Fig. 8.75. (a) Specific heat of κ-$(ET)_2Cu[N(CN)_2]Br$ in the superconducting ($H = 0$) and normal ($H = 14\,T$) state. (b) The anomaly at $T_c = 11.5\,K$ is weakly visible in the inset. (c) Normalized plot of the electronic contribution to the specific heat C_{es} in the superconducting state divided by γT_c as a function of T_c/T. The solid line shows the exponential vanishing of C_{es} towards low T (fit to the data of κ-$(ET)_2Cu(NCS)_2$)

The proposed zero–field nodes of the superconducting gap should result in power–law temperature dependences of the thermal conductivity and the specific heat and finite values at $T = 0$. Indeed, in one thermal–conductivity study a small residual linear contribution was reported [473]; however, it is questionable whether the chosen extrapolation from above $\sim 0.18\,K$ towards low temperatures, assuming a linear electronic and cubic phonon contribution, is justified or not. Recent thermal–conductivity measurements showed that the phonon–scattering length down to lowest temperatures ($T = 0.25\,K$) is strongly influenced by quasiparticle scattering preventing the evolution of the T^3 dependence expected for sample–boundary scattering of phonons [474]. Therefore, further studies are needed to clarify this issue.

Specific heat, C, is a powerful technique for determining whether the superconducting energy gap goes to zero at nodes on the Fermi surface. If the quasiparticle contribution to the specific heat, C_{es}, vanishes with an exponential temperature dependence in the superconducting state, nodes in the energy gap can be ruled out unequivocally. On the other hand, a power–law in T dependence of C_{es} indicates that line or point nodes may be present. However, a power–law dependence in the specific heat needs to be checked

carefully since any extrinsic effect such as a partially normal–conducting sample or an improper subtraction of the non–electronic contributions to C can obscure the exponential temperature dependence and lead to incorrect conclusions.

Measurements of $C(H,T)$ for κ-$(ET)_2Cu[N(CN)_2]Br$ [475] are shown in Fig. 8.75(a) on a double–logarithmic scale. The electronic contribution to C is rather small, only about 1% at $T_c = 11.5\,K$. Therefore, the specific heat anomaly at T_c can only be resolved in a high–resolution experiment (see the enlargement of the data in Fig. 8.75(b)). In a magnetic field of 14 T applied perpendicular to the planes, the sample is in the normal state. Therefore, the data at $H = 14\,T$ comprises the phonon contribution and the normal–state electronic specific heat γT, where the Sommerfeld coefficient $\gamma \approx 25\,mJ/mol\,K^2$. Consequently, C_{es} can be extracted by subtracting the phonon contribution from the C data in $H = 0$. As evidenced in the normalized plot of Fig. 8.75(c), C_{es} vanishes exponentially for κ-$(ET)_2Cu[N(CN)_2]Br$ [475] as well as for three other organic superconductors [474, 476, 477]. These results are in agreement with recent reports by other groups [478, 479]. In fact, all recent specific heat measurements agree on the existence of a complete energy gap in 2D organic superconductors at $H = 0$. However, the $C(H,T)$ measurements are not sensitive to a particular direction in k–space and therefore cannot resolve any possible anisotropy of the superconducting gap.

An analysis of the specific heat jump at T_c yields an interesting trend (Fig. 8.76). For the four superconductors shown, with values of T_c between 3.4 K and 11.5 K, the specific heat jump at T_c is always larger than the weak–coupling value $\Delta C/\gamma T_c = 1.43$ and increases monotonically with increasing T_c [352,475]. This provides direct evidence for an increasing coupling strength with T_c. The dashed lines in Fig. 8.76 represent the weak–coupling ΔC dependence [480], while the solid lines describe strong–coupling behavior; a BCS–like T dependence of the energy gap $\Delta(T)$ scaled by an appropriate parameter has been assumed [481]. Reasonable descriptions of the experimental data are achieved for the gap ratios $\alpha = \Delta(0)/k_B T_c$ given in Fig. 8.76, where $\alpha = 1.76$ in the weak–coupling limit. The coupling strengths λ can be estimated [475] using phenomenological models, yielding values ranging from ~ 0.8 for κ-$(ET)_2I_3$ ($T_c = 3.4\,K$) to 2.5 for κ-$(ET)_2Cu[N(CN)_2]Br$ ($T_c = 11.5\,K$). The large values of λ are in rough agreement with the mass renormalizations extracted from magnetic quantum oscillations [361, 396].

8.4.4 Concluding Remarks

The organic metals and superconductors show a rich variety of novel ground states and cover a broad spectrum of tunable fundamental physical phenomena that are of current interest. One of the most studied, but still very controversial, issues is the nature of the superconductivity. For the 1D Bechgaard salts, a number of recent experiments indicate a triplet superconducting

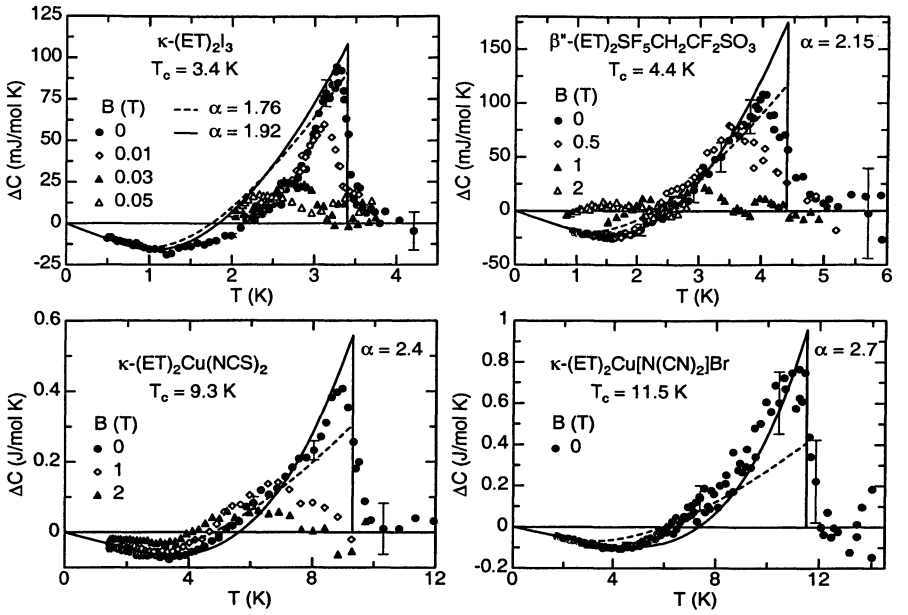

Fig. 8.76. Specific heat in the superconducting state minus the specific heat in the normal state for four different organic superconductors with values of T_c between 3.4 K and 11.5 K. The lines show the predicted BCS behavior for weak coupling (dashed lines, $\alpha = 1.76$) and for strong coupling characterized by various values of the parameter α (solid lines)

state. For the 2D organic superconductors, the experimental situation is unsettled. NMR and thermal–conductivity experiments suggest that the superconducting order parameter is unconventional, whereas the measurements of the specific heat indicate a nodeless gap. In an attempt to solve this puzzling situation, it was suggested that an *s*–wave to *d*–wave gap–symmetry transition could be induced by an in–plane magnetic field [482]. In this theoretical treatment, phonon–mediated superconductivity with a small wavevector was assumed, which could explain such a transition. Although this proposal would resolve the controversial NMR and specific heat results, other predictions of this theory such as the orientation of the *d*–wave gap nodes are at odds with recent experimental results [472]. Further studies, especially experiments that directly probe the phase difference of the superconducting wave function, are highly desirable.

8.5 Layered Cuprate and Ruthenate Superconductors

8.5.1 Introduction

The discovery of superconductivity at $\sim$ 30 K in the La–Ba–Cu–O system by Bednorz and Müller in 1986 ignited a worldwide explosion of research on high temperature superconductivity that still persists after more than one and a half decades. The impetus behind this extraordinary episode in the history of science has been driven by two objectives: the development of a fundamental understanding of high temperature superconductivity and the wide spread use of high temperature superconductors in technological applications. Although an enormous amount of progress has been made on these challenging problems since 1986, many obstacles remain to be overcome before these two objectives can be achieved.

In this Section, we give an overview of the current knowledge and understanding of the fundamental aspects of high T_c superconductivity in cuprates. We begin with a brief introduction to the layered perovskite–like cuprate materials that have been studied the most extensively as well as the structurally related ruthenocuprate magnetic superconductors and the compound Sr_2RuO_4, the leading candidate for p–wave superconductivity. The rest of this section is devoted to a brief survey of the extraordinary superconducting and normal state physical properties of the high T_c cuprate superconductors and a discussion of some of the concepts and notions that have been advanced to account for these properties. Specific topics discussed include: materials, structure and charge carrier doping, superconducting state properties (critical field and current densities, superconducting pairing mechanism, doping dependence of T_c, symmetry of the superconducting order parameter), and normal state properties (non–Fermi liquid behavior, normal ground state, pseudogap, electronic inhomogeneity) and the generic phase diagram. The enormous scope of this subject dictated a very selective choice of the examples cited to illustrate the progress made in this field since its inception in 1986. For comprehensive accounts of specific topics in high T_c superconductivity, the reader is referred to various review articles, such as those that appear in the volumes edited by Ginsberg [483] and by Gschneidner, Eyring and Maple [484]. The materials that are emphasized in this section include the hole–doped superconductors $La_{2-x}M_xCuO_4$ (M = Ba, Sr, Ca, Na), $RBa_2Cu_3O_{7-\delta}$ (R = Y or Ln), $Y_{1-x}Pr_xBa_2Cu_3O_{7-\delta}$, $Bi_2Sr_2CaCu_2O_{8+\delta}$, and the electron-doped superconductors $Ln_{2-x}M_xCuO_{4-y}$ (Ln = Pr, Nd, Sm, Eu; M = Ce, Th).

8.5.2 The Materials

Since 1986, dramatic increases of T_c have been achieved in the layered perovskite–like cuprate superconductors, as illustrated in the plot of the maximum value of T_c vs date in Fig. 8.77. Prior to 1986, the record for the highest value

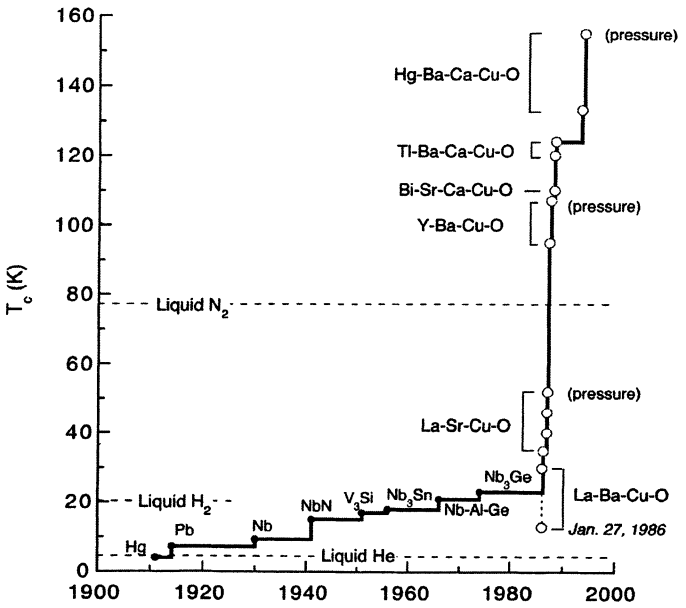

Fig. 8.77. Maximum superconducting critical temperature T_c vs data (Ref. [490])

of T_c ($\sim$ 23 K) was held by the A15 compound Nb_3Ge [485]. Currently, the maximum value of T_c at atmospheric pressure is $\sim$ 133 K for the compound $HgBa_2Ca_2CuO_8$ [486, 487]. When this compound is subjected to high pressures of $\sim$ 30 GPa, the T_c onset increases to $\sim$ 164 K (more than halfway to room temperature!) [488, 489].

The first superconducting oxide system found with T_c values exceeding the 23 K record value held by Nb_3Ge was $La_{2-x}Ba_xCuO_4$, which has a maximum value of T_c of $\sim$ 30 K for $x \approx 0.15$ [491, 492]. Shortly thereafter, $La_{2-x}M_xCuO_4$ systems with M = Sr, Ca, and Na were synthesized that exhibited superconductivity with maximum values of T_c of $\sim$ 40 K for M = Sr [493], $\sim$ 20 K for M = Ca [494], and $\sim$ 20 K for M = Na [495, 496].

The first superconductors with values of T_c exceeding the boiling point of liquid nitrogen (77 K) belong to the $RBa_2Cu_3O_{7-\delta}$ family. Superconductivity was reported to occur for R = Y [497] and all of the lanthanides except Ce and Tb (which do not form the phase) and Pr (which forms the phase, but is insulating and thereby not superconducting) with T_c values that range from $\sim$ 92 K for R = Y to $\sim$ 95 K for R = Nd [498]. Superconductivity at $\sim$ 90 K in the lanthanide analogues of $YBa_2Cu_3O_{7-\delta}$ was discovered independently in laboratories at several institutions throughout the world. (See, for example, Ref. [498] and references cited therein.) Surprisingly, superconductivity with $T_c \sim 85$ K has been reported in $PrBa_2Cu_3O_x$ samples prepared by the traveling floating zone method [499]. However, these materials show large inho-

mogeneity in both lattice parameters and transport and magnetic properties. In the parts of the sample that exhibit bulk superconductivity, the c–axis lattice constant is reported to be larger than that of the nonsuperconducting ceramic polycrystalline or single crystal samples prepared by standard methods. The pressure dependence of T_c of the $PrBa_2Cu_3O_x$ samples is quite large and comparable to values observed in underdoped cuprates. Further research on this fascinating material is clearly warranted, although to date the superconductivity reported for $PrBa_2Cu_3O_x$ has not been confirmed. These results illustrate the complexity of these materials and how sensitive their properties are to the conditions of their growth.

Like most high T_c cuprates, the $La_{2-x}M_xCuO_4$ and $RBa_2Cu_3O_{7-\delta}$ compounds are hole–doped superconductors. The first system of electron–doped cuprate superconductors discovered was $Ln_{2-x}M_xCuO_{4-y}$ (Ln = Pr, Nd, Sm, Eu; M = Ce, Th; $x \sim 0.1 - 0.18; y \approx 0.02$) {(Ln = Pr, Nd, Sm; M = Ce) [500]; (Ln = Nd; M = Th) [501]; (Ln = Pr, Sm; M = Th) [502]; (Ln = Eu; M = Ce) [503].} The highest values of T_c found among the electron–doped superconductors are ~ 25 K.

There has been considerable interest in systems of the type $R_{1-x}Pr_xBa_2Cu_3O_{7-\delta}$, especially for R = Y [245]. This was initially inspired by the puzzling observation that $PrBa_2Cu_3O_{7-\delta}$, when prepared by standard methods, is insulating and nonsuperconducting, whereas the other $RBa_2Cu_3O_{7-\delta}$ compounds that can be formed are metallic and superconducting with values of $T_c \sim 92 - 95$ K, as noted above. The $Y_{1-x}Pr_xBa_2Cu_3O_{7-\delta}$ system is replete with extraordinary physical phenomena including a metal–insulator transition at $x_{cr} \approx 0.55$, a monotonic depression of T_c with x that vanishes near x_{cr} in the metallic phase, a striking crossover in the pressure dependence of T_c from positive to negative with increasing x, a large γT contribution to the low temperature specific heat that is reminiscent of heavy fermion behavior, and Cu^{2+} and Pr^{n+} antiferromagnetic (AFM) ordering in the insulating phase with $T_N(Cu^{2+}) > T_N(Pr^{n+})$, where T_N is the Néel temperature. It has been suggested that these and other peculiar properties of this system are related to hybridization between the Pr localized $4f$ states and the valence band states associated with the conducting CuO_2 planes [504]. A theoretical model that involves the hybridization between the $4f$ states of Pr and the $2p$ states of neighboring oxygen atoms in the $Y_{1-x}Pr_xBa_2Cu_3O_{7-\delta}$ system has, in fact, been developed by Fehrenbacher and Rice [505]. Similar phenomena are found in the related $Y_{1-x}Pr_xBa_2Cu_4O_8$ system which has also been extensively investigated [506]. The striking behavior of the $Y_{1-x}Pr_xBa_2Cu_3O_{7-\delta}$ system is discussed throughout this Section.

In several of the compounds containing R layers, the R ions with partially–filled $4f$ electron shells and magnetic moments have been found to order antiferromagnetically at low temperature [498, 507]. Specific heat data for $RBa_2Cu_3O_{7-\delta}$ with R = Nd, Sm, Gd, Er and Dy that exhibit AFM ordering

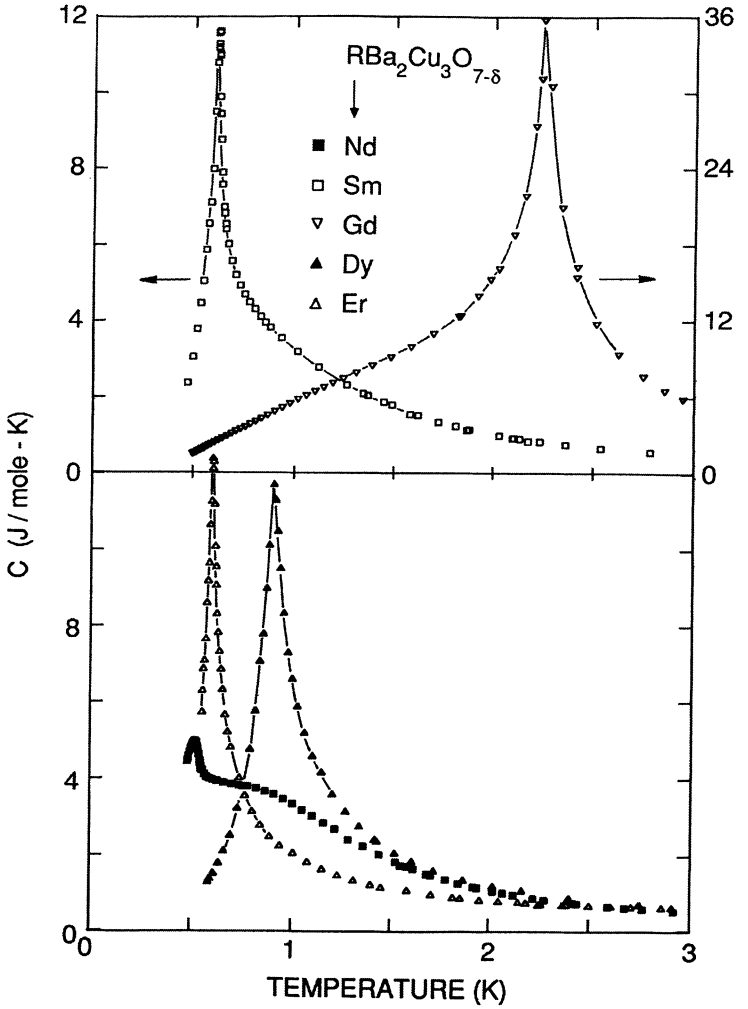

Fig. 8.78. Specific heat C vs temperature between 0.5 K and 3 K for $RBa_2Cu_3O_{7-\delta}$ compounds with R = Nd, Sm, Gd, Dy, and Er, after Ref. [507]

of the R ions at low temperatures reveal pronounced peaks near the Néel temperature T_N as shown in Fig. 8.78 [507].

Several compounds containing CuO_2 and RuO_2 planes have been fabricated in which superconductivity and ferromagnetism, apparently confined to the CuO_2 and RuO_2 planes, respectively, have been reported to coexist with one another microscopically. Examples of these materials include $R_{1.4}Ce_{0.6}RuSr_2Cu_2O_{10-\delta}$ ($T_c \sim 42$ K, Curie temperature $\theta_c \sim 180$ K for R = Gd; $T_c \sim 32$ K, $\theta_c \sim 122$ K for R = Eu) [508] and $GdRuSr_2Cu_2O_8$ ($T_c \sim 46$

K, $\theta_c \sim 132$ K) [509,510]. Magnetic order in the compound $GdRuSr_2Cu_2O_8$ has been studied by means of neutron diffraction measurements by Lynn *et al.* [511]. The Ru magnetic moments order antiferromagnetically at $T_N = 136$ K, coincident with the previously reported onset of ferromagnetism. Neighboring spins are antiparallel in all three directions, with a low temperature moment of 1.18 μ_B along the *c*–axis. These measurements place an upper limit of ~ 0.1 μ_B to any net zero field moment, with fields exceeding 0.4 tesla needed to induce a measureable magnetization. The Gd ions order independently at $T_N = 2.5$ K with the same spin configuration. The value $T_N = 136$ K for AFM ordering of the Ru ions is by far the highest known Néel temperature for antiferromagnetic ordering that coexists with superconductivity. In addition to these rare earth and actinide based cuprates, many other high T_c cuprates have been discovered, a number of which also contain rare earth elements.

The superconducting compound Sr_2RuO_4 has the same crystal structure as the $La_{2-x}M_xCuO_4$ (M = Ba, Sr, Ca, Na) high T_c cuprate superconductors [516]. While the T_c of Sr_2RuO_4 is only $\sim$ 1 K, this compound is of considerable interest because it is the only layered perovskite–like superconductor without Cu and it appears to be a leading candidate for *p*–wave superconductivity. The anisotropy of the superconducting properties of Sr_2RuO_4 is very large ($\gamma = \xi_{ab}/\xi_c \approx 26$), where ξ is the superconducting coherence length. Although this anisotropy is larger than that of $La_{2-x}M_xCuO_4$, the in–plane and c–axis resistivities of Sr_2RuO_4 vary as T^2 at low temperature, indicative of Fermi liquid behavior. Based on similarities to ^{3}He and the existence of closely related oxides such as $SrRuO_3$ that are ferromagnetic, it was suggested [517,518] that Sr_2RuO_4 may exhibit *p*–wave ($L = 1$) spin–triplet superconductivity. In contrast, the cuprate superconductors are generally derived by doping the CuO_2 planes of antiferromagnetic parent compounds by means of chemical substitutions, apparently resulting in superconductivity with spin–singlet pairing in a *d*–wave ($L = 2$) channel.

There is a considerable amount of evidence for unconventional superconductivity in Sr_2RuO_4 [514,515,519]. ^{17}O NMR Knight shift [283] and spin polarized neutron scattering [512] measurements provide the principal evidence for spin–triplet pairing of superconducting electrons in Sr_2RuO_4. These measurements reveal that there is no reduction of the conduction electron spin susceptibility $\chi_s(T)$ in the superconducting state relative to that $\chi_n(T)$ in the normal state. For singlet spin pairing, $\chi_s(T)$ should vanish at low temperatures $T \ll T_c$. Although spin orbit scattering can increase $\chi_s(T)$ for spin–singlet pairing, it is not expected to be strong enough in Sr_2RuO_4 to increase $\chi_s(T)$ to $\chi_n(T)$ [515]. The behavior of $\chi_s(T)$ for the *s*–wave superconductor V_3Si and the unconventional superconductor Sr_2RuO_4, based on spin polarized neutron scattering measurements of Duffy *et al.* [512], are shown in Fig. 8.79. Other evidence for unconventional superconductivity in Sr_2RuO_4 is the extreme sensitivity of the superconductivity to nonmagnetic

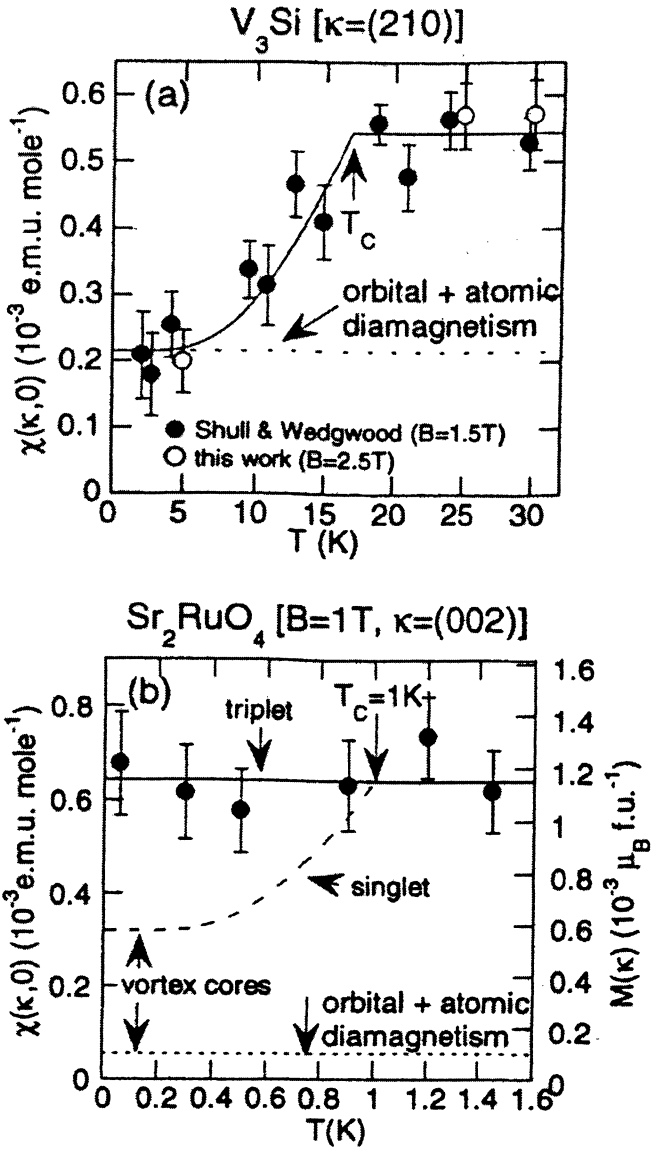

Fig. 8.79. Conduction electron spin susceptibility in the superconducting state χ_s for an s–wave superconductor (V_3Si) and Sr_2RuO_4, based on spin polarized neutron scattering measurements [512]. In (a), the original work of Shull and Wedgewood [513] is confirmed and the data are described well by the Yosida function. In (b), the temperature independence of χ_x for Sr_2RuO_4 is in marked contrast to that expected if Sr_2RuO_4 had singlet pairing, after Ref. [514]

Fig. 8.80. Spin triplet superconducting states corresponding to $\mathbf{d}(\mathbf{k}) = \hat{\mathbf{z}}(k_x + ik_y)$ (left) and $\mathbf{d}(\mathbf{k}) = \hat{\mathbf{x}}k_x + \hat{\mathbf{y}}k_y$ (right). The $\hat{\mathbf{z}}(k_x + ik_y)$ state has an angular momentum along the z–axis (thick arrow) and spins perpendicular in the plane (thin arrows). The $\hat{\mathbf{x}}k_x + \hat{\mathbf{y}}k_y$ state has vanishing total angular momentum because the orbital angular momentum is compensated by the spins of the Cooper pair. Experiments indicate that the superconducting phase in Sr_2RuO_4 is of the type shown in the left panel; i.e., a state with finite angular momentum, after Ref. [515]

impurities; T_c vanishes for Al or Si impurity concentrations corresponding to a mean free path that is comparable to the superconducting coherence length. One of the most intriguing results comes from μSR measurements on Sr_2RuO_4 that reveal an enhancement in the zero field relaxation rate in the superconducting state that is consistent with a superconducting state with broken time reversal symmetry [284]. A variety of experiments indicate that the superconducting energy gap has nodes or very deep minima, although thee form of these nodes is still uncertain.

The spin–triplet superconducting state that seems to be favored by experiments on Sr_2RuO_4 has the form $\mathbf{d}(\mathbf{k}) = \hat{\mathbf{z}}(k_x + ik_y)$. This state and another spin–triplet state are schematically represented in Fig. 8.80 [515]. The $\hat{\mathbf{z}}(k_x + ik_y)$ state has angular momentum along the z–axis (thick arrow) and spins perpendicular in the plane (thin arrows), while the $\hat{\mathbf{x}}k_x + \hat{\mathbf{y}}k_y$ state has vanishing total angular momentum because the orbital angular momentum is compensated by the spins of the Cooper pair [515]. A comprehensive review of the normal and superconducting state properties of Sr_2RuO_4 and the physics of spin–triplet pairing can be found is Ref. [514].

Quantum spin ladder materials have attracted much interest [520, 521]. These materials consist of ladders made of AFM chains of $S = 1/2$ spins coupled by inter–chain AFM bonds. Examples of 2–leg ladder materials are $SrCu_2O_3$ and $LaCuO_{2.5}$; an example of a 3–leg ladder material is $Sr_2Cu_2O_5$. Superconductivity has been discovered in the ladder material $Sr_{0.4}Ca_{13.6}Cu_{24}O_{41.84}$ under pressure with $T_c \approx 12$ K at 3 GPa [522]. Interest in quantum spin ladder materials is partly due to the fact that they are simple model systems for theories of superconductivity based on magnetic pairing mechanisms.

Approximately 100 different cuprate materials, many of which are superconducting, have been discovered since 1986. Several of the more important high T_c cuprate superconductors are listed in Table 8.7, along with the maximum values of T_c observed in each class of materials. Included in the table are examples of abbreviated designations (nicknames) for specific cuprate

Table 8.7. (a) Some important classes of cuprate superconductors and the maximum value of T_c observed in each class. (b) Examples of the abbreviated names (nicknames) used to denote cuprate materials

(a)	
Material	Max. T_c (K)
$La_{2-x}M_xCuO_4$; M = Ba, Sr, Ca, Na	~ 40
$Ln_{2-x}M_xCuO_{4-y}$; Ln = Pr, Nd, Sm, Eu; M = Ce,Th	~ 25
$YBa_2Cu_3O_{7-\delta}$	92
$LnBa_2Cu_3O_{7-\delta}$	~ 95
Ce, Tb do not form phase.	
Pr forms phase; neither metallic nor superconducting.	
$RBa_2Cu_4O_8$	~ 80
$Bi_2Sr_2Ca_{n-1}Cu_nO_{2n+4}$ (n = 1,2,3,4)	(n = 3) 110
$TlBa_2Ca_{n-1}Cu_nO_{2n+3}$ (n = 1,2,3,4)	(n = 4) 122
$Tl_2Ba_2Ca_{n-1}Cu_nO_{2n+4}$ (n = 1,2,3,4)	(n = 3) 122
$HgBa_2Ca_{n-1}Cu_nO_{2n+2}$ (n = 1,2,3,4)	(n = 3) 133

(b)	
Material	Nickname
$YBa_2Cu_3O_{7-\delta}$	YBCO; YBCO–123; Y–123
$Bi_2Sr_2Ca_2Cu_3O_{10}$	BSCCO; BSCCO–2223; Bi–2223
$Tl_2Ba_2Ca_2Cu_3O_{10}$	TBCCO; TBCCO–2223; Tl–2223
$HgBa_2Ca_2Cu_3O_8$	HBCCO; HBCCO–1223; Hg–1223
$La_{1.85}Sr_{0.15}CuO_4$	LSCO
$Nd_{1.85}Ce_{0.15}CuO_{4-y}$	NCCO

materials which we will use throughout this article (e.g., $YBa_2Cu_3O_{7-\delta}$ = YBCO, YBCO-123, Y-123).

It is interesting to note that superconductivity with values of T_c in the neighborhood of 30–40 K has been found in several noncuprate materials: the cubic perovskite $Ba_{1-x}K_xBiO_3$ ($T_c \approx 30$ K) [523,524], the fcc "buckeyball" compound Rb_3C_{60} ($T_c \approx 29$ K) [525,526], and the compound MgB_2 ($T_c \approx 39$ K) [527].

8.5.3 Structure and Charge Carrier Doping

The high T_c cuprate superconductors have layered perovskite–like crystal structures which consist of conducting CuO_2 planes separated by layers comprised of other elements, denoted as A, and oxygen, A_mO_n, and, in some cases, layers of Ln ions [528, 529]. The mobile charge carriers, which can be electrons but are usually holes, are generally believed to reside primarily within the CuO_2 planes. The A_mO_n layers apparently function as charge reservoirs that control the doping of the CuO_2 planes with charge carriers and as spacers that govern the anisotropy of the physical properties of the materials.

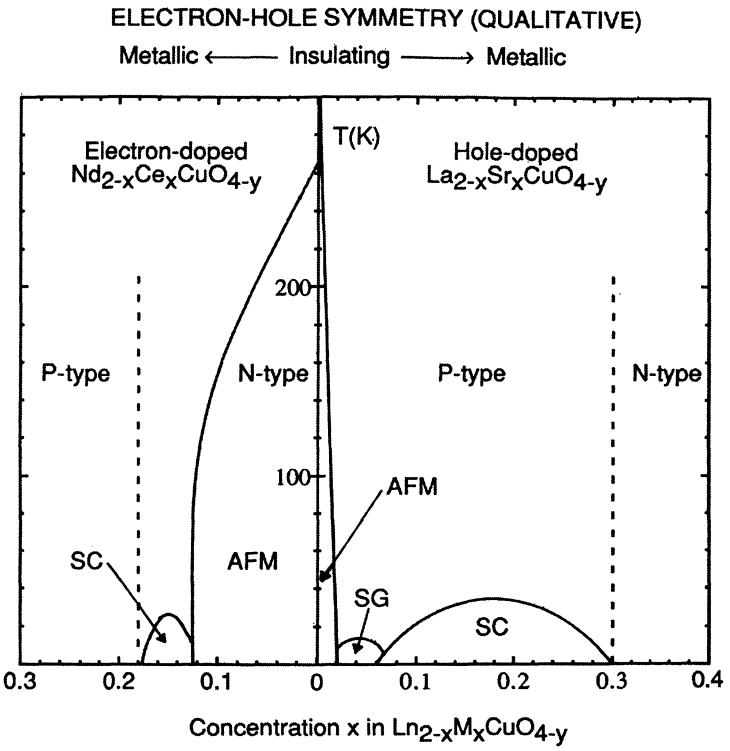

Fig. 8.81. Temperature–dopant concentration ($T - x$) phase diagram delineating the regions of superconductivity and antiferromagnetic ordering of the Cu^{2+} ions for the hole–doped $La_{2-x}Sr_xCuO_4$ and electron–doped $Nd_{2-x}Ce_xCuO_{4-y}$ systems. AFM = antiferromagnetic phase, SG = spin–glass phase, and SC = superconducting phase, after Ref. [530]

Many of the cuprates can be doped with charge carriers and rendered superconducting by substituting appropriate elements into an AFM insulating parent compound. For example, substitution of divalent Sr for trivalent La in the AFM insulator La_2CuO_4 dopes the CuO_2 planes with mobile holes and produces superconductivity in $La_{2-x}Sr_xCuO_4$ with a maximum T_c of ~ 40 K at $x \approx 0.17$ [493]. Similarly, substitution of tetravalent Ce for trivalent Nd in the AFM insulating compound Nd_2CuO_4 apparently dopes the CuO_2 planes with electrons, resulting in superconductivity in $Nd_{2-x}Ce_xCuO_{4-y}$ with a maximum T_c of ~ 25 K at $x \approx 0.15$ for $y \approx 0.02$ [500, 530]. The temperature T vs x phase diagrams for the $La_{2-x}Sr_xCuO_4$ and $Nd_{2-x}Ce_xCuO_{4-y}$ systems are shown in Fig. 8.81 [530].

The $Ln_{2-x}M_xCuO_{4-y}$ electron–doped materials have a tetragonal crystal structure that is similar to that of the $La_{2-x}M_xCuO_4$ hole–doped materials, but without the apical oxygen atoms. The crystal structures of the

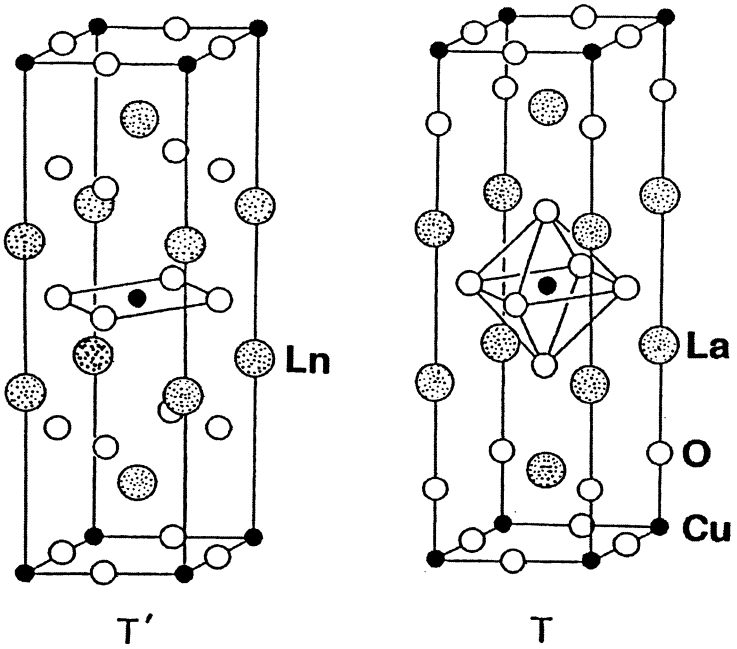

Fig. 8.82. Crystal structures of La_2CuO_4 (T–phase) and Ln_2CuO_4 (Ln = Pr, Nd, Sm, Eu, Gd; T′–phase) parent compounds, after Ref. [530]

La_2CuO_4 and Nd_2CuO_4 parent compounds are displayed in Fig. 8.82 [530]. The $La_{2-x}Sr_xCuO_4$ and $Nd_{2-x}Ce_xCuO_{4-y}$ systems have one CuO_2 plane per unit cell and are referred to as single CuO_2 layer compounds. Other superconducting cuprate systems have more than one CuO_2 plane per unit cell: $LnBa_2Cu_3O_{7-\delta}$ has two CuO_2 planes per unit cell (double CuO_2 layer compound), while $Bi_2Sr_2Ca_{n-1}Cu_nO_x$ has n CuO_2 layers per unit cell (n CuO_2 layer compound) and can be synthesized by conventional methods for $n = 1, 2$, or 3.

8.5.4 Superconducting Properties

Critical field and critical current density

With values of T_c in excess of the boiling temperature of liquid nitrogen (77 K) for some compounds, the high T_c cuprates were immediately recognized as promising candidates for technological applications of superconductivity, since they can be cooled into the superconducting state using liquid nitrogen, closed cycle refrigerators, and other more economical refrigeration techniques. Cuprates such as the $RBa_2Cu_3O_{7-\delta}$ compounds (T_c in the range 92 – 95 K) have enormous critical fields $\sim 10^2$ tesla [498, 531] that are more than adequate for most high–current and high–field technological applications. Shown

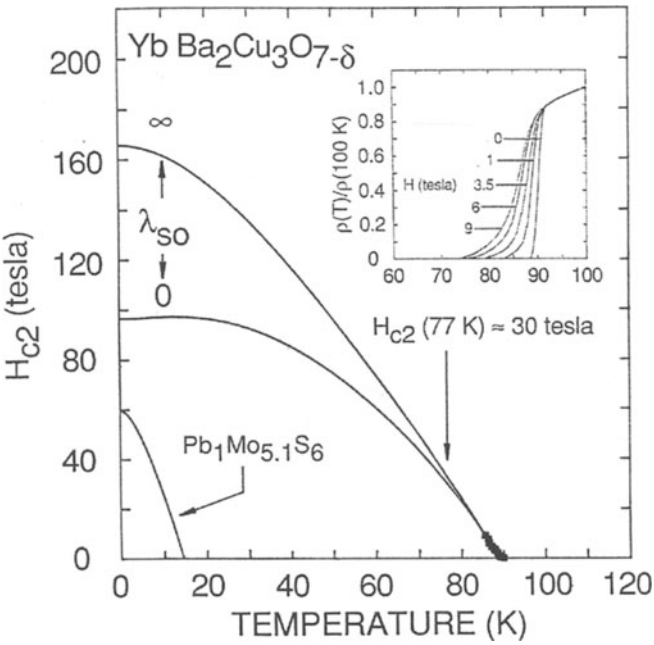

Fig. 8.83. Upper critical field H_{c2} vs temperature for the compound $YbBa_2Cu_3O_{7-\delta}$. The solid lines are based on standard WHH [18] theory for a conventional type II superconductor in the limits of maximum (spin–orbit scattering parameter $\lambda_{so} = 0$) and minimum ($\lambda_{so} = \infty$) paramagnetic limitation and have been fitted to the data near T_c. Inset: Normalized electrical resistivity vs temperature in several magnetic fields between 0 and 9 tesla, after Ref. [501]

in Fig. 8.83 is the resistively determined upper critical field $H_{c2}(T)$ curve for the compound $YbBa_2Cu_3O_{7-\delta}$. Extrapolation of the $H_{c2}(T)$ curves measured between 0 and ~ 10 T to $T = 0$ K, using the theory developed by Werthamer, Helfand, and Hohenberg (WHH) in 1966 without paramagnetic limiting [18], yields a value of $H_{c2}(0) \approx 160$ T [498].

Epitaxially grown thin films of $YBa_2Cu_3O_{7-\delta}$ on single crystal $SrTiO_3$ substrates have critical current densities $J_c \approx 10^6$ A/cm^2 in zero field that decrease relatively slowly with magnetic field, making them suitable for technological applications [532]. Techniques have been devised that yield values of J_c in high fields for in–plane grain oriented thin films of $YBa_2Cu_3O_{7-\delta}$ on flexible substrates at 64 K (pumped liquid nitrogen temperatures) that exceed those of NbTi and Nb_3Sn at liquid helium temperatures [533]. Presently, two of the leading candidates for technological applications of superconductivity are the $RBa_2Cu_3O_{7-\delta}$ and $Bi_2Sr_2Ca_{n-1}Cu_nO_{2n+4}$ ($n = 2,3$) materials. The first generation superconducting tapes and wires are based on both substi-

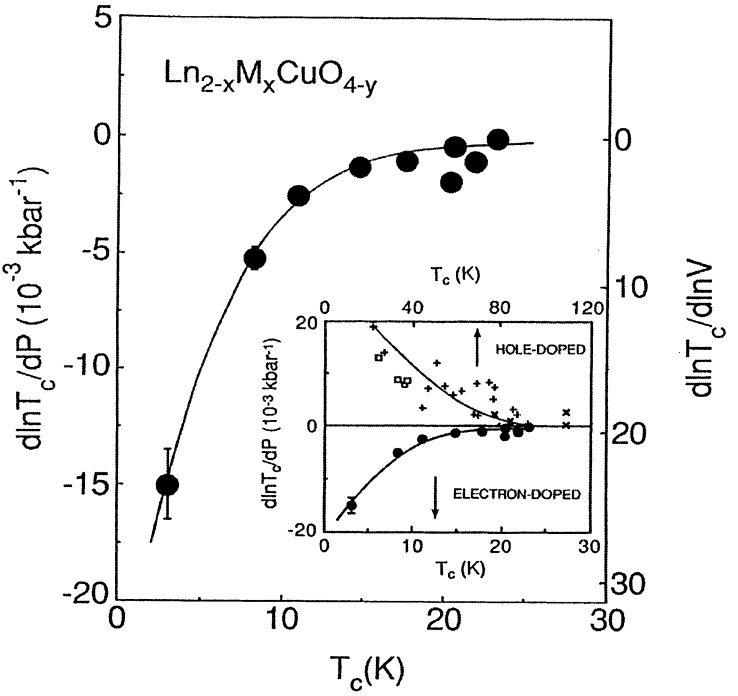

Fig. 8.84. Relative rate of change of T_c with applied pressure P, $\mathrm{d}\ln T_c/\mathrm{d}P$, as a function of T_c for the electron–doped superconductors $Ln_{2-x}M_xCuO_{4-y}$ (Ln = Pr, Nd, Sm, Eu; M = Ce, Th; $x \approx 0.15$; $y \approx 0.03$). Inset: Same data plotted together with similar data for hole–doped superconductors from Ref. [535]. (□: La–based "214"; +: R–based "123"; x: Bi–Sr– and Tl–Ba–Ca–Cu–O materials), after Ref. [536]

tuted and unsubstituted $Bi_2Sr_2Ca_{n-1}Cu_nO_{2n+4}$ (n = 2,3) superconductors prepared by the powder–in–tube technique [534].

Superconducting pairing mechanism

Two features in the $T-x$ phase diagrams for $La_{2-x}Sr_xCuO_4$ and $Nd_{2-x}Ce_xCuO_{4-y}$ in Fig. 8.81 would appear to be relevant to cuprate superconductivity: (i) the electron–hole phase–diagram may provide a constraint on viable theories of high T_c superconductivity in cuprates, and (ii) the proximity of antiferromagnetism suggests that superconducting electron pairing in the cuprates may be mediated by AFM spin fluctuations. An AFM pairing mechanism is consistent with the occurrence of d–wave pairing with $d_{x^2-y^2}$ symmetry that is suggested by experiments on several hole–doped cuprates (discussed later in this article). Several theoretical models (for example, [537, 538]), based on AFM spin fluctuations, have predicted d–wave superconductivity with $d_{x^2-y^2}$ symmetry for the cuprates. In contrast to the apparent electron–hole symmetry in the $T-x$ phase diagrams of hole– and

electron–doped cuprates, there appears to be an interesting electron–hole "antisymmetry" in the pressure dependence of T_c. This is illustrated in Fig. 8.84 which contains a plot of the relative change of T_c with applied pressure, $d\ln T_c/dP$, vs T_c for the electron–doped superconductors and a comparison of these data with similar data for various hole–doped cuprate superconductors [536].

Other features are consistent with non–phonon–mediated pairing in the hole–doped cuprates. The curve of T_c vs carrier concentration can be approximated by an inverted parabola with the maximum value of T_c occurring at an optimal dopant concentration x_0 [539]. (Note that the terminology "under–doped" refers to values of x smaller than the "optimally–doped" value x_0 where T_c is maximized, whereas "over–doped" refers to values of x larger than x_0.) The isotope effect on T_c for optimally–doped material is essentially zero (i.e., $T_c \propto M^{-\alpha}$ with $\alpha \approx 0$; M = ion mass) [540].

An interesting example of the inverted parabolic dependence of T_c on carrier concentration is provided by the $Y_{1-x-y}Ca_yPr_xBa_2Cu_3O_{7-\delta}$ system. In this system, the Ca^{2+} and Pr ions that are substituted for Y^{3+} in $YBa_2Cu_3O_{7-\delta}$ have the effect of "counter–doping" the CuO_2 planes with holes and electrons, respectively. Assuming that each substituted Ca^{2+} ion generates one hole in the CuO_2 planes, analysis of the $T_c(x, y)$ data in terms of a phenomenological model described below indicates that each substituted Pr ion localizes approximately one hole in the CuO_2 planes [542] (see below). The localization of holes is also reflected in the behavior of T_c as a function of Pr concentration x in the $Y_{1-x}Pr_xBa_2Cu_3O_{7-\delta}$ system ($y = 0$). Here, T_c decreases with increasing x as the $Y_{1-x}Pr_xBa_2Cu_3O_{7-\delta}$ system becomes more under–doped and vanishes near the onset of the metal–insulator transition at $x_{mi} \approx 0.55$. The $T - x$ phase diagram for the $Y_{1-x}Pr_xBa_2Cu_3O_{7-\delta}$ system is displayed in Fig. 8.85(b) which shows the behavior of $T_c(x)$ as well as the Néel temperatures $T_N(x)$ for AFM ordering of Cu and Pr magnetic moments [504, 541]. It has been argued that the depression of T_c with x is primarily due to the decrease in the number of mobile holes with increasing Pr concentration, although magnetic pair breaking by Pr may also be involved [541,542] (see below). Shown in Fig. 8.86 (a) are plots of T_c vs Ca concentration y for four Pr concentrations x in the $Y_{1-x-y}Ca_yPr_xBa_2Cu_3O_{7-\delta}$ system [542]. Curves formed by solid and dashed lines represent the equation

$$\begin{aligned} T_c(x, y) &= T_{c0} - A(a - bx + y)^2 - Bx \\ &= T_c(97\text{ K}) - (425\text{ K})(0.1 - 0.95x + y)^2 - (96.5\text{ K})x. \end{aligned} \tag{8.28}$$

The first term is the maximum attainable value of $T_c(97\text{ K})$, the second term represents the effect of hole generation by Ca (y) ions and localization of holes by Pr (x) ions (0.1 is an optimal hole concentration), while the last term describes the overall depression of T_c with x due to pair breaking interactions in the linear low concentration regime. These data illustrate the inverted parabolic dependence of T_c on charge carrier concentration observed

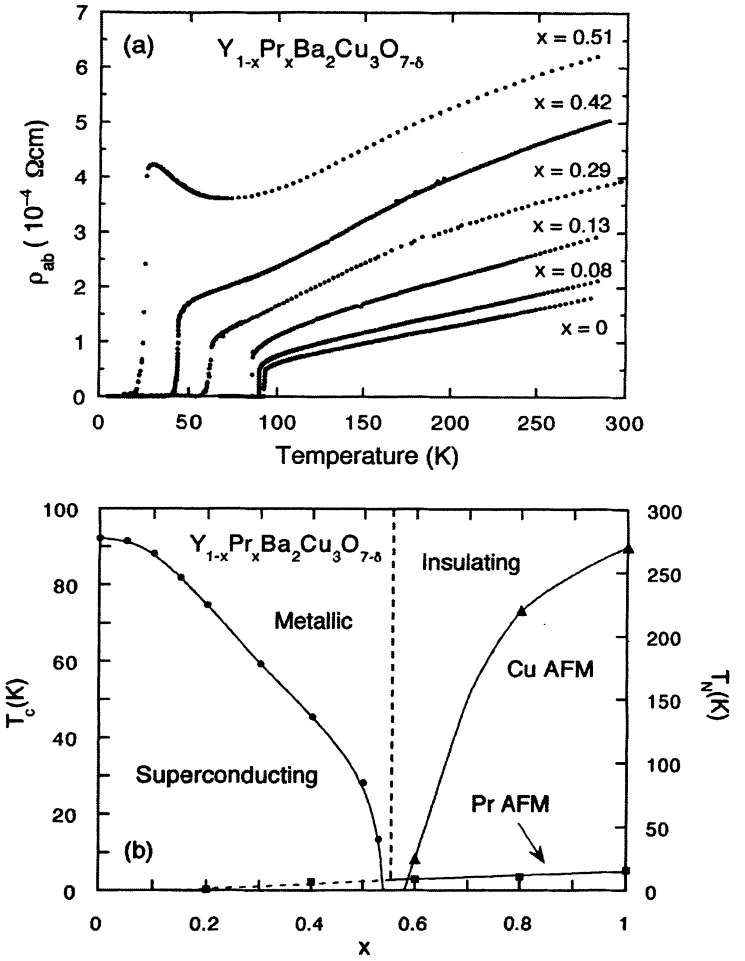

Fig. 8.85. (a) In-plane electrical resistivity ρ_{ab} vs temperature T curves for $Y_{1-x}Pr_xBa_2Cu_3O_{7-\delta}$ ($0 < x < 0.51$) single crystals, after Ref. [504]. (b) Temperature T vs Pr concentration x phase diagram for the $Y_{1-x}Pr_xBa_2Cu_3O_{7-\delta}$ system, delineating metallic, superconducting, insulating, and antiferromagnetically ordered regions, after Ref. [504, 541]

in many superconducting cuprate systems. Displayed in Fig. 8.86 (b) is a plot of T_c vs Pr concentration x. The dashed line represents the function $T_c(x, y = 0) + (96.5\ \mathrm{K})x$ which corresponds to pure hole localization, while the solid line corresponds to the function $T_c(x, y = 0)$ which includes hole localization and pair breaking.

The occurrence of appreciable hybridization between the Pr localized $4f$ electron states and the valence band states associated with the conducting

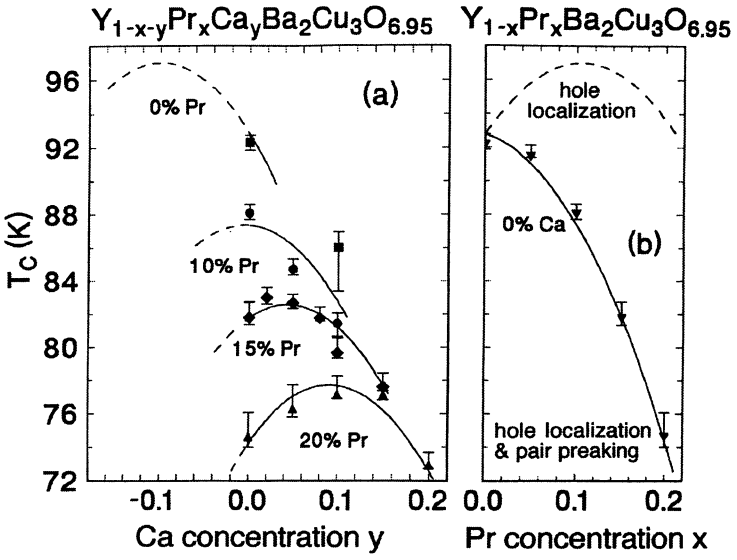

Fig. 8.86. (a) Superconducting critical temperature T_c vs Ca concentration y for four Pr concentrations x in the $Y_{1-x-y}Ca_yPr_xBa_2Cu_3O_{7-\delta}$ system [542]. Curves formed by solid and dashed lines represent Eq. 8.28, as explained in the text. (b) T_c vs Pr concentration x. The dashed line represents the function $T_c(x, y = 0) + (96.5\ \mathrm{K})x$ which describes pure hole localization, and the solid line represents the function $T_c(x, y = 0)$ which includes hole localization and pair breaking, after Refs. [504, 542]

CuO_2 planes was first proposed by Neumeier, Maple, and Torikachvili in 1988 [543] to account for the rapid reduction of T_c and the striking crossover in the pressure dependence of T_c from positive to negative with increasing x in the $Y_{1-x}Pr_xBa_2Cu_3O_{7-\delta}$ system. This proposal was based on similar behavior exhibited by the $La_{1-x}Ce_x$ system described in Section 8.2, in which the rate of depression of T_c by the Ce impurities displayed a strong dependence on pressure that was attributed to the hybridization between the Ce localized $4f$ states and conduction electron states [57]. Direct evidence for Pr localized $4f$-CuO_2 valence band hybridization was obtained from resonant photoemission spectroscopy experiments (RESPES) on the $Y_{1-x}Pr_xBa_2Cu_3O_{7-\delta}$ system by Kang *et al.* [544].

Measurements of the pressure dependence of T_c were repeated by Maple, Paulius, and Neumeier [545] on higher quality $Y_{1-x}Pr_xBa_2Cu_3O_{7-\delta}$ specimens studied at zero pressure by Neumeier and Maple [541]. The results of these experiments are shown in Fig. 8.87 (a) where $\Delta T_c = T_c(P) - T_c(0)$ is plotted vs P for several values of x between 0 and 0.5 [545]. The $\Delta T_c(P)$ data are in qualitative agreement with the earlier results and reveal a dramatic crossover from positive to large negative dependences of T_c on P as the Pr

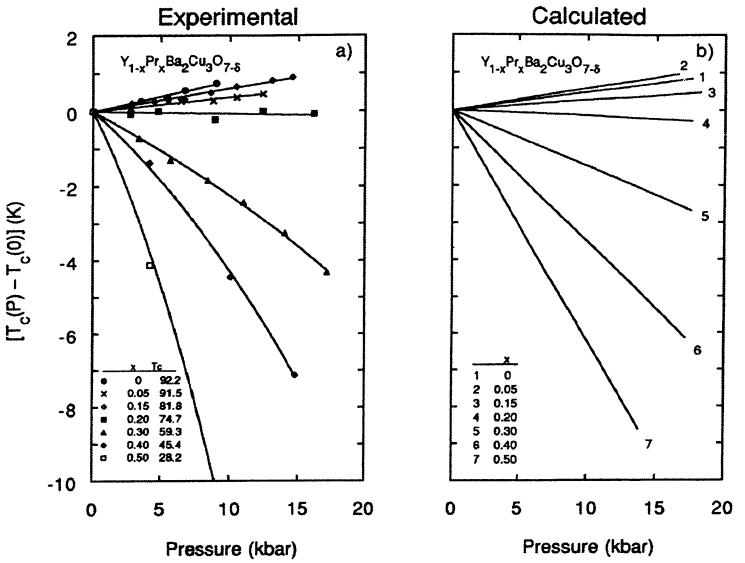

Fig. 8.87. Shift in T_c relative to its value at zero pressure, $T_c(P) - T_c(0)$, of $Y_{1-x}Pr_xBa_2Cu_3O_{7-\delta}$ samples with various Pr concentrations $0 \leq x \leq 0.5$ vs pressure P to 18 kbar. (a) Experimental data. (b) Calculated behavior according to the phenomenological model described in the text, after Ref. [545]

concentration is increased. Earlier measurements of $\rho(T, P)$ on a sample with $x = 0.5$ [541,546] showed that this sample near the metal–insulator transition becomes less metallic under pressure.

An extension of the formula for $T_c(x)$ for the $Y_{1-x}Pr_xBa_2Cu_3O_{7-\delta}$ system to incorporate the effect of applied pressure can also account semiquantitatively for the remarkable variations in T_c with P that have been observed in the $Y_{1-x}Pr_xBa_2Cu_3O_{7-\delta}$ system. The trends in the $T_c(x, P)$ data can be obtained by assuming that the parameters A and a are, to first approximation, independent of P, and that T_{c0}, b and B can be expanded in a power series to first order in P; i.e.,

$$T_{c0}(P) \approx T_{c0}(0) + T'_{c0}(0)P \tag{8.29}$$

$$b(P) \approx b(0) + b'(0)P \tag{8.30}$$

$$B(P) \approx B(0) + B'(0)P \tag{8.31}$$

The best overall fit of the resultant expression for $[\mathrm{d}T_c(x, P)/\mathrm{d}P]_{P=0}$ to the experimental data yields the values $T'_{c0}(0) = 0.048\,\mathrm{K/kbar}$, $b'(0) = 0.0041\,\mathrm{K/kbar}$ and $B'(0) = -0.02\,\mathrm{K/kbar}$ [545]. The increase of b with P is consistent with an increase of the valence (decrease in the $4f$ electron shell occupation number) of Pr with P, which is intuitively reasonable. A

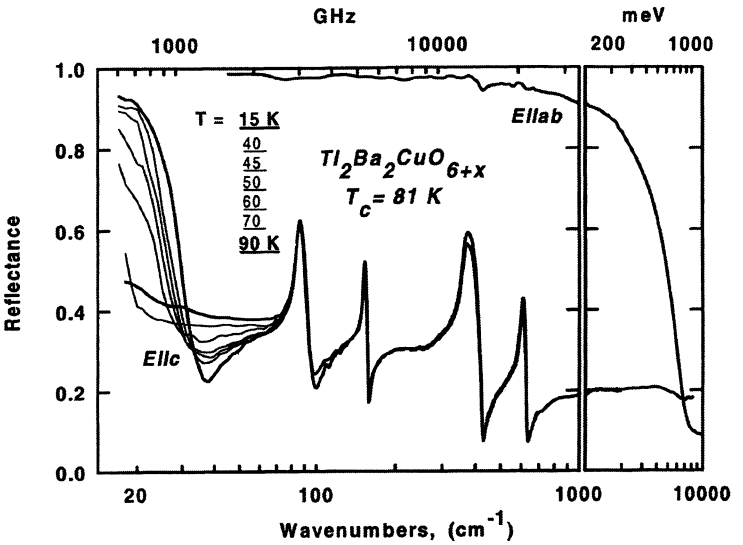

Fig. 8.88. Reflectance of $Tl_2Ba_2CuO_{6+x}$ measured with $E \parallel c$ and $E \parallel ab$ polarizations of incident radiation. The c–axis reflectance is nearly insulating in the normal state but at $T < T_c \approx 80$ K is dominated by the Josephson–like plasma edge, after Ref. [548]

decrease (increase) of the magnitude of the exchange interaction parameter $\mathcal{J}$ with P can be inferred from the decrease of $B'(0)$ with P, depending upon whether the complications associated with the Kondo effect are excluded (included). As discussed in Section 8.2, the Kondo effect is expected (and possibly observed in the specific heat [547]) in metals containing R ions that carry magnetic moments when there is strong hybridization between the localized $4f$ states of the R ion and conduction electron states which generates a large, negative (antiferromagnetic) exchange interaction [6]. However, inclusion of the Kondo effect in the analysis of the $T_c(x, P)$ data is complicated. The calculated $\Delta T_c(x, P)$ curves for x values corresponding to the experimental $\Delta T_c(x, P)$ data presented in Fig. 8.87(a) are shown in Fig. 8.87(b) and give a semiquantitative description of the $\Delta T_c(x, P)$ data over the range $0 \leq x \leq 0.5$, even though the $\Delta T_c(x, P = 0)$ data are only described well for $0 \leq x \leq 0.2$ (see Fig. 8.86(b)).

It is interesting that superconductivity with values of T_c exceeding ~ 40 K has only been observed in layered cuprates which have strongly anisotropic, nearly two–dimensional electronic properties. An important issue for these materials is the nature of interlayer transport and the role it plays in the superconductivity. Reflectance $R(\omega)$ measurements with polarized light reveal that $R(\omega)$ for the electric field E parallel to the CuO_2 planes, $E \parallel CuO_2$, exhibits a metallic response, while $R(\omega)$ for $E \perp CuO_2$ resembles that of ionic insulators with characteristic phonon peaks in the far infrared. This is

illustrated in Fig. 8.88 where R vs ω data for $Tl_2Ba_2CuO_{6+x}$ (Tl2201) [548] are displayed. For temperatures below T_c, a sharp plasma edge at $\omega = 37$ cm^{-1} evolves out of a nearly "insulating" normal state spectrum since the supercurrents flow in all crystallographic directions. In an effort to explore the relationship between changes in the incoherent c–axis conductivity below T_c and the c–axis superfluid density, Basov *et al.* [548] have analyzed the interlayer conductivity of the cuprate high T_c superconductors $Tl_2Ba_2CuO_{6+x}$, $La_{2-x}Sr_xCuO_4$, and $YBa_2Cu_3O_{6.6}$, all of which show incoherent interlayer response in the normal state. The analysis reveals that the magnitude of the superfluid density ρ_s significantly exceeds the weight missing from the real part of the conductivity in the frequency region comparable to the superconducting energy gap 2Δ. This indicates that a significant fraction of ρ_s is derived from mid infrared frequencies. Basov *et al.* [548] suggest that the discrepancy between the magnitude of ρ_s and the spectral weight that is missing from the far infrared part of the conductivity can be interpreted in terms of an interlayer kinetic energy change associated with the superconductivity.

Because of their high values of T_c, short coherence lengths, long penetration depths, and large anisotropy, the cuprate superconductors exhibit a wealth of striking vortex phases and phenomena that are currently being vigorously investigated (For a review, see, for example, [549–553]).

Symmetry of the superconducting order parameter

A great deal of effort has been expended to determine the symmetry of the superconducting order parameter of the high T_c cuprate superconductors [12,554,555]. The pairing symmetry provides clues to the identity of the superconducting pairing mechanism which is essential for the development of the theory of high temperature superconductivity in the cuprates.

Shortly after the discovery of high T_c superconductivity in the cuprates, it was established from flux quantization, Andreev reflection, Josephson effect, and nuclear magnetic resonance (NMR) Knight–shift measurements that the superconductivity involves electrons that are paired in singlet spin states [556]. Possible orbital pairing states include s–wave, extended s–wave, and d–wave states. In the s–wave state, the energy gap $\Delta(\mathbf{k})$ is isotropic; i.e., $\Delta(\mathbf{k})$ is constant over the Fermi surface. This leads to "activated" behavior of the physical properties in the superconducting state for $T \ll \Delta$; e.g., the specific heat $C_e(T)$, ultrasonic attenuation coefficient $\alpha_s(T)$, and NMR spin lattice relaxation rate $1/T_1(T)$ vary as $e^{-\Delta/T}$. For the extended s–wave state, the energy gap $\Delta(T)$ is anisotropic; i.e., $\Delta(\mathbf{k})$ exhibits a variation over the Fermi surface that has the same symmetry as the rotational symmetry of the crystal. Similarly, for the d–wave case, the energy gap $\Delta(\mathbf{k})$ is anisotropic; however, the symmetry is lower than the symmetry of the crystal. The d–wave state that is consistent with most, but not all, of the experiments discussed below has $d_{x^2-y^2}$ symmetry, which can be expressed as $\Delta(\mathbf{k}) = \Delta_0[\cos(k_x a) - \cos(k_y a)]$. For both the extended s–wave and d–wave cases, $\Delta(\mathbf{k})$ vanishes at lines on the Fermi surface, resulting in a density

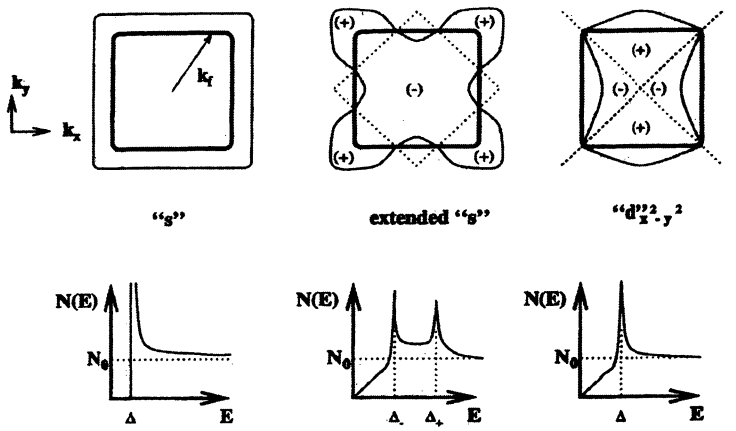

Fig. 8.89. Fermi surface gap functions and densities of states of a superconductor with tetragonal symmetry for various pairing symmetries. The gap functions in the $\mathbf{k}_z = 0$ plane (top) are represented by the light solid lines; distance from the Fermi surface (dark solid lines) gives the amplitude, a positive value being outside the Fermi surface, a negative value inside. The corresponding density of states for one–quasi–particle excitations $N(E)$ is shown below each gap function, with N_0 the normal state value. Gap node surfaces are represented by the dashed lines. Left: The classic s–wave case, where the gap function is constant, with value Δ. This gives rise to a square–root singularity in $N(E)$ at energy $E = \Delta$. Middle: The extended s–wave case derives from pairs situated on nearest–neighbor square lattice sites in real space, with an approximate k–space form of $\cos(k_x a) - \cos(k_y a)$. For the Fermi surface shown here, the gap function has lines of nodes running out of the page. Right: A d–wave function of $x^2 - y^2$ symmetry. The extended s–wave and d–wave functions shown here each have a linear density of states up to order Δ, which measures the maximum gap amplitude about the Fermi surface, after Ref. [12]

of states $N(E)$ that is linear in energy E at low values of E. This leads to "power law" T^n (n = integer) behavior of the physical properties for $T \ll \Delta$; e.g., $C_e(T) \sim T^2$, the superconducting penetration depth $\lambda(T) \sim T$, and $1/T_1(T) \sim T^3$. The definitive determination of the symmetry of the superconducting order parameter requires the determination of both the magnitude and the phase of $\Delta(\mathbf{k})$. Shown in Fig. 8.89 is a schematic diagram of the variation of the energy gap over the Fermi surface and the density of states $N(E)$ vs E for the "s", "extended s", and "$d_{x^2-y^2}$" states [12].

Magnitude of the superconducting order parameter

A number of different types of measurements have been performed on the high T_c cuprate superconductors that are sensitive to $|\Delta(\mathbf{k})|$. These include microwave penetration depth $\lambda(T)$ [557], microwave surface conductivity [558], nuclear magnetic resonance (NMR) relaxation rate $1/T_1(T)$ [559], magnetic field dependence of the electronic specific heat $C_e(T)$ [560], thermal conductivity [561], angle resolved photoemission spectroscopy (ARPES) [562],

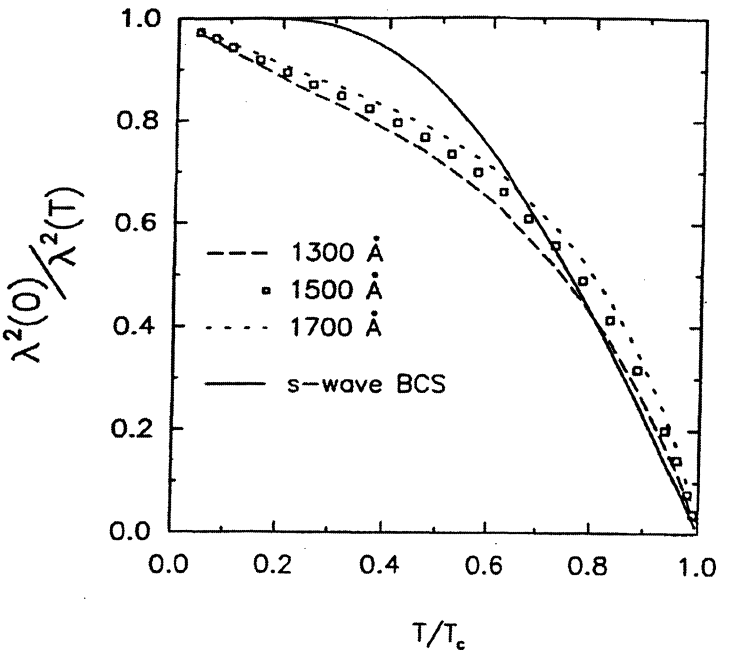

Fig. 8.90. Ratio $[\lambda(0)/\lambda(T)]^2$ extracted from measurements of $\Delta\lambda(T)$ on a $YBa_2Cu_3O_{6.95}$ single crystal, a measure of the superfluid density. The different choices of $\lambda(0)$ (square and long and short dashed curves) used have little effect on the overall shape. The strong linear behavior at low temperatures is clearly different from the s–wave BCS result, after Ref. [557]

quasiparticle tunneling [563, 564] and Raman scattering [565]. The results of these studies are generally consistent with a superconducting state with $d_{x^2-y^2}$ or extended s–wave symmetry for the hole–doped cuprates such as YBCO–123, YBCO–124, LSCO, and BSCCO. Experiments discussed below indicate a dominant component of $d_{x^2-y^2}$ symmetry in the superconducting order parameter of hole–doped cuprates.

Shown in Fig. 8.90 are data for $[\lambda(0)/\lambda(T)]^2$ vs T/T_c, where λ is the London penetration depth for a $YBa_2Cu_3O_{6.95}$ single crystal from the work of Hardy *et al.* [557]. The data clearly deviate from the BCS s–wave behavior (solid line in the figure) and are linear in T at low temperatures. The linear behavior is consistent with the existence of line nodes in the energy gap of a clean d–wave superconductor.

Early electron tunneling [566], microwave penetration depth [567, 568], and Raman spectroscopy [569] measurements on the electron–doped superconductor NCCO indicated that the superconducting order parameter of this material has s–wave symmetry. Superconductivity with d–wave symmetry for hole–doped cuprates and s–wave symmetry for electron–doped

cuprates seems rather surprising, in view of the similarities in the structures of the hole–doped and electron–doped superconductors and the fact that they are both derived from chemical substitution of AFM insulating parent compounds. However, more recent microwave [570, 571], angle–resolved photoemission spectroscopy (ARPES) [572,573], and phase sensitive SQUID microscope (see below) [574] experiments appear to be consistent with a d–wave superconducting order parameter. According to Blumberg *et al.* [575], who recently performed low energy electronic Raman scattering measurements on NCCO single crystals, these seemingly contradictory results can be rationalized in terms of a nonmonotonic form of the $d_{x^2-y^2}$ order parameter. The superconducting gap opens up rapidly with departure from the diagonal nodal directions and reaches a maximum value of $4.4k_BT_c$ at the hot spots that are located closer to the nodes than to the Brillioun zone boundaries where the gap drops to $3.3k_BT_c$. The enhancement of the gap value in the proximity of the hot spots emphasizes the role of antiferromagnetic spin fluctuations for superconductivity in the electron–doped cuprates. Thus, despite strong differences between the electron– and hole–doped cuprates, their superconductivity may have the same order parameter symmetry and originate from a similar mechanism.

Phase of the superconducting order parameter

Several different types of measurements that are sensitive to the phase of $\Delta(\mathbf{k})$ have been performed. These measurements, all of which involve the Josephson effect, include superconducting quantum interference device (SQUID) interferometry [576–578], single junction modulation [579,580], tricrystal ring magnetometry [581–583], c–axis Josephson tunneling [584–588], and grain boundary tunneling [589]. The SQUID interferometry, single junction modulation, and tricrystal ring magnetometry measurements were performed on YBCO, while tricrystal magnetometry experiments have also been carried out on TBCCO. These experiments indicate that the superconducting order parameter in the YBCO and TBCCO hole–doped materials has $d_{x^2-y^2}$ symmetry. However, c–axis Josephson tunneling studies on junctions consisting of a conventional superconductor (Pb) and twinned or untwinned single crystals of YBCO indicate that the superconducting order parameter of YBCO has a significant s–wave component [584, 585]. As noted above, tricrystal ring magnetometry measurements indicate d–wave symmetry for the electron–doped superconductor NCCO [590] which, according to recent low energy polarized electronic Raman scattering studies, has a nonmonotonic $d_{x^2-y^2}$ superconducting order parameter [575].

A new type of c–axis Josephson tunneling experiment in which a conventional superconductor (Pb) was deposited across a single twin boundary of a YBCO single crystal was performed by Kouznetsov *et al.* [591]. The Josephson critical current I_c was measured as a function of magnitude and angle ϕ of magnetic field applied in the plane of the sample. For H aligned perpendicular to the twin boundary, a maximum in I_c as a function of H was observed

at $H = 0$, whereas for H parallel to the twin boundary, a minimum in I_c was observed at $H = 0$. In all samples investigated, a clear experimental signature of an order parameter phase shift across the twin boundary was observed. The results provide evidence for mixed d– and s–wave pairing in YBCO and are consistent with predominant d–wave pairing with $d_{x^2-y^2}$ symmetry and a sign reversal of the s–wave component across the twin boundary.

Recently, $Bi_2Sr_2CaCu_2O_{8-\delta}$ (Bi2212) bicrystal c–axis twist Josephson junction experiments were performed and taken as evidence for a dominant s–wave order parameter for $T < T_c$ [592, 593]. The twist angle ϕ_0 independence of the c–axis Josephson critical current J_c across the twist junction for T just below T_c was interpreted in terms of a dominant s–wave order parameter for all $T \leq T_c$. This experiment is in apparent contradiction to the results of the tricrystal experiments on Bi2212 which indicated a dominant $d_{x^2-y^2}$ wave order parameter component in Bi2212 at low temperatures for both under–doped and over–doped samples [590]. It was recently suggested that these experiments would be compatible if the superconductivity exhibited by Bi2212 were mostly s–wave in the bulk and d–wave on the surface [594]. Critical discussions of these and other phase sensitive experiments on Bi2212 can be found in several recent papers (for example, [595, 596]).

Various mixed s– and d–wave pairing models that have been developed to account for the superconducting properties of the orthorhombic YBCO-123 system are reviewed by Béal–Monod [597].

Multiple superconducting states

An anomaly in the thermal conductivity κ at low temperature of the high T_c superconductor $Bi_2Sr_2Ca(Cu_{1-x}Ni_x)_2O_8$ was reported by Movshovich *et al.* [598]. The anomaly takes the form of a sharp reduction of κ at a temperature $T_c^* \approx 200$ mK, which separates a higher temperature region where κ varies as T^α with α between 1.6 and 1.75 and a lower temperature region where κ is linear in T. The low temperature anomaly was found to be suppressed by the application of a small magnetic field. Movshovich *et al.* proposed that the observed behavior is consistent with a phase transition into a second bulk low temperature superconducting state at T_c^*. They note that the presence of a second superconducting state would constitute direct evidence for unconventional superconductivity in $Bi_2Sr_2CaCu_2O_8$. As noted in Section 8.3, multiple superconducting states have been observed in the heavy fermion superconductors UPt_3 and $U_{1-x}Th_xBe_{13}$ in which the superconducting electrons are also believed to be paired in states with finite angular momentum.

8.5.5 Normal State Properties

It was realized at the outset that the normal state properties of the high T_c cuprate superconductors are unusual and appear to violate the Landau Fermi liquid paradigm [599–603]. Some researchers share the view that it will be necessary to develop an understanding of the normal state before the

superconducting state can be understood, since the normal state properties reflect the electronic structure that underlies high T_c superconductivity.

The anomalous normal state properties first identified in the high T_c cuprate superconductors include the electrical resistivity and Hall effect. The electrical resistivity $\rho_{ab}(T)$ in the ab–plane of many of the hole–doped cuprate superconductors near optimal doping has a linear temperature dependence between T_c and high temperatures $\sim$ 1000 K, with an extrapolated residual resistivity $\rho_{ab}(0)$ that is very small; i.e., $\rho_{ab}(T) \approx \rho_{ab}(0) + cT$, with $\rho_{ab}(0) \approx 0$ and the value of c similar within different classes of cuprate materials [604]. An example of the linear T–dependence of $\rho_{ab}(T)$ is displayed in Fig. 8.85(a) for the $Y_{1-x}Pr_xBa_2Cu_3O_{7-\delta}$ system [504]. In contrast, both $\rho_{ab}(T)$ and $\rho_c(T)$ of the optimally–doped electron–doped cuprate $Sm_{1.83}Ce_{0.17}CuO_{4-y}$ vary as T^2, indicative of three dimensional Fermi liquid behavior in the $La_{2-x}M_xCuO_4$ systems [605].

The Hall coefficient R_H is inversely proportional to T and the cotangent of the Hall angle $\theta_H = R_H/\rho$ varies as T^2; i.e., $\cot\theta_H = \sigma_{xx}/\sigma_{xy} = AT^2 + B$ [607]. This is illustrated in Fig. 8.91 which contains a plot of θ_H vs T^2 calculated for a field of 6 tesla for $Y_{1-x}Pr_xBa_2Cu_3O_{7-\delta}$ single crystals [606]. The linear T–dependence of $\rho(T)$ and the quadratic T–dependence of $\cot(\theta_H)$ have been attributed to longitudinal and transverse scattering rates τ_ℓ^{-1} and τ_t^{-1} that vary as T and T^2, respectively [608]. In the RVB model, the constant and T^2 terms in τ_t^{-1} and, in turn, θ_H, are ascribed to scattering of spinons by magnetic impurities and other spinons, respectively. On the other hand, using the nearly antiferromagnetic Fermi liquid description of planar quasiparticles, Stojkovic and Pines [609] have shown that the anomalous temperature dependence of the Hall angle could result from highly anisotropic scattering at different regions of the Fermi surface. A review of magnetoresistance and Hall effect studies of cuprate superconductors, particularly the electron–doped cuprates $La_{2-x}M_xCuO_4$ and the hole–doped system $Y_{1-x}Pr_xBa_2Cu_3O_{7-\delta}$, can be found in Ref. [610].

Normal ground state

The evolution of the normal ground state of the cuprates as a function of dopant concentration is particularly interesting. This is reflected in the temperature dependences of the *ab*–plane and *c*–axis electrical resistivities $\rho_{ab}(T)$ and $\rho_c(T)$ [612]. Both $\rho_{ab}(T)$ and $\rho_c(T)$ exhibit insulating behavior (i.e., $d\rho/dT < 0$) in the under–doped region, $\rho_{ab}(T)$ is metallic (i.e., $d\rho/dT > 0$) and $\rho_c(T)$ is insulating or metallic in the optimally–doped region, depending on the system, and $\rho_{ab}(T)$ and $\rho_c(T)$ are both metallic in the over–doped region. The linear T–dependence of $\rho_{ab}(T)$ and the insulating behavior of $\rho_c(T)$ suggest two dimensional non–Fermi liquid behavior near the optimally–doped region, whereas the metallic $\rho(T) \sim T^n$ with $n > 1$ reflects a tendency towards three dimensional Fermi liquid behavior in the over–doped region. Measurements in 61–tesla pulsed magnetic fields to quench the superconductivity have been particularly useful in elucidating the evolution

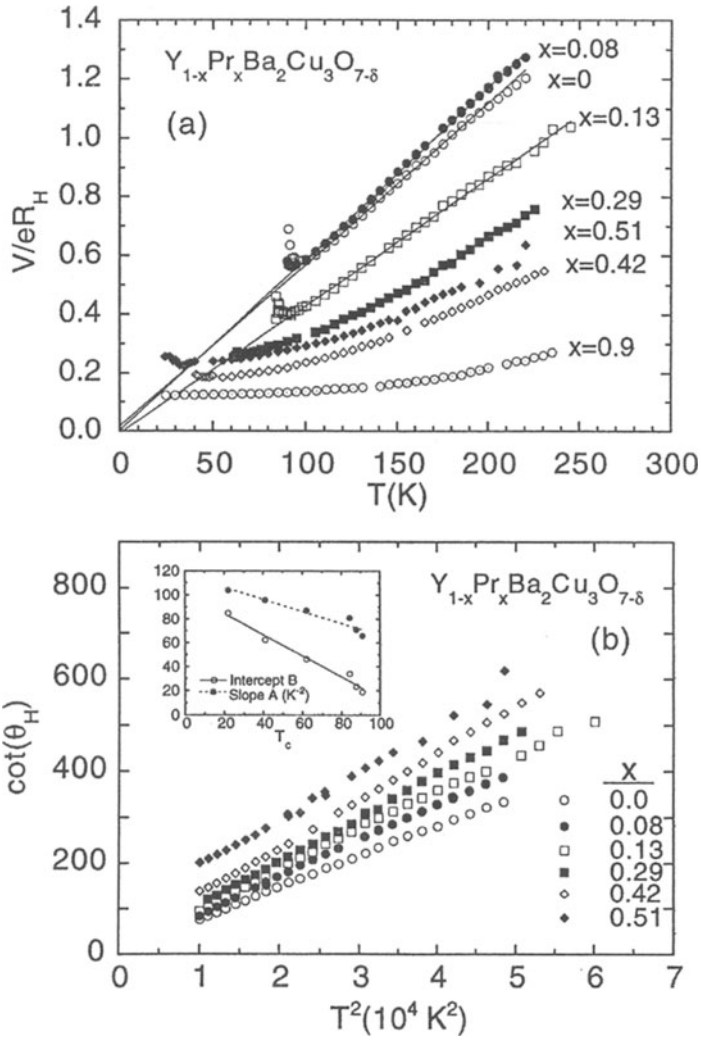

Fig. 8.91. (a) Temperature dependence of the Hall carrier number $n_{\rm H} = V/eR_{\rm H}$ for $Y_{1-x}Pr_xBa_2Cu_3O_{7-\delta}$ single crystals with different x values. The fact that the data for two pairs of x values ($x = 0$, $x = 0.08$, and $x = 0.42$, $x = 0.51$) are out of sequence in the $V/eR_{\rm H}$ vs T plot, but not in the $\cot(\theta_{\rm H})$ vs T^2 plot (see (b) of this figure), could be a result of the error in measuring the thickness of these crystals. The $x = 0.9$ value represents the nominal composition, while the x values of the superconducting samples were estimated by comparing the T_c's of the crystals with those of high quality polycrystalline samples. After Ref. [504]. (b) Cotangent of the Hall angle $\cot(\theta_{\rm H})$ vs T^2 of $Y_{1-x}Pr_xBa_2Cu_3O_{7-\delta}$ single crystals with magnetic field $H = 6$ tesla and $H \parallel c$, after Ref. [606]

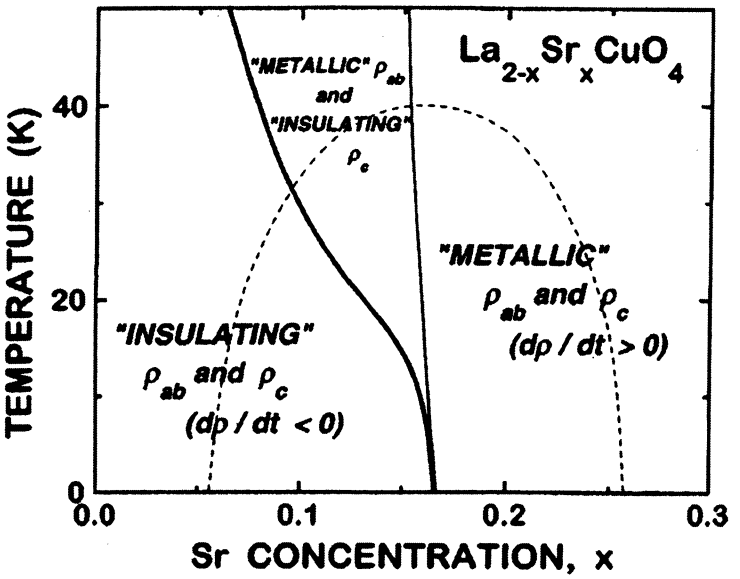

Fig. 8.92. Temperature – Sr concentration ($T - x$) phase diagram of the $La_{2-x}Sr_xCuO_4$ system, after superconductivity has been suppressed by an intense pulsed magnetic field. The insulator–metal crossover occurs near optimum doping and a new insulating regime is revealed, in which the electrical resistivity diverges as the logarithm of the temperature. The dashed line represents the T_c vs x curve in zero field and the two solid lines delineate the insulating ρ_{ab} and ρ_c, metallic ρ_{ab} and insulating ρ_c, and metallic ρ_{ab} and ρ_c regions in the normal state accessed by high magnetic fields, after Ref. [611]

of $\rho_{ab}(T)$ and $\rho_c(T)$ with dopant concentration in the $La_{2-x}Sr_xCuO_4$ system [611]. Both $\rho_{ab}(T)$ and $\rho_c(T)$ were found to exhibit a $-\ln T$ divergence in the under–doped region, indicative of a three dimensional non–Fermi liquid [613]. Shown in Fig. 8.92 is the temperature–Sr concentration ($T - x$) phase diagram of the $La_{2-x}Sr_xCuO_4$ system, after the superconductivity has been suppressed by an intense pulsed magnetic field [611]. The insulator–metal crossover occurs near optimum doping and a new insulating regime is revealed, in which the electrical resistivity diverges as the logarithm of the temperature.

As an example of the evolution of $\rho_{ab}(T)$ and $\rho_c(T)$ with doping, we again refer to the $Y_{1-x}Pr_xBa_2Cu_3O_{7-\delta}$ system. Shown in Fig. 8.93 are $\rho_{ab}(T)$ and $\rho_c(T)$ data for $Y_{1-x}Pr_xBa_2Cu_3O_{7-\delta}$ single crystals in the range of Pr concentrations $0 \leq x \leq 0.55$ [614]. The following features in the $\rho_{ab}(T)$ and $\rho_c(T)$ data in Fig. 8.93 are evident: a nonmonotonic evolution of $\rho_c(T)$ with x, the transformation of both $\rho_{ab}(T)$ and $\rho_c(T)$ from metallic to semiconducting with x, and the coexistence of metallic $\rho_{ab}(T)$ and semiconducting $\rho_c(T)$ for a certain range of doping. The nonmonotonic variation of $\rho_c(T)$ with

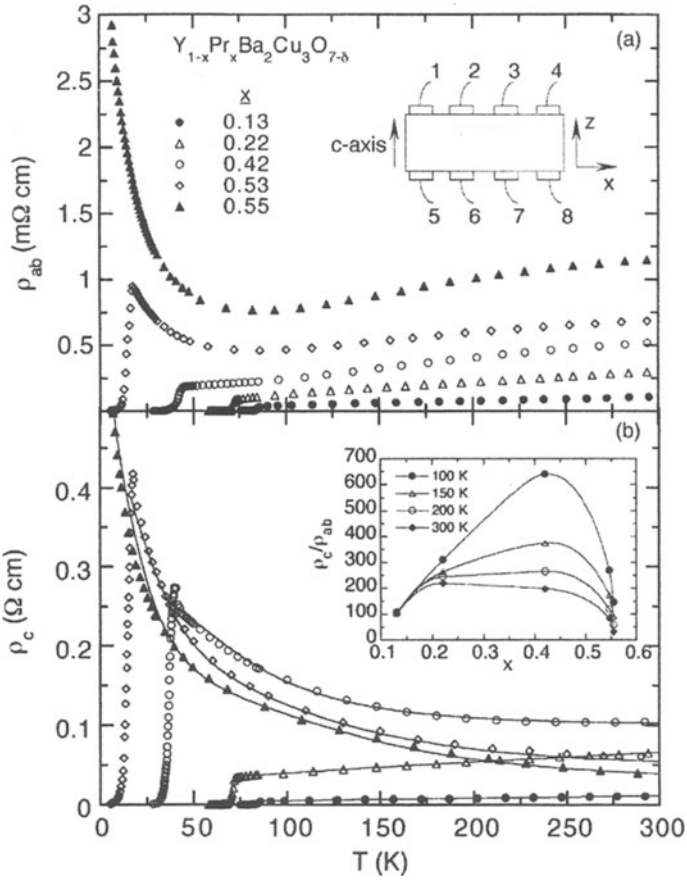

Fig. 8.93. (a) In–plane resistivity $\rho_{ab}(T)$ and (b) out–of–plane resistivity $\rho_c(T)$ for $Y_{1-x}Pr_xBa_2Cu_3O_{7-\delta}$ single crystals. The solid lines in (b) are fits to the data using a model described in Ref. [614]. Inset to (a): The configuration of leads used in the measurements. Inset to (b): Anisotropy ρ_c/ρ_{ab} vs Pr concentration x at different temperatures. The solid lines are guides to the eye, after Ref. [614]

x in Fig. 8.93(b) can be described with a phenomenological model [614] that assumes that the c–axis conductivity takes place via incoherent elastic tunneling between CuO_2 bilayers and CuO chain layers with a gap in the energy spectrum of the CuO chains (solid lines in Fig. 8.93(b)).

Pseudogap

Perhaps the most remarkable aspect of the normal state is the pseudogap in the charge and spin excitation spectra of under–doped cuprates [555]. The pseudogap has been inferred from features in various transport, magnetic, and thermal measurements including $\rho_{ab}(T)$ [616–618]; $R_H(T)$ [619], thermoelectric power $S(T)$ [620], NMR Knight shift $K(T)$ [621], NMR spin–lattice

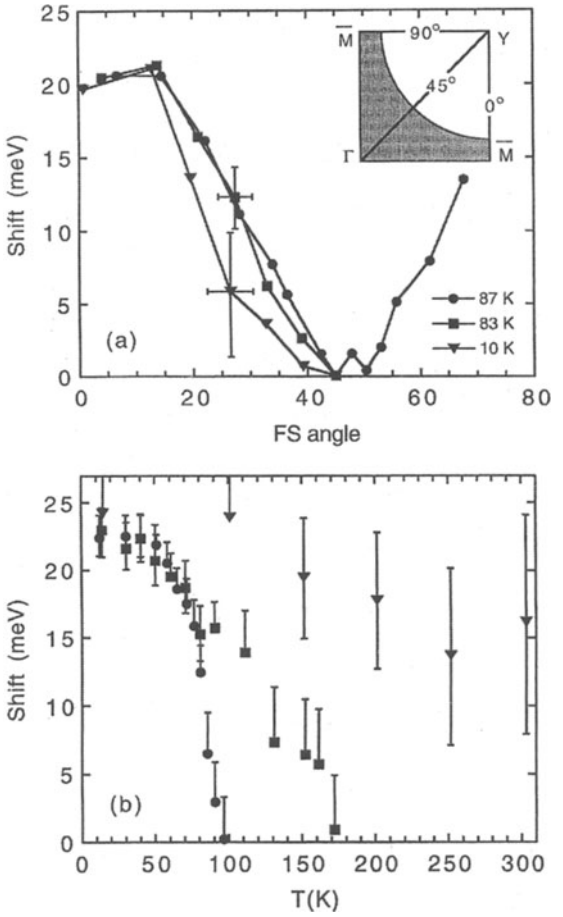

Fig. 8.94. Momentum and temperature dependence of the energy gap estimated from leading edge shifts of ARPES spectra for BSCCO–2212. (a) k–dependence of the gap in the T_c = 87 K, 83 K, and 10 K samples, measured at 14 K. The inset shows the Brillouin zone with a large Fermi surface (FS) closing the (π, π) point, with the occupied region shaded. (b) Temperature dependence of the maximum gap in a near–optimal T_c = 87 K sample (circles), and two underdoped samples with T_c = 83 K (squares) and T_c = 10 K (triangles), after Ref. [615]

relaxation rate $1/T_1(T)$ [622–624], magnetic susceptibility $\chi(T)$ [619], neutron scattering [625], and specific heat $C(T)$ [626], as well as spectroscopic measurements such as infrared absorption [627–629] and ARPES [615, 630].

An example of the features in $\rho_{ab}(T)$ that are associated with the pseudogap can be seen in the $\rho_{ab}(T)$ data displayed in Figs. 8.85(a) and 8.93(a) for the $Y_{1-x}Pr_xBa_2Cu_3O_{7-\delta}$ system. As the system becomes more under–doped with increasing x, $\rho_{ab}(T)$ deviates from linear behavior at higher temperature

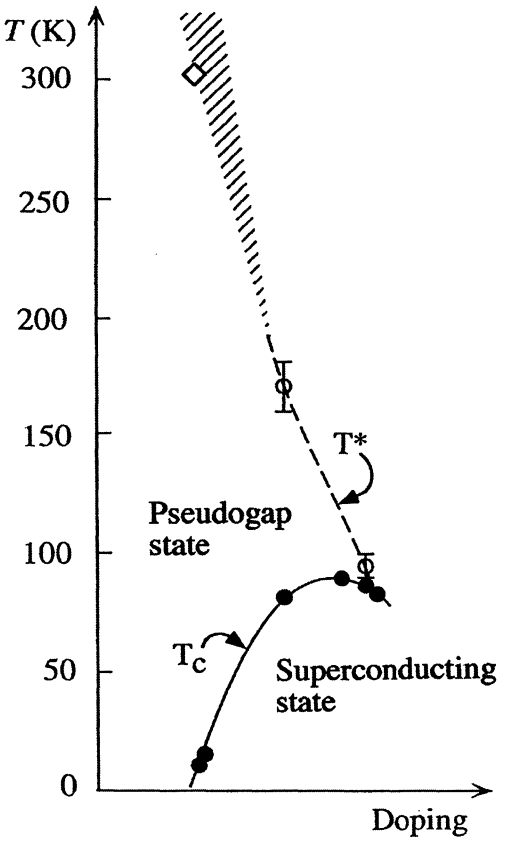

Fig. 8.95. Schematic phase diagram of BSCCO–2212 as a function of doping. The filled symbols represent values of T_c determined from magnetic susceptibility measurements. The open symbols are values of T^* at which the pseudogap closes, derived from the data shown in Fig. 8.94, after Ref. [615]

at a characteristic temperature T^* which represents a crossover into the pseudogap state at $T < T^*$.

The transport, thermal, magnetic, and infrared studies of the pseudogap have been carried out on several cuprate materials, including LSCO, YBCO–123, YBCO–124, and BSCCO–2212, while the ARPES investigations of the pseudogap have mainly focused on BSCCO, although ARPES measurements have also been made on oxygen–deficient YBCO.

The ARPES measurements reveal several striking aspects of the pseudogap. The magnitude of the pseudogap has the same **k**–dependence in the ab–plane as the magnitude of the superconducting energy gap, with maxima in the directions of k_x and k_y and minima at 45° to these directions. In fact, the symmetry is consistent with $d_{x^2-y^2}$ symmetry inferred from Josephson

tunneling measurements on hole–doped cuprates discussed previously. Furthermore, measurements of the temperature dependence of the pseudogap at the angles where it is a maximum show that the superconducting gap grows continuously out of the pseudogap and that the value of the sum of both gaps at low temperatures is constant, independent of the temperature T^* at which the pseudogap opens, or T_c. This is in marked contrast to the situation in conventional superconductors where the energy gap is proportional to T_c.

These features of the pseudogap are illustrated in Fig. 8.94(a) and Fig. 8.94(b) which show the **k**–dependence of the energy gap and the dependence of the maximum gap on temperature from the ARPES measurements of Ding *et al.* [615] on BSCCO–2212 samples with values of T_c of 87 K, 83 K, and 10 K. The pseudogap and superconducting regions for BSCCO–2212 derived from the ARPES measurements of Ding *et al.* [615] are summarized in the temperature T_c vs charge carrier doping plot in Fig. 8.95.

Recently, direct measurements of the quasiparticle density of states (DOS) by scanning tunneling spectroscopy on $Bi_2Sr_2CaCu_2O_{8+\delta}$ (Bi2212) single crystals as a function of oxygen doping and temperature were made by Renner *et al.* [632]. It was found that the shape of the DOS in the superconducting state is essentially doping independent, the pseudogap above T_c scales with the superconducting gap, and the pseudogap is also present in overdoped samples. Both gaps were found to be essentially temperature independent. Tunneling spectra at various temperatures between 4.2 K and 293.2 K for Bi2212 are shown in Fig. 8.96.

In subsequent work, the temperature dependence of the quasiparticle density of states of over–doped $Bi_2Sr_2CuO_{6+\delta}$ (Bi2201) single crystals was measured between 275 mK and 82 K by means of scanning tunneling spectroscopy [633]. Below $T_c = 120$ K, the spectra exhibit a gap with well defined coherence peaks at $\pm\Delta$ greater than about 12 meV, which disappears at T_c. Above T_c, the spectra display a clear pseudogap of the same magnitude, gradually fillng up and vanishing at $T^* \approx 68$ K. This gap value is extremely large for a T_c of 10 K and is ~ 7 times larger than the BCS d–wave prediction $\Delta_{BCS} = 1.8$ meV [634]. This implies a very high ratio $2\Delta_p/k_BT_c \approx 28$, a value even larger than $2\Delta_p/k_BT_c \approx 10$ for Bi2212 at equivalent doping, showing that superconductivity is far from BCS–like in Bi2201, even in the over–doped regime. This work also revealed that the ratio of Δ_p and T^* is the same as found in other high T_c cuprate superconductors. This is illustrated in the plot of T^*/T_c vs $2\Delta_p/k_BT_c$ shown in Fig. 8.97 where it can be seen that the data are well represented by the BCS relation $2\Delta_p/k_BT^* = 4.3$, where T_c has been replaced by T^*. This suggests that T^*, rather than T_c, reflects the mean field critical temperature of cuprate superconductors and favors models which involve precursor pairing as the origin of the pseudogap phase.

Electronic inhomogeneity

Stripes, a complex form of electronic self–organization, have been observed

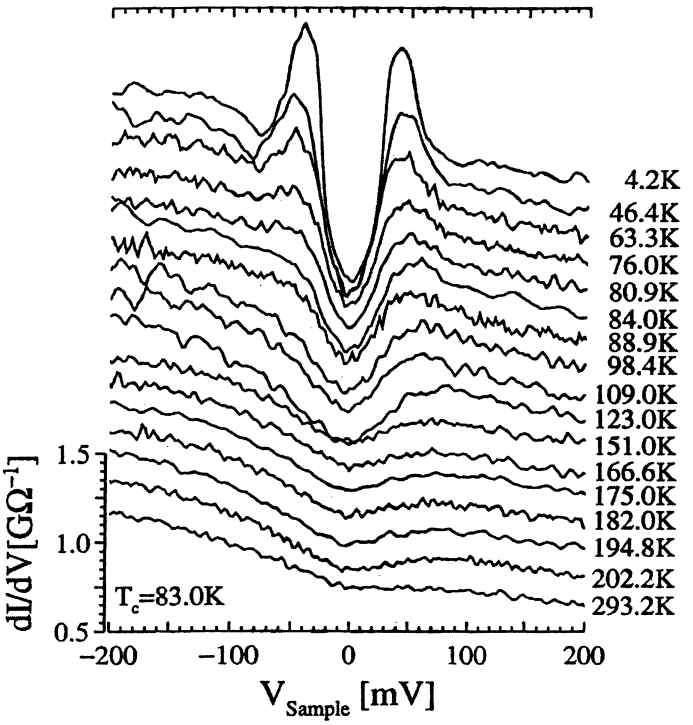

Fig. 8.96. Tunneling spectra for Bi2212 measured at various temperatures indicated in the figure. The conductance scale corresponds to the 293 K spectrum; the other spectra have been offset vertically for clarity, after Ref. [632]

in certain cuprates at low doping near the onset of the superconducting regime [635]. The stripes are believed to consist of mobile charge carriers in the CuO_2 planes that are confined to narrow one–dimensional lines ("charge stripes") and separated by insulating regions which exhibit antiferromagnetic order, similar to that which occurs in the parent Mott insulators such as La_2CuO_4 in which electrons are localized as a result of strongly repulsive electron–electron interactions. Thus, there should be large anisotropy in electrical conductivity between directions parallel and perpendicular to the stripes. The stripes are particulary prominent at low doping where T_c is low and substantially weakened at higher doping where T_c is a maximum. This suggests that stripes and superconductivity compete with one another, and many researchers believe that these two phases arise from a common underlying mechanism. Some reseachers believe that the stripes are actually a precondition for high T_c superconductivity in the cuprates.

The first evidence for static spin and charge order in cuprates was obtained in a neutron scattering study of a single crystal of $La_{1.6-x}Nd_{0.4}Sr_xCuO_4$ by

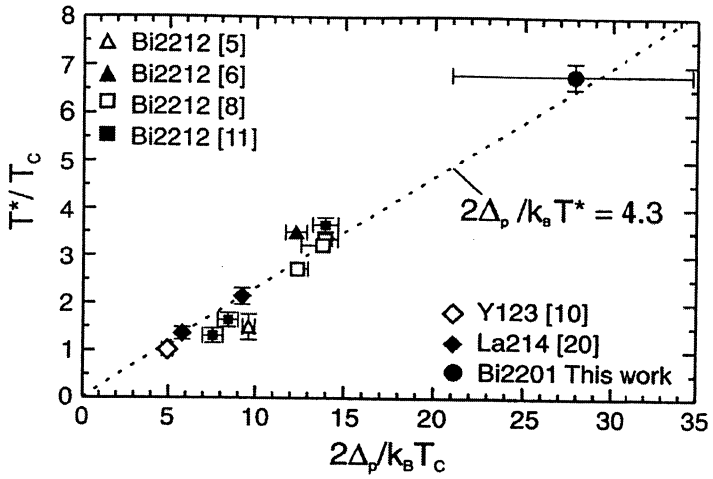

Fig. 8.97. T^*/T_c vs $2\Delta_p/k_BT_c$ for various cuprate superconductors compared to the mean field relation $2\Delta_p/k_BT^* = 4.3$, where T_c has been replaced by T^*. Error bars have been extracted from the references given by Kugler et al. (2001) indicated in the figure, after Ref. [633]

Tranquada *et al.* [636]. In this material, the partial substitution of Nd for La results in a change in crystal structure from the usual low temperature orthorhombic (LTO) phase to the low temperature tetragonal (LTT) phase, and a depression of T_c near $x = 0.125$. The LTO-LTT structural transition occurs at $\sim$ 70 K in $La_{1.6-x}Nd_{0.4}Sr_xCuO_4$ for $x = 0.12$, and evidence for static spin and charge stripes comes from neutron scattering as well as x-ray scattering experiments [636,637]. In the $La_{2-x}Sr_xCuO_4$ system, inelastic neutron scattering experiments have yielded evidence for dynamical two-dimensional spin correlations characterized by an incommensurate wave vector [638–640]. The characteristic wave vectors associated with magnetic scattering in $La_{1.85}Sr_{0.15}CuO_4$ and $La_{1.48}Nd_{0.4}Sr_{0.12}CuO_4$ are essentially identical. Thus, the major difference between the two systems appears to be the static vs dynamic character of the correlations. This similarity suggests that dynamical stripe correlations of both spin and charge exist in superconducting $La_{1.85}Sr_{0.15}CuO_4$. An intriguing question is what roles these dynamical spin and charge stripe correlations play in the anomalous normal state properties and the superconducting pairing mechanism in the cuprates.

Recently, Dumm *et al.* [641] performed infrared (IR) spectroscopy measurements on single crystals of $La_{1.97}Sr_{0.03}CuO_4$, a weakly doped phase of one of the protypical high T_c superconducting systems $La_{2-x}Sr_xCuO_4$. The existence of spin stripes in the $La_{2-x}Sr_xCuO_4$ system has been well documented through extensive neutron scattering and transport studies on this system by Matsuda *et al.* [642]. The IR spectroscopy measurements revealed

anisotropy of both the electronic conductivity and the lattice dynamics. The phonon mode data indicate that the spin stripes may be accompanied by charge ordering which appears to be quasi–static on the time scale of phonon frequencies. Significant anisotropy of the electronic reponse within the CuO_2 planes was found, with enhancement of the conductivity along the stripe direction. The authors conclude that the results uncover a more complex electronic behavior due to stripes that is beyond an idealized picture of strictly one–dimensional charge channels embedded in an antiferromagnetic insulator.

Extensive low temperature scanning tunneling microscopy/spectroscopy (STM/S) studies have been performed on optimally–doped $Bi_2Sr_2CaCu_2O_{8+\delta}$ (Bi2212) [643]. The measurements reveal electronic inhomogeneities that are reflected in spatial variations in both the local density of states spectrum and the superconducting energy gap. These variations are correlated spatially and have a very short length scale of ~ 14 Å.

Recent scanning tunneling spectroscopy studies of the high T_c superconductor $Bi_2Sr_2CaCu_2O_{8+\delta}$ (Bi2212) have revealed weak, incommensurate spatial modulations in the tunneling conductance [644]. Fourier analysis of images of these energy–dependent modulations yield the dispersion of their wave vectors. Comparison of the dispersions with photoemission spectroscopy data indicate that quasiparticle interference, due to elastic scattering between characteristic regions of momentum space, provides a consistent explanation for the conductance modulations, without the need to invoke another order parameter. These results implicate quasiparticle scattering processes as candidates to explain other incommensurate phenomena in cuprates. However, these results do not rule out stripes in Bi2212, but they show that stripes are not needed to explain the undulations on the surface of BSCCO seen earlier by STM.

Generic phase diagram

Based upon investigations on LSCO, YBCO–123, YBCO–124, BSCCO, and other systems, one can construct a generic $T - x$ phase diagram, represented schematically in Fig. 8.98. The phase diagram is very rich and contains insulating, antiferromagnetic, superconducting, pseudogap, two dimensional (2D) non–Fermi liquid like, and three dimensional (3D) Fermi liquid like regions. This version of the phase diagram is similar to the one proposed by Tallon and Loram [645] who examined the temperature dependence of the NMR Knight shift and relaxation rate, entropy, electrical resistivity, infrared conductivity, Raman scattering, ARPES and electron tunneling data. In this phase diagram, the maximum value of T_c occurs at a value of the hole concentration $p_{max} \approx 0.16$, while the critical hole concentration p_{cr} where T^* vanishes (quantum critical point) is $p_{cr} \approx 0.19$.

A number of models and notions have been proposed to explain the part of the phase diagram delineated by the curves of T^* and T_c vs x (for example, [646–653]). Many of these models involve the local pairing of electrons

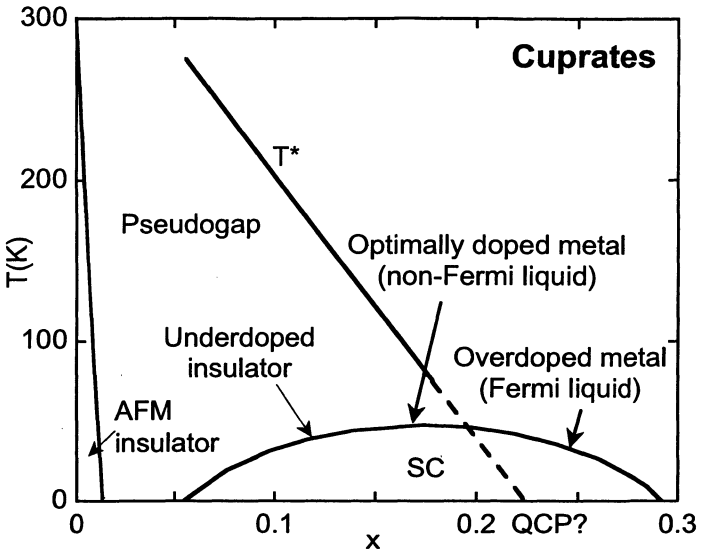

Fig. 8.98. Generic temperature T^*–dopant concentration x phase diagram for cuprates (schematic). The lines labelled T_N and T_c delineate the antiferromagnetic (AFM) and superconducting regions, respectively. The line denoted T^* represents the crossover into the pseudogap state. The dashed line is a linear extrapolation of $T^*(x)$ to a possible quantum critical point (QCP)

(or holes) at the temperature T^* leading to a suppression of the low lying charge and spin excitations and the formation of the normal state pseudogap, followed by the onset of phase coherence at T_c that results in superconductivity. Since the phenomenon of superconductivity involves coherent pairing, a bell shaped curve of T_c vs x results as shown schematically in Fig. 8.99. For example, in resonating valence bond (RVB) models [599,646–649,652], which incorporate spin – charge separation into "spinons" with spin $\sigma = 1/2$ and charge $q = 0$ and "holons" with $\sigma = 0$ and $q = +e$, where e is the charge of the electron, the spinons become paired (spin pseudogap) at T^* and coherent pairing of holons (Bose–Einstein condensation) occurs at T_ϕ, resulting in superconductivity.

As illustrated in Fig. 8.99, the temperature T^* at which the pseudogap forms decreases with doping level x from a value much larger that T_c at low doping to a value comparable to T_c near optimal doping level where T_c is a maximum. Extrapolation of $T^*(x)$ to 0 K suggests that there is a QCP within the superconducting region, as depicted in Fig. 8.99. A number of theories have been developed that relate the high T_c superconductivity in the cuprates to the existence of a QCP where $T^*(x)$ vanishes. It is interesting that superconductivity in certain heavy fermion f–electron materials (e.g., $CeIn_3$, $CePd_2Si_2$) is found in the vicinity of a magnetic QCP and T_c has an

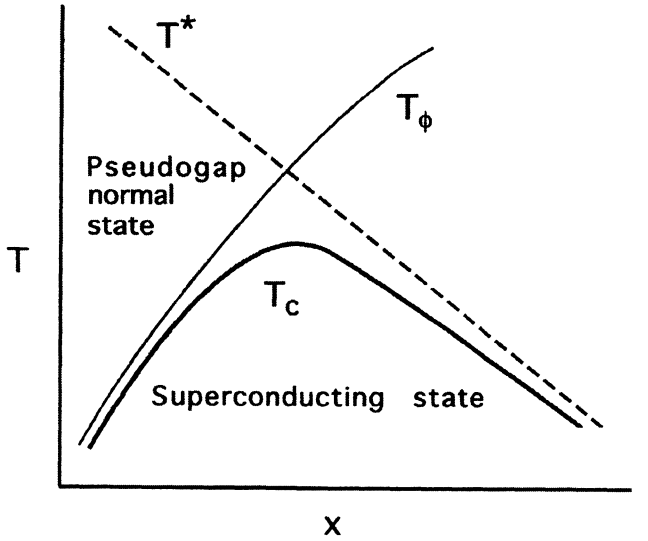

Fig. 8.99. Schematic temperature T^* – dopant concentration x phase diagram for the cuprates. The dashed line labelled T^* represents the temperature below which some type of local pairing occurs leading to a suppression of low energy excitations and the formation of the pseudogap. The solid line labelled T_ϕ denotes the temperature below which phase coherence develops, resulting in superconductivity. The dark solid line labelled T_c delineates the superconducting region

inverted parabolic dependence on pressure, the control parameter. Further evidence for a connection between the pseudogap phase and superconductivity is the similarity in the magnitude of the superconducting energy gap and its variation with direction about the Fermi surface; e.g., as discussed above, the pseudogap and the superconducting gap is BSCCO both have $d_{x^2-y^2}$ symmetry, according to ARPES measurements. Recent Nernst effect measurements the $La_{2-x}Sr_xCuO_4$ system in high magnetic fields have provided evidence for vortices (or vortex–like excitations) at temperatures significantly above T_c in the pseudogap phase [654, 655]. In the Nernst effect, a thermal gradient is applied to the sample in a magnetic field, and vortices are detected by the large transverse electric field produced as the vortices diffuse down the gradient. In underdoped $La_{2-x}Sr_xCuO_4$, the vortex–like excitations extend to a temperature $T_{vortex}(x)$ is much larger than T_c and about one–half of $T^*(x)$ (i.e., $T_{vortex}(x)$ tracks $T^*(x)$) [654]. In overdoped $La_{2-x}Sr_xCuO_4$, the the upper critical field curve $H_{c2}(T)$ does not end at the zero field critical temperature T_c, but at a much higher temperature [655]. These results suggest that T_c corresponds to a loss in phase rigidity, rather that a vanishing of the pairing amplitude. Recently, evidence for vortex–like excitations

above T_c were obtained from in–plane magnetoresistivity measurements on $Y_{1-x}Pr_xBa_2Cu_3O_{7-\delta}$ single crystals [656].

8.5.6 Concluding Remarks

The past two decades of research have consistently yielded a rich variety of new compounds, new phenomena, and new insights into the nature of superconductivity. When heavy–fermion superconductivity was first discovered in $CeCu_2Si_2$ in 1979 by Steglich and coworkers, the coexistence of magnetism and superconductivity had only been established in ternary rare earth compounds such as the rare earth molybdenum chalcogenides RMo_6X_8 (X = S, Se) and the rare earth rhodium borides RRh_4B_4. Since then about 20 different Ce–, Pr–, U–, and Pu–based heavy–fermion superconductors have been discovered and the list will continue to grow. The past few years have seen renewed interest in heavy–fermion superconductors with the discovery of the coexistence of ferromagnetism and superconductivity in UGe_2, URhSi, and, possibly, $ZrZn_2$. The exciting discovery of superconductivity in $PrOs_4Sb_{12}$, which contains two superconducting phases which appear to have different order parameter symmetries, and may have a quadrupolar origin, suggests a new route to unconventional superconductivity. Heavy–fermion superconductors continue to be a fertile area of research and enhance our understanding of superconductivity.

The organic metals and superconductors show a rich variety of novel ground states and cover a broad spectrum of tunable fundamental physical phenomena which are of current interest. One of the most studied but still very controversial issues is the nature of the superconductivity. For the 1D Bechgaard salts a number of recent experiments indicate a triplet superconducting state. For the 2D organic superconductors, the experimental situation is unsettled. NMR and thermal–conductivity experiments suggest that the superconducting order parameter is unconventional, whereas the measurements of the specific heat indicate nodeless gap. In an attempt to solve this puzzling situation, it was suggested that an s–wave to d–wave gap–symmetry transition could be induced by an in–plane magnetic field [482]. In this theoretical treatment, phonon–mediated superconductivity with a small wavevector was assumed, which could explain such a transition. Although this proposal would resolve the controversial NMR and specific heat results, other predictions of this theory such as the orientation of the d–wave gap nodes are at odds with recent experimental results [472]. Further studies, especially experiments that directly probe the phase difference of the superconducting wave function, are highly desirable.

Many of the high Tc cuprate superconductors are derived from antiferromagnetic insulating parent compounds through chemical substitutions that dope the CuO2 planes with electrons or holes. It is widely believed that the pairing mechanism in these material is associated with AFM spin fluctuations. The cuprates have a very rich and interesting T – x phase diagram that

contains AFM, pseudogap, and superconducting phases. The pseudogap gap phase and the superconductivity appear to be intimately related and have energy gaps with the same symmetry. The preponderance of evedence indicates that the superconducting order parameter has d–wave symmetry. However, some experiments indicate that the superconducting order parameter has s–wave symmetry or, at least, a significant s–wave component. The pseudogap temperature T*(x) may vanish in the superconducting phase at a QCP that may be profoundly related to the high Tc superconductivity found in these remarkable materials. An interesting feature that may whose role in the high Tc superconductivity of the cuprates is not yet known is electronic inhomogeneity observed in various experiments (e.g., neutron diffraction, scanning STM). Other high Tc cuprate superconductors will undoubtedly be discovered, and it is not unreasonable that some will have values of Tc greater that the current maximum value of 133 K (at atmospheric pressure). The theory of the normal and superconducting states of the cuprate superconductors represents a significant challenge. The compound Sr_2RuO4 exhibits unconventional superconductivity and is one of the leading candidates for p–wave superconductivity.

8.6 Comparison of the Properties of Different Classes of Novel Superconductors

In this chapter, we have focused on the unconventional superconductivity that is exhibited by three classes of strongly correlated electron materials: heavy fermion f–electron intermetallic compounds, organic compounds, and layered cuprates and ruthenates. For all three classes of materials, there is evidence that the unconventional superconductivity of many of these compounds is anisotropic with an energy gap that vanishes at points on along lines on the Fermi surface. This indicates that the superconducting electrons are paired in singlet or triplet spin states with finite angular momentum $L > 0$. The strongest evidence for superconducting electron pairing with $L > 0$ comes from experiments on the layered perovskite like cuprate high T_c superconductors that probe the magnitude as well as the phase of the superconducting order parameter $\Delta(\mathbf{k})$. These experiments generally indicate that $\Delta(\mathbf{k})$ has $d_{x^2-y^2}$ symmetry in the hole–doped cuprates, although recent twist angle experiments mentioned above suggest s–wave pairing. As discussed earlier in this chapter, the situation with the electron–doped cuprate high T_c superconductors is less clear, with some experiments indicating s–wave pairing and others suggesting d–wave pairing; further research will be required to clarify the situation in this complex group of cuprate superconductors. For the heavy fermion f–electron intermetallic compounds and the organic compounds, a variety of measurements in the superconducting state that probe the magnitude of the superconducting order parameter are consistent with $L > 0$ pairing. These experiments are based on power law T–dependences of

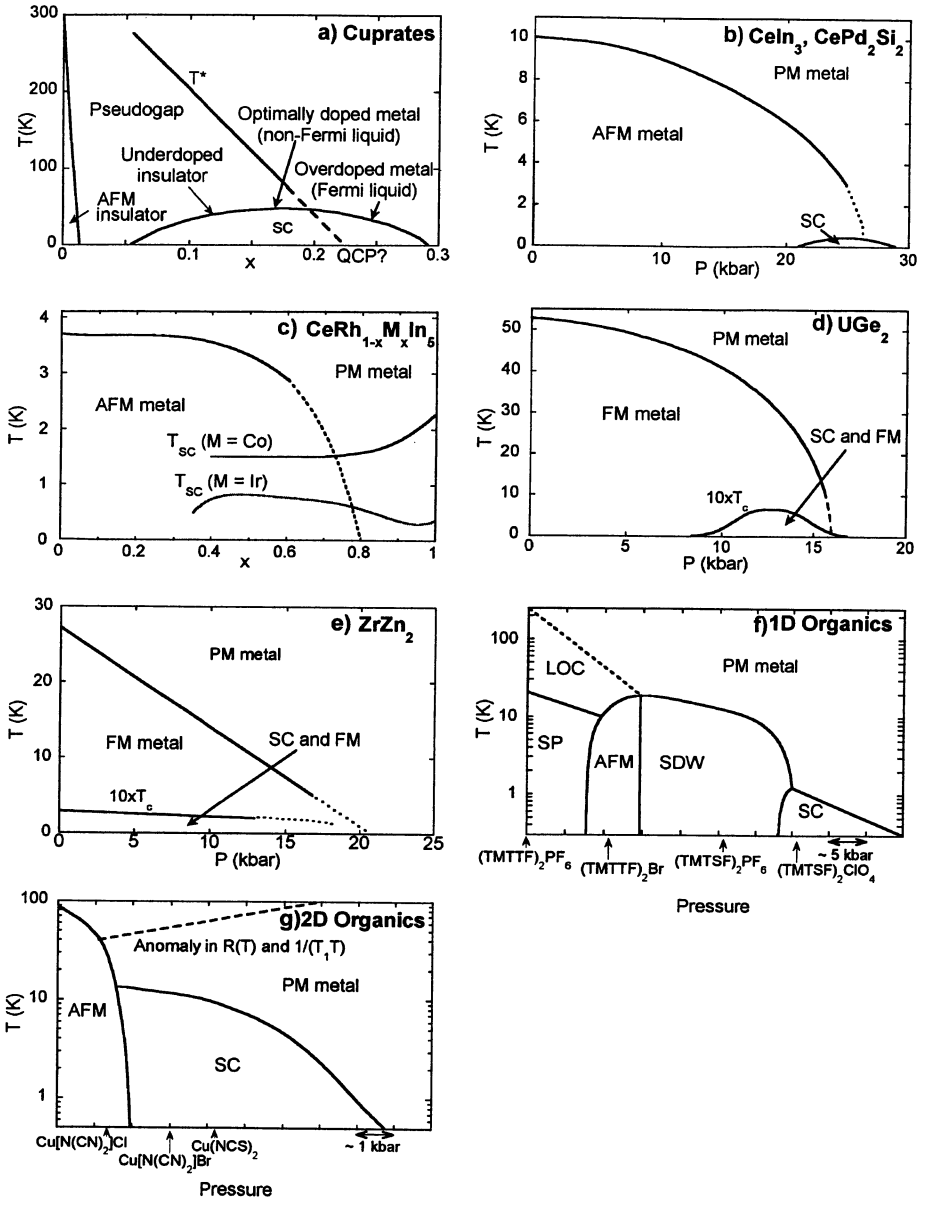

Fig. 8.100. Schematic temperature T^* – dopant concentration x and T^* – pressure P phase diagram for the cuprates: (a) heavy fermion f–electron materials (b)–(e), and organic compounds (f)–(g)

the physical properties in the superconducting state. Since it has not yet been possible to perform experiments that are sensitive to the phase of the superconducting order parameter in these materials, as was done in the cuprates, the case for $L > 0$ pairing in these materials is not as strong as in the cuprates.

In all three classes of materials, magnetically ordered ground states are found in close proximity to the superconducting ground states. This is illustrated by the temperature vs composition ($T - x$) and temperature vs pressure ($T - P$) phase diagrams of the high T_c cuprate, f–electron heavy fermion, and organic superconductors shown in Figs. 8.100 (a)–(g). Although these phase diagrams differ in the extent to which the magnetic and superconducting phases overlap, the overall similarity is compelling and suggests that there is some kind of relationship between magnetism and superconductivity in these materials. In many of the compounds, the curve of T_c vs x or P has an inverted parabolic shape and occurs near a magnetic quantum critical point, where the magnetic fluctuations are expected to be especially strong and extended in temperature and energy, and are thereby effective in mediating superconducting electron pairing. This is dramatically illustrated in the phase diagrams of the heavy fermion compounds $CeIn_3$ and $CePd_2Si_2$ as depicted in Fig. 8.100 (b). It is interesting to note that electron tunneling measurements on the heavy fermion f–electron superconductor UPd_2Al_3 have revealed a feature in the normal state conductance at an energy where magnetic excitations have been identified in inelastic neutron scattering studies on this compound. In addition to superconductivity, non–Fermi liquid behavior in the physical properties is found in examples in all three classes of these materials near magnetic quantum critical points. (The situation is more complex in the f–electron intermetallic compounds where non–Fermi liquid behavior in some systems occurs throughout a large range of concentration and appears to be associated with some type of unconventional Kondo effect.) Experiments on the new heavy fermion filled skutterudite compound $PrOs_4Sb_{12}$ reveal unconventional superconductivity. In this compound, the heavy fermion state and the superconductivity may arise from quadrupolar fluctuations, rather than magnetic fluctuations that are believed to be responsible for the superconducting electron pairing in the unconventional superconductors considered in this chapter. The pseudogap and superconducting phases appear to be intimately related and have energy gaps with the same symmetry (apparently, d-wave symmetry). The pseudogap temperature $T^*(x)$ may vanish in the superconducting phase at a QCP that could be linked to the occurrence of high T_c superconductivity in these remarkable materials. An interesting feature whose role, if any, in the high T_c superconductivity of the cuprates has not yet established is electronic inhomogeneity observed in various experiments (e.g., neutron diffraction, scanning STM).

Acknowledgements

We would like to thank N. P. Butch, N. A. Frederick, T. A. Sayles, and J. D. Thompson for critical comments regarding this Chapter. Invaluable techni-

cal assistance in preparing this manuscript was provided by C. Rosado and C. Rayt. Research support of the U.S. Department of Energy, the National Science Foundation, and the Deutsche Forschungsgemeinschaft is gratefully acknowledged.

References

1. N. D. Mathur, F. M. Grosche, S. R. Julian, I. R. Walker, D. M. Freye, R. K. W. Haselwimmer, and G. G. Lonzarich, Nature **394**, 39 (1998).
2. S. R. Julian, F. V. Carter, F. M. Grosche, R. K. W. Haselwimmer, S. J. Lister, N. D. Mathur, G. J. McMullan, C. Pfleiderer, S. S. Saxena, I. R. Walker, N. J. W. Wilson, and G. G. Lonzarich, J. Magn. Magn. Mat. **177-181**, 265 (1998).
3. S. S. Saxena, P. Agarwal, K. Ahllan, F. M. Grosche, R. K. W. Haselwimmer, M. J. Steiner, E. Pugh, I. R. Walker, S. R. Julian, P. Monthoux, G. G. Lonzarich, A. Huxley, I. Sheikin, D. Braithwaite, and J. Flouquet, Nature **406**, 587 (2000).
4. V. Jaccarino and M. Peter, Phys. Rev. Lett. **9**, 290 (1962).
5. M. B. Maple, in *Magnetism: A Treatise on Modern Theory and Materials*, edited by H. Suhl (Academic, New York, 1973), Vol. 5, Chap. 10, p. 289.
6. M. B. Maple, Appl. Phys. **9**, 179 (1976).
7. in *Superconductivity in Ternary Compounds I, Topics in Current Physics*, edited by Ø. Fischer and M. B. Maple (Springer-Verlag, Berlin, Heidelberg, New York, 1982), Vol. 32, Chap. 1, p. 1.
8. in *Superconductivity in Ternary Compounds II, Topics in Current Physics*, edited by M. B. Maple and Ø. Fischer (Springer-Verlag, Berlin, Heidelberg, New York, 1982), Vol. 34.
9. M. B. Maple, H. C. Hamaker, and L. D. Woolf, in *Superconductivity in Ternary Compounds II, Topics in Current Physics*, edited by M. B. Maple and Ø. Fischer (Springer-Verlag, Berlin, Heidelberg, New York, 1982), Vol. 34, Chap. 4.
10. M. B. Maple, in *Advances in Superconductivity, NATO ASI Series, Series B Physics*, edited by B. Deaver and J. Ruvalds (Plenum, New York, London, 1983), Vol. 100, p. 279.
11. M. B. Maple, Nature **315**, 95 (1985).
12. D. L. Cox and M. B. Maple, Physics Today **48**, 32 (1995).
13. Ø. Fischer, in *Ferromagnetic Materials*, edited by K. H. J. Buschow and E. P. Wohlfarth (Elsevier, New York, 1990), Vol. 5, Chap. 6, p. 465.
14. V. L. Ginzburg, Sov. Phys. JETP **4**, 153 (1957).
15. B. T. Matthias, H. Suhl, and E. Corenzwit, Phys. Rev. Lett. **1**, 92 (1958).
16. B. S. Chandrasekhar, Appl. Phys. Lett. **1**, 7 (1962).
17. A. M. Clogston, Phys. Rev. Lett. **9**, 266 (1962).
18. N. R. Werthamer, E. Helfand, and P. C. Hohenberg, Phys. Rev. **147**, 295 (1966).
19. K. Maki, Phys. Rev. **148**, 362 (1966).
20. W. Buckel and R. Hilsch, Z. Phys. **128**, 324 (1950).
21. C. Herring, Physica **24**, S 184 (1958).
22. H. Suhl and B. T. Matthias, Phys. Rev. **114**, 977 (1959).

23. A. A. Abrikosov and L. P. Gorkov, Zh. Eksp. Teor. Fiz., 39 (1960) 1781; Sov. Phys. JETP **12**, 1243 (1961).
24. J. R. Schrieffer and P. A. Wolff, Phys. Rev. **149**, 491 (1966).
25. J. Friedel, Nuovo Cimento **Suppl. 12**, 1861 (1958).
26. P. W. Anderson, Phys. Rev. **124**, 41 (1961).
27. M. B. Maple, Phys. Lett. **26A**, 513 (1968).
28. C. A. Luengo and M. B. Maple, Solid State Commun. **12**, 757 (1973).
29. W. R. Decker and D. K. Finnemore, Phys. Rev. **172**, 430 (1968).
30. S. Skalski, O. Betbeder-Matibet, and P. R. Weiss, Phys. Rev. **136**, A1500 (1964).
31. Y.-J. Kim and A. W. Overhauser, Phys. Rev. B **49**, 15799 (1994).
32. M. B. Maple, Solid State Commun. **8**, 1915 (1970).
33. P. G. deGennes, J. Phys. Radium **23**, 510 (1962).
34. M. B. Maple, W. A. Fertig, A. C. Mota, L. E. DeLong, D. Wohlleben, and R. Fitzgerald, Solid State Commun. **11**, 829 (1972).
35. G. Riblet and K. Winzer, Solid State Commun. **9**, 1663 (1971).
36. C. A. Luengo, M. B. Maple, and W. A. Fertig, Solid State Commun. **11**, 1445 (1972).
37. H. Armbrüster, H. v. Löhneysen, G. Riblet, and F. Steglich, Solid State Commun. **14**, 55 (1974).
38. S. D. Bader, N. E. Phillips, M. B. Maple, and C. A. Luengo, Solid State Commun. **16**, 1263 (1975).
39. M. B. Maple and Z. Fisk, in *Proc. Eleventh Int. Conf. Low Temp. Phys.*, edited by J. F. Allen, D. M. Finlayson, and D. M. McCall (Elsevier, St. Andrews, Scotland, 1968), p. 1288.
40. P. E. Bloomfield and D. R. Hamann, Phys. Rev. **164**, 856 (1967).
41. J. G. Huber, W. A. Fertig, and M. B. Maple, Solid State Commun. **15**, 453 (1974).
42. A. B. Kaiser, J. Phys. C **3**, 409 (1970).
43. M. B. Maple, J. G. Huber, B. R. Coles, and A. C. Lawson, J. Low Temp. Phys. **3**, 137 (1970).
44. J. G. Huber and M. B. Maple, J. Low Temp. Phys. **3**, 1987 (1970).
45. J. G. Huber and M. B. Maple, Solid State Commun. **8**, 1987 (1970).
46. C. A. Luengo, J. M. Cotignola, J. Sereni, A. R. Sweedler, M. B. Maple, and J. G. Huber, Solid State Commun. **10**, 459 (1972).
47. C. A. Luengo, J. M. Cotignola, J. Sereni, A. R. Sweedler, and M. B. Maple, in *Proc. 13th Int. Conf. Low Temp. Phys., Boulder, Colorado*, edited by K. D. Timmerhaus, W. J. O'Sullivan, and E. F. Hammel (Plenum, New York, London, 1972), p. 585.
48. H. L. Watson, D. T. Peterson, and D. K. Finnemore, Phys. Rev. B **8**, 3179 (1973).
49. D. L. Martin, Proc. Royal Soc. (London) **78**, 1489 (1961).
50. F. W. Smith, J. Low Temp. Phys. **5**, 683 (1971).
51. C. W. Dempesy, private communication of unpublished data; reported in Ref. [44] (1970).
52. E. Müller-Hartmann and J. Zittartz, Phys. Rev. Lett. **26**, 428 (1971).
53. A. Ludwig and M. J. Zuckermann, J. Phys. F **1**, 516 (1971).
54. M. J. Zuckermann, Phys. Rev. **168**, 390 (1968).
55. E. Müller-Hartmann and J. Zittartz, Z. Phys. **234**, 58 (1970).

56. M. Jarrell, Phys. Rev. B; Rapid Commun. **41**, 4815 (1990).
57. M. B. Maple, J. Wittig, and K. S. Kim, Phys. Rev. Lett. **23**, 1375 (1969).
58. J. G. Huber, J. Brooks, D. Wohlleben, and M. B. Maple, in *Magnetism and Magnetic Materials*, edited by C. D. Graham, Jr., G. H. Lander, and J. J. Rhyne (AIP, New York, 1975), Vol. 24, p. 475.
59. S. Ortega, M. Roth, C. Rizzuto, and M. B. Maple, Solid State Commun. **13**, 5 (1973).
60. C. A. Luengo, J. G. Huber, M. B. Maple, and M. Roth, Phys. Rev. Lett. **32**, 54 (1974).
61. C. A. Luengo, J. G. Huber, M. B. Maple, and M. Roth, J. Low Temp. Phys. **21**, 129 (1975).
62. H. B. MacKay, L. D. Woolf, M. B. Maple, and D. C. Johnston, J. Low Temp. Phys. **41**, 639 (1980).
63. M. Ishikawa and Ø. Fischer, Solid State Commun. **24**, 747 (1977).
64. W. Thomlinson, G. Shirane, D. E. Moncton, M. Ishikawa, and Ø. Fischer, Phys. Rev. B **23**, 4455 (1981).
65. R. W. McCallum, D. C. Johnston, R. N. Shelton, and M. B. Maple, Solid State Commun. **24**, 391 (1977).
66. H. C. Hamaker, L. D. Woolf, H. B. MacKay, Z. Fisk, and M. B. Maple, Solid State Commun. **31**, 139 (1979).
67. M. B. Maple, L. D. Woolf, C. F. Majkrzak, G. Shirane, W. Thomlinson, and D. E. Moncton, Phys. Lett. **77A**, 487 (1980).
68. D. E. Moncton, G. Shirane, W. Thomlinson, M. Ishikawa, and Ø. Fischer, Phys. Rev. Lett. **41**, 1133 (1978).
69. P. Fulde and J. Keller, in *Superconductivity in Ternary Compounds II, Topics in Current Physics*, edited by M. B. Maple and Ø. Fischer (Springer-Verlag, Berlin, Heidelberg, New York, 1982), Vol. 34, Chap. 9, p. 249.
70. W. Baltensperger and S. Strassler, Phys. Cond. Materie **1**, 20 (1963).
71. C. F. Majkrzak, S. K. Satija, G. Shirane, H. C. Hamaker, Z. Fisk, and M. B. Maple, Phys. Rev. B **27**, 2889 (1983).
72. R. Nagarajan, C. Mazumkar, Z. Hossain, S. K. Dhar, K. V. Gopolakrishnan, L. C. Gupta, C. Godart, B. D. Padalia, and R. Vijayaraghavan, Phys. Rev. Lett. **72**, 274 (1994).
73. R. J. Cava, H. Takagi, H. W. Zandbergen, J. J. Krajewski, W. F. Peck, Jr., T. Siegrist, B. Batlogg, R. B. van Dover, R. J. Felder, K. Mizuhashi, J. O. Lee, H. Eisaki, and S. Uchida, Nature **367**, 252 (1994).
74. R. J. Cava, H. Takagi, B. Batlogg, H. W. Zandbergen, J. J. Krajewski, W. F. Peck, Jr., R. B. van Dover, R. J. Felder, T. Siegrist, K. Mizuhashi, J. O. Lee, H. Eisaki, S. A. Carter, and S. Vehida, Nature **367**, 146 (1994).
75. J. L. Sarrao, M. C. de Andrade, J. Herrmann, S. H. Han, Z. Fisk, M. B. Maple, and R. J. Cava, Physica C **229**, 65 (1994).
76. H. Eisaki, H. Takagi, R. J. Cava, K. Mizuhashi, J. O. Lee, B. Batlogg, J. J. Krajewski, W. F. Peck, Jr., and S. Uchida, Phys. Rev. B **50**, 647 (1994).
77. R. Movshovich, M. F. Hundley, J. D. Thompson, P. C. Canfield, B. K. Cho, and A. J. Chubakov, Physica C **227**, 381 (1994).
78. M. Xu, P. C. Canfield, J. E. Ostenson, D. K. Finnemore, B. K. Cho, Z. R. Wang, and D. C. Johnston, Physica C **227**, 321 (1994).
79. T. E. Grigereit, J. W. Lynn, Q. Huang, A. Santoro, R. J. Cava, J. J. Krajewski, and W. F. Peck, Jr., Phys. Rev. Lett. **73**, 2756 (1994).

80. P. C. Canfield, P. L. Gammel, and D. J. Bishop, Physics Today **October**, 40 (1998).
81. W. A. Fertig, D. C. Johnston, L. E. DeLong, R. W. McCallum, M. B. Maple, and B. T. Matthias, Phys. Rev. Lett. **38**, 987 (1977).
82. M. Ishikawa and Ø. Fischer, Solid State Commun. **23**, 37 (1977).
83. M. B. Maple, H. C. Hamaker, L. D. Woolf, H. B. MacKay, Z. Fisk, W. Odoni, and H. R. Ott, in *Crystalline Electric Field and Structural Effects in f-Electron Systems*, edited by J. E. Crow, R. P. Guertin, and T. W. Mihalisin (Plenum, New York, 1980), p. 533.
84. D. E. Moncton, D. B. McWhan, J. Eckert, G. Shirane, and W. Thomlinson, Phys. Rev. Lett. **39**, 1164 (1977).
85. D. E. Moncton, D. B. McWhan, P. H. Schmidt, G. Shirane, W. Thomlinson, M. B. Maple, H. B. MacKay, L. D. Woolf, Z. Fisk, and D. C. Johnston, Phys. Rev. Lett. **45**, 2060 (1980).
86. J. W. Lynn, D. E. Moncton, W. Thomlinson, G. Shirane, and R. N. Shelton, Solid State Commun. **26**, 493 (1978).
87. S. K. Sinha, G. W. Crabtree, D. G. Hinks, and H. A. Mook, Phys. Rev. Lett. **48**, 950 (1982).
88. J. W. Lynn, G. Shirane, W. Thomlinson, R. N. Shelton, and D. E. Moncton, Phys. Rev. B **24**, 3817 (1981).
89. L. D. Woolf, S. E. Lambert, M. B. Maple, F. Acker, H. C. Ku, W. Odoni, and H. R. Ott, J. Low Temp. Phys. **51**, 117 (1983).
90. J. Rossat-Mignod, P. Burlet, S. Quźel, A. Benoît, J. Flouquet, R. Horyn, O. Peña, and M. Sergent, J. Physique Lett. **46**, L373 (1985).
91. P. W. Anderson and H. Suhl, Phys. Rev. **116**, 898 (1959).
92. E. I. Blount and C. M. Varma, Phys. Rev. Lett. **42**, 1079 (1979).
93. R. A. Ferrell, J. K. Bhattacharjee, and A. Bagchi, Phys. Rev. Lett. **43**, 154 (1979).
94. H. Matsumoto, H. Umezawa, and M. Tachiki, Solid State Commun. **31**, 157 (1979).
95. M. B. Maple, J. Magn. Magn. Mater. **31-34**, 479 (1983).
96. D. C. Johnston, W. A. Fertig, M. B. Maple, and B. T. Matthias, Solid State Commun. **26**, 141 (1978).
97. H. A. Mook, O. A. Pringle, S. Kawarazaki, S. K. Sinha, G. W. Crabtree, D. G. Hinks, M. B. Maple, Z. Fisk, D. C. Johnston, L. D. Woolf, and H. C. Hamaker, in *Superconductivity in d- and f-Band Metals 1982*, edited by W. Buckel and W. Weber (KFK, Karlsruhe, 1982), p. 201.
98. L. D. Woolf, D. C. Johnston, H. A. Mook, W. C. Koehler, M. B. Maple, and Z. Fisk, Physica B&C **109&110**, 2045 (1982).
99. K. N. Yang, S. E. Lambert, H. C. Hamaker, M. B. Maple, H. A. Mook, and H. C. Ku, in *Superconductivity in d- and f-Band Metals 1982*, edited by W. Buckel and W. Weber (KFK, Karlsruhe, 1982), p. 217.
100. H. C. Ku, F. Acker, and B. T. Matthias, Phys. Lett. **76A**, 399 (1980).
101. H. C. Hamaker, H. C. Ku, M. B. Maple, and H. A. Mook, Solid State Commun. **43**, 455 (1982).
102. H. W. Meul, C. Rossel, M. Decroux, Ø. Fischer, G. Remenyi, and A. Briggs, Phys. Rev. Lett. **53**, 497 (1984).
103. M. S. Torikachvili and M. B. Maple, Solid State Commun. **40**, 1 (1981).

104. M. S. Torikachvili, J. Beille, S. E. Lambert, and M. B. Maple, in *Superconductivity in d- and f-Band Metals 1982*, edited by W. Buckel and W. Weber (KFK, Karlsruhe, 1982), p. 217.
105. M. Decroux, S. E. Lambert, M. S. Torikachvili, M. B. Maple, R. P. Guertin, L. D. Woolf, and R. Baillif, Phys. Rev. Lett. **52**, 1563 (1984).
106. B. B. Schwartz and L. W. Gruenberg, Phys. Rev. **177**, 747 (1969).
107. Ø. Fischer, Helv. Phys. Acta. **45**, 229 (1972).
108. S. Maekawa and M. Tachiki, Phys. Rev. B **18**, 4688 (1978).
109. F. Steglich, J. Aarts, C. D. Bredl, W. Lieke, D. Meschede, W. Franz, and H. Schäfer, Phys. Rev. Lett. **43**, 1892 (1979).
110. D. Aoki, A. Huxley, E. Ressouche, D. Braithwaite, J. Flouquet, J.-P. Brison, E. Lhotel, and C. Paulsen, Nature **413**, 613 (2001).
111. D. Rossi, R. Marazza, and R. Ferro, J. Less-Common Metals **66**, 17 (1979).
112. B. H. Grier, J. M. Lawrence, V. Murgai, and R. D. Parks, Phys. Rev. B **29**, 2664 (1984).
113. G. Knopp, A. Loidl, R. Caspary, U. Gottwick, C. D. Bredl, H. Spille, F. Steglich, and A. P. Murani, J. Magn. Magn. Mat. **74**, 341 (1988).
114. O. Trovarelli, M. Weiden, R. Müller-Reisener, M. Gómez-Berisso, P. Gegenwart, M. Deppe, C. Geibel, J. G. Sereni, and F. Steglich, Phys. Rev. B **56**, 678 (1997).
115. I. R. Harris and G. V. Raynor, J. Less-Common Metals **9**, 7 (1965).
116. H. Hegger, C. Petrovic, E. G. Moshopoulou, M. F. Hundley, J. L. Sarrao, Z. Fisk, and J. D. Thompson, Phys. Rev. Lett. **84**, 4986 (2000).
117. C. Petrovic, R. Movshovich, M. Jaime, P. G. Pagliuso, M. F. Hundley, J. L. Sarrao, Z. Fisk, and J. D. Thompson, Europhys. Lett. **53**, 354 (2001).
118. C. Petrovic, P. G. Pagiluso, M. F. Hundley, R. Movshovich, J. L. Sarrao, J. D. Thompson, Z.Fisk, and P. Monthoux, J. Phys: Condens. Matter **13**, L337 (2001).
119. M. Nicklas, V. A. Sidorov, H. A. Borges, P. G. Pagliuso, C. Petrovic, Z. Fisk, J. L. Sarrao, and J. D. Thompson, Phys. Rev. B **67**, 020506(R) (2002).
120. E. D. Bauer, N. A. Frederick, P.-C. Ho, V. S. Zapf, and M. B. Maple, Phys. Rev. B **65**, 100506(R) (2002).
121. M. W. McElfresh, J. H. Hall, R. R. Ryan, J. L. Smith, and Z. Fisk, Acta Cryst., Sec. C **46C**, 1579 (1990).
122. T. J. Heal and G. I. Williams, Acta Cryst. **8**, 494 (1950).
123. T. T. M. Palstra, A. A. Menovsky, J. van den Berg, A. J. Dirkmaat, P. H. Kes, G. J. Nieuwenhuys, and J. A. Mydosh, Phys. Rev. Lett. **55**, 2727 (1985).
124. C. Geibel, C. Schank, S. Thies, H. Kitazawa, C. D. Bredl, A. Böhm, M. Rau, A. Grauel, R. Caspary, R. Helfrich, U. Ahlheim, G. Weber, and F. Steglich, Z. Phys. B **84**, 1 (1991).
125. C. Geibel, S. Thies, D. Kaczorowski, A. Mehner, A. Grauel, B. Seidel, U. Ahlheim, R. Helfrich, K. Petersen, C. D. Bredl, and F. Steglich, Z. Phys. B **83**, 305 (1991).
126. P. Boulet, A. Daoudi, M. Potel, H. Noël, G. M. Gross, G. André, and F. Bourée, J. Alloys Comp. **247**, 104 (1997).
127. V. H. Tran, R. Troć, and G. André, J. Magn. Magn. Mater. **186**, 81 (1998).
128. C. W. Kimball, P. P. Vaishnava, A. E. Dwight, J. D. Jorgensen, and F. Y. Fradin, Phys. Rev. B **32**, 4419 (1985).

129. J. L. Sarrao, L. A. Morales, J. D. Thompson, B. L. Scott, G. R. Stewart, F. Wastin, J. Rebizant, P. Boulet, E. Collneau, and G. H. Lander, Nature **420**, 297 (2002).
130. M. B. Maple, E. D. Bauer, V. S. Zapf, E. J. Freeman, N. A. Frederick, and R. P. Dickey, Acta Physica Polonica B **32**, 3291 (2001).
131. H. R. Ott, H. Rudigier, Z. Fisk, and J. L. Smith, Phys. Rev. Lett. **50**, 1595 (1983).
132. G. R. Stewart, Rev. Mod. Phys. **56**, 755 (1984).
133. W. Assmus, M. Herrmann, U. Rauchschwalbe, S. Riegel, W. Lieke, H. Spille, S. Horn, G. Weber, F. Steglich, and G. Cordier, Phys. Rev. Lett. **52**, 469 (1984).
134. F. Steglich, C. D. Bredl, W. Lieke, U. Rauchschwalbe, and G. Sparn, Physica B **126**, 82 (1984).
135. P. Gegenwart, C. Langhammer, C. Geibel, R. Helfrich, M. Lang, G. Sparn, F. Steglich, R. Horn, L. Donnevert, A. Link, and W. Assmus, Phys. Rev. Lett. **81**, 1501 (1998).
136. S. Raymond, D. Jaccard, H. Wilhelm, and R. Cerny, Solid State Commun. **112**, 617 (1999).
137. F. M. Grosche, S. R. Julian, N. D. Mathur, and G. G. Lonzarich, Physica B **223-224**, 50 (1996).
138. R. Movshovich, T. Graf, D. Mandrus, M. F. Hundley, J. D. Thompson, R. A. Fisher, N. E. Phillips, and J. L. Smith, Physica B **223-224**, 126 (1996).
139. D. Braithwaite, T. Fukuhara, A. Demuer, I. Sheikin, S. Kambe, J.-P. Brison, K. Maezawa, T. Naka, and J. Flouquet, J. Phys.: Condens. Matter **12**, 1339 (2000).
140. G. Knebel, M. Brando, J. Hemberger, M. Nicklas, W. Trinkl, and A. Loidl, Phys. Rev. B **59**, 12390 (1999).
141. T. C. Kobayashi, T. Miyazu, N. Takeshita, K. Shimizu, K. Amaya, Y. Kitaoka, and Y. Ōnuki, J. Phys. Soc. Jpn. **67**, 996 (1998).
142. G. Knopp, A. Loidl, K. Knorr, L. Pawlak, M. Duczmal, R. Caspary, U. Gottwick, H. Spille, F. Steglich, and P. Murani, Z. Phys. B **77**, 95 (1989).
143. F. R. de Boer, J. C. P. Klaasse, P. A. Veenhuizen, A. Böhm, C. D. Bredl, U. Gottwick, H. M. Mayer, L. Pawlak, U. Rauchschwalbe, H. Spille, and F. Steglich, J. Magn. Magn. Mat. **63-64**, 91 (1987).
144. F. M. Grosche, M. J. Steiner, P. Agarwal, I. R. Walker, D. M. Freye, S. R. Julian, and G. G. Lonzarich, Physica B **281-282**, 3 (2000).
145. I. R. Walker, F. M. Grosche, D. M. Freye, and G. G. Lonzarich, Physica C **282-287**, 303 (1997).
146. R. A. Fisher, F. Bouquet, N. E. Phillips, M. F. Hundley, P. G. Pagliuso, J. L. Sarrao, Z. Fisk, and J. D. Thompson, Phys. Rev. B **65**, 224509 (2002).
147. J. D. Thompson, R. Movshovich, Z. Fisk, F. Bouquet, N. J. Curro, R. A. Fisher, P. C. Hammel, H. Hegger, M. F. Hundley, M. Jaime, P. G. Pagliuso, C. Petrovic, N. E. Phillips, and J. L. Sarrao, J. Magn. Magn. Mat. **226-230**, 5 (2001).
148. R. Vollmer, A. Faißt, H. v. Löhneysen, E. D. Bauer, P.-C. Ho, V. S. Zapf, and M. B. Maple, Phys. Rev. Lett. **90**, 057001 (2003).
149. H. R. Ott, H. Rudigier, Z. Fisk, and J. L. Smith, Physica **127B**, 359 (1984).
150. G. R. Stewart, Z. Fisk, J. O. Willis, and J. L. Smith, Phys. Rev. Lett. **52**, 679 (1984).

151. A. DeVisser, J. J. M. Franse, and A. Menovsky, J. Magn. Magn. Mat. **43**, 43 (1984).
152. S. M. Hayden, L. Taillefer, C. Vettier, and J. Flouquet, Phys. Rev. B **46**, 8675 (1992).
153. M. B. Maple, J. W. Chen, Y. Dalichaouch, T. Kohara, C. Rossel, M. S. Torikachvilli, M. W. McElfresh, and J. D. Thompson, Phys. Rev. Lett. **56**, 185 (1986).
154. T. T. M. Palstra, A. A. Menovsky, and J. A. Mydosh, Phys. Rev. B (Rapid Communications) **33**, 6527 (1986).
155. A. Huxley, I. Sheikin, E. Ressouche, N. Kernavanois, D. Braithwaite, R. Calemczuk, and J. Flouquet, Phys. Rev. B **63**, 144519 (2001).
156. R. Vollmer, C. Pfleiderer, H. v. Löhneyesen, E. D. Bauer, and M. B. Maple, Physica B **312-313**, 112 (2002).
157. I. H. Hagmusa, K. Prokeš, Y. Echizen, T. Takabatake, T. Fujita, J. C. P. Klaasse, E. Brück, V. Sechovský, and F. R. de Boer, Physica B **281&282**, 223 (2000).
158. L. E. DeLong, J. G. Huber, K. N. Yang, and M. B. Maple, Phys. Rev. Lett. **51**, 312 (1983).
159. W. R. Abel, A. C. Anderson, W. C. Black, and J. C. Wheatley, Phys. Rev. **147**, 111 (1966).
160. S. Doniach and S. Engelsberg, Phys. Rev. Lett. **17**, 750 (1966).
161. W. F. Brinkman and S. Engelsberg, Phys. Rev. Lett. **21**, 1187 (1968).
162. H. R. Ott and Z. Fisk, in *Handbook on the Physics and Chemistry of the Actinides*, edited by A. J. Freeman and G. H. Lander (North-Holland, Amsterdam, 1987), Vol. 4, Chap. 2, p. 85.
163. K. G. Wilson, Rev. Mod. Phys. **47**, 773 (1975).
164. W. Lieke, U. Rauchschwalbe, C. B. Bredl, F. Steglich, J. Aarts, and F. R. de Boer, J. Appl. Phys. **53**, 2111 (1982).
165. W. Bao, P. G. Pagliuso, J. L. Sarrao, J. D. Thompson, Z. Fisk, J. W. Lynn, and R. W. Erwin, Phys. Rev. B **62**, 14621(R) (2000).
166. W. Bao, P. G. Pagliuso, J. L. Sarrao, J. D. Thompson, Z. Fisk, J. W. Lynn, and R. W. Erwin, Phys. Rev. B **67**, 099903(E) (2003).
167. W. Bao, P. G. Pagliuso, J. L. Sarrao, J. D. Thompson, Z. Fisk, and J. W. Lynn, Phys. Rev. B **64**, 020401(R) (2001).
168. P. H. Frings, J. J. M. Franse, F. R. de Boer, and A. Menovsky, J. Magn. Magn. Mat. **31-34**, 240 (1983).
169. G. Aeppli, E. Bucher, C. Broholm, J. K. Kjems, J. Baumann, and J. Hufnagl, Phys. Rev. Lett. **60**, 615 (1988).
170. A. Krimmel, P. Fischer, B. Roessli, H. Maletta, C. Geibel, C. Schank, A. Grauel, A. Loidl, and F. Steglich, Z. Phys. B **86**, 161 (1992).
171. A. Schröder, J. G. Lussier, B. D. Gaulin, J. D. Garrett, W. J. L. Buyers, L. Rebelsky, and S. M. Shapiro, Z. Phys. B **86**, 161 (1992).
172. L. E. DeLong, R. P. Guertin, S. Hassanain, and T. Fariss, Phys. Rev. B **31**, 7059 (1985).
173. K. Kadowaki and S. B. Woods, Solid State Commun. **58**, 507 (1986).
174. K. Andres, J. E. Graebner, and H. R. Ott, Phys. Rev. Lett. **35**, 1779 (1975).
175. H. R. Ott, O. Marti, and F. Hulliger, Solid State Commun. **49**, 1129 (1984).
176. V. S. Zapf, E. J. Freeman, E. D. Bauer, J. Petricka, C. Sirvent, N. A. Frederick, R. P. Dickey, and M. B. Maple, Phys. Rev. B **65**, 014506 (2001).

177. U. Rauchschwalbe, Physica B&C **147**, 1 (1987).
178. I. Sheikin, E. Steep, D. Braithwaite, J.-P. Brison, S. Raymond, D. Jaccard, and J. Flouquet, J. Low Temp. Phys. **122**, 591 (2001).
179. R. Movshovich, T. Graf, D. Mandrus, J. D. Thompson, J. L. Smith, and Z. Fisk, Phys. Rev. B **53**, 8241 (1995).
180. D. Jaccard, H. Wilhelm, K. Alami-Yadri, and E. Vargoz, Physica B **259-261**, 1 (1999).
181. G. Knebel, D. Braithwaite, P. C. Canfield, G. Lapertot, and J. Flouquet, Phys. Rev. B **65**, 024425 (2002).
182. T. Tayama, A. Harita, T. Sakakibara, Y. Haga, H. Shishido, R. Settai, and Y. Ōnuki, Phys. Rev. B **65**, 180504(R) (2002).
183. M. B. Maple, J. W. Chen, S. E. Lambert, Z. Fisk, J. L. Smith, H. R. Ott, J. S. Brooks, and M. J. Naughton, Phys. Rev. Lett. **54**, 477 (1985).
184. J. W. Chen, S. E. Lambert, M. B. Maple, Z. Fisk, J. L. Smith, G. R. Stewart, and J. O. Willis, Phys. Rev. B **30**, 1583 (1984).
185. Y. Dalichaouch, M. C. de Andrade, and M. B. Maple, Phys. Rev. B **46**, 8671 (1992).
186. E. D. Bauer, R. P. Dickey, V. S. Zapf, and M. B. Maple, J. Phys.: Condens. Matter **13**, L759 (2001).
187. N. Tateiwa, T. C. Kobayashi, K. Hanazono, K. Amaya, Y. Haga, R. Settai, and Y. Ōnuki, J. Phys.: Condens. Matter **13**, L17 (2001).
188. R. R. Hake, Appl. Phys. Lett. **10**, 189 (1967).
189. See, for example, M. Tinkham, *Introduction to Superconductivity*, (McGraw-Hill, New York, 1975).
190. A. Krimmel, P. Fischer, B. Roessli, C. Geibel, F. Steglich, and A. Loidl, J. Magn. Magn. Mat. **149**, 380 (1995).
191. K. Matsuda, Y. Kohori, and T. Kohara, Phys. Rev. B **55**, 15223 (1997).
192. L. Paolasini, J. A. Paixao, G. H. Lander, A. Delapalme, N. Sato, and T. Komatsubara, J. Phys.: Condens. Matter **5**, 8905 (1993).
193. J. Sticht and J. Kübler, Z. Phys. B **87**, 299 (1992).
194. H. Kita, A. Donni, Y. Endoh, K. Kakurai, N. Sato, and T. Komatsubara, J. Phys. Soc. Jpn. **63**, 726 (1994).
195. B. D. Gaulin, D. Gibbs, E. D. Isacs, J. G. Lussier, J. N. Reimers, A. Schröder, L. Taillefer, and P. Zschack, Phys. Rev. Lett **73**, 890 (1994).
196. N. Metoki, Y. Haga, Y. Koike, and Y. Ōnuki, Phys. Rev. Lett. **80**, 5417 (1998).
197. N. Bernhoeft, N. Sato, B. Roessli, N. Aso, A. Hiess, G. H. Lander, Y. Endoh, and T. Komatsubara, Phys. Rev. Lett. **81**, 4244 (1998).
198. M. Kyogaku, Y. Kitaoka, K. Asayama, C. Geibel, C. Schank, and F. Steglich, J. Phys. Soc. Jpn. **61**, 2660 (1992).
199. H. Tou, Y. Kitaoka, K. Asayama, C. Geibel, C. Schank, and F. Steglich, J. Phys. Soc. Jpn. **64**, 725 (1995).
200. M. Jourdan, M. Huth, J. Hessert, and H. Adrian, Physica B **230**, 335 (1997).
201. S. Nakamura, T. Moriya, and K. Ueda, J. Phys. Soc. Jpn. **65**, 4026 (1996).
202. N. Sato, N. Aso, G. Lander, B. Roessli, T. Komatsubara, and Y. Endoh, J. Phys. Soc. Jpn. **66**, 2981 (1997).
203. M. Jourdan, M. Huth, and H. Adrian, Nature **398**, 47 (1999).
204. M. Kyogaku, Y. Kitaoka, K. Asayama, C. Geibel, C. Schank, and F. Steglich, J. Phys. Soc. Jpn. **62**, 4016 (1993).
205. T. Moriya, in *Spin Fluctuations in Itinerant Electron Magnetism*, edited by P. Fulde (Springer-Verlag, Berlin, 1985).

206. T. Moriya and T. Takimoto, J. Phys. Soc. Jpn. **64**, 960 (1995), and refs. therein.
207. G. G. Lonzarich, in *Electron*, edited by M. Springford, (Cambridge University Press, Cambridge, England, 1997).
208. U. Zülicke and A. J. Millis, Phys. Rev. B **51**, 8996 (1995).
209. M. Nicklas, R. Borth, E. Lengyel, P. G. Pagliuso, J. L. Sarrao, V. A. Sidorov, G. Sparn, F. Steglich, and J. D. Thompson, J. Phys.: Condens. Matter **13**, L905 (2001).
210. V. A. Sidorov, M. Nicklas, P. G. Pagliuso, J. L. Sarrao, Y. Bang, A. V. Balatsky, and J. D. Thompson, Phys. Rev. Lett. **89**, 157004 (2002).
211. G. q. Zheng, K. Tanabe, T. Mito, S. Kawasaki, Y. Kitaoka, D. Aoki, Y. Haga, and Y. Ōnuki, Phys. Rev. Lett **86**, 4664 (2001).
212. Y. Kohori, Y. Yamato, Y. Iwamoto, T. Kohara, E. D. Bauer, M. B. Maple, and J. L. Sarrao, Phys. Rev. B **64**, 134526 (2001).
213. R. Movshovich, M. Jaime, J. D. Thompson, C. Petrovic, Z. Fisk, P. G. Pagliuso, and J. L. Sarrao, Phys. Rev. Lett. **86**, 5152 (2001).
214. K. Izawa, H. Yamaguchi, Y. Matsuda, H. Shishido, R. Settai, and Y. Ōnuki, Phys. Rev. Lett. **87**, 057002 (2001).
215. A. Bianchi, R. Movshovich, N. Oeschler, P. Gegenwart, F. Steglich, J. D. Thompson, P. G. Pagliuso, and J. L. Sarrao, Phys. Rev. Lett. **89**, 137002 (2002).
216. N. Oeschler, P. Gegenwart, M. Lang, R. Movshovich, J. L. Sarrao, J. D. Thompson, and F. Steglich, Phys. Rev. Lett **91**, 076402 (2003).
217. A. Bianchi, R. Movshovich, C. Capan, A. Lacerda, P. G. Pagliuso, and J. L. Sarrao, Phys. Rev. Lett. **91**, 187004 (2003).
218. K. Maki and T. Tsuneto, Progress of Theoretical Physics **31**, 945 (1964).
219. L. W. Gruenberg and L. Gunther, Phys. Rev. Lett **16**, 996 (1966).
220. H. A. Radovan, N. A. Fortune, T. P. Murphy, S. T. Hannahs, E. C. Palm, S. W. Tozer, and D. Hall, Nature **425**, 51 (2003).
221. C. Martin, C. C. Agosta, S. W. Tozer, H. A. Radovan, E. C. Palm, T. P. Murphy, and J. L. Sarrao, cond-mat/0309125 (unpublished).
222. J. Paglione, M. A. Tanatar, D. G. Hawthorn, E. Boaknin, R. W. Hill, F. Ronning, M. Sutherland, L. Taillefer, C. Petrovic, and P. C. Canfield, Phys. Rev. Lett. **91**, 246405 (2003).
223. P. Fulde and R. A. Ferrell, Phys. Rev. **135**, A550 (1964).
224. A. I. Larkin and Y. N. Ovchinnikov, Sov. Phys. JETP **20**, 762 (1965).
225. N. R. Dilley, J. Herrmann, S. H. Han, and M. B. Maple, Phys. Rev. B: Brief Reports **56**, 2379 (1997).
226. G. W. Crabtree, M. B. Maple, W. K. Kwok, J. Herrmann, J. A. Fendrick, N. R. Dilley, and S. H. Han, Physics Essays **9**, 628 (1996).
227. M. B. Maple, M. C. de Andrade, J. Herrmann, R. P. Dickey, N. R. Dilley, and S. H. Han, J. Alloys and Compounds **250**, 585 (1997).
228. M. R. Norman, Phys. Rev. Lett **71**, 3391 (1993).
229. D. Hall, E. C. Palm, T. P. Murphy, S. W. Tozer, Z. Fisk, U. Alver, R. G. Goodrich, J. L. Sarrao, P. G. Pagliuso, and T. Ebihara, Phys. Rev. B **64**, 212508 (2001).
230. R. Settai, H. Shishido, S. Ikeda, Y. Murakawa, M. Nakashima, D. Aoki, Y. Haga, H. Harima, and Y. Onuki, J. Phys.: Condens. Matter **13**, L627 (2001).

231. P. G. Pagliuso, R. Movshovich, A. D. Bianchi, M. Nicklas, N. O. Moreno, J. D. Thompson, M. F. Hundley, J. L. Sarrao, and Z. Fisk, Physica B **312-313**, 129 (2002).
232. Y. Kitaoka, Y. Kawasaki, T. Mito, S. Kawasaki, G. q. Zheng, K. Ishida, D. Aoki, Y. Haga, R. Settai, Y. Onuki, C. Geibel, and F. Steglich, J. Phys. Chem. Solids **63**, 1141 (2002).
233. S. Kawasaki, T. Mito, G. q. Zheng, C. Thessieu, Y. Kawasaki, K. Ishida, Y. Kitaoka, T. Muramatsu, T. C. Kobayashi, D. Aoki, S. Araki, Y. Haga, R. Settai, and Y. Onuki, Phys. Rev. B **65**, 020504R (2001).
234. P. G. Pagliuso, C. Petrovic, R. Movshovich, D. Hall, M. F. Hundley, J. L. Sarrao, J. D. Thompson, and Z. Fisk, Phys. Rev. B **64**, 100503(R) (2001).
235. T. Muramatsu, N. Tateiwa, T. C. Kobayashi, K. Shimizu, K. Amaya, D. Aoki, H. Shishido, Y. Haga, and Y. Onuki, Physica B **312-313**, 140 (2002).
236. T. Mito, S. Kawasaki, Y. Kawasaki, G. q. Zheng, Y. Kitaoka, D. Aoki, Y. Haga, and Y. Onuki, Phys. Rev. Lett **90**, 077004 (2003).
237. G. D. Morris, R. H. Heffner, J. E. Sonier, D. E. MacLaughlin, O. O. Bernal, G. J. Nieuwenhuys, A. T. Savici, P. G. Pagliuso, and J. L. Sarrao, Physica B **326**, 390 (2003).
238. M. C. Aronson, J. D. Thompson, J. L. Smith, Z. Fisk, and M. W. McElfresh, Phys. Rev. Lett. **63**, 2311 (1989).
239. D. L. Cox, Phys. Rev. Lett. **59**, 1240 (1987).
240. D. L. Cox and A. Zawadowski, Adv. Phys. **47**, 599 (1998).
241. C. L. Seaman, M. B. Maple, B. W. Lee, S. Ghamaty, M. S. Torikachivili, J. S. Kang, Z. Liu, J. W. Allen, and D. L. Cox, Phys. Rev. Lett. **67**, 2882 (1991).
242. M. B. Maple, M. C. de Andrade, J. Herrmann, S. H. Han, R. Movshovich, D. A. Gajewski, and R. Chau, Physica C **263**, 490 (1996).
243. D. A. Gajewski, N. R. Dilley, R. Chau, and M. B. Maple, J. Phys.: Condens. Matter **8**, 9793 (1996).
244. See various articles in Proceedings of the Institute for Theoretical Physics Conference on Non-Fermi Liquid Behavior in Metals, Santa Barbara, 1996, P. Coleman, M. B. Maple, and A. J. Millis, eds., J. Phys.: Condens. Matter **8** (1996).
245. M. B. Maple, C. L. Seaman, D. A. Gajewski, Y. Dalichaouch, V. B. Barbetta, M. C. de Andrade, H. A. Mook, H. G. Lukefahr, O. O. Bernal, and D. E. MacLaughlin, J. Low Temp. Phys. **95**, 225 (1994).
246. A. J. Schofield, Contemporary Physics **40**, 95 (1999).
247. G. R. Stewart, Rev. Mod. Phys. **73**, 797 (2001).
248. B. Andraka and A. M. Tsvelik, Phys. Rev. Lett. **67**, 2886 (1991).
249. B. Andraka and G. R. Stewart, Phys. Rev. B. **47**, 3208 (1993).
250. R. Chau and M. B. Maple, J. Phys.: Condens. Matter **8**, 9939 (1996).
251. H. v. Löhneysen, T. Pietrus, G. Portisch, H. G. Schlager, A. Schröder, M. Sieck, and T. Trappmann, Phys. Rev. Lett. **72**, 3262 (1994).
252. H. v. Löhneysen, J. Magn. Magn. Mat. **200**, 532 (1999).
253. O. Trovarelli, C. Geibel, S. Mederle, C. Langhammer, F. M. Grosche, P. Gegenwart, M. Lang, G. Sparn, and F. Steglich, Phys. Rev. Lett. **85**, 626 (2000).
254. F. M. Grosche, S. J. S. Lister, F. V. Carter, S. S. Saxena, R. K. W. Haselwimmer, N. D. Mathur, S. R. Julian, and G. G. Lonzarich, Physica B **239**, 62 (1997).
255. P. Nozières and A. Blandin, J. Phys. (France) **41**, 193 (1980).

256. A. M. Tsvelik, J. Phys. C **18**, 159 (1985).
257. A. W. W. Ludwig and I. Affleck, Phys. Rev. Lett. **67**, 3160 (1991).
258. P. Schlottmann and P. D. Sacramento, Adv. Phys. **42**, 641 (1993).
259. O. O. Bernal, D. E. MacLaughlin, H. G. Lukefahr, and B. Andraka, Phys. Rev. Lett. **75**, 2023 (1995).
260. E. Miranda, V. Dobrosavljević, and G. Kotliar, J. Phys.: Condens. Matter **8**, 9871 (1996).
261. E. Miranda, V. Dobrosavljević, and G. Kotliar, Phys. Rev. Lett. **78**, 290 (1997).
262. A. H. Castro Neto, G. Castilla, and B. A. Jones, Phys. Rev. Lett. **81**, 3531 (1998).
263. J. A. Hertz, Phys. Rev. B **14**, 1165 (1976).
264. A. J. Millis, Phys. Rev. B **48**, 7183 (1993).
265. M. A. Continentino, Phys. Rev. B **47**, 11587 (1993).
266. A. M. Tsvelik and M. Reizer, Phys. Rev. B **48**, 9887 (1993).
267. S. Sachdev, N. Read, and R. Oppermann, Phys. Rev. B **52**, 10286 (1995).
268. Q. Si, J. Phys.: Condens. Matter **15**, S2207 (2003).
269. V. S. Zapf, E. J. Freeman, R. P. Dickey, P.-C. Ho, and M. B. Maple, Physica B **312-313**, 448 (2002).
270. M. B. Maple, A. Amann, R. P. Dickey, E. J. Freeman, C. Sirvent, M. C. de Andrade, and N. R. Dilley, Physica B **281-282**, 332 (2000).
271. Y. Dalichaouch, M. B. Maple, M. S. Torikachvili, and A. L. Giorgi, Phys. Rev. B **39**, 2423 (1989).
272. Y. Dalichaouch, M. B. Maple, J. W. Chen, T. Kohara, C. Rossel, M. S. Torikachvili, and A. L. Giorgi, Phys. Rev. B **41**, 1829 (1990).
273. E. D. Bauer, V. S. Zapf, P.-C. Ho, E. J. Freeman, C. Sirvent, and M. B. Maple, submitted to Phys. Rev. Lett,, 2002.
274. M. Lenkewitz, S. Corsépius, G.-F. v. Blanckenhagen, and G. R. Stewart, Phys. Rev. B **55**, 6409 (1997).
275. V. S. Zapf, N. A. Frederick, K. L. Rogers, K. D. Hof, P.-C. Ho, E. D. Bauer, and M. B. Maple, Phys. Rev. B **67**, 064405 (2003).
276. P. G. Pagliuso, N. O. Moreno, N. J. Curro, J. D. Thompson, M. F. Hundley, J. L. Sarrao, Z. Fisk, A. D. Christianson, A. H. Lacerda, B. E. Light, and A. L. Cornelius, Phys. Rev. B **66**, 054433 (2002).
277. S. Nakatsuji, S. Yeo, L. Balicas, Z. Fisk, P. Schlottmann, P. G. Pagliuso, N. O. Moreno, J. L. Sarrao, and J. D. Thompson, Phys. Rev. Lett. **89**, 106402 (2002).
278. B. E. Light, A. L. Cornelius, P. G. Pagliuso, and J. L. Sarrao, cond-mat/0307394 (unpublished).
279. S. Nakatsuji, D. Pines, and Z. Fisk, cond-mat/0304587 (unpublished).
280. V. S. Zapf, T. A. Sayles, N. A. Frederick, and M. B. Maple (unpublished).
281. C. Pfleiderer and A. D. Huxley, Phys. Rev. Lett. **89**, 147005 (2002).
282. S. Watanabe and K. Miyake, J. Phys. Soc. Jpn. **71**, 2489 (2002).
283. K. Ishida, H. Mukuda, Y. Kitaoka, K. Asayama, Z. Q. Mao, Y. Mori, and Y. Maeno, Nature **396**, 658 (1998).
284. G. M. Luke, Y. Fudamoto, K. M. Kojima, M. I. Larkin, J. Merrin, B. Nachumi, Y. J. Uemura, Y. Maeno, Z. Q. Mao, Y. Mori, H. Nakamura, and M. Sigrist, Nature **394**, 558 (1998).
285. G. R. Stewart, Z. Fisk, J. O. Willis, and J. L. Smith, Phys. Rev. Lett. **52**, 679 (1984).

286. Y. Dalichaouch, M. C. de Andrade, D. A. Gajewski, R. Chau, P. Visani, and M. B. Maple, Phys. Rev. Lett. **75**, 3938 (1995).
287. A. P. Mackenzie, R. K. W. Haselwimmer, A. W. Tyler, G. G. Lonzarich, Y. Mori, S. Nishizaki, and Y. Maeno, Phys. Rev. Lett. **80**, 161 (1998).
288. K. B. Blagoev, J. R. Engelbrecht, and K. S. Bedell, Phil. Mag. Lett. **78**, 169 (1998).
289. K. B. Blagoev, J. R. Engelbrecht, and K. S. Bedell, Phys. Rev. Lett. **82**, 133 (1999).
290. N. I. Karchev, K. B. Blagoev, K. S. Bedell, and P. B. Littlewood, Phys. Rev. Lett. **86**, 846 (200).
291. H. Suhl, Phys. Rev. Lett **87**, 167007 (2001).
292. A. A. Abrikosov, J. Phys.: Condens. Matter **13**, L943 (2001).
293. P. Fulde and J. Keller, in *Superconductivity in Ternary Compounds II, Topics in Current Physics*, edited by M. B. Maple and Ø. Fischer (Springer, Berlin, 1982), Vol. 34, Chap. 9.
294. W. Thomlinson, G. Shirane, J. W. Lynn, and D. E. Moncton, in *Superconductivity in Ternary Compounds II, Topics in Current Physics*, edited by M. B. Maple and Ø. Fischer (Springer, Berlin, 1982), Vol. 34, Chap. 8.
295. C. Pfleiderer, M. Uhlarz, S. M. Hayden, R. Vollmer, H. v. Löhneysen, N. R. Bernhoeft, and G. G. Lonzarich, Nature **412**, 58 (2001).
296. R. A. Fisher, S. Kim, B. F. Woodfield, N. E. Phillips, L. Taillefer, K. Hasselbach, J. Flouquet, A. L. Giorgi, and J. L. Smith, Phys. Rev. Lett. **62**, 1411 (1989).
297. V. Müller, C. Roth, D. Maurer, E. W. Scheidt, K. Lüders, E. Bucher, and H. E. Bömmel, Phys. Rev. Lett. **58**, 1224 (1987).
298. S. Adenwalla, S. W. Lin, Q. Z. Ran, Z. Zhao, J. B. Ketterson, J. A. Sauls, L. Taillefer, D. G. Hinks, M. Levy, and B. K. Sarma, Phys. Rev. Lett. **65**, 2298 (1990).
299. H. v. Löhneysen, Physica B **197**, 551 (1994).
300. R. H. Heffner, J. L. Smith, J. O. Willis, P. Birrer, C. Baines, F. N. Gygax, B. Hitti, E. Lippelt, H. R. Ott, A. Schenck, E. A. Knetsch, J. A. Mydosh, and D. E. MacLaughlin, Phys. Rev. Lett. **65**, 2816 (1990).
301. G. M. Luke, A. Deren, L. P. Le, W. D. Wu, Y. J. Uemura, D. A. Bonn, L. Taillefer, and J. D. Garrett, Phys. Rev. Lett. **71**, 1466 (1993).
302. G. Goll and H. v. Löhneysen, Physica C **317&318**, 82 (1999).
303. S. E. Lambert, Y. Dalichaouch, M. B. Maple, J. L. Smith, and Z. Fisk, Phys. Rev. Lett. **57**, 1619 (1986).
304. R. Joynt and L. Taillefer, Rev. Mod. Phys. **74**, 235 (2002), and references therein.
305. R. H. Heffner and M. R. Norman, Comments Cond. Mat. Phys. **17**, 361 (1996), and references therein.
306. J. A. Sauls, Adv. Phys. **43**, 113 (1994).
307. K. Park and R. Joynt, Phys. Rev. B **53**, 12346 (1995).
308. C. Choi and J. Sauls, Phys. Rev. Lett. **66**, 484 (1991).
309. R. Joynt, J. Phys.: Condens. Matter **2**, 3415 (1990).
310. D.-C. Chen and A. Garg, Phys. Rev. Lett. **70**, 1689 (1993).
311. I. Luk'yanchuk, J. Phys. I **1**, 1155 (1991).
312. P. Kumar and P. Wolfle, Phys. Rev. Lett. **59**, 1954 (1987).
313. F. Kromer, M. Lang, N. Oeschler, P. Hinze, C. Langhammer, F. Steglich, J. S. Kim, and G. R. Stewart, Phys. Rev. B **62**, 12477 (2000).

314. P. Fulde, Physica B **230-232**, 1 (1997).
315. M. B. Maple, P.-C. Ho, N. A. Frederick, V. S. Zapf, W. M. Yuhasz, and E. D. Bauer, Acta Physica Polonica B **34**, 919 (2003).
316. M. B. Maple, P.-C. Ho, V. S. Zapf, N. A. Frederick, E. D. Bauer, W. M. Yuhasz, F. M. Woodward, and J. W. Lynn, J. Phys. Soc. Jpn. **71**, 23 (2002).
317. T. Goto, private communication.
318. Y. Aoki, T. Namiki, S. Ohsaki, S. R. Saha, H. Sugawara, and H. Sato, J. Phys. Soc. Jpn. **71**, 2098 (2002).
319. T. Tayama, T. Sakakibara, Y. Aoki, and H. Sato, J. Phys. Soc. Jpn. **72**, 1516 (2003).
320. S. Watanabe, Y. Kuramoto, T. Nishino, and N. Shibata, J. Phys. Soc. Jpn. **68**, 159 (1999).
321. M. Kohgi, K. Isawa, M. Nakajima, N. Metoki, A. Araki, N. Bernhoeft, J.-M. Mignot, A. Gukasov, H. Sato, Y. Aoki, and H. Sugawara, J. Phys. Soc. Jpn. **72**, 1002 (2003).
322. N. Oeschler, P. Gegenwart, F. Steglich, N. A. Frederick, E. D. Bauer, and M. B. Maple, Acta Phys. Pol. B **34**, 919 (2003).
323. N. Oeschler, P. Gegenwart, F. Weickert, P. Thalmeier, F. Steglich, E. D. Bauer, N. A. Frederick, and M. B. Maple, to be published (unpublished).
324. P.-C. Ho, V. S. Zapf, E. D. Bauer, N. A. Frederick, M. B. Maple, G. Geister, P. Rogl, S. Berger, C. Paul, and E. Bauer, in *Physical Phenomena at High Magnetic Fields - IV*, edited by G. Boebinger, Z. Fisk, L. P. Gor'kov, and A. Lacerda (World Scientific, Singapore, 2002), p. 98.
325. P.-C. Ho, N. A. Frederick, V. S. Zapf, E. D. Bauer, T. D. Do, M. B. Maple, A. D. Christianson, and A. H. Lacerda, Phys. Rev. B **67**, 180508(R) (2003).
326. D. M. Broun, P. J. Turner, G. K. Mullins, D. E. Sheehy, X. G. Zheng, S. K. Kim, N. A. Frederick, M. B. Maple, W. N. Hardy, and D. A. Bonn, cond-mat/0310613, (2003).
327. E. E. M. Chia, M. B. Salamon, H. Sugawara, and H. Sato, cond-mat/0308454, (2003).
328. K. Izawa, Y. Nakajima, J. Goryo, Y. Matsuda, S. Osaki, H. Sugawara, H. Sato, P. Thalmeier, and K. Maki, Phys. Rev. Lett **90**, 117001 (2003).
329. D. E. MacLaughlin, J. E. Sonier, R. H. Heffner, O. O. Bernal, B.-L. Young, M. S. Rose, G. D. Morris, E. D. Bauer, T. D. Do, and M. B. Maple, Phys. Rev. Lett. **89**, 157001 (2002).
330. H. Kotegawa, M. Yogi, Y. Imamura, Y. Kawasaki, G. q. Zheng, Y. Kitaoka, S. Ohsaki, H. Sugawara, Y. Aoki, and H. Sato, Phys. Rev. Lett. **90**, 027001 (2003).
331. R. Balian and N. R. Werthamer, Phys. Rev. **131**, 1553 (1963).
332. Y. Aoki, A. Tsuchiya, T. Kanayama, S. R. Saha, H. Sugawara, H. Sato, W. Higemoto, A. Koda, K. Ohishi, and R. Kadono, Phys. Rev. Lett. **91**, 067003 (2003).
333. M. B. Maple, P.-C. Ho, N. A. Frederick, V. S. Zapf, W. M. Yuhasz, and E. D. Bauer, Physica B **328**, 29 (2003).
334. K. Tenya, N. Oeschler, P. Gegenwart, F. Steglich, N. A. Frederick, E. D. Bauer, and M. B. Maple, Acta Phys. Pol. B **34**, 995 (2003).
335. F. B. Anders, Eur. Phys. J. B **28**, 9 (2002).
336. K. Miyake, H. Kohno, and H. Harima, J. Phys.: Condens. Matter **15**, L275 (2003).

337. M. Ichioka, N. Nakai, and K. Machida, J. Phys. Soc. Jpn. **72**, 1322 (2003).
338. J. Goryo, Phys. Rev. B **67**, 184511 (2003).
339. I. A. Sergienko and S. H. Curnoe, cond-mat/0309382, (2003).
340. D. Jérome, A. Mazaud, M. Ribault, and K. Bechgaard, J. Physique Lett. **41**, L95 (1980).
341. T. Ishiguro, K. Yamaji, and G. Saito, in *Organic Superconductors* (Springer, Berlin, 1998).
342. J. M. Williams, J. R. Ferraro, R. J. Thorn, K. D. Carlson, U. Geiser, H. H. Wang, A. M. Kini, and M. H. Whangbo, in *Organic Superconductors: Synthesis, Structure, Properties, and Theory* (Prentice Hall, Englewood Cliffs, 1992).
343. A. M. Kini, U. Geiser, H. H. Wang, K. D. Carlson, J. M. Williams, W. K. Kwok, K. D. Vandervoort, J. E. Thompsen, D. L. Stupka, D. Jung, and M. H. Whangbo, Inorg. Chem. **29**, 2555 (1990).
344. J. M. Williams, A. M. Kini, H. H. Wang, K. D. Carlson, U. Geiser, L. K. Montgomery, G. J. Pyrka, D. M. Watkins, J. M. Kommers, S. J. Boryschuk, A. V. S. Crouch, W. K. Kwok, J. E. Schirber, D. L. Overmyer, D. Jung, and M. H. Whangbo, Inorg. Chem. **29**, 3272 (1990).
345. H. Kobayashi, Curr. Opin. Solid State Mater. Sci. **2**, 440 (1997).
346. H. Kobayashi, H. Akutsu, H. Tanaka, A. Kobayashi, M. Tokumoto, L. Brossard, and P. Cassoux, Synth. Met. **102**, 1654 (1999).
347. J. Wosnitza, Physica C **317-318**, 98 (1999).
348. M. Lang, Supercond. Rev. **2**, 1 (1996).
349. R. H. McKenzie, Science **278**, 820 (1997).
350. R. H. McKenzie, Comments Cond. Mat. Phys. **18**, 309 (1998).
351. J. Wosnitza, in *Studies of High-Temperature Superconductivity*, edited by A. V. Narlikar (Nova Science Publishers, Huntington, 2000), Vol. 34.
352. J. Wosnitza, Curr. Opin. Solid State Mater. Sci. **5**, 131 (2001).
353. J. Singleton and C. Mielke, Contemp. Phys. **43**, 63 (2002).
354. W. A. Little, Phys. Rev. **134**, A1416 (1964).
355. N. Thorup, G. Rindorf, H. Soling, and K. Bechgaard, Acta. Cryst. **B37**, 1236 (1981).
356. Y. J. Lee, R. M. Nieminen, P. Ordejon, and E. Canadell, Phys. Rev. B **67**, 180505 (2003).
357. P. M. Grant, J. Physique **44**, 847 (1983).
358. K. Bechgaard, C. S. Jacobsen, K. Mortensen, J. H. Pederson, and N. Thorup, Solid State Commun. **33**, 1119 (1980).
359. K. Mortensen, Y. Tomkiewicz, and K. Bechgaard, Phys. Rev. B **25**, 3319 (1982).
360. J. C. Scott, H. J. Pedersen, and K. Bechgaard, Phys. Rev. Lett. **45**, 2125 (1980).
361. J. Wosnitza, in *Fermi Surfaces of Low-Dimensional Organic Metals and Superconductors* (Springer, Berlin, 1996).
362. K. Bechgaard, K. Carneiro, M. Olsen, F. B. Rasmussen, and C. S. Jacobsen, Phys. Rev. Lett. **46**, 852 (1981).
363. T. Adachi, E. Ojima, K. Kato, H. Kobayashi, T. Miyazaki, M. Tokumoto, and A. Kobayashi, J. Am. Chem. Soc. **122**, 3238 (2000).
364. D. Jaccard, H. Wilhelm, D. Jérome, J. Moser, C. Carcel, and J. M. Fabre, J. Phys.: Condens. Matter **13**, L89 (2001).
365. H. Wilhelm, D. Jaccard, R. Duprat, C. Bourbonnais, D. Jérome, J. Moser, C. Carcel, and J. M. Fabre, Eur. Phys. J. B **21**, 175 (2001).

366. D. Jérome, Science **252**, 1509 (1991).
367. F. Guo, K. Murata, A. Oda, Y. Mizuno, and H. Yoshino, J. Phys. Soc. Jpn. **69**, 2164 (2000).
368. M. Miyazaki, K. Kishigi, and Y. Hasegawa, J. Phys. Soc. Jpn. **69**, 997 (2000).
369. M. Ribault, D. Jérome, J. Tuchendler, C. Weyl, and K. Bechgaard, J. Physique Lett. **44**, L953 (1983).
370. P. M. Chaikin, M. Y. Choi, J. F. Kwak, J. S. Brooks, K. P. Martin, M. J. Naughton, E. M. Engler, and R. L. Greene, Phys. Rev. Lett. **51**, 2333 (1983).
371. L. P. Gor'kov and A. G. Lebed, J. Physique Lett. **45**, L433 (1984).
372. D. G. Clarke, S. P. Strong, and P. W. Anderson, Phys. Rev. Lett. **72**, 3218 (1994).
373. S. P. Strong, D. G. Clarke, and P. W. Anderson, Phys. Rev. Lett. **73**, 1007 (1994).
374. T. Lorenz, M. Hofmann, M. Grüninger, L. Freimuth, G. S. Uhrig, M. Dumm, and M. Dressel, Nature **418**, 614 (2002).
375. G. M. Danner and P. M. Chaikin, Phys. Rev. Lett. **75**, 4690 (1995).
376. E. I. Chashechkina and P. M. Chaikin, Phys. Rev. Lett. **80**, 2181 (1998).
377. D. Jérome, J. Physique IV **10**, 69 (2000).
378. P. M. Chaikin, E. I. Chashechkina, I. J. Lee, and M. J. Naughton, J. Phys.: Condens. Matter **10**, 11 301 (1998).
379. G. Rindorf, H. Soling, and N. Thorup, Acta Crystallogr. B **38**, 2805 (1982).
380. R. P. Shibaeva, V. F. Kaminskii, and V. K. Bel'skii, Sov. Phys. Crystallogr. **29**, 638 (1984).
381. J. M. Williams, T. J. Emge, H. H. Wang, M. A. Beno, P. T. Copps, L. N. Hall, K. D. Carlson, and G. W. Crabtree, Inorg. Chem. **23**, 2558 (1984).
382. J. M. Williams, H. H. Wang, M. A. Beno, T. J. Emge, L. M. Sowa, P. T. Copps, F. Behroozi, L. N. Hall, K. D. Carlson, and G. W. Crabtree, Inorg. Chem. **23**, 3839 (1984).
383. A. Kobayashi, R. Kato, H. Kobayashi, S. Moriyama, S. Nishio, K. Kajita, and W. Sasaki, Chem. Lett. **1987**, 459 (1987).
384. H. Urayama, H. Yamochi, G. Saito, S. Sato, A. Kawamoto, J. Tanaka, T. Mori, Y. Maruyama, and H. Inokuchi, Chem. Lett. **1988**, 463 (1988).
385. H. Mori, S. Tanaka, M. Oshima, G. Saito, T. Mori, Y. Murayama, and H. Inokuchi, Bull. Chem. Soc. Jpn. **63**, 2183 (1990).
386. M. Oshima, H. Mori, G. Saito, and K. Oshima, Chem. Lett. **1989**, 1159 (1989).
387. U. Geiser, J. A. Schlueter, H. H. Wang, A. M. Kini, J. M. Williams, P. P. Sche, H. I. Zakowicz, M. L. VanZile, J. D. Dudek, P. G. Nixon, R. W. Winter, G. L. Gard, J. Ren, and M.-H. Whangbo, J. Am. Chem. Soc. **118**, 9996 (1996).
388. I. J. Lee, M. J. Naughton, G. M. Danner, and P. M. Chaikin, Phys. Rev. Lett. **78**, 3555 (1997).
389. I. J. Lee, P. M. Chaikin, and M. J. Naughton, Phys. Rev. B **62**, R14 669 (2000).
390. D. Andres, M. V. Kartsovnik, W. Biberacher, K. Neumaier, and H. Müller, to be published (unpublished).
391. T. Mori, A. Kobayashi, Y. Sasaki, H. Kobayashi, G. Saito, and H. Inokuchi, Bull. Chem. Soc. Jpn. **57**, 627 (1984).
392. T. Mori, A. Kobayashi, Y. Sasaki, H. Kobayashi, G. Saito, and H. Inokuchi, Chem. Lett. **1984**, 957 (1984).
393. H. Kobayashi, R. Kato, A. Kobayashi, Y. Nishio, K. Kajita, and W. Sasaki, Chem Lett. **1986**, 789 & 833 (1986).

394. M. V. Kartsovnik, V. N. Laukhin, S. I. Pesotskii, I. F. Schegolev, and V. M. Yakovenko, J. Physique I France **2**, 89 (1992).
395. K. Oshima, T. Mori, H. Inokuchi, H. Urayama, H. Yamochi, and G. Saito, Phys. Rev. B **38**, 938 (1988).
396. J. Singleton, Rep. Prog. Phys. **63**, 1111 (2000).
397. R. H. McKenzie and P. Moses, Phys. Rev. Lett. **81**, 4492 (1998).
398. P. Moses and R. McKenzie, Phys. Rev. B **60**, 7998 (1999).
399. J. Wosnitza, G. Goll, D. Beckmann, S. Wanka, D. Schweitzer, and W. Strunz, J. Physique I France **6**, 1597 (1996).
400. J. Wosnitza, S. Wanka, J. Hagel, E. Balthes, N. Harrison, J. A. Schlueter, A. M. Kini, U. Geiser, J. Mohtasham, R. W. Winter, and G. L. Gard, Phys. Rev. B **61**, 7383 (2000).
401. J. Wosnitza, S. Wanka, J. Hagel, R. Häussler, H. v. Löhneysen, J. A. Schlueter, U. Geiser, P. G. Nixon, R. W. Winter, and G. L. Gard, Phys. Rev. B **62**, R11 973 (2000).
402. J. Wosnitza, J. Hagel, J. S. Qualls, J. S. Brooks, E. Balthes, D. Schweitzer, J. A. Schlueter, U. Geiser, J. Mohtasham, R. W. Winter, and G. L. Gard, Phys. Rev. B **65**, 180506R (2002).
403. J. Wosnitza, S. Wanka, J. Hagel, H. v. Löhneysen, J. S. Qualls, J. S. Brooks, E. Balthes, J. A. Schlueter, U. Geiser, J. Mohtasham, R. W. Winter, and G. L. Gard, Phys. Rev. Lett. **86**, 508 (2001).
404. H. Mayaffre, P. Wzietek, C. Lenoir, D. Jérome, and P. Batail, Europhys. Lett. **28**, 205 (1994).
405. A. Kawamoto, K. Miyagawa, Y. Nakazawa, and K. Kanoda, Phys. Rev. Lett. **74**, 3455 (1995).
406. M. Dressel, in *Studies of High Temperature Superconductors*, edited by A. Narlikar (Nova Science Publishers, Huntington, 2000), Vol. 34, p. 1.
407. L. Fruchter, A. Aburto, and C. Pham-Phu, Phys. Rev. B **56**, R2936 (1997).
408. M. Inada, T. Sasaki, T. Nishizaki, N. Kobayashi, S. Yamada, and T. Fuakase, J. Low Temp. Phys. **117**, 1423 (1999).
409. R. Kleiner, F. Steinmeyer, G. Kunkel, and P. Müller, Phys. Rev. Lett. **68**, 3294 (1992).
410. P. Müller, in *Advances in Solid State Physics* (Vieweg, Braunschweig, 1994).
411. S. S. P. Parkin, M. Ribault, D. Jérome, and K. Bechgaard, J. Phys. C **14**, 5305 (1981).
412. K. Murata, M. Tokumoto, H. Anzai, K. Kajimura, and T. Ishiguro, Jpn. J. Appl. Phys. **26**, 1367 (1987).
413. J. I. Oh and M. J. Naughton, to be published (unpublished).
414. A. Lebed, Phys. Rev. B **59**, R721 (1999).
415. I. J. Lee, S. E. Brown, W. G. Clark, M. J. Strouse, M. J. Naughton, W. Kang, and P. M. Chaikin, Phys. Rev. Lett. **88**, 017004 (2002).
416. I. J. Lee, D. S. Chow, W. G. Clark, M. J. Strouse, M. J. Naughton, P. M. Chaikin, and S. E. Brown, Phys. Rev. B **68**, 92510 (2003).
417. A. G. Lebed, K. Machida, and M. Ozaki, Phys. Rev. B **62**, R795 (2000).
418. S. Belin and K. Behnia, Phys. Rev. Lett. **79**, 2125 (1997).
419. K. Kuroki, R. Arita, and H. Aoki, Phys. Rev. B **63**, 094509 (2001).
420. R. Brusetti, M. Ribault, D. Jérome, and K. Bechgaard, J. Physique **43**, 801 (1982).
421. A. A. Abrikosov, J. Low Temp. Phys. **53**, 359 (1983).

422. L. P. Gor'kov and D. Jérome, J. Physique Lett. **46**, L643 (1985).
423. M. Miyazaki, K. Kichigi, and Y. Hasegawa, J. Phys. Soc. Jpn. **68**, 3794 (1999).
424. H. Shimahara, Phys. Rev. B **61**, R14 936 (2000).
425. M. Lang, F. Steglich, N. Toyota, and T. Sasaki, Phys. Rev. B **49**, 15 227 (1994).
426. J. Hagel, S. Wanka, D. Beckmann, J. Wosnitza, D. Schweitzer, W. Strunz, and M. Thumfart, Physica C **291**, 213 (1997).
427. S. Wanka, D. Beckmann, J. Wosnitza, E. Balthes, D. Schweitzer, W. Strunz, and H. J. Keller, Phys. Rev. B **53**, 9301 (1996).
428. S. Wanka, J. Hagel, J. Wosnitza, and D. Schweitzer, Synth. Met. **103**, 1996 (1999).
429. D. E. Farrell, C. J. Allen, R. C. Haddon, and S. V. Chichester, Phys. Rev. B **42**, 8694 (1990).
430. S. Kawamata, K. Okuda, T. Sasaki, and N. Toyota, J. Low Temp. Phys. **105**, 1721 (1996).
431. Y. Yeshurun and A. P. Malozemoff, Phys. Rev. Lett. **60**, 2202 (1988).
432. M. Tinkham, Phys. Rev. **129**, 2413 (1963).
433. W. E. Lawrence and S. Doniach, in *Proc. 12th Intern. Conf. Low Temp. Physics, Kyoto, 1970*, edited by E. Kanda (Academic Press of Japan, Tokyo, 1971), Vol. 12, p. 361.
434. V. V. Dorin, R. A. Klemm, A. A. Varlamov, A. I. Budzin, and D. V. Livanov, Phys. Rev. B **48**, 12 951 (1993).
435. M. V. Kartsovnik, G. Y. Logyenov, K. Maki, and N. D. Kushsh, Synth. Met. **103**, 1827 (1999).
436. J. Singleton, J. A. Symington, M.-S. Nam, A. Ardavan, M. Kurmco, and P. Day, J. Phys.: Condens. Matter **12**, L641 (2000).
437. N. Harrison, L. Balicas, J. S. Brooks, and M. Tokumoto, Phys. Rev. B **62**, 14 212 (2000).
438. N. Harrison, C. H. Mielke, A. D. Christianson, J. S. Brooks, and M. Tokumoto, Phys. Rev. Lett. **86**, 1586 (2001).
439. P. Christ, W. Biberacher, M. V. Kartsovnik, E. Steep, E. Balthes, H. Weiss, and H. Müller, JETP Lett. **71**, 451 (2000).
440. J. S. Qualls, L. Balicas, J. S. Brooks, N. Harrison, L. K. Montgomery, and M. Tokumoto, Phys. Rev. B **62**, 10 008 (2000).
441. A. Bjelis, D. Zanchi, and G. Montambaux, J. Physique IV **9**, Pr10 203 (1999).
442. P. Christ, W. Biberacher, H. Müller, K. Andres, E. Steep, and A. G. M. Jansen, Physica B **204**, 153 (1995).
443. N. Harrison, Phys. Rev. B **66**, 121101(R) (2002).
444. S. Uji, H. Shinagawa, T. Terashima, T. Yakabe, Y. Terai, M. Tokumoto, A. Kobayashi, H. Tanaka, and H. Kobayashi, Nature **410**, 908 (2001).
445. L. Balicas, J. S. Brooks, K. Storr, S. Uji, M. Tokumoto, H. Tanaka, H. Kobayashi, A. Kobayashi, V. Barzykin, and L. P. Gor'kov, Phys. Rev. Lett. **87**, 067002 (2001).
446. S. M. D. Soto, C. P. Slichter, A. M. Kini, H. H. Wang, U. Geiser, and J. M. Williams, Phys. Rev. B **52**, 10 364 (1995).
447. H. Mayaffre, P. Wzietek, D. Jérome, C. Lenoir, and P. Batail, Phys. Rev. Lett. **75**, 4122 (1995).
448. K. Kanoda, K. Miyagawa, A. Kawamoto, and Y. Nakazawa, Phys. Rev. B **54**, 76 (1996).

449. S. Kamiya, Y. Shimojo, M. A. Tanatar, T. Ishiguro, H. Yamochi, and G. Saito, Phys. Rev. B **65**, 134510 (2002).
450. F. Zuo, J. S. Brooks, R. H. McKenzie, J. A. Schlueter, and J. M. Williams, Phys. Rev. B **61**, 750 (2000).
451. P. Wzietek, H. Mayaffre, D. Jérome, and S. Brazovskii, J. Phys. I France **6**, 2011 (1996).
452. S. Sadewasser, C. Looney, J. S. Schilling, J. A. Schlueter, J. M. Williams, P. G. Nixon, R. W. Winter, and G. L. Gard, Solid State Commun. **104**, 571 (1997).
453. M. Lang, R. Modler, F. Steglich, N. Toyota, and T. Sasaki, Physica B **194–196**, 2005 (1994).
454. J. Müller, M. Lang, F. Steglich, J. A. Schlueter, A. M. Kini, U. Geiser, J. Mohtasham, R. W. Winter, G. L. Gard, T. Sasaki, and N. Toyota, Phys. Rev. B **61**, 11739 (2000).
455. K. Kanoda, Hyperfine Interact. **104**, 235 (1997).
456. K. Kanoda, Physica C **282-287**, 299 (1997).
457. D. Fournier, M. Poirier, M. Castonguay, and K. D. Truong, Phys. Rev. Lett. **90**, 127002 (2003).
458. A. M. Kini, J. A. Schlueter, B. H. Ward, U. Geiser, and H. H. Wang, Synth. Met. **120**, 713 (2001).
459. A. M. Kini, K. D. Carlson, H. H. Wang, J. A. Schlueter, J. D. Dudek, S. A. Sirchio, U. Geiser, K. R. Lykke, and J. M. Williams, Physica C **264**, 81 (1996).
460. D. Pedron, G. Visentini, R. Bozio, J. M. Williams, and J. A. Schlueter, Physica C **276**, 1 (1997).
461. L. Pintschovius, H. Rietschel, T. Sasaki, H. Mori, S. Tanaka, N. Toyota, M. Lang, and F. Steglich, Europhys. Lett. **37**, 627 (1997).
462. M. Lang, N. Toyota, T. Sasaki, and H. Sato, Phys. Rev. Lett. **69**, 1443 (1992).
463. A. Carrington, I. J. Bonalde, R. Prozorov, R. W. Gianetta, A. M. Kini, J. Schlueter, H. H. Wang, U. Geiser, and J. M. Williams, Phys. Rev. Lett. **83**, 4172 (1999).
464. F. Creuzet, C. Bourbonnais, D. Jérome, D. Schweitzer, and H. J. Keller, Europhys. Lett. **1**, 467 (1986).
465. F. Creuzet, C. Bourbonnais, G. Creuzet, D. Jérome, D. Schweitzer, and H. J. Keller, Physica B **143**, 363 (1986).
466. S. M. D. Soto, C. P. Slichter, H. H. Wang, U. Geiser, and J. M. Williams, Phys. Rev. Lett. **70**, 2956 (1993).
467. D. M. Ginsberg and L. C. Hebel, in *Superconductivity*, edited by R. Parks (Marcel Dekker, New York, 1969), Vol. 1, p. 193.
468. J. M. Schrama, E. Rzepniewski, R. S. Edwards, J. Singleton, A. Ardavan, M. Kurmoo, and P. Day, Phys. Rev. Lett. **83**, 3041 (1999).
469. S. Hill, N. Harrison, M. Mola, and J. Wosnitza, Phys. Rev. Lett. **86**, 3451 (2001).
470. T. Shibauchi, Y. Matsuda, M. B. Gaifullin, and T. Tamegai, Phys. Rev. Lett. **86**, 3452 (2001).
471. T. Arai, K. Ichimura, K. Nomura, S. Takasaki, J. Yamada, S. Nakatsuji, and H. Anzai, Phys. Rev. B **63**, 104518 (2001).
472. K. Izawa, H. Yamaguchi, T. Sasaki, and Y. Matsuda, Phys. Rev. Lett. **88**, 027002 (2002).
473. S. Belin, K. Behnia, and A. Deluzet, Phys. Rev. Lett. **81**, 4728 (1998).

474. J. Wosnitza, S. Wanka, J. Hagel, M. Reibelt, D. Schweitzer, and J. A. Schlueter, Synth. Met. **133-134**, 201 (2003).
475. H. Elsinger, J. Wosnitza, S. Wanka, J. Hagel, D. Schweitzer, and W. Strunz, Phys. Rev. Lett. **84**, 6098 (2000).
476. J. Wosnitza, X. Liu, D. Schweitzer, and H. J. Keller, Phys. Rev. B **50**, 12747 (1994).
477. S. Wanka, J. Hagel, D. Beckmann, J. Wosnitza, J. A. Schlueter, J. M. Williams, P. G. Nixon, R. W. Winter, and G. L. Gard, Phys. Rev. B **57**, 3084 (1998).
478. A. E. Kovalev, T. Ishiguro, J. Yamada, S. Takasaki, and H. Anzai, JETP **92**, 1035 (2001).
479. J. Müller, M. Lang, R. Helfrich, F. Steglich, and T. Sasaki, Phys. Rev. B **65**, 140509(R) (2002).
480. B. Mühlschlegel, Z. Phys. **155**, 313 (1959).
481. H. Padamsee, J. E. Neighbor, and C. A. Shiffman, J. Low Temp. Phys. **12**, 387 (1973).
482. G. Varelogiannis, Phys. Rev. Lett. **88**, 117005 (2002).
483. in *Physical Properties of High Temperature Superconductors*, edited by D. M. Ginsberg (World Scientific, Singapore, New Jersey, London, Hong Kong, 1989-1994), Vol. 1-4.
484. in *Handbook on the Physics and Chemistry of the Rare Earths: High Temperature Superconductors I, II*, edited by K. A. Gschneidner, Jr., L. Eyring, and M. B. Maple (Elsevier, New York, 2001), Vol. 30,31.
485. J. R. Gavaler, Appl. Phys. Lett. **23**, 480 (1973).
486. S. N. Putilin, E. V. Antipov, O. Chmaissem, and M. Marezio, Nature **362**, 226 (1993).
487. A. Schilling, M. Cantoni, J. D. Guo, and H. R. Ott, Nature **363**, 56 (1993).
488. C. W. Chu, L. Gao, F. Chen, Z. J. Huang, R. L. Meng, and Y. Y. Xue, Nature **365**, 323 (1993).
489. M. Nuñez-Regueiro, J.-L. Tholence, E. V. Antipov, J.-J. Capponi, and M. Marezio, Science **262**, 97 (1993).
490. M. B. Maple, in *Handbook on the Physics and Chemistry of the Rare Earths: High Temperature Superconductors I*, edited by K. A. Gschneidner, Jr., L. Eyring, and M. B. Maple (Elsevier, New York, 2001), Vol. 30, Chap. 1, p. 1.
491. J. G. Bednorz and K. A. Müller, Z. Phys. B **64**, 189 (1986).
492. H. Takagi, S. Uchida, K. Kitazawa, and S. Tanaka, Jpn. J. Appl. Phys. **26**, L123 (1987).
493. R. J. Cava, R. B. van Dover, B. Batlogg, and E. A. Rietman, Phys. Rev. Lett. **58**, 408 (1987).
494. K. Kishio, K. Kitazawa, S. Kanbe, T. Yasuda, N. Sugii, H. Takagi, S. Uchida, K. Fueki, and S. Tanaka, Chem. Lett. **Issue 1**, 429 (1987).
495. J. T. Markert, C. L. Seaman, H. Zhou, and M. B. Maple, Solid State Commun **66**, 387 (1988).
496. M. A. Subramanian, J. Gopalakrishnan, C. C. Torardi, T. R. Askew, R. B. Flippen, A. W. Sleight, J. J. Lin, and S. J. Poon, Science **240**, 495 (1988).
497. M. K. Wu, J. R. Ashburn, C. J. Torng, P. H. Hor, R. L. Meng, L. Gao, Z. J. Huang, Y. Q. Wang, and C. W. Chu, Phys. Rev. Lett. **58**, 908 (1987).
498. M. B. Maple, Y. Dalichaouch, J. M. Ferreira, R. R. Hake, B. W. Lee, J. J. Neumeier, M. S. Torikachvili, K. N. Yang, H. Zhou, R. P. Guertin, and M. V. Kuric, Physica B **148**, 155 (1987).

499. Z. Zou, J. Ye, K. Oka, and Y. Nishihara, Phys. Rev. Lett. **80**, 1074 (1998).
500. Y. Tokura, H. Takagi, and S. Uchida, Nature **337**, 345 (1989).
501. J. T. Markert and M. B. Maple, Solid State Commun. **70**, 145 (1989).
502. J. T. Markert, E. A. Early, T. Bjørnholm, S. Ghamaty, B. W. Lee, J. J. Neumeier, R. D. Price, C. L. Seaman, and M. B. Maple, Physica C **158**, 178 (1989).
503. E. A. Early, N. Y. Ayoub, J. Beille, J. T. Markert, and M. B. Maple, Physica C **160**, 320 (1989).
504. M. B. Maple, C. C. Almasan, C. L. Seaman, S. H. Han, K. Yoshiara, M. Buchgeister, L. M. Paulius, B. W. Lee, D. A. Gajewski, R. F. Jardim, C. R. Fincher, Jr., G. B. Blanchet, and R. P. Guertin, J. Superconductivity **7**, 97 (1994).
505. R. Fehrenbacher and T. M. Rice, Phys. Rev. Lett. **70**, 3471 (1993).
506. J. Herrmann, U.-C. Boehnke, M. Krötzsch, B. Lippold, and F. Schlenkrich, Physica C **221**, 76 (1994).
507. J. T. Markert, Y. Dalichaouch, and M. B. Maple, in *Physical Properties of High Temperature Superconductors I*, edited by D. M. Ginsberg (World Scientific, Singapore, 1989), Chap. 6.
508. I. Felner, Y. Asaf, and O. Millo, Phys. Rev. B **55**, R3374 (1997).
509. L. Bauernfeind, W. Widder, and H. F. Braun, J. Low Temp. Phys. **105**, 1605 (1996).
510. C. Bernard, J. L. Tallon, C. Niedermayer, T. Blasius, A. Golnik, E. Brücher, R. K. Kremer, D. R. Noakes, C. E. Stronach, and E. J. Ansaldo, Phys. Rev. B **59**, 14099 (1999).
511. J. W. Lynn, B. Keimer, C. Ulrich, C. Bernhard, and J. L. Tallon, Phys. Rev. B **61**, R14964 (2000).
512. J. A. Duffy, S. M. Hayden, Y. Maeno, Z. Mao, J. Kulda, and G. J. McIntyre, Phys. Rev. Lett. **85**, 5412 (2000).
513. C. G. Shull and F. A. Wedgewood, Phys. Rev. Lett. **16**, 513 (1966).
514. A. P. Mackenzie and Y. Maeno, Rev. Mod. Phys. **75**, 657 (2003).
515. Y. Maeno, T. M. Rice, and M. Sigrist, Physics Today **June**, 42 (2001).
516. Y. Maeno, H. Hashimoto, K. Yoshida, S. Nishizaki, T. Fujita, J. G. Bednorz, and P. Lichtenberg, Nature **372**, 532 (1994).
517. T. M. Rice and M. Sigrist, J. Phys.: Condens. Matter **7**, 643 (1995).
518. G. Baskaran, Physica B **223-224**, 490 (1996).
519. S. R. Julian, A. P. Mackenzie, G. G. Lonzarich, C. Bergemann, R. K. W. Haselwimmer, Y. Maeno, S. Nishizaki, A. W. Tyler, S. Ikeda, and T. Fujita, Physica B **259-261**, 928 (1999).
520. M. Takano, Physica C **263**, 468 (1996).
521. S. Maekawa, Science **273**, 1515 (1996).
522. M. Uehara, T. Nagata, J. Akimitsu, H. Takahashi, N. Môri, and K. Kinoshita, J. Phys. Soc. Jpn. **65**, 2764 (1996).
523. L. F. Mattheis, E. M. Gyorgy, and D. W. Johnson, Jr., Phys. Rev. B **37**, 3745 (1988).
524. R. J. Cava, B. Batlogg, J. J. Krajewski, R. Farrow, L. W. Rupp, Jr., A. E. White, K. Short, W. F. Peck, and T. Kometani, Nature **332**, 814 (1988).
525. M. J. Rosseinsky, A. P. Ramirez, S. H. Glarum, D. W. Murphy, R. C. Haddon, A. F. Hebard, T. T. M. Palstra, A. R. Kortan, S. M. Zahurak, and A. V. Makhija, Phys. Rev. Lett. **66**, 2830 (1991).

526. K. Holczer, O. Klein, S.-M. Huang, R. B. Kaner, K.-J. Fu, R. L. Whetten, and F. Diederich, Science **252**, 1154 (1991).
527. J. Nagamatsu, N. Nakagawa, T. Muranaka, Y. Zanitani, and J. Akimitsu, Nature **410**, 63 (2001).
528. A. W. Sleight, Physics Today **44(June)**, 24 (1991).
529. J. D. Jorgensen, Physics Today **June**, 34 (1991).
530. M. B. Maple, MRS Bulletin XV **No. 6**, 60 (1990).
531. T. P. Orlando, K. A. Delin, S. Foner, E. J. McNiff, Jr., J. M. Tarascon, L. H. Greene, W. R. McKinnon, and G. W. Hull, Phys. Rev. B **36**, 2394 (1987).
532. P. Chaudhari, R. H. Koch, R. B. Laibowitz, T. R. McGuire, and R. J. Gambino, Phys. Rev. Lett. **58**, 2684 (1987).
533. R. Hawsey and D. Peterson, Superconductor Industry **Fall**, (1996).
534. M. Marezio, ISTEC Journal **11 (No. 3)**, 20 (1998).
535. C. Murayama, N. Môri, S. Yomo, H. Takagi, S. Uchida, and Y. Tokura, Nature (London) **339**, 293 (1989).
536. J. T. Markert, J. Beille, J. J. Neumeier, E. A. Early, C. L. Seaman, T. Moran, and M. B. Maple, Phys. Rev. Lett. **64**, 80 (1990).
537. D. J. Scalapino, Physics Reports **250**, 329 (1995).
538. D. Pines, Physica B **199 and 200**, 300 (1994).
539. S. Uchida, Jpn. J. Appl. Phys. **32**, 3784 (1993).
540. J. P. Franck, in *Physical Properties of High Temperature Superconductors IV*, edited by D. M. Ginsberg (World Scientific, Singapore, 1994), Chap. 197, p. 189.
541. J. J. Neumeier and M. B. Maple, Physica C **191**, 158 (1992).
542. J. J. Neumeier, T. Bjørnholm, M. B. Maple, and I. K. Schuller, Phys. Rev. Lett. **63**, 2516 (1989).
543. J. J. Neumeier, M. B. Maple, and M. S. Torikachvili, Physica C **156**, 574 (1988).
544. J.-S. Kang, J. W. Allen, Z.-X. Shen, W. P. Ellis, J. J. Yeh, B. W. Lee, M. B. Maple, W. E. Spicer, and I. Lindau, J. Less-Common Met. **148**, 121 (1989).
545. M. B. Maple, L. M. Paulius, and J. J. Neumeier, Physica C **195**, 64 (1992).
546. M. B. Maple, Y. Dalichaouch, E. A. Early, B. W. Lee, J. T. Markert, M. W. McElfresh, J. J. Neumeier, C. L. Seaman, M. S. Torikachvili, K. N. Yang, and H. Zhou, in *High-T_c Superconductors*, edited by H. W. Weber (Plenum, New York, 1988), p. 29.
547. S. Ghamaty, B. W. Lee, J. J. Neumeier, G. Nieva, and M. B. Maple, Phys. Rev. B **43**, 5430 (1991).
548. D. N. Basov, S. I. Woods, A. S. Katz, E. J. Singley, R. C. Dynes, M. Xu, D. Hinks, C. C. Homes, and M. Strongin, Science **283**, 49 (1999).
549. D. A. Huse, M. P. A. Fisher, and D. S. Fisher, Nature **358**, 553 (1992).
550. G. Blatter, M. V. Feigel'man, V. B. Geshkenbein, A. I. Larkin, and V. M. Vinokur, Rev. Mod. Phys. **66**, 1125 (1994).
551. D. E. Farrell, in *Physical Properties of High Temperature superconductors IV*, edited by D. M. Ginsberg (World Scientific, Singapore, 1994), Vol. IV, Chap. 2, p. 7.
552. E. H. Brandt, Prog. Phys. **58**, 1465 (1995).
553. G. W. Crabtree and D. R. Nelson, Physics Today **April**, 38 (1997).
554. B. G. Levi, Physics Today **May**, 17 (1993).
555. B. G. Levi, Physics Today **January**, 19 (1996).

556. B. Batlogg, in *High Temperature Superconductivity*, edited by K. S. Bedell, D. Coffey, D. E. Meltzer, D. Pines, and J. R. Schrieffer (Addison-Wesley, Redwood City, 1990), p. 37.
557. W. N. Hardy, D. A. Bonn, D. C. Morgan, R. Liang, and K. Zhang, Phys. Rev. Lett. **70**, 3999 (1993).
558. D. A. Bonn, R. Liang, T. M. Riseman, D. J. Baar, D. C. Morgan, K. Zhang, P. Dosanjh, T. L. Duty, A. MacFarlane, G. D. Morris, J. H. Brewer, W. N. Hardy, C. Kallin, and A. J. Berlinsky, Phys. Rev. B **47**, 11314 (1993).
559. J. A. Martindale, S. E. Barrett, K. E. O'Hara, C. P. Slichter, W. C. Lee, and D. M. Ginsberg, Phys. Rev. B **47**, 9155 (1993).
560. K. A. Moler, D. J. Baar, J. S. Urbach, R. Liang, W. N. Hardy, and A. Kapitulnik, Phys. Rev. Lett. **73**, 2744 (1994).
561. H. Aubin, K. Behnia, M. Ribault, R. Gagnon, and L. Taillefer, Phys. Rev. Lett. **78**, 2624 (1997).
562. Z.-X. Shen, D. S. Dessau, B. O. Wells, D. M. King, W. E. Spicer, A. J. Arko, D. Marshall, L. W. Lombardi, A. Kapitulnik, P. Dickenson, S. Doniach, J. DiCarlo, T. Loeser, and C. H. Park, Phys. Rev. Lett. **70**, 1553 (1993).
563. D. Mandrus, J. Hartge, C. Kendziora, L. Mihaly, and L. Forro, Europhys. Lett. **22**, 199 (1993).
564. D. Coffey and L. Coffey, Phys. Rev. Lett. **70**, 1529 (1993).
565. T. P. Deveraux, D. Einzel, B. Stadlober, R. Hackl, D. H. Leach, and J. J. Neumeier, Phys. Rev. Lett. **72**, 396 (1994).
566. Q. Huang, J. F. Zasadzinski, N. Tralshawala, K. E. Gray, D. G. Hinks, J. L. Peng, and R. L. Greene, Nature **347**, 309 (1990).
567. D.-H. Wu, J. Mao, S. N. Mao, J. L. Peng, X. X. Xi, R. L. Greene, and S. M. Anlage, Phys. Rev. Lett. **70**, 85 (1993).
568. S. M. Anlage, D.-H. Wu, J. Mao, S. N. Mao, X. X. Xi, T. Venkatesan, J. L. Peng, and R. L. Greene, Phys. Rev. B **50**, 523 (1994).
569. B. Stadloper, G. Krug, R. Nemetschek, R. Hackl, J. L. Cobb, and J. T. Markert, Phys. Rev. Lett. **74**, 4911 (1995).
570. J. D. Kokales, P. Fournier, L. V. Mercaldo, V. V. Talanov, R. L. Greene, and S. M. Anlage, Phys. Rev. Lett. **85**, 3696 (2000).
571. R. Prozorov, R. W. Giannetta, P. Fournier, and R. L. Greene, Phys. Rev. Lett. **85**, 3700 (2000).
572. N. P. Armitage, D. H. Lu, D. L. Feng, C. Kim, A. Damascelli, K. M. Shen, F. Ronning, Z.-X. Shen, Y. Onose, Y. Taguchi, and Y. Tokura, Phys. Rev. Lett. **86**, 1126 (2001).
573. T. Sato, T. Kamiyama, T. Takahashi, K. Kurahashi, , and K. Yamada, Science **291**, 1517 (2001).
574. C. C. Tsuei and J. R. Kirtley, Rev. Mod. Phys. **72**, 969 (2000).
575. G. Blumberg, A. Koitzsch, A. Gozar, B. S. Dennis, C. A. Kendziora, P. Fournier, and R. L. Greene, Phys. Rev. Lett. **88**, 107002 (2002).
576. D. A. Wollman, D. J. Van Harlingen, W. C. Lee, D. M. Ginsberg, and A. J. Leggett, Phys. Rev. Lett. **71**, 2134 (1993).
577. D. A. Brauner and H. R. Ott, Phys. Rev. B **50**, 6530 (1994).
578. A. Mathai, Y. Gin, R. C. Black, A. Amar, and F. C. Wellstood, Phys. Rev. Lett. **74**, 4523 (1995).
579. D. A. Wollman, D. J. Van Harlingen, J. Giapintzakis, and D. M. Ginsberg, Phys. Rev. Lett. **74**, 797 (1995).

580. J. H. Miller, Q. Y. Ying, Z. G. Zou, N. Q. Fan, J. H. Xu, M. F. Davis, and J. C. Wolfe, Phys. Rev. Lett. **74**, 2347 (1995).
581. C. C. Tsuei, J. R. Kirtley, C. C. Chi, L.-S. Yu-Jahnes, A. Gupta, T. Shaw, J. Z. Sun, and M. B. Ketchen, Phys. Rev. Lett. **72**, 593 (1994).
582. J. R. Kirtley, C. C. Tsuei, J. Z. Sun, C. C. Chi, L. S. Yu-Jahnes, A. Gupta, M. Rupp, and M. B. Ketchen, Nature **373**, 225 (1995).
583. C. C. Tsuei, J. R. Kirtley, M. Rupp, J. Z. Sun, A. Gupta, M. B. Ketchen, C. A. Wang, Z. F. Ren, J. H. Wang, and M. Bhushan, Science **271**, 329 (1996).
584. A. G. Sun, D. A. Gajewski, M. B. Maple, and R. C. Dynes, Phys. Rev. Lett. **72**, 2267 (1994).
585. A. G. Sun, S. H. Han, A. S. Katz, D. A. Gajewski, M. B. Maple, and R. C. Dynes, Phys. Rev. B **52**, R15731 (1995).
586. J. Lesueur, M. Aprili, A. Goulan, T. J. Horton, and L. Dumoulin, Phys. Rev. B **55**, 3308 (1997).
587. A. G. Sun, A. Truscott, A. S. Katz, R. C. Dynes, B. W. Veal, and C. Gu, Phys. Rev. B **54**, 6734 (1996).
588. R. Kleiner, A. S. Katz, A. G. Sun, R. Summer, D. A. Gajewski, S. H. Han, S. I. Woods, E. Dantsker, B. Chen, K. Char, M. B. Maple, R. C. Dynes, and J. Clarke, Phys. Rev. Lett. **76**, 2161 (1996).
589. P. Chaudhari and S.-Y. Lin, Phys. Rev. Lett. **72**, 1084 (1994).
590. C. C. Tsuei and J. R. Kirtley, Phys. Rev. Lett. **85**, 182 (2000).
591. K. A. Kouznetsov, A. G. Sun, B. Chen, A. S. Katz, S. R. Bahcall, J. Clarke, R. C. Dynes, D. A. Gajewski, S. H. Han, M. B. Maple, J. Giapintzakis, J.-T. Kim, and D. M. Ginsberg, Phys. Rev. Lett. **79**, 3050 (1997).
592. Q. Li, Y. N. Tsay, M. Suenaga, R. A. Klemm, G. D. Gu, and N. Koshizuka, Phys. Rev. Lett. **83**, 4160 (1999).
593. A. Bille, R. A. Klemm, and K. Scharnberg, Phys. Rev. B **62**, 661 (2000).
594. K. A. Müller, Phil. Mag. Lett. **82**, 279 (2002).
595. R. A. Klemm, to be published in the Proceedings of the 23rd International Conference on Low Temperature Physics, Hiroshima, Japan, 2002 (unpublished).
596. Y. Takano, T. Hatano, A. Fukuyo, A. Ishii, M. Ohmori, S. Arisawa, K. Togano, and M. Tachiki, Phys. Rev. B **65**, 140513 (2002).
597. M. T. Beal-Monod, Physica C **298**, 59 (1998).
598. R. Movshovich, M. A. Hubbard, M. B. Salamon, A. V. Balatsky, R. Yoshizaki, J. L. Sarrao, and M. Jaime, Phys. Rev. Lett. **80**, 1968 (1998).
599. P. W. Anderson, Science **235**, 1196 (1987).
600. B. G. Levi, Physics Today **March**, 20 (1990).
601. K. Levin, J. H. Kim, J. P. Lu, and Q. Si, Physica C **175**, 449 (1991).
602. R. B. Laughlin, Science **244**, 525 (1988).
603. C. M. Varma, P. B. Littlewood, S. Schmitt-Rink, E. Abrahams, and A. E. Ruckenstein, Phys. Rev. Lett. **63**, 1996 (1989).
604. Y. Iye, in *Physical Properties of High Temperature Superconductors III*, edited by D. M. Ginsberg (World Scientific, Singapore, 1992), Vol. III, Chap. 4.
605. Y. Dalichaouch, C. L. Seaman, C. C. Almason, M. C. de Andrade, H. Iwasaki, P. K. Tsai, and M. B. Maple, Physica B **103**, 308 (1991).
606. C. C. Almasan, S. H. Han, K. Yoshiara, M. Buchgeister, B. W. Lee, L. M. Paulius, D. A. Gajewski, and M. B. Maple, Physica B **199-200**, 288 (1994).
607. T. R. Chien, Z. Z. Wang, and N. P. Ong, Phys. Rev. Lett. **67**, 2088 (1991).

608. P. W. Anderson, Phys. Rev. Lett. **67**, 2092 (1991).
609. B. P. Stojkovic and D. Pines, Phys. Rev. Lett. **76**, 811 (1996).
610. C. C. Almasan and M. B. Maple, in *Handbook on the Physics and Chemistry of the Rare Earths: High Temperature Superconductors II*, edited by K. A. Gschneidner, Jr., L. Eyring, and M. B. Maple (Elsevier, New York, 2001), Vol. 31, Chap. 197, p. 251.
611. G. S. Boebinger, Y. Ando, A. Passner, T. Kimura, M. Okuya, J. Shimoyama, K. Kishio, K. Tamasaku, N. Ichikawa, and S. Uchida, Phys. Rev. Lett. **77**, 5417 (1996).
612. S. L. Cooper and K. E. Gray, in *Physical Properties of High Temperature Superconductors IV*, edited by D. M. Ginsberg (World Scientific, Singapore, 1994), Chap. 3.
613. Y. Ando, G. S. Boebinger, A. Passner, T. Kimura, and K. Kishio, Phys. Rev. Lett. **75**, 4662 (1995).
614. C. N. Jiang, A. R. Baldwin, G. A. Levin, T. Stein, C. C. Almasan, D. Gajewski, S. H. Han, and M. B. Maple, Phys. Rev. B **55**, R3390 (1997).
615. H. Ding, T. Yokoya, J. C. Campuzano, T. Takahashi, M. Randeria, M. R. Norman, T. Mochiku, K. Kadowaki, and J. Giapintzakis, Nature **382**, 51 (1996).
616. B. Bucher, P. Steiner, J. Karpinski, E. Kaldis, and P. Wachter, Phys. Rev. Lett. **70**, 2012 (1993).
617. B. Batlogg, H. Y. Hwang, H. Takagi, R. J. Cava, H. L. Rao, and J. Kwo, Physica C **235-240**, 130 (1994).
618. T. Ito, K. Takenaka, and S. Uchida, Phys. Rev. Lett. **70**, 3995 (1993).
619. H. Y. Hwang, B. Batlogg, H. Takagi, H. L. Kao, J. Kwo, R. J. Cava, J. J. Krajewski, and W. F. Peck, Jr., Phys. Rev. Lett. **72**, 2636 (1994).
620. J. L. Tallon, J. R. Cooper, P. deSilva, G. V. M. Williams, and J. W. Loram, Phys. Rev. Lett. **75**, 4114 (1995).
621. W. W. Warren, Jr., R. E. Walstedt, G. F. Brennert, R. J. Cava, R. Tycko, R. F. Bell, and G. Dabbagh, Phys. Rev. Lett. **62**, 1193 (1989).
622. M. A. Takigawa, P. Reyes, P. C. Hammel, J. D. Thompson, R. H. Heffner, Z. Fisk, and K. C. Ott, Phys. Rev. B **43**, 247 (1991).
623. H. Alloul, A. Mahajan, H. Casalta, and O. Klein, Phys. Rev. Lett. **70**, 1171 (1993).
624. T. Imai, T. Shimizu, H. Yasuoka, Y. Ueda, and K. Kosuge, J. Phys. Soc. Jpn. **57**, 2280 (1988).
625. J. Rossat-Mignod, L. P. Regnault, C. Vettier, P. Bourges, P. Burlet, J. Bossy, J. Y. Henry, and G. Lapertot, Physica C **185-189**, 86 (1991).
626. J. W. Loram, K. A. Mirza, J. R. Cooper, and W. Y. Liang, Phys. Rev. Lett. **71**, 1740 (1993).
627. C. C. Homes, T. Timusk, R. Liang, D. A. Bonn, and W. N. Hardy, Phys. Rev. Lett. **71**, 1645 (1993).
628. D. N. Basov, T. Timusk, B. Dabrowski, and J. D. Jorgensen, Phys. Rev. B **50**, 3511 (1994).
629. A. V. Puchkov, P. Fournier, D. N. Basov, T. Timusk, A. Kapitulnik, and N. N. Kolesnikov, Phys. Rev. Lett. **77**, 3212 (1996).
630. A. G. Loeser, Z.-X. Shen, D. S. Dessau, D. S. Marshall, C. H. Park, P. Fournier, and A. Kapitulnik, Science **273**, 325 (1996).
631. A. Damascelli, Z. Hussain, and Z.-X. Shen, Rev. Mod. Phys. **75**, 473 (2003).

632. C. H. Renner, B. Revaz, J.-Y. Genoud, K. Kadowaki, and Ø. Fischer, Phys. Rev. Lett. **80**, 149 (1998).
633. M. Kugler, Ø. Fischer, C. Renner, S. Ono, and Y. Ando, Phys. Rev. Lett. **86**, 4911 (2001).
634. H. Won and K. Maki, Phys. Rev. B **49**, 1397 (1994).
635. B. G. Levi, Physics Today **June**, 19 (1998).
636. J. M. Tranquada, B. J. Sternlieb, J. D. Axe, Y. Nakamura, and S. Uchida, Nature **375**, 561 (1995).
637. M. V. Zimmermann, A. Vigliante, T. Niemoeller, N. Ichikawa, T. Frello, J. Madsen, P. Wochner, S. Uchida, N. H. Andersen, J. M. Tranquada, D. Gibbs, and J. R. Schneider, Europhys. Lett. **41**, 629 (1998).
638. S.-W. Cheong, G. Aeppli, T. E. Mason, H. Mook, S. M. Hayden, P. C. Canfield, Z. Fisk, K. N. Clausen, and J. L. Martinez, Phys. Rev. Lett. **67**, 1791 (1991).
639. T. E. Mason, G. Aeppli, and H. A. Mook, Phys. Rev. Lett. **68**, 1414 (1992).
640. T. R. Thurston, P. M. Gehring, G. Shirane, R. J. Birgeneau, M. A. Kastner, Y. Endoh, M. Matsuda, K. Yamada, H. Kojima, and I. Tanaka, Phys. Rev. B **46**, 9128 (1992).
641. M. Dumm, S. Komiya, Y. Ando, and D. N. Basov, Phys. Rev. Lett. **91**, 077004 (2003).
642. M. Matsuda, M. Fujita, K. Yamada, R. J. Birgeneau, M. A. Kastner, H. Hiraka, Y. Endoh, S. Wakimoto, and G. Shirane, Phys. Rev. B **62**, 9148 (2000).
643. S. H. Pan, J. P. O'Neal, R. L. Badzey, C. Chamon, H. Ding, J. R. Engelbrecht, Z. Wang, H. Eisaki, S. Uchida, A. D. Gupta, K.-W. Ng, E. W. Hudson, K. M. Lang, and J. C. Davis, Nature **413**, 282 (2001).
644. J. E. Hoffman, K. McElroy, D.-H. Lee, K. M. Lang, H. Eisake, S. Uchida, and J. C. Davis, Science **297**, 1148 (2002).
645. J. L. Tallon and J. W. Loram, Physica C **349**, 53 (2001).
646. Y. Suzumura, Y. Hasegawa, and H. Fukuyama, J. Phys. Soc. Jpn. **57**, 2768 (1988).
647. H. Fukuyama, Prog. Theoret. Phys. **Suppl. 108**, 287 (1992).
648. N. Nagaosa and P. A. Lee, Phys. Rev. B **45**, 966 (1992).
649. M. Randeria, N. Trivedi, A. Moreo, and R. T. Scalettar, Phys. Rev. Lett. **69**, 2001 (1992).
650. V. J. Emery and S. A. Kivelson, Nature **374**, 434 (1995).
651. Y. J. Uemura, in *Proceedings of the 10th Anniversary HTS Workshop on Physics, Materials, and Applications*, edited by B. Batlogg, C. W. Chu, W. K. Chu, D. U. Gubser, and K. A. Müller (World Scientific, Singapore, 1996), p. 68.
652. S.-C. Zhang, Science **275**, 1089 (1997).
653. C. Castellani, C. Di Castro, and M. Grilli, Z. Phys. B **103**, 137 (1997).
654. Z. A. Xu, N. P. Ong, Y. Wang, T. Kakeshita, and S. Uchida, Nature **406**, 486 (2000).
655. Y. Wang, N. P. Ong, Z. A. Xu, T. Kakeshita, S. Uchida, D. A. Bonn, R. Liang, and W. N. Hardy, Phys. Rev. Lett. **88**, 257003 (2002).
656. V. Sandu, E. Cimpoiasu, C. C. Almasan, S. Li, and M. B. Maple, to be published (unpublished).

9 Electronic Theory for Superconductivity in High–T_c Cuprates and Sr_2RuO_4

D. Manske, I. Eremin, and K.H. Bennemann
Institut für Theoretische Physik, Freie Universität Berlin, Germany

9.1 **Introduction** 732
9.2 **Electronic Theory for Hole– and Electron–Doped Cuprates** 750
9.2.1 Electronic Structure and Hamiltonain 751
9.2.2 Eliashberg Theory for the Interaction Between Quasiparticles and Antiferromagnetic Spin Fluctuations 754
9.2.3 Elementary Excitations 760
9.2.4 Dynamical Spin Susceptibility 764
9.2.5 Gap Equation: Singlet and Triplet Cooper–Pairing 767
9.2.6 Superfluid Density n_s 771
9.2.7 Cooper–Pair Phase Fluctuations 773
9.2.8 Tunnelling Spectra 777
9.2.9 Bilayer Effects 780
9.2.10 Electron–Doped Cuprates 782
9.3 **Electronic Theory for Ruthenates (Sr_2RuO_4)** 785
9.3.1 Electronic Structure and Hamiltonain 785
9.3.2 Eliashberg–like Theory for the Coupling of Quasiparticles to Ferromagnetic and Incommensurate Antiferromagnetic Spin Fluctuations 788
9.3.3 Elementary Excitations in Sr_2RuO_4 791
9.3.4 Dynamical Spin Susceptibility: Magnetic Anisotropy 793
9.3.5 Gap Equation: Triplet Pairing and Symmetry of the Superconducting Order Parameter 794
9.4 **Results for Hole– and Electron–Doped Cuprates** 799
9.4.1 Bare Electronic Structure 799
9.4.2 Elementary Excitations 801
9.4.3 Dynamical Spin Susceptibility 810
9.4.4 Order Parameter: Doping Dependence 813
9.4.5 Resonance Peak and Magnetic Coherence 815
9.4.6 Phase Diagram for Electron- and Hole-Doped Cuprates 820
9.4.7 Doping Dependence of the Superfluid Density $n_s(x,T)$ 827
9.4.8 SIS and NIS Tunnelling Spectra 833
9.4.9 Bilayer Effects 836
9.5 **Results for Sr_2RuO_4** 839

K. H. Bennemann et al. (eds.), *The Physics of Superconductors*
© Springer-Verlag Berlin Heidelberg 2004

9.5.1 Electronic Structure 839
9.5.2 Elementary Excitations: Effect of Spin Fluctuations 840
9.5.3 Dynamical Spin Susceptibility, NMR, and INS 842
9.5.4 Superconducting Order Parameter 847
9.5.5 Doping Dependence of Ruthenates 853
9.6 **Summary and Outlook** 855
Appendix A: Derivation of the generalized Eliashberg Equations for the Interaction of Quasiparticles and Spin Fluctuations 857
Appendix B: Numerical Solution Method for the Generalized Eliashberg Equations 861
Appendix C: Derivation of the Quasiparticle Self-Energy 865
Appendix D: Cooper-Pair Phase Fluctuations 868
Acknowledgements 878
References 878

9.1 Introduction

Superconductivity remains one of the most interesting problems in Solid State Physics. During the last years in particular high-transition temperature superconductivity in the cuprates with non-s-wave pairing symmetry and unconventional superconductivity in the isostructural strontiumruthenate (Sr_2RuO_4) also with a non-s-wave symmetry of the superconducting order parameter and triplet Cooper-pairing have been studied. Cuprates and ruthenates have an oxide layered structure with CuO_2-and RuO_2-planes, respectively. These seem to play an important role regarding superconductivity and magnetic activity. For an illustration we show in Fig. 9.1 the crystal structures (in Sr_2RuO_4 the basic element is a RuO_2-plane and the superconducting transition temperature for triplet pairing is T_c=1.5K). Undoped La_2CuO_4 is an antiferromagnetic insulator. Superconductivity occurs only upon doping (Ba instead of La) and reaches a maximum for hole doping $x = 0.15$ with a transition temperature $T_c \approx 40$K [1]. The different behavior of Sr_2RuO_4 and $La_{2-x}Ba_xCuO_4$ is definitely related to the electronic structure of RuO_2 and CuO_2-planes.

Let us emphasize also some differences in the crystal structures of Sr_2RuO_4 and $La_{2-x}Ba_xCuO_4$. Sr_2RuO_4 has pure tetragonal crystal structure. The RuO_6-octahedra are not distorted. On the other hand, in $La_{2-x}Ba_xCuO_4$ the corresponding CuO_6-octahedra are sufficiently distorted. In general, it is an important problem to understand the dependence of T_c based on crystal structure. In Fig. 9.2 we show the crystallographic structures of Bi-based cuprates with various number of CuO_2-layers per unit cell. T_c increases almost linearly from $Bi_2Ba_2CuO_6$ to the $Bi_2Ca_2Ba_2Cu_3O_{10}$. Note, not only

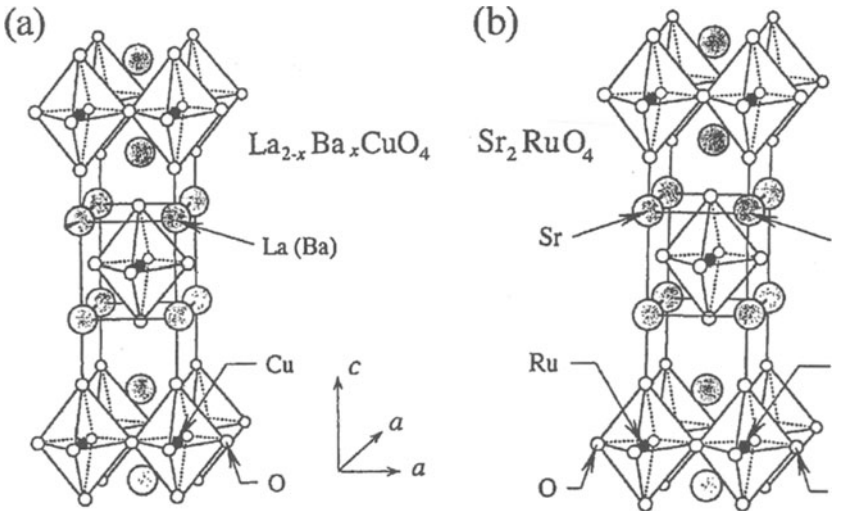

Fig. 9.1. (a) Cuprate singlet superconductor $La_{2-x}Ba_xCuO_4$. (b) Layered perovskite structure of the triplet superconductor Sr_2RuO_4

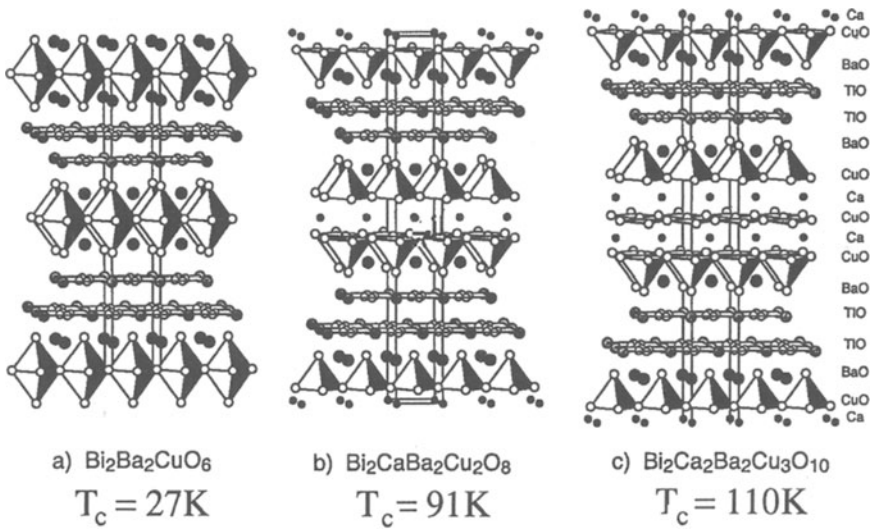

Fig. 9.2. T_c of cuprate crystal structures with various CuO_2-layers: (a) one-layer, (b) two-layer, and (c) three-layer

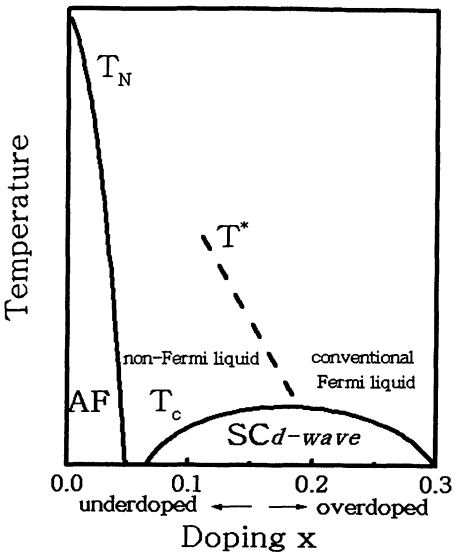

Fig. 9.3. Schematic phase diagram of hole-doped cuprates. High-T_c superconductivity occurs always in the vicinity of an antiferromagnetic phase transition (AF). The superconducting transition temperature as a function of the hole concentration $T_c(x)$ has a characteristic parabola-like shape. The superconducting order parameter is of d-wave symmetry. The normal state can be divided into two parts: In the overdoped region the cuprates behave like a conventional Fermi liquid, whereas in the underdoped regime below a temperature T^* one finds strong antiferromagnetic correlations and non-Fermi-liquid behavior. T^* is a crossover temperature and is called pseudogap temperature, because a normal-state gap opens up in the spin- and charge degrees of freedom. T^* may enter the T_c curve roughly at optimum doping concentration or at overdoped values dependent on the number of CuO_2-planes per unit cell

the number of CuO_2-layers is changing, but also other properties like the strength of the orthorhombic distortions in these materials.

Cuprates

The parent compounds of the cuprate superconductors like La_2CuO_4 or $YBa_2Cu_3O_6$ are quasi-two-dimensional antiferromagnetic insulators. Doping these systems with holes, for example, La_2CuO_4 with strontium or $YBa_2Cu_3O_6$ with oxygen causes a transition from a Mott insulator to a metallic phase. The metallic phase exhibits unconventional superconductivity with non s–wave symmetry of the order parameter and the transition temperature T_c increases with increasing doping towards a maximum value. Further doping decreases T_c. Finally, superconductivity disappears in the overdoped region. Remarkably, despite differences between the phase diagrams of various hole-doped cuprates one can map all of them into one so-called generic

phase diagram as shown in Fig. 9.3. This seems possible if one assumes that Cooper-pairing and normal state dynamics already occur essentially in the CuO_2-plane. Then, the physical properties of each cuprate compound depend mainly on the number of carriers within a CuO_2 plane and the correlation between them.

Besides crystal structures, doping dependence $T_c(x)$, and phase diagram, many important properties have been observed. For example, various experiments indicate for the cuprates $d_{x^2-y^2}$–symmetry of the superconducting order parameter and singlet Cooper–pairing:

$$\Delta_{\mathbf{k}} = \frac{\Delta_0}{2}(\cos k_x - \cos k_y). \tag{9.1}$$

The superconducting transition temperatures may be as high as 150K. Considerable electronic correlations yield a non-Fermi liquid behavior of the elementary excitations in the normal state (below T*). Generally, the behavior of the cuprates depends significantly on the doping concentration x.

Note, regarding the symmetry of the superconducting order parameter in the cuprates, evidence for $d_{x^2-y^2}$-wave pairing in hole–doped cuprates comes from several sources, in particular from nuclear magnetic resonance (NMR) [3], phase sensitive measurements [4–7], penetration depth measurements [8, 9], ARPES [10], and polarization-dependent Raman scattering experiments [11–14]. In contrast to the conventional superconductors, the behavior of the $d_{x^2-y^2}$-wave symmetry of the superconducting order parameter in the first Brillouin Zone (BZ) is very peculiar. In particular, the presence of the line nodes along the diagonal of the BZ and the corresponding changes of sign in the gap function allow different experimental techniques to distinguish a $d_{x^2-y^2}$-wave symmetry from other symmetries, for example from isotropic s-wave symmetry.

In Fig. 9.4 we show NMR/NQR results of Ref. [3] for the temperature dependence of the spin-lattice relaxation rate $1/T_1$ of ^{63}Cu for three different high-T_c cuprate superconductors below T_c. A signature of unconventional superconductivity is the absence of the so-called Hebel–Slichter peak at $T \simeq T_c$ and also the temperature dependence of $1/T_1$: In contrast to a low temperature exponential decay in the case of s-wave pairing, the relaxation rate $1/T_1$ has a rather different dependence on T, namely a power law that one would expect for d-wave symmetry of the superconducting order parameter. Note, for a d-wave gap with line nodes along the diagonals the density of states is not fully gaped and thus allows the quasiparticles to occupy states for energies $|\omega| < 2\Delta_0$ (Δ_0 is the maximal gap at $T = 0$). In an NMR experiments one averages over the first BZ and thus one takes also into account the states at the line nodes. As a result, the temperature dependence of the spin-lattice relaxation follows a power law ($\propto T^3$). As one sees in Fig. 9.4 this is indeed the case for high-T_c cuprate superconductors.

There is another important signature of unconventional superconductivity in the cuprates. Usually, one observes $T_c \propto \Delta_0$ for conventional superconduc-

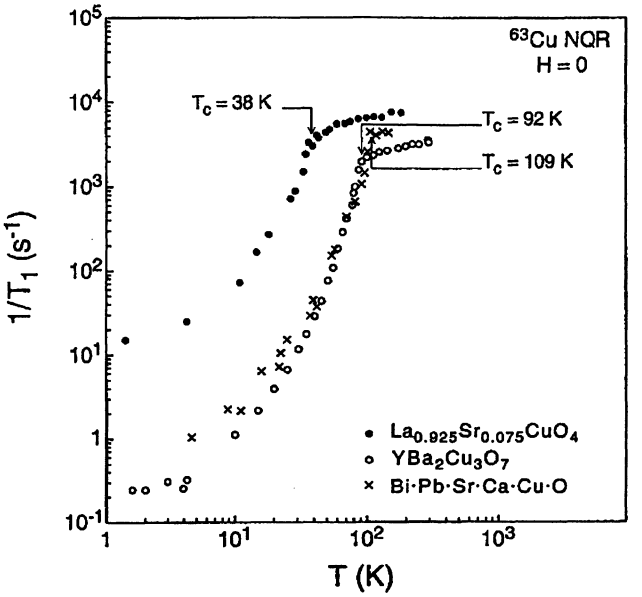

Fig. 9.4. Temperature dependence of the ^{63}Cu NQR spin–lattice relaxation rate for various cuprate superconductors revealing singlet d–wave Cooper-pairing (taken from Ref. [3])

tors ($\Delta_0 = \Delta(T = 0)$). However, in hole-doped cuprates this relation is not generally satisfied and only observed for $x > x_0$. For $x < x_0$ (x_0 = optimal doping), i.e. in underdoped cuprates, T_c is decreasing upon decreasing doping, while the measured Δ_0 becomes larger. As noted by Uemura *et al.* [15] in underdoped cuprates one finds $T_c \propto n_s$ where n_s is a superfluid density. This is shown in Fig. 9.5.

In general, the normal state of the hole-doped cuprates depends sensitively on doping, see Fig. 9.6. The overdoped cuprates behave like a conventional Fermi liquid, whereas the underdoped ones, in particular below the pseudogap temperature T^*, exhibit some unusual properties. For example, a gap is present in the elementary excitation spectrum, strong anisotropies are observed (mainly caused by the quasi-two-dimensional nature of the system), and short-range antiferromagnetic fluctuations exist. This different behavior of underdoped and overdoped crystals can be seen, for example, from ^{63}Cu spin-lattice relaxation rate and the inelastic neutron scattering (INS) intensity in hole–doped cuprates. In the overdoped cuprates $1/T_1T$ increases monotonously as T decreases down to T_c, while in the underdoped ones $1/T_1T$ passes through a maximum at the spin-gap temperature T^* for decreasing T [16]. At the same time similar behavior is observed by INS where in the underdoped cuprates the imaginary part of the spin susceptibility Im $\chi(\mathbf{Q}, \omega)$

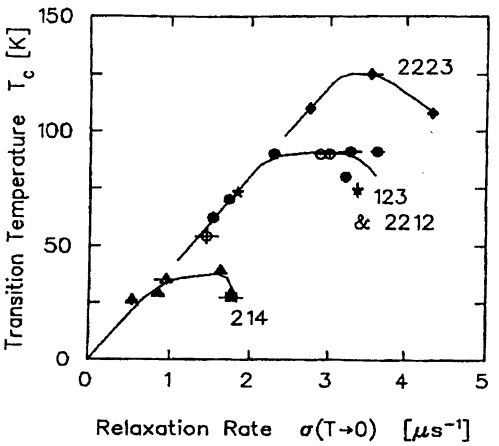

Fig. 9.5. The superconducting transition temperature T_c plotted vs low-temperature muon–spin–relaxation rate σ measured for different high–T_c superconductors see Ref. [15] (214: $La_{2-x}Sr_xCuO_4$, 123: $YBa_2Cu_3O_7$, 2212: $Bi_2Sr_2Ca_2CuO_8$, 2223: $Bi_2Sr_2Ca_2Cu_3O_{10}$). Note, $\sigma(0)$ is proportional to the superfluid density, n_s/m^*

passes at fixed small frequency ω ($\simeq 10-15$meV) through a maximum at T^* for decreasing T [17].

In addition, angle–resolved photoemission spectroscopy (ARPES) experiments on underdoped $Bi_2Sr_2CaCu_2O_{8+\delta}$ show the presence of a 'pseudo'-gap with $d_{x^2-y^2}$–wave symmetry well above T_c also in the charge excitation spectrum [18,19]. Recent tunneling experiments indicate also a presence of a pseudogap in the tunneling spectral density well above T_c [20]. This gap opens below the temperature T^*. Several other experiments including heat capacity [21], transport [22], Raman scattering [23], and, in particular, scanning tunneling spectroscopy [24, 25] confirmed the existence of a pseudogap in the elementary excitations below T^*. To clarify the origin of the pseudogap a few phenomenological models like the Marginal–Fermi–Liquid (MFL) [26], the Nested–Fermi–Liquid [27,28], and Nearly-Antiferromagnetic–Liquid (NAFL) [29] have been developed. These describe the unusual non–Fermi–liquid properties in the normal state of hole–doped cuprates.

In the cuprate superconductors the CuO_2-plane seems to be most important. The surrounding environment of the CuO_2-plane, usually called charge reservoirs, play somehow a passive role supplying charge carriers for the planes. For some cuprates it is possible that also electrons can be doped into the CuO_2-plane. It is remarkable that these so-called electron-doped cuprates differ drastically from the hole-doped ones. Note, the large asymmetry in their phase diagrams see Fig. 9.6:

1. The antiferromagnetism persists in the electron-doped compounds up to

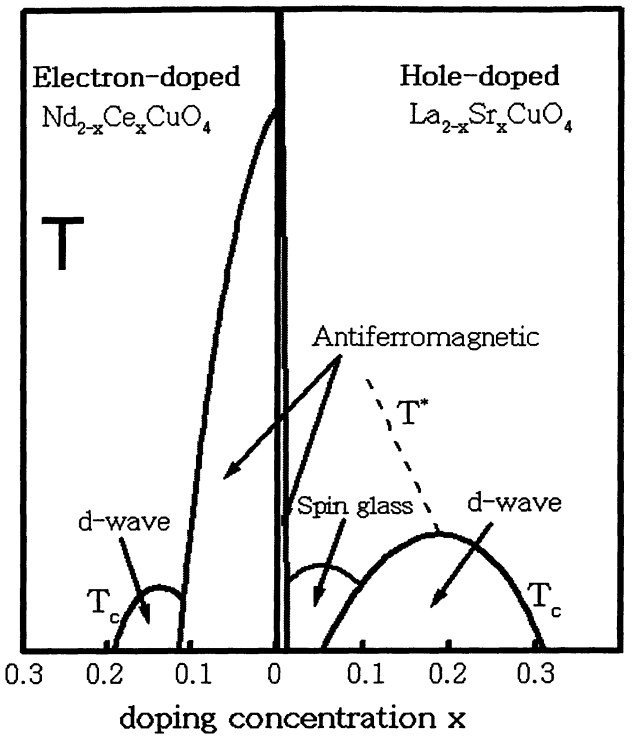

Fig. 9.6. The phase diagram of hole(LSCO)- and electron(NCCO)-doped cuprates, temperature T versus doping concentration x. Note, the asymmetry between electron and hole-doped cuprates. In the case of hole doping the carriers are occupying mainly the oxygen p-band, while for electron doping the carriers occupy the upper Hubbard band of the copper. Note, antiferromagnetism is for rather different doping concentration destroyed in electron- and hole-doped cuprates

x=0.12 or 0.14 [30], while in hole-doped compound $La_{2-x}Sr_xCuO_4$(LSCO) antiferromagnetism disappears already at x = 0.05;

2. Superconductivity in electron–doped cuprate systems occurs in a very narrow doping range (0.14<x<0.17 for $Nd_{2-x}Ce_xCuO_4$(NCCO) [31,43] and has a smaller transition temperature T_c), in the hole-doped LSCO system the doping range for which superconductivity occurs is broader ($0.05 < x < 0.3$). In addition, the behavior of the electron–doped cuprates in the normal and superconducting state is very different in comparison to the hole-doped ones. For example, in the normal state a pseudogap in the excitation spectrum in hole-underdoped cuprates is seen in many experiments [32]. In electron–doped ones the existence of the pseudogap is unclear. In optimally-doped $YBa_2Cu_3O_{6+y}$ (YBCO) and LSCO the in-plane resistivity increases linearly with temperature over a wide range [33] indicating a non-Fermi liquid behav-

ior. In NCCO (x=0.15) the in-plane resistivity is quadratic in temperature [34]. Photoemission spectroscopy studies of a CuO_2-plane show flat energy bands near the Fermi surface (FS) of the high-T_c hole doped cuprates [35]. However, in NCCO one finds a flat band only 300 meV below the FS [36]. Therefore, the question arises: Are the pairing symmetries of the electron and hole-doped cuprates different? It is widely believed that hole-doped are $d_{x^2-y^2}$–wave superconductors. In electron–doped cuprates the symmetry of the order parameter was for a long time under debate. Early measurements of in-plane penetration depth in NCCO have been fitted with an exponential temperature dependence suggesting isotropic BCS type s–wave gap [37] rather than power law decay expected for unconventional superconductors with nodes in the gap function. Thus, recent experiments indicate non-s-wave symmetry and rather $d_{x^2-y^2}$-wave symmetry of the superconducting order parameter. Most recent measurements of the magnetic penetration depth [41,42] have shown that the best fit occurs for dominant $d_{x^2-y^2}$-wave plus small admixture of the s-wave contribution for the underlying gap symmetry. The most convincing evidence for dominant $d_{x^2-y^2}$-wave symmetry in electron-doped NCCO and PCCO at optimal doping came very recently from the phase sensitive experiments [43]. Note, however with increasing doping the symmetry of the superconducting order parameter seems to change towards anisotropic s-wave type [44].

In general, for increasing doping itinerancy increases and antiferromagnetic activity disappears. The strong interplay of antiferromagnetic excitations and superconductivity, is in particular seen by inelastic neutron scattering (INS) and elementary excitations measured by angle–resolved photoemission spectroscopy (ARPES) experiments. The feedback of superconductivity on the spin susceptibility $\chi(\mathbf{q},\omega)$ and the recently observed 'kink' in the dispersions is illustrated in Fig. 9.7 and Fig. 9.8, respectively.

In Fig. 9.7 we show the INS results for optimally-doped $YBa_2Cu_3O_{6.92}$ [45]. Employing linear response theory, the intensity in INS is proportional to the magnetic structure factor that yields the imaginary part of the dynamical spin susceptibility. Thus, INS provides a direct probe of the spin susceptibility, $\chi(\mathbf{q},\omega)$. The normal state spin dynamics can be described approximately at the important antiferromagnetic wave vector $\mathbf{Q} = (\pi,\pi)$ by the Ornstein–Zernicke response function

$$\mathrm{Im}\chi \propto \frac{\omega\,\omega_{sf}}{\omega^2+\omega_{sf}^2} \quad . \tag{9.2}$$

Note, the rapid increase of $\mathrm{Im}\chi$ and the maximum at $\omega = \omega_{sf}$. In the superconducting state the behavior of $\mathrm{Im}\chi$ is very different. The spin excitation spectrum renormalizes strongly and becomes gaped at lower frequencies and then exhibits a sharp so-called 'resonance' peak at an energy ω_{res}. In the case of the optimally-doped YBCO one gets $\omega_{res} = 41\mathrm{meV}$.

The appearance of the resonance peak firstly reported in Ref. [46] suggests a strong renormalization of the spin fluctuation spectrum in the supercon-

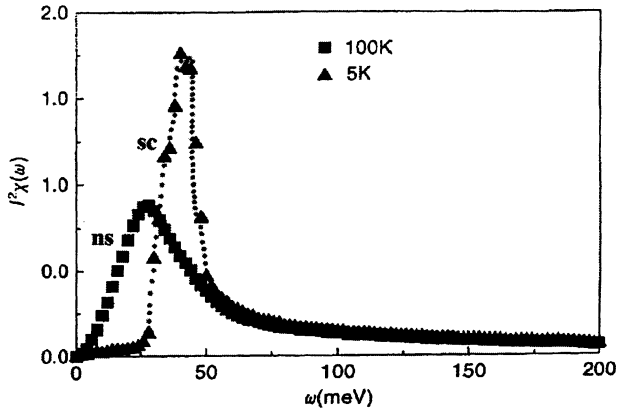

Fig. 9.7. Spin excitation spectrum $I^2\chi(\mathbf{q} = \mathbf{Q}, \omega)$ versus frequency for optimally-doped YBCO as observed by Inelastic Neutron Scattering (INS) experiments in cuprates [45]. In the normal state an Ornstein–Zernike behavior is observed. Note, the feedback of superconductivity ($T = 5\text{K} < T_c$) on the spin susceptibility and the formation of the so-called "resonance" peak at $\omega_{res} = 41\text{meV}$

ducting state that cannot be accounted for by the simple phenomenological form of the spin susceptibility, $\chi(\mathbf{q}, \omega)$ (see Eq. (9.2)). Note, phonon-mediated superconductivity is difficult to reconcile with the appearance of a resonance peak. Thus, the important resonance peak is a fingerprint of Cooper-pairing due to spin excitations. In a recent INS measurements [47] a resonant spin excitation in the overdoped and optimally–doped $Bi_2Sr_2CaCu_2O_{8+y}$ (BSCCO) is also observed with mode energies $E_{res} = 38\text{meV}$ and 43meV, respectively. This observation together with the previous measurements in underdoped phase of YBCO [45,48] indicates for the whole doping range a constant ratio

$$\frac{E_{res}}{k_B T_c} = 5.4 \quad . \tag{9.3}$$

The resonance peak emerged as a key property of the copper oxide superconductors. The observation of a resonance like feature in the superconducting state of single CuO_2–layer cuprate superconductor $Tl_2Ba_2CuO_{6+x}$ near optimal doping seems very important [49]. Note, no resonance peak is observed in electron-doped cuprates.

In view of this one may conclude that the analysis of the spin fluctuation spectrum above and below T_c and its doping dependence is significant for a microscopic theory of cuprate superconductivity.

Similarly important is the behavior of the elementary excitations above and below T_c. Regarding the 'kink' structure shown in Fig. 9.8 we note the following. With certain assumptions ARPES measures the spectral density, $A(\mathbf{k}, \omega)$, of the electrons in the CuO_2–planes. Due to recent developments in ARPES the spectral density can be studied with high accuracy versus

frequency at fixed momentum (so–called Energy Distribution Curves (EDC)) as well as a function of momentum at fixed frequency (so–called Momentum Distribution Curves (MDC)). One of the most important information that

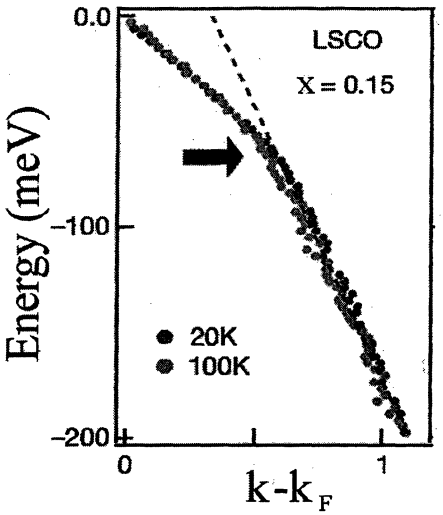

Fig. 9.8. Energy dispersion $\omega(\mathbf{k}-\mathbf{k_F})$ in the nodal direction with respect to the Fermi energy in the first BZ as observed by ARPES for the hole-doped cuprate compound BISSCO at different temperatures [56] versus the normalized momentum relative to the Fermi level. Note, the slope of the curve gives the renormalized group velocities

one gets by analyzing MDC and EDC is the renormalized energy dispersion $\omega_{\mathbf{k}}$ for the elementary excitations. Note, MDC curves are better suited for determining the energy dispersion due to a weaker momentum than frequency dependence of the self-energy, $\Sigma(\mathbf{k},\omega)$.

In Fig. 9.8 we show the results of Lanzara *et al.* [56] for the $(0,0) \rightarrow (\pi,\pi)$ direction in the first Brillouin Zone (BZ). One clearly sees that the curve shows a change in its slope around 50 ± 15meV. This so-called "kink" feature was observed by several groups [57]. Changes in the elementary excitation spectrum due to coupling of the carriers to spin fluctuations are generally expected. The coupling to spin fluctuations should result in rather different frequency and momentum dependencies of the self-energy than in the phonon case. To understand this 'kink' feature in detail is one of the important problems in the theory of high-T_c cuprates.

Note, tunneling spectroscopy allows also to determine the structure of the elementary excitations in cuprates. Originally, the successful analysis of tunneling spectra in conventional superconductors like Pb led to the common acceptance of the electron-phonon mechanism and Eliashberg theory of

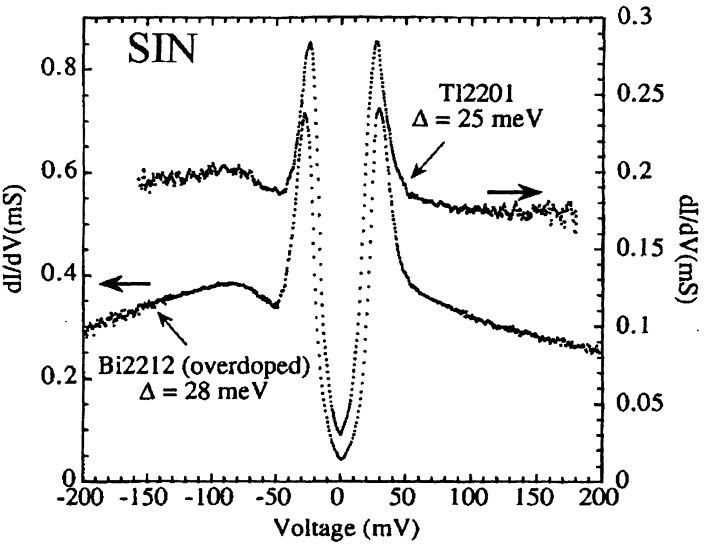

Fig. 9.9. Tunneling Spectra: Comparison of SIN conductances of Tl2201 and slightly overdoped Bi2212 at $T = 4.2$K. The results are taken from Ref. [62]

superconductivity [61]. Similarly, an understanding of the structure in the tunneling spectra in high-T_c cuprates is a central problem.

In Fig. 9.9 we show results for the Superconductor–Insulator-Normal metal (SIN) tunneling conductance $(dI/dV)_s$ normalized to its normal state value for two different cuprate superconductors, $Bi_2Sr_2CaCu_2O_{8+\delta}$ (BISCCO) and $Tl_2Ba_2CuO_6$ (Tl2201) having two and one CuO_2-plane per unit cell, respectively [62]. In both cases the superconducting gaps and T_c are similar demonstrating the essential independence of the observed features on the number of CuO_2-layers. Notice again a non-s-wave character of the superconducting gap, since the tunneling spectra have a characteristic V-shape indicating a presence of states inside the superconducting gap. In addition, further important details are related to the pairing interaction. Immediately after the coherence peak a 'dip–hump' structure is present with a 'hump' approximately at energy $3\Delta_0$, where Δ_0 is the superconducting gap at T=0. This structure is asymmetric with respect to the zero bias, since it occurs only below T_c. It is natural to suggest that the observed structure results from the pairing interaction and reflects the important frequency range of the spin fluctuations relevant for Cooper-pairing. One has to understand the relation of the 'dip-hump' feature to the 'kink' structure seen by ARPES in order to connect both experiments with each other.

This summarizes some key facts about superconductivity in hole– and electron–doped cuprates. We will present an electronic theory for the central problems by studying the interaction between carriers and spin excitations.

Ruthenates

Let us describe now essential properties of triplet Cooper-pairing in Sr_2RuO_4. Superconductivity and magnetic activity in the ruthenates seem intimately related. The character of the magnetic activity is still discussed. One ex-

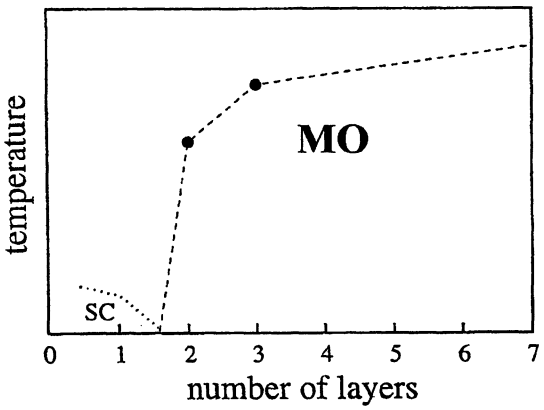

Fig. 9.10. Schematic phase diagram of the ferromagnetic and superconducting systems (Rodllesen–Popper crystals) $Sr_{n+1}Ru_nO_{3n+1}$, taken from Ref. [63]. The number of layers is the parameter which determines the transition between the two phases: MO=magnetically ordered and SC=superconducting

pects in view of triplet Cooper–pairing ferromagnetic spin fluctuations are present in Sr_2RuO_4. This is indirectly confirmed by the results shown in Fig. 9.10 where we plot a schematic phase diagram of the ferromagnetic and superconducting members of the Ruddlesen–Popper series ($Sr_{n+1}Ru_nO_{3n+1}$) as a function of the numbers of RuO_2-layers per unit cell, n. The infinite layer ($SrRuO_3$) is a ferromagnet with $T_{Curie} \approx 165$K. For n=3 one finds $T_{Curie} \approx 148$K and for n=2 $T_{Curie} \approx 102$K. This demonstrates the tendency that T_{Curie} is reduced with decreasing layer number n. This suggests that even for n=1, when supeconductivity occurs, one expects significant ferromagnetic fluctuations. These may play an important role for triplet superconductivity in Sr_2RuO_4.

Similar to the case of cuprates, inelastic neutron scattering (INS) studies reveal the formation of strong incommensurate antiferromagnetic fluctuations(IAF) for the wave vector $\mathbf{Q}= (2\pi/3, 2\pi/3)$ at energy $\omega_{sf} = 6$meV [65] and no signature of ferromagnetic fluctuations. In addition, results for the spin susceptibility $\chi(\mathbf{q},\omega)$ obtained by means of NMR [66] indicate a remarkable temperature-dependent magnetic anisotropy, for illustration see Fig. 9.11.

In general, the spin-lattice relaxation as measured by NMR allows to study different components of the magnetic susceptibility like their transverse and longitudinal parts. One finds that at room temperatures all components

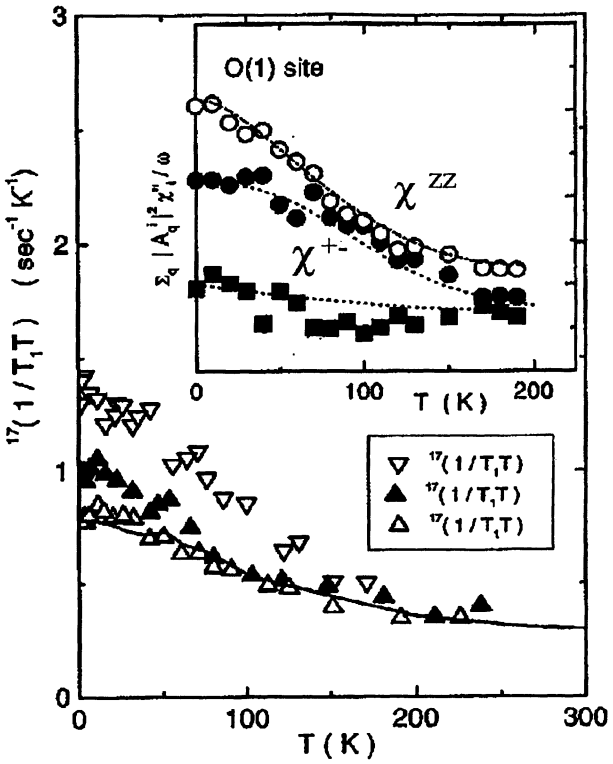

Fig. 9.11. Anisotropic magnetic response of a single RuO_2-plane in the triplet superconductor Sr_2RuO_4 versus temperature in the normal state as observed by NMR experiments [66]. Results are shown for the spin-lattice relaxation on the oxygen nuclei ^{17}O in the RuO_2-plane in terms of $(T_1T)^{-1}$. In the inset the results for the corresponding components of the spin susceptibility (transverse and longitudinal ones) are shown indicating the increase of the magnetic anisotropy upon cooling. χ^{zz} and χ^{+-} refer to the response of the system to the external magnetic field parallel and perpendicular to the RuO_2-plane, respectively

are the same. Then, for decreasing temperature, an isotropic response in the ruthenates is observed. Upon cooling the spin-lattice relaxation starts to differ and the anisotropy reaches a maximum at T=T_c. Therefore, at low temperatures one expects that magnetic anisotropy plays an important role for Cooper-pairing.

In Fig. 9.12 we show experimental results suggesting triplet Cooper-pairing in Sr_2RuO_4. In conventional superconductors the spin part of the Knight shift measured by NMR decreases rapidly below T_c due to formation of singlet Cooper-pairs. On the other hand, in a triplet superconductor with S=1 the spin part of the Knight shift should not change below T_c, since the

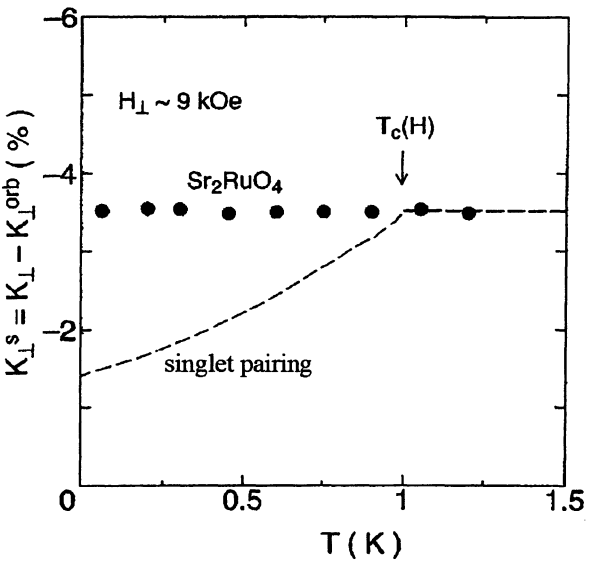

Fig. 9.12. Results for the uniform spin susceptibility, $\chi(\mathbf{q}=0,\omega=0)$ in the superconducting state of cuprates ($YBa_2Cu_3O_7$, dashed curve) and ruthenates measured by NMR ^{99}Ru Knight shift [66]. One clearly sees that in contrast to the singlet Cooper-pairing where the spin susceptibility decreases upon cooling, the Knight shift in Sr_2RuO_4 is unchanged by lowering T below T_c. In case of triplet Cooper-pairing the Knight shift decreases not below T_c, since the polarization induced by the external magnetic field does not change in the superconducting state

polarization induced by the weak external magnetic field and probed by NMR does not change. This behavior is observed in Sr_2RuO_4 by Ishida *et al.* [66] and provides unambiguous evidence for triplet Cooper-pairing [67].

Note, shortly after this discovery p-wave symmetry of the superconducting order parameter and triplet pairing has been suggested by Sigrist and Rice [50] using a phenomenological theory and some analogies between the normal state of ^{3}He and Sr_2RuO_4. In the case of p-wave pairing one has

$$\Delta_p = \Delta_0 \left(k_x + ik_y\right) \quad , \tag{9.4}$$

and thus an order parameter where $|\Delta|$ has no line nodes. Yet it must be remarked that the microscopic theory of triplet Cooper-pairing in Sr_2RuO_4 is still under discussion [51].

In general, assuming an exchange of magnetic fluctuations as responsible for Cooper–pairing like in cuprates, the structure of the spin susceptibility $\chi(\mathbf{q},\omega)$ and the Fermi surface topology should control the superconductivity in the ruthenates. Note, ferromagnetic spin fluctuations dominating over antiferromagnetic ones will cause then triplet paring.

The behavior mentioned above, the magnetic anisotropy, temperature dependence of the Knight shift as well as of the specific heat and other properties, and of the electronic structure (Fermi surface topology) are important characteristics of Sr_2RuO_4 and essential for an electronic theory.

Electronic Theory

Obviously, it is of great interest to have an electronic theory explaining the important normal state behavior and the pairing mechanism for superconductivity in cuprates and ruthenates. In this article we present results obtained by using a Hubbard–like model Hamiltonian and by taking into account the coupling of the elementary excitations to spin fluctuations (which are partially generated by the quasiparticles itself). This coupling may play the most important role for Cooper-pairing. Using an effective second order perturbation theory the interaction of the electrons (or holes) and spin fluctuations leads to the following effective electron-electron interaction shown in Fig. 9.13. Applying a generalized Eliashberg-type theory in the strong coupling

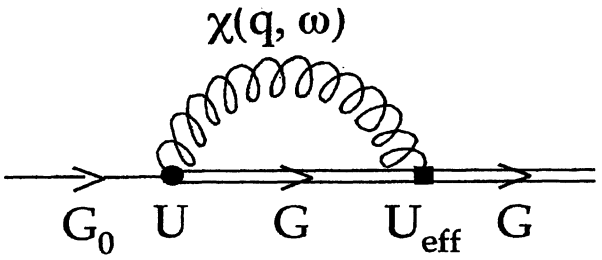

Fig. 9.13. Feynman diagram representing for the cuprates and ruthenates the coupling of the carriers described by a Green's function G (G_0= bare propagator) to magnetic spin fluctuations described by the spin susceptibility $\chi(\mathbf{q},\omega)$. U (U_{eff}) is an effective (renormalized) coupling constant which includes vertex corrections

limit we describe important behavior of hole- and electron-doped cuprates and Sr_2RuO_4. We compare our results critically with experiments. Note, in contrast to phonon-mediated superconductors no Migdal's theorem can be used [92]. In general, Tremblay *et al.* [100], and Chubukov *et al.* [182] have studied the role if vertex corrections of quasiparticle couple to spin fluctuations. They have pointed out that due to $\omega_{sf}/E_F \sim 10^{-2}$ and a flat dispersion around $(\pi, 0)$ they do only change the magnitude of the effective Coulomb interaction U, but the resultant dynamics of vertex corrections may be neglected ($U \rightarrow U_{eff}$). Note, that in the optimally and overdoped cuprates the vertex corrections are small and have positive sign of the Eliashberg coupling. This even enhances the coupling to spin fluctuations [52], but in underdoped cuprates the vertex corrections may get important. However, simply speaking, as long as $U\chi(\mathbf{q},\omega) < 1$, perturbation theory for constructing a pairing potential in the paramagnetic phase should work, unless poles on the bosonic

mode (i.e. in χ) enhance the pair-breaking contribution of the vertex function drastically [53]. Concerning the dynamics, note that the pairing potential is mediated by the same quasiparticles that form the Copper-pairs. Therefore, one has to solve this many-body problem self-consistently. As we will discuss below, the spin susceptibility χ, resulting from d-electrons of Cu, and the gap function that is dominated by a hybridization of p- and d- electrons, strongly interact with each other. Thus, in general one has coupled equations for $\chi\{G, \Delta\}$ and $\Delta\{G, \chi\}$ where G is the Green's function of the coore-sponding electron. Note that in a simple spin-fermion model the feedback of the elementary excitations on the pairing potential is neglected [182]. Simply speaking, electrons (holes) do not only condense into Cooper-pairs, but are also involved in the magnetic activity. Thus, a self-consistent treatment indeed is required.

In a way by employing the trial–and–error principle we hope to find the correct route for a theory which may play the same role as the B.C.S.-theory for the case of electron-phonon interaction with s-wave symmetry singlet Cooper-pairing. Of course, not only the doping dependence of superconductivity in the cuprates, but also the doping dependence of the elementary excitations and of the spin susceptibility $\chi(\mathbf{q}, \omega)$ are important problems to investigate. Despite the same strategy that we apply to cuprates and ruthenates, their behavior is different due to the differences in their electronic structures. Of course, the electronic structure, the energy dispersions and resultant Fermi surface will play an important role as an input for the calculations.

Basic Electronic Structure

For all cuprate compounds (both hole- and electron-doped ones) the degeneracy between $3d$–orbitals is removed by the lattice structure. After some straightforward calculations it can be shown (see Fig. 9.14 (a)) that the hybridized copper and oxygen orbitals separate. The state with highest (lowest) energy has mainly $d_{x^2-y^2}$-wave character. The missing electron (*i.e.* a hole) gives the Cu-ion a spin $\frac{1}{2}$. Thus, in the absence of doping, the cuprate material is well described by a model of mostly localized spin-$\frac{1}{2}$ states. The other orbitals are occupied and therefore can be neglected. However, the strong Coulomb repulsion between holes in the same orbital is so far not taken into account and must be included [68]. Due to large Coulomb repulsion $d_{x^2-y^2}$-orbitals split into two so-called lower and upper Hubbard bands (LHB and UHB), respectively as shown in Fig. 9.14(b). Then, at half-filling the system becomes an insulator. Furthermore, due to a very large U_d the splitting of $d_{x^2-y^2}$-band is so large that the oxygen p-band lies between the UHB and the LHB. The charge transfer gap in cuprates δ ($\delta = \epsilon_p - \epsilon_d$) is smaller than U_d [74, 167].

This has a very interesting consequence for the doping of the CuO_2-plane with holes or electrons. Due to the large Coulomb repulsion the doped hole is mainly in the oxygen p-band. Therefore, in hole-doped cuprates the carriers (holes) occupy mainly hybridized oxygen p-states. Contrary, electron doping

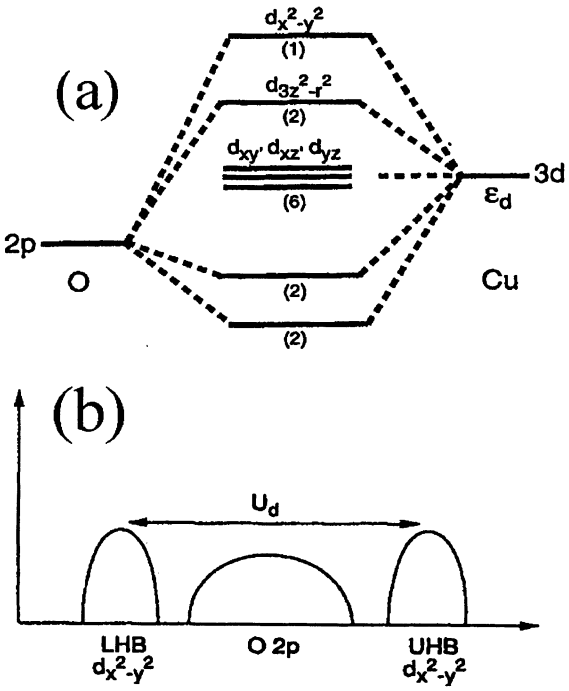

Fig. 9.14. Schematic electronic structure of CuO_2-planes reflecting bonding between a Cu^{2+} and two O^{2-} ions. (a) Initial splitting of the bands taking into account crystal field interaction only. We consider only d-electrons (holes) of Cu and p_x and p_y orbitals of the oxygen. The numbers indicate the occupations of the different levels in the undoped compound. (b) Role of the on-site Coulomb repulsion and the splitting of $3d_{x^2-y^2}$-orbital into a lower (LHB) and upper Hubbard band (UHB). U_d is the Coulomb repulsion between electrons at Copper. Due to $\delta = \epsilon_p - \epsilon_d < U_d$ the cuprates are Mott-Hubbard insulators without doping

means effectively doping of the $d_{x^2-y^2}$-orbital in the UHB. Thus, the carriers in the electron-doped cuprates sit largely at Cu $3d$-sites.

Fig. 9.14(b) suggests that hole- and electron-doped cuprates may under certain assumptions be mapped on to an effective one-band Hubbard model. The difference between hole and electron doping will be reflected by the different parameters of the model and differences of the character of the involved orbitals of the hybridization between p– and d–states. For hole doping the Fermi level lies in the p-band and for electron doping in the UHB. The spin at Cu-sites will induce a spin polarization at the neighboring oxygen sites upon hole doping (see Zhang–Rice singlet formation). This is not the case for electron doping (at Cu-sites). Then one decreases effectively only the number of Cu-spins. Consequently, one gets different behavior of $\chi(\mathbf{q}, \omega)$ and different

doping dependence of antiferromagnetism in the hole– and electron–doped cuprates.

Similarly as for the cuprates we use also a Hubbard-like Hamiltonian for the ruthenates (Sr_2RuO_4). However, we include three bands (α, β, γ) crossing the Fermi-level into the calculations. In Sr_2RuO_4 the formal valence of the

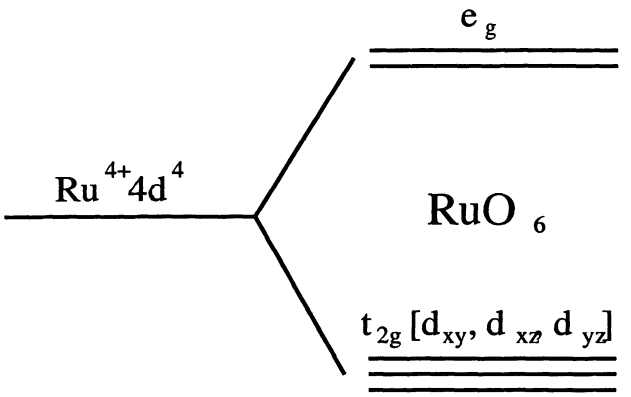

Fig. 9.15. Electronic structure of Sr_2RuO_4. The Ru^{4+} ion corresponds to a $4d^4$ level. The splitting of the e_g and t_{2g} subshells is due to the RuO_6 crystal field. The orbitals d_{xy}, d_{xz}, and d_{yz} cross the Fermi level. Magnetic activity results from the t_{2g} subshell. The RuO_2-plane structure plays an important role

ruthenium ion is Ru^{4+}. This leaves four electrons remaining in the 4*d*-shell. Furthermore, Ru ion sits at the center of a RuO_6-octahedron and the crystal field of the O^{2-} ions splits the five 4*d*-states into threefold (t_{2g}) and twofold (e_g) subshells as illustrated in Fig. 9.15. The negative charge of the O^{2-} ions causes the t_{2g} subshell to lie lower in energy. Note, these orbitals (xz, yz, and xy) have lobes that point between the O^{2-} ions lying along the x, y, and z-axes. Electrons of these orbitals form the Fermi surface and as we have already mentioned the α, β, and γ-bands. We again assume that the most important interaction of the carriers is with spin excitations described by the spin susceptibility $\chi(\mathbf{q},\omega)$ and resulting from Ru α-, β-, and γ-states.

To explain the experimentally observed large anisotropy of the magnetic activity in the RuO_2-plane, see $\chi^{+-}(\mathbf{q},\omega)$ and $\chi^{zz}(\mathbf{q},\omega)$ along the z-direction perpendicular to the planes, we include also spin-orbit coupling for the significant α, β, and γ-bands. Again, we hope that our trial–and–error type philosophy and critical comparison with experiments helps to find the correct theory and explains triplet superconductivity.

In summary, by using a Hubbard–like Hamiltonian we attempt to describe the electronic properties of the layered superconductors Cu-oxides and Ru-oxides. The theory for this spin excitation mediated superconductivity in

cuprates and ruthenates may help also to find a theory for the other novel superconductors like the heavy-fermion ones, $ZrZn_2$, UPt_3, UGe_2, etc.

In the next chapters we describe the electronic theory for calculating (a) the elementary excitations, the self-energy and spectral density (b) the spin susceptibility $\chi(\mathbf{q},\omega)$ and (c) superconductivity and the symmetry of the superconducting order parameter. We present results for various important properties. Finally, we discuss the limitation of our model for the cuprates and ruthenates and give an outlook.

9.2 Electronic Theory for Hole– and Electron–Doped Cuprates

We present now the theory for the interaction between quasiparticles and spin fluctuations in the cuprates and in Sr_2RuO_4. For simplicity we assume that the electronic dynamics is controlled by the CuO_2 and RuO_2–planes, respectively.

For the description of singlet superconductivity in the cuprates we use a one–band model Hamiltonian. The interaction between the carriers (quasiparticles) is described by an effective Coulomb coupling U and the itinerancy of the carriers by a hopping integral t. In the case of hole doping the states of the effective band are mainly the p–states originating from O–atoms. The spin fluctuations arise from the magnetic activity of the Cu–spins and the induced spin polarization of the p–states. In the case of electron doping the effective one–band Hamiltonian describes the hybridized d–states of the UHB (see Fig. 9.14(b)) and U is an effective coupling between the electrons in these states. The spin fluctuations result from the Cu–spins. Upon doping the Cu–spins are quenched and the spin polarization of the band is reduced. We assume itinerant magnetism for the UHB. How physically correct and useful this model is, in particular for hole doped cuprates, must be judged by comparison of the theoretical results with experiments.

For describing triplet Cooper–pairing in Sr_2RuO_4 we also employ a Hubbard Hamiltonian. In contrast to cuprates no doping occurs. In order to derive an electronic theory it is important to take the electronic band structure of the t_{2g}–subshell into account and thus to include the states of the d_{xy}, d_{yz}, and d_{xz}–bands which cross the Fermi level. Magnetic activity arises from itinerant electrons in the Ru d–orbitals. Due to a different topology of the corresponding Fermi surfaces a strong magnetic anisotropy occurs ($\chi^{+-} > \chi^{zz}$) in the normal state. This mainly results from different values of the g–factor for the transverse and longitudinal components of the spin susceptibility (i.e. the matrix elements differ) and from a change of the bare energy dispersion of the d–electrons. Obviously, this will have consequences for the symmetry of the superconducting order parameter. In order to describe this magnetic anisotropy, one must also take into account spin–orbit coupling.

9.2.1 Electronic Structure and Hamiltonian

In the case of the cuprates the calculation of the electronic properties is complicated due to strong electronic correlations [69]. In order to account

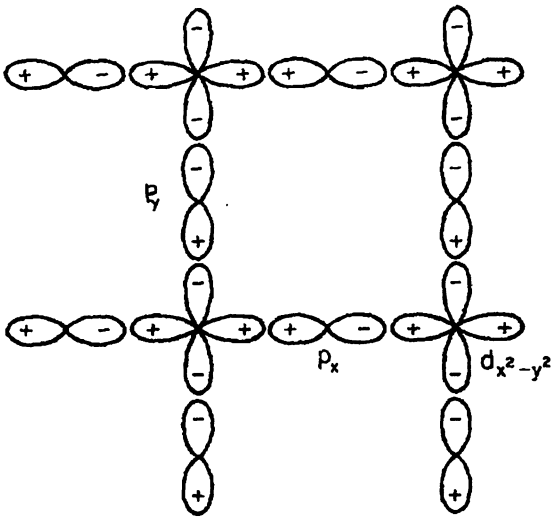

Fig. 9.16. Schematic representation of the electronic structure of a single CuO_2–plane consisting of Cu $d_{x^2-y^2}$–orbitals and the oxygen p_σ–orbitals. Without doping one hole is present in the Cu $d_{x^2-y^2}$–orbital. Via hybridization with oxygen (i.e. superexchange) p–orbitals of two neighboring copper holes interacts antiferromagnetically. This leads to antiferromagnetic ordering of the Cu–spins. The doped holes are mainly in the oxygen p–orbitals due to a large Coulomb repulsion U_d and destroy antiferromagnetism of the copper spins. Also spin frustration occurs. In contrast to this, doping the CuO_2–plane with electrons means effectively occupation of the UHB band and quenching of the Cu–spins and thus weakening of the antiferromagnetism

for them we use a simplifying model that includes the states which originate from the CuO_2–planes and play the most significant role. First, we neglect interlayer coupling of CuO_2–planes.

In Fig. 9.16 we show the electronic structure of a CuO_2–plane. The undoped case corresponds to a half–filled band, i.e. one hole per copper site. The holes are occupying mainly the $d_{x^2-y^2}$–orbitals and interact with each other via superexchange yielding an antiferromagnetic ground state. Due to a large Coulomb repulsion U_d further holes that are doped into the CuO_2–plane are mainly placed on the four oxygen p–states surrounding the copper sites. Thus, the center of mass of these new quasiparticles is still located on the copper sites. Obviously, the spin polarization of the doped holes tends to

suppress the antiferromagnetism. In addition, spin frustration takes place for small hole–doping.

In the case of electron–doped cuprates the doped carriers occupy directly copper $d_{x^2-y^2}$–states. Therefore, the antiferromagnetism is weakened by diluting the copper spins. No spin frustration occurs.

Finally, after doping a reasonable number of carriers into a CuO_2–plane, in both cases –electron or hole doping– one ends up with a non–ordered paramagnetic (metallic) phase that still reveals (short range) antiferromagnetic correlations. The resulting spin excitations are responsible for singlet Cooper–pairing in the cuprates. In our electronic theory we assume that these can be described mainly by itinerant carriers [72].

We use the three–band Hubbard–like model [73]

$$H = \epsilon_d \sum_{i,\sigma} d^+_{i\sigma} d_{i\sigma} + \epsilon_p \sum_{i,\sigma} p^+_{i\sigma} p_{i\sigma} + \sum_{i,j,\sigma} t^{ij}_{pd} \left(d^+_{i\sigma} p_{j\sigma} + \text{h.c} \right) + \sum_{i,j,\sigma} t^{ij}_{pp} \left(p^+_{i\sigma} p_{j\sigma} + \text{h.c} \right) + U_d \sum_i n^d_{i\uparrow} n^d_{i\downarrow} + U_p \sum_i n^p_{i\uparrow} n^p_{i\downarrow} + U_{pd} \sum_{i,j} n^p_{i\uparrow} n^d_{j\downarrow} \tag{9.5}$$

for describing the hole– and electron–doped cuprates. Here, the sums are performed over the copper and oxygen lattice positions both labeled by i and σ refers to the spin. $t^{ij}_{\alpha\beta}$ describes the hopping between the sites i and j and states α and β. $n^d_{i\sigma} = d^+_{i\sigma} d_{i\sigma}$ and $n^p_{i\sigma} = p^+_{i\sigma} p_{i\sigma}$ are the Cu $3d$ and O $2p$ hole densities for site i, respectively. U_d and U_p refer to on–site copper and oxygen Coulomb repulsion, respectively, and U_{pd} accounts for the copper–oxygen interaction.

As we have discussed above, due to strong electronic correlations the undoped cuprates are antiferromagnetic insulators. The chemical potential is lying between the upper Hubbard band of the $d_{x^2-y^2}$–orbital and oxygen p–band (see Fig. 9.17 for an illustration). Upon hole doping the chemical potential lies in the oxygen p–band. The latter hybridizes strongly with copper d–states. As a result the bandwidth of the oxygen band reduces and Zhang–Rice singlets are formed [75]. In the case of electron doping, the chemical potential lies in the copper upper Hubbard band (UHB). Furthermore, due to large values of U_d and of the charge–transfer gap δ, the copper UHB and LHB are well separated in energy. This suggests to use for doped cuprates an effective one–band Hubbard–like Hamiltonian [77]:

$$H = -\sum_{i,j} t_{ij} \left(c^+_{i\sigma} c_{j\sigma} + \text{h.c.} \right) + U \sum_i n_{i\uparrow} n_{i\downarrow} + \ldots \tag{9.6}$$

describing the dynamics of holes in hybridized p–states and of electrons in effective d–states of the UHB. In Eq. (9.6) the $c^+_{i\sigma}$ are fermion creation operators

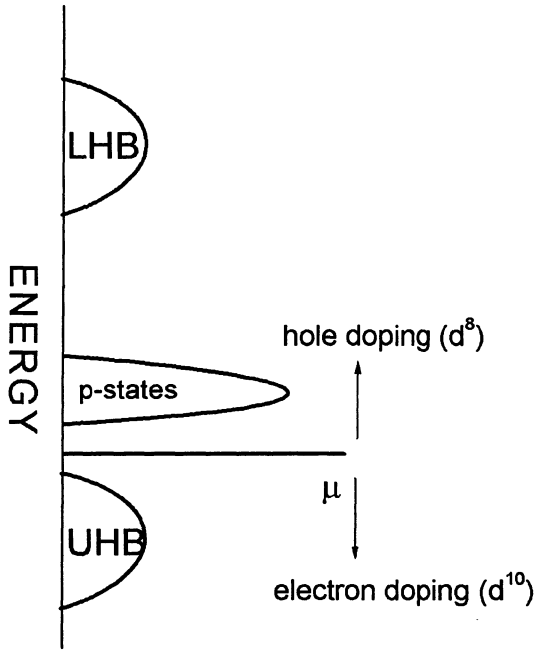

Fig. 9.17. Illustration of the hole and electron doping in cuprates. Without doping due to strong electronic correlations the chemical potential μ lies between the upper Hubbard band (UHB) of the copper $d_{x^2-y^2}$–orbital and oxygen p–states. Upon hole doping the chemical potential shifts towards the oxygen p–band leading to insulator–metal transition. In the case of electron doping the chemical potential lies in the copper UHB. Note, the lower Hubbard band (LHB) of $d_{x^2-y^2}$–states is separated largely in energy from the oxygen p–states due to $U_d \gg \delta$, $\delta = \epsilon_p - \epsilon_d$

for spin σ on sites i of a two–dimensional square lattice, and $n_{i\sigma} = c^+_{i\sigma} c_{i\sigma}$ denotes the density for spin σ. The Hubbard U describes the effective Coulomb interaction between the quasiparticles in the conduction band.

Note, the effective interaction U might be different in hole– and electron–doped cuprates. In the latter case both itinerant behavior and magnetism result from the electrons in the copper d–states of the UHB. In the hole–doped case the hole carriers are located mainly on the oxygen p–states, and the magnetic activity arises mainly from Cu–spins, the localized copper d–holes. These interact with the spins of the doped holes that are present at the oxygen sites. In Eq. (9.6) the interaction of the itinerant electrons with the Cu–spins results from U and the remaining not explicitly given terms take care of the local spin character. Note, the interaction of local spins $\mathbf{S}_i$ with itinerant carriers having spin σ should be of the form $(\boldsymbol{S}_i \cdot \boldsymbol{\sigma})$. For simplicity

one is tempted to simulate this in the case of hole doping by an effective interaction between the band electrons.

Using this physical picture we develop the Eliashberg theory for Cooper–pairing in hole– and electron–doped cuprates. First, we rewrite the effective one–band Hubbard Hamiltonian for the itinerant carriers in momentum space:

$$H = \sum_{\mathbf{k}\sigma} \epsilon_{\mathbf{k}} c^{\dagger}_{\mathbf{k},\sigma} c_{\mathbf{k},\sigma} + \frac{U}{2} \sum_{\mathbf{k}\mathbf{k}'\mathbf{q}\sigma} c^{\dagger}_{\mathbf{k},\sigma} c^{\dagger}_{\mathbf{k}',-\sigma} c_{\mathbf{k}'+\mathbf{q},-\sigma} c_{\mathbf{k}-\mathbf{q},\sigma} + \cdots , \tag{9.7}$$

with the one–band electron (or hole) energy

$$\epsilon_{\mathbf{k}} = -2t \left[\cos(k_x) + \cos(k_y) - 2t' \cos(k_x)\cos(k_y) + \frac{\mu}{2} \right] \quad . \tag{9.8}$$

The dots in Eqs. (9.6) and (9.7) refer to residual interactions, for example resulting from the local character of the Cu–spins. Note, U is an effective interaction for the carriers in the $p-d$–states including largely the effects due to $(\mathbf{S}_i\sigma)$. For a description of the itinerant quasiparticles we assume nearest neighbor and next nearest neighbor hopping described by t and t', respectively. Here and in the following we set the lattice constant equal to one.

Note that the general form of the unrenormalized tight–binding energy dispersion is the same for holes and electrons, but with different parameters used for t and t'. These have to be chosen in agreement with the experimentally observed Fermi surface in hole– and electron–doped cuprates.

9.2.2 Eliashberg Theory for the Interaction Between Quasiparticles and Antiferromagnetic Spin Fluctuations

In general, the interaction between the carriers and spin fluctuations in the cuprates is given by

$$H_{int} = \sum_{\mathbf{q}} \tilde{U}_{eff}(\mathbf{q}) \, \vec{s}(\mathbf{q}) \, \vec{S}(-\mathbf{q}) \quad . \tag{9.9}$$

Here, $\tilde{U}_{eff}$ denotes the effective coupling and $s(\mathbf{q})$ is the spin operator of the itinerant carriers,

$$\vec{s}(\mathbf{q}) = \frac{1}{2} \sum_{\mathbf{k}} \sum_{\sigma\sigma'} c^{+}_{\mathbf{k}+\mathbf{q},\sigma} \, \tau_{\sigma\sigma'} \, c_{\mathbf{k},\sigma'} \quad , \tag{9.10}$$

where τ represents the Pauli matrices. $S(\mathbf{Q})$ is the spin operator referring to the Cu–spins. The corresponding spin–spin correlation function gives the dynamical spin susceptibility, $\chi(\mathbf{q},\omega)$. Due to itinerancy of the Cu spin electrons

the susceptibility χ may be determined by the random phase approximation (RPA). Then,

$$\chi_{RPA}(\mathbf{q},\omega) = \frac{\chi_0(\mathbf{q},\omega)}{1-\tilde{U}\chi_0(\mathbf{q},\omega)} \quad . \tag{9.11}$$

Here, χ_0 is the bare spin susceptibility which is defined via retarded Green's functions for the quasiparticles creating the spin excitation. Then, in second order perturbation theory the effective electron–electron interaction has the form (see Fig. 9.13):

$$V_{eff} = \tilde{U}_{eff}\,\chi_{RPA}(\mathbf{q},\omega)\,\tilde{U} \quad , \tag{9.12}$$

where $\tilde{U}_{eff}$ and $\tilde{U}$ refer to the coupling between the carriers and the spin excitations. $\tilde{U}_{eff}$ includes vertex corrections whereas $\tilde{U}$ denotes the effective coupling. Then the Eliashberg–like system of equations for a superconductor are given by the Green's function ($G^{-1} = G_0^{-1} - \Sigma$) with self–energy:

$$\Sigma(\mathbf{k},\omega) = \tilde{U}_{eff}\,\tilde{U}\sum_{\mathbf{k}'}\sum_{\omega'}\chi_{RPA}(\mathbf{k}-\mathbf{k}',\omega-\omega')\,G(\mathbf{k}',\omega') \tag{9.13}$$

and anomalous self–energy

$$\Phi(\mathbf{k},\omega) = -\tilde{U}_{eff}\,\tilde{U}\sum_{\mathbf{k}'}\sum_{\omega'}\chi_{RPA}(\mathbf{k}-\mathbf{k}',\omega-\omega')\,G(\mathbf{k}',\omega') \times G(-\mathbf{k}',-\omega')\,\Phi(\mathbf{k}',\omega') \quad . \tag{9.14}$$

Here, $\Sigma(\mathbf{k},\omega)$ is the self–energy of the one–particle Green's function $G(\mathbf{k},\omega)$ in the normal state and $\Phi(\mathbf{k},\omega) = \Delta(\mathbf{k},\omega)Z(\mathbf{k},\omega)$ is the corresponding anomalous part. The superconducting order parameter is $\Delta(\mathbf{k},\omega)$. $Z(\mathbf{k},\omega)$ denotes the renormalization function describing the effective mass of the quasiparticles. We employ the Dyson equation yielding

$$G(\mathbf{k},\omega) = \frac{1}{\omega - \epsilon_{\mathbf{k}} + \mu - \Sigma(\mathbf{k},\omega)} \equiv G(k) \quad . \tag{9.15}$$

This system of equations allows to find the superconducting gap and the superconducting transition temperature $T_c(\Delta(T_c) = 0)$. The spin fluctuations and $\chi(\mathbf{q},\omega)$ would act as an input.

Note, on the RPA level also the charge fluctuations may be included. This may be of interest if a charge–density–wave (CDW) or stripe formation occurs. Both may compete for small doping. The superposition of spin and charge fluctuations leads to $\chi = \chi^c + \chi^s$ with

$$\chi^c_{RPA}(\mathbf{q},\omega) = \frac{\chi_0(\mathbf{q},\omega)}{1+\tilde{U}\chi_0(\mathbf{q},\omega)} \quad . \tag{9.16}$$

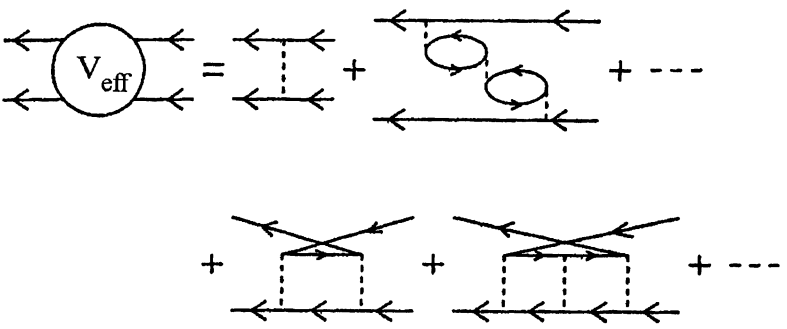

Fig. 9.18. RPA diagrams for the effective pairing interaction V_{eff} for singlet pairing in cuprates resulting from the exchange of longitudinal and transverse spin and charge fluctuations. The solid lines refer to the one–particle Green's function that are taken in accordance with Eqs. (9.15) and (9.17) and the dashed lines denote an effective Coulomb interaction $\tilde{U}$. The first diagram leads to a renormalized chemical potential. The ladder diagrams refer to Cooper–pairing due to spin fluctuations. Note that for singlet pairing only an even number of bubble diagrams occur due to Pauli's principle describing both spin and charge fluctuations. The charge and spin fluctuations can be separated from each other and give rise to the first and second terms in Eqs. (9.21)-(9.22), respectively

Then, in the Nambu representation [89] the 2×2 matrix $\Sigma(\mathbf{k})$ is given by the expression

$$\Sigma(k) = \sum_{k'} V_s(k-k')\,\tau_0\,G(k')\,\tau_0 + \sum_{k'} V_c(k-k')\,\tau_3\,G(k')\,\tau_3 \quad , \tag{9.17}$$

where the τ_α ($\alpha = 0,1,2,3$) are the Pauli matrices and V_s and V_c are the matrix elements of the electron–electron interaction due to spin and charge fluctuations shown in Fig. 9.18. Omitting the first diagram one finds

$$V_s(q) = \frac{3}{2}\,\tilde{U}_{eff}\,\tilde{U}\,\chi_s(q), \qquad V_c(q) = \frac{1}{2}\,\tilde{U}_{eff}\,\tilde{U}\,\chi_c(q) \quad , \tag{9.18}$$

where χ_s and χ_c are the dynamical spin and charge (dielectric) susceptibilities which within RPA are given by

$$\chi_s(q) = \frac{\chi_{s0}(q)}{1-\tilde{U}\chi_{s0}(q)} \qquad \text{and} \qquad \chi_c(q) = \frac{\chi_{c0}(q)}{1+\tilde{U}\chi_{c0}(q)} \quad . \tag{9.19}$$

Here, $\chi_{s0}(q)$ and $\chi_{c0}(q)$ are the corresponding irreducible parts calculated from unrenormalized Green's functions [90].

Obviously, the effective pairing interaction defined in Fig. 9.18 is related to the self–energy Σ shown in Fig. 9.13 and thus to Eq. (9.17) by $V_{eff} = \delta\Sigma/\delta G$. A similar relation holds for the vertex corrections leading to $U \to U_{eff}$. To

a good approximation they have a weak ω–dependence, and therefore do not change the dynamics of the elementary excitations and the spectrum of the superconducting gap too much. Note also, in general the Green's functions used for V_{eff} may be different from those of the carriers who participate in Cooper–pairing. Furthermore, also the form and value of the bare susceptibilities may differ for localized and itinerant magnetism.

The matrix Green's function $\hat{G}(k)$ and the self–energy are related by the Dyson equation (9.15):

$$\hat{G}^{-1} = \begin{pmatrix} G_0^{-1} - \Sigma^G & -\Sigma^F \\ -\bar{\Sigma}^F & \bar{G}_0^{-1} - \bar{\Sigma}^G \end{pmatrix} \quad , \tag{9.20}$$

where Σ^G and Σ^F denote the normal and anomalous part of the self–energy, respectively. Using the diagrams displayed in Fig. 9.18 and employing Matsubara frequencies the self–energies are given by

$$\begin{aligned} \Sigma^G(\mathbf{k}, \imath\omega_n) = \frac{1}{\beta N} \sum_{\mathbf{k}' i\omega_n'} \Bigg[& \frac{1}{2} \tilde{U}_{eff} \tilde{U} \frac{\chi_{c0}(\mathbf{q}, i\nu_m)}{1 + \tilde{U}\chi_{c0}(\mathbf{q}, i\nu_m)} \\ & + \frac{3}{2} \tilde{U}_{eff} \tilde{U} \frac{\chi_{s0}(\mathbf{q}, i\nu_m)}{1 - \tilde{U}\chi_{s0}(\mathbf{q}, i\nu_m)} + \tilde{U}_{eff} \tilde{U} \chi_G(\mathbf{q}, i\nu_m) \Bigg] \\ & \times G(\mathbf{k}', i\omega_n') \end{aligned} \tag{9.21}$$

and

$$\begin{aligned} \Sigma^F(\mathbf{k}, \imath\omega_n) = -\frac{1}{\beta N} \sum_{\mathbf{k}' i\omega_n'} \Bigg[& \frac{1}{2} \tilde{U}_{eff} \tilde{U} \frac{\chi_{c0}(\mathbf{q}, i\nu_m)}{1 + \tilde{U}\chi_{c0}(\mathbf{q}, i\nu_m)} \\ & - \frac{3}{2} \tilde{U}_{eff} \tilde{U} \frac{\chi_{s0}(\mathbf{q}, i\nu_m)}{1 - \tilde{U}\chi_{s0}(\mathbf{q}, i\nu_m)} - \tilde{U}_{eff} \tilde{U} \chi_F(\mathbf{q}, i\nu_m) \Bigg] \\ & \times G(\mathbf{k}', i\omega_n') \quad , \end{aligned} \tag{9.22}$$

where $i\nu_m = i\omega_n - i\omega_n'$. The first and second term refers to charge and spin fluctuations, respectively. Note, the bare susceptibilities can be defined in terms of $\chi_{G,F}$, i.e. $\chi_{c0} = \chi_G - \chi_F$ and $\chi_{s0} = \chi_G + \chi_F$. Both are defined in Appendix A. The term $\tilde{U}_{eff}\tilde{U}\chi_{G,F}$ on the right–hand side compensates for double counting that occurs in second order.

So far, the Eliashberg–like equations have been derived on the imaginary axis and for finite temperatures $\beta^{-1} = k_B T$. This is convenient because of the spectral properties of the corresponding Green's function. However, in order to compare directly with experiment we need the solution of the self–energy equations on the real ω–axis. One possibility would be to solve the generalized Eliashberg equations slightly above the real axis [87]. However, we further want to avoid continuation to the real ω–axis, $z = i\omega_n \rightarrow \omega + i0^+$, after a solution has been obtained. This can lead to numerical uncertainties and instabilities. Therefore, we formulate the generalized Eliashberg equations

from the beginning directly on the real frequency axis. For doing this we use spectral representation of the one–particle Green's functions [84,85]. Details of the calculation are given in Appendix A. After performing the sum over the Matsubara frequencies [96] we arrive at the following set of equations for the quasiparticle self–energy components Σ_ν ($\nu = 0, 3, 1$) with respect to the Pauli matrices τ_ν in the Nambu representation:

$$\Sigma_\nu(\mathbf{k},\omega) = N^{-1}\sum_{\mathbf{k}'}\int_0^\infty d\Omega\,[P_s(\mathbf{k}-\mathbf{k}',\Omega) + (\delta_{\nu 0}+\delta_{\nu 3}-\delta_{\nu 1})\,P_c(\mathbf{k}-\mathbf{k}',\Omega)]\int_{-\infty}^{\infty} d\omega'\,I(\omega,\Omega,\omega')A_\nu(\mathbf{k}',\omega'). \quad (9.23)$$

P_s and P_c refer to spin and charge fluctuations, respectively. The kernel I and the spectral functions A_ν are given by

$$I(\omega,\Omega,\omega') = \frac{f(-\omega')+b(\Omega)}{\omega+i\delta-\Omega-\omega'} + \frac{f(\omega')+b(\Omega)}{\omega+i\delta+\Omega-\omega'} \quad (9.24)$$

and

$$A_\nu(\mathbf{k},\omega) = -\pi^{-1}\,\mathrm{Im}\;[a_\nu(\mathbf{k},\omega)/D(\mathbf{k},\omega)] \quad . \quad (9.25)$$

The denominator is given by

$$D = [\omega Z]^2 - [\epsilon(\mathbf{k})+\xi]^2 - \phi^2 \quad ,$$

Also we use $a_0 = \omega Z$, $a_3 = \epsilon(\mathbf{k}) + \xi$, and $a_1 = \Delta Z$. In Eq. (9.24), f and b denote the Fermi and Bose distribution function, respectively.

The band filling

$$n = 1/N\sum_{\mathbf{k}} n_{\mathbf{k}}$$

is determined with the help of the $\mathbf{k}$–dependent occupation number

$$n_{\mathbf{k}} = 2\int_{-\infty}^{\infty} d\omega f(\omega)[A_0(\mathbf{k},\omega)+A_3(\mathbf{k},\omega)] \quad ,$$

which is calculated self–consistently. Note, this introduces the doping dependence of the superconducting gap, the elementary excitations and spin excitations. The case $n = 1$ corresponds to half filling. The interaction between quasiparticles due to spin and charge fluctuation is given by

$$P_s = (2\pi)^{-1}\tilde{U}_{eff}\,\tilde{U}\,\mathrm{Im}(3\chi_s - \chi_{s0}) \quad ,$$
$$P_c = (2\pi)^{-1}\tilde{U}_{eff}\,\tilde{U}\,\mathrm{Im}(3\chi_c - \chi_{c0}) \quad . \quad (9.26)$$

So far our formulation is quite general and applies similarly to any system with strong interaction of the carriers with spin fluctuations. In case of strong

hybridization between the Cu d–states and the oxygen p–states one may approximately use the same Green's functions for determining $G(\mathbf{k},\omega)$, $\Sigma(\mathbf{q},\omega)$, and $\chi(\mathbf{q},\omega)$. In this effective one–band picture one uses $\tilde{U} = U_{eff}$ [98]. Then, the above expressions constitute a system of coupled equations for the quasiparticles Green's function and Cooper–pairs. These equations must be solved numerically by iterations for a temperature given and fixed parameters t, U, as well as doping x [99]. The spin susceptibility is the important input for determining Σ and G. In general, one expects that $\chi(\mathbf{q},\omega)$ is approximately given by the Ornstein–Zernicke theory, with

$$\chi_{s0} = -\frac{1}{2}T\sum_{k} \text{Tr}\,[G(k)\,\tau_0\,G(k+q)\,\tau_0] \quad , \tag{9.27}$$

and

$$\chi_{c0} = -\frac{1}{2}T\sum_{k} \text{Tr}\,[G(k)\,\tau_3\,G(k+q)\,\tau_3] \quad . \tag{9.28}$$

Here, Tr stands for the trace of the corresponding 2×2 matrix.

In the case of electron–doped cupates we may safely assume that $\chi(\mathbf{q},\omega)$ results from the itinerant quasiparticle states in the upper Hubbard band. Thus, we have $\chi = \chi\{G\}$ with χ_0 given by Eqs. (9.27) and (9.28). This yields a Berk–Schrieffer–type theory for the coupling between electrons described by G and the spin fluctuations described by

$$\chi = \chi_0 + U_{eff}\,\chi_0\,\chi \quad . \tag{9.29}$$

On the other hand, in the the case of hole–doped cuprates the hybridization between the p– and d–states suggest to assume for simplicity that the spin excitations may be determined (at least approximately) by the same quasiparticle states described by $G(\mathbf{k},\omega)$. Hence, we use $\chi = \chi\{G\}$ and for χ the RPA–form and for χ_0 again Eqs. (9.27) and (9.28). This model is supported by the observation of a strong feedback effect of G on χ [45].

In the case of ruthenates the spin excitations described by $\chi(\mathbf{q},\omega)$ result from the quasiparticles of the α–, β–, and γ–states. Hence, the Green's function G is also used for calculating the spin susceptibility, i.e. $\chi = \chi\{G\}$.

In summary, we use for the cuprates and ruthenates a Berk–Schrieffer–type theory for the behavior of the quasiparticles coupling to spin excitations:

$$G = G\{\chi\} \quad , \qquad \chi = \chi\{G\} \quad , \tag{9.30}$$

and determine χ from an electronic theory within RPA. Obviously, the calculation demands a high degree of self–consistency for determining G, the resultant elementary excitations, the spin susceptibility, and for superconductivity. Details of this procedure are given in Appendix B.

The dynamical spin susceptibility χ^s determines the properties of the electronic system. Its peak structure at $\mathbf{Q}_{AF} = (\pi,\pi)$ is important. The latter

arises due to the nesting properties of the Fermi surface. The RPA denominator enhances further this peak structure of the spin susceptibility. The charge fluctuations arise also from the nesting properties, but are not that much enhanced by the RPA denominator. Therefore, the charge fluctuations play a smaller role for Cooper–pairing. However, some other interactions (like electron–phonon interaction or long–range Coulomb repulsion) may change the situation completely and may lead to the enhancement of the dynamical charge susceptibility. This may happen at low doping where the screening is smaller and the lattice distortions can be more important. Although we do not consider these effects explicitly in our electronic theory one can relatively easy incorporate them in our Eliashberg–like theory just by changing mainly the form of χ^c.

9.2.3 Elementary Excitations

For understanding the high–T_c cuprates their elementary excitations are of central significance. First we discuss those in hole–doped cuprates. Using the Green's functions for the elementary excitations (i.e. the local density of states) one gets after continuation to the real ω–axis and for a fixed temperature for the spectral density

$$A(\mathbf{k},\omega) = -\frac{1}{\pi} \frac{\Sigma''(\mathbf{k},\omega)}{\left[\omega - \epsilon_{\mathbf{k}} - \Sigma'(\mathbf{k},\omega)\right]^2 + \left[\Sigma''(\mathbf{k},\omega)\right]^2} \quad . \tag{9.31}$$

Here, $\epsilon_{\mathbf{k}}$ is the bare energy dispersion given by Eq. (9.8) and $\Sigma'(\mathbf{k},\omega)$ and $\Sigma''(\mathbf{k},\omega)$ are the real and imaginary parts of the self–energy, respectively. The renormalized energy dispersion $\omega_{\mathbf{k}}$ of the quasiparticles is given by

$$\omega_{\mathbf{k}} = \epsilon_{\mathbf{k}} + \mathrm{Re}\Sigma(\mathbf{k},\omega) \quad . \tag{9.32}$$

Here, the doping dependence occurs due to a change in the chemical potential of $\epsilon_{\mathbf{k}}$ and in particular from the frequency dependence and also from the doping dependence of the dynamical spin susceptibility $\chi(\mathbf{q},\omega)$.

In Fig. 9.19 we demonstrate the importance of many–body effects due to the self–energy. The renormalization of the dispersion by Σ causes structure in the dispersion, the so–called kink feature. We show the unrenormalized tight–binding energy dispersion $\epsilon_{\mathbf{k}}$ in the normal state along the route $(0,0) \rightarrow (\pi,0) \rightarrow (\pi,\pi) \rightarrow (0,0)$ of the first BZ. Below the Fermi level the measured energy dispersion $\omega_{\mathbf{k}}$ along $(0,0) \rightarrow (\pi,\pi)$ is changed compared to the bare tight–binding case due to the self–energy corrections. We define the kink at the inflection point of the dashed curve where the renormalized dispersion tends to approach again the bare dispersion $\epsilon_{\mathbf{k}}$. Note, the renormalization of $\epsilon_{\mathbf{k}}$ is expected to be anisotropic. Recent studies by Dessau and co–workers [230] reveal no kink structure along $(\pi,0) \rightarrow (\pi,\pi)$ direction in the normal state, but only in the superconducting state.

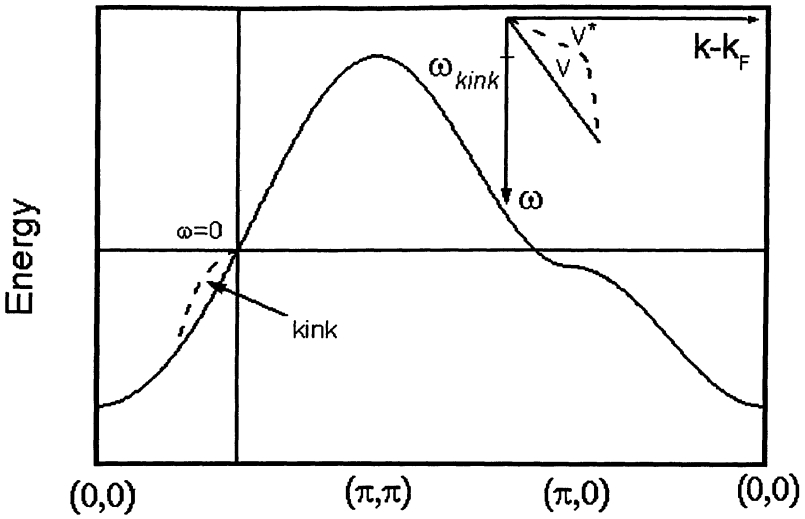

Fig. 9.19. Calculated bare tight–binding energy dispersion for hole–doped cuprates in the normal state using Eq. (9.8). The dashed curve illustrates the changes due to renormalization, $\omega_{\mathbf{k}} = \epsilon_{\mathbf{k}} + \mathrm{Re}\Sigma(\mathbf{k},\omega)$. Due to structure in $\mathrm{Re}\Sigma$ the energy dispersion shows a kink feature along the $(0,0) \rightarrow (\pi,\pi)$ and also other directions in the first Brillouin Zone. The inset shows an enlargement of the kink structure. The maximum deviation from the bare dispersion and also the renormalized velocity of the quasiparticles $v \rightarrow v^*$ reflect the behavior of the self–energy and thus the coupling to spin fluctuations

The self–energy $\Sigma(\mathbf{k},\omega)$ for cuprates is calculated self–consistently using the 2D one–band Hubbard Hamiltonian for the CuO_2–planes and assuming coupling of the quasiparticles to spin fluctuations. The superconducting gap function $\Delta(\mathbf{k},\omega)$ is also calculated self–consistently. As described earlier the full momentum and frequency dependence of the quantities is kept. No further parameter is introduced. It is important to realize that due to the combined effects of Fermi surface topology and $\chi(\mathbf{q} = \mathbf{Q},\omega)$ at the antiferromagnetic wave–vector $\mathbf{Q}_{AF} = (\pi,\pi)$, the $\mathbf{k}$ and ω dependence of $\Sigma(\mathbf{k},\omega)$ become very pronounced and change the dispersion $\omega(\mathbf{k})$.

Most importantly the changes in the electronic dispersion are anisotropic in the first BZ. This is illustrated in Fig. 9.20 where we show the Fermi surface of optimally hole–doped cuprates. Due to the fact that the spin susceptibility $\chi(\mathbf{q},\omega)$ has structure mainly at ω_{sf} and for the transferred wave vector $\mathbf{q} = \mathbf{Q}$ the influence of $\chi(\mathbf{q},\omega)$ on the elementary excitations is expected to be very anisotropic with respect to the different parts of the Brillouin Zone. First, the antiferromagnetic wave vector $\mathbf{Q} = (\pi,\pi)$ connects exactly quasiparticles at the Fermi level close to the $(0,\pi)$ points of the first Brillouin Zone. These quasiparticles experience the strongest coupling to antiferromagnetic spin

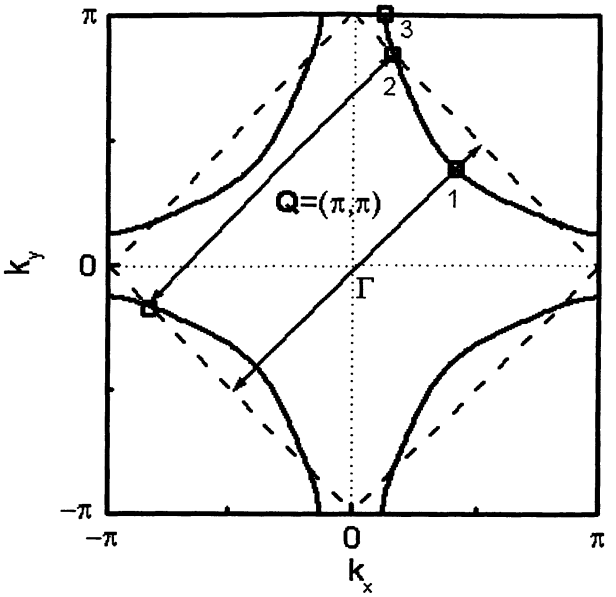

Fig. 9.20. Illustration of the anisotropy of the elementary excitations using the calculated Fermi surface for hole–doped cuprates in the first Brillouin zone (BZ) for a single CuO_2–layer. The anisotropy can be characterized by three different points on the Fermi surface. Point number 1 refers to the diagonal part of the BZ (so–called nodal point or cold spot) and point number 3 refers to the so–called antinodal point close to $(0, \pi)$. The dashed line denotes the magnetic BZ crossing the electronic Fermi surface exactly at the 'hot spots' (labeled number 2). The antiferromagnetic wave vector **Q** connects via scattering by spin fluctuations the two pieces of the Fermi surface mainly at the hot spots. At the $(0, \pi)$ points and along the diagonals the wave vector **Q** connects quasiparticle states below the Fermi level only. Note, the characteristic anisotropic behavior of the elementary excitations may help to distinguish the resultant kink structure from the one which may be caused by electron–phonon coupling

fluctuations. Quasiparticles at the diagonals of the BZ are *not* connected by the **Q** and thus have smaller scattering by spin fluctuations at the Fermi level. The corresponding point on the Fermi surface is called *cold spot* or *nodal point.* Furthermore, the quasiparticle states at the Fermi level close to the $M = (0, \pi)$ point in the first BZ are usually called *antinodal* points. Note, that the quasiparticle states at cold and hot spots which are connected by **Q** lie *close to* the Fermi level. This will be important later for discussing the kink feature. Therefore, we may define three characteristic regions at the Fermi surface regarding their sensitivity to coupling to antiferromagnetic spin fluctuations (see Fig. 9.20).

Furthermore, this feature in $\Sigma(\mathbf{k}, \omega)$ changes the spectral density and the energy dispersion. Using Fig. 9.13 the self–energy on the real axis within the

weak–coupling limit is approximately given by (see Appendix C)

$$\Sigma(\mathbf{k},\omega) \approx -\frac{U^2}{4}\sum_{\mathbf{k}'}\int_0^\infty d\omega' \frac{\mathrm{Im}\chi_{\mathrm{RPA}}(\mathbf{k}-\mathbf{k}',\omega')}{\omega-\omega'-\epsilon_{\mathbf{k}'}}\left[\coth\frac{\omega'}{2T}-\tanh\frac{\omega'-\omega}{2T}\right]. \tag{9.33}$$

Due to the momentum and energy conservation one expects characteristic structure in Σ.

It is important to mention that the self–energy has a strong frequency dependence, while the bare energy dispersion of the carriers $\epsilon_{\mathbf{k}}$ has mostly no frequency dependence. Thus, already in the normal state, $\Sigma(\mathbf{k},\omega)$ has a maximum reflecting a corresponding maximum of Im χ at $\mathbf{q} \approx \mathbf{Q}$ and $\omega \approx \omega_{sf}$. Then, the kink position follows from the pole of the denominator of Eq. (9.33). This leads to the 'kink condition'

$$\omega_{kink} \approx E_{\mathbf{k}-\mathbf{Q}} + \omega_{sf}(x) \quad . \tag{9.34}$$

This gives an estimate of the position of the kink. We will discuss later how ω_{sf} depends on the doping concentration. Note that in the underdoped regime of hole–doped cuprates a normal–state pseudogap with $d_{x^2-y^2}$–wave symmetry opens up below T^* around the antinodal point $(0,\pi)$. This leads to a smaller density of states and therefore to a smaller coupling of holes to spin fluctuations. Furthermore, if the pseudogap is larger than the superconducting gap, no kink structure below T_c should be present along the antinodal direction.

What does happen in the superconducting state? Below T_c the superconducting gap $\phi(\mathbf{k},\omega)$ opens rapidly for decreasing temperature T and becomes maximal in momentum space around the M point reflecting the momentum dependence of the effective pairing interaction. Therefore, the occurrence of a kink structure *only* below T_c in the antinodal direction is a direct fingerprint of the spin excitation spectrum. Furthermore, as we will discuss below Im $\chi(\mathbf{Q},\omega)$ in Eq. (9.33) is peaked at the resonance frequency ω_{res} (roughly at $\omega_{sf}+\Delta$). Therefore, the kink condition in the superconducting states is given by

$$\omega_{kink} \approx E_{\mathbf{k}-\mathbf{Q}} + \omega_{res}(x) \quad . \tag{9.35}$$

Obviously, ω_{sf}, $\Delta(\mathbf{k},\omega)$, and thus ω_{res} depend on the doping concentration x. Their behavior is intimately connected to the doping dependence of the dynamical spin susceptibility $\chi(\mathbf{q},\omega)$ as will be discussed below.

Finally, in order to compare the spectral density of the elementary excitations directly with results for the local density of states measured by angle–resolved photoemission spectroscopy one needs also information about the corresponding matrix elements that are anisotropic and are dependent on the energy of the incident photon. In addition, R. Manzke *et al.* pointed out that polarization–dependent photoemission reveals also fine–structure in

the low energy excitation spectrum that complicates the line–shape analysis of the date [105]. In particular, for a single–layer high–T_c superconductor at optimum hole–doping two maxima dependent on the orientation of the polarization vector are found. Note that, if the tetragonal symmetry of the crystal is broken by the occurrence of a charge–density wave, see related formation of stripes for example, similar effects are expected. Note, in electron–doped cuprates we expect a different behavior which we discuss later.

In underdoped cuprates we study the influence of the pseudogap formation on the spin fluctuations by assuming an additional (to a superconducting) d–wave gap in the electronic excitations

$$E_g(\mathbf{k}) = E_g(0)(\cos k_x - \cos k_y)/2 \quad . \tag{9.36}$$

Below the pseudogap temperature T*, the electronic density of states reduces at the Fermi level due to the gap in the electronic dispersion. Furthermore, most of electronic states at the nested parts of the Fermi surface will be gaped below T*. Therefore, the 'kink' structure in the dispersion will reveal some changes along (0,0)$\rightarrow (\pi, 0)$ in the pseudogap regime. While the origin of the pseudogap is not yet clarified experimentally, it is instructive to see how it affects the elementary excitations and the spin excitations.

9.2.4 Dynamical Spin Susceptibility

One of the most important quantity of our electronic theory is the dynamical spin susceptibility. Note that χ controls the corresponding Cooper–pairing, for example. We assume that the magnetic activity of the Cu–spins may be described by the state of the UHB in the case of electron doping and by the hybridized p– and d–states of the one–band Hamiltonian in the case of hole doping. Then, from the elementary excitations of the quasiparticles we calculate the irreducible parts of the lowest order (Lindhard) spin and charge susceptibility in the normal state

$$\chi_{s0,c0}(\mathbf{q},\omega) = -\sum_{\mathbf{k}} \frac{f(\epsilon_{\mathbf{k}}) - f(\epsilon_{\mathbf{k+q}})}{\epsilon_{\mathbf{k}} - \epsilon_{\mathbf{k+q}} + i\delta} \quad . \tag{9.37}$$

Again, f denotes the Fermi distribution function and $\epsilon_{\mathbf{k}}$ is the energy dispersion. Due to the nesting properties of the Fermi surface χ_{s0} and χ_{c0} (in the following abbreviated with χ_0) are mainly peaked at the antiferromagnetic wave vector $\mathbf{Q} = (\pi, \pi)$ [106]. Using the random phase approximation (RPA) this will be further enhanced, since

$$\chi_{RPA}(\mathbf{q},\omega) = \frac{\chi_0(\mathbf{q},\omega)}{1 - U\,\chi_0(\mathbf{q},\omega)} \quad . \tag{9.38}$$

Like already the Lindhard susceptibility also χ_{RPA} may yield low–energy antiferromagnetic spin fluctuations at a frequency $\omega = \omega_{sf}$ [95].

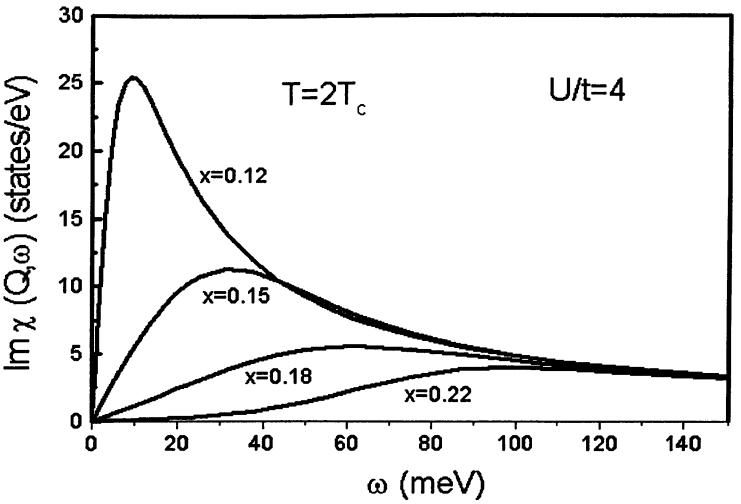

Fig. 9.21. Dynamical spin susceptibility Im $\chi_{RPA}(\mathbf{Q},\omega)$ calculated using RPA and the generalized Eliashberg equations for hole-doped cuprates in the normal state at a temperature $T = 2T_c$ for various doping concentrations, $x = 0.12$ (underdoped), $x = 0.15$ (optimal doping), and $x = 0.18$, $x = 0.22$ (overdoped)

In order to compare our results with inelastic neutron scattering (INS) experiments we calculate the imaginary part of $\chi_{RPA}(\mathbf{Q},\omega)$:

$$\mathrm{Im}\,\chi_{RPA}(\mathbf{Q},\omega) = \frac{\mathrm{Im}\,\chi_0(\mathbf{Q},\omega)}{(1 - U\,\mathrm{Re}\,\chi_0(\mathbf{Q},\omega))^2 + U^2\,(\mathrm{Im}\,\chi_0(\mathbf{Q},\omega))^2} \quad . \tag{9.39}$$

Note, due to the vicinity to an antiferromagnetic instability, Im χ_{RPA} is characterized approximately by an Ornstein–Zernicke behavior [29]

$$\mathrm{Im}\,\chi_{RPA}(\mathbf{Q},\omega) \propto \frac{\omega\,\omega_{sf}}{\omega^2 + \omega_{sf}^2} \quad , \tag{9.40}$$

with a pronounced peak at the wave vector $\mathbf{q} = \mathbf{Q}$ and $\omega = \omega_{sf}$. In order to illustrate this we show in Fig. 9.21 the doping dependence of Im χ_{RPA} at the antiferromagnetic wave vector $\mathbf{Q}$ versus frequency in the normal state.

In the superconducting state the situation is different due to presence of the superconducting gap $\phi(\mathbf{k},\omega) = Z(\mathbf{k},\omega)\Delta(\mathbf{k},\omega)$. The essential behavior follows already from the Lindhard susceptibility χ_0. In the weak-coupling limit ($Z \equiv 1$) χ_0 is of BCS-form [94]:

$$\begin{aligned}\chi_0(\mathbf{q},\omega) = \sum_{\mathbf{k}} \Bigg\{ & \frac{1}{2}\left[1 + \frac{\epsilon_{\mathbf{k}}\epsilon_{\mathbf{k+q}} + \Delta_{\mathbf{k}}\Delta_{k+q}}{E_{\mathbf{k}}E_{\mathbf{k+q}}}\right] \frac{f(E_{\mathbf{k+q}}) - f(E_{\mathbf{k}})}{\omega - E_{\mathbf{k+q}} + E_{\mathbf{k}} + i\delta} \\ & + \frac{1}{4}\left[1 - \frac{\epsilon_{\mathbf{k}}\epsilon_{\mathbf{k+q}} + \Delta_{\mathbf{k}}\Delta_{k+q}}{E_{\mathbf{k}}E_{\mathbf{k+q}}}\right] \frac{1 - f(E_{\mathbf{k+q}}) - f(E_{\mathbf{k}})}{\omega + E_{\mathbf{k+q}} - E_{\mathbf{k}} + i\delta} \\ & + \frac{1}{4}\left[1 - \frac{\epsilon_{\mathbf{k}}\epsilon_{\mathbf{k+q}} + \Delta_{\mathbf{k}}\Delta_{k+q}}{E_{\mathbf{k}}E_{\mathbf{k+q}}}\right] \frac{f(E_{\mathbf{k+q}}) + f(E_{\mathbf{k}}) - 1}{\omega - E_{\mathbf{k+q}} + E_{\mathbf{k}} + i\delta} \Bigg\} . \end{aligned} \tag{9.41}$$

Thus, the imaginary part at the wave vector $\mathbf{Q} = (\pi, \pi)$ is given by

$$\mathrm{Im}\chi_0(\mathbf{Q},\omega) = \frac{1}{2}\sum_{\mathbf{k}} \Big\{ \left[1 - f\left(E_{\mathbf{k}}\right)\right] \delta(\omega + 2E_{\mathbf{k}}) + \left[f\left(E_{\mathbf{k}}\right) - 1\right] \delta(\omega - 2E_{\mathbf{k}}) \Big\} . \tag{9.42}$$

Here, the energy $E_{\mathbf{k}} = \sqrt{\epsilon_{\mathbf{k}}^2 + \Delta_{\mathbf{k}}^2}$ is the dispersion relation of the Cooper pairs in the superconducting state. Due to the density of states of the quasiparticles in the superconducting state the imaginary part of the BCS spin susceptibility has an important characteristic frequency

$$\omega_{DOS} \approx 2\Delta(x,T) \quad .$$

A closer inspection of Eq. (9.39) shows an interesting resonant–like behavior of Im $\chi(\mathbf{q},\omega)$. Generally, one finds that the structure of Im χ is determined by Im χ_0, if $(U\mathrm{Re}\ \chi_0) \neq 1$, and by $(U\mathrm{Re}\ \chi_0) = 1$, if this can be fulfilled. Furthermore, one finds for increasing U that the peak in Im χ shifts to lower energies. Most importantly χ_0 becomes resonantly if the condition

$$\frac{1}{U_{cr}} = \mathrm{Re}\chi_0(\mathbf{q} = \mathbf{Q}, \omega = \omega_{res}) \tag{9.43}$$

is satisfied. Note, this would signal the occurrence of a spin density wave collective mode with energy $\hbar\omega_{res}$. The real part is given (at $T = 0$) by:

$$\mathrm{Re}\ \chi_0(\mathbf{Q},\omega_{res}) = \sum_{\mathbf{k}} \frac{E_{\mathbf{k}}E_{\mathbf{k+Q}} - \epsilon_{\mathbf{k}}\epsilon_{\mathbf{k+Q}} - \Delta_{\mathbf{k}}\Delta_{\mathbf{k+Q}}}{\left(E_k + E_{k+Q}\right)^2 - \omega_{res}^2} \frac{E_{\mathbf{k}} + E_{\mathbf{k+Q}}}{2E_{\mathbf{k}}E_{\mathbf{k+Q}}} . \tag{9.44}$$

Therefore, due to the feedback effect of superconductivity on Im χ its behavior differs drastically from the normal state and yields the formation of the resonance feature at $\mathbf{q} = \mathbf{Q}$ and $\omega = \omega_{res}$ as it is observed in INS experiments. To be more precise, we find for *optimal doping*, where Eq. (9.43) determines the structure of Im χ_{RPA}, the important relation

$$\omega_{res}(T) = 2\Delta_0(T) - \omega_{sf}(T) \quad . \tag{9.45}$$

Thus, physically speaking, the resonance peak appearing in INS experiments only below T_c is mainly determined by the maximum of the superconducting gap, but renormalized by normal state spin excitations. Obviously, Δ_0 and ω_{sf} are doping dependent quantities. On general grounds one expects that

$$\omega_{res}(x) \propto \begin{cases} \omega_{sf}(x), & \text{underdoped cuprates} \\ 2\Delta_0(x), & \text{overdoped cuprates} \end{cases} \tag{9.46}$$

Note, the pseudogap will also affect the properties of the dynamical spin susceptibility below T*. For example, the uniform part of the spin susceptibility $\chi(\mathbf{q} = 0, \omega = 0)$ which is proportional to the density of states will

strongly decrease upon decreasing temperature below T* due to the gap in the electronic spectrum. Later, we will discuss in detail the influence of the pseudogap by using a new energy dispersion $\epsilon_{\mathbf{k}} = \sqrt{(\epsilon_{\mathbf{k}}^0)^2 + E_g(\mathbf{k})^2}$. Similarly the spectrum of the antiferromagnetic spin fluctuations $\mathrm{Im}\chi(\mathbf{Q},\omega)$ will show some structure at energies about $2\mathrm{E}_g(0)$ as follows from Eq. (9.42). Furthermore, the resonant condition, Eq. (9.43), can be fulfilled also below T*, since the pseudogap influences the spin fluctuation spectrum as the superconducting gap below T_c. In the superconducting state the influence of the pseudogap on the dynamical spin susceptibility is expected to be small, since it is believed that both are of *d*–wave type and the superconducting gap and pseudogap are similar in magnitude. In electron–doped cuprates there seems to be no clear evidence for a pseudogap behavior in the elementary excitations and in the spin susceptibility below a certain temperature T^*. However, in an external magnetic field and below T_c tunneling spectroscopy reveals a pseudogap [153]. This will be discussed later.

9.2.5 Gap Equation: Singlet and Triplet Cooper–Pairing

We want to investigate now in more detail how unconventional superconductivity can arise from the exchange of spin fluctuations, from a purely electronic mechanism.

Singlet Cooper–pairing

For this purpose let us first consider the simplified weak–coupling gap equation for singlet pairing ($T = 0$)

$$\Delta(\mathbf{k}) = -\sum_{\mathbf{k}'} \frac{V_s^{eff}(\mathbf{k}-\mathbf{k}')}{2E(\mathbf{k}')}\,\Delta(\mathbf{k}') \quad , \tag{9.47}$$

which is a self–consistency equation for the superconducting order parameter $\Delta(\mathbf{k})$ in momentum space where $\mathbf{k}$ is defined in the first Brillouin zone. $V_s^{eff}(\mathbf{k}-\mathbf{k}')$ represents the effective two–particle pairing interaction in the singlet pairing channel. This is, to a good approximation, proportional to χ_{RPA} if Cooper–pairing due to spin fluctuations is present. Again, the energy $E(\mathbf{k}) = \sqrt{\Delta^2(\mathbf{k}) + \epsilon^2(\mathbf{k})}$ is the dispersion relation of the Bogolubov quasiparticles where $\epsilon(\mathbf{k})$ denotes the bare electronic dispersion of the electrons in the normal state. In contrast to the pairing via electron–phonon coupling the momentum dependence cannot be neglected due to the strong anisotropy of the pairing interaction.

Note that in the BCS theory $V_s^{eff} < 0$ (and V_t^{eff}) is taken as a constant. Therefore, one obtains a solution for $\Delta(\mathbf{k})$ of Eq. (9.47) which is structureless in momentum space [61, 94].

Let us now investigate how it is possible to solve Eq. (9.47) with a *repulsive* pairing potential assuming singlet pairing. Due to the fact that $V_s^{eff} > 0$, one would naively think that there exists no solution. However, this is not so. If one takes into account that $V_s^{eff}(\mathbf{k}-\mathbf{k}')$ might have a strong momentum

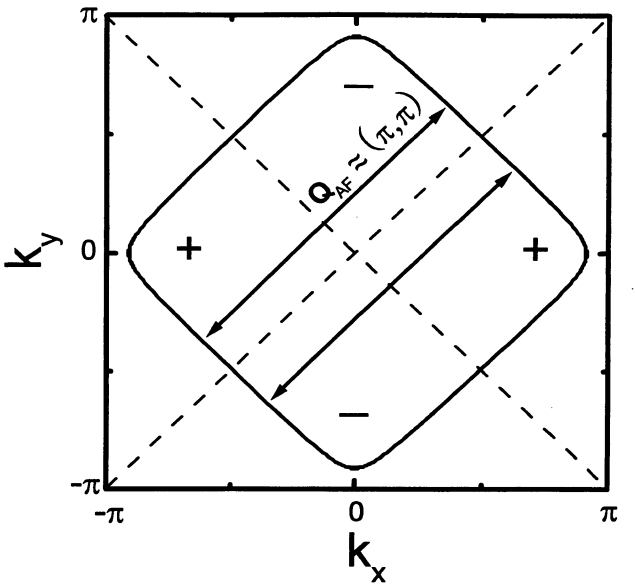

Fig. 9.22. Illustration of the $d_{x^2-y^2}$–symmetry of the superconducting order parameter in the first BZ of hole– and electron–doped cuprates. The +(−) sign corresponds to the sign of the order parameter. Two electrons (holes) at the Fermi surface (solid curve) are coupled by the exchange of antiferromagnetic spin fluctuations peaked at (π, π) yielding to the formation of Cooper–pairs only in the case if the order parameter changes sign. Note, the dashed lines refer to the nodes in the d–wave order parameter $\Delta(\mathbf{k}) = \Delta_0[\cos k_x - \cos k_y]/2$

dependence it is easily seen that indeed the gap equation has a solution. This is illustrated in Fig. 9.22 where we show the first Brillouin zone (BZ) and a Fermi surface which corresponds to the half–filled case of the two–dimensional one–band Hubbard model. This Fermi surface resembles the measured one in the high–T_c superconductor $La_{2-x}Sr_xCuO_4$. For simplicity, we assume also an underlying tetragonal symmetry of the crystal. The behavior of a superconducting order parameter with $d_{x^2-y^2}$–wave symmetry and resultant $\Delta > 0$ and $\Delta < 0$ areas is indicated. If one now assumes that the effective pairing interaction $V_s^{eff}(\mathbf{k} - \mathbf{k}')$ has a strong momentum dependence, for example a large peak at the antiferromagnetic wave vector $\mathbf{q}_{AF} = \mathbf{Q} = (\pi, \pi)$ connecting different parts of the Fermi surface then the gap equation has a solution for $V_s^{eff} > 0$. Note that the wave vector $\mathbf{Q}$ connects areas where Δ is positive with those where $\Delta < 0$. Thus, one finds indeed a solution of Eq. (9.47).

The simplest solution is the $d_{x^2-y^2}$–symmetry gap

$$\Delta(\mathbf{k}) = \Delta_0 \left[\cos k_x - \cos k_y\right]/2 \quad , \tag{9.48}$$

which has nodes along the diagonals. Note, for an effective pairing interaction which is structureless in momentum space such a solution of the gap equation for a d–wave order parameter would not be possible. In fact an order parameter which belongs to an anisotropic s–wave representation (possibly with nodes) would not satisfy the pairing condition mentioned above. In order to solve Eq. (9.47) for a pairing interaction which is peaked at (π, π) one definitely needs an order parameter that changes sign. Therefore, we see that the superconducting gap has less symmetry than the underlying Fermi surface. In addition to a broken gauge invariance ($U(1)$) due to the occurrence of superconductivity a further symmetry is broken (in our case the invariance under a rotation of 90 degrees) we call this 'unconventional'. Notice that this neither implies an electronic pairing mechanism nor a corresponding large value of T_c, but distinction from electron–phonon pairing.

Triplet Cooper–pairing

In the case of triplet Cooper–pairing one has to solve the gap equation

$$\Delta(\mathbf{k}) = -\sum_{\mathbf{k}'} \frac{V_t^{eff}(\mathbf{k}-\mathbf{k}')}{2E(\mathbf{k}')}\,\Delta(\mathbf{k}') \quad , \tag{9.49}$$

where $V_t^{eff}(\mathbf{k}-\mathbf{k}')$ denotes the effective two–particle pairing interaction in the triplet pairing channel. Most importantly, Pauli's principle requires that $V_t^{eff} < 0$, i.e. an *attractive* pairing interaction in momentum space. Note, this is similar to pairing via electron–phonon interaction where the minus sign in front of the right–hand side of Eq. (9.49) is also cancelled. A solution of the gap equation is then relatively easy. In particular, if the transferred momentum $\mathbf{q} = \mathbf{k} - \mathbf{k}'$ is small, one may obtain,for example, a p–wave symmetry of the superconducting order parameter:

$$\Delta_p(\mathbf{k}) = \Delta_0(\sin k_x + i \sin k_y) \quad . \tag{9.50}$$

Note, the condition $\mathbf{q} \approx 0$ is indeed fulfilled in the case of superfluid ^{3}He that is close to a ferromagnetic transition. A similar situation is present in Sr_2RuO_4 (see its phase diagram in Fig. 9.10). This already suggests triplet p–wave symmetry for the order parameter of Sr_2RuO_4. Obviously, the results for $\chi(\mathbf{q}, \omega)$ in cuprates exclude triplet Cooper–pairing.

Finally, let us critically mention that the arguments given above for cuprates and ruthenates are weak–coupling arguments. However, these may be used also in the strong–coupling limit of the pairing process. For example, the linearized version of the gap equation for high–T_c cuprates in the strong–coupling limit is given by

$$\lambda\ \mathrm{Im}\ \Delta(\mathbf{k},\omega)Z(\mathbf{k},\omega) = -\frac{1}{N}\sum_{\mathbf{k}} \int_{-\infty}^{\infty} d\omega'\ [b(\Omega) + f(\Omega - \omega)]$$

$$\times\ [P_s(\mathbf{q},\omega) - P_c(\mathbf{q},\omega)]\ \mathrm{Im}\left[\frac{\Delta(\mathbf{k}',\omega')Z(\mathbf{k}',\omega')}{(\omega Z)^2 - (\epsilon_{\mathbf{k}'} + \xi)^2}\right] \quad , \tag{9.51}$$

where P_s and P_c are defined in Eq. (9.23). However, although lifetime effects of the electrons will lead to a renormalization of the quasiparticles, the weak–coupling arguments given above still remain valid. As in the weak–coupling case, for decreasing temperature T the eigenvalue $\lambda(T)$ increases and passes through unity at $T = T_c$. The derivation of Eq. (9.51) is given in Appendix A.

In general, the superconducting order parameter $\Delta(\mathbf{k}, \omega)$ does not only yield a gap in the single–particle density of states, it also sets the scale for the condensation energy due to the formation of Cooper–pairs. Therefore, one might expect

$$T_c \propto \Delta_0$$

as in conventional superconductors. This is so in overdoped cuprates where the superconducting transition is of mean–field type with corresponding coherence length of Cooper–pairs ($\xi \sim 100\mathring{A}$) and thus global uniform phase of the Cooper–pairing. In contrast to this we will see below that in the underdoped case the number of carriers and density of Cooper–pairs is small and thus the wave functions of Cooper–pairs do not overlap significantly. Under such conditions –also because of the layered structure of cuprates– it is well known that (thermal) fluctuations of the phases of the Cooper–pairs will play an important role for determining T_c. Their corresponding energy scale is given by the superfluid density (or phase stiffness) n_s [87,107,108]. Therefore, in the underdoped regime one already expects from general arguments

$$T_c \propto n_s$$

as observed experimentally by Uemura *et al.* [15]. The calculation of n_s which controls many properties is described in the following section.

To summarize, we have demonstrated on general grounds that for Cooper–pairing via spin fluctuations the underlying Fermi surface topology plays an important role. In particular, for singlet pairing one expects a $d_{x^2-y^2}$–wave order parameter if nesting properties are present. Without nesting one expects no solution for a repulsive pairing interaction. Furthermore, as we will show later the nesting properties of the electron–doped cuprates are weak. Therefore, a competition between repulsive spin–fluctuation–mediated interaction and attractive electron–phonon interaction may result. A a consequence a transition from $d_{x^2-y^2}$–wave order parameter towards anisotropic s–wave symmetry may occur for $T_c \to 0$ and as a function of doping. In the case of (attractive) triplet pairing no nesting properties are needed and p–wave symmetry for the superconducting order parameter would naturally occur if the pairing is dominated by nearly ferromagnetic spin fluctuations. However, if strong nesting would be present, an order parameter with f–wave symmetry could win over p–wave symmetry. We will see later in this article that the symmetry of the superconducting order parameter calculated from a microscopic electronic theory will indeed support these general arguments.

9.2.6 Superfluid Density n_s

We discuss now the behavior of the superfluid density $n_s(\omega, T, x)$. The frequency ω reflects the dynamics of the corresponding quasiparticles and thus lifetime effects. Note, n_s controls the doping dependence of the phase coherence, thermodynamic behavior, the penetration depth, the Nernst effect, Cooper–pair phase fluctuations, etc.

Obviously, the superfluid density n_s is a central property for understanding the superconductivity and dynamics of the cuprates, in particular of underdoped cuprates. The superfluid density $n_s(\omega, T, x)$ may be calculated using the current–current correlation function or equivalently from

$$\frac{n_s}{m} = \frac{2t}{\hbar^2}\,(S_N - S_S), \tag{9.52}$$

where we have introduced for convenience the oscillator strength

$$S_N = \frac{\hbar^2 c}{2\pi e^2 t}\int_{0+}^{\infty} \sigma_1(\omega) d\omega. \tag{9.53}$$

S_S is the value of Eq. (9.53) in the superconducting state. Here, we utilize the f–sum rule for the real part of the conductivity $\sigma_1(\omega)$

$$\int_0^{\infty} \sigma_1(\omega)\, d\omega = \pi e^2 n/2m^* \quad ,$$

where n is the 3D hole density and m^* denotes the effective band mass (in our case for the tight–binding band considered). The conductivity $\sigma(\omega)$ is calculated in the normal and superconducting state using the Kubo formula [96,97]

$$\sigma(\omega) = \frac{2e^2}{\hbar c}\frac{\pi}{\omega}\int_{-\infty}^{\infty} d\omega' \left[f(\omega') - f(\omega'+\omega)\right] \times \frac{1}{N}\sum_{\mathbf{k}} \left[v_{k,x}^2 + v_{k,y}^2\right] \left[N(\mathbf{k},\omega'+\omega)\, N(\mathbf{k},\omega')\, A_1(\mathbf{k},\omega'+\omega)\, A_1(\mathbf{k},\omega')\right]. \tag{9.54}$$

Here, $v_{k,i} = \partial\epsilon_k/\partial k_i$ are the calculated band velocities within the CuO_2–plane and c is the c–axis lattice constant. The spectral functions N and A_1 are defined in Eq. (9.166). Vertex corrections have been neglected. Physically speaking, we are looking for the loss of spectral weight of the Drude peak at $\omega = 0$ that corresponds to excited quasiparticles above the superconducting condensate for temperatures $T < T_c^*$. Then, with the help of above equations we calculate the dynamical conductivity $\sigma(\omega)$ via (e = elementary charge) [96]

$$\frac{n_s(\omega)}{m} = \frac{1}{e^2}\,\omega\,\mathrm{Im}\;\sigma(\omega) \quad , \tag{9.55}$$

where Im $\sigma(\omega)$ has been obtained using Eq. (9.54) from the current–current correlation function and the Kubo formula. Furthermore, the penetration depth $\lambda(x,T)$ is calculated within the London theory [101] by

$$\lambda^{-2} \propto n_s. \quad ,$$

This will be discussed later.

Of course, in particular for underdoped cuprates phase fluctuations of the Cooper–pairs must be included into the calculation of n_s. A generalization of Eq. (9.55) leads to

$$n_s(\mathbf{q},\omega) = \omega \,\mathrm{Im}\, \sigma(\mathbf{q},\omega) \quad . \tag{9.56}$$

Since the conductivity σ can be expressed in terms of a current–current correlation function, n_s is related to $\langle \mathbf{J}(\mathbf{r},t)\cdot\mathbf{J}(0,0)\rangle$ where $J \propto (\psi^*\nabla\psi - \psi\nabla\psi^*)$. Using $\psi(\mathbf{r},t) = |\psi| e^{i\phi(\mathbf{r},t)}$ one arrives at $(\nabla\phi(0,0) = \frac{2e}{c\hbar}\overrightarrow{A}(0,0)$ for frozen amplitude fluctuations, see Appendix D.)

$$n_s \sim \langle \nabla\phi(\mathbf{r},t)\cdot\nabla\phi(0,0)\rangle \quad . \tag{9.57}$$

On general grounds one expects that the phase correlation function $C = \langle \nabla\phi\cdot\nabla\phi\rangle_\phi$ behaves as $C \to 1$ for large doping x and that a Meissner effect occurs only for $C(T) \to 1$ at T_c [104]. (Here, $\langle \nabla\phi\cdot\nabla\phi\rangle\ |_\phi$ means phase averaging).

From this we can calculate $n_s(\mathbf{q},\omega)$ and its doping dependence. For overdoped cuprates and for $T \to 0$ we expect that phase fluctuations play a minor role, see detailed discussion in the next section, while for underdoped cuprates ($x \to 0$) Cooper–pair phase fluctuations should become more and more important. However, for frequencies $\omega \sim 1/time > \omega_{phase}$ the behavior of $n_s(\mathbf{q},\omega)$ should correspond to the case where no phase fluctuations are seen. In this connection $\omega_{phase}^{-1} = \tau_1$ refers to the lifetime of the phase fluctuations. In underdoped cuprates it describes the dynamics of n_s. We estimate the lifetime from $\tau_1 \propto \Delta^{-1} \propto T_c^{-1}$, since the energy change involved in the excitations is of the order of $\Delta e^{i\phi}$. Note that above T_c one has $\langle e^{i\phi}\rangle = 0$ due to phase–incoherent Cooper pairs.

In summary, our mean field results for $n_s(x,T)$ are expected to be approximately valid for overdoped cuprates and also for underdoped cuprates if $T \to 0$ for times shorter than the lifetime of the phase fluctuations. If Cooper–pair phase fluctuations become important the superfluid density is given by Eq. (9.57). Note, for $\mathbf{q} \to 0$, $\omega \to 0$ one gets after phase averaging of $\langle \nabla\phi(\mathbf{r},t)\cdot\nabla\phi(0,0)\rangle \to 0$ at $T = T_c$. Thus, the Meissner effect occurs only for phase–coherent Cooper–pairs. In the following we safely approximate the phase correlation function $\langle \nabla\phi\cdot\nabla\phi\rangle \approx 0$ above T_c. Below T_c one takes $\langle \nabla\phi\nabla\phi\rangle \approx 1$ for simplicity. This is approximately true for Gaussian fluctuations.

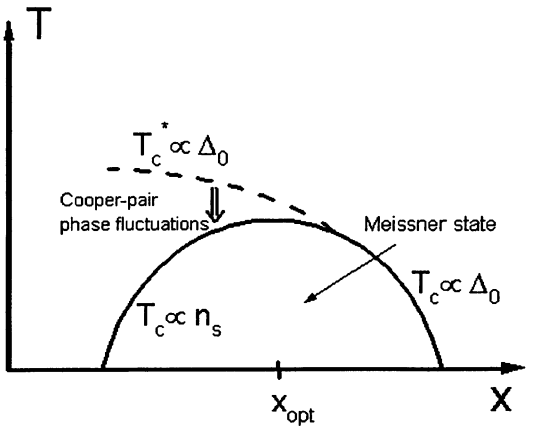

Fig. 9.23. Illustration of the significance of Cooper–pair phase fluctuations in underdoped cuprates with low superfluid density n_s. With the help of the generalized Eliashberg theory one finds below the crossover temperature T_c^* local Cooper–pairs without long–range phase coherence ('pre–formed pairs'). The temperature T_c denotes the superconducting phase transition temperature below which phase coherent Cooper–pairs and the Meissner effect occurs. For $x < x_{opt}$ one gets $T_c^* \rightarrow T_c$ due to phase fluctuations

9.2.7 Cooper–Pair Phase Fluctuations

As mentioned above the cuprates consist of weakly coupled two–dimensional CuO_2 planes. For doping $x \rightarrow 0$ the Cooper–pairs do not overlap much. Therefore, one expects that Cooper–pair phase fluctuations are enhanced. These fluctuations of phase incoherent Cooper pairs destroy the long–range superconducting order and the Meissner effect. In conventional bulk superconductors Cooper–pair phase fluctuations are not relevant, since the large superfluid density leads to strong overlap of Cooper–pairs and the phase fluctuations cost much energy. Thus, in conventional superconductors the superconducting transition is due to the destruction of the Cooper pairs and T_c is proportional to Δ_0 [94]. On the other hand, the observation by Uemura *et al.* that $T_c \propto n_s$ in underdoped hole–doped cuprates [15] indicates that the phase fluctuations drive the transition in these regime. Then, at $T \rightarrow T_c$ where $\Delta F_{phase} \simeq T_c$ phase coherent Cooper–pairs occur. ΔF_{phase} denotes the free energy contribution due to phase fluctuations. Cooper–pairs might exist above T_c and break only up at a crossover temperature around $T_c^* > T_c$. Here, T_c^* is approximately given by the transition temperature one would obtain without phase fluctuations. Note, the Meissner effect takes place only below T_c. This situation is illustrated in Fig. 9.23.

The bulk transition temperature T_c at which phase coherence of the Cooper pairs occurs is determined by the Ginzburg–Landau free energy functional $\Delta F\{n_s, \Delta\}$ where the superfluid density divided by the effective mass

m, $n_s(x,T)/m$, is calculated self–consistently from the current–current correlation function. First, we consider the static case, i.e. $n_s \neq n_s(\omega)$. The doping dependence of the Ginzburg–Landau–like free–energy change (see $n_s(x,T)$) is given by

$$\Delta F = F_S - F_N = -\frac{1}{\beta} \ln \left[\int \mathcal{D}\Delta^\dagger \mathcal{D}\Delta \, e^{-\frac{1}{\hbar} S_{eff}[\Delta^\dagger, \Delta]} \right] \quad . \tag{9.58}$$

The functional integral is taken over the fields $\mathcal{D}\Delta^\dagger = \prod_{\mathbf{r}_i, t_i} d\Delta^\dagger(\mathbf{r}_i, t_i)$. The effective action S_{eff} is defined in Appendix D where we also derive the Dyson equation for the Cooper–pair phase fluctuations on a microscopic level. On phenomenological grounds the Gor'kov equations including the phase fluctuations were derived by Berthod and Giovannini [103]. Equation (9.58) is the basis for determining T_c in the presence of Cooper–pair phase fluctuations. For simplicity, we neglect first the interaction between the amplitude and the phase of Cooper–pairs (see Ref. [104] and Appendix D for details of the interplay between amplitude and phase fluctuations). Then, we write

$$\Delta F = \Delta F_{cond} + \Delta F_{phase} \quad , \tag{9.59}$$

where $\Delta F_{cond} \approx \alpha \{n_s/m^*\} \Delta_0(x)$ is the condensation energy due to Cooper–pairing and $\Delta F_{phase} \approx \frac{\hbar^2 n_s}{2m^*}$ is the loss in energy due to phase incoherent Cooper–pairs. Here, α denotes the available phase space for Cooper–pairs normalized per unit volume and can be estimated in strongly overdoped regime. In contrast to conventional superconductors in cuprates α is smaller mainly due to large size of the unit cell [123–125]. This will be discussed later in connection with Fig. 9.52.

From the interplay between condensation energy and phase fluctuation energy we can estimate the role of phase fluctuations for determining T_c at different doping. One expects that for underdoped cuprates $0.15 > x \rightarrow 0$, phase fluctuations get more important and cost less energy. Thus $\Delta F_{phase} < \Delta F_{cond}$ and consequently $T_c \sim \Delta F_{phase} < \Delta F_{cond} \sim T_c^*$. Note that Cooper–pairs break up thermally at T_c^*. Since $\Delta F_{phase} \propto n_s$ one gets due to Cooper–pair phase fluctuations $T_c(x) \propto n_s(x)$ in the underdoped regime.

In the overdoped case the situation is described by the fact that Cooper–pair phase fluctuations cost too much energy. Phase coherence would break up thermally at a temperature larger then the temperature at which Cooper–pairs are broken up. Thus, only a single phase coherent Cooper pair state occurs, i.e. the Meissner state. The system undergoes a mean–field transition according to a small condensation energy ΔF_{cond} and then $T_c(x) \propto \Delta_0(x)$. Note, the explicit derivation of the free energy functional is given in Appendix D. The Meissner effect only occurs if after phase averaging $n_s(\omega \rightarrow 0) \neq 0$ yielding a London penetration depth

$$\frac{1}{\lambda^2(T)} \propto n_s(T, \omega = 0).$$

Here, n_s refers to the phase averaged superfluid density. Within standard (time–dependent) Ginzburg–Landau theory [104], the superfluid density n_s can be calculated through Eq. (9.57).

To summarize, using this physical picture one already obtains on general grounds a superconducting phase diagram and in particular an optimum T_c and doping concentration as it is illustrated in Fig. 9.23. In particular, calculating ΔF_{cond} and ΔF_{phase} from the generalized Eliashberg equations one finds an optimal doping concentration at $x_{\rm opt} \simeq 0.15$. We get $T_c \propto \Delta F_{cond} \sim \Delta_0$ for overdoped cuprates and $T_c \propto \Delta F_{phase} \sim n_s$ for underdoped cuprates. Clearly, the Meissner effect occurs only for phase coherent Cooper–pairing and $\lambda^{-2} \propto n_s$.

BKT theory for Cooper–pair phase fluctuations

Due to the layered structure of the cuprates and weak interlayer coupling the underdoped cuprates should behave in accordance with the 2D–XY model (except in a narrow critical range around T_c where the 3D–XY is more appropriate) [109, 110]. Thus, the standard theory for the 2D–XY model, the Berezinskii–Kosterlitz–Thouless (BKT) renormalization group theory, should be a reasonable starting point for a study of Cooper–pair phase fluctuations [111–114]. In particular we discuss the determination of T_c with the help of the BKT theory.

The superconducting transition predicted by BKT theory is due to unbinding of fluctuating vortex–antivortex pairs in the superconducting order parameter. Gaussian phase fluctuations are not important, since they do not shift T_c [115]. Since we are mainly interested in the determination of T_c, we first consider the static case where the phase ϕ does not depend on frequency. Then, the phase action is given by

$$S_{phase} = \frac{\tilde{K}}{2} \int d^2r \, (\nabla\phi)^2 \quad , \tag{9.60}$$

where the phase stiffness is related to the superfluid density through $\tilde{K} = n_s(T)\hbar^2/(4m^*T)$. For the cuprates it turns out that the relevant parameters for the unbinding of thermally created vortex–antivortex pairs are the dimensionless stiffness K and the vortex core energy E_{core}. The vortex core energy refers to the energy amount that is needed for the suppression of the superconducting order parameter in the vortex core, i.e. $\Delta(\mathbf{r} \rightarrow \mathbf{r}_{core}) = 0$. This, in general will renormalize the phase stiffness yielding $K \rightarrow K_r$. The stiffness is related to to n_s by

$$K(T) = \beta\hbar^2 \frac{n_s(T)}{m^*} \frac{d}{4} \quad , \tag{9.61}$$

where β denotes again the inverse temperature and m is again the effective mass. d is the average spacing between CuO_2 layers. In our calculations we set d to half the height of the unit cell of $YBa_2Cu_3O_{6+x}$, for example [116]. Note, that the renormalized stiffness K_r is related to the superfluid velocity

through

$$\frac{1}{K_r} = \frac{4m^2}{\hbar^2} \int d^2r \, \langle \mathbf{v}_s(\mathbf{r}) \cdot \mathbf{v}_s(0) \rangle \quad . \tag{9.62}$$

For determining T_c one has to solve the Kosterlitz recursion relations ('flow equations') [111]

$$\frac{dy}{dl} = (2 - \pi K)\, y \tag{9.63}$$

and

$$\frac{dK}{dl} = -4\pi^3 y^2 K^2 \quad . \tag{9.64}$$

Here, $y = e^{-\beta E_c}$ denotes the vortex fugacity. For the vortex core energy we use the approximate result by Blatter *et al.*, i.e. [110]

$$E_{core} = \pi k_B T K \ln \kappa \quad , \tag{9.65}$$

where κ is the Ginzburg parameter. $l = (r/r_0)$ is a logarithmic length scale which relates K to the strength of the vortex–antivortex interaction. For $T > T_c$, note K tends to zero for $l \to \infty$. The interaction at large distances is screened and the largest vortex–antivortex pair unbind. This destroys the Meissner effect and leads to dissipation. On the other hand, bound Cooper–pairs reduce K and thus n_s, but do not destroy superconductivity. After solving Eqs. (9.63)-(9.65) it turns out that that the renormalization of K is very small [116]. Thus, within a good approximation, one can obtain $T_c(x)$ from the simple criterion [111,116–118,121]

$$K(T_c) = \frac{2}{\pi} \quad , \tag{9.66}$$

or

$$\frac{n_s(T_c, x)}{m^*} = \frac{2}{\pi} \frac{4k_B T_c}{\hbar^2 d} \quad . \tag{9.67}$$

The superfluid density $n_s(T, x)$ entering Eq. (9.67) is calculated from the generalized Eliashberg equations using Eqs. (9.57)-(9.54).

Finally, in order to compare our results also with time–dependent measurements we calculate $n_s(\omega, T)$. Regarding the frequency dependence of n_s we mention the following: A dynamical generalization of the BKT theory was developed by Ambegaokar *et al.* [113,236]. It turns out that the critical size for a vortex–antivortex pair is given by

$$r_\omega = \sqrt{\frac{D_\nu}{2\pi\omega}} \quad , \tag{9.68}$$

where D_ν denotes the corresponding diffusion constant. Only pairs with size $r \leq r_\omega$ contribute to the screening. Unfortunately, D_ν is not easy to calculate. In the absence of pinning, the theory by Bardeen and Stephen yields [119]

$$D_\nu^0 = \frac{2\pi c^2 \xi_{ab}^2 \rho_n T}{\phi_0^2 \tilde{d}} \quad , \tag{9.69}$$

where c is the speed of light, $\xi_{ab} \sim r_0/2$ corresponds to the coherence length, ρ_n denotes the normal–state resistivity, $\phi_0 = hc/2e$ is the elementary superconducting flux quantum, and $\tilde{d}$ corresponds to an effective layer thickness. However, in cuprate superconductors, pinning becomes important. Thus, we assume a simple Arrhenius law

$$D_\nu = D_\nu^0 \exp\left(\frac{-E_p}{T}\right) \quad , \tag{9.70}$$

where E_p denotes the corresponding pinning energy barrier. Eqs. (9.70) and (9.69) are inserted into Eq. (9.68) yields a new length scale l in Eqs. (9.63) and (9.64), namely a new upper limit $l = \ln(r_\omega/r_0)$. Thus, we get $n_s(\omega, T)/m^* = \omega \,\mathrm{Im}\, \sigma(\omega)/e^2$ where the conductivity $\sigma(\omega)$ is obtained from the current–current correlation function. Since $1/\omega \sim$ *time*, and *time* say the time of an observation, we expect phase coherence already for $\omega\tau \gg 1$, where τ refers to the lifetime of phase fluctuations.

Resumé

In summary, we have demonstrated on general grounds that the interplay between Cooper–pair condensation energy and phase fluctuation energy already yields an optimal doping concentration. Thus, the phase diagram can be described in the overdoped part by $T_c \propto \Delta_0$ and in the underdoped case by $T_c \propto n_s$. The superconducting transition temperature T_c in underdoped cuprates might be estimated also by the BKT theory. The **dynamical stiffness** $\propto n_s(\omega)$ provides information about the time–scale of Cooper–pair phase fluctuations. In our theory these are treated classically and the coupling between amplitude and phase has been neglected. The results for $n_s(\omega)$ can be compared with time–resolved measurements. Note, that for $\omega > \omega_{phase}$, where ω_{phase} refer to the phase fluctuations, one expects a behavior as in the absence of the phase fluctuations. Thus $n_s(\omega) \to n_s(T, x)$ in the absence of the Copper–pair phase fluctuations. We further would like to mention that phase fluctuations are also related to the formation of vortices. For details see Appendix D.

9.2.8 Tunneling Spectra

A most important verification of the approximate validity of the conventional Eliashberg theory came from electron tunneling experiments. They probe the **k**–averaged quasiparticle excitation spectra in the normal and

superconducting state. Therefore, in the case of singlet pairing in high-T_c cuprates and triplet pairing in ruthenates also important fingerprints of the spin-fluctuation-mediated pairing interaction can be seen. Hence, we analyze now tunneling in superconductor-insulator-normal metal (SIN) and superconductor-insulator-superconductor (SIS) junctions.

Using standard tunneling theory [152] we have

$$H = H_L + H_R + H_T, \tag{9.71}$$

where $H_L(H_R)$ is the Hamiltonian for particles on the left-hand-side (right-hand-side) of the tunnel junction. Note, H contains all many-body effects. Here, in general, $[H_L, H_R] = 0$. H_T denotes the tunnel operator with a matrix element T_{pk}. The total current through the tunnel junction can be expressed as the average rate of change per time t of the number of particles. For example, on the left-hand-side of the junction ($\hbar = 1$),

$$I_{tot}(t) = -e\,\langle \dot{N}_L(t)\rangle = -e\,i\int_{-\infty}^{t} dt'\,\langle\,[N_L(t), H_T(t')]\,\rangle \quad . \tag{9.72}$$

After some algebra [197] one arrives at

$$I_{tot}(t) = I_s(t) + I_J(t),$$

where

$$I_s(t) = e\int_{-\infty}^{\infty} dt'\,\theta(t-t')\,\Big(e^{ieV(t'-t)}\langle\,[A(t), A^+(t')]\,\rangle - e^{ieV(t-t')}\langle\,[A^+(t), A(t')]\,\rangle\Big) \quad , \tag{9.73}$$

and

$$I_J(t) = e\int_{-\infty}^{\infty} dt'\,\theta(t-t')\,\Big(e^{-ieV(t'+t)}\langle\,[A(t), A(t')]\,\rangle - e^{ieV(t+t')}\langle\,[A^+(t), A^+(t')]\,\rangle\Big) \quad . \tag{9.74}$$

Here, I_s refers to the single-particle tunneling and I_J describes tunneling of Cooper-pairs, the Josephson effect. The operator A is given by $A(t) = \sum_{\mathbf{k},\mathbf{p}} T_{\mathbf{kp}} c_{\mathbf{k}}^+(t) c_{\mathbf{p}}(t)$ where $c_{\mathbf{k}}^+$ ($c_{\mathbf{p}}$) refers to the single-particle creation (annihilation) operator entering the Hubbard Hamiltonian, and eV is the applied voltage.

In order to study the single-particle excitations we focus in the following on I_s. A closer inspection of Eq. (9.73) shows that the current can be expressed as $I \propto (G_{red} - G_{adv})$ where G_{red} (G_{adv}) is the retarded (advanced) Green's function that correspond to the operator A. This would lead to $I_s = -2e\,\mathrm{Im}\,(G_{red})$ and is important for SIS junctions. In the case of SIN tunneling one obtains [94, 197]

$$I_s = 2e\sum_{\mathbf{k},\mathbf{p}} |T_{\mathbf{k},\mathbf{p}}|^2 \int_{-\infty}^{\infty} \frac{d\omega}{2\pi} A_R(\mathbf{k},\omega) A_L(\mathbf{p},\omega+eV)\,[f(\omega) - f(\omega+eV)]\ , \tag{9.75}$$

where $f(\omega)$ again denotes the Fermi distribution function and A_L and A_R is the spectral density of the left–hand–side (sc–state) and right–hand–side (n–state) material, respectively. The factor 2 arises from the spin summation. The matrix element $T_{\mathbf{k},\mathbf{p}}$ (i.e. the transfer rate) varies on the energy scale E/E_F which should be negligible if $E \simeq \Delta_0$. Thus, an adequate approximation should be to take $T_{\mathbf{k},\mathbf{p}} = T_0 = const.$

Note, the elementary excitations are entering in Eq. (9.75) via $A(\mathbf{k},\omega)$. In particular, the frequency dependence of the gap, $\phi(\omega)$, reflecting the dynamics of the Cooper–pairing will be of importance. Performing the sum over momenta we obtain the important result that the single–particle density of states $N(\omega)$ is proportional to the dynamical conductivity dI_s/dV (normalized by its normal–state value) for a SIN tunneling junction system measured at $\omega = eV$ with V being the applied voltage:

$$\sigma_{tun}(eV) = \frac{dI_s(eV)}{dV} \propto \sum_{\mathbf{k}} A(\mathbf{k},\omega) = N(\omega) \quad . \tag{9.76}$$

Obviously, below T_c the tunneling density of states $\sigma_{tun}(eV)$ in cuprates reveals interesting structures due to the interaction of quasiparticles with antiferromagnetic spin fluctuations and the opening of the superconducting gap. What is the energy position of these structures? In the superconducting state the spin fluctuation spectrum is peaked at the resonance energy ω_{res}. Thus, the structure in the NIS tunneling occurs at

$$\omega_{res} + \Delta_0 \quad \text{(NIS)} \quad . \tag{9.77}$$

This follows immediately from Eq. (9.75), since he spectral density $A(\mathbf{k},\omega)$ in the superconductor reflects ω_{res} and the shift of the quasiparticle density by Δ_0.

In the case of SIS tunneling the characteristic feature in the tunneling spectrum is shifted to the higher energy

$$\omega_{res} + 2\Delta_0 \quad \text{(SIS)} \quad . \tag{9.78}$$

Again, in addition to ω_{res} each spectral density shifts the energy by Δ_0.

The maximum gap value Δ_0 and the resonance frequency ω_{res} are both doping dependent quantities. As mentioned earlier to a good approximation one finds $\omega_{res}(x) \propto 2\Delta_0(x)$ and $T_c \simeq T_c^* \propto \Delta_0$ in the overdoped case and $\omega_{res}(x) \propto \omega_{sf}(x)$ in underdoped cuprates. Thus, in overdoped cuprates a reduction of spectral weight ('dip') is expected at around $\omega_{res} + \Delta_0 \simeq 3\Delta_0$ (SIN), and in underdoped cuprates at $\omega_{res} + \Delta_0 \simeq \omega_{sf} + \Delta_0$ (SIN). Similarly we get for overdoped cuprates structure at $\omega_{res} + 2\Delta_0 \simeq 4\Delta_0$ (SIS), and for underdoped ones at $\omega_{res} + 2\Delta_0 \simeq \omega_{sf} + 2\Delta_0$ (SIS). Therefore, we may safely conclude that as in the BCS and conventional Eliashberg theory the single–particle tunneling spectrum reflects the density of states and thus provides insight into the strength and dynamics of the Cooper–pairing.

Finally, we would like to mention that for electron–phonon mediated superconductivity the spectrum of the pairing potential is mainly unchanged in the superconducting state with respect to the normal state. Thus, structure in the tunneling spectrum is expected at an energy $\hbar\omega_D$ where ω_D is the Debye frequency. In contrast to this, in the case of spin–fluctuation–mediated Cooper–pairing strong feedback effects are present yielding anisotropic elementary excitations and a renormalized spin spectrum ($\omega_{sf} \rightarrow \omega_{res}$). This leads to the structure described above and is clearly a direct fingerprint of Cooper–pairing by spin fluctuations and is expected for both hole– and electron–doped cuprates. In addition, also the momentum dependence of the superconducting order parameter is reflected in the tunneling spectrum. In particular, for an order parameter with s–wave symmetry resulting from electron–phonon interaction, one finds an isotropic density of states with a gap for frequencies $|\omega| < 2\Delta_0$. In contrast, in the case of unconventional superconductivity where the order parameter has nodes, thermal excitations with energies smaller than $2\Delta_0$ are possible (around the nodes). Using thermodynamic arguments one can easily show that the density of states has a linear slope for $\omega \rightarrow 0$ [28].

Note, additional structure will occur due to Andreev bound–states in SIN and SIS tunneling.

9.2.9 Bilayer Effects

Many high–T_c cuprates contain more than one CuO_2–plane per unit cell like for example YBCO or BISSCO compounds (see Fig. 9.2). So far, our theory has focused mainly on the physical properties of a single CuO_2–plane. Of course, it is desirable to understand how the properties change if several CuO_2–planes per unit cell are present and how the number of CuO_2–layers per unit cell affects $T_c(x)$, for example. Note, the bilayer coupling $t_\perp$ causes

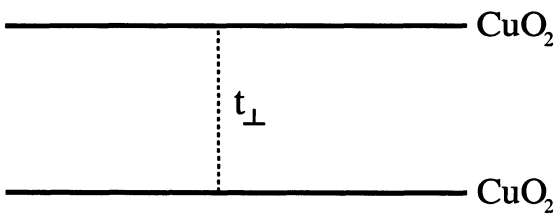

Fig. 9.24. Illustration of the interlayer coupling $t_\perp$ affecting the energy dispersion $\epsilon_{\mathbf{k}}$, Fermi surface and Cooper–pairing across CuO_2–layers

changes of the Fermi surface topology and the dispersion $\epsilon_{\mathbf{k}}$. There is also an interlayer coupling of Cooper–pairs. For several CuO_2–planes per unit cell also effects due to varying hole doping are expected. The simplest situation

is illustrated in Fig. 9.24 where we show schematically the coupling of two CuO_2–planes via the coupling parameter $t_\perp$.

In the following we will present an extension of the generalized Eliashberg–like theory for the case of two coupled CuO_2–planes [149,151]. We start from a Hamiltonian that contains nearest and next nearest neighbor hopping t and tt', respectively, as well as an intra–layer Coulomb repulsion U, an inter–layer interaction V and an inter–layer hopping $t_\perp$. The corresponding Hamiltonian is given by

$$H = H_{int} + H_{hop} \quad , \tag{9.79}$$

and with $U_{eff} = U$

$$H_{int} = U \sum_i n_{il\uparrow} n_{il\downarrow} + \frac{V}{2} \sum_{i \neq j \sigma \sigma' l} n_{il\sigma} n_{jl\sigma'} \quad , \tag{9.80}$$

and

$$H_{hop} = - \sum_{\langle i,j \rangle l \sigma} t_l \, c^\dagger_{il\sigma} c_{jl\sigma} - t_\perp \sum_{i\sigma} c^\dagger_{i1\sigma} c_{i2\sigma} \quad . \tag{9.81}$$

Here, $c^\dagger_{il\sigma}$ ($c_{il\sigma}$) creates (annihilates) an electron on site i in the layer $l = 1$ or $l = 2$ with spin σ and $n_{il\sigma} = c^\dagger_{il\sigma} c_{il\sigma}$. We diagonalize the Hamiltonian with respect to the hopping term. Thus, we perform a transformation in term of the operators $d_{\mathbf{k}\nu\sigma}$ with the help of

$$c_{\mathbf{k}l\sigma} = \sum_\nu S_{l\nu} \, d_{\mathbf{k}\nu\sigma} \quad , \qquad S_{l\nu} = \frac{1}{\sqrt{2}} \begin{pmatrix} e^{-ik_z c} & e^{-ik_z c} \\ e^{-ik_z c} & -e^{-ik_z c} \end{pmatrix} \quad , \tag{9.82}$$

where $\nu = +$ and $\nu = -$ denotes the bonding and antibonding band, respectively, $2c$ is the distance between adjacent planes, and $\mathbf{k}$ is the in–plane momentum. Thus, Eq. (9.81) can be rewritten as

$$H_{hop} = \sum_{\mathbf{k}\sigma} (d_{\mathbf{k}1\sigma}, d_{\mathbf{k}2\sigma}) \begin{pmatrix} \epsilon_+(\mathbf{k}) & 0 \\ 0 & \epsilon_-(\mathbf{k}) \end{pmatrix} \begin{pmatrix} d_{\mathbf{k}1\sigma} \\ d_{\mathbf{k}2\sigma} \end{pmatrix} \quad , \tag{9.83}$$

with

$$\epsilon_\pm = -2t \left[\cos(k_x) + \cos(k_y) - 2t' \cos(k_x) \cos(k_y) + \frac{\mu}{2} \right] \mp t_\perp \quad . \tag{9.84}$$

One is now able to extend the generalized Eliashberg equations as described at the beginning of this chapter. The corresponding Bethe–Salpeter equations separate with respect to band indices into two sets of coupled equations [149,150]. If, for simplicity the inter–plane Coulomb repulsion V is neglected

we find six coupled equations for the self–energy components:

$$\Sigma_{i\nu}(\mathbf{k},\omega) = N^{-1}\sum_{\mathbf{k}'}\sum_{\mu=+,-}\int_0^\infty d\Omega\,[P_s^{\mu\nu}(\mathbf{k}-\mathbf{k}',\Omega) + (\delta_{\nu 0}+\delta_{\nu 3}-\delta_{\nu 1})\,P_c^{\mu\nu}(\mathbf{k}-\mathbf{k}',\Omega)]\int_{-\infty}^{\infty} d\omega'\,I(\omega,\Omega,\omega')A_{i\nu}(\mathbf{k}',\omega') \quad , \tag{9.85}$$

(for a comparison, see Eq. (9.23)). In a shorthand notation we get

$$\Sigma_{ll'}(k) = \sum_{k'} V_{ll'}(k-k')\,G_{ll'}(k') \quad , \tag{9.86}$$

where $V_{ll'}$ is the effective pairing interaction due to spin (and also charge) fluctuations. Obviously, V and thus the dynamical spin susceptibilities $\chi_{s,c}$ are 2×2 matrices in the layer indices, having elements diagonal (χ^{aa}, χ^{bb}) and off–diagonal (χ^{ab}, χ^{ba}) with respect to the layer indices. The components of the spin susceptibility transforming as even and odd with respect to the layer indices are given by $\chi^e = \chi^{aa} + \chi^{bb}$ and $\chi^o = \chi^{ab} + \chi^{ba}$. For identical planes $\chi^{aa} = \chi^{bb}$ and $\chi^{ab} = \chi^{ba}$. The measured susceptibility is then given

$$\chi(\mathbf{q},q_z,\omega) = \chi^e(\mathbf{q},\omega)\cos^2\left(\frac{q_z c}{2}\right) + \chi^o(\mathbf{q},\omega)\sin^2\left(\frac{q_z c}{2}\right) \quad , \tag{9.87}$$

where c is the separation of the layers within a unit cell, $\mathbf{q}$ is the in–lane wave vector, and q_z denotes the component perpendicular to the planes. Note, if in cuprates or ruthenates the spin response in INS experiments would dominate at the wave vector $q_z = \pi$, for example, one would expect that $\chi^o \gg \chi^e$ in Eq. (9.87).

9.2.10 Electron–Doped Cuprates

Although we discussed in the previous chapters already the differences and similarities of electron– and hole–doped cuprates (in particular the evolution of antiferromagnetism as a function of the doping concentration) it is of interest to summarize the significant properties of the electron–doped compounds. The understanding of the phase diagram of the electron–doped cuprates should play a key role in resolving the physics of cuprates in general.

In Fig. 9.25 we show the phase diagram for the metallic phase of electron–doped cuprates. The behavior of T_c upon doping follows a parabolic–like curve with a narrow doping range for which superconductivity occurs. Therefore, despite the rather different behavior of the spin fluctuations in hole– (localized) and electron–doped (itinerant) cuprates the doping dependence of the T_c curve looks similar in hole– and electron–doped cuprates. This suggests the same mechanism for Cooper–pairing and most importantly, indicates the similar role played by the localized and itinerant spin fluctuations.

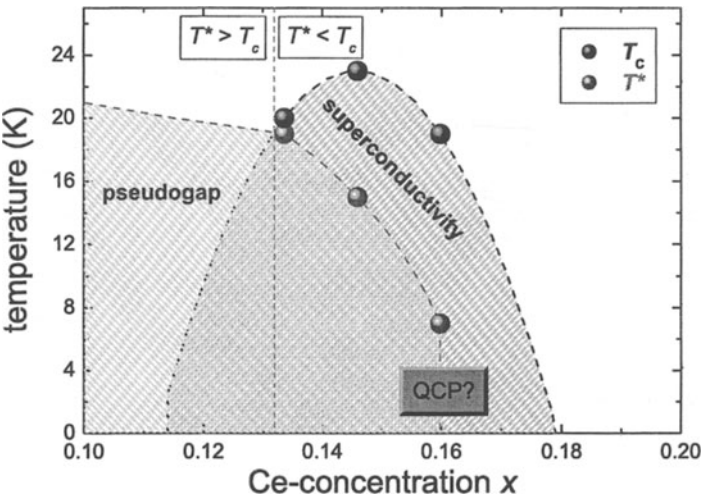

Fig. 9.25. Metallic part of the phase diagram of electron–doped cuprates taken from Ref. [153]. Note, the narrow range of superconductivity in electron–doped cuprates, and the smaller energy scale of the pseudogap. Both hole– and electron–doped cuprates show a similar phase diagram indicating the same mechanism for superconductivity and pseudogap formation. Note, the doping concentration where the pseudogap disappears may be related to a Quantum Critical Point. T^* refers to the pseudogap temperature

The appearance of the 'pseudogap' in the electronic spectrum of electron–doped cuprates has been debated for a long time. Recently its existence in the presence of a high magnetic field has been confirmed by careful tunneling spectroscopy by Alff *et al.* [153]. In particular, it has been found the the pseudogap shows a very similar doping dependence as in hole–doped cuprates, but its temperature range is lower. Moreover, as seen from Fig. 9.25 as in hole–cuprates the energy scale of the pseudogap and superconductivity crosses each other around the optimal doping and the pseudogap disappears in slightly overdoped cuprates. This confirms the close similarity between electron– and hole–doped cuprates regarding most of the properties. It also suggests that the mechanism of superconductivity, symmetry of the superconducting order parameter, and the anomalous normal state properties should have the same origin in both compounds.

In order to discuss the main difference we show in Fig. 9.26 our results for the Fermi surface of the hole– and electron–doped cuprates. These agree well with available experimental data [166]. Remarkably, the differences of the Fermi surfaces in the first BZ in hole and electron–doped cuprates have important consequences for their superconducting and normal state properties. In particular, the antiferromagnetic spin fluctuations which are peaked at $\mathbf{Q} = (\pi, \pi)$ connect different portions of the Fermi surface in hole– and

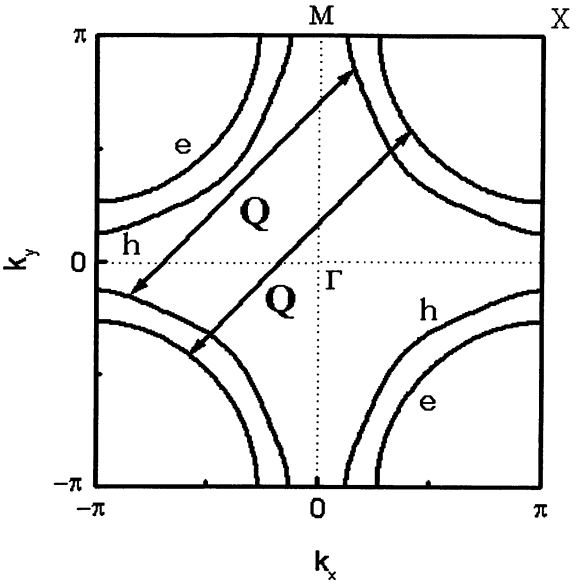

Fig. 9.26. Tight-binding results for the Fermi surface for hole- (h) and electron-doped (e) cuprates at optimal doping. $\Gamma = (0,0)$, M= $(\pi,0)$, and X= (π,π) denote the symmetry points of the first Brillouin zone. Remarkably the topology of the Fermi surface is in both cases hole-like. Q = (π,π) refers to the antiferromagnetic wave vector

electron-doped cuprates as one sees in Fig. 9.26. In the hole-doped cuprates the antiferromagnetic wave vector connects the carriers that lie close to the $M = (\pi,0)$ point of the first BZ. This means that the main scattering by the spin fluctuations occurs in hole-doped cuprates around these points (so called 'hot spots'). On the other hand, in the electron-doped cuprates the antiferromagnetic wave vector $\mathbf{Q}= (\pi,\pi)$ connects carriers that are close to the diagonal of the BZ. Therefore, the main effect of the interaction will occur there. This will be reflected in the asymmetrical behavior of the hole- and electron-doped cuprates.

What are the consequences for the superconducting state? In particular, we expect the appearance of the higher harmonics in the $d_{x^2-y^2}$-wave superconducting order parameter in the electron-doped cuprates, since the Cooper-pairing occurs far from the antinodal M points and close to the diagonals of the Brillouin Zone. Furthermore, due to a weaker (than in hole-doped cuprates) nesting of the Fermi surface the non-Fermi-liquid behavior and antiferromagnetic fluctuations should also be less pronounced in the electron-doped cuprates. Lattice vibrations may play a role for superconductivity in the overdoped part of the electron-doped phase diagram [154].

To summarize, we show that the asymmetry between hole– and electron–doped cuprates is expected due to differences in their Fermi surfaces and density of states. As a result of this, the scattering on spin fluctuations plays a more important role around $M = (\pi, 0)$ points of the BZ in hole–doped cuprates. On the contrary, the scattering on spin fluctuations occurs close to the diagonals of the BZ in the electron–doped cuprates. This will be reflected in the asymmetric behavior between hole– and electron–doped cuprates in the normal and superconducting states.

9.3 Electronic Theory for Ruthenates (Sr_2RuO_4)

We discuss Sr_2RuO_4 in detail, since it exhibits triplet Cooper–pairing as maybe also realized in some Heavy Fermion systems. What causes triplet pairing, since both ferromagnetic and antiferromagnetic spin fluctuations are present in the ruthenates? What is the effect of the strong magnetic anisotropy on superconductivity and its thermodynamic properties?

9.3.1 Electronic Structure and Hamiltonian

We present now the electronic theory for Sr_2RuO_4 which exhibits a superconducting transition temperature $T_c = 1.5$K. Effects involving all bands crossing the Fermi level are expected to play an important role for determining the triplet superconductivity in this compound. We will start the analysis by calculating the electronic structure of Sr_2RuO_4. In Fig. 9.27 we illustrate the basic electronic structure of Sr_2RuO_4. The highly planar structure of

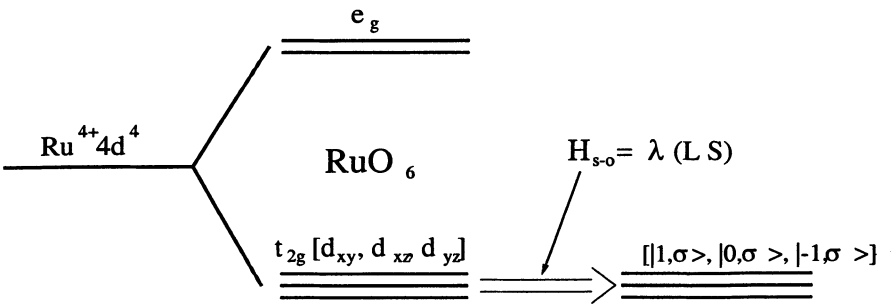

Fig. 9.27. Electronic structure of Sr_2RuO_4 including an effective spin–orbit coupling between d_{xy}, d_{yz}, and d_{xz} states. Due to a mixing of spin and orbital degrees of freedom the new states are characterized by pseudo–spin and pseudo–orbital quantum numbers. Since the spin–orbit coupling H_{s-o} does not break the time–reversal symmetry the Kramers degeneracy between the spin *up* and *down* is not removed

Sr_2RuO_4 prevents substantial energy dispersion along the z–direction. Note

the large interplanar separation of the RuO_6 octahedra. At the same time in the ab–plane neighboring RuO_6–octahedra share O ions which in turn are π–bonded to the Ru ions. Thus, the xy–orbital will form a two–dimensional band, while the xz– and yz–bands have only a restricted one–dimensional character. For the metallic properties one has to take into account intermediate electronic correlations.

Then an effective Hamiltonian for describing the physics in Sr_2RuO_4 is a two–dimensional three–band Hubbard Hamiltonian

$$H = \sum_{\mathbf{k},\sigma} \sum_{\alpha} \epsilon_{\mathbf{k}\alpha} a^{+}_{\mathbf{k},\alpha\sigma} a_{\mathbf{k},\alpha\sigma} + \sum_{i,\alpha} U_\alpha \, n_{i\alpha\uparrow} n_{i\alpha\downarrow} \quad , \tag{9.88}$$

where $a_{\mathbf{k},\alpha\sigma}$ is the Fourier transform of the annihilation operator for the d_α orbital electrons ($\alpha = xy, yz, zx$) and U_α is an effective on–site Coulomb repulsion. The hopping integrals $t_{\mathbf{k}\alpha}$ denote the energy dispersions of the tight–binding bands

$$\epsilon_{\mathbf{k}\alpha} = -\epsilon_0 - 2t_x \cos k_x - 2t_y \cos k_y + 4t' \cos k_x \cos k_y \quad . \tag{9.89}$$

In accordance with LDA calculations [156] and experimental measurements of the Fermi surface and energy dispersions [155] one chooses for d_{xy}–, d_{zx}–, and d_{yz}–orbitals the values for the parameter set $(\epsilon_0, t_x, t_y, t')$ as (0.5, 0.42, 0.44, 0.14), (0.23, 0.31, 0.045, 0.01), and (0.23, 0.045, 0.31, 0.01)eV.

This model was recently applied to Sr_2RuO_4 [157,158,160]. Its electronic properties can explain some features of the spin excitation spectrum in the compound Sr_2RuO_4. However, this model neglects spin–orbit coupling and fails to explain the magnetic anisotropy at low temperatures observed in NMR experiments [161]. It is known that the spin–orbit coupling plays an important role in the superconducting state of Sr_2RuO_4. In particular it was shown by Ng and Sigrist that the spin–orbit coupling lowers the free–energy and effects superconductivity and the symmetry of the superconducting order parameter [158]. The state is characterized by the orbital momentum of the Cooper–pair wave function aligning along the z–direction. This so–called chiral state of the superconducting order parameter is given by

$$\Delta(\mathbf{k}) = \Delta_0 \tilde{\mathbf{z}} (\sin k_x \pm \sin k_y) \quad . \tag{9.90}$$

Another indication of the importance of the spin–orbit coupling is the recent observation of the large spin–orbit coupling in the related insulating compound Ca_2RuO_4 [162].

Therefore, we extend the theory by adding to the Hamiltonian given in Eq. (9.88) the spin orbit coupling:

$$H_{s-o} = \lambda \sum_i L_i \cdot S_i \quad , \tag{9.91}$$

Here, the effective angular momentum L_i operates on the three t_{2g}–orbitals on the site i and $\mathbf{s}_i$ are the electron spins. As in an earlier approach [158]

we restrict ourselves to the three orbitals, ignoring e_{2g}–orbitals and choose the coupling constant λ such that the t_{2g}–states behave like an $l = 1$ angular momentum representation. Moreover, it is known that the quasi–two–dimensional xy–band is separated from the quasi–one–dimensional xz– and yz–bands. Then, one expects that the effect of spin–orbit coupling is small for the xy–band and can be neglected for simplicity. Therefore, we consider the effect of the spin–orbit coupling on xz– and yz–bands only. Then, the kinetic part of the Hamiltonian $H_t + H_{so}$ can be diagonalized and the new energy dispersions are

$$\begin{aligned}\epsilon^{\sigma}_{\mathbf{k},yz} &= (t_{\mathbf{k},yz} + t_{\mathbf{k},xz} + A_{\mathbf{k}})/2,\\ \epsilon^{\sigma}_{\mathbf{k},xz} &= (t_{\mathbf{k},yz} + t_{\mathbf{k},xz} - A_{\mathbf{k}})/2,\end{aligned} \tag{9.92}$$

where $A_{\mathbf{k}} = \sqrt{(t_{\mathbf{k},yz} - t_{\mathbf{k},xz})^2 + \lambda^2}$, and σ refers to a pseudo–spin quantum numbers. The spin–orbit coupling does not break the time–reversal symmetry and therefore the Kramers degeneracy between the spin *up* and *down* is not removed. The resultant Fermi surface consists of three sheets as observed in experiment [155]. Most importantly spin–orbit coupling together with Eq. (9.88) leads to a new quasiparticle which we label by pseudo–spin and pseudo–orbital indices. The unitary transformation $\tilde{U}_{\mathbf{k}}$ connecting old and new quasiparticle states is defined for each wave vector and leads to the following relation between them:

$$\begin{aligned}c^{+}_{\mathbf{k},yz+} &= u_{1\mathbf{k}} a^{+}_{\mathbf{k},yz+} - i v_{1\mathbf{k}} a^{+}_{\mathbf{k},xz+},\\ c^{+}_{\mathbf{k},xz+} &= u_{2\mathbf{k}} a^{+}_{\mathbf{k},yz+} - i v_{2\mathbf{k}} a^{+}_{\mathbf{k},xz+},\\ c^{+}_{\mathbf{k},yz-} &= u_{1\mathbf{k}} a^{+}_{\mathbf{k},yz-} + i v_{1\mathbf{k}} a^{+}_{\mathbf{k},xz-},\\ c^{+}_{\mathbf{k},xz-} &= u_{2\mathbf{k}} a^{+}_{\mathbf{k},yz-} + i v_{2\mathbf{k}} a^{+}_{\mathbf{k},xz-},\end{aligned} \tag{9.93}$$

where

$$u_{m\mathbf{k}} = \frac{\lambda}{\sqrt{(t_{\mathbf{k},yz} - t_{\mathbf{k},xz} \mp A_{\mathbf{k}})^2 + \lambda^2}}, \tag{9.94}$$

and

$$v_{m\mathbf{k}} = \frac{t_{\mathbf{k},yz} - t_{\mathbf{k},xz} \mp A_{\mathbf{k}}}{\sqrt{(t_{\mathbf{k},yz} - t_{\mathbf{k},xz} \mp A_{\mathbf{k}})^2 + \lambda^2}} \quad . \tag{9.95}$$

The '-' and '+' signs refer to $m = 1$ and $m = 2$, respectively.

Note that despite the spin–orbit coupling causing the spin and orbit quantum numbers not to be good ones we can still identify the Cooper–pairing to be triplet or singlet one. This refers then to the pseudo–spin quantum numbers. At the same time, the magnetic behavior of Sr_2RuO_4 becomes very anisotropic due to the fact that both one–particle Green's functions and Lande's g–factors will be different if the magnetic field is applied along c–axis or in the ab–RuO_2 plane. In particular, the anisotropy arises mainly

from the calculations of the Lande's g–factors and in particular their orbital parts. The factors $g_z = \tilde{l}_z + 2s_z$ and $g_+ = \tilde{l}_+ + 2s_+$ are calculated using the new quasiparticle states. The latter consist, for example, of xz– and yz–orbitals which in turn are the combinations of the initial orbital states $|2,+1\rangle$ and $|2,-1\rangle$ mixed due to the crystal field. Then, the matrix elements $\langle|l_+|\rangle$ ($\langle|l_-|\rangle$) are zero for the xz– and yz–orbitals while $\langle|l_z|\rangle$ matrix element is not. Therefore, the longitudinal components of the spin susceptibility of the xz– and yz–band get enhanced in comparison to the transverse one. One of the interesting question that we will analyze later is the effect of spin–orbit coupling on the antiferromagnetic and ferromagnetic fluctuations. This provides insights into a microscopic explanation of the pairing mechanism and allows to calculate the spatial structure of the superconducting order parameter.

9.3.2 Eliashberg–like Theory for the Coupling of Quasiparticles to Ferromagnetic and Incommensurate Antiferromagnetic Spin Fluctuations

For the analysis of the interaction between quasiparticles and spin fluctuations (ferromagnetic and incommensurate antiferromagnetic) we proceed as follows. The form of the electronic theory remains the same as for the case of cuprates and we extend the electronic theory towards a three–band theory as observed in Sr_2RuO_4 [163,164]. In the normal state both self–energy and thermal Green's functions become a matrix of 3×3 form, *i.e.* $G_{i,j,m}(\mathbf{k},\omega_n)$ and $\Sigma_{i,j,m}(\mathbf{k},\omega_n)$, where i,j,m refer to the band indexes of the xy, yz, and xz–orbitals. The corresponding Dyson equation is given by

$$\left[\hat{G}(\mathbf{k},\omega_n)\right]^{-1} = \left[\hat{G}^0(\mathbf{k},\omega_n)\right]^{-1} - \hat{\Sigma}(\mathbf{k},\omega_n), \tag{9.96}$$

where $\hat{G}^0_{i,j,m}(\mathbf{k},\omega_n)$ is the matrix of the bare Green's function determined via the tight–binding energy dispersions for the xy, yz, and xz–bands. The self–energy is given by [164]

$$\Sigma_{i,j,m}(\mathbf{k},\omega_n) = T\sum_{q,l} V^1_{i,j,m}(\mathbf{q},\omega_l) \times G_{i,j,m}(\mathbf{k}-\mathbf{q},\omega_n-\omega_l) \quad , \tag{9.97}$$

where $V^1_{i,j,m}(\mathbf{q},\omega_l)$ is an effective interaction between quasiparticles and spin fluctuations. Similarly as for cuprates it consists of an infinite series of diagram including charge and spin fluctuations. However, some important differences are included in the random phase approximation.

Most importantly we consider now the diagrams shown in Fig. 9.28 with odd number of bubbles that contribute to the triplet pairing. This is in contrast to singlet pairing in cuprates where an even number of bubbles occur (see Fig. 9.18). Furthermore, due to the inclusion of the spin–orbit coupling we expect that the transverse (+-) and the longitudinal (zz) parts of the spin susceptibility are different. Thus, in the RPA series they have to be summed

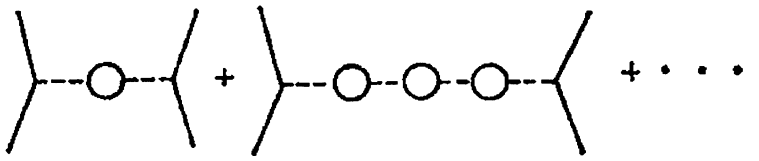

Fig. 9.28. RPA diagrams for triplet Cooper–pairing with odd number of bubbles that refer to longitudinal charge and spin fluctuations

separately. Then the effective pairing interaction in the 3×3 form including transverse and longitudinal spin fluctuations and also charge fluctuations is given by

$$V^1_{i,j,m}(\mathbf{q},\omega_l) = \frac{1}{2}V^{sp,zz}_{i,j,m}(\mathbf{q},\omega_l) + V^{sp,+-}_{i,j,m}(\mathbf{q},\omega_l) + \frac{1}{2}V^{ch}_{i,j,m}(\mathbf{q},\omega_l) \quad , \quad (9.98)$$

where

$$V^{sp,zz} = U^2\frac{\chi_0^{sp,zz}}{1-U\chi_0^{sp,zz}}, \qquad V^{sp,+-} = U^2\frac{\chi_0^{sp,+-}}{1-U\chi_0^{sp,+-}} \quad (9.99)$$

describe coupling to spin density fluctuations and

$$V^{ch} = U^2\frac{\chi_0^{ch}}{1+U\chi_0^{ch}} \quad (9.100)$$

to charge density fluctuations. Here, χ_0^{ch}, $\chi_0^{sp,+-}$ are the irreducible parts of the spin and charge susceptibilities [198]. Note that in the Bethe–Salpeter equation shown diagrammatically in Fig. 9.18 for singlet Cooper–pairing an even number of bubbles and also ladder diagrams occur. In the case of triplet Cooper–pairing the contribution of the ladder diagrams is zero and an odd number bubbles diagrams occur due to Pauli's principle shown in Fig. 9.28. Since the Feynman rules require a (-1) for each loop an extra minus sign enters the gap equation via V_t^{eff} in Eq. (9.49). As described earlier this makes a solution of the gap equation relatively easy.

The magnetism in the ruthenates resulting from the quasiparticles in the t_{2g}–orbital is itinerant and thus the magnetic response is created by the same electrons that form also the Cooper–pairs. Then, for example the irreducible part of the charge susceptibility χ_0^{ch} is defined in terms of the electronic Green's functions (on a square lattice with size N)

$$\chi_0^{ch}(\mathbf{q}) = \frac{1}{N}\sum_{\mathbf{k}} G(\mathbf{k}+\mathbf{q})G(\mathbf{k}), \quad (9.101)$$

where $G(\mathbf{k})$ is the one–electron Green's function (we omit here the band indices for simplicity). The longitudinal and transverse components of the

spin susceptibilities are also calculated in terms of the electronic Green's functions. In contrast to the cuprates in ruthenates $\chi_0^{sp,zz}$ and $\chi_0^{sp,+-}$ are different due to the magnetic anisotropy.

To determine the superconducting transition temperature T_c one must solve the following set of linearized gap equations with eigenvalue $\lambda_\mu(T)$, where μ refers to the band index ($\mu = \alpha, \beta, \gamma$):

$$\lambda_\mu \Delta_{\mu,l,m}(\mathbf{k}, \omega_n) = -\frac{T}{N} \sum_{k',\omega_j,\mu'} V^{(2)}_{\mu,l,m}(\mathbf{k}-\mathbf{k}', \omega_n - \omega_j)\, G_\mu(\mathbf{k}', \omega_j) \times G_{\mu'}(-\mathbf{k}', -\omega_j)\, \Delta_{\mu',l,m}(\mathbf{k}', \omega_j). \tag{9.102}$$

Here, the quantum numbers l and m refer to the orbital and spin state of a Cooper–pair, respectively. Note, T_c is determined from $\lambda_\mu(T_c) = 1$ and the interband coupling will provide a single T_c for all three bands (of course the largest energy gain will be due to the band having the larger density of states).

In order to simplify the discussion we now focus mainly on the γ–band due to its large density of states. In the case of singlet pairing one has $l = 0, 2, ...$ and $m = 0$, and for triplet pairing one gets $l = 1, 3, ...$ and $m = \pm 1$ or $m = 0$. The pairing potential $V^{(2)}$ (taken for singlet or triplet pairing) controls which state gives the lowest energy and determines singlet or triplet Cooper–pairing. Three possibilities may occur:

(a) singlet pairing,
(b) triplet pairing with the total spin $S_z = 0$ of the Cooper–pair wave function,
(c) triplet pairing with the total spin $S_z = \pm 1$.

Note, *a priori* we cannot judge which pairing state is realized in the ruthenates due to the presence of both antiferromagnetic and ferromagnetic fluctuations. Therefore, one has to solve the gap equations for all three possibilities.

Thus, for singlet d–wave pairing we would use for the pairing interaction

$$V_s^{(2)} = \frac{1}{2} V_{sp}^{zz} + V_{sp}^{+-} - \frac{1}{2} V_{ch} \quad . \tag{9.103}$$

leading to the linearized gap equation ($\mu = \gamma, l = 2, m = 0$)

$$\lambda \Delta = -\frac{T}{N} \sum V_s^{(2)} G G \Delta \quad . \tag{9.104}$$

Note, due to magnetic anisotropy we separate the longitudinal and transverse parts of spin fluctuations.

As we will discuss below the magnetic anisotropy that is due to spin–orbit coupling is in particular very important for triplet pairing [158]. We will show

later in section 1.3.5 that it will lift the degeneracy of the three possible triplet states. In order to demonstrate this we separate the gap equation into two parts for $|m| = 1$ and $m = 0$. For triplet pairing with $S_z = \pm 1$ we have

$$V_{tr1}^{(2)} = -\frac{1}{2}V_{sp}^{zz} - \frac{1}{2}V_{ch} \tag{9.105}$$

resulting from the set of diagrams with odd number of bubbles (see Fig. 9.28) yielding

$$\lambda\Delta = -\frac{T}{N}\sum V_{tr1}^{(2)} GG\Delta \quad . \tag{9.106}$$

Finally, for triplet pairing with $S_z = 0$ we get

$$V_{tr0}^{(2)} = \frac{1}{2}\left(V_{sp}^{zz} - V_{sp}^{+-} - V_{ch}\right) \quad , \tag{9.107}$$

and the gap equation

$$\lambda\Delta = -\frac{T}{N}\sum V_{tr0}^{(2)} GG\Delta \quad . \tag{9.108}$$

Obviously, if no magnetic anisotropy would be present, i.e. $\chi^{+-} = 2\chi^{zz}$, one obtains the *same* gap equation for $|m| = 1$ and $m = 0$. Therefore, we safely conclude that the important magnetic anisotropy selects one of the triplet state ($\chi^{zz} > \chi^{+-}$) lifting the degeneracy. As we will discuss in sections 1.3.4 and 1.3.5, ferromagnetic fluctuations favouring triplet pairing are mainly present in χ^{+-} and thus in V_{sp}^{+-}. This will lower the energy for the $m = 0$ triplet state.

Obviously, the magnetic anisotropy described above that enters the Eliashberg–like theory will lead to interesting effects if an external magnetic field h_{ext} is applied. For example, the anisotropy of the ratio $h_{c2}^{\perp}/h_{c2}^{||}$ and its connection to the internal structure of the superconducting order parameter will be discussed in sections 9.3.4 and 9.5.4.

9.3.3 Elementary Excitations in Sr_2RuO_4

The behavior of the elementary excitations in ruthenates is controlled by the spin fluctuations:

$$\omega_{\mathbf{k}} = \epsilon_{\mathbf{k}} + \Sigma(\mathbf{k}, \omega) \quad . \tag{9.109}$$

Here, the self–energy $\Sigma(\mathbf{k}, \omega)$ results mainly from the coupling to spin fluctuations. Clearly, since the anisotropic spin susceptibility $\chi(\mathbf{k}, \omega)$ is the important input for Σ, the self–energy and thus the elementary excitations are affected by the magnetic anisotropy. Note, the spin fluctuations in ruthenates are highly anisotropic. Strong *incommensurate* antiferromagnetic fluctuations

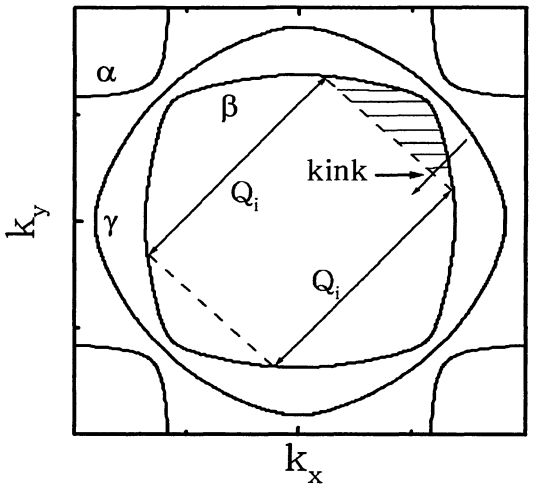

Fig. 9.29. Expected 'kink' structure in Sr_2RuO_4. The Fermi surface in Sr_2RuO_4 consists of three bands. The nesting properties of the $yz(\beta)$–band reveal the formation of two–dimensional incommensurate spin fluctuations at $\mathbf{Q}_i = (2\pi/3, 2\pi/3)$ and $\omega_{sf} \approx 6$meV. The quasiparticles at the β–band reveal a strong renormalization due to scattering by spin fluctuations. Thus, a corresponding 'kink' formation for occupied states below E_F (shaded area) along certain direction in the first BZ as indicated by the arrow may occur

at the wave vector $\mathbf{Q}_i = (2\pi/3, 2\pi/3)$ and $\omega_{sf} = 6$meV are present in Sr_2RuO_4 only in the quasi–one–dimensional $xz(\alpha)$– and $yz(\beta)$–bands. Similar to the cuprates, we expect also the formation of the 'kink' feature due to spin fluctuations as shown in Fig. 9.29. On general grounds a 'kink' structure occurs in the energy dispersion of the β–band below E_F for the quasiparticles that are connected by the corresponding wave vector $\mathbf{Q}_i$ and ω_{sf}. Note, according to the relation

$$\omega_{kink} = \omega_{sf} + \epsilon^{yz}_{\mathbf{k}+\mathbf{Q}_i} \tag{9.110}$$

the 'kink' energy will be smaller than in cuprates due to a lower value of ω_{sf} in the ruthenates.

The quasiparticles in the $xy(\gamma)$–band do not experience the scattering by antiferromagnetic spin fluctuations and interact mainly with weak ferromagnetic fluctuations. Thus, one expects mainly Fermi–liquid–type of behavior for the quasiparticles in the xy–band. Furthermore, due to a small value of the superconducting gap ($\Delta_0 << \omega_{sf}$) there will be no noticeable feedback of superconductivity on the 'kink' feature.

9.3.4 Dynamical Spin Susceptibility: Magnetic Anisotropy

Let us analyze the dynamical spin susceptibility in Sr_2RuO_4. Due to the mixing of the spin and orbital degrees of freedom, the magnetic susceptibility involves also the orbital magnetism which is very anisotropic.

For the calculation of the transverse, χ_l^{+-}, and longitudinal, χ_l^{zz}, components of the spin susceptibility of each band l we use the diagrammatic

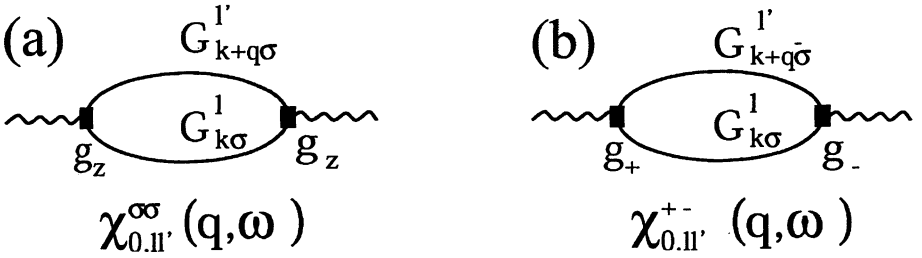

Fig. 9.30. Diagrammatic representation of (a) the longitudinal and (b) the transverse magnetic susceptibility. The full lines represent the electron Green's function with pseudo–spin σ and pseudo–orbital $\tilde{l}$ quantum numbers. The Lande's g–factors are denoted by $g_+ = \tilde{l}_+ + 2s_+$ ($g_- = \tilde{l}_- + 2s_-$) and $g_z = \tilde{l}_z + 2s_z$

representation shown in Fig. 9.30. Note that the Kramers degeneracy is not removed by the spin–orbit coupling, since the latter does not remove the time–reversal symmetry and $G^l_{k+} = G^l_{kz}$. Thus, the anisotropy arises mainly from the calculations of the Lande's g–factors and in particular their orbital parts. The factors $g_z = \tilde{l}_z + 2s_z$ and $g_+ = \tilde{l}_+ + 2s_+$ are calculated using the new quasiparticle states. The latter consist, for example, of xz– and yz–orbitals which in turn are the combinations of the initial orbital states $|2,+1\rangle$ and $|2,-1\rangle$ mixed due to the crystal field. Then, the matrix elements $\langle|l_+|\rangle$ ($\langle|l_-|\rangle$) are zero for the xz– and yz–orbitals while $\langle|l_z|\rangle$ matrix element is not. Therefore, the longitudinal components of the spin susceptibility of the xz– and yz–band get enhanced in comparison to the transverse one. We obtain, for example, for the $|xz\rangle$–states for the transverse susceptibility

$$\chi^{+-}_{0,xz}(\mathbf{q},\omega) = -\frac{4}{N}\sum_{\mathbf{k}}(u_{2\mathbf{k}}u_{2\mathbf{k}+\mathbf{q}} - v_{2\mathbf{k}}v_{2\mathbf{k}+\mathbf{q}})^2\,\frac{f(\epsilon^+_{\mathbf{k}xz}) - f(\epsilon^-_{\mathbf{k}+\mathbf{q}xz})}{\epsilon^+_{\mathbf{k}xz} - \epsilon^-_{\mathbf{k}+\mathbf{q}xz} + \omega + iO^+}\,, \tag{9.111}$$

and for the longitudinal susceptibility

$$\chi^{zz}_{0,xz}(\mathbf{q},\omega) = \chi^{\uparrow}_{xz}(\mathbf{q},\omega) + \chi^{\downarrow}_{xz}(\mathbf{q},\omega)$$

$$= -\frac{2}{N}\sum_{\mathbf{k}}\left[u_{2\mathbf{k}}u_{2\mathbf{k}+\mathbf{q}} + v_{2\mathbf{k}}v_{2\mathbf{k}+\mathbf{q}} + \sqrt{2}(u_{2\mathbf{k}}v_{2\mathbf{k}+\mathbf{q}} + v_{2\mathbf{k}}u_{2\mathbf{k}+\mathbf{q}})\right]^2$$
$$\times \frac{f(\epsilon^{+}_{\mathbf{k}xz}) - f(\epsilon^{+}_{\mathbf{k}+\mathbf{q}xz})}{\epsilon^{+}_{\mathbf{k}xz} - \epsilon^{+}_{\mathbf{k}+\mathbf{q}xz} + \omega + iO^{+}} \quad . \tag{9.112}$$

Here, $f(x)$ is again the Fermi function and $u^2_{\mathbf{k}}$ and $v^2_{\mathbf{k}}$ are the corresponding coherence factors defined in Eqs. (9.94)-(9.95).

For all other orbitals the calculations are similar and straightforward. Note, the magnetic response of the xy–band remains mainly isotropic. This is due to the absence of the nesting features in the xy–band.

Then, one gets within RPA the following expressions for the transverse susceptibility ($\bar{l} = -l$)

$$\chi^{+-}_{RPA,l}(\mathbf{q},\omega) = \frac{\chi^{+-}_{0,l}(\mathbf{q},\omega)}{1 - U\chi^{+-}_{0,l}(\mathbf{q},\omega)} \quad , \tag{9.113}$$

and for the longitudinal susceptibility

$$\chi^{zz}_{RPA,l}(\mathbf{q},\omega) = \frac{\chi^{zz}_{0,l}(\mathbf{q},\omega)}{1 - U\chi^{zz}_{0,l}(\mathbf{q},\omega)} \quad , \tag{9.114}$$

where $\chi^{zz}_{0,l} = \chi^{++}_{0,l} + \chi^{--}_{0,l}$.

These susceptibilities are used in the corresponding pairing interaction for triplet pairing. In order to compare our results with NMR and INS experiments we take

$$\chi^{zz}_{tot} = \sum_{l}\chi^{zz}_{RPA,l} \tag{9.115}$$

and

$$\chi^{+-}_{tot} = \sum_{l}\chi^{+-}_{RPA,l} \quad . \tag{9.116}$$

9.3.5 Gap Equation: Triplet Pairing and Symmetry of the Superconducting Order Parameter

The interesting question in the ruthenates is why does triplet Cooper–pairing with the possible pair states $\psi^{\pm}$

$$|\uparrow\uparrow\rangle \quad , \quad m_z = +1$$
$$|\downarrow\downarrow\rangle \quad , \quad m_z = -1$$

and ψ^0

$$\frac{1}{\sqrt{2}}(|\uparrow\downarrow + |\downarrow\uparrow\rangle) \quad , \quad m_z = 0 \tag{9.117}$$

take place in the presence of strong incommensurate antiferromagnetic spin fluctuations at $\mathbf{Q}_i = (2\pi/3, 2\pi/3)$ originating from the xz– and yz–bands and weaker ferromagnetic fluctuations arising from the xy–band. For the interplay of the antiferromagnetic and ferromagnetic–like spin excitations the magnetic anisotropy, $\chi^{xx}(\mathbf{Q}_i) > \chi^{\pm}(\mathbf{Q}_i)$, is very significant. This anisotropy will also lift the degeneracy of the three possible triplet states and favor for the Cooper–pairs the state

$$\psi^0 \sim \frac{1}{\sqrt{2}}(|\uparrow\downarrow + |\downarrow\uparrow\rangle) \quad .$$

Note, the magnetic anisotropy is caused by spin orbit coupling. The above three triplet Cooper–pair states with magnetic quantum numbers $m_z = \pm 1, 0$ result from the transverse and longitudinal spin excitations. Therefore, the important normal–state result $\chi^{zz}(\mathbf{Q}_i) > \chi^{+-}(\mathbf{Q}_i)$ already suggests lifting of the triplet states degeneracy and the realization of the $m_z = 0$ state $\frac{1}{\sqrt{2}}(|\uparrow\downarrow + |\downarrow\uparrow\rangle)$.

In the case of a dominating γ–band, with a large density of states, it follows almost directly from the Fermi surface topology illustrated in Fig. 9.31 that triplet Cooper–pairing mediated by ferromagnetic excitations occurs.

Of course, the gap equation determines the occurence of the triplet state with $m_z = 0$. Note that the order parameter for triplet Cooper–pairing can be written in the form

$$\Delta_{\mathbf{k}} = \sum_{\mu} d_{\mu}(\mathbf{k})(\sigma_{\mu} i\sigma_2) = \begin{pmatrix} -d_x + id_y & d_z \\ d_z & d_x + id_y \end{pmatrix}. \tag{9.118}$$

Again as in the cuprates all chosen symmetries must be irreducible representations of the D_{4h} crystallographic point group symmetry, since the crystal field potential is very strong in ruthenates as well as in cuprates. The full set of them was found by Sigrist and Rice [146]. Experimentally it is confirmed that in Sr_2RuO_4 (close to T_c) only $d_z = \hat{\mathbf{z}}$ component of the superconducting order parameter is present while $d_x = \hat{\mathbf{x}}$ and $d_y = \hat{\mathbf{y}}$ component are strongly suppressed [66].

For a discussion of the symmetry of the order parameter it is instructive to consider the Fermi surface topology and the structure of $\chi(\mathbf{q})$. Thus, in order to investigate triplet pairing in Sr_2RuO_4 in more detail, we show in Fig. 9.31 its corresponding Fermi surface topology obtained from the three–band Hubbard Hamiltonian discussed earlier in this chapter. However, for simplicity we discuss here only the γ–band which has a high density of states. The effects due to the other bands (α and β) will be analyzed in detail later.

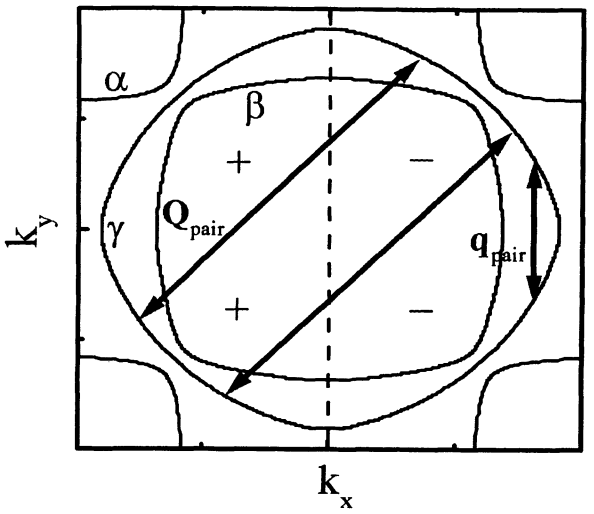

Fig. 9.31. Calculated Fermi surface (FS) topology for Sr_2RuO_4 and symmetry analysis of the superconducting order parameter Δ in the first Brillouin zone. The real part of a p–wave order parameter has the node along k_x=0. The +(−) and the dashed lines refer to the signs of the momentum dependent order parameter of Δ. α, β, and γ denote the FS of the corresponding (hybridized) bands. The Cooper–pairing wave vectors $\mathbf{Q}_i$ and $\mathbf{q}_i$ refer to maxima in the spin susceptibility and provide the main contribution to the pairing instability

For the moment and for simplicity let us discuss only the γ–band in order to study the differences between Sr_2RuO_4 and cuprates.

Sr_2RuO_4 shows a two–dimensional electronic structure which indicates that the Cooper–pairing mainly occurs in the RuO_2–plane. Thus, we discuss first the superconductivity in the RuO_2–plane and then analyze what happens along c–direction.

A closer inspection of Eq. (9.50) shows that $|\Delta_p|^2$ has no nodes. However, Re Δ_p (also Im Δ_p) indeed has a nodal line also displayed in Fig. 9.31. This has important consequences if strong nesting would be present. Then, f–wave symmetry of the superconducting order parameter would win over p–symmetry. This can be seen as follows. Note, the summation over $\mathbf{k}'$ in the first BZ is dominated by the contributions due to $\mathbf{Q}_{pair}$ and the one due to a smaller wave vector $\mathbf{q}_{pair}$ (see $\chi(\mathbf{q},\omega)$). Thus, we obtain approximately for the γ–band contribution (angular quantum number $l = f$ or p)

$$\Delta_l(\mathbf{k}) \approx \sum_i \frac{V_t^{eff}(\mathbf{Q}_i)}{2\epsilon^{\gamma}_{\mathbf{k}+\mathbf{Q}_i}} \Delta_l(\mathbf{k}+\mathbf{Q}_i) + \sum_i \frac{V_t^{eff}(\mathbf{q}_i)}{2\epsilon^{\gamma}_{\mathbf{k}+\mathbf{q}_i}} \Delta_l(\mathbf{k}+\mathbf{q}_i) \quad , \quad (9.119)$$

where the sum is over all contributions due to $\mathbf{Q}_i$ and $\mathbf{q}_{pair}$. The wave vectors $\mathbf{Q}_{pair}$ bridge portions of the FS where Re Δ_p has the opposite sign. Since the

smaller wave vector $\mathbf{q}_{pair}$ bridges areas on the Fermi surface with same *and* opposite signs, its total contributions is almost zero, i.e.

$$\sum_i \frac{V_t^{eff}(\mathbf{q}_i)}{2\epsilon^{\gamma}_{\mathbf{k}+\mathbf{q}_i}} \Delta_l(\mathbf{k}+\mathbf{q}_i) \approx 0 \quad . \tag{9.120}$$

Thus, we find a gap equation where Δ_l is expected to change its sign for an attractive interaction and dominating $\mathbf{Q}_i$ transitions. However, this is not possible! In other words, if the corresponding pairing interaction involves strong nesting similar to cuprates, i.e. a peak of χ_{RPA} at $q \approx \mathbf{Q}_{pair}$, Cooper–pairing and a p–symmetry solution of Eq. (9.50) would not be possible due to $V_t^{eff} < 0$. Nesting properties would suppress p–wave and favor f–wave, and then

$$\Delta_f(\mathbf{k}) = \Delta_0 \hat{\mathbf{z}} (\cos k_x - \cos k_y)(\sin k_x + i \sin k_y) \quad . \tag{9.121}$$

Like the $d_{x^2-y^2}$–wave order parameter in cuprates the f–wave symmetry order parameter has also nodes along the diagonals. Note, $\tilde{\mathbf{z}}$ indicates that only d_z component of the superconducting order parameter is present.

For weaker nesting and for ferromagnetic spin fluctuations one expects that p–wave symmetry wins over f–wave symmetry triplet Cooper–pairing. Obviously, the magnetic anisotropy observed in Sr_2RuO_4 is important for this.

The odd parity of the superconducting order parameter and strong reduction of T_c by non–magnetic impurities suggests that electron–phonon interaction does not cause superconductivity in Sr_2RuO_4. Note, the recently observed negative isotope effect ($\alpha = -0.15$) indicates the complicated dependence of the isotope mass from interaction parameters [165].

One expects on general grounds that the singlet Cooper–pairing will not be realized in the ruthenates. The simple reason behind this is that the antiferromagnetic fluctuations favoring singlet pairing with $d_{x^2-y^2}$–wave symmetry of the superconducting order parameter originate from the quasi–one dimensional xz- and yz-bands. However, the xy-band with only weak ferromagnetic fluctuations has a much larger density of states at the Fermi level. This indicates its large contribution to superconductivity. Therefore, the xy–band will not be unstable with respect to the singlet Cooper–pairing. This is illustrated in Fig. 9.31. Note, we get for $d_{x^2-y^2}$–wave symmetry a change of sign of the order parameter upon crossing the diagonals of the BZ. For the singlet Cooper–pairing the wave vectors around $\mathbf{Q}_i$ connecting areas (+) and (-) contribute constructively to the pairing. Contributions due to $\mathbf{q}_i$ and the background connecting areas with the same sign subtract from the pairing (see Fig. 9.31 with nodes at the diagonals). Therefore, we get that the four contributions due to $\mathbf{q}_i$ in the xy-band do not allow to have $d_{x^2-y^2}$–wave symmetry in the xy–band. Despite the pair–building contribution due to $\mathbf{Q}_i$ one gets that the eigenvalue of the $d_{x^2-y^2}$–wave symmetry in the xy–band is

smaller than for the $f_{x^2-y^2}$–wave symmetry. This is due to the large contribution from $\mathbf{Q}_i$ to the cross–terms for the triplet pairing which are absent for the singlet pairing. For d_{xy}–symmetry where the nodes are along $(\pi,0)$ and $(0,\pi)$ directions we argue similarly. Thus, we may exclude this symmetry.

What is the situation between the RuO_2–planes? First due to a weak dispersion the electronic bands along c–direction one may expect the weak dispersion of the superconducting p–wave gap in a form:

$$\Delta(\mathbf{k}) = \Delta_0 \hat{\mathbf{z}}(\sin k_x a \pm i \sin k_y a)(\cos k_z c + const) \quad . \tag{9.122}$$

Note, that due to the *cosine* function the superconducting gap will have a node for the $k_z = \pi/2c$. On the other hand, the formation of the node in the superconducting order parameter usually reflects the underlying structure of the pairing potential. In our case this is a spin susceptibility which becomes anisotropic due to spin–orbit coupling. In particular, the antiferromagnetic spin fluctuations are polarized along c–direction, while ferromagnetic fluctuations are mainly present in the RuO_2–plane. Then, the polarized antiferromagnetic spin fluctuations could be one of the reason for the node formation away from the RuO_2–plane in Sr_2RuO_4. This we will discuss later.

What happens if an external magnetic field is applied? As in superfluid ^{3}He there exists an interesting effect concerning the possible change of the orientation of the unit vector $d_z = \hat{\mathbf{z}}$ of the superconducting order parameter. In general, the spin susceptibility is a tensor in spin space with principal axes along the preferred directions. Therefore the magnetic energy density

$$f_h = -\frac{1}{2}\sum_{\mu\nu} \chi_{\mu\nu} h_\mu h_\nu \tag{9.123}$$

depends on the orientation of the susceptibility tensor and hence on the order parameter itself. As we have discussed in the Introduction the spin susceptibility of Sr_2RuO_4 in the superconducting state behaves differently for different orientation of the magnetic field. For example for $\mathbf{h} \perp \mathbf{d}$ (i.e an external magnetic field is applied along the a– or b–direction) the susceptibility is unchanged with respect to its normal state value χ_N [209]. On the contrary when $\mathbf{h}||\mathbf{d}$ the susceptibility becomes gapped which temperature dependence is described by the so–called Yoshida function [209]. Therefore, the spin susceptibility in Sr_2RuO_4 depends strongly on the relative orientation of $\mathbf{d}$ and $\mathbf{h}$. In its general form the susceptibility tensor reads

$$\chi_{\mu\nu} = \chi_N^0 \{\delta_{\mu\nu} - \hat{d_\mu}\hat{d_\nu}\,[1 - Y_0(T)]\}, \tag{9.124}$$

where $Y_0(T) = -\int_{-\infty}^{\infty} dE_{\mathbf{k}} \frac{df_{\mathbf{k}}}{dE_{\mathbf{k}}}$ is Yosida function.

One finds that for the magnetic field applied along c–direction, the susceptibility and consequently the magnetic energy gets a contribution which tends to orient $\mathbf{d}$ perpendicular to the magnetic field

$$\Delta f_h = \frac{1}{2}\Delta\chi(\mathbf{d}\cdot\mathbf{h})^2 \,, \tag{9.125}$$

where $\Delta\chi = \chi_N^0(1 - Y_0(T))$. It means that for a relatively large magnetic field applied along c–direction the significant d_x and d_y components in the superconducting order parameter in Sr_2RuO_4 can be induced. This possibility is already known from superfluid ^{3}He. Of course, as in ^{3}He, this effect is relatively small but observable. This is a subject of further experimental studies.

In the following we present results for important properties of the superconducting state. First we discuss superconductivity of cuprates, then that of ruthenates.

9.4 Results for Hole– and Electron–Doped Cuprates

We present results for key properties of cuprate superconductivity using as a model the Hubbard Hamiltonian and Eliashberg–like theory and assuming Cooper–pairing due to spin fluctuations. Important input for the calculations is the electronic band structure. Comparison of the calculations with experiments should further justify the validity of our theory. We find $d_{x^2-y^2}$–wave superconductivity for both hole– and electron–doped cuprates. The elementary excitations and the doping dependent phase diagram are central results.

9.4.1 Bare Electronic Structure

In Fig. 9.32 we present results for the energy dispersion along the route $(0,0) \rightarrow (\pi,0) \rightarrow (\pi\pi) \rightarrow (0,0)$ of the first Brillouin zone for hole– and electron–doped cuprates at optimal doping. We refer as a typical example to $La_{2-x}Sr_xCuO_4$ and $Nd_{2-x}Ce_xCuO_4$. It is known that the position of the flat bands with respect to the Fermi level is described by the ratio of t'/t. Using the fact that in hole–doped cuprates the flat bands lie close to the Fermi energy while in the electron–doped ones they lie much lower this ratio is expected to be small in hole–doped cuprates, while in electron–doped cuprates we approximate $t'/t = -0.3$ in order to describe the experimental results.

The corresponding densities of states are shown in Fig. 9.33. The flat bands reflecting the so–called van–Hove singularity are a common feature of the cuprates having a two–dimensional square lattice. Note again that the bands are at different energies in hole– and electron–doped cuprates. Due to the fact that in hole–doped cuprates the van–Hove singularity lies near the Fermi energy these are closer to an antiferromagnetic instability than the electron–doped ones. Therefore, antiferromagnetic spin fluctuations in the hole–doped cuprates are expected to be much stronger due to the nesting. As a consequence more phase space is available for Cooper–pairing.

Note, this does not contradict the experimental data which indicate a large doping range of antiferromagnetism in electron–doped cuprates. As was shown earlier [167,168] the small doping range of antiferromagnetism in hole–doped cuprates is due to spin frustration that arises from holes at the oxygen

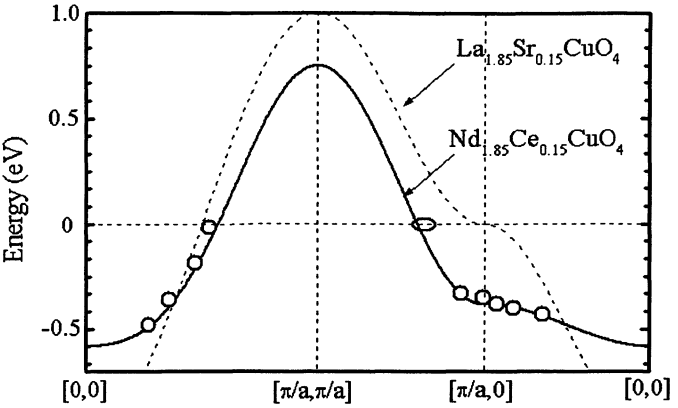

Fig. 9.32. Calculated energy dispersion for the hole– and electron–doped cuprates at optimal doping concentration. We use t=250meV and t′=0 for the hole–doped cuprates (dashed curve) and t=128meV and t′=-0.3 for the electron–doped cuprates (solid curve). The experimental data (open symbols) taken from Ref. [166]. Note, the position of the flat bands in the electron–doped cuprates is 300meV below E_F. On the other hand, in most of the hole–doped cuprates the van–Hove singularity lying close to the Fermi level

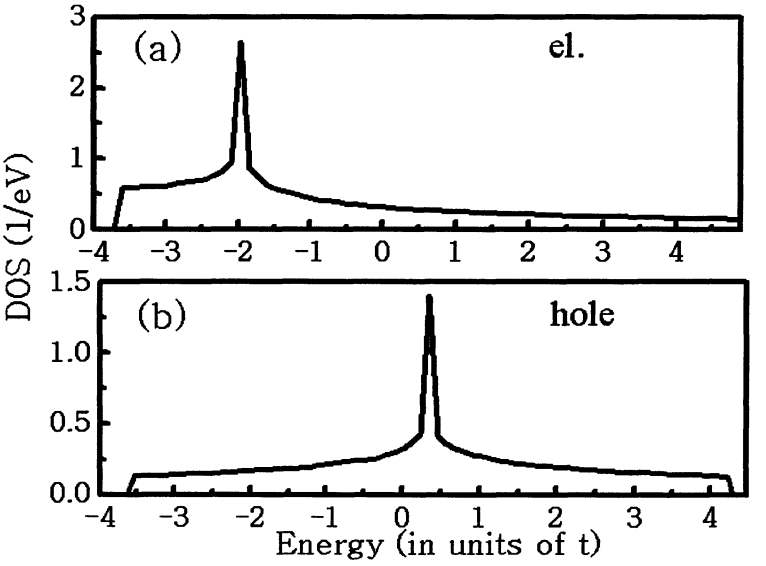

Fig. 9.33. Results for the density of states in (a) electron–doped and (b) hole–doped cuprates using the energy dispersion shown in Fig. 9.32. The so–called van–Hove singularity that originates from the flat part of the conduction bands lies in hole–doped cuprates much closer to the Fermi energy ($\epsilon_F = 0$) than in electron–doped ones

sites. In contrast in the electron–doped cuprates only a dilution of the Cu–spins takes place and thus as a consequence antiferromagnetism occurs over larger doping range.

The input (material–dependent) parameters of the theory will play an important role in our calculations and will explain the observed asymmetry between electron– and hole–doped cuprates. Moreover, since the topology of the Fermi surface and the corresponding position of the flat bands change with doping we also expect the characteristic changes in the behavior of hole– and electron–doped cuprates with doping.

We would like also to note that many of the hole–doped cuprates contain two CuO_2–planes per unit cell and that this requires the inclusion of bilayer effects into our theory. We will study this later, but would like to stress that the main features that will be obtained within a one–band calculation will describe already the main experimental facts of the cuprates.

9.4.2 Elementary Excitations

Let us first discuss the elementary excitations. The results for the spectral density due to the scattering of the carriers by antiferromagnetic spin fluctuations are expected to exhibit fundamental behavior. As we have shown the dispersion of the carriers will be modified by the self–energy, Σ, arising from the coupling of the quasiparticles to antiferromagnetic spin fluctuations:

$$\omega_{\mathbf{k}} = \epsilon_{\mathbf{k}} + \mathrm{Re}\Sigma(\mathbf{k}, \omega).$$

Note, the renormalization of $\epsilon_{\mathbf{k}}$ by $\Sigma(\mathbf{k}, \omega)$ will be characteristically anisotropic.

1. Nodal direction

We start the discussion analyzing the spectral density of hole–doped superconductors in the normal state. The spectral density reveals the elementary excitations and in particular the renormalized energy dispersion. First, we present our results for the spectral density along the nodal $(0,0) \rightarrow (\pi, \pi)$ direction in the first BZ.

In Fig. 9.34 we show the calculated spectral density $N(\mathbf{k}, \omega)$, i.e. the local density of states, as a function of frequency and momentum $\mathbf{k} - \mathbf{k}_F$. The peak positions correspond to the renormalized energy dispersion. Due to coupling of holes to antiferromagnetic spin fluctuations the quasiparticle dispersion changes its slope and shows a pronounced kink feature at the energy $\omega_{kink} \approx 75 \pm 15\mathrm{meV}$.

How can one understand the kink feature in a simple way? At the first glance the occurrence of a kink in the nodal direction seems to be surprising, since the main interaction of the carriers with spin fluctuations occurs at the hot spots. Note, the kink feature is present along the diagonal of the BZ close to the cold spots. However, away from the Fermi level, but close to it (along $(0,0) \rightarrow (\pi, \pi)$), the quasiparticles couple strongly to spin fluctuations. Most

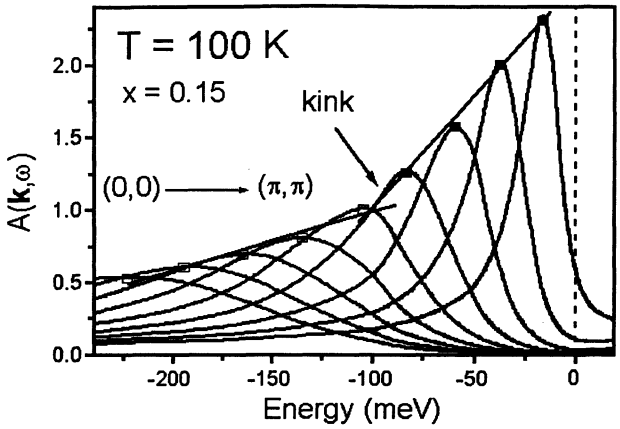

Fig. 9.34. Calculated spectral density $A(\mathbf{k},\omega)$ in the normal state along the nodal $(0,0) \rightarrow (\pi,\pi)$ direction (from left to right) as a function of frequency in the first Brillouin zone (BZ). The peak positions (connected by the solid line to guide the eye) refer to the renormalized energy dispersion $\omega_{\mathbf{k}}$. One clearly sees the kink structure at an energy approximately $\omega_{kink} = 75 \pm 15$meV that results from coupling of the quasiparticles to spin fluctuations

importantly, as follows from Fig. 9.20 the largest scattering will occur at values of $\mathbf{k} - \mathbf{k}_F = \mathbf{Q}$ and $\omega = \omega_{sf}$. From Eq. (9.168) follows

$$\Sigma(\mathbf{k}, i\omega_n) = -T^2 \sum_{\omega_m,\nu_m} \sum_{\mathbf{k}',\mathbf{q}} \tilde{\tau}_0 G(\mathbf{k}-\mathbf{k}', i\omega_n - i\nu_m)\tilde{\tau}_0 U^2 \times \frac{1}{2}\mathrm{Tr}\left[\tilde{\tau}_0 G(\mathbf{k}+\mathbf{q}, i\omega_m + i\nu_m)\tilde{\tau}_0 G(\mathbf{q}, i\omega_m)\right] \quad . \tag{9.126}$$

Then approximating the Green's function

$$G(\mathbf{k}, i\omega_n) \approx G_0(\mathbf{k}, i\omega_m) = \frac{i\omega_n \tilde{\tau}_0 + \epsilon_{\mathbf{k}}\tilde{\tau}_3 - \phi_{\mathbf{k}}\tilde{\tau}_1}{(i\omega_n)^2 - E_{\mathbf{k}}^2} \quad , \tag{9.127}$$

one gets after some algebra with $E_{\mathbf{k}}^2 = \epsilon_{\mathbf{k}}^2 + \phi_{\mathbf{k}}^2$ on the real axis

$$\Sigma(\mathbf{k},\omega) \approx -\frac{U^2}{4} \sum_{\mathbf{k}'} \int_0^\infty d\omega' \frac{\mathrm{Im}\chi_{\mathrm{RPA}}(\mathbf{k}-\mathbf{k}', \omega')}{\omega - \omega' - E_{\mathbf{k}'}} \times \left[\coth\left(\frac{\omega'}{2T}\right) - \tanh\left(\frac{\omega'-\omega}{2T}\right)\right] \quad . \tag{9.128}$$

The imaginary part of the spin susceptibility is approximately given by the Ornstein–Zernicke expression which has a peak structure at the wave vector $\mathbf{q}$ and frequency $\omega = \omega_{sf}$. Furthermore, the self–energy is mainly frequency–dependent, while the bare dispersion of the carriers is not. Then, already in

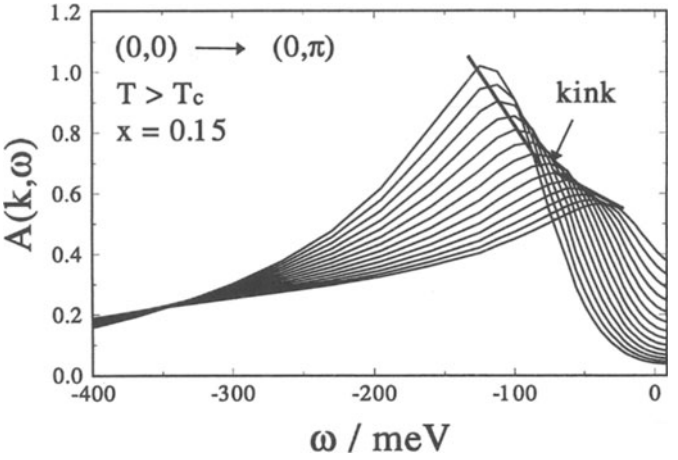

Fig. 9.35. Spectral density $A(\mathbf{k},\omega)$ as a function of frequency along the $(0,0) \rightarrow (0,\pi)$ direction of the first BZ in the normal state calculated from the generalized Eliashberg equations. Again, the peak positions reveal the renormalized energy dispersion $\omega_{\mathbf{k}}$. A kink occurs at similar energy as in the nodal direction. Due to inelastic scattering of holes by spin fluctuations close to $(0,\pi)$, $A(\mathbf{k},\omega)$ becomes also broader. Note that, in contrast to the nodal direction, one does not cross the Fermi level in the $(0,0) \rightarrow (0,\pi)$ direction. Instead, one reaches the flat part of the tight–binding band

the normal state the self–energy $\Sigma(\mathbf{k},\omega)$ has a maximum reflecting a corresponding maximum of Im χ at $\mathbf{q} \approx \mathbf{Q}$ and $\omega' \approx \omega_{sf}$. Then, the kink position follows from the pole of the denominator of Eq. (9.128). This leads to the 'kink condition'

$$\omega_{kink} \approx E_{\mathbf{k}-\mathbf{Q}} + \omega_{sf}(x) \quad . \tag{9.129}$$

Note, this gives an estimate of the position of the kink and explains the behavior of the spectral density $A(\mathbf{k},\omega)$ shown in Fig. 9.34. Furthermore, since the superconducting gap is zero for $\omega = 0$, but not for $\omega = \omega_{sf}$, the kink feature along the nodal direction $(0,0) \rightarrow (\pi,\pi)$ will change only slightly below T_c.

2. $(0,0) \longrightarrow (0,\pi)$ direction

In order to see whether the kink feature is present in other directions of the Brillouin Zone, we show in Fig. 9.35 the evolution of the spectral density along the $(0,0) \rightarrow (0,\pi)$ direction. Despite the fact that along this direction we do not cross the Fermi level, the kink feature is still present and is found at an energy similar to the one for the nodal $(0,0) \rightarrow (\pi,\pi)$ direction. This indicates that the kink feature occurs not only along the $(0,0) \rightarrow (\pi,\pi)$ direction. Instead, the kink is characteristic for all direction where $\mathbf{k}-\mathbf{k}_F \simeq \mathbf{Q}$ and $\omega \simeq \omega_{sf}$. Also below T_c we find that the kink feature is present in

the $(0,0) \rightarrow (0,\pi)$ direction (not shown). Note, that our results are in fair agreement with experimental data [56].

3. Antinodal direction

In Fig. 9.36(a) we show our results for $N(\mathbf{k},\omega)$ along the $(\pi,0) \rightarrow (\pi,\pi)$ route, i.e. the antinodal direction, of the first BZ in the normal state. Note, that the spectral density at the $(0,\pi)$ point is broader than at the antinodal point due to stronger coupling to spin excitations peaked at $\mathbf{q} = \mathbf{Q} = (\pi,\pi)$ as discussed in Fig. 9.20. Clearly, no kink is present.

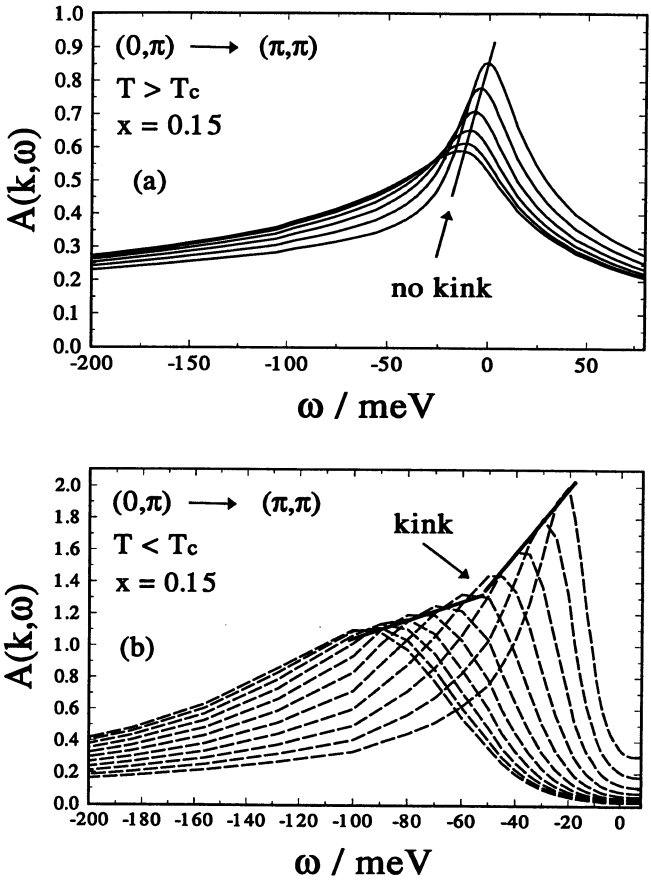

Fig. 9.36. Calculated spectral density $A(\mathbf{k},\omega)$ along the antinodal $(\pi,0) \rightarrow (\pi,\pi)$ direction in the first BZ as a function of frequency in the normal (a) and superconducting (b) state. Due to the flat band close to the Fermi level the spectral density shows no kink structure in the normal state. Below T_c the superconducting gap $\phi(\omega)$ opens yielding a kink structure in the spectral density that occurs at the energies $\omega_{kink} \approx 50 \pm 10$ meV for optimal doping

The absence of a kink structure can be explained with the flat structure of the CuO_2–plane around the M point (see Fig. 9.32) and with the fact that the wavevector is not large enough to bridge antinodal points in the BZ. Simply speaking, for a flat band the frequency dependence of Σ in Eq. (9.32) does not play a significant role and therefore no change of the velocity and no kink structure is present.

What does happen in the superconducting state? Below T_c the superconducting gap $\phi(\mathbf{k},\omega)$ opens rapidly for decreasing temperature T and becomes maximal in momentum space around the M point reflecting the momentum dependence of the effective pairing interaction (see Eq. (9.168)). In addition, due to the frequency dependence of the gap the flat band around M disappears.

In Fig. 9.36(b) we show results for $A(\mathbf{k},\omega)$ at a temperature $T = 0.5T_c$ where the superconducting gap has opened. A kink structure around $\omega_{kink} \approx 50 \pm 10$ meV is present reflecting the magnitude of ϕ. Hence, in the $(\pi,0) \rightarrow (\pi,\pi)$ direction this kink feature is only present below T_c and connected to the feedback effect of ϕ on the elementary excitations. We will show later that this feedback is also important for the resonance peak seen in INS. Note, that the superconducting gap $\phi(\mathbf{k},\omega)$ is calculated self–consistently in our theory and reflecting the underlying spin fluctuations which dominate the pairing potential V_{eff}. Therefore, the occurrence of a kink structure *only* below T_c in the antinodal direction is a *direct* fingerprint of the spin excitation spectrum. Furthermore, as we will discuss below, Im $\chi(\mathbf{Q},\omega)$ entering Eq. (9.128) is peaked at the resonance frequency ω_{res} (roughly at $\omega_{sf} + \Delta$). Therefore, the kink condition is given by

$$\omega_{kink} \approx E_{\mathbf{k}-\mathbf{Q}} + \omega_{res}(x) \quad . \tag{9.130}$$

In Fig. 9.37(a) the frequency dependence of Re $\Sigma(\mathbf{k}_a,\omega)$ in the normal and superconducting state at the antinodal point $\mathbf{k} = \mathbf{k}_a$ is shown. Due to the occurrence of the resonance feature in Im $\chi(\mathbf{Q},\omega)$ and the related feedback of the superconducting gap $\phi(\omega)$, Re Σ shows a pronounced structure below T_c at energies of about $\omega_{res} + \Delta_0$. Also the corresponding imaginary part Im $\Sigma(\mathbf{k} = \mathbf{k}_a,\omega)$ shows a peak below T_c (see Fig. 9.37(b)). This pronounced behavior is responsible for the kink formation along $(\pi,0) \rightarrow (\pi,\pi)$ direction in the BZ.

Therefore, while the kink features are present along $(0,0) \rightarrow (\pi,\pi)$ and $(\pi,0) \rightarrow (\pi,\pi)$ directions in the superconducting state of hole–doped cuprates, their nature is qualitatively different. Along the nodal direction the superconducting gap is zero (for $\omega = 0$) and thus the feedback effect of superconductivity on the elementary and spin excitations is small. Therefore, ω_{sf} determines mainly the kink feature. On the other hand, along the antinodal direction the gap is maximal and yields a strong feedback of superconductivity on χ. Thus, in the superconducting state ω_{res} and Δ_0 yield the kink structure along $(\pi,0) \rightarrow (\pi,\pi)$ direction that is not present in the normal state.

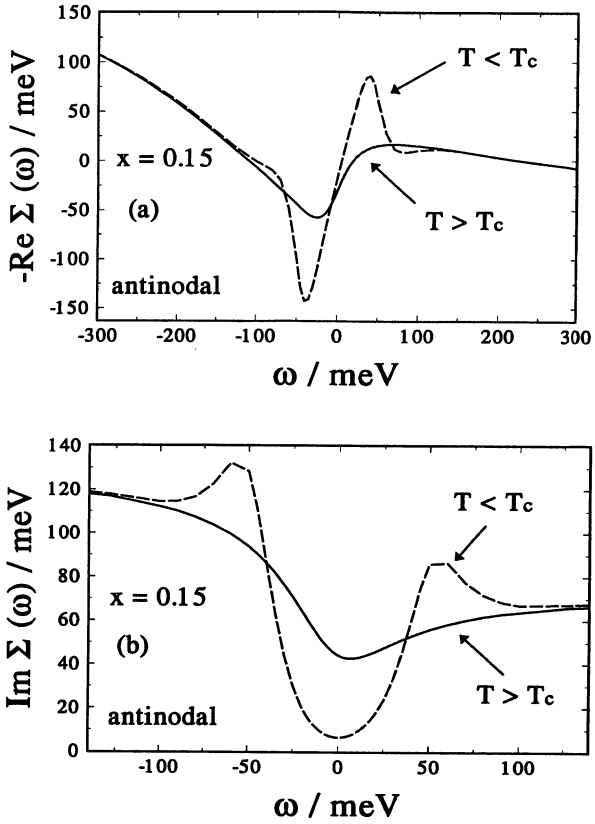

Fig. 9.37. (a) Calculated frequency dependence of the self-energy Re $\Sigma(\mathbf{k}_a, \omega)$ at the antinodal point $\mathbf{k}_a$ of the first BZ in the normal (solid curve) and superconducting state (dashed curve). Due to the feedback effect of the superconducting gap $\phi(\omega)$, a peak (dip) occurs for $\omega > 0$ ($\omega < 0$) which roughly defines the position of the kink structure. (b) The corresponding imaginary part at the antinodal point Im $\Sigma(\mathbf{k} = \mathbf{k}_a, \omega)$ is shown. Again, due to the feedback effect of $\phi(\omega)$, a maximum occurs below T_c. Note, that both Re Σ and Im Σ are not fully antisymmetric (symmetric) with respect to ω at optimum doping $x = 0.15$

Doping dependence of the elementary excitations and their energy renormalization

The different reasons for the kink structures in hole–doped cuprates along different directions in the first BZ will be also reflected in their doping dependence. The results we have shown so far were for optimal doping concentration $x = 0.15$. This refers to a band filling of $n = 0.85$. Note, the superconducting transition temperature T_c behaves differently in the overdoped (OD) and

underdoped (UD) regime:

$$T_c \propto \Delta(T \to 0), \quad \text{OD-regime}$$
$$T_c \propto n_s(T \to 0), \quad \text{UD-regime} \quad ,$$

where n_s is the superfluid density calculated self–consistently from the generalized Eliashberg equations.

In the antinodal $(0,\pi) \to (\pi,\pi)$ direction the kink is only present below T_c due to the feedback of $\phi(\omega)$. In the OD case the gap $\phi(\omega)$ decreases reflecting a mean–field–like behavior. Thus, the energy where the kink occurs must decrease with overdoping:

$$\omega_{kink}(x) \propto \Delta_0(x) \quad . \tag{9.131}$$

This behavior is indeed observed by Dessau and co–workers [230]. Note, the above argument remains true also in the strongly OD case where no resonance peak in Im $\chi(\mathbf{Q},\omega)$ occurs because the feedback effect of $\phi(\omega)$ should always be present.

Regarding the kink along the nodal $(0,0) \to (\pi,\pi)$ direction we note the following: ω_{sf} increases with increasing doping from underdoped to overdoped cuprates. Since ω_{sf} determines the kink position along $(0,0) \to (\pi,\pi)$ direction we expect

$$\omega_{kink}(x) \propto \omega_{sf}(x). \quad . \tag{9.132}$$

This is in qualitative agreement with experimental data [169] (for underdoped regime and optimally doped superconductors). On the other hand, the spectral weight of Im $\chi(\mathbf{Q},\omega)$ decreases drastically with overdoping. Therefore, the coupling of the quasiparticles to spin fluctuations is getting much weaker in the OD case. These two competing effects seem responsible for the non–monotonic and weak doping dependence of the kink position in the nodal direction [230].

Elementary excitations in electron–doped cuprate

Another interesting observation is the asymmetric behavior of hole and electron–doped cuprates. Note, that no kink feature has been reported in the electron–doped cuprates [59]. It is believed that the electron–phonon coupling is much more pronounced in electron–doped cuprates than in hole–doped ones. This is reflected, for example, by the behavior of the resistivity $\rho \propto T^2$ in the normal state at optimum doping and by the transition between $d_{x^2-y^2}$–wave symmetry of the superconducting gap towards anisotropic s–wave as it has been observed in several experiments [60]. Simply speaking, the spin fluctuations in electron–doped cuprates are weaker than in the hole–doped ones yielding a smaller T_c and a smaller superconducting gap [187]. Thus, no kink is present in the nodal direction and also no kink occurs in the $(0,\pi) \to (\pi,\pi)$ direction below T_c. This is related to the fact that the flat band around $(0,\pi)$ lies in electron–doped cuprates well below the Fermi level and, therefore, it cannot be softened due to $\phi(\omega)$.

Summary
Regarding the superconducting state note that in the hole–doped cuprates a strong renormalization of the spin fluctuation spectra occurs due to the feedback effect of superconductivity and that $\Delta_0 \sim \omega_{sf}$ leading to a resonance peak at $\omega = \omega_{res}$. In electron–doped cuprates, the spin excitations do not obey the resonant condition. Thus, only a rearrangement of spectral weight occurs below T_c, but no resonance peak. Therefore, the kink feature is intimately connected with the resonance peak. There is only a small feedback of superconductivity below T_c on Im χ in the electron–doped cuprates due to $\omega_{sf} >> \Delta_0$. Thus, we find also no kink feature in the superconducting state of electron–doped cuprates in the antinodal direction.

Anisotropic scattering rates

The behavior of the self–energy $\Sigma(\mathbf{k}, \omega)$ implies of course corresponding anisotropy for the scattering rate of the quasiparticles and for the conductivity. We discuss now the anisotropy of the scattering rate $\tau^{-1}(\omega)$ of hole–doped cuprates at different points on the Fermi surface.

In Fig. 9.38 we show our results for $\tau^{-1}(\omega)$ at the antinodal point and the nodal point, respectively, for optimal doping (a) and for the overdoped case (b) for various temperatures. In Fig. 9.38(a) one clearly sees that the scattering rate is very anisotropic on the Fermi surface reflecting the anisotropy of the coupling of elementary excitations to spin fluctuations. In particular, $\tau^{-1}(\omega)$ in the normal state is almost three times larger at the antinodal point than at the nodal point. This agrees with recent ARPES experiments [189]. Furthermore, we find that for $\omega \to 0$,

$$\text{Im } \Sigma \propto \omega.$$

This demonstrates non–Fermi liquid behavior in the underdoped and optimally hole–doped cuprates.

In the overdoped cuprates the anisotropy between nodal and antinodal points is strongly reduced and disappears almost for $\omega \to 0$. Most importantly the system then behaves more Fermi–liquid–like. The latter is seen from Fig. 9.38(b) where one observes a crossover from the Im $\Sigma \propto \omega$ to the Im $\Sigma \propto \omega^2$ behavior. This is also in agreement with experimental observation [190].

Below T_c at the antinodal point $\tau^{-1}(\omega)$ for optimal doped reveals a strong feedback at energies

$$\omega \sim \omega_{res} + \Delta_0 \quad ,$$

where ω_{res} refers to the resonant frequency of the spin fluctuations. Note, at the nodal point the effect of superconductivity is rather weak due to the node of the $d_{x^2-y^2}$wave symmetry of the superconducting order parameter.

In the overdoped cuprates below T_c both at the nodal and antinodal points no structure in the frequency dependence of $\tau^{-1}(\omega)$ occurs. The latter is also clear, since spin fluctuations spectrum weakens and does not reveal resonant

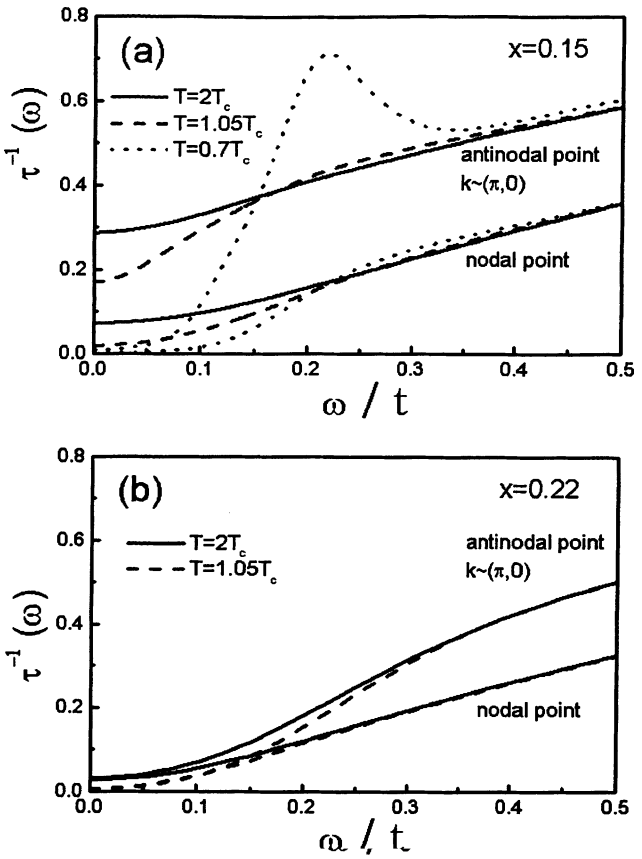

Fig. 9.38. Scattering rate $\tau^{-1}(\omega)$ of optimally (a) and overdoped (b) hole–doped cuprates versus frequency at the nodal and antinodal point of the Brillouin Zone (BZ) and calculated for various temperatures. The anisotropy results from coupling to spin fluctuations and is disappearing in the overdoped case. Thus, a crossover from a non–Fermi liquid to a Fermi liquid behavior occurs. Note also the feedback effect of superconductivity for different parts of the BZ at optimal doping

condition below T_c. This is consistent with the behavior of $\tau^{-1}(\omega)$ above T_c where crossover to Fermi–liquid behavior takes place.

To summarize the doping dependence of the quasiparticle scattering rate we find pronounced non–Fermi liquid behavior in underdoped and optimally doped cuprates (Im $\Sigma \propto \omega$) due to strong scattering of quasiparticles by spin fluctuations. In the overdoped case the crossover to Fermi–liquid–like behavior occurs (Im$\Sigma \propto \omega^2$) that reflects the weakening of the spin fluctuations with increasing doping. In the superconducting state the pronounced spin fluctuations reveal structure in $\tau^{-1}(\omega)$ at the antinodal point of the Brillouin

Zone for underdoped and optimally doped cuprates. Due to weakening of spin fluctuations this structure disappears with increase of doping towards overdoped cuprates. Our results for Fermi–liquid versus non–Fermi–liquid seem quite general and could be used as a basis for systematic studies.

In order to illustrate the influence of the pseudogap E_g on the elementary excitations we have calculated the self–energy including in the energetic dispersion the pseudogap $E_g(\mathbf{k}) = E_g(\cos k_x - \cos k_y)$ ($T^* = 0.1t = 250K$).

In Fig. 9.39 we show the evolution of the imaginary part of the self–energy $\mathrm{Im}\Sigma(\mathbf{k}_a, \omega)$ for decreasing temperature at the antinodal point of the BZ where the pseudogap is maximal. In the pseudogap regime the self–energy shows a gap–like feature up to $2E_g$. The renormalization of the quasiparticle scattering rate leads to the peak at $2E_g$ and it becomes more pronounced for decreasing temperature. Correspondingly this peak in the imaginary part of the self energy at $2E_g$ reveals an enhancement of the $\mathrm{Re}\Sigma$. As a result the quasiparticle effective mass m^* enhances in comparison to its value at $\omega = 0$.

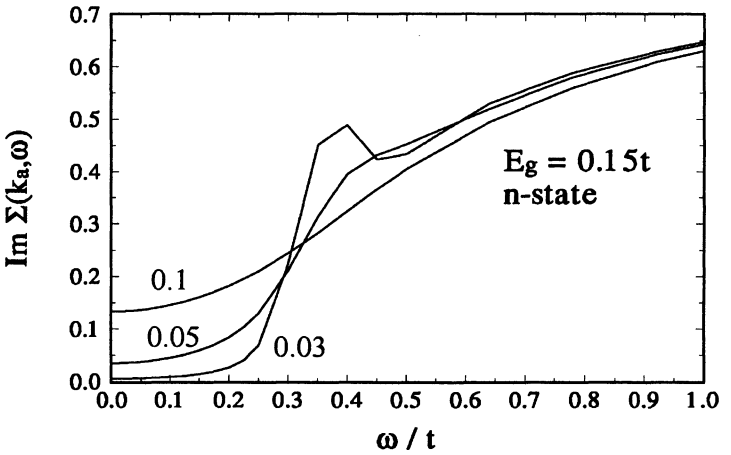

Fig. 9.39. Calculated imaginary part of the self–energy $\mathrm{Im}\Sigma(\mathbf{k}_a, \omega)$ at the antinodal wave vector $\mathbf{k}_a$ and a pseudogap $E_g = 0.15t$ for various temperatures $T = 0.1$, 0.05, and 0.03t in units of t

Our results are in qualitative agreement with complex optical conductivity results on underdoped Bi2212, YBCO, and LSCO compounds [191].

9.4.3 Dynamical Spin Susceptibility

An important quantity in our model is the dynamical spin susceptibility which is calculated in the random–phase–approximation (RPA) for renormalized Green's functions as we have discussed in the previous section. One

of the most important question is how the spin excitation spectrum is changing upon doping in high-T_c cuprates. Due to the nesting properties of the Fermi surface at the wave vector $\mathbf{Q}$ both electron and hole-doped cuprates show an enhancement of the spin response at the antiferromagnetic wave vector which is further augmented by the RPA denominator. These antiferromagnetic fluctuations induced by the itinerant carriers can be characterized by the frequency ω_{sf} of the spin fluctuations where ω_{sf} refers roughly to the peak position in the dynamical spin susceptibility.

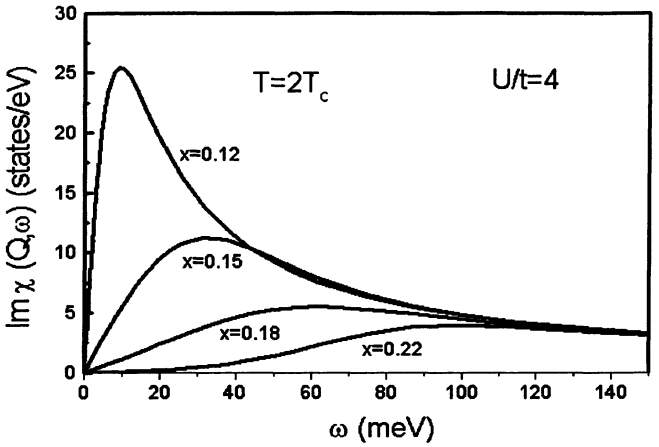

Fig. 9.40. Calculated imaginary part of the dynamical spin susceptibility $\mathrm{Im}\chi(\mathbf{q} = \mathbf{Q}, \omega)$ for the hole-doped cuprates at temperature T=$2T_c$ for different doping concentrations x=0.12 (underdoped), x=0.15 (optimal doping), and x=0.18, x=0.22 (overdoped)

In Fig. 9.40 we show the results of our calculations for $\mathrm{Im}\chi(\mathbf{Q}, \omega)$ versus frequency at different doping concentration. As one sees in the underdoped cuprates $\mathrm{Im}\chi$ shows a sharp peak and follows an Ornstein-Zernicke behavior. The position of the peak defines the spin fluctuation frequency ω_{sf}. With increasing doping ω_{sf} shifts towards larger frequencies and the peak becomes less pronounced. This agrees well with experimental data of INS. This behavior is expected, since for increasing doping the system goes away from the antiferromagnetic instability and therefore ω_{sf} becomes larger. This for example indicates that in the overdoped regime the renormalization of the elementary excitations will be isotropic at different parts of the Fermi surface while in optimally and underdoped materials the strongest scattering takes place at the parts of the Fermi surface that are connected by the wave vector (π, π) (so-called 'hot spots'). These results are consistent with the behavior of the elementary excitations that we have discussed previously.

What is the spin spectrum of the electron-doped cuprates? As expected

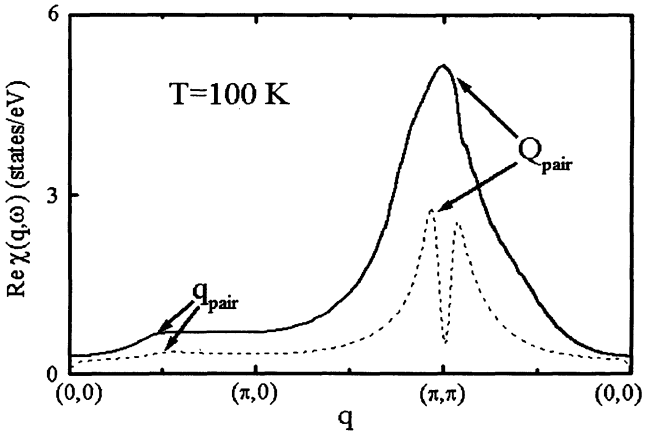

Fig. 9.41. Momentum dependence of the real part of the spin susceptibility for the optimally electron–doped cuprates $\mathrm{Re}\chi(\mathbf{q},\omega)$ along the Brillouin zone route $(0,0) \rightarrow (\pi,0) \rightarrow (\pi,\pi) \rightarrow (0,0)$ at $U/t = 4$, T=100K and $\omega = 0$(solid curve) and $\omega = \omega_{sf} = 0.47t$ (dashed curve). The main contributions to the Cooper–pairing interaction come from the wave vector $\mathbf{q}_{pair}$ and $\mathbf{Q}_{pair}$

the electron–doped cuprates demonstrate also the presence of the antiferromagnetic fluctuations at $\mathbf{Q}$. This is seen in Fig. 9.41 where we plot the behavior of the $\mathrm{Re}\chi(\mathbf{q},\omega)$ along the route $(0,0) \rightarrow (\pi,0) \rightarrow (\pi,\pi) \rightarrow (0,0)$ of the first BZ at $\omega = 0$ and $\omega = \omega_{sf}$. In both cases $\mathrm{Re}\chi$ yields a peak at wave vector $\mathbf{Q}$. However, this peak is much weaker than in hole–doped cuprates due to the weaker nesting properties of the corresponding Fermi surface. The latter can be seen by analyzing the position of the ω_{sf} in the electron–doped cuprates. While in hole–doped cuprates at optimal doping it is of the order of

$$\omega_{sf}^{h} \approx 20meV,$$

in the electron–doped cuprates it is approximately

$$\omega_{sf}^{e} \approx 60meV.$$

Therefore, the effect of the spin fluctuations on the elementary excitations will be weak in the electron–doped cuprates. For example, since the energy scale of the spin fluctuations is large the low–energy properties in electron–doped case will behave more like in the standard Fermi liquid theory (*i.e.* $\Sigma'' \sim \omega^2$). This is suggested experimentally by the quadratic behavior of the electronic part of the resistivity in electron–doped cuprates.

Another important feature is that electron–doped cuprates will behave more like overdoped cuprates, since their spin dynamics is very similar. A consequence is the absence of the 'kink' feature and 'hot spots' in the electron–doped cuprates.

9.4.4 Order Parameter: Doping Dependence

Let us now discuss the superconducting properties of the cuprates. A most important question concerns the symmetry of the superconducting order parameter and its doping dependence in hole– and electron–doped cuprates. Due to the repulsive nature of the spin fluctuation mediated pairing interaction a conventional isotropic s–wave pairing is not possible. Therefore, for singlet pairing the orbital state of the Cooper–pair wave function should be the $l = 2$ representation that corresponds to a d–symmetry of the order parameter. The particular symmetries which might occur in the CuO_2 plane are the ones which belong to the corresponding tetragonal crystal field symmetry D_{4h}. The corresponding representations can be substituted into the gap equation and the symmetry that yields the eigenvalue $\lambda = 1$ at highest temperature is the realized symmetry of the superconducting order parameter in layered cuprates.

The solutions of the generalized Eliashberg equations within the FLEX approximation give the $d_{x^2-y^2}$–wave symmetry of the superconducting order parameter in the CuO_2–plane for both hole and electron doping as shown for demonstration in Fig. 9.42(a) for the electron–doped cuprates at optimal doping. This is easy to understand if one remembers that the main contribution to the pairing comes from the spin susceptibility that is peaked at $\mathbf{Q} \approx (\pi, \pi)$. The latter connects in the hole–doped cuprates the parts of the Fermi surface close to the M points of the BZ. Keeping in mind the repulsive nature of the pairing interaction one sees that in order to have a Cooper–pairing the order parameter has to have different sign at the corresponding parts of the Fermi surface connected by the antiferromagnetic wave vector $\mathbf{Q}$. Then, $d_{x^2-y^2}$–wave symmetry is the most natural solution.

Since the topology of the Fermi surface does not change significantly in the hole–doped cuprates at least in optimally and overdoped cuprates the $d_{x^2-y^2}$–wave symmetry is always the most prominent solution of the gap equation. The situation is different in the electron–doped cuprates where phonons are important and weaker nesting is present. Assuming an exchange of antiferromagnetic spin fluctuations as responsible for Cooper–pairing in electron–doped cuprates we also obtain a $d_{x^2-y^2}$–wave symmetry of the underlying order parameter for the electron–doped cuprates at optimal doping. However, as we have pointed out earlier the topology of the electron–doped cuprates is in such a way that the parts of the Fermi surface connected by the $\mathbf{Q}$ are closer to the diagonals of the BZ rather than to a M points as shown in Fig. 9.42(b). Therefore, even though the symmetry of the superconducting order parameter is still $d_{x^2-y^2}$, the gap structure has some additional features (higher harmonics, see Fig. 9.43) that reflects the structure of the susceptibility χ and the corresponding topology of the Fermi surface.

Hence, it is possible that the symmetry of the superconducting order parameter can change with doping. This in particular may be the case for the overdoped compounds where the nesting becomes weaker. In addition,

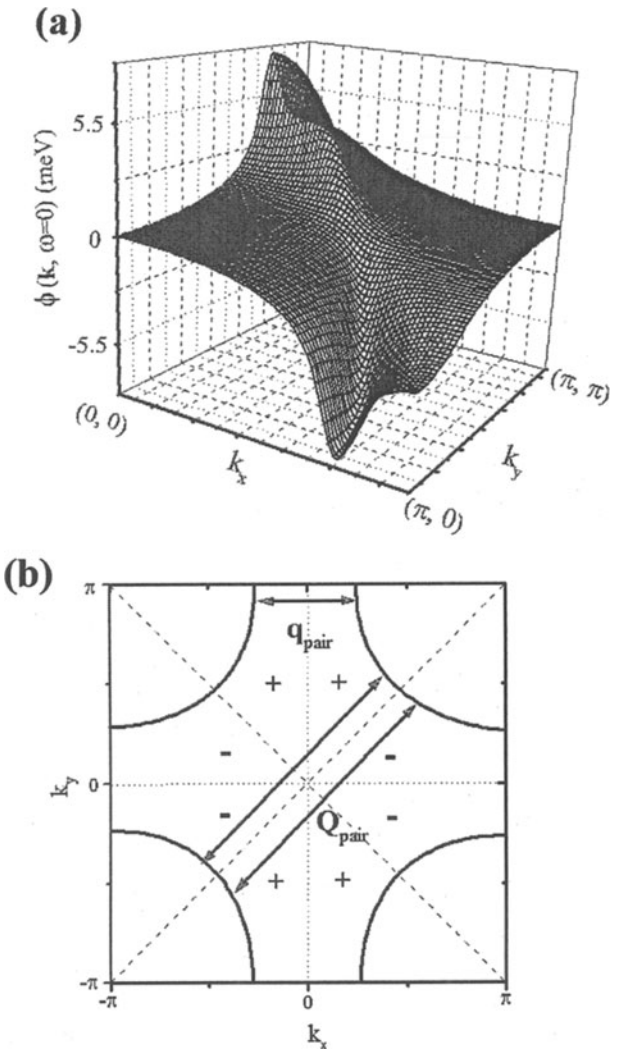

Fig. 9.42. (a) Calculated $d_{x^2-y^2}$–wave superconducting gap at T=0.8 T_c and x=0.15 in the first square of the BZ. (b) Calculated Fermi surface for the optimally electron–doped cuprates. The +(-) signs and dashed lines refer to the signs of the momentum dependence $d_{x^2-y^2}$–wave superconducting gap $\Delta(\mathbf{k}, \omega = 0)$ and its nodes, respectively

if the electron–phonon coupling plays a role it may overcome the repulsive interaction due to spin fluctuations and favor s–wave pairing. In principle, it could happen that the gap symmetry changes from $d_{x^2-y^2}$–wave to the s–wave for $T_c \to 0$, since more Cooper–pair condensation energy may result in nodeless s–wave symmetry.

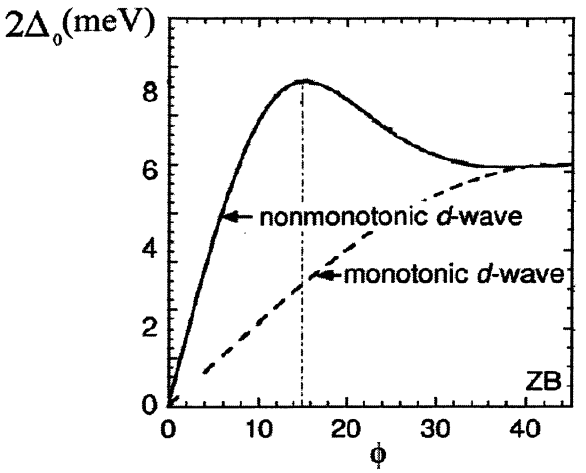

Fig. 9.43. Illustration of the non–monotonic d–wave behavior of the superconducting gap below T_c at T=5K in optimally electron–doped cuprates ($x = 0.15$) along the Fermi surface (the superconducting gap Δ_0 changes from the diagonal of the Brillouin Zone towards zone boundary(ZB) as a function of angle ϕ [40]

It is interesting to mention that phonons may also assist in principle the d–wave pairing if one assumes that the important phonon mode participating in the superconductivity is peaked at $\mathbf{q} \approx (0.4\pi, 0)$ as shown in Fig. 9.42(b). Indeed, the parts of the Fermi surface connected by the wave vector $\mathbf{q}$ have the same sign even for the $d_{x^2-y^2}$–wave pairing. Therefore, an attractive electron–phonon interaction could contribute to the d–wave pairing [187,188].

9.4.5 Resonance Peak and Magnetic Coherence

One of the important consequence of the spin–fluctuation–mediated Cooper–pairing and $d_{x^2-y^2}$–wave symmetry of the superconducting order parameter is the peculiar behavior of the spin dynamics in the superconducting state. The latter in particular occurs due to the fact that the spin fluctuation frequency ω_{sf} is of the same order as the superconducting gap Δ_0, at least in the hole–doped cuprates. One expects that the feedback effect of superconductivity on the spin excitations will be important if the quasiparticles condensing into Cooper–pairs are also partly involved in the spin fluctuation dynamics. Thus, it is important to see whether the experimentally observed 'resonance' peak and 'magnetic coherence' effect can be explained within our self–consistent electronic theory.

Let us start our study with the analysis of the imaginary part of the bare BCS expression for the spin susceptibility (see Eq. (9.41)) at the wave vector

$\mathbf{Q}=(\pi,\pi)$:

$$\mathrm{Im}\chi_0(\mathbf{Q},\omega)=\frac{1}{2}\sum_{\mathbf{k}}\Big\{\left[1-f\left(E_{\mathbf{k}}\right)\right]\delta(\omega+2E_{\mathbf{k}})+\left[f\left(E_{\mathbf{k}}\right)-1\right]\delta(\omega-2E_{\mathbf{k}})\Big\}. \tag{9.133}$$

Here, $f\left(E_{\mathbf{k}}\right)$ denotes the Fermi function and $E_{\mathbf{k}}=\sqrt{\epsilon_{\mathbf{k}}^2+\Delta_{\mathbf{k}}^2}$ is the disper-

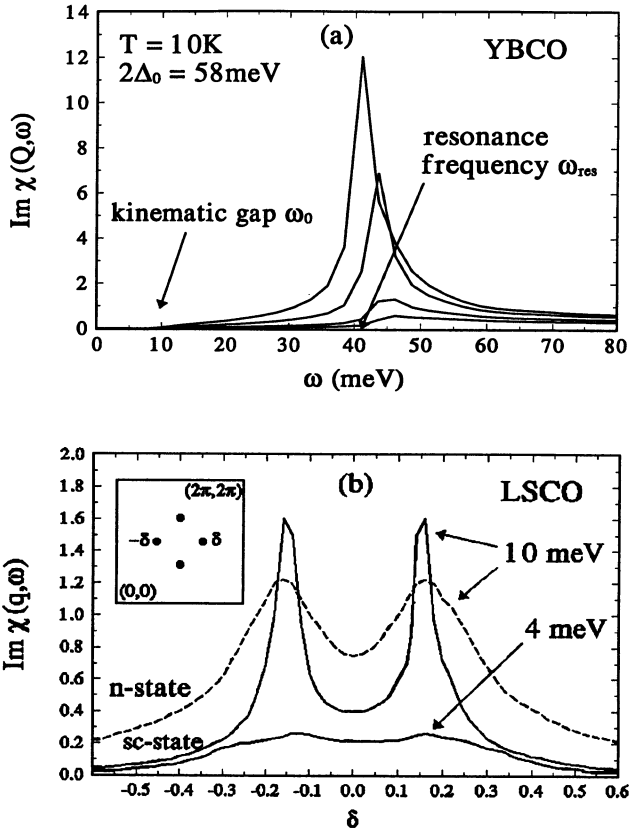

Fig. 9.44. Numerical results for the resonance peak and magnetic coherence in the weak-coupling limit. (a) Imaginary part of the RPA spin susceptibility in units of states/eV versus ω in the superconducting state at wave vector $\mathbf{Q}=(\pi,\pi)$ for U/t=1,2,3, and 4 from bottom to top. We find ω_{res}=41meV. Below the kinematic gap ω_0, $\mathrm{Im}\chi(\mathbf{Q},\omega)$ is zero. (b) Calculated magnetic coherence: the solid curves correspond to the superconducting state whereas the dotted curve is calculated in the normal state. The observed four peaks occur at $\mathbf{Q}_i=(1\pm\delta,1\pm\delta)\pi$ (see inset) and in the figure we show only the peaks at $\mathbf{Q}_i=(1,1\pm\delta)\pi$. In our calculations we find for the parameter of incommensurability δ =0.18

sion of the Cooper pairs in the superconducting state. As one sees from Eq. (9.133) the imaginary part of the BCS spin susceptibility has an important characteristic frequency ω_{DOS} that arises from the density of states of the quasiparticles in the superconducting state which have a gap in their spectrum due to superconductivity. Note, $\omega_{DOS} \approx 2\Delta(x,T)$. In order to describe the effect of spin fluctuations one uses in the simplest case the RPA spin susceptibility. Then, in addition to ω_{DOS} a second characteristic frequency occurs in the RPA spin susceptibility. In particular, one finds that the structure in $\mathrm{Im}\chi(\mathbf{Q},\omega)$ can also be determined by the condition

$$1 = U\mathrm{Re}\chi_0(\mathbf{Q},\omega = \omega_{res})$$

as have been pointed our earlier. Therefore, with increasing U one sees that the peak resulting from ω_{DOS} will shift to lower energies and most importantly will become resonant for $U = U_{cr}$. Note, this signals the occurrence of a spin density wave collective mode.

In Fig. 9.44(a) we present for different values of U our weak coupling results for $\mathrm{Im}\chi(\mathbf{Q},\omega)$ (*i.e.* without taking into account the lifetime effects). In the superconducting state $\mathrm{Im}\chi$ becomes gaped approximately at $2\Delta_0$. With increasing U the peak in $\mathrm{Im}\chi$ shifts to lower frequencies and at $U_{cr} = 4t$ it becomes resonant. Therefore, the resonance peak observed in INS results in our model due to occurrence of superconductivity, but is renormalized by the normal state spin excitations.

Another interesting feature at optimal doping relates to the momentum dependence of $\mathrm{Im}\chi(\mathbf{q},\omega)$ as observed in LSCO. In contrast to some other cuprates the susceptibility is peaked at the incommensurate wave vector $\mathbf{Q}_i = (\pi \pm \delta, \pi \pm \delta)$. In the superconducting state these incommensurate peaks behave rather unusually. With decreasing frequency they first become much more pronounced in comparison to the normal state and at low enough frequency disappear [179,180]. This phenomenon was originally called 'magnetic coherence' due to similarity of the observed effect with the quasiparticle coherence peak that occurs below T_c in the conventional superconductors. Using the parameters of the tight–binding dispersion for LSCO we have found the same behavior of $\mathrm{Im}\chi$ in our calculations [181] as shown in Fig. 9.44(b).

The same is the case for the resonance peak. One sees that in LSCO ω_{sf} is comparable to the superconducting gap and therefore, there is a strong renormalization of the spin spectrum in the superconducting gap. Due to the reduced scattering below T_c the incommensurate peaks at $\mathbf{Q}_i$ become sharper than in the normal state. Furthermore, for decreasing energy the intensity of the peaks will decrease due to a superconducting gap. At energies of about 2meV we do not obtain any well–resolved peaks. This is shown in Fig. 9.44(b).

Using the self–consistent FLEX approach we see that our weak–coupling results do not change drastically. Many experimental facts can be already understood on the basis of $d_{x^2-y^2}$–wave symmetry of the superconducting

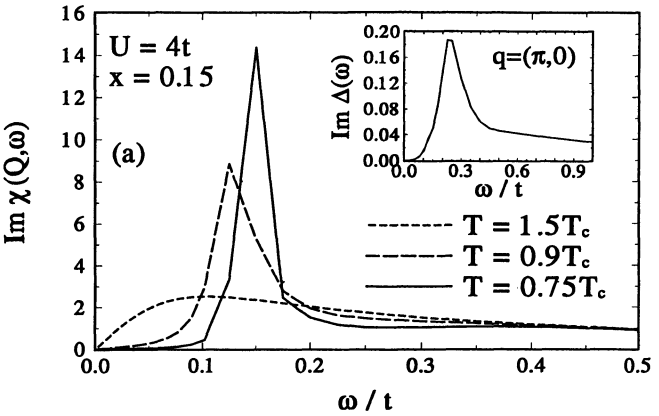

Fig. 9.45. Imaginary part of the RPA spin susceptibility at $\mathbf{Q} = (\pi, \pi)$ calculated using the FLEX approximation. For the normal state we get ω_{sf}=0.1t and in the superconducting state we obtain ω_{res}=0.15t. Assuming t=250 meV we find that 0.16t=40meV. Inset: Imaginary part of the gap function at T=0.075T_c for wave vector $\mathbf{q}$=$(\pi, 0)$

order parameter. However, in the strong–coupling Eliashberg approach the spin excitation spectrum can be studied self–consistently. For example, in Fig. 9.45 we show the FLEX results for Im$\chi(\mathbf{Q}, \omega)$ in the normal and superconducting state. In the normal state the spin fluctuation spectrum shows a peak at ω_{sf} =0.1t. In the superconducting state the resonance peak occur at ω_{res} =41meV and remarkably already at T=0.7T_c the resonance peak is fully developed and does not change further its position in frequency with lowering temperature. This reflects that in the strong–coupling Eliashberg approach the superconducting gap evolves rapidly below T_c and reaches almost its maximum already at T=0.7T_c.

Physically speaking, the resonance peak results from the frequency dependence of the superconducting gap function which is calculated self–consistently, and from the vicinity to a spin–density–wave collective mode which satisfies Eq. (9.43). Since the quasiparticle scattering rate is reduced in the superconducting state the strong– and weak–coupling results do not differ drastically.

It is of general interest to study the doping dependence of the resonance peak in the overdoped and underdoped cuprates. In Fig. 9.46 we show our results for the doping dependence of ω_{res} from underdoped to the overdoped regimes. Note, the ω_{res} is decreasing away from optimal doping. In the overdoped regime the resonance peak is mainly determined by the superconducting gap, since the spin fluctuations get weaker and play a less significant role. The superconducting gap is decreasing in the overdoped cuprates and thus the energy position of the resonance peak will also decrease. In the under-

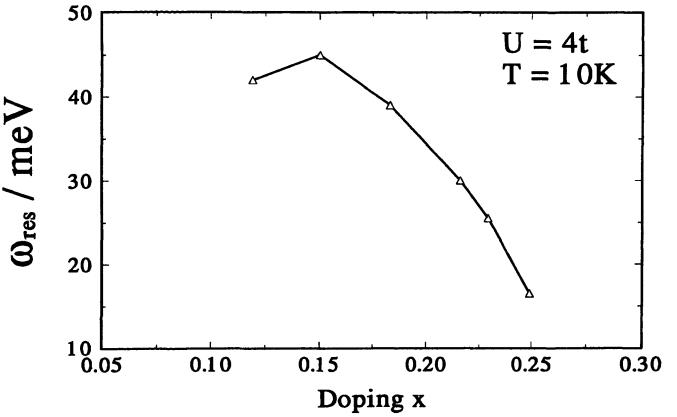

Fig. 9.46. FLEX results for ω_{res} versus doping. Note, in the overdoped regime with $T_c \propto \Delta_0$ we find a constant ratio of ω_{res}/T_c

doped cuprates the situation is different. In this case the system is very close to an antiferromagnetic instability and thus the effect of superconductivity on the formation of the resonance peak consists only of reducing the damping. This helps to satisfy the resonant condition. The frequency position of the resonance peak will be rather set by the normal state frequency ω_{sf}. Since ω_{sf} gets smaller with decreasing doping the resonance peak position also decreases in the underdoped cuprates.

To summarize, we obtain for the position of the resonance:

$$\omega_{res} \approx \begin{cases} \omega_{sf}, & \text{underdoped} \\ 2\Delta_0 - \omega_{sf}, & \text{optimal doping} \\ 2\Delta_0, & \text{overdoped} \end{cases} . \tag{9.134}$$

Here, the optimal doping corresponds approximately to x=0.15 holes per copper site.

Let us also comment on the spin dynamics of the electron–doped cuprates. As we already mentioned the nesting properties in the electron–doped cuprates are much weaker and thus they are far from the antiferromagnetic instability. As a result, calculating $\mathrm{Im}\chi(\mathbf{Q},\omega)$ we find that ω_{sf} becomes larger than in hole–doped cuprates and less pronounced as shown in Fig. 9.47. This has an important consequence also for the feedback of superconductivity. In particular, we find that the resonance condition, i.e. Eq. (9.43), in the electron–doped cuprates cannot be fulfilled and the spin excitations spectrum is only slightly renormalized due to the superconducting gap.

We would like to stress that despite the absence of the resonance peak in electron–doped cuprates the superconducting instability is nevertheless driven by the spin fluctuations. Thus, the appearance of the resonance peak cannot be considered as a proof of the spin–fluctuation induced Cooper–

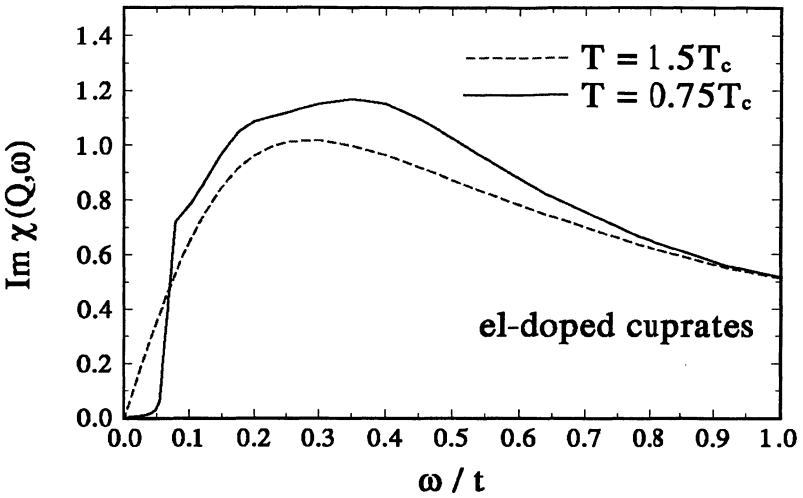

Fig. 9.47. The imaginary part of the spin susceptibility for the electron–doped cuprates above and below T_c at $\mathbf{q}=\mathbf{Q}=(\pi,\pi)$ calculated using the FLEX theory. The calculations are performed for U=4t and for an optimal doping concentration x=0.15. No resonance peak is found. Only a rearrangement of spectral weight due to $\Delta(\omega)$ occurs

paring, since its appearance signals only the occurrence of a spin–density wave collective mode below T_c.

To summarize, we have shown that the spin dynamics in cuprates above and below T_c can be successfully explained on the basis of the one–band Hubbard Hamiltonian and RPA spin susceptibility employing the FLEX approximation. Important features like resonance peak and magnetic coherence occur in the superconducting state of hole–doped cuprates due to the feedback of superconductivity and rearrangement of the normal state spin excitation spectrum calculated within self–consistent Eliashberg approach for various doping concentrations. Our results are also qualitatively similar to the those of the spin–fermion model [182].

9.4.6 Phase Diagram for Electron– and Hole–Doped Cuprates

We demonstrate that our electronic theory assuming the exchange of antiferromagnetic spin fluctuations as a relevant pairing mechanism for singlet pairing in cuprates can account for the main features in the phase diagram of hole–doped cuprates. In particular, we determine the doping dependence of the characteristic temperatures of the phase diagram, namely $T_c^*(x)$, $T_c(x)$, and also T^* at which a gap appears in the spectral density. Below T_c^* we indeed find incoherent Cooper–pairs ('pre–formed pairs') which become phase coherent only below the critical temperature T_c. We will show that phase fluc-

tuations contributing ΔF_{phase} to the free energy lead to a decreasing critical temperature in the underdoped regime, $T_c^* \to T_c$, and thus to the appearance of an optimal doping x_{opt}. It is shown that this result is due to the small superfluid density $n_s(T)$ in the system. Most importantly, we find for $x > x_{opt}$ that Cooper–pair phase fluctuations cost too much energy ($\Delta F_{phase} \propto n_s$) and thus $T_c \propto \Delta_0$, while for $x < x_{opt}$ one gets $T_c \propto \Delta F_{phase}$. Note at T_c the Meissner effect occurs. ΔF_{cond} denotes the contribution to the free energy due to Cooper–pair formation and ΔF_{phase} refers to the contribution due to phase fluctuations of the Cooper–pairs. We compare our results with those of Berezinskii–Kosterlitz–Thouless (BKT) theory as well as with the XY model.

In Fig. 9.48 we show our results for the phase diagram of hole–doped cupra m the linear doped

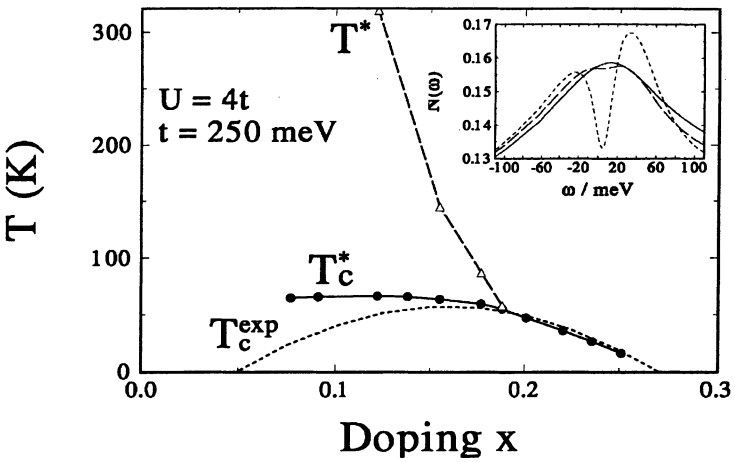

Fig. 9.48. Results for the phase diagram of hole–doped cuprates using the one–band Hubbard model. Cooper–pair phase fluctuations are neglected. Note, $x = 1 - n$ and on–site Coulomb repulsion is $U = 4t$, where t is the nearest neighbor hopping integral. Below the pseudogap temperature T^* (dashed line) one finds a reduction of spectral weight in the density of states at $\omega = 0$ (see inset). T_c^* (solid line) denotes the superconducting transition temperature neglecting Cooper–pair phase fluctuations. The dashed–dotted line corresponds to a phenomenological fit to experimental data [172]. Inset: Density of states $N(\omega)$ in units $1/t$ for doping $x = 0.15$ at temperature $T = 4.5T_c^*$ (solid line), $T = 2.3T_c^* \equiv T^*$ (dashed line), and $T = 1.01T_c^*$ (dotted)

cuprates the results of FLEX calculations and experiment agree well with each other, $T_c^* \approx T_c$ and $T_c \propto \Delta_0(x)$. Due to a weakening of the nesting properties of the Fermi surface upon increasing doping and corresponding

suppression of antiferromagnetic spin fluctuations the superconducting transition temperature goes down and we do not find any superconductivity above x=0.3. On the other hand in the underdoped regime the T_c curve in FLEX approach still slightly increases while in the experiment it decreases and the superconductivity does not exist below x=0.05.

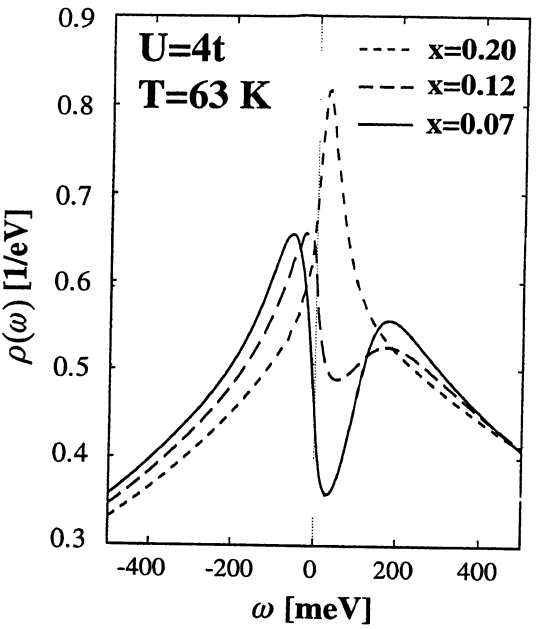

Fig. 9.49. Calculated doping dependence of the pseudogap in the electronic density of states in the normal state of hole–doped cuprates. For small doping the pseudogap appears due to the scattering of quasiparticles by antiferromagnetic spin fluctuations. Note, with decreasing doping the pseudogap increases. This agrees well with experimental data [184]. Moreover, for underdoped cuprates the value of the calculated pseudogap (taken as a distance between the edges) $\Delta_p \approx 80$meV is similar to that measured in underdoped cuprates$\Delta_p^{exp} \approx 88$meV [184]

The slight increase of T_c upon lowering the doping below optimal one is the result of the shape of the Fermi surface and of the large scattering rate that prevent more and more Cooper–pairing. In our model the Fermi surface becomes closer to nesting and thus the corresponding spin fluctuations responsible for superconductivity get enhanced. This indicates that the model we have used in mean–field is not applicable for the underdoped cuprates. In the vicinity of antiferromagnetism the effects of the electronic correlations play an important role. The perturbative approach we are using will not properly account of the correlations. For example, it is known from the ARPES experiments [183] that the shape of the Fermi surface is changing

in hole underdoped cuprates and forms pockets around $(\pi/2, \pi/2)$ points of the BZ which is believed to be a result of the electronic correlations. Also, note a pseudogap opens up in the elementary excitations spectrum, see Fig. 9.49. Furthermore, Cooper–pair phase fluctuations matter and suppress T_c. We will present results for this case later, see Fig. 9.51.

In the Eliashberg formulation of the Cooper–pairing the carriers do not only pair, but also scatter on spin fluctuations. If the scattering is strong some of the quasiparticles will be away from the Fermi level already in the normal state. This forms some dip, *i.e.* the reduction of the spectral weight (so–called pseudogap) in the density of states at the Fermi level as one sees from the inset of Fig. 9.48. In order to investigate the doping dependence of the pseudogap in the density of states more in detail we show in Fig. 9.49 the calculated results for $N(\omega)$ for various doping. One clearly sees that in the overdoped region the density of states is unrenormalized due to weakness of the antiferromagnetic correlation. For decreasing doping the pseudogap at the Fermi level occurs and it increases upon decreasing doping. The pseudogap opens below $T = T^*$. Results for T^* using $U = 4t$ as a function of hole doped are shown in Fig. 9.48. Most importantly our results show good agreement for the doping dependence of the pseudogap. Similar to the NIS tunneling experimental data [184] the pseudogap increases with decreasing doping from overdoped to underdoped cuprates. In Table 9.1 we show our calculated results for T^*

Table 9.1. Results for the calculated pseudogap formation temperature T^* resulting from the scattering of carriers by spin fluctuations for different doping in comparison with experimental data on T^*_{exp} found in YBaCuO–compounds [185].

x	T^* (K)	T^*_{exp} (K)
0.16	100	90
0.15	150	160
0.14	200	190
0.13	310	240

using $U = 4t$ for different doping in comparison with experimental data on YBaCuO–compounds [185]. One notices that our results agree also well on the quantitative level. Moreover, for the underdoped cuprates the calculated magnitude of the pseudogap taken as a distance between edges of two peaks ($\Delta_p \approx 80meV$ at x=0.07) agrees well with experimental value $\Delta_p^{exp} = 88meV$ found for underdoped cuprates [184]. For completeness it remains to be seen whether the same theory can explain also the phase diagram of electron–doped cuprates. In Fig. 9.50 we present the results of FLEX calculations for electron–doped cuprates [187]. Most importantly our mean–field results for the phase diagram are in good agreement with experimental data again for optimally and overdoped region. For example, one sees that the maximal

T_c is smaller than in the hole–doped case. The reasons for this are poorer nesting properties of the Fermi surface in electron–doped case and also the fact that a flat bands lies in NCCO is approximately 300meV below the Fermi level. Another important feature of the phase diagram of the electron–doped

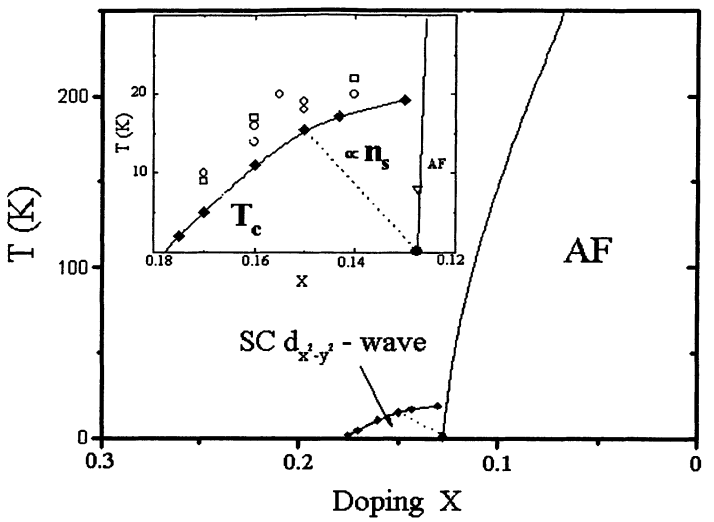

Fig. 9.50. Results for the phase diagram of electron–doped cuprates using the one–band Hubbard model. We neglect Cooper–pair phase and amplitude fluctuations, thus $T_c^* = T_c$. The hole doping concentration is $x = 1 - n$ and the on–site Coulomb repulsion $U = 4t$, where t is the nearest neighbor hopping integral. The inset shows the region of superconductivity.The antiferromagnetic (AF) transition curve is taken from Ref. [186]. The solid curve corresponds to our calculated T_c values [187]. The experimental data are squares from Ref. [192], circles from Ref. [193], triangle from [194]. The dashed curve would correspond to $T_c \propto n_s$ as in hole–doped cuprates

cuprates is the narrower range of superconductivity than in hole–doped case ($0.12 < x < 0.18$ in electron–doped case and $0.05 < x < 0.3$ for hole–doped cuprates). The reason for this is also clear: in the overdoped regime the nesting properties of electron–doped NCCO become rapidly very poor and cannot drive superconductivity. In the underdoped regime one should keep in mind that antiferromagnetism persists in electron–doped case for larger doping. Thus, the superconductivity region will be further destroyed by the antiferromagnetic instability which is competing with the superconducting one.

Similarly to hole–doped cuprates the important question is how T_c lowers in the underdoped regime. Our calculations have shown in agreement with experiment that there is no weak pseudogap above T_c in the underdoped

regime of the electron–doped cuprates in contrast to the hole–doped ones. The reason is clear: The spin fluctuations are less pronounced in the electron–doped cuprates and thus do not produce a dip in the spectral density at the Fermi level.

We present now results for $T_c(x)$ in the underdoped cuprates ($x < x_{opt}$) including Cooper–pair phase fluctuations. The region $x < x_{opt}$ can be experimentally characterized by a T_c which decreases with decreasing hole density x. Furthermore, the so–called Uemura scaling holds [15]. It has been recognized early that a small n_s leads to a reduced stiffness against fluctuations of the phase of the superconducting order parameter [107, 108, 196]. Furthermore, cuprate superconductors consist of weakly–coupled CuO_2 planes so that Cooper–pair phase fluctuations are enhanced also by the reduced dimensionality. Note, in conventional superconductors this is not relevant, since the large superfluid density leads to a typical energy scale of Cooper–pair phase fluctuations much larger than the superconducting energy gap Δ which governs the thermal breaking of a Cooper–pair. Thus, in conventional superconductors $T_c \propto \Delta(T = 0)$ [94]. In contrast to this the observation $T_c \propto n_s$ in underdoped (hole–doped) cuprates indicates that Cooper–pair phase fluctuations drive the superconducting instability. The Cooper–pairs only break up at a crossover temperature $T_c^* > T_c$ and between T_c and T_c^* local phase–incoherent Cooper–pairs exist [107, 108, 120, 121, 196]. Then a transition to superconductivity with phase–coherent Cooper–pairs occurs at $T_c \propto n_s$ [107, 108, 120].

Using results for $n_s(x, T)$ calculated from Kubo formula we get for the underdoped cuprates the phase diagram shown in Fig. 9.51. In the overdoped regime T_c^* is identical with the bulk transition temperature T_c below which a Meissner effect is found. We get in agreement with experiments from our electronic theory $T_c \propto \Delta(T \to 0)$ for overdoped cuprates. In the overdoped cuprates the energy costs due to Cooper–pair phase fluctuations ($\propto n_s/m$) are higher than the condensation energy. Then, Cooper–pair phase fluctuations play minor role for determining T_c in the overdoped cuprates. In contrast to this we find in the underdoped cuprates $T_c \propto n_s(x) \propto T_c^*$. This results from the low superfluid density n_s. At T_c^* phase–incoherent Cooper–pairs are formed and only at $T_c < T_c^*$ one gets phase coherence.

Our theory shows that an optimal doping occurs as a result of replacing for determining T_c the free energy change $\Delta F_{cond}(x)$ due to Cooper–pair condensation for overdoped cuprates by the free energy change ΔF_{phase} gained from phase coherence of the Cooper–pairs. Thus, T_c^{opt} occurs when $\Delta F_{cond} = \Delta F_{phase} \sim n_s$.

In Fig. 9.52 results are shown for $\Delta F(x)$. We find that ΔF_{cond} mainly follows the doping dependence of the mean–field transition temperature T_c^*. The doping dependence of $\Delta F_{phase}(x)$ is given by $n_s(0)/m$. Note, the energy cost due to phase fluctuations has the opposite behavior as the energy gain due to Cooper–pair condensation with respect to the doping concentration x.

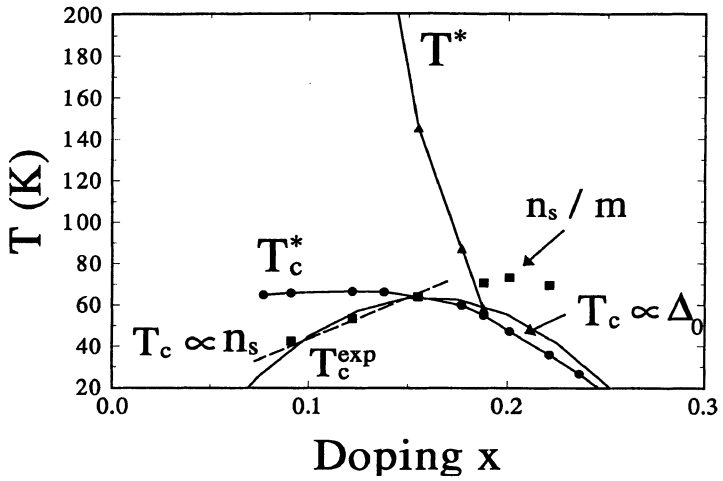

Fig. 9.51. Phase diagram for high-T_c superconductors resulting from a spin fluctuation induced Cooper-pairing including their phase fluctuations. The calculated values for $n_s(0)/m$ (squares) are in good agreement with muon-spin rotation experiments [173]. They determine the energy costs for the Cooper-pair phase fluctuations. T_c^* denotes the temperature below which Cooper-pairs are formed. The dashed curve refers to our calculated results using $n_s(x)$ and gives the observed Uemura scaling $T_c \propto n_s(T=0,x)$ [15]. Below T^* we get a gap structure in the spectral density as observed in tunneling spectroscopy [24, 131]. The solid curve T_c^{exp} refers to experiments describing many hole-doped superconductors [172]

It is remarkable that we get from our electronic theory a crossing of the two energy contributions ΔF_{cond} and ΔF_{phase} at $x \simeq 0.15$ for which the largest T_c is observed. The consequence of this is that we find a non-monotonic doping dependence of $T_c(x)$ and optimal doping at $x \simeq 0.15$ and $T_c \propto n_s$ for underdoped cuprates (and thus the Uemura scaling) .

Physically speaking in the overdoped regime we find a large ΔF_{phase} which means that Cooper-pair phase fluctuations cost much energy. Thus, the system will undergo a mean-field transition involving phase coherent Cooper-pairs and a small condensation energy ΔF_{cond} ($\Delta F_{cond} \sim T_c \propto \Delta_0 < \Delta F_{phase}$). In the underdoped cuprate superconductors the energy gain due to the formation of Cooper-pairs is such that they are broken up to T_c^* and $T_c^* > T_c$. Only at $T \leq T_c$ the phase coherence of the Cooper-pairs occurs.

Note, the coherence length in electron-doped cuprates $\xi_{ab} = 30\mathring{A}$ [153] is much larger than a typical value for the hole-doped ones. This means that all Cooper-pairs overlap well with each other and that almost all electrons are involved in superconductivity. Therefore, one expects that the Cooper-pair phase fluctuations plays much less important role in the electron-doped cuprates than in hole-doped ones.

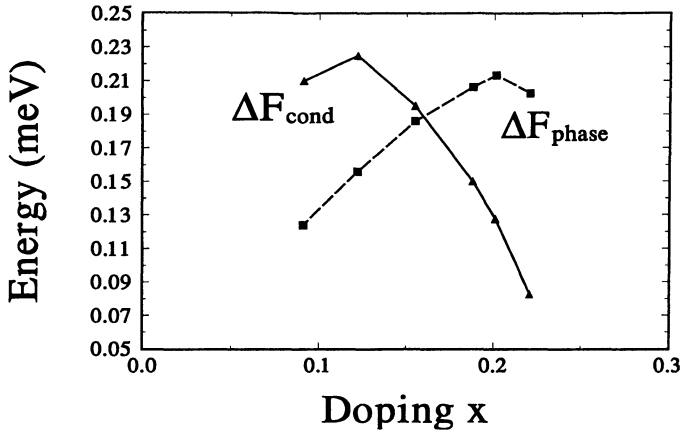

Fig. 9.52. Calculated crossover of the phase–stiffness energy and ΔF_{cond}. $\Delta F_{phase} \propto n_s/m^*$ and the condensation energy is $\Delta F_{cond} \simeq \alpha\{n_s/m\}\Delta_0(x)$. Here, we estimate $\alpha \simeq 2.5 \times 10^{-3}$ (For comparison in conventional superconductor Al $\alpha \approx 0.4$ [122]. Note, in cuprates α is small for two reasons, namely, the number of holes condensed into Cooper–pairs is maximal 50 percent of the whole number of carriers available and, secondly, due to the large size of the unit cell of cuprates). Note, our results for α agree well with other theoretical and experimental estimates [123–125]. Note, $\Delta F_{phase} < \Delta F_{cond}$ implies the two characteristic temperatures T_c^*, where Cooper–pairs are formed at $T_c \sim \Delta_0$, and $T_c \approx \Delta F_{phase} \propto n_s$, where Cooper–pairs become phase coherent

To summarize, we have solved the generalized Eliashberg equations self–consistently and extended them by including Cooper–pair phase fluctuations to calculate some basic properties of the hole–doped cuprate superconductors. The doping dependence of $T_c(x)$ and an improved phase diagram is obtained. In particular we show also results for the condensation energy and for the weak pseudogap temperature T^* below which a small reduction in the spectral density at the Fermi level appears.

9.4.7 Doping Dependence of the Superfluid Density $n_s(x,T)$

In Fig. 9.53 results for the temperature dependence of the superfluid density $n_s(\omega = 0)/n$ (n denotes the normal–state band filling) are given below T_c^* for various doping concentrations. We calculate n_s using the current–current correlation function and standard many–body theory [96]:

$$\frac{n_s(\omega)}{m} = \frac{1}{e^2}\,\omega\,\mathrm{Im}\;\sigma(\omega) \quad , \tag{9.135}$$

Note, according to London's theory, $\lambda_L \propto n_s$, the ratio n_s/n is related to measurements of the (in–plane) penetration depth, for example see microwave experiments. Note, that our calculations show that roughly only 1/3 of the

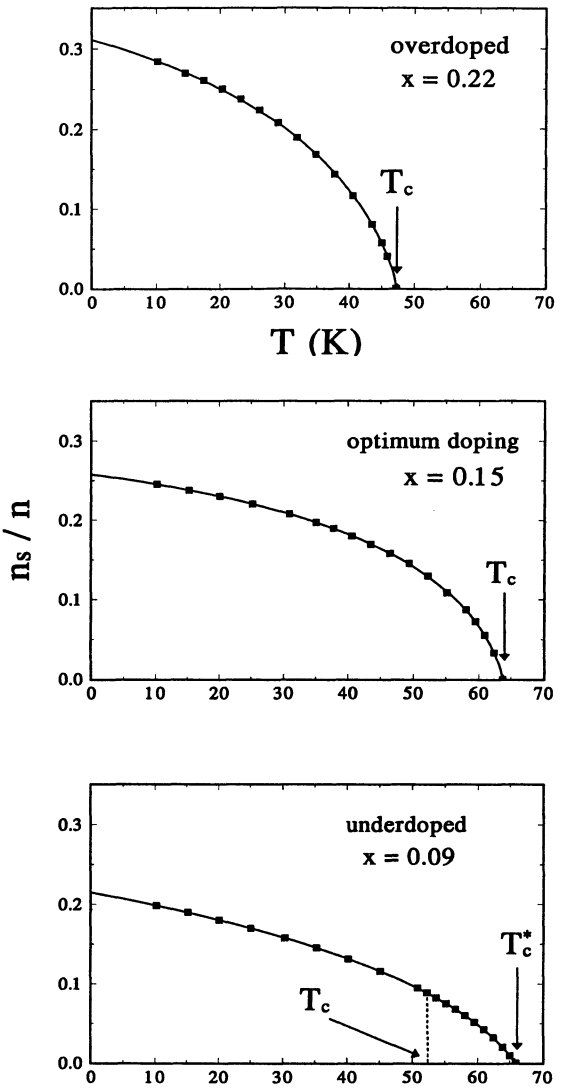

Fig. 9.53. Temperature dependence of the superfluid density $n_s(x,T)$ calculated with the help of Eqs. (9.168) and (9.57)-(9.54) for various hole doping concentrations x. We extrapolate the results to $T \to 0$. At temperature T such that $T_c < T < T_c^*$ Cooper–pairs become phase incoherent, $n_s^0 \to 0$. Our results are in fair agreement with measurements of the in–plane penetration depth by Bonn, Hardy and co–workers [9]. The dashed curve for the underdoped case illustrates the effect of Cooper–pair phase fluctuations according to the (static) Kosterlitz–Thouless theory

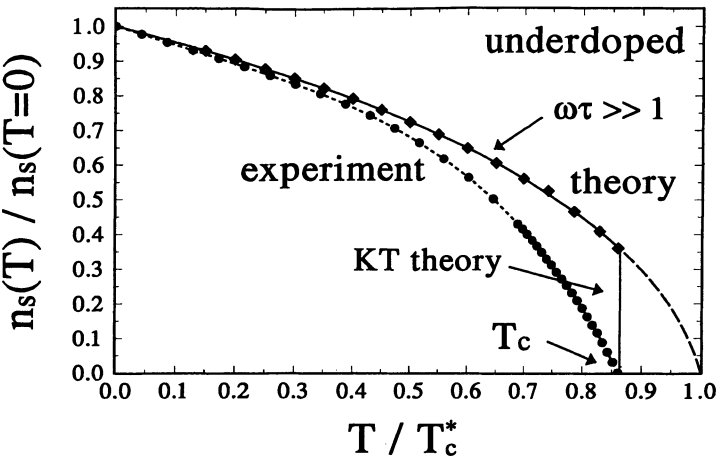

Fig. 9.54. Phase averaged superfluid density for underdoped cuprates. The deviation of experimental (circles) from FLEX results is due to Cooper–pair phase fluctuations with lifetime τ. Taking these into account within BKT–theory one gets results indicated by the vertical line. Note, for the dynamical superfluid density ($t \sim \omega^{-1}$) one expects $n_s(t) \rightarrow n_s$(FLEX) if $\omega\tau >> 1$

holes become superconducting, even for $T \rightarrow 0$. This is typical for a strongly interacting system. For decreasing doping ($x \rightarrow 0$) the curves $n_s(T)$ get flatter and smaller as experimentally observed.

For underdoped cuprates Cooper–pair phase fluctuations are getting important ($T_c^* < T_c$). Then, after averaging over the phases of the Cooper–pairs one expects of course $n_s \rightarrow 0$ for T$\rightarrow T_c$. We illustrate this in Fig. 9.53 where we show experimental results and FLEX–results for underdoped cuprates. Then, a qualitative agreement with the data of Bonn, Hardy and co–workers on $\lambda^2(T=0)/\lambda^2(T)$ concerning the slope of the curves in the vicinity of T_c^* and the linear behavior for $T \rightarrow 0$ is found [9].

In particular the FLEX approximation for the generalized Eliashberg equations yields close to T_c^* a relation $\lambda^3(T=0)/\lambda^3(T) \propto (T_c^* - T)$. The same power law has been found by Kamal *et al.* and has been attributed to critical fluctuations starting about 10K below T_c, since the slope coincides with the critical exponent for the 3D XY model [9]. Here, we obtain this power law from the generalized Eliashberg equations using the FLEX approximation which is purely 2D and does not contain critical fluctuations. Instead, the rapid increase of n_s below T_c^* is due to the self–consistent treatment of the superconducting gap function $\Delta(\omega)$. Thus, we conclude: while 3D critical fluctuations are expected in a very narrow temperature range close to T_c, these are not the origin of the observed power law on the scale of 10K.

In Fig. 9.54 we present the FLEX results for Cooper–pairing phase averaged superfluid density in underdoped superconductors. The effect of phase

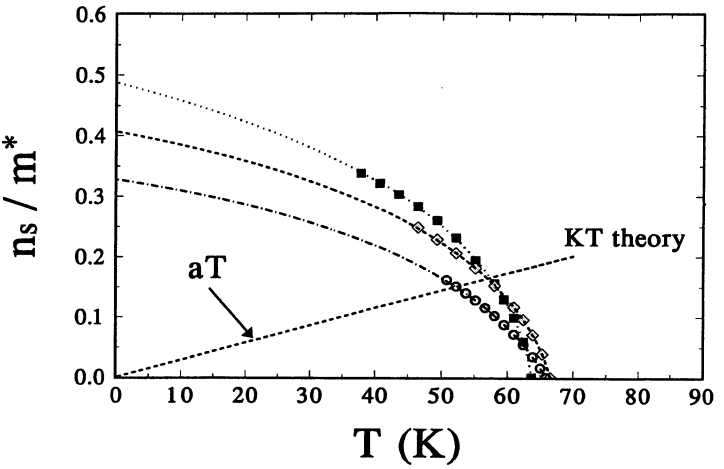

Fig. 9.55. Results for the superfluid density divided by m in units $10^{-2} m_e^{-1} \mathring{A}^{-2}$ as a function of temperature T for various doping concentrations: x=0.155 (squares), x=0.122 (diamonds), x=0.091 (circles). From $n_s(x,T)$, T_c is given as indicated by the intersection with aT, where $1/a = \pi/2$ (BKT theory)

fluctuations can be seen from the discrepancy between experiment [9] and theory. One clearly sees that no Meissner effect results for $T > T_c$, since the phase correlation function $< \nabla\phi(\mathbf{r}) \cdot \nabla\phi(0) >$ becomes zero. The results obtained using static Kosterlitz–Thouless theory (straight line) and the FLEX results (diamonds) for $n_s(x,T)$ are shown. The FLEX results neglect phase fluctuations which is appropriate for $\omega\tau \to \infty$. Of course, in Kosterlitz–Thouless theory we get $n_s \to 0$ at T_c. Note, in our full FLEX calculations we have to use for the phase averaged superfluid density $n_s = n_s^0 \langle \nabla\phi(\mathbf{r}) \cdot \nabla\phi(0) \rangle$ and then also $n_s \to 0$ at T_c. Note that for $T < T_c$ the discrepancy between experimental results and our FLEX calculations indicates the importance of Cooper–pair phase fluctuations below T_c.

In Fig. 9.55 we show results for n_s renormalized due to phase (vortex) fluctuations (see for details Appendix D). The Berezinski–Kosterlitz–Thouless (BKT) theory describes the unbinding of thermally created pancake vortex–antivortex pairs. The relevant parameters are the dimensionless stiffness K and the core energy E_c of vortices. The stiffness is related to n_s

$$K(T) = \frac{\hbar^2}{k_B T} \frac{n_s(T)}{m^*} \frac{d}{4} \tag{9.136}$$

where d is the average spacing between neighboring CuO_2–planes. Hence, $T_c \sim n_s(T_c) K(T_c)$ and $K(T_c)$ is given by BKT. Starting from the smallest vortex–antivortex pairs of size r_0, the pairs are integrated out and their effect is incorporated by an approximate renormalization of K and the fugacity

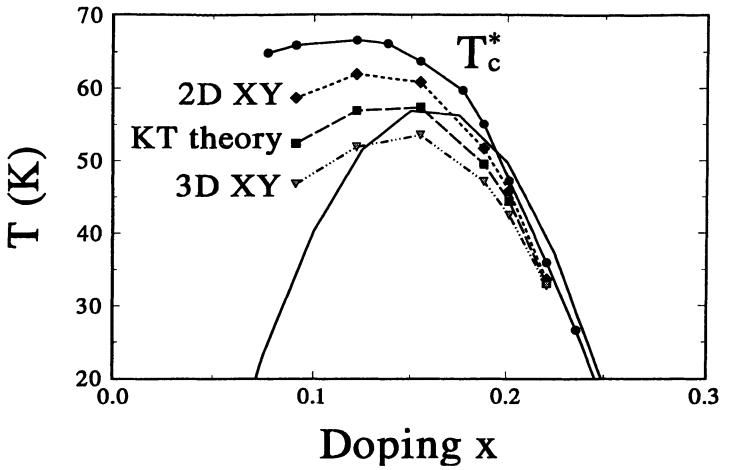

Fig. 9.56. Calculated doping dependence for T_c calculated with the help of the Berezinski–Kosterlitz–Thouless (BKT) theory. For comparison the T_c curves obtained within 2D and 3D X–Y models, and also mean–field result, T_c^* are displayed

$y = e^{-E_c/k_BT}$. As mentioned earlier this leads to the Kosterlitz recursion relation

$$\frac{dy}{dl} = (2 - \pi K)y \quad , \tag{9.137}$$

$$\frac{dK}{dl} = -4\pi^3 y^2 K^2 \quad , \tag{9.138}$$

where $l = \ln(r/r_0)$ is a logarithmic length scale. Bound pairs reduce K and thus n_s, but do not destroy superconductivity. At T_c, K jumps from a universal value of $2/\pi$ to zero. The values of T_c shown in Fig. 9.56 are obtained by numerically integrating Eqs.(9.138) with n_s taken from FLEX results.

In Fig. 9.56 we plot the transition temperature T_c obtained with the help of BKT theory and the temperature T_c^* where Cooper pairs form. For decreasing doping x, T_c^* becomes nearly constant and decreases slightly for the lowest doping level, consistent with the strong decrease of the onset temperature of vortex effects at even lower doping found by Xu et al. [138]. On the other hand, T_c turns down again in the underdoped regime. We have also calculated the superconducting gap Δ_0 extrapolated to $T \to 0$ (not shown). Δ_0 is here defined as half the peak–to–peak separation in the density of states. We find approximately $\Delta_0 \approx T_c^*$. For a comparison the T_c curves obtained within 2D and 3D XY models are also shown. We again find that Cooper–pair phase fluctuations are unimportant in the overdoped regime. Note, $n_s(T, x) \to 0$ for $T \to T_c^*$, since Cooper–pairs disappear at T_c^*.

The transition temperature T_c has to be determined by averaging over the Cooper–pair phase fluctuations. In a Ginzburg–Landau (GL) treatment

the phase is given by the GL wave function $\psi(\mathbf{r},t) = |\psi|e^{i\phi(\mathbf{r},t)}$, where n_s is related to the correlation function $\langle\nabla\phi(\mathbf{r},t)\cdot\nabla\phi(0,0)\rangle$. In the presence of spatial phase fluctuations of $\psi(\mathbf{r})$ the averaged superfluid density $\bar{n}_s = |\bar{\psi}(\mathbf{r})|^2\langle\nabla\phi(\mathbf{r})\cdot\nabla\phi(0)\rangle$ will vanish at T_c so that no Meißner effect occurs above T_c. BKT theory as well as the 2D [141] and 3D XY models [140] predict that T_c is proportional to $n_s(T_c)/m$. Note, T_c as obtained within the 3D XY model is larger than the 2D values, since fluctuations are less important in 3D.

Finally, we calculate the dynamical phase stiffness. Note, the superfluid density can be also obtained from the imaginary part of the conductivity

$$\frac{n_s}{m^*} = \frac{1}{e^2}\lim_{\omega\to 0}\omega\sigma_2^S(\omega) \quad . \tag{9.139}$$

This can be shown with the help of Kramers–Kronig relations. We have recalculated n_s/m^* in this way and find identical results with those obtained from Eq. (9.52). Note, for small wave vector $\mathbf{q}\to 0$ the Eq. (9.139) can be written as

$$\frac{n_s(\omega)}{m^*} = \frac{1}{e^2}\omega\sigma_2^S(\omega) \quad . \tag{9.140}$$

The imaginary part $\sigma_2^S(\omega)$ of the dynamical conductivity is obtained from the FLEX approximation for the dynamical current–current correlation function using the Kubo formula. This is discussed in Appendix D.

The resulting phase stiffness $n_s(\omega)/m^*$ is shown in Fig. 9.57 for x=0.12 (underdoped) at various temperatures. At higher doping the results (not shown) are similar, only the typical frequency scale, which turns to be the low–temperature superconducting gap Δ_0 is reduced. For temperatures $T < T_c^*$ the superfluid density is non–zero at $\omega = 0$ indicating the presence of the Cooper–pair phase fluctuations in the system. On the contrary, for $T = T_c^*$ $n_s(\omega = 0)/m^* = 0$ and thus no dynamical Cooper–pair phase fluctuations are present. Note, for $\omega > 0$ the superfluid density is finite even for $T > T_c^*$. At first glance this is surprising, since the phase is not well defined for $\Delta = 0$. However, the phase action contains also contribution from the time derivative of the phase besides the stiffness term. While the total action vanishes, each term on its own does not. Another interesting observation is that all curves merge together at energies of about $2\Delta_0$. This is expected, since the superfluid density is a current–current correlation function which has a characteristic energy scale at about $2\Delta_0$ in the superconducting state.

Even slightly below T_c^*, $n_s(\omega = 0)/m^*$ obtains a significant finite value, leading to the Meissner effect, and there is a considerable redistribution of weight from energies roughly above twice the low–temperature gap, $2\Delta_0$, to energies below $2\Delta_0$. This redistribution increases with decreasing temperature. Also, a peak develops slightly below Δ_0 followed by a dip around $2\Delta_0$, this structure being most pronounced in the underdoped case. Since Δ_0 is smaller in the overdoped regime, $n_s(\omega)/m^*$ changes more rapidly for small

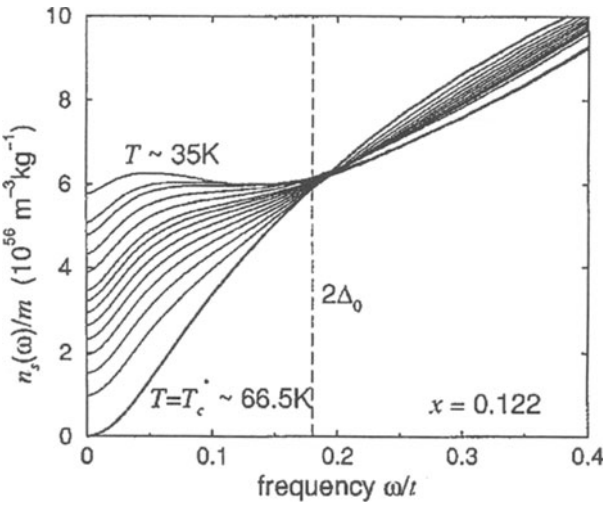

Fig. 9.57. Frequency dependent phase stiffness $n_s(\omega)/m^*$ for doping x=0.12 (underdoped) and various temperatures k_BT/t =0.012, 0.015, 0.016,0.017, 0.018, 0.019, 0.0195, 0.02, 0.0205, 0.021, 0.0215, 0.022, 0.0225, 0.023 (with decreasing $n_s(0)/m^*$). Here, t = 250meV is the hopping integral. The frequency is given in units of t ($\hbar = 1$). At $T_c^* \approx 0.023t/k_B$ = 66.5K, Cooper–pairs start to form. Below T_c^* there is a marked transfer of weight from energies above $2\Delta_0$ to energies below, where Δ_0 is the maximum gap at low temperatures as obtained from the FLEX calculations

ω in this case. It is of course not surprising that $2\Delta_0$ is the characteristic frequency of changes in $n_s(\omega)/m^*$ related to the formation of Cooper–pairs.

To summarize, we analyze here the behavior of the superfluid density $n_s(\omega, T, x)$ which controls the doping dependence of the phase coherence, thermodynamic behavior, the penetration depth, the Nernst effect, Cooper–pair phase fluctuations, etc. Note, we find that the superfluid density plays the most significant role in the underdoped cuprates and determines the superconductivity. We find our results we found to be consistent with the BKT theory.

9.4.8 SIS and NIS Tunneling Spectra

Tunneling spectra are a good measure of the superconducting state. It sheds light on the validity of our electronic theory. Here, we calculate the tunneling spectra for SIS (superconductor/insulator/superconductor) and NIS (normal state metal/insulator/superconductor). Let us see to which extent the spin fluctuation model for superconductivity can explain the fine structures seen by tunneling spectroscopy below T_c in the cuprates (remember the significant success of the BCS and Eliashberg theory of superconductivity due to electron–phonon coupling resulting from the explanation of the fine structures

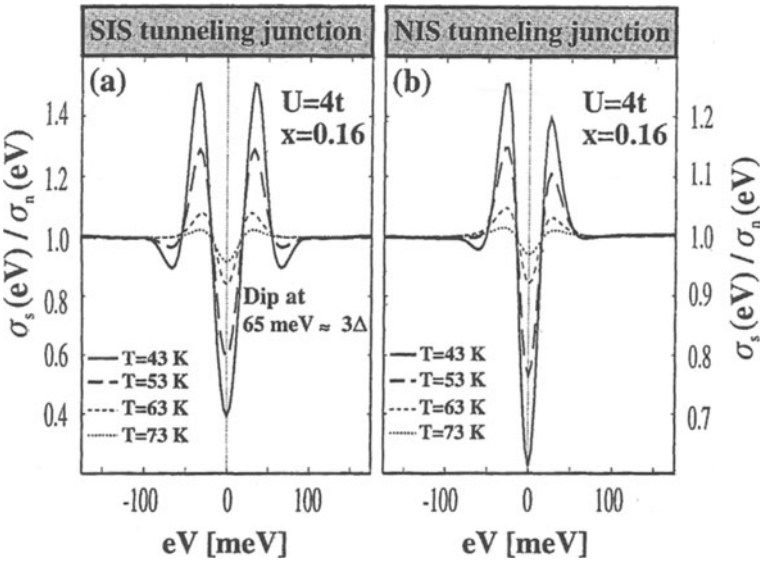

Fig. 9.58. Results for (a) SIS and (b) NIS tunneling conductances $\sigma_s(eV)$ using Cooper–pairing theory due to spin–fluctuation exchange. Both quantities are normalized by the normal state $\sigma_n(eV)$ taken at T=T_c

seen by tunneling spectroscopy in conventional superconductors which exhibits the single–particle excitations spectrum [61]). It is important to relate these features to the spin fluctuation frequency ω_{sf} and resonance frequency ω_{res}. One expects that the remarkable dip structure seen in the single–particle excitation spectrum of various cuprates might be an intrinsic *fingerprint* of a spin–fluctuation induced Cooper–pairing in high–T_c cuprates [220]. It is also interesting to understand why these dip structures occur at different energies in the in–plane normal–insulator–superconductor (NIS) and superconductor–insulator–superconductor (SIS) measurements. Furthermore, while the SIS spectrum is symmetric with respect to the sign of applied voltage the NIS spectra are asymmetric [221, 222].

In Fig. 9.58 we present results [223] for the SIS and NIS spectra at various temperatures obtained using the generalized Eliashberg equations. Remarkably both NIS and SIS tunneling curves show the dip features at $\omega = \omega_{res} + \Delta_0$ and $\omega = \omega_{res} + 2\Delta_0$, respectively. This agrees with experimental data. In order to understand better the origin of these peaks let us remember that the experimental tunneling conductance in NIS is determined by the quasiparticle density of states as discussed in the theory chapter. As we already know the density of states in cuprates is affected by the scattering of the carriers by antiferromagnetic spin fluctuations which are peaked in the superconducting state at ω_{res}. Taking into account that the whole spectrum will be shifted

by the value of the superconducting gap Δ_0 one concludes that the dip seen in the experiments results from the peak in the spin excitations spectra at (π, π) shifted by the superconducting gap. Therefore, the position of the dip

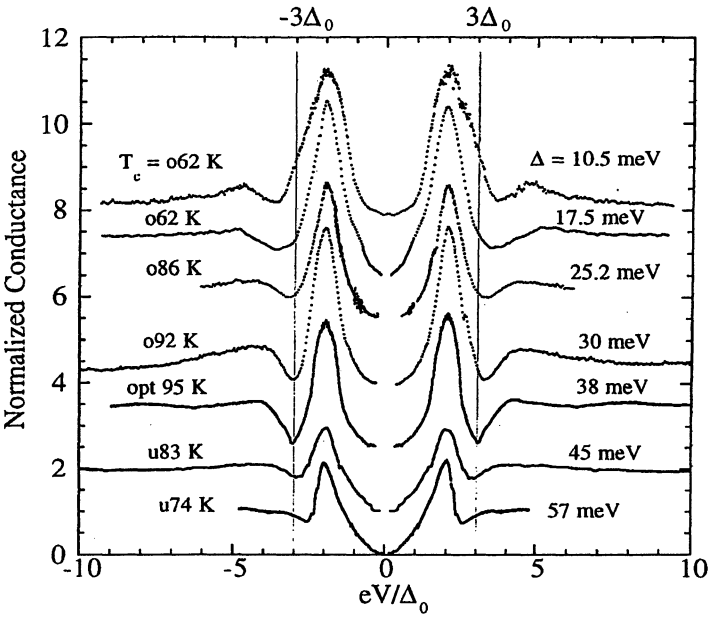

Fig. 9.59. SIS tunneling conductance at various doping levels showing the shift of the dip feature with T_c. Voltage axis is rescaled in units of Δ_0/e, taken from [226]

in NIS is given by:

NIS–dip: $\omega \approx \omega_{res} + \Delta_0$.

In the SIS tunneling both convoluted density of states have to be taken in the superconducting state and thus the dip in SIS occurs at:

SIS–dip: $\omega \approx \omega_{res} + 2\Delta_0$.

This agrees with experiment. Furthermore, in the NIS tunneling the curves are asymmetric due to the fact that one of the density of states has to be taken in the normal state. Thus, the effect will be visible only for the unoccupied states and depends also on the shape of the Fermi surface for the different materials. Therefore, depending on the particular doping level and material the effect may show up for the positive bias voltage or on its negative side.

Our results for SIN and SIS tunneling are similar to those obtained by the spin–fermion model [224]. Regarding the doping dependence of the 'dip' feature we note that it correlates with the doping dependence of the 'resonance

peak' seen in INS. Therefore, the position of the 'dip' feature should have qualitatively similar doping dependence as expected from Fig. 9.46 [225].

In Fig. 9.59 we show the experimental results on SIS tunneling [226]. One clearly sees that the position of the dip does not occur exactly at $3\Delta_0$ but rather at $2\Delta_0 + \omega_{res}$. Furthermore as was argued in Ref. [226] the position of the dip scales similarly to the scaling of the 'resonance' peak seen by INS. Therefore, it appears that dip structure can be considered a strong coupling effect analogous to phonon structures, but the excitations that are responsible for this feature, the spin fluctuations.

Note, the antiferromagnetic spin fluctuations are much weaker in the electron–doped cuprates. As a result the 'dip–hump' feature was not observed in these compounds so far.

9.4.9 Bilayer Effects

Another interesting effect is the bilayer splitting observed in high–T_c cuprates. For a long time it was believed that the enhancement of T_c in two–layer cuprates results from interlayer coupling in the elementary unit cell. The bilayer splitting was observed only recently by means of ARPES experiments [229–231]. As expected the bilayer splitting can be described by the interlayer hopping term

$$2t_\perp \cos k_z \left(\cos k_x - \cos k_y\right)^2 \quad ,$$

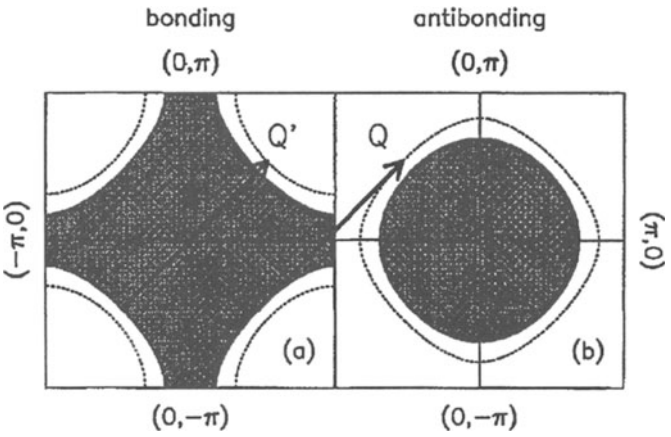

Fig. 9.60. (a) Bonding and (b) antibonding equal energy contours taken from Ref. [232] at optimal doping. The solid lines bounding the shaded regions are the bonding and antibonding Fermi surfaces, respectively. The arrow labeled **Q** corresponds to a (π, π, π) momentum transfer which dynamically nests the bonding Fermi surface with an excited antibonding state shown by the dotted curve. Note, that a momentum transfer **Q'**$=(\pi, \pi, 0)$ fails now to provide nesting

where $t_\perp = 70\text{meV}$. $t_\perp$ describes hopping term between the CuO_2–planes and $k_z = 0$ or π corresponds to the bonding and antibonding bands, respectively. As a result there are two bands crossing the Fermi level as shown in Fig. 9.60.

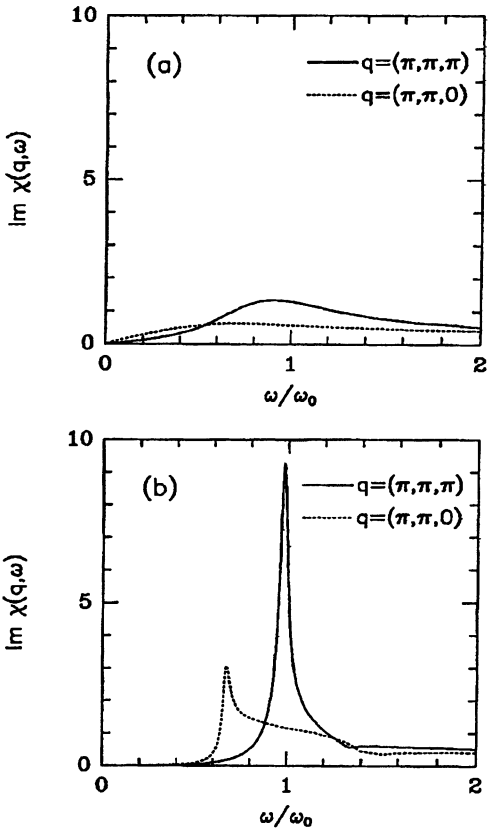

Fig. 9.61. Change of nesting: Results for spin susceptibility $\text{Im}\chi(\mathbf{Q},\omega)$ versus ω for $\mathbf{Q}$'=(π,π,π) (solid curve) and $\mathbf{Q}$= $(\pi,\pi,0)$ (dotted curve) for (a) the normal state at T=T_c and (b) the superconducting state at T=$T_c/2$ taken from [232]. The scales in (a) and (b) are the same for comparison

The change in the Fermi surface topology is important for our theory, since the spin fluctuations are dependent on the amount of the nesting. In the bilayered cuprates due to introduced hopping between neighboring CuO_2–planes the topology of the Fermi surface slightly changes and most importantly the nesting shifts to the three–dimensional antiferromagnetic wave vector $\mathbf{Q}' = (\pi,\pi,\pi)$. This is shown in Fig. 9.60.

The change of the nesting is also seen in the calculation of the spin susceptibility $\text{Im}\chi(\mathbf{q},\omega)$. This is illustrated in Fig. 9.61(a). The peak in $\text{Im}\chi$

in the normal state is more pronounced at **Q'** rather than for **Q** indicating that in the bilayer cuprates the antiferromagnetic fluctuations are essentially three–dimensional. Another interesting feature relates to the resonance peak formation below T_c. Similar to the normal state the 'resonance' peak will be more pronounced for the wave vector **Q'** and stronger in its intensity (see Fig. 9.61(b)) as compared to the one–layer materials. This probably explains why in most cases the resonance peak is visible only in the bilayer cuprates.

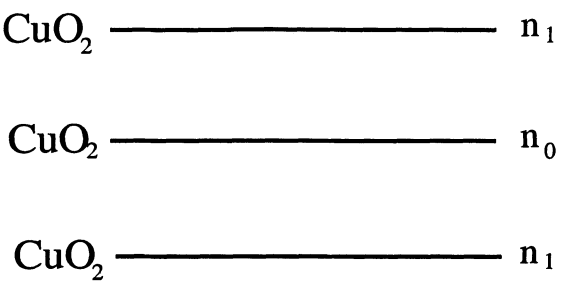

Fig. 9.62. Illustration of the change of the doping concentration of CuO_2–planes in trilayer cuprates. Due to its crystallographic position the inner CuO_2–plane has a smaller doping than the outer ones. Therefore, the inner CuO_2–plane will be underdoped. This effectively may reduces the T_c of the system if further increase the number of layers takes place. For example, it is known that already in five–layered cuprate superconductors the inner CuO_2–plane is undoped and remains insulating

What happens with further increase of the number of CuO_2–planes per unit cell? Already for the three–layer materials due to crystallographic position of the inner CuO_2–plane its doping concentration is sufficiently lower than for the two outer ones as illustrated in Fig. 9.62. Further increase of the number of CuO_2 layers per unit cell does not result in the enhancement of T_c for the same reason. Namely, the inner planes will be less and less metallic and already for five–layered compounds the innner CuO_2 is non–superconducting. This explains the reduction of T_c with increasing number of CuO_2–planes per unit cell, n ($n > 3$).

A final remark we would like to make is on the value of calculated T_c in bilayered cuprates. In the spin fluctuation scenario and using the FLEX approximation T_c enhances in the bilayer cuprates due to enhanced nesting and the corresponding spin fluctuations at **Q'**. However, this depends on the momentum dependence of the hopping term.

Note, in bilayer cuprates the essential physics is unchanged. Therefore, the corresponding 'fingerprints' of the spin fluctuation Cooper–pairing like 'resonance' peak and 'dip' feature seen in INS, and kink structure in the elementary excitations seen in ARPES, and SIS/NIS tunneling spectroscopy

should be present. Further experimental and theoretical studies are expected to support this.

9.5 Results for Sr_2RuO_4

9.5.1 Electronic Structure

We begin the discussion of our results for Sr_2RuO_4 by analyzing their electronic structure. In contrast to the cuprates the electronic structure of the ruthenates is more complicated. For example, according to the LDA calcula-

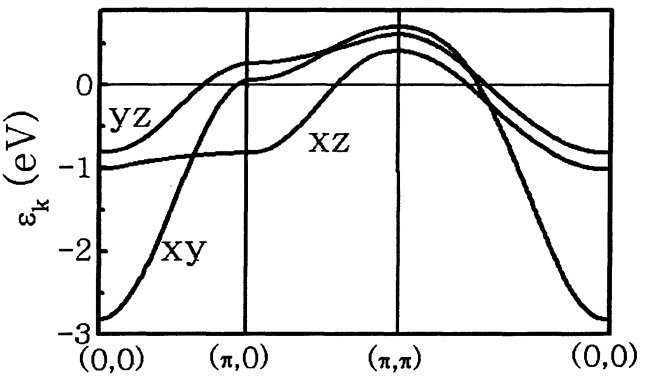

Fig. 9.63. Calculated energy dispersion of the xy, yz, and xz–bands in Sr_2RuO_4 along the route $(0,0) \rightarrow (\pi,0) \rightarrow (\pi,\pi) \rightarrow (0,0)$ in the first BZ. The tight–binding parameters are used. The spin–orbit coupling is taken into account. Note that the energy dispersion of the $xy(\gamma)$–band is two–dimensional, while $xz(\alpha)$–, and $yz(\beta)$–bands are sufficiently one–dimensional as seen from their dispersion

tions there are three bands which cross the Fermi level [157]. Moreover, while one band is quasi–two dimensional (xy), the other two bands (xz, yz) are quasi–one dimensional ones. This is shown in Fig. 9.63 where we present our results for the energy dispersion of the Sr_2RuO_4 in the RuO_2–plane ($k_z = 0$) using the tight–binding parameters and spin–orbit coupling as described before.

The main effect of the spin–orbit coupling on the dispersion is the removal of the degeneracy between xz– and yz–bands as present in the LDA calculation. Therefore, one may say that the spin–orbit coupling acts like a hybridization. On the other hand, the character of the xz– and yz–bands still remains one–dimensional. This also can be recognized in Fig. 9.63. For, example one clearly sees that the xz–band and yz–bands are weakly momentum dependent along $(0,0) \rightarrow (0,\pi)$ and $(0,\pi) \rightarrow (\pi,\pi)$ directions, respectively. At the same time the xy–band is two–dimensional. The reason for this is

the strong overlap between the d_{xy} Ru orbital with the $2p_x$ and $2p_y$ oxygen orbitals. Since Sr_2RuO_4 shows a quasi–two dimensional behavior, it has been proposed originally [50] that only xy–band plays an important role for determining the physical properties of Sr_2RuO_4 in the normal and superconducting states. Actually this is further supported by the fact that the flat region of the xy–band leading to a logarithmic singularity in the density of states (so–called Van–Hove singularity) lies very close to the Fermi level.

Yet note the question about the role of the xz– and yz–bands for determining the physical properties of Sr_2RuO_4 remains unclear. In Fig. 9.64 we show the results for the two–dimensional Fermi surface in ruthenates which consists of two electron–like Fermi surfaces of yz nd xy–bands and hole–like Fermi surface of the xz–band. The filling of each band is approximately 2/3. The important feature that we would like to stress is a strong nesting of the $yz(\beta)$–band at the incommensurate antiferromagnetic wave vector $\mathbf{Q}_i = (2\pi/3, 2\pi/3)$. This is extremely interesting, since it indicates first an importance of the band structure for determining the normal and superconducting properties of Sr_2RuO_4 and secondly it shows the necessity to include into the theoretical analysis all three bands. This is in contrast to the cuprates where the one–band approximation seems to be in order mostly.

9.5.2 Elementary Excitations: Effects of Spin Fluctuations

Unfortunately the complete analysis of the elementary excitations including all three bands and spin–orbit coupling has not been performed so far

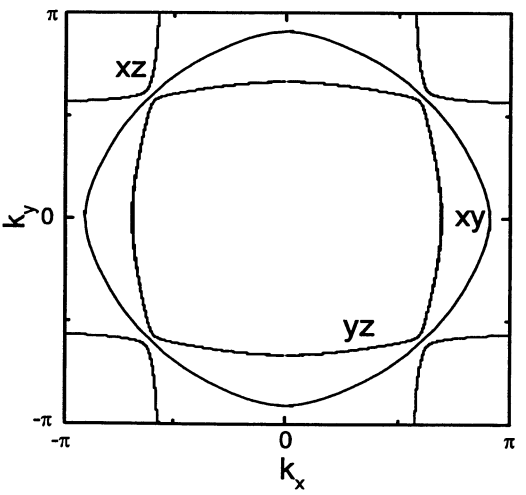

Fig. 9.64. Calculated two–dimensional Fermi surface of Sr_2RuO_4 by taking into account spin–orbit coupling. The Fermi surface consists of three sheets: two with electron–like topology and one with hole–like topology. Spin–orbit coupling acts like a hybridization and removes the degeneracy of the α(xz)– and β(yz)–bands

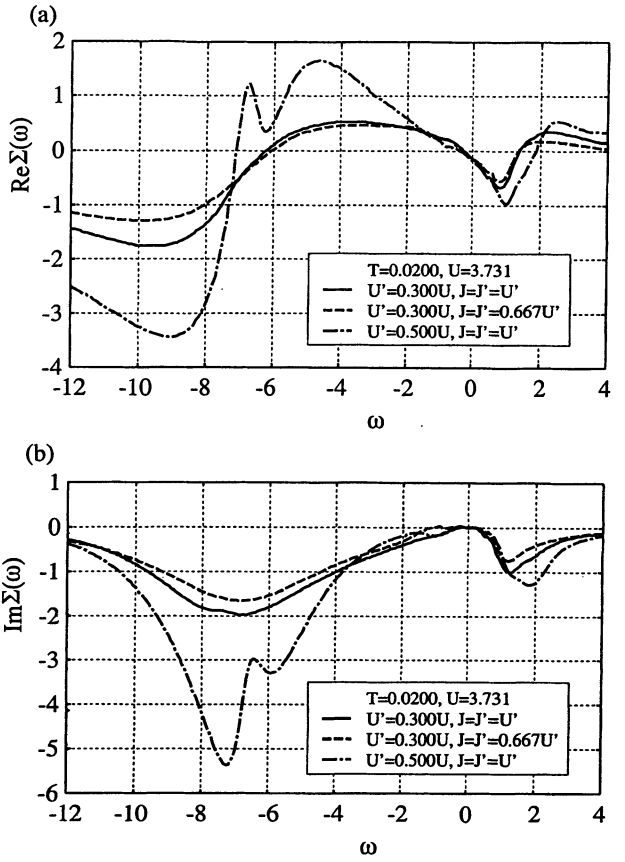

Fig. 9.65. The normal state (a) real and (b) imaginary part of the self–energy for the γ–band taken from Ref. [174]. U, U', and J, J' refer to the intra– and interband Coulomb and Hund's coupling, respectively. Note, that the self–energy $\Sigma(\omega)$ and ω are given in terms of the hopping integral, t

in Sr_2RuO_4. However, there were several attempts to analyze the behavior of the elementary excitations in the 'most important' γ(xy)–band using a perturbation theory up to third order with respect to the on–site Coulomb interaction U. A three–band Hubbard model has been used [174, 175].

In Fig. 9.65 we show the results for the real and imaginary part of the self–energy versus frequency for different values of Coulomb repulsion (intraband U and interband U') and Hund's coupling (J and J') calculated at $\mathbf{k}_F$ for the γ–band. As one can see this band demonstrates the usual Fermi–liquid behavior for different values of the inter–orbit coupling, $\mathrm{Re}\Sigma(\omega) \sim \omega$ and $\mathrm{Im}\Sigma(\omega) \sim \omega^2$ at low energies. Therefore, it is likely that the nesting in α and β–bands does not influence strongly the low–energy excitations of the

γ–band that arise due to a presence of the ferromagnetic–like fluctuations originating also from the γ–band.

On the other hand, at higher energies the self–energy is sensitive to the inter–orbital interaction which can be further observed in the optical conductivity for example. Another important question is the behavior of the self–energy in the α– and β–bands. For example, one expects naively that due to a presence of the strong incommensurate antiferromagnetic fluctuations (IAF) at $(2\pi/3, 2\pi/3)$ and a quasi–one–dimensional character of these bands their self–energy may show a pronounced non–Fermi liquid behavior like in cuprates. Note, experiment does not show any significant deviation from the Fermi–liquid behavior. Further studies are needed.

9.5.3 Dynamical Spin Susceptibility, NMR, and INS

Perhaps one of the most interesting property of the ruthenates is the dynamical spin susceptibility in the normal state. As we discussed in the Introduction the understanding of the temperature dependence of $\chi(\mathbf{q}, \omega)$ is of key significance for determining the superconducting properties in Sr_2RuO_4. Let us study how the two–dimensional three–band Hubbard Hamiltonian together with the spin–orbit coupling can explain the existing experimental data.

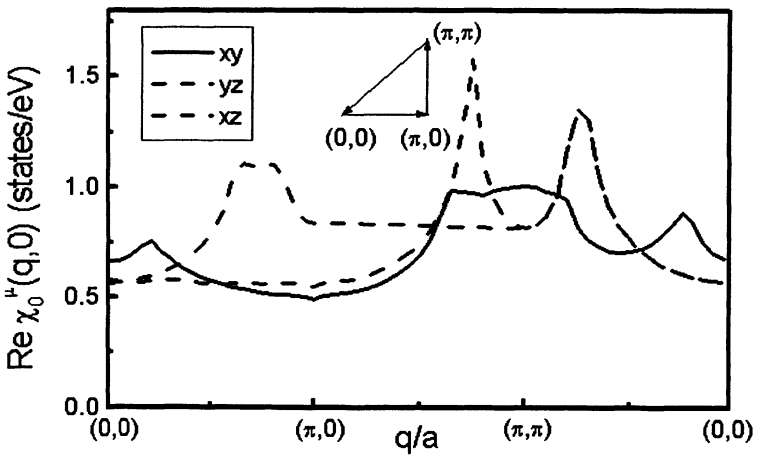

Fig. 9.66. Calculated real part of the Lindhard spin susceptibility χ_0^μ (μ refers to the band indices) in the normal state of Sr_2RuO_4 along the route $(0,0) \rightarrow (\pi,0) \rightarrow (\pi,\pi) \rightarrow (0,0)$ in the first BZ for the three different orbitals (xz,yz, and xy) crossing the Fermi level. Due to the nesting of the xz and yz–bands their susceptibilities show an enhancement at the incommensurate antiferromagnetic wave vector $\mathbf{Q}_i = (2\pi/3, 2\pi/3)$. The response of the xy–band is more isotropic, but significantly larger than in the normal metal due to the vicinity of the Van–Hove singularity

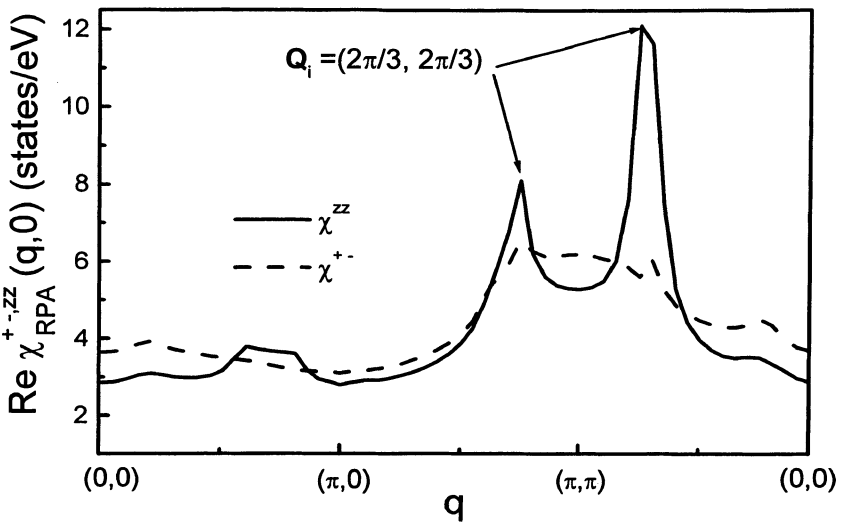

Fig. 9.67. Calculated real part of the longitudinal and transverse components of the total RPA spin susceptibility $\chi^{+-,zz}_{RPA} = \sum_{\mu} \chi^{+-,zz}_{\mu,RPA}$ (μ refers to the band indices) in the normal state of Sr_2RuO_4 along the route $(0,0) \rightarrow (\pi,0) \rightarrow (\pi,\pi) \rightarrow (0,0)$ in the first BZ. Due to spin–orbit interaction the transverse component (χ^{+-}) contains not incommensurate antiferromagnetic fluctuations (IAF) from xz and yz–orbitals, while in the longitudinal component (χ^{zz}) they are enhanced

In Fig. 9.66 we show the results for the Lindhard response functions calculated for the different bands using their tight–binding dispersions. The spin–orbit coupling is not taken into account. As expected due to the pronounced nesting of the xz and yz–bands their susceptibilities display peaks at $\mathbf{Q}_i = (2\pi/3, 2\pi/3)$, while the xy–band does not show any significant feature. The response of the xy–band is enhanced due to the presence of the van–Hove singularity close to the Fermi level. It becomes clear that the features observed by INS relates mainly to the magnetic response of the xz– and yz–bands. However, the present results cannot account for the observed magnetic anisotropy, since both longitudinal and transverse components of the total spin susceptibility are the same if the term which transfers the anisotropy from the orbital subspace into the spin one is neglected. In order to do this we include spin–orbit coupling.

Using the random phase approximation (RPA) for every particular band we calculate the longitudinal and transverse components of the total susceptibility in the RuO_2–plane. Its real parts at $\omega = 0$ are shown in Fig. 9.67. As a result of the spin–orbit coupling the magnetic response becomes very anisotropic along the whole Brillouin Zone. Since the spin and orbital degrees of freedom are mixed now, the orbital anisotropy will be reflected in the magnetic susceptibility. As one sees in Fig. 9.67 the longitudinal component has a pronounced peak at $\mathbf{Q}_i$, while the transverse one does not show

these features at all and is almost isotropic (reproduces mostly the response of the xy–band). In order to understand why the longitudinal susceptibility shows mostly the nesting features of the xz– and yz–bands one has to remember that due to spin–orbit coupling the orbital component of the magnetic susceptibility cannot be excluded. Therefore, the matrix elements such as $\langle i|l_z|j\rangle$ and $\langle i|l_{+(-)}|j\rangle$ have to be taken into account. At the same time the xz– and yz–bands consist of the $|2,+1\rangle$ and $|2,-1\rangle$ orbital states. One sees that while the longitudinal component gets an extra term due to l_z, the transverse component does not, since the transitions between states $|2,+1\rangle$ and $|2,-1\rangle$ are not allowed. Thus, the contribution of the nesting of the xz and yz orbitals to the longitudinal component of the susceptibility is larger than to the transverse one and incommensurate antiferromagnetic fluctuations are almost absent.

In order to see this we show in the inset of Fig. 9.68 the frequency dependence of the longitudinal and transverse components of Imχ calculated for the wave vector $\mathbf{Q}_i = (2\pi/3, 2\pi/3)$. Despite some structure seen in the real part of χ^{+-}_{RPA} at $(2\pi/3, 2\pi/3)$ (see Fig. 9.67) there are no real incommensurate antiferromagnetic fluctuations (IAF) at this wave vector. On the other hand, the structure in χ^{zz}_{RPA} at the same wave vector refers to the IAF fluctuations. The longitudinal component of Imχ reveals a peak at approximately

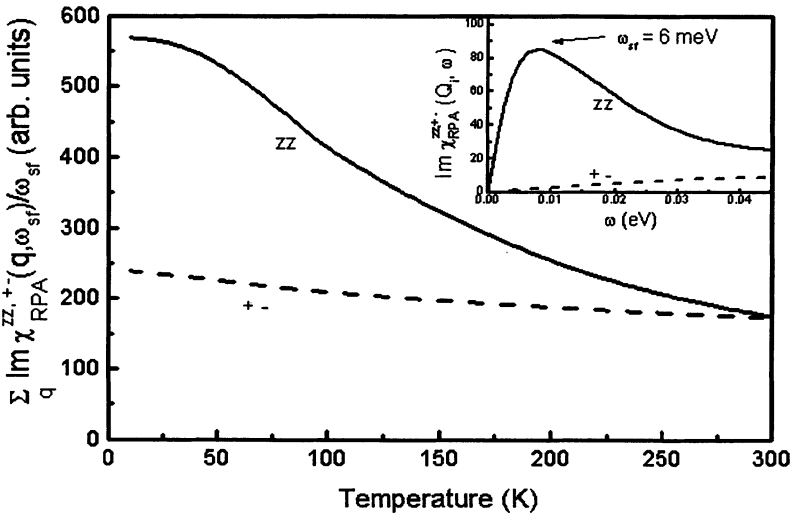

Fig. 9.68. Magnetic anisotropy: Temperature dependence of the imaginary part of the spin susceptibility divided by ω_{sf} and summed over $\mathbf{q}$. Note, zz and $+-$ refer to the out–of–plane (solid curve) and in–plane (dashed curve) components of the RPA spin susceptibility. In the inset we show the corresponding frequency dependence of Im$\chi_{RPA}(\mathbf{Q}_i, \omega)$ at the IAF wave vector $\mathbf{Q}_i = (2\pi/3, 2\pi/3)$ and for $\omega_{sf} = 6$meV

$\omega_{sf} = 6\text{meV}$ in quantitative agreement with INS experimental data [65]. The transverse component is featureless showing the absence of incommensurate antiferromagnetic spin fluctuations. Thus, the fluctuations in the transverse susceptibility are isotropic and ferromagnetic–like. Therefore, antiferromagnetic fluctuations are present only perpendicular to the RuO_2–plane.

In order to demonstrate the temperature dependence of the magnetic anisotropy induced by the spin–orbit coupling we display in Fig. 9.68 the temperature dependence of the quantity

$$\sum_{\mathbf{q}} \frac{Im\chi_{RPA}(\mathbf{q}, \omega_{sf})}{\omega_{sf}}$$

for both components. At room temperatures both longitudinal and transverse susceptibilities are almost identical, since thermal effects wash out the influence of the spin–orbit interaction. With decreasing temperature the magnetic anisotropy increases and at low temperatures we find the important result that the out–of–plane component χ^{zz} is about two times larger than the in–plane one:

$$\chi^{zz} > \chi^{+-}/2 \quad .$$

We also note that our results are in accordance with earlier estimations made by Ng and Sigrist [158]. However, there is one important difference. In their work it was found that the IAF are slightly enhanced in the longitudinal

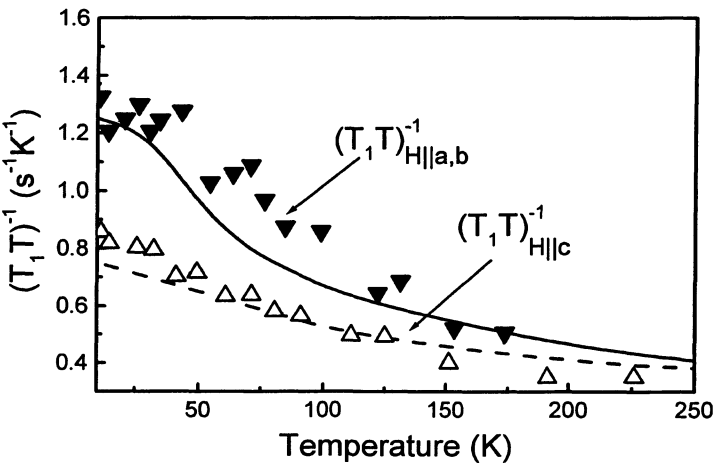

Fig. 9.69. Calculated normal state temperature dependence of the nuclear spin–lattice relaxation rate T_1^{-1} of ^{17}O in the RuO_2–plane for the external magnetic field applied along c–axis (dashed curve) and along the ab–plane (solid curve). Down– and up–triangles are experimental results taken from Ref. [161]

components of the xz– and yz–bands in comparison to the transverse one. In our case we have found that the longitudinal component of the magnetic susceptibility strongly enhances due to orbital contributions. Moreover, we show by taking into account the correlation effects within RPA that the IAF are even further enhanced in the z–direction.

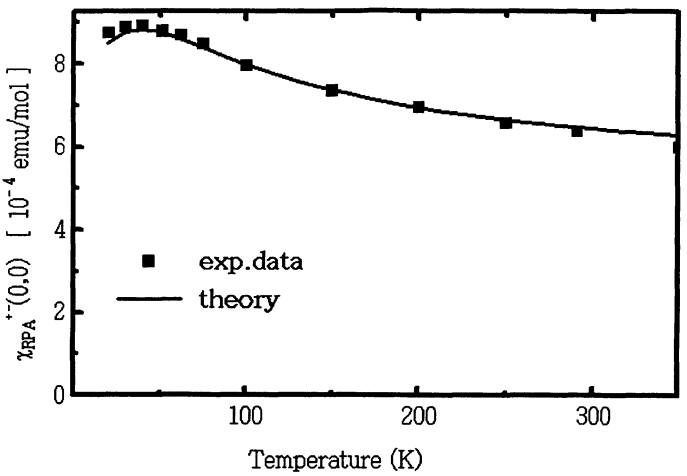

Fig. 9.70. The temperature dependence of the uniform spin susceptibility $\chi^{+-}_{RPA}(0,0)$ calculated using our RPA theory in comparison with the ^{17}O Knight shift measurements in the RuO_2–plane. The peak is due to thermal activation involving xy and yz, xz bands

Finally, in order to compare our results with experimental data we calculate the nuclear spin–lattice relaxation rate T_1^{-1} for the ^{17}O ion in the RuO_2–plane for different external magnetic field orientation (i = a, b, and c):

$$\left[\frac{1}{T_1 T}\right]_i = \frac{2k_B\gamma_n^2}{(\gamma_e\hbar)^2}\sum_{\mathbf{q}}|A^p_{\mathbf{q}}|^2\frac{\chi''_p(\mathbf{q},\omega_{sf})}{\omega_{sf}} \quad , \tag{9.141}$$

where $A^p_{\mathbf{q}}$ is the q–dependent hyperfine–coupling constant perpendicular to the i–direction.

In Fig. 9.69 we show the calculated temperature dependence of the spin–lattice relaxation for an external magnetic field within and perpendicular to the RuO_2–plane together with experimental data. At $T = 250$K the spin–lattice relaxation rate is almost isotropic. Due to the anisotropy in the spin susceptibilities arising from spin–orbit coupling the relaxation rates become increasingly different for decreasing temperature. The largest anisotropy occurs close to the superconducting transition temperature in good agreement for experimental data [161].

It is still important to see whether our theory yields the weak ferromagnetic fluctuations that were observed by means of the NMR Knight shift [176]. The latter probes the magnetic fluctuations around $\mathbf{q}$=0. In Fig. 9.70 we show the results for the temperature dependence of the uniform susceptibility $\chi^{+-}_{RPA}(0,0)$. One sees that a weak temperature dependence in fair agreement with experimental data [176] occurs and arises due to ferromagnetic–like fluctuations mainly of the xy–band. Note, very recently ferromagnetic–like excitations were also observed by means of INS experiments [177]. This also agrees with our results.

9.5.4 Superconducting Order Parameter

Triplet superconductivity in Sr_2RuO_4 is of particular interest. It is important to understand in detail how the triplet Cooper–pairing is realized in this system with ferromagnetic and incommensurate antiferromagnetic spin fluctuations at $\mathbf{Q}_i = (2\pi/3, 2\pi/3)$. We note that the total spin susceptibility $\chi(\mathbf{q},\omega)$ controls the symmetry of the superconducting order parameter. Therefore, the spin–orbit coupling plays an important role for the superconducting state and for determining the symmetry of the superconducting state. First, we present the analysis of the superconducting gap without taking into account the spin orbit–coupling. We assume that exchange of spin fluctuations is responsible for Cooper–pairing. Why is triplet pairing pairing realized despite the strong incommensurate antiferromagnetic fluctuations (IAF) at $\mathbf{Q}_i \approx (2\pi/3, 2\pi/3)$?

For the analysis of superconductivity in Sr_2RuO_4 we take into account that experiment observes non–s–wave symmetry of the order parameter which strongly suggests spin–fluctuation–mediated Cooper pairing. Then assuming spin–fluctuation–induced pairing it is possible to analyze the symmetry of the superconducting state from the gap equation and our calculated results for $\chi(\mathbf{q},\omega)$ with pronounced wave vectors at $\mathbf{Q}_i$ and $\mathbf{q}_i$. The gap equation is for the band i given by:

$$\Delta^i_{\mathbf{k}} = -\sum_{\mathbf{k}',j} [V^{eff}_{\sigma}(\mathbf{k},\mathbf{k}')]^{ij} \frac{\Delta^j_{\mathbf{k}'}}{2E^j_{\mathbf{k}'}} \tanh\left(\frac{E^j_{\mathbf{k}'}}{2k_BT}\right) \quad , \tag{9.142}$$

where $E^i_{\mathbf{k}} = \sqrt{{\epsilon^i_{\mathbf{k}}}^2 + \left[\Delta^i_{\mathbf{k}}\right]^2}$ is the energy dispersion of the band i. Note, the pairing potential $V^{eff}_{\sigma}(\mathbf{k},\mathbf{k}')$ is different for singlet ($\sigma = 0$) and triplet ($\sigma = 1$) Cooper pairing. The eigenvalue analysis of Eq. (9.142) will yield the symmetry with the lowest energy.

For the determination of the pairing potential we use the calculated FS and spin susceptibility for Sr_2RuO_4 and also follow the analysis by Anderson and Brinkmann for ^{3}He [198] and by Scalapino for the cuprates [199]. We compare the results obtained by assuming singlet or triplet pairing.

For triplet pairing the effective pairing interaction is given by

$$\left[V_1^{eff}(\mathbf{k},\mathbf{k}')\right]^{ij} = -\frac{U^2}{2}\left(\frac{\chi_0^{ii}(\mathbf{k}-\mathbf{k}',0)}{1-U\chi_0^{ii}(\mathbf{k}-\mathbf{k}',0)} + \frac{\chi_0^{ii}(\mathbf{k}-\mathbf{k}',0)}{1+U\chi_0^{ii}(\mathbf{k}-\mathbf{k}',0)}\right) - 2U^2\chi_0^{ij}(\mathbf{k}-\mathbf{k}',0) \quad , \tag{9.143}$$

where the last term occurs only for α and β–bands. Note, the first two terms refer to the intraband spin and charge fluctuations, respectively

For singlet pairing the effective pairing interaction has the form [200]

$$\left[V_0^{eff}(\mathbf{k},\mathbf{k}')\right]^{ij} = \frac{U^2\chi_0^{ii}(\mathbf{k}-\mathbf{k}',0)}{1-U\chi_0^{ii}(\mathbf{k}-\mathbf{k}',0)} + \frac{U^3\left[\chi_0^{ii}(\mathbf{k}-\mathbf{k}',0)\right]^2}{1-U^2\left[\chi_0^{ii}(\mathbf{k}-\mathbf{k}',0)\right]^2} - U^2\chi^{ii}(\mathbf{k}-\mathbf{k}',0) \quad . \tag{9.144}$$

Again, the first two terms refer to the spin and charge fluctuations, respectively and the last term avoids double counting. Note, the cross–terms including χ^{ij} are small due to the Pauli principle and thus we neglect them for singlet pairing.

Using appropriate symmetry representations [201] we discuss the solutions of Eq. (9.142) assuming p, d, or f–wave symmetry of the order parameter in the RuO_2–plane:

$$\Delta_p(\mathbf{k}) = \Delta_0\hat{\mathbf{z}}(\sin k_x a + i\sin k_y a), \tag{9.145}$$

$$\Delta_d(\mathbf{k}) = \Delta_0(\cos k_x a - \cos k_y a), \tag{9.146}$$

$$\Delta_{f_{x^2-y^2}}(\mathbf{k}) = \Delta_0\hat{\mathbf{z}}(\cos k_x a - \cos k_y a)(\sin k_x a + i\sin k_y a). \tag{9.147}$$

Here the $\hat{\mathbf{z}}$–unit vector refers to the d_z component of the Cooper–pairs as observed in the experiment [208]. The possible explanation for this we present later. These symmetries of the superconducting order parameter must be substituted into the Eq. (9.142). For simplicity we consider first the solution of Eq. (9.142) in the RuO_2–planes and then discuss what is happening along c–axis. Note, the largest eigenvalue of Eq. (9.142) will yield the symmetry of the superconducting order parameter Δ_l in Sr_2RuO_4.

Solving Eq. (9.142) in the first BZ down to 5K we have found that p–wave symmetry yields the largest energy gain for the $xy-$band, while for the $xz-$ and $yz-$bands the situation is more complicated.

One sees that the gap equations for the $xy-$ and $yz-$, xz–bands can be separated due to their weak interaction. For the xy–band the p–wave is the most stable solution, while for the $xz-$ and $yz-$bands $f_{x^2-y^2}$–wave symmetry yields the largest eigenvalue due to stronger nesting.

Fig. 9.71 characterizes the solutions of Eq. (9.142). Note, a good approximation is to linearize Eq. (9.142) with respect to Δ_l^i, i.e. $E_{\mathbf{k}'}^i \to \epsilon_{\mathbf{k}'}^i$. We use also $\tanh(\epsilon_{\mathbf{k}'}^i/2k_BT) = 1$. Thus, the main contribution to the pairing comes from the Fermi levels. We present our results for the Fermi surface in the RuO_2 plane. The wave vectors $\mathbf{Q}_i$ and $\mathbf{q}_i$ refer to the peaks in $\chi(\mathbf{q},\omega)$. The

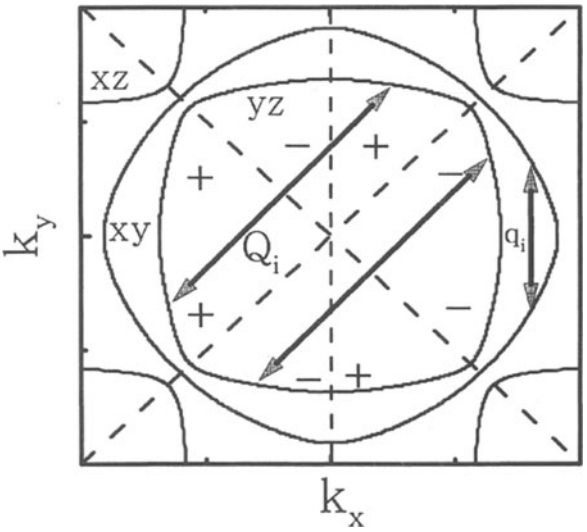

Fig. 9.71. Symmetry analysis of the order parameter for triplet pairing in the first BZ for k_z=0 (solid curves) and $k_z = \pi/2c$ (dotted curves). α, β, and γ denote the FS of the corresponding hybridized bands. The wave vectors $\mathbf{Q}_i$ and $\mathbf{q}_i$ are the pronounced wave vectors resulting from the susceptibility (without spin–orbit coupling). For $f_{x^2-y^2}$–wave symmetry the nodes of the real part of the order parameter are shown (dashed lines) and the regions + (-) where the $f_{x^2-y^2}$–wave superconducting gap is positive (negative). Note, for the real part of a p–wave order parameter the node would occur only along k_x=0

areas with $\Delta_{f_{x^2-y^2}} > 0$ and $\Delta_{f_{x^2-y^2}} < 0$ are denoted by (+) and (-), respectively. Note, the minus sign in Eq. (9.142) is cancelled for triplet pairing. The summation over $\mathbf{k}'$ in the first BZ is dominated by the contributions due to $\mathbf{Q}_i$ for the α– and β–bands and the one due to $\mathbf{q}_i$ for the γ–band.

As can be seen from Fig. 9.71 in the case of $f_{x^2-y^2}$–wave symmetry for the xy–band the wave vector $\mathbf{q}_i$ bridges the same number of portions of the FS with opposite and equal sign. Therefore, for the xy–band no solution with $f_{x^2-y^2}$–wave symmetry is possible. On the other hand, for the xz– and yz–band the wave vector $\mathbf{Q}_i$ bridges portions of the FS with *equal* signs of the $f_{x^2-y^2}$–superconducting order parameter. The eigenvalue of this order parameter is also enhanced due the interband nesting for xz and yz–bands. Thus, superconductivity in the xz– and yz–band in the RuO_2 plane is indeed possible with $f_{x^2-y^2}$–wave order parameter. Therefore, solving Eq. (9.142) for the three band picture we found a competition between triplet p–wave and $f_{x^2-y^2}$–wave superconductivity in the RuO_2–plane.

Also using Eq. (9.144) we can rule out singlet pairing. In particular, assuming $d_{x^2-y^2}$–symmetry for Sr_2RuO_4 the Eq. (9.142) yields an eigenvalue which is lower than in the case of triplet pairing. As can be seen using Fig.

9.71 this is plausible. Note, we get for $d_{x^2-y^2}$–wave symmetry a change of sign of the order parameter upon crossing the diagonals of the BZ. According to Eq. (9.142) wave vectors around $\mathbf{Q}_i$ connecting areas (+) and (-) contribute constructively to the pairing. Contributions due to $\mathbf{q}_i$ and the background connecting areas with the same sign subtract from the pairing (see Fig. 9.71 with nodes at the diagonals). Therefore, we get that the four contributions due to $\mathbf{q}_i$ in the xy–band do not allow to have $d_{x^2-y^2}$–wave symmetry in the xy–band. Despite the pair–building contribution due to $\mathbf{Q}_i$ one gets that the eigenvalue of the $d_{x^2-y^2}$–wave symmetry in the xy–band is smaller than for the $f_{x^2-y^2}$–wave symmetry. This is due to the large contribution from $\mathbf{Q}_i$ to the cross–terms for the triplet pairing which are absent for the singlet pairing. For d_{xy}–symmetry where the nodes are along $(\pi,0)$ and $(0,\pi)$ directions we argue similarly. Thus, we may exclude this symmetry. Thus, we safely conclude that as a result of the topology of the FS and the spin susceptibility we seem to get for p– and f–wave symmetry the strongest pairing. We can definitely exclude d–wave pairing in the RuO_2–plane.

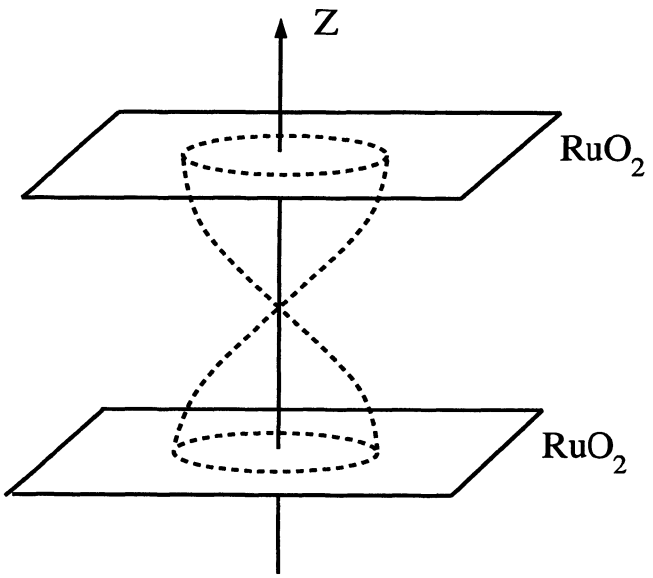

Fig. 9.72. Schematic representation of the possible node formation in the order parameter between the RuO_2–planes (in real coordinate representation) as resulting from the magnetic anisotropy. Here, the amplitude of the order parameter along the z–direction has been drawn in cylindrical coordinates between RuO_2–planes. This seems in agreement with thermal conductivity measurements below T_c [208,210]

Since we found a strong competition between p–wave and $f_{x^2-y^2}$–wave superconductivity in the RuO_2–plane the question arises what is the role of

the c–axis in determining the superconducting properties in Sr_2RuO_4. This question requires an understanding of the role of spin–orbit coupling for the determining the symmetry of the superconducting order parameter?

First, the spin–orbit coupling affects the spin dynamics and as we have shown induces the anisotropy in the spin subspace. In particular the two–dimensional IAF at $\mathbf{Q}_i = (2\pi/3, 2\pi/3)$ align along c–direction. This simply means that the antiferromagnetic moments associated with these fluctuations align along z–direction. At the same time the ferromagnetic fluctuations are in the ab–plane. This is illustrated in Fig. 9.72. Since the interaction in the RuO_2–plane (k_z=0) is mainly ferromagnetic nodeless p–wave pairing is indeed possible and the superconducting order parameter in all three bands will not have nodes and not only for xy–band as before. Note also that the γ-band reveals a high density of states. Therefore, the triplet p–wave pairing without line–nodes will be realized in the RuO_2–plane. On the other hand the state between the RuO_2–plane will be determined mainly by the IAF that are polarized along the c–direction. This implies that the magnetic interaction between the planes has to be rather antiferromagnetic than ferromagnetic. This antiferromagnetic interaction suggests a line of nodes for $\Delta(\mathbf{k})$ between the neighboring RuO_2–planes. In a phenomenological approach this was shown by two groups [202,203]. For example, it was proposed that the symmetry of the superconducting order parameter in Sr_2RuO_4 will have a form

$$\Delta_{\mathbf{k}} = \Delta_0 \tilde{\mathbf{z}} \left(\sin \frac{k_x a}{2} \cos \frac{k_y a}{2} + i \sin \frac{k_y a}{2} \cos \frac{k_x a}{2} \right) \cos \frac{k_z c}{2}. \tag{9.148}$$

Then, due to the magnetic anisotropy induced by spin–orbit coupling a nodeless p–wave pairing is possible in the RuO_2–plane as experimentally observed [208]. Thus, a node would lie between the RuO_2–planes. Indeed as observed by thermal conductivity measurements [208,210] the nodes in the superconducting order parameter are between the RuO_2–planes.

Note, the spin–orbit coupling determines also the orientation of the orbital moment z of the Cooper–pair. In particular, it is convenient to combine the three spin component into a vector $\mathbf{d}(\mathbf{k})$ in spin space. As mentioned earlier this is achieved by the expanding $\Delta_{\mathbf{k}}$ in the three symmetric 2×2 matrices $i\sigma_\mu\sigma_2$, $\mu = 1,2,3$, where σ_μ are the Pauli matrices as

$$\Delta_{\mathbf{k}} = \sum_\mu d_\mu(\mathbf{k})(\sigma_\mu i\sigma_2) = \begin{pmatrix} -d_x + id_y & d_z \\ d_z & d_x + id_y \end{pmatrix}. \tag{9.149}$$

Then, in a triplet superconductor, the pairing state can be represented by the three–dimensional vector $\mathbf{d}(\mathbf{k})$, whose magnitude and direction may vary over the Fermi surface in $\mathbf{k}$–space. Like in ^{3}He several pairing states related to the different orientation of the total spin moment of the Cooper–pair d_z, d_y, d_z may have the same condensation energy under weak–coupling conditions. This degeneracy is related to the spin rotation symmetry being present in ^{3}He (which leads to presence of a so–called B–phase) but is lifted by the

spin–orbit coupling in Sr_2RuO_4 [206]. Then, the analogy of the A–phase–like can realize in Sr_2RuO_4 ($\mathbf{d}(\mathbf{k})_A = (0,0,d_z(k_x \pm ik_y))$) while the B–phase–like might be suppressed ($\mathbf{d}(\mathbf{k})_B = (d_x k_x, d_y k_y, 0)$).

The different orientation of the spin and orbital angular momenta of the Cooper–pair is illustrated in Fig. 9.73 . The important consequence of this

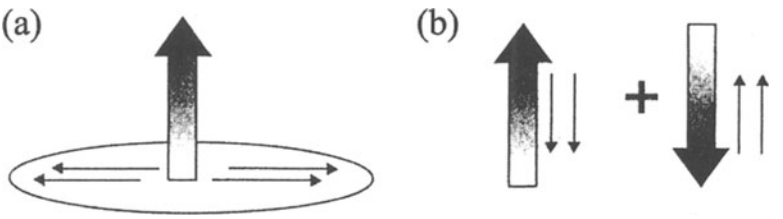

Fig. 9.73. Illustration of the possible superconducting states in Sr_2RuO_4 taken from Ref. [211]. (a) $\Delta(\mathbf{k}) = d_z(\sin k_x + i \sin k_y)$ and (b) $\Delta(\mathbf{k}) = d_x \sin k_x + d_y \sin k_y$ have different spin and total angular momentum. The $\Delta(\mathbf{k}) = d_z(\sin k_x + i \sin k_y)$ superconducting state has an angular momentum along c–axis (thick arrow) and the spin lying in the RuO_2–plane

order parameter is the uncompensated orbital angular momentum of the Cooper–pair (so–called 'chiral' state). Why the chiral state, i.e., $\Delta(\mathbf{k}) = d_z(\sin k_x \pm i \sin k_y)$, is realized in view of our results for the magnetic anisotropy in the normal state shown in Figs. 8.67 and 8.68? To see this, one has to consider the additional contribution of the spin–orbit coupling to the free enerby in the superconducting state $\lambda(\mathbf{l}_{CP} \cdot \mathbf{s})$ where $\mathbf{l}_{CP}$ refers to the orbital moment of a Cooper–pair and $\mathbf{s}$ denotes the electron spin. In a simple mean–field analysis the components of $\mathbf{s}$ are replaced by $\langle s_i \rangle \sim \chi_{ij} \cdot H_j$ where χ_{ij} refers to the transversal (χ_{+-}) and longitudinal (χ_{zz}) component of the magnetic susceptibility. Obviously, due to $\chi_{zz} > \chi_{+-}$ (see Figs. 8.67 and 8.68) the degeneracy between various representation for $\Delta(\mathbf{k})$ is lifted because one gains more energy if the orbital moment of a Cooper–pairs is aligned along the z–direction yielding the chiral state as the lowest one in energy. This state is illustrated in Fig. 9.73(a).

In analogy to ^{3}He, the interesting effects can be observed by applying external magnetic field or external pressure along ab–plane to Sr_2RuO_4. For example, in ^{3}He under pressure the transition from B to A phase has been observed. In Sr_2RuO_4 the situation is the opposite. Superconductivity in Sr_2RuO_4 is already in the A–like phase and therefore, by applying pressure or magnetic field one could cause the transition into B–like phase. However, if the γ–band would become more nested due to external pressure, an f–wave order parameter is possible. Another interesting effect concerns the possible change of the orientation of the unit vector $d_z = \hat{\mathbf{z}}$ of the superconducting order parameter induced by the external magnetic field discussed in

section 9.3.5. It means that for relatively large magnetic field applied along c–direction the significant d_x and d_y components in the superconducting order parameter in Sr_2RuO_4 can be induced. Of course, this effect is relatively small (as also in ^3He) but can be observed.

In summary, Sr_2RuO_4 is a remarkable example of a system where the interplay of ferromagnetic and incommensurate antiferromagnetic fluctuations result in a non–trivial symmetry of the superconducting order parameter. Note, the nesting of $\alpha-$ and β–bands may lead as we have shown to a node formation in the superconducting gap. Although its existence was not yet definitely concluded experimentally it can be verified by applying magnetic field or pressure. Since the antiferromagnetic fluctuations are not helpful for the triplet pairing, one may expect an enhancement of the superconducting transition temperature and the nodeless superconducting gap if the nesting is suppressed. Interestingly this phenomenon was proposed to be responsible for the occurrence of superconductivity in the ferromagnetic phase [207] of unconventional superconductors like $ZrZn_2$ and UGe_2. In particular, we have shown that spin–orbit coupling play an essential role in stabilization of the A–like phase in Sr_2RuO_4 and is responsible for the node formation between neighboring RuO_2–planes.

9.5.5 Doping Dependence of Ruthenates

Comparing ruthenates and cuprates one clearly sees that their behavior differs drastically in the normal state. The ruthenates are good Fermi–liquid systems despite of the presence of IAF at $\mathbf{Q}_i = (2\pi/3, 2\pi/3)$. On the other hand cuprates can be characterized as systems which may behave mainly non–Fermi liquid like. The most remarkable is the doping concentration dependence of the cuprates properties. The electronic correlations are more important in cuprates. The on–site Coulomb repulsion U (which can be roughly estimated as e^2/r where r refers to the radius of the corresponding electronic shell) is much larger than the band width. In the ruthenates which are $4d$–electron systems the effect of correlations is weaker than in cuprates and U is of order of the electronic bandwidth, W. Therefore, one concludes that in ruthenates we are in the intermediate correlation regime. As a result in the ruthenates the correlations are not strong enough to violate Fermi–liquid theory. Nevertheless, correlations in the ruthenates occur as well. This is obvious from Fig. 9.74.

In Fig. 9.74 we show results for the magnetic phase diagram obtained experimentally by Nakatsuji and Maeno [218] for $Ca_{2-x}Sr_xRuO_4$. Despite the fact that introducing Ca does not change the valence in the system the magnetic phase diagram changes completely. First, superconductivity disappears and systems remain paramagnetic metals up to x=0.5. Then, the system becomes a ferromagnetic metal. Most remarkably upon further doping an insulating antiferromagnetic transition occurs.

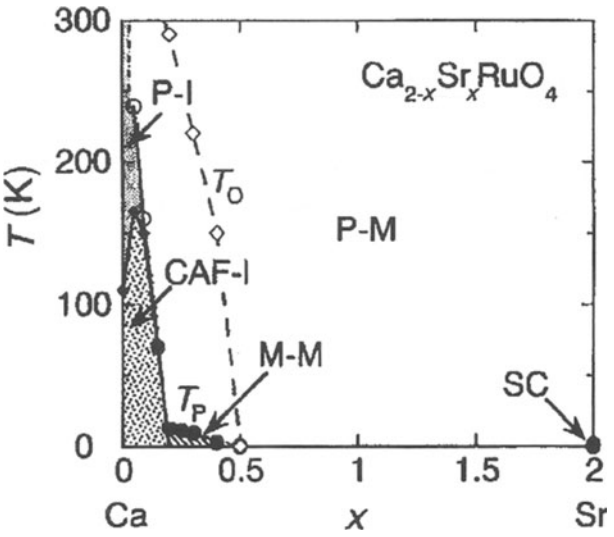

Fig. 9.74. Phase diagram of $Ca_{2-x}Sr_xRuO_4$. P refers to paramagnetic, CAF to canted antiferromagnetic, M to magnetic, SC to the the superconducting phase, –M to the metallic phase, and –I to the insulating phase

Note, introducing Ca instead of Sr ion allows to have structural distortion of the pure tetragonal crystal lattice of Sr_2RuO_4 due to the smaller radius of the Ca ionic sphere. This was discussed by Fang and Terakura [219] by means of LDA calculations. Their main results are shown in Fig. 9.75. First, between $0 < x < 0.5$ the RuO_6 octahedra gets rotated around c–axis. This basically changes the hopping term of the xy–band and most importantly brings the van Hove singularity closer to the Fermi level enhancing the ferromagnetic fluctuations and leading to a ferromagnetic state at $x = 0.5$. Further doping with Ca allows to have not only the rotation of the RuO_6 octahedra, but also its tilting. Thus, hopping in the xz and yz–bands reduces. As a consequence the Coulomb repulsion U will be larger than the bandwidth of the conduction bands. The resulting increase of correlations cause a Mott insulator transition driven by the IAF fluctuations. Further studies of the resistivity in Ca doped samples will justify the proposed scenario.

To summarize the whole section we have shown that Sr_2RuO_4 is one of the first example of a solid state system showing unconventional triplet superconductivity. We have shown that spin fluctuations may explain qualitatively the occurrence of p–wave superconductivity with line nodes between the RuO_2–planes. Furthermore, due to a presence of ferromagnetic and incommensurate antiferromagnetic fluctuations Sr_2RuO_4 seems to be an ideal system where the role and competitions of various spin fluctuations for the formation of superconductivity can be studied in detail. In particular, we have

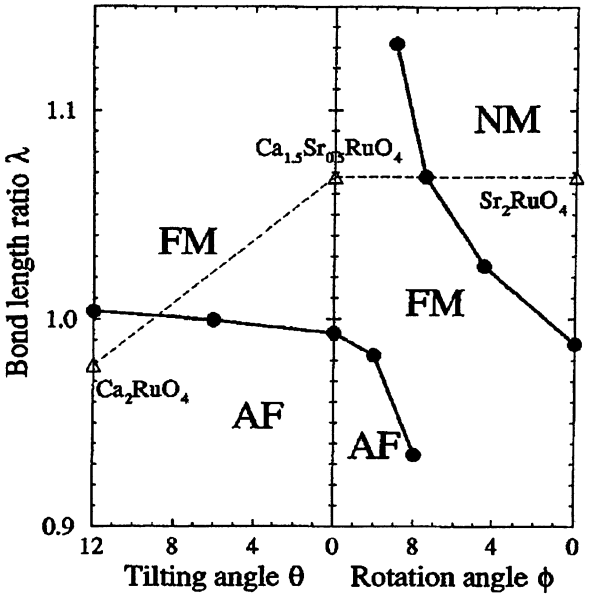

Fig. 9.75. The calculated magnetic phase diagram of Sr_2RuO_4 including structural distortions, taken from Ref. [219]. The solid lines are calculated phase boundaries, while the triangles linked by dashed lines correspond to the experimental data

seen that incommensurate antiferromagnetic spin fluctuations are not helpful for triplet pairing and may result in the formation of line nodes between neighboring RuO_2–planes. The relative simplicity of this compound in comparison to heavy–fermion superconductors could make Sr_2RuO_4 the model system where further interesting and exciting physics (in particular regarding thermodynamical properties, effects due to magnetic and non–magnetic impurities, etc.) will be discovered.

9.6 Summary and Outlook

In this review we present a microscopic theory for the interaction between quasiparticles and spin fluctuations. This is applied to the layered cuprates and triplet superconductor Sr_2RuO_4. For simplicity we assume that the electronic dynamics is essentially controlled by the CuO_2 and RuO_2–planes, respectively.

For the description of singlet superconductivity in the cuprates we employ a one–band model Hamiltonian. The interaction between the carriers (quasiparticles) is described by an effective Coulomb coupling U and the itinerancy of the carriers by a hopping integral t. In the case of hole doping the states of the effective band are mainly the hybridized p–states originating

from the O–atoms. The spin fluctuations arise from the magnetic activity of the Cu–spins and the induced spin polarization of the p–states. In the case of electron doping the effective one–band Hamiltonian describes the hybridized d–states of the UHB and U is an effective coupling between the electrons in these states. The spin fluctuations result from the Cu–spins. Upon doping the Cu–spins are quenched and the spin polarization of the band is reduced. We assume itinerant magnetism for the UHB.

Using this model we have found that the phase diagram, the symmetry of the superconducting order parameter, and the behavior of the elementary and spin excitations in hole– and electron–doped cuprates can be largely understood. Particular interesting behavior we have found for the underdoped cuprates. Due to strong scattering of quasiparticles by antiferromagnetic spin fluctuations a 'weak' pseudogap appears at the Fermi level in the density of states. It increases with decreasing doping concentration. Cooper–pair phase fluctuations in underdoped cuprates are enhanced by the reduced dimensionality and also since phase–incoherent Cooper–pairs do not overlap well resulting in a small n_s. These fluctuations of phase–incoherent Cooper pairs destroy the long–range superconducting order and the Meissner effect. In conventional, bulk superconductors this is not relevant, since the large superfluid density leads to a typical energy scale of phase fluctuations much larger than the superconducting energy gap Δ which governs the thermal breaking of Cooper pairs. Thus, in conventional superconductors the superconducting transition is due to the destruction of the Cooper pairs and T_c is proportional to Δ_0. We have found $T_c \propto n_s$ in underdoped hole–doped cuprates indicating that the phase fluctuations drive the transition. The Cooper–pairs only break up at a crossover temperature around T_c^*, $T_c^* > T_c$. T_c^* is approximately given by the transition temperature one would obtain without phase fluctuations. Between T_c and T_c^* local Cooper–pairs without long–range phase coherence are present. Therefore, we safely conclude that we have a qualitative understanding of the phase diagram in the cuprates. Furthermore, the important elementary excitations and their interdependence with spin excitations (resonance peak) can be well understood within our theory. Our results also shed some light on the asymmetry of hole– and electron–doped cuprates.

For describing triplet Cooper–pairing in Sr_2RuO_4 we also employ a Hubbard Hamiltonian. In order to derive an electronic theory we take the electronic band structure of Sr_2RuO_4 into account. Magnetic activity arises from the itinerant electrons in the Ru d–orbitals. Due to spin–orbit coupling a strong magnetic anisotropy occurs ($\chi^{+-} < \chi^{zz}$) in the normal state . This mainly results from different values of the g–factor for the transverse and longitudinal components of the spin susceptibility (i.e. the matrix elements differ) and from a change of the bare energy dispersion of the d–electrons. Obviously, this and the presence of incommensurate antiferromagnetic and ferromagnetic fluctuations have consequences for the symmetry of the superconducting order parameter. In particular, using spin fluctuation–induced

Cooper–pairing one can understand how p–wave Cooper–pairing with line nodes between neighboring RuO_2–planes may occur.

Despite the relative success of the Eliashberg–like treatment of superconductivity via spin fluctuations exchange in cuprates and ruthenates there remain critical questions. In particular, in the theory of cuprates it is necessary to clarify the role of the vertex corrections and to which extent an effective second order perturbation theory can be applied. Furthermore, in the underdoped cuprates the origin of the pseudogap and the coexistence of short–range weak antiferromagnetism and superconductivity has to be understood. Also the symmetry of the superconducting order parameter in overdoped electron–doped cuprates must be clarified. In the ruthenates the thermodynamical properties remain to be studied in detail. It is of interest to apply our theory also to superconductivity in heavy–fermion systems exhibiting spin fluctuations.

APPENDIX A
Derivation of the Generalized Eliashberg Equations for the Interaction of Quasiparticles and Spin Fluctuations

Here, we present the derivation of the generalized Eliashberg equations for the interaction of quasiparticles and spin fluctuations in a detailed form, however, without discussing the relevancy of the approximations we used. This is discussed in the main text.

We start with the Green's function for itinerant electrons (holes). Using the Nambu notation for the superconducting state [89], the one–particle Green's function is a 2x2–matrix

$$\hat{G}(\mathbf{k}, i\omega_n) = \int_0^\beta d\tau \, e^{i\omega_n \tau} \hat{G}(\mathbf{k}, \tau) \quad , \tag{9.150}$$

where

$$\hat{G}(\mathbf{k}, \tau) = -\langle T_\tau \, \psi_{\mathbf{k}}(\tau) \psi_{\mathbf{k}}^\dagger(0) \rangle \quad , \quad \psi_{\mathbf{k}}(\tau) = \begin{pmatrix} c_{\mathbf{k}\uparrow}(\tau) \\ c_{-\mathbf{k}\downarrow}^\dagger(\tau) \end{pmatrix} \quad . \tag{9.151}$$

We employ the Heisenberg picture:

$$c_{\mathbf{k}\sigma}(\tau) \equiv e^{\tau H} \, c_{\mathbf{k}\sigma} \, e^{-\tau H} \quad , \tag{9.152}$$

and

$$\bar{c}_{\mathbf{k}\sigma}(\tau) \equiv e^{\tau H} \, c_{\mathbf{k}\sigma}^\dagger \, e^{-\tau H} \quad , \tag{9.153}$$

where τ corresponds to an imaginary time. Thus, we define the matrix elements of the one–particle Green's functions as

$$\begin{aligned} G_{\alpha\beta}(\mathbf{k},\tau) &= -\langle T_\tau\, c_{\mathbf{k}\alpha}(\tau) c^\dagger_{\mathbf{k}\beta}\rangle, \\ \bar{G}_{\alpha\beta}(\mathbf{k},\tau) &= -\langle T_\tau\, \bar{c}_{-\mathbf{k}\alpha}(\tau) c_{-\mathbf{k}\beta}\rangle, \\ F_{\alpha\beta}(\mathbf{k},\tau) &= -\langle T_\tau\, c_{\mathbf{k}\alpha}(\tau) c_{-\mathbf{k}\beta}\rangle, \\ \bar{F}_{\alpha\beta}(\mathbf{k},\tau) &= -\langle T_\tau\, \bar{c}_{-\mathbf{k}\alpha}(\tau) c^\dagger_{\mathbf{k}\beta}\rangle \quad . \end{aligned} \tag{9.154}$$

In order to obtain the renormalized single–particle Green's function we solve the Dyson equation

$$\hat{G}^{-1} = \hat{G}_0^{-1} - \hat{\Sigma} \quad . \tag{9.155}$$

This relates the matrix representing the bare propagator $\hat{G}_0$ and its renormalization due to the sum of all irreducible self–energy diagrams $\hat{\Sigma}$ to the dressed propagator $\hat{G}$. The Dyson equation reads in Nambu space

$$\hat{G}^{-1} = \begin{pmatrix} G_0^{-1} - \Sigma^G & -\Sigma^F \\ -\bar{\Sigma}^F & \bar{G}_0^{-1} - \bar{\Sigma}^G \end{pmatrix} \quad , \tag{9.156}$$

where the inverse bare propagator is given by $\hat{G}_0^{-1} = i\omega_n - \epsilon_{\mathbf{k}}$. In the case where the effective pairing interaction V_{eff} is given by the diagrams shown in Fig. 9.18 the self–energy is (for simplicity we put $U_{eff} = U$)

$$\begin{aligned} \Sigma^G(\mathbf{k}, \imath\omega_n) = \frac{1}{\beta N} \sum_{\mathbf{k}' i\omega_n'} \Bigg[\frac{1}{2} U^2 \frac{\chi_{c0}(\mathbf{q}, i\nu_m)}{1 + U\chi_{c0}(\mathbf{q}, i\nu_m)} \\ + \frac{3}{2} U^2 \frac{\chi_{s0}(\mathbf{q}, i\nu_m)}{1 - U\chi_{s0}(\mathbf{q}, i\nu_m)} + U^2 \chi_G(\mathbf{q}, i\nu_m) \Bigg] G(\mathbf{k}', i\omega_n') \quad , \end{aligned} \tag{9.157}$$

and

$$\begin{aligned} \Sigma^F(\mathbf{k}, \imath\omega_n) = -\frac{1}{\beta N} \sum_{\mathbf{k}' i\omega_n'} \Bigg[\frac{1}{2} U^2 \frac{\chi_{c0}(\mathbf{q}, i\nu_m)}{1 + U\chi_{c0}(\mathbf{q}, i\nu_m)} \\ - \frac{3}{2} U^2 \frac{\chi_{s0}(\mathbf{q}, i\nu_m)}{1 - U\chi_{s0}(\mathbf{q}, i\nu_m)} - U^2 \chi_F(\mathbf{q}, i\nu_m) \Bigg] G(\mathbf{k}', i\omega_n') \quad . \end{aligned} \tag{9.158}$$

Here, $i\nu_m = i\omega_n - i\omega_n'$ and N denotes size of a square lattice. The term $U^2\chi_{G,F}$ on the right–hand side compensates for double counting that occurs in second order. Σ^G and Σ^F denote the normal and superconducting part of the self–energy, respectively [88]. χ_{c0} and χ_{s0} correspond to the irreducible charge– and spin susceptibility, respectively, and are given by

$$\begin{aligned} \chi_{c0}(\mathbf{q}, i\nu_m) = -\frac{1}{\beta N} \sum_{\mathbf{k} i\omega_n} [G(\mathbf{k}+\mathbf{q}, i\omega_n + i\nu_m) G(\mathbf{k}, i\omega_n) - \\ F(\mathbf{k}+\mathbf{q}, i\omega_n + i\nu_m) F^\dagger(-\mathbf{k}, i\omega_n)] \\ \equiv \chi_G(\mathbf{q}, i\nu_m) - \chi_F(\mathbf{q}, i\nu_m) \end{aligned} \tag{9.159}$$

and

$$\chi_{s0}(\mathbf{q}, i\nu_m) \equiv \chi_G(\mathbf{q}, i\nu_m) + \chi_F(\mathbf{q}, i\nu_m) \quad . \tag{9.160}$$

Note, on the RPA level also the charge fluctuations are included. This may be of interest if a charge–density–wave (CDW) or stripe formation occurs. Both may compete for small doping. For example, it was pointed out that polarization–dependent photoemission reveals also fine–structure in the low energy excitation spectrum [105]. In particular, for a single–layer high–T_c superconductor at optimum hole–doping two different behavior of the spectral density at $(\pi, 0)$ and $(0, \pi)$ were found indicating their difference. This may indicate the importance of charge fluctuations in cuprates.

Because Re Σ is symmetric and Im Σ is antisymmetric with respect to $i\omega_n$, it is possible to make the following ansatz:

$$\Sigma^G(\mathbf{k}, i\omega_n) = i\omega_n \left[1 - Z(\mathbf{k}, i\omega_n)\right] + \xi(\mathbf{k}, i\omega_n) \tag{9.161}$$

$$\Sigma^F(\mathbf{k}, i\omega_n) = \phi(\mathbf{k}, i\omega_n) \quad , \tag{9.162}$$

where Z and ξ are real and also symmetric with respect to $i\omega_n$. Z describes the renormalization of the quasiparticle mass and ξ corresponds to the renormalization of the bare band energy $\epsilon_{\mathbf{k}}$. This will be also discussed in Appendix C. $\phi(\mathbf{k}, i\omega_n) = Z(\mathbf{k}, i\omega_n)\Delta(\mathbf{k}, i\omega_n)$ denotes the strong-coupling superconducting gap function. In general, the interdependence of elementary excitations with spin excitations leads to strong self–energy effects. If lifetime effects of the elementary excitations are included the superconducting gap will also have a strong frequency dependence.

Note, in the case where Cooper–pair phase fluctuations are unimportant one may choose

$$F(\mathbf{k}, i\omega_n) = e^{2i\alpha} F^*(\mathbf{k}, -i\omega_n) \tag{9.163}$$

and put the phase equal to zero. Thus, no extra equation occurs for $\bar{\phi}(\mathbf{k}, i\omega_n)$.

Then, with the help of Eqs. (9.161) and (9.162) we are able to write down the diagonal and off–diagonal parts of the one–particle Green's function [94]:

$$G(\mathbf{k}, i\omega_n) = \frac{i\omega_n Z(\mathbf{k}, i\omega_n) + \epsilon_{\mathbf{k}} + \xi(\mathbf{k}, i\omega_n)}{\left(i\omega_n Z(\mathbf{k}, i\omega_n)\right)^2 - \left(\epsilon_{\mathbf{k}} + \xi(\mathbf{k}, i\omega_n)\right)^2 - \phi^2(\mathbf{k}, i\omega_n)} \quad , \tag{9.164}$$

and

$$F(\mathbf{k}, i\omega_n) = \frac{\phi(\mathbf{k}, i\omega_n)}{\left(i\omega_n Z(\mathbf{k}, i\omega_n)\right)^2 - \left(\epsilon_{\mathbf{k}} + \xi(\mathbf{k}, i\omega_n)\right)^2 - \phi^2(\mathbf{k}, i\omega_n)} \quad . \tag{9.165}$$

Since we want to solve the generalized Eliashberg equations on the real ω–axis rather than on the Matsubara points on the imaginary axis, we use now the spectral representation of the one–particle Green's function

$$G(\mathbf{k}, i\omega_n) = \int_{-\infty}^{\infty} d\omega \, \frac{N(\mathbf{k}, \omega)}{i\omega_n - \omega}, \quad F(\mathbf{k}, i\omega_n) = \int_{-\infty}^{\infty} d\omega \, \frac{A_1(\mathbf{k}, \omega)}{i\omega_n - \omega}. \tag{9.166}$$

and inserting Eqs. (9.166) into Eqs. (9.159) and (9.160). After performing the sum over the Matsubara frequencies [96] we arrive at

$$\text{Im}\ \chi_{s0,c0}(\mathbf{q},\omega) = \frac{\pi}{N}\int_{-\infty}^{\infty} d\omega'\ [f(\omega') - f(\omega'+\omega)]$$
$$\times \sum_{\mathbf{k}} [N(\mathbf{k}+\mathbf{q},\omega'+\omega)N(\mathbf{k},\omega')A_1(\mathbf{k}+\mathbf{q},\omega'+\omega)A_1(\mathbf{k},\omega')]\,. \qquad (9.167)$$

f denotes the Fermi distribution function.

Thus we arrive at the following set of equations for the quasiparticle self-energy $\Sigma_\nu \quad \nu = 0,\ 3,\ 1$ in the Nambu representation:

$$\Sigma_\nu(\mathbf{k},\omega) = N^{-1}\sum_{\mathbf{k}'}\int_0^\infty d\Omega\ [P_s(\mathbf{k}-\mathbf{k}',\Omega)$$
$$+\ (\delta_{\nu 0}+\delta_{\nu 3}-\delta_{\nu 1})\,P_c(\mathbf{k}-\mathbf{k}',\Omega)]\int_{-\infty}^{\infty} d\omega'\,I(\omega,\Omega,\omega')A_\nu(\mathbf{k}',\omega')\,. \qquad (9.168)$$

These equations have been discussed in the main text. Here, the spin and charge fluctuation interactions are given by

$$P_s = (2\pi)^{-1}U^2\,\text{Im}\ (3\chi_s - \chi_{s0})\,, \qquad \chi_s = \chi_{s0}\,(1-U\chi_{s0})^{-1} \quad , \qquad (9.169)$$

and

$$P_c = (2\pi)^{-1}U^2\,\text{Im}\ (3\chi_c - \chi_{c0})\,, \qquad \chi_s = \chi_{c0}\,(1+U\chi_{c0})^{-1} \quad . \qquad (9.170)$$

A_ν has been defined in Eq. (9.25). Then,

$$\Delta(\mathbf{k},\omega)Z(\mathbf{k},\omega) = -\frac{1}{N\pi}\sum_{\mathbf{k}'}\int_0^\infty d\Omega\ [P_s(\mathbf{k}-\mathbf{k}',\Omega) - P_c(\mathbf{k}-\mathbf{k}',\Omega)]$$
$$\times \int_{-\infty}^{\infty} d\omega'\left[\frac{f(-\omega')+b(\Omega)}{\omega+i\delta-\Omega-\omega'} + \frac{f(\omega')+b(\Omega)}{\omega+i\delta+\Omega-\omega'}\right]$$
$$\times\ \ \text{Im}\left[\frac{Z(\mathbf{k}',\omega')\Delta(\mathbf{k}',\omega')}{D(\mathbf{k}',\omega')}\right], \qquad (9.171)$$

$$\omega Z(\mathbf{k},\omega) = -\frac{1}{N\pi}\sum_{\mathbf{k}'}\int_0^\infty d\Omega\ [P_s(\mathbf{k}-\mathbf{k}',\Omega) + P_c(\mathbf{k}-\mathbf{k}',\Omega)]$$
$$\times \int_{-\infty}^{\infty} d\omega'\left[\frac{f(-\omega')+b(\Omega)}{\omega+i\delta-\Omega-\omega'} + \frac{f(\omega')+b(\Omega)}{\omega+i\delta+\Omega-\omega'}\right]$$
$$\times\ \ \text{Im}\left[\frac{Z(\mathbf{k}',\omega')\omega'}{D(\mathbf{k}',\omega')}\right], \qquad (9.172)$$

and

$$\epsilon_{\mathbf{k}} + \xi(\mathbf{k},\omega) = -(N\pi)^{-1} \sum_{\mathbf{k}'} \int_0^\infty d\Omega \, [P_s(\mathbf{k}-\mathbf{k}',\Omega) + P_c(\mathbf{k}-\mathbf{k}',\Omega)] \times \int_{-\infty}^{\infty} d\omega' \left[\frac{f(-\omega')+b(\Omega)}{\omega + i\delta - \Omega - \omega'} + \frac{f(\omega')+b(\Omega)}{\omega + i\delta + \Omega - \omega'} \right] \times \mathrm{Im}\left[\frac{\epsilon_{\mathbf{k}'} + \xi(\mathbf{k}',\omega')}{D(\mathbf{k}',\omega')} \right]. \tag{9.173}$$

Here, $D(\mathbf{k},\omega) = [\omega Z(\mathbf{k},\omega)]^2 + [\Delta(\mathbf{k},\omega)Z(\mathbf{k},\omega)]^2 - [\epsilon_{\mathbf{k}} + \xi(\mathbf{k},\omega)]^2$ and $b(\omega)$, $f(\omega)$ are the Bose and Fermi distribution functions, respectively.

These are the so–called generalized Eliashberg equations on the real frequency axis. Their detailed numerical solution will be discussed in Appendix B. Note, in contrast to the electron–phonon case the momentum dependence cannot be restricted to the Fermi surface due to the strong anisotropy of the elementary excitations and the pairing interaction.

APPENDIX B
Numerical Solution Method for the Generalized Eliashberg Equations

We discuss the details of the algorithm for the numerical solution of the Eliashberg equations. This is helpful for the programming of the equations. The expressions are presented line by line as these occur in the main program. To achieve the highest accuracy we avoid continuation methods like the Pade–approximation and solve the Eliashberg equation directly on the real–frequency axis. First, one starts with the calculation of the imaginary part of the spin susceptibilities using the tight–binding unrenormalized energy dispersion $\epsilon_{\mathbf{k}}$:

$$\mathrm{Im}\chi_G(\mathbf{q},\omega) = \frac{\pi}{N} \sum_{\mathbf{k}} \int_{-\infty}^{\infty} d\omega \, [f(\omega) - f(\omega+\Omega)] \, N(\mathbf{k},\omega) N(\mathbf{k}+\mathbf{q},\omega+\Omega), \tag{9.174}$$

$$\mathrm{Im}\chi_F(\mathbf{q},\omega) = \frac{\pi}{N} \sum_{\mathbf{k}} \int_{-\infty}^{\infty} [f(\omega) - f(\omega+\Omega)] \, A_1(\mathbf{k},\omega) A_1(\mathbf{k}+\mathbf{q},\omega+\Omega). \tag{9.175}$$

Then, we obtain their real parts via Kramers–Kronig relation:

$$\mathrm{Re}\ \chi_{G,F}(\mathbf{q},\omega) = \frac{1}{\pi} P \int_{-\infty}^{\infty} d\omega \, \frac{\mathrm{Im}\ \chi_{G,F}(\mathbf{q},\omega)}{\omega - \Omega}, \tag{9.176}$$

and define the irreducible charge and spin susceptibilities

$$\chi_{c0} = \chi_G - \chi_F, \quad \chi_{s0} = \chi_G + \chi_F. \tag{9.177}$$

In the next step we calculate the kernels of the Eliashberg equations:

$$P_s \equiv \frac{1}{\pi}\,\mathrm{Im}\,\left[\frac{3}{2}\frac{U^2\chi_{s0}}{1-U\chi_{s0}}\right], \quad P_c \equiv \frac{1}{\pi}\,\mathrm{Im}\,\left[\frac{3}{2}\frac{U^2\chi_{c0}}{1+U\chi_{c0}}\right], \tag{9.178}$$

$$P_G \equiv P_s + P_c - \frac{1}{\pi}\,\mathrm{Im}\,\left[\frac{1}{2}U^2\left(\chi_{s0}+\chi_{c0}\right)\right], \tag{9.179}$$

$$P_F \equiv -P_s + P_c + \frac{1}{\pi}\,\mathrm{Im}\,\left[\frac{1}{2}U^2\left(\chi_{s0}+\chi_{c0}\right)\right], \tag{9.180}$$

and plug them into the equations for determining the imaginary parts of the self–energies

$$\mathrm{Im}\phi(\mathbf{k},\omega) = \frac{\pi}{N}\sum_{\mathbf{q}}\int_{-\infty}^{\infty} d\Omega\,\left[b(\Omega)+f(\Omega-\omega)\right]P_F(\mathbf{q},\omega)A_1(\mathbf{k}-\mathbf{q},\omega-\Omega) \tag{9.181}$$

and

$$\mathrm{Im}\Sigma(\mathbf{k},\omega) = -\frac{\pi}{N}\sum_{\mathbf{q}}\int_{-\infty}^{\infty} d\Omega\,\left[b(\Omega)+f(\Omega-\omega)\right]P_G(\mathbf{q},\omega)N(\mathbf{k}-\mathbf{q},\omega-\Omega). \tag{9.182}$$

The real parts are obtained again via Kramers–Kronig relations:

$$\mathrm{Re}\;\phi(\mathbf{k},\omega) = \frac{1}{\pi}P\int_{-\infty}^{\infty} d\omega'\,\frac{\mathrm{Im}\;\phi(\mathbf{k},\omega')}{\omega'-\omega}, \tag{9.183}$$

$$\mathrm{Re}\;\Sigma^G(\mathbf{k},\omega) = \frac{1}{\pi}P\int_{-\infty}^{\infty} d\omega'\,\frac{\mathrm{Im}\;\Sigma^G(\mathbf{k},\omega')}{\omega'-\omega}. \tag{9.184}$$

The next step calculates the energy shift

$$\xi \equiv \frac{1}{2}\left[\Sigma^G(\mathbf{k},\omega)+\Sigma^{G*}(\mathbf{k},-\omega)\right], \tag{9.185}$$

and the mass renormalization function

$$\omega Z \equiv \omega - \frac{1}{2}\left[\Sigma^G(\mathbf{k},\omega)-\Sigma^{G*}(\mathbf{k},-\omega)\right]. \tag{9.186}$$

This completes the first iteration.

With the obtained results for the energy shift and the renormalization function we calculate the new spectral densities

$$N(\mathbf{k},\omega) = -\frac{1}{\pi}\mathrm{Im}\,\frac{\omega Z+\epsilon_{\mathbf{k}}+\xi}{(\omega Z)^2-(\epsilon_{\mathbf{k}}+\xi)^2-\phi^2} = A_0(\mathbf{k},\omega)+A_3(\mathbf{k},\omega), \tag{9.187}$$

$$A_1(\mathbf{k},\omega) = -\frac{1}{\pi}\mathrm{Im}\,\frac{\phi}{(\omega Z)^2-(\epsilon_{\mathbf{k}}+\xi)^2-\phi^2}, \tag{9.188}$$

and then return to the Eq. (9.174). The procedure is repeated until the convergence is reached. The numerical calculations are performed on a square lattice with 256×256 points in the Brillouin zone and with 200 points on the real ω axis up to $16t$ with an almost logarithmic mesh. The full momentum and frequency dependence of the quantities is kept. The convolutions in $\mathbf{k}$ space are carried out with Fast Fourier Transforms. As we mentioned the real parts of the susceptibilities, gap, and self–energy are calculated with the help of the Kramers–Kronig relations (P denotes the corresponding principal value integration). The spectral functions A_1, $P_{G,F}$, Im ϕ, Im ξ, and Im $\chi_{G,F}$ are antisymmetric and the corresponding real parts are symmetric with respect to ω. Thus the spectral function for the interacting electrons (or holes) $N(\mathbf{k},\omega)$ is separated into a symmetric part A_0 and an antisymmetric part A_3 (see Eq. (9.187)). The corresponding equations for the normal state can be recovered by setting the off–diagonal terms of the self–energy, ϕ, A_1, and χ_F, identically to zero.

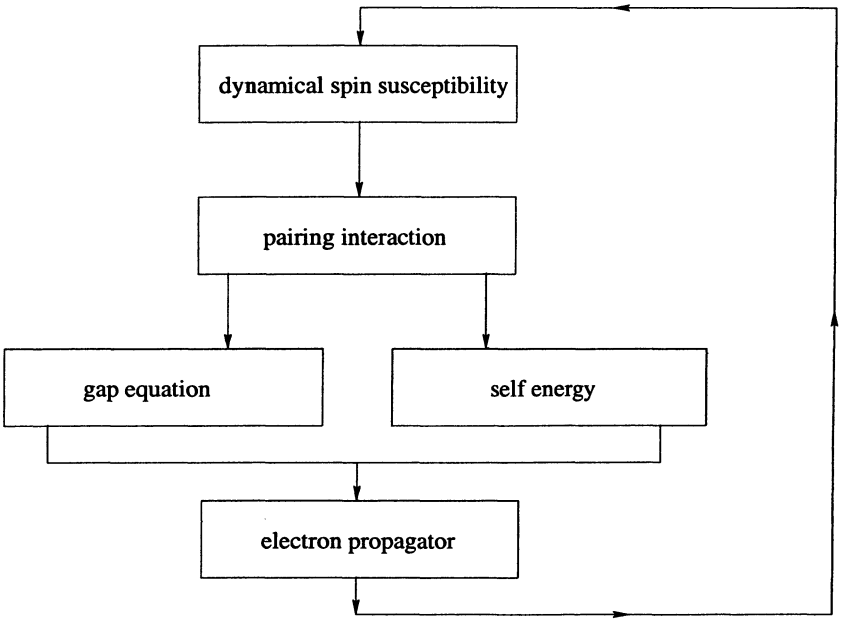

Fig. 9.76. Illustration of the procedure to solve Eliashberg equations. The full momentum and frequency dependence of the quantities is kept. The calculations include pair breaking effects for the Cooper–pairs resulting from lifetime effects of the elementary excitations

For illustration we show in Fig. 9.76 how Eqs. (9.168) - (9.170) are solved: One starts with a dynamical spin susceptibility $\chi(\mathbf{q},\omega)$ and constructs the

effective pairing interaction using Eq. (9.179). Then, the strong–coupling gap equation for the superconducting order parameter $\phi(\mathbf{k},\omega)$ and the corresponding Dyson equation $G^{-1}(\mathbf{k},\omega) = G_0^{-1}(\mathbf{k},\omega) - \Sigma(\mathbf{k},\omega)$ have to be solved, respectively. Having solved these two equations one has new appropriate starting input values for an electron propagator G. This is again used to calculate χ. This procedure is repeated until all equations are solved.

In order to determine the superconducting transition temperature T_c we solve the linearized gap equation, see Eq. (9.183):

$$\lambda(T)\,\mathrm{Im}\;\phi(\mathbf{k},\omega) = -\frac{1}{N}\sum_{\mathbf{k}}\int_{-\infty}^{\infty} d\omega'\;[b(\Omega)+f(\Omega-\omega)]\;P_F(\mathbf{q},\omega) \times \mathrm{Im}\left[\frac{\phi(\mathbf{k}',\omega')}{(\omega Z)^2-(\epsilon_{\mathbf{k}'}+\xi)^2}\right], \qquad \lambda(T_c)=1. \quad (9.189)$$

Here, χ_F in P_F is set to zero identically. For decreasing temperature T the eigenvalue $\lambda(T)$ increases and reaches unity at $T = T_c$. The spectral functions calculated during the solution of Eq. (9.189) are then appropriate starting values for the solution of the equations below T_c. Solving the generalized Eliashberg equations for cuprates we find that below T_c the superconducting gap function has $d_{x^2-y^2}$–wave symmetry for both hole– and electron–doped superconductors. Vertex corrections for the two–particle correlation function are not included. The calculations for Sr_2RuO_4 are performed similarly.

As mentioned earlier there exists an important feedback effect of the self–energy on the spectral functions of the corresponding quasi–particles (dressed holes or electrons). This is in particular the case in the superconducting state. Below T_c a gap appears in the spectral density of the quasiparticles. These not only condense into Cooper–pairs, but also provide the effective pairing interaction $V^{eff}(\mathbf{q},\omega)$. The superconducting gap function $\phi(\mathbf{k},\omega) = Z(\mathbf{k},\omega)\Delta(\mathbf{k},\omega)$ will be calculated self–consistently including all scattering and damping effects. This strong feedback effect has important consequences: for example, the dynamical spin susceptibility $\mathrm{Im}\;\chi_s(\mathbf{Q},\omega)$ shows a rearrangement of its spectral weight for small frequencies $\omega < 2\phi(\mathbf{Q},\omega)$ followed by a peak at approximately $\omega = 2\phi$. Note, for simplicity we restrict our discussion to the antiferromagnetic nesting vector $\mathbf{q} = \mathbf{Q} = (\pi,\pi)$. As discussed in the Introduction this behavior provides an explanation for the observed 'resonance peak' in inelastic neutron scattering in many cuprate superconductors. Therefore, the strong feedback effect of superconductivity on the elementary excitations and thus on $\mathrm{Im}\;\chi_s(\mathbf{Q},\omega)$ can be viewed as a general phenomenon of a strongly interacting system and in particular as an important fingerprint of spin–fluctuation–mediated pairing in cuprate high–T_c superconductors. The opening of the superconducting gap also helps to obtain a kink in the antinodal direction. To demonstrate this interdependence the self–consistent procedure shown in Fig. 9.76 is required.

APPENDIX C
Derivation of the Quasiparticle Self–Energy (weak–coupling case)

In order to discuss the anisotropic $\mathbf{k}$–dependence of the elementary excitations, $\epsilon_{\mathbf{k}} = \epsilon^0_{\mathbf{k}} + \Sigma(\mathbf{k},\omega)$, it is instructive to consider the weak–coupling limit ($Z = 1$) of the generalized Eliashberg equations. Using an one–loop approximation the self–energy is given by:

$$\Sigma(\mathbf{k},\omega) = -T^2 \sum_{\omega_n,\nu_m} \sum_{\mathbf{p},\mathbf{q}} \hat{\tau}_i\, G(\mathbf{k}-\mathbf{p}, i\omega_n - i\nu_m)\, \hat{\tau}_i\, U_{eff}(\mathbf{p}) U(\mathbf{p}) \times \frac{1}{2} \mathrm{Tr}\left[\hat{\tau}_i\, G(\mathbf{p}+\mathbf{q}, i\omega_n + i\nu_m)\, \hat{\tau}_i\, G(\mathbf{k}, i\omega_n)\right] \quad . \tag{9.190}$$

For spin fluctuations we have $\tau_i = \tau_0$. For simplicity we use $U_{eff}U = U^2$ and assume that the Coulomb interaction $U(\mathbf{p})$ is constant. The full Green's function is approximated by its non–interacting part

$$G(\mathbf{k}, i\omega_n) \simeq G_0(\mathbf{k}, i\omega_n) = \frac{i\omega_n \hat{\tau}_0 + \epsilon_k \hat{\tau}_3 - \Delta_k \hat{\tau}_1}{(i\omega_n)^2 - \epsilon_k^2 - \Delta_k^2} \quad . \tag{9.191}$$

Using Eq. (9.191) and introducing the quasiparticle energy dispersion in the superconducting state $E_p^2 = \epsilon_p^2 + \Delta_p^2$ and the coherence factors

$$c_{\pm}(\mathbf{p}+\mathbf{q}, \mathbf{q}) = 1 \pm \frac{\epsilon_{p+q}\epsilon_q + \Delta_{p+q}\Delta_q}{E_{p+q}E_q} \quad , \tag{9.192}$$

we can perform the sum over ω_n in Eq. (9.190). Noting that

$$T \sum_{\omega_n} \frac{1}{(i\omega_n + i\nu_m - y)(i\omega_n - x)} = \frac{f(x) - f(y)}{i\nu_m + x - y}, \tag{9.193}$$

one obtains

$$T \sum_{\omega_n} \frac{1}{2} \mathrm{Tr}\left[G(\mathbf{p}+\mathbf{q}, i\omega_n + i\nu_m)\, G(\mathbf{q}, i\omega_n)\right] = \frac{1}{4}\left[\left[\frac{f(E_q) - f(E_{p+q})}{i\nu_m + E_q - E_{p+q}} + \frac{f(-E_q) - f(-E_{p+q})}{i\nu_m - E_q + E_{p+q}}\right] c_+(\mathbf{p}+\mathbf{q}, \mathbf{q}) + \left[\frac{f(-E_q) - f(E_{p+q})}{i\nu_m - E_q - E_{p+q}} + \frac{f(E_q) - f(-E_{p+q})}{i\nu_m + E_q + E_{p+q}}\right] c_-(\mathbf{p}+\mathbf{q}, \mathbf{q})\right] \quad . \tag{9.194}$$

Eq. (9.194) has to be multiplied by $\frac{i\omega_n - i\nu_m}{(i\omega_n - i\nu_m)^2 - E_{k-p}^2}$ for the $\hat{\tau}_0$-component and by $\frac{1}{(i\omega_n - i\nu_m)^2 - E_{k-p}^2}$ for the $\hat{\tau}_3$– and $\hat{\tau}_1$–component, respectively and summed

over ν_m. Using (n = Bose function) $n(-x) = -(1+n(x))$, $f(-x) = 1-f(x)$ and $-T\sum_{\nu_m} \frac{1}{(i\nu_m - x)(i\nu_m - y)} = \frac{n(x)-n(y)}{x-y}$ in the form

$$-T\sum_{\nu_m} \frac{1}{(i\nu_m - i\omega_n - x)(i\nu_m - y)} = \frac{n(i\omega_n + x) - n(y)}{i\omega_n + x - y}$$

$$= -\frac{f(x) + n(y)}{i\omega_n + x - y} \quad ,$$

we obtain after the analytic continuation $i\omega_n \to \omega + i\eta$ the self–energy. For example, the imaginary part of the self–energy is

$$\text{Im}\ \Sigma_0(\mathbf{k},\omega) = \frac{\pi U^2}{8}\Bigg[\sum_{\mathbf{p}} [f(E_{k-p}) + n(E_{p+q} + \omega)]$$

$$\times \sum_{\mathbf{q}} \Bigg[c_+(\mathbf{p}+\mathbf{q},\mathbf{q})\,[f(E_q) - f(E_{p+q})]$$

$$\times [\delta(\omega + E_{k-p} - E_q + E_{p+q}) - \delta(\omega + E_{k-p} + E_q - E_{p+q})]$$

$$+ c_-(\mathbf{p}+\mathbf{q},\mathbf{q})\,[1 - f(E_q) - f(E_{p+q})] \times$$

$$\times [\delta(\omega + E_{k-p} + E_q + E_{p+q}) - \delta(\omega + E_{k-p} - E_q - E_{p+q})] \Bigg]$$

$$+ \sum_{\mathbf{p}} [f(E_{k-p}) + n(E_{k-p} - \omega)] \sum_{\mathbf{q}} \Bigg[c_+(\mathbf{p}+\mathbf{q},\mathbf{q})\,[f(E_q) - f(E_{p+q})]$$

$$\times\ [\delta(\omega - E_{k-p} + E_q - E_{p+q}) - \delta(\omega - E_{k-p} - E_q + E_{p+q})]$$

$$+\ c_-(\mathbf{p}+\mathbf{q},\mathbf{q})\,[1 - f(E_q) - f(E_{p+q})]$$

$$[\delta(\omega - E_{k-p} - E_q - E_{p+q}) - \delta(\omega - E_{k-p} + E_q + E_{p+q})] \Bigg] \Bigg] . \qquad (9.195)$$

We introduce the susceptibility in the superconducting state

$$\chi(\mathbf{p}, i\nu_m) = -T\sum_{\omega_n}\sum_{\mathbf{q}} \frac{1}{2}\,\text{Tr}\,[G(\mathbf{p}+\mathbf{q}, i\omega_n + i\nu_m)G(\mathbf{q}, i\omega_n)]$$

$$= -\frac{1}{4}\sum_{\mathbf{q}} \Big[\, c_+(\mathbf{p}+\mathbf{q},\mathbf{q})\,[f(E_q) - f(E_{p+q})]$$

$$\times \left[\frac{1}{i\nu_m + E_q - E_{p+q}} - \frac{1}{i\nu_m - E_q + E_{p+q}}\right]$$

$$+ \quad c_-(\mathbf{p}+\mathbf{q},\mathbf{q})\,[1 - f(E_q) - f(E_{p+q})]$$

$$\times \left[\frac{1}{i\nu_m - E_q - E_{p+q}} - \frac{1}{i\nu_m + E_q + E_{p+q}}\right] \quad . \tag{9.196}$$

Then,

$$\mathrm{Im}\Sigma_0(\mathbf{k},\omega) = \frac{U^2}{2}\sum_{\mathbf{p}} [-[f(E_{k-p}) + n(E_{k-p}+\omega)]\ \mathrm{Im}\ \chi(\mathbf{p},\omega + E_{k-p})$$
$$\times\ [f(E_{k-p}) + n(E_{k-p}-\omega)]\ \mathrm{Im}\ \chi(\mathbf{p},\omega - E_{k-p})] \quad . \tag{9.197}$$

With the help of $f(x) + n(y) = \frac{1}{2}\left[\coth\left(\frac{y}{2T}\right) - \tanh\left(\frac{x}{2T}\right)\right]$ one finds the important result

$$\mathrm{Im}\Sigma_0(\mathbf{k},\omega) = -\frac{U^2}{4}\sum_{\mathbf{p}} \int_{-\infty}^{\infty} d\omega' \left[\coth\left(\frac{\omega'}{2T}\right) - \tanh\left(\frac{\omega'-\omega}{2T}\right)\right]$$
$$\times\ \mathrm{Im}\ \chi(\mathbf{k}-\mathbf{p},\omega')\,\delta(|\omega-\omega'| - E_p) \quad . \tag{9.198}$$

Therefore, the anisotropy of the spin excitations (weighted by the density of states) is intimately related to the anisotropy of the self-energy of the elementary excitations. The strength of this anisotropy is controlled by U^2. Thus, it is clear that spin dynamics will control the quasiparticle behavior in cuprates. As a result one expects an important feedback of spin fluctuations on quasiparticle dynamics. In particular the characteristic spin fluctuation frequencies in the normal (ω_{sf}) and superconducting (ω_{res}) will determine the characteristic features in the energy dispersion.

For the $\hat{\tau}_1$- and $\hat{\tau}_3$-component of Σ one obtains similar results. It is instructive to write them in a unified way using the nesting approximation. In this approximation one assumes that the main contribution to the momentum sum comes from Im χ at the nesting vector $\mathbf{Q} = (\pi,\pi)$. Then, the self-energy does not longer depend on $\mathbf{k}$ and one can write ($\nu = 0, 1, 3$):

$$\mathrm{Im}\ \Sigma_\nu(\omega) = -\frac{U^2}{4}\int_{-\infty}^{\infty} d\omega' \left[\coth\left(\frac{\omega'}{2T}\right) - \tanh\left(\frac{\omega'-\omega}{2T}\right)\right]$$
$$\times \mathrm{Im}\ \chi(\mathbf{Q},\omega)\, N_\nu(|\omega-\omega'|) \quad , \tag{9.199}$$

where

$$N_0(x) = \sum_{\mathbf{p}} \delta(|x| - E_p)\,, \quad N_1(x) = -\mathrm{signx}\sum_{\mathbf{p}} \frac{\Delta_p}{E_p}\delta(|x| - E_p)\,,$$

$$N_3(x) = \text{signx} \sum_{\mathbf{p}} \frac{\epsilon_p}{E_p} \delta(|x| - E_p) \quad . \tag{9.200}$$

This completes the derivation of the self–energy in the weak–coupling case. In a strong-coupling case the procedure described in Appendix A has to be used. Then, it is possible to obtain the self–energy only numerically.

APPENDIX D
Cooper–Pair Phase Fluctuations

As suggested by the observation of $T_c \propto n_s$ for the underdoped cuprates [15] and by the small superfluid density, $n_s << n$ for $x \to 0$, and also by the weakly coupled two–dimensional CuO_2 planes, one expects that Cooper–pair phase fluctuations are important. These fluctuations of phase–incoherent Cooper pairs will destroy the long–range superconducting order and the Meissner effect. In conventional, bulk superconductors these phase fluctuations are not relevant, since for large superfluid density the phase fluctuations are energetically too costly. Thus, in conventional superconductors the superconducting transition is due to the destruction of the Cooper pairs and T_c is proportional to Δ_0 [94]. Note, the superconducting energy gap Δ governs the thermal breaking of Cooper pairs. Clearly, the observation by Uemura *et al.* that $T_c \propto n_s$ in underdoped hole–doped cuprates [15] indicates that Cooper–pair phase fluctuations are important [107,108,120]. The Cooper–pairs break up only at a crossover temperature around $T_c^* > T_c$ where T_c^* is approximately given by the transition temperature one would obtain without phase fluctuations and where at T_c Cooper–pairs get phase coherent. Between T_c and T_c^* local Cooper–pairs without long–range phase coherence are present.

In the following, we discuss phase fluctuations and their influence on elementary excitations, Meissner effect, interplay of phase and amplitude fluctuations, and superconducting transition temperature T_c.

Role of phase and amplitude fluctuations for determining T_c We start from the expression for the free energy of a superconductor:

$$\Delta F \equiv F_S - F_N = -\frac{1}{\beta} \ln \left\{ \int \mathcal{D}\Delta^\dagger \mathcal{D}\Delta e^{-\frac{1}{\hbar} S_{\text{eff}}[\Delta^\dagger, \Delta]} \right\}, \tag{9.201}$$

where $S_{\text{eff}}[\Delta^\dagger, \Delta]$ is the effective action obtained after integrating out the fermion variables. This is a functional of the Cooper–pair field $\Delta(t, \mathbf{r})$. Note, Eq. (9.201) is *exact*. The BCS theory is obtained from the saddle–point of the effective action. The simplest case corresponds to taking $\Delta = \Delta_0 = \text{const}$. Then the free energy becomes

$$\Delta F = -\frac{1}{\beta} \text{Tr} \ln[\mathbf{G}^{-1}(\Delta_0^*, \Delta_0)] + \frac{\Omega}{V_0} |\Delta_0|^2, \tag{9.202}$$

where $\mathbf{G}$ is the Nambu–Gorkov matrix Green's function, $V_0 > 0$ is the coupling constant, and Ω is the volume of the system. Minimization of ΔF gives the BCS gap equation.

To start the study the effect of phase fluctuations in superconductors we make the change of variables

$$\Delta(\tau, \mathbf{r}) = \rho(\tau, \mathbf{r}) e^{i\theta(\tau, \mathbf{r})}. \tag{9.203}$$

Let us write $\rho(\tau, \mathbf{r}) = \rho_0 + \delta\rho(\tau, \mathbf{r})$ and for the phase $\theta(\tau, \mathbf{r}) = \theta_0 + \delta\theta(\tau, \mathbf{r})$ and expand the effective action up to quadratic fluctuations in $\delta\rho$ and $\delta\theta$. The effective action then becomes

$$\begin{aligned} S_{\text{eff}} \approx \frac{\beta}{2} \sum_{\mathbf{q},n} [&\Pi_{\rho\rho}(\omega_n, \mathbf{q}) \delta\rho(\omega_n, \mathbf{q}) \delta\rho(-\omega_n, -\mathbf{q}) \\ &+ \Pi_{\theta\theta}(\omega_n, \mathbf{q}) \delta\theta(\omega_n, \mathbf{q}) \delta\theta(-\omega_n, -\mathbf{q})]. \end{aligned} \tag{9.204}$$

Note, we are not considering terms involving both the phase and amplitude fluctuations. These terms are often very small at low frequencies. Thus, to lowest order we can write

$$\Delta F = \Delta F_{\text{cond}} + \Delta F_{\text{phase}}, \tag{9.205}$$

where

$$\Delta F_{\text{cond}} = -\frac{1}{\beta} \ln \int \mathcal{D}\delta\rho \, \exp\left[-\frac{\beta}{2} \sum_{\mathbf{q},n} \Pi_{\rho\rho}(\omega_n, \mathbf{q}) \delta\rho(\omega_n, \mathbf{q}) \delta\rho(-\omega_n, -\mathbf{q}) \right] \tag{9.206}$$

gives the condensation energy, and

$$\Delta F_{\text{phase}} = -\frac{1}{\beta} \ln \int \mathcal{D}\delta\theta \exp\left[-\frac{\beta}{2} \sum_{\mathbf{q},n} \Pi_{\theta\theta}(\omega_n, \mathbf{q}) \delta\theta(\omega_n, \mathbf{q}) \delta\theta(-\omega_n, -\mathbf{q}) \right], \tag{9.207}$$

is the Cooper–pair energy gained due to phase coherence. In the low frequency and momentum limit we have

$$\Pi_{\theta\theta}(\omega_n, \mathbf{q}) = -\chi(\omega_n, \mathbf{q}) \omega_n^2 + \Lambda_{\mu\nu}(\omega_n, \mathbf{q}) q_\mu q_\nu, \tag{9.208}$$

where $\chi(\omega_n, \mathbf{q})$ is the density–density correlation function and

$$\Lambda_{\mu\nu} = \frac{n}{m} \delta_{\mu\nu} - \beta \langle j_\mu(\omega_n, \mathbf{q}) j_\nu(-\omega_n, \mathbf{q}) \rangle, \tag{9.209}$$

is the phase stiffness. In the limit $\omega \to 0$ and $\mathbf{q} \to 0$ the expression $\Lambda_{\mu\nu}$ gives the superfluid density divided by the effective mass, n_s/m. Thus, one gets approximately from $\Delta F_{phase}(0) \sim k_B T_c$ and $\Delta F_{phase} \propto n_s$, which results for $\Delta F_{cond} > \Delta F_{phase}$, that $T_c \propto n_s$

Quantum mechanically the role of the phase fluctuations is expressed by phase and particle number which are conjugate operators:

$$[\hat{\theta}, \hat{N}] = i\hbar. \tag{9.210}$$

Here, $\hat{N}$ denotes the Cooper–pair particle number operator. Thus, an immediate consequence of Eq. (9.210) is the uncertainty relation

$$\Delta\theta\Delta N \sim \hbar. \tag{9.211}$$

A rough estimate gives $\Delta N \sim n_s(0)$ and thus

$$\Delta\theta \sim \frac{1}{n_s(0)}. \tag{9.212}$$

Therefore, phase fluctuations are very important in systems having a small value of the zero–temperature superfluid density. This is precisely the case for the cuprate superconductors in the underdoped regime [108]. Indeed, since $n_s(0) \propto x$, where x is the hole concentration, we see that $\Delta\theta \sim 1/x$. As a result of Cooper–pair phase fluctuations and vortex condensation we have that

$$\Delta\theta \propto \frac{1}{T_c}. \tag{9.213}$$

Therefore, we obtain from Eq. (9.212) that the reduction of T_c in underdoped cuprates due to Cooper–pair phase fluctuations is given by

$$T_c \sim n_s(0). \tag{9.214}$$

Therefore, for small doping phase fluctuations are very important.

Meissner effect

Let us now estimate the role played by the coherent phase fluctuations for the Meissner effect. Writing $\psi = \sqrt{n_s}e^{i\phi}$ and taking into account the phase fluctuations only, one finds that the free energy is given by

$$F[n_s, \phi] = \int_0^\beta d\tau \int d^2r n_s \left[\frac{1}{4}\left(\nabla_\mu\phi + \frac{2e}{c\hbar}A_\mu\right)^2 + \eta(\partial_\tau\phi)^2\right]. \tag{9.215}$$

Then using

$$\sigma_{\nu\mu} = \frac{\hbar}{\omega_\nu}\int d^2r \int d\tau \frac{\delta^2 \ln Z}{\delta A_\mu(\tau, \mathbf{r})\delta A_\nu(0)} e^{i\omega_\nu\tau + i\mathbf{qr}}, \tag{9.216}$$

where Z is the partition function ($Z = \int \mathcal{D}\psi^*\mathcal{D}\psi exp(-F[\psi^*, \psi])$), we find for the conductivity after phase averaging

$$\sigma_{\mu\nu}(\mathbf{q}, i\omega_\nu) = \frac{\pi n_s}{R_Q\omega_\nu}\left(-\delta_{\mu\nu} + \frac{q_\nu q_\mu}{4\eta\omega_\nu^2 + q^2}\right). \tag{9.217}$$

The analytic continuation to the real frequencies yields for $q \rightarrow 0$

$$\sigma_{\mu\nu}(\mathbf{q}=0,\omega_\nu) = -\frac{\pi n_s}{R_Q}\delta_{\mu\nu}\left(\frac{i}{\omega}+\pi\delta(\omega)\right), \tag{9.218}$$

which implies perfect conductivity and for $\omega \rightarrow 0$

$$< j_\mu >= -\frac{\pi n_s}{R_Q}\left(\delta_{\mu\nu}-\frac{q_\mu q_\nu}{q^2}\right)A_\nu. \tag{9.219}$$

This demonstrates the occurrence of a Meissner effect below T_c in the superconducting phase in presence of the phase fluctuations and shows that phase fluctuations are indeed importnant.

Effect of the phase fluctuations on the elementary excitations: Dyson's equation

In order to calculate the density of states for a d–wave superconductor in the presence of Cooper–pair phase fluctuations, one has to derive the corresponding Dyson equation for the elementary excitations. If one considers the Fourier transformation of the spectral density of the pairing interaction P_s, it turns out that the effective pairing potential V_{eff} is *attractive* on nearest neighbor sites in real space [82]. Thus we start with

$$H = -t\sum_{\langle i,j\rangle}\sum_{\sigma} c^\dagger_{i\sigma}c_{j\sigma} + \text{h.c.} - \mu\sum_i n_i + V_{eff}\sum_{\langle i,j\rangle} c^\dagger_{i\uparrow}c^\dagger_{j\downarrow}c_{j\downarrow}c_{i\uparrow}, \tag{9.220}$$

where $V_{eff} < 0$. In order to evaluate the free energy and correlation functions of the system one has to evaluate the partition function (Φ, Φ^* = Grassmann variables):

$$\mathcal{Z} = \int \mathcal{D}(\Phi,\Phi^*)\, \mathrm{e}^{-\mathcal{S}[\Phi^*,\Phi]} \quad ,$$

where the action is given by

$$\mathcal{S}[\Phi^*,\Phi] = \int_0^\beta d\tau \quad \left[\sum_{i\sigma}\Phi^*_{i\sigma}(\partial_\tau-\mu)\Phi_{i\sigma} + t\sum_{\langle ij\rangle\sigma}\Phi^*_{i\sigma}\Phi_{j\sigma} + V_{eff}\sum_{\langle ij\rangle}\Phi^*_{i\uparrow}\Phi^*_{j\downarrow}\Phi_{j\downarrow}\Phi_{i\uparrow}\right] .$$

We now come to the derivation of the propagator for Cooper–pair phase fluctuations and the corresponding self–energy equations. For this purpose one has to integrate out the electronic degrees of freedom. This leads to

$$\mathcal{S}_{eff}[\varphi] = \mathcal{S}^{BCS}_{eff}(\Delta^0) + \frac{1}{\beta}\sum_{qn}\varphi(q,i\nu_n)\left[\mathcal{D}_\varphi(q,i\nu_n)\right]^{-1}\varphi(-q,-i\nu_n). \tag{9.221}$$

or diagrammatically

$$\mathcal{S}_{\rm eff}[\varphi] - \mathcal{S}_{eff}^{BCS}(\Delta^0) =$$ 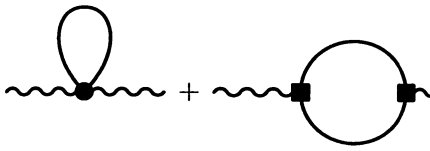 (9.222)

where the vertices, which couple the quasiparticles (holes) and the phases, are given by

$$\hat{\Gamma}_0^1(k,k') = \frac{i}{2}\left[(ik - ik')\,\hat{\tau}_3 - (\epsilon_{\mathbf{k}} - \epsilon_{\mathbf{k}'})\,\hat{\tau}_0\right] =$$ 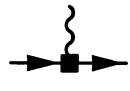 (9.223)

$$\hat{\Gamma}_0^2(k,k',k'') = \frac{1}{8}\left[\epsilon_{\mathbf{k}} - \epsilon_{\mathbf{k}-\mathbf{k}''} - \epsilon_{\mathbf{k}''+\mathbf{k}'} + \epsilon_{k'}\right]\hat{\tau}_3 =$$ 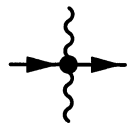 (9.224)

and $\hat{\tau}_i$ are the corresponding Pauli matrices. The BCS part of the effective action is given by

$$\mathcal{S}_{eff}^{BCS}(\Delta^0) = -\mathrm{Tr}\ln\left[-\hat{\mathcal{G}}_0^{-1}\right] + \beta N\,\frac{|\Delta^0|^2}{|V_{eff}|} \quad . \tag{9.225}$$

In Eq. (9.221) $\mathcal{D}_\varphi(q,i\nu_n) = \langle\langle\varphi(q,i\nu_n)\,\varphi(-q,-i\nu_n)\rangle\rangle$ is the propagator of the corresponding phase of a Cooper-pair given by [121]

$$\begin{aligned}\mathcal{D}_\varphi(q,i\nu_n) = 8\Big[& -\chi_0(q,i\nu_n)\,(i\nu_n)^2 \\ & -(i\nu_n)\sum_\alpha\left[\Pi^{\alpha\rho}(q,i\nu_n) + \Pi^{\rho\alpha}(q,i\nu_n)\right]2\sin\frac{q_\alpha}{2} \\ & +\sum_{\alpha\beta}\rho^{\alpha\beta}(q,i\nu_n)\,(2\,\sin\frac{q_\alpha}{2})\,(2\,\sin\frac{q_\beta}{2})\Big]^{-1} \quad ,\end{aligned} \tag{9.226}$$

with the phase stiffness $\rho^{\alpha\beta}(q,i\nu_n) = \mathrm{T}^{\alpha\beta} + \Pi^{\alpha\beta}$. Π and T are the current–current correlation function and mass operator, respectively [96]. It is

$$\Pi^{\alpha\beta}(q,i\nu_n) = \frac{1}{\beta N}\sum_{kn'} v^\alpha_{k-\frac{q}{2}}\,v^\beta_{k-\frac{q}{2}}\mathrm{Tr}\left[\hat{\mathcal{G}}_0(k,i\omega_{n'})\,\hat{\mathcal{G}}_0(k-q,i\omega_{n'}-i\nu_n)\right] \quad , \tag{9.227}$$

$$\mathrm{T}^{\alpha\beta} = \frac{1}{N}\sum_k t_k^{\alpha\beta}\,(n_{k\uparrow} + n_{k\downarrow}) \quad . \tag{9.228}$$

In analogy to Kadanoff and Baym we are now able to calculate the dressed Green's functions and their corresponding self–energies [144, 145]. If we consider Cooper–pair phase fluctuations and treat them up to second order, it is [121]

$$\hat{\mathcal{G}}(k, i\omega_n) = \hat{\mathcal{G}}_0(k, i\omega_n) - \hat{\mathcal{G}}_0(k, i\omega_n)\, \hat{\Sigma}^{\varphi\varphi}(k, i\omega_n)\, \hat{\mathcal{G}}(k, i\omega_n) \quad , \tag{9.229}$$

or diagrammatically

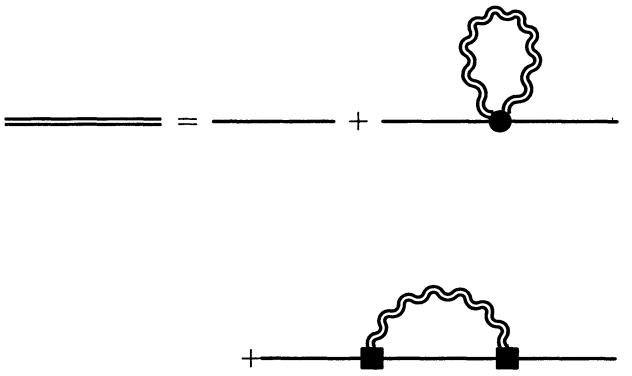

(9.230)

where the normal and anomalous part of the self–energy due to Cooper–pair phase fluctuations are given by [143]

$$\Sigma^{\mathcal{G}}(k, i\omega_n) = \frac{1}{4\beta N} \sum_{q,n'} [(i\nu_{n\prime})^2 - 2\, i\nu_{n\prime}\, (\epsilon_k - \epsilon_{k-q}) + (\epsilon_k - \epsilon_{k-q})^2] \times \mathcal{G}_0(k-q, i\omega_n - i\nu_{n\prime})\, \Pi^{\varphi\varphi}(q, i\nu_n) \quad , \tag{9.231}$$

$$\Sigma^{\mathcal{F}}(k, i\omega_n) = \frac{1}{4\beta N} \sum_{q,n'} [(i\nu_{n\prime})^2 + (\epsilon_k - \epsilon_{k-q})^2] \times \mathcal{F}_0(k-q, i\omega_n - i\nu_{n\prime})\, \Pi^{\varphi\varphi}(q, i\nu_n) \quad . \tag{9.232}$$

The vertices are given above. Furthermore, in the diagrammatic representation $\hat{\mathcal{G}}_0$ is the dressed Green's function (given in Appendix A) within the FLEX approximation that includes, in particular, the scattering by spin fluctuations.

Finally, these self–energy corrections must be added to their counterparts Σ^G and Σ^F resulting from the exchange of spin fluctuations alone in Eq. (9.156). Then, one can perform for $\hat{\mathcal{G}}$ an analytical continuation to the real ω–axis and solve the corresponding equations. Of course, the current–current correlation function Π has to be calculated self–consistently using Eq. (9.226) describing the propagation of Cooper–pair phase fluctuations.

Interplay of phase and amplitude fluctuations

So far we assume that the phase and amplitude fluctuations are decoupled.

The next step is to study the interplay between them. At low frequencies and momenta this is equivalent to consider an incompressible charged fluid with $\nabla \cdot \mathbf{v}_s = 0$, where $\mathbf{v}_s$ is the superfluid velocity. Therefore, in the hydrodynamic limit the phase–decoupled free energy leads to a constant charge density, i.e. the amplitude fluctuations are essentially frozen in the low energy limit. To see this in a simple way, note that the hydrodynamics of a charged fluid is described by the non–linear Schrödinger–like equation of the Cooper–pair wave function:

$$\frac{\partial \rho^2}{\partial t} + \nabla \cdot (\rho^2 \mathbf{v}_s) = 0 \tag{9.233}$$

and

$$\hbar \frac{\partial \theta}{\partial t} = -\frac{m}{2}\mathbf{v}_s^2 + 2eV - \frac{\hbar^2}{2m}\left(\frac{1}{\rho}\nabla^2 \rho\right). \tag{9.234}$$

Here, V is the electric potential and generally $\mathbf{v}_s = \hbar[\nabla\theta - (2e/c\hbar)\mathbf{A}]/m$, with $\mathbf{A}$ being the vector potential minimally coupled to the phase gradient. Eq. (9.233) is just the continuity equation. In the above hydrodynamic equations the phase and amplitude of the Cooper pair are coupled. When the amplitude is frozen, the continuity equation gives us the incompressibility condition $\nabla \cdot \mathbf{v}_s = 0$, which implies up to other gauge–equivalent solutions $\nabla\theta = 2e\mathbf{A}/(c\hbar)$. In this case Eq. (9.233) yields

$$\hbar \frac{\partial \theta}{\partial t} = 2eV, \tag{9.235}$$

which is just Josephson's voltage–phase relation.

What happens to the interplay if the doping concentration is changed? At optimal doping the phase and amplitude fluctuations are equally important. Note, the critical temperature T_c is then at its highest value. However, with further increasing doping the critical temperature decreases, now not due to phase fluctuations which become negligible in the overdoping regime, but due to increasing itinerancy with $\chi \to 0$, i.e. the pairing field disappears.

Note, in general like in magnetism (ferromagnetism) phase and amplitude fluctuations of the order parameter are coupled and one would get for $\Delta = |\Delta|e^{i\phi}$ that $|\Delta| \to 0$ affects $\langle \nabla\phi \nabla\phi \rangle$ and vica versa.

Using Ginzburg–Landau theory it is easy to see that amplitude fluctuations decrease T_c. Consider the inverse susceptibility $\chi^{-1}(T)$, with $T > T_c$, in a Ginzburg–Landau (GL) description. We have

$$\chi^{-1}(T) = a_0(T - T_0) + u\langle |\psi|^2 \rangle, \tag{9.236}$$

where T_0 is the mean–field critical temperature and u is the GL interaction. In the overdoped regime the CuO_2 planes are more strongly coupled and the Cooper pairs tunnel coherently between the planes. Thus, we calculate $\langle |\psi|^2 \rangle$

in three dimensions. Considering an isotropic system for simplicity we have the self-consistent equation

$$\chi^{-1}(T) = a_0(T - T_0) + u \int \frac{d^3p}{(2\pi)^3} \frac{1}{p^2 + \chi^{-1}(T)}$$
$$= a_0(T - T_0) + \frac{u\Lambda}{2\pi^2} - \frac{u}{4\pi}\sqrt{\chi^{-1}(T)}, \tag{9.237}$$

where Λ is a cutoff. We see that the critical temperature is

$$T_c = T_0 - \frac{u\Lambda}{2\pi^2}, \tag{9.238}$$

which is indeed lower than T_0.

This T_c reduction and the one due to phase fluctuations are, however, fundamentally different regarding the way by which the superconducting state is destroyed. In the underdoped cuprates the phase fluctuations are expected to relate to the formation of vortices and the superconducting phase is destroyed due to the proliferation of thermally and quantum excited vortices. Thus, the non-superconducting phase can be thought of as a phase where the vortices are condensed. Note, the vortex condensation in underdoped cuprates may in part be responsible for the suppression of spectral weight and non-Fermi liquid behavior.

In a simple Eliashberg-like treatment of T_c in which fluctuations of the superconducting condensate are neglected (see Fig. 9.48), the temperature $T_c^* \propto \Delta(T \to 0)$ is equal to the mean-field temperature T_0. Therefore, fluctuations are reducing $T_c < T_c^*$.

The role of transverse phase fluctuations in the BKT theory and in determining T_c:

How to connect the Berezinskii-Kosterlitz-Thouless (BKT) theory to the Eliashberg-like theory in the presence of vortices? For this let us write the following simple effective Hamiltonian density containing both the phase and cooper-pair particle number:

$$\mathcal{H} = \frac{1}{2g}\hat{N}^2 + \frac{n_s(T)\hbar^2}{4m}(\nabla\hat{\theta})^2. \tag{9.239}$$

Note, the above Hamiltonian describing a continuum limit also an array of Josephson weak-link junctions. If we identify $\hat{N}$ as the "momentum" operator conjugated to the phase operator $\hat{\theta}$ [see Eq. (9.210)], we see that in Eq. (9.239) the first term on the RHS corresponds to the kinetic energy, while the second one is the potential energy. The partition function of the system can be written as the functional integral

$$Z = \int [\prod_{\tau,\mathbf{r}} d\theta(\tau,\mathbf{r}) dN(\tau,\mathbf{r})] \exp\left[-\frac{1}{\hbar}S(\theta,N)\right] \tag{9.240}$$

and the action is given by

$$S(\theta, N) = \int_0^\beta d\tau \int d^2r(-iN\ \partial_\tau\theta + \mathcal{H}). \tag{9.241}$$

After performing the Gaussian integral over $N(\tau, \mathbf{r})$ we obtain the effective action containing only the phase $\theta(\tau, \mathbf{r})$:

$$S_{\text{phase}} = \int_0^\beta d\tau \int d^2r\mathcal{L}(\theta), \tag{9.242}$$

where the Lagrangian is given by

$$\mathcal{L} = \frac{g}{2}(\partial_\tau\theta)^2 + \frac{n_s(T)\hbar^2}{4m}(\nabla\theta)^2. \tag{9.243}$$

Let us now turn to a determination of T_c with the help of the BKT theory. We make the approximation that θ is independent of the Matsubara time. Then we can write the phase action as

$$S_{\text{phase}} = \frac{\tilde{K}}{2} \int d^2r(\nabla\theta)^2, \tag{9.244}$$

where the phase stiffness $\tilde{K}$ is related to the superfluid density through $\tilde{K} = n_s(T)\hbar^2/(4mT)$. The superfluid density can be computed from a Hamiltonian like the Hubbard model employing a many–body treatment as the FLEX approximation and the Kubo formula. In the case of the cuprates it is useful to introduce an additional parameter d giving the average distance between the CuO_2 planes such that the new phase stiffness is given by

$$K(T) = \beta\hbar^2 \frac{n_s(T)}{m} \frac{d}{4} \quad , \tag{9.245}$$

In our calculations we set d to half the height of the unit cell of $YBa_2Cu_3O_{6+x}$. The renormalized phase stiffness can be expressed as

$$\begin{aligned} \frac{1}{K_R} &= \frac{4m^2T}{\hbar^2 dn_s(T)} \\ &= \frac{4m^2}{\hbar^2} \int d^2r\langle \mathbf{v}_s(\mathbf{r}) \cdot \mathbf{v}_s(0)\rangle. \end{aligned} \tag{9.246}$$

In order to compute the correlation function involving the superfluid velocity, we have to split the gradient of the phase between the longitudinal (regular) and transverse (singular) contributions. The transverse fluctuations account for the vortices. We have then

$$v_{s,\mu}(\mathbf{r}) = \partial_\mu\varphi(\mathbf{r}) + 2\pi\varepsilon_{\mu\nu}\partial_\nu \int G(\mathbf{r} - \mathbf{r}')n(\mathbf{r}') \quad , \tag{9.247}$$

where $G(\mathbf{r}-\mathbf{r}')$ satisfies the equation $-\nabla^2 G(\mathbf{r}-\mathbf{r}') = \delta^2(\mathbf{r}-\mathbf{r}')$. The *vortex density* can be written as $n(\mathbf{r}) = \sum_i q_i \delta^2(\mathbf{r}-\mathbf{r}_i)$, where $q_i = \pm 1$. As is well known, the statistical mechanics of two–dimensional vortices can be mapped on a Coulomb gas [233]. Using the Coulomb gas scenario the superfluid density can be related to the vortex density correlation function in momentum space. One finds [234]

$$\frac{n_s}{n_s^0} = 1 - \frac{2\pi}{T}\Lambda^2 \lim_{k\to 0}\langle n(k)n(-k)\rangle \quad , \tag{9.248}$$

where n_s^0 is the bare superfluid density and Λ is a cutoff.

Starting from the smallest vortex–antivortex pairs of size r_0, the pairs are integrated out and their effect is incorporated by an approximate renormalization of K and the fugacity $y = e^{-\beta E_c}$. Then, from Eqs. (9.246) and (9.247) we obtain the BKT recursion relations [235]:

$$\frac{dy}{dl} = (2-\pi K)\, y \quad , \qquad \frac{dK}{dl} = -4\pi^3 y^2 K^2 \quad . \tag{9.249}$$

For the vortex core energy we use the approximate result by Blatter *et al.*, i.e.

$$E_{core} = \pi k_B T K \ln\kappa \quad , \tag{9.250}$$

where κ is the Ginzburg parameter. $l = \ln(r/r_0)$ is a logarithmic length scale which relates K to the strength of the vortex–antivortex interaction. For $T > T_c$, K tends to zero for $l \to \infty$, so that the interaction at large distances is screened and the largest vortex–antivortex pair unbind. This destroys the Meissner effect and leads to dissipation. On the other hand, bound Cooper–pairs reduce K and thus n_s, but do not destroy superconductivity. After solving Eqs. (9.249) and (9.250) it turns out that that the renormalization of K is very small. Thus, within a good approximation, one can obtain $T_c(x)$ from the simple criterion

$$K(T_c) = \frac{2}{\pi}, \qquad \text{or} \qquad \frac{n_s(T_c,x)}{m} = \frac{2}{\pi}\,\frac{4k_B T_c}{\hbar^2 d} \tag{9.251}$$

which we have used in the main text.

Let us turn now to the ω–dependence of the Cooper–pair phase fluctuations. A dynamical generalization of the BKT theory was developed by Ambegaokar *et al.* [234, 236]. It turns out that the critical size for a vortex–antivortex pair is given by (see Eq. (8.68))

$$r_\omega = \sqrt{\frac{D_\nu}{2\pi\omega}} \quad ,$$

where D_ν denotes the corresponding diffusion constant. In the absence of pinning, the theory by Bardeen and Stephen yields [119]

$$D_\nu^0 = \frac{2\pi c^2 \xi_{ab}^2 \rho_n T}{\phi_0^2 \tilde{d}} \quad ,$$

where c is the speed of light, $\xi_{ab} \sim r_0/2$ corresponds to the coherence length, ρ_n denotes the normal–state resistivity, $\phi_0 = hc/2e$ is the elementary superconducting flux quantum, and $\tilde{d}$ corresponds to an effective layer thickness. For the pinning we assume an Arrhenius law given by Eq. (8.70). Eqs. (8.69) and (8.70) are inserted into Eq. (8.68) yielding a new length scale l in Eqs. (9.249), namely a new upper limit $l = \ln(r_\omega/r_0)$. Then, one finds

$$\frac{n_s(\omega)}{m} = \frac{1}{e^2}\,\omega\,\mathrm{Im}\;\sigma_S(\omega) \quad , \tag{9.252}$$

where $\sigma_S(\omega)$ is the difference between the total dynamical conductivity in the superconducting state and its value in the normal state. It can be obtained from the current–current correlation function and the Kubo formula using the generalized Eliashberg equations described in Appendix A.

Acknowledgements
We thank L. Tewordt, C. Timm, J. Schmalian, F. Nogueira, D. Morr, J. Fink and M. Peter for many useful discussions.

References

1. J.G. Bednorz and K.A. Müller, Z. Phys. B **64**, 189 (1986).
2. A.W. Hewat, In: *Materials and Crystallographic Aspects of High-T_c Superconductivity*, edited by E. Kaldis, NATO ASI Series, Vol. 263 (Kluwer-Dordrecht 1994), p.17.
3. Y. Kitaoka, K. Ishida, F. Fujiwara, T. Kondo, K. Asayama, M. Horvatic, Y. Berthier, P. Butaud, P. Segransan, C Berthier, H. Katayana-Yoshida, Y. Okabe, and T. Takahashi, In: *Strong Correlations and Superconductivity*, Springer series in Solid-State Sciences 89, edited by H. Fukuyama, S. Maekawa, and A.P. Malozemoff, (Springer, Berlin 1989) p. 262.
4. D. A. Wollmann, D. J. van Harlingen, W. C. Lee, D. M. Ginsberg, and A. J. Leggett, Phys. Rev. Lett. **71**, 2134 (1993).
5. J.R. Kirtley, C.C. Tsuei, J.Z. Sun, C.C. Chi, L.S. Yu-Jahnes, A. Gupta, M. Rupp, and M.B. Ketchen,, Nature (London) **373**, 225 (1995).
6. C.C. Tsuei, J.R. Kirtley, M. Rupp, J.Z. Sun, A. Gupta, and M.B. Ketchen, Science **272**, 329 (1996).
7. C. C. Tsuei, J. R. Kirtley, Rev. of Mod. Phys. **72**, 969 (2000).
8. W. N. Hardy, D. A. Bonn, D. C. Morgan, R. Liang, and K. Zhang, Phys. Rev. Lett. **70**, 3999 (1994).
9. S. Kamal, Ruixing Liang, A. Hosseini, D. A. Bonn, and W. N. Hardy, Phys. Rev. B **58**, R8933 (1998); S, Kamal, D. A. Bonn, Nigel Goldenfeld, P. J. Hirschfeld, Ruixing Liang, and W. N. Hardy, Phys. Rev. Lett. **73**, 1845 (1994).
10. Z. X. Shen *et al.*, Phys. Rev. Lett. **70**, 1553 (1993).
11. M. C. Krantz and M. Cardona, J. Low Temp. Phys. **99** 205 (1995).
12. D. Einzel and R. Hackl, J. Raman Spectroscopy **27**, 307 (1996).
13. T. P. Devereaux and D. Einzel, Phys. Rev. B **51**, 16336 (1995); **54** 15547 (1996).
14. D. Manske, C. T. Rieck, R. Das Sharma, A. Bock, and D. Fay, Phys. Rev. B **56**, R2940 (1997).

15. Y.J. Uemura *et al.*, Phys. Rev. Lett. **62**, 2317 (1989).
16. For a review, see C. P. Slichter in *Strongly Correlated Electronic Systems*, edited by K. S. Bedell *et al.* (Addison Wesley, Reading, MA, 1994)
17. L.P. Regnault, P. Bourges, P. Burlet, J.Y. Henry, J. Rossat-Mignod, Y. Sidis, C. Vettier, Physica B **213-214**, 48 (1995).
18. D.S. Marshall, D.S. Dessau, A.G. Loeser, C-H. Park, A.Y. Matsuura, J.N. Eckstein, I. Bozovic, P. Fournier, A. Kapitulnik, W.E. Spicer, and Z.-X. Shen, Phys. Rev. Lett. **76**, 4841 (1996).
19. J.M. Harris, Z.-X. Shen, P.J. White, D.S. Marshall, M.C. Schabel, J.N. Eckstein, and I. Bozovic, Phys. Rev. B **54**, R15655 (1996).
20. Ch. Renner, B. Revaz, J.-Y. Genoud, K. Kadowaki, and Ø. Fischer, Phys. Rev. Lett. **80**, 149 (1998).
21. J.W. Loram, K.A. Mirza, J.R. Cooper, and W.Y. Liang , Phys. Rev. Lett. **71**, 1740 (1993); J. W. Loram *et al.*, J. Superconductivity **7**, 234 (1994).
22. B. Batlogg, H. Y. Hwang, H. Takagi, R. J. Cava, H. L. Kao, and J. Kwo, Physica C **235-240**, 130 (1994).
23. R. Nemetschek, M. Opel, C. Hoffmann, P.F. Mueller, R. Hackl, H. Berger, L. Forro, A. Erb, and E. Walker, Phys. Rev. Lett. **78**, 4837 (1997); G. Blumberg, M. Kang, M.V. Klein, K. Kadowaki, and C. Kendziora, Science **278**, 1427 (1997).
24. Ch. Renner, B. Revaz, J.-Y. Genoud, K. Kadowaki, and Ø. Fischer, Phys. Rev. Lett. **80**, 149 (1998).
25. A. K. Gupta and K.-W. Ng, Phys. Rev. B **58**, R8901 (1998).
26. C. M. Varma, Phys. Rev. Lett. **63**, 1996 (1989).
27. A. Virosztek and J. Ruvalds, Phys. Rev. B **42**, 4064 (1990).
28. J. Ruvalds, C. T. Rieck, J. Zhang and A. Virosztek, Science **256**, 1664 (1992).
29. A. J. Millis, H. Monien, and D. Pines, Phys. Rev. B **42**, 167 (1990).
30. G.M. Luke, L.P. Le, B.J. Sternlieb, Y.J. Uemura, J.H. Brewer, R. Kadono, R.F. Kiefl, S.R. Kreitzman, T.M. Riseman, C.E. Stronach, M.R. Davis, S. Uchida, H. Takagi, Y. Tokura, Y. Hidaka, T. Murakami, J. Gopalakrishnan, A.W. Sleight, M.A. Subramanian, E.A. Early, J.T. Markert, M.B. Maple, and C.L. Seaman, Phys. Rev. B **42**, 7981 (1990).
31. Y. Tokura, H. Takagi, and S. Uchida, Nature **337**, 345 (1989).
32. T. Timusk and B. Statt, Rep. Prog. Phys. **62**, 61 (1999).
33. H. Takagi, B. Batlogg, H.L. Kao, J. Kwo, R.J. Cava, J.J. Krajewski, and W.F. Peck, Phys. Rev. Lett. **69**, 2975 (1992).
34. C.C. Tsuei, A. Gupta, and G. Koren, Physica C **161**, 415 (1989).
35. D.S. Dessau, Z.-X. Shen, D.M. King, D.S. Marshall, L.W. Lombardo, P.H. Dickinson, A.G. Loeser, J. DiCarlo, C.-H Park, A. Kapitulnik, and W.E. Spicer, Phys. Rev. Lett. **71**, 2781 (1993); A.A. Abrikosov, J.C. Campuzano, and K. Gofron, Physica C **214**, 73 (1993).
36. D.M. King, Z.-X. Shen, D.S. Dessau, B.O. Wells, W.E. Spicer, A.J. Arko, D.S. Marshall, J. DiCarlo, A.G. Loeser, C.H. Park, E.R. Ratner, J.L. Peng, Z.Y. Li, and R.L. Greene, Phys. Rev. Lett. **70**, 3159 (1993).
37. S.M. Anlage, D.-H. Wu, J. Mao, S.N. Mao, X.X. Xi, T. Venkatesan, J.L. Peng, and R.L. Greene, Phys. Rev. B **50**, 523 (1994); D.H. Wu, J. Mao, S.N. Mao, J.L. Peng, X.X. Xi, T. Venkatesan, R.L. Greene, and S.M. Anlage, Phys. Rev. Lett. **70**, 85 (1993).

38. W.N. Hardy, D.A. Bonn, D.C. Morgan, R. Liang, and K. Zhang, Phys. Rev. Lett. **70**, 3999 (1993); D.A. Bonn, S. Kamal, K. Zhang, R. Liang, D.J. Baar, E. Klein, and W.N. Hardy, Phys. Rev. B **50**, 4051 (1994).
39. B. Stadlober, G. Krug, R. Nemetschek, and R. Hackl, Phys. Rev. Lett. **74**, 4911 (1995).
40. G. Blumberg, A. Koitzsch, A. Gozar, B.S. Dennis, C.A. Kendziora, P. Fournier, and R.L. Greene, Phys. Rev. Lett. **88**, 107002 (2002).
41. R. Prozorov, R.W. Gianetta, P. Furnier, and R.L. Greene, Phys. Rev. Lett. **85**, 3700 (2000).
42. J.D. Kokales, P. Furnier, L.V. Mercaldo, V.V. Talanov, R.L. Greene, and S.M. Anlage, Phys. Rev. Lett. **85**, 3696 (2000).
43. C.C. Tsuei and J.R. Kirtley, Phys. Rev. Lett. **85**, 182 (2000).
44. J.A. Skinta, M.-S. Kim, T.R. Lemberger, T. Greibe, and M. Naito, Phys. Rev. Lett. **88**, 207005 (2002).
45. P. Bourges, in *Gap Symmetry and Fluctuatios in High-Tc Superconductors*, eds. J. Bok, G. Deutscher, D. Pavuna and S. Wolf (Plenum Press, NY, 1998).
46. J. Rossat-Mignod, L.P. Regnault, C. Vettier, P. Bourges, P. Burlet, J. Bossy, J.Y. Henry, L. Lapertot, Physica C **185-189**, 86 (1991).
47. H. He, Y. Sidis, P. Bourges, G.D. Gu, A. Ivanov, N. Koshizuka, B. Liang, C.T. Lin, L.P. Regnault, E. Schoenherr, and B. Keimer, Phys. Rev. Lett. **86**, 1610 (2001).
48. H.F. Fong, P. Bourges, Y. Sildis, L.P. Regnault, A. Ivanov, G.D. Gu, N. Koshizuka, and B. Keimer, Nature **398**, 588 (1999); P. Dai, H.A. Mook, S.M. Hayden, G. Aeppli, T.G. Perring, R.D. Hunt, and F. Dogan, Science **284**, 1344 (1999).
49. H. He, P. Bourges, Y. Sidis, C. Ulrich, L.P. Regnault, S. Pailhes, N. . Berzigiarova, N.N. Kolesnikov, and B. Keimer, Science **295**, 1045 (2002).
50. T.M. Rice and T.M. Sigrist, J. Phys.: Condens. Matter **7**, L643 (1995).
51. I. Eremin, D. Manske, and K.H. Bennemann, Europhys. Lett. **58**, 871 (2002).
52. P. Monthoux, Phys. Rev. B **55**, 15261 (1997); A. Chubukov, P. Monthoux, and D.K. Morr, Phys. Rev. B **56**, 7789 (1997).
53. If so, then the usual perturbation theory breaks down [54] and a non-perturbative approach has to be used as suggested for example in Ref. [55].
54. J.R. Schrieffer, J. Low Temp. Phys. **99**, 397 (1995).
55. N.E. Bickers and D.J. Scalapino, cond-mat/0010480 (unpublished).
56. A. Lanzara, P.V. Bogdanov, X.J. Zhou, S.A. Kellar, D.L. Feng, E.D. Lu, T. Yoshida, H. Eisaki, A. Fujimori, K. Kishio, J.-I. Shimoyama, T. Nodall, S. Uchida, Z. Hussain, Z.-X. Shen, Nature (London) **412**, 510 (2001).
57. Originally the kink feature was attributed to a coupling of the itinerant carriers to phonons, in particular, to a longitudinal optical phonon mode at 60meV which was observed to behave anomalously in several experiments [58]. However, this interpretation has several disadvantages. The first one relates to the fact that the inelastic scattering rate in hole-doped cuprates is linear with frequency or temperature (whichever is larger) which can be hardly explained using conventional electron-phonon coupling. Also in electron-doped cuprates there is no kink present [59] and the electronic part of the resistivity follows a quadratic behavior at low temperatures indicating conventional Fermi liquid behavior. It is not clear how both features can be explained assuming the same electron-phonon coupling.

58. R. J. McQueeney, Y. Petrov, T. Egami, M. Yethiraj, G. Shirane, and Y. Endoh, Phys. Rev. Lett. **82**, 628 (1999).
59. Z.-X. Shen, A. Lanzara, S. Ishihara, N. Nagaosa, cond-mat/0108381 (unpublished).
60. J.A. Skinta, T.R. Lemberger, T. Greibe, and M. Naito, Phys. Rev. Lett. **88**, 207003 (2002); J.A. Skinta, M.-S. Kim, T. Greibe, and M. Naito, *ibid*, 207005 (2002).
61. J.R. Schrieffer, D.J. Scalapino, and J.W. Wilkins, Phys. Rev. Lett. **10**, 336 (1963).
62. J.F. Zasadzinski, L. Ozyuzer, M. Miyakawa, D.G. Hinks, and K.E. Gray, Physica C **341-348**, 867 (2000).
63. M. Sigrist, D. Agterberg, A. Furusaki, C. Honerkamp, K.K. Ng, T.M. Rice, and M.E. Zhitomirsky, Physica C **317-318**, 134 (1999).
64. P. Bourges, in *Gap Symmetry and Fluctuatios in High-Tc Superconductors, eds. J. Bok, G. Deutscher, D. Pavuna and S. Wolf, Plenum Press, NY, 1998.*
65. Y. Sidis, M. Braden, P. Bourges, B. Hennion, S. NishiZaki, Y. Maeno, and Y. Mori, Phys. Rev. Lett. **83**, 3320 (1999).
66. K. Ishida, H. Mukuda, Y. Kitaoka, Z.Q. Mao, H. Fukuzawa, and Y. Maeno, Phys. Rev . B **63**, 060507 (2001).
67. Although the decisive and unambiguous evidence for spin-triplet Cooper-pairing from in-plane ^{17}O and ^{99}Ru Knight shift data, it is important to note that $H_{c2}^{||}$ (parallel to the c-axis) is too small for NMR measurements. Therefore, strictly speaking the present Knight shift data do not fully reinforce Sr_2RuO_4 to be a triplet superconductor. In order to complete the picture, further studies, for example tunneling experiments along the c-axis, are necessary.
68. Actually neglecting interactions, one would have expected La_2CuO_4 to be metallic with a half-filled conduction band. As we know this is not true and this material is an antiferromagnetic insulator. Therefore, double occupancy should be energetically not favorable due to Coulomb repulsion.
69. As we know from the experiment the parent cuprate compounds are antiferromagnetic insulators. At the same time by applying a local-density-approximation calculation on undoped cuprates one finds that the system should be metallic with one hole per unit cell that satisfies the formal valences of La^{3+}, O^{2-}, and Cu^{2+} [70] that is inconsistent with experiment. The neglection of the electronic correlations of strong local Coulomb repulsion is responsible for this.
70. W.E. Pickett, Rev. Mod. Phys. **61**, 433 (1989).
71. However, the question about the exclusion of the apical oxygen and upper copper orbitals (in particular, $d_{3z^2-r^2}$) is still debated in some studies. This in particular concerns the asymmetry between hole- and electron-doped cuprates, since the latter do not have the apical oxygen. Thus, one may speculate that possible asymmetry between hole- and electron-doped cuprates may arise at least partly from there. This is still a subject of experimental and theoretical clarification.
72. We assume that the Cu-spins are part of the $p-d$ hybridized states.
73. V.J. Emery, Phys. Rev. Lett. **58**, 2794 (1987).
74. J. Zaanen, G.A. Sawatzky, and J.W. Allen, Phys. Rev. Lett. **55**, 418 (1985).
75. F.C. Zhang and T.M. Rice, Phys. Rev. B **37**, 3759 (1988).

76. G. Baumgärtel, J. Schmalian, and K.H. Bennemann, Phys. Rev. B **48**, 3983 (1993).
77. Note, the validity of the effective one-band hamiltonian for the hole-doped cuprates has has been also justified from a microscopic consideration of Baumgärtel, Schmalian and Bennemann [76] on the basis of $p-d$ Hamiltonian using a slave-boson technique [78].
78. G. Kotliar, and A.E. Ruckenstein, Phys. Rev. Lett. **57**, 1362 (1986).
79. P. Monthoux and D. Pines, Phys. Rev. B **47**, 6069 (1993).
80. N. E. Bickers, D. J. Scalapino, and S. R. White, Phys. Rev. Lett. **62**, 961 (1989); N. E. Bickers and D. J. Scalapino, Ann. Phys. (N.Y.) **193**, 206 (1989).
81. C.-H. Pao and N. E. Bickers, Phys. Rev. Lett. **72**, 1870 (1994); Phys. Rev. B **51**, 16310 (1995).
82. D. J. Scalapino, Phys. Rep. **250**, 329 (1995).
83. P. Monthoux and D. J. Scalapino, Phys. Rev. Lett. **72**, 1874 (1994).
84. T. Dahm and L. Tewordt, Phys. Rev. Lett. **74**, 793 (1995).
85. M. Langer, J. Schmalian, S. Grabowski, and K.H. Bennemann, Phys. Rev. Lett. **75**, 4508 (1995).
86. H.-B. Schüttler and C.-H. Pao, Phys. Rev. Lett. **75**, 4504 (1995).
87. J. Schmalian, S. Grabowski, and K. H. Bennemann, Phys. Rev. B **56**, R509 (1997).
88. L. Tewordt, J. Low Temp. Phys. **15**, 349 (1974).
89. Y. Nambu, Phys. Rev. **117**, 648 (1960).
90. Note, including charge fluctuations effects might be of interest in connection with lattice distortions and stripe formation. Superconductivity and charge density wave formation may coexist to some extent in the cuprates.
91. N. F Berk and J. R Schrieffer, Phys. Rev. Lett. **17**, 433 (1966).
92. A. B. Migdal, Zh. Eksp. Teor. Fiz **34**, 1438 (Soviet Phys.- JETP **34**, 996 (1958)).
93. G. Grimvall, *The Electron-Phonon Interaction in Metals*, North Holland, Amsterdam (1981).
94. J. R Schrieffer, *Theory of Superconductivity* (Addison-Wesley, Redwood City, 1964)
95. Note that the doping dependence of χ is controlled by the chemical potential via band filling. On general grounds we expect that for doping $x \to 0$ in particular spin density excitations and charge density excitations compete with each other.
96. G. D. Mahan *Many-Particle Physics* (Plenum Press, New York, 1981)
97. S. Wermbter and L. Tewordt, Physica C **211**, 132 (1993).
98. Note, $\tilde{U} = U_{eff}$ neglects differences between the itinerant carriers and the (local) Cu-spins.
99. Note, that one has to use the solution of the generalized Eliashberg equations in order to solve the corresponding two-particle vertex equations. This yields vertex corrections and thus a renormalized Coulomb interaction $U \to U_{eff}$. In Ref. [100] it has been argued that vertex corrections are –to a good approximation– frequency independent, and therefore the dynamics of the coupling of elementary excitations and spin excitations remain unchanged. In view of our calculations this seems to be in good agreement with experiment.
100. Y. M. Vilk and A.-M. S. Tremblay, J. Phys. I France **7**, 1309 (1997).
101. F. London and H. London, Proc. Roy. Soc. (London) **A149**, 71 (1935).

102. As for magnetism (Heisenberg or itinerant magnets) one expects in general interaction between the amplitude and the phase.
103. B. Giovannini, and C. Berthod, Phys. Rev. B **63**, 144516 (2001).
104. In analogy to ferromagnetism like in Ni we expect $n_s^0/n_s = \langle \nabla\Phi(\mathbf{r},t)\nabla\Phi(0)\rangle$. Note, it is straightforward to map our electronic theory on a lattice (Wannier type representation) and then to derive from the product of the anomalous Green's functions, $\{\mathcal{F}\cdot\mathcal{F}^*\}$, a contribution to the free energy of the form $n_s\cos\Theta_{ij}$ as used by Chakraverty *et al.* [107]. Here, Θ_{ij} is the angle between the phase of neighboring Cooper-pairs. Approximately, one has $n_s = n_s^0\bar{\Theta}_{ij}$, with $\bar{\Theta}_{ij} = 1$ for $T < T_c$ and $\bar{\Theta}_{ij} = 0$ for $T > T_c$
105. R. Manzke, R. Müller, C. Janowitz, M. Schneider, A. Krapf, and H. Dwelk, Phys. Rev. B **63**, 100504 (2001).
106. Note, in general χ_{s0} and χ_{c0} can be peaked at different wave vectors depending on the additional interaction included in a model.
107. B.K. Chakraverty, A. Taraphder, and M. Avignon, Physica C **235-240**, 2323 (1994); B.K. Chakraverty, and T.V. Ramakrishnan, *ibid*, **282-287**, 290 (1997).
108. V.J. Emery and S.A. Kivelson, Nature (London) **374**, 434 (1995).
109. M. V. Feigel'mann, Zh. Eksp. Teo. Fiz. **76**, 784 [Sov. Phys. JETP **49**, 395 (1989)].
110. G. Blatter, M. V. Feigel'mann, V. B. Geshkenbein, A. I. Larkin, and V. M. Vinokur, Rev. Mod. Phys. **66**, 1125 (1994).
111. V. L. Berezinskii, Zh. Eksp. Teo. Fiz. **61**, 1144 (1971) [Sov. Phys. JETP **34**, 610 (1972)]; J. M. Kosterlitz and D. J. Thouless, J. Phys. C **6**, 1181 (1973); J. M. Kosterlitz, *ibid* **7**, 1046 (1974).
112. M. R. Beasley, J.E. Mooij, and T. P. Orlando, Phys. Rev. Lett. **42**, 1165 (1979); S. Doniach and B. A. Hubermann, Phys. Rev. Lett. **42**, 1169 (1979); B. I. Halperin and D. R. Nelson, J. Low Temp. Phys. **36**, 599 (1979); L. A. Turkevich, J. Phys. C **12**, L385 (1979).
113. P. Minnhagen, Rev. Mod. Phys. **59**, 1001 (1987).
114. A. Kovner and B. Rosenstein, Phys. Rev. B **42**, 4748 (1990).
115. This is true in three dimensions. Of course, in the 2D case Gaussian fluctuations destroy the long-range order yielding $T_c = 0$, but the mean-field transition is still unchanged.
116. C. Timm, D. Manske, and K. H. Bennemann, Phys. Rev. B **66**, 094515 (2002).
117. In FLEX theory the fluctuations of the ordered antiferromagnetic state in the paramagnetic metallic regime are treated *beyond* the mean-field level. However, the fluctuations of the superconducting condensate were neglected in earlier treatments. A detailed comparison between $n_s(\omega)$ within the XY model and the FLEX approximation is given in Refs. [116,118]
118. D. Manske and K. H. Bennemann, Physica C **341-348**, 83-86 (2000); D. Manske, T. Dahm, and K.H. Bennemann, Phys. Rev. B **64**, 144520 (2001).
119. J. Bardeen and and M. J. Stephen, Phys. Rev. **140**, 1197A (1965).
120. J. Schmalian, S. Grabowski, and K.H. Bennemann, Phys. Rev. B **56**, R509 (1997).
121. F. Schäfer, C. Timm, D. Manske, and K. H. Bennemann, J. Low Temp. Phys. **117**, 223 (1999).
122. J.C. Swihart, D.J. Scalapino, and Y. Wada, Phys. Rev. Lett. **14**, 106 (1965).
123. M.R. Norman, M. Randeria, B. Janko, and J.C. Campuzano, Phys. Rev. B **61**, 14742 (2000).

124. R. Haslinger and A.V. Chubukov, cond-mat/0303140 (unpublished).
125. J.L. Tallon and J.W. Loram, Physica C **349**, 53 (2001).
126. W. W. Warren, R.E. Walstedt, G.F. Brennert, R.J. Cava, R. Tycko, R.F. Bell, and G. Dabbagh, Phys. Rev. Lett. **62**, 1193 (1989).
127. H. J. Tao, F. Lu, and E. J. Wolf, Physica C **282-287**, 1507 (1997).
128. Ch. Renner, B. Revaz, J.-Y. Genoud, K. Kadowaki, and Ø. Fischer, Phys. Rev. Lett. **80**, 149 (1998).
129. H. Takagi *et al.*, Phys. Rev. Lett. **69**, 2975 (1992).
130. D. Matthey, S. Gariglio, B. Giovannini, and J. M. Triscone, Phys. Rev. B **64**, 024513 (2001).
131. N. Miyakawa, J.F. Zasadzinski, L. Ozyuzer, P. Guptasarma, D.G. Hinks, C. Kendziora, and K.E. Gray, Phys. Rev. Lett. **83**, 1018 (1999).
132. P. C. E. Stamp, L. Forro, and C. Ayache Phys. Rev. B **38**, 2847 (1988).
133. S. N. Artemenko, I. G. Gorlova, and Y. I. Latyshev, Phys. Lett. A **138**, 428 (1989).
134. S. Martin, A.T. Fiory, R.M. Fleming, G.P. Espinosa, and A.S. Cooper, Phys. Rev. Lett. **62**, 677 (1989).
135. N. C. Yeh and C. C. Tsuei, Phys. Rev. B **39**, 9708 (1989).
136. T. Freltoft, H. J. Hensen, and P. Minnhagen, Solid State Comm. **78**, 635 (1991).
137. A. K. Pradhan, S.J. Hazell, J.W. Hodby, C. Chen, Y. Hu, and B.M. Wanklyn, Phys. Rev. B **47**, 11374 (1993).
138. Z. A. Xu, N. P. Ong, Y. Wang, T. Kakeshita, S. Uchida, Nature **406**, 486 (2000)
139. Y. Wang, Z. A. Xu, T. Kekeshita, S. Uchida, S. Ono, Y. Ando, and N. P. Ong, cond-mat/0108242.
140. J. Adler, C. Holm, and W. Janke, Physica A **201**, 581 (1993).
141. P. Olsson and P. Minnhagen, Physica Scripta **43**, 203 (1991).
142. C. Meingast, V. Pasler, P.Nagel, A. Gykov, S. Tajima, and P. Olsson, Phys. Rev. Lett. **86**, 1606 (2001).
143. F. Schäfer, D. Manske, and K.H. Bennemann, unpublished.
144. G. Baym and L. P. Kadanoff, Phys. Rev. **124**, 287 (1961).
145. G. Baym, Phys. Rev. **127**, 1391 (1962).
146. M. Sigrist and T.M. Rice, Z. Phys.B: Condensed Matter **68**, 9 (1987).
147. H.-J. Kwon and A. T. Dorsey, Phys. Rev. B **59**, 6438 (1999).
148. T. M. Rice, Phys. Rev. **140**, A1889 (1965).
149. T. Dahm, D. Manske, and L. Tewordt, Phys. Rev. **B** 54, 6640 (1996).
150. S. Grabowski, J. Schmalian, M. Langer, and K.H. Bennemann, Phys. Rev. B **55**, 2784 (1997).
151. G. Hildebrand, E. Arrigoni, J. Schmalian, and W. Hanke, Eur. Phys. J. B **8**, 195 (1999).
152. M.H. Cohen, L.M. Falicov, and J.C. Phillips, Phys. Rev. Lett. **8**, 316 (1962).
153. L. Alff, Y. Krockenberger, B. Welter, R. Gross, D. Manske, and M. Naito, Nature **422**, 698 (2003).
154. For $T_c \rightarrow 0$ a competition between quasiparticles coupling to spin fluctuations and phonons may in principle cause for energetic reasons a change from $d_{x^2-y^2}$-symmetry to s-symmetry of the superconducting order parameter. Such a scenario could be formulated using Ginzburg-Landau theory.
155. A. Damascelli *et al.*, Phys. Rev. Lett. **85**, 5194 (2000).

156. A. Liebsch, and A. Lichtenstein, Phys. Rev. Lett. **84**, 1591 (2000)
157. I.I. Mazin and D.J. Singh, Phys. Rev. Lett. **82**, 4324 (1999).
158. K.K. Ng, and M. Sigrist, Europhys. Lett. **49**, 473 (2000).
159. Note, χ^{+-} is the response to an external magnetic field $H_{||}$ parallel to the RuO_2-plane, similarly χ^{zz} is the response to $H_{\perp}$ perpendicular to the RuO_2 plane.
160. D. K. Morr, P. F. Trautmann, and M. J. Graf, Phys. Rev. Lett. **86**, 5978 (2001).
161. K. Ishida, H. Mukuda, Y. Minami, Y. Kitaoka, Z.Q. Mao, H. Fukazawa, and Y. Maeno, Phys. Rev. B**64**, 100501(R) (2001).
162. T. Mizokawa, L.H. Tjeng, G.A. Sawatzky, G. Ghiringhelli, O. Tjernberg, N.B. Brookes, H. Fukazawa, S. Nakatsuji, and Y. Maeno, Phys. Rev. Lett. **87**, 077202 (2001).
163. H. Kontani, and K. Ueda, Phys. Rev. Lett. **80**, 5619 (1998).
164. K. Kuroki, M. Ogata, R. Arita, and H. Aoki, Phys. Rev. B **63**, 060506(R) (2001).
165. Z.Q. Mao, Y. Maeno, Y. Mori, S. Sakita, S. Nimori, and M. Udagawa, Phys. Rev. B **63**, 144514 (2001).
166. D. M. King, Z.-X. Shen, D.S. Dessau, B.O. Wells, W.E. Spicer, A.J. Arko, D.S. Marshall, J. DiCarlo, A.G. Loeser, C.H. Park, E.R. Ratner, J.L. Peng, Z.Y. Li, and R.L. Greene, Phys. Rev. Lett. **70**, 3159 (1993).
167. G. Baumgärtel, J. Schmalian, and K.H. Bennemann, Phys. Rev. B **48**, 3983 (1993).
168. C. Timm and K.H. Bennemann, Phys. Rev. Lett. **84**, 4994 (2000).
169. T. Valla, A.V. Fedorov, P.D. Johnson, and S.L. Hulbert, Phys. Rev. Lett. **82**, 2179 (1999).
170. J. Ruvalds, C.T. Rieck, S. Tewari, J. Thoma, and A. Virosztek, Phys. Rev. **B 51**, 3797 (1995).
171. Z. X. Shen, A. Lanzara, and N. Nagaosa, preprint cond-mat/0102244 (unpublished).
172. J.L. Tallon, C. Bernhard, H. Shaked, R.L. Hittermann, and J.D. Jorgensen, Phys. Rev. B **51**, 12911 (1995).
173. C. Bernhard, J.L. Tallon, Th. Blasisus, A. Golnik, and Ch. Niedermeyer, Phys. Rev. Lett. **86**, 1614 (2001).
174. T. Nomura and K. Yamada, J. Phys. Soc. Jpn. **69**, 1856 (2000); ibid, cond-mat/0203453 (unpublished).
175. K. Kuroki, M. Ogata, R. Arita, and H. Aoki, Phys. Rev. B **63**, 060506 (2001).
176. T. Imai *et al.*, Phys. Rev. Lett. **81**, 3006 (1998).
177. M. Braden, Y. Sidis, P. Bourges, P. Pfeuty, J. Kulda, Z. Mao, and Y. Maeno, cond-mat/0206304 (unpublished).
178. J.R. Schrieffer, *Theory of superconductivity* (Addison-Wesley, 1988).
179. T.E. Mason, A. Schröder, G. Aeppli, H.A. Mook, and S.M. Hayden, Phys. Rev. Lett. **77**, 1604 (1996).
180. B. Lake, G. Aeppli, T.E. Mason, A. Schroder, D.F McMorrow, K. Lefmann, M. Isshiki, M. Nohara, H. Takagi, and S.M. Haydon, Nature (London) **400**, 43 (1999).
181. D. Manske, I. Eremin, and K.H. Bennemann, Phys. Rev. B **63**, 054517 (2001).
182. A.V. Chubukov, D. Pines, and J. Schmalian, in *The Physics of Superconductors Vol.1* (Edts. K.H. Bennemann, J.B. Ketterson, Springer 2002).

183. A. Ino, C. Kim, M. Nakamura, T. Yoshida, T. Mizokawa, A. Fujimori, Z.-X. Shen, T. Kakeshita, H. Eisaki, and S. Uchida, Phys. Rev. B **65**, 094504 (2002).
184. Ch. Renner, B. Revaz, J.-Y. Genoud, K. Kadowaki, and Ø. Fischer, Phys. Rev. Lett. **80**, 149 (1998).
185. G.V.M. Williams, J.L. Tallon, and J.W. Loram, Phys. Rev. B **58**, 15053 (1998).
186. G. Baumgärtel, J. Schmalian, and K.H. Bennemann, Phys. Rev. B **48**, 3983 (1993).
187. D. Manske, I. Eremin, and K.H. Bennemann, Phys. Rev. B **62**, 13922 (2000).
188. T.S. Nunner, J. Schmalian, and K.H. Bennemann, Phys. Rev. B **59**, 8859 (1999).
189. S.V. Borisenko, A.A. Kordyuk, T.K. Kim, A. Koitzsch, M. Knupfer, M.S. Golden, J. Fink, M. Eschrig, H. Berger, and R. Follath, Phys. Rev. Lett. **90**, 207001 (2003).
190. Z.M. Yusof, B.O. Wells, T. Valla, A.V. Fedorov, P.D. Johnson, Q. Li, C. Kendziora, S. Jian, and D. G. Hinks, Phys. Rev. Lett. **88**, 167006 (2002).
191. A.V. Puchkov, D.N. Basov, and T. Timusk, J. Phys. Condens. Matter **8**, 10049 (1996).
192. E.F. Paulus *et al.*, Solid State Commun. **73**, 791 (1990).
193. H. Takagi, S. Uchida, and Y. Tokura, Phys. Rev. Lett. **62**, 1197 (1989).
194. G. Liang, J. Chen, M. Croft, K.V. Ramanujachary, M. Greenblatt, and M. Hegde, Phys. Rev. B **40**, 2646 (1989).
195. V.J. Emery and S.A. Kivelson, Nature **374**, 434 (1995).
196. S. Doniach and M. Inui, Phys. Rev. B **41**, 6668 (1990).
197. G.D. Mahan, *Many-Particle Physics* (Plenum Press, New-York and London, 1990).
198. A.J. Layzer and D. Fay, *Proc. Int. Low Temp. Conf.*, St. Andrews (LT-11), Academic Press, London, (1968); P.W. Anderson and W.F. Brinkmann, in *"The physics of liquid and solid Helium"*, eds. K.H. Bennemann and J.B. Ketterson (V. 2, Wiley-Interscience, 1978).
199. N.F. Berk and J.R. Schrieffer, Phys. Rev. Lett. **17**, 433 (1966); D.J. Scalapino, Phys. Rep. **250**, 329 (1995).
200. Note, the second term in V_0 comes from ladder diagrams which due to the Pauli principle do not contribute to the triplet pairing.
201. Y. Hasegawa, K. Machida, and M. Ozaki, J. Phys. Soc. Jpn. **69**, 336 (2000).
202. M.E. Zhitomirsky, and T.M. Rice, Phys. Rev. Lett. **87**, 057001 (2001).
203. J.F. Annett, G. Litak, B.L. Gyorffy, and K.I. Wysokinski, cond-mat/0109023 (unpublished).
204. G.M. Luke, Y. Fudamoto, K.M. Kojima, M.I. Larkin, J. Merrin, B. Nachumi, Y.J. Uemura, Y. Maeno, Z.Q. Mao, Y. Mori, H. Nakamura, and M. Sigrist, Nature **394**, 558 (1998).
205. K. Ishida, H. Mukuda, Y. Kitaoka, A. Asayama, Z.Q. Mao, Y. Mori, and Y. Maeno, Nature **396**, 658 (1998).
206. K.K. Ng and M. Sigrist, Europhys. Lett. **49**, 473 (2000).
207. K.G. Sandeman, G.G. Lonzarich, A.J. Schofield, cond-mat/0210552 (unpublished).
208. K. Izawa, H. Takahashi, H. Yamaguchi, Y. Matsuda, M. Suzuki, T. Sasaki, T. Fukase, Y. Yoshida, R. Settai, and Y. Onuki, Phys. Rev. Lett. **86**, 2653 (2001).

209. For more detailed discussion on the behavior of the spin susceptibility see D, Vollhardt and P. Woelfle, in "*The superfluid phases of Helium*^{3}" (Taylor and Francis, London, 1990).
210. M.A. Tanatar, M. Suzuki, S. Nagai, Z.Q. Mao, Y. Maeno, and T. Ishiguro, Phys. Rev. Lett. **86**, 2649 (2001).
211. Y. Maeno, T.M. Rice, and M. Sigrist, Phys. Today **54**, 42 (2001).
212. K. Yoshida, Y. Maeno, S. Nishizaki, and T. Fujita, Physica C **263**, 519 (1996).
213. D.F. Agterberg, Phys. Rev. Lett. **80**, 5184 (1998).
214. T.M. Riseman *et al.*, Nature **396**, 242 (1998).
215. Z.Q. Mao, Y. Maeno, S. Nishizaki, T. Akima, and T. Oshigiro, Phys. Rev. Lett. **84**, 991 (2000).
216. D.F. Agterberg, Phys. Rev. B **64**, 052502 (2001).
217. M. Sigrist, J. Phys. Soc. Jpn. **69**, 1290 (2000).
218. S. Nakatsuji, and Y. Maeno, Phys. Rev. Lett. **84**, 2666 (2000).
219. Z. Fang and K. Terakura, Phys. Rev. B **64**, 020509(R) (2001).
220. J.F. Zasadzinski, this book, Vol.1.
221. D. Mandrus, L. Forro, and D. Koller, and L. Mihaly, Nature **351**, 460 (1991).
222. J.F. Zasadzinski, Bull. Am. Phys. Soc. **37**, 668 (1992).
223. S. Grabowski, Ph.D. thesis, Berlin (1996).
224. A.V. Chubukov, D. Pines, and J. Schmalian, this book, Vol.1, p. 495.
225. Finally, we would like to note also that recently it was argued [227] that in many cases the 'dip feature' seen in bilayer cuprates can be produced by the effects of bilayer splitting. However, recent studies of the one-layer Tl-based cuprates [228] confirm the presence of the 'dip' feature indicating its intrinsic relation to the 'resonance' peak. In order to identify the 'dip' position seen in bilayer cuprates and its relation to the 'resonance' peak further studies are necessary.
226. J.F. Zasadzinski, L. Qzyuzer, N. Miyakawa, K.E. Gray, D.G. Hinks, and C. Kendziora, Phys. Rev. Lett. **87**, 067005 (2001).
227. A.A. Kordyuk, S.V. Borisenko, T.K. Kim, K. Nenkov, M. Knupfer, M.S. Golden, J. Fink, H. Berger, R. Follath, cond-mat/0110379.
228. J.F. Zasadzinski, L. Ozyuzer, N. Miyakawa, D.G. Hinks, and K. E. Gray, Physica C **341-348**, 867 (2000).
229. A.A. Kordyuk, S.V. Borisenko, M.S. Golden, S. Legner, K.A. Nenkov, M. Knupfer, J. Fink, H. Berger, L. Forro, and R. Follath, Phys. Rev. B **66**, 014502 (2002).
230. Y.-D. Chuang, A.D. Gromko, A. Fedorov, Y. Aiura, K. Oka, Y. Ando, H. Eisaki, S.I. Uchida, and D.S. Dessau, Phys. Rev. Lett. **87**, 117002 (2001).
231. D. L. Feng *et al.*, Phys. Rev. Lett. **86**, 5550 (2001).
232. N. Bulut and D.J. Scalapino, Phys. Rev. B **53**, 5149 (1996).
233. J.M. Kosterlitz and D.J. Thouless, J. Phys. C **6**, 1181 (1973).
234. P. Minnhagen, Phys. Rev. B **23**, 5745 (1981).
235. D. R. Nelson and J. M. Kosterlitz, Phys. Rev. Lett. **39**, 1201 (1977).
236. V. Ambegaokar, B. I. Halperin, D. R. Nelson, and E. D. Siggia, Phys. Rev. Lett. **40**, 783 (1978); V. Ambegaokar and D. Seitel, Phys. Rev. B **19**, 1667 (1979); V. Ambegaokar, Halperin, D. R. Nelson, and E. D. Siggia, Phys. Rev. Lett. **21**, 1806 (1980).

10 Heavy Fermion Superconductivity

Peter S. Riseborough Dept. of Physics, Polytech Univ., NewYork, USA
George M. Schmiedeshoff Occidental College, Dept. of Phys., Calif., USA
James L. Smith National Laboratory of Los Alamos, Nevada, USA

10.1 **Overview** 890
10.2 **Introduction** 892
10.2.1 Multiple Superconducting Phases 896
10.2.2 Interplay of Superconductivity and Magnetism 901
10.2.3 Quasi–Particles and Collective Excitations 905
10.2.4 Possible Pairing Mechanisms 917
10.2.5 The Symmetry of the Order Parameter 925
10.3 **Properties of the Normal State** 951
10.3.1 Thermodynamic Properties 956
10.3.2 Transport Properties 972
10.3.3 Dynamic Magnetic Properties 985
10.4 **Properties of the Superconducting State** 1007
10.4.1 Thermodynamic Properties 1007
10.4.2 Transport Properties 1014
10.4.3 Dynamic Magnetic Properties 1037
10.5 **Heavy Fermion Superconducting Compounds** 1054
10.5.1 UPt_3 1056
10.5.2 $CeCu_2Si_2$ 1058
10.5.3 UBe_{13} 1058
10.5.4 Thoriated UBe_{13} 1059
10.5.5 URu_2Si_2 1060
10.5.6 UPd_2Al_3 1060
10.5.7 UNi_2Al_3 1061
10.5.8 $CeRhIn_5$ 1061
10.5.9 $CeIrIn_5$ 1062
10.5.10 $CeCoIn_5$ 1062
10.5.11 $CeIn_3$ 1062
10.5.12 $CePd_2Si_2$ 1063
10.5.13 $CeRh_2Si_2$ 1063
10.5.14 $CeCu_2Ge_2$ 1063
10.5.15 $PrOs_4Sb_{12}$ 1064
10.5.16 U_2PtC_2 1064
10.5.17 Related Materials 1064
10.6 **The Conclusion** 1066
Acknowledgements 1066
References 1066

K. H. Bennemann et al. (eds.), *The Physics of Superconductors*
© Springer-Verlag Berlin Heidelberg 2004

10.1 Overview

When the BCS theory appeared in 1957, Bernd Matthias felt it did not do everything. He thought that it worked for the p–electron superconductors such as lead and tin, but the transition metal superconductors such as niobium and vanadium were still unexplained. Aside from his instinct, it was that here the isotope effect was all over the map. This led him to uranium, where his student Hunter Hill did the isotope effect for uranium and found that the orthorhombic α–phase had a backward mass squared dependence and that the cubic γ–phase looked BCS-like. This was Hunter's thesis work, and the experiment was difficult enough that those who did not like the result could ignore it. Bernd was also drawn to the U_6X superconducting compound with X = Mn, Co, Fe, and Ni. In these compounds, the T_c scaled with the moments, that is, they followed the Slater–Pauling curve. These were the first superconductors discovered that formed with $3d$ magnetic elements.

The heavy–fermion ground state arises at low temperature. Near room temperature, these metals have magnetic moments whose magnetic susceptibility suggest that they would order antiferromagnetically at low temperature. However somewhere below 50 K, unexpected behavior shows up. The electrical resistivity is high for a metal, and the magnetic ordering does not occur. The heat capacity below 10 K is quite large and seems consistent with the presence of magnetic moments. However, when some compounds became superconducting with the heat capacity indicating that the large value was due to the superconducting electrons instead of the magnetic moments, it seemed wrong. It was as if the rocks in a stream bed began to flow instead of the water. There is still no accepted explanation for such behavior.

In 1975 Bucher *et al.* noted that the compound UBe_{13} had become superconducting with a somewhat large critical field [1]. They said it was likely that pure uranium filaments were present in the sample, and the superconductivity was hence an impurity effect. In 1978, Franz *et al.* reported in a footnote that the compound $CeCu_2Si_2$ had become superconducting [2], but in this case there was not a simple explanation for an impurity effect. In both cases the authors were clearly wondering what had happened but knew it could not be correct. Steglich continued to pursue the superconductivity and in 1979 reported that is was genuine [3]. As a superconducting material, it seemed ordinary except for the heat capacity that was about a thousands times too large. Steglich coined the name of heavy–fermion superconductor by associating the huge heat capacity with a huge mass for the conduction electrons, which was the only parameter that could be adjusted. So there was a superconductor with a heat capacity for the superconducting electrons that was as large as that usually associated with fixed magnetic moments. People who were paying attention considered it an oddity, and little happened.

In 1983 Ott *et al.* rechecked Bucher's result and found UBe_{13} to have properties remarkably similar to those of $CeCu_2Si_2$ [4]. Polycrystalline and single–crystalline samples were made at Los Alamos and seen to be supercon-

ducting. Heat–capacity measurements at Zürich showed that indeed a huge heat capacity was in the superconducting electrons. The condensed–matter physics community began to take notice, and measurements of many other properties began in earnest on both compounds. It was noticed that the temperature dependence of the heat capacity in the superconducting state was not an exponential, as seen in known superconductors and as predicted by the Bardeen Cooper Schrieffer theory, but rather it was a power law. This suggested that a gap had not opened everywhere on the Fermi surface (Ott *et al.* 1984) [5]. This is similar to the pairing in superfluid ^{3}He, which is non–s–wave pairing. This was the first possible example of an exotic superconductor, one in which the Cooper pairs have a symmetry that is not isotropic or almost so. Some theorists sharpened their pencils, and the people in Los Alamos and Zürich were wondering about the analogy to ^{3}He because the smoking gun for low–symmetry superconductors would be more than one superconducting phase.

Then in 1984, Stewart *et al.* reported that UPt_3 was superconducting and was another candidate for a low–symmetry superconductor [6]. They had been studying it as a spin–fluctuating material when it went superconducting at low temperatures. While UBe_{13} and $CeCu_2Si_2$ were not good Fermi liquid metals (later to become its own field as non–Fermi liquid materials), UPt_3 fit the many–body models of Fermi liquids perfectly. The theorists began work and had much success at describing this ground state. However, how the state occurred was and is the mystery of heavy–fermion superconductors.

Also in 1984, Smith *et al.* began putting impurities into UBe_{13} and found a strange non–monotonic depression of the superconducting transition temperature with the addition of thorium [7]. In 1985, heat–capacity measurements in Zürich showed two huge superconducting transitions, and the analogy to ^{3}He and the proof of low–symmetry superconductivity was made [8]. The first material, $CeCu_2Si_2$, remained an s–wave superconductor. So by 1986, all of the measurements that anyone could think of were being performed around the world, and review articles were being printed such as Fisk *et al.* 1986 [9] and Fisk *et al.* 1988 [10]. These also cover non–superconducting heavy–fermion systems that became identifiable once the properties of the superconductors were well known. Many theses were being written, and the old men of superconductivity were thanking the younger experimentalists for breathing new life into superconductivity. Order seemed to be at hand.

Then late in 1986, Bednorz and Müller published their work on high–temperature superconductivity [11], and an avalanche cut a huge swath through condensed–matter physics leaving many subjects deserted. As it developed that high–temperature superconductors were also non–s–wave, theorists were well prepared. Only two example of transitions between superconducting states have been found in oxides (Movshovich *et al.* 1998 [12] and Mota *et al.* 1999 [13]), and these results are not widely known or accepted. However, all of the modern techniques that came from the original scan-

ning tunnelling microscope have, in the 1990's, permitted workers to directly measure the symmetry of the superconducting energy gap.

The compound UPt_3 had one more surprise left. In 1989, Fisher *et al.* discovered a second bump in the heat capacity of the superconducting transition [14]. Workers all over the world took the old samples out of their drawers to remeasure this because all had missed it, and it was confirmed to have two superconducting phases. It was soon seen that the magnetic–field–and–temperature phase diagram had three superconducting phases, and the theoretical description of them was under control quickly.

Now, we have heavy–fermion superconductors and high–temperature superconductors both without an accepted model for how these ground states occur. New theory is still needed. One recent development is the possibility of quantum critical points at zero temperature that hold some promise of explaining the general phase diagrams for both of these superconductors, which usually have an antiferromagnetic state in them. There is a feeling that some larger theoretical picture may emerge and show us all new physics. It is also true that in Germany and Japan, there are now major experimental institutes engaged in the search for more heavy–fermion materials with the usual name now of highly–correlated electron systems. And of course, theoretical work is underway everywhere.

10.2 Introduction

The first heavy–fermion superconductor $CeCu_2Si_2$ was discovered by Steglich [3] in 1979. Despite intense skepticism from members of the scientific community, Steglich demonstrated that stoichiometric $CeCu_2Si_2$ underwent a transition to a superconducting state at the critical temperature $T_c = 0.7$ K. This material was regarded as a unique anomaly until several other materials were discovered which had the same distinctive normal state properties. Some of these heavy–fermion materials [4,6] even have similar unusual superconducting phases. This class of heavy–fermion materials can be loosely categorized as systems that are in close proximity to a magnetic instability, and have the characteristic properties that at high temperatures, the system exhibits evidence of local moments; at low temperatures, the system resembles a Fermi liquid with very heavy quasi–particle masses. The heavy–fermion materials are based on elements from the lanthanide or actinide series which have incomplete f shells. The f derived electronic states retain a lot of their ionic character in that they are almost localized and experience large electronic interactions attributable to the smallness of the radius of the ionic f orbitals. The heavy–fermion materials are those in which there is a delicate balance between the strong ionic coulomb interactions that tend to localize the electrons and yield local magnetic moments, and the hybridization with extended band states that tends to delocalize the f electrons. The delicate balance is responsible for the temperature dependent cross–over from the high temperature

local moment regime to the low temperature regime of itinerant f electron behavior. At high temperatures, the magnetic moments are manifested via the Curie–Weiss variation of the magnetic susceptibility with Curie constants almost equal the full ionic magnetic moments, and also through a Kondo–like logarithmic temperature variation of the electrical resistivity indicating resonant scattering of conduction electrons from independent local moments. In the low temperature regime, the strong electron–electron interactions show up as strong renormalizations of the properties of the itinerant electrons. The excitations of the interacting electron gas include quasi–particle excitations that closely resemble the excitations of a non–interacting electron gas. The quasi–particles have dispersion relations that form narrow correlated f bands close to the Fermi energy. The quasi–particle masses, as inferred from the coefficient, γ, of the low temperature linear T term of the specific heat, can be as large as 1000 free electron masses. The masses of the heavy quasi–particle are assumed to have evolved from the entropy released during the transformation of the high temperature magnetic moments. The specific heat coefficient γ determined from the normal state of $CeCu_2Si_2$ is roughly 1100 mJ/mole K^2, while that of the paramagnetic heavy–fermion $CeCu_6$ [15] system is 1300 mJ/mole K^2. The low temperature susceptibilities $\chi(T)$ are also enhanced above the values of the Pauli paramagnetic susceptibilities inferred from the density of states obtained via LDA calculations. The values of the low temperature susceptibilities can be as large as 28×10^{-3} e.m.u./mole for $CeCu_6$ and 16×10^{-3} e.m.u./mole for $CeRu_2Si_2$ [16]. A measure of the relative strengths of enhancements experienced by the susceptibility and the specific heat is given by the Wilson ratio,

$$R_W = \frac{\pi^2 k_B^2 \chi(0)}{3\mu_B^2 \gamma} \tag{10.1}$$

which has the ideal value of unity for the non–interacting electron gas. However, the values of the Wilson ratio found for most heavy–fermion systems are also close to unity. Comparison of the γ values and the low temperature limit of the magnetic susceptibilities with the densities of states at the Fermi energy found in LDA electronic structure calculations [17] indicate that the quasi–particle masses are enhanced by factors as large as 25, presumably due to strong electron–electron interactions. This interpretation is supported by the observation of a $T^3 \ln T$ term in the specific heat of UPt_3, which is characteristic of spin–fluctuations driven by strong electron–electron interactions. In addition, the low temperature electrical resistivities of some materials, such as $CeCu_6$, show $\rho(T) = \rho(0) + A\,T^2$ variations where the coefficient A takes on large values. The large value of A is indicative of the formation of a Fermi liquid state in which the resistivity is dominated by scattering between the heavy quasi–particles. In this interpretation, the value of A is a measure of the inverse square of the renormalized Fermi energy. The most direct and definitive evidence proving the existence of the heavy Fermi liquid state is given by the measurement of de Haas – van Alphen oscillations [18, 19]. In

a number of materials, large quasi–particle mass enhancements have been found over significant portions of the Fermi surface. The large quasi–particle masses inferred for some or all portions of the Fermi surface correlate well with the measured value of γ. Evidence of the strong magnetic correlations is provided by the fact that, in many heavy–fermion systems, the addition of small amounts of impurities allows the strong electron interactions to drive the system magnetic. This suggests that the heavy–fermion systems may be in the vicinity of a quantum critical point and that the extremely large mass enhancements are produced by the nearly critical magnetic fluctuations. Unlike the U heavy–fermion systems, the Ce systems seem to show properties that are attributable to strongly localized fluctuating f magnetic moments, so that a large part of the mass enhancement for the Ce heavy–fermion compounds may result from the local moment fluctuations.

Large mass enhancements can also be inferred from the normal state specific heats of the uranium heavy–fermion superconductors UBe_{13} [4], UPt_3 [6] and URu_2Si_2 [20, 21], which have magnitudes that are of the same order as in the heavy–fermion Ce compounds. The observed γ values are 1100 mJ/mole K^2 for UBe_{13}, 400 for UPt_3, and 60 mJ/mole K^2 for URu_2Si_2. The magnetic susceptibilities χ, in the low temperature normal state, are also enhanced. For UBe_{13}, which has a cubic structure, the low temperature normal state susceptibility has a value of 14×10^{-3} e.m.u./mole. In UPt_3, which has hexagonal symmetry, the susceptibility is anisotropic, having the value of 4×10^{-3} e.m.u./mole for fields along the c–axis and 8.1×10^{-3} in the basal plane. In URu_2Si_2, which has tetragonal symmetry, the susceptibility is 4.9×10^{-3} for fields along the c–axis and 1.5×10^{-3} e.m.u./mole in the perpendicular directions. Fermi liquid analyses of the specific heat and susceptibility are complicated by the existence of unusual low temperature magnetic phases and correlations. In fact, while the large values of the χ and γ may be considered as indicative of the formation of a highly enhanced Fermi liquid, the resistivity of UBe_{13} is still large $\sim 100 \mu\Omega$cm, and although rapidly varying, it shows no evidence of a T^2 variation setting in before the superconducting transition occurs [1]. The large magnitude of the specific heat jump that occurs at the superconducting transition temperature, T_c, shows that the electrons that take part in the formation of the heavy–fermion state form the Cooper pairs. That is, the normalized jump discontinuity $(C_s - C_n) / C_n$ is of the order of unity, similar to the B.C.S value of 1.43, which indicates that the superconducting electrons have heavy masses (see Fig. 10.1). A similar conclusion is arrived at by a thermodynamic analysis of the extremely large initial slopes of the upper critical fields $(\partial H_{c2}/\partial T)_{T_c}$ [22–24] which is about – 42 T/K for UBe_{13}.

The equilibrium superconducting state is that which minimizes the total energy, including the strong Coulomb interaction between the f electrons that

[1] However, when magnetic fields large enough to suppress the superconductivity are applied, UBe_{13} does exhibit a T^2 term in the resistivity.

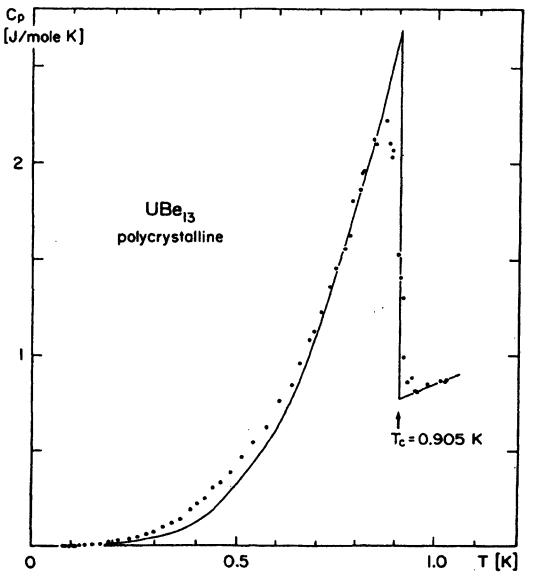

Fig. 10.1. Low temperature specific heat of UBe_{13} measured by Ott. *et al.* (1985) [5]. The magnitude of the jump in the specific heat at T_c is comparable to the magnitude of the linear T term in the normal state. This suggests that the heavy quasi–particles of the normal state form the Cooper pairs. For comparison, the specific heat calculated for a strong coupling ABM p–wave superconductor is shown by the solid line. The temperature dependence is indicative that the quasi–particle density of states is gapless

gives rise to the enhanced masses in the Ce and U heavy–fermion materials. The superconducting electrons could form Cooper pairs with finite angular momentum, l, which could lower the Coulomb repulsion between the pairing electrons as the pair wave function vanishes at the origin. The decrease in the large Coulomb energy could offset the increase in kinetic energy due to the orbital motion. The finite angular momentum of the pairs could also lead to the superconducting gap at the Fermi energy falling to zero at either isolated zeros or lines, giving rise to a finite density of states for low–energy quasi–particle excitations. These point zeros and line zeros give rise to power law variations with T for various physical properties, which are in contrast to the exponentially activated behavior usually observed in s–wave superconductors. Such power law variations have been found in experiments [5,25–31] and show conclusive evidence of low–energy excitations. However, the observed power laws have not led to a consensus as to whether they are caused by either point zeros or line zeros in the order parameter. This lack of consensus could be due to the complications of either pair breaking effects of impurities in

anisotropic superconductors or due to collective fluctuations. In either case, heavy–fermion superconductors are examples of exotic superconductors.

10.2.1 Multiple Superconducting Phases

Soon after the discovery of the uranium heavy–fermion superconductors, it was noticed that some heavy–fermion superconductors exhibited multiple superconducting phases. This discovery gave strong support to the hypothesis that the superconductivity involved exotic pairings. Motivated by the discovery of the power law temperature variations and the implications about the zeros in the gap, Ott *et al.* [8] doped the superconductors with impurities to find their effect on the superconducting transition temperature T_c, as it is well known that non–magnetic impurities suppress anisotropic pairing. It was found that substitution of just a few percent of Th atoms on the U sites in UBe_{13} produced a large non–monotonic change in T_c and also reduced the value of the resistivity at constant T [7]. Measurements of the specific heat showed a spectacular result namely, that for Th concentrations in the range $0.01 < x < 0.06$, the specific heat shows two jumps that have comparable discontinuities (see Fig. 10.2). The upper transition is associated with a large Meissner effect and has a maximum T_{c1} near 0.6 K in this range of x, whereas the second transition occurs at T_{c2}, which is approximately 0.4 K. The existence of the second transition in the doped samples was confirmed by sound velocity and ultrasonic attenuation experiments [32]. The sound veloc-

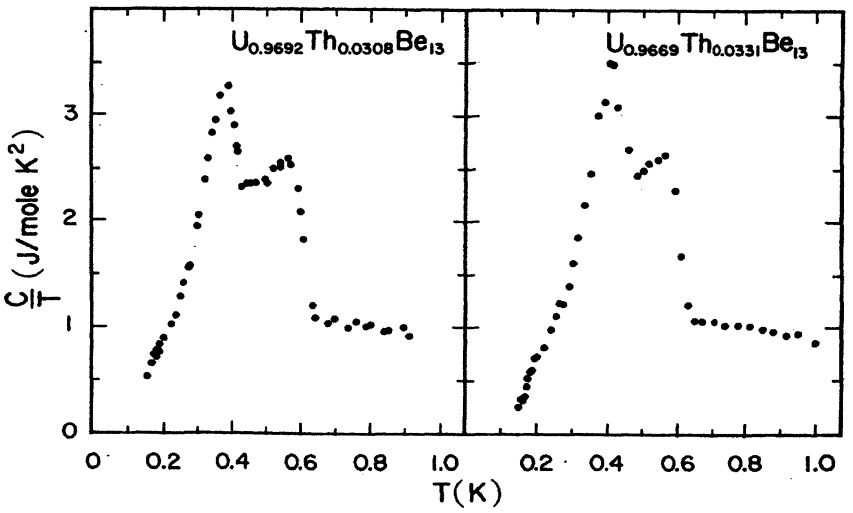

Fig. 10.2. The temperature dependence of the specific heat of $U_{1-x}Th_xBe_{13}$ compounds, for $x = 0.0308$ and $x = 0.0331$ showing the double transition measured by Ott. *et al.* (1985) [8]

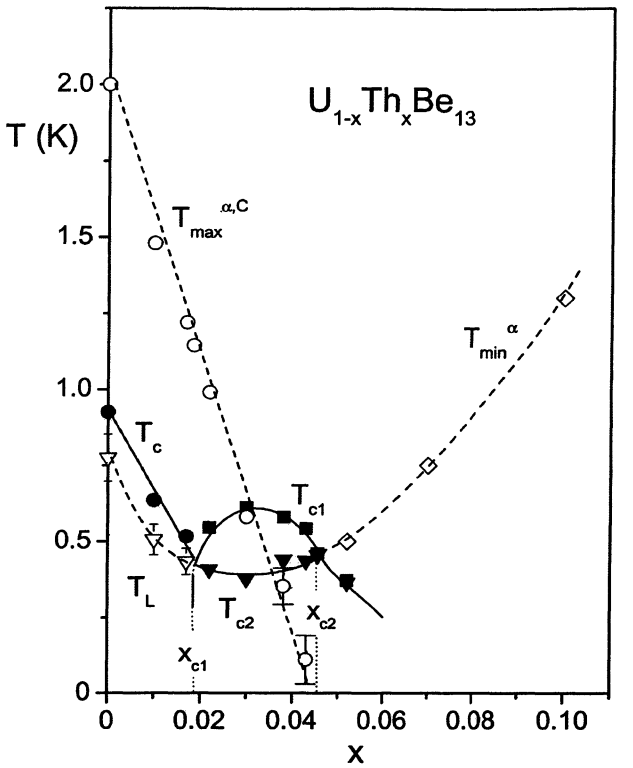

Fig. 10.3. A $T - x$ phase diagram for $U_{1-x}Th_xBe_{13}$. Filled symbols denote phase transitions and open symbols indicate anomalies in the specific heat (C) and thermal expansion (α). The solid vertical line at $x = x_1$ represents a phase boundary established by the specific heat measurements under pressure of Zieve *et al.* [500]. [After Oeschler *et al.* (2003), [496]]

ity showed a pronounced minimum at T_{c2}, while the attenuation showed a λ peak. The second superconducting phase was assigned as having some intrinsic weak magnetic character. The magnetic nature of the second transition was later confirmed via improved muon spin resonance measurements [33], which show that weak magnetic moments of the order 10^{-3} μ_B are formed below T_{c2} but only in the concentration range $0.01 < x < 0.06$. The phase diagram is shown in Fig. 10.3. The existence of two superconducting phases, in analogy with the phase diagram of ^{3}He, is further evidence of the unconventional nature of the superconducting order parameter. If the system were an s–wave superconductor and the Fermi surface were isotropically gapped at T_{c1}, it seems very unlikely that the large jump in the specific heat at T_{c2} would be due to a weak magnetic transition that merely coexists with the superconducting transition. If the superconducting gap is anisotropic hav-

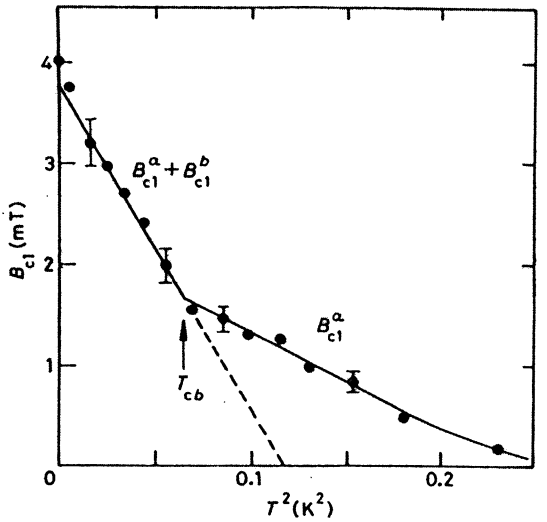

Fig. 10.4. The lower critical field H_{c1} of $U_{1-x}Th_xBe_{13}$ for $x = 0.03$, as measured by Rauchschwalbe *et al.* (1987) [36]. The temperature of the kink indicates the existence of a second transition

ing nodes, the electronic states in the vicinity of nodes could take part in a magnetic transition and could result in the small size of the moments [34]. However, it still remains unlikely that magnetic ordering of these states could produce a large jump in the specific heat. An alternate possibility is that the second transition is between two distinct unconventional superconducting phases, one of which may involve broken time reversal symmetry [35]. This alternate possibility was given credence by the measurements performed by Rauchschwalbe *et al.* [36] where $H_{c1}(T)$ showed a quadratic T dependence with a coefficient that abruptly changes at T_{c2} (see Fig. 10.4). This suggests that the lower transition is between two superconducting phases that have different types of order parameters. The faster temperature variation of H_{c1} below T_{c2} is interpretable as due to an increase in the superconducting condensation energy.

Careful measurements on UPt_3 also revealed the presence of two jumps in the specific heat [14] with critical temperatures separated by 60 mK. The specific heat jumps for two different samples of UPt_3 are shown in Fig. 10.5. The application of a magnetic field in the basal plane reduces both transition temperatures [37], but the 60 mK splitting observed at $H = 0$ is diminished and the transitions merge at a critical point ($H_{c2}(T) = 5$ kOe and $T = 380$ mK). The H – T phase diagram of UPt_3 is shown in Fig. 10.6. A definite kink in the temperature derivative of $H_{c2}(T)$ had been previously observed at this field [38,39]. The splitting between the two jumps in the specific heat depends on the direction of the applied field. Application of a field parallel to

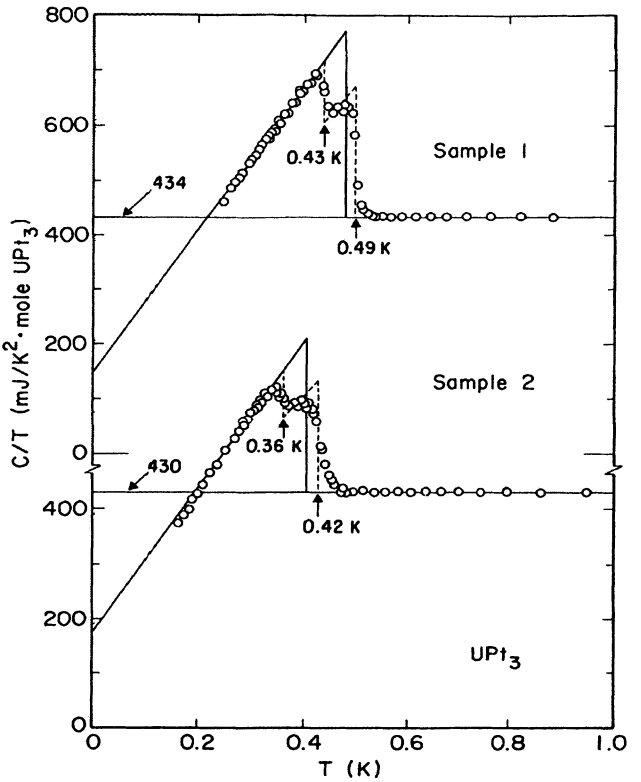

Fig. 10.5. The double transition in the specific heat found in two samples UPt_3 found by Fisher *et al.* (1989) [14]

the c direction does not reduce the splitting between the transitions, and for this field direction, the critical field does not show any discontinuity in the slope of $H_{c2}(T)$ up to the highest measured fields (7.5 kOe). The lower critical field, $H_{c1}(T)$, has a similar dependence on the orientation of the field [40]. A sharp kink in the temperature dependence of H_{c1} was observed for fields in the basal plane, and no kink was found for fields parallel to the c–axis. Evidence for further structure in the H–T phase diagram was provided by ultrasonic attenuation measurements. Early on, Qian *et al.* [41] and Müller *et al.* [42] observed a λ anomaly in the ultrasonic attenuation, just below T_c for longitudinal waves at H= 0. The position of the attenuation peak splits at higher fields, and the peak continues deep within the superconducting state as a cusp–like feature. Initially, the attenuation experiments were given scant attention by the scientific community, but given the preponderance of evidence for multiple superconducting phases, ultrasonic measurements are now recognized as providing excellent evidence for a phase boundary between different superconducting phases [43]. For H fields in the basal plane, this phase

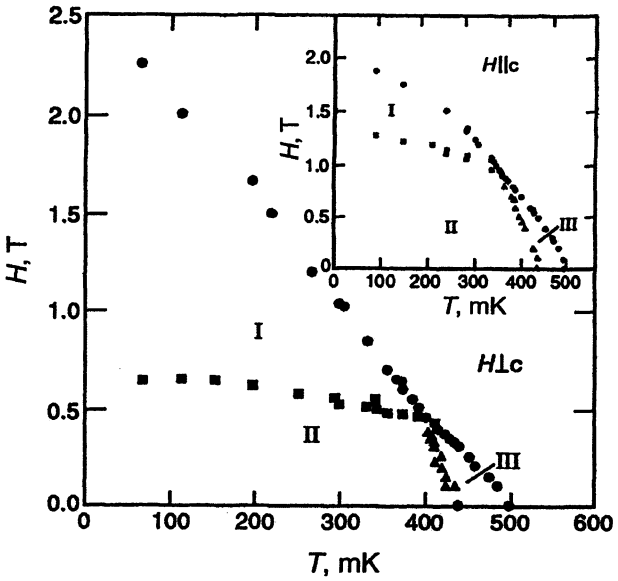

Fig. 10.6. The temperature–field phase diagram of UPt_3, as deduced from sound-velocity measurements of Adenwalla *et al.* (1990) [44]. The applied field is in the basal plane. The inset shows the phase diagram when the applied field is directed along the c axis. The low field boundary separating the mixed and the Meissner phases is not shown

boundary appears to join up with the phase boundaries obtained from the two specific heat jumps at the very point where the splitting between the jumps disappears. The complete phase diagram of UPt_3 has been obtained from anomalies in the measured velocity of acoustic phonons [44, 45]. The phase diagram in the $H - T$ plane shows the existence of five superconducting phases in contrast to the two usually observed in type II superconductors. The phase diagram contains two distinct Meissner phases in addition to three mixed phases. The transition to the superconducting phase of UPt_3, at zero field and ambient pressure, occurs at a temperature of 0.5 K, which is well below the Néel temperature of $T_N \sim 6K$ at which a small moment antiferromagnetic phase occurs. The application of uniaxial or hydro–static pressure shows that the splitting between the zero field superconducting transitions disappears above a critical pressure [46, 48, 49]. As shown in Fig. 10.7, the pressure at which the two jumps in the specific heat merge coincides with the pressure where the antiferromagnetism also disappears [46]. This suggests that the appearance of multiple superconducting phases in UPt_3 is intimately related to the occurrence of magnetic ordering.

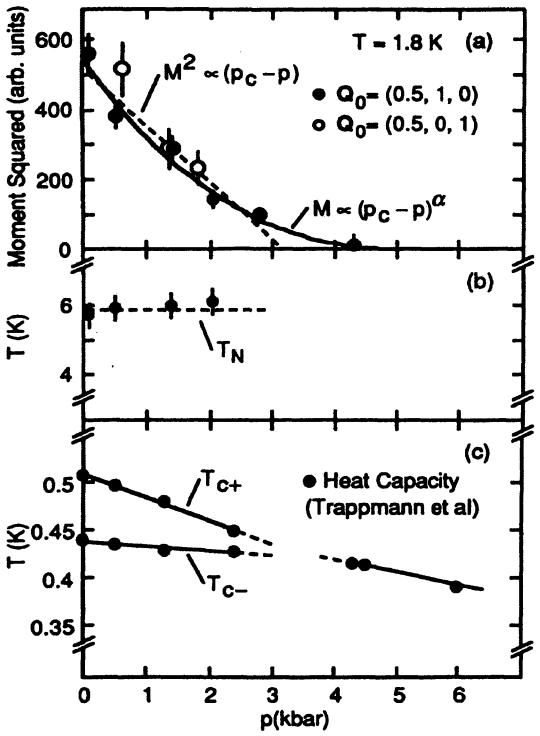

Fig. 10.7. The integrated intensity of the magnetic peaks $(\frac{1}{2}, 1, 0)$ and $(\frac{1}{2}, 0, 1)$ of UPt_3 at $T = 1.8$ K as a function of hydrostatic pressure [46] is shown in (a). The magnetic Bragg peak intensity should correspond to the square of the order parameter. The Néel temperature T_N, as determined from the integrated intensities, is shown as a function of pressure in (b). The critical pressure at which the magnetism disappears coincides with the pressure at which the specific heat jumps merge [47]

10.2.2 Interplay of Superconductivity and Magnetism

A further notable characteristic of the heavy–fermion superconductors is that, with the exception of UBe_{13}, UGe_2, and URhGe, the superconducting phases coexist with antiferromagnetic correlations which have characteristic temperatures, usually T_N, that can be roughly an order of magnitude greater than the corresponding superconducting critical temperatures. The strengths of the antiferromagnetic correlations are weakest for the systems that show the largest mass enhancements, such as $CeCu_2Si_2$, UPt_3 and $U_{1-x}Th_xBe_{13}$, where the size of the moments is at most minute, of the order of 0.03 μ_B. Muon spin resonance experiments on these three materials indicate that magnetic fluctuations have extremely long characteristic time scales. On the other hand, the more recently discovered compounds URu_2Si_2, UNi_2Al_3 [50] and

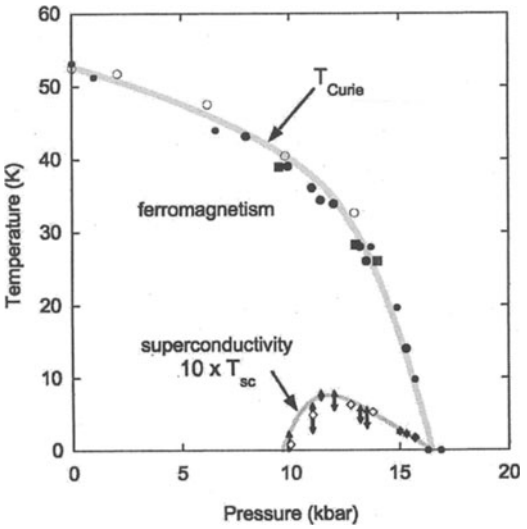

Fig. 10.8. The pressure–temperature phase diagram of the ferromagnetic superconductor UGe_2 [65]. The Curie temperature were determined from the susceptibility (filled circles), resistivity (open circles) and neutron diffraction (squares). The onset and completion of the resistive superconducting transition are shown by the filled triangles. Note the change of scale for the superconducting transition temperature

UPd_2Al_3 [51] have much smaller γ coefficients which, if estimated above the respective Néel temperatures, are only as large as 150 mJ / mole K^2. The γ values below the Néel temperatures are reduced, indicating a partial gapping of the Fermi surface. These moderately enhanced materials have T_N's that can be as high as 14.5 K and have ordered magnetic moments that range up to 0.85 μ_B.

For a long time, $CeCu_2Si_2$ was the only known Ce based heavy–fermion superconductor at ambient pressure. However, this compound suffered from materials problems namely, a small change in stoichiometry could result in the ground state changing from superconducting to antiferromagnetic. Very recently it was found that $CeIrIn_5$ and $CeCoIn_5$ superconduct at $T_c = 0.4$ and $T_c = 2.3$ K, respectively [52,53]. Furthermore, these materials are almost always single crystals and apparently do not suffer from the same problems as exhibited by $CeCu_2Si_2$. These new heavy–fermion superconductors have a quasi–two–dimensional structure. They are quite anisotropic and exhibit well defined crystal field excitations at high temperatures [54] and at low temperatures show de Haas – van Alphen oscillations characteristic of anisotropic Fermi surfaces [55, 56]. More important, they show that the superconductivity occurs in the vicinity of magnetism [57]. The quasi–two–dimensional nature of the materials and the anisotropy of the magnetically ordered states is favorable for the existence of large amplitude magnetic fluctuations in the

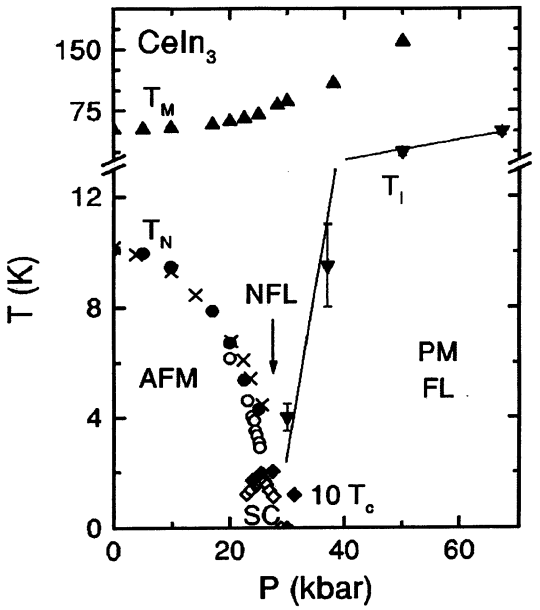

Fig. 10.9. The pressure–temperature phase diagram of the antiferromagnetic superconductor $CeIn_3$ [63]. The Neel temperature and superconducting transition temperatures are denoted by T_c and T_N, respectively. Note that T_c is scaled by a factor of 10. T_M denotes the temperature of the maximum in the resistivity, while T_I indicates a temperature at which the system crosses over into a Fermi liquid phase

superconducting state. In the superconducting state, the specific heat, thermal conductivities [58, 59] and NMR $1/T_1$ relaxation rates [60, 61] show the power law temperature variations, which are consistent with the superconducting order parameter having lines of nodes. Since these materials share many common features with cubic $CeIn_3$, which is also antiferromagnetic and superconducts ($T_c \approx 200$ mK) at pressures greater than 25 kbar [62], together they form a family of materials in which the effect of structure (such as the role of dimensionality or magnetic anisotropy) on the interplay of superconductivity and magnetism can be investigated.

Since it was a commonly held belief that ferromagnetism is detrimental to superconductivity, it was a great surprise when superconductivity was discovered in the ferromagnetic phase of UGe_2 [64]. As shown in Fig. 10.8, the superconducting phase in UGe_2 occurs for pressures in the range of 1 to 1.5 GPa [65] where the material is ferromagnetically ordered. As the pressure is increased from 1 to 1.5 *GPa*, the critical temperature for ferromagnetic ordering shows indications of rapidly decreasing from about 30K to 0, while the maximum superconducting transition temperature is only 0.7K and falls

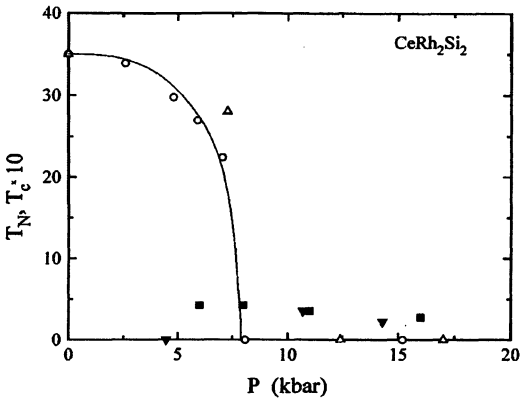

Fig. 10.10. The pressure temperature phase diagram of the antiferromagnetic superconductor $CeRh_2Si_2$ [67]. The solid symbols represent the superconducting transition temperature T_c, while the open symbols denote the Neel temperature T_N

to zero at a pressure where the ferromagnetism disappears. *URhGe* which goes superconducting at ambient pressure for temperatures below 0.25K, also has a ferromagnetic Curie temperature $T_c = 9.5$K which is unusually small [66]. Since uniform internal magnetic fields are pair breaking for the singlet–pairs of a BCS superconductor, it has been suggested that in these systems the Cooper pairs are in a triplet state. However, if this is the case, there seems to be no compelling reason as to why the superconducting phase should be restricted to only occur inside the ferromagnetic phase. On the other hand, if the ferromagnetic state can be described strictly as a local Fermi liquid [68], then it has been rigorously shown [69] that there is an attractive s–wave interaction and the triplet interaction is identically zero. Furthermore, a mean field analysis shows that a singlet superconducting state in a ferromagnet may survive if the pair breaking due to the uniform internal field is sufficiently strong [70].

The observation of the superconducting phase within ferromagnetic and antiferromagnetic phases with low transition temperatures shows that the heavy–fermion materials are often correlated with the proximity of a quantum critical point [71–73]. At a quantum critical point, the large amplitude low frequency magnetic fluctuations could produce appreciable contributions to physical properties that are different from those expected of highly renormalized quasi–particles. The existence of large amplitude magnetic fluctuations associated with the quantum critical point leads to another exciting possibility namely, that the superconducting pairing mechanism for the quasi–particles is primarily mediated by low–energy spin–fluctuations [74]. Either the characteristic frequency of the low–energy spin–fluctuations or the mass renormalizations associated with the heavy quasi–particles presum-

ably, could be responsible for setting the low values of the superconducting transition temperatures, T_c. Generally, heavy–fermion superconductors have superconducting transition temperatures in the range between 0.2 and 3 K. The compound $PuCoGa_5$ provides a notable exception to this statement, as it has a T_c of about 18.5 K, which is the highest reported T_c for a heavy–fermion superconductor [75]. The low values of T_c found in most heavy–fermion superconductors are in stark contrast with the very large critical temperatures found in the other well known examples of exotic superconductivity – the high temperature superconducting cuprates.

10.2.3 Quasi–Particles and Collective Excitations

At high temperatures, the properties of heavy–fermion systems can often be described in terms of a set of local moments coupled to a sea of conduction electrons. At temperatures below a characteristic temperature, sometimes known as the coherence temperature, the properties show evidence that the excitations have large spatial extents. Below the coherence temperature, the transport properties indicate that the scattering from the spin degrees of freedom start to freeze out and that the electronic excitations extend throughout the crystal. For sufficiently low temperatures, one may expect that the properties will be described by the quasi–particle excitations of Landau Fermi liquid theory. However, in a few of the heavy–fermion systems, the Fermi liquid state is never completely formed before superconductivity sets in. In these cases one expects that, below the coherence temperature, the properties may be determined by the low–energy excitations that include both the collective excitations, such as phonons and spin–waves, as well as the quasi–particle excitations.

Quasi–Particle Excitations

Elementary excitations can be categorized either as quasi–particles or as collective excitations. The quasi–particle excitations are in one–to–one correspondence with the excitations of the non–interacting system. The quasi–particle excitations have a close similarity to the single–electron excitations of a non–interacting electron gas. The properties of these quasi–particles are most readily seen through inspection of the one–electron thermal Green's function [76] defined by the expectation value of the time ordered product of the thermal average

$$G^{\alpha,\beta}_{\underline{k},\underline{k}'}(\tau) \;=\; -\,\frac{1}{\hbar}\;{<}\mid \hat{T}\; a_{\underline{k}',\beta}(\tau)\; a^{\dagger}_{\underline{k},\alpha}(0) \mid {>} \quad . \tag{10.2}$$

The Green's function represents the time evolution of the probability amplitude for a single electron to be added to the Bloch state with wave vector $\underline{k}$ and spin σ. The electron creation and annihilation operators are evaluated in the imaginary time representation where they evolve according to the

prescription

$$a_{\underline{k},\alpha}(\tau) \;=\; \exp\left[\;+\; \frac{\hat{H}\,\tau}{\hbar} \right] a_{\underline{k},\alpha}(\tau)\; \exp\left[\;-\; \frac{\hat{H}\,\tau}{\hbar} \right] . \tag{10.3}$$

Due to periodic translational invariance and spin rotational invariance of the normal state, the Green's function is diagonal in the wave vector and spin indices

$$G^{\alpha,\beta}_{\underline{k},\underline{k}'}(\tau) \;=\; \delta_{\alpha,\beta}\; \delta_{\underline{k},\underline{k}'}\; G(\underline{k};\tau) \, . \tag{10.4}$$

The Fourier transform of the diagonal Green's function is defined via

$$G(\underline{k};\tau) \;=\; k_B\, T \sum_n G(\underline{k}; i\hbar\omega_n)\; \exp\left[\;-\; i\;\omega_n\;\tau \right] , \tag{10.5}$$

where

$$\hbar\,\omega_n \;=\; k_B\, T\, \pi\, (\, 2\, n \;+\; 1\,) \tag{10.6}$$

are the Matsubara frequencies. The interacting Green's function is expressed in terms of the non–interacting Green's function $G^0(\underline{k}, i\omega_n)$ and the self–energy $\Sigma(\underline{k}, i\omega_n)$ through Dyson's equation

$$\left[\; G(\underline{k}; i\hbar\omega_n) \;\right]^{-1} \;=\; \left[\; G^0(\underline{k}; i\hbar\omega_n) \;\right]^{-1} \;-\; \Sigma(\underline{k}; i\hbar\omega_n) \, , \tag{10.7}$$

where the non–interacting Green's function is evaluated as

$$\left[\; G^0(\underline{k}; i\hbar\omega_n) \;\right]^{-1} \;=\; i\;\hbar\;\omega_n \;-\; e(\underline{k}) \;+\; \mu \, . \tag{10.8}$$

The pole of the non–interacting Green's function is at the single–electron Bloch energy $e(\underline{k}) - \mu$, and measures the excitation energy relative to the Fermi energy. The self–energy represents the change in the Green's function due to the interactions. The Fermi energy of the interacting system, μ, is determined by the pole of the Green's function at $\omega_n \;=\; 0$, which leads to

$$\mu \;=\; e(\underline{k}_F) \;+\; \Sigma(\underline{k}_F; 0) \, , \tag{10.9}$$

where $\underline{k}_F$ is a Bloch vector on the Fermi surface. The thermal Green's function is related to the $T \;=\; 0$ Green's function via analytic continuation $i\;\hbar\omega_n \;\rightarrow\; E$. The correspondence between quasi–particle excitations and the single–electron excitations of the non–interacting system follows from the expansion of the self–energy near the Fermi energy. For energies close to the Fermi energy, the Green's function can be re–written as

$$\begin{aligned} \left[\; G(\underline{k}; E) \;\right]^{-1} &\approx E \left(1 - \frac{\partial \Sigma(\underline{k}; E)}{\partial E} \right)\Bigg|_{\omega=0} - e(\underline{k}) - \Sigma(\underline{k}; 0) + \mu - i Im \Sigma(\underline{k}; E) \\ &= \left(\;1 \;-\; \frac{\partial \Sigma(\underline{k}; E)}{\partial E} \;\right)\Bigg|_{\omega=0} \left[\;E \;-\; E_{\underline{k}} \;+\; \frac{i\;\hbar}{2\;\tau^*_{\underline{k}}(E)} \right] . \end{aligned} \tag{10.10}$$

The interaction produces a linear superposition of the electron in a Bloch state $\underline{k}$ with one–electron states surrounded by a cloud of electron–hole pairs. The quasi–particle weight, $Z_{\underline{k}}^{-1}$, represents the fraction of this superposition that corresponds to the bare Bloch electron. The fraction is less than unity $Z_{\underline{k}} > 1$, and $Z_{\underline{k}}$ is given in terms of the frequency derivative of the self–energy by

$$Z_{\underline{k}} = 1 - \left. \frac{\partial \Sigma(\underline{k}; E)}{\partial E} \right|_{E=0} . \tag{10.11}$$

The quasi–particle energy $E_{\underline{k}}$, measured from the Fermi energy μ, and the decay rate are given by

$$E_{\underline{k}} = e(\underline{k}) + \Sigma(\underline{k}; E_{\underline{k}}) - \mu ,$$

$$E_{\underline{k}} \approx Z_{\underline{k}}^{-1} \Big(e(\underline{k}) + \Sigma(\underline{k}; 0) - \mu \Big) , \tag{10.12}$$

and

$$\frac{\hbar}{2\, \tau_{\underline{k}}^{*}(E)} = - Z_{\underline{k}}^{-1}\, Im\, \Sigma(\underline{k}; E + i\delta) \tag{10.13}$$

respectively. Since the imaginary part of the Green's function is proportional to the single–particle density of states, the self–energy can be viewed as a renormalization of the single–electron excitation energies $e(\underline{k})$, yielding the quasi–particle energy $E_{\underline{k}}$. The imaginary part of the self–energy can be viewed as providing the width or lifetime of the single–particle state. As shown by Luttinger [77], the imaginary part of the self–energy near the Fermi energy due to electron–electron interactions vanishes proportional to E^2, if perturbation theory converges. The small magnitude of the lifetime is due to the Pauli exclusion principle which reduces the phase space allowed for electron–electron scattering. The smallness of the lifetime of low–energy excitations has the effect that the spectrum resembles that of a non–interacting electron gas in which the quasi–particle masses are enhanced by a factor of $Z_{\underline{k}}$. The quasi–particle states are extremely long lived, not only because of the vanishing of the lifetime due to electron–electron interactions but also because the residual lifetime resulting from elastic scattering by impurities is enhanced by the factor of $Z_{\underline{k}}$. Due to the extremely small magnitude of the lifetime of quasi–particles at the Fermi energy, the Fermi energy is well defined and the effect of electron–electron interactions does not change the volume enclosed by the Fermi surface [77]. It is found that, in de Haas – van Alphen experiments on some of the heavy Fermion systems, the multi–sheeted Fermi surfaces enclose volumes that are consistent with Luttinger's theorem being valid. For heavy–fermion systems, the $\underline{k}$ dependence of the self–energy is considered to be small, and the frequency dependence is extremely rapid. Thus,

the quasi–particles are expected to be extremely heavy and long–lived but have little spectral weight. Also, a large portion of the weight is expected to lie in the broad incoherent portion of the spectral density.

Since the quasi–particles are governed by Fermi–Dirac statistics, their contributions to thermodynamic quantities have asymptotic low temperature variations that are similar to those of the non–interacting electron gas. In particular, the entropy S of the gas of quasi–particles is given by

$$S = -k_B \sum_{\sigma,\underline{k}} \left[(1 - f(E_{\underline{k}})) \ln[1 - f(E_{\underline{k}})] + f(E_{\underline{k}}) \ln[f(E_{\underline{k}})] \right] . \quad (10.14)$$

Hence, the quasi–particles give rise to a linear T contribution in the low temperature electronic specific heat. However, the coefficient γ, instead of just reflecting the electronic density of states, is given by the density of quasi–particle energies at the Fermi surface

$$\rho_{qp}(E) = \sum_{\underline{k}} \delta(E - E_{\underline{k}}) ,$$

$$\rho_{qp}(0) \sim \sum_{\underline{k}} Z_{\underline{k}} \, \delta(\mu - e(\underline{k}) + \Sigma(\underline{k}; 0))) , \quad (10.15)$$

which is enhanced over the electronic density of states $\rho(\mu)$ by a factor Z similar to the Fermi surface average of $Z_{\underline{k}}$. Comparison of the low temperature electronic specific heat coefficient γ and electronic structure calculations, yields an estimate of the wave function renormalization Z of approximately 25 for highly enhanced systems such as UPt_3. The heavy quasi–particle masses in some or all parts of the Fermi surface can also be inferred from the amplitude of the de Haas – van Alphen oscillations in the magnetization [78]. The signatures of the gas of heavy quasi–particles may also be expected to show up in transport properties, albeit modified by the residual interactions between the quasi–particles. The temperature dependence of the d.c. resistivity of the enhanced Fermi liquid state is dominated by the transport scattering rate. If the self–energy is roughly k independent, the transport scattering rate should coincide with the scattering rate $\frac{1}{\tau}$ found from the imaginary part of the self–energy since the conductivity vertex corrections are expected to be small. For low temperatures and samples of high purity, Matheissen's rule is expected to apply. In this case, the scattering rate is additive, and $\frac{1}{\tau}$ is expected to be composed of a sum of a temperature independent term $\frac{1}{\tau_0}$ due to the potential scattering from isolated impurities, a quadratic Baber term caused by the quasi–particles scattering off of each other, and a negligibly small T^5 term expected from electron–phonon scattering

$$\frac{1}{\tau} = \frac{1}{\tau_0} + A\,T^2 + B\,T^5 . \quad (10.16)$$

If the impurity scattering can be treated in the Born approximation, then, due to the approximate invariance of the density of states at the Fermi energy,

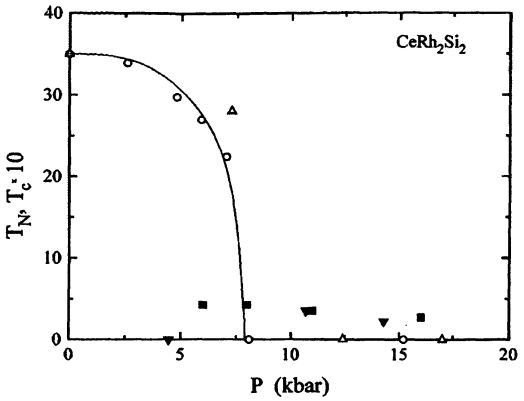

Fig. 10.11. The optical conductivity $\sigma(\omega)$ of single crystals and polycrystals of UPt_3 at $T = 1.2$ K and $T = 20$ K [79]. The data show the growth of the narrow quasi–particle Drude peak at low temperatures

the impurity scattering rate $\frac{1}{\tau_0}$ is not directly renormalized by the electron–electron interactions. The T^2 Baber term has its origin in the Pauli–exclusion principle limiting the phase space available for scattering of low–energy electrons, and is exactly the same physics behind the E^2 variation of the imaginary part of the self–energy. Since Baber scattering involves the scattering of two quasi–particles, the scattering rate is enhanced by a factor proportional to Z^2. The residual d.c. conductivity does not directly depend on the real part of the self–energy and is, therefore, un–renormalized. Alternately, the d.c. residual resistivity is un–renormalized due to the small magnitude of the velocity vertex correction, and due to the cancellation of the wave function renormalization in the ratio of the renormalized quantities

$$\frac{\tau^*}{m^*} \approx \frac{\tau}{m} \tag{10.17}$$

and also because the electron density n is unchanged by electron–electron interactions. This last fact is seen by noting that n is proportional to the Fermi surface volume which, according to Luttinger's theorem, is independent of the strength of electron–electron interactions. Despite the absence of significant renormalization of the d.c. conductivity, the renormalized lifetimes do show up as extremely narrow widths of the Drude peak [79–81]

$$Re\left[\,\sigma(\omega)\,\right] = \frac{n\,e^2\,\tau^*}{m^*}\,\frac{1}{1 + \omega^2\,\tau^{*\,2}} \tag{10.18}$$

observed in measurements of the dynamical conductivity $\sigma(\omega)$ at low temperatures. The frequency dependence of the measured conductivity $\sigma(\omega)$ for UPt_3 [79], is shown in Fig. 10.11 for low and high temperatures. Basically, if

one has a fixed concentration of impurities, and hence a fixed mean free path, then the quasi–particle lifetime is just determined by the quasi–particle velocity $\hbar\, k_F/m^*$, which is reduced by the large quasi–particle mass. Therefore, the enhanced effective mass results in an enhancement of the lifetime due to impurity scattering. At higher frequencies, one expects that inelastic scattering processes should become important and the quasi–particle weight should acquire a frequency dependence. The frequency dependence of the scattering rate and the quasi–particle renormalization are expected to be related by causality and other requirements. In particular, the optical sum rule [82] relates the integral of the optical conductivity over all frequencies to the total number of electrons in the system

$$\int_0^\infty d\omega\ Re\left[\ \sigma(\omega)\ \right] = \frac{\pi}{2}\,\frac{n\,e^2}{m_e}\,, \tag{10.19}$$

where n is the density of electrons and m_e is the electron mass. Similarly, the integrated intensity of the low frequency Drude peak

$$\int_0^{\omega_0} d\omega\ Re\left[\ \sigma(\omega)\ \right] = \frac{\pi}{2}\,\frac{n(\omega_0)\,e^2}{m^*} \tag{10.20}$$

can be used to define the number of coherent quasi–particles $n(\omega_0)$ and their weight Z^{-1} [83], whereas the higher energy structure is due to the incoherent excitations. The existence of the quasi–particle Drude peak has been confirmed in UPt_3, $CeAl_3$ and $CeCoIn_5$ [79, 80, 84], however, it has not been observed in UBe_{13} [85] where it is doubtful that a Fermi liquid is formed at temperatures higher than the superconducting T_c. In the cases where the Fermi liquid is fully formed, it is not expected that good agreement will be found between the optical effective mass, whose definition involves the Fermi surface average of the inverse quasi–particle mass, and the Fermi surface average quasi–particle mass obtained from specific heat. The disagreement is expected to be marked specially if the de Haas – van Alphen experiments show both light and heavy quasi–particle excitations co–existing on the Fermi surface.

In systems like UBe_{13}, the Fermi liquid phase is not completely formed before superconductivity sets in, therefore, the thermodynamic and transport properties may be directly affected by the collective excitations of the electrons. In addition, the large mass renormalization Z of the quasi–particles might also be attributable to the existence of low frequency collective excitations, such as local spin–fluctuations or more extended magnetic excitations that are precursors of long–ranged magnetic ordering. The collective excitations are directly amenable to experimental observation and also may mediate residual interactions between the quasi–particles, and therefore, they could be responsible for the superconducting pairing.

Collective Excitations

Since the normal states of heavy–fermion materials are characterized by a

large quasi–particle density of states near the Fermi–level, they are susceptible to entropy–driven instabilities, which reduce the density of states at the Fermi energy. This tendency is manifested by the sensitivity of the normal state to small amounts of added impurities that can lead to an instability towards states with spontaneously broken symmetries. If the interactions are short–ranged and the symmetry that is broken is continuous, Goldstone's theorem [86] is valid. Goldstone's theorem ensures that the system will support a branch of collective excitations with a zero threshold energy that dynamically restores the spontaneously broken symmetry. The order parameter acts as the collective coordinate for the zero energy collective excitations. The spin–waves with $\underline{q} \approx 0$ in a ferromagnet, the antiferromagnetic spin–waves near the critical wave vector(s) $\underline{Q}_c$, and the transverse sound waves in a periodic solid, form well known examples of these Goldstone collective modes. Similar boson–like collective excitations are expected to occur in the disordered or high temperature state as precursors to the instabilities. In the disordered state, these boson modes are expected to have extremely long lifetimes and have excitation spectra that form broad continua. A well known example of these precursor modes is provided by the paramagnon fluctuations in Pd, which occur as Pd is very close to an instability to a ferromagnetic state [87–89]. It is expected that, as the temperature is lowered through the instability, these pre–critical modes will merge together with the critical fluctuations and, eventually, the (Goldstone) spin–wave modes will emerge in the ordered state. There is a growing body of evidence that suggests that heavy–fermion systems are in the vicinity of a quantum critical point, implying that the system supports large amplitude critical fluctuations due to a nearby $T = 0$ phase transition. One expects that the properties of the material should show scaling behavior due to the quantum critical point. The critical fluctuations near a quantum critical point are expected to have a different nature than those associated with a finite temperature transition as they cannot be treated classically [71–73]. The zero–point quantum fluctuations replace the role of the thermally–driven fluctuations. Since the dynamics are inextricably linked to the statics at a quantum critical point, the phase space of the magnetic fluctuations is given by $(\omega, \underline{k})$. If the characteristic frequency scales as ξ^{-z}, where ξ is the magnetic correlation length and z is the dynamical exponent, then the effective dimensionality of the phase space for a $T = 0$ quantum critical point is given by $d_{eff} = d + z$. Hence, as the effective dimensionality d_{eff} differs from the dimensionality d of the classical critical point, one expects to find different types of scaling relations at a quantum critical point. The search for the ultimate description of quantum critical fluctuations is an actively ongoing field of research.

The simplest starting point for these theories of the collective spin–fluctuation modes lies in the Random Phase Approximation (RPA) [90,91]. The RPA is the crudest approximation that captures the physics of the Gaussian fluctuations and is most certainly expected to fail near the quantum crit-

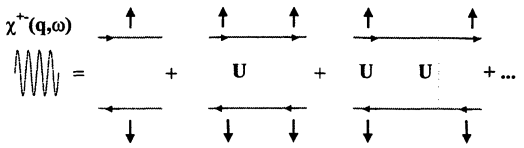

Fig. 10.12. The diagrammatic representation of the Feynmann diagrams leading to the RPA expression for the transverse spin–fluctuations. The directed solid lines denote the one–electron Green's functions. The vertical arrows represent the directions of the electronic spins. The dashed vertical line represents the on–site Coulomb interaction U

ical point. In most approaches, one assumes that the Coulomb interaction is highly screened, and this results in a Hubbard point contact interaction U between electrons of opposite spins. Within the quasi–particle treatment, the band energies $e(\underline{k})$ should be replaced by the quasi–particle energies $E_{\underline{k}}$, and the interaction should be expressed in terms of the Landau Fermi–liquid parameters. However, we shall, in the rest of this section, be consistent with the usual formulation of RPA as a one parameter Fermi liquid, in which the interaction between the quasi–particles is denoted by U. Since we shall neglect the vertex corrections to the susceptibility, we shall also suppress all the factors of Z^{-1}, while it is true that Fermi liquid corrections should renormalize U to $U\ Z^{-2}$. Although the results are derived on the basis of a one band Hubbard model, they can easily be extended to a two band or Anderson Lattice model [92]. The transverse susceptibilities are expressed in terms of multiple scattering processes involving an up–spin electron with a down–spin hole shown in Fig. 10.12 [90,91], yielding

$$\chi^{+-}(\underline{q};\omega) \ = \ \frac{\mu_B^2\ \chi_0(\underline{q};\omega)}{1\ -\ U\ \chi_0(\underline{q};\omega)}\ , \tag{10.21}$$

where $\chi_0(\underline{q};\omega)$ is the non–interacting Lindhard susceptibility, given by

$$\chi_0(\underline{q};\omega) \ = \ \frac{1}{N}\ \sum_{\underline{k}}\ \left[\ \frac{f(e(\underline{k}))\ -\ f(e(\underline{k}+\underline{q}))}{\hbar\,\omega\ -\ e(\underline{k})\ +\ e(\underline{k}+\underline{q})\ +\ i\,\delta}\ \right]\ . \tag{10.22}$$

In the RPA, a magnetic instability of the paramagnetic state towards an ordered state with ordering wave vector $\underline{Q}$ is obtained when the static susceptibility $\chi(\underline{Q};0)$ diverges, which occurs due to the vanishing of a denominator. This happens when the generalized Stoner criterion is fulfilled,

$$1 \ = \ U\ \chi_0(\underline{Q};0)\ , \tag{10.23}$$

where $\chi_0(\underline{Q};0)$ is the reduced non–interacting susceptibility. The paramagnetic state is unstable for values of U greater than a critical value U_c where the equality of (10.23) first holds, at any value of $\underline{Q}$. The type of instability,

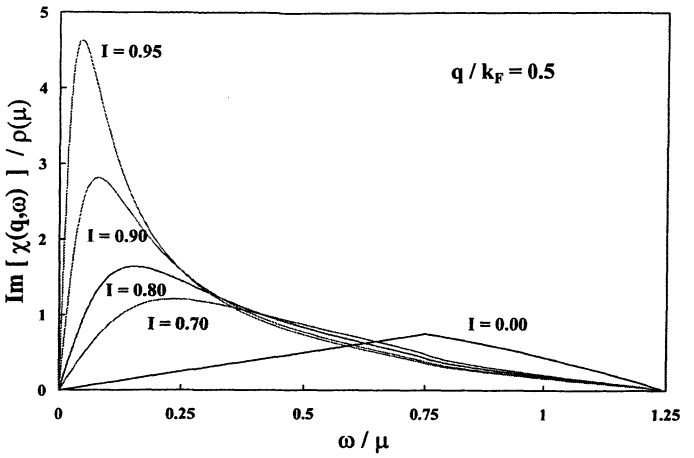

Fig. 10.13. The frequency variation of $Im\ \chi(\underline{q};\omega)$ for fixed $\underline{q}$. The parameter I is given by $I = U\ \rho(\mu)$. The damped spin–fluctuations soften and grow in amplitude as the quantum critical point is approached. [After Doniach (1967)]

determined by $\underline{Q}$ and the critical value of U at which it occurs, is governed by both the quasi–particle band structure and the state of occupation of the bands. If $\chi_0(\underline{Q};0)$ is largest at $\underline{Q} = 0$, the system is expected to become unstable to a ferromagnetic state at a critical value of U determined by the usual Stoner criterion for ferromagnetism, $1 = U_c\ \rho(\mu)$. For perfect nesting tight–binding bands at half filling, one finds that $\chi(\underline{Q};0)$ diverges for $\underline{Q} = \pi\ (1,1,1)$, leading to an instability towards an antiferromagnetic state for U greater than the critical value of $U_c = 0$ [93]. In general, for U values close to the critical value U_c, the static susceptibility evaluated at the relevant $\underline{Q}$ is enhanced, and the imaginary part of the susceptibility undergoes a similar enhancement. Since the imaginary part of the susceptibility is a measure of the spectrum of magnetic excitations, the enhanced RPA expressions

$$Im\left[\ \chi^{+,-}(\underline{q};\omega)\ \right] = \frac{\mu_B^2\ Im\ \chi_0^{+,-}(\underline{q};\omega)}{[\ 1 - U\ Re\ \chi_0^{+,-}(\underline{q};\omega)\ ]^2 + [\ U\ Im\ \chi_0^{+,-}(\underline{q};\omega)\ ]^2} \tag{10.24}$$

show the propensity for low frequency large amplitude spin–fluctuation excitations, as shown in Fig. 10.13. Near the instability, the magnetic excitation spectrum consists of a continuum of low–energy (quasi–elastic) and over–damped precritical fluctuations from which, on increasing U above U_c, a branch of sharp spin–wave excitations are expected to emerge in the magnetically ordered state.

The large amplitude spin–fluctuations are also expected to give rise to a renormalization of the quasi–particles. The change in the energies of the quasi–particles shows up in the RPA self–energy due to the emission and

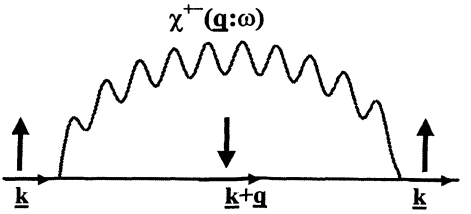

Fig. 10.14. The RPA expression for the up–spin electron self–energy $\Sigma(\underline{k}; E)$. The one–electron Green's function is denoted by the directed line, and the spin–fluctuation by a wavy line. In this process, an up–spin electron of momentum $\underline{k}$ emits a spin–fluctuation of momentum $\underline{q}$, thereby flipping its spin

absorption of spin–waves, which flip the spin of the electron (see Fig. 10.14). The quasi–particle weight of the low frequency excitations is reduced as the scattering from the large amplitude spin–fluctuations reduces the probability that the electron remains in a spatially extended Bloch state. For a nearly ferromagnetic system, this leads to a logarithmic enhancement of the linear term in specific heat [88,89] via

$$C \propto k_B T \ln \left| 1 - U \rho(\mu) \right| . \tag{10.25}$$

Using a Fermi liquid approach, Carneiro and Pethick [94] have shown that long wavelength collective fluctuations can also lead to a $T^3 \ln T$ term in the specific heat similar to that found in paramagnon theories [95]. Likewise, the collective fluctuations also can lead to an enhancement of the quasi–particle scattering rate which in turn, leads to an enhanced T^2 term in the electrical resistivity [87,96]. The precise form of the renormalization found in RPA does depend crucially on the type of magnetic instability (ferromagnetic, incommensurate spin density wave, antiferromagnetic) that is being approached. For example, in quantum phase transitions with finite ordering wave vectors $\underline{Q}$, electrons are resonantly scattered by magnetic fluctuations between portions of the Fermi surface that are connected by the vector $\underline{Q}$ (see Fig. 10.15). This leads to the occurrence of hot lines on the Fermi surface where the quasi–particles are extremely short lived and, therefore, are not well–defined. The size of these hot regions is proportional to $\sqrt{T}$. On the other hand, for a ferromagnetic quantum critical point, the entire Fermi surface is subject to critical scattering. The different nature of the critical scattering results in different power law temperature dependences of various physical quantities [97]. For example, the leading non–analytic part of the free energy ΔF is given by

$$\Delta F = \sum_{\underline{q}} \int_0^\infty \frac{d\omega}{\pi} \left[N(\omega) + \frac{1}{2} \right] Im \left[\ln U \chi(\underline{q}; \omega) \right] , \tag{10.26}$$

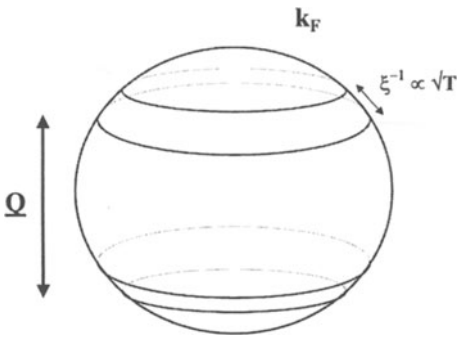

Fig. 10.15. Hot lines on a Fermi surface. The dynamic susceptibility becomes critical at wave vector $\underline{Q}$. The electrons on the two lines of the Fermi surface which are connected by wave vector $\underline{Q}$ are subject to resonant scattering. The width of the hot lines is given by ξ^{-1}, which is proportional to $\sqrt{T}$

where $N(\omega)$ is the Bose–Einstein distribution function, and the spin–fluctuation propagator either has the form

$$\chi(\underline{q};\omega)^{-1} \sim (1 - I) + a\left(\frac{q}{k_F}\right)^2 + i\,b\left(\frac{\hbar\,\omega\,k_F}{\mu\,q}\right) \tag{10.27}$$

near a ferromagnetic instability or has the form

$$\chi(\underline{q};\omega)^{-1} \sim (1 - I) + a\,\frac{(\underline{q} - \underline{Q})^2}{k_F^2} + i\,b\left(\frac{\hbar\,\omega}{\mu}\right) \tag{10.28}$$

near an antiferromagnetic instability. For a d dimensional system that is above the critical dimensionality, at a quantum critical point where $I = 1$, this produces a leading $T^{1+d/3}$ temperature dependence of ΔF for a ferromagnetic quantum critical point, but near an antiferromagnetic quantum critical point ΔF has a $T^{1+d/2}$ dependence. The temperature dependence of ΔF gives rise to the non–analytic temperature dependences of the C/T ratio.

Close to a quantum critical point, where both thermaland quantum critical fluctuations are important, the properties are expected to be significantly different from the properties calculated using simple RPA. At finite temperatures and in the quantum critical region, the effect of coupling among the different modes of spin–fluctuations becomes important [98]. The theories of Moriya [91], Hertz [71] and Millis [73] predict that three dimensional electronic systems at a quantum critical point have an effective dimensionality greater than the upper critical dimension and, hence, are dominated by Gaussian spin–fluctuations, albeit highly renormalized by mode–mode coupling. In this case, the hyperscaling relation is not expected to be obeyed. The strength of the mode–mode coupling is expected to vanish at zero temperature. It is generally believed that the region over which the Fermi liquid

behavior is found, is smaller for systems which are close to exhibiting a magnetic instability. Furthermore, as the quantum critical point is approached, the Fermi liquid power laws are expected to be gradually replaced by other types of non–universal power laws. For example, the T^2 variation of the resistivity found in the Fermi liquid regime of a clean three–dimensional metal is expected to be replaced by a $T^{\frac{5}{3}}$ variation at a ferromagnetic quantum critical point or a $T^{\frac{3}{2}}$ variation at an antiferromagnetic quantum critical point. These power laws are intermediate between the low temperature Fermi liquid T^2 variation and the linear T variation found within RPA at higher temperatures and are consistent with expectations based on the shrinking temperature range over which Fermi liquid behavior is to be observed. The simple power laws obtained using self–consistent spin–wave theory are only expected to be recovered at low temperatures. Furthermore, the scaling behavior expected from the quantum critical point is expected to be severely modified by the effects of disorder [99, 100]. In the case of an antiferromagnetic quantum critical point in a clean system, the hot lines are not expected to dominate drastically the low temperature physical properties, since the hot lines have a limited extent. For example, the contributions of the hot lines to the conductivity are expected to be shorted out by the normal regions of the Fermi surface [101]. However, the presence of impurities leads to $\underline{k}$ not being a good quantum number since electrons are inelastically scattered between different portions of the Fermi surface. Hence, the mixing between different $\underline{k}$ values results in all the electrons on the Fermi surface participating in the critical scattering [100].

Table 10.1. Quantum critical exponents for physical properties.

$d = 3$	Ferro	Antiferro
C/T	$-\ln T$	$\gamma - \alpha\sqrt{T}$
$\Delta\chi_{\underline{Q}}^{-1}$	$T^{\frac{4}{3}}$	$T^{\frac{3}{2}}$
$\Delta\rho$	$T^{\frac{5}{3}}$	$T^{\frac{3}{2}}$
$d = 2$	Ferro	Antiferro
C/T	$T^{-\frac{1}{3}}$	$-\ln T$
$\Delta\chi_{\underline{Q}}^{-1}$	$-T\ln T$	$-T\ /\ \ln T$
$\Delta\rho$	$T^{\frac{4}{3}}$	T

In general, the power laws found in heavy–fermion systems do not coincide with those found in the above–mentioned type of two or three dimensional theories (shown in Table(10.1).). One possible cause for this discrepancy is perhaps due to the heaviness of the quasi–particle masses. That is, in the above theories, the electron dynamics are assumed to occur on a fast energy scale compared with the slow critical fluctuations, therefore the fast electron

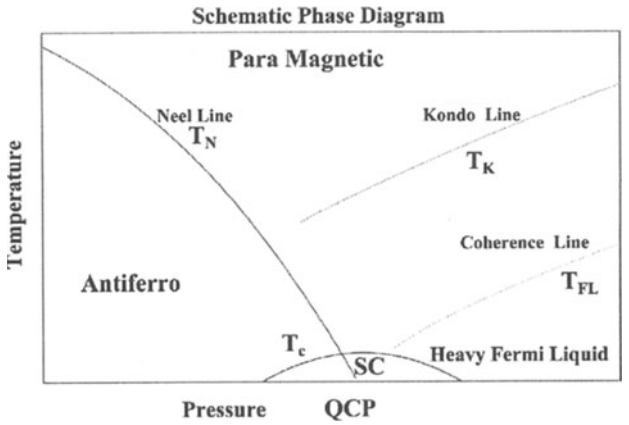

Fig. 10.16. A schematic pressure–temperature phase diagram near a Quantum Critical Point (Q.C.P.). The solid lines T_N and T_c, respectively, denote the transition temperatures to the Néel and superconducting phases. The dashed lines represent the characteristic temperatures associated with the Kondo effect, T_K and the low temperature Fermi Liquid T_{FL}

dynamics can be integrated out. For systems with high effective masses, such descriptions may no longer be appropriate [102]. Related ideas about the lack of scaling being caused by the breakdown of the quasi–particle concept have been expressed by Coleman [103]. An alternate possible cause for the discrepancy could be due to the nature of the assumed theoretical model [2]. Generally, it has been assumed that strong electron–electron interactions, which give rise to the formation of heavy quasi–particles and strong magnetic fluctuations, are unfavorable for the formation of superconducting pairs. However, the observation of superconducting phases only in the immediate vicinity of quantum critical points, as sketched in Fig. 10.16, challenges the assumption. These observations suggest that the large amplitude quantum critical fluctuations might even be responsible for the occurrence of the superconductivity. The two most outstanding questions about the superconductivity in heavy–fermion systems concern the nature of the pairing mechanism and the symmetry of the superconducting order parameter.

10.2.4 Possible Pairing Mechanisms

The interaction mechanism that is responsible for pairing electrons in common superconductors is mediated by phonons. Fröhlich [104] predicted that

[2] The Moriya, Hertz, Millis theory assumes the validity of a non–degenerate one–band model, whereas multi–band models, with orbital degeneracy and strong spin–orbit coupling, appear to be more appropriate for describing heavy–fermion systems. These other models may be in a different universality class and, hence, have other critical exponents.

the superconducting transition temperature T_c should be proportional to a typical phonon frequency. Furthermore, as the phonon frequency squared is inversely proportional to the mass of the ions, M, Fröhlich predicted that the transition temperature should vary as

$$T_c \propto M^{-\frac{1}{2}} . \tag{10.29}$$

This dependence of T_c on the mass was confirmed by experiments by Maxwell [105] and Reynolds *et al.* [106] who measured T_c for samples composed of different isotopes. This isotope effect has been observed in a number of simple materials such as Hg, Pb, Mg, Sn, Tl. For these simple metals, the retarded electron–electron attraction, due to the charged ions over screening the Coulomb interaction [107], has a simple mass dependence. The isotope effect is much smaller or even almost absent in transition metals and compounds such as Ru and Os, where the electrons are more localized and the relative strength of the Coulomb repulsion is large [108]. In $\alpha - U$, a large isotope effect even occurs with a positive exponent [109], but detailed calculations show that the superconductivity is still phonon mediated [110]. The absence of an isotope effect does not necessarily imply non–phonon mediated electron–electron interactions but merely that simplifying circumstances that lead to Fröhlich's isotopic mass dependence are not present. As heavy–fermion systems have extremely heavy quasi–particle masses due to large electron–electron interactions, one does not expect isotope experiments to provide direct evidence of the nature of the pairing mechanism. Furthermore, for systems that appear to be on the verge of a magnetic instability [111,112], it is possible that the collective excitations of the spin system could provide an alternate or complementary mechanism to the phonon mediated interaction.

Many different pairing mechanisms have been proposed for heavy–fermion superconductors, ranging from electron–phonon coupling [113,114] to ferromagnetic and antiferromagnetic spin–fluctuations [115–117]. The main problem posed in developing a microscopic description of the superconductivity lies with the lack of knowledge of the normal state because of its strong electron correlations. A commonly used approach that describes the formation of the superconducting state starts from assuming the validity of a Fermi liquid description of the normal state. In what follows, we shall outline this approach to superconductivity. However, as some heavy–fermion superconductors show no evidence that a Fermi liquid state has formed before the superconducting transition has occurred, this approach is not on a firm basis. Second, as the Fermi liquid approach neglects the effect of the collective fluctuations, it does not address the role that the low–frequency spin–fluctuations play in suppressing the superconducting transition. The proper starting point for a microscopic description of electron–phonon mediated superconductivity lies in the Eliashberg equations [118,119] in which the superconducting gap, or order parameter, is related to a time varying quantity $\Sigma^{(a)}_{\alpha,\beta}(\underline{k};\tau)$, which is the anomalous or pair self–energy in the superconducting state. The gap pa-

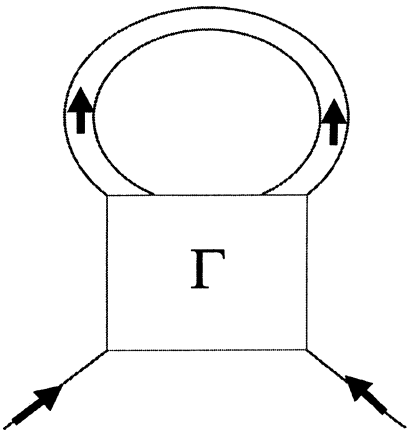

Fig. 10.17. The Feynmann diagram associated with the anomalous self–energy $\Sigma^{(a)}(\underline{k};\hbar\omega)$. The solid square represents the irreducible vertex interaction $\Gamma(\underline{q};\hbar\omega)$. The directed double lines represent the fully renormalized Green's function

rameter in the quasi–particle spectra, $\Delta_{\alpha,\beta}(\underline{k};i\hbar\omega_n)$, is defined in terms of the anomalous self–energy and wave function renormalization via

$$\Delta(\underline{k};\omega_n) \;=\; \frac{\Sigma^{(a)}(\underline{k};i\hbar\omega_n)}{Z_{\underline{k}}(i\hbar\omega_n)}\;. \tag{10.30}$$

The self–energy $\Sigma^{(a)}_{\alpha,\beta}(\underline{k};i\hbar\omega_n)$ is depicted diagrammatically in Fig. 10.17. A rigorous derivation of the Eliashberg equations for the self energies relies on the validity of Migdal's theorem [120], which states that the vertex correction is tiny, of the order of the square root of the ratio of the electron to the ion mass $\sim 10^{-3}$. There are no analogous theorems known for couplings to other bosonic modes such as spin–waves [121], but nevertheless, it is still hoped that similar equations may describe superconducting pairing mediated by other bosonic mechanisms. In the Eliashberg equations, the gap can be expressed in terms of the spectral density associated with the bosonic pairing mechanism and the spectral density of the electrons forming the Cooper pairs. In the presence of strong interactions, the spectral densities include appropriate self energies, and the pairing interaction is manifested through an irreducible vertex interaction, $\Gamma(\underline{k},\underline{k}+\underline{q};i\hbar\omega_m,i\hbar\omega_n)_{\alpha,\beta;\mu,\nu}$. Terms corresponding to the irreducible vertex interaction due to the exchange of bosons are shown in Fig. 10.18. The self–energy, the gap, and the irreducible vertex interaction should all be calculated self consistently. The linearized gap equation, which

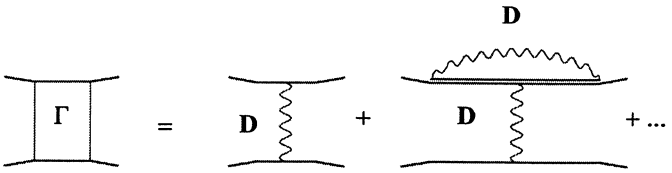

Fig. 10.18. The Feynmann diagram expansion of the irreducible vertex interaction $\Gamma(\underline{q};\hbar\omega)$ in terms of bosonic excitations. The boson propagators, $D(\underline{q}';\hbar\omega')$, are represented by the wavy lines

determines T_c for the various pairings, is given by

$$\Delta_{\alpha,\beta}(\underline{k};i\hbar\omega_n) = -k_B T_c \frac{1}{N}\sum_m \sum_{\underline{q}} \sum_{\mu,\nu} \Gamma(\underline{k},\underline{k}+\underline{q};i\hbar\omega_m,i\hbar\omega_n)_{\alpha,\beta;\mu,\nu} \times G_\mu(\underline{k}+\underline{q};i\hbar\omega_m)\, G_\nu(-\underline{k}-\underline{q};-i\hbar\omega_m)\, \Delta_{\mu,\nu}(\underline{k}+\underline{q};i\hbar\omega_m). \tag{10.31}$$

The normal state becomes unstable to the superconducting state that has the highest T_c in the case of no degeneracy. The criterion for a further instability of superconducting phase to phases with other types of pairings must be determined on the basis of minimization of the Free energy. In the case of strong electron–phonon coupling, the vertex corrections are limited by Migdal's theorem [120] to be smaller than the bare vertex interaction by factors at least as small as 10^{-2}. These corrections are negligibly small and, therefore, have the effect that the self-energies can be calculated with extremely good accuracy. In such cases, the Eliashberg equations have been solved. Such calculations are reviewed in references [122,123]. For heavy–fermion superconductors, the physics is not so clear and, despite the absence of experimental confirmation, the validity of a Fermi liquid picture is often assumed. Under this assumption, the imaginary time Green's functions in the vicinity of the Fermi energy may be replaced by their quasi–particle contributions. In particular, the quasi–particle masses are changed from the band mass m_b by the wave function renormalization to $Z\, m_b$, the quasi–particle lifetimes τ_0 are increased to $Z\,\tau_0$ and the strength of the quasi–particle pole is reduced from unity by a factor Z^{-1}. The enhanced quasi–particle masses are simply absorbed into a re–definition of $e(\underline{k}) - \mu$ as the normal state quasi–particle energies $E_{\underline{k}}$. If the electron–phonon coupling was proven to be the mechanism responsible for heavy–fermion superconductivity, the ratio of the quasi–particle masses to the ionic masses are no longer negligible so, even in this case, Migdal's theorem and the Eliashberg equations may be of doubtful validity. Even though retardation plays an important role in superconductivity, an approximation that has been frequently used consists of replacing the vertex function by an appropriate interaction potential evaluated on the Fermi surface. In this

approximation, the interaction potential contains the effect of the instantaneous Coulomb repulsion, and the linearized gap equation simplifies to take the weak–coupling BCS form [124],

$$\Delta_{\alpha,\beta}(\underline{k}) \;=\; Z^{-2}\,\frac{1}{N}\sum_{\underline{q}}\sum_{\mu,\nu}\Gamma(\underline{k},\underline{k}+\underline{q})_{\alpha,\beta;\mu,\nu}\;\Delta_{\mu,\nu}(\underline{k}+\underline{q}) \times\left[\frac{1\;-\;f(E_{\nu,\underline{k}+\underline{q}})\;-\;f(E_{\mu,-\underline{k}-\underline{q}})}{E_{\nu,\underline{k}+\underline{q}}\;+\;E_{\mu,-\underline{k}-\underline{q}}}\right]. \tag{10.32}$$

This differs from the usual BCS theory of simple superconductors in that the wave function renormalization Z^{-1} is now explicitly included, and also, there is an implicit difference in that the dispersion relations are those of the heavy quasi–particles. The spin dependence of the quasi–particle energies may be important for the occurrence of superconductivity within a magnetically ordered phase. The summation over $\underline{q}$ can be performed by introducing an integration over the density of states which is cut off at a frequency, ω_c, characteristic of the bosons responsible for the pairing

$$\begin{aligned}
&\Delta_{\alpha,\beta}\,(\hat{k}) = \\
&\qquad Z^{-2}\sum_{\mu,\nu}\int\frac{d\Omega}{4\pi}\Gamma(\hat{k},\hat{k}')_{\alpha,\beta;\mu,\nu}\Delta_{\mu,\nu}(\hat{k}')\int_{-\hbar\omega_c}^{+\hbar\omega_c}dE\rho_{qp}(E)\left(\frac{1-2f(E)}{2E}\right)\\
&=\; Z^{-1}\,\rho(\mu)\sum_{\mu,\nu}\int\frac{d\Omega}{4\pi}\,\Gamma(\hat{k},\hat{k}')_{\alpha,\beta;\mu,\nu}\,\Delta_{\mu,\nu}(\hat{k}')\;\times\\
&\times\;\left(\left[1-2f(\hbar\omega_c)\right]\cdot\ln\frac{\hbar\omega_c}{k_BT}\;+\;2\int_0^{\frac{\hbar\omega_c}{k_BT}}dx\;\ln x\;\frac{\partial}{\partial x}\left(\frac{1}{\exp x\;+\;1}\right)\right)\\
&=\; Z^{-1}\rho(\mu)\sum_{\mu,\nu}\int\frac{d\Omega}{4\pi}\Gamma(\hat{k},\hat{k}')_{\alpha,\beta;\mu,\nu}\Delta_{\mu,\nu}(\hat{k}')\left(\left[1-2f(\hbar\omega_c)\right]\ln\frac{\hbar\omega_c}{k_BT}+\ln\frac{2\gamma}{\pi}\right),
\end{aligned} \tag{10.33}$$

where we have ignored any spin polarization in the quasi–particle bands. Usually, the Fermi function $f(\hbar\omega_c)$ is neglected under the assumption that $\hbar\omega_c > k_BT_c$, which usually holds for phonon mediated pairing. However, this assumption may not be appropriate for spin–fluctuation mediated pairing near a quantum critical point. In such cases, a strong coupling approach may have to be used. In the above expression, the electron density of states $\rho(\mu)$ is un–enhanced by the interactions but is multiplied an explicit factor of Z^{-1}. As pointed out by Varma [125], this leads to an expression for T_c similar to the BCS weak–coupling form except that the exponent is increased by a factor of Z, i.e.,

$$k_BT_c \;=\; 1.14\;\hbar\omega_c\;\exp\left[-\left(\frac{Z}{\Gamma\rho(\mu)}\right)\right], \tag{10.34}$$

where Γ is the Fermi surface average of $\Gamma(\hat{k}, \hat{k}')$. Thus, the mass renormalization Z could depress T_c. The value of T_c in heavy–fermion superconductors could also be low due to a small ω_c in the prefactor [126] as well as in the exponent due to the appearance of the Fermi functions.

The relationship between the nature of spin–fluctuations and the singlet or triplet character of the pairing is found by expanding both the on–Fermi surface vertex function and the order parameter in spherical harmonics. The expansions are

$$\Gamma(\hat{k}, \hat{k}')_{\alpha,\beta;\mu,\nu} = \sum_{l,m} \Gamma(l)_{\alpha,\beta;\mu,\nu} \, Y_m^l(\hat{k})^* \, Y_m^l(\hat{k}') \tag{10.35}$$

and

$$\Delta_{\mu,\nu}(\hat{k}) = \sum_{l,m} \Delta_{\mu,\nu}(l,m) \, Y_m^l(\hat{k}) \, . \tag{10.36}$$

The orthogonality of the spherical harmonics Y_m^l, leads to an independent linearized gap equation for each l value. Furthermore, if the spin dependence of the vertex function is of the form

$$\Gamma(l)_{\alpha,\beta;\mu,\nu} = (\, U_l \, \delta_{\alpha,\beta;\mu,\nu} - J_l \, \vec{\sigma}_{\alpha;\nu} \, . \, \vec{\sigma}_{\beta;\mu} \,) \, , \tag{10.37}$$

where U_l is an effective direct Coulomb repulsion and J_l is an effective exchange, then, with the aid of the identity

$$\left(S \, (S+1) - 2 \, \frac{3}{4} \right) \delta_{\alpha,\beta;\mu,\nu} = \frac{1}{2} \, \vec{\sigma}_{\alpha;\nu} \, . \, \vec{\sigma}_{\beta;\mu} \, , \tag{10.38}$$

where S is the total spin of the Cooper pair, one can show that the equations for the different T_c's are

$$1 = \ln \frac{k_B T_c}{\hbar \omega_c} \, Z^{-1} \, \rho(\mu) \, (\, U_l + 3 \, J_l \,) \tag{10.39}$$

for singlet T_c's with $S = 0$ and even l, while

$$1 = \ln \frac{k_B T_c}{\hbar \omega_c} \, Z^{-1} \, \rho(\mu) \, (\, U_l - J_l \,) \tag{10.40}$$

for triplet T_c's with $S = 1$ and odd l. The normal state becomes unstable to the angular momentum pairing state with the highest T_c. In the case where a set of order parameters have degenerate T_c's, the instability first occurs to the state with the linear combination of the order parameters that corresponds to the lowest free energy [127,128]. Large values of U_0, from the direct Coulomb repulsion, are unfavorable for s–wave pairing. However, U_0 represents the residual interactions between a pair of quasi–particles and is represented by a Fermi liquid parameter F_0 which is unknown, apriori, and it could have a

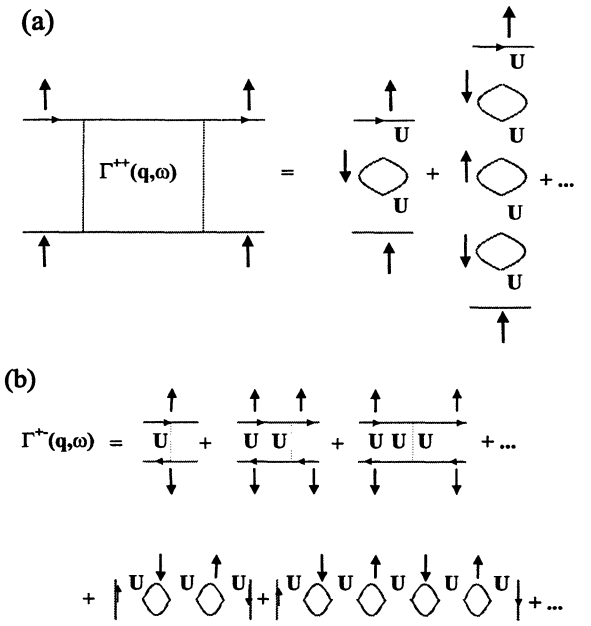

Fig. 10.19. The RPA expression for the irreducible interaction between a pair of electrons with parallel spins is depicted in terms of Feynmann diagrams in (a). The interaction between electrons with anti–parallel spins is shown in (b). The interaction not only involves the longitudinal spin–fluctuations but also transverse spin–fluctuations

quite small magnitude in which case s–wave pairing might still occur. It is also seen that the $\underline{q}$ dependence of the effective exchange interaction strongly influences the tendency for singlet versus triplet pairing [129, 130].

In analogy to the paramagnetic spin–fluctuation pairing mechanisms [131–133] proposed for ^{3}He, a number of authors [115–117] have investigated the effect of incommensurate or antiferromagnetic spin–fluctuations within the RPA. The effective interaction between a pair of electrons with parallel spins is shown in Fig. 10.19a. The dashed lines represent the local Coulomb interaction, and the directed lines represent the one–electron Green's functions. These diagrams only contain odd numbers of bubbles due to the spin–dependent nature of the Coulomb repulsion U and are related to the longitudinal or z–z components of the magnetic susceptibility. The resulting interaction between parallel spin electrons at the Fermi energy is given by

$$\Gamma(\underline{k},\underline{k}')_{\sigma,\sigma:\sigma,\sigma} = -\frac{U^2\,\chi_0(\underline{k}-\underline{k}';0)}{1-U^2\,\chi_0^2(\underline{k}-\underline{k}';0)}\,, \tag{10.41}$$

where $\chi_0(\underline{q};0)$ is the static limit of the appropriate transverse, non–interacting, reduced susceptibility, having the usual Lindhard form.

The effective interaction between electrons with anti–parallel spins is given by the sum of three terms, one being the on site Coulomb repulsion U, another term stemming from the transverse susceptibility, and the last term originates from the remaining part of the longitudinal susceptibility. These terms are depicted diagrammatically in Fig. 10.19b and are evaluated as

$$\Gamma(\underline{k},\underline{k}')_{\sigma,-\sigma;-\sigma,\sigma} = U + \frac{U^3\chi_0^2(\underline{k}-\underline{k}';0)}{1 - U^2\,\chi_0^2(\underline{k}-\underline{k}';0)} + \frac{U^2\,\chi_0(\underline{k}+\underline{k}';0)}{1 - U\,\chi_0(\underline{k}+\underline{k}';0)} \,. \tag{10.42}$$

For values of U in the vicinity of the critical value U_c, the susceptibilities for $\underline{q} \sim \underline{Q}$ are enhanced as are the effective quasi–particle interactions of Eqn. (10.41) and Eqn. (10.42). Thus, one expects the effective interaction to be highly peaked at $\underline{q}$ values closely connected to the $\underline{Q}$ values of the quantum critical point. Due to the increase in the amplitude of the spin–fluctuations as the quantum critical point is approached, the superconducting interaction in the paramagnetic phase is expected to be largest just at the quantum critical point. In the magnetically ordered phase, the transverse spin–fluctuations are expected to transform into a branch of undamped Goldstone modes. However, as shown by Schrieffer *et al.* [134], the Goldstone modes of the antiferromagnetically ordered state of an isotropic material do not produce superconducting pairing. Due to the loss of the low–energy transverse spin–fluctuation modes as a pairing mechanism in the ordered phase and as the amplitude (longitudinal) modes are expected to acquire a mass, one expects that the superconducting pairing will diminish deep within the magnetically ordered phase [3]. Hence, the superconductivity is expected to occur only in close proximity to a quantum critical point.

In comparing the relative tendencies of the nearly ferromagnetic and nearly antiferromagnetic spin–fluctuations in producing triplet or singlet pairings [129,130], it is useful to re–write the momentum transfers for on–Fermi surface processes as $|\,\underline{k} \pm \underline{k}'\,|^2 = 2k_F^2\,(1 \pm \cos\theta)$, where $\cos\theta = \hat{k}\,.\,\hat{k}'$. Then, with the use of the addition theorem for spherical harmonics, one finds

$$J_l = \frac{2\,l\,+\,1}{4} \int_0^{\pi} d\theta\, \sin\theta\, P_l(\cos\theta)\, \frac{U^2\,\chi_0(\underline{k}-\underline{k}';0)}{1 - U\,\chi_0(\underline{k}-\underline{k}';0)} \,, \tag{10.43}$$

where $P_l(x)$ are the Legendre polynomials. If the system is close to a ferromagnetic instability, the effective interaction due to the spin–fluctuations is

[3] The combined effect of spin–orbit coupling and crystalline anisotropy in a heavy–fermion system may result in the magnetic order parameter losing its continuous symmetry. Hence, the nature of the soft–modes at the transition may change. In such cases, it might be expected that the soft–modes may remain effective in producing superconducting pairing within the magnetically ordered phase.

enhanced and positive for momentum transfers of magnitude $q = 2k_F \sin\frac{\theta}{2} \sim 0$, and from the properties of the Legendre function, one expects that the strengths of J_l are positive ($P_l(1) = 1$) and decrease with increasing l due to the increasing number of nodes of $P_l(\cos\theta)$. This, combined with a large value of U_0, may forbid s–wave singlet pairing and leads to the conclusion that ferromagnetism may favor triplet spin pairing with $l = 1$. That is, a ferromagnetic exchange between distant electrons can stabilize triplet pairs [135]. On the other hand, if the proximity to a spin density wave phase enhances the susceptibility at non–zero $\underline{q}$ values in regions where the odd l values of $P_l(\cos\theta)$ are negative ($P_l(-1) = (-1)^l$), triplet pairing may be unfavorable. However, even l singlet pairing may still occur as it is stabilized by the antiferromagnetic exchange. Such a simple analysis of the strength of the various pairings is not expected to hold in real materials with multi–sheeted Fermi surfaces but is crucially controlled by the structure of the Fermi surface of the normal state [74].

The usual weak–coupling description of superconducting states, developed by Bardeen Cooper and Schrieffer [124], has a starting point that assumes the normal state electronic system is in the Fermi liquid state. The superconducting pairing interaction is introduced, which then produces the instability to the superconducting state. To the extent that the pairing interactions can be treated in the mean–field approximation, the quasi–particle concept remains valid in the superconducting state. The absence of a significant lifetime for the quasi–particle states essentially follows from the same reasoning as in the normal state, namely, that the Pauli–exclusion principle significantly reduces the amount of phase space available for scattering processes. In this mean–field description, the quasi–particle dispersion relations $E_{\sigma,\underline{k}}$ have forms that depend on the nature of the superconducting order parameters. For the majority of conventional superconductors, the normal state is well described by Fermi liquid theory, and the transition to the superconducting state closely follows the mean–field predictions. However, measurements on some heavy–fermion systems show that the systems have not settled into the Fermi liquid phase before the superconducting transition occurs. Thus, the validity of the use of the quasi–particle concept is dubious. Nevertheless, it may be expected that some features of the heavy–fermion superconducting states are robust in that they only depend on underlying symmetries and thus, would be common to the mean–field description in terms of quasi–particles as well as a more rigorous treatment.

10.2.5 The Symmetry of the Order Parameter

The symmetry of the superconducting order parameter, or more precisely the vanishing of the gap at the Fermi energy, does lead to anomalous temperature dependences of specific heat and transport properties far below T_c. An early series of such experiments which were devised to elucidate the symmetry did lead to the conclusion that the superconducting gap does vanish somewhere

on the Fermi surface [5,25–31] but was equivocal on the detailed nature of the order parameter. Nevertheless, in the following we shall examine the possible symmetries of the gap function and their experimental manifestations. These considerations shall then be applied to the various heavy–fermion compounds in subsequent sections.

The Cooper pairs are characterized by the pairing function, which is defined by the expectation value of the product of two electron annihilation operators, $a_{\sigma,\underline{k}}$, as

$$\Phi_{\alpha,\beta}(\underline{k}) = < \mid a_{\alpha,\underline{k}}\, a_{\beta,-\underline{k}} \mid > , \tag{10.44}$$

where α, and β denote the spin values quantized along the z axis. We shall consider the equilibrium state in which the center of mass of the pairs are at rest. For convenience we shall, as in the case of superfluid ^{3}He [136], assume spherical symmetry and also neglect spin–orbit scattering. Neither of these assumptions are valid for heavy–fermion systems [137]. For f electrons, spin–orbit coupling is known to be strong, and the anisotropy caused by the crystalline environment also needs to be accounted for. So, both these assumptions need to be abandoned in a proper description of heavy–fermion superconductors. As their abandonment only complicates the presentation [138, 139] but does not invalidate the general approach being outlined, we shall make use of these assumptions for pedagogical purposes. This approach mirrors the historical development of the theoretical description of heavy–fermion superconductivity, which often proceeded by analogy with ^{3}He.

The singlet pairing function is written as the anti–symmetrized product

$$\Phi^s(\underline{k}) = < \mid (a_{\uparrow,\underline{k}}\, a_{\downarrow,-\underline{k}} - a_{\downarrow,\underline{k}}\, a_{\uparrow,-\underline{k}}) \mid > . \tag{10.45}$$

The triplet pairing functions can be expressed in terms of the components organized by the eigenvalues of S_z as

$$\Phi^t_{S_z=1}(\underline{k}) = < \mid a_{\uparrow,\underline{k}}\, a_{\uparrow,-\underline{k}} \mid >$$
$$\Phi^t_{S_z=0}(\underline{k}) = < \mid (a_{\uparrow,\underline{k}}\, a_{\downarrow,-\underline{k}} + a_{\downarrow,\underline{k}}\, a_{\uparrow,-\underline{k}}) \mid > .$$

and

$$\Phi^t_{S_z=-1}(\underline{k}) = < \mid a_{\downarrow,\underline{k}}\, a_{\downarrow,-\underline{k}} \mid > . \tag{10.46}$$

From consideration of the fermion anti–commutation relations, one finds that the singlet pairing function is even in $\underline{k}$ whereas the triplet wave function is odd in $\underline{k}$. By considering the effects of various symmetries on an arbitrary pairing wave function, one finds that in this case, one can parameterize an arbitrary pairing function in terms of a scalar singlet $\Phi^s(\underline{k})$ and a (vector) triplet $\vec{\Phi}^t(\underline{k})$ pairing function via

$$\Phi_{\alpha,\beta}(\underline{k}) = \frac{1}{2} \left[\left(\Phi^s(\underline{k}) + \vec{\sigma}.\vec{\Phi}^t(\underline{k}) \right) i\, \sigma_y \right]_{\alpha,\beta} . \tag{10.47}$$

The unitary operator $i\,\sigma_y$ occurs as a consequence of the spin operator $\vec{\sigma}$ being odd under time reversal symmetry and also as the anti–symmetric Pauli matrix has the effect that

$$i\,\sigma_y\,\vec{\sigma}\,(-i\,\sigma_y) = -\vec{\sigma}^{*}\,. \tag{10.48}$$

The direction of the triplet ordering is given in terms of the matrix elements of the vector pairing function

$$\vec{\Phi}^{t}(\underline{k}) = \left[-\Phi^{t}_{S_z=1}(\underline{k})\,(\hat{x}+i\hat{y}) + \Phi^{t}_{S_z=0}(\underline{k})\,\hat{z} + \Phi^{t}_{S_z=-1}(\underline{k})\,(\hat{x}-i\hat{y}) \right]. \tag{10.49}$$

If the pairing interaction is of the form

$$\hat{H}_{int} = \frac{1}{N}\sum_{\underline{k},\underline{q}}\sum_{\alpha,\beta,\mu,\nu} V(\underline{k},\underline{q})_{\beta,\alpha:\,\mu,\nu}\; a^{\dagger}_{\beta,-\underline{k}}\; a^{\dagger}_{\alpha,\underline{k}}\; a_{\mu,\underline{q}}\; a_{\nu,-\underline{q}}\,, \tag{10.50}$$

then the pairing potential can be expressed as the average

$$\Delta_{\alpha,\beta}(\underline{k}) = \frac{1}{N}\sum_{\underline{q}}\sum_{\mu,\nu} V(\underline{k},\underline{q})_{\beta,\alpha:\,\mu,\nu}\;\Phi_{\mu,\nu}(\underline{q})\,. \tag{10.51}$$

The above equation shows that the symmetry of the pairing potential is related to the pairing function. By analogy to Eqn. (10.47), one can then write the pairing potential as

$$\Delta_{\alpha,\beta}(\underline{k}) = \frac{1}{2}\left[\left(D(\underline{k}) + \vec{\sigma}\,.\,\vec{d}\,(\underline{k}) \right) i\,\sigma_y \right]_{\alpha,\beta}. \tag{10.52}$$

The three different S_z components of the spin triplet pairing potential are assigned the amplitudes which are related to the components of $\vec{d}^{\,t}$ via

$$\begin{aligned} -\,d_{S_z=1} &= d_x - i\,d_y\,, \\ d_{S_z=0} &= d_z\,, \\ d_{S_z=-1} &= d_x + i\,d_y\,. \end{aligned} \tag{10.53}$$

One can expand the singlet pairing potential in the spherical harmonics $Y^{l}_{m}(\hat{k})$ as

$$D(\underline{k}) = \sum_{l,m} D^{l}_{m}(k)\; Y^{l}_{m}(\hat{k})\,, \tag{10.54}$$

where due to the symmetry imposed by fermion anti–commutation relations $D(\underline{k}) = D(-\underline{k})$, only even values of l contribute. Likewise, the components of the triplet pairing potential can also be expanded in the same way

$$d_{S_z}(\underline{k}) = \sum_{l,m} d^{l}_{m,S_z}(k)\; Y^{l}_{m}(\hat{k})\,, \tag{10.55}$$

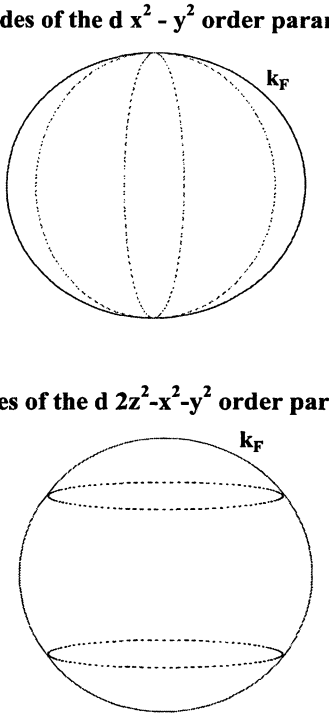

Fig. 10.20. Positions of the lines of nodes for d–wave superconductors, in momentum space. The dashed lines represent the lines of zeros of the superconducting order parameter on the spherical Fermi surface (indicated by the solid line). (a) The lines of nodes of the $d_{x^2-y^2}$ order parameter consists of a pair of great circles which intersect at the poles. (b) The lines of nodes for the $d_{2z^2-x^2-y^2}$ phase consists of two non–intersecting circles

but as the pairing potential is anti–symmetric in $\underline{k}$ $d_{S_z}(\underline{k}) = -d_{S_z}(-\underline{k})$, only the odd values of l contribute. Thus, singlet pairing only occurs with even values of l and triplet pairing only occurs with odd values of l. It is noted that in anisotropic crystals, singlet and triplet pairing remain mutually exclusive if the symmetry group contains an inversion symmetry $\underline{k} \rightarrow -\underline{k}$.

The BCS mean–field Hamiltonian [124] can be expressed in terms of the pairing potentials as

$$\hat{H}_{MF} = \sum_{\alpha,\underline{k}} \left(e_\alpha(\underline{k}) - \mu \right) a^\dagger_{\alpha,\underline{k}} \, a_{\alpha,\underline{k}} + \sum_{\alpha,\beta,\underline{k}} \left(\Delta_{\alpha,\beta}(\underline{k}) \, a^\dagger_{\beta,-\underline{k}} \, a^\dagger_{\alpha,\underline{k}} + \Delta^*_{\alpha,\beta}(\underline{k}) \, a_{\alpha,\underline{k}} \, a_{\beta,-\underline{k}} \right) . \tag{10.56}$$

This apart from a constant term, can be re–expressed as

$$\hat{H}_{MF} = \frac{1}{2}\left[\sum_{\alpha,\underline{k}}(e_\alpha(-\underline{k}) - \mu)a^\dagger_{\alpha,-\underline{k}}a_{\alpha,-\underline{k}} - \sum_{\alpha,\underline{k}}(\, e_\alpha(\underline{k}) - \mu)\; a_{\alpha,\underline{k}}a^\dagger_{\alpha,\underline{k}}\right] + \sum_{\alpha,\beta,\underline{k}}\left(\; \Delta_{\alpha,\beta}(\underline{k})\; a^\dagger_{\beta,-\underline{k}}\; a^\dagger_{\alpha,\underline{k}} \;+\; \Delta^*_{\alpha,\beta}(\underline{k})\; a_{\alpha,\underline{k}}\; a_{\beta,-\underline{k}}\;\right). \quad (10.57)$$

A four component column operator, Ψ, is introduced

$$\Psi(\underline{k}) = \begin{pmatrix} a_{\uparrow,-\underline{k}} \\ a_{\downarrow,-\underline{k}} \\ a^\dagger_{\uparrow,\underline{k}} \\ a^\dagger_{\downarrow,\underline{k}} \end{pmatrix},$$

where the first two components (and the last two) are conjugate pairs, whereas the first and fourth (and second and third) are time reversal partners. This notation allows the BCS Hamiltonian to be written in matrix form

$$\hat{H}_{MF} = \frac{1}{2}\sum_{\underline{k}} \Psi^\dagger(\underline{k})\; \tilde{H}_{MF}(\underline{k})\; \Psi(\underline{k})\,, \quad (10.58)$$

where the matrix is given by

$$\tilde{H}_{MF}(\underline{k}) =$$

$$\begin{pmatrix} e_\uparrow(-\underline{k}) & 0 & -\,d_{S_z=1}(\underline{k}) & d_{S_z=0}(\underline{k}) + D(\underline{k}) \\ 0 & e_\downarrow(-\underline{k}) & d_{S_z=0}(\underline{k}) - D(\underline{k}) & d_{S_z=-1}(\underline{k}) \\ -\,d^*_{S_z=1}(\underline{k}) & d^*_{S_z=0}(\underline{k}) - D^*(\underline{k}) & -\,e_\uparrow(\underline{k}) & 0 \\ d^*_{S_z=0}(\underline{k}) + D^*(\underline{k}) & d^*_{S_z=-1}(\underline{k}) & 0 & -\,e_\downarrow(\underline{k}) \end{pmatrix}. \quad (10.59)$$

This mean–field Hamiltonian has quasi–particle excitation energies that can be expressed as

$$E_{\sigma,\underline{k}} = \pm\sqrt{(e(\underline{k}) - \mu)^2 + |D(\underline{k})|^2 + |\,\vec{d}\,(\underline{k})|^2 - \sigma\,|\,i\;\vec{d}\,(\underline{k}) \wedge \vec{d}^{\,*}(\underline{k})\,|}\,, \quad (10.60)$$

where $\sigma = \pm 1$. Consider the term inside the square root that is proportional to a vector product and σ, this term is real. When the vector product is zero

the pairing is said to be unitary, and when it is non–zero the pairing is non–unitary. In the non–unitary state, the spin degeneracy is lifted and a staggered spin density will occur, which is a consequence of the spontaneous breaking of time reversal symmetry.

One important characteristic of unconventional superconductivity is that the gap at the Fermi surface may vanish for specific $\underline{k}$ values, which are the nodes of the order parameter. For singlet superconductivity, the gap vanishes when $\mid D(\underline{k}) \mid^2 = 0$ at the Fermi surface $e(\underline{k}) = \mu$ [4]. For triplet superconductivity, the gap vanishes when

$$\mid \vec{d}(\underline{k}) \mid^2 \pm \mid i\, \vec{d}(\underline{k}) \wedge \vec{d}^{\,*}(\underline{k}) \mid = 0 \tag{10.61}$$

at $e(\underline{k}) = \mu$. In the non–unitary state, it is possible that the gap may vanish for only one spin direction.

The vanishing of the superconducting gap at the nodes does produce a finite density of states for quasi–particle excitations that may be revealed in thermodynamic, transport, and spectroscopic measurements. Although several experiments were performed with the intention of establishing the existence of and characterizing the nodes, the results were often conflicting. In retrospect, the lack of consensus concerning the nature of the nodes is not surprising as even Nb based superconductors show various deviations from strict singlet s–wave BCS behavior.

For singlet s–wave superconductivity in an isotropic system, there are no nodes. Thus, for an isotropic singlet superconductor, the existence of nodes is related to the formation of pairs with non–zero angular momenta. The singlet pairing d–wave state, $d_{x^2-y^2}$, seems increasingly certain to be the symmetry of the high temperature superconducting phase of $YBa_2Cu_3O_7$, which has an extremely anisotropic perovskite structure. The order parameter for this phase has the long wavelength form $D(\underline{k}) \propto (k_x^2 - k_y^2)$, and so the gap vanishes at lines of nodes which form two great circles with a relative orientation of $\frac{\pi}{2}$ and the circles intersect at the poles as shown in Fig. 10.20a. Another type of d–wave ordering is the $d_{2z^2-x^2-y^2}$ in which there are two separate planes where $D(\underline{k}) = 0$ that intersect with Fermi energy in circles. As shown in Fig. 10.20b, one circle is in the $k_z = + k_f/\sqrt{3}$ plane and the other in the $k_z = - k_f/\sqrt{3}$ plane.

There are three triplet p–wave states which have been extensively studied in the context of ^{3}He. These are all unitary states, and the first one we shall consider is given by

$$\vec{d}(\underline{k}) \propto \hat{x}\, k_x + \hat{y}\, k_y + \hat{z}\, k_z \tag{10.62}$$

which corresponds to the Balian–Werthamer (BW) phase [140]. This pairing corresponds to one with angular momentum $\vec{J} = \vec{L} + \vec{S} = 0$, as can be

[4] The diagonal part of the self–energy has been neglected.

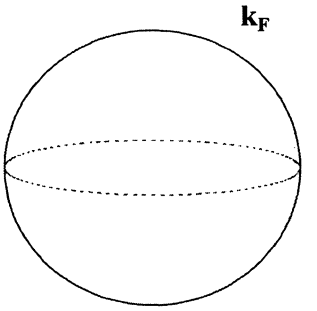

Fig. 10.21. The line of nodes of the order parameter for the polar phase of a p–wave superconductor is located on the equatorial circle on the Fermi surface

seen from re–writing the gap function as

$$\vec{d}\,(\underline{k}) \propto k \left(\sin\theta \cos\phi\, \hat{x} + \sin\theta \sin\phi\, \hat{y} + \cos\theta\, \hat{z} \right)$$
$$\propto \sqrt{\frac{2\pi}{3}}\, k \left[\left(\hat{x} - i\hat{y} \right) Y_1^1 - \left(\hat{x} + i\,\hat{y} \right) Y_{-1}^1 + \sqrt{2}\,\hat{z}\, Y_0^1 \right] \tag{10.63}$$

which, on comparing with Eqn. (10.49) and noting the normalization of $\Phi_{S_z=0}$, is easily identifiable as a state with $\vec{J} = 0$. The gap has a constant magnitude over the Fermi energy, and so the gap does not vanish for any $\underline{k}$ values in the BW state. The BW pairing is realized in the B phase of superfluid ^{3}He.

Another state is the Anderson–Brinkman–Morell (ABM) phase [141],

$$\vec{d}\,(\underline{k}) \propto \hat{z}\,(\,k_x + i\,k_y\,) = \hat{z}\,k\,\sin\theta\,\exp[\,i\,\varphi\,] \tag{10.64}$$

which is identified as the state with $S_z = 0$ and $L_z = \hbar$. Thus, $\vec{S}$ and $\vec{L}$ are perpendicular to each other. For the ABM phase, the gap at the Fermi surface vanishes at the point nodes where $k_x = k_y = 0$. The ABM pairing is realized in the A phase of superfluid ^{3}He.

The third state is the polar phase, p_z, where

$$\vec{d}\,(\underline{k}) \propto \hat{z}\,k_z\,. \tag{10.65}$$

This state has $S_z = 0$ and $L_z = 0$. As shown in Fig. 10.21, the gap function vanishes at the line node in the equatorial plane where $k_z = 0$.

The above singlet and triplet states may be appropriate for isotropic systems but are not appropriate for crystals of lower symmetry. However, due

to a symmetry breaking transition, the Cooper pairs may still have a point group symmetry lower than the full point group symmetry of the crystalline lattice. The various possible types of pairings in crystalline environments of different symmetries with spin–orbit coupling have been tabulated by Anderson [142], Volovik and Gor'kov [139], and also by Blount [138]. The possible pairings, neglecting spin–orbit coupling, were enumerated by Ozaki *et al.* [143]. We shall first discuss the effect of the periodic lattice and then the effect of spin–orbit coupling.

Crystal Symmetry

The periodic symmetry of the crystalline lattice breaks full rotational symmetry and, therefore, angular momentum is no longer a good quantum number. The basis functions of the rotational group can no longer be used to describe the pairing. However, the basis functions appropriate to the point group can be used. We shall focus the discussion on the O_h group, the tetragonal group D_{4h}, and the hexagonal group D_{6h}, which are relevant to UBe_{13}, $CeCu_2Si_2$ and URu_2Si_2, and UPt_3. For an irreducible representation with dimensionality d, the scalar or vector order parameter can be expressed as a linear combination of the degenerate partner basis functions $\phi_i(\hat{k})$ (scalar or vector), times functions of the invariants of the full point group [5], $f_n(\hat{k})$. The degenerate partners are expressed in the form $\sum_n \phi_{i,n}(\hat{k}) f_n(\hat{k})$. Thus, for example, the vector order parameter is expressed as

$$\vec{d}(\hat{k}) = \sum_{i=1}^{i=d} C_i \left[\sum_n \vec{\phi}_{i,n}(\hat{k})\, f_n(\hat{k}) \right] \tag{10.66}$$

and an analogous equation holds true for the singlet order parameter $D(\underline{k})$. The summation over n runs through d and $3d$ values respectively, for singlet and triple pairings [144]. A specific example found in Table(10.2) for singlet pairing in cubic symmetry is the doubly degenerate $\Gamma_3^+(E_g)$ representation in which the degenerate partners basis functions have the form

$$\begin{aligned} \phi_1(\hat{k}) &= \sum_{n=2;4} (k_x^n + k_y^n - 2k_z^n) f_n(\hat{k}) \,, \\ \phi_2(\hat{k}) &= \sum_{n=2;4} (k_x^n - k_y^n) \,, f_n(\hat{k}) \end{aligned} \tag{10.67}$$

where the $f_n(\hat{k})$ have the form $a_n + b_n k^2 + c_n(k_x^4 + k_y^4 + k_z^4) + \ldots$. Likewise, for cubic symmetry, the singly degenerate triplet pairing $\Gamma_1^-(A_{1u})$ representation found in Table(10.3) has the basis function

$$\vec{\phi}_1(\hat{k}) = \sum_{n=1;3;5} (\hat{x}\, k_x^n + \hat{y}\, k_y^n + \hat{z}\, k_z^n)\, f_n(\hat{k}) \,. \tag{10.68}$$

[5] It is possible that the functions $f_n(\hat{k})$ vanish at some $\underline{k}$ points, thereby producing nodes in the order parameter. However, the set of nodes that are produced in this way will still have the full point group symmetry of the lattice.

The coefficients C_i multiplying the degenerate partner basis functions are arbitrary and are determined only by the spontaneous symmetry broken state. The invariant functions $f_n(\hat{k})$ corresponding to the admixtures of the different angular momentum components are well defined for each representation and should be determined by minimization of the free energy. The tetragonal symmetry singlet and triplet representation basis functions are given in Table(10.4) and Table(10.5) respectively. The basis for the non–degenerate singlet pairings in the tetragonal $\Gamma_3^+(B_{1g})$ representation is written, with different notation $k_\pm = k_x \pm ik_y$, as

$$\phi_1(\hat{k}) = (k_x^2 - k_y^2)\, f(\hat{k}) = Re\ k_+^2\ f(\hat{k})\,, \tag{10.69}$$

where the expansion of the invariant function no longer has a quadratic term in the modulus of $\underline{k}$ but instead, has the different form $f(\hat{k}) = a + bk_z^2 + c(k_x^2 + k_y^2) + \ldots$. The triplet pairing in a D_{4h} structure belonging to the representation $\Gamma_1^-(A_{1u})$ has the form given by,

$$\vec{\phi}_1(\hat{k}) = \hat{z}k_z f_0(\hat{k}) + \sum_{n=1;3} (\hat{x}k_x^n + \hat{y}k_y^n) f_n(\hat{k})\,. \tag{10.70}$$

Even though the crystal field mixes states of different angular momentum, one can usually identify the pairing states via the dominant components of the orbital angular momentum. For example, in the cubic group with spin singlet pairing shown in Table(10.2), we identify the nodeless one dimensional $\Gamma_1^+(A_{1g})$ representation with s–wave pairing and the lowest components of the $\Gamma_3^+(E_g)$ $(n = 2)$ and $\Gamma_5^+(T_{2g})$ $(n = 0)$ representations as the crystal field split members of the five dimensional d–wave pairing basis. Likewise, for triplet pairing in the cubic group shown in Table(10.3), we can identify the one dimensional basis (formed by selecting the $n = 1$ component) of $\Gamma_1^-(A_{1u})$ and the two dimensional basis (also formed by selecting $n = 1$) of $\Gamma_3^-(E_u)$ as the crystal field split three dimensional p–wave pairing basis functions. The node structure for the non–degenerate representations can be found. For example, in a cubic structure with singlet pairing, the high symmetry reduces the number of non–degenerate representations to two. These are the $\Gamma_1^+(A_{1g})$ phase, which is nodeless and the $\Gamma_2^+(A_{2g})$ phase, where the order parameter vanishes on six distinct planes. In the $\Gamma_2^+(A_{2g})$ phase, the six planes intersect the three dimensional Fermi surface on six distinct arcs, giving six lines of nodes on the Fermi surface. In a structure with lower symmetry such as the tetragonal structure, the number of non–degenerate singlet representations is four. The possible singlet phases in D_{4h} are shown in Table(10.4). In addition to the nodeless $\Gamma_1^+(A_{1g})$ phase, one finds the two non degenerate $\Gamma_3^+(B_{1g})$, and $\Gamma_4^+(B_{2g})$ phases, which each produce two lines of nodes as expected for d–wave pairing, and finally the order parameter for the $\Gamma_2^+(A_{2g})$ pairing vanishes on four planes giving four lines of nodes.

For triplet pairing, the occurrence of nodes is generally rarer than for singlet pairings since the three components of $\vec{d}(k)$ must vanish simultane-

Table 10.2. Singlet Pairing Basis Functions for in the Cubic Group O_h. The forms of the degenerate partners are shown. As explained in the text, the components labelled by n must be multiplied by an invariant function $f_n(k)$ and summed over n to yield a degenerate partner. The degenerate partners are separated by commas.

Representation	Basis Functions
$\Gamma_1^+(A_{1g})$	1
$\Gamma_2^+(A_{2g})$	$(k_x^2 - k_y^2)(k_y^2 - k_z^2)(k_z^2 - k_x^2)$
$\Gamma_3^+(E_g)$	$2k_z^n - k_x^n - k_y^n \ , \ k_x^n - k_y^n$ n = 2 ; 4
$\Gamma_4^+(T_{1g})$	$k_x k_y (k_x^n - k_y^n) \ , \ k_y k_z (k_y^n - k_z^n) \ , \ k_z k_x (k_z^n - k_x^n)$ n = 2 ; 4 ; 6
$\Gamma_5^+(T_{2g})$	$k_x k_y k_z^n \ , \ k_y k_z k_x^n \ , \ k_z k_x k_y^n$ n = 0 ; 2 ; 4

ously. The need to satisfy three conditions may be expected to reduce the dimensions of the nodes from a surface to a set of isolated points, which need not lie on the Fermi surface. Inspection of Table(10.3) shows that this is the case for the O_h $\Gamma_1^-(A_{1u})$ phase where the components vanish on orthogonal planes producing isolated zeros not on the Fermi surface, so the gap has no nodes. The components of the order parameter for the highly symmetric non–degenerate $\Gamma_2^-(A_{2u})$ phase each vanish on three planes. This leads to the order parameter vanishing on the four lines $k_x = \pm k_y = \pm k_z$, which intersect the Fermi surface in eight points, resulting in eight point nodes.

The detailed node structure of degenerate representations depends on the spontaneous symmetry breaking between the degenerate partners. In the singlet case, the phase of the order parameter $D(\underline{k})$ can always be chosen to be zero and so $D(\underline{k})$, if it vanishes, does so on surfaces that intersect the Fermi surface in curves. Examples of this are found in both the triply degenerate O_h $\Gamma_5^+(T_{2g})$ and the doubly degenerate $\Gamma_3^+(E_g)$ singlet pairing representations. It is seen that if the system spontaneously selects any one of the degenerate partners, the order parameter will vanish on two distinct planes leading to two lines of nodes. Also, if the effects of the higher order angular momentum contributions are minimal, an arbitrary linear combination of degenerate partner basis functions also makes the order parameter vanish on two surfaces leading to two curved lines of nodes. The analogous case for the singlet D_{4h} symmetry is given by the doubly degenerate $\Gamma_5^+(E_g)$ representation, which also can yield lines of nodes. One of the line nodes is the intersection of the plane $k_z = 0$ with the Fermi surface.

Table 10.3. Triplet Pairing Basis Functions in the Cubic O_h group. The vector $\underline{k}$ is just the radial vector given by $\hat{x}k_x + \hat{y}k_y + \hat{z}k_z$. The components of the symmetric partners are separated by colons, whereas the symmetric partners are separated by commas.

Representation	Basis Functions
$\Gamma_1^-(A_{1u})$	$\hat{x}k_x^n + \hat{y}k_y^n + \hat{z}k_z^n$ n = 1 ; 3 ; 5
$\Gamma_2^-(A_{2u})$	$\hat{x}k_x^n(k_y^2 - k_z^2) + \hat{y}k_y^n(k_z^2 - k_x^2) + \hat{z}k_z^n(k_x^2 - k_y^2)$ n = 1 ; 3 ; 5
$\Gamma_3^-(E_u)$	$\hat{x}k_x^n - \hat{y}k_y^n$, $\hat{x}k_x^n + \hat{y}k_y^n - 2\hat{z}k_z^n$ n = 1 ; 3 ; 5 $(k_x^n - k_y^n)\underline{k}$, $(2k_z^n - k_x^n - k_y^n)\underline{k}$ n = 2 ; 4 $\hat{x}k_x^5k_z^2 - \hat{y}k_y^5k_z^2 + \hat{z}k_z^5(k_x^2 - k_y^2)$, $\hat{x}k_x^5(k_z^2 - 2k_y^2) + \hat{y}k_y^5(k_z^2 - 2k_x^2) + \hat{z}k_z^5(k_x^2 + k_y^2)$
$\Gamma_4^-(T_{1u})$	$k_x^m(\hat{y}k_z^n - \hat{z}k_y^n)$, $k_y^m(\hat{z}k_x^n - \hat{x}k_z^n)$, $k_z^m(\hat{x}k_y^n - \hat{y}k_x^n)$; n = 1 ; 3 ; 5 m = 0 ; 2 $\hat{x}k_yk_z(k_y^2 - k_z^2)k_x^n$, $\hat{y}k_zk_x(k_z^2 - k_x^2)k_y^n$, $\hat{z}k_xk_y(k_x^2 - k_y^2)k_z^n$; n = 1 ; 3 ; 5
$\Gamma_5^-(T_{2u})$	$k_z^m(\hat{y}k_x^n + \hat{x}k_y^n)$, $k_x^m(\hat{z}k_y^n + \hat{y}k_z^n)$, $k_y^m(\hat{x}k_z^n + \hat{z}k_x^n)$; n = 1 ; 3 ; 5 m = 0 ; 2 $\hat{z}k_xk_yk_z^n$, $\hat{x}k_yk_zk_x^n$, $\hat{y}k_xk_zk_y^n$; n = 1 ; 3 ; 5

With triplet pairing, the phase of the order parameter can also be chosen to be real in the unitary case. However, in this case, due to the stringent requirement that if $\vec{d}(\underline{k})$ is to vanish, three equations to be satisfied, the only nodes which occur usually are point nodes. These may be satisfied by symmetry, as in the tetragonal $\Gamma_2^-(A_{2u})$ pairing shown in Table(10.5) where, if $f_2 = f_3 = 0$, symmetry dictates that the order parameter vanishes on the line $k_x = k_y = 0$. In this case, the gap that develops on the Fermi surface has isolated nodes at the poles.

However, line nodes also can be obtained for triplet phases. As Blount has noted [138], the vanishing of the order parameter on a surface can be achieved since the rotational invariance in spin space can reduce the number of independent components of $\vec{d}$ to two and thus lead to a line of nodes on the Fermi surface. An example of this is given in the O_h group with the $\Gamma_3^-(E_u)$ irreducible representation where, if $\vec{d}$ spontaneously chooses to lie in the $\underline{k}$ direction, then $\vec{d}(\underline{k})$ vanishes on two surfaces and leads to two lines of nodes

Table 10.4. Singlet Pairing Basis Functions in the Tetragonal D_{4h} group.

Representation	Basis Functions
$\Gamma_1^+(A_{1g})$	1
$\Gamma_2^+(A_{2g})$	$k_y k_x (k_x^2 - k_y^2)$
$\Gamma_3^+(B_{1g})$	$k_x^2 - k_y^2$
$\Gamma_4^+(B_{2g})$	$k_x k_y$
$\Gamma_5^+(E_g)$	$k_z k_x \ ; \ k_z k_y \ , \ k_z k_x^3 \ ; \ k_z k_y^3$

on the Fermi surface. This type of situation is expected to be forbidden when the effect of spin–orbit coupling is taken into consideration. The irreducible

Table 10.5. Triplet Pairing Basis Functions in the Tetragonal D_{4h} group. The value $k_x \pm ik_y$ is denoted by $k_\pm$ and the vector $\hat{x} \pm i\hat{y}$ is denoted by $\hat{r}_\pm$. The upper and lower signs $\pm$ in the doubly degenerate E_u representation correspond to the degenerate partners.(n = 0 ; 2)

Representation	Basis Functions
$\Gamma_1^-(A_{1u})$	$\hat{z}\, k_z \ ; \ Re\, \hat{r}_- k_+ \ ; \ Re\, \hat{r}_+ k_+^3$
$\Gamma_2^-(A_{2u})$	$Im\, \hat{r}_- k_+ \ ; \ Im\, \hat{r}_+ k_+^3 \ ; \ \hat{z}\, k_z\, Im\, k_+^4$
$\Gamma_3^-(B_{1u})$	$\hat{z}\, k_z\, Re\, k_+^2 \ ; \ Re\, \hat{r}_+ k_+ \ ; \ Re\, \hat{r}_- k_+^3$
$\Gamma_4^-(B_{2u})$	$\hat{z}\, k_z\, Im\, k_+^2 \ ; \ Im\, \hat{r}_+ k_+ \ ; \ Im\, \hat{r}_- k_+^3$
$\Gamma_5^-(E_u)$	$\hat{z}\, k_\pm^{n+1} \ ; \ k_z\, \hat{r}_\pm k_\pm^n \ ; \ k_z\, \hat{r}_\pm k_\mp^{n+2}$

representations for singlet and triplet pairings of the hexagonal group D_{6h} are shown in Table(10.6) and Table(10.7).

In addition to the point group symmetry, the superconducting order parameter must also have the same translational symmetry as the lattice. In particular, the order parameter must be periodic in the Brillouin zone and should also reflect any other translation symmetry element present in the space group. The functions given in the tables correspond to the long wavelength limit form of the order parameters. Some possible forms of the order

parameters with the correct translational symmetry have been examined for the case of UPt_3 [145,146].

Table 10.6. Singlet Pairing Basis Functions in the Hexagonal D_{6h} group. The value $k_x \pm ik_y$ is denoted by $k_\pm$. The upper and lower signs $\pm$ in the doubly degenerate E_g representations correspond to the degenerate partners.

Representation	Basis Functions
$\Gamma_1^+(A_{1g})$	1
$\Gamma_2^+(A_{2g})$	$Im\ k_+^6$
$\Gamma_3^+(B_{1g})$	$k_z\ Im\ k_+^3$
$\Gamma_4^+(B_{2g})$	$k_z\ Re\ k_+^3$
$\Gamma_5^+(E_{1g})$	$k_z\ k_\pm\ ;\ k_z\ k_\mp^5$
$\Gamma_6^+(E_{2g})$	$k_\pm^2\ ;\ k_\mp^4$

Spin–Orbit Coupling

In the presence of spin–orbit coupling, the electrons spin quantized about any fixed axis is no longer a good quantum number, however, the electron does have a well defined magnetic moment. The magnetic moment is an axial vector and can be expressed in terms of a $\underline{k}$ dependent gyromagnetic ratio $g_{i,j}$ which couples to the electron spins via

$$m_i(\underline{k}) \;=\; \frac{1}{2} \sum_j g_{i,j}(\underline{k})\ \sigma_j \ . \tag{10.71}$$

Then, in second quantized form, the magnetic moment operator is given by the expression

$$\hat{\vec{M}}(\underline{k}) \;=\; \frac{1}{2} \sum_{\alpha,\beta} a_\alpha^\dagger(\underline{k}) \left(\vec{m}(\underline{k}) \right)_{\alpha,\beta} a_\beta(\underline{k}) \tag{10.72}$$

The expectation value of this operator can be expressed in terms of the one–electron density matrix $\rho_{\alpha,\beta}(\underline{k}) \;=\; <\mid a_\alpha^\dagger(\underline{k})\ a_\beta(\underline{k}) \mid >$, as

$$<\mid \hat{\vec{M}}(\underline{k}) \mid > \;=\; Trace\left[\vec{m}(\underline{k})\ \rho(\underline{k}) \right] . \tag{10.73}$$

Since the Zeeman splitting of the electron in a Bloch state $\underline{k}$ is given by the eigenvalues, $\pm\ E_z(\underline{k})$, of the Hamiltonian

$$H_Z \;=\; -\ \vec{M}(\underline{k}) \cdot \vec{H} \ . \tag{10.74}$$

Table 10.7. Triplet Pairing Basis Functions in the Hexagonal D_{6h} group. The value $k_x \pm ik_y$ is denoted by $k_\pm$ and the vector $\hat{x} \pm i\hat{y}$ is denoted by $\hat{r}_\pm$. The *Re* and *Im* terms in the doubly degenerate E_u representations correspond to the degenerate partners.

Representation	Basis Functions
$\Gamma_1^-(A_{1u})$	$\hat{z}\, k_z \;;\; Re\, \hat{r}_+\, k_- \;;\; Re\, \hat{r}_+\, k_+^5$
$\Gamma_2^-(A_{2u})$	$Im\, \hat{r}_+\, k_- \;;\; Im\, \hat{r}_+\, k_+^5 \;;\; Im\, \hat{z}\, k_z\, k_-^6$
$\Gamma_3^-(B_{1u})$	$Im\, \hat{z}\, k_-^3 \;;\; Im\, \hat{r}_+\, k_z\, k_+^2 \;;\; Im\, \hat{r}_+\, k_z\, k_-^4$
$\Gamma_4^-(B_{2u})$	$Re\, \hat{z}\, k_-^3 \;;\; Re\, \hat{r}_+\, k_z\, k_+^2 \;;\; Re\, \hat{r}_+\, k_z\, k_-^4$
$\Gamma_5^-(E_{1u})$	$Re\, \hat{z}\, k_+ \;;\; Re\, \hat{r}_+\, k_z \;;\; Re\, \hat{r}_-\, k_z\, k_+^2$; $Re\, \hat{z}\, k_-^5 \;;\; Re\, \hat{r}_-\, k_z\, k_-^4 \;;\; Re\, \hat{r}_+\, k_z\, k_-^6$, $Im\, \hat{z}\, k_+ \;;\; Im\, \hat{r}_+\, k_z \;;\; Im\, \hat{r}_-\, k_z\, k_+^2$; $Im\, \hat{z}\, k_-^5 \;;\; Im\, \hat{r}_-\, k_z\, k_-^4 \;;\; Im\, \hat{r}_+\, k_z\, k_-^6$
$\Gamma_6^-(E_{2u})$	$Re\, \hat{r}_+\, k_+ \;;\; Re\, \hat{z}\, k_z\, k_+^2 \;;\; Re\, \hat{r}_-\, k_+^3$; $Re\, \hat{r}_-\, k_-^3 \;;\; Re\, \hat{r}_+\, k_-^5 \;;\; Re\, \hat{z}\, k_z\, k_-^4$, $Im\, \hat{r}_+\, k_+ \;;\; Im\, \hat{z}\, k_z\, k_+^2 \;;\; Im\, \hat{r}_-\, k_+^3$; $Im\, \hat{r}_-\, k_-^3 \;;\; Im\, \hat{r}_+\, k_-^5 \;;\; Im\, \hat{z}\, k_z\, k_-^4$

Then the splitting of the eigenvalues is found from H_Z^2 independent of the choice of basis. As the Hamiltonian is a Hermitian operator, the eigenvalues are found in terms of the g factors as

$$E_Z(\underline{k})^2 \;=\; \frac{1}{4}\, \vec{H} \,.\, \tilde{g}(\underline{k})^t\, \tilde{g}(\underline{k}) \,.\, \vec{H} \,. \tag{10.75}$$

This shows that, even though the spin is not a good quantum number, the pairing states can be determined in terms of a quasi–spin, independent of the basis, as had been assumed by Anderson [142]. The order parameter still takes on the same form in that it is still composed of either a scalar or a scalar product of an axial vector with $\vec{m}(\underline{k})$

$$\Delta_{\alpha,\beta}(\underline{k}) \;=\; \left(\left[D(\underline{k}) \;+\; \vec{d}\,(\underline{k}) \,.\, \vec{m}(\underline{k}) \right] \left(i\, \sigma_y \right) \right)_{\alpha,\beta} \,. \tag{10.76}$$

The results derived in the presence of spin–orbit coupling go smoothly over into the zero spin–orbit case, as can be seen by expressing the order parameter in the form

$$\Delta^\dagger(\underline{k})\, \Delta(\underline{k}) \;=\; \left| D(\underline{k}) \right|^2 + \left(\vec{m}(\underline{k}) \,.\, \vec{d}\,(\underline{k}) \right) \left(\vec{d}^{\,*}(\underline{k}) \,.\, \vec{m}(\underline{k}) \right) . \tag{10.77}$$

With the use of the Pauli identity, this procedure yields the same expression for the quasi–particle eigenvalues as Eqn. (10.60), but in which $\vec{d}\,(\underline{k})$ is merely replaced by $\vec{d}\,(\underline{k})\ g(\underline{k})$. Thus, most of the formal results for the superconducting quasi–particles found without spin–orbit coupling also hold when it is present. In particular, one expects that the characteristic energy dependence of the superconducting quasi–particle density of states will be unaffected by spin–orbit scattering.

Quasi–Particle Density of States

The density of states for single quasi–particle excitations for anisotropic superconducting states have distinctly different forms which are determined by whether the gap is nodeless, has isolated nodes, or lines of nodes and also the slope with which the gap falls to zero. The quasi–particle density of states $\rho_{qp}(E)$ is given by

$$\rho_{qp}(E) \ = \ \frac{1}{2} \sum_{\underline{k},\pm} \delta(\ E \ \pm \ E_{\sigma,\underline{k}}\ ) \ . \tag{10.78}$$

On assuming singlet s–wave pairing, one finds the BCS result

$$\rho_{BCS}(E) \ = \ \rho(\mu) \ \frac{|\ E\ |}{\sqrt{E^2 \ - \ |\ \Delta_0\ |^2}} \tag{10.79}$$

for $|E| > \Delta_0$, otherwise $\rho_{BCS}(E) = 0$. Here $\rho(\mu)$ is the normal phase density of states that has been assumed to be constant near the Fermi energy and $D(k_F) = \Delta_0$. Since this s–wave phase shows a gap of width $2\ |\Delta_0|$ all the way around the position of the normal state Fermi surface, a number of physical quantities show simple exponentially activated behavior in the low temperature regime where the temperature dependence of the superconducting gap is small. For the anisotropic singlet $d_{x^2-y^2}$ pairing, the density of states is given by

$$\rho_{d_{x^2-y^2}}(E) \ = \ \frac{\rho(\mu)\ |E|}{4\pi} \int_0^{2\pi} d\phi \int_0^{\pi} d\theta \frac{\sin\theta}{\sqrt{E^2 \ - \ |\Delta_0|^2 \sin^4\theta \cos^2 2\phi}} \ . \tag{10.80}$$

As the order parameter vanishes on two great circles, $\cos 2\phi = 0$, on the Fermi surface, the density of states is proportional to $E\ \ln E$ as $E/\Delta_0 \rightarrow 0$. The $d_{2z^2-x^2-y^2}$ order parameter of a cubic material also has two lines of nodes, which results in the density of states

$$\rho_{d_{2z^2-x^2-y^2}}(E) \ = \ \frac{\rho(\mu)\ |E|}{2} \int_0^{\pi} d\theta \frac{\sin\theta}{\sqrt{E^2 \ - \ \frac{1}{4}\ |\ \Delta_0\ |^2\ (\ 1 \ - \ 3\cos^2\theta\ )^2}} \tag{10.81}$$

that also tends to zero linearly for small E. The quasi–particle density of states for these particular singlet phases are shown in Fig. 10.22. The quasi–particle density of states for the phases $d_{x,y}$, $d_{x,z}$ and $d_{y,z}$ should be identical

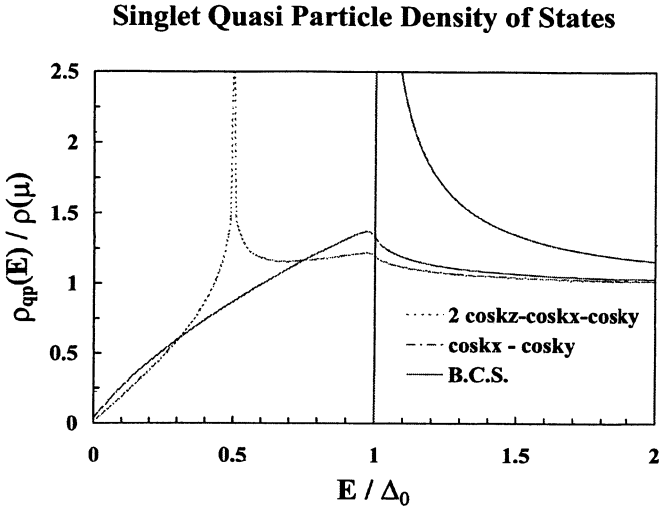

Fig. 10.22. The quasi–particle density of states $\rho_{qp}(E)$ for selected singlet superconducting phases, in the clean limit. The BCS s–wave state has a true gap in the quasi–particle density of states, and a singularity at the gap edge. The maximum superconducting gap is denoted by Δ_0. The d–wave phases have states with energies below Δ_0

with $\rho_{d_{x^2-y^2}}(E)$. For an isotropic system, the most stable d–wave phase [127] corresponds to a linear combination of the even m order parameters

$$D(\hat{k}) \propto \left[\frac{1}{\sqrt{2}} Y_0^2(\hat{k}) + \frac{1}{2} \left(Y_2^2(\hat{k}) - Y_{-2}^2(\hat{k}) \right) \right] \tag{10.82}$$

which only has point nodes. Therefore, the quasi–particle density of states varies as E^2 for small E, as shown in Fig. 10.23.

For triplet pairing, the differing node structures yield different forms for the quasi–particle density of states. The density of states is given in terms of an integration over the direction of $\underline{k}$,

$$\rho_{S=1}(E) = \frac{1}{8\pi} \rho(\mu) \int d\Omega \sum_{\sigma} Re \left[\frac{|E|}{\sqrt{E^2 + |\vec{d}(\hat{k})|^2 - \sigma |i \vec{d}(\hat{k}) \wedge \vec{d}^*(\hat{k})|}} \right] . \tag{10.83}$$

We shall describe the relation between the order parameter and the quasi–particle density of states for the well known p–wave states. The BW state, having an isotropic gap and no nodes, has the same density of states as the singlet s–wave phase given by the BCS expression, but where Δ_0 is given by the magnitude of $\vec{d}$ at the position of the normal state Fermi surface.

The ABM state order parameter given in spherical polar coordinates is $\vec{d} = \hat{z}\,\Delta_0\,\sin\theta\,e^{i\,\phi}$, and so the quasi–particle density of states in the ABM phase is found from

$$\rho_{ABM}(E) = \frac{\rho(\mu)\,|E|}{4\pi}\int_0^{2\pi} d\phi \int_0^{\pi} d\theta \frac{\sin\theta}{\sqrt{E^2 - |\,\Delta_0\,|^2\,\sin^2\theta}}$$
$$= \frac{\rho(\mu)\,E}{2\Delta_0}\,\ln\left|\frac{E + \Delta_0}{E - \Delta_0}\right| . \tag{10.84}$$

Thus, the density of states in the ABM phase has a weak logarithmic singularity at $E = \Delta_0$ and falls to zero as $E \to 0$ like E^2, due to the presence of isolated nodes. In the polar state, $\vec{d} = \hat{z}\,\Delta_0\,\cos\theta$, so the density of states is given by

$$\rho_{p_z}(E) = \frac{\rho(\mu)\,|E|}{4\pi}\int_0^{2\pi} d\phi \int_0^{\pi} d\theta \frac{\sin\theta}{\sqrt{E^2 - |\,\Delta_0\,|^2\,\cos^2\theta}}$$
$$= \frac{\pi\,\rho(\mu)\,|E|}{2\Delta_0} \qquad \Delta_0 > |E|$$
$$= \frac{\rho(\mu)\,E}{\Delta_0}\,\arcsin\left[\frac{\Delta_0}{E}\right] \qquad \Delta_0 < |E| . \tag{10.85}$$

Thus, due to the presence of a line of nodes in the polar phase, the quasi–particle density of states at lower energies only falls to zero linearly in E, as $E \to 0$. This should be contrasted with the ABM phase, which has isolated point nodes where the density of states goes to zero quadratically with E. The larger density of states at low energies for polar phase with its line nodes compared with the ABM phase with its point nodes, is compensated by the decrease in the peak of the quasi–particle density of states. That is, the polar state only shows a slight enhancement at Δ_0 where the density of states only has a cusp, but the ABM state shows a divergence. The quasi–particle density of states for the singlet BCS state is shown together with the $d_{2z^2-x^2-y^2}$ state and the $d_{x^2-y^2}$ in Fig. 10.22. The singularities and cusps are due to the gaps having extremal points at the position of the normal state Fermi surface. The quasi–particle density of states for the triplet BW, ABM, and polar states are shown in Fig. 10.24. The low–energy behavior of these quasi–particle density of states are quite distinct, having different power law dependences in E. The different power laws are due to the differences in the node structure of the superconducting gap. These power law dependences may be expected to show up in thermodynamic properties far below T_c, albeit modified by the effects of impurity scattering and collective excitations.

Pair Breaking Impurities

In an s–wave superconductor, the effect of non–magnetic impurities is min-

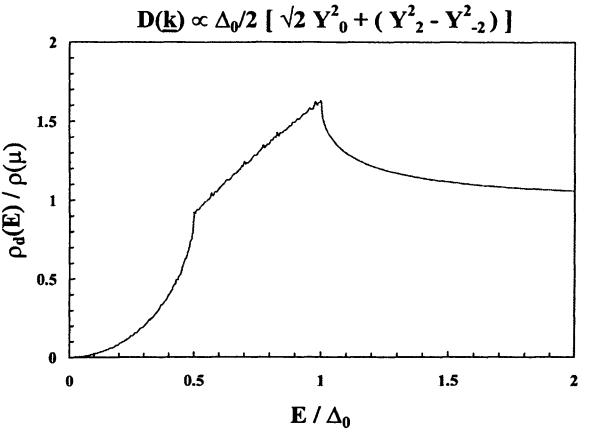

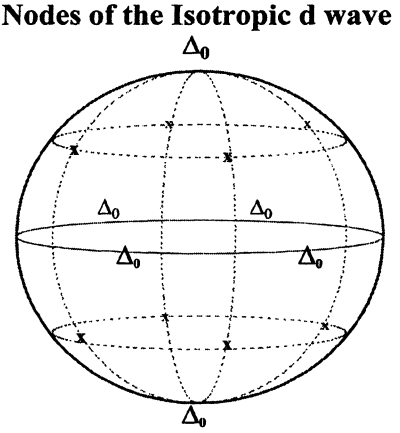

Fig. 10.23. The quasi-particle density of states $\rho_d(E)$ for an isotropic d-wave phase, with the order parameter $| D(\hat{k}) | = \frac{\Delta_0}{2} [(3 \cos^2\theta - 1)^2 + 3 \sin^2 2\varphi \sin^4\theta]^{\frac{1}{2}}$. Since the order parameter has eight point nodes as the quasi-particle density of states is proportional to E^2 for small E. Also, since the order parameter only attains its maximum value of Δ_0 at six isolated points, the density of states does not diverge

imal [6] and results in a pair weakening effect, which can be absorbed into

[6] The variation of T_c for Sn with a concentration of In impurities was studied by Coles [148]. The T_c showed a sharp initial drop which saturated for In concentrations of about 2%. The initial drop of T_c is attributed to the impurities destroying the anisotropy of the Fermi surface. This is not a violation of Anderson's theorem since it strictly only applies to systems with isotropic Fermi surfaces. The almost constant value of T_c which is found for In concentrations greater than 2% is a verification of Anderson's theorem.

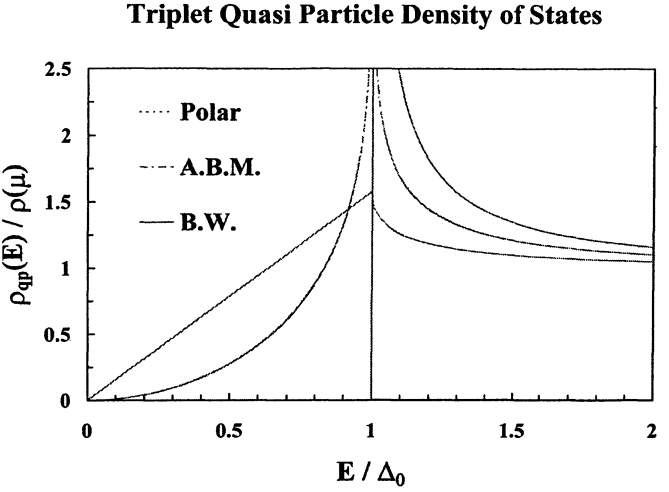

Fig. 10.24. The quasi–particle density of states $\rho_{qp}(E)$ for selected triplet p–wave superconducting states, in the clean limit. The density of states of the BW phase is identical to that of the BCS s–wave phase. The ABM phase and polar phases have states below Δ_0. The ABM or axial state shows a quadratic energy dependence for energies below Δ_0, while the polar state has a linear energy dependence

a reduction of the pairing potential or density of states. Anderson's theorem [149], which describes the effect of non–magnetic impurities in s–wave superconductors, can be stated as, " A static external perturbation, that neither breaks time reversal invariance nor produces a spatial variation of the order parameter, does not produce a change in the thermodynamic properties of a superconductor." Since the order parameters of anisotropic superconductors are inhomogeneous, Anderson's theorem no longer applies and the effect of impurities is analogous to that of magnetic impurities in s–wave superconductors [150, 151]. The analogy is complete in that significant concentrations of impurities may produce significant changes in the low–energy density of states leading to the removal of any remaining gaps. The changes in the low–energy variation of the quasi–particle density of states lead to variances in the power law temperature dependences expected from analysis of the simple node structures of clean materials [152–154].

The types of effect caused by non–magnetic impurities in anisotropic superconductors can be seen by examining the density of states in the superconducting state in which the impurity potential, U_0, is short–ranged and is treated as a small perturbation. The density of states can be obtained from the trace of the Green's function in the superconducting state. To treat the pairing in the superconducting state, one introduces the four by four matrix

Green's function $G(\underline{k};\tau)$ describing the four component fields, via

$$G(\underline{k};\tau) \;=\; -\,\frac{1}{\hbar}\;\; <\mid \hat{T}\;\Psi(\underline{k},\tau)\;\Psi^{\dagger}(\underline{k},0)\mid >\,, \tag{10.86}$$

where $\hat{T}$ is Wick's time ordering operator. The upper and lower two by two diagonal blocks have matrix elements that are related to the usual Green's functions

$$G_{\alpha,\beta}(\underline{k},\underline{k}';\tau) \;=\; -\,\frac{1}{\hbar}\;\; <\mid \hat{T}\;a_{\underline{k},\alpha}(\tau)\;a^{\dagger}_{\underline{k}',\beta}(0)\mid >\;. \tag{10.87}$$

The upper and lower two by two off–diagonal blocks represent the anomalous Green's functions, as introduced by Gor'kov [147]. The elements of the anomalous Green's functions are written as

$$F_{\alpha,\beta}(\underline{k},\underline{k}';\tau) \;=\; \frac{1}{\hbar}\;\; <\mid \hat{T}\;a_{\underline{k},\alpha}(\tau)\;a_{-\underline{k}',\beta}(0)\mid > \tag{10.88}$$

and

$$F^{\dagger}_{\alpha,\beta}(\underline{k},\underline{k}';\tau) \;=\; \frac{1}{\hbar}\;\; <\mid \hat{T}\;a^{\dagger}_{-\underline{k},\alpha}(\tau)\;a^{\dagger}_{\underline{k}',\beta}(0)\mid >\;. \tag{10.89}$$

Within the mean–field approximation, the Fourier Transform of the Green's functions are given by the solutions of the coupled equations

$$\begin{aligned}&(\;i\;\hbar\,\omega_n\;-\;e(\underline{k})\;+\;\mu\;)\;G_{\alpha,\beta}(\underline{k},\underline{k}';i\hbar\omega_n)\;+\;\sum_{\gamma}\;\Delta_{\alpha,\gamma}(\underline{k})\;F^{\dagger}_{\gamma,\beta}(\underline{k},\underline{k}';i\hbar\omega_n)\\&\;=\delta_{\alpha,\beta}\;\delta(\underline{k}-\underline{k}')\end{aligned} \tag{10.90}$$

and

$$\begin{aligned}&(\;i\;\hbar\,\omega_n\;+\;e(\underline{k})\;-\mu\;)\;F^{\dagger}_{\alpha,\beta}(\underline{k},\underline{k}';i\hbar\omega_n)\;+\;\sum_{\gamma}\;\Delta^{*}_{\alpha,\gamma}(\underline{k})\;G_{\gamma,\beta}(\underline{k},\underline{k}';i\hbar\omega_n)\\&\;=0\end{aligned} \tag{10.91}$$

In the unitary states, these equations have the solution,

$$\begin{aligned}&G_{\alpha,\beta}\;(\underline{k},\underline{k}';i\hbar\omega_n)\;=\\&-\;\frac{(\;i\;\hbar\,\omega_n\;+\;e(\underline{k})\;-\;\mu\;)}{\hbar^2\omega_n^2\;+\;(\;e(\underline{k})\;-\;\mu\;)^2\;+\;\Delta^{\dagger}(\underline{k})\;\Delta(\underline{k})}\;\delta_{\alpha\beta}\;\delta(\underline{k}-\underline{k}')\end{aligned} \tag{10.92}$$

and

$$F^{\dagger}_{\alpha,\beta}(\underline{k},\underline{k}';i\hbar\omega_n) = +\frac{\Delta^{*}_{\alpha,\beta}(\underline{k})}{\hbar^2\omega_n^2+(\;e(\underline{k})-\mu\;)^2+\Delta^{\dagger}(\underline{k})\Delta(\underline{k})}\delta(\underline{k}-\underline{k}')\;. \tag{10.93}$$

The order parameter is determined from the non–linear equation

$$\Delta_{\alpha,\beta}(\underline{k}) \;=\; -\,k_B\,T\sum_{n,\underline{q}}\sum_{\mu,\nu} V(\underline{k},\underline{q})_{\beta,\alpha;\mu,\nu}\;F_{\mu,\nu}(\underline{q},\underline{q};i\hbar\omega_n) \tag{10.94}$$

which yields Δ as a function of temperature. We assume a low concentration of impurities, c_0, that are randomly distributed and act as point scatterers. The matrix self–energy can be calculated as

$$\Sigma(\underline{k};i\hbar\omega_n) \;=\; c_0\sum_{\underline{p}} U_0\;\rho_4\;G(\underline{p};i\hbar\omega_n)\;\rho_4\;U_0\;, \tag{10.95}$$

where ρ_4 is the 4×4 Dirac matrix that is written in block diagonal form as

$$\rho_4 \;=\; \begin{pmatrix} I & 0 \\ 0 & -I \end{pmatrix}. \tag{10.96}$$

Here, I is the unit two by two matrix. The Green's functions have to be calculated self–consistently. In the unitary case, the diagonal and non–diagonal elements in the self–energy can be evaluated and do give rise to a renormalization of the frequency and order parameter. The renormalizations are given by the solution of the coupled equations

$$\begin{aligned} i\,\hbar\,\tilde{\omega}_n &= i\,\hbar\,\omega_n + c_0\sum_{\underline{p}} U_0^2\;\frac{i\,\hbar\,\tilde{\omega}_n\;+\;(\,e(\underline{p})\;-\;\mu\,)}{\hbar^2\tilde{\omega}_n^2\;+\;(\,e(\underline{p})-\mu\,)^2\;+\;\tilde{\Delta}^{\dagger}(\underline{p})\;\tilde{\Delta}(\underline{p})}\;, \\ \tilde{\Delta}_{\alpha,\beta}(\underline{k}) &= \Delta_{\alpha,\beta}(\underline{k}) + c_0\sum_{\underline{p}} U_0^2\frac{\tilde{\Delta}_{\alpha,\beta}(\underline{p})}{\hbar^2\tilde{\omega}_n^2+(e(\underline{p})-\mu)^2+\tilde{\Delta}^{\dagger}(\underline{p})\tilde{\Delta}(\underline{p})}\;. \end{aligned} \tag{10.97}$$

The energy $e(\underline{p})$ is odd about the Fermi energy and so, for systems with electron–hole symmetry, the term proportional to $e(\underline{p})-\mu$ drops out in the diagonal parts of the self–energy matrix. Thus, impurity scattering only results in a frequency dependent renormalization of ω_n. For s–wave scattering, subject to Anderson's theorem, the off–diagonal term produces an identical frequency dependent renormalization of the gap. Thus, for s–wave scattering in the Born approximation, one finds the explicit form for the renormalizations

$$\begin{aligned} i\tilde{\omega}_n &= i\omega_n + \pi c_0 U_0^2\rho(\mu)\frac{i\tilde{\omega}_n}{\sqrt{\hbar^2\tilde{\omega}_n^2+|\tilde{D}_s(k_F)|^2}}\;, \\ \tilde{D}_s(\underline{k}) &= D_s(\underline{k}) + \pi c_0 U_0^2\rho(\mu)\frac{\tilde{D}_s(k_F)}{\sqrt{\hbar^2\tilde{\omega}_n^2+|\tilde{D}_s(k_F)|^2}}\;. \end{aligned} \tag{10.98}$$

Hence the ratio of $\tilde{\omega}_n/\tilde{D}_s$ is unchanged from the un–renormalized value ω_n/D_s. Furthermore, the quasi–particle density of states is unaltered since it only depends upon the ratio $\tilde{\omega}_n/\tilde{D}_s$. The equation that determines the order parameter remains unchanged. Thus, the critical temperature of an s–wave superconductor is not substantially reduced by the presence of the impurities. These conclusions are in accord with Anderson's theorem.

For triplet pairing, the gap is an odd function of $\underline{p}$ and so, due to the summation over the direction of $\underline{p}$, the off–diagonal self–energy vanishes identically. Hence, we have

$$i\,\tilde{\omega}_n = i\,\omega_n + \pi\,c_0\,U_0^2\,\rho(\mu)\int \frac{d\Omega_{\underline{p}}}{4\,\pi}\,\frac{i\,\tilde{\omega}_n}{\sqrt{\hbar^2\tilde{\omega}_n^2 + |\,\vec{\tilde{d}}(\underline{p})\,|^2}}$$

and

$$\vec{\tilde{d}}(\underline{k}) = \vec{d}(\underline{k})\,. \tag{10.99}$$

Therefore, Anderson's theorem does not apply to triplet superconductors. The effect of impurities reduce the critical temperature T_c, as can be seen from the linearized gap equation

$$1 = k_B\,T_c\,\pi\sum_{n=0}^{n_c}\frac{<V(k_F,k_F)>\,\rho(\mu)}{|\,\hbar\,\omega_n\,| + \pi\,c_0\,|\,U_0\,|^2\,\rho(\mu)}\,, \tag{10.100}$$

where the summation is cut–off at n_c, which is determined by a frequency range ω_c in which the pairing interaction is attractive $\hbar\,\omega_c = (2n_c + 1)\,\pi\,k_BT$, and $<V(k_F,k_F)>$ is the Fermi surface averaged value of the pairing interaction. The summation depends logarithmically on the cut off. The linearized gap equation can be re–written as

$$\frac{1}{k_B\,T_c\,\pi\,<V(k_F,k_F)>\,\rho(\mu)} = \sum_{n=0}^{n_c}\frac{1}{|\,\hbar\,\omega_n\,|} + \sum_{n=0}^{\infty}\left(\frac{1}{|\,\hbar\,\omega_n\,| + \pi\,c_0\,|\,U_0\,|^2\,\rho(\mu)} - \frac{1}{|\,\hbar\,\omega_n\,|}\right). \tag{10.101}$$

The critical temperature obtained for the dirty system should be compared with the expression for the critical temperature T_{c0} obtained for the clean system

$$1 = k_B\,T_{c0}\,\pi\sum_{n=0}^{n_c}\frac{<V(k_F,k_F)>\,\rho(\mu)}{|\,\hbar\,\omega_n\,|}\,. \tag{10.102}$$

On identifying the $\frac{2\,\pi}{\hbar}\,c_0\,|\,U_0\,|^2\,\rho(\mu)$ as being equal to the impurity scattering rate $\frac{1}{\tau}$ as evaluated in the Born approximation, and using the expression for

T_{c0} for the clean system, one finds that non–magnetic impurities depress T_c in an anisotropic superconductor according to

$$\ln\left(\frac{T_{c0}}{T_c}\right) = \psi\left(\frac{1}{2} + \frac{\hbar}{4\,\pi\,k_B T_c \tau}\right) - \psi\left(\frac{1}{2}\right), \tag{10.103}$$

where ψ is the digamma function. This formula is similar to the formula derived by Abrikosov and Gor'kov that describes the depression of T_c caused by spin–flip scattering by impurities in an s–wave superconductor [150]. The analogy to scattering by paramagnetic impurities in an s–wave superconductor is complete in that large enough impurity scattering can also lead to gapless superconductivity.

We shall explicitly examine the transition to the gapless phase for some triplet phases [153]. On analytically continuing from $i\,\hbar\,\omega_n \rightarrow E + i\delta$ one finds

$$\lim_{i\hbar\omega_n \rightarrow E} Im\left[\, i\,\hbar\,\tilde{\omega}_n \,\right] = \pi\, c_0 \mid U_0 \mid^2 \rho_{qp}(E)\,, \tag{10.104}$$

where the self consistency equation for $s = i\,\hbar\,\tilde{\omega}_n$ is given by

$$s - E = i\,\frac{\hbar}{2\,\tau}\int \frac{d\Omega_{\underline{k}}}{4\,\pi}\,\frac{s}{\sqrt{s^2 - \mid \vec{d}(\hat{k}) \mid^2}}\,. \tag{10.105}$$

For the Balian–Werthamer phase, where $\vec{d}\,(\underline{k}) = \Delta_0\,\hat{k}$, the above equation reduces to

$$s - E = i\,\frac{\hbar}{2\,\tau}\,\frac{s}{\sqrt{s^2 - \mid \Delta_0 \mid^2}}\,. \tag{10.106}$$

The gap energy is the threshold value of E_g below which s is real and is given by the critical value of s determined from the equation

$$\frac{\partial E}{\partial s} = 1 + i\,\frac{\hbar}{2\,\tau}\,\frac{\mid \Delta_0 \mid^2}{(\,s^2 - \mid \Delta_0 \mid^2\,)^{\frac{3}{2}}} = 0\,. \tag{10.107}$$

The solution for s results in the gap being given by

$$E_g = \Delta_0\left[\,1 - \left(\frac{\hbar}{2\,\tau\,\Delta_0}\right)^{\frac{2}{3}}\,\right]^{\frac{3}{2}}. \tag{10.108}$$

The gap is reduced by increasing the impurity scattering rate, and the gap first falls to zero when $\frac{\hbar}{2\,\tau} = \Delta_0$ in the regime where Δ_0 and T_c are still finite. For larger impurity scattering rates, the BW phase is gapless.

For the ABM phase, where $\vec{d}\,(\underline{k}) = \hat{z}\,\Delta_0\,\sin\theta\,e^{i\,\phi}$, one finds

$$s - E = i\,\frac{\hbar}{4\,\tau\,\Delta_0}\,s\,\ln\left(\frac{s + \Delta_0}{s - \Delta_0}\right). \tag{10.109}$$

The density of states at $E = 0$ is found from the solution for $s(0)$

$$s(0) = 0 \ , \qquad for \quad \left(\frac{\hbar}{4\,\tau\,\Delta_0}\right) < \frac{1}{\pi}$$
$$s(0) = i\,\Delta_0\,\cot\left(\frac{2\,\tau\,\Delta_0}{\hbar}\right) \ , \qquad for \quad \left(\frac{\hbar}{4\,\tau\,\Delta_0}\right) > \frac{1}{\pi} \tag{10.110}$$

which shows the transition to a gapless phase for large impurity scattering rates. In the gapless phase, the zero energy quasi–particle density of states is given by

$$\rho_{ABM}(0) = -\,\frac{2\,\tau\,\Delta_0}{\hbar}\,\rho(\mu)\,\cot\left(\frac{2\,\tau\,\Delta_0}{\hbar}\right) \qquad for \quad \left(\frac{\hbar}{4\,\tau\,\Delta_0}\right) > \frac{1}{\pi}\,. \tag{10.111}$$

For finite E, the equation for $s(E)$ can be solved iteratively in powers of E. For low impurity scattering rates, one finds the solution

$$s = \frac{E}{\left[1 - \left(\frac{\pi\,\hbar}{4\,\tau\,\Delta_0}\right)\right]} + i\,\frac{E^2\,\hbar}{2\,\tau\,\Delta_0^2}\,\frac{1}{\left[1 - \left(\frac{\pi\,\hbar}{4\,\tau\,\Delta_0}\right)\right]^3} + \ldots \tag{10.112}$$

which yields a density of states which varies as E^2 for low energies

$$\rho_{ABM}(E) = \rho(\mu)\left(\frac{E}{\Delta_0}\right)^2 \frac{1}{\left[1 - \left(\frac{\pi\,\hbar}{4\,\tau\,\Delta_0}\right)\right]^3} + \ldots \tag{10.113}$$

due to isolated point nodes. The coefficient of the E^2 term in the quasi–particle density of states diverges at a critical value of the scattering rate

$$1 = \left(\frac{\pi\,\hbar}{4\,\tau\,\Delta_0}\right) \tag{10.114}$$

at which point the ABM phase becomes gapless as the isolated nodes grow into regions of finite area.

For the polar phase, a similar analysis yields

$$s - E = i\left(\frac{\hbar}{2\,\tau\,\Delta_0}\right) s\,\arcsin\left(\frac{\Delta_0}{s}\right). \tag{10.115}$$

This has the solution at $E = 0$ which is always given by

$$s(0) = i\,\frac{\Delta_0}{\sinh\left(\frac{2\,\tau\,\Delta_0}{\hbar}\right)} \tag{10.116}$$

and hence, the quasi–particle density of states is

$$\rho_{p_z}(0) = \rho(\mu) \frac{\left(\frac{2\,\tau\,\Delta_0}{\hbar}\right)}{\sinh\left(\frac{2\,\tau\,\Delta_0}{\hbar}\right)} . \tag{10.117}$$

This shows that the critical impurity scattering rate for producing a gapless phase is zero. Thus, the line nodes grow into regions of finite area, and the superconductivity becomes gapless, even for the slightest concentration of impurities. The calculated quasi–particle density of states for these three p–wave states are shown in Fig. 10.25, for various impurity scattering rates.

The above analysis were based on the assumption that the impurity scattering potential is sufficiently weak so that the Born approximation is adequate. However, in heavy–fermion systems, the large value of the quasi–particle density of states invalidates the above approach, as was first pointed out by Pethick and Pines [155]. The increased strength of the scattering mechanism can lead to marked modifications of the low–energy variation of the quasi–particle density of states. Within the limit of low impurity concentration, one can sum the series of multiple scattering processes involving the same impurity to yield the T–matrix result for the impurity self–energy

$$\Sigma(\underline{k}; i\hbar\omega_n) = c_0 \sum_{\underline{p}} U_0\, \rho_4\, G(\underline{p}; i\hbar\omega_n) \left[1 - \sum_{\underline{p}''} U_0\, \rho_4\, G(\underline{p}''; i\hbar\omega_n) \right]^{-1} \rho_4\, U_0 \tag{10.118}$$

A dimensionless measure of the strength of the scattering from a single impurity is given by the normal state phase shift δ_0, which is given by

$$\tan\,\delta_0 = -\,\pi\, U_0\, \rho(\mu) \tag{10.119}$$

for the case of low–energy scattering and electron–hole symmetry. The limit of resonant scattering ($\delta_0 = \pm\,\frac{\pi}{2}$) can be treated similarly to the weak scattering results, and the quasi–particle density of states is given by

$$\rho_{qp}(E) = \rho(\mu)\; Re\left[\int \frac{d\Omega_{\underline{k}}}{4\,\pi} \frac{s}{\sqrt{s^2 - |\,\vec{d}(\hat{k})\,|^2}} \right], \tag{10.120}$$

where $s(E)$ is found from

$$\frac{c_0}{\pi\,\rho(\mu)} \frac{i}{s - E} = \int \frac{d\Omega_{\underline{k}}}{4\,\pi} \frac{s}{\sqrt{s^2 - |\,\vec{d}(\hat{k})\,|^2}} . \tag{10.121}$$

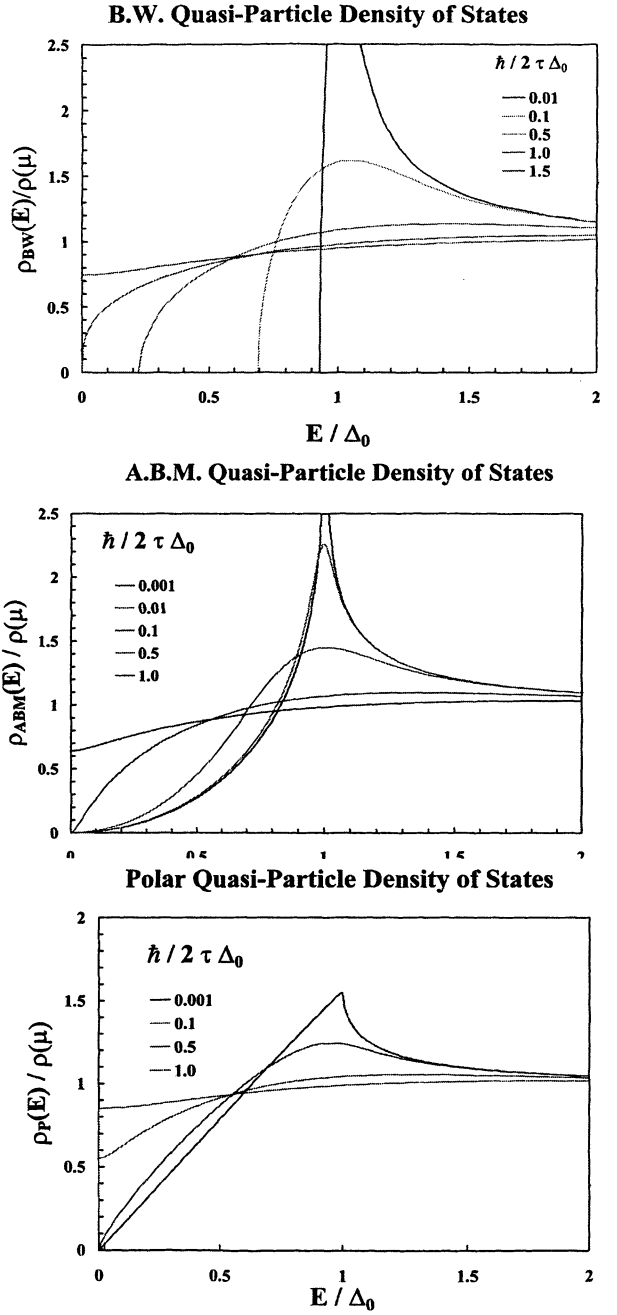

Fig. 10.25. The quasi–particle density of states for various phases of p–wave superconductors, and different strengths of the impurity scattering rate Γ. The impurity scattering rate is evaluated in the Born approximation [After Ueda and Rice (1985), [153]]

In this limit, the low–energy density of states is different from the density of states found in the Born approximation. For example, the consistency relation for the ABM state can be solved at $E = 0$ to yield

$$s(0) = i \frac{1}{\pi} \sqrt{\frac{c_0}{2\,\rho(\mu)\,\Delta_0}} \quad , \qquad for \quad 1 \gg |\, s(0)\,| \, . \tag{10.122}$$

Thus, the quasi–particle density of states is gapless for arbitrarily small concentrations of impurities and has the value

$$\rho_{ABM}(0) = \rho(\mu) \sqrt{\frac{c_0}{2\,\rho(\mu)\,\Delta_0}} \tag{10.123}$$

which is a non–analytic function of the concentration, c_0. This result for resonant scattering is in contrast to the Born approximation result for the ABM phase where there is a finite critical value of the impurity scattering rate. Furthermore, as shown in Fig. 10.26, for resonant impurity scattering, the ABM and polar states have low–energy maxima in the quasi–particle density of states [156]. As the order parameter is traceless, the balance between the diagonal and off–diagonal self–energy terms is also destroyed in the anisotropic singlet pairing phases. Generally, the different scaling behavior of the frequency and gap destroys the invariance of the quasi–particle density of states and leads to an increase in the number of low–energy states. Thereby, the simple power law dependences of the quasi–particle density of states and the concomitant power law dependences of the low temperature thermodynamic properties that are expected from the symmetry of the order parameter are spoiled. However, the power law dependences expected from the quasi–particle excitation spectrum could also be spoilt by the effect of collective excitations. The manner in which collective excitations affect the spectrum of excitations in the normal state and in the superconducting state is much less well understood.

10.3 Properties of the Normal State

Many properties of the normal state of heavy–fermion materials definitively show the existence of a characteristic temperature that marks the cross–over from the high temperature local moment phase to the low temperature non–magnetic phase. In the literature on Ce heavy–fermion materials, this characteristic temperature is often referred to as the Kondo temperature, T_K, since the high temperature phase shows properties characteristic of a set independent local moments that spin–flip scatter with the conduction electrons. In this high temperature regime, the local moments can be viewed in terms of the single–impurity Anderson model [157]. In the Anderson model, the local f states are broadened by the mixing with the conduction band

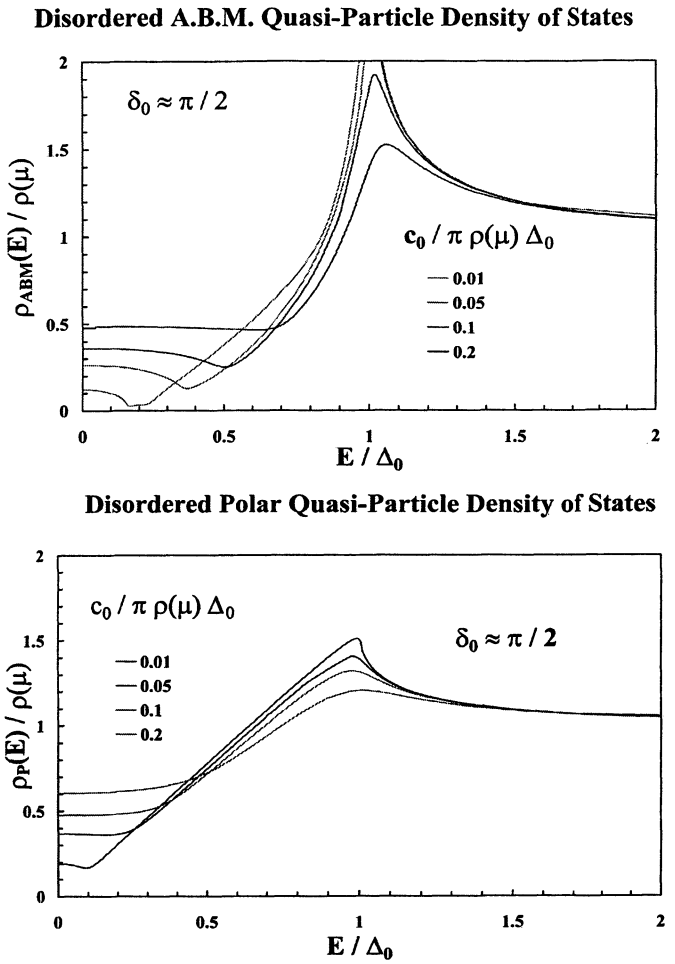

Fig. 10.26. The quasi–particle density of states for the ABM and polar p–wave superconducting phases, for different strengths of the impurity scattering. The scattering is treated in the T–matrix approximation. Resonant scattering occurs when the phase shift is given by $\delta_0 = \frac{\pi}{2}$, i.e., $\cot \delta_0 = 0.0$. The Born Approximation corresponds to the limit of large $\cot \delta_0$. [After Hirschfeld *et al.* (1986), [156]]

density of states. The width of the virtual bound state Δ is approximately given by the Fermi–Golden rule expression

$$\Delta = \pi \rho(\mu) \mid V \mid^2 , \tag{10.124}$$

where $\rho(\mu)$ is the conduction band density of states at the Fermi energy, and V is the hybridization matrix element. An on–site local Coulomb interaction U tends to prevent multiple occupancy of the f level. When $U > \Delta$ and when

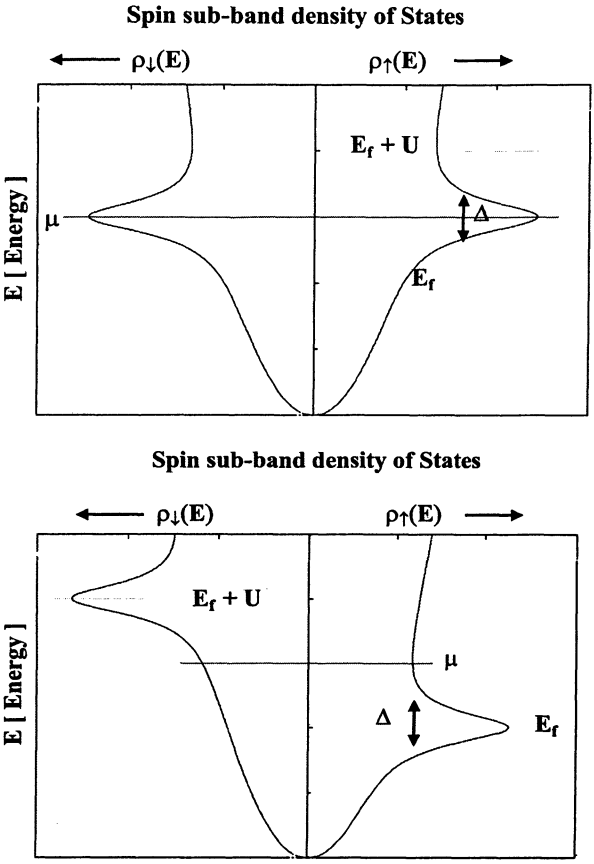

Fig. 10.27. The density of states of the single–impurity Anderson model, as calculated in the Hartree–Fock approximation. The density of states is composed of the sum of the conduction band contribution and a contribution from the f state on the impurity. In the mixed valent limit, shown in upper figure, the virtual bound state is unpolarized. The virtual bound state is located at the energy $E_f + U\, n_f/2$. In the Kondo limit where the local moment is present, the virtual bound state is spin split, as shown in lower figure. [After Anderson (1961), [157]]

the f level is almost singly occupied, a Hartree–Fock treatment [157] yields a solution which possesses a local magnetic moment. In the local moment or Kondo regime, the impurity f density of states is spin–split and broadened, as is shown in Fig. 10.27. However, this solution is only approximate since spin–rotational invariance has been broken locally, and the residual interactions between the local moment and the conduction electrons are expected to flip the local moment and hence, restore the broken symmetry. These residual interactions were investigated by Schrieffer and Wolf [158], who mapped the

local moment limit of the single–impurity Anderson model onto the single–impurity Kondo model. In the single–impurity Kondo model [159], the repeated spin–flip scattering between the local moment and the conduction electrons results in the formation of a singlet bound state. The properties of the Kondo model show scaling with the energy of the bound state which is $k_B T_K$. The Kondo temperature for a spin one–half impurity is estimated to be of the order of

$$k_B\, T_K \;\sim\; \rho(\mu)^{-1}\, \exp\left[\, \frac{\pi\,(\,E_f\,-\,\mu\,)}{2\,\Delta}\,\right], \tag{10.125}$$

where E_f is the energy of a single electron in the f state of the isolated impurity. Due to the presence of the exponential factor, the Kondo temperature is expected to be much smaller than Δ. For temperatures above T_K, the bound state is thermally depopulated, and the high temperature properties may be adequately described by low order perturbation expansions [160]. However, as the temperature is decreased below the Kondo temperature, the resonant nature of the scattering increases and weak–coupling perturbation approximation fails, since the model scales to a strong–coupling fixed point [161,162]. Near this fixed point, the properties scale with T/T_K and are qualitatively described by a gas of non–interacting quasi–particles residing in a narrow virtual bound state of width $k_B T_K$ located near the Fermi energy (see Fig. 10.28). The exact Bethe–Ansatz solution [163–165] of the model shows that the low temperature properties are those of a local Fermi liquid. In the local Fermi liquid, the low temperature susceptibility is enhanced relative to the linear T coefficient of the specific heat by a factor that depends on the degeneracy, N, of the ground state magnetic configuration. For large degeneracies, the relative enhancement or Wilson ratio is simply $N/(\,N\,-\,1\,)$.

Although the Wilson ratio and the scaling property of the Kondo impurity model are in reasonable agreement with experimental results on dilute Ce systems, Nozières has questioned whether the results of the simple Kondo model can be directly applied to concentrated Ce compounds [166]. In particular, in the Kondo model the screening of a local moment only involves electrons within $k_B T_K$ of the Fermi–level. For a concentrated compound in which the moments on each f ion are screened by a number of conduction electrons localized around each of them, the number of conduction electrons required for screening is far greater than the number $k_B T_K \rho(\mu)$ allowed for by the solution of the single impurity model. If instead, one assumes that the screening electrons remain itinerant and only form a resonance instead of a bound state, the spin–flip interaction of the conduction electrons with the local moments may still produce a non–magnetic state in which the local moments are slowly fluctuating. That is, Nozières argument does not apply if the conduction electrons responsible for the screening remain itinerant [167]. In this case, one must abandon the purely local description at sufficiently low temperatures.

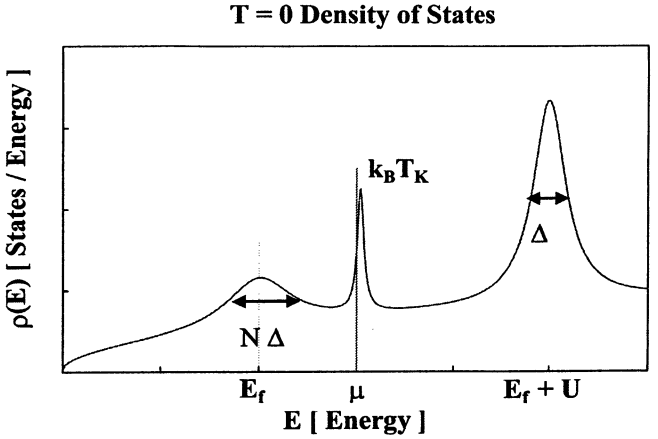

Fig. 10.28. A schematic plot of the $T = 0$ density of states for the N–fold degenerate single–impurity Anderson model, in the Kondo limit. The f contribution to the density of states has features at energies of E_f and $E_f + U$. In addition, at low temperatures, a narrow Kondo resonance of width $k_B T_K/N$ occurs at an energy $k_B T_K$ above the Fermi energy

It is more likely that the Kondo paradigm contains the generic physics of local electronic correlations observed in the heavy–fermion materials. This has lent credence by the recent discovery, based on the infinite dimensional limit $d \rightarrow \infty$, that strongly correlated metals can have physical properties which qualitatively resemble those of localized magnetic impurities [168–170]. The limit $d \rightarrow \infty$ of most many–body models is usually exactly soluble via mean–field theory and can be scaled such that it can be exactly mapped onto a non–trivial effective local impurity model. In the resulting dynamical mean–field theory, the local fluctuations on the neighboring lattice sites are treated as being governed by an effective single–impurity Anderson model in which the hybridization to the conduction electron density of states has to be determined self–consistently [171,172]. This theoretical approach is more promising than that of the single impurity Kondo model, as it decouples the temperature scale of the resonant magnetic scattering in the high temperature regime, and the temperature scale below which the low temperature Fermi liquid forms [173]. In addition to the questions posed by Nozières, it is quite unclear how the U compounds could be directly described by simple Kondo impurity models in which the $5f$ states are assigned as belonging to a unique magnetic configurations. It seems more likely that the U systems may be described by more general many–body models such as multi–band Hubbard models, which may also be described by dynamical mean–field theory. The application of dynamical mean–field theory to heavy–fermion systems is limited by its failure to describe non–local correlations. As dynamical mean–field theory omits the effect of non–local spin–fluctuations, and as quantum

critical points occur when the non–local magnetic correlations dominate over the local spin–fluctuations [88], dynamical mean–field theory is expected to be inadequate close to quantum critical points.

For some heavy–fermion compounds, the characteristic temperatures T_K inferred from thermodynamic, transport, magnetic and other spectroscopic probes, are quite consistent. However, even for these systems, the low temperature thermodynamic properties do show the existence of other low–energy scales that are often attributed either to Fermi liquid formation or the onset of spatial coherence or spatial magnetic correlations. In the quantum critical point description, this coherence temperature is identified as the cross–over temperature at which the physics of the quantum critical point gives way to the physics of the Fermi liquid fixed point [175, 176]. In a phase space that is extended, as for instance when pressure is applied, the line of cross–over points is experimentally accessible since physical quantities should exhibit extrema on parallel lines. The phenomenon of coherence is most clearly manifested in transport phenomena, though it does also show up directly in high resolution spectroscopic measurements on single crystals [177]. The phenomenon of coherence falls beyond the scope of the exactly soluble single impurity Kondo models or dynamical mean–field theory and, therefore, still lacks an adequate theoretical description.

10.3.1 Thermodynamic Properties

The Specific Heat

The low temperature specific heats of the normal state phase of heavy–fermion systems are dramatically different from ordinary metals. The extrapolated value of the ratio of the specific heat to the temperature

$$\lim_{T \to 0} \frac{C(T)}{T} = \gamma \tag{10.126}$$

can be of the order of 1 J / mole K^2, which is 1000 times larger than the corresponding ratio for Cu. In many heavy–fermion systems, notably UBe_{13}, $CeCu_2Si_2$, $CeAl_3$ and $CeCu_6$, the ratio $C(T)/T$ shows an increase with decreasing temperatures, at low temperatures, and shows signs of saturation. For UBe_{13} and $CeAl_3$ the upturn starts at a scale of the order of 10 K. The heat capacity of UBe_{13} is shown in Fig. 10.29. The large magnitudes of the extrapolated specific heat coefficients γ are attributed in part to the flat quasi–particle dispersion relation arising from the small hybridization between the f orbitals and the states on the ligand atoms and in part due to the average of the quasi–particle mass enhancement, $Z_{\underline{k}}$. The assignment of the large value of the γ coefficient as being due to enhanced quasi–particles is found to be consistent with de Haas–van Alphen measurements. For UPt_3 and UAl_2, the specific heat has the form

$$C(T) = \gamma T + \delta T^3 \ln T + \beta T^3 \tag{10.127}$$

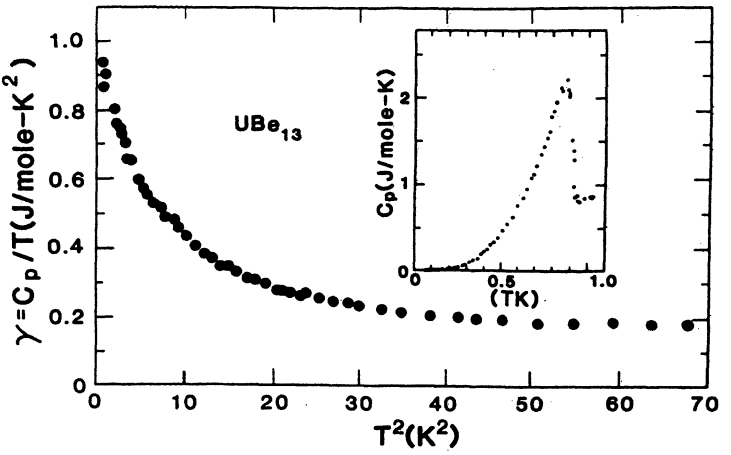

Fig. 10.29. The specific heat in the normal state of UBe_{13} divided by temperature as a function of T^2. [After Ott *et al.* (1983) [4]]. Note the upturn at low temperatures and the large extrapolated value at $T = 0$ as compared to the value of 0.07 mJ/mole/K^2 for Cu

for temperatures up to 20 K. The low temperature specific heat of UPt_3 and the fit to this form are shown in Fig. 10.30. The above form and the sign of δ are compatible with a Fermi liquid that exhibits large amplitude, long wavelength, collective fluctuations such as ferromagnetic spin–fluctuations [88,89,94,95]. The values of the coefficients β are also quite large compared with values expected from phonon contributions in normal metals and probably could also have a significant electronic component. The entropies calculated from the enhanced low temperature specific heats have values comparable to those of a disordered set of independent moments on the f ions, suggesting a magnetic origin of the enhancement. This conclusion is strengthened for UAl_2 by the finding [178,179] that an applied magnetic field actually suppresses the low temperature upturn in C/T.

An unusual feature of the specific heat of some heavy–fermion systems is that they seem to indicate that the fluctuations are of a local character and reside mainly on the f ions. For example, on substituting La for Ce in $CeCu_6$, the temperature dependence of the specific heat of $Ce_xLa_{1-x}Cu_6$ per Ce ion is independent of x, for $1 > x > 0.5$, indicating that the large specific heat of this Ce compound is dominated by local processes [180]. A similar conclusion was previously drawn from dilution studies of $CePb_3$ [181], where it was found that the properties simply scale with the Ce concentration. The specific heats per mole Ce of diluted $CePb_3$ and $CeCu_6$ are shown in Fig. 10.31. This type of scaling behavior should be contrasted with the behavior found in dilution studies of $CeCu_2Si_2$, $CeAl_3$ and UBe_{13}. In stoichiometric $CeAl_3$, the C/T ratio shows a small maximum around $T = 0.3$K [182], and on doping

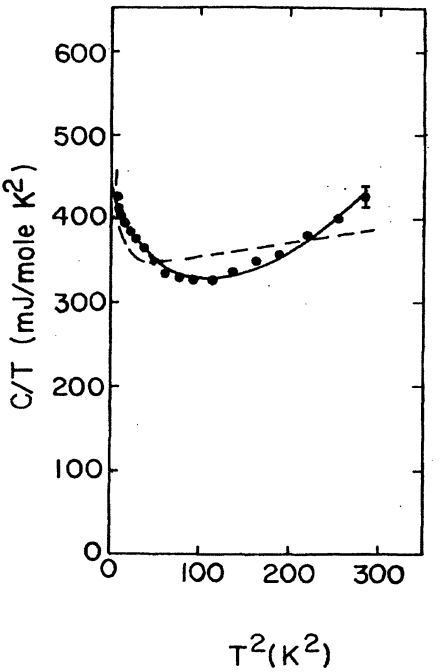

Fig. 10.30. The low temperature specific–heat ratio $C(T)/T$ versus T^2 for UPt_3. The solid line is a fit to $C(T) = \gamma T + \delta T^3 \ln T$. The dashed line is a fit to $\gamma T + \beta T^3 + \delta/T$. [After Stewart *et al.* (1984), [6]]

substitutionally for Ce with La, the peak moves up to higher temperatures. However, the Kondo temperature decreases with doping [183]. Calculations based on single impurity models show that the low temperature peak is not simply due to the Kondo effect in the presence of crystal fields [184, 185]. Therefore, it has been speculated that the peak is either due to the onset of magnetic correlations or is a manifestation of structure in the quasi–particle density of states caused by the coherence of the lattice.

There exists a similar low temperature peak in the specific heat of UBe_{13} near $T = 2$K which is suppressed and moves towards lower temperature on substituting 3 percent of U by Th [186]. Substitutional doping on the U sites of UBe_{13} by a few percent of impurities leads to a rapid decrease in the γ value. The introduction of roughly 3 % concentration of impurities leads to a depression of γ by roughly 30 %. These studies suggest that the value of γ crucially depends on the U – Be separation. Stoichiometric $CeCu_2Si_2$ seems to be on the critical phase boundary between a phase that exhibits magnetic correlations at low temperatures, the A phase and a phase that superconducts at low temperatures, the S phase. A generalized phase diagram of $CeCu_2Si_2$ is shown in Fig. 10.32. The A and S phases seem to coexist in stoichiometric

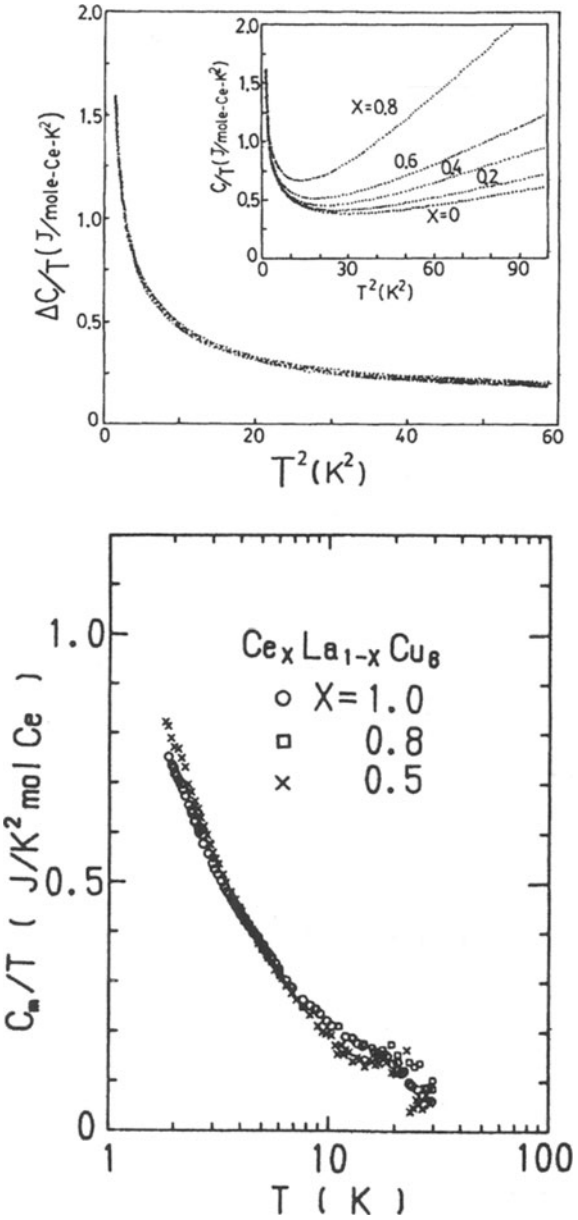

Fig. 10.31. (a) The excess specific heat per mole Ce, ΔC versus T^2 for $Ce_{1-x}La_xPb_3$ samples with $x = 0.0$, 0.2, 0.4, 0.6 and 0.8. Insert: The total specific heat per molar formulae unit divided by T for the same samples. [After Lin *et al.* (1987), [181]]. (b) The specific heat per mole Ce for $Ce_xLa_{1-x}Cu_6$ with $x = 1$, 0.8 and 0.5, plotted versus T. The insert shows the low T data. [After Õnuki and Komatsubara (1987), [180]]

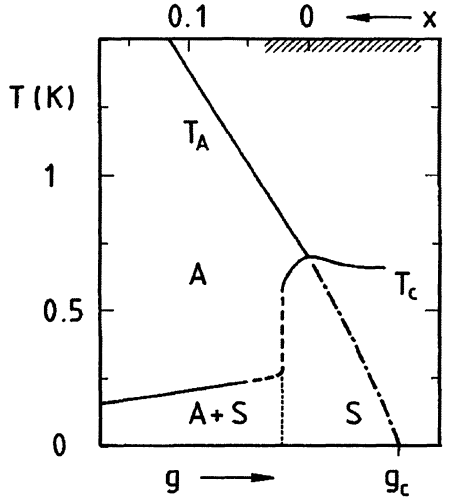

Fig. 10.32. A schematic phase diagram for $CeCu_2Si_2$ at zero field, indicating the existence ranges for a spin density wave–like phase (A), superconductivity (S), and the coexistence ranges (A+B). The abscissa is an effective coupling constant g which is proportional to x in $CeCu_2(Si_{1-x}Ge_x)_2$ or to the composition in homogeneous $CeCu_2Si_2$. [After Gegenwart *et al.* (1998), [191]]

single crystals [187]. In this case, altering the composition can result in the stabilization of the separate phases [188, 189]. The A phase shows a specific heat due to heavy quasi–particles perhaps including a $T^3 \ln T$ contribution arising from ferromagnetic spin–fluctuations [190]. In the presence of applied magnetic fields sufficiently large to suppress the superconductivity, the S phase appears and has a non–Fermi–liquid like temperature dependence of the specific heat [191]

$$\frac{C}{T} = \gamma_0 - A\,T^{\frac{1}{2}} \,. \tag{10.128}$$

This non–analytic temperature variation indicates that the material is either close to a quantum critical point in which non–local correlations are developing, or that there is a significant amount of local disorder as has been inferred from neutron measurements of the nuclear pair distribution function [192].

The Magnetic Susceptibility

The magnetic susceptibilities of heavy–fermion systems show temperature driven cross–overs between forms reminiscent of local moments and low temperature Pauli–like susceptibilities. This is illustrated in Fig. 10.33, which shows the temperature dependence of the susceptibilities for UBe_{13} and $CeAl_3$. At high temperatures, the susceptibilities can be fit by the form

$$\chi(T) = n\,\frac{\mu_{eff}^2}{3\,k_B\,(\,T - \Theta\,)}\,, \tag{10.129}$$

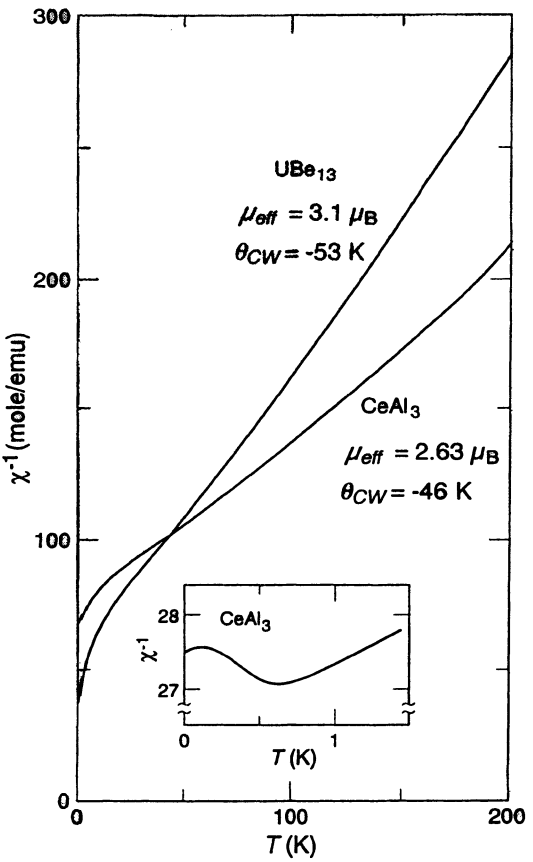

Fig. 10.33. The temperature dependence of the magnetic susceptibility $\chi(T)$ for UBe_{13} and $CeAl_3$ plotted as $\chi^{-1}(T)$. The effective moments and Curie–Weiss temperature obtained from high temperature fits are also shown. At low temperatures, the temperature variation of $\chi(T)$ for $CeAl_3$ weakens and becomes Pauli–paramagnetic, as shown in the inset

where μ_{eff} is the size of the effective magnetic moment, n is the density of local moments, and Θ is the Curie–Weiss temperature. The values of the effective moment μ_{eff} are nearly that of the free ionic moments, and the values of the Curie–Weiss temperature Θ are usually negative, suggesting antiferromagnetic interactions between the local moments.

At lower temperatures, the susceptibilities cross–over to Pauli–paramagnetic susceptibilities that show large enhancements similar to those of the specific heat γ coefficients. The cross–over from Curie–Weiss like to Pauli–paramagnetic like susceptibilities seems to occur at higher temperatures than the temperatures at which the C/T ratios build up [193, 194]. The magni-

Table 10.8. High Temperature Properties of the Normal State. Anisotropic properties of crystals are given along the principal directions in the form of "a/b/c".

Material	Θ (K)	μ_{eff} (μ_B)	$\rho(T = 300K)$ ($\mu\Omega$ cm)
UCu_5	284	3.52	286
UAl_2	245	3.1	190
UPt_3	50 / 170	2.5 / 2.37	230 / 135
U_2Zn_{17}	105	3.3	110
URu_2Si_2	65	3.51	324 / 169
UBe_{13}	53	3.1	107
UPd_2Al_3	47	3.2	140 / 200
UCd_{11}	23	3.45	80
UGe_2	- 34	2.7	156
$CeCu_2Si_2$	140	2.68	90
$CeCu_6$	59 / 59 / 8	2.6 / 2.67 / 2.46	70
$CeAl_3$	46	2.63	65

tudes of the measured γ and $\chi(0)$ can be compared indirectly by using the model of non–interacting electrons. For the gas of non–interacting electrons, the Pauli–susceptibility is given by

$$\chi(0) \;=\; 2\,\mu_B^2\,\rho(\mu)\,, \tag{10.130}$$

where $\rho(\mu)$ is the density of states, per spin, at the Fermi energy, and the specific heat coefficient is given by

$$\gamma \;=\; 2\,\frac{\pi^2}{3}\,k_B^2\,\rho(\mu)\,. \tag{10.131}$$

Therefore, a plot of γ versus $\chi(0)$ for hypothetical non–interacting electron systems should yield a straight line with slope given by

$$\frac{\pi^2}{3}\left(\frac{k_B}{\mu_B}\right)^2. \tag{10.132}$$

As shown by Fisk *et al.* [195] (see Fig. 10.34), the heavy–fermion systems have γ and $\chi(0)$ values that lie close to the same line. Therefore, as the Wilson ratio is close to unity, this indicates that the enhancements of the susceptibilities have similar magnitudes to the specific heat enhancements.

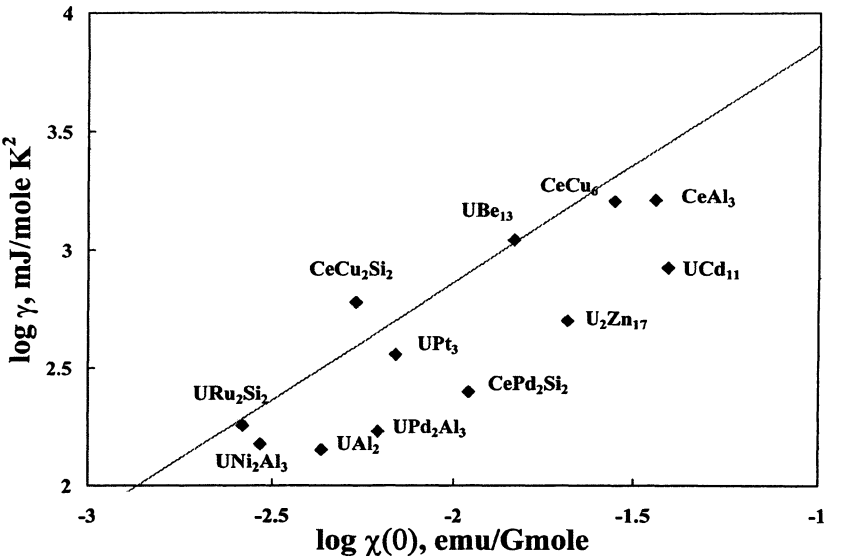

Fig. 10.34. A log–log plot of the limiting values, per mole f material, of C/T in mJ/mole K^2 and χ in emu/Gmole for selected heavy fermion compounds. The straight line represents the relation for non–interacting electrons. [After Fisk *et al.* (1987), [195]]

From a Fermi liquid point of view, one would expect that the uniform static susceptibility should show an enhancement, S, given by

$$S = \frac{m^*/m_b}{1 + F_0^a}, \tag{10.133}$$

where F_0^a is the spin antisymmetric interaction between a pair of quasi–particles with angular momentum $l = 0$. However, the specific heat is just enhanced by the factor

$$m^*/m_b . \tag{10.134}$$

Thus, the χ to γ ratio yields information about the spin–dependent interaction between the quasi–particles. In most Ce compounds, both enhancements seem to be due to single–site processes. This can be seen by inspection of the susceptibility of $Ce_xLa_{1-x}Cu_6$ per Ce ion, which is independent of x in the range $1 > x > 0.1$. The susceptibilities of $Ce_xLa_{1-x}Cu_6$ and $Ce_xLa_{1-x}Pb_3$ are shown in Fig. 10.35. The similarity of the curves suggests that the large susceptibility, like the large specific heat, is dominated by local processes involving the f electrons. Since the spin–orbit split ground state of the Ce^{3+} ion corresponds to $J = 5/2$ and degeneracy of 6, the ratio of the susceptibility to γ term predicted by the single–site Kondo model should be very similar to

the ratio for non–interacting electrons. On the other hand, in UBe_{13} doped substitutionally on the U sites [196], the susceptibility seems to scale linearly with the number of U atoms, while the γ coefficient per U atom is rapidly reduced by dilution. This suggests that an appreciable fraction of the mass enhancement in UBe_{13} is not due to a single–site magnetic Kondo process. A similar conclusion has been drawn from dilution studies of UPt_3 [197], which show that dilution can result in the suppression of the specific heat by up to 50 % of the stoichiometric value while the uniform static susceptibility is barely affected. These conclusions are consistent with measurements of the de Haas – van Alphen oscillations on a number of U and Ce compounds, which show that the quasi–particles are itinerant and form part of the Fermi surface, albeit with a very small dispersion of the bands.

de Haas–van Alphen oscillations

Measurements of the magnetization in high fields and at low temperatures show oscillations as a function of the inverse field. The presence of the oscillations has long been held as an indicator that the quasi–particles are itinerant, form part of the Fermi surface, and are long lived. The oscillations are due to the existence of Landau peaks in the density of states, which are a consequence of the quantized orbital motion of the quasi–particles in the presence of an applied field. As the applied field is increased, the energy separation between consecutive Landau peaks increases linearly with the field, and the oscillations occur as the peaks in the density of states move through the Fermi energy. The fundamental periods of the oscillations are related to the extremal cross–sectional areas of the Fermi surface perpendicular to the applied field. For non–interacting electrons, the fundamental oscillation stemming from each electron orbit around an extremal area is governed by the Lifschitz – Kosevich formula

$$M_z \;=\; A\,\cos\left(\frac{\hbar\,c\,S}{e\,H_z}\;+\;\phi\right), \tag{10.135}$$

where S is the extremal area of $\underline{k}$ space enclosed by the quasi–particle orbiting around the Fermi surface, and ϕ is a phase reflecting the Zeeman splitting between the bands of different spins. The amplitude of the oscillations, A, is given by

$$A \sim V\;\frac{k_B\,T\,S}{2\,\pi^2}\,\sqrt{\frac{e}{\hbar\,c\,H_z}}\,\exp\left[\;-\;\frac{2\,\pi^2\,m_b\,c}{\tau\,e\,H_z}\;\right]\,cosech\left[\frac{2\pi^2 m_b c k_B T}{\hbar e H_z}\right], \tag{10.136}$$

where τ is the lifetime due to scattering processes and m_b is the effective mass deduced from the dispersion relation of the non–interacting electrons at the Fermi surface. The scattering rate, $1/\tau$, is usually introduced in an ad–hoc manner. The contribution from each extremal area contributes to the

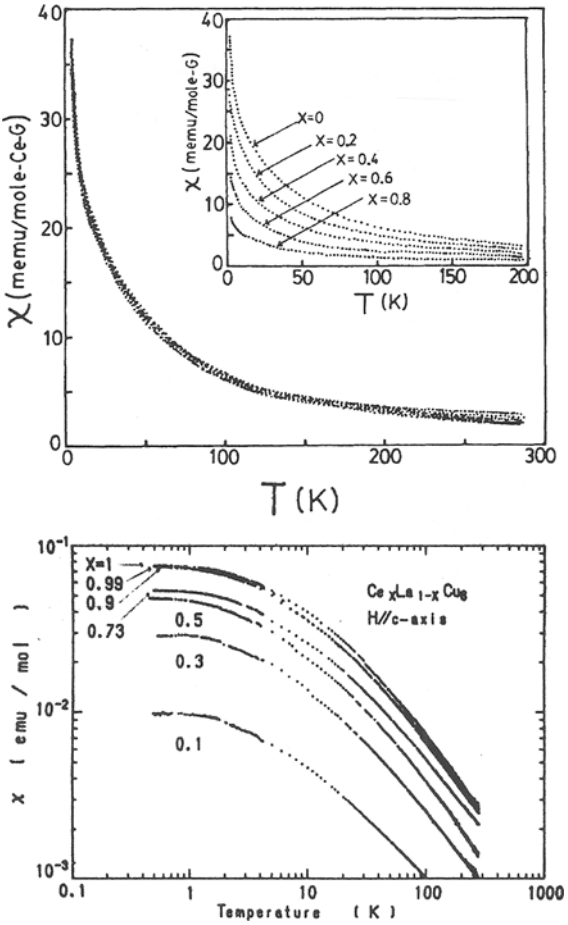

Fig. 10.35. (a) The magnetic susceptibility per mole Ce, $\chi(T)$ versus T for $Ce_{1-x}La_xPb_3$ samples with $x = 0.0$, 0.2, 0.4, 0.6 and 0.8. Insert: The total susceptibility per molar formula unit for the same samples. [After Lin *et al.* (1987), [181]]. (b) The magnetic susceptibility per mole formula unit for $Ce_xLa_{1-x}Cu_6$, plotted versus T. [After Ōnuki and Komatsubara (1987), [180]]

signal with the weight given by

$$\sqrt{\frac{2\,\pi}{\left|\frac{\partial^2 S}{\partial k_z^2}\right|}}\,, \tag{10.137}$$

where k_z is the component of the wave–vector parallel to the field. This factor expresses the weight of an extremal cross–section relative to that of an extremal section of a spherical Fermi surface of the same size, S. Since Fermi surfaces are often multi–sheeted, the measured areas are typically compared

with the results of electronic structure calculations. For most simple metals, the experimentally determined areas are usually in excellent agreement with the LDA calculations. Since the oscillations originate from the Landau peaks in the density of states passing through the Fermi energy, broadening, either due to the Fermi function or from the effect of impurity scattering on the Landau peaks, is expected to wash out the oscillations. Therefore, one expects that the oscillations should only be measurable at extremely low temperatures ($T < 1\ K$), for high fields, and for very high quality samples having very low residual resistivities.

The Lifschitz–Kosevich formula must be modified when the effect of electron–electron interactions are introduced. First, the spin–splitting phase factor ϕ may be exchange enhanced and may become field–dependent [198]. Phenomenologically, one is also led to expect that the scattering rate should be identified with the imaginary part of the self–energy evaluated on the Fermi surface and that the real part of the self–energy may also be expected to appear as an addition to the imaginary part. In the thermal average which is performed by transforming to a sum over Matsubara frequencies ω_n, the real part of the self–energy contains a term proportional to $(1 - Z(0))\omega_n$, and therefore, produces a correction of order $\pi k_B T$. In the small H/T limit, the additional term originating from the real part of the self–energy can be combined with the $k_B T$ dependence in the argument of the cosech term in the non–interacting formulae, thereby replacing the band mass m_b by the quasi–particle mass m^*. Thus, the temperature dependence of the amplitude of the oscillations can be used to deduce the quasi–particle effective masses. As the linear T term in the specific heat–capacity is related to the average of the quasi–particle masses on the Fermi surface, one may be able to compare the average of the quasi–particle masses observed in de Haas–van Alphen experiments with the specific heat. However, in attempting to make this comparison, it is important to note that some portions of the Fermi surface may not have been observed in the de Haas – van Alphen experiments. As can seen from Eq. (10.136), the amplitudes of the heavier branches are expected to be quite small and may easily be missed. Also, in the case where the γ coefficient depends on the magnitude of the applied field, as it should if the quasi–particle mass enhancements are of magnetic origin, the average quasi–particle mass should be compared with the specific heat measured under comparable fields. It should be noted that the amplitude factor contains the ratio of the quasi–particle mass to the quasi–particle lifetime so, if the mass enhancements arise from a local process, the quasi–particle mass enhancement factor should cancel with the enhancement of the quasi–particle lifetime. This cancellation occurs much in the same way as the cancellation of the enhancements in the residual resistivity $\rho(0)$ that occurs when the self–energy is k independent. This implies that the impurity scattering should not be significantly more effective in reducing the amplitude of the oscillations than in metals with comparable density of states.

The de Haas – van Alphen oscillations were observed in measurements on $CeCu_6$, $CeCu_2Si_2$, UCd_{11}, UPt_3, UPd_2Al_3, URu_2Si_2 and $CeRu_2Si_2$ for temperatures between 200 and 100 mK and fields up to 18 T. Despite many valiant attempts, measurements on UBe_{13} have failed to yield de Haas van – Alphen oscillations [199]. In most of these materials, sheets of the Fermi surface with large effective masses have been found. The extremal areas inferred for UPt_3 are in good agreement with the Fermi surface geometry found from electronic structure calculations [200,201]. The effective masses inferred from the amplitude can be factors of 10 to 30 times larger than those found in LDA band structure calculations [202,203], and the heavy masses found range from 25 m_e to 200 m_e. This suggests that the quasi–particle mass enhancements due to electron–electron interactions, are extremely large. The Fermi surface average of the observed effective masses produces a quasi–particle density of states that is in rough agreement with the γ value of UPt_3. Whereas in UPt_3 the quasi–particles at the Fermi surface have large effective masses, the effective masses found in $CeCu_6$ are smaller [206] and are in the range of 6 to 80 m_e. However, as the specific heat of $CeCu_6$ is appreciably larger than that of UPt_3, one suspects that the bands with heavier masses were not observed. This situation also seems to be definitely the case for $CeCu_2Si_2$ in which only small masses of 4 to 6 m_e have been observed [204]. The observation of the heavy mass sheets of the Fermi surface in UPt_3, but not in $CeCu_6$ and $CeCu_2Si_2$, is probably due to the higher quality of the UPt_3 samples. Also, part of the discrepancy between the de Haas – van Alphen effective masses and the specific heat of $CeCu_6$ measured in zero field [205,206] is accounted for, if the field dependence of the specific heat is considered [207,208]. The decrease of the effective mass with applied magnetic field is taken as an indication that spin–flip excitations are responsible for part of the mass renormalizations, and that application of the field quenches the spin–flip scattering processes. The lack of agreement between the specific heat and de Haas – van Alphen effective masses in URu_2Si_2 is very notable in that the only effective masses that have been found, so far, are in the range of 15 to 25 m_e, and these only yield about 16 percent of the total γ value [209,210]. Likewise for UCd_{11} [213], the only effective masses observed are only in the range of 2 to 11 m_e. As previously mentioned, the difficulty of observing heavy quasi–particle mass branches of the Fermi surface is due to the exponentially small amplitudes of their oscillations. However, both light and heavy quasi–particle masses can be found in the same compound such as in $CeRu_2Si_2$, where the observed masses are in the range of 1 to 120 m_e [214].

Some heavy–fermion materials undergo meta–magnetic like transitions at high fields in which the magnetizations undergo rapid change with respect to magnetic field at a critical value of the field H_m. The meta–magnetic transitions become sharper at lower temperatures. These highly non–linear susceptibilities indicate either that the systems are on the verge of undergoing

an instability to a magnetically ordered phase [7] or that a spin–split branch of quasi–particles crosses the Fermi surface. For example, URu_2Si_2 may undergo as many as three transitions, located at $H_{m1} = 35.9$ T , $H_{m2} = 36.1$ T and $H_{m3} = 39.7$ T. The three transitions in URu_2Si_2 have been observed in transport properties [215] as well as in the magnetization [266]. UPt_3 has a meta–magnetic transition at $H_m = 20$ T while $H_m = 18$ T for UPd_2Al_3 ; $H_m = 8$ T for $CeRu_2Si_2$ and a very much weaker meta–magnetic transition occurs in $CeCu_6$ at a critical field of $H_m = 2$ T. Above these fields, the effective masses rapidly decrease with increasing field [217,218]. For example, in UPd_2Al_3, the effective masses found below $H_m = 18$ T are as large as 45 m_e [219], but for fields above H_m, the effective masses found are 31 and 5.4 free electron masses [220].

De Haas – van Alphen oscillations have also been observed in the mixed states of type II superconductors such as $NbSe_2$ [221], Nb_3Sn, V_3Si [222] and YNi_2B_2C [223]. This effect is probably due to the existence of unpaired quasi–particle particles which can be quantized into Landau levels similar to the manner in which the quasi–particles in the normal state are quantized into Landau levels. De Haas – van Alphen measurements have been performed in the superconducting states of UPd_2Al_3 and URu_2Si_2, and oscillations were observed to persist until the strength of the applied field was reduced substantially below H_{c2}. Since the estimated diameters of the cyclotron orbits are factors of 10 greater than the vortex lattice spacing, the unpaired quasi–particles apparently must traverse through the superconducting regions. The frequencies of the oscillations remain unchanged in the superconducting state, however, the quasi–particle masses and scattering rates inferred from a Fermi liquid like analysis are altered. For example, the branch with mass of 5.4 m_e found in the normal state of UPd_2Al_3 was also observed in the superconducting state, but the inferred effective mass was further reduced to 3.0 m_e.

[7] For a paramagnetic system close to a magnetic instability, one expects that the free–energy expressed as a function of the magnetization M could have a local minimum at $M \neq 0$, in addition to the global minimum at $M = 0$. The application of a magnetic field may cause the energy of the local minimum to be lowered, thereby stabilizing it at the critical field H_m associated with the meta–magnetic transition. The criterion for the occurrence of a meta–magnetic transition can be easily calculated for the Stoner model. In the Stoner model, the magnetization–field relation is given by

$$M = 2\mu_B^2 HS\rho(\mu)\left[1 + \frac{1}{6}\left[\left(\frac{\rho''}{\rho}\right) - 3\left(\frac{\rho'}{\rho}\right)^2\right]\mu_B^2 H^2 S^3 + \ldots\right], \qquad (10.138)$$

where $S = (1 - U\,\rho(\mu))^{-1}$ is the Stoner enhancement factor. The terms non–linear in H can be large due to the appearance of extra powers of S. The cubic term may be negative either if the density of states at the Fermi energy is close to a maximum or if it is rapidly varying. If non–linear terms in M are negative, then meta–magnetic transitions may occur at critical fields. Thus, meta–magnetic transitions may be expected to occur in the vicinity of quantum critical points.

Phenomenologically, the amplitude of oscillations could be expected to be reduced due to the decrease in the number of unpaired quasi–particles and also due to the smearing of the Fermi energy in the superconducting state. The latter phenomenon could also appear as an increase in the quasi–particle scattering rate consistent with the observations in the superconducting state of URu_2Si_2 [210]. The appearance of de Haas–van Alphen oscillations in the superconducting state is surprising since it undermines a commonly held belief that observability of the oscillations is a signature of the existence of a sharply defined Fermi surface and the long lifetime of the quasi–particles. Furthermore, it is surprising as it definitively shows that such oscillations can also be observed in non–Fermi–liquid states.

Table 10.9. Low Temperature Normal State Properties (Extrapolated to $T = 0$).

Material	γ (mJ mole f ion^{-1} K^{-2})	$\chi(0)$ (10^{-3} emu /mole)	A ($\mu\Omega$ cm K^{-2})	$\rho(0)$ ($\mu\Omega$ cm)
$CeAl_3$	1620	36	35	0.77
$CeCu_6$	1600	28	$\sim$ 120	15 / 9.2 / 8.3
UBe_{13}	1100	14.7	-	17
$CeCu_2Si_2$	600	4 / 8	10.7	4.8
UCd_{11}	840	39	-	
U_2Zn_{17}	500	19 / 24	-	
UPt_3	360	8.1 / 4.4	1.6 / 0.61	0.23 / 0.59
UPd_2Al_3	170	8.1 / 2.2	$\sim$ 0.3	3.5
URu_2Si_2	180	1.5 / 4.9	0.17 / 0.10	1.27
UNi_2Al_3	150	3.3 / 2.2		
UAl_2	142	4.3	10.7	4.8
UGe_2	100	-	$\sim$ 0.25	0.26
$CePd_2Si_2$	250	11	-	1.4
$CeRh_2Si_2$ (P=0)	21	2.9 - 3.2	0.8	0.75
$CeIn_3$	100	11	-	0.6
$CeRhIn_5$ (P=0)	60	4 - 22	-	0.4
$CeIrIn_5$	750	9 - 20	-	$\sim$ 0.1
$CeCoIn_5$	350	4 - 7	-	3

Magnetic Instabilities

Several of the heavy–fermion materials undergo instabilities to magnetically ordered states at lower temperatures. The most frequently found type of ordering is antiferromagnetic, however, ferromagnetic phases have been iden-

tified in UGe_2, URhGe $CeRu_2Ge_2$, $CeGe_2$, and $CeSi_x$. The values of γ found from extrapolation above the ordering temperatures are generally about a factor of 1.2 to 3 times higher than the γ values found from extrapolating below the ordering temperatures. This indicates that the antiferromagnetic order may have produced a partial gapping of the Fermi surfaces. Exceptions to this are given by $CeAl_3$, UCu_5 and UPt_3, where the extrapolated γ values are larger in the magnetically ordered phases. These findings are consistent with the general observation that the entropy found by integrating below the ordering temperature is about 30 percent less than entropy expected from a simple Fermi liquid picture, i.e., γ may still be growing below T_N and the Fermi liquid may have not been completely formed when T has been decreased to T_N.

The values of the ordered moments are smaller than those associated with the free ion values. This is sometimes attributed to the screening of the f moments by the conduction electrons. However, in view of Nozières arguments for Ce compounds and the existence of reduced moment ordering in U compounds, it seems apparent that the itinerant nature of the f electrons is involved in the reduction of the moments. In some compounds such as $CeAl_3$ and URu_2Si_2, the magnetic ordering appears to be inhomogeneous, only occurring in a small fraction of the sample volume [224]. It seems likely that these samples are also inhomogeneous. The magnitude of the moments on the atoms in the magnetically ordered volume can be large, of the order of 0.5 μ_B per f atom but the moment averaged over the sample can be as small as 0.03 μ_B per f atom, as found for URu_2Si_2. It has been found [225] that in URu_2Si_2, application of pressures of up to 1.5 GPa produces an increase in the size of the ordered moment to a value of the order of 0.25 μ_B per U atom but only produces a slight increase in T_N. The magnetic ordering shows up in the specific heat of $CeAl_3$ as a faint and sample dependent anomaly at the ordering temperature that considerably increases in magnitude on dilution. As shown in Fig. 10.36, the specific heat jump observed in stoichiometric URu_2Si_2 is quite large [20, 21]. The small magnitude of the volume averaged ordered moment in URu_2Si_2 seems inconsistent with the large value of the entropy associated with the specific heat anomaly at T_N. The specific heat jump is about 5.82 J/mole–K, and the entropy ΔS associated with the anomaly has a magnitude of about 0.17 $Nk_B \ln 2$. On the other hand, Landau mean–field theory suggests that the magnitude of the entropy of the transition should be of the order of

$$\Delta S \sim N k_B \left(\frac{\mu_{sat}}{\mu_{eff}}\right)^2, \tag{10.139}$$

where μ_{sat} is the $T = 0$ saturation value of the sub–lattice magnetization; and μ_{eff} is the paramagnetic moment ($\mu_{eff} \approx 3.51\ \mu_B$), as obtained from fitting the susceptibility above T_N to a Curie–Weiss law. The large discrepancy between the observed and inferred magnitudes of the anomalous entropy

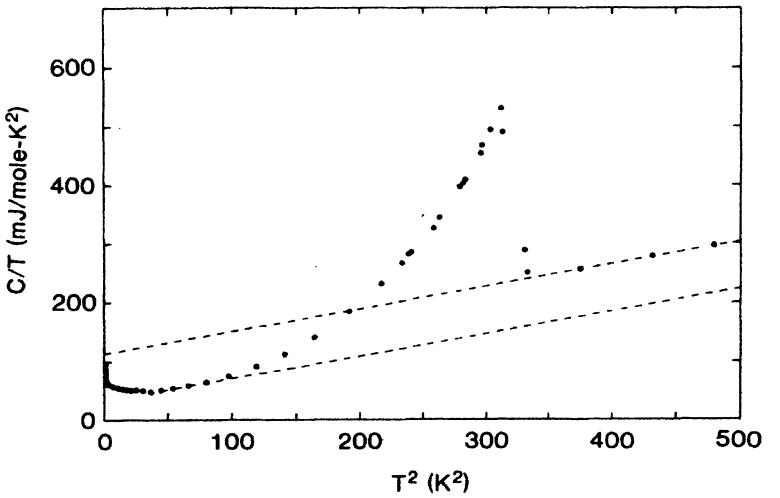

Fig. 10.36. The specific heat jump of the "hidden order" phase transition of URu_2Si_2. The specific heat ratio C/T is plotted as a function of T^2. A mean field–like jump occurs at $T_N \approx 17.5$ K which is associated with the "hidden order" phase transition. [After Maple *et al.* (1986), [21]]

has been taken as indicating that another type of ordering occurs simultaneously with the antiferromagnetism. However, although the other type of ordering has been searched for, it has not yet been identified.

An alternate paradigm for heavy–fermion materials is provided by the model of a highly enhanced Fermi liquid close to a quantum critical point. In this picture, the large enhancements are caused by the slow, large amplitude, critical magnetic fluctuations. Due to the close proximity of the critical point, one may expect various physical quantities to obey scaling laws [72]. In this case, one expects that the properties may be expressed in terms of the $\underline{q}$ dependent magnetic susceptibility $\chi(\underline{q}, T)$ which expresses the response of the system to a staggered magnetic field $H(\underline{q})$. The absence of a large $\chi(0,0)/\gamma$ ratio indicates that the dominant magnetic fluctuations that occur are not localized around $q = 0$. This is consistent with the observation that most heavy–fermion systems undergo instabilities to antiferromagnetic phases. Likewise, since the transport scattering rate is dominated by processes involving large scattering angles θ due to the weighting factor of $(1 - \cos\theta)$, measurements of transport properties might also be expected to provide information on the magnitude of the wave–vectors of the magnetic fluctuations in the absence of competing instabilities and complicated multi–sheeted Fermi surfaces.

Table 10.10. Properties of the Magnetically Ordered State.

Material	T_N (K)	Ordered Moment M (μ_B)	γ (mJ K^{-2} mole f ion^{-1})
$CeAl_3$	1.6	-	1300
$CeCu_2Si_2$	0.8	$\sim$ 0.1	1000
UCd_{11}	5	-	250
U_2Zn_{17}	9.7	0.8	200
UPt_3	5.0	0.02	450
UPd_2Al_3	14.5	0.85	150
URu_2Si_2	17.5	-	65
UNi_2Al_3	4.6	0.24	120
UGe_2	$T_c(P = 1\ GPa) = 34$	$M(P = 0) = 1.4$	-
$CePd_2Si_2$	10.2	0.7	250
$CeRh_2Si_2$	36	1.8	21
$CeIn_3$	10.2	0.65	100
$CeRhIn_5$ (P=0)	3.8	0.15	60

10.3.2 Transport Properties

Electrical Resistivity

The room temperature resistivities of heavy–fermion compounds are quite large, of the order of 100 $\mu\ \Omega cm^{-1}$, most probably due to spin disorder scattering. As seen in Fig. 10.37, the resistivity of some materials such as $CeCu_2Si_2$, $CeAl_3$, UBe_{13} and U_2Zn_{17}, shows an increase with decreasing temperature. This type of temperature dependence is unusual for simple metals but is characteristic of the Kondo effect often found in materials containing isolated and disordered magnetic impurities. In this subset of heavy–fermion materials, the upturn in the resistivity follows a logarithmic temperature dependence that results from the conduction electrons resonantly spin–flip scattering from isolated magnetic impurities, as calculated in third order perturbation theory [160]. If, at high T, the conduction electrons are assumed to be scattered by localized moments, the conductivity is given by

$$\sigma(T) = \frac{e^2\ k_F^3}{3\ \pi^2\ m}\ I^{(0)}\ , \tag{10.140}$$

where

$$I^{(n)} = \int_{-\infty}^{+\infty} dE \left(-\frac{\partial f}{\partial E} \right) \frac{E^n}{Im\ \Sigma_c(E)} \tag{10.141}$$

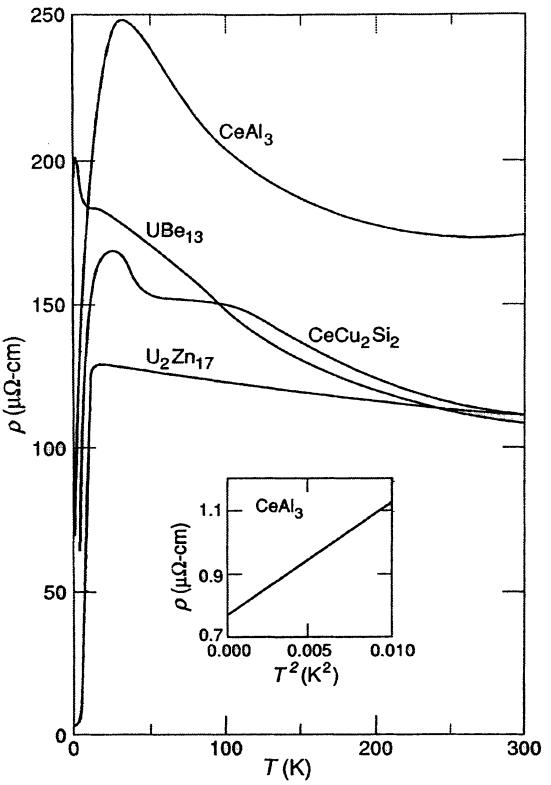

Fig. 10.37. The temperature dependence of the electrical resistivity of the heavy fermion compounds U_2Zn_{17}, $CeAl_3$, $CeCu_2Si_2$ and UBe_{13}. The inset shows the low temperature T^2 variation of the resistivity found in $CeAl_3$

and where $\Sigma_c(E)$ is the conduction electron self–energy. For independent local moments the imaginary part of the self–energy is given by

$$Im\ \Sigma_c(E) \ = \ \pi \mid V \mid^2 \rho_f(E,T)\ , \tag{10.142}$$

where $\rho_f(E,T)$ is the temperature dependent f density of states, and V is the hybridization matrix elements. For $T < T_K$, a narrow (possibly crystal field split) Kondo resonance forms at an energy T_K above μ. The temperature dependent crystal–field split $\rho_f(E,T)$ expected from the single–impurity Anderson model is shown in Fig. 10.38. Thus, the resistivity is expected to reflect any crystal–field splitting that may be present. As seen in Fig. 10.39, there are two peaks in the resistivity of $CeCu_2Si_2$ [226] both of which can be attributed to spin–flip scattering from the $J = \frac{5}{2}$ crystal field split states of the Ce^{3+} ion. The position of the higher temperature peak ($\sim$ 160 K) is associated with the crystal field splitting between the multiplets of the lowest spin–orbit split $J = \frac{5}{2}$ level of the Ce^{3+} ions. The 160 K peak is

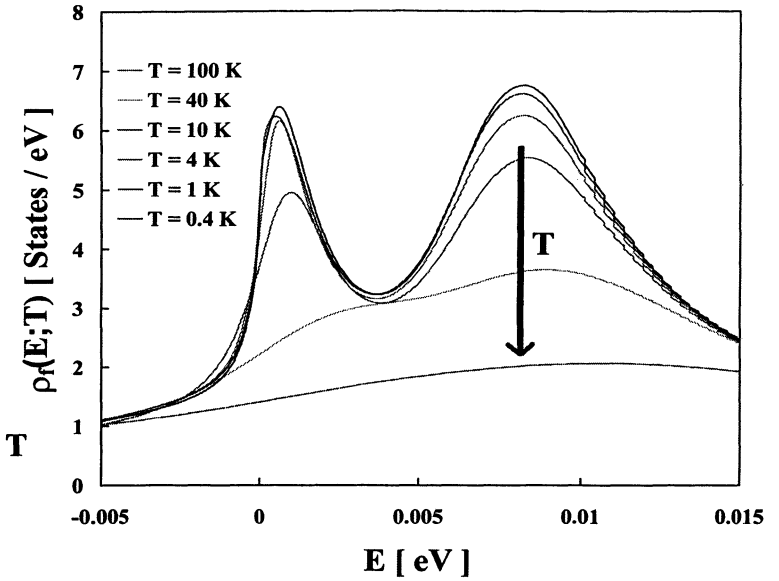

Fig. 10.38. The calculated energy dependence of the f electron density of states $\rho_f(E,T)$ for the single–impurity Anderson model, at various temperatures. The calculation is appropriate to describe a Ce ion in a cubic environment. The temperature dependent Kondo peak, above the Fermi energy, is split by the crystalline electric field. The spectrum was calculated using the non–crossing approximation

produced by the freezing out of transitions into the higher crystal field split states [164,227]. For temperatures greater than the crystal field splitting, the conduction electrons participate in scattering events in which the Ce^{3+} ions are scattered between all the crystal field split states of the $J = \frac{5}{2}$. However, for temperatures below the crystal field splitting of the lowest multiplet, only the lowest crystal field multiplet contributes to the scattering rate. Hence, as the coefficient of the ln T term in the resistivity is determined by the effective degeneracy of the local moments, the drop in effective degeneracy produces the second peak in $\rho(T)$ for $CeCu_2Si_2$. In contrast to Ce systems [228–232], U based heavy–fermion systems show little evidence of crystal field splittings or, if they do, are ambiguous [234–236]. For single impurity spin–flip scattering, the logarithmic temperature variation of the resistivity is expected to cease near T_K, below which the resistivity should show a Fermi liquid like $\rho(T) = \rho(0) - A\,T^2$ temperature variation with a resistivity maximum only occurring at zero temperature. In contrast to theoretical results for the single–impurity Kondo model, for heavy–fermion materials such as $CeAl_3$, $CeCu_2Si_2$, $CeCu_6$, URu_2Si_2 and UBe_{13}, the observed Kondoesque increase in the resistivity is followed by a rapid decrease with decreasing temperature. The decrease is often attributed to the onset of coherence in the set of f moments. Above the coherence temperature, the f moments are as-

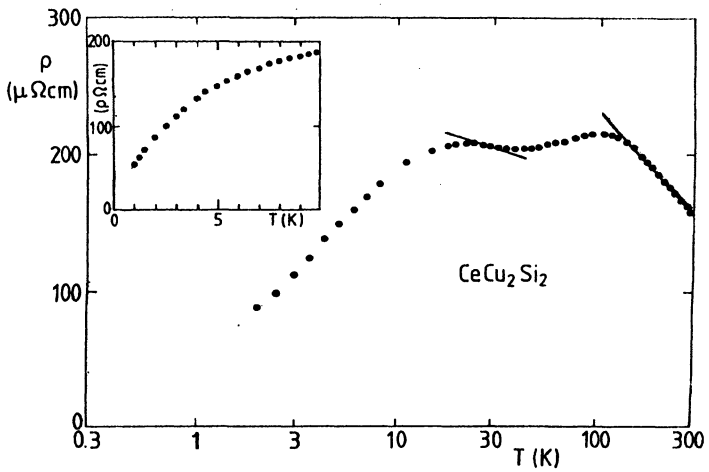

Fig. 10.39. The temperature dependence of the electrical resistivity of $CeCu_2Si_2$, plotted on a logarithmic temperature scale. The two regions where the resistivity shows an approximate $\ln T$ dependence are indicated by the solid lines. [After Franz *et al.* (1979), [226]]

sumed to be independent and have uncorrelated fluctuations whereas at low temperatures, the moments are assumed to approximately align over large spatial regions. The fluctuations responsible for preventing perfect alignment are assumed to have a collective character, and it is these fluctuations that are assumed to provide the dominant inelastic scattering process that freezes out as T is reduced to zero. In URu_2Si_2, the broad peak in the resistivity occurs at 50 K where it attains a value of 3000 $\mu\Omega$cms and then shows a rapid decrease at lower temperatures. The decrease is briefly interrupted at $T_N = 17.5$ K, where the resistivity shows a slight, but abrupt, increase due to ordering [21]. The increase in the resistivity is understood in terms of a partial gapping of the Fermi surface and is consistent with the change in the extrapolated C/T ratio from 112 mJ/mole K^2 above T_N to 65.5 mJ/mole K^2 below T_N. In UBe_{13}, the peak in the resistivity is remarkably sharp; the peak occurs at 2.5 K and has a value of the order of 200 $\mu\Omega$cm. On the other hand, UPt_3 and UAl_2 do not show Kondoesque maxima in the resistivities but just decrease with decreasing temperature. The low temperature resistivities of $CeCu_6$, $CeAl_3$, UAl_2, UPt_3, UGe_2 under pressure and YbBiPt show $\rho(T) = \rho(0) + A\,T^2$ temperature variations characteristic of electron–electron scattering. The coefficients of the T^2 terms are enormous as they seem to scale with the square of the γ term in the specific heat [237], in agreement with the argument involving highly enhanced quasi–particles. The large A coefficients are, therefore, taken as indicating the mutual scattering of quasi–particles in a highly enhanced Fermi liquid. Although a large T^2 coef-

ficient was also observed in the resistivity of $CeCu_2Si_2$, it has been suggested that this is not a true manifestation of the existence of a Fermi liquid in that by suppressing the superconductivity through the application of a magnetic field, a $T^{3/2}$ temperature variation is observed in S type samples [191]. Since the specific heat of S type samples also shows non–Fermi–liquid like behavior, it has been suggested that the non–Fermi–liquid is caused by the existence of a quantum critical point, but could also be due to structural disorder [192].

The residual resistivities $\rho(0)$ of heavy–fermion materials are sensitive to the presence of disorder and impurities. Often the residual resistivity is found to have a magnitude comparable to that of common metals with similar levels of impurities. However, in cases where the f ion is substituted by a non–magnetic impurity, the resulting residual resistivities are quite large. This has led to the concept of the Kondo hole in which a substitutional non–magnetic impurity at an f site of a heavy–fermion system produces a scattering phase shift of $\frac{\pi}{2}$ relative to the coherent resonant scattering of the lattice of f ions. Since the difference of the phase shifts is close to $\frac{\pi}{2}$, the scattering of the substitutional non–magnetic impurity is similar to the scattering produced by a magnetic impurity in a simple metal [238]. Basically, the large residual resistance of a Kondo hole in a heavy–fermion metal can be attributed as being due to the persistence of the large mass renormalization of the current carrying quasi–particle in the presence of disorder. This is to be expected as current can only be carried by states that are spatially extended. On the other hand, the scattering time at the site of the non–magnetic impurity is not expected to be renormalized by the mass enhancement factor as the scattering is purely a local phenomenon taking place on the non–magnetic impurity ion. The identification of the wave function renormalization Z with the ratio Δ/k_BT_K then yields a residual resistivity that is governed by the characteristic Kondo scattering rate of the missing f ion.

Magneto–Resistance

Since large amplitude fluctuations of the magnetic moments are assumed to be responsible for the transport scattering rate, the field dependence of the resistivity or longitudinal magneto–resistance should be quite illuminating. Basically, the application of a sufficiently large magnetic field could result in a partial ordering of the moments thereby suppressing the magnetic fluctuations and producing a reduction of the resistivity. This expectation is borne out in experiments on $CeCu_6$ [239] and in the normal state of UBe_{13} [240,241] which show large negative magneto–resistances, $\Delta\rho(H)$,

$$\frac{\Delta\rho(H)}{\rho(0)} = \frac{\rho(H) - \rho(0)}{\rho(0)} . \tag{10.143}$$

On the other hand, for both $CeAl_3$ [242,243] and $CeCu_2Si_2$ [242], the magneto–resistance is negative at sufficiently high temperatures and changes sign at temperatures comparable to the cross–over temperature. The high temperature magneto–resistance shows a scaling with field which can be understood

in terms of models of magnetic scattering from single impurities [244,245] in which Zeeman splitting suppresses the incoherent resonant scattering. However, the single impurity models fail at low temperatures where the incoherent magnetic scattering ceases [240,246]. In this low temperature limit, one expects that the resistivity will be dominated by impurity scattering and that the magneto–resistance should follow the scaling implied by Koehler's law. In UBe_{13}, the low temperature magneto–resistance is very large, negative, and anisotropic, which is indicative that the magnetic fluctuations responsible for the scattering of the conduction electrons are also anisotropic [247]. For UPt_3 and UAl_2, which have no maxima in the resistivity, the magneto–resistances are positive [248]. A positive transverse magneto–resistance is often found in common metals with multi–sheeted Fermi surfaces. In these common metals, the Lorentz force produces different shifts of the various sheets of Fermi surface that only produce a zero transverse current when their contributions are combined. The Lorentz force acting on the transverse current components produces a positive magneto–resistance. Therefore, the positive magneto–resistances found at low temperatures can be regarded as providing signatures that the quasi–particles are itinerant.

The Hall Effect

The application of a static magnetic field perpendicular to the direction current flow in a metal, produces a voltage drop in a direction that opposes the Lorentz force acting on the moving electrons. The Hall coefficient, R_H, describes the dependence of the ratio of the transverse electric field to the current on the strength of the applied field. In conventional metals, the Hall coefficient is almost temperature independent and provides information about the density and the sign of the charge carriers. However, in heavy–fermion systems, the Hall coefficient is about two orders of magnitude larger than in conventional metals and is also highly temperature dependent. At room temperature, the Hall coefficient is usually positive and initially increases with decreasing temperature and then goes through a maximum. The maximum has been observed in $CeCu_6$ [249], $CeCu_2Si_2$ [250], UBe_{13} [251] and UPt_3 [252]. The temperature dependence of the Hall coefficient of UPt_3 is shown in Fig. 10.40. For systems for which the resistivity has a maximum, the temperatures of the maximum in the Hall coefficients and the temperatures of the corresponding resistivity maxima are comparable [249]. The high temperature variation of the Hall coefficient is interpreted in terms of the combination of the usual Hall effect due to the Lorentz force and also from skew scattering. The skew scattering results from the scattering of conduction electrons from a set of independent magnetic impurities. The skew scattering involves the polarization of the moments by the applied magnetic field which also produces a spin–splitting in the impurity f density of states. The spin–orbit coupling on the impurity results in interference between the $l = 3$ and $l = 2$ angular momentum channels [253]. The extreme sensitivity of the narrow quasi–particle density of states at the Fermi energy has been

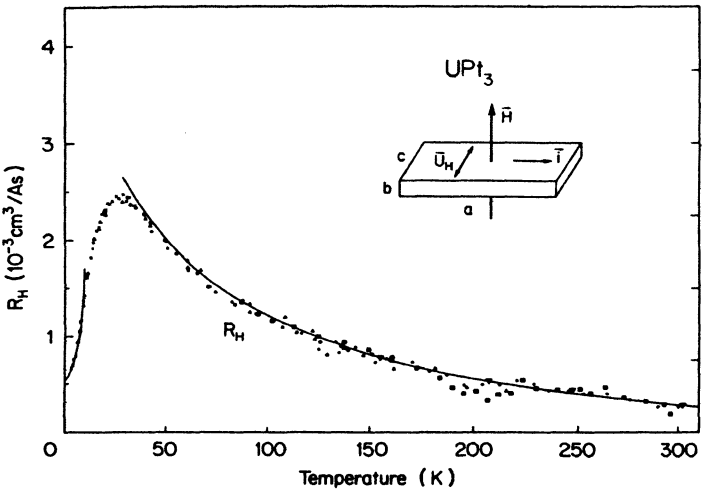

Fig. 10.40. The temperature dependence of the Hall coefficient of UPt_3 measured in a 4–T field. [After Schoenes and Franse (1986), [252].] The solid line is a fit to an expression for incoherent skew scattering

identified [254] as the source of the very large magnitude of the Hall coefficient. The anomalous skew scattering from independent local moments does reproduce the high temperature behavior of the Hall coefficient but fails to predict the maximum in the Hall coefficient, which is followed by a rapid drop at lower temperatures. The drop in the Hall coefficient has been interpreted as signifying the onset of coherence between the fluctuating parts of the local magnetic moments. In some heavy–fermion materials such as UAl_2, the Hall coefficient changes sign at low temperatures. Similar sign changes in R_H can be found in materials that have multi–sheeted Fermi surfaces.

Thermopower

It is expected that the low temperature limit of the thermopower S should be un–renormalized by the quasi–particle mass enhancement. Nevertheless, the measurement is expected to reflect the strong interactions as it should provide a measure of the logarithmic derivative of the imaginary part of the self–energy. This can be seen from the usual expression of the linear T contribution in terms of the ratio of two correlation functions

$$S = -\beta \frac{K^{11}}{K^{12}} , \tag{10.144}$$

where K^{11} involves the time ordered current–current correlation function, and K^{12} involves the heat flux–current correlation function

$$K^{11} = \frac{1}{3} \int_0^\beta d\tau \, \exp\left[i \, \omega \, \tau \right] \, < T_\tau \, \underline{j}(\tau) \cdot \underline{j}(0) > ,$$

$$K^{12} = \frac{1}{3} \int_0^\beta d\tau \, \exp\left[i \, \omega \, \tau \right] \, < T_\tau \, \underline{j}_Q(\tau) \cdot \underline{j}(0) > , \qquad (10.145)$$

where $\underline{j}$ is the current density and $\underline{j}_Q$ is the heat flux. The Seebeck coefficient can be approximately evaluated as

$$S = - \frac{1}{| e | T} \frac{I^{(1)}}{I^{(0)}} . \qquad (10.146)$$

When the above expression is analyzed using the Sommerfeld expansion, one finds the relation

$$S = \frac{\pi^2}{3} \frac{k_B^2 \, T}{| e |} \frac{\left(\frac{\partial \, Im \, \Sigma(E)}{\partial E} \right)}{Im \, \Sigma(E)} \Bigg|_{E=0} \qquad (10.147)$$

which also shows that S should vanish linearly with T at low temperatures. The measured thermopowers show considerable variation both with compound and with temperature but do share one common characteristic, which is that the magnitude of S is about an order of magnitude larger than common metals. At 4 K, the thermopower of UBe_{13} is -11 μVK^{-1} [255] and has decreased to -25 μVK^{-1} just below 1 K where the superconductivity sets in. At high temperatures, the thermopowers of $CeCu_2Si_2$ [2] and UAl_2 [256] are both positive, and have magnitudes of 15 μVK^{-1} and 40 μVK^{-1}, respectively, while in the same temperature range S for UPt_3 is negative with a magnitude of about -12 μVK^{-1}. The compound $CeCu_2Si_2$ has a shallow maximum in S of about 20 μVK^{-1} at 170 K, which seems to be connected with the crystal field splitting observed in this compound, while the thermopower of UPt_3 appears to have an even shallower minimum of -12 μVK^{-1} near 200 K. The thermopower of UPd_2Al_3 is large and shows a monotonic decrease with decreasing temperature [257]. These slow variations of S in the high temperature region, are to be contrasted with the variations [258] found in $CeCu_6$ and $CeAl_3$, where S decreases from about 40 to 10 μVK^{-1} as T is increased from 50 and 300 K. The thermopower of UPt_3 changes sign at 24 K, and has a positive peak at about 8 K. The thermopower in $CeCu_2Si_2$ changes sign at 75 K from positive to negative with decreasing temperature, and there is a deep minimum (-35 μVK^{-1}) at 20 K near the cross–over temperature. This is followed by a small positive maxima at a temperature of 0.2 K. The thermopower of $CeAl_3$ [259] is similar to $CeCu_2Si_2$ in that it goes through a minimum (-4 μVK^{-1} at 3.5 K), changes sign near the crossover temperature, and shows a small positive maximum at an even lower temperature ($\sim$ 0.3 K). However, $CeCu_6$ has three positive maxima [258], while

UAl_2 only shows one negative minimum before tending to zero linearly with T [256]. This rich variety of behavior is not reconcilable with the behavior of a single impurity Kondo model in which the scattering is dominated by the position of the Kondo resonance with respect to the Fermi–level. For Ce impurities, the model predicts that S has a positive maximum at the Kondo or cross–over temperature and falls to zero as $T \rightarrow 0$. The richness of the low temperature variations of the thermo electric power, like the Hall effect and the de Haas van Alphen measurements, suggests that the electronic structure contains a number of quasi–particle bands with high effective masses near the Fermi energy.

Thermal Conductivity

The thermal conductivity of metals, unlike the electrical conductivity, has contributions from the non–equilibrium distribution of phonons as well as from the quasi–particles. Thus, one may write

$$\kappa = \kappa_L + \kappa_e \tag{10.148}$$

where κ_L represents the lattice contribution and κ_e is the electronic contribution. There is no simple experimental way to decouple these two terms without recourse to theory. It is expected that, at sufficiently low temperatures, one will have

$$\kappa_L \propto T^2 , \tag{10.149}$$

when the phonon scattering is due to electron–phonon interactions, and if the mean free path is less than the size of the crystal. Otherwise, one expects

$$\kappa_L \propto T^3 \tag{10.150}$$

when the phonons mainly scatter from the surfaces of the crystal. At temperatures much greater than the Debye temperature, $T \gg \Theta_D$, one expects that the lattice contribution to the thermal conductivity will have the temperature dependence

$$\kappa_L \propto \frac{1}{T} . \tag{10.151}$$

These considerations lead one to conclude that, at sufficiently low temperatures, the quasi–particle contribution is the dominant term in the thermal conductivity. The quasi–particle contribution to the thermal conductivity is usually written as

$$\kappa_e = \frac{\pi^2}{9} k_B T \left(v^2 \tau \rho_{qp}(E) \right) \Big|_{E=0} , \tag{10.152}$$

where τ is the scattering rate, and v is the quasi–particle velocity ($\tau \sim Z\tau_0$ and $v \sim \frac{\hbar}{Z} \frac{k_F}{m_b}$). The two factors of the mass renormalization Z, occurring in

the quasi–particle velocities, are expected to cancel with a similar factor in the quasi–particle density of states and also with one factor of Z in the quasi–particle lifetime. Hence, the overall magnitude of the electronic contribution of the low temperature thermal conductivity should not differ significantly from that of a normal metal, for reasons similar to why the d.c. electrical conductivity is also unrenormalized. Thus, one expects that the Lorentz number, $L(T)$, defined by

$$L(T) = \frac{\kappa_e(T)}{T\,\sigma(T)} \tag{10.153}$$

should have a value similar to the value L_0 predicted for purely elastic scattering

$$L_0 = \frac{\pi^2}{3}\left(\frac{k_B}{e}\right)^2 . \tag{10.154}$$

For purely elastic scattering, the Lorentz number, involving the ratio of the appropriate conductivity tensors, is expected to be isotropic. Since inelastic scattering results in a reduction of the quasi–particles' energies, in addition to the reduction in the quasi–particle current, the Lorentz number is expected to be reduced below L_0 when inelastic scattering is also present. Since stoichiometric heavy–fermion materials often show sizeable T^2 terms in the low temperature electrical resistivity which are attributed to (inelastic) electron–electron scattering, one expects that when the T^2 term is larger than the residual resistivity, $L(T)$ should have a value close to that for purely elastic Baber scattering [260]

$$L_{elas} = L_0\left(\frac{36}{\pi^2} - 3\right) . \tag{10.155}$$

However, for lower temperatures such that the quasi–particle–quasi–particle scattering term becomes negligible compared with the residual resistivity, one should recover higher values of $L(T)$ close to the Lorentz number L_0. These expectation are very nearly borne out by experiments on the normal states of $CeAl_3$, $CeCu_6$, $CeCu_2Si_2$ and UPt_3. In $CeAl_3$ [259,261,262], the Lorentz number exhibits a minimum value of 0.75 L_0 at 0.5 K, which is larger than the theoretical limit of 0.65 L_0, and it overshoots the elastic limit yielding a weak maximum at 1.1 L_0 at 50 mK. The temperature of the minimum roughly agrees with the temperature where the T^2 term dominates the resistivity. For $CeCu_6$, the Lorentz number falls to a minimum value smaller than L_0 at a temperature of about 0.3 K, which is close to the temperature of 0.15 K where the T^2 term in the resistivity first becomes apparent as it cools [263]. The extrapolated data show that $L(T)$ approaches L_0 at 20 mK, in agreement with the arguments concerning the freezing out of the inelastic scattering processes. For $CeCu_2Si_2$, the low T value of $L(T)$ appears to be L_0 [2,264]. At

low temperatures, the inferred phonon contribution to κ_L of $CeCu_2Si_2$ has a T^2 variation [264] as expected from electron–phonon scattering. The phonon contribution κ_L starts to become larger than the electronic component at the temperature of 1 K where on cooling the T^2 term in the resistivity first becomes apparent [264]. For UPt_3, the minimum value of 0.45 occurs at a temperature of the order of 2 K [265, 266]. Since UBe_{13} does not form a Fermi liquid, it is not surprising that the Lorentz number is not constant but instead varies approximately linearly with temperature [28,267].

For temperatures greater than the coherence temperature, the Fermi liquid analysis of κ_e is expected to fail. However, in the temperature regime where $T > T_K$, one expects that Ce based heavy–fermion materials will resemble a metal in which the conduction electrons scatter off of a set of independent disordered magnetic moments. In this temperature regime, the thermal conductivity from the electrons may be calculated perturbatively [268]. The result for the Lorentz number $L(T)$ can be approximately expressed in the form

$$L(T) = \frac{1}{e^2\,T}\left(\frac{I^{(2)}}{I^{(0)}} - \left(\frac{I^{(1)}}{I^{(0)}}\right)^2\right), \tag{10.156}$$

where $I^{(n)}$ is defined by Eqn. (10.141). The Lorentz number is also expected to depend strongly on the crystal field splittings [269]. The crystal field splitting in $CeCu_2Si_2$ is assumed to give rise to a minimum in the Lorentz number at the temperature around 80 K. In this high temperature regime, the Lorentz number can be appreciably greater than L_0. This result is caused by the large temperature induced shift of the f density of states away from the Fermi energy for $T > T_K$. The experiments are consistent with this trend: However, the lattice contribution to κ_L is no longer negligible and may be several times greater than the quasi–particle contribution. This hypothesis is supported by the comparison of measurements on $CeCu_2Si_2$ with the reference material $LaCu_2Si_2$. In fact, if the phonon contribution κ_L is completely ignored in the data analysis, the Lorentz number is about a factor of twenty times greater than L_0. The inferred presence of a large phonon contribution is also supported by the conclusion that the theoretical calculated values of $L(T)$, using the independent Kondo impurity model, are unable to account for electronic contributions to $L(T)$ of this magnitude. Likewise, for UPt_3, the phonon contribution has been identified as being important above 3.5 K [29] and may be responsible for up to a maximum of 4.5 L_0 of the Lorentz number at $T = 24$ K inferred from the raw data [266]. The Lorentz number for $CeCu_6$, in the high temperature regime [270] qualitatively resembles $L(T)$ for UPt_3, having a maximum at $T \sim 20$ K where it attains a value of about 2.5 L_0 but falls towards L_0 at higher temperatures.

Ultrasonic Attenuation

Ultrasonic experiments measure the attenuation and velocities of sound waves and, through the electron–phonon interaction, provide information about the

electronic system. At temperatures much lower than the Debye temperature, the attenuation of the sound wave due to anharmonic phonon interactions should be negligible, and the electron–phonon interaction should provide the dominant contribution to the attenuation. In this case, one expects a strong similarity between the ultrasonic attenuation coefficient and the electrical conductivity. Just like the optical conductivity $\sigma(\omega)$ yields the lifetime of a photon, the ultrasonic attenuation $\alpha_{\underline{q},\hat{\epsilon}}(\omega)$ yields the lifetime of a phonon. This similarity is expected since, for many purposes, the effect of a phonon can be interpreted in terms of the effect of the accompanying electric field. In analogy with the conductivity, one expects that in the limit $q \rightarrow 0$, the renormalization of the scattering rate will cancel with the mass enhancement. Thus, in the long wavelength limit, the ultrasonic attenuation is expected to be unrenormalized. The most noticeable difference between ultrasonic attenuation and optical absorption occurs through the extremely different magnitudes of the velocities of the corresponding waves. If the conditions allow the heavy quasi–particles to co–move with the sound wave, it becomes possible for the quasi–particles to surf–ride and continuously absorb energy from the sound wave. For example, if a longitudinally polarized sound wave with phase velocity $\frac{\omega}{q}$ propagates through a gas of heavy quasi–particles, it strongly perturbs the quasi–particles with velocities almost parallel and almost equal to the phase velocity of the wave. In the frame of reference travelling with the wave, the quasi–particle is at rest and experiences an essentially time independent electric field. The electric field continuously transfers energy from the wave to the quasi–particles that have the same velocity. If there is a slight mismatch in the velocities, quasi–particles with lower velocities than the wave draw energy from the wave and accelerate, whereas quasi–particles that are moving faster lose energy and slow down. This results in the rate of energy loss of the wave being proportional to the derivative of the distribution of quasi–particle velocities, which is evaluated at the velocity of sound. At temperatures below those at which the heavy quasi–particles are being formed, the Fermi velocity is comparable to the sound velocity in contrast to normal metals. So the attenuation of sound waves may be expected to be larger than in ordinary metals. On the other hand, due to the approximate equality between the sound velocities [271], the Born–Oppenheimmer approximation no longer applies and the sound wave may have to adjust adiabatically to the quasi–particles' motions. The induced coupling of the phonon modes can also lead to damping. It is found that the ultrasonic attenuation for $CeCu_6$, UPt_3, and UBe_{13} have magnitudes comparable to that of ordinary metals [27]. This suggests that the magnitude of the coupling between the quasi–particle and sound wave is reduced from that observed in normal metals due to the appearance of vertex corrections. Nevertheless, the strong electron–phonon coupling shows up in other elastic properties. In ordinary metals, the attenuation is relatively featureless and is described by

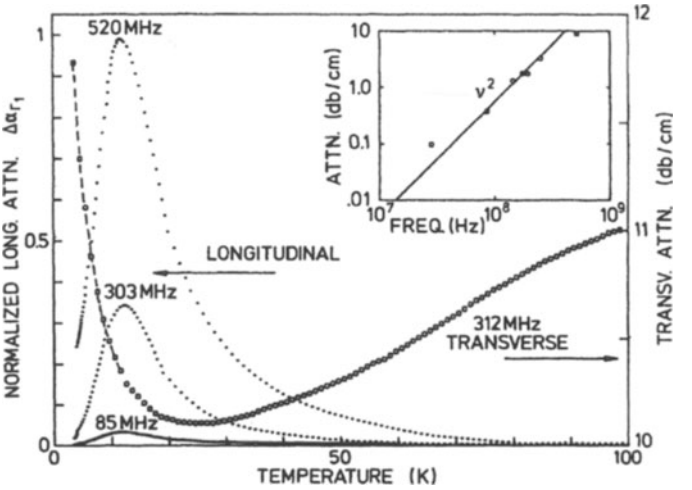

Fig. 10.41. The temperature dependence of the transverse (312MHz, q || b, u||c) and longitudinal ultrasonic attenuation coefficients $|alpha(\nu)$ of UPt_3 at various frequencies ν. The longitudinal data are normalized to the 520–MHz peak. The inset shows the ν^2 dependence. [After Müller *et al.* (1986), [272]]

a Drude–like formula,

$$\alpha(\omega) = \frac{\omega^2 \tau}{1 + \omega^2 \tau^2} \frac{\lambda^2 \rho(\mu)}{\rho c^3} , \tag{10.157}$$

where λ is the electron–phonon coupling, c is the velocity of sound, and ρ is the mass density. In heavy–fermion compounds at high temperatures, the magnitude and frequency dependence of the attenuation is reasonably similar to normal metals. However, anomalous temperature dependences are observed in the low temperature quasi–particle phases. The temperature dependence of the attenuation of longitudinal sound in UPt_3 shows an anomalous peak at 12 K [272], and has an amplitude that scales with the square of the frequency of sound. The temperature dependence of the attenuation coefficient is shown in Fig. 10.41. Since the anomaly is only present in the absorption of longitudinal sound but not of transverse sound, the origin of this peak has been ascribed by Schotte *et al.* [273] to the existence of a breathing mode. In the breathing mode, the lattice adjusts locally to the state of the f ion, and vice versa. Thus, the sound waves are coupled to the heavy quasi–particle bands. This type of coupling is also expected to modify the phonon dispersion relations due to hybridization with the quasi–particle bands. At temperatures above 12 K, the heavy quasi–particle masses have not fully formed, and so the coupling becomes incoherent. Thus, the effect of an increase in temperature results in a reduction of the attenuation coefficient. Since in the model of Schotte *et al.* the sound wave mainly couples to the

thermally excited quasi–particles, the coupling is ineffective in attenuating sound at temperatures lower than 12 K. Therefore, the sound wave attenuation diminishes for temperatures lower than the peak temperature. At still lower temperatures, but still in the normal state, the attenuation coefficient of UPt_3 decreases proportional to T^2 with increasing temperatures [30]. This is indicative of the T^2 dependence of the quasi–particle scattering rate. The observation of an anomalous peak in the phonon density of states [274] provides supporting evidence for the validity of the breathing mode picture of UPt_3. The attenuation of longitudinal sound waves in $CeCu_6$ [275] is somewhat similar to that of UPt_3 in that it shows a peak below a temperature of 10 K. However, unlike UPt_3, the intensity of the peak in $CeCu_6$ scales linearly with frequency. Furthermore, the peak broadens and shifts to higher temperatures with increasing phonon frequency.

10.3.3 Dynamic Magnetic Properties

Just as the effects of the collective magnetic fluctuations and the low temperature gas of heavy quasi–particles show up in the transport and thermodynamic properties of heavy–fermion materials, the effects of these excitations also show up in the magnetic properties.

Nuclear Magnetic Relaxation

In the presence of an applied static magnetic field, a nuclear spin relaxes to its ground state through interaction with the fluctuations of the electronic magnetic moments. On assuming that the coupling is weak so that the Born Approximation is valid, the longitudinal relaxation rate $1/T_1$ can be expressed in terms of the hyperfine field coupling $A_{hf}(\underline{r} - \underline{r}')$ between the nuclear spin point $\underline{r}'$ to the magnetization density $\underline{M}(\underline{r})$ and the dynamic susceptibility $\chi^{+,-}(\underline{q};\omega)$ via

$$\frac{\hbar}{T_1} = k_B\, T\, \frac{1}{N} \sum_{\underline{q}} \left| A_{hf}(\underline{q}) \right|^2 \left[\frac{Im\ \chi^{+,-}(\underline{q};\omega_N)}{\hbar\, \omega_N} \right] . \tag{10.158}$$

In this, $A_{hf}(\underline{q})$ is the spatial Fourier transform of the hyperfine field, and ω_N is the nuclear Larmor frequency which, in conventional metals, can be neglected as it is much smaller than the lowest energy scale for the electrons. The dynamic magnetic susceptibility is the spatial and temporal Fourier transform of the quantity $\chi^{\alpha,\beta}(\underline{r};t)$ defined by the causal correlation function involving the commutator of the components of the magnetization density

$$\chi^{\alpha,\beta}(\underline{r};t) = -\frac{i}{\hbar} < | \left[M^{\alpha}(\underline{r};t)\ ,\ M^{\beta}(0;0) \right] | > \Theta(t)\ , \tag{10.159}$$

where $\Theta(t)$ is the Heaviside step function. In the paramagnetic state, the susceptibility tensor is spin rotationally invariant so one has

$$\chi^{x,x}(\underline{r};t) = \chi^{y,y}(\underline{r};t) = \chi^{z,z}(\underline{r};t) = \frac{1}{2}\, \chi^{+,-}(\underline{r};t)\ . \tag{10.160}$$

Due to the Shiba relation [276], one expects that, for a local paramagnetic Fermi liquid in the limit $\omega \rightarrow 0$, the imaginary part of the susceptibility should satisfy the equation

$$\lim_{\omega \rightarrow 0} (2 J + 1) \frac{J (J + 1)}{3} \frac{Im \chi^{z,z}(0;\omega)}{\hbar \omega} = \pi \left(\frac{\chi^{z,z}(0;0)}{g \mu_B} \right)^2 . \quad (10.161)$$

This suggests that, with a $\underline{q}$ independent hyperfine coupling, the longitudinal nuclear relaxation rate of heavy–fermion systems should vary as the square of the low temperature static susceptibility or the square of the γ coefficient in the specific heat, much the same as the correlation between the coefficient of the T^2 term of the resistivity and the linear T term in the specific heat found by Kadowaki and Woods [237]. For materials such as UBe_{13} [277], the scaling with the square of the quasi–particle density of states is not followed due to the $\underline{q}$ dependence of the coupling and vertex corrections. Nevertheless, magnetic relaxation experiments on heavy–fermion compounds at low temperatures do show the linear T Korringa relaxation rate with an enhanced magnitude, indicating the existence of heavy quasi–particles.

The Knight shift K is a shift in the nuclear resonance field which provides a measure of the induced field at the site of the nucleus due to the polarization of the electronic system. It is often found that the induced field is dominated by the bulk static susceptibility $\chi^{z,z}(0;0)$ of the f electrons and so can be used as an estimate of the strength of the average hyperfine field

$$K = \frac{A_{hf}}{g_N \mu_N} \chi^{z,z}(0;0) . \quad (10.162)$$

Assuming a local isotropic hyperfine field and isotropic $\underline{q}$ independent magnetic fluctuations, one finds the dimensionless Korringa product

$$S = k_B T K^2 \frac{T_1}{\hbar} \quad (10.163)$$

has the theoretical value

$$S_0 = \frac{(2 J + 1) J (J + 1)}{6 \pi} \left(\frac{g_e \mu_B}{g_N \mu_N} \right)^2 \quad (10.164)$$

for ions with magnetic moment J. Corrections must be made to this relation for heavy–fermions compounds with anisotropic susceptibilities. The magnitude of the Korringa ratio is defined as $S S_0$. Since the relaxation rate involves a sum over all $\underline{q}$, deviations from the ideal value of the Korringa ratio may be used to infer the relative magnitude of the $\underline{q}$ averaged susceptibility to the uniform ($\underline{q} = 0$) susceptibility.

The Knight shift and the longitudinal relaxation rate can be used to estimate the typical frequency of local moment fluctuations. Assuming a phenomenological $\underline{q}$ independent relaxational form for the dynamic susceptibility

$$\chi^{z,z}(\omega) = \chi^{z,z}(0) \frac{\Gamma}{\Gamma - i \hbar \omega} , \quad (10.165)$$

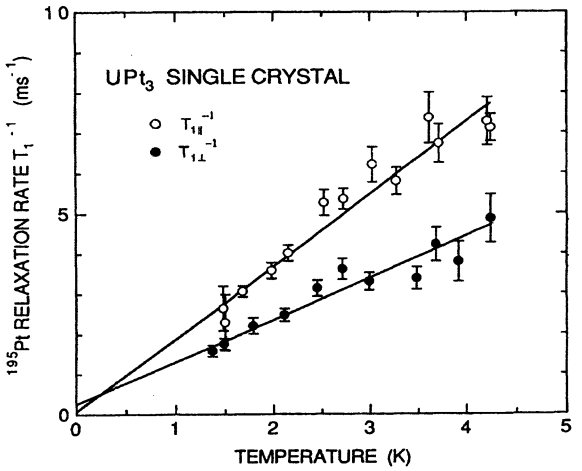

Fig. 10.42. The temperature dependence of the spin–lattice relaxation rate $1/T_1$ for ^{119}Pt in UPt_3. The relaxation rate is anisotropic and the results are measured with the static field applied parallel and perpendicular to the crystal c–axis. [After Vithayathil *et al.* (1991), [278]]

where Γ is the relaxation rate, one finds that, if $\hbar\,\omega_N \ll \Gamma$, the transverse relaxation rate can be expressed in terms of the limit

$$\lim_{\omega_N \to 0} \frac{Im\ \chi^{z,z}(\omega_N)}{\hbar\,\omega_N} = \frac{\chi^{z,z}(0)}{\Gamma}\,. \tag{10.166}$$

Thus, the spin–fluctuation energy is estimated as

$$\Gamma = 2\,k_B\,T\,\frac{T_1}{\hbar}\,|\,A_{hf}\,|^2\,\chi^{z,z}(0) \tag{10.167}$$

Above the Néel temperature, the NMR longitudinal relaxation rate of UPt_3 is linear in T [31], but below T_N, has a large anisotropic coefficient that varies from 1810 to 1050 $\mathrm{sec}^{-1}\,\mathrm{K}^{-1}$ for fields parallel and perpendicular to the crystalline c–axis [278]. The anisotropy of the relaxation rate (shown in Fig. 10.42) is accompanied by a large anisotropic Knight shift [279] which reflects the anisotropy of the bulk susceptibility. From estimates of the hyperfine field taken from the Knight shift, a $\underline{q}$ averaged fluctuation energy Γ of the order of 9 meV was deduced from the measurements. This energy is quite large when compared with the temperature scale over which the large specific heat γ value develops. The Korringa ratio was found to be of the order of 1.2, which indicates that the system supports low–energy paramagnon excitations, consistent with the finding of a $T^3 \ln T$ term in the low temperature specific heat.

The linear T dependence of the longitudinal relaxation rate in UBe_{13} has been observed for temperatures less than $T = 1.5$ K, which is much lower

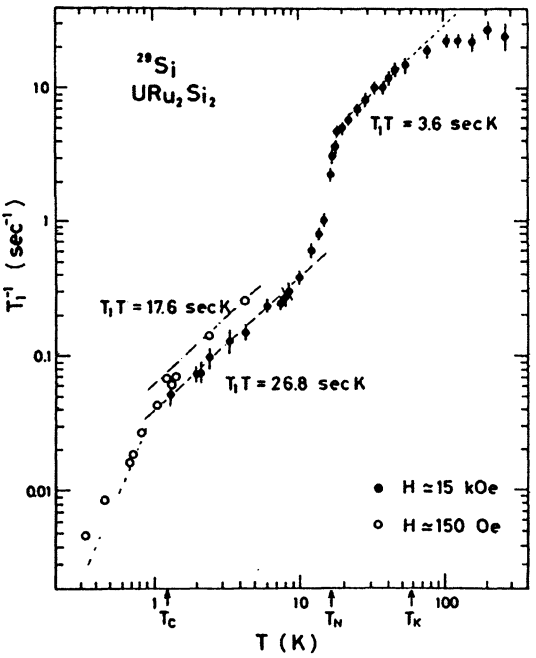

Fig. 10.43. The temperature dependence of the spin–lattice relaxation rate $1/T_1$ for ^{29}Si in external field (open circles) and ^{105}Ru in zero field (solid circles) in URu_2Si_2. The relaxation rate shows an abrupt change at the hidden ordering temperature T_N and at the superconducting transition temperature T_c. [After Kohra *et al.* (1987), [281]]

than the temperature of 10 K, where the specific heat enhancement starts forming. The Korringa ratio is only 0.3, which is much reduced from the ideal value, suggesting the presence of strong antiferromagnetic correlations [280].

Below the temperature of about $T = 70$ K, the longitudinal relaxation rate of URu_2Si_2 follows the Korringa linear T dependence indicative of the formation of a Fermi liquid. This linear dependence is interrupted at the Néel temperature of $T_N = 17.5$ K, and the relaxation rate again follows a linear law a little below T_N, but with a reduced coefficient [281, 282]. The temperature dependence of $1/T_1$ for URu_2Si_2 is shown in Fig. 10.43. The data does not show any sign of a spin–wave contribution to the relaxation process. For non–interacting quasi–particles, the coefficient of the T term in the Korringa rate is proportional to the square of the quasi–particle density of states. Thus, the drop in the coefficient of T found on entering the Néel state is indicative of a partial gapping of the Fermi surface. This is consistent with the drop in the specific heat γ from 180 mJ mol^{-1} K^{-2} above to 50 mJ mol^{-1} K^{-2} below the transition. Although no direct evidence of antiferromagnetic ordering was observed in NMR measurements at ambient pressure, experiments

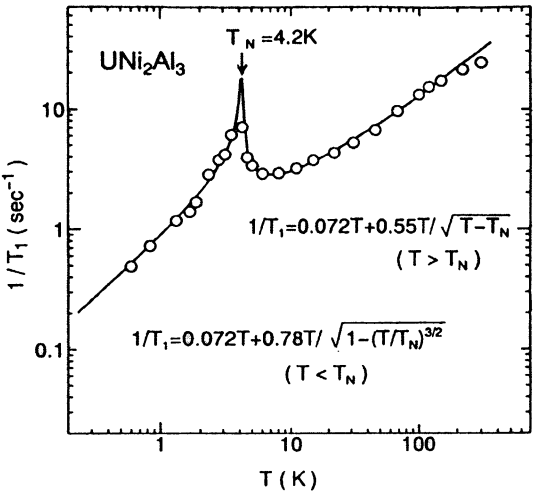

Fig. 10.44. The temperature dependence of the spin–lattice relaxation rate $1/T_1$ for ^{27}Al in UNi_2Al_3. [After Kyogaku *et al.* (1993), [283]]

at $P = 8.3$ k bar [224] show a well defined splitting of the resonance line at T_N. The splitting is consistent with the staggered exchange splitting from a type I antiferromagnetic structure. In addition, the NMR spectra showed a substantial contribution from the un–split resonance line that continued, but diminished in intensity as the temperature was reduced below the Néel temperature. Since the magnitude of the staggered exchange field starts levelling off below 15 K, and as the ratio of intensities of the split and un–split lines continuously change with T, it has been suggested that regions of antiferromagnetism and paramagnetism coexist inside the single crystal sample but with temperature dependent volume fractions. The interpretation based on the temperature and pressure dependent volume fractions of the two phases is consistent with the spontaneous magnetic moments inferred from neutron diffraction experiments under pressure [225]. However, as the magnitude of the specific heat jump at T_N does not scale with the volume fraction, it has been suggested that another (as yet unknown) type of ordering also occurs at T_N.

The temperature dependence of $1/T_1$ of UPd_2Al_3 [283] is very similar to that found in URu_2Si_2, in that it shows a Korringa rate that shows a partial reduction of the density of states at the Fermi energy on entering the magnetically ordered state. The properties of UNi_2Al_3 are quite different from UPd_2Al_3, in that the Korringa law does not apply above $T_N = 4.2$ K, and any linear T coefficient is quite small. As seen in Fig. 10.44, the magnetic transition is marked by a peak in $1/T_1$, which is indicative of strongly antiferromagnetically coupled local moments. At lower temperatures, superconductivity occurs before any linear T region develops. When a sufficiently

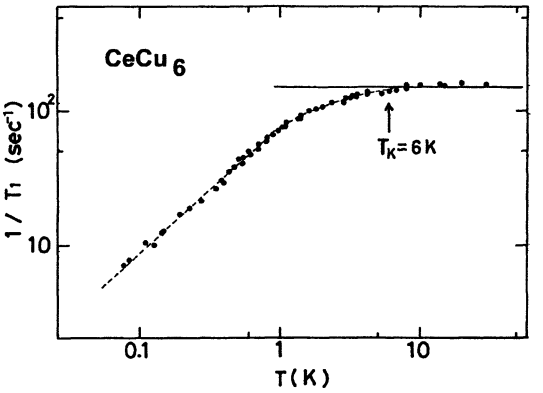

Fig. 10.45. The temperature dependence of the spin–lattice relaxation rate $1/T_1$ for ^{63}Cu (crosses) in $CeCu_6$ and ^{29}Si (solid circles) in $CeRu_2Si_2$. [After Kitaoka *et al.* (1985), [284]]

large magnetic field is applied to suppress the superconductivity, a linear T dependence can be resolved.

The longitudinal magnetic relaxation rates have been measured at the Cu site of $CeCu_6$ [284] and at the Cu and Si sites of $CeCu_2Si_2$ [277,285,286]. In $CeCu_2Si_2$, the low temperature relaxation rate varies linearly with T up to $T = 5$ K, but has a coefficient of proportionality of 5 sec^{-1} K^{-1}. This large value of the slope should be contrasted with the corresponding slope of 0.025 sec^{-1} K^{-1} found in the compound $LaCu_2Si_2$, which does not contain any f electrons. The enhanced value of the low temperature relaxation rate is even more apparent in $CeCu_6$, where $1/T_1$ follows a linear Korringa law below about $T = 0.2$ K with a slope of 88 sec^{-1} K^{-1} [284]. The relaxation rates for $CeCu_6$ and $CeRu_2Si_2$ are shown in Fig. 10.45. At higher temperatures, the relaxation rate of $CeCu_6$ starts changing form and shows a plateau associated with the cross–over temperature T_K of 12 K, and above this, it shows a slow decrease with increasing temperature due to the Curie–like variation of the susceptibility. From the temperature variation of the longitudinal relaxation rate, one finds that the low temperature Fermi liquid in $CeCu_6$ only starts forming at a temperature lower than the cross–over temperature by a factor of 60, whereas for UBe_{13} this ratio is estimated to be about 9. It is noteworthy that the result for $CeCu_6$ does not show the scaling expected from the single–impurity Anderson model, despite the fact that the non–local contributions to the magnetic response found from neutron scattering are estimated as being only 10% . However, the ratio found for UBe_{13} is more in line with the expectation based on the single–impurity Anderson model [287] despite the presence of strong antiferromagnetic correlations as indicated by the Korringa ratio.

The transverse magnetic relaxation rate $1/T_2$ provides information about processes whereby the nuclear spin precession is dephased and does not involve transitions where there is a change of Zeeman energy. On neglecting the effects of static random local fields, the transverse relaxation rate is given by perturbation theory as

$$\left(\frac{\hbar}{T_2}\right)^2 = \frac{3}{4} I(I+1) \mid A_{hf} \mid^4 \left[\frac{1}{N} \sum_{\underline{q}} \chi^2(\underline{q}) - \left(\frac{1}{N} \sum_{\underline{q}} \chi(\underline{q}) \right)^2 \right] \tag{10.168}$$

which measures the non–uniform component or $\underline{q}$ variation of the static susceptibility. For systems close to a magnetic instability in which $\chi(\underline{q})$ peaks up around a ordering vector $\underline{Q}$, one expects that the susceptibility may have an Ornstein–Zernicke form with a correlation length ξ,

$$\chi(\underline{q}) = \frac{\chi(\underline{Q})}{1 + \mid \underline{q} - \underline{Q} \mid^2 \xi^2} \,. \tag{10.169}$$

Thus, one finds that

$$\left(\frac{\hbar}{T_2}\right)^2 \propto \xi^{-3} \chi^2(\underline{Q}) \tag{10.170}$$

and as, from the simple scaling hypothesis $\chi(\underline{Q}) \propto \xi^2$, one has

$$\frac{1}{T_2} \propto \xi^{\frac{1}{2}} \,. \tag{10.171}$$

Thus, one expects $1/T_2$ to be enhanced in the vicinity of a magnetic phase transition. Furthermore, in the ordered state, the precession frequency is expected to be changed due to the presence of static magnetic moments or local fields. This information can be used to provide information about the size of the ordered moments.

In addition to $1/T_2$ relaxation rates, NMR linewidths are also sensitive to local static magnetic fields [288]. This has provided some additional information on the $T = 17.5$ K transition in URu_2Si_2. In this compound it was found that, for temperatures above T_N, the linewidth is linearly–dependent on the field and has an anisotropy similar to that of the sample's magnetization. However, below T_N, the measurements also show an additional isotropic, field–independent, contribution to the linewidth which is shown in Fig. 10.46. The temperature dependence of the isotropic component is similar to that expected from a mean–field transition that occurs at T_N. Since at ambient pressures the signal is predominantly from the paramagnetic regions of the sample, and as (unlike the magnetic ordering) the field–independent contribution to the width is isotropic, the authors suggest that the width is due to the coupling to the unknown or "hidden" order parameter.

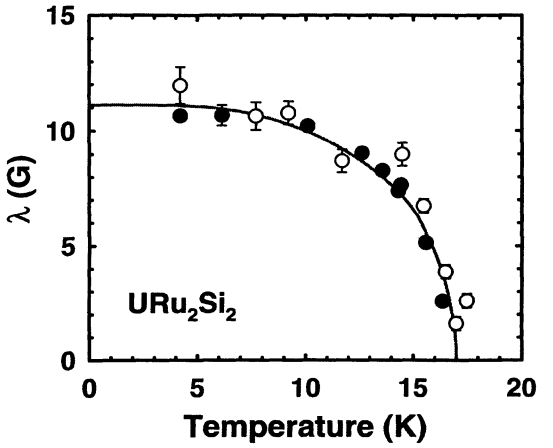

Fig. 10.46. The temperature dependence of the anomalous component of the ^{29}Si line width $\lambda(T)$ in URu_2Si_2. Open circles H $\parallel$ to c, solid circles H $\perp$ to c. [After Bernal *et al.* (2001), [288]]

Muon spin relaxation works in much the same way as NMR, but the zero field precession rate is much more sensitive to ordered magnetic moments with small magnitudes. Also as the muon precession frequency is extremely slow, μSR is effective in discriminating between slowly varying magnetic order and static order. Therefore, muon spin relaxation measurements have played a particularly important role in identifying magnetic phase transitions, specially as the transition to magnetically ordered phases of heavy–fermions may or may not be accompanied by specific heat anomalies. In the case of UPt_3, Cooke *et al.* [289] discovered the existence of magnetic ordering at $T_N = 5$ K through the zero field muon spin relaxation line width $1/T_2$, even though no corresponding specific heat anomaly was observed at the transition. The transverse relaxation rate showed the growth of an additional contribution below T_N corresponding to an increase in the local fields due to a very small moment of order 0.01 μ_B. The small magnitude of the ordered moment is presumably responsible for the absence of a specific heat anomaly at T_N. The existence of magnetic ordering was rapidly confirmed by neutron scattering experiments [290]. However, later muon resonance experiments on better quality samples no longer showed this feature in the muon relaxation rate [291]. This discrepancy is presumably caused by the exact cancellation of the field due to the ordered moment at the muon sites which is disrupted by the presence of disorder and thereby revealing a finite staggered magnetization.

In URu_2Si_2, the magnetic transition is accompanied by a large change in the specific heat at $T_N = 17.5$ K, but the size of the average ordered magnetic moments found from neutron and x–ray scattering are only of the

order of 0.03 μ_B. Although transverse relaxation rates and Knight shift measurements do indicate that magnetic ordering occurs, the static ordered magnetic moments inferred from the muon measurements [292,293] are an order of magnitude smaller than the average magnetic moments found from the neutron scattering experiments at ambient pressure. Due to the large magnitude of the specific heat jump and the small magnitude of the averaged ordered moments, it has been suggested [294–296] that the primary ordering is non–magnetic. However, polarized diffraction experiments and a symmetry analysis seem to rule out higher order multipolar transitions [297]. Also, measurements in applied fields do not yield evidence for exotic types of multiple spin correlations [298].

In $CeAl_3$, by contrast with URu_2Si_2 where a large specific heat anomaly is found at T_N, only a slight and sample dependent specific heat anomaly has been observed. However, the muon spin resonance spectrum shows evidence that magnetic order develops in $CeAl_3$ at $T = 1.5$ K [299,300]. Furthermore, near $T = 0.7$ K where the susceptibility shows a maximum, the ordered moment is quite sizeable and has been reported to be as large as 0.5 μ_B [301]. The lack of correlation between the size of the ordered moments and the size of the specific heat jump is not understood. However, the magnetic ordering does appear to show up in the resistivity of single crystals where a T^3 variation has been observed [302]. The T^3 variation is indicative of the existence of a low–energy branch of spin–wave excitations.

Evidence for static magnetic order in $CeCu_2Si_2$ in zero field and longitudinal field muon spin relaxation has been reported [303] just above the superconducting transition temperature $T_c = 0.7$ K. The inferred size of the ordered magnetic moments is of the order of 0.1 μ_B. However, the intensity of the NQR line decreases monotonically with decreasing temperature and shows no anomalous broadening associated with ordered magnetic moments [304,305]. The magnetic ordering persists in the superconducting phase and competes with the superconductivity [306–308]. Investigations show evidence that the superconductivity and magnetic ordering may exist in separate thermodynamic phases, but these are phases for which T_c and T_N coincide in the best quality samples. Application of a magnetic field suppresses the superconductivity transition temperature but (initially) has no effect on T_N. The zero field muon spin relaxation experiments show two components that decay at rates that differ by about an order of magnitude [308]. The data can be interpreted in terms of the sample existing in two separate phases: the superconducting phase and a magnetic A phase. An estimate of the weight of these two phases can be made based on the amplitudes of the two components. For temperatures above the superconducting transition, the proportion of the A phase increases with decreasing T, reaching a maximum at T_c with a value of $\frac{3}{4}$. The magnitude of the specific heat jump at the superconducting transition seems to scale with the relative weights of the two phases. As the temperature is lowered, the volume fraction associated with the superconduc-

tor grows by expelling the A phase and saturates at about a volume fraction of $\frac{2}{3}$. The relative weights of the superconducting phase and the A phase are extremely sensitive to the deviations from stoichiometry of Ce [189]. Doping experiments have shown that substitutionally doping Th on the Ce sites can lead to the formation of an antiferromagnetic state with a significantly larger magnetic ordering temperature for Th concentrations of only about 7 %.

Neutron Scattering Cross–section

The most direct way of obtaining information about the magnetic excitations in a material is through inelastic neutron scattering experiments in which momentum $\hbar\underline{q}$ and energy $\hbar\omega$ are transferred between the neutron and the sample. The neutron interacts with the electronic spins via a dipolar interaction and yields information about the imaginary part of the dynamic susceptibility. The differential scattering cross–section for an unpolarized beam of neutrons due to purely magnetic scattering, is given by

$$\frac{d^2\sigma}{d\omega d\Omega} = N\left(\frac{g_n e^2}{g\mu_B m_e c^2}\right)^2 \frac{k}{k'}\left[1+N(\omega)\right]\left|F(q)\right|^2 \sum_{\alpha,\beta} Im\chi^{\alpha,\beta}(\underline{q};\omega) \times\left(\delta_{\alpha,\beta}-\hat{q}_\alpha\hat{q}_\beta\right). \tag{10.172}$$

Here, $F(q)$ is the atomic form factor for the magnetic moments, k and k' are the magnitude of the incident and scattered neutron wave vectors, and $N(\omega)$ is the Bose–Einstein distribution function. The above expression should also be multiplied by the Debye–Waller factor due to zero point and thermally excited lattice vibrations.

Generally, the low–energy dynamic magnetic response of a heavy–fermion system is interpreted as the sum of a large quasi–elastic relaxation contribution that is $\underline{q}$ independent and $\underline{q}$ dependent terms associated with spatial magnetic correlations. The relaxational component is of the form

$$Im\left[\chi(q;\omega)\right] = A\,\frac{\hbar\,\omega\,\Gamma}{\hbar^2\,\omega^2+\Gamma^2} \tag{10.173}$$

which is indicative of local moment fluctuations. The width of the quasi–elastic peak seems to saturate at low temperatures but increases with increasing T at higher temperatures. The $\underline{q}$ independence and the temperature variation of the width Γ found in some $\bar{C}e$ systems [229,230,309] are similar to the behaviors found in the single–impurity Anderson model [310], where

$$\Gamma(T) \sim \Gamma(0) + B\sqrt{T}\,. \tag{10.174}$$

The temperature dependence of the quasi–elastic linewidth of $CePb_3$ is shown in Fig. 10.47. The product of the zero temperature limit of the linewidth and

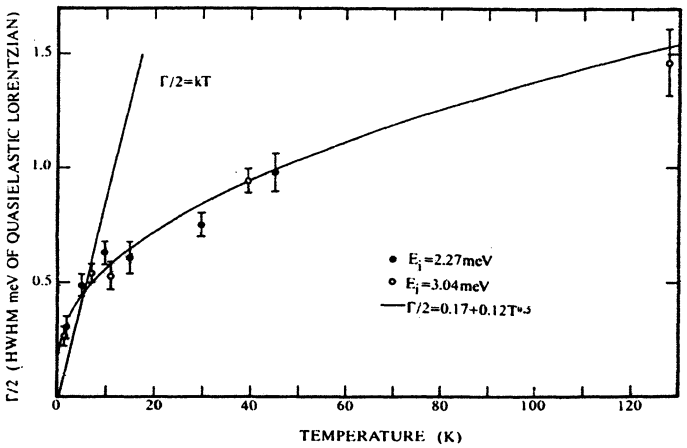

Fig. 10.47. The temperature dependence of the experimentally determined half-width Γ of the quasi-elastic peak in $CePb_3$. [After Balakrishnan *et al.* (1989), [313]]

the linear T term in specific heat, $\Gamma(0)$ γ, should scale inversely with the Wilson ratio. For $CeAl_3$ [309], $CeCu_6$ and $CeRu_2Si_2$ [311, 312] respectively, the product has magnitudes of 0.77, 0.67 and 0.70 J meV/mole/K^2 , even though the widths show considerable variation with $\underline{q}$. By contrast, in $CePb_3$ where no $\underline{q}$ dependence was observed [313], the product is only 0.034, whereas the Wilson ratio obtained from thermodynamic measurements at the same temperatures is of the order of unity [181]. Similar narrow quasi-elastic peaks are found in U heavy-fermion systems [314] and can have a wide range of values for the product $\Gamma(0)$ γ. The narrow quasi-elastic response can also be interpreted as the response of a gas of heavy quasi-particles in a very narrow band. The $\underline{q}$ dependent contributions may signify fluctuations associated with long-ranged order or competing types of short-ranged order. In particular, the quasi-particle contribution to the susceptibility should show up at very low temperatures as a narrow quasi-elastic peak at small energy and momentum transfers. The intensity of the peak should be proportional to the quasi-particle weight but may be significantly reduced by spin-orbit scattering. For the cerium heavy-fermion compounds [228, 229, 231–233], the higher energy spectra also show inelastic peaks due to crystal field excitations. As seen in Fig. 10.48, the localized crystal field excitations can be reasonably described by the single impurity Anderson model.

Inelastic neutron scattering experiments on UPt_3 show the existence of a local relaxational component to the response which has a width of $\Gamma = 9$ meV [315]. The experimental data are shown in Fig. 10.49. The $\underline{q}$ dependence is associated with three different types of magnetic correlations. Long wavelength ferromagnetic (0,0,0) fluctuations gradually start developing below 150 K [316] and show a $\underline{q}$ dependent energy width $\Gamma(q) \propto q$. These

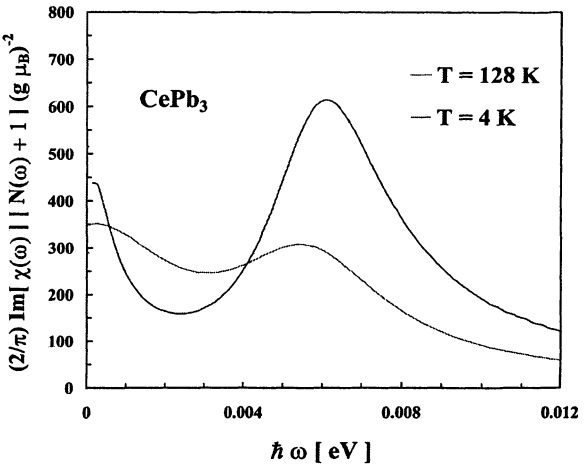

Fig. 10.48. The neutron inelastic scattering cross–section calculated in the NCA, for the single impurity Anderson model with parameters appropriate for $CePb_3$. The spectrum consists of a low energy quasi–elastic peak and an inelastic peak due to crystal field excitations in a cubic environment

fluctuations are similar to paramagnons since, for $q \rightarrow 0$ fluctuations, one expects

$$1 - U \ Re\, \chi_0(\underline{q};\omega) \sim 1 - U\, \rho(\mu) + O\left(\frac{q}{k_F}\right)^2 \tag{10.175}$$

and

$$Im\, \chi_0(\underline{q};\omega) \sim \frac{\pi}{4}\, \rho(\mu) \left(\frac{\hbar\, \omega\, k_F}{\mu\, q} \right). \tag{10.176}$$

Within RPA, this behavior of the quasi–particle susceptibility produces the pre–critical fluctuations appropriate to a damped, but conserved, order parameter. The paramagnon fluctuations could be responsible for the $T^3 \ln T$ term observed in the specific heat and the value of the large Korringa ratio [278, 279] . In addition to the (0,0,0) fluctuations, there are two types of antiferromagnetic modes in the spectrum. A quasi–elastic peak starts developing below $T = 30$ K centered at momentum transfers of $(0, 0, 1)$ and is characterized by a large energy width $\Gamma \sim 5$ meV [317, 318]. This signifies the presence of a rapidly changing short–ranged magnetic order in which the two uranium ions in the unit cell are antiferromagnetically coupled. This produces an antiferromagnetic correlation between the spins along the c axis and a ferromagnetic correlation between the spins in the basal plane. The intensity of the inelastic peak decreases as $\underline{q}$ is varied away from $(0, 0, 1)$. The width of the peak $\Delta q \sim \xi^{-1}$ provides a measure of the correlation

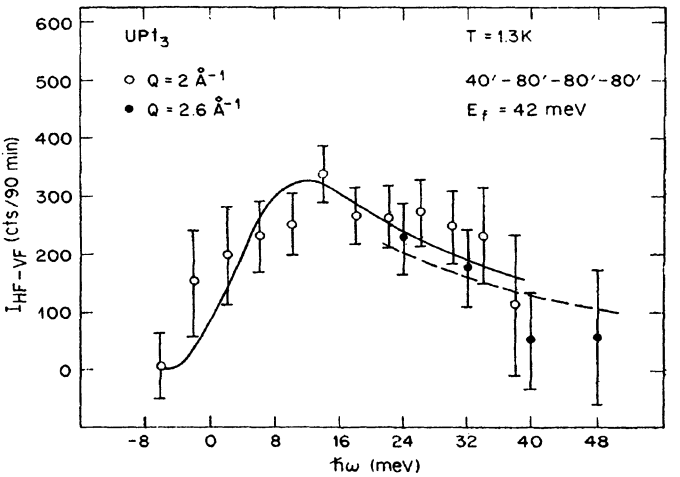

Fig. 10.49. The 9 meV quasi–elastic peak observed in polarized beam inelastic neutron scattering experiments on UPt_3. [After Aeppli *et al.* (1985), [315]]

length ξ. The anisotropy of the correlation length in UPt_3 suggests that fluctuating in–plane ferromagnetic correlations are present for temperatures as large as $T = 100$ K. The second type of antiferromagnetic fluctuations is associated with a wave–vector of $(\frac{1}{2}, 0, 1)$ which develops at $T = 18$ K and peaks at a frequency of the order of 0.2 meV. Magnetic ordering occurs at this wave–vector below the critical temperature of $T_N = 5$ K, as evidenced by the development of magnetic Bragg peaks at $(\frac{1}{2}, 0, 1)$, since the magnetic Bragg peak intensities are (apart from the temperature dependent Debye–Waller factor) proportional to the square of the sub–lattice magnetization. The magnetic moments are in the basal plane of the hexagonal structure and are aligned parallel to the propagation vector $\underline{Q} \equiv (\frac{1}{2}, 0, 0)$. The magnitude of the ordered moments found through neutron diffraction experiments are anomalously small. The measured ordered moment only attain the value of 0.02 μ_B per U ion just above the superconducting transition temperature T_c [290]. The temperature dependence of the intensity of the magnetic Bragg peak of UPt_3 is shown in Fig. 10.50. The temperature dependence of the magnitude of the sub–lattice magnetization $\underline{M_Q}(T)$ follows the scaling law

$$| \underline{M_Q}(T) | \propto (T_N - T)^{\beta} \tag{10.177}$$

for $T_N > T$, where $\beta \sim 0.5$. The value of the critical exponent is not consistent with the values expected for three dimensional ordering of localized magnetic moments. Similar values of β are also found in other systems with anomalously low magnetizations such as URu_2Si_2 at ambient pressure. The critical exponents β found for other magnetically ordered heavy–fermion systems with larger moments such as UNi_2Al_3, UPd_2Al_3 and U_2Zn_{17}, have

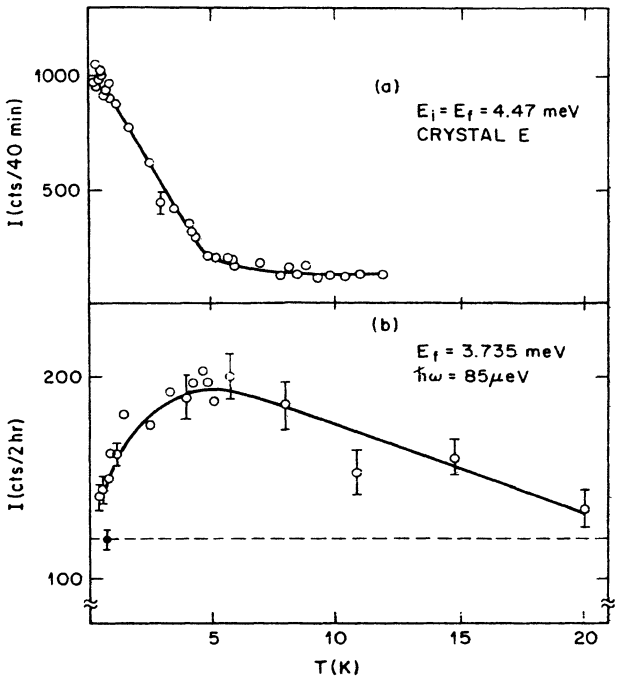

Fig. 10.50. (a) The temperature dependence of the elastic scattering intensity at $q = (\frac{1}{2}, 0, 1)$. For purposes of comparison, (b) shows the temperature dependence of scattering with energy transfers of 85 μeV at $q = (0.52, 0, 0.99)$. [After Aeppli *et al.* (1988), [319]]

values close to 0.35 which are within the range expected for three dimensional ordering of localized moments. For comparison, we show the temperature dependence of the magnetic Bragg peak intensity of UPd_2Al_3 in Fig. 10.51. The correlation lengths associated with the Bragg peaks of UPt_3 remain finite above and below T_N, and are of the order of 250 – 500 Å [319]. As the cross–section for elastic Bragg scattering is proportional to the energy conserving Dirac delta function $\delta(\omega)$, measurements of the elastic Bragg peaks involve windows of energy transfers which includes the point $\omega = 0$. Thus, the Bragg intensity also contains contributions from low–energy critical scattering, which have finite correlation lengths. Since the Bragg peaks were observed to have finite correlation lengths, questions are raised as to the nature of the ordering whether it is quasi–static short–ranged ordering, or whether it is long–ranged ordering that is interrupted by the presence of defects [320]. Muon spin resonance experiments confirmed the presence of magnetic ordering at $T_N \sim 5$ K [289, 321]. As the temperature is reduced from just above the superconducting transition temperature, the intensity of the antiferromagnetic Bragg peaks shows a sudden change of slope as it starts

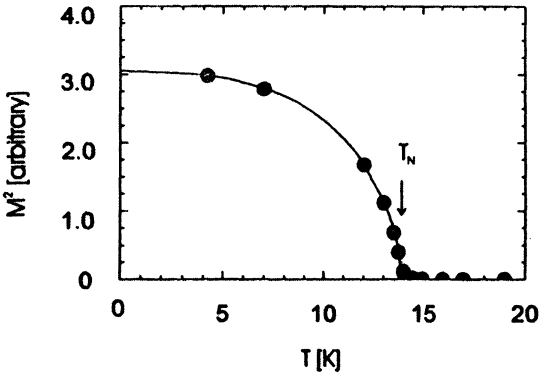

Fig. 10.51. The temperature dependence of the intensity of the $(0, 0, \frac{1}{2})$ antiferromagnetic Bragg peak in UPd_2Al_3. [After Petersen *et al.* (1994), [344]]

to decrease. This indicates that the antiferromagnetic ordering coexists and competes with the superconductivity [322].

Inelastic neutron scattering experiments on UBe_{13} [323, 324] at $T \sim 10$ K show an approximately $\underline{q}$ independent relaxational paramagnetic response with a large quasi–elastic width $\Gamma = 14$ meV. The approximate $\underline{q}$ independence of the inelastic scattering cross–section is indicative of the localized nature of the magnetic fluctuations. At energy transfers less than 2 meV [314], there is another roughly $\underline{q}$ independent quasi–elastic component to the spectrum, of width $\Gamma \sim 1.6$ meV at $T = 1.0$ K, which decreases to 1.0 meV at $T = 0.6$ K. If these smaller values of $\Gamma(0)$ are combined with the specific heat coefficient γ, the product $\gamma\,\Gamma(0)$ has a value of 1.7 which is closer to the values found for Ce heavy–fermion compounds. Antiferromagnetic like correlations are apparent in the quasi–elastic spectrum at momentum transfers $(\frac{1}{2}, \frac{1}{2}, 0)$ below a temperature of 30 K [325], but no long–ranged magnetic order was found.

Neutron scattering experiments on URu_2Si_2 show an instability to an antiferromagnetically ordered state below $T_N = 17.5$ K with average ordered magnetic moments of only $\mu \sim 0.03\mu_B$ [326] or $0.023\ \mu_B$ per U [327]. The value of the ordered moment increases when pressure is applied, becoming as large as $0.25\ \mu_B$ per U atom at $P = 1.3$ GPa [225]. The measured value of the critical exponent for magnetic order parameter is $\beta \sim 0.5$ at ambient pressure. However, for URu_2Si_2, the comparison of NMR and neutron diffraction experiments under pressure [224] indicate that magnetism only occurs in a small temperature dependent fraction of the sample volume and that, if the temperature dependence of the volume is accounted for, the critical exponent β falls within the normal range. Initial reports suggested that the correlation length ξ remained finite and was of the order 200 to 400 Å. Later, it was found that the correlation length is sample dependent and that the Bragg peaks of the highest quality samples were resolution limited [328].

The ordering found is consistent with a Type I antiferromagnetic structure in which the spins align parallel in planes perpendicular to the tetragonal c–axis and are anti–parallel between planes. Since "hidden ordering" has been suggested as the cause of the large specific heat jump at T_N, neutron diffraction measurements were performed using polarized beams and applied fields. However, these experiments show no evidence of the "hidden ordering" [297, 298].

At temperatures of the order of $T = 50$ K, the inelastic scattering spectrum of URu_2Si_2 [329] shows the presence of a broad quasi–elastic response of width $\Gamma \sim 6$ meV, suggesting that the spins have relaxational dynamics. Below the Néel temperature, the inelastic scattering spectra show that both sharp spin–wave like excitations and broad relaxational spin–fluctuations coexist in the antiferromagnetic state. At $T = 1$ K, there are well defined dispersive spin–wave peaks along the $(1, q, 0)$ direction that have a minimum excitation energy of 1.8 meV at the Antiferromagnetic zone boundary [330] which is located at $q = 0$. The dispersion relation for these magnetic excitations is shown in Fig. 10.52. The longitudinal character of the spin–wave excitations, the Ising–like nature of the magnetic ordering, and the existence of a gap, all indicate that there is considerable anisotropy in the magnetic interactions at low temperatures. The spin–wave excitations are rapidly damped out above the Néel temperature T_N. The spectrum of magnetic fluctuations in the energy range between 4 and 12 meV appears to have a short correlation length, of the order of the lattice spacing, in that the intensity decreases slowly as $\underline{q}$ is varied away from $\underline{Q} = (1, 0, 0)$. The response in this energy range seems to be associated with Stoner excitations of the gas of heavy quasi–particles. Since URu_2Si_2 has a large magnetic anisotropy, and as it may play an important role in the formation of superconductivity, inelastic scattering measurements were made with the view of identifying the source of the anisotropy [331]. Although crystal–field like features were observed at the high energies of 49, 99 and 158 meV, these features had widths of 64, 36 and 89 meV, which are comparable with the splittings. This indicates that the f states in URu_2Si_2 are much more strongly hybridized with the conduction band states than in the Ce heavy–fermion compounds, and perhaps, have a large mixed valent character. Like UPt_3, the intensity of the antiferromagnetic Bragg peak in URu_2Si_2 is diminished at the onset of the superconducting transition [332].

The inelastic neutron scattering spectra of cerium based heavy–fermion compounds are different from the uranium based heavy–fermion compounds in that they show clear evidence of crystal field splittings. An example is given by the inelastic neutron scattering spectra of $CeAl_3$ [233], which is shown in Fig. 10.53. Like the uranium compounds, the cerium compounds also show the existence of an almost $\underline{q}$ independent quasi–elastic peak which develops at low temperatures, but in the low temperature limit, the widths

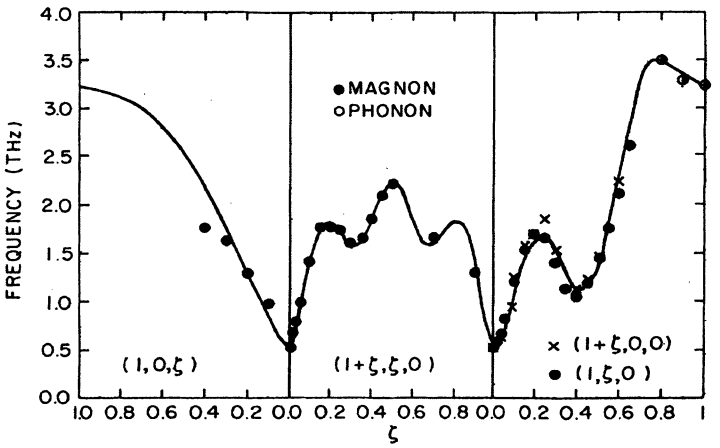

Fig. 10.52. The dispersion relation of a sharp magnetic excitation observed in URu_2Si_2. The dispersion relation is shown in the $(1,0,\zeta)$, $(1+\zeta,\zeta,0)$ and $(1,0,\zeta)$ directions. It should be noted that the dispersion relation does not go soft, as is expected for isotropic antiferromagnetic spin waves, but instead shows a gap. The existence of a gap is indicative of magnetic anisotropy. [After Broholm *et al.* (1991), [330]]

attain smaller values. For example, the width found in $CeCu_2Si_2$ [229,333] is of the order of 1 meV, and is less than 0.5 meV for $CeAl_3$ [309].

In $CeCu_6$, the magnetic fluctuations exhibit an Ising–like anisotropy along the b axis. Two different components of quasi–elastic magnetic scattering were identified [334,335]. The first component which becomes apparent at temperatures below 10 K, has an almost $\underline{q}$ independent quasi–elastic response with a width that follows a $\sqrt{T}$ temperature variation and has a residual width, $\Gamma(0)$, of the order of 0.4 meV. The second component consists of a narrower $\underline{q}$ dependent quasi–elastic peak that starts developing below $T = 3$ K. For the Ce compounds, unlike the U compounds, the magnitude of the residual $\underline{q}$ independent quasi–elastic width seems to correlate well with the large low temperature specific heat γ values. The magnetic spectrum of $CeCu_6$ has a $\underline{q}$ dependent component which shows a peak at a frequency of the order of 0.2 meV, and the $\underline{q}$ dependence is indicative of incommensurate antiferromagnetic fluctuations with the pair of propagation vectors $(1 \pm \delta, 0, 0)$, where $\delta = 0.15$. The correlation length, ξ, in $CeCu_6$ was found to be anisotropic, and saturates below $T = 1.5$ K to values of the order of 4 Å along the c–axis and 10 Å along the a–axis [334], indicating that the order is definitely short–ranged. The temperature dependence of the various widths are shown in Fig. 10.54, and the temperature dependence of the correlation lengths are shown in Fig. 10.55. The $\underline{q}$ dependent component of the total spectrum is

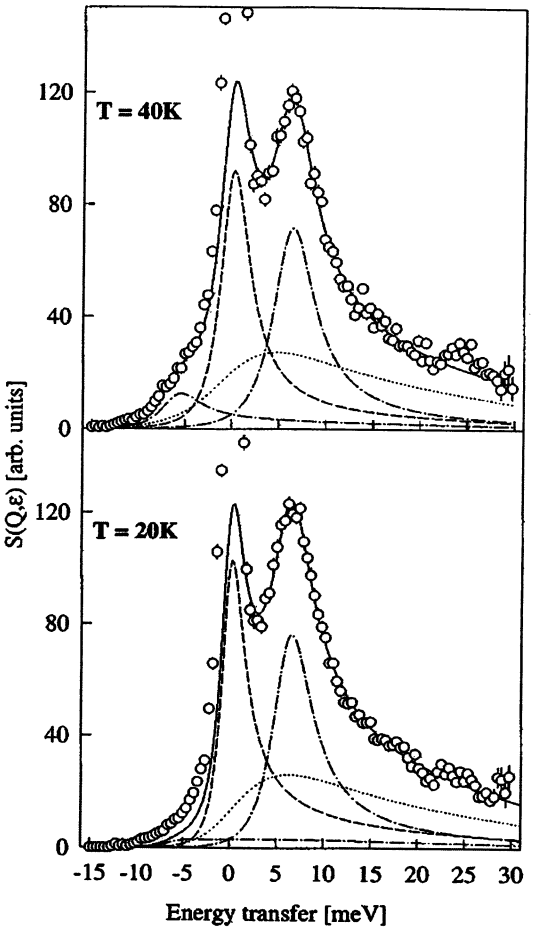

Fig. 10.53. The inelastic neutron scattering cross–section of $CeAl_3$. The spectrum shows a quasi–elastic contribution and a crystal field excitation. [After Goremychkin *et al.* (1999), [233]]

estimated to be much smaller than the local component by a factor of about 10.

The introduction of Au impurities substitutionally for Cu can drive paramagnetic $CeCu_{6-x}Au_x$ to an antiferromagnetic quantum critical point. The critical concentration is $x_c \approx 0.1$. The thermodynamic and transport properties of the disordered compound have anomalous temperature dependences in the vicinity of the quantum critical point. For example, the specific heat contains a T ln T term and the low temperature resistivity is linear in T [336]. For $x > x_c$, the system has incommensurate order with three pairs of Bragg peaks located very near to the values $(1 \pm 0.15, 0, 0)$, identified in

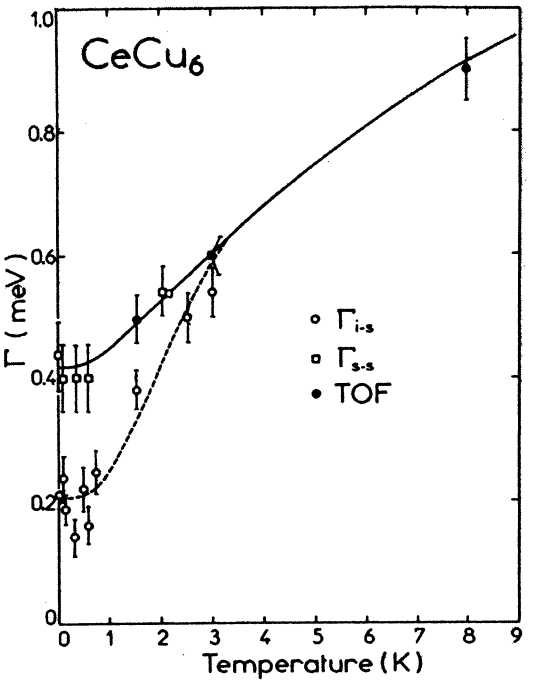

Fig. 10.54. The temperature variation of the single–site and inter–site contributions to the line–width $\Gamma(T)$, for $CeCu_6$. [After Rossat–Mignod *et al.* (1988), [334]]

the stoichiometric compound [337]. At the quantum critical point, the Bragg peaks broaden into ridges which connect into a "butterfly" shaped critical line [338]. The extended region of q space were this type of critical scattering occurs is shown in Fig. 10.56. The anomalous critical exponents at the quantum critical point led Rosch *et al.* [339] to speculate that the magnetic fluctuations were two–dimensional, despite the underlying electronic system being three–dimensional. At the quantum critical point, the width of the magnetic response may be expected to vanish at $T = 0$, for an isotropic magnetic system, as the magnetic excitations soften. This has led Schröder *et al.* [340] to examine the energy dependence for $\underline{q}$ on the critical "butterfly" and look for a $\hbar\omega/k_BT$ scaling, with the functional form

$$Im\ \chi(\underline{Q};\omega,T) \sim T^{-\alpha}\ g(\omega/T)\ , \tag{10.178}$$

where $g(\omega/T)$ is a universal scaling function. The scaling behavior is shown on a double logarithmic plot, for the best fit value of the exponent $\alpha = \frac{3}{4}$. The scaled data are shown in Fig. 10.57. This critical scaling behavior seems not to be just confined to the region of critical scattering since the static susceptibility also follows a modified Curie–Weiss form

$$\chi(T)^{-1} = \chi(0)^{-1} + a\,T^{\alpha} \tag{10.179}$$

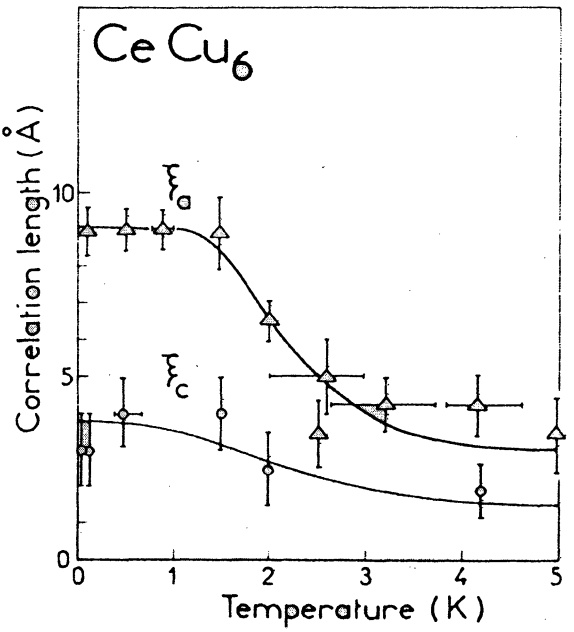

Fig. 10.55. The temperature variation of the correlation lengths $\xi(T)$ for inter–site correlations along the a and c axes, for $CeCu_6$. [After Rossat–Mignod *et al.* (1988), [334]]

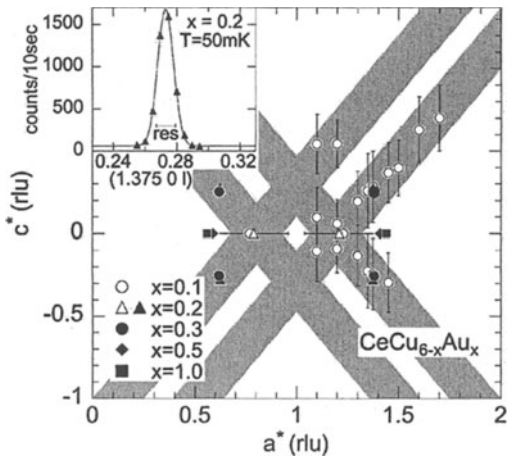

Fig. 10.56. The region of q space where critical scattering occurs for $Ce(Au_xCu_{6-x})$. The region of critical scattering forms a "dog's bone" or "butterfly". The insert shows a resolution limited Bragg peak for $x = 0.2$ and $T = 50$ mK. [After Stockert *et al.* (1998), [338]]

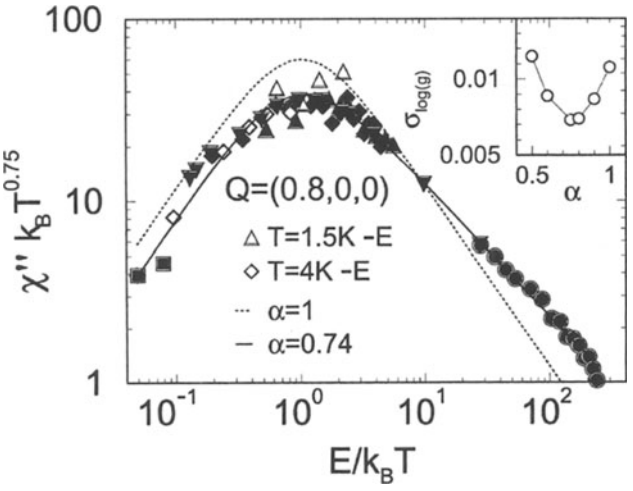

Fig. 10.57. The ω/T scaling of $Im[\ \chi(\omega,T)\ ]$ on the critical "butterfly" for $Ce(Au_xCu_{6-x})$. The scaling is shown on a log – log plot. The inset shows that the optimal value of α is close to 0.74. [After Schroeder *et al.* (1998), [340]]

with the exponent $\alpha = \frac{3}{4}$, as opposed to the Curie–Weiss value, $\alpha = 1$. Similar scaling has also been observed in the scattering cross–section of non–Fermi–liquid disordered compound $UCu_{5-x}Pd_x$ [341], with $x \sim 1$ and $x \sim 1.5$. However, in this case, the best critical exponent is $\alpha = \frac{1}{3}$ which indicates that the form of the scaling is non–universal. The magnetic response for $x \sim 1$ shows a $\underline{q}$ dependence which is similar to that of the stoichiometric, antiferromagnetic, compound with $x = 0$. However, for $x = 1.5$, this $\underline{q}$ dependence was not observed [342]. This was interpreted as signalling the cross–over from a quantum critical region to a quantum disorder region. The implications of these non–universal scaling results are not currently understood.

Neutron diffraction experiments on UPd_2Al_3 and UNi_2Al_3 show that these materials both undergo transitions to antiferromagnetic ordered phases [343]. UPd_2Al_3 orders magnetically at $T_N = 14.3$ K, and has a magnetic structure comprised of spins ferromagnetically aligned in the basal plane parallel to the a direction. The sheets of ferromagnetically aligned spins are coupled antiferromagnetically with the sheets of spins in the neighboring planes. This arrangement corresponds to the wave–vector $\underline{Q} = (0, 0, \frac{1}{2})$. The quasi–elastic peaks centered on the magnetic ordering vectors become resolution limited Bragg peaks in the antiferromagnetic phase. The Bragg peak intensities are consistent with the saturated magnetic moment having the magnitude of 0.85 μ_B per U. The critical exponent β is close to the value 0.326 expected for a three dimensional Ising system. The inelastic spectrum clearly shows the existence of a spin–wave mode with a peak position that disperses almost

linearly from an energy transfer close to zero at $\underline{q} = (0,0,\frac{1}{2})$ to 3 meV at $\underline{q} = (0,0,0.6)$. Thus, to within the experimental resolution, the spectrum shows the existence of dispersive spin–wave like excitations [344]. The line shape resembles an inelastic peak and, unlike conventional spin–waves, is subjected to significant broadening which is of the order of 1 meV. Higher resolution measurements show that as the temperature is lowered below T_N, in addition to the peak due to the propagating spin–waves, a quasi–elastic peak with a $\underline{q}$ dependent width of about 0.5 meV can be resolved [345,346].

At the superconducting transition of UPd_2Al_3, the intensity of the $(0,0,\frac{1}{2})$ Bragg peak shows that the sub–lattice magnetization undergoes a sharp but small (1%) decrease with decreasing temperature. This indicates that superconductivity and magnetism coexist and compete [343,347]. A superconducting gap was observed in the spin–wave spectrum below T_c [348]. The gap is marked by an inelastic peak at the magnetic Bragg vector which shows a sharp increase in intensity below T_c. The gap switches on more rapidly than expected from the BCS theory and saturates at a value of $\Delta(0) \geq 0.36$ meV. This results in the ratio $2\ \Delta(0)\ /\ k_B\ T_c \geq 4.6$ instead of the value 3.5 expected from BCS theory [349]. The observation of the superconducting gap in the inelastic neutron scattering spectra makes UPd_2Al_3 unique, and the observation of any $\underline{q}$ dependence should enable the symmetry of the order parameter to be obtained by direct methods.

Magnetic ordering in UNi_2Al_3 is found to occur below a temperature $T_N = 4.6$ K. Neutron diffraction measurements [350] show incommensurate magnetic order with ordering wave vectors $\underline{Q} = (\frac{1}{2} \pm \delta, 0, \frac{1}{2})$ where $\delta = 0.11$ and the ordered moments are only 0.24 μ_B per U. The critical exponent was found to have the value $\beta \sim 0.345$ as expected for a three dimensional $x-y$ system. The widths of the Bragg peaks correspond to long coherence lengths of the order of 400 Å. The field dependence of the magnetic structure suggests that the magnetic moments align along the a direction in the basal plane and that the magnitude and sense of the moments are modulated [351]. Inelastic neutron scattering experiments [352] were unable to identify any spin–wave like excitations but did show a low–energy quasi–elastic peak which is strongly localized around the incommensurate wave vector. The energy width of the quasi–elastic peak decreases with decreasing temperatures, saturating to a value of the order of 0.6 meV. However, a more recent study [353] has investigated the spectrum at energy transfers in the range of 2 to 10 meV. It was found that there was a ridge of high intensity on a line segment near the incommensurate ordering vectors $(\frac{1}{2} \pm \delta, 0, \frac{1}{2})$ and there was also a well localized maximum around the wave–vector $(0,0,\frac{1}{2})$. These peaks have widths of the order of 6 meV and start developing at temperatures below 80 K. In fact, for energy transfers greater than 0.5 meV ($\approx k_B\ T_N$), the intensity of the commensurate peak dominates over the incommensurate peak. That is, above this energy, the magnetic fluctuations of incommensurate UNi_2Al_3 strongly resemble those of commensurate UPd_2Al_3. In contrast to UPd_2Al_3,

no superconducting gap was observable in the magnetic excitation spectrum of UNi_2Al_3 below the transition temperature.

10.4 Properties of the Superconducting State

10.4.1 Thermodynamic Properties

The Specific Heat

The entropy of the gas of quasi–particles is given by the formula

$$S = -k_B \sum_{\sigma,\underline{k}} \Big[(1 - f(E_{\sigma,\underline{k}})) \ln[1 - f(E_{\sigma,\underline{k}})] + f(E_{\sigma,\underline{k}}) \ln[f(E_{\sigma,\underline{k}})] \Big] \ . \quad (10.180)$$

Therefore, for unitary phases, the quasi–particle contribution to the specific heat is given by

$$C_{qp}(T) \ = \ \frac{4}{T} \int_0^\infty dE \ \rho_{qp}(E) \left(E^2 - \frac{T}{2} \frac{\partial \Delta_0^2}{\partial T} \right) \left(- \frac{\partial f}{\partial E} \right) \quad (10.181)$$

which involves the average of the temperature derivative of the square of the quasi–particle energy, evaluated at the position of the normal state Fermi surface. Since, in the mean–field approximation, the square of the gap has a finite slope for T just below T_c and is zero above, the specific heat has a discontinuity at T_c. In BCS theory, the magnitude of the jump has the value given by $3.03 \ \Delta_0^2(0) \ \rho(\mu) \ / \ T_c$. Thus, the value of the specific heat jump found in weak–coupling BCS theory when normalized by the normal state specific heat, is given by

$$\frac{\Delta C(T_c)}{C(T_c)} = \frac{C_s \ - \ C_n}{C_n} = \frac{12}{7 \ \xi(3)} = 1.426 \quad (10.182)$$

This ratio is a measure of the quantity

$$\frac{1}{2 \ k_B^2 \ T_c} \left(\frac{\partial \Delta_0^2(T)}{\partial T} \right) \Big|_{T_c} \sim \left(\frac{\Delta_0(0)}{k_B \ T_c} \right)^2 . \quad (10.183)$$

The values of the specific heat jumps for strong coupling materials tend to be higher than the BCS value. For example the normalized jump for Pb is as large as 2.71. This trend is understood as being due to inelastic scattering processes [354, 355] which tend to suppress T_c more than $\Delta_0(0)$. With the exception of UBe_{13}, the heavy–fermion superconductors have normalized specific heat discontinuities which either are of the same order as or are smaller than the BCS ratio. The values of the specific heat jumps show large variations which are mainly due to differences in sample quality. In UPt_3, the largest specific heat jumps are found in the samples with the sharpest transitions and highest T_c's. In UPt_3 and URu_2Si_2, the transitions found are

usually broad, while UBe_{13} shows the sharpest transition. The broadness of the transition initially found in UPt_3 was responsible for masking the double peak structure of the specific heat observed in higher quality samples. The deviation of the jump from the BCS value is indicative of anisotropic superconductivity as weak–coupling calculations indicate that the magnitude of the jump is diminished as the density of low–energy quasi–particle states increases [8]. Thus, for example, the normalized specific heat jumps for the pristine BW, ABM and polar triplet states are, respectively, calculated as $\frac{12}{7\,\xi(3)} \sim 1.426$, $\frac{10}{7\,\xi(3)} \sim 1.188$ and $\frac{20}{21\,\xi(3)} \sim 0.792$, and decrease along with T_c as the concentration of non–magnetic impurities is increased. The temperature dependence of the specific heats for various p–wave superconducting phases are shown in Fig. 10.58. In heavy–fermion superconductors, which generally are type II superconductors, the jump in the specific heat occurs at lower temperatures when magnetic fields, H, are applied. The jump marks the instability of the normal state to a vortex state. The relation between the temperature and field provides the temperature dependence of the upper critical field $H_{c2}(T)$. A λ like anomaly is expected to occur in the specific heat at a lower temperature where the applied field H is equal to the lower critical field $H_{c1}(T)$. At this temperature, the usual Abrikosov magnetization–field relation has an infinite slope which implies a similar temperature variation of the entropy, and produces the λ anomaly. Good examples of this second anomaly is found in V and Nb superconductors [356, 357].

Low Temperatures

The low–energy power law energy dependence of the quasi–particle density of states could be expected to show up in power law temperature dependence of the low temperature electronic specific heat, for $T \ll T_c$. For these temperatures, the order parameter is expected to have saturated, and so then, if one considers the Fermi liquid as being well formed, the quasi–particle contribution is given by

$$C_{qp}(T) \;=\; \frac{4}{T} \int_0^\infty dE\; \rho_{qp}(E)\; E^2 \left(-\frac{\partial f}{\partial E} \right) . \tag{10.184}$$

This yield an exponentially activated behavior of the specific heat, $C_{qp}(T) \sim 9.17\; \gamma\; T_c\; \exp[\, -\, \Delta_0\; /\; k_B T\,]$, for states like the BCS or BW states which have no nodes; a T^3 variation for the low temperature specific heat in the ABM phase with isolated nodes and a T^2 variation for the polar (p_z) or $d_{2z^2-x^2-y^2}$ phase with lines of nodes. However, the experimentally determined low temperature specific heats of the superconducting heavy–fermion uranium compounds are described by

$$C(T) \;=\; \gamma_s\; T \;+\; \epsilon_s\; T^n \,, \tag{10.185}$$

[8] More precisely, assuming a separable pairing interaction, the normalized specific heat jump yields a measure of the angular variation of the gap over the Fermi surface. It is equal to the BCS value of the discontinuity times the ratio of the square of the second moment of the gap to the fourth moment.

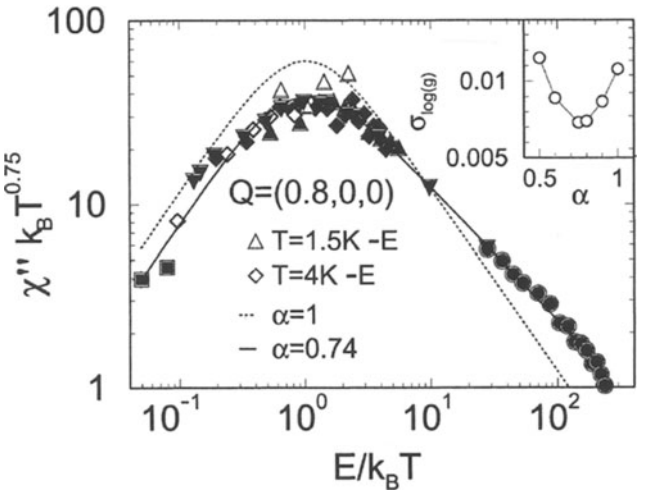

Fig. 10.58. The temperature dependent specific heat normalized to the normal state specific heat at T_c calculated for various p–wave superconducting phases. The magnitude of the normalized discontinuity at T_c decreases from ≈ 1.4, to 1.2 to 0.8 along the series BW, ABM and polar. The low temperature specific heat shows an exponential variation for the BW state, whereas the low temperature specific heats of the ABM and polar phases show power law temperature variations which are consequences of the types of nodes in the order parameters

where γ_s is sample dependent. The residual γ_s has often been attributed to either the existence of a normal component, or due to a gapless phase caused by pair breaking impurities. For example, in UPt_3 the coefficient of the residual linear T term takes values between 265 and 56 mJ mole^{-1} K^{-2} depending on sample quality [14]. This suggests that between 50 % and 16 % of the normal state Fermi surface is ungapped for these samples. The value of the exponent n is 2 for UPt_3, whereas $n = 3$ for UBe_{13} and UPd_2Al_3. The specific heat of URu_2Si_2 shows a quadratic temperature variation [358], and the smallest γ_s value reported is 4 mJ mole^{-1} K^{-2} and the largest is 13 mJ mole^{-1} K^{-2}. The smaller magnitude of the ratio γ_s/γ for URu_2Si_2 is perhaps not surprising since it has been estimated that about 30 % of the Fermi surface remains ungapped below the 17.5 K transition. In $CeCu_2Si_2$, the temperature dependence of the specific heat below T_c is non–exponential, and can be fitted via a T^2 variation close to the critical temperature but shows a T^3 variation at low temperatures down to 50 mK. A residual value of γ_s of the order of 24 mJ mole^{-1} K^{-2} has been reported [359]. This number suggests that only 4 % of the original Fermi surface is ungapped in the superconducting state of $CeCu_2Si_2$. The values of the exponents, n, suggests that there are nodes in the superconducting gap, however, the pair breaking effects of impurities may alter the temperature dependence [152–154] and may also lead to a gapless

phase. This is consistent with the observation that materials with the broadest transitions tend to have the largest values of γ_s. As the heavy–fermion superconductors may be in the vicinity of quantum critical point, the Fermi liquid may not have been fully formed before the superconducting transition occurs as is true for UBe_{13}, and as the specific heat provides a measure of the density of all low–energy excitations and not just quasi–particles, it may prove difficult to disentangle the various factors which affect the temperature dependence of the specific heat.

The Critical Fields

The thermodynamic critical field H_c of a superconductor is determined by equating the energy of the magnetic field to the difference in free energies between the superconducting and normal states

$$V_o \frac{H_c^2(T)}{8\pi} = F_n - F_s \,, \tag{10.186}$$

where V_o is the volume. At $T = 0$ this reduces to the condensation energy of the superconducting state

$$V_o \frac{H_c^2(T)}{8\pi} = U_n - U_s = \frac{1}{2}\rho(\mu) \int \frac{d\Omega}{4\pi} \, Trace \, \Delta(\underline{k})\Delta^\dagger(\underline{k}) \,. \tag{10.187}$$

Here. $\rho(\mu)$ is the single–particle density of states at the Fermi energy and $\Delta(\underline{k})$ is the gap function. For an s–wave superconductor at finite temperatures $F = U - TS$ with $U_n - U_s = \frac{1}{2}\rho(\mu)\Delta_0^2(T)$ and the temperature dependent gap is determined from

$$\frac{1}{\rho(\mu)V} = \int_0^{\hbar\omega_c} d\xi \, \frac{\tanh\left(E/2k_BT\right)}{E} \,, \tag{10.188}$$

where $-V$ is the potential for scattering a pair of electrons (assumed constant in BCS theory), ω_c is a cutoff frequency (usually the Debye frequency), $E = \sqrt{\xi^2 + \Delta_0^2}$, and the entropy of the superconducting state is

$$S_s = -2k_B\rho(\mu) \int_0^{\hbar\omega_c} d\xi \, \left[f(E)\ln f(E) + (1 - f(E))\ln(1 - f(E))\right] \,, \tag{10.189}$$

where $f(E) = 1/(e^{E/k_BT} + 1)$.

When solved numerically, in either the strong or weak coupling limit, the solution of the above equations differs from

$$H_c(T) = H_c(0) \left[1 - \left(\frac{T}{T_c}\right)^2\right] \tag{10.190}$$

by no more than a few percent. Meissner flux expulsion and zero resistivity disappear at H_c and the normal state is recovered. (It is interesting to note

that Eqn. (10.190), a good approximation to the BCS result, follows from a two–fluid model of superconductivity proposed by Gorter and Casimir in 1934. In this model the free energy of the normal state is taken to be $-\frac{1}{2}\gamma T^2$ and the free energy of the superconducting state is a constant [360].)

In a type–I superconductor the only critical field is H_c discussed above. In a type–II superconductor, quantized flux vortices appear in fields greater than the lower critical field H_{c1}, and superconductivity persists to fields as high as the upper critical field H_{c2} where the normal cores of the vortex lattice overlap and the zero resistance state is destroyed. The creation of the vortex state becomes energetically favorable when the Ginzburg–Landau parameter $\kappa > 1/\sqrt{2}$ ($\kappa = \lambda/\xi$ where λ is the penetration depth and ξ is hereafter the coherence length. When $\kappa \gg 1$ (an appropriate limit for the heavy–fermion superconductors) the Ginzburg–Landau equations can be solved to give

$$H_c = \frac{\Phi_o}{2\sqrt{2}\pi\mu_o\lambda\xi}, \tag{10.191}$$

$$H_{c1} = H_c\frac{\ln\kappa}{\sqrt{2}\kappa} = \frac{\Phi_o}{4\pi\mu_o\lambda^2}\ln\left(\frac{\lambda}{\xi}\right), \tag{10.192}$$

$$\text{and } H_{c2} = \sqrt{2}\ \kappa\ H_c = \frac{\Phi_o}{2\pi\mu_o\xi^2}\ . \tag{10.193}$$

Here, Φ_o is the flux quantum (similar results for anisotropic systems are summarized elsewhere [361]). In the high κ limit generally appropriate for the heavy–fermion superconductors, H_c is very nearly the geometric mean of H_{c1} and H_{c2}. In fact, there are three Ginzburg–Landau parameters which depend on T, l/ξ (where l is the mean free path), and the degree of anisotropy of the impurity scattering. However, the various κ_i differ from κ by no more than 20% [362], and we will not pursue the matter here.

Many early theories of the upper critical field focused on the maximum attainable field associated with a single limiting factor. An example of such a limiting factor, frequently encountered in the heavy–fermion superconductors, is the field dependence of the normal state free energy caused by the coupling to the paramagnetic spins. Since the spin susceptibility of spin–singlet superconductors vanishes at $T = 0$, the Pauli limiting field $H_p(0)$ is defined as the field at which the free energy of the normal state with spin susceptibility χ_n equals the condensation energy of the superconducting state. At $T = 0$, the definition takes the form

$$\frac{1}{2}\ \chi_n\ H_p^2(0)\ =\ \frac{1}{2}\ \rho(\mu)\ \Delta_0^2(0). \tag{10.194}$$

H_p, sometimes known as the Chandrasekhar [363] or Clogston [364] limit, can be significantly enhanced when spin–orbit coupling is strong. At $T = 0$

$$H_{p,so}(0) = \left(\frac{\hbar}{6\lambda_{so}\Delta(0)}\right)^{1/2} H_p(0), \tag{10.195}$$

where λ_{so} is the spin–orbit coupling parameter. Since the zero temperature limit of the spin susceptibilities of spin–triplet superconductors are generally expected to be either non–zero or anisotropic, the upper critical field may be expected to exceed $H_p(0)$ in spin–triplet phases. In particular, for a spin–triplet superconductor, a field applied parallel to the direction of the Cooper pairs spin will not be subject to the Pauli limit but fields with components in the perpendicular directions will produce pair breaking [365].

Perhaps the most commonly used and successful framework to interpret $H_{c2}(T)$ measurements on "classic" Type II superconductors is that developed by Werthamer, Helfand, Hohenberg, and Maki (WHHM) [366,367]. WHHM solved the Ginzburg–Landau equations incorporating both orbital and spin paramagnetic effects in addition to both nonmagnetic and spin–orbit scattering. The resulting H_{c2} curves are qualitatively similar to the shape of Eqn. (10.190) featuring a linear temperature dependence below T_c that gently rolls over to a constant as $T \to 0$ (in other words, $H_{c2}(T)$ exhibits negative curvature or none at all). Since these predictions, which work so well with classic Type II superconductors, generally fail (except in the broadest terms) with heavy–fermion superconductors, we will not pursue this approach here but refer the reader to the overview and compilation of formulas presented by Orlando *et al.* [368]. Strong coupling can also cause significant deviations from the behaviors discussed above and we refer the reader to the overview of Carbotte [123]. Critical field anisotropy can originate from an anisotropic Fermi surface (sometimes characterized by an effective mass tensor [361]), an anisotropic order parameter, or magnetism for example.

Specific predictions for the upper critical fields resulting from anisotropic order parameters (or combinations thereof) have been made by a number of authors. In many cases, such as the p–wave ABM state for example [369,370], these order parameters lead to a characteristic anisotropy of H_{c2} even though the temperature dependence remains similar to that of the WHHM model. In other cases the temperature dependence is also affected, and can result in the positive curvature which is so inconsistent with the WHHM model [371,372]. A good overview of these issues can be found in the review article by Sigrist and Ueda [154].

The appearance of a non–uniform superconducting state, independently predicted in the mid–60's by Fulde and Ferrell [373] and Larkin and Ovchinnikov [374], below $T/T_c \approx 0.55$ and in fields near H_{c2} has sometimes been invoked to explain the unusual shapes of the upper critical fields exhibited by the heavy–fermion superconductors. The so–called FFLO state is one in which the internal magnetic field breaks a number of the spin–singlet Cooper pairs, and produces a uniform flow of the condensate. This state is stabilized when the current of the Cooper pair condensate is compensated by a counter flow of the quasi–particle gas. This FFLO state is suppressed by impurities and results in an additional first–order phase transition to the (relatively more uniform) vortex lattice state [375].

Many features of the models discussed above are consistent with the heavy electrons themselves entering the superconducting state. For example, standard thermodynamics shows that [376]

$$\left(\frac{\Delta C}{T}\right)\Big|_{H_{c2}(T)} = \left(\frac{\partial H_{c2}}{\partial T}\right)^2 \left[\left(\frac{\partial M}{\partial H}\right)_s - \left(\frac{\partial M}{\partial H}\right)_n\right]. \tag{10.196}$$

Thus, the large initial slope of the upper critical field and the low values of T_c are related to the large effective masses of the electrons forming the Cooper pairs. Parameters characterizing the critical field curves of the heavy–fermion superconductors are collected in Table 10.11.

The upper critical field of UPt_3 reflects the three underlying superconducting states meeting a tetra–critical point (at 0.39 K and 0.44 T) which manifests as a sharp kink in $H_{c2}(T)$ when fields are applied along the c–axis. The anisotropy of $H_{c2}(T)$ reverses sign near 0.2 K: above (below) this temperature H_{c2} is larger (smaller) with fields applied along the c–axis than with fields applied within the basal plane. There have been fewer measurements of the lower critical field of UPt_3 owing, in part perhaps, to the difficulty of these measurements. All of the measurements are consistent with a sharp increase in slope near the transition between the lower temperature B phase and higher temperature A phase though the existence and size of the anisotropy is somewhat less certain. An increase in slope is consistent with the appearance of a second order parameter which would increase the condensation energy. A deeper discussion of the critical fields of UPt_3 can be found in the recent review article by Joynt and Taillefer [377].

The upper critical field of the best single crystal samples of UBe_{13} shows a broad region of positive curvature setting in near $T_c/2$ which has been interpreted as evidence for the FFLO state discussed above [378,379]. Sharp features in $H_{c2}(T)$ (or, more correctly, the irreversibility curve) of UBe_{13}, suggesting additional phases in either the superconducting or normal state have been reported [380] but as yet there is no consensus on the existence of such features. An anisotropy consistent with lines of zeros for the gap function has been reported [381,382] but has not been confirmed [383]. Despite the unusual shape of the upper critical field, the lower critical field of a polycrystal sample of UBe_{13} exhibits the usual quadratic temperature dependence [384], however, we are unaware of any measurements on single crystals at this time.

In $CeCu_2Si_2$, the upper critical field exhibits a broad, shallow maximum centered near 0.2 K the origin of which is uncertain but suggestions have included "(1) exchange–enhanced 'polarization fields' between (residual) Ce moments, (2) 'Kondo–type' pair breaking from these residual moments, and (3) competition between the (phonon–mediated) attraction and Coulomb repulsion between those slowly moving heavy–fermions whose velocity is already comparable to the velocity of sound" [22]. At low temperatures, the upper critical field with fields applied along the c–axis is about 20% larger than when they are applied along the a–axis. The size of this anisotropy decreases

monotonically as T_c is approached. In earlier studies, the anisotropy vanished near T_c near which the slopes of the critical field curves were equal [22]. More recently, however, a small anisotropy has been observed to exist very close to T_c where the slopes vary from 23 T/K with fields along the a–axis to 18.5 T/K with fields along the c–axis [385]. The few measurements of the lower critical field of $CeCu_2Si_2$ show a short region of positive curvature just below T_c [384,386].

Table 10.11. The Superconducting parameters of some heavy fermion superconductors. Values separated by slashes characterize a–axis/c–axis anisotropy (* under pressure).

Material	T_c (K)	$\frac{\Delta C(T_c)}{C(T_c)}$	$H_{c2}(0)$ (T)	$-\frac{dH_{c2}}{dT}\|_{T_c}$ (T/K)	$H_{c1}(0)$ (mT)	Refs.
UPt_3	0.55	1.0	2.5 / 2.0	4.5 / 7.7	3.0	[377,480,497]
$CeCu_2Si_2$	0.69	1.27	2 / 2.4	23	2.3	[387,480,497]
UBe_{13}	0.9	2.5	12	42	4.5	[387,480,497]
URu_2Si_2	1.5	0.82	13 / 3	4 / 14	1.4	[480,497]
UPd_2Al_3	2.0	1.2	3.0 / 3.6	4.3	1.0	[480,497]
UNi_2Al_3	1.0	0.5	1.5	1.4	1.4	[480,497]
$CeRhIn_5$	2.1*	0.36	~ 16	14		[57,521]
$CeIrIn_5$	0.4	0.76	9.3 / 5.3	4.8 / 2.5		[522]
$CeCoIn_5$	2.3	4.5	11.7 / 5.0	24.0 / 11.4	2.5 / 9.5	[522,523,525]
$CeIn_3$	0.18*		0.45	3.2		[63,529]
$CePd_2Si_2$	0.52*		2	13		[529,531]
$CeRh_2Si_2$	0.35*		.35	1.4		[67]
$CeCu_2Ge_2$	0.7*		2	11		[534]
$PrOs_4Sb_{12}$	1.85	3	2.2	1.9	23	[536,540,541]
U_2PtC_2	1.47			9		[542]

10.4.2 Transport Properties

At sufficiently low temperatures, transport properties are determined by the properties of the quasi–particle excitations and, unlike thermodynamic properties, are essentially affected by scattering. If the temperature is so low that inelastic scattering from low–energy collective fluctuations is frozen out, then elastic impurity scattering may be expected to provide the dominant scattering mechanism. However, it is not appropriate to treat the impurity scattering in the Born approximation since it leads to a scattering time that has the same energy dependence as the quasi–particle density of states and which would lead to similar temperature dependences as in the normal state. This

is in contradiction to experimental observation. Hence, as pointed out by Pethick and Pines [155], it appears as if the impurity scattering is resonant.

Thermal Conductivity

The electronic contribution to the thermal conductivity can be calculated via linear response theory. The thermal conductivity can be expressed in terms of the heat flux correlation function. The thermal conductivity tensor $\kappa_{i,j}(T)$ can be written as the limit $\omega \rightarrow 0$ of the expression [389]

$$\kappa_{i,j}(T) = -\frac{1}{\hbar\, T}\left(\frac{\partial\, Im\, K^R_{i,j}(\omega)}{\partial\omega}\right)\Big|_{\omega=0}, \tag{10.197}$$

where

$$K^R_{i,j}(\omega) = \frac{\hbar^2}{8m^2}\int\frac{dE_1}{2\pi}\int\frac{dE_2}{2\pi}\frac{(E_1+E_2)^2}{E_1-\hbar\omega-E_2-i\delta}\Big(f(E_2)-f(E_1)\Big) \times\sum_{\underline{k}} k_i k_j Trace\Big(ImG(\underline{k};E_1)\rho_4 ImG(\underline{k};E_2)\rho_4\Big)_{av} \tag{10.198}$$

and where the Trace is over the matrix Green's function $G(\underline{k};\omega)$ defined by Eqn. (10.86). This expression is to be averaged over the distribution of impurities. This type of analysis produces the standard result [9]

$$\kappa_{i,j} = \frac{1}{T}\sum_{\sigma,\underline{k}} v_i(\underline{k})\, v_j(\underline{k})\, \tau(E_{\underline{k}})\, E^2_{\underline{k}}\left(-\frac{\partial f}{\partial E_{\underline{k}}}\right) \tag{10.199}$$

in which $\underline{v}(\underline{k})$, $E_{\underline{k}}$ and $\tau(E_{\underline{k}})$, respectively, are the quasi–particle velocity, the quasi–particle energy and the quasi–particle lifetime.

Singlet Pairing

For the case of isotropic singlet pairing and in the Born approximation, the rate of scattering of a quasi–particle from state $\underline{k}$ to state $\underline{k}'$ by non–magnetic impurities is given in terms of the quasi–particle density of states by

$$\frac{1}{\tau(E_{\underline{k}})} = \frac{1}{\tau_0}\frac{\rho_{BCS}(E_{\underline{k}})}{\rho(\mu)}\left(1-\frac{|\,\Delta_0\,|^2}{E^2_{\underline{k}}}\right), \tag{10.200}$$

where the normal state scattering rate due to a concentration of randomly distributed non–magnetic impurities, c_0, is given by

$$\frac{1}{\tau_0} = \frac{2\,\pi}{\hbar}\, c_0\, \rho(\mu)\, |\, U_0\,|^2\,. \tag{10.201}$$

[9] This expression for the thermal conductivity of a superconductor was derived by O. Betbeder–Matibet and P. Nozières, using a Boltzmann equation approach (O. Betbeder–Matibet and P. Nozières, Ann. Phys. (N.Y.) 51, 392 (1969)). This result is obtained when the self–energy due to impurity scattering is small compared with $k_B\, T$.

The quasi–particle velocity is defined by

$$\underline{v}(\underline{k}) = \frac{1}{\hbar}\frac{\partial E_{\underline{k}}}{\partial \underline{k}} = \frac{\hbar \underline{k}}{m}\left(\frac{e(\underline{k}) - \mu}{E_{\underline{k}}}\right), \tag{10.202}$$

where the order parameter has been assumed to be approximately independent of the magnitude of $\underline{k}$. Hence, the coherence factor in the expression for the quasi–particle lifetime $\tau(E_{\underline{k}})$ will cancel with a factor of

$$\left(\frac{e(\underline{k}) - \mu}{E_{\underline{k}}}\right)^2 \tag{10.203}$$

in the expression for $v_i(\underline{k})\ v_j(\underline{k})$. On combining these expressions, and on replacing the sum over $\underline{k}$ by integrals over the solid angle and the magnitude of k, one finds that the conductivity tensor is given by

$$\kappa_{i,j} = \frac{2\tau_0}{T}\left(\frac{\hbar k_F}{m}\right)^2 \int \frac{d\Omega}{4\pi}\hat{k}_i\hat{k}_j \int_{-\infty}^{+\infty} de \frac{\rho^2(e)}{\rho_{BCS}(E)} E^2\left(-\frac{\partial f}{\partial E}\right). \tag{10.204}$$

The integral over the solid angle $d\Omega$ causes the off–diagonal components of the tensor to vanish, and yields equal diagonal components. The tensor is given by

$$\kappa_{i,j} \approx \delta_{i,j}\frac{4\tau_0}{3T}\left(\frac{\hbar k_F}{m}\right)^2 \rho(\mu) \int_{\Delta_0}^{\infty} dE\ E^2\left(-\frac{\partial f}{\partial E}\right). \tag{10.205}$$

In this expression, the factor of the quasi–particle density of states is absent as we have used the Born approximation for the quasi–particle lifetime. On evaluating the integral at low temperatures, where $k_B\ T \ll \Delta_0$, one finds

$$\kappa_{i,j}(T) = \delta_{i,j}\ \frac{4\ \tau_0}{3\ T}\left(\frac{\hbar k_F}{m}\right)^2 \rho(\mu)\ \Delta_0^2\ \exp\left[-\beta\ \Delta_0\right]. \tag{10.206}$$

Therefore, the quasi–particle component to the thermal conductivity tensor of a BCS superconductor is thermally activated and is isotropic.

For the case of anisotropic pairing, the Born approximation for the scattering rate is given in terms of the quasi–particle density of states by

$$\frac{1}{\tau(E_{\underline{k}})} = \frac{1}{\tau_0}\frac{\rho_{qp}(E_{\underline{k}})}{\rho(\mu)}, \tag{10.207}$$

since the angular integration over the final state momentum $\underline{k}'$ has caused the term in the coherence factor which is bi–linear in the order parameter to vanish. Since the cancellation between the coherence factor in the lifetime and the factors in the quasi–particle velocity does not occur for anisotropic

pairing, the quasi–particle contribution to the thermal conductivity tensor is given by

$$\kappa_{i,j} = \frac{2\,\tau_0}{T}\left(\frac{\hbar k_F}{m}\right)^2 \int \frac{d\Omega}{4\,\pi}\,\hat{k}_i\,\hat{k}_j \int_{-\infty}^{+\infty} de\,(\,e\,-\,\mu\,)^2\,\frac{\rho^2(e)}{\rho_{qp}(E)}\left(-\frac{\partial f}{\partial E}\right)$$
$$= \frac{4\,\tau_0}{T}\left(\frac{\hbar k_F}{m}\right)^2 \rho^2(\mu) \int \frac{d\Omega}{4\pi}\hat{k}_i\hat{k}_j \int_{|D(\hat{k})|}^{\infty} dE \frac{E\sqrt{E^2 - |D(\hat{k})|^2}}{\rho_{qp}(E)}\left(-\frac{\partial f}{\partial E}\right). \tag{10.208}$$

On interchanging the order of the integrations, one obtains the result

$$\kappa_{i,j} = \frac{4\tau_0}{T}\left(\frac{\hbar k_F}{m}\right)^2 \rho^2(\mu) \int_0^{\infty} dE \frac{E}{\rho_{qp}(E)}\left(-\frac{\partial f}{\partial E}\right) I_{i,j}(E)\,, \tag{10.209}$$

where the factor $I_{i,j}(E)$ describes the anisotropy, and is given by

$$I_{i,j}(E) = \int \frac{d\Omega}{4\pi}\hat{k}_i\hat{k}_j\sqrt{E^2 - |D(\hat{k})|^2}\,. \tag{10.210}$$

The integration only runs over the solid angles for which the argument of the square root is positive. Assuming the validity of this expression, one observes that there exists a possibility that the anisotropy of the thermal conductivity tensor may provide information about the locations of the nodes of the order parameter.

For illustrative purposes, we shall consider the d–wave order parameter with $m = 1$,

$$D(\hat{k}) = \Delta_0\,\sin 2\theta\,\exp[\,i\,\varphi\,] \tag{10.211}$$

This order parameter has a line of nodes in the equatorial plane and two isolated point nodes, one at each of the poles. Hence, the quasi–particle density of states is linearly proportional to E at low energies and is logarithmically divergent at $E = \Delta_0$. The thermal conductivity tensor only has diagonal components and is isotropic in the x–y plane. The anisotropy of the tensor is governed by the angular integrals

$$I_{z,z}(E) = \frac{\Delta_0}{2}\int d\theta\,\sin\theta\,\cos^2\theta\,\sqrt{\left(\frac{E}{\Delta_0}\right)^2 - \sin^2\,2\theta}\,,$$
$$I_{x,x}(E) = \frac{\Delta_0}{4}\int d\theta\,\sin\theta\,\sin^2\theta\,\sqrt{\left(\frac{E}{\Delta_0}\right)^2 - \sin^2\,2\theta}\,, \tag{10.212}$$

where the integration only runs over the ranges of θ where the argument of the square root is positive. For small E, these integrals are proportional to E^4/Δ_0^4 and E^2/Δ_0^2 respectively. The differences in the behavior occurs because, at low energies, the line of nodes has more weight than the point

nodes and the factor of $\cos^2\theta$ in the z component of the tensor is limited to be smaller than $E^2/4\Delta_0^2$ while $\sin^2\theta \approx 1$. Hence, for temperatures such that $k_B\,T \ll 0.2\,\Delta_0$, one expects that $\kappa_{z,z}(T) \propto T^3$, while $\kappa_{x,x}(T) = \kappa_{y,y}(T) \propto T$. The different temperature dependence of the components of the thermal conductivity tensor reflect the presence of the line of nodes in the equatorial plane.

Any anisotropic behavior of $\kappa(T)$ is expected to be extremely difficult to observe experimentally, since a slight misalignment of the crystal, the presence of domains or grain boundaries etc., may cause the measured thermal conductivity to be dominated by the largest component of the tensor.

Triplet Pairing

In the case of triplet pairing, the quasi–particle contribution to the thermal conductivity can be written in a form analogous to the thermal conductivity for anisotropic singlet pairing. The tensor can be expressed as

$$\kappa_{ij}(T) = \frac{\hbar^2 k_F^2}{m^2 k_B T^2}\rho(\mu)\int_0^\infty dE E sech^2\frac{\beta E}{2}\tau(E)I_{i,j}(E)\,, \tag{10.213}$$

where $\tau(E)$ is the scattering time and $I_{i,j}(E)$ is given by

$$I_{i,j}(E) = \int \frac{d\Omega}{4\,\pi}\,\hat{k}_i\,\hat{k}_j\,\sqrt{E^2 - |\,\vec{d}\,(\hat{k})\,|^2}\,. \tag{10.214}$$

In the BW phase, the order parameter is nodeless and so, the thermal conductivity is diagonal, isotropic and exponentially activated. Thus, the thermal conductivity in the BW phase is similar to the thermal conductivity of the BCS state.

For the ABM state, the low temperature thermal conductivity is anisotropic. As the magnitude of the order parameter varies as $|\,\vec{d}\,(\hat{k})\,| = \Delta_0\,\sin\theta$, the factor of k_i^2 in the diagonal components of the thermal conductivity tensor introduces an extra factor of E^2/Δ_0^2 in the low–temperature limit of the transverse components compared with the longitudinal component. The longitudinal thermal conductivity is estimated as

$$\kappa_{\|}(T) = \frac{\hbar^2 k_F^2}{k_B\,T^2\,m^2}\,\rho(\mu)\int_0^\infty dE\;E\;sech^2\frac{\beta\,E}{2}\,\tau(E)\frac{E^3}{|\,\Delta_0\,|^2} \tag{10.215}$$

and the transverse components are estimated as

$$\kappa_{\perp}(T) = \frac{\hbar^2 k_F^2}{k_B T^2\,m^2}\rho(\mu)\int_0^\infty dE E sech^2\frac{\beta E}{2}\tau(E)\frac{E^5}{|\Delta_0|^4}\,. \tag{10.216}$$

In the Born Approximation, since $\rho_{ABM}(E)$ varies as E^2 and thus $\tau(E) \propto E^{-2}$, the longitudinal component of the thermal varies as $\kappa_{\|}(T) \propto T$ whereas the transverse components vary as $\kappa_{\perp}(T) \propto T^3$.

For the polar state, where $|\,\vec{d}\,(\hat{k})\,| = \Delta_0\,\cos\theta$ which vanishes along the equatorial plane, the transverse and longitudinal components of the thermal

conductivity tensor are given by

$$\kappa_{\perp}(T) = \frac{\hbar^2 k_F^2}{k_B T^2 m^2} \rho(\mu) \int_0^{\infty} dE\ E\ sech^2 \frac{\beta E}{2}\ \tau(E) \frac{E^2}{|\Delta_0|} \quad (10.217)$$

and

$$\kappa_{\parallel}(T) = \frac{\hbar^2 k_F^2}{k_B T^2 m^2} \rho(\mu) \int_0^{\infty} dE E sech^2 \frac{\beta E}{2} \tau(E) \frac{E^4}{|\Delta_0|^3}\ . \quad (10.218)$$

In the polar state, the quasi–particle density of states is given by $\rho_{p_z}(E) \propto E$, hence $\tau(E) \propto E^{-1}$. Thus, one has $\kappa_{\parallel}(T) \propto T^3$ and $\kappa_{\perp}(T) \propto T$. It should be noted that the anisotropy in the T dependence of $\kappa(T)$ is switched between the polar and the ABM states [390].

Since $\Delta_0 \gg k_B T$, the above results imply that the linear T term will dominate the experimentally determined temperature variation of the thermal conductivity of either a polar or an ABM state. In general, a linear T dependence is expected for states with either point or line nodes. Also, if the Lorentz number found in the normal state is constant, as is expected if impurities provide the dominant scattering mechanism, the thermal conductivity in the superconducting state should have a magnitude which is very similar to the normal state value. The above results were obtained using the Born approximation. However, it has been argued that, even in the normal state, it is not valid to treat impurity scattering within the Born approximation since the impurity scattering may be resonant, i.e., close to the unitarity limit.

If the impurity scattering is resonant and $k_B T \gg \hbar/2\tau$, then in the ABM phase one has $\tau(E) \sim \tau_0$, while $\tau(E) \propto E \ln^2 E$ in the polar phase. Thus, for resonant scattering, the leading T dependences for the components of the thermal conductivity for the ABM phase are expected to be $\kappa_{\parallel}(T) \propto T^3$ and $\kappa_{\perp}(T) \propto T^5$. The polar phase has the opposite anisotropy to the ABM phase, however, additional factors of $\ln^2 T$ multiply the leading low–temperature powers of T. That is, for the polar phase, $\kappa_{\parallel}(T) \propto T^5 \ln^2 T$ and $\kappa_{\perp}(T) \propto T^3 \ln^2 T$. In general, it is expected that for strong scattering by dilute impurities such that the T–matrix approximation is valid [156, 391], the orientationally averaged thermal conductivity $\kappa(T)$ should follow a T^3 law if the order parameter has point nodes or should follow a T^2 law if the order parameter has line nodes.

However, the resonant impurity scattering may be sufficiently large to cause the superconducting quasi–particle density of states to be finite at zero energy. In this case, it has been shown [393] that the low–energy superconducting quasi–particles may be strongly localized, even when the normal state quasi–particles are not. This results in a universal expression for the d.c. limit of the electrical conductivity of the superconducting state which is finite and independent of the disorder. As a consequence, for $k_B T \ll \hbar/2\tau$, a Wiedemann–Franz like relation holds [394]. This relation shows that, in the very low temperature limit, the superconductor's thermal conductivity $\kappa(T)$

should also be linear in T, irrespective of the node structure. Furthermore, the largest component of $\kappa_{i,j}(T)$ can also be independent of impurity scattering for certain types of order parameter [394]. These results can be understood by recognizing that the effect of strong impurity scattering is to randomize the Fermi surface, thereby acting to restore its approximate spherical symmetry.

The electronic contribution to the thermal conductivity of UBe_{13} does not follow the exponentially activated law expected from BCS theory but shows a T^2 variation in the superconducting state at relatively high temperatures (between 0.8 and 0.1 K) which could be indicative of lines of nodes in the order parameter [28]. However, this assignment is contrary to the assignment of point nodes made on the basis of the T^3 variation observed in the specific heat. Experiments on some samples show that, below 100 mK, $\kappa(T)$ varies linearly with T

$$\kappa(T) \;=\; \alpha_s \, T \,, \tag{10.219}$$

where $\alpha_s \;=\; 0.03$ mW $K^{-2}cm^{-1}$ [267]. The temperature dependence of κ for the two different temperature regimes found in this sample of UBe_{13} are shown in Fig. 10.59. However, other samples do not show any noticeable linear temperature dependences [395]. This seems to indicate that the thermal conductivity is extremely sensitive to the quality of the sample.

The temperature dependence of the thermal conductivity of UPt_3 also does not follow an exponential activation law but has a temperature variation which can be fit by the sum of a T and a T^2 term [29,396,397]

$$\kappa(T) \;=\; \alpha_s \, T \;+\; \beta_s \, T^2 \,. \tag{10.220}$$

The value of the coefficient of the linear T term, α_s, was found to vary from sample to sample, varying from 0.55 to 12 mW K^{-2} cm^{-1}. The magnitude of the coefficient β_s of the T^2 term in UPt_3 can be as large as 60 mW K^{-3} cm^{-1} [397] which is two orders of magnitude greater than the corresponding coefficient in UBe_{13}. The strength of the T^2 term in the $\kappa(T)$ of UPt_3 is also much larger than the corresponding term found from the $\kappa(T)$ of $CeCu_2Si_2$ [398], for which $\beta_s \;\sim\; 1.8$ mW K^{-3} cm^{-1} and $\alpha_s \;\sim\; 0.28$ mW K^{-2} cm^{-1}. Although an anisotropy of $\kappa(T)$ was detected in UPt_3 [399], the anisotropy is fully developed in the normal state and $\kappa(T)$ becomes more isotropic for temperatures below the second superconducting transition. An analysis of the measurements favors an order parameter with a form similar to $Y_1^2(\theta,\varphi)$ but did not conclusively identify the symmetry of the gap.

The lack of agreement with expectations based on simple quasi–particle theories and elastic impurity scattering is perhaps not surprising, since the validity of the quasi–particle description of the normal state of both UBe_{13} and $CeCu_2Si_2$ is questionable.

Ultrasonic Attenuation

Measurements of the ultrasonic attenuation should allow the temperature dependence and the anisotropy of the gap to be determined. Within BCS

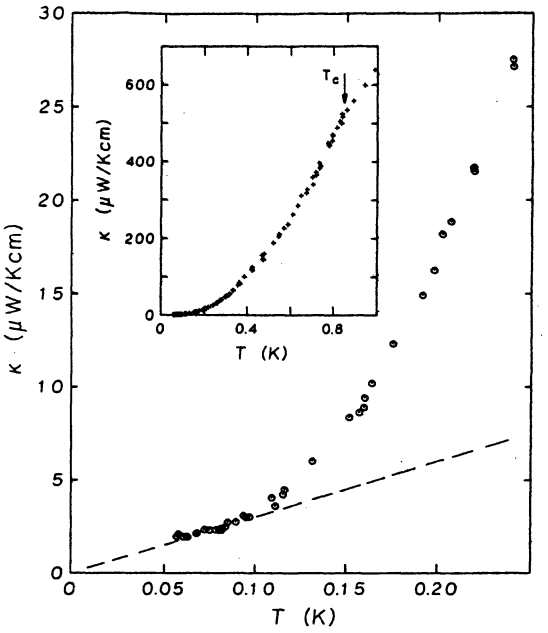

Fig. 10.59. The temperature dependence of the thermal conductivity κ of UBe_{13}, at low temperatures. The dashed line represents a possible linear term $\kappa(T) = \alpha_s T$. The insert shows the temperature dependence of κ in a wider temperature range which extends up to T_c. [After Ravex *et al.* (1987), [267]]

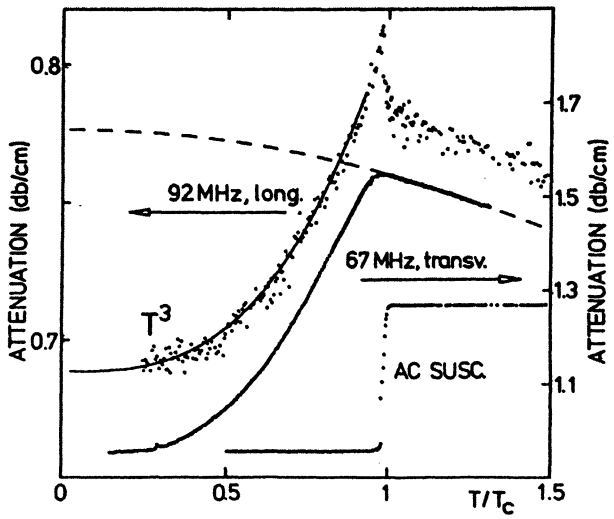

Fig. 10.60. The temperature dependence of the attenuation rate for longitudinal and transverse sound in UPt_3. [After Müller *et. al* (1986), [404]]

theory, and even with s–wave pairing, the attenuation coefficients for longitudinal and transverse sound are different. This difference occurs since a longitudinal sound wave merely produces a time–dependent scalar potential which acts on the electrons, whereas a transverse sound wave produces a transverse electromagnetic field and hence, is subject to the Meissner effect. The Meissner effect has the effect of reducing the coupling strength between the electrons and the transverse phonons and, therefore, reduces the transverse attenuation rate just below the superconducting transition [400, 401]. This mechanism is held to be responsible for an almost discontinuous drop in the attenuation rate for shear waves in Al [402] and In [403] at T_c. Below the transition temperature, the evolution of the superconducting gap leads to a further reduction of the attenuation rate. This behavior is in direct contrast with the ultrasonic attenuation of the heavy–fermion superconductors UPt_3 [42, 404–406], UBe_{13} [26] and URu_2Si_2 [407], where peaks have been found in the ultrasonic attenuation just below T_c.

A sharp peak in the longitudinal attenuation coefficient was observed in UBe_{13} in the form of a λ–like anomaly at a temperature just below the superconducting transition temperature of 0.8 K [26]. A similar sharp λ–like peak for the attenuation of longitudinal sound waves in UPt_3 was found at a temperature of about 500 mK [404]. A less pronounced and more rounded peak was also seen in the attenuation of transverse sound waves in UPt_3 [405,406]. The peak in URu_2Si_2 [407] is of the form of a rounded λ–like anomaly and has a maximum at a temperature of ~ 1.25 K, which is below the superconducting transition T_c of 1.35 K. Initially, it had been speculated that these peaks have their origin in the collective modes of the superconducting order parameter, similar to the collective modes observed in ^{3}He. However, in this case, the analogy with ^{3}He is flawed. Since the crystals do not posses continuous rotational symmetries, but only have the discrete rotational symmetries contained in their point groups, the collective excitations are not Goldstone modes. If spin–orbit scattering is strong in these U compounds, the frequencies of the collective modes of the order parameter could have magnitudes similar to the superconducting gaps. Furthermore, these collective modes are only expected to be well defined [129, 408] at very low temperatures in very clean materials. Since the peaks in the attenuation coefficient occur at temperatures just below the critical temperatures, and since there appears to be a residual zero energy density of states due to impurity scattering, the collective modes are expected to be over–damped, therefore, this explanation seems unlikely. An alternate viewpoint was provided by Coffey [409], who related the peak in the attenuation to the enhanced quasi–particle masses which makes the velocity of sound comparable to the Fermi velocity. In this picture, the conductivity enters the expression for the longitudinal attenuation rate, thereby producing a screening of the electron–phonon coupling. As in the normal state conductivity, the mass enhancement factor produces a sharp low–frequency Drude peak in the conductivity. Although this effect is

also predicted for a BCS state, it is stronger in anisotropic superconducting states where the low–energy quasi–particle density of states is finite, and so, the screening is more effective.

Low Temperatures

As a precursor to the discussion of the anisotropy in $\alpha_{\underline{q}}(T)$, we shall first examine the ultrasonic attenuation in an ordinary singlet superconductor. For a singlet superconductor, the attenuation rate is approximated by the Fermi Golden Rule expression

$$\alpha_{\underline{q},\hat{\epsilon}} = 2\pi|\lambda_{\underline{q},\hat{\epsilon}}|^2 \sum_{\underline{k},\sigma} \left(1 + \frac{(e(\underline{k})-\mu)(e(\underline{k}+\underline{q})-\mu) - D(\underline{k})\ D(\underline{k}+\underline{q})}{E_{\underline{k}} E_{\underline{k}+\underline{q}}}\right) \times (\ f(E_{\underline{k}}) - f(E_{\underline{k}+\underline{q}}))\delta(\ E_{\underline{k}+\underline{q}} - E_{\underline{k}} - \hbar\omega_{\underline{q},\hat{\epsilon}})\ , \tag{10.221}$$

where $\lambda_{\underline{q},\hat{\epsilon}}$ is the electron–phonon coupling strength, and $\omega_{\underline{q},\hat{\epsilon}}$ is the frequency of a phonon with wave–vector $\underline{q}$ and polarization $\hat{\epsilon}$. The summation over $\underline{k}$ can be separated into an integral over the magnitude of k (or $e(\underline{k})$) and an integral over the polar angle, θ, defined with respect to $\underline{q}$. For an s–wave superconductor, the angular integral can be replaced by an integral over the magnitude of $e(\underline{k}+\underline{q})$ where the range of integration runs between $e(k-q)$ and $e(k+q)$. The range of this transformed integral is shown in Fig. 10.61. Conservation of energy $E_{\underline{k}+\underline{q}} = E_{\underline{k}} + \hbar\omega_{\underline{q}}$ demands that the only $\underline{k}$ values that contribute to the attenuation are those which are close to the equatorial plane of the Fermi surface, if $v_F > c$ and $k_F > q$, as shown in Fig. 10.62. Since the term in the coherence factor proportional to $e(\underline{k}+\underline{q}) - \mu$ is anti–symmetric under the integration, it vanishes, thereby yielding the expression

$$\alpha_{\underline{q},\hat{\epsilon}} = \frac{m^2}{\pi q\hbar^4}|\lambda_{\underline{q},\hat{\epsilon}}|^2 \int_0^\infty de(\underline{k}) \int_{e(k-q)}^{e(k+q)} de(\underline{k}+\underline{q}) \left(1 - \frac{D(\underline{k})D(\underline{k}+\underline{q})}{E_{\underline{k}}E_{\underline{k}+\underline{q}}}\right) \times (f(E_{\underline{k}}) - f(E_{\underline{k}+\underline{q}}))\delta(E_{\underline{k}+\underline{q}} - E_{\underline{k}} - \hbar\omega_{\underline{q},\hat{\epsilon}})\ , \tag{10.222}$$

which, since $\omega_{\underline{q}}$ is small, simplifies to

$$\begin{aligned}\alpha_{\underline{q},\hat{\epsilon}} &= \frac{m^2\ \omega_{\underline{q}}}{\pi\ q\ \hbar^4}\ |\ \lambda_{\underline{q},\hat{\epsilon}}\ |^2 \int_0^\infty de(\underline{k}) \int_{e(k-q)}^{e(k+q)} de(\underline{k}+\underline{q}) \left(\frac{e(\underline{k})\ -\ \mu}{E_{\underline{k}}}\right)^2 \\ &\quad \times \left(-\frac{\partial f(E_{\underline{k}})}{\partial E_{\underline{k}}}\right) \delta(\ E_{\underline{k}+\underline{q}}\ -\ E_{\underline{k}}\ -\ \hbar\omega_{\underline{q},\hat{\epsilon}}\ ) \\ &= \frac{m^2\ \omega_{\underline{q}}}{\pi\ q\ \hbar^4}\ |\ \lambda_{\underline{q},\hat{\epsilon}}|^2 \int_{\Delta_0}^\infty dE_{\underline{k}} \left(-\frac{\partial f(E_{\underline{k}})}{\partial E_{\underline{k}}}\right).\end{aligned} \tag{10.223}$$

In this expression, the coherence factors have cancelled with the quasi–particle density of states. Thus, in a BCS superconductor, the attenuation coefficient $\alpha(T)$ should follow the law

$$\alpha(T)\ \propto\ f(\Delta_0(T))\ , \tag{10.224}$$

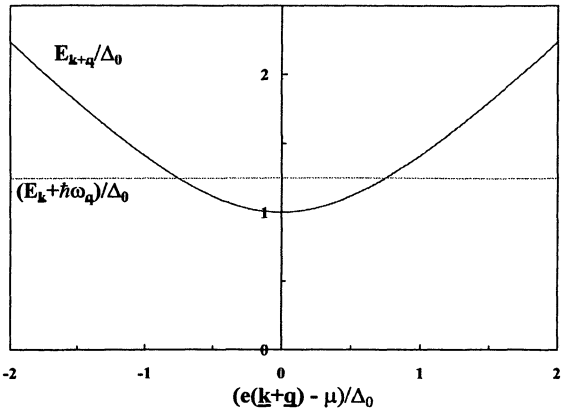

Fig. 10.61. The range of the integration over over energy in eqn(10.222), representing the integration over the polar angle θ

where $f(x)$ is the Fermi function and $\Delta_0(T)$ is the superconducting gap. Thus, for temperature far below T_c, the attenuation coefficient should be thermally activated

$$\alpha(T) \sim \exp\left[- \beta \Delta_0 \right] . \tag{10.225}$$

The above derivation emphasizes that, if $\underline{q}$ is defined as the polar axis, it is the electrons which have $\underline{k}$ vectors near the equatorial plane of the spherical Fermi surface that provide the dominant contribution to the attenuation of sound waves. Furthermore, since the contribution from this region of $\underline{k}$ space is weighted by a function depending on $E_{\underline{k}}/k_B T$, the presence of nodes of the order parameter within this equatorial plane may result in a power law temperature dependence of $\alpha_{\underline{q}}(T)$.

To illustrate the origin of the anisotropy, consider the clean limit of a polar–like superconductor with a line of nodes in the equatorial plane of the Fermi surface [410]. When the propagation vector $\underline{q}$ is aligned precisely along the polar axis $\vec{d}$, the attenuation process primarily involves excitations on the line of nodes and, therefore, the attenuation coefficient resembles that of the normal state. However, if the direction of $\underline{q}$ is slightly rotated, the attenuation will only involve the low energy excitations near two isolated points on the line of nodes. Hence, one expects that the attenuation coefficient $\alpha_{\underline{q}}(T)$ will vary linearly with T. The coefficient of the linear T term will depend sensitively on the angle $(\vec{d}.\ \hat{q})$. For an ABM–like state, one may expect that if the $\underline{q}$ vector is oriented in a plane exactly perpendicular to the direction of $\vec{d}$ [10], the low–energy excitations will predominately be near the isolated point

[10] For the A.B.M. state $\vec{d}$ is in the direction of the polar axis.

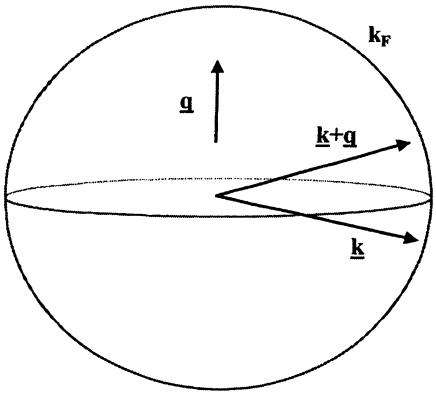

Fig. 10.62. Typical reciprocal space geometry of electrons involved in the attenuation of sound with wave vector $\underline{q}$, in the clean limit. The electrons which are primarily involved in the attenuation process are located near the equator of the Fermi surface

nodes. In this case, one expects that in this case, the attenuation coefficient should vary linearly with T. For other orientations the density of low energy excitations is reduced, so $\alpha_{\underline{q}}(T)$ is expected to be proportional to T^2.

The heavy–fermion superconducting materials are not in the clean limit. However, similar types of anisotropic results and pseudo–selection rules have been obtained for systems with resonant impurity scattering and high concentrations [156,411,412]. For example, in the dirty limit, the attenuation of transverse sound waves [413] is proportional to

$$\alpha_{\underline{q},\hat{\epsilon}}(\omega) \propto \omega^2 \sum_{\underline{k}} \left(-\frac{\partial f}{\partial E_{\underline{k}}} \right) \tau_{\underline{k}}(E) \left(\frac{\xi(\underline{k})}{E_{\underline{k}}} \right)^2 \left[\hat{k}.\hat{q} \right]^2 \left[\hat{k}.\hat{\epsilon} \right]^2 , \qquad (10.226)$$

where $\xi(\underline{k}) \equiv e(\underline{k}) - \mu$. For a superconductor with a line of nodes and at low temperatures, the largest contribution comes from $\underline{k}$ values close to the nodes. Due to the geometric factors, the attenuation is small if either the propagation vector $\underline{q}$ or the polarization $\hat{\epsilon}$ is directed towards the nodes and is larger for other orientations. Hence, even in the dirty limit, the anisotropy can be used to determine the positions of the nodes in the superconductors order parameter.

In the heavy–fermion superconductors UBe_{13} and UPt_3, the low temperature attenuation coefficient have power law temperature dependences, suggesting that the gaps are anisotropic and have nodes. The exponent of the power law temperature–dependence not only varies with the direction of propagation but also depends upon the polarization of the sound waves.

For the hexagonal compound UPt_3, Müller *et al.* [404] measured the attenuation coefficient for both longitudinal and transverse sound propagating

along the c–axis. At temperatures sufficiently below T_c, the transverse [404] and longitudinal waves [27, 30] seemed to show a T^2 dependence of the attenuation rate. However, a fit to the attenuation of longitudinal sound over a wider temperature range, yields a T^3 dependence [404]. The attenuation of transverse sound waves propagating in the basal plane is dependent upon the direction of the polarization. Transverse sound waves propagating in the basal plane but with polarizations also in the basal plane, showed an attenuation which is linear in T [405]. This is in direct contrast with the attenuation of transverse waves propagating in the basal plane, but with the polarization along the c–axis, which have an attenuation coefficient that shows a T^2 or T^3 [406] temperature dependence. Since the polarization dependence vanishes in the normal state, this is strong evidence that the anisotropy is a feature of the superconducting state. However, the nature of the order parameter is not easily discerned from these experiments. For a polar–like state with lines of nodes, the longitudinal attenuation should have a quasi–linear T dependence or, for an ABM–like state with point nodes, the attenuation should vary as T^2 [156, 411]. The experimental observations of the longitudinal attenuation rate, therefore, favor an interpretation based on ABM–like states [410, 414] and rule–out polar–like states. However, the T dependences found in the transverse sound wave experiments of Shivaram *et al.* [405] do not fit the predictions for ABM–like states with point nodes but instead fit the theoretical results for polar–like states with lines of nodes.

For UBe_{13}, measurements below 0.9 K [26] showed that the attenuation of longitudinal sound waves followed a T^2 variation which implies the existence of an ABM–like state with point nodes.

Electromagnetic Response

The electromagnetic absorption spectra of an s–wave superconductor has been calculated by Mattis and Bardeen [415], using the Kubo formulae. On assuming non–conservation of momentum, either caused by the presence of impurities or by the samples surface, the absorption spectrum is given by the integral

$$\frac{\sigma_s}{\sigma_n} = \int_{-\infty}^{\infty} dE \rho_{BCS}(E)\rho_{BCS}(E-\hbar\omega)\left(\frac{f(E-\hbar\omega)-f(E)}{\hbar\omega}\right)\left(1+\frac{\Delta_0^2}{E(E-\hbar\omega)}\right) \tag{10.227}$$

for $\hbar\omega > 2\Delta_0$. At $T = 0$, the absorption is evaluated in terms of the complete elliptical integral functions $E(x)$ and $K(x)$ as

$$\frac{\sigma_s}{\sigma_n} = \left(1+\frac{2\,\Delta_0}{\hbar\omega}\right)E\left(\frac{\hbar\omega-2\Delta_0}{\hbar\omega+2\Delta_0}\right) - \left(\frac{4\,\Delta_0}{\hbar\omega}\right)K\left(\frac{\hbar\omega-2\Delta_0}{\hbar\omega+2\Delta_0}\right) \tag{10.228}$$

for $\hbar\omega > 2\Delta_0$. At $T = 0$ where no thermally excited quasi–particles are present, the optical conductivity is zero for frequencies in the range

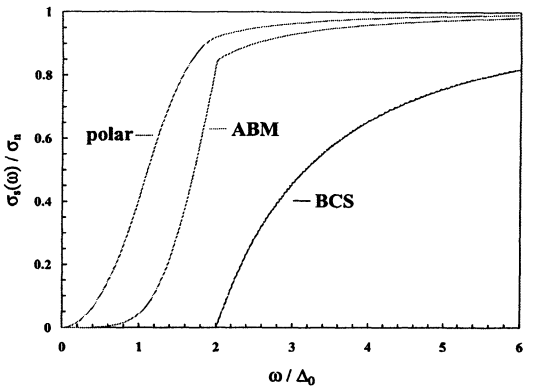

Fig. 10.63. The frequency dependence of the real part of the $T = 0$ optical conductivity calculated for various superconducting phases. The BCS phase conductivity exhibits a threshold at $\hbar\omega = 2\Delta_0$. The ABM and polar phases have nodes in the order parameter, therefore, the respective conductivities should show power law variations at low frequencies

$2\ \Delta_0\ >\ \hbar\ \omega\ >\ 0$. At higher frequencies, the incident photon can be absorbed through a process in which a Cooper pair is broken and two quasi–particles are created. Since the coherence factors are reduced near the gap edge, the a.c. conductivity shows a continuous increase above the threshold frequency and approaches the normal state conductivity at frequencies much greater than the gap frequency. Thus, as seen in Fig. 10.63, the area under the theoretically predicted curve $\sigma_s(\omega)$ is smaller than found in the normal state. The ω variation of $\sigma(\omega)$ calculated by Mattis and Bardeen is in agreement with experiments on In [416]. There is also good agreement between the theoretical and experimentally observed temperature dependence of $\sigma(\omega)$ for example, as found from measurements of the microwave surface impedance of Zn [417].

As shown by Tinkham and Ferrell [418], the inequality $\sigma_s(\omega) < \sigma_n(\omega)$, which is valid for all finite frequencies, has the consequence that the optical sum rule

$$\int_0^\infty d\omega\ \sigma(\omega)\ =\ \frac{\pi\ n\ e^2}{2\ m} \tag{10.229}$$

is not satisfied, if the integration is performed down to a finite cut off ϵ at the lower limit. Hence, the conductivity must have a zero frequency delta function spike in order to satisfy the optical sum rule. This spike represents the absorption of energy from d.c. electric fields which produce accelerated supercurrents. This spike is of special significance as causality connects the $\delta(\omega)$ contribution to the real part of the conductivity to a $1/\omega$ variation in the imaginary part of the conductivity. The existence of the $1/\omega$ term shows that supercurrent will flow in response to a uniform d.c. vector potential $\vec{A}$,

thereby screening the external magnetic field. The ensuing non–local relation is similar to the (local) London relation

$$\vec{J}(\underline{r}) = -\frac{c}{4\,\pi\,\lambda_L^2}\,\vec{A}(\underline{r}) \tag{10.230}$$

which involves the London penetration depth λ_L. Within the BCS theory, the penetration depth $\lambda(T)$ should have a leading exponential low temperature variation [419]. The calculated temperature dependence of the penetration depth is given by

$$\frac{\lambda(T)}{\lambda(0)} - 1 \propto T^{-\frac{1}{2}} \exp\left[-\frac{\Delta_0}{k_B\,T} \right], \tag{10.231}$$

since the Fermi surface is completely gapped in s–wave superconductors.

For anisotropic superconductors which have nodes in the order parameter, one expects very different results. First, since the angular average of the order parameter vanishes, and since the tensorial nature of the conductivity has been ignored, the coherence factors are reduced to unity. Hence, the expression analogous to that of Mattis and Bardeen for the dirty limit of the absorption spectrum is just given by the convolution of the quasi–particle density of states

$$\frac{\sigma_s}{\sigma_n} = \int_0^{\hbar\omega} dE \rho_{qp}(E)\rho_{qp}(E-\hbar\omega)\left(\frac{f(E-\hbar\omega)-f(E)}{\hbar\omega}\right). \tag{10.232}$$

Secondly, due to the existence of nodes, the quasi–particle density of states is finite and, therefore, the conductivity is expected to be finite down to zero frequency. For an order parameter with point nodes, one expects that the above expression for the conductivity should vary as ω^4 at low frequencies while for an order parameter with line nodes, one expects an ω^2 variation. The electromagnetic absorption spectra for the BCS, ABM and polar states are shown in Fig. 10.63. For a more general description of electromagnetic absorption, incorporating the tensorial nature of the conductivity and the effects of impurity scattering, the interested reader is referred to the article of Hirschfeld *et al.* [420]. From an analysis of this type, Lee [393] found the surprising result that the $\omega \rightarrow 0$ limit of the conductivity has value which is universal and independent of the impurity scattering rate. However, if the impurity scattering is sufficiently strong, Lee [393] has shown that the electronic states in the superconducting phase may be localized even though the electronic states in the normal state are not. The increased tendency for localization of the superconducting electrons is caused by the reduction of the effective dimension of the space in which the quasi–particles close to the nodes are free to move. The localization leads to the a.c. conductivity being dominated by the thermal activation of quasi–particle excitations across the mobility gap, despite any power law energy variation of the quasi–particle density of states near the Fermi energy.

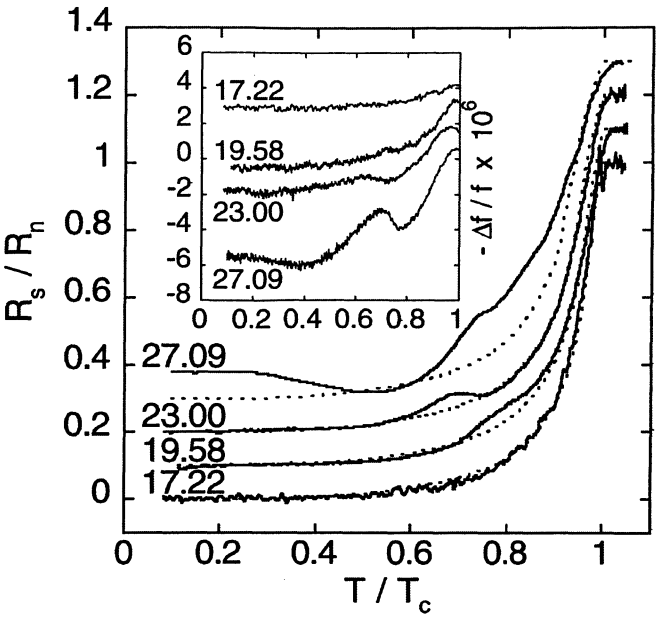

Fig. 10.64. The temperature dependence of the surface resistance of UBe_{13}, for various frequencies. The surface resistance was normalized to unity at T_c and zero at $T = 0$. Each curve is labelled by the measurement frequency in GHz. Anomalous structures are seen for temperatures in the interval $T_c > T > 0.8\ T_c$. The dotted lines are fits to the Mattis–Bardeen theory for an s–wave superconductor. The inset shows the resonant frequency shift. [After Feller *et al.* (2002), [423]]

The temperature dependence of the surface–impedance of UBe_{13} has been measured [421], and compared with theoretical predictions based on the BCS state. The value of Δ_0/k_BT_c was treated as an adjustable parameter. The experimentally determined surface–reactance shows a coherence peak just below T_c, which is well reproduced by Mattis–Bardeen theory [415], and less well so by the theory of Skalski *et al.* [422] which incorporates the effect of a finite spin–flip scattering rate caused by magnetic impurities. However, a single value of Δ_0/k_BT_c does not fit the data at all frequencies, which indicates that the order parameter corresponds to $l \neq 0$. In fact, subsequently anomalous structure (shown in Fig. 10.64) was identified [423] in the surface–resistance of UBe_{13} below $0.8\ T_c$, which was attributed to collective excitations of an $l \neq 0$ superconducting order parameter.

Since, as seen in Fig. 10.63, the spectral weight below twice the maximal gap $2\Delta_0$ is diminished below the normal state conductivity, the zero–frequency delta function present in $\sigma_s(\omega)$ is also expected to exist in the anisotropic superconducting phases, albeit with reduced weight. On employing the Kramers–Kronig relations, one can infer that the penetration depth

should have a power law temperature dependence of the form

$$\frac{\lambda(T)}{\lambda(0)} - 1 \propto \left(\frac{T}{T_c}\right)^n , \tag{10.233}$$

where the exponent n depends on the node structure of the superconducting order parameter. Power law temperature variations of the penetration depth have been observed in heavy–fermion superconductors for example, a T^2 power law dependence has been observed in UBe_{13} [424]. By contrast, in UPt_3 the superfluid density measured by μSR experiments [425, 426] was also found to have a power law temperature dependence but one in which the exponent is anisotropic. Since the main contribution to the superfluid density is governed by the nodes in the superconducting order parameter, the magnetic field dependence of the penetration depth can be significant. Yip and Sauls [427] have suggested that this non–linear Meissner effect might be used to probe the momentum space positions of the nodes in the order parameter. However, Li *et al.* [428] find that in general, the non–local nature of the electromagnetic response does mask any non–linear Meissner effect, except under special circumstances.

Tunnelling measurements

Measurements of quasi–particle tunnelling at sufficiently low temperatures are expected to yield the quasi–particle density of states $\rho_{qp}(E)$. We assume that the tunnelling occurs between a normal metal with a relatively featureless density of state $\rho_N(E) \sim \rho(\mu)$ and a superconductor, and that the tunnelling matrix element T is independent of $\underline{k}$. If a bias voltage V is applied across the junction, the tunnelling current I is given by

$$I = \frac{2\pi}{\hbar} e|T|^2 \int_{-\infty}^{\infty} dE \rho_N(E - eV)\rho_{qp}(E)\Big[f(E - eV) - f(E)\Big] . \tag{10.234}$$

The coherence factors do not enter the above expression [429], since the quasi–particle wave functions are reduced to the normal state wave functions in the barrier region. Hence, if the differential conductance σ is defined by

$$\sigma = \left(\frac{dI}{dV}\right) \tag{10.235}$$

the differential tunnelling conductance is evaluated as

$$\sigma(V) = \frac{2\pi}{\hbar} e^2|T|^2\rho(\mu) \int_{-\infty}^{\infty} dE \rho_{qp}(E)\left(-\frac{\partial f}{\partial E}\right)\Big|_{E-eV} . \tag{10.236}$$

At sufficiently low temperatures, the expression for the tunnelling conductance reduces to

$$\sigma(V) \propto \rho_{qp}(eV) . \tag{10.237}$$

Hence, a measurement of the voltage dependence of the quasi–particle tunnelling conductance should yield the quasi–particle density of states [430]. Likewise, a similar analysis of quasi–particle tunnelling between two superconductors should yield the joint density of states with features at the sum and difference of the characteristic energies of the superconducting density of states for the two materials. For two s–wave superconductors at finite temperatures, a discontinuity occurs in the tunnelling current for a voltage V_+ corresponding to the sum of the two superconducting gaps, while a weak temperature dependent logarithmic singularity occurs in the current at the voltage V_- corresponding to the difference of the gaps [430,431]

$$\begin{aligned} e\,V_+ &= \Delta_1 + \Delta_2\,, \\ e\,V_- &= |\,\Delta_1 - \Delta_2\,|\,. \end{aligned} \tag{10.238}$$

The observation of the quasi-particle density of states and, therefore, the characteristic van–Hove singularities and the low–energy variation, should provide information about the nature of the order parameter. However, it should be noted that the presence of the surface may locally distort the superconducting phase [432]. In this case, the tunnelling matrix elements may become orientational dependent and the local density of states may differ from the bulk quasi–particle density of states.

The best tunnelling measurements obtained to date are those on UPd_2Al_3. The junctions consisted of high quality UPd_2Al_3 films which were separated from the strong coupling superconductor Pb by a thin layer of Al [433]. A small magnetic field was applied in order to suppress the superconductivity of Pb. For temperatures below the superconducting transition of UPd_2Al_3, the tunnelling conductance developed a minimum at zero bias voltages and a large peak structure at a voltage of the order of 0.24 mV. The large peak structure resembles the van Hove singularities often found in superconducting quasi–particle density of states at Δ_0 (see Figs. 10.23 and 10.24). On identifying this voltage with the gap energy, one finds that the universal ratio $\Delta_0(0)/k_BT$ is of the order of 3.71 [434]. The differential conductance also showed a fainter peak at a voltage of 1.25 mV, which was attributed to strong coupling corrections. These features in the density of states are assumed to originate from coupling to unusual antiferromagnetic spin excitations seen in inelastic neutron scattering experiments [349,435]. By contrast, the interpretation of tunnelling experiments on $CeCu_2Si_2$ is not so clear cut. The tunnel junctions were constructed from $CeCu_2Si_2$ which were separated by a thin oxide layer from an overlayer of Pb. The measurements showed that, for temperatures below the T_c of $CeCu_2Si_2$, the tunnelling conductance resembles the superconducting density of states of Pb but is superimposed with very small features that were attributed to a gapless superconducting quasi–particle density of states of $CeCu_2Si_2$ [436].

Point Contact Spectroscopy

The difficulty of fabricating good tunnel junctions and the small tunnelling

probabilities associated with oxide layers has hampered tunnelling experiments. On the other hand, measurements of the differential conductance of point–contacts between a superconductor and metal are expected to produce larger currents. In this case, the Cooper pair wave function of the superconductor extends into the metal and Andreev reflection may occur [437] along with the usual single–particle transfer process. That is, an electron of momentum $\underline{k}$ incident on the boundary between the metal and superconductor may combine with a normal state electron of momentum $-\underline{k}$ to form a Cooper pair that subsequently resides within the superconducting condensate. This process can be viewed as an incident electron, with energy $E < \Delta_0$, inside the metal being scattered from the surface of the superconductor and emerging in the metal as a reflected hole, thereby transferring a net charge of 2 e across the junction. The role of Andreev reflection in point contact spectroscopy on conventional s–wave superconductors was pointed out by Blonder *et al.* [438]. Since the conductance depends on an interface potential which in part models the decay of the pairing potential in the normal metal, the conductance smoothly evolves between the result for classic tunnelling expressed by Eqn. (10.236) and the extreme Andreev limit. In the extreme Andreev limit, the conductance of an s–wave superconductor – metal contact shows a zero bias peak which is twice as great as the normal state conductance of the junction. The magnitude of the peak height of the normalized conductance is two since a charge of 2 e is transferred across the junction for each normal–metal electron with energy $E < \Delta_0$ that falls incident on the surface. The conductance recovers to the normal state value at higher voltages ($e\,V > \Delta_0$) as other electron transfer processes gradually take over. Bruder extended the analysis of Andreev reflection to the case of unconventional superconductors [439] and found that the energy of the peak is extremely dependent on the type of superconducting order parameter and the direction of the incident electron's momentum. In the usual geometry of point contact measurement, the electrons have varying angles of incidence with the boundary and, therefore, conductance measurements yield weighted orientational averages of functions of the order parameter.

Early Point contact tunnelling measurements were made on UPt_3 and UBe_{13} and various metals [440, 441] but did not lead to reliable estimates of the gaps for the heavy–fermion superconductors. Later, measurements on UPt_3 [442–444] showed that distinct minima in the differential conductance – voltage relation occur for current flow along the c–axis but are generally absent for current flow in the basal plane. The differential conductance shows significant variation with the surface treatment. These results indicate that the superconducting order parameter has an anisotropic dependence on $\underline{k}$. The amplitude of the zero bias peak, when normalized to the conductance at large voltages, is an order of magnitude smaller than expected from theory. A similar discrepancy with the theoretical magnitude of the peak was found in URu_2Si_2 [445]. On defining the strength of the zero bias conductance

peak as the area between $\sigma(V)$ in the superconductor and the normal state background, the strength vanished close to T_{c2}. The vanishing of the strength between T_{c1} and T_{c2} is very surface sensitive but indicates that Andreev reflection is suppressed in the A phase. A similar reduction of the strength was found when a magnetic field was applied in the basal plane.

Point contact measurements on URu_2Si_2 [445] are of particular interest since they showed a gap with magnitude of approximately 10 meV opened up in the conductance spectrum near the transition temperature of 17.5 K. As also observed in point contact measurements in UPt_3 [443], the shape of the zero bias conduction peak for URu_2Si_2 is consistent with an order parameter that has lines of nodes [445].

In contrast to the very small magnitude of the zero bias conductance peak found in UPt_3 and URu_2Si_2, the magnitude of the conductance peak in UBe_{13} [446] is roughly a factor of 5 times larger than the theoretical value for an *s*–wave superconductor. The enhancement of the zero bias anomaly was attributed to the formation of an Andreev surface state, which can occur if there is a non–trivial dependence on the angle subtended by the nodes of the order parameter to the normal to the interface [447]. As the bias voltage was increased, the zero bias conductance peak of UBe_{13} was followed by a minimum which was reduced from the normal state value and then showed a sharp increase as it recovered to the normal state value. The variation of the differential conductivity with voltage is shown in Fig. 10.65. The sharp increase occurred at a temperature–dependent voltage which was of the order of magnitude 0.25 mV at 330 mK. Such sharp changes of the conductance have not been observed for *s*–wave superconductors but have been predicted to occur at the gap voltage $e\,V = \Delta_0$ for junctions with anisotropic superconductors [447]. If the temperature dependent characteristic voltage is interpreted as being the magnitude of the order parameter $\Delta_0(T)$, then UBe_{13} would correspond to a universal ratio $2\Delta_0(0)/k_BT_c$ of about 6.7 which is far greater than the BCS value of 3.5, and is also greater than the ratio predicted for most *p*–wave phases (ABM 4.6, polar 4.9) but is more comparable with the value of 6.2 predicted for the $m = 0$ *d*–wave phase.

Josephson Tunnelling

Josephson tunnelling involves the tunnelling of Cooper pairs between two superconductors [448]. A d.c. tunnel current may appear even in the absence of an applied voltage but also appears as an a.c. current if a voltage is applied. The a.c. current is expressed in terms of the phase difference between the wave functions of the two superconductors

$$I(t) = I_0 \sin\left(\frac{2\,eV\,t}{\hbar} + \Delta\varphi\right). \tag{10.239}$$

The phase difference not only has contributions from the intrinsic phases of the superconductors but also has contributions from any magnetic vector potential that may be present at the junction. When integrated over the finite size of the contact, this term can give rise to a Frauenhofer diffraction

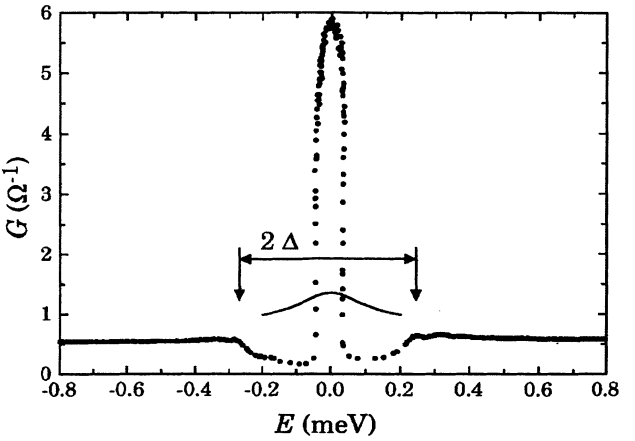

Fig. 10.65. The differential conductivity of a UBe_{13}-Au point contact at $T = 330$ mK, as a function of voltage. The height of the zero–bias anomaly is roughly five times greater than is expected for an s–wave superconductor. The solid line shows an estimate of the Kondo contribution to $G(V)$. [After Wälti *et al.* (2000), [446]]

pattern [449]. The leading order contribution to the Josephson coupling can be calculated using second order perturbation theory [448]. To lowest order there should be no Josephson current between a singlet and triplet superconductor [450], since spin is conserved in the tunnelling process. However, even in this case, spin–orbit interaction and higher order processes may produce a non–zero Josephson current. If the tunnelling is due to a fourth order process, the Josephson frequency is expected to be given by $4\ eV/h$. Since the presence of the surface locally violates certain rotational symmetries contained in the point group, it is possible for relatively large Josephson currents to flow between superconductors with different orbital symmetries. In fact, the magnitude of the order parameter at the surface may even vary with the relative orientation of the boundary and the node directions. Due to this, it is possible to extract the symmetry of the order parameter from Josephson tunnelling measurements [451]. However, the Josephson effect is a very weak effect and sensitive to impurities and inhomogeneities, since the total coupling energy for a conventional Josephson junction is estimated to be only of the order of 1 eV. For the heavy–fermion systems, the preparation and characterization of good surfaces and junctions represent formidable experimental problems. Therefore, there has been only limited progress in the investigation of the Josephson effect in heavy–fermion superconductors.

A d.c. Josephson current was found to exist between $CeCu_2Si_2$ and Al [440]. The Josephson current vanished at the T_c of $CeCu_2Si_2$ with applied magnetic fields greater than the upper critical field of Al but smaller than the critical field of $CeCu_2Si_2$. Hence, the tunnelling current involved the superconducting phases of both materials. The application of magnetic fields

produced irregular Frauenhofer diffraction patterns which were smeared out. The smearing was attributed to the irregular geometry of the junctions. As the observed value of the critical current was quite large, having a maximum magnitude that is 80 % of the BCS value, it appears as if the Josephson coupling is of second order [452] and not of fourth order. Furthermore, since Al is known to be a singlet superconductor, the large coupling strength indicates that $CeCu_2Si_2$ is also a singlet superconductor.

No Josephson currents were found to flow across weak links between UPt_3 surfaces [440]. However, a Josephson current, with an irregular Frauenhofer pattern and well defined Shapiro steps was observed between UPt_3 and Nb in a superconductor – normal metal – superconductor junction [453]. The critical current measured for junctions where the current flow is primarily along the c–axis of the UPt_3 single crystal is significantly larger than for junctions where the current flows along the basal plane. The critical current temperature relations show clear kinks at the lower critical temperature T_{c2}. For temperatures below T_{c2}, the slope of the critical current – temperature relation is large for current flow along the c–direction, and smaller for current flow in the basal plane. For temperatures above T_{c2}, the slope of the critical current temperature relation for flow in the basal plane changes to a larger value but the curve representing flow along the c–axis is rather flat. The change in the anisotropy at T_{c2} seems to indicate that the anisotropy in the current flow is related to the unconventional nature of the superconductivity in UPt_3. It should be noted that, since the anisotropy measurements were made on junctions with different surfaces, the apparent anisotropy possibly could reflect a difference in the properties of the interfaces. A much larger anisotropy was inferred from measurements of Josephson currents through point contacts between URu_2Si_2 and Nb [454] where no current was observed for contacts aligned parallel to the c–axis but finite currents were found for contacts aligned parallel to the a–b directions. The absence of Josephson currents flowing along the c–axis could, however, have many other possible causes.

No Josephson tunnelling currents were observed to flow across a weak link between two surfaces of UBe_{13}. In a junction between Al and UBe_{13}, superconductivity was introduced in UBe_{13} by the proximity effect for temperatures below the superconducting transition of Al but above the superconducting transition for UBe_{13}. In this temperature regime, a weak Josephson current was observed between these materials. A proximity induced Josephson current was also found to occur across a point contact between UBe_{13} and Ta at temperatures below T_c for Ta and above T_c for UBe_{13}. This Josephson current was destroyed as the temperature was lowered below the T_c of UBe_{13} [455,456]. This was taken as evidence that the superconducting order parameter of UBe_{13} competes with the superconductivity of Ta and hence, are of different symmetry. The analysis presented in Ref. [456] suggested that the Cooper pairs were spin–triplet, however, spin–singlet d–wave pairing would

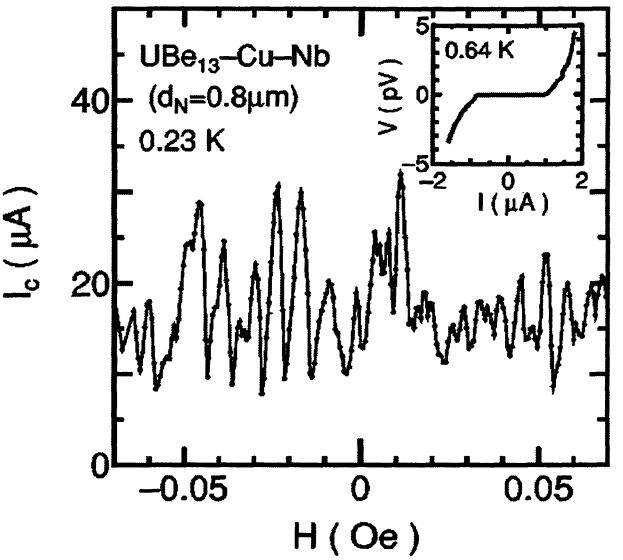

Fig. 10.66. The field dependence of the Josephson current through a UBe_{13}-Nb junction. The irregular Frauenhoffer pattern suggests that the junction is not uniform. The inset shows the $I-V$ curve showing the critical Josephson current. [After Shibata *et al.* (1999), [458]]

be more consistent with the experimental observations. In particular, when illuminated with microwave radiation of frequency ω, the current d.c. voltage relation exhibited Shapiro steps of magnitude $\Delta V = \hbar\omega/2e$, instead of $\Delta V = \hbar\omega/4e$ as would be expected for a fourth order Josephson coupling between singlet and triplet superconductors [450, 457]. The interpretation of these experiments is enigmatic since a conventional Josephson tunnelling current, with an irregular Frauenhofer pattern (see Figs. 10.66 and 10.67) and conventional Shapiro steps (shown in Fig. 10.68), was observed at temperatures below 0.94 K between UBe_{13} and Nb in a fairly well defined superconductor – normal metal – superconductor geometry [458]. The Shapiro steps were observed to have a magnitude of $\Delta V = \hbar\omega/2e$, as expected for a second order Josephson coupling between two singlet superconductors. On the other hand, the magnitudes of the critical currents were remarkably small, being two orders of magnitude smaller than the critical currents observed in UPt_3. However, as the critical currents were limited by heating, it was not possible to determine whether the magnitude of the Josephson coupling in UBe_{13} was consistent with the tunnelling being due to a fourth order process or a second order process.

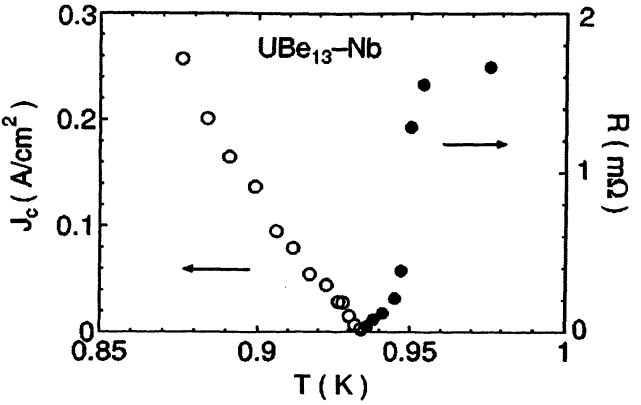

Fig. 10.67. The temperature dependence of the critical Josephson current J_c and the junction resistance R, near T_c for a UBe_{13}-Nb junction. After Shibata *et al.* (1999), [458]

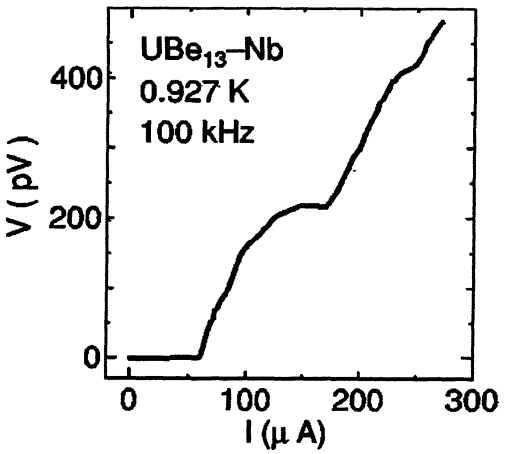

Fig. 10.68. The $I(V)$ relation for a UBe_{13}-Nb junction, showing conventional Shapiro steps when an ac current of frequency 100 kHz is superimposed on the dc current. [After Shibata *et al.* (1999), [458]]

10.4.3 Dynamic Magnetic Properties

Nuclear Magnetic Resonance

As previously mentioned, nuclear magnetic resonance experiments yield several important quantities: the Knight shift and the nuclear spin relaxation rates which are $1/T_1$ the longitudinal relaxation rate, and the transverse relaxation rate $1/T_2$. The changes in behavior of these quantities on entering

the superconducting phase does give information about the nature of the density of magnetic excitations in the superconductor.

The Knight shift

The Knight shift has many contributions, one important contribution provides a measure of the local part of the static susceptibility of the itinerant electrons which produces a magnetic polarization at the nuclear site. For heavy–fermion superconductors, the normal state Knight shift is expected to be dominated by the enhanced Pauli spin susceptibility, though spin–orbit coupling will introduce an orbital part. However, in the superconducting state, the Knight shift is expected to be dominated by the diamagnetic susceptibility produced by the supercurrent shielding the external field. The Pauli spin susceptibility will be modified by the superconductivity, and provide information about the pairing. The zero field susceptibility is defined as a derivative of the magnetization $\chi(T) = (\frac{\partial M}{\partial H})$. The magnetization that is produced by the electronic spins aligning with a magnetic field applied along the z–axis is given by

$$M_z = \left(\frac{g\mu_B}{2}\right) \sum_{\underline{k}} \left[f(E_{\uparrow,\underline{k}}) - f(E_{\downarrow,\underline{k}}) \right] \tag{10.240}$$

which is expressed in terms of the Fermi–distribution for quasi–particles with spin σ and quasi–particle energy $E_{\sigma,\underline{k}}$. The field dependence of the quasi–particle energies depends on the type of spin pairing, so we shall discuss the different types of spin pairings separately.

Singlet Pairing

For singlet pairing, the magnetic field couples to the spins of the quasi–particles via the Zeeman energies. As can be seen from inspection of the matrix in Eqn. (10.58), only the time reversal partners pair when $\vec{d}(\underline{k}) \equiv 0$. The quasi–particles consist of broken pairs, i.e., electrons of spin σ and holes of spin $-\sigma$. Since a down–spin hole has the same Zeeman energy as an up–spin electron, the quasi–particle energies depend on the magnetic field through

$$E_{\sigma,\underline{k}} = E_{H=0,\underline{k}} - \left(\frac{g\mu_B \sigma H}{2}\right) \tag{10.241}$$

and so the spin susceptibility takes the usual form

$$\chi_{S=0}(T) = 4\left(\frac{g\mu_B}{2}\right)^2 \int_0^\infty dE\ \rho_{S=0}(E) \left(-\frac{\partial f}{\partial E}\right). \tag{10.242}$$

The BCS density of states should be used in the above expression, for an s–wave superconductor. In this case, the susceptibility tends to zero as $T \to 0$ in an exponentially activated way $\chi_{BCS}(T) \sim \exp[-\Delta_0/k_B T]$. The exponential vanishing of the spin susceptibility occurs as the electrons form singlet

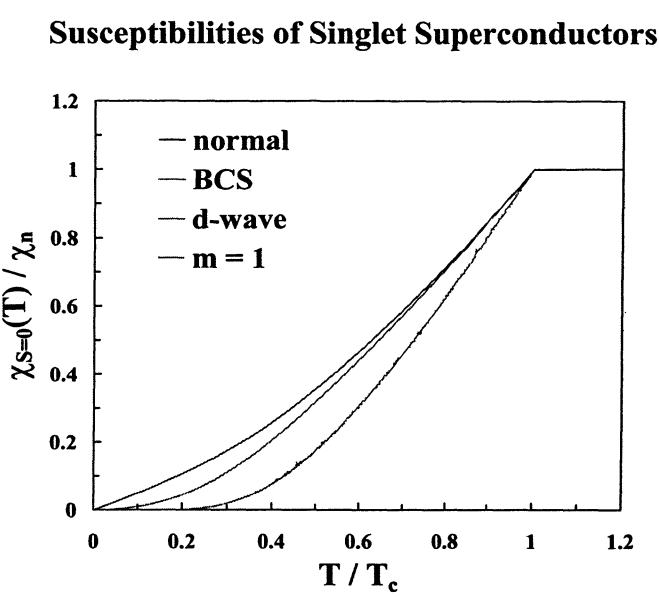

Fig. 10.69. The calculated spin susceptibilities of singlet superconducting phases. The susceptibilities are normalized to the normals state susceptibility. The susceptibilities in the singlet superconducting phases all vanish as $T \rightarrow 0$. The susceptibility of the BCS phase is given by the Yosida function, which vanishes exponentially at low temperatures. The susceptibilities of the isotropic and $m = 1$ d–wave phases vary as powers of the temperature, at low temperatures

pairs in the ground state, and the finite spin moment is caused by thermal population of quasi–particles [459]. For a singlet superconductor that has point nodes, the density of states varies as E^2 at low energies and, therefore, one expects that $\chi_{S=0}(T) \propto T^2$ for $T \ll T_c$. Whereas for a singlet superconductor which has line nodes, the density of states is given by $\rho_{S=0}(E) \propto E$ at low energies, hence one obtains $\chi_{S=0}(T) \propto T$. The temperature dependence of the calculated spin susceptibility expected for various singlet spin superconducting phases is shown in Fig. 10.69.

Thus, in the spin singlet phases, the spin susceptibility could be expected to vanish as $T \rightarrow 0$. However, spin–orbit coupling will produce a residual susceptibility that depends on the ratio of the superconducting coherence length, ξ_0, to the mean free path due to spin–orbit scattering, l_{so}. In the presence of spin–orbit coupling, the spin is no longer a good quantum number for the single–particle eigenstates and the spin–up and spin–down states are mixed. In the limit that the strength of the spin–orbit coupling $\lambda \vec{L} . \vec{S}$ is so large that $\lambda \gg \Delta_0$, the average value of σ_z for a single particle state tends to zero. The spin susceptibility is, therefore, reduced. From the Kramers–Kronig relations, one observes that a significant contribution to the normal state

$\chi(T)$ comes from single–particle states with excitation energies of the order of the spin–orbit scattering rate $\hbar/\tau_{so}$ which is, by assumption, greater than Δ_0. As an opening up of a superconducting gap at the Fermi energy is not expected to change the contribution of these higher energy states, one finds that the susceptibility in the superconducting state can remain comparable in magnitude to the normal state value. According to Anderson [460, 461], the normalized susceptibility should have the two limits. The limit of strong spin–orbit scattering is defined by $l_{so} \ll \pi \xi_0$, where $\xi_0 = \hbar v_F/\pi \Delta_0$ and $l_{so} = v_F \tau_{so}$, and the limit of weak spin–orbit scattering is defined by $l_{so} \gg \pi \xi_0$. In the limit of strong spin–orbit scattering, the normalized susceptibility is given by [462]

$$\frac{\chi_{BCS}(0)}{\chi_n} \approx 1 - \frac{8\, l_{so}}{3\, \pi\, \xi_0} . \tag{10.243}$$

For weak spin–orbit scattering, the susceptibility ratio is given by

$$\frac{\chi_{BCS}(0)}{\chi_n} \approx \frac{3\, \pi\, \xi_0}{8\, l_{so}} . \tag{10.244}$$

Hence, the existence of a partial Meissner effect at $T = 0$ does not necessarily imply the presence of either triplet or gapless superconducting phases.

Triplet Pairing

For triplet pairing, the above argument indicates that a finite susceptibility could be expected to arise due to the $S = 1$ spin of the Cooper pairs. The way the susceptibility depends on the orientation of the field $\vec{H}$ relative to the direction of $\vec{d}$, for a direction of $\vec{d}$ independent of $\underline{k}$, is described below.

First, if $\vec{d}$ is parallel to $\vec{H}$ for all $\underline{k}$, then, as $\vec{H}$ is the direction of quantization of σ, $\vec{d}$ is parallel to $\hat{z}$ and so $S_z = 0$. Since $d_{S_z=0}$ is the only finite component of the order parameter, the off–diagonal blocks in the mean–field Hamiltonian Eqn. (10.58) are proportional to σ_x. And so, as in the singlet case, only the same time reversal partner states are coupled. Thus, one obtains the same Zeeman type of coupling as the singlet case, $E_{\sigma,\underline{k}} = E_{H=0,\underline{k}} - \frac{1}{2}\,(\, g\mu_B \sigma H\,)$, and the susceptibility is given by the same expression as Eqn. (10.242) but with the appropriate triplet density of states.

$$\begin{aligned}\chi_{S=1,\parallel}(T) &= 2\left(\frac{g\mu_B}{2}\right)^2 \sum_{\underline{k}} \left(-\frac{\partial f}{\partial E_{\underline{k}}}\right) \\ &= 4\left(\frac{g\mu_B}{2}\right)^2 \int_0^\infty dE\; \rho_{S=1}(E) \left(-\frac{\partial f}{\partial E}\right) .\end{aligned} \tag{10.245}$$

Hence, the spin susceptibility has a linear T variation for a density of states with lines of nodes or a T^2 variation with point nodes.

Secondly, if $\vec{H}$ is perpendicular to $\vec{d}$ for all $\underline{k}$, then, as $\vec{d}$ is perpendicular to $\hat{z}$, the pairs are in a linear combination of states with $S_z = \pm 1$. The

off–diagonal blocks of the mean–field Hamiltonian are of diagonal form and only couple electrons and holes with the same spin directions. Then, the quasi–particle energies are given by

$$E^2_{\sigma,\underline{k}} = \left[e(\underline{k}) - \mu - \left(\frac{g\mu_B \sigma H}{2}\right) \right]^2 + \left| d_x(\underline{k}) + i\sigma d_y(\underline{k}) \right|^2 . \quad (10.246)$$

Furthermore, since

$$\left(\frac{\partial E_{\sigma,\underline{k}}}{\partial H}\right) = -\left(\frac{g\mu_B \sigma}{2}\right)\left(\frac{\partial E_{\sigma,\underline{k}}}{\partial e_\sigma(\underline{k})}\right), \quad (10.247)$$

the expression for $\chi_{S=1,\perp}(T)$ has the form

$$\chi_{S=1,\perp}(T) = \sum_\sigma \left(\frac{g\mu_B \sigma}{2}\right)^2 \rho(\mu) \int_{-\infty}^{+\infty} de \left(\frac{\partial E_\sigma}{\partial e}\right)\left(-\frac{\partial f(E_\sigma)}{\partial E_\sigma}\right)$$
$$= 2\left(\frac{g\mu_B}{2}\right)^2 \rho(\mu) . \quad (10.248)$$

Hence, in this case, the uniform static spin susceptibility retains the normal state value. In general, for triplet pairing, the orientational average of $\chi_{S=1}(T)$ will have a magnitude of 2/3 the normal state susceptibility.

The sum of the quasi–particle energies are lowered when $\vec{H}$ is perpendicular to $\vec{d}(\underline{k})$. For an isotropic system like ^{3}He, and a pairing vector which has a direction independent of $\underline{k}$ such as in the ABM phase, the vector $\vec{d}$ will rotate to remain perpendicular to the field and the susceptibility will remain constant. On the other hand, heavy–fermion systems are expected to have strong spin–orbit coupling and crystalline anisotropy, therefore, the direction of $\vec{d}$ is expected to remain constant when $\vec{H}$ is applied. If the material has an anisotropy such that spins have an easy axis or plane, then $\chi_{S=1}$ for that phase will be reduced if $\vec{H}$ tilts away from the axis or plane. In such cases of strong anisotropy, the susceptibility tensor is given by the directional average

$$\chi^{i,j}_{S=1}(T) =$$
$$2\left(\frac{g\mu_B}{2}\right)^2 \sum_{\underline{k}} \left(-\frac{\partial f}{\partial E_{\underline{k}}}\right)\left[\frac{d^*_i(\underline{k}) d_j(\underline{k})}{\underline{d}^*(\underline{k}).\underline{d}(\underline{k})} + \left(\frac{\partial E_{\underline{k}}}{\partial e_{\underline{k}}}\right)\left(\delta_{i,j} - \frac{d^*_i(\underline{k}) d_j(\underline{k})}{\underline{d}^*(\underline{k}).\underline{d}(\underline{k})}\right)\right] \quad (10.249)$$

In the BW phase the zero temperature susceptibility is 2/3 of the normal state value, this occurs as the $\underline{k}$ averaged value of $\vec{d}^{\,2}$ has one component parallel to $\vec{H}$ which is suppressed, the other two components retain their normal values. The calculated spin susceptibilities expected for various triplet superconducting phases is shown in Fig. 10.70. The above discussion indicates

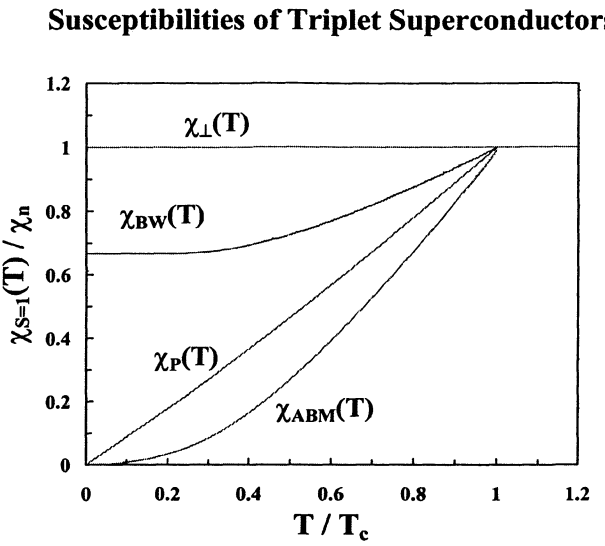

Fig. 10.70. The calculated spin susceptibilities of triplet superconducting phases. The susceptibility for the BW phase is isotropic. The susceptibilities of the ABM and polar phases are anisotropic, if the order parameter is pinned by the lattice. The susceptibilities vanish at low temperatures for applied fields which are parallel to the Cooper pair spin but remain unaffected for fields oriented perpendicular to the spin

that, if the behavior of the hyperfine field is known (perhaps extrapolated from the normal state), the temperature dependence of the Knight shift in the superconducting state can yield information about the nature of the pairing.

In pure UBe_{13}, the muon Knight shift [321] exhibits a large reduction below T_c with a magnitude similar to that found in weak coupling s–wave superconductors. The Knight shifts found for Th [321] and B doped samples [463] show no appreciable changes on entering the superconducting states which is consistent with the formation of spin–singlet Cooper pairs but with strong spin–orbit scattering or gapless phases caused by impurity scattering. The anisotropic Knight shift observed in $CeCu_2Si_2$ [464, 465] undergoes a significant reduction in the superconducting state, similar to the behavior observed in UBe_{13}. The reduction found in $CeCu_2Si_2$ is consistent with the vanishing of the spin susceptibility at zero temperature, as expected for a spin–singlet superconducting phase. In $CeCoIn_5$ [60], the decrease of the ^{59}Co Knight shift in the superconducting state is large for fields along the c–axis and is hardly noticeable for fields in the perpendicular directions. However, the lack of any decrease in the perpendicular directions was attributed to a large temperature independent contribution to the susceptibility from the Co

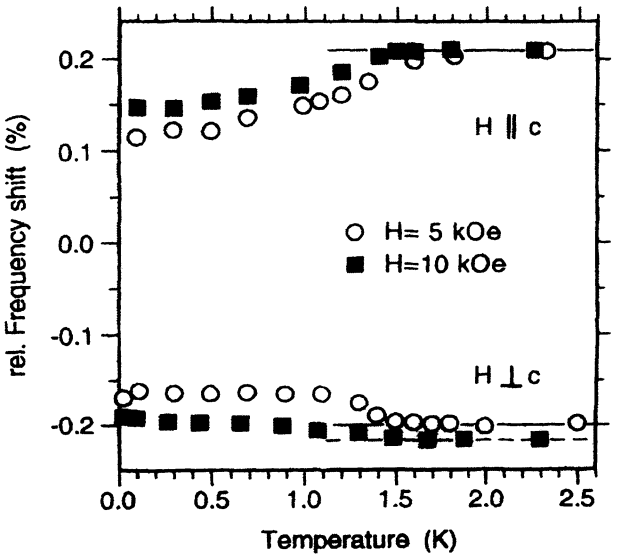

Fig. 10.71. Temperature dependence of the muon Knight shifts in UPd_2Al_3, for fields applied parallel and perpendicular to the c axis. [After Feyerherm *et al.* (1994), [468]]

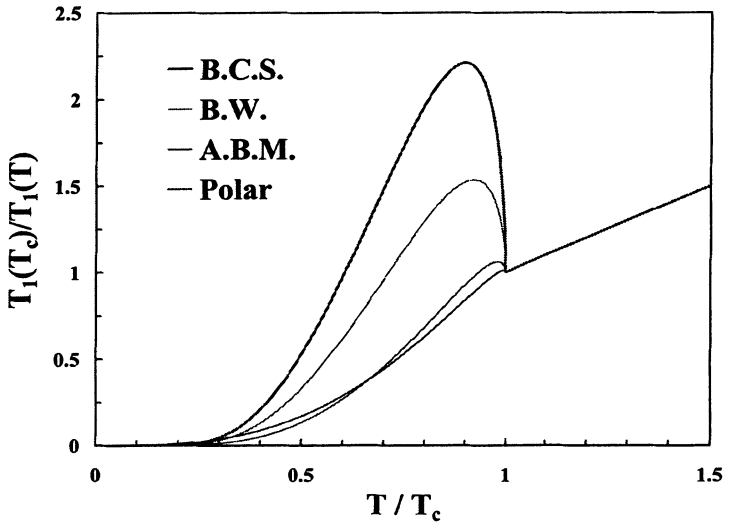

Fig. 10.72. The calculated temperature dependence of the spin-lattice relaxation rate $1/T_1$ for the BCS, BW, ABM and polar phases. The rates are normalized to the normal state relaxation rate at T_c. A Hebel–Slichter peak occurs below T_c for the BCS and BW phases, but is absent for the ABM and polar phases

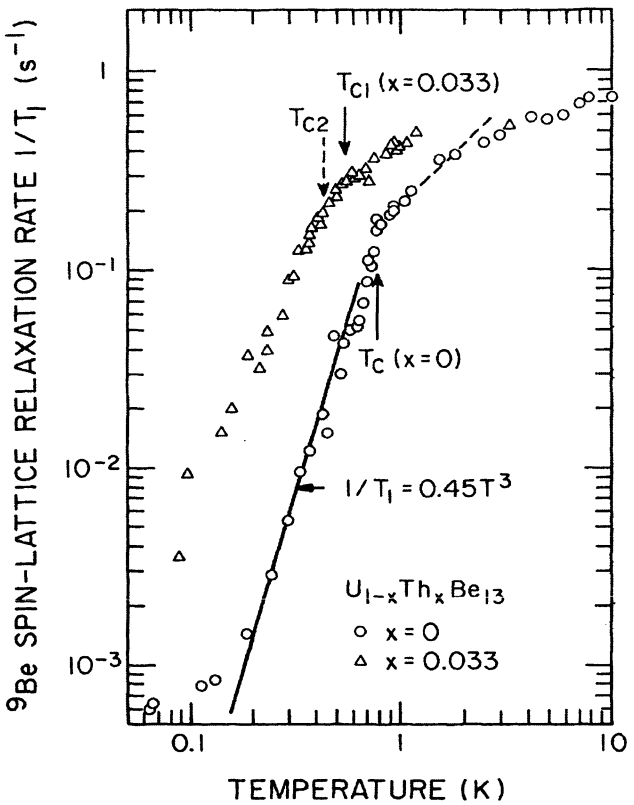

Fig. 10.73. The temperature dependence of the ^{9}Be nuclear spin relaxation rate $1/T_1$ in $U_{1-x}Th_xBe_{13}$, for $x = 0$ and $x = 0.033$. The solid line is a fit to a T^3 power law below T_c, and the dashed line is the normal state Korringa law. [After MacLaughlin *et al* (12984), [25]]

3d orbitals. The observation of a smaller but isotropic decrease in the Knight shift of ^{115}In below T_c is supportive of a superconducting state which involves spin–singlet Cooper pairs.

The Knight shift has been measured in the superconducting state of single crystals of UPt_3 [466, 467]. For large fields [466], no appreciable change was observed on entering the superconducting phase for all directions of the applied field. However, a later study [467] showed a very small decrease occurred for fields aligned along either the b–axis or c–axis but only for fields such that $H_a < 5$ kOe and $H_c < 2$ kOe. This was interpreted as showing evidence for spin–triplet pairing, in which the superconducting vector order parameter is pinned to the lattice for small applied fields but for sufficiently large fields is free to rotate so as to follow the direction of the applied field.

This explanation rests on the unjustified assumption of very weak spin–orbit coupling in UPt_3 and also does not explain the extremely small magnitude of the change of Knight shift that occurs when the order parameter is pinned. However, since the crystals were of very high quality, the absence of a reduction of the spin susceptibility at low temperatures is not attributable to spin–orbit or to impurity scattering in a spin–singlet superconducting phase.

Although the normal state susceptibility and the μSR Knight shift of UPd_2Al_3 are anisotropic, the small and anisotropic change in the Knight shift which occurs below T_c has been taken as evidence that the electrons form spin–singlet Cooper pairs. An analysis of the normal state data indicates that part of the anisotropy originates in the coupling. The dipole contribution is estimated to be three times stronger than the hyperfine field coupling. Although a small anisotropic change in the Knight shift is observed as the temperature is decreased below T_c, the analysis attributes the change to an isotropic reduction of the f spin susceptibility [468]. The reduction has a magnitude of 11% which is only compatible with spin–singlet pairing of the quasi–particles if one partitions the f susceptibility into separate quasi–particle and local moment contributions. This is in direct contrast with conclusions from Al NMR Knight shift studies of the isostructural compound UNi_2Al_3. The Knight shift measurements of UNi_2Al_3 have been interpreted as indicating that the quasi–particles form triplet–spin Cooper pairs [469]. Since the crystals are not axially symmetric, the crystals contain two inequivalent Al sites. As a consequence, the experiments on UNi_2Al_3 show two distinct NMR peaks for magnetic fields applied parallel to the a–axis. In UNi_2Al_3, the Knight shift predominantly comes from the hyperfine coupling which has a similar magnitude to that found in UPd_2Al_3. However, on reducing T below T_c, the Knight shift observed for one peak did not show a change comparable to that found in UPd_2Al_3 and hence, it is argued that these measurements provide evidence for triplet–spin superconductivity. Due to the much larger $1/T_1$ contribution to the peak width for fields along the c–axis, these experiments were unable to determine if the Knight shift exhibits the full anisotropic Meissner behavior expected from a spin–triplet superconductor.

Longitudinal Nuclear Spin Relaxation

The temperature variation of the Spin Lattice relaxation rate $1/T_1$ can be drastically changed at the onset of superconductivity. This occurs as a result of the change in the quasi–particle excitation spectrum but also is due to a modification of the matrix elements for the coupling of the quasi–particle excitations to the nuclear spins. As the modification of the matrix elements of the coupling interaction, known as the coherence factor, involves the gap function, $1/T_1$ could provide additional information about the symmetry of the superconducting phase. The relaxation rate for a spin distribution aligned along the z axis is driven by spin–flip fluctuations, and is given by the ex-

pression

$$1/T_1 \;=\; k_B T\,(g\mu_B)^2\,\frac{1}{N}\sum_{\underline{q}} A(\underline{q})^2\left[\frac{Im\;\chi^{+,-}(\underline{q};\omega_N)}{\hbar\,\omega_N}\right], \qquad (10.250)$$

where ω_N is the nuclear Larmor frequency, and $A(\underline{q})$ is the averaged strength of the local hyperfine field. The factor $Im\;\chi^{+,-}(\underline{q};\omega)$ represents the density of states for magnetic spin–flip fluctuations. A typical value of the nuclear Larmor frequency is $\hbar\omega_N \sim 10^{-7}$ meV and so, for all but in systems with exceptionally slow spin–fluctuations, one may approximate ω_N by $\omega_N = 0$. This approximation could be expected to fail near a quantum critical point. Just to illustrate the nature of the coupling to the superconductivity, we shall replace the full susceptibility by the lowest order polarization part or quasi–particle susceptibility.

The first step in evaluating the imaginary part of the susceptibility is to express the spin–flip operators in terms of the four component fields $\Psi(\underline{k})$, so the spin raising operator $\hat{\sigma}^+(\underline{q})$ is given by

$$\hat{\sigma}^+(\underline{q}) \;=\; \Psi^\dagger(-\underline{k}-\underline{q})\begin{pmatrix}\sigma^+ & 0\\ 0 & -\sigma^-\end{pmatrix}\Psi(-\underline{k})\,, \qquad (10.251)$$

where σ^+ and σ^- are the 2×2 Pauli spin matrices. The spin lowering operator $\hat{\sigma}^-(\underline{q})$ is given by

$$\hat{\sigma}^-(\underline{q}) \;=\; \Psi^\dagger(-\underline{k}-\underline{q})\begin{pmatrix}\sigma^- & 0\\ 0 & -\sigma^+\end{pmatrix}\Psi(-\underline{k})\,. \qquad (10.252)$$

In general, the matrix $\tilde{\sigma}^i$ corresponding to a spin operator $\hat{\sigma}^i$ is a 2×2 block diagonal matrix with the upper and lower diagonal elements given, respectively, by σ^i and $(\,i\sigma_y\,)\,\sigma_i\,(\,-i\sigma_y\,)$, where the lower diagonal element reflects the effect of time reversal on the spins. The lowest order contribution to the susceptibility tensor $\chi^{\alpha,\beta}(\underline{q};\omega)$ is given be expressed in terms of the Fourier transform of the imaginary time single–particle Green's functions. These Green's functions are defined in terms of the Wick's time ordered product of two four–component fields

$$G(\underline{k};\tau) = -<\mid \hat{T}\;\Psi(\underline{k},\tau)\Psi^\dagger(\underline{k},0)\mid>\;. \qquad (10.253)$$

The susceptibility tensor can be written as the analytic continuation onto the real frequency axis of the trace

$$\chi^{\alpha,\beta}(\underline{q};\nu_m) =$$
$$k_B T\left(\frac{g\mu_B}{2}\right)^2\frac{1}{N}\sum_{n,\underline{k}}\frac{1}{2}TraceG(\underline{k}+\underline{q};i\hbar(\omega_n+\nu_m))\tilde{\sigma}^\beta G(\underline{k};i\hbar\omega_n)\tilde{\sigma}^\alpha\,, \qquad (10.254)$$

where ω_n are the fermion Matsubara frequencies, $\hbar\omega_n = \pi\, k_B T\, (2n+1)$ and ν_m is a boson Matsubara frequency. For unitary states where $\tilde{H}^2_{MF}$ is diagonal, the quasi–particle contribution to the Fourier transformed Green's function can be written as

$$G(\underline{k}; i\hbar\omega_n) = -\, Z^{-1}\, \frac{(\, i\,\hbar\,\omega_n + \tilde{H}_{MF}\,)}{\hbar^2\,\omega_n^2 + E^2_{\underline{k}}}\,. \tag{10.255}$$

Hence, on evaluating Eqn. (10.254) and continuing the imaginary frequency $i\,\nu_m$ onto the real ω axis, the energy difference components of the imaginary part of the susceptibility tensor are given by the expression,

$$\begin{aligned} Im[\chi^{\alpha,\beta}(\underline{q};\omega)] = Z^{-2}\,\pi\left(\frac{g\mu_B}{2}\right)^2 \frac{1}{N}\sum_{\underline{k}}\int_{-\infty}^{+\infty} dE\left[\, f(E) - f(E+\hbar\omega)\,\right] \\ \times\,\frac{1}{2}\,Trace\left(\frac{(\,E + \tilde{H}_{MF}\,)\,\tilde{\sigma}^{\beta}(\,E + \hbar\omega + \tilde{H}_{MF}\,)\,\tilde{\sigma}^{\alpha}}{4\,E\,(\,E+\hbar\omega\,)}\right) \\ \times\left[\,\delta(E - E_{\underline{k}})\,\delta(E+\hbar\omega - E_{\underline{k}+\underline{q}}) + \delta(E+E_{\underline{k}})\,\delta(E+\hbar\omega+E_{\underline{k}+\underline{q}})\,\right] \end{aligned} \tag{10.256}$$

This represents a quasi–elastic process involving scattering from the thermal population of quasi–particles. The factors in front of the spin operators, as modified by the matrix nature of $\tilde{\sigma}$, produce the coherence factors. Since the coherence factors differ between the singlet and triplet pairing cases, we shall discuss them separately.

Singlet Pairing

In this case, the spin–flip excitation spectrum is obtained as

$$\begin{aligned} Im[\chi^{+,-}(\underline{q};\omega)] = \pi Z^{-2}\left(\frac{g\mu_B}{2}\right)^2 \frac{1}{N}\sum_{\underline{k}}\int_{-\infty}^{+\infty} dE\left[f(E) - f(E+\hbar\omega)\right] \\ \times\left(1 + \frac{\xi(\underline{k})\xi(\underline{k}+\underline{q}) + D(\underline{k})D(\underline{k}+\underline{q})}{E_{\underline{k}}E_{\underline{k}+\underline{q}}}\right) \\ \times\left[\delta(E - E_{\underline{k}})\delta(E+\hbar\omega - E_{\underline{k}+\underline{q}}) + \delta(E+E_{\underline{k}})\delta(E+\hbar\omega+E_{\underline{k}+\underline{q}})\right]. \end{aligned} \tag{10.257}$$

The two summations over $\underline{k}$ and $\underline{k}+\underline{q}$ in Eqn. (10.250) when combined with Eqn. (10.257) have the effect that the bi–linear term in $\xi(\underline{k}) = e(\underline{k}) - \mu$, which is anti–symmetric about the Fermi energy, vanishes. Also, since for singlet superconductivity, the order parameter is an even function of $\underline{k}$ these terms are retained. Then, in the s–wave phase, the relaxation rate is given

by

$$\hbar/T_1 = \pi k_B T Z^{-2} (g\mu_B)^2 A^2 \int_0^\infty dE \left(-\frac{\partial f}{\partial E} \right) \left[1 + \left(\frac{\Delta_0}{E} \right)^2 \right] \rho_{BCS}(E)^2 \,, \tag{10.258}$$

where we have set $\omega_N = 0$, and A is the local hyperfine field. The above expression indicates that a peak in $1/T_1$ should occur just at the superconducting transition. The peak occurs since the BCS density of states diverges at $E = \Delta_0$, which yields a divergence in the integrand in the superconducting state. The logarithmic divergence of $1/T_1$ in the superconducting state is actually suppressed by small residual anisotropy in the gap and also by the quasi–particle lifetimes. As the derivative of the Fermi function

$$\left(-\frac{\partial f}{\partial E} \right) \Big|_{E=\Delta_0} \tag{10.259}$$

has its largest value in the superconducting state at $T = T_c$, the above argument indicate that a peak in $1/T_1$ occurs just at T_c. The resulting experimentally observed peak is known as the Hebel–Slichter peak [470], and is often seen in weak–coupling s–wave superconductors. The peak actually occurs at roughly 0.8 T_c. This reduced temperature and the suppression of the logarithmic divergence is well described by interactions between thermally excited phonons and the quasi–particles [471]. Fibich found that the temperature dependence of the rate could be expressed as

$$\frac{\hbar}{T_1} \propto 2 k_B T f(\Delta_0) \left[1 + \frac{\Delta_0}{k_B T} (1 - f(\Delta_0)) \ln \left(2 \left(\frac{2\Delta_0}{\Gamma(T)} \right)^{4/3} \right) \right] , \tag{10.260}$$

where $\Gamma(T)$ represents the imaginary part of the gap which is a characteristic energy for quasi–particle scattering from a thermal distribution of phonons, $\Gamma(T) \sim (k_B T)^2/\hbar\omega_D$. However, in strong–coupling s–wave systems, quasi–particle interactions and lifetime effects can substantially suppress the peak. At low temperatures, $T \ll T_c$, the relaxation rate is expected to show a thermally activated temperature variation, $1/T_1 \propto \exp[-\Delta_0 / k_B T]$.

Triplet Pairing

The coherence factors in the triplet or p–wave pairing phases should be replaced by

$$\left(1 + \frac{Re[\xi(\underline{k})\xi(\underline{k}+\underline{q}) - (\hat{z} \,.\, \vec{d}\,(\underline{k}))(\vec{d}^{\,*}(\underline{k}+\underline{q}) \,.\, \hat{z})]}{E_{\underline{k}} E_{\underline{k}+\underline{q}}} \right) . \tag{10.261}$$

Since $\xi(\underline{k}) = e(\underline{k}) - \mu$ is an odd function about the Fermi energy and $\vec{d}\,(\underline{k})$ is an odd function of $\underline{k}$, the bi–linear terms vanish, leaving a coherence factor of

unity. Hence, the rate is given in terms of an integration over an appropriate quasi–particle density of states squared for the p–wave phase.

$$\hbar/T_1 = \pi\ k_B T\ Z^{-2}\ (g\mu_B)^2\ A^2 \int_0^\infty dE \left(-\frac{\partial f}{\partial E}\right) \rho_{S=1}(E)^2\ . \quad (10.262)$$

We note that the weak logarithmic divergence of the density of states in the ABM phase is integrable, and the Hebel–Slichter peak is also completely absent in the polar phase.

At low temperatures in the BW phase, the same type of exponentially activated behavior is recovered as in the BCS phase. The low temperature form of $1/T_1$ in the ABM phase is given by

$$\hbar/T_1 \ = \ 4!\ \pi\ \frac{(g\mu_B)^2\ A^2\ Z^{-2}\ \rho(\mu)^2}{\Delta_0^4}\ (\ k_B T\ )^5 \quad (10.263)$$

and in the polar phase

$$\hbar/T_1 \ = \ \pi\ \frac{\pi^2 (g\mu_B)^2\ A^2\ Z^{-2} \rho(\mu)^2}{2\Delta_0^2}\ (\ k_B T\ )^3\ , \quad (10.264)$$

where the inequality $T \ll T_c$ should hold for both expressions. Thus, the characteristic energy dependence associated with the distribution of nodes could govern the low temperature quasi–particle contribution to the spin–lattice relaxation rate. Also, the quasi–particle contribution to the relaxation rate should remain unrenormalized. However, it should be noted that only the lowest order polarization part of the susceptibility has been considered but the higher order interactions between the quasi–particles and vertex corrections are also important. The vertex corrections may be expected to partially cancel the effect of the self–energy which is responsible for Z. The interactions are responsible for adding the low–energy collective spin–fluctuations to the continuum of single quasi–particle Stoner excitations.

The spin–lattice relaxation rates of the heavy–fermion superconductors UBe_{13} [25], UPt_3 [472], $CeCu_2Si_2$ [474], UPd_2Al_3 [473] and $CeIrIn_5$ [60, 61] do not show any evidence of a Hebel–Slichter peak at T_c, but instead show a cross–over between a linear T–like Korringa variation above T_c to an approximate T^3 variation in the superconducting state. In UPt_3, the T^3 law is only followed closely in the restricted temperature range between 0.1 and 0.3 K, which is far below the superconducting transition temperature ($T_c \sim 0.5$ K). However, in UBe_{13}, UPd_2Al_3 and to a lesser extent $CeCu_2Si_2$, the T^3 dependence holds right up to T_c. Since the gap $\Delta_0(T)$ is expected to be rapidly varying with T in this temperature region, the T^3 variation should not be interpreted in terms of the power law energy dependence of the quasi–particle density of states. The power law T dependence due to the energy dependence of the quasi–particle density of states is expected to be restricted to occur in a temperature regime far below T_c. In UBe_{13}, the approximate T^3

variation crosses over to a linear T variation at the lowest measured temperatures [475]. The coefficient of the linear T term is observed to increase with doping [463], which is consistent with the picture of a gapless superconducting phase caused by resonant impurity scattering of Cooper pairs with non–zero angular momentum, $l \neq 0$. Although no low temperature linear T regimes were identified in the relaxation rates of UPd_2Al_3 [473], $CeCu_2Si_2$ [474] and $CeCoIn_5$ [60], at the lowest measured temperatures, the data do show indications of departures from the T^3 power law variation which are consistent with linear T variations.

Neutron Scattering Cross–section

Perhaps one of the potentially most powerful probes of the nature of the order parameter would be inelastic neutron scattering measurements. The scattering cross–section not only provides a measure of the spectrum of the magnetic fluctuations of the quasi–particles but also, via the dependence on polarization and the direction of the momentum transfer $\hbar\underline{q}$, the anisotropy in the coherence factors. The main limitations of this method are due to the strong residual interactions between the quasi–particles that result in the large amplitude spin–fluctuations, and the loss of intensity needed for polarized scattering. The gaps that could be observed in the inelastic neutron scattering cross–section may be expected to be of the order of $2\Delta_0$ which, for the heavy–fermion superconductors, could be expected to range between 0.3 meV and 1 meV.

The magnetic scattering cross–section of an incident beam of unpolarized neutrons is related the imaginary part of the dynamic susceptibility via,

$$\frac{d^2\sigma}{d\omega d\Omega}(\underline{q};\omega) = \gamma_0^2 \frac{k_f}{k_i} \frac{|F(\underline{q})|^2}{g^2\mu_B^2} [1 + N(\omega)] \sum_{\alpha,\beta} Im[\chi^{\alpha,\beta}(\underline{q};\omega)](\delta_{\alpha,\beta} - \hat{q}_\alpha \hat{q}_\beta) \ , \tag{10.265}$$

where $\hbar\underline{q}$ and $\hbar\omega$ refer to the momentum and energy transfer of the neutron, and $F(\underline{q})$ is the atomic form factor. The summation over β corresponds to experiments in which the polarization of the scattered beam is not observed. It should be noted that the dipole nature of the interaction between the neutron and the electron spins results in the neutron only interacting with the spin components transverse to the momentum transfer $\underline{q}$. The imaginary part of the dynamic susceptibility contains the Raman scattering type of process expressed in Eqn. (10.256), and a pair–breaking scattering process. The quasi–elastic or Raman scattering process involves the scattering of the neutrons from thermally excited quasi–particles. These low–energy fluctuations formed the basis for the discussion of NMR experiments, and are expected to vanish in the limit of zero temperature. The spectrum originating from processes in which pairs in the condensate are broken and where the resulting quasi–particles are then scattered across the gap is given by the energy sum terms in Eqn. (10.254). These terms remain finite at zero temperature. The

energy loss contribution to the pair–breaking process is evaluated as

$$Im[\chi^{\alpha,\beta}(\underline{q};\omega)] = Z^{-2}\pi\left(\frac{g\mu_B}{2}\right)^2 \frac{1}{N}\sum_{\underline{k}}\left[1 - f(E_{\underline{k}}) - f(E_{\underline{k}+\underline{q}})\right]$$
$$\times \frac{1}{2}Trace\left(\frac{(E_{\underline{k}} - \tilde{H}_{MF})\tilde{\sigma}^{\beta}(E_{\underline{k}+\underline{q}} + \tilde{H}_{MF})\tilde{\sigma}^{\alpha}}{4E_{\underline{k}}E_{\underline{k}+\underline{q}}}\right)\delta(\hbar\omega - E_{\underline{k}} - E_{\underline{k}+\underline{q}}) \,. \tag{10.266}$$

Here, we have only considered the quasi–particle contribution. The value of the trace depends upon the character of the superconductivity. Again, we consider the singlet pairing case separately from triplet pairing.

Singlet Pairing

Conventional singlet pairing superconductors are paramagnetic, so one retains spin rotational invariance

$$\frac{1}{2}\, Im[\chi^{+,-}(\underline{q};\omega)] = Im[\,\chi^{z,z}(\underline{q};\omega)] = Im[\chi^{x,x}(\underline{q};\omega)] = Im[\chi^{y,y}(\underline{q};\omega)] \,. \tag{10.267}$$

The imaginary part of the quasi–particle susceptibility is found as

$$Im[\chi^{+,-}(\underline{q};\omega)] = \pi(g\mu_B)^2 Z^{-2}\frac{1}{N}\sum_{\underline{k}}\left[1 - f(E_{\underline{k}}) - f(E_{\underline{k}+\underline{q}})\right]$$
$$\times\left(\frac{(E_{\underline{k}} - \xi(\underline{k}))(E_{\underline{k}+\underline{q}} + \xi(\underline{k}+\underline{q})) - D(\underline{k})D(\underline{k}+\underline{q})}{4E_{\underline{k}}E_{\underline{k}+\underline{q}}}\right)\delta(\hbar\omega - E_{\underline{k}} - E_{\underline{k}+\underline{q}}) \,. \tag{10.268}$$

The scattering cross–section for pair–breaking scattering processes vanishes identically in the limit $\underline{q} \rightarrow 0$ so, for this $\underline{q}$ value, neutron scattering only occurs through processes involving the Raman scattering from thermally activated quasi–particles. In this limit, the non–zero part of the quasi–particle contribution involves coherence factors of unity and would manifest itself by a narrow zero energy delta function like peak with strength proportional to Z^{-1}, in the absence of spin–orbit scattering.

For finite $\underline{q}$, the cancellation in the coherence factors for the pair breaking processes is incomplete. For s–wave pairing, the pair breaking process has a threshold at the maximum value of the superconducting gap $\hbar\,\omega = 2\,\Delta_0$, for $0 < q < 2\,k_F$. For non s–wave pairing phases where there are nodes in the order parameter, interesting possibilities occur when the system is close to an antiferromagnetic instability. In this case, one expects that in the normal state, there should be a quasi–elastic peak from magnetic fluctuations that should show softening at the $\underline{q}$ value $\underline{Q}_c$ which corresponds to the magnetic Bragg peak of the (hypothetical) ordered state [476]. The magnetic fluctuations are expected to decay into quasi–particle excitations. Therefore, the

height and width of the quasi–elastic peak is governed by the quasi–particle density of states. As the temperature is lowered and the normal state becomes unstable to a superconducting state, the low–energy quasi–particle density of state is suppressed since the superconducting gap opens up on portions of the Fermi surface. This may result in the quasi–elastic neutron scattering peak at $\underline{Q}_c$ transforming into a narrow low–energy resonance for $\hbar\,\omega\ <\ 2\,\Delta_0$. The height of the peak is expected to have an inverse correlation with the maximum value of the superconducting gap. Furthermore, the ω dependence of the low–energy edge of the resonance should either show a ω or ω^2 variation depending upon the existence of either line nodes or point nodes in the gap. The sharp peak is expected to rapid broaden and disperse to higher energies as $\underline{q}$ is varied away from $\underline{Q}_c$. Excitations of a similar type have been observed in the superconducting state of magnetically ordered UPd_2Al_3 [346,348,435,477]. The spectra of the transverse excitations found in the polarized inelastic neutron scattering spectra, at $\underline{q} = \underline{Q}_c$, are shown in Fig. 10.74.

Triplet Pairing

The pair breaking scattering cross–section for triplet superconductors is governed by

$$Im[\chi^{i,i}(\underline{q};\omega)] = \pi(g\mu_B)^2 Z^{-2}\frac{1}{N}\sum_{\underline{k}}\left[1-f(E_{\underline{k}})-f(E_{\underline{k}+\underline{q}})\right]\delta(\hbar\omega - E_{\underline{k}}-E_{\underline{k}+\underline{q}})$$
$$\times\ Re\left(\frac{(E_{\underline{k}}-\xi(\underline{k}))(E_{\underline{k}+\underline{q}}+\xi(\underline{k}+\underline{q}))+\vec{d}\,(\underline{k})\,\vec{d}^{\,*}(\underline{k}+\underline{q})-2d_i(\underline{k})d_i^*(\underline{k}+\underline{q})}{4E_{\underline{k}}E_{\underline{k}+\underline{q}}}\right). \tag{10.269}$$

In the limit $\underline{q}\ \rightarrow\ 0$, the coherence factors relevant to unpolarized experiments remain finite, in contrast with the singlet phase. This is because the vector $\vec{d}$ takes over the role of the momentum transfer $\underline{q}$, in defining the coupling of the neutron's spin to the electronic magnetic moments. The energy dependence of the various limiting forms of the unpolarized neutron cross–section are given by

$$\propto\ \pi\ \rho(\mu)\ \frac{\Delta_0^2}{\hbar\omega}\ \frac{2}{\sqrt{\hbar^2\omega^2\ -\ 4\ \Delta_0^2}}\ ,\qquad \hbar\omega\ \geq\ 2\ \Delta_0\ , \tag{10.270}$$

for the BW phase,

$$\propto\ \frac{\pi\ \rho(\mu)}{4\ \hbar\omega\ \Delta_0}\left[\left(\hbar^2\omega^2\ +\ 4\ \Delta_0^2\right)\ \ln\left[\frac{\sqrt{\hbar\omega\ +\ 2\ \Delta_0}}{\sqrt{\hbar\omega\ -\ 2\ \Delta_0}}\right]-\ \frac{\Delta_0\ \hbar\omega}{2}\right] \tag{10.271}$$

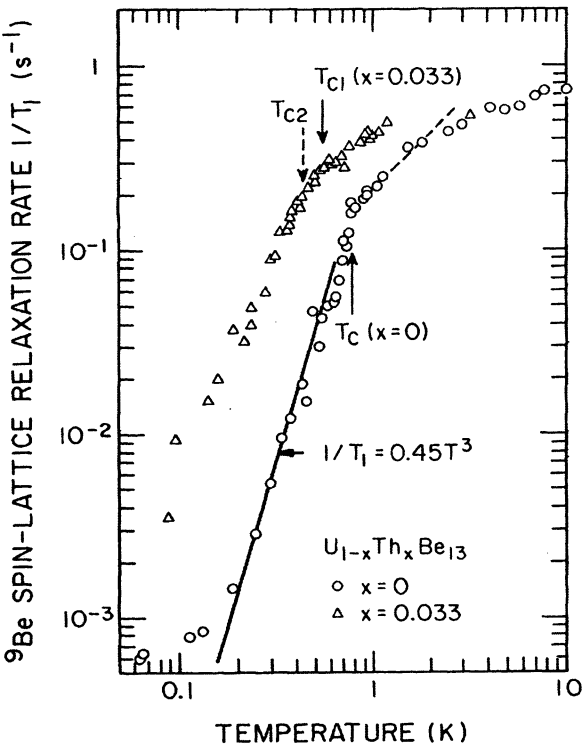

Fig. 10.74. The inelastic polarized neutron scattering cross-section for UPd_2Al_3 at the antiferromagnetic Bragg point $\underline{Q}$. The longitudinal and transverse response is shown by open and closed circles, respectively. At this $\underline{q}$ value, the spectra shows that the quasi-elastic peak due to an overdamped spin-wave evolves into a resonant mode as T is decreased below the superconducting transition temperature. [After Bernhoeft *et al.* (1998), [435]]

in the ABM phase, while the polar phase cross–section is proportional to

$$\propto \frac{\pi^2 \rho(\mu)\hbar\omega}{8\Delta_0} \quad , \quad 2\Delta_0 \geq \hbar\omega$$
$$\propto \pi\rho(\mu)\left(\sin^{-1}\frac{2\Delta_0}{\hbar\omega} - \frac{2\Delta_0}{\hbar^2\omega^2}\sqrt{\hbar^2\omega^2 - 4\Delta_0^2}\right) \quad , \; 2\,\Delta_0 \leq \hbar\omega \; . \qquad (10.272)$$

These are shown in Fig. 10.75. The non–analyticities stem from the characteristic energy dependences of the quasi–particle density of states. The $q = 0$ spectra could lead to a unique identification of triplet superconducting phases, however, neutron scattering experiments at low momentum transfers are difficult to perform. Therefore, the observation of the energy and momentum dependences of low–energy resonances corresponding to the

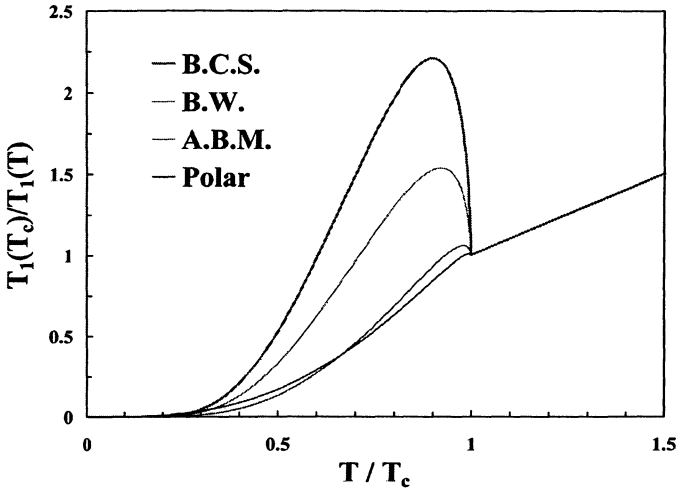

Fig. 10.75. The calculated $T \to 0$ limit of the imaginary part of the uniform ($q = 0$) frequency dependent susceptibility of p-wave superconducting phases, normalized to the density of states at the Fermi energy. The BW phase exhibits a square root singularity at $\hbar\omega = 2\Delta_0$. The imaginary part of the $q = 0$ dynamic susceptibility for the ABM phase exhibits a square root singularity at the maximum gap and a ω^2 variation at low frequencies. The polar phase shows a linear ω variation at low frequencies

quasi–elastic paramagnon or anti–paramagnon excitations of the normal state could be used to determine the nature of superconducting states. In particular, in triplet superconductors, there exists a possibility for observing a double–peaked structure in the low–energy magnetic response, corresponding to the different behavior of magnetic fluctuations perpendicular and parallel to the vector superconducting order parameter.

10.5 Heavy Fermion Superconducting Compounds

Elsewhere in this chapter, the underlying theoretical and experimental approaches to the problem of heavy fermion superconductivity are discussed in detail. In this section we consider the heavy fermion superconductors on a compound–by–compound basis. For each compound we provide a brief introduction and an overall "snapshot" of the physical picture that is developing for each compound at the time this review was written (mid 2003). Our focus is on the nature and origin of the superconducting states themselves. One cannot, of course, completely understand the superconducting states without a clear understanding of the normal state that they arise from, so the fact that the heavy fermion problem has not yet been solved represents an intrinsic limitation in our endeavor. We assume that the reader is familiar with the

general characteristics of the heavy fermion state either from reading other sections in this chapter or from any of the excellent review articles that exist such as those by Stewart [479], Hess, Riseborough, and Smith [480], or Grewe and Steglich [301] for example.

In a recent review article focused on the heavy fermion superconductors, Brison *et al.* [481] (citing an earlier review by Ott [482]) identify the central questions in the field, questions that date from the earliest heavy fermion superconductors studied:

- Does the pairing mechanism involve magnetic interactions?
- What is the symmetry of the superconducting order parameter and the topology of the gap function?
- What is the nature of the interplay between magnetic order (when it exists) and superconductivity?

In another recent review of unconventional pairing in superconductors Annett [483] identifies five "classes" of experimental evidence for unconventional superconductivity:

- Class 1: Experiments consistent with a multi–component order parameter, such as those experiments showing multiple superconducting phases in UPt_3 (Ref's [14] and [44] for example). These experiments constitute "definitive proof" of an unconventional superconducting state.
- Class 2: Experiments that measure the macroscopic order parameter symmetry, such as Josephson interference effects. Such experiments have been very useful in studies of the cuprates. Several heavy fermion compounds show Josephson critical currents. Measurements consistent with anisotropic order parameters exist but overall these difficult experiments have not yet been accomplished in the heavy fermion compounds as successfully as in the cuprates.
- Class 3: Measurements of the electronic spin susceptibility in the superconducting state which tends to zero as $T \rightarrow 0$ for singlet pairing and remains finite for triplet or higher order pairing, measurements such as the Knight shift of thoriated UBe_{13} [484,485] for example.
- Class 4: Experiments demonstrating that the Fermi surface average of the gap function is zero (usually through the failure of Anderson's theorem), experiments such as resistivity measurements probing the sensitivity of T_c to non–magnetic impurities. If the average is non–zero, Anderson's theorem can be applied and the superconducting state is not easily destroyed by non–magnetic impurities. Results consistent with this effect have been reported for UPt_3 [486,487].
- Class 5: Experiments consistent with the gap function vanishing at line and/or point nodes on the Fermi surface. Such a structure results in power–law temperature dependences for a host of measurable quantities such as the specific heat, ultrasonic attenuation, or thermal conductivity [488]. Such power–law dependences (as opposed to the exponential

temperature dependence associated with a uniform s–wave gap) are ubiquitous in the heavy–fermion superconductors.

10.5.1 UPt_3

Since the discovery of superconductivity by Stewart *et al.* [6], UPt_3 has arguably become the most extensively studied of all the heavy fermion superconductors. It now seems safe to assert that unconventional superconductivity in UPt_3 has been unambiguously established. A comprehensive review on UPt_3 by Joynt and Taillefer [377] has recently appeared, it contains an extensive survey of the literature and an in–depth analysis of the state of contemporary research.

Superconductivity in hexagonal UPt_3 ($T_c^+ = 0.53$ K) condenses out of a "heavy" normal state characterized by a resistivity that decreases monotonically with falling temperature and a spin fluctuation–like term in the specific heat, both of which are unusual in heavy fermion superconductors. Experiments show that UPt_3 is an extreme Type II superconductor (with a Ginzburg–Landau parameter of about 44 in the A–phase) in the clean limit [377].

A tendency toward magnetism manifests as a peak in the magnetic susceptibility near 18 K which evolves into a metamagnetic transition near 20 T at low temperatures. A subtle, small–moment ($\sim 0.02\mu_B$/U–atom oriented along a* in the basal plane with domain sizes of about 150 Å), antiferromagnetic order appears at $T_N \sim 5$ K which seems to be intimately related to the superconducting phase diagram as discussed below. The inability to detect a feature associated with T_N using techniques other than neutron scattering (such as μSR, NMR, or virtually any thermodynamic measurement) suggests that the moments are not static, but fluctuate at a very high rate [490].

UPt_3 exhibits three distinct superconducting phases: the A phase occurs at the onset of superconductivity in ambient fields, the B phase appears at $T_c^- = T_c^+ -$ 50 mK, below the onset of the A phase and extends to $T = 0$ (the B–phase is the ground state). The proximity of T_c^+ and T_c^- suggests that they may arise from degenerate states split by some perturbation, the most likely candidate being the antiferromagnetic order. The C phase exists in magnetic fields above about 0.4 T. (One could argue that there are, in fact, five phases since the A and B phases each have a Meissner state below H_{c1} and a vortex state above H_{c1}.) A schematic of the high field superconducting phase diagram is shown in Fig. 10.76, the four phase boundaries shown meet at a true tetracritical point near (0.38 K, 0.8 T) with $H \parallel c$ and (0.43 K, 0.8 T) with $H \perp c$. Also shown in Fig. 10.76 are figures characterizing the gap structures of the E_{2u} model [491], a solid candidate for the multi–component order parameter characterizing the superconducting states of UPt_3 in terms of spin–triplet, f–wave pairing. This approach describes the unusual shape and anisotropy of the upper critical field very well with paramagnetic limiting for fields along the c–axis [492].

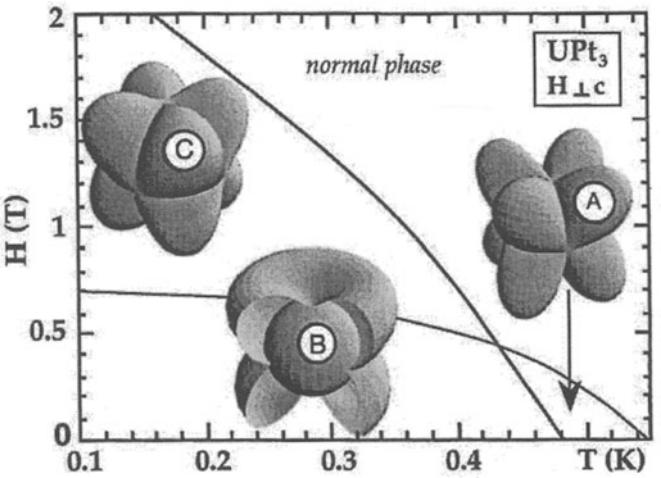

Fig. 10.76. A schematic phase diagram of the three high field superconducting states of UPt_3, together with the hypothetical corresponding gap structures of the E_{2u} model: a rotation of the azimuthal line nodes distinguishes the A and C phases, the B phase has only a second-order point node on the c-axis. [After Brison *et al.* (2000), [481]]

The interplay between superconductivity and magnetism is demonstrated most clearly by neutron–scattering and specific heat experiments under pressure: the antiferromagnetism is suppressed while the two superconducting transitions at T_c^+ and T_c^- appear to merge into one. Within experimental resolution, the superconducting transitions merge at the same pressure (about 3 kbar) that destroys antiferromagnetism [46], a most compelling result.

Candidate theories for the order parameter of UPt_3 include two–dimensional representations where a small coupling to the antiferromagnetism splits the energies of two degenerate states, mixed representations where the two zero field superconducting transitions involve gap functions that are not related by symmetry (so the splitting of T_c^+ and T_c^- is "accidental", unrelated to the antiferromagnetism), and others. Virtually all of the candidate theories result in an odd–parity order parameter; the reader is referred to Joynt and Taillefer [377] for an in–depth discussion.

The identification of the pairing mechanism remains one of the most important and least understood aspects of the work on the heavy fermion superconductors in general and the situation for UPt_3 is no exception. It is generally assumed that mechanism involving the exchange of spin fluctuations, similar to that of superfluid ^3He [136], and that the Cooper pairs are in a triplet state.

10.5.2 $CeCu_2Si_2$

Tetragonal $CeCu_2Si_2$ was the first heavy fermion superconductor discovered [3]. The close proximity of superconductivity and magnetism in $CeCu_2Si_2$ is highlighted by the sensitivity of the ground state to the details of sample preparation and stoichiometry. Quite a bit of work was required to sort out the ground state which can be either bulk superconducting (S–type), magnetic (A–type), both (A/S–type), or "a related phase" (X–type) which is probably magnetic; there is also a high field magnetic phase (the B–phase) and recent high field magnetization studies are consistent with the A and B phases being spin density wave phases [493]. The best single crystals are of the A/S type [494] which becomes superconducting at 0.68 K just below the onset of the magnetic A–phase at 0.70 K. μSR measurements show that the superconducting state competes with the magnetic state (consistent with an SDW state which will compete with superconductivity for the Fermi surface) and that the two states do not coexist microscopically [308]. Given this proximity of low temperature states it is not surprising that $CeCu_2Si_2$ exhibits non–Fermi Liquid behavior in its specific heat and electrical resistivity [191]. It is also not surprising that the superconducting properties of $CeCu_2Si_2$ show significant sample dependences.

In studies of several off–stoichiometry single crystal samples of $CeCu_2Si_2$, the anisotropic upper critical fields can sometimes be fit by a standard s–wave model with significant Pauli limiting and sometimes not [387] though the overall shape is qualitatively consistent with conventional superconductivity. The superconductivity of $CeCu_2Si_2$ is in the clean limit and exhibits a strong Type II character with a typical Ginzburg–Landau parameter in the 50–56 range.

Early studies of the superconducting states of a wide range of samples do not show significant evidence for unconventional superconductivity [387]. A more recent study, however, shows evidence for two different kinds of superconducting states from samples with only slightly different stoichiometry. The two sample groups show a T^2 dependence for the superconducting specific heat but opposite pressure dependences for T_c, d–wave superconductivity has been proposed [495].

10.5.3 UBe_{13}

UBe_{13} (along with $CeCu_2Si_2$ and other heavy fermion superconductors that also show a magnetic phase transition) is frequently characterized as a non–Fermi Liquid superconductor [496] because the superconducting state appears (near $T_c = 0.9$ K) before Fermi liquid behavior has a chance to set in (though the application of modest pressures and/or magnetic fields causes the Fermi liquid state to emerge above T_c [498]). Of all the known heavy fermion superconductors UBe_{13} has the largest effective mass and one of the few compounds with cubic symmetry. UBe_{13} does not appear to order magnetically,

though there is some evidence for field–induced small–moment magnetism coexisting with the superconducting state above about 5 T it has not been confirmed [499]. The resistivity of UBe_{13} is enormous, near 100 $\mu\Omega-$cm just above T_c, leading to an electronic mean–free–path of only a few lattice spacings in length and (not surprisingly) dirty–limit superconductivity.

Many of the initial measurements on UBe_{13}, such as the specific heat, NMR spin–lattice relaxation rate, and London penetration depth exhibit power–law temperature dependences suggesting the presence of line–nodes in the gap function. Tunneling measurements have also resulted in evidence for Andreev surface bound–states [446]. More recent measurements of the specific heat and thermal expansion on higher quality single crystals show an unusual temperature dependence suggestive of a line of "anomalies" in the H–T plane that has been interpreted in terms of antiferromagnetic fluctuations associated with a quantum critical point [496]. This behavior is especially intriguing in samples doped with thorium, a subject we will return to in another section.

Measurements of the lower critical field show the quadratic temperature dependence characteristic of a conventional superconducting state, but the shape of the upper critical field is quite unusual, exhibiting significant positive curvature in the best samples. Recent measurements of the upper critical field under pressure yield a series of H_{c2}(T,P) curves that are well fit by a strong coupling theory incorporating an FFLO state in high magnetic fields. These results are also consistent with a non–phonon–mediated coupling mechanism [379].

Evidence for unconventional superconductivity in UBe_{13} is mounting but the nature of the anomalies described above have yet to be incorporated into a coherent picture of the superconducting state.

10.5.4 UBe_{13} with Th

The phase diagram of $U_{1-x}Th_xBe_{13}$ is shown in Fig. 10.3. Doping non–magnetic thorium onto the uranium sites depresses T_c non–monotonically and a second phase transition appears at a lower temperature (T_{c2}) in the thorium concentration range of about 2% to 4%. Though not as well established experimentally as the multiple superconducting phase diagram of UPt_3, pressure studies, lower critical field measurements (showing a sharp upward kink at T_{c2} [36]) and the size of the specific heat jumps suggest that the colder phase transition separates one kind of superconducting state from another. On the other hand, the observation of small moment magnetism below T_{c2} ($\mu \sim 10^{-3}\mu_B$/U–atom [33]) suggests that this lower state may be magnetic, perhaps a spin–density–wave state coexisting with the superconductivity.

Recent studies of the phase diagram utilizing both specific heat and thermal expansion measurements are shown in Fig. B where the open symbols denote the "anomalies" discussed in the section on pure UBe_{13} and the solid

symbols represent phase transitions [496]. There is an intriguing correlation suggesting that the anomalies in the pure compound evolve into the colder phase of the thoriated compounds. Also shown in Fig. B is a vertical solid line near a thorium concentration $x_{c1} \approx 0.02$ representing the pressure studies of Zieve *et al.* [500] who find clear evidence for a vertical phase boundary separating the two regions.

Theoretical efforts to understand this unusual phase diagram include multiple superconducting states and the onset of antiferromagnetism [501], broken time–reversal symmetry at T_{c2} [502], a "freezing" of the antiferromagnetic fluctuations associated with proximity to a quantum critical point [496], and a "ferrisuperconductivity" theory involving a multi–component order parameter and the appearance of a charge density wave state at T_{c2} [503].

10.5.5 URu_2Si_2

Tetragonal URu_2Si_2 enters the superconducting state near 1.5 K, a temperature about ten times colder than the temperature where it enters into a state of "hidden order". The term "hidden order" denotes an unknown phase with which the superconductivity coexists and which is presently the subject of much current study and debate. Long thought to be a transition to a small–moment ($\mu = 0.03\mu_B$/U–atom) antiferromagnetic state, it has also been recognized for a long time that the size of the specific heat jump is much larger than one would expect for such a transition. Recent neutron diffraction [225] and NMR measurements under pressure [224] have led to the suggestion that the magnetism is from a minority phase, though this matter is still under active discussion [504]. A resolution of this issue will impact our understanding of the superconducting state which, according to recent neutron scattering measurements, is coupled to the magnetic order [505].

Evidence for unconventional superconductivity manifests in specific heat measurements consistent with a line of nodes in the gap function [506] and by anisotropic point contact measurements of the Josephson current between URu_2Si_2 and Nb, a result which suggests that the order parameter must have even parity [454] (*e.g. d*–wave). The upper critical field is strongly anisotropic, strongly Pauli limited along the c–axis, and exhibits a positive curvature consistent with *d*–wave symmetry [507]. It has been pointed out that this interpretation violates the symmetry required of a simple antiferromagnet [508], but with recent measurements suggesting that the magnetism may not be intrinsic the original argument remains an important part of the picture of unconventional superconductivity developing for this compound [509].

10.5.6 UPd_2Al_3

The superconducting state of UPd_2Al_3 condenses near T_c= 2.0 K out of a coexisting antiferromagnetic state (T_N= 14.5 K) with atomic–like moments ($\mu = 0.85\mu_B$/U–atom) aligned in the hexagonal basal plane [51, 343, 510].

NMR measurements of the nuclear relaxation time [511] and the thermal conductivity [512] are consistent with a line of nodes in the gap function, while Knight shift measurements and a Pauli limited upper critical field indicate even parity pairing [513]. But the most important development in UPd_2Al_3 derives from the fact that relatively high quality thin films, with a T_c near 1.6 K only slightly reduced from the bulk T_c, have been fabricated for tunnelling experiments. These experiments reveal a strong coupling to an excitation whose energy nearly matches a magnetic excitation clearly visible in neutron scattering measurements [433,477]. Taken together, these exciting experimental results constitute the strongest evidence for a magnetic mechanism (in this case magnetic excitons) for superconductivity yet discovered.

10.5.7 UNi_2Al_3

Though similar in many respects to isostructural UPd_2Al_3, there are clear differences in the unconventional superconducting state of UNi_2Al_3. Superconductivity appears near 1 K and coexists with an incommensurate spin density wave state with a (relatively) small magnetic moment (about 0.2 μ_B/U–atom) that appears near 4.5 K [514,515]. As with the Pd compound, NMR measurements of the temperature dependence of T_1 suggest the presence of line nodes in the gap [516]. The upper critical field of UNi_2Al_3 is well fit by the conventional WHHM theory without paramagnetic limiting [517,518] while measurements of the Knight shift show that the spin susceptibility does not change on crossing T_c and down to 50 mK [469], both of these results are consistent with a spin–triplet superconducting state.

10.5.8 $CeRhIn_5$

The tetragonal crystal structure of $CeRhIn_5$ (and that of $CeIrIn_5$ and $CeCoIn_5$ discussed below) can be thought of as layers of $CeIn_3$ separated by layers of $RhIn_2$ leading to a quasi–two–dimensional electronic structure. Some features of this sub–family of heavy fermion superconductors, such as a proximity to antiferromagnetism, may therefore be similar to the cuprate superconductors [57]. However, unlike the isostructural compounds $CeIrIn_5$ and $CeCoIn_5$ (both of which are heavy fermion superconductors at ambient pressure), $CeRhIn_5$ is a heavy fermion antiferromagnet at ambient pressure with a Néel temperature $T_N = 3.8$ K. In the antiferromagnetic state the Ce spins (0.37 μ_B/Ce–atom) form a helical structure along the c–axis, a structure characterized by an incommensurate wave vector [519]. The magnitude of the internal field created by the Ce spins decreases linearly with applied pressure while T_N remains nearly constant [520]. At a critical pressure near $P_c \sim 15$ kbar specific heat measurements suggest that the antiferromagnetic state is abruptly replaced by a superconducting state whose critical temperature (about 2.1 K) is surprisingly pressure independent [521]. More recent NQR measurements show that the two states coexist homogeneously at a

pressure of 17.5 kbar. At 21 kbar the spin–lattice relaxation rate exhibits a T^3 temperature dependence and no coherence peak, suggesting a line node in the gap function. A T^2 term in the superconducting specific heat is also consistent with line nodes [521].

10.5.9 $CeIrIn_5$

Nearly antiferromagnetic $CeIrIn_5$ shows quadratic and linear temperature dependences of the superconducting specific heat and thermal conductivity (in the "universal limit") respectively [58] along with a T^3 temperature dependence of the spin–lattice relaxation rate with no Hebel–Slichter coherence peak [60,61]. All of these experimental results are consistent with line nodes in the gap function. The upper critical field is anisotropic but of a conventional shape that does not yield strong experimental evidence either for or against Pauli limiting [522].

10.5.10 $CeCoIn_5$

Just at the edge of an antiferromagnetic quantum critical point, tetragonal $CeCoIn_5$ exhibits the highest critical temperature ($T_c = 2.3$ K) of the heavy fermion superconductors and an enormous specific heat jump at T_c. Several experimental results are consistent with line nodes in the energy gap: T^2 and T^3 temperature dependences of the superconducting specific heat and thermal conductivity respectively [58] and a T^3 temperature dependence of the spin–lattice relaxation rate with no Hebel–Slichter coherence peak [60]. The Knight shift decreases for both parallel and perpendicular directions to the tetragonal c axis in the superconducting state, which shows that the spin susceptibility decreases with decreasing temperature consistent with spin singlet pairing [60]. A $d_{x^2+y^2}$ state has been proposed for $CeCoIn_5$ based on thermal conductivity measurements which reveal a fourfold symmetry in the a–b plane, characteristic of a superconducting gap with nodes along the ($\pm\pi$, $\pm\pi$) directions [59]. Also consistent with such a state, several groups report that the phase transition at H_{c2} is first–order in high fields [59,524].

The lower critical field shows a linear temperature dependence [525], while the upper critical field exhibits an unusual low temperature shape and hysteresis [526]. Both critical fields are anisotropic. Strong indications of an FFLO state in $CeCoIn_5$ [524] have been confirmed with the observation of a second–order phase boundary just below H_{c2} at low temperature [527].

10.5.11 $CeIn_3$

It is not unreasonable to think of cubic $CeIn_3$ as the parent compound of the previous three heavy fermion superconductors. Under ambient pressure $CeIn_3$ is a heavy fermion antiferromagnet with an ordering temperature $T_N = 10.2$

K, an ordered moment of 0.65 μ_B/Ce–atom, and a wave vector in the [111] direction [528]. As pressure is applied T_N is depressed and eventually vanishes near a temperature of about 0.18 K at a critical pressure of about 26 kbar, below this temperature antiferromagnetism is replaced by a superconducting state [529]. This P–T phase diagram, similar to that observed in several high–T_c compounds, has been shown to be characteristic of magnetically mediated superconductivity [529]. Measurements of the spin–lattice relaxation time at a pressure of 26.5 kbar do not show a coherence peak [530] though the upper critical field (at the same pressure) can be described by a conventional strong coupling model in the clean limit [63]. Existing experimental results are not inconsistent with unconventional superconductivity in this important compound, especially given its P–T phase diagram, but, as with most of the heavy fermion superconductors (especially those below), more work is required to identify the symmetry of the order parameter.

10.5.12 $CePd_2Si_2$

Evolving from a heavy fermion antiferromagnet to a heavy fermion superconductor under applied pressure, the P–T phase diagram of $CePd_2Si_2$ is similar to that of $CeIn_3$ and suggests that the superconductivity of $CePd_2Si_2$ is also magnetically mediated [529]. The disappearance of antiferromagnetism does not quite coincide with the maximum superconducting critical temperature (as it does in $CeIn_3$) of about 0.52 K which occurs near an applied pressure of 5 GPa. The shape of the upper critical field at this pressure is not inconsistent with conventional superconductivity though there appear to be some deviations at the lowest temperatures [531]. Another study shows that the upper critical field is well described by a weak–coupling, clean–limit model with a slightly anisotropic orbital limit and a strongly anisotropic paramagnetic one [532].

10.5.13 $CeRh_2Si_2$

The P–T phase diagram of $CeRh_2Si_2$ is qualitatively similar to that of $CePd_2Si_2$ and $CeIn_3$ (discussed above) where antiferromagnetism (ambient pressure T_N = 36 K) is replaced by superconductivity near a critical pressure of 9 kbar and a critical temperature of 0.35 K [67]. The upper critical field is not inconsistent with that of a conventional Type II superconductor though the transition widths are wide and the data are sparse.

10.5.14 $CeCu_2Ge_2$

Superconductivity at very high pressures has been reported for $CeCu_2Ge_2$. Similar to other Ce compounds discussed above, the antiferromagnetic order (T_N = 4.7 K at ambient pressure) is suppressed between 7 and 10 GPa and

is replaced by a superconducting state which appears below a temperature of about 0.6 K. The critical temperature is nearly pressure independent up to about 13 GPa after which it increases rapidly to a maximum value of almost 2 K near 16 GPa before vanishing near 20 GPa [533]. The upper critical field shows significant Pauli limiting consistent with singlet pairing [534].

10.5.15 $PrOs_4Sb_{12}$

Discovered just last year, cubic $PrOs_4Sb_{12}$ is the only known Pr based heavy fermion superconductor so far. Thermal conductivity [535] and specific heat [536] measurements suggest the presence of two distinct superconducting states featuring point–nodes in the gap function (an unusual feature in heavy fermion superconductors). No Hebel–Slichter peak is observed in the temperature dependence of the spin–lattice relaxation time, although an exponential temperature dependence at low temperatures suggests that the gap function is isotropic [537]. An exponential temperature dependence is also found for the magnetic penetration depth as deduced from μSR measurements [538]. A small internal magnetic field, appearing just below T_c is clearly visible in the μSR measurements of Aoki *et al.* [539], consistent with a multi–component order parameter which, in turn, is consistent with multiple superconducting states. The upper critical field is of a conventional shape and does not show evidence of Pauli limiting [540]. The lower critical field, on the other hand, exhibits a pronounced positive curvature even at the lowest temperatures [541]. Lastly, we note that the presence of a field–induced antiferro–quadrupolar ordered phase just above the upper critical field suggests that quantum quadrupole fluctuations of the Pr ions may play a role in the superconducting mechanism.

10.5.16 U_2PtC_2

The lowest effective mass of all the heavy fermion compounds we discuss belongs to U_2PtC_2 which may be considered as intermediate between the heavy fermion superconductors and less–anomalous uranium based superconductors such as U_6Fe. Though the critical temperature is appreciable ($T_c = 1.47$ K) we are unaware of any clear evidence for unconventional superconductivity in this compound owing to a lack of experimental studies.

10.5.17 Related Materials

Lastly, we discuss several superconductors that are not usually considered to be heavy fermion superconductors but which show a "family resemblance" in the sense that all are examples of superconductivity in strongly correlated electron systems.

UGe_2, URhGe, and $ZrZn_2$

The topic of ferromagnetic superconductivity might be said to date from 1957

and the seminal work of Ginzburg [543]; a number of excellent reviews covering the work of the intervening decades exist [544] most recently by Flouquet *et al.* [545]. A most intriguing possibility for the following compounds is that superconductivity and ferromagnetism involve the *same* electrons.

Superconductivity in orthorhombic UGe_2 appears near a pressure of 12 kbar just below the pressure at which ferromagnetism is suppressed [64]. The maximum critical temperature $T_c = 0.7$ K occurs at 12 kbar where the Curie temperature is still about 30 K and the size of the ordered moment is about 1 μ_B/U–atom. Estimates of the internal field created by the ferromagnetic order are of order 100 T so triplet pairing seems likely. The shape of the upper critical field is anisotropic and strongly pressure dependent, exhibiting re–entrant behavior near a pressure of 13.2 kbar [546]. A p–wave superconducting state has been proposed that coexists with the itinerant ferromagnetism [547]. At ambient pressure, ferromagnetism appears at 9.5 K in orthorhombic URhGe followed by superconductivity near 0.3 K [66]. The upper critical field of a polycrystal exhibits a conventional shape. Triplet superconductivity is expected given the large internal fields associated with the 0.5 μ_B/U–atom moments. Cubic $ZrZn_2$ is also an ambient pressure superconductor ($T_c = 0.3$ K) where the superconductivity appears out of an itinerant ferromagnetic state ($T_C = 28.5$ K with an ordered moment of 0.17 μ_B/f.u.) [548]. The upper critical field shows a qualitatively conventional shape. Recent theoretical work suggests a multi–component order parameter with nodes in the gap function [549]. Clearly a great deal of work remains to be done to characterize the superconducting states of these intriguing compounds.

$PuNiGa_5$

The final compound we discuss in this section is the tetragonal plutonium–based compound $PuNiGa_5$ which exhibits the highest critical temperature ($T_c = 18.5$ K) ever observed for an f–electron compound [75]. $PuNiGa_5$ (and $PuRhGa_5$ which is reported to superconduct at 8.7 K [550]) exhibits the same crystal structure as the Ce 1–1–5 compounds discussed above, aspects of the Fermi surface structure are also quite similar [551]. Recent electronic structure calculations suggest that the superconductivity is caused by the pairing of plutonium 5f electrons [552]. Measurements of the upper critical field near T_c, fit to a conventional WHHM form, suggest that the critical field reaches 74 T at $T = 0$ which would exceed the Pauli limit. The lower critical field at 5 K is estimated to be about 350 Oe which, in turn, permits an estimate of 32 for the Ginzburg–Landau parameter.

We close this section by referring to Table(10.11) containing various superconducting parameters of the heavy fermion superconductors we have discussed above. The significant number of empty spaces is just one piece of evidence suggesting the opportunities still awaiting experimentalists in this mature yet steadily growing field of research.

10.6 The Conclusion

Superconductivity in novel materials exhibits many interesting properties. One may assume that in particular new systems, alloys, compounds will also in the future offer new exciting phase–transitions and superconductivity.

Acknowledgements
This work at Temple University was supported by the US Department of Energy, Office of Basic Energy Sciences, through award no. DEFG02–01ER45872.

References

1. E. Bucher, J. P. Maita, G. W. Hull, R. C. Fulton, and A. S. Cooper, (1975), "Electronic Properties of Beryllides of Rare–Earth and Some Actinides," *Phys. Rev. B*, **11**, 440.
2. W. Franz, A. Grießel, F. Steglich, and D. Wohlleben, (1978), "Transport Properties of $LaCu_2Si_2$ and $CeCu_2Si_2$ Between 1.5 K and 300 K," *Z. für Physik B*, **31**, 7.
3. F. Steglich, J. Aarts, C. Bredl, W. Lieke, D. Meschede, W. Franz, and H. Schäfer, (1979), "Superconductivity in the Presence of Strong Pauli Paramagnetism: $CeCu_2Si_2$," *Phys. Rev. Lett.*, **43**, 1892.
4. H. R. Ott, H. Rudigier, Z. Fisk, and J. L. Smith, (1983), "UBe_{13}: An Unconventional Actinide Superconductor," *Phys. Rev. Lett.*, **50**, 1595.
5. H. R. Ott, H. Rudigier, T.M. Rice, K. Ueda, Z. Fisk, and J. L. Smith, (1984), "*P*–Wave Superconductivity in UBe_{13}," *Phys. Rev. Lett.*, **52**, 1915.
6. G. R. Stewart, Z. Fisk, J. O. Willis, and J. L. Smith, (1984), "Possibility of Coexistence of Bulk Superconductivity and Spin Fluctuations in UPt_3," *Phys. Rev. Lett.*, **52**, 679.
7. J. L. Smith, Z. Fisk, J. O. Willis, B. Batlogg, and H. R. Ott, (1984), "Effects of Impurities on the Properties of the Heavy Fermion Superconductor UBe_{13}," *J. Appl. Phys.*, **55**, 1996.
8. H. R. Ott, H. Rudigier, Z. Fisk, and J. L. Smith, (1985), "Phase Transition in the Superconducting State of $U_{1-x}Th_xBe_{13}$ (x=0-0.06)," *Phys. Rev. B*, **31**, 1651.
9. Z. Fisk, H. R. Ott, T. M. Rice, and J. L. Smith, (1986), "Heavy–Electron Metals," *Nature*, **320**, 124.
10. Z. Fisk, D. W. Hess, C. J. Pethick, D. Pines, J. L. Smith, J. D. Thompson, and J. O. Willis, (1988), "Heavy–Electron Metals: New Highly Correlated States of Matter," *Science*, **239**, 33.
11. J. G. Bednorz, and K. A. Müller, (1986), "Possible High–T_c Superconductivity in the Ba–La–Cu–O System," *Z. für Physik B*, **64**, 189.
12. R. Movshovich, M. A. Hubbard, M. B. Salamon, A. V. Balatsky, R. Yoshizaki, J. L. Sarrao, and M. Jaime, (1998), "Low–temperature anomaly in thermal conductivity of $Bi_2Sr_2Ca(Cu_{1-x}\ Ni_x)_2O_8$: Second superconducting phase?" *Phys. Rev. Lett.*, **80**, 1968.
13. A. C. Mota, E. Dumont, A. Amann, and Y. Maeno, (1999), "Transition into a low temperature superconducting phase of unconventional pinning in Sr_2RuO_4," *Physica B*, **261**, 934.

14. R. A. Fisher, S. Kim, B. W. Woodfield, N. E. Phillips, L. Taillefer, K. Hasselbach, J. Flouquet, A. L. Giorgi, and J. L. Smith, (1989), "Specific Heat of UPt_3: Evidence of Unconventional Superconductivity," *Phys. Rev. Lett.*, **62**, 1411.
15. G. R. Stewart, Z. Fisk, and M. S. Wire, (1984), *Phys. Rev. B*, **30**, 482.
16. J. -M. Mignot, J. Flouquet, P. Haen, F. Lapierre, L. Puech, and J. Voiron, (1988), *J. Mag. Mag. Mat.*, **76-77**, 97.
17. T. Oguchi, A. J. Freeman, and G. Crabtree, (1986), *Phys. Lett. A*, **117**, 428.
18. L. Taillefer, R. Newbury, G. G. Lonzarich, Z. Fisk, and J. L. Smith, (1987), *J. Mag. Mag. Mat.*, **63-64**, 372.
19. L. Taillefer, and G. G. Lonzarich, (1988), *Phys. Rev. Lett.*, **60**, 1570.
20. T. T. M. Palstra, A. M. Menovsky, A. J. Dirkmaat, P. H. Kes, G. J. Nieuwenhuys, and J. A. Mydosh, (1985), *Phys. Rev. Lett.*, **55**, 2727.
21. M. B. Maple, J. W. Chen, Y. Dalichaouch, T. Kohara, C. Rossel, M. S. Torikachvili, M. W. McElfresh, and J. D. Thompson, (1986), *Phys. Rev. Lett.*, **56**, 185.
22. W. Assmus, M. Herrmann, U. Rauchschwalbe, S. Riegel, W. Lieke, H. Spille, S. Horn, G. Weber, F. Steglich, and G. Cordier, (1984), *Phys. Rev. Lett.*, **52**, 469.
23. M. B. Maple, J. W. Chen, S. E. Lambert, Z. Fisk, J. L. Smith, H. R. Ott, J. S. Brooks, and M. J. Naughton, (1985), *Phys. Rev. Lett.*, **54**, 477.
24. J. W. Chen, S. E. Lambert, M. B. Maple, Z. Fisk, J. L. Smith, G. R. Stewart, and J. O. Willis, (1984), *Phys. Rev. B*, **30**, 1583.
25. D. E. MacLaughlin, Cheng Tien, W. G. Clark, M. D. Lan, Z. Fisk, J. L. Smith, and H. R. Ott, (1984), *Phys. Rev. Lett.*, **53**, 1833.
26. B. Golding, D. J. Bishop, B. Batlogg, W. H. Haemmerle, Z. Fisk, J. L. Smith, and H. R. Ott, (1985), *Phys. Rev. Lett.*, **55**, 2479.
27. B. Batlogg, D. J. Bishop, B. Golding, E. Bucher, J. Hufnagl, Z. Fisk, J. L. Smith, and H. R. Ott, (1986), *Phys. Rev. B*, **33**, 5906.
28. D. Jaccard, J. Flouquet, Z. Fisk, J. L. Smith, and H. R. Ott, (1985), *J. Phys.* (Paris), **46**, L 811.
29. J. J. M. Franse, A. Menovsky, A. de Visser, C. D. Bredl, U. Gottwick, W. Lieke, H. M. Mayer, U. Rauchschwalbe, G. Sparn, and F. Steglich, (1985), *Z. für Physik B*, **59**, 15.
30. D. J. Bishop, C. M. Varma, B. Batlogg, E. Bucher, Z. Fisk, and J. L. Smith, (1984), *Phys. Rev. Lett.*, **53**, 1009.
31. Y. Kohori, T. Kohara, H. Shibai, Y. Oda, T. Kaneko, Y. Kitaoka, and K. Asayama, (1987), *J. Phys. Soc. Jpn.*, **56**, 2263.
32. B. Batlogg, D. Bishop, B. Golding, C. M. Varma, Z. Fisk, J. L. Smith, and H. R. Ott, (1985), *Phys. Rev. Lett.*, **55**, 1319.
33. R. H. Heffner, J. L. Smith, J. O. Willis, P. Birrer, C. Baines, F. N. Gygax, B. Hitti, E. Lippelt, H. R. Ott, A. Schenck, E. A. Knetsch, J. A. Mydosh, and D. E. MacLaughlin, (1990), *Phys. Rev. Lett.*, **65**, 2816.
34. K. Machida, and M. Kato, (1987), *Phys. Rev. Lett.*, **58**, 1986.
35. M. Gulácsi, and Zs. Gulácsi, (1989), *Phys. Rev. B*, **39** 12352.
36. U. Rauchschwalbe, F. Steglich, G. R. Stewart, A. L. Giorgi, P. Fulde, and K. Maki, (1987), *Europhys. Lett.*, **3**, 751.
37. K. Hasselbach, L. Taillefer, and J. Flouquet, (1989), *Phys. Rev. Lett.*, **63**, 93.
38. U. Rauchschwalbe, U. Ahlen, F. Steglich, D. Rainer, and J. J. M. Franse, (1985), *Z. für Physik B*, **66**, 379.

39. B. S. Shivaram, T. F. Rosenbaum, and D. Hinks, (1986), *Phys. Rev. Lett.*, **57**, 1259.
40. B. S. Shivaram J. J. Ganon Jr., and D. Hnks, (1989), *Phys. Rev. Lett.*, **63**, 1723.
41. Y. J. Qian, M. F. Xu, A. Schenstrom, H. P. Braun, J. B. Ketterson, D. Hinks, M. Levy, and B. K. Sarma, (1987), *Solid State Commun.*, **63**, 599.
42. V. Müller, C, Roth, D. Maurer, E. W. Scheidt, K. Lüders, E. Bucher, and H. E. Bömmel, (1987), *Phys. Rev. Lett.*, **58**, 1224.
43. A. M. Shenstrom, M. F. Xu, Y. Hong, D. Bein, M. Levy, B. K. Sarma, S. Adenwalla, Z. Zhao, T. Tokayasu, D. W. Hess, J. B. Ketterson, J. A. Sauls, and D. G. Hinks, (1989), *Phys. Rev. Lett.*, **62**, 332.
44. S. Adenwalla, S. W. Lin, Q. Z. Ran, Z. Zhao, J. B. Ketterson, J. A. Sauls, D. Hinks, M. Levy, and B. K. Sarma, (1990), *Phys. Rev. Lett.*, **65**, 2298.
45. G. Bruls, D. Weber, B. Wolf, P. Thalmeier, B. Lüthi, A. de Visser, A. A. Menovsky, (1990), *Phys. Rev. Lett.*, **65**, 2294.
46. S. M. Hayden, L. Taillefer, C. Vettier, and J. Flouquet, (1992), *Phys. Rev. B*, **46**, 8675.
47. T. Trappmann, H. von Löhneysen, and L. Taillefer, (1991), *Phys. Rev. B*, **43**, 13714.
48. D. S. Jin, S. A. Carter, B. Ellman, T. F. Rosenbaum , and D. G. Hinks, (1992), *Phys. Rev. Lett.*, **68**, 1579.
49. M. Bouhkny, G. L. Bullock, B. S. Shivaram, and D. G. Hinks, (1994), *Phys. Rev. B*, **50**, 8985.
50. C. Geibel, S. Theis, D. Kaczorowski, A. Mehner, A. Grauel, B. Seidel, U. Ahlheim, R. Helfrich, K. Petersen, C. D. Bredl, and F. Steglich, (1991), *Z. für Physik B*, **83**, 305.
51. C. Geibel, C. Shank, S. Theis, H. Kitazawa, C. D. Bredl, A. Bohm, M. Rau, A. Grauel, R. Caspary, R. Helfrich, U. Ahlheim, G. Weber, and F. Steglich, (1991), *Z. für Physik B*, **84**, 1.
52. C. Petrovic, R. Movshovich, M. Jaime, P. G. Pagliuso, M. F. Hundley, J. L. Sarrao Z. Fisk, and J. D. Thompson, (2001), *Europhys. Lett.*, **53**, 354.
53. C. Petrovic, P. Pagliuso, M. F. Hundley, R. Movshovich, J. D. Thompson, Z. Fisk, and P. Monthoux, (2001), *J. Phys. C.M.*, **13**, L 337.
54. T. Takeuchi, T. Inoure, K. Sugiyama, D. Aoki, Y. Haga, K. Kindo, and Y. Õnuki, (2001), *J. Phys. Soc. Jpn.*, **70**, 877.
55. Y. Haga, Y. Inada, H. Harima, K. Oikawa, M. Murakawa, H. Nakawaki, Y. Tokiwa, D. Aoki, H. Shishido, S. Ikeda, N. Watanabe, and Y. Õnuki, (2001), *Phys. Rev. B*, **63**, 060503(R).
56. H. Shishido, R. Settai, D. Aoki, S. Ikeda, H. Nakawaki, N. Nakamaura, T. Iizuka, Y. Inada, K. Sugiyama, T. Takeuchi, K. Kindo, T. C. Kobayashi, Y. Haga, H. Harima, Y. Aoki, T. Namiki, H. Sato, and Y. Õnuki, (2002), *J. Phys. Soc. Jpn.*, **71**, 162.
57. H. Hegger, C. Petrovic, E. G. Moshpoulo, M. F. Hundley, J. L. Sarrao, Z. Fisk, and J. D. Thompson, (2000), *Phys. Rev. Lett.*, **84**, 4986.
58. R. Movshovich, M. Jaime, J. D. Thompson, C. Petrovic, P. G. Pagliuso, Z. Fisk, and J. L. Sarrao, (2001), *Phys. Rev. Lett.*, **86**, 5152.
59. K. Izawa, H. Yamaguchi, Y. Matsuda, H. Shishido, R. Settai, and Y. Õnuki, (2001), *Phys. Rev. Lett.*, **87**, 057002.
60. Y. Kohori, Y. Yamato, Y. Iwamoto, T. Kohara, E. D. Bauer, M. B. Maple, and J. L. Sarrao, (2001), *Phys. Rev. B*, **64**, 134526.

61. G-Q. Zheng, K. Tanabe, T. Mito, S. Kawasaki, Y. Kitaoka, D. Aoki, Y. Haga, and Y. Õnuki, (2001), *Phys. Rev. Lett.*, **85**, 4664.
62. I. R. Walker, F. M. Grosche, D. M. Freye, and G. G. Lonzarich, (1997), *Physica C*, **282**, 303.
63. G. Knebel, D. Braithwaite, P. C. Canfield, G. Lapertot, and J. Flouquet, (2001), *Phys. Rev. B*, **65**, 024425.
64. S. S. Saxena, P. Agarwal, K. Ahilan, F. M. Grosche, R. K. W. Haselwimmer, M. J. Steiner, E. Pugh, I. R. Walker, S. R. Julian, P. Monthoux, G. G. Lonzarich, A. Huxley, I. Sheikin, D. Braithwaite, and J. Flouquet, (2000), *Nature*, **406**, 587.
65. A. Huxley, I. Sheikin, E. Ressouche, N. Kernavanois, D. Braithwaite, R. Calemczuk, and J. Flouquet, (2001), *Phys. Rev. B*, **63**, 144519.
66. D. Aoki, A. Huxley, E. Ressouche, D. Braithwaite, J. Flouquet, J. -P¿ Brison, E. Lhotel, and C. Paulsen, (2001), *Nature*, **413**, 613.
67. R. Movshovich, T. Graf, D. Mandrus, J. D. Thompson, J. L. Smith, and Z. Fisk, (1996), *Phys. Rev. B*, **53**, 8241.
68. I. E. Dzyaloshinskii, and P. S. Kondratenko, (1976), *Sov. Phys. J.E.T.P.*, **43**, 1036.
69. K. B. Blagoev, J. R. Engelbrecht, and K. S. Bedell, (1998), *Phil. Mag. Lett.*, **78**, 169.
K. B. Blagoev, J. R. Engelbrecht, and K. S. Bedell, (1999), *Phys. Rev. Lett.*, **82**, 133.
70. N. I. Karchev, K. B. Blagoev, K. S. Bedell and P. B. Littlewood, (2001), *Phys. Rev. Lett.*, **86**, 846.
71. J. A. Hertz, (1976), *Phys. Rev. B*, **14**, 1165.
72. M. A. Continentino, (1994), *Phys. Rep.*, **239**, 180.
73. A. J. Millis, (1993), *Phys. Rev. B*, **48**, 7183.
74. D. Fay, and J. Appel, (1985), *Phys. Rev. B*, **32**, 6071.
75. J. L. Sarrao, L. A. Morales, J.D. Thompson, B. L. Scott, G. R. Stewart, F. Wastin, J. Rebizant, P. Boulet, E. Colineau, and G. H. Lander, (2002), *Nature*, **420**, 297.
76. A. A. Abrikosov, L. P. Gor'kov, and I. E. Dzyaloshinki, *Methods of Quantum Field Theory in Statistical Physics*, (Dover Publications, New York, (1975)).
77. J. M. Luttinger, and J. C. Ward, (1960), *Phys. Rev.*, 118, 1417.
J. M. Luttinger, (1960), *Phys. Rev.*, **119**, 1153.
J. M. Luttinger, (1961) *Phys. Rev.*, **121**, 942.
78. M. Springford, and A. Wasserman, (1996), *Adv. in Phys.*, **45**, 471.
79. S. Donovan, A. Schwartz, and G. Grüner, (1997), *Phys. Rev. Lett.*, **79**, 1401.
80. A. M. Awasthi, L. DeGiorgi, G. Grüner, Y. Dalichaouch, and M. B. Maple, (1993), *Phys. Rev. B*, **48**, 10 692.
81. L. DeGiorgi, M. Dressel, G. Grüner, P. Wachter, N. Sato, and T. Komatsubara, (1994), *Europhys. Lett.*, **25**, 3111.
82. W. Kohn, (1964), *Phys. Rev.*, **A 171**, 133.
83. L. DeGiorgi, (1999), *Rev. Mod. Phys.*, **71**, 687.
84. E. J. Singley, D. N. Basov, E. D. Bauer, and M. B. Maple, (2002), *Phys. Rev. B*, **65**, 161101(R).
85. F. Bommeli, L. DeGiorgi, P. Wachter, F. B. Anders, and A. V. Mitin, (1997), *Phys. Rev. B*, **56**, R1001.
86. J. Goldstone, (1961), *Nuovo Cimento*, **19**, 154.

87. A. I. Schindler, and B. R. Coles, (1968), *J. Appl. Phys.*, **39**, 956.
88. S. Doniach, and S. Engelsberg, (1966), *Phys. Rev. Lett.*, **17**, 750.
89. N. F. Berk, and J. R. Schrieffer, (1966), *Phys. Rev. Lett.*, **17**, 433.
90. T. Izuyama, D. J. Kim, and R. Kubo, (1963), *J. Phys. Soc. Jpn.*, **18**, 1025.
91. T. Moriya, *Spin Fluctuations in Itinerant Magnets*, (Springer Verlag, Berlin, (1985)).
92. P. S. Riseborough, and D. L. Mills, (1980), *Phys. Rev. B*, **21**, 5338.
93. D. R. Penn, (1966), *Phys. Rev.*, **142**, 350.
94. G. M. Carneiro, and C. J. Pethick, (1975), *Phys. Rev. B*, **11**, 1106.
95. W. F. Brinkman, and S. Engelsberg, (1968), *Phys. Rev.*, **169**, 417.
96. P. Lederer, and D. L. Mills, (1968), *Phys. Rev.*, **165**, 837.
97. T. Moriya, (1970), *Phys. Rev. Lett.*, **24**, 1433.
98. T. Moriya, and T. Takimoto, (1995), *J. Phys. Soc. Jpn.*, **64**, 960.
99. S. Sachdev, and J. Ye, (1992), *Phys. Rev. Lett.*, **69**, 2411.
100. A. Rosch, (1999), *Phys. Rev. Lett.*, **82**, 4280.
101. R. Hlubina, and T. M. Rice, (1995), *Phys. Rev. B*, **51**, 9534.
102. B. L. Altshuler, L. B. Ioffe, and A. J. Millis, (1995), *Phys. Rev. B*, **52**, 5563.
103. P. Coleman, (1999), *Physica B*, **259-261**, 353.
104. H. Fröhlich, (1950), *Phys. Rev.*, **79**, 845.
105. E. Maxwell, (1950), *Phys. Rev.*, **78**, 477.
106. C. A. Reynolds, B. Serin, W. H. Wright, and L. B. Nesbitt, (1950), *Phys. Rev.*, **78**, 487.
107. J. Bardeen, and D. Pines, (1955), *Phys. Rev.*, **99**, 1140.
108. J. W. Garland, (1967), *Phys. Rev.*, **153**, 460.
109. R. D. Fowler, J. D. G. Lindsay, R. W. White, H. H. Hill, B. T. Mathias, (1967), *Phys. Rev. Lett.*, **19**, 892.
110. H. Capellmann, and J. R. Schrieffer, (1968), *Phys. Rev. Lett.*, **21**, 1060.
111. J. O. Willis, J. D. Thompson, Z. Fisk, A. de Visser, J. J. M. Franse, and A. A. Menovsky, (1985), *Phys. Rev. B*, **31**, 1654.
112. N. Tateiwa, T. C. Kobayashi, K. Hanazono, K. Amaya, Y. Haga, R. Settai, and Y. Ōnuki, (2001), *J. Phys. C.M.*, **13**, L17.
113. H. Razafimandimby, P. Fulde, and J. Keller, (1984), *Z. für Physik B*, **54**, 111.
114. H. Jichu, A. D. S. Nagi, B. Jin, T. Matsuura, and Y. Kuroda, (1987), *Phys. Rev. B*, **35**, 1692.
115. M. T. Beal Monod, C. Bourbonnais, and V. J. Emery, (1986), *Phys. Rev. B*, **34**, 7716.
116. D. J. Scalapino, E. Loh, and J. E. Hirsch, (1986), *Phys. Rev. B*, **34**, 8190 also D. J. Scalapino, E. Loh, and J. E. Hirsch, (1987), *Phys. Rev. B*, **35**, 6694.
117. K. Miyake, S. Schmitt-Rink, and C. M. Varma, (1986), *Phys. Rev. B*, **34**, 6554.
118. G. M. Eliashberg, (1960), *Sov. Phys. J.E.T.P. Lett.*, **11**, 696.
119. D. J. Scalapino, J. R. Schrieffer, and J. W. Wilkins, (1966) *Phys. Rev.*, **148**, 263.
D. J. Scalapino, in R. D. Parks, *Superconductivity*, (Marcel Dekker Publishers, New York (1969)).
120. A. B. Migdal, (1958), *Sov. Phys. J.E.T.P.*, **7**, 996.
121. J. A. Hertz, K. Levin, and M. T. Beal-Monod, (1976), *Solid State Commun.*, **18**, 803.
122. P. B. Allen, and B. Mitrović, *Solid State Physics*, Vol. 37, Edited by H. Ehrenreich, F. Seitz, and D. Turnbull, (Academic Press, New York, (1982)).

123. J. P. Carbotte, (1990) *Rev. Mod. Phys.*, **62**, 1027.
124. J. Bardeen, L. N. Cooper, and J. R. Schrieffer, (1957), *Phys. Rev.*, **108**, 1175.
125. C. M. Varma, unpublished.
126. G. A. Gehring, and L. E. Major, (1994), *J. Phys. C.M.*, **6**, 495.
127. D. J. Thouless, (1960), *Ann. Phys.*, **10**, 553.
128. N. D. Mermin, (1974), *Phys. Rev. A*, **9**, 868.
129. P. Wölfle, (1979), *Rep. Prog. Phys.*, **42**, 269.
130. J. W. Serene, and D. Rainer, (1983), *Phys. Reports*, **101**, 221.
131. P. W. Anderson, and W. F. Brinkman, (1973), *Phys. Rev. Lett.*, **30**, 1108.
132. W. F. Brinkman, J. W. Serene, and P. W. Anderson, (1974), *Phys. Rev. A*, **10**, 2386.
133. D. Fay, (1975), *Phys. Lett. A*, **51 A**, 356.
134. J. R. Schrieffer, X. G. Wen, and S. C. Zhang, (1989), *Phys. Rev. B*, **39**, 11663.
135. S. Nakajima, (1973), *Prog. Theor. Phys.*, **60**, 1101.
136. A. J. Leggett, (1975), *Rev. Mod. Phys.*, **47**, 331.
137. P. W. Anderson, (1984), *Phys. Rev. B*, **30**, 1549.
138. E. I. Blount, (1985), *Phys. Rev. B*, **32**, 2935.
139. G. E. Volovik, and L. P. Gor'kov, (1985), *Sov. Phys. J.E.T.P.*, **61**, 843.
140. R. Balian, and N. R. Werthamer, (1963), *Phys. Rev.*, **131**, 1553.
141. P. W. Anderson, and P. Morel, (1961), *Phys. Rev.*, **123**, 1911.
142. P. W. Anderson, (1984), *Phys. Rev. B*, **30**, 4000.
143. M. Ozaki, K. Machida, and T. Ohmi, (1985), *Progr. Theor. Phys.*, **74**, 221.
M. Ozaki, K. Machida, and T. Ohmi, (1986), *Progr. Theor. Phys.*, **745**, 442.
144. S. Yip, and A. Garg, (1993), *Phys. Rev. B*, **48**, 3304.
145. M. R. Norman, (1990), *Phys. Rev. B*, **41**, 170.
146. M. R. Norman, (1994), *Phys. Rev. B*, **50**, 6904.
147. L. P. Gor'kov, (1958), *Sov. Phys. J.E.T.P.*, **7**, 505.
148. B. R. Coles, (1962), *I.B.M. J. Res. Dev.*, 6, 68.
149. P. W. Anderson, (1959), *J. Phys. Chem. Solids*, **11**, 26.
150. A. A. Abrikosov, and L. P. Gor'kov, (1963), *Sov. Phys. J.E.T.P. Lett.*, **12**, 143.
151. K. Maki, in R. D. Parks, *Superconductivity*, (Marcel Dekker Publishers, New York (1969)).
152. L. P. Gor'kov, and P. A. Kalugin, (1985), *Sov. Phys. J.E.T.P.*, **41**, 253.
153. K. Ueda, and T. M. Rice, *Theory of Heavy Fermions and Valence Fluctutaions*, (Springer Verlag, Berlin, (1985)).
154. M. Sigrist, and K. Ueda, (1991), *Rev. Mod. Phys.*, **63**, 239.
155. C. J. Pethick, and D. Pines, (1986), *Phys. Rev. Lett.*, **57**, 118.
156. P. Hirschfeld, D. Vollhardt, and P. Wölfle, (1986), *Solid State Commun.*, **59**, 111.
157. P. W. Anderson, (1961), *Phys. Rev.* , **124**, 41.
158. J. R. Schrieffer, and P. A. Wolf, (1966), *Phys. Rev.*, **149**, 491.
159. A. C. Hewson, *The Kondo Problem to Heavy Fermions*, (Cambridge University Press, Cambridge, (1993)).
160. J. Kondo, (1964), *Prog. Theor. Phys.*, **32**, 37.
161. P. W. Anderson, (1970), *J. Phys. C*, **3**, 2439.
162. K. G. Wilson, (1975), *Rev. Mod. Phys.*, **47**, 773.
163. N. Andrei, K. Furuya, and J. H. Lowenstein, (1983), *Rev. Mod. Phys.*, **55**, 331.

164. A. Tsvelik, and P. Wiegmann, (1983), *Adv. in Phys.*, **32**, 453.
165. P. Schlottmann, (1989), *Phys. Reps.*, **181**, 1.
166. P. Nozières, (1985), *Ann. Phys.*, **10**, 19.
167. P. Nozières, (1998), *Eur. J. Phys. B*, **6**, 447.
168. J. Friedel, and C. M. Sayers, (1977), *J. Phys.* (Paris), **38**, 697.
169. E. Muller-Hartmannn, (1989), *Z. für Phys. B*, **74**, 507.
170. D. Vollhardt, and W. Metzner, (1989), *Phys. Rev. Lett.*, **62**, 324.
171. A. Georges, G. Kotliar, W. Krauth, and J. Marcello, (1996), *Rev. Mod. Phys.*, **68**, 13.
172. Th. Pruschke, M. Jarrell, and J. K. Freericks, (1995), *Adv. in Phys.*, **44**, 187.
173. S. Burdin, A. Georges, and D. Grempel, (2000), *Phys. Rev. Lett.*, **85**, 1048.
174. S. Doniach, (1977), *Physica B*, **91**, 231.
175. M. Continentino, G. Japiassu, and A. Troper, (1989), *Phys. Rev. B*, **39**, 9734.
176. M. Continentino, (1993), *Phys. Rev. B*, **47**, 11587.
177. A. J. Arko, P. S. Riseborough, A. B. Andrews, J. J. Joyce, A. N. Tahvildar-Zadeh, and M. Jarrell, *Handbook of The Physics and Chemistry of Rare Earths, Vol. 26*, K. A. Gschneidner, and L. Eyring eds., (Elsevier Science B.V., Amsterdam, (1999)).
178. R. J. Trainor, M. B. Brodsky, and H. V. Culbert, (1975), *Phys. Rev. Lett.*, **34**, 1019.
179. G. R. Stewart, A. L. Giorgi, B. L. Brandt, S. Foner , and A. J. Arko, (1983), *Phys. Rev. B*, **28**, 1524.
180. Y. Ōnuki, and T. Komatsubara, (1987), *J. Mag. Mag. Mat.*, **63&64**, 281.
181. C. L. Lin, A. Wallash, J. E. Crow, T. Mihalisin, and P. Schlottmann, (1987), *Phys. Rev. Lett.*, **58**, 1232.
182. G. Lapertot, R. Calemczuk, C. Marcenant, J.Y. Henry, J. X. Boucherle, J. Flouquet, J. Hammann, R. Cibin, J. Cors, D. Jaccard, and J. Sierro, (1993), *Physica B*, **186-188**, 454.
183. B. Andraka, C. S. Jee, and G. R. Stewart, (1995), *Phys. Rev. B*, **52**, 9462.
184. R. Pietri, K. Ingersent, and B. Andraka, (2001), *Phys. Rev. Lett.*, **86**, 1090.
185. P. S. Riseborough, (2003), *Phys. Rev. B*, **67**, 045102.
186. J. S. Kim, and G. R. Stewart, (1995), *Phys. Rev. B*, **51**, 16 190.
187. G. Bruls, B. Wolf, D. Finsterbusch, P. Thalmeier, I. Kouroudis, W. Sun, W. Assmus, B. Lüthi, M. Lang, K. Gloos, F. Steglich , and R. Modler, (1994), *Phys. Rev. Lett.*, **72**, 1754.
188. F. Steglich, P. Buschinger, P. Gegenwart, M. Lohmann, R. Helfrich, C. Langhammer, P. Hellmann, L. Donnevert, S. Thomas, A. Link, C. Geibel, M. Lang, G. Sparn, and W. Assmus, (1996), *J. Phys. C.M.*, **8**, 9909.
189. R. Modler, M. Lang, C. Geibel, C. Schank, R. Muller-Reisener, P. Hellmann, A. Link, G. Sparn, W. Assmus, F. Steglich, (1995), *Physica B*, **206&207**, 586.
190. M. Ishikawa, N. Takeda, P. Ahmet, V. Karaki, and H. Ishimoto, (2001), *J. Phys. C.M.*, **13**, L25.
191. P. Gegenwart, C. Langhammer, C. Geibel, R. Helfrich, M. Lang, G. Sparn, F. Steglich, R. Horn, L. Donnevert, A. Link, W. Assmus, (1998), *Phys. Rev. Lett.*, **81**, 1501.
see also P. Gegenwart, M. Lang, A. Link, G. Sparn, C. Geibel, F. Steglich, and W. Assmus, (1999), *Physica B*, **259&261**, 403.
see also P. Gegenwart, M. Lohmann, M. Lang, R. Helfrich, C. Langhammer, M. Koppen, C. Geibel, F. Steglich, and W. Assmus, (1997), *Physica B*, **230&232**, 527.

192. J. D. Thompson, H. Hegger, D. Louca, G. H. Kwei, R. Movshovich, C. Petrovic, and J. L. Sarrao, (2000), *J. Alloys and Compds.*, **303&304**, 239.
193. M. McElfresh, M. B. Maple, J. O. Willis, D. Schiferl, J. L. Smith, Z. Fisk, and D. L. Cox, (1993), *Phys. Rev. B*, **48**, 10395.
194. B. Andraka, (1995), *Phys. Rev. B*, **52**, 16031.
195. Z. Fisk, H. R. Ott, and J. L. Smith, (1987), *J. Less-Common Metals*, **133**, 99.
196. J. S. Kim, B. Andraka, C. S. Jee, S. B. Roy, and G. R. Stewart, (1990), *Phys. Rev. B*, **41**, 11 073.
197. G. Frauenberger, M. Baldus, and G. R. Stewart, (1993), *Phys. Rev. B*, **47**, 3204.
198. P. S. Riseborough, (1984), *Phys. Stat. Solidi B*, **122**, 161.
199. N. Harrison, A. L. Cornelius, H. Harima, K. Takegahara, J. A. Detwiler, G. M. Schmiedeshoff, J. C. Cooley, and J. L. Smith, (2000), *Phys. Rev. B*, **61**, 1779.
200. L. Taillefer, R. Newbury, G. G. Lonzarich, Z. Fisk, and J. L. Smith, (1987), *J. Mag. Mag. Mat.*, **63&64**, 372.
201. N. Kimura, T. Komatsubara, D. Aoki, Y. Ōnuki, Y. Haga, E. Yamamaoto, H. Aoki, and H. Harima, (1998), *J. Phys. Soc. Jpn.*, **67**, 2185.
202. C. S. Wang, M. R. Norman, R. C. Albers, A. M. Boring, W. E. Pickett, H. Krakauer, N. E. Christiensen, (1987), *Phys. Rev. B*, **35**, 7260.
203. M. R. Norman, R. C. Albers, A. M. Boring, and N. E. Christiensen, (1988), *Solid State Commun.*, **68**, 245.
204. M. Hunt, P. Meeson, P. -A. Probst, P. Reinders, M. Springford, W. Assmus, and W. Sun, (1990), *J. Phys. C.M.*, **2**, 6859.
205. P. H. P. Reinders, M. Springford, P. T. Coleridge, R. Boulet, and D. Ravot, (1986), *Phys. Rev. Lett.*, **57**, 1631.
206. S. Chapman, M. Hunt, P. Meeson, P. H. P. Reinders, M. Springford, and M. Norman, (1990), *J. Phys. C.M.*, **2**, 8123.
207. G. R. Stewart, B. Andraka, C. Quitmann, B. Treadway, Y. Shapira, and E. J. McNiff, Jr., (1988), *Phys. Rev. B*, **37**, 3344.
208. K. Satoh, T. Fujita, Y. Maeno, Y. Ōnuki, and T. Komatsubara, (1988), *J. Mag. Mag. Mat.*, **76&77**, 128.
209. C. Bergemann, S. R. Julian, G. J. McMullan, B. K. Howard, G. G. Lonzarich, P. Lejay, J. P. Brison, and J. Flouquet, (1997), *Physica B*, **230**, 348.
210. H. Ohkuni, Y. Inada, Y. Tokiwa, K. Sakurai, R. Settai, T. Honma, Y. Haga, E. Yamamoto, Y. Ōnuki, H. Yamagami, S. Takahashi, and T. Yanagisawa, (1999), *Philos. Mag. B*, **79**, 1045.
211. Y. Inada, H. Ohkuhni, M. Hedo, Y. Tokiwa, K. Sakura, Y. Haga, E. Yamamoto, T. Honma, and Y. Ōnuki, (1999), *Physica B*, **259**, 642.
212. H. Yamagami, and N. Hamada, (2000), *Physica B*, **284**, 1295.
213. A. L. Cornelius, A. J. Arko, J. L. Sarrao, and N. Harrison, (1999), *Phys. Rev. B*, **59**, 13542.
214. G.G. Lonzarich, (1988), *J. Mag. Mag. Mat.*, **76&77**, 1.
215. K. Bakker, A. de Visser, A. A. Menovsky, and J. J. M. Franse, (1993), *Physica B*, **186-188** 720.
216. A. de Visser, F. R. de Boer, A. A. Menovsky, and J. J. M. Franse, (1987), *Sol. State Commun.*, **64**, 527.
217. H. Aoki, S. Uji, A. K. Albesaard, and Y. Ōnuki, (1993), *Phys. Rev. Lett.*, **71**, 2110.
218. S. R. Julian, F. S. Tautz, G. J. McMullan, and G. G. Lonzarich, (1994), *Physica B*, **199&200**, 63.

219. Y. Inada, A. Ishiguro, J. Kimura, N. Sato, A. Sawada, T. Komatsubara, and H. Yamagami, (1995), *Physica B*, **206&207**, 33.
220. T. Terashima, C. Haworth, M. Takashita, H. Aoki, N. Sato, and T. Komatsubara, (1997), *Phys. Rev. B*, **55**, 13369.
221. J.E. Graebner, and M. Robbins, (1976), *Phys. Rev. Lett.*, **36**, 422.
222. F. M. Mueller, D. H. Lowndes, Y. K. Chang, A. J. Arko, and R. S. List, (1992), *Phys. Rev. Lett.*, **68**, 3928.
223. M. Heinecke, and K. Winzer, (1995), *Z. für Physik B*, **98**, 147.
224. K. Matsuda, Y. Kohori, T. Kohara, K. Kuwahara , and H. Amitsuka, (2001), *Phys. Rev. Lett.*, **87**, 2031.
225. H. Amitsuka, M. Sato, N. Metoki, M. Yokohama. K. Kuwahara, T. Sakakibara, H. Morimoto, S. Kawarazaki, Y. Miyako, and J. A. Mydosh, (1999), *Phys. Rev. Lett.*, **83**, 5114.
226. W. Franz, F. Steglich, and D. Wohlleben, (197(0. *J. Phys.* (Paris) Colloque, **C5**, 342.
227. B. Cornut, and B. Coqblin, (1972), *Phys. Rev. B*, **5**, 4541.
228. A. P. Murani, K. Knorr, K. H. J. Buschow, *Crystal Field Effects in Metals and Alloys* A. Furrer, ed., (Plenum Press, New York, (1977)), 268.
229. S. Horn, E. Holland-Moritz, M. Lowenhaupt, F. Steglich, H. Scheuer, A. Benoit, and J. Flouquet, (1981), *Phys. Rev. B*, **23**, 3171.
230. A. Loidl, G. Knopp, H. Spille, F. Steglich, and A. P. Murani, (1989), *Physica B*, **156&157**, 794.
231. E. A. Goremychkin, and R. Osborn, (1993), *Phys. Rev. B*, **47**, 14280.
232. E. A. Goremychkin, and R. Osborn, (1993), *Phys. Rev. B*, **47**, 14580.
233. E. A. Goremychkin, R. Osborn and I. L. Sashin, (1999), *J. Appl. Phys.*, **85**, 6046.
234. G. J. Nieuwenhuys, (1987), *Phys. Rev. B*, **35**, 5260.
235. P. Santini, and G. Amoretti, (1994), *Phys. Rev. Lett.*, **73**, 1027.
236. H. Amitsuka, and T. Sakakibara, (1994), *J. Phys. Soc. Jpn.*, **63**, 736.
237. K. Kadowaki, and S. B. Woods, (1986), *Solid State Commun.*, **58**, 507.
238. J. M. Lawrence, J. D. Thompson, and Y. Y. Chen, (1985), *Phys. Rev. Lett.*, **54**, 2537.
239. Y. Ōnuki, Y. Shimizu, and T. Komatsubara, (1985), *J. Phys. Soc. Jpn.*, **54**, 304.
240. B. Batlogg, D. J. Bishop, E. Bucher, B. Golding Jr., A. P. Ramierez, Z. Fisk, and J. L. Smith, (1987), *J. Mag. Mag. Mat.*, **63&64**, 441.
241. B. Andraka, G. R. Stewart, (1994), *Phys. Rev. B*, **49**, 1259.
242. U. Rauchschwalbe, F. Steglich, A. de Visser, and J. J. M. Franse, (1987), *J. Mag. Mag. Mat.*, **63&64**, 347.
243. G. Remenyi, A. Briggs, J. Flouquet, O. Laborde, and F. Lapierre, (1983), *J. Mag. Mag. Mat.*, **31-34**, 407.
244. B. Horvatic, and V. Zlatic, (1984), *Phys. Rev. B*, **30**, 6717.
245. P. Schlottmann, (1987), *Phys. Rev. B*, **35**, 5279.
246. B. Andraka, (1995), *Phys. Rev. B*, **52**, 16031.
247. Y. Haga, E. Yamamoto, T. Honma, A. Nakamura, M. Hedo, S. Araki, H. Ohkuni, and Y. Ōnuki, (1999), *Physica B*, **259-261**, 627.
248. G. R. Stewart, Z. Fisk, J. O. Willis, and J. L. Smith, (1984), *Physica B*, **127**, 448.
249. F. P. Milliken, T. Penney, F. Holtzberg, and Z. Fisk, (1988), *J. Mag. Mag. Mat.*, **76&77**, 201.

250. F. G. Aliev, N. B. Brandt, V. V. Moschalkov, and S. M. Chudinkov, (1983), *Solid State Commun.*, **47**, 693.
251. T. Penney, J. Stankiewicz, S. von Molnar, Z. Fisk, J. L. Smith, and H. R. Ott, (1986), *J. Mag. Mag. Mat.*, **54-57**, 370.
252. J. Schoenes, and J. J. M. Franse, (1986), *Phys. Rev. B*, **33**, 5138.
253. A. Fert, and O. Jaoul, (1972), *Phys. Rev. Lett.*, **28**, 303.
254. P. Coleman, P. W. Anderson, and T. V. Ramakrishnan, (1985), *Phys. Rev. Lett.*, **55**, 414.
255. D. Jaccard, J. Flouquet, Z. Fisk, and J. L. Smith, (1985), *J. Phys. Lett.*, **46**, L811.
256. H. Armbruster, W. Franz, W. Schlabitz, and F. Steglich, (1979), *J. Phys. Colloq.*, **C4**, 40, 150.
257. A. Grauel, D. Fromm, C. Geibel, F. Steglich, N. Sato, and T. Komatsubara, (1993), *Int. J. Mod. Phys. B*, **7**, 50.
258. F. Steglich, U. Rauchschwalbe, U. Gottwick, H. M. Mayer, G. Sparn, N. Grewe, U. Poppe, and J. J. M. Franse, (1985), *J. Appl. Phys.*, **57**, 3054.
259. D. Jaccard, and J. Flouquet, (1985), *J. Mag. Mag. Mat.*, **47&48**, 45.
260. L. Colquitt Jr., H. R. Frankhauser, and F. J. Blatt, (1971), *Phys. Rev. B*, **4**, 292.
261. H. R. Ott, O. Marti, and F. Hulliger, (1984), *Solid State Commun.*, **49**, 1129.
262. J. Flouquet, P. Haen, C. Marcenat, P. Lejay, A. Amato, D. Jacaard, and E. Walker, (1985), *J. Mag. Mag. Mat.*, **52**, 85.
263. H. Sato, J. Zhao, W. P. Pratt Jr., Y. Ōnuki, and T. Komatsubara, (1987), *Phys. Rev. B*, **36**, 8841.
264. G. Sparn, W. Leike, U. Gottwick, F. Steglich, and N. Grewe, (1985), *J. Mag. Mag. Mat.*, **47&48**, 521.
265. A. Sulpice, P. Candit, J. Chaussy, J. Flouquet, D. Jacaard, P. LeJay, and J. L. Tholence, (1986), *J. Low Temp. Phys.*, **62**, 39.
266. A. de Visser, A. Menovsky, and J. J. M. Franse, (1987), *Physica B*, **147**, 81.
267. A. Ravex, J. Flouquet, J. L. Tholence, D. Jaccard, and A. Mayer, (1987), *J. Mag. Mag. Mat.*, **63&64**, 400.
268. A. K. Bhattacharjee, and B. Coqblin, (1976), *Phys. Rev. B*, **13**, 3441.
269. A. K. Bhattacharjee, and B. Coqblin, (1988), *Phys. Rev. B*, **38**, 338.
270. E. Brück, A. Nowack, N. Hohn, H. Paulus, and A. Freimuth, (1986), *Z. für Physik B*, **63**, 155.
271. B. Lüthi, (1985), *J. Mag. Mag. Mat.*, **52**, 70.
272. V. Müller, D. Maurer, K. de Groot, E. Bucher, and H. E. Bömmel, (1986), *Phys. Rev. Lett.*, **56**, 248.
273. K. D. Schotte, D. Föster, and U. Schotte, (1986), *Z. für Physik B*, **64**, 165.
274. R. Mock, and G. Güntherodt, (1989), *Z. für Physik B*, **74**, 315.
275. S. -W. Lin, S. Adenwalla, J. B. Ketterson, M. Levy, and B. K. Sarma, (1992), *J. Low. Temp. Phys.*, **89**, 217.
276. H. Shiba, (1975), *Prog. Theor. Phys.*, **54**, 967.
277. D. E. MacLaughlin, (1985), *J. Mag. Mag. Mat.*, **47&48**, 121.
278. J. P. Vithayathil, D. E. MacLaughlin, E. Koster, D. Ll. Williams, and E. Bucher, (1991), *Phys. Rev. B*, **44**, 4705.
279. Y. Kohori, H. Shibai, T. Kohara, Y. Oda, Y. Kitaoka, and K. Asayama, (1988), *J. Mag. Mag. Mat.*, **76&77**, 478.
280. H. R. Ott, H. Rudigier, E. Felner, Z. Fisk, and J. L. Smith, (1986), *Phys. Rev. B*, **33**, 126.

281. T. Kohra, Y. Kohori, K. Assayama, Y. Kitaoka, M. B. Maple, and M. S. Torikachvilli, (1987), *Jpn. J. Appl. Phys.*, **26**, 1247.
282. Y. Kohori, (1996), *J. Phys. Soc. Jpn.*, **65**, 679.
283. M. Kyogaku, Y. Kitaoka, K. Assayama, C. Geibel, C. Schank, and F. Steglich, (1993), *J. Phys. Soc. Jpn.*, **62**, 4016.
284. Y. Kitaoka, Y. Fujiwara, Y. Kohori, K. Asayama, Y. Õnuki, and T. Komatsubara, (1985), *J. Phys. Soc. Jpn.*, **54**, 3686.
285. J. Aarts, F. R. de Boer, and D. E. MacLaughlin, (1983), *Physica B*, **121**, 162.
286. Y. Kitaoka, K. Ueda, T. Kohara, K. Asayama, Y. Õnuki, and T. Komatsubara, (1985), *J. Mag. Mag. Mat.*, **52**, 341.
287. M. Jarrell, J. Gubernatis, and R. N. Silver, (1991), *Phys. Rev. B*, **44**, 5347.
288. O. O. Bernal, C. Rodrigues, A. Martinez, H. G. Lukefahr, A. A. Menovsky, and J. A. Mydosh, (2001), *Phys. Rev. Lett.*, **87**, 196402/3.
289. D. W. Cooke, R. H. Heffner, R. L. Hutson, M. E. Schillaci, J. L. Smith, J. O. Willis. D. E. MacLaughlin, C. Boekema, R. L. Lichti, A. B. Denison, and J. Oostens, (1986), *Hyperfine Interactions*, **31**, 425.
290. G. Aeppli, E. Bucher, A. I. Goldman, G. Shirane C. Broholm, and J. K. Kjems, (1988), *J. Mag. Mag. Mat.*, **76&77**, 385.
291. P. Dalmas de Réotier, A. Yaouanc, R. H. Heffner, P. C. M. Gubbens, and C. T. Kaiser, (2000), *Phys. Rev. B*, **61**, 6377.
292. D. E. MacLaughlin, D. W. Cooke, R. H. Heffner, R. L. Hutson, M. W. McElfresh, M. E. Schillaci, H. D. Rempp, J. L. Smith, J. O. Willis, E. Zirngiebl, C. Boekema, R. L. Lichti, and J. Oostens, (1988), *Phys. Rev. B*, **37**, 3153.
293. E. A. Knetsch, A. A. Menovsky, G. J. Nieuwenhuys, J. A. Mydosh, A. Amato, R. Feyerherm, F. N. Gygax, A. Schenck, R. H. Heffner, and D. E. MacLaughlin, (1993), *Physica B*, **186-188**, 300.
294. L. P. Gor'kov, (1991), *Europhys. Lett.*, **16**, 301.
295. L. P. Gor'kov, and R. Sokol, (1992), *Phys. Rev. Lett.*, **69**, 2586.
296. V. Barzykin, and L. P. Gor'kov, (1993), *Phys. Rev. Lett.*, **70**, 2479.
297. M. B. Walker, W. J. L. Buyers, Z. Tun, W. Que, A. A. Menovsky, and J. D. Garrett, (1993), *Phys. Rev. Lett.*, **71**, 2630.
298. T. E. Mason, W. J. L. Buyers, T. Petersen, and J. D. Garrett, (1995), *J. Phys. C.M.*, **7**, 5089.
299. S. Barth, H. R. Ott, F. N. Gygax, B. Hitti, E. Lippelt A. Schenck, C. Baines, B. van der Brandt, T. Konter, and S. Mango, (1987), *Phys. Rev. Lett.*, **59**, 2991.
300. S. Barth, H. R. Ott, F. N. Gygax, B. Hitti, E. Lippelt, and A. Schenck, (1988), *J. Mag. Mag. Mat.*, **76&77**, 455.
301. F. Steglich, and N. Grewe, *Handbook on the Physics and Chemistry of Rare Earths*, K. A. Gschneidner Jr. and L. Eyring, eds., Volume 14, (North Holland Publishers, Amsterdam, (1991)).
302. D. Jaccard, R. Cibin, J. L. Jorda, and J. Flouquet, (1987), *Jpn. J. Appl. Phys.*, **26**, 517.
303. Y. J. Uemura, W. J. Kossler, X. H. Yu, H. E. Schone, J. R. Kempton, C. E. Stronach, S. Barth, F. N. Gygax, B. Hitti, A. Schenck, C. Baines, W. F. Lankford, Y. Õnuki, and T. Komatsubara, (1989), *Phys. Rev. B*, **39**, 4726.
304. H. Nakamura, Y. Kitaoka, T. Iwai, H. Yamada, and K. Asayama, (1992), *J. Phys. C.M.*, **4**, 473.
305. Y. Kitaoka, H. Nakamura, T. Iwai, K. Asayama, U. Ahlheim, C. Geibel, C. Schank, and F. Steglich, (1992), *J. Phys. Soc. Jpn.*, **60**, 2122.

306. H. Nakamura, Y. Kitaoka, H. Yamada, and K. Asayama, (1988), *J. Mag. Mag. Mat.*, **76&77**, 517.
307. G. M. Luke, A. Keren, K. Kojima, L.P. Le, B. J. Sternlieb, W. D. Wu, Y. J. Uemura, Y. Ōnuki, and T. Komatsubara, (1994), *Phys. Rev. Lett.*, **73**, 1853.
308. R. Feyerherm, A. Amato, C. Geibel, F. N. Gygax, P. Hellmann, R. H. Heffner, D. E. MacLaughlin, R. Mueller-Reisener, G. J. Nieuwenhuys, A. Schenck, and F. Steglich, (1995), *Physica B*, **206&207**, 596.
see also: R. Feyerherm, A. Amato, C. Geibel, F. N. Gygax, P. Hellmann, R. H. Heffner, D. E. MacLaughlin, R. Mueller-Reisener, G. J. Nieuwenhuys, A. Schenck, and F. Steglich, (1997), *Phys. Rev. B*, **56**, 699.
309. A. P. Murani, K. Knorr, K. H. J. Buschow, A. Benoit, and J. Flouquet, (1980), *Solid State Commun.*, **36**, 523.
310. N. E. Bickers, D. L. Cox and J. W. Wilkins, (1987), *Phys. Rev. Lett.*, **54**, 230.
see also N. E. Bickers, D. L. Cox, and J. W. Wilkins, (1987), *Phys. Rev. B*, **36**, 2306.
311. L. P. Regnault, W. A. C. Erkelens, J Rossat-Mignod, P. Lejay, and J. Flouquet, (1988), *Phys. Rev. B*, **38**, 4481.
312. J. L. Jacoud, L. P. Regnault, J. Rossay-Mignod, C. Vettier, P. LeJay, and J. Flouquet, (1989), *Physica B*, **156&157**, 818.
313. G. Balakrishnan, D. McK Paul, and N. R. Bernhoeft, (1988), *Physica B*, **156&157**, 817.
314. G. H. Lander, S. M. Shapiro, C. Vettier, and A. J. Dianoux, (1992), *Phys. Rev. B*, **46**, 5387.
315. G. Aeppli, E. Bucher, and G. Shirane, (1985), *Phys. Rev. B*, **32**, 7579.
316. N. R. Bernhoeft, and G. G. Lonzarich, (1995), *J. Phys. C.M.*, **7**, 7325.
317. G. Aeppli, A. I. Goldman, G. Shirane, G. Aeppli, E. Bucher, and M. C. Lux-Steiner, (1987), *Phys. Rev. Lett.*, **58**, 808.
318. A. I. Goldman, G. Shirane, G. Aeppli, E. Bucher, and J. Hufnagl, (1987), *Phys. Rev. B*, **36**, 8523.
319. G. Aeppli, E. Bucher, C. Broholm, J. K. Kjems, J. Baumann, and J. Hufnagl, (1988), *Phys. Rev. Lett.*, **60**, 615.
320. P. A. Midgely, S. M. Hayden, L. Taillefer, B. Bogenberger, and H. von Löhneysen, (1993), *Phys. Rev. Lett.*, **70**, 678.
321. R. H. Heffner, D. W. Cooke, A. L. Giorgi, R. L. Hutson, M. E. Schillaci, H. D. Rempp, J. L. Smith, J. O. Willis, D. E. MacLaughlin, C. Boekema, R. L. Lichti, J. Oostens, and A. B. Dension, (1989), *Phys. Rev. B*, **39**, 11345.
322. G. Aeppli, D. Bishop, C. Broholm, E. Bucher, K. Siemensmeyer, M. Steiner, and N. Stuesser, (1989), *Phys. Rev. Lett.*, **63**, 676.
323. A. I. Goldman, S. M. Shapiro, D. E. Cox, J. L. Smith, and Z. Fisk, (1985), *Phys. Rev. B*, **32**, 6042.
324. A. I. Goldman, S. M. Shapiro, G. Shirane, J. L. Smith, and Z. Fisk, (1986), *Phys. Rev. B*, **33**, 1627.
325. S. Coad, A. Heiss, D. F. McMorrow, G. H. Lander, G. Aeppli, Z. Fisk and G. R. Stewart, S. M. Hayden, and H. A. Mook, (2000), *Physica B*, **276-278**, 764.
326. C. Broholm, J. K. Kjems, W. J. L. Buyers, P. Mathews, T. T. M. Palstra, A. A. Menovsky, and J. A. Mydosh, (1987), *Phys. Rev. Lett.*, **59**, 1467.
327. B. Fak, C. Vettier, J. Flouquet, P. Lejay, and J. M. Mignot, (1995), *Physica B*, **206&207**, 415.

328. T. E. Mason, B. D. Gaulin, J. D. Garrett, Z. Tun, W. J. L. Buyers, and E. D. Isaacs, (1990), *Phys. Rev. Lett.*, **65**, 3189.
329. U. Walter, M. Lowenhaupt, W. Schlabitz, and C. K. Loong, (1986), *Phys. Rev. B*, **33**, 7875.
330. C. Broholm, H. Lin, P. T. Mathews, T. E. Mason, W. J. L. Buyers, M. F. Collins, A. A. Menovsky, J. A. Mydosh, and J. K. Kjems, (1991), *Phys. Rev. B*, **43**, 12809.
331. J -G. Park, K. A. McEwen, and M. J. Bull, (2002), *Phys. Rev. B*, **66**, 094502.
332. T. Honma, Y. Haga, E. Yamamoto, N. Metoki, Y. Koike, H. Ohkuni, and Y. Ōnuki, (1999), *Physica B*, **259**, 646.
333. C. Stassis, B. Batlogg, J. P. Reimka, J.D. Axe, G. Shirane, and Y. J. Uemura, (1986), *Phys. Rev. B*, **33**, 1680.
334. J. Rossat-Mignod, L. P. Regnault, J. L. Jacoud, C. Vettier, P. Lejay, J. Floquet, E. Walker, D. Jaccard, and A. Amato, (1988), *J. Mag. Mag. Mat.*, **76&77**, 376.
335. G. Aeppli, H. Yoshizawa, Y. Endoh, E. Bucher, J. Hufnagl, Y. Ōnuki, and T. Komatsubara, (1986), *Phys. Rev. Lett.*, **57**, 122.
336. H. von Löhneysen, (1996), *J. Phys. C.M.*, **8**, 9689.
337. A. Schröder, J.W. Lynn, R.W. Erwin, M. Lowenhaupt, and H. von Löhneysen, (1994), *Physica B*, **199-200**, 47.
338. O. Stockert, H. von Löhneysen, A. Rosch, N. Pyka, and M. Lowenhaupt, (1998), *Phys. Rev. Lett.*, **80**, 5627.
339. A. Rosch, A. Schröder, O. Stockert, and H. von Löhneysen, (1997), *Phys. Rev. Lett.*, **79**, 159.
340. A. Schröder, G. Aeppli, E. Bucher, R. Ramazashvili, and P. Coleman, (1998), *Phys. Rev. Lett.*, **80**, 5623.
341. M. C. Aronson, R. Osborne, R. A. Robinson, J. W. Lynn, R. Chau, C. L. Seaman, and M. B. Maple, (1995), *Phys. Rev. Lett.*, **75**, 725.
342. R. Osborn, M. C. Aronson, B. D. Rainford, M. B. Maple, R. Chau, and K. H. Andersen, (1997), *Physica B*, **241**, 859.
343. A. Krimmel, P. Fischer, B. Roessli, H. Maletta, C. Geibel, C. Schank, A. Grauel, A. Loidl, and F. Steglich, (1992), *Z. für Physik B*, **86**, 161.
344. T. Petersen, T. E. Mason, G. Aeppli, A. P. Ramierez, E. Bucher, and R. R. Kleimann, (1994), *Physica B*, **199&200**, 151.
345. N. Sato, N. Aso, G.H. Lander, B. Roessli, T. Komatsubara, and Y. Endoh, (1997), *J. Phys. Soc. Jpn.*, 66, 1884.
346. N. Bernhoeft, B. Roessli, N. Sato, N. Aso, A. Heiss, G. H. Lander, Y. Endoh, and T. Komatsubara, (1999), *Physica B*, **259-261**, 614.
347. N. Metoki, Y. Haga, Y. Koike, N. Aso, and Y. Ōnuki, (1997), *J. Phys. Soc. Jpn.*, **66**, 2560.
348. N. Metoki, Y. Haga, Y. Koike, and Y. Ōnuki, (1998), *Phys. Rev. Lett.*, **80**, 5417.
349. N. Metoki, Y. Koike, Y. Haga, T. Honma, M. Sato, Y. Ōnuki, N. Kimura, K. Maesawa, H. Amitsuka, M. Yokoyama, K. Kuwahara, and Y. Miyako, (2000), *Physica B*, **280**, 362.
350. A. Schroder, J. G. Lussier, B. D. Gaulin, J. D. Garrett, W. J. L. Buyers, L. Rebelsky, and S. M. Shapiro, (1994), *Phys. Rev. Lett.*, **72**, 136.
351. J. G. Lussier, M. Mao, A. Schroder, J. D. Garrett, B. D. Gaulin, S. M. Shapiro, and W. J. L. Buyers, (1997), *Phys. Rev. B*, **56**, 11749.

352. N. Aso, B. Roessli, N. Bernhoeft, R. Calemczuk, N. K. Sato, Y. Endoh, T. Komatsubara, A. Heiss, G. H. Lander, and H. Kadowaki, (2000), *Phys. Rev. B*, **61**, 11867.
353. B. D. Gaulin, M. Mao, C. R. Weibe, Y. Qiu, S. M. Shapiro, S. H. Lee, and J. D. Garrett, (2002), *Phys. Rev. B*, **66**, 174520.
354. Y. Wada, (1964), *Rev. Mod. Phys.*, **36**, 253.
355. J. C. Swihart, D. J. Scalapino, and Y. Wada, (1965), *Phys. Rev. Lett.*, **14**, 106.
356. D. K. Finnemore, T. F. Stromberg, and C. A. Swenson, (1966), *Phys. Rev.*, **149**, 231.
357. R. Radebaugh, and P. H. Keesom, (1966), *Phys. Rev.*, **149**, 217.
358. W. Schlabitz, J. Baumann, B. Pollit, U. Rauchschwalbe, H.M. Mayer, U. Ahlheim, and C.D. Bredl, (1986), *Z. für Physik B*, **62**, 171.
359. F. Steglich, C.D. Bredl, W. Lieke, U. Rauchschwalbe, and G. Sparn, (1984), *Physica B*, **126**, 82.
360. J. R. Schrieffer, *Theory of Superconductivity*, (W.A. Benjamin, Inc., Reading, (1964)).
361. Terry P. Orlando, and Kevin A. Delin, *Foundations of Applied Superconductivity*, (Addison-Wesley, Reading, (1991)).
362. G. Eilenberger, (1967), *Phys. Rev.*, **153**, 584.
363. B. S. Chandrasekhar, (1962), *Appl. Phys. Lett.*, **1**, 7.
364. A. M. Clogston, (1962), *Phys. Rev. Lett.*, **9**, 261.
365. I. A. Luk'yanchuk, and V. P. Minnev, (1987), *Sov. Phys. J.E.T.P.*, **66**, 1168.
366. N. R. Werthamer, E. Helfand, and P. C. Hohenberg, (1966), *Phys. Rev.*, **147**, 295.
367. K. Maki, (1966), *Phys. Rev.*, **148**, 362.
368. T. P. Orlando, E. J. McNiff Jr., S. Foner, and M. R. Beasley, (1979), *Phys. Rev. B*, **19**, 4545.
369. K. Scharnberg, and R. A. Klemm, (1980), *Phys. Rev. B*, **22**, 5233.
370. K. Scharnberg, and R. A. Klemm, (1985), *Phys. Rev. Lett.*, **54**, 2445.
371. Robert Joynt, (1990), *Phys. Rev. B*, **41**, 4271.
372. M. Prohammer, and J. P. Carbotte, (1990), *Phys. Rev. B*, **42**, 2032.
373. P. Fulde, and R. A. Ferrell, (1964), *Phys. Rev.*, **135**, 550.
374. A. I. Larkin, and Y. N. Ovchinnikov, (1965), *Sov. Phys. J.E.T.P.*, **20**, 762.
375. L. W. Gruenberg, and L. Gunther, (1966), *Phys. Rev. Lett.*, **16**, 996.
376. B. B. Goodman, (1962), *Phys. Lett.*, **1**, 215.
377. R. Joynt, and L. Taillefer, (2002), *Rev. Mod. Phys.*, **74**, 235.
378. F. Thomas, B. Wand, T. Luhmann, P. Gegenwart, G. R. Stewart, F. Steglich, J. P. Brison, A. Buzdin, L. Glemot, and J. Flouquet, (1996) *J. Low Temp. Phys.*, **102**, 117.
379. L. Glemot, J. P. Brison, J. Flouquet, A. I. Buzdin, I. Sheikin, D. Jaccard, C. Thessieu, and F. Thomas, (1999), *Phys. Rev. Lett.*, **82**, 169.
380. G. M. Schmiedeshoff, Z. Fisk, and J. L. Smith, (1992), *Phys. Rev. B*, **45**, 10544.
381. N. E. Alekseevskii, V. I. Nizhankovskii, V. N. Narozhnyi, E. P. Khlybov, and A. V. Mitin, (1986), *J. Low Temp. Phys.*, **64**, 87.
382. F. G. Aliev, V. Kovachik, V. V. Moshchalkov, V. V. Pryadun, N. E. Alekseevskii, A. V. Mitin, N. Agrait, S. Vieira, and R. Villar, (1991), *J. Low Temp. Phys.*, **85**, 359.

383. P. J. C. Signore, B. Andraka, G. R. Stewart, and M. W. Meisel, (1995), *Phys. Rev. B*, **52**, 10315.
384. U. Rauchschwalbe, W. Lieke, C. D. Bredl, F. Steglich , J. Aarts, K. M. Martini, and A. C. Mota, (1982), *Phys. Rev. Lett.*, **49**, 1448.
385. I. Sheikin, D. Braithwaite, J. -P. Brison, W. Assmus, and J. Flouquet, (2000), *J. Low Temp. Phys.*, **118**, 113.
386. A. Pollini, A. C. Mota, P. Visani, R. Pittini, G. Juri, and T. Teruzzi, (1993), *J. Low Temp. Phys.*, **9-**, 15.
387. U. Rauchschwalbe, (1987), *Physica B*, **147**, 1.
388. R. D. Parks, *Superconductivity*, (Marcel Dekker Publishers, New York (1969)).
389. V. Ambegokar, and A. Griffin, (1965), *Phys. Rev.*, **137**, A 1151.
390. L. Coffey, T. M. Rice, and K. Ueda, (1985), *J. Phys. C*, **18**, L 813.
391. S. Schmitt-Rink, K. Miyake, and C. M. Varma, (1986), *Phys. Rev. Lett.*, **57**, 2575.
392. P. Hirschfeld, P. Wölfle, and D. Einzel, (1988), *Phys. Rev. B*, **37**, 83.
393. P.A. Lee, (1993), *Phys. Rev. Lett.*, **71**, 1887.
394. M. J. Graf, S. -K. Yip, J. A. Sauls, and D. Rainer, (1996), *Phys. Rev. B*, **53**, 15147.
395. H. R. Ott, E. Felder, A. Bernasconi, Z. Fisk, J. L. Smith, L. Taillefer, and G. Lonzarich, (1987), *Jpn. J. Appl. Phys.*, 26, Suppl. **26-3**, 1217.
396. D. Jaccard, J. Flouquet, P. Lejay, and J. L. Tholence, (1985), *J. Appl. Phys.*, **57**, 3082.
397. K. Behnia, L. Taillefer, J. Flouquet, D. Jaccard, K. Maki, and Z. Fisk, (1991), *J. Low. Temp. Phys.*, **84**, 261.
398. F. Steglich, U. Ahlheim, J. J. M. Franse, N. Grewe, D. Rainer, and U. Rauchschwalbe, (1985), *J. Mag. Mag. Mat.*, **52**, 54.
399. B. Lussier, B. Ellman, and L. Taillefer, (1994), *Phys. Rev. Lett.*, **73**, 3295.
400. T. Tsuneto, (1961), *Phys. Rev.*, **121**, 402.
401. L. P. Kadanoff, and I. I. Falko, (1964), *Phys. Rev.*, **136**, A 1170.
402. L. T. Claiborne Jr., and R. W. Morse, (1964), *Phys. Rev.*, **136**, A 893.
403. K. Fossheim, (1967), *Phys. Rev. Lett.*, **19**, 81.
404. V. Müller, D. Maurer, E. W. Scheidt, Ch. Roth, K. Lüders, E. Bucher, and H. E. Bömmel, (1986), *Solid State Commun.*, **57**, 319.
405. B. S. Shivaram, J. H. Jeong, T. F. Rosenbaum, and D. G. Hinks, (1986), *Phys. Rev. Lett.*, **56**, 1078.
406. P. Thalmeier, B. Wolf, D. Weber, R. Blick, G. Bruls, and B. Lüthi, (1992), *J. Mag. Mag. Mat.*, **108**, 109.
407. K. J. Sun, A. Schenstrom, B. K. Sarma, M. Levy, and D. G. Hinks, (1989), *Phys. Rev. B*, **40**, 11284.
408. L. D. Landau, (1957), *Sov. Phys. J.E.T.P.*, **5**, 101.
409. L. Coffey, (1989), *Phys. Rev. B*, **40**, 715.
L. Coffey, (1987), *Phys. Rev. B*, **35**, 8440.
410. S. N. Coppersmith, and R. A. Klemm, (1986), *Phys. Rev. Lett.*, **56**, 1870.
411. K. Scharnberg, D. Walker, H. Monien, L. Tewordt, and R. A. Klemm, (1986), *Solid State Commun.*, **60**, 535.
412. B. Arfi, and C. J. Pethick, (1988), *Phys. Rev. B*, **38**, 2312.
413. J. Moreno, and P. Coleman, (1996), 53, R2995.
414. J. P. Rodriguez, (1985), *Phys. Rev. Lett.*, **55**, 250.
415. D. C. Mattis, and J. Bardeen, (1958), *Phys. Rev.* **111**, 412.

416. D. M. Ginsberg, and M. Tinkham, (1960), *Phys. Rev.*, **118**, 990.
417. S. A. Zemon, and H. A. Boorse, (1966), *Phys. Rev.*, **146**, 309.
418. M. Tinkham, and R. A. Ferrell, (1959), *Phys. Rev. Lett.*, **2**, 331.
419. J. Halbritter, (1971), *Z. für Physik*, **243**, 201.
420. P. J. Hirschfeld, P. Wölfle, J. A. Sauls, D. Einzel, and W. O. Putikka, (1989), *Phys. Rev. B*, **40**, 6695.
421. S. -W. Lin, C. T. Lin, B. K. Sarma, G. R. Stewart, and J. B. Ketterson, (1996), *Phys. Lett. A*, **217**, 161.
422. S. Skalski, O. Betbeder-Matibet, and P. R. Weiss, (1964), *Phys. Rev.*, **136**, A 1500.
423. J. R. Feller, C. -C. Tsai, J. B. Ketterson, J. L. Smith, and B. K. Sarma, (2002), *Phys. Rev. Lett.*, **88**, 247005.
424. D. Einzel, P. J. Hirschfeld, F. Gross, B. S. Chandrasekhar, K. Andres, H. R. Ott, J. Beuers, Z. Fisk, and J. L. Smith, (1986), *Phys. Rev. Lett.*, **56**, 2513.
425. C. Broholm, G. Aeppli, R. N. Kleinman, D. R. Harshman, D. J. Bishop, E. Bucher, D. Ll. Williams, E. J. Ansaldo, and R. H. Heffner, (1990), *Phys. Rev. Lett.*, **65**, 2062.
426. A. Yaouanc, P. Dalmas de Réotier, A. Huxley, J. Flouquet, P. Bonville, P. C. M. Gubbens, and A. M. Mulders, (1998), *J. Phys. C.M.*, **10**, 9791.
427. S. K. Yip, and J. A. Sauls, (1992), *Phys. Rev. Lett.*, **69**, 2264.
428. M. R. Li, P. J. Hirschfeld, and P. Wölfle, (1998), *Phys. Rev. Lett.*, **81**, 5640.
429. J. Bardeen, (1962), *Phys. Rev. Lett.*, **9**, 147.
J. Bardeen, (1960), *Phys. Rev. Lett.*, **6**, 57.
430. I. Giaever, (1960), *Phys. Rev. Lett.*, **5**, 147.
I. Giaever, and K. Megerle, (1961), *Phys, Rev.*, **122**, 1101.
431. J. Nicol, S. Shapiro, and P. H. Smith, (1960), *Phys. Rev. Lett.*, **5**, 461.
432. V. Ambegaokar, P. G. deGennes, and D. Rainer, (1974), *Phys. Rev. A*, **9**, 2676.
433. M. Jourdan, M. Huth, and H. Adrian, (1999), *Nature*, **398**, 47.
434. M. Huth, M. Jourdan, and H. Adrian, (2000), *Physica B*, **281&282**, 882.
435. N. Bernhoeft, N. Sato, B. Roessli, N. Aso, A. Heiss, G. H. Lander, Y. Endoh, and T. Komatsubara, (1998), *Phys. Rev. Lett.*, **81**, 4244.
436. I. Iguchi, T. Yasuda, Y. Õnuki, and T. Komatsubara, (1987), *Phys. Rev. B*, **35**, 8873.
437. A. F. Andreev, (1964), *Sov. Phys. J.E.T.P.*, **19**, 1228.
438. G. E. Blonder, M. Tinkham, and T. M. Klapwijk, (1981), *Phys. Rev. B*, **25**, 4515.
439. Ch. Bruder, (1990), *Phys. Rev. B*, **41**, 4017.
440. U. Poppe, (1985), *J. Mag. Mag. Mat.*, **52**, 157.
441. A. Nowack, A. Heinz, F. Oster, D. Wohlleben, G. Güntherodt, Z. Fisk, and A. Menovsky, (1987), *Phys. Rev. B*, **36**, 2436.
442. G. Goll, H. von Löhneysen, I.K. Yanson, and L. Taillefer, (1993), *Phys. Rev. Lett.*, **70**, 2008.
443. G. Goll, C. Bruder, and H. von Löhneysen, (1995), *Phys. Rev. B*, **52**, 6801.
444. C. Obermair, G. Goll, H. von Löhneysen, I.K. Yanson, and L. Taillefer, (1998), *Phys. Rev. B*, **57**, 7506.
445. K. Hasselbach, J. R. Kirtley, and P. Lejay, (1992), *Phys. Rev. B*, **46**, 5826.
446. Ch. Wälti, H. R. Ott, Z. Fisk, and J. L. Smith, (2000), *Phys. Rev. Lett.*, **84**, 5616.

447. Y. Tanaka, and S. S. Kashiwaya, (1995), *Phys. Rev. Lett.*, **74**, 3451.
448. B. D. Josephson, (1962), *Physics Lett.*, **1**, 251.
449. R. C. Jaklevic, J. Lambe, J. E. Mercereau, and A. H. Silver, (1965), *Phys. Rev. A*, **140**, 1628.
450. J. A. Pals, W. van Haeringen, and M. H. van Maaren, (1977), *Phys. Rev. B*, **15**, 2952.
451. J. R. Kirtley, C. C. Tsuei, J. Z. Sun, C. C. Chi, L. S. Yu-Jahes, A. Gupta, M. Rupp, and M. B. Ketchan, (1995), *Nature*, **373**, 225.
452. V. Ambegaokar, and A. Baratoff, (1963), *Phys. Rev. Lett.*, **10**, 486.
453. A. Sumiyama, S. Shibata, Y. Oda, N. Kimura, Y. Haga, and Y. Ōnuki, (1998), *Phys. Rev. Lett.*, **81**, 5213.
454. S. Wasser, A. Nowack, W. Schlabitz, A. Freimuth, O. E. Kvitnitskaya, A. A. Menovsky, and C. Bruder, (1998), *Phys. Rev. Lett.*, **81**, 898.
455. S. Han, K. W. Ng, E. L. Wolf, H. F. Braun, L. Tanner, Z. Fisk, J. L. Smith, and M. R. Beasley, (1981), *Phys. Rev. B*, **32**, 7567.
456. S. Han, K. W. Ng, E. L. Wolf, A. J. Millis, J. L. Smith, and Z. Fisk, (1986), *Phys. Rev. Lett.*, **57**, 238.
457. E. V. Thuneberg, and V. Ambegaokar, *Phys. Rev. Lett.*, **60**, 365 (1988).
458. S. Shibata, A. Sumiyama, Y. Oda, Y. Haga, and Y. Ōnuki, (1999), *Phys. Rev. B*, **60**, 3076.
459. K. Yosida, (1958), *Phys. Rev.*, **110**, 769.
460. P. W. Anderson, (1959), *Phys. Rev. Lett.*, **3**, 325.
461. A. A. Abrikosov, and L. P. Gor'kov, (1962), *Sov. Phys. J.E.T.P.*, **15**, 752.
462. K. Miyake, and K. Asayama, (2000), *Phys. Rev. B*, **62**, 11363.
463. E. T. Ahrens, R. H. Heffner, P. C. Hammel, A. P. Reyes, J. D. Thompson, J. L. Smith, and W. G. Clark, (1999), *Phys. Rev. B*, **59**, 1432.
464. Y. Kitaoka, H. Tou, K. Ishida, N. Kimura, Y. Ōnuki, E. Yamamoto, Y. Haga, and K. Maezawa, (2000), *Physica B*, **281&282**, 878.
465. K. Ueda, Y. Kitaoka, H. Yamada, Y. Kohori, T. Kohara, and K. Asayama, (1987), *J. Phys. Soc. Jpn.*, **56**, 867.
466. H. Tou, Y. Kitaoka, K. Asayama, N. Kimura, Y. Ōnuki, E. Yamamoto, and K. Maezawa, (1996), *Phys. Rev. Lett.*, **77**, 1374.
467. H. Tou, Y. Kitaoka, K. Ishida, K. Asayama, N. Kimura, Y. Ōnuki, E. Yamamoto, Y. Haga, and K. Maezawa, (1998), *Phys. Rev. Lett.*, **80**, 3129.
468. R. Feyerherm, A. Amato, F.N. Gygax, A. Schenck, C. Geibel, F. Steglich, N. Sato, and T. Komatsubara, (1994), *Phys. Rev. Lett.*, **73**, 1849.
469. K. Ishida, D. Ozaki, T. Kamatsuka, H. Tou, M. Kyogaku, Y. Kitaoka, N. Tateiawa, N.K. Sato, N. Aso, C. Geibel, and F. Steglich, (2002), *Phys. Rev. Lett.*, **89**, 37002.
470. L. C. Hebel, and C. P. Slichter, (1957), *Phys. Rev.*, **107**, 901.
L. C. Hebel, and C. P. Slichter, (1959), *Phys. Rev.*, **113**, 1504.
471. M. Fibich, (1965), *Phys. Rev. Lett.*, **14**, 561.
472. Y. Kohori, T. Kohara, H. Shibai, Y. Oda, Y. Kitaoka, and K. Asayama, (1988), *J. Phys. Soc. Jpn.*, **57**, 395.
473. K. Matsuda, Y. Kohori, and T. Kohara, (1997), *Phys. Rev. B*, **55**, 15223.
474. K. Ishida, Y. Kawasaki, K. Tabuchi, K. Kashima, Y. Kitaoka, K. Asayama, C. Geibel, and F. Steglich, (1999), *Phys. Rev. Lett.*, **82**, 5353.
475. C. Tien, and I. M. Jiang, (1989), *Phys. Rev. B*, **40**, 229.
476. P. S. Riseborough, (2002) *J. Jpn. Phys. Soc. Suppl.* **71**, 344.
see also P. S. Riseborough, (2002), *Physica B*, **312-313**, 19.

477. N. Sato, N. Aso, K. Miyake, R. Shiina, P. Thalmeier, G. Varlogiannis, C. Geibel, F. Steglich, P. Fulde, and T. Komatsubara, (2001), *Nature*, **410**, 340.
478. K. Satoh, S. W. Yun, I. Umehara, Y. Ōnuki, S. Uji, T. Shimizu, and H. Aoki, (1992), *J. Phys. Soc. Jpn.*, **61**, 1827.
479. G. R. Stewart, (1984), *Rev. Mod. Phys.*, **56**, 755.
480. D. W. Hess, P. Riseborough, and J. L. Smith in *Encyclopedia of Applied Physics* (VCH, Weinheim, 1993), Vol. 7, p. 435.
481. J. P. Brison, L. Glémot, H. Suderow, A. Huxley, S. Kambe, and J. Flouquet, (2000), *Physica B*, **280**, 165.
482. H. R. Ott, *Prog. in Low Temp. Phys.*, v. 11 (Elsevier, Amsterdam, 1987) p. 215.
483. J. F. Annett, (1999) *Physica C* **317-318**, 1.
484. R. H. Heffner, D. W. Cooke, Z. Fisk, R. L. Hutson, M. E. Schillaci, J. L. Smith, J. O. Willis, D. E. MacLaughlin, C. Boekema R. L. Lichti, A. B. Denison, and J. Oostens, (1986), *Phys. Rev. Lett.*, **57**, 1255.
485. J. E. Sonier, R. H. Heffner, D. E. MacLaughlin, G. J. Nieuwenhuys, O. Bernal, R. Movshovich, P. G. Pagliuso, J. Cooley, J. L. Smith and J D. Thompson, (2000), *Phys. Rev. Lett.*, **85**, 2821.
486. M. C. Aronson, T. Vorenkamp, Z. Koziol, A. de Visser, K. Bakker, J. J. M. Franse, and J. L. Smith, (1991), *J. Appl. Phys.*, **69** 5487 .
487. H. G. M. Duijn, N. H. van Dijk, A. de Visser, and J. J. M. Franse, (1996), *Physica B*, **224**, 44 .
488. C. M. Varma, (1985), *Comments Solid State Phys.*, **11**, 221.
489. Zuyu Zhao, F. Behroozi, S. Adenwalla, Y. Guan, J. B. Ketterson, Bimal K. Sarma, and D. G. Hinks, (1991), *Phys. Rev. B*, **43**, 13721.
490. R. J. Keizer, A. de Visser, A. A. Menovsky, J. J. M. Franse, B. Fak, and J.-M. Mignot, (1999), *Phys. Rev. B*, **60**, 6668.
491. J. A. Sauls, (1994), *Adv. Phys.*, **43**, 113.
492. C. H. Choi and J. A. Sauls, (1991), *Phys. Rev. Lett.*, **66**, 484.
493. T. Tayama, M. Lang, T. Lühmann, F. Steglich, and W. Assmus, (2003), *Phys. Rev. B*, **67**, 214504.
494. F. Steglich, P. Gegenwart, C. Geibel, R. Helfrich, P. Hellmann, M. Lang, A. Link, R. Modler, G. Sparn, N. Buttgen, A. Loidl, (1996), *Physica B*, **223 & 224**, 1.
495. M. Ishikawa, N. Takeda, M. Koeda, M. Hedo, and Y. Uwatoko, (2003), *Phys. Rev. B*, **68**, 024522.
496. N. Oeschler, F. Kromer, T. Tayama, K. Tenya, P. Gegenwart, G. Sparn, F. Steglich, M. Lang, G. R. Stewart, (2003), *Acta Phys. Pol. B*, **34** 255.
497. R. H. Heffner and M. R. Norman, (1996), *Comments Cond. Mat. Phys.*, **17**, 361.
498. J. D. Thompson, M. W. McElfresh, J. O. Willis, Z. Fisk, J. L. Smith, and M. B. Maple, (1987), *Phys. Rev. B*, **35**, 48.
499. G. M. Schmiedeshoff, Z. Fisk, and J. L. Smith, (1992), *Phys. Rev. B*, **48**, 16417.
500. R. J. Zieve, D. S. Jin, T. F. Rosenbaum, J. S. Kim and G. R. Stewart, (1994), *Phys. Rev. Lett.*, **72**, 756.
R. J. Zieve, R. Duke, and J. L. Smith, (2003), "Pressure and linear heat capacity in thoriated UBe_{13}", preprint.
501. P. Kumar, and P. Wölfle, (1987) , *Phys. Rev. Lett.*, **59**, 1954.

502. M. Sigrist, and T. M. Rice, (1989), *Phys. Rev. B*, **39**, 2200.
503. V. Martisovits, G. Zaránd, and D. L. Cox, (2000), *Phys. Rev. Lett.*, **84** 5872.
504. N. Bernhoeft, G. H. Lander, M. J. Longfield, S. Langridge, D. Mannix, E. Lidström, E. Colineau, A. Hiess, C. Vettier, F. Wastin, J. Rebizant, and P. Lejay, (2003), *Acta Phys. Pol.*, **34**, 1367.
505. Tetsuo Honma, Yoshinori Haga, Etsuji Yamamoto, Naoto Metoki, Yoshihiro Koike, Hitoshi Ohkuni, Norihito Suzuki and Yoshichika Ōnuki, (1999), *J. Phys. Soc. Jpn.*, **68**, 338.
506. K. Hasselbach, J. R. Kirtley, and J. Flouquet, (1993), *Phys. Rev. B*, **47**, 509.
507. L. E. de Long, D. Togliatti, G. W. Lehman, W. -K. Kwok, G. W. Crabtree, K. G. Vandervoort, D. G. Hinks, (1990), *Physica* B, **163**, 499.
508. P. Thalmeier, (1991), *Phys. Rev. B*, **44** 7120.
509. R. Joynt, W. K. Kwok, G. W. Crabtree, D. G. Hinks, and L. DeLong, (1991), *Phys. Rev. B*, **44**, 7122.
510. L. Paolasini, J. A. Paixao, G. H. Lander, A. Delapalme, N. Sato, and T. Komatsubara, (1993), *J. Phys. Cond. Mat.*, **5**, 8905.
511. K. Gloos, R. Modler, H. Schimanski, C. D. Bredl, C. Geibel, F. Steglich, A. I. Buzdin, N. Sato, and T. Komatsubara, (1993), *Phys. Rev. Lett.*, **70**, 501.
512. M. Hiroi, M. Sera, N. Kobayashi, Y. Haga, E. Yamamoto, and Y. Ōnuki, (1997), *J. Phys. Soc. Jpn.*, **66**, 1595.
513. M. Jourdan, M. Huth, S. Mouloud, and H. Adrian, (1998), *J. Mag. Mag. Mat.*, **177-181**, 294.
514. A. Schröder, J. G. Lussier, B. D. Gaulin, J. D. Garrett, W. J. L. Buyers, L. Rebelsky and S. M. Shapiro, (1994), *Phys. Rev. Lett.*, **72**, 136.
515. Y. J. Uemura and G. M. Luke, (1993), *Physica B*, **186-188**, 223.
516. H. Tou, Y. Kitaoka, T. Kamatsuka, K. Asayama, C. Geibel, F. Steglich, S. Süllow and J. A. Mydosh, (1997), *Physica B*, **230-232**, 361.
517. Y. Dalichaouch, M. C. de Andrade, and M. B. Maple, (1992), *Phys. Rev. B*, **46**, 8761.
518. N. Sato, N. Koga, and T. Komatsubara, (1996), *J. Phys. Soc. Jpn.*, **65**, 1555.
519. Wei Bao, P. G. Pagliuso, J. L. Sarrao, J. D. Thompson, Z. Fisk , J. W. Lynn and R. W. Erwin, (2000), *Phys. Rev. B*, **62**, R14621.
Wei Bao, P. G. Pagliuso, J. L. Sarrao, J. D. Thompson, Z. Fisk, J. W. Lynn, and R. W. Erwin, (2001), *Phys. Rev. B*, **63**, 219901.
520. T. Mito, S. Kawasaki, G.-q. Zheng, Y. Kawasaki, K. Ishida, Y. Kitaoka, D. Aoki, Y. Haga, and Y. Ōnuki, (2001), *Phys. Rev. B*, **63**, 220507.
521. R. A. Fisher, F. Bouquet, N. E. Phillips, M. F. Hundley, P. G. Pagliuso, J. L. Sarrao, Z. Fisk, and J. D. Thompson, (2002), *Phys. Rev. B*, **65**, 224509.
522. R. Movshovich, A. Bianchi, M. Jaime, M. F. Hundley, J. D. Thompson, N. Curro, P. C. Hammel, Z. Fisk, P. G. Pagliuso, and J. L. Sarrao, (2002), *Physica B*, **312-313**, 7.
523. S. Ikeda, H. Shishido, M. Nakashima, R. Settai, D. Aoki, Y. Haga, H. Harima, Y. Aoki, T. Namiki, H. Sato, Y. Ōnuki, (2001), *J. Phys. Soc. Jpn.*, **70**, 2248.
524. A. Bianchi, R. Movshovich, N. Oeschler, P. Gegenwart, F. Steglich, J. D. Thompson, P. G. Pagliuso, and J. L. Sarrao, (2002), *Phys. Rev. Lett.*, **87**, 057002.
525. S. Majumdar, M. R. Lees, G. Balakrishnan, and D. McK. Paul, (2003), *Phys. Rev. B*, **68**, 012504.

526. T. P. Murphy, Donavan Hall, E. C. Palm, S. W. Tozer, C. Petrovic, Z. Fisk, R. G. Goodrich, P. G. Pagliuso, J. L. Sarrao, and J. D. Thompson, (2002), *Phys. Rev. B*, **65**, 100514.
527. H. A. Radovan, N. A. Fortune, T. P. Murphy, S. T. Hannahs, E. C. Palm, S. W. Tozer, and D. Hall, (2003), *Nature*, **425**, 51.
528. J. M. Lawrence and S. M. Shapiro, (1980), *Phys. Rev. B*, **22**, 4379.
529. N. D. Mathur, F. M. Grosche, S. R. Julian, I. R. Walker, D. M. Freye, R. K. W. Haselwimmer, and G. G. Lonzarich, (1998), *Nature* **394**, 39.
530. S. Kawasaki, T. Mito, Y. Kawasaki, G.-q. Zheng, Y. Kitaoka, H. Shishido, S. Araki, R. Settai, and Y. Ōnuki, (2002), *Phys. Rev. B*, **66**, 054521.
531. S. Raymond, and D. Jaccard, (2000), *Phys. Rev. B*, **61**, 8679.
532. I. Sheikin, E. Steep, D. Braithwaite, J.-P. Brison, S. Raymond, D. Jaccard, and J. Flouquet, (2001), *J. Low Temp. Phys.*, **122**, 591.
533. E. Vargoz and D. Jaccard, (1998), *J. Mag. Mag. Mat.*, **177-181**, 294.
534. T. C. Kobayashi, T. Miyazu, N. Takeshita, K. Shimizu, K. Amaya, Y. Kitaoka, and Y. Ōnuki, (1998), *J. Phys. Soc. Jpn.*, **67**, 996.
535. K. Izawa, Y. Nakajima, J. Goryo, Y. Matsuda, S. Osaki, H. Sugawara, H. Sato, P. Thalmeier, and K. Maki, (2003), *Phys. Rev. Lett.*, **90**, 117001/1.
536. R. Vollmer, A. Faißt, C. Pfleiderer, H. v. Löhneysen, E. D. Bauer, P.-C. Ho, V. Zapf, and M. B. Maple, (2003), *Phys. Rev. Lett.*, **90**, 057001/1.
537. H. Kotegawa, M. Yogi, Y. Imamura , Y. Kawasaki, G.-q. Zheng, Y. Kitaoka, S. Ohsaki, H. Sugawara, Y. Aoki, and H. Sato, (2003), *Phys. Rev. Lett.*, **90**, 027001/1.
538. D. E. MacLaughlin, J. E. Sonier, R. H. Heffner, O. O. Bernal, Ben-Li Young, M. S. Rose, G. D. Morris, E. D. Bauer, T. D. Do, and M. B. Maple, (2002), *Phys. Rev. Lett.*, **89**, 157001/1.
539. Y. Aoki, A. Tsuchiya, T. Kanayama, S. R. Saha, H. Sugawara, H. Sato, W. Higemoto, A. Koda, K. Ohishi, K. Nishiyama, and R. Kadono, (2003), *Phys. Rev. Lett.*, **91**, 067003/1.
540. E. D. Bauer, N. A. Frederick, P.-C. Ho, V. S. Zapf, and M. B. Maple, (2002), *Phys. Rev. B*, **65**, 100506.
541. P.-C. Ho, N. A. Frederick, V. S. Zapf, E. D. Bauer, T. D. Do, M. B. Maple, A. D. Christianson and A. H. Lacerda, (2003), *Phys. Rev. B*, **67** 180508.
542. G. P. Meisner, A. L. Giorgi, A. C. Lawson, G. R. Stewart, J. O. Willis, M. S. Wire, and J. L. Smith,)1984), *Phys. Rev. Lett.*, **53**, 1829.
543. V. Ginzburg, (1957), *Sov. Phys. JETP*, **4**, 153.
544. See, for example, the articles collected in *Superconductivity in Ternary Compounds* vol. 2, ed. by M. B. Maple and Ø. Fischer (Springer-Verlag, Berlin, 1982).
545. J. Flouquet, A. Huxley, D. Braithwaite, F. Hardy, G. Knebel, V. Mineev, E. Ressouche, D. Aoki, and J. P. Brison, (2003), *Acta Phys. Pol. B*, **34**, 275.
546. I. Sheikin, A. Huxley, D. Braithwaite, J. P. Brison, S. Watanabe, K. Miyake, and J. Flouquet, (2001), *Phys. Rev. B* **64**, 220503.
547. T. R. Kirkpatrick, and D. Belitz, (2003), *Phys. Rev. B*, **67**, 024515.
548. C. Pfleiderer, M. Uhlarz, S. M. Hayden, R. Vollmer, H. v. Löhneysen, N. R. Bernhoeft, and G. G. Lonzarich, (2001), *Nature*, **412**, 58.
549. K. V. Samokhin and M. B. Walker, (2002), *Phys. Rev. B*, **66**, 174501.
550. F. Wastin *et al.* (to be published).
551. Takahiro Maehira, Takashi Hotta, Kazuo Ueda, and Akira Hasegawa, (2003), *Phys. Rev. Lett.*, **90**, 207007/1.

552. I. Opahle and P. M. Oppeneer, (2003), *Phys. Rev. Lett.*, **90**, 157001/1.

11 Superfluid ^{3}He and the Cuprate Superconductors

A. J. Leggett
Department of Physics, University of Illinois, USA

11.1 **Introduction: Bose Condensation and Cooper Pairing**.....1087
11.2 **The Normal State: Is the Fermi–Liquid Picture Valid?** ... 1094
11.3 **Response Functions: The MIR Peak in the Cuprates**.....1098
11.4 **The Cooper–Paired States of Superfluid ^{3}He and the Cuprates: General Considerations**.....1100
11.5 **Symmetry of the Order Parameter**.....1107
11.6 **Conclusion**.....1111
11.6 **Summary**.....1111
Acknowledgements.....1112
References.....1112

11.1 Introduction: Bose Condensation and Cooper Pairing

This chapter is devoted to a comparison of two apparently very different physical systems, superfluid liquid ^{3}He and the cuprate superconductors. What these two systems have in common–at least according to almost universal belief–is that they are systems of Fermi particles, already very degenerate,in which not only are the "quasi–dielectronic molecules" which we call Cooper pairs formed, but once formed are automatically forced to occupy a *single* two–particle state, as regards both their center–of–mass motion and their internal structure. This phenomenon is very reminiscent of the phenomenon of Bose condensation which is almost universally believed to occur in the boson system liquid ^{4}He below the λ–point, and has in the last few years been spectacularly demonstrated in a second Bose system, trapped ultracold monatomic alkali gases. It is therefore appropriate to start this chapter with a brief discussion of the more easily understood phenomenon of simple Bose condensation and its relationship to the apparently more complex behavior associated with Cooper pairing in degenerate Fermi systems.

Let's consider, first, a simple system of N bosons for which the internal structure and any internal degrees of freedom can be neglected. Such a system is realized, at least in the context of the low–energy phenomena of interest to us, in liquid ^{4}He and also in the boson alkali gases to the extent that one and only one hyperfine species is present (and we can safely neglect effects such as the bending of the quantization axis in space etc.: see Ref. [1], Section IV.E).The total particle number N is assumed to be large compared to unity.

K. H. Bennemann et al. (eds.), *The Physics of Superconductors*
© Springer-Verlag Berlin Heidelberg 2004

While various definitions of Bose or Bose–Einstein condensation (BEC) have been proposed in the literature, the conceptually simplest (and the one most appropriate to the alkali gases) seems to me to be that given many years ago by Penrose and Onsager [2], which goes roughly as follows. Consider an arbitrary many–body state of the system (which need not be in or even close to thermal equilibrium) and define the single–particle density matrix $\hat{\rho}_1(\mathbf{r}, \mathbf{r}', t)$ in the standard way. Since this quantity, regarded as a matrix in its indices is from its definition Hermitian, it may be diagonalized by choosing an appropriate basis of single–particle eigenfunctions (which need not be eigenfunctions of the Hamiltonian, and will in the general case be time–dependent). Let's now examine the eigenvalues of $\hat{\rho}_1$. There are two cases of prime interest: (A)All eigenvalues are of order unity (not of order of the total particle number N). We call such a state of the system "normal" (i.e. not Bose–condensed). (B)One eigenvalue is of order N, the rest of order 1. In this case we say we have ("simple") Bose–Einstein condensation (BEC). The large eigenvalue is called the "number of condensed particles" and denoted N_o so that the ratio N_o/N is the "condensate fraction", and the unique single–particle eigenfunction (in general time–dependent) associated with this special eigenvalue is called the "condensate wave function", $\chi_o(\mathbf{r}, t)$ or when multiplied by a factor, the "order parameter". The above discussion (or considerations involving the so–called "spontaneous breaking of U(1) symmetry", which are in effect equivalent though to my mind conceptually less satisfactory) is the standard basis for discussion of BEC systems in the literature. It should be noted that by itself it fails to answer two obvious questions, namely: (1) why should *any* eigenvalue of the single–particle density matrix ever be of order N?, (2) why should not *more than one* eigenvalue be of order N? The most obvious answer to question (1) is that (as shown by Einstein in his original 1925 paper) for a free Bose gas in thermal equilibrium the result follows from an explicit calculation, and that (contrary to the view expressed by some of his contemporaries) it is reasonable to expect this result to be robust against small departures from equilibrium and/or weak interatomic interactions. (In fact, it was shown many years ago by Gavoret and Nozières [3] that so long as perturbation theory in the interactions converges, the system indeed shows BEC in equilibrium at $T = 0$). The second question is more tricky. For a Bose system with weak *repulsive* interatomic interactions, it turns out that macroscopic occupation of more than one single–particle state is energetically very costly, because of the "Fock" term in the mean–field energy (which has a sign opposite to that in the more familiar Fermi case). Consequently, the effect of a weak interatomic interaction is actually to reinforce and stabilize "simple" BEC. By contrast, a weak attraction between atoms favors macroscopic occupation of several different single–particle states (a phenomenon sometimes called "fragmentation"), or what turns out to be effectively equivalent "collapse" of the system in real (coordinate) space. The general belief, which seems consistent with existing experiment, is that in an alkali Bose

gas with weakly attractive interatomic interactions no stable BEC state is possible.

If we confine ourselves from now on to the repulsive case, the existence of BEC has many spectacular consequences. The most direct one is a characteristic phenomenon seen in the alkali gases when they are confined, as is the usual experimental situation, called a harmonic trap: Above the temperature of transition to the BEC state the atoms have a thermal distribution which is little different from the classical Maxwell one and the atomic cloud therefore has a width determined by the condition that the potential at its edge should be of order kT. When BEC sets in, however, a finite fraction of the atoms (which at low temperatures is nearly equal to one) by definition occupies a *single* one–particle state. In thermal equilibrium, for a noninteracting gas, this would be the harmonic–oscillator groundstate, and since the width of the latter is much smaller than that of the thermal cloud, a very narrow and high peak in the density should rise out of the thermal background. In real life the repulsive interactions broaden the (self–consistently determined) condensate wave function so that it is appreciably wider than the harmonic groundstate, but the effect is still spectacular; it was in fact the first experimental evidence for the onset of BEC.

A second spectacular manifestation of the effects of BEC is the complex of phenomena which are usually lumped together under the name of "superfluidity", and which generally speaking take a cleaner form in He–II (the phase of liquid ^{4}He below the λ–point) than in the alkali gases. The reason for this has to do with the different potential "geometries" in the two cases. The question of exactly what are the conditions for each of the characteristic phenomena of superfluidity to occur in a given system and geometry is a quite subtle one (see e.g. Ref. [1]), Section VI), but it seems clear that a necessary condition for the most striking manifestation, that of persistent flow in a ring geometry, is a sufficiently strong interatomic repulsion. It is easily shown that a noninteracting Bose gas, even when Bose–condensed, will not show this effect.

Finally, it should be remarked that while the ^{4}He atom has no "internal" degrees of freedom (at least to the extent that it remains in its electronic groundstate), in the case of the BEC alkali gases there exists such an internal degree of freedom, namely that associated with the electron and nuclear spin, neither of which is zero. As a result, in the general case the description of BEC in these systems is more complicated than that given above, and in particular, even when all interactions are repulsive, the occurrence of "fragmented" condensates cannot be excluded; see e.g. Ref. [1], Section V.D.

I now turn to the Fermi case. As pointed out long ago by Yang [4], in this case there are rigorous theorems which forbid the single–particle density matrix to have a macroscopic eigenvalue or indeed any eigenvalue greater than 1, as one would intuitively expect. However, there is nothing to prevent the *two–particle* density matrix defined explicitly below from having one or

more macroscopic eigenvalues. We can look at this question intuitively by considering our N–fermion system at zero temperature and make (at present for no obviously good reason!) the following ansatz for the groundstate

$$\Psi_N(\mathbf{r}_1\mathbf{r}_2..\mathbf{r}_N : \sigma_1\sigma_2..\sigma_N) = \mathcal{A}\ \phi_i(\mathbf{r}_1, \mathbf{r}_2\sigma_1\sigma_2)\phi_j(\mathbf{r}_3\mathbf{r}_4\sigma_3\sigma_4)....$$
$$\phi_w(\mathbf{r}_{N-1}\mathbf{r}_N\sigma_{N-1}\sigma_N) \quad , \tag{11.1}$$

where $\mathcal{A}$ is the operator which antisymmetrizes the expression with respect to simultaneous interchange of the coordinates and spins of any two fermions. We do not yet specify whether any two or more of the subscripts $i, j...w$ are identical. Provided the antisymmetrization is properly carried out, there are no a priori constraints in this respect. Intuitively, an ansatz of the form (11.1) (with an appropriately "bound" form of the ϕ's) could correspond to pairing of the fermions (say for definiteness electrons) into a sort of "di–electronic molecules" in as many different states as there are different values of the subscript. We can now ask for the number of "molecules" in each different state, and in particular whether one or several states are macroscopically occupied. The analogy with BEC of simple bosonic systems is then obvious.

Actually, the above approach, while perhaps helpful to one's intuition, is of limited practical usefulness. The reason is that the literal interpretation of a many–body wave function of the form (11.1) in terms of "molecules" which are in the states ϕ_i is useful, if at all, only in the limit that the effective "radius" of the pair states described by the functions $\phi_i(\mathbf{r}_1\mathbf{r}_2\sigma_1\sigma_2)$. That is the range of the variable $|\ \mathbf{r}_1 - \mathbf{r}_2\ |$ over which the function is of appreciable weight is small compared to the mean interparticle distance. A condition which may be fulfilled in for example liquid deuterium but is certainly not in most of the systems of interest in the present context which are predominantly in recisely the opposite limit (range of ϕ much *greater* than mean interparticle distance). In this limit (sometimes called the "BCS" as opposed to the "Bose" limit), the "molecular" wave functions ϕ_i, while certainly definable,have little physical significance. A much more useful quantity is the two–particle density matrix $\hat{\rho}_2$ defined (at T = 0) by

$$\hat{\rho}_2(\mathbf{r}_1\sigma_1\mathbf{r}_2\sigma_2 : \mathbf{r}_1'\sigma_1'\mathbf{r}_2'\sigma_2' : t) \equiv \langle\ \psi^\dagger_{\sigma_1}(\mathbf{r}_1)\psi^\dagger_{\sigma_2}(\mathbf{r}_2)\psi_{\sigma_3}(\mathbf{r}_3)\psi_{\sigma_4}(\mathbf{r}_4)\ \rangle\ . \tag{11.2}$$

This in some sense automatically takes into account the complications introduced by the need for antisymmetrization. For example, the expressions for expectation values of two–particle quantities such as the potential energy, or more precisely for the contributions to them from the formation of "pairs", look horribly complicated when expressed in terms of the ϕ_i. However, when written in terms of $\hat{\rho}_2$ have a very simple form, in fact one exactly analogous to the familiar expressions for the two–particle case. See e.g. Ref. [5]. Thus, for any quantitative purpose it is highly desirable to work in terms of $\hat{\rho}_2$.

The quantity $\hat{\rho}_2$ is defined for an arbitrary state of the system as a function of the four coordinate–plus–spin variables $\mathbf{r}_1\sigma_1, \mathbf{r}_2\sigma_2$ and the time t. Let us

for pedagogical convenience temporarily ignore the spin coordinates, fix t and regard $\hat{\rho}_2$ as a matrix with respect to the *pair* of indices $\mathbf{r}_1\mathbf{r}_2$, which replaces the single index $\mathbf{r}$ in the Bose case. (We could of course equally well have chosen to consider the pair $\mathbf{r}_1, \mathbf{r}_3$, but there is a reason for the present choice). As in the Bose case, the matrix is Hermitian and can thus be diagonalized. Let the eigenvalues be denoted n_i and the corresponding eigenfunctions be χ_i. The a priori constraints on the n_i are quite weak (see Yang's original paper [4]), and in particular there is nothing to forbid one or more of them being of order N. Thus, just as in the Bose case, it is possible to define (simple) "quasi–BEC" by the condition that one *and only one* of the n_i's is of order N and also, if we wish, "fragmented quasi–BEC" by the statement that more than one is of order N. However, it turns out that, at least for the systems of interest in the present context, fragmented quasi–BEC is likely to be relevant only under conditions so extreme that they have probably not been realized experimentally [6].

As is well–known, the state realized in conventional superconductors, and also in superfluid ^{3}He and the cuprate superconductors, is almost universally believed to correspond in the above language to "simple BEC", and the entities which are condensed are called Cooper pairs. The concept of a Cooper pair in the abstract perhaps not totally well defined, but one can as a matter of definition think of it as the object whose wave function $\chi_o(\mathbf{r}_1\mathbf{r}_2) \equiv F(\mathbf{r}_1\mathbf{r}_2)$ is just the eigenfunction of $\hat{\rho}_2$ corresponding to the single macroscopic eigenvalue. It is worth noting that the actual eigenvalue N_0 (which one might regard as the "number of condensed Cooper pairs"), while it is "of order of" the total particle number N,is quite a small fraction of order kT_c/ϵ_F of N, at least in the cases of interest to us here. It may also be noted that in contrast to the Bose case an attractive interparticle interaction is usually conducive to (simple) quasi–BEC (as in the original BCS theory) rather than the reverse.

The "pair wave function" or "order parameter" $F(\mathbf{r}_1\mathbf{r}_2)$ (often written as $\langle\psi(\mathbf{r}_1)\psi(\mathbf{r}_2)\rangle$) may be expressed as a function of the center–of–mass coordinate $\mathbf{R} = (\mathbf{r}_1 + \mathbf{r}_2)/2$ and the relative coordinate $\mathbf{r} \equiv \mathbf{r}_1 - \mathbf{r}_2$ (and the spins, which we can now safely put back in). In the case of the conventional superconductors the general belief is that the dependence on the "internal" degrees of freedom (relative coordinate and spin) is uniquely fixed,in the groundstate and more generally in thermal equilibrium, by the energetics, so that the Cooper pairs resemble the ^{4}He atom in having effectively no internal variable. On the other hand, there is nothing which excludes a priori the possibility that one or more "internal" symmetries are spontaneously broken in the groundstate, so that the pairs have one or more "orientational" degrees of freedom, analogously to the hyperfine degree of freedom in the BEC alkali gases. We will see below that this situation is in fact realized both in superfluid ^{3}He and in a sense in the cuprates.

Obvious differences, and some similarities

At first sight the physical systems formed by the superfluid phases of liquid

^{3}He on the one hand, and the cuprate superconductors on the other could hardly be more different. In fact, as already remarked, at the level of superficial inspection just about the only thing they have in common is that both are Fermi systems in which the formation of Cooper pairs leads to the characteristic phenomena of superfluidity (superconductivity). There are many obvious differences. I now list some of them.

The first and most obvious difference is of course that in the case of the cuprates, as in all metallic superconductors, the relevant fermions (electrons) are charged, whereas in liquid ^{3}He they are neutral. This has the consequence that the "macroscopic quantum phenomena" characteristic of the paired superfluid state look at first sight very different in the two systems. However, this is something we are already used to in the context of the analogy between superfluidity in ^{4}He and "old–fashioned" superconductivity (see e.g. Ref. [7]), so it is not necessary to discuss it further here.

A second glaring difference is that the electrons in the cuprates as in all metals move in the background of a periodic crystalline lattice, whereas in liquid ^{3}He the atoms move in free space. Actually, the difference is even more pronounced; whereas in most traditional superconductors it is at least not a bad zeroth–order approximation to treat the conduction electrons as moving freely in three–dimensional space, the cuprates have a strongly layered structure, so that the approximation of free motion, to the extent that it is valid at all, can be applied only for the motion parallel to the CuO_2 planes; for motion along the third axis (c–axis) it is certainly essential to take the lattice into account from the start.

A third difference lies in the degree of sensitivity to parameters which can be varied. Liquid ^{3}He at temperatures of the order of the superfluid transition temperature T_c is about as pure a system as one can find in nature: any chemical or even isotopic (^{4}He) impurities rapidly condense on the walls of the experimental cell, so that the only parameters which can be meaningfully varied are the macroscopic thermodynamic ones, pressure and magnetic field and of course temperature. As we shall see, the onset temperature and nature of the superfluid state does in fact depend in an interesting way on those variables. By contrast, superconductivity in the cuprates, while to some extent sensitive to pressure and field, is much more dramatically influenced by other variables, in particular by the details of the chemical stoichiometry. This in most cases is variable over a wide range and by the presence of various trace elements such as Zn.

Why, then, is there any hope at all that any of the extensive research done on superfluid ^{3}He could have any relevance to the cuprates? One can think immediately of three arguments in this direction, although to be sure none of them is a priori overwhelming. First, consider the ratio of the transition temperature T_c to the Fermi temperature T_F (the fact that there is no completely unambiguous definition of the latter quantity for a strongly interacting system need not worry us, since we are interested only in orders

of magnitude). For the classic pre–1975 superconductors T_c always lies below 25K, while T_F is typically $\sim 3\times10^4$K. Thus, the ratio T_c/T_F is never greater than $\sim10^{-3}$ and often considerably smaller. For the cuprates T_c this can be up to 160K, and T_F can be plausibly argued to be as small as a few thousand K. Thus, T_c/T_F is typically of order 3×10^{-2}, Finally, for liquid ^{3}He T_c is of the order 3 mK and T_F of order 0.5K, so that the ratio is $\sim10^{-2}$. We see that in this respect the cuprates are considerably closer to ^{3}He than they are to the classic superconductors. The heavy–fermion systems have an even larger ratio ($\sim$0.2) of T_c/T_F, if T_F is defined in terms of the low–temperature effective mass.

A second and perhaps more fundamental reason has to do with possible mechanisms of Cooper pairing. As is well known in the BCS theory which is believed to describe the classic superconductors the mechanism is an effective attraction resulting from the exchange of virtual phonons. It is an important feature of the BCS theory that the mediating excitation (the phonon) is primarily associated with the ionic cores, i.e. with a system different from the conduction electrons which form the Cooper pairs. On the other hand, it seems almost certain for the heavy–fermion superconductors, and at least probable for the cuprates, that phonons do not play the dominant role and that the origin of Cooper pairing must therefore be sought in the conduction–electron system itself. In this respect the situation is similar to that in liquid ^{3}He, where there simply is nothing outside the ^{3}He atoms. In this system, trivially, the mechanism of pairing must reside within the system of paired fermions.

Finally, there is the question of the symmetry of the order parameter (pair wave function). In the classic superconductors this is believed to be isotropic, or more accurately to have the symmetry of the lattice. Formally, the order parameter transforms according to the identity representation of the symmetry group of the Hamiltonian. By contrast, in superfluid ^{3}He it is by now almost universally believed that the order parameter is of "exotic" form, i.e. does not have the (orbital) symmetry (in this case SO(3)) of the underlying Hamiltonian, and more specifically that is of the p–wave form, though different in detail for the different superfluid phases (see Section 11.5). It is by now generally though not universally believed that in the cuprates, while the symmetry group of the CuO_2 planes is exactly or approximately that of the square, the order parameter has the so–called $d_{x^2-y^2}$ form. So again it transforms according to a nontrivial representation of the symmetry group of the Hamiltonian. Once more, some heavy–fermion systems may be even closer to superfluid ^{3}He systems in this respect. The pairing state in UPt_3 is widely believed to be of p–wave type. Actually, this resemblance between ^{3}He and the cuprates or the heavy–fermion systems may not be quite as significant as it looks at first sight, see Section 11.5. However, it has undoubtedly played a role in the historical development of the analysis of cuprate superconductivity.

11.2 The Normal State: Is the Fermi–Liquid Picture Valid?

It is convenient for the purpose of the present discussion to focus on a single–plane cuprate such as Tl–2201 or Hg–1201, thus setting aside some questions which are specific to the multilayer systems such as YBCO. Furthermore, I shall make two assumptions which, while not universally agreed, would probably win the consent of a large majority of the relevant community: (a) In the normal or in the superconducting state, most of the interesting phenomena are primarily associated with the behavior of the conduction electrons in the CuO_2 planes. Moreover, the process of electron transfer from one plane to the next is sufficiently weak that it may be neglected to a first approximation. (b) The kinetic energy of the ions (i.e. phonons) does not play an important role. Then, at least to a first approximation, the system of fermions we need to consider in the cuprates consists of the conduction electrons which move within the single CuO_2 planes in the "external" potential provided by the static ionic lattice and interact with the standard Coulomb interaction. This is screened by the core electrons associated with the ions. To a first approximation it is reasonable to approximate the effects of the screening by (a single number) the real high frequency dielectric constant ϵ_∞. At a similar level of approximation liquid ^{3}He may be viewed as a system of neutral atoms with total (nuclear) spin 1/2 obeying Fermi statistics and interacting via a short–range potential of the van der Waals type. (The small nuclear dipole–dipole interaction plays an important role in the superfluid phase, see Section 11.5, but can be neglected to a first approximation in the normal phase). In both cases the inter–fermion interactions are in some sense "strong". The repulsive part of the van der Waals interaction in ^{3}He approximates a hard core at interatomic distances $\lesssim 2.5\mathring{A}$, while the interatomic spacing in the liquid at melting pressure is $\sim 3.4\mathring{A}$. In the case of the cuprates the interaction of two conduction electrons on the same lattice site is believed to be of the order of 10 eV. This is more than an order of magnitude greater than the Fermi energy of a noninteracting system of the same density.

It was precisely in the context of a three–dimensional neutral Fermi system, such as (normal) liquid ^{3}He, that Landau developed his celebrated theory of a Fermi liquid. [8] While it is conventional to define what one means by a Fermi liquid in terms of the behavior of the microscopic Green's functions of the system, for our purposes a less technical description similar to that used in Landau's first paper [8] will suffice. Crudely speaking, a Fermi liquid is a Fermi system such that if we start from the noninteracting gas, perturbation theory in the interaction strength converges. As a result the character of the groundstate and low–lying excited states (or more accurately the vast majority of the latter) is similar to that of the corresponding states of the noninteracting gas. To be a little more concrete, the excited energy eigenstates of the system can be specified quite generally by enumerating the *difference* $\delta n\ (\mathbf{p}\sigma)$ between the number $n(\mathbf{p},\sigma)$ of particles in momentum state $\mathbf{p}$ and

with spin[1] σ and its value in the groundstate: evidently $\delta n(\mathbf{p}\sigma)$ is 0 or +1 for $|\mathbf{p}| > p_F$ and 0 or -1 for $|\mathbf{p}| < p_F$, where the Fermi momentum p_F is uniquely fixed as a function of density n ($p_F^3 = 3\pi^2 n$). The quantity $n(\mathbf{p}\sigma)$ defined in this way (taking $n(\mathbf{p}\sigma) \equiv \theta(p_F - |\mathbf{p}|)$ by definition in the groundstate) is usually called the "number of quasiparticles in state $(\mathbf{p}\sigma)$". It is clear that generally speaking the lowest–lying energy eigenstates will be those where only a few $\delta n(\mathbf{p}\sigma)$ are different from zero. The interacting system is now said to be a Fermi liquid if the structure of the (interacting) groundstate and *low–lying* excited states is such that to a good approximation the latter can be labeled by a set of quantities $\{\delta n(\mathbf{p}\sigma)\}$ having the above property ($\delta n(\mathbf{p}\sigma) =$ 0 or +1 for $|\mathbf{p}| > p_F$, $\delta n(\mathbf{p}\sigma) = 0$ or -1 for $|\mathbf{p}| < p_F$). Furthermore the energy can be expanded in the $\delta n(\mathbf{p}\sigma)$ as follows

$$E\{\delta n(\mathbf{p}\sigma)\} = E_o + \sum_{\mathbf{p}\sigma} \epsilon(\mathbf{p}) \delta n(\mathbf{p}\sigma) + \frac{1}{2} \sum_{pp'\sigma\sigma'} f(\mathbf{p}\mathbf{p}'\sigma\sigma') \delta n(\mathbf{p}\sigma) \delta n(\mathbf{p}'\sigma'), \tag{11.3}$$

where the groundstate energy E_o is a constant. The coefficients ϵ and f have as $|\mathbf{p}| \to p_F$ the following behavior

$$\epsilon(\mathbf{p}) = const.(|\mathbf{p}| - p_F), \quad f(\mathbf{p}\mathbf{p}'\sigma\sigma') = \text{independent of } |\mathbf{p}|, |\mathbf{p}'|,$$
$$f \equiv (dn/d\epsilon)^{-1} \sum_i (F_l^s + F_l^a \sigma\sigma') P_l(\hat{\mathbf{p}} \cdot \hat{\mathbf{p}}'), \tag{11.4}$$

where $dn/d\epsilon$ is the single–particle density of states at the Fermi surface and P_l the Legendre polynomial. (Clearly, the noninteracting system is the special case $\epsilon = (p_F/m)(|\mathbf{p}| - p_F)$, $f = 0$). The above expression for the energy, which is strictly diagonal in the quantities $\delta n(\mathbf{p}\sigma)$, is never exactly valid in an interacting system, because of terms in the Hamiltonian which lead to mutual scattering of quasiparticles between states with different $\mathbf{p},\sigma$; however, arguments based on the Pauli principle show that it is self–consistent to take the probability of scattering to tend to zero as $(|\mathbf{p}| - p_F)^2$, that is, faster than the excitation energy of the quasiparticle in question (see e.g. Ref. [9]).

It is worth noting that in the above discussion it is *not* assumed that the interaction terms in the Hamiltonian conserve the total momentum $\mathbf{P}$ (or spin $\mathbf{S}$) of the system. The question of whether or not there is a one–one correspondence, as above, between the groundstate and low–lying states of the interacting and noninteracting systems is independent of that consideration. If the total momentum is in fact conserved, as e.g. in the case of liquid ^{3}He, then the quasiparticle states (low–lying approximate energy eigenstates) are exact eigenstates of total momentum with eigenvalue

$$\mathbf{P} = \sum_p \mathbf{p} \delta n(\mathbf{p}\sigma) \tag{11.5}$$

[1] For notational simplicity I ignore here the fact that the spin should strictly be treated as a vector, in particular as regards its occurrence in f: see e.g. Ref. [9].

(and one can make a similar statement for the total spin). In the opposite case, the labeling is still valid, but the total momentum operator is in general not diagonal in the basis formed by the quantity $\delta n(\mathbf{p}\sigma)$.

It should be strongly emphasized that for any given real–life system of fermions the validity of Landau Fermi–liquid theory is an *assumption*, which can almost never be proved from first principles, but at best can be substantiated by comparison of the predictions made on that hypothesis with experiment. It should be stressed that some of these predictions are nontrivial, in the sense that the number of predicted relations between different experimental quantities is larger than the number of a priori undetermined parameters needed to characterize the fundamental quantities $\epsilon(\mathbf{p})$ and $f(\mathbf{p}\mathbf{p}'\sigma\sigma')$.

Is liquid ^{3}He in fact a Fermi liquid? If in the definitions one were to treat "low–lying" as meaning "with (single–quasiparticle) energies much less than 1K but much greater than 3mK", then all the evidence is that the answer is yes. Whenever the properties of liquid ^{3}He in the normal phase well below 100 mK have been measured, it has always proved possible to fit the results into the framework of Fermi–liquid theory (though cf. end of Section 11.4). However, the very existence of the superfluid phases shows that by a technically accurate definition liquid ^{3}He is ironically *not* a Fermi liquid. Indeed, the excitation energies of the *very* low–lying excited states relative to the groundstate are of the generalized BCS form (see Section 11.4) and certainly do not correspond to expressions (11.3) and (11.4). This situation is usually summed up by saying that liquid ^{3}He in the *normal* state behaves as a Fermi liquid. It then follows that the phenomenon of Cooper pairing can be discussed on the basis of this picture, see Section 11.4.

As already remarked, the Landau Fermi–liquid theory was originally developed with specific reference to liquid ^{3}He, which is both neutral and translation–invariant. The generalization of the theory to a charged but still translationally invariant system was made soon thereafter by Silin [10]. In effect, one simply generalizes the philosophy of the standard random phase approximation by using the original Landau theory to calculate the "local" responses and then, when necessary, replacing the external electric field by the sum of the external field and that produced self–consistently by the charge response of the system itself. The generalization to the case of a finite crystalline potential is a little more tricky and is discussed for example in Ref. [11]. The simplest formulation is probably to start by ignoring the inter–conduction electron interactions and solving for the eigenstates of the single–particle terms in the Hamiltonian (kinetic plus lattice potential energy); in this way one generates the usual Bloch–wave states, which are eigenstates not of total momentum $\mathbf{P}$ but rather of total quasimomentum $\mathbf{K}$, and are labeled correspondingly by a quasimomentum index $\mathbf{k}$ and spin σ. The resulting system is the analog of the noninteracting gas in the translation–invariant case. Then one turns on the interaction and *assumes* that the resulting groundstate and low–lying excited states can be put into one–one correspondence with these

of the starting ("noninteracting") state. It is important to note that, because of the possibility of umklapp processes, the interaction does not conserve the total quasimomentum $\mathbf{K}$; hence while one can still *label* the resulting states by $\delta n(\mathbf{k}, \sigma)$, $\mathbf{k}$ no longer has the physical interpretation of true quasimomentum (and in fact the operator $\hat{\mathbf{K}}$ is nondiagonal in the $\delta n(\mathbf{k}, \sigma)$ basis). This observation has some importance in the context of the discussion of the "mid–infrared" peak in the cuprates: see next Section.

Is the normal state of the cuprates a Fermi liquid (in the same sense as that in which the normal state of ^{3}He can be said to be a Fermi liquid)? This is one of the most hotly debated questions in the theory of cuprate superconductivity, and to discuss it we need to define it carefully. Let us first ask the question: Suppose we could somehow cool the system down to zero temperature while forbidding the superconducting transition to occur. Would the resulting "groundstate" and low–lying excited states conform to the definition of a Fermi liquid? In the case of liquid ^{3}He (where there is apparently no practical way of suppressing the superfluid transition, so that this really is only a thought–experiment) the answer is almost certainly yes. In the case of the cuprates, there are real–life possibilities of suppressing the superconducting transition, in particular (a) by the application of a sufficiently strong magnetic field and (b) by doping the CuO_2 planes with certain types of impurity such as Zn. Although for practical reasons rather few systematic studies have been done of the resultant state an answer seems to be emerging which is rather intriguing [12]: There appears to be a critical concentration $p_c \sim 0.19$ of the hole–doping parameter p (no. of holes per CuO_2 units) such that for $p > p_c$ the lowest–lying states indeed have Fermi–liquid like character. However, to the left of this point in the phase diagram (i.e. for $p < p_c$) the behavior appears to be qualitatively different, with the system tending continuously towards an *insulating* state as the temperature falls towards zero. If this is really the correct picture, then it is not entirely clear that the question "does the normal state of the cuprate superconductors behave as a Fermi liquid?" has any clearly defined meaning. Of course one could in any case argue that the system placed in a strong ($\sim$30–60T)magnetic field, or doped substantially with Zn impurities, is not "the same" system as a true (superconducting) cuprate, and that therefore no conclusions can be drawn from experiments of the above type. In that case it is conceivable that the true situation is the following: If one, by theoretical fiat rather than by any realistically available experimental means, could forbid the formation of Cooper pairs in the (pure, zero–field) system while cooling it to zero, then the "groundstate" and low–lying states would indeed be of Fermi–liquid type, as in the corresponding thought–experiment with ^{3}He. However, in both cases we should expect the Fermi–liquid description to break down badly when the temperature becomes some (small) fraction of T_F, let us say for example $0.1T_F$. Now, in the case of ^{3}He, ($T_c/T_F \sim 10^{-2}$) this "breakdown" temperature is still some way above T_c, so that there is a fairly wide temperature

regime (3mK $\lesssim$ T $\lesssim$ 50 mK) where a well–defined Fermi–liquid behavior is seen. On the other hand, in the cuprates the breakdown temperature could be so little above the observed T_c that no clear Fermi–liquid regime is seen. It has to be said, however, that this scenario, while perhaps plausible for the higher–temperature compounds such as the Tℓ and Hg series, is much less so for compounds such as (optimally doped) Bi–2201 where T_c is only in the range 10–30K, and to defend it one has to argue that such compounds are in some way untypical, even in the normal state, of the cuprates as a whole.

A point which has been widely noticed is that while at optimal doping the resistivity of the cuprates is rather accurately linear in T, it appears to cross over to the T^2 form characteristic of Fermi–liquid theory as one increases the doping p ("overdopes"). Other experimental properties, where they have been measured, also appear to approximate better the Fermi–liquid predictions with overdoping. This observation appears entirely consistent with the hypothesis that the crossover observed as a function of p in samples where T_c has been suppressed to zero is indeed characteristic of the behavior of a (hypothetical) pure, zero–field sample in the absence of pair formation. Exactly what are the implications of this scenario for the interpretation of the finite–T behavior as a function of p is at present a hotly debated issue.

11.3 Response Functions: The MIR Peak in the Cuprates

One of the most universal properties of the superconducting cuprates (though it is also found in nonsuperconducting ones) is the so–called midinfrared peak in the optical spectrum. The most dramatic way of bringing out this feature is to plot as a function of frequency not, as is conventionally done, the raw data (reflectance) or the (inferred) real part of the conductivity, but rather the so–called loss function $L(\omega) \equiv$ - Im $\epsilon^{-1}(\omega)$ (where $\epsilon(\omega)$ is the $\mathbf{q} \to 0$ limit of the complex transverse dielectric constant $\epsilon_\perp(\mathbf{q}\omega)$). For a conventional metal described by the Drude theory this quantity would have a narrow peak at the plasma frequency ω_p, which is typically of the order of a few eV, and for ω small compared to ω_p (but large compared to the scattering rate Γ) would be very small. For a more realistic (band) model $L(\omega)$ should of course have features corresponding to inter–band transitions, but unless the band gap ΔE is anomalously small there should still be a regime $\Gamma << \omega << \Delta$E when it is small. The experimental behavior of $L(\omega)$ in the cuprates is very characteristic and very different from these expectations. $L(\omega)$ is small below $\sim$0.1eV, but there is a wide and strong peak extending from about that point to $\sim$ 1-1.5 eV (the exact upper limit depends on the system), at which point L drops precipitously almost to zero, thereafter slowly increasing again. (See for example Ref. [13]).

Because this "midinfrared" (MIR) peak occurs in nonsuperconducting cuprates as well as the superconducting ones, it has often been regarded as

irrelevant to the mechanism of superconductivity. However, already several years ago it was established [14] that the transition to the superconducting state is accompanied by a change in the reflectance in the MIR regime of the order of 1%, about two orders of magnitude larger than expected in a naive BCS–type theory, and recent ellipsometric measurements [15,16] have strongly confirmed this result. Thus, while it is at present unclear exactly what relation these phenomena have to the mechanism of superconductivity, they can certainly not be dismissed as totally irrelevant to it. Thus it becomes a more urgent question to understand the origin of the MIR peak.

It is tempting to regard this peak, along with the linear–in–T resistivity, the anomalous T–dependence of the Hall effect, etc., as evidence that the normal state of the cuprates cannot be a Fermi liquid. I shall now demonstrate, using the analogy with liquid ^{3}He, that this argument is not convincing and that it is perfectly consistent to interpret the MIR peak as simply the "incoherent background" on a Fermi–liquid picture. Since the quantity $\epsilon(\omega)$ is, apart from a factor of ω^{-2}, just the (transverse) current–current correlation function in the limit $\mathbf{q} \rightarrow 0$, it is necessary to analyze the behavior of such functions in the Fermi–liquid scenario.

Consider then some quantity A(**r**t) which may or may not be locally conserved. Define the corresponding response function $\chi_{AA}(\mathbf{r}t,\mathbf{r}'t')$ in the standard way (see. e.g. Ref [17], Chapter 2), take its Fourier transform $\chi_{AA}(\mathbf{q}\omega)$ with respect to the variable $\mathbf{r}-\mathbf{r}'$ and $t-t'$, and consider the limit $\mathbf{q} \rightarrow 0$. It now turns out that in Fermi–liquid theory one has the following result. If A(**r**t) is a locally conserved quantity, then in the static limit the correlation function $\chi_{AA}(\mathbf{q}\omega)$ can be expressed entirely in terms of the properties of the low–lying (quasiparticle) states, and generally speaking has a rather simple generic form (which however involves the values of relevant Landau parameters F_s^l, F_a^l). In particular, the region of ω for which there is finite spectral weight ($Im\chi_{AA}(\mathbf{q}\omega)\neq 0$) tends to zero as $\mathbf{q} \rightarrow 0$. Thus, in the case of liquid ^{3}He, we expect that the correlation functions of the three conserved quantities N (particle number), **S** and **P** will have no spectral weight at finite frequencies in the limit $\mathbf{q} \rightarrow 0$. Experiments on ultrasound properties appear consistent with this expectation in the case of N. The correlation functions of **S** and **P** are more difficult to measure. On the other hand, consider some quantity such as the spin current Λ which is not locally conserved (in the case of spin current it is easily verified that it can be changed in a collision, even though the total spin and total current are each locally conserved). In this case there will be some contribution to $\chi_{AA}(\mathbf{q}\omega)$ from the quasiparticle states, and this contribution will have zero weight at finite frequencies as $\mathbf{q} \rightarrow 0$. However, there is also a contribution from nonquasiparticle states, sometimes called the "background" contribution, even in the limit $\mathbf{q} \rightarrow 0$. Physically, the process involved may be regarded as the "undressing" of a quasiparticle by turning off part of its screening cloud. In the case of the spin current it turns out that one can actually calculate the relative contribution

Z_b of this background to the sum rule

$$\int Im \frac{\chi_{\Lambda\Lambda}(\mathbf{q}\omega)}{\omega} = \frac{N}{m} \quad .$$

In fact we have

$$Z_b = 1 - \frac{m}{m^*} \frac{1}{1 + F_1^a/3} \, . \tag{11.6}$$

Since for ^{3}He at melting pressure the ratio m^*/m is about 6, while F_1^a is not very different from zero, the contribution of the background is about 80% of the whole!

Now let's turn to the cuprates. In this case, while total particle number and spin are still locally conserved, the current **J** is not, because of the effects of the crystalline potential. One's first instinct in this situation is to re–express **J** as a sum of terms respectively diagonal and nondiagonal in the band index, and then to argue that the nondiagonal terms involve interband transitions. Thus these will have zero weight below the energy ΔE corresponding to the relevant band gap, while the diagonal terms can be treated just like the (true) current in the translation–invariant case and thus will have zero weight at finite ω in the limit of $\mathbf{q} \to 0$. However, this is not correct, because in the presence of umklapp processes, although the total quasimomentum **K** commutes with the single–particle terms in the Hamiltonian, it does not commute with the interaction. Hence the quantity $\chi_{JJ}(\mathbf{q}\omega)$ can have finite spectral weight in the region $\omega << \Delta$E, even in the limit $\mathbf{q} \to 0$. (It should perhaps be cautioned that "ΔE" here should refer to the band gap of the *noninteracting* system: in the presence of strong interaction it is not obvious that ΔE even retains any clear meaning). Thus, there is no a priori objection to fitting the MIR peak into a Fermi–liquid picture.

11.4 The Cooper–Paired States of Superfluid ^{3}He and the Cuprates: General Considerations

As noted in Section 11.2, in the case of liquid ^{3}He there is a regime of more than a decade in temperature where the system appears to behave as a Fermi liquid in the sense of Landau. Indeed, normal ^{3}He is often regarded as the paradigm of such a system. This region is bounded below by the onset of superfluidity, which is almost universally believed to be a consequence of the onset of Cooper pairing. It is therefore natural to try to construct a theory of the paired (superfluid) state which as it were takes off from the Fermi liquid description of the normal state. A system so described is often referred to as a "superfluid Fermi liquid". Before doing so I very briefly review the most salient properties of the superfluid states. For details see eg. Ref. [19], or Chapter 4 of Ref. [9].

Actually, what is most striking about the phase diagram of liquid ^{3}He below 3 mK is that the superfluid "state" actually corresponds not to one but to three different phases, which are conventionally known as the A, B, and A_1 phases. The B phase is stable over most of the P–T plane in magnetic fields of less than a few kG; the A phase is stable, in zero field, at high pressures and temperatures $\gtrsim 0.7T_c$, and also stable in fields $\gtrsim 6kG$ for arbitrary pressure, while the A_1 phase occupies, in finite magnetic field, a thin sliver of the phase diagram between the A (or B) and normal phases. The B phase appears to be isotropic as regards most of its properties and its thermodynamics appear to be qualitatively similar to those of a classic (BCS) superconductor. In particular, the data on the specific heat are consistent with its vanishing exponentially as T $\rightarrow$ 0. By contrast, the A phase shows considerable anisotropy, e.g. in the ultrasonic attenuation, and its thermodynamics is different from the standard BCS–like behavior. In particular, the specific heat appears to tend to zero as T$\rightarrow$0 as a power law rather than exponentially. As regards the paramagnetic susceptibility (which, remember, in the case of ^{3}He is due entirely to the nuclear spins), this falls rapidly in the B phase to a value as T$\rightarrow$0 of about 1/3 of the normal–state value, while in the A phase it is independent of temperature and very nearly (but not quite!)equal to the normal–state value. The properties of the A_1 phase are generally similar to those of the A phase. It should be mentioned that although these three new phases have been referred to from the very earliest days as the "superfluid" phases of ^{3}He, the evidence for superfluidity as such is very much more circumstantial than in the case of ^{4}He. In fact, had one not had theoretical ideas developed in the context of ^{4}He and metallic superconductors to guide one, it seems likely that the phenomenon would have remained hidden for even longer than the 15 years or so for which it went undetected in ^{4}He(He-II).

Let us now discuss how to formulate the theory of Cooper pairing in a system such as ^{3}He which above T_c appears to be behaving as a normal Fermi liquid. A simple semi–phenomenological way to do this is as follows. We simply define operators $\alpha^+_{\mathbf{p}\sigma}, \alpha_{\mathbf{p}\sigma}$ which create and destroy Landau quasiparticles rather than real atoms (e.g. when acting on the interacting groundstate, the operator $\alpha^+_{\mathbf{p}\sigma}\alpha_{\mathbf{p}'\sigma'}(\mid \mathbf{p} \mid > p_F, \mid \mathbf{p}' \mid < p_F)$ creates a state with $\delta n(\mathbf{p}\sigma) = +1$ and $\delta n(\mathbf{p}'\sigma') = --1$). These operators rather obviously satisfy Fermi statistics, and in general have the same status in the context of the groundstate and low–lying states of the interacting system as do the original fermion operators $a^+_{\mathbf{p}\sigma}, a_{\mathbf{p}\sigma}$ with respect to the corresponding states of the noninteracting system. Then, in addition to the "Fermi–liquid" terms (11.3) in the Hamiltonian, which are diagonal in the δn–representation, one introduces a BCS–like "pairing" term of the usual general form. Formulated in terms of the quasiparticle operators $\alpha^+_{p\sigma}, \alpha_{p\sigma}$ one has

$$\hat{V}_{pair} = \sum_{\substack{\mathbf{p}\mathbf{p}' \\ \alpha\beta\gamma\delta}} V(\mathbf{p},\mathbf{p}' : \alpha,\beta,\gamma,\delta)\alpha^+_{\mathbf{p}\alpha}\ \alpha^+_{-\mathbf{p}\beta}\alpha_{-\mathbf{p}'\gamma}\alpha_{\mathbf{p}\prime\delta}\ . \tag{11.7}$$

This term is actually a special case of the "scattering" terms which as already pointed out are left out in Eq. (11.3). It is intuitively clear that the effect of such a term is likely to be qualitatively similar to that of the BCS pairing term in a Fermi gas. It will induce a collective bound state of the Cooper type, but with the individual fermion components of the pair being Landau quasiparticles rather than real fermions. However, the internal configuration of the pair need not have s–wave symmetry as in the classic superconductors. Rather, the effective angular spin and angular momentum of the pair will correspond to that "channel" in which the projection of the pairing interaction V is most attractive (negative). A system which is well described by this procedure is often called a "superfluid Fermi liquid" (SFL).

It is clear that the role of the single–particle energy in all this is just as in the BCS case, the only difference being that the free mass m is replaced by the effective mass m^*. What about the last term in Eq. (11.3), involving the Landau interaction function $f(\mathbf{pp}'\sigma\sigma')$, which has no obvious analog in the BCS theory? The crucial point is that, as discussed in Ref. [18], this term only comes into play when there is some macroscopic "polarization" of the system, and the formation of Cooper pairs does not lead to such polarization (at least in the approximation of "particle–hole symmetry". This is thought to be very good for ^{3}He). Thus, at first sight at least, the value of the transition temperature T_c should be a function only of m^* and the coefficients V in Eq. (11.7), and should be totally insensitive to the Landau f–function. This should also be true of these properties of the paired state (for example the specific heat) which do not refer, either explicitly or implicitly, to any macroscopic polarization; however, these properties (e.g. the spin susceptibility and normal density) which do involve such polarization should be sensitive to the Landau function, i.e. to the relevant F_l^s's or F_l^a's. As an example, the ratio of the spin susceptibility $\chi(T)$ in an (s–wave–paired) superfluid state to its normal–state value χ_n which in the BCS theory is just the Yoshida function Y(T), should be given for a superfluid Fermi liquid by the expression

$$\frac{\chi(T)}{\chi_n} = (1+F_0^a)\ \frac{Y(T)}{1+F_0^a Y(T)}\ . \tag{11.8}$$

Although this expression tends to 1 for $T \to T_c$ and to zero for $T \to 0$, its shape as a function of temperature may be quite different from that of the function Y(T). Similar remarks apply to the normal density $\rho_n(T)$ as a function of T. For a much more detailed discussion, see e.g. Ref. [18] which uses the notation $Z_0 \equiv 4F_0^a$.

At first sight, then the theory of a superfluid Fermi liquid is nothing but the theory of a superfluid Fermi "gas" as described by BCS plus the set of molecular fields associated with the Landau parameters F_l, F_l^a. And indeed, it turns out that once the nature of the pairing states is currently chosen and T_c itself fitted from experiment, such a description gives predictions for the properties of the superfluid phase in question as a function of T/T_c which are quantitatively accurate typically at the level of a few percent and often

better. As we shall see, this observation is actually quite puzzling, but let us first briefly pause to identify the relevant pairing states.

It is by now almost universally believed, on the basis of NMR and other experimental signatures, that the pairing states corresponding to the observed A, B and A_1 phases of ^{3}He all correspond to Cooper pairs formed in a state with total spin 1 and total (apparent) orbital angular momentum 1 (i.e. a p–state), but with different combinations of spins and orbital angular momenta within this class. More specifically, the Fourier–transformed order parameter (pair wave function) $F_{\mathbf{k},\alpha\beta} \equiv \langle a_{\mathbf{k}\alpha} a_{-\mathbf{k}\beta} \rangle$ is in the case of the A phase a product of a spin function which by an appropriate choice of axis can be written $2^{-1/2}$ $(\uparrow_1\downarrow_2 + \downarrow_1\uparrow_2)$, i.e. corresponds to $S = 1$, $S_z = 0$. And the orbital function which, by an appropriate choice of the orbital axis can be written as proportional to $k_x + ik_y$, i.e. corresponds to $L = L_z = 1$. The A_1 phase has an identical orbital wave function, but the spin function can now be written as simply $\uparrow_1\uparrow_2$ ($S = S_z = 1$: only one spin species undergoes pairing!). The B phase is a bit more subtle; it is what in atomic physics would be called a $^3P_0$ state, but with the spins rotated through a finite angle relative to the orbital angular momenta. For more details see Section 11.6.

The rather good agreement of the predictions of the simple SFL picture with the experimentally observed properties of superfluid ^{3}He is actually rather surprising at first sight, for the following reason: Unlike in the classic metallic superconductors where there is a natural energy cutoff of the order of the Debye energy for the pairing interaction $\hat{V}_{pair}$ in liquid ^{3}He not only is there no obvious such cutoff, but we do not know a priori where the pairing terms came from in the first place. Recall, this is a pairing interaction between *quasiparticles*, not between real atoms, and we have very little quantitative knowledge of the "structure" of a quasiparticle. In any event, there seems no good reason why the pairing interaction should not extend up to energies where the BCS assumption of a constant density of states breaks down badly, or why it should not itself depend substantially on the magnitude of the momenta $\mathbf{p}$ and $\mathbf{p}'$. Why do these complications not affect the temperature–dependence of the measured quantities?

The answer to this dilemma (or at least a large part of it) was given in a classic 1962 paper [20] by Anderson and Morel which long predates the experimental discovery of pairing in ^{3}He. Imagine that the original inter–quasiparticle pairing interaction indeed has the above properties, but that the characteristic scale ϵ_0 over which the strength of V, the density of states etc., varies is much larger than the experimentally measured T_c. Then one can choose an intermediate energy cutoff ϵ_c such that $T_c \ll \epsilon_c \ll \epsilon_0$, and take into account the "scattering" into pair states of energy $|\ \epsilon\ | > \epsilon_c$ by a standard multiple–scattering (t–matrix) procedure. As a result we get a problem where the pairing interaction operates only within a "shell" of width $2\epsilon_c$ around the (quasiparticle) Fermi energy, with a (single–spin) density of states $N(0) \equiv \frac{1}{2}\left(\frac{dn}{d\epsilon}\right)$ and pairing interaction V which is constant as a function of energy (i.e.

of $|\mathbf{p}|$ within this shell). This is, just the original BCS assumption generalized to include possible angular dependence of V. Thus, all the unknowns are buried in the quantities N(0) and $V(\hat{\mathbf{p}}, \hat{\mathbf{p}}')$. The transition temperature T_c is determined by N(0) and the magnitude of the most attractive component V_ℓ of V. The angular dependence of the order parameter reflects the identity of this "most attractive" component. Thus once T_c and the symmetry is determined everything else goes exactly according to the BCS prescriptions and there are no further unknowns.

The above discussion leaves one major question unanswered: Why should there be more than one stable superfluid phase, even in zero external magnetic field? As mentioned above, all the evidence is that both the A and B phases are spin triplet p–wave states but with different forms of the order parameter. Such a situation cannot occur in a simple BCS–type theory with a single fixed value V_1 of the interaction in the p–wave channel. In such a theory the B phase is the unique free energy minimum. The generally accepted explanation, originally given by Anderson and Brinkman [21], is that because the effective interaction between quasiparticles is strongly renormalized and the renormalization process is itself sensitive to the pairing state, the "effective" value of V_1 is slightly different for the A and B phases, and this small difference is enough to stabilize the A phase, even at zero field, in a small region of the P–T plane. This effect is formally of order $(T_c/T_F)^2$ and is a correction to the simple superfluid Fermi–liquid picture. A comprehensive discussion of all corrections which appear to this order has been given by Serene and Rainer [22].

Now let us turn to the superconducting cuprates, and suppose that we take the transition temperature T_c of a given compound from experiment and consider the superconducting–state properties as functions of the reduced temperature T/T_c. Consider first those bulk properties which within the BCS theory are only indirectly sensitive to the energy gap $\Delta(T)$. Examples are the specific heat, spin susceptibility and superfluid density which is measured in the standard way by the penetration depth. Then the most salient qualitative observation is that the general pattern of the temperature–dependence of these quantities, at least in the optimally doped and overdoped regimes, is very similar to that expected in a superfluid Fermi liquid. Indeed, if we restrict ourselves to "not too low" temperatures (say $T/T_c \gtrsim 0.2$), it is actually quite difficult to distinguish the system from a classic BCS superconductor with s–wave pairing! The characteristic effects associated with the "exotic" nature of the order parameter mostly come into play only at the lowest temperatures, see next Section. For a reason to be discussed in the next Section, it does not make a lot of sense to ask whether we can fit the temperature–dependences at say the 1% level by using a SFL model. In the "underdoped" region of the phase diagram the situation is less clear. For example, the specific heat and the spin susceptibility show considerable

"precursor" effects at temperatures above T_c. From this alone it is clear that they cannot follow the SFL predictions.

If one considers phenomena such as angle–resolved photoemission or tunnelling which, at least in a BCS superconductor, are direct measures of the energy gap $\Delta(\mathrm{T})$, then even at optimal doping (or in the overdoped regime) the agreement with the SFL model is more problematic. The ratio $\Delta(0)/T_c$ inferred from this data is often much larger than the BCS value 1.76, and in addition it is not always even clear that the "gap" $\Delta(\mathrm{T})$ inferred from these data actually tends to zero in the limit $\mathrm{T} \rightarrow T_c$. This pattern is amplified in the underdoped regime, when a feature which looks suspiciously reminiscent of an energy gap (the "pseudogap") persists in the data up to several times T_c. To summarize, the data seem to be qualitatively consistent with an SFL picture at optimal doping and in the overdoped regime, but not in the underdoped regime. This is not particularly surprising, since we saw in Sections 11.2 and 11.3 that a similar statement could be made about the normal phase.

It is interesting to ask, does there exist a quantitative test of SFL theory in the cuprates? Recall that in the case of normal ^{3}He, the normal state does permit such a quantitative test, see Section 11.2. Rather serendipitously, it turns out that the answer is yes, as pointed out by Chiao *et al.* [23]. They note that according to recent theory [24] in a superconductor with the order parameter symmetry believed to be characteristic of the cuprates and described by the SFL model the low–temperature limit of the thermal conductivity divided by T is independent of the impurity concentration and a function only of two parameters which are measured independently in ARPES experiments. Thus, if the SFL model applies, from the ARPES data it should be possible to predict the thermal conductivity with no free parameters. It turns out that such a prediction works essentially perfectly for optimally doped BSCCO, so that one can say that the SFL model is at least not excluded for this system. One cannot of course say that this proves it to be right, since it is possible that the SFL model is a special case of a more general class of models which makes the same prediction. In principle, further tests of this quantitative type are possible by using data on e.g. the low–temperature specific heat, but the quality of the data at present is inadequate for this. It should further be noted that while the prediction of the SFL model for the $\mathrm{T} \rightarrow 0$ temperature–dependence of the penetration depth involves a Landau parameter which cannot be independently measured. The value required for this parameter in order to fit the data is quite "reasonable" (i.e. ~ 1, not ~ 10 or 0.1!).

A final question of interest concerns the "size" of the Cooper pairs, and the related issue of their possible "pre–formation". Although the definition of the "size" (or "radius") ξ of the pairs is to some extent a matter of convention, a natural choice is that it is the root–mean square radius associated with the so–called "anomalous average" $\mathrm{F}(\mathrm{r}) \equiv \langle \psi_\alpha(0)\psi_\beta(\mathbf{r})\rangle$ which characterizes

the paired state (the real–space Fourier transform of the quantity entering (11.10) below, i.e. the single macroscopically occupied eigenfunction of $\hat{\rho}_2$). For a simple BCS model ξ is then only weakly temperature–dependent and of order of magnitude $\hbar v_F/\pi k_B T_c$ (i.e. equal, up to a numerical factor of order unity, to the "Pippard coherence length" ξ_0).

As is well known, for the classic superconductors such as Al the quantity ξ is of order 10^3-$10^4 \mathring{A}$. This is typically several orders of magnitude greater than the interparticle spacing a. It is this state of affairs which is the key to the remarkable success of the BCS (mean–field) theory of superconductivity. An equivalent way of looking at it is to note that the ration a/ξ_0 is up to a factor of order unity equal to $\Delta/\epsilon_F (\sim T_c/T_F)$. The pair binding energy Δ is very small compared to the Fermi energy ϵ_F, so that the pair formation process affects only a fairly thin shell of states around the Fermi surface. If on the other hand it were to turn out that ξ is comparable to a (or Δ or kT_c or to ϵ_F) then we should expect fluctuations around the mean–field solution to play a major role. In particular we might get a substantial range of temperature where Cooper pairs are formed locally, but do not undergo the "quasi–Bose–Einstein condensation" characteristic of the BCS state. The scenario is sometimes referred to as that of "pre–formed pairs." In the extreme limit $\xi << a$, the picture would be one of tightly bound di–electronic (bosonic) "molecules" which form at some high temperature T_0 and then undergo Bose condensation at a much lower, unrelated, temperature $T_{BEC} << T_0$.

As remarked in Section 11.1, the ratio T_c/T_F is considerably larger for both ^{3}He and the cuprate superconductors than for classic superconductors such as Al. If we work in terms[2] of the Cooper–pair radius ξ, then it turns out that for ^{3}He ξ varies from about 200 $\mathring{A}$ at melting pressure to about 1200 $\mathring{A}$ at saturated vapor pressure. This is large compared to the interparticle spacing ($\sim 3\ \mathring{A}$). It is therefore not surprising that superfluid ^{3}He appears to be very well described by the mean–field BCS theory. In the case of the cuprates, it is not entirely clear that we should continue to use the estimate $\xi \sim \hbar v_F/\pi k T_c$. If however we do so, and take the value of v_F (for BSCCO) from ARPES measurements, see eg. Ref. [23], we find that at optimal doping ξ is typically $\sim 50\mathring{A}$, while if we take the relevant "interparticle spacing" to be that of the extra holes doped into the CuO_2 planes it is about $8\mathring{A}$ at optimal doping. Thus, the ratio ξ/a is only ~ 6. Away from optimal doping it increases. If we take this result seriously, it implies that while we are by no means in the limit of "di–electronic" molecules, we should expect fluctuations to give substantial corrections to the mean–field theory; such effects are indeed seen in the cuprates, most spectacularly in the macroscopic electromagnetic properties. A particular prediction, as noted above, would be that there should be a fairly substantial regime of temperature where pairs are formed but are not Bose condensed. In this regime the "local" properties of the system

[2] Working in terms of a/ξ rather than T_c/T_F has the advantage that the quantity a ($\equiv n^{-1/3}$ where n is the relevant particle density) is better defined than T_F.

should be similar to those of the superconducting phase, but there should be no long–range order and hence no superconductivity (in the sense of zero resistance or a Meissner effect). A substantial school of thought [25] claims that the so–called "strange metal" regime of the cuprates which appears on the underdoped side of the phase diagram is exactly the instantiation of this prediction, and in particular that the approximately defined line of anomalies in the experimental properties usually denoted by T*(p) corresponds to the onset of pair formation (which, just as in the case of the formation of ordinary diatomic molecules, is expected to be gradual rather than by a phase transition). Whether such a scenario can explain the properties of the "strange metal" regime quantitatively or even qualitatively is at present the subject of vigorous controversy. Parenthetically, it is amusing that following early suggestions along these or similar lines for the cuprates, it has been proposed [26] that normal ^{3}He–usually taken to be our paradigmatic Fermi liquid, see Section 11.2, may itself be described by a scenario of this general type.

11.5 Symmetry of the Order Parameter

Perhaps the most striking difference between superfluid ^{3}He and the cuprates on the one hand, and the classic superconductors on the other, is that while in the latter case the order parameter is believed to have the same symmetry as the lattice, in both ^{3}He and the cuprates the general belief is that it is "exotic", that is, transforms according to a nontrivial representation of the symmetry group G of the Hamiltonian. This may well also be true in the case of certain heavy–fermion and organic superconductors. For the moment, I will assume that in each case the order parameter corresponds to a single irreducible representation of G. This point will be briefly re–examined below.

In the case of liquid ^{3}He, where there is no lattice, the symmetry group is (to the extent that we ignore the small nuclear dipole–dipole interaction) a product of the group $SO(3)_{orb}$ of rotations in orbital coordinate space and the group $SU(2)_{sp}$ corresponding to rotations in spin space; we need SU(2) rather then SO(3) because of the double–valued character of the spin functions. For a complex (Cooper pair) of two particles of spin 1/2 the relevant irreducible representations of SU(2) correspond to a singlet and a triplet, and on the basis of the behavior of the spin susceptibility it is almost universally believed that both the A and the B phases correspond to the triplet. Under all but very special circumstances, the Pauli principle then implies that the orbital wave function is odd–parity, i.e. corresponds to "angular momentum" ℓ = 1,3,5... All the evidence is that in both A and B phases ℓ is equal to 1. Thus, in both the A and B phases of ^{3}He the Cooper pairs have $\ell = S = 1$. Of course, this statement does not characterize the pairing state uniquely, since we have 3 possible Zeeman substates corresponding to spin and 3 to orbital angular momentum, thus 9 possible states in all. The most compact characterization

of the order parameter turns out to be through the quantity

$$\mathbf{d}(\mathbf{k}) \equiv (i\sigma_y\boldsymbol{\sigma})_{\alpha\beta}\langle a^+_{\mathbf{k}\beta}a^+_{-\mathbf{k}\alpha}\rangle\,, \tag{11.9}$$

where the components of $\boldsymbol{\sigma}$ are the Pauli matrices. The quantity $\mathbf{d}(\mathbf{k})$ automatically behaves as a vector in spin space, and because of the $\ell = 1$ requirement must also transform as a vector in orbital space. The forms of $\mathbf{d}(\mathbf{k})$ inferred from NMR and other evidence to correspond to the A and B phases of ^{3}He are as follows: For the A phase $\mathbf{d}(\mathbf{k})$ is given up to a multiplying constant by

$$\mathbf{d}(\mathbf{k}) = \hat{\mathbf{d}}(\mathbf{k}\cdot(\hat{\mathbf{n}}_1 + i\hat{\mathbf{n}}_2))\,, \tag{11.10}$$

where $\hat{\mathbf{d}}$ is a real vector in spin space and $\hat{\mathbf{n}}_1$ and $\hat{\mathbf{n}}_2$ are a pair of mutually orthogonal (real) unit vectors in orbital space. It is conventional to define a third unit vector $\hat{\boldsymbol{\ell}}$ by $\hat{\boldsymbol{\ell}} \equiv \hat{\mathbf{n}}_1 \times \hat{\mathbf{n}}_2$. The physical interpretation is that in the A phase the pairs have total spin 1 and spin projection 0 on the (spin–space) axis $\hat{\mathbf{d}}$, and in orbital space have "apparent" angular momentum 1 along the(orbital–space) axis $\boldsymbol{\ell}$. To discuss the B phase, it is convenient to start from the state $\mathbf{d}(\mathbf{k}) = \mathbf{k}$. In this state the apparent orbital angular momentum is always directed oppositely to the spin, so this is what in the language of atomic physics would be denoted as a $^3P_0$ state. The actual state of ^{3}He–B is believed to be obtained by rotating the spin coordinate system relative to the orbital one through an angle θ around an axis $\hat{\boldsymbol{\omega}}$. To minimize the dipole–dipole energy θ has to be $\cos^{-1}(-1/4) \approx 104°$, but the axis $\hat{\boldsymbol{\omega}}$ is fixed only by higher–order effects. The resulting state, while it has $\langle\mathbf{L}\rangle = \langle\mathbf{S}\rangle = 0$, has a finite value of the quantity $\langle\mathbf{L}\times\mathbf{S}\rangle$ directed along $\hat{\boldsymbol{\omega}}$. For further details see e.g. Ref. [9].

In the case of the single–plane cuprates, it is most natural to regard the pair wave function as defined within a single CuO_2 plane, with transfer between neighboring planes effected by a Josephson–type mechanism. Then to the extent that we neglect spin–orbit interaction, the relevant symmetry group is the product of the orbital symmetry group, which is exactly or approximately that of the square, C_{4v}, times the group $SU(2)_{spin}$. Again, the possible spin representations are singlet or triplet, and the evidence from the NMR behavior strongly favors the singlet. This then suggests that the orbital state has even parity. The even–parity irreducible representations of C_{4v} are four in number, and are denoted in the formal notation of group theory A_{1g}, A_{2g}, B_{1g} and B_{2g}, or informally s (or s^+), g(or s^-), $d_{x^2-y^2}$ and d_{xy}, respectively. There is by now rather convincing evidence (see e.g. Ref. [27]) that, at least in these cuprates where phase interference experiments have been done (YBCO, Tℓ-2201, Bi-2212...) the symmetry of the order parameter is $d_{x^2-y^2}$ (B_{1g}). There is a strong suspicion that this is so for all the superconducting cuprates.

Here it is necessary to emphasize an important distinction: The orbital symmetry group SO(3) of ^{3}He (as well as the spin group $SU(2)_{sp}$) is continuous. Thus, once one has specified not just the irreducible representation

involved (in this case $\ell = S = 1$) but also the "nature" of the state (e.g. A–like or B–like), the only freedom left over is the "orientation" in orbital and/or spin space, e.g. for an A–like state the vectors $\hat{\boldsymbol{\ell}}$ and $\hat{\mathbf{d}}$. It is clear that the free energy must be independent of those in the neglect of the small nuclear dipole–dipole interaction. This has the consequence that if one makes the hypothesis that the SFL model is exact for ^{3}He and chooses a particular state, e.g. A or B, one can calculate the free energy and most of the relevant experimental quantities exactly as a function of T/T_c and of the Landau parameters. It thus makes sense to try to quantify the small discrepancies from these predictions, cf. e.g. Ref. [22]. By contrast, the orbital group C_{4v} of the cuprates consists of discrete operations ($\pi/2$ rotations and reflections), so the statement that the symmetry of the order parameter is d_{x2-y2} tells us only that it changes sign under $\pi/2$ rotations and also under reflections in a 45° crystal axis. This still allows a wide variety of dependencies on $\mathbf{k}$, from a simple form to a complicated form with several nodes other than the 4 in the 45° direction which are imposed by symmetry alone. Consequently, the statement that the system behaves as a SFL does not uniquely determine the free energy and other quantities as functions of T/T_c and the Landau parameters: to obtain such a result one needs a specific microscopic model which fixes quantities such as the single–quasiparticle energy and the effective pairing interactions as detailed functions of $\mathbf{k}$ as the latter varies around the Fermi surface.

A second difference associated in part with the different structure of the groups SO(3) and C_{4v} is that in the former case "continuous" mixing–in of irreducible representations other than the principal one allowed, whereas in the latter this requires a second phase transition (on this point, see Section 11.3 of Ref. [28]). Thus the absence of any observed second phase transition in the essentially pure tetragonal[3] crystal Tℓ-2201 is strong evidence that the bulk order parameter is pure d_{x2-y2}, while the pairing state of ^{3}He–A (though not ^{3}He–B) may have a small admixture of other odd–parity orbital states ($\ell = 3,5...$). In practice this seems very unlikely to produce quantitatively significant corrections.

In general, the fact that the order parameter of a given system is "exotic" (i.e. has symmetry lower than that of the Hamiltonian) has a number of interesting consequences. First, in most such cases the order parameter, and hence the energy gap which is crudely speaking proportional to it will have nodes at one or more points on the Fermi surface. This means that the number of normal quasiparticles excited at low temperatures will be proportional to a power of T rather then exponentially small. Consequently, experimental quantities such as the specific heat which are crudely proportional to the amount of normal component will themselves have a power–law behavior. Such power–law behavior is indeed observed in the cuprates, in particular

[3] For cuprates such as YBCO with appreciable orthorhombic anisotropy the analysis becomes rather messier, see e.g. Ref. [28].

in the NMR properties and the deviation of the penetration depth from its zero–temperature limit. This is strong evidence for the existence of nodes of the gap which are also observed more directly in ARPES experiments. To be sure, the mere existence of nodes is not peculiar to exotic pairing states – an s–wave (A_{1g}) state, provided it is of the so–called "extended" type, can also have them – but the salient point is that a $d_{x^2-y^2}$ state, because it must (by definition!) change sign under reflection in any 45° axis, necessarily has nodes at these points, which is exactly where they are observed in ARPES.

In the above argument, it was taken for granted that the energy gap $\Delta(\mathbf{k})$ is simply proportional to the orbital order parameter. This is indeed the case for spin singlet pairing, where the order parameter can be expressed as a simple product of a trivial spin factor (the singlet state) and an orbital factor. For spin triplet pairing the situation is in general a little more complicated. In this case it turns out (at least for the so–called "unitary" class of states which includes the A and B states) that the gap $\Delta(\mathrm{k})$ is proportional to the quantity $|\mathbf{d}(\mathbf{k})\ |^{1/2}$. We see that the B–phase gap is *uniform* over the Fermi surface and thus has no nodes, while the A–phase gap is proportional to $(\mathbf{k}\cdot\boldsymbol{\ell})2$ and so has two nodes in the directions $\pm\hat{\boldsymbol{\ell}}$. Consequently, we expect that the properties of ^{3}He–B should behave as a function of temperature, similarly to those of a classic (s–wave) superconductor, (e.g. the specific heat should decrease exponentially in the limit $\mathrm{T} \rightarrow 0$), while for ^{3}He–A we should get power–law behavior qualitatively similar to that seen in the cuprates. But at the very lowest temperatures (lower than currently accessible) the thermodynamics should be dominated by bosonic collective excitations such as spin waves. This prediction appears consistent with existing experiments, although lower–temperature measurements would be needed to confirm it definitively [9].

A second consequence of exotic pairing in general is that various experimentally measured quantities may show an anisotropy over and above that prescribed by the Hamiltonian. Examples of such behavior in superfluid ^{3}He include the A–phase ultrasonic attenuation, which depends on the angle of the sound propagation vector relative to the characteristic orbital vector $\hat{\boldsymbol{\ell}}$, and the magnetic susceptibility, which depends on the angle of the field relative to the characteristic spin vector $\hat{\mathbf{d}}$. In ^{3}He–B the orbital and spin properties are individually isotropic, but the effect of the rather subtle anisotropy in the correlation of the spin and orbital coordinates comes out in the NMR behavior, which is sensitive to just such correlations and indeed depends on the direction of the static field relative to the "spin–orbit rotation vector" $\hat{\boldsymbol{\omega}}$. In the cuprates the most obvious signature of anisotropy is in the ARPES data. While one would expect (and finds) the spectra to be somewhat different along the crystal axes and at 45° even in the normal phase, this difference is strongly accentuated in the superconducting phase, since as already described a gap develops which is finite along the axes but zero in the 45° directions.

A third class of phenomena related to exotic pairing has to do with possible variations of the characteristic "orientation" in space and/or in time. Here there is a very substantial difference between ^{3}He and the cuprates. In the former case, if for definiteness we consider the A phase, the characteristic orbital vector $\hat{\boldsymbol{\ell}}$ and spin vector $\hat{\mathbf{d}}$ are pinned only very weakly in bulk (by effects such as the nuclear dipole–dipole interaction, residual heat flows etc.: see Ref. [29], Section X), and as a result such spatial and/or temporal variation of the orientation is quite commonplace and of great interest both experimentally and theoretically, see e.g. Ref. [9]. By contrast, in the cuprates there is no question of spin "orientation" since the state is a singlet, and the "orientation" of the orbital wave function is firmly pinned by the crystal axes. The only remaining freedom is to exchange the + or − signs on the four "lobes" of the pair wave function. Since this merely multiplies the total pair wave function by a − sign, one might think it would have no physical significance. Indeed for a spatially uniform situation this is true. However, it is precisely this subtle degree of freedom which allows, in a spatially nonuniform setup, the rather spectacular Josephson (quantum phase interference) experiments which are the most convincing evidence in favor of the d_{x2-y2} symmetry assignment, see e.g. Ref. [27].

11.6 Conclusion

From the discussion in this chapter the reader might draw the conclusion that the phenomenon of superfluidity in liquid ^{3}He has been any help in understanding cuprate superconductivity. Note, the vast differences between the two systems and the few similarities. However, such a conclusion would, I think, miss a crucial point: In the history of research on Cooper pairing in Fermi systems, superfluid ^{3}He was the very first case of a system where the pairing was neither of the conventional (s–wave) symmetry nor due to exchange of entities (phonons) different from those being paired. These features had been anticipated theoretically. It is difficult to overestimate the role of the experimental discovery of superfludity in ^{3}He in opening the minds of the community to the idea that superconducting (or superfluid) long–range order might be a very generic phenomenon and that the detailed properties of systems sharing it might be very different from those of the classic superconductors. Certainly, such an expectation has been spectacularly realized in the cuprates; and to my mind it is entirely possible that it will in the future have other equally spectacular realizations elsewhere.

11.7 Summary

This chapter compared the phenomenon of superfluidity in liquid ^{3}He with that of superconductivity in the cuprates. It discussed, inter alia, the similarities and differences of the two systems in the normal state with particular

attention to the ^{3}He analog of the "mid–infrared peak" seen in the cuprates, the extent to which the superfluid state in either or both systems can be regarded as a "superfluid Fermi liquid", and the differences in the consequences of the "exotic" order–parameter symmetry believed to be common to the two superfluid phases.

Acknowledgements
This work was supported by the National Science Foundation under grant NSF–MR–99–86199.

References

1. A.J. Leggett, Rev. Mod. Phys. **73**, 307 (2001).
2. O. Penrose and L. Onsager, Phys. Rev. **104**, 576 (1956).
3. P. Gavoret and P. Nozières, Ann. Phys. **28**, 349 (1964).
4. C.N. Yang, Rev. Mod. Phys. **34**, 694 (1952).
5. A.J. Leggett, in *Electron*, ed. M. Springford, Cambridge University Press, Cambridge 1997.
6. A.J. Leggett, in *Bose–Einstein Condensation*, ed. A. Griffin, D.W. Snoke, and S. Stringain, Cambridge University Press, Cambridge 1995.
7. W.F. Vinen, in R. D. Parks, ed., *Superconductivity*, (Marcel Dekker, New York 1969), Vol. II., p. 1167.
8. L.D. Landau, Zh. Eksp. Teor. Fiz. **30**, 1058 (1956): translation, Soviet Physics JETP **3**, 920 (1957).
9. D. Vollhardt and P. Wölfle, *The Superfluid Phases of ^{3}He*, Taylor and Francis, London (1990).
10. V.P. Silin, Zh. Eksp. Teor. Fiz. **33**, 495 (1957): translation, Soviet Physics JETP **6**, 387 (1958).
11. B.L. Jones and J.W. McClure, Phys. Rev. **143**, 133 (1966).
12. G.S. Boebinger *et al.*, Phys. Rev. Letters **77**, 5417 (1996).
13. T. Timusk and D.B. Tanner, in D.M. Ginsberg (ed.), *Physical Properties of High–Temperature Superconductors*, Vol. I. (World Scientific, Singapore 1989), p. 339.
14. M.J. Holcomb, C.L. Perry, J.P. Collman and W.A. Little, Phys. Rev. B**53**, 6739 (1996).
15. M. Rübhausen, A. Gozar, M.V. Klein, P. Guptasarma and D.G. Hinks, Phys. Rev. B**63**, 224514 (2001).
16. H.J. Molegraaf, C. Presura, D. van der Marel, P.H. Kes and M. Li, Science **295** 2239 (2002).
17. D. Pines and P. Nozières, *The Theory of Quantum Liquids*, W.A. Benjamin, New York 1966.
18. A.J. Leggett, Phys. Rev. **140** A, 1869 (1965).
19. J.C. Wheatley, Revs. Mod. Phys. **47**, 415 (1975).
20. P.W. Anderson and P. Morel, Phys. Rev. **123**, 1911 (1961).
21. P.W. Anderson and W.F. Brinkman, Phys. Rev. **30**, 1108 (1973).
22. J.W. Serene and D. Rainer, Phys. Rep. **101**, 221 (1983).
23. M. Chiao, R.W. Hill, C. Lupien, L. Taillaer, P. Lambert, R. Gagnon and P. Fournier, Phys. Rev. B**62**, 3554 (2000).

24. A.C. Durst and P.A. Lee, Phys. Rev. B **62**, 1270 (2000).
25. M. Randeria and N. Trivedi, J. Phys. Chem. Solids **59**, 1754 (1998).
26. J.P. Bouchand and C. Lhuillier, Z. Phys. B **75**, 283 (1989).
27. C.C. Tsuei and J.R. Kirtley, Rev. Mod. Phys. **72**, 969 (2000).
28. J.F. Annett, N. D. Goldenfeld and A.J. Leggett, in D.M. Ginsberg, ed., *Physical Properties of High Temperature Superconductors*, World Scientific, Vol. V, Singapore 1996.
29. A.J. Leggett, Rev. Mod. Phys. **47**, 331 (1975).

Author Index

A

Abeles, B., 26, 27, 32, 50, 52
Abrikosov, A.A., 265, 559, 624, 947
Achkir, D., 529
Aebi, P., 192
Aeppli, G., 423, 997, 998
Akamatu, H., 454
Alexander, S., 52
Allen, J.W., 265, 423
Allen, P.B., 423
Ambegaokar, V., 776, 877
Andersen, O., 265
Anderson, P.W., 265, 580, 847, 1103, 1104
Ando, Y., 156, 417, 419, 423
Andraka, B., 532
Andreev, A.F., 103
Aoki, Y., 630, 1064
Arai, T., 524
Arko, A., 265
Armbrüster, H., 568
Armitage, N.P., 423
Arrigoni, E., 380
Ashcroft, N., 173
Auerbach, A., 423

B

Bader, S.D., 568
Balakrishnan, G., 995
Baltensperger, W., 575
Bandyopahyay, B., 31
Bandyopay, S., 33
Bansil, A., 173, 265
Bardeen, J., 1, 777, 877, 925, 1026–1028
Basov, D.N., 146, 423, 685
Batlogg, B., 265
Bauer, E.D., 555
Baym, G., 67, 873
Beasley, M.R., 423
Becca, F., 378, 380
Bechgaard, K., 636
Bednorz, J.G., 1, 3, 668, 891
Bennemann, C., VI
Bennemann, K.H., 1, 14, 21, 731
Bergman, D., 52
Bernal, O.O., 992
Bernhoeft, N., 1053
Berthod, L., 774
Betbeder–Matibet, O., 1015
Bianchi, A., 607–609
Biggs, T., 504
Birgeneau,R.J., 423
Blatter, J., 776
Blonder, G.E., 1032
Bloomfield, P.E., 566, 569
Blount, E.I., 580, 935
Blumberg, G., 688
Boninsegni, M., 383
Bonn, D.A., 423, 828
Bontemps, N., 418
Borisenko, S.V., 192
Brinkmann, W.F., 847, 1104
Brison, J.P., 1055, 1057
Broholm, C., 1001
Bruder, C., 1032
Bucher, E., 890
Buckel, W., 14, 15, 21

C

Calandra, C., 379
Campuzano, J.C., 167, 185
Carbotte, J., 1012
Carneiro, G.M., 914
Carrington, A., 661
Castro Neto, A.H., 423
Chakravarty, S., 357, 423
Chandrasekhar, V., 54
Chen, S.J., 142
Chernyshev, A.L., 382
Chiao, M., 1105

Chubukov, A., 746
Coffey, L., 1022
Cohen, R., 52
Coles, G.R., 942
Cooke, D.W., 992
Cooper, L., 1, 925
Corenzwit, E., 558
Cosentini, A.C., 378

D

Dagotto, E., 288, 383, 423
Dai, P.C., 423
Damascelli, A., 168
Davis, J.C.S., 423
Dayan, M., 52
de Gennes, P., 100
Decker, W.R., 563
Dempesy, C.W., 571
Dessau, D.S., 185, 760, 807
Deutscher, G., 14, 24, 42, 45
Di Castro, C., 423
Ding, H., 185, 192, 206, 249, 265, 696
Dorsey, A.T., 497
Dressel, M., 529, 540
Dumm, M., 698
Dynes, R.C., 423

E

Eilenberger, G., 71, 82
Eisaki, H., 423
Eisenberg, E., 378
Elsinger, H., 533
Emery, V., 378, 379, 383
Engelsberg, S., 242
Eremin, I., 21, 731
Eschrig, M., 265
Eyring, V., 668

F

Falci, G., 37
Fehrenbacher, R., 670
Feller, J.R., 1029
Fenichel, H., 52
Ferrell, R., 580, 607, 1012, 1027
Feyerherm, R., 1043
Fibich, M., 1048
Filler, T., 52
Finkelstein, A., 423
Finnemore, D.K., 563
Fisher, M.P.A., 329, 423, 892
Fisk, Z., 891
Flouquet, P., 1065
Fröhlich, H., 917
Fradkin, E., 382, 423
Franz, W., 975
Fretwell, H., 192, 265
Fujimori, A., 265
Fukuyama, H., 518, 535
Fukuzumi, Y., 139
Fulde, P., 537, 607, 1012

G

Garland, J., 14
Gavoret, J., 1088
Geballe, T.H., 423
Gerber, A., 52
Gershenson, M., 52
Ginsburg, D.M., 668
Giovannini, B., 774
Girlando, A., 517
Gofron, K., 265
Goodrich, R.G., 117
Gor'kov, L., 559, 947
Goremychkin, E.A., 1002
Graebner, J.E., 532
Granath, M., 423
Grave, I., 52
Grewe, N., 1055
Grigereit, T.E., 577
Gromko, A.D., 261
Grunbaum, E., 52
Gschneidner, K.A., 668
Gunther, L., 45
Guptasarma, P., 265

H

Hagel, J., 509
Hallwachs, E., 173
Hamann, D.R., 566, 569
Hardy, W.N., 828
Harrison, N., 656
Harshman, D.R., 529
Hasegawa, Y., 531, 535
Helfand, E., 678, 1012
Hellberg, S., 378, 379, 383, 392
Herbut, I.F., 136
Herring, C., 559
Hertz, J.A., 173, 915
Hess, D.W., 1055
Hielsch, R., 14
Hinks, D., 265
Hirsch, J.E., 288
Hirschfeld, P., 952, 1028
Hohenberg, P.C., 678, 1012
Hussain, Z., 168

I

Ichikawa, N., 404, 418
Imer, J.N., 206
Imry, Y., 45, 52
Ioffe, J., 32
Ishida, Y., 745
Ito, H., 492, 499
Izawa, K., 526, 606, 631, 632

J

Jérome, D., 454, 488, 636, 642
Jaccarino, V., 584, 586
Jacobsen, C.S., 473
Jeckelmann, E., 371
Johnson, P., 265
Johnson, P.D., 423
Joynt, R., 1013, 1056, 1057

K

Köppen, M., 540
Kadanoff, L., 67, 873
Kadowaki, K., 265, 592, 986
Kaiser, A.B., 568
Kallin, C., 423
Kamal, S., 340, 829
Kaminski, A., 198, 265
Kang, J.S., 682
Kanoda, K., 479, 490
Kapitulnik, A., 423
Kataev, V., 478
Kawamoto, A., 479
Kee, H.-Y., 423
Keller, H., 161
Ketterson, J.B., 1
Kim, Y.-B., 423
Kini, A.M., 540
Kino, H., 518
Kivelson, S.A., 326
Klein, O., 529
Kohn, W., 289
Kohra, 988
Komatsubara, T., 959
Kondo, Y., 519
Kornelsen, K., 474
Kosevich, A.M., 466
Kouznetsov, K.A., 688
Kozlov, M.E., 475
Kromer, F., 540
Kugler, M., 698
Kund, M., 485
Kupriyanov, M.Y., 92, 93
Kyogaku, M., 603, 989

L

Lang, M., 453, 660
Langhammer, C., 540
Lanzara, A., 256, 261, 741
Larkin, A.I., 67, 82, 607, 1012
Laughlin, B., 265
Le, L.P., 530, 531
Lebed, A., 651
Lee, P.A., 1028
Lee, Y.S., 423
Lefebvre, S., 492
Leggett, A.J., 1087

Li, M.R., 1030
Li, Z.Z., 265
Lifshitz, E.M., 61, 466
Lin, H.Q., 479
Lindenfeld, P., 52
Lindroos, M., 173
Liu, W.V., 382
Loh, J.E., 288
Lonzarich, 615
Lonzarich, G.G., 605
Loram, J.W., 294, 699
Ludwig, A., 570
Luengo, C.A., 563, 568, 571
Lukichev, V.F., 92, 93
Luttinger, J.M., 289
Lynch, D.L., 168

M

Mühlschlegel, B., 21
Müller, J., 453
Müller, K.A., 1, 3, 161, 668, 891, 899
Müller, V., 984, 1021, 1025
Müller–Hartmann, E., 570
Maclaughlin, D.E., 1044
Maeno, Y., 853
Maki, K., 525, 537, 540, 607, 1012
Manousakis, E., 378, 379, 383, 392
Manske, D., 21, 731
Manzke, R., 763
Maple, M.B., 555, 563, 668, 682
Martin, D.L., 571
Martinis, J.M., 105
Matsuda, A., 138, 603
Matsuda, M., 698
Matsumoto, H., 580
Matthias, B.T., 558, 559, 890
Mattis, D.C., 1026–1028
McKenzie, R.H., 646
McLean, W., 52
Merchant, L.M., 333
Mesot, J., 211, 265
Meul, H.W., 584–586
Millis, A.J., 615, 915
Miyake, K., 622
Mochiku, T., 265
Moessner, P., 327, 328
Molegraaf, H.J.A., 279
Moller, K.A., 423
Momono, N., 115, 150, 151
Moncton, D.E., 579
Montgomery, L.K., 471
Mook, H.A., 423
Morel, P., 1103
Moriya, T., 519, 615, 915
Morris, G.D., 612
Moses, P., 646
Mota, A., 891
Movshovich, R., 689, 891

N

Nakatsuji, S., 853
Nakazawa, Y., 532, 533
Nayak, C., 380, 423
Neumeier, J.J., 682
Noack, R.M., 310, 370
Noda, T., 419
Nogueira, F., 21
Norman, M.R., 167
Nowack, A., 476
Nozières, P., 43, 954, 955, 1015, 1088
Nussinov, Z., 423

O

Ōnuki, Y., 959
Oganesyan, V., 422
Olson, C., 168, 185, 206, 265
Ong, N.P., 423
Ono, S., 155, 157
Onsager, L., 1088
Orenstein, J., 423
Orlando, T.P., 1012
Ott, H.R., 890, 896, 1055
Ovadyahu, Z., 52
Ovchinnikov, Y.N., 67, 82, 607, 1012
Overhauser, A.W., 564

P

Paglione, J., 609
Panagopoulos, C., 145
Parks, R.D., 21
Pauling, L., 327
Paulius, L.M., 682
Pendry, J., 173
Penrose, O., 1088
Peter, M., 21, 586
Pethick, C.J., 914, 949, 1015
Pines, D., 690, 949, 1015
Pintschovius, L., 523
Pistolesi, F., 43
Pitaevskii, L., 61
Poilblanc, D., 379
Polchinski, J., 344
Presland, M.R., 112
Putikka, W.O., 378, 379

Q

Qian, Y.J., 899

R

Raffy, H., 265
Rainer, D., 71, 1104
Randeria, M., 167, 176
Rappaport, M., 52
Rauchschwalbe, U., 898
Ravex, A., 1021
Regel, A., 32
Rice, T.M., 670, 745, 795, 950
Riera, S., 383
Rimberg, A.J., 336
Riseborough, P.S., 888, 1055
Rokhsar, D.S., 326
Rommer, S., 375, 376
Rosch, A., 1003
Rosenkranz, S., 265
Rossat–Mignod, J., 580, 1003, 1004

S

Sachdev, S., 423
Saito, G., 458
Santadner–Syro, A.F., 279
Sasaki, T., 540
Sato, T., 265
Sauls, J.A., 1030
Saxena, S.S., 621
Scalapino, D.J., 242, 288, 358, 372, 373, 375, 379, 381, 385, 423, 847
Schön, G., 83
Schaich, W.L., 173
Schlueter, J.A., 540
Schmalian, J., 519, 524
Schmid, A., 83
Schmiedeshoff, G.M., 888
Schneider, T., 111
Schotte, K.D., 984
Schröder, A., 1003, 1005
Schrieffer, B., 265
Schrieffer, J.R., 1, 242, 243, 287, 423, 924, 925, 953
Schweitzer, D., 540
Segawa, K., 153, 154
Semba, K., 138
Senthil, T., 329
Serene, J.W., 71, 1104
Sethna, J.P., 326
Shankar, R., 344, 345
Shapira, Y., 42, 52
Shen, Z.X., 168, 185, 206, 207, 243, 265, 419, 423
Shibata, S., 1036, 1037
Shih, C.T., 379, 383
Shin, C.S., 379
Shull, C.G., 673
Sidorov, V.A., 612
Sigrist, M., 745, 795, 1012
Silin, V.P., 1096
Sinha, S.K., 579
Skalski, S., 561, 563, 564, 1029
Smith, F.W., 571
Smith, J.L., 888, 891, 1055
Smith, N.V., 176
Sondhi, S.L., 327, 328, 423
Sorella, S., 383, 384

Spivak, B.I., 423
Steglich, F., 540, 702, 890, 892, 1055
Stephen, M.J., 777, 877
Stewart, G.R., 891, 958, 1055, 1056
Stockert, O., 1004
Stojkovic, B.P., 690
Strassler, S., 575
Suhl, H., 558, 559, 580
Sulzbach, E.v., 21

T

Taillefer, L., 212, 1013, 1056, 1057
Takahashi, T., 265
Takeuchi, T., 265
Takigawa, M., 535
Tallon, J.L., 699
Tanatar, M.A., 486
Tayama, T., 631
Thoma, H., 471
Timusk, T., 423
Tinkham, M., 655, 1027
Torikachvili, M.S., 682
Toyota, N., 540
Tranquada, J.M., 422, 423, 698
Tremblay, J., 746
Trugman, S.A., 358, 389
Tsuneto, T., 607

U

Ueda, K., 950, 1012
Uemura, Y.J., 136, 145, 736, 770, 773, 868
Ullah, S., 497
Usadel, K.D., 88

V

Valla, T., 423
van der Marel, D., 418
Varma, C., 265, 580, 921
Veal, B., 265
von Löhneysen, H., 626

W

Wang, N.L., 474
Watanabe, S., 622
Watson, H.L., 571
Wedgewood, F.A., 673
Wen, X.G., 329
Werthamer, N.R., 678, 1012
White, S.R., 369, 372, 375, 379–381, 385
Wilczek, F., 380
Wilhelm, F., 99
Wohlman, O.E., 52
Wolf, P.A., 953
Won, H., 525
Woods, S.B., 986
Worrington, T., 52
Wosnitza, J., 540, 555

X

Xiao, S., 149

Y

Yamaji, K., 517
Yip, S.K., 1030
Yokoya, T., 265

Z

Zaanen, J., 409, 423
Zachar, O., 382, 423
Zaitsev, A.V., 92
Zapf, V.S., 555
Zeyher, R., 523
Zhang, S-C., 423
Zhao, G.M., 115
Zhou, X.J., 423
Zieve, R.J., 1060
Zittartz, J., 570
Zuckermann, M.J., 570
Zuo, F., 658
Zwicknagl, G., 523

Subject Index

A

ABM phase, 941, 947, 1012, 1018, 1019, 1024, 1026, 1041, 1049
activation energy, 485
adiabatic limit, 352
AFM
– fluctuations, 606
– insulator, 676
– superconductor, 617
– transition, 611
AG theory, 561, 571
Aharonov–Bohm type magnetic flux, 106
Al–Ge mixtures, 37
amorphous, 27
– Al_2O_3, 26
– metals, 14
amplitude
– fluctuations, 330, 868, 873
– spin, 307
Anderson
– model, 912, 954, 994
– theorem, 943, 945
Anderson–Brinkman–Morell phase, 931
Andreev
– interferometer, 106, 107
– reflection, 685
– surface bound–states, 1033, 1059
angle–resolved photoemission (ARPES), 169, 282
angular momentum pairing state, 922
anion ordering, 483, 484, 535
anisotropic Knight shift, 1042
anisotropy, 123, 132, 137, 151, 203, 217, 693
– correlation length, 997
– organic superconductors, 159
– parameter, 496, 510
anomalous
– Green's functions, 944
– metallic state, 336
– skew scattering, 978
– T–dependence, 1099
anti–paramagnon excitations, 1054
antibonding, 183, 184
antiferromagnet, 118, 277, 286
– correlations, 298, 355
– doped, 401
-- cuprates, 398
– exchange energy J, 394
– exchange interaction, 565
– hole pair motion
-- frustration, 389, 390
– instability, 915
– insulating state, 297
– one hole, 388
– order, 482, 489, 493
– phases, 5, 300
– spin fluctuations, 471, 476, 477, 479, 516, 519, 918
– two holes, 389
ARPES, 6, 168, 169, 176, 185, 202–204, 210, 211, 229, 230, 234, 238, 253, 256, 263, 265, 287, 291, 319, 688, 701, 1110
– dispersion, 263
– intensity, 179, 180, 190, 192, 193, 197, 198, 259, 315
– lineshape, 179, 195, 200
– matrix elements, 189
-- polarization dependence, 201
– photocurrent, 230
– response, 311
– spectra, 179, 183, 187, 214, 216, 259, 694
-- EDCs, 179
-- MDCs, 179
Aslamazov–Larkin/Maki–Thompson contribution, 656

attenuation
– coefficient, 1023
– rate
–– drop, 1022
– transverse sound waves, 1025

B

B_{c_1}, 504, 507, 509
B_{c_2}, 496, 504–511, 513–515, 536, 537
$B_{c_{th}}$, 497, 504, 507, 509
B–phase gap, 1110
BaKBiO, 280
Balian–Werthamer
– p–wave order parameter, 632
– phase, 930, 947
band
– filling, 464, 465
– structure, 456, 464, 502, 518
– width, 456, 467, 491, 519
BCS, 502, 515, 516, 519, 528, 533
– coherence factors, 205
– expression, 52
– interaction parameter, 50, 51
– result, 505, 508, 523, 524, 533, 535, 939
– superconductivity, 134, 287, 1105
– theory, 1, 264, 329, 890, 891, 921, 1090
BCS–Eliashberg theory, 280, 285, 352
BCS–Eliashberg–Migdal theory, 402
Bechgaard salts, 457–459, 483, 534–536, 636, 639, 643, 659
Bechgaard superconductors, 649
BEDT–TSF, 457, 493, 494
BEDT–TTF, 457, 458, 493, 494, 503, 521, 636
Berezinskii–Kosterlitz–Thouless theory, 775, 821, 830, 875
Berry phase, 360
Bethe–Ansatz solution, 954
Bethe–Salpeter equation, 781, 789
BETS, 457, 463, 471, 493, 506, 637
– λ-$(BETS)_2FeCl_4$, 656
$Bi_2Sr_2CuO_{6+\delta}$, 113
Bi2212, 168
bilayer
– effects, 780
– material, 187
– splitting, 200, 202, 836
–– Bi2212, 199
–– effects, 261
BiO layers, 168
bipolarons, 353, 354
Bloch state, 907, 1096
Bogoliubov quasiparticle energy, 203
Bogoliubov–Valatin transformation, 79
Boltzmann equation, 83
bonding, 183
Born approximation, 80, 562, 945, 985
Born–Oppenheimmer approximation, 983
Bose–Einstein condensation, 21, 700, 1087–1091
Bose–Einstein distribution function, 915
bosonic
– collective excitation, 1110
– system, 136
bosonization, 304
bosonized Hamiltonian, 306, 362
boundary conditions, 91–93, 95
Bragg peaks, 999
Brillouin zone, 194, 195, 206, 229, 262, 761, 768
broken symmetry, 300, 301
BSCCO, 701
BW phase, 1041, 1049

C

C_{60}, 280
– molecules, 280
c–axis tunnelling, 291
canonically conjugate variables, 18
capacitance C, 17, 32

carrier concentration, 456, 472, 494, 497
CDW, 14, 309
– coupling, 323
– fluctuations, 300, 351
– ground state, 323
– insulators, 351
– operators, 306
– phase, 363
– susceptibility, 300
$CeCoIn_5$, 609, 611, 1062
$CeCu_2Ge_2$, 1063
$CeCu_2Si_2$, 587, 589, 901, 1058
$CeCu_6$, 968
$CeIn_3$, 11, 605, 1062
$CeIrIn_5$, 1062
$CeMIn_5$, 587, 606, 611, 621
$CePd_2Si_2$, 605, 1063
$CeRh_2Si_2$, 1063
$CeRhIn_5$, 1061
cerium heavy–fermion compounds, 995
$CeRu_2Si_2$, 968
Chandrasekhar/Clogston limit, 1011
charge
– carrier doping, 675
– excitation, 312, 314, 693
– fluctuation, 118
– imbalance, 82
– Luttinger exponent, 350
– ordering
-- self–organized, 396
– phases, 307
– stripe correlations, 301
– stripes, 403, 406
– transfer, 456, 464, 465
-- salts, 13
charging up behavior, 16
chemical potential, 184
Chevrel
– compounds, 283
– phase, 572, 574, 658
chiral state, 786
coherence
– factor, 203, 865
– length, 47, 121, 332, 335, 495, 497, 505–507, 509, 510, 529–531, 770
-- superconducting, 101
– peaks, 292
coherent
– Bose–condensed state, 354
– resonant scattering, 976
collective
– excitation, 905, 910
– fluctuations, 914
– mode, 252, 766, 818
commutator equation, 18
competing magnetic interactions, 582
competing order, 283
complex order parameter, 330
condensation energy, 133, 145, 147, 263, 264, 1010, 1011
conductance, 37, 99, 100, 1022
conductivity, 133, 134
conventional
– metals, 277
– superconductors, 2, 277
cooling–rate dependence, 485–487, 492, 534, 535
Cooper channel, 346, 347
Cooper pair, 336, 904, 926, 932, 1091, 1105
– localization, 119
– phase coherence, 17
– radius, 1106
Cooper–pairing, 2, 10, 1087
– ^{3}He, 1101
– phase–coherent, 4
– triplet, 8
correlated electron gas, 184, 422
correlation
– function, 308, 370, 978
-- pair field, 370
– length, 112, 153, 357, 991
-- exponent, 153

Coulomb
– blockade, 16, 31, 32, 50, 336
-- model, 33
– energy, 17, 42
– interaction, 136, 280
– pseudopotential, 281
– repulsion, 280
– retardation, 280
coupling between grains, 334
coupling mode–mode, 915
critical
– behavior, 120, 124, 141
-- quantum, 130
– current density, 47, 677
– exponent, 135, 148, 159, 917, 997
– field, 47, 607, 652, 677, 968, 1010
-- anisotropy, 1012
-- upper, 47–49
– film thickness, 116
– fluctuations, 911
– phenomena, 299
– point, 134, 148
– scattering, 916
– temperature, 43, 49, 567, 570, 573, 669
crossover, 130
– 3D–2D, 116, 158
– critical behavior, 338
– doping tuned, 161
– metal to insulator, 153
– scale, 301
– temperature, 227
crystal
– field, 973, 1000
– field multiplet, 974
– growth, 458
– structure, 733
-- La_2CuO_4, 677
-- Sr_2RuO_4, 732
– symmetry, 932
crystalline anisotropy, 924
crystallites
– metallic and dielectric, 29
cuprate superconductors, 121, 277, 297, 675, 698, 1091
– undoped state, 386
cuprates, 1, 6, 21, 136
– electron gas, 422
– electron–doped, 782
Curie temperature, 618
Curie–Weiss, 590, 970, 1003
– temperature, 561, 562
current
– correlation function, 173
– density, 72

D

$d_{x^2-y^2}$ symmetry, 701
d–wave superconductivity, 136, 518–520, 524, 529, 530, 535, 536
DC conductivities, 133
de Gennes/Ginzburg–Landau theory, 102
de Haas–van Alphen measurement, 956
de Haas–van Alphen oscillations, 13, 647, 893, 902, 964, 966, 969
Debye temperature, 50, 980
Debye–Waller factor, 324, 994
degenerate representations, 934
degenerate triplet pairing, 932
deGennes factor, 564
density of states, 9, 51, 199, 466, 475, 478, 479, 490, 502, 503, 509, 523, 686
– superconducting, 244
– tunneling, 292
density wave, 457, 471, 476, 481, 489, 492, 502, 519
– correlations, 366
– unidirectional, 394
di–electronic molecules, 1106
diamagnetic susceptibility, 125
dielectric
– barriers, 29
– crystal, 29
– layer, 28

differential conductivity, 602
diffusion, 28, 49
– coefficient, 49, 87, 88, 98
– equation, 56, 90
– mechanism, 29
digamma function, 947
dimensional
– 1D Luther–Emery liquid, 327
– 1D organic superconductors, 649
– 2D
–– organic superconductors, 653
–– QSI criticality, 137, 156
–– QSI to 3D–QSN criticality, 161
–– quantum critical points, 132
–– weak localization, 156
– 2D organic superconductors, 655, 658
– 3D condensation mechanism, 152
– crossover, 302, 316, 320, 357, 411
dimerization, 458, 459, 461, 464, 465, 467, 490
Dingle temperature, 466
dip/hump structure, 243
dipole matrix elements, 172
dirty limit, 85, 134
discrete translational symmetry, 403
discretization, 16
disorder, 116, 152, 161, 336, 459, 460, 471, 482–485, 487, 488, 492, 531, 534
dispersion, 183, 186, 205
dissipation, 336
DMRG, 381
– methods, 375, 380
– study, 377, 386
domain walls, 306
dopant concentration, 123, 138
doped
– antiferromagnet, 328, 386
– hole concentration, 387
– hole critical concentration, 392
– ladders, 365
doping dependence, 112, 248
– anisotropy, 112
– dispersion, 250
– spectra, 251
– superconducting peak, 252
DOS, 200
Drude peak, 910, 1022
Drude–like formula, 984
dynamic
– conductivity, 909
– critical exponent, 153
– magnetic properties, 985, 1037
– magnetic response, 994
– mean field theory, 321, 956
– stripes, 383
– susceptibility, 10, 985
dynamical phase stiffness, 832
dynamical stripe array, 321
Dyson equation, 65, 755, 757, 788, 871, 906

E

eclipsed conformation, 460
EDC, 183, 189, 197, 198, 201, 206–208, 258, 412
– dispersion, 190
effective
– electron mass, 10
– exchange, 922
– Hamiltonian, 318, 353
– interaction, 924
– mass, 32, 467, 468, 473, 495, 507
Ehrenfest relation, 631
eigenvalues, 938
Einstein
– oscillator, 352
– relation, 48
elastic scattering, 80, 85
electric current, 57, 90, 98
electrical resistance, 30, 38, 572, 592, 595, 618, 623, 972
– in–plane, 681
electrochemical potential, 82
electromagnetic absorption spectra, 1028
– ABM, 1028

- BCS, 1028
- polar states, 1028
electromagnetic response, 1026
electron
- π orbital, 456, 458, 462, 464, 489, 503, 527
- σ orbital, 456, 464
- doped cuprates, 676, 782
- doped superconductors, 680
- fractionalization, 329
- hole symmetry, 949
- nematic phase, 409
- tunneling, 602
electron–electron
- correlations, 467–469, 472, 489, 516
- interaction, 174, 351, 893, 917
- scattering, 244
electron–molecular–vibration (EMV), 475, 521
electron–phonon coupling, 174, 349, 422, 467–469, 473, 475, 489, 520, 522, 918, 920
- constant, 476, 502, 523
- strength, 1023
electronic
- dispersion, 185
- inhomogeneity, 696
- liquid crystals, 407
- specific heat coefficient, 908
electrostatic energy, 16, 32
elementary excitations, 303, 310, 311, 328, 760, 764, 791, 801, 807, 840, 905
Eliashberg theory, 754, 757, 861, 918, 920
energy dispersion, 760, 788
energy gap, 202, 1110
energy spectrum, 16, 194
entropy, 908, 970
equilibrium distribution function, 92
$ErRh_4B_4$, 578–580, 623
ethylene conformation, 460, 485, 492
ethylene endgroups, 460, 471, 479, 485, 486, 492, 521, 523, 527, 531
Euclidean action, 345
eutectic systems, 26
exchange field, 12, 20, 584, 586
exchange interaction, 356, 560
exotic pairing, 1111
extended Bloch state, 914

F

Fe, 11
Fermi Arcs, 217
Fermi crossing, 220, 235, 248
Fermi energy, 43, 170, 560, 906, 907
Fermi function, 170, 176, 177, 181, 189, 199, 263
Fermi Golden rule, 171, 952, 1023
Fermi liquid, 256, 277, 283, 284, 321, 344, 463, 464, 470, 471, 474, 479, 592, 808, 812, 905, 1094, 1097
- behavior, 348, 672
- marginal, 261
- non, 196, 264
- normal state, 278
- parameter, 212, 922
- phase, 910
- planar, 355
- superfluid, 1102, 1104
- theory, 1098
Fermi sea, 290
Fermi surface, 177, 180, 181, 184–186, 188, 192, 195, 197, 199, 205, 207, 209, 212, 219, 223, 224, 229, 257, 287, 291, 347, 419, 464, 467, 473, 476, 479, 481, 482, 489, 491, 492, 504, 507, 517–519, 926
- anisotropic, 1012
- antibonding, 204
- Bi(Pb)–2212, 225
- Bi2201, 199
- Bi2212, 199, 200
- Bilayer–split, 203
- determination, 188

- gap functions, 686
- instability, 287, 408
- optimally doped, 199
- UD, 223
- with doping, 222
Fermi surface nesting, 642
Fermi velocity, 211, 596
Fermi–Dirac statistics, 908
fermionic degrees of freedom, 349
ferromagnetic
- exchange interaction, 561
- instability, 915
- phase, 393
- superconductors, 1064
Feynman diagram, 244, 260
FFLO state, 1012
final state lifetimes, 229
finite-size scaling, 125
fixed point, 127, 128
- Hamiltonian, 362
fluctuating stripes, 407
fluctuation, 121, 161, 297, 402, 1106
- charge density wave, 305
- gapless, 307
- phase, 329
- singlet pairing, 308
- spin density wave, 305
- thermal phase, 334
- triplet pairing, 308
flux
- quantization, 685
- quantum, 1011
forward scattering interactions, 362
Fröhlich superconductivity, 656
fractionalization, 310
- electron, 325
fractionalized excitations, 318
fragmented condensates, 1089
Frauenhofer diffraction pattern, 1034
free energy, 10, 45, 1011
- density, 34, 118, 150
Friedel–Anderson model, 560, 572
Fulde–Ferrell–Larkin–Ovchinnikov (FFLO) state, 509, 513, 538, 656

G

gap, 203, 206, 207, 209, 210, 248, 1105
- doping dependence, 210
- equation, 767, 769, 794
- function, 212
- leading edge, 235
- miscibility, 391
- node surface, 686
- parameter, 290
- Peierls, 351
- spin, 308
- superconducting, 212, 229, 242
-- *d*–wave, 291
gapless
- excitation, 178
- phase, 948
- spin wave excitation, 355
- superconductivity, 564
gauge transformation, 74
Gaussian fluctuations, 911
Giaever tunnelling, 44
Ginzburg
- criterion, 655
- number, 497
Ginzburg–Landau, 112
- equations, 1011, 1012
- free energy, 774
- Hamiltonian, 121
- parameter, 1056, 1058
- theory, 10, 44, 45, 136, 775
- type analysis, 12
glass–like transition, 479, 485, 491, 492, 531
Goldstone mode, 285, 355, 358, 924
- collective, 911
Goldstone's theorem, 355, 911
Gor'kov equation, 78, 84
gradient expansion, 67, 69, 196
grain size, 27, 28
- distribution, 38
grains, 17, 336
granular
- Al, 31

– films, 27, 31
– insulating phase, 42
– insulators, 39
– materials, 27, 42
– structure
–– transport, 31
– superconductors, 14, 331
Green's function, 179, 228, 263, 905, 906, 944
– advanced, 62
– quasiclassical, 71, 75, 80
– retarded, 62, 84
group $SU(2)_{spin}$, 1108
gyromagnetic ratio, 937

H

H_{c1}, 653
H_{c2}, 5, 653
– enhancement, 649
H–bonding, 461, 504
Haldane's conjecture, 356
Hall
– coefficient, 690, 977
– constant, 30, 33
Hall effect, 30, 977, 1099
Hamilton–Jacobi equations, 18
Hamiltonian
– one–band model, 750
Hartree–Fock
– stripes, 381
– theory, 395
– treatment, 381, 953
heat capacity, 36–39, 41, 890
Heaviside step function, 985
heavy quasi–particle masses, 892
heavy–fermion, 594, 895, 907, 971
– f–electron material, 556, 587
– compounds, 556, 587
– metals, 1, 9, 10, 21, 1054
– superconductor, 590, 593, 597, 689, 892, 902, 905, 920, 1007, 1025, 1055
–– local–moment, 634
–– magnetically ordered, 621
–– uranium, 896
Hebel–Slichter coherence peak, 603, 662, 664, 735, 1049
Heisenberg
– antiferromagnet, 355
– ladder, 356, 368, 369
– model, 356, 357, 369
– phase, 376
helicity modulus, 121, 337
Helium–B, 1108
Hertz/Millis theory, 615
$HgBa_2CuO_{4+\delta}$, 113
high temperature superconductivity, 1, 279, 430, 670
highest occupied molecular orbital (HOMO), 464, 465, 475, 502
hole
– density, 381, 385
– localization, 682
– pockets, 184
holons, 327
Holstein model, 282, 352
– interacting electrons and phonons, 352
hopping integral, 182
Hubbard band
– lower, 182
– upper, 182, 747
Hubbard chains, 366
Hubbard Hamiltonian, 366
– one–band, 754
– three–band, 371, 752, 786
Hubbard ladders, 368, 369
– doped, 370
Hubbard model, 282, 364, 367, 369, 386, 391
– negative U, 352
– point contact interaction, 912
– related systems, 386
– rings, 367
– two dimensional, 377
Hund's rule, 560
– multiplet, 619
hybridization matrix element, 952

hydro-static pressure, 900
hypercubic lattice, 337
hyperfine coupling, 604, 985, 986, 1048

I

imaginary time representation, 905
impurities, 483, 943, 1097
– magnetic, 943
in–plane penetration depth, 132
incoherent excitations, 910
incommensurability, 8, 304
incommensurate
– magnetic peaks, 404, 1006
– order, 1002
inelastic neutron scattering, 296, 405, 599, 600, 995, 999
infinitesimal RG transformation, 347
infrared conductivity, 294
insulating quantum antiferromagnets, 354
insulator transition, 31
interaction U_{eff}, 184
interchain coupling, 316
intergrain
– conductance, 32, 41
– coupling, 39
– tunneling
-- matrix element, 40
interlayer
– magnetoresistance, 655
– resistance, 648
intermolecular electron–phonon coupling, 475, 476, 523
interplay
– superconductivity and magnetism, 901
intrinsic pinning, 662
inverse adiabatic limit, 352, 354
inverse photoemission, 230
irreducible representation
– G, 1107
irreversibility line, 510–512, 531
Ising model, 112
isotope effect, 139, 140, 486, 503, 504, 521, 659, 918
– coefficient, 140
-- inverse, 141
isotropic
– antiferromagnetic couplings, 356
– stripe fluid, 408

J

Jaccarino–Peter field–compensation effect, 657
Josephson
– coupling, 40, 42, 44, 318, 323, 334, 409, 510, 1034, 1036
-- inter–stripe, 323
-- intergrain, 46
– current, 18, 1034, 1035
– effect, 4, 17, 495, 685, 688, 778
– energy, 17
– equations, 18, 41
– junction, 2, 14, 134, 146
– length, 357
– plasma edge
-- like, 684
– plasma resonances, 649
– tunneling, 688, 696, 1033
-- c–axis, 688
– voltage–phase relation, 874
– vortices, 510, 512

K

Kadowaki–Woods plot, 594
Keldysh Green's function, 61, 63, 65, 66, 75, 77
– quasiclassical, 83
kinematic constraints, 312
kinetic energy
– driven stripe formation, 411
– driven superconducting pairing, 361, 418
kinetic equation, 88, 91
kink, 261
– condition, 763, 803, 805

– dispersion, 262
– energy, 261
– structure, 740, 801
Knight shift, 7, 292, 294, 604, 651, 685, 746, 986, 1038, 1044
– μSR, 1045
Koehler's law, 977
Kohn–Luttinger theorem, 392
Kondo
– effect, 613, 958
– interaction, 590
– model, 954, 974
– resonance, 973
– temperature, 565, 566, 951, 954, 958
Kondo–Heisenberg model, 355
Korringa rate, 986, 987, 989
Kosterlitz recursion relation, 831
Kramers–Kronig
– relations, 253, 1029
– transformation, 230, 231, 242, 255
Kubo formula, 771, 825

L

$La_{2-x}Sr_xCuO_4$, 113
ladder systems, 374
lambda
– point, 1087, 1089
– transition, 121
Lanczos techniques, 365, 377, 379
Landé g–factor, 560
Landau
– Fermi–liquid theory, 395, 689, 1096
–– mean–field, 970
–– stripes, 395
– free energy, 394
– interaction function, 1102
– parameter, 1102, 1105
– quantization, 656
Landau–Ginzburg theory, 34, 394, 421
Landau–levels, 14
Lande's g–factors, 793
Larkin–Ovchinnikov state, 12, 14, 20
lattice instabilities, 284
law of corresponding states, 564, 571
layered perovskite–like crystal, 675
layered structure, 644
– organic metals, 644
layered superconductors, 112, 146, 158, 668
LDA calculations, 893
lifetime, 229
– phonon, 983
Lifschitz–Kosevich formula, 964, 966
Lindhard susceptibility, 764, 912
line nodes, 941, 949
linear response theory, 1015
linearized gap equation, 921, 946
lineshape, 259
– EDC, 181
– MDC, 181
– peak/dip/hump, 240
– photoemission, 228
– spectral, 253
linewidth, 175, 208, 1003
liquid ^{3}He, 1097
liquid ^{4}He, 1087, 1089
Little's model, 454, 517
local
– Fermi liquid, 904
– hyperfine field, 1046
– moment fluctuations, 994
localization, 42, 136
localized magnetic moments, 557, 586, 951, 972
lock–in transition, 510
London
– penetration depth, 112, 332, 1059
– relation, 1028
– theory, 772, 827
long–range order, 152, 1107
longitudinal nuclear relaxation rate, 986

longitudinal relaxation rate, 985, 986
Lorentz
- force, 977
- invariance, 308
- number, 981, 982
- transformations, 313
Lorentzian lineshape, 181, 198, 246, 256
- MDC, 198, 254
loss function, 1098
lower critical field, 899
- UPt_3, 1013
lowest unoccupied molecular orbital (LUMO), 464
LSCO, 405
$LuRh_4B_4$, 579
Luther–Emery liquid, 308, 316, 362, 363
Luttinger exponent, 362, 363, 409
Luttinger liquid, 196, 306, 361–363, 470, 473, 474, 642

M

M/I transition, 33
magnetic
- anisotropy, 7, 790, 793, 797
- Bragg peak, 997
- coherence, 815
- field, 114, 120, 123, 152
-- induced superconductivity, 584
- fluctuations, 705, 904
- flux, 3, 360
- instability, 968, 969
- moment operator, 937
- order, 970, 992, 1055
- penetration depth, 122
- phases
-- $NdRh_4B_4$, 576
- quantum critical point, 7
- relaxation effects, 653
- resonant mode energy, 248
- response
-- width, 1003
- scattering
-- cross–section, 1050
- susceptibility, 578, 618, 960
- torque, 125, 127
magnetization, 590, 1038
magneto–resistance, 976
- oscillations, 645
Maki parameter, 607
many–body
- effects, 467
- renormalization, 174
Marginal–Fermi–Liquid (MFL), 261, 737
mass
- enhancement, 894
- renormalization, 242, 922
matrix element, 171, 191, 193, 194, 199, 222, 241
matrix self–energy, 945
Matsubara frequencies, 906, 1047
Mattis–Bardeen theory, 1029
MDC, 197, 198, 313, 314, 412
- dispersion, 199, 255
mean free path, 32
mean–field
- critical temperature, 696
- Hamiltonian, 928, 1041
- transition temperature, 497, 498, 506
Meissner effect, 4, 773, 832, 870, 896, 1022
Meissner flux expulsion, 1010
Meissner–Ochsenfeld effect, 1
Meissner–phase, 10
melting
- line, 129, 130
- stripes, 408
- transition, 128, 153
metal–insulator boundary, 159
MgB_2, 280
microwave surface conductivity, 686
midinfrared (MIR) peak, 1098, 1100
Migdal's theorem, 919
mixed representation, 68

mode model, 244
model
– $t-J$, 358, 378, 386, 394
-- doped ladders, 370
-- ladders, 365, 368, 369
-- square, 359
-- two dimensional, 377
– $t-J-V$, 392
momentum distribution, 195, 353
Monte Carlo simulations, 364, 365, 377, 380, 383, 384, 392
Mott insulator, 228, 284, 285, 336, 398
Mott limit, 354
Mott's minimum metallic conductivity criterion, 32
Mott–Hubbard insulating state, 483, 489, 518, 519, 659
multilayer systems, 1094
multiple superconducting phases, 625, 689, 896
muon Knight shift, 993, 1042

N

Néel ordered antiferromagnetic states, 327, 355, 392
Néel temperature, 599, 603, 605, 902, 987, 1000
$Na_xCoO_2(H_2O)$
– intercalated, 21
Nambu representation, 756, 758
Nambu–Gor'kov Green's functions, 94
nano–size grains, 37
nanostructured superconductors, 24
nematic phase, 408
Nernst effect, 701
nested–Fermi–Liquid, 737
nesting, 464, 476, 479, 482, 489, 490, 504, 519
neutron
– cross–section, 994, 1050
– data, 251, 253
– diffraction, 1005
– mode, 260
– resonance, 250, 259, 260
– scattering, 405, 406, 412, 999
NMR, 297, 989, 999, 1050, 1103
– Cu, 292
– linewidths, 991
– longitudinal relaxation rate, 987
– spin–lattice relaxation rate, 663, 1059
nodal
– quasiparticles, 253, 291, 321
– spin liquid, 427
node structures, 940
non–analytic function, 951
non–bonding states, 183
non–centrosymmetric anion, 459, 483
non–degenerate representation, 933
non–equilibrium Green's function, 61, 76
non–equilibrium properties, 70, 89
non–Fermi liquid, 278, 310, 349, 411, 587, 606, 610, 613, 617, 690, 976, 1058
– materials, 891
non–linear Meissner effect, 1030
non–Lorentzian, 181
non–spin–flip scattering, 86
nonequilibrium
– electron distribution, 58
– persistent currents, 656
noninteracting
– Bose gas, 1089
– fermions, 313
nonlinear response function, 173
normal state, 178, 184
– Bi2212, 185
– resistivity, 27
– susceptibility, 1045
normalized Gaussian, 208
novel superconductors, 2, 703
nuclear
– Larmor frequency, 1046
– magnetic relaxation, 985

– magnetic resonance, 597, 603, 986, 1037

O

odd–parity, 1107
one band Hubbard model, 912
one loop
– beta function, 348
– diagrams, 346
– RG equations, 347, 349
one–step model, 172
optical
– conductivity, 298, 418, 1026
– phonon, 352
– sum rule, 1027
optimal doped, 153
– Bi2212, 201
orbital symmetry group SO(3), 1108
orbital wave function, 1107
order parameter, 43, 46, 290, 309, 495, 506, 509, 510, 512, 515, 517, 520, 521, 524, 529, 534, 535, 735, 745, 767, 795, 813, 938, 945, 1091, 1107–1109
– p–type, 8
– amplitude, 329
– CDW, 322
– phase, 688, 935
– superconducting, 8, 384, 686
– symmetry, 290, 660, 685, 686, 925, 1006
– vector, 932
ordered
– moments, 970
– stripes, 277
organic
– materials, 1, 13, 21
– metals, 643
– superconductors, 13, 636, 637, 647, 649, 660, 666
Ornstein–Zernicke theory, 739, 759, 765, 811
orthorhombicity, 405
– Bi2201, 182
– Bi2212, 182
overdoped, 420
– Bi2212, 202
overlap integral, 464, 469, 473, 476, 488, 502, 507

P

P–T phase diagram, 1063
p–wave states, 1104
packing, 456, 459–461, 503
pair
– binding energy, 367, 369, 371
-- doping dependence, 370
– breaking impurities, 941
– currents thermally induced, 337
– field
-- $d_{x^2-y^2}$, 372–374
– tunnelling interaction, 362
– wave function, 1091
pairing, 282, 301, 917
– ^{3}He, 1103
– collective, 288
– correlations, 366, 372
– kinetic energy driven, 418
– potential, 927
– state
-- UPt_3, 1093
– symmetry, 289
pancake vortices, 510, 511, 527
paramagnetic
– impurities, 283, 559
– state, 912
particle–hole channels, 203, 204, 346
path integral formulation, 117
Pauli
– Clogston limit, 651
– limit, 1012
– limiting field, 504, 505, 508, 509, 513, 515, 537
– matrices, 307, 387, 1046, 1108
– principle, 925, 1095
– susceptibility, 591, 960
Pb–Ge mixtures, 48
Peak/Dip/Hump, 200, 202, 240, 248

Peierls
- gap, 351
- metal–insulator transition, 636
- renormalization, 350
- state, 327
- transition, 640
penetration depth, 3, 119, 121, 136, 139, 141, 203, 487, 495, 505, 507, 509, 520, 528–531, 661, 686, 1028, 1029, 1105
- magnetic, 660
percolation
- behavior, 40
- correlation length, 29, 47, 48
- localization, 31
- random structure, 29
- threshold, 30
perfect nesting, 913
periodic table, 2
perovskite–like cuprate materials, 668
perturbation
- beta function, 348
- renormalization group, 304, 317
- RG analysis, 344, 348, 361
- theory, 353
phase
- A, 1108
- charge, 307
- shift, 949
- stiffness, 337
- transition, 115, 151
phase coherence, 101, 119, 130, 329
- long–range, 108
phase diagram, 6, 9, 11, 20, 115, 152, 284, 301, 302, 309, 397, 403, 410, 613, 641, 820, 1059
- $H-T$, 632, 634, 650
- $P-T$, 658
- $T-P$, 612
- $t-J$ model, 393
- cuprates, 420, 700, 701, 704
- generic, 699
- $La_{2-x}Sr_xCuO_4$, 692
- liquid ^{3}He, 1101
- magnetic, 619
- superconducting gap symmetry, 633
- $U_{1-x}Th_xBe_{13}$, 627
- UGe_2, 12
- UPt_3, 626
- $ZrZn_2$, 624
phase difference, 106
phase fluctuations, 5, 283, 299, 330, 421, 772, 825, 868, 871
- classical, 336
- quantum, 336
- stiffness, 337
- thermal, 336
phase ordering, 282, 331, 335
phase separation, 374, 376, 378, 391, 393, 396, 400
- boundary, 379
- Coulomb frustrated, 394, 396, 403
phase–twisting field, 121
phases A,B,A_1, 1101, 1103
phonons, 261, 399, 422
photoemission, 171, 175
- intensity, 175
- matrix elements, 192
- process, 172
- selection rules, 172
photon flux, 173
pinning, 509–513, 530, 531
planar quasiparticles, 690
plasma frequency, 1098
point contact, 1031–1033, 1035
point group symmetry, 932, 936
polar phase, 931
polarization selection rules, 188
polymer polyacetylene, 351
preformed Cooper pairs, 327, 1105
$PrOs_4Sb_{12}$, 629, 633, 636, 1064
proximity
- coupled systems, 97
- coupled wire, 97
- effect, 102

pseudogap, 5, 43, 214, 215, 217, 221, 225–228, 248, 286, 291, 296, 297, 300, 301, 316, 406, 693, 695, 696, 701, 703, 1105
– anisotropy, 222
– phase, 231
– regime, 43, 223, 252
– scales, 411
– self–energy, 238
– temperature, 703
pseudoternary system, 582, 583
$PuCoGa_5$, 633, 634

Q

quantized flux vortices, 1011
quantum
– antiferromagnets, 326, 354
– critical behavior, 358
– critical exponents, 916
– critical fluctuations, 31, 116, 131, 144, 157–159, 313, 915
– critical line, 156
– critical point, 21, 152, 604, 904, 911, 912, 915, 917, 924, 956, 1003
– ferromagnet, 914
– Hall effect, 401, 410, 642
– Hall nematic phases, 401
– insulator transition, 157
– nonlinear sigma model, 357
– phase transition, 135, 143, 149, 152, 153, 158, 291, 604
– spin ladder materials, 674
quantum Monte Carlo simulations, 379
quasi–1D superconductors, 303
– cuprates, 412
quasi–Bose–Einstein condensation, 1106
quasi–classical
– equations, 91
– Green's function, 94
quasi–dielectronic molecules, 1087
quasi–one–dimensional organic metals, 638
quasi–particle, 184, 318, 905, 911
– approximation, 70, 83
– density of states, 939
– energy gap, 43
– excitations, 185, 336, 686, 905, 929
– operators, 1101
– peak, 225, 248, 250
– spectrum, 290
– thermally activated, 1051
– velocity, 1016
– weight, 907
quasi–static stripe fluctuations, 322
quasi–two dimensional, 168, 170
– organic metals, 643
quasi-1D physics, 321
quasiclassical approximation, 70

R

Raman scattering, 687, 1050, 1051
random
– percolating structure, 26, 52
–– transport, 30
– phase approximation, 755, 843, 911
rare earth rhodium borides, 572
reduced dimensionality, 158
reflectance, 684, 1099
relaxation rate, 1048
– ^{63}Cu, 294
– NMR, 686
renormalization, 176, 945
– group method, 281
– of the effective interactions, 346
– of the quasi–particles, 913
resistivity, 30, 101, 137–139, 150, 293, 295, 332, 334, 981
– $(TMTSF)_2X$ salts, 640
– c–axis, 295
– electrical, 592, 595
– in–plane, 693
– maximum, 471, 483
– threshold, 138
resolution effects, 229

resonance
– impurity scattering, 951, 1019
– peak, 299, 739, 815
– position, 819
resonating valence bond (RVB), 228, 326, 700
response function, 173, 1099
retardation, 287, 344, 348
RG transformation, 344, 350
ring exchange interaction, 328
RMo_6S_8 compounds, 574
RPA, 321, 911
– self-energy, 913
Ruddlesen–Popper series, 743
Ruderman–Kittel–Kasuya–Yosida, 561
ruthenates, 1, 6, 21
RVB phase, 427

S

S–N–S–N transition sequence, 586
saddle point singularity, 199
sandwiches, 20
scaling, 120, 130, 158, 362, 498, 499, 916
– function, 127, 129, 134, 151, 153
– hypothesis, 991
– relation, 132, 137, 143, 144, 157
– theory, 117
scanning tunnelling microscope, 892
scattering rate, 297, 964
Schottky, 630
– contribution, 630
Schrieffer–Wolff transformation, 560
screening length, 50
screening parameter, 51
secular equation, 182
selection rules, 171
self-energy, 174, 179, 229, 230, 238, 242, 259, 260, 757, 761, 907
– anomalous, 919
– electron, 228
– impurity, 949
– pseudogap, 238
– temperature dependence, 233
self-organized structure, 316
shadow bands, 187
Shapiro steps, 1035, 1036
Shubnikov phase, 649, 656, 662
Shubnikov–de Haas oscillations, 642, 645
sine–Gordon theory, 305, 362
single
– grain behavior, 33
– impurity Anderson model, 990
– particle
-- state lifetime, 907
– stripe, 380
– tight binding electron band, 352
single–particle
– scattering rate, 238
singlet
– formation
-- Zhang–Rice, 748
– pair tunnelling, 361
– pairing, 926, 1015, 1038, 1047, 1051
-- *d*–wave, 309
– states, 931
SIS tunneling, 202
Slater–Pauling curve, 890
small grains, 15, 16, 35
smectic
– fixed point, 325
– stripe phase, 323
SNS junction, 106
soft–modes, 924
soliton excitations, 306
Sommerfeld coefficient, 609, 648
specific heat, 125, 126, 132, 142, 293, 569, 588, 594, 599, 608, 614, 630, 635, 665, 667, 671, 893, 956, 960, 1007, 1008
– Bi2212, 211
– coefficient, 591
– jump, 596, 666
– logarithmic enhancement, 914

spectral
– conductance, 99
– density, 240, 760
– function, 174, 176, 177, 194, 203, 207, 208, 220, 237, 250, 263, 310, 311, 318, 319
-- Bi2212, 201
-- Nambu, 245
-- normal state, 263
-- single particle, 318
– lineshape, 174, 253
– peak, 233, 235
– supercurrent, 107
– thermal conductance, 103
– weight, 214, 294
spin
– amplitudes, 307
– density wave, 277, 905, 1000
-- ladder systems, 374
-- operators, 306
-- peak, 601
– excitations, 8, 305, 308, 312, 693
– glass freezing, 617
– liquid, 327
– moments, 381
– order, 284
– relaxation
-- longitudinal nuclear, 1045
– rotational invariance, 308, 363, 1051
– stripes, 382, 403
-- formation, 406
-- order, 405
spin fluctuation, 14, 893, 904, 913
– antiferromagnetic, 923
– energy, 987
– excitation, 913
– incommensurate, 405, 923
– local, 910
– pairing mechanism, 923
– propagator, 915
– theory, 616
spin gap, 299, 314, 356, 366–369, 371, 400
– phase, 308
– proximity effect, 361
spin susceptibility, 673, 1039
spin–charge separation, 313, 325, 326, 329
spin–flip, 954
– excitation spectrum, 1047
– fluctuations, 1045
– scattering, 19, 87, 972
spin–lattice relaxation rate, 603, 664, 1049
spin–mean free path, 20
spin–orbit coupling, 787, 788, 845, 924, 937, 977, 1011, 1022, 1040, 1041, 1051
spin–Peierls order, 400
spin–singlet state, 504, 505, 508, 513, 515, 527, 535
spin–split bands, 14
spin–triplet state, 505, 534–536, 538, 674, 1012
– superconducting, 674
spinless fermions, 308, 360
spinons, 329
spiral SDW, 403
SQUID, 688
Sr_2RuO_4, 672, 673
staggered conformation, 460
static stripes, 383
Stoner
– criterion, 912
-- ferromagnetism, 913
– enhancement factor, 968
– excitations, 1000
stripe
– correlations, 399
– dynamics, 325
– fluctuations, 323, 324, 409
– formation, 301, 378, 396
-- ladders, 374
– glasses, 396
– liquid phases, 325, 394, 396
– order, 284, 298
-- doped antiferromagnets, 395

stripes, 316, 324, 377, 382, 384, 394, 399, 401, 403, 418, 696
– conducting, 416
– insulating, 416
strong
– attractive interactions, 282
– coupling, 252, 351
– repulsive interactions
-– between electrons, 288
sub–lattice magnetization, 997, 1006
sum rule, 176, 195
superconductivity
– s–wave, 535, 941
– t–J model, 383
– anisotropic, 1028
– antiferromagnetic, 573, 576, 577
– B.C.S., 2
– Bechgaard, 649
– cuprates, 285, 403, 675, 698
– electron–doped, 680
– energy gap, 600
– ET–based, 644
– ferromagnetic, 559, 577, 1064
– field induced, 14
– fluctuation, 420, 497, 506, 653
– granular, 46, 51
– heavy–fermion, 588, 590, 593, 597, 689
– high temperature, 365, 401
-– mechanism, 402, 416
– history, 2
– insulator, 40, 41
– insulator transition, 336
– layered
-– Cuprates, Ruthenates, 668
– local, 365
– magnetic field induced, 584, 656
– magnetic interactions, 558
– magnetically–ordered, 572
– MgB_2, 21
– occurrence, 2
– order parameter, 302
– organic, 647, 649, 660, 666
– pairs, 917
– PdH–systems, 14
– phase, 300, 899
– quantum dots, 21
– slab, 132
– structure interdependence, 21
– susceptibility, 314, 367, 368
– transition temperature, 5, 682, 894
– triplet, 18
– two–fluid model, 1011
– type–I, 3, 1011
– type–II, 3, 9, 121, 595, 1011
– unconventional, 672
superconductor–metal bilayer, 104
supercurrent, 107, 112
superfluid, 136, 1089
– ^{3}He, 121, 891, 931, 1041, 1091, 1100, 1101, 1111
– density, 133, 329, 330, 332, 337, 687, 771, 825, 1030
– Fermi liquid, 1112
– phase stiffness, 330
– transition, 124
– velocity, 775
superlattice, 187, 188
– Bi2212, 185
surface–impedance
– UBe_{13}, 1029
susceptibility, 36, 306, 893, 924
– enhancement, 963
– spin, 36
– tensor, 985, 1046
symmetry, 1107
– group G, 1107
– pair wavefunction, 288

T

T_c enhancement, 52
T–matrix, 949
TCNQ, 456
theory
– BCS, 1, 890, 891
– Berezinskii–Kosterlitz–Thouless, 775, 821, 830, 875

– Ginzburg–Landau, 10, 44, 45, 775
– Ornstein–Zernicke, 759
– tunneling, 778
thermal
– 3D–XY fluctuations, 159
– coefficients, 58
– conductivity, 60, 103, 104, 203, 212, 238, 980, 1015, 1018, 1020
–– tensor, 1017
–– UBe_{13}, 1020
– critical behavior, 124
– current, 57, 75
– density of electronic states, 296
– diffusion coefficient, 103
– driven fluctuations, 911
– excitations, 330
– fluctuations, 159, 330, 915
– phase fluctuations, 334
thermodynamic
– limit, 368
– properties, 956, 1007
thermoelectric
– effects, 73, 98
– power, 61, 593, 978, 979
thin films, 157
Thouless
– expression, 41
– length, 101
three–current correlator, 174
tight–binding description, 187, 199
time reversal symmetry, 8, 328
$TmRh_4B_4$, 576
TMTSF, 457, 494, 636, 637
– $(TMTSF)_2X$ salts, 639
TMTTF, 457
Tomonaga–Luttinger
– model, 306, 313–315
topological
– doping, 395
– order, 329
transformation
– granular to amorphous, 29
transition
– metal to insulator, 29, 42, 49
– temperature, 3, 48, 136, 140, 611
transport properties, 972, 1014
transverse
– dielectric constant, 1098
– excitations spectra, 1052
– magnetic relaxation rate, 991
– relaxation rate, 987
– sound waves, 1026
– susceptibilities, 912
triplet
– p–wave states, 930
– Cooper–pairing, 1, 904, 925, 927, 931, 932, 935, 940, 946, 1018, 1040, 1048, 1052
Trugman terms, 388, 389
TTF, 456–458
tunnel junction, 4, 18, 19, 31, 1031
tunneling, 37, 251, 334, 335, 1030
– current, 20, 1030
– data, 238
– spectra, 240, 697, 833
– spectroscopy, 741
– spin polarized, 20
– theory, 778
two dimensional stripe order, 366
two–particle density matrix, 1089
type–II superconductivity, 6, 595, 653, 678
– vortex dynamics, 654

U

U_2PtC_2, 1064
$U_{1-x}Th_xBe_{13}$, 587, 625
UBe_{13}, 589, 896, 901, 910, 1007, 1025, 1058, 1059
UGe_2, 11, 587, 621, 623, 624, 901, 903, 1064
ultrasonic attenuation, 896, 982, 1020, 1022
umklapp processes, 1100
uncertainty relation, 18
unconventional superconductivity, 672, 703, 930
underdoped, 386, 405

UNi_2Al_3, 1061
unitary states, 930
universality, 123, 132, 917
– classes, 152
UPd_2Al_3, 587, 598, 902, 1060
upper critical field, 634, 649, 1011, 1013, 1059
– H_{c2}, 575, 598, 678
UPt_3, 587, 589, 625, 628, 891–893, 898, 901, 956, 977, 987, 1025, 1044, 1056, 1057
URhGe, 587, 901, 1064
URu_2Si_2, 617, 901, 968, 1060
Usadel equation, 21, 85, 94, 97

V

valence fluctuations, 590
van der Waals radius, 458, 459
van–Hove singularities, 1031
variational Monte Carlo calculations, 379
vector pairing function, 927
vector potential, 74, 122, 124
– fluctuations, 121
vertex correction, 10, 174, 212, 755, 771, 919, 922, 1049
volume fraction, 30
vortex
– excitations, 337, 701
– fluid transition, 116, 120, 152
– formation, 3
– glass, 116, 152
-- quantum, 120, 153
– lattice, 116, 128, 152, 1012
– liquid, 130
– melting, 116, 124, 152
– phase, 10, 685
– solid, 116

W

Ward identities, 355, 356
wave function renormalization, 919
weak coupling
– renormalization group approach, 344
– superconductor, 51
weak screening, 50
weakly coupled grains, 39
Wick's
– time ordered product, 1046
– time ordering operator, 944
Wiedemann–Franz relation, 1019
Wigner
– distribution function, 67
– representation, 65
Wigner–Eckhart theorem, 360
Wilson ratio, 592, 893, 954, 962, 995

X

XY
– critical
-- behavior, 128, 148
-- line, 123
-- point, 133
-- properties, 126
– model, 336, 338, 775, 829
– universality, 118, 124, 128

Y

$YBa_2Cu_3O_{7-\delta}$, 126
YBCO, 213, 405
Yoshida function, 798, 1102

Z

Zeeman, 1107
– splitting, 558, 964, 977
zero
– bias conductance, 1010, 1032, 1033
– field susceptibility, 1038
– point quantum fluctuations, 911
Zhang–Rice singlet, 752
$ZrZn_2$, 1064